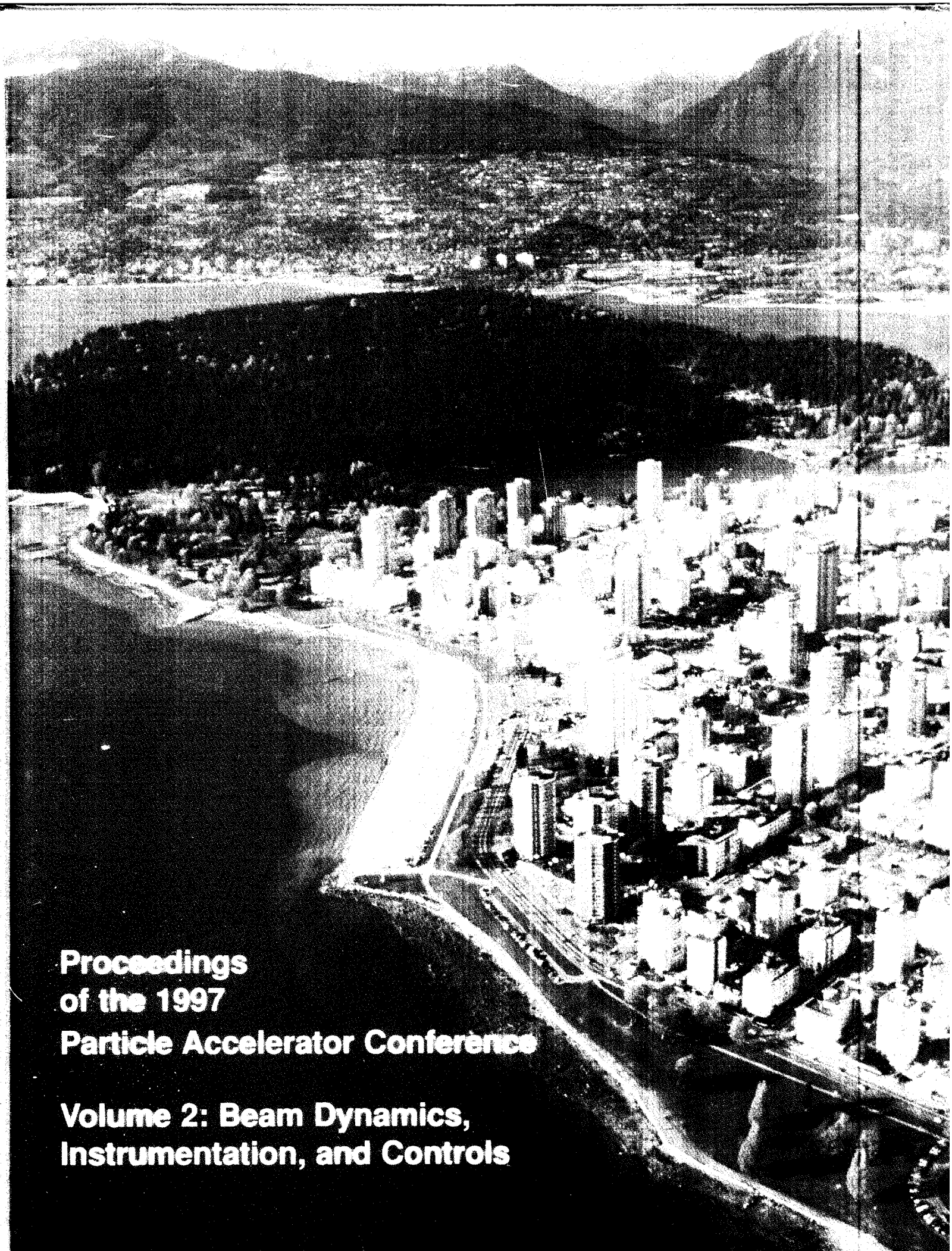

Proceedings of the 1997 Particle Accelerator Conference

Volume 2: Beam Dynamics, Instrumentation, and Controls

DISTRIBUTION STATEMENT A
Approved for Public Release
Distribution Unlimited

Proceedings of the 1997 Particle Accelerator Conference

19990326 076

Vancouver, B.C., Canada
12–16 May 1997

Editors
M. Comyn, M.K. Craddock, M. Reiser, J. Thomson

Volume 2 of 3
Beam Dynamics, Instrumentation and Controls

Organized by
TRIUMF
University of Maryland

Held under the joint auspices of
Institute of Electrical and Electronics Engineers
(Nuclear and Plasma Sciences Society)
American Physical Society
(Division of Physics of Beams)

Sponsored by
US Department of Energy
National Science Foundation
Office of Naval Research

IEEE

The American Physical Society

DTIC QUALITY INSPECTED 4

PROCEEDINGS OF THE 1997 PARTICLE ACCELERATOR CONFERENCE

Copyright and Reprint Permission: Abstracting is permitted with credit to the source. Libraries are permitted to photocopy beyond the limits of U.S. copyright law for private use of patrons those articles in this volume that carry a code at the bottom of the first page, provided the per-copy fee indicated in the code is paid through the Copyright Clearance Center, 222 Rosewood Drive, Danvers, MA 01923. For other copying, reprint, or republication permission, write to the IEEE Copyrights Manager, IEEE Operations Center, 445 Hoes Lane, Piscataway, NJ 08855-1331. All rights reserved.
Copyright © 1998 by The Institute of Electrical and Electronics Engineers, Inc.

IEEE Catalog Number: 97CH36167 (softbound)
97CB36167 (casebound)

Library of Congress Number: 88-647453

ISBN Softbound: 0-7803-4376-X
ISBN Casebound: 0-7803-4377-8
ISBN Microfiche: 0-7803-4378-6
ISBN CD-ROM: 0-7803-4379-4

Additional copies of this publication are available from

IEEE Operations Center
P. O. Box 1331
445 Hoes Lane
Piscataway, NJ 08855-1331
USA

Phone: 1-800-678-IEEE (1-800 678-4333)
1-732-981-0060
1-732-981-1393
FAX: 1-732-981-9667 (FAX)
Telex: 833-233
E-mail: customer.service@ieee.org

OUTLINE OF CONTENTS

VOLUME 1

PLENARY AND SPECIAL SESSIONS; ACCELERATORS AND STORAGE RINGS

OPENING PLENARY SESSION 1
SPECIAL SESSION 16
FINAL PLENARY SESSION 29
HIGH-ENERGY HADRON ACCELERATORS AND COLLIDERS 47
High-Energy Hadron Accelerators and Colliders 89
Beam Injection, Extraction, Transport and Targetry W 156
Beam Injection, Extraction, Transport and Targetry X 207
LEPTON ACCELERATORS AND COLLIDERS 281
Electron Storage Rings and Accelerators 324
Circular Electron Colliders 363
Muon Colliders 393
LINEAR COLLIDERS 425
Linear Collider Beam Dynamics 467
Linear Collider Structure 518
Linear Colliders (Other) 557
ADVANCED CONCEPTS 611
New Acceleration Techniques 633
LIGHT SOURCES AND FREE ELECTRON LASERS 698
Synchrotron Radiation Facilities 742
Free Electron Lasers 871
LOW- AND MEDIUM-ENERGY ACCELERATORS AND RINGS 915
Proton Synchrotrons and Storage Rings 959
Low- and Medium-Energy Circular Accelerators 1027
RFQ Linacs 1078
Proton and Ion Linacs 1111
Electron Linacs 1197
Electrostatic and Other Accelerators 1224
PULSED-POWER AND HIGH-INTENSITY BEAMS 1230
Pulsed Power Accelerators 1254
Pulsed Power Technology 1269

VOLUME 2

BEAM DYNAMICS, INSTRUMENTATION AND CONTROLS

SINGLE-PARTICLE BEAM DYNAMICS AND OPTICS 1331
Lattice Design and Optics 1371
Maps, Tracking and Dynamic Aperture 1418
Error Effects, Experiments, Spin Dynamics 1460
Other Single-Particle Beam Dynamics 1493
MULTIPARTICLE BEAM DYNAMICS I 1532
Instabilities and Cures (High Energy) 1575
Wake Field 1658
Impedance 1700

Beam-Beam Interaction 1759
Beam Cooling 1792
Other Multiparticle Beam Dynamics 1810
MULTIPARTICLE BEAM DYNAMICS II 1837
High-Current Dynamics 1858
Space Charge 1882
BEAM INSTRUMENTATION 1971
Short-Bunch Instrumentation 1996
Instrumentation Electronics 2023
Tune Measurement 2052
Beam Position Monitors 2069
Emittance and Profile Instrumentation 2149
Other Beam Instrumentation 2207
INSTABILITIES AND FEEDBACK 2276
Feedback Systems (including Beam) 2290
CONTROLS AND COMPUTING 2395
Control Systems W 2437
Control Systems X 2487
Computer Codes W 2538
Computer Codes X 2606

VOLUME 3
SUBSYSTEMS, TECHNOLOGY AND APPLICATIONS

SOURCES AND INJECTORS 2657
Particle Sources (including Polarized Sources) 2696
RF Guns and Linac Injectors 2787
RADIOFREQUENCY SYSTEMS 2879
Room-Temperature RF 2920
Superconducting RF 3072
RF Sources/Systems 3111
Related Hardware 3174
MAGNETS 3201
Room-Temperature Magnets 3227
Superconducting Magnets 3338
Power Supplies 3449
Insertion Devices 3491
VACUUM, ALIGNMENT, RADIATION MONITORING AND OTHER TECHNOLOGY 3542
Vacuum Technology 3580
Alignment and Survey 3645
Radiation Monitoring and Safety 3669
Other Subsystems Technology and Components 3687
APPLICATIONS OF ACCELERATORS 3770
Medical Therapy 3813
Medical Isotope Production 3834
High-Power Accelerator Applications 3848
Electron Beam Processing 3854
Non-Destructive Evaluation and Other Applications 3866

CONTENTS OF VOLUME 2

SINGLE-PARTICLE BEAM DYNAMICS AND OPTICS

Chair: R. Servranckx

Beam Dynamics in SLC *(Invited)* — *Ralph W. Assmann* 1331
Rigorous Integration of Maps and Long-Term Stability *(Invited)* — *K. Makino* 1336
Analytic Nonlinear Methods for Beam Optics *(Invited)* — *J. Irwin* 1341
Nonlinear Dynamics Issues for Quasi-Isochronous Storage Rings *(Invited)* — *D. Jeon, M. Bai, C.M. Chu, X. Kang, S.Y. Lee, A. Riabko, X. Zhao* 1346
Lattice Design for a High-Power Infrared FEL *(Invited)* — *D.R. Douglas* 1351
Overview of the LHC Dynamic Aperture Studies — *M. Böge, A. Faus-Golfe, J. Gareyte, H. Grote, J.-P. Koutchouk, J. Miles, Q. Qing, T. Risselada, F. Schmidt, S. Weisz* 1356
Global and Local Horizontal-Vertical Decoupling — *L.C. Teng* 1359
Analytic Lattice Design with *BeamOptics* — *B. Autin, T. D'Amico, V. Ducas, M. Martini, E. Wildner* 1362
Experimental Measurement of High-Gradient Standing Wave Accelerator Transport Matrix — *S. Reiche, J.B. Rosenzweig, L. Serafini* 1365
Application of Cremona Approximation to One-Turn Maps for the Large Hadron Collider — *Alex J. Dragt, Dan T. Abell* ..... no manuscript submitted
Method of Strong Focusing — *V.E. Shapiro* 1368

Lattice Design and Optics

A Standard FODO Lattice with Adjustable Momentum Compaction — *D. Trbojevic, E. Courant* 1371
Beam-Based Calibration of the Linear Optics Model of ELSA — *J. Keil, D. Husmann* 1373
Lattices for Medical Synchrotrons Employing Active Scanning — *M. Benedikt* 1376
Matching to Gantries for Medical Synchrotrons — *M. Benedikt, C. Carli* 1379
Beam Optics Issues for the Antiproton Decelerator — *P. Belochitskii, C. Carli, T. Eriksson, R. Giannini, S. Maury, D. Möhl, F. Pedersen* 1382
Longitudinal Radiation Excitation of Quasi-Isochronus Storage Ring "New SUBARU" — *Y. Shoji, A. Ando, H. Tanaka, M. Takao, K. Soutome* 1385
Lattice Design of BTCF Storage Ring — *N. Huang, L.H. Jin, W.B. Liu, D. Wang, Z.T. Wei, C.H. Yu* 1388
The Focusing Structure of the Prague Proton Synchrotron for Hadron Therapy — *A.Y. Molodozhentsev, I.N. Ivanov, V.K. Makoveev, G.I. Sidorov, K. Prokesh, J. Sedlak, M. Kuzmiak* 1391
Dynamic Aperture with Multipoles of Special Quadrupole Magnets in the KEKB Interaction Region — *H. Koiso, H. Nakayama, K. Oide, M. Tawada* 1394
Magnetic Optics for Proton Radiography — *C. Thomas Mottershead, John D. Zumbro* 1397
Design of Double Storage Rings at MUSES — *N. Inabe, T. Katayama* 1400
Ion Optical Design of the BRF-FNAL-SAIC-UW PET Accelerator — *D.J. Larson, D. Sun, P.E. Young, F.M. Bieniosek, J.-F. Ostiguy, R.J. Pasquinelli, M. Popovic* 1403
Optics for SOLEIL at 2.5 GeV — *P. Nghiem, P. Brunelle, J.-L. Laclare, M.-P. Level, A. Nadji, J. Payet, M. Sommer, A. Tkatchenko* 1406
Emittance Study of Combined Function TBA Lattice at SRRC — *Min-Huey Wang, Peace Chang, K.T. Hsue, C.C. Kuo, C.S. Hsue* 1409
Beam Optics for the Target Beam Lines of the European Spallation Source — *V. Ziemann* 1412
Intrinsic Third Order Aberrations in Electrostatic and Magnetic Quadrupoles — *R. Baartman* 1415

Maps, Tracking and Dynamic Aperture

Canonical Particle Tracking and End Pole Matching of Helical Insertion Devices — *Godehard Wüstefeld, Michael Scheer* 1418
Orbit Dynamics for Unstable Linear Motion — *G. Parzen* 1421
Particle Motion Inside and Near a Linear Half-Integer Stopband — *G. Parzen* 1424
Particle Motion in the Stable Region Near the Edge of a Linear Sum Resonance Stopband — *G. Parzen* 1427
The Linear Parameters and the Decoupling Matrix for Linearly Coupled Motion in 6-Dimensional Phase Space — *G. Parzen* 1430
Dynamic Aperture of the Storage Ring VEPP-2M in Round Beam Mode — *I.A. Koop, A.P. Lysenko, I.N. Nesterenko, Yu.M. Shatunov, A.A. Valishev* 1433

Tracking Studies for the LHC Optics Version 4 at Injection Energy — *M. Böge, F. Schmidt* 1436
Estimates for Long-Term Stability for the LHC — *M. Böge, F. Schmidt* 1439
A More Robust and Flexible Lattice for LHC — *A. Faus-Golfe, H. Grote, J.-P. Koutchouk, T. Risselada, A. Verdier, S. Weisz* 1442
Inverse Logarithm Decay of Long-Term Dynamic Aperture in Hadron Colliders — *M. Giovannozzi, W. Scandale, E. Todesco* 1445
Dynamic Aperture Study on the Beijing Tau-Charm Factory Design — *Q. Qin, Z.T. Wei, N. Huang, A.M. Xiao* 1448
Computation of the Dynamic Aperture of 2D Generic Maps Using Invariant Manifolds — *Massimo Giovannozzi* 1451
An Orbit and Dispersion Correction Scheme for the PEP-II — *M.H.R. Donald, Y. Cai, H. Shoaee, G. White* ... 1454
Experimental Non Linear Beam Dynamics Studies at SPEAR — *A. Terebilo, C. Pellegrini, M. Cornacchia, J. Corbett, D. Martin* 1457

Error Effects, Experiments, Spin Dynamics

Overcoming Weak Intrinsic Depolarizing Resonance with Energy-Jump — *H. Huang, L. Ahrens, J.G. Alessi, M. Bai, K.A. Brown, G. Bunce, P. Cameron, P. Ingrassia, A.E. Kponou, K. Krueger, S.Y. Lee, A.U. Luccio, Y.I. Makdisi, F. Mariam, M. Okamura, L. Ratner, K. Reece, T. Roser, H. Sato, H.M. Spinka, N. Tsoupas, D.G. Underwood, W. van Asselt, N.W. Williams, A. Yokosawa* 1460
Nonlinear Beam Dynamics Study at the VEPP-4M — *V. Kiselev, E. Levichev, V. Sajaev, V. Smaluk* 1463
Dynamic Aperture Study in the VEPP-4M Storage Ring — *V. Kiselev, E. Levichev, V. Sajaev, V. Smaluk* 1466
Sorting Strategies for the CERN-LHC Dipoles — *R. Bartolini, W. Scandale, M. Giovannozzi, E. Todesco* 1469
Investigation of Chromaticity Sharing at the Cornell Electron Storage Ring — *S. Henderson, R. Littauer, B. McDaniel, T. Pelaia, R. Talman, E. Young* 1472
Beam Dynamics with Noise in Superferric Very Large Hadron Collider ("Pipetron") — *V.D. Shiltsev* 1475
Overcoming Intrinsic Spin Resonance by Using an AC Dipole — *M. Bai, L. Ahrens, J.W. Glenn, H. Huang, S.Y. Lee, L. Ratner, T. Roser, M. Syphers, W. van Asselt, A. Yokosawa* 1478
First Test of Orbit Response Matrix in Proton Storage Ring — *C.M. Chu, M. Ball, G. East, B. Hamilton, D. Jeon, X. Kang, L. Kiang, S.Y. Lee, K.Y. Ng, A. Pei, A. Riabko, T. Sloan* 1481
Test of Optics Diagnostics in ATF — *K. Kubo, K. Oide, J. Urakawa, T. Okugi* 1484
Effect of RF Phase Modulation on the Longitudinal Beam Dynamics — *Min-Huey Wang, L.H. Chang, Peace Chang, K.T. Hsu, C.C. Kuo, W.K. Lau, C.S. Hsue* 1487
Measurement of the Variation of Machine Parameters and the Effect of the Power Supplies Ripple on the Instantaneous Tunes at SPEAR — *A. Terebilo, C. Pellegrini, M. Cornacchia, J. Corbett, D. Martin* 1490

Other Single-Particle Beam Dynamics

Some Results of the Advanced Photon Source Beam Lifetime Studies — *Hana M. Bizek* 1493
The Extended Touschek Lifetime — *Hana M. Bizek* 1496
"Integrable Accelerator" Structure for Round Beams with Soliton-Like Force — *V.V. Danilov* 1499
Wavelet Approach to Accelerator Problems, I. Polynomial Dynamics — *A. Fedorova, M. Zeitlin, Z. Parsa* 1502
Wavelet Approach to Accelerator Problems, II. Metaplectic Wavelets — *A.N. Fedorova, M.G. Zeitlin, Z. Parsa* 1505
Wavelet Approach to Accelerator Problems, III. Melnikov Functions and Symplectic Topology — *A.N. Fedorova, M.G. Zeitlin, Z. Parsa* 1508
Some Interaction Peculiarities of Relativistic Particles with UHF Electric Field of High Intensity at Large Distances — *O.P. Korovin, V.O. Naidenov, E.O. Popov* 1511
Nonlinear Longitudinal Dynamics Studies at the ALS — *J.M. Byrd, W.-H. Cheng, F. Zimmermann* 1514
Energy Acceptance and Touschek Lifetime Calculations for the SOLEIL Project — *A. Nadji, G. Flynn, J.-L. LaClare, M.-P. Level, P. Nghiem, J. Payet* 1517
Simulations of Non-Linear Beam Dynamics Effects Due to an Electromagnetic Elliptical Wiggler — *L. Tosi, B. Diviacco, R.P. Walker, G. Wuestefeld, M. Scheer, S. Werin* 1520
Dispersion in the Presence of Strong Transverse Wakefields — *Ralph W. Assmann, Alex Chao* 1523
Review of Image Effects on Particle Beams in Cylindrical Pipes — *C.K. Allen, M. Reiser* 1526
A Multimedia Tutorial for Charged-Particle Beam Dynamics — *Richard R. Silbar* 1529

MULTIPARTICLE BEAM DYNAMICS I

Chair: J. Bisognano, *Thomas Jefferson National Accelerator Facility*

Energy Dependence of Beam-Beam Interactions at LEP *(Invited)* — *H. Burkhardt* 1532
Beam Dynamics Problems for a $\mu^+ - \mu^-$ Collider *(Invited)* — *D. Neuffer* 1537
Collisions of Resonantly Coupled Round Beams at the Cornell Electron-Positron Storage Ring (CESR) — *E. Young, S. Henderson, R. Littauer, B. McDaniel, T. Pelaia, R. Talman* 1542
Longitudinal Beam Instabilities in the Barrier RF System — *Y.H. Chin* 1545
Strong Longitudinal Focusing and Microwave Instability in Storage Rings — *Y. Wu, V.N. Litvinenko* ..... no manuscript submitted
Microwave Instability at Transition Crossing in the KEK-PS — *K. Takayama, D. Arakawa, J. Kishiro, K. Koba, T. Toyama, M. Yoshii* 1548
Fractional Filling Induced Landau Damping of Longitudinal Instabilities at the ESRF — *O. Naumann, J. Jacob* 1551
Effects of Incoherent Space Charge Forces on the Fast Head-Tail Instability — *Michael Blaskiewicz* 1554
First Operation of the Superconducting Electron Cooler at the Storage Ring TARN II — *T. Tanabe, I. Katayama, S. Ono, K. Chida, T. Watanabe, Y. Arakaki, K. Noda, T. Honma, Y. Haruyama, M. Saito, T. Odagiri, K. Hosono, T. Yosiyuki, M. Hosino, I. Watanabe* 1557
Lasers and Laser-Cooling Used for Studies of Beam Dynamics — *N. Madsen, M. Drewsen, L.H. Hornekær, A. Labrador, J.S. Nielsen, P. Shi, J.S. Hangst, J.P. Schiffer, V.A. Lebedev* 1560
First Observations of a "Fast Beam-Ion Instability" at the ALS — *J.M. Byrd, A.W. Chao, S. Heifets, M.G. Minty, T.O. Raubenheimer, J.T. Seeman, G.V. Stupakov, J. Thomson, F. Zimmermann* 1563
The Experimental Study on Beam-Photoelectron Instability in BEPC — *Z.Y. Guo, H. Huang, S.P. Li, D.K. Liu, L. Ma, Q. Qin, L.F. Wang, J.Q. Wang, S.H. Wang, C. Zhang, F. Zhou, Y.H. Chin, H. Fukuma, S. Hiramatsu, M. Izawa, T. Kasuga, E. Kikutani, Y. Kobayashi, S. Kurokawa, K. Ohmi, Y. Sato, Y. Suetsugu, M. Tobiyama, K. Yokoya, X.L. Zhang* 1566
Operation and Performance of Bunch Precompression for Increased Current Transmission at the SLC — *M.G. Minty, R. Akre, F.J. Decker, J. Turner* 1569
Ultra-Short Bunches by Using a Quasi-Continous Compressor Scheme in a Long Beam Transfer Line — *H. Schlarb, R. Brinkmann* 1572

Instabilities and Cures (High Energy)

Compensation of Longitudinal Coupled-Bunch Instability in the Advanced Photon Source Storage Ring — *K.C. Harkay, A. Nassiri, J.J. Song, Y.W. Kang, R.L. Kustom* 1575
Fast Transverse Instability in the NSNS Accumulator Ring — *A.G. Ruggiero, M. Blaskiewicz* 1578
$e - p$ Instability in the NSNS Accumulator Ring — *Alessandro G. Ruggiero, Mike Blaskiewicz* 1581
Microwave Instability Thresholds — *S.Y. Zhang* 1584
Longitudinal Coupled-Bunch Instability Around 1 GHz at the CERN PS Booster — *F. Caspers, M. Chanel, H. Schönauer, L. Søby, M. D'Yachkov* 1587
Beam Intensity Limits in the Main Injector through Transition with a Normal Phase Jump Scheme — *C.M. Bhat, J.A. MacLachlan* 1590
Longitudinal Instability Due to the Randomness of Higher Mode Frequencies of RF Cavity — *Soon-Kwon Nam, T.Y. Kim* 1593
Experimental Observations of the Ion-Related Coupled Bunch Instability in a Bunch Train in TRISTAN AR — *H. Fukuma, Y. Chin, S. Kato, E. Kikutani, S. Kurokawa, S. Matsumoto, K. Ohmi, Y. Suetsugu, M. Tobiyama, K. Yokoya, X.L. Zhang* 1596
Beam Loss at the Beginning of Acceleration in the KEK-PS Main Ring — *T. Toyama, D. Arakawa, I. Igarashi, J. Kishiro, K. Koba, K. Takayama* 1599
Bunch Lengthening and Energy Spread Increasing in Electron Storage Rings — *J. Gao* 1602
Theory of Single Bunch Transverse Collective Instabilities in Electron Storage Rings — *J. Gao* 1605
Theoretical Investigations on Multibunch Instabilities in Electron Storage Rings and Linear Accelerators — *J. Gao* 1608
Recent Experimental Evidence for the Los Alamos Proton Storage Ring Beam Instability — *M.A. Plum, D.H. Fitzgerald, D. Johnson, J. Langenbrunner, R. Macek, F. Merrill, P. Morton, B. Prichard, O. Sander, M. Shulze, H.A. Thiessen, T.S. Wang, C. Wilkinson* 1611
Increase of the Transverse Strong Head-Tail Instability Threshold by an Alternating Chromaticity — *Wen-Hao Cheng, Andrew M. Sessler, Jonathan S. Wurtele* 1614

The Electron-Cloud Instability in PEP-II: An Update — *M.A. Furman, G.R. Lambertson* 1617
Saturation of the Ion Transverse Instability — *S. Heifets* 1620
A Coupled-Bunch Ion Instability in the SLC Electron Damping Ring — *P. Krejcik* 1623
Ion Effects in the SLC Electron Damping Ring — *P. Krejcik, D. Pritzkau, T. Raubenheimer, M. Ross, F. Zimmermann* 1626
Saw-Tooth Instability Studies in the Stanford Linear Collider Damping Rings — *B.V. Podobedov, R.H. Siemann* 1629
Fast Ion Instability in Real Lattice — *G.V. Stupakov* 1632
Nonlinear Dynamics of Single Bunch Instability — *G.V. Stupakov, B.N. Breizman, M.S. Pekker* 1635
Stablization of the Spectral Intensity Fluctuations with the Higher Order Mode Frequency Tuners — *Ch. Wang, L.H. Chang, S.S. Chang, Y.I. Chang, C.C. Kuo, C.Y. Lai, W.K. Lau, M.C. Lin, S.J. Lin, G.H. Luo, T.T. Yang* 1638
Shielding Transient Self-Interaction of a Bunch Entering a Circle from a Straight Path — *R. Li, C.L. Bohn, J.J. Bisognano* 1641
Analysis on the Steady-State Coherent Synchrotron Radiation with Strong Shielding — *R. Li, C.L. Bohn, J.J. Bisognano* 1644
Landau Damping of the Weak Head-Tail Instability for Beams with Quadratic Amplitude-Dependent Betatron Tunes and Binomial Amplitude Distributions — *H.J. Tran, S.R. Koscielniak* 1647
Preliminary Measurement of Energy-Spread Change Resulting from the Resistive-Wall Instability — *H. Suk, J.G. Wang, Y. Zou, S. Bernal, M. Reiser* 1650
Space-Charge Effects on the Beam Resonance Instability — *M.B. Ottinger, T. Tajima, K. Hiramoto* 1653
Longitudinal Coupled Bunch Instabilities in the JHP 50 GeV Main Ring — *T. Uesugi, Y. Mori, S. Machida, C. Ohmori, Y. Chin* 1656

Wake Field

Coherent Radiation of an Electron Bunch Moving in an Arc of a Circle — *E.L. Saldin, E.A. Schneidmiller, M.V. Yurkov* 1658
Wakefields of Short Bunches in the Canal Covered with Thin Dielectric Layer — *A. Novokhatski, A. Mosnier* . 1661
Measurement of the Longitudinal Wake Potential in the Photon Factory Electron Storage Ring — *Kazuhiro Tamura, Toshio Kasuga, Makoto Tobiyama, Takashi Obina, Akira Mochihashi, Baogen Sun* 1664
Weak-Strong Simulation of Beam-Photoelectron Instability in a Positron Storage Ring — *K. Ohmi* 1667
Equivalent Circuit Study of Beam-Loading Using a Moment Method — *T.F. Wang, S. Machida, Y. Mori, C. Ohmori* 1670
Collective Centroid Oscillations as an Emittance Preservation Diagnostic in Linear Collider Linacs — *C.E. Adolphsen, K.L.F. Bane, W.L. Spence, M.D. Woodley* 1673
Beam Loading Compensation in the NLCTA — *C. Adolphsen, T. Lavine, C. Nantista, R. Ruth, J. Wang, D. Yeremian* 1676
Emittance Dilution through Coherent Energy Spread Generation in Bending Systems — *P. Emma, R. Brinkmann* 1679
Single Bunch Stability in PEP-II LER — *S. Heifets, G. Sabbi* 1682
Geometrical Wake of a Smooth Flat Collimator — *G.V. Stupakov* 1685
Synchrotron Radiation Wake in Free Space — *G.V. Stupakov* 1688
Effects of the Landau Cavity on the Electron Beam — *L.H. Chang, Ch. Wang, W.K. Lau* 1691
Beam Breakup in a Microtron — *Byung C. Yunn, Lia Merminga* 1694
Beam Loading Optimized Filling Patterns for Partially Filled Storage Rings — *S.A. Bogacz* 1697

Impedance

A Potpourri of Impedance Measurements at the Advanced Photon Source Storage Ring — *N.S. Sereno, Y.-C. Chae, K.C. Harkay, A. Lumpkin, S.V. Milton, B.X. Yang* 1700
Beam Impedance Study for the BESSY-II Storage Ring — *S. Khan* 1703
The Coupling Impedance of the RHIC Injection Kicker System — *H. Hahn, A. Ratti* 1706
Design of a Heavily Damped Superconducting Cavity for SOLEIL — *A. Mosnier, S. Chel, X. Hanus, A. Novokhatski, G. Flynn* 1709
Stability Diagrams for Landau Damping — *J. Scott Berg, Francesco Ruggiero* 1712
An Impedance Data Base Program for LEP2 and the LHC — *O. Brüning* 1715

The HOM Study of CESR RF Cavities Studied Using a Single Circulating Bunch — *A. Temnykh, D. Hartill, S. Belomestnykh, R. Kaplan* 1718
Controlling the Resistive Wall Instability in the Fermilab Main Ring — *D. Capista, D. McGinnis, J. Steimel, I. Kourbanis, D. Still* 1721
Impedance Scaling and Impedance Control — *W. Chou, J. Griffin* 1724
Measurement of the Kicker Coupling Impedances in the SIS and ESR at GSI — *Udo Blell* 1727
Impedance Studies for BEPC — *F. Zhou, Z.Y. Gou, S.H. Wang, G.W. Wang, C.X Tang* 1729
Beam Coupling Impedances of Obstacles Protruding into Beam Pipe — *Sergey S. Kurennoy* 1732
Improvements in Curing Coupled Bunch Instabilities at ELETTRA by Mode Shifting after the Installation of the Adjustable Higher Order Mode Frequency Shifter (HOMFS) — *M. Svandrlik, A. Fabris, C. Pasotti* . 1735
Estimate of the Impedance Due to Wall Surface Roughness — *K.L.F. Bane, C.K. Ng, A.W. Chao* 1738
Longitudinal Beam-Transfer-Function Measurements at the SLC Damping Rings — *M.G. Minty, F. Zimmermann* 1741
Analytic and Numerical Analysis of the Longitudinal Coupling Impedance of an Annular Cut in a Coaxial Liner — *Alexei V. Fedotov, Robert L. Gluckstern* 1744
General Analysis of the Longitudinal Coupling Impedance of a Rectangular Slot in a Thin Coaxial Liner — *Alexei V. Fedotov, Robert L. Gluckstern* 1747
Resonant Effects in the Longitudinal Coupling Impedance of a Rectangular Slot in a Coaxial Liner — *Alexei V. Fedotov, Robert L. Gluckstern* 1750
Path Integral Computation of Laslett Coefficients in Pipes with Arbitrary Transverse Geometry — *S. Petracca, F. Ruggiero, V. Galdi, I. Pinto* 1753
Influence of Resistive Wall Impedance on the VSX Light Source — *N. Nakamura, T. Koseki* 1756

Beam-Beam Interaction

Two Examples of Integrable Systems with Round Colliding Beams — *V.V. Danilov, E.A. Perevedentsev* 1759
Beam-Beam Effects Simulation for VEPP-2M with the Flat and the Round Beams — *I.N. Nesterenko, D.N. Shatilov, E.A. Simonov* 1762
A Luminosity Monitor Using the Coherent Beam-Beam Interaction — *David Sagan, John Sikora, Stuart Henderson* 1765
The Incoherent Long Range Beam-Beam Interaction in CESR — *Alexander Temnykh, David Sagan* 1768
Measurement and Simulation of Nonlinear Beam-Beam Mode Coupling in the Fermilab Tevatron — *S. Assadi, C.S. Mishra* 1771
Beam-Beam Simulations with Crossing Angle in TEV33 — *V.D. Shiltsev* 1774
Evaluation of "Round Colliding Beams" for Tevatron — *V.V. Danilov, V.D. Shiltsev* 1777
A Study on Beam-Beam Interactions for BTCF — *C. Zhang, N. Huang, K. Hirata* 1780
Dispersion in the Interaction Point — *S. Petracca, K. Hirata* 1783
Effect of Noise in Beam-Beam Interaction — *Yuri K. Batygin, Takeshi Katayama* 1786
Beam-Beam Simulations with Non-Gaussian Distributions for SLC and SLC-2000 — *K.L.F. Bane, P. Chen, F. Zimmermann* 1789

Beam Cooling

High Current Magnetized Plasma Discharges and Electron Beams for Capture and Cooling of Charged Leptons and Hadrons — *Ady Hershcovitch* 1792
Linac-Based Electron Cooling Device — *N.S. Dikansky, V.V. Parkhomchuk, V.M. Petrov, V.G. Shamovsky, A.N. Smirnov, P.D. Vobly, V.N. Volkov* 1795
The Coupling-Cavity Scheme for Three-Dimensional Laser Cooling — *T. Kihara, H. Okamoto, Y. Iwashita, K. Oide* 1798
Design and Analysis of a Cooling Insertion Lattice for Optical Stochastic Cooling — *A. Zholents, M. Zolotorev, W. Wan* 1801
An Amplifier for Optical Stochastic Cooling — *A. Zholents, M. Zolotorev* 1804
Simulation of Beam Bunching with Electron Cooling for the Ion Storage Ring of RIKEN RI-Beam Factory Project — *M. Takanaka, T. Katayama* 1807

Other Multiparticle Beam Dynamics

Generation of Sub-Picosecond X-Ray Pulses at BESSY-II — *S. Khan* 1810
Energy Loss of Proton and Lead Beams in the CERN-SPS — *J. Arnold, T. Bohl, H. Burkhardt, R. Cornali, K. Cornelis, G. Engelmann, R. Giachino, A. Hofmann, M. Jonker, T. Linnecar, M. Meddahi, L. Normann, E. Shaposhnikova, A. Wagner, B. Zotter* 1813
Beam Echoes in the CERN SPS — *O. Brüning, T. Linnecar, F. Ruggiero, W. Scandale, E. Shaposhnikova, D. Stellfeld* 1816
Observation and Simulation of Beam Tails in LEP — *I. Reichel, H. Burkhardt, G. Roy* 1819
Synchrotron Oscillation Driven by RF Phase Noise — *Kern W. Ormond, Joseph T. Rogers* 1822
Numerical Solution for Fokker-Planck Equations in Accelerators — *M.P. Zorzano, H. Mais, L. Vazquez* 1825
Multibunch Collision Scheme in BEPC — *L.F. Wang, C. Zhang, Z.Y. Guo, S.H. Wang* 1828
Emittance Measurement from the Decay Rate of Coherent Oscillation through Nonlinear Filamentation — *S. Kamada, N. Akasaka, K. Ohmi* 1831
Effect of Diffusion on Bunched Beam Echo — *G.V. Stupakov, A.W. Chao* 1834

MULTIPARTICLE BEAM DYNAMICS II

Chair: K-J. Kim, *Lawrence Berkeley National Laboratory*

Advances in 3D Electromagnetic Finite Element Modeling *(Invited)* — *E.M. Nelson* 1837
Experimental Results on Beam Halo *(Invited)* — *G. Haouat* 1841
Core and Halo Particle Dynamics of High Intensity Proton Beams — *M. Pabst, K. Bongardt, A.P. Letchford* ... 1846
The Fine Structure of the Longitudinal Machine Impedance Observed with Single Bunches — *T. Bohl, T.P.R. Linnecar, E. Shaposhnikova* 1849
Equipartitioning and Halo Due to Anisotropy — *Ingo Hofmann* 1852
Design and Development of an Electron Recirculator for Study of High-Current Beam Dynamics — *J.G. Wang, S. Bernal, P. Chin, J.J. Deng, Y. Li, M. Reiser, H. Suk, M. Venturini, Y. Zou, T. Godlove, R.C. York* .. 1855

High-Current Dynamics

Parasitic Energy Loss in the LEP Superconducting Cavities — *G. Arduini, O. Brüning, G. Cavallari, P. Gayet, G. Geschonke, E. Haebel, A. Hofmann, M. Jimenez, O. Meincke, G. Morpurgo, G. Roy, H. Schmickler, J. Uythoven, A. Wagner, B. Zotter* 1858
Transmission Line Analysis of Beam Deflection in a BPM Stripline Kicker — *George J. Caporaso, Yu-Ju Chen, Brian Poole* 1861
Space-Charge Forces of a DC Beam in a Continuous Bend — *Yu-Jiuan Chen* 1864
Diode and Final-Focus Simulations for DARHT — *Thomas P. Hughes, Dale R. Welch, Randolph L. Carlson* 1867
Influence of Ion Channel on Electron Beam Propagation — *Han S. Uhm, E.H. Choi, J.J. Ko, H.M. Shin* 1870
Simulations of Bunch Precompression at High Currents in the SLC Damping Rings — *K.L.F. Bane, M.G. Minty, A.W. Chao* 1873
Measurement of the Longitudinal Wakefield in the SLAC Linac — *K.L.F. Bane, F.-J. Decker, J.T. Seeman, F. Zimmermann* 1876
Analytic Expressions for Longitudinal Schottky Signals from Beams with Gaussian Momentum Distribution — *V. Ziemann* 1879

Space Charge

Proton Injection and RF Capture in the National Spallation Neutron Source — *A.U. Luccio, J. Beebe-Wang, D. Maletic, F.W. Jones* 1882
Transverse Instability in High Intensity Proton Rings — *S.Y. Zhang, W.T. Weng* 1885
Compensation of Bend-Plane Emittance Growth in a 180 Degree Bend — *David H. Dowell* 1888
Coherent Synchrotron Radiation Induced Emittance Growth in a Chicane Buncher — *David H. Dowell, Patrick G. O'Shea* 1891
Free Energy Relaxation in a Drift-Tube Linac — *Nathan A. Brown, George H. Gillespie, Barrey W. Hill* 1894
High Current Beam Dynamics for the Upgraded UNILAC — *W. Barth, L. Dahl, J. Glatz, J. Klabunde, U. Ratzinger, A. Schempp* 1897
Considerations on Particle Dynamics in a Heavy Ion DTL — *Horst Deitinghoff, Giovanni Parisi* 1900
Bunch Space Charge Limits in an RTM — *V.I. Shvedunov, H. Euteneuer, K.-H. Kaiser* 1902

Comparative Study of Accelerating Structures Proposed for High Power Linac — *A. Kolomiets, S. Yaramishev* 1905
Intensity Dependence of Betatron Resonances Observed at the KEK-PS — *Y. Shoji, D. Arakawa, J. Kishiro, K. Koba, S. Machida, K. Marutsuka, Y. Mori, C. Ohmori, H. Sato, M. Shirakata, H. Takagi, K. Takayama, T. Toyama, M. Yoshii* 1908
Halo Formation from Axisymmetric Breathing Beams — *Masanori Ikegami, Hiromi Okamoto* 1911
Emittance Growth of an Intense Electron Beam in a Focusing Channel — *B.E. Carlsten* 1914
Beam Matching and Halo Control — *W. Lysenko, Z. Parsa* 1917
Equipartitioning in a High Current Proton Linac — *Lloyd M. Young* 1920
Numerical Simulation Studies of the LBNL Heavy-Ion Beam Combiner Experiment — *W.M. Fawley, P. Seidl, I. Haber, A. Friedman, D.P. Grote* 1923
A Scaled Beam-Combining Experiment for Heavy Ion Inertial Fusion — *P.A. Seidl, C.M. Celata, W.W. Chupp, A. Faltens, W.M. Fawley, W. Ghiroso, K. Hahn, E. Henestroza, S. MacLaren, C. Peters* 1926
Theory of Longitudinal Beam Halo in RF Linacs: I. Core/Test-Particle Formulation — *John J. Barnard, Steven M. Lund* 1929
Theory of Longitudinal Beam Halo in RF Linacs: II. Envelope-Particle Resonances — *Steven M. Lund, John J. Barnard* 1932
Self-Pinched Transport Theory for the SABRE Ion Diode — *Dale R. Welch, C.L. Olson, D.L. Hanson* 1935
Emittance Growth and Particle Diffusion Induced by Discrete-Particle Effects in Intense Beams — *Renato Pakter, Chiping Chen* 1938
Prevention of Halo Formation in High Brightness Beams — *Yuri K. Batygin* 1941
New Classes of Uniform Distributions for Charged Particles in Longitudinal Magnetic Field — *O. Drivotin, D. Ovsyannikov* 1944
The Calculation, Simulation, and Measurement of Longitudinal Beam Dynamics in Electron Injectors — *B. Dunham, H. Liu, R. Kazimi* 1947
Stability and Halo Formation in Axisymmetric Intense Beams — *Robert L. Gluckstern, Sergey S. Kurennoy* ... 1950
KV-Beam in a Dispersive Channel — *M. Venturini, M. Reiser* 1953
Longitudinal Focusing of Space-Charge Dominated Beams in the UMD Electron Ring — *J.J. Deng, J.G. Wang, M. Reiser, T. Godlove* 1956
Injector Design for a Model Electron Ring at the University of Maryland — *T.F. Godlove, S. Bernal, J.J. Deng, Y. Li, M. Reiser, J.G. Wang, Y. Zou* 1959
High Beam Current Handling in the HF Main Ring — *S. Machida, Y. Mori, C. Ohmori, Y. Ishi, S. Shibuya, M. Tomizawa* 1962
Space Charge Dominated Envelope Dynamics of Asymmetric Beams in RF Photoinjectors — *J.B. Rosenzweig, S. Anderson, Luca Serafini* 1965
Beam Dynamics in an Integrated Plane Wave Transformer Photoinjector at S- and X-Band — *J.B. Rosenzweig, X. Ding, D.T. Palmer, C. Pellegrini, L. Serafini, D. Yu* 1968

BEAM INSTRUMENTATION

Chair: A. Lumpkin, *Argonne National Laboratory*

Picosecond-Resolution 'Slice' Emittance Measurement of Electron Bunches *(Invited)* — *Ilan Ben-Zvi, Joe X. Qiu, Xijie Wang* 1971
Electron Beam Instrumentation Techniques Using Coherent Radiation *(Invited)* — *D.X. Wang* 1976
A Laser-Heterodyne Bunch-Length Monitor for the SLC Interaction Point — *T. Kotseroglou, R. Alley, D. McCormick, S. Horton-Smith, K. Jobe, P. Raimondi, M.C. Ross, T. Shintake, F. Zimmermann* 1981
Laser Based Sub-Picosecond Electron Bunch Characterization Using 90° Thomson Scattering — *W.P. Leemans, P. Volfbeyn, M. Zolotorev, K-J. Kim, S. Chattopadhyay, R.W. Schoenlein, A.H. Chin, T.E. Glover, P. Balling, C.V. Shank* 1984
Synchrotron Radiation Interferences Between Small Dipoles at LEP — *C. Bovet, A. Burns, F. Méot, M. Placidi, E. Rossa, J. de Vries* 1987
Electron Bunch Length Diagnostic with Coherent Smith-Purcell Radiation — *D.C. Nguyen* 1990
A High Resolution Electron Beam Profile Monitor — *W.S. Graves, E.D. Johnson, P.G. O'Shea* 1993

Short-Bunch Instrumentation

The Argonne Wakefield Accelerator: Diagnostics and Beam Characterization — *M. Conde, W. Gai, R. Konecny, X. Li, J. Power, P. Schoessow, N. Barov* 1996
Time-Resolved Imaging of Electron and Positron Beams at APS — *A.H. Lumpkin, B.X. Yang* 1999

Optical Transition Radiation Measurements on the ELETTRA Linac — *D. Giove, C. De Martinis, G. D'Auria, M. Ferianis, C. Rossi, A. Variola* 2002
Measuring the RMS Length of Short Electron Pulses with an RF Cavity and a Beam Position Monitor — *Steven J. Russell* 2005
Device for the Electron Bunch Length Measurement of 1-5 mm RMS — *V.E. Kaljuzhny, D.V. Kostin, N.P. Sobenin, S.N. Yarigin, A.A. Zavadtsev, M. Dohlus, N. Holtkamp* 2008
A New Frequency-Domain Method for Bunch Length Measurement — *M. Ferianis, M. Pros, A. Boscolo* 2011
Mechanical Design of the HER Synchrotron Light Monitor Primary Mirror for the PEP-II B-Factory — *Edward F. Daly, Alan S. Fisher, Nadine R. Kurita, J. Brian Langton* 2014
Sub-Picosecond Electron Bunch Length Measurement — *Chitrlada Settakorn, Michael Hernandez, Helmut Wiedemann* 2017
Measuring Longitudinal Distribution and Bunch Length of Femtosecond Bunches with RF Zero-Phasing Method — *D.X. Wang, G.A. Krafft* 2020

Instrumentation Electronics

The Algebraic Reconstruction Technique (ART) — *D. Raparia, J. Alessi, A. Kponou* 2023
Noise Reduction on the LEP Bunch Current Measurement System — *A. Burns, B. Halvarsson, H. Jakob, H. Schmickler* 2026
A Beamloss Diagnostic System for CESR — *S. Henderson* 2029
A New Flying Wire System for the Tevatron — *W. Blokland, G. Vogel, J. Dey* 2032
A High Speed, Multi-Sampling Data Acquisition System for Beam Diagnostics — *Ming-Jen Yang* 2035
Low Intensity Beam Diagnostics with Microchannel Plate Detectors — *G. Cuttone, C. De Martinis, Paolo Finocchiaro, Dario Giove, Guido Raia, Alberto Rovelli* 2038
Design of a VXI Module for Beam Phase and Energy Measurements for LEDA — *J.F. Power, J.D. Gilpatrick, M.W. Stettler* 2041
Description and Operation of the LEDA Beam Position/Intensity Measurement Module — *C.R. Rose, M.W. Stettler* 2044
Design Study for an Undulator Photon Beam Position and Profile Monitor — *Ian C. Hsu, C.-T. Wang, P.-C. Lai* 2047
An RF Signal Processing Module for the SPS Orbit Observation System Upgrade — *W.R. Rawnsley, K. Fong, S. Fang, J.P. Papis* 2049

Tune Measurement

Characterization of Beam Dynamics in the APS Injector Rings Using Time-Resolved Imaging Techniques — *B.X. Yang, A.H. Lumpkin, M. Borland, K. Harkay, A. Nassiri* 2052
Lattice Function Measurements in the Fermilab Accumulator Ring — *M. Church* 2055
Realtime Tune Measurements in Slow-Cycling Accelerators — *D. Herrup* 2058
Tune Measurement Methods in the Fermilab Main Ring — *D. Still, I. Kourbanis, D. Capista* 2061
Automatic Beam Position Control at LASREF — *M.A. Oothoudt, C. Pillai, M.V. Zumbro* 2064
Mechanical Design of a Pinger System for the LBNL Light Source Accelerator — *W. Thur, J. Akre, A. Gavidia, J. Guigli* 2067

Beam Position Monitors

Performance of the Upgraded NSLS Beam Position Monitors — *R.J. Nawrocky, J. Keane* 2069
A Compact BPM for the Fermilab Main Injector — *J. Fitzgerald, J. Crisp* 2072
Upgrade of the BPM System for the BEPC Storage Ring — *Li Ma, Ping Shi* 2075
Bunch Shape Monitors for the DESY H^- Linac — *A.V. Feschenko, A.V. Liiou, A.N. Mirzojan, A.A. Menshov, P.N. Ostroumov, N. Holtkamp, C. Kleffner, M. Nagl, I. Peperkorn* 2078
Design and Commissioning of Beam Position Monitors in the IUCF Cooler Injector Synchrotron — *M.S. Ball, B.J. Hamilton, D. Bilodeau* 2081
Measurement of Injection Orbit Using a Single Pass BPM System at the PF Ring — *T. Honda, M. Katoh, A. Ueda, M. Tadano, Y. Kobayashi, T. Mitsuhashi* 2084
Calibration for KEKB Beam Position Monitors — *Kotaro Satoh, Masaki Tejima* 2087
Comparison of Beam-Position-Transfer Functions Using Circular Beam-Position Monitors — *J.D. Gilpatrick* 2090
The LEDA Beam-Position Measurement System — *C.R. Rose, J.D. Gilpatrick, M.W. Stettler* 2093
Orbit Measurement and Correction in the LNLS Synchrotron Light Source — *R.H.A. Farias, L.C. Jahnel, Liu Lin, D. Macedo, F.S. Rafael, A.R.D. Rodrigues, P.F. Tavares* 2096

Real Time Dispersion Measurements at the MIT-Bates Linac — *K. Jacobs, S. Bradley, A. Carter, B. McAllister, C. Sibley, F. Wang* 2099
Beam Size Effects on Beam Position Measurements in Proton Synchrotron — *T. Nakagawa* 2102
Two Frequencies Cavities for Beam Position Monitor — *V.E. Kaljuzhny, D.V. Kostin, M.W. Lalayan, O.S. Milovanov, N.P. Sobenin, S.N. Yarigin, N. Holtkamp* 2104
Beam-Based Offset Calibration of the PLS BPM — *J.Y. Huang, D.H. Jung, K.H. Kim, S.H. Nam, M. Yoon, I.S. Ko* 2107
Calibration of the Beam-Position Monitor System for the SLAC PEP-II B Factory — *R. Johnson, S. Smith, N. Kurita, K. Kishiyama, J. Hinkson* 2110
A Two-Bunch Beam Position Monitor — *E. Medvedko, R. Aiello, S. Smith* 2113
Effect of TE Mode Power on the PEP-II LER BPM System — *J. Corlett, C.-K. Ng, S.R. Smith* 2116
Detection of Beam Induced Dipole-Mode Signals in the SLC S-Band Structures — *M. Seidel, C. Adolphsen, R. Assmann, D.H. Whittum* 2119
Beam Position Monitor System for PEP-II — *Stephen R. Smith, G. Roberto Aiello, Linda J. Hendrickson, Ronald G. Johnson, Mark R. Mills, Jeff J. Olsen* 2122
Optics Measurement Resolution and BPM Errors — *Yu-Chiu Chao* 2125
Linear Optics Correction in the CEBAF Accelerator — *V.A. Lebedev, M. Bickley, J. Bisognano, S. Schaffner, J. van Zeijts, G.A. Krafft, M. Tiefenback, W.A. Watson III, B. Yunn* 2128
1 nA Beam Position Monitoring System — *Rok Ursic, Roger Flood, Chip Piller, Edward Strong, Larry Turlington* 2131
Beam Position Monitors Inside the FEL-Undulator at the TESLA Test Facility Linac — *R. Lorenz, H. Henke, T. Kamps, U. Hahn, M. Wendt* 2134
First Operating Experiences of Beam Position Monitors in the TESLA Test Facility Linac — *R. Lorenz, M. Sachwitz, H.J. Schreiber, F. Tonisch, M. Castellano, P. Patteri, F. Tazzioli, L. Catani* 2137
The Closed Orbit Measuring System at the DELTA Synchrotron Radiation Facility — *A. Jankowiak, K. Wille* 2140
Development of a Resistive Beam Position/Current Monitor for the UMD Electron Ring — *H. Suk, J.G. Wang, S. Bernal, M. Reiser* 2143
Performance of the Single-Pass Position Monitor at SOR-RING — *Hirofumi Kudo, Kenji Shinoe, Hiroyuki Takaki, Tadashi Koseki, Norio Nakamura, Yukihide Kamiya, Tohru Honda* 2146

Emittance and Profile Instrumentation

A Scanning Target Profile Monitor for the Slow Extracted Beam at the AGS — *K.A. Brown, I.H. Chiang, D. Gassner, J. Geller, J.W. Glenn, J. Hock, G.A. Smith, J. Tuozzolo, R. Witkover, E. Zitvogel* 2149
A Prototype Ionization Profile Monitor for RHIC — *R. Connolly, P. Cameron, W. Ryan, T.J. Shea, R. Sikora, N. Tsoupas* 2152
A Multi-Wire Beam Profile Monitor in the AGS — *H. Huang, W. Buxton, V. Castillo, J.W. Glenn, G. Mahler, M. Syphers, W. van Asselt, R.L. Witkover, S.Y. Zhang* 2155
RADON Reconstruction in Longitudinal Phase Space — *V. Mane, J. Wei, S. Peggs* 2158
Orbit Compensation for the Time Varying Elliptically Polarized Wiggler with Switching Frequency at 100 Hz — *O. Singh, S. Krinsky* 2161
A Turn-By-Turn Vertical Profile Monitor — *R. Scott Smith, Stuart Henderson, D. Hartill, Tong Chen, R.H. Siemann* 2164
Fermilab Main Ring Ion Profile Monitor System — *J.R. Zagel, J.L. Crisp, A.A. Hahn, Patrick G. Hurh* 2166
First Test Results of a Residual Gas Beam Profile Monitor — *V. Variale, N. Ceci, V. Valentino, G. Lamanna, T. Clauser, V. Stagno, A. Dainelli, M. Poggi* 2169
A Longitudinal Phase Space Monitor at the Photon Factory Storage Ring — *Y. Kobayashi, M. Izawa* 2171
Study of a Non-Intrusive Electron Beam Radius Diagnostic — *Thomas J.T. Kwan, Barbara G. DeVolder, John C. Goldstein, Charles M. Snell* 2174
Preliminary Results of RMS Emittance Measurements Performed on the Sub-Picosecond Accelerator Using Beam Position Monitors — *Steven J. Russell* 2177
Spectral Fluctuations of Incoherent Radiation and Measurement of Longitudinal Bunch Profile — *M.S. Zolotorev, G.V. Stupakov* 2180
A Turn by Turn Photon Beam Profile Observation by a Laser Beam Saturated Photodiode — *Ian C. Hsu, C.-H. Lee, G.-T. Cheng* 2183
Beam Profile Monitors in the NLCTA — *C. Nantista, C. Adolphsen, R.L. Brown, R. Fuller, J. Rifkin* 2186
An RF Bunch-Length Monitor for the SLC Final Focus — *F. Zimmermann, G. Yocky, D. Whittum, M. Seidel, P. Raimondi, C.K. Ng, D. McCormick, K. Bane* 2189

Analysis of a Novel Diffractive Scanning-Wire Beam Position Monitor (BPM) for Discriminative Profiling of Electron vs. X-Ray Beams — *R. Tatchyn* 2192
Analysis of a Single-Shot Longitudinal Bunch Profiling System Based on an Ultra-Short Pulse Ti:Sapphire Laser — *R. Tatchyn* 2195
High Power Beam Profile Monitor with Optical Transition Radiation — *J.-C. Denard, P. Piot, K. Capek, E. Feldl* 2198
An Emittance Measurement System for a Wide Range of Bunch Charges — *B. Dunham, D. Engwall, A. Hofler, M. Keesee, R. Legg* 2201
A Multislit Transverse-Emittance Diagnostic for Space-Charge-Dominated Electron Beams — *P. Piot, J. Song, R. Li, G.A. Krafft, D. Kehne, K. Jordan, E. Feldl, J.-C. Denard* 2204

Other Beam Instrumentation

Status of the APS Diagnostics Undulator Beamline — *B.X. Yang, A.H. Lumpkin, G.A. Goeppner, S. Sharma, E. Rotela, I.C. Sheng, E. Moog* 2207
Tests of APS X-Ray Transmitting Beam Position Monitors at ESRF — *Deming Shu, Juan Barraza, Tuncer Kuzay, Graham Naylor, Pascal Elleaume* 2210
Observations of Secondary Emission Chamber Degradation from Very High Intensity Proton Beams at the AGS — *K.A. Brown, I.H. Chiang, A. Pendzick, T. Tallerico* 2213
Performance of the RHIC Injection Line Instrumentation Systems — *T.J. Shea, R.L. Witkover, P. Cameron, R. Connolly, W.A. Ryan, G.A. Smith, E. Zitvogel* 2215
RHIC Beam Loss Monitor System Design — *R. Witkover, E. Zitvogel, R. Michnoff* 2218
Instrumentation for Low Energy Electron Measurements — *Cheng-Yang Tan* 2221
A Proposed New HOM Monitoring System on the SRS — *P.A. McIntosh* 2223
Online Calculation of Tevatron Collider Luminosity Using Accelerator Instrumentation — *A.A. Hahn* 2226
A Beam Monitoring & Calibration System for High-Power Electron Linacs — *V.L. Uvarov, S.P. Karasyov, S.V. Maryokhin, R.I. Pomatsalyuk, S.Yu. Prokopenko, I.N. Shlakhov, S. Tenishev* 2229
LEDA and APT Beam Diagnostics Instrumentation — *J.D. Gilpatrick, T.R. Hodapp, K.F. Johnson, D.G. Martinez, R.P. Martinez, J.F. Power, C.R. Rose, R.E. Shafer, R.B. Shurter, M. Stettler* 2232
PEP-II Bunch-by-Bunch Current Monitor — *M.J. Chin, J.A. Hinkson* 2235
Optical Beam Diagnostics for the LNLS Synchrotron Light Source — *R.H.A. Farias, L.C. Jahnel, Liu Lin, P.F. Tavares* 2238
Vibration Measurement for Instrumentation and Diagnostics — *S. Sarkar, E. Ilhoff, C. Sibley, S.B. Soong, S. Wells, E. Tsentalovich, T. Zwart, J. Shaw* 2241
Option of Method for Electron Bunch Phase Distribution Monitoring — *A. Tron, I. Merinov, V. Smirnov* 2244
Space Charge Effect in Secondary Electron Monitors — *A. Tron* 2247
Equipment for Beam Current and Electron Energy Monitoring During Industry Irradiation — *A.A. Zavadtsev* 2250
Design and Initial Commissioning of Beam Diagnostics for the PEP-II B Factory — *A.S. Fisher, D. Alzofon, D. Arnett, E.L. Bong, B. Brugnoletti, B. Collins, E. Daly, A. Gioumousis, R. Johnson, A. Kulikov, N. Kurita, J. Langton, D. McCormick, R. Noriega, S. Smith, V. Smith, R. Stege, M. Bjork, M. Chin, J. Hinkson, R. McGill, T. Suwada* 2253
Beam Current Monitors in the NLCTA — *Christopher Nantista, Chris Adolphsen* 2256
Real-Time Beam Loss Monitoring System and its Application at SRRC — *K.T. Hsu, K.K. Lin, C.H. Kuo, Y.C. Liu* 2259
Methods of Orbit Correction System Optimization — *Yu-Chiu Chao* 2262
Automated Path Length and M_{56} Measurements at Jefferson Lab — *D. Hardy, J. Tang, R. Legg, M. Tiefenback, M. Crofford, G.A. Krafft* 2265
Analyzing Measurements of Nonlinear Transfer Functions with Tschebyshev Polynomials — *G.A. Krafft* 2268
Beam-Based Phase Monitoring and Gradient Calibration of Jefferson Laboratory RF Systems — *M.G. Tiefenback, K. Brown* 2271
A High Power Faraday Cup to Measure Extracted Beam Current from the Bates South Hall Ring — *J. Shaw, R. Averill, S. Kowalski, S. Sarkar, C. Sibley, S. Sobczynski, W. Turchinetz* 2274

INSTABILITIES AND FEEDBACK

Chair: R. Talman, *Cornell University*

Laser Manipulation of Beams *(Invited)* — *S. Chattopadhyay* ..... no manuscript submitted
Photoemission Instabilities: Theory and Experiment *(Invited)* — *Joseph T. Rogers* 2276
Commissioning of the APS Real-Time Orbit Feedback System — *J. Carwardine, G. Decker, K. Evans Jr., A. Hillman, F. Lenkszus, R. Merl, A. Pietryla* 2281
Control of Multibunch Longitudinal Instabilities and Beam Diagnostics Using a DSP-Based Feedback System — *D. Teytelman, R. Claus, J. Fox, H. Hindi, R. Larsen, I. Linscott, S. Prabhakar, W. Ross, A. Young, A. Drago, M. Serio, G. Stover* 2284
Global Orbit Feedback Utilizing Analog and Digital Technologies — *O. Singh, Y. Tang, S. Ramamoorthy, S. Krinsky, L.H. Yu* 2287

Feedback Systems (including Beam)

Evaluation of the Global Orbit Correction Algorithm for the APS Real-Time Orbit Feedback System — *J. Carwardine, K. Evans Jr.* 2290
Characterization and Equalization of the AC Responses of the Corrector Magnets for the APS Local Orbit Feedback System — *C. Doose, S.H. Kim* 2293
Simulation of the APS Storage-Ring RF Accelerating System — *C. Schwartz, A. Nassiri, Y. Kang, R.L. Kustom* . 2296
Multiple Control for Feedback Tuning of the Advanced Photon Source Storage Ring/Booster RF Cavities — *T.L. Smith* 2299
An Example of a Digital Synthesis Approach to DSP Design: The AGS Transverse Damper — *K.A. Brown, G.A. Smith, V. Wong* 2302
Longitudinal Coupled Bunch Instabilities on the NSLS X-Ray Ring — *R.W. Klaffky, W. Broome, R. D'Alsace, S.L. Kramer, M.G. Thomas, J.M. Wang* 2305
AGS Slow Extracted Beam Improvement — *I. Marneris, G. Danowski, J. Sandberg, A. Soukas* 2308
RF Control System for the SC Cavity of the Tesla Test Facility Injector — *A. Mosnier, S. Chel, B. Phung Ngoc, J.M. Tessier* 2311
Emittance Preservation in the PS Complex — *B. Autin, L. Giulicchi, A. Jansson, M. Lindroos, A. Lombardi, M. Martini, K. Schindl* 2314
Observation of a Longitudinal Coupled Bunch Instability with Trains of Bunches in CESR — *Michael Billing* 2317
A Design and Performance Analysis Tool for Superconducting RF Systems — *T. Schilcher, S.N. Simrock, L. Merminga, D.X. Wang* 2320
Observation and Cure of Longitudinal Coupled-Bunch Instabilities in the Fermilab Main Ring — *S. Assadi, I. Kourbanis, D. McGinnis, J. Steimel* 2323
Digital Low Level RF Systems for Fermilab Main Ring and Tevatron — *B.E. Chase, B. Barnes, K. Meisner* ... 2326
Damping of Injection Oscillations — *V.M. Zhabitsky* 2329
Strategy for Developing Fast Bunch Feedback Systems for KEKB — *E. Kikutani, M. Tobiyama* 2332
Study of Bunch by Bunch Feedback System in TRISTAN-AR — *M. Tobiyama, E. Kikutani* 2335
APT LLRF Control System Model Results — *A. Regan, C. Ziomek* 2338
Algorithms and Implementation of APT Resonant Control System — *Yi-Ming Wang, Amy Regan* 2341
Status of the PEP-II Transverse Feedback Systems — *W. Barry, J. Corlett, M. Fahmie, J. Greer, G. Lambertson, C. Pike* 2344
Beam Test of the Acceleration System with the DDS in HIMAC Synchrotron — *M. Kanazawa, K. Noda, E. Takada, M. Kumada, A. Itano, S. Watanabe, Y. Morii* 2347
Transverse Beam Feedback System in the PLS — *J.Y. Huang, M.K. Park, M. Kwon, M. Yoon, I.S. Ko* 2350
The Design of the ELETTRA Fast Local Feedback System — *C.J. Bocchetta, D. Bulfone, A. Galimberti, D. Giuressi, M. Lonza, R. Sergo, C. Scafuri, L. Tosi, R. Visintini* 2353
First Operational Results with the ELETTRA Fast Local Feedback System — *C.J. Bocchetta, D. Bulfone, A. Galimberti, D. Giuressi, M. Lonza, R. Sergo, C. Scafuri, L. Tosi, R. Visintini* 2356
Commissioning Experience with the PEP-II Low Level RF System — *P. Corredoura, S. Allison, R. Claus, W. Ross, L. Sapozhnikov, H.D. Schwarz, R. Tighe, C. Yee, C. Ziomek* 2359
Design and Verification of Controllers for Longitudinal Oscillations Using Optimal Control Theory and Numerical Simulation: Predictions for PEP-II — *H. Hindi, S. Prabhakar, J. Fox, D. Teytelman* 2362
Gap Voltage Feed-Forward Board for PEP-II Low Level RF System — *W. Ross, R. Claus, L. Sapozhnikov* 2365
VXI Based Multibunch Detector and QPSK Modulator for the PEP-II/ALS/DAΦNE Longitudinal Feedback System — *A. Young, J. Fox, D. Teytelman* 2368

Local Feedback Experiment in the Taiwan Light Source — *C.H. Kuo, K.T. Hsu, Jenny Chen, K.K. Lin, C.S. Chen, R.C. Sah* 2371
Digital Global Orbit Feedback System Developing in SRRC — *C.H. Kuo, K.K. Lin, C.J. Wang, Jenny Chen, J.S. Chen, C.S. Chen, K.T. Hsu* 2374
Developement of a Digital Longitudinal Damper for the TLS Storage Ring — *W.K. Lau, S.J. Lin, M.S. Yeh, L.H. Chang, T.T. Yang, K.T. Hsu, M.H. Wang, C.C. Kuo* 2377
Optimising Injection into CELSIUS with a Steering Feedback and Beta-Matching System — *Ahmad Mohammadzadeh* 2380
Development of Digital Feedback Systems for Beam Position and Energy at the Thomas Jefferson National Accelerator Facility — *J. Karn, M. Chowdhary, A. Hutton, V. Lebedev, R. Legg, P. Letta, H. Shoaee, W. Watson, J. van Zeijts* 2383
Design and Implementation of a Slow Orbit Control Package at Thomas Jefferson National Accelerator Facility — *J. van Zeijts, S. Witherspoon, W.A. Watson* 2386
Robinson-Type Criteria for Beam and RF Cavity with Delayed, Voltage-Proportional Feedback — *Shane Koscielniak* 2389
Study of Orbit Feedback Systems for the TESLA Linear Collider — *R. Lorenz, I. Reyzl, S. Sabah* 2392

CONTROLS AND COMPUTING

Chair: R. Humphrey, *Stanford Linear Accelerator Center*

Object Oriented Programming Interfaces for Accelerator Control *(Invited)* — *Lawrence T. Hoff* 2395
A Portable Accelerator Control Toolkit *(Invited)* — *W.A. Watson III* 2398
Experience with EPICS in a Wide Variety of Applications *(Invited)* — *Martin R. Kraimer, Matthias Clausen, William Lupton, Chip Watson* 2403
The Procedure Execution Manager and Its Application to Advanced Photon Source Operation — *M. Borland* 2410
Data Warehouse on the Web for Accelerator Fabrication and Maintenance — *A. Chan, G. Crane, I. MacGregor, S. Meyer* 2413
COSY INFINITY Version 7 — *Martin Berz* 2416
A Solving Module of an Expert System for Nonlinear Beam Dynamics — *S. Andrianov, A. Dvoeglazov* 2419
Designing a Portable Architecture for Intelligent Particle Accelerator Control — *W. Klein, C. Stern, G. Luger, E. Olsson* 2422
A Hybrid Numerical Method for Orbit Correction — *Greg White, Tom Himel, Hamid Shoaee* 2425
Electron Multipactor Code for High-Power RF Devices — *S. Humphries Jr., D. Rees* 2428
Eigenmodes of Microwave Cavities Containing High-Loss Dielectric Materials — *S.J. Cooke, B. Levush* 2431
Status of Unified Accelerator Libraries — *Nikolai Malitsky, Richard Talman* 2434

Control Systems W

Innovative Aspects of the SDL Control System — *W.S. Graves, S.K. Feng, P.S. Pearson, J.D. Smith* 2437
Control and Operational Models for Vacuum Equipment — *P. Strubin, N. Trofimov* 2440
PC-Based Applications Programming on the SRS Control System — *B.G. Martlew, H.L. Owen, M.J. Pugh, B.R. Rawlinson, S.L. Smith* 2443
The Usage of Transient Recorders in the Daily HERA Machine Operation — *R. Bacher, M. Clausen, P. Duval, L. Steffen* 2446
A High Reliability Accelerator Control System — *J. Callahan, J. Collins, A. Qualls, W. Hunt* 2449
Nuclotron Control System — *V. Andreev, V. Gorchenko, A. Kirichenko, A. Kovalenko, I. Kulikov, V. Monchinsky, S. Romanov, B. Sveshnikov, A. Tsarenkov, B. Vasilishin, M. Voevodin, V. Volkov* 2452
Use of a Virtual Accelerator for a Development of an Accelerator Control System — *Noboru Yamamoto* 2455
Operation Logging System Using the Database for Synchrotron Radiation Beam Lines at the Photon Factory — *Noriichi Kanaya, Seiji Asaoka, Hideki Maezawa* 2458
Integrating Commercial and Legacy Control Systems With EPICS — *J.O. Hill, K.U. Kasimer, J.B. Kowalkowski* 2461
Completion of the LANSCE Proton Storage Ring Control System Upgrade - A Successful Integration of EPICS into a Running Control System — *S.C. Schaller, E.A. Bjorklund, N.T. Callaway, G.P. Carr, J.A. Faucett, M.A. Oothoudt, D.J. Ostrem* 2464
Automating ELETTRA Operation with "One Button Machine" — *D. Bulfone, F. Potepan, C. Scafuri* 2467
Operator Interface for the PEP-II Low Level RF Control System — *S. Allison, R. Claus* 2470

Network Upgrade for the SLC: PEP-II Network — *M. Crane, M. Call, S. Clark, F. Coffman, T. Himel, T. Lahey, E. Miller, R. Sass* 2473
Network Upgrade for the SLC: Control System Modifications — *M. Crane, R. Mackenzie, R. Sass, T. Himel* ... 2476
Using WWW in SRRC Control System — *J.S. Chen* 2479
The Design of the Control System for ANKA — *S. Avsec, B. Jeram, G. Mavric, M. Plesko, J. Stefan* 2481
Automated Startup of the CEBAF 45 MeV Injector — *D. Kehne, P. Letta, B. Dunham, R. Kazimi* 2484

Control Systems X

Applications Toolkit for Accelerator Control and Analysis — *M. Borland* 2487
A Bunch Clock for the Advanced Photon Source — *Frank R. Lenkszus, Robert J. Laird* 2490
Embedded Controllers, Field Bus and a Modular IO Concept: Central Elements of BESSY II Controls — *J. Bergl, B. Kuner, R. Lange, I. Müller, R. Müller, G. Pfeiffer, J. Rahn, H. Rüdiger* 2493
RHIC Beam Permit and Quench Detection Communications System — *C.R. Conkling Jr.* 2496
The RHIC Real Time Data Link System — *H. Hartmann* 2499
Evaluation of IEEE 1394 Serial Bus for Distributed Data Acquisition — *T.J. Shea, J. Mead, P. Cerniglia, C. Degen* 2502
Precision Timing Control System — *Robert E. Meller* 2505
Implementation of a New RF Monitoring System for the SRS Using LabVIEW — *M.J. Pugh, A.R. MacDonald* 2508
Commissioning of SPring-8 Linac Control System — *H. Sakaki, H. Yoshikawa, T. Asaka, T. Hori, Y. Itoh, A. Kuba, A. Mizuno, S. Suzuki, T. Taniuchi, K. Yanagida, H. Yokomizo* 2511
Improvements to the LANSCE Accelerator Timing System — *L.J. Rybarcyk, F.E. Shelley Jr.* 2514
A Components Database Design and Implementation for Accelerators and Detectors — *S. Meyer, A. Chan* ... 2517
Arc Detection and Interlock Module for the PEP-II Low Level RF System — *R. Tighe* 2520
Automatic Lattice Parameters Measurement Tools at SRRC — *Jenny Chen, C.S. Chen, K.K. Lin, K.T. Hsu* 2523
Orbit Correction Using Virtual Monitors at Jefferson Lab — *Yu-Chiu Chao, Bruce Bowling, Johannes van Zeijts, William A. Watson III, Sue Witherspoon* 2526
Pulse Selection Control for the IR FEL Photocathode Drive Laser — *K. Jordan, R. Evans, O. Garza, R. Hill, M. Shinn, J. Song, D. Venhaus* 2529
Experience With Vsystem in a Wide Variety of Applications — *Peter N. Clout, Robert T. Westervelt* 2532
Tuning and Optimization at Brookhaven and Argonne: Results of Recent Experiments — *W. Klein, C. Stern, M. Kroupa, R. Westervelt, G. Luger, E. Olsson* 2535

Computer Codes W

Spin Tracking Study of the AGS — *Haixin Huang, Thomas Roser, Alfredo Luccio* 2538
An Interactive Beam Line Simulator Module for RHIC — *W.W. MacKay* 2541
Modeling RHIC Using the Standard Machine Format Accelerator Description — *F. Pilat, C.G. Trahern, J. Wei, T. Satogata, S. Tepikian* 2544
3-D Numerical Field Calculations of CESR's Upgraded Superconducting Magnets — *Z. Greenwald, S. Greenwald* 2547
Wake Fields of a Bunch on a General Trajectory Due to Coherent Synchrotron Radiation — *M. Dohlus, A. Kabel, T. Limberg* 2550
Application of the GSM Method and TD Computation of the Long Range Wake in Linear Accelerator Structures — *A. Jöstingmeier, M. Dohlus, C. Rieckmann, A.S. Omar* 2553
Enhancements to the Longitudinal Dynamics Code ESME — *J. MacLachlan, J.-F. Ostiguy* 2556
Optics Elements for Modeling Electrostatic Lenses and Accelerator Components I. Einzel Lenses — *George H. Gillespie, Thomas A. Brown* 2559
The Particle Beam Optics Interactive Computer Laboratory for Personal Computers and Workstations — *George H. Gillespie, Barrey W. Hill, Hendy Martono, John M. Moore, Nathan A. Brown, Michael C. Lampel, R. Chris Babcock* 2562
Lorentz Group Lie Algebra Map of Ultra-Relativistic Radiating Electron — *H. Kawaguchi, K. Tsubota, T. Honma* 2565
PLATO, a Program Library for the Analysis of 4D Nonlinear Transverse Motion — *M. Giovannozzi, E. Todesco, A. Bazzani, R. Bartolini* 2568
Parallel Algorithms for the Analysis of Nonlinear Betatronic Motion — *M. Giovannozzi, E. McIntosh* 2571
Further Improvements in TRACE 3-D — *D.P. Rusthoi, W.P. Lysenko, K.R. Crandall* 2574
Applications of the General Particle Tracer Code — *S.B. van der Geer, M.J. de Loos* 2577

The Computer Program LIAR for the Simulation and Modeling of High Performance Linacs — *R. Assmann, C. Adolphsen, K. Bane, P. Emma, T.O. Raubenheimer, R. Siemann, K. Thompson, F. Zimmermann* 2580
LEGO: A Modular Accelerator Design Code — *Y. Cai, M. Donald, J. Irwin, Y.T. Yan* 2583
Lattice Commissioning Strategy for the B-Factory — *M. Lee, Y. Cai, J. Corbett, H. Shoaee, D. Whittum, G. White, Y. Yan* 2586
Transverse Wakefield Analysis for the NLC & JLC Detuned Structures on a Parallel Computer — *Xiaowei Zhan, Kwok Ko* 2589
MAPA: Implementation of Standard Interchange Format and Use of Analyzing Lattices — *Svetlana G. Shasharina, John R. Cary* 2592
Ion Optical Stray Field Analysis of an ESR Dipole — *B. Schillinger, T. Weiland, B. Langenbeck* 2594
Development of the ACCSIM Tracking and Simulation Code — *F.W. Jones* 2597
A Graphical User Interface for RELAX3D — *F.W. Jones* 2600
HESHBEAM - A Program with a Graphical User Interface for Calculation of the Luminosity Spectrum and the Differential Luminosity — *H. Heydari, H. Schulte* 2603

Computer Codes X

Tracking Routines for General Insertion Devices — *Michael Scheer, Godehard Wüstefeld* 2606
Simulation of Multipacting in RF Cavities and Periodical Structures — *A.V. Grudiev, D.G. Myakishev, V.P. Yakovlev* 2609
Consideration of DC Space Charge Effects in the Modal Analysis of Aperture Coupled-Cavities — *A. Jöstingmeier, M. Dohlus, C. Rieckmann, A.S. Omar* 2612
A Self-Consistent Beam Loaded Traveling Wave Accelerator Model for Use in TRACE 3-D — *M.C. Lampel* 2615
Monte Carlo Simulation of Nonlaminar DC Beam Including the Influence of Self-Fields — *G. Zapalac* 2618
Use of the LANA Code for the Design of a Heavy Ion Linac — *D.V. Gorelov, P.N. Ostroumov, R.E. Laxdal* 2621
Relativistic Klystron Two-Beam Accelerator Simulation Code Development — *S.M. Lidia, R.D. Ryne* 2624
Measured and Theoretical Characterization of the RF Properties of Stacked, High-Gradient Insulator Material — *T.L. Houck, G.J. Caporaso, C.C. Shang, S.E. Sampayan, N.E. Molau, M.L. Krogh* 2627
Wake Properties of a Stripline Beam Kicker — *Brian R. Poole, George J. Caporaso, Wang C. Ng* 2630
BBU Design of Linear Induction Accelerator Cells for Radiography Application — *C.C. Shang, Y.-J. Chen, G.J. Caporaso, T.L. Houck, N.E. Molau, S.D. Nelson, W.C. Wang, J. Fockler, S. Gregory* 2633
A Flexible-Variable Truncated Power Series Algebra in Zlib — *Y.T. Yan, Y. Cai, J. Irwin* 2636
A Field-Cancellation Algorithm for Constructing Economical Planar Permanent Magnet (PM) Multipoles with Large High-Quality Field Apertures — *R. Tatchyn* 2639
Aperture Calculation of AURORA-2D Compact Electron Storage Ring with Superconducting Wiggler — *H. Tsutsui, T. Takayama, T. Hori* 2642
Numerical Simulation and RF Model Measurements of the New GSI IH-DTL — *B. Krietenstein, T. Weiland, U. Ratzinger, R. Tiede, S.A. Minaev* 2645
Broad-Band Impedance of LHC Shielded Bellows — *Misha D'yachkov, Francesco Ruggiero* 2648
GdfidL: A Finite Difference Program with Reduced Memory and CPU Usage — *W. Bruns* 2651
Expression Templates for Truncated Power Series — *John R. Cary, Svetlana G. Shasharina* 2654

BEAM DYNAMICS IN SLC[1]

Ralph W. Assmann
Stanford Linear Accelerator Center, Stanford University, Stanford CA 94309

Abstract

Beam dynamics issues affect many different aspects of the SLC performance. This paper concentrates on the multi-particle beam dynamics in the linac and the associated limitations that are imposed on the overall SLC performance. The beam behavior in the presence of strong wakefields has been studied in order identify ways to optimize the performance and to predict the expected emittances in high performance linacs. Emittance measurements and simulations are presented for the SLAC linac and are compared in detail. As the overall SLC performance depends on the accelerator stability, the tuning stability is discussed. Results are shown and the consequences for the performance of the SLC are discussed.

1 INTRODUCTION

The Stanford Linear Collider (SLC), the world's first linear collider, is now in its eighth year of operation. The SLC delivers e^+e^- collisions at a center-of-mass energy of 91.2 GeV and explores the Z-resonance. It provides the unique opportunity to experimentally explore the beam dynamics that is relevant to high performance linear colliders. Limitations can be assessed, theoretical and numerical models can be checked and possible optimization schemes can be tested. There are many crucial ingredients to the understanding and successful operation of a linear collider. This paper concentrates on the beam dynamics in the SLAC linac.

The 30 years old SLAC linac, upgraded for SLC, has a length of 3 km and accelerates electron and positron beams from an initial beam energy of 1.19 GeV to about 47 GeV. The accelerating gradient of the S-Band (2.856 GHz) structures is about 17 MeV/m. In the ideal case the normalized transverse beam emittances $\gamma\varepsilon_x$ and $\gamma\varepsilon_y$ are conserved during acceleration. However, unavoidable imperfections in connection with dipole mode wakefields can cause large emittance dilutions. An increase in the transverse beam emittances directly limits the achievable luminosity L:

$$L = f_{rep} \cdot \frac{N_e^2}{4\pi\sqrt{\varepsilon_x\,\varepsilon_y}\sqrt{\beta_x^*\,\beta_y^*}} \qquad (1)$$

Beam disruption is neglected here. The repetition rate f_{rep}, the β-functions β_x^* and β_y^* at the interaction point and the beam current N_e are to a large extent determined by the machine design. The magnitude of the transverse emittances, however, are largely determined by imperfections in the linac. The understanding of the multi-particle beam dynamics in the SLAC linac is crucial in order to minimize the emittance dilutions, to achieve maximum tuning stability and to optimize the integrated luminosity.

2 WAKEFIELDS IN THE SLAC LINAC

In the SLAC linac high current bunches (about 6 nC or $3.5\ 10^{10}$ particles) are accelerated to 47 GeV. The particles induce dipole wakefields in the RF structures, causing subsequent beam deflections. In the easiest case a single bunch is described by two particles ("head" and "tail"), each carrying half the bunch charge. As the head particle enters off-center into the structure it excites a transverse dipole wakefield that causes a deflection of the tail particle. The tail beam ellipse is offset with respect to the head beam ellipse and the projected emittance is increased. The principle of wakefield generated emittance dilution is illustrated in Figure 1.

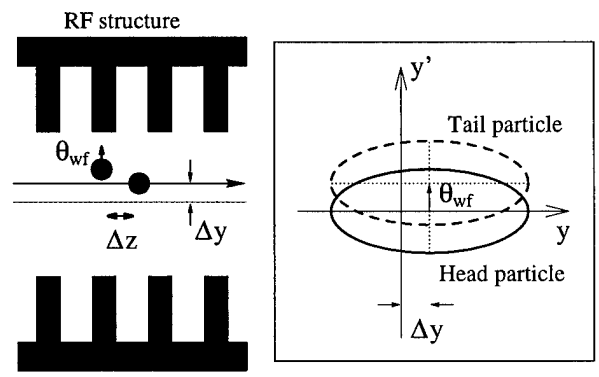

Figure 1 Principle of a wakefield generated increase in the projected emittance. A single bunch is represented by two particles. The projected beam emittance is increased due to a wakefield kick θ_{WF}.

The calculated wakefield functions in the SLAC linac are shown in Figure 2 as a function of distance Δz (e.g. between head and tail particle). The transverse wakefield deflection θ_{WF} in a structure with length L_{struc} is obtained from the transverse wakefield function WF_{transv}:

$$\theta_{WF} = WF_{transv}(\Delta z) \cdot \frac{Q_1\, L_{struc}}{E_2} \cdot \Delta y_1 \qquad (2)$$

[1] Work supported by the Department of Energy, contract DE-AC03-76SF00515.

Two slices, a leading slice "1" and a trailing slice "2" are considered. Slice "1" excites the wakefield with its charge Q_1 and its offset Δy_1. Taking into account the distance Δz between the slices and the energy E_2 of slice "2", the deflection angle is obtained. Wakefield deflections θ_{WF} are always induced if the beam does not travel through the centers of all accelerating structures. The important measure for wakefield generated emittance dilution is therefore the RMS structure misalignment with respect to the beam.

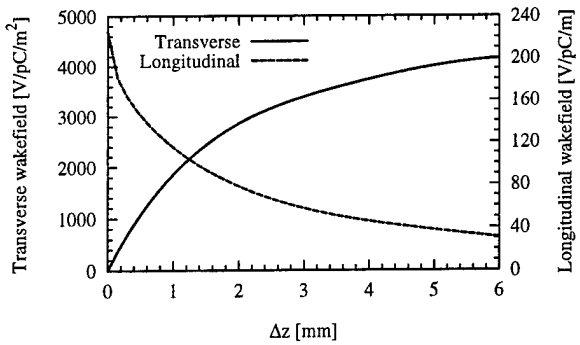

Figure 2 Calculated transverse and longitudinal wakefield functions for the SLC [1].

Modeling

The behavior of intense beams in the presence of strong wakefields and multiple interacting imperfections can be described accurately with numerical computer programs. The simulations for this paper were done with the new "LIAR" program [2]. This program allows to calculate chromatic, dispersive and wakefield generated emittance dilutions in a misaligned linac. Table 1 summarizes the default parameters that were used for the SLAC linac simulations.

Linac optics	Split-tune lattice [3] (July 1996)
Bunch population	$3.5\ 10^{10}$
Longitudinal bunch shape	42 MV compressor voltage (measured) [4]
Initial $\gamma\varepsilon_x$ / $\gamma\varepsilon_y$	30 / 3.5 mm-mrad
Quadrupole misalignment	100 μm (rms x, y)
BPM to quad misalignment	100 μm (rms x, y)
Structure misalignment (12 m girders)	200 μm (rms x, y)

Table 1 Default parameters for the linac simulations.

BNS damping

In addition to emittance dilutions, transverse wakefields can cause beam-breakup. In a two particle model, the wakefield deflections induced from the oscillating head particle defocus the tail particle until it falls behind 90° in betatron phase advance. Travelling 90° behind the oscillating head particle, wakefield deflections then add up resonantly and the tail is driven to higher and higher oscillation amplitudes.

This resonant beam-breakup can be avoided if so-called "BNS-damping" is implemented. Using the slope of the accelerating RF, an energy difference is between head and tail is induced ("correlated energy spread"). With a proper choice of RF phases, the defocusing wakefield effects for the tail can then be cancelled by chromatic effects from the quadrupoles. Ideally, the normalized amplitude of a betatron oscillation is one along the whole linac (same trajectories of head and tail).

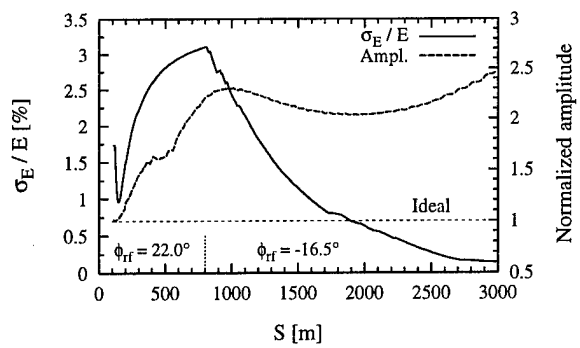

Figure 3 Simulated energy spread and normalized amplitude of a betatron oscillation along the SLAC linac.

Figure 3 illustrates the BNS setup that was used in the SLAC linac during the 1996 run. The beam was located at RF phases of +22° and -16.5°, leading to a 5% reduction in available beam acceleration. Several boundary conditions limit the efficiency of BNS that can be achieved in the SLAC linac:

1. There is no efficient BNS energy spread in the beginning of the linac.
2. The energy spread must be reduced to 0.15% at the end of the linac in order to meet the Final Focus chromatic bandwidth.
3. The RF phases must not become to large. Enough beam acceleration must be maintained in order to accelerate the beams to 46.6 GeV.

The efficiency of BNS in the SLAC linac is illustrated in Figure 3 with the normalized amplitude of a betatron oscillation. It grows by a factor of 2.5, indicating only partial BNS damping. For SLC, BNS is limited by the available beam acceleration in the linac. Note, that a stronger lattice would allow to implement better BNS damping. For a comparison of the measured and simulated normalized amplitude see [5].

3 EMITTANCE TRANSPORT

The principle of wakefield generated growth in the projected emittance was illustrated in Figure 1. If the trajectories are steered flat (minimizing the BPM readings) the residual emittance growth in the SLAC linac is unacceptably large. This is illustrated in Figure 4 for the

vertical plane. The normalized emittance is simulated to grow by about 27 mm-mrad in x and 21 mm-mrad in y. Without wakefields, dispersion dilutes the emittance by 5.1 mm-mrad in x and 3.9 mm-mrad in y. Emittance growth is clearly dominated by wakefields.

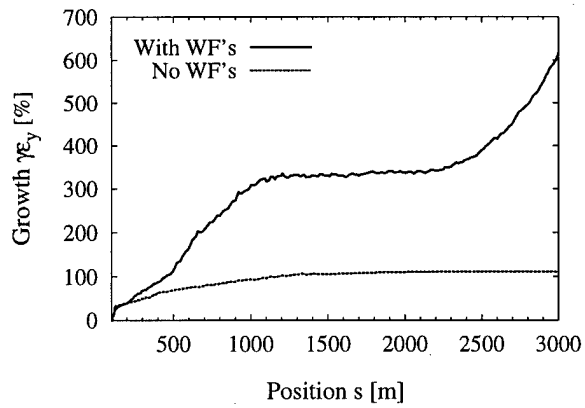

Figure 4 Simulated average vertical emittance along the linac for flat trajectories, with and without wakefields.

In 1991 so called "oscillation bumps" were introduced to optimize the emittances [6]. Betatron oscillations are generated along the linac in order to induce head-to-tail deflections that cancel the existing wakefield "banana"-shape of the linac bunch. A theoretical description is given in [2].

Typically two bumps are used parasitically during SLC operation in order to empirically minimize the measured emittances in sector 11 and sector 28 of the linac (the linac is divided into 30 sectors). The two bumps represent 16 degrees of freedom (2 x 2 phases x 2 planes x 2 beams). As an emittance measurement takes several minutes, emittance tuning requires typically several hours. Figure 5 shows a measured horizontal trajectory after emittance optimization.

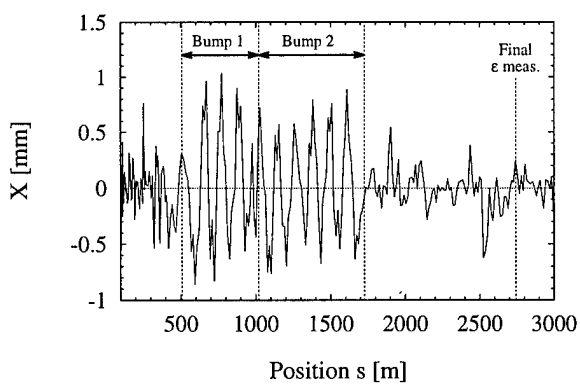

Figure 5 Horizontal linac trajectory with bumps during record luminosity on June 21st.

The simulated average vertical emittance growth after bump optimization is shown in Figure 6. The normalized emittance is reduced to the level expected from the linac dispersion at the locations of the emittance measurements. The bumps work well and compensate essentially all wakefield effects. The emittance after optimization is limited by dispersion which also is reduced somewhat by the bumps. Note that the emittance in Figure 6 grows rapidly in the end of the linac. Wakefield effects are uncompensated after the emittance measurement near the end of the linac. This growth is reduced through the use of synchrotron light screens just before the arcs at 3000 m..

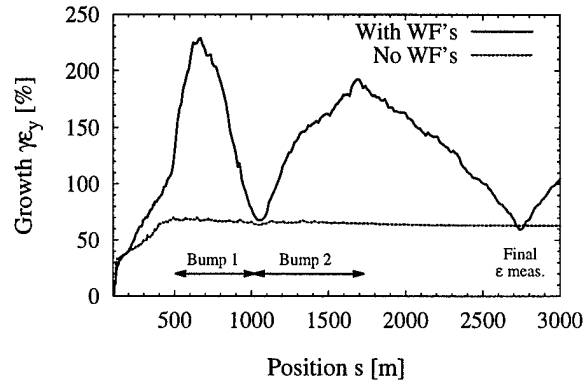

Figure 6 Simulated average vertical emittance along the linac after bump optimization.

Emittance performance in 1996

The linac beam emittances are measured regularly during the SLC operation. Every two hours the measurements are saved into a database that tracks the history of important accelerator and beam parameters. The database values for emittance measurements were analyzed for the 1996 SLC run.

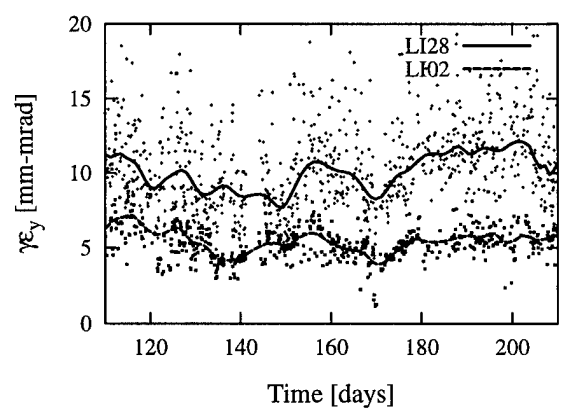

Figure 7 Measured vertical emittances against time for the beginning (LI)2) and end (LI28) of the SLAC linac. The data covers the period from April 1st to July 31st.

The vertical electron emittances in the beginning and end of the SLAC linac are shown in Figure 7. In order to summarize the 1996 emittance performance, the emittance measurements at the end of the linac were analyzed as a function of the incoming emittance. The results are shown in Figure 8 where they are compared to

simulation results. Emittance measurements were filtered in order to eliminate flyers outside of two standard deviations around the average.

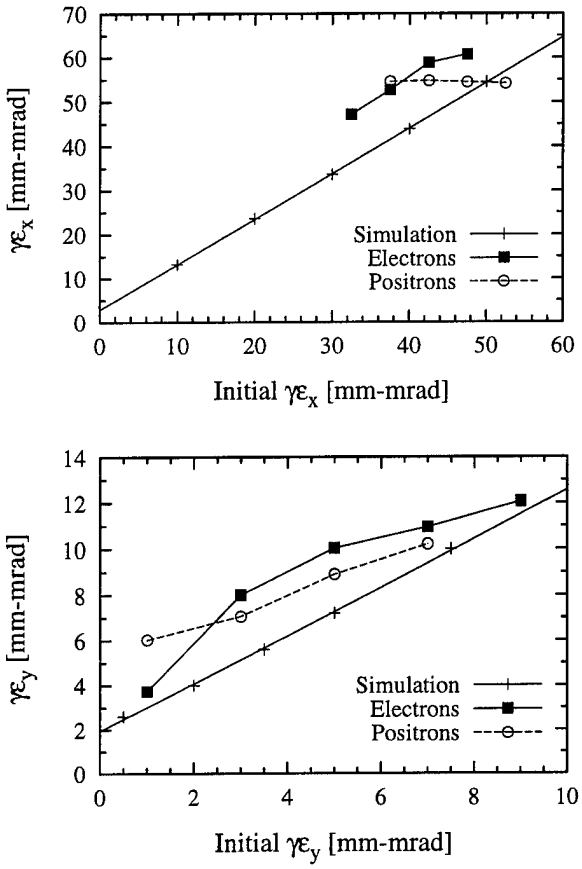

Figure 8 Normalized horizontal and vertical emittances at sector 28 against the initial values. Simulation results for electrons are compared to the electron and positron average performance during the 1996 run. Statistical errors are too small to be visible.

The simulation results can be parameterized in the form:

$$\gamma\varepsilon_{28} = \kappa \cdot \gamma\varepsilon_{initial} + \Delta\gamma\varepsilon_{wf} \qquad (3)$$

Multiplicative emittance growth is characterized by κ, while wakefield generated emittance growth is additive and is described by the term $\Delta\gamma\varepsilon_{wf}$. Fits to the simulation results provide:

- $\kappa = 1.03$, $\Delta\gamma\varepsilon_{wf} = 2.83$ (27) mm-mrad (electron X)
- $\kappa = 1.06$, $\Delta\gamma\varepsilon_{wf} = 1.95$ (21) mm-mrad (electron Y)

The simulated additive emittance growth without bump optimization is indicated in brackets. Multiplicative emittance growth is expected to be small. The measured 1996 emittances indeed do not provide any indication for large multiplicative emittance growth (larger than expected slope).

The measured growth $\Delta\gamma\varepsilon_{wf}$ is determined from the 1996 data for the average injected emittance:

- $\gamma\varepsilon_{initial} = (36.3 \pm 4.1)$ mm-mrad (electron X)
- $\gamma\varepsilon_{initial} = (5.0 \pm 1.5)$ mm-mrad (electron Y)
- $\gamma\varepsilon_{initial} = (44.0 \pm 3.9)$ mm-mrad (positron X)
- $\gamma\varepsilon_{initial} = (2.4 \pm 1.0)$ mm-mrad (positron Y)

The numbers indicate the 1996 average values and their standard deviations. With those injected emittances one obtains from Figure 9:

- $\Delta\gamma\varepsilon_{wf} \sim 13$ mm-mrad (electron X)
- $\Delta\gamma\varepsilon_{wf} \sim 5$ mm-mrad (electron Y)
- $\Delta\gamma\varepsilon_{wf} \sim 11$ mm-mrad (positron X)
- $\Delta\gamma\varepsilon_{wf} \sim 4$ mm-mrad (positron Y)

The average additive emittance growth in the SLAC linac is reduced by factors of more than 2 in x and more than 4 in y due to bumps. However, the emittance growth is still larger than the simulated performance by ~ 9 mm-mrad in x and ~ 2.5 mm-mrad in y. This discrepancy can be explained to a large extent by the tuning stability in the linac. Note, that the predicted performance was almost achieved for electrons with small incoming vertical emittances. Occasionally emittance growth as small as 1 mm-mrad was measured in the SLAC linac.

Tuning stability

Once the final beam emittance has been optimized in the SLAC linac, the trajectory looks similar to that shown in Figure 5. The trajectory and the phase relations of structure and quadrupole errors must be kept constant in order to maintain the optimized emittance. Any drift in the beam optics will cause additional wakefield emittance growth.

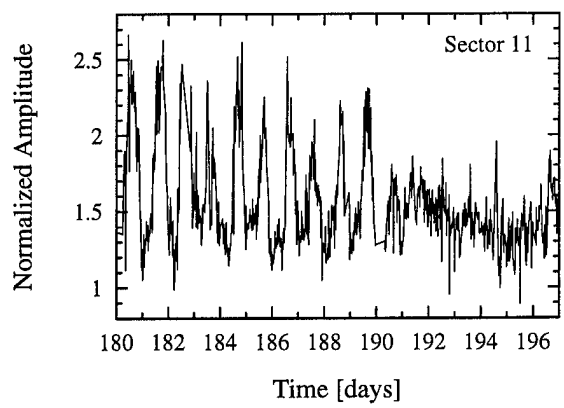

Figure 9 Variation of the normalized amplitude of a betatron oscillation in sector 11 of the SLAC linac. A fix was applied on day 191 [7,11].

The SLAC linac is subject to large day-night variations in the beam optics. The beam phase advance changes by up to 130° and the amplitude growth of an incoming betatron oscillation varies by factors of about 2. An example is shown in Figure 9 for the location between the two linac bumps. It is immediately clear that the bump optimization is heavily disturbed by those changes in the beam optics.

As day-night transitions occur every 12 hours and the bump optimization takes several hours itself, bumps are tuned constantly. The measured average emittance

growth is significantly increased beyond the simulated value that assumes full optimization. The emittance stability can be quantified from the observed spread in emittance measurements (compare Figure 7). The spread in the final linac emittances agrees well for electrons and positrons and one obtains:

- $\sigma_\varepsilon = 5.9$ mm-mrad (x)
- $\sigma_\varepsilon = 2.8$ mm-mrad (y)

Correcting for the spread of the incoming emittances (see above) the emittance spread generated in the linac is calculated to be 4.5 mm-mrad in x and 2.4 mm-mrad in y. The larger spread in x may indicate less frequent tuning. The relative emittance increase (important for luminosity reduction) is smaller in x than in y. The difference $\Delta\varepsilon_{unexplained}$ between the measured average emittances in the linac and the predicted values can be expressed in terms of emittance stability:

- $\Delta\varepsilon_{unexplained} \sim 1.5\ \sigma_\varepsilon$ (x)
- $\Delta\varepsilon_{unexplained} \sim 1\ \sigma_\varepsilon$ (y)

It is not unreasonable to assume a 1 σ loss of emittance performance due to continual tuning of linac bumps and large day-night variations.

Pulse-to-pulse jitter

The typical SLAC linac trajectory looks similar to the one shown in Figure 6. It was already pointed out that wakefields change the beam optics. The phase advance and the normalized strength of a betatron oscillation are a function of the wakefield strength. Because the amplitude of wakefield deflections depends on the bunch length and current, any change in those parameters will change the beam optics and the beam trajectory. Incoming charge and current jitter translates into transverse position jitter. This was studied in [7].

If BNS damping is not fully implemented (as in the SLAC linac) a betatron oscillation will also cause emittance growth. It is important to note that transverse beam jitter translates into emittance jitter. The measured SLC beam emittance, measured over many hundred pulses, is increased. This effect must be studied further.

Limitations and alternatives

The present performance of the SLAC linac is limited by the stability of the beam optics. Long oscillation bumps are especially sensitive against optics changes. Several ideas have been proposed to determine the structure to beam offsets in the SLC and then to steer the beam through structure centers [8,9,10]. No bumps would be needed and errors are corrected on a local scale.

In order to evaluate this approach we consider the expected emittance without wakefields and without bumps. Simulations predict a dispersive emittance growth of 5.1 mm-mrad in x and 3.9 mm-mrad in y. This must be compared to the measured average emittances during the 1996 run: 12 mm-mrad in x and 4.5 mm-mrad in y. Perfect elimination of wakefield deflections in y will bring only a slight improvement, if dispersion remains uncorrected. Steering through the structure centers will even increase the RMS beam to quadrupole offset and therefore the expected dispersive emittance growth.

6 SUMMARY

Multi-particle beam dynamics in the SLC linac was discussed with an emphasis on the emittance transport. The emittance optimization, done with linac bumps, was shown to work very well. Wakefield generated and dispersive emittance growths are optimized simultaneously.

The emittance performance during the 1996 run was shown to agree within 1-1.5 standard deviations of its measured variation with simulations. The average performance was limited by the tuning stability of the linac. Occasionally emittance growth as small as 1 mm-mrad was measured in the vertical plane. Though the large horizontal emittances are suspicious, the data does not indicate larger than expected multiplicative emittance growth.

New optimization methods, that avoid the usage of bumps, will only then significantly improve the emittance performance, if dipole wakefields and dispersion are optimized simultaneously.

7 ACKNOWLEDGEMENTS

I wish to thank R. Siemann for his active interest and support. I further thank A. Chao, F.J. Decker, N. Phinney, P. Raimondi, T. Raubenheimer, M. Ross, G. Stupakov and F. Zimmermann for many stimulating discussions.

REFERENCES

[1] K. Bane and P. Wilson. Proc. 11th Int. Conf. On High Energy Accelerators, CERN 1980, p.592.
[2] R. Assmann et al, "LIAR - A computer program for the modeling and simulation of high performance linacs". SLAC/AP-103.
[3] F.J. Decker et al., "Long-range wakefields and split-tune lattice at the SLC". SLAC-PUB-7259 (1996).
[4] R.H. Holtzapple. Stanford University, PhD Thesis 1996.
[5] R. Assmann et al, "Monitoring of the SLC optics with a diagnostic pulse". These proceedings.
[6] J. Seeman et al, "The introduction of trajectory oscillations to reduce emittance growth in the SLC linac". SLAC-PUB-5705 (1992).
[7] C. Adolphsen et al, "Beam Trajectory Jitter in the SLC Linac". PAC95.
[8] R. Assmann et al, "Observation and Analysis of Static Deflections from Transverse Long-Range Wakefields in the SLC". These proceedings.
[9] F.J. Decker et al, "Super-ASSET: A Technique for Measuring and Correcting Accelerator Structure Misalignments at the SLC.". These proceedings.
[10] M. Seidel et al, "Detection of Beam-Induced Dipole-Mode Signals in the SLC S-Band Structures". These proceedings.

RIGOROUS INTEGRATION OF MAPS AND LONG-TERM STABIITY

Kyoko Makino*, Department of Physics and Astronomy and National Superconducting Cyclotron Laboratory, Michigan State University, East Lansing, MI 48824

Abstract

In spite of its importance, it has been very difficult to estimate long-term stability of particles in repetitive systems in a fully rigorous way. One of the main causes of the difficulty is the inaccuracy of the maps of the system; while to any fixed order they can be computed easily using Differential Algebraic (DA) techniques, it has so far not been possible to determine bounds for the remainders. Another difficulty is that most methods to rigorously formulate the problem lead to the need for global optimization of highly complex multi-dimensional objective functions. The Remainder-enhanced Differential Algebraic (RDA) method, an extension of the DA method that simultaneously provides rigorous bounds for the remainders, can solve both problems. The Taylor maps are evaluated rigorously with interval remainders, using the verified integral method within the framework of RDA. And rigorous RDA global optimization allows to efficiently get bounds on long-term stability.

1 INTRODUCTION

The problem to estimate the long-term stability of weakly nonlinear systems finds its origin in the detailed study of the solar system. Many perturbative methods for repetitive motion have been developed from this question. The question of long-term stability of particles in repetitive systems like circular accelerators and storage rings is one of new applications in this category.

High order Taylor transfer maps of the action on phase space describe the motion of particles very well. The differential algebraic (DA) techniques [1] [2] [3] [4] have offered a very elegant and accurate way to obtain such transfer maps. Typically derivatives of up to order ten in six variables are needed, so other methods are far from providing a robust way to study the weakly nonlinear behavior of beams.

Recently, ideas of Lyapunov, Nekhoroshev and others triggered an analysis of stability in particle accelerator based on approximate invariants[5][6][7], and the question of long-term stability can be re-cast into a highly complicated optimization problem [6] [8]. Figure 1 shows tracking pictures of a repetitive system described by a six dimensional Taylor map in the sixth order in actual coordinates and in normal form coordinates, where in the latter case the motion is seen as approximately stable. The deviations from invariance directly relate to the time for particles to be lost. The deviation functions, which are multidimensional polynomials up to roughly 500th order, consist of about 10^5 floating-point operations. The irregularity of the functions as well as the high dimensionality makes the question very troublesome for conventional optimization methods. The sharpness of the bounds of the functions is important in order to guarantee a large number of stable turns, but in reality the functions have a very large number of local maxima. To be useful, the maxima have to be sharp to about 10^{-6}, and for some applications to 10^{-12}. Figure 2 shows the deviations from a normal form invariant circle in Figure 1 as a function of two angles. Interval methods give a mathematically rigorous estimate, but complicated functions like ours cannot avoid a severe blow-up problem, the control of which is the key to get a practical estimate.

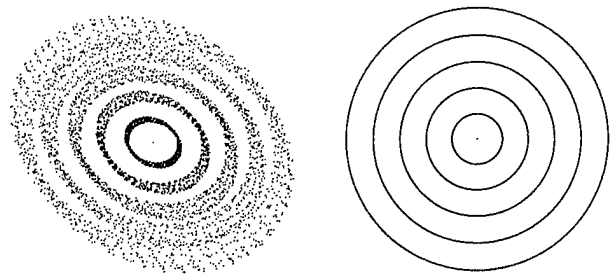

Figure 1: Tracking pictures of a repetitive system. The left is in particle optical coordinates x and $a = p_x/p_0$, and the right is in normal form coordinates.

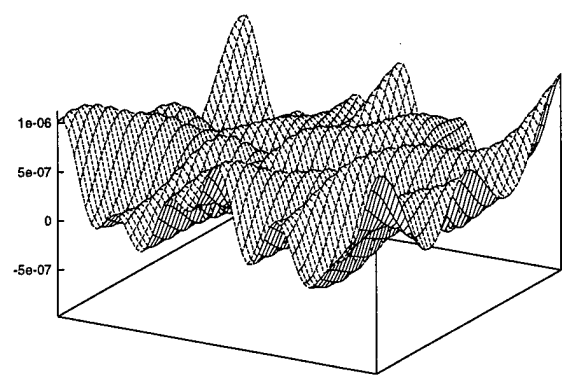

Figure 2: Deviation from normal form invariance of a repetitive system.

A new technique, the method of Remainder-enhanced Differential Algebras (RDA) [9][10][11][12], combines the DA technique to express the model function by a Taylor polynomial, and interval computation to evaluate the interval bound of the Taylor remainder. The resulting error bounds are usually rather sharp, in particular at higher or-

* Work in collaboration with Martin Berz, Department of Physics and Astronomy and National Superconducting Cyclotron Laboratory, Michigan State University, East Lansing, MI 48824.

0-7803-4376-X/98 /$10.00 © 1998 IEEE

ders. In normal form theory, it is known that if the transfer map has a converging Taylor series in normal form coordinates, the system is stable. So the sharpness of the remainder term of the deviation function is the key to the problem. Thus, the RDA method now can give a practical answer to the question.

To complete the question, the other important aspect is to have rigorous Taylor transfer maps to describe the weakly nonlinear systems. This paper discusses the theory for rigorous integration of ordinary differential equations within the framework of RDA, which enables to obtain rigorous Taylor transfer maps[13]. The method has been implemented in the code COSY INFINITY[14][15], and the paper covers some example calculations.

2 RIGOROUS COMPUTATION BY INTERVAL METHODS

An interval represents a number on computers in a rigorous way, by rounding the number downwards to the lower bound and upwards to the upper bound. It can also represent an extended domain of numbers. These two features enable interval calculations on computers to make reliable statements. However, in practice, interval methods have some severe disadvantages, which make the mere interval method useless for calculation of complicated functions: The width of resulting intervals scales with the width of original intervals; and a blow-up occurs in extended calculations, which can be seen in the simple example, $[a,b]-[a,b]=[a-b,b-a]\neq[0,0]$. Furthermore, a difficulty exists in case of multiple dimensions d with n sampling points, because computational expense scales with n^d.

A new approach, the Remainder-enhanced Differential Algebraic (RDA) method, provides remedy to these disadvantages of interval computations[9].

3 REMAINDER-ENHANCED DIFFERENTIAL ALGEBRAS

3.1 Taylor Models

A C^∞ function $f:[\vec{a},\vec{b}]\subset R^v\to R$ can be expressed by the n-th order Taylor polynomial P_n expanded around the reference point $\vec{x}_0$ and a remainder ε_n as $f(\vec{x})=P_n(\vec{x}-\vec{x}_0)+\varepsilon_n(\vec{x}-\vec{x}_0)$. Let the interval I_n be such that $\forall\vec{x}\in[\vec{a},\vec{b}]$, $\varepsilon_n(\vec{x}-\vec{x}_0)\in I_n$. Then

$$\forall\vec{x}\in[\vec{a},\vec{b}],\quad f(\vec{x})\in P_n(\vec{x}-\vec{x}_0)+I_n.$$

Because of the special form of the Taylor remainder term ε_n, in practice usually the remainder decreases as $|\vec{x}-\vec{x}_0|^{n+1}$. Hence, if $|\vec{x}-\vec{x}_0|$ is chosen to be small, the interval remainder bound I_n can become very small. We say a pair (P_n,I_n) is an n-th order Taylor model of f.

3.2 Taylor Models for addition, multiplication and intrinsic functions

The question now is how to efficiently determine Taylor models for any arbitrary functional dependency that can be expressed on a computer[9]. The key is to begin with the Taylor model for the identity function, which is trivial, and then successively build up Taylor models for the total function from its pieces. This requires methods to determine Taylor models for sums and products from those of the summands or factors.

Let the functions $f,g:[\vec{a},\vec{b}]\subset R^v\to R$ have Taylor models $(P_{n,f},I_{n,f})$, $(P_{n,g},I_{n,g})$. Then an n-th order Taylor model for $f+g$ is obviously obtained as

$$(P_{n,f}+P_{n,g},I_{n,f}+I_{n,g}).$$

An n-th order Taylor model for $f\cdot g$ is obtained as

$$\begin{aligned}&(P_{n,f\cdot g},I_{n,f\cdot g}),\quad\text{where}\\ I_{n,f\cdot g}\;=\;&B(P_{n,f}\cdot P_{n,g}-P_{n,f\cdot g})+B(P_{n,f})\cdot I_{n,g}\\ &+B(P_{n,g})\cdot I_{n,f}+I_{n,f}\cdot I_{n,g},\end{aligned}$$

with $B(P)$ denoting a bound of the polynomial P. The key idea of computing Taylor models for intrinsic functions is to employ Taylor's theorem of the function under consideration.

3.3 Taylor Models for Derivations and Anti-derivations

For many practical problems, in particular the efficient solution of differential equations, it is actually important to complement the set of operations by a derivation ∂, as well as its inverse ∂^{-1}, similar as in other differential algebraic approaches.

Given an n-th order Taylor model (P_n,I_n) of a function f, we can determine a Taylor model for the indefinite integral $\partial_i^{-1}f=\int f\,dx_i'$ with respect to variable i. The operator ∂_i^{-1}on the space of Taylor models is defined as

$$\begin{aligned}&\partial_i^{-1}(P_n,I_n)\\ =\;&\left(\int_0^{x_i}P_{n-1}dx_i',\;(B(P_n-P_{n-1})+I_n)\cdot B(x_i)\right).\end{aligned}$$

Similar to the case of the Differential Algebra on the set of Truncated Power Series, and following one of the main thrusts of the theory of Differential Algebras, we will use these for the solution of the initial value problem

$$\frac{d}{dt}\vec{r}(t)=\vec{F}(\vec{r}(t),t),\tag{1}$$

where $\vec{F}$ is continuous and bounded. We are interested in both the case of a specific initial condition $\vec{r}_0$, as well as the case in which the initial condition $\vec{r}_0$ is a variable, in which case our interest is in the flow of the differential equation

$$\vec{r}(t)=\mathcal{M}(\vec{r}_0,t).$$

3.4 Example computation

We made a comparison computation to show how the new method works to obtain a rigorous bound. We used a deviation function from a normal form invariance used in Figures 1 and 2 to get a bound within the domain intervals $[.04, .06]$ in each six coordinate variables. To get the rough idea of the actual size, we made a real number scan at 1000 random points and at 3^6 points at edges and center in each dimension. The bound of values by the scan is

```
[-.3121185581961283E-05,0.4212429306152572E-04].
```

The mere interval computation gave the bound

```
[-4.471335284762441     , 4.807741733133240     ],
```

which is rigorous but useless because of a severe blow-up. Now, the remainder bound carried by the sixth order Taylor model computation is

```
[-.5358533718862318E-05,0.5358814729171932E-05]
```

and it added up to a total bound of

```
[-.3466186723563667E-04,0.5352931790602934E-04].
```

The comparison with the estimate by the scan shows the practical strength of the RDA method.

4 VERIFIED INTEGRAL WITH TAYLOR MODELS

Our goal is now to determine a Taylor model for the flow $\mathcal{M}(\vec{r}_0, t)$ of the differential equation (1). The remainder bound should be fully rigorous for all initial conditions $\vec{r}_0$ and times t that satisfy

$$\vec{r}_0 \in [\vec{r}_{01}, \vec{r}_{02}] = \vec{B}, \quad t \in [t_0, t_1].$$

In particular, $\vec{r}_0$ itself may be a Taylor model, as long as its range is known to lie in $\vec{B}$.

Since conventional numerical integrators don't provide rigorous estimates for the integration error but only approximate estimates, we have to start from scratch from the foundations of the theory of differential equations[13].

4.1 Schauder's Fixed Point Theorem

We re-write the differential equation as an integral equation

$$\vec{r}(t) = \vec{r}_0 + \int_{t_0}^{t} \vec{F}(\vec{r}(t'), t')\, dt',$$

noting that the initial value problem has a (unique) solution if and only if the corresponding integral equation has a (unique) solution. Now we introduce the operator $A : \vec{C}^0[t_0, t_1] \rightarrow \vec{C}^0[t_0, t_1]$ on the space of continuous functions from $[t_0, t_1]$ to R^v via

$$A\left(\vec{f}\right)(t) = \vec{r}_0 + \int_{t_0}^{t} \vec{F}\left(\vec{f}(t'), t'\right) dt'.$$

Then the problem of finding a solution to the differential equation is transformed to a fixed-point problem on the space of continuous functions

$$\vec{r} = A(\vec{r}).$$

We will now apply Schauder's fixed point theorem to rigorously obtain a Taylor model for the flow.

Theorem (Schauder): *Let A be a continuous operator on the Banach Space X. Let $M \subset X$ be compact and convex, and let $A(M) \subset M$. Then A has a fixed point in M, i.e. there is an $\vec{r} \in M$ such that $A(\vec{r}) = \vec{r}$.*

4.2 Strategy to Satisfy the Requirements of Schauder's Theorem

In our specific case, $X = \vec{C}^0[t_0, t_1]$, the Banach space of continuous functions on $[t_0, t_1]$, equipped with the maximum norm, and the integral operator A is continuous on X. The process to apply Schauder's theorem consists of the following steps:

- Determine a family Y of subsets of X, the Schauder Candidate Sets. Each set in Y should be compact and convex, it should be contained in a suitable Taylor model, and its image under A should be in Y.
- Using differential algebraic methods on Taylor models, determine an initial set $M_0 \in Y$ that satisfies the inclusion property $A(M_0) \subset M_0$. Then all requirements of Schauder's theorem are satisfied, and M_0 contains a solution.
- Iteratively generate the sequence $M_i = A(M_{i-1})$ for $i = 1, 2, 3, \ldots$. Each M_i also satisfies $A(M_i) \subset M_i$, and we have $M_1 \supset M_2 \supset \ldots$. We continue the iteration until the size stabilizes sufficiently.

4.3 Schauder Candidate Sets

For the first step, it is necessary to establish a family of sets Y from which to draw candidates for M_0. Let $(\vec{P} + \vec{I})$ be a Taylor model depending on time as well as the initial condition $\vec{r}_0$. Then we define the associated set $M_{\vec{P}+\vec{I}}$ as follows:

$$\begin{aligned} M_{\vec{P}+\vec{I}} &\subset \vec{C}^0[t_0, t_1]; \text{ and for } \vec{r} \in M_{\vec{P}+\vec{I}}: \\ \vec{r}(t_0) &= \vec{r}_0 \\ \vec{r}(t) &\in \vec{P} + \vec{I}\, \forall t \in [t_0, t_1]\, \forall \vec{r}_0 \\ |\vec{r}(t') - \vec{r}(t'')| &\leq k|t' - t''|\, \forall t', t'' \in [t_0, t_1]\, \forall \vec{r}_0. \end{aligned}$$

In the last condition, k is a bound for $\vec{F}$, which exists because $\vec{F}$ is continuous and the solutions can cover only a finite range over the interval $[t_0, t_1]$. The last condition means that all $\vec{r} \in M_{\vec{P}+\vec{I}}$ are uniformly Lipschitz with constant k. Define the family of candidate sets Y as

$$Y = \bigcup_{\vec{P}+\vec{I}} M_{\vec{P}+\vec{I}}.$$

4.4 *Convexity, Compactness, and Invariance of Schauder Candidate Sets*

Let $M \in Y$. Then M is convex, because $\vec{x}_1, \vec{x}_2 \in M \Rightarrow \alpha\vec{x}_1 + (1-\alpha)\vec{x}_2 \in M \; \forall \alpha \in [0,1]$.

Furthermore, M is compact, i.e. any sequence in M has a clusterpoint in M. To see this, let $(\vec{x}_n)$ be a sequence of functions in M. Then by definition of M, $(\vec{x}_n)$ is uniformly Lipschitz, and thus uniformly equicontinuous. $(\vec{x}_n)$ is also uniformly bounded, and hence according to the Ascoli-Arzela Theorem, has a uniformly convergent subsequence. Since the $\vec{x}_n$ are continuous, so is the limit $\vec{x}^*$ of this subsequence, and since M is closed, the limit $\vec{x}^*$ is in M.

Finally, A maps Y into itself, and the uniform Lipschitzness follows because $\vec{F}$ is bounded by k.

4.5 *Satisfying the Schauder Inclusion Requirement with Differential Algebraic Methods*

The only remaining requirements for Schauder's theorem is to find a Taylor model $\vec{P} + \vec{I}$ such that

$$A(\vec{P} + \vec{I}) \subset \vec{P} + \vec{I}.$$

This condition can be checked computationally using the differential algebraic operations on the set of Taylor models. To succeed with the inclusion requirement depends on finding suitable choice for $\vec{P}$ and $\vec{I}$. Furthermore, it is desirable to have $\vec{I}$ tight. Both benefit from the choice of a polynomial $\vec{P}$ that is already "close" to the true solution of the ODE.

Attempt sets M^* of the form

$$M^* = M_{\vec{P}^* + \vec{I}^*}, \quad \text{where} \quad \vec{P}^* = \mathcal{M}_n(\vec{r}_0, t),$$

the n-th order Taylor expansion of the flow of the ODE. It is to be expected that $\vec{I}^*$ can be chosen smaller and smaller as the order n of $\vec{P}^*$ increases.

This requires the knowledge of the n-th order flow $\mathcal{M}_n(\vec{r}_0, t)$, including time dependence. It can be obtained by iterating in conventional DA. To this end, one chooses an initial function $\mathcal{M}_n^{(0)}(\vec{r}, t) = \mathcal{I}$, where $\mathcal{I}$ is the identity function, and then iteratively determines

$$\mathcal{M}_n^{(k+1)} =_n A(\mathcal{M}_n^{(k)}).$$

In case $\vec{F}$ is origin preserving, this process converges to the exact DA result $\mathcal{M}_n$ in exactly n steps.

Now try to find $\vec{I}^*$ such that

$$\mathcal{M}_n + \vec{I}^* \subset A(\mathcal{M}_n + \vec{I}^*),$$

the Schauder inclusion requirement. The suitable choice for $\vec{I}^*$ requires experimenting, but is greatly simplified by the observation

$$\begin{aligned} \vec{I}^* &\supset \vec{I}^{(0)}, \quad \text{where} \\ \mathcal{M}_n(\vec{r}, t) + \vec{I}^{(0)} &= A(\mathcal{M}_n(\vec{r}, t) + [\vec{0}, \vec{0}]). \end{aligned}$$

Evaluating the right hand side in the RDA yields a lower bound for $\vec{I}^*$, and a benchmark for the size to be expected. Now iteratively try

$$\vec{I}^{(k)} = 2^k \cdot \vec{I}^{(0)},$$

until a computational inclusion is found, i.e.

$$A(\mathcal{M}_n(\vec{r}, t) + \vec{I}^{(k)}) \subset \mathcal{M}_n(\vec{r}, t) + \vec{I}^{(k)}.$$

4.6 *Iterative Refinement of the Inclusion*

Once a computational inclusion has been determined, the solution of the ODE is known to be contained in the Taylor model $\mathcal{M}_n(\vec{r}, t) + \vec{I}^{(k)}$. Set $\vec{I}_{(1)} = \vec{I}^{(k)}$; since the solution is a fixed point of A, it is even contained in

$$A^k(\mathcal{M}_n(\vec{r}, t) + \vec{I}_{(1)}) \quad \text{for all } k.$$

Furthermore, the iterates of A are shrinking in size, i.e.

$$A^k(\mathcal{M}_n(\vec{r}, t) + \vec{I}_{(1)}) \subset A^{k-1}(\mathcal{M}_n(\vec{r}, t) + \vec{I}_{(1)}) \; \forall k.$$

So the width of the remainder bound of the flow can be decreased by iteratively determining

$$\mathcal{M}_n(\vec{r}, t) + \vec{I}_{(k)} = A(\mathcal{M}_n(\vec{r}, t) + \vec{I}_{(k-1)}),$$

until no further significant decrease in size is achieved. As a result,

$$\mathcal{M}_n(\vec{r}, t) + \vec{I}_{(k)}$$

is the desired sharp inclusion of the flow of the original ODE.

5 EXAMPLES OF INTEGRATION

In this section, we will provide two examples for the practical use and performance of the method discussed above. The first example is to test the integration algorithm; it is the motion on a circle defined by the differential equations and initial conditions

$$\dot{x} = -y, \quad \dot{y} = x, \quad x(0) = 1, \; y(0) = 0.$$

The integration from 0 to 2π was performed using tenth order Taylor models with a fixed step size of $\pi/36$. The resulting interval inclusions based on double precision interval arithmetic are

```
+1.00000000E+00+[-.43837892E-13,+0.43837892E-13]
-0.63043563E-14+[-.43587934E-13,+0.43587934E-13].
```

Another example is to analyze the motion of a charged particle in a homogeneous dipole magnet. The flow of the differential equation over a region of initial conditions is determined. The integration was carried out through the dipole with the deflection radius of 1m over a deflection angle of 36 degrees with a fixed step size of 4 degrees. The initial conditions of four phase space variables, x,

$a = p_x/p_0$, y and $b = p_y/p_0$, are within the domain intervals

$$[-.02, .02] \times [-.02, .02] \times [-.02, .02] \times [-.02, .02],$$

and the Taylor polynomial describing the dependence of the four final coordinate values on the four initial coordinate values was determined. The order in time and initial conditions was chosen to be 12, and the step size was estimated so as to ascertain an overall accuracy below 10^{-9}; since no automatic step size control was utilized, the estimate proved conservative and the actual resulting error was somewhat lower:

```
[-0.4496880372277553E-09,+0.3888593417126594E-09]
[-0.1301070602141642E-09,+0.1337099965985420E-09]
[-0.3417079805637740E-10,+0.3417079805637740E-10]
[-0.0000000000000000E+00,+0.0000000000000000E+00]
```

The resulting Taylor polynomials describing the dependence of final on initial coordinates were compared with those obtained by our particle optics code COSY INFINITY[14][15], and agreement was found. A further check was to compare a large collection of rays through the dipole obtained by COSY INFINITY with ones through the results of the flow calculated by the verified integrator. For all rays studied, the difference between the final coordinates determined geometrically by the dipole element in COSY INFINITY and those predicted by the twelfth order Taylor polynomial were within the calculated remainder bounds.

6 OUTLOOK

Automatic step size and order control is expected to allow the integrator to automatically assure pre-specified accuracy goals at nearly optimal speed.

For the study of rigorous long-term stability, the development of other invariant classes based on wavelets, or possibly Fourier-splines is important, as well as the utilization of multi-turn maps and the development of more sophisticated understanding of actual escape mechanisms. Finally, the method discussed here will facilitate a modification of existing accelerator lattices to minimize occurring invariant defects.

7 ACKNOWLEDGEMENTS

We are grateful for the financial support of this research to the Department of Energy, Grant No. DE-FG02-95ER40931, and the Alfred P. Sloan Foundation.

8 REFERENCES

[1] M. Berz. Differential algebraic description of beam dynamics to very high orders. *Particle Accelerators*, 24:109, 1989.

[2] M. Berz. Arbitrary order description of arbitrary particle optical systems. *Nuclear Instruments and Methods*, A298:426, 1990.

[3] M. Berz. *High-Order Computation and Normal Form Analysis of Repetitive Systems, in: M. Month (Ed), Physics of Particle Accelerators*, volume AIP 249, page 456. American Institute of Physics, 1991.

[4] M. Berz. Modern map methods for charged particle optics. *Nuclear Instruments and Methods*, 363:100, 1995.

[5] R. L. Warnock and R. D. Ruth. Long–term bounds on nonlinear Hamiltonian motion. *Physica D*, 56(14):188–215, 1992. also SLAC–PUB–5267.

[6] M. Berz and G. Hoffstätter. Exact bounds of the long term stability of weakly nonlinear systems applied to the design of large storage rings. *Interval Computations*, 2:68–89, 1994.

[7] G. H. Hoffstätter. *Rigorous bounds on survival times in circular accelerators and efficient computation of fringe–field transfer maps*. PhD thesis, Michigan State University, East Lansing, Michigan, USA, 1994. also DESY 94-242.

[8] M. Berz, G. Hoffstätter, W. Wan, K. Shamseddine, and K. Makino. COSY INFINITY and its applications to nonlinear dynamics. *in: Computational Differentiation: Techniques, Applications, and Tools*, SIAM, 1996.

[9] K. Makino and M. Berz. Remainder differential algebras and their applications. *in: Computational Differentiation: Techniques, Applications, and Tools*, SIAM, 1996.

[10] M. Berz. Differential algebras with remainder and rigorous proofs of long-term stability. In *Fourth Computational Accelerator Physics Conference*. AIP Conference Proceedings, 1996.

[11] M. Berz. From Taylor series to Taylor models. In *Proceedings, First Accelerator Theory Institute*. AIP, 1997.

[12] K. Makino and M. Berz. Implementation and applications of Taylor model methods. *Reliable Computing*, submitted, 1997.

[13] M. Berz and K. Makino. Integration of ODEs and flows with differential algebraic methods on Taylor models. *Reliable Computing*, submitted, 1997.

[14] M. Berz. COSY INFINITY Version 7 reference manual. Technical Report MSUCL-977revised, National Superconducting Cyclotron Laboratory, Michigan State University, East Lansing, MI 48824, 1996.

[15] M. Berz. COSY INFINITY version 7. In *1997 Particle Accelerator Conference*. these proceedings, 1997.

ANALYTIC NONLINEAR METHODS FOR BEAM OPTICS

J. Irwin†, SLAC, 2575 Sand Hill Rd., Menlo Park, CA, USA 94025

Abstract

In recent years there have been major advances in the computation and use of high-order maps for the design, optimization and operation of beamlines. We will describe five practical examples for both linear and circular colliders.

1 INTRODUCTION

The range of meaning for the word "analytical" extends from a hand-derived formula to be used by hand, to a computer-derived formula to be used by hand (eg. with a symbolic manipulation program), to a computer-derived expression to be seen only by a computer. There is an increasing degree of complexity as one proceeds through these types. The hand-derived/hand-used is especially important for the first stages of beamline design, the computer-derived/hand-used is especially important for use in the operation and tuning of an existing beamline, and computer-derived/computer-used is useful in the intermediate and final stages of beamline design. We will describe five examples, covering a full range of complexity. From least to most complex these examples will be:

- use of similarity transformations (FFTB design, SLC diagnosis)
- statistical maps (SSC smear and tune-shift)
- aberrations (SLC upgrade)
- resonance basis and nPB tracking (PEP-II design)
- kick factorization (possibly LHC).

2 LIE OPERATOR BASICS

The Lie operator and associated algebra are valuable tools to understanding the examples to be described. We introduce them briefly here. See reference [1].

2.1 Lie operators

For R a constant, the equation $\frac{d}{dt}f = Rf$ has the solution $f(t+\Delta t) = e^{\Delta t R} f(t)$. This equation could equally well be written $f(t+\Delta t) = e^{\Delta t \frac{d}{dt}} f(t)$, which is now true for a very large class of functions f(t). We will be concerned with a class of functions $f(x(s), p_x(s), ...)$ where $x(s)$ is the particle position, and the differential operator, d/ds, is given by a Hamiltonian. Symbolically $\frac{d}{ds} = -:H(x, p_x, ..):$ where $:H:f = \{H, f\}$ and where $\{.. ,..\}$ is the symbol for the Posson bracket. In other words

$$f(s+\Delta s) = e^{\Delta s \frac{d}{ds}} f(s) = e^{-\Delta s:H:} f(x, p_x, ..)$$

We often drop the ": ... :" notation when no confusion can arise.

2.2 Composition laws

The usefulness of the Lie operator symbol lies in the three following properites:

1. Concatenation. If the Hamiltonian H changes abruptly from a function H_1 in a segment Δs_1 to a function H_2 in a segment Δs_2, then the result of transporting through the two adjacent segments is $e^{-\Delta s_1 :H_1:} e^{-\Delta s_2 :H_2:}$.

2. Composition (BCH law). For generator functions A and B, there is a generator C, such that $e^A e^B = e^C$ where C is given by a perturbation series of Poisson brackets: $C = A + B + \frac{1}{2}\{A, B\} + ...$

3. Similarity. For generator functions A and B, $e^A e^B e^{-A} = e^{e^A(B)}$. This law says that the simlarity transform of a Lie operator is given by the Lie operator with an approriately transformed generator. This law looks rather special, but has wide applicability.

2.3 Representation of elements and beamlines

From the concatenation law it is clear that a beamline can be represented by a product of Lie operators. This result is enhanced by the fact that element misplacements can be represented by coordinate transformations specified by Lie operators inserted between elements. Likewise fringe fields, edge angles, and overlapping fields (eg. a quadrupole sitting in a solenoid) all can be faithfully represented by the appropriate Lie operators.[2]

2.4 Dragt-Finn map representation

We have stated that any element can be represented by a Lie operator and a beamline can be represented by a product of such operators. There are a variety of means by which these operator products can be composed to find a Lie operator representation for the entire beamline. The final result usually takes the form of a product of a linear operator, specified either by a matrix or a Lie operator, and a purely nonlinear operator. More often the beamline map is determined by tracking through the elements with

†Work supported by the Department of Energy, contract DE-AC03-76SF00515.

a power series to determine a power series representation of the beamline map. Using the factorizaiton result derived by Dragt and Finn any power series which represents a symplectic map can be represented by the product of a linear map and a nonlinear Lie operator. [3]

2.5 Normal forms

Normal form factorizations apply to closed rings. In rings one often seeks a representation of the form

$$M e^{G} = e^{A} \mathrm{Re}^{h} e^{-A}$$

where M is the linear map for the ring, G in the generator of the remainder nonlinear map, R is a block-diagonal rotation matrix, h is a generator that depends only on action operators, and A is the generator of a similarity transformation that maps the phase-space invariant surfaces of the original map, when they exist, onto a product of toroids. [4]

This normal form may be found formally but will only be accurate under limited conditions that are difficult to specify precisely. It is important to distinguish between properties of the one-turn map, which will generally be well behaved and continuous in all the variables defining it, and the "iterated map" which may have a range of behaviors, including of course, chaotic motion. Hence the normal form, which can only represent very regular behavior, can not represent the full range of expected properties of the iterated map.

3. STATISTICAL MAPS

During a design process, one must assign statistical values to many element properties, such as multipole strengths and magnet positions. One must then study an ensemble of machines to be sure that all have acceptable behavior. It would be advantageous if one could avoid the map composition process for all rings in the statistical sample, and assign statistical values directly to map coefficients. The following work describes the first foray into such territory [5]. This work also provides valuable insight into how the nonlinear generator of the one-turn map is related to the nonlinearities of beamline elements.

3.1 The motive

The SSC design group had chosen a quantity called smear, which was roughly the rms spread of the invariant action, along with tune-shift-with-amplitude, to characterize the behavior of lattices prior to studying their long-term behavior. Since these quantities depended on the random seed determining each lattice, a large computational effort was required to determine smear for a statistical sample of each basic design. Forest showed that these quantities could be found using Lie methods. Bengtsson and Irwin included closed-orbit effects and firmly established that the results of the calculation and tracking were identical, including the Fourier decomposition of the smear. Weeks of computational time were reduced to minutes.

3.2 The method

Starting with the representation of the one-turn map as a product of Lie operators, each representing an element, one first solves for corrector strengths to find a satisfactory closed orbit. For the phase advances of the SSC lattice and the location of correctors and BPMs, one could do this quite simply using a local bump algorithm. With the corrector strengths determined, operators could be introduced to represent them.

The principal step is to write each element map as a product of two linear maps bracketing a remainder containing the chromaticity and nonlinear multipole terms. Similarity transformations can now be used to move all linear maps to the front of the line. The result is that the variables in the remainder map generators are replaced by a linear sum expressing the coordinate at the center of the element location as a function of the position and momenta at the end of the beamline.

Since the remainders are small maps, the BCH law can now be used to find the nonlinear generator of the one-turn map. The first term in the BCH law is just the sum of the element remainder generators.

The apparent complexity of a 100 km ring conaining a variety of nonlinear terms spread out along the circumference is replaced by a linear matrix and one nonliner map specified by a polynomial starting with third order terms. The polynomial is given, to first order, as a sum of the polynomials of the nonlinearities in the ring, each written as a function of the position and momenta at the end of the ring. The situation could hardly be simpler!

Furthermore using the BCH theorem there is a clear prescription how to find next order terms so that they can be calculated and compared to the first order terms. This approach is a usual perturbation theory in the strength of element nonlinearity strength. Its advantage is simplicity and clarity.

Most of the multipole strengths contain a stochastic variable. The sum of stochastic variables can be represented as a stochastic variable. In this way one finds directly an expression for the map with stochastic variables in coefficients.

3.3 Smear and tune-shift-with-amplitude

One can next look at the normal form expression to find the generator of the simlarity transformation in terms of the one-turn nonlinear map generator. At this step the tune of the ring enters explicitly. Finally the generator of the tune-shift-with-amplitude can be found. There is a complication that important terms in this expression are second order in the sextupole terms of the one-turn generator.

4. KICK FACTORIZATION

A kick map, which for example might represent an impulse approximation for an element, has a generator

that depends on only one phase space variable. It leaves the variable x unchanged and increments the momenta by a function of the position. A generalization of the kick would be a map whose generator was a coordinate transformation of a kick generator. These have also been referred to as a jolts.

4.1 The motive

Kick maps and products of kick maps are very easy and fast to evaulate. They are guaranteed sympletic because no truncation is required. Since the one-turn map is the result of adding together a bunch of kicks in the case where each element is represented by a symplectic kick factorization, it is natural to ask whether given a one-turn generator one could find a factorization, hopefully with a much smaller number of factors, that would faithfully represent it. If so, the one turn-map could be tracked very rapidly to study the long-term behavior so important in proton machines.

4.2 The method

One posits a set of kicks with simple, but specified phase-space rotations between them [6]. The number of kicks is determined by the number of terms required to represent the highest order polynomial.

One first solves a linear equation for the coefficients of the third order polynomials. Next one determines the fourth-order effects of these polynomials, subtracts these terms from the original one-turn map and fits the remainder by a sum of fourth-order polynomials, and so on.

4.3 Improvements

Rotations between kicks can be specified by a set of points in a 2D plane, where the x coordinate is the horizontal-plane rotation angle, and the y coordinate is the vertical-plane rotation angle. One quickly realizes that, if the points are on a coordinate grid, an unusually large number of points is required because of a degeneracy. So one is led to tilt this grid slightly. Techniques developed by Abell and Dragt [7] have shown that there is an optimal angle for this tilt. They have also studied other groups of linear maps between kicks, in search of a "best choice".

5. USE OF SIMILARITY TRANSFORMATIONS

Final focus systems for linear colliders are unusal in that the nonlinearities are necessarily very strong. If uncorrected, the chromaticity of the final doublet in the Next Linear Collider (NLC) design would give an rms size to the beam that is about 100 times larger than its linear size. This huge chromatic term is compensated by a pair of sextupoles separated by a -I section upstream from the doublet, and these chromatic kicks coming via the presence of dispersion in these sextupoles must in turn be several times smaller than the sextupole kicks themselves to insure good system bandwidth. These nonlinearities cannot be dealt with effectively, or with any insight, using the BCH theorem.

However because the sextupole nonlinearities must cancel out, there must be a structure in the beamline that insures this. This structure is, of course, the -I module between them. Placing the sextupole at each end of the -I, and removing linear terms, as described in section 3, we see that we are looking at a simlarity transformation, where the generator of the similarity transform is the sextupole generator.

5.2 Chromatic-correction section map

The remainder generator for the -I between sextupoles contain chromatic terms of the form

$$a_n x^2 \delta^n + b_n p_x^2 \delta^n + ..$$

along with similar terms in y. There are no xp_x terms if the -I section is forward-backward symmetric. The generator of the sextupole is of the form:

$$G_S = \frac{k_S}{3!}[(x \pm \eta\delta)^3 - 3(x \pm \eta\delta)y^2]$$

$$= \frac{k_S}{3!}[x^3 - 3xy^2 + 3\eta^2 x\delta^2 \pm 3\eta(x^2 - y^2)\delta + .]$$

To form the similarity transform, we add and subtract two times the chromatic term on the left hand side. This leaves a residuual chromatic term twice the size of the term in the sextupole generator, and a sturcture which is a pure similarity transform [8]. The map for this module may now be determined precisely by replacing p_x by $p_x - \frac{\partial G_S}{\partial x}$, and similarly for p_y. This transformed generator has the property that no large terms remain. The chromaticty term has been removed. It must be moved through the final telescope to cancel the chromaticity of the final doublet, producing another similarity structure to evaluate. And the sextupole terms are gone. What is left is a transform of the -I chromatic terms by the presence of the sextupoles. Since the derivative of G_S is second order, and this is squared, the highest order aberration which arises from the linear chromaticity of the -I will be of fifth order.

Besides determining an important high order aberration, which by design must be kept acceptably small, we have established that there are no additional terms. We have found a very consise expression for these aberrations which can be used in determining optimal design parameters (length, b functions, dispersion) for final focus design [9].

5.3 Similarity transformation generality

The considerations of the preceding paragraph are surprisingly general. Often one asks questions such as, "How bad can the launch conditions be?" or "How large can a misalignement be?". Since it is presumed that there will be a corrector to compensate steering, or a change in

a quadrupole to compensate a mismatch, all of these questions resolve themselves in a similarity transfrom structure. [10]

6. ABERRATIONS

Each term in the nonlinear beamline generator corresponds to a unique aberration. These terms will be small by design, even for beamlines with large nonlinearities.

6.1 Final focus system upgrade

In evaluating existing, and typically non-ideal beamlines, one will use symbolic manipulator programs or truncated power series agebras to determine the beamline map. Investigation of the generator will reveal what aberrations are dominating the beamline. Modifications to eliminate the aberrations can be considered. Before a recent upgrade, the dominant aberration on the SLC final focus beamline was the term $\delta^2 p_y^2$, a second-order (in δ) chromaticity term. This term could be corrected by putting a quadrupole in the final telescope [11]. Since there is a large first order chromaticity at each end of this telescope, small phase advance changes between these terms produces the second order term. This can be seen by evaluating the Poisson bracket $\{p_{x1}^2, p_{x2}^2\} = p_{x1} p_{x2} \{p_{x1}, p_{x2}\} \approx p_{x1}^2 \{p_{x1}, p_{x2}\}$.

7. RESONANCE BASIS

For rings it is more informative to write the nonlinear one-turn map generator in a resonance basis. The transform to this basis is linear, hence easy to perform. It plays an important role in the normal form theory. The generator of a ring will have many, many terms and in general it is impossible to determine the effect of an aberration by looking at its strength. However in the course of the PEPII design a graphic display was developed [12] to monitor the strengths of these aberrations. This proved useful for two reasons:
inadvertent mistakes in the input lattice, where quickly spotted, and several general lessons were learned. One important lesson concerned the strength of chromatic terms (anything quadratic in phase-space variables with a d dependence). This is of course well-known, but the required conditions became more quantitative.

8. NPB TRACKING

In the design process, many what-if questions naturally arise. What if we were able to change the strength of a particular resonance? What if we changed the tune? These questions can be answered if one can reliably track with the map.

8.1 The nPB tracking method

Because one contemplated asking questions about changes in resonance strengths, it was natural to seek a method to track in an action-angle basis. It was a great surprise to find that one could, and with excellent speed. The method consists of applying the map to the standard phase-space variables x, p_x, .. but evaulating the resulting Poisson brackets in the action-angle variables. Astonishingly this can be done without ever evaluating a sine or cosine, or square root. See reference [12] for details. Results were compared to element-by-element tracking to establish that the dynamic aperture determinations were identical.

8.2 Swimps and swamps

A SWIMP is an acronym we have given to a "switched map". A switched map is derived from the one-turn map of a beamline by altering it in some interesting way. The most important SWIMPs used in the PEPII design process were those for which the one-turn phase advance of the linear map was changed while the nonlinear map remained unchanged. Since the phase trombone of PEPII is located in a benign section of beamline, this can correspond quite closely to a real situation. Varying the tune over one quadrant of the tune plane, and looking at the dynamic aperture, resulted in what has been called a SWAMP plot. In this way the behavior of our lattices could be studied in the entire tune plane, rather than just one point. [13]

9. SUMMARY

An example of an analytical result in nonlinear beam optics was presented for five distint levels of complexity. Starting from the lowest, these examples were:

- use of similarity transformations to determine design equations for linear collider final focus systems
- use of the BCH law to determine a statistical sample of one-turn maps for proton rings
- use of the nonlinear generator to find and correct aberrations in a beamline map, or monitor resonance strengths in a ring map
- description of an action-angle based tracking algorithm that allows one to determine dynamic apertures of electron rings in the entire tune plane
- description of a kick factorization method for a one-turn map that may be used to rapidly determine the long-term behavior of proton rings

10 ACKNOWLEDGEMENTS

All of the methods described rely on the Lie operator methods introduced into accelerator physics by A. Dragt. My first exposure to these methods came through collaboration with E. Forest in the SSC design group. I especially thank these two pioneers, and my inspiring, creative collaborators over the past ten years: J. Bengtsson, Y. Cai, T. Chen, G. Roy, N. Walker, Y. Yan, and F. Zimmermann.

REFERENCES

[1] For a recent overview of this subject and bibliography we recommend A. J. Dragt, 'Maps past, present, and future'. Part. Accel. **54**, (1996)

[2] E. Forest, Mm. Reusch, D. Bruhwiler, and A. Amiry, 'The correct local description for tracking in rings', Part. Accel. **45**, 65 (1994)

[3] A. Dragt and J. Finn, 'Lie series and invariant functions for anlytic symplectic maps', J. Math. Phys. **17**, 2215 (1976)

[4] E. Forest, M. Berz, and J. Irwin, 'Normal form methods for complicated periodic systems', Part. Accel **24**, 91 (1989)

[5] E. Forest, 'Analytical computation of the smear', SSC-95 (1987), and J. Bengtsson and J. Irwin, 'Analytical calculations fo smear and tune shift', SSC-232 (1990)

[6] J. Irwin, 'A multi-kick factorization algorithm for nonlinear maps', SSC--228 (1989).

[7] D. Abell, 'Analytical properties and Cremona approximation of transfer maps for Hamiltonian systems', U. of Maryland physics department, PhD thesis (1995)

[8] G. Roy, 'Analysis of the optics of the final focus test beam using Lie algebra based techniques', PhD Thesis, SLAC Report-397 (1992]

[9] F. Zimmermann, R. Helm and J. Irwin, Optimization of the NLC final focus system, SLAC-PUB-6791.

[10] J. Irwin, N. Walker and M. Woodley, 'Using Lie algebra methods to analytically study non-perturbative effects in beam lines', SLAC-PUB-5920 (1992)

[11] N. Walker, J. Irwin, and M. Woodley, 'Third order corrections to the SLC final focus, SLAC-PUB-6205 (1993)

[12] Y. T. Yan, J. Irwin, and T. Chen, 'Resonance basis maps and nPB tracking for dynamic aperture studies', SLAC-PUB-7179, June 96

[13] Y. T. Yan, Y. Cai, D. Ritson, T. Chen, and J. Irwin, 'Swamp plots for dynamic aperture studies of PEPII lattices', SLAC-PUB-6876

NONLINEAR DYNAMICS ISSUES FOR QUASI-ISOCHRONOUS STORAGE RINGS *

D. Jeon, M. Bai, C. M. Chu, X. Kang, S. Y. Lee, A. Riabko, X. Zhao
Indiana University Cyclotron Facility
2401 Milo B. Sampson Lane, Bloomington, IN 47405

Abstract

The synchrotron equation of motion in quasi-isochronous (QI) storage rings was transformed to a universal Weierstrass equation, where solution is given by Jacobian elliptic functions. Scaling properties of QI Hamiltonian were derived. The effects of phase space damping and the sensitivity of particle motion to external harmonic modulation were studied. We found that rf phase modulation is particularly enhanced in QI storage rings. This means that the operators of QI storage rings should pay special attention to rf phase modulation. Exact formula and sum rules for resonance strength coefficients were derived. In the presence of radiation damping and rf phase modulation, QI system exhibits a sequence of period-two bifurcation enroute towards global chaos (instability) in a region of modulation tune. The critical modulation amplitude for the onset of global chaos shows a cusp as a function of modulation tune. This cusp was shown to arise from the transition from the 2:1 to the 1:1 parametric resonances. We also studied the effect of rf voltage modulation and found that the tolerance of rf voltage modulation is much larger than that of rf phase modulation.

1 INTRODUCTION

Very short electron bunches, e.g. sub-millimeter in bunch length, can be important for such applications as time resolved experiments, next generation light sources, coherent synchrotron radiation, and damping rings for the next linear colliders. A possible method for producing short bunches is to reduce the phase slip factor η or the momentum compaction factor α_c for electron storage rings because beam bunch width is proportional to $\sqrt{|\eta_0|}$ for small bunches inside the bucket. Thus a short bunch regime is equivalent to the condition of a small $|\eta_0|$. Since η is related to the the revolution frequency deviation (see Eq. (1)), the condition of small $|\eta|$ is also called the quasi-isochronous (QI) condition. Because of its potential benefit, interest in the physics of low α_c lattice have recently grown [1-7]. This paper is a review of [8, 9]. The aspects of stochastic dynamics of QI system was also studied [10].

Including the velocity difference between the off momentum particle and the synchronous particle, the fraction deviation of the revolution frequency is given by

$$\frac{\Delta\omega}{\omega_0} = -\eta\delta = -\left(\eta_0 + \eta_1\delta + \cdots\right)\delta, \tag{1}$$

where η_0 and η_1 are the first order and the second order phase slip factors and where $\delta = \Delta p/p_0$. For most of storage rings, the truncation of the phase slip factor at the η_1 term is a good approximation.

Using (ϕ, δ) as conjugate phase space coordinates,where ϕ is the rf phase angle, synchrotron mapping equations are given by

$$\delta_{n+1} = \delta_n + \frac{eV}{\beta^2 E}[\sin(\phi_{n+1}+\phi_s) - \sin\phi_s] - 2\pi\lambda\delta_n, \tag{2}$$

$$\phi_{n+1} = \phi_n + 2\pi h(\eta_0\delta_{n+1} + \eta_1\delta_{n+1}^2), \tag{3}$$

where the subscript stands for the revolution number, V is the rf voltage, h is the harmonic number, ϕ_s is the synchronous phase, and λ is the damping decrement. Under QI condition, $\eta_1\delta^3$ term is not negligible and should be included. Neglecting the friction term, the difference equation can be cast into the Hamiltonian given by

$$H = \frac{1}{2}h\eta_0\delta^2 + \frac{1}{3}h\eta_1\delta^3 + \frac{eV}{2\pi\beta^2 E}[\cos(\phi+\phi_s) + \phi\sin\phi_s], \tag{4}$$

$$\approx \frac{1}{2}h\eta_0\delta^2 + \frac{1}{3}h\eta_1\delta^3 - \frac{eV\cos\phi_s}{4\pi\beta^2 E}\phi^2, \tag{5}$$

where $\theta = s/R$ serves as the time coordinate, and R is the mean radius of the storage ring.

2 PARTICLE HAMILTONIAN IN QI STORAGE RINGS

For synchrotron storage rings operating near the isochronous condition, the small amplitude synchrotron tune is given by

$$\nu_s = \sqrt{\frac{heV|\eta_0\cos\phi_s|}{2\pi\beta^2 E_0}}, \tag{6}$$

where βc and E_0 are the velocity and the energy of the beam. Using $t = \nu_s\theta$ as the time variable and using (x, p) as the conjugate phase space coordinates, where

$$x = -\frac{\eta_1}{\eta_0}\frac{\Delta p}{p_0}, \quad p = \frac{dx}{dt}, \tag{7}$$

the synchrotron Hamiltonian for particle motion in QI storage rings is given by

$$H = \frac{1}{2}p^2 + \frac{1}{2}x^2 - \frac{1}{3}x^3. \tag{8}$$

* Work supported by DOE, Grant No. DOE-DE-FG02-93ER40801, and the NSF, Grant No. PHY-9512832.

The "energy" E of the autonomous Hamiltonian is a constant of motion with $E \in [0, \frac{1}{6}]$ for particles inside the bucket. Figure 1 shows the potential energy and the stable bucket area for the Hamiltonian.

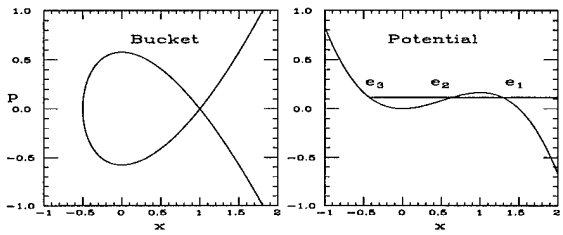

Figure 1: Stable bucket on the left and the potential energy.

The equation of motion for a particle with energy E is given by

$$\left(\frac{dx}{dt}\right)^2 = \frac{2}{3}x^3 - x^2 + 2E. \tag{9}$$

Letting $u = \frac{1}{\sqrt{6}}t$ and $\wp = x$, the equation of motion is transformed to the standard Weierstrass equation:

$$\left(\frac{d\wp(u)}{du}\right)^2 = 4(\wp - e_1)(\wp - e_2)(\wp - e_3), \tag{10}$$

where the turning points, $e_1 \geq e_2 \geq e_3$, are given by

$$e_1 = \frac{1}{2} + \cos(\xi),\ e_2 = \frac{1}{2} + \cos(\xi - 120°),$$
$$e_3 = \frac{1}{2} + \cos(\xi + 120°),\ \xi = \frac{1}{3}\arccos(1 - 12E).$$

For particles inside the separatrix, the discriminant is positive, i.e. $\Delta = 648E(1 - 6E) > 0$, and the Weierstrass $\wp$ function can be expressed in terms of the Jacobian elliptic function:

$$x(t) = e_3 + (e_2 - e_3)\mathrm{sn}^2\left(\sqrt{\frac{e_1 - e_3}{6}}t|m\right), \tag{11}$$

$$m = \frac{e_2 - e_3}{e_1 - e_3} = \frac{\sin\xi}{\sin(\xi + 60°)} \leq 1. \tag{12}$$

The period and the tune of the elliptic function are given by

$$T = 2\sqrt{6}\frac{K(m)}{\sqrt{e_1 - e_3}}, Q = \frac{2\pi}{T} = \frac{\pi[\sqrt{3}\sin(\xi + 60°)]^{1/2}}{\sqrt{6}K(m)}. \tag{13}$$

In the original accelerator coordinate system, the synchrotron tune becomes

$$Q_s = \nu_s Q = \nu_s \frac{\pi[\sqrt{3}\sin(\xi + 60°)]^{1/2}}{\sqrt{6}K(m)}. \tag{14}$$

Figure 2 shows $Q(E)$ as a function of energy. In particular, we note that the synchrotron tune decreases to zero very sharply near the separatrix, which causes parametric resonances induced by the time dependent perturbation to overlap one another and gives rise to chaos.

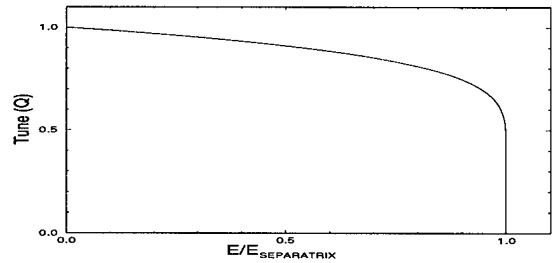

Figure 2: Tune Q as a function of E.

2.1 *Action-angle variables*

The action of a Hamiltonian torus is:

$$J = \frac{1}{8}\sqrt{\frac{2}{3}}(e_2 - e_3)^2(e_1 - e_3)^{1/2}F\left(\frac{2}{3}, -\frac{1}{2}; 3; m\right), \tag{15}$$

where $F\left(\frac{2}{3}, -\frac{1}{2}; 3; m\right)$ is a hypergeometric function given by

$$F\left(\frac{2}{3}, -\frac{1}{2}; 3; m\right) = 1 - \frac{1}{4}m - \frac{5}{128}m^2 - \frac{7}{512}m^3 - \ldots.$$

Using the generating function

$$F_2 \equiv \int_{e_3}^{x} p dx, \tag{16}$$

the angle variable is given by:

$$\psi = \frac{\partial F_2}{\partial J} = \sqrt{\frac{6}{e_1 - e_3}}QF(w|m) = Qt, \tag{17}$$

where Q is the synchrotron tune given by Eq. (13) and $F(w|m)$ is the incomplete elliptic integral of the first kind given by:

$$F(w|m) = \int_0^w \frac{dz}{\sqrt{1 - m\sin^2 z}},\ w = \arcsin\sqrt{\frac{x - e_3}{e_2 - e_3}}. \tag{18}$$

2.2 *The bucket area*

The bucket area is the area in phase space in which charged particles can be accelerated without loss. So the bigger the bucket area is, the more charged particles can be accelerated. The bucket area A in (x, p) is

$$A = 2\pi J_{sep} = \oint_{sep} p dx = \frac{6}{5}. \tag{19}$$

Thus the bucket area A_B in (ϕ, δ) is given by

$$A_B = \frac{6}{5}\left(\frac{|\eta_0|^{5/2}}{|\eta_1|^2}\right)\left(\frac{2\pi h\beta^2 E}{eV|\cos\phi_s|}\right)^{1/2}. \tag{20}$$

In contrast to the nominal synchrotron Hamiltonian, the bucket area of the QI Hamiltonian increases with *decreasing* rf voltage V and $|\cos\phi_s|$. Note also that the bucket area is proportional to $|\eta_0|^{5/2}/|\eta_1|^2$. For a lattice with a small η_0, a proper correction for η_1 becomes necessary in order to provide a stable phase space for the beam bunch.

3 DYNAMICS WITH RF PHASE MODULATION

3.1 *Without damping*

In the presence of rf phase modulation and without damping, the Hamiltonian is given by

$$H = \frac{p^2}{2} + \frac{x^2}{2} - \frac{x^3}{3} + \omega_m B x \cos \omega_m t, \quad (21)$$
$$= H_0 + \omega_m B x \cos \omega_m t, \quad (22)$$

where the effective modulation amplitude is

$$B = \frac{\eta_1 a}{\eta_0 \nu_s} \sim \frac{|\eta_1|}{|\eta_0|^{3/2}}, \quad (23)$$

$\omega_m = \nu_m / \nu_s$ is the normalized modulation tune, a and ν_m are the rf phase modulation amplitude and tune. Note that B is greatly enhanced for QI storage rings.

3.1.1 Expansion of phase space coordinates

x can be expressed as a function of (J, ψ) as follows:

$$x(t) = g_0(J) + \sum_{n=1}^{\infty} g_n(J) \cos(n\psi), \quad (24)$$

where

$$g_0 = e_3 + (e_1 - e_3) \frac{K(m) - E(m)}{K(m)},$$
$$g_n = (e_1 - e_3) \frac{2\pi^2}{K^2(m)} \frac{(-1)^n n q^n}{1 - q^{2n}},$$
$$q = e^{-\pi K'/K} = \frac{m}{16} + 8\left(\frac{m}{16}\right)^2 + 84\left(\frac{m}{16}\right)^3 + \ldots,$$
$$\psi = \frac{\pi}{2K(m)} \sqrt{\frac{e_1 - e_3}{6}} \nu_s \theta = Q \nu_s \theta = Q t, \quad (25)$$

where $K(m)$ and $E(m)$ are the complete elliptic integrals of the first and second kind and $K'(m) = K(1-m)$.

The expansion coefficients satisfy the sum rule:

$$\sum_{n=1}^{\infty} g_n^2(J) = 2 g_0 (1 - g_0). \quad (26)$$

Since $g_0 = 1$ on the separatrix, the strength of all harmonics must vanish on the separatrix.

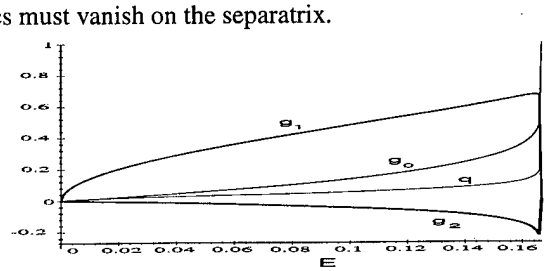

Figure 3: Plot of g_0, g_1, g_2 and the parameter q. g_1 is related with the 1:1 parametric resonance and g_2 with the 2:1 resonanace. As ispredicted by sum rule, all the strength functions go to zero at the separatrix.

3.1.2 Whisker map

Since $Q(E)$ drops sharply near the separatrix, all the parametric resonances $n : l$ satisfying $\omega_m \approx \frac{n}{l} Q(E_{n:l})$ overlap near the separatrix, thus forming a stochastic layer. The width of stochastic layer can be estimated using the whisker map.

The energy change rate due to the time-dependent perturbation is given by

$$\frac{dH_0}{dt} = \frac{\partial H_0}{\partial t} + [H_0, H] = -\omega_m B p \cos \omega_m t. \quad (27)$$

Using the separatrix orbit:

$$x_{sx}(t) = 1 - \frac{3}{\cosh t + 1}, \quad p_{sx}(t) = \frac{3 \sinh t}{(\cosh t + 1)^2}, \quad (28)$$

the energy change in one complete revolution is given by

$$\Delta E = -\omega_m B \int_{-\infty}^{\infty} p_{sx}(t - t_0) \cos \omega_m t dt$$
$$= \frac{6\pi \omega_m^3 B}{\sinh \pi \omega_m} \sin \phi, \quad (29)$$

where $\phi = \omega_m t_0$. The revolution period near the separatrix is given by

$$T(E) = 2\sqrt{\frac{6}{e_1 - e_3}} K(m) \approx \ln\left(\frac{144}{|\frac{1}{6} - E|}\right). \quad (30)$$

Thus the whisker map is given by

$$E_{n+1} = E_n + \frac{6\pi \omega_m^3 B}{\sinh \pi \omega_m} \sin \phi_n, \quad (31)$$
$$\phi_{n+1} = \phi_n + \omega_m \ln\left(\frac{144}{|\frac{1}{6} - E_{n+1}|}\right). \quad (32)$$

Related figure might be found (Fig. 3) in [9] which is omitted for limitation on space. The width of stochastic layer, estimated from the linearized whisker map, is

$$|E - \frac{1}{6}| \leq \frac{3\pi \omega_m^4 B}{2 \sinh \pi \omega_m}.$$

3.2 *With damping*

Including damping force, the equation of motion becomes:

$$x'' + A x' + x - x^2 = -\omega_m B \cos \omega_m t, \quad (33)$$

where

$$A = \frac{\lambda}{\nu_s} = \frac{U_0 J_E}{2\pi E_0 \nu_s} \sim \frac{1}{|\eta_0|^{1/2}}, \quad B = \frac{\eta_1 a}{\eta_0 \nu_s} \sim \frac{|\eta_1|}{|\eta_0|^{3/2}}. \quad (34)$$

It is worth pointing out that both the damping coefficient A and the phase modulation amplitude B are amplified as a result of scaling of the transformation into normalized phase space coordinates, because for QI storage rings, the value of $|\eta_0|$ is orders of magnitude smaller than the usual storage rings.

3.2.1 Melnikov integral method

The Melnikov integral method has often been applied to study the chaotic transition of many dynamical systems. If the stable and unstable orbits from a hyperbolic fixed point cross each other, the dynamical system becomes homoclinic, which is an indicator of chaotic motion. Calculating the distance between the two orbits perturbatively, the Melnikov integral becomes

$$D = -\int_{-\infty}^{\infty} \left[\omega_m B p_{sx}(t-t_0)\cos\omega_m t - A p_{sx}^2(t-t_0)\right] dt, \tag{35}$$

where x_{sx} and p_{sx} are the separatrix orbit. After integration, it becomes:

$$D = -\frac{6\pi\omega_m^3 B \sin\omega_m t_0}{\sinh \pi\omega_m} - \frac{6A}{5}, \tag{36}$$

and the condition for global chaos is

$$B_{cr} = \frac{A}{5\pi}\frac{\sinh\pi\omega_m}{\omega_m^3}. \tag{37}$$

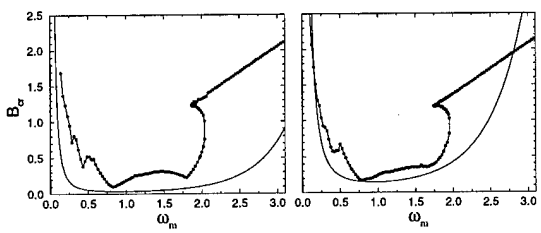

Figure 4: B_{cr} for $A = 0.05$ (on the left) and for $A = 0.2$. Solid line is for Melnikov integral method and solid circle for numerical simulation.

The Melnikov integral method provides only a rough estimation for low modulation frequency $\omega_m \leq 2$. For high modulation frequency, it overestimates the stable region of parameter space. In short, the Melnikov integral method is a measure of rough estimation only for low modulation frequency.

3.2.2 Attractor solution for 1:1 prametric resonance

The attractor solution for the 1:1 parametric resonance can be obtained by harmonic linearization method. Let the ansatz be :

$$x = X_0 + X_1\cos(\omega_m t + \xi_1), \tag{38}$$

then the following relations are obtained:

$$\omega_m^2 B^2 = A^2\omega_m^2 X_1^2 + \left(\omega_m^2 - \sqrt{1-2X_1^2}\right)^2 X_1^2, \tag{39}$$

$$\tan\xi_1 = \frac{-A\omega_m}{\omega_m^2 - \sqrt{1-2X_1^2}}, \tag{40}$$

$$X_0 = \frac{1}{2}\left(1-\sqrt{1-2X_1^2}\right). \tag{41}$$

It should be noted that $X_1 = \frac{1}{\sqrt{2}}$ represents the maximum oscillation amplitude for which this dynamical system is stable. Setting the maximum tolerable modulation amplitude for the 1:1 parametric resonance is given by

$$B_{cr,1:1} = \frac{1}{\sqrt{2}}\sqrt{A^2+\omega_m^2}. \tag{42}$$

This is almost a linear funtion of ω_m for large ω_m.

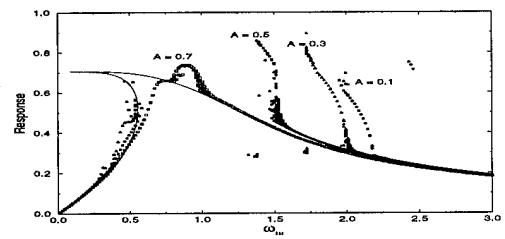

Figure 5: X_1 obtained numerically for modulation amplitude $B = 0.5$ with damping parameter $A = 0.1, 0.3, 0.5$, and 0.7 respectively. Solid lines correspond to the solution of Eq. (39) for $A = 0.7$ and $B = 0.5$. Two characteristic features are (1) the threshold tune of the 2:1 parametric resonance decreases with increasing damping parameter A, and (2) the appearance of very strong stop band around $\omega_m \approx 1$ for the 1:1 resonance.

3.2.3 Attractor solution for 2:1 parametric resonance

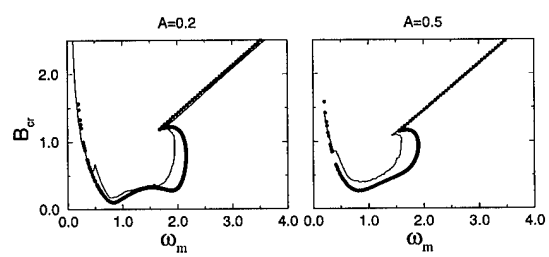

Figure 6: Plot of critical modulation amplitude B_{cr} for $A = 0.2$ (left) and $A = 0.5$ (right). Solid circles of bootshape are obtained from 1:1 Eq. (39) and 2:1 Eq. (46) resonances and solid circles of straight line from Eq. (42). Thin solid line from numerical simulation.

The periodic attractor solution associated with the 2:1 parametric resonance can be obtained by using the ansatz:

$$x(t) = X_0 + X_1\cos(\omega_m t + \xi_1) + y(t). \tag{43}$$

The equation of motion for $y(t)$ is then given by

$$y'' + Ay' + [1 - 2X_0 - 2X_1\cos(\omega_m t + \xi_1)]\, y \approx 0. \tag{44}$$

Let the solution of this damped Mathieu equation be

$$y(t) = X_{1/2}(s)\cos\left(\frac{\omega_m}{2}t + \xi_{1/2}\right). \tag{45}$$

The condition for Mathieu instability can also be obtained by assuming $X_{1/2} \sim e^{st}$ with $s \geq 0$, i.e.

$$A^2\frac{\omega_m^2}{4} + \left(\frac{\omega_m^2}{4} - \sqrt{1-2X_1^2}\right)^2 \leq X_1^2. \tag{46}$$

The boot-shaped curve (in solid circle) describes the onset of period-two bifurcation (Mathieu instability) obtained from Eq. (39) and setting equality to Eq. (46). The "straight line" defining the maximum tolerable modulation amplitude B_{cr} is in well agreement with the curve of Eq. (42). In conclusion, the stability of QI storage ring is determined mainly by the 1:1 and 2:1 parametric resonances. And it should be noted that the "cusp" structure is reproduced from the theory of these two resonances.

3.2.4 Chaos through period-two bifurcation

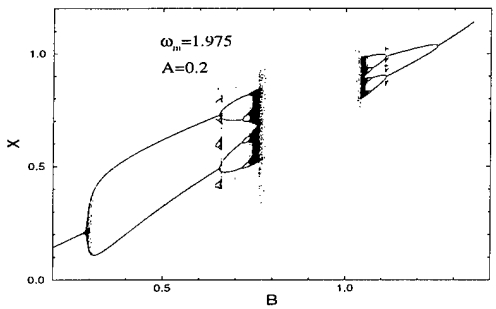

Figure 7: The attractors as a function of modulation amplitude B at the modulation frequency $\omega_m = 1.975$ and the damping coefficient $A = 0.2$.

The upper "mirror" structure corresponds to the "cusp" structure in Fig. 4. This clearly shows chaos through a series of period-two bifurcation and this phenomenon occurs only for $\omega_m \leq 2$ due to 2:1 parametric resonance. Systematic patterns of bifurcation are observed. Clearly period-two bifurcation can be attributed to 2:1 parametric resonance and occurs in the vicinity of this particular parametric resonance, i.e., $\omega_m \leq 2 + \epsilon$ where ϵ is a small positive number.

4 DYNAMICS WITH RF VOLTAGE MODULATION

In the presence of rf voltage modulation and damping force, the equations of motion in normalized phase space are

$$p' = x - x^2, \quad x' = -p - bp\cos\omega_v t - Ax, \tag{47}$$

where

$$\frac{\Delta V}{V} = b\cos\omega_v t. \tag{48}$$

The Melnokov integral method was applied again to study the chaotic transition, which is given by

$$\begin{aligned} D &= \int_{-\infty}^{\infty} \left(x_{sx}(t) - x_{sx}^2(t)\right)\left[bp_{sx}(t)\cos\omega_v(t+t_0)\right. \\ &+ \left. Ap_{sx}(t)\right]dt, \qquad (49) \\ &= \frac{3\pi\sin\omega_v t_0}{4\sinh\pi\omega_v} b\omega_v^2\left(\omega_v^2+1\right)\left(1-\omega_v^2\right) + \frac{6A}{5}, \qquad (50) \end{aligned}$$

where x_{sx} and p_{sx} are the separatrix orbit. The condition for a homoclinic structure near the separatrix is given by

$$b_{cr} = \frac{2A\sinh\pi\omega_v}{\pi\omega_v^2\left(\omega_v^2+1\right)\left|\omega_v^2-1\right|}. \tag{51}$$

It should be pointed out that the dynamical system is infinitely stable for the modulation frequency of $\omega_v \approx 1$.

Numerical simulation revealed that QI system is very stable against voltage modulation. Due to limited space, interested readers are asked to refer to [9] for detailed discussion and figure (Fig. 12). Like the phase modulation, the Melnikov integral method also gives only a rough idea of stable region especially for low modulation frequency ω_v but generally overestimates the stability region for high frequency region.

5 CONCLUSION

We have transformed the synchrotron equation of motion in the QI regime into a universal Weierstrass equation, where the solution is expressed in Jacobian elliptic function. The phase space coordinates are expanded in action-angle variables. The strength function vanishes at the center of bucket and at the separatrix. Higher harmonic parametric resonances become more important near the separatrix. The effective damping coefficient A for the QI Hamiltonian is proportional to $|\eta_0|^{-1/2}$. And the effective modulation amplitude B is proportional to $|\eta_1|/|\eta_0|^{3/2}$ (it is particularly enhanced). For rf phase modulation, the Melnikov integral method is a measure of rough estimation of the transition to global chaos only for $\omega_m \leq 2$. The role of parametric resonances in transition to chaos was identified for rf phase modulation. For $\omega_m \geq 2$, the stability is mainly determined by the 1:1 parametric resonance. For $\omega_m \leq 2$, the 2:1 parametric resonance on top of the 1:1 resonance makes the SFP of the 1:1 resonance unstable and bifurcate (Mathieu instability). A sequence of period-two bifurcation enroute to global chaos is a characteristic for $\omega_m \leq 2$. The effects of rf voltage modulation of QI dynamical system turns out to be insensitive.

6 REFERENCES

[1] C. Pelligrini and D. Robin, Nucl. Inst. Methods, A **301**, 27 (1991).

[2] D. Robin, E. Forest, C. Pelligrini, A. Amiry Phys. Rev. E **48**, 2149 (1993); H. Bruck *et al.*, IEEE Trans. on Nucl. Science NS**20**, 822 (1973).

[3] L. Liu *et al.*, Nucl. Inst. and Methods **A329**, 9 (1993).

[4] H. Hama, S. Takano and B. Isoyama, Nucl Inst. and Methods **A329**, 29 (1993). S. Takano, H. Hama and G. Isoyama, Japan J. of Appl. Phys. **32**, 1285 (1993).

[5] A. Nadji *et al.*, Proceedings of the 4th European particle accelerator conference, p. 128 (1994).

[6] D. Robin, H. Hama, and A. Nadji, Lawrence Berkeley Technote LBL-37758 (1995).

[7] D. Robin *et al.*, SLAC-PUB-95-7015 (1995).

[8] A. Riabko *et al*, Phys. Rev. E **54**, 815 (1996).

[9] D. Jeon *et al*, Phys. Rev. E **54**, 4192 (1996).

[10] M. Bai *et al*, Phys. Rev. E **55**, 3493 (1997).

LATTICE DESIGN FOR A HIGH-POWER INFRARED FEL

D. R. Douglas, Thomas Jefferson National Accelerator Facility,
12000 Jefferson Avenue, Newport News, VA 23606-1909 USA

Abstract

A 1 kW infrared FEL for industrial, defense, and related scientific applications, is being built at Jefferson Lab. It will be driven by a compact energy-recovering CW superconducting radio-frequency (SRF) linear accelerator. Stringent phase space requirements at the wiggler, low beam energy, and high beam current subject the design to numerous constraints. This report addresses these issues and presents a design solution for an accelerator transport lattice meeting the requirements imposed by physical phenomena and operational necessities.

1 PROJECT OVERVIEW

A high-power FEL is under construction at Jefferson Lab. Driven by a compact, SRF-based energy-recovering CW linac (parameters of which are in Table 1), it will produce a 1 kW, 3–6.6 μm photon beam.

Table 1: Driver Accelerator Parameter List

Injection kinetic energy	10 MeV
Beam kinetic energy at wiggler	42 MeV
Beam kinetic energy at dump	10 MeV
Beam current	5 mA
Normalized rms design emittance	<13 mm-mrad
FEL extraction efficiency	0.5 %
$\delta p/p$, rms before wiggler:	0.5 %
full after wiggler:	5 %

The driver accelerator comprises a 10 MeV injector, a linac based on a single Jefferson Lab cryomodule containing eight SRF cavities, a wiggler and optical cavity, and an energy-recovery recirculation arc (to limit cost and technical risk by reducing RF power requirements in the linac). Construction ends in October 1997; operations follow immediately to produce first light by February 1998. High-power end-user service commences in summer 1998. Funding for the project is provided by the Office of Naval Research, the DOE, the Commonwealth of Virginia, and several industrial members of the Laser Processing Consortium. Further project and design information is available elsewhere in these proceedings [1] and on the World Wide Web as a link from http://www.jlab.org/.

2 DESIGN REQUIREMENTS

2.1 Fundamental Requirements

The driver transport system must meet two fundamental requirements. First, it must deliver to the FEL an electron beam with a properly configured phase space. Second, it must transport the "spent" beam from the wiggler back through the accelerating structure for energy recovery.

The first requirement is imposed by the FEL system [2], which is based on a cavity resonator with low (~1/2%) extraction efficiency and modest instantaneous power output. High average output power is achieved by using a high repetition rate; this avoids many of the difficulties of low-rep-rate, high-peak-power systems. The FEL is optimized to use a 42 MeV, 5 mA beam of 135 pC bunches delivered at 37.425 MHz; a beam with normalized rms emittance below 13 mm-mrad and $(\delta p/p)_{rms}$~0.5% is required. Electron beam/optical mode overlap requirements demand betatron matching into the wiggler; the peak current needed for the design FEL gain requires longitudinal phase space management by bunch length compression to an rms length of ~1 psec at the wiggler.

The second requirement embodies the use of energy recovery to reduce RF power demands, cost, and radiation effects by using the recirculated beam to drive the RF cavities. As the full momentum spread after the wiggler will be 5%, this creates a need for large transport system acceptance.

2.2 Physical Phenomena/System Constraints

These requirements couple to many physical phenomena and constraints. The system design must be simple and economical to meet cost and schedule constraints. Low instantaneous FEL power and high repetition rate suggest use of a CW driver; the project time scale leads to use of standard Jefferson Lab SRF components. Transverse matching and longitudinal phase space management requirements at the wiggler imply quadrupole telescopes and a bunch length compressor are needed. High current and low energy suggest collective effects may be important. To avoid space-charge-driven beam quality degradation, a moderately high injection energy is needed [3]. Beam breakup (BBU) and other impedance-driven instabilities must be avoided [4]. Coherent synchrotron radiation (CSR) must be managed to preserve beam emittance [5]. RF stability must be assured, particularly in transient regimes such as FEL turn-on and initiation of energy recovery [6].

The energy-recovery transport must have large acceptance to limit beam losses from a 5% momentum spread beam. Control of beam envelopes and lattice aberrations must be provided over a large volume of phase space. Variable momentum compaction is needed to allow energy compression and optimization of RF stability during energy recovery. This reduces the momentum spread, and enhances the stability, of the 10 MeV energy-recovered beam during transport to the dump.

Project constraints and physical effects eliminate most candidate system configurations. Jefferson Lab cryomod-

0-7803-4376-X/98 /$10.00 © 1998 IEEE

ules cannot simultaneously accelerate (decelerate) two beams moving in opposite directions due to constraints on RF phases in adjacent cavities. Use of existing hardware designs (to meet cost and schedule goals) therefore excludes any geometry accelerating and energy recovering with anti-parallel beams. Concepts using multiple cryomodules or custom RF components are eliminated by cost.

FEL placement in the system is dictated by the relative importance of various physical phenomena. Partial or complete recirculation before the wiggler avoids transport of the large momentum spread "spent" beam, simplifying energy recovery but leaving CSR- and space-charge-driven emittance growth as a potential problem. We therefore locate the FEL immediately downstream of the linac. This choice reduces the impact of CSR and space charge, at a possible cost of increased complexity in the energy recovery transport. It also allows for "straight-ahead" operation of the machine (without energy recovery) to drive the FEL at low powers during initial operation.

3 DESCRIPTION OF SOLUTION

3.1 Detailed System Design Specifications

The design concept (Figure 1) comprises a 10 MeV injector, a single eight-cavity Jefferson Lab cryomodule accelerating to 42 MeV, transport to the wiggler, and energy-recovery transport from wiggler through module to a beam dump. Specifications exist for each of these segments. The module-to-wiggler transport must provide transverse matching and bunch length compression. The energy-recovery transport must have large momentum acceptance (>5%) and variable momentum compaction (similar in magnitude to that of the module-to-wiggler compression).

Other specifications are global. Beam spots and envelopes should be modest throughout the system ($\beta < 25$–30 m). Components must be simple, robust, low cost, and, if possible, in the Jefferson Lab inventory. As the beam energy is low, dipoles will bend through large angles and focus strongly; the effects of dipole edges, gaps, and field rolloff must be incorporated in design computations. Finally, the system should avoid aggravating collective effects such as CSR, BBU, wake fields, or space charge.

3.2 Transport to the Wiggler

A four-quadrupole telescope in the injector provides betatron matching into the driver linac; an achromatic line transports beam from the telescope to the linac axis. The linac comprises a single high-gradient cryomodule, and accelerates the beam by 32 MeV. RF focusing controls the beam envelopes; the beam will be accelerated 12.5° off crest, so as to slew the longitudinal phase space in preparation for bunch length compression before the wiggler.

After the cryomodule, a quadrupole telescope (two triplets) betatron matches the beam to the wiggler. An achromatic four-dipole chicane between the triplets separates optical cavity and electron beam components while compressing the bunch length. The chicane geometry is limited by the allowable momentum compaction. Larger chicanes provide more space, but lead to higher momentum compactions and more jitter in time of flight; to maintain FEL pulse/electron beam synchronism with the available RF stability, the momentum compaction must be modest ($|M_{56}| < 0.3$ m).

Studies indicate space charge is not important in full-energy segments of the system [7]; single-particle design tools can be used for the 42 MeV transport. Space charge does, however, affect motion in the injector and the module. Injection matching and the beam phase space just after the module thus depend on current. The machine will use a fixed single-bunch charge (60 pC for first light, 135 pC for full power), and vary the average current by altering the repetition rate. Wake-field effects will be small, so space charge effects will not be dependent on repetition rate, but only on the bunch charge. A separate solution for the injector-to-module and module-to-wiggler matches will therefore be used for each bunch-charge state.

3.3 Energy-Recovery Transport

After the wiggler, the electron beam (with a full momentum spread of ~5%) is transported through a recirculation arc to the cryomodule for energy recovery. A second six-quadrupole telescope is used to betatron match into the recirculation arc. This avoids beam envelope mismatch, large spot sizes, aggravated optical aberrations, error sensitivities, and potential beam loss. As in the transport to the wiggler, a dipole chicane embedded in the telescope moves the electron beam around the optical cavity; this chicane lengthens bunches, reducing peak currents and alleviating potential space charge and CSR effects.

The transport arc is an isochronous, large-momentum-acceptance beamline based on the MIT/Bates Linear Accelerator Center recirculator [8]. Dipole parameters

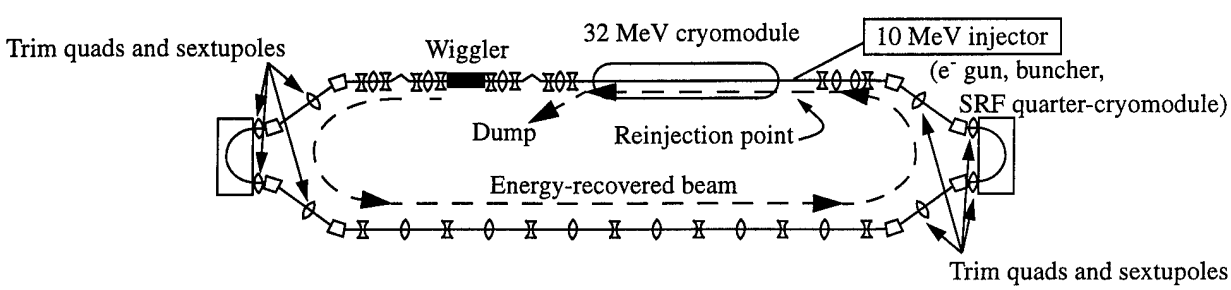

Figure 1: Design concept for Jefferson Lab 1 kW IR FEL driver accelerator.

(bend and edge angles) and drift lengths are set to provide M_{56}=0 from wiggler to reinjection point, and, across each end loop, achromatic, betatron stable motion in x (with a tune of 5/4) and imaging transport (M_y=-I) in y. The end loops are joined by six 90° FODO cells. $M_{x,y}$=-I over the backleg, giving M_x=I and M_y=-I and, with reflective symmetry about the center of the backleg, suppression of aberrations over the full arc. The symmetry giving this suppression can be imposed due to the choice of wiggler placement immediately after the linac. Each end loop has four trim quads for dispersion and compaction control; M_{56} can be varied over ±0.25 m. Each also has four sextupoles to suppress aberrations. T_{166}, T_{266}, and T_{566} are set to zero; others are controlled by the choice of system parameters. The system path length is nominally 501.5 RF wavelengths; this can be varied by ±1/2 wavelength by trim steering in the 180° bends.

After the beam is returned to the linac axis, a four-quad telescope matches it into the module for energy recovery. This is not strictly necessary, as RF focusing will provide adequate beam envelope control during energy recovery. It is introduced to simplify installation of upgrades, which, due to reduced RF focusing at higher energy, require extra matching.

Beam viewers based on optical transition radiation (OTRs) and electromagnetic beam position monitors (BPMs) provide diagnostic information throughout the machine [9]. A diagnostic is placed approximately every quarter betatron wavelength. Trim dipoles are placed adjacent to the diagnostics for orbit correction and diagnostic steering. The wiggler-to-arc transport and FODO backleg are instrumented to support studies investigating CSR effects [10]. Bunch arrival time/beam phase monitors are placed before and after the cryomodule for measurement and correction of transport system path lengths and momentum compactions.

The beam path footprint lies within a rectangle 5.75 m by 48 m. Table 2 provides a component summary for the driver transport system from back end of injector quarter-cryomodule to reinjection point.

Table 2: Transport System Components

Line	Bends	Quads	6-poles	H/V correctors	BPM/OTR
Injection line	3	4	0	4/4	2/3
Match to wiggler	7	6	0	3/3	3/6
Match to recirc.	4	6	0	3/3	3/3
Recirculation	10	21	8	16/11	19/8
Reinjection match	2	4	0	2/2	2/0

4 SYSTEM PERFORMANCE

4.1 Linear Optics

Figure 2 displays beam envelopes and dispersions from injection through the cryomodule during energy recovery. They are everywhere well behaved, implying that error sensitivities will be low and that apertures available in standard Jefferson Lab cavities (70 mm) and quadrupoles (54 mm) will be adequate to transport beams of the design emittance (13 mm-mrad, normalized) with low losses. BBU threshold estimates based on lattices of this character indicate that such instabilities will be avoided [11].

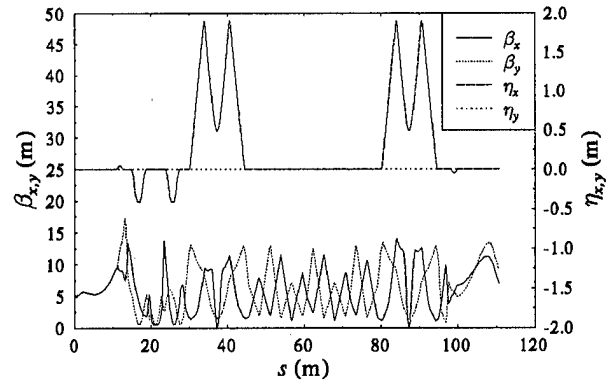

Figure 2: Driver beam envelopes and dispersions.

4.2 Aberration Analysis

Second-order aberrations are modest; good behavior is thus expected. The T_{336}, T_{346}, T_{436}, and T_{446} chromatic aberrations for transport from wiggler to reinjection point are of concern. These couple to steering errors at the wiggler to produce dispersive effects at reinjection leading to spot growth. Effort was made to limit their values to order 100 (m/(m-rad) for T_{336}, m/rad^2 for T_{346},...) or smaller; this, coupled with the stringent steering (~30 μm/30 μrad) to give electron beam/optical mode overlap required for FEL operation [12], will limit spot growth at reinjection to order 1 mm or less.

Higher-order aberration analysis was performed using various numerical tools. To certify the calculations, the principal design tool, DIMAD [13], was compared to the higher-order model TLIE [14]. Simulations showed the two codes to be generally consistent [15]. Nonlinear effects beyond second order were found to be significant and were modeled in qualitatively similar fashion by both programs.

4.3 Chromatic Performance

Chromatic performance has been investigated in detail to ensure large momentum acceptance. Momentum scans of lattice and beam properties have been performed for the module-to-wiggler and wiggler-to-module transports. System behavior is adequate over a 6% momentum range. We observe a significant variation of phase advance with momentum. This is not a serious problem in this single-pass system, but can give rise to phase space distortions in certain cases, one of which will be described during a following discussion of energy recovery. Typical system performance is shown in Figure 3, which displays a horizontal beam envelope momentum scan from wiggler to reinjection point. Note that no untoward chromatic variations are observed. Worst-case variations yield peak beam envelopes of ~35 m, a factor three times the nominal peak of order 13 m and well within the system acceptance.

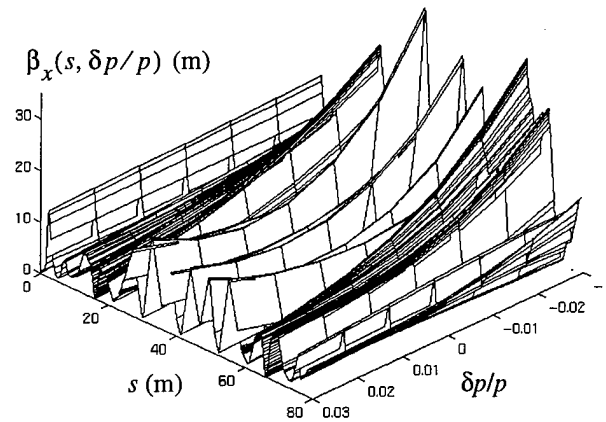

Figure 3: Momentum scan of horizontal beam envelope from wiggler to reinjection point.

4.4 Geometric Performance

Geometric aberrations have also been studied in detail. Ray-tracing simulations at a normalized emittance of 130 mm-mrad (10 times the design rms value) show only modest phase space distortion ($\Delta\varepsilon/\varepsilon \leq 0.3$) over the full momentum acceptance of the system. Figure 4 presents an image at the reinjection point of 130 mm-mrad transverse phase spaces launched at the wiggler with various momentum offsets between -3% and +3%; little phase space distortion and only modest beam envelope variations are visible.

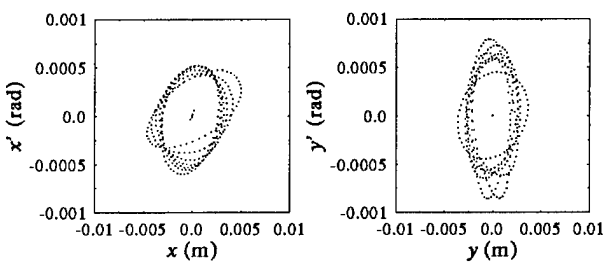

Figure 4: Geometric aberration analysis ray-trace results.

These analyses have similarly shown the system exhibits little betatron phase variation with amplitude. We therefore conclude that the geometric performance of this beamline is acceptable to at least 10 times the nominal emittance. This result holds for simulations using either equal or unequal horizontal and vertical initial emittance, implying the system exhibits little inherent horizontal/vertical coupling as well.

4.5 Simulation of Energy Recovery

Energy recovery has been simulated (without space charge) to verify lattice performance. An initial 6-sigma/6-dimensional phase space was gaussian-loaded at the center of the wiggler with 10000 particles using design beam envelopes, emittances, and a 1% rms momentum spread. This population was ray-traced to 10 MeV after the cryomodule. Figure 5 shows the resulting phase spaces; the upper plots show the phase space for ideal transport; the lower show the same data with a 1 mm initial vertical offset of the beam. We observe growth of the vertical phase space due to the aforementioned T_{336} aberration/chromatic variation of the vertical phase advance with momentum. We note that FEL operation requires steering to an orbit error of ~30 μm to ensure overlap of the electron beam and optical mode [16]; under these circumstances, the resulting spot size growth will be negligible.

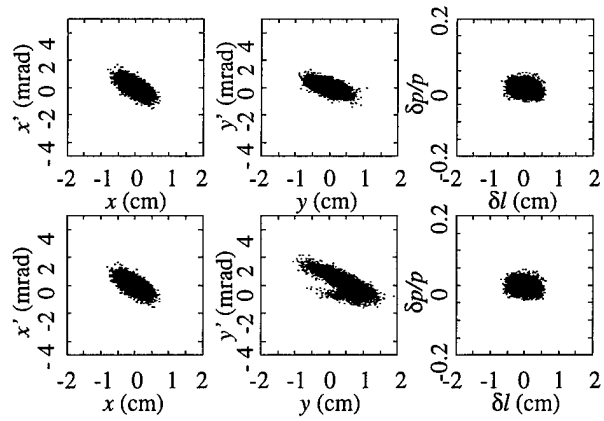

Figure 5: Ray-trace simulation of energy recovery. Upper row: ideal transport; lower row: 1 mm injection error in y.

5 ERROR EFFECTS

Error effects have been studied to develop component specifications and evaluate machine sensitivities. An aggressive project schedule has led us to explore error effects analytically and generate an "error budget", which was subsequently to be verified numerically. During energy recovery, the beam can occupy 1/3 to 1/2 of the machine physical aperture; we therefore require that beam size growth due to all known error sources be limited to ~10% of the nominal spot size. Analysis of the effect of any single error source was used to set tolerances that ensure beam spot growth is limited to the 0.1–1% range. A sum in quadrature over all errors will then be limited as desired. Simulations are being used to certify that this budget is sufficient (though perhaps more conservative than necessary) to meet machine performance targets. Error tolerances characteristic of the recirculation transport are given in Table 3.

Table 3: Typical Error Tolerances for System Components

Error		Dipole	Quad	Comments
Alignment		1 mm	0.5 mm	rms transverse
Excitation	DC	10^{-3}	10^{-3}	DC rms field error
	AC	10^{-5}	10^{-4}	rms AC "ripple"
Field quality	$\Delta B/B$	10^{-4}		variation over aperture
	$\Delta B/B$		10^{-3}	error at half aperture
	K_1	0.27 ± 0.05		end-field rolloff integral

We find that the system response to errors is generally similar to, or weaker than, that of the CEBAF linac, confirming the suitability of using standard Jefferson Lab components. The transport dipoles are an exception to this rule. In these magnets, the bend angles, dispersions, and

beam size are large; good field control and quality are needed. Effort was expended to ensure that dipole fields are uniform throughout the magnet working aperture, end-fields are well characterized, and power supply regulation is adequate to avoid ripple-driven beam quality degradation. All main dipoles will be excited in series to suppress ripple effects. A program of magnet prototyping and measurement has led to designs that provide stray field control and well-defined end-field rolloff. Information from this prototype effort [17] has been incorporated into the transport system optical design. Optics designs were done using the TRANSPORT second-order fringe-field model [18] with $K_1 = 0.27$ (based on field maps of a prototype) and K_2 neglected.

Most analytically derived tolerances were confirmed numerically. Simulations indicate a baseline array of BPMs, OTRs and steerers placed roughly every quarter wavelength in betatron phase will allow machine operation in the presence of the anticipated errors and avoid beam quality degradation. Figure 6 displays orbits from wiggler to reinjection point before and after correction for on- and off-momentum transport of ten randomly selected error sets consistent with the error budget.

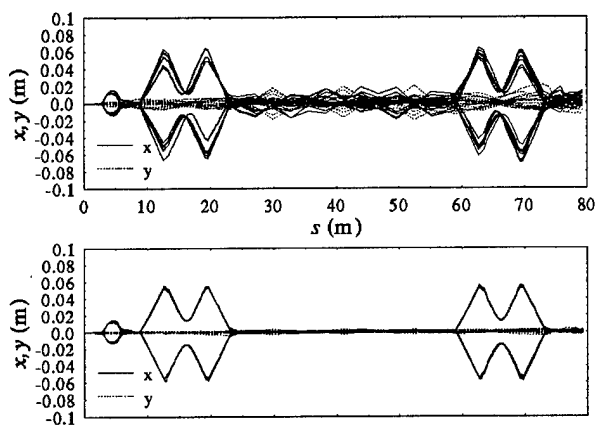

Figure 6: Orbits with errors before (top) and after (bottom) correction on and off momentum (at ±3 %).

For each "random seed", the simulations examined correction of the central orbit and all performance criteria discussed in Section 4, including chromatic behavior of the orbit (off-momentum orbits, dispersions, and momentum compactions) and beam behavior about the orbit (beam and lattice properties), large amplitude behavior (geometric aberrations and phase space distortion), and horizontal/vertical coupling. All simulations indicate that machine performance is acceptable for errors within the error budget. Studies are ongoing and will be extended to include field inhomogeneities in magnets and cavities, and to model space charge effects through the full acceleration and energy recovery cycle. The focus will then shift to commissioning and operational processes such as alternate orbit-correction algorithms, dispersion/momentum compaction adjustment, lattice/beam phase space matching, error resolution, and correction of lattice properties

6 ACKNOWLEDGMENTS

The work reported here reflects the effort of all members of the Jefferson Lab FEL Team and Accelerator Design Department. I would like to thank Dr. Fred Dylla, Dr. Court Bohn, and Dr. Joe Bisognano of Jefferson Lab for their support and guidance, and Dr. Jay Flanz of the Northeast Proton Therapy Center at Massachusetts General Hospital for considerable design assistance. This work was supported by U.S. DOE Contract DE-AC05-84ER40150 and the Office of Naval Research.

7 REFERENCES

[1] C. L. Bohn on behalf of the Jefferson Lab FEL team., "Recirculating Accelerator Driver for a High-Power Free-Electron Laser: A Design Overview," these proceedings.

[2] S. Benson and the Jefferson Lab FEL Team, "An Overview of the Jefferson Lab IR FEL Program," presented at the 18th International Free Electron Laser Conference, Rome, August 1996.

[3] H. Liu, J. Benesch, S. Benson, J. Bisognano, D. Douglas, G. Neil, D. Neuffer, C. Sinclair, and B. Yunn, "Modeling of Space Charge Dominated Performance of the CEBAF FEL Injector," *Nucl. Instrum. and Methods A* 358 (1995) 475–478.

[4] B. Yunn, unpublished.

[5] R. Li, C. Bohn, and J. Bisognano, "Shielding Effect on the Transient Self-Interaction of a Bunch Entering a Bend," these proceedings.

[6] L. Merminga, J. J. Bisognano, and J. R. Delayen, "Energy Stability in Recirculating, Energy Recovering Linacs in the Presence of an FEL," in the Proceedings of EPAC 96; L. Merminga, G. A. Krafft, D. X. Wang, and B. C. Yunn, "Longitudinal Beam Dynamics with Space Charge in an FEL Driver Accelerator," these proceedings.

[7] H. Liu, private communication; B. Yunn, unpublished.

[8] J. B. Flanz and C. P. Sargent, "Operation of an Isochronous Beam Recirculation System," *Nucl. Instrum. and Methods A* 241 (1985) 325–333.

[9] G. A. Krafft, K. Jordan, D. Kehne, J.-C. Denard, P. Piot, S. Benson, E. Feldl, J. Song, and R. Ursic, "Electron Beam Diagnostics for Jefferson Lab's High-Power Free Electron Laser," these proceedings.

[10] C. L. Bohn *et al.*, *op. cit.*

[11] B. Yunn, unpublished.

[12] S. Benson and G. Neil, private communication.

[13] R. V. Servranckx, K. L. Brown, L. Schachinger, and D. Douglas, "Users Guide to the Program DIMAD," SLAC Report 285 UC-28 (A), May 1985.

[14] J. van Zeijts and F. Neri, "The Arbitrary Order Design Code TLIE 1.0," in *Proceedings of the Workshop on Nonlinear Effects in Accelerators*, (IOP Publishing, 1993).

[15] R. Li, unpublished.

[16] S. Benson and G. Neil, *op. cit.*

[17] J. Karn, G. Biallas, A. Guerra, and L. Harwood, "Magnetic Measurements of the Prototype Dipole for the IR-FEL at the Thomas Jefferson National Accelerator Facility," these proceedings.

[18] K. Brown, "A First- and Second-Order Matrix Theory for the Design of Beam Transport Systems and Charged Particle Spectrometers," SLAC Report 75, June 1982.

OVERVIEW OF THE LHC DYNAMIC APERTURE STUDIES

M. Böge, A. Faus-Golfe, J. Gareyte, H. Grote, J.-P. Koutchouk, J. Miles,
Q. Qing, T. Risselada, F. Schmidt, S. Weisz,
CERN, Geneva, Switzerland

Abstract

The dynamic aperture (D.A.) of the LHC is estimated by tracking a thin-lens model of the lattice over a real machine time of 9 seconds. This raw result is then processed to predict the D.A. over longer times and realistic conditions. We discuss the reliability and limits of the method, the phenomena limiting the D.A. and scaling laws used for fast estimates. The long-term dynamic aperture at injection is close to the requirements, with prospects of further improvements.

1 INTRODUCTION

In the LHC, the accumulation of the beam will take 7 minutes. Prior to this operation, the machine optics will have to be tuned. Experience from other colliders indicates that this step may take from 30 minutes to several hours, depending on the previous history of the magnets. The luminosity lifetime at peak energy is expected to be about 10 hours. Consequently the lifetime of a single beam must be significantly larger than one and ten hours respectively to allow efficient operation. Its estimation is however out of reach of present computers. Instead we resort to computing the dynamic aperture (D.A.) which is the largest stable transverse amplitude in a connected domain for a sample of 'typical' particles circulating in a simplified model of the accelerator. Even this computation is very demanding and is limited in practice to about 10 seconds of real LHC time. Using the results of additional studies, especially measurements of the D.A. in the SPS and HERA, the simulation results are extrapolated to realistic times and accelerator characteristics.

2 MODEL OF THE LHC MACHINE

The D.A. of LHC at injection is dominated by systematic multipoles in the superconducting dipoles. The sextupole b_3 and decapole b_5 are corrected by small coils at the end of each dipole. After correction with an accuracy better than 10%, these multipoles do not limit the D.A. The other allowed systematic multipoles are weak by design and contribute little to the D.A. The non-allowed multipoles, in particular a_4, b_4, a_3 may have significantly large bias inside a production line and limit seriously the D.A. For the time being we assume eight independent production lines, each one being used to equip one arc. The average values of the multipoles are drawn from a Gaussian distribution cut at 1.5σ. This severe cut reflects the capability of measuring and correcting trends during the fabrication.

At injection, the multipole errors considered are those measured about 15 minutes after the end of magnet cycling. The consequences of the decay of the persistent currents and their spread from magnet to magnet, the ramp-induced multipoles related to the inter-strand resistance of the superconducting cable and the ramping rate have not been taken into account so far. Our scaling laws indicate that they should not degrade the D.A significantly even though they produce an increase of linear coupling.

The model of the machine includes a realistic description of the misalignment errors and linear imperfections. The closed orbit and linear coupling are corrected with the methods available in control rooms to 1 mm rms and a residual closest tune approach of less than 0.001. The fractional betatron tunes are chosen to be .28/.31. Tune scans have yet to be performed for the new optics and error table.

3 METHODS FOR CALCULATING THE DYNAMIC APERTURE

The evaluation of the D.A. is limited mainly by the computing resources and our ability to analyse the large quantity of data generated by tracking codes. Most of the choices about the methods result from these limitations.

Each real magnet is represented by one thin lens, providing symplecticity and fast integration. In collision, a finer model of the low-β triplet quadrupoles (localization of the imperfections and edges properly represented) is yet to be implemented.

Sixty different imperfect machines are tracked to estimate the lower bound of the stable motion (D.A.) with a confidence level of 95%. A coarse tracking is done first to localize the D.A., followed by fine mesh tracking just below the coarse D.A. estimate.

To ensure a realistic sampling of initial conditions, 90 initial x_i and y_i are chosen within a range of 3σ, with $x_i/y_i = 1$ for equal emittances and β-functions in the two planes. The momentum deviation is initialized to 1.7 σ_e. Studies [1] showed an insignificant loss of D.A. when going closer to the bunch edge. The three corresponding phases are initialized to zero as they naturally sample their phase space from turn to turn. Each initial condition is in fact a pair of two near-by particles ('Lyapunov pairs') whose distance is used to detect the onset of a chaotic motion. In the course of tracking, the variation of the amplitude ratio x_i/y_i is usually small. A coarser tracking is occasionally done for five different amplitude ratios and used to estimate the loss of D.A. with respect to $x_i/y_i = 1$. A computer cluster made of 10 powerful workstations (the NAP Project [2]) is dedicated to tracking with either Sixtrack [3] or MAD [4]. The estimate of the 'conventional' D.A. as

0-7803-4376-X/98 /$10.00 © 1998 IEEE

defined above, takes less than 2 days of computation.

Certain machines are tracked up to 10^6 or 10^7 turns (10 minutes of LHC time). The survival plots are fitted to a conjecture law to extrapolate to longer times. The onset of chaos is used as a qualitative indication and may represent a pessimistic estimate of the D.A. The effect of the ripple of the magnetic fields was studied for 60 machines [5] and the result is included in the interpretation of the D.A. provided by tracking.

For a fast evaluation of the D.A., the concept of D.A. per multipole d_n turns out to be surprisingly effective. The D.A. is tracked for a relevant value of one multipole n one at a time [6]. For a α-times larger value of multipole n, the equation of motion remains invariant if the amplitudes (and the D.A.) are divided by $\alpha^{1/(n-2)}$. The D.A. for a set of multipoles is obtained by combining the d_n's following the conjecture in [7]:

$$d_n(b_n = \alpha) = \frac{d_n(b_n = 1)}{\alpha^{1/(n-2)}} \qquad \frac{1}{d^4} = \sum_n \frac{1}{d_n^4} \qquad (1)$$

So far, these scaling laws are verified to better than 10% by tracking in all cases considered.

4 TARGET DYNAMIC APERTURE

Table 1: *Relation between required and target D.A.'s.*

Source or Uncertainty	Impact	D.A. in σ
Target D.A. at 10^5 turns		12.0
Finite mesh size	-5%	
Initial to average amplitude	-5%	
Amplitude ratio x_i/y_i	-5%	
Extrapolation to 4 10^7 turns	-7%	9.6
Time dependent multipoles	-10%	
Ripple	-10%	7.8
safety margin	-20%	6.2

The halo of the injected beam will be cut at 3σ in the injector. To allow for injection errors and orbit drifts, the primary collimator will be positioned at 6σ [8]. To avoid perturbing the collimation by non-linearities, we require the D.A. to be at least 6σ. This corresponds to observed good conditions in SPS and HERA. The particles in the beam secondary halo survive for up to 100 turns and may reach an amplitude of 9σ. The amplitude smear must then stay within limits to maintain a good collimation efficiency. In Table 1, the target D.A.for tracking is computed back from the required actual D.A.. The safety margin reflects the discrepancy between calculated and measured D.A.'s as observed in the SPS and HERA. The target D.A. from tracking should be 12σ. It could reduce to 10.5σ if time dependent effects and safety margins are not independent and combined quadratically.

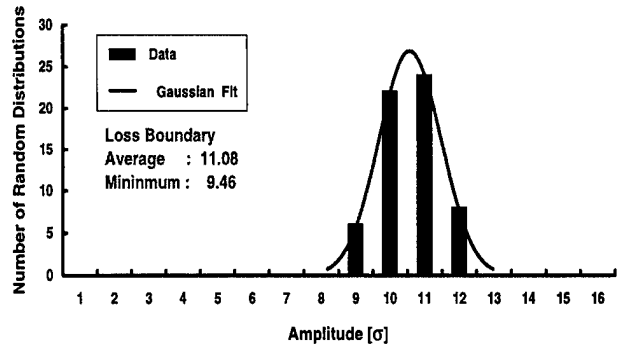

Figure 1: Distribution of D.A.'s

5 RESULTS AND ANALYSIS

5.1 *Dynamic aperture*

The latest results [5] were calculated for LHC version 4.3 [8] which has a lattice without tune split and a cell phase advance very close to 90° . The imperfection table 9607 was used. Figure 1 shows that the minimum D.A. is 9.5σ.

5.2 *Survival plot*

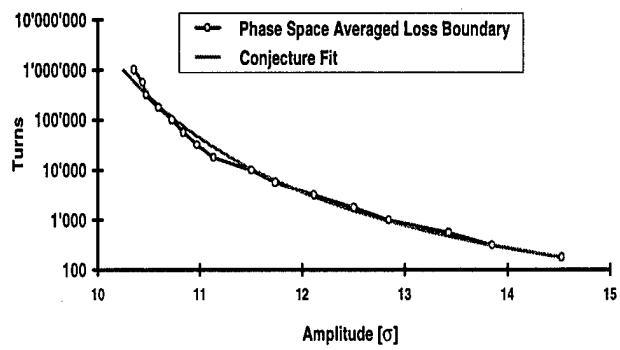

Figure 2: Fitting law for the averaged D.A.

After proper averaging in phase space [9], an inverse logarithmic law fits well the LHC D.A. data (Figure 2) and seems to allow a reasonable extrapolation from 10^5 to 4×10^7 turns.A further loss of 7% can be predicted.

5.3 *Contributions to the onset of unstable motion*

The linear imperfections meaning corrected closed orbits (1 mm rms), a corrected betatron coupling and a residual β-beating of 10%, account for a loss of 5% of D.A.

Figure 3 shows that the amplitude detuning is only correlated with the D.A. when it is sufficiently large ($\delta Q >$ 0.005 at the D.A.).

The main limitation of the D.A. comes from a_4 and b_4. Figure 4 shows that the D.A. is significantly increased by correcting the average values of a_4 and b_4 with additional coils at the end of each dipole. The difference coupling resonances ($2Q_x - 2Q_y$ and $Q_x - Q_y$) driven by these multipoles appear well correlated with the D.A. results [10],

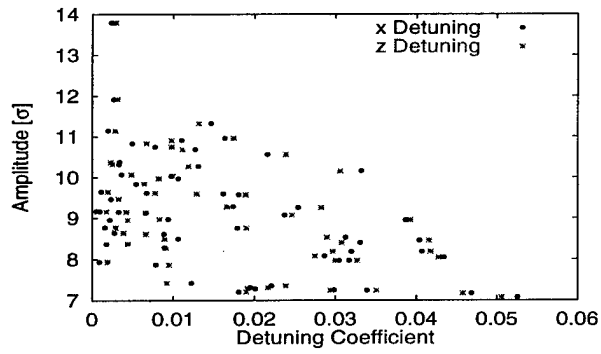

Figure 3: Relation between D.A. and amplitude detuning $\partial Q/\partial J$ in mm^{-2}

suggesting that an improvement will be obtained from the new optics with a tune split.

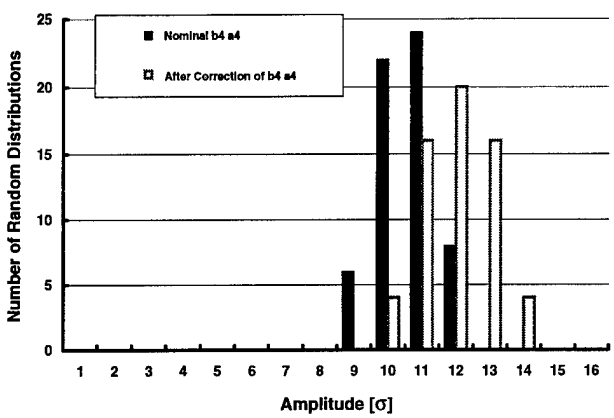

Figure 4: Effect of a_4, b_4 on the D.A.

5.4 *Influence of the second beam at injection*

The beams cross at an angle of ± 150 μrad and are separated by ± 1mm in the orthogonal plane. This gives an almost uniform separation of about 7σ. Optionally the scheme can be rotated by 45^0 to minimize the beam-beam tune footprint. Tracking has revealed a clear reduction of the 10^5-turn D.A. from over 10σ to less than 7σ (Figure 5) with 4 interaction regions. In the new version 5 of the LHC optics, an additional quadrupole allows a reduction of the β_{max} in the triplet quadrupoles, thereby increasing the beam separation to 11σ.

5.5 *D.A. at collision energy*

The aim of the first tracking campaign carried out at collision energy was to evaluate the requirements for the field quality in the low-β triplet. For that purpose, an extreme situation with four physics insertions ($\beta^* = 0.5$ m) and the nominal crossing angle of $\pm 100\mu$rad was considered.

Tuning	D.A. (σ)
$\beta^* = 6$ m	37.7
$\beta^* = 0.5$ m	10.0

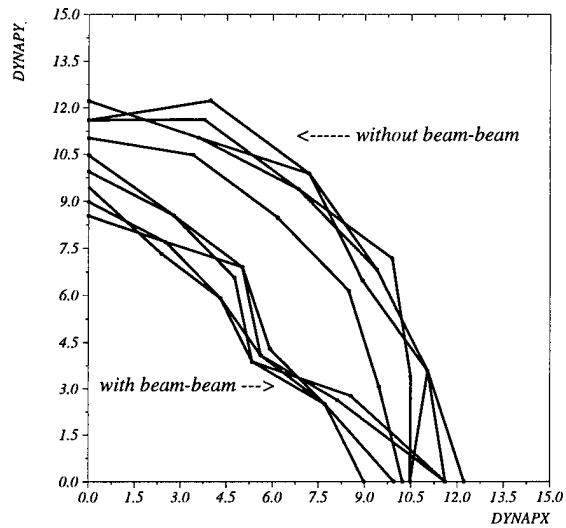

Figure 5: D.A. with/without a second beam at 7σ

The beam-beam effect was disregarded. With the first estimates of the multipole field errors in the low-β triplet, 6D tracking [11] shows clearly that the D.A. is only limited by the triplet errors and more precisely by a large b_{10} component which will be reduced by design.

6 CONCLUSIONS

Given the cost of safety margins, considerable care is being taken to describe in the most realistic way the LHC magnetic fields and the particle dynamics. The D.A., computed by element-by-element tracking, appears to be just sufficient at injection. We aim to gain a safety margin of 20% by reducing or correcting the dominant errors a_4, b_4 and a_3. The effect of the systematic normal and skew octupoles could be reduced in the new optics with tune split. At collision energy, without beam-beam effect, the D.A. is limited to 10σ by the b_{10} of the low-β quadrupole which will be reduced.

7 REFERENCES

[1] F. Schmist, LHC Project Note 30, 1996.

[2] E. McIntosh *et al.*, Montreux 95.

[3] F. Schmidt, CERN SL/94-56(AP),1994.

[4] H. Grote and F.C. Iselin, CERN/SL/90-13rev4(AP), 1995.

[5] M. Böge, F. Schmidt, this conference.

[6] Q. Qin, S. Weisz, LHC Project Note 42, 1996.

[7] V. Ziemann, Particle. Acc. Vol.55,pp.141-150, 1996.

[8] *LHC Conceptual Design* (CERN/AC/95-05(LHC), 1995.

[9] M. Giovannozzi *et al.*,LHC Project report 45, 1997.

[10] Y. Cai, J.P. Koutchouk, LHC Project Note 75, 1996.

[11] A. Faus-Golfe & A. Verdier, EPAC96, 1996.

GLOBAL AND LOCAL HORIZONTAL-VERTICAL DECOUPLING

L. C. Teng
Advanced Photon Source, Argonne National Laboratory
9700 South Cass Avenue, Argonne, Illinois 60439 USA

Abstract

In this paper we investigate systematically the global and local effects of horizontal-vertical couplings on the beam and the measurement and control of these couplings. Piecemeal studies have been made on these subjects by different authors [1, 2, 3]. For completeness, their results are integrated here wherever appropriate. This brings the understanding and execution of the coupling correction to the same degree of completeness as that of the closed orbit correction.

1 GENERAL PROPERTIES OF SYMPLECTIC 4×4 MATRICES

A 4×4 matrix is conveniently written as

$$T = \left(\begin{array}{c|c} M & m \\ \hline n & N \end{array}\right). \tag{1}$$

The cross separates the matrix into four 2×2 matrices. The symplectic conjugate of T is

$$T^+ \equiv \left(\begin{array}{c|c} S & 0 \\ \hline 0 & S \end{array}\right)\left(\begin{array}{c|c} \tilde{M} & \tilde{n} \\ \hline \tilde{m} & \tilde{N} \end{array}\right)\left(\begin{array}{c|c} \tilde{S} & 0 \\ \hline 0 & \tilde{S} \end{array}\right) = \left(\begin{array}{c|c} M^+ & n^+ \\ \hline m^+ & N^+ \end{array}\right) \tag{2}$$

where

$$S \equiv \begin{pmatrix} 0 & 1 \\ -1 & 0 \end{pmatrix} = \text{unit symplectic matrix.}$$

T is symplectic if $T^+T = 1$, namely $T^+ = T^{-1}$ = inverse.

A symplectic matrix can be parameterized as:

$$T = \left(\begin{array}{c|c} M & 0 \\ \hline 0 & N \end{array}\right)\left(\begin{array}{c|c} 1 & F \\ \hline -F^+ & 1 \end{array}\right) = \left(\begin{array}{c|c} M & MF \\ \hline -NF^+ & N \end{array}\right) \tag{3}$$

or as

$$T \equiv RPR^+$$

$$\text{with } R = \left(\begin{array}{c|c} \cos\psi & D\sin\psi \\ \hline -D^+\sin\psi & \cos\psi \end{array}\right), \quad P = \left(\begin{array}{c|c} A & 0 \\ \hline 0 & B \end{array}\right). \tag{4}$$

In the first form, Eq. (3), the 2×2 matrices M, N, and F are not symplectic, but the number of free parameters are reduced from 12 to 10 by the relations $\det M = \det N = (1 + \det F)^{-1}$. In the second form, Eq. (4), A, B, and D are all symplectic 2×2 matrices. Together with ψ, this form contains again the requisite ten parameters. Relations among the various forms are:

$$\begin{cases} A = M - Dn\tan\psi & D = h/\sqrt{\det h} \\ B = N + D^+ m\tan\psi & \tan 2\psi = \dfrac{\sqrt{\det h}}{\frac{1}{2}\mathrm{Tr}(N-M)} \end{cases}, \tag{5}$$

where the fundamental coupling matrix h is

$$h \equiv m + n^+ = MF - FN^+.$$

2 ONE-TURN TRANSFER MATRIX

We write the coordinate 4-vector of the transverse phase space as $\begin{pmatrix} X \\ Y \end{pmatrix}$ with $X \equiv \begin{pmatrix} x \\ x' \end{pmatrix}_o$ and $Y \equiv \begin{pmatrix} y \\ y' \end{pmatrix}$, and denote by T the 4×4 symplectic one-turn transfer matrix. Equation (4) shows that the decoupled principal coordinate 4-vector is

$$\begin{pmatrix} U \\ V \end{pmatrix} \equiv R^+\begin{pmatrix} X \\ Y \end{pmatrix} \quad \text{with } U = \begin{pmatrix} u \\ u' \end{pmatrix}, V \equiv \begin{pmatrix} v \\ v' \end{pmatrix} \tag{6}$$

and is transferred by the decoupled matrix P.

The principal betatron tunes (eigen-tunes) are given as usual by

$$\cos 2\pi\nu_u = \frac{1}{2}\mathrm{Tr}A, \quad \cos 2\pi\nu_v = \frac{1}{2}\mathrm{Tr}B. \tag{7}$$

From Eq. (5) we can derive the relationship

$$(\cos 2\pi\nu_v - \cos 2\pi\nu_u)^2 = \left[\frac{1}{2}\mathrm{Tr}(N-M)\right]^2 + \det h. \tag{8}$$

The ten parameters of T are all functions (lattice functions) of the coordinate s around the closed orbit and are written as

Six principal lattice functions:

$\alpha_u \ \beta_u \ \phi_u$ (from A)

$\alpha_v \ \beta_v \ \phi_v$ (from B)

Four coupling lattice functions:

a, b, c, d (ad - bc = 1)

$$\left[\text{from } D = \begin{pmatrix} a & b \\ c & d \end{pmatrix}\right]$$

and ψ.

For the coupling lattice functions, ψ gives the overall strength of coupling and D gives the specific mode of coupling. For example, a and d give the angles of rotation of the principal axes u and v from x and y, and b gives the fraction of the amplitudes of x and y coupled over to those of v' and u'.

0-7803-4376-X/98 /$10.00 © 1998 IEEE

3 COUPLING ELEMENTS

There are two types of coupling elements: the skew quadrupole (SQ) and the solenoid (SL). The transfer matrix across an SQ is

$$T_{SQ} = \frac{1}{2}\left(\begin{array}{c|c} 1 & 1 \\ \hline -1 & 1 \end{array}\right)\left(\begin{array}{c|c} f & 0 \\ \hline 0 & g \end{array}\right)\left(\begin{array}{c|c} 1 & -1 \\ \hline 1 & 1 \end{array}\right)$$

$$= \frac{1}{2}\left(\begin{array}{c|c} g+f & g-f \\ \hline g-f & g+f \end{array}\right), \tag{9}$$

where

$$f = \begin{pmatrix} \cos\sqrt{q}s & \frac{1}{\sqrt{q}}\sin\sqrt{q}s \\ -\sqrt{q}\sin\sqrt{q}s & \cos\sqrt{q}s \end{pmatrix}$$

$$g = \begin{pmatrix} \cosh\sqrt{q}s & \frac{1}{\sqrt{q}}\sinh\sqrt{q}s \\ \sqrt{q}\sinh\sqrt{q}s & \cosh\sqrt{q}s \end{pmatrix}$$

and $q \equiv \frac{1}{B\rho}\frac{\partial B_x}{\partial x}$.

The transfer matrix across an SL is

$$T_{SL} = \left(\begin{array}{c|c} e & 0 \\ \hline 0 & e \end{array}\right)\left(\begin{array}{c|c} \cos ks & \sin ks \\ \hline -\sin ks & \cos ks \end{array}\right), \tag{10}$$

where

$$e = \begin{pmatrix} \cos ks & \frac{1}{k}\sin ks \\ -k\sin ks & \cos ks \end{pmatrix} \quad \text{with } k \equiv \frac{1}{2}\frac{B_z}{B\rho}.$$

For "thin" elements these become

$$T = \left(\begin{array}{c|c} I & K \\ \hline -K^+ & I \end{array}\right) \quad \text{with} \quad \begin{cases} K_{SQ} = \begin{pmatrix} 0 & 0 \\ qs & 0 \end{pmatrix} \\ K_{SL} = \begin{pmatrix} ks & 0 \\ 0 & ks \end{pmatrix} \end{cases}. \tag{11}$$

If in a lattice there are a number of thin coupling elements, the one-turn transfer matrix is

$$T = \left(\begin{array}{c|c} M & 0 \\ \hline 0 & N \end{array}\right)_{on}\left(\begin{array}{c|c} I & K \\ \hline -K^+ & I \end{array}\right)_n \cdots \left(\begin{array}{c|c} I & K \\ \hline -K^+ & I \end{array}\right)_1\left(\begin{array}{c|c} M & 0 \\ \hline 0 & N \end{array}\right)_{1o} \tag{12}$$

$$= \left(\begin{array}{c|c} M & 0 \\ \hline 0 & N \end{array}\right)_o\left(\begin{array}{c|c} I & F \\ \hline -F^+ & I \end{array}\right),$$

where

$$F \equiv \sum_i M_{oi}K_iN_{io} \text{ and } K_i = K_{SQ} \text{ or } K_{SL},$$

and $\left(\begin{array}{c|c} M & 0 \\ \hline 0 & N \end{array}\right)_o$ is the uncoupled one-turn matrix from location o around back to o. In F we have taken only linear terms in K_i of the thin (weak) coupling elements.

4 GLOBAL DECOUPLING

There are two primary global features that are affected by coupling—the betatron tunes and the emittances. Other quantities affected are derivatives of these two, such as the chromaticity.

4.1 Minimum Separation between Eigentunes

The minimum separation between eigentunes is governed by the relation given as Eq. (8) and was studied in detail in Ref. 3. It is important to note that the left-hand side of Eq. (8) is independent of s. To make it vanish, i.e., to make $\nu_u = \nu_v$ in fractional parts, one has to tune both terms on the right-hand side to zero at some location s. The equation then ensures that these terms are zero everywhere around the ring. The first term, Tr(N-M), is tuned mainly by the normal lattice quadrupoles and the second term, det h, is tuned by the skew quadrupoles. In general, two SQs are necessary to compensate all error couplings in the ring (from roll errors of quadrupoles and vertical orbit distortions in sextupoles) to give det h = 0.

For normal operation of the ring, however, $\nu_u \neq \nu_v$ in fractional parts, and the lattice can be decoupled (det h = 0) only at specific locations. In a synchrotron radiation storage ring it is desirable to be decoupled at insertion devices. Local decoupling is, thus, useful.

4.2 Emittance Coupling

Two bilinear invariants were given in Ref. 2. The relevant one here is

$$W_u = U^+J_uU = (X^+J_uX)\cos^2\psi + (Y^+D^+J_uDY)\sin^2\psi$$
$$- (X^+J_uDY + Y^+D^+J_uX)\sin\psi\cos\psi, \tag{13}$$

where

$$J_u = \begin{pmatrix} \alpha_u & \beta_u \\ -\gamma_u & -\alpha_u \end{pmatrix}$$

and

$$X^+ = \tilde{X}\tilde{S} = \text{symplectic conjugate.}$$

The concept and formulation of the 2-dimensional emittances ε_x and ε_y for a beam of particles moving in the 4-dimensional phase space are not well defined, but the following observations are useful.

1. Setting first Y = 0, then X = 0, we get the projections on the 2-dimensional coordinate planes which, when averaged around the ring and averaged over the particles, may be defined as the emittances. This gives

$$\begin{cases} \varepsilon_x \equiv \overline{(X^+ J_u X)}\,\overline{\cos^2\psi} \\ \varepsilon_y \equiv \overline{(Y^+ D^+ J_u D Y)}\,\overline{\sin^2\psi} \end{cases}. \tag{14}$$

2. When the ring is not coupled $\psi = 0$ and we have $\varepsilon_y = 0$ and $\varepsilon_x = \overline{(X^+ J_u X)} \equiv \varepsilon_o$ = total emittance.
3. The symplectic D-transformation $D^+ J_u D$ is area preserving.

These considerations lead to the identification

$$\begin{cases} \varepsilon_x = \varepsilon_o \overline{\cos^2\psi} = \varepsilon_o(1 - \overline{\sin^2\psi}) \\ \varepsilon_y = \varepsilon_o \overline{\sin^2\psi} \end{cases}. \tag{15}$$

To measure $\overline{\sin^2\psi}$, we get from Eq. (5)

$$\frac{\overline{\det h}}{(\cos 2\pi\nu_v - \cos 2\pi\nu_u)^2} = \overline{\sin^2 2\psi} = 4\overline{\sin^2\psi}\left(1 - \overline{\sin^2\psi}\right), \tag{16}$$

where $\overline{\det h}$ can be calculated from the strengths of the two SQs after they are tuned to give zero eigen-tune separation, namely $\nu_u = \nu_v$.

5 LOCAL DECOUPLING

For local decoupling we leave the one-turn transfer matrix and concentrate on the transfer matrix over the local section of lattice, say, from -s to s. If the decoupling is to be at o, one generally needs four SQs on either side of o tuned such that F = 0 for the transfer matrix from -s to s and that, for the transfer matrix from o to s, F has an appropriate value to cancel the existing value at o. In Ref. 3 certain symmetric arrangements of the SQs were suggested to simplify the calculation and the design.

In a synchrotron radiation storage ring one generally wants the lattice to be decoupled at the straight sections for insertion devices, but the number of installed SQs is generally much less than eight per straight section. Thus, we have a least squares problem of minimizing coupling in all straight sections with a small number of available SQs. For this and for many procedures discussed earlier we need the Beam Coupling Monitor (BCM) to measure the coupling. The most direct way to measure the coupling is to impart an orbit deflection in one plane using correction dipoles and measure the orbit distortion produced in the other plane using BPMs. If the orbit deflection imparted is $\begin{pmatrix}\delta X \\ \delta Y\end{pmatrix}$ and the orbit distortion immediately downstream is written as $\begin{pmatrix}X \\ Y\end{pmatrix}$, from orbit closure we get after one revolution

$$\left(\begin{array}{c|c} M & m \\ \hline n & N \end{array}\right)\begin{pmatrix}X \\ Y\end{pmatrix} + \begin{pmatrix}\delta X \\ \delta Y\end{pmatrix} = \begin{pmatrix}X \\ Y\end{pmatrix}. \tag{17}$$

We make two separate measurements:

1. δX only $(\delta Y = 0)$, Eq. (17) gives

$$\begin{cases} nX = (1 - N)Y \\ mY = (1 - M)X - \delta X \end{cases} \tag{18}$$

2. δY only $(\delta X = 0)$, Eq. (17) gives

$$\begin{cases} mY = (1 - M)X \\ nX = (1 - N)Y - \delta Y \end{cases} \tag{19}$$

The first ones of Eqs. (18) and (19) are independent of the specific values of the deflections and are most useful. In terms of F they are

$$\begin{cases} F^+ X = (1 - N^{-1})Y & (\delta X \text{ only}) \\ FY = -(1 - M^{-1})X & (\delta Y \text{ only}) \end{cases}. \tag{20}$$

The four scalar equations obtained by applying one each of δX and δY deflections are not independent. To get independent equations we can apply, say, two independent horizontal deflections $\delta X_1 = \begin{pmatrix}1 \\ 0\end{pmatrix}$ and $\delta X_2 = \begin{pmatrix}0 \\ 1\end{pmatrix}$. The four scalar equations so obtained from the first of Eq. (20) are independent and will determine all four elements of F from which we can calculate ψ. The whole procedure could be automated and the BCM, although not as fast as the BPM, should be able to give the readings in a few seconds.

The remainder of the procedure is identical to that for closed orbit correction. The BCM measurement is performed for each individual SQ to get the response matrix elements and some least-squares algorithm, e.g., the convenient Singular Value Decomposition procedure, is then used to minimize, say, the values of ψ at all the BCM locations.

6 ACKNOWLEDGMENT

Work is supported by the U.S. Department of Energy, Office of Basic Energy Sciences, under Contract No. W-31-109-ENG-38.

7 REFERENCES

[1] L. Teng, Fermilab Report FN-229, 1971.
[2] D. Edwards and L. Teng, IEEE Trans. Nucl. Sci., NS-20, No. 3, p. 885 (1973).
[3] S. Peggs, IEEE Trans. Nucl. Sci., NS-30, No. 4, p. 2460 (1983).

ANALYTIC LATTICE DESIGN WITH *BeamOptics*

B.Autin, T. D'Amico, V. Ducas, M. Martini, E. Wildner
CERN, PS Division, 1211 Geneva 23, Switzerland

Abstract

In contrast with light optics, high-energy particle optics has no rotational symmetry and its analytical treatment becomes rapidly intractable by hand. One way to improve the situation is to parametrize specific modules with the help of a symbolic program. The code *BeamOptics*, with its full symbolic, numerical and graphical functions is a tool for lattice analysis and design and it is applied to specific optical modules.

1 INTRODUCTION

Optics has been for centuries a fully analytic science. This is true for light and charged-particle optics as long as the focusing elements have a rotational symmetry. Magnetic alternating-gradient structures opened new realms in optics, but at the expense of a loss of analytic description for most devices with the exception of the FODO cell and its variants. The reason for this increased complexity lies in the special symmetries of the magnetic fields, in the fact that focusing in one plane means de-focusing in the other plane and that overall focusing is obtained with at least two elements. Moreover, classical optics deals with ray tracing whilst particle optics is better described by the beam envelope than by individual rays. To cope with this situation, a number of numerical codes with internal optimization procedures have been written. However, as stated by K. Brown in his introduction to *TRANSPORT* [1], they are "superb at solving the mathematics of the problem but not the physics".

The alternative proposed with *BeamOptics* consists of restoring the analytic description by using symbolic computing which has been invented precisely to do by computer the calculations that are intractable by hand. It would be naive to think that symbolic computing is a universal panacea. Limitations may appear in the management of the memory space, in the computing time and in the interpretation of the output. It is nevertheless useful to study modules for which the number of variables is equal to the number of constraints. The problem is then deterministic and amenable to exact solutions. *BeamOptics* has all the functions to determine the geometry of a transfer line or of a circular machine, to trace a trajectory, the orbit dispersion, the variation of the path length with momentum, the β-function and the betatron phase advance. It has also a library of modules that can be used for regular periods, orbit manipulation and betatron matching. It is this aspect which will be developed and the examples of isochronous periods and of a matching triplet are thoroughly treated.

2 REGULAR PERIODS

For both technical and economical reasons, a machine must be as regular as possible. In addition to the classical types of cells, *BeamOptics* contains codes for quasi-isochronous periods whose theory and functionalities are presented.

2.1 Classical periods

FODO and triplet cells are fully described in *BeamOptics* using the thin lens approximation. Thin elements can be transformed into long ones but the properties of the cells are slightly changed due to effects like the edge focusing of the dipoles. A real beam line l derived from a thin lens model can be converted into a period by using the function `Period[l]`. If a line has a mirror symmetry, the calculations are simplified in the function `HalfPeriod` which assumes that the longitudinal derivatives of the β-function and of the orbit dispersion are zero at the ends.

2.2 Quasi-isochronous period

When particles of different momenta rotate at the same revolution frequency, the machine is said to be isochronous. This regime may be necessary when transition is to be avoided or when the bunch length has to be small. It can only occur if the orbit length decreases with momentum since the velocity always increases with momentum. The ratio α_p of the relative change of orbit length $\Delta L/L$ to the relative momentum error $\Delta p/p$ is the momentum compaction and it is related to the orbit dispersion D and to the radius of curvature ρ of the central orbit by the expression

$$\alpha_p = \frac{1}{L}\int_0^L \frac{D}{\rho}\,ds\,.$$

The orbit dispersion observed at a point of curvilinear abscissa s is given as a function of the β-function and of the betatron phase advance μ by

$$D(s) = -\frac{\sqrt{\beta(s)}}{\sin Q\pi}\int_s^{s+L}\sqrt{\beta(t)}\cos(-Q\pi + |\mu(t)-\mu(s)|)\,\frac{dt}{\rho(t)}$$

The variable t is the abscissa along the orbit in the dipoles. The sign of the dispersion changes abruptly when the tune Q traverses an integer value. It is therefore in the vicinity of an integer tune that D and α_p can be negative. The problem is to find a structure which can be tuned

0-7803-4376-X/98 /$10.00 © 1998 IEEE

near an integer. In a regular FODO cell, this is impossible unless an irregularity, like *missing magnets*, is introduced in the bending magnet distribution. The tune of the period made of n cells of betatron phase advance μ_0 is close to the integer

$$h = n\frac{\mu_0}{2\pi}.$$

In this type of period, the de-coupling is complete between the focusing and the dispersion (Figure 1). The position of the missing magnets is determined by such considerations as the maximum orbit dispersion and the space to be reserved to kicker and septum magnets.

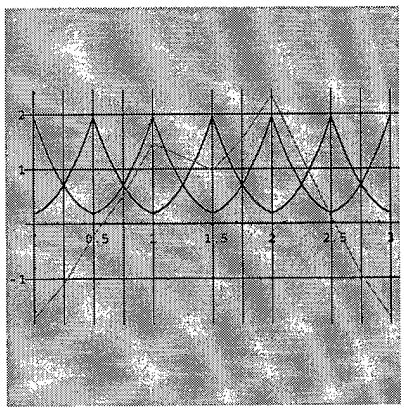

Figure: 1 Horizontal (red) and vertical (blue) β-functions and orbit dispersion (green) in a 3-cell quasi-isochronous period.

The *BeamOptics* function for a quasi-isochronous period is simply `IsoPeriod[n,options]` where n is the number of cells. In the absence of optional arguments, the beam line is tuned at the zero momentum compaction near the resonance closest to $\pi/2$ with two missing magnets about $\pi/2$ apart. In addition to the beam line and its characteristic functions, the function returns the range of integer resonances and the symbolic expressions of the input orbit dispersion and of the path length as functions of the phase advance per cell. Using the symbolic output, the period can be studied for a wide range of phase advances per cell (Figure 2).

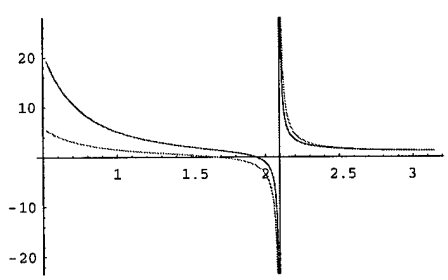

Figure: 2 Variations of the incremental path length (red) and input orbit dispersion (green) in a missing magnet 3-cell period with the phase advance per cell.

Optional arguments are related to the scaling parameters: cell length and deflection per magnet, to the position of the missing magnets and to the choice of the resonance.

The negative dispersion lattices have a few other peculiarities. The change in length of the off-momentum orbits can be perceived only if the orbit dispersion is plotted about the curved reference orbit, this facility exists only in *BeamOptics* and is provided by the function `AbsoluteBeamPlot`. The calculation of the instantaneous time constants of the beam blow-up due to intra-beam scattering is often simplified by averaging the variations of the orbit dispersion. This is clearly not justified when the momentum compaction is close to zero. The `IBS` function of *BeamOptics* returns the time constants in the horizontal, vertical and longitudinal phase planes as the result of a numerical integration of the various integrals without any approximation. The computing time is rather long but the results can serve as a reference for faster but approximate methods.

3 INSERTIONS

In large machines and especially in colliders, long straight sections, the insertions, are dedicated to injection, extraction, RF cavities and experimental areas. They are usually matched to the arcs in two steps, first by canceling the orbit dispersion and its longitudinal derivative using a *dispersion suppressor* and then by achieving the required beam shape. Orbit dispersion and betatron motion are thus de-coupled.

3.1 Dispersion suppressor

There is a great variety of dispersion suppressors; some act on the focusing, others on the bending structure. In any circumstance, a linear system of two equations with two unknowns x and y has to be solved:

$$D(x,y) = 0 \quad \frac{d}{ds}D(x,y) = 0,$$

the orbit dispersion and its derivative being taken at the end of the suppressor. The *BeamOptics* function is `DSuppressor[l, DVector[D,D'],{x,y}]` where l is a symbolic beam line and some of whose elements are functions of x or y and D and D' are the components of the input dispersion vector.

3.2 Betatron matching

Betatron matching is the most difficult problem in lattice design because it is basically non linear. It consists of finding a 4-parameter module which maps input to output horizontal and vertical phase plane ellipses. There is no substantial loss of generality in assuming that the boundary conditions are not arbitrary but of type I or II:

$$\beta_x = \beta_y \quad \alpha_x + \alpha_y = 0 \quad (I)$$
$$\alpha_x = 0 \quad \alpha_y = 0 \quad (II)$$

In this spirit, telescopes [2,3,4,5], single lens and doublet matching devices [6,7], quarter and half wavelength

transformers [2,6] have been developed. Research is being pursued and, as an example, the properties of a symmetric triplet (Figure 3) will be discussed. Can indeed the general β- matching problem be solved using the two focal lengths f_1 and f_2 of the quadrupoles and the distances l and d as unknowns? The theory of this module [8] shows that the solutions, when they exist, are given by a cubic equation. The *BeamOptics* function:

`MatchingTriplet[`$\sigma_{h1}, \sigma_{h2}, \sigma_{v1}, \sigma_{v2}$`]`,

where σ denotes the function `Sigma[β,α]`, solves this equation and returns the beam line and its properties.

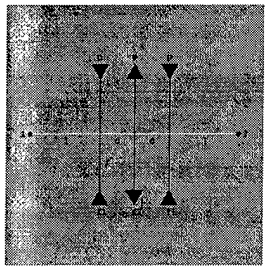

Figure: 3 Symmetric triplet as a matching device.

A graphical output (Figure 4) is shown for the special values:

$$\beta_{x1} = 2m \qquad \beta_{y1} = 1m \quad \alpha_{x1} = \alpha_{y1} = 0$$
$$\beta_{x2} = \beta_{y2} = 3m \quad \alpha_{x2} = -1 \qquad \alpha_{y2} = 1$$

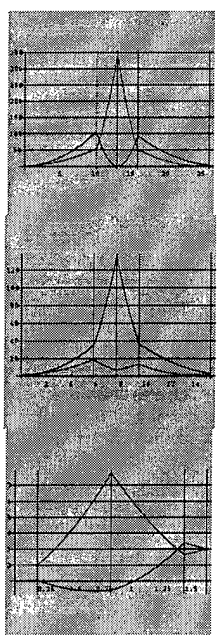

Figure: 4 Matching solutions using a symmetric triplet.

The type of solution strongly depends on the length l. It has also to be noted that l is a scaling parameter and each type of solution can generate a family of solutions by varying l at the cost of changing the β values at point 2. This may nevertheless be acceptable if there is enough room to add a quarter-wavelength transformer to achieve the required boundary conditions.

This problem also reveals the special case

$$f_1 = -f_2 = f\ .$$

The device may then be an interesting alternative to a doublet for the final focus of a round beam. With the extra-notations

$$\gamma = \frac{1+\alpha^2}{\beta} \qquad \alpha_0 = \sqrt{\beta_1\gamma_2 + \beta_2\gamma_1 - 2},$$

the parameters can be expressed simply:

$$f = \frac{\alpha_2}{\gamma_1 - \gamma_2} \qquad l = \left|\frac{f}{\alpha_2}\right|\sqrt{\alpha_0\left(\alpha_0 + |\alpha_2|\right)} \qquad d = |f|\sqrt{1 + \left|\frac{\alpha_2}{\alpha_0}\right|}$$

and it is sufficient to specify the β-value at point 1 and the σ_h value at point 2 in the `MatchingTriplet` function. Figure 5 shows the graphics output of

`MatchingTriplet[1, Sigma[10,-1]]`

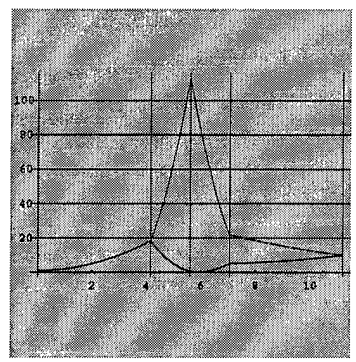

Figure: 5 Special matching solution using a symmetric triplet with equal focal lengths.

5 CONCLUSION

The program *BeamOptics* is a tool of analysis and design of accelerator lattices made of bending magnets and quadrupoles. It can generate the analytic expressions that describe an optical module and contains a library of fully documented and easy to use functions. Last, due to the functional style which avoids the risk of interference between existing and new functions, the program can be upgraded at will by the user to address a specific problem.

6 ACKNOWLEDGEMENTS

The program *BeamOptics* uses *Mathematica* [9] and *Geometrica*, an application of *Mathematica* for exact drawing and geometry.

REFERENCES

[1] K. L. Brown and S.K. Howry, SLAC-91 (1970).
[2] K. L. Brown and R. V. Servrancks, in *Physics of High Energy Particle Accelerators*, AIP Conf. Proc. No. 127, 62-138 (1983).
[3] O. Napoly, CERN/LEP-TH/89-69.
[4] B.W. Montague, F. Ruggiero, CERN, CLIC Note 37.
[5] B. Autin, E. Wildner, in *Proceedings of EPAC'96*, THP030G (1996).
[6] B. Autin, in *Particle World*, Vol.2, No. 3, 74-80(1991).
[7] B. Autin, in *New Computing Techniques in Physics Research II*, 763-771 (World Scientific, 1992).
[8] T. D'Amico, G. Guignard, *These proceedings.*
[9] S. Wolfram, *Mathematica* (Addison Wesley, 1991).

EXPERIMENTAL MEASUREMENT OF HIGH-GRADIENT STANDING WAVE ACCELERATOR TRANSPORT MATRIX

S. Reiche, DESY, Hamburg, Germany
J.B. Rosenzweig, University of California, Los Angeles, USA
L. Serafini, INFN-Milano, Milan, Italy

Abstract

This paper presents an experimental study of the transverse beam dynamics of an electron beam in a high-gradient, standing wave linear accelerator. A 3.6 MeV beam from the UCLA RF Photoinjector (SATURNUS) is injected at various phases and rf field amplitudes into the plane wave transformer (PWT) linac (peak acceleration 40 MeV/m), and its transverse dynamics measured by a corrector magnet sweeping method. This method allows us to reconstruct the transverse matrix elements, which are compared to analytical predictions(J.B. Rosenzweig and L.Serafini, Physical Review E 49, 1599 (1994)). The determinant of the experimentally derived matrix is found to be the ratio of the initial to final momentum, verifying the theory, and providing direct evidence of adiabatic damping of transverse trace space.

1 INTRODUCTION

With the rise in use of high gradient radio-frequency linear accelerators (rf linacs), in devices such as rf photoinjectors[1] and linear collider test facilities[2], there has been increased attention placed on the strong transverse focusing effects present in these devices. These effects, which are due both to first order transient effects at the entrance and exit of a linac, and to second order ponderomotive (alternating gradient) effects in the body of the periodic linac structure, are of primary importance in understanding the beam transport in moderate energy sections ($5 < \gamma = E/m_e c^2 < 100$) of electron accelerators. While theoretical analyses of the focusing properties of linacs date back to the 1960's[3, 4], recent work has produced a more detailed understanding of the ponderomotive force[5], and analytical solutions of these equations for arbitrary acceleration phase and spatial harmonic content of the rf fields have been found[6], which led to a matrix description of the trace space transport.

This matrix treatment of beam dynamics in high gradient rf linacs, as well as the underlying analytical model for the averaged (over an rf period) transverse forces, have formed the underpinning of much recent work, from the optics of linear collider test facilities[2], to the full theory of space-charge dominated beam dynamics in rf photoinjectors[7]. While these implementations of the theory have been compared positively with computer simulation, there has, however, been no effort to date to verify the theoretical advances with experiment. This paper therefore presents a first such verification.

2 THEORY

The trace space transport matrix corresponding to a rf linac, which upon multiplication of a transverse trace space vector, *e.g.* (x, x') , gives the mapping of this vector through the linac, has recently been derived for arbitrary rf phase, amplitude, and spatial harmonic content in the linac. Including all terms to second order in the average accelerating gradient $eE_0 \cos(\phi) \equiv \gamma' m_e c^2$, where E_0 is the amplitude of the synchronous ($\nu_\phi \cong c$) spatial harmonic wave component of the rf field, and $\phi = \omega t - kz$ is the phase defined with respect to the maximum acceleration in this wave, the action of a ponderomotive force can obtained to second order by averaging over the fast alternating gradient first order forces and the induced lowest order oscillatory motion, as[5, 6]

$$\overline{F_r} = \eta(\phi) \frac{(qE_0)^2}{8\gamma m_0 c^2} r \tag{1}$$

with

$$\eta(\phi) \equiv \sum_{n=1}^{\infty} b_n^2 + b_{-n}^2 + 2b_n b_{-n} \cos(2\phi). \tag{2}$$

The coefficients b_n are the Floquet amplitudes of the spatial harmonics, defined by the expression, valid for an ultra-relativistic ($\nu_b \cong c$) electron

$$E_z \equiv E_0 \mathrm{Re}\left[\sum_{n=-\infty}^{\infty} b_n e^{i(2k_0 nz + \phi)}\right] \tag{3}$$

where $k_0 = \psi/d = \omega/c$ and ψ is the rf phase shift per period of the linac, with $\psi = \pi$ in the structure considered here.

From the averaged force, the differential equation governing the *seculat* trajectory of the electron, about which the fast oscillations induced in first order are performed, is derived. Its general solutions, given in matrix form, can be found in Ref. 6. At the ends of an rf structure, there are first order transient angular kicks associated with entering and exiting the fringing field which are not immediately cancelled in first order by a nearby kick. These kicks, again valid when considering the secular trajectory, are given by $\pm\gamma'/2\gamma$, for the exit and entrance regions, respectively. Multiplying the matrices associated with the entrance, interior, and exit of the linac, we have the full trace space transport matrix,

$$M = \tag{4}$$

$$\begin{bmatrix} \cos(\alpha) - \sqrt{\frac{2}{\eta(\phi)}} \cos(\phi)\sin(\alpha) & \sqrt{\frac{8}{\eta(\phi)}} \frac{\gamma_i}{\gamma'} \cos(\phi)\sin(\alpha) \\ -\frac{\gamma'}{\gamma_f}\left[\frac{\sin(\phi)}{\sqrt{2\eta(\phi)}} + \frac{\sqrt{\eta(\phi)}}{\sqrt{8}\cos(\phi)}\right]\sin(\alpha) & \frac{\gamma_i}{\gamma_f}\left[\cos(\alpha) + \sqrt{\frac{2}{\eta(\phi)}}\cos(\phi)\sin(\alpha)\right] \end{bmatrix}$$

0-7803-4376-X/98 /$10.00 © 1998 IEEE

Here $\alpha = \frac{\sqrt{\eta(\phi)}}{\sqrt{8}\cos(\phi)} \ln(\gamma_f/\gamma_i)$, with γ_i and γ_f the initial and final Lorentz factors of the electron, respectively, which are simply related by $\gamma_f = \gamma_i + \gamma' L$, with L equal to the length of the linac section, with $\gamma' m_e c^2$ equal to the averaged (over a period of the linac) acceleration gradient.

3 THE EXPERIMENT

The linac used for the present experiments is a component of the UCLA Photoinjector, a rf accelerating section which boosts the energy of a 3.6 MeV photoelectron beam extracted from a high gradient 1.5 cell π-mode rf gun to approximately 12.8 MeV at maximum in these experiments. This linac is constructed of a novel, high shunt impedance design known as a plane-wave transformer[8] (PWT), and has non-negligible spatial harmonic content (*e.g.* $\eta(0) = 1.23$). The experimental arrangement is nearly ideal for observing the focusing and adiabatic damping predicted by the matrix given in Eq. 4. This is due to a number of advantages, the first being that the beam can be viewed as essentially point-like for the purpose of centroid measurements, as it has a short rms phase extent, $\sigma_\phi \cong 1°$ (as determined by coherent transition radiation[9] measurements), it has a low rms normalized emittance, measured as $\epsilon_n < 10^{-5}$ m-rad, and moderately large charge per bunch, $Q \cong 200$ pC. This charge is large enough to clearly observe the photoelectrons over the dark-current background, yet small enough that collective effects on the centroid motion, such as transverse wake-fields, can be neglected.

The additional advantage this arrangement offers is that the matrix elements to be measured are most strongly dependent on the ratio γ_f/γ_i, and on γ'. The PWT is by nature a high gradient linac ($\gamma' \leq 50\ \mathrm{m}^{-1}$), with moderate length $L = 42$ cm, and thus to obtain a large value γ_f/γ_i one only need inject with a relatively small initial energy $\gamma_i m_e c^2$. This energy cannot, however, be made arbitrarily small due to the constraint that $\nu_b \cong c$, and a related requirement that the relative energy gain per period of the linac be much smaller than unity, both of which are required in order to guarantee the validity of Eq. 4. Thus the injection energy given by the rf gun (which must in fact produce a relativistic beam due to its extraction dynamics) is nearly ideal for maximizing the matrix elements given in Eq. 4.

In order to determine the transfer matrix of the PWT linac, the centroid of the photo-electron beam is measured using a differential steering technique originally developed to calibrate the beam energy after the gun. For this measurement, the current I of steering (or kicker) magnet K1 is swept while monitoring the centroid position of the electron beam on the downstream phosphor screen P1. The momentum of the beam is determined from the differential change of the centroid position dx_c/dI with current I. The near-axis field $\int B_y(I,z)dz$ of the horizontally-deflecting steering magnets was determined with Hall probe measurements, and the phosphor screens and related video calibrations performed before the experiments.

This method of the momentum determination helps establish the initial conditions of the beam, and also forms the technical basis for the matrix element measurements. As it is difficult to determine the actual electromagnetic center of the linac with respect to the insertable phosphor diagnostics, we were forced to use a differential steering technique. In this case, one of the low energy magnets previous to the linac (K1 or K2) was swept, while observing the centroid motion of the beam downstream of the linac (P2 or P3). The four combinations of the steering magnets and observation points, along with knowledge of the drift lengths, integrated field of the steering magnets, and precise calibration of the video images of the phosphor screens, give four measured quantities which allow reconstruction of the linac transport matrix.

4 RESULTS

In the initial round to experiments, the dependence of the matrix elements on linac injection phase was measured. For each phase, we swept through eight different currents in the steering magnets, and obtained a linear fit to the resulting centroid motion at the phosphor screens. Three noticeable effects were the source of small errors in this method: (1) a large amount of dark current emitted from the gun, (2) transverse centroid injection errors arising from cathode drive laser pointing jitter, and (3) a slow drift in the photocathode drive laser injection phase. This third effect allowed data to be taken over only a limited time span, with all data taken in a single session to ensure the reproducibility of conditions.

The data resulting from these measurements give the calculated values of the centroid sweep rate using the transport derived from the M-matrix and the relevant drift matrices. There is fairly good agreement for all four measurement sets between the predictions and data over all phases where reliable measurements could be made, with a slightly larger sensitivity on phase offsets from the crest displayed by the data. Note that there are larger errors associated with two measurements made at screen P3 for phases of -2.2 and +10 degrees. The P3 data was inherently more difficult to obtain, because the photoelectron beam was much larger in size than at P2, and the two more uncertain points suffered from large interference from the dark current background at their specific running conditions.

The data are inverted to give the elements of the M-matrix, with the results shown in Figs. 1. The relative experimental uncertainty shown by the error bars is larger than for the data sets due to the higher order sensitivity introduced by the inversion process. Also shown in Figs. 1 are the theoretical predictions for the M-matrix. Since the matrix elements were more sensitive to the experimental noise in the data, we also fit the data to a quadratic in ϕ, and then used the resulting filtered data function in the inversion routine to generate a smooth fit in ϕ for the matrix elements. As can be seen, this fit agrees quite well with theoretical predictions.

As a final check on the validity of these data sets, and to independently verify the adiabatic damping component of

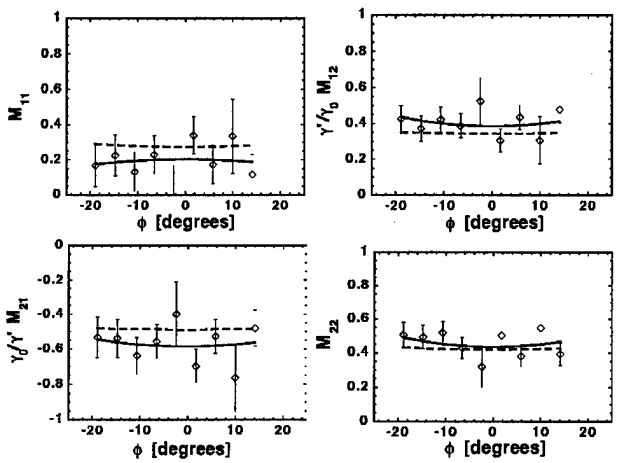

Figure 1: Matrix elements of the transverse trace space map M of the PWT linac as a function of phase ϕ. The values obtained from inverting a quadratic fit to the raw data are drawn by a solid line, the theoretical values by a dashed line. The matrix elements M_{12} and M_{21} are weighted by the factors γ'/γ_0 and γ_0/γ', respectively, to normalize all matrix elements.

the transformation, in Fig. 2 (left) we display the experimentally derived values of det(M), as well as the predicted values, γ_i/γ_f. Because of the form of the algebraic relation between the determinant and the matrix elements, the relative experimental uncertainty in det(M) is no larger than for the elements themselves. We have also plotted the values of det(M) obtained from the quadratic fit to the raw data. Not too surprisingly, this produces agreement with theory as consistent as the agreement found for the matrix elements.

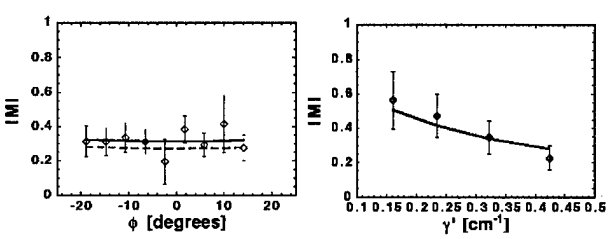

Figure 2: Determinant of the transverse trace space map for different acceleration phases ϕ (left) and gradients γ' (right). The values for the inverted fit to the data for the phase dependency are represented by a solid line, and for the theoretical predictions by a dashed line.

In order to complete a parametric study of the predictions of Eq. 4, and explore the adiabatic damping effects in more detail, we undertook a set of measurements of the matrix elements' dependence on E_0. In this case the rf attenuator was used to lessen the power fed into the linac, yielding, after resetting the phase to optimal acceleration, final beam energies of 7.1, 8.7, 10.6 and 12.8 MeV, or average accelerating fields of E_o =8.3, 12.1, 16.6, and 21.9 MV/m, respectively. This data can then be inverted as before to give the matrix elements. These experimentally derived determinants are plotted in Fig. 2 (right), along with the predicted values of γ_i/γ_f. This plot, which shows the expected behavior quite well is, taken along with Fig. 2 (left), convincing direct evidence for the adiabatic damping of transverse "action", or area, in trace space.

5 CONCLUSION

In conclusion, these sets of measurements have provided a first verification of the theoretical model developed in Refs. 5 and 6 of linear transverse dynamics of electrons undergoing simultaneous strong acceleration as well as first and second order transverse focusing in an rf linac. The matrix treatment of the dynamics predicted by this model has been directly tested, with the experimentally derived matrix elements in fairly close agreement with the model derived elements. The determinants of the matrices obtained in this manner have been shown to display the expected dependence, det(M) $= \gamma_i/\gamma_f$, giving direct evidence for the adiabatic damping of trace space area. Some deviations from theoretically predicted matrix elements themselves were noticeable, however, especially in the data obtained at lower acceleration gradient.

6 ACKNOWLEDGMENTS

This work performed with partial support from U.S. Dept. of Energy grants DE-FG03-90ER40796 and DE-FG03-92ER40693, the Sloan Foundation grant BR-3225 and the Deutscher Akademischer Austauschdienst (German academic exchange program).

7 REFERENCES

[1] K.J. Kim, *Nucl. Instruments and Methods A* **275**, 201 (1989).

[2] TESLA Test Facility Linac Conceptual Design Report, Ed.D. Edwards (DESY, Hamburg, 1995).

[3] E. Chambers, Stanford High Energy Physics Laboratory Report (Stanford, 1965).

[4] R. Helm and R. Miller, in *Linear Accelerators*, Eds. Pierre M. Lapostolle and Albert L. Septier (North-Holland, Amsterdam, 1969).

[5] S.C. Hartman and J.B. Rosenzweig, *Phys. Rev. E* **47**, 2031 (1993).

[6] J.B. Rosenzweig and L. Serafini, *Phys. Rev. E* **49**,1599 (1994).

[7] L. Serafini and J.B. Rosenzweig, TESLA report 96-12 (DESY, Hamburg, 1996), also submitted to *Phys. Rev. E.*

[8] R. Zhang, *et. al., Proc. of the 1995 Part. Accel. Conference*, 1102 (IEEE, 1995); D. Swenson, in *Proc. of the 1988 European Part. Accel. Conf.* p.1418 (World Scientific, 1989).

[9] U. Happek, A.J. Sievers, and E.B. Blum, *Phys. Rev. Lett.* **67**, 2962 (1991).

METHOD OF STRONG FOCUSING

V.E. Shapiro * TRIUMF, 4004 Wesbrook Mall, Vancouver, B.C., Canada V6T 2A3

Abstract

New methods for focusing and stabilization of the motion of charged and polarized neutral particles by electromagnetic fields are described. The idea is to rotate highly inhomogeneous fields in time so that the coupling of particles' orthogonal oscillations near the focal axis is substantially modulated. Unlike the field alternation without rotation which is used throughout for strong focusing in systems like beam transport, accelerators, and traps, the rotation in such devices opens up new ways for focusing and trapping not only in a point or an axis but also in an orbit or cylindrical surface. It can give much tighter confinement, helps overcome space charge and aberrations problems and provides flexible monitoring of several beams.

1 INTRODUCTION

The strong focusing, i.e. the average focusing effect of frequently alternating focusing and defocusing fields, gains new properties suitable for beam line applications by exploring the field rotation about the optic axis rather than familiar non-rotating field alternation. The proposals and discussion have been concentrated on the strong focusing with magnetic or electric static quadrupoles rotating helically in space, e.g. [1-11]. Recently but independently and for problems of magnetic traps for neutral particles, the author found new methods of tight trapping by means of highly non-uniform fields rotating in time rather than in space. We suggest that the strong focusing with the electric and magnetic fields rotating in time can be effectively explored also in beam line applications for charged particles, particularly in radio frequency quadrupole accelerators and systems, providing a more diverse and flexible control of beam optics. In this paper, we will focus on general specifics of the proposed strong focusing. Basically, there is a correlation between the strong focusing under the fields varying in time and that of in space and we will pay attention to some features not discussed in the literature on static helical structures. The specifics of magnetic focusing of neutral particles will be briefly elucidated at the end of the discussion.

2 BASIC EQUATIONS

The analysis will be based on a special though a rather representative model, a continuously rotating quadrupole system for which the analytical calculations become tractable. The equations of transversal motion of a charged particle near the optic axis will be

$$\begin{aligned} \ddot{x} &= kx\cos(2\Omega t) + ky\sin(2\Omega t) + ax + g\dot{y} + f_x, \\ \ddot{y} &= kx\sin(2\Omega t) - ky\cos(2\Omega t) + ay - g\dot{x} + f_y \quad (1) \end{aligned}$$

where k is related to the strength of the quadrupole rotating at frequency Ω and a to the strength of the (smoothed) rf defocusing, beam space-charge and other forces assumed axially symmetric and static; g is related to the gyro factor of longitudinal magnetic field, it allows us to see similarities and interlacing with the effect of rotating quadrupole; f are other forces, neglected unless specified otherwise. With t replaced by longitudinal coordinate z and with $f = g = 0$, this is a familiar type of equations considered in the literature devoted to strong focusing with helical quadrupole static structures. A combined space-time rotation of the quadrupole is governed by the equations of same type.

The rotating quadrupole, unlike the alternating, non-rotating, gives rise to the modulation of both the partial frequencies of the orthogonal oscillations about the optic axis and the coupling between these oscillations. This additional modulation enhances the strong focusing effect and enriches it with new, gyroscopic-like properties.

3 FIELD ARRANGEMENT

The time rotation, say, of an electric planar quadrupole field can be created by a.c. current of frequency 2Ω driving out of phase two identical quads of parallel (along z) electrodes with each quad creating a standard four-electrode planar quadrupole field geometry centered at the axis of symmetry. The two quads are turned about z by angle $\pi/4$ with respect to each other, i.e. in case of thin electrodes they form, in cross section, the apices of a rectilinear octagon. As a result, the lines of the a.c. field created by one quad are orthogonal to the lines of the other and shifted in time phase by $\pi/2$. The same idea of creating the rotating field with two conventional a.c. field configurations which are out of phase and ensemble with orthogonal field lines can be explored for the arranging of the rotation of a multi-pole field. For the field of multipole-number N rotating at frequency Ω, the frequency of a.c. current should be $N\Omega$.

The doubling of the field poles will impose additional tolerance limits on the mechanical arrangement of the system, being the price for more effective and versatile functions elucidated below.

4 STABILITY CONDITIONS

In the rotating frame $\mathbf{R} = (X_1, X_2, z)$ with the coordinates X_1, X_2 in the directions coinciding with the principal axes

* Email: vshapiro@triumf.ca

0-7803-4376-X/98 /$10.00 © 1998 IEEE

of the rotating quadrupole, the equations of particle motion (1) reduce to the form

$$\begin{aligned} \ddot{X}_1 &= (a+k)X_1 + 2(\Omega+g)\dot{X}_2 + \Omega^2 X_1 + F_1, \\ \ddot{X}_2 &= (a-k)X_2 - 2(\Omega+g)\dot{X}_1 + \Omega^2 X_2 + F_2. \end{aligned} \quad (2)$$

The terms proportional to Ω represent Coriolis forces and to Ω^2 centrifugal; $F_{1,2}$ are related to $f_{1,2}$ via the rotation transformation,

$$F_1 + iF_2 = \exp(i\Omega t)(f_x + if_y).$$

Let us analyse the system (2) for $F_{1,2} = 0$. The equilibrium state is at $X_{1,2} = 0$ and the normal oscillations near the z axis are of the form $\exp(\pm i\Omega_\pm)$ where

$$\Omega_\pm^2 = \check{\Omega}^2 - \check{a} \pm \sqrt{k^2 - 4\check{a}\check{\Omega}^2} \quad (3)$$

and

$$\check{\Omega} = \Omega + g, \quad \check{a} = a - g^2.$$

The regime of stable focusing requires the conditions of $\Omega_\pm^2 > 0$, otherwise defocusing occurs via an instability which is parametric in the picture of fixed coordinate frame. The stability condition on k and Ω is given by

$$\check{a} < \check{\Omega}^2, \quad 4\check{a}\check{\Omega}^2 < k^2 < \left(\check{a} + \check{\Omega}^2\right)^2 \quad (4)$$

and is represented by the green shaded region in the figure. The yellow shaded region is a familiar shape in conventional strong focusing systems, it corresponds to the model (1) with the x-y coupling terms $\sim \sin(2\Omega t)$ omitted and $\check{a} = a$. As seen from the region at $g^2 - a < 0$, the rotating quadrupole gives stable focusing with considerably smaller gradients k's. The rotation also resists the influence of short-range field inhomogeneities, since no parametric resonance instabilities arise near $(g^2 - a) = n^2(\Omega + g)^2$ with $n = 2, 3, ...$

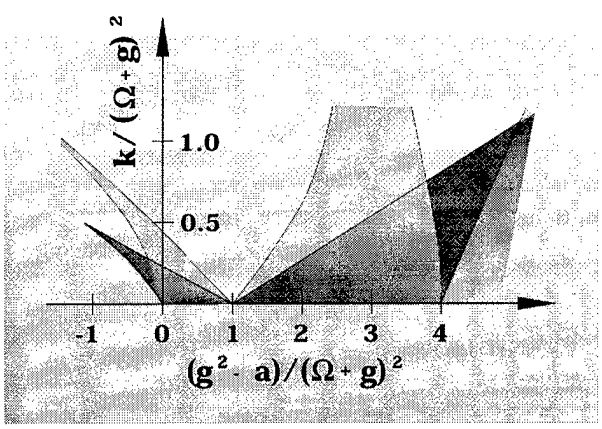

5 FOCUSING STRENGTH AND INDUCED GYROSCOPY

In the fixed frame, the transversal particle motion is a superposition of four harmonics of frequencies $\Omega \pm \Omega_\pm$ of elliptical polarization. These four frequencies are displaced asymmetrically with respect to zero, pointing to a specific gyroscopic modulation of the motion which may be 100 % depending on initial conditions. The case of fast rotation, $k \ll \Omega^2$, gives an idea of characteristic trends. Then both kinds of parametric influence in Eq. (1), $\sim \cos(2\Omega t)$ and $\sim \cos(2\Omega t)$, contribute equally to the average focusing force. This force is radial and its gradient

$$k_o = \frac{k^2}{4\Omega^2} \quad (5)$$

is twice as powerful as that of the alternating, non-rotating quadrupole of same strength k. As k/Ω^2 increases, the focusing becomes stronger than twice, since the modulated coupling $\sin(2\Omega t)$ gives rise to both the net radial forces and the net gyro forces similar to the terms $\sim g$ in (1). Within leading approximation, the corresponding gyroscopic factor

$$g_o = \frac{k^2}{8\Omega^3}. \quad (6)$$

The g_o gives the scale of the modulation frequency. In next order approximation in k/Ω^2, the averaged dynamics is modified by this gyro force similarly to the effect of the terms $\sim g$ in (1), renorming a to $a - g_o^2$. This enhances the net focusing force with k/Ω^2 by about 20% in a certain interval inside the stability region. The focusing strength can be considerably more than doubled by the use of rotating multi-pole fields.

6 FOCUSING WITH ROTATING MULTI-POLE FIELDS

The fact that the rotation of non-uniform fields with multi-pole numbers higher than quadrupole can be rather effective for the focusing is evident from the following. The higher the number of a multi-pole component, the weaker its contribution to the overall focusing action in the vicinity of rotation axis. The contribution, however, rapidly increases with the distance from the axis. The action of synchronously rotating multi-pole fields results in the appearing in Eq.. (2) of forces $F_{1,2}$ with polynomial dependence on X_1 and X_2 and independent of t. The equilibrium states are given by the algebraic equations in $X_{1,2}$

$$X_s = -F_s/(\Omega^2 + a + k_s) \quad (7)$$

with $s = 1, 2$, $k_s = \pm k$ respectively. The roots of (7) represent a number of orbiting states of frequency Ω of different orbital radius and different azimuth. The oscillations in close vicinity of such states obey the linearized equations of the same type discussed above and, hence, the same analysis of stability and other properties can be applied. The strength of focusing, being proportional to the square of gradients $F_{1,2}$, increases sharply with the multi-pole number and the radius of equilibrium orbit and this considerably favours the confinement. In addition to enlarging the area of strong focusing, new schemes can be arranged for flexible monitoring of several beams, overcoming space charge and aberrations problems.

An important novel property is the ability to provide focusing not only in the axis of rotation, but in a finite radius cylindrical surface. This can be arranged without higher multi-pole fields. The rotation of quadrupole field is then combined with the synchronous rotation about the same z-axis of transversal uniform field. For example, for the focusing with electric fields, the uniform component can be generated by two quads of electrodes that provide the rotating quadrupole. The driving frequency of the uniform component should be Ω, rather than 2Ω, and each of the two quads should be operated in the dipole mode (rather than quadrupole) so that now the orthogonal dipole fields are driven out of phase. The additional uniform field results in the particle dynamics being governed by the same equations (2) except that the equilibrium state of $X_{1,2}$ is shifted from the center of rotation, as given by Eq. (7), with $F_{1,2}$ equal to the instant components of the rotating uniform field at $t = 0$. In the fixed coordinate frame the shifted state is an orbital motion of frequency Ω and the rotating uniform field controls the azimuth and radius of the orbit. Note that though the motion equations for small displacements from this orbit coincide with (2), the confinement in this state differs from that of vanishing uniform field component since a harmonic of frequency Ω (synchronously rotating with the field) arises in addition to the four harmonics corresponding to the formal normal modes.

7 MAGNETIC TRAPPING OF NEUTRAL PARTICLES

The strong focusing with rotating highly non-uniform fields can be effective for focusing and confinement of both charged particles and neutral polarized particles. Let us briefly consider its application to trapping of neutral spin-polarized particles with magnetic fields rotating at a frequency Ω small compared to the frequency scale Ω_Z of Zeeman splitting of the spectrum of the trapped particles in the field. In such conditions the magnetic polarization μ of the particles follows the direction of instant field $\mathbf{B}(\mathbf{r}, t)$ adiabatically and the magnetic force field is potential. For the particles with vector μ antiparallel to $\mathbf{B}$, the magnetic force potential

$$V = \mu B$$

where $\mu = |\mu| = const > 0$ and $B = |\mathbf{B}|$. The potential is singular at $B = 0$ and is not harmonic, $\Delta V \neq 0$. We found that, in such conditions the strong focusing with rotating non-uniform fields has unique advantages for tighter, stable confinement of polarized neutral particles.

In particular, the 3D trapping of remarkable characteristics occurs when the field is of the form

$$\mathbf{B} = \mathbf{B}_{st}(\mathbf{r}) + \mathbf{b}(t, \mathbf{r}) \tag{8}$$

where $\mathbf{B}_{st}$ is a static quadrupole field of axial symmetry with the symmetry axis z in vertical direction and $\mathbf{b}$ is a sum of uniform and quadrupole planar fields synchronously rotating about axis z. In the rotating frame coordinates, the equilibrium state of the trapped particle is where the force potential

$$U(\mathbf{R}) = \mu B(\mathbf{R}) + Mgz - M\Omega^2(X_1^2 + X_2^2)/2$$

(Mgz is the gravity potential) is minimum. The equilibrium state $\mathbf{R} = \mathbf{R}_o$ represents a planar orbit and is most effective for confinement when the vertical component of the static field $\mathbf{B_{st}}(\mathbf{R_o})$ is small compared to the magnitude of the planar rotating field $\mathbf{b}(\mathbf{R_o})$. The dynamics of particle transversal oscillations near the equilibrium orbit is described approximately by the equations of structure (2). Details of the analysis are in [12]. It is important that the radius of equilibrium orbit can be reduced to zero by the variation of the rotating uniform field. This allows considerable decrease of current loads in the coils of the magnetic field and results in cardinal improvement of trapping characteristics. Not only the confinement, but also the polarization alignment of the trapped particles over their cloud is improved since the area of singularity of magnetic potential (the main contributor to the polarization misalignment) is removed.

In addition, the trapping with rotating fields of considered geometry opens up new, vast possibilities for magnetic separation and evaporative cooling of polarized neutral particles, since the equilibrium orbit radius critically depends on the gradient of rotating quadrupole field and on the rotation frequency Ω via a resonance denominator. The corresponding orbit resonance frequency differs from that of parametric resonance and both can be controlled independently in such a way as to enhance the differences in equilibrium states and stability of particles with different μ/M.

8 REFERENCES

[1] L.C. Teng, Argonne Report ANLAD-55 (Febr. 1959).

[2] F. Krienen, CERN/SC-129 and CERN 57-28.

[3] M. Morpurgo, CERN - SC/4114/141.

[4] S. Ohnuma, TRIUMF Report TRI-69-10 (1969).

[5] G. Salardi, E. Zanazzi and F. Uccelli, Nucl. Instr. and Meth. **59**, 152 (1969).

[6] R.M. Pearce, Nucl. Instr. and Meth. **83**, 101 (1970).

[7] R.L. Gluckstern, Proc. of 1979 Linear Accelerator Conf., Montauk Point, New York, p. 245.

[8] R.L. Gluckstern and R.F. Holsinger, Nucl. Instr. and Meth. **187**, 119 (1981).

[9] D. Raparia, Proc. of 1990 Linear Accelerator Conf., Albuquerque, p. 405.

[10] Y. Mori, A.Taggi, T. Okuyama, M. Kinsho, H. Yamamoto, T. Ishida and Y. Sato, Proc. of 1992 Linear Accelerator Conf., Ottawa, Ontario Canada -AECL-10728, Vol. 2, p. 642.

[11] K. Masek and T.R. Sherwood, CERN/PS 95-30 (HI) (1995).

[12] V.E. Shapiro, Phys. Rev. A **47**, 2, R1019 (1996).

A STANDARD FODO LATTICE WITH ADJUSTABLE MOMENTUM COMPACTION *

D. Trbojevic and E. Courant
Brookhaven National Laboratory, Upton, NY, 11973, USA

Abstract

An existing lattice made of identical FODO cells can be modified to have adjustable momentum compaction. The modified lattice consists of repeating superperiods of three FODO cells where the cells have different horizontal phase advances. This allows tuning of the momentum compaction or γ_t (transition) to any desired value. A value of the γ_t could be an imaginary number. A drawback of this modification is relatively large values of the dispersion function (two or three times larger than in the regular FODO cell design). This scheme also requires an additional quad bus for the modified cells.

1 INTRODUCTION

Particles travel along the reference orbit in an accelerator ring with momentum p_0 and period of revolution T_0. If they have a momentum deviation Δp, the time of the arrival a the point of observation will be different. An offset in the revolution period ΔT is given by:

$$\frac{\Delta T}{T_0} = \left(\alpha - \frac{1}{\gamma^2}\right)\frac{\Delta p}{p_0}\,, \qquad (1)$$

where α, the *momentum compaction* is a property of the lattice, and $\eta = \alpha - \gamma^{-2}$ is called the *phase-slip factor*; γ is the Lorentz relativistic factor for the on-momentum particle. The momentum compaction factor is a measure of the path length difference between the off-momentum particle and the on-momentum particle. The transition energy γ_t is the energy at which η vanishes, i.e. it equals $1/\sqrt{\alpha}$. In many accelerators γ_t lies in the acceleration range. We shall show that an existing FODO lattice can be modified so as to make γ_t either very large or even imaginary (negative α). This could be used to for example to avoid having to cross transition, or to make zero momentum compaction *isochronous* storage rings.

The momentum compaction of a lattice, to the first order, is an integral of the dispersion function D through the dipoles:

$$\alpha = \frac{1}{C_0}\oint \frac{D(s)}{\rho(s)}ds\,, \qquad (2)$$

where ρ is the radius of curvature and s is the longitudinal path length measured along the reference orbit with a circumference C_0. There are many ways to devise an accelerator lattice with either fixed or adjustable value of the momentum compaction [1],[3],[4],[5]. Vladimirski and Tarasov [1] propose use of reverse bend dipoles to make the momentum compaction negative. Teng [6] shows that a straight section with a phase advance of π can make the dispersion closed orbit negative at dipoles. Iliev [3] and Guignard [4] use a harmonic approach, where the betatron function is modulated to produce negative values of the momentum compaction by way of resonance conditions. We have reported earlier [5] and [8] the use of flexible-momentum compaction lattices to minimize dispersion values.

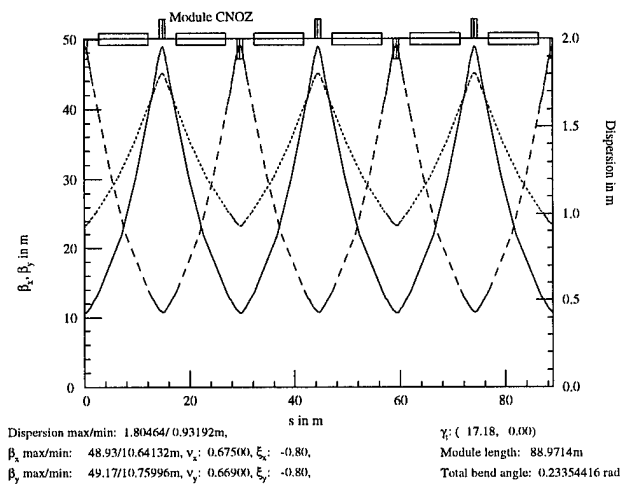

Figure 1: Courant-Snyder functions in the three RHIC cells under normal operating conditions.

2 NORMALIZED DISPERSION FUNCTION

The dispersion function D needs to be adjusted through the FODO cell to obtain a different integral of its values through dipoles. Because the dispersion function satisfies a second order inhomogeneous differential equation of motion [7] it is useful to use the normalized dispersion function with components ξ and χ as previously defined [5]:

$$\xi = \sqrt{\beta_x}D' - \frac{\beta_x'}{2\sqrt{\beta_x}}D, \quad \chi = \frac{1}{\sqrt{\beta_x}}D, \qquad (3)$$

where β_x and β_x' are respectively the horizontal betatron amplitude function and its derivative [7], ξ and χ are projections of the normalized dispersion vector.

3 FODO CELLS WITH ADJUSTABLE MOMENTUM COMPACTION

As an example we modify the lattice of the Relativistic Heavy Ion Collider (RHIC) at Brookhaven National Laboratory, where the dipole length is $L_d = 9.45m$ and the

* Work performed under the auspices of the U.S. Department of Energy

cell length is $L_c \simeq 29.6m$. In our example we use superperiods of three cells as previously proposed by Guignard [4]. Figure 1 shows the Courant-Snyder functions for three cells under the standard operating conditions.

We chose a point of reflection symmetry of the orbit functions at the middle of the three cells. We modify the quadrupole strengths so as to obtain a negative momentum compaction.The quadrupole strengths which make the momentum compaction negative, with $\gamma_t = i358$, are presented in Table 1.

Table 1

Q. Strengths	κ(1/m)
κ_{QDA}	0.05648
κ_{QF}	0.07330
κ_{QD}	0.09634
κ_{QFC}	0.13057

The normalized dispersion plot for this case is shown in figure 2.

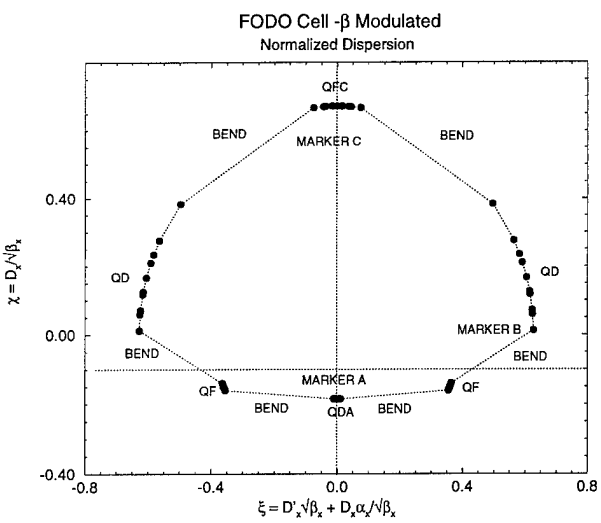

Figure 2: Normalized Dispersion function within the β modulated three FODO cells.

Figure 3 shows the orbit functions β_x, β_y and D in the modified cells (the centers of symmetry are at QDA and QFC).

We see that the penalty paid for making the dispersion negative is almost a doubling of the maximum β_x and β_y function and of the dispersion funcion. In addition the tunes ν_x and ν_y are changed substantially.

4 CONCLUSION

The momentum compaction of the standard FODO cell lattice could be adjusted by the modulating the *betatron functions* to any desired values with the drawback of larger values of the dispersion and betatron functions. A range of dispersion function offsets, obtained by the quad adjustments, falls within twice of the optimum FODO cell dispersion

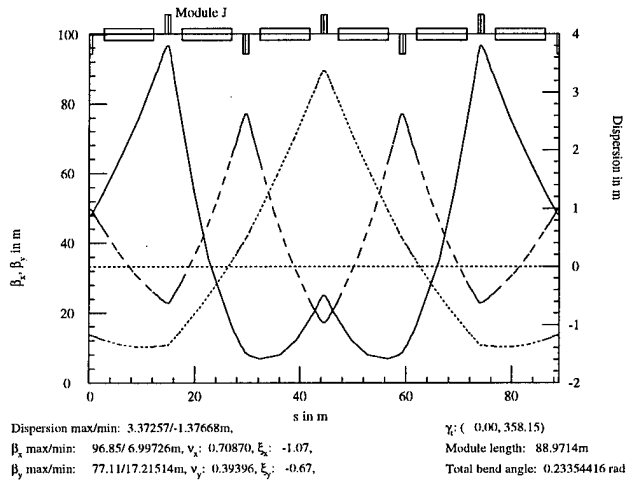

Figure 3: Courant-Snyder functions in three β perturbed cells.

values. The maximum values of β_x and β_y are less than two times the values at optimum betatron tunes ($\nu = \pi/2$). The beam size was less than $\sqrt{2}$ larger. This report shows that a resonance condition ([4], [3]) was not necessary to achieve different values of the momentum compaction within standard FODO cells. We used an existing FODO lattice to accommodate the momentum compaction value, but we do not recommend it the lattice of a new accelerator.

5 REFERENCES

[1] V.V. Vladimirski and E.K. Tarasov, " Theoretical Problems of the Ring Accelerators", USSR Academy of Sciences, Moscow (1955).

[2] T. Riesselada, *Design of Quadrupole schemes to modify Gamma Transition*, CERN PS/90-51 (1990).

[3] A.I. Iliev, "Analytic Approach to Design of High Transition Energy Lattice with Modulated β Function", Proc. of 1991 IEEE Part. Accel. Conf., 1991, San Francisco, California, pp 1907-1909.

[4] G. Guignard, "A Lattice with no Transition and Largest Aperture", Proc. of 1989 IEEE Part. Accel. Conf., March 20-23, 1989, Chicago, IL, pp 915-917.

[5] D. Trbojevic, D. Finley, R. Gerig, and S. Holmes, "Design Method for High Energy Accelerator without Transition Energy", Proc. of Second European Particle Accelerator Conference, Nice, France, June 1990, pp 1536-1538.

[6] L.C. Teng, "Infinite Transition-energy Synchrotron Lattice using π-straight Section", Part. Acc. **4**, pp. 81-85 (1972);

[7] E.D. Courant and H.S. Snyder, "Theory of the Alternating Gradient Synchrotron", Ann. Phys. **3**, 1 (1958).

[8] S. Y. Lee, K.Y. Ng, D. Trbojevic, "Minimizing dispersion in flexible-momentum compaction lattices", Physical Review E, Vol. 48, Number 4, October 1993, pp. 3040-3048.

BEAM-BASED CALIBRATION OF THE LINEAR OPTICS MODEL OF ELSA

J. Keil, D. Husmann, University of Bonn, Physics Institute,
Nußallee 12, 53115 Bonn, Germany

Abstract

The Electron Stretcher Accelerator (ELSA) of Bonn University is used to provide an external electron beam of high duty factor in the energy range from 0.5–3.5 GeV for fixed target experiments. In the near future polarized electron beams will be accelerated up to the highest energies. In order to avoid depolarization of the beam by imperfection and intrinsic resonances the control of the closed orbit and the symmetry of the ring lattice has to be improved. For calibration of the optics model of ELSA the orbit response matrix has been measured and fitted with help of the program CALIF. The strengths of the two quadrupole families and the relative scaling factors for the beam position monitors and corrector magnets have been determined this way. The results of the fits and a comparison with measurements of the optical functions of ELSA will be presented.

1 INTRODUCTION

Since 1987 Bonn University operates the Electron Stretcher Accelerator ELSA [1] which is used to deliver a nearly continuous electron beam to three fixed target experiments in the energy range between 0.5 GeV and 3.5 GeV. The accelerator facility consists of two LINACs equipped with polarized and unpolarized electron guns, a rapid cycling booster synchrotron (50 Hz) and the main ring ELSA (fig. 1). Using a third integer resonance the pulses injected from the booster into ELSA are slowly extracted for a duration of up to a minute and delivered to one of three external experiments.

To some extend ELSA is used as a partially dedicated light source. Currents of more than 250 mA can be stored in ELSA at 1.6 GeV and lifetimes of up to 3 hours for 15 mA at 2.3 GeV have been achieved, which are merely vacuum limited.

The ELSA lattice was designed with a two-fold symmetry and is composed of 16 FODO cells build up in two arcs and two straight sections. Integrated into the arcs are missing-magnet dispersion suppressors to provide vanishing dispersion in the straight sections containing the injection magnets, RF cavities and sextupoles used for the resonance extraction. Besides the two quadrupole families there are four sextupoles for chromaticity correction per plane and four sextupoles to drive the third integer resonance used for extraction.

One of the main goals in the future will be the acceleration of a polarized electron beam up to an energy of 3.5 GeV. In order to avoid the depolarization due to imperfection and intrinsic resonances, correction methods (harmonic correction and tune jumping) have to be applied [6].

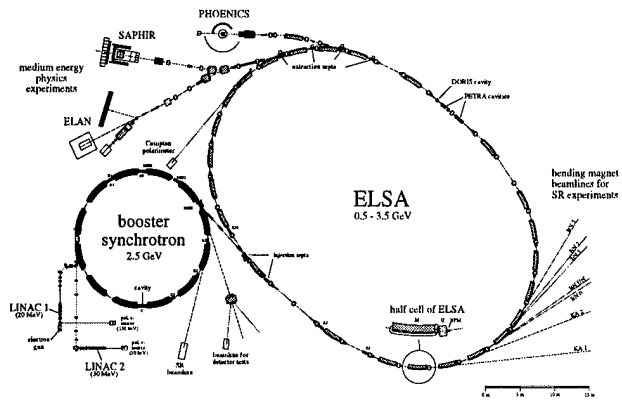

Figure 1: Layout of the facility ELSA

For an appropriate correction a better knowledge of the optics is necessary, because some of the depolarizing resonances are suppressed due to the supersymmetry of the lattice. This symmetry is broken by gradient errors and by a nonzero orbit in the sextupole magnets.

The calibration of the internal polarimeter of ELSA will be done by using the self-polarization of the beam. The appearence of reasonable polarization depends strongly on the control of the closed orbit in the quadrupoles. We will adopt the method of k-modulation of single quadrupoles [5] to center the beam in the quadrupoles and to find the offset between the center of the BPM and the magnetic center of the nearby quadrupole. For the reconstruction of the position of the beam in the quadrupoles the exact knowledge of the optics is mandatory.

2 THEORY

The method of beam-based calibration of the optics model uses the analysis of the measured orbit response matrix $\bar{\mathbf{C}}$ [2] [4]. The elements of the response matrix

$$\bar{\mathbf{C}}_{ij} = \frac{\Delta x_i}{\Delta \theta_j} \tag{1}$$

are defined as the change of the beam position Δx_i at the beam position monitor (BPM) i due to a change of the kick $\Delta\theta_j$ of the corrector magnet j.

The theoretical response matrix $\mathbf{C}$ is expanded to first order in the fit parameters (for instance the gradients of single quadrupoles k_l) using an accelerator modeling program. Each matrix element $\bar{\mathbf{C}}_{ij}$ depends on the BPM gain x_i and the corrector scale factor y_j. This results in the fol-

0-7803-4376-X/98/$10.00 © 1998 IEEE

lowing equation:

$$x_i \bar{\mathbf{C}}_{ij}\, y_j = \mathbf{C}_{ij} + \sum_l \frac{\partial \mathbf{C}_{ij}}{\partial k_l} \delta k_l \quad . \tag{2}$$

For the solution of this least-square problem it has to be taken into account, that for each plane all BPM gain factors x_i can be increased when all corrector scaling factors y_j are reduced at the same time and vice versa. In the computer program CALIF [2], which we used for the analysis of the measured orbit response matrix $\bar{\mathbf{C}}$, two methods are implemented to deal with this degeneracy of the problem.

The first one uses an alternating fitting of the BPM gains x_i in combination with the focusing strengths k_l and the corrector scalings y_j in combination with the k_l.

The other method is to solve the linear equation system for the fit parameters and to remove the degeneracy of the problem by using the singular value decomposition[3]. In addition this fit considers, that a kick $\Delta\theta_i$ of a corrector at a place with non-vanishing dispersion D_x leads to an energy change of

$$\frac{\Delta E}{E} = \frac{\Delta\theta_i D_x}{\alpha C_0} \tag{3}$$

in a machine with momentum compaction factor α and circumference C_0, which effects the measured data of all BPMs.

3 MEASUREMENTS

For the closed orbit correction of ELSA, 24 BPMs (both planes), 16 horizontal and 17 vertical corrector magnets are available. Therefore the orbit response matrix $\mathbf{C}$ has $48 \times (16 + 17) = 1584$ matrix elements, which can be used for fitting the optics model and the BPM and corrector scaling factors.

In order to reduce the number of fit parameters of the optics model all chromatic and extraction sextupoles were turned off. Otherwise additional focusing and defocusing fields emerging from the nonzero orbit in these nonlinear elements would appear.

The measurement of the response matrix was done automatically and took about one hour. The current change was equal for all corrector magnets and created closed orbit deviations with peak amplitudes of several millimeters.

4 ANALYSIS

The measured response matrix was then analyzed with the help of the computer code CALIF. The set of the 48 BPM gain factors x_i, the 33 scaling factors of the corrector magnets y_j and the two quadrupole strengths k_l of the main quadrupole families were chosen as fit parameters.

We used both methods implemented in CALIF to deal with the degeneracy of the BPM/corrector scaling problem. Both methods converged to nearly the same solution. The corrector scale factors y_j were fitted with an relative error of ≈ 1.4 % and the BPM gains x_i with ≈ 2 %. For the rms resolution of the BPMs we found values between 200

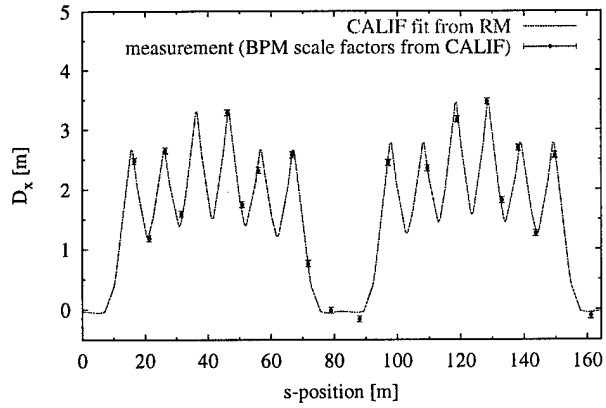

Figure 2: Measurement of the horizontal dispersion function (the BPM data were scaled with the gain factors obtained from the CALIF fit) and prediction from the fitted optics model

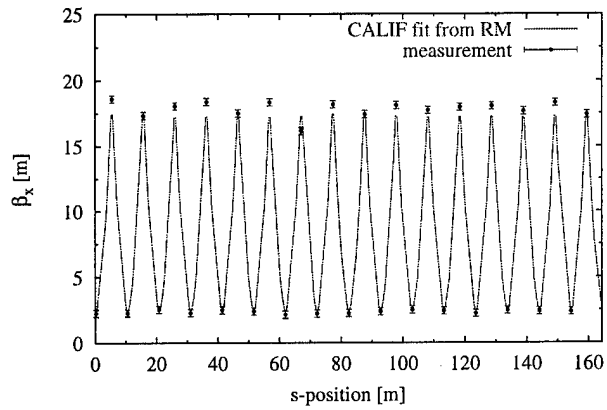

Figure 3: Measurement of the horizontal beta function and prediction from the fitted optics model for the ELSA lattice

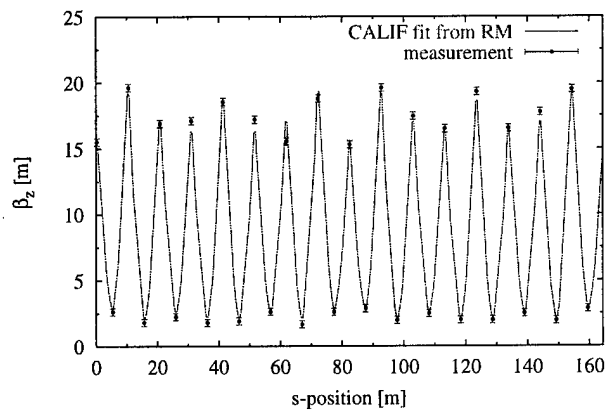

Figure 4: Measurement of the vertical beta function and prediction from the fitted optics model for the ELSA lattice

and 300 μm, which are in good agreement to our previous experiences with the BPM system.

At first we checked whether the fit reconstructed the right scaling factors of the two different types of corrector magnets in use at ELSA. In places with less space a shorter version of the corrector with about 70 % field strength had been installed. CALIF successfully found all these correctors and was also able to find the three magnets with interchanged polarity (a fact which was already known).

In order to decide if the fit converged to the right solution, predictions from the optics model have to be compared with independently measured data. One such value is the tune of the machine, because in no place it entered into the analysis of the response matrix. We found that the tunes agreed very well with the tunes computed from the model. The differences between the measured and the computed tune from the model were $\Delta Q_x = 0.002$ in the horizontal and $\Delta Q_z = -0.001$ in the vertical plane.

Other parameters, which can be checked, are the optical functions of the machine. The dispersion function can be calculated from the well known expression

$$D_x = -\alpha \Delta x \frac{f_{\mathrm{RF}}}{\Delta f_{\mathrm{RF}}} \quad , \tag{4}$$

by measuring the displacement of the beam Δx due to the change in the RF frequency f_{RF}.

In figure 2 the dispersion function predicted from the fitted optics model and the measured data are plotted. The measured data were rescaled with the BPM gain factors obtained from the fit. The measured data without this rescaling had deviations of several ten percent from the theoretical values.

The beta functions were measured by k-modulation of the 32 quadrupoles. For the purpose of the precise measurement of the position of the BPMs with respect to the magnetic center of the nearby quadrupoles we installed a k-modulation system [5], which allows to change the focusing strength of a single quadrupole of up to $\Delta k/k = \pm 1$ % using an additional power supply. From the tune shift ΔQ and the effective magnetic field length l_{eff} the mean beta function

$$\bar{\beta} = \frac{4\pi \Delta Q}{\Delta k \, l_{\mathrm{eff}}} \tag{5}$$

in the quadrupole can be calculated.

The measured data and the prediction from the fitted optics model for the beta functions are shown in figures 3 and 4. As we fitted only the strength of the quadrupole families, it is not possible to model effects like the beating of the beta functions evoked from gradient errors of single quadrupoles.

The fit of the measured response matrix predicted that the quadrupole strengths have to be increased by 2.9 ‰ for the F-quadrupoles and 0.4 ‰ for the D-quadrupoles in contrast to our current theoretical model of ELSA. Thereupon we investigated the quadrupole power supplies and found that this deviation was partially caused by a faulty balancing in one of the power supplies and a DAC scaling error.

We also tried to include the strengths of the 32 single quadrupoles in the set of fit parameters. Unfortunately, this fit failed and pairs of quadrupoles with strength deviations of nearly equal size but reversed signs showed up. The probable reason for this behaviour is the unequal distribution of the corrector magnets due to lack of space along the circumference of ELSA, leading to quadrupole pairs with no corrector in between.

5 CONCLUSIONS AND PLANS

With the analysis of the measured response matrix it was possible to fit the two quadrupole families of ELSA and the BPM and corrector scale factors. The tunes calculated from the model fit closely to the measured values. Also the optical functions are in good agreement with the measured data. We were able to determine the gain factors of the BPMs and found some faulty hardware.

In the future we plan to increase the number of correctors to allow also the measurement of single quadrupole gradient errors, which we were not able to fit so far. The old BPM system will be substituted by a new one with a much higher resolution, offering to fit also for other parameters like the s-positions or the tilts of the elements.

6 ACKNOWLEDGEMENTS

The authors would like to thank Volker Ziemann from 'The Svedberg Laboratory' (Uppsala University) for using the program CALIF, his support with the program and interesting discussions.

7 REFERENCES

[1] K.H.-Althoff et al.: 'ELSA – One Year Experience with the Bonn Electron Stretcher Accelerator', Particle Accelerators 27 (1990) 101.

[2] J. Corbett, M. Lee, V. Ziemann: 'A Fast Model-Calibration Procedure for Storage Rings', SLAC-PUB-6111 and PAC 1993.

[3] W. Press, S. Teukolsky, W. Vetterling, B. Flannery: 'Numerical Recipes in C: The Art of Scientific Computing', Cambridge Univ. Press, 1996.

[4] D. Robin, G. Portmann, H. Nishimura, J. Safranek: 'Model Calibration and Symmetry Restoration of the Advanced Light Source', EPAC 1996.

[5] P. Röjsel: 'A beam position measurement system using quadrupole magnets magnetic centra as the position reference', Nucl. Inst. and Meth., A343 (1994) 374.

[6] C. Steier, D. Husmann: 'Correction of Depolarizing Resonances in ELSA', these proceedings.

LATTICES FOR MEDICAL SYNCHROTRONS EMPLOYING ACTIVE SCANNING

M. Benedikt, CERN/PS, CH-1211 Geneva 23, Switzerland

Abstract

Medical synchrotrons fall naturally into two categories; those using passive scattering techniques to spread the beam over the irradiation field and those using active scanning techniques to perform a high-precision conformal treatment of the tumour. The latter category is the newer generation that requires slower, more stable beam spills, achieved by the use of a third-integer extraction. These machines work below transition and for the stability of the stack, waiting outside the resonance, the chromaticity should be negative. This imposes strict constraints on the lattice for the application of the Hardt condition that aligns the separatrices of different momenta. This in turn affects the lattice between the electrostatic and magnetic septa, which should be, as close as possible, an achromatic transfer. It is also important that the extraction separatrices grow in a balanced way to economise the machine aperture. Since the separatrices occupy the same space at all energies, the 'good-field' region cannot be relaxed at higher energies as is normal in machines dominated by adiabatic damping. A sample lattice is presented to illustrate these points.

1 INTRODUCTION

Hadron-therapy can be based on protons or light ions. Extraction energies up to 400 MeV/u are needed for carbon ions, which requires a maximum magnetic rigidity of 6.5 Tm. Typically, such machines have a circumference of less than 80 m and small tune values. The use of a third-integer resonant extraction extends the beam spill time sufficiently to perform on-line dosimetry at the patient and to switch the beam on and off according to the dose required.

The uniformity of the spill, and the achieved dose distribution, depend critically on the method of extraction, on the lattice design and the stability of the power converters. It should also be remembered that such a machine will be in a hospital environment and therefore reliability, manoeuvrability of equipment and simplicity of operation will all be major concerns. The requirements on the spill are rather strict; the momentum spread of the extracted beam should be small, to make full use of the sharp dose localisation due to the Bragg peak, and the mean energy and the spread must not vary within a single spill, as this would cause a moving beam spot at the patient and an uncontrolled correlation between position and depth.

2 BASIC LATTICE DESIGN

The design shown below was developed from two achromatic, one-to-one mapping arcs ($\mu_x = \mu_z = 2\pi$). Each arc bends 180° and has a closed dispersion bump. This type of arc is extremely useful at the start of matching in a symmetric structure, as it will accept any Twiss input values and return them at the exit, always with the same phase advance. The arc was based on four 90° FODO cells, in which the F-quadrupoles were later split to form a FOFODO cell with longer drift spaces after each pair of dipoles. Alternatively, this can be described as a series of triplets, in which the β_x is kept small and the vertical focusing of the rectangular dipoles is used to limit the peaks in β_z. The smaller β_x is important at the maximum of the dispersion for the aperture and at the dipoles to limit the generation of the dispersion.

The arcs have then been detuned by changing the lengths of the drift sections to accommodate a betatron core, an internal dumping system and the electrostatic septum. The arcs are joined by two dispersion-free straight sections that are adjusted for the magnetic septum, the resonance sextupole and the rf and injection insertions. The lattice functions (Fig. 1) were adapted to the needs of each insertion with the help of a third quadrupole family, resulting in the final tune values of $Q_x = 1.67$ and $Q_z = 1.72$. The lattice has a superperiodicity of two with a mirror symmetry within each superperiod.

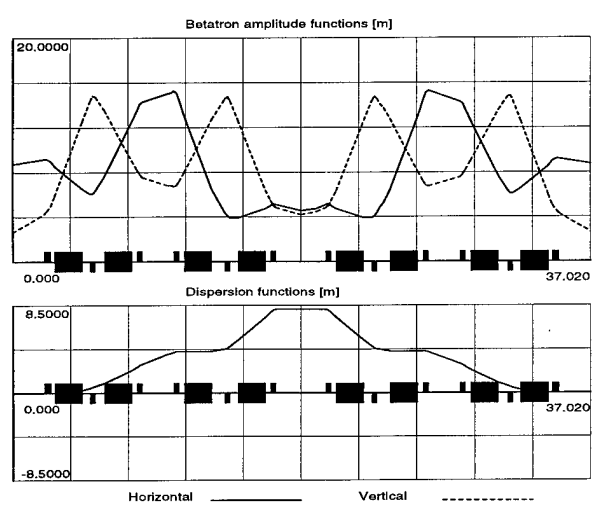

Figure 1: Lattice functions for one superperiod of the ring

An advantage of the split F-structure is that the beta-functions are quasi constant in the long straight sections whereas in a FODO, they vary rapidly across drift spaces and tune changes can alter values at the extraction septa more easily. The smooth Twiss-functions avoid high focusing strengths. The quadrupoles are low-field, straight-pole units and the dipoles are H-type units with rectangular edge focusing, 1.85 m long. The sagitta of ± 4.5 cm is just acceptable in a straight magnet which has the advantage of being simple to construct.

3 EXTRACTION

3.1 Sextupole magnets

The main parameters that determine the phase-space geometry for a third-integer resonance are the chromaticity and the resonance excitation, both of which are controlled by sextupoles. To simplify operation, one would like to have independent handles on these two parameters. In the lattice shown, this is achieved by placing the resonance sextupole in one of the dispersion-free sections so that it has no chromatic effect. For an independent control of the chromaticity, the two-fold symmetry of the lattice and a horizontal tune close to an even number ($Q_h = n \pm 1/3$, with n even) are used. Two sextupole magnets of equal strength are positioned in the dispersion region of the arcs on opposite sides of the ring, so that the resonance driving term is zero. The vertical chromaticity is adjusted in a similar way. To get some degree of orthogonality, the horizontal chromaticity sextupoles are at a large β_x, small β_z and the converse applies to the vertical ones.

3.2 Electrostatic Septum

When the beam enters the resonance, there will be a range of momentum and emittance values that define a boundary between the stable and unstable regions, which is given by the width of the stop band for the third-integer resonance, as

$$\left| Q'_x \frac{\Delta p}{p} \right| = \sqrt{\varepsilon_x} \sqrt{\frac{1}{48\sqrt{3}\pi}} |S|, \qquad (1)$$

where S is the normalised resonance sextupole strength, ε_x the horizontal emittance and Q'_x the absolute chromaticity, $dQ_x/(dp/p)$. The dispersion function at the electrostatic septum will spread the separatrices so that particles with different momenta reach the septum with different angles. The condition to set the optics so that all the extraction separatrices are superimposed (Fig. 2) to give minimum losses on the electrostatic septum is known as the Hardt condition [1],

$$D_n \cos\alpha + D'_n \sin\alpha = -\frac{4\pi}{S} Q'_x, \qquad (2)$$

where D_n and D'_n are the normalised dispersion and its derivative and α is the angle measured from the X-axis in the anticlockwise direction to the perpendicular from the origin to the separatrix. For this condition, the normalised dispersion vector should be perpendicular to the separatrices. This then allows the superposition, using a large (absolute) chromaticity, which gives a small momentum spread for the extracted beam, as can be seen from (1). The large chromaticity also increases the tune spread of the beam, giving a defense against power supply ripple during extraction.

For a typical angle of 20° to 50° between the X-axis and the extraction separatices, $D_n > 0$ and $D'_n < 0$ are needed (Fig. 2). The fact that negative chromaticity is required to ensure the stability of the stack [2], together with the above geometrical considerations, fixes the position of the electrostatic septum in the outer half of the vacuum chamber. This result is independent of whether the stack is positioned above or below the resonance in tune. In the lattice, the electrostatic septum is positioned 230° downstream from the resonance sextupole in the long straight section in the second half of the arc, where $D_n = 1\ m^{1/2}$ and $D'_n = -2\ m^{1/2}$, as required for the Hardt condition. The angle between the extraction separatrices and the normalised dispersion vector is 80° and the separatrices are superimposed for $Q'_x = -4$.

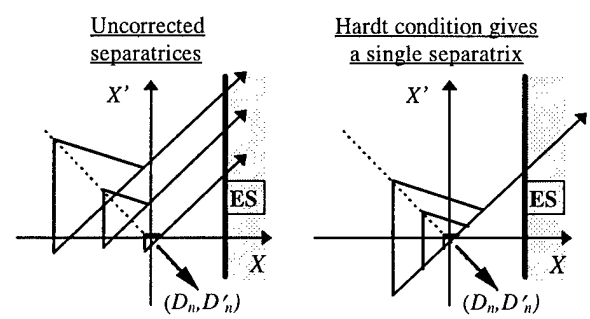

Figure 2: Extraction separatrices at electrostatic septum

3.3 Magnetic Septum

The magnetic extraction septum is positioned in the gap created by the kick of the electrostatic septum. In order to minimise the required voltage, both septa should be located at a large β_x and the phase separation should be close to 90°. A phase advance of 270° is less convenient as it puts the magnetic septum to the inside and the extracted beam has to be transported through a longer distance, which in a small machine means that the crossing of a chromaticity sextupole is unavoidable.

The gap for the magnetic septum will be reduced due to the momentum spread of the extracted beam if the transfer from the electrostatic to the magnetic septum is not achromatic which is the case in the example lattice. To keep this effect small, the magnetic septum is best positioned in the dispersion free section just after the last dipole magnet of the arc. The phase advance between the

septa is 55°, which gives 82% of the maximum gap opened by the kick of the electrostatic septum. The horizontal beta-functions at the septa are $\beta_{xES} = 15$ m and $\beta_{xMS} = 9$ m, which with a kick of 2.5 mrad gives a gap of 24 mm. For an electrostatic septum of 1 m length, the corresponding voltage at top energy (400 MeV/u C^{6+}) is 34 kV/cm. The gap reduction due to the non-achromatic transfer is 2.8($\Delta p/p$) [m]. For the example lattice, with a momentum spread of 0.001, the reduced gap of 21 mm is still adequately wide to allow the magnetic septum to be placed outside the vacuum which improves the reliability of the system. The layout of the extraction elements is shown in Fig. 3.

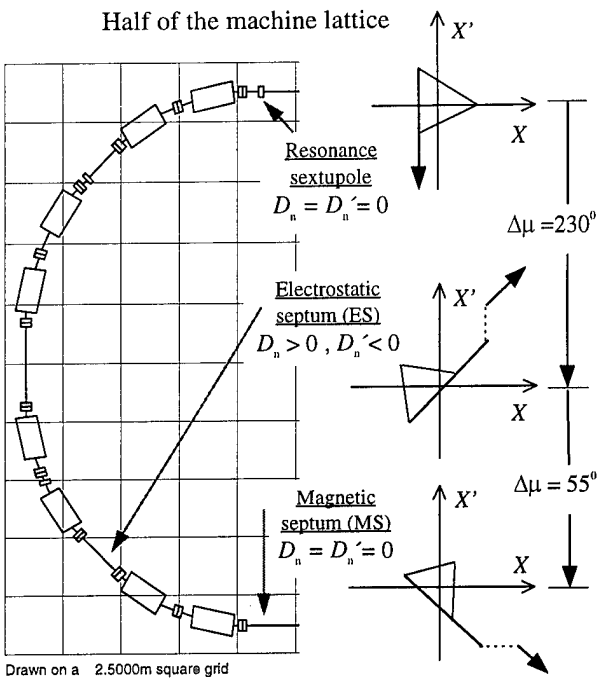

Figure 3: Layout of extraction elements

3.4 Extraction method

The choice of the extraction method will influence the spill characteristics. The Hardt condition is only effective if the resonance is stationary, i.e. if the beam is moved into the resonance e.g. by a betatron core [3,4] or with rf-noise [5]. In this case, the beam is always extracted from the same radial position in the machine, with mean momentum and momentum spread remaining unchanged during the spill. Therefore no dynamic orbit, focusing or tune corrections are required. The time structure of the spill can be improved by increasing the velocity in tune with which particles enter the resonance. One possibility is to slowly accelerate an unbunched beam with a large momentum spread into the resonance and to front-end this slow acceleration with an empty rf-bucket positioned over the resonance [6].

4 CONCLUSIONS

In any machine design there are essential requirements and desirable features. Inevitably there are conflicts, and compromises are needed. For example, reducing the dipole gap height often has high priority on grounds of power, whereas in a medical synchrotron the power dissipation is less important than optimum lattice functions and low-ripple power converters for the extraction. The lattice presented meets the extraction requirements. The only compromise is the transfer from the electrostatic to magnetic septum, which is not entirely achromatic but the required kick is very modest and there is no problem in opening sufficient gap for the magnetic septum. The resonance is stationary during extraction, as are all transverse beam parameters. This is an essential requirement for a stable spill since it avoids the need for dynamic corrections of orbits, tuning and resonance excitation, and delivers a beam with constant energy and momentum spread.

5 ACKNOWLEDGMENTS

This work constitutes a preparatory lattice design for a medical synchrotron and was carried out within the framework of the Proton Ion Medical Machine Study (PIMMS), which is a collaboration between CERN, GSI, Med-AUSTRON and TERA that is hosted by the PS-Division in CERN. The author would like to thank the members of the collaboration for many helpful discussions and Phil Bryant for introducing him to lattice design.

6 REFERENCES

[1] W. Hardt, Ultraslow extraction out of Lear (transverse aspects), CERN, internal report PS/DL/LEAR Note 81-6.

[2] W. Schnell, B. Zotter, A simplified criterion for transverse stability of a coasting beam, and its application to the ISR, CERN-ISR-GS-RF/76-26

[3] L. Badano, S. Rossi, Characteristics of a betatron core for extraction in a proton-ion medical synchrotron, to be published.

[4] J.C Ciret, Extraction du faisceau de Saturne II par acceleration betatronique. Le Gephyrotron, GERMA 76.02/IE-117.

[5] S. van der Meer, Stochastic extraction, A low ripple version of resonant extraction, CERN/PS/AA, 78-6

[6] R. Cappi, Ch. Steinbach, Improvement of the low frequency duty factor of slow extraction by rf phase displacement, PAC 1981, Washington.

MATCHING TO GANTRIES FOR MEDICAL SYNCHROTRONS

M. Benedikt, C. Carli, CERN/PS , CH-1211 Geneva 23, Switzerland

Abstract

Treatment of tumours by hadron-therapy is greatly improved if the patient can be irradiated from different directions. This task is performed by a gantry, i.e. a section of beam line that can be rotated around the patient. The gantry optics have to be designed in such a way that the beam at the patient is independent of the rotation angle. The various matching techniques are briefly reviewed in the light of the current development in medical synchrotrons towards active scanning, which requires a small, high-precision beam spot at the patient. In particular, beam delivery systems with rotators are discussed.

1 INTRODUCTION

In a medical machine the designer has the problem of matching the beam coming from the accelerator to the rotating gantry, as shown in Figure 1.

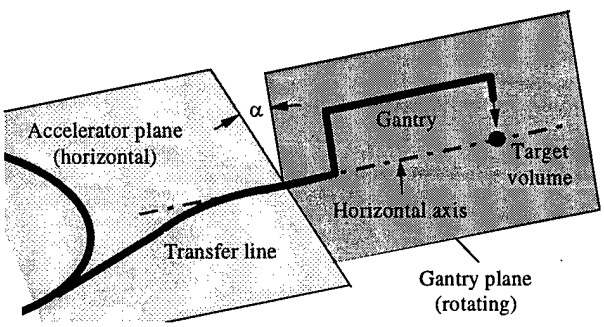

Figure 1: Schematic view of a rotating gantry.

The following requirements have to be fulfilled independent of the rotation angle:

- Constant spot size and shape at the treatment volume.
- No correlation between momentum and position.
- No change of the beam optics inside the gantry.

There appear to be only two methods, that satisfy all the above requirements, and a third method (one to one gantry) that partially fulfills them.

Consider a vector **y**, containing the transverse phase-space coordinates of a particle. The statistical average of any distribution of particles in phase space is then given by the σ-matrix [1] defined as

$$\sigma = \left\langle \mathbf{y}\,\mathbf{y}^{\mathrm{T}} \right\rangle ,$$

where the brackets mean the expectation value. For an uncoupled beam, all elements coupling the horizontal and the vertical phase space vanish and the σ-matrix is of the form shown below,

$$\sigma_{uc} = \begin{pmatrix} \langle x^2 \rangle & \langle xx' \rangle & 0 & 0 \\ \langle x'x \rangle & \langle x'^2 \rangle & 0 & 0 \\ 0 & 0 & \langle z^2 \rangle & \langle zz' \rangle \\ 0 & 0 & \langle z'z \rangle & \langle z'^2 \rangle \end{pmatrix} .$$

With the definition of the statistical emittance,

$$E_x = \sqrt{\langle x^2 \rangle \langle x'^2 \rangle - \langle xx' \rangle^2} ,$$

the relationship between the σ-matrix and the Twiss formalisms is found as,

$$\gamma_x = \frac{\langle x'^2 \rangle}{E_x}, \qquad \alpha_x = -\frac{\langle xx' \rangle}{E_x}, \qquad \beta_x = \frac{\langle x^2 \rangle}{E_x}$$

2 SYMMETRIC BEAM METHOD

In the symmetric beam method, the gantry is matched directly to the fixed beam line coming from the accelerator. To obtain the same beam behaviour inside the gantry and at the patient, independent of rotation, the beam has to be symmetric at the gantry entrance. The necessary symmetry conditions can be derived by the use of the σ-matrix. For an uncoupled beam the σ-matrix at the end of the fixed beam line, just in front of the gantry is given by:

$$\sigma = \begin{pmatrix} E_x\beta_x & -E_x\alpha_x & 0 & 0 \\ -E_x\alpha_x & E_x\gamma_x & 0 & 0 \\ 0 & 0 & E_z\beta_z & -E_z\alpha_z \\ 0 & 0 & -E_z\alpha_z & E_z\gamma_z \end{pmatrix} ,$$

and after a rotation, **R**, the new σ-matrix is given by

$$\sigma_2 = \mathbf{R}\sigma_1\mathbf{R}^{\mathrm{T}} .$$

When the incoming beam is rotationally symmetric, the matrix σ_2 will be independent of the rotation angle. Therefore the following constraints have to be fulfilled at the entry to the gantry:

$$E_x\beta_x = E_z\beta_z \qquad E_x\alpha_x = E_z\alpha_z \qquad E_x\gamma_x = E_z\gamma_z ,$$

0-7803-4376-X/98 /$10.00 © 1998 IEEE

which means that the following beam- and optics properties are required:

- Equal emittances $E_x = E_z$.
- Equal Twiss parameters $\beta_x = \beta_z$, $\alpha_x = \alpha_z$, $\gamma_x = \gamma_z$.
- Zero dipersion function $D = 0$, $D' = 0$.

Thus the beam must be symmetric in real space and of identical shape in the two transverse phase spaces. It is not sufficient to have only a physically 'round' beam at the gantry entrance. To have equal Twiss parameters in both planes is not very limiting in practice but the constraint of equal emittances is a severe problem for resonant extraction from a synchrotron. Therefore this method is best suited for a cyclotron based facility.

3 ONE TO ONE GANTRY METHOD

For this method, the gantry must be a 1:1 or 1:-1 mapping, achromatic structure, with phase advances being multiples of π for both transverse planes. For simplicity $\mu_x=\mu_z=2\pi$ is considered. The transfer matrix for the gantry is the 4x4 unit matrix **I**. The gantry rotation is described with a rotation matrix $\mathbf{R}_\alpha$. The overall matrix $\mathbf{M}_0$, from the end of the fixed beam line to the treatment volume, is then given by:

$$\mathbf{M}_0 = \mathbf{M}_{gantry}\mathbf{R}_\alpha = \mathbf{I}\mathbf{R}_\alpha = \begin{pmatrix} \cos\alpha & 0 & \sin\alpha & 0 \\ 0 & \cos\alpha & 0 & \sin\alpha \\ -\sin\alpha & 0 & \cos\alpha & 0 \\ 0 & -\sin\alpha & 0 & \cos\alpha \end{pmatrix}.$$

Thus, the beam seen from the gantry, is rotated at the treatment volume by the negative gantry angle -α. This rotation cannot be avoided but if the beam at the gantry entrance is symmetric in real space, the patient will always 'see' the same particle distribution. Therefore

$$E_x\beta_x = E_z\beta_z \qquad \text{and} \qquad D = 0\,,\, D' = 0$$

are required at the gantry entrance. The disadvantage of the one-to-one gantry method is that, as long as the beam does not fulfill all the conditions of the symmetric beam method, the beam is coupled inside the gantry, resulting in changing beam envelopes.

4 ROTATOR METHOD

In the rotator method [2] an insertion containing only quadrupoles is placed just in front of the gantry. This section of beam line (*the rotator*) is then rotated in proportion to the gantry rotation.

4.1 Basic principle

Consider a section of bending-free transfer line with betatron phase advances of 2π in the horizontal and π in the vertical plane with a transfer matrix of the form

$$\mathbf{M}_{rot} = \begin{pmatrix} 1 & 0 & 0 & 0 \\ 0 & 1 & 0 & 0 \\ 0 & 0 & -1 & 0 \\ 0 & 0 & 0 & -1 \end{pmatrix}$$

If this line is physically rotated by half the gantry angle ($\alpha/2$) the overall transfer matrix $\mathbf{M}_0$ from the end of the fixed beam line through the rotator to the gantry entrance is obtained as,

$$\mathbf{M}_0 = \mathbf{R}_{\alpha/2}\mathbf{M}_{Rot}\mathbf{R}_{\alpha/2} = \mathbf{M}_{Rot}.$$

The final overall transfer matrix maps the incoming normal modes directly to those of the gantry without any cross-coupling and independent of the gantry angle.

$$\begin{pmatrix} x \\ x' \\ z \\ z' \end{pmatrix}_{\text{Gantry}} = \begin{pmatrix} 1 & 0 & 0 & 0 \\ 0 & 1 & 0 & 0 \\ 0 & 0 & -1 & 0 \\ 0 & 0 & 0 & -1 \end{pmatrix} \begin{pmatrix} x \\ x' \\ z \\ z' \end{pmatrix}_{\text{Input}}$$

The dispersion function (D,D') is automatically rotated and matched at the same time, since in a bending-free region, the dispersion function acts like a betatron oscillation. This can be used for a simplified gantry design (i.e. fewer quadrupole magnets, shorter gantry). Additional advantages are:

- No requirements on the beam symmetry at the gantry entrance.
- Dispersion at the gantry entrance can be finite.
- Uncoupled beam inside the gantry.

The rotator method is best suited for a slow extracted beam from a synchrotron that has unequal emittances in the transverse planes.

4.2 Rotator design

In the above theory, the only visible constraint on the design of rotators is that the phase advances must be 2π and π. However, one has to be aware that the overall transfer matrix does not contain any information about beam sizes and chromatic effects inside the structures. A rotation by $\pi/2$ is equivalent to a change from focusing to defocusing in the rotator and therefore FODO structures lead to very large fluctuations of the Twiss functions and beam sizes due to the opposite signs of α_x and α_z at the entrance. For this reason, rotators should be designed with approximately equal Twiss parameters for the transverse planes at the entrance, which ensures a controlled beam behaviour at any rotation angle. Figure 2 shows a design example, the structure consists of two doublets that match the equal Twiss functions at the entrance ($\beta_x = \beta_z = 4$ m, $\alpha_x = \alpha_z = 0$) into a FODO channel that gives the required phase advances of $\mu_x = 2\pi$ and $\mu_z = \pi$.

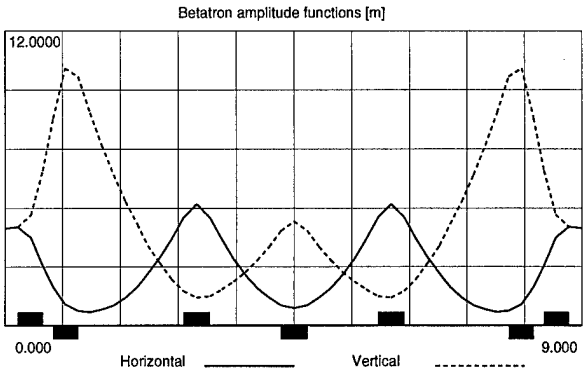

Figure 2: Twiss functions for Doublet FODO rotator.

4.3 Extension modules

To deliver beam to different gantries with only one rotator a modular beam delivery system can be used [3]. 'Extension modules' with optical properties similar to the rotator are inserted between the rotator and the different gantries. These modules are fixed in the accelerator plane. They must be achromatic sections of transfer line with phase advances of $n \cdot \pi$ in the transverse planes. Modules that provide a deflection must therefore have a closed dispersion bump. Figure 3 shows a 60° deflecting extension module based on the Doublet FODO rotator.

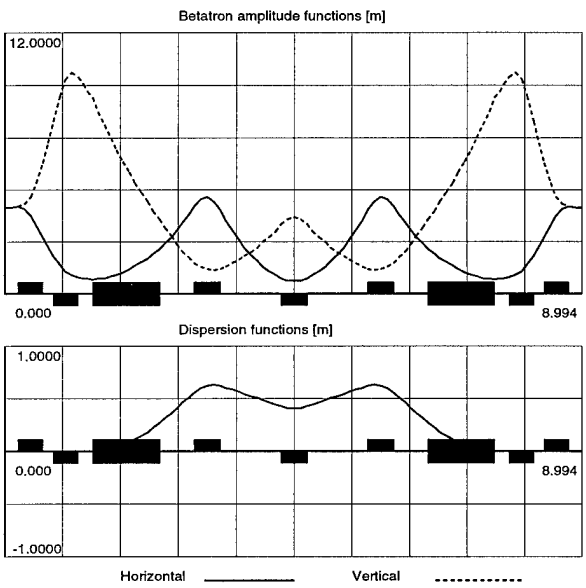

Figure 3: Extension module providing 60° deflection

Two C-shaped dipoles have been inserted such that they give a closed dispersion bump. Powering the dipoles deflects the beam towards one gantry. To send the beam to a different gantry, the dipoles are not powered and the beam goes straight through the first dipole, where the structure is continued with the standard rotator lattice. Figure 4 illustrates the geometry, the first two quadrupoles are commonly used by the deflecting and the straight-through extension modules.

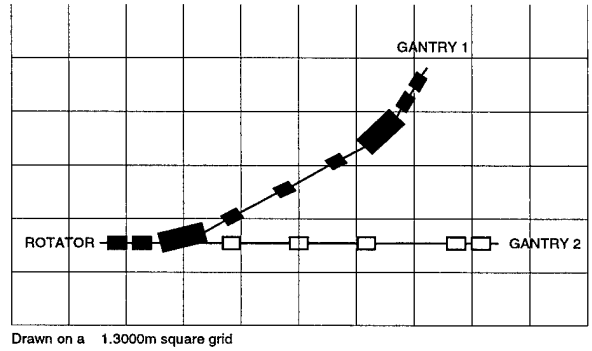

Figure 4: Geometry of deflection and straight-through extension modules.

5 CONCLUSIONS

In this paper the different techniques for matching therapy beams to gantries are reviewed. The methods can be summarised as follows:

Symmetric Beam Method:

- Requires a fully symmetric beam, i.e. equal emittances and Twiss functions at gantry entrance.
- The dispersion must be zero at the gantry entrance.
- Well suited for beams from cyclotrons.

One-to-one Gantry Method:

- Phase advances in the gantry must be multiples of π in both transverse planes.
- Requires a symmetric beam in real space at the gantry entrance.
- The dispersion must be zero at the gantry entrance.
- Beam sizes change inside the gantry.
- Suited for beams from synchrotrons and cyclotrons, but non-perfect matching.

Rotator Method:

- Requires an additional quadrupole lattice section with phase advances of 2π and π in the transverse planes. This insertion (*rotator*) has to be rotated proportional to the gantry angle.
- In principle, no restrictions on the beam symmetry.
- In principle, no restrictions on the dispersion function which may simplify the gantry design.
- Well suited for beams from synchrotrons and cyclotrons.

6 REFERENCES

[1] J. Buon, A statistical description of a particle beam subjected to a linear and coupled betatron motion, LAL/RT 96-03.

[2] L. C. Teng, private communications, Fermilab, laboratory notebook (Jan. 1970), Oct. 1986.

[3] M. Benedikt, C. Carli, Optical design of a beam delivery system using a rotator, CERN/PS 96-41.

BEAM OPTICS ISSUES FOR THE ANTIPROTON DECELERATOR

P. Belochitskii, JINR, RU-141 980 Dubna, Russia
C. Carli, T. Eriksson, R. Giannini, S. Maury, D. Möhl, F. Pedersen,
CERN, CH-1211 Geneva 23, Switzerland

Abstract

The deceleration of the beam down to 0.1 GeV/c in the ring previously used as Antiproton Collector (AC) at 3.5 GeV/c, requires a number of modifications to the lattice. The insertion of the electron cooling, needed to cool the antiproton beam at low energy, implies the re-arrangement of quadrupoles. The optical functions then need to be readjusted in order to keep the large acceptance and to cope with the electron and stochastic cooling environment. Calculations of the linear optics and of the acceptance are reported. Tests of beam deceleration in the AC show the need for closed-orbit correction at low momentum in addition to the static correction by the movement of the quadrupoles available in the present configuration. The deceleration tests will be discussed and a correction system, which includes trim supplies on the main bending magnets, will be described.

1 THE ELECTRON COOLING INSERTION

The present AC lattice [1] is made of 28 FODO cells with two straight sections of about 28 m length each, two of 15 m length and four densely packed arcs. The 28 m straight sections have no orbit dispersion whereas the 15 m sections have a small dispersion. To satisfy the topology imposed by the injection and ejection lines special 'half-quadrupoles' are used in the injection/extraction section and some quadrupoles are transversally displaced in the other 28 m straight section in order to maintain symmetry.

For efficient operation as an Antiproton Decelerator [2,3] electron cooling is needed at low energy. The electron cooling device should be located in a straight section where the dispersion is zero and beta functions of 5-10 m are desired. To gain space for the cooler, the central quadrupole of the long straight section opposite to the injection section is removed and the two adjacent F-quadrupoles are shifted towards the next D-lenses. The rematching of the optics is done by decreasing the distance between the closest two lenses on either side of the cooler.

The required strength for these new D-lenses is beyond the values obtainable with the AC quadrupoles, so two identical quadrupoles are needed side by side using AC spares. The new layout of this section in shown in Fig. 1.

2 AD LATTICE

The very large acceptance requirements are $\Delta p/p = \pm 3\%$ and $A_h = A_v = 240\pi$ mm·mrad, as in the present AC, in order to capture about 5×10^7 $\bar{p}$/shot. Other conditions such as the phase advance between the pick-ups and the kickers of the stochastic cooling systems, and between injection/ejection septum and kickers, have also to be maintained close to their present values.

The optical functions are shown in Fig. 2. The horizontal envelope is larger ($\beta_H \cong 18$ m instead of 12 m in the AC) and the vertical envelope is similar to the one of the AC except in the first quadrupole of the cooling insertion where β_V is 20 m. For both machines, the dispersion function remains the same.

The working point ($Q_h = 5.28$, $Q_v = 5.19$ instead of $Q_h \cong Q_v \cong 5.45$ in the AC) has been chosen as a result of an optimization of the acceptance in the presence of the cooling insertion and the other constraints mentioned.

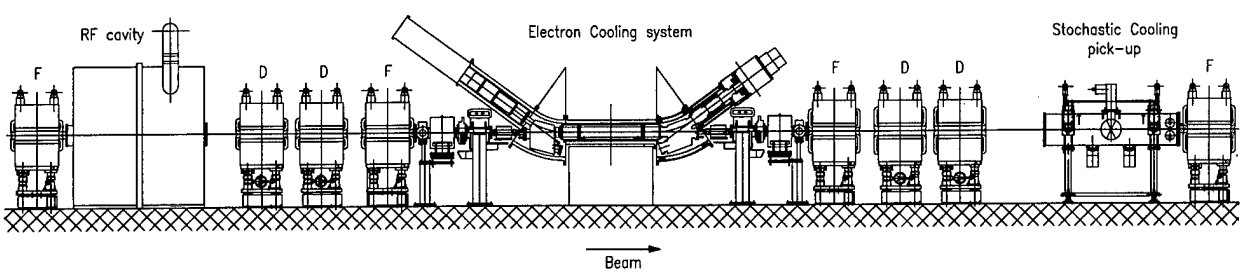

Fig.1: Layout of the Electron Cooling insertion.

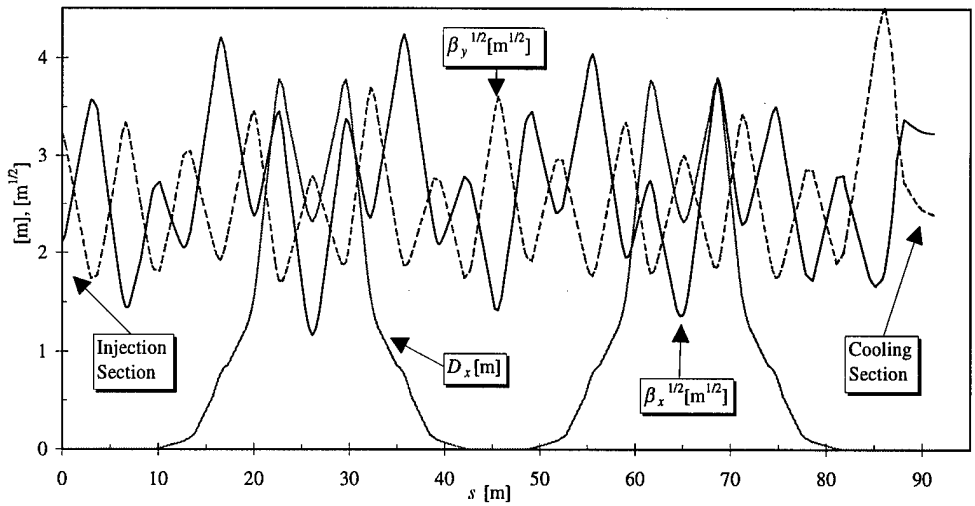

Fig. 2: Envelope functions ($\sqrt{\beta_h}, \sqrt{\beta_v}$) and dispersion function D for the AD. The plot is for one half of the ring, starting in the middle of the injection section and finishing in the cooling section.

3 TESTS ON THE AC

Machine study sessions in parallel with the physics runs during 1995/1996 were used to decelerate a test beam of about 10^9 protons to the lowest possible momentum and to identify the problems. A few decelerations were done with antiprotons ($N = 5 \times 10^7$) to demonstrate that it is feasible, but most decelerations were done with protons ($N = 5 \times 10^9$), where beam diagnostics to measure tunes and orbits are available. For that, the existing tunable ferrite cavity (1.6 MHz, normally used for rebunching of antiprotons prior to extraction from the AC) was modified to cover a frequency range of 1 to 2 MHz and a field sensing coil was installed in one of the ring bending magnets. A software package was written to control the ramping magnet currents which are adjusted based on beam measurements.

A plot of the fraction of the beam surviving after deceleration to different momenta is shown in Fig. 3. The lowest beam momentum obtained with enough protons left to measure orbits and tunes was 12% of maximum momentum (430 MeV/c). The ramping from 100% to 20% in this experiment took approx. 120 s. The design goal for the AD machine is deceleration to 3% in about 10 s. We believe that the remaining losses are a combination of transverse emittance blow-up due to poor vacuum and reduced acceptance due to poor orbit. The limiting factors at 430 MeV/c were:

- Quad-trim power supply regulation working below a current of about 2 A.
- Slow deceleration (software ramping) combined with poor vacuum leading to excessive emittance blow-up due to multiple Coulomb scattering.
- Tune measurements impossible with present system (50 MHz Schottky pick-up).
- Poor tracking (current regulation) limiting deceleration speed.
- Stability of field sensing coil and/or B-train generator.
- Reduced acceptance due to orbit errors.

Both horizontal and vertical orbits were measured as a function of momentum.

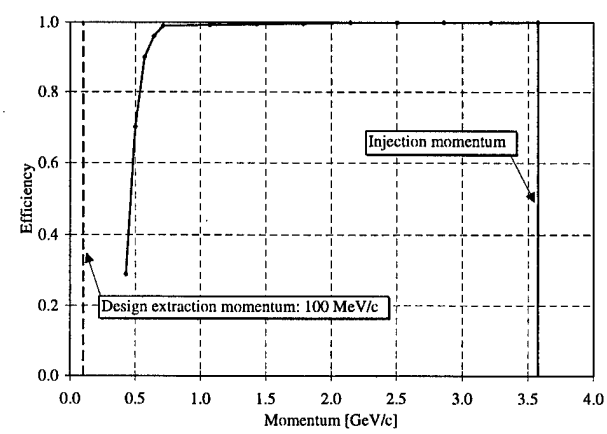

Fig. 3: Beam survival during deceleration of a pencil beam of about 10^9 protons as a function of momentum.

These experiments clearly showed the need for closed-orbit correction at low energy. In fact, horizontal excursions of ±30 mm (Fig. 4) were measured at 430 MeV/c even though the orbit was carefully corrected at 3.57 GeV/c by the present 'static' system of moving the quadrupoles. The orbit variations are probably due to saturation asymmetries at high energy and to remanence asymmetries at low energies.

The measured beam positions in the straight sections down to 430 MeV/c are shown in Fig. 4.

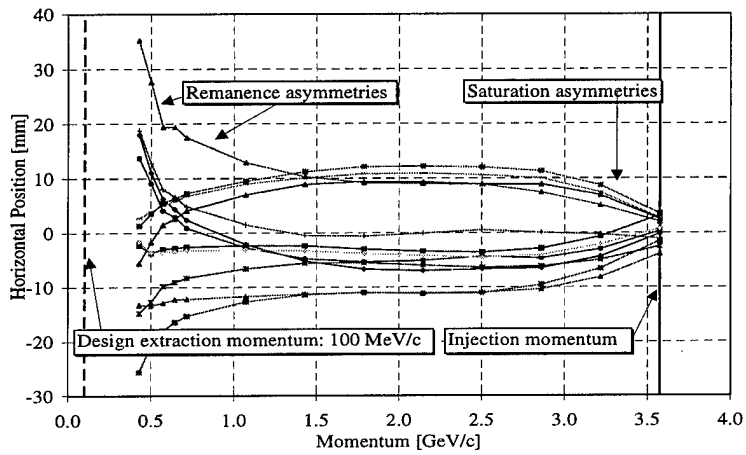

Fig. 4: Horizontal orbit distortion vs. momentum measured at 12 pick-ups in the AC. At 3.57 GeV/c the orbit was corrected (acceptance optimized) by adjustment of the quadrupole positions.

4 ORBIT CORRECTION

To extrapolate the orbit distortions to low energies a formula: $\chi_0 = A+B/p$ was fitted through all, but the two highest measured momenta. Extrapolation to 100 MeV/c indicated distortions up to ±150 mm and ±15 mm for the horizontal and vertical planes, respectively.

The scheme retained for horizontal orbit correction is based on trim supplies that will be available on the bending magnets plus a few additional correctors that will be installed in the long straight section and especially on both sides of the electron cooling insertion.

It has been decided to connect the 24 magnets in groups of adjacent pairs thus needing a total of 12 trimming supplies. Application of a MICADO algorithm [4] gives the residual distortion of the horizontal orbit at 100 MeV/c smaller than 15 mm, as indicated in Fig. 5.

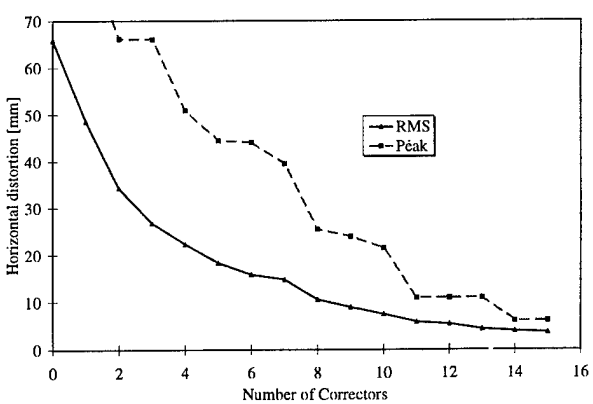

Fig. 5: Residual distortion of the horizontal orbit (in mm) at the pick-up locations after correction using *n* correctors in the AC.

With 14 vertical correction dipoles, installed in locations where space can be made available, the vertical closed-orbit distortions at 100 MeV/c are reduced from 15 mm to about 4 mm.

Together with the static correction (quadrupole movement), this system can be used for an orbit correction to better than ±15 mm horizontally and ±5 mm vertically in the entire energy range, at least for the errors extrapolated from the present AC.

5 CONCLUSION

All the identified limitations will be eliminated by appropriate upgrades during the course of the AD project. Modification of the AC lattice and an orbit correction scheme have been found which should permit electron cooling and efficient beam deceleration to 100 MeV/c. Work is underway to confirm and improve the scheme.

REFERENCES

[1] H. Koziol and S. Maury, 'Parameter List for the Antiproton Accumulator Complex (AAC)', Edition 1994, CERN/PS 95-15, 1995.

[2] S. Baird, D. Berlin, J. Boillot, J. Bosser, M. Brouet, J. Buttkus, F. Caspers, V. Chohan, D. Dekkers, T. Eriksson, R. Garoby, R. Giannini, O. Grobner, J. Gruber, J.Y. Hémery, H. Koziol, R. Maccaferri, S. Maury, C. Metzger, K. Metzmacher, D. Möhl, H. Mulder, M. Paoluzzi, F. Pedersen, J.P. Riunaud, C. Serre, D.J. Simon, G. Tranquille, J. Tuyn, B. Williams: 'Design Study of the Antiproton Decelerator: AD', CERN/PS/96-43 (AR), 1996.

[3] S. Baird, D. Berlin, J. Boillot, J. Bosser, M. Brouet, J. Buttkus, F. Caspers, V. Chohan, D. Dekkers, T. Eriksson, R. Garoby, R. Giannini, O. Grobner, J. Gruber, J.Y. Hémery, H. Koziol, R. Maccaferri, S. Maury, C. Metzger, K. Metzmacher, D. Möhl, H. Mulder, M. Paoluzzi, F. Pedersen, J.P. Riunaud, C. Serre, D.J. Simon, G. Tranquille, J. Tuyn, and A. Van der Schueren: 'The Antiproton Decelerator (AD)', this conference.

[4] B. Autin, Y. Marti, 'Closed Orbit Correction of A.G. Machines Using a Small Number of Magnets', CERN-ISR-MA/73-17,1973.

LONGITUDINAL RADIATION EXCITATION OF QUASI-ISOCHRONUS RING 'New SUBARU'

Y. Shoji, A. Ando, LASTI, Himeji Institute of Technology,
2167 Shosha, Himeji-shi, Hyogo-ken, 671-22 JAPAN,
H. Tanaka, M. Takao and K. Soutome, SPring-8, Kamigori, Ako-gun, Hyogo-ken, 678-12 JAPAN

Abstract

The longitudinal radiation excitation is a diffusion process in time axis which came from the stochastic fluctuation of where the photo-emission takes place. Usually this radiation excitation hides behind the well-known radiation excitation of energy spread. However in a quasi-isochronous ring, it dominates over the bunch stretch owing to the radiation excitation of energy spread. We give an analytical expression for the equilibrium state within linear optics including this excitation. Some consequencies of this excitation is calculated using parameters of New SUBARU.

1 INTRODUCTION

A quasi-isochronus storage ring has an advantage in forming ultra short bunch, which has many applications. It is expected to offer higher luminosity in a collider, a very short pulsed synchrotron light and hopefully a higher peak current of an electron beam. The idea of utilizing a quasi-isochronous ring to shorten the bunch length comes from a well-known expression that the equilibrium bunch length is proportional to the square root of the linear momentum compaction factor $\sqrt{\alpha}$ [1]. The shortening of the equilibrium bunch length by means of reducing α is demonstrated at several synchrotron light source rings [2, 3, 4, 5, 6, 7, 8]. Their studies showed that an intensity effct, a potential well distortion or instabilities, restricts the bunch to shorten when non-linear part of the momentum compaction factor is corrected. The limit to the bunch shortening with low beam current was not clarified until we introduced an idea of *longitudinal radiation excitation* [9].

The idea of the longitudinal excitation is a heating by the stochastic fluctuation of where the photo-emission takes place in a ring. If the photo-emission takes place at the first bending dipole from the RF, the electron goes around most part of the ring with lower energy compared with the starting one. On the other hand, if the photo-emission happens at the last bending dipole, the electron goes around most part of the ring with starting energy and finishes the revolution with the same energy as the previous case. When α is positive, the revolution time of the former case is shorter than that of the latter. This stochastic variation produces a heating in time axis. In usual storage rings the longitudinal excitation is buried in the energy spread excitation and hardly can be observed. On the other hand, in a quasi-isochronous storage ring the longitudinal excitation becomes remarkable, since one can reduce α to zero but can not do the longitudinal excitation. In this report the quantity of this effect is calculated using the New SUBARU storage ring.

Table 1: Parameters of New SUBARU ring.

Electron energy	$E_0 =$	1.5 GeV
Circumference	$L_0 =$	118.716 m
Revolution period	$T_0 =$	396 ns
Momentum compaction factor	$\alpha =$	-0.0012
		$\sim$ +0.0011
Natural energy spread	$\sigma_{EN} =$	0.072 %
Longitudinal damping time	$1/\kappa_s =$	3.42 ms
RF voltage gradient	$V' =$	550 kV/ns
Bending angle of normal B	$\theta =$	34 degrees
Bending angle of invert B	$\theta_c =$	-8 degrees
Curvature of radius	$\rho_0 =$	3.22 m

New SUBARU [10] is a name of the project to construct an 1.5 GeV synchrotron light source ring in the SPring-8 site using the 1.0 GeV Linac as an injector. Laboratory of Advanced Science and Technology for Industry (LASTI) of Himeji Institute of Technology is in charge of the construction collaborating with SPring-8. The storage ring is of a race track type with two fold symmetry. Table1 summarizes main storage ring parameters. It has 6 quasi-isochronus and achromatic bending cells and 6 dispersion free straight sections. A type of the bending cell is a quasi-isochronus TBA using a small invert dipole as a middle bend in order to control α.

2 LONGITUDINAL RADIATION EXCITATION

2.1 *Analytical expression of the longitudinal excitations*

To derive analytical expressions for the longitudinal excitation, we assume the followings; (a) circulating electrons or positrons are ultra-relativistic, (b) the ring has only one RF gap, (c) the absolute value of curvature radius in bending dipoles is constant.

We assume that the RF gap is located at $s = 0$ or $s = L_0$, where s is the azimuthal coordinate and L_0 is the circumference of a ring. At the lowest order of perturbation, the change of path length in one turn caused by N photo-emissions is expressed by

$$\Delta L = \sum_j^N \int_{s_j}^{L_0} \frac{\eta(s)}{\rho(s)} \frac{u_j}{E_0} ds \,. \tag{1}$$

where $\eta(s)$, $\rho(s)$ and E_0 are respectively the horizontal dispersion function, the radius of curvature and the synchronous energy. Symbols u_j is the energy loss produced by the jth photo-emission at the azimuthal location s_j. In

0-7803-4376-X/98/$10.00 © 1998 IEEE

this paper Δ stands for the change by the photo-emissions in one turn, while δ stands for a displacement from the barycenter.

The displacement in relative energy by N photo-emissions and that of the arriving time from the reference are

$$\frac{\Delta E}{E_0} = \sum_j^N \frac{u_j}{E_0}, \tag{2}$$

$$\Delta\tau = \frac{T_0}{L_0}\sum_j^N \int_{s_j}^{L_0} \frac{\eta(s)}{\rho(s)}\frac{u_j}{E_0} ds, \tag{3}$$

where T_0 is a revolution period. Introducing the incomplete momentum compaction factor $\tilde{\alpha}(s_j)$ defined by

$$\tilde{\alpha}(s_j) = \frac{1}{L_0}\int_{s_j}^{L_0} \frac{\eta(s)}{\rho(s)} ds, \tag{4}$$

Eq. (3) is simply rewritten by

$$\Delta\tau = T_0 \sum_j^N \frac{u_j}{E_0}\tilde{\alpha}(s_j). \tag{5}$$

For the sake of a convenience we write the variance of $\tilde{\alpha}$ as I_α, which is calculated only from the geometrical parameters of a ring:

$$I_\alpha = \frac{1}{L_0^2}\left\langle\left[\int_{s_j}^{L_0}\frac{\eta(s)}{\rho(s)}ds - \langle\tilde{\alpha}\rangle L_0\right]^2\right\rangle. \tag{6}$$

The variances of $\Delta E/E_0$ and $\Delta\tau$ are calculated as

$$\left\langle\left\langle\left(\frac{\Delta E}{E_0} - \left\langle\left\langle\frac{\Delta E}{E_0}\right\rangle\right\rangle\right)^2\right\rangle\right\rangle = \langle N\rangle\left\langle\frac{u^2}{E_0^2}\right\rangle, \tag{7}$$

$$\left\langle\left\langle\left\langle(\Delta\tau - \langle\langle\langle\Delta\tau\rangle\rangle\rangle)^2\right\rangle\right\rangle\right\rangle = T_0^2 I_\alpha \langle N\rangle\left\langle\frac{u^2}{E_0^2}\right\rangle, \tag{8}$$

where the brackets $\langle\ \ \rangle$ represent an average over N, over photon energy or over s_j only at the bending dipoles.

2.2 *Equilibrium energy spread and bunch length*

To calculate the equilibrium bunch length, we start with a matrix equation of the linearized synchrotron oscillation in a storage ring. A single turn transfer of a synchrotron oscillation is described by

$$X_n = AX_{n-1} + D_n. \tag{9}$$

Here the vectors X_n and D_n denote respectively the state of a particle in the synchrotron oscillation phase space and the radiation excitation in the nth turn and A is a transfer matrix including radiation damping. The state vector X_n is defined at just before the RF gap ($s = L_0$) by

$$X_n = \begin{pmatrix} \left.\frac{\delta E}{E_0}\right|_n \\ \left.\delta\tau\right|_n \end{pmatrix}, \tag{10}$$

where $(\delta E/E_0)|_n$ and $\delta\tau|_n$ are the relative energy displacement and the arriving time displacement from the barycenter at just before the RF gap in the nth turn. The one turn transfer matrix A is written as

$$A = \begin{pmatrix} 1 - 2\kappa_s T_0 & \frac{eV'}{E_0}(1 - 2\kappa_s T_0) \\ -\alpha T_0 & 1 - \alpha T_0 \frac{eV'}{E_0} \end{pmatrix}. \tag{11}$$

where V' and κ_s are the gradient of the RF acceleration voltage and the radiation damping coefficient. The vector D_n is described by

$$D_n = \begin{pmatrix} \left.\frac{\Delta E}{E_0}\right|_n - \left\langle\left\langle\frac{\Delta E}{E_0}\right\rangle\right\rangle \\ \left.\Delta\tau\right|_n - \langle\langle\langle\Delta\tau\rangle\rangle\rangle \end{pmatrix}. \tag{12}$$

The suffix n in the averaging brackets is omitted because the averaged values are independent of the turn number n. When $\alpha eV' > 0$ the equibrium state X_∞ exists whether the eigen values of A are complex or real. That is

$$X_\infty = \sum_{m=0}^{\infty} A^m D_m. \tag{13}$$

Although the energy spread is constant over a circumference, the equilibrium bunch length varies along s. The state vector after infinite turns at any place s in the ring $X_\infty(s)$ is given by a transformation from $X_\infty = X_\infty(L_0)$ as follows

$$\begin{pmatrix} 1 & 0 \\ -\tilde{\alpha}(s) T_0 & 1 \end{pmatrix} X_\infty(s) = X_\infty. \tag{14}$$

The equilibrium energy spread is given by the variance of the energy displacement of $X_\infty(s)$, that is

$$\sigma_E^2 = \frac{1 + (\Omega^* T_0)^2 I_\alpha/\alpha^2}{1 - \left(\frac{1}{2}\Omega^* T_0\right)^2}\sigma_{EN}^2 \tag{15}$$

with

$$(\Omega^* T_0)^2 = \frac{\alpha eV'}{E_0} T_0. \tag{16}$$

Here σ_{EN}^2 is the natural energy spread given by

$$\sigma_{EN}^2 = \frac{1}{4\kappa_s T_0}\langle N\rangle\left\langle\frac{u^2}{E_0^2}\right\rangle. \tag{17}$$

2.3 *Intrinsic Bunch Shortening Limit*

The variance of the equilibrium bunch length $\sigma_\tau^2(s)$ depends on $\tilde{\alpha}(s)$, therefore a function of position in the ring. If we can choose any value as $\tilde{\alpha}(s)$, $\sigma_\tau^2(s)$ takes a minimum

$$\sigma_{\tau,\min}^2 = \left[1 + (\Omega^* T_0)^2 \frac{I_\alpha}{\alpha^2} + \frac{4(\kappa_s T_0)^2 I_\alpha}{\alpha^2 + (\Omega^* T_0)^2 I_\alpha}\right] \times \left(\frac{\alpha}{\Omega^*}\right)^2 \sigma_{EN}^2 \tag{18}$$

at

$$\tilde{\alpha}(s) = \frac{\alpha}{2}\left[1 - \frac{4\kappa_s T_0 I_\alpha}{\alpha^2 + (\Omega^* T_0)^2 I_\alpha}\right]. \quad (19)$$

In the case of a sufficiently small α, Eq. (18) is approximated as

$$\sigma^2_{\tau,\min} \approx T_0^2\left[I_\alpha + 4\left(\frac{\kappa_s E_0}{eV'}\right)^2\right]\sigma^2_{EN}. \quad (20)$$

One can easily confirm that I_α approaches to a nonzero constant as $\alpha \to 0$ and that $\sigma_{\tau,\min}$ has a lower limit. Because $4[(\kappa_s E_0)/(eV')]^2$ is always positive, $\sigma_{\tau,\min}$ cannot be smaller than

$$\sigma^2_{\tau,0} = T_0^2 I_\alpha \sigma^2_{EN}. \quad (21)$$

This is an intrinsic limit of the bunch length determined by the ring geometrical parameters I_α, T_0 and σ^2_{EN}.

2.4 *Variance of the incomplete momentum compaction factor I_α*

In a conventional ring the continuous increase of $\tilde{\alpha}(s)$ around the ring is very much larger than a oscillating part of $\tilde{\alpha}(s)$, so

$$I_\alpha = \frac{1}{12}\alpha^2$$

is a good approximation. However in a quasi-isochronus ring, sections with positive and negative $\tilde{\alpha}$ appear alternatively. In a quasi-isochronus ring using TBA cell with invert dipole,

$$\begin{aligned} I_\alpha &= \left(\frac{\rho_0}{L_0}\right)^2\left(\frac{\theta^6}{252}\right) \\ &\times \left[1 + \frac{2\theta_c}{3\theta}\left(1 + \frac{\theta_c^3}{20\theta^3}\right)\left(1 - \frac{\theta_c}{2\theta} + \frac{\theta_c^2}{4\theta^2}\right)\right] \end{aligned} \quad (22)$$

at the isochronus limit. Here θ and θ_c are bending angles of the normal the invert bend, respectively. We have assumed that both θ and θ_c are much less than unity.

3 CONSEQUENCES OF LONGITUDINAL RADIATION EXCITATION

The most important consequence of the longitudinal radiation excitation is the existance of the intrinsic bunch shortening limit. Now we know the final goal of the study on the quasi-isochronus operation. We also predict the energy shift from the bunch head to the tail, represented by Eq. (19).

The other consequence is a restriction to the isochronus ring FEL (ISRFEL) [11]. Its basic idea is that in isochronus or quasi-isochronus storage ring the electrons remain trapped in the optical potential wells formed by the laser fields. Such a design eliminates the heating by the reconstruction of microbunches taking the advantage of radiation damping in a storage ring. However, according to our calculations any shorter bunch than $\sigma_{\tau,0}$ cannot exist stationary in any linear potential. Consequently ISRFEL with shorter wave length than several times $\sigma_{\tau,0}$ is forbidden. In New SUBARU $\sigma_{\tau,0}$ was calculated to be about 0.12ps (=0.035mm). therefore ISRFEL has a possibility only in over a few tenth milli meter wave region.

The other consequence is the supression of collective beam instability of ultra-high frequency. The longitudinal radiation excitation reduces any fine time structure in a beam, such as density modulation, energy modulation, and transversal oscillation. The diffusion constant in time axis is

$$\begin{aligned} \kappa_t &= \left\langle\!\left\langle\!\left\langle (\Delta\tau - \langle\!\langle\!\langle \Delta\tau \rangle\!\rangle\!\rangle)^2 \right\rangle\!\right\rangle\!\right\rangle / T_0 \\ &= 4\kappa_s T_0^2 I_\alpha \sigma^2_{EN}. \end{aligned} \quad (23)$$

This would reduce the modulations of harmonic number n with damping coefficient of $(2\pi n/T_0)^2\,\kappa_t$.

In New SUBARU, we compare this damping coefficient with that of the Landau damping of longitudinal microwave instability, using coasting beam approximation. We used $n = 10T_0/\sigma_\tau$. The result says at smaller α than 2×10^{-6} the diffusion by the longitudinal radiation excitation dominates over the Landau damping in New SUBARU.

4 ACKNOWLEDGMENT

The authors wish to thank Dr. S. Daté and Dr. Miyahara in SPring-8 for useful suggestions and helpful discussions. We also thank Professor T. Mochizuki in Himeji Institute of Technology for the special encouragement.

5 REFERENCES

[1] M. Sands, *Proc. of International School of Physics Enrico Fermi* Course **46**, *Physics with Intersecting Storage Ring*, edited by B. Touschek (Academic Press, San Diego, 1971), p. 257.

[2] S. Krinsky, *et al.*, *AIP Conference Proceedings* **249**, edited by M. Month and M. Dienes (1992), p. 762.

[3] H. Hama, *et al.*, Nucl. Instr. & Meth. **A329**, 29 (1993).

[4] P. Tran, *et al.*, *Proc. of 1993 IEEE PAC*, p. 173.

[5] D. Robin, *AIP Conference Proceedings* **367**, edited by E.B. Blum, M. Dienes and J.B. Murphy, (1995), p. 181.

[6] L. Farvacque, *AIP Conference Proceedings* **367**, (1995), p. 245.

[7] J.L. Laclare, *Proc. of the 10th ICFA beam dynamics workshop on 4th generation light source*, (ESRF,Grenoble,1996).

[8] A. Nadji, *et al.*, Nucl. Instr. & Meth. **A378**, 376 (1996).

[9] Y. Shoji, *et al.*, Phys. Rev. E **54**, R4556 (1996).

[10] A. Ando, 'VUV and SOFT X-RAY LIGHT SOURCE "New SUBARU"', this proceedings.

[11] D. Deacon and J. Madey, Phys. Rev. Lett. **44**, 449(1980)

LATTICE DESIGN OF BTCF STORAGE RING

N. Huang, L.H. Jin, W.B. Liu, D. Wang, Z.T. Wei, C.H. Yu
IHEP, Chinese Academy of Sciences, P.O. Box 918-9, Beijing 100039, P.R. of China

Abstract

This paper will describe the latest improved optics design of Beijing Tau-Charm Factory (BTCF). It has larger dynamic aperture for the high luminosity mode, higher luminosity with longer Touschek lifetime for the monochromator mode, compared with previous design[2]. Some study results of spin matching of polarization mode will be presented here.

1 INTRODUCTION

In terms of the goals of the machine [1], the lattice is designed to take the high luminosity mode as the first priority, meantime to be compatible with the polarized beam collision mode and monochromator mode.

2 OPTICS

The BTCF consists of two rings , one above the other, with one interaction point (IP). Each ring is 53 m wide and 165 m long with a circumference of 385.4 m. The two rings are vertically separated about 1.67m. Each ring can be divided into four main parts: The interaction region (IR), two polarization insertions, two arcs and a utility region with injection section. (see Figure 1). The main lattice parameters for the high luminosity mode and monochromator scheme are listed in Table 1. The lattice functions of the whole ring for the high luminosity mode are shown in Figure 2.

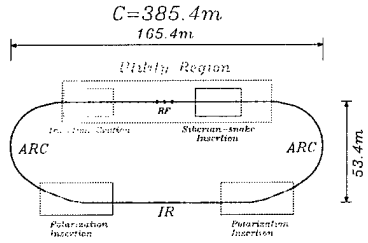

Figure 1: Schematic diagram of the BTCF storage ring.

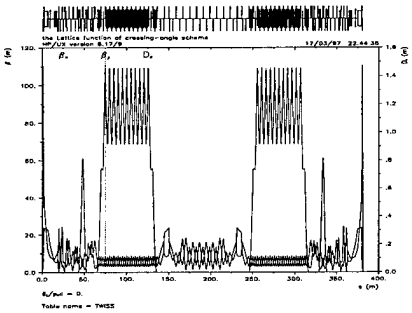

Figure 2: Twiss parameters of the high luminosity mode.

3 INTERACTION REGION

At each side of the IP there are a micro-beta insertion and a vertical separation insertion. Figure 3 shows the magnet layout in the region.

Table 1: Main lattice parameters for the high luminosity mode.

Mode	High Lumi.	Monochr.
Circumference (m)	385.4	385.4
Normal Energy (GeV)	2.0	1.55
Crossing angle at IP (mrad)	2.6×2	0.0
Bending radius (m)	8.33	8.33
Beta-functions at IP (m) Hori./Verti.	0.66/0.01	0.01/0.15
Dispersion-functions at IP (m) Hori./Verti.	0.0/0.0	0.0/0.45
Natural horizontal emittance (nmrad)	138	83 36(with wig.)
Vertical emittance (nmrad)	2.1	5.3
Tunes,Hori./vert.	11.75/11.76	12.21/12.23
Natural chromaticity, H/V	-17/-35	-36/-31
Momentum compaction	0.014	0.014
Momentum spread (10^{-4})	6	7.8(with wig.)
Damping time,H/V/Longi.(ms)	30/30/15	26/61/90
Number of benches	86	29
Particle per bench (10^{10})	5.4	9.3
Beam-beam parameters ξ_x/ξ_y	0.044/0.04	0.018/0.015
Luminosity ($10^{33} cm^{-2} s^{-1}$)	1.0	0.2
Energy spread at CM (MeV)	1.7	0.14

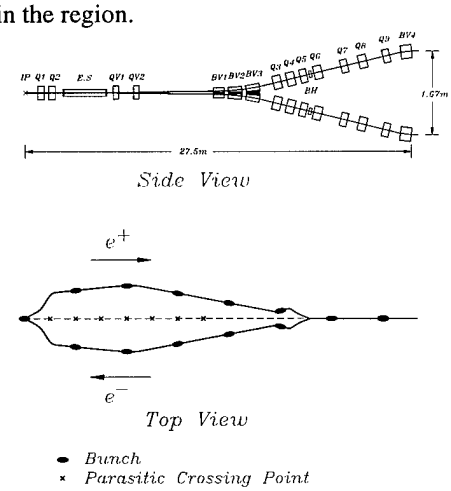

Figure 3: Magnet layout in the interaction region.

The two iron-free superconducting quadrupoles (Q1 and Q2) are used to achieve the micro-beta function at the IP. Q1 is 0.9 m away from the IP. Q1 and Q2 are protruded into the detector. The distance between Q1 and Q2 is kept 0.3 m. The maximum field gradients of Q1 and Q2 are respectively 29 T/m and 20 T/m with a length of 0.5 m. After colliding at the IP, the two beams are initially separated by an electrostatic separator ES, located 0.6 m away from Q2, with a length of 3.2 m. The ES field is limited below 1.5 MV/m to avoid the risk of sparking due to a significant quantity of synchrotron radiation. The vertical off-set quadrupole QV1 (0.5 m away from the ES) is used to further increase beam separation so that a sufficient separation

is obtained to install the vertically bending septum magnets. Three vertical bending septum magnets BV1, BV2, and BV3 further finish the beam separation. The bending angle of BV3 is increased by 10 mrad and the length of IR is 1 m shorter than the previous design [2]. The last vertical bending magnet BV4 brings the beam back onto horizontal orbit.

Six quadrupoles are arranged to finish focusing and vertical dispersion matching between BV3 and BV4. The length of Q3, Q4, Q6 and Q8 is 0.6 m, while the length of Q7, Q9 is 0.5 m. Owing to the insufficient separation of the two beams, the outer radii of Q3, Q4 have to be strictly confined in one direction as 160 mm and 230 mm respectively. The maximum gradient of these quadrupoles is 15 T/m.

For the high luminosity mode, a pair of horizontal deflecting dipoles (BH), symmetrically placed just where the horizontal phase advance from the IP is π, produces a closed orbit distortion between the two BHs and makes the two beams collide at a small horizontal crossing angle (referred to the crossing angle scheme). As Figure 3 shows, the BH lies in between Q5 and Q6 and the maximum field of 0.06 T. The phase advance between ES and BV4 is about 2π so that the vertical dispersion produced by the ES, BV1, BV2 and BV3 can be suppressed. The maximum vertical dispersion function is about 0.2 m in this region.

For the monochromator mode, the polarity of Q1, Q2, Q6 has to be changed, and Q4, Q8 and BHs are switched off. The lattice functions of this region are shown in Figure 4.

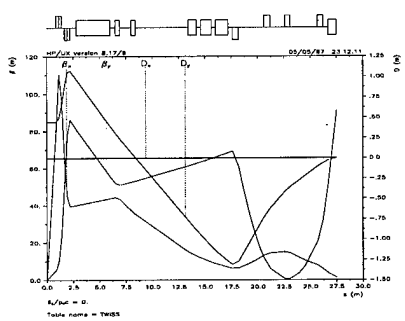

Figure 4: Lattice functions of the IR for the monochromator mode.

This mode requires that there be vertical dispersions opposite in sign and equal in value at the IP for the electron and positron. The dispersion value is changed from 0.35m to 0.45m comparing with the previous design [2] in order to increase luminosity.

The opposite dispersions can be produced by the vertical deflecting components (ES, BV1, BV2, BV3 and BV4), which make the electron and the positron into different directions. The central particle trajectory between ES and BV3 in this mode differs from the crossing angle scheme due to larger deflecting angle of ES at the strength (1.5 MV/m). The difference is canceled after BV3 by adjusting the magnitude of off-set quadrupoles QV1 and vertical septums BV1, BV2 and BV3. The phase advance between ES and BV4 is close to π in order to suppress the vertical dispersion.

Behind BV4 is the polarization insertion which only does matching to arc except polarization mode. There are beta-function matching section and spin rotator section.

3.1 Arc

Each arc consists of 14 FODO cells, including 10 normal cells with 60° phase advance and one dispersion suppressor at each end of an arc, one of which contains two FODO cells with 2 normal bending magnets missed. Each dispersion superessors close to the IR has a special bending magnet with independent power supply. The length of each normal bending magnet is 0.96m with the bending angle of 6.605°. The length of each cell is 5.12 m. The drift space of 0.6 m is provided for hardware between the dipole and the quadrupole. In this fashion, the emittance can be controlled easily by adjusting wigglers in this region.

For the monochromator mode, the lattice is almost the same as above except eight Robinson wigglers in each ring are used for redistributing the damping partition number between J_x and J_ϵ [3, 4]. For this mode, the luminosity increases as the beam energy spread increases. When the Robinson wigglers decrease the emittance, it happens to increase the energy spread. Choosing the parameters of each Robinson wiggler (4 blocks) as the effective length of 0.84 m (total length is 1.32 m) with the dipole bending radius 14m and the gradient strength 1.2 m^{-2}, J_x increases from 1 to 2.34 and J_ϵ reduces from 2 to 0.66. As a result the emittance gets to about 36 nmrad and the energy spread increases to 8×10^{-4} from natural energy spread 4.6×10^{-4} at 1.55GeV. Figure 5 shows the lattice functions in the arc.

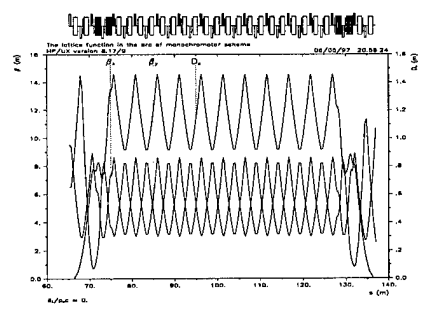

Figure 5: Lattice functions in arc for the monochromator mode.

3.2 Utility Region

A long straight region lies on the side opposite from the IR. It consists of the injection insertion and four regular FODO cells as well as two beta-function matching sections. Figure 6 gives the lattice functions in this region. The Each quadrupole here is 0.4 m long with the maximum gradient of 15 T/m. The kickers and Lambertson magnet are arranged in one injection insertion. The RF cavities are located in the regular cells which can provide over 3.2 m long drift spaces. The working points can be adjusted in this region.

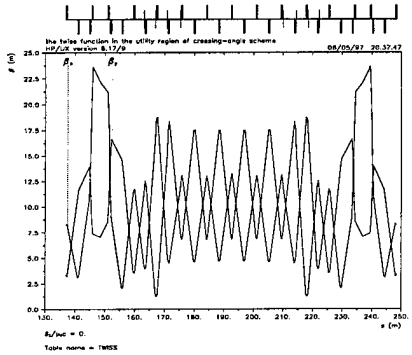

Figure 6: Lattice functions in the utility region for the high luminosity mode, (for the monochromator mode is almost the same).

3.3 Spin Rotator Section

The longitudinal polarization scheme at around 2.0 GeV adopted in current BTCF design is symmetric solenoid spin rotator.

The rotator in each side of IR consists of one Double Bend Achromat section (19.8° $\sim$ 21.5°), and two superconducting solenoids (9.63 T) which are switched off in non-polarization mode, and many quadrupoles for the local coupling compensation and other matching. To reach an applicable polarization level the spin-matching must be applied to suppress the strong depolarization effects even for the perfectly aligned machine. The 'partial' spin-matching by adjusting 25 quadrupole strengths results in remarkable enhancement in depolarization time (100 minutes, see Figure 7) and equilibrium polarization level. Change in helicity can easily be achieved by reversing the field direction of solenoid. However the detailed studies show that more modifications in lattice design are needed to optimize the performance of polarization operation mode [5].

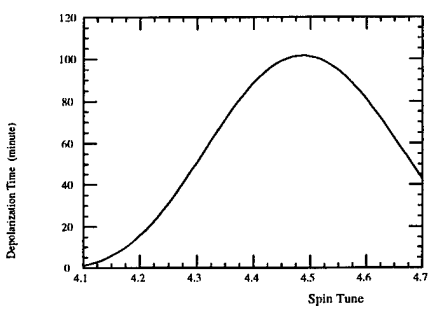

Figure 7: Depolarization time with spin-matching at 2.0 GeV.

4 TRACKING STUDIES

The tracking and simulations (without imperfections) are evaluated with the code MAD [6]. Except for the chromaticity sextupoles, no other correctors have been installed into the linear lattice. Simulations in six dimension are done for 2000 turns which corresponds to 1/12 damping time. Chromaticities in both transverse planes are corrected to a slightly positive value.

For the high luminosity mode, 48 sextupoles with five families are distributed in the arcs of each ring. Without any errors considered, the dynamic aperture of $20\sigma_x \times 15\sigma_y$ is obtained at the energy spread of $\pm 0.6\%$ with fully-coupled situation. Figure 8 gives the dynamic aperture of the high luminosity mode (without errors).

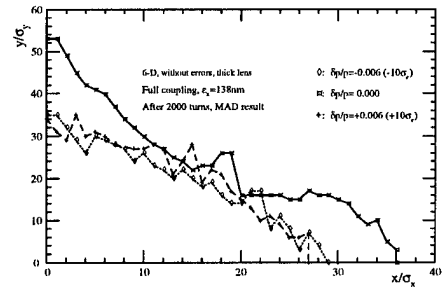

Figure 8: The dynamic aperture of the high lumi. mode.

5 TOUSCHEK LIFETIME AND DYNAMIC APERTURE OF MONOCHROMATOR MODE

5.1 Touschek Lifetime

In order to increase Touschek lifetimeτ_T large beam size and energy acceptance(E_{acc}) is necessary. So the normal cell with 60° phase advance is used in the arc to increase the dynamic aperture and energy acceptance and emittance (ϵ_x=35 nmrad with wigglers).

The results calculated by the code ZAP [7] show: when ϵ_x=13nm, ϵ_y=2nm, E_{acc}=8e-3, it has τ_T=0.5hrs . when ϵ_x=35nm, ϵ_y=5.3nm, E_{acc}=8e-3,9e-3,10e-3,11,e-3, it has τ_T=1.0hrs,1.3hrs, 1.7hrs, 2.1hrs respectively .

5.2 Dynamic Aperture

For the monochromator mode, 48 sextupoles of nine families are distributed in the arcs of each ring.The initial tracking results in six dimensions with full coupling is shown that dynamic aperture is $15\sigma_x \times 11\sigma_y$ with $\delta p = \pm 0.008$

6 CONCLUSION

The current lattice design is feasible to meet the requirement of the BTCF. The three operation modes have been compatible in one magnet lattice. Obviously, more detailed work is still needed on the aspects of the dynamic aperture and polarization.

7 REFERENCES

[1] Y.Z. Wu, "Beijing Tau-Charm Factory Design Study", this proceedings.

[2] "The Feasibility Report of Beijing Tau-Charm Factory", IHEP-BTCF, Report-03, October 1996

[3] K. W. Robinson, "Radiation Effects in Circular Accelerator", Phys, Rev 111, 373 (1958)

[4] Y. Baconnier, et al, Nuclear Instruments and Methods A 234 (1985) 244

[5] D. Wang, to be published

[6] H.Grote, F.C.Iselin, "The MAD Program", CERN/SL/90-13 (AP), 1990

[7] M.S. Zisman, et al, "ZAP User's Manual", LBL-21270, 1986

THE FOCUSING STRUCTURE OF THE PRAGUE PROTON SYNCHROTRON FOR HADRON THERAPY

A.Yu.Molodozhentsev, I.N.Ivanov, V.K.Makoveev, G.I.Sidorov
Laboratory of Particle Physics,
Joint Institute for Nuclear Research
Dubna, Moscow region, 141980 Russia and
K.Prokesh, J.Sedlak , M.Kuzmiak
"Oncology 2000" Foundation, Prague, Czech Republic

Abstract

This paper reports a lattice design of a dedicated proton synchrotron for hadron therapy. This synchrotron, named as a Prague Medical Synchrotron (PRAMES), will be used as a kernel of an accelerator complex of a Prague Oncological Hospital (Czech Republic). The synchrotron will be able to accelerate high-intensity proton beam of $6.25 \cdot 10^{10}$ protons per pulse till the energy of 60÷220 MeV with the 1 Hz repetition rate. The active scanning of tumours is assumed. To satisfy this requirement, the slow (third-order) extraction scheme is analysed. The single turn injection of the proton beam is utilised to get the trapped proton beam with small transverse emittance on the injection energy of 12 MeV. The developed focusing structure of the ring has two superperiods with two long straight sections to install the injection, acceleration and extraction systems. Each period is composed of two achromatic cells to provide, first of all, a high efficiency of the slow extraction. The cell consists of two rectangular dipole magnets with the 45 degree bending angle and 22.5 degree edge angle at both ends, and a triplet of quadrupole lenses. To adjust the working point to the slow extraction, an additional quadrupole triplet in the superperiod is utilised. The output horizontal and vertical tunes are 2.666 and 1.8, respectively. The slow extraction scheme of the accelerated proton beam is discussed in the paper.

1 INTRODUCTION

A good clinical experience with proton-beam radiotherapy has stimulated the interest in designing and constructing dedicated hospital-based machines for this purpose. Reliability and simplicity without loosing the required parameters of the machine, should be considered, first of all, to design this accelerator. The technological and economic requirements for these machines are of great importance for an industrial approach. A synchrotron meets the machine requirements better than a linear accelerator or a cyclotron [1]. The dedicated proton synchrotron is built in the Loma Linda University Medical Center (USA). There are several projects offered in different countries (USA, Japan, Italy, China). Most of the proposed medical synchrotrons are based on the weak-focusing structure to get a compact design.

Specifications for such a machine are not hard but a consensus is necessary on several key requirements [2]. Extraction energy of the proton beam should be from 60 MeV till 220 MeV with the energy variability less than 0.4 MeV to treat the cancer at different depth. The average beam current should be, at least, 10 nA for reasonably short treatment periods of time. The injection energy may be small. The minimum value of this energy can be estimated using the Laslett tune shift. But the accelerator complex for cancer therapy should be able to produce the short-lived radiopharmaceuticals for the proton emission tomography (PET). Then it is necessary to find some compromise between an injection energy and cost of the injector. A low current injector can be accommodated by using multiturn injection but this additional complexity should be avoided in a medical accelerator. The single-turn injection is chosen.

The transverse emittance and momentum spread should be as small as possible. Real normalised transverse emittance for the proton linear accelerator is equal to 0.6π μm.rad, then one can assume the normalised emittance of the trapped beam of 1π μm.rad and the momentum spread of ± 0.003 on the injection energy.

The PRAMES has been designed to accelerate the 12 MeV high-intensity proton beam from a RFQ/DTL linac to the maximum output energy of 220 MeV. To satisfy the requirements of the slow extraction, the focusing structure of the dedicated proton synchrotron for the cancer therapy is proposed. The lattice design is based on the achromatic cells with conventional warm dipole magnets. The repetition rate is chosen of 1 Hz to have a sufficient time duration for the slow extraction. Using the active scanning of the tumour with protons for a single spill, the tumour will get at least $5 \cdot 10^{10}$ protons per pulse. The spill time could be till 250 ms. The slow extraction using the third-order radial resonance determines the working point position. The strong-focusing lattice has been analysed to get good controlled transverse dimensions of the proton beam.

0-7803-4376-X/98 /$10.00 © 1998 IEEE

2 PRAMES LATTICE DESIGN

The general layout of the PRAMES lattice is shown in Figure 1.

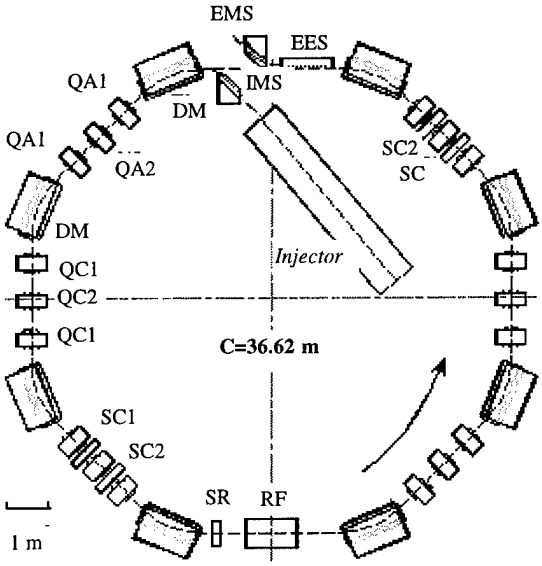

Figure 1: General layout of the ring of the PRAMES.

The main parameters of the PRAMES are listed in Table 1.

Table 1

Output kinetic energy (MeV)	60 ÷ 220
Energy variability (MeV)	< 0.4
Energy variability accuracy (MeV)	< ± 0.35
Average current (nA): patient / acceleration	7.8 / 10
Repetition rate (Hz)	1
Norm. transverse emittance(π.μm)	1
Number protons per pulse: patient (active scanning) acceleration	$48 \cdot 10^{10}$ $6.25 \cdot 10^{10}$

The developed focusing structure of the ring has a race-track configuration with two long straight sections to install the injection, acceleration and extraction systems. To minimise the β-function and the dispersion function, the double bend achromat with the focusing triplet (QA1-QA2-QA1) is utilised. The dipole magnets (DM) are the rectangular magnets with the bending angle of 45°. To minimise the coil current, the maximum magnetic field is equal to 1.2 T. The working point position can be optimised by the adjusting triplet of the quadrupole lenses (QC1-QC2-QC1). The lattice of the synchrotron has two sorts of the sextupole lenses. The sextupoles in the arcs with a finite dispersion are grouped into two families (SC1, SC2). They only influence on the chromaticity. The sextupole lens (SR) in the non-dispersion straight section influences only on the beam behaviour near the third-order resonance line.

The lattice parameters are listed in Table 2. The focusing structure of the ring is calculated using the MAD and the AGILE programs.

Table 2

Main parameters of the Prague proton synchrotron

I. Proton Beam Properties (round beam)	Proton Energy (MeV)	
	12	220
Momentum (MeV/c)	150.535	679.123
Rigidity (Tm)	0.502	2.265
Acc. Emittance (π μm)	6.232	1.381
Energy spread	±0.003	±0.0014
Orbit Period (μsec)	0.77	0.208
Incoh.Vt. Tune Shift @ $6.25 \cdot 10^{10}$ protons	-0.052	-0.009
II. Lattice Parameters		
Circumference (m)	36.62	
Dipole magnet field (T): min / max	0.26599 / 1.2	
Straight Section (m)	3.5	
Bending Radius (m)	1.88768	
Effective Length of the dipole magnet (m)	1.4825	
Dipole Edge Angle (deg)	22.5	
Number of Quadrupoles: achromatic + adjusting	12 + 6	
Max.Quad.Strength (m^{-2})	5.0	
Betatron tune on the extraction: ν_x / ν_z	2.666 / 1.8	
β-functions (220MeV) β_x (m) : max / avegare β_z (m) : max / average	7.089 / 3.037 8.46 / 3.6297	
Dispersion (m): max / av	1.026 / 0.3337	
Chromaticity (ξ_x , ξ_z) natural corrected	-4.977 , -3.627 -4.981 , -3.609	
Transition energy	5.562	
Working region H/V,mm	80 / 55	

The magnet field uniformity in the dipole magnet of the ring should be less than $5 \cdot 10^{-4}$. The vertical dimension of the working region is determined by the vertical beam size on the injection energy. But in a machine uisng a slow extraction, the good-field region required for the extraction becomes the important characteristics in the horizontal plane. The "stable" region during extraction will occupy the same horizontal space at all energies. Then the horizontal "good" field region should be the same for both - the injection and extraction energies. The horizontal size of the working region is equal to 80 mm for the electrostatic septum (EES) described below.

3 RESONANCE EXTRACTION

The tumour is treated with the spatial definition of a voxel (e.g. 5×5×2 mm^3). The spill must be uniform. It requires a relatively long, high-quality spill. The extracted beam should have the same extraction trajectory amd momentum spread throughout the spill time. To avoid losses of the particles in the extraction elements, the achromatic cells are used for the focusing structure design.

The amplitude selection method is chosen from possible extraction techniques. This classic method needs the minimum of equipment. The spill can be switched on and off using special quadrupoles. The developed focusing structure of the synchrotron has two families of the adjusting quadrupole lenses to lead the working point on the different extraction energy to the resonance line $8\nu_x=3$ (Figure 2).

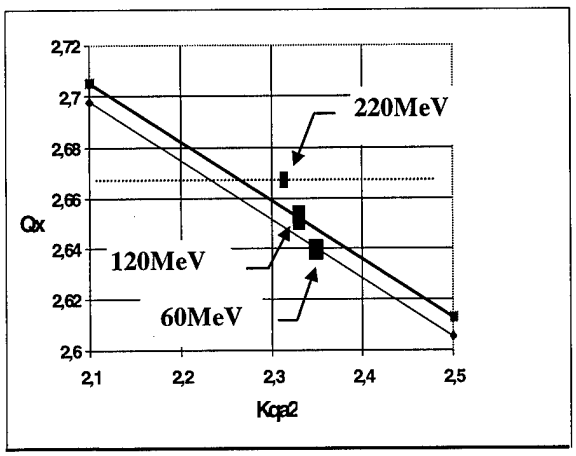

Figure 2: Variation of the horizontal betatron tune for different kinetic energy to lead to the third-order resonance line $3Q_x=8$. The strength of the second (focusing) quadrupole lense is fixed (Kqa1=-1.28957 m^{-2}).

To ensure transverse stability for the extracted beam, the chromaticity of the lattice should be negative. The natural chromaticities of the proposed structure are -4.977 (horizontal) and -3.627 (vertical). Correction of the chomaticity is determined by the extracted beam quality.

The third-order resonance is driven by a sextupole perturbation of the resonance sextupole lense (SR) installed in the zero-dispersion long drift space. The effective length of the sextupole lenses is equal to 15 cm. The normalized strength of the resonance sextupole is equal to 12.8 $m^{(-1/2)}$.

Two families of the sextupole lenses (SC1, SC2) are placed in the non-zero dispersion arcs of the ring to correct the chromaticity and escape the angular dispersion of the extracted particles with different momentum

The normalized strength of the sextupoles are less than 0.1 $m^{(-1/2)}$. The corrected chromaticities of the proposed structure are -4.981 (horizontal) and -3.609 (vertical). The horizontal phase space of the extracted beam is presented in Figure 3. The kinetic energy of the proton is equal to 220 MeV with the relative momentum spread of ± 0.0014. Calculation of the slow extraction is performed using the AGILE program.

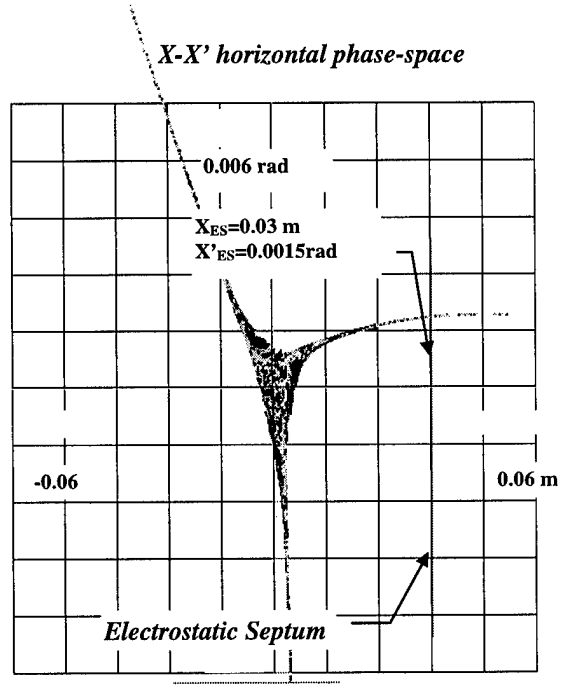

Figure 3: The horizontal phase-space for the third-order resonance extarction of the accelerated particles (on the entrance into the electrostatic septum).

A high efficiency (98%) of the extracted particles is an important requirement for this machine. Then the elements of the extraction channel are the electrostatic (EES) and magnetic septa (EMS). The both elements are located in the zero-dispersion long drift space. The electrostatic septum has to be designed with the 0.05 mm wire diameter. The distance between the circulating beam and the wires of the electrostatic septum is assumed to be more than 25 mm. The gap between the plates of the septum is equal to 10 mm. The length is equal to 1200 mm. The applied voltage is 40 kV. The developed focusing structure of the ring allows to provide a sufficient deviation of the extracted beam from the circulating one to install the first magnetic septum with the blade thickness about 10 mm.

REFERENCES

[1] U.Amaldi, M.Grandolfo and L.Picardi Editors: The TERA project and the design of compact proton accelerators (The TERA Collaboration), 1995.

[2] M.Goitein: Proc. Medical Workshop on Accelerators for Charged-Particle Beam Therapy, Fermilab (January 24-25,1985) p.41.

DYNAMIC APERTURE WITH MULTIPOLES OF SPECIAL MAGNETS IN THE KEKB INTERACTION REGION

H. Koiso, H. Nakayama, K. Oide, and M. Tawada,
KEK, 1-1 Oho, Tsukuba, Ibaraki 305, Japan

Abstract

At KEKB, six quadrupoles of special shapes are placed in the interaction region. Those quadrupoles are accompanied by higher-order multipole components which are prominent sources to degrade the dynamic aperture, and which even affect the linear optics because the design orbit passes through one of the special quadrupoles off-axis. In order to represent realistic field distributions of those quadrupoles obtained by hardware design, we take the higher-order multipoles up to 21st into account in our simulation. Using this model, we have redesigned the linear lattice and have estimated tolerances on the magnitudes of multipole components.

1 INTRODUCTION

KEKB[1] is an 8 GeV + 3.5 GeV electron-positron double-ring collider with small vertical beta function at the interaction point (IP) ($\beta_y^* = 1$cm) and short bunch spacing (59 cm). In order to separate both beams, a finite beam crossing angle of 22 mrad is adopted, and eight special quadrupole magnets listed in Table 1 are installed near IP. Two final-focus quadrupoles are superconducting magnets which work on both beams. The other six are iron-core magnets with special shapes to let the counter-rotating beam pass through unaffectedly.

Magnet	r_b (mm)	B' (T/m)	x_{max} (mm)	y_{max} (mm)	Beam
QC2LE	60	3.2	67.5	13.3	$e^- \downarrow$
QC2LP	40	6.1	56.9	10.2	$e^+ \uparrow$
QC1LE	38	-14.2	22.4	20.7	$e^- \downarrow$
QCSL (IP)	(75)	-21	13.3	19.9	$e^- \downarrow e^+ \uparrow$
QCSR	(75)	-21	14.2	24.3	$e^- \downarrow e^+ \uparrow$
QC1RE	70	-13.2	28.5	26.6	$e^- \downarrow$
QC2RP	45	2.9	68.6	11.9	$e^+ \uparrow$
QC2RE	60	10.8	69.2	16.3	$e^- \downarrow$

Table 1: Special quadrupole magnets near IP. In the first column, r_b is the bore radius, B' the field gradient, x_{max}andy_{max} the maximum amplitudes of the injected beam in the horizontal and vertical planes. The positive sign of B' means horizontal-focusing.

In spite of the small beta function, a chromaticity correction scheme with noninterleaved sextupoles[2] provides a large dynamic aperture for the bare lattice of KEKB. After canceling main transverse nonlinearity of sextupoles, the dynamic aperture is limited by small residual terms such as the nonlinear Maxwellian fringe field of final quadrupoles. The iron-core quadrupoles near IP accompany higher-order multipole components which may degrade the dynamic aperture. In this paper, we discuss how to treat the multipole components and examine their effects on the beam dynamics mainly in the high-energy ring (HER), because HER is strongly affected by the multipoles of the vertical-focusing quadrupoles named QC1LE and QC1RE placed next to the superconducting ones.

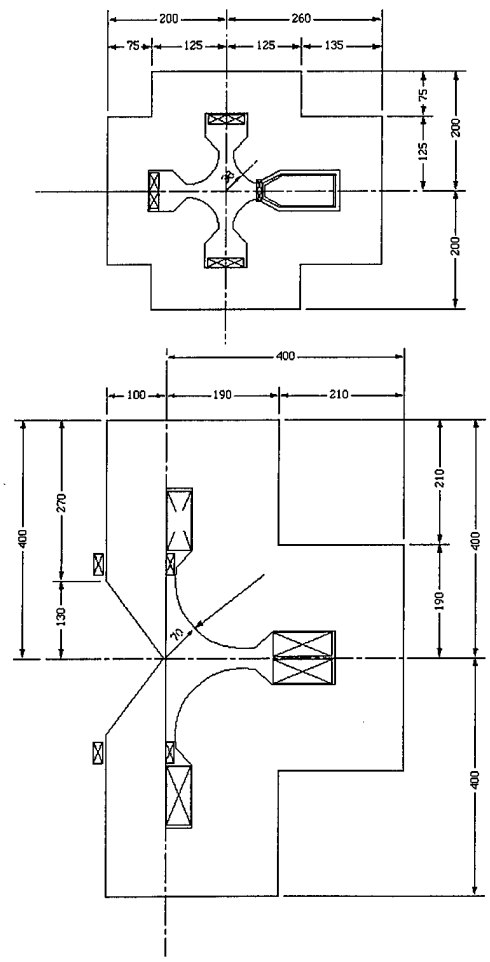

Figure 1: Schematic view of QC1LE (above) and QC1RE (below). A field free space is embedded in QC1LE. The other four quadrupoles have shapes like QC1LE.

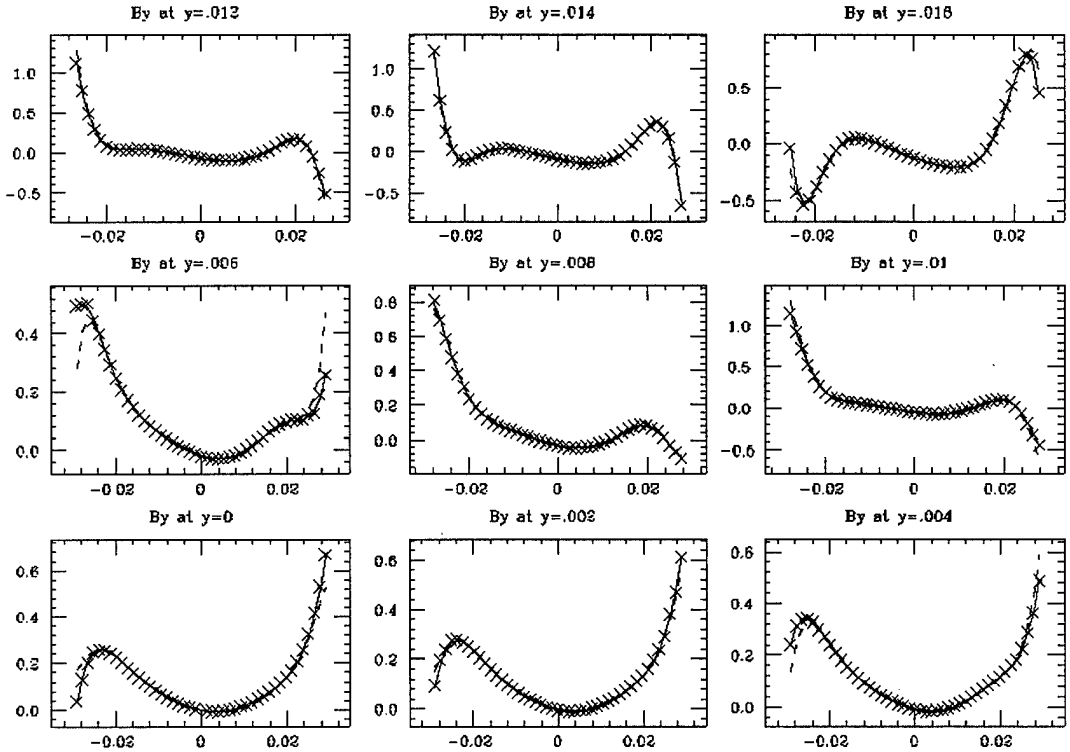

Figure 2: A part of the fitting results of the QC1LE multipoles. The crosses show the data obtained by OPERA-2d. The solid and dashed lines depict the fitting results with the multipoles up to $n = 21$ and 14, respectively. The dashed line deviates from the data near the edge of the fitting region ($x^2 + y^2 < (0.03)^2$). Each graph collects the data at $y = constant$. The horizontal axis is the horizontal position x in meter, and vertical axis is the B_y in Gauss, respectively.

2 MULTIPOLE EXPANSION

The six iron-core quadrupoles have been designed based on two-dimensional field calculations by OPERA-2d[3]. One of the quadrupoles, QC1RE, is a half quadrupole, and the rest are full quadrupoles with field free space for the counter-rotating beam as shown in Fig. 1. In order to derive the multipole components, we express the magnetic fields, B_x and B_y as

$$B_y(x,y) + iB_x(x,y) = B_0 \sum_{n=0}^{N} (b_n + ia_n)(x+iy)^n. \quad (1)$$

After subtracting the main quadrupole component, the data B_x and B_y obtained by the OPERA-2d calculation are fitted in the standard least-square method with parameters b_n in the region which covers the physical aperture. The skew components a_n are set to be zero since all the quadrupoles have symmetry with respect to the horizontal median plane.

Figure 2 shows an example of fitting for QC1LE. Introducing b_n up to $n = 21$, the field data at 537 points are represented well with the residuals smaller than 0.1 Gauss which is consistent to the estimated errors in the field calculation. The other five quadrupoles are also fitted with the same accuracy in the same way. The merit of this fitting method is to fully utilize the field data over the region where the beam may exist. All calculations concerning the data fitting in this section, and optics matching and tracking in the next section have been done by the code SAD[4] developed at KEK.

3 EFFECTS ON DYNAMIC APERTURE

To estimate the effect of the multipoles, at the first step, we compare the dynamic aperture with and without the multipoles of QC1LE out of the four special quadrupoles in HER. Since the design orbit passes through QC1LE on-axis, we need not redesign the linear optics even when the multipoles are included. (The design orbit also lies on-axis in the horizontal-focusing full quadrupoles.) The strengths of sextupoles are also not reoptimized with the multipoles.

The dynamic aperture has been estimated by six-dimensional full-symplectic tracking using SAD. The $2(n+1)$-pole magnets up to $n = 21$ with a finite effective length are treated consistently in SAD. Each magnet is subdivided into many pieces along the beam axis. The number of pieces is increased until the results of tracking converge. The nonlinear Maxwellian fringe field at the edge of the magnet is also involved in the tracking not only for the main quadrupole but for the multipoles.

As shown in Fig. 3(a), the multipole components drastically decrease the transverse dynamic aperture near the on-momentum region. The dynamic aperture at QC1LE is $(x, y) = (2.9\text{cm}, 2.7\text{cm})$ which is a few mm larger than

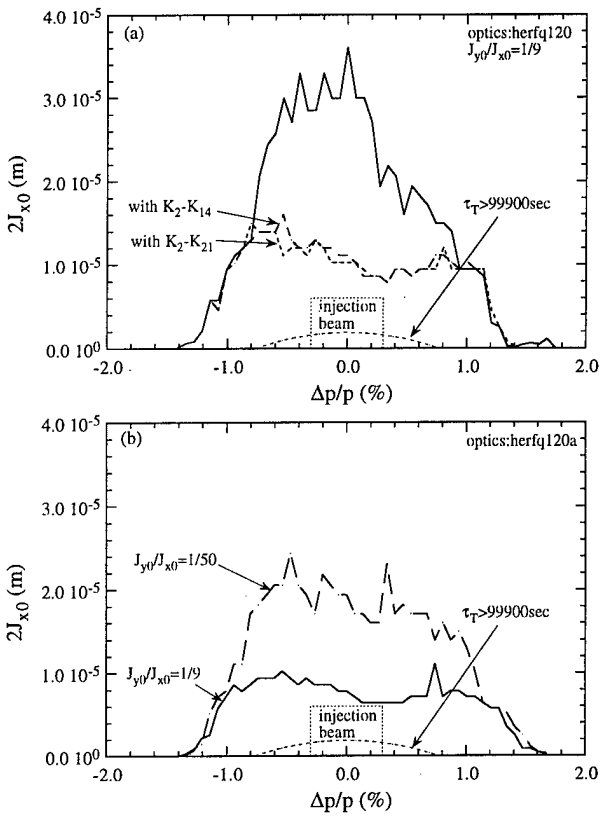

Figure 3: Dynamic aperture of HER with the multipole components of special quadrupoles. (a) with (dashed lines) and without (solid line) the multipoles of QC1LE. (b) with the multipoles of all the special quadrupoles.

the physical aperture. This result is reasonable since the magnetic field is cared only inside the physical aperture in the magnet design, thus it deviates rapidly from the ideal quadrupole outside the physical aperture. The two types of multipole expansion up to $n = 14$ and $= 21$ do not make a significant difference in the dynamic aperture.

In the next step, we take the multipoles of all special quadrupoles including QC1RE into account. Because the design orbit goes through QC1RE at 44.55 mm off-axis, we must redesign the linear lattice with the multipoles of QC1RE and must readjust the strengths of the sextupoles as well. Figure 3(b) shows the dynamic aperture with the multipoles of all special quadrupoles. The dynamic aperture decreases again compared with Fig. 3(a), but still satisfies the requirement for beam injection ($2J_{x0} = 6 \times 10^{-6}$m at the momentum deviation of $\pm 0.3\%$) and is cocsistent with the the physical aperture at QC1RE as shown in Fig. 4. We assume the vertical-to-horizontal coupling of the coherent oscillation at injection J_{y0}/J_{x0} to be 1/9 in the tracking.

In the case of a smaller coupling ($J_{y0}/J_{x0} = 1/50$), the dynamic aperture is improved considerably beyond the physical aperture as shown in Figs. 3(b) and 4.

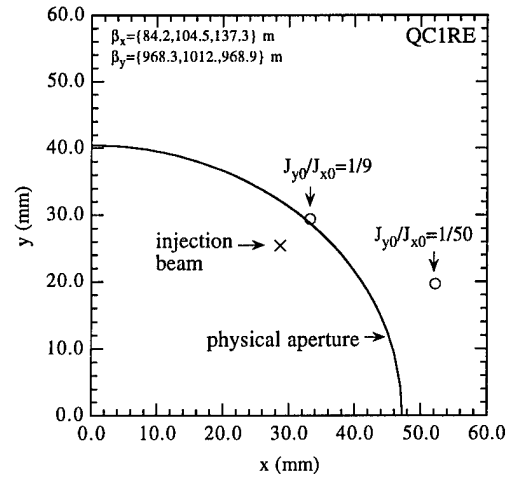

Figure 4: Physical and dynamic apertures at QC1RE. The origin is set at 44.55 mm from the center of QC1RE.

4 CONCLUSIONS

The iron-core quadrupoles with special shapes near IP have been designed by the two-dimensional field calculation. The magnetic field distributions of those quadrupoles have been expressed well with the higher-order multipole components up to 21st over the range which covers the physical aperture. Although the dynamic aperture of HER has been drastically degraded by those multipoles, it is still larger than the physical aperture at QC1LE and QC1RE, and satisfies the requirement for beam injection.

5 ACKNOWLEDGMENTS

We thank S.-I. Kurokawa, K. Satoh and N. Toge for useful comments and discussions and S. Takasaki for preparing the pictures.

6 REFERENCES

[1] 'KEKB B-Factory Design Report', KEK-Report 95-7, 1995.

[2] K. Oide and H. Koiso, Phys. Rev. E47, 2010(1993). H. Koiso and K. Oide, Proc. 1995 Part. Accel. Conf. at Dallas, TAG11, 2780(1995).

[3] OPERA-2d, Vector Fields Limited, Oxford, England.

[4] Information on SAD is available at http://www-acc-theory.kek.jp/SAD/sad.html.

MAGNETIC OPTICS FOR PROTON RADIOGRAPHY*

C. Thomas Mottershead and John D. Zumbro, Los Alamos National Laboratory,
Los Alamos, New Mexico 87545

Abstract

High energy protons of 10 to 50 GeV can be used to radiograph dense objects. Because the transmitted beam particles undergo multiple coulomb scattering (MCS) in the object, a magnetic lens system is used to focus the particles exiting each point of the object onto a distant image plane. Without the lens, the MCS would seriously blur the radiographic image. Correlations can be introduced in the illuminating beam to cancel a major part of the chromatic and geometric aberrations in the lens, while providing locations inside the lens where the rays are sorted by MCS angle. This allows the introduction of angle cut apertures to aid material identification. The requirement for a matched multistage lens system with successively smaller angle-cut apertures leads to the use of minus-identity (-I) lenses, in which the angle sorting is in the longitudinal mid plane of the lens, and the exit beam correlations are the same as the input correlations. A single stage -I lens has been successfully tested at Brookhaven with 10-GeV protons and another is being used in dynamic experiments with 0.8-GeV protons at Los Alamos. The resolution achievable at higher energies is briefly surveyed.

1 PROTON RADIOGRAPHY

A proton beam passing through a dense homogeneous object of material (Z,A) is depleted by removal collisions, with an attenuation length $\lambda_T = (n\sigma_T)^{-1}$ dependent on the density n of nuclei, and the total nuclear cross section $\sigma_T \propto A^{2/3}$. The surviving protons undergo millions of small coulomb scatterings that produce a roughly gaussian angular distribution at the exit surface of the object. The half-width, in milliradians, of this multiple coulomb scattering (MCS) exit cone [1] is

$$\phi_c = \frac{14.1}{p\beta}\sqrt{\frac{L}{L_R}}\left[1+\tfrac{1}{9}log_{10}\left(\frac{L}{L_R}\right)\right], \qquad (1)$$

where p is the beam momentum in GeV/c, L is the path length through the object, and $L_R \propto Z^2/A$ is the radiation length of the material. Appropriate weighted averages for the path length ratios are applicable to real inhomogenous objects. The proton radiographic image is formed by a magnetic lens downstream of the object. The lens refocuses the MCS exit cone from each point of the object back to a corresponding point in the detector plane. A second requirement on the magnetic optics is to provide a location where the rays are sorted by MCS angle, so an aperture can block the larger angles. Points in the image where the aperture will pass the entire exit cone would be unaffected, but other points, having an angular width greater than the aperture acceptance, would be recorded with reduced intensity. A series of radiographs made with different angle cut apertures thus opens the possibility of discriminating material type as well as density.

2 THE IDENTITY LENS

The first-order transfer matrix **R** of an imaging lens maps a particle with initial coordinates (x,θ) to a final position $x_f = R_{11}x + R_{12}\theta$. Point-to-point imaging means $R_{12} = R_{34} = 0$, so the final position is independent of the initial angle. This requires at least a quadrupole doublet. One-to-one (inverted) imaging, meaning $R_{11} = R_{33} = -1$, requires at least a triplet, but quadruplets are preferred because they can produce the same beam excursions in both planes.

A quadrupole beamline is reflection symmetric if its second half is the mirror image of the first half, meaning the sequence of drifts and quads is traversed in the reverse order and with the opposite signs for the magnetic fields. The symmetry forces $R_{34} = R_{12}$, and $R_{43} = R_{21}$ so a reflection symmetric lens always focuses simultaneously in both planes. It also forces $R_{33} = R_{22}$, and $R_{44} = R_{11}$, so the 1:1 condition occurs simultaneously in both planes as well.. Russian quadruplets [2,3] of the form +A-B+B-A are an example of reflection symmetry.

If the first half of the beamline is itself reflection symmetric, then the second half is the same as the first, and the lens consists of two identical cells. In this case, if the transfer matrix of one cell is **M**, that of the whole lens is given (in each plane) by the 2x2 matrix identity

$$\mathbf{R} = \mathbf{M}^2 = -\mathbf{I}\,det(\mathbf{M}) + \tau\mathbf{M}, \qquad (2)$$

where $\tau \equiv Tr(\mathbf{M}) \equiv M_{11} + M_{22}$ is the trace of **M**. The determinant $det\,\mathbf{M} = 1$ for beamline matrices. When the trace $\tau = 0$, we have an identity lens with **R=-I**.

An identity lens preserves beam correlations because the output phase space is an inverted copy of the input. Therefore multistage systems can be built by simply stacking identical identity lenses in series. Since **-I** commutes with everything, including a drift matrix, an identity lens actually images an entire 3D volume surrounding the object.

In the simplest case, the cell **M** is a doublet, defined by only four parameters: the outside drifts f, the inside drift s between the quads, and the length and strength $(L, \pm G)$ of the two quads. Any one of these can be adjusted to set $\tau = 0$.

3 CHROMATIC CANCELLATION

The chromatic aberration coefficients define the final position errors for particles off the design momentum. The matrix elements in general are functions of the fractional

* Work supported by United States Dept. of Energy

momentum deviation $\Delta \equiv \delta p/p$, so the final position of an off-momentum ray with initial coordinates (x, θ) is

$$x_f = R_{11}(\Delta)x + R_{12}(\Delta)\theta \tag{3}$$

Suppose now that the initial beam is strongly correlated, as if it came from a (virtual) point source a distance L upstream of the entry plane of the lens. Such a beam would lie along the line $\theta = wx$ in phase space, where $w = L^{-1}$ is the beam correlation coefficient. Real particles exit the object at angle $\theta = wx + \varphi$, where φ represents all deviations from the correlation line due to both MCS in the object and non-zero emittance in the illuminating beam. To first order in Δ, the final position of this particle is (primes indicate momentum derivatives):

$$x_f = R_{11}x + R_{12}\theta + (R_{11}' + wR_{12}')x\Delta + R_{12}'\varphi\Delta + \cdots \tag{4}$$

If we choose the correlation coefficient w so that

$$R_{11}' + wR_{12}' = 0, \quad \text{or} \quad w = -R_{11}'/R_{12}' \tag{5}$$

all position dependent chromatic aberrations vanish. The contribution of the $R_{11}' \equiv T_{116}$ (TRANSPORT notation) term is canceled by the principal coefficient $C_x \equiv R_{12}' \equiv T_{126}$. With $R_{12} = 0$, and $R_{11} = -1$, the final position is

$$x_f = -x + C_x\varphi\Delta. \tag{6}$$

The remaining chromatic aberration depends only on the deviation angle φ. We call a beam with this correlation chromatically matched. K. Brown [4] has pointed out that $R_{11}' = T_{116}$ vanishes if the diagonal elements of **M** are zero. This requires 3 or 4 quads per cell, but has the advantage that parallel illumination with w=0 is the matched beam.

4 ANGLE SORTING

The angle cut aperture must be placed where the rays are completely sorted by MCS angle. This always occurs in the midplane of a chromatically matched identity lens. If **M** is the transport matrix of the first cell, Eq.(2) gives the matrix elements of the whole lens for off-momentum particles:

$$R_{jk}(\Delta) = -\delta_{jk} + \tau(\Delta)M_{jk}(\Delta). \tag{7}$$

The momentum derivatives of these at the origin $\Delta = 0$ are

$$R_{jk}' \equiv \left.\frac{dR_{jk}}{d\Delta}\right|_{\Delta=0} = M_{jk}\frac{d\tau}{d\Delta} + \tau\left.\frac{dM_{jk}}{d\Delta}\right|_{\Delta=0} = \tau' M_{jk}, \tag{8}$$

because the lens is focused with $\tau(0) = 0$. Therefore

$$R_{11}' + wR_{12}' = \tau'(M_{11} + wM_{12}) = 0, \tag{9}$$

implying that after the first cell, the position of the rays depends only on φ, not on x. This is angle sorting:

$$x_{mid} = (M_{11} + wM_{12})x + M_{12}\varphi = M_{12}\varphi. \tag{10}$$

5 THE ILLUMINATING BEAM

The required phase space correlations are provided by a matching section just upstream of the object. This section must also expand the beam to fully illuminate the field-of-view. The expansion is provided by either a diffuser, or a quadrupole lens, which increases the angular size of the beam as it enters a long drift. Other, larger quadrupoles then adjust the beam parameters to best fit the required correlation line $\theta = wx$ in each plane. In the usual beam moments notation $\langle x\theta \rangle \equiv -\alpha\varepsilon$ and $\langle x^2 \rangle \equiv \beta\varepsilon$, where e is the beam emittance. The final β must be set to produce the required beam size. Then α is adjusted to minimize the mean square deviation from the correlation line. The minimum is $\langle \phi^2 \rangle = \beta/\varepsilon$, obtained when $\alpha = -w\beta$. The residual incident emittance angles are added in quadrature to the multiple coulomb scattering angles produced by the object.

6 THE BROOKHAVEN EXPERIMENT

The first test of such a system was carried out in Experiment 920 at Brookhaven National Laboratory in July 1996. Available 8Q48 quadrupoles running near their maximum field of 12.5 T/m were set up as an identity lens. Another 8Q48 and a pair of 12Q30 quads were used for the matching lens to properly illuminate the object out to 7 cm from the axis. Fig.1 shows the layout, with boxes indicating the location and size of the quadrupoles, and vertical lines marking the object and image planes. A 3 mm tantalum plate was used to spread the 10 GeV test beam into an 18.6m drift. Two sigma beam envelopes in x and y from this diffuser are shown. Fig.2 shows a log-ratio attenuation image of a tungsten step wedge taken with this lens. The image is 15 cm square, bounded by the intersection of two elongated ellipses, which are the images of the limiting beam pipe from different locations in the x and y planes.

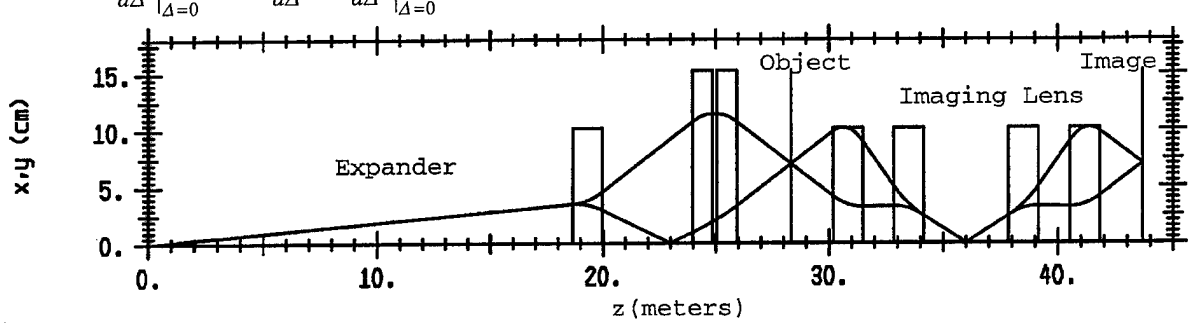

Figure 1: Beam Expander and Identity Lens set up in the A1 beam line at the AGS.

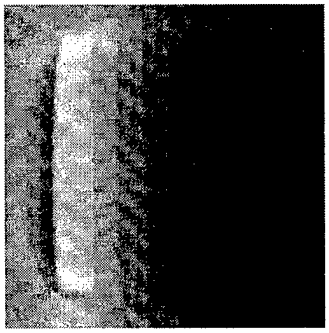

Figure 2: Experimental Image of a Tungsten Step Wedge.

7 FIELD OF VIEW

The field-of-view (FOV) is an important measure of the performance of a magnetic lens. Here we define the FOV as the maximum initial x or y coordinate that a particle can have and still travel all the way through the lens without striking a limiting aperture. This clearly depends on the initial angle $\theta = wx + \varphi$, making the FOV a function of the deviation angle φ. Fig 3 shows matched rays scattered at φ=0, $\pm 5mR$ and $\pm 10mR$ from points spaced at 2 cm in the object plane of the Brookhaven test lens. Note the angle sorting at the midplane. The x-position at z of a ray with initial coordinates (x, φ) is

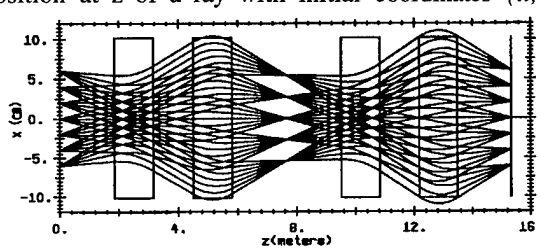

Figure 3: X-plane Ray Traces in the BNL A1 Identity Lens

given [5] by the "sinelike" and "cosinelike" rays $S(z) \equiv M_{12}(z)$, and $C(z) \equiv M_{11}(z)$ characterizing the map out to z. The ray that just reaches the limiting aperture $a(z)$ at z is

$$x_{ap}(z) = (a(z) - S(z)\varphi)/(C(z) + wS(z)) \qquad (11)$$

The FOV is the largest possible x for each φ. This is the smallest $x_{ap}(z)$ for any z, and may be obtained by a numerical search. Fig. 4 shows this function for the BNL lens with and without the matching correlation. The endpoint of both curves at 13 mR is the maximum angle the lens will transmit from a point on axis. Without correlations, the FOV at φ=10 milliradians is only 1.1 cm. With them, it increases to 5.4 cm, about half of the actual quad aperture/

8 HIGH ENERGY LENS SURVEY

To assess the ultimate performance of magnetic lenses for proton radiography, we note that the dominant lens error is chromatic aberration of the form $C_x \varphi \Delta$, and both ϕ and Δ scale inversely with the beam momentum. Better resolution is therefore expected with higher beam

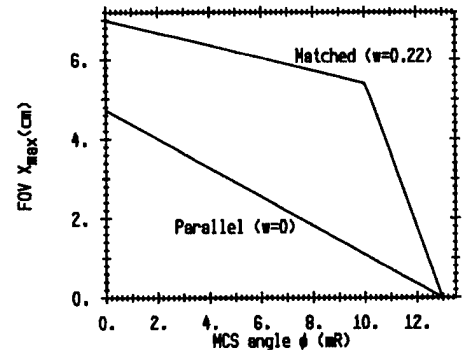

Figure 4: Field of View of BNL Lens (cm)

energy. The chromatic coefficients (C_x, C_y) scale with the overall length of the imaging lens. Shortening the lens requires higher field gradients, suggesting the use of superconducting quadrupoles. The FOV scales with the aperture or pole tip radius a of the quadrupoles. For an estimate of lens performance at high energy, assume a pole tip field of B=5 Tesla, a focal standoff drift of f=2m, and no space between the quads in a cell. For aperture a, the gradient will be G=B/a T/m. We adjust quad length L to achieve focus, and plot in Fig. 5 the chromatic error $C_x \varphi \Delta$ vs. a (roughly the FOV diameter) for a series of energies: 10, 20, 30, 50, and 100 GeV. The chromatic error scale is for a reference object which produces φ=10mR and Δ=0.01 RMS at 10 GeV. The error rises with aperture because G decreases, requiring longer quads, but is below 0.1 mm with a 15cm FOV for this object at 50 GeV.

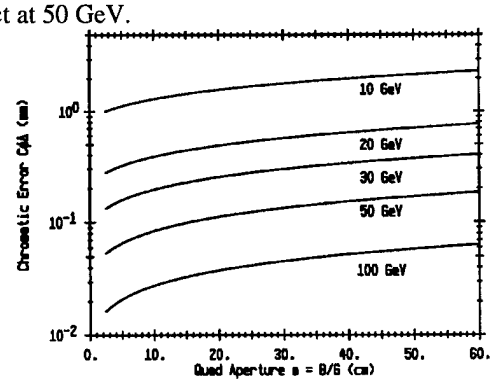

Figure 5. Scaled Chromatic Blur vs. Quad Aperture

ACKNOWLEDGMENTS

The authors would like to thank K. L. Brown, F. R. Neri, C. L. Morris, H. A. Thiessen, P. L. Walstrom, and H. J. Ziock for numerous helpful discussions on this subject.

REFERENCES

[1] 'Review of Particle Data Properties', Particle Data Group, Rev. Mod. Phys. 56, No.2, pS50, April 1984
[2] 'Beam Optics of Quadrupole Probe-forming Systems', W. Grime and F. Watt, Hilger, Bristol, 1984, p28.
[3] A. D. Dymnikov, T. Ya Fishkova, and S. Ya Yavor Sov. Phys.-Tech. Phys, 10, 822, 1965
[4] K. L. Brown, private communication
[5] 'The Optics of Charged Particle Beams', D. C. Carey, Harwood Pub., 1987, p.27

DESIGN OF DOUBLE STORAGE RINGS AT MUSES

N. Inabe, RIKEN, Wako, Saitama 351-01, Japan
T. Katayama, Center for Nuclear Study, School of Science, Univ. of Tokyo, Tanashi, Tokyo 188, Japan

Abstract

Double storage rings (DSR) will play a role to perform various experiments of collision or merging of radio-isotope beams with ions, electron beams and X-rays produced from an undulator. The experiments will be performed at two crossing points. One is for collision of RI beam with electron with crossing angle 20 mrad. Another is for merging for ion beams with angle of 170 mrad. To perform these expriments with high luminosity, electron beam has two different operation modes. The emittance of 10^{-6} m*rad is prepared for the collison with RI and that of 10^{-8} m*rad is done for production of high brilliant X-ray.

1 INTRODUCTION

The DSR is an experimental colliding rings planned in Radio Isotope Beam Factory at RIKEN[1]. In the DSR a variety of unique experiments are envisaged through the collisions of RI beam with electron beam, collision of RI beam with X-ray produced from undulator and merging of RI (ion) beams. To perform these experiments with high luminosity electron beam is required to have two different operation modes. One is a mode to have emittance of the 10^{-6} m*rad (large emittance mode, L.E.M) at energy of 1 GeV. This mode is used for collision with RI beam. Another is to have emittance of 10^{-8} m*rad (small emittance mode, S.E.M) at 2.5 GeV to produce high brilliant X-ray from the undulator. Ion beam is required to have a large maximum energy of 14.6 Tm (800 MeV/u for A/Z=3) and is operated by third mode (ion mode, I.M).

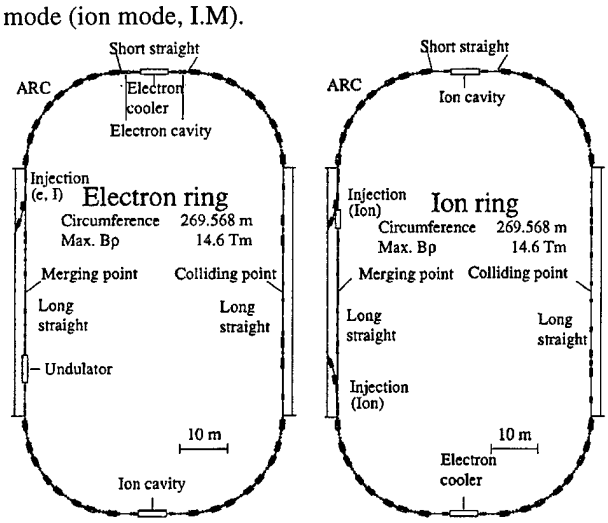

Fig. 1 Two rings in the DSR. 1a is an electron ring and 1b is an ion ring.

The DSR is composed of an electron ring and an ion ring shown in Fig. 1a and b. The electron ring stores not only electron beam but also ion beam for the merging experiment. The ion ring stores only ion beam. The circumference of each ring is 269.568 m which is 8 times larger than that of injéctor superconducting ring cyclotron. Each ring has four arcs, two long straight sections and two short straight sections.

The arc section is designed to adjust emittance of electron beam. In each long straight section, two rings cross vertically. One crossing point is used for the collision of RI beam with electron beam with collison angle 20 mrad (colliding section). In the colliding section configurations of magnets for the electron and ion ring are different because clearance is small due to small crossing angle. Another crossing point is used for merging of ion beams with merging angle of 170 mrad. (merging section) In the merging section the undulator and insertion devices are also located. Electron beam is injected into the electron ring with multi-turn injection method. Ion beam is inserted into both rings with one turn. Short straight sections are used for an electron cooler and RF cavities. The electron cooler is prepared to supress the beam instabilities and to make a short bunch of ion beam. In the following section, details of each section will be described.

2 DESIGN OF EACH SECTION

2.1 Arc Section

Figure 2 shows configuration of the arc in the DSR for both S.E.M and L.E.M. Small emittance can be produced by making small dispersion in dipole magnet.

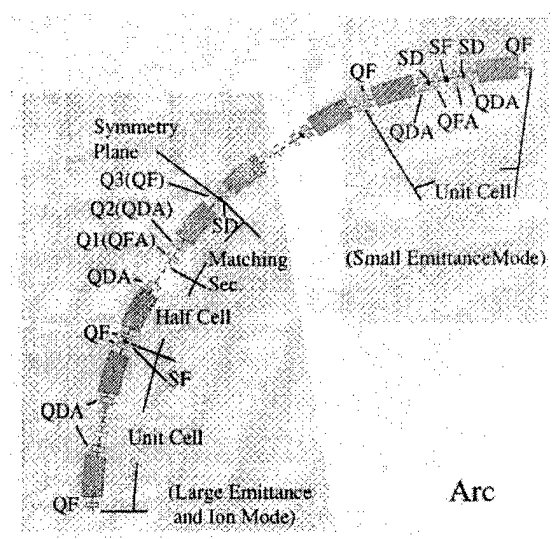

Fig. 2 Compositon of the arc section.

For the S.E.M the arc consists of four unit cells with Double Bend Achromat (DBA) structure. The DBA structure is achieved by the quadrupole magnets for focus (QFA) and those for defocus (QDA). The other quadrupole magnets (QF) are used to fulfill a periodic condition of the cell. Fig. 3 shows β and dispersion functions of the cell. Beta functions fulfill the periodic condition. From the result that dispersion is 0 outside the dipole magnets, one can see that DBA structure is achieved in the cell. The horizontal emittance is almost decided by the cell because there are no horizontal bending magnet except for arcs. The obtained value of horizontal emittance is 13.9 nm*rad at 2.5 GeV. The value is small enough for the S.E.M.

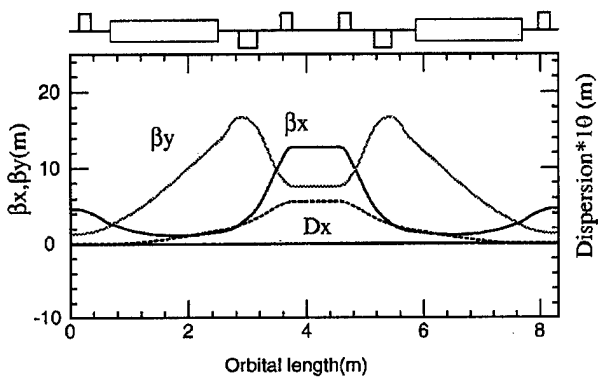

Fig. 3 β and dispersion functions in the unit cell for S.E.M.

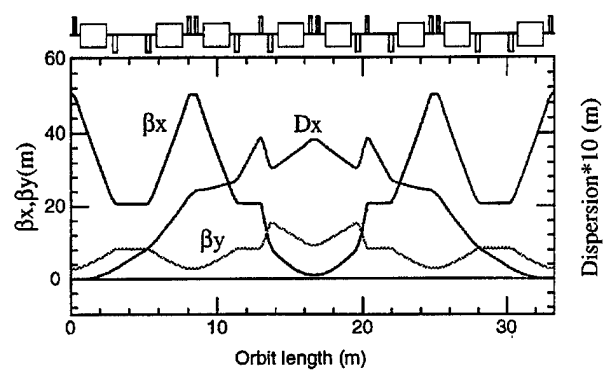

Fig. 4 β and dispersion functions in the arc for L.E.M.

For the L.E.M, emittance is made large by abandoning DBA structure and making large dispersion in dipole magnet. As shown in Fig. 2 the center of the arc is a symmetry plane of β and dispersion functions. The half arc consists of an unit cell, a half cell and a matching section. In the unit and half cell the QFA's are not used to enlarge dispersion in the dipole magnets. In the matching section three quadrupole magnets (Q1, Q2 and Q3) are adjusted to make the symmetry plane at the center of the arc. Figure 4 shows β and dispersion functions of the arc for this mode. Both functions have symmetry plane at the center and a region out of the arc is dispersion free. The obtained value of emittance is 0.76 μm*rad, which fulfills requirements.

For the I.M the composition of the arc is the same as that of the L.E.M. However, since magnetic rigidity of ion beam is much larger than that of L.E.M, focusing powers of quadrupole magnets are adjusted to be weaker than those of the L.E.M. The tendency of the β and dispersion functions are similar. The region out of the arc is also dispersion free in the mode.

2.2 *Colliding Section*

Figure 5 shows a configuration of the magnet in this section. The crossing angle is chosen as small as possible to get large luminosity. In Fig. 5 path of the electron beam is shown by black arrows and that of the ion beam is shown by white arrows. The electron beam goes to the colliding point with parallel to horizontal plane using two dipole magnets with bending angle 15°. The ion beam goes to the point with angle of 20 mrad (1.145°) after bending down with 10° and bending up with 8.855°.

The small β values of the both beams at colliding point are also chosen in order to get high luminosity. The β values of the electron beam for both horizontal and vertical direction are 0.02 m and those of the ion beam are 0.1 m[3]. To get small β values a quadrupole doublet (QD1) is located at a distance of 1.5 m from the colliding point. The ion beam also passes through the doublet. Since focusing power of the doublet is small for the ion beam additional quadrupole doublet (QDI2) is located at rather long distance from the crossing point. The long distance (7.5 m) is to keep clearance from the beam-line of the electron. The other quadrupole magnets are used to match the emittance of each beam.

The calculated β and dispersion functions of electron and ion beams are shown in Fig. 6 and 7 respectively. In the calculation the central orbit of the ion beam in the quadrupole doublet is assumed to be in the center of the QD1 and QD1'. The maximum β values of the electron beam are 113 m for horizontal direction and 750 m for vertical. The small β value of horizontal direction comparing with that of vertical one is required to prepare large acceptance for electron beam to be inserted by multiturn horizontally. For the ion beam the maximum β values are 1223 m (35 mm in beam size) for horizontal and 970 m for vertical. The large β for the ion mode is due to long distance between the QDI2 and the crossing point.

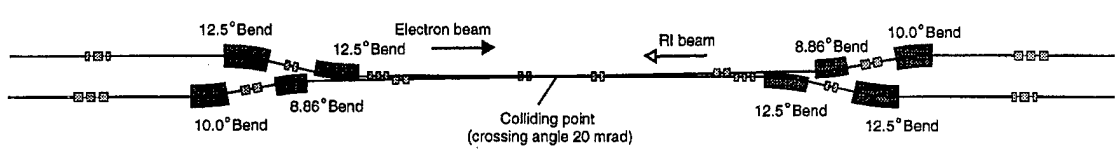

Fig. 5 Side view of the colliding section.

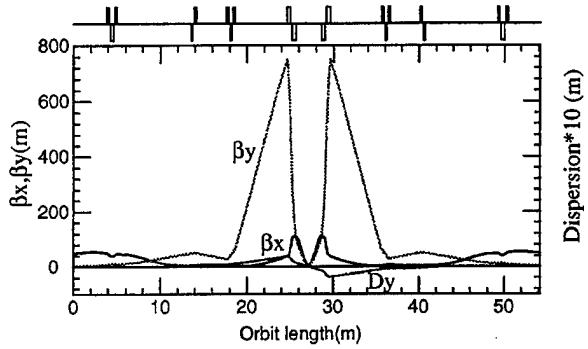

Fig. 6 β and dispersion functions in the colliding section of the electron ring.

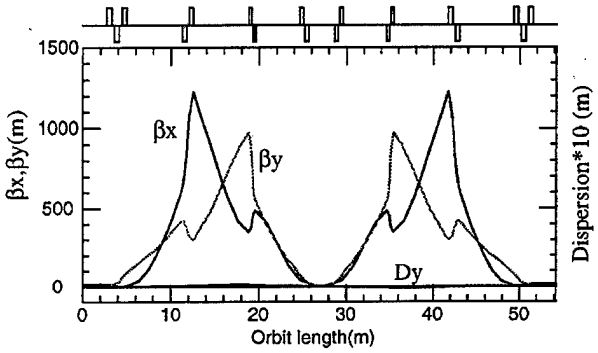

Fig. 7 β and dispersion functions in the colliding section of the ion ring.

2.3 Merging Section

Figure 8 shows a configuration of the magnets for the merging section. The path of the ion beams are shown by two arrows in fig. 8. The crossing angle, 10° is chosen by the requirement of experiments.

Small values of β are also chosen in the mode to get large luminosity. The values of β are 0.6 m for both direction. To get small β value quadrupole doublet is inserted at distance of 3.5 m from the crossing point. To match the emittance several quadrupoles are inserted the section. The configurations of the quadrupole magnets of two beam lines are all the same. The maximum β value in this section is 102 m for horizontal and 58 m for vertical. The small β value in the whole region compared with the that of the colliding section is because the β of crossing point of the merging section is larger than that of the colliding section.

The beam of the undulator is required to be small and pararell for the electron beam of S.E.M. The requirement is fulfilled by inserting of a quadrupole triplet between the arc and the undulator. The obtained β is about 2 m over all the section.

2.4 Short Straight Section

The short straight section is used for the electron cooling of the ion beam. For efficient electron cooling the ion beam should be parallel and have small size. In the section four quadrupole magnets are inserted and make the required beam. The obtained β value is about 7 m over all the section.

3 RING PARAMETERS OF DSR

After the design of each section we calculated the ring parameters for each operation mode. For I.M, two cases are calculated. One is for collision with electron beam (I.M-C). Another is for merging (I.M-M).

The obtained parameters of the four modes are summarized in Table 1. Large chromaticities of L.E.M and I.M-C are originated from large β values and strong filed gradients of quadrupole magnets in the colliding section. That for S.E.M is due to DBA structure of the arc. Natural chromaticity is corrected using sextupoles as shown in Fig. 2.

		S.E.M	L.E.M	I.M-C	I.M-M
Tune	βx	16.105	6.754	6.235	5.637
	βy	9.105	8.163	5.018	5.732
Chromaticity					
	ξx	-29.7	-37.7	-62.7	-11.4
	ξy	-34.7	-90.7	-47.6	-10.3
Transition γ		85.19	4.857	5.071	5.071
Momentum compaction		0.0014	0.042	0.039	0.039
Max. β (m)	βx	24.5	113	1223	102
	βy	51.9	750	970	57.8
β at colliding section (m)	βx*	8.5	0.02	0.1	4.2
	βy*	10.5	0.02	0.1	4.8
β at merging section (m)	βx*	3.9	5.0	10.0	0.6
	βy*	23.4	5.0	10.0	0.6

Table 1 Parameters of the DSR for several modes.

REFERENCES

[1] Yano et al., in these Proceedings.
[2] Wakasugi et al., in these Proceedings.
[3] Katayama et al., proc. of STORI 96, to be published.

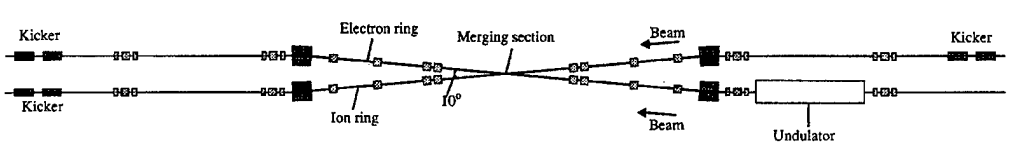

Fig. 8 Side view of the merging section.

ION OPTICAL DESIGN OF THE BRF-FNAL-SAIC-UW PET ACCELERATOR

D.J. Larson, D. Sun, P.E. Young
SAIC, 4161 Campus Point Ct., San Diego, CA 92121
F.M. Bieniosek, J.-F. Ostiguy, R.J. Pasquinelli, M. Popovic, C.W. Schmidt
Fermilab, P.O. Box 500, Batavia, IL 60510 USA*

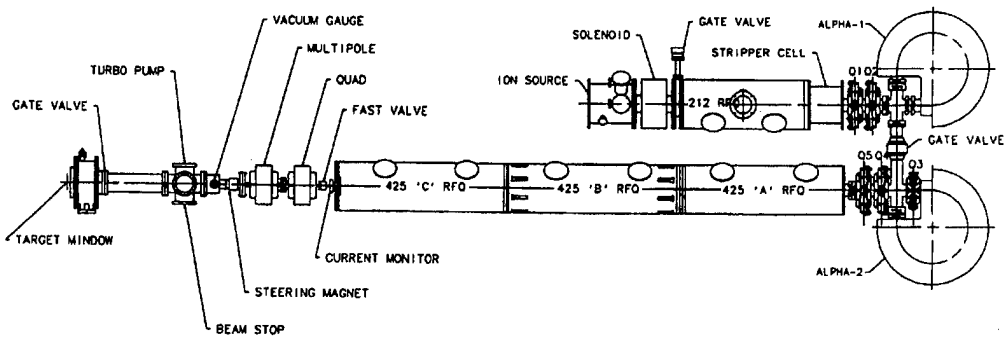

Figure 1. The PET Accelerator. Scale - Dipoles Have 30.48-cm Bend Radius.

Abstract

Production of positron emitting radioactive isotopes ^{18}F, ^{15}O, ^{11}C and ^{13}N for use in positron emission tomography is important for medical imaging. The present state of the production art is to use cyclotrons to accelerate deuterons to an energy range in the 10's of MeV and impinge the deuterons on appropriate targets. An alternative approach is to use a cascade of RFQ's to accelerate ^{3}He ions to 10-MeV as the bombarding particles. Due to the lower background radiation, a ^{3}He accelerator requires far less shielding than a cyclotron, in addition to other advantages. This paper will discuss briefly the end to end ion optics design of an RFQ based ^{3}He PET accelerator. Emphasis will be on the medium energy beam transport (MEBT) portion. The MEBT required a solution to the difficult problem of matching two RFQ's while allowing room for a gas jet stripper. Our solution to this problem could be modified to allow a match between high power RFQ's and linacs, a problem faced by several possible future accelerators.

1 INTRODUCTION

The ^{3}He PET Accelerator[1] is shown in Figure 1. In order to get sufficient ^{3}He beam current out of the source, $^{3}He^{+}$ is accelerated in the source to 20-keV. A low energy beam transport (LEBT) section matches the $^{3}He^{+}$ beam into an initial 212.5-MHz RFQ wherein it is accelerated to 1-MeV. Since $^{3}He^{++}$ is needed for the latter acceleration stages (to keep length manageable) a MEBT section strips and focuses the beam prior to entering the subsequent RFQ's. (At 1-MeV beam energy efficient stripping is possible using a gas jet stripper.) The $^{3}He^{++}$ beam is then accelerated in three 425-MHz RFQ's to a final beam energy of 10.5-MeV. A high energy beam transport (HEBT) section flattens and focuses the beam onto the PET production target.

In the absence of an all encompassing accelerator code, the optics of the PET accelerator was designed using a number of complimentary codes. Each section, source, LEBT, 212.5-MHz RFQ, MEBT, 425-MHz RFQ and HEBT, was studied with a design tool most applicable to that section, and a careful matching was done to translate the output of one code into the input of the next.

This report only highlights the design philosophy of the PET accelerator. For more detailed information on various beam sections the reader is referred to PET collaboration internal reports.[2]

2 ION SOURCE, LEBT & 212.5 MHz RFQ

The ion source has been studied by the ray tracing code EGUN (by Herrmannsfeldt of SLAC), and is consistent with experiments. The plasma temperature was varied until EGUN produced an emittance equal to what was measured at the end of the LEBT. The distance between the source plasma and the extraction electrode was varied within know tolerance until the current output from EGUN matched the measured current output of the source. The EGUN study was done up to the point where electron neutralization of the space charge is expected to begin.

*Operated by the Universities Research Association Inc, under contract with the U.S. Department of Energy.

Since the beam is unbunched in the LEBT, the LEBT has been studied with TRACE 2-D. The design followed from a detailed analysis of emittance measurements done in July, 1996. The emittance measurements were done for a variety of solenoid settings, and a consistent modeling of the LEBT was obtained for this set of measurements. The model which obtained the closest fit to the data implied that the beam was highly space charge neutralized, and that the beam at the exit of the source was close to a waist. The EGUN runs are consistent with a waist at the source exit.

The Pre-stripper RFQ Design was performed during a previous phase of the project using PARMTEQ, which is a space charge inclusive, particle tracking code.

3 MEBT DESIGN

The MEBT, which matches the beam out of the 212.5-MHz RFQ and into the 425-MHz RFQ string, has proven to be the most challenging portion of the accelerator to design and implement. Due to space and vacuum constraints, a design based on a near-symmetric, 540-degree isochronous triple focus bend has been adopted. The output of the 212.5-MHz RFQ is a small (~2-mm radius), tightly bunched, rapidly debunching beam. The input to the 425-MHz RFQ requires that the beam be even smaller (~1-mm radius), be tightly bunched and be converging in one transverse plane while diverging in the other. High current (28-mA average in the macro pulse) makes space charge concerns important. The chosen MEBT design appears in Figure 2.

3.1 Design Principles and Codes Used

The first guiding principle for the MEBT design is that of isochronicity. By developing a design for the MEBT that is isochronous at an energy of 1-MeV, all particles will traverse the MEBT region in the same amount of time. Since the particles are tightly bunched when they leave the 212.5-MHz RFQ, the beam is equally bunched when it enters the 425-MHz RFQ. Isochronicity requires that there be a great deal of dispersion in a long bending region, since it is dispersion in a bend region that leads to higher momentum particles traversing a longer path, and it is this longer path that allows them to have the same transit time. Computer analysis could only achieve the condition of isochronicity if 540 degrees of bending was accomplished. The design of a 540-degree bend also led to a condition where the overall PET accelerator was shortened by folding; this is important to keep the total device size manageable.

The second guiding principle is that of symmetry. Having a triple waist in the center of the drift between two double focusing (n = 0.53) 270-degree dipole bends (the cross-over arm) ensures that the beam evolution in each dipole is a mirror image of the other. Since the longitudinal phase space is also symmetric about that point, this leads to a condition where the dispersion and the dispersion gradient are both zero as the beam leaves the second 270-degree magnet. This symmetry also leads to cancellation of some higher order optics effects.

The third guiding principle is that of tunability. The fringe field behavior of the magnets and the amount of space charge neutralization (caused by trapped electrons in the beam) can not be known exactly in advance. To allow for operation in the presence of these uncertainties seven tunable electromagnetic quadrupoles were designed into the system.

The fourth guiding principle is separability. While not totally separable, the two quadrupoles placed in the cross-over arm are in a region of high dispersion and have a predominant effect on the longitudinal optics, with only a small effect on the transverse optics.

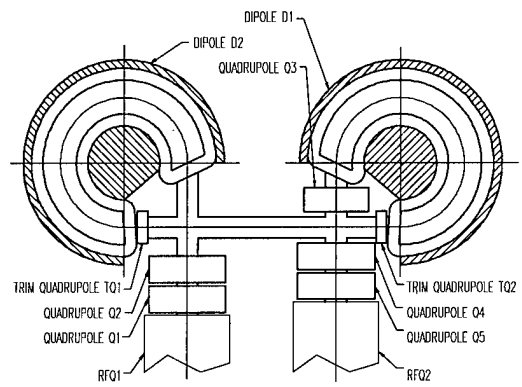

Figure 2. PET MEBT layout.

The MEBT has been studied in great detail using TRANSPORT, TRACE 3-D, and SCAT. TRANSPORT was used to check the zero space charge limit of the design, while TRACE 3-D and SCAT (a 2D code) were used to check space charge inclusive operation. Of these codes, only TRACE 3-D had all the features desired. The TRACE 3-D output for the MEBT design is shown in Figure 3.

3.2 Space Charge

A major concern of the device design was the self space charge of the ^{3}He beam. Analysis indicated that full space charge forces would lead to severe emittance dilution for a gaussian beam distribution, and would also lead to focal point shift as a function of beam current. In the worst (gaussian) case, 40-50% of the beam was predicted to be lost due to space charge emittance growth, and a pulse to pulse and intra pulse current consistency of 5% would be required to adequately control the position of the final focal point. It was realized in advance that the beam distribution might be quasi-parabolic or quasi-uniform and this would alleviate the problem of emittance growth. It was also realized that electron neutralization might off set the problems of space charge entirely.

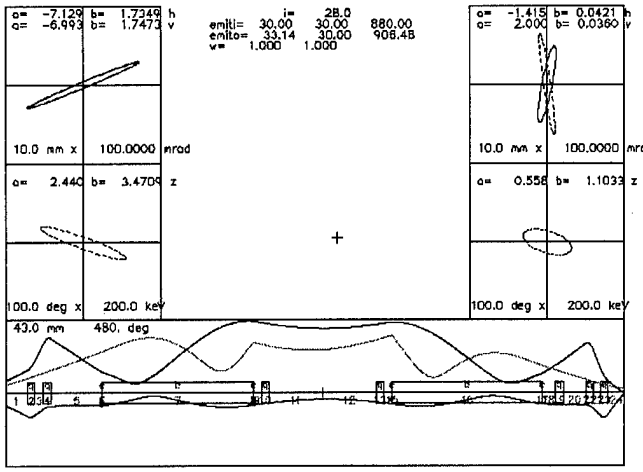

Figure 3. TRACE 3-D Output Graphics - MEBT Design.

3.3 Tolerances

An important issue in the MEBT development was a specification of tolerances for the magnetic components in the system. One of the basic rules of thumb for accelerator design is violated in the MEBT design, in that beam half size varies from under one-mm to 43-mm as the beam evolves throughout the MEBT. A usual rule of thumb is to keep the beam within a factor of 10 in size during traversal through a system. But this rule comes about because of the role of magnetic field errors. A small error in field where the beam is large contributes a relatively large angular error to the beam phase space, creating emittance dilution. Awareness of this danger led to a careful consideration of field quality in each of the MEBT components. Analysis and tracking studies indicated that the 270-degree dipoles were particularly prone to causing emittance growth. This led to a field tolerance of plus or minus 1.6-Gauss out of the 4.1-kG dipole field for the good field region of the dipole. This led in turn to a four conic section shim requirement on the dipole pole face[3], with the pole face machined to half mil accuracy.

Magnetic tolerances for the quadrupoles[3] were not as severe, with a 10-G field error being allowable. (This is because of the relatively short length of these quadrupoles.) Tolerances for tilt, role, yaw and transverse misalignment were also derived; none of these tolerances proved difficult to implement.

3.4 MEBT Operation

While MEBT operation has been demonstrated with values close to the nominal design values for magnetic excitation, experiment has proven the utility of the tunable devices. Emittance scans done at the end of the MEBT show output MEBT horizontal emittance varying between 30 π mm-mr (90% beam, normalized) to 200 π mm-mr depending upon the settings of the quadrupoles in the cross-over arm. (This shows the effect of dispersion varying as a function of cross-over arm quadrupole strength.) While the nominal settings of the cross-over arm quadrupoles are zero (the edge angles of the 270-degree magnets are designed to arrange this) experimental operation of these quadrupoles requires significant excitation. Variations between the design nominal values and experimental values for the remaining MEBT quadrupoles were also observed.

The most telling success of the MEBT operation is in the beam transmission through the first downstream RFQ. Transmission is in excess of 60%. At no point in the experimental operation is space charge causing deleterious effects. For more information on MEBT operation, see our companion paper[4].

4 425-MHz RFQ STRING AND HEBT

The Post-stripper RFQ string was designed using PARMTEQ. For our application it is best to use several RFQ's to reach the design energy of 10.5-MeV. (Conflicting modes are more difficult to suppress as length is increased. Also, as a practical matter, commercial construction of the vanes is limited by the length of material that can be machined in a single piece.) We have modified the PARMTEQ code so that a direct particle tracking could be performed in the short regions between each of the three RFQ's. Extensive studies of the RFQ string were done with many different scenarios. Current, emittance, particle number, and random seeds were all varied.

The HEBT for the PET accelerator has a function of delivering the 10.5-MeV He^3 beam to a target window. The HEBT line consists of drifts, a quadrupole, and a multipole magnet. The quadrupole, and the quadrupole component of the multipole, provide appropriate focusing to match the beam to the target. The higher order fields of the multipole have been used to arrange a more uniform beam density at the target window, lowering the peak target heating. The HEBT was designed using TURTLE.

REFERENCES

[1] Ralph Pasquinelli, et al., `A 3He++ RFQ Accelerator for the Production of PET Isotopes', PAC-97, 9B.09.

[2] PET collaboration internal reports: D.J. Larson, `LEBT 96'; `MEBT 95'; `MEBT 96'; and `HEBT 96' and D. Sun, `Report on End to End Simulation of RFQ A, B and C'; all reports can be obtained from the office of the PET project manager, Ralph Pasquinelli.

[3] N. Chester, et al., `Magnet Development for the BRF Positron Emission Tomography Accelerator', PAC-97, 2P.09.

[4] F.M. Bieniosek, et al., `Charge Stripper and MEBT for the 3He RFQ Accelerator', PAC-97, 7P.111.

OPTICS FOR SOLEIL AT 2.5 GEV[1]

P. Nghiem°, P. Brunelle*, J.-L. Laclare°, M.-P. Level°, A. Nadji°, J. Payet°°, M. Sommer*, A. Tkatchenko°°

° Projet SOLEIL, DRIF CNRS, Av. de La Terrasse, Bât. 5, 91198 Gif sur Yvette, France
* LURE, Centre Universitaire Paris-Sud, Bât. 209 A, 91405 Orsay Cedex, France
°° CEA Saclay, LNS, Groupe Théorie, 91191 Gif sur Yvette

Abstract

We analyse here the different steps of the optimization procedure and present the new lattices obtained at 2.5 GeV. In order to assure easy commissioning and comfortable operation, special attention has been paid to minimize error sensitivity and maximize dynamic aperture and energy acceptance for all proposed operating points.

1. INTRODUCTION

Following the decision to increase the energy of the SOLEIL ring from 2.15 GeV to 2.5 GeV [1], new optics have to be optimized. While keeping the basic structure described in Table 1 and especially the same ring circumference, one aims to obtain at least the excellent performances achieved at the previous energy, in terms of emittance, brilliance, error sensitivity, dynamic aperture, energy acceptance, etc. [2].

Table 1. SOLEIL basic structure.

Circumference	336.55 m
Type	DB (A)
Number of superperiods	4
Number of cells/period	4
Long straights	4 x ~14 m
Medium straights	8 x ~ 7 m
Dipoles	32 in 1 family
Quadrupoles (2 types)	160 in 8 families
Sextupoles	112 in 8 families

2. OPTIMIZATION PROCEDURE

High brilliance criteria combined with low structure periodicity often induce large sextupole strengths and small dynamic aperture. To overcome these difficulties, we have adopted the following optimization procedure in five steps :

• *1st step*, Tune and Emittance. Select the regions in the tune diagram where not only low emittance can be obtained, but also where there is a minimum of systematic destructive resonances together with a minimum sensitivity to dipolar and quadrupolar errors. Optionally, one can also try to have tunes near to a coupling resonance in order to better control horizontal/vertical coupling, and also vertical tune below half integer in order to avoid or reduce resistive wall instabilities. In the study at the previous energy, we already found out three 'good' regions [2]. One region is free of resonances but the emittance is not so small, an other one allows to achieve the smallest emittance but with a rather small dynamic aperture, and a third region which is a good compromise between the two previous ones. This last region is selected to start with the present studies : $\nu_x \sim 18.3$, $\nu_z \sim 8.3$.

• *2nd step*, Beta Functions. They should be chosen by taking into account the criteria of low emittance which defines β_x inside dipoles, high brilliance from insertions which constrains mainly β_z, minimum beam stay clear for injection which asks for a reasonable ratio of β_{max}/β_{inj}, low error sensitivity and low chromaticity which impose low β_{max}. Globally, we search also for a maximum of symmetry and regularity of β functions along the lattice which are useful for the sextupole compensation associated with the regular induced phase advance, so as for the machine operation where it is convenient to have same β's in equivalent sections.

• *3rd step*, Sextupole position. It seems fundamental that the lower sextupole strengths are, the better will be dynamic aperture and energy acceptance. For this reason, sextupoles should be located where β_x and β_z are well decoupled and this should happen in at least 2 such positions where the dispersion η_x is large.

• *4th step*, Chromaticity Correction and Dynamic Aperture Optimization. These two purposes are achieved by separate sextupoles in Chasman Green-like lattices and by the same ones in dispersion distributed lattices. We optimize the dynamic aperture only at nominal energy (dp/p=0), on the basis of analytical formulae where only first order quantities are involved [3], [4]. One can first minimize some specific low order resonance strengths but this is in general not necessary, especially when the first step is fairly done. The strategy consists mainly in minimizing the first order amplitude distorsions of sextupolar resonances and adjusting the linear terms of tune shifts with betatron excursion $(d\nu/dy)_0$ to avoid the crossing of destructive resonances.

• *5th step*, Momentum Acceptance. When the previous steps are well achieved, we have in general a very good momentum acceptance and no extra optimization is necessary. When the momentum acceptance is nevertheless small, we set one sextupole after an other at fixed strengths and go back to the 4th step with the

[1] Work supported by CNRS, CEA, MENESR.

remaining sextupoles in order to flatten as far as possible the dependence in dp/p of tunes or β's.

3. RESULTS

It is important to apply scrupulously these five steps, to not hesitate to go back to the first step if necessary and to discard solutions which lead to bad compromises. The 3rd step for example is very important, its achievement often implies a re-arrangement of magnetic elements and sometimes a change of the circumference. In the study at the previous energy where the dipole field was 1.56 T, the circumference of 336 m has been imposed by the sextupole location optimization.

Now, designing the machine for a higher energy, we have also searched to decrease the dipole field to 1.4 T. But it induced a too important lengthening of dipoles, leading to a larger vertical chromaticity and bad locations of sextupoles. By balancing in an other way the straight lengths, the dynamic aperture becomes acceptable but remains less comfortable than previously. As each performance comes back to its previous level only when the circumference is lengthened by 10 m, this solution was abandoned.

In opposition, with the same dipole field as previously and simply by an increase of the dipole length while consequently shortening the medium straight, performances are not noticeably deteriorated and this solution was adopted. Table 2 summarizes the main features of the low emittance and Chasman Green-like lattices. All calculations have been performed with the BETA code [6].

Table 2. Lattice main features.

Lattice type	Low emittance	Chasman Green-like
Emittance	3.1 nm.rad	9.6 nm.rad
Tunes ν_x / ν_z	18.28 / 8.38	18.30 / 8.32
β_x / β_z max	28.6 m / 18.5 m	28.9 m / 19.4 m
β_x / β_z in long straights	10.0 m / 8.0 m	10.1 m / 8.0 m
β_x / β_z in medium straights	4.2 m / 1.3 m	4.5 m/ 1.3 m
Norm. nat. chromaticity H / V	-3.03 / -2.66	-3.34 / -2.74
Relative energy spread	9.24 10^{-4}	9.24 10^{-4}
Dispersion max / long straights / medium straights	0.28 m / 0.18 m / 0.12 m	0.5 m / 0.0 m / 0.0 m
Momentum compaction factor	4.76 10^{-4}	6.42 10^{-4}

The emittance is lowered by a factor of 3 from the Chasman Green-like lattice when the dispersion is distributed, although the two lattice types have about the same tunes and beta functions. For the sake of simplicity, in the following we will only discuss the low emittance lattice case which can be considered as the standard lattice, knowing that the results for the Chasman Green-like case are at least as good.

The beta functions displayed in Fig. 1 satisfy well the criteria of the above 2nd step and allow to reach the targeted brilliance with appropriate undulators [1].

With reasonable sextupole strengths and while cancelling the natural chromaticities, the dynamic aperture at nominal momentum presented at Fig.2a is at least comparable to the vacuum chamber. The tune variation with betatron excursion in Fig. 2b illustrates the method of acting on $(d\nu/dy)_0$ to avoid the crossing of destructive resonances. In the horizontal phase space (z = 0) of Fig. 2.c, the relative regularity of motion attests the limited effects of resonances in the stable zone. A detailed exploration of the space phase by 2nd order tracking shows the presence of islands when the tune verifies $m\nu_x = n$, with m, n integers and n not always a multiple of the lattice period. Provided that random magnetic errors are kept small, one can consider that the dynamic aperture is not reduced since these islands are surrounded by stable regions. We suppose that the closed orbit is almost perfectly corrected, that quadrupolar default resonances are compensated with independent quadrupole power supplies, and finally that higher multipolar errors are below tolerances. Anyway, an other sextupole tuning avoiding to have $m\nu_x = n$ is available with slightly smaller dynamic apertures.

The energy acceptance is very large. Fig. 3 shows that dynamic apertures for momentum deviations up to ± 6% are still not negligible. Indeed, as can be seen in Fig. 4, the tune dependence in momentum deviation is still flat within this range and integer tunes are reached for dp/p larger than ± 10 %. These results are necessary to obtain a comfortable Touschek lifetime which is larger than 10 h in all operating modes [5]. It has to be noticed that synchrotron motion is not yet taken into account in dynamic aperture calculation but one can expect that it will induce only a marginal change.

The sensitivity to magnetic errors is relatively low. With standard dipolar errors defined as

- quadrupole misalignment : $\sigma_{x,z} = 1\ 10^{-4}$ m
- dipole field error : $\sigma_B / B = 1\ 10^{-3}$
- dipole misalignment : $\sigma_{s,z} = 5\ 10^{-4}$ m,

$$\sigma_{\theta s} = 2\ 10^{-4} \text{ rad}$$

a set of 100 samples following a gaussian distribution truncated at 3 rms deviations indicates that there are up to 96 % of stable cases. For 10 samples of these errors divided by a factor of 2 (after first turn steering or by use of girders), the dynamic aperture as displayed in Fig. 5, is still large.

4. CONCLUSION

The above decomposition of lattice optimization into five steps could appear to be trivial, nevertheless a scrupulous application of these steps seems to be necessary. The strategy is in fact simple : to keep in mind at each step the final objectives in terms of brilliance, acceptance, error sensitivity... As failing in any of these steps could compromise the final result, one has very often to go back to the first step. So this procedure is very time consuming but it seems that it is the price to pay for this kind of 3rd generation machine where one has to conciliate very high brilliance and comfortable operation.

Results so obtained are fully satisfying, but further studies remain to be done concerning effect of synchrotron motion, of insertion devices, etc.

5. REFERENCES

[1] J.-L. Laclare et al., "Status of the SOLEIL project", This conference.

[2] P. Brunelle et al., "SOLEIL : optics and performances of the source", report APD SOLEIL/A/95-03.

[3] P. Audy, Thesis, Université Paris-Sud, Orsay, France, 1989.

[4] P. Audy et al., report LNS 89-14, 1989.

[5] A. Nadji et al., "Energy acceptance and Touschek lifetime calculation for the SOLEIL project", This conference.

[6] J. Payet et al., BETA code, LNS version.

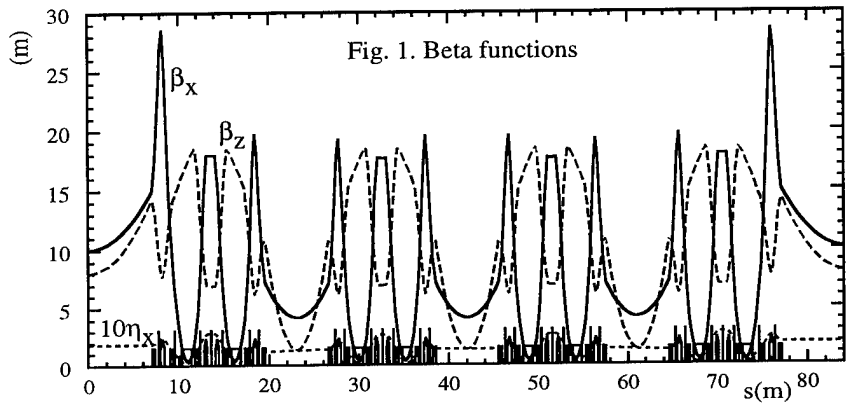

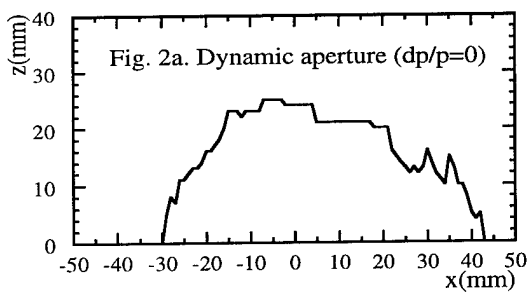

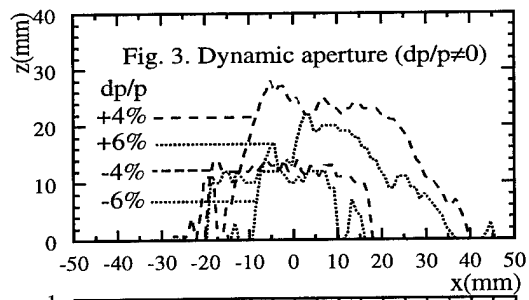

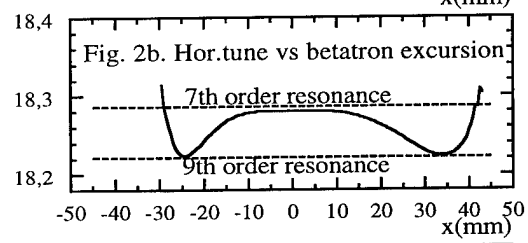

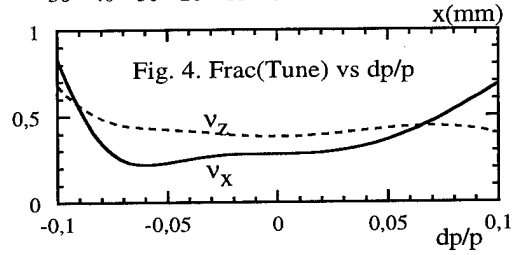

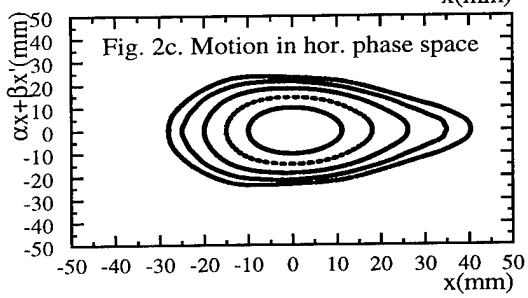

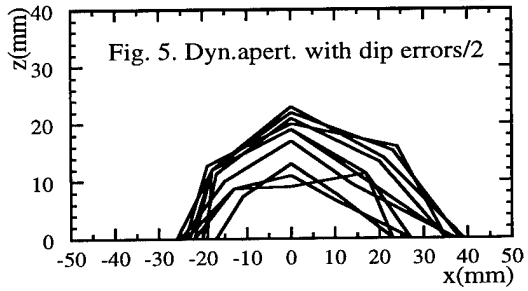

EMITTANCE STUDY OF COMBINED FUNCTION TBA LATTICE AT SRRC

Min-Huey Wang, Peace Chang, K.T. Hsu, C.C. Kuo and C.S. Hsue*,
SRRC, No.1, R & D Road VI, SBIP, Hsinchu 300, Taiwan, R.O.C.
National Tsing Hua University, Hsinchu 300, Taiwan, R.O.C.*

Abstract

In order to provide more flexible light source to the users, the emittance of the SRRC TBA lattice was studied. Several ways to reduce or enlarge the emittance of the lattice had been studied. The smaller emittance of the ring had been approached by releasing the dispersion free constraints in the long straight section. The results of the emittance study are described in this paper.

1 INTRODUCTION

As a third generation light source, a major goal of SRRC is to achieve higher photon brightness. In addition to the insertion devices installed in long straight sections to enhance the photon flux, the improvement of ring lattice design to minimize the beam emittance has also been studied. Several ways to reduce or enlarge the emittance of the lattice had been studied.

The natural beam emittance of an electron storage ring is determined by the equilibrium of radiation damping with quantum fluctuation[1]. For a non isomagnet magnet the natural beam emittance is:

$$\varepsilon_x = \frac{\sigma_{x\beta}^2(s)}{\beta(s)} = \frac{C_q\gamma_0^2 < \frac{H}{\rho^3} >}{J_x < \frac{1}{\rho^2} >}. \tag{1}$$

The natural beam emittance of an isomagnet magnet is given as:

$$\varepsilon_x = \frac{C_q\gamma_0^2 < H >_{\mathrm{mag}}}{J_x\rho}. \tag{2}$$

Where $C_q = 3.84 \times 10^{-13}m$ is the quantum coefficient, γ_0 the electron energy over the electron rest mass energy, ρ the bending radius of the dipole magnet and J_x is damping partition number of the bending plane. The H function is defined as: $H = \gamma D^2 + 2\alpha DD' + \beta D'^2$, where α, β, γ are the Courant and Synder (twiss) parameters[2]. D is the dispersion function and D' is the derivative of the dispersion function with respect to the path length. $< H >_{\mathrm{mag}}$ means averaging over the bending magnet. The minimum beam emittance of an isomagnet ring is[3]

$$\varepsilon_{me} = \frac{1}{4\sqrt{15}}\frac{C_q\gamma_0^2\theta^3}{J_x}. \tag{3}$$

Here θ is the bending angle of the dipole. However as is proved by S.Y. Lee[4] that it is impossible for an isomagnet TBA or QBA with equal dipole length to achieve the above minimum beam emittance. The length of the inner dipole should be $3^{1/3}$ times the length of the outer dipole. The achievable equilibrium beam emittance of the isomagnetic sector equal dipole length TBA lattice at small angle approximation is

$$\varepsilon^*_{\mathrm{METBA}} = 1.1064\frac{C_q\gamma_0^2\theta^3}{4\sqrt{15}J_x}. \tag{4}$$

In this report the minimum emittance of SRRC TBA lattice is derived. The study of the adjustment of the ring lattice to achieve different beam emittance is reported. An feasible operation path of the ring to achieve the lower emittance lattice is also given.

2 THE STUDY OF THE BEAM EMITTANCE OF SRRC COMBINED FUNCTION TBA LATTICE

The SRRC is a six-fold symmetry TBA lattice with a mirror symmetry from the middle of the second bend in the arc[5]. There are four pairs of quadrupoles in each superperiod, three(Q1, Q2 and Q3) in the long straight section and one(Q4) in the achromat. The combined function dipole is rectangular of length 1.22 m, bending radius 3.495 m and gradient 0.37.

Using similar procedures as in reference[4], the H function averaged through a combined sector magnet is given by:

$$\begin{aligned}
< H >_{\mathrm{mag}} &= H_0 + (\alpha_0 D_0 + \beta_0 D_0')\theta E(q) - \frac{1}{3}(\gamma_0 D_0 \\
&\quad + \alpha_0 D_0')\rho\theta^2 F(q) + \frac{\beta_0}{3}\theta^2 A(q) \\
&\quad - \frac{\alpha_0}{4}\rho\theta^3 B(q) + \frac{\gamma_0}{20}\rho^2\theta^4 C(q) \\
H_0 &= \gamma_0 D_0^2 + 2\alpha_0 D_0 D_0' + \beta_0 D_0'^2 \\
A(q) &= -\frac{(6q - 3\sinh 2q)}{4q^3} \\
B(q) &= \frac{6q - 8\cosh q + 2\sinh 2q}{q^4} \\
C(q) &= \frac{30q - 40\sinh q + 5\sinh 2q}{q^5} \\
E(q) &= -\frac{2(1 - \cosh q)}{q^2} \\
F(q) &= \frac{6(q - \sinh q)}{q^3}
\end{aligned}$$

0-7803-4376-X/98/$10.00 © 1998 IEEE

Where $q = \sqrt{|K|}l$, l is the length of the dipole, $K = -(k - \frac{1}{\rho^2})$, k is the gradient of the combined function magnet and ρ is the bending radius. β_0, α_0, γ_0, D_0, D_0' are the value of the twiss parameters and dispersion function at the beginning of the dipole. By setting $D_0 = D_0' = 0$ and minimize the $< H >_{\text{mag}}$ with respect to initial twiss function, the minimum $< H >_{\text{mag}}$ for the outer dipoles is obtained

$$< H >_{\text{outer}} = \frac{\sqrt{16AC - 15B^2}}{4\sqrt{15}} \rho\theta^3.$$

The $< H >_{\text{mag}}$ for the center dipole minimized with respect to initial dispersion function is given by:

$$< H >_{\text{center}} = \rho\theta^3 \frac{1}{12}(\frac{\beta_0}{l}\bar{A} - \alpha_0\bar{B} + \frac{4}{15}l\gamma_0\bar{C})$$

$$\bar{A} = 4A - 3E^2, \;\; \bar{B} = 3B - 2EF, \;\; \bar{C} = \frac{9}{4}C - \frac{5}{4}F^2$$

By applying the symmetry condition of betatron function at the center dipole and the matching of dispertion function between center dipole and outer dipoles, the value of the twiss parameter at the beginning of the center dipole and the minimum $< H >_{\text{center}}$ can be determined. The initial values of β_0, α_0 and γ_0 are $1.25388l$, 0.49743, $\frac{0.99487}{l}$. The same results can also be applied to rectangular dipole magnet. For SRRC q is 0.654875. The minimum emittance of the combined rectangular magnet of SRRC is given by:

$$\begin{aligned} \varepsilon &= \frac{C_q\gamma_0^2}{J_x\rho_0}(\frac{2}{3} < H >_{\text{outer}} + \frac{1}{3} < H >_{\text{center}}) \\ &= 1.1797\frac{C_q\gamma_0^2\theta^3}{4\sqrt{15}J_x} \end{aligned} \quad (5)$$

For small angle limit, this is reduced to equation (5). The minimum emittance of SRRC is 5.97×10^{-9}m.rad

The operational emittance of SRRC is 2.115×10^{-8}m.rad which is 2.5 times larger than the value of possible minimum beam emittance. An attempt to achieve a feasible operation with lower beam emittance is tried. The quadrupole strength of the designed lattice had been modified to try to fit the matching condition of the minimum beam emittance. However the real components are not free to move in space. With this constraint the original design of SRRC lattice is near a local minimum of beam emittance. Without changing hardware components and still keeping achromatic condition, the reduction of beam emittance by adjusting the strength of quadrupoles is very little. In order to further reduce the beam emittance a few systematic searches had been tried in the study. The first is to change the strength of Q2 stepwisely while keeping the strength of the other three quadrupoles the same. The change of the strength of Q2 does not reduce the beam emittance much. The adjustable range of Q2 strength to obtain a stable solution is from 2.78 m^{-2} to 3.18 m^{-2}. Another study is moving the position of Q4 slightly and varying the strength of Q4 to preserve the achromatic condition. From the study we can have a lower emittance lattice which is 70% lower of the nominal value. But in real operation the movement of the quadrupole is not feasible. Without moving the quadrupole position and still keeping the achromatic condition, it is hard to reduce the beam emittance. Therefore we release the achromatic condition in the long straight section. The tune of lattice is matched to the operational value by adjusting the strengths of Q1, Q2 and Q3. The results of Q4 strength and tune matching is shown in Table 1.

Table 1: The natural beam emittance with different strength of Q4.

Q4	ϵ_0	ν_x	ν_y	$\frac{\sigma_p}{p}$
m^{-2}	10^{-8} (m.rad)			10^{-4}
2.51	5.11	7.247	4.097	6.91
2.61	3.39	7.247	4.097	6.64
2.71	2.12	7.247	4.097	6.47
2.81	1.45	7.247	4.097	6.37
2.857	1.39	7.247	4.097	6.35
2.91	1.49	7.247	4.097	6.33
3.01	2.28	7.247	4.097	6.34
3.11	3.75	7.247	4.097	6.40
3.21	5.74	7.247	4.097	6.53

From Table 1 it shows that the minimum emittance 1.39×10^{-8}m.rad, occurs at Q4 strength of 2.857 m^{-2}. By varying the strength of Q4, different value of emittance is derived. The reason to match the tune close to the operational tune will be discussed below. In the next section we take the minimum emittance derived in this case as an example to apply to the storage ring. The transversal beam size σ_x and σ_y of the nominal lattice and the lower emittance lattice is shown in Figure 1.

3 EXPERIMENT OF APPLYING THE LOWER EMITTANCE LATTICE TO THE STORAGE RING

Firstly, we tried to inject the beam with lower emittance lattice. However, the dispersion function is smaller at the sextupole position and the need of the strength of sextupole to correct the chromaticity is higher. The higher sextupole settings shrink the dynamic aperture and it was hard to inject beam. An alternative method is to switch to the lower emittance lattice after beam was stored. The advantage to keep the tune of the lower emittance lattice close to the operational one was with no beam loss during the lattice transition. If the tune of the two lattice is far away then the probability to cross the resonance and cause beam loss during the lattice transition is increased. However at the beginning of the experiment we still encountered beam loss during lattice transition. The problem was solved by finding a path to avoid the fifth difference resonance line in tune space which might be the cause of beam loss in the previous experiment. The path with and without beam loss

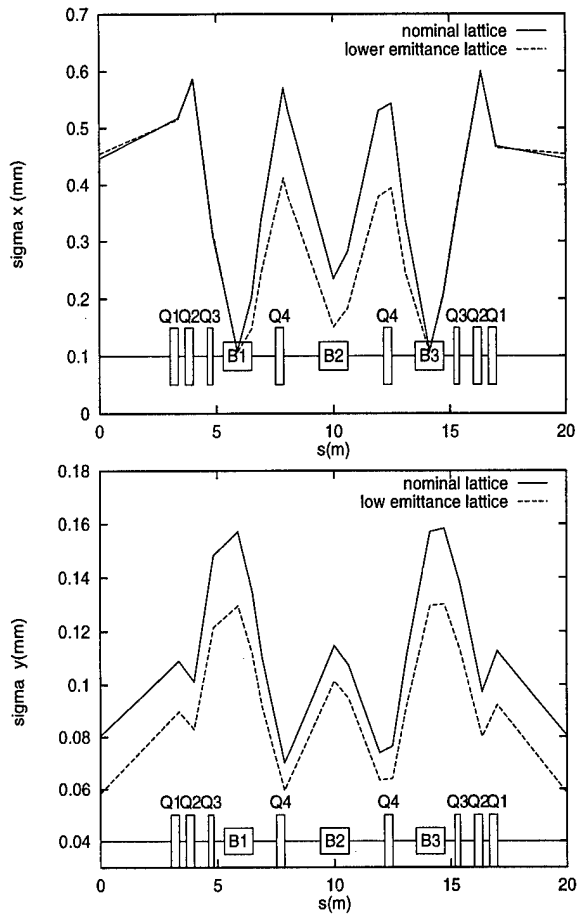

Figure 1: The transversal beam size of the operational lattice and the low emittance lattice.

in tune space is shown in Figure 2. The dispersion function which affected the beam emittance was measured and compared to the simulation value is shown in Figure 3.

4 DISCUSSION

A lattice with lower beam emittance derived from the original operation lattice is presented. The beam emittance is reduced by 35%. An operational path to change the ring lattice from the nominal lattice to a lower beam emittance lattice without beam loss was achieved. A table of quadrupole power supply setting is established for the control system to transit the lattice to lower emittance automatically. By using the same algorithm different value of beam emittance lattice is applicable to the SRRC storage ring.

5 REFERENCES

[1] 'The Physics of Electron Storage Rings — An Introduction', Mathew Sands, SLAC-121.

[2] 'Theory of the Alternating-Gradient Synchrotron', E.D. Courant, H.S Snyder, Ann. Phys. 3, 1.

[3] 'Particle Accelerator Physics', H. Wiedemann, Vol.1, p.406, Spring-Verlag.

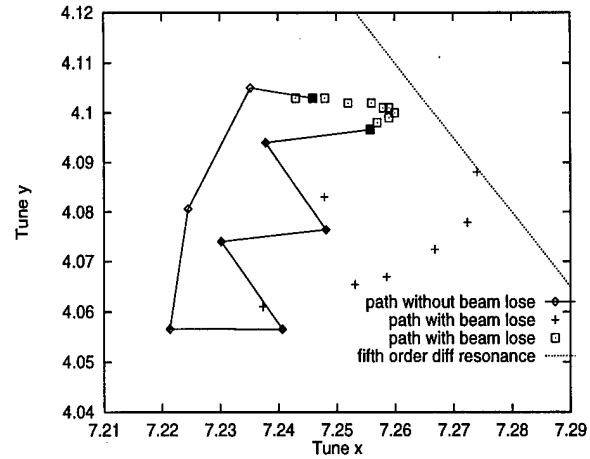

Figure 2: The transitional path from operational lattice to the low emittance lattice in the tune space.

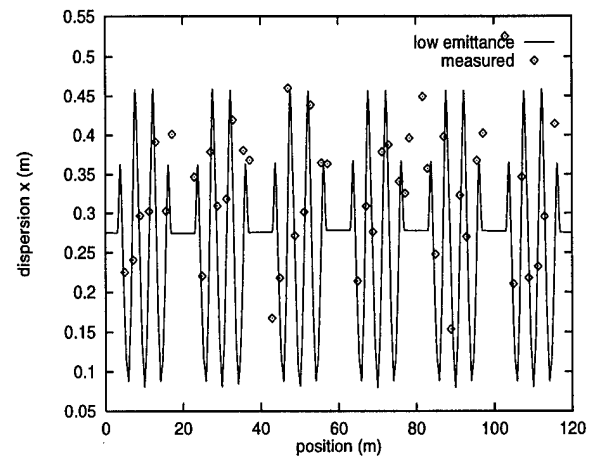

Figure 3: The measured dispersion function and modeled dispersion function of low emittance lattice.

[4] 'Emittance Optimization in Three and Multiple-Bend Achromats', S.Y. Lee, Phys. Rev. E54, 1940(1996).

[5] 'Lattice Design of SRRC 1.3 GeV Storage Ring', C.S. Hsue, C.C Kuo, J.C. Lee and M.H. Wang, 1991 PAC conference proceedings, p.2670.

BEAM OPTICS FOR THE TARGET BEAM LINES OF THE EUROPEAN SPALLATION SOURCE

V. Ziemann, The Svedberg Laboratory, S-75121 Uppsala, Sweden

Abstract

The beam optical design of the he target beam line complex of the European Spallation Source is discussed. These beam lines join beams from two 1.334 GeV accumulator rings and deliver the beam to a beam dump, a 1 MW target, a 5 MW target, and a transmission muon target in the beam line to the 5 MW target.

1 INTRODUCTION

The target beam line complex of the European Spallation Source (ESS) joins beams from both accumulator rings and delivers the beam (see Fig. 1) to a beam dump, a 1 MW target, a 5 MW target, and a transmission muon target in the beam line to the 5 MW target.

The previous beam optical design of the target beam lines [1] was based on modules made of quadrupole triplets, rather similar to those used in the accumulator rings. This, however, entails comparatively high quadrupole excitations and limited flexibility of tuning the beta functions and dispersion.

Here we start from an entirely different perspective [2]. As a basic building block of the beam line complex we use 90° and 60° FODO cells with a cell length of 8 m and 12 m, respectively. The former are used to limit the length of the beam line and the latter are only used in the long 10 Hz line to save magnets and reduce their excitation. FODO cells with 90° or 60° phase advance in both planes have rather nice beam optical properties:

- It is possible to use a large number of equally designed magnets, which reduces the cost.
- The horizontal and vertical beta functions are oscillating out of phase, i.e. β_x is large in focusing quadrupoles where β_y is small. This allows almost independent control of the horizontal and vertical plane and four consecutive quadrupoles allow to control $\beta_x, \alpha_x, \beta_y, \alpha_y$.
- Placing bending magnets with equal/opposite bending angle 180°/360° betatron phase apart cancels their contribution to the dispersion.
- Displacing a 180°-section longitudinally by making the drift space before the section a little longer and making the drift space following the section a little shorter generates beta beat inside the 180°-section only, but does not affect the beta functions outside.
- Powering two consecutive focusing quadrupoles in a 90° lattice equally only produces a local beta beat between the two quadrupoles, but does not affect the beta functions outside.[1] This feature can be exploited to tune non-zero dispersion without perturbing the beta functions.
- The required elliptic target spot size is easily achievable by letting the beam expand in a drift space following the last two quadrupoles which can be used to tune the spot size on target.

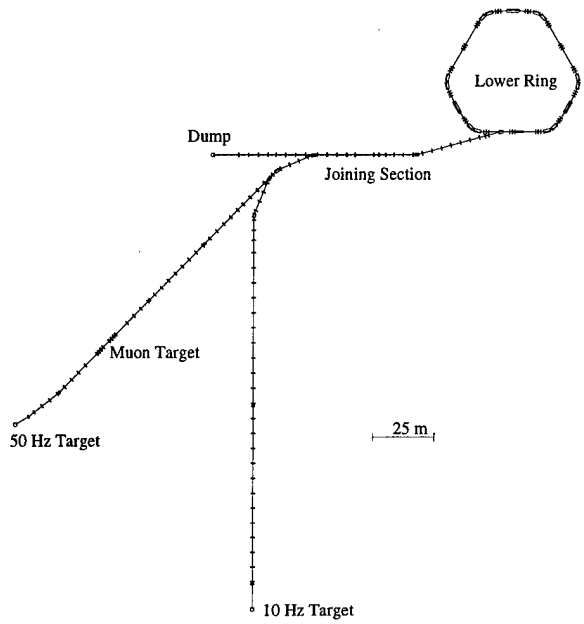

Figure 1: *Layout of the ESS Target Beam Lines.*

The beam delivered from the accumulator rings has a design emittance of $30\,10^{-6}\,\pi$ m rad. The aperture requirement throughout the ESS target beam line complex is set to

$$\text{Aperture} > \sqrt{480\,10^{-6}\beta} + 6\,10^{-3}D + 3\,\text{mm} \qquad (1)$$

where β is the beta function, D is the absolute value of the dispersion, and the 3 mm is the thickness of the vacuum chamber wall. Orbit errors and misalignment are absorbed in $480\,10^{-6}\pi$m rad.

2 BEAM OPTICS

After exiting the rings the beam must be matched into a 90° FODO line using 4 consecutive quadrupoles. Af-

[1] This is correct for thin quadrupoles. Long quadrupoles generate aberrations proportional to higher order in the quadrupole excitation.

0-7803-4376-X/98 /$10.00 © 1998 IEEE

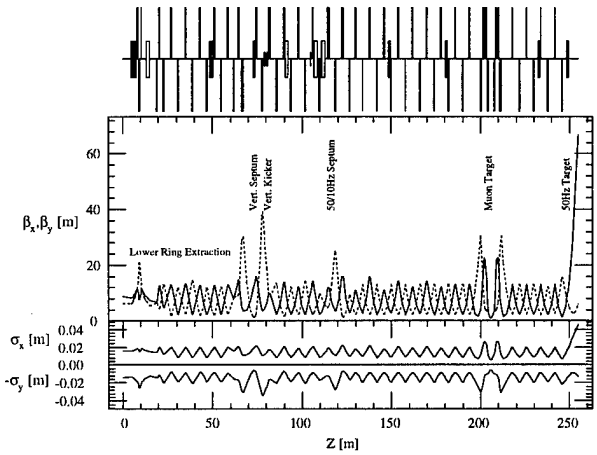

Figure 2: *Beam lines to the 50 Hz Target.*

ter cancelling the dispersion generated by the ring septum with two short 0.6 m long bending magnets and fine tuning the dispersion by the method explained above, the upper beam is bend downwards and joined with the beam from the lower ring in a vertical septum magnet and a kicker. The section leading the upper beam which is 2 m above the lower beam down is 15 m long and called the "elevator". The 360° vertical phase advance through the elevator that is needed to cancel the vertical dispersion is generated by a powerful quadrupole triplet (gradient = 8.5 T/m). The outermost quadrupole is 5.2 m away from the center of the vertical bending magnets and, taking the beam chamber radius into account results in a moderate half-height restriction of those magnets of 0.62 m. The magnets in the lower line a pushed away from the joining septum, resulting in a 0.8 m half-height restriction for the closest quadrupole in the lower line. After the joining septum the beam line is matched into a 90° FODO lattice.

Most of the magnets in the joining section have rather modest requirements with a few notable exception: (i) The triplet in the elevator has the cross section of the standard quadrupole, but is 50 % longer. (ii) The joining septum limits the aperture to 3 sigmas in order to allow sufficient blade thickness. (iii) The associated vertical kicker is about 15 % stronger than the ring extraction kicker. (iv) One non-standard quadrupole between between the kicker and the septum is required in order to accomodate the kicked orbit.

The next special area is the first switch yard which leads the beam to the dump target if the first 22.5° bending magnet is turned off. The beam enters the dump line through a zero degree port of the C-type bending magnet. The first four quadrupoles in the dump line are pushed away from the bending magnet by 0.8 m. This allows staggering of these quadrupoles with those in the 50 Hz line. The rest of the dump line consists of regular 90° quadrupoles. The rms beam spot size on the dump is 4.4 by 4.4 cm, but can be tuned easily with the last two quadrupoles, which are 10.28 m away from the dump and may have to be made radiation hard.

If the first 22.5° bending magnet is turned on the beam is bend into the 50 Hz line. This bending magnet generates dispersion of up to 1.5 m which is cancelled with a second 22.5° C-type bending magnet before the beam enters the second switch yard. There every fifth pulse is kicked into the the bending channel of two septum magnets that deflect the beam by 22.5° and lead it to the 10 Hz target. If the switching magnet is turned off, the beam enters the 50 Hz beam line where the first four quadrupoles are pushed away from the septum to allow staggering. After an initial matching section the beam is vertically elevated by 4.3 m to ground level and encounters the muon target where the beta functions are focused to 1 m. The interaction point is 1.5 m away from the face of the closest quadrupoles. The optics is designed to keep the maximum beta functions in the 30 m range and the gradients below 7.5 T/m such that standard quadrupoles can be used, even though they have to be radiation hard. The length of the muon target is chosen to be a multiple of the normal 90° cell length such that it can be substituted by regular FODO cells. After exiting the muon target the beam is bend by two 7.5° bending magnets onto the 50 Hz target that is 5.4 m after the final (possibly radiation hard) bending magnet. On target the rms beam size is 4.4 by 1.3 cm but can be tuned by the last two quadrupoles.

As already mentioned above every fifth pulse is directed into the deflecting channel of two septum magnets that bend the beam into the 10 Hz line. The orbit and beam sizes between the switching magnet and the septum are optimized such that standard quadrupoles can be used. The septum magnets generate dispersion which is cancelled in another 22.5° C-type bending magnet 180° phase advance downstream. Immediately following the last bending magnet the phase advance per cell is changed to 60° in order to reduce the number of quadrupoles in the long beam line to the 10 Hz target. Before the target the beam is brought up 4.3 m to ground level. In order to cancel the dispersion the two 3.4° bending magnets have to be 6 cells apart. The dis-

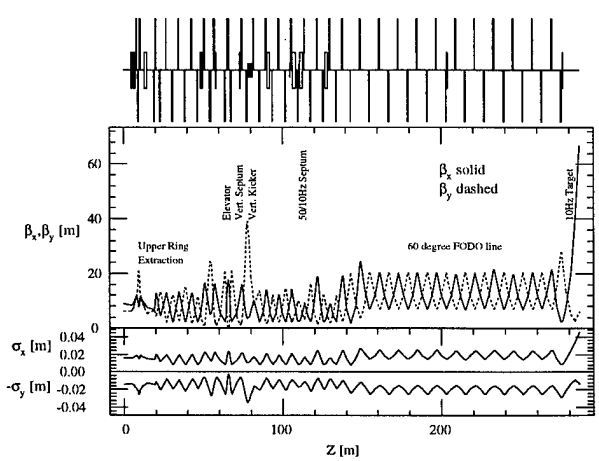

Figure 3: *Beam lines to the 10 Hz Target.*

tance between the last bending magnet and the 10 Hz target is 10.1 m in which the beam expands to 4.4 by 1.3 cm but can be tuned with the last two quadrupoles.

3 DIRECT LINAC BEAM TO 50 HZ TARGET

In order to allow the direct linac beam impinge on the 50 Hz target with its much reduced emittance of $0.6\,10^{-6}\pi$m rad, the regular 90° FODO quadrupoles after the muon target can be turned off and the muon target quads can be used to tune the spot size. With the reduced emittance we were able to produce rms beam sizes on the 50 Hz target of 4.4 by 1.3 cm without excessive quadrupole excitations. If the regular quadrupoles after the muon target are connected in series to their own power supply this feature will not incur any extra costs from the beam optics point of view. In this mode of operation one has to keep in mind the very large sensitivity of the target position on the quadrupole misalignment. The amplification factor is on the order of 200 for some quadrupoles such that 0.3 mm misalignment leads to 60 mm offset on the target which is about 1.5 rms beam sizes. Thus one has to carefully align the magnets between the muon target and the 50 Hz target.

4 MAGNETS

The large beam power of the 1.334 GeV proton beams and large emittances of $30\,10^{-6}\,\pi$ m rad together with the requirement for small beam losses implies to use large aperture magnets. We propose to mostly use two types of standard quadrupoles. The short .A quadrupoles are 0.40 m long and have standard radius 0.11 m. They are used in the 60° and 90° FODO lines. They should be designed for a maximum gradient of 75 kG/m. The long .B quadrupoles are 0.60 m long and have standard radius 0.14 m. They are used when the integrated gradient needs to be higher or the radius needs to be larger. They should be designed for maximum gradient 70 kG/m. A small number of special quadrupoles are also needed and will be discussed in the respective sections.

All bending magnets are rectangular bends (they do not focus in the bend plane, but in the other plane) and they come in two varieties: The .S bending magnets are 0.6 m long and the .L are 1.8 m long C-type magnets, which allow extracting beams through a zero-degree port. This feature is needed at the dump-line junction. Both .S and .L magnets are designed for a peak field of 16 kG.

5 MUON TARGET

The Muon Target section is designed such that it has a length that is a multiple of the normal FODO cell length, such that initially it can be replaced by standard FODO quads. The distance of the Interaction point and the final quad is 1.5 m and the minimum beta function is 1 m in both planes. These specifications are achieved by using a standard triplet optics that is matched into the 90° FODO line. The maximum beta functions are 30 m. The magnets in the Muon target area QD24.M.B,...,QD27.M.B must be constructed to withstand a high radiation dose.

6 TUNING AND DIAGNOSTIC

In order to correct the orbit we propose to use 26 horizontal and 26 vertical orbit correctors together with 45 beam position monitors at critical places in the target beam line complex. The correctors should provide 3.5 mrad kick angle and should be placed around beam pipes with 0.11 m and 0.14 m radius.

A total of 8 current monitors are needed. Two should be placed near the first quadrupole in the upper and lower ring extraction beam lines, one after the joining septum, one in the dump line, and one near the start and end of the 50 Hz and 10 Hz lines, respectively.

In order to match the beam properly into the respective beam lines a total of 30 beam size monitors (harps) are required. Half of them to measure the horizontal and half to measure the vertical beam size. In the dump, 50 Hz and 10 Hz line they should be arranged in groups of 4 in order to measure the complete incoming beam's matrix. To each of the beam size measuring section corresponds a tuning section of normally four quadrupoles on individual power supplies that allow to control the proper matching of the beam into the beam lines.

There will be 3 m long beam loss monitors placed every 4 m along the beam lines, resulting in a total number of 163. Information about the beam position on the targets will be generated by thermo-couplers on the target.

7 ACKNOWLEDGEMENTS

Discussions with D. Reistad, TSL and A. Simonsson, MSL are gratefully acknowledged. Special thanks to A. Simonsson for preparing Fig. 1. Most of the magnet data reported here are supplied by E. Zaplatin and K. Ziegler, HMI. The discussion about diagnostics reported here profitted greatly by discussions with S. Møller, Univ. Aarhus and many other participants at various workshops.

8 REFERENCES

1. B. Anderberg, L. Nilsson, D. Reistad, A. Simonsson, C. Stålnacke, *ESS Target Beam Lines,* ESS 95-21-R.

2. V. Ziemann, *New Optics of the ESS Target Beam Lines,* ESS-96-66-R, Dec. 1996.

INTRINSIC THIRD ORDER ABERRATIONS IN ELECTROSTATIC AND MAGNETIC QUADRUPOLES

R. Baartman, TRIUMF, 4004 Wesbrook Mall, Vancouver, B.C., Canada, V6T 2A3

Abstract

Intrinsic aberrations are those which occur due to the finite length of the desired field configuration. They are often loosely ascribed to the fringing field. This is misleading as it implies that the effects can be minimized by shaping the fields. In fact, there is an irreducible component related to the broken symmetry. It is present even in the hard-edge limit, and moreover, the other (soft-edge) effects can be simply ascribed to the intrinsic aberration spread over a finite length.

We rederive the aberration formulas for quadrupoles using a Hamiltonian formalism. This allows for an easy comparison of electrostatic and magnetic quadrupoles. For different combinations of large and small emittances in the two transverse planes, it is found that in some situations electrostatic quadrupoles have lower aberrations, while in others, magnetic quadrupoles are better. As well, we discuss the ways in which existing transport codes handle quadrupole fringe fields. Pitfalls are pointed out and improvements proposed.

1 INTRODUCTION

A common prescription for quadrupole design is that the beam occupy no more than a certain fraction, usually 1/2 to 3/4, of the aperture. Another common prescription is that the longer the quadrupole is compared with its bore diameter, the better. As well, it is common practice to carefully round the ends of the poles. We show that none of these common practices can be validated by the quadrupole dynamics up to 3rd order in force.

The misconceptions are perpetuated by existing transport codes like GIOS[1] and COSY[2], because they allow one to make calculations with no fringe fields. Then when fringe fields are included, aberrations increase. In fact, the no-fringe-field cases are non-physical and such calculations should not be permitted in transport codes. The aberrations in question are not caused by the fringe fields, but by the broken symmetry inherent in a quadrupole of finite length.

We start with the quadrupole Hamiltonian and find canonical transformations for both the electrostatic and magnetic cases which eliminate the derivatives of the quadrupole strength up to 4th order. In this way, we easily reproduce the known aberration formulas, but with additional physical insight.

2 THEORY

2.1 Electrostatic

When using the longitudinal position as independent variable, the Hamiltonian H is just the longitudinal momentum:

$$H = -\sqrt{p_0^2 - 2mq\Phi - p_x^2 - p_y^2}. \tag{1}$$

The electrostatic potential is $\Phi(x, y, z)$ and p_0 is the reference momentum. We will benefit from cleaner and more transparent notation if momenta are measured in units of p_0. This has the additional benefit that to first order, $p_x = x'$. Additionally, we let the potential Φ in units of the reference kinetic energy $p_0^2/(2m)$. Then

$$H = -\sqrt{1 - \Phi - p_x^2 - p_y^2}. \tag{2}$$

We expand the square root to 4th order in coordinates and ignore the constant:

$$H \approx \frac{1}{2}(\Phi + p_x^2 + p_y^2) + \frac{1}{8}(\Phi + p_x^2 + p_y^2)^2. \tag{3}$$

To the same order, Laplace's equation gives for the expansion of the quadrupole potential:

$$\Phi = V(z)(x^2 - y^2) - \frac{V''(z)}{12}(x^4 - y^4). \tag{4}$$

The final Hamiltonian, correct to 4th order is

$$\begin{aligned} H &= \frac{1}{2}\left[V\left(x^2 - y^2\right) - \frac{V''}{12}(x^4 - y^4) + p_x^2 + p_y^2\right] \\ &\quad + \frac{1}{8}\left[V\left(x^2 - y^2\right) + p_x^2 + p_y^2\right]^2. \end{aligned} \tag{5}$$

The trouble with applying this to simple cases like thin lenses and hard-edge limits is the presence of $V''(z)$, which becomes singular in those limits. In most cases, one sacrifices physical insight and simply traces particles with this Hamiltonian, using a more-or-less realistic function $V(z)$. For example, the approach taken in GIOS[1] is to leave it up to the user to specify 'fringe field integrals' such as $\int V^2 dz$ through the fringe fields. However, this leaves much room for error; different integrals may not be realistic or consistent with each other. Moreover, if one needs to solve Laplace's equation to find fringe field integrals, one might as well use the solution directly in a ray-tracing code. If one does go through this exercise, one discovers that the higher order aberrations are relatively insensitive to the 'hardness' of the quadrupole edges. This leads one

0-7803-4376-X/98/$10.00 © 1998 IEEE

to suspect that the aberrations are dominated by an intrinsic effect which has nothing to do with the detailed shape of the fringing field. Such is indeed the case.

It turns out to be possible to find a canonical transformation which eliminates the derivatives of $V(z)$. In our case, we wish to retain terms to 4th order in the Hamiltonian (3rd order on force), and the transformation $(x, p_x, y, p_y) \rightarrow (X, P_X, Y, P_Y)$ has generating function

$$G(x, P_X, y, P_Y) = xP_X + yP_Y + \frac{V'}{24}(x^4 - y^4) + -\frac{V}{6}(x^3 P_X - y^3 P_Y). \tag{6}$$

To the same order, this yields the transformation

$$\begin{aligned} x &= X + \frac{V}{6}X^3 \\ p_x &= P_X - \frac{V}{2}X^2 P_X + \frac{V'}{6}X^3. \end{aligned} \tag{7}$$

The y-transformation is obtained by replacing x, p_x, X, P_X with y, p_y, Y, P_Y and V with $-V$. Note that outside the quadrupole, the transformed coordinates are the same as the original ones.

This yields the transformed Hamiltonian H^*:

$$\begin{aligned} H^* &= \frac{V}{2}(X^2 - Y^2) + \frac{1}{2}(P_X^2 + P_Y^2) + \\ &+ \frac{1}{8}(P_X^2 + P_Y^2)^2 - \frac{V}{4}(X^2 + Y^2)(P_X^2 - P_Y^2) \\ &+ \frac{7V^2}{24}(X^4 + Y^4) - \frac{V^2}{4}X^2 Y^2. \end{aligned} \tag{8}$$

We can identify the terms: the first two are the usual linear ones; the third term is not related to the electric field (it is small and due to the fact that $x' \neq p_x$ or, equivalently, $\tan\theta \neq \sin\theta$); the 4th term is also small and arises because a particle going through the quadrupole at an angle is inside the quad for slightly longer than one which remains on axis. See ref. [3] for more complete physical derivation of the individual terms.

The dominating higher order terms are the last two terms in eqn. 8. Since there are no derivatives of V, we can directly write down the aberrations in the thin-lens limit:

$$\Delta p_x = \frac{-1}{f^2 L}\left(\frac{7}{6}x^3 - \frac{1}{2}xy^2\right), \tag{9}$$

with a similar expression for Δp_y. L and f are the quadrupole's effective length and focal length. The fractional focal error is found by dividing by the linear part $\Delta_0 p_x = -x/f$:

$$\frac{\Delta f_x}{f} = \frac{1}{fL}\left(\frac{7}{6}x^2 - \frac{1}{2}y^2\right) \tag{10}$$

for x, and similarly for y.

2.2 *Magnetic*

In magnetic fields, the canonical momentum $\vec{p}$ contains the vector potential $\vec{A}$ so that the time-based Hamiltonian is

$$H_\tau = \frac{1}{2m}\left|\vec{p} - q\vec{A}\right|^2 \tag{11}$$

As before, we use the invariant $p_0 \equiv \sqrt{2mH_\tau}$ to normalize the momenta, convert to z as independent variable, and expand the square root, keeping terms up to 4th order:

$$\begin{aligned} H &\approx -A_z + \frac{1}{2}\left[(p_x - A_x)^2 + (p_y - A_y)^2\right] + \\ &+ \frac{1}{8}\left[(p_x - A_x)^2 + (p_y - A_y)^2\right]^2. \end{aligned} \tag{12}$$

To this order, the vector potential for quadrupole strength $k(z)$ is

$$\begin{aligned} A_x &= -\frac{k'}{4}xy^2, \quad A_y = \frac{k'}{4}x^2 y \\ A_z &= -\frac{k}{2}(x^2 - y^2) + \frac{k''}{48}(x^4 - y^4), \end{aligned} \tag{13}$$

and the Hamiltonian can be written:

$$\begin{aligned} H &= \frac{1}{2}\left[k\,(x^2 - y^2) - \frac{k''}{24}(x^4 - y^4) + p_x^2 + p_y^2\right] + \\ &+ \frac{k'xy}{4}(yp_x - xp_y) + \frac{1}{8}(p_x^2 + p_y^2)^2. \end{aligned} \tag{14}$$

The generating function which will eliminate derivatives of k is

$$G(x, P_X, y, P_Y) = xP_X + yP_Y + \frac{k'}{48}(x^4 - y^4) + -\frac{k}{12}\left[(x^3 + 3xy^2)P_X - (3x^2 y + y^3)P_Y\right], \tag{15}$$

which, to the same order yields transformation

$$\begin{aligned} x &= X + \frac{k}{12}(X^3 + 3XY^2) \\ p_x &= P_X - \frac{k}{4}\left[(X^2 + Y^2)P_X - 2XYP_Y\right] + \frac{k'}{12}X^3, \end{aligned} \tag{16}$$

and similarly for (y, p_y). The transformed Hamiltonian is

$$\begin{aligned} H^* &= \frac{k}{2}(X^2 - Y^2) + \frac{1}{2}(P_X^2 + P_Y^2) + \\ &+ \frac{1}{8}(P_X^2 + P_Y^2)^2 - \frac{k}{4}(X^2 + Y^2)(P_X^2 - P_Y^2) \\ &+ \frac{k^2}{12}(X^4 + Y^4) + \frac{k^2}{2}X^2 Y^2. \end{aligned} \tag{17}$$

Notice the similarity to eqn. 8: in fact all terms are identical except the last two, which only differ in their coefficients. Applying the same procedure as in the electrostatic case, we write down the fractional change in focusing strength:

$$\frac{\Delta f_x}{f} = \frac{1}{fL}\left(\frac{1}{3}x^2 + y^2\right) \tag{18}$$

3 DISCUSSION

Formulas 10 and 18 are handy for quickly evaluating the importance of 3rd order aberration. They also show that for fixed focal length, the **only** way of reducing the aberration is by lengthening the quadrupole; the fraction of aperture used is not important; for a given effective length, the absolute size of the aperture is not important; the shape of the ends of the electrode is not important.

Comparing the two formulas, we see that for roundish beams ($x \approx y$), electrostatic and magnetic quads yield similar aberrations: they are in the ratio of $\frac{7}{6} : \frac{4}{3}$. For cases where one transverse dimension is large compared with the other, and it is important to maintain the quality in the larger dimension, magnetic quads are better by a factor of $\frac{7}{2}$. However, for the more common case where it is more important to maintain the quality of the higher quality dimension, electrostatic quads win by a factor of 2.

Results from using the above Hamiltonians are in agreement with those from using the commonly used codes GIOS and COSY, provided fringe field cards are used. In both of those codes it is possible to perform a 3rd order calculation with quads which have no fringe fields. This gives incorrect and actually completely unphysical results. In essence, omitting the fringe field cards in those codes describes a situation where the particle traverses non-Maxwellian fields. For example, GIOS, since it does not use the scalar value of the potential field, does not obey conservation of energy when fringe field cards are omitted.

The hard-edge case is correctly described in GIOS by including fringe field cards and setting the quadrupole aperture to zero, or, equivalently, setting all the fringe field integrals to zero. This is a useful approximation since the results are usefully close to reality and yet one needs not worry about specifying realistic fringe field integrals. This does not work in COSY, since a zero aperture forces an infinitesimal integration step-size. A better solution would be to build in the hard-edge kicks and use these as default when no fringe field is specified.

The required hard-edge kicks at the entrance to the quadrupole are derived directly from equations 7 and 16. The reason is that we know that the transformed coordinates (X, P_X, Y, P_Y) do not experience any singular forces in the hard-edge limit. Therefore, the kicks for those coordinates are all zero. So the kicks for the untransformed (x, p_x, y, p_y) for the electrostatic case are,

$$\begin{aligned} \Delta x &= \frac{V}{6}x^3 \\ \Delta p_x &= \frac{-V}{2}x^2 p_x \\ \Delta y &= \frac{-V}{6}y^3 \\ \Delta p_y &= \frac{V}{2}y^2 p_y, \end{aligned} \tag{19}$$

and for the magnetic case are,

$$\begin{aligned} \Delta x &= \frac{k}{12}(x^3 + 3xy^2) \\ \Delta p_x &= \frac{-k}{4}\left[(x^2+y^2)p_x - 2xyp_y\right] \\ \Delta y &= \frac{-k}{12}(3x^2y + y^3) \\ \Delta p_y &= \frac{k}{4}\left[(x^2+y^2)p_y - 2xyp_x\right]. \end{aligned} \tag{20}$$

The kicks at the exit are, of course, opposite in sign. These agree with the GIOS case of zero fringe field integrals. See ref. [1].

4 REFERENCES

[1] H. Matsuda and H. Wollnik *Third Order Transfer Matrices for the Fringing Field of Magnetic and Electrostatic Quadrupole Lenses* NIM **103**, p. 117 (1972).

[2] M. Berz *Computational Aspects of Design and Simulation: COSY INFINITY* NIM **A298**, p. 473 (1990).

[3] R. Baartman *Aberrations in Electrostatic Quadrupoles* TRI-DN-95-21 (TRIUMF internal note, 1995).

CANONICAL PARTICLE TRACKING AND END POLE MATCHING OF HELICAL INSERTION DEVICES

Godehard Wüstefeld, Michael Scheer, BESSY II Project
Rudower Chaussee 5, Geb. 15.1, 12489 Berlin, Germany

Abstract

The low emittance 1.7 GeV synchrotron radiation light source BESSY II [1] is presently under construction in Berlin-Adlershof [1]. For the generation of circularly polarized radiation two helical insertion devices (IDs) will be installed [2]. A discussion of beam dynamical effects for such devices is given with special attention to sextupole-like fields of IDs and their compensation by the end poles.

1 INTRODUCTION

The BESSY II storage ring offers 14 out of 16 straight sections for IDs. Two helical undulators of the Sasaki-type [3] will be installed to provide users with up to 1300 eV polarized photon beams. The undulators will be built with NdFeB magnets having a period length of 56 mm (30 periods total) and a minimum half gap of 7.5 mm. Each device will be operated in a double undulator setup mode, where the two halfs of one device are used to generate different polarized photon beams which are separated by about $\pm 200 \mu rad$ deflection. A fast chopper is used for polarization switching up to 100 Hz [2]. A photon flux density of $1.7 \cdot 10^{13} photons/s\, mm^2 0.1\% BW 0.1A$ is expected at a degree of polarization of $P_c = 0.72$ for the 5th harmonic and a flux density of $1.8 \cdot 10^{14} photons$ with a polarization of $P_c = 0.99$ for the 1st harmonic. They can be tuned to obtain any degree of polarization, from circular to linear (both horizontal and vertical) for photon energies up to 1300 eV.

Particle tracking methods are applied to verify that these IDs are tolerable for the storage ring. Special attention is given to the effect of the end poles. It is shown that the modeling of the IDs has to be done together with a well matched end pole configuration to obtain stable particle oscillation amplitudes. If these end poles are included in the calculations, only weak interactions of the electron beam with the IDs are predicted.

2 MODELING OF THE TRACKING ROUTINE

The helical undulator consists of 4 long parallel beams of alternating rows of permanent magnets. A variable gap between the upper and the lower row adjusts the on-axis field. The upper left and the lower right row can simultaneously be shifted with respect to the two other rows. This phase shift results in a magnetic field of arbitrary ellipticity. The scalar potential V [4] of the periodic part of the field is obtained by a superposition of the 4 row contributions (x =horizontal, y =vertical and z =longitudinal axis) $V = b_0(V_1 + V_2 + V_3 + V_4)/8$, with

$$V_1 = (e^{+k_y y} cx_- / k_y + e^{+k_z y}/k_z) sz_+$$

$$V_2 = (e^{+k_y y} cx_+ / k_y + e^{+k_z y}/k_z) sz_-$$

$$V_3 = (e^{-k_y y} cx_+ / k_y + e^{-k_z y}/k_z) sz_+$$

$$V_4 = (e^{-k_y y} cx_- / k_y + e^{-k_z y}/k_z) sz_-,$$

and $cx_\pm = \cos(k_x(x \pm x_0))$, $sz_\pm = \sin(k_z z \pm \psi/2)$.

This analytical expression for the scalar potential describes the B_y- and B_x-field with an error of a few percent in the parameter range of interest compared with results of numerical magnet codes. For the present study the parameters choosen are: field strength parameter $b_0 = 1T$, horizontal gap separation $x_0 = 0.02m$, longitudinal period length $\lambda_z = 2\pi/k_z = 0.056m$, horizontal period length $\lambda_x = 2\pi/k_x = 0.0896m$, which yields a vertical $\lambda_y = 2\pi/k_y = 0.0475m$. The parameter ψ measures the shift of the two rows with respect to the other ones. At $\psi = 0$ a magnetic field of $0.6T$ is obtained on the ID axis.

In [5] an approximated solution of the Hamilton-Jacobi differential equation

$$\partial F/\partial z + H = 0$$

is presented in terms of an analytical Taylor series expansion of the generating function F. A Hamiltonian function of the type

$$H = (p_x - A_x)^2/2 + (p_y - A_y)^2/2 - A_z$$

is used, were A_x, A_y and A_z are the components of the magnetic vector potential divided by the magnetic stiffness $B\rho$ of the electrons. For the present study F is expanded up to the third order with respect to the transverse momenta p_x and p_y and a third variable $b_0/B\rho$ which is proportional to the scaled vector potentials. To obtain the tracking routine the scalar potential V is used as an input for the computer algebraic code REDUCE [6]. With this code parts for an existing FORTRAN mapping module are generated in an automatic way. This mapping routine is extremely fast [7], it can take several periods of the ID in a single step, and it is symplectic because of the generating function approach.

3 MATCHING OF THE END POLES

To obtain helical oscillations of electrons in an ID the potential function has approximately to be like $V \propto a(x,y)\cos k_z z + b(x,y)\sin k_z z$, where the derivatives of $a(x,y)$ and $b(x,y)$ describe the horizontal and

[1]funded by the Bundesministerium für Bildung, Wissenschaft, Forschung und Technologie and by the Land Berlin

0-7803-4376-X/98/$10.00 © 1998 IEEE

vertical magnetic field shifted by 90 degrees.

The end poles match the closed orbit from the outside of the ID to a wiggling, periodic orbit inside the ID and back to the outside. Ideally this is done without any residual closed orbit kick or shift of the beam at the exit. To achieve a well matched orbit, two integrals over the fields in both planes B_y and B_x have to vanish, i.e.

$$I_1 = \int_{-L}^{L} B_y dz \equiv 0 \text{ and } I_2 = \int_{-L}^{L}\int_{-L}^{z} B_y dz' dz \equiv 0,$$

and for the other plane as well. This can be achieved by pure dipole-fields, without any higher order field components. However, sextupole-like fields of the ID have to be matched in addition by the end poles [8].

From the potential function terms can be derived which characterize sextupole-like fields:

$$\partial^3 V/\partial x^3,\ \partial^3 V/\partial x^2 \partial y,\ \partial^3 V/\partial x \partial y^2 \text{ and } \partial^3 V/\partial y^3$$

at $x = y = 0$. These fields have the same order as the two-dimensional sextupole fields. Because of the three-dimensional character of the ID fields there are 4 terms, compared with two expressions (skew and normal) in the two-dimensional case. For the ID one expects an oscillation of these terms along the beam axis with a zero value on average. The amplitude of these oscillations could be large, for example the term $\partial^3 V/\partial y^3$ integrated over half a period could yield as much as 80 T/m for the suggested helical ID. For comparison, the correction sextupoles of the BESSY II optics reach values of 50 T/m. With respect to these fields the ID can be considered as an alternating series of strong sextupole kicks.

There is some similarity between the strong oscillation of the sextupole fields and the oscillation of the dipole fields for the ID. Collins distortion functions [9] are very well suited to demonstrate the effect of these sextupole-like fields. In his note an algorithm is given which can be applied to these fields [8]. Instead of 5 distortion functions for normal two-dimensional sextupoles there are now 7 in case of an ID without skew terms.

If only a single sextupole-like kick inside the ID is considered as a source of distortion neglecting other effects the distortion functions B_i ($i = 1 - 7$) become very simple. All of them can be written as:

$$B_i = \frac{1}{2} s_i(z) \cos(\delta_i + \phi_{i0} - \phi_i) / \sin(\phi_{i0}),$$

where the phase around the ring is $2\phi_{i0}$ and B_i is evaluated outside the ID at ϕ_i. The longitudinal position z and the phases are defined in such a way that $z = \phi_i = \delta_i = 0$ at the same point. All phases are scaled, dependent on the type i of the distortion function. There are 4 different δ_i-scalings:

$$\delta_{1,5} = \tilde{\varphi_x},\ \delta_2 = 3\tilde{\varphi_x},\ \delta_{3,6} = 2\tilde{\varphi_y} + \tilde{\varphi_x},\ \delta_{4,7} = 2\tilde{\varphi_y} - \tilde{\varphi_x},$$

and similar relations for skew terms (exchange x and y). $\tilde{\varphi_x}$ and $\tilde{\varphi_y}$ are the unscaled horizontal and vertical betatron phases. Similar relations are valid for ϕ_i and ϕ_{i0}. Also the sextupole kicks are scaled. The strength of the kick is proportional to an infinitesimal 'kick-length' Δz and to the sextupole-like field given by the partial derivatives of the potential function multiplied by scaling factors of the local beta functions:

$$s_{1,2}(z) = \frac{1}{3} \Delta z V_{yxx} \beta_x \sqrt{\beta_x}$$

$$s_{3,4}(z) = \frac{1}{6} \Delta z V_{yyy} \beta_x \sqrt{\beta_y}$$

$$s_{5,6,7}(z) = \frac{1}{3} \Delta z V_{yxx} \beta_y \sqrt{\beta_x}$$

For the evaluation of a particular B_i sextupole kicks and phase functions with equal indices have to be combined.

The distortion function B_i can be decomposed into a $\cos(\phi_i - \phi_{i0})$- and a $\sin(\phi_i - \phi_{i0})$-wave. The amplitudes A_c and A_s of these waves for an extended source $s_i(z)$ are proportional to the integrals

$$A_c \propto \int_{ID} s_i(z) \cos \delta_i dz \text{ and } A_s \propto \int_{ID} s_i(z) \sin \delta_i dz.$$

Ideally these amplitudes should be zero to minimize optics distortions. If the phase advance over the ID is small, $\sin \delta_i$ is proportional to z and $s_i(z)$ can be replaced by the unscaled sextupole strength $s(z) = V_{yyy}$, V_{yyx}, V_{yxx} and V_{xxx}, respectively, and setting the beta functions constant. The condition for vanishing A_c and A_s can further be simplified by partial integration:

$$A_c \approx \int_{-L}^{L} s(z) dz \equiv 0,\ A_s \approx \int_{-L}^{L}\int_{-L}^{z} s(z') dz' dz \equiv 0.$$

In this approximation the sextupole fields are matched only due to the ID itself, independent of the machine optics. In this limit all distortion functions can be canceled with a single, properly placed end pole kick. These integrals are of the same type as those of the closed orbit condition, but now applied to the sextupole-like fields. In the potential approximation introduced above the $\cos k_z z-$like term is naturally matched, because the integrals for the closed orbit and for the sextupole matching become zero, whereas at least the $\sin k_z z-$like term requires special end poles.

In case this simplification fails, one has to include the z-dependence of the beta functions as well into the matching. Locations for IDs with fast changing beta functions (low beta insertions) could be critical, or if more complicated symmetries than these simple cos- and sin-expressions are applied.

For example in Fig. 1 the distortion function B_1 is shown. In the $i = 1$ case all scaled phases can be replaced by the corresponding horizontal beta phase value.

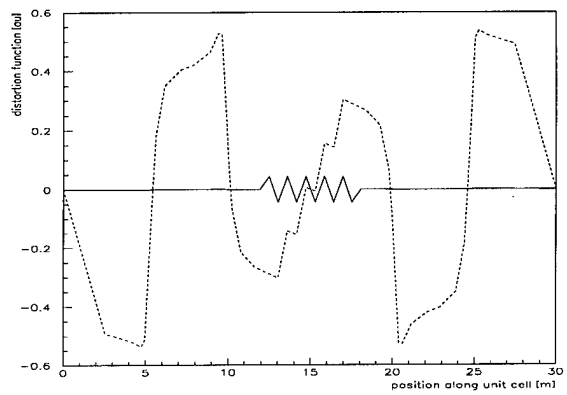

Figure 1: Distortion function B_1 for the matched (line) and unmatched (dotted line) case along one BESSY II cell.

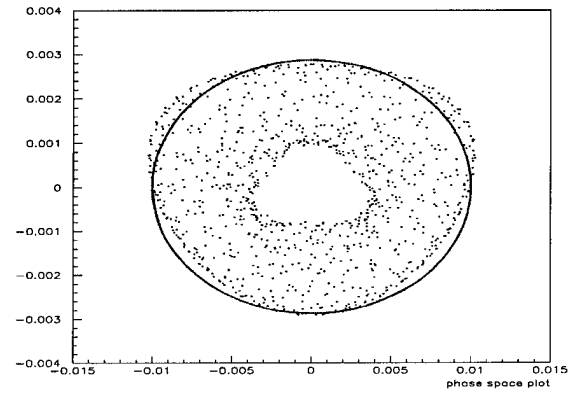

Figure 2: Vertical phase space plot for the matched (line) and unmatched (dots) case.

The distortion generated by the sextupole-like kicks of the ID is plotted for one lattice cell. In this figure the number of ID-periods is reduced to 4, to see clearly the oscillation of the distortion function inside the ID. The distortion is large and spreads out along the cell if no end poles are applied (dotted line). If the parameters are adjusted to the ID parameters, the size of the distortion function is about the same as the one produced by the correction sextupoles of the ring optics. The line in Fig. 1 shows the same configuration but with matched end poles. It is clearly seen that the distortion is nearly perfectly enclosed within the ID, like a closed sextupole bump.

These two situations are compared in Fig. 2 on the basis of tracking simulations for the correctly modeled ID inserted in a linear BESSY II optics. A particle is started in the straight section with 1 cm amplitude in both planes and tracked for 1000 turns. The unmatched case (dots) shows a large smear due to the sextupole fields of the ID. The effect of a good matching is clearly visible, the phase space figure shows a nearly perfect circle. The matching is achieved by an end pole configuration on either side of the ID, each one composed by two poles. These poles are simulated by a step length of the generating function over half a longitudinal period length using the potential function given above, but with reduced field amplitudes. At the entrance side the first half pole has a strength of $+\frac{1}{4}V$ and the second half pole has a strength of $-\frac{3}{4}V$. At the exit side the sequence is reversed, using $+\frac{3}{4}V$ and $-\frac{1}{4}V$. Applying these end poles both closed orbit and distortion functions are well matched. In the matched case the effect of the helical device on the BESSY II optics can be ignored. If the tracking is done with all 14 insertions and one of these replaced by a helical device, no reduction of the dynamic aperture is seen.

4 CONCLUSION

A matched end pole design is required for (not only helical) IDs to damp closed orbit and distortion function oscillations. Both effects can be canceled by properly adjusted end poles. For the full tuning range of the shift parameter ψ of the helical device no effects on the BESSY II dynamic aperture is seen. The required sextupole corrections are in first approximation independent of the ring optics. In case of fast changing beta functions inside the ID the correction has to be done including the ring optics.

5 ACKNOWLEDGEMENTS

It is a pleasure to thank Lidia Tosi from ELETTRA/Trieste for valuable discussions on this subject.

6 REFERENCES

[1] E. Jaeschke, "Status of the High Brilliance Synchrotron Light Source BESSY II", these proceedings

[2] J. Bahrdt at al., "A Double Undulator for the Production of Circularly Polarized Light at BESSY II", Proceedings of the 1996 European Particle Accelerator Conference, Barcelona (Spain)

[3] S. Sasaki et al., "Design of a New Type of Planar Undulator for Generating Variably Polarized Radiation", Nucl. Instr. Meth. **A331**,p.763 (1993)

[4] Johannes Bahrdt, private communication, BESSY, 1996

[5] G. Wüstefeld, "Particle Tracking with Generating Functions of Magnetic Fringing Fields", Proceedings of the IEEE 1995 Particle Accelerator Conference, Dallas (USA), 1995, p. 2868

[6] A. C. Hearn, REDUCE 3.6, ©A.C.Hearn, RAND, Santa Monica, CA 90407-2138,USA (reduce@rand.org)

[7] M. Scheer et al. "Tracking Routines for General Insertion Devices", these proceedings

[8] G. Wüstefeld, "Distortion Functions for Insertion Devices", unpublished note, BESSY, 1997
e-mail: wuestefeld@bessy.de

[9] T. L. Collins, "Distortion Functions", Fermilab-84/114, 1984, FNAL, Batavia, IL 60510 USA

ORBIT DYNAMICS FOR UNSTABLE LINEAR MOTION

G. Parzen*, Brookhaven National Laboratory, Upton, NY 11973 USA

Abstract

A treatment is given of the orbit dynamics for linear unstable motion that allows for the zeros in the beta function and makes no assumptions about the realness of the betatron and phase functions. The phase shift per turn is shown to be related to the beta function and the number of zeros the beta function goes through per turn. The solutions of the equations of motion are found in terms of the beta function.

1 INTRODUCTION

In the case of linear unstable motion, the beta function can be zero at some points in the lattice. Because of the zeros in the beta function, and other assumptions often made about the realness of the beta function and phase function, the usual treatment given for stable motion does not carry over to the case of unstable motion. A treatment is given below, that allows for the zeros in the beta functions and does not make assumptions about the realness of the betatron and phase functions.

It will be shown that the solutions of the equations of motion can be written in the form

$$\begin{aligned} x &= \beta^{\frac{1}{2}} \exp(\pm\psi) \\ \psi &= P\int_{s_0}^{s} \frac{ds}{\beta} + i\frac{\pi}{2}N_z \end{aligned} \qquad (1\text{-}1)$$

N_z is the number of times $\beta(s)$ goes through zero between s_0 and s. P indicates the principle value of the integral. The solutions of the equations of motion can also be written as

$$x = \exp[\pm\mu s/L]f(s) \qquad (1\text{-}2)$$

where $f(s)$ is periodic and L is the length of one turn. It will be shown that for unstable motion

$$\begin{aligned} \mu &= 2\pi(g + iq/2) \\ q &= \frac{1}{2}N_z \\ g &= \frac{P}{2\pi}\int_0^L \frac{ds}{\beta} \end{aligned} \qquad (1\text{-}3)$$

where N_z is the number of zeros the beta function goes through in one turn. P indicates the principle value of the integral.

Often, the case of unstable linear motion is found when a gradient perturbation is applied to a lattice whose unperturbed ν-value is close to $q/2$, q being some integer. In this case, perturbation theory will show [1] that the solutions have the form given by Eq. (1-1) where $q/2$ is the half integer close to the unperturbed to the ν-value. In the general case, where the unstable motion cannot be viewed as due to a perturbing gradient then the value of q is given by $\frac{1}{2}N_z$ where N_z is the number of zeros in the beta function in one turn.

It will also be shown that near a zero of the beta function at $s = s_1$, ψ will become infinite and the dominant term is ψ is given by

$$\psi \sim \pm\frac{1}{2}\log(s - s_1) \qquad (1\text{-}4)$$

See [4] for more details.

2 THE DEFINITION OF THE BETA FUNCTION

The linear parameters can be defined in terms of the elements of the one period transfer matrix. The 2×2 transfer matrix, M, is defined by

$$\begin{aligned} x(s) &= M(s, s_0)x(s_0) \\ x &= \begin{pmatrix} x \\ p_x \end{pmatrix} \end{aligned} \qquad (2\text{-}1)$$

The one period transfer matrix is defined by

$$\hat{M}(s) = M(s + L, s) \qquad (2\text{-}2)$$

where the lattice is assumed to be periodic with the period L. The matrix M is assumed to be symplectic

$$\begin{aligned} M\overline{M} &= I \\ \overline{M} &= \tilde{S}\tilde{M}\,S \\ S &= \begin{pmatrix} 0 & 1 \\ -1 & 0 \end{pmatrix} \quad I = \begin{pmatrix} 1 & 0 \\ 0 & 1 \end{pmatrix} \end{aligned} \qquad (2\text{-}3)$$

$\tilde{S}$ is the transpose of S. Also $|M| = 1$ where $|M|$ is the determinant of M. One can show that $\hat{M}(s)$ and $\hat{M}(s_0)$ are related by

$$\hat{M}(s) = M(s, s_0)\hat{M}(s_0)M(s_0, s) \qquad (2\text{-}4)$$

It follows from Eq. (2-4) that $\hat{M}_{11} + \hat{M}_{22}$, the trace of $\hat{M}$, is independent of s. For unstable motion it is assumed that $|\hat{M}_{11} + \hat{M}_{22}| > 2$. This may be shown to lead to unstable exponentially growing motion.

One can now introduce the constant parameter μ defined by

$$\cosh\mu = \frac{1}{2}\left(\hat{M}_{11} + \hat{M}_{22}\right) \qquad (2\text{-}5)$$

If $\hat{M}_{11} + \hat{M}_{22}$ is positive, then μ will be real. However if $\hat{M}_{11} + \hat{M}_{22}$ is negative then μ has to have the imaginary

* Work performed under the auspices of the U.S. Department of Energy.

part $iq\pi$ where q is an odd integer. In general, one can write

$$\begin{aligned} \mu &= \mu_R + iq\pi \\ \cosh\mu_R &= \frac{1}{2}\left|\hat{M}_{11} + \hat{M}_{22}\right| \end{aligned} \tag{2-6}$$

where q is an even integer if $\hat{M}_{11} + \hat{M}_{22}$ is positive, and q is an odd integer when $\hat{M}_{11} + \hat{M}_{22}$ is negative.

μ is related to the eigenvalues of $\hat{M}$, λ_1 and λ_2, where $\lambda_1 + \lambda_2 = \hat{M}_{11} + \hat{M}_{22}$ and $\lambda_1\lambda_2 = 1$ from $|\hat{M} - \lambda I| = 0$. It follows from Eq. (2-5) that

$$\begin{aligned} \lambda_1 &= \exp(\mu) \\ \lambda_2 &= \exp(-\mu) \end{aligned} \tag{2-7}$$

One can define the linear parameters, β, α, γ, using the elements of the one period transfer matrix. If one uses the form of the transfer matrix often used [2] for stable motion the linear parameters will be imaginary for unstable motion. To make the linear parameters real, they will be defined here in terms of the one period transfer matrix as

$$\hat{M} = \begin{bmatrix} \cosh\mu + \alpha\sinh\mu & \beta\sinh\mu \\ \gamma\sinh\mu & \cosh\mu - \alpha\sinh\mu \end{bmatrix} \tag{2-8}$$

$$\beta\gamma = 1 - \alpha^2$$

β, α, γ are then given in terms of $\hat{M}_{ij}$ as

$$\begin{aligned} \beta &= (-1)^q \hat{M}_{12}/\sinh\mu_R \\ \alpha &= (-1)^q(\hat{M}_{11} - \hat{M}_{22})/2\sinh\mu_R \\ \gamma &= (1-\alpha^2)/\beta \end{aligned} \tag{2-9}$$

Eq. (2-6) does not specify the sign of μ_R. One can define the sign of μ_R to be always positive. Then β, α, γ can then be computed from the $\hat{M}_{ij}$ using Eq. (2-9). It will be seen later that the sign of $\beta(s)$ can change within a period, and $\beta(s)$ can be zero at certain values of s for unstable motion.

2.1 *Differential Equations for β, α, γ*

It is assumed that the linearized equations of motion can be written as

$$\begin{aligned} \frac{dx}{ds} &= A_{11}x + A_{12}p_x \\ \frac{dp_x}{ds} &= A_{21}x + A_{22}p_x \\ A_{11} + A_{22} &= 0 \end{aligned} \tag{2-10}$$

In the large accelerator approximation, $A_{11} = A_{22} = 0$ and $A_{12} = 1$. one can show that

$$\frac{d\hat{M}}{ds} = A\,\hat{M} - \hat{M}\,A. \tag{2-11}$$

A is the 2×2 matrix whose elements are the A_{ij} of Eq. (2-10). Replacing $\hat{M}$, using Eq. (2-8), in Eq. (2-13) gives the result

$$\begin{aligned} \frac{d\beta}{ds} &= 2A_{11}\beta - 2A_{12}\alpha \\ \frac{d\alpha}{ds} &= -A_{21}\beta + A_{12}\gamma \\ \frac{d\gamma}{ds} &= 2A_{21}\alpha - 2A_{11}\gamma \end{aligned} \tag{2-12}$$

2.2 *Differential Equation for β*

In this section, the differential equation for β will be obtained without making any assumptions about the form of the solutions of the equations of motion. For the sake of simplicity, the derivation will be given for the large accelerator case which assumes $A_{11} = A_{22} = 0$ and $A_{12} = 1$.

Introducing b, where $\beta = b^2$, one can then find (see [4] for details)

$$\begin{aligned} \frac{d^2b}{ds^2} + Kb + \frac{1}{b^3} &= 0 \\ b &= \beta^{\frac{1}{2}}. \end{aligned} \tag{2-13}$$

3 SOLUTIONS OF THE EQUATIONS OF MOTION AND THE BETA FUNCTION

For stable motion, the role of the beta function in the solutions of the equations of motion is well known. A similar result will be found here for unstable motion. The treatment usually given for stable motion, does not carry over to unstable motion because of the assumptions usually made about the realness of the betatron and phase functions, and the absence of zeros in the beta function.

Let us write the solutions of the equations of motion as

$$\begin{aligned} x &= b\exp(\psi) \\ b &= \beta^{\frac{1}{2}} \end{aligned} \tag{3-1}$$

where β and b have been defined by Eq. (2-8). Then b has been shown to obey, see Eq. (2-13),

$$\begin{aligned} \frac{d^2b}{ds^2} &+ Kb + \frac{1}{b^3} = 0 \\ K &= -A_{21} \end{aligned} \tag{3-2}$$

x then obeys the equations

$$\frac{d^2x}{ds^2} + Kx = 0 \tag{3-3}$$

Putting the form of x assumed in Eq. (3-1) into Eq. (3-3), and using Eq. (3-2) for b one gets

$$\frac{d^2\psi}{ds^2} + \frac{2}{b}\frac{db}{ds}\frac{d\psi}{ds} + \left(\frac{d\psi}{ds}\right)^2 - \frac{1}{b^4} = 0 \tag{3-4}$$

Putting $f = d\psi/ds$ one gets

$$\frac{df}{ds} + \frac{2}{b}\frac{db}{ds}f + f^2 - \frac{1}{b^4} = 0 \tag{3-5}$$

The solutions of Eq. (3-5) are

$$f = \pm(1/b^2) = \pm 1/\beta. \tag{3-6}$$

Thus

$$\psi = \pm \int_{s_0}^{s} \frac{ds}{\beta} \tag{3-7}$$

and the two solutions of the equations of motion are

$$x = \beta^{\frac{1}{2}} \exp\left(\pm \int_{s_0}^{s} \frac{ds}{\beta}\right) \tag{3-8}$$

One may note that in deriving Eq. (2-8) no assumption was made about the realness of β or ψ. However, there is a problem with the result for unstable motion, as in the case of unstable motion $\beta(s)$ will go through zero. To evaluate the integral when $\beta(s)$ has zeros, Eq. (3-2) will be replaced by

$$\psi = \lim_{\epsilon \to 0} \int_{s_0}^{s} \frac{ds}{\beta - i\epsilon} \tag{3-9}$$

where ϵ is a positive small quantity. It can be shown that Eq. (3-9) gives (see section 4)

$$\psi = P \int_{s_0}^{ds} \frac{ds}{\beta} + \sum_{s_n} \frac{i\pi}{|\beta'(s_n)|} \tag{3-10}$$

where s_n are the locations of the zeros of $\beta(s)$ from s_0 to s. P represents the principle part of the integral.

One can also show that $\beta'(s) = \pm 2$ at the zeros of $\beta(s)$. Since $\beta\gamma = \alpha^2 - 1$, then $\alpha = \pm 1$ when $\beta = 0$. Since $\beta' = -2\alpha$, $\beta' = \mp 2$ when $\beta = 0$. One can now write Eq. (3-10) as

$$\psi = P \int_{s_0}^{s} \frac{ds}{\beta} + \frac{i\pi}{2} N_z \tag{3-11}$$

where N_z is the number zeros in $\beta(s)$ in s_0 to s.

One may notice that the imaginary part of ψ has on an unusual dependence on s. It is constant in between zeros of $\beta(s)$ and jumps by $\pi/2$ at each zero of $\beta(s)$. One can use Eq. (3-11) to find the change in ψ over one turn, $\psi(s + L) - \psi(s)$, and find

$$\psi(s + L) - \psi(s) = P \int_{s}^{s+L} \frac{ds}{\beta} + iq\pi \tag{3-12}$$

where $2q$ is the number of zeros in $\beta(s)$ in one turn, and L is the length of one turn. For simplicity, it is being assumed that the period L is one turn. Since $\beta(s)$ is a periodic function, the number of zeros of $\beta(s)$ in one turn has to be even. If one defines the tune as the imaginary part of $\psi(s + L) - \psi(s)$ divided by 2π, then one has

$$\text{tune} = q/2. \tag{3-13}$$

Eq. (4-13) shows the connection between the tune and the number of zeros in the beta function in one turn. The real part of $\psi(s_0 + L) - \psi(s_0)$ gives the exponential growth in one turn. If one defines the exponential growth factor, g, to be the real part of $\psi(s + L) - \psi(s)$ divided by 2π

$$g = \frac{P}{2\pi} \int_{s}^{s+L} \frac{ds}{\beta} \tag{3-14}$$

See [4] for details.

4 PHASE FUNCTION RESULTS WHEN β HAS ZEROS

In this section, the result for the phase function, ψ, given by Eq. (3-10) will be derived. Also, the behavior of ψ when s is near the zeros of $\beta(s)$ will be studied. First, let us consider the case where

$$\psi = \lim_{\epsilon \to 0} \int_{s_0}^{s} \frac{ds}{\beta - i\epsilon} \tag{4-1}$$

$\epsilon > 0$, and one assumes there is only one zero for $\beta(s)$ at $s = s_1$ between $s = s_0$ to $s = s$. Then, one can write

$$\psi = P \int_{s_0}^{s} \frac{ds}{\beta} + \int_{s_1-\delta}^{s_1+\delta} \frac{ds}{\beta - i\epsilon} \tag{4-2}$$

where $\delta \to 0$ but $\delta \gg \epsilon$. P stands for the principle part of the integral. Near s_1 one can write $\beta = \beta'(s_1)(s - s_1) + \ldots$ and find

$$\begin{aligned} \int_{s_1-\delta}^{s_1+\delta} \frac{ds}{\beta - i\epsilon} &= \int_{s_1-\delta}^{s_1+\delta} \frac{ds}{\beta'(s_1)(s - s_1) - i\epsilon} \\ &= \frac{1}{\beta'(s_1)} \int_{-\delta}^{\delta} d\bar{s} \frac{(\bar{s} + i\bar{\epsilon})}{\bar{s}^2 + \bar{\epsilon}^2}, \ \bar{s} = s - s_1, \ \bar{\epsilon} = \epsilon/\beta'(s_1) \\ &= \frac{1}{\beta'(s_1)} \frac{i\bar{\epsilon}}{|\bar{\epsilon}|} \pi \\ &= \frac{1}{|\beta'(s_1)|} i\pi \end{aligned} \tag{4-3}$$

If there are many zeros between s_0 to s at $s = s_n$ one then finds

$$\psi = P \int_{s_0}^{s} \frac{ds}{\beta} + \sum_{s_n} \frac{i\pi}{|\beta'(s_n)|} \tag{4-4}$$

It can be shown that near a zero of $\beta(s)$, like $s = s_1$, ψ becomes infinite like

$$\psi \sim \pm \frac{1}{2} \log(s - s_1) \tag{4-5}$$

see [4] for more details and results.

5 REFERENCES

[1] G. Parzen, Particle motion inside and near a linear half–integer stopband, BNL Report, BNL-62036 (1995).

[2] E.D. Courant and H.S. Snyder, Theory of the alternating gradient synchrotron, Ann. Phys. 3, 1 (1958).

[3] J.S. Bell, Hamiltonian Mechanics, CERN Accelerator school proceedings, CERN 87-03 (1987); Rutherford Lab. Report AERE T/R 1114 (1953).

[4] G. Parzen, Orbit dynamics for unstable linear motion, BNL Report, BNL-63074 (1996).

PARTICLE MOTION INSIDE AND NEAR A LINEAR HALF-INTEGER STOPBAND

G. Parzen*, Brookhaven National Laboratory, Upton, NY 11973 USA

Abstract

This paper studies the motion of a particle whose tune is inside and near a linear half-integer stopband. Results are found for the tune and beta functions in the stable region close to an edge of the stopband. It is shown that the eigenvalues and the eigenfunctions of the transfer matrix are real inside the stopband. All the results found are also valid for small accelerators where the large accelerator approximation is not used.

1 INTRODUCTION

Inside a linear-half integer stopband the particle motion can be unstable and grow exponentially. The eigenvalues and eigenfunctions of the transfer matrix are shown to be real inside the stopband. In the stable region near an edge of the stopband, the tune varies rapidly and the beta function becomes infinite as the unperturbed tune approaches the edge of the stopband. Results are found for the tune and beta function in the stable region near an edge of the stopband. It is found that the beta function becomes infinite inversely as the square root of the distance of the unperturbed tune from the edge of the stopband.

2 RESULTS WHEN THE TUNE IS IN THE STOPBAND

It will be assumed that in the absence of the perturbing fields, the tune of the particle is ν_0 and that the motion is stable when ν_0 is close to $q/2$, where q is an integer.

It is assumed that a perturbing field is present which is given on the median plane by

$$\Delta B_y = -G(s)x \tag{2-1}$$

$G(s)$ is periodic in s and contains the field harmonics that can excite the stopband around $\nu_0 = q/2$.

Introducing η defined by

$$\eta = x/\beta^{1/2}, \tag{2-2}$$

where β is the beta function of the unperturbed field, the equation of motion can be written as

$$\begin{aligned} \frac{d^2\eta}{d\theta^2} &+ \nu_0^2\eta = f \\ f &= \nu_0^2\beta^{3/2}\Delta B_y/B\rho \\ f &= -\nu_0^2\beta^2 G\eta/B\rho \\ B\rho &= pc/e,\ d\theta = ds/\nu_0\beta \end{aligned} \tag{2-3}$$

The final results found below are valid for small accelerators that require the use of the exact linearized equations. See [7] for details.

Eq. (2-3) can be written as

$$\begin{aligned} \frac{d^2\eta}{d\theta^2} + \nu_0^2 &= -2\nu_0 b(\theta)\eta \\ b(\theta) &= \frac{1}{2}\nu_0\beta^2 G/B\rho \end{aligned} \tag{2-4}$$

Because $b(\theta)$ is periodic a solution for η will have the form

$$\eta = \exp(i\nu_s\theta)h(\theta) \tag{2-5}$$

where $h(\theta)$ is periodic. It is assumed that the tune ν_0 will change to ν_s because of the perturbing field. Thus η can be assumed to have the form

$$\begin{aligned} \eta &= A_s\exp(i\nu_s\theta) + \sum_{r\neq s} A_r\exp(i\nu_r\theta) \\ \nu_r &= \nu_s + n \end{aligned} \tag{2-6}$$

where n is some integer but $n \neq 0$. For a zero perturbing field the solution for η is $\eta = A\exp(i\nu_0\theta)$. Thus for small perturbing fields it can be assumed that

$$\begin{aligned} \nu_s &\simeq \nu_0 \\ A_r &\ll A_s \text{ for } r \neq s \end{aligned} \tag{2-7}$$

Putting Eq. (2-6) into Eq. (2-4), one obtains a set of equations for the A_r

$$\begin{aligned} (\nu_r^2 - \nu_0^2)A_r &= 2\nu_0\sum_{\bar{r}} b_{r\bar{r}}A_{\bar{r}} \\ b_{r\bar{r}} &= \frac{1}{2\pi}\int_0^{2\pi} d\theta\, b(\theta)\exp(-i\nu_r\theta + i\nu_{\bar{r}}\theta) \\ \nu_r &= \nu_s + n \end{aligned} \tag{2-8}$$

It is assumed that ν_0 is near $\nu_0 = q/2$, q being an integer. The stopband is defined as the range of ν_0 for which the tune, ν_s, in the presence of the perturbation given by Eq. (2-2) has a non-zero imaginary part. One can write ν_s as

$$\nu_s = \nu_{sR} - ig \tag{2-9}$$

It will be shown that inside the stopband, where $g \neq 0$, then

$$\nu_{sR} = q/2 \tag{2-10}$$

This may be shown as follows. Let μ be the phase shift for a period, and $\mu = 2\pi\nu_s$ where the period has been assumed

* Work performed under the auspices of the U.S. Department of Energy.

to be one turn or 2π in θ. Let T be the transfer matrix for one period. Then one has

$$\cos\mu = \frac{1}{2}(T_{11} + T_{22}), \tag{2-11}$$

and one sees that $\cos\mu$ is real even inside the stopband since the T_{ij} are real. One also has

$$\begin{aligned}\cos\mu &= \cos 2\pi(\nu_{sR} - ig) = \cos(2\pi\nu_{sR})\cosh(2\pi g) \\ &+ i\sin(2\pi\nu_s R)\sin(2\pi g)\end{aligned} \tag{2-12}$$

In order for $\cos\mu$ to be real, one has to have either $g = 0$ or, if $g \neq 0$, $2\pi\nu_{sR} = n\pi$, where n is some integer. Thus, inside the stopband where $g \neq 0$,

$$\nu_{sR} = n/2 \tag{2-13}$$

In order to have continuity when the perturbation goes to zero, one has $n = q$ and

$$\nu_{sR} = q/2 \tag{2-14}$$

Now let us return to the problem of computing the growth factor, g, using perturbation theory. One sees from Eq. (2-8) that when $\nu_0 \simeq q/2$, then one of the A_r becomes comparable to A_s, and this is the A_r for which $\nu_r = \nu_s - q$, $\nu_r \simeq -q/2$. Thus in the above iterative procedure for finding η, one will assume for the initial guess for η,

$$\begin{aligned}\eta &= A_s\exp(i\nu_s\theta) + A_{\bar{s}}\exp(i\nu_{\bar{s}}\theta) \\ \nu_{\bar{s}} &= \nu_s - q\end{aligned} \tag{2-15}$$

From Eq. (2-8) one finds

$$(\nu_r^2 - \nu_o^2)A_r = 2\nu_0 b_{rs}A_s + 2\nu_0 b_{r\bar{s}}A_{\bar{s}} \tag{2-16}$$

$$\nu_r = \nu_s + n \quad \text{or} \quad \nu_r = \nu_{\bar{s}} + n = \nu_s - q + n$$

For $r = s$ and $r = \bar{s}$ one obtains 2 equations for A_s and $A_{\bar{s}}$

$$\begin{aligned}(\nu_s^2 - \nu_0^2)A_s &= 2\nu_0 b_{s\bar{s}}A_{\bar{s}} \\ (\nu_{\bar{s}}^2 - \nu_0^2)A_{\bar{s}} &= 2\nu_0 b_{\bar{s}s}A_s \\ \nu_{\bar{s}} &= \nu_s - q\end{aligned} \tag{2-17}$$

In Eq. (2-17), it has been assumed, for simplicity sake, that $b_{ss} = 0$. This can be accomplished by redefining ν_0 to be $\nu_0 + b_0$.

In order for Eqs. (2-17) to have a solution, one must have

$$\begin{aligned}(\nu_s^2 - \nu_0^2)(\nu_{\bar{s}}^2 - \nu_0^2) &= 4\nu_0^2|b_{s\bar{s}}|^2 \\ \nu_{\bar{s}} &= \nu_s - q\end{aligned} \tag{2-18}$$

Eq. (2-18) determines ν_s. If one writes $\nu_s = \nu_{sR} - ig$, one finds

$$\left[(\nu_{sR} - ig)^2 - \nu_0^2\right]\left[(\nu_{sR} - q - ig)^2\right] = 4\nu_0^2|\Delta\nu|^2 \tag{2-19}$$

where $\Delta\nu = b_{s\bar{s}}$

$$\Delta\nu = \frac{1}{4\pi}\int_0^L ds\,\beta\exp(-iq\theta)G/B\rho \tag{2-20}$$

$$\nu_{sR} = q/2 \tag{2-21}$$

$$\begin{aligned}(q/2 - \nu_0)^2 + g^2 &= |\Delta\nu|^2 \\ g &= \pm\left\{|\Delta\nu|^2 - (q/2 - \nu_0)^2\right\}^{1/2}\end{aligned} \tag{2-22}$$

3 TUNE NEAR THE EDGE OF A STOPBAND

In this section, a result will be found for the tune in the stable region outside the stopband but close to one of the edges of the stopband. It will be shown that close to the edge of a stopband,

$$|\nu - q/2| = \{2|\Delta\nu|\,|\nu_0 - \nu_e|\}^{1/2} \tag{3-1}$$

ν is the tune in the presence of the gradient perturbation, ν_e is the edge of the stopband, $\nu_e = q/2 \pm |\Delta\nu|$. $|\Delta\nu|$ is the half-width of the stopband. Eq. (3-1) shows that when ν_0 is close to an edge of the stopband, ν_e, ν varies rapidly with ν_0, and the slope of the ν vs. ν_0 curve is vertical at $\nu_0 = \nu_e$.

To find ν in the stable region outside the stopband, where $\nu_0 - q/2| > |\Delta\nu|$, one goes back to the derivation given for ν inside the stopband, starting with Eq. (2-19). Eq. (2-22) shows that for $|\nu_0 - q/2| > |\Delta\nu|$ the only acceptable solution is $g = 0$, and Eq. (2-19) can be written as

$$(\nu - \nu_0)(|\nu - q| - \nu_0) = |\Delta\nu|^2 \tag{3-2}$$

where we have put $\nu_s = \nu$.

Assuming that ν_0 is just below the stopband edge $\nu_e = q/2 - |\Delta\nu|$, put $\nu_0 = \nu_e - \epsilon$ and $\nu = q/2 - \delta$ into Eq. (3-2), where ϵ and δ both approach zero as ν_0 approaches the stopband edge. We find

$$\delta = \{\epsilon(\epsilon + 2|\Delta\nu|)\}^{1/2} \tag{3-3}$$

The top edge of the stopband can be treated in the same way and both results can be combined into the one result

$$\begin{aligned}|\nu - q/2| &= \{|\nu_0 - \nu_e|(|\nu_0 - \nu_e| + 2|\Delta\nu|)\}^{1/2} \\ \nu_e &= q/2 \pm |\Delta\nu|\end{aligned} \tag{3-4}$$

Very close to the stopband edge, $|\nu_0 - \nu_e| \ll |\Delta\nu|$, one finds

$$|\nu - q/2| = \{2|\Delta\nu||\nu_0 - \nu_e|\}^{1/2} \tag{3-5}$$

Thus, as ν_0 approaches a stopband edge, ν approaches $q/2$, and $d\nu/d\nu_0$ become infinite like $1/|\nu_0 - \nu_e|^{1/2}$.

A result can be found for the beta function in the stable region outside the stopband, but close to one of the edges of the stopband. It can be shown that close to edge of a stopband (see [7] for details)

$$[(\beta - \beta_0)/\beta_0]_{\max} = [2|\Delta\nu|/|\nu_0 - \nu_e|]^{1/2} \tag{3-6}$$

ν_e is the edge of the stopband, $\nu_e = q/2 \pm |\Delta\nu|$. $|\Delta\nu|$ is the half-width of the stopband. ν_0, β_0 are the unperturbed tune and beta function. Eq. (3-6) shows that when ν_0 approaches the edge of the stopband, $(\beta - \beta_0)/\beta_0$ becomes infinite like $1/|\nu_0 - \nu_e|^{1/2}$.

4 COMMENTS ON THE RESULTS

Others have worked on this subject and there is some overlap between the contents of this paper and their work. P.A.

Sturrock[2] obtained results for the stopband width and the growth parameter g at the center of the stopband. E.D. Courant and H. Snyder[3] obtained the result for the width of the stopband. H. Bruck[4] showed that the solutions of the equation of motion at the edge of the stopband are stable. He also states that the real part of ν is constant at $q/2$ across the stopband without giving a proof of this. A.A. Kolomensky and A.N. Lebedev[5] obtained results for the stopband width and the growth parameter g at the center of the stopband. H. Wiedemann[6] obtained the result for the width of the stopband using a method similar to that used by Courant and Snyder.

The new results in this paper include the following. The result given for the tune ν near the edge of the stopband, ν_e, $|\nu - q/2| = [2|\Delta\nu||\nu_e - \nu_0|]^{1/2}$. The result given for the beta function near the edge of the stopband, $[(\beta - \beta_0)/\beta_0]_{\max} = [2|\Delta\nu|/|\nu_e - \nu_0|]^{1/2}$. The proof given showing that the real part of ν is constant over the stopband at $q/2$ does not depend on perturbation theory, and the result follows from the symplectic properties. The result that all the results found in this paper will also hold for a small accelerator where the large accelerator approximation is not used. The result given for the solutions of the equations of motion when ν_0 is inside the stopband, and the proof that the eigenfunctions and eigenvalues of the transfer matrix are real inside the stopband. See [7] for more details.

5 REFERENCES

[1] G. Parzen, Linear orbit parameters for the exact equations of motion, BNL Report, BNL-60090 (1994).

[2] P.A. Sturrock, Static and dynamic electron optics, Cambridge Univ. Press, London (1955).

[3] E.D. Courant and H.S. Snyder, Theory of the alternating gradient synchrotron, Annals. of Physics, Vol. 3, p. 1 (1958).

[4] H. Bruck, Circular particle accelerators, (1965), English translation Los Alamos Report, LA-TR-72-10 Rev.

[5] A.A. Kolomensky and A.N. Lebedev, Theory of cyclic accelerators, North Holland Publishing Co., Amsterdam (1966).

[6] H. Wiedemann, Particle accelerator physics, Springer-Verlag, Berlin (1993).

[7] G. Parzen, Particle motion inside and near a linear half-integer stopband, BNL Report BNL-62036 (1995).

PARTICLE MOTION IN THE STABLE REGION NEAR THE EDGE OF A LINEAR SUM RESONANCE STOPBAND

G. Parzen*, Brookhaven National Laboratory, Upton, NY 11973 USA

Abstract

This paper studies the particle motion when the tune is in the stable region close to the edge of linear sum resonance stopband. Results are found for the tune and the beta functions. Results are also found for the two solutions of the equations of motion. The results found are shown to be also valid for small accelerators where the large accelerator approximation may not be used.

1 INTRODUCTION

This paper studies the motion of a particle whose tune is near an edge of a linear sum resonance stopband. It is assumed that the tune is not near any other linear resonance, and the motion is dominated by the linear sum resonance. It is assumed that the linear sum resonance is being driven by a skew quadrupole field perturbation. When the unperturbed tune ν_{x0}, ν_{y0} is close to the resonance line $\nu_x + \nu_y = q$, q being an integer, the particle motion can be unstable. Results are found for the tune and the beta functions when the unperturbed tune is in the stable region but close to an edge of the stopband. Results are also found for the two solutions of the equations of motion. All the results found are shown to be also valid for small accelerators where the large accelerator approximation may not be used. See [14] for more details.

2 RESULTS WHEN THE TUNE IS INSIDE THE STOPBAND

It will be assumed that in the absence of the perturbing fields, the tune of the particle is given by ν_{x0}, ν_{y0}, the x and y motions are uncoupled, and that the motion is stable when ν_{x0}, ν_{y0} is close to the line $\nu_{x0} + \nu_{y0} = q$, where q is an integer. It is assumed that a perturbing field is then added which is given by the skew quadrupole field

$$\begin{aligned} \Delta B_x &= -B_0 a_1\, x \\ \Delta B_y &= B_0 a_1\, y \end{aligned} \tag{2-1}$$

a_1 is the skew quadrupole multipole and $a_1 = a_1(s)$. B_0 is some standard field, usually the field in the main dipoles of the lattice.

The coupled equations of motion can be written as

$$\begin{aligned} \frac{d^2}{d\theta_x^2}\eta_x &+ \nu_{x0}^2\eta_x = b_x\,\eta_y \\ \frac{d^2}{d\theta_y^2}\eta_y &+ \nu_{y0}^2\eta_y = b_y\,\eta_x \end{aligned} \tag{2-2}$$

$$\begin{aligned} b_x &= -\nu_{x0}^2\beta_x(\beta_x\beta_y)^{\frac{1}{2}}a_1/\rho \\ b_y &= -\nu_{y0}^2\beta_y(\beta_x\beta_y)^{\frac{1}{2}}a_1/\rho \end{aligned}$$

One can assume that η_x has the form

$$\begin{aligned} \eta_x &= A_s\exp(i\nu_{xs}\theta_x) + \sum_{r\neq s} A_r\exp(i\nu_{xr}\theta_x) \\ \nu_{xr} &= \nu_{xs} + n, \quad n \text{ an integer}, n \neq 0 \end{aligned} \tag{2-3a}$$

where for small enough a_1, $A_r \ll A_s$ and $\nu_{xs} \to \nu_{x0}$ for $a_1 \to 0$. For the corresponding form for η_y one might assume for η_y

$$\begin{aligned} \eta_y &= \sum_r B_r\exp(i\nu_{yr}\theta_y) \\ \nu_{yr} &= \nu_{xs} + n \end{aligned} \tag{2-3b}$$

where $B_r \ll A_s$ for small enough a_1.

It will be seen below, that the solution assumed for η_y Eq. (2-3b) is valid if one is not near the sum resonance $\nu_x + \nu_y = q$, q being an integer. When ν_{x0}, ν_{y0} are close to the sum resonance $\nu_x + \nu_y = q$, then one of the B_r will become as large as A_s and this is the B_r for which $\nu_{yr} = \nu_{xs} - q$. This is shown below. Thus, one assumes for η_y the solution with the form

$$\begin{aligned} \eta_y &= B_{\bar{s}}\exp(i\nu_{y\bar{s}}\theta_y) + \sum_{r\neq\bar{s}} B_r\exp(i\nu_{yr}\theta_y) \\ \nu_{y\bar{s}} &= \nu_{xs} - q \\ \nu_{yr} &= \nu_{xs} + n, \quad n \neq -q \end{aligned} \tag{2-3c}$$

Here $B_r \ll A_s$ but $B_{\bar{s}} \simeq A_s$. It is being assumed that ν_{x0}, ν_{y0} are not close to any other resonance other than $\nu_x + \nu_y = q$.

Putting this assumed form for η_x, η_y into the differential equations Eq. (2-2), and assuming for the initial guess

$$\begin{aligned} \eta_x &= A_s\exp(i\nu_x\theta_x) \\ \eta_y &= B_{\bar{s}}\exp(i\nu_{y\bar{s}}\theta_y) \\ \nu_{y\bar{s}} &= \nu_{xs} - q = -(q - \nu_{xs}) \end{aligned} \tag{2-4}$$

one finds that, see [14] for details,

$$\begin{aligned} (\nu_{xs}^2 - \nu_{x0}^2)(\nu_{y\bar{s}}^2 - \nu_{y0}^2) &= 4\nu_{x0}\nu_{y0}|\Delta\nu_x|^2 \\ \Delta\nu_x &= \frac{1}{4\pi}\int_0^L ds(\beta_x\beta_y)^{\frac{1}{2}}(a_1/\rho) \\ &\exp[-i(\nu_{x0}\theta_x + (q-\nu_{x0})\theta_y)] \end{aligned} \tag{2-5}$$

To solve Eq. (2-5) one puts

$$\nu_{xs} = \nu_{xsR} - ig_x$$

* Work performed under the auspices of the U.S. Department of Energy.

where ν_{xsR} and g_x are both real, which gives the equation

$$(\nu_{xsR} - ig_x - \nu_{x0})(q - \nu_{xsR} + ig_x - \nu_{y0}) = |\Delta\nu_x|^2 \quad (2\text{-}6)$$

Eq. (2-6) then gives

$$\begin{aligned} g_x^2 &+ [\frac{1}{2}(q - \nu_{x0} - \nu_{y0})]^2 = |\Delta\nu_x|^2 \\ g_x &= \pm\left\{|\Delta\nu_x|^2 - [\frac{1}{2}(q - \nu_{x0} - \nu_{y0})]^2\right\}^{1/2} \end{aligned} \quad (2\text{-}7)$$

Results can be found for η_x and η_y which are correct to first order in the perturbation and when ν_{x0}, ν_{y0} is inside the stopband or in the stable region near an edge of the stopband. η_x, η_y are given by Eqs. (2-3). For the ν_x mode

$$\begin{aligned} \eta_x &= A_s \exp(i\nu_{xs}\theta_x) + \sum_{r\neq s} A_r \exp(i\nu_{xr}\theta_x) \\ \eta_y &= B_{\bar{s}} \exp(i\nu_{y\bar{s}}\theta_y) + \sum_{r\neq s} B_r \exp(i\nu_{yr}\theta_y) \\ \nu_{y\bar{s}} &= \nu_{xs} - q \\ \nu_{yr} &= \nu_{xs} + n, \quad n \neq -q \\ \nu_{xr} &= \nu_{xs} + n, \quad n \neq 0 \end{aligned} \quad (2\text{-}8)$$

Results and details for η_x, η_y are given in [14].

3 THE TUNE NEAR THE EDGE OF A STOPBAND

In this section, a result will be found for the tune in the stable region outside the stopband but close to an edge of the stopband. It will be shown that close to an edge of the stopband the tune of the ν_x mode is given by

$$\begin{aligned} |\nu_x - \frac{1}{2}(\nu_{x0} + q - \nu_{y0})| &= \{\epsilon_x|\Delta\nu_x|\}^{\frac{1}{2}} \\ \epsilon_x &= |q \pm 2|\Delta\nu_x| - \nu_{x0} - \nu_{y0}| \end{aligned} \quad (3\text{-}1)$$

ν_x is the tune of the ν_x mode, ϵ is the distance from ν_{x0}, ν_{y0} to the edge of the stopband. In the $\pm$, the $+$ sign is for the upper edge, and the $-$ sign for the lower edge. When ν_{x0}, ν_{y0} reaches the edge of the stopband, then $\epsilon = 0$, and $\nu_x = \frac{1}{2}(\nu_{x0} + q - \nu_{y0})$ is the real part of the tune inside the stopband.

Eq. (3-1) shows that near the stopband edge, ν_x varies rapidly with ϵ_x. As one reaches the edge of the stopband, ϵ_x goes to zero and $d\nu_x/d\epsilon_x$ becomes infinite like $\epsilon_x^{-\frac{1}{2}}$.

To find ν_x in the stable region outside the stopband, where $|q - \nu_{x0} - \nu_{y0}| > 2|\Delta\nu_x|$, one goes back to the derivation given in section 2 for ν_x inside the stopband, starting with

$$(\nu_x - \nu_{x0})(q - \nu_x - \nu_{y0}) = |\Delta\nu_x|^2 \quad (3\text{-}2)$$

Because of the condition that ν_x is outside the stopband or

$$|q - \nu_{x0} - \nu_{y0}| > 2|\Delta\nu_x| \quad (3\text{-}3)$$

one sees that one must have $g_x = 0$.

Let us assume that we start with ν_{x0}, ν_{y0} below the lower stopband edge and let ν_{x0}, ν_{y0} approach the lower stopband edge. The equation of the lower stopband edge is given by

$$q - \nu_{x0} - \nu_{y0} = 2|\Delta\nu_x| \quad (3\text{-}4)$$

when ν_{x0}, ν_{y0} arrive on the lower stopband edge, then ν_x will arrive at the value $\nu_x = \frac{1}{2}(\nu_{x0} + q - \nu_{y0})$. Thus below the stopband edge one can write

$$\nu_x = \frac{1}{2}(\nu_{x0} + q - \nu_{y0}) - \delta_x \quad (3\text{-}5)$$

where $\delta_x \to 0$ when ν_{x0}, ν_{y0} arrive at the stopband edge. We then find

$$\begin{aligned} \nu_x - \nu_{x0} &= \frac{1}{2}(q - \nu_{x0} - \nu_{y0}) - \delta_x \\ q - \nu_x - \nu_{y0} &= \frac{1}{2}(q - \nu_{x0} - \nu_{y0}) + \delta_x \end{aligned} \quad (3\text{-}6)$$

and Eq. (3-2) becomes

$$\begin{aligned} [\frac{1}{2}(q - \nu_{x0} - \nu_{y0})]^2 - \delta_x^2 &= |\Delta\nu_x|^2 \\ \delta_x &= \left\{[\frac{1}{2}(q - \nu_{x0} - \nu_{y0})]^2 - |\Delta\nu_x|^2\right\}^{\frac{1}{2}} \end{aligned} \quad (3\text{-}7)$$

Eq. (3-7) gives ν_x in the stable region near the stopband. It can be put in another form that indicates the dependence on the distance from ν_{x0}, ν_{y0} to the stopband edge.

Below the stopband, one writes

$$\epsilon_x = q - 2|\Delta\nu_x| - \nu_{x0} - \nu_{y0} \quad (3\text{-}8)$$

where ϵ_x indicates the distance from ν_{x0}, ν_{y0} to the stopband edge which is given by Eq. (3-4). When ν_{x0}, ν_{y0} is on the stopband edge and $\nu_{x0} + \nu_{y0} = q - 2|\Delta\nu_x|$ then $\epsilon_x = 0$.

Using Eq. (3-8) to replace $q - \nu_{x0} - \nu_{y0}$ by $\epsilon_x + 2|\Delta\nu_x|$ in Eq. (3-7) one finds

$$\delta_x = \{\epsilon_x(|\Delta\nu_x| + \epsilon_x/4)\}^{\frac{1}{2}} \quad (3\text{-}9)$$

Eq. (3-9) can then be written so as to hold both above and below the stopband to give

$$\begin{aligned} \left|\nu_x - \frac{1}{2}(\nu_{x0} + q - \nu_{y0})\right| &= \{\epsilon_x(|\Delta\nu_x| + \epsilon_x/4)\}^{\frac{1}{2}} \\ \epsilon_x &= |q \pm 2|\Delta\nu_x| - \nu_{x0} - \nu_{y0}| \end{aligned} \quad (3\text{-}10)$$

where ϵ_x is the distance from ν_{x0}, ν_{y0} to the stopband edge. One uses the $+$ sign for the upper stopband edge and the $-$ sign for the lower edge.

Close to the stopband edge, where $\epsilon_x \ll |\Delta\nu_x|$ then Eq. (3-10) gives the result

$$\left|\nu_x - \frac{1}{2}(\nu_{x0} + q - \nu_{y0})\right| = \{\epsilon_x\,|\Delta\nu_x|\}^{1/2} \quad (3\text{-}11)$$

Equations (3-10) and (3-11) give the tune of the ν_x mode, ν_x, near the stopband edge. The result for the tune of the ν_y

mode, ν_y, may be found by making the substitution $\nu_x \rightarrow \nu_y$, $\nu_{x0} \rightarrow \nu_{y0}$, $\nu_{y0} \rightarrow \nu_{x0}$, $|\Delta\nu_x| \rightarrow |\Delta\nu_y|$.

If one varies the unperturbed tune, ν_{x0}, ν_{y0}, so that the tune approaches the edge of the stopband, the tune on the stopband edge depends on the value of ν_{x0}, ν_{y0} when the unperturbed tune arrives at the stopband edge. The stopband edges are given by the two lines

$$\nu_{x0} + \nu_{y0} = q \pm 2|\Delta\nu|$$

where it is assumed that $|\Delta\nu_x| = |\Delta\nu_y| = |\Delta\nu|$ and the $+$ sign is for the upper edge and the $-$ sign for the lower edge.

The tune of the ν_x mode at the stopband edge is then given by

$$\begin{aligned} \nu_x &= \frac{1}{2}(\nu_{x0} + q - \nu_{y0}) \\ \nu_x &= \nu_{x0} \pm |\Delta\nu| \end{aligned} \tag{3-12}$$

where the $+$ sign is for the lower edge and the $-$ sign for the upper edge.

The tune of the ν_y mode at the stopband edge is given by

$$\nu_y = \nu_{y0} \pm |\Delta\nu|$$

One may note, that at the stopband edge

$$\begin{aligned} \nu_x + \nu_y &= \nu_{x0} + \nu_{y0} \pm 2|\Delta\nu| \\ \nu_x + \nu_y &= q \end{aligned} \tag{3-13}$$

and the ν_x, ν_y lies on the resonance line.

Eqs. (3-6) and (3-7) can also be rewritten as, for the ν_x mode and below the resonance line,

$$\begin{aligned} \nu_x &= \nu_{x0} + 0.5D\left\{1 - [(\frac{2\Delta\nu}{D})^2]^{\frac{1}{2}}\right\} \\ D &= q - \nu_{x0} - \nu_{y0} \\ \Delta\nu &= \Delta\nu_x \simeq \Delta\nu_y \end{aligned} \tag{3-14}$$

Results for the beta functions near the edge of the stopband are given in [14].

4 COMMENTS ON THE RESULTS

Others have worked on this subject and there is an overlap between the contents of this paper and their work. These previous papers [4–13] give results for the stopband width and for the growth rate inside the stopband.

The results in this paper include the following:

1. Results for the tune in the stable region near an edge of the stopband. The results show that as ν_{x0}, ν_{y0} approach the edge of the stopband, the tunes of the two normal modes ν_x and ν_y begin to change rapidly and when ν_{x0}, ν_{y0} reach the stopband edge then ν_x and ν_y lie on the resonance line $\nu_x + \nu_y = q$. These final values of ν_x, ν_y, when ν_{x0}, ν_{y0} reach the stopband edge, are approached like $\epsilon^{\frac{1}{2}}$, where ϵ is the distance from ν_{x0}, ν_{y0} to the stopband edge.
2. Results for the beta functions of the normal modes, β_x, β_y, in the stable region near the edge of a stopband. The results show that β_x, β_y do not become infinite when ν_{x0}, ν_{y0} approach the stopband edge, unless ν_{x0}, ν_{y0} are near the half integer resonances $v_x = m/2$, or $v_y = n/2$, m and n being integers.
3. Results for the 2 solutions of the equations of motion in the stable region near a stopband edge and in the unstable region.
4. The above results hold also for small accelerators, where the exact equations of motion have to be used and the large accelerator approximation is not valid. For small accelerators, one needs the restriction that the perturbing field gradients do not shift the closed orbit.

5 REFERENCES

[1] G. Parzen, Linear orbit parameters for the exact equations of motion, BNL Report, BNL–60090 (1994).

[2] G. Parzen, Particle motion in the stable region near the edge of a linear half–integer resonance, BNL report, BNL–62036 (1995).

[3] D. Edwards and L. Teng, Parameterization of linear coupled motion in periodic systems, Proc. 1973 IEEE PAC, p. 885 (1973).

[4] P.A. Sturrock, Static and dynamic electron optics, Cambridge Univ. Press, London (1955).

[5] R. Hagedom, Stability and amplitude ranges of two–dimensional non–linear oscillations with a periodic hamiltonian, CERN 57-1 (1957).

[6] A. Schoch, Theory of linear and non-linear perturbations of betatron oscillations in an alternating gradient synchrotron, CERN 57-21 (1957).

[7] E.D. Courant and H.S. Snyder, Theory of the alternating gradient synchrotron, Ann, Phys. 3, 1 (1958).

[8] A.A. Kolomensky and A.N. Lebedev, Theory of cyclic accelerators, North Holland Publishing Co. (1966).

[9] G. Ripken, Untersuchugen zur Strahlführung und Stabsilitat der Teilchen bewegung, DESY R1-7014 (1970).

[10] W.P. Lysenko, Nonlinear betatron oscillations, Particle Accelerators 5, 1 (1973).

[11] G. Guignard, The general theory of all sum and difference resonances in three–dimensional magnetic field in a synchrotron, CERN 76-06 (1976).

[12] G. Guignard, A general treatment of resonances in accelerators, CERN 78-11 (1978).

[13] H. Wiedenmann, Particle Accelerator Physics II, Springer–Verlag, New York (1995).

[14] G. Parzen, Particle motion in the stable region near the edge of a linear sum resonance, BNL Report, BNL-62456 (1995).

THE LINEAR PARAMETERS AND THE DECOUPLING MATRIX FOR LINEARLY COUPLED MOTION IN 6 DIMENSIONAL PHASE SPACE

G. Parzen*, Brookhaven National Laboratory, Upton, NY 11973 USA

Abstract

It will be shown that starting from a coordinate system where the 6 phase space coordinates are linearly coupled, one can go to a new coordinate system, where the motion is uncoupled, by means of a linear transformation. The original coupled coordinates and the new uncoupled coordinates are related by a 6×6 matrix, R. It will be shown that of the 36 elements of the 6×6 decoupling matrix R, only 12 elements are independent. A set of equations is given from which the 12 elements of R can be computed from the one period transfer matrix. This set of equations also allows the linear parameters, the β_i, α_i, $i = 1, 3$, for the uncoupled coordinates, to be computed from the one period transfer matrix.

1 THE DECOUPLING MATRIX, R

The particle coordinates are assumed to be x, p_x, y, p_y, z, p_z. The particle is acted upon by periodic fields that couple the 6 coordinates. The linearized equations of motion are assumed to be

$$\begin{aligned} \frac{dx}{ds} &= A(s)x \\ x &= \begin{bmatrix} x \\ p_x \\ y \\ p_y \\ z \\ p_z \end{bmatrix}, \end{aligned} \tag{1-1}$$

where the 6×6 matrix $A(s)$ is assumed to be periodic in s with the period L. Note that the symbol x is used to indicate both the column vector x and the first element of this column vector. The meaning of x should be clear from the context. The 6×6 transfer matrix $\mathrm{T}(s, s_0)$ obeys

$$\begin{aligned} x(s) &= \mathrm{T}(s, s_0)x(s_0) \\ \frac{d\mathrm{T}}{ds} &= A(s)\mathrm{T} \end{aligned} \tag{1-2}$$

It is assumed that the motion is symplectic so that

$$\mathrm{T}\overline{\mathrm{T}} = I, \quad \overline{\mathrm{T}} = \tilde{\mathrm{S}}\tilde{\mathrm{T}}\,\mathrm{S} \tag{1-3}$$

where I is the 6×6 identity matrix, $\tilde{\mathrm{T}}$ is the transpose of T and the 6×6 matrix S is given by

$$\mathrm{S} = \begin{bmatrix} 0 & 1 & 0 & 0 & 0 & 0 \\ -1 & 0 & 0 & 0 & 0 & 0 \\ 0 & 0 & 0 & 1 & 0 & 0 \\ 0 & 0 & -1 & 0 & 0 & 0 \\ 0 & 0 & 0 & 0 & 0 & 1 \\ 0 & 0 & 0 & 0 & -1 & 0 \end{bmatrix} \tag{1-4}$$

The 6×6 transfer matrix $\mathrm{T}(s, s_0)$ has 36 elements. However, the number of independent elements is smaller because of the symplectic conditions given by Eq. (2-3). There are 15 symplectic conditions or $(k^2 - k)/2$ where $k = 6$. The transfer matrix T then has 21 independent elements.

One can also introduce the one period transfer matrix $\hat{\mathrm{T}}(s)$ defined by

$$\hat{\mathrm{T}}(s) = \mathrm{T}(s + L, s) \tag{1-5}$$

$\hat{\mathrm{T}}(s)$ is also symplectic and has 21 independent elements.

One now goes to a new coordinate system where the particle motion is not coupled. The coordinates in the uncoupled coordinate system will be labeled u, p_u, v, p_v, w, p_w. It is assumed that the original coupled coordinate system and the new uncoupled coordinate system are related by a 6×6 matrix $R(s)$

$$\begin{aligned} x &= R\,u \\ u &= \begin{bmatrix} u \\ p_u \\ v \\ p_v \\ w \\ p_w \end{bmatrix} \end{aligned} \tag{1-6}$$

$R(s)$ will be called the decoupling matrix.

One can introduce a 6×6 transfer matrix for the uncoupled coordinates called $P(s, s_0)$ such that

$$u(s) = P(s, s_0)u \tag{1-7}$$

and one finds that

$$P(s, s_0) = R^{-1}(s)\mathrm{T}(s, s_0)R(s_0) \tag{1-8}$$

one can also introduce the one period transfer matrix $\hat{P}(s)$ defined by

$$\begin{aligned} \hat{P}(s) &= P(s + L, s) \\ \hat{P}(s) &= R^{-1}(s + L)\hat{\mathrm{T}}(s)R(s) \end{aligned} \tag{1-9}$$

* Work performed under the auspices of the U.S. Department of Energy.

The decoupling matrix is defined as the 6×6 matrix that diagonalize $\hat{P}(s)$, which means here that when the 6×6 matrix $\hat{P}$ is written in terms of 2×2 matrices it has the form

$$\hat{P} = \begin{bmatrix} \hat{P}_{11} & 0 & 0 \\ 0 & \hat{P}_{22} & 0 \\ 0 & 0 & \hat{P}_{33} \end{bmatrix} \tag{1-10}$$

where $\hat{P}_{ij}$ are 2×2 matrices. $\hat{P}$ will be called a diagonal matrix in the sense of Eq. (1-10).

The definition given so far of the decoupling matrix R, will be seen to not uniquely define R and one can add the two conditions on R that it is a symplectic matrix and it is a periodic matrix. The justification for the above is given by the solution found for $R(s)$ below.

Because $\mathrm{T}(s, s_0)$ and $R(s)$ are symplectic, it follows that $P(s, s_0)$ and $\hat{P}(s)$ are symplectic. Eq. (1-8) can be rewritten as

$$\begin{aligned} P(s, s_0) &= \overline{R}(s)\, \mathrm{T}(s, s_0)\, R(s_0) \\ \hat{P}(s) &= \overline{R}(s)\, \hat{\mathrm{T}}(s)\, R(s) \end{aligned} \tag{1-11}$$

It also follows that the 2×2 matrices has 3 independent elements as $|\hat{P}_{11}| = |\hat{P}_{22}| = |\hat{P}_{33}| = 1$. Eq. (1-12) can be written as

$$\hat{\mathrm{T}}(s) = R(s)\, \hat{P}(s)\, \overline{R}(s) \tag{1-12}$$

Eq. (1-12) shows that R has 12 independent elements, as $\hat{\mathrm{T}}$ has 21 independent elements and $\hat{P}$ has 9 independent elements. As R has only 12 independent elements, one can suggest that R has the form, when written in terms of 2×2 matrices,

$$R = \begin{bmatrix} q_1 I & R_{12} & R_{13} \\ R_{21} & q_2 I & R_{23} \\ R_{31} & R_{32} & q_3 I \end{bmatrix} \tag{1-13}$$

where q_1, q_2, q_3 are scalar quantities, the R_{ij} are 2×2 matrices and I is the 2×2 identity matrix. The matrix in Eq. (1-13) appears to have 27 independent elements. However, R is symplectic and has to obey the 15 symplectic conditions, and this reduces the number of independent elements to 12. The justification for assuming this form of R, given by Eq. (1-13), will be provided below where a solution for R will be found assuming this form for R.

Using Eq. (1-13) for R and the symplectic conditions, one can, in principle, solve Eq. (1-12) for R and $\hat{P}$ in terms of the one period matrix $\hat{\mathrm{T}}$. This was done by Edwards and Teng[1] for motion in 4-dimensional phase space where $\hat{\mathrm{T}}$ has 10 independent elements, R has 4 independent elements and $\hat{P}$ has 6 independent elements. An analytical solution of Eq. (1-12) for the 6-dimensional case was not found. However, a different procedure for finding $\hat{P}$ and R will be given by finding the eigenvectors of $\hat{P}$, using the eigenvectors of the one period matrix, $\hat{\mathrm{T}}$.

The 2×2 matrices P_{11}. P_{22}, P_{33} which make up $\hat{P}$ each have 3 independent elements and can be written in the form

$$\begin{aligned} \hat{P}_{11} &= \begin{bmatrix} \cos\psi_1 + \alpha_1 \sin\psi_1 & \beta_1 \sin\psi_1 \\ -1/\gamma_1 \sin\psi_1 & \cos\psi_1 - \alpha_1 \sin\psi_1 \end{bmatrix} \\ \gamma_1 &= (1 + \alpha_1^2)/\beta_1 \end{aligned} \tag{1-14}$$

with similar expressions for $\hat{P}_{22}$ and $\hat{P}_{33}$ Eq. (1-14) and the similar expressions for $\hat{P}_{22}$, $\hat{P}_{33}$ can be used to define the three beta functions β_1, β_2 and β_3.

2 THE LINEAR PARAMETERS β, α, AND ψ AND THE EIGENVECTORS OF THE TRANSFER MATRIX

In this section, the eigenvectors of the one period transfer matrix, $\hat{P}$, will be found and expressed in terms of the linear periodic parameters β, α and ψ. These will be used below to compute the linear parameters from the one period transfer matrix $\hat{\mathrm{T}}$. They will also be used to find the three emittance invariants ϵ_1, ϵ_2 and ϵ_3 and to express them in terms of the linear parameters β_i, α_i, $i = 1, 3$.

The uncoupled transfer matrix obeys

$$\begin{aligned} \frac{d}{ds} &= P(s, s_0) = B(s)\, P(s, s_0) \\ B &= \overline{R}\, A\, R + \frac{d\overline{R}}{ds} \end{aligned} \tag{2-1}$$

This follows from Eq. (1-2) and Eq. (1-11).

One sees from Eq. (2-1) that $B(s)$ is a periodic matrix, $B(s+L) = B(s)$. It can also be shown that B is a periodic, diagonal matrix similar to $\hat{P}$. See [6] for details.

As the 2×2 matrix B_{11} is periodic, one can show[2] that the eigenvector of the transfer matrix for $\overline{u}$ is

$$\begin{aligned} \overline{u}_1 &= \begin{bmatrix} \beta_1^{1/2} \\ \beta_1^{1/2}(-\alpha_1 + i) \end{bmatrix} \exp(i\psi_1) \\ \tilde{\overline{u}}_1^{*}\, S\, u_1 &= 2i \end{aligned} \tag{2-2}$$

with the eigenvalue $\lambda_1 = \exp(i\mu_1)$. $\beta_1(s)$, $\alpha_1(s)$ are periodic functions and the phase function $\psi_1 = \mu_1 s/L + g_1(s)$ where $g_1(s)$ is periodic.

One can now write down the eigenvectors of the $\hat{P}$ matrix using Eq. (2-2). These eigenvectors will be called $u_1, u_2, u_3, u_4, u_5, u_6$, each of which is a 6×1 column vector with the eigenvalues $\lambda_1 = \exp(i\mu_1)$, $\lambda_3 = \exp(i\mu_2)$, $\lambda_5 = \exp(i\mu_3)$, $\lambda_2 = \lambda_1^*$, $\lambda_4 = \lambda_3^*$ and $\lambda_6 = \lambda_5^*$.

3 COMPUTING THE LINEAR PARAMETERS β, α, ψ FROM THE TRANSFER MATRIX

An important problem in tracking studies is how to compute the linear parameters, β, α, ψ, defined in section 3, from the one period transfer matrix. The one period transfer matrix can be found by multiplying the transfer matrices of each of the elements in a period. A procedure is given below for computing the linear parameters, which also computes the decoupling matrix R from the one period transfer matrix.

The first step in this procedure is to compute the eigenvectors and their corresponding eigenvalues for the one period transfer matrix $\hat{\mathrm{T}}$. This can be done using one of the standard routines available for finding the eigenvectors of a real matrix. $\hat{\mathrm{T}}$ is assumed to be known. In this case,

there are 6 eigenvectors indicated by the 6 column vectors x_1, x_2, x_3, x_4, x_5 and x_6. Because $\hat{T}$ is a real 6×6 matrix, $x_2 = x_1^*$, $x_4 = x_3^*$, $x_6 = x_5^*$. The corresponding eigenvalue for x_1 is $\lambda_1 = \exp(i\mu_1)$ and the eigenvalue for x_2 is $\lambda_1^* = \exp(i\mu_1)$. In a similar way, λ_2, λ_2^* are the eigenvalues for x_3 and x_4, and λ_3, λ_3^* are the eigenvalues for x_5 and x_6. One can show that (see [6] for details).

$$\begin{aligned} \psi_1 &= ph(x_1) \\ 1/\beta_1 &= Im(p_{x1}/x_1) \\ \alpha_1 &= -\beta_1 Re(p_{x1}/x_1) \end{aligned} \tag{3-1}$$

where Im and Re stand for the imaginary and real part, and ph indicates the phase.

Using Eq. (3-1), one can find the linear parameters β_1, α_1, and ψ_1 from the eigenvector x_1 of $\hat{T}$. A procedure can be given for computing the entire R matrix. See [6] for details.

4 THE THREE EMITTANCE INVARIANTS

Three emittance invariants will be found for linear coupled motion in 6-dimensional phase space. Expressions will be found for these invariants in terms of β_i, α_i. A simple and direct way to find the emittance invariants is to use the definition of emittance suggested by A. Piwinski[4] for 4-dimensional motion. This is given by

$$\epsilon_1 = |\,\tilde{x}_1 \;\; S\,x|^2 \tag{4-1}$$

x is a 6×1 column vector representing the coordinates x, p_x, y, p_y, z, p_z. x_1 is a 6×1 column vector which is an eigenvector of the one period transfer matrix $\hat{T}$. x_1 is assumed to be normalized so that

$$\tilde{x}_1^* \;\; S\,x_1 = 2i \tag{4-2}$$

One first notes that ϵ_1 given by Eq. (4-1) is an invariant since $\tilde{x}_1 \;\; S\,x$ is a Lagrange invariant as x_1 and x are both solutions of the equations of motion. Eq. (3-1) then represents an invariant which is a quadratic form in x, p_x, y, p_y, z, p_z. This result can be expressed in terms of the linear parameters β_1, α_1 by evaluating ϵ_1 in the coordinate system of the uncoupled coordinates. Since the uncoupled coordinates, represented by the column vector u, is related to x by the symplectic matrix R,

$$\epsilon_1 = |\tilde{u}_1 \; S\,u|^2 \tag{4-3}$$

u_1 is an eigenvector of the one period matrix $\hat{P}$, and one sees that because of Eq. (1-11),

$$x_1 = R\,u_1 \tag{4-4}$$

one can now use the result for u, given by Eq. (2-5) and find that

$$\begin{aligned} \epsilon_1 &= \frac{1}{\beta_1}\left[(\beta_1 p_u + \alpha_1 u)^2 + u^2\right] \\ \epsilon_1 &= \gamma_1 u^2 + 2\alpha_1 u p_u + \beta_1 p_u^2 \\ \gamma_1 &= (1+\alpha_1)^2/\beta_1 \end{aligned} \tag{4-5}$$

5 REFERENCES

[1] D.A. Edwards and L.C. Teng, Parameterization of Linear Coupled Motion, Proc. IEEE PAC73, p. 885, 1973.

[2] G. Parzen, Linear Orbit Parameters for the Exact Equations of Motion, BNL Report AD/RHIC-124, BNL-60090, 1993.

[3] G. Parzen, Emittance and Beam Size Distortion due to Linear Coupling, Proc. IEEE PAC93, p. 489, 1993.

[4] A. Piwinski, Intra-Beam Scattering in the Presence of Linear Coupling, DESY Report, DESY 90-113 (1990).

[5] E.D. Courant and H.S. Snyder, Theory of the Alternating Gradient Synchrotron, Annals of Physics 3, p. 1 (1958).

[6] G. Parzen, The Linear Parameters and the Decoupling Matrix for Linearly Coupled Motion in 6 Dimensions, BNL Report BNL-61522 (1995).

DYNAMIC APERTURE OF THE STORAGE RING VEPP-2M IN ROUND BEAM MODE.

I.A. Koop, A.P. Lysenko, I.N. Nesterenko, Yu.M. Shatunov, A.A. Valishev,
Budker Institute of Nuclear Physics, 11 Lavrentyev av.,630090 Novosibirsk, Russia

Abstract

This paper describes dynamic aperture limitation of VEPP-2M in round beam operation due to chromaticity correction sextupoles and a way of lattice optimisation. First order canonical perturbation theory is used to estimate influence of sextupoles on dynamic aperture. The estimates are compared with tracking results.

1 INTRODUCTION

Electron-positron collider VEPP-2M is a machine operating in the energy range $2E$ from 0.36 to 1.38 GeV. Its reconstruction to the round beam operation mode is in progress to test the round beam concept experimentally [1].

The existing and proposed beam and optics parameters are summarized in the Table 1.

VEPP-2M: BEAM AND OPTICS PARAMETERS			
Parameters		**flat beam**	**round beam**
Circumference, m	C	17.88	17.88
RF frequence, MHz	f_0	200	200
Momentum compaction	α	0.167	0.206
Emittances, cm · rad	ε_x	$1.1 \cdot 10^{-5}$	$1.7 \cdot 10^{-5}$
	ε_z	$1.3 \cdot 10^{-7}$	$1.7 \cdot 10^{-5}$
Energy loss/turn, keV	ΔE_0	4.9	5.0
Dimensionless	δ_x	$3. \cdot 10^{-6}$	$3.7 \cdot 10^{-6}$
damping	δ_z	$4.8 \cdot 10^{-6}$	$3.7 \cdot 10^{-6}$
decrements	δ_s	$1.1 \cdot 10^{-5}$	$1.2 \cdot 10^{-5}$
Energy spread	σ_ε	$3.6 \cdot 10^{-4}$	$3.6 \cdot 10^{-4}$
β_x at IP, cm	β_x	45	5.0
β_z at IP, cm	β_z	4.5	5.0
Betatron tunes	ν_x, ν_z	3.05,3.1	3.1,3.1
Particles/bunch	e^-, e^+	$2 \cdot 10^{10}$	$6.7 \cdot 10^{10}$
Tune shifts	ξ_x, ξ_z	0.02,0.05	0.1,0.1
Luminosity, $cm^{-2} \cdot s^{-1}$	L_{max}	$\sim 5 \cdot 10^{30}$	$\sim 1 \cdot 10^{32}$

Table 1: Comparative parameters of VEPP-2M beams for existing flat beams option ("wiggler-on") and round beams option. (Energy 510 MeV)

Because of significant changes in the machine lattice and increase of natural chromaticity, the chromaticity correction scheme has to be seriously reviewed.

2 VEPP-2M LATTICE PROPERTIES

The present magnetic lattice of VEPP-2M has four mirror-symmetric periods with low β^*−functions in interaction regions (IR), which are provided by two quadrupole doublets. Chromaticity correction is performed by 16 sextupoles of two families Sx and Sz situated near the corresponding quadrupoles (the dispersion is non-zero in the IRs). Due to symmetry and betatron phase advance between members of one family close to π, this scheme is well-compensated and the dynamic aperture is determined by other reasons.

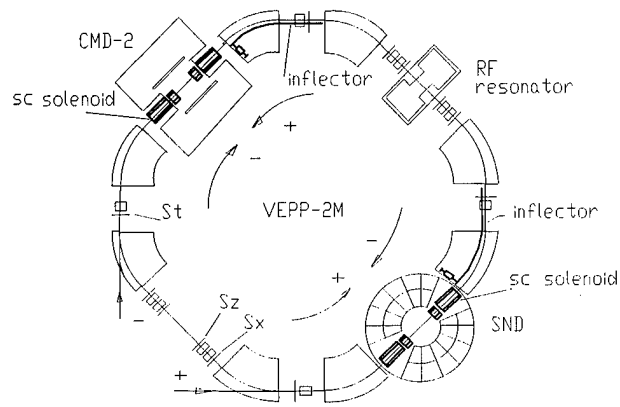

Figure 1: VEPP-2M modification for the round beam mode.

The main idea of VEPP-2M lattice modification to round beam mode is to replace the quadrupole doublets in the IRs by SC solenoids accomodated inside the detectors (fig. 1). As far as the dispersion is now zero over the IR, the compensation of the betatron tune chromaticities is possible only in the arcs. Unfortunately, the remaining there eight sextupoles can not compensate relatively high natural chromaticity ($\gamma\frac{\partial\nu_x}{\partial\gamma} = \gamma\frac{\partial\nu_z}{\partial\gamma} = -13$) without significantly reducing dynamic aperture.

The way out was found in installing one additional "compensating" sextupole family St.

3 NONLINEAR RESONANCES

The design operating point for the round beam mode is $\nu_x = \nu_z = 3.1$. Thus, the nearest sextupole resonances are:

$3 \cdot \nu_x = 10$	$\nu_x = 3$
$3 \cdot \nu_x = 9$	$2 \cdot \nu_z - \nu_x = 3$
$2 \cdot \nu_z + \nu_x = 9$	$2 \cdot \nu_z + \nu_x = 10$

Each resonance amplitude is defined by the relevant harmonic of the Hamiltonian [2]:

$$H(J, \psi, \theta) = \sum h_{m_x, m_z, n}(J) \cdot e^{i(m_x\psi_x + m_z\psi_z + n\theta)}$$

0-7803-4376-X/98 /$10.00 © 1998 IEEE

Here J is the action variable, ψ is the betatron phase, $\theta = s/R_0$; R_0 is the gross radius. For sextupoles:

$$h_{3,0,n} = J_x^{3/2} \cdot \left[\frac{R_0^2}{24 \cdot B\rho} \cdot \oint \frac{ds}{2\pi} S \beta_x^{3/2} e^{i(3\chi_x + n\theta)} \right]$$

$$h_{1,0,n} = J_x^{1/2} J_z \cdot \left[\frac{3R_0^2}{24 \cdot B\rho} \cdot \oint \frac{ds}{2\pi} S (\beta_x^{3/2} - 2\beta_x^{1/2}\beta_z) e^{i(\chi_x + n\theta)} \right]$$

$$h_{1,\pm 2,n} = J_x^{1/2} J_z \cdot \left[\frac{3R_0^2}{24 \cdot B\rho} \cdot \oint \frac{ds}{2\pi} S \beta_x^{1/2} \beta_z e^{i(\chi_x \pm 2\chi_z + n\theta)} \right]$$

Where $S = \partial^2 B_z / \partial x^2$ is the sextupole gradient, $\chi_{x,z}(s) = \int ds/\beta_{x,z} - \nu_{x,z} s$. Now we can apply the first order canonical perturbation theory [3]. If we consider *one* isolated sextupole resonance, for example $\nu_x = 3$ (detuning $\epsilon = \nu_x - 3$), with the amplitude h, the averaged Hamiltonian in the variables J and slow phase $\Phi = \psi_x - 3\theta$ is:

$$H = \epsilon \frac{R_0}{2} J_x + h J_x^{3/2} cos(\Phi)$$

The dynamic aperture limitation is given by the Hamiltonian stationary points:

$$\frac{\partial H}{\partial \Phi} = 0 \qquad \frac{\partial H}{\partial J_x} = 0$$

From these equations we obtain $J_{th} = \frac{4}{9}(\frac{R_0}{2}\frac{\epsilon}{|h|})^2$. And $X_{max} = \sqrt{J_{th}\beta}$ is the limit of the stable motion. One easily sees that the lower is $|h|$, the higher is X_{max}. In fact, the reality is much more complicated, as all the rest harmonics are not zero. But in our case this simplification is applicable because this resonance prevails (see table 2). Of course we should take into account unharmonicity of the ring ($\frac{\partial \nu}{\partial a^2}$).

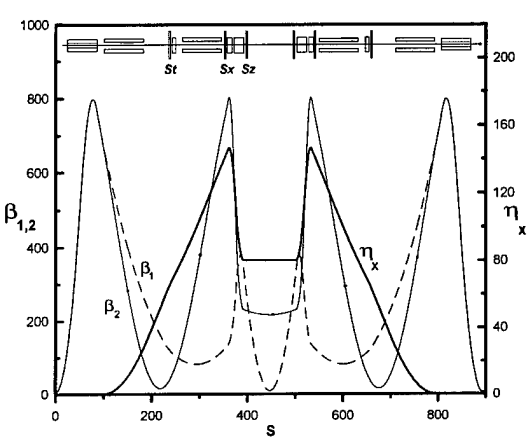

Figure 2: Lattice functions of modified VEPP-2M (Half of period).

4 LATTICE OPTIMISATION

As it has been already mentioned, we needed an additional sextupole family to improve the lattice properties. Position for this family was chosen in accordance with the lattice functions and available place in the existing ring.

A good place was found in the "technical" drift (fig. 2), where dispersion is non-zero, and the β – functions vary strongly enough ($\beta_1/\beta_2 = 5.7$).

The sextupole strengths were optimised to obtain the lowest Hamiltonian harmonics. Total unharmonicity of the ring is negative if we take into account sextupoles and non-linear edges of quadrupoles and solenoids (fig 3).

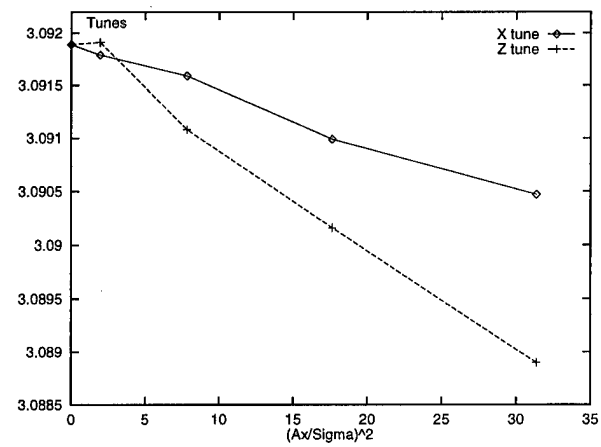

Figure 3: Betatron tunes versus amplitude.

Thus, the most attention was paid to the harmonic $h_{1,0,3}$. Table 2 shows comparison of different resonances amplitudes for two and three sextupole families.

	Sx,Sz	Sx,Sz,St
$3\nu_x = 10$	24.8	10.1
$\nu_x = 3$	201.5	151.7
$3\nu_x = 9$	45.5	9.5
$2\nu_z - \nu_x = 3$	52.1	39.0
$2\nu_z + \nu_x = 9$	56.3	20.1
$2\nu_z + \nu_x = 10$	114.2	62.7

Table 2: Resonance amplitudes (relative units).

The final parameters of the chromaticity correction sextupoles are:

Family	Length (m)	$\frac{\partial^2 B_z}{\partial x^2}$ (T/m^2)
Sx	0.0395	205
Sz	0.0505	-456
St	0.09	-835

Table 3: Sextupole parameters

5 RESULTS

Application of the third chromaticity correction family has strongly reduced all the sextupole harmonics. After optimisation, the dynamic aperture was calculated by tracking a particle through the lattice with averaging over the initial betatron phase. As the tracking has shown, the dynamic aperture increased from 7.8σ with two families to 14.5σ with three, which is considered to be satisfactory for the machine operation. The calculated dynamic aperture shape is shown in fig. 4.

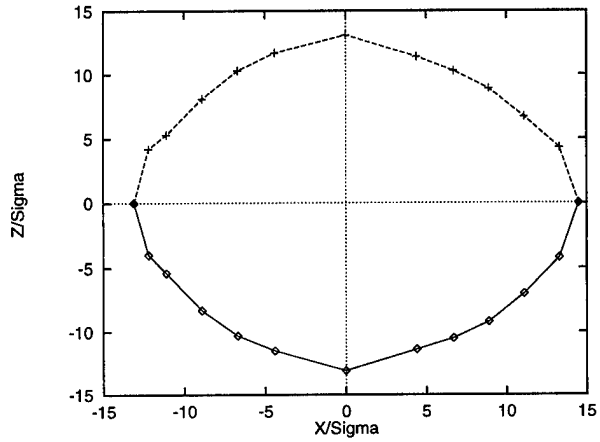

Figure 4: Dynamic aperture (tracking data).

6 ACKNOWLEDGEMENTS

The authors wish to thank E.A. Perevedentsev for enlightening discussions and help in compiling this text.

7 REFERENCES

[1] A.N.Filippov et al.: 'Proc. of the 15th Int. Conf. High Energy Acc.', Hamburg (1992), p.1145

[2] N.S.Dikansky and D.V.Pestrikov: 'The physics of intense beams and storage rings.' New York: American Inst. of Physics, (1994)

[3] G.Guignard: 'Chromaticity: nonlinear aberrations.', in Proc. of CERN Acc. School, Oxford (1985), p.91

TRACKING STUDIES FOR THE LHC OPTICS VERSION 4 AT INJECTION ENERGY

M. Böge and F. Schmidt, CERN

Abstract

Extensive Tracking Studies have been performed for a realistic model of the LHC at the injection energy of 450 GeV. The underlying model contains all static multipole magnet errors and linear imperfections. The imperfect machines are corrected using control room techniques. The paper gives estimates for the dynamic aperture (Dyn.Aper.) for 60 different realizations of errors for the versions 4. To get a better picture of the dynamics the emittance ratios are varied to sample a large fraction of the phase space. Phase space averaged apertures are compared with averages over different imperfect machines for selected emittance ratios. Lastly it is checked if the reduced systematic a_4 and b_4 multipolar components of the main bending magnets remain an important aperture limitation.

1 INTRODUCTION

During the long injection period of about 15 minutes that is needed to fill the LHC with 2835 bunches per beam the particles have to survive in guiding and focusing fields with large high order multipolar errors. These errors result from the magnets which are superconducting and without field shaping material in order to reach the highest possible fields. Besides the geometric part there are large persistent current contributions. The latter are important at injection energy in particular because the ratio between top and injection energy is large ($\approx$ 15.5). The same reason makes it difficult to built a power supply system that achieves, at injection level, a current ripple of a few ppm only. Moreover, the fact that the magnets are produced by different suppliers introduce additional uncertainties in the error components around the machine.

All these effects have to be considered to arrive at a meaningful estimate for the Dyn.Aper. . For this purpose a multiple processor system with shared memory architecture [1] has been acquired recently which has the fastest floating point performance below the supercomputer level. The tracking programs [2, 3] have been optimized with considerable effort. Nevertheless, the system is still far from being able to track a large hadron collider like the LHC in real time. In fact only 1% of the total injection time can be covered by systematic numerical studies assuming an acceptable response time. This paper therefore attempts to give an estimate of the Dyn.Aper. for the full injection period using an extrapolation technique based on a recently discovered relation between the phase space averaged Dyn.Aper. and the number of turns [8].

2 TRACKING PREREQUISITES

Each node of the mentioned multiple processor system allows to track one particle once around the LHC lattice including all errors in about 1.4 ms. The total throughput of the 10 processors is therefore roughly 7,000 per second and $600 \cdot 10^6$ turns day. Even though these numbers seem to be large at first sight, they are not large when compared to the actual computational needs:

- To cover the injection time some 10^7 turns have to be tracked.
- The Dyn.Aper. has to be found in the full six–dimensional phase space.
- 60 representations of the random errors (seeds) have to be tracked for each case to find a lower bound of the Dyn.Aper. . This lower bound does exclude an even lower Dyn.Aper. with a 95% probability [5].

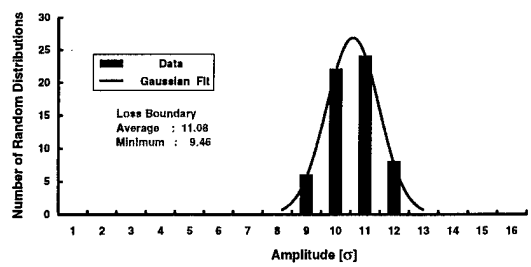

Figure 1: *Histogram of Dyn.Aper. (60 seeds) for the nominal LHC lattice including a Gaussian fit*

- Many cases have to be studied to obtain a good understanding of what causes the reduction of the Dyn.Aper. and to test if there are cures to improve it.

3 EXPLORATION OF PARAMETER SPACE

Owing to the above reasoning it is necessary to find ways to sample only a fraction of the large parameter space while still obtaining the essential information about the Dyn.Aper. . This is done in the following fashion:

- The angular phase in a single tracking run is not varied. Instead as many tracking data as possible are kept to reconstruct the sampling of the phase space in subsequent post–processing runs.
- Both transverse amplitudes are varied while keeping the ratio between the emittances constant. In most cases a ratio equal to one has been used called the "45° case". K=$atan\sqrt{e_{II}/e_I}$ can be varied between 0° to

0-7803-4376-X/98 /$10.00 © 1998 IEEE

90°, with e_I and e_{II} the emittances of mode I and II respectively. Figure 2 shows how the Dyn.Aper. depends on this emittance ratio.

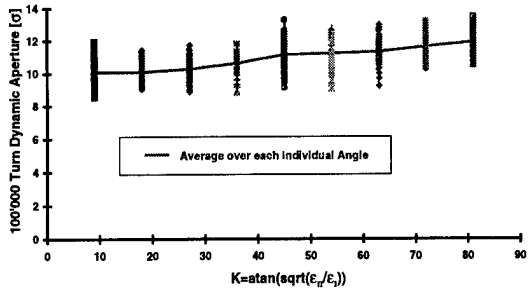

Figure 2: *Dyn.Aper. versus emittance ratio*

- In the longitudinal plane the relative momentum is fixed to a deviation of 0.00075 which is 75% of the bucket half size. This is sufficiently close to the bunch edge and at the same time avoids the vicinity of the separatrix with its very special properties. Moreover in Ref. [6] it has been found for LHC version 4.1 that the Dyn.Aper. tends to decrease weakly towards larger relative momentum deviations.

- The Dyn.Aper. is determined in in the following way: in a first step a rough estimate of the Dyn.Aper. is found. In a second step the amplitude is varied from well below up to this rough border in very fine amplitude steps. This allows to pick up small nests in the amplitude range where particles have short survival times. To this end 30 pairs of particles per beam sigma are used and in most cases a total of 300 particles are tracked. In fact it is observed that this fine amplitude scan guarantees an error of about –0.5%. Spreading the 30 pairs over 3σ can easily result in an overestimation of the Dyn.Aper. by 2σ.

Therefore the simulation time needed for one single case with 60 seeds, 300 particles, 5 emittance ratios and tracked for just 10^5 turns requires two full weeks of the cpu–time and 100% availability of the computer system. Of course not all cases can be studied in such depth. One possible shortcut is to gain a factor of 5 by tracking the 45° case only and applying a correction factor for the emittance ratio variation which has been derived from a thorough systematic study.

4 REDUCTION FACTORS

This correction is part of a sequence of reduction factors that are applied to arrive at an estimate for the 10^7 turn Dyn.Aper.. In detail, the following steps are considered:

- Traditionally the Dyn.Aper. has been stated as a function of initial amplitude. Of course it is much better to use the average amplitude, obtained via postprocessing, to avoid local deviations due to phase space distortions. In the LHC case it leads to a variation of the Dyn.Aper. between +4% and -5%. To be safe a correction factor of 0.95 is applied.

- a 5% reduction to cover the error introduced by the finite step size of the amplitude has to be taken into account.

- The above mentioned correction factor for the variation of emittance ratios is about 0.97.

- To cover the effect of the linear imperfections a reduction factor of 0.93 is used (see below).

- The inverse logarithmic conjecture [8] has been thoroughly checked for the LHC. This study is documented in a separate contribution to this conference [9]. Here the conjecture is used to derive the Dyn.Aper. at 10^7 turns from the tracking data obtained at up to 10^5 turns. The reduction factor turns out to be about 0.93. It goes without saying that the conjecture has been checked for several cases at 10^6 turns. 3 runs have even been extended to 10^7 turns.

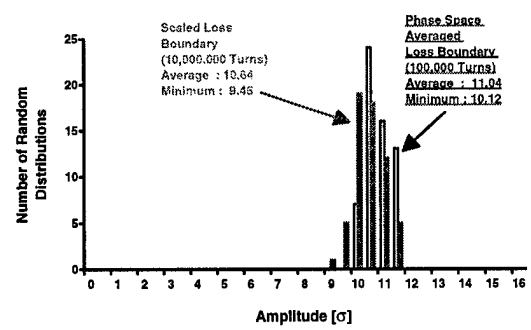

Figure 3: *Scaling of the loss bound histogram from* 10^5 *to* 10^7 *turns*

- Besides the magnetic errors it is equally important to consider the power supply ripple which tends to make particle motion weakly chaotic in large fractions of the phase space. The performed preliminary studies together with the experimental experience [4] suggest a reduction factor of about 0.93.

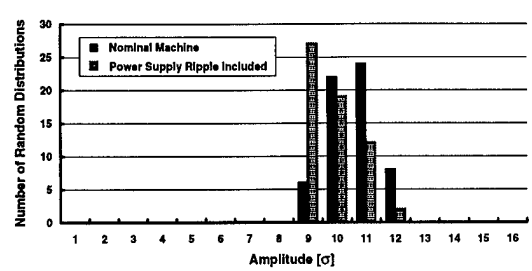

Figure 4: *Effect of ripple on Dyn.Aper.*

- Lastly a reduction factor of 0.8 is applied for all unknown effects. This seems to be adequately pessimistic when comparing tracking results with experiments at various existing machines [4].

A linear addition of these effects, which is of course a pessimistic assumption, reduces the Dyn.Aper. at 10^7 turns to about 56% of the 10^5 turns Dyn.Aper..

It should be noted that this may not even be sufficient as not all all known effects are included up to now like tolerances of the magnetic errors and all the dynamic effects which are most important at the beginning of the ramp. These will be evaluated in the near future and added to the above list.

5 TRACKING RESULTS

The histogram in Figure 1 visualises the loss boundaries (10^5 turns, 45° case) of 60 different seeds for the nominal LHC lattice and its Gaussian fit which is consistent with the distribution. The minimum and the average value is determined to be 9.5σ and 11σ respectively.

For the same number of machine realizations a scan has been performed in order to find the dependence of the Dyn.Aper. on the emittance ratio (see Figure 2). The average value for the individual ratios increases monotonically with the emittance ratio. This feature remains to be explained. It should be noted that the 45° case coincides with the arithmetic average value of the angular distribution as well as with the phase space average within 2%. Although this agreement cannot be generalised it can be used as a justification for the strategy to track the 45° case and to check the dependence on the angle for selected cases only.

This scan shows that in order to get a realistic lower bound of the Dyn.Aper. a further reduced of 3% has to be applied.

The scaling of the Dyn.Aper. to 10^7 turns using phase space averaged data from 100 to 10^5 turns lowers the average of the distribution by 4% and the minimum by 7% (see Figure 3).

It is well known that power supply ripple in conjunction with nonlinearities lead to a reduction of the Dyn.Aper. [4]. Lacking a proper electrical model of the LHC transmission line the SPS tune modulation spectrum has been used and scaled to the LHC case. With tune modulation switched on the loss boundary distribution becomes asymmetric with its peak shifted towards lower amplitude values (Figure 4). The average and minimum value is reduced by 7% and 1% respectively.

In the presence of linear imperfections the average Dyn.Aper. is reduced by 4% and the minimum by 7%. In

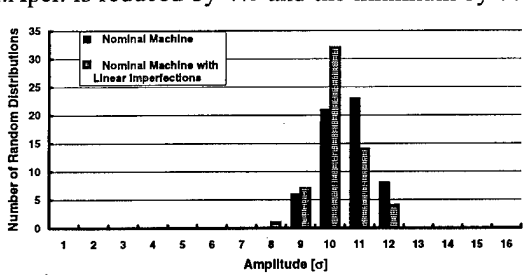

Figure 5: *Effect of linear imperfections on the Dyn.Aper.*

Ref. [7] it has been demonstrated that a correction of the large octupolar components leads to significant increase of the Dyn.Aper . In response to this study the estimates for the b_4 and a_4 have been revised and it was found possible to lower them by a factor of 3 and 2 respectively. As expected these reduced errors lead to a loss boundary distribution halfway between the two extreme cases as seen in Figure 6. It remains to be investigated if a correction of the residual octupoles is still needed.

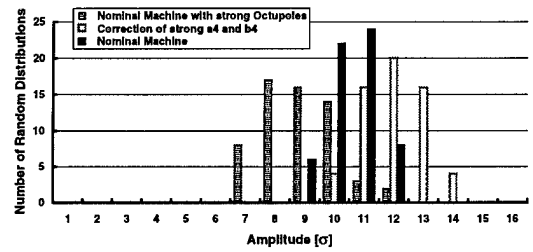

Figure 6: *Histograms of Dyn.Aper. for cases with large octupolar components, large but corrected and reduced values respectively*

6 CONCLUSIONS

An extensive study of the Dyn.Aper. of the LHC version 4 at injection energy has been performed. The Dyn.Aper. is found to be roughly 9.5σ for the nominal LHC lattice including realistic errors. Various potential influences on the Dyn.Aper. have been addressed in detail: transverse emittance ratio, uncorrected multipolar components b_4, a_4, linear imperfections and power supply ripple. The dedicated multiprocessor system allows to do systematic studies of about 1% of the LHC injection period. In addition, the available pre– and postprocessing tools can handle the simultaneous variation of several tracking parameters.

To estimate the Dyn.Aper. at 10^7 turns a sequence of reduction factors have been applied to the data obtained at 10^5 turns. Taking into account all known effects and using an estimate for the unknowns the actual Dyn.Aper. is expected to be about a factor of two smaller with respect to the tracking results.

7 ACKNOWLEDGEMENTS

We would like to thank E. McIntosh from the CERN computer division for his enthusiastic support in all hard– and software aspects of our studies.

8 REFERENCES

[1] E. McIntosh et al. , LHC95 workshop, Montreux, 1995.
[2] F. Schmidt, CERN SL/94–56 (AP).
[3] H. Grote and F.C. Iselin, CERN SL 90–13 (AP) (Rev. 4).
[4] W. Fischer et al. , Phys. Rev. E Vol. 55.
[5] H. Grote, private communication.
[6] F. Schmidt, LHC Project Note 30.
[7] M. Böge et al. ,LHC Project Report 31.
[8] M. Giovannozzi et al. , LHC Project Report 45.
[9] M. Böge et al. , these proceedings.

ESTIMATES FOR LONG–TERM STABILITY FOR THE LHC

M. Böge and F. Schmidt *, CERN

Abstract

Since about 10 years survival plots have been used to evaluate single–particle long–term stability. In a recent paper (M. Giovannozzi et al.) this concept has been reviewed, using a dynamic aperture (Dyn.Aper.) definition based on the average over different ratios of emittances. It has been shown that the survival times evaluated according to this procedure decay with the inverse of the logarithm of the number of turns in several different systems. In this paper the validity of this conjecture is tested in the case of the latest LHC lattice which has been studied extensively.

The inverse log conjecture also predicts a non–zero Dyn.Aper. at infinite times called D_∞. The tracking data are analysed for LHC lattice to determine the relation between D_∞ and the onset of chaos determined through Lyapunov exponents. Two different methods to automate the prediction of the Lyapunov exponent are tested and are compared with D_∞.

1 INTRODUCTION

In Ref. [1] (see also Ref. [2]) it has been shown that for several dynamical systems the evolution of the Dyn.Aper. $D(N)$ as a functions of turn number N is well described by the following equation here called the *Inverse Log Conjecture*:

$$D(N) = D_\infty \left(1 + \frac{b}{log_{10}(N)}\right). \qquad (1)$$

The D_∞ can be interpreted as the Dyn.Aper. after an infinite number of turns while the b appears to be a measure of the range of amplitude where particle loss will take place, e.g. a value $b = 3$ means that after 1'000 turns the Dyn.Aper. is still a factor of two larger than D_∞. For this relation to work a precondition is to average the Dyn.Aper. over the four dimensional phase space as described in Ref. [3]:

$$D(N) = \left(\int_0^{\pi/2} [D_\alpha(N)]^4 \sin(2\alpha) d\alpha\right)^{1/4}, \qquad (2)$$

where α is related to emittance ratio ϵ_{II}/ϵ_I by:

$$\alpha = atan\sqrt{\epsilon_{II}/\epsilon_I}, \qquad (3)$$

e.g. ($\alpha = 45°$) corresponds to a emittance ratio of ($\epsilon_{II}/\epsilon_I = 1$). As the tracking for the LHC is usually done in the full six dimensional phase space one could argue that an average over the six dimensions is needed. This is not done for the following reasons: firstly the nonlinear coupling between longitudinal and transverse planes is small which allows the separate treatment of the longitudinal plane, secondly for the LHC tracking the initial conditions in the longitudinal phase space are not varied but fixed to one set of pessimistic and therefore large values and lastly the tracking effort would have to be increased by another factor of ten. One aim of this report is to check the conjecture for the LHC version 4 which has been extensively studied (see Ref.[4]). Another aim is the understanding of the relation between D_∞ and the onset of chaos.

* *This research was supported in part by the National Science Foundation under Grant No. PHY94-07194.*

2 FITTING TECHNIQUE

One can rewrite Eq. 1 as follows:

$$D(N) \cdot \log_{10}(N) = D_\infty \cdot \log_{10}(N) + D_\infty \cdot b, \qquad (4)$$

where $\log_{10}(N)$ is treated as an independent variable. Thus D_∞ denotes the slope and $D_\infty \cdot b$ the offset of a linear function which describes $D(N) \cdot \log_{10}(N)$. A linear regression yields both quantities with a certain error Δ. The error of $D(N)$ is calculated to be:

$$\Delta(D(N)) = \Delta(D_\infty) + \Delta(D_\infty \cdot b)\frac{1}{log_{10}(N)} \qquad (5)$$

It should be noted that the multiplication of $D(N)$ with $\log_{10}(N)$ in Eq. 4 puts a stronger weight on loss boundaries at larger turn numbers N where they are most relevant.

3 CONJECTURE TEST

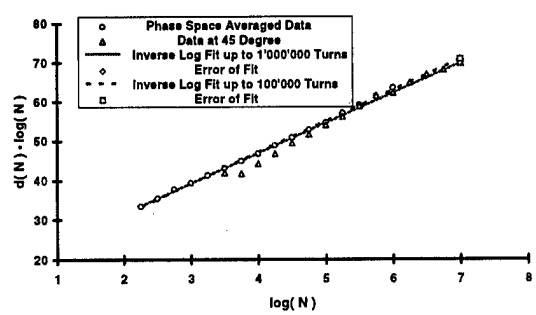

Figure 1: *Fits of Eq. 4 from* 10^2 *to* 10^5 *and* 10^6 *as well as the extrapolation to* 10^7 *turns for one realization of the imperfect LHC*

Figure 1 summarises the tracking data and the fitting result for one realization of the imperfect LHC: the tracking has been performed for 17 emittance ratios up to 10^6 turns. For the emittance ratio of one ($\alpha = 45°$) the tracking has been prolonged to 10^7 turns. A linear regression fit according to Eq. 4 is performed up to 10^5 and 10^6 turns. The fits

are extrapolated to 10^7 turns and quoted with their errors. The data for $\alpha = 45°$ which deviate from the phase space averaged data at small turn numbers are consistent with both fits beyond 10^6 turns within their errors. Moreover, reducing the number of angles to 9 changes the predicted D_∞ by a mere 1.1%. A bit worrying is the fact that the fit-

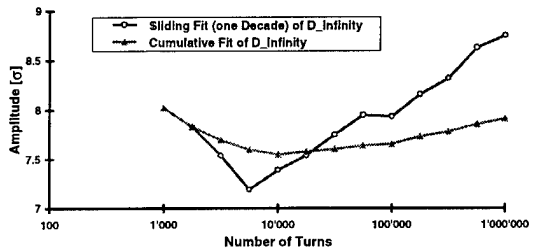

Figure 2: *D_∞ determined from a cumulative fit and a sliding fit*

ted D_∞ is increasing by 3%. Figure 2 shows that this is due to the fact that the sliding fit of D_∞ is increasing monotonically after a few thousand of turns, i.e. the Dyn.Aper. decreases less rapidly than the linear fit does imply. Applying the conjecture fit to 60 machine representations (Figure 3) reveals a small anti correlation between D_∞ and b which could mean that the linear relation of Eq. 4 is based on a too simple assumption. On the other hand the figure also

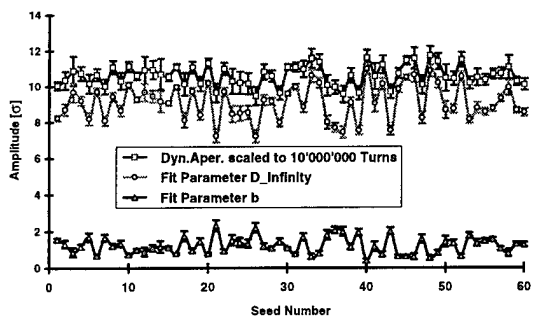

Figure 3: *Scaled Dyn.Aper. and the conjecture fit parameters D_∞ and b*

shows that the fit constants and the Dyn.Aper. scaled from 10^5 to 10^6, using the inverse log conjecture, have small errors. Even though the fit parameters may not have a clear physical meaning the two parameter fit may still be useful to extrapolate the Dyn.Aper. to larger turn numbers. To check this assumption emittance ratio scans have been extended up to 10^6 turns for 5 different seeds (see Figure 4). The fit involving data up to 10^5 turns and the tracking data for 10^6 turns agree within the error bars of the extrapolation.

4 CHAOS AND D_∞

Since many years the chaotic boundary has been used to estimate the long–term Dyn.Aper. (see Ref. [5]). D_∞ determined from the conjecture fit should agree with the onset of chaos because both quantities describe the stability

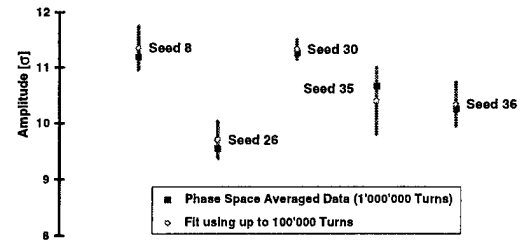

Figure 4: *Comparison of tracked and scaled Dyn.Aper.*

boundary in phase space. Agreement of the two independent methods would give D_∞ a physical meaning at least in a heuristic manner. It is well known that there cannot be a rigorous non–zero loss boundary over infinite number of turns in a system with more than two degrees of freedom due to the loss of particles in the Arnold web (see Ref.[6]). However tracking studies for various systems have clearly shown that there always seems to be a hard core of stability in the amplitude space which is equivalent to a non–zero D_∞. Two models have been tested: the four dimen-

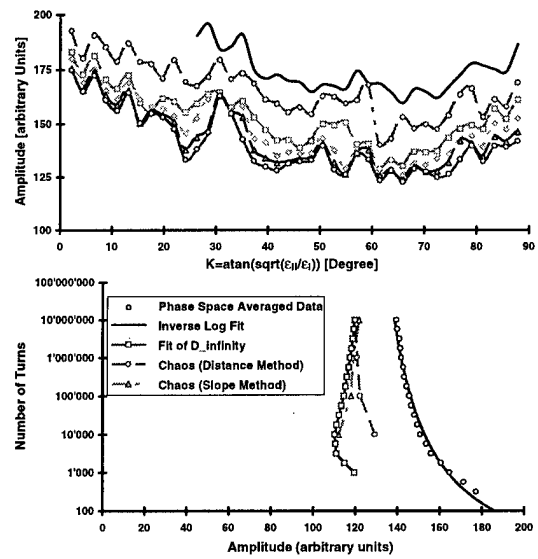

Figure 5: *The Hénon model* – **Top:** *Stable amplitude versus emittance ratio between 10^2 and 10^7 turns,* **Bottom:** *Survival plot, conjecture fit and chaos boundary*

sional Hénon model and the LHC case for which the conjecture fit is shown in Figure 1. Due to its simplicity the first model can be tracked for a large number of angles and turn numbers (40 and 10^7 respectively) while the LHC can be tracked for only 17 angles and 10^6 turns. The LHC study has required two weeks of CPU time of a powerful 10 processor workstation cluster [7]. The **Top** part of figure 5 and 6 depict the Dyn.Aper. versus emittance ratio, a curve is shown for each decade of turn numbers. It should be noted however that the tunes of the latter have been carefully chosen [8] (Q_x=0.168, Q_z=0.201) to obtain a sizeable chaotic regime while for the LHC the tunes (Q_x=63.28, Q_z=63.31) are placed where the Dyn.Aper. is expected to be at its optimum value. For the phase space

averaged Dyn.Aper. the conjecture fit agrees well with the tracking data in both cases (see **Bottom** part of Figure 5 and 6). Chaos is detected by tracing the path of two initially close–by particles. This method is preferred over the original one introduced by Benettin et al. [9] as in this context the most sensitive measure is more relevant than the precise knowledge of the Lyapunov exponent. Owing to the fact

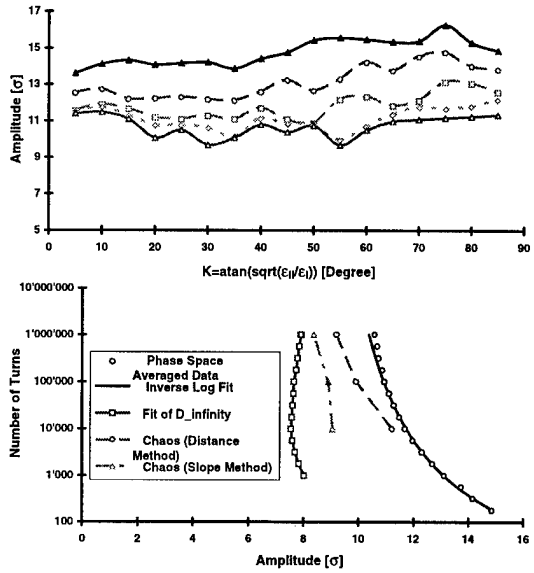

Figure 6: *The LHC* – **Top:** *Stable amplitude versus emittance ratio between* 10^2 *and* 10^6 *turns,* **Bottom:** *Survival plot, conjecture fit and chaos boundary*

that the automatic detection of the onset of chaos is much more difficult than the reliable but time consuming inspection by eye a new approach has been attempted. Two different values can be automatically extracted from the tracking data: the first method uses a threshold of the distance in phase space which is larger than the final separation of any two regular (initially close–by) particles at the end of the tracking, the second method calls motion chaotic once the slope, calculated from the evolution of the distance in phase space in a double logarithmic scale, is outside a certain interval of slope values (for regular motion the slope is one). In the following these techniques are called the **distance** and the **slope** method respectively. The distance method is certainly safe due to its definition. However, it is an optimistic estimate because weakly chaotic particles may not have enough time to separate beyond the chosen threshold. The slope method is less precisely defined: it may be also optimistic in the case where the motion is so weakly chaotic, that the slope is not affected, but it may be pessimistic because it can pick up large oscillations of particles which are close to some resonance but nevertheless regular. The slope method is preferable because it is more consistent with the inspection by eye. It should be mentioned that both methods can be improved by using frequency analysis [10] which allows to eliminate most of the regular oscillations of the evolution of the distance in phase space. In the case of the Hénon model the slope method is pessimistic and very close to the D_∞ fit. From the above discussion it is not surprising that D_∞ itself varies widely as a function of turns. As expected the distance method is optimistic at low turn numbers. At 10^7 turns, however, all three curves converge to almost the same point. It should be noted that this behavior has been reproduced at two other tune working points (Q_x=0.201, Q_z=0.168 and Q_x=0.201, Q_z=0.112). For the LHC the distance and the slope method are both optimistic. Also in this case the latter agrees quite well with D_∞ at large turn numbers. It is clear from these dependencies that the motion of particles in the LHC case reveals very weak chaotic behavior over a large range of amplitudes.

In both models the fit of D_∞ appears to be pessimistic in an intermediate turn number regime. In fact, in all studied LHC cases D_∞ is a too pessimistic estimate of long–term stability.

5 CONCLUSION

The inverse log conjecture has been thoroughly tested for the LHC version 4. Although doubts remain about the physical meaning of D_∞ and b the fit can be used to extrapolate the Dyn.Aper. from 10^5 to 10^6 turns. There are indications that this extrapolation can be further extended to 10^7 turns. The chaos and D_∞ border seem to converge for large turn numbers for both the Hénon and the LHC model.

6 ACKNOWLEDGEMENTS

7 ACKNOWLEDGEMENTS

We would like to thank E. Todesco for discussing the conjecture fit for the Hénon model with one of the authors at the Santa Barbara workshop.

8 REFERENCES

[1] M. Giovannozzi et al., CERN LHC Project Report **45** (1996); M. Giovannozzi et al., Beam Dynamics Newsletter **12** (1996).

[2] M. Giovannozzi et al., these proceedings.

[3] E. Todesco and M. Giovannozzi, Phys. Rev. E **53**, (1996) 4067.

[4] M. Böge and F. Schmidt, these proceedings.

[5] F. Schmidt et al., Part. Accel. **35**, pp. 249–256 (1991).

[6] B.V. Chirikov, Physics Reports **52**, pp. 263–379, (1979).

[7] E. McIntosh et al., LHC95 workshop, Part. Accel. **54** (1995).

[8] E. Todesco, private communication.

[9] Benettin et al., Phys. Rev. A **14**, (1976) 2338.

[10] R. Bartolini and F. Schmidt, LHC Project Report **98**.

A MORE ROBUST AND FLEXIBLE LATTICE FOR LHC

A. Faus-Golfe, H. Grote, J.-P. Koutchouk, T. Risselada, A. Verdier, S. Weisz,
CERN, Geneva, Switzerland

Abstract

To correct more efficiently the arc dispersion , the exact antisymmetry of the LHC optics is now broken, except in the low-β triplets common to the two rings. A new quadrupole is added between the experimental insertions and the dispersion suppressors and several arc quadrupoles are complemented by a small trim quadrupole. The larger number of parameters gives flexibility to the lattice and allows a partial separation of the optical functions, with a decrease of the total number of quadrupole units. It is possible to change rather freely the phase advances of the arc cells. The nominal tunes are split by 4 units to reduce coupling. The β^* tuning range in the experimental low-β is significantly increased, allowing e.g. a larger beam separation at injection. The super-periodicity of LHC remains 1. We plan to study whether it can be increased within the LHC hardware constraints.

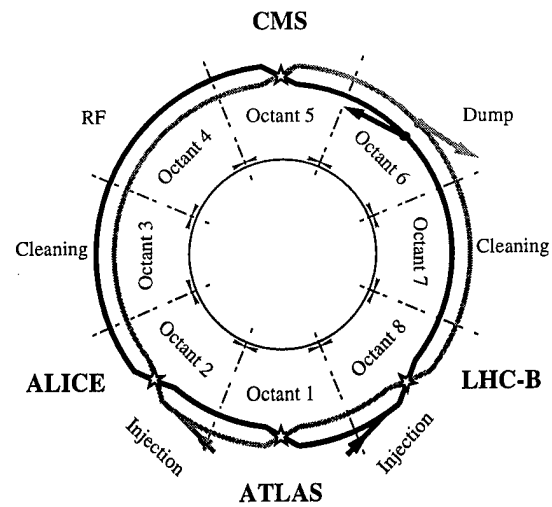

Figure 1: layout of LHC

1 INTRODUCTION

The common low-β triplet in the LHC insertions is naturally antisymmetric for the two counter-rotating beams. An antisymmetric excitation of the two triplets on either side of the interaction point (IP) allows the same sequence of magnetic fields to be experienced by the two beams along their respective paths. This elegant principle had been extended to the whole rings, leading to a simplified design [1] of LHC by reducing drastically the number of parameters.

However in order to cope with a possibly large systematic skew quadrupolar imperfection, the betatron tunes must be split by several units [3]. This requires to break the exact antisymmetry. A second motivation arises from the requirements of robustness and flexibility: the dispersion function cannot be antisymmetric in a plane ring; its suppression by an antisymmetric scheme caused optical distortions and a lack of robustness [2]. In the new version 5 of the LHC optics, the antisymmetry, although underlying, is not imposed, opening a larger parameter space and requiring new methods.

2 THE LHC ARCS

The LHC is composed of 8 arcs separated by 8 insertions. Each arc is made of 23 standard FODO cells. The horizontal and vertical cell betatron phase advances are close to 90° $\pm$ 2° yielding a tune split of 2 units in the arcs. Enough gradient is available to split the tunes by up to 8 units, which is optimal for the compensation of systematic resonances in each arc. However the nominal phase advance is purposely chosen close to 90° to avoid a significant dephasing between the sextupoles of the same family (45° at most) in the 4 family scheme required in collision.

3 DISPERSION SUPPRESSION

The aim of the dispersion suppressors (D.S.) is four-fold:

- guide the LHC beam in the LEP tunnel,
- cancel the dispersion arising in the arc,
- cancel the dispersion arising in the separation/recombination dipoles D1/D2,
- cancel the dispersion caused by the horizontal crossing angle at the IP.

The LHC straight-sections have a limited adaptability: their phases are constrained (collimation sections);the space is restricted (long decay of the large β-function) and the number of parameters is small. The D.S. therefore has to act as an optical buffer, allowing an independent tuning of the arc cells and of the insertions. However economy favours the use of standard arc dipoles and quadrupoles in series with the arc which increases further the difficulty.

The LEP dispersion suppressor, which defines the geometry of the tunnel, is made of 3.5 cells with a 90° phase advance, optimized to suppress the dispersion. With the 2.5-longer LHC dipoles and quadrupoles, only two LHC cells can be fitted in the D.S. tunnel. It is still possible to follow accurately the LEP tunnel (Figure 2) but the dispersion is only reduced by a factor of 2. Quadrupoles have to be used to cancel it. Due to the approximate antisymmetry, on one side of the IP, only one of the 5 D.S. quadrupoles is both focusing and efficient (at a place where the dispersion is large). It is thus necessary to complement the D.S. sec-

0-7803-4376-X/98 /$10.00 © 1998 IEEE

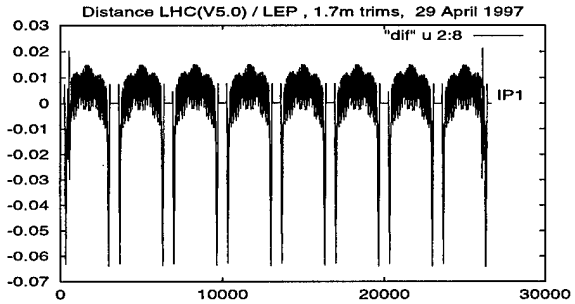

Figure 2: Transverse distance between LHC and LEP in m.

tion proper by the first quadrupole of the arc, thereby using 2.5 cells for the D.S.. In this way, the dispersion can be suppressed but the horizontal optics can hardly be changed due to a lack of parameters. Some additional trim quadrupoles are foreseen in the arc to recover a flexibility however limited by the physical aperture of the arc elements. On the other side of the IP, the D.S, with two efficient focusing quadrupoles, is tuned differently and is more flexible. In spite of the mentioned limitations, the new D.S. is robust. It allows a large adaptability of the arc and, combined to the straight-section, a reasonable flexibility of the insertions.

4 EXPERIMENTAL INSERTIONS

The counter-rotating beams cross at four non-equidistant locations around the LHC circumference (Figure 1). Two of the experimental insertions are designed to provide the highest luminosities while the two others are combined with the beam injection systems. All these insertions are built along the same principle (Figure 3):

- the low-β triplets, optimal for round beams, are common to the two rings. The quadrupole lengths and positions are optimized to power each triplet in series, with a gradient independent of β^*, allowing to tune each ring independently.
- the combination/separation dipoles D1 and D2 bring the two beams into collision and back into their respective rings.
- the matching section, increased to 4 two-in-one quadrupoles allows an extended tuning range of β^* from more than 12 to 0.5 m and beyond.

4.1 High Luminosity Insertions

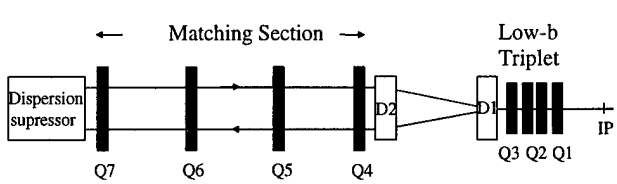

Figure 3: Lay-out of the experimental insertions

The large forward flux of particles produced at the IP's requires to use warm dipoles for D1. This fixes the distance between D1 and D2 and constrains the space available for the matching quadrupoles. In the injection optics, a β^* of 12 m (or even 20 m if required), maximizes the acceptance of the low-β triplet, allowing a large beam separation. The collision β^* of 0.5m is obtained with an adjustment of the normalized gradients of the four matching quadrupoles only. The total phase advances of the insertions can be varied at constant β^*, a criterion of robustness. The number of parameters is however not sufficient to fix the phase advances from the IP to the arc. It is small enough not to decrease the efficiency of the 4-family sextupole scheme.

4.2 Combined Injection/Experimental Insertions

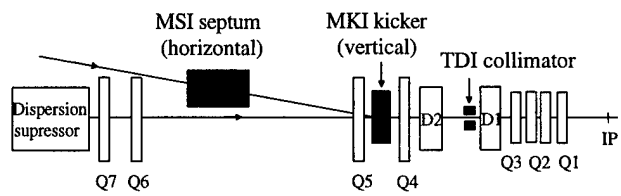

Figure 4: lay-out of the injection

In LHC version 5, the incoming beam is bent horizontally by the septum magnet (MSI) and kicked vertically (MKI) onto its orbit (Figure 4). The absorber (TDI) has to protect the machine and experiments in case of misfiring. This requires the vertical phase advance from MKI to TDI to exceed 70° [5]. This condition can be satisfied if the Q4 quadrupole is defocusing; Q5 then enhances the efficiency of the kicker magnet. The polarity of the machine is thus defined. To maximize the drift space for injection elements, D1 and D2 are super-conducting which is allowed by the lower luminosity of these insertions. In Point 8, which hosts a single arm spectrometer, the collision point is displaced longitudinally by 11.25 m to best explot the existing LEP cavern. The matching section allows continuous tuning of β^* from 250 m to 12 m and from 20 m to 0.5 m as requested by the experiments. The robustness is equivalent to that of the experimental insertion except at injection where no flexibility is left.

5 SERVICE INSERTIONS

Cleaning Insertions: The size of the secondary halo after passing the betatron collimators at 6σ and 7σ is decreased to 8.5 σ by increasing the modulation of $\mu_y - \mu_x$ in the insertion. A separate study [4] shows that this result is optimum.

RF and Instrumentation: Point 4 is dedicated to RF and instrumentation. The dispersion vanishes in the RF cavities. In the absence of other constraints, it is the most flexible of the LHC insertions: the phase can be varied by $\pm 0.2 * 2\pi$ and β^* from 19m to 1000m.

Dump: The dump insertion is essentially identical to the

former design [1] with a septum common to the two rings and quadrupoles of enlarged aperture.

6 GLOBAL PARAMETERS

The D.S.'s provide naturally a tune split of 2 units. The betatron tunes are adjusted with the arcs to 63.28/59.31 at injection, and 63.31/59.32 in collision. With 2 sextupole families, the non-linear chromatic aberration in collision (Figure 5) would be too large [6] for chromaticity measurement or a further reduction of β^*. The LHC will have 4 families of sextupole.

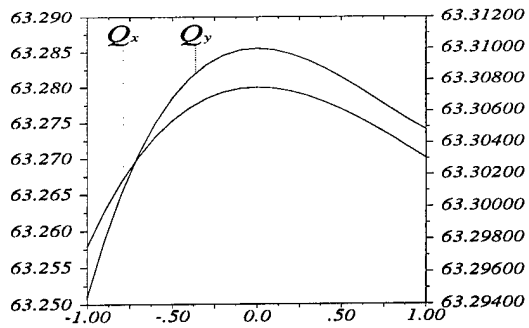

Figure 5: Tune versus relative momentum over ±0.001

7 CORRECTION SYSTEMS

Closed Orbit: An x/y beam position monitor and a dipole corrector are foreseen at each quadrupole.

Tune-shifts: the two LHC rings share the focusing and defocusing quadrupole circuits. To adjust each ring separately 8 small quadrupoles connected in 2 families are placed at both extremities of each arc. The maximum tune shift is limited by optical aberrations to ±0.5. This is sufficient to compensate for different focusing errors in the two rings and to explore the tune space between the integer and half-integer resonances. Larger tune shifts are of course possible in the two rings simultaneously.

Chromaticity: the chromaticity arising from the quadrupoles is corrected by sextupoles placed close to the arc quadrupoles. As the optics flexibility is insufficient to control the phase advance between IP's, four families of sextupoles are needed.

Dipole Field Harmonics b_3 and b_5: The persistent currents in the dipoles cause a chromaticity of some 500 units expected to vary by 30% during injection and snap-back. This effect is corrected by sextupolar spool-pieces in the dipole ends.The decapole, detrimental to the dynamic aperture, is corrected in the same way.

Betatron Coupling: 16 skew quadrupole pairs (at $\pi/2$) correct the coupling arising in the arc from the a_2 in the dipoles. A few skew quadrupoles placed at 90° in $(\mu_x - \mu_y)$ in the insertions form a second family.

Landau Damping: 144 short octupoles in the arc, powered in F and D circuits, damp the dipole and higher-order coherent transverse modes at 7 TeV [7]. At injection energy, instabilities are suppressed by feedback and the direct space-charge tune spread.

8 FLEXIBILITY

The optics flexibility necessary to produce tune shifts or tune splits by at least 4 units is now part of the nominal design. Experience with other colliders (ISR, LEP) shows that optics changes over the machine lifetime go much beyond what is required by tune shifts/splits. Care must be taken that the lenses located in the arcs and the D.S.'s but used to correct or adapt the insertions can face possibly changing requirements in the insertions.

We use the adaptability of the betatron phase as an index of flexibility. The present achievement is about ±0.2 (in tune units) in the experimental and RF insertions. This is sufficient to cope with small displacements of quadrupoles and with the equalization of the betatron phase advance between the two high luminosity collision points. Reaching a higher symmetry in phase advance or controlling the phase advance between the IP and the arcs seems presently both out of reach and not justified. The additional quadrupole added in the matching sections of the experimental insertions provides the flexibility mentioned above. The RF insertion is less constrained and was designed with this goal in mind. The other insertions however still show very little flexibility and work is continuing to improve them. The arc cell itself is already constrained by the 4 family sextupole scheme and the optimization of the dynamic aperture at injection. The sextupole scheme in the arc is able to cope with a reduction of β^* by a factor of 2.

9 CONCLUSION

The optics of LHC, while retaining the main options of its former versions, has been profoundly reworked to allow robustness and minimal provisions for flexibility. While the main goal, a large split between the betatron tunes, was satisfied, more stringent requirements have emerged: the protection of the low-β quadrupoles against mis-injected beams and the effect of the long-range beam-beam interaction on the dynamic aperture at injection. In both cases, the implemented flexibility allowed to face the requirements. Further studies are necessary to attempt providing some more flexibility in the strongly constrained insertions such as the collimation and dump insertions by reconsidering the flexibility of the focusing in the dispersion suppressors.

10 REFERENCES

[1] *LHC Conceptual Design* (CERN/AC/95-05(LHC), 1995)

[2] A. Faus-Golfe *et al.*, paper MOP030L,EPAC96, 1996.

[3] J.P. Koutchouk, paper MOP029L,EPAC96, 1996.

[4] D. Kalchev, this conference.

[5] J. B. Jeanneret, LHC Project Note 40, 1996.

[6] F. Schmidt, LHC Project Note 38, 1996.

[7] J. Gareyte *et al.*, LHC Project report 91Rev, 1997.

INVERSE LOGARITHM DECAY OF LONG-TERM DYNAMIC APERTURE IN HADRON COLLIDERS*

M. Giovannozzi†, INFN, Sezione di Bologna, Italy
W. Scandale, CERN, Geneva CH 1211
E. Todesco, Dipartimento di Fisica Università di Bologna, Italy

Abstract

The long-term behaviour of the non-linear single-particle dynamics is considered for the 4D Hènon map. The dynamic aperture is defined as the average of the particle loss boundary over several ratios of emittances. Using this definition, survival plots turn out to decay with the inverse of the logarithm of the number of turns. We also compare the extrapolation of the dynamic aperture with the prediction of the maximal Lyapunov exponent.

1 INTRODUCTION

Modern hadron colliders based on superconducting magnets suffer from the unavoidable effect of field-shape distortions, particularly harmful during the injection plateau. This critical period can last a large number of turns making difficult to evaluate the single-particle stability with computer simulations. In the case of the CERN Large Hadron Collider [1], the injection process will last for 10^7 turns. On the other hand, numerical simulations based on symplectic tracking can hardly reach $10^5 - 10^6$ turns, also in consideration of the fact that a dense sampling of the phase space is crucial to obtain significant results. Three main approaches have been proposed in the past to speed-up the investigations on beam stability: the determination of the onset of chaotic behaviour using the maximal Lyapunov exponent [2, 3], the evaluation of the drift in the space of approximated invariants carefully evaluated through numerical methods [4], and the visualization of the dynamic aperture reduction with increasing number of turns through survival plots [5, 6, 7].

In this paper, we investigate the survival plots of the 4D Hènon map, with extended numerical methods.

The Hènon map [8] represents a simplified model of 4D betatronic motion where the coupling with longitudinal dynamics and the modulation of the linear frequencies are neglected. Using this map, we investigate the dynamics with numerical simulations and we propose phenomenological scenarios to interpret the results. We recall a way to define the dynamic aperture [9] and we compute it as a function of the number of turns N. The result can be interpolated with a three-parameter formula, justified in terms of the Nekhoroshev and KAM theorems. The interpolation fits very well with the numerical data and agrees with the prediction of the onset of chaos provided by the Lyapunov exponent. Our results can be extended to a more realistic accelerator model, describing 6D motion including the ripple effect [10, 11].

2 ANALYSIS OF THE PHASE SPACE

We consider a grid of initial conditions on the plane (x, y), with $p_x = p_y = 0$ and we track the orbit for a large number of turns. From the tracking results, we evaluate the number of turns N up to which the particle is stable and the two nonlinear frequencies (ν_x, ν_y) of the motion. The frequencies are computed using an interpolation of the FFT plus Hanning filter [12]. For regular trajectories the frequencies are well defined with precision of the order of $1/N^4$ [12]. For chaotic orbits instead the frequencies are not defined and the algorithm provides values that vary along the discrete time N, and that do not converge for $N \to \infty$.

The results are presented in various forms.

Long-term plot: each initial condition (x, y) is plotted using a different marker according to the number of turns N at which particle loss occurs.

Network of resonances: only the initial conditions (x, y) locked on resonances are drawn: they satisfy

$$q\nu_1 + p\nu_2 = l + \epsilon \qquad q, p, l \in \mathbf{Z} \tag{1}$$

We use the value $\epsilon = 10^{-4}$. This plot directly displays the size of resonances, their position in phase space, and their relation with the dynamic aperture shown in the long-term plot.

Survival plot: the survival time N is shown as a function of D, the average value of the initial conditions stable for N turns.

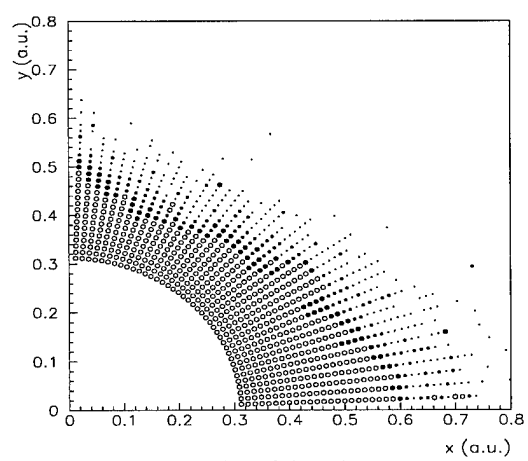

Figure 1: Long-term plot of the Hènon map at $\nu_x = 0.168$, $\nu_y = 0.201$: empty circles represent initial conditions stable up to 10^7 turns; full circles represent unstable initial conditions (smaller circles correspond to shorter stability times).

* Work partially supported by EC Human Capital and Mobility contract Nr. ERBCHRXCT940480.

† Present address: CERN PS Division

In Fig. 1 a dense long-term plot for the Hénon map with linear frequencies $\nu_x = 0.168$, $\nu_y = 0.201$ is shown. A rectangular grid of initial conditions is iterated for at most 10^7 turns. In the inner region all the particle are stable for at least 10^7 turns. There are no holes, at least at the resolution used of our grid scan. After that, one finds a rather irregular but sharp border of instability: outside the border, one has a chaotic sea of initial conditions that are lost between 10^6 and 10 turns.

In Fig. 2 the network of resonances for the same model of Fig. 1 is shown. One finds very large stable resonances; moreover, the mechanism of particle loss due to the diffusion along the resonant channels or due to resonance crossing does not seem to be very relevant. The bulk of long-term losses occurs in the wide chaotic band where no resonance structures are visible. This chaotic band is characterized by isolated points locked on low order resonances, that appear in the figure as a set of scattered dots. The same mechanism of loss has been observed for other values of the betatron frequencies and for other models, as a 4D model of the LHC [3].

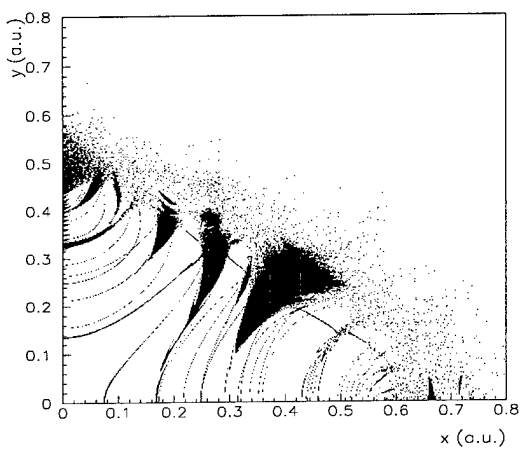

Figure 2: Network of resonances of the Hènon map at $\nu_x = 0.168$, $\nu_y = 0.201$: black dots represent initial conditions locked on resonances up to order 15.

From these results we conclude that there is a rather sharp border that separates stable from unstable initial conditions for the considered number of turns ($10^7 - 10^8$); long-term particle losses mainly occur in wide chaotic bands where all the integrable structure has been wiped out; the mechanism of diffusion along the resonant channels and due to resonance crossing are rather weak.

3 DYNAMIC APERTURE AND ASSOCIATED ERRORS

In a previous work [9] we defined the dynamic aperture as the average radius over the phase space area stable for N turns. Particles are started along a 2D polar grid in the coordinate space (x, y):

$$x = r\cos\theta \qquad y = r\sin\theta \tag{2}$$

with p_x p_y equal to zero. Let $r(\theta; N)$ be the last stable initial condition along θ before the first loss at a turn number lower than N occurs. The dynamic aperture is

$$D = \left(\int_0^{\pi/2} [r(\theta; N)]^4 \sin 2\theta d\theta\right)^{1/4}. \tag{3}$$

This definition differs from the usual one [6, 7], where, to speed up simulations, the scan is made only along the diagonal of the space (x, y).

When the definition (3) is implemented in a computer code, one has to carry out two discretizations: one over the radial variable r and one over the angular variable θ. Let $\Delta r = (r_{max} - r_{min})/N_r$ and $\Delta\theta = \pi/2N_\theta$ be the step size in r and θ respectively. The total error associated with the dynamic aperture estimate can be obtained using gaussian sum in quadrature

$$\Delta D = \sqrt{\left(\frac{\partial D}{\partial r}\frac{\Delta r}{2}\right)^2 + \left(\frac{\partial D}{\partial \theta}\frac{\Delta\theta}{2}\right)^2}. \tag{4}$$

To estimate the derivatives of D, we replace (3) with the simple average over θ

$$D = \frac{2}{\pi}\int_0^{\pi/2} r(\theta; N)d\theta \equiv < r(\theta; N) > . \tag{5}$$

Using this formula the associated error reads

$$\Delta D = \sqrt{\frac{(\Delta r)^2}{4} + < |\frac{\partial r}{\partial \theta}| >^2 \frac{(\Delta\theta)^2}{4}} \tag{6}$$

Therefore, to optimize the integration steps, Δr must be equal to $\Delta\theta$ times $< |\frac{\partial r}{\partial \theta}| >$.

4 PREDICTION BASED ON EXTRAPOLATION

In Fig. 3 we show $D(N)$ versus N for the same model of Fig. 1, carrying out simulations up to 10^8 turns. A very fine phase space scan (120 radial steps from 0.3 to 0.8 and 60 angular steps) has been used in order to obtain a very high accuracy (error of the order of 1%).

We interpolate the dynamic aperture with an inverse logarithmic law. Indeed, the phase space is divided into two regimes. An inner region where almost all the phase space is foliated into KAM tori, except a very small fraction where the Arnold diffusion can take place over the resonance web [14]. This region appears in simulations as a "full" domain of initial conditions stable for extremely high number of turns. Its average radius is called D_∞. An outer region where almost all the foliation of phase space in KAM tori has been destroyed, and only a wide chaotic sea is left. Since we are close to the last KAM torus, we assume that in this region the particles escape to infinity with the rate provided by the Nekhoroshev estimate [15]:

$$N(r) = N_0 \exp\left(\frac{r_*}{r}\right)^{1/\kappa}, \tag{7}$$

where $N(r)$ is the number of turns that are estimated to be stable for particles with initial amplitude smaller than r.

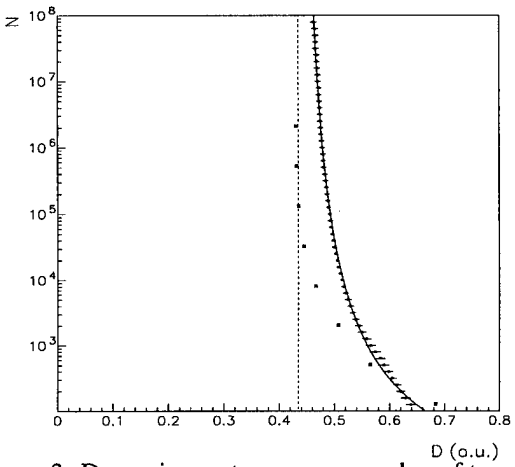

Figure 3: Dynamic aperture versus number of turns (dots) for the Hènon map at $\nu_x = 0.168$, $\nu_y = 0.201$; analytic interpolation (solid line) and extrapolation at infinity (dotted line). Prediction of the chaotic border according to the Lyapunov exponent (stars). The error bars are computed according to Eq. (6).

Using the information from KAM theorem (the existence of a positive D_∞) and from the Nekhoroshev theorem (the inverse log decaying of the dynamic aperture), one obtains the following equation

$$D(N) = D_\infty \left(1 + \frac{b}{\log^\kappa(N/N_0)}\right) \tag{8}$$

We tried to interpolate the data shown in Fig. 3 with this formula using three free parameters D_∞, b and the exponent κ. We fixed N_0 to one by using the heuristic argument that $D(1) = \infty$.The solution is found by minimizing the value of the χ^2 function, i.e.

$$\chi^2 = \frac{1}{J-3}\sum_{j=1}^{J}\frac{(D(N_j) - \hat{D}(N_j))^2}{\sigma_i} \tag{9}$$

where the interpolated dynamic aperture $\hat{D}(N_i)$ according to Eq. (8) is evaluated at the turn number N_i, and $\sqrt{\sigma_i}$ is the error estimated through Eq. (6). It turns out that it is rather difficult to determine the exponent with a high precision. For instance, if we consider all the exponents that provide a χ smaller than 0.7, that corresponds in our case to a confidence level of 95%, we obtain $\kappa \in [0.9, 2]$. The optimal exponent for our case turns out to be around 1.5. The interpolation is shown in Fig. 3 as a solid line, and agrees very well with tracking data. Indeed, a refined version of the Nekhoroshev theorem [16] leads to the estimate $\kappa = (1+d)/2$, where d is the number of degrees of freedom of the particle motion. In our case we have $\kappa = 1.5$. This is in agreement with our simulations, however the theoretical estimate of κ is still quite controversial. For instance in the older Ref. [17, 18] the expected value of κ for our case was estimated to be 3. Additional checks for higher dimensions would be highly desirable in order to cross-check the optimal estimate of the exponent with the validity of our scenario.

We have also computed the estimate of the chaotic border through the Lyapunov exponent, using the same type of definition for the dynamic aperture, where now $r(\theta)$ is the amplitude of the particle immediately before the first particle along θ whose Lyapunov exponenet is greater than an appropriate threshold as described in Ref.[3]. The results are shown in Fig. 3. The Lyapunov guess of the chaotic border seems to converge rather rapidly (when compared to tracking) to the value of D_∞.

Finally we evaluated the error on D_∞ by computing the interval of 95 % confidence level around the interpolating function (8), and we found $D_\infty = 0.4750 \pm 0.0018$. The error is so small mostly because of the large number of turns used in the survival plot and of the fine grid scan applied in the evaluation of $D(N)$.

5 ACKNOWLEDGEMENTS

We wish to thank Prof. Turchetti for relevant contributions to the analysis and to the interpretation of the tracking data. Special thanks to S. Bongini, M. Böge, J. Ellison, J. Irwin, F. Schmidt and B. Warnock, for constructive discussions.

6 REFERENCES

[1] The LHC Study Group, *CERN–LHC* **95-05** (1995).

[2] Schmidt, F., Willeke, F., and Zimmermann, F. , *Part. Accel.* **35** 249 (1991).

[3] Giovannozzi, M., Scandale, W., and Todesco, E., *Part. Accel.*, 65-4 (1997) p.165.

[4] Warnock, R. L., and Ruth, R. D., *Physica D* **56** 188 (1992).

[5] Chao, A., *AIP Conf. Proc.* **230** 203 (1990).

[6] Yan, Y. *SSC* **500** (1991).

[7] Galluccio, F., and Schmidt, F., *Third European Particle Accelerator Conference* Gif sur Yvette: Edition Frontiéres (1993) pp. 640–42.

[8] Hénon, M., and Heiles, C., *Astr. J.* **69-1** 73 (1964).

[9] Todesco, E., Giovannozzi M., *Phys. Rev. E* **53** 4067 (1996).

[10] Böge, M., and Schmidt, F., these proceedings.

[11] Giovannozzi, M., Scandale, W., and Todesco, E., in preparation.

[12] Bartolini, R., Bazzani, A., Giovannozzi, M., Scandale, W., and Todesco, E., *Part. Accel.* **52** 147 (1996).

[13] Turchetti, G., private communication.

[14] Siegel, C. L., and Moser, J., *Lectures in celestial mechanics*, Berlin: Springer Verlag, 1971.

[15] Nekhoroshev, N., *Russ. Math. Surv.* **32** 1 (1977).

[16] Bazzani, A., and Turchetti, G., *Chaotic Dynamics: Theory and Practice* New York: Plenum Press 59 (1991).

[17] Turchetti, G., *Number theory and physics* Berlin–Heidelberg: Springer Verlag 223 (1990).

[18] Bazzani, A., Marmi S., and Turchetti, G., *Cel. Mech.* **47** 333 (1990).

DYNAMIC APERTURE STUDY ON BEIJING τ-CHARM FACTORY DESIGN

Q. Qin, Z.T. Wei, N. Huang, A.M. Xiao
Institute of High Energy Physics, Chinese Academy of Sciences
P.O.Box 918, Beijing 100039, China

1 INTRODUCTION

The Beijing τ-Charm Factory (BTCF) is a two-ring collider, with the beam energy of 2 GeV, including both crossing-angle and monochromator schemes. Some brief parameters of the ring are shown in table 1. The dynamic aperture behaves as a crucial role in the design of collider, especially the particle factories. The arrangement of chromaticity sextupoles, which influence the dynamic aperture mainly as considered, is illustrated in the following section. The 6-dimensional simulations were done with MAD code mainly, while SIXTRACK was also used for comparison and cross-checking. High order multipolar components for magnets were assigned in the tracking. To improve the dynamic aperture of the machine, the lattice has been made some progress, and the mono-chromator scheme has also been upgraded as well. In this paper, only the dynamic aperture simulations on the crossing-angle scheme are described.

Table 1: Main parameters of the BTCF storage ring[1]

Beam energy (GeV)	2.0
Circumference (m)	385.447
Crossing angle at IP (mrad)	5.2
β-function at IP (m/m)	0.65/0.01
Betatron tunes Q_x/Q_y	11.8/12.6
Momentum compaction	0.014
Natural chromaticity Q'_x/Q'_y	-20/-36
Natural emittance (nm)	153
Energy spread	5.84×10^{-4}
Synchrotron tune	0.068
Total current per beam (A)	0.57
Number of bunches	86
Luminosity ($cm^{-2}s^{-1}$)	1×10^{33}

2 SEXTUPOLE INSTALLATION AND LATTICE EVOLUTION

In the design of Preliminary Lattice (PL) for BTCF storage ring[1], two families of chromaticity sextupoles have been set. They are interleaved with different phase advance between the SD's and the SF's (SD stands for the defocusing sextupole, while SF the focusing one.). The phase advance of each cell in the arc is around 60°. This brings about the diminishing of the dynamic aperture of the storage ring, as shown in the following sections. To overcome the shortcoming of the lattice and increase the dynamic aperture, an Improved Lattice (IL) with different sextupoles array has been developed[2]. In the IL, we arranged the sextupoles again according to the theory of W vector proposed by B.Montague[3] and changed the phase advance of cell to exact 60°. The sextupoles are still interleaved, but with same phase advance between SD's and SF's. At last, the tunes have been changed to near 11.25 in horizontal and 12.25 in vertical. This Improved Lattice has a better dynamic aperture compared with the Preliminary Lattice, even with the effects of multipolar components of magnets.

3 ERROR ASSIGNMENT

The stable area in phase space is affected by the non-linear fields introduced by magnet imperfections or by the beam-beam effect. The non-linearities are measured in terms of the high-order coefficients a_n and b_n of the complex field expansion (European convention)

$$B_y + iB_x = B_1 \sum_n (b_n + ia_n)(z/R_r)^{n-1} \qquad (1)$$

where B_1 is the nominal vertical magnetic field, B_y and B_x are the actual components of the field in the vertical and horizontal planes, R_r is the reference radius, and $z = x + iy$.

In the light of the experience of BEPC and other machine, such as PEP[4], only random or rms. errors with Gaussian distribution for dipoles and normal quadrupoles are given to the simulations. Both systematic and random errors for the superconducting insertion quadrupoles near the collision point are introduced in the tracking program. Table 2 shows the expected field pertubations of dipoles and quadrupoles.

Neither field strength error, nor roll error, nor misalignment has been put into simulation because we don't install any correctors except for chromaticity sextupoles. All the three kinds of above errors could be compensated by dipolar or skew quadrupolar correctors. The parallel studies are still under way.

4 TRACKING ON DYNAMIC APERTURE

The dynamic aperture is defined as the maximum initial amplitude of particles which have to survive for suitable time in electron ring. Above a certain oscillation amplitude the particle motion becomes unstable. A large dynamic aperture is required for a reliable lattice of storage

0-7803-4376-X/98/$10.00 © 1998 IEEE

Table 2: Field errors expected for tracking (in units of 10^{-4} at R_r=1cm)

Random errors in dipole				Random errors in quadrupole			
b_1	0.000	a_1	0.000	b_1	0.000	a_1	0.000
b_2	0.000	a_2	0.000	b_2	0.000	a_2	0.000
b_3	0.174	a_3	0.000	b_3	0.220	a_3	0.000
b_4	0.008	a_4	0.000	b_4	0.013	a_4	0.000
b_5	0.003	a_5	0.000	b_5	1.46E-3	a_5	0.000
b_6	0.000	a_6	0.000	b_6	5.73E-4	a_6	0.000
b_7	0.000	a_7	0.000	b_7	0.000	a_7	0.000
b_8	0.000	a_8	0.000	b_8	0.000	a_8	0.000
b_9	0.000	a_9	0.000	b_9	0.000	a_9	0.000
b_{10}	0.000	a_{10}	0.000	b_{10}	9.216E-7	a_{10}	0.000
b_{11}	0.000	a_{11}	0.000	b_{11}	0.000	a_{11}	0.000
b_{12}	0.000	a_{12}	0.000	b_{12}	0.000	a_{12}	0.000
b_{13}	0.000	a_{13}	0.000	b_{13}	0.000	a_{13}	0.000
b_{14}	0.000	a_{14}	0.000	b_{14}	5.734E-10	a_{14}	0.000

Field errors in superconducting quadrupole Q1							
Systematic errors				Random errors			
b_2	0.000	a_2	0.000	b_2	0.000	a_2	0.000
b_3	0.000	a_3	0.000	b_3	2.64E-2	a_3	0.000
b_4	0.000	a_4	0.000	b_4	3.04E-3	a_4	0.000
b_5	0.000	a_5	0.000	b_5	3.49E-4	a_5	0.000
b_6	0.000	a_6	0.000	b_6	4.01E-5	a_6	0.000
b_7	0.000	a_7	0.000	b_7	4.61E-6	a_7	0.000
b_8	0.000	a_8	0.000	b_8	5.30E-7	a_8	0.000
b_9	0.000	a_9	0.000	b_9	6.09E-8	a_9	0.000
b_{10}	0.000	a_{10}	0.000	b_{10}	7.00E-9	a_{10}	0.000
b_{11}	0.000	a_{11}	0.000	b_{11}	8.05E-10	a_{11}	0.000
b_{12}	0.000	a_{12}	0.000	b_{12}	9.25E-11	a_{12}	0.000
b_{13}	0.000	a_{13}	0.000	b_{13}	1.06E-11	a_{13}	0.000
b_{14}	0.000	a_{14}	0.000	b_{14}	1.22E-12	a_{14}	0.000
b_{15}	0.000	a_{15}	0.000	b_{15}	1.41E-13	a_{15}	0.000
b_{18}	-8.54E-14	a_{18}	0.000	b_{18}	0.000	a_{18}	0.000

Field errors in superconducting quadrupole Q2							
Systematic errors				Random errors			
b_2	0.000	a_2	0.000	b_2	0.000	a_2	0.000
b_3	-6.20E-2	a_3	0.000	b_3	5.59E-2	a_3	0.000
b_4	2.41E-2	a_4	0.000	b_4	1.32E-2	a_4	0.000
b_5	1.97E-3	a_5	0.000	b_5	3.12E-3	a_5	0.000
b_6	-3.69E-4	a_6	0.000	b_6	7.38E-4	a_6	0.000
b_7	0.000	a_7	0.000	b_7	1.75E-4	a_7	0.000
b_8	0.000	a_8	0.000	b_8	4.13E-5	a_8	0.000
b_9	0.000	a_9	0.000	b_9	9.76E-6	a_9	0.000
b_{10}	0.000	a_{10}	0.000	b_{10}	2.31E-6	a_{10}	0.000
b_{11}	0.000	a_{11}	0.000	b_{11}	5.45E-7	a_{11}	0.000
b_{12}	0.000	a_{12}	0.000	b_{12}	1.29E-7	a_{12}	0.000
b_{13}	0.000	a_{13}	0.000	b_{13}	3.05E-7	a_{13}	0.000
b_{14}	0.000	a_{14}	0.000	b_{14}	7.20E-8	a_{14}	0.000
b_{15}	0.000	a_{15}	0.000	b_{15}	1.70E-9	a_{15}	0.000
b_{18}	0.000	a_{18}	0.000	b_{18}	0.000	a_{18}	0.000

ring, not only due to efficient injection, but long lifetime under collision conditions and other reasons.

A modified thin lens model has been applied in the simulation on dynamic aperture for BTCF. In this model, each thick lens quadrupole is separated into two pieces of thin lens with a space of 2/3 length of the thick lens between two thin lenses. This makes the thin lens model approach the real machine with smaller beta-beatings and closer quadrupole strengths[5].

In BTCF, the injection takes place in the horizontal plane for both rings. To evaluate the injection aperture we launch particles at the injection point and determine the aperture in terms of transverse position coordinates measured from the central orbit. In injection, the vertical beam size is taken from the fully-coupled emittances. An aperture, including 16 rms horizontal beam sizes and 7 rms vertical beam sizes within nearly $10\sigma_e$ of the nominal injection energy, i.e., $16\sigma_x \times 7\sigma_y \times 10\sigma_e$, is required for injection.

In the colliding-beam conditions, particles are launched at the interaction point. The dynamic aperture of 10σ in both transverse planes and $10\sigma_e$ in energy deviation is taken into account. The fully-coupled emittances are also considered.

All the tracking and simulations (with or without imperfections) were evaluated with the code MAD[6] in 6D, and cross-checked with SIXTRACK[7]. Except for chromaticity sextupoles, no any other correctors have been installed into the linear lattice. Simulations are done for 2000 turns, which corresponds to 1/12 damping time, at several amplitudes. Chromaticities in both transverse planes are corrected to a slightly positive value.

Figure 1 and 2 depict the β functions and tunes as functions of energy deviation in the crossing-angle scheme in PL, while figure 3 and 4 show the same parameters in IL. The dynamic aperture in transverse planes with or without energy deviation and multipolar errors is plotted in figures 5 and 6 for both PL and IL lattices, while figure 7 compares the results from MAD and SIXTRACK under the same conditions of tracking. The magnetic multipolar imperfection causes the decrease of dynamic aperture, especially in the vertical plane. The results obtained from MAD and SIXTRACK could be considered similar in tracking to a certain extent. The simulation for 24000 turns, i.e., one damping time, has also been studied. The dynamic aperture only reduces reasonably 1 or 2 σ in both transverse planes.

5 CONCLUSION

The chromaticity sextupoles remain the key reason in dynamic aperture, from the changing of the sextupoles arrangement and the evolution of the lattice. The improved lattice of BTCF gives a larger dynamic aperture than the preliminary lattice. With the multipolar imperfections of magnets, the dynamic aperture decreases about 10σ in vertical plane, but still satisfies the needs of injection and collision. Compared with the results from SIXTRACK, MAD gives similar outcome in the simulation.

6 ACKNOWLEDGEMENTS

The authors are grateful to the useful discussion with Prof. L.M. Chen of IHEP. We wish to thank Dr. F. Schmidt and Dr. H. Grote for their help on the codes of simulation. Our gratitude is also to be expressed to the AP group of IHEP for strong supports.

7 REFERENCES

[1] 'Feasibility Study Report on Beijing Tau-Charm Factory', IHEP-BTCF Report-03, Oct. 1996.

[2] Z.T.Wei, Master dissertation, 1997.

[3] B.W.Montague, 'Chromatic Effects and Their First-Order Correction', CERN 87-03, 1987.

[4] PEP-II, 'An Asymmetric B Factory Conceptual Design Report', June 1993.

[5] Q.Qin, 'A Thin Lens Approximation of LHC Linear Lattice', CERN SL-Note/95-68 (AP), 1995.

[6] H.Grote, F.C.Iselin, 'The MAD Program', CERN/SL/90-13 (AP), 1990.

[7] F.Schmidt, 'SIXTRACK, Version 1.2', CERN/SL/94-56 (AP), 1994.

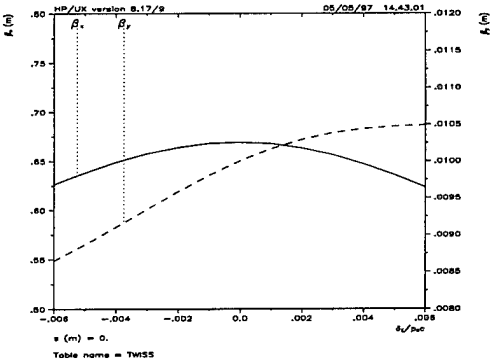

Figure 1: β-fuction vs energy deviation in PL

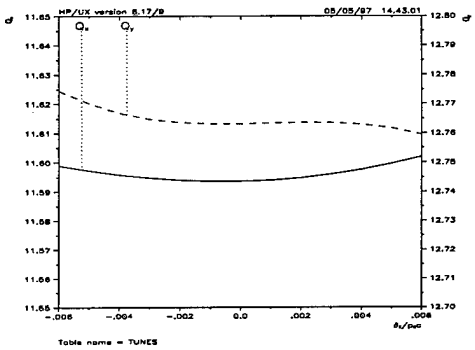

Figure 2: Tunes vs energy deviation in PL

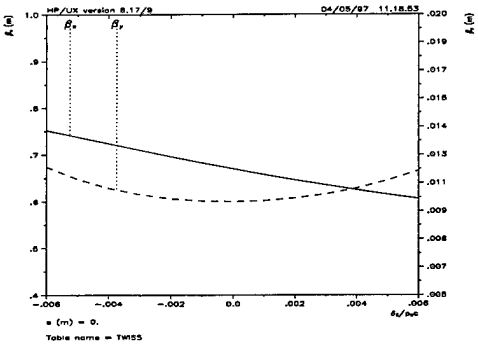

Figure 3: β-fuction vs energy deviation in IL

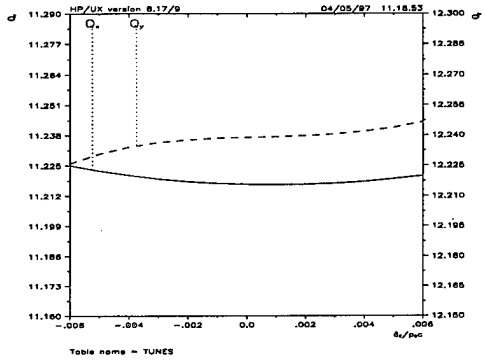

Figure 4: Tunes vs energy deviation in IL

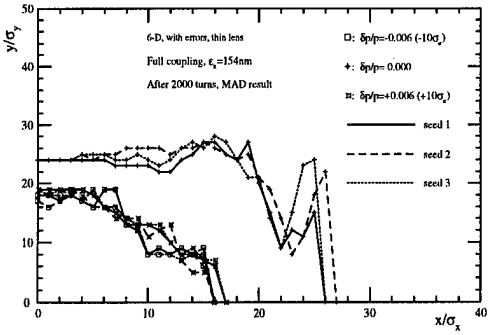

Figure 5: Dynamic aperture with errors of PL

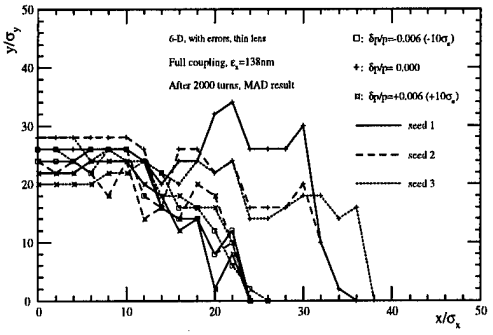

Figure 6: Dynamic aperture with errors of IL

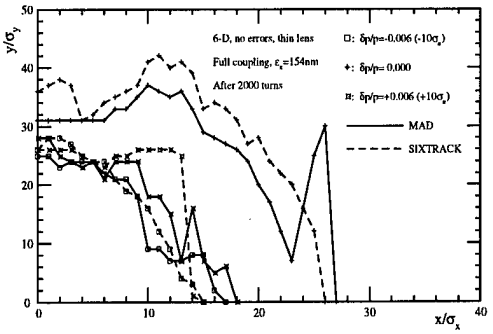

Figure 7: Comparison of results from MAD and SIX-TRACK

COMPUTATION OF THE DYNAMIC APERTURE OF 2D GENERIC MAPS USING INVARIANT MANIFOLDS

Massimo Giovannozzi*, INFN Sezione di Bologna, ITALY

Abstract

In this paper the phase-space of generic 2D area-preserving polynomial mappings is studied. These mappings modelize the transverse dynamics of a flat beam in a circular machine dominated by nonlinear magnetic errors. In particular, the problem of computing the dynamic aperture, i.e. the region in phase-space where stable motion occurs, is considered. The main result is that the boundary of the stability domain is given by the invariant manifolds emanating from the outermost unstable fixed point of low period (one or two). This study extends previous results obtained for reversible area-preserving polynomial maps of the plane.

1 INTRODUCTION

One of the main topics in the study of nonlinear Hamiltonian systems is the determination of the region in phase-space where bounded motion occurs (also called stability domain or dynamic aperture). For two-dimensional nonlinear systems, it is possible to define unambiguously an area in phase-space where the motion is stable for arbitrarily long periods. Around the origin, which is usually chosen to be a stable fixed point, there are closed curves (1D KAM tori), and wherever the nonlinear frequency satisfies a resonant condition, the invariant curves are broken into islands. When nonlinearities are dominant, one reaches a stability border beyond which a fast escape to infinity occurs. This stability border is what we have called the dynamic aperture. In this picture the KAM tori separate different phase-space domains: therefore, there exists a last connected invariant curve whose interior represents a set of stable initial conditions. Outside this curve, there can only be islands of stability, scattered in the sea of initial conditions which escape to infinity.

The evaluation of the stability domain is not only an important issue from a theoretical point of view, but also a key problem in many applications. For instance, the size of the stability domain is the main source of concern in the design of a circular particle accelerator. This parameter imposes tight constraints on the magnetic lattice of the machine and a good insight into the sources of instabilities is necessary to ensure good performance.

Our approach to the problem of determining the stability domain of a 2D polynomial map, which generalizes the results of [1–3], consists in computing the invariant manifolds of the outermost hyperbolic fixed point. Thanks to the homoclinic and/or heteroclinic intersections, the invariant manifolds related with different fixed points are connected with each other generating the homoclinic tangle. This structure is shown to be the border of the stability domain. A result obtained by Friedland and Milnor [4], allows the proof of the existence of hyperbolic fixed points of low period (one or two) for generic area-preserving polynomial maps of the plane, thus showing that our method is generically applicable to determine the stability domain.

2 POLYNOMIAL MAPS AND FIXED POINTS

2.1 *A classification Theorem*

In 1969 [5], Hénon showed that every quadratic mapping of the plane can be reduced to the simple form

$$(x, y) \xmapsto{\mathbf{h}_2} (y, y^2 + c - \delta x), \tag{1}$$

where the parameter δ represents the constant jacobian. Friedland and Milnor [4] found a way to generalize the result obtained by Hénon to arbitrary degree polynomial maps. The result of their studies can be summarized as follows

THEOREM 1 *Every polynomial map can be written as the composition of*

$$(x_0, x_1) \xmapsto{\mathbf{h}_{d_1}} (x_1, x_2) \xmapsto{\mathbf{h}_{d_2}} \cdots \xmapsto{\mathbf{h}_{d_m}} (x_m, x_{m+1}), \tag{2}$$

where $\mathbf{h}_{d_i}$ is a generalized Hénon map, namely

$$\mathbf{h}_{d_i}(x, y) = (y, p_i(y) - \delta_i x) \tag{3}$$

and $p_i(y)$ is a polynomial of degree $d_i \geq 2$. This composition can be chosen so that the leading coefficient, i.e. the coefficient of the highest degree, in each polynomial p_i is ± 1, and so that the next highest coefficient is zero. The resulting normal form is unique up to a finite number of choices.

Thus every polynomial transformation is defined inductively by $x_{i+1} = p_i(x_i) - \delta_i x_{i-1}$, with

$$p_i(x_i) = \pm x_i^{d_i} + (\text{terms of degree} \leq d_i - 2). \tag{4}$$

It is readily seen that this normal form depends on exactly $d_1 + \cdots d_m$ parameters.

2.2 *Fixed points of area-preserving maps*

A fixed point of a polynomial map $\mathbf{g}$ is a root of the equation

$$\mathbf{g}(x, y) = (x, y). \tag{5}$$

* Present address: CERN PS Division

0-7803-4376-X/98/$10.00 © 1998 IEEE

The solutions of Eq. (5) can be classified by considering the trace of the linearization $\mathbf{g}_L$ around the fixed point. In the area-preserving case, the situation is as follows

$$|\mathrm{Tr}(\mathbf{g}_\mathrm{L})| \begin{cases} < 2 & \text{the fixed point is } \textit{elliptic} \\ = 2 & \text{the fixed point is } \textit{parabolic} \\ > 2 & \text{the fixed point is } \textit{hyperbolic} \end{cases} \tag{6}$$

In the first case the fixed point is *stable* while in the third case it is *unstable*. The following result can be proved:

THEOREM 2 *Given an area-preserving polynomial map* $\mathbf{g}$ *of degree* d *then*

- *the outermost fixed point is always hyperbolic if* d *is even or* d *is odd and the leading term is positive;*
- *the outermost fixed point of* $\mathbf{g}^2$ *is always hyperbolic if* d *is odd and the leading term is negative.*

3 INVARIANT MANIFOLDS

For a hyperbolic fixed point $\mathbf{x}_\mathrm{hyp}$, the eigenvectors of the linearization of the map $\mathbf{g}_\mathrm{L}$ around $\mathbf{x}_\mathrm{hyp}$ define two linear sets in the plane, along which the motion induced by the linearized map has an expanding or a contracting behaviour.

We can extend these sets to the original nonlinear map $\mathbf{g}$, i.e. it is possible to define two manifolds emanating from the unstable fixed point, called $\mathcal{W}^\mathrm{u}(\mathbf{x}_\mathrm{hyp})$ and $\mathcal{W}^\mathrm{s}(\mathbf{x}_\mathrm{hyp})$, having the same expanding (superscript u) or contracting (superscript s) behaviour. The eigenvectors of $\mathbf{g}_\mathrm{L}$ are tangential to $\mathcal{W}^{\mathrm{u,s}}(\mathbf{x}_\mathrm{hyp})$ at the fixed point.

The invariant manifolds have at least the hyperbolic fixed point as intersection. An additional intersection, $\mathbf{x}_\mathrm{hom}$, is either called homoclinic or heteroclinic depending on whether the two intersecting manifolds emanate from the same hyperbolic fixed point. Provided the two manifolds are non-tangential at the point $\mathbf{x}_\mathrm{hom}$, it can be proven that the set of intersections is countable. Therefore, unless the two manifolds coincide completely, which occurs in the integrable case, they will oscillate around each other.

Due to the area-preserving character of the map, the area enclosed between two successive intersections remains constant. As the period of the motion tends to infinity approaching the hyperbolic fixed point, the distance between successive intersections decreases exponentially, leading to larger and larger oscillations close to the hyperbolic fixed point.

Efficient algorithms have been developed [6] to construct the whole sets $\mathcal{W}^{\mathrm{u,s}}(\mathbf{x}_\mathrm{hyp})$. They allow the reconstruction of the invariant manifolds with a uniform accuracy using a relatively small number of initial conditions together with efficient interpolation schemes.

For the purpose of this study, a simpler approach has been implemented. In fact, it turns out, that it is sufficient to iterate many times a set of initial conditions belonging to a small part of these manifolds in the vicinity of $\mathbf{x}_\mathrm{hyp}$. Moreover, these initial conditions can be chosen on the eigenvalues of the linearized map provided their distance to the hyperbolic fixed point is sufficiently small.

4 STABILITY DOMAIN

4.1 Analytical results

The stability domain $\mathcal{K}$ of a polynomial map $\mathbf{g}$ is defined as the region in phase-space where stable motion occurs. An initial condition (x_0, y_0) is stable if the sequence of iterates $(x_n, y_n) = \mathbf{g}^n(x_0, y_0)$ is bounded for both positive and negative n. One can prove [4] that $\mathcal{K}$ is compact and of positive Lebesgue measure.

Consider the following set

$$\partial\mathcal{K} = \mathcal{W}^\mathrm{s}(\mathbf{y}_\mathrm{hyp}) \bigcup \mathcal{W}^\mathrm{u}(\mathbf{y}_\mathrm{hyp}), \tag{7}$$

where $\mathbf{y}_\mathrm{hyp}$ is the outermost hyperbolic fixed point. In case the degree of $\mathbf{g}$ is odd and the coefficient of the leading term is negative, the hyperbolic fixed point used in Eq. (7) refers to the second iterate of the map $\mathbf{g}^2$, while in the other cases it represents the fixed point of $\mathbf{g}$. It is readily seen that $\partial\mathcal{K}$ is invariant under the dynamics generated by $\mathbf{g}$, hence, an orbit cannot cross this set. The geometrical structure of $\partial\mathcal{K}$ is extremely complex. In fact, the invariant manifolds emanating from different hyperbolic fixed points of the map or its second iterate, present homoclinic and, possibly, heteroclinic intersections. This ensures that $\mathcal{K}$ encloses a finite region of phase-space. Furthermore, the manifolds emanating from hyperbolic fixed points of higher period, i.e. solutions of

$$\mathbf{g}^m(x, y) = (x, y) \tag{8}$$

might also have intersections with $\partial\mathcal{K}$: the result is a dense network of manifolds emanating from the outermost hyperbolic fixed point, with an infinite number of intersections.
The dynamics outside $\mathcal{K}$ is trivial: no bounded motion can occur and the same happens for points trapped inside the homoclinic tangle.

Finally, points belonging to the region inside $\partial\mathcal{K}$ are stable, as they cannot leave this region without crossing $\partial\mathcal{K}$, and violating the invariance property.

4.2 Numerical results

The result presented in this paper have been obtained with the program GIOTTO [7]. GIOTTO allows the study of the dynamics of 2D systems using numerical tools (such as frequency analysis, evaluation of Lyapunov exponents, visualization of phase-space portrait, computation of fixed

point computation and evaluation of homoclinic tangle) as well as analytical tools (such as normal forms).

The first model analyzed consists of a polynomial map of degree six

$$\mathbf{h}_6 = \mathbf{h}_2 \circ \mathbf{h}_3, \tag{9}$$

where

$$\mathbf{h}_3 = (y, y^3 + \alpha y + \beta - x) \qquad \mathbf{h}_2 = (y, y^2 + \gamma - x). \tag{10}$$

The parameters have been set equal to the following values $\alpha = -0.856$, $\beta = -0.164$, $\gamma = -0.120$. In Fig. 1,

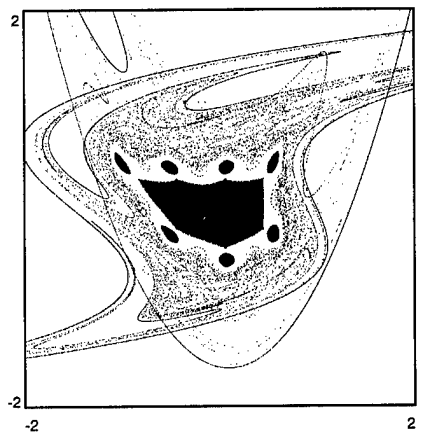

Figure 1: Stability domain (black area) and the invariant manifolds emanating from the unstable fixed point of period one of $\mathbf{h}_6$.

the key result is shown (the black area represents the set $\mathcal{K}$). This has been computed by simply iterating the map $\mathbf{h}_6$ over a rectangular grid of initial conditions and plotting the initial conditions which stay bounded after 10000 turns. On top of the set $\mathcal{K}$, $\partial\mathcal{K}$ is superimposed. It is apparent that $\partial\mathcal{K}$ bounds $\mathcal{K}$.

The next step would be to consider an odd degree map. The chosen models are:

$$\mathbf{h}_{9\pm} = \mathbf{h}'_{3\pm} \circ \mathbf{h}_3, \tag{11}$$

where

$$\mathbf{h}'_{3\pm} = (y, \pm y^3 + \alpha y + \beta - x) \qquad \mathbf{h}_3 = (y, y^3 + \gamma y + \delta - x). \tag{12}$$

The parameters have been set equal to $\alpha = -0.712$, $\beta = -0.272$, $\gamma = 0.268$, $\delta = 0.680$ for $\mathbf{h}_{9+}$, while $\alpha = -0.172$, $\beta = 0.352$, $\gamma = 0.916$, $\delta = 0.348$ for $\mathbf{h}_{9-}$ has been chosen. In Fig. 2 the set $\mathcal{K}$ is depicted together with $\partial\mathcal{K}$. The outermost fixed point is hyperbolic and it can be used to construct the invariant manifolds and the set $\partial\mathcal{K}$. Finally, in Fig. 3 the two sets $\mathcal{K}$ and $\partial\mathcal{K}$ (relative to the fixed point of period two) are shown. It is clearly seen that the homoclinic tangle generated by either the unstable fixed point of period one or the unstable fixed point of period two represents the border of the region of stable

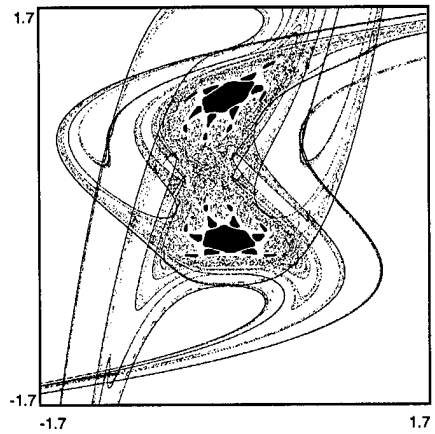

Figure 2: Stability domain (black area) and invariant manifolds emanating from the outermost unstable fixed point of period one for $\mathbf{h}_{9+}$.

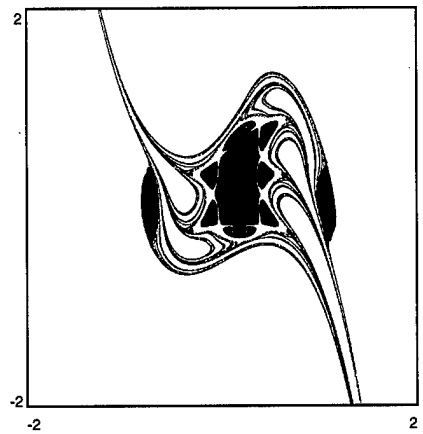

Figure 3: Stability domain (black area) and invariant manifolds from the outermost unstable fixed point of period two for $\mathbf{h}_{9-}$.

motion for $\mathbf{h}_{9+}, \mathbf{h}_{9-}$. Although the phase-space topology of the three models presented here is completely different, nevertheless the information on the hyperbolic fixed points of low period is sufficient to reconstruct the border of the stability domain, thanks to the phenomenon of homoclinic and heteroclinic intersections.

5 REFERENCES

[1] M. Giovannozzi, Phys. Lett. **A182** (1993) 255.

[2] A. Bazzani, M. Giovannozzi, G. Servizi, E. Todesco and G. Turchetti, Physica **D64** (1993) 66.

[3] M. Giovannozzi, Phys. Rev. E **53** (1996) 6403.

[4] S. Friedland and J. Milnor, Ergod. Th. & Dynam. Sys. **9** (1989) 67.

[5] M. Hénon, Q. Appl. Math. **27** (1969) 291.

[6] D. Hobson, J. of Comp. Phys. **104** (1993) 14.

[7] D. Bortolotti, M. Giovannozzi, G. Servizi, E. Todesco and M. N. Vrahatis, Int. J. Mod. Phys. **C6** (1995) 651.

AN ORBIT AND DISPERSION CORRECTION SCHEME FOR PEP-II *

M.H.R. Donald, Y. Cai, H. Shoaee and G.White
Stanford Linear Accelerator Center, Stanford University, Stanford, CA 94309 USA

Abstract

A scheme of simultaneously correcting the orbits and dispersion has been implemented in the simulation code [1] and on-line control system [2] for PEP-II [3]. The scheme is based on the eigenvector decomposition method. An important ingredient of the scheme is to choose the optimum eigenvectors that minimize the orbit, dispersion and corrector strength. Simulations indicate this to be a very effective way to control the vertical residual dispersion.

1 INTRODUCTION

To achieve optimum luminosity in a storage ring it is vital to control the residual vertical dispersion. In the original PEP storage ring, a scheme [4] to control the residual dispersion function was implemented using the ring orbit as the controlling element. The "best" orbit not necessarily giving the lowest vertical dispersion. A similar scheme has been implemented in both the on-line control code [2] and in the simulation code LEGO [1]. The method involves finding the response matrices (sensitivity of orbit/dispersion at each Beam-Position-Monitor (BPM) to each orbit corrector) and solving in a least squares sense for minimum orbit, dispersion function or both. The optimum solution is usually a subset of the full least squares solution.

2 RESPONSE MATRICES

The orbit response matrices for a beamline (R_{12}) and a closed ring (C_{12}) are well known.

In a beamline The response to an orbit corrector at position s_p observed as a change in orbit at position s_o is given by for $\mu_{s_o} > \mu_{s_p}$

$$y_o = \sqrt{\beta_p \beta_o}\Theta_p \sin(\mu_{s_o} - \mu_{s_p}) \tag{1}$$

for $\mu_{s_o} < \mu_{s_p}$

$$y_o = o \tag{2}$$

In a closed ring the response to an orbit corrector at position s_p, observed as a change in orbit at position s_o is given by

$$y_o = \frac{\sqrt{\beta_p \beta_o}}{2\sin\pi\nu}\Theta_p \cos(\pi\nu + \mu_1 - \mu_2) \tag{3}$$

where μ_1 and μ_2 denote the smaller and larger of the phases at the corrector/monitor positions respectively.

The response matrices for the dispersion function can be found by differentiating these expressions with respect to $\delta = dp/p$ the relative momentum.

In a beamline we observe how equation 1 changes as a function of momentum. β_p, β_o, μ_p and μ_o all depend on momentum, as does Θ_p the applied kick from the corrector.

$$\begin{aligned}\frac{dy_o}{d\delta} &= \frac{1}{\Theta_p}\frac{d\Theta_p}{d\delta}y_o \\ &+ \frac{1}{2}\left[\frac{1}{\beta_o}\frac{d\beta_o}{d\delta} + \frac{1}{\beta_p}\frac{d\beta_p}{d\delta}\right]y_o \\ &+ \left[\frac{d\mu_1}{d\delta} - \frac{d\mu_2}{d\delta}\right]\frac{y_o}{\tan(\mu_2 - \mu_1)}\end{aligned} \tag{4}$$

We find the derivative of the first term to be

$$\frac{d\Theta_p}{d\delta} = -\Theta_p$$

In the LEGO code the derivatives $\frac{1}{\beta_p}\frac{d\beta}{d\delta}$ and $\frac{d\mu}{d\delta}$ are found by a finite difference method. The Twiss parameters are evaluated at momenta slightly below and slightly above the nominal momentum and the finite differences in β and ν are recorded.

In a closed ring we observe how equation 3 changes as a function of momentum. As before β_p, β_o, μ_p and μ_o and Θ_p all depend on momentum, but in this case the dependence of the machine tune ν on momentum must also be taken into account.

$$\begin{aligned}\frac{dy_o}{d\delta} &= \frac{1}{\Theta_p}\frac{d\Theta_p}{d\delta}y_o \\ &- \frac{\pi}{2}\frac{1}{sin^2\pi\nu}\sqrt{\beta_p\beta_o}\cos(\mu_1 - \mu_2)\Theta_p\frac{d\nu}{\delta} \\ &+ \frac{1}{2}\left[\frac{1}{\beta_o}\frac{d\beta_o}{d\delta} + \frac{1}{\beta_p}\frac{d\beta_p}{d\delta}\right]y_o \\ &- \tan(\pi\nu + \mu_1 - \mu_2)\left[\frac{d\mu_1}{d\delta} - \frac{d\mu_2}{d\delta}\right]y_o\end{aligned} \tag{5}$$

Alternatively the D_{12} matrix for the ring can be found from the expression [6]

$$\frac{dy_m}{d\delta} = \frac{\sqrt{\beta_m\beta_c}}{2\sin\pi\nu}\Theta_c\left\{\sum_{qs}\begin{bmatrix}\frac{(-K1+K2\eta)}{2\sin\pi\nu}\beta_{qs} \\ \cos(\pi\nu - |\mu_m - \mu_{qs}|) \\ \cos(\pi\nu - |\mu_c - \mu_{qs}|) \\ -\cos(\pi\nu - |\mu_m - \mu_c)\end{bmatrix}\right\} \tag{6}$$

where the change in orbit due to a corrector change is tracked through every quadrupole and sextupole and the momentum dependence of the kicks is summed around the ring. Note that, although this equation gives the vertical dispersion function, the dispersion function used for the kick (η) is the horizontal dispersion function. The subscripts m, c and qs refer to monitor, corrector and quadrupole or sextupole respectively. A similar expression can be found for the response in a beamline.

* Work supported by the Department of Energy under Contract No. DE-AC03-76SF00515

3 THE MICADO METHOD

Knowing the response of the orbit/dispersion to a change in strength of each orbit corrector we can solve for the change in corrector strengths required to correct the measured orbit/dispersion. If y is the orbit generated by a corrector set x and the response matrix is M

$$y = Mx \tag{7}$$

and the solution is

$$x = M^{-1}y \tag{8}$$

for a square matrix.

$$x = (M^tM)^{-1}y \tag{9}$$

is the the least squares solution of a non-square system of equations.

The MICADO [5] package uses The Householder Transform method to solve the least squares problem, but at the reduction of each column of the matrix the intermediate result is stored. the pivot is chosen on the basis of which column matches the measured orbit best.

The net result is that the first solution obtained picks out a single corrector that best corrects the orbit/dispersion. The next column chosen finds the corrector that (in conjunction with the first corrector) best corrects the orbit/dispersion, and so on.

4 THE EIGENSOLUTION METHOD

The equation

$$y = Ax \tag{10}$$

is solved in the least squares sense by pre-multiplying by M^t

$$A^tAx = A^ty \tag{11}$$

and then decomposing the matrix A^tA into its eigenvalues (a diagonal matrix D) and eigenvectors (a square matrix U).

$$\begin{aligned} & y &=& Ax \\ & A^ty &=& A^tAx \\ but & A^tA &=& UDU^t \\ therefore & A^ty &=& UDU^tx \\ & x &=& UD^{-1}U^tA^ty \end{aligned}$$

The terms U^tA^ty result in a column vector, the values of which indicate how well each of the orthogonal eigenvectors best fit the data. Ordering the eigenvalues and eigenvectors on these numbers allows applying a subset of the eigensolution determined on how well the data fits. The size of the eigenvalues is also important however, the larger the eigenvalue, the more sensitive the correction is, a small change in strength giving a large change in the correction. In a ring, for example, the largest eigenvectors correspond to eigenvectors with patterns close to the betatron tune of the machine. The eigenvectors (and eigenvalues) are ordered on the *product* of the best fit and the eigenvalue.

After the eigenvectors and eigenvalues are ordered, the correction (-x) is found by multiplying out $D^{-1}U^tA^ty$ then summing the corrector sets $U_{ij}(D^{-1}U^tA^ty)_j$ for each corrector i

5 MERITS OF THE METHODS

Both methods overcome one of the problems of the full solution. In the presence of noise (BPM errors, machine errors and an otherwise non-perfect machine model) and a possibly ill-conditioned matrix, the strength of the correctors can suddenly jump to very large values when trying to correct for non-physical BPM readings. Cutting the solution short (fewer correctors or corrector sets) gives acceptable solutions with weaker correctors.

The MICADO method tends to pick out the most effective individual correctors to give an acceptable orbit/dispersion and is used often in correcting the orbit with very few correctors. The eigensolution method is particularly useful for correction of the dispersion function, where patterns in the orbit are used for the correction. Either method may be used to correct orbit, dispersion or a weighted combination of the two. In PEP-I a weighting factor, where 2 cm of dispersion was worth 1 mm of orbit, proved to be satisfactory.

6 SIMULATIONS USING LEGO

Simulations have been performed using the code LEGO to check out the on-line code and also to simulate start-up of the High Energy Ring of PEP-II with alignment, field setting and multipole errors. A typical simulation would:

- correct first turn orbits until a stable machine results
- correct closed orbits both horizontal and vertical
- correct vertical dispersion
- correct orbit and dispersion together

Table 1 shows the result of just such a simulation on PEP-II with expected tolerances on alignment, field setting and multipole errors on all elements. In this case the rms of the quadrupole roll errors was increased from the expected 0.5 mr to the value 2 mr.

Figure 1 shows how the rms of the corrector strengths grows steadily while the rms of the residual dispersion function falls rapidly at first then more slowly. This figure corresponds to the first dispersion correction of table 1. The rms of the measured dispersion function (reduced from 40.25 mm to 5.67 mm) was close to the predicted rms value of 3.87 mm.

Figure 2 shows how the correction goes unstable when all the corrector sets are chosen (full correction). For the 145 correctors and 151 BPMs in the High Energy Ring it is best to take no more than 50 sets, then measure the dispersion function (and orbit) and repeat the correction. The case shown is the same as that shown in table 1. and figure 1 except that the correction was not stopped at 50 sets. The

Table 1: Results of a simulated correction

Action	Horizontal orbit (mm)	Vertical orbit (mm)	Vertical dispersion (mm)
First turn orbits	21.559	14.220	
Correct H orbit	4.380	11.662	
Correct V orbit	3.628	0.990	
Closed orbits	4.384	0.575	34.053
Correct H orbit	0.552	1.122	40.248
Correct V orbit	0.248	0.100	41.265
Correct V orbit again		0.0285	40.438
Correct V dispersion		1.794	5.676
Correct dispersion again		1.808	3.927
Correct both orbit and dispersion		0.792	11.188

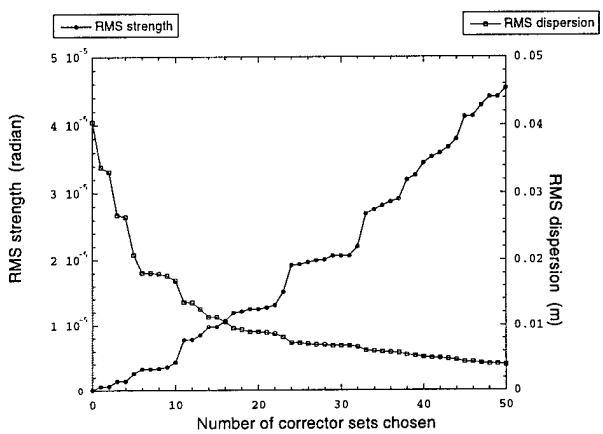

Figure 1: A correction of the vertical dispersion function showing how the strength of the orbit correctors increases while the rms of the dispersion function decreases. Only the first 50 corrector sets are recorded

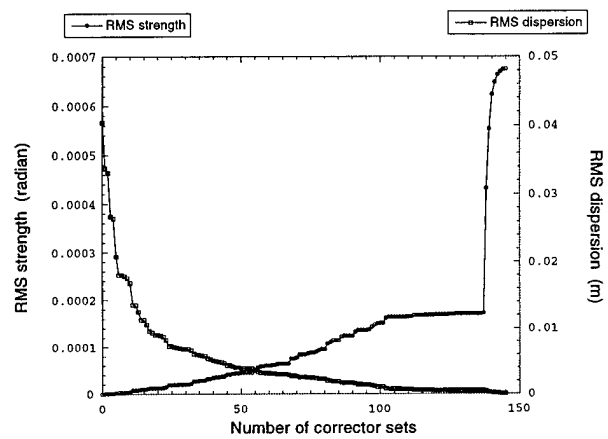

Figure 2: The same correction as figure 1 but in this case the predictions for all 145 corrector sets are shown

results for the case of full correction were very much worse than those for the limited correction. It was predicted that the rms of the dispersion would be 0.04 mm. On measurement it was found to be 15 mm. much worse than previously, the orbit was also much worse at 6.24 mm.

7 SUMMARY

The scheme for control of unwanted residual dispersion function has been implemented, both on-line and in the simulation code LEGO. The on-line code has been checked against the simulation code. Simulations indicate that the scheme will work well when the two storage rings of the PEP-II B-Factory are commissioned.

8 REFERENCES

[1] Y. Cai, M.H.R. Donald, J. Irwin and Y.T. Yan, "LEGO: A Modular Accelerator Design Code," these proceedings.

[2] N. Phinney and H. Shoaee, "SLC Control System – Status and Development," Proc. of 1987 Particle Accelerator Conference, Washington D.C., March 1987.

[3] "PEP-II: An Asymmetric B Factory," Conceptual Design Report, SLAC-418, June 1993.

[4] M.H.R. Donald *et al.*, "Some Schemes for On-Line Correction of the Closed Orbit, Dispersion and Beta Functions in PEP," Proc. of 1981 Particle Accelerator Conference, March 1981.

[5] B. Autin and Y. Marti, "Closed Orbit Correction of A.G. Machines using a Small Number of Magnets," CERN/ISR-MA/73-17, March 1973.

[6] A.W. Chao, Martin J. Lee, E. Linstadt, N.C. Spencer, "Online Orbit and Dispersion Correction Schemes for PEP," (SLAC) PEP-0318, Oct 1979.

EXPERIMENTAL NON LINEAR BEAM DYNAMICS STUDIES AT SPEAR[1]

A.Terebilo, C.Pellegrini, University of California, Los Angeles, CA 90024
M.Cornacchia, J.Corbett, D.Martin, SLAC, Stanford University, Stanford, CA 94309

Abstract

The frequency map analysis of a Hamiltonian system [1],[2],[3] recently introduced to accelerators physics in combination with turn-by-turn phase space measurements opens new experimental opportunities for studying non linear dynamic in storage rings. In this paper we report on the experimental program at SPEAR having the goal of measuring the frequency map of the machine. In this paper we discuss the accuracy of the instantaneous tune extraction from experimental data and demonstrate the possibility of the frequency map measurement.

1 TURN-BY-TURN PHASE SPACE MONITOR

We have previously reported on experimental beam dynamics studies at SPEAR and hardware used for this purpose [4], [5]. We have upgraded the electronics following the BPM base-band processor in order to achieve higher resolution by adding 6 channels of custom built high speed low noise track and holds serving as a front end for 14-bit Pentek™ ADCs in the VME mainframe. The resolution achieved in the single pass is 125 μm for current per bunch 3mA. We have modified the fast kicker triggering circuitry to initiate the data acquisition cycle at fixed phase with respect to AC to avoid the influence of the 60 Hz ripple in the magnetic field [6]. The control of the data acquisition has also been automated using LabView™ running on Pentium™ workstation for effective use of machine time dedicated to accelerators physics.

2 INSTANTANEOUS TUNE EXTRACTION

We apply Numerical Analysis of Fundamental Frequency (NAFF) to a subset of numerically or experimentally obtained turn-by-turn trajectories starting at turn m containing N turns

$$f_n, \text{ where } n = m...m+N-1, \qquad (1)$$

f_n represents turn-by-turn data for one of the canonical variables. We search for the fundamental frequencies $\nu_{m,N}^{(k)}$ that maximize the absolute value of the correlator:

$$I(\nu_{m,N}^{(k)}) = \sum_{n=m}^{m+N-1} f_n \exp\left(-i2\pi \cdot \nu_{m,N}^{(k)} n\right)\chi_{m-n} \qquad (2)$$

$$\chi_n = \sin(\pi \cdot n / N)$$

These frequencies extracted from the numerical tracking data asymptotically converge for $N \to \infty$ to the tunes (winding numbers) associated with invariant surfaces in the phase space.

If the method is applied to experimental tracking data, the interpretation of these frequencies needs to be modified for two reasons:

1. due to synchrotron radiation in electron machine the particle does not stay on the invariant tori.
2. BPMs measure the trajectory in the phase space of the center of mass of a distribution which differs from a single particle trajectory due to decoherence[6].

Given a subset of the center of mass trajectory data (1) NAFF picks out the *instantaneous* (associated with particular starting turn m) tunes $\nu_{m,N}^{(k)}$, that make an approximation of (1) in the form

$$f_n = \sum_k a_{m,N}^{(k)} \cos\left(2\pi \cdot \nu_{m,N}^{(k)} n + \psi_{m,N}^{(k)}\right)\chi_{m-n} \qquad (3)$$

The instantaneous amplitudes $a_{m,N}^{(k)}$ can be computed afterwards by chi-square fitting.

3 ACCURACY OF THE INSTANTANEOUS TUNE EXTRACTION

We find it necessary to investigate the accuracy of the instantaneous tune extraction in order to be able to interpret the results correctly. Although the functions $\exp(-i2\pi \cdot \nu \cdot n)$ can serve as basis vectors, the correlator (2) is not a legitimate projection operator for any finite N. Therefore the method will introduce systematic errors due to the finite number of turns used. Systematic errors also increase by several orders of magnitude as the tune approaches to an integer or half integer.

We numerically tested the accuracy of the NAFF by applying it to a test sequence

$$f_n = A\cos\left(2\pi \cdot n\nu + \psi\right) + R_n(\sigma)$$

where $R_n(\sigma)$ Gaussian white noise.

[1] Work supported by US DOE grant DE_FG03-92ER40793 and contract DOE-AC03-76SF00515, Office of Basic Energy Sciences, Division of Chemical Sciences.

The error on Fig.1. is the r.m.s. error for tunes and phases randomly seeded in the range 0.05 ... 0.45 and 0 - $\pi/2$ respectively.

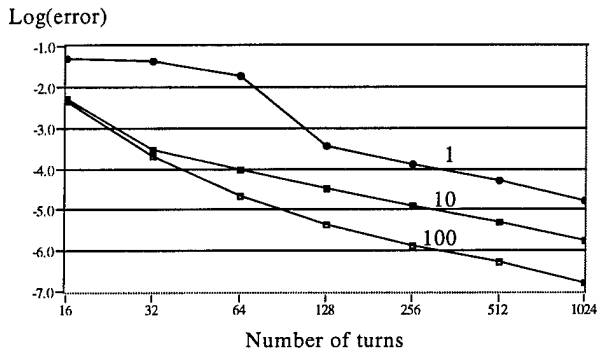

Fig.1 r.m.s. error for a range of experimentally useful numbers of turns and signal to noise ratios.

4 PROPOSED AND CARRIED OUT EXPERIMENTS, RESULTS AND DISCUSSION

4.1 Frequency map measurements.

Frequency map analysis [1][2][3] provides a useful visualization of the dynamics of a Hamiltonian system. The non linear resonance lines act as attractors or repellers in the tune space. Since the width of the resonant structures associated with high order resonances is within the achievable resolution of the method, we have started experiments to extract the frequency map experimentally.

The frequency map (footprint) on Fig.2. is obtained by numerical tracking with initial conditions chosen on a uniform grid in J_x, J_y action space. For each initial condition the particle is tracked for 1024 turns and the horizontal and vertical tunes are computed using NAFF. The linear working point of SPEAR (7.166;5.26) is in the upper right corner.

The four octupoles installed in SPEAR introduce positive horizontal tune shift with horizontal amplitude[5], so a transverse kick places the instantaneous tunes in a new point in the tune space different from the linear working point.

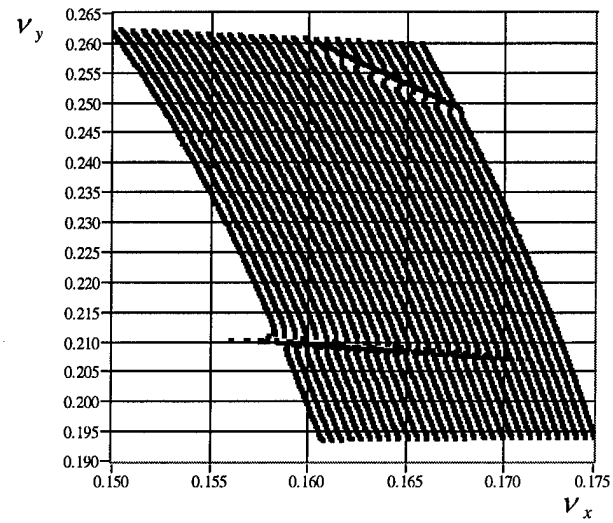

Fig.2 Frequency map of the SPEAR model.

To detect the presence of a resonant line we tune the machine such that linear working point is slightly above it. We then follow the evolution of the tunes after applying a horizontal kick. The experiment was conducted with 5mA in a single bunch stored in the machine.

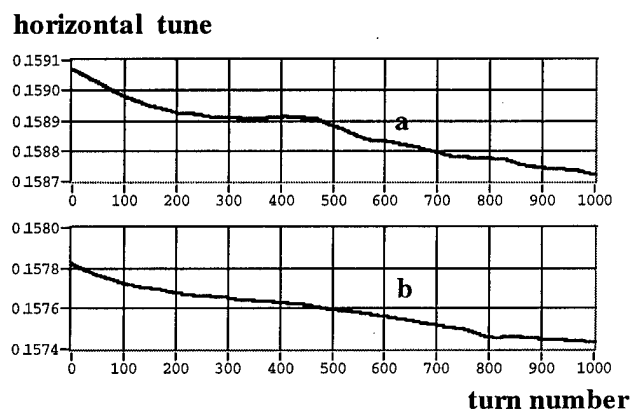

Fig.3 Experimental evidence of the $3\nu_x + 2\nu_y = 32$ resonance crossing. Horizontal tune vs. turn number for 2 different nearby linear working points set approximately to (a) (7.158 ;5.261) and (b) (7.157 ; 5.261)

In case (a), after the kick the instantaneous tune point starts on the other side of the resonance line due to the positive horizontal tune shift with amplitude and then crosses the line as the amplitude decreases. The flat part of the upper graph is a manifestation of the resonance crossing. In case (b), the linear tune is chosen below the line so it is not crossed.

4.2 Modulation of instantaneous tune and amplitude with synchrotron frequency.

It is can be seen from Fig.1. that even for N=32, the accuracy of the NAFF method is between 1×10^{-3} and 1×10^{-4}. In SPEAR, the synchrotron period is ~50 turns. This suggests that we should be able to resolve the

modulation of the transverse tunes at the synchrotron frequency due to coherent synchrotron oscillations and centroid amplitude modulations due to the decoherence-recoherence effect, and due to non-zero energy spread within the bunch [7]. All these effects were indeed observed using instantaneous tune measurements.

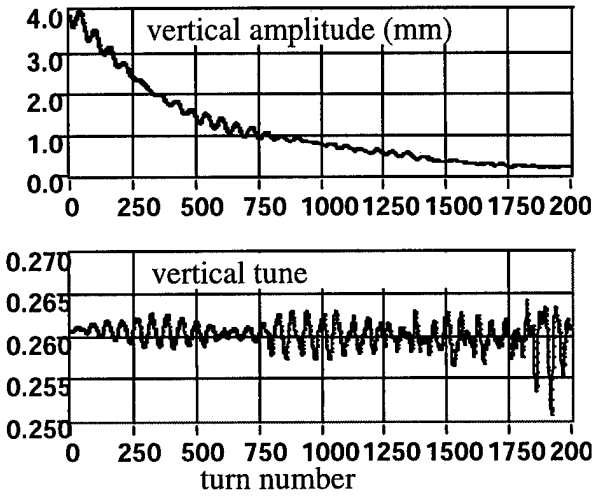

Fig.4 Evolution of the instantaneous vertical tune $\nu_{m,32}^{(y)}$ and amplitude $a_{m,32}^{(y)}$ as a function of turn number.

5 CONCLUSIONS

The instantaneous tune extraction technique can be applied to experimental tracking data with reasonable accuracy. Frequency map can be experimentally determined using the existing turn-by-turn phase space measurement techniques and NAFF instantaneous tune extraction.

6 ACKNOWLEDGEMENTS

The authors express their appreciation to D.Gough, G.Johnson, D.Mostoffi, J.Yang. for their contribution in the design and building of the electronics for the data acquisition system. We greatefully acknowledge the input into the program at earlier stages by P.Tran. We also thank H.D.Nuhn, M.Lee, D.Robin, E.Todesco for useful and inspiring discussions.

REFERENCES

[1] H.Dumas, J.Laskar: 'Global Dynamics and Long-Time stamility in Hamiltonian systems via numerical frequency analysis', Phys. Rev. Lett. 70, 2975 (1993)

[2] J.Laskar, 'Frequency analysis for multi-dimensional syatems', Physica D67 (1993) 257 - 281

[3] J.Laskar, D.Robin: 'Applications of frequency map analysis to the ALS',Proc. of the International Workshop on Single-Particle Effects in Large Hadron Colliders, Montreux, Switzerland (1995)

[4] P.Tran,C.Pellegrini, M.Cornacchia, M.Lee, W.Corbett: 'Non linear beam dynamics experimental program at SPEAR' IEEE PAC 1995 p. 3323

[5] P.Tran et.al 'Measurement of the octupole induced tune shifts at SPEAR' AIP Conf. Proc. Vol. 315, 1994

[6] A.Terebilo, C.Pellegrini, M.Cornacchia, J.Corbett, D.Martin:'Measurement of time variation of machine parameters', these proceedings.

[7] S.Y.Lee:'Review of nonlinear beam dynamics experiments' AIP Conf.Proc. (1992) 131 p.249-264.

OVERCOMING WEAK INTRINSIC DEPOLARIZING RESONANCES WITH ENERGY-JUMP*

H. Huang[1], L. Ahrens[1], J.G. Alessi[1], M. Bai[2,3], K.A. Brown[1], G. Bunce[1], P. Cameron[1], P. Ingrassia[1], A.E. Kponou[1], K. Krueger[3], S.Y. Lee[2], A.U. Luccio[1], Y.I. Makdisi[1], F. Mariam[1], M. Okamura[5], L. Ratner[1], K. Reece[1], T. Roser[1], H. Sato[4], H.M. Spinka[3], N. Tsoupas[1], D.G. Underwood[3], W. van Asselt[1], N.W. Williams[1], and A. Yokosawa[3]

(1) Brookhaven National Laboratory, Upton, NY 11973, USA
(2) Department of Physics, Indiana University, Bloomington, IN 47405, USA
(3) Argonne National Laboratory, 9700 Cass Ave., Argonne, IL 60493, USA
(4) KEK, 1-1 Oho, Tsukuba-shi, Ibaraki-ken, 305, Japan
(5) RIKEN, Wako, Saitama, 351-01, Japan

Abstract

In the recent polarized proton runs in the AGS, a 5% partial snake was used successfully to overcome the imperfection depolarizing resonances. Polarized proton beam was accelerated up to the required RHIC injection energy of 25 GeV. However, significant amount of polarization was lost at $0+\nu_y$, $12+\nu_y$ and $36+\nu_y$, which is believed to be partially due to the coupling resonances. To overcome the coupling resonance, an energy-jump was generated by rapidly changing the beam circumference using the powerful AGS rf system. It clearly demonstrates that the novel energy-jump method can successfully overcome coupling resonances and weak intrinsic resonances.

1 INTRODUCTION

The spin vector of an orbiting particle in a synchrotron obeys the Thomas-BMT equation [1], where the dynamics of spin motion can be characterized by the spin tune ν_s, which is defined as the number of spin precessions per revolution about a stable spin direction. The acceleration of polarized beam will encounter depolarizing resonances whenever the spin precession frequency exactly matches the frequency with which the protons encounter depolarizing horizontal magnetic fields. For an ideal accelerator, where orbiting particles experience only the vertical guide field, the spin tune is equal to $G\gamma$, where $G = 1.7928$ is the anomalous G-factor of the proton, and γ is the relativistic Lorentz factor. The resonance condition for imperfection depolarizing resonances arises when $\nu_s = G\gamma = n$, where n is an integer. The condition for intrinsic depolarizing resonances arises when $\nu_s = G\gamma = kP \pm \nu_y$, where k is an integer, ν_y is the vertical betatron tune, and P is the superperiodicity. For the Brookhaven Alternating Gradient Synchrotron (AGS), $P = 12$ and $\nu_y \approx 8.8$.

Traditionally, the imperfection depolarizing resonances are compensated with the tedious harmonic correction method and the intrinsic depolarizing resonances are overcomed with tune-jump method[2]. The polarized proton runs of experiment E-880 at the AGS aim to demonstrate the feasibility of polarized proton acceleration using a 5% partial Siberian snake [3]. In the first run it was shown that a 5% snake is sufficient to avoid depolarization due to the imperfection resonances [4]. The results are shown in Fig. 1 as open circles and dashed lines. The pulsed tune-jump quadrupoles were not powered in this run. Although some depolarization at intrinsic resonances are expected, the level of the depolarization does not agree with a simple model calculation. A spin tracking study using SPINK [5] was then performed and it showed that there is an extra resonance adjacent to the intrinsic resonance which causes further depolarization [6]. This additional resonance can be easily understood as a linear coupling effect. Since the solenoidal 5% partial snake introduces considerable linear coupling between the two transverse betatron motions, the vertical betatron motion has also a component with the horizontal betatron frequency. As a consequence, the beam will see an additional resonance, the so-called coupling resonance at $G\gamma = 0 + \nu_x$, besides the intrinsic resonance at $G\gamma = 0 + \nu_y$. Besides the linear coupling effect, the synchrotron motion also causes some additional depolarization but to a smaller extent.

The second run showed that it is possible to use the tune jump method in the presence of the partial snake. A new record high energy for accelerated polarized proton beam of 25 GeV was reached with about 12% beam polarization left. Again no polarization was lost due to the imperfection resonances and depolarization from most intrinsic resonances was avoided with the tune jump quadrupoles. However, as can be seen from Fig. 1, significant amount of polarization was lost at $G\gamma = 0 + \nu_y$, $12 + \nu_y$ and $36 + \nu_y$. The first two of these three resonances were successfully crossed previously when the partial snake was not installed. It is believed that the losses are partially due to the coupling resonances. The tune jump method changes the vertical

* Work performed under the auspices of the U.S. Dept. of Energy

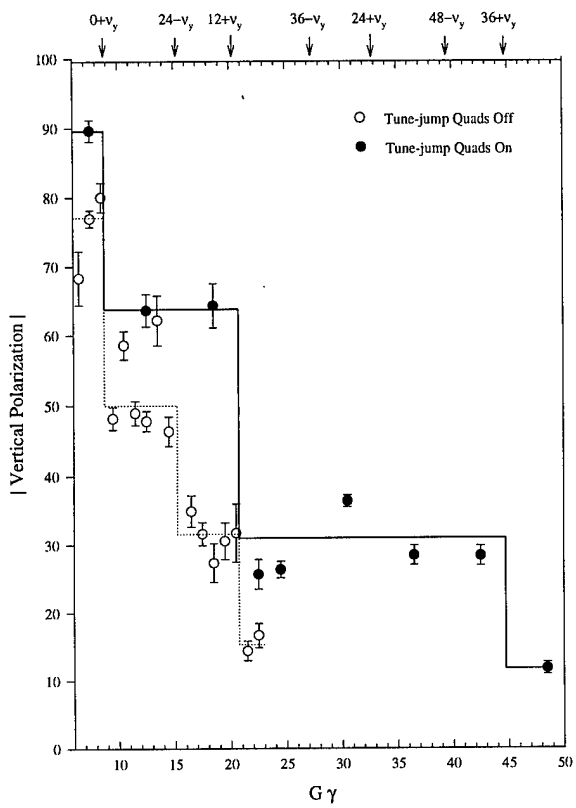

Figure 1: Results of AGS 5% partial snake test. The measured absolute value of the vertical polarization at $G\gamma = n + \frac{1}{2}$ up to $G\gamma = 48.5$. The open circles are the results without the tune-jump quadrupoles and the solid points are the results with the tune-jump quadrupoles.

betatron tune within less than one revolution to effectively make the resonance crossing speed very fast. However, the coupling resonance is still crossed at the normal crossing speed and can cause polarization loss. The strength of the tune jump quadrupoles is not sufficient to jump the last resonance $G\gamma = 36 + \nu_y$. Instead, we attempted to induce spin flip at this resonance but were only partially successful. A spin tracking shows that the amount of depolarization observed agrees with the effect of the strong coupling resonance at $G\gamma = 36 + \nu_x$.

2 OVERCOME THE COUPLING RESONANCES

As shown in the simulations, it is clear that the unexpected depolarization level after crossing the strong intrinsic resonances is due to the combined effect of the coupling resonance and synchrotron oscillation. The coupling resonance strength can be decreased by separating the tune. However, separating the two tunes for more than 0.5 unit does not help, because the source of the coupling is localized at the snake solenoid. The ratio of the coupling resonance strength to the intrinsic resonance strength with a 5% partial snake and 0.1 unit tune separation is about 0.06. With a larger tune separation of 0.3, the ratio goes down to 0.03. Also, since the coupling resonances are generally weak, the acceleration rate can be maximized to minimize the depolarization at the coupling resonance. With a 25π mm-mrad polarized beam in the AGS, the coupling resonances adjacent to the weak intrinsic resonances such as $24 - \nu_y, 24 + \nu_y$ and $48 - \nu_y$ will have little effect with the regular acceleration rate $\alpha = 4.5 \times 10^{-5}$. But the coupling resonances adjacent to the strong intrinsic resonances such as $0 + \nu_y, 12 + \nu_y, 36 - \nu_y$ and $36 + \nu_y$ will cause significant depolarization. This ratio makes it impossible to cross them at a single speed without losing polarization. Using a very slow crossing speed could fully flip spin after the intrinsic resonance, but on the other hand, it also increases the depolarization from the coupling resonances. Even the traditional tune-jump quadrupole method is challenged. The tune jump method changes the betatron tunes in less than one orbit turn to effectively make the resonance crossing speed very fast. If the two tunes are separated, the coupling resonance is crossed by the beam at the normal crossing speed which causes depolarization. Moreover, the tune jump can increase the beam emittance and increase the strengths of subsequent coupling and intrinsic resonances. In short, the benefits of all these methods will be reduced or diminished without extra efforts to overcome the coupling resonances.

To eliminate the coupling resonances, one can think of compensating the linear coupling globally. Two sets of strong skew quadrupoles could compensate the linear coupling of the solenoidal partial snake globally. However, with a global decoupling, the orbit is flat globally but not locally, which means that at certain locations, the coupling will be non-zero and may still cause some problem. One possible way is to eliminate only the coupling resonance closest to the intrinsic resonance instead of eliminating everyone. Some further simulation is needed to test the idea. Practically, the skew quadrupoles in the AGS are not strong enough to compensate the coupling of the solenoidal snake.

When the intrinsic resonances are crossed with coherent betatron oscillation excited with an AC dipole [7], slow acceleration rate or tune-jump, the coupling resonances can be crossed using a fast energy-jump at the resonance. This novel energy-jump method was used to cross the coupling resonance and the results are summarized in Fig. 2. In the experiment, an acceleration rate which was only 5% of the regular one was used to induce more spin flip at the intrinsic resonance $G\gamma = 0 + \nu_y = 8.8$, while an energy-jump at about half of the regular acceleration rate was generated to cross the coupling resonance at $G\gamma = 0 + \nu_x = 8.6$. The energy-jump was accomplished by rapidly changing the beam circumference by 88 mm using the powerful AGS rf system. Because of the large momentum spread of the beam indicated as a hashed band in the lower part of Fig. 2, not all the beam particles are crossing the resonance during the jump unless the jump timing is carefully adjusted. From the beam momentum distribution, the ratio of the final to the initial polarization as a function of jump timing T_{jump} can be predicted and is shown as the solid line in the top half of Fig. 2. It shows good agreement with the data.

It clearly demonstrates that the novel energy-jump method can successfully overcome coupling resonances and weak intrinsic resonances.

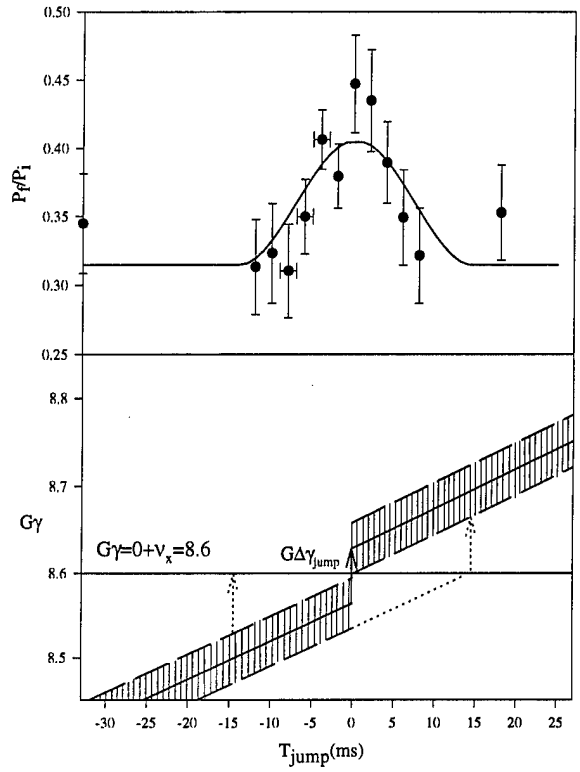

Figure 2: Energy jump data and schematics. In the top half, solid points are the experiment data, the solid line is the predicted curve, where P_f is the beam polarization measured after crossing both $G\gamma = 0 + \nu_x = 8.6$ and $G\gamma = 0 + \nu_y = 8.8$, and P_i is the beam polarization before the crossing. Bottom half shows the energy jump scheme. $G\gamma_{jump}$ is the amount of change of $G\gamma$ during the jump. The intrinsic resonance line $G\gamma = 0 + \nu_y = 8.8$ is not shown.

3 OUTLOOK

In the future, a novel scheme of overcoming strong intrinsic resonances is going to be tested, which is to use an AC dipole[7],[8]. Full spin flip can be achieved with a stronger artificial AC spin resonance excited by an AC dipole at a modulation tune ν_m. If we choose the AC spin resonance location $K_{AC} = n \pm \nu_m$ near the intrinsic spin resonance, the spin motion will be dominated by the AC dipole resonance and the spin near the intrinsic resonance will adiabatically follow the spin closed orbit of the AC spin resonance. With the AC dipole, a new dominant resonance near the intrinsic resonance is introduced, instead of enhancing the intrinsic resonance and also the coupling resonance strength, as has been proposed earlier[9]. Spin tracking studies for the AGS ring have indicated that this scheme should work. The energy-jump method can then be used for the residual coupling resonances and the weak intrinsic resonances.

4 REFERENCES

[1] L.H. Thomas, Phil. Mag. **3**, 1 (1927); V. Bargmann, L. Michel, V.L. Telegdi, Phys. Rev. Lett. **2**, 435 (1959).

[2] F.Z. Khiari, et al., Phys. Rev. D**39**, 45 (1989).

[3] T. Roser, High Energy Spin Physics: 8th International Symposium, Minneapolis in 1988, AIP Conference Proceedings, **187**(1989) 1442.

[4] H. Huang, et al., Phys. Rev. Lett. **73**, 2982 (1994).

[5] A. Luccio, BNL Report, BNL-52481(1995).

[6] H. Huang, T. Roser, A. Luccio, These Proceedings.

[7] M. Bai, et al., These Proceedings.

[8] M. Bai, S.Y. Lee, H.Huang, T. Roser, M. Syphers, "Overcoming the Intrinsic Spin Resonance Using Resonance Island Created by RF Dipole", AGS/RHIC/SN No. 055.

[9] T. Roser, Proceedings of the 10th International Symposium on High Energy Spin Physics, Nagoya, (1992) 429.

NONLINEAR BEAM DYNAMICS STUDY AT THE VEPP-4M

V. Kiselev, E. Levichev, V. Sajaev, V. Smaluk
Budker Institute of Nuclear Physics, Novosibirsk 630090, RUSSIA

Abstract

Nonlinear dynamics of transverse beam motion has been studied experimentally at the VEPP-4M electron-positron collider. One aspect of nonlinear beam behaviour described in this paper is the amplitude-dependent tune shift near nonlinear resonances. The measurement results are presented and compared with the theoretical prediction.

1 INTRODUCTION

Despite the progress in explanation of nonlinear phenomena in circular accelerators, there still is a gap between computer simulations or analytical predictions and reality. To reduce this gap, many dedicated experiments have been performed in both hadron and lepton machines in recent years. Rather complete and well-prepared reports can be found in Ref.[1],[2].

As it was recently found [3], the dynamic aperture of VEPP-4M is strongly affected by magnetic field nonlinearities. The measured value of the dynamic aperture does not follow the lattice model with nonlinear components computed from direct magnetic measurements. In order to explain this discrepancy, nonlinear motion features were measured extensivelly at the VEPP-4M storage ring in 1995-1996.

This paper concerns the study of nonlinear detuning under various experimental conditions. The amplitude-dependent tune shift was studied for both sextupole and octupole perturbation using a FFT spectrum of coherent beam oscillation excited by fast kicker. The experimental data agree quite well with the tracking simulation and model prediction.

2 HARDWARE DESCRIPTION

The VEPP-4M storage ring is a 6 GeV racetrack electron-positron collider with a circumference of 366 m. The study was performed at an injection energy of 1.8 GeV. To produce coherent transverse motion, the beam is kicked vertically or horizontally by pulsed electromagnetic kickers. Oscillation of the beam centroid and beam intensity are measured turn-by-turn with a beam position monitor (BPM) $SRP3$ for up to 4096 revolutions. The rms displacement resolution is $\sigma_{x,z} \simeq 70\mu$m in a 1 to 5 mA beam current range.

For a theoretical prediction the following sources of magnetic field nonlinearity were taken into account :

1. 32 vertical and horizontal sextupole corrections distributed along the magnets in the arcs (two families, DS and FS).
2. Lumped sextupoles $SES2$, $NES2$ and $SES3$, $NES3$ located symmetrically around the interaction point.
3. Quadratic field component produced by the arc magnet pole shape (two families, SSF and SSD).
4. Octupole correction coils incorporated in the arc magnet main coils (32 corrections, two families, SRO and NRO).

Because of high beta-function values ($\simeq$120 m), a bulk of natural chromaticity of the ring is produced by the final focus quadrupoles ($\simeq$50% in a horizontal plane and $\simeq$60 % in a vertical plane). This chromaticity is locally compensated by the $SES2/NES2$ and $SES3/NES3$ sextupoles. Hence, we can expect that the influence of these sextupoles on the nonlinear dynamics should be emphasized.

3 AMPLITUDE-DEPENDENT TUNE SHIFT

Coherent beam oscillation is fired by several kicker pulses with different amplitudes, and tune was extracted from a FFT spectrum of 1024 revolutions. To avoid decoherence and various damping mechanisms, a special algorithm is developed to extract beam displacement from first 30-50 revolutions. The accuracy of the tune measurement is better than $2 \cdot 10^{-4}$. Before kick measurement the following preparatory adjustments and calibrations are made:

1. Beta-functions are measured in the $SRP3$ pickup station: β_z =12 m, β_x =4 m (model values are β_z =13.2 m, β_x =4.5 m).
2. Tune-current dependence is measured ($\delta\nu_x = -3 \cdot 10^{-4}$ mA^{-1}, $\delta\nu_z = -1.3 \cdot 10^{-3}$ mA^{-1}) and taken into account. To reduce this effect, in every kick series the beam intensity is dropped down for less than 0.3 mA.
3. The linearity and absolute kick amplitude calibration is made by scrapers with accuracy better than 0.1mm.

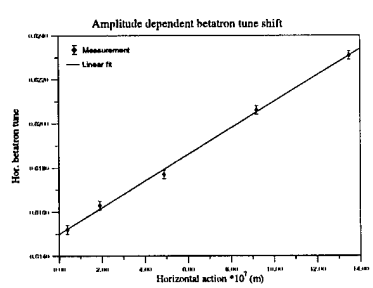

Figure 1: Typical amplitude dependence of the betatron tune.

For both octupole and sextupole perturbation, the nonlinear tune shift is proportional to the squared initial beam

0-7803-4376-X/98/$10.00 © 1998 IEEE

displacement (Fig.1). A general 2D form of the amplitude-dependent tune shift can be expressed as (a second order approximation):

$$\Delta\nu_x(a_x, a_z) = C_{11} \cdot 2J_x + C_{12} \cdot 2J_z,$$
$$\Delta\nu_z(a_x, a_z) = C_{21} \cdot 2J_x + C_{22} \cdot 2J_z,$$

where C_{nm} depends on particular perturbative potential. The measured and estimated coefficient values are listed in Table:

$C_{nm} \cdot 10^4$ (m^{-1})	Theory	Experiment
C_{11}	50	3900
C_{12}	-840	-1400
C_{21}	-840	-1750
C_{22}	-830	-1400

The difference in theoretical and experimental C_{11} made us explore systematically the horizontal nonlinearity of the ring. The later may be induced by octupole and/or sextupole (in second order) errors that we did not consider in our model simulation. To distinguish, which one defines C_{11} in our case, we used the difference between the determination of the octupole and sextupole tune shift. For an octupole potential the horizontal tune shift is independent on an initial tune value:

$$\Delta\nu_x^{(o)}(J_x) = \frac{J_x}{16\pi}\int_0^C \mathcal{O}(s)\beta_x^2(s)ds + o(J_x^2), \qquad (1)$$

where C is the machine circumference and $\mathcal{O}(s) = (d^3B_z(s)/dx^3)/B\rho$ is the effective octupole strength. Sextupole tune shift on the contrary depends on an initial tune near the resonance $3\nu_{x0} \simeq m$ in a resonant way and can be written as

$$\Delta\nu_x^{(s)}(J_x) \simeq -J_x \cdot 36\,\frac{A_{3m}^2}{3\nu_x - m} + o(J_x^2),$$

where A_{3m} is the azimuthal harmonic of the sextupole Hamiltonian.

The measured horizontal tune shift as a function of an initial tune ν_{x0} in the vicinity of the resonance $3\nu_{x0} = 26$ is shown in the top of Fig.2. To fit the computed curve with the data points, we should move the curve in positive direction by a value $\Delta\nu_x^{(o)}/2J_x \simeq 3500$ m^{-1} independently of initial tunes. We can propose that this value is the octupole contribution to the total tune shift.

To verify validity of this assumption, first, we controled octupole perturbation by the octupole correctors SRO/NRO, distributed along the ring arcs. Changing their excitation current from 0 A to -0.5 A provides a decrease of the average level of the $C_{11}(\nu_{x0})$ for all the unperturbed working points ν_{x0} to a magnitude $\Delta\nu_x^{(o)}/2J_x \simeq 1700$ m^{-1}, while its resonant behaviour remains the same.

Next, we reduced the sextupole driving term responsible for the resonance $3\nu_{x0} = 26$. The excitation current of the $SES2/NES2$ sextupoles was decreased from 8 A to 4.4 A and the relevant sextupole harmonic became twice

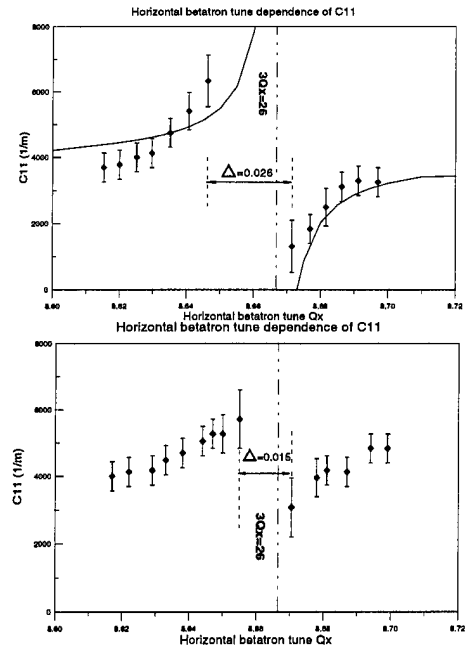

Figure 2: C_{11} behaviour near a resonance $3\nu_x = 26$ with normal (top) and reduced (bottom) sextupole driving term. Data points are measured; the curve is predicted.

as less. Uncompensated chromaticity was corrected by the sextupole coils in the regular arc magnets. One can see that the average level of the detuning retains, while the sextupole contribution is reduced. It is clearly seen from the resonance stopband Δ that was defined as a distance between the points where the beam lifetime became as low as 300÷400 s.

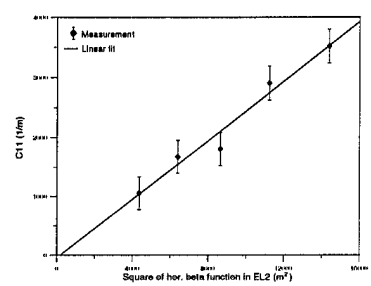

Figure 3: Dependence of the C_{11} coefficient on the β_x^2 value in the FF quadrupoles.

A detailed tracking study points out to the final focus (FF) quadrupoles $EL1/EL2$ as a most probable source of the octupole error. Otherwise we should suppose an unrealistically high nonlinear error in regular arc quadrupoles. It was shown in Ref.[4], that quadrupole edge fields can produce large detuning; however, in our case the relevant contribution to the C_{11} coefficient is ten times as less as the measured one. That is why we suspected that the octupole error was distributed in the FF quadrupoles.

Following this indication, we have done a set of measurements. **1.** According to (1), first we measured quadratic

dependence of the octupole detuning on β_x. The excitation current in the quadrupoles $EL1/EL2$ was changed, the tune point was adjusted back by the arc quadrupole magnets, the chromaticity was compensated and closed orbit distortion was corrected. The results of the measurement are presented in Fig.3 where C_{11} is shown as a function of β_x^2 in the FF quadrupoles. From this result we can estimate the value of the octupole errors as follows: $\mathcal{O} \simeq 0.5$ G/cm^3 $= 8.1$ m^{-4}.

2. Employing steering coils around the interaction region gives a possibility of measuring integrated magnetic field distribution by an electron beam. We can produce a local symmetric or antisymmetric orbit bump in the horizontal plane as it is shown in Fig.4, keeping closed orbit distortion in the rest of the ring within 0.5 mm, and measure the betatron tune shift caused by the

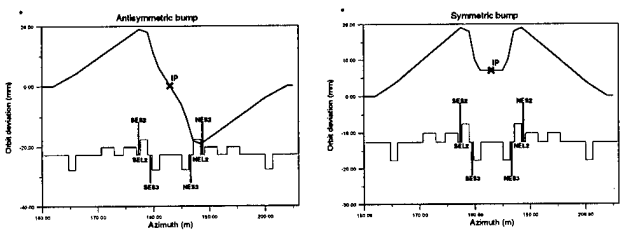

Figure 4: Closed orbit bump to measure the integrated magnetic field distribution by electron beam around the interaction point (IP). Left - antisymmetric, right - symmetric.

magnetic nonlinearities. In case of the symmetric bump the main contribution to the tune shift is provided by the chromatic sextupoles SES/NES, located inside the bump. In case of the antisymmetric bump the sextupole contribution is substracted and measured betatron tune shift as a function of orbit displacement x in the FF quadrupoles unambiguously demonstrates presence of integrated octupole nonlinearity (Fig.5).

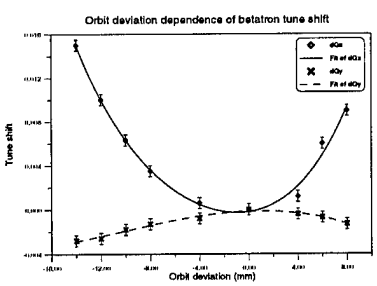

Figure 5: Betatron tune shift as a function of orbit deviation in the FF quadrupoles in case of the antisymmetric bump.

Using least square fitting of this curve one can easy extract the octupole contribution to the gradient error. In our case it gives us the octupole error in the FF quadrupole $\mathcal{O} \simeq 0.5$ G/cm^3 that agrees well with the previous estimation.

3. Due to the symmetry of the vector magnetic potential, a dodecapole componet B_5 is an inherency of a quadrupole field. For an ideal quadrupole magnetic field is represented as

$$B_z = B_1 x + \frac{1}{5!} B_5 x^5 + ...$$

Hence the octupole component in a quadrupole lens is proportional to the dodecapole and squared closed orbit distortion $\mathcal{O} \propto B_5 x_{co}^2$. To check it, we made a symmetric local bump in the FF region and study the horizontal amplitude-dependent tune shift as a function of x_{co}. The result is depicted in Fig.6. Estimation of the dodecapole value gives $B_5 \simeq 0.2$ G/cm^5 $\simeq 2.4 \cdot 10^4$ m^{-6}.

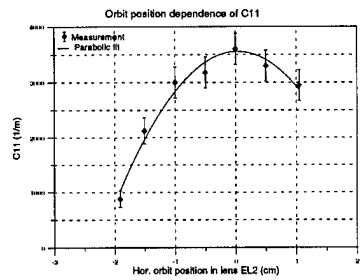

Figure 6: C_{11} coefficient as a function of the COD in the FF quadrupoles.

These measurements seem to point out the FF quadrupoles as a probable source of strong horizontal detuning due to octupole field error $\mathcal{O} \simeq 0.5$ G/cm^3 (1.8 GeV). Unfortunately, direct field measurement gives only half of this value and the reason for this discrepancy was not understood yet.

4 CONCLUSION

We studied amplitude-dependent tune shift at the VEPP-4M electron-positron collider. The measurements were performed by the single turn-by-turn BPM technique. The experiments indicate that the features of our nonlinear system are strongly influenced by octupole perturbation that does not follow from the model lattice representation. All measurement results agree well with the theoretical prediction if we assume small (about 0.5 G/cm^2) octupole error in the final focus qudrupoles. Unfortunately, direct magnetic measurement provides only one half of the required value.

5 REFERENCES

[1] J.Gareyte. Experimantal evidence of transverse nonlinear phenomena in accelerators, *Part. Accel.* **27** , 187-196 (1990).

[2] W.Fischer, M.Giovannozzi and F.Schmidt. The dynamic aperture experiment at the CERN SPS, CERN SL/95-96(AP), 1995.

[3] V.Kiselev, E.Levichev, V.Sajaev, V.Smaluk. Dynamic aperture measurement at the VEPP-4M storage ring. *Part.Accel.*(in printing).

[4] Forest E.*et al.* (1994). Sources of amplitude-dependent tune shift in the PEP-II design and their compensation with octupoles. - Proc. of EPAC'94, London, **2**, 1033-1035.

DYNAMIC APERTURE STUDY AT THE VEPP-4M STORAGE RING

V. Kiselev, E. Levichev, V. Sajaev, V. Smaluk
Budker Institute of Nuclear Physics, Novosibirsk 630090, RUSSIA

Abstract

Dynamic aperture has been studied experimentally at the VEPP-4M electron-positron collider. A transverse bunch motion was excited by fast kickers. The beam intensity and the amplitude of the coherent oscillations were measured turn-by-turn by the BPM. In this paper the technique of determining the dynamic/physical aperture is described. Several methods of increasing the dynamic aperture are discussed. The results of computer simulation and simple model analytic prediction explaining the experimental data are presented.

1 INTRODUCTION

In Ref.[1] the results of the measurements of nonlinear phase trajectories and amplitude-dependent tune shift at VEPP-4M are discussed. Here we concentrate on the aperture limitation study due to the nonlinear magnetic field.

The measurements were performed at the injection energy of 1.8 GeV with the following beam parameters: horizontal emittance ϵ_x =35 nm, betatron tunes ν_x =8.620 and ν_z =7.572, natural chromaticity ξ_x =-13.6 and ξ_z =-20.6, revolution period τ =1.2 μs. Large contribution of the final focus quadrupoles to the natural chromaticity ($\simeq$50 % in the horizontal direction and $\simeq$ 60 % in the vertical direction) is compensated by the near-by sextupoles of $SES2$ and $NES2$ families (6 lenses). The residual chromaticity is corrected in the arcs by 32 sextupole corrections distributed along the dipole magnets (DS and FS families).

The dynamic aperture is measured by the coherent beam motion excitation[2],[3]. Coherent betatron motion is excited by fast electromagnet kickers in the horizontal or vertical planes. To measure the beam displacement and the intensity of every revolution BPM $SRP3$ in the turn-by-turn mode is used[4]. The measured BPM resolution (rms) in this mode for the beam current range of 1-5 mA equals $\simeq$ 70 μm for both directions.

2 DYNAMIC APERTURE MEASUREMENT TECHNIQUE

The measurement of the coherent beam motion allows to determine dynamic or physical aperture as a displacement at which the beam intensity loss occurs - the same way it does in the computer tracking. But contrary to simulation where a single particle is tracked, in experiment we deal with a beam of a finite size and current. The later can cause many effects (coherent and incoherent) which obscure the precise aperture measurement. Hence, the beam loss study has been carried out before performing a dynamic aperture measurement. We expected that the particles would be lost very fast outside the stable motion boundary because their amplitude grows exponentially when the nonlinear motion becomes unstable.

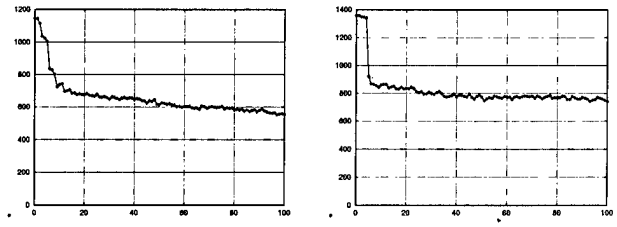

Figure 1: A fast beam loss onto the dynamic (left) and physical (right) aperture. The first 100 revolutions are shown.

This study shows that:

1. When the kick amplitude is low, the BPM does not indicate the intensity reduction: all particles move inside the acceptance along the stable trajectories.
2. At some intermediate kick amplitude a long term beam loss appears. The typical time interval for this loss is about 10 ms, and it occurs because of the particle distribution cut off by the aperture limitation. During this time many other effects (including damping) can take place, so it is difficult to extract the information about the dynamic aperture from these measurements.
3. And only starting with the high enough amplitude of the kick, a short time (20-50 turns) beam loss is observed (Fig.1). Only this loss corresponds to the dynamic aperture limitation because of the fast growth of the particle displacement outside the stable region.

The total intensity decreases include both long and short term parts but only the last one defines the aperture limitation unambiguously.

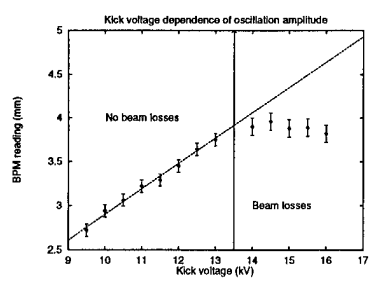

Figure 2: BPM coordinate reading as a function of the kick voltage.

Apart from the beam intensity, the BPM also measures the position of the beam center of mass. The initial amplitude of the coherent oscillations is computed for the first 30

0-7803-4376-X/98/$10.00 © 1998 IEEE

turns to cancel all damping effects. For low amplitudes, the BPM coordinate reading X_p linearly depends on the kick voltage $X_p = KU$. However, when the fast beam loss is observed, this dependence drastically declines from the linear one (Fig.2). To explain this fact we have assumed that the beam center of mass $X_p(U)$ differs from the actual kick amplitude X_0 just after the kick because some beam portion is lost and several dozens revolutions are not enough for the quantum effects to restore the initial beam distribution. This fact should be taken into account when the dynamic aperture is measured by BPM.

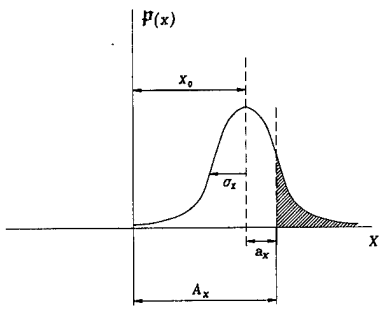

Figure 3: Beam is kicked onto the boundary of the dynamic or physical acceptance (left - phase space, right - beam distribution).

To verify our assumption, we consider the beam kicked onto the boundary of the dynamic or physical acceptance $A_x = a_x + X_0$ (see Fig.3). For the Gaussian distribution $\mathcal{P}(x, x')$ with the rms beam size σ_x, the ratio of the beam intensity inside the stable phase area to the initial one $æ = I_1/I_0$ is given by the error function

$$æ = 1/2 \pm \frac{1}{2}\mathrm{erf}(\frac{a_x}{\sqrt{2}\sigma_x}),$$

where "+" ("-") is taken when $æ > 1/2$ ($æ < 1/2$). Assuming that $A_x \gg \sigma_x$, we can integrate $\mathcal{P}(x, x')$ over x' from $-\infty$ to $+\infty$. After the beam distribution tail is lost outside the stable acceptance, the BPM coordinate may be written as

$$X_p = X_0 - \sigma_x \frac{1}{æ\sqrt{2\pi}} \exp(-\frac{a_x^2}{2\sigma_x^2}) = X_0 - \sigma_x F(æ),$$

where $X_0 = KU$ is the linear kick amplitude. Knowing the value of æ, one can find $F(æ)$. In the reasonable range of $æ = 0.2 \div 1$, $F(æ)$ can be approximated as

$$F(æ) \simeq 1.6(1 - æ).$$

Fig. 4 shows the measured value of $\Delta X(æ) = X_0 - X_p(æ) = \sigma_x F(æ)$. The horizontal rms beam size extracted from these data $\sigma_x = 0.5 \pm 0.12$ mm corresponds quite well to that obtained by the beam lifetime measurements with a movable scraper ($\sigma_x = 0.55$ mm).

From these measurements we can conclude that the fast beam loss (for 20-50 beam revolutions) actually relates to the aperture limitation, while the long term beam intensity

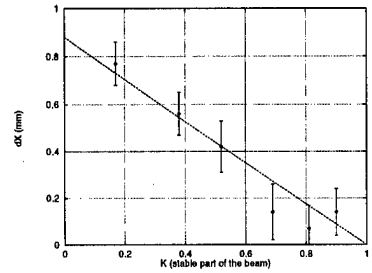

Figure 4: Measured dependence of $\Delta X(æ)$

measurements can include many different effects. For the dynamic aperture measurement we proceed as follows:

1. The coefficient $K = X_p/U$ is found at the low kick amplitude.
2. The kick voltage is increased till the half beam is lost after the first 20 revolutions, $æ = I_{20}/I_0 \simeq 0.5$.
3. The dynamic aperture is defined according to $A_x = KU_{0.5}$.

For a typical VEPP-4M lattice at the injection energy, the measured aperture limitations at the azimuth of BPM station $SRP3$ are

$$A_x = 4.5\,, \quad A_z = 5.1\,,$$
$$\sigma_x = 0.55\,, \quad \sigma_z = 0.42\,,$$
$$\beta_x = 4\,, \quad \beta_z = 12\,,$$

Now the question is how to distinguish which one aperture, dynamic or physical, limits the stable area? To answer this question we have measured the beam loss at the movable scraper. The scraper moves toward the beam orbit with a step as small as 0.1 mm and the fast beam loss is studied. Fig.1 shows the beam loss without scraper and when the latter is inserted into the vacuum chamber. One can see that if the boundary of the motion is determined by the scraper, the beam intensity drops sharply during the first revolutions, while for the dynamic aperture limitation several dozens turns are required to get particles out of the stable area.

In case of VEPP-4M, we have the dynamic aperture for the horizontal plane and the physical aperture for the vertical plane.

3 THEORY ANALYSIS

The VEPP-4M model lattice tracking demonstrates the horizontal dynamic aperture twice as large as the measured one.

The sextupole-induced horizontal resonance that is easily reached from the nominal tune $\nu_x = 8.62$ is $3\nu_x = 26$, and the phase space measurement shows typical triangle shape of the phase trajectories[1]. That's why to explain the discrepancy between the tracking and experiment, we consider analytically the horizontal dynamic aperture in the

vicinity of the resonance $3\nu = m$. This isolated resonance can be described with the following Hamiltonian,

$$H_r = \delta J_x + \alpha J_x^2 + \sqrt{(8)} A_3 J_x^{3/2} cos 3\phi_x,$$

where J_x and ϕ_x is the action and angle variables, $\delta = \nu_x - m/3$ is the distance from the resonance, α is the nonlinearity, and A_3 is the resonance driving term (azimuthal Fourier harmonic of the sextupole perturbation)

$$A_3 = \frac{1}{12\sqrt{2}} \int_0^{2\pi} \beta_x^{3/2} \frac{B"}{B\rho} cos(3(\psi_x - \nu_x\theta) + m\theta) d\theta.$$

The action variable relates to the transverse displacement as $x(s) = \sqrt{2\beta_x(s)J_x}$. The stable motion is limited by two points which correspond to the action J_{x1} ($\phi_x = 0$) and J_{x2} ($\phi_x = \pi$). The first point is a resonance fixed point and can be found from

$$\frac{\partial H_r}{\partial J_x} = 0, \quad \frac{\partial H_r}{\partial \phi_x} = 0.$$

The second point J_{x2} is defined by the invariant Hamiltonian $H_r(J_{x1}, 0) = H_r(J_{x2}, \pi)$ that gives a fourth power equation which can be solved numerically.

To calculate the horizontal dynamic aperture we will use the experimental results presented in Ref.[1]. For our tune point $\nu_x = 8.620$ the measured sextupole perturbation harmonic equals $A_3 \simeq -2.8$ m$^{-1/2}$. This value reasonably corresponds to the model one. On the contrary, the measured nonlinearity is much more large than that obtained from the VEPP-4M model lattice. The experimental data show $\alpha = 3200$ m^{-1}. The study indicates the octupole field errors in the final focus quadrupoles (where the betatron functions reach the value more than 100 m) as a possible source of this nonlinearity. Using these values, we can obtain the following dynamic aperture at the azimuth of BPM $SRP3$ ($\beta_x = 4$ m):

$$A_x = (+5.1, \quad -3.3). \tag{1}$$

The measured dynamic aperture ($A_x = 4.5$ mm) is obtained from the oscillations amplitude averaged over several dozens turns, hence to compare it with the theory result we need to take from (1) the mean absolute value which equals $A_x = 4.2$ mm. The ideal VEPP-4M lattice gives the aperture of $A_x = (+10, \quad -5)$ that is significantly larger than the measured one.

Apart from the analytic estimation, computer tracking of the realistic lattice has been performed with the octupole field incorporated into the final focus quadrupoles to provide the measured detuning effect. The tracking results agree with the theoretical results.

4 DYNAMIC APERTURE INCREASE

To open the dynamic aperture we need to reduce either the resonance driving term A_3 or nonlinearity α. We have verified each of these ways as well as combined both of them.

As the strong final focus sextupoles $SES2$ and $NES2$ strongly contribute to the harmonic A_3, we have decreased their excitation current from 8.4 A to 4.3 A. The residual chromaticity was compensated by the distributed sextupole correctors in the arcs.

As was shown in Ref.[1], in our case the horizontal nonlinearity is defined by the octupole perturbation. So, we have used the octupole coils in the arcs (which are not energized in the routine operation mode) to decrease the nonlinearity by a factor of 1.7.

The first way (sextupole harmonic reduction) results in the horizontal aperture enhancing up to 7 mm, which is more than 1.5 times larger than the initial one. On the contrary, the octupole corrections do not provide significant aperture increase (5.4 mm). Measurements done after combining the two approaches indicate that the aperture increased up to 5.9 mm which is less than that obtained with the sextupole correction only.

The latter seems to be rather strange because the tracking for all three cases shows that the best result (up to 10 mm) is obtained in case when two kinds of corrections are used simultaneously. A possible explanation is that the octupole perturbation excites additional high order resonances which create obstacles to the aperture increasing.

5 CONCLUSION

In conclusion, we have experimentally measured the dynamic aperture of the VEPP-4M storage ring using the turn-by-turn particle tracking system. As it was found for VEPP-4M, the horizontal aperture is limited by the nonlinear fields, while the vertical one is defined by the physical limitation.

The stable motion boundary, obtained with the single resonance approximation, shows good agreement with the measurement results.

We have increased the horizontal aperture by the sextupole resonance driving term reduction. But we failed to do the same by the detuning compensation with the octupole field corrections. We suspect that this might be due to the additional higher-order resonances excited by the octupole corrector.

6 REFERENCES

[1] V.Kiselev, E.Levichev, V.Sajaev, V.Smaluk. Nonlinear beam dynamics study at VEPP4-M. The Proc. of the EPAC'96, v2, pp.896-898, 1996.

[2] P.L.Morton et al. A diagnostic for dynamic aperture.- SLAC-PUB-3627, 1985.

[3] S.Y.Lee et al. Experimental determination of a nonlinear Hamiltonian in a synchrotron.- Phys.Rev.Let v.67, No.27, 1991.

[4] A.Dubrovin at al. Applications of beam diagnostic system at the VEPP-4 complex. The Proceedings of the EPAC'96, v2, pp.1585-1587, 1996.

SORTING STRATEGIES FOR THE LHC DIPOLES

R. Bartolini, W. Scandale
CERN, CH-1211 Geneva 23, Switzerland
M. Giovannozzi, E. Todesco
INFN, Sezione di Bologna, V. Irnerio 46, I-40126 Bologna, Italy

1 INTRODUCTION

Unavoidable field-shape imperfections are present in the superconducting magnets of modern hadron colliders, due to mechanical tolerances, persistent currents, design imperfections, coil deformations and iron saturation. The residual multipolar errors, typically of the order of a few units in 10^{-4} at the usual reference radius of 1 cm, have a detrimental effect on the stability of the particle orbits. A sound design of the machine layout, with well focused orbit functions and a suited set of multipolar correctors, may help in improving the beam stability. However, the dynamic aperture (hereafter DA), may strongly depend on the random part of the multipolar imperfections and on the specific distribution of the errors along the machine azimuth. In such a case, sorting strategies can be applied to provide the mutual compensation of the residual errors. This procedure is quite demanding, therefore it is crucial to evaluate in detail the expected beneficial effects on beam dynamics. In fact, all the magnets have to be carefully measured as they are manufactured and qualified in terms of the random imperfections. In addition, a sizeable number of magnets must be available for sorting before the final installation.

Two techniques are proposed for sorting the LHC dipoles. The first one uses the perturbative analysis of the nonlinear betatron motion to find dynamical quantities which allow to evaluate rapidly the DA. These quantities are called Quality Factors (hereafter QF) [1, 2]: the search of a satisfactory rearrangement is performed by generating random permutations of the magnetic elements, selecting the permutation which optimises the QF and hence the DA. The effectiveness of this method depends on the degree of correlation of the QF with the numerical estimate of the dynamic aperture. The second approach is based on the local cancellation of the random errors by pairing the magnets with similar errors in magnitude and sign and placing the pairs in strategic positions along the azimuth of the accelerator. We refer to these methods as deterministic algorithms [3, 4].

In Section 2 we present in detail the sorting strategies. In Section 3 we apply them to a realistic LHC model. Conclusions are drawn in Section 4.

2 SORTING STRATEGIES

2.1 *Analytical indicators of the dynamic aperture*

A good arrangement of the magnets along the azimuth of the accelerator can be found by comparing a sufficiently large number of random permutations [5]. Each permutation produces a different lattice with a different DA and the search is stopped when a satisfactory value of the DA is found. The direct calculation of the DA is extremely time consuming and allows to explore only a very limited number of permutations. It is therefore necessary to find dynamical quantities which can be computed much faster while being well correlated with the DA, in order to explore more configurations. The perturbative theory of the betatron motion provides a powerful tool to parametrise the effects of non linearities on beam dynamics and to build analytical indicators of the DA. The QF considered in this paper are either the tuneshift or the strength of a certain resonance.

The first step of the sorting procedure is the analysis of the correlation of various QF with the DA. A QF is retained if it allows to better disentangle the good realizations (i.e. the ones with a large DA) from the bad ones. The second step consists in generating a set of random permutations of the errors and for each permutation to compute only the QF. The permutation which gives the minimum value of the QF is selected. The third and last step of this technique consists in the verification of the effectiveness of the sorting strategy. The analysis of the correlation of the QF's with the DA is made typically considering only the 4D betatronic motion, and the short-term DA. We therefore have to check, a posteriori, that the sorted sequence is more stable for long-term tracking, including synchrotron motion and various tune ripple sources. It is also interesting to verify whether the improvement is robust with respect to significant changes of the working point of the machine. This last step will be treated in a separate paper in preparation.

The DA is calculated by tracking particles for 10^3 turns, with different initial conditions on a polar grid in the plane (x, y) assuming zero initial momenta. The coordinates of the last stable particle on each radius are retained and the value of the DA is given by the average of the radius over the different angles. The QF's used are defined in Ref. [2] and they were calculated with the FORTRAN code PLATO [6].

2.2 *Deterministic algorithms*

Local compensation schemes allow to define deterministic algorithms to rearrange the magnetic elements along the azimuth of the accelerator. They are based on the pairing of magnets with similar random errors which mutually compensate by an appropriate location in the lattice.

Pairing at zero phase advance. Taking into account that two adjacent dipoles have close values of the optical functions and almost the same betatron phase, one can obtain a local compensation scheme by placing in adjacent posi-

0-7803-4376-X/98/$10.00 © 1998 IEEE

tions two errors equal in strength but with opposite signs. In the LHC cell the average phase advance between two dipoles is approximately 15 degrees and the optical functions vary by less than 50%. This method will be denoted by Sort-1 in what follows.

Pairing at 180 or 360 degrees. Two equal and opposite errors are quite well compensated at 360 degrees, while equal errors with the same sign cancel at 180 degrees, assuming that the motion is quasi-linear between the two locations. In the LHC, each cell contains 6 dipoles and the phase advance is about 90 degrees. Positions separated by 24 (12) magnets correspond to a phase advance of 360 (180) degrees. In these positions the optical functions are the same. Therefore one can easily obtain quasi-local compensation of the errors. This method will be denoted as Sort-2.

2.3 *Mixed techniques*

It is possible to define sorting procedures based on more than one of the previous strategies. The pairing of two adjacent magnets can be improved by a compensation at 360 degrees. In this case 4 dipoles are paired. This method will be denoted as Sort-3. Furthermore, the techniques based on the QF's can be used in combination with deterministic algorithms. In this case the compensated pairs of magnets are considered as a new unit and the permutations are generated not on the single magnets but on the pairs. In fact we found very effective to combine the QF's analysis on permutations of blocks of 4 dipoles previously paired with the Sort-3 method. This method will be denoted as Sort-3-QF, where QF is the dynamical quantity which has been minimised.

3 THE LHC MODEL

The LHC model used in our simulation is the old LHC version 2, with the injection optics. It is made of 8 octants, each of them carrying 16 dipoles in the dispersion suppressor region and 144 dipoles in the arcs. Each arc is composed of 24 FODO cells each carrying 6 dipoles. The overall number of dipoles is 1280. The set of 376 chromatic sextupoles is considered in the simulations. The distribution of the random errors is assumed to be Gaussian truncated at 3 σ and the σ of the multipolar coefficients used in the simulation are given in Table 1. We assume that the magnets will be installed as the production goes on. Only a limited number of dipoles will be stored and available for sorting. We applied the sorting strategies on groups of 144 dipoles. Two extreme cases were analysed in detail: dipoles with only random b_3, and dipoles with the full set of random errors given in Table 1.

3.1 *Random b_3*

We applied the deterministic algorithms to a set of 100 realizations of the random errors. Furthermore we analysed the correlation of the QF's related to the tuneshifts and the strength of several resonances. Several of those were found

Table 1: Random errors in the LHC dipoles at injection, in unit 10^{-4} referred to a radius of 1 cm.

Order	Normal	Skew
1	-	-
2	0.372	1.227
3	0.882	0.186
4	0.055	0.186
5	0.083	0.041
6	0.014	0.022
7	0.012	0.011
8	0.005	0.005
9	0.003	0.004
10	0.002	0.002
11	0.001	0.001

to be well correlated as shown in Fig. 1(a) and (b). The correlations can vary when the dipoles are paired, i.e. with the scheme Sort-3 as shown in Fig. 1 (c) and (d). Some

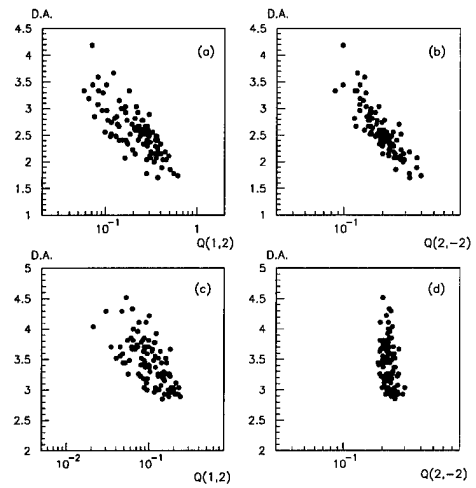

Figure 1: Correlation of DA and QF for 100 random realizations of b_3: (a) norm of (1,2), (b) norm of (2,-2). After the pairing of the dipoles according to the scheme Sort-3, the same correlation plots are shown in (c) and (d) respectively.

QF's lose their correlation with the dynamic aperture after the pairing of the dipoles while others are still well correlated. This implies that the process of pairing acts only on particular resonant terms as, for instance, the strength of the resonance $(2, -2)$. The QF's which are still correlated can be used to improve the DA: the norm of the resonance $(1, 2)$ has been used to sort a set of 100 random realizations of the errors. The characteristics of the distribution of the DA and the results of the sorting strategies are reported in Table 2. The average value over 100 realizations is denoted by $< \rho >$ and the R.M.S. by σ_ρ. The improvement of the DA due to the sorting of the cases with an initially small value of the DA are denoted as 'Worst Cases' in Table 2. The effect of sorting on the DA can be put in evidence by plotting the relative gain in DA as a function of the DA of the unsorted realizations of the errors, as shown in Fig. 3.

Table 2: Characteristics of the DA distribution over 100 random realizations of b_3, with different sorting procedures.

	$<\rho>$	σ_ρ	Gain	Worst Cases
unsorted	2.57	0.44	-	
sort-1	3.24	0.39	26%	74%
sort-2	3.02	0.37	18%	53%
sort-3	3.45	0.38	35%	82%
sort-3-$Q(1,2)$	3.78	0.42	48%	91%

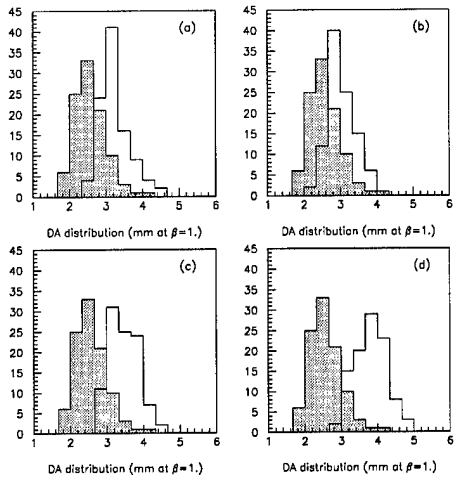

Figure 2: DA distribution over 100 random realizations of b_3 paired and sorted with $Q(1,2)$; the DA is given in normalized mm at $\beta_x = 1$ m.

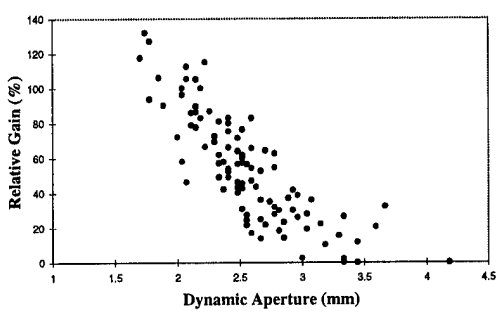

Figure 3: Relative gain as a function of the DA of the unsorted sequence of random errors for 100 realizations. Random b_3.

3.2 *All random errors*

We applied the deterministic algorithm described in Sec. 2.2 to the case where all the random errors up to the 11-th order are considered in the dipoles. The correlation of the QF's was also investigated generating permutation of the block of magnets previously paired. Owing to the presence of multipoles of order as high as 11, the one turn map has to be calculated at the same order. Resonances up to 10-th order were investigated and the norm of the resonance $(7,-1)$ was chosen to select the best permutation

Table 3: Characteristics of the DA distribution over 100 random realizations of all the random errors, with different sorting procedures.

	$<\rho>$	σ_ρ	Gain	Worst Cases
unsorted	1.57	0.09	-	-
sort-1	1.63	0.07	4%	13%
sort-2	1.64	0.05	4%	15%
sort-3	1.65	0.07	5%	15%
sort-3-$Q(7,-1)$	1.68	0.05	7%	17%

of the blocks obtained from the Sort-3 method. The effects on the DA were investigated on a set of 100 random realizations of the errors and the results are reported in Table 3 and in Fig. 4. The improvement of the dynamic aperture is still non negligible especially for the worst cases.

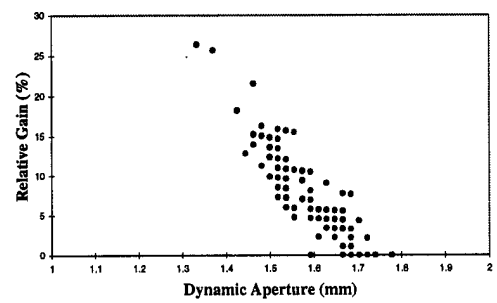

Figure 4: Relative gain as a function of the DA of the unsorted sequence of random errors for 100 realizations. All random errors.

4 CONCLUSIONS

We presented several sorting strategies and their application to a simplified LHC model with only random errors. The effect of sorting on the dynamic aperture is particularly significant for the worst realizations of the random errors, and improvements larger than 25% were found for the most complicated cases where all multipolar errors up to order 11 are included in the dipoles. The analysis of the robustness of these improvements is in progress in more recent LHC lattice models.

5 REFERENCES

[1] F. Willeke, DESY HERA **87–12** (1987).

[2] M. Giovannozzi, R. Grassi, W. Scandale, E. Todesco, Phys. Rev. **E 52**, pp (1995). 3093–3101

[3] W. Scandale, L. Wang, CERN SPS (AMS) **89–22** (1987).

[4] D.M. Ritson, CERN LHC Project Note **53** (1996).

[5] R. Bartolini, M. Giovannozzi, W. Scandale, E. Todesco, CERN LHC Project Note **38** (1995).

[6] M. Giovannozzi, E. Todesco, A. Bazzani, R. Bartolini, CERN PS (AP) **96-12** (1996).

[7] A. Bazzani, E. Todesco, G. Turchetti and G. Servizi, CERN **94–02** (1994).

INVESTIGATION OF CHROMATICITY SHARING AT THE CORNELL ELECTRON STORAGE RING

S. Henderson, R. Littauer, B. McDaniel, T. Pelaia, R. Talman, E. Young,
Laboratory of Nuclear Studies, Cornell University, Ithaca, NY 14853*

Abstract

A potential advantage of the "Möbius" scheme, or any other strongly coupled lattice, is that the normal-mode oscillations are damped at rates which depend on both the horizontal and vertical chromaticities. This opens up the possibility of maintaining adequate damping even for quite negative chromaticity in one plane, provided the other is appropriately increased to compensate. This "chromaticity sharing" has been observed at CESR by introducing resonant coupling with weak skew quadrupoles and observing the coherent damping rates of shock-excited betatron oscillations.

1 INTRODUCTION

Chromaticity compensation is required in high-energy storage rings to avoid instability due to the head-tail (H-T) effect [1, 2]. We define the chromaticity of a lattice as

$$Q' = dQ/d\delta \tag{1}$$

where Q is the betatron tune and δ is the fractional deviation from nominal momentum. The natural chromaticity of a lattice is negative, which produces a positive growth rate α in the lowest (dipole, $m = 0$) H-T mode; damping ($\alpha \leq 0$) requires $Q' \geq 0$. Ordinarily, sextupoles are introduced in the lattice to make $Q' \geq 0$ in both the x and y planes of oscillation.[1]

A sextupole produces *opposite* chromaticity changes in x and y. Thus at least two families of sextupoles are required, so placed as to yield a net positive correction in both planes. To the extent that the x and y sextupoles have opposing effects, their individual strengths can become relatively large, particularly for the y sextupoles, which are less effective because they tend to be in regions of small dispersion. Strong sextupoles reduce the dynamic aperture of the lattice.

A potential advantage of the Möbius scheme proposed by Talman [3] is that normal-mode oscillations, containing both x and y components, should be damped at a rate that depends on both α_x and α_y, an effect we call *chromaticity sharing*. It promises to maintain H-T stability with a less restrictive choice of sextupoles; instead of both $Q'_x \geq 0$ and $Q'_y \geq 0$, the criterion becomes $Q'_x W_x + Q'_y W_y \geq 0$, where W_x, W_y are factors describing the relative magnitudes of the x and y wake fields affecting the bunch.

Talman [4] has generalized the two-macroparticle model of the H-T effect to include $x - y$ coupling. The two coupled modes of interest show equal growth rates of the form

$$\alpha \propto \frac{I\hat{\delta}}{Q_s}(Q'_x W_x + Q'_y W_y) \tag{2}$$

where I is the bunch current, $\hat{\delta}$ is a typical peak momentum deviation, and Q_s is the momentum-oscillation tune. (An additional term which depends on the coupling strength S, $(Q'_x - Q'_y)(W_x - W_y)\frac{S^2/2}{Q_s^2 - S^2}$, small everywhere except near $S \simeq Q_s$, has been neglected.) In this model, constant H-T damping–the same for both coupled modes–occurs along a line in the Q'_x, Q'_y plane of slope $-W_x/W_y$.

Alternatively, one can ascribe a chromaticity directly to each of the normal coupled modes. When the lattice is at resonance (equal *fractional* tunes, $q_x = q_y \equiv q_0$), turning on a coupling element splits the tunes into upper and lower normal modes: $q_{U,L} = q_0 \pm \frac{1}{2}S$, where the tune split S is a measure of the coupling strength. If $Q'_x \neq Q'_y$, a particle off-momentum by δ is detuned from resonance by $D = (Q'_x - Q'_y)\delta$; the mode tunes, centered on $\bar{q} = q_0 + \frac{1}{2}(Q'_x + Q'_y)\delta$, are then separated by $\sqrt{S^2 + D^2}$.

Figure 1 shows q_U and q_L as a function of δ for an extreme case, $Q'_x = 20, Q'_y = -10, S = 0.026$. The curves are what is measured by a tune tracker in *steady-state* conditions when the beam is taken off-momentum by changing the RF frequency. Particles within a CESR bunch might typically have $\delta = \pm 1.5\sigma_\delta \simeq \pm 10^{-3}$, detuning them from resonance, for the case illustrated, by $D \simeq 0.01 - 0.02$, which is of the same order as the coupling strength S. (Möbius coupling will be dramatically stronger.)

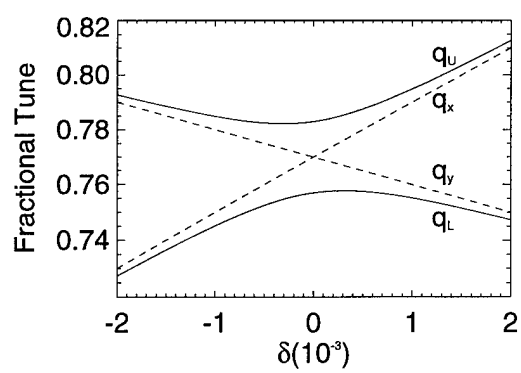

Figure 1: The dependence of the normal mode tunes on energy for $Q'_x = 20, Q'_y = -10, S = 0.026$.

* Work supported by the National Science Foundation

[1] Because $Q' > 0$ produces a positive growth rate in the higher H-T modes, Q' is generally set to zero or only slightly positive. Then the higher modes, with smaller form factors and wake-field coefficients, are stabilized adequately by radiation and Landau damping.

Clearly, if δ varies slowly enough for the modes to retain their identity ($S \gg Q_s$), the chromaticity of each mode is highly nonlinear, which might be expected to lead to decoherence (Landau damping). Such effects would of course not appear in the simple two-superparticle model. On the other hand, if δ changes so rapidly as to mix the modes ($S \ll Q_s$), the effective chromaticity may become that associated with the *average* tune $\bar{q}$, that is $\frac{1}{2}(Q'_x + Q'_y)$. In fact, δ oscillates at frequency $Q_s f_0$; in CESR, $Q_s \simeq 0.05$, comparable to the "tune" S of beats between the modes.

Since tune-tracking studies do not duplicate the conditions of momentum oscillations, we concentrated on measurements of α, the coherent damping rate of shock-excited betatron oscillations. Initially we pursued the expectations described by equation 2.

2 EXPERIMENTAL

We measured the coherent damping rates by shock-exciting the beam with a fast kicker and observing the response of beam-position monitor signals on a fixed-tune spectrum analyzer (bandwidth = 2 kHz, i.e., $\Delta q \simeq 5 \times 10^{-3}$). The analyzer displayed the damping envelope logarithmically, allowing–after subtraction of the incoherent radiation damping rate $\alpha_R \simeq 38\ \mathrm{s}^{-1}$–determination of the coherent damping rate α.

The accelerator lattice used for these experiments was optimized for studying round-beam collisions at CESR; it is described in an accompanying paper [5]. Chromaticity correction is accomplished with sextupoles in two families. Q'_x and Q'_y are independently controlled by simultaneously varying the strengths of the two families; we verified that Q'_x and Q'_y were linear functions of the sextupole strengths and that the x and y chromaticity controls were orthogonal. The H-T damping rates in each plane depended linearly on the associated chromaticity over the range for which a stable beam could be maintained ($0 \leq Q' \leq 12$). The H-T damping coefficients (measured at ~5 mA beam current) were $d\alpha_x/dQ'_x = -5.54\ \mathrm{s}^{-1}\mathrm{mA}^{-1}$ and $d\alpha_y/dQ'_y = -6.19\ \mathrm{s}^{-1}\mathrm{mA}^{-1}$, indicating that the wakefield coefficients are in the ratio $W_x/W_y = 0.89$.

The machine was taken to resonance (typically to within $D_0 \leq 2 \times 10^{-3}$) and globally decoupled. Two skew quadrupoles placed symmetrically with respect to the interaction point were then powered to introduce the desired coupling strength S. In this coupled lattice, the measured normal-mode damping rates depended neither on the orientation of the kick nor of the pickup electrodes (x or y).

3 RESULTS

3.1 *Weak Coupling ($S < Q_s$)*

To check equation 2, we started from a somewhat arbitrary point ($Q'_x \simeq 4, Q'_y \simeq 0$) and followed contours of constant α_U or α_L in the Q'_x, Q'_y plane. The damping rates of the two modes were generally quite different, contrary to the prediction of the two-particle model; the two contours shown in figure 2 correspond to $\alpha_U = 92\ \mathrm{s}^{-1}$ and $\alpha_L = 15\ \mathrm{s}^{-1}$. Data are shown for two coupling strengths, $S = 0.012$ and 0.026. The range of data represents the range of Q' over which a stable beam could be maintained along these contours with this coupling.

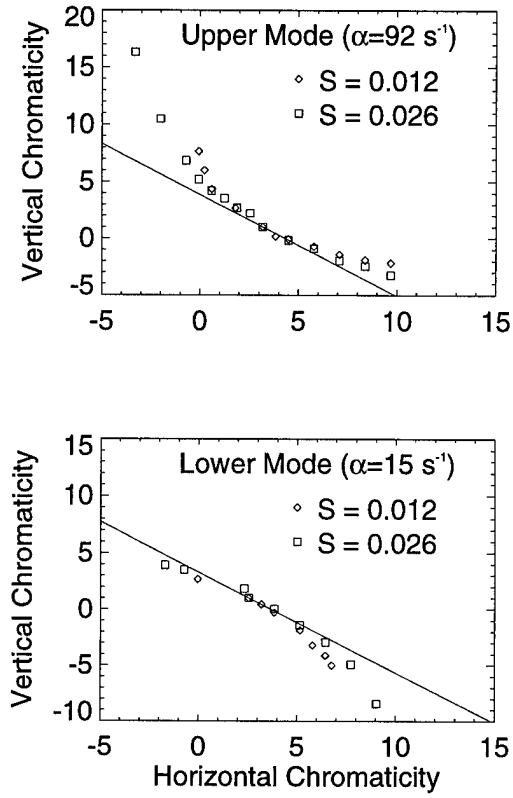

Figure 2: Contours of constant damping rate in the Q'_x, Q'_y plane for the two coupled modes.

The curves demonstrate that there is chromaticity sharing, even for relatively weak coupling. (For comparison, straight lines with the expected slope $-W_x/W_y = -0.89$ are included on the plots.) However, the contours are not straight; their curvature, opposite for α_U and α_L, is only slightly reduced by stronger coupling. Most importantly, the disparity between α_U and α_L calls for explanation.

To investigate the possibility that the physical orientation of the modes in the vacuum chamber played a role, we reversed the sign of the skew quadrupoles, thus interchanging the orientation of the U and L modes. This had a systematic effect only at small Q', that is, for small damping rates ($\simeq 10\ \mathrm{s}^{-1}$). The larger observed damping rates therefore appear to be linked to the modes themselves, not their spatial orientation. We always found $\alpha_U > \alpha_L$.

3.2 *Intermediate Coupling ($S \simeq Q_s$)*

Upon increasing the coupling strength to 0.039 we found it possible to maintain a stable beam over a much larger range of Q', although some conditions could not be approached

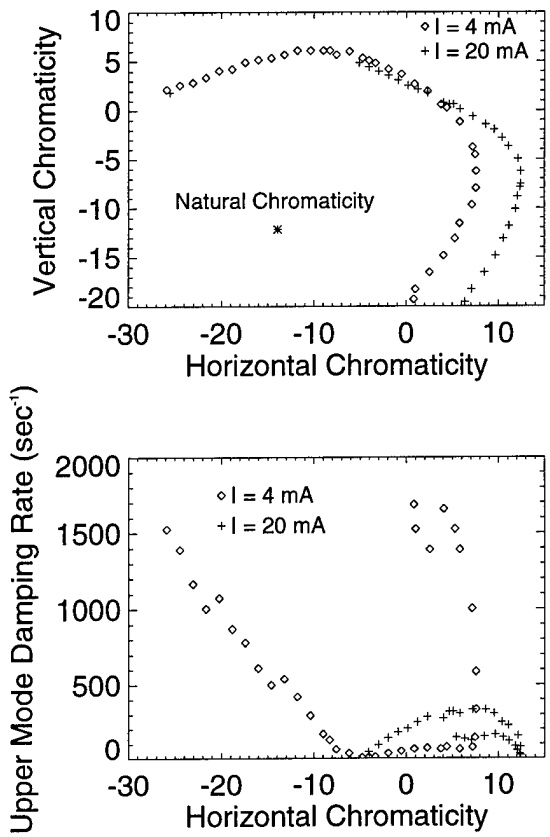

Figure 3: (Upper) Contours of constant damping rate for the lower frequency mode for coupling $S = 0.039$. Contours corresponds to $\alpha_L = 14\ \mathrm{s}^{-1}$ (4 mA) and $\alpha_L = 20\ \mathrm{s}^{-1}$ (20 mA). (Lower) Corresponding damping rate of the upper frequency mode recorded at each point of the contour.

directly by following a contour of constant α. Figure 3 shows contours of constant α_L for two widely different beam currents. Also shown on the lower portion of the figure are the corresponding α_U recorded at each point of the contour. The striking feature is that, for highly negative Q' in either plane, stability is obtained with much smaller positive Q' in the other plane than would be called for with simple chromaticity sharing. In fact, at each end of the contour one family of sextupoles is turned off completely, leaving Q' in the corresponding plane much more negative than the natural value for the lattice ($\simeq -12$), owing to the effect of the other sextupole family. At these extreme points, the damping rate of the upper mode is quite large.

3.3 *Qualitative Investigations*

This unexpected behavior suggests a decoherence phenomenon due to the large spread in tunes (figure 1), an idea supported by the fact that at extreme settings–for example, $Q'_x \simeq 20, Q'_y \simeq -20$ –both modes are heavily damped ($\alpha_{U,L} > 1000\ \mathrm{s}^{-1}$) even at low beam current (2 mA). However, though the coherent oscillation signal disappeared in times well below 1 ms, the optical image nevertheless retained considerable enlargement for times comparable to the interval between the kicks (which occurred at 60 s^{-1}). Clearly, the oscillations quickly become incoherent and individual particle amplitudes are damped only at the low radiation rate, 38 s^{-1}.

If there is decoherence, it should contribute Landau damping independently of the beam current, to an extent determined by the tune modulation produced by momentum oscillations. That is consistent with the general shape of the constant-α contours at extreme Q'. (An attempt to change the momentum oscillations by lowering the RF voltage from an overvoltage of 6× to 4× revealed no significant change in damping rates.)

Apparently, in the intermediate coupling regime ($S \simeq Q_s$), the tune split is large enough for the modes to assert themselves; the momentum oscillations lead to a spread in tunes. The non-linear chromaticity leads naturally to decoherence; unlike the familiar case of linear chromaticity, a particle executing momentum oscillations *does not* return to its initial betatron phase after one synchrotron period. Furthermore, particles with different longitudinal oscillation amplitudes arrive at slightly different phases following one oscillation period, giving rise to decoherence.

4 CONCLUSION

The expected chromaticity sharing in a coupled lattice is confirmed; it occurs even for weak coupling. For intermediate coupling, however, damping mechanisms other than the head-tail effect appear to become dominant. These are tentatively identified as effects of decoherence, produced by the large tune modulation during momentum oscillations, and the nonlinear chromaticity of the coupled modes. Further work–especially in the Möbius regime–is planned.

5 ACKNOWLEDGEMENTS

We would like to thank the CESR Operations staff for their help with these experiments.

6 REFERENCES

[1] M. Sands, SLAC-TN-69-8, C. Pellegrini, Nuovo Cim. **64A**, 477 (1969).

[2] R. Talman, NIM, **193**, 423 (1982), R.D. Kohaupt, DESY 80/22 and DESY M-80/19, (1980).

[3] R. Talman, Phys. Rev. Lett. **74**, 1590(1995).

[4] R. Talman, "Theory of Head-Tail Chromaticity Sharing," CBN-97-17

[5] E. Young *et al.*, "Collisions of Resonantly Coupled Round Beams at the Cornell Electron-Positron Storage Ring (CESR)", these proceedings.

BEAM DYNAMICS WITH NOISE IN SUPERFERRIC VERY LARGE HADRON COLLIDER ("PIPETRON")

V. D. Shiltsev, FNAL * M.S.345, P.O. Box 500, Batavia, IL 60510, USA

Abstract

We study transverse and longitudinal beam dynamics in "Pipetron" collider under influence of external noises.

1 INTRODUCTION

Several proposals of the "beyond-LHC" large colliders with 30–100 TeV beam energy and luminosity of 10^{33} – -10^{35} $s^{-1}cm^{-2}$ have been considered in recent years. Two approaches can be distinguished in the trend – namely, smaller circumference ring with high magnetic field dipoles based on high-T_c technology [1], and (presumably) lower cost option of a micro-tunnel low-field superferric magnet machine with large circumference [2]. The later – often referred as "Pipetron" – is a subject of this article. Table 1 shows relevant parameters of the collider [3].

Table 1: Parameters of "Pipetron"

Proton Energy,	E_p, TeV	100
Circumference,	C, km	1000
Luminosity,	L, $s^{-1}cm^{-2}$	10^{35}
Intensity,	N_p/bunch	$4.1 \cdot 10^{10}$
No. of Bunches,	N_b	25000
RMS emittance,	ϵ_n, $10^{-6}\,m$	1
Long. emittance (rms),	A, eV·sec	0.3
Bunch length (rms),	σ_s, cm	10
Rev. frequency,	f_0, Hz	300
Interaction focus	β^*, cm	10
Beam-beam tune shift	ξ_p	0.005

The collider consists of thousands of magnetic elements, and their field imperfections can seriously affect proper machine operation. Depending on the frequency band one can distinguish two mechanisms of beam perturbations in circular accelerator. Slow processes (with respect to revolution period) produce a distortion of the closed orbit of the beam. At higher frequencies (comparable with the revolution frequency), noises cause direct emittance growth.

2 TRANSVERSE EMITTANCE GROWTH

Effect of Transverse Kicks The primary sources which lead to emittance growth in large hadron colliders are quadrupoles (quad) jitter and high-frequency variations of the bending magnetic field in dipoles. Both sources produce angular kicks and excite coherent betatron oscillations. After decoherence time (determined mostly by beam-beam non-linearities, $N_{decoh} = 1200$ turns) filamentation or dilution process due to tune spread within the beam transforms the coherent oscillations into the emittance increase. If the kick amplitude $\Delta\theta$ varies randomly from turn to turn with variance of $\delta\theta^2$, one can estimate the transverse emittance growth as:

$$\frac{d\epsilon_n}{dt} = \frac{1}{2} f_0 \gamma \sum_i^{all\,kicks} \Delta\theta_i^2 \beta_i = \frac{1}{2} f_0 \gamma \delta\theta^2 < \beta > N \quad (1)$$

where $< \beta >$ is the average beta function, γ is relativistic factor, and N is the number of elements which produce uncorrelated kicks. Two major sources of the dipole kicks are fluctuations δB of the bending dipole magnetic field B_0 which give horizontal kick of $\delta\theta = \theta_0(\delta B/B_0)$ ($\theta_0 = 2\pi/N_d$ is bending angle in each dipole, N_d is total number of dipoles); and transverse quadrupole magnets displacements δX (e.g. due to ground motion) which lead to kick of $\delta\theta = \delta X/F$, where F is the quadrupole focusing length.

Non-"white" noise can be described by frequency-dependent power spectral density(PSD) $S_{\delta\theta}(f)$, and causes the emittance growth with rate of [4] $\frac{d\epsilon_n}{dt} = \gamma f_0^2 \sum_i \left(\beta_i \sum_{n=-\infty}^{\infty} S_{\delta\theta}(f_0|\nu - n|)\right)$ which consists of the sum of PSDs of angular kicks produced by the i-th source at frequencies of $f_0|\nu - n|$, n is integer, the lowest of them is fractional part of the tune times revolution frequency $f_1 = \Delta\nu f_0$.

Beam lifetime in the Pipetron is about $\tau_c = 5$ hours (determined mostly by longitudinal intrabeam scattering [5] $\tau_{\parallel}^{IBS} \approx 6$ hrs, while synchrotron radiation transverse damping time is about 42 hours). Let us constrain that external noise should lead to less than 10% emittance increase while the beam circulates in the accelerator, then we get tolerable the noise-induced emittance growth rate of $\frac{d\epsilon_n}{dt} \leq 0.1 \frac{\epsilon_n}{\tau_c} = 5.6 \cdot 10^{-12}\, m/s$. Taking into consideration 500-m long FODO cell (i.e. $L = 250$m) focusing structure with $\mu = 90^o$ phase advance per cell [3] one can estimate the tune $\nu \simeq 500$, total number of focusing quadrupoles as $N_q = 4000$ and about the same number of dipoles N_d. Now, the acceptable transverse emittance growth rate requires:

a) the PSD of single quadrupole transverse vibration is limited by the value of $\sum_n S_{\delta X}(f_0|\nu - n|) \approx S_{\delta X}(f_0 \Delta\nu) \leq 2 \cdot 10^{-11} \frac{\mu m^2}{Hz} = 20 \frac{pm^2}{Hz}$, where $\Delta\nu$ is fractional part of ν;

b) or the rms amplitude of turn-to-turn jitter of each quadrupole (white noise in frequency band f_0) $\delta X_{rms} \leq 7.6 \cdot 10^{-11}$m;

c) and a tolerable level of bending magnetic field fluctuations to its mean value B_0 in the dipole: $\left(\delta B/B_0\right)_{rms} \leq 3.4 \cdot 10^{-10}$.

Measured Ground Motion Let us make a comparison of the above calculated constraints with experimental data on ground motion. Fig.1 presents PSDs of ground velocity

* Operated by Universities Research Association, Inc., under contract with the US Department of Energy

$S_x(f)(2\pi f)^2$ in units of $(\mu m/s)^2/Hz$ for the USGS "New Low Noise Model" – a minimum of the PSD observed by geophysicists worldwide – and data from accelerator facilities of HERA, KEK, CERN, SLAC, and FNAL (see references in [5]). These spectra indicate that: 1) accelerators are essentially "noisy" places; 2) ground vibrations above 1 Hz are strongly determined by cultural noises – they manifest themselves as numerous peaks in Fig.1; 3) even among accelerator sites the difference is very large, that gives a hint for the Pipetron builders.

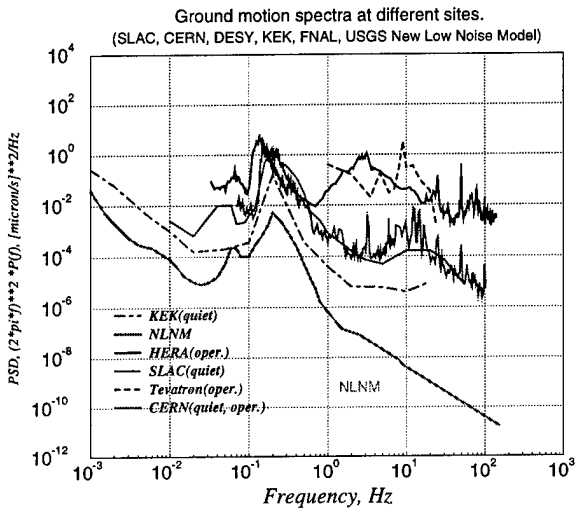

Figure 1: Measured ground velocity spectra.

Below 1 Hz the ground motion amplitude is about 0.3-1 μm due to remarkable phenomena of "7-second hum". This hum is waves produced by oceans – see a broad peak around 0.14 Hz in Fig.1 – with wavelength of about $\lambda \simeq 30$ km. It produces negligible effect on Pipetron, because λ is much bigger than typical betatron wavelength $2\pi\beta \simeq 2$ km. Investigations of spatial characteristics of the fast ground motion have shown that above 1-4 Hz the correlation significantly drops at dozens of meters of distance between points.

Table 2 compares requirements for the Pipetron with three particular tunes $\Delta\nu = 0.18$, 0.31 and 0.45 and experimental data.

Table 2: PSD of Ground Motion (in $(pm)^2/Hz$)

$\Delta\nu$	0.18	0.31	0.45
$f_1 = \Delta\nu f_0$	54 Hz	93 Hz	135 Hz
Pipetron tolerance	**20**	**20**	**20**
SLAC (quiet)	100	-	-
DESY (tunnel)	10^5	7000	1700
CERN (tunnel)	300	20	-

One can see that none of the accelerator data shows vibrations which are less than the Pipetron requirements, although PSDs at higher frequencies (say $f_1 = 135$ Hz) are much less than at lower frequency of 54 Hz, and, therefore, larger $\Delta\nu$ – closer to half integer resonance – are preferable from this point of view. At $\Delta\nu = 0.18$ one needs the vibration power reduction factor of $R = 5 - 5000$. We have not enough experimental data on dipole field fluctuations at 50-150 Hz which may drastically increase the emittance growth.

Feedback System A transverse feedback frequency allows one to suppress the emittance growth caused by excitation of the betatron oscillations simply by damping the coherent beam motion faster then they decohere. The system monitors the dipole offset X of the beam centroid and tries to correct it by dipole kicks θ which are proportional to the offset, applied a quarter of the betatron oscillation downstream. We operate with dimensionless amplification factor g of the system (gain) which is equal to $g = \frac{\theta\sqrt{\beta_1\beta_2}}{X}$, where β_1 and β_2 are the beta-functions at the positions of the pick up and the kicker electrodes respectively. In the limit of $g \ll 1$ the decrement due to the feedback is equal to $\frac{1}{2}f_0 g$, i.e. the amplitude of the betatron oscillations being reduced $1/e$ times after $2/g$ revolution periods. Theory of the feedback (see e.g. [4]) gives the transverse emittance evolution formula:

$$\frac{d\epsilon_n}{dt} = \left(\frac{4\pi\delta\nu_{rms}}{g}\right)^2\left[\left(\frac{d\epsilon_n}{dt}\right)_0 + \frac{\gamma f_0 g^2}{2\beta_1}X^2_{noise}\right], \quad (2)$$

$g \gg 4\pi\delta\nu_{rms}$, where emittance growth rate without feedback $(d\epsilon_n/dt)_0$ is given by (1), X_{noise} is the rms noise of the system (presented as equivalent input noise at the pick-up position), and $\delta\nu_{rms}$ is the rms tune spread within a beam.

Major source of the tune spread (and, consequently, decoherence) is nonlinear beam-beam force which results in the rms tune spread of $\delta\nu_{BB} \approx 0.167\xi = 8.4 \cdot 10^{-4}$.

Analytical consideration of the feedback system resulted in maximum useful gain factor $g_{max} \simeq 0.3$ – there is no reduction of the emittance growth rate with further increase of g because of higher-(than dipole)-order kicks effect, the system noise contribution grows, while the coherent tune shift due to feedback becomes too large, and affects multibunch beam stability in presence of resistive wall impedance.

Therefore, maximum reduction factor $R_{max} = (g_{max}/4\pi\Delta\nu_{BB})^2$ is about 800 for the Pipetron design parameter of $\xi = 0.005$, while the minimum practical gain which still can lead to the damping is about $4\pi\delta\nu_{BB} \approx 0.01$.

As it is seen from (2), feedback noise also leads to emittance growth and its relative contribution grows as $\propto g^2$. Taking the beta function at the pick-up $\beta_1 = 500$m we get limit on the rms noise amplitude:

$$X_{noise} \ll \left[\frac{2\beta_1(d\epsilon_n/dt)_0}{f_0(4\pi\delta\nu_{BB})^2\gamma}\right]^{1/2} \approx 1.4\,\mu m. \quad (3)$$

Power of the output amplifier of the system depends on maximum noise amplitude of the proton beam oscillations and is estimated to be about 50 kW for a bunch-by-bunch system[5].

RF Phase Noise Turn-to-turn jitter of the RF phase $\Delta\phi$ results in fast momentum variation $(\Delta p/p) = (eV_0/E_p)\Delta\phi$ which leads to an instant change of the horizontal orbit of $\Delta X = D_x(\Delta p/p)$, where D_x is the dispersion function at

the RF cavities. Measured $\Delta\phi$ is found to be two orders of magnitude less than estimated tolerances [5] that take the jitter out of list of Pipetron problems.

3 LONGITUDINAL EMITTANCE GROWTH

The RF phase errors at frequencies of the order of synchrotron one $f_s = \nu_s f_0$ and higher lead to the longitudinal emittance growth of:

$$\frac{dA}{dt} = \frac{eV_0}{f_{RF}}\frac{d\phi^2}{dt} = \frac{eV_0}{f_{RF}} 2\pi f_0^2 \nu_s^2 S_\phi(f_0\nu_s), \qquad (4)$$

where $\omega_s = 2\pi\nu_s f_0 > 0$, S_ϕ is the PSD of the phase noise

The synchrotron frequency $f_0\nu_s$ varies from 3.1 Hz at the beginning of the ramp to 0.33 Hz at the end of the ramp at 100 TeV, and then it is about 0.076 Hz during the collision time with $V_0 = 20$ MeV RF.

If one requires less than 10% emittance increase during half an hour of ramp time τ_R, than the tolerance on the phase jitter PSD in $f_{RF} = 450$ MHz RF system is $S_\phi(\omega_s) = \frac{0.1 A f_{RF}}{\tau_R(eV_0)\pi\omega_s^2} \approx \frac{6.4\cdot 10^{-6}}{\omega_s^2}$. Measurements with the SSC RF system HP8662 synthesizer [6] show that in frequency band of 1-100 Hz the PSD of phase noise can be approximated by $S_\phi(\omega_s) = \frac{1.3\cdot 10^{-5}}{\omega^{2.65}}$, that is only twice the tolerance at frequencies about 1 Hz. Equivalent rms phase jitter tolerance is $\delta\phi \simeq \sqrt{\omega_s S_\phi(\omega_s)} \approx 0.3$ mrad at $f_s = 3$ Hz.

The same 10% tolerance for 5 hours of the collision operation with $eV_0 = 20$ MeV gives $S_\phi(\omega_s) \approx \frac{1.2\cdot 10^{-5}}{\omega_s^2}$ that is very close to the measured PSD.

We can conclude that with minor improvement of the RF phase stability with respect to the SSC synthesizer, no longitudinal feedback will probably be required.

Another possible source of the RF phase errors, the change of the circumference due to non-zero dispersion function D_x at the position of dipole kick [7], is found to give negligible contribution to the emittance growth [5].

4 CLOSED ORBIT DISTORTIONS

Alignment Tolerances The rms closed orbit distortion dX_{COD} is proportional to the rms error dX of quads alignment, and if these errors are not correlated, then in the FODO lattice we can get:

$$dX_{COD}^2 = \frac{\beta dX^2}{4sin^2(\pi\nu)}\sum_i \frac{\beta_i}{F_i^2} = \frac{\beta N_q tg(\mu/2) dX^2}{Lsin^2(\pi\nu)}. \qquad (5)$$

Let us take the "safety criteria", i.e. ratio of maximum allowable COD to the rms one, equal to 5, then for maximum COD of dX_{COD}^{max}=1 cm (this is about half aperture of the vacuum chamber) at the focusing lenses where $\beta_F = 765$ m ($L = 250$ m, $\mu = 90^o$) we get requirement on the rms alignment error of $dX \approx 15$ μm (here we take $\Delta\nu = 0.31$). This value sets a challenging task, its solution needs the most sophisticated alignment techniques and two questions arise in this connection: 1) temporal stability of the magnets positions; and 2) applicability of the beam-based alignment.

Slow Ground Motion Numerous data on uncorrelated slow ground motion support an idea of "space-time ground diffusion". An empirical rule that describes the diffusion – so called "the ATL law" [8] – states the rms of relative displacement dX (in any direction) of two points located at a distance L grows with time interval $T < dX^2 >= ATL$, where A is site dependent coefficient of the order of $10^{-5\pm1}$ $\mu m^2/(s\cdot m)$.

The ground diffusion should cause corresponding closed orbit diffusion (COD) in accelerators [1] with rms value over the ring approximately equal to $\langle dX_{COD}^2\rangle \simeq 2\sqrt{ATC}$. It clearly shows that the diffusive orbit drift is not very sensitive to the focusing lattice type (only the circumference C plays role), in particular, there is almost no difference between the combined- and separated-function lattices responses on the ATL-like diffusion.

If one applies the ATL law with $A \approx 4\cdot 10^{-5}$ $\mu m^2/(s\cdot m)$ to the Pipetron (see [5]) then rms COD at $\beta_{max} = 850$ m is equal to $dX_{COD} \approx 800[\mu m]\sqrt{T[hrs]}$. Requirement of "safe" rms COD of 2 mm yields in T=6.3 hours of mean time between necessary realignments to an initial "smooth" orbit. It does not seem to be an easy task to do it mechanically, even with use of robots, especially taking into account 15 μm precision of the procedure. "Beam-based alignment" technique looks as an appropriate method but requires numerous (of the order o the number of quads) correctors with 4.3 Tm maximum strength.

5 CONCLUSIONS.

Preceding consideration shows that natural and man-made vibrations at Pipetron can lead to dangerous transverse emittance growth rate (high-frequency part of spectrum) and closed orbit distortions (at low frequencies). The transverse feedback system can drastically reduce the emittance increase. Sophisticated alignment methods are necessary to keep Pipetron beam on a "golden orbit".

It seems reasonable to carry out "on-site" ground motion studies and magnet vibrations measurements, as well as get data on long-term tunnel movements, the RF phase and amplitude stability, and dipole field jitter.

I acknowledge valuable comments and useful discussions with G.W.Foster, D.Neuffer, D.Finley, P.Colestock, E.Malamud (FNAL) and G.Stupakov(SLAC).

6 REFERENCES

[1] S.Peggs *et.al*, *Proc EPAC'96*, Barcelona, p377.

[2] G.W.Foster, E.Malamud, FERMILAB-TM-1976 (1996)

[3] D.Neuffer, FERMILAB-TM-1964 (1995).

[4] V.Lebedev, *et.al*, *Part. Accel.*, Vol.44, No.3-4, p.147 (1994).

[5] V. Shiltsev, FERMILAB-TM-1987 (1996).

[6] H.-J.Shih, *et.al*, *Part. Accel.*, Vol.43(3) (1994), p.159.

[7] M.Syphers, *et.al*, *Proc. 1993 IEEE PAC*, Washington, p.420.

[8] V.Parkhomchuk*et.al*, *Part. Accel.*, v.46 (1994), p.241.

[9] R.Brinkmann, J.Rossbach, *Nucl. Instr. Meth.*, v. A350 (1994), N.1-2, p.8.

[1] observed in HERA [9]

OVERCOMING INTRINSIC SPIN RESONANCE BY USING AN AC DIPOLE*

M. Bai[1,2,3], L. Ahrens[2], J.W. Glenn[2], H. Huang[2], S.Y. Lee[1], L. Ratner[2]
T. Roser[2], M.J. Syphers[2], W. van Asselt[2], A. Yokosawa[3]
[1]Department of Physics, Indiana University, Bloomington, IN 47405, USA
[2]Brookhaven National Laboratory, Upton, NY11973, USA
[3]Argonne National Laboratory, 9700 Cass Ave., Argonne, IL 60493, USA

Abstract

Depolarization from an intrinsic spin resonance can be avoided by adiabatically exciting a coherent betatron oscillation. Experimental results of creating sustained coherent betatron oscillations in the Brookhaven National Laboratory AGS, and relevant spin tracking calculations are discussed.

1 INTRODUCTION

Intrinsic spin resonance is one of the major types of spin depolarizing resonances. It is caused by vertical betatron oscillations sampling the radial focusing field. The resonance condition is $G\gamma = KP \pm \nu_z$, where K is an integer, P is the number of superperiods, ν_z is the vertical betatron tune, $G = 1.79$ is the anomalous g-factor for the proton, γ is the Lorentz factor, and $G\gamma$ is the number of spin precession per orbit revolution.

For an isolated resonance with resonance strength ϵ at a constant acceleration rate $\alpha = \frac{d(G\gamma)}{d\theta}$ and θ as the bending angle, Froissart-Stora formula gives the ratio of the initial polarization P_i before passing through this resonance to the final polarization P_f after passing through it.

$$\frac{P_f}{P_i} = 2e^{-\pi\frac{|\epsilon|^2}{2\alpha}} - 1 \qquad (1)$$

Based on Eq. 1, to avoid depolarization from spin resonances, coherent vertical betatron oscillation can be induced to increase the resonance strengt of all particles to a level that an adiabatic spin flip will be induced with the normal acceleration rate of the synchrotron.

In this application, a controlled oscillation is adiabatically produced with a high frequency dipole magnet slowly energized to its final field amplitude and likewise slowly de-energized. Then the particle beam emittance is preserved.

This can easily be understood by studying the motion in a phase space frame which is rotating at the AC dipole oscillating frequency. Consider a particle influenced by a single horizontally oriented AC dipole field of length ℓ at a location in the accelerator where the vertical betatron amplitude function is β_z. The field oscillates according to $B_x = B_{\rm m}\cos 2\pi\nu_m n$, where $B_{\rm m}$ is the amplitude of the AC dipole field, $\nu_{\rm m}$ is the modulation tune defined as the oscillating frequency divided by the accelerator's revolution frequency, and n is the number of revolutions about the accelerator.

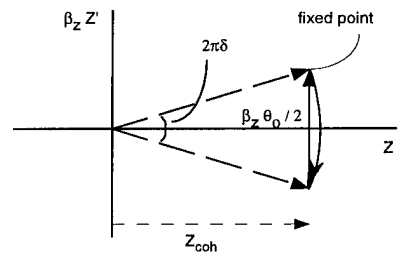

Figure 1: Phase space motion in the rotating frame at the maximum betatron amplitude location.

In this frame, the net rotation angle per turn of a particle's phase space vector is $2\pi\delta$, with $\delta \equiv \nu_z - (k - \nu_{\rm m})$ where k is an integer and ν_z is the vertical betatron tune. The AC dipole field deflects the trajectory through an angle $\theta = B_x\ell/(B\rho)$. Since the dipole field is oscillating at the same frequency as the rotating frame, the time average change of Z' in this frame is just half the amplitude of the modulated angular deflection:

$$\langle Z'\rangle = \frac{1}{2}(B_{\rm m}\ell)/(B\rho) \equiv \frac{1}{2}\theta_0. \qquad (2)$$

Therefore, the coherent betatron oscillation amplitude is given by

$$2\pi\delta \cdot Z_{coh} = \langle Z'\rangle\beta_z \rightarrow Z_{coh} = \frac{B_{\rm m}\ell}{4\pi(B\rho)\delta}\,\beta_z. \qquad (3)$$

Eq. 3 shows that the coherent betatron oscillation amplitude is proportional to the maximum dipole field strength and inversely proportional to the distance from the resonant tune. This equation can also be obtained by working out the Hamiltonian[1].

2 EXPERIMENTAL TESTS IN THE AGS

To investigate the feasibility of this procedure, tests were performed in the Brookhaven AGS with unpolarized beam during a recent Heavy Ion Physics run. The AC dipole was located where the vertical betatron function was about 16.6 m[2].

* The work performed under the auspices of the US Department of Energy

2.1 Experimental Set-up

For the beam tests, the AC dipole was linearly ramped up in about 3 ms and kept at full amplitude for about 4 ms then ramped back to zero in another 3 ms. During acceleration in the AGS, the revolution frequency changes as the particle momentum increases. The AGS beam RF signal was used as the external clock for an arbitrary function generator to generate the sine wave with fixed tune. Thus, by multiplying this sine wave with the magnet's strength amplitude envelope, an amplitude modulated sine wave with a fixed tune was obtained.

The experiment was performed in the AGS with Au^{+77} beam. Its normalized emittance (95%) was about 5π mm-mrad and the rms beam size at the working energy (1.1 GeV/c per nucleon) is about 3.9 mm at a maximum amplitude function location.

Transverse beam position measurements[2] were obtained with a pick-up electrode (PUE) located 4.5 betatron oscillations downstream of the AC dipole, where the vertical amplitude function is 15.4 m. The beam transverse profile was measured using the exsiting AGS IPM (Ionization Profile Monitor) system[2].

2.2 Results

The coherence amplitude as a function of distance between the AC dipole modulation tune from the intrinsic betatron tune was measured both during acceleration as well as at fixed energy in the AGS. The AC dipole modulation tune function was held fixed and the betatron tune was changed to produce different tune separations.

A typical example of the readback from the AC dipole current transformer as a function of revolution number is shown in the bottom portion of Fig. 2. Here, the full dipole strength is 2.82 G-m and its modulation tune is 0.75.

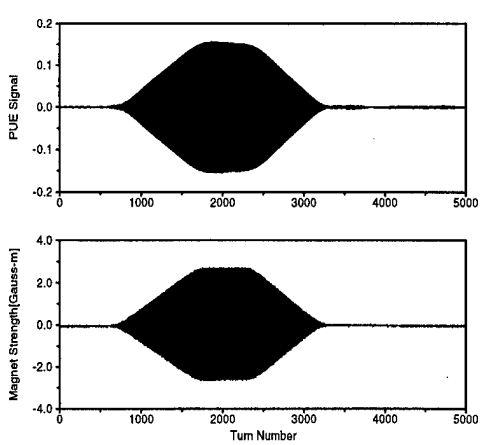

Figure 2: Transverse displacement (top) and AC dipole magnet field amplitude (bottom) as a function of revolutions about the AGS.

The top part of Fig. 2 is the beam's average vertical displacement sampled turn-by-turn. It shows that the coherent betatron motion nicely follows the AC dipole field amplitude shown in the bottom portion of the figure. The intrinsic betatron tune is 8.745.

Results from a typical emittance scan is shown in Fig. 3.

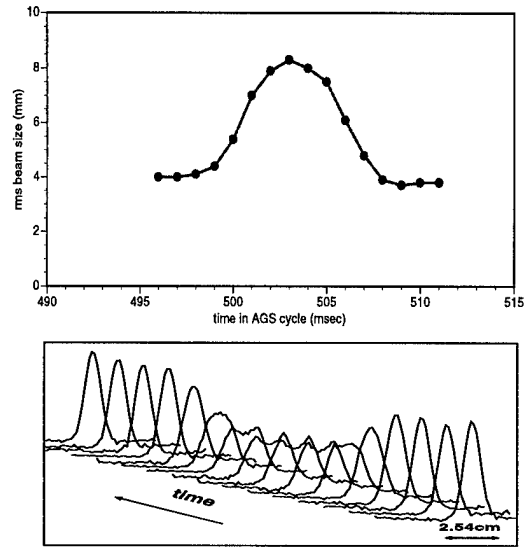

Figure 3: Measured transverse rms beam size versus time in AGS cycle (top). Corresponding beam profiles versus time in AGS cycle (bottom).

The top portion of the figure shows the beam size (rms, in mm) versus time, with measurements taken in 1 ms intervals. The bottom part of the figure shows a mountain range plot of the corresponding vertical beam profiles. The broadening of the distribution and narrowing as the AC magnet turns off is evident.

The measurement time of the IPM system was 3 ms, and hence the beam circles the AGS roughly 900 times during the measurement. Thus, the rms beam size shown in the plot is the time averaged value. The maximum "measured" rms beam size is related to the actual rms beam size, σ_o, and the oscillation amplitude Z_{coh} generated by the AC dipole by

$$\sigma_{meas} = \sigma_o \sqrt{1 + \frac{1}{2}\left(\frac{Z_{coh}}{\sigma_o}\right)^2}. \qquad (4)$$

The fact that the measured rms beam size returns to its previous value indicates that the process was indeed adiabatic and that the beam emittance was preserved.

The ratio of the measured coherent amplitude to dipole field amplitude is shown in Fig. 4 as a function of different tune separations between the modulation tune and the betatron tune. During this set of measurements, the momentum was held fixed at 1.1 GeV/c per nucleon. This particular ratio is shown because when the tunes were placed near resonance without reducing the dipole field amplitude, the oscillation amplitude would become large enough to induce beam loss. Thus, only smaller amplitude oscillations provided meaningful measurements at these tune separations.

For a tune separation of 0.01, the largest amplitude oscillation which could be maintained without significant beam loss was 2.6 times the rms beam size.

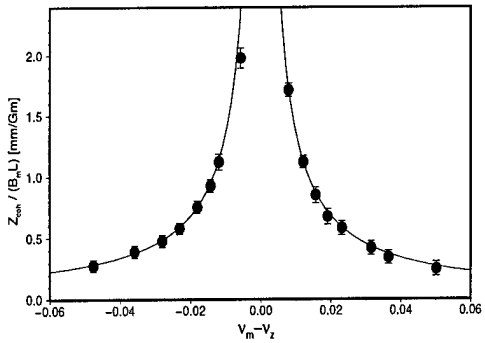

Figure 4: Normalized betatron oscillation amplitude versus δ. The solid line is the predicted curve using Eq. 3.

A similar set of measurements is depicted in Fig. 5, where in this case the beam is being accelerated at a rate of $\dot{\gamma} \equiv \frac{d\gamma}{dt} = 2.44$ sec^{-1} The arbitrary function generator was used to generate the appropriate sine wave with the AGS beam RF signal used as the clock signal. Fig. 5 shows that by accurately fixing the tune separation, the general features of the AC dipole induced coherent betatron oscillations are the same for acceleration and storage.

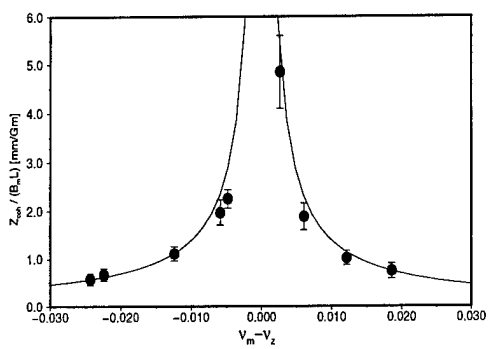

Figure 5: Normalized betatron oscillation amplitude versus δ. The solid line is the predicted curve using Eq. 3.

3 SPIN TRACKING

Multiple particle spin tracking was done with AGS polarized proton parameters. Fig. 6 shows the simulation of crossing $G\gamma = 0 + \nu_z$, where the vertical betatron tune $\nu_z = 8.65$ and the horizontal betatron tune $\nu_x = 8.85$. The normalized 95 % transverse emittance $\epsilon_x = \epsilon_y = 15\pi$mm-mrad. The acceleration rate $\alpha = 4.5 \times 10^{-5}$. The modulation tune ν_m is 0.01 away from ν_z. The spin is fully flipped at $G\gamma = 8, 9$ by the 5% partial snake. The spin flip at the $G\gamma = 0 + \nu_z$ is enhanced from 59% to 95 % by the AC dipole running at the field strength 20G-m. Further improvement can be achieved by obtaining smaller beam emittance or closer distance between the modulation tune ν_m and the vertical betatron tune ν_z.

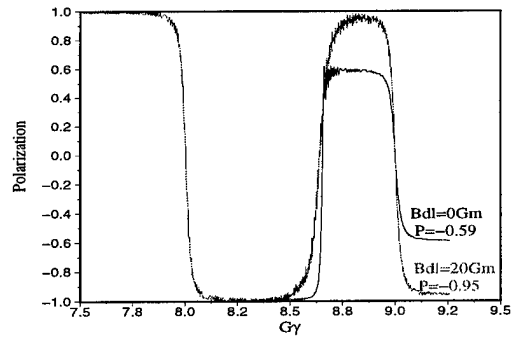

Figure 6: Spin tracking results

4 CONCLUSION

Sustained coherent transverse beam oscillations have been achieved in the AGS using a high frequency AC driven dipole magnet. The amplitude of the oscillations using the present system has been as large as 2.6 times the rms beam size, and the oscillations were held at this level for over 1000 revolutions. By adiabatically increasing and decreasing the dipole field amplitude during this procedure, the transverse emittance of the beam was left unaffected. To set the scale, had an oscillation of that amplitude been left to oscillate freely, the beam emittance would have increased by a factor of 7 after filamentation. This result provides encouragement that this technique can be used to induce spin flip of polarized proton beams in synchrotrons when crossing strong intrinsic depolarizing resonances during acceleration. Another application of this device in a polarized beams storage ring would be the reversal of the polarization direction of the beam. By slowly sweeping the frequency of the modulated dipole field through the spin precession frequency of the storage ring, an adiabatic spin flip can be induced, thus reversing the polarization direction of each individual particle in the storage ring without increasing the beam emittance. This can be useful for reducing systematic errors in polarized beam experiments.

4.1 Acknowledgments

The authors would like to thank A. Dunbar, D. Gassner, J. Reich, P. Sampson, R. Sanders, G. Smith, C. Whalen, N. Williams, K. Zeno for their help during the experiment.

5 REFERENCES

[1] M. Bai, S. Y. Lee, H. Huang, T. Roser, M. Syphers, "Overcoming the Intrinsic Spin Resonance using Resonance Island created by RF Dipole," AGS/RHIC/SN No. 055

[2] M. Bai et al,"Adiabatic Excitation of Coherent Betatron Oscillation with an AC Dipole field", to be submitted to Phys. Rev. E.

FIRST TEST OF ORBIT RESPONSE MATRIX IN PROTON STORAGE RING

C.M. Chu, M. Ball, G. East, B. Hamilton, D. Jeon, X. Kang, L.L. Kiang*,
S.Y. Lee, K.Y. Ng†, A. Pei, A. Riabko, T. Sloan,
Indiana University Cyclotron Facility
2401 Milo B. Sampson Lane, Bloomington IN 47405

Abstract

The Orbit Response Matrix method is applied to experimentally determine the Cooler ring optics at the Indiana University Cyclotron Facility (**IUCF**). We have carried out two experiments in Oct. and Nov. 1996 to measure the orbit response of the IUCF Cooler Ring. An analysis software was adopted from the NSLS, BNL[1]. In our analysis, strength error in quadrupoles and steering dipoles, and amplifier gain in BPMs are included as fitting parameters. However, effects of the linear and non-linear coupling are excluded in our preliminary analysis. Since the resolution of our BPM system is of the order of 10 μm, we will address the effect of BPM resolution on the applicability of the orbit response matrix method in proton storage rings.

1 INTRODUCTION

Orbit response matrix method has been applied to measure and to calibrate the linear optics in electron storage rings for many years[2, 3, 4, 5, 6]. The method can be used to calibrate the strength and the roll of magnets such as quadrupoles and orbit steerer, or gain factor and roll of beam position monitors (**BPMs**). In the IUCF Cooler ring, from time to time we encountered difficulty on tuning beam due to unknown device calibration error. Therefore we would like to apply the orbit response matrix method to calibrate the Cooler ring. This would be the first test of orbit response matrix in a proton storage ring, although there is no fundamental difference between an electron ring and a proton ring as far as the method concerning.

The response matrix is defined as

$$X_i = M_{ij}\theta_j, \tag{1}$$

where $\mathbf{M}$ is either the measured or model response matrix, θ is the vector of changes in steering magnet strengths, and $\mathbf{X}$ is the vector of the resulting change in the particle orbit. The basic idea for the response matrix method is to minimize the difference between the measured and model matrices, $\mathbf{M_{meas}}$ and $\mathbf{M_{mod}}$, respectively. To perform the minimization we define a vector $\mathbf{V}$ as

$$V_k/\sigma_l = \frac{dV_k/\sigma_l}{dx_m}\Delta x_m, \tag{2}$$

where $V_k = |M_{mod_{ij}} - M_{meas_{ij}}|$ is the difference between the model calculated from either MAD[7] or COMFORT[8] program, and the measured orbit response matrices, with k running over all the data points which equals to the multiplication of the number of steering magnets varied and the number of BPMs used; σ_l's are measured BPM noise levels which act as weights to different BPMs; x_m's are the parameters varied to minimize the difference between the model and measured response matrix which can be quadrupole strengths, corrector strengths, the BPM gains, or dispersion correction. Note that σ_k is determined by measuring the orbit many times without changing any corrector strengths. The χ^2 to be minimized is given by

$$\chi^2 = \sum_k \frac{V_k^2}{\sigma_l^2}. \tag{3}$$

By iteratively solving linear Eqs. 2, the χ^2 can be minimized and a fitted model can be obtained.

The IUCF Cooler is a proton storage ring with electron cooling. The ring's circumference is about 86.80 m. A unique feature of the Cooler ring is a straight section with electron cooling, which can greatly reduce the proton beam's momentum spread. There are many multiply linked orbit steering magnets in the cooling section in order to maintain the proton beam closed orbit as well as to confine the cooling electron beam in the cooling section. To avoid much complication, we excluded those steering magnets in our fitting program. In our analysis, there are 36 quadrupole magnets, 2 horizontal and 15 vertical steering magnets, and 19 horizontal and 17 vertical BPMs. We varied the steering magnets one by one and recorded all the BPM data. Thus the number of data points is $(19 + 17) \times (2 + 15) = 612$.

2 ORBIT RESPONSE EXPERIMENT

For our analysis, we exclude any linear and nonlinear coupling. A single BPM response time can be adjusted from 20 to 100 ms depending on the precision requirement. Our experiment was set at 50 ms for each BPM and a total of 2 s for BPM data taking in one Cooler cycle. The BPM resolution is about $0.01 \sim 0.04$ mm.

Before we started taking orbit response data, the linear betatron coupling in the ring had to be minimized[9, 10], where the beam is kicked in one direction and tuned to minimize the observed motion in the orthogonal plane. This effect can be maximized if the X and Y tunes are close to each other. We used a spectrum analyzer to observe the beating oscillations due to the linear betatron coupling fol-

* also at National Tsing Hua University, Taiwan
† Fermilab, P.O. Box 500, Batavia, IL 60510

0-7803-4376-X/98/$10.00 © 1998 IEEE

lowing either a horizontal or a vertical kick. The linear coupling resonance can be corrected by maximizing the beat period of the transverse oscillations using a pair of skew quadrupoles.

However, in this experiment, there was still a non-negligible linear coupling in the ring. This linear coupling effect would contribute to systematic error. A horizontal closed orbit plot following a vertical kick is shown in Fig.1.

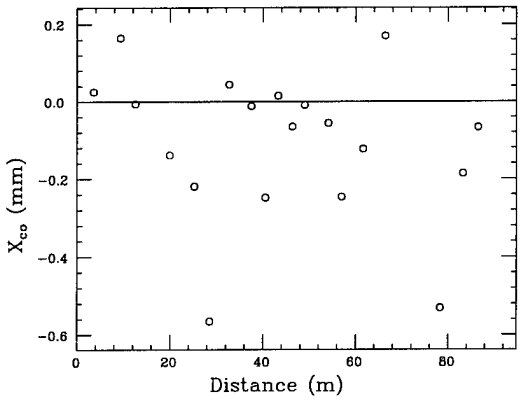

Figure 1: Horizontal closed orbit displacement after a vertical kick after linear coupling minimization. The large non-zero data shows there is still a significant coupling effect.

In the data analysis, the orbit response is assumed to be in a linear range. Thus the next step is to check the linearity of the kicking strength for each kicker versus the orbit response. Fig. 2 shows a typical vertical closed orbit versus steering magnet strength in a high β section.

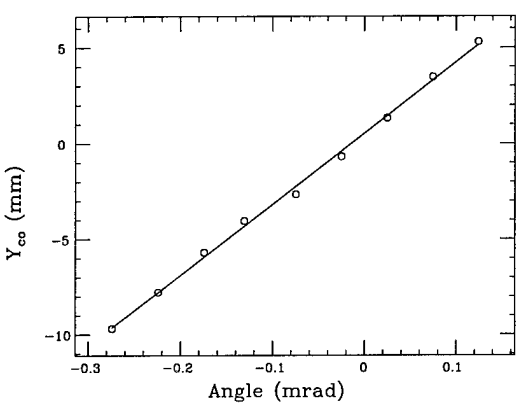

Figure 2: Vertical closed orbit displacement vs. steering magnet strength. The solid line is a fit.

For each run, we set the Cooler cycle time to about 10 s and took 10 consecutive orbit measurements for each steering magnet strength, and averaged over the 10 readouts to get one BPM closed orbit data. Because of the ring instability, we could only calculate each BPM noise level by averaging over about 10 repeated runs. The noise level of BPMs ranges from 0.03 to 0.1 mm.

3 DATA ANALYSIS AND RESULTS

For the parameters to fit, there are 36 quadrupole gradients, 19 horizontal and 17 vertical BPM gains, 2 horizontal and 15 vertical steering magnet strengths, and 2 $\Delta p/p$'s for the 2 horizontal steering magnets. To sum up the above parameters, we then have a total of 91 parameters to fit.

A computer program called *LOCO* (Linear Optics from Closed Orbit) was adopted from the NSLS, BNL. Originally we tried to fit the quadrupole gradients first. However, because the quadrupole gradients are nonlinear and the number of quadrupole gradients (36) is too large, it is very difficult to find a converged solution in the fitting routine efficiently. Therefore, the fitting strategy we used was to fit only the 17 steering magnet strengths first; after the program converged, added the 19 horizontal BPM gain factors; once it done, then included the 17 vertical BPM gain factors; then added the energy correction for the 2 horizontal steering magnets; and finally included the 36 quadrupole gradients. The χ^2 for each step is listed in Table 1.

Table 1: The Orbit Response fitting results.

Fit Parameters Included	χ^2
2 horizontal and 15 vertical kickers	$\sim$ 9500
2 horizontal, 15 vertical kickers and 19 horizontal BPMs	$\sim$ 9400
2 horizontal, 15 vertical kickers, 19 horizontal and 17 vertical BPMs	$\sim$ 1300
2 horizontal, 15 vertical kickers, 19 horizontal, 17 vertical BPMs and 2 horizontal kicker energy corrections	$\sim$ 1300
2 horizontal, 15 vertical kickers, 19 horizontal, 17 vertical BPMs, 2 horizontal kicker energy corrections and 36 quadrupole gradients	$\sim$ 360

The best fit to both vertical and horizontal closed orbit for a typical steering magnet is shown in Fig. 3 and Fig. 4, respectively. Although for some steering magnets there are field clamps on and thus quadrupole effect appearing, we were still able to calibrate the vertical steering magnet field strength to about 10% of accuracy. For the best fit, the vertical closed orbit error is within a standard deviation. However, because there are only 2 horizontal steering magnets included in the analysis, the horizontal fit result is not conclusive.

According to our fit result, we did point out a vertical steering magnet's wrong field strengths by more than 50%. This was proved by measuring the current out of the power supply and the distance between the kicker pole tips.

A difficulty of operating the IUCF Cooler ring is that the beam would not be stored without several sextupole magnets on. This means that we are not able to fit the normal quadrupole gradients without sextupole components.

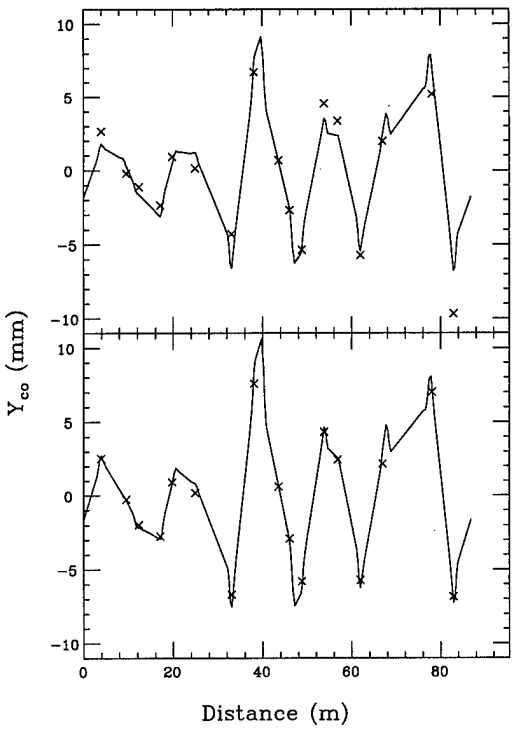

Figure 3: The model and measured vertical closed orbit displacement before (top) and after (bottom) fit. The solid lines are calculated model using COMFORT.

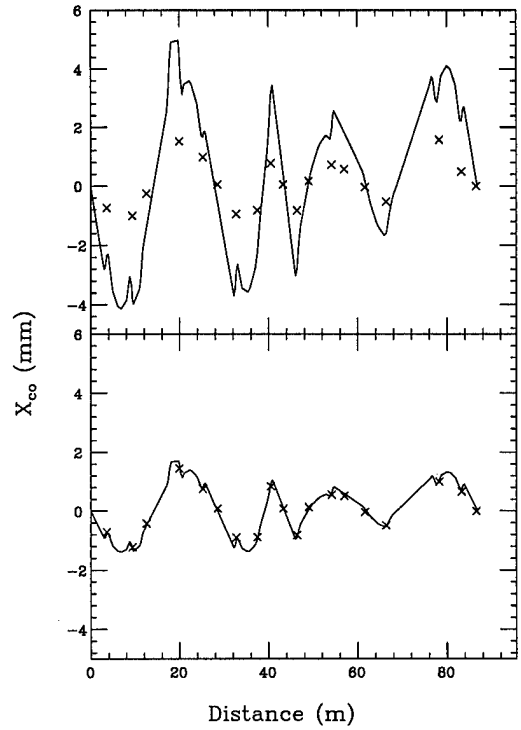

Figure 4: The model and measured horizontal closed orbit displacement before (top) and after (bottom) fit. The solid lines are calculated model using COMFORT.

Therefore, there is an unavoidable systematic error due to the sextupole effect.

4 CONCLUSION

In general, the orbit response matrix method could be applied to a proton storage ring. At the IUCF Cooler ring, a fundamental problem for the accuracy of the orbit response matrix is that there are only 2 independent steering magnets included in the analysis. Furthermore, due to the insufficiency of the data points, the linear coupling effect can not be taken into account. A direct solution to these problems is to install more horizontal steering magnets.

5 ACKNOWLEDGMENTS

We would like to thank James Safranek for the original analysis software and valuable advice. Dick Yoder and Bill Manwaring's help developing the on-line BPM data aquisition was appreciated. We also thank the entire IUCF operation group for their help.

6 REFERENCES

[1] J. Safranek, private communication.

[2] J. Safranek and M.J. Lee, "Calibration of the X-Ray Ring Quadrupoles, BPMs, and Orbit Correctors Using the Measured Orbit Response Matrix", Proceedings of Orbit Correction and Analysis in Circular Accelerators Workshop, AIP Conf. Proc. No. **315**, 128 (1994).

[3] J. Safranek and M.J. Lee, "Calibration of the X-Ray Ring Quadrupoles, BPMs, and Orbit Correctors Using the Measured Orbit Response Matrix",Proceedings of the 1994 European Particle Accelerator Conference, 1027.

[4] J. Bengtsson and M. Mdedahi, "Modeling of Beam Dynamics and Comparison with Measurements for the Advanced Light Source", Proceedings of the 1994 European Particle Accelerator Conference, 1021.

[5] J. Safranek, "Experimental Determination of Linear Optics Including Quadrupole Rotations", Proceedings of the 1995 IEEE Particle Accelerator Conference, 2817.

[6] D. Robin *et al.*, "Model Calibration and Symmetry Restoration of the Advanced Light Source", Proceedings of the 1996 European Particle Accelerator Conference, to be published.

[7] H. Grote and F.C. Iselin, The MAD Program (Methodical Accelerator Design), Version 8.1, User's Reference Manual, CERN/SL/90-13(AP) (1991).

[8] L. Sanchez *et al.*, COMFORT (Control of Machine Functions, Orbits, and Trajectories) Version 4.0, unpublished.

[9] J.Y. Liu *et al.*, Phys. Rev. E **49**, 2347 (1994).

[10] T. Sloan, private communication.

[11] W.H. Press *et al.*, Numerical Recipes in Fortran, The Art of Scientific Computing, 2nd ed., Cambridge University Press (1992).

TEST OF OPTICS DIAGNOSTICS IN ATF

K. Kubo, K. Oide, J. Urakawa,
High Energy Accelerator Research Organization (KEK), Tsukuba, Ibaraki 305, Japan and
T. Okugi, Tokyo Metropolitan University, Hachioji, Tokyo 192-03, Japan

Abstract

In beam operations, corrections and measurement of beam qualities, it is important to know the optics of the beam lines. Because there are always some errors in strength of magnets, actual optics will be different from the model. Errors of quadrupole strength of magnets are estimated by changing strength of steering magnets and measuring beam positions. The method of the error estimation and test results in Damping Ring of ATF, Accelerator Test Facility at KEK, will be reported.

1 INTRODUCTION

As reported in another paper [1], we have started commissioning of the damping ring of ATF in January. It is very important to understand the optics of the ring, which can be different from the calculated one due to errors of magnetic fields. The ATF Damping Ring has a race-track shape which has two arc sections and two straight sections. In the arc sections, there are 36 combined bending magnets which are defocusing in horizontal direction and 72 quadrupole magnets which are focusing in horizontal direction. In the straight sections, there are 30 quadrupole magnets. Errors of quadrupole strengths of the quadrupole magnets and the combined bending magnets have been estimated using beams, by steering beam and measuring the orbit in down stream. The measured response coefficients are fit by errors of strength of quads, beam position monitors (BPM) and steerings.

2 METHOD OF ERROR ESTIMATION

In a beam line, let $R_{12}(i,j)$ and $R_{34}(i,j)$ be the response coefficients of j-th BPM to i-th steering magnet, in horizontal direction and vertical direction respectively,

$$\begin{aligned} x_i &= R_{12}(i,j)x'_j \\ y_i &= R_{34}(i,j)y'_j \end{aligned} \qquad (1)$$

where x_i and y_i are position change at the i-th BPM and x'_j and y'_j are change of kick angles at the j-th steering magnet.

Let $R_{12,mo}(i,j)$ and $R_{34,mo}(i,j)$ be the model response coefficient of i-th BPM to j-th steering magnet in horizontal and vertical directions. And define error of the coefficients as follows.

$$\begin{aligned} \Delta R_{12}(i,j) &= R_{12}(i,j) - R_{12,mo}(i,j) \\ \Delta R_{34}(i,j) &= R_{34}(i,j) - R_{34,mo}(i,j) \end{aligned} \qquad (2)$$

Assume the errors come from errors of strength of quadrupoles between the steer and the BPM and calibration factors of the steer and the BPM as follows.

$$\begin{aligned} k_m &= k_{m,mo} + \Delta k_m \\ x'_j &= (1+\Delta S_j)x'_{j,mo} \\ y'_j &= (1+\Delta S_j)y'_{j,mo} \\ y_i &= (1+\Delta B_{y,i})y_{i,mo} \\ x_i &= (1+\Delta B_{x,i})x_{i,mo} \end{aligned} \qquad (3)$$

where left hand sides express real values, '$_{mo}$' means value from the model. Δk_m is error of k-value. ΔS_j, $\Delta B_{x,i}$ and $\Delta B_{y,i}$ are relative errors of calibration factors of j-th steer, i-th BPM in horizontal and vertical, respectively.

We assume all errors are small and take up to the first order of them. When kick angle at the i-th steering changed by x'_j and y'_j, beam position change and angle change at m-th quad in horizontal and vertical directions, x_m, y_m, x'_m and y'_m are

$$\begin{aligned} x_m &= R_{12}(j \to q_m)x'_j \\ y_m &= R_{34}(j \to q_m)y'_j \\ x'_m &= R_{22}(j \to q_m)x'_j \\ y'_m &= R_{44}(j \to q_m)y'_j \end{aligned} \qquad (4)$$

where $R(j \to q_m)$ is the transfer matrix from j-th steer to m-th quad. The change of kick angles just after the quad due to the position change in both directions are $\delta x'_m = -k_m x_m$ and $\delta y'_m = k_m y_m$. The change of position at i-th BPM, x_i and y_i are

$$\begin{aligned} x_i &= R_{11}(q_m \to i)x_m + R_{12}(q_m \to i)x'_m - R_{12}(q_m \to i)k_m x_m \\ y_i &= R_{33}(q_m \to i)y_m + R_{34}(q_m \to i)y'_m + R_{34}(q_m \to i)k_m y_m \end{aligned} \qquad (5)$$

where $R(q_m \to i)$ is the transfer matrix from the quad to the i-th BPM. Then, the response coefficients are

$$\begin{aligned} R_{12}(i,j) = {} & R_{11}(q_m \to i)R_{12}(j \to q_m) \\ & + R_{12}(q_m \to i)R_{22}(j \to q_m) \\ & - R_{12}(q_m \to i)k_m R_{12}(j \to q_m) \end{aligned}$$

$$\begin{aligned} R_{34}(i,j) = {} & R_{33}(q_m \to i)R_{34}(j \to q_m) \\ & + R_{34}(q_m \to i)R_{44}(j \to q_m) \\ & + R_{34}(q_m \to i)k_m R_{34}(j \to q_m) \end{aligned} \qquad (6)$$

From above equations, taking the first order of errors, error of the response coefficients are

0-7803-4376-X/98/$10.00 © 1998 IEEE

$$\Delta R_{12}(i,j) = -\sum_m R_{12}(q_m \to i)\Delta k_m R_{12}(j \to q_m) - \Delta S_j R_{12,mo}(i,j) + \Delta B_{x,i} R_{12,mo}(i,j)$$

$$\Delta R_{34}(i,j) = \sum_m R_{34}(q_m \to i)\Delta k_m R_{34}(j \to q_m) - \Delta S_j R_{34,mo}(i,j) + \Delta B_{y,i} R_{34,mo}(i,j) \quad (7)$$

where index m runs for all quadrupoles between j-thsteering magnet and i-th BPM.

In principle, when the number of pairs of steering magnet and BPM times two is larger than sum of the number of quadrupoles, steerings and two times of number of BPMs, errors can be estimated from linear fitting from equation (7).

3 MEASUREMENT AND ANALYSIS

3.1 Measurement of response coefficients

Before the measurement, orbit correction using steering magnets were performed to store as much beam as possible.

We changed every steering magnets along the ring and measure beam positions at BPMs. In the measurement, sextupole magnets were turned off to make the response linear. Because our BPM system measures beam positions in a single turn, the ring was considered as a transport line starting at the changed steering magnet, and beam positions of the first turn were measured at BPMs after the magnet. It means that beam passes only once before every position measurement and complexities from multi-turns are avoided.

In the ring, there were 46 horizontal and 40 vertical steering magnets available and 83 BPMs were available and used for this measurement.

For each steering magnet, beam positions were measured with three different current settings, -0.8A, 0A and +0.8A from the original setting. Change of 0.8A corresponds to change of kick angle by 0.85 mrad for the operated beam energy, 0.95 GeV. Because a part of beam was lost far downstream for some settings, data of BPMs only in 50m after changed steering magnets were used for the analysis. To reduce the statistical error of BPMs and effects of jitters, data were taken for 25 pulses for each setting. To estimate the response coefficients, difference of averaged positions with three settings were used for a least square fitting. The position difference was fitted as a linear function of the difference of the set current for each pair of steering magnet and BPM. So far, the horizontal-vertical coupling has been neglected in this analysis. The slopes of the fit represent the response coefficients. The statistical errors of the responses from the measurement are estimated from the errors of average positions in the fittings which was set to be $\sigma_x/\sqrt{n-1}$ and $\sigma_y/\sqrt{n-1}$ where σ_x and σ_y are r.m.s. of measured positions with the same setting and n is the number of pulses for which the beam positions were measured successfully. The error includes both resolution of the BPMs and jitters of the beam.

3.2 Fitting orbit with energy offset

Because we measured the first turn orbit, the beam energy can be different from the energy determined by the bending field of the ring. We estimated the energy offset comparing measured average orbit and calculated dispersion in the first arc section. Plots in Figure 1 shows averaged horizontal beam positions at BPMs in the first arc section. Using the optics model, position, angle and energy offset at the entrance of the arc section were fitted as -1100 μm, 801 μrad and 0.2% of the energy determined by the bending field, respectively. The line in the figure shows the orbit using the fitting. Analysis bellow assumes this estimated offset of the beam energy.

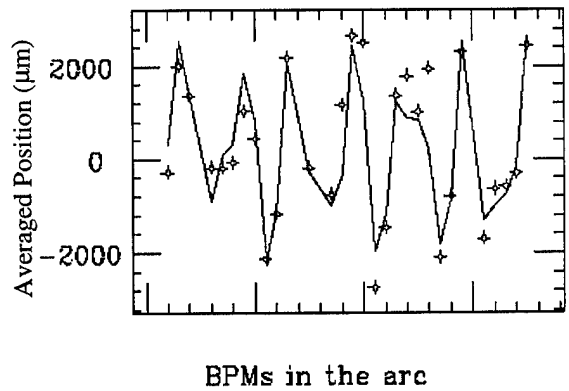

Fig. 1, Average positions at BPMs in the first arc section (plots) and fitted orbit (line).

3.3 Estimation of Machine Errors

Response coefficients $R_{12}(i,j)$ and $R_{34}(i,j)$ are calculated from the current-position responses, multiplied by given factors of kick angles vs. current settings of steering magnets. Figure 2(a) and (b) show measured response coefficients vs. model response coefficients in horizontal and vertical directions, respectively.

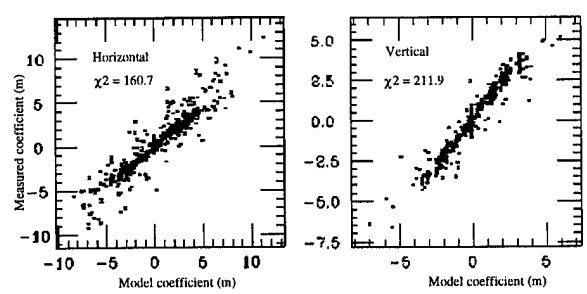

Fig.2, Measured response coefficients vs. model coefficients before fitting, (a) in horizontal direction and (b) in vertical direction.

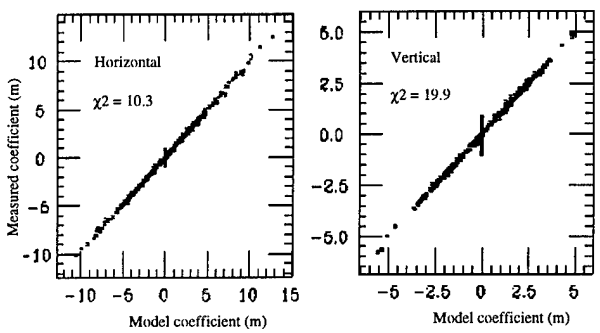

Fig.3, Measured response coefficients vs. model coefficients after fitting, (a) in horizontal direction and (b) in vertical direction.

Errors of quadrupole strengths of magnets, calibration factors of BPMs and current to kick angle factors of steering magnets are fitted using the methods described in section 2. Because the strength of 28 quads called QF1R were very small, their errors were not included in the fitting.

The fitting calculated 108 errors of quadrupole strengths, 86 errors of steering magnets' factors and 166 errors of BPMs' calibration factors. Figure 4 shows estimated relative errors of k-values of magnets, $\Delta k_m / k_{m,mo}$. Large error bars in this figure correspond to quads whose strength are very small. Figure 3(a) and (b) show measured response coefficients vs. model response coefficients in horizontal and vertical directions, respectively, after correction of the model using estimated errors. The corrected model well agrees with the measurement.

The parameters of the model and current setting of each power supply was corrected based on this fitting. After the correction, measured transverse tunes are different from the model by 0.15 in horizontal and 0.02 in vertical where the total tunes are about 15 and 9, respectively. Before the correction, the difference had been more than 0.5 in both directions. More measurements and test of the validity of the correction in detail will be performed near future.

Plots distribute on vertical lines in the figures 3(a) and (b) suggest x-y coupling or rotations of quads, steerings and/or BPMs. The coupling will be studied near future.

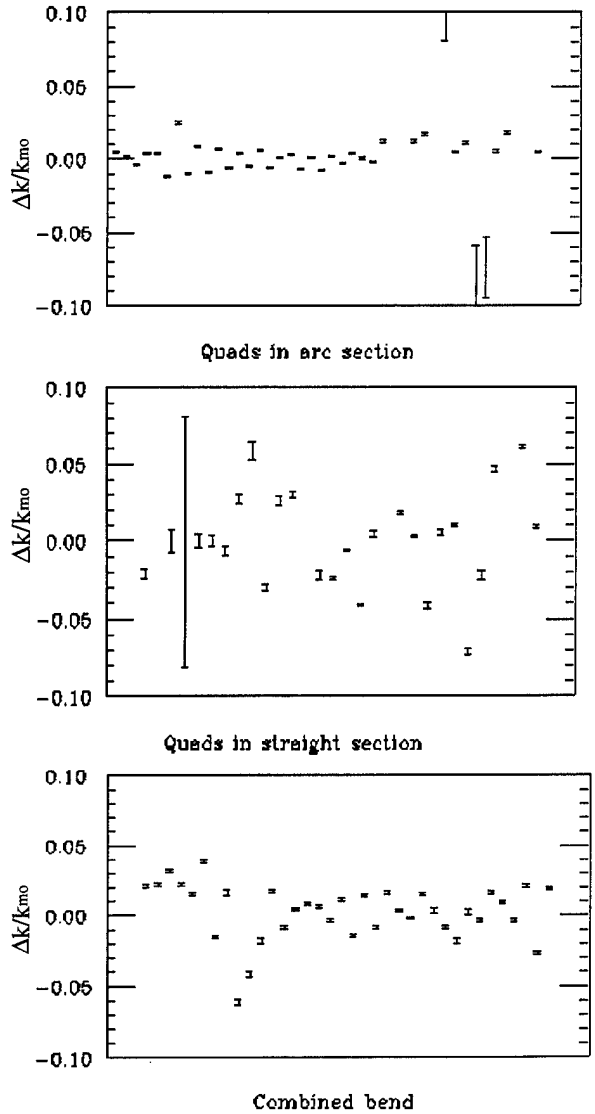

Fig. 4, Fitted relative errors of k-values, quads in arc sections, quads in straight sections and combined bends are shown separately.

4 ACKNOWLEDGMENTS

The authors thank all members of the ATF collaboration group, especially E. Gianfelice, H. Hayano, T. Naito, N. Terunuma and F. Zimmerman for machine setup and preparing and joining the data taking.

REFERENCES

[1] J. Urakawa, in this conference

EFFECT OF RF PHASE MODULATION ON THE LONGITUDINAL BEAM DYNAMICS

Min-Huey Wang, L.H. Chang, Peace Chang, K.T. Hsu, C.C. Kuo, W.K. Lau and C.S. Hsue*,
SRRC, No.1, R & D Road VI, SBIP, Hsinchu 300, Taiwan, R.O.C.
National Tsing Hua University, Hsinchu 300, Taiwan, R.O.C.*

Abstract

When the frequency of the RF noise is close to the synchrotron frequency, it will cause longitudinal beam instability. In order to study the effect of the instability, a sinusoidal phase modulation was applied to the RF system. The beam instability was observed with a streak camera. The oscillation amplitude and frequency of the beam versus the frequency of applied phase modulation was measured. The beam splitting into two beamlets in the same RF bucket was also observed when the frequency of phase modulation was close to the synchrotron frequency.

1 INTRODUCTION

Third generation synchrotron light sources are low emittance machines. Any small error source may cause instabilities of the beam stored in the ring. The RF system is a dominating factor of the longitudinal beam instabilities. If the arrival time of the particle at the RF cavity relative to the RF wave is modulated , the effect on the synchrotron motion is equivalent to RF phase modulation. Error sources such as RF noise, RF klystron power supply ripple, driven RF phase shifter, synchrotron-betatron coupling or even wake fields could cause RF phase modulation. To study the instabilities caused by RF phase modulation on the beam, a sinusoidal phase modulation was applied to the RF system and a Hamamatsu C5680 streak camera was used to observe the effects on the synchrotron motion at SRRC. In this report we will discuss the longitudinal beam dynamics with RF phase modulation, the experimental set up, the process of experiment and the results. The theoretical prediction is compared with the experimental results.

2 LONGITUDINAL BEAM DYNAMICS WITH RF PHASE MODULATION

We consider the case when the RF phase is modulated by a sinusoidal function $a\ \sin(2\pi f_m t)$ with amplitude a and modulation frequency f_m or modulation tune $\nu_m = \frac{2\pi f_m}{\omega_0}$, where ω_0 is the revolution angular frequency. The coupled differential equation for the phase deviation relative to the synchronous phase ϕ, and its conjugate δ defined by $\frac{h\eta}{\nu_s}\frac{\epsilon}{E_0}$ with η the slip factor, h the harmonic number, $\nu_s = \sqrt{\frac{heV_{RF}|\eta\cos\phi_s|}{2\pi E_0}}$ the natural synchrotron tune, ϵ the energy deviation relative to energy E_0 of synchronous particle, become:

$$\frac{d\phi}{d\theta} = \nu_s\delta \tag{1}$$

$$\frac{d\delta}{d\theta} = \frac{h\eta}{2\pi E_0\nu_s}[eV_{RF}\sin(\phi_s + \phi + a\sin\nu_m\theta) - U] \tag{2}$$

Where $\theta = \omega_0 t$ is the revolution angle, ϕ_s the synchronous phase, and U the radiation energy loss, which depends on the energy of the particles. The equation of motion of the RF phase modulation becomes:

$$\frac{d^2\phi}{d\theta^2} - \frac{4\nu_s^2}{h\eta}\mid\tan\phi_s\mid\frac{d\phi}{d\theta} + \nu_s^2(\sin\phi + \mid\tan\phi_s\mid(\cos\phi - 1)) = a\nu_s^2\sin\nu_m\theta\cos\phi \tag{3}$$

The damping rate of SRRC is about 100 s^{-1} and is much smaller than the synchrotron angular frequency $\omega_s = 1.8\times10^5 s^{-1}$. So we will neglect the damping term in the following discussion. The Hamiltonian may now be written as

$$H = \frac{1}{2}\nu_s\delta^2 + \nu_s(1-\cos\phi) + \nu_s\mid\tan\phi_s\mid(\sin\phi - \phi) - a\nu_s\sin\nu_m\theta\sin\phi \tag{4}$$

Employing a canonical transformation to the action-angle variables (ψ, J), the Hamiltonian becomes:

$$H = (\nu_s - \nu_m)J - \frac{\nu_s}{16}J^2 - \frac{\sqrt{2J}}{2}a\nu_s\cos\psi + \Delta H(\psi, J, \theta) \tag{5}$$

with $J = \frac{1}{2}(\delta^2 + \phi^2)$, $\psi = (\arctan(-\frac{\delta}{\phi}) - \nu_m\theta - \frac{\pi}{2})$, Where ΔH is a superposition of terms oscillating at frequency of even harmonics of ν_m[1]. Near the resonance $\nu_s \approx \nu_m$ the dominating term of the Hamiltonian is given by

$$< H >= (\nu_s - \nu_m)J - \frac{\nu_s}{16}J^2 - \frac{\nu_s a\sqrt{2J}}{2}\cos\psi, \tag{6}$$

which is a function of the modulation frequency and amplitude. In terms of the variables $\tilde{\phi} = \sqrt{2J}\ \cos\psi, \tilde{\delta} = \sqrt{2J}\ \sin\psi$ the Hamiltonian becomes:

$$< H >= -\frac{1}{64}\nu_s\tilde{\delta}^4 + \frac{1}{64}(32(\nu_s - \nu_m) - 2\nu_s\tilde{\phi}^2)\tilde{\delta}^2 + \frac{1}{64}(-\nu_s\tilde{\phi}^4 + 32(\nu_s - \nu_m)\tilde{\phi}^2 - 32a\nu_s\tilde{\phi}) \tag{7}$$

The local extrema of the Hamiltonian occurs on the $\tilde{\phi}$ axis where $\frac{\partial H}{\partial\tilde{\phi}} = 0$, $\frac{\partial H}{\partial\tilde{\delta}} = 0$. For $\tilde{\delta} = 0$ the Hamiltonian becomes:

$$H = \frac{1}{64}(-\nu_s\tilde{\phi}^4 + 32(\nu_s - \nu_m)\tilde{\phi}^2 - 32a\nu_s\tilde{\phi}) \tag{8}$$

0-7803-4376-X/98 /$10.00 © 1998 IEEE

The local extrema are determined by

$$\tilde{\phi}^3 - 16(1 - \frac{\nu_m}{\nu_s})\tilde{\phi} + 8a = 0 \qquad (9)$$

Depending on the value of $\nu_m - \nu_s(1 - \frac{3}{16}(4a)^{2/3})$, there are three different kinds of solutions for the cubic equation[2]. For $\nu_m < \nu_s(1 - \frac{3}{16}(4a)^{2/3})$ there are three unequal real roots, corresponding to two stable fixed points(SFP) and one unstable fixed point(UFP) in the $\tilde{\phi}, \tilde{\delta}$ phase space. For $\nu_m = \nu_c \equiv \nu_s(1-\frac{3}{16}(4a)^{2/3})$ all the roots are real and at least two roots are equal. In this case a SFP and a UFP are merged together. The modulation tune ν_c is called the bifurcation tune. When $\nu_m > \nu_s(1 - \frac{3}{16}(4a)^{2/3})$ only one real solution exits. In summary, as the modulation frequency is increased with fixed modulation amplitude, the outer SFP and UFP moved inward toward the origin in the $\tilde{\phi}$, $\tilde{\delta}$ space while the inner SFP moved outward. Figure 1 shows the tori-0(tori passing origin) of Hamiltonian in equation(7) with the value of Hamiltonian equals 0 at modulation amplitude 0.02827 and modulation tune $0.9\nu_s$, $0.956\nu_s$ and ν_s which presented the cases for $\nu_m < \nu_c$, $\nu_m = \nu_c$ and $\nu_m > \nu_c$ respectively. The tori-0 for $\nu_m = 0.944\nu_s$ is also a separatrix and passes USF is also shown in Figure 1. The tracking results of equation (1) and (2) under the same conditions of Figure 1 but neglecting the damping effect are shown in Figure 2. Figure 2 shows the effect of time dependent terms ΔH in equation(7) which is neglected completely in Figure 1.

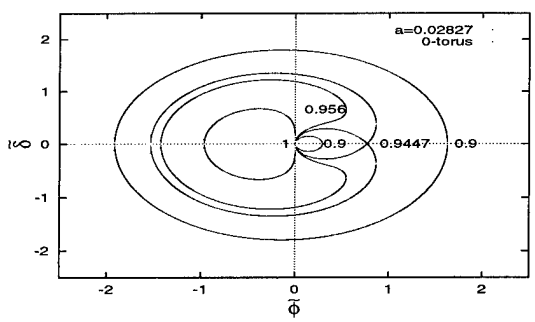

Figure 1: The phase space of RF phase modulation at modulation amplitude 0.02827 and modulation tune 0.9, 0.9447, 0.956 and 1 respectively.

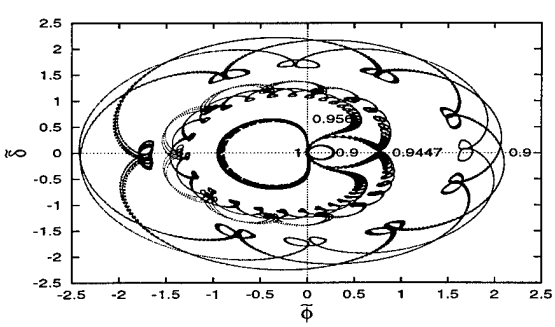

Figure 2: The phase space tracking of RF phase modulation at modulation amplitude 0.02827 and modulation tune 0.9, 0.9447, 0.956 and 1 respectively.

3 EXPERIMENTAL SET UP AND PROCEDURE

The TLS at the SRRC is a 1.3 GeV synchrotron light source. The circumference of the ring is 120m. The revolution time of the ring is 400ns. The frequency of RF cavity is 500 MHz and the harmonic number is 200. The momentum compaction factor of the ring is 6.78×10^{-3}. The natural energy spread is 6.6×10^{-4}. In order to study the beam instability of the ring a Hamamatsu C5680 streak camera was set up at SRRC[3]. In this experiment the synchroscan mode of streak camera combined with the dual time base extender is used to observe the turn by turn electron bunch motion. An amplitude of $\pm$ 0.02827 radian phase modulation was applied to the RF system. The source of the phase modulation was generated by a signal generator applied to the phase lock amplifier to generate a phase shift to the RF cavity. In this experiment the single bunch mode beam current was of 1.5 mA and one RF gap voltage was 400kV. The natural synchrotron tune is 8.08×10^{-3}. The RF bucket energy acceptance is 1.029×10^{-2}, which corresponds to 1.696 radian of RF phase angle. The RF bucket acceptance restricts the allowed beam oscillation amplitude. The modulation frequency applied to the beam was roughly scanned from 1 kHz to 40 kHz with 1 kHz step. Then smaller steps with 0.1 kHz per step were swept from 18 kHz to 22 kHz. The behavior of the longitudinal beam motion was recorded with the streak camera.

4 EXPERIMENTAL RESULTS AND DISCUSSIONS

At modulation frequency 18 kHz the beam was observed to start oscillation with a small amplitude. The oscillation amplitude of the beam increased as the modulation frequency was increased. At modulation frequency 19.4 kHz a beam with a large oscillation amplitude started to show up. As the modulation frequency was increased the intensity of beam with large oscillation increased and the intensity of the beam with small oscillation decreased. At modulation frequency 19.8 kHz the beam with small oscillation disappeared. As the modulation frequency was increased further the oscillation amplitude of the large oscillation beam decreased. At modulation frequency 22 kHz there remained very tiny beam motion. The beam motion captured by the streak camera at the modulation frequency from 19.4 kHz to 19.8 kHz was shown in Figure 3. The splitting of the beam into two beamlets were clearly shown in the figure. The oscillation frequency of the beam under the RF phase modulation from modulation frequency 18 kHz to 22 kHz were measured and is displayed in Figure 4. In Figure 4 the tracking results of oscillation frequency at the same RF phase modulation is also shown. The tracking result is an average of hundred particles with different initial values. The oscillation amplitude of beam versus the modulation frequency is shown in Figure 5.

As mentioned in section 2, if the modulation frequency is below bifurcation tune, it is possible for two beamlets to exist in the same RF bucket. Particles with smaller energy

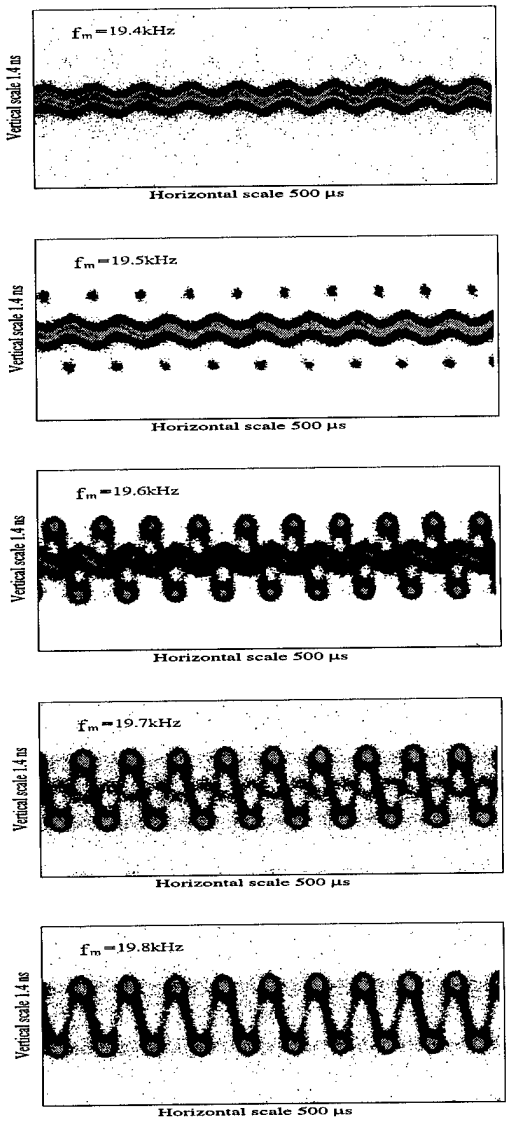

Figure 3: The beam motion observed on the streak camera at modulation amplitude 0.02827 and modulation frequency 19.4 kHz, 19.5 kHz, 19.6 kHz, 19.7 kHz and 19.8 kHz, respectively.

will circulate the inner SFP, while particles with higher energy will circulate the outer SFP. The particles around the inner SFP or outer SFP can interchange through the separatrix. For fixed modulation frequency, the maximum oscillation amplitude of particles around the inner SFP increases as the energy of particles increases, while the maximum oscillation amplitude of particles around the outer SFP decreases as energy increases. For fixed particle energy as shown in Figure 1, the oscillation amplitude of particles around the inner SFP increases as modulation frequency increases. For particles around the outer SFP the oscillation amplitude decreases as modulation frequency increases. At lower modulation frequency the energy and oscillation amplitude of particles around the outer SFP is too large to be accepted in the RF bucket. This explains why at lower

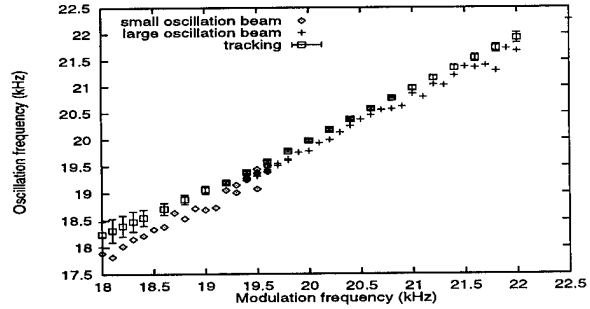

Figure 4: The measured and tracking oscillation frequency at different modulation frequency.

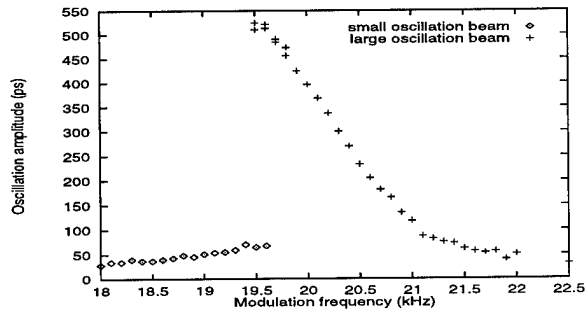

Figure 5: The measured oscillation amplitude at different modulation frequency.

modulation frequency the particles around the outer SFP were not observed. In Figure 3 at modulation frequency 19.5 kHz, the measured large oscillation amplitude was 510 ps which corresponded to 1.6 radian phase oscillation and was below the RF bucket acceptance. From the measurements as shown in Figure 5 the oscillation amplitude of the particles around the outer SFP decreases as modulation frequency increases which is consistent with the discussion in section 2. At modulation frequency 19.8 kHz the small oscillation beam disappeared. However the theoretical bifurcation frequency in this case is 19.3 kHz. The small discrepancy between measured and theoretical values need further investigations.

5 ACKNOWLEDGEMENTS

We would like to thank professor S.Y. Lee for the helpful discussion on this topic during his stay at SRRC.

6 REFERENCES

[1] S.Y. Lee et al., Phys. Rev. Lett 67(1991) 3768; M. Ellison et al., Phys. Rev. Lett 70(1993) 591; H. Huang, et al., Phys. Rev. E 48(1993) 4678.

[2] M. Abramowitz & I.A. Stegun, 'Handbook of Mathematical Functions', National Bureau of standard.

[3] M. H. Wang, et al., Proc. EPAC96, Barcelona(1996)1120; M. H. Wang, et al., Proc. IEEE PAC, (1995)2971.

MEASUREMENT OF THE VARIATION OF MACHINE PARAMETERS AND THE EFFECT OF THE POWER SUPPLIES RIPPLE ON THE INSTANTANEOUS TUNES AT SPEAR[1]

A.Terebilo, C.Pellegrini, University of California, Los Angeles, CA 90024
M.Cornacchia, J.Corbett, D.Martin, SLAC, Stanford University, Stanford, CA 94309

Abstract

For long term stability analysis time variation of tunes is important. We have proposed and tested a technique for measuring the magnitude of this variation. This was made possible by using tune extraction algorithms that require small number of turns thus giving an instantaneous tune of the machine. In this paper we demonstrate the measured effect of the tune modulation with 60 Hz power supplies ripple, power line interference from SLAC linac operating at 30 Hz repetition rate, and non-periodic variation.

1 MOTIVATION

The effect of time dependence of the Hamiltonian on the short and long term stability has been studied before analytically and numerically [1][2][3]. For practical application of the results of these studies one needs to know the magnitude of such variation. If the primary source is the ripple in the power supplies and consequently in the magnetic field, a straightforward measurement of its magnitude would require either precise Hall probe measurements and/or careful calculations of the filtering effect of the magnet iron cores and vacuum chamber at the harmonics of 60 Hz [4]. Alternatively one could use turn-by-turn BPM measurements that have become standard for non-linear dynamics studies in the past few years in combination with recent tune extraction techniques from the turn-by-turn data [5],[6].

2 MEASUREMENT AND INSTANTANEOUS TUNE EXTRACTION TECHNIQUE

For measurement we used the turn-by-turn transverse phase space monitor described in [7] and its upgrade [8]. Transverse betatron oscillations of a single bunch are excited by a pair (horizontal and vertical) of fast kickers. Following the kick the transverse position of the bunch at two BPM locations is recorded every turn. We have modified the fast kicker triggering circuitry to initiate data acquisition at a controlled phase with

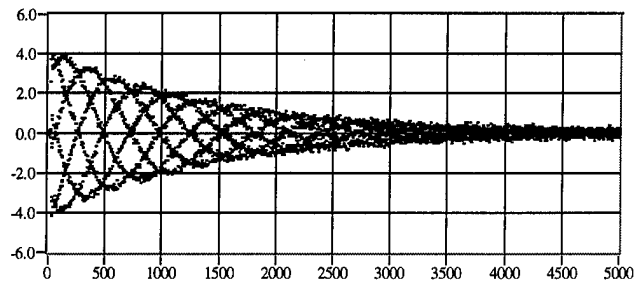

Fig.1 Horizontal centroid position (mm) vs. turn number

respect to AC. A typical response of the bunch centroid to a kick as detected at one BPM is shown on Fig.1.

We compute the instantaneous tune $\nu_{m,N}$ associated with N consequent turns starting at turn m by maximizing the absolute value of the correlator

$$I(\nu_{m,N}) = \sum_{n=m}^{m+N-1} f_n \cdot \exp\left(-i2\pi \cdot \nu_{m,N}, n\right)\chi_n \quad (1)$$

where f_n bunch position at the n - th turn and
χ_n weight function, we use $\sin(\pi \cdot n / N)$

Having computed $\nu_{m,N}$ this way we chi-square fit the amplitude $a_{m,N}$ in the fitting function

$$g_n = a_{m,N} \cos\left(2\pi \cdot \nu_{m,N} n + \psi\right) \quad (2)$$

The accuracy of instantaneous tune extraction algorithm in application to realistic data was numerically tested [8]. For N = 256 that we use for the measurements described in this paper and betatron amplitudes > 1.5 mm, the frequency error is < 0.00005. The modulation of the transverse tune due to the coherent longitudinal oscillations having a period of ~50 turns is averaged out. This accuracy should allow reliable detection of the tune variation of magnitude ~1×10^{-3} which may result from ripple in the guiding and focusing fields, modulation of

[1] Work supported by US DOE grant DE_FG03-92ER40793 and contract DOE-AC03-76SF00515, Office of Basic Energy Sciences, Division of Chemical Sciences.

the RF parameters at harmonics of AC, or the non-harmonic ground motion and power supplies drift.

If the machine is tuned sufficiently far from low order resonances the non linear tune shift with amplitude to the first order is

$$\nu_x = \nu_x^{(0)} + h_{xx} J_x + h_{xy} J_y + \ldots,$$
$$\nu_y = \nu_y^{(0)} + h_{yy} J_y + h_{yx} J_x + \ldots \qquad (3)$$

We extrapolate measured $\nu_{m,N}$ vs. $a^2_{m,N}$ to zero amplitude by fitting a second order polynomial.

3 RESULTS AND INTERPRETATION

3.1 Non periodic variation

In the first test ~200 kicks were applied during a 5 min period maintaining constant relative phase with respect to AC to separate the tune variation not related to the power supply ripple. The $\nu_{m,N}$ vs. $a^2_{m,N}$ was computed for each kick and the extrapolation of the tune to zero amplitude was performed. Few of these plots are shown for kicks approximately 1 s apart in Fig. 2.

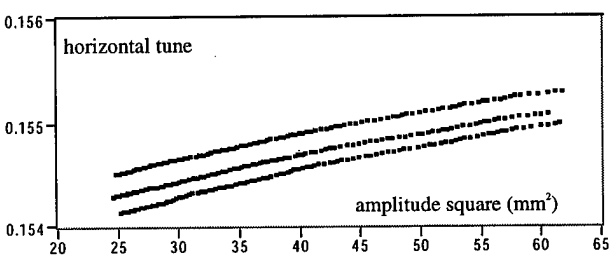

Fig.2 Horizontal tune vs. amplitude square for 3 consequent kicks.

The difference in ν_x between these graphs is ~5×10e^{-4} which is an order of magnitude greater then combined error of the tune extraction method and measurement error. Therefore it should be interpreted as physical tune variation.

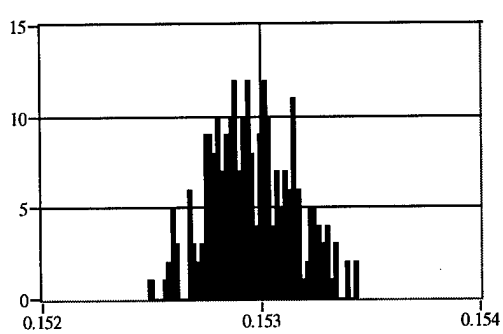

Fig.3 Distribution of horizontal tunes at 0 amplitude measured over 5 min. period at fixed phase relative to AC.

The distribution of horizontal tunes extracted from 200 kicks (Fig.3.) has FWHM of 4×10e^{-4}.

3.2 Periodic tune modulation

For the second test relative phase with respect to the AC was varied. The horizontal and vertical tune modulation is shown on Fig. 4, 5 and 6.

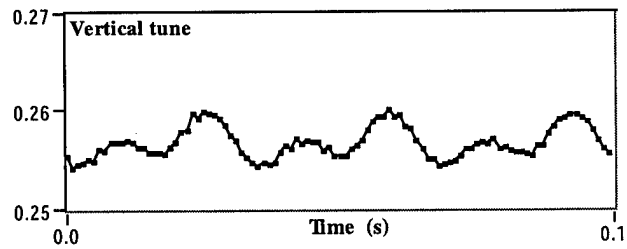

Fig.4 Modulation of vertical tune

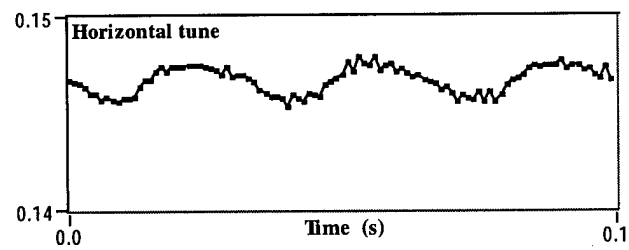

Fig.5. Modulation of horizontal tune

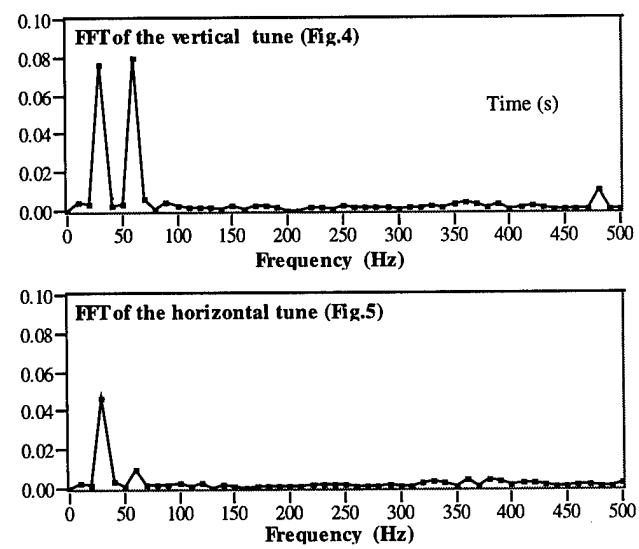

Fig. 6. Spectral analysis of the tune modulation

Figures 4 and 5 show strong 30 Hz power line interference from SLAC linac operating at this repetition rate. The peak to peak magnitude of the tune modulation is 0.002 and 0.006 for horizontal and vertical tunes, respectively. It is factor of 4 greater than non-periodic

tune variations seen when the measurements are done phase locked to the ripple.

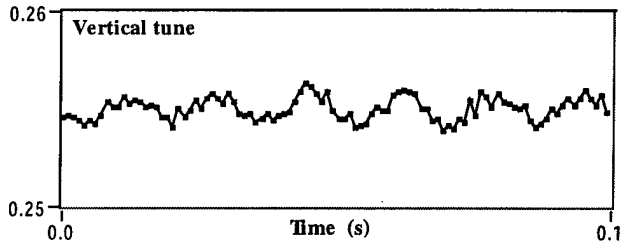

Fig.7 Modulation of vertical tune , no 30Hz power line interference

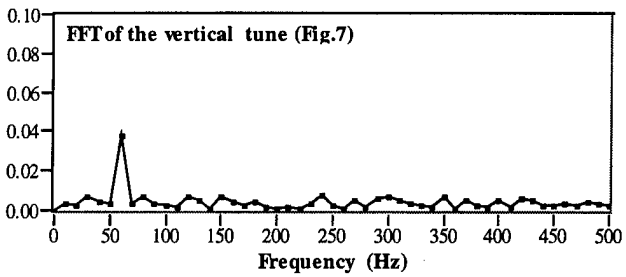

Fig. 8 Spectral analysis of the tune modulation

The data on fig.7 is taken on the day when SLAC linac was operating at 120 Hz. The strongest component in the tune modulation is 60 Hz. The measured peak-to- peak vertical tune modulation is 0.002. The horizontal one is smaller then non-periodic part Fig.3.

4 CONCLUSIONS

We demonstrated a technique for measuring the time variation of the tunes. The following experimental results were obtained:

Non-periodic variation of the tunes	horizontal vertical	$4\times10e^{-4}$ not measured
Peak-to-peak , SLAC linac operating at 30 Hz	horizontal vertical	$2\times10e^{-3}$ $6\times10e^{-3}$
Peak-to-peak, SLAC Linac operating at120 Hz	horizontal vertical	$<4\times10e^{-4}$ $2\times10e^{-3}$

5 ACKNOWLEDGEMENTS

The authors would like to thak D.Gough, G.Johnson, D.Mostoffi for their contribution in the design and building of the electronics for data acquisition system and fast kicker instrumentation.

REFERENCES

[1] A.Bazzani et.Al :'Diffusion in stochastically and periodically modulated Hamiltonian systems',AIP Conf . Proc. (1995) 344 p.68 - 77

[2] A.Bazzani et.Al:'A study of effects of tune modulation in non linear maps', AIP Conf . Proc. (1995) 344 p.345 - 360

[3] G.V.Stupakov: 'Quasi-closed orbit in a harmonically perturbed magnetic field', AIP Conf . Proc. 292 p.267 - 272

[4] P.Burla, D.Cornuet, K.Fischer, P.Leclere, F.Schmidt: 'Power Supply Ripple Study at SPS', AIP Conf. Proc. 326

[5] H.Dumas, J.Laskar: 'Global Dynamics and Long-Time stamility in Hamiltonian systems via numerical frequency analysis', Phys. Rev. Lett. 70 , 2975 (1993)

[6] J.Laskar, D.Robin: 'Applications of frequency map analysis to the ALS' ,Proc. of the International Workshop on Single-Particle Effects in Large Hadron Colliders, Montreux, Switzerland (1995)

[7] P.Tran, C.Pellegrini, M.Cornacchia, M.Lee,W.Corbett: 'Non linear beam dynamics experimental program at SPEAR', IEEE PAC 1995 p. 3323

[8] A.Terebilo, C.Pellegrini, M.Cornacchia, J.Corbett, D.Martin: 'Non linear dynamics studies at SPEAR', these proceedings

SOME RESULTS OF THE ADVANCED PHOTON SOURCE BEAM LIFETIME STUDIES

Hana M. Bizek
Advanced Photon Source, Argonne National Laboratory
9700 South Cass Avenue, Argonne, Illinois 60439 USA

Abstract

Total beam lifetime consists of two components: the residual-gas-scattering lifetime and Touschek lifetime. The residual-gas lifetime is comprised of the elastic and inelastic scattering on electrons and elastic and inelastic scattering on nuclei. Touschek scattering involves scattering of particles within the bunch. One usually calculates only the elastic scattering on nuclei (single Coulomb scattering) and inelastic scattering on nuclei (bremsstrahlung) of the residual-gas-scattering lifetime component. Experience gained from computing the beam lifetime in the Advanced Photon Source (APS) storage ring shows that the electron scattering should not be neglected, particularly the inelastic contribution. Given the measured quantities from the APS storage ring, one can compare theoretical predictions with experimental results. Uncertainties in calculating the various contributions to lifetime will be discussed.

1 INTRODUCTION

Formulas exist [1, 2] to calculate both the residual-gas and Touschek components of the total beam lifetime. The inverse of the total beam lifetime is the sum of the inverses of the individual components.

The residual-gas component depends on the physical and energy apertures and on the properties of the gas mixture remaining in the storage ring, including the gas pressure. It is made up of elastic scattering on electrons, inelastic scattering on electrons, elastic scattering on nuclei (single Coulomb scattering) and inelastic scattering on nuclei (bremsstrahlung). The scattering on nuclei predominates, but scattering on electrons should not be neglected. Particularly elastic scattering on electrons contributes to the residual-gas lifetime. The Touschek component depends on the energy acceptance, momentum spread (which is related to bunch length), bunch current, Twiss parameters, dispersion, and coupling coefficient.

All such quantities are recorded in computer files for analysis. The experimentally observed lifetime is also recorded. This author has written a computer program that accepts this experimental data, computes the theoretically predicted lifetime, and compares this lifetime to the experimental value.

2 RESIDUAL-GAS LIFETIME COMPONENT

The presence of the residual gas, quantified by its pressure, may cause the positrons to either hit the wall or be ejected out of the bunch and get lost. The nature of gases present in the APS storage ring and their partial pressure was provided by John Noonan [3]:

Mass 2 (H_2)	48%
Mass 18 (H_2O)	24%
Mass 28 (CO/N_2)	23%
Mass 44 (CO_2) and remainder	5%

The gas density is related to pressure by:

$$P = \rho k T \tag{1}$$

where P is absolute pressure, ρ is gas density, $T = 300°K$ is absolute temperature and k is the Boltzmann constant (1.38×10^{-23} J/°K).

Given the pressure from data for a particular run, the above data can be used to calculate the loss rates of each gas in the mixture. The total residual-gas loss rate is the sum of loss rates of individual gases comprising the residual gas mixture. Total lifetime is the inverse of the total loss rate.

The formulas for each process of the residual-gas component are discussed below.

- Elastic scattering on nuclei leads to an angular kick for the betatron motion in the vertical direction:

$$R_{eln} = \frac{2\pi r_e^2 Z^2 c\rho}{\gamma^2}\left(\frac{\langle\beta_y\rangle\beta_y}{b^2}\right) \tag{2}$$

- Bremsstrahlung on nuclei leads to an energy loss for the circulating positrons:

$$R_{brn} = \frac{16 r_e^2 Z^2 c\rho}{411}\ln\frac{183}{Z^{1/3}}\left(\ln\frac{1}{\varepsilon_{acc}} - \frac{5}{8}\right) \tag{3}$$

- Elastic scattering on electrons results in transferring part of the positrons' incident energy to the electrons of the residual gas:

$$R_{ele} = \frac{2\pi r_e^2 Z c\rho}{\gamma}\frac{1}{\varepsilon_{acc}} \tag{4}$$

- Inelastic scattering on electrons leads to photon emission:

$$R_{ine} = \frac{16 r_e^2 Z c\rho}{411}\left(\ln\frac{2.5\gamma}{\varepsilon_{acc}} - 1.4\right)\left(\ln\frac{1}{\varepsilon_{acc}} - \frac{5}{8}\right) \tag{5}$$

where r_0 is the classical electron radius, c is the speed of light, Z and ρ are, respectively, the atomic number and the density of the residual gas, γ is the design energy divided by the rest energy of the positrons, $\langle\beta_y\rangle$ is the average vertical beta function around the ring, β_y is the vertical beta function at insertion, b is the vertical half-aperture, and ε_{acc} is the energy acceptance.

0-7803-4376-X/98/$10.00 © 1998 IEEE

Solving Eq. (1) for ρ and substituting this into Eqs. (2) through (5) yields the loss rate of each process as a function of pressure. The loss rate is computed for each gas. The loss rates are added and the inverse is taken to compute the residual-gas component of the beam lifetime.

3 TOUSCHEK LIFETIME COMPONENT

The formulas for the Touschek component are

$$\frac{1}{\tau_T} = \frac{\sqrt{\pi} r_0^2 c N}{\gamma^2 (\delta p_x)^3 V} \int_{\varepsilon_{acc}}^{\infty} \frac{1}{u^2}\left(\frac{u}{\varepsilon_{acc}} - \frac{1}{2}\ln\left(\frac{u}{\varepsilon_{acc}}\right) - 1\right) exp(-u) du \quad (6)$$

$$\text{and } \varepsilon_{acc} = \left(\frac{\Delta p_{acc}}{\gamma \delta p_x}\right)^2, \quad (7)$$

where δp_x is related to the rms angular divergence, and V is the bunch volume [4]. The number of positrons in the bunch N is proportional to the bunch current I_b according to

$$I_b = eN\frac{c}{C}, \quad (8)$$

where e is the unit charge of a positron and $C = 1104$ m is the circumference of the APS storage ring.

In the lifetime calculation the bunch current is not measured directly, because no equipment is available at present. Rather, the beam current and number of filled buckets is available, so the bunch current is obtained by dividing the beam current by the number of buckets filled. This is only an approximation; a direct measurement of the bunch current is preferable.

The bunch length σ_l is a function of current I_b. From the available data, E. Crosbie [5] obtained the best fit. The empirical formula he provides is

$$\sigma_l = 7.344 + 1.388 I_b \quad (9)$$

with σ_l in mm and I_b in mA.

The coupling coefficient and energy acceptance are measured independently. Their values are 2.9% and 0.74%, respectively. The low value of the energy acceptance is attributed to high chromaticity, although the details are unknown.

4 ANALYSIS AND PRESENTATION OF RESULTS

In this report we ask: what values of the various quantities read from the input files will produce computed lifetime results that are comparable to the measured lifetime? First we take the measured quantities, including the measured lifetime, and write them to a file. The computer code uses this output file to compute the various lifetimes according to Eqs. (2) through (7) as well as the total beam lifetime. If the curves coincide (they never do), then the theoretical predictions are consistent with experimental results.

The input data are obtained from files that monitor many quantities of the storage ring. Each day is identified by its date, both Julian and conventional. SDDS tools developed by Michael Borland [6] are used to manipulate the data in those files. For this calculation all quantities (pressure, rf voltage, etc.) are expressed as a function of time of day. Therefore the time of day is the independent variable.

The runs of the storage ring are divided into two categories: machine studies and user runs. The machine studies analyze the overall performance of the storage ring and measure things such as energy acceptance, coupling coefficient, and other properties of the beam. The user runs set up experimental environments for the users. The purpose of the Advanced Photon Source is to provide high-energy X-rays for the users to use in their experiments. The user runs fulfill this purpose.

Beam lifetime studies are performed on selected user runs. The criterion is the continuity and smoothness of the measured beam lifetime curve over a prolonged period, say 7-10 hours. Before deciding whether or not a particular run is suitable for analysis, a plot of the measured lifetime as a function of time of day should be studied.

A standard run is one in which all quantities used in computing the beam lifetime come from the accelerator. Figure 1 displays computed total beam lifetime as well as the individual components, namely, the residual-gas component obtained from Eqs. (2) through (5) and the Touschek component obtained from Eqs. (6) and (7). The residual-gas component is further split into its major contributing processes, that is, the elastic scattering on nuclei obtained from Eq. (2) and bremsstrahlung obtained from Eq. (3). Figure 2 displays the total beam lifetime, contributions to the total beam lifetime from elastic scattering on nuclei and electrons obtained from Eqs. (2) and (4), contributions to the total beam lifetime from inelastic scattering on nuclei and electrons obtained from Eqs. (3) and (5), and Touschek lifetime. Figure 3 compares graphically the measured and computed total beam lifetime. In order to improve the readability of the graphical representations of the results, the lifetime axis is expressed in logarithmic scale.

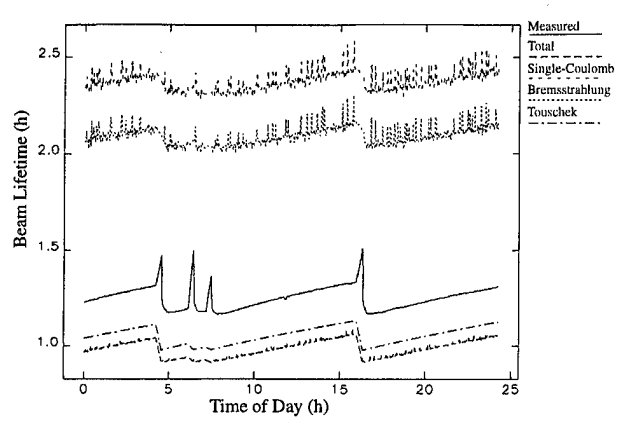

Figure 1: Measured and computed total lifetime, single-Coulomb lifetime, bremsstrahlung lifetime, and Touschek lifetime. The various lifetimes are in log scale.

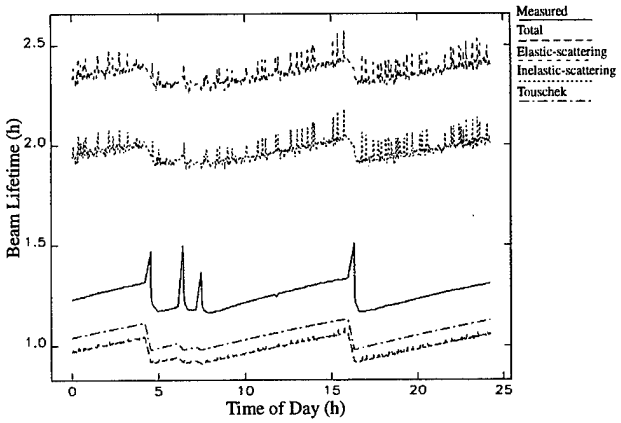

Figure 2: Measured and computed total lifetime, elastic-scattering lifetime, inelastic-scattering lifetime, and Touschek lifetime. The various lifetimes are in log scale.

Figures 1 through 3 represent the standard run. When changing some quantity to try to improve the beam lifetime, we direct our attention to Figure 3. Figure 4 shows the comparison of the computed and measured beam lifetimes if we increase the energy acceptance from 0.74% to 1%. The lifetime curves come closer together, improving consistency.

This investigation shows that better consistency can be achieved if the energy acceptance can be increased from 0.74% to 1%. The energy acceptance ought to be measured again to see if it can be made larger. If the comparison between the measured and computed lifetime is still poor, then other factors, such as the pressure, should be varied.

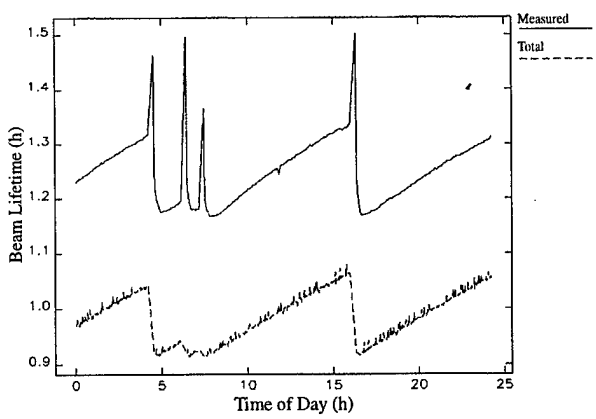

Figure 3: Measured and computed total lifetime. The various lifetimes are in log scale.

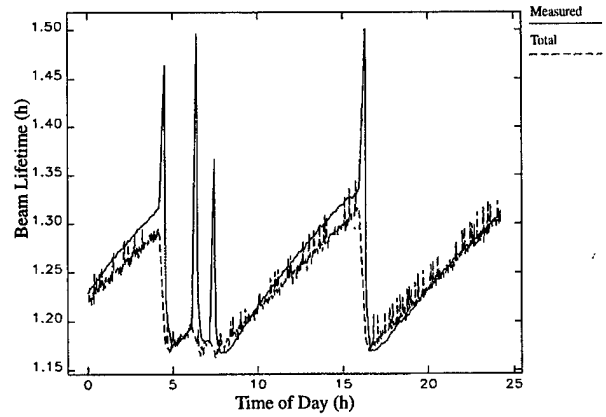

Figure 4: Measured and computed total lifetime with change in energy acceptance, as described in the text. The various lifetimes are in log scale

5 ACKNOWLEDGMENTS

The author wishes to thank Dr. Michael Borland for his assistance with the SDDS tools that produce the figures and with developing a general algorithm using these tools. Thanks also to Dr. Louis Emery for providing information about the user runs of the APS storage ring that were valuable in this calculation. This work was supported by the U.S. Department of Energy, Office of Basic Energy Sciences, under Contract No. W-31-109-ENG-38.

6 REFERENCES

[1] H. Bruck, "Circular Particle Accelerators," Los Alamos National Laboratory, LA-TR-72-10, Rev.

[2] J. LeDuff, "Currents and Current Density Limitations in Existing Electron Storage Rings," *Nucl. Instr. and Meth*, A239, (1985).

[3] John Noonan, private communication.

[4] M. S. Zisman, S. Chattopadhya, J. J. Bisognano, "ZAP User's Manual," LBL--21270, December 1986.

[5] Edwin A. Crosbie, private communication.

[6] Michael Borland, "A Self-Describing File Protocol for Simulation Integration and Shared Postprocessors," Proc. of the 1995 Particle Accelerator Conference, pp. 2184-2186 (1996).

THE EXTENDED TOUSCHEK LIFETIME

Hana M. Bizek
Advanced Photon Source, Argonne National Laboratory
9700 South Cass Avenue, Argonne, Illinois 60439 USA

Abstract

Scattering of particles within the bunch is called Touschek scattering. If large enough, such an energy transfer may eject the particle out of the bunch. If a particle is scattered in the dispersive region, it will induce a horizontal betatron oscillation which will be coupled into vertical motion when it passes through skew components. The amount of coupling is expressed in terms of the coupling coefficient, χ. If the coupling coefficient is large enough, the resulting vertical oscillations may exceed the normally small vertical admittance of the ring. Thus the particles may be lost even though the energy loss is within the momentum acceptance. The lifetime associated with this loss mechanism is called the extended Touschek lifetime. In the usual Touschek lifetime calculation, the lifetime increases as the coupling increases. Including the effect of the vertical oscillation results in a decrease of Touschek lifetime beyond some coupling value.

1 INTRODUCTION

Users of synchrotron radiation sources need hours to complete their experiments. Thus the beam of the Advanced Photon Source (APS) storage ring at Argonne National Laboratory is assumed to circulate stably for a minimum of 10 hours.

The main contributions to the total beam lifetime come from residual gas scattering and Touschek scattering. The residual gas scattering is comprised mostly of single-Coulomb scattering and bremsstrahlung. The single-Coulomb scattering or bremsstrahlung involves elastic or inelastic collisions between the bunch and the surrounding residual gas. Touschek scattering involves scattering of particles within the bunch. A particle may be ejected out of the bunch.

When introducing dispersion into the beam lifetime, we direct our attention to Touschek scattering. A particle passing through the dispersive region will induce a horizontal betatron oscillation which, when passing through skew components, will be coupled into vertical motion. If the coupling coefficient χ is large enough, the resulting vertical oscillations may exceed the small vertical admittance of the ring. The inclusion of this loss mechanism is called the extended Touschek lifetime. The residual-gas lifetime and the extended Touschek lifetime will reduce the total beam lifetime, causing it to slip below the minimum lifetime.

The program ZAP [1] has been altered to take into account the possible loss due to induced betatron oscillations. At each lattice position the energy loss required to produce, by coupling, a vertical oscillation that exceeds the vertical aperture is calculated. When this energy loss is less than the rf bucket half-height, it replaces the rf bucket half-height in the Touschek integral.

2 THE TOUSCHEK INTEGRAL

The normal Touschek lifetime, derived in Bruck [2], increases with increasing coupling coefficient. However, if horizontal oscillations in the dispersive region are included, an increased coupling coefficient can lead to vertical oscillation, which may exceed the normally small vertical apertures. When one includes this effect, one sees that increased coupling leads to decreased lifetime.

A bunch traveling in the dispersive region of the storage ring loses momentum Δp_1. This produces a horizontal betatron displacement η and its derivative η', given as:

$$x = \eta\left(\frac{\Delta p_1}{p_0}\right) \text{ and } x' = \eta'\left(\frac{\Delta p_1}{p_0}\right) \tag{1}$$

where p_0 is the design momentum. This displacement and slope leads to the Courant-Snyder invariant

$$W_x = \left(\frac{\Delta p_1}{p_0}\right)^2 \frac{1}{\beta_x}\left(\eta^2 + \left(\beta_x\eta' - \frac{1}{2}\beta_x'\eta\right)^2\right) = \left(\frac{\Delta p_1}{p_0}\right)^2 \boldsymbol{H}, \tag{2}$$

where $\boldsymbol{H}$ is the so-called Sands factor [3]; this is shown in Fig. 1 for the APS half-sector of length L = 13.8 m. Then the coupling coefficient χ is the ratio of the Courant-Snyder invariants $W_{y;max}/W_{x;max}$. The maximum W_y is determined by the vertical admittance, A_y

$$W_{y;max} = A_y = \frac{a^2}{\beta_y}, \tag{3}$$

where a is the vertical half-aperture, and β_y is the vertical β-function, at the center of the insertion region. β_y = 10 m at insertion of the APS storage ring, and a is assumed to be 2 mm, 3 mm, and 4 mm. Combining Eqs. (2) and (3) we obtain

$$\left(\frac{\Delta p_1}{p_0}\right) = \left(\frac{\Delta p_1}{\gamma}\right) = \sqrt{\frac{a^2}{\chi\beta_y\boldsymbol{H}}}, \tag{4}$$

$$\varepsilon_1 = \left(\frac{\Delta p_1}{\gamma\delta p_x}\right)^2. \tag{5}$$

The extended Touschek lifetime integral is

$$\frac{1}{\tau_{eT}} = \frac{\sqrt{\pi}r_0^2 cN}{\gamma^2(\delta p_x)^3 V}\int_{\varepsilon_0}^{\infty}\frac{1}{u^2}\left(\frac{u}{\varepsilon_1} - \frac{1}{2}\ln\left(\frac{u}{\varepsilon_1}\right) - 1\right)\exp(-u)du, \tag{6}$$

where r_0 is the classical electron radius, c is the speed of light, N is the number of positrons per bunch, γ is the design energy divided by the rest energy of the positrons, δp_x is related to the rms angular divergence, and V is the

0-7803-4376-X/98 /$10.00 © 1998 IEEE

bunch volume [1]. In this equation ε_0 is the smaller of either ε_1 or ε_{rf}. The design momentum p_0 in Eqs. (4) and (5) is written in units of m_0c so that, for relativistic particles, $p_0 = m_0\gamma v/m_0c \approx \gamma$. The lower limit in Eq. (5) depends on the Twiss parameters, the dispersion and its derivative, the coupling coefficient χ, and the vertical half-aperture a.

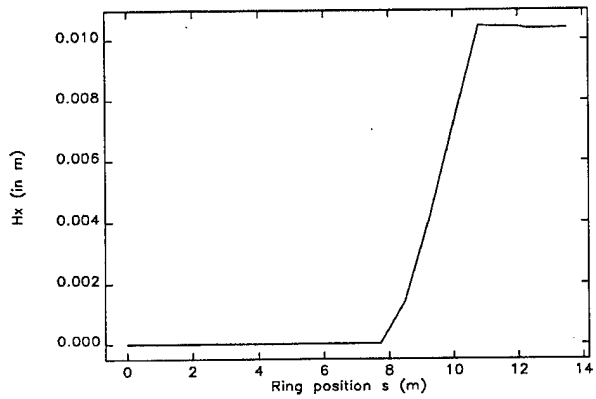

Figure 1: Sands factor.

3 THE METHOD OF CALCULATION

The extended Touschek integral in Eq. (6) and the lower limit in Eq. (5) are evaluated using the modified code ZAP. ZAP has the option of calculating the normal Touschek lifetime or the extended Touschek lifetime. If the latter option is used, the user inputs the vertical half-aperture a in mm, followed by β_y, the vertical β-function at the center of the insertion region in m.

The routine on the extended Touschek lifetime treats betatron oscillations produced in the dispersive region. The dispersive region is typified by the non-zero Sands factor $\boldsymbol{H}$. If $\boldsymbol{H} = 0$, the lower limit will be ε_{rf}.

If $\boldsymbol{H} \neq 0$, then ZAP calculates the lower limit due to betatron oscillations produced in the dispersive region via Eqs. (4) and (5). If $\varepsilon_1 < \varepsilon_{rf}$, then ε_1 is used in Eq. (6) and the loss mechanism of extended Touschek lifetime is used; otherwise the loss mechanism of normal Touschek lifetime is used. Having decided what the lower limit will be, ZAP proceeds to evaluate the Touschek integral.

ZAP accepts horizontal and vertical emittances rather than the coupling coefficient. Those are calculated by

$$\varepsilon_x = \frac{\varepsilon_n}{1+\chi} \quad \text{and} \quad \varepsilon_y = \frac{\chi\varepsilon_n}{1+\chi}, \tag{7}$$

where $\varepsilon_n = 8.2 \times 10^{-9}$ m-rad is the natural emittance of the APS storage ring.

From the synchrotron radiation loss one obtains the synchrotron frequency. In the present calculation if we assume the synchrotron radiation loss is due to dipoles only, then the synchrotron frequency is 1.96 kHz. The energy spread is assumed to be 1.8×10^{-3} and 3.6×10^{-3} for bunch lengths of 1 cm and 2 cm, respectively.

4 ANALYSIS OF RESULTS

In general, the total beam lifetime is the inverse of the sum of the inverses of residual gas and Touschek lifetimes. If the limits due to oscillations in the dispersive region are included, the Touschek lifetime is replaced by extended Touschek lifetime. We thus have

$$\frac{1}{\tau_{tot-nT}} = \frac{1}{\tau_{gas}} + \frac{1}{\tau_{nT}} \quad \text{total with normal Touschek} \tag{8}$$

$$\frac{1}{\tau_{tot-eT}} = \frac{1}{\tau_{gas}} + \frac{1}{\tau_{eT}} \quad \text{total with extended Touschek} \tag{9}$$

where τ_{gas} is the residual gas lifetime, τ_{nT} is the normal Touschek lifetime, τ_{eT} is the extended Touschek lifetime, $\tau_{tot\text{-}nT}$ is the total beam lifetime with normal Touschek lifetime and $\tau_{tot\text{-}eT}$ is the total beam lifetime with extended Touschek lifetime. The total beam lifetimes are displayed in Figs. 2 through 5 for vertical half-apertures of 2 mm, 3 mm, and 4 mm, as shown in the legends to those figures. In the legends "normal" stands for $\tau_{tot\text{-}nT}$, calculated via Eq. (9), and "extended" stands for $\tau_{tot\text{-}eT}$, calculated via Eq. (10).

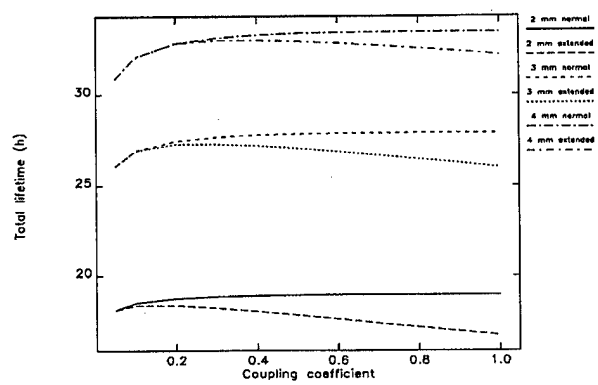

Figure 2: Total beam lifetime with and without extended Touschek lifetime for 5.22-mA bunch current, 0.028 bucket half-height and 2-cm rms bunch length.

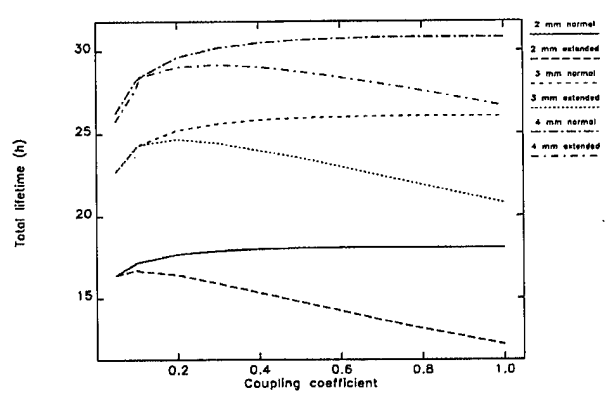

Figure 3: Total beam lifetime with and without extended Touschek lifetime for 5.22-mA bunch current, 0.028 bucket half-height and 1-cm rms bunch length.

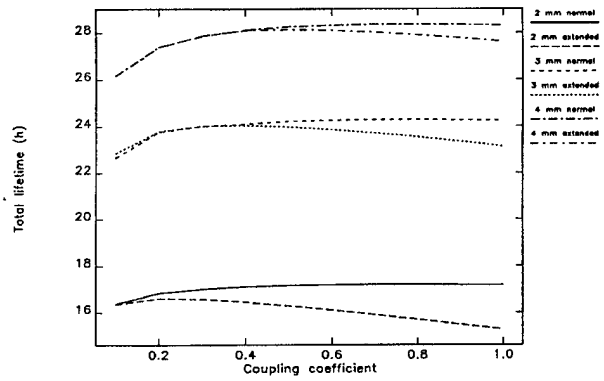

Figure 4: Total beam lifetime with and without extended Touschek lifetime for 5.22-mA bunch current, 0.02 bucket half-height and 2-cm rms bunch length.

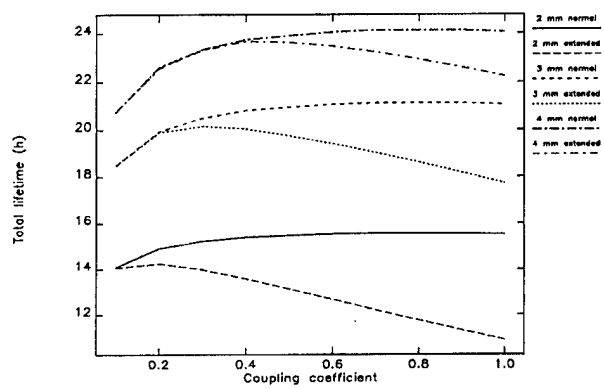

Figure 5: Total beam lifetime with and without extended Touschek lifetime for 5.22-mA bunch current, 0.02 bucket half-height and 1-cm rms bunch length.

For a given coupling coefficient, $\tau_{tot\text{-}eT}$ is always smaller than $\tau_{tot\text{-}nT}$. For a fixed coupling coefficient χ, the difference between $\tau_{tot\text{-}nT}$ and $\tau_{tot\text{-}eT}$ quantifies the influence of oscillations in the dispersive region. The difference increases with increasing coupling and decreasing vertical half-aperture, for fixed beam current, fixed rms bunch length, and fixed rf bucket half-height. The difference also increases with decreasing rms bunch length if all other parameters are kept fixed. This is seen from Figs. 2 and 3 on one hand, and Figs. 4 and 5 on the other.

The influence of betatron oscillations in the dispersive region may cause the total lifetime to slip below the minimum lifetime for optimum storage ring operation, or come perilously close to doing so. This can happen even for pressures as low as 1 nTorr if the rf bucket half-height, the rms bunch length, and the vertical half-aperture are small enough and the coupling coefficient is large enough. In Fig. 5 we have such a case. For 2-mm vertical half-aperture and 100% coupling, $\tau_{tot\text{-}eT}$ is 10.9 hours, while $\tau_{tot\text{-}nT}$ is 15.52 hours. (The minimum lifetime for optimum operation of the APS storage ring is 10 hours.) For a pressure of just 1.2 nTorr, the residual-gas lifetime is about 15.66 hours and the extended Touschek lifetime is about 26 hours, which means that the total beam lifetime, from Eq. (10), is 9.51 hours. The inescapable conclusion is: *under certain conditions, inclusion of betatron oscillations in the dispersive region may cause the total beam lifetime to become quite small, even at low pressures.* With higher pressures the situation can only get worse, because the residual-gas lifetime will be correspondingly lower. In such a case, not only bunches with very high coupling, but even bunches of lower coupling may be affected.

Under normal operating conditions the contribution to the lifetime resulting from oscillations in the dispersive region is not seen, because the coupling is too low. For example, in the APS storage ring the coupling is about 3%. The extended Touschek lifetime is not really different from the normal Touschek lifetime in this case.

5 ACKNOWLEDGEMENTS

The author wishes to thank Dr. Glenn A. Decker for suggesting this problem and Dr. Edwin A. Crosbie for assistance and valuable discussions. Work is supported by the U.S. Department of Energy, Office of Basic Energy Sciences, under Contract No. W-31-109-ENG-38.

6 REFERENCES

[1] M. S. Zisman, S. Chattopadhya, J. J. Bisognano, "ZAP User's Manual," LBL-21270, December 1986.

[2] H. Bruck, "Circular Particle Accelerators," Los Alamos National Laboratory, LA-TR-72-10, Rev.

[3] Matthew Sands, "The Physics of Electron Storage Rings," SLAC 121, May 1979.

"INTEGRABLE ACCELERATOR" STRUCTURE FOR ROUND BEAMS WITH A SOLITON-LIKE FORCE

V.V. Danilov, Budker Institute of Nuclear Physics, 630090, Novosibirsk, Russia

Abstract

This work is devoted to finding the integrable systems for accelerators with strong nonlinear fields. Among all the solutions there is one with a soliton-like force; one of the invariants for this system is a quartic in momentum polynomial. Another one is angular momentum, so this system is related with round beams. Such a field can be made by solenoidal focusing field, so the soluthion presents an example of integrable accelerator with regular nonlinear motion.

All this shows the relation of general theory of integrable systems with particular theory of accelerators; it might initiate applications of Lie groups to equations in partial derivatives for finding "integrable" lattices of accelerators.

1 INTRODUCTION

In high energy circular aceelerators and storage rings the betatron motion of particles can be perfectly described by 2D Hamiltonian, whose form corresponds to the usual non-relativistic motion with a time-dependent force. For such a case there is no possibility to analyse motion of particles by analytical formulas because of the stochasticity of trajectories in phase space. Only the special Hamiltonians give regular motion. For this we need, for example, 2 commuting integrals of motion.

In this paper it is shown, that system with presented below Hamiltonian has 2 commuting integral of motion. Hamiltonian H is (for simplicity particle's mass is equal to 1):

$$H = p_x^2/2 + p_y^2/2 + f_1(t) \cdot r^2/4 + g(r)/4. \qquad (1)$$

where $r = \sqrt{x^2 + y^2}$ and f_1 satisfies

$$f_1''' + 8 \cdot f_1 \cdot f_1' - 3 \cdot h \cdot f_1 = 0.$$

This reminds the equation for a traveling wave solution $f(x - ct)$ of the Korteweg–de Vries equation:

$$f''' + f \cdot f' - c \cdot f' = 0.$$

After changing f_1 to $f/8$ and $3h$ to c in the equation for f_1, we come to the last one.

Hamiltonian (1) depends only on the radius $r = \sqrt{x^2 + y^2}$, so one of the integrals is the angular momentum. In the next section we'll show, how to construct 1D systems with polynomial in momentum integrals of motion, and show, that the presented above system has an additional quartic in momentum invariant.

2 1D DYNAMICAL SYSTEMS WITH INVARIANTS, POLYNOMIAL IN MOMENTUM

Further we use the method of finding integrable systems, proposed by Whittaker [1].

Following [2], we construct here a family of continuous time-dependent 1D Hamiltonians which have a quadratic invariant, and thus the respective motion in 1.5D is integrable. Consider a general form of invariant quadratic in momentum p, assuming that the coefficients A, B, V are arbitrary functions of time t and coordinate x:

$$I = \frac{1}{2}(Ap - B)^2 + V\,,$$

$A \neq 0$. Equating its total time derivative to zero, we account for the Hamiltonian equations of motion $\dot{x} = p$, $\dot{p} = f$, where the unknown force f depends on t, x

$$\frac{dI}{dt} = (Ap - B)\Big(A_x p^2 + (A_t - B_x)p + Af - B_t\Big) + V_x p + V_t \equiv 0\,,$$

the subscripts here denote the respective partial derivatives. The vanishing coefficients of each power of p yield a set of equations in partial derivatives for the four unknown functions: f is to be found along with A, B, V.

First of all, $A_x = 0$, and $A = A(t)$ is an arbitrary function of time. Then we take $A_t - B_x = 0$, whence:

$$B(x,t) = \dot{A}x + A^2\dot{D}\,,$$

with an arbitrary $D(t)$; dots denote the time derivatives. We choose here the special form of arbitrary additive function of time for future convenience.

The last two equations form a set of equations specifying the unknowns f and V:

$$A(Af - B_t) + V_x = 0 \qquad (2)$$
$$-B(Af - B_t) + V_t = 0 \qquad (3)$$

The force f is thus expressed via V, B, A:

$$f = -\frac{V_x}{A^2} + \frac{B_t}{A}\,, \qquad (4)$$

and V is determined by the homogeneous equation in partial derivatives of the 1st order:

$$B\,V_x + A\,V_t = 0$$

Its characteristic curve $x(t)$ is then obtained from the equation:

$$\frac{dx}{dt} = \frac{B}{A} = \frac{\dot{A}x + A^2\dot{D}}{A}\,.$$

0-7803-4376-X/98/$10.00 © 1998 IEEE

Integration gives the lines of constant level of V:

$$X \equiv \frac{x}{A(t)} - D(t) = const\,.$$

Hence,

$$V(x,t) = U\Big(\frac{x}{A(t)} - D(t)\Big)\,,$$

where $U(X)$ is an arbitrary function.

Thus we conclude, that the general solution to our problem of integrable system in 1.5D with quadratic invariant is generated with three arbitrary functions: $A(t)$, $D(t)$, and $U(X)$. The corresponding force f is then found from (4):

$$f = -\frac{1}{A^3}U' + \frac{1}{A}(\ddot{A}x + (A^2\dot{D})^{\cdot})\,.$$

The Hamiltonian of this system can be found from the expression for f:

$$\mathcal{H}(x,p,t) = \frac{p^2}{2} + \frac{1}{A^2}U(\frac{x}{A} - D) - \frac{A\ddot{A}}{2}(\frac{x}{A})^2 - (A^2\dot{D})^{\cdot}\frac{x}{A}\,,$$

and the final form of the desired invariant is:

$$I = \frac{1}{2}(Ap - \dot{A}x - A^2\dot{D})^2 + U(\frac{x}{A} - D)\,.$$

It's possible to find by this method invariants of arbitrary order in momentum. It's shown in [3], that cubic in momentum invariants and corresponding forces may be found from linear equations also (like in quadratic in momentum case).

2.1 *Integrable systems for round beams*

So now we know, how to construct 1D integrable systems. What is the difference between a common 1D case and 2D systems with conservation of the angular momentum? Actually a 2D system with the angular momentum conservation can be reduced to a 1D system with the 'centrifugal' force $\mathcal{M}^2/x^3$. But the difference is in the condition, that the second invariant for this system must exist for each value of $\mathcal{M}$. For $\mathcal{M} = 0$ we have a usual 1D system, so the desired integrable system for round beams gives a common 1D integrable motion, but in general the converse statement is not true (an additional invariant may exist only for zero angular momentum, for example). So the family of integrable systems for round beams is less than the family of common 1D integrable systems.

2.2 *Integrable systems with soliton-like forces*

Let's take the simplest quartic polynomial as an invariant:

$$I = p^4 + A(x,t)\cdot p^2 + B(x,t)\cdot p + C(x,t);$$

here we omit the cubic terms at all, A, B, C are unknown functions. After differentiation of this invariant w.r.t. to time we should have zero coefficients of each power of p (since $dI/dt = 0$), so we have the following set of equations:

$$\begin{aligned} 4F + \frac{\partial A}{\partial x} &= 0 \\ \frac{\partial A}{\partial t} + \frac{\partial B}{\partial x} &= 0 \\ 2\cdot A\cdot F + \frac{\partial B}{\partial t} + \frac{\partial C}{\partial x} &= 0 \\ BF + \frac{\partial C}{\partial t} &= 0, \end{aligned} \tag{5}$$

where $F = \dot{p}$ is the force.

Let's suppose, that we have found some solution of these equations. Now we want, that $F + \mathcal{M}^2/x^3$ be also a solution of the previous set of equations. From the first line of (5) we see, that A has to be transformed into $A + 2\mathcal{M}^2/x^2$, and B stays unchanged.[1]

Let's eliminate the function C from the equations. We can just take the partial derivative of the third equation in (5) w.r.t. to t, and the partial derivative of the forth one w.r.t. to x, and subtract one from another. We have:

$$2\frac{\partial(A\cdot F)}{\partial t} + \frac{\partial^2 B}{\partial t^2} = \frac{\partial(B\cdot F)}{\partial x}.$$

Let's put here the new A and F. We have:

$$2(A_t\cdot F + A\cdot F_t) + 4\mathcal{M}^2/x^2\cdot F_t + 2\mathcal{M}^2/x^3\cdot A_t + B_{tt} =$$
$$B_x(F + \mathcal{M}^2/x^3) + B(F_x - 3\mathcal{M}^2/x^4);$$

here A, B, F are the old functions independent of $\mathcal{M}$, subscripts t, x mean partial derivatives w.r.t. to t, x.

We want to get solutions for an arbitrary value of the angular momentum, so we demand, that each coefficient at any power of $\mathcal{M}$ should vanish. So, from the previous equation we obtain two ones (without $\mathcal{M}$); adding to them the first two equations of (5) we have:

$$\begin{aligned} 4F + A_x &= 0 \\ A_t + B_x &= 0 \\ 3A_t\cdot F + 2A\cdot F_t + B_{tt} &= B\cdot F_x \\ 4F_t\cdot x^2 + 2A_t\cdot x &= B_x\cdot x - 3B. \end{aligned} \tag{6}$$

This is a set of four equations for three unknown functions. A check for consistency is needed in general, in order to verify the existence of any solutions.

To eliminate now F and B, we take F from the first and B_x from the second equation and substitute these in the last one (having taken its time derivative). After that we get an equation for A:

$$x^2 A_{xxt} - xA_{xt} = 0.$$

All the solutions are:

$$A = f_1(t)x^2 + f_2(t) + g(x);$$

[1] This is not the only way of transformation of A and B. For example, A may get a term, which depends on time and momentum. But here we are looking for the simplest solutions.

here f_1, f_2, g are free functions.

After that we have to use one more equation for A, B, F, namely the third one in the set (6). At first, let's express F and B using the solution for A. From the first equation of (6) we have:

$$4F = -2f_1(t) \cdot x - g'(x),$$

and from the second and last ones we have:

$$3B = -3(f_1'(t) \cdot x^3 + f_2'(t) \cdot x) + 2f_1'(t) \cdot x^3.$$

Let's put $f_2 = 0$ for saving calculations (the case $f_2 \neq 0$ can be treated in the same way, but with more complications). Then $B = -f_1' x^3/3$.

The third equation of (6) now reads:

$$-3f_1'(t) \cdot x^2 \cdot \frac{2f_1(t) \cdot x + g'(x)}{4} - (f_1(t) \cdot x^2 + g(x)) f_1'(x) \cdot x$$

$$-f'''(t) \cdot x^3/3 = f_1'(t) \cdot x^3 \cdot \frac{2f_1(t) + g''(x)}{12}.$$

We rewrite it in a more compact form:

$$(-8/3 \cdot f_1(t) f_1'(t) - f_1'''(t)/3) \cdot x^3 =$$

$$f_1'(t)(3g'(x)x^2/4 + g''(x) \cdot x^3/12 + g(x) \cdot x).$$

Having thus separated the variables, we now have:
1. $f_1(t) = const$, g is an arbitrary function of x. It's the case of the invariant quadratic in momentum; now we have it squared.
2.

$$3g'(x)x^2/4 + g''(x) \cdot x^3/12 + g(x) \cdot x = -h \cdot x^3, \quad (7)$$

where h is an arbitrary constant. For $f_1(t)$ we have:

$$f_1''' + 8 \cdot f_1 \cdot f_1' - 3 \cdot h \cdot f_1 = 0. \quad (8)$$

This reminds the equation for a traveling wave solution $f(x - ct)$ of the Korteweg–de Vries equation:

$$f''' + f \cdot f' - c \cdot f' = 0.$$

After changing f_1 to $f/8$ and $3h$ to c in (8), we come to this equation. Then we can find g from (7). Our force then is equal to

$$F(x,t) = -f_1(t) \cdot x/2 - g'(x)/4.$$

So, the presented above method gives an analytical tool aimed at finding integrable systems for round beams (or, even for systems with more complicated integrals of motion, than the angular momentum).

3 ACKNOWLEDGEMENTS

The author thanks E.Perevedentsev for fruitful discussions and careful reading this paper.

4 REFERENCES

[1] E.T. Whittaker, "A treatise on the Analytical Dynamics of Particles and Rigid Bodies", Cambridge, Cambridge University Press (1964).

[2] V.V. Danilov and E.A. Perevedentsev, "Invariants for Nonlinear Accelerator Optics and Round Colliding Beams", *Proc. VII ICFA Beam Dynamics Workshop on Beam-Beam Issues for Multibunch, High Luminosity Circular Colliders*, Dubna, 18-20 May 1995, Dubna (1996), p.167.

[3] V.V. Danilov and E.A. Perevedentsev, "Analytical 1D Method of Increasing the Dynamic Aperture in Storage Rings", *Proc. EPAC'96*, Barcelona (1996), p.893.

WAVELET APPROACH TO ACCELERATOR PROBLEMS, I. POLYNOMIAL DYNAMICS

A. Fedorova and M. Zeitlin*
Institute of Problems of Mechanical Engineering,
Russian Academy of Sciences, Russia, 199178, St. Petersburg, V.O., Bolshoj pr., 61,
Z. Parsa†
Dept. of Physics, Bldg. 901A, Brookhaven National Laboratory, Upton, NY 11973-5000, USA

Abstract

This is the first part of a series of talks in which we present applications of methods from wavelet analysis to polynomial approximations for a number of accelerator physics problems. In the general case we have the solution as a multiresolution expansion in the base of compactly supported wavelet basis. The solution is parametrized by solutions of two reduced algebraical problems, one is nonlinear and the second is some linear problem, which is obtained from one of the next wavelet constructions: Fast Wavelet Transform, Stationary Subdivision Schemes, the method of Connection Coefficients.

In this paper we consider the problem of calculation of orbital motion in storage rings. The key point in the solution of this problem is the use of the methods of wavelet analysis, relatively novel set of mathematical methods, which gives us a possibility to work with well-localized bases in functional spaces and with the general type of operators (including pseudodifferential) in such bases. Our problem as many related problems in the framework of our type of approximations of complicated physical nonlinearities is reduced to the problem of the solving of the systems of differential equations with polynomial nonlinearities with or without some constraints. In this paper we consider as the main example the particle motion in storage rings in standard approach. Starting from Hamiltonian, which described classical dynamics in storage rings and using Serret–Frenet parametrization, we have after standard manipulations with truncation of power series expansion of square root the corresponding equations of motion:

$$\frac{d}{ds}x = \frac{p_x + H\cdot z}{[1+f(p_\sigma)]}; \tag{1}$$
$$\frac{d}{ds}p_x = \frac{[p_z - H\cdot x]}{[1+f(p_\sigma)]}\cdot H - [K_x^2 + g]\cdot x + N\cdot z$$
$$+K_x\cdot f(p_\sigma) - \frac{\lambda}{2}\cdot(x^2 - z^2) - \frac{\mu}{6}(x^3 - 3xz^2);$$
$$\frac{d}{ds}z = \frac{p_z - H\cdot x}{[1+f(p_\sigma)]};$$
$$\frac{d}{ds}p_z = -\frac{[p_x + H\cdot z]}{[1+f(p_\sigma)]}\cdot H - [K_z^2 - g]\cdot z$$
$$+N\cdot x + K_z\cdot f(p_\sigma) - \lambda\cdot xz - \frac{\mu}{6}(z^3 - 3x^2z);$$
$$\frac{d}{ds}\sigma = 1 - [1 + K_x\cdot x + K_z\cdot z]\cdot f'(p_\sigma) -$$
$$\frac{1}{2}\cdot\frac{[p_x + H\cdot z]^2 + [p_z - H\cdot x]^2}{[1+f(p_\sigma)]^2}\cdot f'(p_\sigma)$$
$$\frac{d}{ds}p_\sigma = -\frac{1}{\beta_0^2}\cdot\frac{eV(s)}{E_0}\cdot\sin\left[h\cdot\frac{2\pi}{L}\cdot\sigma + \varphi\right]$$

Then we use series expansion of function $f(p_\sigma)$ and the corresponding expansion of RHS of equations (1). In the following we take into account only an arbitrary polynomial (in terms of dynamical variables) expressions and neglecting all nonpolynomial types of expressions, i.e. we consider such approximations of RHS, which are not more than polynomial functions in dynamical variables and arbitrary functions of independent variable s ("time" in our case, if we consider our system of equations as dynamical problem). The first main part of our construction is some variational approach to this problem, which reduces initial problem to the problem of solution of functional equations at the first stage and some algebraical problems at the second stage. We consider also two private cases of our general construction. In the first case (particular) we have for Riccati equations (particular quadratic approximations) the solution as a series on shifted Legendre polynomials, which is parameterized by the solution of reduced algebraical (also Riccati) system of equations. This is only an example of general construction. In the second case (general polynomial system) we have the solution in a compactly supported wavelet basis. Multiresolution expansion is the second main part of our construction. The solution is parameterized by solutions of two reduced algebraical problems, one as in the first case and the second is some linear problem, which is obtained from one of the next wavelet construction: Fast Wavelet Transform (FWT), Stationary Subdivision Schemes (SSS), the method of Connection Coefficients (CC). Our problems may be formulated as the systems of ordinary differential equations $dx_i/dt = f_i(x_j, t)$, $(i, j = 1, ..., n)$ with fixed initial conditions $x_i(0)$, where f_i are not more than polynomial functions of dynamical variables x_j and have arbitrary dependence of time. Because of time dilation we can consider only next time interval: $0 \le t \le 1$. Let us consider a set of functions $\Phi_i(t) = x_i dy_i/dt + f_i y_i$ and a set of functionals $F_i(x) = \int_0^1 \Phi_i(t)dt - x_i y_i \mid_0^1$, where $y_i(t)(y_i(0) = 0)$ are dual variables. It is obvious that the initial system and the system $F_i(x) = 0$ are equivalent. In part 3 we consider

* e-mail: zeitlin@math.ipme.ru
† e-mail: parsa@bnl.gov

0-7803-4376-X/98/$10.00 © 1998 IEEE

symplectization of this approach. Now we consider formal expansions for x_i, y_i:

$$x_i(t) = x_i(0) + \sum_k \lambda_i^k \varphi_k(t) \quad y_j(t) = \sum_r \eta_j^r \varphi_r(t), \quad (2)$$

where because of initial conditions we need only $\varphi_k(0) = 0$. Then we have the following reduced algebraical system of equations on the set of unknown coefficients λ_i^k of expansions (2):

$$\sum_k \mu_{kr} \lambda_i^k - \gamma_i^r(\lambda_j) = 0 \quad (3)$$

Its coefficients are $\mu_{kr} = \int_0^1 \varphi_k'(t)\varphi_r(t)dt$, $\gamma_i^r = \int_0^1 f_i(x_j, t)\varphi_r(t)dt$. Now, when we solve system (3) and determine unknown coefficients from formal expansion (2) we therefore obtain the solution of our initial problem. It should be noted if we consider only truncated expansion (2) with N terms then we have from (3) the system of $N \times n$ algebraical equations and the degree of this algebraical system coincides with degree of initial differential system. So, we have the solution of the initial nonlinear (polynomial) problem in the form

$$x_i(t) = x_i(0) + \sum_{k=1}^{N} \lambda_i^k X_k(t), \quad (4)$$

where coefficients λ_i^k are roots of the corresponding reduced algebraical problem (3). Consequently, we have an parametrization of solution of initial problem by solution of reduced algebraical problem (3). But in general case, when the problem of computations of coefficients of reduced algebraical system (3) is not solved explicitly as in the quadratic case, which we shall consider below, we have also parametrization of solution (4) by solution of corresponding problems, which appear when we need to calculate coefficients of (3). As we shall see, these problems may be explicitly solved in wavelet approach. Next we consider the construction of explicit time solution for our problem. The obtained solutions are given in the form (4), where in our first case we have $X_k(t) = Q_k(t)$, where $Q_k(t)$ are shifted Legendre polynomials and λ_k^i are roots of reduced quadratic system of equations. In wavelet case $X_k(t)$ correspond to multiresolution expansions in the base of compactly supported wavelets and λ_k^i are the roots of corresponding general polynomial system (3) with coefficients, which are given by FWT, SSS or CC constructions. According to the variational method to give the reduction from differential to algebraical system of equations we need compute the objects γ_a^j and μ_{ji}, which are constructed from objects:

$$\begin{aligned}
\sigma_i &\equiv \int_0^1 X_i(\tau)d\tau = (-1)^{i+1}, \quad (5)\\
\nu_{ij} &\equiv \int_0^1 X_i(\tau)X_j(\tau)d\tau = \sigma_i\sigma_j + \frac{\delta_{ij}}{(2j+1)},\\
\mu_{ji} &\equiv \int X_i'(\tau)X_j(\tau)d\tau = \sigma_j F_1(i,0) + F_1(i,j),\\
&F_1(r,s) = [1-(-1)^{r+s}]\hat{s}(r-s-1),\\
&\hat{s}(p) = \begin{cases} 1, & p \geq 0 \\ 0, & p < 0 \end{cases}\\
\beta_{klj} &\equiv \int_0^1 X_k(\tau)X_l(\tau)X_j(\tau)d\tau = \sigma_k\sigma_l\sigma_j +\\
&\alpha_{klj} + \frac{\sigma_k\delta_{jl}}{2j+1} + \frac{\sigma_l\delta_{kj}}{2k+1} + \frac{\sigma_j\delta_{kl}}{2l+1},\\
\alpha_{klj} &\equiv \int_0^1 X_k^* X_l^* X_j^* d\tau =\\
&\frac{1}{(j+k+l+1)R(1/2(i+j+k))} \times\\
&R(1/2(j+k-l))R(1/2(j-k+l)) \times\\
&R(1/2(-j+k+l)),
\end{aligned}$$

if $j+k+l = 2m, m \in Z$,and $\alpha_{klj} = 0$ if $j+k+l = 2m+1$; where $R(i) = (2i)!/(2^i i!)^2$, $Q_i = \sigma_i + P_i^*$, where the second equality in the formulae for $\sigma, \nu, \mu, \beta, \alpha$ hold for the first case. Now we give construction for computations of objects(5) in the wavelet case. We use some constructions from multiresolution analysis: a sequence of successive approximation closed subspaces V_j: $...V_2 \subset V_1 \subset V_0 \subset V_{-1} \subset V_{-2} \subset ...$ satisfying the following properties: $\bigcap_{j\in\mathbf{Z}} V_j = 0$, $\overline{\bigcup_{j\in\mathbf{Z}} V_j} = L^2(\mathbf{R})$, $f(x) \in V_j <=> f(2x) \in V_{j+1}$ There is a function $\varphi \in V_0$ such that $\{\varphi_{0,k}(x) = \varphi(x-k)_{k\in\mathbf{Z}}\}$ forms a Riesz basis for V_0. We use compactly supported wavelet basis: orthonormal basis for functions in $L^2(\mathbf{R})$. As usually $\varphi(x)$ is a scaling function, $\psi(x)$ is a wavelet function, where $\varphi_i(x) = \varphi(x-i)$. Scaling relation that defines φ, ψ are

$$\begin{aligned}
\varphi(x) &= \sum_{k=0}^{N-1} a_k\varphi(2x-k) = \sum_{k=0}^{N-1} a_k\varphi_k(2x),\\
\psi(x) &= \sum_{k=-1}^{N-2} (-1)^k a_{k+1}\varphi(2x+k)
\end{aligned}$$

Let be $f : \mathbf{R} \longrightarrow \mathbf{C}$ and the wavelet expansion is

$$f(x) = \sum_{\ell\in\mathbf{Z}} c_\ell\varphi_\ell(x) + \sum_{j=0}^{\infty}\sum_{k\in\mathbf{Z}} c_{jk}\psi_{jk}(x) \quad (6)$$

The indices k, ℓ and j represent translation and scaling, respectively

$$\varphi_{jl}(x) = 2^{j/2}\varphi(2^j x - \ell), \psi_{jk}(x) = 2^{j/2}\psi(2^j x - k)$$

The set $\{\varphi_{j,k}\}_{k\in\mathbf{Z}}$ forms a Riesz basis for V_j. Let W_j be the orthonormal complement of V_j with respect to V_{j+1}. Just as V_j is spanned by dilation and translations of the scaling function, so are W_j spanned by translations and dilation of the mother wavelet $\psi_{jk}(x)$. If in formulae (6) $c_{jk} = 0$ for $j \geq J$, then $f(x)$ has an alternative expansion in terms

of dilated scaling functions only $f(x) = \sum_{\ell \in \mathbf{Z}} c_{J\ell}\varphi_{J\ell}(x)$. This is a finite wavelet expansion, it can be written solely in terms of translated scaling functions. We use wavelet $\psi(x)$, which has k vanishing moments $\int x^k \psi(x) d(x) = 0$, or equivalently $x^k = \sum c_\ell \varphi_\ell(x)$ for each k, $0 \leq k \leq K$. Also we have the shortest possible support: scaling function DN (where N is even integer) will have support $[0, N-1]$ and $N/2$ vanishing moments. There exists $\lambda > 0$ such that DN has λN continuous derivatives; for small $N, \lambda \geq 0.55$. To solve our second associated linear problem we need to evaluate derivatives of $f(x)$ in terms of $\varphi(x)$. Let be $\varphi_\ell^n = d^n\varphi_\ell(x)/dx^n$. We derive the wavelet - Galerkin approximation of a differentiated $f(x)$ as $f^d(x) = \sum_\ell c_l \varphi_\ell^d(x)$ and values $\varphi_\ell^d(x)$ can be expanded in terms of $\varphi(x)$

$$\phi_\ell^d(x) = \sum_m \lambda_m \varphi_m(x), \quad \lambda_m = \int_{-\infty}^{\infty} \varphi_\ell^d(x)\varphi_m(x)dx$$

The coefficients λ_m are 2-term connection coefficients. In general we need to find

$$\Lambda_{\ell_1\ell_2\ldots\ell_n}^{d_1 d_2 \ldots d_n} = \int_{-\infty}^{\infty} \prod \varphi_{\ell_i}^{d_i}(x)dx \tag{7}$$

For Riccati case we need to evaluate two and three connection coefficients

$$\begin{aligned} \Lambda_\ell^{d_1 d_2} &= \int_{-\infty}^{\infty} \varphi^{d_1}(x)\varphi_\ell^{d_2}(x)dx, \quad d_i \geq 0, \\ \Lambda^{d_1 d_2 d_3} &= \int_{-\infty}^{\infty} \varphi^{d_1}(x)\varphi_\ell^{d_2}(x)\varphi_m^{d_3}(x)dx \end{aligned}$$

According to CC method [7] we use the next construction. When N in scaling equation is a finite even positive integer the function $\varphi(x)$ has compact support contained in $[0, N-1]$. For a fixed triple (d_1, d_2, d_3) only some $\Lambda_{\ell m}^{d_1 d_2 d_3}$ are nonzero : $2 - N \leq \ell \leq N - 2$, $2 - N \leq m \leq N - 2$, $|\ell - m| \leq N - 2$. There are $M = 3N^2 - 9N + 7$ such pairs (ℓ, m). Let $\Lambda^{d_1 d_2 d_3}$ be an M-vector, whose components are numbers $\Lambda_{\ell m}^{d_1 d_2 d_3}$. Then we have the first key result: Λ satisfy the system of equations

$$\begin{aligned} A\Lambda^{d_1 d_2 d_3} &= 2^{1-d}\Lambda^{d_1 d_2 d_3}, \; d = d_1 + d_2 + d_3, \\ A_{\ell,m;q,r} &= \sum_p a_p a_{q-2\ell+p} a_{r-2m+p} \end{aligned}$$

By moment equations we have created a system of $M + d + 1$ equations in M unknowns. It has rank M and we can obtain unique solution by combination of LU decomposition and QR algorithm. The second key result gives us the 2-term connection coefficients:

$$\begin{aligned} A\Lambda^{d_1 d_2} &= 2^{1-d}\Lambda^{d_1 d_2}, \quad d = d_1 + d_2, \\ A_{\ell,q} &= \sum_p a_p a_{q-2\ell+p} \end{aligned}$$

For nonquadratic case we have analogously additional linear problems for objects (7). Also, we use FWT and SSS for computing coefficients of reduced algebraic systems. We use for modelling D6,D8,D10 functions and programs RADAU and DOPRI for testing.

As a result we obtained the explicit time solution (4) of our problem. In comparison with wavelet expansion on the real line which we use now and in calculation of Galerkin approximation, Melnikov function approach, etc also we need to use periodized wavelet expansion, i.e. wavelet expansion on finite interval. Also in the solution of perturbed system we have some problem with variable coefficients. For solving last problem we need to consider one more refinement equation for scaling function $\phi_2(x)$: $\phi_2(x) = \sum_{k=0}^{N-1} a_k^2 \phi_2(2x - k)$ and corresponding wavelet expansion for variable coefficients $b(t)$: $\sum_k B_k^j(b)\phi_2(2^j x - k)$, where $B_k^j(b)$ are functionals supported in a small neighborhood of $2^{-j}k$.

The solution of the first problem consists in periodizing. In this case we use expansion into periodized wavelets defined by $\phi_{-j,k}^{per}(x) = 2^{j/2}\sum_Z \phi(2^j x + 2^j \ell - k)$. All these modifications lead only to transformations of coefficients of reduced algebraic system, but general scheme remains the same. Extendeed version and related results may be found in [1]-[6].

This research was supported in part by the "New Ideas for Particle Accelerator Programs" under the National Science Foundation Grant No. PHY94-07194.

1 REFERENCES

[1] A.N. Fedorova, M.G. Zeitlin: Preprint IPME **96** (1993)

[2] A.N. Fedorova, M.G. Zeitlin, M.G.: Proc. of 22 Summer School'Nonlinear Oscillations in Mechanical Systems' St. Petersburg (1995) 89.

[3] A.N. Fedorova, M.G. Zeitlin: Proc. of 23 Summer School 'Nonlinear Oscillations in Mechanical Systems' St. Petersburg (1996) 322.

[4] A.N. Fedorova, M.G. Zeitlin: Proc. 7th IEEE DSP Workshop, Norway (1996) 409.

[5] A.N. Fedorova, M.G. Zeitlin: Proc. 2nd IMACS Symp. on Math. Modelling, ARGESIM Report **11** (1997) 1083.

[6] A.N. Fedorova, M.G. Zeitlin: EUROMECH-2nd European Nonlinear Oscillations Conf. (1996) 79.

[7] A. Latto, H.L. Resnikoff and E. Tenenbaum: Aware Technical Report AD910708 (1991).

[8] A.N. Fedorova, M.G. Zeitlin, Z. Parsa: This Proceedings

WAVELET APPROACH TO ACCELERATOR PROBLEMS, II. METAPLECTIC WAVELETS

A. Fedorova and M. Zeitlin*
Institute of Problems of Mechanical Engineering,
Russian Academy of Sciences, Russia, 199178, St. Petersburg, V.O., Bolshoj pr., 61,
Z. Parsa†
Dept. of Physics, Bldg. 901A, Brookhaven National Laboratory, Upton, NY 11973-5000, USA

Abstract

This is the second part of a series of talks in which we present applications of wavelet analysis to polynomial approximations for a number of accelerator physics problems. According to the orbit method and by using construction from the geometric quantization theory we construct the symplectic and Poisson structures associated with generalized wavelets by using metaplectic structure and corresponding polarization. The key point is a consideration of semidirect product of Heisenberg group and metaplectic group as subgroup of automorphisms group of dual to symplectic space, which consists of elements acting by affine transformations.

1 INTRODUCTION

In this paper we continue the application of powerful methods of wavelet analysis to polynomial approximations of nonlinear accelerator physics problems. In part 1 we considered our main example and general approach for constructing wavelet representation for orbital motion in storage rings. But now we need take into account the Hamiltonian or symplectic structure related with system (1) from part 1. Therefore, we need to consider instead of compactly supported wavelet representation from part 1 the generalized wavelets, which allow us to consider the corresponding symplectic structures. By using the orbit method and constructions from the geometric quantization theory we consider the symplectic and Poisson structures associated with Weyl– Heisenberg wavelets by using metaplectic structure and the corresponding polarization. In part 3 we consider applications to construction of Melnikov functions in the theory of homoclinic chaos in perturbed Hamiltonian systems.

In wavelet analysis the following three concepts are used now: 1). a square integrable representation U of a group G, 2). coherent states over G 3). the wavelet transform associated to U.

We have three important particular cases:
a) the affine $(ax+b)$ group, which yields the usual wavelet analysis

$$[\pi(b,a)f](x) = \frac{1}{\sqrt{a}} f\left(\frac{x-b}{a}\right)$$

b). the Weyl-Heisenberg group which leads to the Gabor functions, i.e. coherent states associated with windowed Fourier transform.

$$[\pi(q,p,\varphi)f](x) = \exp(i\mu(\varphi - p(x-q))f(x-q)$$

In both cases time-frequency plane corresponds to the phase space of group representation.
c). also, we have the case of bigger group, containing both affine and Weyl-Heisenberg group, which interpolate between affine wavelet analysis and windowed Fourier analysis: affine Weyl–Heisenberg group [7]. But usual representation of it is not square–integrable and must be modified: restriction of the representation to a suitable quotient space of the group (the associated phase space in that case) restores square – integrability: $G_{aWH} \longrightarrow$ homogeneous space. Also, we have more general approach which allows to consider wavelets corresponding to more general groups and representations [8], [9]. Our goal is applications of these results to problems of Hamiltonian dynamics and as consequence we need to take into account symplectic nature of our dynamical problem. Also, the symplectic and wavelet structures must be consistent (this must be resemble the symplectic or Lie-Poisson integrator theory). We use the point of view of geometric quantization theory (orbit method) instead of harmonic analysis. Because of this we can consider (a) – (c) analogously.

2 METAPLECTIC GROUP AND REPRESENTATIONS

Let $Sp(n)$ be symplectic group, $Mp(n)$ be its unique twofold covering – metaplectic group. Let V be a symplectic vector space with symplectic form (,), then $R \oplus V$ is nilpotent Lie algebra - Heisenberg algebra:

$$[R,V]=0, \quad [v,w]=(v,w)\in R, \quad [V,V]=R.$$

$Sp(V)$ is a group of automorphisms of Heisenberg algebra.

Let N be a group with Lie algebra $R \oplus V$, i.e. Heisenberg group. By Stone– von Neumann theorem Heisenberg group has unique irreducible unitary representation in which $1 \mapsto i$. This representation is projective: $U_{g_1}U_{g_2} = c(g_1,g_2)\cdot U_{g_1g_2}$, where c is a map: $Sp(V)\times Sp(V) \to S^1$, i.e. c is S^1-cocycle.

But this representation is unitary representation of universal covering, i.e. metaplectic group $Mp(V)$. We give this representation without Stone-von Neumann theorem.

* e-mail: zeitlin@math.ipme.ru
† e-mail: parsa@bnl.gov

0-7803-4376-X/98/$10.00 © 1998 IEEE

Consider a new group $F = N' \bowtie Mp(V)$, $\bowtie$ is semidirect product (we consider instead of $N = R \oplus V$ the $N' = S^1 \times V$, $S^1 = (R/2\pi Z)$). Let V^* be dual to V, $G(V^*)$ be automorphism group of V^*.Then F is subgroup of $G(V^*)$, which consists of elements, which acts on V^* by affine transformations.
This is the key point!

Let $q_1, ..., q_n; p_1, ..., p_n$ be symplectic basis in V, $\alpha = pdq = \sum p_i dq_i$ and $d\alpha$ be symplectic form on V^*. Let M be fixed affine polarization, then for $a \in F$ the map $a \mapsto \Theta_a$ gives unitary representation of G: $\Theta_a : H(M) \to H(M)$

Explicitly we have for representation of N on H(M):

$$(\Theta_q f)^*(x) = e^{-iqx} f(x), \quad \Theta_p f(x) = f(x-p)$$

The representation of N on H(M) is irreducible. Let A_q, A_p be infinitesimal operators of this representation

$$A_q = \lim_{t\to 0} \frac{1}{t}[\Theta_{-tq} - I], \quad A_p = \lim_{t\to 0} \frac{1}{t}[\Theta_{-tp} - I],$$

then

$$A_q f(x) = i(qx)f(x), \quad A_p f(x) = \sum p_j \frac{\partial f}{\partial x_j}(x)$$

Now we give the representation of infinitesimal basic elements. Lie algebra of the group F is the algebra of all (non-homogeneous) quadratic polynomials of (p,q) relatively Poisson bracket (PB). The basis of this algebra consists of elements $1, q_1, ..., q_n, p_1, ..., p_n, q_iq_j, q_ip_j, p_ip_j, \quad i,j = 1, ..., n, \quad i \le j,$

$$PB\ is \quad \{f,g\} = \sum \frac{\partial f}{\partial p_j}\frac{\partial g}{\partial q_i} - \frac{\partial f}{\partial q_i}\frac{\partial g}{\partial p_i}$$

and $\{1, g\} = 0 \quad for$ all g,

$\{p_i, q_j\} = \delta_{ij}$,

$\{p_iq_j, q_k\} = \delta_{ik}q_j, \{p_iq_j, p_k\} = -\delta_{jk}p_i$,

$\{p_ip_j, q_k\} = \delta_{ik}p_j + \delta_{jk}p_i, \{p_ip_j, p_k\} = 0$,

$\{q_iq_j, q_k\} = 0, \{q_iq_j, p_k\} = -\delta_{ik}q_j - \delta jkq_i$

so, we have the representation of basic elements
$f \mapsto A_f : 1 \mapsto i, q_k \mapsto ix_k$,

$$p_l \mapsto \frac{\delta}{\delta x^l}, p_iq_j \mapsto x^i \frac{\partial}{\partial x^j} + \frac{1}{2}\delta_{ij},$$
$$p_kp_l \mapsto \frac{1}{i}\frac{\partial^k}{\partial x^k \partial x^l}, q_kq_l \mapsto ix^kx^l$$

This gives the structure of the Poisson manifolds to representation of any (nilpotent) algebra or in other words to continuous wavelet transform.

3 THE SEGAL-BARGMAN REPRESENTATION

Let

$$z = \frac{1}{\sqrt{2}}(p - iq), \quad \bar{z} = \frac{1}{\sqrt{2}}(p + iq),$$

$p = (p_1, ..., p_n)$, F_n is the space of holomorphic functions of n complex variables with $(f,f) < \infty$, where

$$(f,g) = (2\pi)^{-n} \int f(z)\overline{g(z)}e^{-|z|^2} dpdq$$

Consider a map $U : H \to F_n$, where H is with real polarization,F_n is with complex polarization, then we have

$$(U\Psi)(a) = \int A(a,q)\Psi(q)dq,$$

where

$$A(a,q) = \pi^{-n/4} e^{-1/2(a^2+q^2)+\sqrt{2}aq}$$

i.e. the Bargmann formula produce wavelets.We also have the representation of Heisenberg algebra on F_n :

$$U\frac{\partial}{\partial q_j}U^{-1} = \frac{1}{\sqrt{2}}\left(z_j - \frac{\partial}{\partial z_j}\right),$$
$$Uq_jU^{-1} = -\frac{i}{\sqrt{2}}\left(z_j + \frac{\partial}{\partial z_j}\right)$$

and also : $\omega = d\beta = dp \wedge dq$, where $\beta = i\bar{z}dz$.

4 ORBITAL THEORY FOR WAVELETS

Let coadjoint action be

$$< g \cdot f, Y > = < f, Ad(g)^{-1}Y >,$$

where $<,>$ is pairing $g \in G$, $f \in g^*$, $Y \in \mathcal{G}$.

The orbit is $\mathcal{O}_f = G \cdot f \equiv G/G(f)$.

Also,let A=A(M) be algebra of functions, V(M) is A-module of vector fields, A^p is A-module of p-forms. Vector fields on orbit is

$$\sigma(\mathcal{O}, X)_f(\phi) = \frac{d}{dt}(\phi(\exp tXf))\Big|_{t=0}$$

where $\phi \in A(\mathcal{O})$, $f \in \mathcal{O}$. Then $\mathcal{O}_f$ are homogeneous symplectic manifolds with 2-form

$$\Omega(\sigma(\mathcal{O}, X)_f, \sigma(\mathcal{O}, Y)_f) = < f, [X, Y] >,$$

and $d\Omega = 0$. PB on $\mathcal{O}$ have the next form

$$\{\Psi_1, \Psi_2\} = p(\Psi_1)\Psi_2$$

where p is $A^1(\mathcal{O}) \to V(\mathcal{O})$ with definition $\Omega(p(\alpha), X) = i(X)\alpha$. Here $\Psi_1, \Psi_2 \in A(\mathcal{O})$ and $A(\mathcal{O})$ is Lie algebra with bracket $\{,\}$.

Now let N be a Heisenberg group. Consider adjoint and coadjoint representations in some particular case.

$N = (z,t) \in C \times R, z = p + iq$; compositions in N are $(z,t)\cdot(z',t') = (z+z', t+t'+B(z,z'))$, where $B(z,z') = pq' - qp'$. Inverse element is $(-t, -z)$. Lie algebra n of N is $(\zeta, \tau) \in C \times R$ with bracket $[(\zeta,\tau),(\zeta',\tau')] = (0, B(\zeta,\zeta'))$. Centre is $\tilde{z} \in n$ and generated by (0,1); Z is a subgroup $\exp \tilde{z}$. Adjoint representation N on n is given by formula

$$Ad(z,t)(\zeta,\tau) = (\zeta, \tau + B(z,\zeta))$$

Coadjoint:
for $f \in n^*$, $g = (z,t)$,

$$(g \cdot f)(\zeta,\zeta) = f(\zeta,\tau) - B(z,\zeta)f(0,1)$$

then orbits for which $f|_{\bar{z}} \neq 0$ are plane in n^* given by equation $f(0,1) = \mu$. If $X = (\zeta,0)$, $Y = (\zeta',0)$, $X,Y \in n$ then symplectic structure is

$$\Omega(\sigma(\mathcal{O},X)_f,\sigma(\mathcal{O},Y)_f) =< f,[X,Y] >= f(0,B(\zeta,\zeta'))\mu B(\zeta,\zeta')$$

Also we have for orbit $\mathcal{O}_\mu = N/Z$ and $\mathcal{O}_\mu$ is Hamiltonian G-space.

5 KIRILLOV CHARACTER FORMULA OR ANALOGY OF GABOR WAVELETS

Let U denote irreducible unitary representation of N with condition $U(0,t) = \exp(it\ell) \cdot 1$, where $\ell \neq 0$,then U is equivalent to representation T_ℓ which acts in $L^2(R)$ according to

$$T_\ell(z,t)\phi(x) = \exp\left(i\ell(t+px)\right)\phi(x-q)$$

If instead of N we consider E(2)/R we have S^1 case and we have Gabor functions on S^1.

6 OSCILLATOR GROUP

Let O be an oscillator group,i.e. semidirect product of R and Heisenberg group N.

Let H,P,Q,I be standard basis in Lie algebra o of the group O and H^*, P^*, Q^*, I^* be dual basis in o^*. Let functional f=(a,b,c,d) be

$$aI^* + bP^* + cQ^* + dH^*.$$

Let us consider complex polarizations

$$h = (H,I,P+iQ), \quad \bar{h} = (I,H,P-iQ)$$

Induced from h representation, corresponding to functional f (for $a > 0$), unitary equivalent to the representation

$$W(t,n)f(y) = \exp(it(h-1/2)) \cdot U_a(n)V(t),$$

where

$$\begin{aligned} V(t) &= \exp[-it(P^2+Q^2)/2a], \\ P &= -d/dx, \quad Q = iax, \end{aligned}$$

and $U_a(n)$ is irreducible representation of N, which have the form $U_a(z) = exp(iaz)$ on the center of N.
Here we have: U(n=(x,y,z)) is Schrödinger representation, $U_t(n) = U(t(n))$ is the representation,which obtained from previous by automorphism (time translation) $n \longrightarrow t(n)$; $U_t(n) = U(t(n))$ is also unitary irreducible representation of N.

$$V(t) = \exp(it(P^2+Q^2+h-1/2))$$

is an operator, which according to Stone–von Neumann theorem has the property

$$U_t(n) = V(t)U(n)V(t)^{-1}.$$

This is our last private case, but according to our approach we can construct by using methods of geometric quantization theory many "symplectic wavelet constructions" with corresponding symplectic or Poisson structure on it. Very useful particular spline–wavelet basis with uniform exponential control on stratified and nilpotent Lie groups was considered in [9].

Extended version and related results may be found in [1]-[6].

This research was supported in part under "New Ideas for Particle Accelerators Program" NSF-Grant no. PHY94-07194.

7 REFERENCES

[1] A.N. Fedorova, M.G. Zeitlin: Proc. of 22 Summer School'Nonlinear Oscillations in Mechanical Systems' St. Petersburg (1995) 97.

[2] A.N. Fedorova, M.G. Zeitlin: Proc. of 23 Summer School 'Nonlinear Oscillations in Mechanical Systems' St. Petersburg (1996) 322.

[3] A.N. Fedorova, M.G. Zeitlin: Proc. 4 Int. Congress on Sound and Vibration, Russia (1996) 1483.

[4] A.N. Fedorova, M.G. Zeitlin: Proc. 7th IEEE DSP Workshop, Norway (1996) 409.

[5] A.N. Fedorova, M.G. Zeitlin: Proc. 2nd IMACS Symp. on Math. Modelling, ARGESIM Report **11**, Austria (1997) 1083.

[6] A.N. Fedorova, M.G. Zeitlin: EUROMECH-2nd European Nonlinear Oscillations Conf. (1996) 79.

[7] C. Kalisa, B. Torresani: N-dimensional Affine Weyl–Heisenberg Wavelets preprint CPT-92 P.2811 Marseille (1992).

[8] T. Kawazoe: Proc. Japan Acad. **71** Ser. A (1995) 154.

[9] P.G. Lemarie: Proc. Int. Math. Congr., Satellite Symp. (1991) 154.

[10] A.N. Fedorova, M.G. Zeitlin, Z. Parsa, This Proceedings.

WAVELET APPROACH TO ACCELERATOR PROBLEMS, III. MELNIKOV FUNCTIONS AND SYMPLECTIC TOPOLOGY

A. Fedorova and M. Zeitlin*
Institute of Problems of Mechanical Engineering,
Russian Academy of Sciences, Russia, 199178, St. Petersburg, V.O., Bolshoj pr., 61,
Z. Parsa†
Dept. of Physics, Bldg. 901A, Brookhaven National Laboratory, Upton, NY 11973-5000, USA

Abstract

This is the third part of a series of talks in which we present applications of methods of wavelet analysis to polynomial approximations for a number of accelerator physics problems. We consider the generalization of our variational wavelet approach to nonlinear polynomial problems to the case of Hamiltonian systems for which we need to preserve underlying symplectic or Poissonian or quasicomplex structures in any type of calculations. We use our approach for the problem of explicit calculations of Arnold–Weinstein curves via Floer variational approach from symplectic topology. The loop solutions are parametrized by the solutions of reduced algebraical problem – matrix Quadratic Mirror Filters equations. Also we consider wavelet approach to the calculations of Melnikov functions in the theory of homoclinic chaos in perturbed Hamiltonian systems.

1 INTRODUCTION

In this paper we continue the application of powerful methods of wavelet analysis to polynomial approximations of nolinear accelerator physics problems. In part I we considered our main example and general approach for constructing wavelet representation for orbital motion in storage rings. Now we consider two problems of nontrivial dynamics related with complicated differential geometrical and symplectic topological structures of system (1) from part I. In section 2 we give some points of applications of wavelet methods from parts I, II to Melnikov approach in the theory of homoclinic chaos in perturbed Hamiltonian systems. In section 3 we consider another type of wavelet approach, which gives a possibility to parametrize Arnold–Weinstein curves or closed loops in Hamiltonian systems by generalized refinement equations or Quadratic Mirror Filters equations.

2 ROUTES TO CHAOS

Now we give some points of our program of understanding routes to chaos in some Hamiltonian systems in the wavelet approach [1]-[9]. All points are:

1. A model.
2. A computer zoo. The understanding of the computer zoo.
3. A naive Melnikov function approach.
4. A naive wavelet description of (hetero) homoclinic orbits (separatrix) and quasiperiodic oscillations.
5. Symplectic Melnikov function approach.
6. Splitting of separatrix... $\longrightarrow$stochastic web with magic symmetry, Arnold diffusion and all that.

1. As a model we have two frequencies perturbations of particular case of system (1) from part I:

$$\begin{aligned}
\dot{x}_1 &= x_2 \\
\dot{x}_2 &= -ax_1 - b[\cos(rx_5) + \cos(sx_6)]x_1 - \\
&\quad dx_1^3 - mdx_1x_3^2 - px_2 - \varphi(x_5) \\
\dot{x}_3 &= x_4 \\
\dot{x}_4 &= ex_3 - f[\cos(rx_5) + \cos(sx_6)] - gx_3^3 - \\
&\quad kx_1^2x_3 - gx_4 - \psi(x_5) \\
\dot{x}_5 &= 1 \\
\dot{x}_6 &= 1
\end{aligned}$$

or in Hamiltonian form

$$\begin{aligned}
\dot{x} &= J \cdot \nabla H(x) + \varepsilon g(x, \Theta), \\
\dot{\Theta} &= \omega, \quad (x, \Theta) \in R^4 \times T^2, \\
T^2 &= S^1 \times S^1,
\end{aligned}$$

for $\varepsilon = 0$ we have:

$$\dot{x} = J \cdot \nabla H(x), \quad \dot{\Theta} = \omega \tag{1}$$

2. For pictures and details one can see [3], [8]. The key point is the splitting of separatrix (homoclinic orbit) and transition to fractal sets on the Poincare sections.
3. For $\varepsilon = 0$ we have homoclinic orbit $\bar{x}_0(t)$ to the hyperbolic fixed point x_0. For $\varepsilon \neq 0$ we have normally hyperbolic invariant torus T_ε and condition on transversally intersection of stable and unstable manifolds $W^s(T_\varepsilon)$ and $W^u(T_\varepsilon)$ in terms of Melnikov functions $M(\Theta)$ for $\bar{x}_0(t)$.

$$M(\Theta) = \int_{-\infty}^{\infty} \nabla H(\bar{x}_0(t)) \wedge g(\bar{x}_0(t), \omega t + \Theta) dt$$

* e-mail: zeitlin@math.ipme.ru
† e-mail: parsa@bnl.gov

0-7803-4376-X/98/$10.00 © 1998 IEEE

This condition has the next form:

$$M(\Theta_0) = 0$$
$$\sum_{j=1}^{2} \omega_j \frac{\partial}{\partial \Theta_j} M(\Theta_0) \neq 0$$

According to the approach of Birkhoff-Smale-Wiggins we determined the region in parameter space in which we observe the chaotic behaviour [3], [8].

4. If we cannot solve equations (1) explicitly in time, then we use the wavelet approach from part I for the computations of homoclinic (heteroclinic) loops as the wavelet solutions of system (1). For computations of quasiperiodic Melnikov functions

$$M^{m/n}(t_0) = \int_0^{mT} DH(x_\alpha(t)) \wedge g(x_\alpha(t), t + t_0) dt$$

we used periodization of wavelet solution from part I.

5. We also used symplectic Melnikov function approach

$$\begin{aligned} M_i(z) &= \lim_{j\to\infty} \int_{-T_j^*}^{T_j} \{h_i, \hat{h}\}_{\Psi(t,z)} dt \\ d_i(z,\varepsilon) &= h_i(z_\varepsilon^u) - h_i(z_\varepsilon^s) = \varepsilon M_i(z) + O(\varepsilon^2) \end{aligned}$$

where $\{,\}$ is the Poisson bracket, $d_i(z,\varepsilon)$ is the Melnikov distance. So, we need symplectic invariant wavelet expressions for Poisson brackets. The computations are produced according to part II.

6. Some hypothesis about strange symmetry of stochastic web in multi-degree-of freedom Hamiltonian systems [9].

3 WAVELET PARAMETRIZATION IN FLOER APPROACH.

Now we consider the generalization of our wavelet variational approach to the symplectic invariant calculation of Arnold–Weinstein curves (closed loops) in Hamiltonian systems [10]. We also have the parametrization of our solution by some reduced algebraical problem but in contrast to the general case where the solution is parametrized by construction based on scalar refinement equation, in symplectic case we have parametrization of the solution by matrix problems – Quadratic Mirror Filters equations [11].

The action functional for loops in the phase space is [10]

$$F(\gamma) = \int_\gamma pdq - \int_0^1 H(t, \gamma(t)) dt$$

The critical points of F are those loops γ, which solve the Hamiltonian equations associated with the Hamiltonian H and hence are periodic orbits. By the way, all critical points of F are the saddle points of infinite Morse index, but surprisingly this approach is very effective. This will be demonstrated using several variational techniques starting from minimax due to Rabinowitz and ending with Floer homology. So, (M, ω) is symplectic manifolds, $H : M \to R$, H is Hamiltonian, X_H is unique Hamiltonian vector field defined by

$$\omega(X_H(x), v) = -dH(x)(v), \quad v \in T_x M, \quad x \in M,$$

where ω is the symplectic structure. A T-periodic solution $x(t)$ of the Hamiltonian equations

$$\dot{x} = X_H(x) \quad \text{on } M$$

is a solution, satisfying the boundary conditions $x(T) = x(0), T > 0$. Let us consider the loop space $\Omega = C^\infty(S^1, R^{2n})$, where $S^1 = R/\mathbf{Z}$, of smooth loops in R^{2n}. Let us define a function $\Phi : \Omega \to R$ by setting

$$\Phi(x) = \int_0^1 \frac{1}{2} < -J\dot{x}, x > dt - \int_0^1 H(x(t)) dt, \quad x \in \Omega$$

The critical points of Φ are the periodic solutions of $\dot{x} = X_H(x)$. Computing the derivative at $x \in \Omega$ in the direction of $y \in \Omega$, we find

$$\begin{aligned} \Phi'(x)(y) &= \frac{d}{d\epsilon} \Phi(x + \epsilon y)|_{\epsilon=0} = \\ & \int_0^1 < -J\dot{x} - \nabla H(x), y > dt \end{aligned}$$

Consequently, $\Phi'(x)(y) = 0$ for all $y \in \Omega$ iff the loop x satisfies the equation

$$-J\dot{x}(t) - \nabla H(x(t)) = 0,$$

i.e. $x(t)$ is a solution of the Hamiltonian equations, which also satisfies $x(0) = x(1)$, i.e. periodic of period 1. Periodic loops may be represented by their Fourier series:

$$x(t) = \sum_{k \in \mathbf{Z}} e^{k2\pi Jt} x_k, \quad x_k \in R^{2k},$$

where J is quasicomplex structure. We give relations between quasicomplex structure and wavelets in part IV. But now we use the construction [11] for loop parametrization. It is based on the theorem about explicit bijection between the Quadratic Mirror Filters (QMF) and the whole loop group: $LG : S^1 \to G$. In particular case we have relation between **QMF**-systems and measurable functions $\chi : S^1 \to U(2)$ satisfying

$$\chi(\omega + \pi) = \chi(\omega) \begin{bmatrix} 0 & 1 \\ 1 & 0 \end{bmatrix},$$

in the next explicit form

$$\begin{aligned} \begin{bmatrix} \hat{\Phi}_0(\omega) & \hat{\Phi}_0(\omega+\pi) \\ \hat{\Phi}_1(\omega) & \hat{\Phi}_1(\omega+\pi) \end{bmatrix} &= \chi(\omega) \begin{bmatrix} 0 & 1 \\ 1 & 0 \end{bmatrix} \\ &+ \chi(\omega+\pi) \begin{bmatrix} 0 & 0 \\ 0 & 1 \end{bmatrix}, \end{aligned}$$

where

$$\left|\hat{\Phi}_i(\omega)\right|^2 + \left|\hat{\Phi}_i(\omega+\pi)\right|^2 = 2, \quad i = 0, 1.$$

Also, we have symplectic structure on LG

$$\omega(\xi,\eta) = \frac{1}{2\pi}\int_0^{2\pi} < \xi(\theta), \eta'(\theta) > d\theta$$

So, we have the parametrization of periodic orbits (Arnold–Weinstein curves) by reduced QMF equations.

Extended version and related results may be found in [1]-[9].

This research was supported in part under "New Ideas for Particle Accelerator Program" NSF-Grant no. PHY94-07194.

4 REFERENCES

[1] A.N. Fedorova, M.G. Zeitlin: Proc. of 22 Summer School'Nonlinear Oscillations in Mechanical Systems' St. Petersburg (1995) 89.

[2] A.N. Fedorova, M.G. Zeitlin: Proc. of 22 Summer School'Nonlinear Oscillations in Mechanical Systems' St. Petersburg (1995) 97.

[3] A.N. Fedorova, M.G. Zeitlin: Proc. of 22 Summer School'Nonlinear Oscillations in Mechanical Systems' St. Petersburg (1995) 107.

[4] A.N. Fedorova, M.G. Zeitlin: Proc. of 23 Summer School 'Nonlinear Oscillations in Mechanical Systems' St. Petersburg (1996) 322.

[5] A.N. Fedorova, M.G. Zeitlin: Proc. 7th IEEE DSP Workshop, Norway (1996) 409.

[6] A.N. Fedorova, M.G. Zeitlin: Proc. 2nd IMACS Symp. on Math. Modelling, ARGESIM Report **11**, Austria (1997) 1083.

[7] A.N. Fedorova, M.G. Zeitlin: EUROMECH-2nd European Nonlinear Oscillations Conf. (1997) 79.

[8] A.N. Fedorova, M.G. Zeitlin: EUROMECH-2nd European Nonlinear Oscillations Conf. (1997) 153.

[9] A.N. Fedorova, M.G. Zeitlin: Proc. of 24 Summer School'Nonlinear Oscillations in Mechanical Systems' St. Petersburg (1997).

[10] E. Hofer, E. Zehnder: Symplectic Topology, Birkhauser (1994).

[11] M. Holschneider, U. Pinkall: CPT-94 P.3017 Marseille (1994).

[12] A.N. Fedorova, M.G. Zeitlin, Z. Parsa: This Proceedings.

SOME INTERACTION PECULIARITIES OF RELATIVISTIC PARTICLES WITH UHF ELECTRIC FIELD OF HIGH INTENSITY AT LARGE DISTANCES

O.P. Korovin, V.O. Naidenov, E.O. Popov

A.F.Ioffe Physical-Technical Institute, Russian Academy of Sciencies, 194021, St-Petersburg, Russia

ABSTRACT

Interaction of relativistic charged particles with high intensity UHF electric field has been studied. Magnetic component of the field is taken equal to zero. It is shown that interaction process has some peculiarities depending on ratio between input particle energy and field intensity. In particular, an acceleration of part of monoenergetic electron beam on account of other part with simultenious energy transfer from the beam to the field is possible.

MATHEMATICAL MODEL

Mathematical model of particle movement is taken from [1]. Equation of movement:

$$\frac{dmv}{dt} = qE + q(v \times B), \qquad (1)$$

here $m = \frac{m_0}{\sqrt{1-\beta^2}}$ – mass; m_0 - rest mass of the particle; v – velocity of the particle; c – velocity of light; q – charge of the particle.

Magnetic field is equal to zero:

$$\omega \frac{dmv}{d\vartheta} = qE_0 \sin\vartheta = \frac{qV_0}{h}\sin\vartheta, \qquad (2)$$

hence

h – interaction distance, V_0 -amplitude of microwave field.

After integrating equation (2) we introduce function $A(\vartheta)$:

$$A(\vartheta) = \frac{\beta}{(1-\beta^2)^{1/2}} = \frac{\beta_e}{(1-\beta_e^2)^{1/2}} + \left(\frac{qV_0}{m_0c^2}\right)\left(\frac{\lambda}{2\pi h}\right)[\cos\vartheta_e - \cos\vartheta], \qquad (3)$$

where $\beta = \frac{v}{c}$, λ – wavelength, β_e, ϑ_e - are the relative velocity of the particle and initial phase (phase of the field at start of interaction).

The equation (3) governs the movement of the particle in the alternating electric field. The path traversed by the particle in this field depending on entrance phase is calculated by formula:

$$S = \frac{c}{\omega}\int_{\vartheta_e}^{\vartheta_h} \frac{A(\vartheta)d\vartheta}{\left[1+A^2(\vartheta)\right]^{1/2}}. \qquad (4)$$

On the basic of this mathematical model a software for calculation of relativistic charged particle with UHF was developed. This software allows determination of particle energy, interaction time, description the dependence of the path traversed by the particle from the time etc., i.e. gives full description of interaction process. It can be used for a particle of any mass, energy and charge interacting with electric field of arbitrary frequency and intensity.

RESULTS AND DISCUSSION

For calculation the following initial parameters were set: frequency and intensity of the UHF electric field, energy and input phase of the electron. Varying the input phase from 0 to 360 degrees with 1 or 3 degree's step one can reveal the process of interaction with monoenergetic electron beam. To test the validity of the calculations the other problem of interaction of electron with 3-dimensional field of standing wave in rectangular waveguide was solved. The outlined problem represents the special case of 3-dimensional field. In spite of the fact that these were different problems and their solutions were performed mathematically in a different way, the results of calculations by both programs coincide within the accuracy less than 0.1%. This confirms the reliability of results.

The calculations have been performed in the frequency range 0.8-3 GHz, field intensity varying from 100 kV/m up to 100 MV/m. The input energy of electrons varied from 7 keV to 700 MeV. Fig.1 illustrates the typical dependence of maximal energy acquired by electrons from interaction distance (upper curve) and average energy acquired (or lost) by electron with input phase from 0 to 2π (lower curve). The input electron energy was 7 MeV,

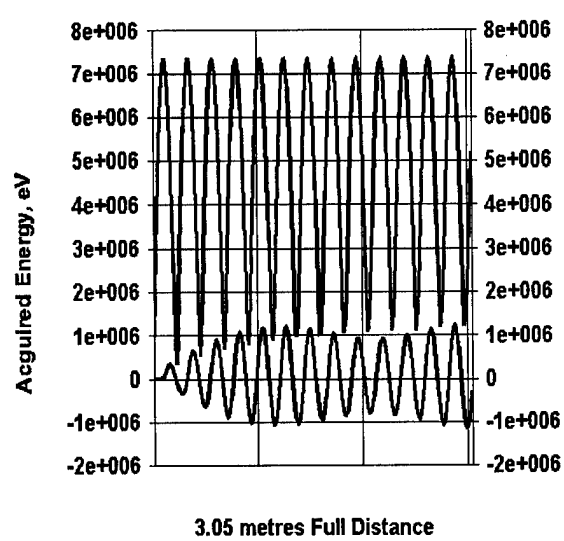

Fig.1.

field intensity (amplitude value) 100 MeV, frequency 1.3 GHz. Data analysis leads to the following conclusion:

1) At a relative to wavelength long distance of $\lambda/3$ electron acquires 6.45 MeV, i.e. ~80% of maximal energy which they could obtain in a permanent field of the same intensity. Average energy obtained by all electrons with input phase from 0 to 2π is close to zero. That means, the acceleration of electrons could be performed on account of other electrons of the same constant monoenergetic beam. This circumstance can be useful for superconducting resonators.
2) At the distance of $\lambda/2$ maximal accelerated are electrons with zero input phase. They obtain 64.3% from the maximal energy which could be acquired in the permanent field of the same intensity. This value is practically the same for relativistic electrons of different energies.
3) Maximum of acquired energy is repeated exactly through the distance equal to wavelength λ.
4) Minimal value of maximal electron energy is also repeated through the distance λ and has tendency to increase slowly with distance.
5) At the distance approximately equal ~$5/4\lambda$ (28cm) electrons with input phase near to zero acquire energy of ~4.5 MeV whereas average energy balance shows transmission of energy from electron beam to the field. This effect could be observed only for relativistic electrons at large interaction distances. On Fig.2 the dependence of the electron energy distribution from the input phase for the 28 cm interaction distance is presented. It is seen, that maximal energy (~4.5 MeV) is acquired by electrons with input phase near zero, and ~5 MeV of energy is lost by electrons with input phase near 180°.

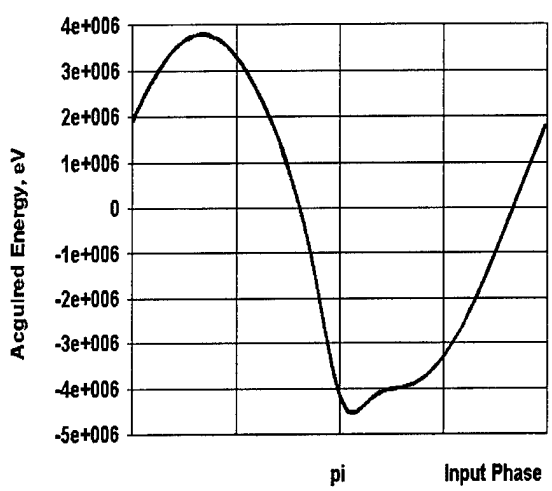

Fig.2.

6) At the distance of 31 cm electrons acquire maximum of energy 6.5 MeV without taking energy from the field.
7) On Fig.3 the input phase dependence of electron energy distribution at the distance of 3.01 m is presented. At this distance electron with input phase 0 acquire minimum of energy, whereas electrons with phase close to 180° lose totally their energy.

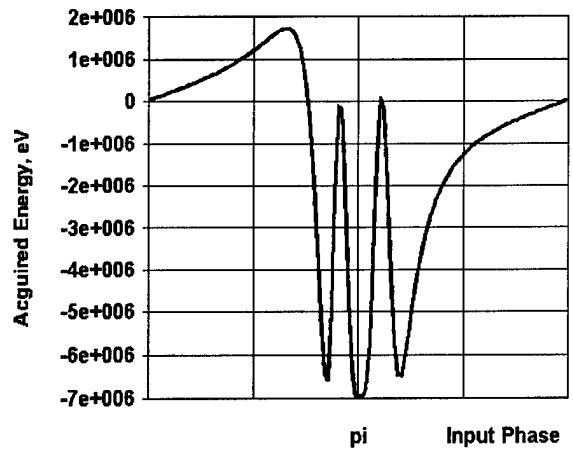

Fig.3.

8) To compare relativistic and nonrelativistic electron interaction with UHF field at large distances Fig.4 is presented. Electrons have input energy of 1 MeV, field intensity is equal 100 MV/m, frequency is equal 1.3 GHz. Special features noted above are absent on these curves.

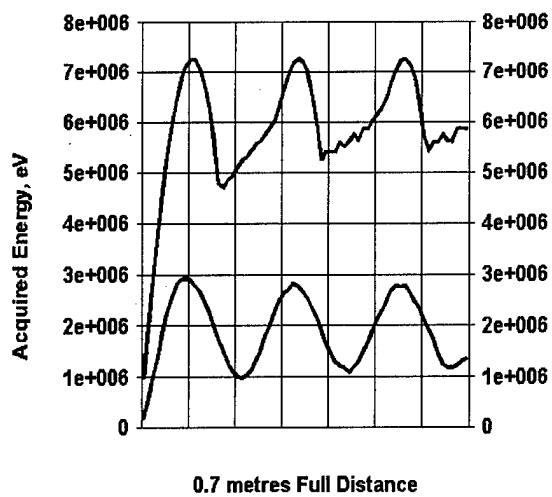

Fig.4.

CONCLUSION

The above mentioned peculiarities are specific only to relativistic electrons by definite ratios between field intensity, frequency, electron input energy. They can be used for acceleration of permanent monoenergetic electron beam with simultaneous energy transmission from beam to the field, bunched beam braking and in other cases, like movement in cosmic fields.

ACKNOWLEDGMENTS

Authors would like to thank Rozova I.V. for making part of computations and Popov S.O. for help in writing physical ActiveX library and testing the program.

REFERENCES

[1] Coleman P. D. Theory of the Rebatron - a Relativistic Electron Bunching Accelerator//N.Y.: Journal of Applied Physics. 1957. v. 28, [1] 9. p. 927–936.

NONLINEAR LONGITUDINAL DYNAMICS STUDIES AT THE ALS *

J. M. Byrd†, W-H Cheng†, F. Zimmermann§
†Lawrence Berkeley National Laboratory, One Cyclotron Road, Berkeley, California 94720
§Stanford Linear Accelerator Center, Stanford, California 94309

Abstract

We present an account of our efforts to understand unexpected observations in the course of performing measurements of the longitudinal beam transfer function. As the amplitude of excitation was increased, we observed a notch in the middle of the peak amplitude response of the transfer function. Our observations are explained by a bifurcation in the amplitude due to the nonlinearity of the oscillations, demonstrated by measurements of the longitudinal bunch profile using a streak camera.

1 INTRODUCTION

Beam transfer function (BTF) techniques are common in accelerators. In its simplest form, a swept frequency drive is used to excite beam oscillations in order to measure the synchrotron or betatron tunes. The BTF can also be used to measure the beam impedance and various other machine parameters. While engaged in such measurements at the Stanford Linear Collider damping ring (SLCDR), one of us observed an unusual phenomenon in the longitudinal transfer function[1]. As the level of excitation was increased, a deep notch appeared in the amplitude response of the BTF. In similar studies at the Advanced Light Source (ALS), we were able to reproduce the results observed at the SLCDR. In the course of further investigations at the ALS, we were led into the rich field of nonlinear dynamics and were treated to some stimulating observations of beam behavior. This paper describes our investigations and the physics which explains our observations.

2 MEASUREMENTS

In the fall of 1996, we began a program of machine studies using the longitudinal BTF to measure various machine parameters. In general, a network or FFT signal analyzer is used to excite longitudinal oscillations via phase modulation of the RF voltage. Beam oscillations are detected using a standard phase detection technique. A more complete description of the experimental setup is given in reference [2]. The BTF is defined as the relative amplitude and phase of the beam response to excitation as a function of frequency. Shown in Figure 1 is a plot of the amplitude and phase of single bunch longitudinal BTF measurements as a function of increasing excitation. For this case, the excitation frequency was swept from lower to higher frequency.

At small excitation amplitudes, the BTF agrees with theory[2]. However, we were surprised to see the distortion of the BTF as the excitation was increased, particularly the deep notch and sudden 180 degree phase shifts in both the amplitude and phase. We resolved to uncover its source. Because longitudinal oscillations are well known to be nonlinear, especially at larger amplitudes, we looked in the direction of a nonlinear effect.

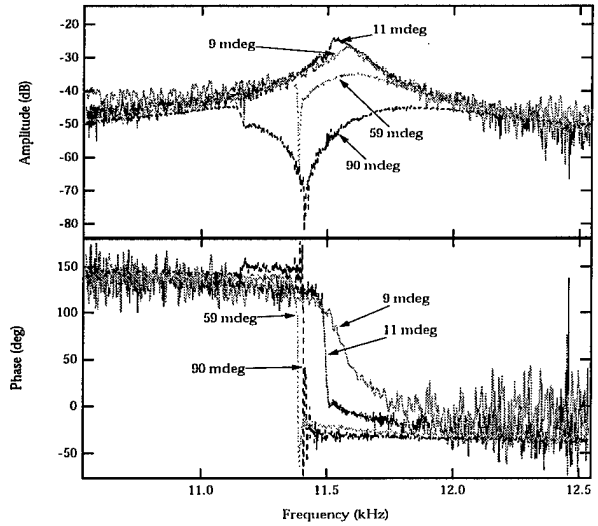

Figure 1: Amplitude and phase of longitudinal beam transfer functions for increasing frequency sweeps as a function of drive amplitude.

To make a more detailed study of the longitudinal dynamics near the notch in the transfer function, we used a streak camera (SC) to observe the evolution of the longitudinal distribution as the modulation frequency sweeps upward through the synchrotron frequency. A schematic diagram of the Hamamatsu C5680 SC is shown in Figure 2. The SC works by converting the time structure of an optical light pulse into vertical deflection at the CCD camera. In our experiments, the vertical deflection plates are driven by a 125 MHz sinusoidal voltage synchronized to the beam. In addition, there is an optional slow horizontal deflection which allows observation of the longitudinal profile as a function of time. The time scale of the horizontal sweep can be adjusted to observe several turns or thousands of turns. For sweep times longer than several hundred turns, individual turns can no longer be resolved and so the longitudinal profile appears as a continuous line across the image.

Shown in Figure 3 are images of the longitudinal profile vs. time for three modulation frequencies (f_m): below the frequency where the notch appears in the BTF, at the notch

* This work was supported by the U.S. Dept. of Energy under Contract Nos. DE-AC03-76SF00098 and DE-AC03-76SF00515.

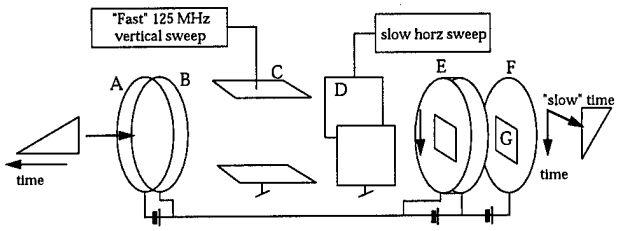

Figure 2: Schematic diagram of the streak camera in synchroscan mode with dual sweep. A: phothcathode, B: accel. mesh, C: vert. deflection electrode, D: horz. defl. electrode, E: microchannel plate F: phosphor screen, G: CCD camera.

frequency, and above. The darker area represents higher intensity. For example, in Figure 3a, the sinusoidal pattern of the distribution is due to the phase modulations (the nominal RMS bunch length is 15-20 psec.) At this level of excitation, the bunch has oscillation amplitude of about 100 psec peak–peak. At the notch frequency, the bunch appears to split into two separate beamlets, oscillating with different amplitudes and out of phase by 180 degrees. Above the notch, the original bunch pattern disappears and only the second bunch pattern is evident.

Assuming that the streak camera profiles correctly indicate the presence of two beamlets in the same RF bucket, then an explanation for the notch in the BTF data presents itself. The phase detector for the BTF is sensitive only to *net* dipole phase oscillations of the bunch. As the modulation frequency passes through the notch, at some frequency the dipole moment of the two islands cancels.

Although the mystery of the notch in the BTF is solved, the question remains as to why the beamlets are formed. Fortunately, the theory of nonlinear longitudinal oscillations in the presence of phase modulation is well documented[3]. We provide here only a qualitative discussion of the theory.

Consider a driven harmonic oscillator (HO) which has a frequency dependence on the oscillation amplitude such that the frequency decreases at larger amplitudes. When the HO is driven near resonance, it reaches larger amplitudes which causing a detuning to lower frequencies. Synchrotron oscillations can be modeled in this form. If the longitudinal coordinates are expressed in a frame rotating with the modulation frequency, we can plot the phase space of the oscillations as shown in Figure 4. The two stable fixed points are marked A and B; C is unstable. The outer island corresponds to the point at 11 kHz on the upper branch of the response curve as shown in Figure 5. One characteristic feature of the response is that below some frequency, there are two stable amplitude responses while above this frequency there is a single stable response. The transition between these two is known as a bifurcation. Note that the outer island in the phase space representation moves to larger phase as the modulation frequency decreases below the bifurcation frequency. Radiation damping is ignored.

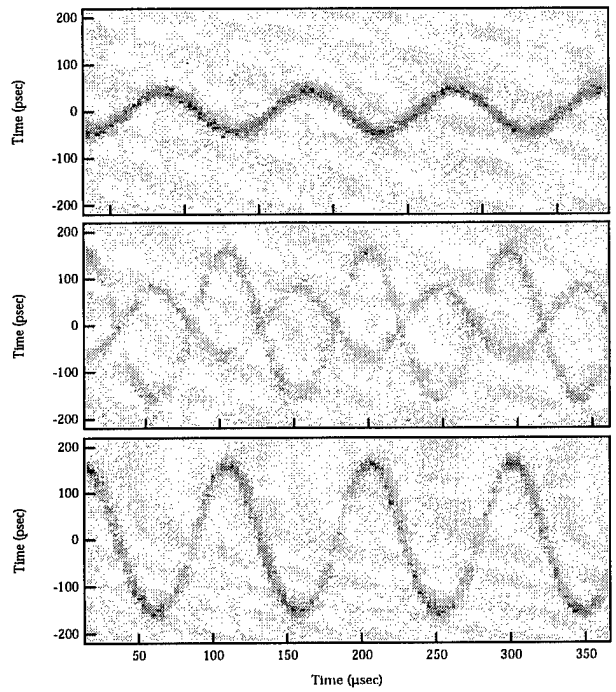

Figure 3: Images of the longitudinal profile (in psec) vs.time using the streak camera in dual scan mode: top) f_m below frequency of notch in BTF; middle) f_m at frequency of notch; bottom) f_m above notch frequency.

Consider a situation where both islands A and B are populated with electrons. In the lab frame, we observe the projection of the distribution on the horizontal axis in Figure 4 as the phase space diagram rotates about the origin. When the islands are situated as shown, the two beamlets are at their maximum separation in phase (or time). When the phase space has rotated by 90 degrees, the beamlets are coincident in phase but at their maximum energy separation. Figure 3a corresponds to the situation where there are two stable islands but only island B is populated. In Figure 3b, the modulation frequency has increased and islands A and B are populated but oscillating at different amplitudes. In Figure 3c, the modulation frequency is above the bifurcation frequency and only island A is stable.

Another issue is the mechanism for electrons to go from one stable island to another. We believe that the dominant diffusion mechanism is Touschek scattering. In this process, an elastic collision between electrons within a bunch has a finite probability of transferring enough energy to the longitudinal momentum such that the electrons are no longer within the RF bucket. Typically, the electrons scattered outside the momentum acceptance are lost. For the case of two stable islands as shown above, electrons are scattered outside the separatrix of island B whereupon the majority are damped into island A. To test this hypothesis,

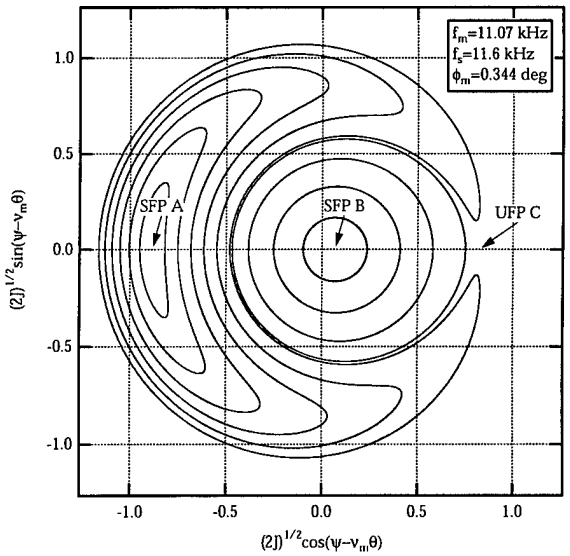

Figure 4: Phase space diagram in a frame rotating at the modulation frequency. The two stable fixed points are shown.

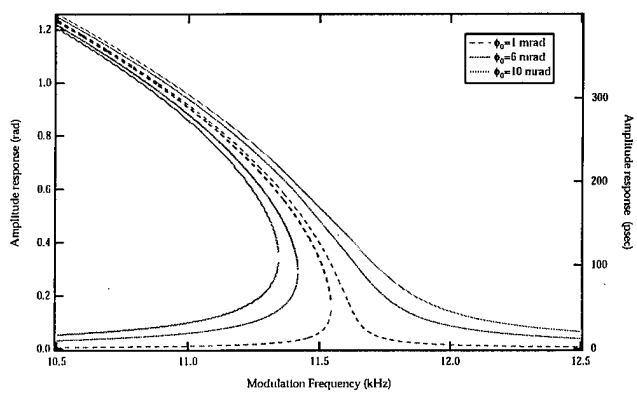

Figure 5: Response of driven longitudinal oscillations for 3 excitation amplitudes. The nominal synchrotron frequency is 11.6 kHz.

we modulated at a fixed frequency and recorded the longitudinal profile vs. time. An example is shown in Figure 6. The diffusion into the outer island is evident as well as a small decrease in the inner island. We extracted the diffusion rate by comparing the relative rate of increase of the peak signal in the outer island compared to the inner island.

A plot of the diffusion rates as a function of modulation frequency for several beam currents is shown in Figure 7. Calculations of the scattering rate using the separatrix of island B as the momentum acceptance show approximate agreement with the measurements. We are currently analyzing this in more detail.

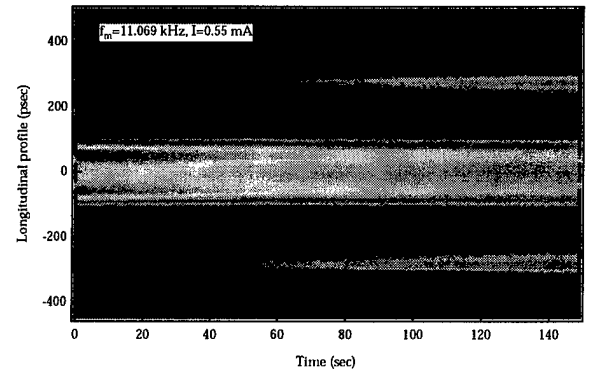

Figure 6: Longitudinal profile vs time at a fixed modulation frequency and amplitude showing diffusion from the inner to the outer island.

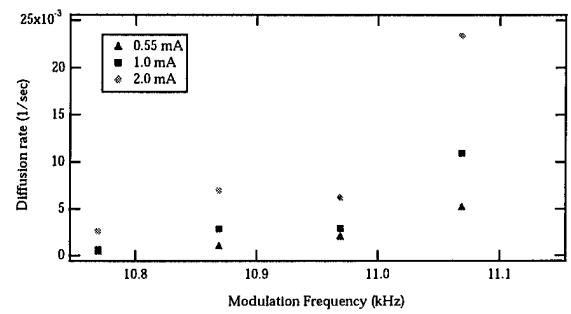

Figure 7: Diffusion rates as a function of modulation frequency for 3 different bunch currents.

3 CONCLUSIONS

The behavior of the BTF for upward swept frequency excitation at large amplitudes can be understood through the nonlinear dynamics of synchrotron oscillations. The notch in the BTF is explained by the presence of two beamlets formed in the two stable islands below the bifurcation frequency. Similar effects are observed for downward swept excitation. We hope that the diagnostics of nonlinear longitudinal dynamics can be extended further to be useful in understanding topics such as higher order momentum compaction, collective effects, and Touschek and intrabeam scattering. We are grateful to Prof. S.Y. Lee for helpful discussions.

4 REFERENCES

[1] M. Minty, F. Zimmermann, *Longitudinal beam transfer function measurements at the SLC damping rings*, these proceedings.

[2] J. Byrd, *Longitudinal beam transfer function diagnostics in the ALS*, these proceedings.

[3] H. Huang, et. al.,*Experimental determination of the Hamiltonian for synchrotron motion with rf phase modulation* Phys. Rev. E **48**, 4678, 1993. G. Tsironis, S. Peggs, T. Chen, *Tune modulation, Mathieu stability, and the driven pendulum*1990 EPAC, p 1753.

ENERGY ACCEPTANCE AND TOUSCHEK LIFETIME CALCULATIONS FOR THE SOLEIL PROJECT[1]

A. Nadji°, G. Flynn*, J.-L. Laclare°, M.-P. Level°, P. Nghiem°, J. Payet°°

°Projet SOLEIL, DRIF CNRS, Av. de La Terrasse, Bât. 5, 91198 Gif sur Yvette, France
*LURE, Centre Universitaire Paris-Sud, Bât. 209 A, 91405 Orsay Cedex, France
°°CEA Saclay, LNS, Groupe Théorie, 91191 Gif sur Yvette

Abstract

Touschek scattering is an important beam lifetime limiting effect for the SOLEIL storage ring and the dominant one for high single bunch current operation. The Touschek relevant energy acceptance may be determined by the radiofrequency system, dynamic aperture or vacuum chamber physical aperture. In the latter two cases, Touschek induced betatron oscillations must be considered. We present energy acceptance and Touschek lifetime calculations for SOLEIL in the presence of these three limitations taking into account the non-linear chromatic orbit as well as energy variation of the optical functions. In light of these considerations, Touschek lifetime lattice optimization will be discussed.

1. INTRODUCTION

One approach to improving the Touschek lifetime (τ_T) is to increase the energy acceptance $\left(\tau_T \propto \varepsilon_{acc}^{>2}\right)$ which may be determined by the RF bucket momentum height, by the aperture of the vacuum chamber or by the dynamic aperture if the induced amplitude after a Touschek scattering exceeds one of these two transverse limits.

To ensure a large longitudinal energy acceptance (± 6 %), the RF system (using superconducting cavities) will provide a peak voltage of more than 3 MV.

The aim of this paper is to present calculations of the ε_{acc} and the corresponding τ_T in the presence of the three limitations indicated above. These calculations have been performed taking into account non-linear chromatic closed orbit effects as well as energy variation of the optical functions. In addition, the presence of a small vertical aperture in narrow gap undulators may also limit τ_T in the presence of transverse coupling. Calculations supporting this result will also be presented.

Finally, we will shortly discuss a method for increasing τ_T by acting on the so-called lattice H function.

2. NON-LINEAR CALCULATIONS OF THE ENERGY ACCEPTANCE

A Touschek scattering event results in an instantaneous change in particle energy δ. As a result the particle reference orbit, initially assumed to be zero everywhere, is suddenly replaced by the chromatic orbit defined by : $x_{ch}(s) = \eta(s)\delta$, where $\eta(s)$ is the dispersion function. The well-known solution for the particle oscillation envelope subsequent to a collision located at s* is given by :

$$x_{max}(s) = \eta(s)\delta + \sqrt{\beta(s)H(s^*)}\ \delta \qquad (1)$$

where : $H(s^*) = \gamma(s^*)\eta^2(s^*) + 2\alpha(s^*)\eta(s^*)\eta'(s^*) + \beta(s^*)\eta'^2(s^*)$

The first term in (1) is due to the chromatic closed orbit while the second results from induced betatron motion.

We have observed that straightforward application of (1), as done in ZAP [1], is in general insufficient for two reasons. First, with extremely large sextupoles, the chromatic closed orbit is not strictly proportional to δ but contains higher order terms which, for the large ε_{acc} of interest, can have a very significant effect. Secondly the optical functions (but not η and η') entering into the expression for H(s*), are those which hold for the energy δ. Since these functions all vary with energy, this effect should also be taken into account.

In order to account for these higher order effects in δ, a module for the automatic calculation of ε_{acc} and τ_T has been integrated into the BETA code [2]. The algorithm used is as follows :

The general non-linear closed orbit Δx, and the optical functions are all calculated as functions of δ and s.

The dynamic aperture A_{dyn}, in betatron amplitude, is determined as a function of δ using the turn by turn tracking module of BETA.

The horizontal invariant physical aperture is calculated as a function of δ by :

$$A_{phys}(\delta) = \underset{s\in[0,s_{max}]}{\mathrm{Min}}\left\{\frac{\left(X_{vc} - \Delta x(s,\delta)\right)^2}{\beta_x(s,\delta)}\right\} \qquad (2)$$

where X_{vc} is the vacuum chamber half-width.

These two transverse acceptances are then combined into a single acceptance, which is symmetric and monotonic because of the synchrotron oscillation :

$$A(\delta) = \underset{\delta'\in[-\delta,\delta]}{\mathrm{Min}}\left\{\mathrm{Min}\left[A_{phys}(\delta'), A_{dyn}(\delta')\right]\right\} \qquad (3)$$

Next one calculates the invariant betatron amplitude induced by a change in energy occuring at the location s* by :

$$a_{induced}(s^*,\delta) = \frac{\left(\Delta x(s^*,\delta)\right)^2}{\beta_x(s^*,\delta)} + \beta_x(s^*,\delta)\left[\Delta x'(s^*,\delta) - \frac{\beta_x'(s^*,\delta)\Delta x(s^*,\delta)}{2\beta_x(s^*,\delta)}\right]^2 \qquad (4)$$

[1] Work supported by CNRS, CEA, MENESR.

The local transverse energy acceptance is then calculated by solving the equation :

$$A(\varepsilon_t(s)) - a(s,\varepsilon_t(s)) = 0 \qquad (5)$$

Because of the symmetric and monotonic nature of $A(\delta)$, this equation can have at most two solutions which we call $\varepsilon_{t\pm}$. The overall energy acceptance is then given by :

$$\varepsilon_{acc\pm}(s) = \mathrm{Min}\left[\varepsilon_{RF}, \varepsilon_{t\pm}(s)\right] \qquad (6)$$

Finally the Touschek loss rates are calculated by the well known formula for each of the two solutions and the total loss rate thus becomes :

$$\frac{1}{\tau_{T1/2}} = \frac{1}{2}\left[\frac{1}{\tau^{+}_{T1/2}(\varepsilon^{+}_{acc}(s))} + \frac{1}{\tau^{-}_{T1/2}(\varepsilon^{-}_{acc}(s))}\right] \qquad (7)$$

which is averaged over the machine to give the global inverse Touschek lifetime.

3. RESULTS OBTAINED IN THE HORIZONTAL PLANE

The calculations have been performed for the standard low emittance (3 nm.rad) and Chasman-Green (9 nm.rad) lattices. Nevertheless, we will give here detailed results obtained only for the standard lattice and mention only briefly the Chasman-Green optics.

Figure 1 shows the dynamic and the physical apertures calculated as a function of δ. One can note the asymmetry between the positive and the negative sides of δ. For a X_{VC} less than 35 mm, the physical aperture is always smaller than the dynamic one.

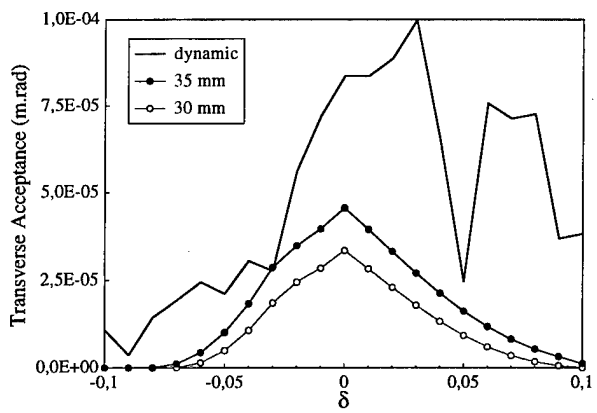

Fig. 1. Dynamic and physical apertures as a function of δ.

The induced betatron amplitude calculated as a function of s and δ, using equation (4) also shows asymmetric behaviour. The figure 2 gives a result obtained in the center of a long straight section. The amplitude for positive δ is much greater than that for negative values. This is due to the large positive value of the second order dispersion η_2 ($\Delta x = \eta_1\delta + \eta_2\delta^2 + \ldots$) at this location. In the center of the achromat, the amplitude curve is reversed because of the sign inversion of η_2 (Fig. 2). Taking into account this asymmetry, the solution of equation (6) will give two different energy acceptance solutions. An example of this result can be seen in figure 3, where the difference is clearely explained by the considerations given above.

One can also note that obviously, ε_{acc} is the most reduced in the center of the achromat (η_{xmax}) and in the medium length straight sections (η_x = 0.13 m and weak β_x = 4 m)[3].

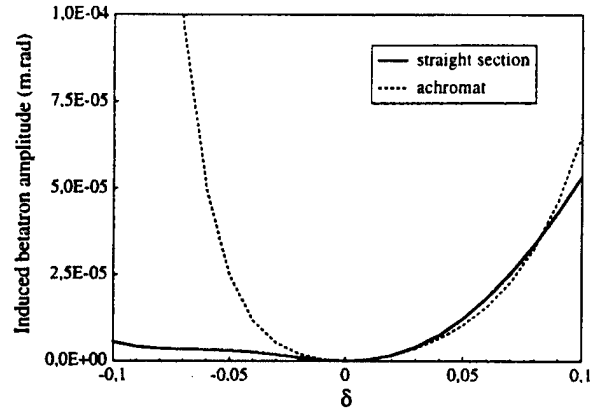

Fig. 2. Example of induced betatron amplitude.

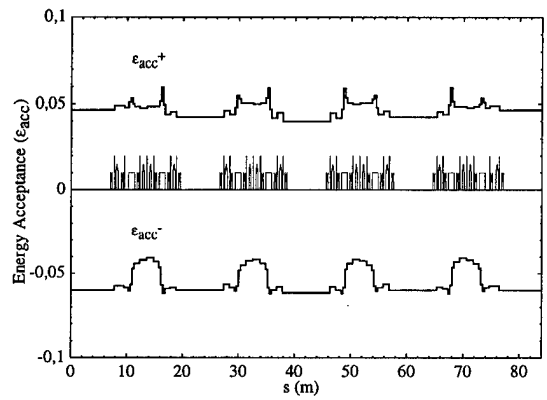

Fig. 3. Energy acceptance variation along the ring.

The difference between the linear and non-linear calculations is illustrated by the figure 4. This points out that the linear calculation of τ_T is optimistic (42 h versus 27 h) and that, in our case the contribution of the sextupole effect cannot be neglected.The contributions of the non-linear chromatic orbit and the variation of optical functions with energy have been studied separately and the most important contribution is that due to the first effect.

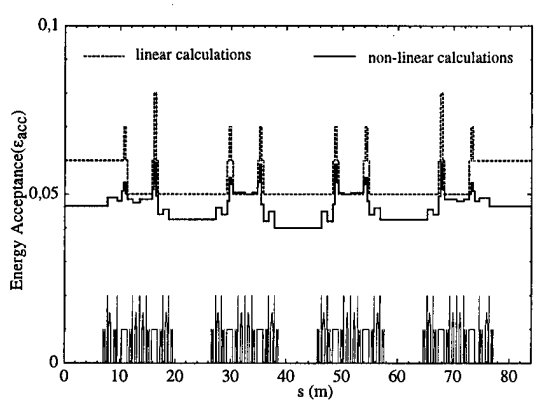

Fig. 4. Linear and non-linear calculations.

The results of ε_{acc} calculations as a function of the physical aperture in the presence of the two other limitations suggest that a stay clear of ±35 mm in the horizontal plane is a reasonable compromise. This corresponds to a τ_T of 36 h for the multibunch operation mode [I_b = 1.26 mA (I_t = 500 mA) ; κ^2 = 0.01 ; ε_{RF} = 5.1 % (V_{RF} = 3 MV) and $\sigma_{\ell n}$ = 13 ps]. No bunch lengthening was taken into account.

For many technical reasons, the injection septum magnet will be placed inside the vacuum chamber. The calculations show that it must be located at 23 mm at least from the vacuum chamber center in order to avoid any related Touschek lifetime reduction.

In the case of the Chasman-Green optics, the induced betatron amplitudes are almost symmetric in δ as are the energy acceptances and loss rates. The difference between the linear and non-linear τ_T calculations is only 16 %.

4. RESULTS IN THE VERTICAL PLANE

For the time structure mode, we will operate with a high current in a single bunch or in a few bunches. The τ_T will be the dominant contribution to the overall beam lifetime. Normally, one expects that strong coupling between horizontal and vertical betatron motion will increase the bunch volume and therefore increase τ_T.

The vertical vacuum chamber is restricted in several places of the ring by the undulators gaps to 15 mm (a vertical vacuum chamber half-height of 6.5 mm) in order to provide high brilliance for photon energies up to 10 keV [4].

Supposing zero vertical dispersion, all vertical betatron motion will be due to transverse coupling and thus the vertical betatron amplitude will be given by :

$$a_z\,(s^*,\delta) = \kappa^2\, a_x\,(s^*, \delta) \qquad (8)$$

The τ_T has been calcultated as a function of the coupling. In figure 5 we can see that the expected increase in τ_T saturates rapidly and falls beyond κ^2 = 80 %. This result is directly related to the vertical stay clear at undulator locations.

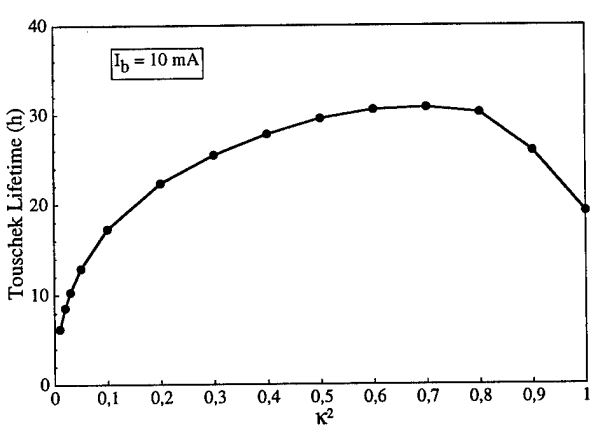

Fig. 5. Touschek lifetime as a function of the coupling.

5. EXAMPLE OF TOUSCHEK EFFECT OPTIMISED LATTICE

Starting from Touschek scattering calculation generalized to include the effects of dispersion [5], one can say that, for the motion around the chromatic closed orbit, τ_T varies approximately as :

$$\frac{1}{\tau_T} \approx \int_s^{s+C} \frac{H^b(s)}{V_B(s)}\, ds \qquad (9)$$

where b is a constant equal to values between 1 and 4 depending on the range of variation of the ξ parameter of the well-known function $C(\xi)$ appearing in the Touschek lifetime expression. H(s) and $V_B(s)$ are respectively the so-called H function (cf. 2) and the bunch volume both calculated everywhere in the ring.

Considering this interesting indication, simulations to minimize $\int H(s)\, ds$ have been undertaken keeping the emittance, tunes and betatron functions nearly unchanged. Preliminary results show an 11 % decrease in $\int H(s)\, ds$ and a corresponding 22 % increase in τ_T, consistent with (9), where in our case, b is about 2 and V_B is nearly constant.

6. CONCLUSION

We show that when the Touschek scattering occurs with large energy deviation in dispersion sections, it is necessary to consider the non-linear chromatic closed orbit as well as the variation of the optics with energy. If only the linear effects are considered (ZAP code for example), the calculations can be optimistic by a factor of 2.

In the high intensity bunch mode, the increase of the coupling between horizontal and vertical betatron motions do not give the hoped for increase in Touschek lifetime because of the limited vertical stay clear. Notice that there is no IBS effect at the nominal energy.

To increase the single bunch current threshold we prefer using a feedback system instead of increasing the vertical chromaticity in order to avoid reducing the large energy acceptance.

An interesting reflexion concerning Touschek effect lattice optimization shows that if the dispersion is distributed in such a way that the so-called H function is minimized everywhere in the machine, the Touschek lifetime can be substantially increased.

Nonetheless further work on this subject is needed as calculations done so far do not completely take into account the effects of non-linear betatron motion nor tune modulation resonances due to synchrotron oscillations.

7. ACKNOWLEDGEMENTS

We would like to mention the fruitful discussions on this subject with our colleagues of the SLS project.

8. REFERENCES

[1] M.S. Zisman et al., ZAP code.
[2] J. Payet et al., BETA code LNS version.
[3] P. Nghiem et al., this conference.
[4] J.-L. Laclare et al., this conference.
[5] J. Le Duff, LAL-RT 88-08.

SIMULATIONS OF NON-LINEAR BEAM DYNAMICS EFFECTS DUE TO AN ELECTROMAGNETIC ELLIPTICAL WIGGLER

L. Tosi, B. Diviacco and R. P. Walker, Sincrotrone Trieste, Italy
G. Wüstefeld and M. Scheer, BESSY, Berlin
S. Werin, MAX-lab, Sweden

Abstract

We present the results of extensive beam dynamic simulations that have been carried out in order to study the non-linear effects of an electromagnetic elliptical wiggler, presently under construction for ELETTRA, using different symplectic tracking methods implemented in the codes BETA and RACETRACK.

1 INTRODUCTION

A novel electromagnetic elliptical wiggler (EEW) has been designed and is currently under construction for the ELETTRA facility [1]. The device is designed in order to provide a source of circularly polarised light in the VUV/Soft X-ray region with a variable helicity up to 100 Hz switching rate. The device has a maximum vertical on-axis field of 0.5 T, a horizontal field of 0.1 T, and 15 periods of length 0.212 m.

In this report we present the results of extensive beam dynamic simulations that have been carried out in order to study the non-linear effects of the device and to optimise its performance in ELETTRA. It has already been noticed in previous simulations [2,3] that the introduction of a helical insertion device in the ELETTRA lattice may lead to significant reduction in the dynamic aperture due to the non-linear terms present in the extra field components compared to standard plane insertion devices. It was expected therefore that special care would have to be taken in the design of the pole shapes in order to assure the least impact on the beam dynamics within the mechanical and magnetic possibilities of the design. For this purpose, extensive simulations have been carried out for various pole configurations with the two codes BETA and RACETRACK. Since 3D magnetic field calculations showed that the transverse field distributions differed significantly from the standard model based on circular and hyperbolic functions [4], and also the existence of higher longitudinal harmonics, the two codes have been modified in order to include a more realistic transverse and longitudinal field distribution. Section 2 deals firstly with the field representation, while the results of the simulations are presented and compared in Section 3.

2 MODEL OF THE WIGGLER FIELD

In order to accurately model the magnetic field produced by the wiggler it has to be taken into account that due to the large period to gap ratio, the longitudinal distribution of the fields is non-sinusoidal, with strong odd harmonics present, and also that due to the unusual geometry of the poles, the transverse field distribution is quite complex (see fig. 1).

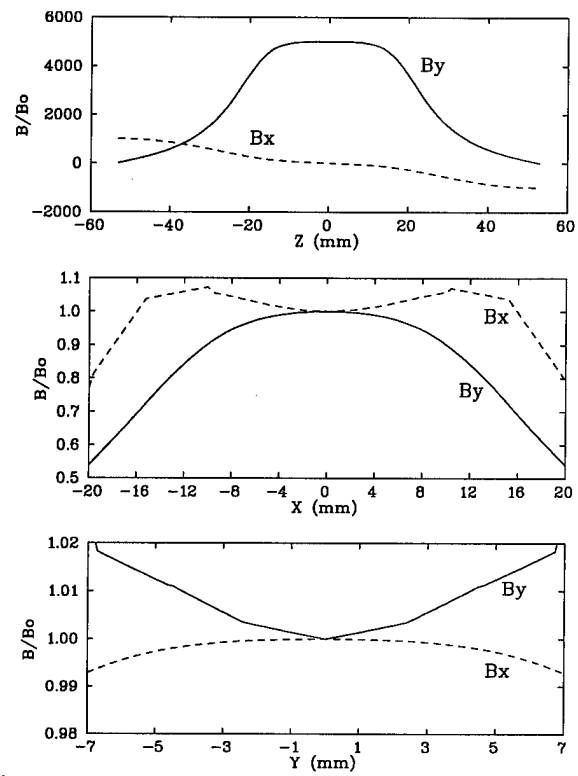

Figure 1. Field distributions along the wiggler axis (upper) and transversely in the horizontal (x) and vertical (y) directions.

A suitable description of the field can be obtained using a polynomial expansion for the off-axis field variation in the following form:

$$\phi_h = \sum_n B_{hn}\{x + a_{2hn}x^3 + b_{2hn}y^2x + a_{3hn}x^5 + b_{3hn}y^2x^3 + c_{3hn}y^4x + a_{4hn}x^7 + b_{4hn}y^2x^5 + c_{4hn}y^4x^3 + d_{4hn}y^6x\}\cos nkz$$

$$\phi_v = \sum_n B_{vn}\{y + a_{2vn}y^3 + b_{2vn}x^2y + a_{3vn}y^5 + b_{3vn}x^2y^3 + c_{3vn}x^4y + a_{4vn}y^7 + b_{4vn}x^2y^5 + c_{4vn}x^4y^3 + d_{4vn}x^6y\}\sin nkz$$

where ϕ_h and ϕ_v are the scalar potentials corresponding to the horizontal and vertical poles respectively, and $k=2\pi/\lambda 0$. The coefficients are derived by fitting the expressions above to the Fourier-analysed computed field distribution. The fit is in practice performed only in the horizontal plane, the remaining terms being derived by the following relations, imposed by Maxwell's equations :

0-7803-4376-X/98/$10.00 © 1998 IEEE

$$6a_{2v1} = k^2 - 2b_{2v1} \qquad 6a_{2v3} = 9k^2 - 2b_{2v3}$$
$$6b_{3v1} = k^2 b_{2v1} - 12c_{3v1} \qquad 6b_{3v3} = 9k^2 b_{2v3} - 12c_{3v3}$$
$$6c_{4v1} = k^2 c_{3v1} - 30d_{4v1} \qquad 6c_{4v3} = 9k^2 c_{3v3} - 30d_{4v3}$$
$$20a_{3v1} = k^2 a_{2v1} - 2b_{3v1} \qquad 20a_{3v3} = 9k^2 a_{2v3} - 2b_{3v3}$$
$$20b_{4v1} = k^2 b_{3v1} - 12c_{4v1} \qquad 20b_{4v3} = 9k^2 b_{3v3} - 12c_{4v3}$$
$$42a_{4v1} = k^2 a_{3v1} - 2b_{4v1} \qquad 42a_{4v3} = 9k^2 a_{3v3} - 2b_{4v3}$$

By comparing the fit with the actual field distribution at arbitrary positions it was concluded that sufficient accuracy was obtained using only the 1st and 3rd harmonics. In order to evaluate the effects of different pole profiles on the beam dynamics, various shapes of both the horizontal and the vertical poles have been considered. Figure 2 shows the transverse distribution of the two field components under the respective poles for different pole profiles. Not shown are the variations in the other plane, namely By(y) and Bx(x). The fits also demonstrated the different transverse variations for the 1st and 3rd harmonics, a flat variation of the total field being due to a different curvature of the 1st and 3rd harmonics.

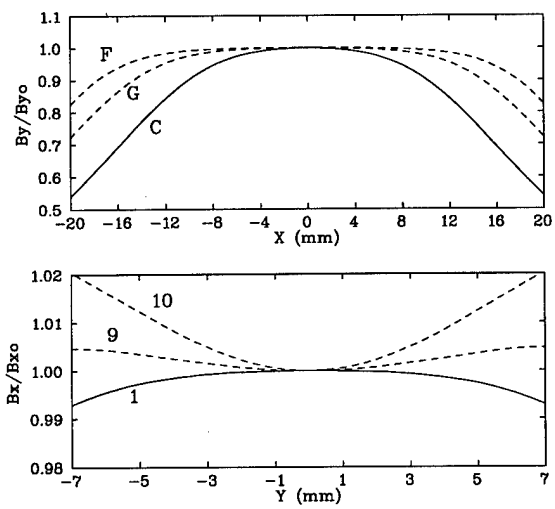

Figure 2. Field distributions due to various vertical (upper) and horizontal (lower) pole profiles.

3 BEAM DYNAMICS

New tracking routines, which take into account the polynomial expression of the field described in the previous section, have been added to the codes BETA and RACETRACK. Both integration methods implemented in the codes are symplectic up to second order [5,6]. In order to check the correct functioning of the two routines, comparisons of tracking results and phase space plots were firstly made. The results show an overall good agreement with occasional differences of 1 mm, which can be considered within the precision of the methods. During this process however the importance of setting the correct initial conditions at the entrance and at the exit of a helical insertion device emerged. In reality, insertion devices have end poles which set the particles on the

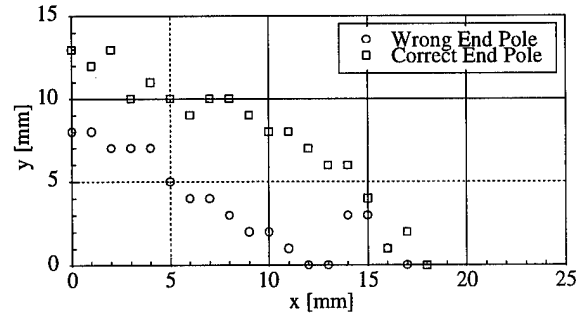

Figure 3. Comparison of tracking results with correct and incorrect treatment of the end poles.

appropriate trajectory but which however are not included in the model. In order to simulate these, both codes shifted the particle's coordinates and angles by a constant amount corresponding to the closed orbit. It was found that this procedure was not sufficient to guarantee the correct entrance and exit conditions, especially at large amplitudes due to the non-linear nature of the fields. The two codes adopted different equivalent solutions to overcome the problem. While BETA has included an end pole on either side of the device of reduced field amplitude [7], RACETRACK has adopted the solution of imposing the continuity of the conjugate momenta by adjusting properly the slope. Figure 3 shows the effect on the dynamic aperture when incorrect conditions are used. The problem of the end poles arises also in the case of a planar device, if the model takes a sine variation longitudinally.

Four particles with different initial conditions were tracked over 1000 turns and for 0.0 and ±2.5% energy deviation corresponding to the ELETTRA momentum acceptance. The linear effects of the EEW on the optics are modest, giving rise to tune shifts less than 0.01 and beta asymmetries less than 5% in both planes. In this respect, retuning of the machine to the nominal tunes of 0.3 horizontally and 0.2 vertically did not lead to any significant improvement of the dynamics.

Figure 4 illustrates the dynamic aperture investigating different pole configurations for the vertical field. The three different cases correspond to the pole shapes specified in the previous section. It can be seen that the major differences occur at small horizontal amplitudes,

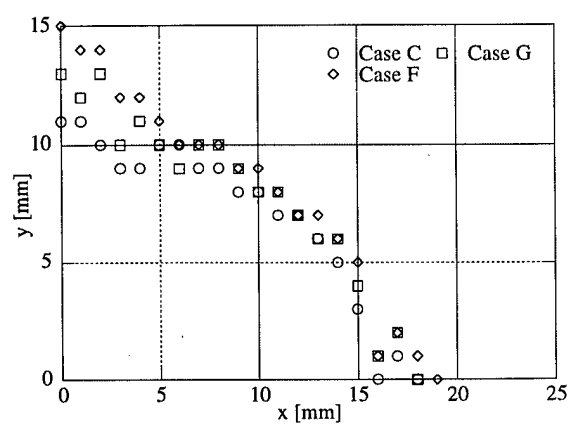

Figure 4. Comparison of dynamic apertures for various vertical pole profiles.

but with vertical amplitudes which are anyway outside the 15 mm full physical aperture of the machine. Tracking particles which were off momentum by ± 2.5% showed also no substantial differences between the three investigated cases. Thus case C, being the optimal configuration from the iron saturation point of view, was chosen as the final design for the vertical pole.

Figure 5 shows the dynamic aperture for different horizontal field configurations, using case C for the vertical poles. Here, the difference among the various cases is even less pronounced, thus Pole 1 was chosen for the final design. Figure 6 instead compares the dynamic apertures of the device with its final poles with the bare lattice when one introduces the 15 mm physical aperture of the machine at the entrance and exit of the device.

Dynamic apertures computations were also performed including all of the five plane insertion devices presently installed in ELETTRA. The result is shown in figure 7.

During the pole shape optimization, also the influence of the presence of the third harmonics was investigated by setting to zero the corresponding field amplitudes. Results showed that the dynamics are determined mainly by the first harmonic.

Another important issue which was investigated is the effect of a positioning error of the device. This was studied by creating in both planes symmetric and asymmetric bumps in the device of 1.0 mm and 0.5 mm with 0.34 mrad respectively. Even though a slight increase in the coupling was noticed, there was no substantial difference in the dynamic apertures with respect to the non-misaligned case.

4 CONCLUSION

The correct procedure for treatment of insertion device end fields in tracking routines has been determined. Simulations show that the EEW should have only a minor effect on the beam dynamics in ELETTRA.

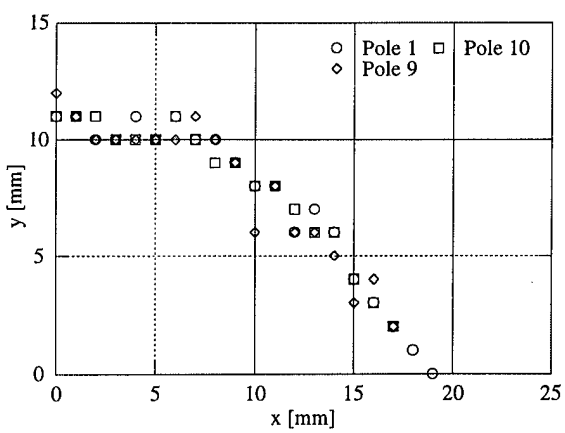

Figure 5. Comparison of dynamic apertures for various horizontal pole profiles.

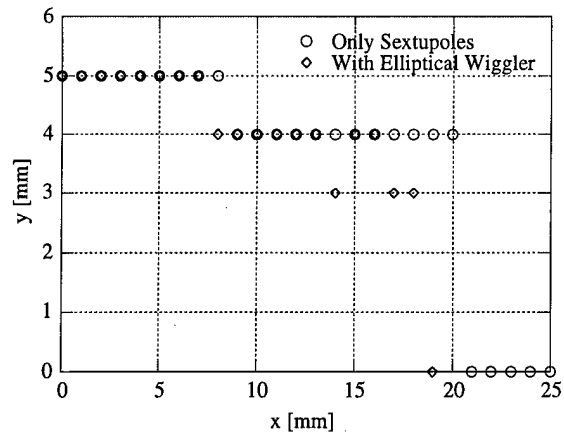

Figure 6. Dynamic aperture of the EEW including the physical aperture of the vacuum chamber.

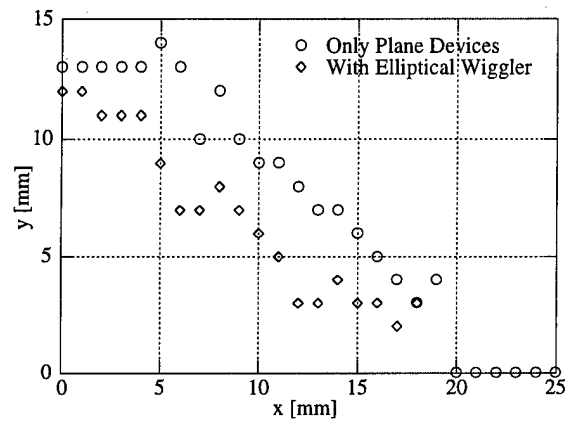

Figure 7. Comparison of dynamic aperture of the EEW with other ELETTRA insertion devices.

REFERENCES

[1] R.P. Walker et al.: `Design of an Electromagnetic Elliptical Wiggler for ELETTRA', this conference.

[2] L. Tosi et al.: 'Effect of Non-planar Undulators on Beam Dynamics in ELETTRA', Proceedings of the Particle Accelerator Conference, San Francisco, USA, 1991.

[3] C.J. Bocchetta et al.: 'Studies of the Effects of an Elliptical Wiggler in ELETTRA', Proceedings of the European Particle Accelerator Conference, Berlin, Germany, 1992.

[4] R.P. Walker: 'Main Features of Electron Motion in General Helical Fields', Sincrotrone Trieste Technical Note, ST/M-TN-89/41, 1989.

[5] M. Scheer et al.: 'Tracking Routines for Arbitrary Insertion Devices', this conference.

[6] R. Nagaoka et al.: 'An Improved Scheme for Integrating the Particle Motion through the Insertion Device in RACETRACK', Sincrotrone Trieste Internal Report, ST/M-90/6, 1990.

[7] G. Wüstefeld: 'Canonical Particle Tracking and End Pole Matching of Helical Insertion Devices', this conference.

DISPERSION IN THE PRESENCE OF STRONG TRANSVERSE WAKEFIELDS*

Ralph W. Assmann and Alex Chao
Stanford Linear Accelerator center, Stanford University, Stanford, CA 94309

Abstract

To minimize emittance growth in a long linac, it is necessary to control the wakefields by correcting the beam orbit excursions. In addition, the particle energy is made to vary along the length of the bunch to introduce a damping, known as the BNS damping, to the beam break-up effect. In this paper, we use a two-particle model to examine the relative magnitudes of the various orbit and dispersion functions involved. The results are applied to calculate the effect of a closed orbit bump and a misaligned structure. It is shown that wake-induced dispersion is an important contribution to the beam dynamics in long linacs with strong wakefields like SLC.

1 WAKE INDUCED DISPERSION (TWO-PARTICLE MODEL)

Consider a linac with uniform betatron focusing and no acceleration. Introduce an orbit kick θ at $s = 0$. The betatron equation of motion for a particle with relative energy error δ is

$$x''(s) + \frac{k_\beta^2}{1+\delta}x(s) = \frac{\theta}{1+\delta}\delta(s), \tag{1}$$

with the solution

$$x(s) = \frac{\theta}{k_\beta\sqrt{1+\delta}}\sin(\frac{k_\beta s}{\sqrt{1+\delta}}). \tag{2}$$

When $k_\beta s\delta \ll 1$, one may expand (2) in δ, i.e.

$$x(s) = x_0(s) + \eta(s)\delta + \mathcal{O}(\delta^2), \tag{3}$$

with

$$x_0(s) = \frac{\theta}{k_\beta}\sin k_\beta s$$

and the dispersion function $\eta(s) = -\frac{\theta}{2}(s\cos k_\beta s + \frac{1}{k_\beta}\sin k_\beta s)$. When $k_\beta s \gg 1$, the dispersion effect can clearly be important. When $k_\beta s\delta \ll 1$ is not satisfied, we will have to use Eq.(2) instead of Eq.(3).

We next consider a two-particle model for the kicked beam. The motion of the leading macroparticle (considered to be on-momentum) of the beam is given by $x = x_0(s)$. Let $N/2$ be the number of electrons in the leading and the trailing macroparticles, γ be the design energy Lorentz factor, W_1 be the wake function per cavity period, and L be the cavity period length. Let $y(s)$ designate the orbit deviation of the trailing macroparticle. We have

$$\begin{aligned} y''(s) + \frac{k_\beta^2}{1+\delta}y(s) &= \frac{\theta}{1+\delta}\delta(s) \\ &- \frac{Nr_0W_1}{2\gamma L(1+\delta)}\frac{\theta}{k_\beta}\sin k_\beta s, \end{aligned} \tag{4}$$

where r_0 is the classical electron radius. In Eq.(5), we have assumed the leading and the trailing macroparticles have the same design betatron frequency. This is the case when there is no BNS damping. The case with BNS damping is to be treated later.

The solution to Eq.(5) is

$$\begin{aligned} y(s) = x(s) - \frac{\Upsilon\theta}{k_\beta L_0}\frac{2}{k_\beta\delta}\cdot \\ \left(\sin k_\beta s - \sqrt{1+\delta}\sin\frac{k_\beta s}{\sqrt{1+\delta}}\right) \end{aligned} \tag{5}$$

where we have defined a dimensionless parameter

$$\Upsilon = -\frac{Nr_0W_1L_0}{4\gamma Lk_\beta}. \tag{6}$$

The first term on the right hand side of Eq.(6) is the direct response of the trailing macroparticle to the orbital kick and is the same as Eq.(2). The second term is the driven response to the wakefield.

When $k_\beta s\delta \ll 1$, we can expand (6) in δ to obtain

$$\begin{aligned} y(s) &= y_0(s) + [\eta(s) + \xi(s)]\delta + \mathcal{O}(\delta^2) \\ y_0(s) &= x_0(s) - \frac{\Upsilon\theta}{k_\beta L_0}(s\cos k_\beta s - \frac{1}{k_\beta}\sin k_\beta s) \\ \xi(s) &= -\frac{\Upsilon\theta}{4k_\beta L_0}\cdot \\ &\quad \left(k_\beta s^2\sin k_\beta s - s\cos k_\beta s + \frac{1}{k_\beta}\sin k_\beta s\right) \end{aligned} \tag{7}$$

where $y_0(s)$ is the usual beam break-up response to wake fields, and $\xi(s)$ is the wake-induced dispersion function.

Note that $\xi(s)$ is doubly resonantly driven as evidenced by its containing a term proportional to s^2. When Υ and $k_\beta L_0$ are both $\gg 1$, the ratio among the four quantities is

$$\xi\delta : y_0 : \eta\delta : x_0 \approx \frac{\Upsilon k_\beta L_0\delta}{4} : \Upsilon : \frac{k_\beta L_0\delta}{2} : 1. \tag{8}$$

Comparing ξ with η near the end of linac, the magnitude of ξ is larger by a factor of $\Upsilon/2$. This indicates the wake-induced dispersion may be an important consideration in a long linac such as the SLC or the NLC.

* Work supported by the Department of Energy, contract DE-AC03-76SF00515.

In the above analysis, acceleration has been ignored. When acceleration is taken into account, we need to replace the expression (7) by

$$\Upsilon = -\frac{N r_0 W_1 L_0}{4\gamma_f L k_\beta} \ln \frac{\gamma_f}{\gamma_i}, \tag{9}$$

where $\gamma_{i,f}$ refer to the initial and final beam energies of the linac.

For the SLC, if we take $N = 5 \times 10^{10}$, $W_1 = -0.7$ cm^{-2}, $L_0 = 3$ km, $L = 3.5$ cm, and $k_\beta = 0.06$ m^{-1}, and let the beam be accelerated from 1 GeV to 50 GeV, we find $\Upsilon = 14$. If we further take $\delta = 0.5\%$, we find $\xi\delta : y_0 : \eta\delta : x_0 \approx 3.1 : 14 : 0.45 : 1$.

One may ask what happens when a BNS damping is imposed. In this case, the leading macroparticle sees a focusing gradient k_β, therefore $x(s), x_0(s)$ and $\eta(s)$ remain given by Eqs.(2-4). However, the trailing particles see a stronger focusing with

$$y''(s) + \frac{(k_\beta + \Delta k_\beta)^2}{1+\delta} y(s) = \frac{\theta}{1+\delta}\delta(s) - \frac{N r_0 W_1}{2\gamma L(1+\delta)} \frac{\theta}{k_\beta} \sin k_\beta s \tag{10}$$

which has the solution

$$y(s) = \frac{\theta}{(k_\beta + \Delta k_\beta)\sqrt{1+\delta}} \sin\left(\frac{k_\beta s + \Delta k_\beta s}{\sqrt{1+\delta}}\right) - \frac{2\Upsilon\theta}{k_\beta L_0} \frac{1}{1+\delta-(1+\frac{\Delta k_\beta}{k_\beta})^2} \left[\frac{1}{k_\beta}\sin k_\beta s - \frac{\sqrt{1+\delta}}{k_\beta + \Delta k_\beta} \sin\left(\frac{k_\beta s + \Delta k_\beta s}{\sqrt{1+\delta}}\right)\right]. \tag{11}$$

The BNS condition is to choose Δk_β such that

$$(1 + \frac{\Delta k_\beta}{k_\beta})^2 = 1 + \frac{2\Upsilon}{k_\beta L_0}. \tag{12}$$

When (13) is satisfied, the orbit of a trailing particle whose $\delta = 0$ is identical to that of the leading macroparticle, i.e. $y(s, \delta = 0) = x_0(s)$, thus minimizing the beam emittance growth due to wake fields. The question now is what happens to the wake-induced dispersion effect. With the BNS condition (13), Eq.(12) reads

$$y(s) = x_0(s) + \frac{\theta\delta}{k_\beta(\delta - \frac{2\Upsilon}{k_\beta L_0})} \left[\sqrt{\frac{1+\frac{2\Upsilon}{k_\beta L_0}}{1+\delta}} \sin\left(k_\beta s \sqrt{\frac{1+\frac{2\Upsilon}{k_\beta L_0}}{1+\delta}}\right) - \sin k_\beta s\right]. \tag{13}$$

One sees a resonance response when $\delta = \frac{2\Upsilon}{k_\beta L_0}$. This is because then the tail particle has a betatron focusing strength $\frac{k_\beta + \Delta k_\beta}{\sqrt{1+\delta}} = k_\beta$.

Typically we have $\frac{\Upsilon}{k_\beta L_0} \ll 1$ (and thus $\Delta k_\beta \ll k_\beta$) and $\delta \ll 1$. If we further have the condition $k_\beta s\delta \ll 1$ and $\delta \ll \frac{2\Upsilon}{k_\beta L_0}$, then we can write

$$y(s) \approx x_0(s) + \xi(s)\delta, \tag{14}$$

where

$$\xi = -\frac{\theta L_0}{2\Upsilon}[\sin(k_\beta s + \frac{\Upsilon}{L_0}s) - \sin k_\beta s]. \tag{15}$$

This is a very small dispersion. We have, instead of Eq.(9),

$$\xi\delta : y : \eta\delta : x = \frac{k_\beta L_0 \delta}{2\Upsilon} : 1 : \frac{k_\beta L_0 \delta}{2} : 1. \tag{16}$$

Note that $y(s)$ in (15) does not contain a term $\eta(s)\delta$ as Eq.(8) did. Note also that inspite of BNS, ξ is not identical to η, although y is made identical to x by the BNS condition. There is therefore a dispersive mismatch between the head and the tail of the bunch due to a mismatch between $\xi\delta$ and $\eta\delta$. The increase in the beam emittance is

$$\Delta\epsilon = \frac{k_\beta}{2}(\frac{1}{2}\theta L_0 \sigma_\delta)^2 \tag{17}$$

In order for this effect to be negligible, we need the condition, even when the BNS condition is perfectly satisfied,

$$\theta L_0 \sigma_\delta \ll \sigma_\beta, \tag{18}$$

where σ_β is the betatron beam size.

2 CLOSED π BUMPS

So far, we have considered the case of an uncorrected betatron oscillation, induced by a single kick θ. We now study a closed π-bump that is implemented with two kicks θ that are located at $s = 0$ and $s = \pi/k_\beta$. The orbit and dispersion functions for the second kick are obtained by substituting s with $s - \pi/k_\beta$. For example, $x_0(s) \to x_0'(s - \pi/k_\beta)$.

The orbit function $\tilde{x}_0$ downstream of the π-bump is just the sum of x_0 and x_0'. With Eq.(3) we obtain immediately $\tilde{x}_0 = 0$, indicating that the bump is closed. Doing the same excercise for the tail orbit and the dispersion functions we obtain from Eqs.(4) and (8):

$$\begin{aligned} \tilde{\eta}(s) &= \eta(s) + \eta(s - \pi/k_\beta) = -\frac{\theta\pi}{2k_\beta}\cos(k_\beta s) \\ \tilde{y}_0(s) &= -\frac{\pi\Upsilon\theta}{k_\beta^2 L_0}\cos k_\beta s \\ \tilde{\xi}(s) &= -\frac{\pi\Upsilon\theta}{4k_\beta^2 L_0}[(2k_\beta s - \pi)\sin k_\beta s - \cos k_\beta s]. \end{aligned} \tag{19}$$

We obtain the well known result that a closed π-bump is not closed for the dispersion η, and generates a dispersion oscillation with constant amplitude. The π-bump is also not closed for the tail orbit. If the BNS condition is satisfied the bump is closed for both head and tail particle. The results are important because the orbit after steering can be described by a superposition of π-bumps (90 degree lattice). The wake kick during the orbit bump, together with the energy offset of the tail particle, gives rise to a wake-induced dispersion which increases linearly with s.

3 DISPERSION FROM A MISALIGNED STRUCTURE

The kick θ above applied both to head and tail particle, as from quadrupole offsets or dipole correctors. In the case of a structure offset, the head induces a dipole wakefield that deflects the tail particle by $\hat{\theta}$. The head orbit is not disturbed and we can write:

$$x_0(s) = 0 \quad , \quad y_0(s) = \frac{\hat{\theta}}{k_\beta} \sin k_\beta s. \tag{20}$$

Orbit correction (without BPM errors) requires that the sum of head and tail trajectory is zero ($x_0(s) + y_0(s) = 0$). This is achieved by applying a kick $\theta = -\hat{\theta}/2$ to both particles. Assuming BNS and $\delta = 0$ we get:

$$x_0(s) = -y_0(s) = \frac{\theta/2}{k_\beta} \sin k_\beta s. \tag{21}$$

The centroid trajectory is zero as required, but head and tail particle perform uncorrected betatron oscillations. The centroid dispersion η_{tot} is:

$$\begin{aligned} \eta_{tot} &= -\left(\frac{\hat{\theta}}{2} + \frac{\theta}{2}\right)(s \cos k_\beta s + \frac{1}{k_\beta} \sin k_\beta s) \\ &- \frac{\theta L_0}{2\Upsilon}[\sin(k_\beta s + \frac{\Upsilon}{L_0} s) - \sin k_\beta s]. \end{aligned} \tag{22}$$

Because the tail dispersion ξ that is induced by the "corrector" kick θ is small (see Eqs.(17)), we can neglect it here. With $\theta = -\hat{\theta}/2$ we obtain:

$$\eta_{tot} \approx -\frac{\hat{\theta}}{4}(s \cos k_\beta s + \frac{1}{k_\beta} \sin k_\beta s) \tag{23}$$

The centroid dispersion η_{tot} that is generated by a misaligned structure grows resonantly with s and therefore becomes large for long linacs.

The orbit due to a misaligned quadrupole and after trajectory correction can be described by a π-bump through the quadrupole center (90 degree lattice). The resulting dispersion downstream of the closed bump was given in Eq.(20). Comparing this to Eq.(24), we see that the dispersion generated from a misaligned structure can become larger than the dispersion from a misaligned quadrupole after orbit correction. The ratio between them is of the order of $(\hat{\theta}/\theta) \cdot (k_\beta L_0/2\pi)$ at the end of the linac. Due to its resonant growth in s, dispersion from a misaligned structure becomes larger than the one from a misaligned quadrupole though $\hat{\theta} < \theta$ for the same misalignment. The importance of wake-induced dispersion was indeed shown in SLC simulations done with the computer program LIAR [1]. Figure 1 shows that wakefield generated dispersion in the SLC becomes larger than quadrupole generated dispersion for large bunch charges.

4 CONCLUSION

The orbit and dispersion functions in the presence of wakefields have been calculated. It was shown that the dispersion effect of an orbit kick is made much worse by the presence of the wakefields in the absence of BNS damping. The effect of this large wake-induced dispersion is found to be suppressed but not removed when BNS condition is introduced. The results were used to evaluate the effects of a closed orbit π-bump and a misaligned structure. The dispersion generated from a structure offset was shown to grow resonantly with s *after* trajectory correction. Therefore, wakefield generated dispersion can become much larger than the dispersion from misaligned quadrupoles. Simulations for the SLC linac confirmed this behavior [2].

As centroid dispersion with strong wakefields is mainly generated by structure offsets, a dispersion measurement can be used to determine the structure errors. We can envision new and improved algorithms to optimize emittance in linacs with strong wakefields. For example, emittance might be optimized by empirically adjusting structure movers so as to minimize the measured centroid dispersion.

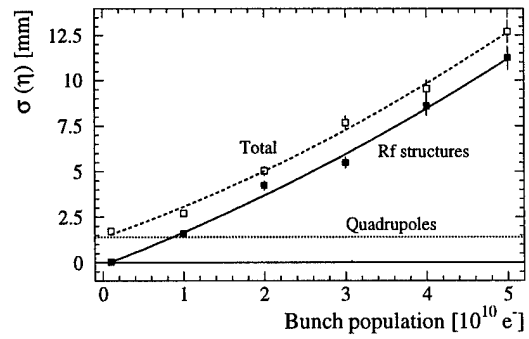

Figure 1: Simulated RMS dispersion as a function of bunch population at the end of the SLC linac and after orbit correction. The dotted line shows the dispersion without wakefields. The points indicate simulation results with wakefields. The filled points show a case where only the RF structures were misaligned. Finally, the open points show the total dispersion, if quadrupole and BPM errors are included. It is seen that centroid dispersion is mainly generated by structure offsets for the SLC at high bunch current. Even with a flat centroid trajectory (filled points), the centroid dispersion can become large.

5 ACKNOWLEDGEMENTS

We would like to thank Robert Siemann, Ron Ruth and Tor Raubenheimer for stimulating discussions.

6 REFERENCES

[1] R. Assmann et al, "LIAR - A Computer Program for the Modeling and Simulation of High Performance Linacs". SLAC/AP-103.

[2] R. Assmann et al., "Dispersion measurements and studies for the SLC linac". To be published.

REVIEW OF IMAGE EFFECTS FOR PARTICLE BEAMS IN CYLINDRICAL PIPES

C. K. Allen†, Techno-Sciences, Inc., 10001 Derekwood Lane, Suite 204, Lanham, MD 20706 and
M. Reiser††, Institute for Plasma Research, University of Maryland, College Park, MD 20742

Abstract

The effects of a perfectly conducting beam pipe are examined for both a centered continuous beam and a centered bunched beam. A set of coupled, ordinary differential equations is derived for each case. These equations describe the dynamics of the rms beam envelopes along the design trajectory. Finally, an example application is presented for the bunched beam situation.

1 INTRODUCTION

For some time we have been investigating the image effects from a cylindrical beam pipe on beam dynamics, in particular for space-charge dominated beams [1,2,3]. By image effects we mean, of course, the action of the charges induced on the pipe from the beam's space charge. Here we review the most useful conclusions of these investigations. Specifically, sets of ordinary differential equations are presented which describe the dynamics of the rms beam envelopes. These results are essentially the continuation of work initiated by Sacherer in the early 1970's [4].

1.1 Ellipsoidal Symmetry and Equivalent Beams

We restrict our attention to particle beams having elliptical symmetry for continuous beams and ellipsoidal symmetry for bunched beams. The results are applicable to quadrupole focusing systems for the continuous beam case (and, of course, solenoidal systems). However, we further restrict our attention to the axisymmetric situation in the bunched beam case. Since we are primarily interested in the longitudinal effects, this simplifies the analysis so that most of the results can be expressed analytically in terms of elementary functions (otherwise, elliptical integrals would appear in the final system). The longitudinal results still apply in an average sense to bunched beams having quadrupole symmetry.

All the results presented here are expressed in terms of an equivalent uniform beam. As Sacherer discovered, the statistical dynamics of the beam (i.e., the rms envelopes) are only loosely coupled, if at all, to the actual distribution of the beam. Therefore, we choose our model to be the uniform beam, since it has well-defined envelopes (unlike a gaussian or a thermal distribution). The equivalent beam principle tells us that the actual beam may be modeled by a uniform beam so long as both beams have the same second spatial moments and rms emittances. The differential equations given here describe the beam envelopes of the equivalent uniform beam.

1.2 Further Limitions

The major short-coming of the analysis is that is does not describe a self-consistent situation. Specifically, our model for the self-fields of the beam does not consistently couple with the beam dynamics. The net result is that there is no model for rms emittance growth in the beam. However, in the space-charge dominated situation this drawback is of little concern. In this case the beam dynamics are dominated by the self-fields of the beam and thermal effects play only a minor role. Moreover, these beams tend toward a uniform distribution and it has beam shown that in the bunched beam case that the equilibrium (stationary) distribution is closely approximated by an ellipsoid [5].

1.3 Moment Equations

The general idea of the analysis is to take moments of the equations of motion with respect to the particle beam distribution. The Vlasov equation then allows the time derivative operator and the moment operator to commute. The net result is a set of coupled, ordinary differential equations involving the moments. We concentrate on the second order moments. Letting $\langle\cdot\rangle$ denote the moment operator with respect to the particle beam distribution, we find the following [6]:

$$\langle x^2\rangle'' - \frac{[\langle x^2\rangle']^2}{2\langle x^2\rangle} + \frac{2k_x(\zeta)}{\gamma m v^2}\langle x^2\rangle - \frac{2q}{\gamma^3 m v^2}\langle xE_x\rangle - \frac{2\tilde{\epsilon}_x^{\,2}}{\langle x^2\rangle} = 0,$$
$$\langle y^2\rangle'' - \frac{[\langle y^2\rangle']^2}{2\langle y^2\rangle} + \frac{2k_y(\zeta)}{\gamma m v^2}\langle y^2\rangle - \frac{2q}{\gamma^3 m v^2}\langle yE_y\rangle - \frac{2\tilde{\epsilon}_y^{\,2}}{\langle y^2\rangle} = 0,$$
$$\langle z^2\rangle'' - \frac{[\langle z^2\rangle']^2}{2\langle z^2\rangle} + \frac{2k_z(\zeta)}{\gamma m v^2}\langle z^2\rangle - \frac{2q}{\gamma m v^2}\langle zE_z\rangle - \frac{2\tilde{\epsilon}_z^{\,2}}{\langle z^2\rangle} = 0.$$

where ζ is the path length along the design trajectory, the prime indicates differentiation with respect to ζ, γ is the relativistic factor, v is the bunch velocity (assumed constant), q and m are the particles' charge and mass, respectively, the $k_\alpha(\zeta)$'s are the "spring constants" of the focusing system, the $\tilde{\epsilon}_\alpha$'s are the rms emittances, and the E_α are the self electric fields. In the above system we have assumed that the individual magnetic self-fields in the beam frame are negligible but the collective magnetic field is not. Our task is now consigned to the determination of the moments $\langle\alpha E_\alpha\rangle$.

2 CONTINUOUS BEAMS

Here we assume that the beam is continuous along the

†email: cka@glue.umd.edu
††email: mreiser@glue.umd.edu

0-7803-4376-X/98 /$10.00 © 1998 IEEE

design trajectory and that the ζ variations are slow enough to allow for an accurate 2D transverse plane analysis. To find the moment $\langle xE_x\rangle$ with images we employed a Green's function technique. By expanding Green's function in a trigonometric series (in polar coordinates), we can identify the self-field terms corresponding to the induced (image) charges on the beam pipe. Taking the moments of these fields we get [2]

$$\langle xE_x\rangle = \frac{Q}{4\pi\epsilon_0}\left[\frac{\langle x^2\rangle^{1/2}}{\langle x^2\rangle^{1/2}+\langle y^2\rangle^{1/2}} + \frac{2\langle x^2\rangle}{b^4}\left(\langle x^2\rangle - \langle y^2\rangle\right)\right] + O\left(\frac{\langle x^2\rangle^2}{b^8}\right),$$

where b is the radius of the beam pipe, Q is the charge per cross-section, and $O(\cdot)$ indicates the standard order notation. The first term was originally calculated by Sacherer and is the free-space self-field contribution. The second term represents the contribution due to the induced charges from the distribution's quadrupole moment. The last term is meant to say that the image forces due to the higher order moments of the charge distribution (octupole moments and up) scale as $\langle x^4\rangle^2/b^8$, etc. Note that the above expression is independent of the distribution, this condition leads to the notion of equivalent beams.

Substituting the above equation and an analogous one for the y direction into the moment equations includes the lowest order effects from images. Translating the resulting moment equations into the equations for the equivalent uniform beam yields the result

$$X'' + \kappa_x(\zeta)X - \frac{2K}{X+Y} - \frac{\epsilon_x^2}{X^3} - \frac{K}{4b^4}(X^3 - XY^2) = 0,$$
$$Y'' + \kappa_y(\zeta)Y - \frac{2K}{X+Y} - \frac{\epsilon_y^2}{Y^3} - \frac{K}{4b^4}(Y^3 - YX^2) = 0,$$

where $X(\zeta)$ and $Y(\zeta)$ are the beam envelopes, the $\kappa_\alpha(z)=k_\alpha(z)/(\gamma mv^2)$ are the focusing functions, and $K=qI/(2\pi\epsilon_0\gamma mv^3)$ is the generalized beam perveance [7] (I being the beam current). The quantities ϵ_x and ϵ_y are the effective emittances of the beam given by $4\tilde{\epsilon}_x$ and $4\tilde{\epsilon}_y$, respectively. These equations are recognized as the standard KV coupled-envelope equations with the addition of a term (for each equation) accounting for the dominant image effects. Since the beam is centered and has elliptical symmetry, $\langle x^3\rangle$ is zero and the next image term will be an octupole term.

One may see that the image effects do not play a large role in the beam dynamics. However, for beams with large eccentricities we have seen this role to be significant. Matching sections, overall, will probably be more susceptible to image effects since the beam envelopes tend to make larger excursions through them.

3 BUNCHED BEAMS

As mentioned in the introduction we restrict our attention to the axisymmetric case and use cylindrical coordinates (r,z) where $r^2=x^2+y^2$. Therefore, the bulk of the analysis is the determination of the moments $\langle rE_r\rangle$ and $\langle zE_z\rangle$. Although for the free-space situation these moments may be determined analytically in terms of elementary functions, they are not simple expressions. Therefore, we simply present the results of the analysis for the equivalent uniform ellipsoid. The interested reader is referred to [3] for the details. We have

$$R'' + \kappa_r(\zeta)R - \frac{3K}{4\sqrt{5}}\frac{1}{R^2}W_r\left(\frac{Z}{\sqrt{2}R}\right) - \frac{45K}{2}\frac{R\cdot A_f(R,Z)}{(Z^2-R^2)^{3/2}} - \frac{\epsilon_r^2}{R^3} = 0$$
$$Z'' + \kappa_z(\zeta)Z - \frac{3\gamma^2K}{2}\frac{1}{Z^2}W_z\left(\frac{Z}{\sqrt{2}R}\right) + \frac{45\gamma^2K}{2}\frac{Z\cdot A_f(R,Z)}{(Z^2-R^2)^{3/2}} - \frac{\epsilon_z^2}{Z^3} = 0$$

where $R(\zeta)$ and $Z(\zeta)$ are the beam envelopes, and ϵ_r and ϵ_z are the effective emittances given by $5/2\tilde{\epsilon}_r$ and $5\tilde{\epsilon}_z$, respectively. The functions W_r and W_z come from the free-space self-fields and the function A_f represents the image field effects on the dynamics. This function depends upon the actual distribution profile of the particle beam, indicated by the label f. The function $A_f(R,Z)$ actually has a simpler representation as given below.

$$A_f(R,Z) \equiv \begin{cases} A_f\left(\dfrac{b}{\sqrt{Z^2-R^2}}\right) & \text{for } Z>R, \\ 0 & \text{for } Z<R, \end{cases}$$

(The zero value for A_f comes from the fact that image effects are negligible whenever $Z<R$.) Thus, we see that A_f really depends upon only one parameter. The graphs of A_f for several different distributions are shown in Fig. 2. The expression for W_r and W_z are given below.

$$W_r(s) \equiv \begin{cases} \dfrac{1}{2}\dfrac{1}{(\frac{1}{2}-s^2)^{3/2}}\arctan\dfrac{\sqrt{\frac{1}{2}-s^2}}{s} - \dfrac{s}{\frac{1}{2}-s^2} & \text{for } s\in[0,\tfrac{1}{\sqrt{2}}), \\ \dfrac{s}{s^2-\frac{1}{2}} - \dfrac{1}{2}\dfrac{1}{(s^2-\frac{1}{2})^{3/2}}\operatorname{arctanh}\dfrac{\sqrt{s^2-\frac{1}{2}}}{s} & \text{for } s\in(\tfrac{1}{\sqrt{2}},\infty), \end{cases}$$

and

$$W_z(s) \equiv \begin{cases} \dfrac{s^2}{\frac{1}{2}-s^2} - \dfrac{s^3}{(\frac{1}{2}-s^2)^{3/2}}\arctan\dfrac{\sqrt{\frac{1}{2}-s^2}}{s} & \text{for } s\in[0,\tfrac{1}{\sqrt{2}}), \\ \dfrac{s^3}{(s^2-\frac{1}{2})^{3/2}}\operatorname{arctanh}\dfrac{\sqrt{s^2-\frac{1}{2}}}{s} - \dfrac{s^2}{s^2-\frac{1}{2}} & \text{for } s\in(\tfrac{1}{\sqrt{2}},\infty). \end{cases}$$

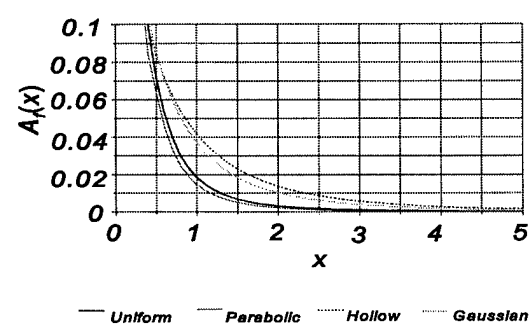

Figure 1: Function $A_f(x)$ for different distributions

In the space-charge dominated situation the uniform distribution is of primary importance. The expression for A_f in this case is given below

$$A_f(x) = \int_{-\infty}^{+\infty} \frac{K_0(|\omega| x)}{I_0(\omega x)} \left(\frac{3\cos\omega}{\omega^2} - \frac{3\operatorname{sinc}\omega}{\omega^2} + \operatorname{sinc}\omega \right) \left(\frac{\cos\omega}{\omega^2} - \frac{\operatorname{sinc}\omega}{\omega^2} \right) d\omega .$$

This expression may be integrated numerically to form a table of values for $A_f(x)$ (for interpolation). Once done the differential system may be integrated using standard numerical techniques. We may also express in terms of an infinite series of Bessel functions

$$\begin{aligned} A_f(x) &= -\frac{61}{450}\pi - \frac{\pi}{15}\ln\left(\frac{x}{4}\right) \\ &+ \sum_{n=1}^{\infty} \frac{2\pi}{\alpha_n^2 J_1^2(\alpha_n)} \left(\frac{x}{\alpha_n} + \frac{x^2}{\alpha_n^2} \right) \\ &\cdot \left(\frac{x}{\alpha_n}\sinh\frac{\alpha_n}{x} - \frac{3x^2}{\alpha_n^2}\cosh\frac{\alpha_n}{x} + \frac{3x^3}{\alpha_n^3}\sinh\frac{\alpha_n}{x} \right) e^{-\frac{\alpha_n}{x}} . \end{aligned}$$

This expression is convenient for asymptotic analysis.

3.1 A Simple Example

To illustrate the utility of these results we have simulated a simple transport system for bunched particle beams. The transport system has uniform focusing in the radial direction and periodic focusing in the longitudinal direction. The focusing functions for the z direction is shown in Fig. 2a. We have used a "hard-edge" function for $\kappa_z(\zeta)$. The period of $\kappa_z(\zeta)$ is 25cm, the pulse length is 5cm, with maximum value 200m^{-2}. The constant value of $\kappa_r(\zeta)$ is 100m^{-2}. The beam parameters are given as follows: K=0.01, ϵ_r=5×10^{-5}m-rad, ϵ_z=2×10^{-5}m-rad, and γ=1.

The matched beam solution in free space is shown in Fig. 2b while the matched beam solution including a pipe with radius b=5cm is shown in Fig. 2c. In both situations the top curves is the Z envelope. Obviously, the pipe has a substantial effect on the beam dynamics in this case. Note the coupling between the radial and longitudinal motion. Both planes oscillate synchronously, in phase with the longitudinal envelope equation, as they travel down the beam axis.

4 CONCLUSIONS

In the continuous beam case the image effects are relatively minor but can become a factor if the beam undergoes extreme eccentricities . It would seem to be sound policy to design systems which minimizes image effects and the extended KV equations offer a simple formula to analytically determine when they may become troublesome.

In the bunched beam case image effects become unavoidable whenever $Z>R$. The designer must account for these effects in beam transport systems. The differential equations presented herein provide a way to simulate bunch behavior, at least in the space-charge dominated regime.

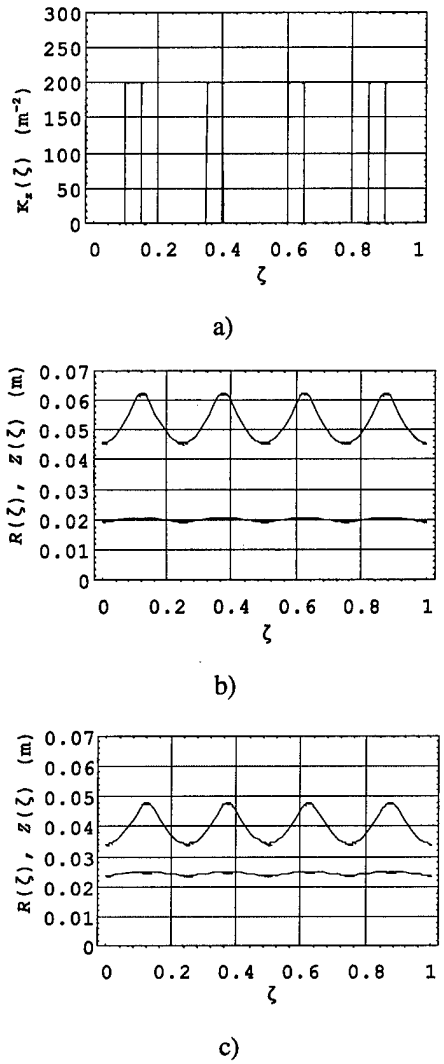

Figure 2: Bunched beam example

5 REFERENCES

[1] C.K. Allen, N. Brown, and M. Reiser, "Image Effects for Bunched Beams in Axisymmetric Systems", *Particle Accelerators*, Vol. 45 (1994), pp. 149-165.

[2] C.K. Allen and M. Reiser, "Image Effects of Cylindrical Pipes on Continuous Beams", *Phys. Rev. E*, Vol. 54, No. 3 (1996), pp. 2884-2888.

[3] C.K. Allen and M. Reiser, "Bunched Beam Envelope Equations Including Images from a Cylindrical Pipe", *Phys. Rev. E*, (to be published in Vol. 55, No. 6, 1997).

[4] F.R. Sacherer, "RMS Envelope Equations with Space Charge", *IEEE Trans. Nucl. Sci.*, Vol. NS-18 (1971), p. 1106.

[5] C.K. Allen and M. Reiser, "Zero-Temperature Equilibrium for Bunched Beams", *Particle Accelerators*, Vol. 48 (1995), pp. 193 -211.

[6] C.K. Allen, "Image Effects and Optimal Control of Space-Charge Dominated Particle Beams", Ph.D. dissertation, University of Maryland, 1996, Chapt. 1.

[7] For a description of this parameter see M. Reiser, *Theory and Design of Charged Particle Beams* (Wiley, 1994), pp. 197, 257.

A MULTIMEDIA TUTORIAL FOR CHARGED-PARTICLE DYNAMICS

Richard R. Silbar, WhistleSoft, Inc., 168 Dos Brazos, Los Alamos, NM 87544
E-Mail: silbar@whistlesoft.com; Web Page: http://www.whistlesoft.com/~silbar/

Abstract

We are developing a computer-based tutorial for charged-particle beam optics. The tutorial, "*Accelerators and Beams*," will be delivered on Macintosh and Windows platforms. It uses multimedia techniques to enhance the student's rate of learning and length of retention of the material. As such, it integrates our interactive On-Screen Laboratories™ with hypertext, line drawings, photographs, animation, video, and sound. We are targeting a broad audience from technicians to graduate students in science and engineering. There will be both an academic version and specialized versions for companies that have particular training needs. The tutorial content is about equivalent to a one-semester course at the upper undergraduate level. At this time we have about a third of the material available in prototype form.

1 INTRODUCTION

In late 1993 the DOE solicited Small Business Innovative Research (SBIR) proposals for a "novel apparatus for teaching beam optics." WhistleSoft, Inc., then a newly-formed company in Los Alamos, NM, responded with a proposal to develop a self-paced, interactive multimedia tutorial on the subject.

We were awarded a grant for such a project, now entitled "*Accelerators and Beams*," and have since moved into Phase II of the project. Since beginning Phase II we have been authoring the tutorial directly for both Windows and Macintosh computers. The first piece of the tutorial, *Vectors*, will be published this summer. The remaining pieces of the course will be completed and published over the next year.

This paper reports our progress on this ambitious project and gives of flavor of what the final tutorial will look like.

2 TUTORIAL CONTENT

The content of the course is roughly equivalent to a three-hour semester course at a university, although our intended target audience is broader than just upper-undergraduate university audiences. An important feature is the ability of the student to choose to work at a comfortable level of detail. We indicate these levels – "Introductory," "Intermediate," and "Advanced" – by a color-coded background, but an alternative labeling could just as well be "Technician," "Junior Engineer," and "Physicist." The presentation ranges accordingly from one which is mostly text and graphics to one which is mathematical and abstract. We have developed materials at each of these levels. Most of our effort so far has been at the Introductory Level, since it is more difficult to shape the material at this level into a form appropriate for student consumption.

The tutorial has twelve content modules:

1. Overview (an "Overture")
2. Forces, Electricity & Magnetism
3. Motion in a Magnetic Field
4. Focussing Elements, I
5. Beams, Beam Sizes, Phase Space
6. Matrix Beam Optics
7. DC Acceleration
8. Focussing Elements, II
9. Periodic Transport
10. Space Charge
11. Radiofrequency Cavities and Linacs
12. Using Professional Design Software

The difficulty of the material obviously increases as one gets into the later modules, but the goal is to always have something accessible at the Introductory Level throughout the tutorial.

In addition to these twelve content modules, we also have three "refresher modules" on topics that the student might want to brush up on:

A. Vectors
B. Matrices
C. Special Relativity

In a sense these modules are like appendices in a textbook.

At this point in time we have nearly complete prototypes of three of the modules (Topics 2, 3, and 5). The first refresher module, *Vectors*, has been scheduled for publication by Physics Academic Software in July 1997. We will describe the content of these modules below.

0-7803-4376-X/98/$10.00 © 1998 IEEE

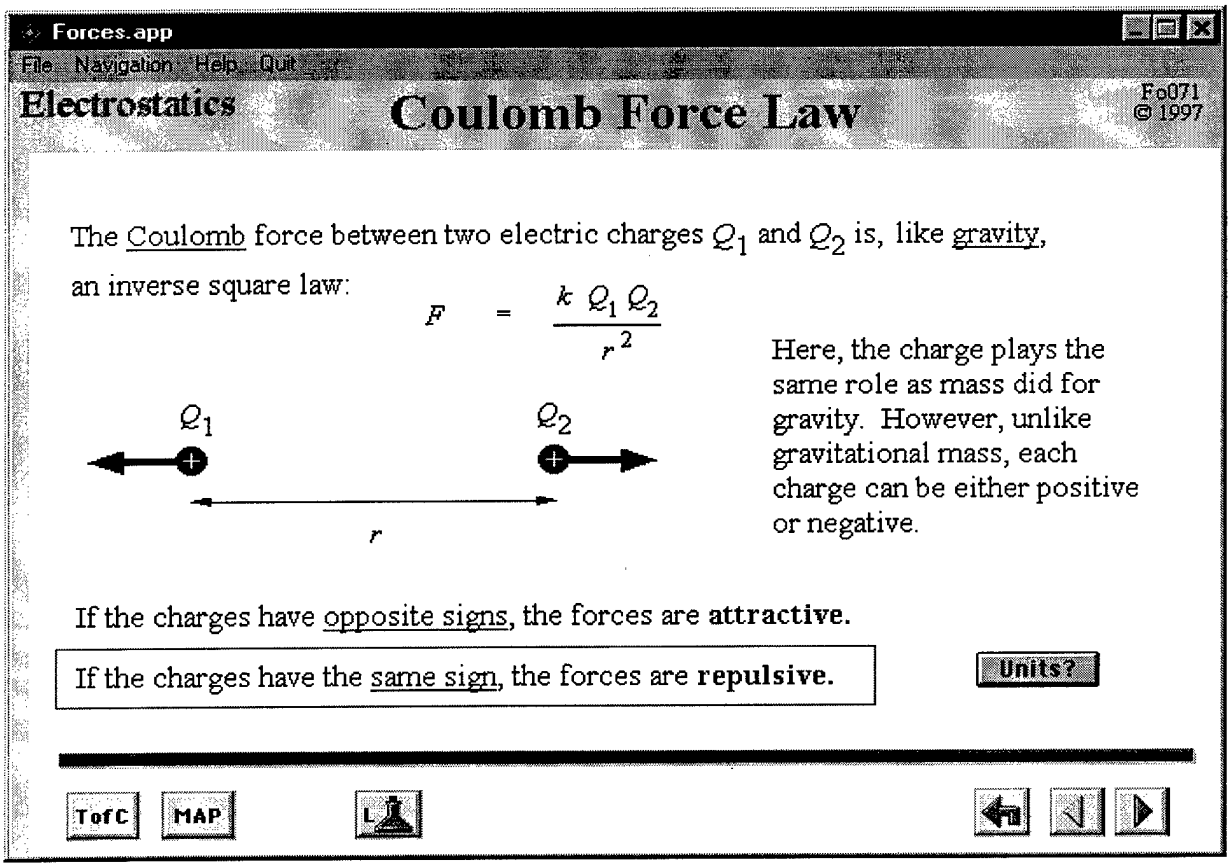

Figure 1. A typical page from *Forces* module.

3 THE PRODUCTION TEAM

A multimedia project necessarily involves a wide variety of talents. WhistleSoft is fortunate to be leading a very capable team. The people who have so far been deeply involved in this project, along with their specialties, are:

Andrew A. Browman, physicist (domain expert)
Charles S. Brownrigg, design and authoring
Richard K. Cooper, original principal investigator
Catherine Malloy, instructional and graphic design
J. Patrick McGee, senior programmer
William C. Meade, physicist and senior programmer
Robert A. Williams, senior programmer

Cooper and McGee are no longer involved with the project. All these people are local to Los Alamos.

3 TOPIC 2: FORCES

We decided to begin, in Phase II, with something a little less difficult than an Overture. Topic 2 reviews forces and motion, with an emphasis on electromagnetism, the fundamental force of importance for accelerator physics. A somewhat more broadly oriented version of Topic 2 will be submitted to the *Computers in Physics* software contest at the end of May, 1997.

Topic 2 opens with a title page (splash screen) while loading initialization files, and then proceeds to a Table of Contents page. The subtopics covered in this module are:

1. Fundamental Quantities
2. History; Quick Tour of Fundamental Forces.
3. Forces and Motion
4. Electrostatic Forces
5. Electromagnetic Forces

One can return to this page by means of an always-present "T of C" button (see Fig. 1). When one of these sections (which are blue-underlined hyperlinks, as in a World-Wide Web browser) has been visited, the link after return is purple instead of blue. When the student has viewed *all* pages of a section, a red check mark appears beside that entry.

An alternative way of navigating through the material of the tutorial is available by clicking on the "Map" button. also in the lower left corner of Fig. 1. The Concept Map page displays ellipse- and box-objects which are hyperlinked to tutorial content pages. The Map Button is always available to the user. On returning to the Map after having looked at some of the content

frames, you have an indication of where you have been in this module, as the ellipses and boxes for the concepts you have visited are outlined in purple instead of blue. A red star indicates the page that you just came from.

A variety of other navigational transitions can be accessed through the navigational control buttons at the bottom of the window (see Fig. 1) and through a pull-down menu in the window's title-bar. One of these is a Go Back button, which retraces the path taken by the student. The Table of Contents and Map pages also have button which takes the student to an Index, which is also hyperlinked to its subjects.

A typical content page illustrating Coulomb's Law for electrostatic forces is shown in Fig. 1. The student has gotten to this point through a series of progressive disclosures. At this point he or she has the choice of several interactions, including going to the next page (or the previous one) in this section. The (upper) blue underlined words are hypertext links going to related pages, including a short historical vignette on Charles Augustin de Coulomb. (The lower blue words alternate the force arrows between attractive and repulsive.) Clicking the Units button at the lower right takes the student to a sidebar-page that discusses the physical units of the quantities in the force law equation. Finally, the button at the bottom left with the Erlenmeyer flask takes to student to a "laboratory" which imparts the feel of just how fast the "long-ranged" electric force falls off with distance.

On other pages, there are buttons which take the student to self-test questions, usually multiple choice in nature but with useful explanations and guidance for the wrong choices of answers. The student can gauge his or her progress by calling up a Report Card (in the Help pull-down menu) detailing how many pages have been visited, how many questions have been attempted, and how many of those were answered correctly.

Another important aspect of the tutorial is our use of two- and three-dimensional animations to impart the sense of a page's concept. For example, the concept of conservation of momentum is helped by a simple 2D animation involving a cannon recoiling from shooting its ball. For discussion of the electromagnetic forces (which involve a lot of use of the Right Hand Rule) we use more complicated 3D animations involving "moving camera" points of view.

For now, we have use the sound sense only sparingly in this module. Buttons click when "pressed" and there are short sound effects associated with actions on the screen, but we have eschewed providing narrative sound files to go with each content page. This has been partly inspired by a hope to keep this module small enough to be deliverable on diskettes rather than CD-ROMS.

In its present state, the Forces Topic has 71 content pages, 10 question and answer pages, and 6 On-Screen Laboratories.™

4 TOPIC 3: MOTION IN EM FIELDS

This module deals with cyclotron motion of a charged particle moving in a (uniform) magnetic field, with magnetic rigidity, and touches on cyclotrons and spectrometers. In the near future, we will add an Intermediate Level section on the Wien Filter (motion in crossed electric and magnetic fields) and an Advanced Level section on magnetrons.

The module has only very recently been converted from an earlier version to a form more consistent with the tutorial style guide. As a result, it is in a rougher state than the *Forces* module. It is also smaller in size. At the time of the PAC97 conference it has 9 content pages, many "stubs" referring back to pages in Topic 2, and one interactive laboratory. In addition to the two missing sections mentioned above, it will need filling out with questions and more laboratories.

5 TOPIC 5: BEAM SIZE, PHASE SPACE, BEAM ENVELOPES, AND SPACE CHARGE EFFECTS

This module has the most advanced materials of the prototypes that we have built so far. It too has only recently been converted to the new tutorial style. It incorporates many of the same features as described for Topic 2, but with a more extensive use of sound in the form of narrations accompanying the content pages. Also, here, we have experimented with jump-outs and returns from an ancillary piece which consititutes a Glossary of Beam Dynamics Terms.

As can be judged from the section title above, Topic 5 is a more lengthy module than Topic 3. At the time of this writing it has 31 content pages. It too will need filling out with more self-test questions and laboratories.

6 ACKNOWLEDGEMENTS

The WhistleSoft development team has had the benefit of many useful suggestions from a large number (~100) of user testers of our prototype modules.

The tutorial prototypes discussed in this paper have been authored mainly using Macromedia's Authorware software package, but with content prepared using other software such as Macromedia's Extreme 3D, Macromedia's FreeHand, Adobe Photoshop and Adobe Premiere.

We want to acknowledge the encouragement and support for this project of Richard Rinkenberger, Gerald Peters, and David Sutter of the Department of Energy's Division of High Energy and Nuclear Physics, in the Office of Energy Research.

ENERGY DEPENDENCE OF BEAM-BEAM INTERACTIONS AT LEP

H. Burkhardt, CERN, Geneva, Switzerland

Abstract

LEP has been operated for several years at beam energies around 45 GeV and more recently at beam energies of 65 and 86 GeV, thus covering about a factor of two in beam energies.

Vertical beam-beam tune shifts exceeding 0.04 were reached at all energies.

At the lower energies, emittance increase using wigglers was used successfully to avoid excessive beam blow-up and flip-flop from beam-beam interactions and allowed to operate safely at the beam-beam limit throughout fills lasting typically 10 hours. Significant non-Gaussian tails were observed in the vertical plane and have limited the maximum current in collisions.

At the higher energies, the best performance in terms of luminosity and beam-beam tune shift demands higher currents per bunch and minimization of emittances. Vertical to horizontal emittance ratios below 0.5 % have been achieved.

1 INTRODUCTION

The following quantities will be used:

e, m_e, r_e	:	electron charge, mass and classical radius
f	:	revolution frequency, 11245.5 Hz
i	:	bunch current
E	:	beam energy

The interaction of the particles of one beam with the electromagnetic fields of the other produces a horizontal and vertical tune spread of:

$$\xi_x = \frac{r_e\, m_e\, i\, \beta_x^*}{2\pi\, e\, f\, E\, \sigma_x^2 (1 + \frac{\sigma_y)}{\sigma_x)}}$$

$$\xi_y = \frac{r_e\, m_e\, i\, \beta_y^*}{2\pi\, e\, f\, E\, \sigma_x \sigma_y (1 + \frac{\sigma_y)}{\sigma_x)}}$$

These formulas apply Gaussian shaped bunches, colliding head on. The quantities ξ_x and ξ_y are referred to as beam-beam tune shift parameters. For flat beams ($\sigma_y \ll \sigma_x$) we can write in good approximation:

$$\xi_x = \frac{r_e m_e}{2\pi e f E} \cdot \frac{i\, \beta_x^*}{\sigma_x^2} = \frac{r_e m_e}{2\pi e f E} \cdot \frac{i}{\varepsilon_x}$$

$$\xi_y = \frac{r_e m_e}{2\pi e f E} \cdot \frac{i\, \beta_y^*}{\sigma_x \sigma_y}$$

For the ratio of the tune shift parameters we obtain:

$$\frac{\xi_y}{\xi_x} = \frac{\beta_y^*}{\beta_x^*} \frac{\sigma_x}{\sigma_y} = \sqrt{\frac{\beta_y^* \varepsilon_x}{\beta_x^* \varepsilon_y}}$$

Horizontal and vertical beam-beam tune shift parameters are equal if the ratio of vertical to horizontal β functions at the interaction point (β_y^*/β_x^*) is equal to the emittance ratio $\kappa = \varepsilon_y/\varepsilon_x$. The luminosity per interaction region is :

$$\mathcal{L} = \frac{i^2 k}{4\pi e^2 f \sigma_x \sigma_y} = \frac{E\, i\, k\, \xi_y}{2 e r_e m_e\, \beta_y^*}$$

For constant beam size, the beam-beam tune shift parameters increase linearly with current and the luminosity with current squared.

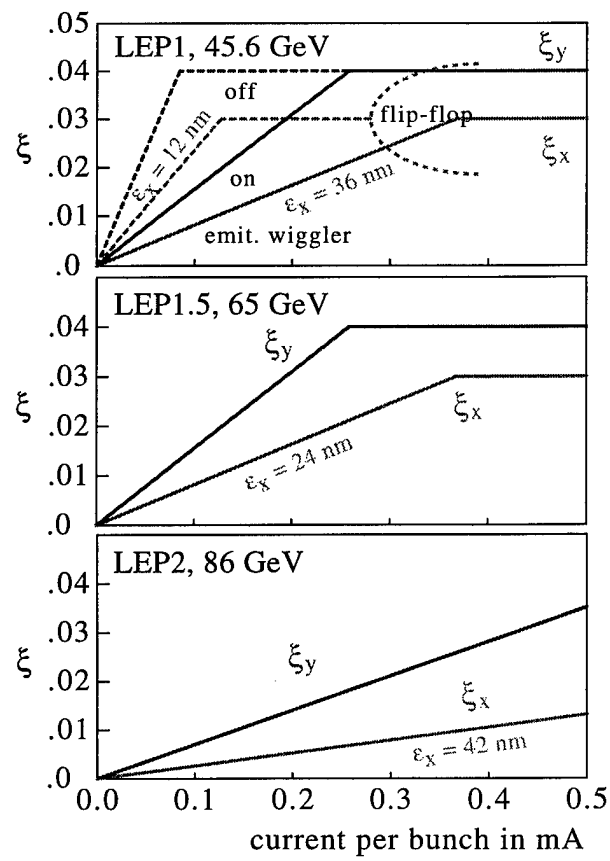

Figure 1: Illustration of the expected behavior of ξ with current for $\beta_x^* = 2.5$ m, $\beta_y^* = 0.05$ m and an emittance ratio $\kappa = 0.5$ %. The vertical beam-beam tune shift parameter was assumed to saturate at 0.04 and the horizontal beam beam tune shift parameter at 0.03.

0-7803-4376-X/98/$10.00 © 1998 IEEE

For higher currents, the beam-beam interaction will lead to an increase in beam sizes and to saturation of the beam-beam tune shift parameters at values of typically 0.04 for a well tuned machine. This is referred to as operation at the beam-beam limit: Emittances and luminosity increase linearly with current. The highest luminosity performance is obtained for operation at the beam-beam limit (at maximum ξ) throughout the whole fill. Fig. 1 illustrates the expected behavior of the beam-beam tune shift parameters as function of the bunch current.

For a given optics, the horizontal emittance scales with beam energy squared. ξ_x and the damping time are proportional to E^{-3}. At LEP1, the beam-beam limit can be reached for very low currents (0.1 mA). To collide safely higher currents and to avoid uncontrolled unequal emittance blow-up (flip-flop), the horizontal emittance is increased using a wiggler in a dispersive region.

2 LEP1, E=45.6 GEV

LEP was operated in the years 1989 to 1995 at beam energies close to 45.6 GeV for the production of Z-Bosons [1]. It took several years until beam-beam tune shifts exceeded values of 0.04.

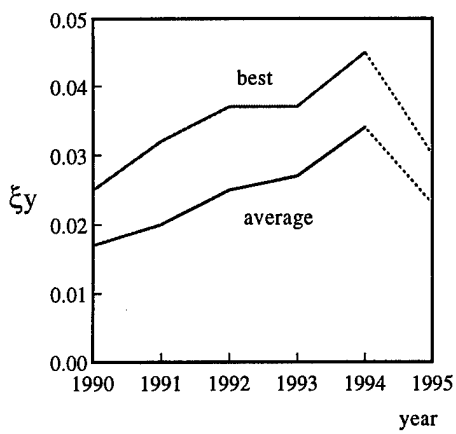

Figure 2: Best and average vertical beam-beam tune shift ξ_y for 6 years of operation at LEP1 energies.

Fig. 2 shows the average and best vertical beam-beam tune shift parameters reached during the years of LEP1 operation. The best values with some comments on the operation are listed below:

1990: ξ_y = .025, odd integer tunes 71/77 for low coupling, 60° phase advance.

1991: ξ_y = .032, even integer tunes 70/76 for improved beam-beam tune shift.

1992: ξ_y = .037, from 60° to 90° phase advance in both planes, realignment of LEP, emittance control.

1993: ξ_y = .037, 90°/60° optics, from 4+4 to 8+8 bunches using the Pretzel scheme, introduction of golden orbits.

1994: ξ_y = .045, no change compared to 1993, operational optimization based on golden orbits.

1995: ξ_y = .030, 12+12 bunches using bunch trains and vertical separation.

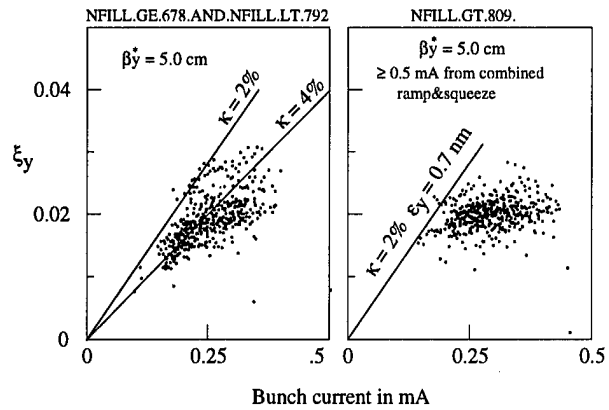

Figure 3: Vertical beam-beam tune shift parameter ξ_y as function of bunch current as observed earlier (left) and later (right) in 1991.

In Fig. 3, it can be seen, that operation at LEP1 energies became only beam-beam limited later in 1991. The vertical beam-beam tune shift parameter started to saturate on average at values of about 0.02. In 1992, the phase advance was increased to 90°, resulting in 12 nm horizontal emittance (compared to 35 nm with 60°). Using a wiggler in a dispersive region, the horizontal emittance could be adjusted between 12 and 36 nm. This was very successful and allowed stable operation with ξ_y regularly exceeding values of 0.03 as can be seen in Fig. 4.

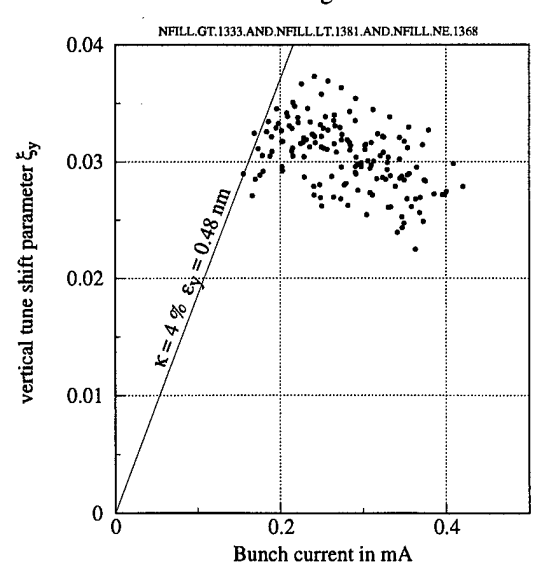

Figure 4: Vertical beam-beam tune shift parameter ξ_y in 1992 for 4+4 bunches,

LEP beams are colliding in four interaction points. Up to 1992, LEP was filled with 4 electron and 4 positron

bunches. Local vertical separation was used to avoid unwanted collisions. From 1993 on, regular operation was using 8+8 bunches with horizontal separation in the arcs of LEP using the Pretzel scheme [2]. Residual vertical and horizontal separation was minimized and allowed beam-beam tune shifts similar to the best 4+4 operation. Still, fills with similar currents resulted in luminosities and vertical beam-beam tune shift parameters ξ_y varying significantly ($\pm$ 30 %). Vertical orbit corrections had significant effects on luminosity. However, it was not sufficient to reach a small rms in the vertical orbit. Correcting back to the particular structure of a vertical orbit saved in conditions with excellent beam-beam tune shift ("golden orbit") gave reproducibly good results. 1994 optics and running conditions were unchanged compared to 1993. Stable operation at one single beam energy and extensive use of reloading and reproducing "golden orbits" resulted in excellent and rather reproducible performance with vertical beam-beam tune shifts exceeding 0.04 on many occasions, as can be seen in Fig. 5. "Golden orbits" are obtained empirically starting from a well corrected machine. The vertical orbit is modified by many small local and global vertical corrections and the result on luminosity recorded. The ingredients of a "golden orbit" are not exactly known, but certainly include a minimization of the vertical dispersion at the interaction points and of the coupling between the horizontal and vertical planes.

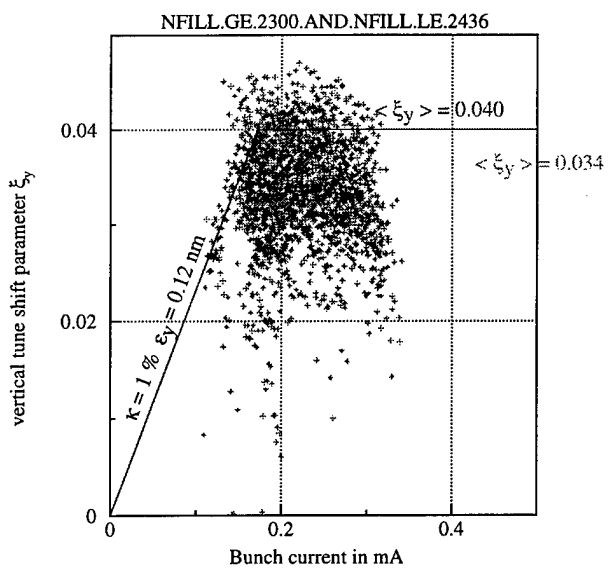

Figure 5: ξ_y dependence on current in final Pretzel operation. The expected behavior for an emittance ratio of κ=1% and a maximum ξ_y=0.04 is also shown.

Fig. 6 shows luminosity, currents, beam-beam tune shift and inverse beam-beam lifetimes for one of the best fills at LEP1 energies.

Beam lifetimes in LEP are well understood [3]. Single beam lifetimes are typically 45 hours at LEP1 energies and

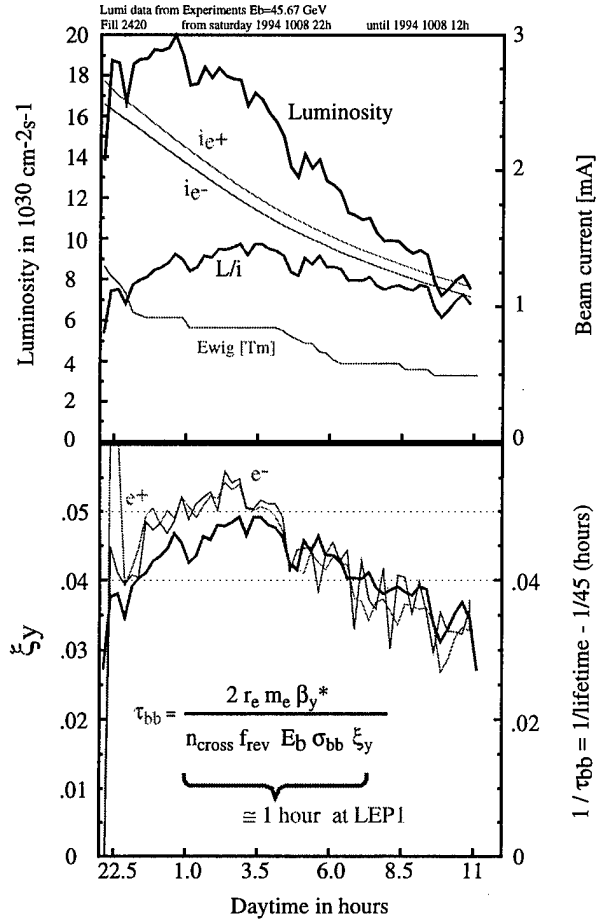

Figure 6: Luminosity, currents, beam-beam tune shift parameter ξ_y and inverse beam-beam lifetimes of a very good fill at LEP1 with 8+8 bunches in the Pretzel scheme.

mainly due to beam particles lost in Compton scattering on thermal photons, originating from the black body radiation of the beam pipe. In collisions, the lifetime decreases to typically 20 hours. The dominant process is radiative Bhabha scattering or beam-beam Bremsstrahlung. The lifetime in collisions τ_{bb} is inversely proportional to ξ_y, as shown in the lower part of Fig. 6. Extra losses at high currents are explained by scraping of non-Gaussian tails. At a low level, non-Gaussian tails were always observed in LEP both in the horizontal and the vertical plane and even without collisions. They can be explained to a large extent by scattering processes and off-momentum particles as described in [4].

The amount of non-Gaussian tails can increase significantly for high currents and beam-beam tune shifts. The maximum useful current, that could safely be collided at LEP1 energies was in fact limited to about 0.4 mA per bunch by background and lifetime problems due to the presence of strong non-Gaussian tails, mainly in the vertical plane.

Differences in intensities between the various electron and positron bunches up to a level of about 10 % did not cause any problems.

The performance in terms of vertical beam-beam tune shift decreased in 1995 when 12+12 bunches were collided using bunch trains with vertical separation. This was attributed to residual vertical separation [5].

3 LEP1.5, E=65 GEV

LEP1 operation was stopped in october 1995. More superconducting radio frequency cavities were installed. This allowed in November 1995 to raise the beam energy to 65 GeV. The same optics with with 90°/60° phase advance was used as previously at LEP1 energies. The natural horizontal emittance at 65 GeV is then $\varepsilon_x = 24$ nm. New record levels in beam-beam tune shift of $\xi_y = 0.05$ and peak luminosities of $L = 2.6 \cdot 10^{31} \mathrm{cm}^{-2}\mathrm{s}^{-1}$ with only 4+4 bunches were obtained within 10 days of operation at this new energy.

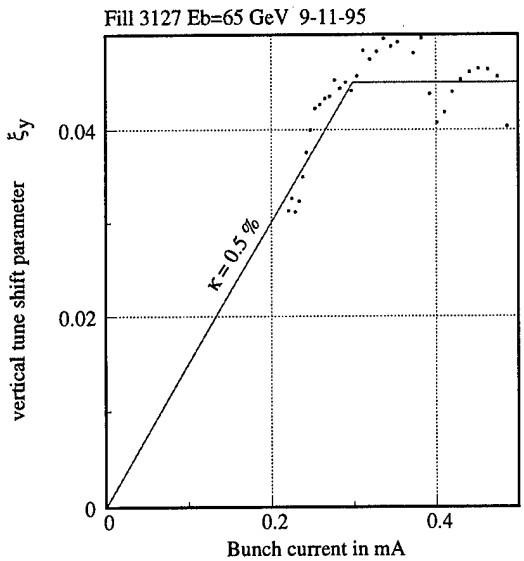

Figure 7: ξ_y dependence on bunch current observed at a beam energy of 65 GeV. The data is shown as dots and the expected behavior for an emittance ratio κ=0.5% and a maximum ξ_y=0.045 as line.

Fig. 7 shows the vertical beam-beam tune shift for a fill at 65 GeV. If we extrapolate the straight line in Fig. 7 we obtain an unperturbed vertical beam-beam tune shift of about 0.08 at a current of 0.5 mA. There were no lifetime nor background problems when currents of 0.5 mA were collided at 65 GeV. The size of both beams increased symmetrically and there was no need for emittance control at this energy. It was possible to close collimators relatively tight without lifetime problems. In spite of the higher currents per bunch, there were less non Gaussian beam tails than at LEP1 energies [6].

4 LEP2, E=86 GEV

After adding many more superconducting cavitities in the shutdown between 1995 and 1996 and in a short stop in summer 1996, it was possible to raise the beam energy to 86 GeV [7]. The natural horizontal emittance at this energy is $\varepsilon_x = 42$ nm for the 90°/60° lattice.

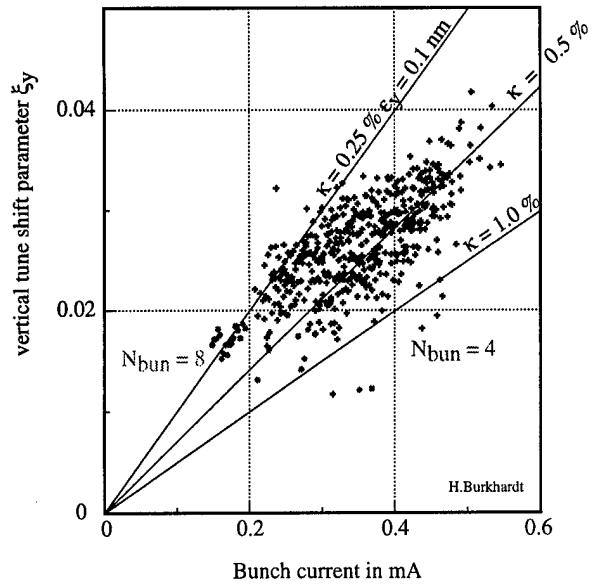

Figure 8: 90°/60° optics, ε_x=42 nm, 86 GeV

Fig. 8 shows the observed dependence of vertical beam-beam tune shift on current. Vertical tune shifts exceeded 0.04 at the highest bunch currents that were available without any sign of saturation. The straight lines show the expected behavior for several emittance ratios. Vertical emittances down to 0.1 nm corresponding to an emittance ratio of only 0.25 % were obtained in some cases.

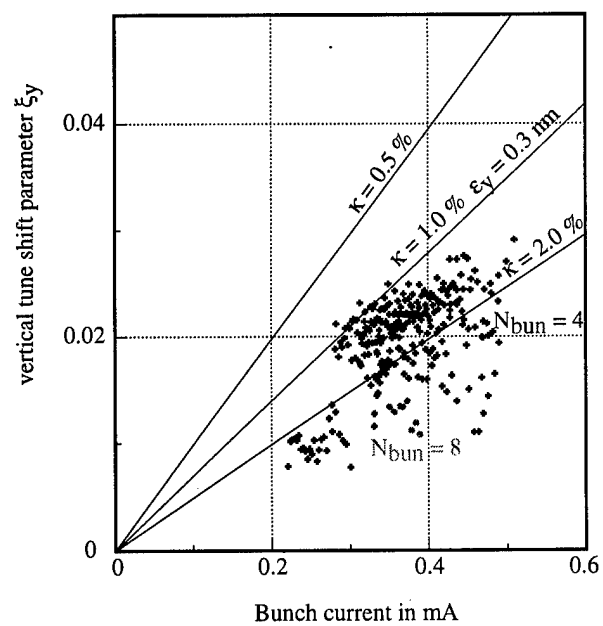

Figure 9: 108°/90° optics, ε_x=30 nm, 86 GeV

There was an attempt to decrease the horizontal emittance through an increase in the horizontal phase advance: An optics with 108°/90° phase advance and a natural horizontal emittance of $\varepsilon_x = 30$ nm at 86 GeV was used for

the last three weeks of operation in 1996. Fig. 9 shows the observed vertical beam-beam tune shifts as function of current. The vertical emittance was larger than previously and overall performance did not improve [8].

Plans for 1997 are to return for regular operation to the well known $90°/60°$ optics and to attempt to reduce the horizontal emittance by an increase in the horizontal damping partition to a value of $J_x \approx 1.5$. The impedance of LEP will be decreased by the removal of normal conducting cavities and it should be possible to increase the current per bunch. Since there were no signs yet of a saturation in the vertical beam-beam tune shift at LEP2 energies, we hope this year to reach new record levels of maybe $\xi_y = 0.06$.

5 SUMMARY, CONCLUSION

We described observations of beam-beam interactions in LEP, based on 7 years of operation, covering about a factor of two in beam energies from 45 to 86 GeV.

Beam lifetimes are well understood at all energies in LEP and accounted for by particle scattering processes.

The vertical beam-beam tune shift parameter ξ_y exceeded 0.04 at all energies. Good performance needs a well corrected machine and careful operational tuning (golden orbit).

The main observations at the three energies can be summarized as follows:

LEP1, 45.6 GeV : Using an optics with 90° phase advance in the horizontal plane and a wiggler placed in a region with dispersion, it was possible to adjust the horizontal emittance between 12 and 36 nm, and to operate safely at the beam-beam limit in fills lasting over 10 hours. The maximum useful current in collision was limited to about 0.4 mA by non-Gaussian transverse beam tails, generating background to the experiments and reducing the beam lifetime.

LEP1.5, 65 GeV: Going from 45.6 to 65 GeV implied an increase of the horizontal emittance from 12 to 24 nm and a reduction of the damping times by nearly a factor of three. Operation was very stable, there were less non-Gaussian tails and no problem to collide currents of 0.5 mA. Vertical beam-beam tune shifts up to about 0.05 were reached after only 10 days of operation at the new energy.

LEP2, 86 GeV: Most of the operation at this energy was based on the same optics with 90° phase advance in the horizontal plane as used at lower energies. The natural horizontal emittance at this energy is 42 nm. Vertical beam-beam tune shifts increased linearly with current, reaching 0.04 without any signs of saturation. An attempt to improve performance using the higher phase advance of 108° in the horizontal plane was not so successful. Plans for this year are to return to the 90° phase advance optics and to reduce the horizontal emittance by an increase of the horizontal damping partition.

6 REFERENCES

[1] G. Arduini *et al.* LEP1 Operation, 1989–1995. In V. Suller and Ch. Petit-Jean-Genaz, editors, *Proceedings of the 5th European Particle Accelerator Conference*, volume 1, pages 286–288, 1996.

[2] R. Bailey *et al.* LEP Operation in 1993 with the Pretzel Scheme. In V. Suller and Ch. Petit-Jean-Genaz, editors, *Proceedings of the 4th European Particle Accelerator Conference*, volume I, pages 439–441, 1994.

[3] H. Burkhardt and R. Kleiss. Beam Lifetimes in LEP. In V. Suller and Ch. Petit-Jean-Genaz, editors, *Proceedings of the 4th European Particle Accelerator Conference*, volume II, pages 1353–1355, 1994.

[4] I. Reichel, H. Burkhardt and G. Roy. Observation and Simulation of Beam Tails in LEP. These proceedings.

[5] W. Herr *et al.* Experience with Bunch Trains in LEP. These proceedings.

[6] I. Reichel. The Loss Monitors at High Energy. In J. Poole, editor, *Proceedings of the 6th Workshop on LEP Performance*, pages 137–140, 1996.

[7] S. Myers. LEP2: Present and Future Performance and Limitations. These proceedings.

[8] D. Brandt *et al.* Low Emittance Lattices for LEP2. These proceedings.

BEAM DYNAMICS PROBLEMS FOR A μ^+-μ^- COLLIDER

D. Neuffer
Fermilab, P. O. Box 500, Batavia IL 60510

Abstract

A μ^+-μ^- collider requires a high-intensity proton source for π-production, a high-acceptance π-μ decay channel, a μ-cooling system, a rapid acceleration system, and a high-luminosity collider ring for the collision of short, intense μ^+-μ^- bunches. Significant beam-dynamics problems exist in each of these systems. These problems and some paths to solutions are discussed in this paper.

1. INTRODUCTION

Recently considerable interest has developed in the possibility of a high-energy high-luminosity μ^+-μ^- Collider,[1,2,3] and a multi-laboratory collaboration has been formed to study this concept. Table 1 shows some possible parameters for a 4 TeV collider with a luminosity of $L = 10^{35}$ $cm^{-2}s^{-1}$, as well as parameters of a potential 400 GeV first collider, and Fig. 1 shows a conceptual view of the components of such a facility. The collider requires a high-intensity proton source for π-production, a high-intensity π-production target with a high-acceptance π-μ decay channel, a μ-cooling system to cool the beams to collider requirements, a rapid acceleration system, and a high-luminosity collider ring for the collision of short, intense μ^+-μ^- bunches. Each of these components poses significant beam-dynamics problems.

The critical property of muons in a collider is that the muons decay, with a lifetime of $\tau_\mu = 2.2\ (E_\mu/m_\mu)$ μs. This means that μ-beam stability is only needed for a few hundred turns in the μ^+-μ^- collider, but it also means that obtaining high luminosity requires compressing the muons into ultra-high intensity bunches. The expression for luminosity (for equal intensity round beams) is:

$$L = \frac{f_0 n_S n_b \gamma_\mu N_\mu^{\ 2}}{4\pi\varepsilon_N \beta^*},$$

where n_S is the luminosity lifetime (in turns) in the collider, n_b is the number of colliding bunches in each beam, N_μ is the number of muons per bunch, $\gamma_\mu = (E_\mu/m_\mu)$, ε_N is the normalized emittance, and β^* is the collider focusing parameter, with the beam size at collisions given by $\sigma^2 = \varepsilon_N\beta^*/\gamma_\mu$. High luminosity requires maximizing N_μ within minimal beam sizes, and that implies significant beam dynamics challenges. In the following sections we will review the beam dynamics problems in each of the successive components of the collider system, referencing more detailed studies and suggested solutions from our collaborators and indicate what we consider the most critical unresolved problems.

The primary difficulties are single-particle beam dynamics problems. However, if these single-particle problems are solved, then multiparticle problems, such as collective instabilities and beam-beam limits, will occur, and these multiparticle beam dynamics problems must also be solved to obtain high luminosity.

Table 1: Parameter list for μ^+-μ^- Colliders

Parameter	Symbol	Top Demo	4TeV
Collision Energy	$2\,E_\mu$	400	4000 GeV
Energy per beam	E_μ	200	2000 GeV
Luminosity	$L=f_0 n_s n_b N_\mu^2/4\pi\sigma^2$	5×10^{32}	$10^{35}cm^{-2}s^{-1}$
Source Parameters			
Proton energy	E_p	10	30 GeV
Protons/pulse	N_p	$2\times2.5\times10^{13}$	$4\times3\times10^{13}$
Pulse rate	f_0	15	15Hz
μ acceptance	μ/p	0.2	.2
μ-survival	N_μ/N_{source}	0.3	.33
Collider Parameters			
Collider radius	R	120	1200m
μ /bunch	$N_{\mu\pm}$	1.5×10^{12}	2×10^{12}
Number of bunches	n_B	1	2
Storage turns	$2n_s$	1800	1800
Norm. emittance	ε_N	10^{-4}	5×10^{-5}m-rad
μ-beam emittance	$\varepsilon_t=\varepsilon_N/\gamma$	5.3×10^{-8}	2.5×10^{-9}m-rad
Interaction focus	β_0	1	0.3 cm
Beam size at IR	$\sigma=(\varepsilon\beta_0)^{1/2}$	23	2.1μm

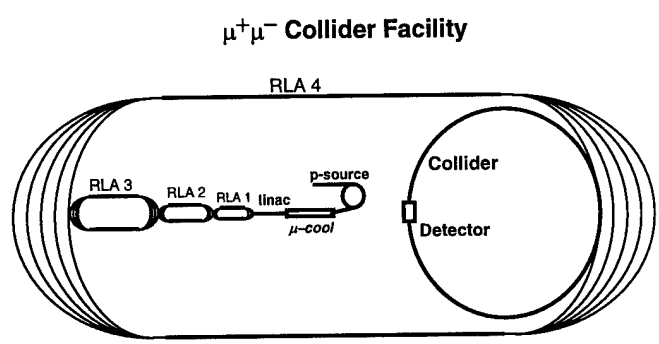

Figure 1 Overview of a μ^+-μ^- Collider facility showing p-source, μ-Cooling, recirculating-linac acceleration (RLA) and collider.

2. PROTON SOURCE

The collider requires an intense source of protons for $\pi \Rightarrow \mu$ production. The baseline design requires intensity comparable to that proposed for a KAON factory, but with the significant difference that the beam is bunched to short bunch lengths when extracted onto targets for π-production (4 bunches of 2.5×10^{13} at ~1 ns or I =

0-7803-4376-X/98/$10.00 © 1998 IEEE

$eNc/((2\pi)^{1/2}\sigma_z) \cong 1600$ A peak current). This short bunch would certainly surpass various instability thresholds and strategies to reach this intensity are being developed.[4]

At injection, the key limitation is transverse space charge and the beam would be injected within a long bunch so that the peak current is small enough to keep the total space charge tune shift less than 0.25—0.5. The beam then bunches as it is accelerated, and coherent transverse and longitudinal instabilities become a concern. Longitudinal instability is avoided by placing the beam energy always "below transition", which means using a flexible-momentum compaction lattice.[5] It may also be possible to cancel space-charge impedances by adding inductive elements to the transport.

Compression to peak current is obtained by bunching at the end of the acceleration cycle or after extraction, with possible combination of separate bunches on the target. Simulations which include space charge and impedance effects are being developed to test these compression conditions. Also experiments on the BNL AGS are being developed in which the limits of bunch compression in an existing ring are explored at parameters near μ^+-μ^- driver conditions.[6]

3. π-PRODUCTION AND μ-COLLECTION

Another key difficulty occurs in the targetry and collection of secondary π and μ beams, where we require collection of ~0.1 μ per primary proton.[7] The current strategy is to immerse the production target in a 20-T solenoid, so that most π's are trapped. This is followed by a 5T solenoid transport which accepts most of the low energy μ's (100—600 MeV/c) produced by π-decay. (see fig. 2 An rf system within that decay transport reduces the energy spread by "rf rotation", in which the faster particles decelerate while slower ones accelerate. This transforms the short-bunch beam on target producing a large momentum spread in μ's to a longer μ-bunch with reduced $\delta p/p$.[1] The key beam dynamics problems here are in developing a high-acceptance transport for the μ-beam, both for large $\delta p/p$ and transverse ε_T, and in obtaining an appropriate bunch-rotation rf system.

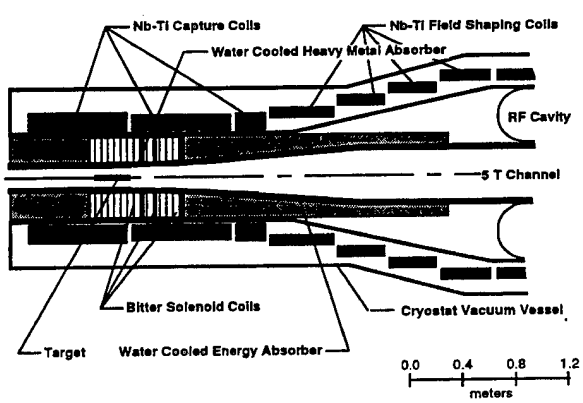

Figure 2 Capture solenoid and match to transport for $\pi \rightarrow \mu$ decay + rf rotation (from ref. 1).

Solutions have been found in using a multiharmonic 30—150 MHz rf system embedded in a 5—8T short-period solenoid transport, and verified by simulations. Energy selection in the μ-decay can be used to select a relatively high polarization in the μ-beams (see fig. 3).[8]

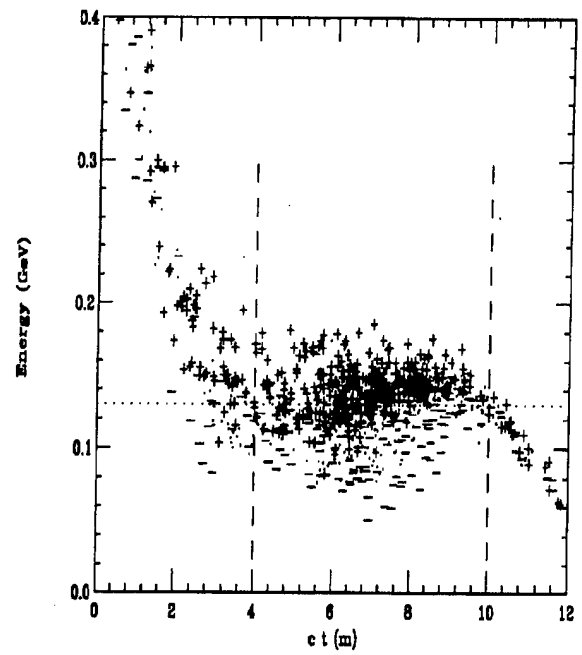

Figure 3 μ-beam at end of rf rotation. + and - signs refer to + and- polarization. (from ref. 8)

4. μ-COOLING

After rf rotation the beam still has both a large momentum spread ($\delta p/p \cong 10\%$) and transverse phase space $\varepsilon_T \cong 0.015$ m-rad). The μ^+-μ^- Collider concept relies on ionization cooling to compress the beam phase-space volume to obtain high luminosity. This cooling method has been described by Skrinsky et al.[2] and by Neuffer.[3] In ionization cooling, the beam loses transverse and longitudinal momentum while passing through a material medium, and regains only longitudinal momentum in acceleration cavities. Cooling by large factors requires successive stages of energy loss and reacceleration (20 to 50 stages).[1,8] Since ionization cooling does not directly cool the beam longitudinally, these stages must include wedge absorbers at non-zero dispersion to exchange longitudinal and (cooled) transverse phase-space.

The differential equation for rms transverse cooling is:

$$\frac{d\varepsilon_T}{ds} = -\frac{1}{\beta^2 E}\frac{dE}{ds}\varepsilon_T + \frac{\beta_\perp E_s^2}{2\beta^3 m_\mu c^2 L_R E} \qquad (1)$$

where the first term is the frictional cooling effect and the second is the multiple scattering heating term. Minimal heating requires that $\beta_\perp$, the betatron focusing amplitude at the absorber, be small, and that L_R, the absorber radiation length, be large (light elements; i.e. Li or Be). The energy loss mechanism also causes energy-loss straggling, which

naturally sets rms $\delta p/p$ at the ~4% level, even with longitudinal cooling.

The beam dynamics problems in μ-cooling include the beam-material interactions intrinsic to the cooling process, the single-particle beam transport problems associated with obtaining strong foci at the absorbers, the chromatic effects of ~4% $\delta p/p$, dispersion and transverse matching at wedge absorbers, as well as longitudinal motion control with rf reacceleration, and the multiparticle constraints imposed by space-charge and wake-fields in the short intense bunches, where the beam intensifies as it is cooled.

Lattices for cooling have been developed and a favored design includes sequences of solenoid "FOFO" cells with rf cavities and LiH absorbers at low-β foci of the lattice. Another desirable focusing situation is obtained by confining the cooling beam within a high-current Li (or Be) rod which both focuses and cools the beam. The transport must include arc segments with wedges for cooling longitudinally; obtaining large $\delta p/p$ acceptance configurations with cooling and transport stability is nontrivial.[9]

An outline design scenario for μ-cooling has been developed, and critical sections of the cooling section have been simulated.[10,11] Figure 4 displays transverse phase space before and after a cooling section which cools transverse phase space by 25×.[12] However an integrated design including the full complexity of the beam transports, reacceleration and bunching, and including nonlinear beam

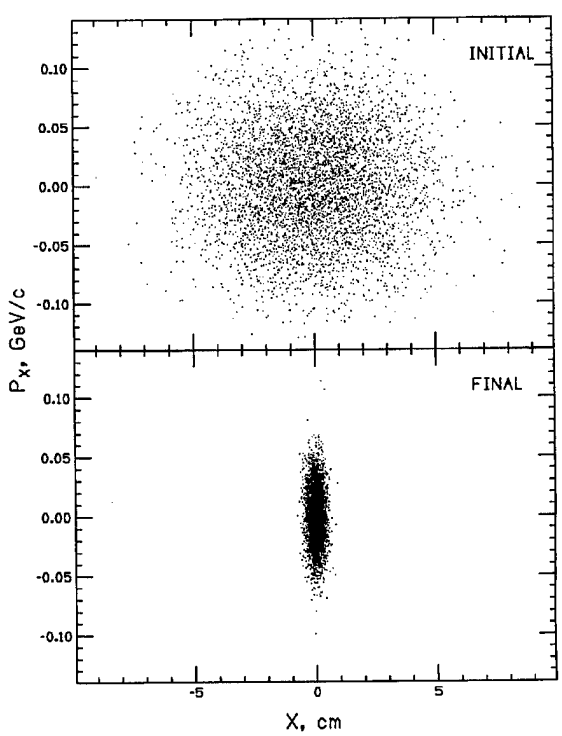

Figure 4 Transverse phase space (p_x-x) before and after a cooling channel which reduces ε_T from 0.01 to 0.0004 m-rad.

dynamics coupled with the ionization interactions has not yet been developed and simulated. Initial cooling experiments verifying cooling efficiency must also be developed.

5. μ-ACCELERATION

Acceleration must be completed before μ-decay. This constraint can be written as the equation:

$$eV_{rf}' >> \frac{m_\mu c^2}{L_\mu} \cong 0.16 \text{ MeV/m},$$

where eV_{rf}' is the acceleration rate, and L_μ is the μ decay length (660m). Relatively fast acceleration is required, and two alternatives have been developed: recirculating linacs (RLAs) or very rapid-cycling synchrotrons (RCS).[13] In both cases significant challenges exist in obtaining acceleration without phase-space dilution. Simulations show that longitudinal matching is relatively straightforward, and transverse matching is possible.[14] However precise matching in rapid-cycling systems may be difficult, and beam decay within the transport and acceleration must be tolerated. Collimation for e's from μ-decay will be required, particularly at the entrances of arcs.

Acceleration of high intensity bunches is required. Wake fields from short, high-intensity bunches can be large. From TESLA 1300 MHz cavity calculations, wake fields at the level of $k_\parallel \cong 10$ V/pC/m may be expected. $k_\parallel$ is expected to vary as $1/a^2$ and $1/\lambda^2$ and $1/\sigma^{1/2}$, where a is the cavity aperture, λ is the acceleration wavelength and σ is the bunch length. [15,16] Calculations indicate that the wakefield would limit bunch intensities to ~2×10^{12} with 1300 MHz rf in a RLA scenario. The longitudinal dynamics is microtron-like and off-crest acceleration enables compensation of the linear part of the wakefields, with synchrotron-like phase stability.[14] Longer wavelength and large aperture rf systems are favored for maximal bunch intensities.

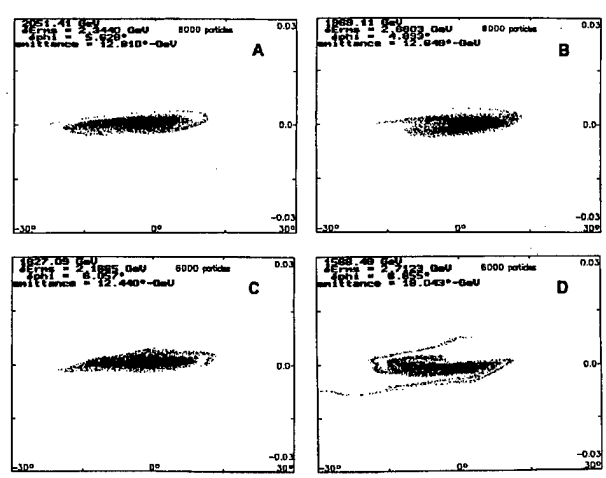

Figure 5 Simulation results of RLA acceleration of beam to 2 TeV with wakefields, for Nμ = 0, 1, 2, and 4×10^{12} (A, B, C and D, respectively) (from ref. 14).

6. μ-COLLIDER

After acceleration to full energy, the μ^+-μ^- beams are inserted into a storage ring for multiturn collisions at full energy until μ-decay. The number of storage turns before decay is ~300B, where B is the mean ring bending field in T, or ~2000 turns at B=6.7 T. High luminosity requires that the beams be focussed to small spots and short bunches at the interaction points (IPs). It also implies high beam densities and that could allow multiparticle instabilities.

The short-bunch requirement (~3mm) implies a nearly isochronous ring to avoid bunch-lengthening and that is obtained by using a flexible momentum compaction lattice for the Collider arcs. In these arcs the dispersion oscillates with an average value near zero, so that the momentum compaction (the variation of path length with momentum) $\alpha_p = 1/\gamma_T^2 = (\delta C/C)/(\delta P/P)$ is near zero ($\alpha_p \sim 10^{-5}$—10^{-8} in recent designs).

The small focus at the IP(σ=2μ, β=0.003m) with the geometric and chromatic acceptance requirements is a significant design challenge. A design has been developed which uses final focusing triplets of 10 T quads (10 cm radius), where β_{max} = 100km, and chromaticity correction inserts of ~300m (containing quads, dipoles and sextupoles) on each side of the IP. [17,18] The lattice has adequate dynamic apertures of $\delta p/p \sim \pm 0.15\%$ with 5σ beam amplitudes.

The peak currents associated with 3mm bunches of 2×10^{12} μ (13000A) pose the possibility of coherent instabilities. For $\alpha_p \cong 10^{-8}$, there is no longitudinal motion within the μ lifetime and the beam motion is e^--linac-like, with the linac length given by the μ decay length, with instability modes such as the possibility of head-tail beam breakup, and with possible solutions such as BNS damping.[19]

For $\alpha_p \cong 10^{-5}$, there are ~10 synchrotron oscillations /μ-lifetime. The usual synchrotron stability criteria for longitudinal and transverse impedances $Z_{L,}$, $Z_\perp$ may be applied:

$$\left|\frac{Z_L}{n}\right| < F\frac{E|\eta|}{e\beta^2 I_{peak}}\left(\frac{\Delta E}{E}\right)^2 \quad ; \quad Z_\perp < \frac{4\pi m\gamma\,\beta\omega_\beta c}{eI_{peak}}\Delta\nu\,,$$

obtaining $Z_L/n < \sim 0.022\Omega$, but these are moderated by the finite μ-lifetime. [20]

Cheng et al. [21,22] have analyzed potential longitudinal and transverse instabilities in a tracking code that includes linear and non-linear α_p, wakefields (including resistve-wall, rf cavities and broad-band resonators), and μ-decay. They find acceptable dynamics at $Z_L/n = 0.1\Omega$ with $\alpha_p = -10^{-5}$, $\delta p/p$ =0.15%, and 1GV of 3000MHz rf. (Synchrotron dynamics with negative α_p was preferable to isochronous motion.) The simulations did not include advanced stabilization methods such as BNS damping, multiharmonic rf, alternating chromaticity, etc., although these may added in the future.

Another critical limitation in collider rings is set by the beam-beam interaction, the nonlinear interaction at the collision points. The beam-beam tune shift $\Delta\nu_{BB}$ is given by:

$$\Delta\nu_{BB} = \frac{N_\mu r_\mu}{4\pi\varepsilon_N}\,,$$

and is chosen to be ~0.05 in the parameters of Table 1. Simulations by P. Chen[23] and by M. Furman[24] have shown some hour-glass and disruption effects but general stability with the beam-beam interaction for the μ-lifetime. Somewhat larger $\Delta\nu_{BB}$ can be tolerated; figure 6 shows simulation results with $\Delta\nu_{BB}$=0.05, 0.10 and 0.15 and only the largest value shows luminosity loss.

Stupakov and Chen[25] and Skrinsky[26] have suggested that even larger $\Delta\nu_{BB}$ could be tolerated if the collision points were immersed in a plasma or in solid Li, which would neutralize the beam-beam force. The μ-material interaction rates and multiple scattering in the plasma or Li are tolerably small within the μ-lifetime; however, detector backgrounds may increase.

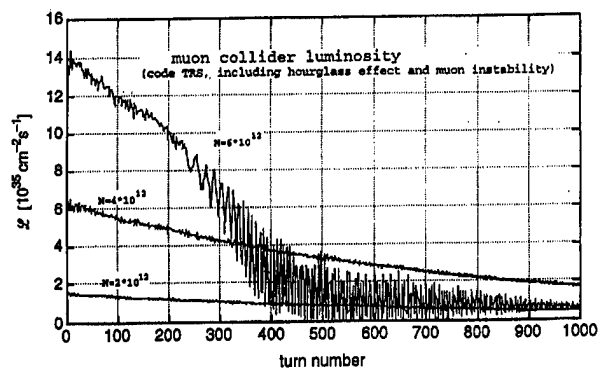

Figure 6 Simulation results of strong-strong beam-beam interactions with μ-decay at $\Delta\nu_{BB}$ = 0.05, 0.10, and 0.15. Luminosity is lost only at $\Delta\nu_{BB}$ = 0.15.[24]

7. THE FIRST (LOW-ENERGY) μ-COLLIDER

The first μ^+-μ^- collider would be a lower-energy machine (possibly at 100×100 to 200×200 GeV), designed both to test the basic concepts as well as to provide significant physics at the Higgs or Top mass, and may be at somewhat lower intensity. Palmer has extrapolated from the high-energy case to set low-energy collider parameters.[27] Assuming equal $\Delta\nu_{BB}$, equal-aperture IP quads and equal 6-D emittances, it is found that σ, β^* and ε_T should vary as $E_\mu^{-1/3}$. Instability constraints are relaxed by almost an order of magnitude,[21] and the lower energy makes strong focusing (to a larger β^*) somewhat easier. β_{max} at the IP quads is reduced by an order of magnitude to < 10km; which makes the chromaticity correction easier and a special insertion may not be needed. Proton driver and beam-cooling requirements would be somewhat similar for lower and high energy machines, except that the transverse cooling may be reduced by a factor of 2—4. The beam dynamics of lower-energy machines is

overall somewhat easier but still quite difficult, and a low-energy machine would be suitable as an initial research machine.

8. DISCUSSION

We have discussed some of the beam dynamics problems associated with the challenge of a μ^+-μ^- Collider, and outlined some of the recent research toward solving these. (In this review we have not included discussion of other problems - detector problems, cost issues and radiation control, etc. These are discussed by Palmer.[27]) However the beam dynamics problems are not yet completely defined, and complete solutions are not yet obtained. Much research and invention is needed toward obtaining complete and optimal solutions, and we hope the present discussion will assist in stimulating that research.[28]

We acknowledge the assistance of the many contributors to the μ^+-μ^- collider studies, based at BNL, Fermilab, LBL, and other universities and laboratories, including R. Palmer, R. Noble, A. Tollestrup, A. Sessler, J. C. Gallardo, and many others.

REFERENCES

[1] $\mu^+\mu^-$ Collider - A Feasibility Study, BNL-52503, Fermi-Lab-Conf.-96-092, LBNL-38946 (1996), presented at the Snowmass workshop (1997).

[2] A. N. Skrinsky and V.V. Parkhomchuk, Sov. J. Nucl. Physics 12, 3(1981), E. A. Perevedentsev and A. N. Skrinsky, Proc. 12th Int. Conf. on High Energy Accel., 485 (1983).

[3] D. Neuffer, Fermilab Note FN-319, July 1979, D. Neuffer, Particle Accelerators 14, 75 (1983), D. Neuffer, Proc. 12th Int. Conf. on High Energy Accelerators, 481 (1983), D. Neuffer, Nucl. Inst. and Meth. A350, 27 (1994).

[4] J. Norem et al., paper 4W.25, this PAC proceedings (1997)

[5] S. Y. Lee, K. Y. Ng, and D. Trbojevic, Phys. Rev. E48, 3040 (1993).

[6] J. Norem et al. "Bunch Shortening Experiments in the Fermilab Booster and the AGS", 4W.24, this PAC 1997 proceedings.

[7] N. V. Mokhov, R. J. Noble, and A. Van Ginneken, Proc. Montauk Workshop, AIP Conf. Proc. 372, 61 (1996).

[8] R. Palmer, A. Tollestrup, A. Sessler, to appear in Proc. 1996 Workshop on the future of High Energy Physics, Snowmass.

[9] R. Fernow J. C. Gallardo, and R. Palmer, paper 4W.26, this PAC proceedings (1997).

[10] A. Van Ginneken, Nucl. Inst. and Meth. A362, 213 (1995).

[11] D. Neuffer and A. Van Ginneken, Fermilab Pub-96-451, to be published in Nucl. Inst. and Meth. A (1997).

[12] D. Neuffer and A. Van Ginneken, paper 4W.31, these PAC 1997 proceedings.

[13] D. Summers et al., paper 3C.04, this PAC 1997 proceedings.

[14] D. Neuffer, Nucl. Inst. and Meth. A384, 263 (1997).

[15] A. Mosnier and O. Napoly, Proc. 15th Int Conf. On High Energy Accelerators, ed. J. Rossbach, p 963 (1992).

[16] A. Novokhatski and A. Mosnier, these PAC 1997 proceedings.

[17] A. Garren et al., Nucl. Phys. B (Proc. Suppl.) 51A, 148 (1997).

[18] A. Garren, C. Johnstone and K. Ng, "Recent Progress on a Lattice for a 2-TeV Muon Collider", 4W.34, this PAC 1997 proceedings.

[19] K.-Y. Ng, "Beam Stability Issues in a Quasi-Isochronous Muon Collider", Proc. Montauk Workshop, AIP Conf. Proc. 372, 224 (1996).

[20] W.-H. Cheng, A. M. Sessler, and J. S. Wurtele, "Studies of Collective Instabilities in Muon Collider Rings", AIP Conf. Proc. 372, 206 (1996).

[21] W.-H. Cheng, A. M. Sessler, and J. S. Wurtele, "Longitudinal Behavior in a Muon Collider Ring", unpublished, February 1997.

[22] W. H. Cheng et al., paper 4W.33, these PAC 1997 proceedings.

[23] P. Chen, Nucl. Phys. B (Proc. Suppl.) 51A, 179 (1997).

[24] M. Furman, Proc.1996 Snowmass workshop on Future Directions in High Energy Physics (1997).

[25] I. Stupakov and P. Chen, Phys. Rev. Lett. 6, 3715 (1996).

[26] A. N. Srinsky, unpublished (1996).

[27] R. Palmer, paper 6B.02, this 1997 PAC proceedings.

[28] Proc. Orcas I. Workshop on μ^+-μ^- Colliders (1997).

COLLISIONS OF RESONANTLY COUPLED ROUND BEAMS AT THE CORNELL ELECTRON-POSITRON STORAGE RING (CESR)

E. Young, S. Henderson, R. Littauer, B. McDaniel, T. Pelaia, R. Talman,
Wilson Synchrotron Laboratory, Cornell University, Ithaca, NY 14853*

Abstract

As a first step toward testing the proposed "Möbius" scheme[1], we used existing CESR elements to collide round, rather than flat, beams. The tune shift parameter, ξ, was inferred from the beam profiles and current, was compared to the tune shift of the coherent beam-beam π mode, and was corroborated by luminosity measurement. Values of ξ up to 0.09 were achieved without significant lifetime reduction.

1 INTRODUCTION

For round beams ($\epsilon_x = \epsilon_y = \epsilon, \beta_x^* = \beta_y^* = \beta^* \rightarrow \sigma_x^* = \sigma_y^* = \sigma^*$), the well known expressions for the tune shift parameter and the luminosity, written in terms of the emittance, $\epsilon = \sigma^2/\beta$, become

$$\xi = \frac{r_e}{4\pi\gamma e f}\frac{I}{\epsilon}, \quad L = \frac{I^2}{4\pi e^2 f \beta^* \epsilon} = \frac{\gamma}{e r_e}\frac{\xi I}{\beta^*}, \qquad (1)$$

where I is the current per beam. For a given ξ, L for a round beam is twice as large as for a flat beam; moreover, there is hope of achieving higher values of ξ with a round beam[2]. For dissimilar beams, equation (1) for the luminosity becomes

$$L = \frac{I_+ I_-}{2\pi e^2 f \beta^* (\epsilon_+ + \epsilon_-)}. \qquad (2)$$

Simulations of round beams in collision show considerable promise, especially in the "Möbius" scheme proposed by Talman[1].[1] If a CESR lattice is tuned to the coupling resonance ($Q_x - Q_y =$ integer), sufficient x-y coupling can be achieved using existing skew quadrupoles in CESR to make equal transverse emittances, $\epsilon_x = \epsilon_y$. The present interaction region (IR) quadrupoles can produce $\beta_x^* = \beta_y^*$, but only for relatively large values of β^*. While this limits the luminosity attainable with round beams, it does not prevent large ξ, which is independent of β^*; thus the present experiment focuses on ξ, rather than luminosity.

Since the bunch currents were sometimes not equal and the beam-beam blowup was often not symmetrical during these experiments, we consider separately the tune shift parameter experienced by each beam:

$$\xi_\pm = \frac{r_e}{4\pi\gamma e f}\frac{I_\mp}{\epsilon_\mp}. \qquad (3)$$

A weak-strong unbalance can entrench itself if the stronger beam, by producing a large ξ, blows up the weak beam and thus reduces the ξ that it experiences itself.

During collisions there are two primary coherent modes of beam motion, analogous to the normal modes of coupled pendulums. One mode has the same frequency as single beam motion. The other mode, called the π mode, is shifted to a higher frequency. The relationship between the tune shift of the coherent beam-beam π mode, ΔQ_π, and the tune shift parameter, ξ, is

$$\cos 2\pi(Q_o + \Delta Q_\pi) = \cos 2\pi Q_o - 2\pi\lambda\xi_{\rm av}\sin 2\pi Q_o, \quad (4)$$

where $\xi_{\rm av} = \frac{1}{2}(\xi_+ + \xi_-)$. For an (unrealistic) linearized interaction, $\lambda = 2$. For more realistic models of round Gaussian beams, Yokoya and Koiso[3], and independently Alexahin[4], find $\lambda = 1.21$, assuming $\epsilon_+ = \epsilon_-$ and $I_+ = I_-$. The derating factor λ has not been derived for the case of unequally blown up bunches.

2 EXPERIMENTAL CONDITIONS

2.1 Machine Conditions

The design parameters for the round beam lattice are shown in table 1. The fractional tunes match the optimum operating point as found in simulation studies.[2] At the outset of the experiment, the betatron phase advance around the ring was measured and corrected[5] to conform to the design parameters. The resulting β functions agreed with the design values to within about 5%.

Table 1: Lattice parameters for round beam experiment.

Tunes	$Q_x = 10.77$
	$Q_y = 9.77$
IP β-functions	$\beta_x^* = \beta_y^* = 0.30$ m
IP dispersion	$\eta_x^* = \eta_y^* = 0.0$ m
Emittances	$\epsilon_x = \epsilon_y = \frac{1}{2}\epsilon_{x,\rm flat}$
	$= 62.0$ nm-rad

* Work supported by the National Science Foundation.

[1] A complete test of the "Möbius" insert requires considerable hardware effort, namely the installation of 45° rolled quadrupoles and stronger interaction region (IR) quadrupoles to produce small β^*. The experiments described in this paper were intended to test some aspects of round beam collisions before this hardware was available. A Möbius section has since been installed and awaits testing. Optics with smaller β^* will become available after the planned installation of superconducting IR quadrupoles in 1998.

[2] In a few tune scans done in the weak/strong regime, deterioration of beam-beam performance was seen at an average fractional tune of about 0.8, in rough agreement with predictions for the simulations. All results reported here are for collisions at the design tune.

The CLEO detector solenoid was left at its usual field of 1.5 T, and compensation of this field was achieved by rolling quadrupoles on either side of the interaction point (IP) by small angles (minimum tune separation < 0.002). After that, a pair of skew quadrupoles was powered to produce the intended transverse coupling, which splits the observed tunes into upper and lower normal modes, where the tune split is a measure of the coupling strength. During these experiments, the tune split was typically 0.012. We collided single bunches of electrons and positrons. At the crossing point on the opposite side of the ring, the electron and positron bunches were separated vertically with an electrostatic bump.

2.2 *Diagnostics*

Existing monitors, which image synchrotron light onto a linear CCD photodiode array, were used to monitor the vertical profile. The output of these profile monitors was digitized and later fitted to a Gaussian plus a linear background, an example of which is shown in figure 1. Inferring the absolute vertical emittance, $\epsilon_y = \sigma_y^2/\beta_y$, requires knowledge of the optical magnification of the synchrotron light monitor and of β_y at the source point of the synchrotron light. These parameters are somewhat uncertain, as evidenced by the unequal values of ϵ_0 measured for positrons (51 ± 2 nm-rad) and electrons (61 ± 2 nm-rad). We normalize the scale factors to bring both values of ϵ_0 to their average, 56 nm-rad.[3] No horizontal scanners were available. The horizontal emittance was assumed to equal the vertical emittance due to the substantial coupling; this is consistent with the shape of the light image as seen on a TV monitor.

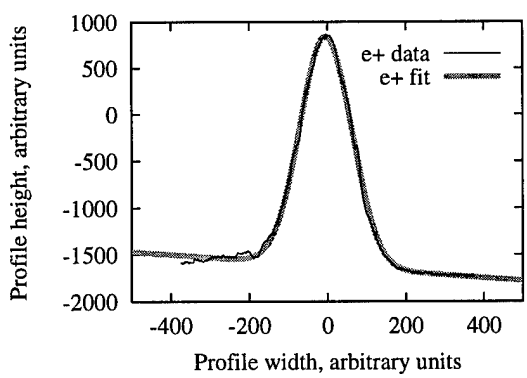

Figure 1: An example of the digitized beam profile and the Gaussian fitted to it. In the digitizer units, $\sigma = 58.6$, which corresponds to $\epsilon = 67.5$ nm-rad.

The coherent mode frequencies were monitored by a spectrum analyzer connected to pickup electrodes. During collisions the two coupled transverse modes and the corresponding coherent beam-beam π modes were easily identifiable in most cases. During most runs the π mode shift was slightly different for the two coupled modes, as shown in figure 2. The reason for this is not known. For calculating ξ, the average of the two tune splits, $\overline{\Delta Q_\pi}$, was used.

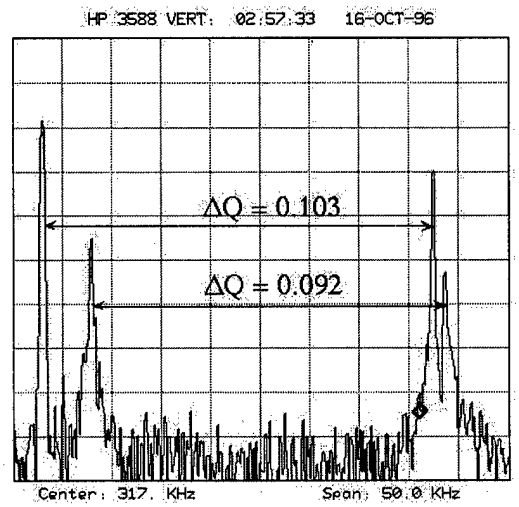

Figure 2: Spectrum of colliding beams showing all four modes. The average tune split seen here, $\overline{\Delta Q_\pi} = 0.098$, was the maximum tune split achieved.

During two runs, the luminosity was measured by the standard method using CLEO endcap detectors to monitor Bhabha scattering.

3 RESULTS

3.1 *Beam Blowup*

An important effect of the beam-beam interaction is the increase of the colliding beam emittance over that of the unperturbed single beam. If this blowup increases more quickly than proportionally to the current, then further gains in tune shift cannot be made by increasing the current. Figure 3 shows the emittance blowup factors for each beam, $b_\pm \equiv \epsilon_\pm/\epsilon_0$, as a function of the tune shift parameter experienced, $\xi_\pm$. The electrons are consistently blown up more than the positrons, an (unexplained) tendency also observed during flat beam operation of CESR. As the upper limit of these curves was approached ($\xi_- \rightarrow 0.09$), it became progressively harder to bring the beams into collision without loss; however, once in collision the beam lifetimes did not differ significantly from the pre-collision lifetimes. Furthermore, over the range of our data ($I_{\text{per beam}}$ up to 22 mA), no limiting tune shift saturation is evident.

3.2 *π Mode Tune Shift*

For each run we compared the observed tune shift, $\overline{\Delta Q_\pi}$ to the value calculated from our measured ξ_{av} via equation (4). Unfortunately, the applicable derating factor λ has not

[3]Equality of positron and electron emittances to within 1% was confirmed by inserting scrapers into the vertical aperture until the beam lifetime of a single bunch of positrons or electrons reached a predetermined value.

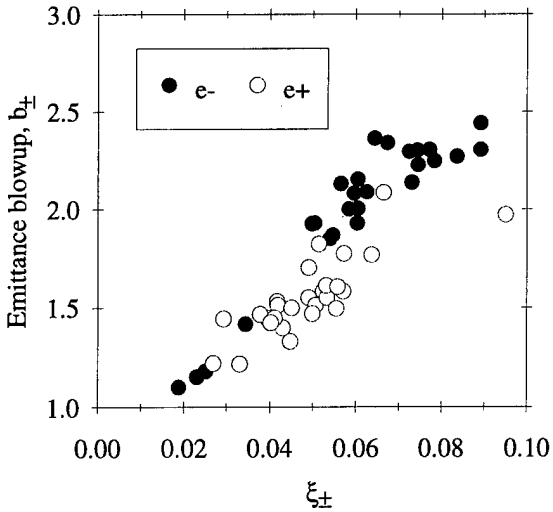

Figure 3: The emittance blowup of each beam, $b_\pm$ as a function of the tune shift parameter which it experienced, $\xi_\pm$.

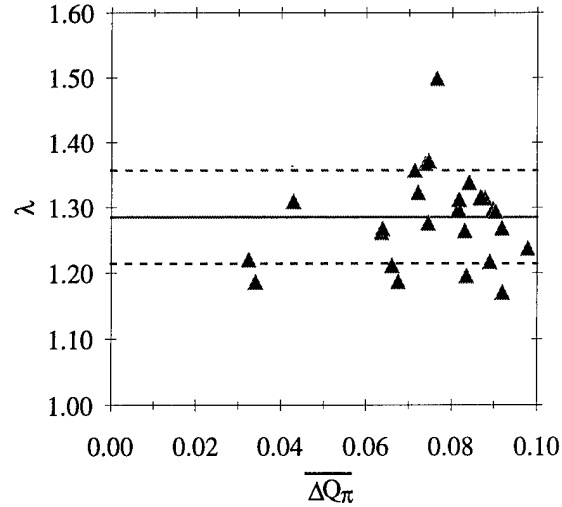

Figure 4: The calculated factor λ vs. ΔQ_π. $\lambda_{\rm av} = 1.28 \pm 0.07$ is indicated by the horizontal lines.

been derived for the case $\epsilon_+ \neq \epsilon_-$. Figure 4 shows that our results correspond to values of λ in the range 1.28 ± 0.07.[4]

3.3 *Luminosity*

As a further consistency check, the luminosity as measured by the CLEO endcap detector was recorded during two runs, and the beam profiles and currents were recorded several times during those runs from which the theoretical luminosity was calculated. Table 2 shows that there was good agreement between the measured luminosity and the luminosity predicted by equation (1).

Table 2: The luminosity calculated from I and ϵ and the measured luminosity at different times during two runs.

$I_{\rm per\ beam}$ in mA ($\pm$ 2%)	L in 10^{31} cm^{-2} s^{-1} Calculated ($\pm$ 10%)	Measured ($\pm$ 5%)
19.5	0.95	0.97
21.6	1.10	0.95
21.1	1.12	1.06
19.1	0.95	0.93

[4]For round beams with unequal currents per beam (but equal emittances), Yokoya and Koiso[3] find that λ increases from 1.21 to 1.28 as the current ratio becomes 2:1. Had we chosen to normalize our emittances to the lattice value ($\epsilon_0 = 62$ nm-rad), we would have obtained $\lambda = 1.43$; normalizing to the scraper result ($\epsilon_0 = 51$ nm-rad) would have yielded $\lambda = 1.18$.

4 CONCLUSION

These experiments demonstrate the feasibility and promise of collisions of beams made round via strong coupling. Tune shift parameters of the same order ($\xi \rightarrow 0.09$) as those in simulations were reached with only moderate emittance blowup and without significant lifetime reduction.

5 REFERENCES

[1] R. Talman, Phys. Rev. Lett., v. 74, p. 1590 (1995).

[2] S. Krishnagopal and R. Siemann, *Proc. 1989 IEEE Part. Accel. Conf.*, p. 836 (1989).

[3] K. Yokoya and H. Koiso, Part. Acc., v. 27, p. 181 (1990).

[4] Y. I. Alexahin, "On the Landau Damping and Decoherence of Transverse Dipole Oscillations in Colliding Beams," CERN-SL-96-64 AP (1996).

[5] D. Sagan, D. Rubin, and S. Greenwald, *Proc. EPAC '96* (1996).

LONGITUDINAL BUNCHED-BEAM INSTABILITIES IN A BARRIER RF SYSTEM

Y. H. Chin and H. Tsutsui, KEK, 1-1 Oho, Tsukuba-shi, Ibaraki-ken, 305, Japan

Abstract

This paper deals with theoretical and numerical analysis of longitudinal instabilities in a barrier RF system. A theory was developed to formulate using the Vlasov equation and the synchrotron- energy mode expansion. The result can be expressed in a form of eigenvalue matrix. A simulation code ECLIPS (Evaluation Code for Longitudinal Instabilities in a Proton Synchrotron) was also developed. Both were applied to the JHF 50GeV proton synchrotron at injection. They show excellent agreements. The results demonstrate that the microwave and the negative mass instabilities in a bunched beam can be explained by mode-coupling instabilities.

1 INTRODUCTION

The barrier RF system[1] has been proposed as a new method to achieve a high beam current by creating a very flat bunched beam. Unlike in a conventional RF system, particles are drifting freely between two discreet single-turn RF waveforms at which they suddenly receive repelling forces to turn around. The particle trajectory results in an squarish shape in the phase space. The bunch length can be easily controlled by changing the distance between two barriers. The synchrotron motion tends to become very slow (of the order of 10 Hz at the JHF[2]), while its frequency spread becomes comparable to the synchrotron frequency itself. An idea of higher harmonic cavity is aimed to create a similar RF environment[3].

The collective stability of the beam due to wake fields in a barrier RF system may resemble that in a coasting beam, provided that the wave length of the beam density modulation is shorter than the bunch length and the instability growth is much faster than the synchrotron oscillation. Such a coasting beam approximation has beam made for years to allow the usage of the Keil-Schnell-Boussard criterion to a long proton bunch. It is, however, not clear what should replace the Keil-Schnell-Boussard criterion when the coasting beam approximation is inappropriate in a bunched-beam.

A more direct approach, based on the bunched-beam mode expansion of the phase space density, has been proposed by Sacherer[4]. This is an attempt to explain the microwave and negative mass instabilities in a bunched beam in terms of couplings between different synchrotron modes. The mode-coupling offers a possible explanation for existence of the threshold. However, his formalism lacks the Landau damping effect due to a synchrotron frequency spread (or energy spread), which plays an essential role in a coasting beam to set the threshold. Therefore, his mode-coupling theory fails to make a transition to the coasting beam theory.

Our goal is to construct a theory proper bunched-beam longitudinal instabilities in a barrier RF system with the Landau damping effect included and without the coasting beam approximation. The correct treatment of the synchrotron frequency spread in the squarish barrier bucket can be done by describing the synchrotron motion using action-angle variables[5]. From numerical comparisons between the theory and simulations, we can show that the coasting beam instabilities are indeed transformed to mode-coupling instability in a long bunch.

2 VLASOV ANALYSIS

In this section, we briefly outline the formalism. The phase space particle trajectory in the barrier bucket is illustrated in Fig. 1:

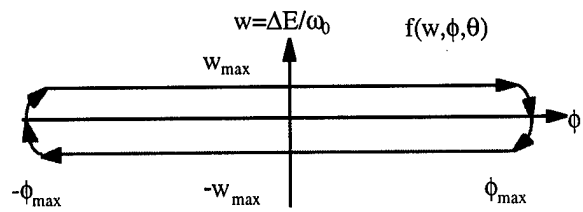

Figure 1: Phase space trajectory in a barrier bucket.

where ΔE is the energy deviation from the average energy E_0, ω_0 is the revolution frequency, and ϕ is the relative position of particle in a bunch in angle. We use θ, the angular position of particle in a ring, as an independent variable. Let us approximate this trajectory by a square for simplicity. The constant of motion (action I) is the area confined by the square trajectory:

$$I = \frac{1}{2\pi}\int dw d\phi = \frac{2}{\pi}\phi_{\max} w_{\max} \tag{1}$$

The corresponding angle variable is the phase of the particle oscillation around the trajectory:

$$\psi \equiv \omega_s t = -\frac{\eta}{\beta^2}\cdot\frac{\pi\omega_0^2}{2\phi_{\max}E_0}\cdot w_{\max} t \tag{2}$$

where η is the slippage factor, βc is particle velocity and

$$\omega_s \equiv \nu_s(I)\omega_0 = -\frac{\eta}{\beta^2}\cdot\frac{\omega_0^2}{E_0}\left(\frac{\pi}{2\phi_{\max}}\right)^2 I \tag{3}$$

is the synchrotron frequency proportional to I.

The evolution of phase space distribution $f(I,\psi,\theta)$ obeys the Vlasov equation:

$$\frac{\partial f}{\partial\theta} + \psi'\frac{\partial f}{\partial\psi} + I'\frac{\partial f}{\partial I} = 0 \tag{4}$$

where a prime means taking the derivative with respect

0-7803-4376-X/98 /$10.00 © 1998. IEEE

to θ. We solve the above equation by the perturbation technique. Since I and ψ are the canonical variables, the perturbed part of $f(I,\psi,\theta)$ can be factorized to separate functions for each of them. The angle dependent function can be Fourier expanded due to the periodicity with period 2π. The phase space distribution can be thus written as

$$f(I,\psi,\theta) = f_0(I) + \sum_{m=-\infty}^{\infty} f_m(I)\exp(im\psi)\exp(-i\Omega\theta) \qquad (5)$$

Here, the integer m stands for synchrotron mode number. The line charge density $\rho(\phi)$ corresponding to the perturbed part of the phase space distribution is given by

$$\rho(\phi) = \frac{2}{\frac{2}{\pi}\phi_{\max}} \cdot \sum_{m=-\infty}^{\infty} \begin{bmatrix} i\sin(m\frac{\phi}{\phi_{\max}}\frac{\pi}{2}) \\ \cos(m\frac{\phi}{\phi_{\max}}\frac{\pi}{2}) \end{bmatrix} \cdot \int_0^{\infty} f_m(I)dI \qquad (6)$$

The upper and lower terms in the bracket correspond to odd and even integers of m, respectively. Figure 2 shows $\rho(\phi)$ for the lowest three synchrotron modes.

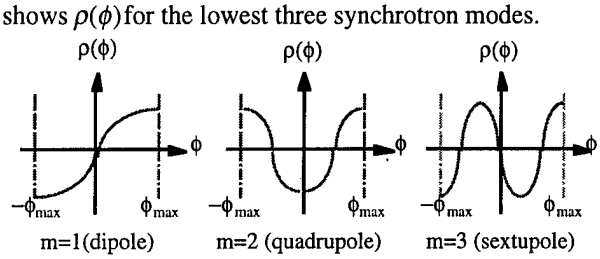

Figure: 2 The line charge density $\rho(\phi)$ for m=1 (dipole), m=2 (quadrupole) and m=3 (sextupole) modes.

Using the impedance $Z(\omega/\omega_0)$ and the Fourier transform of $\rho(\phi)$, $\tilde{\rho}(\nu)$, we can write

$$I' = -e^2 N \frac{\phi_{\max}}{\pi^2}\mathrm{sgn}(w)\sum_{p=-\infty}^{\infty} Z(p+\Omega)\tilde{\rho}(p+\Omega) \times \exp(-i(p+\Omega)\phi - i\Omega\theta) \qquad (7)$$

$$\psi' = \nu_s(I) \qquad (8)$$

where N is the number of particles in a bunch. Substitution of Eqs. (5), (7) and (8) into Eq. (4) yields an integral equation for $f_m(I)$:

$$(\Omega - m\nu_s(I))f_m(I) = i\frac{2eI_b m}{\pi^3\omega_0}\sum_{n=-\infty}^{\infty}\frac{df_0(I)}{dI}i^{n-m}\int_0^{\infty} f_n(I')dI' \times \sum_{p=-\infty}^{\infty}\frac{Z(p+\Omega)}{p+\Omega}C_m^*(p+\Omega)C_n(p+\Omega) \qquad (9)$$

where I_b is the circulating current and

$$C_m(q) = \frac{q\frac{2}{\pi}\phi_{\max}\begin{bmatrix} i\cos(q\phi_{\max}) \\ \sin(q\phi_{\max}) \end{bmatrix}}{m^2 - \left(q\frac{2}{\pi}\phi_{\max}\right)^2} \qquad (10)$$

The same rule as in Eq. (6) is applied to Eq. (10).

Let us solve Eq. (9) by expanding the unknown function $f_m(I)$ using a complete set of orthogonal polynomials The choice of appropriate polynomials depends on the unperturbed distribution $f_0(I)$ (the initial energy distribution). For a Gaussian distribution, it is the Laguerre polynomials. After lengthy calculation, Eq. (9) transforms to a matrix eigenvalue equation for Ω and an expansion coefficient vector $\mathbf{a}$:

$$\Omega\mathbf{I}\cdot\mathbf{a} - \mathbf{N}\cdot\mathbf{a} = \mathbf{M}\cdot\mathbf{a} \qquad (11)$$

where $\mathbf{I}$ is the unit matrix and the elements of other matrixes are explicitly given by

$$N_{nl}^{mk} = -m\frac{\pi\eta}{\sqrt{2}\phi_{\max}\beta^2}\left(\frac{\Delta E}{E_0}\right)_{rms}\delta_{mn}L_{kl} \qquad (12)$$

$$L_{kl} = \int_0^{\infty}\sqrt{x}e^{-x}L_k(x)L_l(x)dx \qquad (13)$$

$$M_{nl}^{mk} = -im\frac{\sqrt{2}I_b}{\pi^{5/2}\phi_{\max}(\Delta E/E_0)_{rms}E_0/e}i^{n-m}\delta_{k0}\delta_{l0} \times \sum_{p=-\infty}^{\infty}\frac{Z(p+\Omega)}{p+\Omega}C_m^*(p+\Omega)C_n(p+\Omega) \qquad (14)$$

Here, $L_k(x)$ is the Laguerre polynomials.

3 NUMERICAL EXAMPLES

Table 1 summaries the main parameters of JHF 50 GeV proton synchrotron at injection. The resonator model is used to characterize the impedance of the ring.

Table 1: Main parameters of JHF 50 GeV ring.

Injection energy, E_I	3 GeV
Circumference, C	1442 m
Design circulating current, I_b	6.65 A
Slippage factor, η	-0.05
Half bunch length in angle, $\phi_{\max}$	150 degree
RMS energy spread, $(\Delta E/E_0)_{rms}$	0.212%
RMS synchrotron frequency, $\Omega_0/2\pi$	16.96 Hz
Impedance of the ring at peak, R_s	10 kΩ
Resonant frequency, f_r	3.4 MHz
Q-value	1

Figure 3 shows the coherent synchrotron mode frequencies (normalized by Ω_0) and the growth rate as a function of the circulating current. Several modes start to couple at about 5A, signaling the onset of instabilities. Figure 4 shows the time evolution of the rms energy spread at 5A for various initial energy spread. One can see that the energy distribution stops to blow up when the initial energy spread is about 0.2%, in a good agreement with the analytical result (a slow increase of the energy spread attributes to non-compensation of the energy loss due to wake fields in simulations). Though not shown here, the phase space plot shows an uniform particle density after a blow-up of the energy spread. This is a signature of the microwave instability. The 5A threshold for circulating current is lower than the design value of 6.65A, which suggests a need of reducing the impedance.

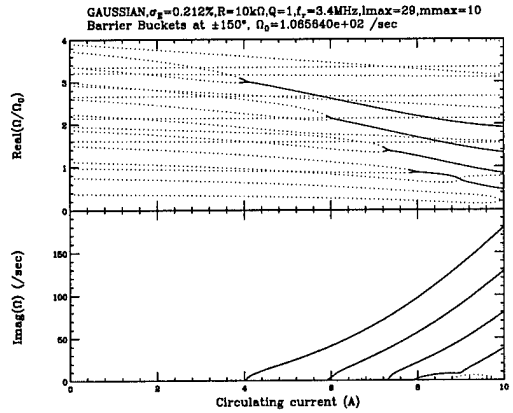

Figure 3: Coherent synchrotron mode frequencies and the growth rate versus the circulating current (theory).

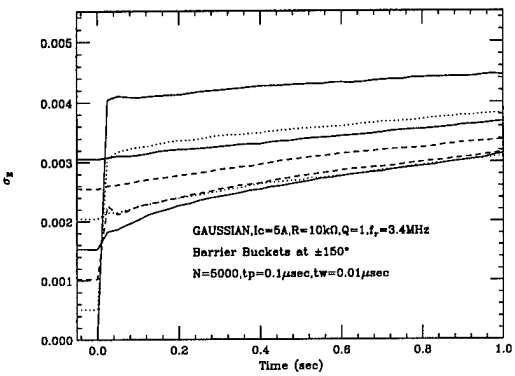

Figure 4: Time evolution of the rms energy spread for various initial spread (simulations).

Next, let us apply to a pure inductive impedance. The inductance is chosen to be equal to that of the resonator model at low frequency. The coasting beam theory predicts the excitation of negative mass instability. Figure 5 shows the coherent synchrotron mode frequencies and the growth rate versus the circulating current. Many synchrotron modes couple simultaneously with their negative mode partners (they are mirror images with respect to the $\Omega=0$ line) at about 9A. The growth rate increases very rapidly after the mode-couplings. Figure 6 shows the time evolution of the rms energy spread at 9A for various initial energy spread. The threshold of energy spread appears to be around 0.21%, in a good agreement with the analytical result again. Figure 7 shows the phase space distribution after the instability ceased for the initial energy spread of 0.05%. Strong concentration of particles can be observed at several places as expected for the negative mass instability. According to the coasting beam theory, the negative mass instability has the same threshold for all coasting beam modes "n" for a pure inductive impedance. This behavior agrees with the simultaneous onset of mode-coupling instabilities of all synchrotron modes as seen in Fig. 5. Another important point is that the real part of mode frequencies vanishes after mode-couplings. Namely, the modes stop moving in phase space, while they grow. This behavior corresponds to the characteristic of the negative mass instability that the crests of beam density are fixed in the beam frame.

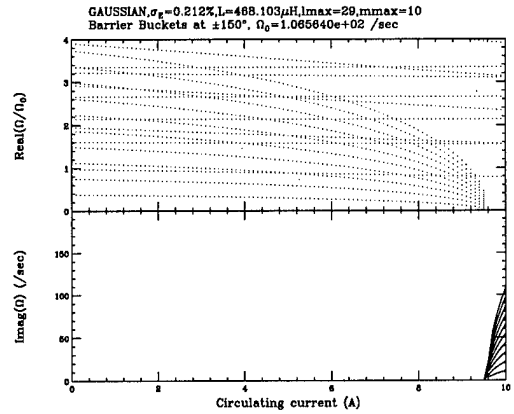

Figure 5: Coherent synchrotron mode frequencies and the growth rate for the inductive impedance (theory).

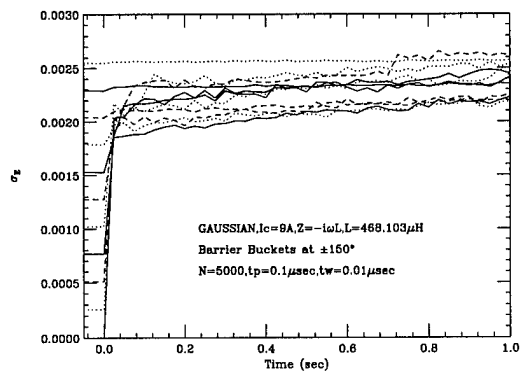

Figure 6: Time evolution of the rms energy spread for various initial spread for the inductive impedance (simulations).

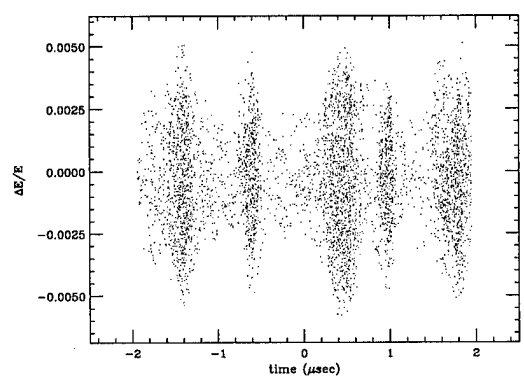

Figure 7: The phase space distribution after the instability ceased for the initial energy spread of 0.05% (simulations).

REFERENCES

[1] J.E. Griffin et. al., IEEE Trans. NS-30, 3502 (1983).
[2] KEK Report JHP-30 (1996).
[3] A. Hofmann and S. Myers, LEP Lote 158 (1979).
[4] F. Sacherer, IEEE Trans. NS-24, 1393 (1977).
[5] Y.H. Chin, Nucl. Instr. Methods, 215, 501 (1983).

MICROWAVE INSTABILITY AT TRANSITION CROSSING IN THE KEK-PS

K. Takayama, D. Arakawa, J. Kishiro, K. Koba, T. Toyama, and M. Yoshii
High Energy Accelerator Research Organization (KEK)
1-1 Oho, Tsukuba, Ibaraki 305 Japan

Abstract

Microwave instability in the KEK proton synchrotron was systematically studied Temporal evolution of the microwave instability was clearly explained with a proton-klystron model. Beam position monitors and cavity-like vacuum chambers have been idetified as its driving sources. Replacement of these high impedance materials has been confirmed to reduce the growth of the instability to the expected level.

1 INTRODUCTION

The KEK 12GeV PS has been subject to serious damage of the microwave instability (MI) at transition crossing (TC) since the beginning of its operation[1]. Since KEK-PS's impedance budget has been never concerned, a lot of high impedance materials as discussed later are *periodically* located along the ring, following lattice components. The observed threshold beam current for the M.I. and size of Landau daming due to γ_t-jump are different in order of magnitude from that of the theoretical estimation based on the existing broad-band model. In the recent article[2], simulation works and experimental test of the longitudinal impedance, extensive beam experiments of the MI at TC, a proton-klystron model capable of consistently explaining the experimental results, and their comparison was presented. In the last summer, two-thirds of resonant impedance devices to which the MI can be attributed has been replaced by low impedance ones. Its results will be reported in addition to brief review of the article [2].

2 EXPRIMENTAL RESULTS

A single bunch(500MeV) from the booster ring was injected into the 12GeV-PS ring waiting with standing RF-buckets of harmonic 9. The beam intensity(1-5x10^{11} /ppp) was controlled by changing the H^- beam spill-length hitting a stripping carbon-foil in the booster, the RF frequency is ~7MHz, and the synchronous phase is switched from 15^0 to 165^0 at TC. To elucidate the dependence of the MI on phase-mixing speed, the size of γ_t-jump, $\Delta\gamma_t$, was varied up to 0.25 for 0.5msec Longitudinal bunch information was a signal from the fast wall-current monitor with ~2GHz resolution.

The MI observed in the KEK-PS always grows from the tail portion. Fig.1 shows a typical evolution of the bunch-shape which is projected on the time-axis. Below transition the MI never evolves to an observable level, just after TC it dramatically starts to grow within 1 msec near 1GHz, then a fraction goes away from the bunch-center. High frequency(400MHz-12GHz) components of the beam-induced signal on the vertical plate in the beam position monitor(BPM) were obtained by a spectrum analyzer; the 1.23GHz component is remarkable after TC when the instability occurs. This component is related to the MI and its frequency is in agreement with the modulation frequency observed in the bunch profile.

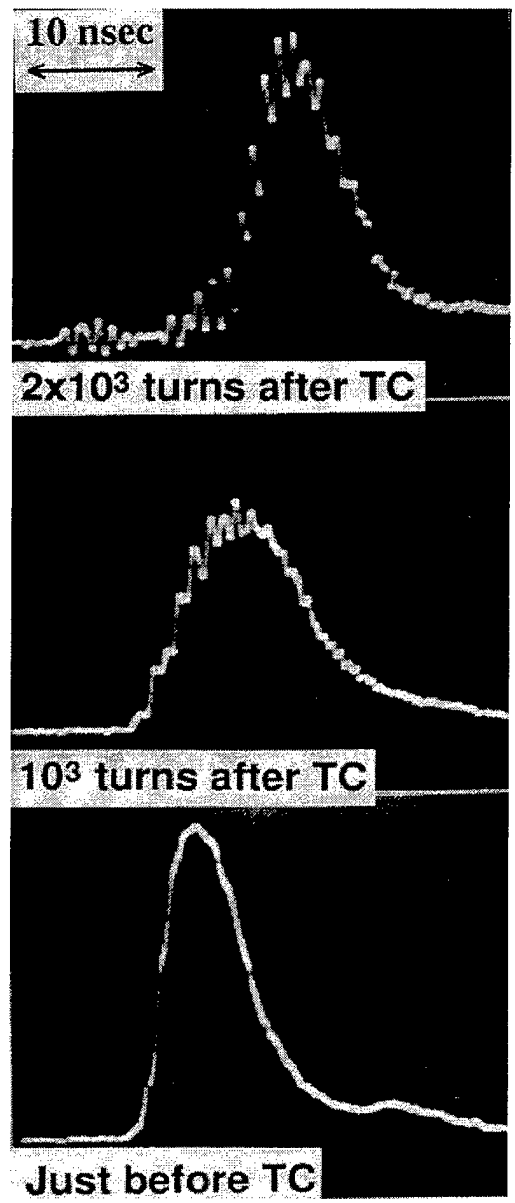

Fig.1. Bunch Profiles from -1 msec to +2msec (t=0 msec: transition)

Fig.2 shows the ratio as a function of the particle number per bunch. Beyond some critical value of particle number the blow-up becomes obvious. The dependence of the emittance blow-up on a size of γ_t-jump is depicted in Fig.3 for a fixed beam current of $N=5\times10^{11}$.

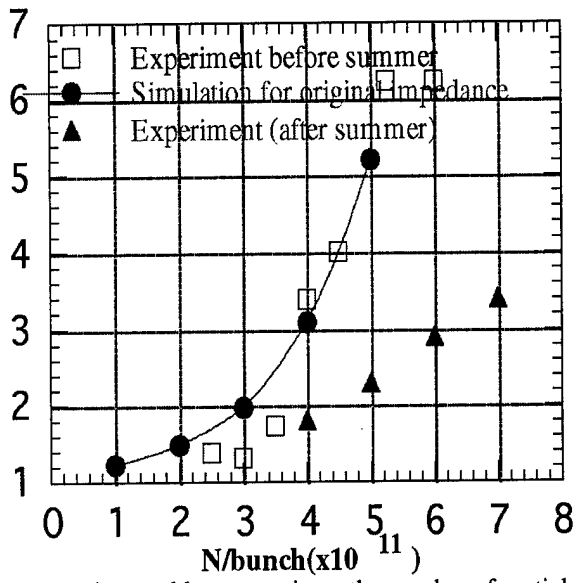

Fig.2. Emittance blow-up ratio vs the number of particles

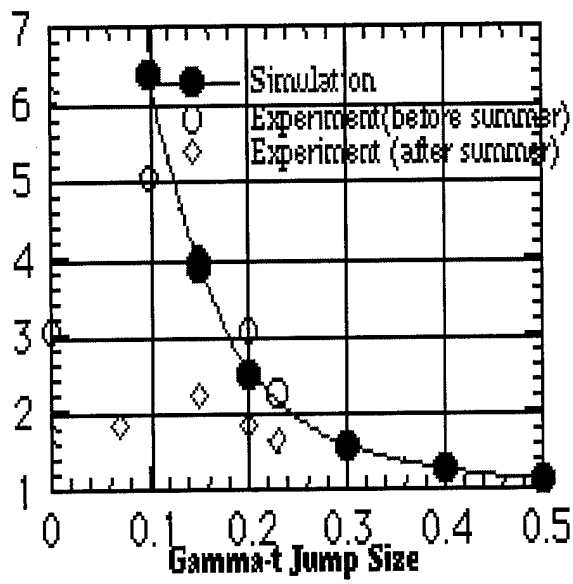

Fig.3. Emittance blow-up ratio vs the size of γ_t jump($\Delta\gamma_t$)

3 IMPEDANCE CALCULATION & MEASUREMENTS

Resonant structures(RS) capable of exciting the observed MI have been identified as a result of MAFIA calculations and impedance measurements at the test-bench. As shown in Table, the BPM and cavity-like vacuum-chamber(CVC) which are placed at each side of vacuum chamber in the lattice quadrupole magnets have a large shunt-impedance. In the numerical simulations, a magnitude of R_{shunt}/Q obtained by the MAFIA calculations and measurements has been used, which are in agreement to each other in order of magnitude; while the quality factor was treated as a kind of free parameter because a loaded Q in the actual ring is not satisfactorily estimated.

Table 1
Resonant Impedance(measurement/calculation)

	$\omega_\lambda/2\pi$ (GHz)	Q	R_{shunt} (Ω)	R/Q (Ω)
BPM	0.636/0.667	77/2650	$1.5\times10^3/2.6\times10^4$	19.4/9.8
	/1.13	/3769	$/6.2\times10^4$	/16.3
	1.498/1.377	230/8222	$5.3\times10^3/3.3\times10^3$	23/40
CVC	/1.44	/4846	$/1.4\times10^5$	/28.8
	/1.84	/4048	$/1.9\times10^5$	/46.6

4 PROTON-KLYSTRON MODEL

In the model highly RS are periodically distributed along the beam-path and wake fields excited by the bunch-head can affect the bunch-tail. Member change in a global-scale between the bunch-head and -tail scarcely occurs near transition. All of excited RS can be regarded as idling cavities. Build-up of the wakes in each RS is treated in a formulation of the forced excitation of a damped harmonic-oscillator, as discussed in the reference [2].

5 SIMULATION RESULTS

The temporal-evolution of a bunch was numerically obtained. As seen in Fig.4, the simulation reproduces the essential aspects of the experimental result: (1) no notable growth of the MI below TE, (2) its rapid growth just after the TC, (3) run away of a bunch-fraction, and (4) large blow-up of the emittance after the TC-process.

General features of the MI are (a) efficient energy transfer from beam to microwaves is resulted from the deceleration of the micro-structure's core, yielding the drift of the cores in the negative direction of the momentum space, (b) the interaction between wakes and the beam tends to occur in the bunch-tail owing to the finite Q-value, (c) the convection of the micro-structure formation toward the bunch-head is crucial from the same reason as that of (b). According to (b) and (c), the particles located in the region of $E>E_s$ and $\phi>\phi_s$ below the TE and $E<E_s$ and $\phi>\phi_s$ above the TE can contribute to the evolution of the MI. Since the wake's phase coincides with the motion of micro structure's core, the particles located in the other side of momentum-space are affected by the wake in counter phase, suffering a rapid modulation in their motion. Below the TE a fraction of decelerated microbunch core necessarily falls into the region of $E<E_s$ where the fraction is forced to move in the opposite direction of the phase ϕ; the microbunch formation is likely to be wiped out. Thus the MI is not able to evolve to a level comparable to that above the TE.

In the early-stage (≤400 turns) bunching and

amplification proceed like that in a microwave amplifier such as free-electron lasers; the repeated synchrotron-rotation in the micro-bucket doesn't occur but particles almost drift in the momentum-space. A fraction of the micro structure placed in the decelerating phase is rapidly decelerated, amplifying the microwaves. The microwaves' phase follows the motion of the decelerated fraction because electro-magnetic waves are amplified at the expense of the kinetic energy of protons. Consequently the other fraction having been placed in the accelerating phase falls into the decelerating phase to turn to contribute to further microstructure formation. This looks like eruption in the bunch-tail (see the middle of Fig.4).

Simulation results indicated that for the fixed value of R_{shunt}/Q=10 ohm and $(\Delta\gamma_t)$=0.15 the bunch eruption due to the MI is remarkable beyond $N_0=3\times10^{11}$ as seen in Fig.2. Simulations showed larger suppression of the MI as the size of $d\gamma_t/dt(=2(\Delta\gamma_t)_{max}/\Delta t)$ increases (see Fig.3) and are in good agreement with the experimental results. The fast phase-mixing in a case of the large $(\Delta\gamma_t)_{max}$ is likely to prevent the MI from growing up. There is a notable difference in the region of small size of $d\gamma_t/dt$ where the nonlinear kinematics effects are dominant and a beam bunch asymmetrically stretches in the direction of $\Delta p/p>0$. There the momentum spread in the bunch tail exceeds the momentum aperture; accordingly a significant fraction of the bunch tail is lost. To confirm the relative importance of the broad-band space-charge impedance in the present MI, space-charge forces were turned off; there any notable change in the eruption-like feature was not found.

6 RESONANT IMPEDANCE REDUCTION

During the summer shutdown, the two-thirds of highly resonant impedance device pairs (BPM and CVC) have been replaced by newly designed ones. The new BPM is an elctrostatic type. Its R_{Shunt}/Q is reduced by a factor of 2 or 3 according to the MAFIA calculation. The resonant frequency of the dominant mode moves to 342MHz. In the new CVC the original cavity-like structure is discarded and the evacuation port is shilded by RF slits. As a result, a magnitude of resonant impedance is neglible small. The emittance blow-up ratio has been measured in the same way. The results are put in Figs2,3. Certainly, the emittance blow-up ratio has notably decreased as expected, although the MI itself is still observed to evolve at some level.

7 CONCLUSION

The systematic experimental results of the MI at TC and their theoretical explanation were presented. The countermeasure employed to suppress the MI was reported. The particular aspects of eruption-like breakup just after TC and its evolution from the tail-half which have never been anticipated by the conventiona

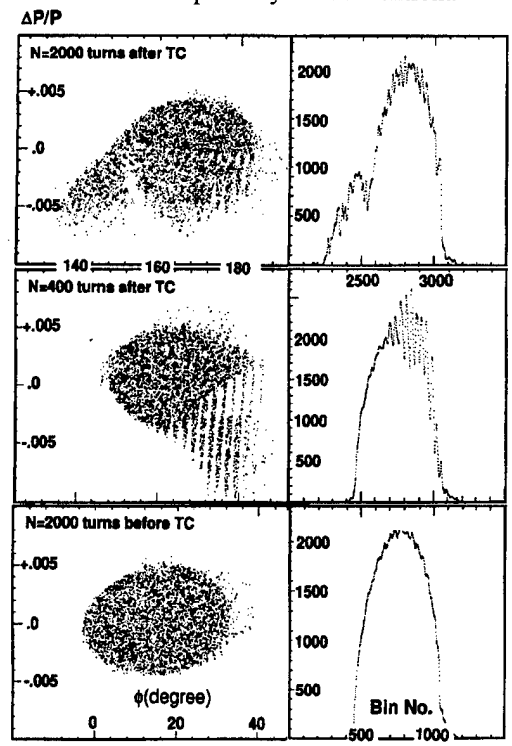

Fig.4. Typical simulation results of TC

l collective instability theory and simulation where a cumulative feature of the beam-cavity interaction in a finite time-period is not taken into account, were clearly manifested by the proton-klystron model. The TC in the KEK-PS may provide the germinal situation of a large-scale proton klystron which was proposed as a possible power source for linear colliders[3].

8 ACKNOWLEDGEMENTS

The authors wish to thank KEK-PS members for their interest and continual support through this work. T.Kubo deserves our thanks for providing various information on the vacuum devices and arrangment of replacement works. One of authors(K.T.) acknowledges Prof. S.Y.Lee and Dr. J.Wei for useful discussions and comments.

9 REFERENCES

[1] Y.Mizumachi and K.Muto, *IEEE Trans. on Nucl. Sci.* **NS-28, No. 3**, 2563 (1981), S.Ninomiya and T.Ieiri, private communication (1995).

[2] K.Takayama, D.Arakawa, J.Kishiro, K.Koba, and M.Yoshii, *Phys. Rev. Lett.***78**, 871 (1997).

[3] E.Perevedentsev and A.Skrinsky, *Proc. of 12th Int. Conf. on High-Energy Accelerators*, 508(1983).

FRACTIONAL FILLING INDUCED LANDAU DAMPING OF LONGITUDINAL INSTABILITIES AT THE ESRF

O. Naumann, J. Jacob, ESRF, Grenoble

Abstract

Longitudinal coupled bunch instabilities are a major obstacle for the increase of beam current in modern electron storage rings. At the ESRF, threshold limits for multi-bunch operation have been considerably increased by using fractional fillings, from about 60 mA for a homogeneous filling to well beyond the nominal intensity of 200 mA for a filling of one third of the circumference. The gap in the bunch train induces a modulation of the cavity voltage and a subsequent spread in synchrotron frequencies. This results in additional Landau damping. An appropriate set of coupled equations, which completely models the problem, has been derived. With slight simplifications one obtains analytical formulae which still accurately describe the observed effect. The theoretical results have been soundly confirmed by experiments carried out at the ESRF.

1 INTRODUCTION

Longitudinal coupled bunch instabilities (LCBIs) arise from the resonant coupling of multi-bunch modes (MBMs) with higher order modes (HOMs) in RF cavities. Avoiding the resonance by tuning away the HOMs is one remedy, reduction of the coupling by damping the HOM or staying at low beam currents is another. In the present paper we show how, additionally, Landau damping [1] can be used in high energy electron storage rings to maintain strong beam current levels. It is routinely applied at the ESRF in combination with a dedicated temperature regulation system [2].

In section 2 we use a set of coupled equations to treat the combined effect of Landau damping coming from different synchrotron frequencies of the individual bunches and the strong natural synchrotron damping in a high energy storage ring. We also present methods to accurately calculate current thresholds. Section 3 gives results on the determination of the frequency spread induced by the beam loading due to a fractional filling. We employ this to compute the threshold current. In section 4 we present experimental results that validate our theory.

Unless stated otherwise we use standard ESRF parameters [2], [3]. Notably the revolution time is $T_0 = 2.8\ \mu$s, the revolution frequency $\omega_0/(2\pi) = 355$ kHz, the energy $E_0 = 6$ GeV, the loss per turn $U_0 = 4.75$ MeV, the momentum compaction factor $\alpha = 1.9 \cdot 10^{-4}$, the harmonic number $h = 992$, the natural damping constant $\delta_\mathrm{n} = 277$ Hz the mean synchrotron frequency $f_\mathrm{s} = \omega_\mathrm{s}/(2\pi) = 1.97$ kHz and the peak cavity voltage $\widehat{V} = 8$ MV. HOMs with shunt impedances up to about 4 MΩ have to be considered at the ESRF, mainly at 500 and 910 MHz.

2 LCBI MODEL WITH A SPREAD IN SYNCHROTRON FREQUENCIES

2.1 Interaction Equations

For short bunches, rigid bunch MBMs are responsible for LCBIs. We model the beam in the storage ring as N rigid bunches, obeying synchrotron equations with frequencies $\omega_{\mathrm{s}k}$ spread over a range $\Delta\omega_\mathrm{s}$:

$$\ddot{\tau}_k + 2\delta_\mathrm{n}\dot{\tau}_k + \omega_{\mathrm{s}k}^2\tau_k = 0 \quad , \quad k = 1, \ldots, N \qquad (1)$$

τ_k is the temporal displacement of bunch k w.r.t. a synchronous particle at phase $\phi_{\mathrm{s}k}$. It is well known that

$$\delta_\mathrm{n} \approx \frac{U_0}{T_0 E_0} \quad , \quad \omega_{\mathrm{s}k}^2 = \frac{\alpha}{T_0 E_0/e}\left.\frac{\mathrm{d}V}{\mathrm{d}\tau}\right|_{\phi_{\mathrm{s}k}} \quad . \qquad (2)$$

Distinct $\omega_{\mathrm{s}k}$ arise from a modulation of $\mathrm{d}V/\mathrm{d}\tau$ and $\phi_{\mathrm{s}k}$.

An MBM giving rise to a synchrotron sideband in the beam spectrum at $(n + mh)\omega_0 + \omega$ can be described by

$$\tau_k(t) = \widehat{\tau}_k \mathrm{e}^{\mathrm{j}(\omega t + 2\pi n k/h)} \quad , \quad k = 1, \ldots, N \qquad (3)$$

where n is the MBM number, $\widehat{\tau}_k$ the complex amplitude and ω the common complex frequency of the bunch oscillation. Due to its high Q, an HOM is excited only by spectral lines near ω_HOM. Developing the phase modulated beam signal up to first order yields an expression for the HOM-voltage to be added to the energy budget of each bunch, linear in each $\widehat{\tau}_k$. Using this and the ansatz (3) in (1), we acquire a system of coupled equations for the $\widehat{\tau}_k$ and ω:

$$(-\omega^2 + \mathrm{j}2\omega\delta_\mathrm{n} + \omega_{\mathrm{s}k}^2)\widehat{\tau}_k = \mathrm{j}H\sum_{i=1}^{N} I_i\widehat{\tau}_i \qquad (4)$$

with $k = 1, \ldots, N$. Here I_i is the DC current in bunch i, the total current is $I_\mathrm{b} = \sum_{i=1}^{N} I_i$. H is given by

$$H = \omega_\mathrm{HOM} Z_\mathrm{HOM}\frac{\alpha}{T_0 E_0/e} \qquad (5)$$

with Z_HOM the impedance of the HOM (linac-Ohms).

2.2 Dispersion Relation

Eq. (4) leads to the dispersion relation

$$1 = \sum_{1=k}^{N}\frac{\mathrm{j}HI_k}{\omega_{\mathrm{s}k}^2 - \omega^2 + 2\delta_\mathrm{n}\mathrm{j}\omega} \quad . \qquad \text{(DR)}$$

Its N solutions ω_i are the eigenfrequencies of the system (4). For small currents the ω_i are near $\omega_{\mathrm{s}i} + \mathrm{j}\delta_\mathrm{n}$, increasing I_b will move them. The stability limit is reached at the threshold current I_th, where the first of the ω_i becomes purely real. Fig. 1 shows how the rhs of (DR) maps the positive real axis ($0 < \omega < \infty$). As in feedback theory, the system is instable if the critical point 1 is encircled.

0-7803-4376-X/98 /$10.00 © 1998 IEEE

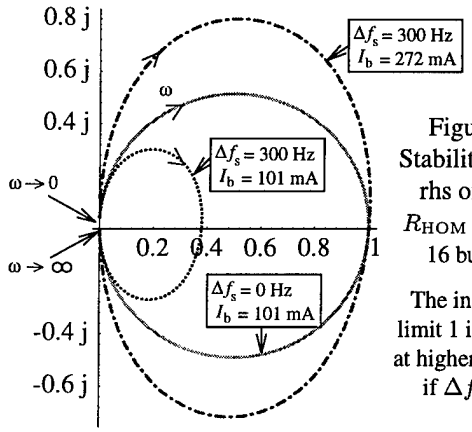

Figure 1: Stability traces, rhs of (DR) $R_{\mathrm{HOM}} = 2\,\mathrm{M}\Omega$ 16 bunches

The instability limit 1 is reached at higher currents, if $\Delta f_{\mathrm{s}} > 0$.

2.3 *Eigenvalue Approach*

The eigenvalues (μ_i) of the matrix obtained from eq. (4)

$$\begin{pmatrix} \mathrm{j}HI_1 - \omega_{\mathrm{s}1}^2 & \mathrm{j}HI_2 & \cdots & \mathrm{j}HI_N \\ \mathrm{j}HI_1 & \mathrm{j}HI_2 - \omega_{\mathrm{s}2}^2 & \cdots & \mathrm{j}HI_N \\ \vdots & \vdots & \ddots & \vdots \\ \mathrm{j}HI_1 & \mathrm{j}HI_2 & \cdots & \mathrm{j}HI_N - \omega_{\mathrm{s}N}^2 \end{pmatrix}$$

are related to the solutions ω_i by $\mu_i = \omega_i^2 - 2\delta_{\mathrm{n}}\mathrm{j}\omega_i$ and it is easier to compute them than to evaluate (DR) directly. An iteration in I_{b} yields I_{th}, as shown in Fig. 2. This illustrates best what Landau damping means here: because of the frequency spread energy is continuously transferred from the HOM excited MBM to the other MBMs. A narrow band feedback on the $n = 0$ MBM could be applied to damp the LCBI, as is addressed in [4].

Using natural damping we are reversing this idea: *all* MBMs now damp the *single* MBM that actively participates in the LCBI. In fact, the MBMs that do not couple back to the HOM dissipate their energy freely due to δ_{n}. Note that this scheme attacks *any* LCBI.

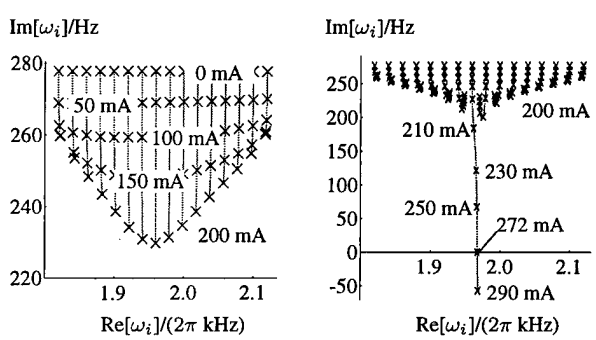

Figure 2: Evolution of the ω_i with I_{b}. $R_{\mathrm{HOM}} = 2\,\mathrm{M}\Omega$, 16 bunches, $\Delta f_{\mathrm{s}} = 300$ kHz.

2.4 *Simplifications for the Calculation of I_{th}*

In the worst case the crest of the HOM impedance will be exactly on the synchrotron sideband, then H is real. Knowing that at the threshold the dominating solution ω of (DR) is real, we have two equations for I_{th} and ω:

$$I_{\mathrm{th}} = \frac{N}{2\delta_{\mathrm{n}} H\omega}\left(\sum_{k=1}^{N}\frac{I_k/I_{\mathrm{th}}}{(\omega_{\mathrm{s}k}^2-\omega^2)^2+4\delta_{\mathrm{n}}^2\omega^2}\right)^{-1} \quad (6)$$

$$0 = \sum_{k=1}^{N}\frac{I_k(\omega_{\mathrm{s}k}^2-\omega^2)}{(\omega_{\mathrm{s}k}^2-\omega^2)^2+4\delta_{\mathrm{n}}^2\omega^2\delta_{\mathrm{n}}} \quad . \quad (7)$$

They are appropriate numerically for small N.

For equally populated bunches and sufficient natural damping, ω will be given approximately by the root mean square $\omega_{\mathrm{s}} = \sqrt{1/N\sum_{k=1}^{N}\omega_{\mathrm{s}k}^2}$. We write the total frequency spread as $\Delta\omega_{\mathrm{s}}$ and assume an even distribution in frequencies. Then in the case of many bunches we can replace the sum in eq. (6) by an integral and find a simple *analytical formula*:

$$I_{\mathrm{th}}(\Delta\omega_{\mathrm{s}}) = \frac{\omega_{\mathrm{s}}}{H}\frac{\Delta\omega_{\mathrm{s}}}{\arctan(\Delta\omega_{\mathrm{s}}\tau_{\mathrm{nat}}/2)} \quad . \quad (8)$$

Eq. (8) is a very good approximation for solutions obtained by the eigenvalue method or eqs. (6) and (7), as long as $\Delta\omega_{\mathrm{s}}/N \ll \omega_{\mathrm{s}}$. Note that

$$I_{\mathrm{th}}(\Delta\omega_{\mathrm{s}}) \begin{cases} \to & 2\delta_{\mathrm{n}}\omega_{\mathrm{s}}/H \quad \text{for } \Delta\omega_{\mathrm{s}} \to 0 \\ \approx & \dfrac{2\omega_{\mathrm{s}}}{\pi H}\left(\Delta\omega_{\mathrm{s}} + 4\dfrac{\delta_{\mathrm{n}}}{\pi}\right) \quad \text{for } \Delta\omega_{\mathrm{s}} \gg 2\delta_{\mathrm{n}} \end{cases}$$

For $\Delta\omega_{\mathrm{s}} \to 0$ the well known threshold formula is recovered, for large spreads the contributions of natural damping and Landau damping add up.

2.5 *Threshold Current Calculations*

As can be perceived in fig. 3, Landau damping in conjunction with natural damping is more effective at higher energies and for lower values of R_{HOM}. For the ESRF it allows an increase of the beam current by more than a factor 3. Low energy machines, however, may have difficulties in countering strong HOMs just by using this effect, as it does not change orders of magnitude.

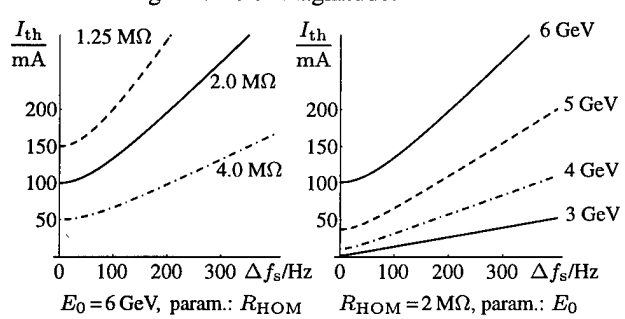

Figure 3: $I_{\mathrm{th}}(\Delta\omega_{\mathrm{s}})$ from eq. (8), $f_{\mathrm{HOM}} = 500$ MHz.

3 EFFECT OF FRACTIONAL FILLINGS

When filling only a fraction of the storage ring circumference, beam loading strongly modulates the cavity voltage. This gives the bunches different zero motion positions (see fig. 4) and different synchrotron frequencies (cf. eq. (2)).

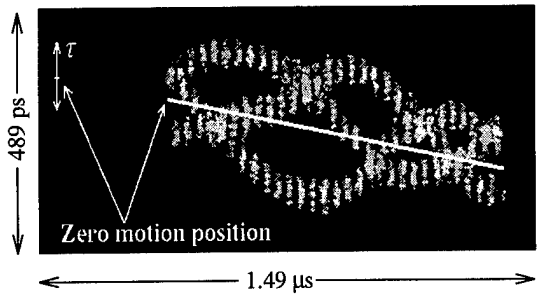

Figure 4: Instability in a 1/3 filling.
Streak camera image, 154 mA, HOM at 911 MHz

The resulting increase of the instability threshold can be calculated with the results of the preceding section if we have quantitative knowledge of the distribution of the ω_{sk}.

Since the beam loading itself is influenced by the position of each bunch, we have contrived an iterative process which converges towards the zero motion positions of all bunches. This fix-point problem has been treated numerically: fig. 5 shows how the overall spread changes with I_b and the filling ratio p.

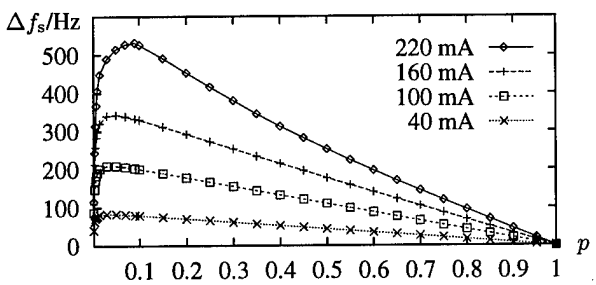

Figure 5: $\Delta\omega_s(p)$, calculated numerically.

Knowing $\omega_{sk}(I_b, p)$, we can determine the threshold current by solving the following equation for I_b:

$$I_b = I_{th}\left[(\omega_{sk}(I_b, p))_{k=1,\ldots,N}\right] \tag{9}$$

where I_{th} from eqs. (6) or (8) is used. Fig. 6 shows $I_{th}(p)$ in analogy to fig. 3. Since raising the beam current increases the spread of the ω_{sk}, self-stabilization is observed for smaller fractions and nonviolent HOMs: Landau damping overcomes the normal LCBI growth rate for any current (e.g. at 6 GeV for $p \leq 0.4$, if $R_{HOM} \leq 2\,M\Omega$).

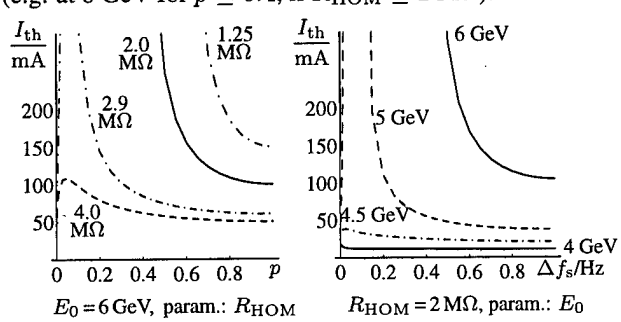

Figure 6: $I_{th}(p)$ from eq. (9), $f_{HOM} = 500$ MHz.

4 EXPERIMENTAL RESULTS

The theoretical results presented so far have been verified by experiments at the ESRF. By means of the temperature control system of the RF-cavities we deliberately tuned HOMs onto a synchrotron sideband. Varying the beam current and observing the presence or absence of longitudinal oscillations (cf. Fig. 4) the threshold current was determined. We present some results for an LCBI due to an HOM at 500 MHz and MBM number 417.

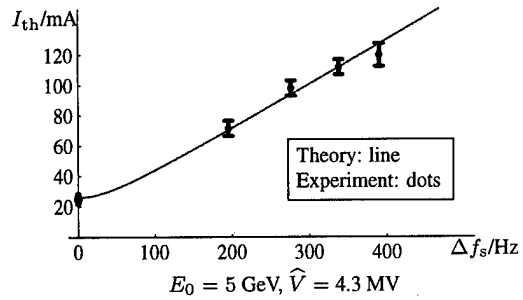

Figure 7: $I_{th}(\Delta f_s)$, theory and experiment.

A direct validation of the results in section 2 was possible at 5 GeV by operating one of the two RF units at $(h+1)\omega_0$, cf. fig. 7 and [2]. The spread in synchrotron frequencies due to the modulation $\Delta\widehat{V}$ is obtained from $\Delta\omega_s/\omega_s = (1 + \tan^2\phi_s)\Delta\widehat{V}/(2\widehat{V})$.

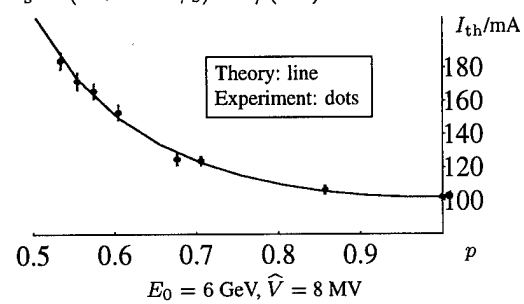

Figure 8: $I_{th}(p)$, theory and experiment.

Fig. 8 shows a striking confirmation of the results from section 3. However, we experienced some deviations for fractions $p \lesssim 0.4$ on strong HOMs around 910 MHz, with measured thresholds below theoretical predictions.

5 CONCLUSIONS AND OUTLOOK

A theory of Landau damping of LCBIs incorporating natural damping was elaborated and the spread in synchrotron frequencies from beam loading due to fractional fillings was computed. This was verified by experiments. Fractional fillings are a simple and efficient way to fight LCBIs in high energy storage rings, our results permit the deliberate choice of the appropriate filling ratio at the ESRF [3]. However, to allow high intensity operation in homogeneous fillings at 6 GeV, direct modulation is envisaged in the near future [2].

6 REFERENCES

[1] H. Hereward: 'The elementary theory of Landau damping', CERN 65-20, Geneva, 1965

[2] J. Jacob et al.: 'Construction of a 3rd RF Acceleration Unit for the ESRF Storage Ring', Proc. EPAC 96, p. 1970

[3] J.-M. Filhol, L. Hardy: 'Status report on the ESRF', PAC 97, these proceedings

[4] R.D. Kohaupt: 'The Theoretical Study of a New Multi-Bunch Damping Mechanism', Z. Phys. C 37, 159-164 (1987)

EFFECTS OF INCOHERENT SPACE CHARGE FORCES ON THE FAST HEAD-TAIL INSTABILITY

M. Blaskiewicz*, AGS Dept. BNL, Upton NY 11973-5000 USA

Abstract

The effects of incoherent space charge forces on the fast head-tail instability are studied numerically. It is found that incoherent space charge forces can dramatically increase the threshold current for a fixed wall impedance.

1 PHYSICAL MODEL AND SIMULATION ALGORITHM

For the purposes of beam dynamics one transverse and the longitudinal degrees of freedom are considered. Let θ denote the machine azimuth, which increases by 2π each turn and will be used as the time-like variable. The time is denoted by t and ω_0 is the angular revolution frequency of a synchronous particle. Consider a single particle and let $\tau(\theta) = t - \theta/\omega_0$ denote the time delay between this particle reaching θ and the synchronous particle reaching θ. The longitudinal equation of motion for a single particle is approximated as

$$\frac{d^2\tau}{d^2\theta} + Q_s^2\tau = 0, \tag{1}$$

where Q_s is the synchrotron tune. The single particle equation of motion for the transverse degree of freedom x is approximated as

$$\begin{aligned}\frac{d^2x}{d^2\theta} &= -Q_x^2x + C_{sc}\rho(\theta,\tau)(x - < x(\theta,\tau) >) \\ &+ \int_{-T}^{\tau} d\tau' W(\tau-\tau')\rho(\theta,\tau') < x(\theta,\tau') > . \end{aligned} \tag{2}$$

In equation (2) Q_x is the bare betatron, $C_{sc} \geq 0$ characterizes the peak strength of the incoherent space charge force, and $\rho(\theta,\tau)$ is the line density of the particles which vanishes for $|\tau| > T$, the half length of the bunch. The transverse center of the beam as a function of azimuth and delay is $< x(\theta,\tau) >$, and the causal coherent forces due to wall impedances are characterized by the wake potential $W(\tau)$. Extending the model to include chromaticity and long range wake forces is straightforward, but will not be considered here.

Equations (1) and (2) are solved by particle tracking. The bunch is modeled as N interacting macro-particles. The equations of motion for kth macro-particle are taken to be

$$\begin{aligned}\frac{d^2\tau_k}{d^2\theta} &= -Q_s^2\tau_k \\ \frac{d^2x_k}{d^2\theta} &= -Q_x^2x_k + \frac{C_{sc}}{N}\sum_{j=1}^{N}(x_k - x_j)\lambda(\tau_k-\tau_j) \\ &+ \frac{1}{N}\sum_{j=1}^{N} x_j\hat{W}(\tau_k-\tau_j). \end{aligned} \tag{3, 4}$$

In equation 4 the new functions $\lambda(\tau)$ and $\hat{W}(\tau)$ are introduced to smooth out the particle-particle forces. If one takes the limit $N \to \infty$ and then takes the limits of $\lambda(\tau)$ going to a delta function and $\hat{W}(\tau) \to W(\tau)$, equation (2) is recovered.

The number of macro-particles is controlled using the parameter n_ℓ. The initial longitudinal variables, τ_k, and $v_k = d\tau_k/(Q_s d\theta)$, are selected by considering the subset of lattice points $(T_k, V_k) = ((k_\tau + 1/2)/n_\ell, (k_v + 1/2)/n_\ell)$, with k_τ and k_v integers, which are inside the unit circle. The initial longitudinal coordinates of a macro particle are derived via

$$(\tau_k, v_k) = L(T_k, V_k)\left(1 - (1 - R_k^2)^{1/(1+\mu)}\right)^{1/2}/R_k,$$

where the parameter μ determines the bunch shape and $R_k^2 = T_k^2 + V_k^2$. The smoothed density in longitudinal phase space is proportional to $(L^2 - \tau^2 - v^2)^\mu$, and results in a line density $\propto (L^2 - \tau^2)^{\mu+1/2}$. During the simulation the longitudinal variables were updated once per turn using a rotation with angle $2\pi Q_s$. Figure 1 illustrates the selection of longitudinal coordinates.

The initial values of the transverse variables x_k and $p_k = dx_k/d\theta$ were obtained using a random number generator. The transverse dynamics consists of two parts, single particle dynamics and multiparticle dynamics. The scheme involves a single particle update followed by a multiparticle update and is repeated M times per turn. The application of collective forces once per turn, as is usually done in lepton machines [1], is not sufficient since space charge tune shifts are large. The single particle update is given by a transfer matrix with a bare betatron phase advance $2\pi Q_x/M$. The multiparticle update consists of a kick from the space charge and wake forces. The space charge kick is given by

$$F_k = \hat{C}_{sc}\sum_{j=1}^{N}(x_k - x_j)\lambda(\tau_k - \tau_j), \tag{5}$$

where $\hat{C}_{sc} = 2\pi C_{sc}/NM$. The kick due to the wake potential is

$$F_k = \frac{2\pi}{NM}\sum_{j=1}^{N} x_j\hat{W}(\tau_k - \tau_j). \tag{6}$$

* Work supported by United States Department of Energy

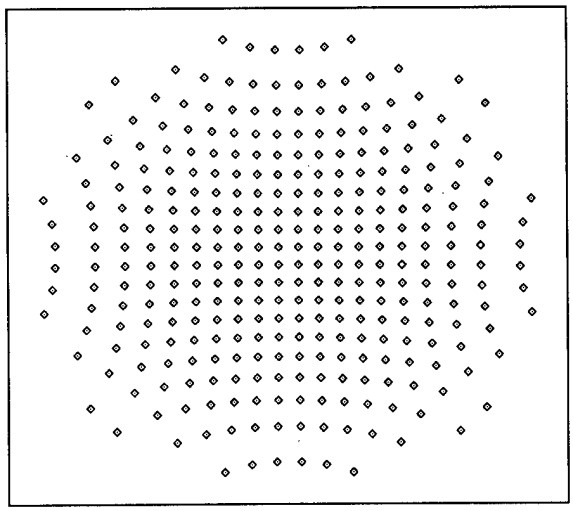

Figure 1: Initial longitudinal coordinates for $n_\ell = 10$ and $\mu = 1$. There are $316 \approx \pi n_\ell^2$ macro-particles.

On the surface, equations (5) and (6) appear to require $O(N^2)$ operations to obtain the kicks for all N macroparticles. This would make simulations with large N untenable. For appropriate choices of $\lambda(\tau)$ and $\hat{W}(\tau)$ the operation count drops to $O(N\log(N))$. The trick is to generalize the phasor technique which is usually employed to retain the cumulative effects of multiple passages through a resonant structure[2].

The smoothing functions

$$\lambda(\tau) = \exp(-\alpha|\tau|),$$

where $\int \lambda d\tau = 2/\alpha = \tau_e$ is the equivalent duration of $\lambda(\tau)$, and

$$\lambda_2(\tau) = (1+\alpha|\tau|)\exp(-\alpha|\tau|)$$

with $4/\alpha = \tau_e$ can be summed efficiently. The algorithm for $\lambda_2(\tau)$ is an obvious generalization of the algorithm for $\lambda(\tau)$, which is presented in detail.

Sort the values of τ_j so that $\tau_j \leq \tau_{j+1}$, which is an $O(N\log N)$ process with standard algorithms[3]. Equation (5) is given by

$$F_k/\hat{C}_{sc} = x_k S1_k^- - S2_k^- + x_k S1_k^+ - S2_k^+, \qquad (7)$$

where

$$\begin{aligned} S1_k^- &= \sum_{j=1}^{k} e^{\alpha(\tau_j - \tau_k)}, \\ S2_k^- &= \sum_{j=1}^{k} x_j e^{\alpha(\tau_j - \tau_k)}, \\ S1_k^+ &= \sum_{j=k+1}^{N} e^{\alpha(\tau_k - \tau_j)}, \\ S2_k^+ &= \sum_{j=k+1}^{N} x_j e^{\alpha(\tau_k - \tau_j)}. \end{aligned} \qquad (8)$$

To calculate the sums one starts with $S_N^+ = 0$, $S_0^- = 0$ and uses

$$\begin{aligned} S1_{k+1}^- &= e^{\alpha(\tau_k - \tau_{k+1})} S1_k^- + 1, \\ S2_{k+1}^- &= e^{\alpha(\tau_k - \tau_{k+1})} S2_k^- + x_{k+1}, \\ S1_{k-1}^+ &= e^{\alpha(\tau_{k-1} - \tau_k)}(S1_k^+ + 1), \\ S2_{k-1}^+ &= e^{\alpha(\tau_{k-1} - \tau_k)}(S2_k^+ + x_k), \end{aligned} \qquad (9)$$

Note that these recurrence relations are stable and that the kicks for all N particles require $O(N)$ calculations after the particles have been sorted in arrival time. The sorting procedure is done when the τ_k s are updated, once per turn.

Next, consider the kick due to the transverse wake field. A smoothed version of the step function wake given by $W(\tau) = W$ for $\tau > 0$ and $W(\tau) = 0$ for $\tau < 0$ is

$$\hat{W}(\tau) = C_W \int_{-\infty}^{\tau} \lambda(\tau')d\tau', \qquad (10)$$

where C_W is a constant and $\lambda(t) = \exp(-\alpha|\tau|)$, as before. Adjusting the constant so that $\hat{W}(\tau) \to W$ as $\tau \to \infty$ yields

$$F_k = \frac{2\pi W}{NM}\left[S0_k^- - S2_k^-/2 + S2_k^+/2\right], \qquad (11)$$

where

$$S0_k^- = \sum_{j=1}^{k} x_j.$$

For a resonator impedance with resonant frequency ω_r and quality factor Q_r the wake kick on particle k is given by

$$F_k = \sum_{j=1}^{k} x_j W_r \sin[\tilde{\omega}(\tau_k - \tau_j)]e^{-\omega_r(\tau_k - \tau_j)/2Q_r}, \qquad (12)$$

where $\tilde{\omega} = \omega_r\sqrt{1 - 1/4Q_r^2}$. Using $\exp(i\phi) = \cos(\phi) + i\sin(\phi)$ a complex sum similar to $S2_k^-$ is obtained.

2 SIMULATION RESULTS

The algorithm described in the previous section has been implemented in fortran code. Results with the smoothing function $\lambda_2(\tau)$ and the step function wake will be presented. Values of n_ℓ, μ, Q_s, τ_e, Q_x, M, W, and the peak value of the incoherent space charge tune shift ΔQ_{sc} were chosen. For the results presented here $M = 24$, $Q_x = 2.9$, and $Q_s = 0.01 \to 0.1$.

The simulations were allowed to continue until the betatron oscillation showed a clear exponential growth rate. The growth rate of the exponential was identified as the growth rate of the most unstable mode. The values of the

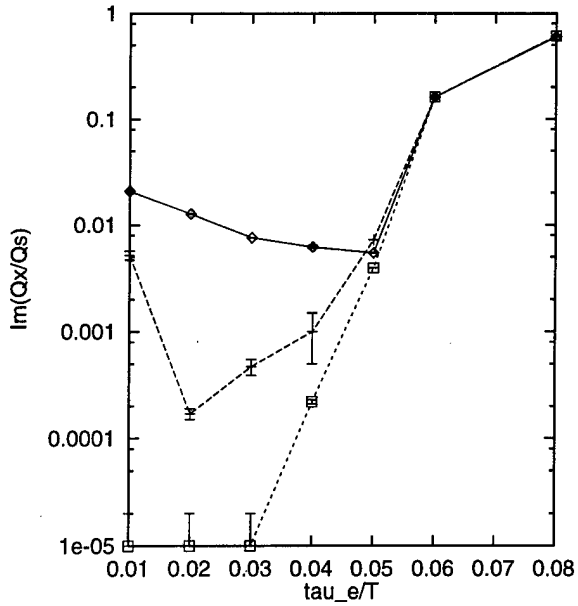

Figure 2: $Im(Q_x/Q_s)$ versus τ_e/T with $\mu = 1$ and $\Delta Q_{sc}/Q_s = 20$ for various values of n_ℓ: $n_\ell = 25$, solid line; $n_\ell = 50$, long dash; $n_\ell = 100$, short dash. The value of the step function wake was five times larger than the threshold value with $\Delta Q_{sc} = 0$.

growth rate were insensitive to the seed value of the random number generator and were the same in both single and double precision.

Figure 2 shows the growth rate of the most unstable mode as a function of τ_e/T for a system which would be highly unstable in the absence of space charge forces. From the figure the best values of τ_e were 0.05, 0.02 and 0.01 for n_ℓ = 25, 50, and 100, respectively.

Figure 3 shows $Im(Q_x/Q_s)$ versus $\Delta Q_{sc}/qs$. While there is a noticeable rise in growth rate after the initial decay $Im(Q_x/Q_s)$ stays below 1% of its value in the absence of space charge. A threshold value of $\Delta Q_{sc}/Q_s = 2$ is inferred from this plot

Figure 4 is the main result. The threshold value of the wake potential increases with space charge tune shift. Results for smooth ($\mu = 1$) and boxcar ($\mu = -1/2$) line densities are similar. If real beams behave in this way the fast head tail instability will rarely, if ever, be seen in low energy hadron machines.

3 REFERENCES

[1] D. Brandt, G.L. Sabbi, B. Zotter EPAC94 pg 1066 (1994).

[2] A. W. Chao, bf Physics of Collective Beam Instabilities in High Energy Accelerators, Wiley , pg 214, (1993).

[3] see *eg.* W.H. Press, B.P. Flannery, S.A. Teukolsky, W.T. Vetterling **Numerical Recipes**, Cambridge University Press, (1986).

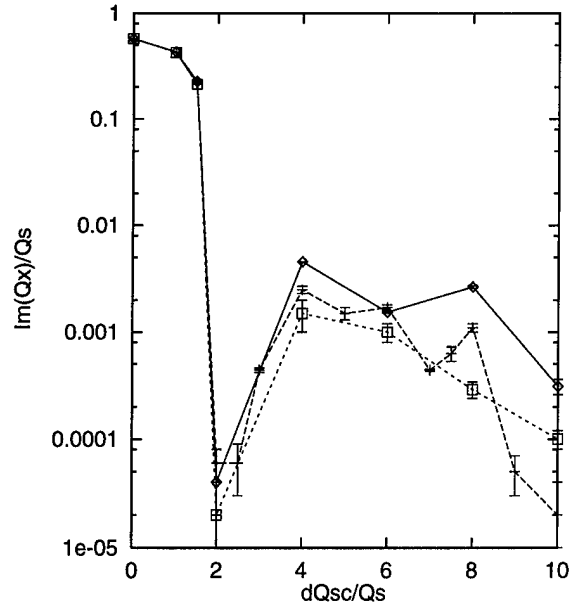

Figure 3: $Im(Q_x/Q_s)$ versus $\Delta Q_{sc}/Q_s$ with $\mu = 1$ for various values of n_ℓ.: $n_\ell = 25$, solid line; $n_\ell = 50$, long dash; $n_\ell = 100$, short dash. The value of the step function wake was 2.5 times larger than the threshold value with $\Delta Q_{sc} = 0$.

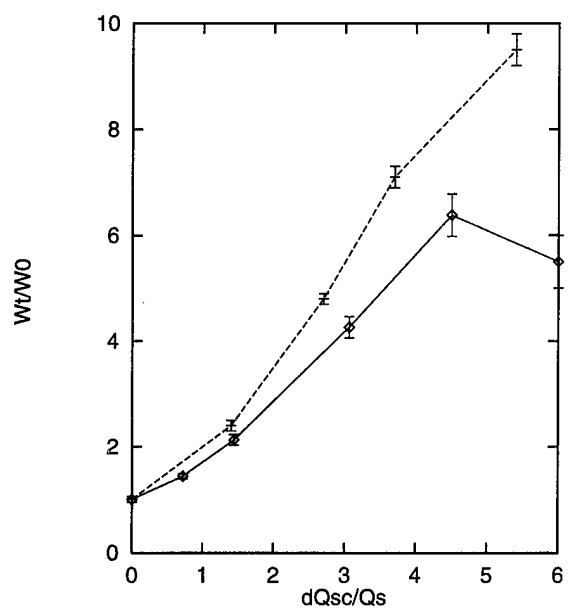

Figure 4: Threshold wake in units of the threshold wake for $\Delta Q_{sc} = 0$ versus $\Delta Q_{sc}/Q_s$ for different line densities: $\mu = 1$, solid line; $\mu = -1/2$, long dash.

FIRST OPERATION OF THE SUPERCONDUCTING ELECTRON COOLER AT THE STORAGE RING TARN II

T. Tanabe, I. Katayama, S. Ono, Center for Nuclear Study, Univ. of Tokyo, Tanashi, Tokyo, Japan
K. Chida, T. Watanabe, Y. Arakaki, High Energy Accelerator Research Organization, Tanashi, Tokyo
K. Noda, T. Honma, National Institute of Radiological Sciences, Anagawa, Chiba
Y. Haruyama, M. Saito, Kyoto Prefectural Univ., Kyoto
T. Odagiri, Tokyo Institute of Technology, Meguro-ku, Tokyo
K. Hosono, Himeji Institute of Technology, Himeji
T. Yosiyuki, M.Hosino, Keihin Product Operations, Toshiba Corporation, Yokohama and
I. Watanabe, New Energy Technology Department, Toshiba Corporation, Chiyoda-ku, Tokyo

Abstract

A superconducting electron cooler with an adiabatic expansion factor of 100 was designed and constructed at the TARN II ring for high-precision experiments and high-speed cooling. The gun solenoid is a liquid-helium-free superconducting magnet with a 20-cm room-temperature bore, which can produce a high magnetic field of up to 3.5 T. An electron beam is expanded from a diameter of 5 mm to 50 mm in a gradually decreasing solenoid field from 3.5 T to 0.035 T. With this cooler it can be expected to reach an electron temperature on the order of 1 meV. The cooler first came into operation in November, 1996. The spectrum of the dissociative recombination, $^3HeH^+ + e \rightarrow {}^3He + H$, clearly showed a dramatic decrease in the electron-beam temperature compared with our previous data measured at an expansion factor of 10 with a normal-conducting solenoid.

1 INTRODUCTION

The electron cooler [1] at the TARN II ring has mainly been used for atomic physics experiments since 1989. In the electron cooling device, the electron beam is guided by a uniform magnetic field directed parallel to the beam axis, which is strong enough to counteract the radial space-charge force. The electrons starting at the cathode have thermal energies of ~ 0.1 eV. The longitudinal temperature ($T_{\|}$) in the beam rest frame, however, is strongly reduced by the acceleration process, while the transverse temperature ($T_{\perp}$) remains unaffected. In most electron coolers used so far, the typical longitudinal temperature was on the order of ~ 0.1 meV at electron energies of a few keV, while the transverse temperature was fixed at ~ 0.1 eV. Thus, the transverse temperature is much higher than the longitudinal temperature.

When the electron beam is used for atomic-collision experiments and for cooling, the longitudinal and transverse temperatures play important roles in somewhat different ways. In electron-ion collision experiments with a resonant relative energy of E_{res} , the energy resolution (δE) is given by

$$\delta E = (1/2)kT_{\|} + kT_{\perp} \pm \sqrt{2E_{res}kT_{\|}}, \qquad (1)$$

where the energy widths are given by $\delta E_{\|} = (1/2)kT_{\|}$ and $\delta E_{\perp} = kT_{\perp}$. Thus, $T_{\|}$ limits the energy resolution at high relative energies, whereas $T_{\perp}$ limits the energy resolution at low relative energies. For electron cooling, a reduction of either temperature leads to an increase of the cooling force.

There is a method used to reduce the transverse temperature with the thermocathode, in which the electron gun is placed in a magnetic field stronger than the guiding field on the remaining beam path, thus resulting in an adiabatic expansion of the electron beam upon entering the lower field region. This method allows the transverse temperature to decrease in the cooling region by a factor given by the ratio of the field strengths involved [2]. The cooler at TARN II was converted to such a new-generation cooler with a gun solenoid field of 5 kG, aiming at an expansion factor of $\sim$ 10, and came into operation in 1994. With this improvement, the transverse electron temperature was reduced to $\sim$ 10 meV, and, thus, faster cooling and higher resolution experiments have been realized [3]. As a next step, we planned to attain even higher expansion ratios of up to 100, which should lead to a transverse temperature on the order of 1 meV. However, a solenoid field higher than 5 kG is almost impossible when using a normal conducting coil and, inevitably, a superconducting coil is required. We thus, designed a superconducting electron cooler, by modifying the electron-gun region, but keeping the remaining parts of the existing electron cooler unaltered. A feature of the superconducting solenoid is that it is liquid-helium free [4], resulting in easy operation and compactness. The new cooler was first implemented in the fall of 1996.

2 ADIABATIC EXPANSION OF AN ELECTRON BEAM

In a uniform solenoid field, an electron has a helical orbit along a magnetic-field line, and the Lorentz force is directed perpendicular to the guiding line of the orbit along the magnetic field. However, if the magnetic-field lines diverge, the Lorentz force acting on the electron also has a

0-7803-4376-X/98/$10.00 © 1998 IEEE

component along the guiding line, resulting in acceleration in the longitudinal direction. The increase in the longitudinal energy means a decrease in the transverse energy due to energy conservation.

When an electron moves sufficiently slowly along the varying axial field, the relation

$$\frac{E_\perp}{B} = \text{const.} \tag{2}$$

holds, which is equivalent to the adiabatic invariance of the orbital magnetic moment associated with the electron motion. The condition that the adiabatic invariants are conserved can be more precisely described by introducing an adiabaticity parameter (ξ) as follows:

$$\xi = \frac{\lambda_c}{B}\left|\frac{dB}{dz}\right|, \tag{3}$$

where λ_c is the spiral length of the cyclotron motion, given by $\lambda_c = 2\pi\sqrt{2m_eE_\parallel}/eB$. The transition is adiabatic if $\xi \ll 1$.

If the axial field strength is reduced from the initial value (B_0) to a final value (B), the transverse energy ($E_\perp$) is reduced according to $E_\perp = (B/B_0)E_{\perp 0}$, where $E_{\perp 0}$ and $E_\perp$ are the initial and final transverse energies, respectively. Here, we call B_0/B the expansion factor. The electron-beam radius (R) increases from the initial value (R_0) according to the relation $R = R_0\sqrt{B_0/B}$. Assuming an expansion factor of 100, $\delta E_\perp$ is reduced to $\sim$ 1 meV as $\delta E_{\perp 0} \sim 0.1$ eV.

The increase in the longitudinal energy spread due to adiabatic expansion is negligible at high energies. Therefore, for the adiabatic expansion, changes in the longitudinal temperature compared with the standard arrangement are not expected.

3 DESIGN AND CONSTRUCTION OF THE SUPERCONDUCTING ELECTRON COOLER

In the new cooler, the electron beam is expanded by a factor of 100 in cross-sectional area in a gradually decreasing field from 3.5 T to 35 mT.

3.1 Electron Gun

The electron-gun optics consists of a flat cathode with a diameter of 5 mm, a Pierce electrode, an anode and an acceleration column. Electrons are extracted by the anode voltage, and then further accelerated by an acceleration column of up to 20 kV in a uniform solenoid field. The perveance of the electron gun is 1 μ P and the maximum current is expected to be 1 A at a gun-anode voltage of 10 kV. The actual design of the gun region is shown in Fig.1.

3.2 Superconducting magnet

The refrigerator-cooled NbTi magnet[4] realizes easy operation and compactness in the present design. The superconducting magnet shown in Fig. 1 has a 20 cm room-temperature bore, and is approximately 1 m in axial length.

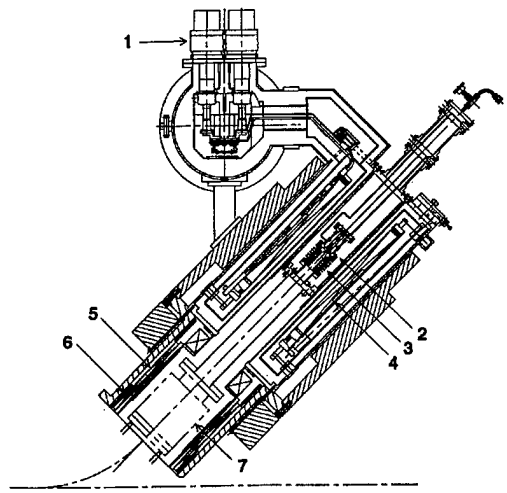

Figure 1: Layout of the electron gun region: (1) refrigerator, (2) electron gun, (3) acceleration tube, (4) superconducting solenoid, (5) normal-conducting solenoid, (6) steering coil, (7) NEG pump.

The magnet can produce a 3.5 T central field at a coil temperature of about 5 K. There is also a small superconducting coil which produces a reverse field, which helps the main field to decrease slightly more steeply. In order to make the field in the gun region more uniform, the outer winding of the main coil has a notch. Thus, a field uniformity of $\pm 10^{-3}$ was realized by the superconducting coil system. There are also normal conducting coils, which are used smoothly to join the superconducting field to the subsequent toroidal field, while keeping ξ as small as possible. Helmholz coils can steer the electron beam in both the horizontal and vertical directions. All of the coils are covered by thick mild-steel return yokes. The main purpose of the return yoke is to prevent any leakage field to the outer region of the superconducting coil. The maximum leakage field from the superconducting coil is about 20 G on the beam line. The ramping rate of the magnet is 3.5 T/30 min. The coil temperature became stabilized at 4.8 K for 3.5 T, although it increased up to 5.4 K during ramping.

3.3 Electron Trajectories

The electron trajectories were studied using the SLAC program [5]. The results of field measurements include errors; this unsteady field results in a significant increase in the transverse electron temperature when tracing the electron trajectories in the variable-field region. By correcting to a smooth change of the magnetic field, the correct temperatures were obtained. Fig. 2 shows a longitudinal magnetic field on the axis and typical electron trajectories in the gun region. Fig.3 repesents the radial velocity for one electron trajectories starting from 0.35 mm off axis. During a decrease in the magnetic field, the radial velocity first increase and then decreases. After adiabatic passage, a reduction in the velocity oscillation amplitude by a factor of 10 can be

observed in Fig. 3.

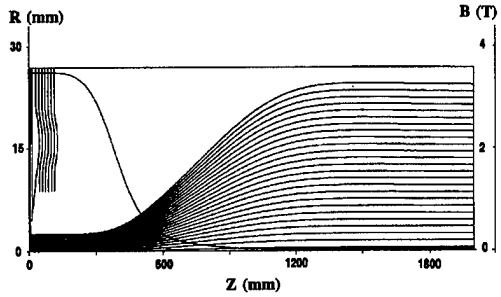

Figure 2: Longitudinal magnetic field on the axis and typical electron trajectories in the gun region at an energy of 2.5 keV and a current of 0.1 A.

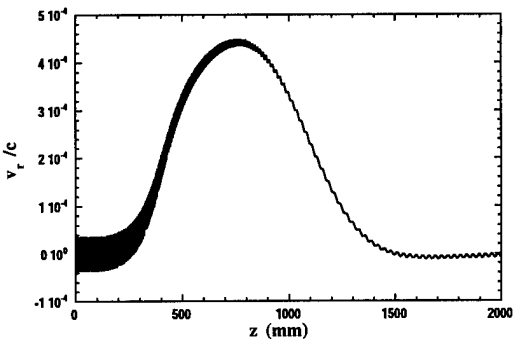

Figure 3: Radial velocity for an electron ray starting from a radius of 0.35 mm at the cathode. The maximum adiabaticity parameter is about 0.05.

4 OPERATION OF THE SUPERCONDUCTING ELECTRON COOLER

The evidence concerning improvements of the electron-beam temperature can be obtained by observing the change in the spectra of the electron-capture process. The fine structure for the dissociative recombination of $^3HeH^+$ was found with a low-temperature electron beam adiabatically expanded by a factor of about 10. Atomic physics theory, however, predicts that the spectrum should have more structure along with a decrease in the electron temperature. We measured the dissociative recombination spectrum for 15-MeV $^3HeH^+$ with the colder electron beam expanded by a factor of 100. The obtained spectrum is compared with our previous results in Fig. 4. As can be seen in this figure, the spectrum changed dramatically, which is clear evidence of a temperature decrease. We further measured the dissociative recombination spectrum of HD^+. Comparison of the spectrum with atomic physics theory indicates that the transverse temperature decreased to the order of 1 meV.

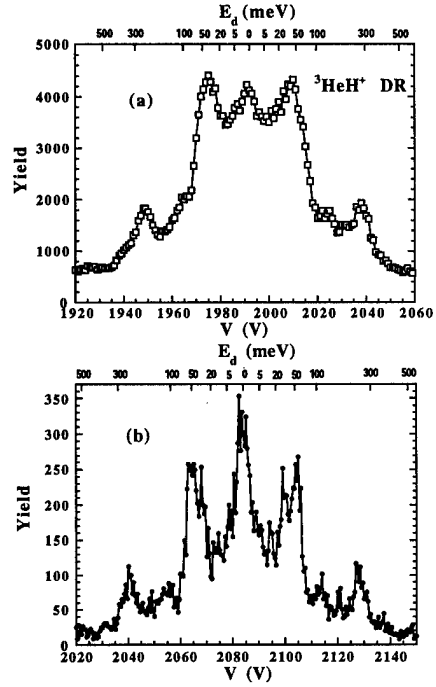

Figure 4: Comparison of the dissociative recombination spectra of $^3HeH^+$ measured at expansion factors of (a) 10 and (b) 100.

5 SUMMARY

The superconducting electron cooler with an expansion factor of 100 came into operation for the first time. An extreme decrease of electron temperatures, probably down to the order of 1 meV, was observed. The liquid-helium-free superconducting magnet realized a compact design and easy operation.

6 ACKNOWLEDGEMENTS

The authors thank the cyclotron staff for their helpful cooperation. This work was performed under Grant-in-Aid for Scientific Research (A) of the Ministry of Education, Science, Sports and Culture.

7 REFERENCES

[1] T.Tanabe et al., 'Electron Cooling Experiments at INS', Nucl. Instr. and Methods, **A307**, 7 (1991).

[2] H.Danared et al., 'Electron Cooling with an Ultracold Electron Beam', Phys. Rev. Lett. **72**, 3775 (1994).

[3] T.Tanabe et al., 'Dissociative Recombiantion of HD^+ with an Ultracold Electron Beam in a Cooler Ring', Phys. Rev. Lett. **75**, 1066 (1995).

[4] T.Tanabe et al., 'Liquid-Helium Free Superconducting Electron Cooler at the Storage Ring TARN II', EPAC96, p.1190.

[5] W.B.Herrmansfeldt, 'Electron Trajectory Program', SLAC-**226** (1979). .

LASERS AND LASER-COOLING USED FOR STUDIES OF BEAM DYNAMICS

N. Madsen, M. Drewsen, L.H. Hornekær, A. Labrador, J.S. Nielsen, P. Shi, and J.S. Hangst,
Institute of Physics and Astronomy, University of Aarhus, Denmark and
J.P. Schiffer, Argonne National Laboratory, Illinois, USA and
V.A. Lebedev, CEBAF, USA

Abstract

A new technique for measuring the transverse profile of ion beams, using laser induced flourescence, is presented. The technique employs the resonant interaction of laser light with a beam of circulating ions in a storage ring. The light from the spontaneous decay of the excited ions is imaged by an optical system onto a high resolution CCD, making it possible to extract the beam's transverse spatial distribution. The first results from this technique, including studies of the transverse to longitudinal coupling in a circulating, laser-cooled ion beam, are presented.

1 INTRODUCTION

The creation and behavior of dense cold (i.e. having a very small velocity spread) ion beams in storage rings are of interest for many storage ring applications. In this paper we present a new technique for measuring the transverse size of an ion beam. The technique utilizes laser induced flourescence and so is especially applicable to beams where laser cooling [1] is utilized.

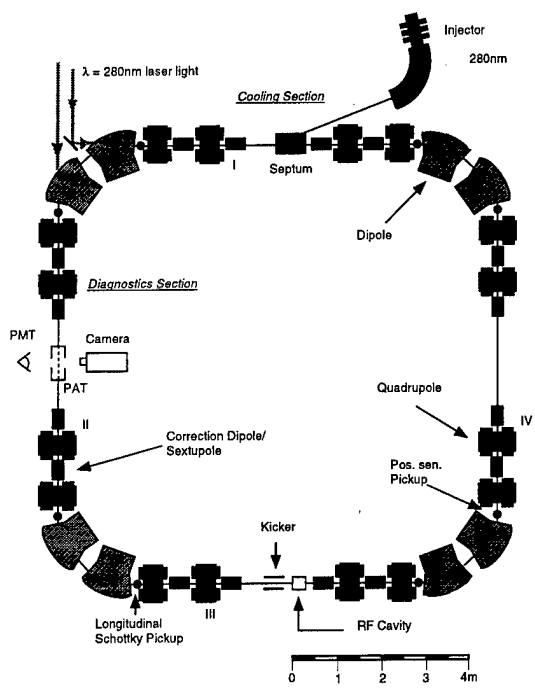

Figure 1: The ASTRID Storage Ring.

2 LASER-COOLING IN ASTRID

At the ASTRID storage ring (figure (1) [3]) we have applied the technique of laser cooling to create and study dense, cold ion beams. Two means are used for the study of the longitudinal degree of freedom. The technique of laser induced flourescence (LIF) involves an ion beam which passes through a cylindrical tube (called Post Acceleration Tube (PAT)) which can be excited by a dc voltage, thereby locally changing the ions velocity and thus the Doppler-shifted resonant frequency of the optical transition. By sweeping the voltage on the tube we can bring different velocity classes of the ion beam into resonance with the laser, and thereby measure the longitudinal velocity distribution [4]. An alternate method monitors the fluctuations induced on a longitudinal pickup (Schottky-noise [5]) by fluctuations in the total beam intensity. From the frequency spectrum of these fluctuations we can, under certain conditions, extract the longitudinal velocity distribution. This technique is sensitive to coherent behavior in the beam, ideal for the study of charge density waves etc. [4]. As the laser cooling force in a storage ring only applies to the longitudinal degrees of freedom, the coupling between the longitudinal and the transverse motion is of major interest. The situation is complicated by the fact that the 'coldest' state of ions in a storage ring is one with constant angular velocity rather than constant linear velocity, though the regime where this becomes important has probably not yet been reached. Several schemes to enhance the transverse to longitudinal coupling have been suggested [6]-[7].

3 TRANSVERSE DIAGNOSTICS

Other, more limited, techniques have been used for transverse diagnostics with varying degrees of success. For instance, non-destructive measurements of the transverse degree of freedom can, in some cases, be done by extracting the amplitude of the betatron sidebands in the Shottky-noise spectrum of a coasting beam induced in a transverse pickup [5]. This method, however, requires fairly intense beams, and furthermore doesn't directly reveal the transverse shape of the beam. A limitation is imposed by the fact that laser cooling induces large distortions of the Schottky-noise signal [4]. Alternatively, a residual-gas ionization beam profile monitor (BPM) has be used to detect the ionization products from collisions between beam particles and rest gas. This technique has been employed at the TSR storage ring in Heidelberg [8]. The technique has a reported spatial resolution of 260(50)μm, and a typical count rate

0-7803-4376-X/98 /$10.00 © 1998 IEEE

for laser cooling conditions (singly charged ions, $\sim 1\mu$A current) of $\sim 300\ s^{-1}$. The cold space charge dominated beam radius in ASTRID for $\sim 10^8$ particles is 1mm and the resolution of the BPM is not sufficient for detailed study of space charge dominated beams, and definitely not for future studies of crystalline beams. Furthermore it is not desirable for the study of ultra-cold beams that the technique relies on collisions with the (hot) rest gas.

In the light of these considerations we have implemented a system to measure the beam profile by imaging the flourescent light from the laser-excited ion beam onto a high resolution, low noise CCD camera.

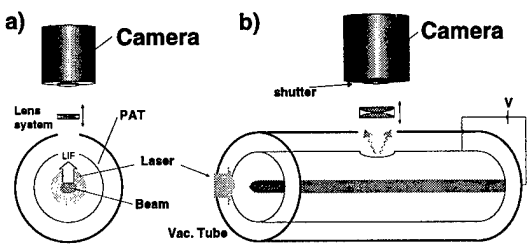

Figure 2: Schematic drawing of two perspectives of the CCD camera setup.

The camera (setup shown in figure 2) can be used to observe the ion beam either vertically or horizontally. The section of beam observed by the camera passes through the above mentioned PAT. In front of the CCD is a mechanical shutter which can be controlled externally, thereby making it possible to image the ion beam at different times after injection. The shutter has an open/close time of order 6ms. The magnification and focus of the system can be calibrated by inserting a plate with marks of known distances. This is also the way to measure the laser profile, i.e. by making the laser incident on a diffuser, and imaging the distribution on the CCD.

The current CCD system consists of a cryogenically cooled CH260 camera head from Photometrics with a Tektronix TK1024AB CCD chip with 1024x1024 square pixels with a side length of 24 microns. Thus the limiting resolution is $\sim$ 24 microns with a magnification of 1, which is a resonable magnification as the beam sizes observed are between 2 and 10 mm wide (FWHM). As explained above the system images the flourescent light from the ion beam interaction with an overlapping resonant laser in the beam pipe. In order to simplify the analysis of the images the spatial intensity distribution of the laser beam needs to be uniform in the appropriate plane. This is done by actively sweeping a strongly focused (FWHM $\sim$ 1mm) laser beam spatially in the desired plane.

The sensitivity of the described system relies on the available laser power, as more laser power generates more flourescent light. To avoid the laser exerting a force on the ion beam while probing, the CCD system images the ion beam inside the PAT. The PAT is held at a voltage ($\sim$ 400 V) thus making it possible to have the ions on resonance inside the PAT and far off resonance outside. The PAT is rather short compared to the cooling section, and no influence of the laser on the ion beam has been observed. Uncooled ion beams with linear densities down to $1.6{\cdot}10^5 m^{-1}$ have been imaged. The main limiting factor for the system is the readout noise of the CCD, as the dark current is extremely low. This means that the present system, by binning the CCD pixels in the beam direction[1], easily can measure beams with linear densities in the string regime [2]. Thus this method of transverse beam diagnostics offers high sensitivity and resolution and is at the same time completely nondestructive.

A further feature of the described system is that the measurements are dispersion free. As the width of the electronic transition is small compared to the uncooled longitudinal velocity spread (in our case an uncooled beam has a spread of order 700 m/s where as the ion fraction in velocity space resonant with the laser has a FWHM of order 13 m/s), the system probes only a narrow velocity class, and the imaged beam profile is a measure of the horizontal beam emittance without the need to consider dispersion. This of course also means that we can measure the dispersion by detuning the laser and probing the horizontal distribution of different velocity classes, this is illustrated in figure 3.

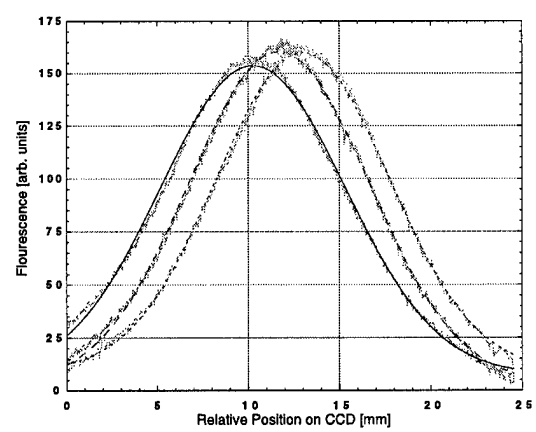

Figure 3: Horizontal beam profiles measured for different longitudinal velocities of a particular beam. The lines are gaussian fits to the data. The solid line is Δv = -279.6m/s, the long-dashed line is Δv=0, and the short-dashed line is Δv = 279.6m/s. For clarity the three curves have been renomalized to the same height.

4 LASER COOLING RESULTS

The ASTRID storage ring (figure 1) [3] was used to store 100 keV $^{24}Mg^+$ ions. The beam is bunched by a sinusoidally varying longitudinal electric field in the beam path. The bunching frequency is the 16th harmonic of the revolution frequency. One counter propagating laser, produced by frequency-doubling 560 nm light from two ring-dye lasers, overlaps the ion beam in one straight section (8 m) of the

[1]Binning means that the charges in a given number of adjecant pixels are added before readout.

storage ring (figure 1). The ultraviolet light, which can be frequency-tuned over a range of 20 GHz, drives the $(3^2S_{1/2}) \leftrightarrow (3^2P_{3/2})$ electronic transition used for laser cooling [9]. By scanning the laser frequency from large red detuning (with respect to the resonant frequency of an ion circulating at the ideal orbit) the particles can be cooled to temperatures of order 1 Kelvin [10].

Experiments have been started with this new technique involving a CCD camera, to explore the transverse phase space as a function of longitudinal cooling. In figure 4 we first show results from observing an uncooled beam of ions. This plot clearly shows the expected nondependence on the number of particles of the transverse size for an uncooled beam. Furthermore we can observe that the ratio of sizes between the two dimensions is ~ 2.2, in good agreement with expections from the calculated beta functions of β_x =11.56m and β_y =2.64m.

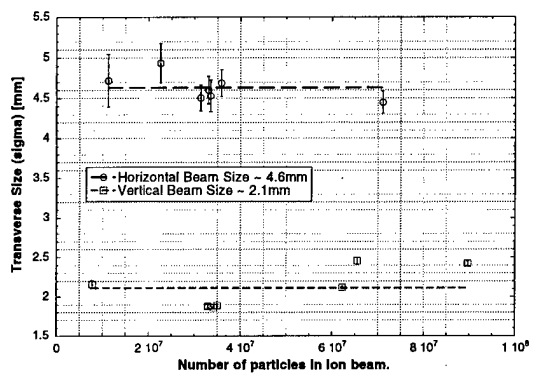

Figure 4: Horizontal and vertical beam sizes measured for uncooled beams having various particles numbers (measured bunch lengths (FWHM) = 1.00m±0.05m). The longitudinal velocity spread is of order 600 m/s for all measurements.

When laser cooling is applied to the above beams, a dramatic decrease of the transverse sizes has been observed. This is shown in figure 5. This figure shows how the transverse dimensions of the ion beam decreases with decreasing longitudinal velocity spread, thus demonstrating the existence of coupling between the longitudinal and transverse motion in a bunched ion beam, earlier demonstrated in a coasting beam [11]. The measurements were done with betatron tunes of Q_x =2.282 and Q_y =2.821. The longitudinal to transverse coupling was observed to disappear at certain betatron tunes, this is believed to be due to tune resonances, and will be investigated further.

5 CONCLUSION

We have demonstrated a new velocity selective technique for measuring ion beam profiles. The technique is applicable for any ion having a closed electronic transition for interaction with laser light. Furthermore it is completely nondestructive, and offers resolutions in the μm regime, which is necessary for observing beam crystallization (shell structures) [12], as has already been done in ion trap experiments [13].

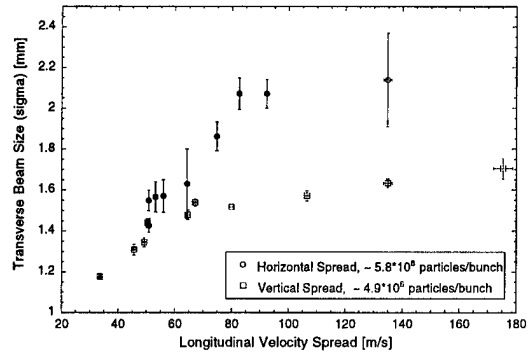

Figure 5: Horizontal and vertical beam profiles measured for different longitudinal velocity spreads. The beam currents are not the same because the measurements weren't done simultaneously, but other measurements showed that these results do not depend sensitively on beam current.

We have furthermore confirmed the presence of a longitudinal to transverse coupling in a laser-cooled ion beam, and observed that the strength of the coupling depends strongly on the betatron tunes. We are currently working on gaining more insight into the behavior of the coupling under varying conditions, which has implications for the ultimate limit for cold ion beams and thus beam crystallisation.

6 ACKNOWLEDGEMENTS

This work was supported by the Danish National Research Foundation through the Aarhus Center for Advanced Physics, and by the U.S. Department of Energy, Nuclear Physics Division, under Contract W-31-109-Eng-38.

7 REFERENCES

[1] T. Hänsch and A. Schawlow, Opt. Comm. **13**, 68 (1975).

[2] R.W. Hasse and J.P. Schiffer, Ann. Phys. **203**, 419 (1990)

[3] S.P. Møller, in Proceedings of the 1991 IEEE Particle Accelerator Conference, IEEE 91CH3038-7, 2811 (1991).

[4] J.S. Hangst *et al.*, Phys. Rev. Letts. **74**, 86 (1995).

[5] D. Boussard, Proc. CERN Accelerator School, vol. 2, Oxford, 1985, ed. S. Turner (CERN 87-03, Geneva, 1987), p. 416.

[6] H. Okamoto, A.M.Sessler and D.Möhl, Phys. Rev. Lett. **72**, 3977 (1994).

[7] H. Okamoto, Phys. Rev. E **50**, 4982 (1994).

[8] B. Hochadel et al., Nucl. Inst. & Meth. A **343**, 401 (1994).

[9] J.S.Nielsen, Opt. Lett. **20**, 840 (1995)

[10] J.S. Hangst *et al.*, Phys. Rev. Letts. **74**, 4432 (1995)

[11] H.J. Miesner *et al.*, Phys. Rev. Letts. **77**, 623 (1996)

[12] A. Rahman and J.P. Schiffer, Phys. Rev. Letts. **57**, 1133 (1986).

[13] S.L. Gilbert et al., Phys. Rev. Lett. **60**, 2022 (1988) and G. Birkl et al., Nature **357**, 310 (1992)

FIRST OBSERVATIONS OF A "FAST BEAM-ION INSTABILITY" AT THE ALS*

J. Byrd†, A. Chao§, S. Heifets§, M. Minty§, T.O. Raubenheimer‡*,
J. Seeman§, G. Stupakov§, J. Thomson†, F. Zimmermann§
†Lawrence Berkeley National Laboratory, Berkeley, California 94720
§Stanford Linear Accelerator Center, Stanford, California 94309
‡CERN, PS Division, CH-1211, Geneva 23, Switzerland

Abstract

We report the results of experiments on a "fast beam-ion instability"[1] at the Advanced Light Source (ALS). This ion instability, which can arise even when the ions are not trapped over multiple beam passages, will likely be important for many future accelerators. In our experiments, we filled the ALS storage ring with helium gas, raising the pressure approximately two orders of magnitude above the nominal pressure. With gaps in the bunch train large enough to avoid conventional (multi–turn) ion trapping, we observed a factor of 2–3 increase in the vertical beam size along with coherent beam oscillations which increased along the bunch train.

1 INTRODUCTION

Ion trapping has long been recognized as a potential limitation in electron storage rings. The ions, generated by beam-gas collisions, become trapped in the negative potential of the beam and accumulate over multiple beam passages. The trapped ions are then observed to cause a number of deleterious effects such as an increasing beam phase space, a broadening and shifting of the beam transverse oscillation frequencies (tunes), collective beam instabilities, and beam lifetime reductions[2, 3]. All of these effects are of concern for the next generation of accelerators, such as the B-factories or damping rings for future linear colliders, which will store high beam currents with closely spaced bunches and ultra-low beam emittances.

One of the standard solutions used to prevent ion trapping is to include a gap in the bunch train which is long compared to the bunch spacing. In this case, the ions are first strongly-focused by the passing electron bunches and then over-focused in the gap. With a sufficiently large gap, the ions can be driven to large amplitudes where they form a diffuse halo and do not affect the beam.

In this paper, we describe experiments that study a new regime of transient ion instabilities predicted to arise in future electron storage rings [1], and linacs with bunch trains. These future rings and linacs, which will be operated with higher beam currents, small transverse beam emittances, and long bunch trains, will use ion clearing gaps to *prevent* conventional ion trapping. But, while the ion clearing gap may suppress the conventional ion instabilities, it will not suppress a transient beam-ion instability where ions generated and trapped during the passage of a *single* train lead to a fast instability. While both conventional and transient ion instabilities have the same origin, namely ions produced by the beam, they have different manifestations and, more importantly, the new transient instability can arise even after the conventional ion instability is cured. This new instability is called the "Fast Beam-Ion Instability" (FBII). In many future rings, the FBII is predicted to have very fast growth rates, much faster than the damping rates of existing and proposed transverse feedback systems, and thus is a potential limitation.

To study the FBII, we performed experiments at the ALS, a 1.5 GeV electron storage ring. At the nominal ALS pressure of about 0.24 nTorr, the FBII is not evident. To study the instability, we intentionally added helium gas to the storage-ring vacuum system until the residual gas pressure was increased about 80 nTorr. This brought the predicted growth rate of the instability at least an order of magnitude above the growth rate of conventional multi-bunch instabilities driven by the RF cavities and above the damping rate of the transverse feedback system (TFB) in the ALS and, thereby, established conditions very similar to those in a future storage ring. We then filled the ring with a relatively short train of bunches, suppressing conventional ion instabilities. In the following, we will first briefly describe This paper describes the experiment and results in more detail.

2 FAST BEAM-ION INSTABILITY

The FBII can be compared with beam break–up in a linear accelerator. In a transport line or a storage ring with a large clearing gap, the ions are not trapped over multiple beam passages. Regardless, during a single passage of the beam, ions are created by each passing bunch which leads to a linear increase of the ion density along the bunch train. These collective oscillations of the ions in the beam's potential well drive the transverse oscillations of the beam at the ion oscillation frequency which in turn resonantly drives the ions to larger amplitudes. The result is an exponential growth of the vertical bunch offsets as a function of both the distance along the train and the distance along the accelerator. Furthermore, only the "slow" (phase velocity less than c) wave will be driven by the ions. The amplitude growth along the train is a distinct signature of a single-pass effect while the second statement implies that

* This work was supported by the U.S. Department of Energy under Contract Nos. DE-AC03-76SF00098 and DE-AC03-76SF00515.

the Fourier spectrum of the signal seen on a beam position monitor will consist of many lower betatron sidebands peaking at the ion oscillation frequency which is a distinct signature of all beam–ion instabilities.

Because the beam–ion interaction is very nonlinear, the FBII will saturate when the oscillations reach amplitudes comparable to the beam size. At this point, the instability growth slows and the transverse oscillations of individual bunches begin to filament due to a spread in betatron frequencies. The resulting distribution depends on the speed with which the beam filaments, the damping, the nonlinearity of the beam-ion force, and the effect of any feedback which is acting to damp coherent oscillations. Thus, depending on parameters, the FBII will cause either the amplitude of the coherent oscillations or, if the bunches have filamented, the size of bunches to increase along the length of the train.

3 EXPERIMENTAL SETUP

The relevant parameters of the ALS are average horizontal and vertical beam sizes of 160 and 30 μm, harmonic number of 328, and betatron tunes of 14.28 (x) and 8.18 (y).

To increase the FBII growth rate so that the instability should be observable in the ALS, we added He gas to the vacuum system. The motivation for using He gas is that the vertical emittance growth from Coulomb scattering was only an 18–20% effect and that calculations indicated that an achievable level of He pressure (<100 nTorr) would give a growth rate of the FBII much faster than the damping rate of the TFB system. For all experimental conditions we expected He ions to be linearly unstable over multiple beam passages. During normal operation, the average pressure with beam is about 0.25 nTorr. To reach the high He pressure it was necessary to turn off all of the active ion pumps except for one pump on either side of the RF cavities. He was added through gas inlet ports located on either side of these pumps, balancing the gas distribution throughout the ring. By adjusting the gas inlet rate, we could maintain an average pressure of ~80 nTorr of He around the ring. The three residual gas analysers indicated that He was the dominant gas species by an order of magnitude; H and Ar were the next most populous species.

The experiments were all performed using the vertical, horizontal, and longitudinal feedback systems[4] to damp coupled–bunch instabilities driven by RF cavity and resistive wall impedances. In this mode, the coupled bunch oscillations are successfully damped by the feedback systems, as is the case for nominal pressure, while oscillations driven by the faster ion instability are not damped during their initial growth. For the conditions in the experiments presented below, the damping rate of the vertical feedback system was about (400 μs)$^{-1}$/mA.

Synchrotron radiation[5] from a bend magnet is used to image the transverse beam profile. Unfortunately the setup of the beamline does not allow measurement of the beam size at different points along the bunch train but instead

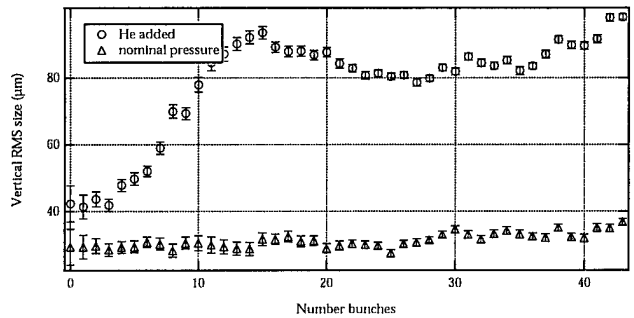

Figure 1: RMS vertical beam size vs. the number of bunches for nominal and elevated pressure conditions.

simply measures the projected size of the entire train. We also observed the frequency spectrum of the dipole moment of the beam using an HP70000 spectrum analyser. One of the BPMs for the transverse feedback system was used as the input to the spectrum analyser.

4 RESULTS

The experimental procedure was to record the synchrotron light image and vertical beam spectrum for a variety of bunch train lengths and bunch currents where conventional trapping of He was not expected. The measurements were made at the nominal pressure and at the elevated pressure after introducing He. We also measured the beam size for single bunches at both nominal and elevated pressure to ascertain the beam-size increase from Coulomb beam-gas scattering, which was of the order of 15-20%, in agreement with calculations.

We studied the onset of the instability by recording the beam behavior as the length of the bunch train was slowly increased. Starting with a single bunch of 0.5 mA, we slowly filled consecutive bunches. Shown in Figure 1 is a plot of the RMS vertical beam size as a function of the number of bunches continuing up to a total of 45 bunches. Also shown is the corresponding vertical beam size at nominal pressure. With He gas, the beam size strongly increased when the number of bunches exceeded 8. The FBII theory predicts that the growth rate for the 8th bunch under these conditions is about (1 ms)$^{-1}$, approximately equal to the feedback damping rate for a current of 0.5 mA/bunch.

The spectrum of coherent vertical oscillations for several different cases is shown in Figure 2. The frequency axis is scaled by the revolution frequency and only the first 164 revolution harmonics are shown. For simplicity, we have plotted the difference of the amplitude of lower and upper sidebands. The coherent vertical sidebands were not present at the nominal pressure. As He was added, a pattern of lower sidebands appeared with a peak amplitude at a frequency near that predicted by FBII simulations. As the beam current was increased, the coherent signal shifted in frequency as expected. A comparison of the frequency of coherent oscillations from experiments and theory shows good agreement. However, we did not observe a coher-

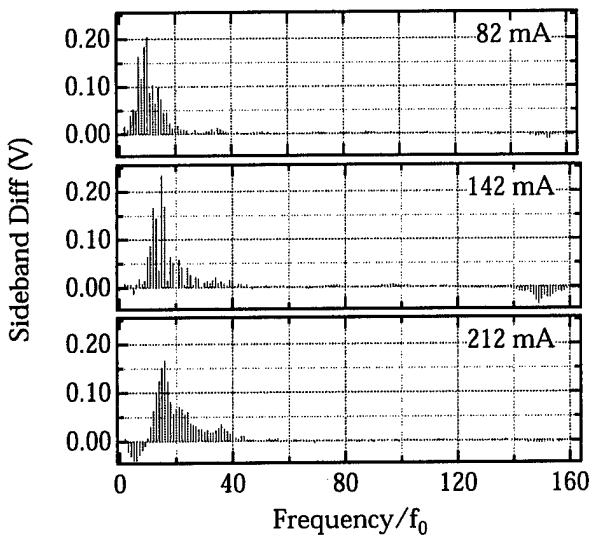

Figure 2: Vertical betatron sidebands measured in the 240/328 fill pattern for three different currents.

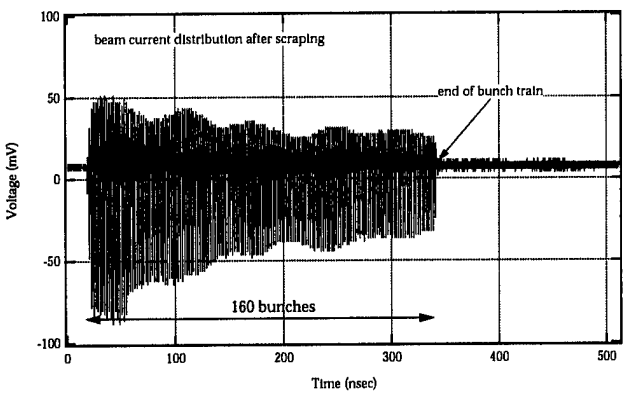

Figure 3: Beam current along the bunch train for 160 bunches after moving a vertical aperture close to the beam. The nonuniform loss pattern shows the increasing vertical oscillations (or beam size) along the bunch train.

ent signal for all cases even though we always observed a vertical blowup. The reason for this is not yet understood. One possible explanation is that for large growth rates the coherent vertical oscillations filament, only leaving an enhanced vertical size. We hope to resolve this question in future experiments.

We were able to measure the relative amplitude of oscillations (or the relative beam size) by moving a vertical aperture (i.e. scraper) close to the beam and detecting the relative current loss along the bunch train. Figure 3 shows the signal from a beam position monitor showing the relative current along the bunch train after scraping the beam. Starting from a uniform current distribution along the train, the scraper reduces the bunch population in the tail about 2.5 times more than that of the leading bunches, indicating that the instability increases along the train. The gradual loss of current along the bunch train demonstrates the transient nature of the instability, which is one of the main predictions of the FBII theory.

5 SUMMARY

In experiments at the ALS, we have made observations of an ion instability in a regime where conventional ion trapping is not expected. Our observations are qualitatively consistent with the FBII. In addition, we have measured the onset of the instability as a function of the bunch-train length. The beam size started to increase significantly with a bunch train of about 8–10 bunches which, based on the *expected* feedback performance, is very close to where the FBII is predicted to become significant. In the future, we plan further experiments to determine why the coherent signals do not always appear although the beam is clearly blown up, to make detailed measurements of the beam size and centroid motion along the bunch train, and to measure the instability growth times as a function of different parameters, especially vacuum pressure.

6 REFERENCES

[1] T.O. Raubenheimer and F. Zimmermann, *Phys. Rev. E*, **52:** 5487–5498 (1995); G.V. Stupakov, T.O. Raubenheimer and F. Zimmermann, *Phys. Rev. E*, **52:** 5499–5504 (1995); G.V. Stupakov, *Proc. of the Int. Workshop on Collective Effects and Impedance for B-Factories, KEK Proceedings* **96-6**, p. 243 (1996); S.A. Heifets, *PEP-II AP-Note:***95-20** (1995).

[2] R. Alves Pires et al., *Proc. 1989 Part. Accel. Conf.*, Chicago, p. 800.

[3] D. Sagan and A. Temnykh, *Nucl. Instr. and Meth.* **A 344:** 459 (1994).

[4] W. Barry, J. Byrd, J. Corlett, G. Lambertson, C. C. Lo, *Proc. of the 1994 EPAC*, July 1994.

[5] R. Keller, T. Renner, D. J. Massoletti, *Proc. of the 7th Beam Instr. Workshop* (1996).

THE EXPERIMENTAL STUDY ON BEAM-PHOTOELECTRON INSTABILITY IN BEPC

Z.Y.Guo, H.Huang, S.P.Li, D.K.Liu, L.Ma, Q.Qin, L.F.Wang, J.Q.Wang, S.H.Wang, C.Zhang, F.Zhou, IHEP, Beijing, China

Y.H.Chin, H.Fukuma, S.Hiramatsu, M.Izawa, T.Kasuga, E.Kikutani, Y.Kobayashi, S.Kurokawa, K.Ohmi, Y.Sato, Y.Suetsugu, M.Tobiyama, K.Yokoya, X.L.Zhang, KEK, Tsukuba-shi, Japan

Abstract

A vertical coupled bunch instability explained as the photoelectron instability (PEI) was observed in the Photon Factory at KEK. To further investigate the instability, the experiments on the PEI have been carried out in Beijing Electron Positron Collider (BEPC) with the collaboration between IHEP, China and KEK, Japan. Many interesting phenomena have been observed for different sets of parameters.

1 INTRODUCTION

A vertical instability was observed in the PF at KEK when the machine was operated with the multibunch positron beam years ago[1] and the similar instability has been also observed in BEPC recently. This instability is a coupled bunch oscillation with a low threshold current of a few 10 mA in both machines. The broad distribution of the betatron sidebands can be observed when the instability occurs. From the spectrum of the betatron sidebands, one cannot find any HOM at the corresponding frequency in RF cavities. It is also hard to be suppressed even by filling positrons partially in RF buckets. This instability does not occur in electron beam at the same conditions. It was explained as the photoelectron instability (PEI)[2].

A computer code has been developed to simulate the PEI. The number of photons emitted by a positron throughout a ring circumference is proportional to the energy of the photon.

The photoelectrons start at the surface of beam pipes and are propagated while receiving the electric force from the following positron bunches. One can consider the force as the wake field to cause the coupled bunch instability. The characteristics of the instability can be estimated by applying the existent instability theory as [3]

$$\Omega_m - \omega_y = \frac{-n_e c T_0}{4\pi\gamma \nu_y n_b N_b} \sum_{k=1}^{k_0} k \frac{d\bar{\nu}_y}{dy} e^{2\pi k i(m+\nu_y)/N_b} \qquad (1)$$

where N_b is the bunch number, n_e the particle number in a bunch, k the range of the wake, ν_y the vertical betatron tune and v_y the velocity of the photoelectron.

The particle factories like B-factories and Tau-charm factories will be built in the world and will be operated at the high current with many bunches of the electron and positron being stored in their respective rings. Therefore, one should investigate the PEI in the existing positron rings. To study the PEI experimentally, a series of machine studies on the PEI in BEPC were proposed [4].

The BEPC has been operated as a collider as well as a synchrotron radiation source with the maximum single beam current of 150 mA from 1.3 to 2.2 GeV. It is possible to provide a variety of the bunch loading pattern on the beam level of the PEI observation. The PEI is simulated for BEPC with the different beam current I_b and the bunch number N_b[5]. In the BEPC diagnostic system, there are several types of beam monitors which have been working well for years. The instruments for the observation of the PEI are prepared by both sides of IHEP and KEK. At present a spectrum analyzer, HP8568B with 1.5 GHz bandwidth, connected with a button pickup is used for the beam spectrum observation.

The machine studies have been progressed in BEPC to survey the PEI in details since last June under the cooperation between IHEP and KEK. The investigated effects on the PEI include: chromaticities, bunch space, emittance, beam energy, RF frequency, distributed ion bumps, betatron tunes, magnetic field, RF voltage, etc. This paper describes the experimental observations and some analyses.

2 OBSERVATION

2.1 Main Characteristics of the PEI

The coupled bunch instability was observed in the positron beam with a low threshold current about 9.4 mA at 1.3 GeV and the full filling with 160 bunches uniformly[6]. The vertical betatron sidebands $nf_0 \pm f_y$ by each revolution frequency were observed on the spectrum analyzer where f_y is the vertical betatron frequency and f_0 the revolutionary frequency. The typical observed vertical sidebands compared to the corresponding growth rate calculated with the phenomenological model are shown in Figure 1, where the solid curves are the calculated growth rate and the vertical lines are the distribution of the observed vertical sidebands. The sidebands were observed at the beam current of 9.6 mA with 158 bunches. The vertical oscillation can also be observed on the synchrotron light monitor. The stability is quite sensitive with the vertical

0-7803-4376-X/98/$10.00 © 1998 IEEE

chromaticity at the threshold current and significantly depends on the bunch spacing.

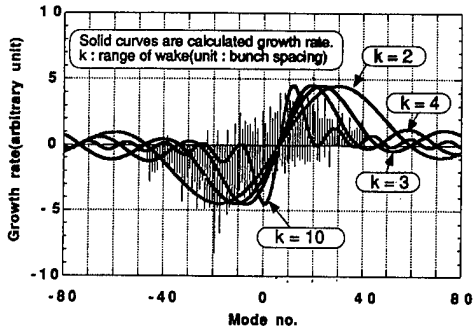

Figure 1: The vertical betatron sidebands and the calculated growth rate of the instability

2.2 Influence of the Chromaticity

The chromaticity influence on the instability is clear especially near the threshold current. The vertical sidebands disappeared when the vertical chromaticity increased by 1 or 2 from the normal value of 4 at the beam current slightly above the threshold of the instability. On the contrary, the vertical sidebands appeared when the chromaticity decreased at the beam current slightly below the threshold. In this way, the threshold current of the instability can be easily determined by adjusting the chromaticity. We did many tests of the chromaticity effect at the different conditions and near the threshold current of the instability. The mechanism of the chromaticity is understood as the head tail damping and the Landau damping.

2.3 Effect of the Bunch Spacing

Most observation of our experiment is done under the condition of the full filling with 160 bunches uniformly. To investigate the bunch spacing dependence, we injected the positron to every other two buckets, i.e. 80 bunches uniformly in the ring. The threshold current of the instability is about 40 mA as the vertical betatron sidebands appeared when the ξ_y changes to 2.8. This result can be explained as the wake field of the photoelectron decreases quickly along the bunch spacing. However, this effect is much stronger than it was predicted by the simulation[5].

2.4 Energy Dependence

To survey the energy dependence of the instability, we scan the beam energy from 1.3 GeV to 2.2 GeV at the beam current about 15 mA. The amplitude of the vertical sidebands slightly decreased at 2.0 GeV and can be affected by the chromaticity. At 2.2 GeV the vertical sidebands disappeared. The sideband distribution is shown in Figure 2. It shows that the sidebands of the instability do not depend on the energy obviously at the beam current above the threshold. We also scan the energy from 1.55 GeV to 2.1 GeV at the beam current about 10.3 mA which is near the threshold. The vertical chromaticity was changed at several energies to obtain the threshold value at which the sidebands disappear. The relation between the beam energy and the vertical chromaticity at the threshold value is shown in Figure 3. It can also be seen that the energy influence on the instability is not very strong. This is another feature of the PEI which can be distinguished from other single beam instabilities in the storage ring.

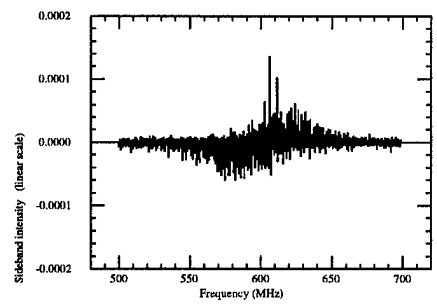

Figure 2-a: Sidebands at the energy of 1.55 GeV

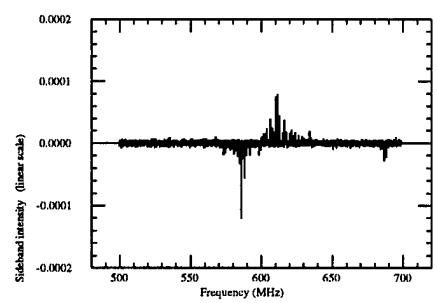

Figure 2-b: Sidebands at the energy of 2.0 GeV

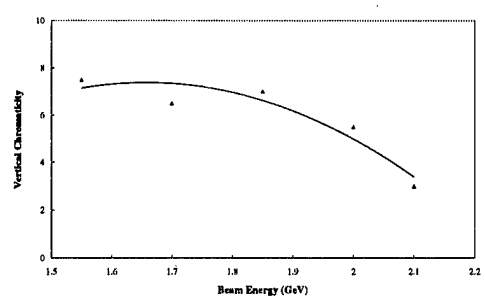

Figure 3: Energy dependence of the PEI

The number of the photon is proportional to the beam energy while the beam instability gets weaker at higher energy from Eq. (1). The beam emittance and the radiation damping time are scaled with square and third power of the beam energy. The number of photoelectrons increases with the beam energy. The energy dependence of the instability should be considered synthetically in this way.

2.5 Influence of the RF Frequency

If the distance between the center of the position beam and the wall of the beam tube is changed, the distribution of the photoelectron should be modified. We change the beam orbit by changing the RF frequency. When the beam current is near the threshold, we change the RF frequency ± 20 kHz respectively which corresponds to a horizontal orbit change of ± 4 mm in average. The amplitude of the sideband is a little weaker at the RF frequency change of –20 kHz than that of +20 kHz as shown in Figure 4. These effects should also be synthesized with the emittance because the emittance variation can be raised from the frequency change.

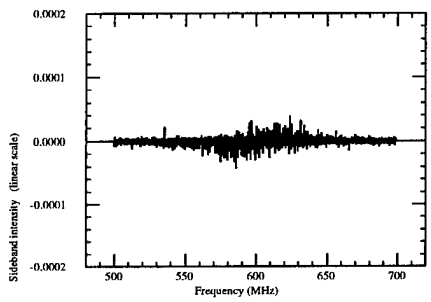

Figure 4-a: The RF frequency influence of –20 kHz

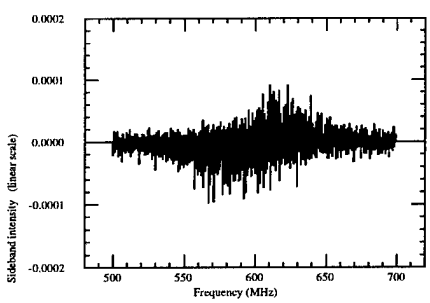

Figure 4-b: The RF frequency influence of +20 kHz

2.6 Other Related Effects

It was reported[7] that the leakage electrostatic field from the distributed ion pump traps the photoelectron and then the photoelectron instability could be resulted. The structure of the BEPC distributed ion pump is similar to that of the CESR but the calculated leakage electrostatic field is about 50 times weaker at the beam orbit center[8]. The distribution of the vertical sidebands was compared in the case of the pumps being turned on and off, but the phenomena of the instability were not changed any more.

The observation shows that the transverse and longitudinal tunes do not affect the vertical sidebands of the PEI when they are changed in a stable region. The phenomena of the instability are not influenced when the RF voltage is changed. The horizontal magnetic field effect on the PEI was also tested by increasing the field of all vertical correctors to 10, 20 and 40 Gausses, there was no experiment evidence to be observed. The threshold currents are almost the same at the conditions of a bunch train with the same bunch spacing but different bunch current and different bunch gap. The emittance dependence of the instability has been observed, but the effect is not clear because the sextupole configuration is also changed simultaneously.

2.7 Beam Spectrum in Electron Filling

The different phenomena were observed in the electron beam under the same conditions as the position beam. Many observation is carried out above the PEI threshold current with the electron beam. The vertical sidebands were only observed at $2f_{rf}$ and $3f_{rf}$ but not at other revolution harmonics. It shows that the instability is only for the position beam as an unique characteristic in position storage rings.

2.8 HOM of RF Cavity

To distinguish the HOM of RF cavity effect on the PEI, a positron beam near the threshold current of the instability was stored and the HOM signal from cavities was observed through loop pick ups below and above the threshold of the instability. No signals corresponding to the HOM was observed. This observation indicates that the PEI does not relate to the HOM of BEPC cavities.

3 DISCUSSION

The positron multibunch instability observed in BEPC is very similar to that observed in PF. The dependence of the instability on the related parameters is studied in more detail. The experiment in BEPC shows that the observed instability seems to be a common phenomenon in positron storage rings, so it is very meaningful to study the instability for such modern positron rings like B factories and Tau-charm factories. Further analytic and simulation studies are in progress.

4 ACKNOWLEDGMENTS

The authors are grateful to the BEPC staffs for their excellent corporation. Many discussions with M.Tigner of CESR and Le Duff of ORSAY are very helpful.

REFERENCES

[1] M.Izawa, et. al., Phy. Rev. Let., Vol. 74, 1995
[2] K.Ohmi, Phy. Rev. Let., Vol. 75, 1995
[3] A.Chao, *Physics of collective Beam Instabilities in High Energy Accelerators*, 1993
[4] Z.Y.Guo et. al., EPAC'96, 1996
[5] C.Zhang, PEI/MD-Note/96-03, 1996
[6] H.Fukuma, et. al., IHEP-KEK/PEI/MD-03, 1996
[7] J.Rogers, CBN, 95-2, 1995
[8] Q.L.Peng, Private communication, 1997

OPERATION AND PERFORMANCE OF BUNCH PRECOMPRESSION FOR INCREASED CURRENT TRANSMISSION AT THE SLC *

M.G. Minty, R. Akre, F.J. Decker, J. Turner
SLAC, Stanford, CA 94309, USA

Abstract

As the beam currents at the SLC are increased, transverse aperture restrictions in the ring-to-linac transport line (RTL) become increasingly important. The RTL contains a bunch compressor which introduces a large energy variation across the bunch and hence a larger transverse beam size. Since 1994 the compressor amplitude has been operating at higher than design voltage. While advantangeous for shaping the bunch distribution, this increased the bunch energy spread and therefore resulted in more beam loss. Moreover, due to current-dependent bunch lengthening in the damping ring, the higher the beam current, the more the current loss. To avoid such losses, the bunch length may be precompressed in the damping ring. Until recently, bunch precompression with high beam currents was not stable. In this paper we identify the reasons for the difficulties, describe the changes made to accomodate bunch precompression, and discuss performance aspects after implementation. The estimated increase in current at the interaction point is 15%.

1 INTRODUCTION

The current loss in the RTL is shown in Fig. 1. This loss has two identified sources: current-dependent bunch lengthening in the damping ring and bunch compression in the RTL. As shown in the measurements by Holtzapple [1], the scaling of the bunch length σ_z on damping ring cavity voltage V_c is $\sigma_z \propto V_c^{\frac{1}{4}}$ at high current. This is weaker than the usual square root law (which was shown to be valid at low beam current). The data of Fig. 1, which were obtained with $V_c = 680$ kV, show a 28% transmission loss (23% taking into account the relative calibration between the toroids) at a beam current consisting of two bunches of 4.5×10^{10} particles per bunch (ppb). At a nominal operating voltage of 800 kV and 4.0×10^{10}, the loss was 13%.

The second source of current loss is related to (standard) bunch compression in the RTL which takes place in two steps: first, a cavity is used to introduce an energy-phase correlation within the bunch, then in the high dispersion region following the cavity, the bunch length is compressed due to the energy-dependent path length. Letting z_r, δ_r and z_l, δ_l denote the longitudinal position z and relative energy δ in the ring (r) and linac (l), respectively, a particle within the bunch is transported as

$$z_l = z_r + R_{56}\delta_l \text{ and } \delta_l = \delta_r + \frac{eV}{E}\cos\phi, \qquad (1)$$

* Work supported by the Department of Energy, contract DE-AC03-76SF00515

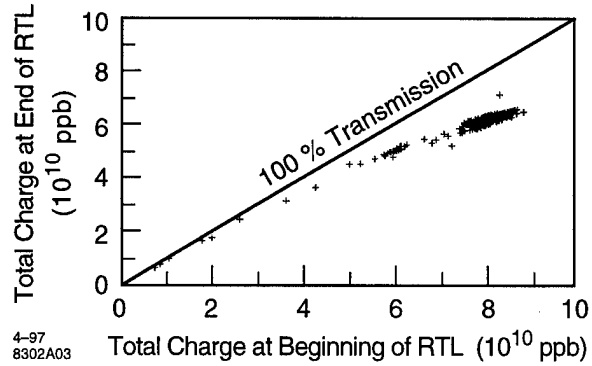

Figure 1: RTL transmission without precompression.

where R_{56} is a lattice parameter which maps phase into energy from the compressor cavity to the linac, e is the electron charge, V is the compressor voltage, $E = 1.19$ GeV is the beam energy, and ϕ is the relative phase of the particle with respect to the zero crossing of the compressor voltage. Recently the compressor amplitude has been operated at higher than design voltage [2]. While advantageous for shaping the longitudinal beam distribution, this increased the energy spread of the bunch by about 30%. From Eq. (1) beam losses can occur in regions of high dispersion η and limited horizontal apertures (since $x = \eta\delta$).

2 BUNCH PRECOMPRESSION ANALYSIS

To minimize these losses, the bunch length may be precompressed [3] by manipulation of the cavity voltage in the damping ring. Previous studies have shown that a single step change in the cavity voltage results in a longitudinal phase space mismatch which elongates the bunch and that the resulting beam phase oscillation may be eliminated while amplifying the bunch length oscillation by application of a second, appropriately timed, step change to the cavity voltage. Implementation of bunch precompression was only moderately stable, however, due to unexplained beam variations.

To better understand the source of the observed instabilites, bunch precompression was subsequently analyzed using a more detailed model [4] of the damping ring rf system including feedback loops, which are used to regulate the cavity voltage and beam phase, and a realistic (nonlinear) klystron. Within that model, the centroid motion of the beam phase ϕ in the damping ring is given by the harmonic solution

$$\ddot{\phi} + \frac{\alpha\omega e\dot{V}}{E\omega T}\phi = 0, \qquad (2)$$

where $\alpha = 0.0147$ is the momentum compaction factor, $\omega = 2\pi \times 714$ MHz is the angular rf frequency, and $T =$

117.6471 ns is the revolution period.

Simulations showed that the newly incorporated direct loop [5] (which is used to regulate transient beam loading[6]) caused the klystron to saturate due to the effective increase in cavity bandwidth: at high gain, therefore, the cavity voltage could not track the requested change. Simulations showed that would be no significant compromise if the loop gain were reduced. As shown in Fig. 2, a factor of 2 reduction in loop gain hardly affects the cavity voltage or beam phase regulation.

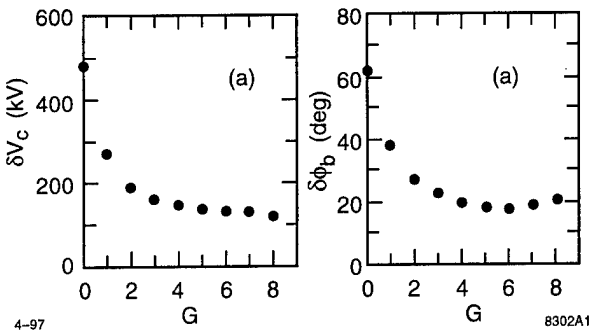

Figure 2: Simulation of peak-to-peak cavity voltage δV_c and beam phase $\delta\phi_b$ variations at injection as a function of direct loop gain G with $V_c = 800$ kV and 2 bunches containing 4×10^{10} ppb.

Following the derivation in Ref. [7], the single-particle model of the rf system was expanded to include estimates for the bunch length and energy spread. Defining the longitudinal emittance ϵ as $\epsilon^2 = \langle\phi^2\rangle\langle\delta^2\rangle - \langle\phi\delta\rangle^2$ and defining the second moments of the distribution to be $\sigma_\phi{}^2 = \langle\phi^2\rangle$, and $\sigma_\delta{}^2 = \langle\delta^2\rangle$, the equation of motion for the bunch length and energy spread are

$$\begin{aligned} \ddot{\sigma_\phi} - \omega_s{}^2\sigma_\phi &= (\alpha\omega_s)^2\frac{\epsilon^2}{\sigma_\phi{}^3} \\ \ddot{\sigma_\delta} - \omega_s{}^2\sigma_\delta &= \frac{(e\dot{V})^2}{E\omega T}\frac{\epsilon^2}{\sigma_\phi{}^3} \end{aligned} \tag{3}$$

with $\dot{V} = \omega V \sin\phi_b$. In deriving Eqs. 3 has been assumed, as in Ref. [7], the commutativity of the time derivative and average over the bunch distribution, which is valid ignoring intrabunch beam dynamics. The effect of short-range wakefields are analyzed in Ref. [8].

Using the reduced direct loop gain to avoid klystron saturation, the predicted cavity voltage and observables are shown in Fig. 3 as a function of time. The double-impulse step changes in the cavity voltage result as expected in an coherent bunch length reduction while the coherent dipole rotation is cancelled.

3 IMPLEMENTATION

Shown in Fig. 4 (to be compared with Fig. 3) are the measured cavity voltage (measured using a diode detector), bunch length (obtained from a peak current measurement,

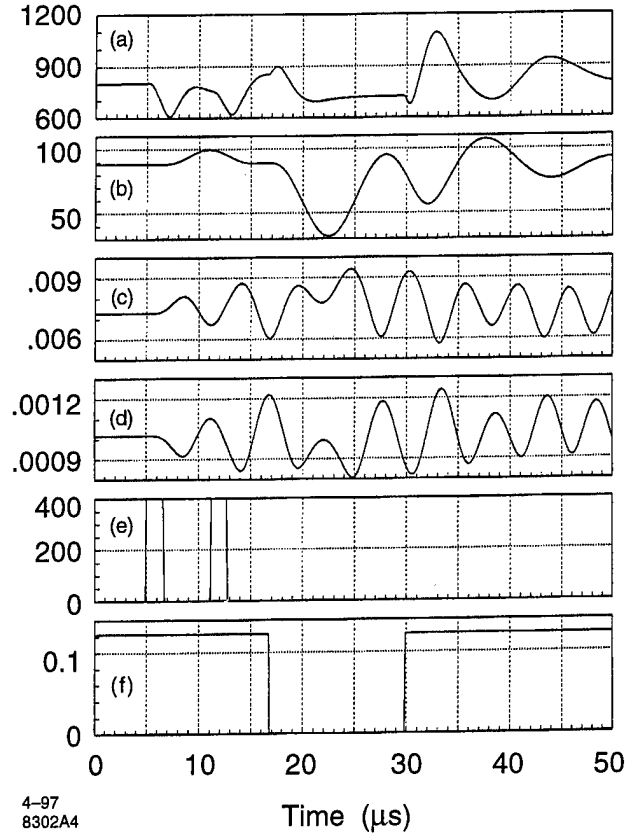

Figure 3: Simulations of bunch precompression parameters. Plotted as a function of time are the cavity voltage [kV] (a), the beam phase [deg] (b), the bunch length [m] (c), the relative beam energy [%] (d), the command for the requested voltage change [kV] (e), and the dc beam current [A] (f).

which is inversely proportional to bunch length, using a single stripline of a position monitor), and mean energy of the beam during precompression. The centroid energy was measured using a horizontal beam position monitor in a region of high dispersion in the damping ring. In the future, we plan to digitize the beam centroid and energy to monitor stability and compare with expectation. The increase in transmission measured during preliminary tests is shown in Fig. 5.

4 PERFORMANCE

When precompression was turned on with reduced direct feedback gain, we detected no change in the beam jitter (position, intensity, and energy) or in the backgrounds at the interaction point (IP). Shown in Fig. 6 is the electron charge at the IP and the precompression command signal; the increase in the average electron beam current is about 10% with precompression. In addition, since electron pulses are used to make positron pulses, the increased electron current yielded higher positron current. The positron current at the IP was observed to increase gradually over a time period of about one week.

Bunch precompression was later implemented in the

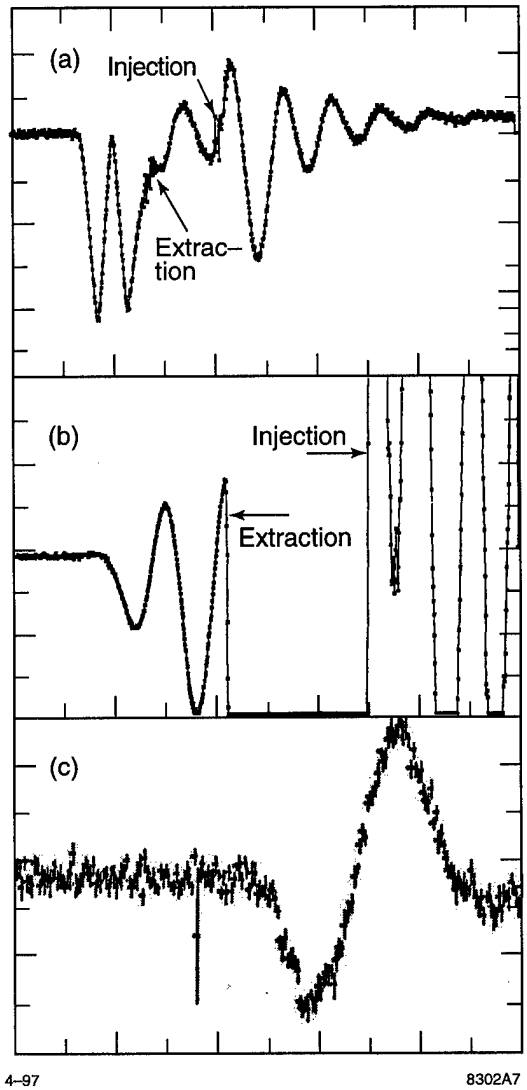

Figure 4: Measured cavity voltage [50 kV/dvsn, 10 μs/dvsn] (a), peak current [10%/dvsn (based on cross-reference with Fig. 3), 5 μs/dvsn] (b), and centroid energy [50 μm or 0.77%/dvsn, 20 turns or 2.34 μs/dvsn] (c).

positron damping ring. Unlike with electrons, however, the luminosity was not observed to increase. The reason for this is not understood. Possible reasons include increased wakefield effects (by the leading positron bunches on the trailing electron bunches), increased bunch length jitter (which is predicted [9] to result in increased orbit jitter), or to a yet undetermined effect.

Acknowledgements The authors gratefully acknowledge R. Siemann for encouraging studies in the area of increased current transmission. The hardware aspects of this project were greatly facilitated by G.R. Barillas, M. Mitchell, and D.A. Steele. We also thank M. Ross and N. Phinney for their support and help with data acquisition.

5 REFERENCES

[1] R. Holtzapple, Ph.D. thesis, Stanford University (1996).

[2] F.J. Decker, R. Holtzapple, T. Raubenheimer, SLAC-PUB-6604, LINAC94, Tsukuba, Japan (1994).

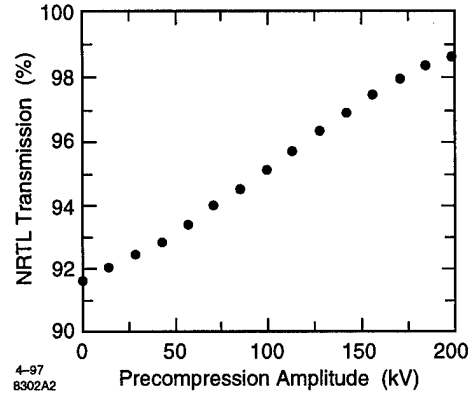

Figure 5: Increase in transmission in the RTL as a function of precompression depth. During the measurement, the timing parameters (i.e. the duration of each step change in the cavity voltage and the spacing between each of the two step changes) were held fixed.

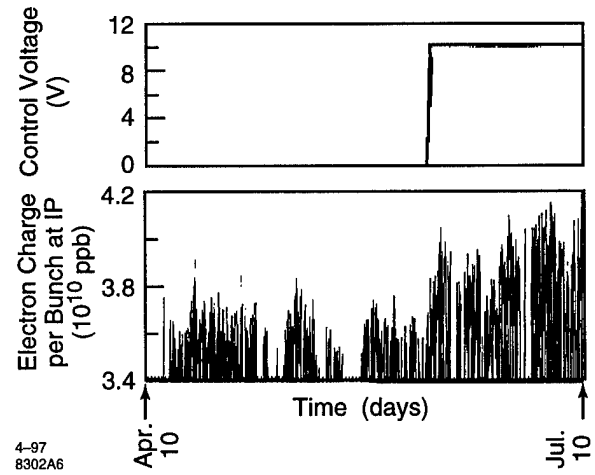

Figure 6: Precompression command signal and electron beam current measured at the IP as a function of time.

[3] F.J. Decker, T. Limberg, J. Turner, "Precompression of Bunch Length in the SLC Damping Rings", HEACC'92, Hamburg (1992).

[4] M. Minty and R. Siemann, "Heavy Beam Loading in Storage Ring Radio Frequency Systems", *Nucl. Instr. and Meth. A*, **376** (1996) 301-318.

[5] P. Krejcik *et al*, "RF Feedback for Beam Loading Compensation in the SLC Damping Rings", Proc. IEEE PAC, Washington, DC (1993).

[6] M.G. Minty *et al*, "Operating Experience with High Beam Currents and Transient Beam Loading in the SLC Damping Rings", Proc. IEEE PAC, Dallas, TX (1995).

[7] A.W. Chao, "Physics of Collective Beam Instabilities in High Energy Accelerators", J. Wiley (1993).

[8] K.L.F. Bane *et al*, "Simulation of Bunch Precompression at High Currents in the SLC Damping Rings", these proceedings, see 9V45.

[9] R. Assmann and F. Zimmermann, SLAC-PUB-8269, to be published in Proc. LINAC96 Conf., Geneva, Switzerland (1996).

ULTRA-SHORT BUNCHES BY USING A QUASI-CONTINUOUS COMPRESSOR SCHEME IN A LONG BEAM TRANSFER LINE

H. Schlarb and R. Brinkmann, DESY, Notkestr.85, D-22603 Hamburg, Germany

Abstract

Integration of an X-Ray Free Electron Laser facility is planned in the TESLA design for a future e^+e^- Linear Collider. In the present scheme, the FEL drive beam is transported to a central user facility in a several km long beamline. In this paper we present how the longitudinal wakefield effect for short bunches in combination with a special beamline magnetic lattice can be used to obtain compression down to an rms-bunch length in the range of a few μm. Peak current of more than 50 kA would enable the X-Ray FEL facility to generate photon wave lengths in the sub-Angstrom regime.

1 DESIGN OF THE TRANSFER LINE

In the current design for a future Tera Electron Volt Super Conducting Linear Accelerator (TESLA) the drive beam for the X-Ray FEL is compressed to a bunch length of $\sigma_z = 25\,\mu$m and accelerated in the LINAC to energies of E_0 =15 to 50 GeV. After 3 km the beam is kicked into a 12 km long transfer line and transported to the central user facility, close to the high energy physics laboratories. An intensive study of wakefields, excited in resistive beam pipes and in the TESLA acceleration modules, opens up the possibility to start with an initial bunch length of 50 μmand end with rms-values of 2 μm. In the design proposed here the bunch compression takes place over several stages using the longitudinal properties of the wakefields in combination with compressor modules situated along the beamline. The stages can be decomposed as follows:

- **Pre-compression:** using the LINAC wakefields ($\sigma_z = 50\,\mu$m$\rightarrow 5\,\mu$m)
- **Over-compression:** interchange of the tail and the head of the bunch ($\sigma_z = 5\,\mu$m$\rightarrow 8\,\mu$m)
- **Compensation:** energy correlation from the LINAC wakefields is eliminated by the resistive wall wakefields ($\sigma_z = 5\,\mu$m)
- **Correlation:** rebuilding of an energy correlation using again the resistive wall wakefields ($\sigma_z = 5\,\mu$m)
- **Final Compression:** using energy correlation of the previous stage ($\sigma_z = 5\,\mu$m$\rightarrow 2\,\mu$m)

In order to simulate the various stages a 1-dimensional numerical code has been written. The initial beam parameters are given in the following table :

Quantity		Units	Value
Energy	E_0	GeV	30.0
Long. Emittance	ϵ_z	keV mm	25.0
Charge	Q_0	nC	1.0
Bunch length	σ_z (rms)	μm	50.0
Peak current	I_{peak}	kA	2.4

Following points are considered:

- Random distribution in the long. phase space
- Wakefields (resistive tube & LINAC)
- Compaction factor in the compressor modules
- Space charge effects.

2 COMPRESSOR MODULES

A special beamline magnetic lattice, 240 m long, with a closed dispersion trajectory and a tuneable positive momentum compaction[1] of α_c = 1-3·10^{-5} is used to compress the bunch. One module consists of three dipoles (bend-radius = 1.2 km, length = 5, 10, 5 m) and FODO-cell structure ($\beta_{x,y}^{aver}$ = 20 m, 22.5 m).

3 WAKEFIELDS

In the present scheme the longitudinal correlation between energy and position inside the bunch is generated by the electromagnetic fields co-travelling with the bunch.

3.1 *Resistive Wall Wakefields*

Wakefields induced in a cylindrically tube of finite conductivity are well understood. Analytical solutions for the delta wake potential in the ultra-relativistic limit, up to any multipole order[2], have been derived in [1, 2, 3]. It has been shown that the short range wakefields can be decomposed in a high frequency ($k_r = \sqrt{3}/\zeta_0$) strongly damped ($\alpha_r = 1/\zeta_0$) oscillator and an additional diffusion term. The characteristic length ζ_0 will be given by

$$\zeta_0 = \left(\frac{2b^2}{Z_0\sigma_0}\right)^{1/3} \qquad (1)$$

where b denotes the radius, σ_0 the conductivity of the wall material and Z_0 =120 π the impedance of vacuum. For a stainless steel tube σ_0 =1.4·$10^6\,\Omega^{-1}$m^{-1} and a radius of

[1]Definition of α_c is given by $\Delta L/L \equiv \alpha_c \Delta E/E$ where L denotes the length of the module and E the energy of the particles.

[2]In the following only the monopole term is considered. The higher orders ($n > 0$) inherent by the fraction $(r/b)^{2n}$ where r denotes the transverse off-set of the beam from the center of the pipe. They can be neglected for ($r \ll b$).

0-7803-4376-X/98/$10.00 © 1998 IEEE

$b = 5$ cm the characteristic length is $\zeta_0 = 211\mu$m. For two point-like particles the longitudinal monopole wake potential reads[3][4][2]

$$W_{0,\|}(\zeta) = -\frac{Z_0 c}{\pi b^2}\left(\frac{4}{3}e^{-\alpha_r\zeta}\cos(k_r\zeta) - \frac{12\sqrt{2}}{3\pi}\int_0^\infty dx\,\frac{x^2 e^{-x^2\alpha_r\zeta}}{x^6+8}\right) \quad (2)$$

with ζ the distance between the source charge and the test charge. For velocities v smaller than the speed of light c the effective bunch length at the wall and the retarded effect of the 'radiated' electromagnetic fields produced by the image current modify the delta wake potential for very short distances $|\zeta| < b/\gamma$, where γ denotes the Lorentz factor. The longitudinal delta wake potential per unit length as a function of ζ is shown in Fig.1.

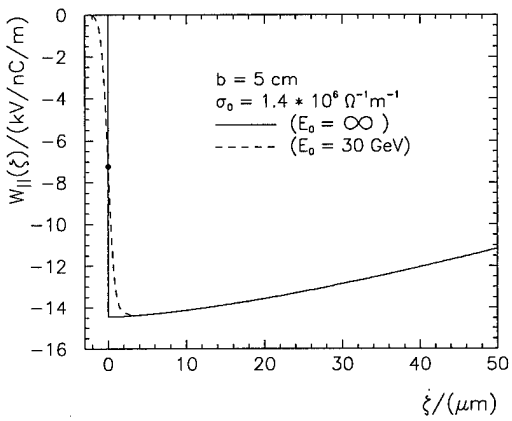

Figure 1: Delta wake potential

For distances in the range $b/\gamma < \zeta \ll \zeta_0$ the short range wakefields act purely capacitive and the forces are independent of ζ. The wake potential for a charge distribution with a rms-bunch length σ_z in the above range will be given by integration of the charge longitudinally. In the special case of a Gaussian charge distribution the longitudinal wake potential will be approximately given by the error-function (see Fig.2).

The energy correlation produced by the bunch due to the resistive wall wakefields is linear at the center of the bunch and obeys automatically the desired phase relation. This behavior of **self-regulated** correlation can not be produced by an off-crest phase acceleration of the beam in a LINAC. For very short bunch lengths an off-crest acceleration will fail anyway since the amplitude of the generated wakefields grows quadratically with the resonance frequency of the cavities ($W_\| \propto f_{res}^2$), while the resulting compensation will only be proportional to the f_{res} ($dE/dz \propto f_{res}$).

[3]The dc-model of conductivity has been used. In case of $\zeta_0 \approx \tau c$ where τ denotes the relaxation time of the conduction electron ($\tau \sim 10^{-15}\,s^{-1}$) the frequency-dependent Ohm's law has to be used. For ourer parameter set it can be neglected.

[4]The anomalous skin effect has not been taken into account. The assumption is justified for materials of poor conductivity if the penetration-depth $\delta = \sqrt{2c/\omega_c Z_0\sigma_0}$ at the cut-off frequency $\omega_c = b/\gamma c$ is much larger than the mean free-path $l = v_F\tau$ of the conducting electrons.

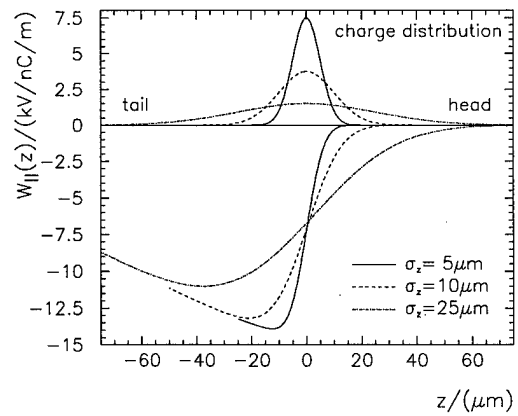

Figure 2: Wake potential for Gaussian charge distr.

3.2 *Wakefields of the TESLA Module*

The longitudinal wakefields for one TESLA module, 10.4 m long, consisting of 8 cavities has been calculated [4]. The results are shown in Fig.3 together with the wake produced by the 8th cavity normalized to one module. It can be seen that both wake potentials can be used for a pre-compression of the bunch coming from the LINAC. The latter, being more linear over the bunch, would lead to a better performance. Since the wakefields for several modules are not yet available the average wake potential (solid curve) is used for numerical simulations. We expect that the LINAC-wakefields of 250 modules (3 km) will look more like the wake of the 8th cavity (dashed curve). This would increase the efficiency of the compressor scheme by 30%.

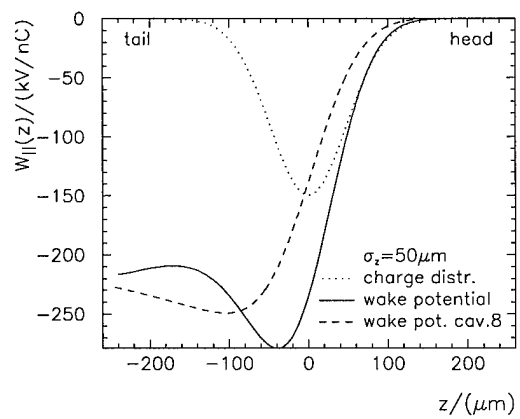

Figure 3: Wake potential of one TESLA module

4 RESULTS

4.1 *Longitudinal Charge and Energy Distribution*

The nonlinearities of the wake potentials at the tails of the bunch reduces the efficiency of such a method. The present simulation shows that approximately 50% of the initial charge can be compressed to extremely small values of less than 2 μm shown in Fig.4(a). The energy distribution of the core of the bunch is shown in Fig.4(b) and reflects essentially the longitudinal emittance of the initial bunch. The two typical peaks at the edges of the energy dis-

tribution are caused by the over-compression in the second stage. This stage is mainly used to increase the efficiency and the stability of the compressor scheme. Note that the LINAC can run with an on-crest acceleration phase, since no compensation of the wakefields is needed.

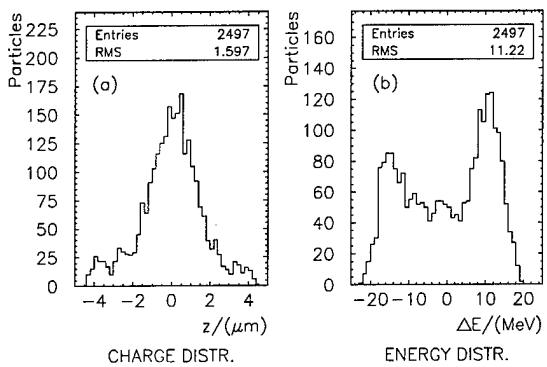

Figure 4: Longitudinal charge distribution (a) and energy distribution (b) for 50% of the initial charge Q_0; the peak current reach $I_{peak} = 50\,\mathrm{kA}$.

Finally the bunch in the longitudinal phase space at the end of the transfer line is shown in Fig.5. The tails of the bunch have to be removed by collimation.

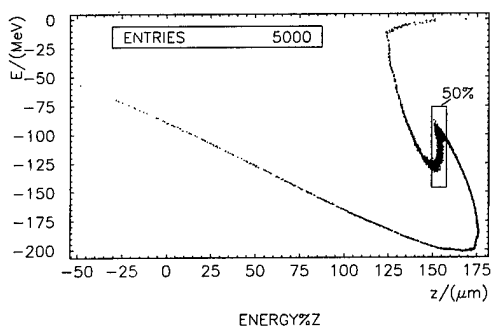

Figure 5: Longitudinal phase space distribution of the particles at the end of the compression scheme; E = 0 corresponds to the initial beam energy $E_0 = 30\,\mathrm{GeV}$.

4.2 *Stability of the Compression scheme*

An important question is the stability of such a scheme for different initial bunch parameters since the energy correlation is generated by the bunch itself. This has been studied in detail for bunch to bunch charge fluctuations up to $\pm 20\%$ while the other parameters have been kept constant. The results are given in Fig.6(a) and (b). The variation is limited to reasonable values for the bunch length, the peak current and the energy spread.

5 OPEN QUESTIONS

The presented values for the peak current are orders above any existing and planned machine so that we expect additional limiting effects for the practical realization of such a compression method. One of these is the coherent synchrotron radiation (CSR)[5] generated in the bending system of the compressor modules for a bunched beam. This

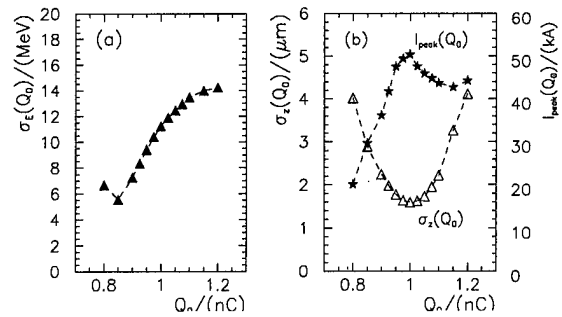

Figure 6: The rms-energy distribution (a) and the rms-bunch length together with peak current (b) for 50% of the initial charge Q_0 as a function of Q_0.

tail-head effect may lead to a coupling between the coherent energy spread generated by the CSR and the transverse (bending) plane coordinates through the chromatic transfer function of the particular beamline. This effect is under study and first estimations shows that this can be the limiting effect for our scheme. It is in principle possible to cancel this effect [6], but the final bunch length will be limited to values somewhat larger than shown above.

6 CONCLUSION

We have presented how the longitudinal wakefield effect can be used to obtain bunch lengths below 2 μm and peak currents above 50 kA with an efficiency of 50%. The concept of over-compression lead to a first order compensation of bunch to bunch charge fluctuations and guarantee the stability of the quasi-continuous compressor scheme up to $\Delta Q_0 \approx \pm 10\%$.

7 ACKNOWLEDGEMENTS

One of the author wishes to thank A. Novokhatski and A. Piwinski for the helpful discussions about the properties of wakefields.

8 REFERENCES

[1] O.Henry & O.Napoly, "The Resistive-Pipe Wake Potentials for Short Bunches", Part. Acc., Vol. 35, pp. 235-247,1991

[2] K. Bane, "The Short Range Resistive Wall Wakefields", SLAC-AP-87, (June 1991)

[3] K. Yokoya, "Resistive Wall Impedance of Beam Pipes of General Cross Section", Part. Acc., Vol. 41, pp. 221-248,1993

[4] A. Novokhatski & A. Mosnier, "Short Range Potentials for a Chain of TESLA cavities", DAPNIA/SEA-96-08, (Nov. 1996)

[5] Ya. S. Derbenev et. al., "Microbunch Radiative Tail-Head Interaction", DESY, (Sep. 1995)

[6] P. Emma & R. Brinkmann, "Emittance Dilution Through Coherent Energy Spread Generation in Bending Systems", contribution to this conference

COMPENSATION OF LONGITUDINAL COUPLED-BUNCH INSTABILITY IN THE ADVANCED PHOTON SOURCE STORAGE RING

K. C. Harkay, A. Nassiri, J. J. Song, Y. W. Kang, R. L. Kustom
Advanced Photon Source, Argonne National Laboratory
9700 South Cass Avenue, Argonne, Illinois 60439 USA

Abstract

A longitudinal coupled-bunch (CB) instability was encountered in the 7-GeV storage ring. This instability was found to depend on the bunch fill pattern as well as on the beam intensity. The beam spectrum exhibited a coupled-bunch signature, which could be reproduced by an analytical model. The oscillations were also observed on a horizontal photon monitor. The beam fluctuations exhibited two periodicities, which were found to be correlated with the rf cavity temperatures. This correlation is consistent with the measured temperature dependence of the higher-order mode (HOM) frequencies [1]. The HOM impedance drives the beam when brought into resonance with the CB mode by the temperature variation. Increasing the inlet cavity water temperature suppressed the instability. The experimental results are compared to an analytical model which characterizes the fill-pattern dependence. Studies to identify the offending HOMs are also presented.

1 INTRODUCTION

The Advanced Photon Source (APS) is a national facility that produces brilliant x-rays for use in scientific and industrial research. Selected parameters for the 7-GeV positron storage ring (SR) are found in Table 1. The nominal stored current is 100 mA, with a design goal of 300 mA. A variety of bunch fill patterns have been employed to meet the needs of the x-ray users and to optimize performance of the beam position monitors (BPMs) in orbit control. Typically, between 40 and 200 bunches are stored out of a possible 1296. It was discovered that some of these fill patterns give rise to a longitudinal CB instability.

Table 1: Nominal APS Storage Ring Parameters

Circumference		1104	m
Revolution frequency	f_{rev}	271.55	kHz
Harmonic number	h	1296	
rf frequency	f_{rf}	351.927	MHz
rf gap voltage	V_{rf}	8.5 - 9.5	MV
Bunch length, FWHM		100	ps
Synchrotron frequency	f_s	1.8 - 2.0	kHz
Synch rad. energy loss /turn	U	5.45	MeV
Damping time, longitudinal	τ_D	4.73	ms

The coupled-bunch instability is an intensity-dependent collective effect that is driven by long-range wakefields such as those produced in the excitation by the beam of high-Q HOMs in the rf accelerating cavities. Under appropriate resonance conditions and with sufficient current, growing beam fluctuations develop, possibly resulting in beam loss. The oscillations occur at harmonics of the synchrotron frequency, modulating specific rotation harmonics in the frequency spectrum of the beam current. There are $\pm$ h/2 possible coupled-bunch modes, n, in which the phase of the νth bunch is $2\pi n\nu/h$. When the instability was first encountered in the SR, the oscillation amplitude was found to be cyclical, growing and decaying over several minutes. It was quickly found that the amplitude variations correlated closely with temperature variations in several rf cavities. The experimental observations and instability compensation are described first. Following is a discussion of the likely driving rf cavity HOM and characterization of the unstable fill patterns.

2 OBSERVATIONS

The SR beam spectrum was observed using the raw signal from a non-zero dispersion BPM button, and the transverse beam size and centroid motion were observed using a bending magnet x-ray pinhole diagnostic signal. The pinhole signal is processed in real-time at a rate less than f_s; therefore, synchrotron oscillations result in an effective horizontal beam size growth. For unstable fill patterns, the beam lifetime was markedly poor, and 100 mA typically could be reached only with difficulty due to beam losses during injection. The particular bunch fill pattern is denoted as M×N, where M is the number of groups, or trains, of N consecutive bunches in a train. The bunch trains can be placed in a symmetric or asymmetric configuration around the ring.

Beam spectra for a symmetric, 4×12 bunch pattern are shown in Figs. 1 and 2, cycling between a stable and unstable state, respectively. A span of one f_{rf} is shown at a high harmonic, since the peak of the CB signals are near (bunch length)$^{-1}$. The beam current is about 100 mA. The envelope of a model 12-bunch train matches the envelope of the rotation harmonics of the data in Fig. 1. The unstable beam spectrum exhibits a coupled-bunch signature. When an interbunch phase advance corresponding to a CB mode of n=

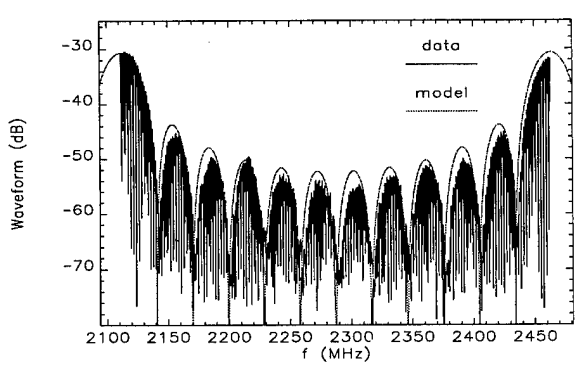

Figure 1: Stable beam spectrum, 4×12 bunch pattern.

0-7803-4376-X/98/$10.00 © 1998 IEEE

540 was introduced in the crude model, using a maximum displacement of 7 degs of rf phase (55 ps), the result shows qualitative agreement with the data in Fig. 2.

In a uniformly-filled ring, the CB spectrum is periodic in $f_{rf}/2$. When the fill pattern is non-uniform, the CB spectrum is highly degenerate. Synchrotron sidebands from several CB modes may be aliased onto every revolution harmonic. This is evidenced in the asymmetric pattern of f_s sidebands in Fig. 3 for the unstable 4×12 fill pattern.

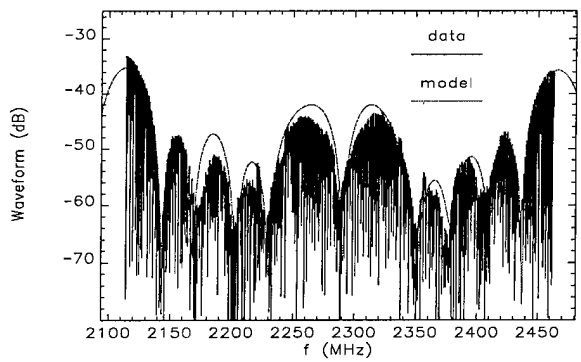

Figure 2: Unstable beam spectrum, 4×12 bunch pattern.

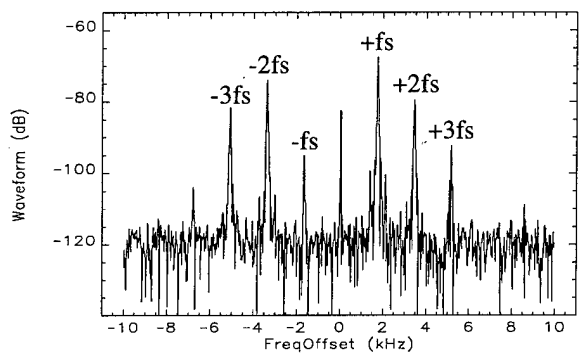

Figure 3: Unstable beam spectrum, centered at $7f_{rf} + f_{rev}$.

2.1 *Correlation with Rf Cavity Temperature*

The cyclical nature of the longitudinal oscillations is seen in Fig. 4, which shows the apparent horizontal beam size over two hours for an unstable fill pattern during a 100-mA store. The maxima correlate with the CB signal in Fig. 2. The beam current decays to 85 mA during this time; the CB fluctuations persist below 75 mA. Two distinct periodicities are seen: 3-4 min and 15-20 min. Little motion is seen in the horizontal centroid or in the vertical plane.

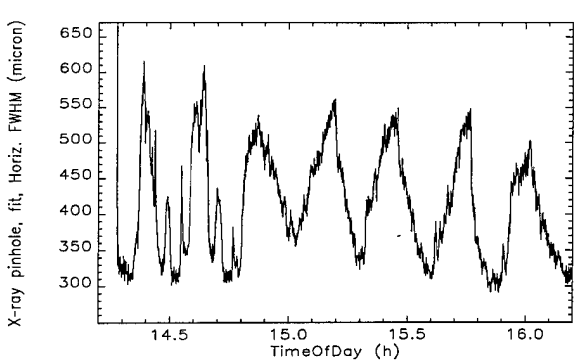

Figure 4: Fluctuating horizontal beam size, 100-mA store.

The rf cavity center temperatures in two of the four sectors over the same period reveal in Fig. 5 a direct correlation with the horizontal beam size variations. This observation is consistent with the view that the HOM frequencies are shifting into and out of resonance with a beam harmonic as the cavity temperatures vary. The measured temperature variation of the HOM frequencies is reported in Ref. 1.

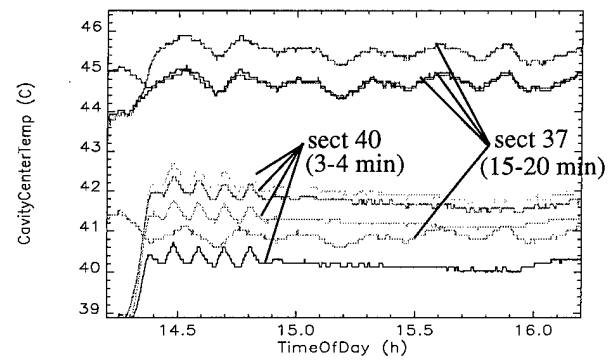

Figure 5: Rf cavity temperature variation in two sectors.

2.2 *Instability Compensation*

The beam appeared to become unstable when the cavity temperatures cycled to their minimum values; therefore, the cavity water supply temperatures were increased in an attempt to shift the HOMs out of resonance with the beam. Sector 37 water temperature was increased by 1.5°F and sector 40 was increased by 1°F. The CB instability was thereby essentially suppressed on following stores (Fig. 6).

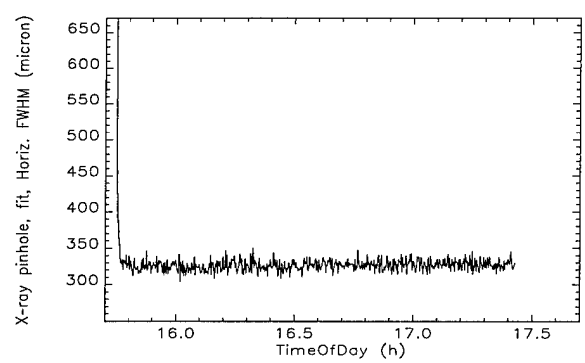

Figure 6: Constant horizontal beam size, 100-mA store, after CB instability compensation.

3 DRIVING RF CAVITY HOM

In the coupled-bunch instability theory, a resonance condition exists between one or more HOM frequencies, f_{HOM}, and the f_{rf} harmonics, p, the f_{rev} harmonics, n, the f_s harmonics, m, and the coherent mode frequencies, Ω_m [2]:

$$f_{HOM} = pf_{rf} \pm nf_{rev} \pm mf_s \pm \Omega_m \approx pf_{rf} \pm nf_{rev}.$$

Because f_s and Ω_m are much smaller than f_{rev}, the expression is simplified as shown on the RHS.

The CB mode envelope in Fig. 2 is centered around 154 MHz from either rf harmonic; therefore, the CB mode is near $\pm 154/f_{rf} \times h = \pm 570$. Plugging this value of n into the expression above for different values of p gives the candidate frequencies listed in Table 2. The one frequency

closest to an rf cavity HOM is 1210 MHz [3]. This is the TM_{013} monopole mode, which has a relatively large temperature response consistent with the results of section 2.2.

Table 2: Possible Driving Frequencies of CB Mode

p	n=570	n=1296-570=726
5	1914 MHz	1958 MHz
4	1562	1606
3	1210	1254
2	858	902
1	506	550

Measurements of the beam-excited rf cavity HOM spectra for different bunch patterns also suggest that the TM_{013} mode is involved in the observed CB instability. The spectra were measured using E-type probes in the rf cavities. High-resolution measurements centered on a rotation harmonic revealed a large upper synchrotron sideband, excited when the beam was unstable (Fig. 7).

The excited HOMs were also measured over a wide frequency range with a resolution bandwidth $\geq f_{rev}$ for stable and unstable beam conditions. These are shown compared to the beam CB spectrum in Fig. 8. The lines marked show increased excitation in one cavity when the beam is unstable. The leftmost marked line is the 1210-MHz mode. The others are possibly aliased lines; the cavity probe detects true HOMs as well as beam power. It should be noted that the coupling of the cavity E-probe varies from mode to mode, and therefore, additional HOMs may be excited by the unstable beam but not revealed by the probe.

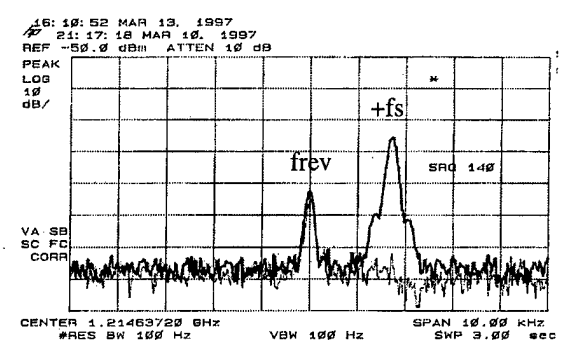

Figure 7: Rf cavity signals centered on 1214.64 MHz.

4 DISCUSSION

Detailed measurements for the symmetric 4×12 bunch fill pattern were presented thus far to demonstrate the character of the CB instability in the storage ring. A number of observations follow, based on studies of about a dozen different patterns. For each unstable pattern, the same CB mode was observed in the beam, implying the same HOM is responsible. Suppressing the instability by raising the cavity temperatures suggests this is truly driven by a long-range, high-Q impedance. The instability threshold was near 100 mA; it did not appear for, say 25 mA in a single train. If short-range wakefields are involved, they are not the dominant effect. However, transient beam-loading cannot be neglected in a partially-filled ring [4].

The CB instability seemed to depend on the bucket interval between the first bunches of each train. The bucket interval for the symmetric, unstable patterns was a multiple of 108. For the observed CB mode, this spacing ensures that synchrotron oscillations of the first bunches of each train are in phase. When the symmetry was broken using the same M×N bunches but with a bucket interval of 250 instead of 324, the instability was not observed. A curious sensitivity to the length of the train was seen. Increasing the train length by only one additional bunch could stabilize or destabilize the beam. Finally, the instability is nearly always in a saturated state, thus the growth rate is difficult to determine. The driving impedance based on a minimum growth rate of τ_D (synchrotron damping) is overestimated for the partially-filled ring.

A detailed spectral analysis of the bunch train and cavity response is planned to address some of these effects. A modification to an existing passive HOM damper design is also planned to increase coupling to the TM_{013} mode [5].

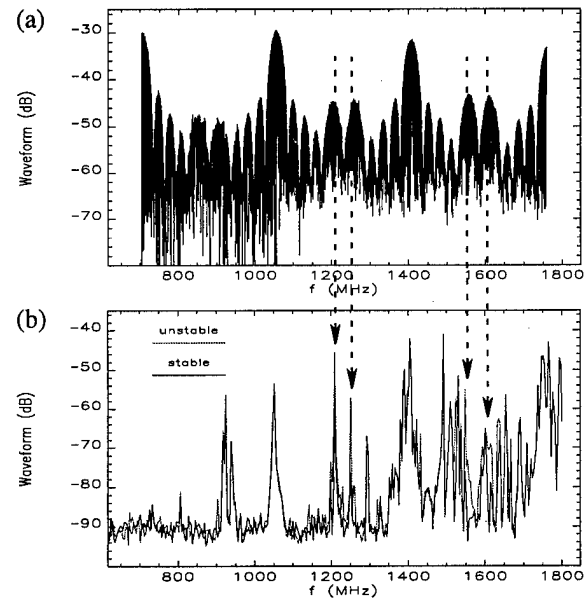

Figure 8: (a) Unstable beam CB spectrum, 4×12 bunch pattern vs. (b) excited HOM spectrum in rf cavity.

5 ACKNOWLEDGMENTS

Work is supported by the U.S. Department of Energy, Office of Basic Energy Sciences, under Contract No. W-31-109-ENG-38. The authors thank A. Lumpkin, ANL, for assistance with the x-ray pinhole diagnostics, and P. Colestock, FNAL, for insightful discussions.

6 REFERENCES

[1] J. Song et al., "Higher-Order Modes of Storage Ring RF Cavities and their Interaction with the Beam at the APS ," these proc.

[2] F. Sacherer, "A Longitudinal Stability Criterion for Bunched Beams," IEEE Trans. Nucl. Sci., NS-20, No. 3, 825 (1973).

[3] T. Smith, "Mode Identification and Cavity Stretching for the Prototype Storage Ring Cavity," ANL Note LS-194 (1992).

[4] K. Thompson and R. Ruth, "Trans. and Long. CB Instab. in Trains of Closely Spaced Bunches," Proc. IEEE PAC, 792 (1989).

[5] J. Song, Y.W. Kang, R. Kustom, Proc. 1993 PAC, 1057 (1993).

FAST TRANSVERSE INSTABILITY IN THE NSNS ACCUMULATOR RING

Alessandro G. Ruggiero and Mike Blaskiewicz
AGS Department, Brookhaven National Laboratory, Upton, NY 11973.

*Abstract**

This paper reports on the results of investigation of possible fast transverse instabilities in the NSNS Accumulator Ring. The instability may be caused by the presence of stripline devices like kicker magnets, the active damper system, and by the RF cavities, and the sharp steps of the vacuum pipe. The instability can be overcome by adopting aluminum as the material of the vacuum chamber, and by smoothing the shape of the vacuum pipe. Still the growth time of the instability remains short especially for the mode in proximity of the betatron tune.

1 THE NSNS ACCUMULATOR RING

The function of the Accumulator Ring is to take the 1.0 GeV proton beam from the Linac and convert the long Linac beam pulse of about 1 ms into a 0.5 microsecond beam in about 1100 turns. The bunch compression occurs during the injection process, and the beam is immediately extracted at the end of the process. The final beam has an intensity of 2.08 x 10^{14} protons per pulse, resulting in 2 MW average beam power at 60 Hz repetition rate. The lattice of the Accumulator Ring is a simple FODO lattice with four-fold symmetry [1]. The salient design parameters are shown in Table 1.

2 THE RING VACUUM PIPE

The main parameters that enter the investigation of the coherent transverse instability are the dimension and the shape of the vacuum chamber, and the resistivity of the wall. The NSNS Accumulator Ring is made of three sections with different vacuum chamber shape and size. The analysis that was made uses formulae that apply strictly to circular geometry. Thus we have approximated the rectangular vacuum chamber by a circular one, and, by taking an average of the pipe dimension around the ring, we have assumed a pipe with an internal radius b = 10 cm. The material of the vacuum chamber is stainless steel for 15% of the circumference, and aluminum for the rest.

3 TRANSVERSE BEAM DIMENSION

The betatron emittance has the same value in the two planes of oscillation. We adopted the criterion to define the total emittance ε_{tot} as 5 times the rms emittance ε_{rms}. Define the average values of the envelope functions $<\beta_{H,V}> = R / Q_{H,V}$, with R the average closed orbit radius and $Q_{H,V}$ the betatron tunes. The average rms beam size in the vertical and horizontal plane are given by $\sigma_{H,V}^2 = <\beta_{H,V}> \varepsilon_{rms}$. This is the contribution from the betatron motion alone, to which we should add the contribution in the horizontal plane from the relative momentum spread δ in the beam, which is $\sigma_E = <\eta> \delta$, where $<\eta> = R / \gamma_T^2$ is the average value of the dispersion around the ring. The total beam relative momentum spread Δ is given in Table 1. The rms value δ is 1/5 of the full value.

Table 1: Parameters of the NSNS Accumulator Ring

Average Power	2 MW
Kinetic Energy	1.0 GeV
Circumference, 2π R	220.7 m
Number of Protons, N	2.08 x 10^{14}
Betatron Tunes, $Q_{H/V}$	5.82 / 5.82
Transition Energy, γ_T	4.93
Full Betatron Emittance, ε_{tot}	120 π mm mrad
Space-Charge Tune-Shift	< 0.2
Total Bunch Area, S	10 eV-s
Full Bunch Length, L	546.6 ns
Full Momentum Spread, Δ	1.6 %
Average Beam radius, a	3.80 cm
Average Pipe Radius, b	10 cm

4 LONGITUDINAL BEAM DIMENSION

The total bunch area is S = 10 eV-s. We shall assume a single RF cavity system for the bunch compression. The requirement is a beam gap, free of any particles, of 294.7 ns and a full bunch length L = 546.6 ns. Assuming again, as usual, a ratio of factor 5 between total and rms values, we can estimate the rms bunch length σ and rms momentum spread δ. The RF system operates at the harmonic number h = 1, and there is thus a single beam bunch, which we assume to hold a cos-square distribution.

* Research on the NSNS is sponsored by the Division of Material Sciences, U.S. Department of Energy, under contract number DE-AC05-96OR22464 with Lockheed Martin Energy Research Corporation for Oak Ridge National Laboratory.

0-7803-4376-X/98/$10.00 © 1998 IEEE

5 THE FAST TRANSVERSE INSTABILITY

The synchrotron period is 0.9 ms, so that the beam bunch will complete only one full synchrotron oscillation before it is extracted. The growth rate of any transverse instability, in order to have a consequence to the beam disruption and loss, will have to be considerably larger than the synchrotron frequency. This situation is characterized as a fast transverse instability, where the synchrotron motion can be neglected and the beam bunch can be treated as a chopped section of coasting beam. The well-known coasting beam theory [2,3] can then be applied.

A coherent perturbation may develop around the contour of the beam bunch. The wavelength of this perturbation has to be at least the bunch length. This sets a lower limit to the perturbation frequency. In terms of the revolution harmonic number this limit is $n > 5$. The upper limit is set by the cut-off due to the presence of the vacuum chamber which is given by $n < \gamma R/b \sim 726$. Outside this range a transverse coherent instability cannot be expected.

6 THE THEORY OF TRANSVERSE COHERENT INSTABILITIES FOR COASTING BEAMS

The stability condition, in terms of the transverse coupling impedance Z_T, is

$$|Z_T| < E_0 \pi Q_{H,V} \beta \gamma [|(n - Q_{H,V}) \eta + \xi_{H,V}| (\Delta p/p) + \delta\nu] / e I_p R = Z_{beam} \quad (1)$$

where $\Delta p/p$ is the FWHM value of the beam momentum spread, E_0 is the proton rest energy, $\xi_{H,V}$ the chromaticity , and $\delta\nu$ the betatron tune spread from non linear elements like octupole magnets. I_p is the peak current of the bunch

$$I_p = Ne / (2\pi)^{1/2} \sigma. \quad (2)$$

In absence of Landau damping, one can estimate the growth rate of the coherent instability

$$\tau^{-1} = I_p r_p \mathrm{Re}(Z_T) / e Q_{H,V} \gamma Z_0 \quad (3)$$

where $Z_0 = 377$ ohm, and $r_p = 1.535 \times 10^{-18}$ m.

As we shall see below, we are in a case where the space charge contribution to the coupling impedance dominates. The frequency of the coherent instability suffers a large shift. This is an indication that there is no Landau damping naturally built within the beam large enough to compensate for the shift, unless this is introduced externally. The real frequency shift of the coherent instability is given by

$$\Delta\omega = I_p r_p \mathrm{Im}(Z_T) / e Q_{H,V} \gamma Z_0 \quad (4)$$

7 THE TRANSVERSE COUPLING IMPEDANCE

There are four major contributions [4] to the transverse coupling impedance. The space-charge contribution dominates in a low-energy storage ring:

$$Z_T = i R Z_0 (a^{-2} - b^{-2}) / \beta^2 \gamma^2. \quad (5)$$

Next, we have the contribution from the wall resistivity:

$$Z_T = (1 - i) R [2 R Z_0 \rho_W / \beta (n - Q_{H,V})]^{1/2} / b^3. \quad (6)$$

By virtue of the deflection theorem [4], the longitudinal coupling impedance Z/n can be translated into an equivalent transverse coupling impedance:

$$Z_T = 2 R Z / \beta b^2 (n - Q_{H,V}). \quad (7)$$

The wall components included in the deflection mode analysis are: bellows, striplines for the beam position monitors and the active damper system, kicker magnets, vacuum chamber steps, vacuum ports, and RF cavities [5].

A large contribution to the real part of the impedance comes from the vacuum chamber steps. The longitudinal coupling impedance from M single steps (uncoupled) was estimated originally by H. Hereward [6]

$$Z/n = 2 M (1 - i\pi) Z_0 (W - 1)^2 b / 2\pi^2 R \quad (8)$$

for $n < n_W = 2\pi R / 2b (W - 1)$, and for $n > n_W$

$$Z/n = Z_0 M (W - 1) / 2\pi n \quad (9)$$

where $W = b_2 / b_1$ is the ratio of the outer dimension b_2 to the inner dimension b_1 of the step.

According to this formula a substantial resistive contribution occurs in the low frequency range. One should point out that very likely this result really applies only to wavelengths which have about the pipe dimension, that is in the proximity of the cut-off. Moreover, steps come in pairs, an entrance followed by an exit discontinuity. Thus, one deals in reality with resonating cavities rather than single de-coupled steps. The contribution represented by Eq.s (8 and 9) has been originally included in the analysis also for very low frequencies, but we believe that otherwise it should really be neglected.

Though it was clearly demonstrated that relation (7) between longitudinal and transverse coupling impedance holds well for stripline devices, like beam position monitors, kickers and the damper system [7], there are some questions about its validity for cavity-like objects, like bellows, vacuum chamber steps, vacuum ports, and RF cavities. Nonetheless, also for these components we have calculated the longitudinal coupling impedance [5] and have then derived the transverse coupling impedance in combination with Eq.(7).

8 THE NSNS ACCUMULATOR RING

Figure 1 is the display of the total expected transverse coupling impedance versus the harmonic number n for the

NSNS Accumulator Ring. The peak around n = 6 is caused by the dependence with the betatron tunes as shown both in Eq.s (6 and 7).

To determine the stability of the beam, we calculate the difference $|Z_T| - Z_{beam}$, taking $\delta\nu = 0$. It is seen that the beam is unstable for all modes $n < 100$. The beam is stable for large mode numbers as a consequence of the frequency compaction factor η.

The growth time τ of the instability, in absence of Landau damping, is plotted in Figure 2. The minimum is $\tau = 5.3$ μs for n = 6. At n = 7 the growth time $\tau = 40$ μs, and at n = 8, $\tau = 91$ μs.

Finally, Figure 3 is the plot of the real frequency shift $\Delta\omega$, divided by the angular revolution frequency $2\pi f_0$. Since the shift is only a small fraction of one harmonic, the possibility of overlapping of neighboring stopbands (mode coupling) seems to be excluded. Moreover, $\Delta\omega / 2\pi f_0$ is about the amount of tune spread which is required to make the motion stable.

9 HOW TO REDUCE THE GROWTH RATE OF THE INSTABILITY

The major concern is obviously the instability for those modes in proximity of the betatron tune. The fewer modes below n = 6 are not relevant in this analysis, since they cannot be excited by the beam. The worst case is represented by the mode n = 6. All the modes n > 20 have growth times of at least half a millisecond, and thus have no significant consequences to the beam performance. The imaginary part of the transverse coupling impedance is essentially given by the space-charge term. The contribution from the other components are entirely negligible.

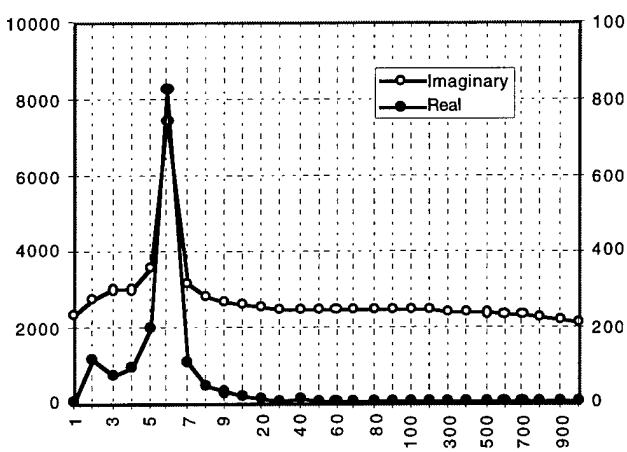

Figure 1. The Transverse Coupling Impedance Z_T (in kohm/m) vs. the Harmonic Number n.

But the largest contribution to the resistive part of the impedance at n = 6 comes (in the order) from the kicker magnets (409 kohm/m), the vacuum chamber steps (168 kohm/m), the RF cavities (147 kohm/m), and the striplines of the active damper system (103 kohm/m). The contribution from the wall resistivity is very small (2.8 kohm/m) when compared to the other components. At the same time the resistive contribution of the beam position monitor is only 2.7 kohm/m

Lowering the betatron tune from 5.8 to 5.2 causes an increase of the instability grow time by a factor of four. At n = 6 now $\tau = 21$ μs. Though this is a significant improvement, nevertheless clearly is not enough. We have pointed out that there are four major components which need very careful engineering design to lower their resistive contribution.

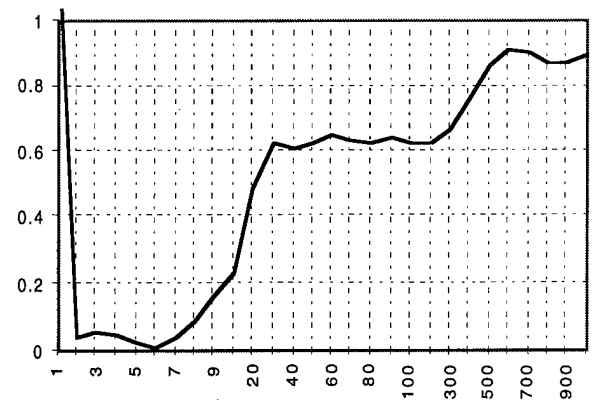

Figure 2. Growth time τ of the Instability (in ms).

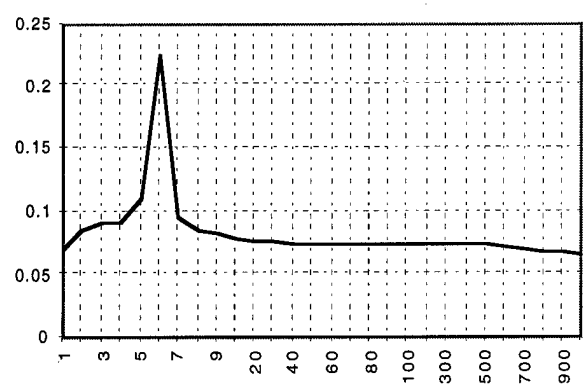

Figure 3. The Real Frequency-Shift $\Delta\omega / 2\pi f_0$.

10 REFERENCES

[1] W.T. Weng et al. These Proceedings.

[2] L.J. Laslett, V.K. Neil, A.M. Sessler, Rev. Sci. Instr., 36, 436, (1965).

[3] K. Hubner, A.G. Ruggiero, V.G. Vaccaro, Proc.7th Int. Conf. on High Energy Accel., Yerevan, p. 343, (1969)

[4] F. Sacherer, Proc. of 9th Int. Conf. on High Energy Accele., SLAC, p. 347, (May 1974).

[5] A.G. Ruggiero, BNL/NSNS Technical Notes No. 27 and 28. April, 1997.

[6] H. Hereward, CERN / ISR - DI / 75-47 (Oct. 1975).

[7] A.G. Ruggiero and V.G. Vaccaro, Internal Report LNF-69/70, Frascati (Italy), Nov. 1969.

e-p INSTABILITY IN THE NSNS ACCUMULATOR RING

Alessandro G. Ruggiero and Mike Blaskiewicz
AGS Department, Brookhaven National Laboratory, Upton, NY 11973.

*Abstract**

It has been speculated that the intensity limitation observed in the Los Alamos Proton Storage Ring (PSR) is caused by a coherent instability [1] induced by the presence of pockets of electrons generated by scattering with the molecules of the vacuum residual gas. A theoretical explanation of the e-p instability of course does exist [2], and is similar to the one developed for the ion-induced instability in electron storage rings. Considering the large beam power (2 MW) involved in the NSNS Accumulator Ring [3], and the consequences caused by even a small amount of beam loss, we need to carefully assess the effects of electrons that may be generated in the vacuum chamber.

1 SOURCES OF ELECTRONS

Electrons may be generated in a variety of ways. Negative ions traverse the stripping foil during injection. The average power associated to the electrons is 2.2 kW, corresponding to 1 GeV primary beam with an average power of 2 MW. Leaving the foil, the electrons will drift forward and enter the fringe field region of a 2.5 kG bending magnet [4], which is part of the horizontal set-up for the beam multiturn injection. The trajectory of the electrons in that region is a semicircle of 10 cm diameter, at the end of which they are collected by a water-cooled copper and graphite collector, disposed parallel to the motion of the incoming beam. The acceptability cryterion is that no more than 10^{-4} electrons per protons are left behind in the stripping foil region.

The second mechanism of electron production is the loss of protons on the vacuum chamber wall. If a proton hits the wall, electrons may be desorbed, which in turn may hit the wall again, and desorb more electrons through a process known as "multipactoring". The effect of this mechanism is controlled by minimizing the loss of the protons to the wall. The design requirement for this purpose is a total loss not exceeding 10^{-4} of the total proton beam intensity, which is achieved by allowing a factor larger than two between physical acceptance and full beam emittance all around the ring, and by insertion of collimators/scrapers in conveniently chosen locations to intercept the beam halo. Also, the vacuum chamber will be made of titanium-coated aluminum, to eliminate or considerably reduce electron desorbtion and multipactoring.

Probably the source of electrons with more serious consequences to the beam stability is the vacuum residual gas. For economic reasons, and simplicity, we have opted for an average pressure of 10^{-9} Torr equivalent nitrogen. The vacuum chamber of the NSNS Accumulator Ring has a large aperture with an average radius b = 10 cm all the way around. Other parameters are shown in Table 1.

Table 1: Parameters of the NSNS Accumulator Ring

Beam Kinetic Energy	1.0 GeV
Beam Average Power	2.0 MW
Number of Protons, N_T	2.08×10^{14}
No. of Injected Turns	1100
Revolution Period, T_0	841.3 ns
Bunch Length, T	546.6 ns
Beam Gap, τ	294.7 ns
Beam Average Radius, a	38 mm
Pipe Radius, b	100 mm
Circumference, $2\pi R$	220.7 m
Betatron Tune (H and V)	5.82
Average Vacuum Pressure	10^{-9} Torr (equiv. N_2)

2 RESIDUAL GAS IONIZATION

The assumed average vacuum pressure corresponds to a residual gas density $n = 6 \times 10^7$ atoms / cm^3 at normal conditions. The expected average ionization cross-section is $\sigma_i = 1.2 \times 10^{-18}$ cm^2. The rate of electron production is then given by

$$d\, n_e / dt \;=\; \beta\, c\, n\, \sigma_i\, N(t) \qquad (1)$$

where N(t) is the number of protons which varies during injection according to $N(t) = N_r\, t$, with $N_r = N_T / T_{inj} = 2.25 \times 10^{17}$ protons / s. At the end of the injection process, the beam has been longitudinally compressed and is immediately extracted. Integration of (1) gives

$$\chi \;=\; n_e / N_T \;=\; 1/2\; \beta\, c\, n\, \sigma_i\, T_{inj} \qquad (2)$$

that is a beam charge neutralization $\chi = 0.09$ %.

*Research on the NSNS is sponsored by the Division of Material Sciences, U.S. Department of Energy, under contract number DE-AC05-96OR22464 with Lockheed Martin Energy Research Corporation for Oak Ridge National Laboratory.

3 MOTION OF THE ELECTRONS

To understand the dynamics of the electrons it is necessary to have an idea of the motion in the various components that make up the Accumulator Ring. For this purpose, we shall assume that the proton beam bunch is a cylinder with dimensions given in Table 1, with transverse and longitudinal uniform charge distribution. The beam intensity varies linearly with time during the injection process. We shall assume that the bunch length L remains approximately unchanged, and that the betatron emittance varies linearly with time. Then, the charge density $N(t) / L a^2$ is constant throughout the multi-turn injection process.

4 MOTION IN THE DRIFTS

The equations of motion are very simple. In the region where the beam bunch is present

$$d^2 (x,y) / dt^2 + \Omega_e^2 (x,y) = 0 \qquad (3)$$

In the beam gap region the motion is a pure drift, where the electrons have an opportunity to leave the beam and reach the vacuum chamber wall. It will require a transverse velocity $v_e = 0.34 \times 10^6$ m / s to escape, which corresponds to an energy of 0.33 eV, less than the 2 keV potential energy in the proton beam. Thus most of the electrons produced by the residual gas ionization, in the drift regions, will be able to escape the beam. It derives that the neutralization coefficient χ given by equation (2) is expected to be considerably lower by several orders of magnitude.

In the presence of the proton bunch, the bouncing angular frequency

$$\Omega_e^2 = 2 N(t) r_e c^2 / a^2 L \qquad (4)$$

where $r_e = 2.82 \times 10^{-15}$ m, and $L = \beta c T = 143$ m. The bouncing frequency is constant during the injection process: $\Omega_e / 2\pi = 113.6$ MHz.

Each electron receives a periodic transverse attractive kick when is traversing the proton bunch, followed by a drift between two consecutive passages. The system of Eq.s (3) can be solved with the matrix method. The transfer matrix over one period, which includes one beam gap and one beam bunch, is

$$M = \begin{vmatrix} \cos\phi - \Omega_e \tau \sin\phi & (1/\Omega_e) \sin\phi + \tau \cos\phi \\ -\Omega_e \sin\phi & \cos\phi \end{vmatrix} \qquad (5)$$

where $\alpha = \Omega_e \tau / 2$ and $\phi = \Omega_e T$. The stability of motion, that is of electron trapping, is determined by the condition $| \mathrm{Tr}\, M | < 2$, that is

$$| \cos\phi - \alpha \sin\phi | < 1 \qquad (6)$$

It is seen that when the beam is completely debunched, that is $\tau = 0$, the motion is always stable and the electrons are trapped. But with a beam gap of $\tau = 295$ ns the motion is unstable.

One can also estimate the time that is required for the electrons to leave the beam and reach the wall, since that is also given by the trace itself of the transfer matrix if we write,

$$| \cos\phi - \alpha \sin\phi | = \cosh \mu \qquad (7)$$

The escape rate is $1 / \tau_{esc} = \mu / T_0$, which for $\tau = 295$ ns gives $\tau_{esc} = 178$ ns. The actual number of electrons present in the vacuum chamber in a drift section is then given by the balance of the escape rate and the production rate, that is when

$$d n_e / dt = \beta c n \sigma_i N(t) - n_e / \tau_{esc} = 0 \qquad (8)$$

At the end of the injection process, we estimate that 0.7×10^8 electrons remain in a drift section, which yields a neutralization coefficient $\chi = 3.4 \times 10^{-7}$.

5 BEAM LEAKAGE IN THE BUNCH GAP

It has been speculated [1] that the ep instability observed in the PSR ring could be caused by an amount of proton beam which leaked in the bunch gap. In the NSNS Accumulator Ring the design calls for the provision of an rf system which compresses the beam in a single bunch during the injection process. The system will guarantee a gap completely clear of beam to a level of 10^{-4} of the total proton intensity. In the case that a small fraction η of the proton beam could be present in the gap, the transfer matrix (5) will be modified to yield a new stability condition

$$| 2 \cos\phi_B \cos\phi_G - (\Omega_G / \Omega_B + \Omega_B / \Omega_G) \sin\phi_B \sin\phi_G | < 2 \qquad (9)$$

where

$$\Omega_B^2 = \Omega_e^2 (1 - \eta), \qquad \Omega_G^2 = \Omega_e^2 \eta \qquad (10)$$

$$\phi_B = \Omega_B T, \qquad \phi_G = \Omega_G \tau \qquad (11)$$

It is seen that already with a 1% of the proton beam leaked in the bunch gap, stability and instability conditions alternate during the injection process. For larger value of η, the chances of electron trapping increases considerably. It is thus important that the bunching process will exclude protons to penetrate the gap at a rate larger than 0.1% of the total proton intensity.

6 MOTION IN THE BENDING MAGNETS

To evaluate the motion of the electrons in a dipole magnet,

one has to modify Eq.s (3) to include the contribution from the dipole field. Within the bunch the equations of motion are

$$d^2x / dt^2 + \Omega_e^2 x = - \Omega_L \, dz / dt \quad (12a)$$

$$d^2y / dt^2 + \Omega_e^2 y = 0 \quad (12b)$$

$$d^2z / dt^2 = \Omega_L \, dx / dt \quad (12c)$$

where $\Omega_L = e B / m_e c$ is the angular Larmor frequency with B the strength of the bending field. Within the bunch gap $\Omega_e = 0$. Thus the vertical motion remains unchanged as in the drift sections, with the same consequences that have been described earlier. The horizontal and longitudinal components of the motion are now coupled to each other through the bending field. The motion on the horizontal plane is dominated by a tight precession movement at the Larmor frequency. In the NSNS Accumulator Ring, B = 0.74 Tesla and Ω_L = 124 GHz.

7 MOTION IN THE QUADRUPOLE MAGNETS

All the components of motion are now coupled to each other by the quadrupole gradient G. Moreover the equations of motion are now nonlinear and difficult to solve exactly. In the interval of the beam bunch Eq.s (12) are modified as follows:

$$d^2x / dt^2 + \Omega_e^2 x = - K_L \, x \, dz / dt \quad (13a)$$

$$d^2y / dt^2 + \Omega_e^2 y = K_L \, y \, dz / dt \quad (13b)$$

$$d^2z / dt^2 = K_L (x \, dx / dt - y \, dy / dt) \quad (13c)$$

where $K_L = e G / m_e c$. Within the bunch gap again $\Omega_e = 0$. Eq.s (13) can be partially integrated to show that

$$dz / dt = v_{init} + K_L (x^2 - y^2) / 2 \quad (14)$$

is a prime integral.

The system of Eq.s (13) can be integrated with some approximations in special cases [5]. For instance, in the case $x^2, y^2 << a^2$ and $dz / dt \sim 0$, one can show that the motion is unstable at least on one plane of oscillations. On the other hand, if one takes x = 0 and y ~ a, it can be seen that $K_L a^2 / 2$ is much larger than v_{init}. In this case there is a large frequency variation with the amplitude of the electron motion. This spread will quickly smear any coherent motion that may appear within the electron beam which cannot then feedback to the proton beam motion.

8 THE E-P INSTABILITY

A coherent instability of the proton beam bunch can be triggered by the electromagnetic interaction with the cloud of electrons, when both beams have a finite displacement of the centers of mass Y_p and Y_e. The equations for Y_p and Y_e are then [1,2,5]

$$d^2Y_p / dt^2 + \Omega_\beta^2 Y_p = (\chi \, r_p / \gamma \, r_e) \, \Omega_e^2 (Y_e - Y_p) \quad (15a)$$

$$d^2Y_e / dt^2 = \Omega_e^2 (Y_p - Y_e) \quad (15b)$$

where Ω_β is the angular betatron frequency. We shall look for a solution of the form

$$Y_{p,e} = \overline{Y}_{p,e} \exp i (k\theta - \Omega t) \quad (16)$$

where Ω is an unknown collective angular frequency, which we expect to be a complex quantity, θ is the angular coordinate around the circumference of the ring, and k is a mode number which, of course, is expected to have only integer values. It is to be noticed that

$$d Y_p / dt = -i (\Omega - k\omega_0) Y_p \quad (17a)$$

$$d Y_e / dt = -i \Omega Y_e \quad (17b)$$

where $\omega_0 = 2\pi f_0$. Substituting (16) into the system of Eq.s (15), and requiring that the resulting determinant of the amplitudes $\overline{Y}_p$ and $\overline{Y}_e$ vanishes, give the following dispersion relation

$$1 = \Omega_p^2 / [(\Omega - k\omega_0)^2 - \Omega_\beta^2] + \Omega_e^2 / \Omega^2 \quad (18)$$

where

$$\Omega_p^2 = (\chi \, r_p / \gamma \, r_e) \, \Omega_e^2 \quad (19)$$

and $r_p = 1.535 \times 10^{-18}$ m.

The dispersion relation (18) is then solved to derive Ω versus the mode number k. The growth rate of the instability is given by the imaginary part of Ω.

The results for the NSNS Accumulator Ring are summarized as follows [5]. It is seen that with $\chi = 1\%$ three modes k = 152, 153 and 154 are unstable. But if $\chi < 0.1\%$ the instability can be avoided by letting the betatron tune change between 5.5 and 5.8.

9 REFERENCES

[1] T. Wang et al., Proc. 1993 PAC, Washington, DC, May 1993. Volume 5 of 5, page 3297.

[2] D. Neuffer et al., *Nucl. Instr. and Meth.* **A321**, 1 (1192).

[3] W.T. Weng et al.. These Proceedings.

[4] L.N. Blumberg and Y.Y. Lee, BNL/NSNS Technical Note No. 003. November 1, 1996.

[5] A.G. Ruggiero and M. Blaskiewicz, BNL/NSNS Technical Notes No. 8 and 35. 1997.

MICROWAVE INSTABILITY THRESHOLDS

S.Y. Zhang
Brookhaven National Laboratory, Upton, NY 11973, USA *

Abstract

Taking the first orthogonal polynomials in the conventional radial mode expansion in the eigenvalue type perturbation approach, the usual Keil-Schnell criteria for the microwave instabilities can be obtained. In this way, a close relationship between the two approaches is established. The existing results are reviewed, and some comments and modifications are made.

1 INTRODUCTION

A brief review of beam instability analyses shows that its development either belongs to a Vlasov-equation-evolved perturbation approach, or belongs to a Keil-Schnell-criterion type approach. In the first approach, see [1] and the references therein, both azimuthal and radial expansions are used to explore the particle distribution evolutions. Current direction is to include the potential well deformation, see for example [2], and to include the effect of Landau damping, see for example [3]. The development is unlikely to give rise to analytical solutions that can be easily used. On the other hand, the second approach uses crude beam profile (with an exception for the longitudinal coasting beams) to estimate the instability threshold for both bunched and coasting beams. General results can be found in [4] and the references therein. These results have been proved very useful and often provide guidance to the development and improvement of accelerators. The crude beam profile, however, has certainly imposed limitations in the application.

In this report, we show that the use of the first orthogonal polynomials in the perturbation approach can give rise to identical results obtained by the Keil-Schnell type criteria. This is owing to the fact that, in general, the first orthogonal polynomial represents the most prominent radial mode. In this way, a close relationship between the two approaches is established. Therefore, comments will be made regarding to the limitation and possible error in the applications of the simplified criteria. Some modifications will then be developed, if necessary.

2 TRANSVERSE INSTABILITY

Using the first orthogonal polynomial for the azimuthal mode $m = 0$, setting $\beta \approx 1$, the bunched beam dynamic equation becomes,

$$\omega - \omega_\beta = \frac{jeI_0}{2Rm_0\gamma\omega_\beta} \sum_{n=-\infty}^{\infty} Z_T(n)\Lambda_{0,1}^2(n') \qquad (1)$$

where ω_β is the betatron frequency, R is the machine radius. The average beam current is $I_0 = Ne\omega_0/2\pi$, where N is the number of particles, and ω_0 is the revolution frequency. Also $Z_T(n)$ is the transverse impedance, and $\Lambda_{0,1}(n)$ is the spectrum of the first orthogonal polynomial for $m = 0$, where n represents the effective spectrum line, r represents the radial position. The notation n' denotes the chromatic effect. The equivalence $\sum_{n=-\infty}^{\infty} Z_T(n)\Lambda_{0,1}^2(n') = \sum_{n=-\infty}^{\infty} Z_T(n'')\Lambda_{0,1}^2(n)$ is used in this article, where n'' denotes the frequency shift equals n' but in the opposite direction.

Consider the normalized Gaussian distribution in phase space,

$$\psi_0(r) = \frac{2}{\pi r_\ell^2} e^{-2r^2/r_\ell^2} \qquad (2)$$

where r_ℓ is the half bunch length in radius. The transverse weight function is defined as $W_T(r) = \psi_0(r)$.

In the following, the instability threshold will be obtained by the rule of thumb, which is,

$$|\Delta\Omega| < \Delta\omega \qquad (3)$$

where $\Delta\Omega$ is the coherent frequency shift, and $\Delta\omega$ is the rms or the half width of half maximum frequency spread.

2.1 Bunched Beam

An estimate of the bunched beam instability threshold can be obtained using $\Lambda_{0,1}^2(n') \approx 1/2\pi$ in (1),

$$\left| \sum_{n=-\infty}^{\infty} Z_T(n) \right| < \frac{4\pi R m_0 \gamma \omega_\beta}{eI_0} \Delta\omega \qquad (4)$$

The criterion given in the equation (5.62) of [4] can be written as,

$$\left| \sum_{n=-\infty}^{\infty} Z_T(n) \right| < \frac{2\omega_\beta \gamma T_0^2}{N r_0 c} \Delta\omega \qquad (5)$$

Using $r_0 = e^2/m_0c^2$, $T_0 = 2\pi/\omega_0$, $\omega_0 = \beta c/R$, the equation (5) becomes identical to (4).

For a long bunch with a narrow spectrum, the error of using (4) can be large, mainly owing to the use of $\Lambda_{0,1}^2(n') \approx 1/2\pi$, the peak of the power spectrum. Also the chromatic effect can introduce uncertainties.

For an improved estimate, therefore, we need to use,

$$\Lambda_{0,1}(n) = \frac{1}{\sqrt{2\pi}} e^{-n^2 r_\ell^2/8} \qquad (6)$$

Substituting (6) into (1), and considering the chromatic effect, we get,

$$\left| \sum_{n=-\infty}^{\infty} Z_T(n'') e^{-n^2 r_\ell^2/4} \right| < \frac{4\pi R m_0 \gamma \omega_\beta}{eI_0} \Delta\omega \qquad (7)$$

* Work performed under the auspices of the U.S. Dept. of Energy

- A criterion is given in [5], which can be written as,

$$\left|\bar{Z}_T(n'')\right| < \frac{2\omega_\beta \gamma E_0 z_L}{ec^2 I_0}\Delta\omega \tag{8}$$

where z_L is the full bunch length, and $\bar{Z}_T(n'')$ is the averaged impedance over the width of the bunch spectrum. The summation on the right side of (1) can be approximately taken as,

$$\sum_{n=-\infty}^{\infty} Z_T(n)\Lambda_{0,1}^2(n') \approx \bar{Z}_T(n'')\frac{2R}{z_L} \tag{9}$$

Substituting (9), using $m_0 = E_0/c^2$, the equation (1) becomes

$$\left|\bar{Z}_T(n'')\right| < \frac{\omega_\beta \gamma E_0 z_L}{ec^2 I_0}\Delta\omega \tag{10}$$

Which differs from (7) by a factor of 0.5.

- A better formalism is presented in the equation (18) in [6]. With $m = 0$, it can be written as,

$$\left|\frac{\sum_{n=-\infty}^{\infty} Z_T(n)h_0(n')}{\sum_{n=-\infty}^{\infty} h_0(n')}\right| < \frac{2\omega_\beta \gamma m_0 z_L}{eI_0}\Delta\omega \tag{11}$$

The left side is called the *effective impedance*, where $h_0(n')$ is the power spectrum of the bunch. If only the first orthogonal polynomial is used, we have $h_0(n') = \Lambda_{0,1}^2(n')$. The redundancy in the equation (11) involving the effective impedance is shown as the follows. Using $r_\ell = z_L/2R$, we can write,

$$\sum_{n=-\infty}^{\infty} h_0(n) = 2\int_0^\infty \frac{1}{2\pi}e^{-n^2 r_\ell^2/4}dn \approx \frac{2R}{\sqrt{\pi}z_L} \tag{12}$$

Applying this equation into (11), the bunch length z_L is cancelled. Since the information of the bunch length has been represented by the bunch spectrum $h_0(n')$ in the numerator of the effective impedance, this triple representation of the bunch length can be seen as redundancy. In comparison, the use of the total effective impedance shown in the left side of (7) seems to be more straightforward. Substituting (12) into (11), we get,

$$\left|\sum_{n=-\infty}^{\infty} Z_T(n'')e^{-n^2 r_\ell^2/4}\right| < \frac{8\sqrt{\pi}Rm_0\gamma\omega_\beta}{eI_0}\Delta\omega \tag{13}$$

This differs from (7) by a factor of 1.13.

2.2 *Coasting Beam*

For a coasting beam, the power spectrum of the perturbation is a delta function at a frequency n_1 with an amplitude $1/2\pi$. The equation (1), therefore, is modified as,

$$\omega - \omega_\beta = \frac{jeI_0}{2Rm_0\gamma\omega_\beta}\sum_{n=-\infty}^{\infty} Z_T(n)\frac{\delta(n-n_1)}{2\pi} \tag{14}$$

then the instability threshold can be estimated as,

$$\underline{|Z_T(n_1)| < \frac{4\pi Rm_0\gamma\omega_\beta}{eI_0}\Delta\omega} \tag{15}$$

The criterion given in the equation (5.91) of [4] is,

$$|Z_T(n)| < \frac{2\omega_\beta\gamma T_0^2}{Nr_0 c}\Delta\omega \tag{16}$$

which is identical to the equation (15).

- The equation (4) in [5] can be written,

$$|Z_T(n)| < \frac{8FE_0\gamma\omega_\beta}{eI_0 R\omega_0^2}\Delta\omega \tag{17}$$

which can be written as,

$$|Z_T(n)| < \frac{8FRm_0\gamma\omega_\beta}{eI_0}\Delta\omega \tag{18}$$

Taking $F = 1$, this equation differs from (15), which is less tight, by a factor of 0.64.

3 LONGITUDINAL INSTABILITY

Using the first orthogonal polynomial, for the $m = 1$ mode, the longitudinal beam dynamic equation in [1] becomes,

$$\omega - \omega_S = \frac{j2\pi\omega_S I_0}{V\cos\phi_S}\sum_{n=-\infty}^{\infty}\frac{Z_L(n)}{n}\Lambda_{1,1}^2(n) \tag{19}$$

where ω_S is the synchrotron frequency, and ϕ_S is the synchronous phase, V is the RF gap voltage per ring, and $Z_L(n)/n$ is the longitudinal impedance. For a Gaussian distribution with the half bunch length r_ℓ, the longitudinal weight function is,

$$W_L(r) = -\frac{\partial\psi_0(r)}{\partial r}\frac{1}{r} = \frac{8}{\pi r_\ell^4}e^{-2r^2/r_\ell^2} \tag{20}$$

3.1 *Bunched Beam*

Using the equations (19) and the approximation,

$$\Lambda_{1,1}(n) \approx \frac{n}{2\sqrt{\pi}} \tag{21}$$

the bunched beam instability threshold is written as,

$$\left|\sum_{n=-\infty}^{\infty} nZ_L(n)\right| < \frac{2V\left|\cos\phi_S\right|}{\omega_S I_0}\Delta\omega \tag{22}$$

where $\Delta\omega$ is the synchrotron frequency spread. The corresponding equation (5.69) in [4] is,

$$\left|\sum_{n=-\infty}^{\infty} nZ_L(n)\right| < \frac{2\omega_S\gamma(2\pi R)^2}{Nr_0|\eta|c^2\omega_0}\Delta\omega \tag{23}$$

Using $\omega_S^2 = -\omega_0^2 e\eta V\cos\phi_S/2\pi E$, the equation (23) is shown to be the same as (22).

This criterion is indeed very crude, owing to that in arriving (21), the approximation of the Bessel function $J_1(nr) \approx nr/2$ is used, which is only valid in a small range $nr < 1$.

An improvement to this criterion, therefore, can be made by using,

$$\Lambda_{1,1}(n) = \frac{n}{2\sqrt{\pi}} e^{-n^2 r_\ell^2/8} \tag{24}$$

Substituting (24) into (19), we get,

$$\left| \sum_{n=-\infty}^{\infty} n Z_L(n) e^{-n^2 r_\ell^2/4} \right| < \frac{2V\,|\cos\phi_S|}{\omega_S I_0} \Delta\omega \tag{25}$$

- The result in the equation (5) in [7] can be written, for $m = 1$ and the harmonic number $h = 1$, as,

$$\left| \frac{\sum_{n=-\infty}^{\infty} (Z_L(n)/n)\, h_1(n)}{\sum_{n=-\infty}^{\infty} h_1(n)} \right| < \frac{6B^3 V\,|\cos\phi_S|}{\omega_S I_0} \Delta\omega \tag{26}$$

where $h_1(n) \approx \Lambda_{1,1}^2(n)$ is the power spectrum of the bunch, and $B = r_\ell/\pi$ is the bunching factor. Note that we have,

$$\sum_{n=-\infty}^{\infty} h_1(n) = 2\int_0^\infty \frac{n^2}{4\pi} e^{-n^2 r_\ell^2/4} dn \approx \frac{1}{\pi^{7/2} B^3} \tag{27}$$

Substituting (27) into (26), using (24), we get,

$$\left| \sum_{n=-\infty}^{\infty} n Z_L(n) e^{-n^2 r_\ell^2/4} \right| < \frac{1.37V\,|\cos\phi_S|}{\omega_S I_0} \Delta\omega \tag{28}$$

which differs from (25) by a factor of 0.69. Again we consider that the use of the equation (25) is more straightforward than (26) with the effective impedance.

3.2 *Coasting Beam*

The Landau damping in the longitudinal coasting beam is the most explored one. Together with the dispersion relation, the stability diagram can be plotted on the real and imaginary impedance plane. Compared with the others, this is the only case that no external focusing presented, therefore, one may expect that this case should be completely different from the others.

The successful application of the coasting beam instability criterion to the bunched beams, i.e. the Boussard criterion, has opened the door to think that at least for the long bunches and/or strong instability, the effect of the synchrotron focusing is not irreplaceable. It is found that using an equivalence

$$\omega_S \approx \Delta\omega \tag{29}$$

and the local current, the bunched beam criteria is closely related with the coasting beam criteria. To establish the relation, using,

$$\frac{1}{|\eta|}\frac{\Delta\omega}{\omega_0} = \left(\frac{\Delta p}{p}\right)_{rms} = \frac{\omega_S r_\ell}{2\,|\eta|\,\omega_0} \tag{30}$$

we find that the equation (29) is equivalent to $r_\ell = 2$. For this case, the beam power spectrum is still a delta function, but the amplitude is no longer constant. Since the amplitude of a delta function equals the area of the function, i.e. $\sum_{n=-\infty}^{\infty} \Lambda_{1,1}^2(n)$, removing the impedance $Z_L(n)/n$ out of the summation on the right side of (19), we get,

$$\left| \frac{Z_L(n)}{n} \right| < \frac{E r_\ell^4}{2\sqrt{2} e |\eta| \omega_0^2 I_0} (\Delta\omega)^2 \tag{31}$$

Substituting $r_\ell = 2$, the equation (31) becomes,

$$\left| \frac{Z_L(n)}{n} \right| < \frac{5.66E}{e|\eta|\omega_0^2 I_0} (\Delta\omega)^2 \tag{32}$$

The Keil-Schnell criterion shown in the equation (5.131) in [4] can read,

$$\left| \frac{Z_L(n)}{n} \right| < \frac{0.68\gamma T_0^3}{2\pi N r_0 |\eta|} (\Delta\omega)^2 \tag{33}$$

where the tri-elliptical spectrum is used. This equation can be written the same as (32), except that the factor 5.66 becomes 4.27.

- The equation (1) in [5] can be written,

$$\left| \frac{Z_L(n)}{n} \right| < \frac{F\gamma E_0 |\eta|}{e I_0} \left(\frac{\Delta p}{p}\right)^2 \tag{34}$$

where the form factor F is a unity. Since $\Delta p/p$ is the full momentum spread at half height, using $\Delta p/p = 2(\Delta p/p)_{rms}$, the equation (34) is the same as (32), except that the factor 5.66 becomes 4.

4 REFERENCES

[1] S.Y. Zhang and W.T. Weng, BNL60557, 1994.

[2] K. Oide and K. Yokoya, KEK 90-10, 1990.

[3] S.Y. Zhang and W.T. Weng, Proc. Workshop on Beam Instabilities in Storage Rings, p.230, Hefei, China, 1994.

[4] A. Chao, *Physics of Collective Beam Instabilities in High Energy Accelerators*, Wiley, New York, 1994.

[5] W. Schnell, CERN 77-13, p.231, 1977.

[6] F. Sacherer, 9th Conf. High Energy Particle Accelerators, p.347, 1974.

[7] F. Sacherer, IEEE Trans. Nucl. Sci., Vol.NS-24, p.1393, 1977.

[8] B. Zotter and F. Sacherer, CERN 77-13, p.175, 1977.

LONGITUDINAL COUPLED-BUNCH INSTABILITY AROUND 1 GHZ AT THE CERN PS BOOSTER

F. Caspers, M. Chanel, H. Schönauer, L. Søby, CERN, CH-1211 Geneva 23, Switzerland
M. D'Yachkov, TRIUMF, 4004 Wesbrook Mall, Vancouver, B.C., Canada V6T 2A3

Abstract

The fast-growing "Ring 4" instability occurring at intensities above 6.5×10^{12} protons in the top one of the four rings of the CERN PS Booster (PSB) is finally explained by an asymmetry in the 40 vacuum pump manifolds common to all rings. Impedance measurements (by wire method) and numerical calculations show a sharp resonant peak (Q~2000) at 1100 MHz and shunt impedances two times higher for the Ring 4 ports as compared to the other rings. This factor is sufficient to explain that the threshold of the instability falls below the maximum intensity only in Ring 4. A final, but labor-intensive and expensive, cure consists of inserting short-circuiting sleeves into all 160 beam ports. Results of beam and impedance measurements and the planned cure will be presented and discussed.

1 INTRODUCTION

For a number of years, a longitudinal instability occurring solely in Ring 4 above a threshold of ~6.5 10^{12} protons is observed in the PS Booster: During acceleration, around 700 MeV, all bunches develop a fast-growing tail sometimes causing loss of a few percent of the beam. The only coherent signals observed on a wide-band wall current monitor are short bursts visible on all revolution harmonics above 800 MHz up to 1.5 GHz. Although there are a number of vacuum tanks and cavities susceptible to drive the instability, they are either common or identical to all four rings. In order to determine whether these cavity-like objects could be the culprits, and whether there is a peculiarity on the level of Ring 4, impedance measurements on spares of the 40 vacuum pump manifolds (vertical connections between the stacked rings) were performed recently.

2 OBSERVATIONS AND EXPERIMENTS

Fig. 1 is a waterfall snapshot of the onset of the instability. Minute tails appear simultaneously on the trailing edge of all bunches. Viewed on a slower vertical time scale, it appears obvious that they are the projection of asymmetric tails rotating in phase space at their local synchrotron frequency. Once the phase space asymmetry has smeared out, the bunches show tails on both edges that continue to grow over some tens of milliseconds. Then one sees peaks on a fixed-tuned spectrum analyzer whenever a revolution harmonic sweeps across. Already at intensities just above threshold this growth exceeds the bucket limits and causes loss of a few percent of the circulating beam a few ms later.

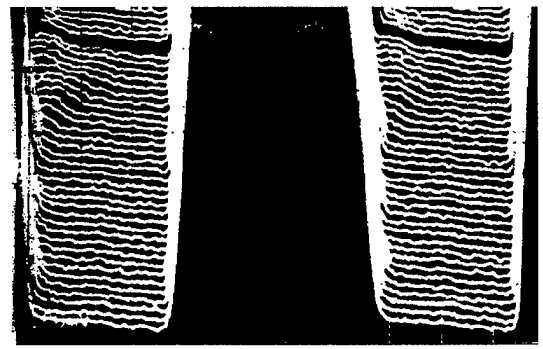

Figure 1: Waterfall display (30 turns between traces, time increases from bottom to top) of the visible onset of the instability. Bunch length is ≈65 ns, bunch height about four times the vertical oscilloscope range.

Recently, the instantaneous bunch spectrum above 900 MHz of the instability was measured with a 5 Gsample/s scope with FFT processor and found to be centered around 1 GHz. Although the spectrum resembles that of Sacherer's sinusoidal modes, it is wider by a factor six than what would be expected from the bunch length.

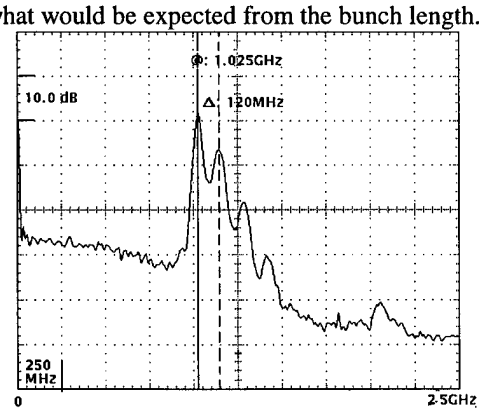

Figure 2: FFT spectrum of the instability. Only the upper half of the spectrum is present, because the wall current monitor signal is filtered through a 900 MHz cut-off high-pass to remove the overwhelming stationary bunch structure.

3 THEORETICAL CONSIDERATIONS

Before the results of the impedance measurements described below were known, only rough estimates of the impedances needed to drive the beam unstable existed. Straightforward application of the Keil-Schnell-Boussard

0-7803-4376-X/98/$10.00 © 1998 IEEE

criterion [1] gives rather low values for the resistive threshold of the order of 25 kΩ, about the shunt impedance of one single cavity. This criterion holds for wide-band impedances or resonators with Q < 100. Using Sacherer's theory of mode coupling [2], recently applied to the Fermilab Main Injector by Ng [3], one finds that for higher Q values R_s/Q rather than R_s only determines the threshold. Similar result were found also for Gaussian beams [4]. The case of the PSB manifolds with a resonance Q of 2400 is still different: Only one of the many lines of the (coupled-) bunch spectrum can interact with the cavity at one time. This raises the threshold impedance to the order of 1MΩ. Figure 3 depicts the numerical computation for the Sacherer model of the threshold intensity along the PSB cycle for a resonator shunt impedance of 700 kΩ. The curve refers to the in-phase (n=0) coupled-bunch mode, which has the lowest threshold, but the four other coupled-bunch modes are not very different, contrary to the single-bunch mode whose threshold is one magnitude higher. The coasting beam threshold for a shunt impedance of 30 kΩ is plotted for comparison. It yields similar threshold intensities to those computed numerically for the resistor-damped manifolds.

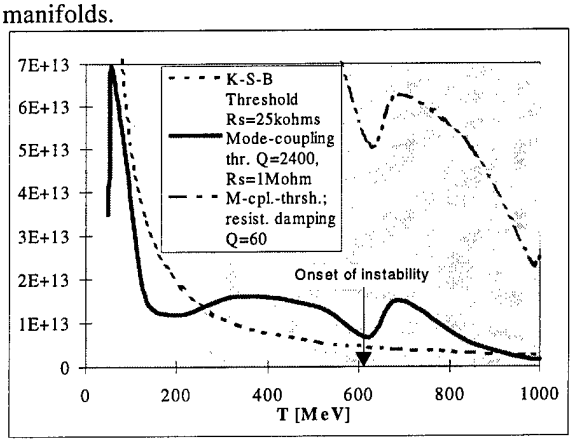

Figure 3: Threshold intensities as function of kinetic energy for K-S-B and mode-coupling criteria. Although the thresholds are comparable, the shunt impedance is 25 kΩ for K-S-B and 1 MΩ (25 kΩ for damped resonators) for the mode-coupling theory of bunched beams .

4 IMPEDANCE MEASUREMENTS: METHOD AND RESULTS

Of the three spare manifolds made available by the Vacuum Group, #1and #2 were slightly different from standard, featuring additional lateral ports (closed here) for insertion of pick-up electrodes. In all beam ports, the beam is shielded from the cavity above and below by strip-like short-circuits. A visual inspection revealed an unexpected feature of all manifolds, namely that the Ring 4, is shielded only from below, probably because it was felt at design that the proximity of the top wall of the manifold made a proper short-circuit superfluous. Hence the level 4 resonator volume is indeed of different shape.

Coupling impedances are determined by the standard method of measuring the S parameters of a wire crossing the test object at the location of the beam, with some precautions to assure a good match at the ports. The impedance of the test object can be calculated from the S_{21} parameter [5]. For the measurements, 500 mm long standard beam pipes were clamped to the manifold at the ring port under test, and closed with a special flange allowing the soldering of terminating resistors of 270 Ω to the wire under mechanical tension. The resistors were chosen to match the characteristic impedance of ~320 Ω of the wire in the vacuum chamber, to 50 Ω. The beam pipe sections were chosen rather long in order not to detune resonances with long evanescent fields into adjacent beam pipes (many cavity modes are beyond waveguide cut-off). In some cases the closed ends of the vacuum pipes were filled with rubber foam to damp the propagating modes above cut-off. Due to the damped propagating modes these measurements are more easily to interpret because the 'baseline' is well-defined.

Another measurement consists of measuring the cavity resonances and their bandwidths by introducing short coupling wires at the gauge ports on the top of the manifold instead of the wire crossing. By checking the S_{11} and S_{22} parameters it was verified that the probes were only weakly coupled to the cavity in order not to reduce the resonator Q by external loading. From these measurements, one can expect to find the true resonance frequency and Q values in the absence of the perturbing wire.

Ring port	Mani-fold	Conditions	Wire Measurement				
	#		f_{res} MHz	Δf MHz	Q	R_s kΩ	R_s/Q Ω
4			1100	0.44	2499	62	24.8
3			1211	0.804	1506	18	12.0
2			1225	1.02	1201	9.5	7.9
1			1220	0.596	2047	19.5	9.5
	1						
4		Foam	1097	0.57	1925	46	23.9
4		Foam + long damping res.	1097	18.2	60	1.7	28.2
4		Foam+2 res.	1097	56.7	19	0.92	47.5
1		Foam	1225	5.25	233	2.55	10.9
4	2	Foam	1090	4	273	7.2	26.4
4		Foam	1097	0.69	1590	36	22.6
3		Foam	1239	1.1	1126	13.6	12.1
2	3	Foam	1237	1.8	687	7.7	11.2
1		Foam	1233	1.6	771	7.8	10.1
4		Foam+long damping res.	1083	18.5	59	1.4	23.9
			Probe Measurement				
4	3	Couplers into gauge ports	1055	0.44	2400	54.2 [1)]	22.6 [2)]
				1) computed from R_s/Q 2)taken from wire measurem't			

Table 1: Measured Impedances of PSB Pump Manifolds

The S parameters were measured with a HP 8753C network analyser. Data were dumped via GPIB and Labview software to a Toshiba Laptop. Table 1 compiles the impedances and Q values (determined by measuring or interpolating the 3 dB bandwidths of the resonance peaks). It also includes the impedances of Ring 4 cavities damped by insertion of a ceramic tube coated with a resistive layer. The R_s/Q values, being essentially a geometry factor, remain practically unchanged. One notices the outstanding differences between Ring 4 level and the others:

1. Wire measurements show resonance frequencies of 1225 - 1230 MHz for the Ring 1-3 cavities and of 1100 MHz for Ring 4.
2. Equivalent shunt impedances are of the order of 40 kΩ for Ring 4 and of 8-18 kΩ for the other rings. Q-values scatter considerably between 700 and 2000, but
3. R_s/Q values are consistently distributed around 24 Ω for Ring 4 and around 11 Ω for the Rings 1 - 3.

5 NUMERICAL COMPUTATIONS

The results of the measurements were corroborated by numerical finite-differences computation of the wake field of a short bunch (5 ns long), from which coupling impedances can be calculated. The longitudinal impedances found for (a) Ring 1-3 cavities with two short-circuit strips, and (b) the Ring 4 cavity with only one short-circuit strip are published in [6].

Their main features are:

1. The cut-off frequencies (and the resonance frequencies) for the structures are slightly different (frequency of the Ring 4 cavity = 1.0 GHz, and of the Ring 1 - 3 cavity = 1.15 GHz).
2. Impedances at resonance are significantly different; it looks as though R_s/Q (which should be proportional to the integral of $\int R(\omega)d\omega$ of the Ring 4 cavity) is approx. 2.5 times higher than the R_s/Q for the Ring 1-3 cavity.
3. There is also a big difference in transverse impedances of the structures.

6 POSSIBLE CURES

An efficient measure to reduce the coupling impedance of the manifolds is the insertion of flexible perforated sleeves into all beam ports. As the manifolds support all the vacuum pumping system, this is a laborious operation which is envisaged for the next PSB shutdown. Although the insertion of damping resistors is much easier, it is not proposed as it is not feasible for the rings 1-3 and the predictable instability threshold is lower compared to the one obtained by short-circuiting sleeves.

7 CONCLUSIONS

Both wire measurements of longitudinal coupling impedance and wake field calculations agree that the pump manifolds act as individual high-Q resonators for each ring, where Ring 4 stands out by a factor ~2.5 w.r.t. the other rings both in R_s (~50 kΩ) and R_s/Q (~25). Q values vary over the measurements but can reach values >2000.

Resonance frequencies (measured 1.055 GHz and calculated 1 GHz) for the Ring 4 cavities are also lower by about 130 MHz with respect to the other levels. There is a difference of 50 MHz between calculations and wire measurements. These results suggest that the pump manifolds might indeed be the driving impedance of the 'Ring 4 Instability', distinguishing this ring from the others.

Straightforward application of the Keil-Schnell-Boussard criterion for stability yields for the observed threshold intensity an impedance of the order of 25 kΩ. This would fit the measurements if there were only one manifold in the ring or if the resonances of the present 40 manifolds do not overlap.

Application of mode-coupling theory for extremely narrow resonances, which interact with only one spectral line of a mode, yields impedance thresholds of the order of 1 MΩ, which is possible only if the resonance curves of the manifolds strongly overlap. From the resonance frequencies measured on three manifolds (two coincide, while the third is 6 MHz lower), this seems not impossible but it is difficult to guess the whole distribution. A scatter of the resonance frequencies may also explain the intriguing fact, that adding 10 manifolds in 1993 has changed neither the threshold of the instability nor the ensuing blow-up. In spite of the open questions, the evidence is convincing enough to justify the cure of short-circuiting all ports by flexible sleeves. In the case of a cure by systematic insertion of damping resistors, individual resonant impedances will certainly overlap and their superposition may dangerously approach the coasting-beam criterion.

8 ACKNOWLEDGEMENTS

We would like to thank the PS Section of the Vacuum Group for their efficient help in the preparation of the measurement.

REFERENCES

[1] D. Boussard, 'Observation of microwave longitudinal instabilities in the CPS', CERN/LabII/RF/75-2 (1975); E. Keil, W.Schnell, 'Concerning longitudinal stability in the ISR', CERN/ISR/TH/RF/ 69-48 (1969) .

[2] F. J. Sacherer, 'Bunch lengthening and the microwave instability', Trans. IEEE Nucl. Sc. NS-24, 1393 (1977), and CERN/PS/BR 77-6 (1977).

[3] K. Y. Ng, 'Mode-coupling instability and bunch lengthening in proton machines', Proc. of the 1995 Part. Acc. Conf. 2977 (1995), Dallas 1995 .

[4] T. Bohl, T. P. Linnecar, E. Shaposhnikova, 'Measuring the resonance structure of accelerator impedance with single bunches' CERN-SL-96-62 RF (1996), and this Conference.

[5] F. Caspers in 'RF Engineering for Particle Accelerators', CERN Accelerator School Proceedings CERN 92-03, p.128 .

[6] F. Caspers, H. Schönauer, L. Soby, 'Impedance measurements on Booster manifolds', CERN PS/HI/Note 96-15 (1996).

BEAM INTENSITY LIMITS IN THE MAIN INJECTOR THROUGH TRANSITION WITH A NORMAL PHASE JUMP SCHEME

C. M. Bhat and J. A. MacLachlan
Fermi National Accelerator Laboratory*, P.O. Box 500, Batavia, IL 60510

Abstract

The Fermilab Main Injector, which is under construction, will be a high intensity proton synchrotron and will be capable of accelerating (decelerating) protons and antiprotons from 8.9 GeV/c to 150 GeV/c (150 GeV/c to 8.9 GeV/c). Presently, the plan is to accelerate or decelerate the beam through the transition energy of 20.49 GeV, using basic normal phase jump scheme. Efficient deceleration of $\bar{p}$ through the Main Injector is crucial for the success of the Recycler Ring Project. We have performed extensive longitudinal beam dynamics simulations for both modes of operation to determine the beam intensity limits and other properties. We present the latest results of calculation and their implications.

1 INTRODUCTION

Upgrading the proton beam intensity in the Main Injector (MI) is important for the high energy $p\bar{p}$ collider physics programs at the Fermilab Tevatron and for several proposed fixed target experiments using the Main Injector beam. Recently, it has been shown that with "slip stacking" [1] the proton beam intensity in the Main Injector at 8 GeV can be increased by a factor of two (or more) over the design bunch intensity [2] of 6×10^{10} particles per bunch (ppb). During the slip stacking, two batches of 84 proton bunches from the 8 GeV Fermilab Booster will be injected into the Main Injector with a small momentum offset; then they are brought together by rf coalescing. Finally, these high intensity bunches will be accelerated from 8 GeV to 120 GeV or 150 GeV through the transition energy of 20.49 GeV. Though the expected bunch area of the beam from the Booster is as small as 0.1 eV-sec [3], after slip stacking the final emittance will be in the range of 0.2-0.35 eV-sec. Passing transition with normal phase jump scheme at high longitudinal space charge density generally poses many problems. In this paper we have made an attempt to investigate any problem associated with acceleration of high intensity bunches through transition without changing the base line lattice of the Main Injector.

The Main Injector has four basic types of acceleration cycles, viz., $\bar{p}$ production, MI Fixed Target slow spill and fast spill and, Tevatron collider. In the first three modes of operations the beam will be accelerated up to 120 GeV and in the collider mode the beam will be accelerated up to 150 GeV. In all these cases, the rate of change of momentum at transition is fixed (see Table 1) and and the maximum number of protons per bunch is expected to be about 15×10^{10}. Hence, one may encounter the general problems of transition crossing in all these cases.

Another issue addressed here is the deceleration of $\bar{p}$'s from 150 GeV to 8 GeV. We plan to recycle the unused $\bar{p}$'s at the end of each collider runs of the Tevatron. The $\bar{p}$'s will be decelerated from 1 TeV to 150 GeV and injected into the Main Injector. The longitudinal bunch area of the beam at 150 GeV is expected to be about 3 eV sec and the $\bar{p}$ intensity per bunch will be 7×10^{10}. This beam will be further decelerated to 8 GeV to store in a Recycler Ring which is being built in the MI tunnel [4].

Here we have performed longitudinal beam dynamics simulations using ESME [5] for both acceleration of high intensity bunches and deceleration of large emittance bunches by including space charge force and realistic beam pipe impedance. In this report we present some of the important findings of our studies.

2 ACCELERATION OF HIGH INTENSITY BUNCHES IN MAIN INJECTOR

It is known that the acceleration of bunches of charged particles across transition energy in a proton synchrotron needs special precautions [6]. In the baseline design of the Main Injector we plan to use only the rf phase jump scheme, i.e., switching the rf phase from ϕ to $\pi - \phi$ as the beam is accelerated through transition energy. Table 1 lists the design parameters of the Main Injector. Since the dp/dt at transition is about 250 GeV/c per second the non-adiabatic time is only about 2.1 msec. Hence the bunches are not very prone to emittance dilution. Because in addition there is approximately 1.5% momentum aperture, one might be able to accelerate the high intensity bunches across transition without any beam loss or significant dilution in the beam area.

Sudden change in rf phase along with the space-charge force of the particles in a bunch induce bunch oscillation at transition. These oscillations are known to be the one of the causes for emittance growth after transition. However, in the Main Injector a quadrupole oscillation damper like the one used in the present Main Ring will be installed to reduce bunch oscillations induced by transition crossing. This damper will be activated about 20 msec after transition crossing. Hence to identify any problems associated with transition crossing it is sufficient to perform simulations for about 100 msec around transition energy. In our simulation this quadrupole damper is not included.

The parameters of the Main Injector relevant to the simulations performed here are listed in Table 1. During transition crossing the space charge force and beam pipe

* Operated by Universities Research Association, Inc. under contract No. DE-AC02-76CH03000 with the U. S. Department of Energy

impedance play significant role. To reduce the beam pipe impedance special designs were developed to shield vacuum pump connections, bellows and any undesirable steps in the ring. Plans have also been made to reduce the impedance arising due to special structures of Lambertson magnets at extraction and injection regions. A conservative estimate of the $Z_{||}/n = 1.6\ \Omega$ [3]. However for simulation, we take $Z_{||}/n = 3\ \Omega$ which gives some safety margin.

Table I. The Main Injector parameters.

Mean radius of FMI	528.3019 m
γ_t (nominal)	21.838
$\dot{\gamma}_t$	267 sec^{-1}
α_1^a	0.002091
Maximum RF Frequency and RF Voltage	4 MV for 53 MHz 15 kV for 106 MHz 60 kV for 2.5 MHz 15 kV for 5 MHz
Protons ϵ_l at 8 GeV Injection I_{Bunch} at 8 GeV	 0.1–0.35 eVs 6–15 $\times 10^{10}$
Anti-protons ϵ_l at 150 GeV Injection I_{Bunch} at 150 GeV	 3–4 eVs 5–7 $\times 10^{10}$
Coup. imp. $Z_{||}/n$	3 Ω
Beam pipe wave guide	1.5–2.2 GHz cutoff
cutoff frequency Transverse Beam size(a)	 2.2 – 5 mm
Beam pipe Radius (b)	5.8 cm (m)

[a] α_1 is the second order term in the expansion of path length.

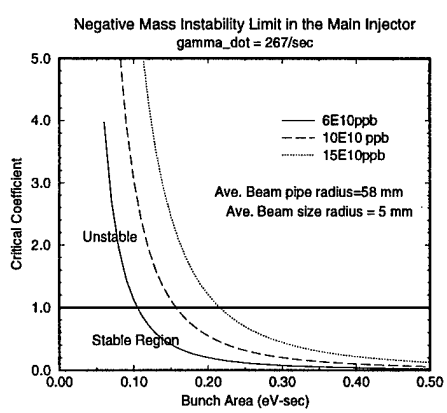

Figure 1: Negative mass instability limits [7] for beam intensity and emittance in the Main Injector. All ESME simulation results presented here pertain to beam properties corresponding to the stable region.

ESME simulations have been carried out using 10^6 macro particles per bunch and ignoring the beam current components above 14 GHz. We avoid negative mass instability by observing the stability limits calculated by W. Hardt [7]. Figure 1 illustrates the negative mass instability limits for three beam intensities as a function of bunch area. The frequency range used in the ESME simulations does display the qualitative features of negative mass instability for low emittance beam.

Figure 2 shows phase space distribution for the highest beam intensity bunch discussed here. We find that the phase space density is almost unchanged across transition.

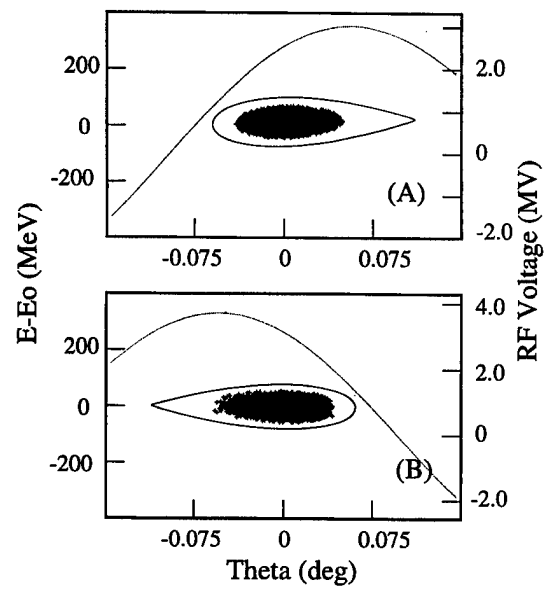

Figure 2: Phase space distribution (i.e., ΔE vs $\theta = \Delta\phi$) of 0.25 eV-sec proton bunch in an accelerating rf bucket in the Main Injector with 53 MHz rf system. The closed contours represent the buckets for the case at 20 msec (A) before (B) after transition. The rf wave form is also shown. The cases shown are for 15×10^{10} ppb.

From these simulations we found that with the normal phase jump scheme in the Main Injector the beam bunches with 15×10^{10} ppb and emittance 0.25 - .35 eV-sec can be accelerated through transition without any noticeable emittance growth and with no beam loss. If the beam longitudinal emittance is less than about 0.20 eV-sec then one might expect considerable emittance growth due to negative mass instability.

3 DECELERATION OF $\bar{P}$ BEAMS

For deceleration of $\bar{p}$, we have investigated two different types of accelerator cycle. In the first method the 3 eV-s beam bunch is captured at 150 GeV using 53 MHz rf buckets (h = 588, V_{rf} = 0.5 MV). Then the bunch is rotated with a 2.5 MHz system (h = 28, V_{rf} = 35 kV) and is matched. The typical matching voltage was about 400 V. Then the bunch is divided in to several bunches by raising the h = 588 rf voltage adiabatically. This takes less than 300 ms at 150 GeV. Thus a 3 eV-s beam bunch is distributed among 11 to 13 bunches. Finally this train of bunches is deceler-

ated to 8 GeV in less than 2 sec. In this process we noticed about a factor of 2 emittance growth and up to about 5% beam loss at transition mainly arising from to non-linear effects on the larger central bunches.

In the second method, the transferred bunch of $\bar{p}$ from Tevatron is decelerated from 150 GeV to 25 GeV in about 1.7 sec using h=588 system. On a "front porch" at 25 GeV, about 1.8 sec, the $\bar{p}$ bunch is transferred to a h=28 bucket with V_{rf}=60 kV and is rotated. At the end of bunch rotation the rf voltage is set to match the beam (i.e., lowered to $\leq$300 V) and raised adiabatically to shrink the bunch. An overall 10% emittance growth is observed during the bunch rotation and shrinking. This bunch is further decelerated using h=28 system. Since the V_{rf}(max) for the h=28 system is limited to 60 kV, the deceleration from 25 GeV to 8 GeV is performed rather slowly. In the scheme proposed here this part of the deceleration is performed in two steps. The deceleration from 25 GeV to 15 GeV with dp/dt $\approx$ -2.5 GeV/c-sec; the later part is carried out with dp/dt$\approx$ -1.4 GeV/c-sec. Thus the entire deceleration process for four bunches of $\bar{p}$'s takes about 12.5 sec. We find no beam loss and the maximum emittance growth is about 9%.

Figures 3 shows the ramp curve for the second method. Various types of rf manipulations performed during deceleration are indicated. Figure 4 shows the phase space distribution from ESME simulation for a decelerating $\bar{p}$ bunch with initial longitudinal beam emittance 3 eV-s and with 7×10^{10} $\bar{p}$pb. We find that the phase space density is almost unchanged across transition.

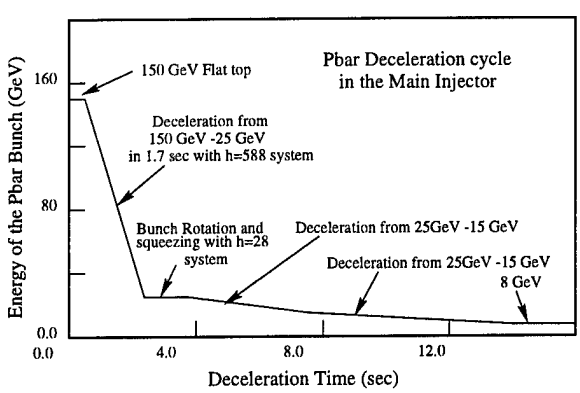

Figure 3: A 12.5 sec long $\bar{p}$ Deceleration cycle used for simulation.

The second method for deceleration has some disadvantages, though the quality of the beam is maintained through out the process. The disadvantages are that since the entire process takes rather long, it might result in an unacceptably long time to decelerate all 36 (or 99) $\bar{p}$ bunches from the Tevatron. Also there is some concern about the stability of the Main Injector magnetic field quality if the magnet current is varied very slowly. However, we are convinced that the longer deceleration time at low magnet current should not pose a problem operationally. For the first method the deceleration the time involved is small; hence is still a good choice.

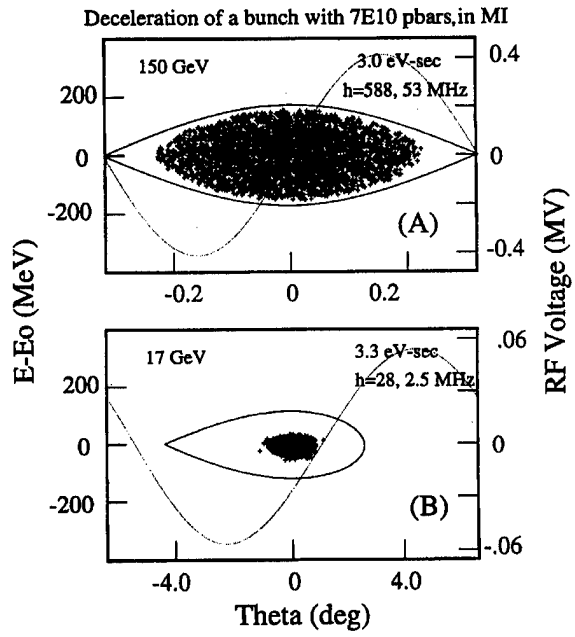

Figure 4: (ΔE vs $\Delta\phi$) distribution of the particles in a decelerating bucket of Main Injector. A) 53 MHz rf system at 150 GeV, B) 2.5 MHz rf system at 17 GeV. For other details see caption of Fig. 3.

4 SUMMARY

We have performed multi-particle beam dynamics simulations for both acceleration and deceleration of beam In the Main Injector. We find that bunches with 15×10^{10} protons and with longitudinal emittance of 0.25 eV-s can be accelerated through transition with out any dilution. For deceleration we investigated two methods of operation, the choice between them will depend on the relative importance of cycle time and deceleration efficiency in an optimized recycling scenario.

5 REFERENCES

[1] S. Shukla, J. Marriner and J. Griffin (Private communication m 1997)

[2] The Fermilab Main Injector Technical Design Handbook (1994, updated 1997).

[3] Run II Design Hand Book (1995).

[4] "Fermilab Recycler Ring Technical Design Report",edited by G. Jackson, FERMILAB-TM-1981

[5] J. MacLachlan, Computer code ESME.

[6] A. Sorenssen, Part. Accelerators, Vol. 6, 114 1975.)

[7] W. Hardt *et al., Proceedings of the 8th International Conference on High Energy Accelerators*, (Geneva, 1971) p. 323.

LONGITUDINAL INSTABILITY DUE TO THE RANDOMNESS OF HIGHER MODE FREQUENCIES OF RF CAVITY

Soon-Kwon Nam and T. Y. Kim
Department of Physics, Kangwon National University, Chuncheon 200-701, Korea

Abstract

The resonance frequencies, shunt impedances and Q-values for the higher order modes in our designed cavity are calculated by the computer codes URMEL and MAFIA. The longitudinal instabilities for the higher order modes are calculated by the eigen mode analysis of Sacherer's integral equation. The growth rates and the tune shifts in the electron storage ring are calculated by considering the randomness of the higher mode frequencies of a cavity due to the construction errors. The results with the construction errors are compared to those of without error cases for the dipole mode and quadrupole mode.

1 THE EIGENVALUE EQUATION AND INSTABILITIES

The method of analysis of longitudinal instabilities is that of Sacherer's [1] whose main result is an integral equation for the eigen mode and eigenfrequencies of the longitudinal bunch oscillations. Our method of analysis is based on Zotter's formalism [2, 3] which is the eigenmode analysis of Sacherer's integral equation without mode coupling for a Gaussian beam and Chin's method [4]. Sacherer's integral equation can be reduced to the eigenvalue equation by expanding the radial mode function in orthogonal polynomials and the eigenvalue equation is written by

$$\det(M - \delta\nu I) = 0 \tag{1}$$

where the matrix M is the interaction matrix which is no longer diagonal and $\delta\nu$ is the relative complex tune shift. The infinite number of solutions for the eigenvalue is specified by the radial modes and azimuthal modes. The real part of the coherent frequency shift gives the real coherent mode frequency shift and the imaginary part gives the instability growth rates. The complex tune shifts of coherent oscillations for a single resonator impedance can be calculated by solving the eigenvalue equation. For the calculations of the growth rates and the tune shifts in the our designed storage ring, we have to consider the randomness of higher mode frequencies due to the construction errors of the cavities. Each impedance peak can contribute to both the growth rate and the damping rate of the Robinson instability according to the position of the impedance peak with respect to the harmonics of the revolution frequency. The Monte Carlo method is used to calculate the average values and rms spreads of the complex tune shifts due to both the accelerating mode impedance and randomly distributed higher mode impedances.

Table 1: Main parameters for calculations

Energy	2 GeV
Average machine radius	26.866 m
Synchrotron tune	0.0059
Revolution frequency	1.78 MHz
Momentum compaction factor	0.0024
Bunch length	0.01 - 0.1 cm
Harmonic number	282
RF frequency	501.96 MHz
Peak voltage	1.5 MV
Cavity length	40 cm
Cavity diameter	46.03 cm

2 THE TUNE SHIFTS AND GROWTH RATES WITH STATISTICAL ANALYSIS

The instability by the statistical analysis have been studied by many authors [4, 5, 6]. Especially, Chin took the impedance of a cavity, not a single cell to take into account the actual fields seen by particles. The resonance frequencies, shunt impedances and Q-values for the higher order modes in our designed cavity with the length of 40 cm, diameter 46.03 cm, peak voltage 1.5 MV and frequency 501.96 MHz and R/Q 58.89 ohm are calculated by the computer codes URMEL [7] and MAFIA [8]. We need random numbers with a distribution that is different from a uniform one. The general approach to obtain a set of random numbers with a given distribution is to start with a uniform set and change it into the one required. We assume that the spread in the higher mode frequencies due to the construction errors of cavities is a Gaussian with standard deviation σ. The magnitude of σ at resonant frequency f_r is estimated by using the formula of the pill box cavity. Thus the standard deviation σ is given by the relative construction error ϵ as $\sigma \sim \epsilon f_r$. We assume the relative construction error of the designed RF cavity is 0.5×10^{-3} for these calculations. The beam parameters used in our calculations are the energy of 2 GeV, average machine radius of 26.866 m, momentum compaction factor 0.0024, betatron tune 6.29, revolution frequency 1.78 MHz, synchrotron tune 0.0059 and bunch length 0.01 to 0.1 cm as shown in Table 1.

The results for the tune shifts versus the bunch length are shown in Fig. 1 and 2 for two azimuthal modes of the dipole where the bunches move rigidly as they execute longitudinal synchrotron oscillations and quadrupole where the bunch head and tail oscillate longitudinally out of phase and three radial modes. Fig. 1 shows the relation-

0-7803-4376-X/98 /$10.00 © 1998 IEEE

ship between the tune shifts and the bunch length for the azimuthal mode m=1(dipole mode) and the radial modes of k=0, 1 and 2.

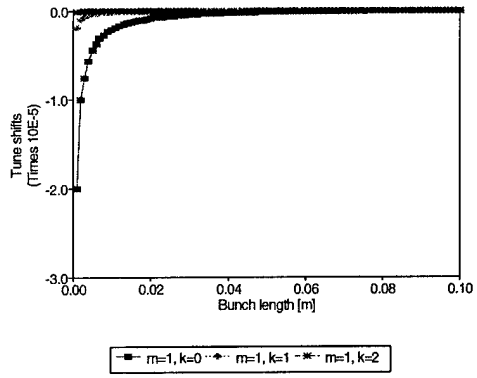

Figure 1: The relationship between the tune shifts and the bunch length for m=1 and k=0, 1 and 2.

Fig. 2 shows the relationship between the tune shifts and the bunch length for the azimuthal mode m=2(quadrupole mode) and the radial modes k=0, 1 and 2. In Fig.1 and 2, Tune shifts are not sensitive to bunch length as bunch lengthen in both cases of the dipole and quadrupole modes.

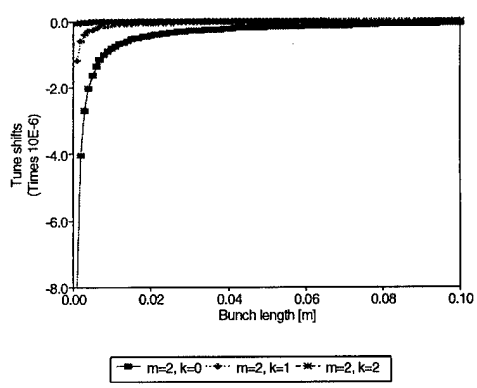

Figure 2: The relationship between the tune shifts and the bunch length for m=2 and k=0, 1 and 2.

Fig. 3 and 4 show the comparison of the growth rates and the tune shifts for with and without errors in the case of m=1 and k=0. Fig. 5 and 6 give the comparison of the growth rates and the tune shifts for with and without errors in the case of m=2 and k=0. The growth rates with and without errors give the maximum error deviation of about a factor of ten by the statistical analysis. For the tune shifts with and without errors, the maximum error deviations are increased by a factor of four. We have calculated the growth rates and the tune shifts for the several hundred cases and considered several data to get the maximum deviation of the tune shifts and growth rates of coherent synchrotron oscillation due to randomly distributed RF cavity impedances.

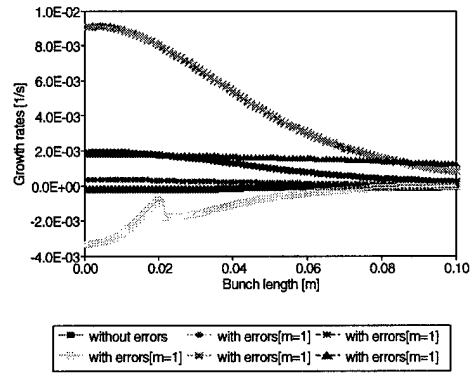

Figure 3: The relationship between the growth rates and the bunch length with and without errors for m=1 and k=0.

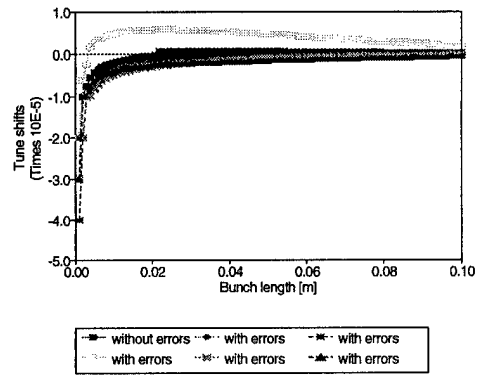

Figure 4: The relationship between the tune shifts and the bunch length with and without errors for m=1 and k=0.

The longitudinal radiation damping rate at 2 GeV storage ring is about 222 sec^{-1}, large enough to stabilize the dipole and quadrupole modes for various azimuthal modes. The contributions of higher modes in these calculations are not sensitive to the spread of resonances due to the construction errors of the designed cavity.

3 CONCLUSION

The longitudinal instabilities for the higher order were calculated by the eigenmode analysis of Sacherer's integral equation. The growth rates and the tune shifts in the electron storage ring were calculated by considering the randomness of the higher mode frequencies of a cavity due to the construction errors. Tune shifts were not sensitive to bunch length as bunch lengthen in both cases of the dipole and quadrupole modes. The results with the construction errors were compared to those of without errors for the dipole mode and quadrupole mode. The growth rates with and without errors gave the maximum error deviations of about a factor of ten by the statistical analysis. For the tune shifts with and without errors, the maximum error deviations are increased by a factor of four. But the growth rates, even in any cases, were small enough compared to the ra-

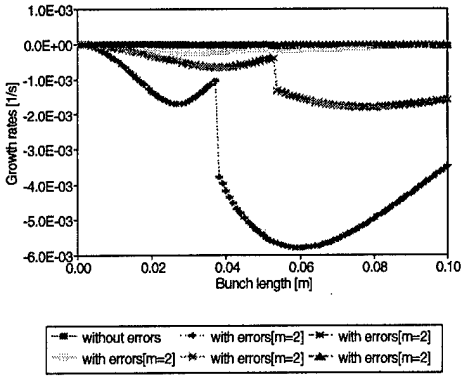

Figure 5: The relationship between the growth rates and the bunch length with and without errors for m=2 and k=0.

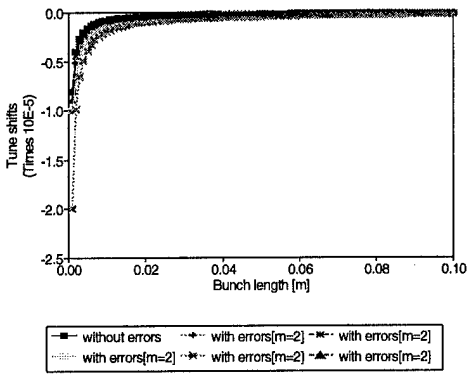

Figure 6: The relationship between the tune shifts and the bunch length with and without errors for m=2 and k=0.

diation damping time of 4.5 ms in our storage ring. The results also indicated that the deviations of the growth rates and the tune shifts due to higher modes of cavities were not sensitive to the construction errors of cavities if they are about 0.5×10^{-3}.

4 REFERENCES

[1] F. J. Sacherer, IEEE Trans. **NS-24**, 1393 (1977).

[2] B. Zotter, CERN SPS/81-18, 1 (1981).

[3] B. Zotter, CERN/ISR-TH/80-03, 1 (1981).

[4] Y. Chin, KEK 81-20, 3 (1982).

[5] C. Pellegrini and M. Sands, PEP-258, 1(1977).

[6] C. Y. Yao and A. Chao, SLAC-PUB-2680, 1(1981).

[7] T. Weiland, Nucl. Instr. Methods, **NS-216**, 329(1983).

[8] The Mafia collaboration(1988).

EXPERIMENTAL OBSERVATIONS OF THE ION-RELATED COUPLED BUNCH INSTABILITY IN A BUNCH TRAIN IN TRISTAN AR

H. Fukuma, Y. Chin, S. Kato, E. Kikutani, S. Kurokawa, S. Matsumoto, K. Ohmi, Y. Suetsugu, M. Tobiyama, K. Yokoya, X. L. Zhang,
Accelerator Laboratory, High Energy Accelerator Research Organization(KEK),
Oho 1-1, Tsukuba-shi, Ibaraki-ken, Japan

Abstract

An experiment was carried out in TRISTAN AR for the search of the fast beam-ion instability(FBII). A train of 100 bunches with 2ns spacing was stored with the help of the transverse bunch feedback system. The nitrogen gas was intentionally leaked into the inside of the vacuum duct to enhance the ion effect. The oscillation patterns were recorded by the beam position monitor system which is capable of storing the transverse position of every bunch up to 1600 turns. The spectra of the bunch oscillation were also measured by a spectrum analyzer. This paper describes the results of the experiment and also discusses the possible explanation of them in terms of the FBII.

1 INTRODUCTION

It is well known that ions which are produced via ionization of residual gas by the beam can be trapped along the orbit due to the attractive force of the electron beam. The trapped ions may affect to the beam motion and cause the instability called ion trapping. The ion trapping is usually avoided by leaving the bunch gap in which the ions are over-focused and eventually disappear. In high intensity rings such as the KEKB the instability may occur even in single passage of the bunch train because enormous ions are created at each bunch passage. The ions created by the head bunch give a kick to trailing bunches. The disturbance to the bunches may resonantly grow along the bunch train. The oscillation amplitude also increases toward the end of the train. This instability is called the fast beam-ion instability (FBII)[1,2,3]. The FBII may affect to the performance of the KEKB because the growth time of the FBII is estimated to be less than 1ms which is merginal value for the bunch feedback system. Though it is very imortant to study the FBII experimentally, only one experiment on the FBII has been reported[4]. Thus we tried to directly observe the buch motion caused by the FBII in TRISTAN AR. This paper describes the results of the experiment.

2 THEORY

According to the linear theory by K. Yokoya[3], the center of mass position $y_n(s)$ of the unstable mode against ion perturbation is given by

$$y_n(s) \approx a_n e^{i(\Theta n - ks)}, \tag{1}$$

where k is the betatron wave number, s a distance along the orbit, n the bunch index counted from the head of the bunch train and Θ the phase advance of the ion oscillation between the arrival time interval of two adjacent bunches which is expressed as

$$\Theta = \sqrt{\frac{2zNm\, r_e L}{A M_N \Sigma_y (\Sigma_x + \Sigma_y)}}. \tag{2}$$

Here, z is the electrovalence, A the mass nunber of the ion, L the distance between bunches, N the number of electrons per bunch, $\Sigma_{x,y}$ the convolution of the beam size of electrons and ions, m and M_N the mass of an electron and a nucleon and r_e the classical electron radius. The conjugate mode $e^{i(-\Theta n - ks)}$ is damped.

The amplitude blowup factor G is approximately given by

$$G = \left|\frac{a_n(s)}{a_0}\right| \approx 1 + \frac{1}{\Gamma}\exp\left[\sqrt{\Gamma + (\alpha_0 \Theta n)^2} - \alpha_0 \Theta n\right] \tag{3}$$

where Γ is a constant defined in ref. [3] and proportional to Θ, s and n^2. α_0 ($\approx$0.077) represents the non-linear smearing of the ion center-of-motion. Equation (3) shows that the amplitude of the motion rapidly increases along the bunch train.

3 EXPERIMENTAL SETUP

The experiment was carried out as a part of the high beam current experiments at the TRISTAN AR[5]. Principal parameters of the AR are shown in Table 1.

The vaccum pressure of the AR is maintained by the ion pumps and non-evapolated getter pumps. The pressure is monitored by 15 cold cathode gauges(CCGs). In the experiment the nitrogen gas was intentionally leaked into the vacuum duct to increase the growth rate of the FBII. The pressure near the injection point of the gas was measured by a residual gas analyzer(RGA). After the leak of the gas the partial pressure of the gas-component whose atomic number is 28, P_{28}, was increased to 6.0 x 10^{-6} Torr at the RGA. The pressure distribution around the injection point of the gas was calculated from the reading of the RGA and the pumping speed of the vacuum pumps[6]. From the calculated pressure distribution and the reading of CCGs we obtained the average value of P_{28}

0-7803-4376-X/98./$10.00 © 1998 IEEE

Table: 1 TRISTAN AR parameters.

Beam energy(GeV)	2.5
Circumference(m)	377
RF frequency(MHz)	508.5808
Harmonic number	640
Revolution frequency(kHz)	795
Natural emittance(m)	4.46×10^{-8}
Average beta functions(H/V) (m)	8.7 / 9.4
Betatron tunes(H/V)	10.14 / 10.25

of 8.4×10^{-8} Torr. The vertical emittance growth by Coulomb scattering was estimated to be 3.8×10^{-10}m[7]. Before the leak of the gas vacuum pressure was 7×10^{-9} Torr.

Main instrument for the experiment was the beam position monitor(BPM) system[8] which was installed in the AR to study the prototype of the bunch feedback system for the KEKB. The signals from up- and bottom-button pickups were both converted to 2GHz signals using cable-delay and fed to the hybrid to make a difference of two signals. The difference-signal was mixed with the reference signal with the frequency of 4 x RF frequency (f_{RF}), then fed to the low pass filter and finally put into the two-tap filter board which can store the data of 1M bytes after digitizing the input signal with an 8-bit ADC. The ADC count U is expressed as $U = k_m\ y\ I_b$, where y is the vertical beam position and I_b the bunch current. The constant k_m was determined to be 46 count/mm/mA by making orbit bumps at the pick up. The trigger for the data taking by the BPM system was generated freely without synchronization with any signal.

As an auxiliary instrument a spectrum analyzer HP8562E(13.2GHz) connected with a vertical button pick up was used for taking the beam spectrum. The observed frequency range was $3f_{RF}$ to $4\ f_{RF}$. From the noise level of the beam spectrum, detectable oscillation amplitude was estimated to be larger than 30μm at the beam current of 100mA. The beam oscillation was also observed by the synchrotron light(SL) monitor.

The beam size was measured by a photodiode arrays. But at present we are not sure whether the monitor is reliable or not because it gives two times larger horizontal beam size than design value in the single bunch operation. In calculations of the growth time and Θ we used the beam size calculated from the design value of horizontal emittance and an estimated vertical-horizontal emittance ratio κ. For the calculation of κ the vertical r.m.s.-misalignment of the quadrupoles $\sigma_y(q)$ was estimated by the closed orbit(c.o.) without orbit correction which was obtained from the measured c.o. and corrector strength. The vertical r.m.s.-misalignment of the sextupoles was assumed to be equal to $\sigma_y(q)$ and the r.m.s.-rotational error of the magnets was also assumed to be 0.2mr. A simulation based on these errors shows that κ is less than 1 % after the orbit correction. Taking account of the emittance growth by Coulomb scattering the total κ is estimated to be several %.

Throughout the experiment the transverse bunch feedback system was employed to store the beam current of several hundred mA. The vertical damping time of the bunch feedback system was estimated to be 800 μs at the bunch current of 4mA[8]. Assuming κ of 2 % and P_{28} of 8.4×10^{-8} Torr the linear theory predicts the growth time of 140μs which is much shorter than the damping time of the bunch feedback system.

4 EXPERIMENTAL PROCEDURE AND RESULTS

A train of 100 bunches was stored with 2ns spacing. This means that about five sixths of RF buckets were left without the bunches. A calculation based on the conventional ion trapping theory[9] shows that the ions are not trapped in our experimental conditions, i.e. absolute value of the trace of the ion motion matrix is larger than 2.

Before the leak of the nitrogen gas we confirmed that the vertical betatron sidebands observed by the spectrum analyzer were disappeared at the beam current of 260 mA. Then we leaked into the gas in the ring. The vertical betatron sidebands remained down to the beam current of 173 mA. Then we added more gas. The beam was injected to 190 mA. Vacuum pressure was 8.4×10^{-8} Torr as described in section 3. The intermittent vertical oscillation, which was not observed before and at the first leak of the gas, appeared in the SL monitor. Beam loss accompanied with the oscillation was not observed. Strong vertical betatron sidebands were observed in the spectrum taken by the spectrum analyzer. The spectrum distribution shows that the large lower sidebands appear below 10th revolution harmonics as expected by the theory(See Figure 1). We also observed upper sidebands whose origin is not understood yet. The sidebands were observed down to 57 mA.

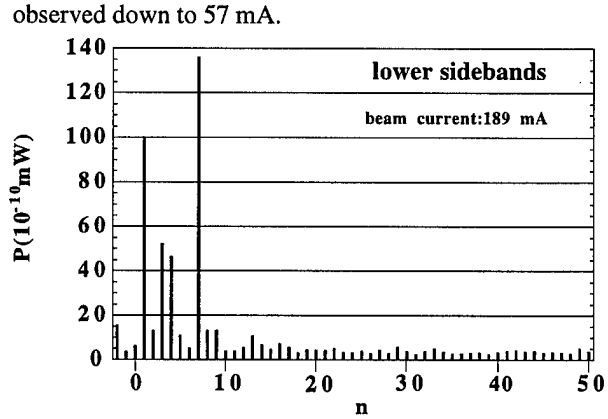

Figure 1: Spectrum of lower betatron sidebands at the frequency of $3\ f_{RF}+nf_r - f_\beta$, where f_r and f_β are the revolution and betatron frequency, respectively.

The bunch oscillation was taken by the BPM system after adding the gas. As the oscillation includes a

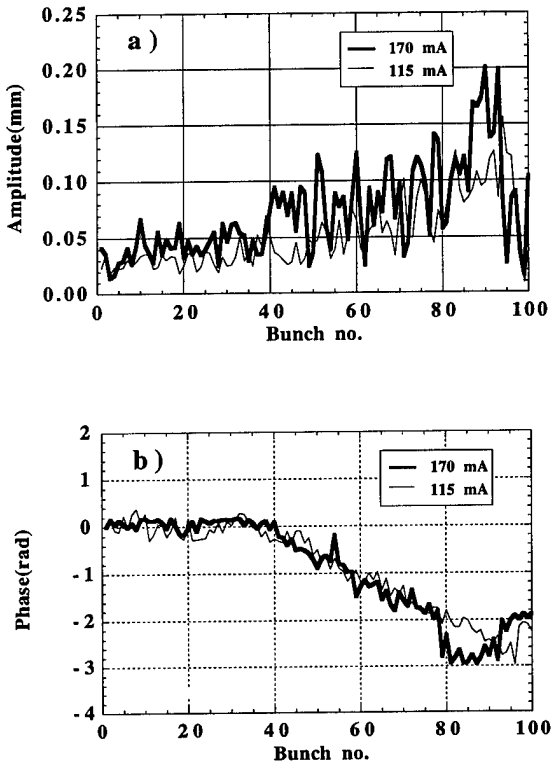

Figure 2: Amplitude a) and phase b) along the bunch train.

large component of synchrotron oscillation we applied Fourier analysis to the data of 1600 turns. The amplitude was normalized by the bunch current because the distribution of the bunch current was not uniform due to the short beam life of about 10-15 min. The obtained amplitude and phase are shown in Fig. 2 a) and b), respectively. Two set of the data were taken in same beam fill but at different beam current of 170 and 115 mA. Fig. 2 a) clearly shows the amplitude growth along the bunch train. The maximum amplitude is about 200μm at the beam current of 170 mA. As the amplitude of 200μm is well above the sensitivity of the spectrum analyzer and the sidebands were not observed by the spectrum analyzer at almost same current before adding the gas, we conclude that the observed oscillation was caused by the addition of the gas.

Fig. 2 b) shows that the phase decreases along the bunch train, which exhibits the oscillation mode is unstable as expected by the theory. The total phase shift from head to tail of the bunch train is about 3 radians. Assuming κ of 2 % the linear theory gives three times larger phase shift than the observation. We may need further study of the beam size to discuss the difference between observed and predicted phase shift. Eq. (2) shows that Θ is expected to be changed by 20% when the beam current decreases from 170 to 115 mA. In Fig. 2 b) expected change of Θ is not clear.

5 SUMMARY

An experiment for the search of the FBII was carried out at the TRISTAN AR. We observed the vertical coupled bunch oscillation caused by adding the nitrogen gas into the ring, which indicates the instability is ion-related. The amplitude of the oscillation along the bunch train increases from head to tail of the bunch train. The decrease of the oscillation phase along the bunch train shows that the unstable mode of the oscillation is excited. The phase shift from head to tail of the train agrees with the linear theory of the FBII within factor of 3. The growth rate of the instability is less than several ms which is the damping time of the bunch feedback system. Observed characteristics of the instability such as being ion-related, the oscillation amplitude increasing along the bunch train, short growth time of the instability and the phase shift from head to tail of the train which agrees with the theory within factors of magnitude shows that the observed instability can be interpreted as the FBII.

Further simulation studies and data analysis are in progress.

6 ACKNOWLEDGEMENTS

The authors thank to N. Akasaka for providing the software for the spectrum analyzer. They also thank the members of the AR experiment group, especially K. Akai and Y. Funakoshi, for stable operation during the experiment.

REFERENCES

[1] T. O. Raubenheimer and F. Zimmermann: 'Fast beam-ion instability. I. Linear theory and simulations', Phys. Rev. E, 52, 5487(1995).

[2] G. V. Stupakov et al.: 'Fast beam-ion instability. II. Effect of ion decoherence', Phys. Rev. E, 52, 5499(1995).

[3] 'KEKB B-Factory Design Report', KEK Report 95-7, 5-17(1996).

[4] J. Byrd et al.: 'Ion Instability Experiments on the ALS', SLAC-PUB-7389(1996).

[5] Y. Funakoshi et al.: 'High beam current experiments for the KEKB conducted at the TRISTAN Accumulation Ring', in these proceedings.

[6] K.Kanazawa: 'On the pressure distribution of a ring accelerator:A Green's function approach', J.Vac. Soc. Technol.A6, 3002(1988).

[7] K.Kanazawa: 'Emittance and vacuum pressure', OHO'91(Lecture note of high energy accelerator seminer), VII-1(1991).

[8] M. Tobiyama and E. Kikutani: 'STUDY OF BUNCH BY BUNCH FEEDBACK SYSTEM IN TRISTAN-AR', in these proceedings.

[9] Mark Q. BARTON : 'ION TRAPPING WITH ASYMMETRIC BUNCH FILLING OF THE NSLS VUV RING', Nucl. Instr. and Meth. A 243, 278(1986).

BEAM LOSS AT THE BEGINNING OF ACCELERATION IN THE KEK-PS MAIN RING

T. Toyama, D. Arakawa, S. Igarashi, J. Kishiro, K. Koba, K. Takayama
High Energy Accelerator Research Organization (KEK), 1-1 Oho, Tsukuba, Ibaraki 305 Japan

Abstract

Towards the intensity up-grade of the KEK-12GeV-PS, the beam loss at the beginning of acceleration should be removed. The loss observed around 80 ms after the beginning of acceleration results from the horizontal head-tail instability. The instability occurs due to a large change in the chromaticity produced by the sextupole field induced in the beam-pipe of the dipole magnets. The horizontal chromaticity moves into a positive region just around 80 ms after the beginning of acceleration. The longitudinal mode 0, 1 and 2 have been observed.

1 INTRODUCTION

The operating point, (ν_x, ν_y), has been changed from (7.12, 7.21) to (7.12, 5.21) since January 1996, expecting a reduction of the space-charge induced effects[1]. After the modification, the beam loss emerges around 80 ms after the beginning of acceleration (P2). Chromaticity control using one of the two sextupole families has been the most effective cure to suppress the beam loss. The observation using the position monitor revealed that the instability is caused by a horizontal coherent dipole motion, which was identified as the Head-Tail Instability (HTI) of longitudinal mode, mainly, $\ell = 0$. The beam loss around 80 ms after P2 has almost vanished by properly exciting sextupoles.

2 EXPERIMENTAL RESULTS

The typical profile of the horizontal coherent dipole oscillation is shown in Fig.1. In Fig.2 the growth of the oscillation is shown in the lower trace and the beam intensity in the upper trace. The signals are sampled at the timing of the bunch center, 5 k samples per division. The start point of the trace is 50 ms after P2. The instabilities occur repeatedly even decreasing beam intensity. Around 80 ms from P2 the mode $\ell = 0$ was mostly observed. On the other hand the mode $\ell = 1$, 2 or some mixtures were observed at the neighbour of the above time region.

It is well known that the head-tail motion of mode $\ell = 0$ is unstable in the positive chromaticity region under the transition energy and has no instability threshold in the beam intensity[2]. The chromaticity is controlled by two families of correction sextupoles. Their main tasks are to correct the chromaticity after the transition energy because the sign of the phase slippage factor $\eta = \alpha - 1/\gamma^2$ changes, and to correct during slow beam extraction for controlling the betatron tune spread. The power supplies are unipolar and not stable near zero current. Therefore they are excited by a current more than about 2 A.

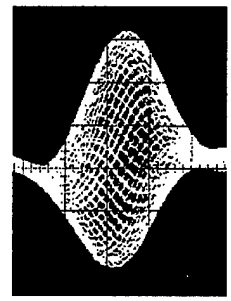

Figure 1: Horizontal coherent oscillation.

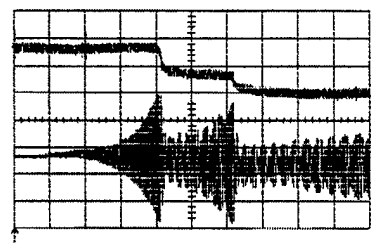

Figure 2: Growth of the coherent oscillation. Upper trace: beam intensity ($10^{11} protons/div$), lower trace: coherent oscillation, abscissa: 5 k samples/div.

Near injection energy, there are some other contributions to the chromaticity other than natural chromaticity and the one from the correction sextupoles, which are not negligible small [3]: a remnant of the correction sextupoles, a sextupole component of the dipole and quadrupole magnets, and an eddy current in the dipole beam-pipe. Calculated contributions are $\xi_{x\,natural} = -7.95$, $\Delta\xi_{x\,remnant} = 1.90$, $\Delta\xi_{x\,di} = -1.63$, $\Delta\xi_{x\,quad} = 0.75$ at the injection energy, $\Delta\xi_{x\,eddy} = 6.19$ at 100 ms after P2 and in addition from the correction sextupoles $\Delta\xi_{x\,sext} = 3.2$ at the injection energy. Here the chromaticity is defined as $\xi = \Delta\nu/(\Delta p/p)$ and the eddy current contribution is estimated using a two-parallel-plate approximation for the beam pipe [4]: $\partial^2 B_y/\partial x^2 = 2\mu_0\sigma(h/g)\dot{B}$, where μ_0 is the permiability of the vacuum, σ the conductivity of the beam pipe, h the thickness of the beam pipe and g the gap height of the magnet.

Taking the energy dependence of the chromaticity into account as

$$\xi_x(t) = \xi_{x\,natural} + \Delta\xi_{x\,sext} + \Delta\xi_{x\,di} + \Delta\xi_{x\,quad} + \Delta\xi_{x\,remnant}\frac{B(0ms)}{B(t)} + \Delta\xi_{x\,eddy}\frac{\dot{B}(t)/B(t)}{\dot{B}(100ms)/B(100ms)}$$

we obtain the time evolution of the chromaticity, which is shown with the measured chromaticity in Fig.3. The solid

0-7803-4376-X/98/$10.00 © 1998 IEEE

line and the filled circles are the calculated and measured results, respectively, for the operation in which the beam loss occurs due to the uncorrected chromaticity at (7.12, 5.21). The calculation including the eddy current effect well agrees with the measured result and well explains the beam loss around 80 ms from P2, when the chromaticity moves into the positive region around 80 ms from P2.

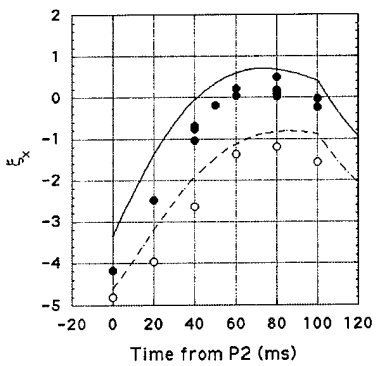

Figure 3: Horizontal chromaticity after the acceleration start.

The natural chromaticity is $\xi_x = -9.22$ for the previous operating point, (7.12, 7.21). Now we can understand the reason why the head-tail instability emerged when changing the operating point. The increase of the natural chromaticity, $\sim$ 1.3, caused zero crossing of the horizontal chromaticity around 80 ms after P2 and forced the horizontal coherent motion, mainly, of mode 0 unstable and resulted in the beam loss.

Since the incoherent space charge tune shift has no effect for the transverse dipole mode, we need some other stabilizing effects. The cure has been achieved by the defocusing sextupole family (S_D) because of the power supply polarity. Corresponding chromaticities are plotted in Fig.3 by the broken line (calculated result) and the open circles (measured result).

Another cure was tried using an octupole magnet. The instability was suppressed by Landau damping at the tune spread of $\sim$ $100\epsilon_x$ (Fig.4), which is consistent with the simulation result described below.

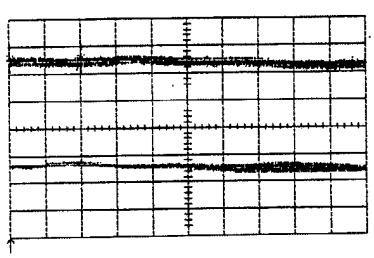

Figure 4: Damping of the coherent oscillation by the octupole magnet. Upper trace: beam intensity ($10^{11} protons/div$), lower trace: coherent oscillation, abscissa: 5 k samples/div.

3 HTI SIMULATION AND DYNAMIC APERTURE

To understand the qualitative feature of the observed HTI a multi-particle simulation code has been developed. In the code the continuous focusing model was employed for the purpose of saving a computation time, transverse wakes were assumed to be constant along the ring, and the synchrotron oscillation was taken account of in the form of changes in energy and phase every turn. Accordingly the change in betatron tune resulted from the finite value of chromaticity was given every turn. Meanwhile, effects due to an octupole magnet were included as a delta-function like kick which was near the real situation in the experiment.

The product of constant wake and beam intensity is a key parameter to determine the instability. Unfortunately the magnitude of wake in the KEK-PS was unknown. Here the product was dealt as a free parameter. To elucidate effects of the chromaticity on the growth of the HTI for different modes, the simulation results are shown in Fig.5. As expected from the theoretical prediction, the mode with a large positive growth has been confirmed to vary as a function of the chromaticity. General features of Landau-damping due to the nonlinear tune-spread have been simulated assuming octupole fields. The maximum size of the oscillation amplitude of beam-centroid is depicted as a function of turn-number in Fig.6, where its saturation and succeeding damping are found. These are typical features of Landau Damping.

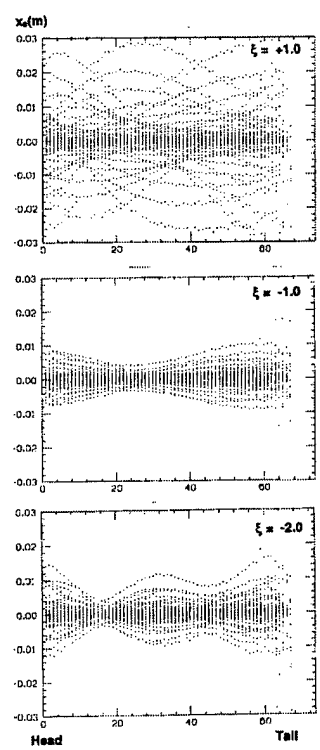

Figure 5: Motion of beam-centroid for different magnitude of the chromaticity.

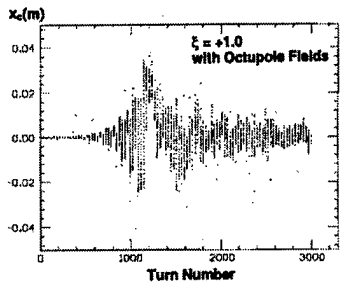

Figure 6: Simulation of Landau damping with octupole magnet fields.

There are some methods to cure the HTI. As mentioned above one is to control chromaticity in a delicate manner by the correction sextupoles and another is to stabilize by Landau damping using octupoles. The excitation of these magnets may reduce the dynamic aperture. Therefore we have examined the dynamic aperture, developing a simulation code by including nonlinear elements, such as sextupole and octupole magnets. A phase space vector (x,x') is multiplied by the transfer matrix in the linear field components and x' is shifted at each nonlinear field component using the thin lens approximation. Poincaré map, (x,$\alpha x + \beta x'$) is plotted in Fig.7 when 16 sextupole magnets were considered to be in an operating condition of suppressing HTI and the induced sextupole field component in the dipole beam-pipe are considered to be localized at the center of the dipole magnets.

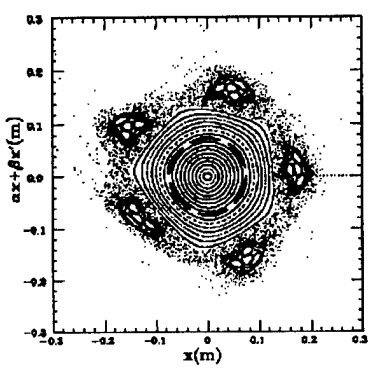

Figure 7: Dynamic aperture with the sextupole excitation and the eddy current.

Besides the correction by the sextupole magnets, Poincaré map is depicted considering the single octupole excitation with the same configuration of the experiment. In this case the dynamic aperture is greatly reduced as shown in Fig.8. More larger dynamic aperture will be obtained by the symmetrically distributed octupole magnets.

4 SUMMARY

Summarizing the present operation at the beam intensity of $\sim 5 \times 10^{12}$ protons per pulse (9 bunches), the instability is almost suppressed by exciting the defocusing sextupole

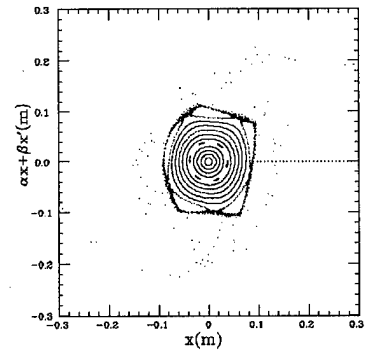

Figure 8: Dynamic aperture with the octupole excitation and the eddy current.

family (S_D). The observed behavior of the HTI is well explained by the simulation and the existing theory.

We are further investigating the HTI, which comprises single- and multi-bunch effects, and will optimize the cure.

5 ACKNOWLEDGEMENTS

The authors wish to thank KEK-PS members for their interest and continual support through this work. They wish to thank Prof. I. Yamane and Prof. H. Sato for calling their attention to the present problem. They also wish to thank Dr. M. Shirakata and Dr. M. Uota for helping in the experiment and giving usefull comments.

6 REFERENCES

[1] S. Machida and Y. Shoji, AIP Conf. Proc. 377 (1995) p.160, S. Machida, Nucl. Instr. Meth. A 384 (1997) 316. and Y. Shoji et. al., these proceedings.

[2] A. Chao, "Physics of collective beam instabilities in high energy accelerators", John Wiley & Sons, Inc., 1993 and the references there in.

[3] A. Ando, et. al.: IEEE Trans. on Nucl. Sci. NS-24, No.3 (1977) p.1530 , A. Ando, et. al.: Proc. of MT-5 (1975) p.63, Y. Shoji: KEK Internal Report, SR-316 (1995) (in Japanese).

[4] D. A. Edwards and M. J. Syphers, "An Introduction to the Physics of High Energy Accelerators", John Wiley & Sons, Inc., 1993.

BUNCH LENGTHENING AND ENERGY SPREAD INCREASING IN ELECTRON STORAGE RINGS

J. Gao, Laboratoire de L'Accélérateur Linéaire, IN2P3-CNRS
et Université de Paris-Sud, 91405 Orsay cedex, France

Abstract

A theory of bunch lengthening and energy spread increasing in electron storage rings is established by introducing the concept of collective random excitations. Analytical formulae are established to calculate the equilibrium bunch length and the energy spread in the whole current range. Some experimental results are compared with those predicted by the theory and the comparison results are quite well.

1 INTRODUCTION

The phenomenon of bunch lengthening as a single bunch effect in an electron storage ring was first observed in ACO [1] at Orsay and later in other machines.

The first empirical formula [1] found in ACO to describe the variation of the bunch duration (σ_τ) with respect to the average bunch current (I_b) and the beam energy (E), written

$$\sigma_\tau^2(\mathrm{ns}) = \sigma_{\tau 0}^2(\mathrm{ns})\left(1 + 2\times 10^{-3}\frac{I_b(\mathrm{mA})}{E^4(\mathrm{GeV})\sigma_\tau(\mathrm{ns})}\right) \tag{1}$$

had a great impact on the potential well distortion (PWD) theory of longitudinal instabilities in electron storage rings established afterwards [2] [3]. The theories largely used to describe the bunch lengthening phenomenon are potential well distortion and microwave instability [4] theories. However, as stated by Chao [5] and Gareyte [6] the field of bunch lengthening is still an open area to more detailed investigations and analytical explanations.

In this paper, we try to give a theory which describes the variations of the bunch length and the energy spread with respect to the bunch current covering the whole current range.

2 NATURAL BUNCH LENGTH AND ENERGY SPREAD

It is well known that in an electron storage ring [7] an electron will lose its energy due to synchrotron radiations. Since this radiation is compensated by the rf cavities in the ring there exists a damping effect on the synchrotron oscillation with the corresponding damping time $\tau_\varepsilon = 2T_0/\frac{d\mathcal{U}_0}{dE}$, where T_0 is the revolution period, $\mathcal{U}_0$ is the synchrotron energy lost per electron per turn, and E is the electron energy. In reality, the synchrotron radiation energy loss is in the form of randomly emitted photons, and this random quantum excitations together with the previously mentioned synchrotron radiation damping effects result in the *single particle* equilibrium energy spread, σ_{ε_0}, and *single particle* "bunch length", σ_{z_0}, expressed as

$$\sigma_{\varepsilon_0}^2 = \frac{\tau_\varepsilon}{4} < \mathcal{N}_p < u_p^2 >> \tag{2}$$

and

$$\sigma_{z_0}^2 = \left(\frac{c\alpha}{\Omega_s E}\right)^2 \sigma_{\varepsilon_0}^2 \tag{3}$$

where $\mathcal{N}_p$ is the total number of photons emitted per electron per second at a dipole of bending radius R, u_p is the photon energy, α is the momentum compaction factor, γ is the normalized electron energy, Ω_s is the synchrotron oscillation angular frequency, and

$$\mathcal{N}_p < u_p^2 >= \frac{55e^2c^2\hbar\gamma^7}{96\sqrt{3}\pi\epsilon_0 R^3} \tag{4}$$

What is very important to realize is that the physical meaning of single particle "bunch length" σ_{z_0} which describes the range of the *uncertainty* of the longitudinal position of the particle due to random quantum radiation excitations.

3 BUNCH LENGTHENING AND ENERGY SPREAD INCREASING

3.1 Potential well distortion

It is known that the mechanism for the potential well distortion which affects the bunch length, mainly due to the imaginary part of the impedance, is a static one, and the energy spread of the bunch is not affected [5]. It is useful to recall the corresponding general formulae from the potential well distortion theory, which are expressed as follows [2] [3]

$$\mathbf{R}_z^2 = 1 + \frac{C'_{PWD} I_b}{\mathbf{R}_z} \tag{5}$$

$$\mathbf{R}_\varepsilon = 1 \tag{6}$$

The author of this paper, however, would believe that eq. 5 should be modified as follows:

$$\mathbf{R}_z^2 = 1 + \frac{C_{PWD} I_b}{\mathbf{R}_z^{1.5}} \tag{7}$$

where I_b is the bunch current, $\mathbf{R}_z = \sigma_z/\sigma_{z_0}$ and $\mathbf{R}_\varepsilon = \sigma_\varepsilon/\sigma_{\varepsilon_0}$. The analytical expression of C_{PWD} and the physical reason for the modification from eq. 5 to eq. 7 are given in ref. 8.

0-7803-4376-X/98/$10.00 © 1998 IEEE

3.2 Collective random excitations

In this paper, we want to show that the resistive part of the impedance can lead to bunch energy spread increasing and bunch lengthening, and we will introduce this mechanism step by step.

• A bunch of length σ_z with N_e particles will lose a kinetic energy W over one turn, and $W = e^2 N_e^2 \mathcal{K}_{||}^{\text{tot}}(\sigma_z)$, where $\mathcal{K}_{||}^{\text{tot}}(\sigma_z)$ is the longitudinal loss factor of the machine for one turn, which depends on the bunch length σ_z.

• The position of each particle inside the bunch is totally unpredictable. No matter where the particle is, after one synchrotron oscillation period T_s, each particle has experienced all the longitudinal positions in the bunch and each particle will lose in average an amount of energy $\mathcal{U}_w = e^2 N_e \mathcal{K}_{||}^{\text{tot}}(\sigma_z)$ per turn.

• The rf accelerating cavities in the ring will compensate W for the bunch and $\mathcal{U}_w$ for each particle per turn in average.

• At the time $t = t_i$, a particle will find its longitudinal random position inside the bunch at z_i which corresponds to a synchrotron phase ϕ_i. Since the longitudinal wake potential varies with respect to the longitudinal position, a particle at one longitudinal position will lose an energy $\mathcal{U}_i$ after one turn.

• Since rf cavities provide each particle with an average energy gain $\mathcal{U}_w$ after each revolution, the net energy gain of the particle after one turn will be $\Delta E_i = \mathcal{U}_w - \mathcal{U}_i$. Apparently, if the particle is located at the very front of the bunch (denoted position 1) after one turn it will lose nothing due to the collective wake potential, however, it gets from rf cavities a gain of energy $\mathcal{U}_w$, and its corresponding $\Delta E_1 = \mathcal{U}_w$. The second characteristic position for the particle in the bunch is $\Delta E_2 = 0$ which means the energy lost due to the wake potential is exactly compensated by the rf cavities. The third characteristic case is $\Delta E_3 = -\mathcal{U}_w$ which corresponds to the longitudinal position where the particle feels the maximum wake potential. It is easy to know that $-\mathcal{U}_w \leq \Delta E_i \leq \mathcal{U}_w$. As stated above, after one synchrotron oscillation the average of ΔE_i over T_s will be zero, and ΔE_i can be reasonably written as

$$\Delta E_i = \mathcal{U}_w \sin(\Omega_s t - \phi_i) \tag{8}$$

where ϕ_i is a random variable. The time interval to have ΔE_i and ΔE_{i+1} is the revolution period T_0. Eq. 8 decribes a stationary random collective excitation process on the energy of a particle in the bunch.

Including now the synchrotron damping effect, the effect of the random kick on the particle energy can be written as

$$\Delta E_i = \mathcal{U}_w \exp\left(-\frac{t - t_i}{\tau_\varepsilon}\right) \sin(\Omega_s (t - t_i)) \tag{9}$$

Having revealed the random process, we will calculate the rms value of the corresponding energy spread. This can be done by using Campbell's theorem [9] which gives

$$\sigma_{\varepsilon,w}^2 = \frac{\mathcal{U}_w^2}{4T_0}\tau_\varepsilon \tag{10}$$

Combining the effects from the quantum radiation and the collective random excitations (both random processes are statistically independent), one gets finally the resultant energy spread

$$\begin{aligned}\sigma_\varepsilon^2 &= \sigma_{\varepsilon_0}^2 + \sigma_{\varepsilon,w}^2 \\ &= \sigma_{\varepsilon 0}^2 \left(1 + \frac{\mathcal{U}_w^2}{T_0 < \mathcal{N}_p < u_p^2 >>}\right)\end{aligned} \tag{11}$$

The bunch length connects with the bunch energy as follows

$$\begin{aligned}\sigma_z^2 &= \left(\frac{c\alpha}{\Omega_s E}\right)^2 \sigma_\varepsilon^2 \\ &= \sigma_{z_0}^2 \left(1 + \frac{\mathcal{U}_w^2}{T_0 < \mathcal{N}_p < u_p^2 >>}\right)\end{aligned} \tag{12}$$

Defining $\mathbf{R}_\iota = \sigma_\iota / \sigma_{\iota 0}$, where ι represents either the bunch length or energy spread, for an isomagnetic ring one gets

$$\mathbf{R}_\iota^2 = \left(1 + \frac{144\epsilon_0 (eRN_e \mathcal{K}_{||}^{\text{tot}}(\sigma_z)^2}{55\sqrt{3}\hbar c \gamma^7}\right) \tag{13}$$

The dependence of $\mathcal{K}_{||}^{\text{tot}}$ on the bunch length can be expressed as

$$\mathcal{K}_{||}^{\text{tot}} = \mathcal{K}_{||,0}^{\text{tot}} \left(\frac{\sigma_{z_0}}{\sigma_z}\right)^\varsigma \tag{14}$$

where $\mathcal{K}_{||,0}^{\text{tot}}$ is the longitudinal loss factor at $\sigma_z = \sigma_{z_0}$, and σ_{z_0} is the natural bunch length. If SPEAR scaling law [10] is used (for example), $\varsigma \approx 1.21$ (each machine has its own ς), and eq. 13 can be written as

$$\mathbf{R}_\iota^2 = 1 + \frac{\mathcal{C}(R_{av} R I_b \mathcal{K}_{||,0}^{\text{tot}})^2}{\gamma^7 \mathbf{R}_\iota^{2.42}} \tag{15}$$

where

$$\mathcal{C} = \frac{576\pi^2 \epsilon_0}{55\sqrt{3}\hbar c^3} \tag{16}$$

$I_b = eN_e c / 2\pi R_{av}$ and R_{av} is the average radius of the ring.

Now it is time for us to combine the effects from both potential well distortion and collective random excitations. Including eqs. 7 and 6 into eq. 15, eq. 15 ($\iota = z$) becomes

$$\mathbf{R}_z^2 = 1 + \frac{C_{PWD} I_b}{\mathbf{R}_z^{1.5}} + \frac{\mathcal{C}(R_{av} R I_b \mathcal{K}_{||,0}^{\text{tot}})^2}{\gamma^7 \mathbf{R}_z^{2.42}} \tag{17}$$

and eq. 15 ($\iota = \varepsilon$) remains

$$\mathbf{R}_\varepsilon^2 = 1 + \frac{\mathcal{C}(R_{av} R I_b \mathcal{K}_{||,0}^{\text{tot}})^2}{\gamma^7 \mathbf{R}_z^{2.42}} \tag{18}$$

What should be pointed out is that $\mathcal{C}$ is a positive number, however, C_{PWD} can be negative if the momentum compaction factor, α, is negative. The procedure to get the information about the bunch lengthening and the energy spread increasing is firstly to solve eq. 17 and find $\mathbf{R}_z(I_b)$, and then calculate $\mathbf{R}_\varepsilon(I_b)$ by putting $\mathbf{R}_z(I_b)$ into eq. 18.

When the bunch current is high enough to neglect the effect of PWD, one has $\mathbf{R}_\varepsilon \approx \mathbf{R}_z$ which means that energy spread increasing and bunch lengthening are almost correlated.

To finish this section, we point out that the third term in eq. 17 might correspond to the so-called turbulent bunch lengthening observed in the experiments.

4 COMPARISON WITH EXPERIMENTAL RESULTS

In this section we use the theory developed above to explain the experimental bunch lengthening measurement results in the storage rings of BEPC and Super-ACO. In the following, we shall fit the experimental bunch lengthening curves by eq. 17 and extract the information on the total loss factor at the natural bunch length for the corresponding machines.

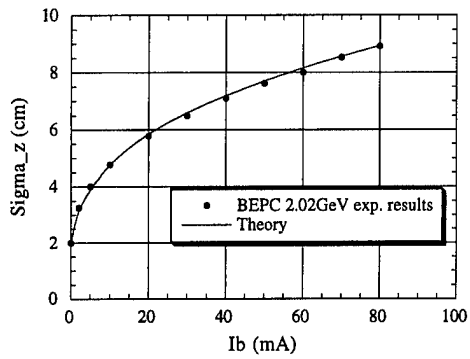

Figure 1: Comparison between BEPC ($R = 10.345$ m and $R_{av} = 38.2$ m) experimental results and the theoretical results at 2.02 GeV with σ_{z_0}=2 cm. The continuous line is the fitted curve of the theory. The dark points are the BEPC 2.02 GeV experimental results.

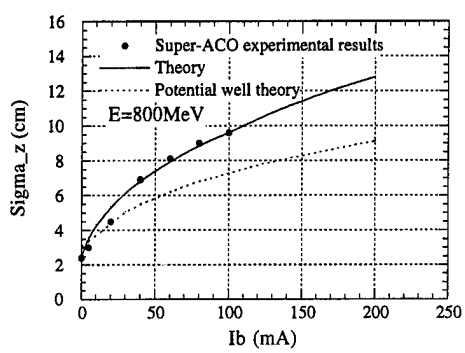

Figure 2: Comparison between Super-ACO ($R = 1.7$ m and $R_{av} = 11.5$ m) experimental results, the theoretical results and the potential well distortion theory predictions at 800 MeV with σ_{z_0}=2.4 cm. The continuous and the dotted lines are the fitted curves of the new and the potential well distortion theories, respectively. The dark points are the Super-ACO 800 MeV experimental results.

Firstly, we look at BEPC (Beijing Electron Positron Collider) [11]. Fig. 1 shows the comparison results between the new theory and the experimental results [11]. By fitting one finds $\mathcal{K}_{||,0}^{\text{tot}} = 3.82$ V/pC at $\sigma_{z_0} = 2$ cm which corresponds $\mathcal{K}_{||}^{\text{tot}} = 1.65$ V/pC at $\sigma_z = 4$ cm by using SPEAR scaling. The recent experimental result [12] shows that $\mathcal{K}_{||}^{\text{tot}} = 1.5$ V/pC at $\sigma_z = 4$ cm which agrees quite well with the theoretical result.

Secondly, Super-ACO [13] is considered and the comparison results are shown in Fig. 2. From the experimental curve one finds $\mathcal{K}_{||,0}^{\text{tot}} = 3.6$ V/pC at $\sigma_{z_0} = 2.4$ cm. The total loss factor of the machine at $\sigma_z = 3$ cm is calculated as 2.22 V/pC by using TBCI [14], and the $\mathcal{K}_{||}^{\text{tot}}$ obtained from the experimental bunch lengthening curve is 2.76 V/pC for the same bunch length by using SPEAR scaling. What should be mentioned is that the experimental results shown in Fig. 2 correspond to the case of positive momentum compaction factor $\alpha = 0.0148$.

More comparisons results can be found in ref. 15.

5 CONCLUSION

In this paper a bunch lengthening theory is established and it is demonstrated that the longitudinal resistive part impedance of the machine (loss factor) increase the bunch length and the energy spread due to collective random excitation effects. Some comparisons between experimental and theoretical results are made and the agreements are quite well.

6 ACKNOWLEDGEMENTS

I would like to thank J. Le Duff for useful discussions and critical comments.

7 REFERENCES

[1] R. Belbeoch et al., Proceedings of the national conference on particle accelerators, No. 1 (Moscow, 1968) p. 129 (in Russian).

[2] C. Pellegrini and A.M. Sessler, *Nuovo Cimento*, **3A** (1971) p. 116.

[3] J. Haissinski, *Nuovo Cimento*, **18B** (1973) p. 72.

[4] D. Boussard, CERN LabII/RF/int./75-2 (1975).

[5] A.W. Chao, "Physics of collective beam instabilities in high energy accelerators", Wiley, New York, 1993.

[6] J. Gareyte, Advances of accelerator physics and technologies, (Editor H. Schopper), World Scientific, 1993, p. 67.

[7] M. Sands, SLAC-121 (1970).

[8] J. Gao, personal note to be published.

[9] J.J. Freeman, "Principles of noise", John Wiely & Sons, Inc. p. 99.

[10] P.B. Wilson, et al., IEEE Trans. on Nucl. Sci. Vol. NS-24, No. 3, June 1977, p. 1211.

[11] Z. Guo, et al., Proceedings of PAC95, Dallas TX (1995) p. 2955.

[12] M. Tigner, Private communication, 03/04/1997.

[13] A. Nadji, et al., Proceedings of EPAC96, Barcelona (1996) p. 676.

[14] P. Brunelle, thèse, 1990.

[15] J. Gao, LAL/RT 97-01, February 1997.

THEORY OF SINGLE BUNCH TRANSVERSE COLLECTIVE INSTABILITIES IN ELECTRON STORAGE RINGS

J. Gao, Laboratoire de L'Accélérateur Linéaire, IN2P3-CNRS
et Université de Paris-Sud, 91405 Orsay cedex, France

Abstract

In this paper, concerning the fast single bunch transverse instability, it is believed that the elimination of the Landau damping is the cause of this type of instability different from the mode-coupling theory. An analytical expression for the threshold current is established.

For a storage ring collider, it is analytically proved that there exists a maximum beam-beam tune shift $\xi_{y,max}$. The analytical expression of $\xi_{y,max}$ is established.

1 INTRODUCTION

The single bunch collective effects in the transverse planes of an electron storage ring can cause fast transverse instabilities when the bunch current surpasses a distinct threshold value. In section 2, the mechanism of this instability is shown to be the elimination of the Landau damping and the corresponding analytical expression of the bunch current threshold is established. In section 3, we will show why there exist a maximum beam-beam tune shift in an electron storage ring collider, and an analytical expression for the maximum beam-beam tune shift is given.

2 SINGLE BUNCH FAST TRANSVERSE COLLECTIVE INSTABILITY

In an electron storage ring the maximum single bunch current is usually limited by a fast transverse bunch size blow-up in the vertical plane when the single bunch current passes an obvious threshold as was observed in PETRA [1] and the other machines. Nowadays, the theoretical explanation to this phenomenon is based on the so-called transverse mode coupling theory originally proposed by Kohaupt [1] and enriched by many others [2][3][4]. However, the stability criterion is very empirical and there are still some ambiguities on the description of the physical pictures. In this section we try to give another explanation to this single bunch transverse collective instability based on the principle of Landau damping.

In a real particle accelerator the mechanism of Landau damping guarantees the stability of the coherent motion of the ensemble of particles in a bunch. The mechanism of Landau damping, however, can be destroyed if the coherent oscillation frequency is shifted outside of the spectrum of the incoherent oscillation frequencies of the ensemble of particles, which is believed to be just the case for the single bunch transverse collective instability. To describe mathematically the process let's look at the vertical betatron oscillation which is more problematic than that in the horizontal plane. Ignoring the variation of β_y with s, one may write

$$y = Bcos\phi \tag{1}$$

$$y' = -\frac{B}{\beta_y}sin\phi \tag{2}$$

where $\phi = s/\beta_y$ and $y' = P_\perp/P_0$. The energy of the coherent vertical betatron oscillation is therefore expressed as

$$E_\perp = \frac{y_c}{\beta_y}E_0 \tag{3}$$

were y_c denotes the amplitude of the collective betatron oscillation and E_0 is the particle energy. The shift of the coherent betatron oscillation frequency can be calculated by using Boltzmann and Ehrenfest theorem which states that for a periodical and linear working lossless engine, the product of energy and the period time is invariant for adiabatic deformation [5], and one has

$$\frac{\Delta\nu_{y,c}}{\nu_y} = \frac{\Delta E_\perp}{E_\perp} \tag{4}$$

where $\nu_y = f_y/f_0$, f_y and f_0 are the vertical betatron and the revolution frequency, respectively. The energy variation in eq. 4 can be easily calculated by using the concept of transverse loss factor $\mathcal{K}_\perp^{tot}$ of the storage ring over one turn, and

$$\Delta E_\perp = \frac{e^2 N_e \mathcal{K}_\perp^{tot}(\sigma_z) y_c}{\nu_y} \tag{5}$$

where N_e is the particle number in the bunch and σ_z is the bunch length. Combining eqs. 3, 4, and 5, one has

$$\Delta\nu_{y,c} = -\frac{e^2 N_e \mathcal{K}_\perp^{tot}(\sigma_z) < \beta_{y,c} >}{E_0} \tag{6}$$

where β_y has been replaced by $< \beta_{y,c} >$ which is the average beta function in the rf cavity region where the transverse wakefield is more important. The dispersion of the incoherent vertical betatron oscillation frequency is expressed as

$$\sigma_{\nu_{y,inc}} = |\xi_{c,y}|\nu_y \frac{\sigma_{\varepsilon 0}\mathbf{R}_\varepsilon}{E_0} \tag{7}$$

where $\sigma_{\varepsilon 0}$ is the natural energy spread, $\mathbf{R}_\varepsilon = \sigma_\varepsilon/\sigma_{\varepsilon 0}$ and $\xi_{c,y}$ is the chromaticity in the vertical plane (usually positive to control the head-tail instability). To shift the coherent frequency totally out of the incoherent frequency spectrum, one needs

$$\Delta\nu_{y,c} = -4\sigma_{\nu_{y,inc}} \tag{8}$$

and one gets finally the instability threshold current

$$I_{b,fast}^{th} = \frac{4 f_y \sigma_{\varepsilon 0}\mathbf{R}_\varepsilon |\xi_{c,y}|}{e < \beta_{y,c} > \mathcal{K}_\perp^{tot}(\sigma_z)} \tag{9}$$

0-7803-4376-X/98 /$10.00 © 1998 IEEE

In fact $\mathbf{R}_\varepsilon$ and $\mathcal{K}_\perp^{tot}(\sigma_z)$ are the functions of I_b, eq. 9, therefore, should be solved in a consistent way. It is useful to express $\mathcal{K}_\perp^{tot}(\sigma_z)$ as $\mathcal{K}_\perp^{tot}(\sigma_z) = \mathcal{K}_{\perp,0}^{tot}/\mathbf{R}_z^\Theta$, where $\mathcal{K}_{\perp,0}^{tot}$ is the value at the natural bunch length, $\mathbf{R}_z = \sigma_z/\sigma_{z0}$, and Θ is a constant. The variations of $\mathbf{R}_\varepsilon$ and $\mathbf{R}_z$ with respect to the bunch current I_b can be obtained by solving longitudinal single bunch motion as shown in ref. 6. It is important to note that by increasing the chromaticity one can push the threshold bunch current upwards.

The threshold current from the coupling mode theory is shown as follows [3][4]

$$I_{b,coupling}^{th} = \frac{F f_s E_0}{e < \beta_{y,c} > \mathcal{K}_\perp^{tot}(\sigma_z)} \tag{10}$$

The difference between eq. 9 and eq. 10 comes from that the mode coupling theory requires $\Delta\nu_{y,c} = F\nu_s$ instead of $\Delta\nu_{y,c} = -4\sigma_{\nu_{y,inc}}$, where F is a variable depending on the bunch length.

Now we take the parameters of Super-ACO for example. Using $< \beta_{y,c} >= 5$ m, $E_0 = 800$ MeV, $\nu_y = 1.7$, $\xi_{c,y} = 1$ and $\mathcal{K}_{\perp,0}^{tot} = 303(\text{V/pC/m})/\mathbf{R}^\Theta$ with $\sigma_{z0} = 2.4$ cm and $\Theta = 0.7$ [7], it is found that $I_{b,fast}^{th} = 140$ mA as shown in Fig. 1.

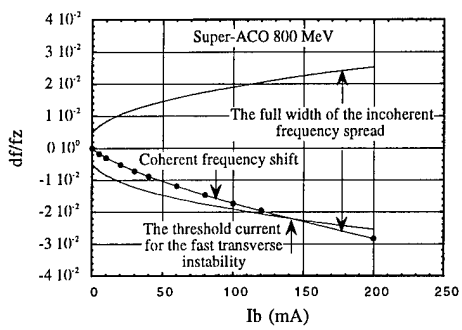

Figure 1: The fast transverse instability is caused by the elimination of the Landau damping (the coherent oscillation frequency is shifted out of the spectrum of the incoherent oscillations).

3 INCREASE OF THE TRANSVERSE BUNCH DIMENSIONS DUE TO BEAM-BEAM EFFECT AND THE MAXIMUM TUNE SHIFT

The luminosity of a circular collider can be expressed as

$$L = \frac{I_{beam}\gamma\xi_y}{2er_e\beta_y^*}\left(1 + \frac{\sigma_y^*}{\sigma_x^*}\right) \tag{11}$$

where r_e is the electron radius, β_y^* is the beta function value at the interaction point, γ is the normalized particle energy, σ_x^* and σ_y^* are the bunch transverse dimensions after the pinch effect, respectively, I_{beam} is the circulating current of one beam, and

$$\xi_y = \frac{N_e r_e \beta_y^*}{2\pi\gamma\sigma_y^*(\sigma_x^* + \sigma_y^*)} \tag{12}$$

is the vertical beam-beam tune shift. Experiments show that when the bunch current is larger than a certain threshold ξ_y will not be able to surpass a maximum value $\xi_{y,max}$. In the following we try to explain this phenomenon and give an anlytical expression for $\xi_{y,max}$.

At each interaction point particles in a bunch will be deflected transversely by the counter-rotating bunch. According to the linear theory of beam-beam dynamics [8], one knows that for two equal charge Gaussian bunches after each collision, the average beam-beam kicks of each particle in the horizontal and the vertical planes are expressed as follows

$$\delta x' = -\frac{2N_e r_e x}{\gamma\sigma_{x,+}^*(\sigma_{x,+}^* + \sigma_{y,+}^*)} \tag{13}$$

$$\delta y' = -\frac{2N_e r_e y}{\gamma\sigma_{y,+}^*(\sigma_{x,+}^* + \sigma_{y,+}^*)} \tag{14}$$

where $\sigma_{x,+}^*$ and $\sigma_{y,+}^*$ are the bunch transverse dimensions just before the interaction point. In fact, these kicks are random and they will move the zero-current equilibrium transverse beam sizes to the new values which depend on the bunch current.

Let's look first at the horizontal plane. Following the arguments in ref. [9], the betatron oscillation is described as follows

$$x = a\sqrt{\beta_x}\cos\phi \tag{15}$$

with

$$a^2 = \frac{1}{\beta_{x,s}}\{x_s^2 + (\beta_{x,s}x_s' - \frac{1}{2}\beta_{x,s}' x_s)^2\} \tag{16}$$

where the subscript s denotes an arbitrary longitudinal position. At the position s there are sudden changes for x_s and x_s' due to the synchrotron quantum radiation excitations:

$$\delta x_s = -D(s)\frac{u_p}{E_0} \tag{17}$$

$$\delta x_s' = -D_s'\frac{u_p}{E_0} \tag{18}$$

where $D(s)$ is the dispersion function and u_p is the energy of one synchrotron radiation photon. Summing all the excitations up, the natural horizontal emittance is found to be

$$\epsilon_{x0} = \frac{\tau_x Q_x}{4} \tag{19}$$

where

$$Q_x = \frac{< \mathcal{N}_p < u_p^2 > \mathcal{H}(s) >}{E_0^2} \tag{20}$$

$$\mathcal{H}(s) = \frac{1}{\beta_{x,s}}\{D(s)^2 + (\beta_{x,s}D_s' - \frac{1}{2}\beta_{x,s}' D(s))^2\} \tag{21}$$

and

$$\tau_x = \frac{2E_0}{J_x < \mathcal{P}_p >} \tag{22}$$

where J_x is the damping partition number, $\mathcal{N}_p$ is the local rate of synchrotron photon emission, and $< \mathcal{P}_p >$ is the

average synchrotron radiation power for one turn. For the vertical plane, similarly, one gets

$$\epsilon_{y0} = \frac{\tau_y Q_y}{4} \tag{23}$$

where

$$Q_y = \frac{< \mathcal{N}_p < u_p^2 > \beta_y(s) >}{2\gamma^2 E_0^2} \tag{24}$$

and

$$\tau_y = \frac{2E_0}{< \mathcal{P}_p >} \tag{25}$$

Assuming that there are N_{IP} interaction points in the machine, if one includes in eq. 18 the N_{IP} independent random kicks $\delta x'$ expressed in eq. 13 (similarly in the vertical plane), one gets the new equilibrium horizontal and vertical emittances

$$\epsilon_x = \epsilon_{x0}\left(1 - \frac{(e^2 N_e \mathcal{K}_{IP,BB,x})^2 N_{IP}\tau_x}{4T_0 E_0^2}\right)^{-1} \tag{26}$$

and

$$\epsilon_y = \epsilon_{y0}\left(1 - \frac{(e^2 N_e \mathcal{K}_{IP,BB,y})^2 N_{IP}\tau_y}{4T_0 E_0^2}\right)^{-1} \tag{27}$$

where T_0 is the revolution period, and

$$\mathcal{K}_{IP,BB,x} = \frac{\beta_x^*}{2\pi\epsilon_0\sigma_{x,+}^*(\sigma_{x+}^* + \sigma_{y,+}^*)} \tag{28}$$

$$\mathcal{K}_{IP,BB,y} = \frac{\beta_y^*}{2\pi\epsilon_0\sigma_{y,+}^*(\sigma_{x,+}^* + \sigma_{y,+}^*)} \tag{29}$$

For an isomagnetic ring, one gets

$$\epsilon_x = \epsilon_{x0}\left(1 - \frac{3\epsilon_0 R(eN_e\mathcal{K}_{IP,BB,x})^2 N_{IP}}{2m_0c^2\gamma^5 J_x}\right)^{-1} \tag{30}$$

and

$$\epsilon_y = \epsilon_{y0}\left(1 - \frac{3\epsilon_0 R(eN_e\mathcal{K}_{IP,BB,y})^2 N_{IP}}{2m_0c^2\gamma^5}\right)^{-1} \tag{31}$$

where R is the local bending radius.

For a flat bunch ($\sigma_{y,+}^* << \sigma_{x,+}^*$), from eq. 31 one knows that

$$\sigma_{x,+}^*\sigma_{y,+}^* > \left(\frac{3RN_{IP}(eN_e\beta_y^*)^2}{8\pi^2\epsilon_0 m_0 c^2\gamma^5}\right)^{1/2} \tag{32}$$

Defining

$$H = \frac{\sigma_{x,+}^*\sigma_{y,+}^*}{\sigma_x^*\sigma_y^*} \tag{33}$$

where H is a measure of the pinch effect. Keeping in mind the physics of beam-beam effect at the interaction point, one can write

$$H = \frac{H_0\sqrt{N_{IP}}}{\gamma} \tag{34}$$

Combining eqs. 12, 32 and 34 one gets finally

$$\xi_y \leq \xi_{y,max} = \frac{H_0}{2\pi\gamma}\sqrt{\frac{T_0}{\tau_y}} \tag{35}$$

or, for an isomagnetic case

$$\xi_y \leq \xi_{y,max} = H_0\sqrt{\frac{\gamma r_e}{6\pi R}} \tag{36}$$

We have therefore found the analytical expression for $\xi_{y,max}$ and explained the well-known phenomenon in circular colliders that $\xi_y \leq \xi_{y,max}$. From eq. 35 it is clear that for fixed γ and T_0, $\xi_{y,max} \propto 1/\sqrt{\tau_y}$. The experimentally reached maximum H_0 is found to be about $\frac{1}{6} \times 10^6$. In fact, eqs. 35 and 36 are valid for the round beam also.

By using eqs. 35 or 36, $\xi_{y,max}$ can be calculated instead of assumed when a new machine is designed. Taking Beijing Tau-Charm Factory parameters for example [10], one finds $\xi_{y,max} = 0.043$ with $R = 8.58$ m and $\gamma = 3914$ (2GeV).

4 CONCLUSION

A new current threshold expression for the fast transverse instability is established based on the concept of the elimination of the Landau damping which shows the dependance of the threshold current on the chromaticity. For a storage ring collider, it has been proved analytically that there exsits a maximum value for the beam-beam tune shift, and an analytical formaule is given for the $\xi_{y,max}$.

5 ACKNOWLEDGEMENTS

The author thanks J. Le Duff for the useful discussions.

6 REFERENCES

[1] R.D. Kohaupt, "Transverse instabilities in PETRA", 11th Int. Conf. on High Energy Accelerators, CERN, 1980, p. 562.

[2] K. Satoh and Y. Chin, "Transverse mode coupling in a bunched beam", Nucl. Instr. and Meth. 207 (1983) p. 309.

[3] B. Zotter, "Mode-coupling or "transverse turbulence" of electron or positron bunches in the SPS and LEP", LEP note 363 (1982).

[4] B. Zotter, "Current limitations in LEP due to vacuum chamber bellows", LEP note 528 (1985).

[5] H. Klein, "Basic concept I", CERN 92-03 (1992) p. 97.

[6] J. Gao, "Bunch lengthening and energy spread increasing in electron storage rings", These proceedings.

[7] P. Brunelle, "Etude théorique et experimentale des faisceaux dans l'anneau VUV SUPER-ACO", thèse, 1990.

[8] E. Keil, "Beam-beam dynamics", CERN 95-06, p. 539.

[9] M. Sands, "The physics of electron storage rings, an introduction" SLAC-121 (1970).

[10] BTCF group, "Feasibility study report on Beijing Tau-Charm Factory", IHEP-BTCF report 01, Dec. 1995.

THEORETICAL INVESTIGATION ON MULTIBUNCH INSTABILITIES IN ELECTRON STORAGE RINGS AND LINEAR ACCELERATORS

J. Gao, Laboratoire de L'Accélérateur Linéaire, IN2P3-CNRS
et Université de Paris-Sud, 91405 Orsay cedex, France

Abstract

In this paper we establish simple analytical criteria for the loaded quality factors of the dipole modes in the accelerating rf structures to prevent the multibunch instabilities in electron storage rings and linear accelerators.

1 INTRODUCTION

In the modern circular and future linear colliders, the option of multibunch operation mode has to be adopted to guarantee the required luminosity. Due to the long range transverse wake potentials, the transverse motion of a bunch in a bunch train can be influenced by the precedent bunches. If the long range transverse wake potentials are not properly controlled multibunch instabilities can occur and the luminosity will be degraded. The classical treatment of the multibunch instabilities can be found in ref. 1 for example. In this paper we try to treat the problem in a different way. We assume that each bunch is represented by a point charge and the detailed discussion about the single bunch longitudinal and transversal instabilities in electron storage rings can be found in refs. 2 and 3.

A charged particle executes betatron oscillation in circular and linear accelerators can be regarded as an independent damped linear oscillator if there is no long range transverse wake potentials permitting the particle "talking" to its neighbours. The mechanisms of damping come from the synchrotron radiation in electron storage rings and the adiabatic acceleration in linear accelerators, respectively. The quality factor of this oscillator is related to the damping time and the betatron oscillation frequency. When the long range wake potentials are strong enough the particles in the bunch train will begin to be coupled from one to another and the independent oscillators become a chain of coupled oscillators with losses, and the betatron oscillation energies of the particles upstream can be transmitted to those of the particles downstream, known as multibunch instabilities. The physical picture described above is similar to that of a coupled rf cavity chain. Now, let's look at a chain of coupled rf cavities with losses which has been studied in detail in ref. 4, one finds that to prevent the coupling between cavities the criterion $K_c Q < 2$ should be satisfied, where K_c is the coupling coefficient in the dispersion curve and Q is the quality factor of the corresponding mode. By analogy, one can find the criteria under which the multibunch instabilities can be prevented in storage rings and linear accelerators.

2 MULTIBUNCH INSTABILITIES IN ELECTRON STORAGE RINGS

Particles in a storage ring execute betatron oscillations. If we neglect the effect of synchrotron radiation excitation and the long range wake potentials, the betatron motion of each bunch can be simplified as a damped oscillator expressed as

$$y = A\cos\left(\omega_y \frac{s}{c}\right)\exp\left(-\frac{\omega_y}{2Q_{y,r}}\left(\frac{s}{c}\right)\right) \tag{1}$$

where y denotes the transverse deviation in horizontal plane x or vertical plane z from the design orbit, ω_y is the angular betatron frequency, and $Q_{y,r}$ (the subscript r denotes the storage ring case) is the quality factor of the oscillator expressed

$$Q_{y,r} = \frac{\omega_y E_0}{<\mathcal{P}_0> J_y} \tag{2}$$

where $<\mathcal{P}_0>$ is the average synchrotron radiation power for one turn, E_0 is the particle energy, J_y is the radiation damping partition number with $J_{y=x} = 1 - \mathcal{D}$ and $J_{y=z} = 1$ $(-2 < \mathcal{D} < 1)$. In reality, however, charged particles interact with the environment and produce long range wake potentials which make the independent oscillating oscillator become a coupled oscillator chain. The coupling coefficient $K_{c,r}$ between the two successive bunches can be calculated from the coherent frequency change due to the long range wake potential similar to the single bunch case [3]

$$\left|\frac{\Delta\nu_{y,c}}{\nu_y}\right| = \frac{e^2 N_e W'_\perp(s_b)\overline{\beta_{y,c}}}{\nu_y E_0} \tag{3}$$

where $W'_\perp(s_b)$ (V/C/m) is the long range dipole wake potential of one turn and of unit transverse displacement, s_b is the distance between two successive bunches, N_e is the particle population in the bunch, $\overline{\beta_{y,c}}$ is the average beta function at the position of the rf cavities, and ν_y is the tune number. By analogy with a coupled rf cavity chain, one finds the coupling coefficient expressed as follows

$$K_{c,r} = 2\left|\frac{\Delta\nu_{y,c}}{\nu_y}\right| \tag{4}$$

According ref. 4, one knows that under the condition

$$K_{c,r} Q_{y,r} < 2 \tag{5}$$

there will be no coupling between two successive oscillators. From eqs. 2 and 4, one finds

$$W'_\perp < \frac{<\mathcal{P}_0> J_y}{2\pi f_0 e^2 N_e \overline{\beta_{y,c}}} \tag{6}$$

0-7803-4376-X/98 /$10.00 © 1998 IEEE

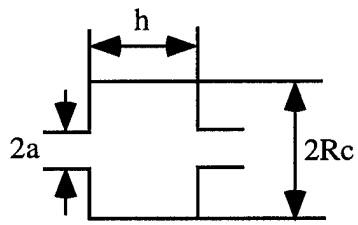

Figure 1: A single rf cavity.

where f_0 is the revolution frequency. For an isomagnetic ring

$$W'_{\perp} < \frac{\gamma^4 J_y}{6\pi\epsilon_0 \rho N_e \overline{\beta_{y,c}}} \tag{7}$$

where ρ is the local bending radius and γ is the normalized particle energy. In a storage ring the accelerating rf cavities are the main components which produce long range wake potentials (narrow band impedance). In the following one considers only the TM_{110} mode in the accelerating rf cavities since $W'_{\perp}(s_b) \approx W'_{\perp,110}(s_b)$ for the long range wake potential. The TM_{110} mode wake potential can be expressed as

$$W'_{\perp,110} = N_c h \frac{2cK_1}{\omega_{rf,1} a^2} \sin(\omega_{rf,1}\frac{s_b}{c}) \times$$

$$\exp\left(-\frac{\omega_{rf,1}}{2Q_{1,r}}\left(\frac{s_b}{c}\right)\right) \exp\left(-\frac{\omega_{rf,1}^2 \sigma_z^2}{2c^2}\right) \tag{8}$$

where N_c is the number of the cavities in the ring, h is the inner length of the cavity, σ_z is the rms bunch length (σ_z is used to calculate the transverse wake potential and the point charge assumption is still valid), $\omega_{rf,1}$ and $Q_{1,r}$ are the angular frequency and the loaded quality factor of the dipole mode, respectively. According to ref. 5, K_1 in eq. 8 corresponding to a single cavity can be expressed analytically as follows

$$K_1 = \frac{J_1^2\left(\frac{u_{11}}{R_c}a\right)}{\epsilon_0 \pi R_c^2 J_2^2(u_{11})} S(x_1)^2 \tag{9}$$

$$S(x) = \frac{\sin x}{x} \tag{10}$$

$$x_1 = \frac{h u_{11}}{2R_c} \tag{11}$$

$$\omega_{rf,1} \approx \frac{c u_{11}}{R_c} \tag{12}$$

where R_c is the cavity radius, a is the iris radius as shown in Fig. 1, and $u_{11} = 3.832$ is the first root of the first order Bessel function. $\omega_{rf,1}$ in eq. 12 can be rather precisely determined by using the analytical formulae from perturbation methods [6][7]. Being pessimistic, we assume $\sin(\omega_{rf,1}\frac{s_b}{c}) = 1$ and find consequently from eq. 7 that

$$\exp\left(-\frac{\omega_{rf,1}}{2Q_{1,r}}\left(\frac{s_b}{c}\right)\right) <$$

$$\frac{\gamma^4 \omega_{rf,1} a^2 J_y}{12\pi c \epsilon_0 \rho N_c h N_e K_1 \overline{\beta_{y,c}} \exp\left(-\frac{\omega_{rf,1}^2 \sigma_z^2}{2c^2}\right)} \tag{13}$$

and

$$Q_{1,r} < \frac{u_{11} s_b}{2R_c ln\left(\frac{12\pi\epsilon_0 \rho R_c N_c h N_e K_1 \overline{\beta_{y,c}} \exp\left(-\frac{u_{11}^2 \sigma_z^2}{2R^2}\right)}{\gamma^4 u_{11} a^2 J_y}\right)} \tag{14}$$

To reach the required loaded $Q_{1,r}$, waveguide type higher order mode couplers can be installed on the accelerating rf cavities and the dimensions of the coupling apertures can be determined analytically as shown in ref. 8. From eq. 14 one can find the condition under which the dipole mode need not to be damped. This condition is simply that $Q_{1,r} \to \infty$ (this condition is somewhat strong but very useful since it doesn't depend on the specific unloaded dipole mode quality factor) when N_e satisfies

$$N_e \leq N_e^* = \frac{\gamma^4 u_{11} a^2 J_y}{12\pi\epsilon_0 \rho R_c N_c h K_1 \overline{\beta_{y,c}} \exp\left(-\frac{u_{11}^2 \sigma_z^2}{2R^2}\right)} \tag{15}$$

Taking Beijing Tau-Charm Factory (BTCF) parameters for example, from eq. 14 one gets $Q_{1,r} = 99$ with $s_b = 12$ m, $R_c = 0.224$ m, $h = 0.22$ m, $a = 0.044$ m, $K_1 = 1.4 \times 10^{11}$ (V/C/m), $N_c = 12$, $N_e = 1.5 \times 10^{11}$, $\overline{\beta_{y,c}} = 10$ m, $\sigma_z = 0.01$ m, $J_{y=z} = 1$, $\rho = 8.58$ m, and $E_0 = 2$ GeV. This result justifies what has been found in ref. 10.

3 MULTIBUNCH INSTABILITIES IN LINEAR ACCELERATORS

In a linear accelerator the physical picture is a little bit different from that in a storage ring. The betatron motion can still be written as that in eq. 1, the quality factor, however, is expressed as

$$Q_{y,L} = \frac{\omega_y E_0}{ceE_z} \tag{16}$$

where E_z is the accelerating gradient and the subscript L in this section denotes linear accelerator case. The damping effect is due to the fact that a particle is accelerated continuously and the betatron oscillation is adiabatically damped [9]. The relative coherent betatron oscillation frequency variation due to the long range transverse wakefield is

$$\left|\frac{\Delta\omega_{y,c}}{\omega_y}\right| = \frac{2\pi e^2 N_e c W'_{\perp,L}(s_b)\overline{\beta_y}}{\omega_y E_0} \tag{17}$$

where $W'_{\perp,L}(s_b)$ (V/C/m^2) is the long range transverse wakefield strength of unit transverse displacement and $\overline{\beta_y}$ is the average beta function value in the linac. In the following one considers only the TM_{110} mode in the accelerating rf structures since $W'_{\perp,L}(s_b) \approx W'_{\perp,L,1}(s_b)$ for the long range wakefield, where $W'_{\perp,L,110}(s_b)$ is the TM_{110} wakefield expressed as

$$W'_{\perp,L,110} = \frac{2cK_{1,L}}{\omega_{rf,1,L} a^2} \sin(\omega_{rf,1,L}\frac{s_b}{c}) \times$$

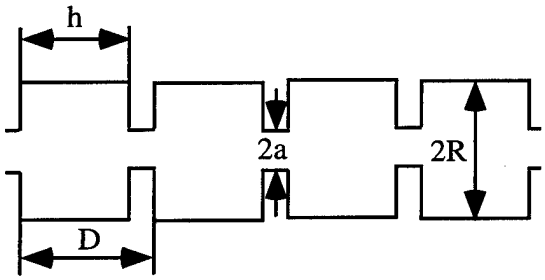

Figure 2: A disk-loaded accelerating structure.

$$\exp\left(-\frac{\omega_{rf,1,L}}{2Q_{1,L}}\left(\frac{s_b}{c}\right)\right)\exp\left(-\frac{\omega_{rf,1,L}^2\sigma_z^2}{2c^2}\right)F(s_b) \quad (18)$$

where $\omega_{rf,1,L}$ and $Q_{1,L}$ are the synchronous frequency and the loaded quality factor of the TM_{110} mode passband, respectively, and $F(s)$ is the wakefield reduction function comes from the detuning effect (for a constant impedance accelerating structure $F \equiv 1$). According to ref. 5, one knows that

$$K_{1,L} = \frac{hJ_1^2\left(\frac{u_{11}}{R}a\right)}{\epsilon_0\pi DR^2J_2^2(u_{11})}S(x_{1,L})^2 \quad (19)$$

$$x_{1,L} = \frac{hu_{11}}{2R} \quad (20)$$

$$\omega_{rf,1,L} \approx \frac{cu_{11}}{R} \quad (21)$$

where D is the period length of the accelerating structure, h is the inner cavity length, a and R are the iris and the cavity radius, respectively, as shown in Fig. 2. Knowing

$$K_{c,L} = 2\left|\frac{\Delta\omega_{y,c}}{\omega_y}\right| \quad (22)$$

and letting $Q_{y,L}K_{c,L} < 2$, one finds

$$W'_{\perp,L,1} < \frac{E_z}{2\pi eN_e\overline{\beta_y}} \quad (23)$$

Taking $\sin(\omega_{rf,1,L}\frac{s_b}{c}) = 1$ for the pessimistic case, one finds

$$\exp\left(-\frac{\omega_{rf,1,L}}{2Q_{1,L}}\left(\frac{s_b}{c}\right)\right) < \frac{E_z\omega_{rf,1,L}a^2}{4\pi ceN_eRK_{1,L}\overline{\beta_y}\exp\left(-\frac{\omega_{rf,1,L}^2\sigma_z^2}{2c^2}\right)F(s_b)} \quad (24)$$

and

$$Q_{1,L} < \frac{u_{11}s_b}{2Rln\left(\frac{4\pi eN_eRK_{1,L}\overline{\beta_y}\exp\left(-\frac{u_{11}^2\sigma_z^2}{2R^2}\right)F(s_b)}{E_zu_{11}a^2}\right)} \quad (25)$$

Similar to the storage ring case, one gets the condition under which no higher order mode coupler is needed

$$N_e \le N_e^* = \frac{E_zu_{11}a^2}{4\pi eRK_{1,L}\overline{\beta_y}\exp\left(-\frac{u_{11}^2\sigma_z^2}{2R^2}\right)F(s_b)} \quad (26)$$

Here we give an example of an ideal detuned S-band linear accelerating structure. From eq. 25 one finds $Q_{1,L}$=2740 with $s_b = 5$ m, $R = 0.04$ m, $h = 0.0292$ m, $D = 0.035$ m, $a = 0.01$ m, $K_{1,L} = 10\times10^{12}$ (V/C/m), $N_e = 2\times10^{10}$, $\overline{\beta_y} = 85$ m, $\sigma_z = 0.005$ m, $F(s_b)$=0.0065, and $E_z = 17$ MV/m. If a constant impedance structure is used then $Q_{1,L}$=187 for the the same set of parameters.

4 CONCLUSION

In this paper we give simple criteria to determine the loaded quality factors of the dipole modes in the accelerating rf structures which are responsible for the multibunch instabilities in electron storage rings and linear accelerators. The relation between the beam and the machine parameters are well established, and the analytical criteria can be served as scaling laws to optimize the machine performance.

5 REFERENCES

[1] A. Chao, "Physics of collective beam instabilities in high energy accelerators", John Wiley & Sons, Inc. 1993.

[2] J. Gao, "Bunch lengthening and energy spread increasing in electron storage rings", these Proceedings.

[3] J. Gao, "Theory of single bunch transverse collective instabilities in electron storage rings", these Proceedings.

[4] J. Gao, "The criterion for the coupling states between cavities with losses", *Nucl. Instr. and Meth.* **A325** (1995) 661-662.

[5] J. Gao, "Analytical formulae and the scaling laws for the loss factors and the wakefields in disk-loaded periodic structures", *Nucl. Instr. and Meth.* **A381** (1996) 174-177.

[6] J. Gao, "Analytical formulae for the frequency changes due to openning apertures on cavity walls", *Nucl. Instr. and Meth.* **A311** (1992) 437.

[7] J. Gao, "Analytical approach and scaling laws in the design of disk-loaded travelling wave accelerating structures", *Particle Accelerators*, **Vol. 43(4)** (1994) pp. 235-257.

[8] J. Gao, "Analytical researches on the accelerating structures, wakefields, and beam dynamics for future linear colliders", LAL 96-45, May 1996, memoir for the habilitation to direct researches, Université de Paris-Sud, Centre d'Orsay, p. 90.

[9] H. Wiedemann, "Particle Accelerator Physics I", Springer-Verlag, 1993, p. 61.

[10] BTCF group, "Feasibility study report on Beijing Tau-Charm Factory", IHEP-BTCF report 01, December 1995.

RECENT EXPERIMENTAL EVIDENCE FOR THE LOS ALAMOS PROTON STORAGE RING BEAM INSTABILITY

M.A. Plum, D.H. Fitzgerald, D. Johnson, J. Langenbrunner, R.J. Macek, F. Merrill, P. Morton, B. Prichard, O. Sander, M. Shulze, H.A. Thiessen, T.S. Wang, C.A. Wilkinson,
Los Alamos National Laboratory, Los Alamos, NM 87545

Abstract

The peak intensity of the PSR is limited by a fast transverse instability. In 1996 we started a project to upgrade the PSR to 200 μA at 30 Hz, which requires operation above the instability threshold achieved with our present rf system. We have, therefore, resumed our experimental program to understand and control the instability. In this paper we will present our latest data.

1 INTRODUCTION

A fast transverse instability has been observed [1] in the Los Alamos Proton Storage Ring (PSR) when the injected beam intensity reaches more than about 2 x 10^{13} protons per pulse. In the present operating intensity of the PSR (70 μA average @ 20 Hz), the instability is controlled by injecting with a notch or gap in the beam bunch greater than 90 ns and by applying sufficient rf buncher voltage (~7 kV with ramping). However, with our program to upgrade the PSR to 200 μA average at 30 Hz, we must improve our understanding of the cause and control of the instability to assure the success of the upgrade. Also, the neutron-scattering community is designing the next-generation accelerator-driven neutron spallation sources. These new machines may exhibit the same instability seen at PSR because they will have peak proton intensities greater than 10^{14} protons per pulse.

Experimental results indicate that electrons trapped within the proton beam most likely drive the PSR instability (e-p instability). In the e-p instability, coupled oscillations of low energy electrons and beam protons develop when electrons are trapped and oscillate in the potential well of the proton beam. In recent experiments we have measured the relative signal strength in the betatron sidebands, the effects of beam in the gap, the effects of clearing electrodes, and tune shift as a function of beam intensity. We have also explored operating at a higher vertical betatron tune.

The PSR is a fast-cycling high-current storage ring designed to accumulate beam over a macropulse (typically about 600 μs) from the Los Alamos Neutron Science Center (LANSCE) linac by multi-turn injection and to compress that beam into a short single-turn extracted pulse (~0.25 μs), which drives the short-pulse neutron spallation source. The beam storage time is typically less than 10 μs. Important parameters include a kinetic energy of 797 MeV, circumference of 90.1 m, revolution frequency of 2.8 MHz, and betatron tunes of $\nu_h \approx 3.17$ and $\nu_v \approx 2.14$.

2 BETATRON SIDEBANDS

We have measured the signal strength in the betatron sidebands by digitizing beam position monitor data and computing fast Fourier transforms. We used both a short stripline beam position monitor with peak sensitivity at about 400 MHz, and a capacitive beam position monitor with a frequency response up to about 100 MHz. The combination of these two pickups allows us to measure a broad range of frequencies. The usual method of viewing sidebands with a spectrum analyzer is not very useful at the PSR because the beam lifetime is only a few milliseconds due to beam loss incurred from the continual passage of the stored beam through the stripper foil. Beam conditions also vary slightly from pulse to pulse, so it is best to acquire all the data in a single pulse. We digitize the signals at 1 GS/s for up to 2 million samples, and analyze the data off line.

Our results show that at the onset of the instability the signal power grows in the lower (slow wave) sidebands, which is typical of many instabilities. As shown in Fig. 1, the power first appears at about 175 MHz, then begins to spread out to the lower sidebands at higher and lower frequencies. For the e-p instability, we expect [1] the signal power to appear at frequency

$$f = \frac{1}{2\pi}\sqrt{\frac{2Nr_e c^2(1-\eta_e)}{\pi b(a+b)R}}$$

where η_e is the neutralization factor, N is the number of protons, r_e is the classical electron radius, c is the speed of light, a and b are the elliptical beam dimensions, and R is the machine radius. At typical PSR parameters (doubling the average N to take into account the peak bunch density), f = 160 MHz.

One test of the e-p instability is to measure the frequency dependence of the signal power as a function of the beam intensity. It should scale as the square root of the number of protons in the ring. We have done this

0-7803-4376-X/98 /$10.00 © 1998 IEEE

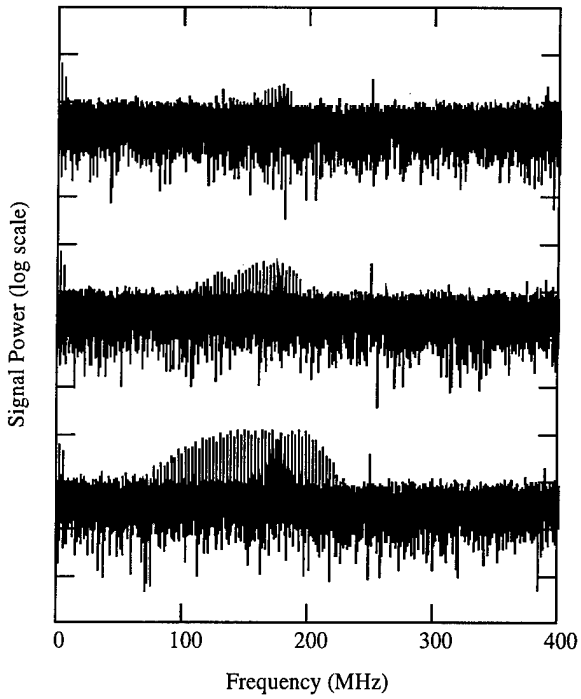

Fig. 1. Sideband power growing in time. The middle spectrum is 60 μs after the top spectrum, and the bottom is 160 μs after the top. All three spectra are from a single beam pulse.

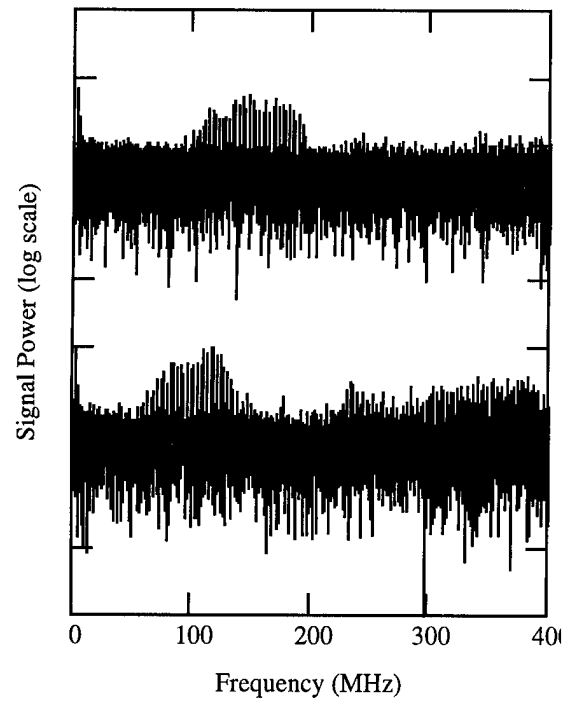

Fig. 2. The signal power at half intensity peaks at lower frequency. The intensity of the upper spectrum is twice that of the lower spectrum. The beam conditions are the same except for the beam intensity and the buncher voltage.

experiment, and we found that decreasing the number of protons by a factor of two (and lowering the buncher voltage to keep the beam unstable) shifts the signal power from about 150 MHz to about 100 MHz. This is almost exactly what one would expect (150 MHz / $\sqrt{2}$ = 106 MHz). Examples of the spectra for the two cases are shown in Fig. 2.

3 VERTICAL BETATRON TUNE

The vertical betatron tune setting is another "dial" that we have found to affect the instability threshold. There is a significant increase in the threshold when the tune is increased by an integer, (i.e., from ~2.14 to ~3.14). The mechanism for this effect might be Landau damping because of the increase in chromatic tune spread at higher tunes. Further evaluation is needed regarding the exploitation of a higher vertical tune. The impact of changes needed for higher-tune operation also needs more study. For example, it may require increased performance from the bump magnets that are part of the direct H^- injection upgrade, and it will change the Twiss parameters of the beam in the extraction line.

Recent tests of operating the PSR at the higher tune show an increase in the instability threshold of about 50%. The accumulation and storage beam losses are roughly twice the normal losses, and beam losses in the transport line to the spallation target are about the same as the normal losses. The higher accumulation and storage losses are consistent with model calculations, which show that the losses are primarily due to increased passages of the circulating beam through the stripper foil, due to the change in lattice parameters at the stripper foil location. We will be able to correct for the latter effect after our upgrade to direct H^- injection (in 1998).

4 BEAM IN THE GAP

Most models of the e-p instability require a mechanism for trapping electrons. In the PSR, if the gap between the head and the tail of the bunch is perfectly clear, then as the gap circulates around the circumference of the machine, any electrons in the beam pipe would self-repel and be lost to the beam pipe walls, thus clearing any electrons. However, if there is just a small amount of beam in the gap, electrons could be trapped.

We have recently conducted experiments designed to purposely inject beam into the gap and measure the effect on the instability threshold. Beam was injected into the gap by manipulating the chopper in the low energy transport area of the linac. By inhibiting the chopper that normally creates a 250-ns-on – 107-ns-off pattern for thousands of pulses, we injected beam for a full 357 ns for just a small number of pulses. We found that injecting beam into the gap significantly lowered

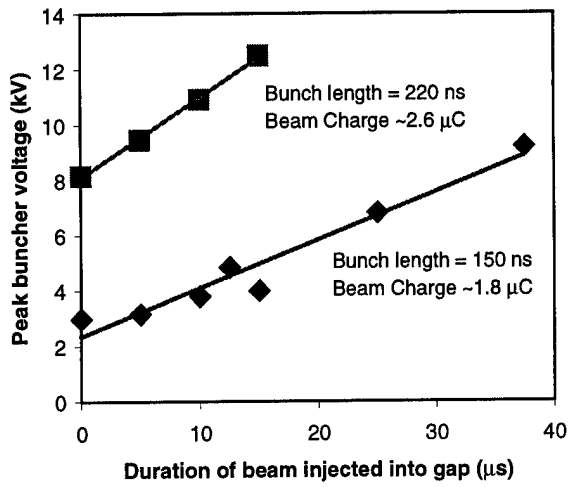

Fig. 3. The instability threshold is decreased (more buncher voltage is required) when beam is injected into the gap. The straight lines are linear fits to the data.

the instability threshold. Our data is shown in Fig. 3. We see from the figure a linear dependence between the threshold and the beam in the gap.

We also measured the beam in the gap by firing the extraction kickers early and extracting any beam that may be in the gap to a current transformer in the extraction line. Using this technique, we conclude that without purposely injecting beam in the gap there is about 15 mA in the gap by the end of the injection cycle for normal operating intensities.

5 CLEARING ELECTRODES

Clearing electrodes have been tried in PSR with limited success in raising the threshold for the PSR instability. During the 1996-97 extended maintenance period we installed small clearing electrodes in sections 1, 2, and 5 to add to previously-installed electrodes in sections 0, 3, and 4. By reconfiguring as clearing electrodes the extraction kicker electrodes in sections 7 and 8, we can bias electrodes of various sizes in 8 out of the 10 straight sections in PSR. Recent experiments using these electrodes have not shown a reproducible effect on the instability threshold.

It is difficult to estimate in detail how much the clearing electrodes suppress the number or density of electrons that are trapped (it is the trapped electrons that would cause the e-p instability – not the ones that are immediately lost), thus making it difficult to form an expectation for the effectiveness of the clearing electrodes. It can be argued that because we have not used clearing electrodes in all sections of the ring we may have missed a pocket that is effective in causing the instability. We plan to continue to study these and other measures for suppressing electron production and trapping. One promising avenue may be low secondary emission vacuum chamber coatings such as TiN.

6 COHERENT TUNE SHIFT

The simple application of the Laslett tune shift formula predicts a large (~0.1) tune shift for the PSR that could result in shifting the tune onto the integer resonance. This scenario has been proposed as a possible explanation of the PSR instability. To determine the importance of tune shift we have measured it as a function of beam intensity by kicking [2] the beam with short (~300 ns) pulses in the vertical plane, and counting the number of coherent betatron oscillations for several hundred microseconds. Our results are shown in Fig. 4.

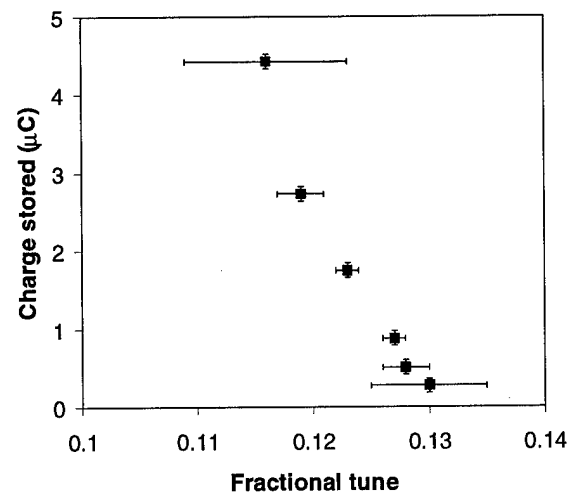

Fig. 4. Tune shift as a function of beam intensity.

We see that at our present operating intensity (3.5 μC), the tune shift is about 0.012. When we complete our upgrade to 200 μA at 30 Hz (6.67 μC), the tune shift will be about 0.023. The data shown in Fig. 4 is our first attempt at systematically measuring tune shifts. In future development periods, we hope to improve the accuracy of our measurements.

7 SUMMARY

Understanding and controlling the PSR beam instability has recently taken on new importance due to design considerations for our upgrade plans and for the next-generation neutron spallation sources. We have recently made a number of new measurements to characterize the instability. Our results add support to the hypothesis that we have an e-p instability. However, more work is needed to understand the electron-creation process and how to control it.

REFERENCES

[1] D. Neuffer et. al., Nucl. Inst. and Meth. A321 (1992) 1-12.
[2] T.W. Hardek and H.A. Thiessen, 1991 IEEE Part. Acc. Conf. (1991) 866.

INCREASE OF THE TRANSVERSE STRONG HEAD-TAIL STABILITY THRESHOLD BY AN ALTERNATING CHROMATICITY *

Wen-Hao Cheng[1], Andrew M. Sessler[2], and Jonathan S. Wurtele[1,2]
[1]Department of Physics, University of California, Berkeley
Berkeley, California 94720
[2]Lawrence Berkeley National Laboratory
Berkeley, California 94720

Abstract

It has been shown that [1], the transverse head-tail instability can be suppressed by modulating the chromaticity over a synchrotron period. In this work, we demonstrate that the threshold of the strong head-tail instability can be significantly increased by the alternating chromaticity (AC). We present results of multi-particle simulation and a new criterion for the SHT instability.

1 INTRODUCTION

The transverse collective beam instability induced by the coupling impedances in a storage ring has two categories: head-tail (HT) and strong head-tail (SHT) instabilities [2]. The HT instability is generated by the chromaticity in a ring, and has no stability threshold. The transverse SHT instability (also known as the transverse microwave instability) occurs when the betatron tune shift is larger than the synchrotron tune, and limits the current carrying capacity in a storage ring. In a previous work [1], we analyzed a new method for suppression of the HT instability by means of variation of the chromaticity over a synchrotron period. Both analytical and numerical studies suggest that a threshold can be developed, and it can be increased to a value larger than the standard SHT stability threshold. The underlying physical mechanisms of the damping scheme are rotation of the head-tail phase (such that the chromatic effect causing the instability is cancelled out in a synchrotron period) and Landau damping (due to the incoherent betatron tune spread generated by the alternating chromaticity.) In this paper, we demonstrate that the AC scheme not only provides damping for the HT instability, but also increases the threshold of the SHT instability. Going beyond the discussions provided in Ref. [1], we provide more simulaton results, and a new approximate SHT stability criterion.

2 DAMPING MECHANISMS

The transverse chromaticity is defined as

$$\xi = \frac{\Delta\omega_\beta/\omega_{\beta 0}}{\delta}, \tag{1}$$

where $\omega_{\beta 0}$ is the betatron angular frequency of the on-momentum particle, and $\delta = \triangle p/p$ is the relative momentum difference. With the AC scheme, the chromaticity is assumed to vary as

$$\xi(s) = \xi_0 + \xi_1 \sin\phi(s), \tag{2}$$

which is a function of "time" s, where s measures the distance around the ring, $\phi(s) = \omega_s s/c$, ω_s is the synchrotron angular frequency, and ξ_0 is the constant (DC) chromaticity. It is well-known that [2], the DC part of chromaticity engenders the HT instability. The AC part is introduced to provide an incoherent tune spread that suppresses the coherent instability without causing additional instabilities [1]. This incoherent chromatic tune spread can be estimated as

$$\sigma_\nu \approx \nu_{\beta 0}\xi_1\sqrt{\langle\delta^2\sin^2\phi\rangle} = \sqrt{\frac{3}{8}}\nu_{\beta 0}\xi_1\sigma_\delta = \sqrt{\frac{3}{8}}\nu_s\chi_1, \tag{3}$$

for a Gaussian beam, where $\nu_{\beta 0} = \omega_{\beta 0}/\omega_0$, ω_0 is the revolution angular frequency, $\sigma_\delta = (\omega_s/c\eta)\sigma_z$, σ_z is the rms bunch length,

$$z = r_z\cos\phi, \quad \delta = (\omega_s/c\eta)r_z\sin\phi, \tag{4}$$

(r_z, ϕ) are the action-angle variables in the longitudinal phase space, the bracket $\langle\rangle$ means a longitudinal phase-space average, and $\chi_{(0,1)} = \omega_{\beta 0}\xi_{(0,1)}\sigma_z/c\eta$ is the DC(AC) phase shift between head and tail of a bunch. The AC incoherent tune spread contributes to Landau damping and decoherence. Unlike its DC counterpart, the AC part of the chromaticity deos not lead to HT instabilities [1]. It is simply because of an otherwise accumulating chromatic effect during the synchrotron oscillation is cancelled out if the sign of the chromaticity is reversed within a synchrotron period. As the alternating chromaticity contributes to Landau damping without inducing instabilities, one may use an AC amplitude as large as possible (within the tolerance of dynamic aperture reduction) to push up the SHT stability threshold, so as to achieve a higher bunch current in a storage ring.

In short, the underlying mechanisms for the AC shceme are: Landau damping and rotation of the head-tail phase.

3 TOLERANCE

Here, we need to note that, it is known [3] that the chromaticity (DC part) could prevent the transverse modes from

* Work supported by the U.S. Department of Energy under contract No. EDDEFG-03-95ER-40936 and DE-AC03-76SF00098

coupling (which the mode-coupling results in the SHT instability) until a higher current limit is reached, if ξ_0 is large enough. However, the HT instability occurs when $\xi_0 \neq 0$, and the the emittance growth could be unacceptable. By using the AC scheme, there is no HT instability. The only foreseeable limitaion would be the reduction of dynamic aperture due to resonances. As the damping of the HT instability (when $\chi_0 \neq 0$) by the AC scheme has been well studied [1], we focus on the effect of a pure AC scheme, i.e., $\chi_0 = 0$, in the following study.

According to Eq. (1), the normalized amplitude of variation of the incoherent betatron tune due to ξ_1 is

$$\left|\frac{\Delta\nu_\beta}{\nu_{\beta 0}}\right| = |\xi_1\delta| \approx \xi_1\sigma_\delta = \frac{\nu_s}{\nu_{\beta 0}}\chi_1. \quad (5)$$

In most applications, the synchrotron tune is much smaller than the betatron tune. Typically, $\nu_s/\nu_{\beta 0} \approx 10^{-4} \sim 10^{-3}$. Assuming a lattice can tolerate 0.2% variation of $\Delta\nu_\beta/\nu_{\beta 0}$, and if $\nu_s/\nu_{\beta 0} = 10^{-4}$, then the maximum AC amplitude one can employ is $\chi_1 = 20$. A larger tolerance of dynamic aperture reduction on $|\Delta\nu_\beta/\nu_{\beta 0}|$ and a smaller value of $\nu_s/\nu_{\beta 0}$ would allow a larger χ_1, which would in turn allow a higher SHT stability limit (as will be shown.)

4 NEW APPROXIMATE SHT STABILITY CRITERION

Let's now define a dimensionless parameter

$$\Upsilon = \Delta\nu/\nu_s, \quad (6)$$

which measures the ratio of the coherent betatron tune shift (due to coupling impedances) to the synchrotron tune. This parameter can be expressed in terms of accelerator parameters as

$$\Upsilon = \pi N r_0 \langle W_\perp\rangle c^2/8\gamma C\omega_{\beta 0}\omega_s, \quad (7)$$

where $r_0 = e^2/m_0c^2$, $N = \int dz'\rho(z')$ is the number of particles in a bunch, $\langle W_\perp\rangle = (1/N)\int_{-\infty}^{\infty} dz'\rho(z')W(z - z')$ is the averaged bunch wake, C is the circumference, γ is the relativistic factor. It can easily be shown that [2], by a two-particle model, the SHT stability limit is

$$\Upsilon \lesssim 1, \quad (8)$$

for a uniform wake function. For a realistic wake function, which is not uniform, the criterion is still valid, except that the bunch wake $\langle W_\perp\rangle$ is associated with a geometric factor. This stability threshold is consistent with the transverse Boussard criterion [4]. Note that, here $\Delta\nu$ is different with the chromatic tune shift, $\Delta\nu_\beta$, shown in Eq. (5). The imaginary part of the modes appears, when the real part of transverse modes couple at where the coherent betatron tune shifts approximately in the amount of synchrotron tune. Instabilities occurs when the mode frequencies are complex. This qualitative description is clearly manifested by Eqs. (6) and (8). Conversely, one can approximate the incoherent tune spread generated from the synchrotron oscillation as, $\sigma_\nu \sim \nu_s$, the stability limit reads

$$\Delta\nu \lesssim \sigma_\nu. \quad (9)$$

Now, with the AC, the incoherent tune spread including the AC [cf. Eq. (3)], is

$$\sigma_\nu \sim \nu_s(1 + \sqrt{3/8}\chi_1). \quad (10)$$

The SHT stability threshold can then be approximately increased from $\Upsilon_{SHT} \simeq 1$ to

$$\Upsilon_{SHT} \simeq 1 + \sqrt{3/8}\chi_1. \quad (11)$$

Of course, Eq. (11) is only an estimate. A rigorous evaluation of a new SHT instability threshold, for the AC scheme, should be obtained from the complete dispersion relation, in which Landau damping is included by the method of singular eigenfunction expansion. In this way, the eigenvalues of the azimuthal mode are exactly computed, and the new threshold Υ_{SHT} is where the modes couple. Detailed formulation can be found in Ref. [1]. Exact calculation of the azimuthal mode coupling is underway.

5 MULTI-PARTICLE SIMULATION

A simulation code has been developed, which follows the motion of macro-particles that are initially loaded with a bi-Gaussian distribution in both longitudinal and transverse phase spaces. The transverse (for either vertical or horizontal) equation of motion for a particle in a bunch is

$$y''(z,s) + \frac{\omega_\beta^2(\delta)}{c^2}y(z,s) = -\frac{r_0}{\gamma C}\int_z^\infty dz'\rho(z')W_\perp(z-z')y(z',s), \quad (12)$$

where $y\,(z)$ is the transverse (longitudinal) oscillation amplitude with respect to the bunch center, and $' = d/ds$. The longitudinal motion is prescribed by Eq. (4). Eqs. (4) and (12) are transformed into a 4-D map for particle's longitudinal and transverse motions.

Specifically, the code simulates a bunched beam traversing a ring with a transverse impedance. The momentum P_y is changed by the kick of the transverse wake force, where $P_y = (c/\omega_{\beta 0})y'$. Particle's betatron oscillation is carried out by a rotation matrix, where $\omega_\beta(\delta) = \omega_{\beta 0}(1+\xi_1\delta\sin\phi)$ is used for the betatron angular frequency. A uniform transverse wake function is used. No longitudinal wake force is included. Results are numerically converged when the number of macro-particles simulated is larger than 400. Numerical values of accelerator parameters used in the simulations can be found in Ref. 1. In general, only two parameters are important to the dynamics studied in this work: Υ and χ_1, which provide scaling laws for accelerator parameters.

The curve of $\langle y\rangle$ presented in this paper is the bunch centroid motion averaged over a synchrotron period. It is defined as

$$\langle y\rangle(\tau_n) = \left[\frac{1}{2N_s+1}\sum_{i=\tau_n-N_s}^{\tau_n+N_s}\bar{y}^2(i)\right]^{1/2}, \quad (13)$$

$$\bar{y}(i) = \frac{1}{N_m}\sum_{m=1}^{N_m} y_m(i), \quad (14)$$

where N_m is the number of macro-particles used in the simulations, τ_n is the number of turn, and N_s is the integer part of $1/\nu_s$. The curve of $\varepsilon_{\rm rms}$ presented in Fig. 1(b) is the rms emittance of the phase space P_y vs. y.

In Figs. 1, we show the simulation results for the stabilization of the SHT instability by a large enough χ_1, when $\Upsilon = 1.65$ and $\chi_0 = 0$. In Fig. 2, simulation results of the excitation of $\langle y \rangle$ and $\varepsilon_{\rm rms}$ at the 8000th turn are shown in the χ_1 vs. Υ space. It can be clearly seen that, the excitations of the bunch centroid and emittance, due to the SHT instability, are significantly suppressed when the AC scheme is implemented. Large χ_1 gives large reduction of the instability growth. Simulation results of the bunch centroid motion agree with the approximate SHT stability threshold [cf. Eq. (11)]. A noteworthy implication of Fig. 2 is that, although the bunch centroid motion is stabilized when χ_1 exceeds the threshold value estimated, the emittance growth requires a much larger χ_1 such that the level of growth is acceptable. As large requirement of χ_1 involves tolerance of dynamic aperture reduction, tolerance of emittance growth when operating above the standard SHT threshold will thus rely on tolerance of dynamic aperture reduction. These tolerance depend on practical applications, and are left for future studies.

6 CONCLUSION

We have shown that, by using the AC scheme, the SHT stability threshold can be increased by the AC scheme, and the bunch excitations of the centroid motion and the emittance growth due to the SHT instability are significantly suppressed. The underlying mechanisms are Landau damping and rotation of the head-tail phase. The tolerance of dynamic aperture reduction is discussed in terms of the AC part of the head-tail phase χ_1. Simulations for the bunch centroid motion agrees with the approximation of the new SHT stability threshold.

7 REFERENCES

[1] W.-H. Cheng, A. M. Sessler, and J. S. Wurtele, "Damping of the Transverse Head-Tail Instability by Periodic Modulation of the Chromaticity", to be published in Physical Review Letters; Lawrence Berkeley National Laboratory Report, LBNL-39642 (1996); W.-H. Cheng, A. M. Sessler, and J. S. Wurtele, "Varying Chromaticity: A Damping Mechanism for the Transverse Head-Tail Instability", submitted to Physical Review E; Lawrence Berkeley National Laboratory Report, LBNL-39717 (1996).

[2] A. W. Chao, *Physics of Collective Instabilities in High Energy Accelerators*, (John Wiley & Sons, New York, 1993).

[3] M.-P. Level, "The Cure of Transverse Mode Coupling Instability in Super-Aco", Proc. 4th Adv. ICFA Beam Dynamics Workshop on Collective Effects in Short Bunches, KEK, 1990, p. 101.

[4] D. Boussard, CERN Lab II/RF/Int 75-2 (1975).

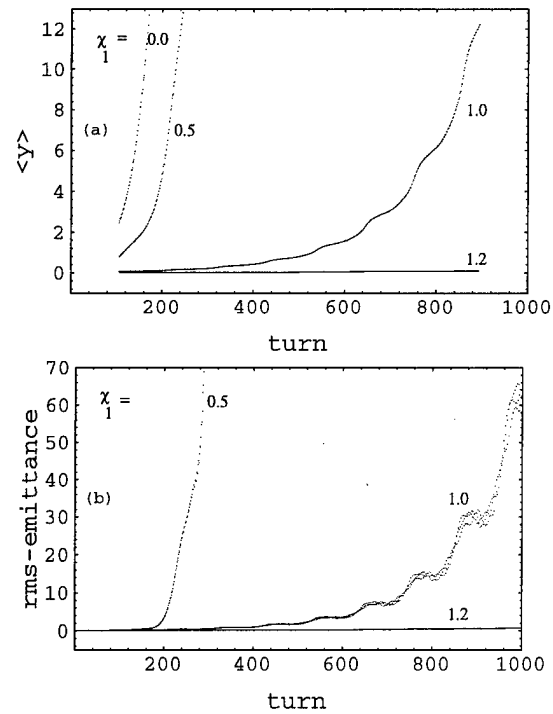

Figure 1: Multi-particle simulation results showing stabilization of the SHT motions of (a) the centroid, and (b) the rms-emittance of a Gaussian beam by χ_1, where the standard SHT stability limit is $\Upsilon_{SHT} = 1$ (when $\chi_1 = 0$.) In these figures, $\chi_0 = 0$, $\Upsilon = 1.65$. According to Eq. (11), when $\chi_1 = 1.2$, $\Upsilon_{SHT} = 1.73$.

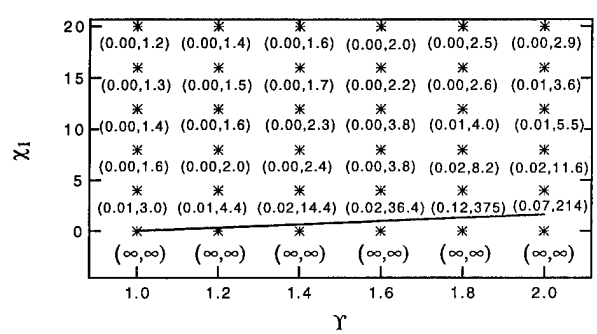

Figure 2: Simulation results of the bunch exciations when Υ is above the SHT stability limit. The numerical values attached beneath the points (*) are $(\langle y \rangle, \Delta\varepsilon_{\rm rms})$, where $\langle y \rangle$ is the averaged centroid motion at the 8000th turn, and $\Delta\varepsilon_{\rm rms} = \varepsilon_{\rm rms}(8000)/\varepsilon_{\rm rms}(0)$. The approximate new stable limit (the solid line) are plotted according to the criterion estimated in Eq. (11). The region above the solid line is stable for the bunch's centroid motion. When $\chi_1 = 0$, the standard SHT stability limit is $\Upsilon_{SHT} = 1$.

THE ELECTRON-CLOUD INSTABILITY IN PEP-II: AN UPDATE

M. A. Furman and G. R. Lambertson, LBNL† MS 71–259, Berkeley, CA 94720, USA

Abstract

We present an update on the estimate of the growth time of the multi-bunch transverse instability in the PEP-II collider arising from the interaction of the positron beam with the accumulated electron cloud. We estimate the contributions to the growth rate arising from the dipole magnets and from the pumping straight sections. We emphasize those quantities upon which the instability is most sensitive. The simulation includes measured data on the secondary emission yield for TiN-coated samples of the actual vacuum chamber. Although our analysis is still in progress, we conclude that the instability risetime is of order 1 ms, which is well within the range controllable by the feedback system.

1 INTRODUCTION

A novel type of fast coupled-bunch instability was identified some two years ago at the Photon Factory at KEK when operating with a positron beam [1], and has been subsequently reproduced at the BEPC machine [2]. The initial suggestion that its origin is an electron cloud [1] in the vacuum chamber that couples the transverse motion of successive bunches has been endorsed by simulations for these and other machines [3,4,5] and analytic work [6]. A related multi-bunch instability induced by electrons is observed in the CESR collider [7].

Here we report an update on our previous estimate [4] of the electron-cloud instability (ECI) growth time that is expected for the PEP-II [8] low-energy ring (LER), obtained from our simulation code "POSINST." While certain input data needs to be sharpened, and numerical issues in the simulation need to be refined, we currently conclude that the growth time for the multibunch coherent dipole instability is in the range 1–2 ms.

2 SIMULATION

Our simulation has been developed in the same spirit as in Ref. 3. We study separately the electron cloud in the pumping straight sections and in the dipole bending magnets since these two elements comprise most of the ring. It is legitimate to separate the problem in this fashion because the longitudinal drift of the electron cloud is slow and because, as it turns out, the range of the wake function is short compared to the betatron wavelength. As a result, it is a good approximation to simply add up the contributions to the wake function from such individual elements in the ring.

The PEP-II vacuum chamber has an elliptical cross-section of semi-axes (a,b)=(4.5,2.7) cm, with an antechamber slot of full height 1.5 cm on the outer-radius side. The electric field of the bunches is calculated taking into account this elliptical geometry boundary condition (however, for simplicity, we use the approximation that the chamber is closed). Further details are described in our previous report [4]. The main new improvement is the inclusion of the space-charge forces from the electron cloud.

2.1 *Geometry of the arcs.*

The LER, which contains the 3.1-GeV positron beam, has six arcs. For the purposes of studying the ECI, we make the simplifying assumption that each arc is composed only of 32 dipole bending magnets and 32 pumping straight sections. The dipole magnets are 0.45 m in length and are evenly spaced by a distance of 7.6 m center-to-center, and the pumping straight sections span the distance between each pair of magnets. The model also assumes that the six utility straight sections, each 121.6 m long, are empty.

2.2 *Photoemission.*

We have refined the computation of the energy spectrum and geometrical distribution of the synchrotron radiation photons generated by the positrons. The PEP-II vacuum chamber has an antechamber on the outer-radius side through which ~99% of these photons escape and thus are inconsequential for our purposes. The remaining ~1% of the photons, which are emitted with relatively large opening angle, strike the vacuum chamber wall just above and just below the slot with an average energy of ~15 eV and a mean grazing angle of ~15 mrad (the critical energy is 4.8 keV). On average, each positron in any given bunch generates ~0.02 such low-energy photons when it traverses any given dipole bending magnet. Some 20% of these photons land on the bending magnet immediately downstream of the emitting dipole, and the remaining ~80% land in the two pumping sections downstream of the emitting dipole.

If the photon reflectivity R of the chamber walls is close to 0, the photons yield photoelectrons upon first striking the wall. If, on the other hand, R is close to 1, the photons bounce inside the chamber many times before yielding photoelectrons. In the first case, the photoelectrons are generated along narrow strips just above and just below the chamber slot; in the second case, the photons get redistributed more or less uniformly both azimuthally and transversely in the chamber, so that the photoelectrons are generated almost uniformly throughout. Since we have not yet measured the

†Work supported by the US Department of Energy under Contract No. DE-AC03-76SF00098.

0-7803-4376-X/98 /$10.00 © 1998 IEEE

reflectivity of the vacuum chamber, in our simulations we study the two extreme cases, R=0 and R~1.

We assume a quantum efficiency Y=1, meaning that one photoelectron is ejected per photon that *penetrates* the wall (not per photon that *hits* the wall). By using this definition of the quantum efficiency, we substantially decouple the knowledge of R from the photoemission process. Thus, for the nominal charge of 5.6×10^{11} positrons per bunch, an average of $\sim1\times0.02\times5.6\times10^{11}=1.1\times10^{10}$ photoelectrons are generated per bunch passage in the region downstream from any given dipole magnet. It can be shown that this quantity is *independent of the value of R* provided R is not extremely close to 1.

The photoelectrons are generated with a mean energy of 5 eV and an rms width also of 5 eV. The simulation represents each burst of these photoelectrons with a fixed number of "macroparticles," typically 1000 per bunch passage, and follows these (and the ensuing secondary electrons) for up to 1000 bunch passages.

3 RESULTS

When an electron strikes the surface it can emit secondary electrons. The basic quantity that describes the process is the secondary emission yield (SEY) δ, which is a function of the incident electron energy and angle, and the surface material. The secondary emission process is taken into account in detail [4] in our simulation because, for the particular case of the PEP-II LER parameter regime, the ECI depends in a non-smooth fashion on δ. In practice, it is the *effective secondary emission* $\bar{\delta}$ that plays the crucial role in determining the intensity of the electron cloud. By definition, $\bar{\delta}$ is the SEY folded with the energy-angle spectrum of the electrons that hit the wall. If $\bar{\delta}>1$, a chain reaction ensues, so that the number of electrons grows rapidly until the space-charge forces are strong enough that a saturation is reached, roughly corresponding to the beam neutralization level. If $\bar{\delta}<1$, on the other hand, the chamber walls act as a net absorber of electrons, and an equilibrium is reached when the number of electrons absorbed per bunch passage equals the number of photoelectrons generated in such a time interval.

The PEP-II vacuum chamber is made of aluminum, which is normally covered with a layer of oxide. Recent measurements [9] for actual vacuum chamber samples (duly cleaned) show that δ peaks at a value ~2 at an incident energy ~250 eV at normal incidence. Our simulation results show that such a value is high enough that $\bar{\delta}>1$ both in the pumping sections and in the dipole magnets. The electron cloud saturates at the average beam neutralization density of 1.26×10^{7} electrons/cm^3, and the resultant ECI growth rate is very fast. As a consequence of this, we are coating [10] the chambers with a 1000-Å thick layer of TiN, which has a measured [9] peak value δ ~1.1. It then turns out that $\bar{\delta}<1$ both for the bending magnets and the pumping straight sections, so that the chain reaction is avoided. All results discussed below take into account such a coating.

3.1 Pumping straight sections

If we assume that R~1, the electron cloud saturates at an average density $\sim4.7\times10^{5}$ electrons/cm^3, which is ~1/27 of the beam neutralization level (one should keep in mind, however, that the distribution itself is time dependent and not perfectly uniform, as seen in Fig. 1). The contribution to the ECI growth rate from all the pumping straight sections in the ring is $\tau^{-1}\sim1100$ s^{-1}. If we assume R=0, then $\tau^{-1}\sim1400$ s^{-1}, and the average density at saturation is ~1/21 of the beam neutralization level.

At these relatively low densities the space-charge force is expected to have a minor effect on the dynamics; we have verified that this is the case. Since the computation of the space-charge effect is by far the most computationally-expensive part of the simulation, neglecting it amounts to a considerable savings of CPU and wall-clock time (our simulations are carried out on a Cray C90 computer at NERSC).

3.2 Dipole bending magnets

In this case the magnetic field confines the electrons in the cloud to move in tight vertical helices whose radius is typically a few microns, and whose cyclotron frequency is $\nu=eB/2\pi mc$=21 GHz. Since the rms bunch length (in time units) is σ=33 ps, the electrons typically perform ~1 cyclotron revolution during a bunch passage. This means that bunch length effects are expected to be important, as we have verified. The main consequence of the cyclotron-phase averaging of the beam-electron interaction is the severe suppression (relative to the impulse approximation) of the horizontal component of the momentum transferred to the electrons in the cloud. An analytic estimate of this suppression factor yields

$$\exp\left(-(2\pi\nu\sigma)^2/2\right)\approx5.9\times10^{-5} \qquad (1)$$

which implies that the kick experienced by an electron is essentially purely vertical. A correct simulation, therefore, requires representing the bunch-electron interaction by many kicks, which is accomplished by dividing the bunch longitudinally into several slices. We have carried out spot-checks, however, that show that the results can be accurately obtained, for the PEP-II parameter regime, by resorting to the short-cut of using the impulse approximation and then suppressing the horizontal component of the kick for each electron by the factor given in Eq. (1).

If we assume R~1, the electron cloud saturates at an average density $\sim3.1\times10^{5}$ electrons/cm^3, which corresponds to ~1/41 of the beam neutralization level, and the contribution to the growth rate of the ECI from all the dipole magnets in the ring is $\tau^{-1}\sim38$ s^{-1}.

If we assume R=0, the photoelectrons are generated only along narrow strips just above and just below the

antechamber slot. Due to the trapping effect of the magnetic field, the electrons remain confined to a narrow vertical region at the outer edge of the chamber, which is ~4.5 cm away from the beam. In this case, the ionization of the residual gas by the beam produces most of the electrons near the beam orbit. However, our simulations show that, even assuming a vacuum pressure 150 times larger than the nominal specification of 1 nTorr, the contribution to τ^{-1} from the dipoles is only ~1.5 s^{-1}.

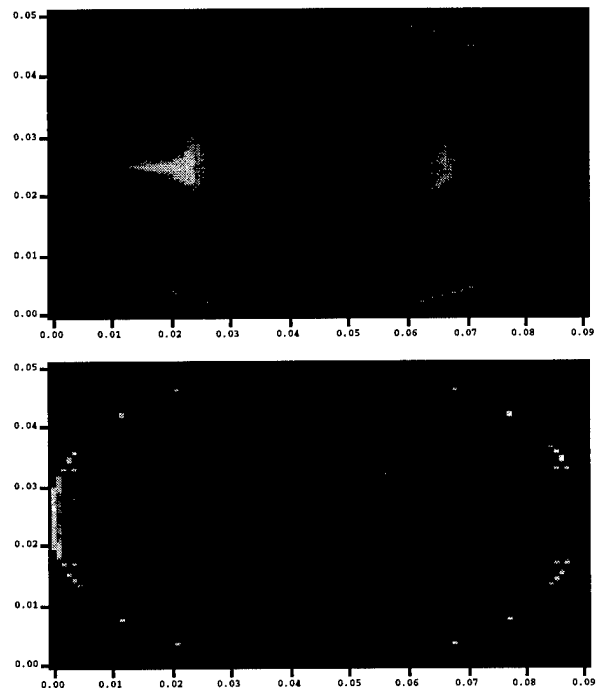

Fig. 1. Image plots of the electron cloud for R~1. Top: pumping straight section. Bottom: dipole bending magnet. The beam orbit is at the center of the ellipse. The antechamber slot is at the right side of the chamber. Brighter colors represent higher local density, and the ratio between the peak density and the average is ~2. The units of both scales are meters.

4 CONCLUSIONS

We conclude from our simulations results that the growth time of the ECI for the PEP-II positron beam is τ~1 ms, and is dominated by the pumping straight sections. Such a growth time is within the range controllable by the feedback system [11].

For R~1, the pumping straight sections dominate the ECI growth rate by a factor ~30:1 over the bending magnets, mainly due to their length. By removing this length factor we obtain τ^{-1}/L~0.80 s^{-1}/m for the pumping sections and τ^{-1}/L~0.44 s^{-1}/m for the bending magnets. These numbers are in a ratio ~2:1, which is in qualitative agreement with the ratio of the corresponding average equilibrium densities of the cloud, and is due to the difference in the beam-cloud dynamics in these two regions with and without magnetic field.

By scaling the above results by the average electron density at equilibrium, we estimate the growth rate of the ECI in the absence of a TiN coating to be ~20–40 times larger than for a coated chamber. In this case the ECI growth rate is fairly insensitive to the detailed values of R, Y and the SEY.

We have thus far assumed a certain specific form for the incident-angle dependence of the SEY, based on standard phenomenology [12]. In the near future we will incorporate the actual measured dependence; we do not expect that our results will change appreciably from those presented here.

We have yet to evaluate the contribution to the ECI growth rate from other magnets and regions of the ring, and to assess the effects of a temporary increase of the SEY from potential air exposure of the chamber. Furthermore, our analysis thus far applies to the coherent dipole multibunch mode in linear (i.e., small amplitude) approximation, and the growth rates have been obtained by computing the dipole wake function assuming that the bunches are rigid charges. Therefore our approach does not shed any light on the ECI at saturation amplitudes, nor about higher-order coherent modes. Such effects remain to be investigated by more complete simulation techniques.

ACKNOWLEDGMENTS

We are grateful to S. Heifets, K. Kennedy, R. Kirby, F. King, A. Zholents, F. Zimmermann and M. Zisman for valuable discussions, to NERSC for supercomputer support, and to J. Peters for his help in making such computer resources available to us.

REFERENCES

[1] M. Izawa, Y. Sato and T. Toyomasu, Phys. Rev. Lett. **74**, 5044 (1995).
[2] Z. Y. Guo et al, Proc. EPAC96, Barcelona, Spain, June 10-14, 1996, p. 1042.
[3] K. Ohmi, Phys. Rev. Lett. **75**, 1526 (1995).
[4] M. A. Furman and G. R. Lambertson, Proc. EPAC96, Barcelona, Spain, June 10-14, 1996, p. 1087.
[5] F. Zimmermann, LHC Project Report 95, 27 February 1997.
[6] S. Heifets, Proc. Intl. Workshop on Collective Effects and Impedance for B Factories (CEIBA95), Tsukuba, Japan, 12-17 June 1995, Y. H. Chin, ed., p. 295, and references therein.
[7] T. Holmquist and J. T. Rogers, Proc. EPAC96, Barcelona, Spain, June 10-14, 1996, p. 319 and references therein.
[8] PEP-II: An Asymmetric B Factory–Conceptual Design Report, June 1993, LBL-PUB-5379/SLAC-418/CALT-68-1869/UCRL-ID-114055/UC-IIRPA-93-01.
[9] R. Kirby and F. King, private communications.
[10] K. Kennedy, H. Hartneck, H. Hsieh, G. Millos, M. Benapfl and R. Kirby, these proceedings.
[11] W. Barry, J. Corlett, M. Fahmie, J. Greer, G. Lambertson and C. Pike, these proceedings.
[12] See, e.g., H. Seiler, J. Appl. Phys. **54**, R1 (Nov. 1983).

SATURATION OF THE ION TRANSVERSE INSTABILITY *

S. Heifets, SLAC, Stanford, CA 94309, USA

Abstract

Fast Ion Instability is studied in the nonlinear regime. It is shown that exponential growth of the linear regime is replaced in this case by the linear dependence on time. Numeric and analytical results are presented describing the beam profile and the beam spectrum in both regimes.

1 INTRODUCTION

The Fast Ion Instability discovered recently [1] has been studied numerically and confirmed experimentally [2]. The transverse instability is caused by the interaction of a train of bunches with the residual gas. Ions produced by transversely offset bunches in the head of a train induce oscillations of the tail of the train. The ions may be cleared out by a gap after one revolution, but the memory remains in the train. Amplitude of oscillations initially grows as $exp\sqrt{t/t_c}$ until the amplitude of a bunch centroid is of the order of the transverse rms σ of a bunch. The initial rise time of the oscillations of a bunch centroid was found to be a fraction of a millisecond, even taking into account the spread of ion frequencies [3]. This is too fast to be observed in experiments directly.

The exponential regime is limited by the nonlinearity of the beam-ion interaction. As a result, exponential growth at large amplitudes is replaced by a linear dependence of the amplitude on time [4], and only this nonlinear regime can be observed experimentally.

The dynamics of the instability in the nonlinear regime is quite complicated. Additional to the nontrivial interference of the perturbations of the beam by the ions excited by different bunches in the train, the instability in the nonlinear regime essentially depends on the feedback damping and noise in the system while experiments without feedback are hardly possible due to the adverse effects of traditional multibunch instabilities. All that make necessary numerical studies of the instability. Simulations include effects of the feedback and random noise describing the time dependence of the train profile and the beam spectrum.

2 ANALYSIS OF INSTABILITY

Vertical motion of electrons of the n-th bunch on the k-th turn is described by the equation [4]

$$\frac{\partial^2 y(t,z)}{\partial t^2} + \omega_b^2 y(s,z) = \tag{1}$$

$$-\kappa\sigma_y \int_0^z dz' f[y(t,z) - Y(t, ct - z - kC, z')] \tag{2}$$

* Work supported by the Department of Energy, contract DE-AC03-76SF00515

where ω_b is betatron frequency,

$$\kappa = \frac{4r_e}{\gamma s_b \sigma_x \sigma_y}\frac{dN_i}{ds}, \tag{3}$$

and dN_i/ds is the ion production rate per bunch proportional to pressure p.

Similarly, the motion of the ions is described by the equation

$$\frac{\partial^2 Y(t,s,z)}{\partial t^2} = \omega_i^2 \sigma_y f[y(t, ct - kC - s) - Y(t,s,z)]. \tag{4}$$

Here ω_i is ion frequency, and function $f(\xi)$ in the RHS of Eq. (2) is either $f(\xi) = \xi/\sigma_y$ for $|\xi| < 1$ (the linear regime), or $f(\xi) = \xi/|\xi|$ for $|\xi| > 1$, in saturation regime, and depends only on the sign of ξ.

In the linear regime, these equations were considered in the original paper [1]. In this case, the solution is

$$y(t,z) = a(t,z)e^{i(\omega_b \pm \omega_i)z/c - i\omega_b t} + c.c., \tag{5}$$

$$Y(t,s,z) = A(t,s,z)e^{-i\omega_b s/c \pm i\omega_i(t-s/c)} + c.c.. \tag{6}$$

The solution grows in time only for the upper sign

$$a(t,z) = a_0 e^{\sqrt{t/t_c}}, \qquad \frac{1}{ct_c} = \frac{\kappa\omega_i z^2}{4\omega_b}, \tag{7}$$

with the quasi-exponentially growth found in the original paper [1]. Correspondingly, the spectrum of the BPM signal

$$V(t) \propto \sum_{n,k} \delta(t - kC - ns_b/c) y(t, ns_b) \tag{8}$$

consists of the betatron side-bands at frequencies $\omega = l\omega_r \mp \omega_b$, $l = 0, 1..$ with the envelope centered at the ion frequency with the lower side-bands having amplitudes larger than that of the upper side-bands and growing in time.

In the nonlinear regime, the RHS in the Eqs. (2) and (4) depends on the function $f(\xi)$. We can expect that the variation of the argument ξ in time is similar to variation of the RHS in the linear regime, that is proportional to $e^{i(\omega_b \pm \omega_i)z/c - i\omega_b t}$ in the equation for $y(t,z)$ and $e^{-i\omega_b s/c \pm i\omega_i(t-s/c)}$ in the equation for $Y(t,s,z)$. In the strongly nonlinear regime, the spectrum of the RHS is a spectrum of a step-function which changes sign with the periods of betatron or ion oscillations. The spectrum of $f(\xi)$ in Eq. (1) and Eq. (4)) contains in this case harmonics of ω_b and ω_i correspondingly. The amplitudes of the harmonics roll off slowly as $1/n$ for the n-th harmonic. In the nonlinear regime, the ions motion is a superposition of ion frequency harmonics. The amplitudes of harmonics don't grow in time but, without the feedback system, their number does. The RHS of Eq. (2) has always a harmonic

oscillating with the betatron frequency. As the result, the amplitude of the bunch centroid motion linearly increases in time.

$$A(n_b) \simeq \frac{\kappa s_b^2 n_b n_t \beta_y}{2} \frac{t}{T_r}. \tag{9}$$

The linear growth described by Eq. (14) replaces the quasi-exponential growth of the linear regime, see Eq. (11), when amplitude is of the order of transverse beam size rms.

3 MODEL FOR SIMULATIONS

To simulate the instability we use a simplified model describing each bunch in a train of n_b bunches as a single macroparticle which goes around the ring in steps equal to s_b. All bunches get a kick from each group of ions at the new location of individual bunches

$$\bar{y}_b' = y_b' - \kappa s_b^2 \beta_y f(y_b - Y_i) \tag{10}$$

and each group of ions gets a kick

$$\bar{Y}_i' = Y_i' + (\omega_i \tau_b)^2 f(y_b - Y_i). \tag{11}$$

Each bunch generates an ion macroparticle with the offset equal to the offset of a bunch, and all ions are killed at the location of the ring just left by the last bunch in the train. To model variation of the rms beam size around the ring, the ion frequencies and the kicks to the bunches are periodically modulated with the period equal to 1/12-th of the circumference of the ring (periodicity of the ALS lattice). The feedback was modeled as a single additional kick for each bunch per turn

$$\bar{y}_b'(s) = y_b'(s) + g y_b(s - \pi\beta_y/2). \tag{12}$$

The gain g defines amplitude damping time $\tau_d = 2T_r/g$. Random kick uniformly distributed within the range $\pm a_{ns}$ was added to the RHS of Eq. (17) to simulate noise.

Most of the simulations were carried out for the ALS-like ring with the revolution period $T_r = n_t \tau_b$, $n_t = 328$, $\tau_b = 2$ ns, for the bunch train of $n_b = 50$ bunches, and He gas ($A = 4$). The bunch parameters were: $N_b = 4 \times 10^9$, $\sigma_x = 165\mu$, and $\sigma_y = 27\mu$. The betatron tune was $\nu_y = 8.18$, and the ion frequency with these parameters was 50.8 MHz. The pressure was increased to 2μTorr and the damping time of the feedback system to $\tau_d = 0.1$ ms to speed up simulations. Initially there were no ions in the ring, and initial conditions were $y_b = y_b' = 0$ for all but the first bunch, for which initial offset of $y_b = 1.0 \times 10^{-4}$ (in units of σ_y) and $y_b' = 0$ were taken. Results for different amplitude of the noise a_{ns} and modulation $\Delta\omega_i/\omega_i$ are described below.

4 RESULTS OF THE SIMULATIONS

Fig. 1 shows growth of the amplitude of the last bunch in the train with number of turns. Dependence is shown in logarithmic and natural scales. In the left hand side, results are shown with the feedback system turned down ($1/\tau_d = 0$), without noise (amplitude of the noise $a_{ns} = 0$) and with the amplitude of modulation of ion frequencies mod $= \Delta\omega_i/\omega_i = 0$ or mod $= 0.5$. Initially, result clearly corresponds to the quasi-exponential growth of the linear regime with the parameter $t_c = 0.41\mu s$ in accordance with Eq. (7. Later, the growth of the dimensionless amplitude is only linear with time and in agreement with Eq. (17), which gives the rate $dA/dn = 0.05$.

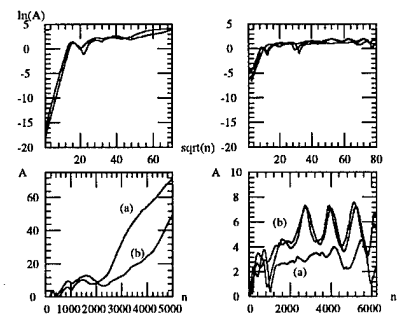

Figure 1: Amplitude of the last bunch vs number of turns in regular (above) and logarithmic (below) scales. Note transition from exponential to linear growth. Left: noise and feedback turned off. (a) mod=0, (b) mod=0.5. Right: (a) $\tau_{fdb} = 0.1$ ms, $a_{ns} = 0.01$, mod=0.5; (b) $\tau_{fdb} = 0.1$ ms, $a_{ns} = 0.002$, mod=0.5; (dots) $\tau_{fdb} = 0.1$ ms, $a_{ns} = 0.002$, mod=0.

Results with the feedback turned on ($\tau_d = 0.1$ ms) are shown in the right hand side of Fig. 1. After initial growth, the amplitude of the last bunch oscillates around some steady level. Effect of the ion frequency modulation in the saturation is small, see two curves without modulation and with the amplitude of modulation mod $= 0.5$.

The variation of the beam profile can be understood from the following. Initially, the amplitude of a bunch grows according to the linear theory and much faster for the bunches in the tail of the train then in the head. Later, however, the feedback takes over and suppresses oscillations of the bunches in the head of the train to zero amplitudes. As a result, the growth rate and the amplitudes of the following bunches decrease and the bunch number with the amplitude $A = 1$ increases in time. Oscillations with large amplitudes retain only in the very tail of the train and, eventually, all oscillations are damped out.

If we now, additionally to the feedback, turn on the noise, the beam profile goes to a steady-state, see Fig. 2. Without the instability, the equilibrium amplitude of a bunch in units of σ would be

$$A_\infty = \sqrt{y_b^2 + y_b'^2} = \sqrt{a_{ns}^2 \tau_d / 6T_r}. \tag{13}$$

For the parameters used in simulations, $T_r = 0.656\mu s$ and $\tau_d = 0.1$ ms, this amplitude corresponds to the nonlinear regime $A_\infty > 1$ for the amplitude of the noise $a_{ns} > 0.2$ If the amplitude is smaller than that, the head of the train oscillates in the linear regime, and the transition to the nonlinear regime takes place somewhere closer to the train tail.

With the instability, the beam profile oscillates around almost triangular shape with amplitudes larger in the tail

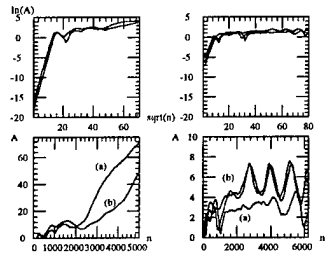

Figure 2: Snap-shot of the beam profile. Amplitude vs bunch number. Vertical scale is blown up 12.5 times. $\tau_{fdb} = 0.1$ ms, mod=0. Case (a) $a_{ns} = 0.01$, case (b) $a_{ns} = 0.002$. Curve $a_{ns} = 0.002$, mod=0 is shown in two cases and is basically the same as in the case (b).

of the train. This beam profile was observed experimentally [5]. The steady-state amplitudes depend on the feedback and are smaller for smaller τ_d. Comparison of the beam profile with different level of the noise shows that the maximum excitation of the beam is not monotonic function of the amplitude of the noise a_{ns} and may be larger for smaller noise although it goes down again at larger a_{ns}. Possible explanation is mentioned above.

The ion frequency modulation reduces the rate of the instability [3]. Effect is quite noticeable in the linear regime, but affects less the steady state amplitudes which are mostly given by the relation between the feedback and the noise.

The beam spectrum at small number of turns has all features of the linear regime: envelope is centered at the ion frequency, $f_i/f_r = 33.3$, see Fig. 3, and the upper sidebands have lower amplitudes then lower side-bands. On the longer time scale, the spectrum changes: more harmonics with frequencies $f_i \pm nf_b$ appear and the ion frequency decreases due to the increase of the amplitudes of ion. In the extreme nonlinear case, ions oscillate in a potential well $U = k_i^2|Y|$ and have frequencies depending on the amplitudes $A = max(y_i)$,

$$\frac{f}{f_r} = \frac{n_t \omega_i \tau_b}{4\sqrt{2A}}, \tag{14}$$

where ω_i is ion frequency in the linear regime. In the nonlinear regime, where the interaction between ions and bunches depend mostly on the sign of the relative position of the bunch and ion centroid, there is no reason to expect that the spectrum is centered around the ion frequency which is typical for the dipole signal of the linear regime. It should be noted, that for relatively low noise level, the head of the train can have small amplitudes corresponding to the linear regime while the tail of the train at the same time may be in the nonlinear regime.

The beam spectrum in the nonlinear regime with feedback and noise initially is much wider than that in the linear regime, Fig. 4, but with time only relatively few harmonics with low frequencies survive.

Calculations with the train of 100 bunches lead to similar results scaled correspondingly with the number of bunches.

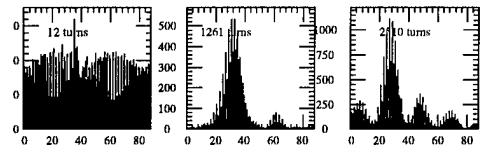

Figure 3: Snap-shot of the beam spectrum. Amplit. vs revolution harmonic number. Feedback, noise, and modulation are off.

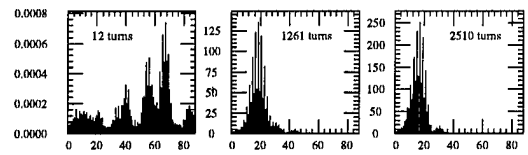

Figure 4: Beam spectrum. $\tau_{fdb} = 0.1$ ms, $a_{ns} = 0.01$, mod=0.5.

5 CONCLUSION

Ion-induced fast transverse instability is constrained by nonlinear effects. Nonlinear effects stop quasi-exponential growth of the amplitude and only the linear with time growth remains. The feedback damping suppresses the bunch oscillations first in the head of the train, effectively reducing the train length and, therefore, the growth rate of the instability. With the noise, the beam takes the typical triangular shape with the profile determined by relation between noise and the feedback. The spectrum of the beam become wider and flatter comparing to the spectrum predicted by the linear theory. Details of the spectrum again depend on the noise and feedback. This may explain unstable character of the spectrum in the experiments.

Acknowledgments

I thank J. Byrd, A. Chao, G. Stupakov, F. Zimmermann for useful discussions.

6 REFERENCES

[1] T. Raubenheimer, F. Zimmermann. Interaction of a Charged Particle Beam with Residual Gas Ions or Electrons, SLAC, January, 1995

[2] J. Byrd, A. Chao, S. Heifets, M. Minty, T. Raubenheimer, J. Seeman, G. Stupakov, J. Thomson, F. Zimmermann, Measurements of a Fast Beam-Ion Instability at the ALS, PAC 1997, Vancouver, Canada

[3] G. Stupakov, T. Raubenheimer, F. Zimmermann. Effect of Ion Decoherence on Fast Beam-Ion Instability, SLAC, January, 1995

[4] S. Heifets, Saturation of the Ion Induced Transverse Blow-up Instability, SLAC-PUB-6959, January 1996

[5] J. Byrd, Preliminary measurements of the FII, PAC 1996

A COUPLED-BUNCH ION INSTABILITY IN THE SLC ELECTRON DAMPING RING*

P. Krejcik, Stanford Linear Accelerator Center, Stanford University, Stanford, CA 94309 USA

Abstract

Under abnormally poor vacuum conditions in the electron damping ring, described in a companion paper at this conference, an emittance blowup was observed related to a transverse instability. The instability was only observed with two bunches in the ring, and could not be seen with single bunch operation, even at the same total beam current as for the two bunches. Measurements of the transverse Beam Transfer Function indicate strong coupling between the two bunches when ions are present. This is described in terms of a simple model where the oscillating ion cloud provides the coupling between the two bunches. The frequency shift due to coupling can also cause the ion cloud to become unstable, and disappear, when the betatron tune of the electron bunch is just below the 1/2 integer.

1 INTRODUCTION

An instability has been observed in the 1.2 GeV SLC electron damping ring relating to the poor vacuum conditions following an accidental venting and contamination of the ring. The instability causes a large amount of emittance blowup, particularly in the vertical plane, which has been addressed in a companion paper at this conference[1]. Many of the observations point to a multi-bunch effect rather than a single bunch emittance growth phenomenon. The signature of the instability, the appearance of strong vertical betatron sidebands in the bunch spectrum, persists down to low intensities of $1 \cdot 10^{10}$ total number of electrons when two bunches are present. However, single bunch intensities as high as $4 \cdot 10^{10}$ electrons do not show such sidebands in the bunch spectrum. The emittance growth of single bunches also clearly decreases at lower intensities, whereas the emittance growth with two bunches is large over a wide range of operating currents.

One important conclusion from the observations of the ion effects in the SLC damping ring is that the ions are only able to be captured during a brief interval after injection while the beam is large. Once the beam has damped to small dimensions the critical mass for an ion to be captured gets quite large. Since we continue to observe ion related emittance growth at long store times this implies that the ion cloud that formed after injection has also shrunk in transverse dimension with the beam. If the ion cloud had not shrunk with the beam those ions would have large amplitude oscillations and be lost from the beam.

This paper concentrates on the coupling aspect of the instability. Measurement techniques were developed to distinguish the coupling from other beam instability modes. A simple model is used to demonstrates how the measured transverse beam transfer function can distinguish between coupled and non-coupled bunches. The change in the instability behavior with the vertical tune can also be interpreted in light of the coupling mechanism. The tune shift of the beam and the shift in frequency of the coherent dipole oscillations of the ion cloud depend upon the modes that are possible in the presence of coupling. Under certain tune conditions the ion cloud is found to be able to shake free of the beam and the instability stops.

2 MEASUREMENT METHODS

The amplitude response of the beam gives some indications of the presence of ions, as described in reference[1]. At CESR the technique has been developed to infer the ion density from the amplitude response using a linear model [2]. A complete characterization of the Beam Transfer Function (BTF) in the presence of ions requires the measurement of both phase and amplitude response, as has been performed for unbunched beams in the CERN antiproton rings [3]. The output from the network analyzer drives a broadband transverse kicker through a 50 W amplifier, as illustrated in figure 1. A stripline kicker is used so the current measured in the stripline is proportional to the kick received by the beam and is used as the reference signal for the BTF. The beam response is measured at another stripline and low-pass filtered to remove the power generated at high frequencies by the short bunches. The signal to noise ratio is improved by using a low noise pre-amplifier in the signal path.

The network analyzer used on these measurements is a conventional swept frequency instrument that acquires the data over several seconds. The beam is stored during this time and has therefore reached its equilibrium emittance. Although data can be retrieved while the damping ring is cycling through many injection and extraction cycles, it is difficult to interpret because of the varying beam conditions. The data presented here is all for stored

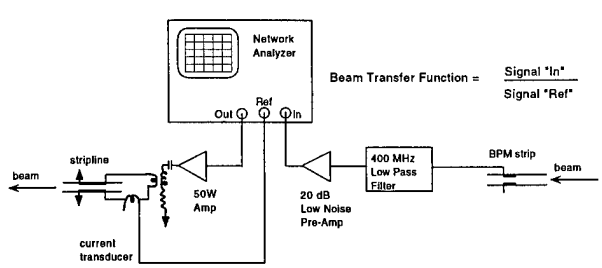

Figure 1: Measurement of the transverse beam transfer function with a network analyzer driving the beam and measuring the response at a stripline monitor.

* Work supported by Department of Energy Contract DE-AC03-76SF00515.

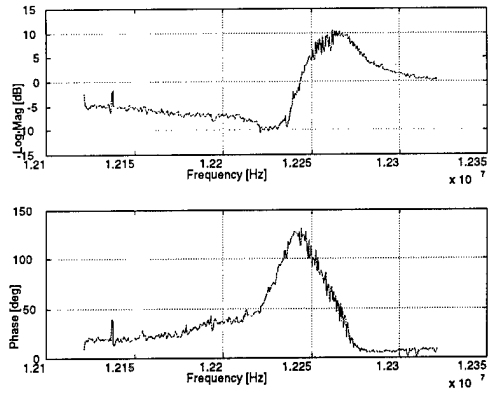

Figure 2: Measured magnitude and phase response for two bunches of $4 \cdot 10^{10}$ electrons each at $f_0+\nu_y$.

beams. Plans are under way to use a synthesized sweep instrument that can be gated on during specific intervals of the store.

3 MEASUREMENT RESULTS

The first case shown in figure 2 is for two bunches of $4 \cdot 10^{10}$ electrons each, which is close to the nominal intensity for SLC operation. The amplitude and phase response do not show a single resonance response as might be expected. The phase does not make a net change as it passes through the resonance, but returns close to its starting value. The tune spread in the electron beam can be deduced from the width of the amplitude response.

The second case in figure 3 is for a single bunch with the same bunch charge as in the previous example. The tune spread in the amplitude response is comparable in both cases. However, a large difference is seen in the phase response between the single and two bunch cases. The phase makes a net change as the frequency is swept through the resonance in the single bunch case.

The third case in figure 4 is again for a single bunch but at a reduced intensity of $1 \cdot 10^{10}$ electrons. The tune spread seen in the amplitude response is reduced, but the phase response shows the same behavior as for high intensities, with a net phase change across the resonance.

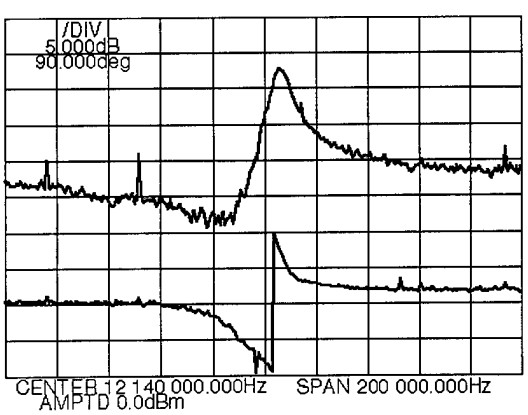

Figure 3: Measured magnitude and phase response for one bunch of $4 \cdot 10^{10}$ electrons at $f_0+\nu_y$.

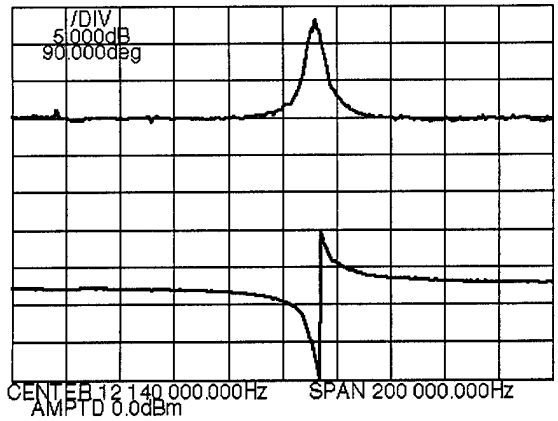

Figure 4: Measured magnitude and phase response for one bunch of $1 \cdot 10^{10}$ electrons at $f_0+\nu_y$.

4 COUPLED BUNCH MODEL

In a simple model the transverse dipole motion of the bunch can be described as an oscillator with natural frequency ω_n and damping ratio ζ. If coupling is included between the two bunches the coupling force is represented by the coupling frequency ω_c and for completeness a damping ratio ζ_c for the coupling is also included. The equations of motion for the phases of bunch 1, ϕ_1, and bunch 2, ϕ_2, are

$$\begin{aligned} \ddot{\phi}_1 + (\zeta + \zeta_c)\dot{\phi}_1 + (\omega_n^2 + \omega_c^2)\phi_1 + \omega_c^2\phi_2 + \zeta_c\dot{\phi}_2 = 0 \\ \ddot{\phi}_2 + (\zeta + \zeta_c)\dot{\phi}_2 + (\omega_n^2 + \omega_c^2)\phi_2 + \omega_c^2\phi_1 + \zeta_c\dot{\phi}_1 = 0 \end{aligned} \quad (1)$$

The coupled bunch motion has two modes, an 0-mode (n=0) and a π-mode (n=1) where the two bunches are in phase or out of phase respectively. The frequency of these two modes is given by

$$\omega^2 = \omega_n^2 \pm \omega_c^2 \quad (2)$$

where the π-mode is shifted up in frequency due to coupling. Note that this amounts to an additional tune shift above that already caused by the focusing effect of the ions on a single bunch.

Equation (1) represents a fourth-order system from which the transfer function can be deduced. The amplitude and phase response versus frequency (Bode plot) is shown in figure 5 for this system. The frequency scale is normalized so that the natural frequency ω_n=1 in the plot. The characteristic behavior of the coupled system is that the frequency sweeps through two resonances, with the phase increasing at the first resonance and then decreasing to the starting value as the second resonance is passed.

The modeled behavior of the fourth-order system resembles very closely the measured response of the two bunch system in figure 2. Note also that the measured two bunch response was at a sideband of an odd revolution harmonic, corresponding to a n=1 mode for the bunch oscillation.

As a comparison, a similar frequency analysis is shown for the single bunch case. The simple oscillator for a single bunch is a second-order system whose transfer

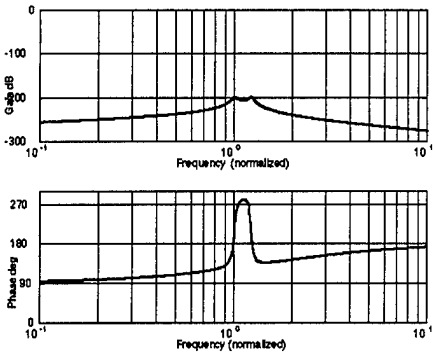

Figure 5: The predicted magnitude and phase response for a 4th-order coupled oscillator model.

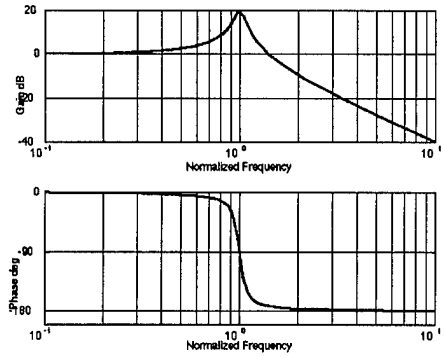

Figure 6: The predicted magnitude and phase response for a 2nd-order single oscillator model.

function may be simply written using control system formalism as

$$G(s) = \frac{\omega_n^2}{s^2 + 2\zeta\omega_n s + \omega_n^2}, \qquad s = j\omega \tag{3}$$

The transfer function has the well-known frequency response of a second-order system, shown in figure 6. Comparing with the measured single bunch response in figures 3 and 4 one can see a similar net phase change across the resonance.

The control system formalism is a useful tool for analyzing the coupling since it is evident that the coupled oscillators can be modeled as two sequential transformations of the type in equation (3). The first transformation corresponds to the single bunch response and the second to the coupling term, so that the complete transfer function can be written as

$$G(s) \times G_c(s) = \frac{\omega_n^2}{s^2 + 2\zeta\omega_n s + \omega_n^2} \times \frac{\omega_c^2}{s^2 + 2\zeta_c\omega_c s + \omega_c^2} \tag{4}$$

which represents the 4th-order system in equation (1).

5 ION CLOUD BEHAVIOR

The modeling above supports the existence of coupling between the bunches. It is further concluded that the coupling is due to ions, since the effect was not seen before the vacuum contamination occurred and the coupling is also not seen in the SLC positron damping ring where no ion trapping occurs. In the introduction it was noted that the ion cloud must shrink with the beam as it damps, in order to account for the persistence of the ions into the store. The small (~70 μm) beam sizes in the damping ring are good candidates for two-stream instabilities to occur as described in plasma physics. That is, the centroids of the electron bunch and the ion cloud will begin to oscillate with respect to each other. The oscillations are self limiting since at larger amplitudes the electron bunch samples the nonlinear 1/r field of the ion cloud. The classical multi-turn instability is discussed, for example in references [4,5].

If we try and include the ion cloud as a third bunch in the model we end up with a sixth-order system describing the phases ϕ_1, ϕ_2 and ϕ_3. This is of limited use since the measurement system only detects the position of the electron bunches and not the ion cloud. However, it is useful to note that there are three oscillation modes present, n=0, 1 and 2. In the n=0 mode the three bunches are in phase, but in the n=1 and n=2 modes the two electron bunches are out of phase and the ion cloud is in phase with either one bunch or the other. Since the ion cloud is always out of phase with one bunch its frequency is always shifted upward according to equation (2).

The expected frequency shift of the ions can account for some of the tune behavior seen with the beam. It has been observed that operating with the vertical tune just below the 1/2 integer resonance cures some of the emittance growth problems due to the instability. If the ion cloud dipole mode frequency is shifted upward by the coupling the ions will be sitting in closer proximity to the 1/2 integer resonance and their amplitude may grow until they are expelled from the beam. The sudden tune jumps observed under these conditions might also be due to changes in the dipole modes as the ion density changes.

Only the coherent dipole motion of the electron bunches have been considered so far. Transverse quadrupoles can also be driven by the coupling in the ion space charge, but can remain hidden from normal dipole pickups, as was the case with the antiproton beams in references [3,5].

6 REFERENCES

[1] P. Krejcik, D. Pritzkau, T. Raubenheimer, M. Ross, F. Zimmermann, "Ion Effects in the SLC Electron Damping Ring", Paper 2V18, these proceedings.

[2] D. Sagan, A. Temnykh, "Observations of the Coherent Beam-Ion Interaction in the CESR Storage Ring", NIM. A344, p.459-469, (1994).

[3] G. Carron et al., "Observation of Transverse Quad-rupole Mode Instabilities in Intense Cooled Antiproton Beams", Proc. 1989 PAC, IEEE p.803, (1989).

[4] G. Koshkarev and P. Zenkevich, "Resonance of Coupled Transverse Oscillations in Two Circular Beams", Particle Accelerators 3, p. 1, (1972).

[5] R. Alves Pires et al., "On the Theory of Coherent Instabilities due to Coupling between a Dense Cooled Beam and Charged Particles from the Residual Gas", Proc. 1989 PAC, IEEE p.800, (1989).

ION EFFECTS IN THE SLC ELECTRON DAMPING RING*

P. Krejcik, D. Pritzkau, T. Raubenheimer, M. Ross, F. Zimmermann,
Stanford Linear Accelerator Center, Stanford University, Stanford, CA 94309 USA

Abstract

We report on the ion-related beam behavior in the electron damping ring during unusually poor vacuum conditions in the weeks that followed a catastrophic kicker chamber failure that contaminated the ring vacuum system. The vacuum gradually improved over several months of beam operation, during which time the vertical emittance remained blown up by a factor of 2. The emittance blowup was accompanied by a transverse instability that produced jitter in the extracted beam size. Both the characteristic spectrum of self-excited betatron sidebands and the emittance blowup exhibited a threshold behavior with beam current and vacuum pressure. This behavior depended strongly on the betatron tune and it was found that the ion effects could be minimized by operating just below the 1/2 integer resonance.

1 INTRODUCTION

The SLC damping rings damp 1.19 GeV beams of either electrons or positrons at a 120 Hz repetition rate with transverse damping times of approximately 3.5 ms. Under normal operating conditions the extracted beams have a $3\cdot10^{-5}$ m normalized horizontal emittance by $0.2\cdot10^{-5}$ m normalized vertical emittance. The high-voltage kicker magnets for injection and extraction of the beam use ceramic vacuum chambers to allow for fast, pulsed operation. In the electron ring one such ceramic chamber fractured as a result of arcing around the chamber and combustion products from magnet insulation were drawn into the vacuum system as it vented to atmosphere.

In order to proceed with the SLC operation as quickly as possible no general cleaning of the vacuum system was done, apart from replacing vacuum chambers in the proximity of the failed magnet. To aid in the lengthy beam processing of the vacuum system that followed, several additional pumps were added to the system, bearing in mind that the ring was already closely packed with components.

Even after the ring vacuum reached acceptable pressure to operate at full current and at the full repetition rate, it was found that the emittance had increased considerably, especially in the vertical plane and that the extracted beam size fluctuated wildly from pulse to pulse. The exact nature of the beam degradation depended on an interrelation between such factors as beam intensity, number of bunches, tune and coupling parameters, duty cycle and recovery from trips in the machine protection interlocks.

2 EMITTANCE AND BEAM LIFETIME

The extracted beam can be profiled on a wire scanner and figure 1 shows the vertical beam profiles in the cases of one and two bunches in the ring. The intensity per bunch is $3.5\cdot10^{10}$ electrons in each case but the vertical beam size increases from 60 μm for one bunch to 200 μm and very non-Gaussian for two bunches. This is to be compared to the 40 μm beam sizes that were obtained under good vacuum conditions, independent of the number of bunches.

The poor vacuum also reduced the beam lifetime to around 150 s, and had some dependency on the total beam current, but not on the number of bunches.

The ion densities that are reached in the ring can be calculated from an ionization rate

$$\dot{\lambda}_{ion} \approx 4\times10^{11}\,\mathrm{m}^{-1}\mathrm{s}^{-1}\,\frac{p}{100\mathrm{nTorr}} \qquad (1)$$

taking carbon monoxide as a typical species with a 2 mbarn cross section. If full neutralization were to occur a line density of $\lambda_{neut}\approx1.6\cdot10^{9}$ m^{-1} would be achieved after about 6 ms store time at a pressure $p=10^{-7}$ Torr. However, doubly ionized ions, whose production cross section is about the same as for singly ionized, are lost from the beam so the

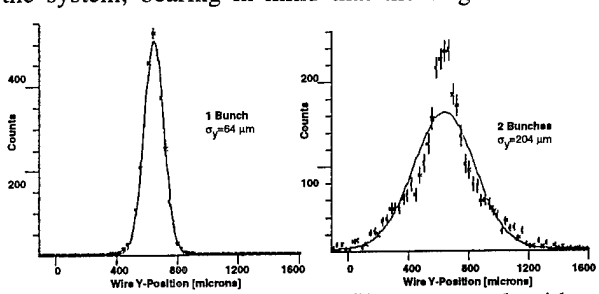

Figure 1: Extracted beam profiles measured with a vertical wire scanner for 1 bunch (left) and 2 bunch operation (right).

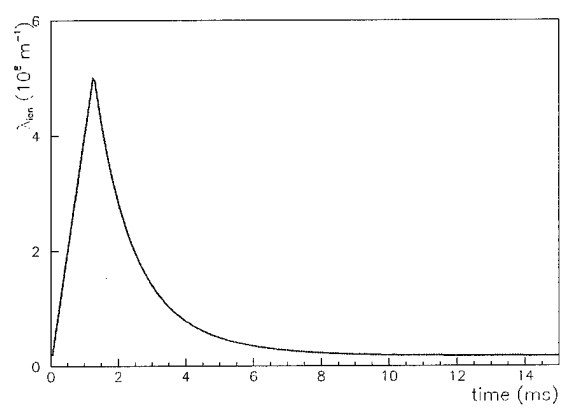

Figure 2: Predicted ion line density, increasing linearly with time then decreasing with the beam size.

* Work supported by Department of Energy Contract DE-AC03-76SF00515.

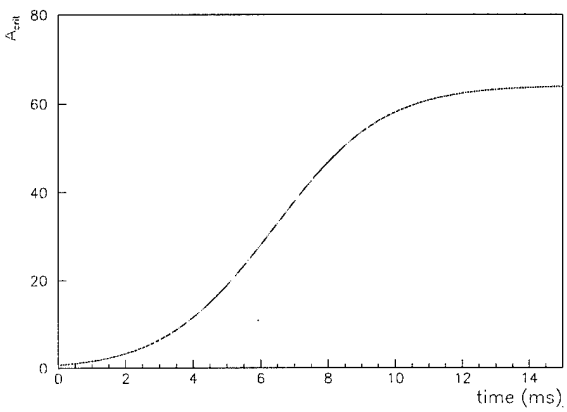

Figure 3: The critical ion mass (a.m.u.) above which ions can be trapped, increases during the store as the beam size shrinks.

equilibrium ion density will not exceed the neutral gas density [1]. The resulting line density depends on the shrinking beam size during the store, as seen in fig. 2.

The critical mass above which an ion is trapped

$$A_{crit} = \frac{N_{tot} C r_p Q}{n_b^2 2\sigma_y(\sigma_x + \sigma_y)} \qquad (2)$$

also depends on horizontal and vertical beam sizes σ_x and σ_y, and in fig. 3 it is seen that the lighter ions can only become trapped immediately after injection. Here we have a total number of electrons, $N_{tot}=8\cdot10^{10}$, the number of bunches, $n_b=2$, ring circumference $C=35$ m, ion charge Q (in units of e) and classical proton radius r_p. The calculated beam size assumes an injected emittance $\gamma\varepsilon_{x0}=\gamma\varepsilon_{y0}\approx20\cdot10^{-5}$ m and energy spread $\delta\approx0.01$ and final emittances of $\gamma\varepsilon_x\approx3\cdot10^{-5}$ m and $\gamma\varepsilon_y\approx0.2\cdot10^{-5}$ m and $\delta\approx7\cdot10^{-4}$. Also assumed are $\beta_x\approx0.7$ m and $\beta_y\approx2.5$ m, $\eta_x\approx0.1$ m, $\tau_{x,y}\approx3.1$ ms $\tau_\delta\approx1.5$ ms.

The ions can reduce the beam lifetime through either bremsstrahlung or single-Coulomb scattering [2]. A combination of these at an ion density of $2\cdot10^8$ m^{-1} is consistent with the observed beam lifetime.

3 TRANSVERSE INSTABILITIES

Ion scattering alone does not account for the large discrepancy in beam sizes between one and two bunch operation. Evidence for a transverse instability causing pulse-to-pulse fluctuations in beam size is also seen in the form of self-excited betatron tune lines in the bunch spectrum, shown in fig. 4. When the beam is stored by disabling the extraction kicker, strong betatron sidebands can be seen around the 8.5 MHz revolution harmonics, even up to 200 MHz. The side-bands correspond to the vertical tune, with some lower amplitude activity also evident at the horizontal tune frequency. The instability can persist for over a minute as the beam intensity decays. On the shorter time

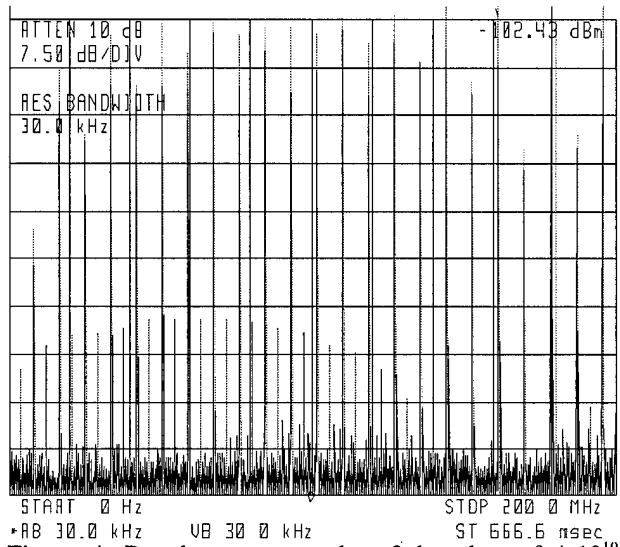

Figure 4: Bunch spectrum when 2 bunches of $4\cdot10^{10}$ electrons each are stored, showing a large number of self excited vertical betatron sidebands.

scale between injection and extraction during normal ring operation the fluctuations in extracted beam size can be linked to rapid variations in the amplitude of the vertical betatron sidebands. In fig. 5 the spectrum analyzer is tuned to one such sideband frequency and the frequency span put to zero so that the sweep detects amplitude changes over a 20 ms interval, triggered at injection. After some milliseconds of damping the amplitude of the betatron motion increases with a sub-millisecond growth time until some self-limiting amplitude is reached and the beam damps once more. This process repeats itself irregularly several times during the store.

It seems reasonable to conclude that ions are captured when the beam is large at injection and remain trapped as the beam shrinks. Even though the critical mass threshold is passed as the beam shrinks, preventing further trapping of ions, the ions, once trapped, can remain in the beam potential.

The horizontal and vertical frequency at which the ions oscillate in the beam potential is given by

$$f_{x,y} = \frac{c}{2\pi}\left(\frac{N_{tot} 2 r_p \nu}{C\sigma_{x,y}(\sigma_x + \sigma_y)A}\right)^{1/2} \qquad (3)$$

and is shown in fig. 6 as a function of time as the beam size decreases, for two different ion masses, A (in a.m.u.). The ion frequencies are below 30 MHz and consequently too low to account for the observed sideband frequencies in the bunch spectrum. The spectral lines observed at 100 MHz frequencies can only be due to transverse dipole modes of the bunch.

4 TUNE RELATED BEHAVIOR

The additional focusing force from the ion cloud produces an upward tune shift, $\Delta\nu$, in both the horizontal, x, and vertical, y, planes, given by

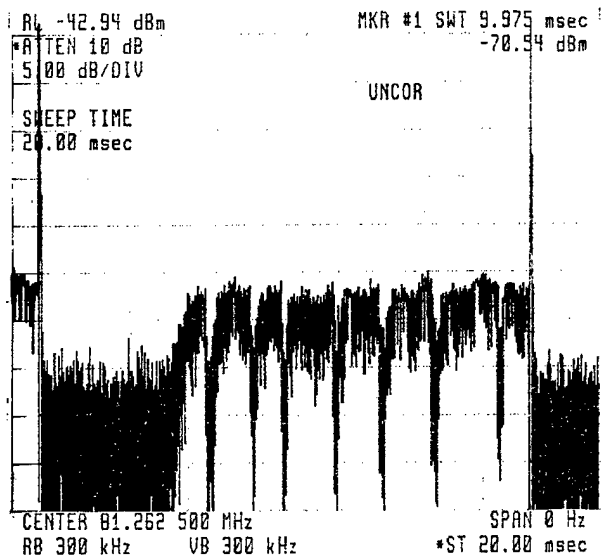

Figure 5: Time dependence of the amplitude of the vertical sideband at $10f_0-\nu_y$, over a period of 20 ms starting at injection (left hand peak).

$$\Delta\nu_{x,y} = \frac{r_p \beta_{x,y} \lambda_{ion} CQ}{\gamma 2\pi\sigma_{x,y}\left(\sigma_x + \sigma_y\right)} \qquad (4)$$

assuming the ion distribution is Gaussian with the same transverse dimensions as the beam. At ion densities equal to the residual gas density the expected tune shifts are $\Delta\nu_x \approx 0.007$ and $\Delta\nu_y \approx 0.05$. If ion densities closer to full neutralization are assumed in order to be consistent with the observed beam lifetime, the expected tune shifts become quite large at 0.07 and 0.5 in x and y respectively.

Several techniques have been employed to measure the tunes and tune shifts. The self-excited betatron lines can be observed with a gated, digital-signal-processing spectrum analyzer (Tektronix 3052) over short time intervals between injection and extraction. For long store times a conventional sweep spectrum analyzer (HP 70000) was also used to measure tunes as the intensity gradually decayed. The transverse betatron modes can also be excited by a broadband rf kicker while the driving frequency is swept through the resonance. Using this technique single bunch vertical tune shifts of 0.022 have been observed with $4 \cdot 10^{10}$ electrons. A technique of using gated white noise centered around the tune frequency while observing on the gated spectrum analyzer have also been tried [3]. After the first few milliseconds of store time, when the ion density is highest according to fig. 2, the driven tune response is difficult to detect. This maybe due to the very large tune spread that accompanies the tune shift, making coherent motion of the bunch difficult to resolve.

A particularly interesting behavior of the tunes was seen when two bunches were stored and allowed to decay over several minutes. The vertical tune had been set close to the 1/2 integer at 3.44 because of the evidence for clearing of the ions from the beam at this working point. After the intensity had

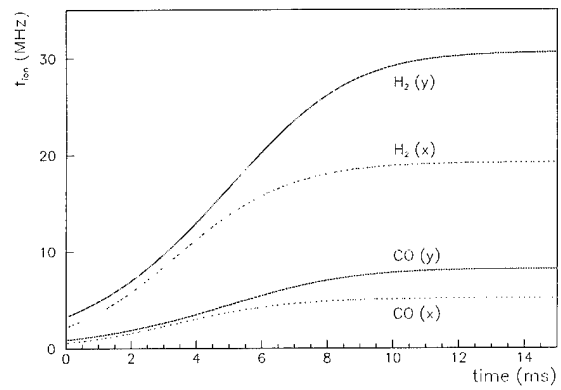

Figure 6: Expected oscillation frequencies for two different ion species as a function of store time during which the beam shrinks.

decayed by approximately a half from the initial $4 \cdot 10^{10}$ electrons, the vertical tune made a spontaneous upward jump of 0.022. The event history could be recalled on the waterfall display of the Tektronix 3052 spectrum analyzer, where one sees the tune line at the beginning of the store as both large in amplitude and with a small frequency spread. After the tune jump the amplitude decreases and the tune spread increases to about .002.

The tune jump is probably the result of a sudden change in the ion population, but it only occurs at vertical tunes just below the 1/2 integer and not at tunes just above the 1/2 integer. Coherent instabilities due to the interaction of an ion cloud and a coasting beam have been analyzed [4] and resonant clearing effects discussed in terms of changing ion frequencies at different beam size locations. In our case a clearing mechanism may be at work through transverse shaking which is discussed in terms of coupled bunch modes in a companion paper at this conference[5]. Since making this observation of clearing the ions the vertical tune has been routinely kept close to the 1/2 integer to minimize emittance growth due to ions.

5 ACKNOWLEDGMENTS

The authors thank R. H. Siemann for his contributions to the beam observations.

6 REFERENCES

1. Y. Baconnier and G.Brianti, "The Stability of Ions in Bunched Machines", CERN/SPS/80-2(DI), 1980.
2. A. Piwinski, "Beam Losses and Lifetime", CERN85-19, 1985.
3. D. Pritzkau and R. H. Siemann, priv. communication.
4. R. Alves Pires et al., "On the Theory of Coherent Instabilities due to Coupling between a Dense Cooled Beam and Charged Particles from the Residual Gas", Proc. 1989 PAC, IEEE p.800, (1989).
5. P. Krejcik, "A Coupled-Bunch Ion Instability in the SLC Electron Damping Ring", Paper 2V17, these proceedings.

SAW-TOOTH INSTABILITY STUDIES IN THE STANFORD LINEAR COLLIDER DAMPING RINGS †

B.V. Podobedov and R.H. Siemann

Stanford Linear Accelerator Center, Stanford University, Stanford, CA 94309 USA

Abstract

Experimental results of the instability studies are being reported. The system built gives a BPM-derived single bunch 'instability signal'. The signal was recorded simultaneously with the longitudinal density bunch profiles obtained from the synchrotron light with the high resolution Hamamatsu streak camera. Correlation of the instability signal with the streak camera profiles has been found. For the strongly developed instability state the dominant mode structure was obtained.

1 INTRODUCTION

It's been reported earlier [1] that the installation of new SLC damping ring vacuum chambers eliminated the saw-tooth instability as a major obstacle for increasing the collider performance. However, the instability didn't go away as it was predicted by simulations. On the contrary, the threshold went down from 3×10^{10} to $1.5\text{-}2\times10^{10}$ particles per bunch. The new instability has a similar limiting behavior, but it apparently limits itself at a much lower level and doesn't affect the shape (and transport properties) of the extracted bunch as severely as the old one.

Here is a brief summary of the new instability properties from [1]. The instability is longitudinal and has a clear threshold behavior. It occurs with either one or two bunches in the ring suggesting a single bunch phenomenon. The presence of instability can be detected by a wire scanner in a dispersive region of the extraction line. It shows a rapid growth of the energy spread as a function of the bunch current above the threshold. More detailed information can be obtained with a spectrum analyzer connected to a beam position monitor (BPM) electrode. It detects the instability sidebands of high frequency revolution harmonics. The sidebands are about f_{inst}~180kHz apart from the rotation harmonics which is almost twice the (low current) synchrotron frequency f_{s0}=100kHz. That suggests that the instability has a predominantly quadrupole mode. The time evolution of the instability can be studied using the spectrum analyzer as a receiver set to a sideband frequency. It shows a different behavior for different current and/or RF voltage settings. The typical pattern is that the instability signal exponentially rises out of noise a few ms after injection and then oscillates in amplitude by 10-20dB with rise and fall times in the 250-500μs range which is comparable with the longitudinal damping time of ~1.9ms [2].The phase of the oscillations appears random with respect to injection.

Those studies did not give *quantitative* answers to important questions such as

- What is the phase space structure of unstable bunches?
- What is the instability effect on the subsequent acceleration in the linac?
- What is the physics of instability?

For the experiment reported here we concentrated on the first question. However, the hardware we developed also provided a tool to investigate the second. As for the last question, several instability mechanisms have been proposed [5-9]. But the referenced papers do not make quantitative predictions, and it is unclear which, if any, applies to our rings. We believe this paper will give more experimental input to address this important question.

2 SETUP AND HARDWARE

2.1 Experimental setup

As it was mentioned in [1] the instability properties in both electron and positron damping rings were similar. Due to some technical reasons the latter was chosen for the present experiment. The ring parameters can be found in [2]. There are two bunches circulating exactly opposite to each other during normal SLC operation. Each bunch is stored for 16ms before extraction, and the next bunch is injected in the middle of the store of the previous one.

There were two major beam diagnostic channels. Synchrotron light was analyzed by the streak camera, while

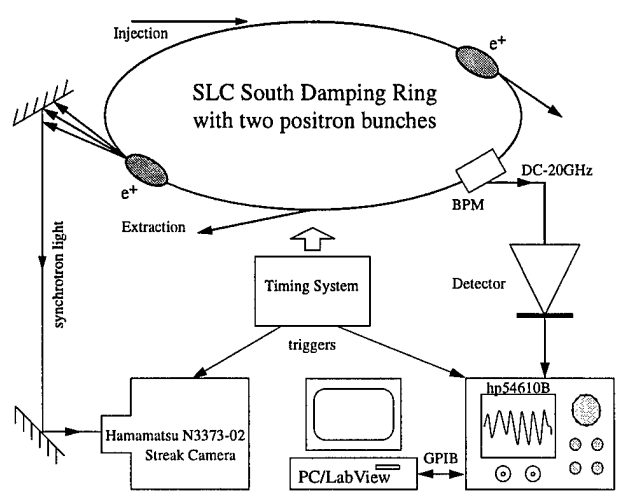

Figure 1. Experimental setup

†Work supported by DOE contract DE-AC03-76SF00515

the high frequency BPM signal was processed and digitized by an oscilloscope. The key part of the experiment was simultaneous data acquisition; hence the timing was important. Both the camera and the scope were triggered on the same trigger pulse (locked to the injection cycle) provided by the SLC timing system. The streak camera profiles were recorded by its own computer while the scope traces were saved on a PC connected via GPIB bus.

2.2 Streak camera

The main device in the setup is the Hamamatsu N3373-02 streak camera with a cooled CCD head. This camera proved to be extremely valuable to study static beam properties [2]. However, mapping the dynamic bunch behavior after the onset of instability is a challenge due to some limitations of the camera. The main one is the slow acquisition speed of a few frames per minute. This prohibits taking multiple pictures within one store not to mention the instability period. One way to make sense from the profiles taken during different stores is to use an external 'instability signal' that measures the instability state when each profile is taken. The second major element in the setup, the BPM signal detector, provides that reference.

2.3 Detector

Instability phase space information is contained in the sidebands of the revolution harmonics [3]. Macroscopic phase space structure with symmetry m (m=1 for dipole, m=2 for quadrupole, etc.) creates sidebands at $nf_{rev} \pm mf_s$, n=0,1,... Measuring the radial phase space structure requires a calibrated, wideband pickup, but phase space orientation can be measured by the phase of any single sideband which could be determined after downmixing.

To observe significant instability amplitude one has to work at a relatively high frequency $f \sim m/2\pi\sigma$ where σ is the bunch length. For our bunch length f>10GHz is required. Squaring a pickup signal gives i) a DC term, dominated by the sum of the squares of the amplitudes of the rotation harmonics, ii) a signal at the instability frequency, f_{inst}, that arises from products of the rotation harmonics with signals at frequencies $nf_{rev} \pm f_{inst}$, and iii) higher frequency products. The second of these is the one of interest. It has considerably improved signal to noise as compared to downmixing a single instability sideband.

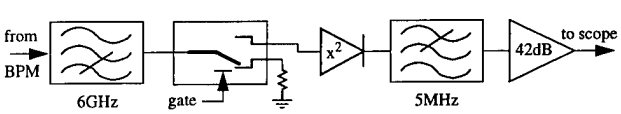

Figure 2. Detector schematic

The detector (Fig. 2) consists of a front end 6GHz high-pass filter to cut the overall power which is dominated by lower frequencies. The next element is a fast SPDT RF switch (with one output port normally terminated) gated at f_{rev}=8.5MHz. Gate delay and width were adjusted to pass the signal only from the bunch the streak camera was looking at. The next element is a square law crystal detector followed by a 5MHz low-pass filter which cuts higher frequency products. The resulting signal is fed into an audio amplifier (about 42dB gain at f_{inst}, 0 at DC) with the output connected to an oscilloscope.

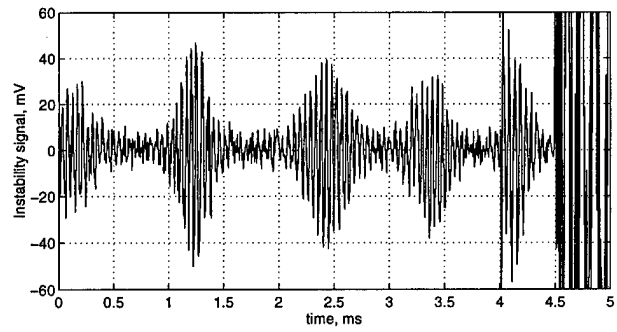

Figure 3. Instability signal after the detector

A typical signal is shown on Fig. 3. Extraction occurs at t=4.5ms, and the spike at 4ms is caused by external modulation of the RF voltage [4]. We can clearly see the instability growing and damping in bursts of about 1ms feature size. The higher frequency component of these bursts is, in fact, f_{inst}.

This detector has a number of applications beyond the experiment reported in this paper. First, the signal from the bunch that is about to be extracted can be correlated with the downstream bunch behavior. It was measured that the instability could be one of the most significant jitter sources for SLC [4]. Second, the detector allowed us to study the cross-talk between the two bunches in the ring correlating the signals coming from two ports of the switch [to be published].

3 DATA TAKING AND PROCESSING

The experiment consisted of repeatedly taking the streak camera profile and simultaneously recording the detector signal. The scope time range was 100μs/screen - enough to cover about 20 instability periods. Both the camera and the scope were triggered on the same timing pulse always coming ~0.5ms before extraction and before any external modulation. The scope trigger position was adjusted so that the streak camera picture was shot exactly in the middle of the trace (Fig. 4). A total of 589 profiles were taken in the time-frame of several days under roughly the same running conditions.

The individual streak camera profiles didn't require processing other than a calibration [2]. Bringing all the profiles to the common time reference was less obvious, since the centroid position information was lost due to substantial (>30ps) trigger jitter. Whether there is any dipole motion of the bunch can be directly checked with a spectrum analyzer. The instability never causes measurable sidebands near f_s, so all the movements of the profiles

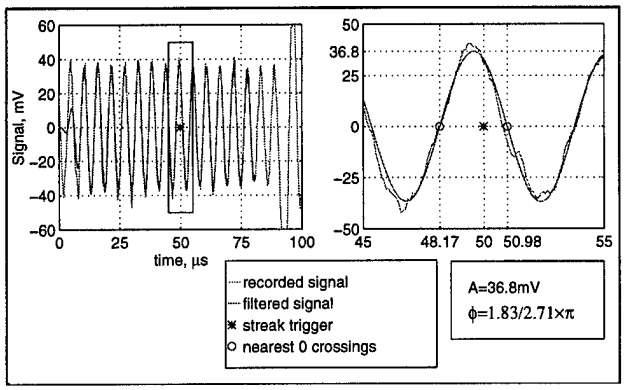

Figure 4. Extracting the instability phase and amplitude from the detector signal

on the streak camera screen were caused by trigger imperfections.This allowed us to find the zero dipole moment time point for each profile and assign t=0 to it.

The instability amplitude and phase at the moment of the streak camera shot were obtained from the scope traces (Fig. 4). To eliminate extraction related effects the last 20% of each trace was discarded and the rest was digitally filtered to reduce the noise (filtering details aren't important). We defined the phase of instability based on zero crossings of the filtered signal. For the amplitude we picked the maximum deviation of that signal in the 20μs region centered at the shot moment. Of course, the phase makes sense only when the amplitude is large, i.e. a burst and the shot coincide.

4 MAIN RESULTS

We ended up with a few hundred streak camera profiles each tagged with the instability amplitude and phase obtained from the scope traces. To study large amplitudes we selected the profiles with the instability amplitude between 20 and 40mV. Those 295 profiles were binned according to their phases. The average shapes for the $+\pi/2\pm\pi/4$ and $-\pi/2\pm\pi/4$ phase bins, and the overall average profile are shown in Fig. 5. The main changes as the phase

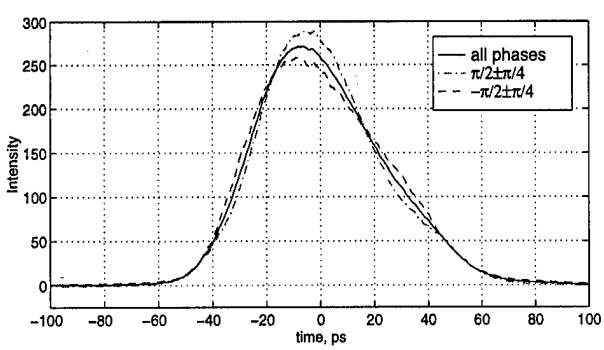

Figure 5. High instability amplitude case: average profiles for different instability phases

varies happen near the top as well as about 30ps into the head and into the tail. We found that the profile height at those regions varied in a sine-like fashion versus instability phase. Since this is a manifestation of the phase space rotation we defined the instability structure as $\delta\rho(\tau_i) = \langle(\rho_k(\tau_i) - \rho_0(\tau_i))/\sin\phi_k\rangle_k$, where ρ_k are all the profiles with corresponding phases ϕ_k, k=1,2,...295, ρ_0 is the phase-averaged profile (Fig. 5, solid) and angle brackets denote the median value.

The structure obtained is plotted on Fig. 6. It is very much like a projection of a quadruple mode (sketched in the corner). The ratio of the positive peak area to the one under ρ_0 is about 3% which measures the amount of redistributed particles creating the quadrupole structure.

For the low amplitude case we found the average profile, and it is similar to ρ_0 for high amplitudes. That means that the difference between the beam distributions when the instability is high or low is less than our sensitivity and the characteristic feature size on Fig. 6.

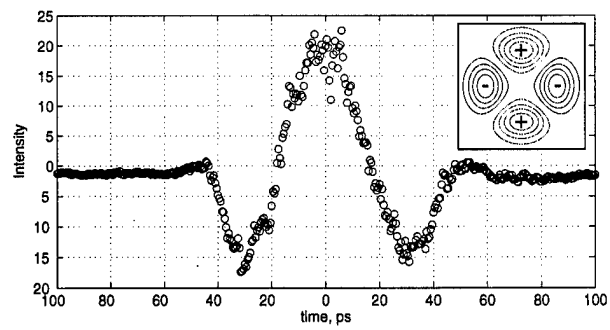

Figure 6. High amplitude instability structure

5 SUMMARY AND CONCLUSIONS

We have built a BPM signal processing circuit that proved to be valuable for single bunch longitudinal diagnostics in a multibunch environment. Combining that detector with the streak camera we have measured the phase space features for the strongly developed saw-tooth instability. The instability is predominantly quadrupole and contains approximately 3% of the beam. In addition, the average profile at large instability amplitudes is the same as the distribution at small amplitude. These facts make it likely that the instability can be interpreted with perturbation techniques.

We plan to continue our instability studies with upgraded hardware and with theoretical work.

REFERENCES

[1] K. Bane et al, Proc 1995 PAC, 3105 (1995).
[2] R.L. Holtzapple, Ph.D. thesis, Stanford University (1996).
[3] R.H. Siemann, AIP Conf. Proc. 184, 430 (1989).
[4] F.-J. Decker et al, Proc Linac 96, Geneva, 143 (1996).
[5] R. Baartman, M.D'Yachkov, Proc 1995 PAC, 3119 (1995).
[6] K. Bane, K. Oide, Proc 1995 PAC, 3112 (1995).
[7] A. Chao et al, Proc 1995 PAC, 3040 (1995).
[8] S. Heifets, Phys. Rev. E, 54, 2889 (1996).
[9] G. Stupakov et al, Phys. Rev. E, 55, #5, (1997).

FAST ION INSTABILITY IN REAL LATTICE

G. V. Stupakov
Stanford Linear Accelerator Center, Stanford University, P.O. Box 4349, Stanford, CA 94309

Abstract

The ionization of residual gas by an electron beam in an accelerator generates ions that can resonantly couple to the beam through a wave propagating in the beam-ion system. The original theory of the Fast Ion Instability [1, 2] was developed assuming both a constant external focusing and the beam size. The theory predicts an instability in which an initial perturbation grows as $\sim \exp(\alpha\sqrt{t})$. In the present paper we consider a more realistic model that takes into account variation of the beta function in the lattice and associated with it variation of the beam size. We find that, in combination with ion decoherence effect, the spatial inhomogeneity can result in 1) purely exponential growth, $\sim \exp(\Gamma t)$, and 2) typically smaller growth rates. Detailed calculations are performed for the lattice of the Advanced Light Source at the LBL.

1 INTRODUCTION

A fast beam-ion instability which is caused by the interaction of a single electron bunch train with the residual gas ions [1, 2] can be of potential danger in future high-current, low-emittance accelerators. The instability mechanism is the same in both linacs and storage rings assuming that the ions are not trapped from turn-to-turn. The ions generated by the head of the bunch train oscillate in the transverse direction and resonantly interact with the betatron oscillations of the subsequent bunches, causing the growth of the initial perturbation of the beam. First experimental observation of the fast ion instability on the Advanced Light Source at the LBL has been recently reported in [3].

The original model of the instability developed in Ref. [1, 2] neglected the spatial variation of the beta function and ion frequency along the beam path. Evidently, this assumption somewhat overestimates the growth rate of the instability because it exaggerates the synchronism between the oscillations of ions located in different positions. It turns out that inclusion of the effect of the ion frequency variation indeed weakens the instability [4]. This effect is especially important for TBA and Chasman-Green lattices used in some synchrotron light sources and characterized by large excursions of the beta function within the cell. In this paper, we study the fast ion instability with account of the spatial inhomogeneity of ion and beam parameters.

For the sake of simplicity, we focus on the interaction of an electron beam with ions, although similar effects apply to a positron beam trapping free electrons. We also assume a one-dimensional model that treats only vertical linear oscillation of the beam and ion centroids.

As in Refs. [1, 2], we adopt a model that treats the bunch train as a continuous beam. This model is applicable if the distance between the bunches l_b is smaller than the betatron wavelength, $l_b \ll c/\omega_\beta$, and the ion oscillation wavelength, $l_b \ll c/\omega_i$.

2 THEORY

We will use the following equation of motion from [2] in which we now include the effect of spatial variation of parameters along the beam path,

$$\frac{\partial^2 y(s,z)}{\partial s^2} + K(s) y(s,z) = -\kappa(s) \int_0^z z' \frac{\partial y(s,z')}{\partial z'} D(s, z-z')\, dz', \qquad (1)$$

where y is the offset of the centroid of the beam as a function of longitudinal position s and the variable z measures the distance along the bunch train, $z = ct - s$, $K(s)$ is the focusing strength of the lattice, D is the decoherence function of the ions, and κ is the coefficient responsible for the beam-ion interaction,

$$\kappa \equiv \frac{4\dot{\lambda}_{ion} r_e}{3\gamma c \sigma_y (\sigma_x + \sigma_y)}, \qquad (2)$$

where γ denotes the relativistic factor for the beam, r_e is the classical electron radius, $\sigma_{x,y}$ is the horizontal and vertical rms-beam size respectively, and $\dot{\lambda}_{ion}$ is the number of ions per meter generated by the beam per unit time. For a given cross section σ_i for collisional ionization, we have

$$\dot{\lambda}_{ion}[\mathrm{m}^{-1}\mathrm{s}^{-1}] \approx 0.9 \cdot 10^9 \sigma_i n_e p_{gas}, \qquad (3)$$

where n_e is the number of electrons in the beam per meter, p_{gas} is the residual gas pressure in torr, and σ_i is the cross section in Mbarns (σ_i is about 2 Mbarns for carbon monoxide ionized by 40 GeV electron beam). The decoherence function is determined by the following relation,

$$D(s,z) = \int d\omega_i \cos(\omega_i z/c) f(s, \omega_i), \qquad (4)$$

where $f(s,\omega_i)$ is the distribution function of ions over the frequency of transverse oscillations ω_i normalized so that $\int f(s,\omega_i)\, d\omega_i = 1$. The decoherence function represents the oscillation of the centroid of an ensemble of ions which is initially offset from the equilibrium position by one unit.

We will also assume that the interaction between the beam and the ions is small,

$$c^2 \kappa l \ll \omega_i^2,\ \omega_\beta^2, \qquad (5)$$

0-7803-4376-X/98/$10.00 © 1998 IEEE

so that the instability develops on a time scale which is much larger than both the betatron period and the period of ion oscillations. Typically this inequality is easily satisfied in the experiment. In such a situation, the most unstable solution of Eq. (1) can be represented as a betatron wave propagating in the beam with a varying amplitude,

$$y(s,z) = \mathrm{Re}A(s,z)\sqrt{\beta(s)}e^{-i\psi(s)+i\omega_{i0}z/c}, \quad (6)$$

where the complex amplitude $A(s,z)$ is a 'slow' function of its variables,

$$\left|\frac{\partial \ln A}{\partial s}\right| \ll \frac{\omega_\beta}{c}, \quad \left|\frac{\partial \ln A}{\partial z}\right| \ll \frac{\omega_{i0}}{c}, \quad (7)$$

$\beta(s)$ is the beta function, $\psi(s)$ is the betatron phase, and ω_{i0} is the averaged over the ring ion frequency, $\omega_{i0} = C^{-1}\int d\omega ds\omega f(s,\omega)$, where C is the circumference of the ring. For a fixed z and constant A, the s-dependence in Eq. (6) describes a pure betatron oscillation, while, for a fixed s (that is in the ion rest frame), the z-dependent part implies oscillations with the frequency ω_{i0}. Hence the wave resonantly couples the ions and the electrons.

It is reasonable to assume that, with a good accuracy, the variation of the ion frequency from point to point does not change the shape of the ion distribution function but only shifts it along the frequency axis,

$$f(s,\omega_i) = F(\omega_i - \omega_{i0} - \delta\omega_i(s)), \quad (8)$$

where $\delta\omega_i(s)$ is the deviation of the local ion oscillation frequency in the center of the beam from ω_{i0}. We will also assume that $\delta\omega_i$ is small, $\delta\omega_i(s) \ll \omega_{i0}$; in the opposite case, when $\delta\omega_i$ is comparable to ω_{i0}, the large variations of the ion frequency should strongly suppress the instability.

Substituting Eqs. (4), (6), and (8) into Eq. (1) and neglecting the second derivative $\partial^2 A/\partial s^2$ on the right hand side gives the following equation

$$\frac{\partial A(s,z)}{\partial s} = \frac{\kappa\omega_{i0}\beta}{2c(2+i\beta')}\int_0^z z'dz'A(s,z')e^{-i\omega_{i0}(z-z')} \times \int d\omega_i f(s,\omega_i)\left[e^{-i\omega_i(z-z')} + e^{i\omega_i(z-z')}\right]. \quad (9)$$

If we now assume that the length of the bunch train l is much larger than the ion wavenumber, $l\omega_i/c \gg 1$, and recall that the ion frequency ω_i is close to ω_{i0}, we conclude that the first term in the brackets rapidly oscillates with the frequency $\approx 2\omega_{i0}$, whereas the second term is a relatively smooth function of $(z-z')$. Clearly, the second term makes the dominant contribution. Leaving only this term in the equation leads to the following expression for the amplitude A,

$$\frac{\partial A(s,z)}{\partial s} = \frac{\kappa\omega_{i0}\beta}{2c(2+i\beta')}\int_0^z z'A(s,z')\hat{D}(s,z-z')\,dz', \quad (10)$$

where

$$\hat{D}(s,z) = e^{i\delta\omega_i(s)z/c}D_0(z), \quad (11)$$

and

$$D_0(z) = \int d\omega F(\omega)e^{i\omega z/c} \quad (12)$$

is the decoherence function in the homogeneous case (see Ref. [2]).

It has been shown in Ref. [2] that the decoherence function $D_0(z)$ can be approximated by the following expression, $D_0(z) = (1+i\alpha\omega_{i0}z/c)^{-1/2}$, where $\alpha = 3/8$ is a numerical factor. This function decays very slowly as $z \to \infty$, which explains why the effect of decoherence (equivalent, in some sense, to Landau damping) only insignificantly decreases the growth rate of the instability [2]. Mathematically, slow decay manifests itself in the fact that $\int_0^\infty D_0(z)dz$ does not converge at infinity.

Situation completely changes for inhomogeneous case. Now, because of the presence of the oscillating factor in Eq. (11), the integral $\int_0^\infty \hat{D}(s,z)dz$ converges almost everywhere (except the points where $\delta\omega_i = 0$), and we can introduce a (complex) decoherence length l_d:

$$l_d(s) = \int_0^\infty \hat{D}(s,z)\,dz. \quad (13)$$

A simple picture of instability arises in the limit of short decoherence length

$$|l_d| \ll l. \quad (14)$$

In this limit, the main contribution to the integral on the right-hand side of Eq. (10) comes from the region where $z' \approx z$, and we can put $z'A(z')$ out of the integral substituting z for z',

$$\frac{\partial A(s,z)}{\partial s} = \Lambda(s,z)A(s,z), \quad (15)$$

where

$$\Lambda(s,z) = \frac{\kappa(s)\omega_{i0}\beta(s)zl_d(s)}{2c(2+i\beta'(s))}. \quad (16)$$

The solution to the last equation is,

$$A(s,z) = A_0(z)\exp\left[\int_0^s \Lambda(s',z)ds'\right], \quad (17)$$

which means that the instability develops with the averaged growth rate Γ

$$\Gamma(z) = c\langle \mathrm{Re}\Lambda(s,z)\rangle. \quad (18)$$

where the angular brackets denote averaging over a period of the lattice (or circumference in a circular accelerator). As a matter of fact, $\Gamma(z)$ is a linear function of z.

Equation (16) predicts how the growth rate scales with the parameters of the beam and the vacuum pressure. For large variation of the ion frequency, $\delta\omega_i/\omega_{i0} > 0.3$, the decoherence length l_d is inversely proportional to the ion frequency, $l_d \sim c/\omega_i 0$, and we obtain the following rough

estimate for the maximal growth rate at the end of the bunch train,

$$\Gamma \sim \frac{c\kappa(s)\beta l}{4}. \tag{19}$$

This equation gives a scaling of the growth rate of the instability with the bunch current I_b, number of bunches in the train n_b, and the vacuum pressure p,

$$\Gamma \propto p n_b I_b = pI, \tag{20}$$

where $I = n_b I_b$ is the total beam current. This scaling differs from the regime when $|l_d| \gg l$ studied in Refs. [1, 2] where the characteristic time τ of the instability scales as $\tau^{-1} \propto p n_b^2 I_b^{3/2}$.

3 GROWTH RATE OF THE INSTABILITY FOR THE ALS EXPERIMENT

Using Eq. (18) we calculated the growth rate of the fast ion instability for the conditions of the dedicated experiment in the Advanced Light Source at the LBL [3]. The horizontal and vertical beta functions for one period of the ALS lattice are shown in Fig.1. We assumed the following parameters in the calculation: beam energy 1.5 GeV, accelerator circumference 196.8 m, bunch spacing 0.61 m, vertical emittance 9.4×10^{-11} m, horizontal emittance 4.1×10^{-9} m.

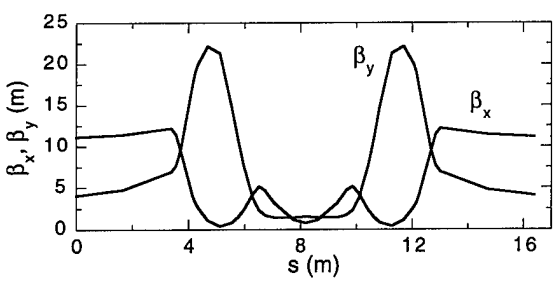

Figure 1: Plot of horizontal and vertical β-functions in the ALS. Only one period of the lattice is shown.

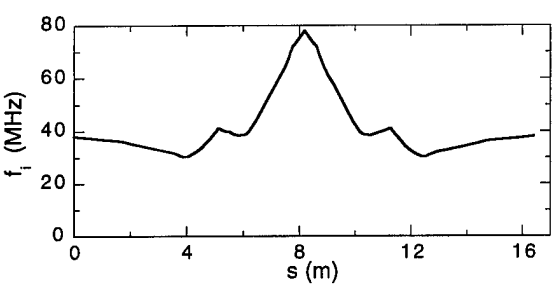

Figure 2: Frequency of *He* ion oscillations as a function of position for the lattice shown in Fig. 1. Beam current $I = 0.2$ A, number of bunches $n_b = 240$.

We also assumed a residual *He* gas of pressure $p = 80$ nTorr [3] and used the ionization cross section of 0.15 Mbarn [5]. The variation of the ion frequency along the beam path in one period of the ring is shown in Fig 2, and the ratio of the calculated decoherence length given by Eq. (13) and the bunch train length l is shown in Fig. 3. One sees that the inequality (14) holds almost everywhere except for two positions in the half-period of the ring. The average ion frequency for this case is 41 MHz, with the rms spread of about 12 MHz.

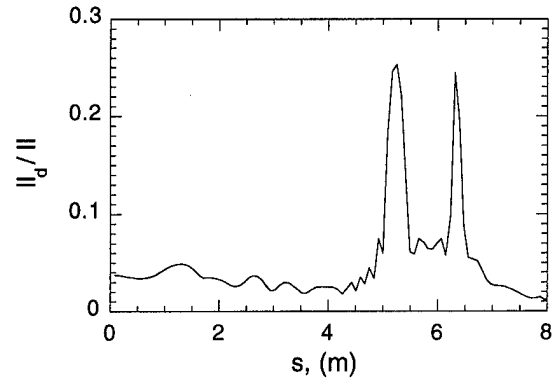

Figure 3: Absolute value of the ratio of the decoherence length and the train length as a function of position in a half of the ALS period.

Table 1: Inverse growth rate of the instability

I, A	n_b	Γ^{-1}, ms
0.2	240	0.40
0.1	240	0.83
0.2	150	0.34
0.2	320	0.42

The results of the calculations for several different regimes are given in Table 1. The growth times predicted by Eq. (18) turns out to be orders of magnitude larger than predicted by the theory that assumes a constant ion frequency in the ring. The growth rate for a given total current is almost independent of the train length, in accordance with the scaling law (20).

4 REFERENCES

[1] T. O. Raubenheimer and F. Zimmermann. *Phys. Rev. E*, **52**, 5487, (1995).

[2] G. V. Stupakov, T. O. Raubenheimer, and F. Zimmermann. *Phys. Rev. E*, **52**, 5499, (1995).

[3] J. Byrd et al. Paper 3B.11, these proceedings; to be published in *Physical Review Letters*.

[4] G.V. Stupakov. *Proceedings of the International Workshop on Collective Effects and Impedance for B-Factories (CEIBA95)*, Tsukuba 12-17 June, 1995, KEK Proceedings 96-6, Aug. 1996, p. 243.

[5] Tables and Graphs of Electron-Interaction Cross Section from 10 eV To 100 GeV Derived from LLNL Evaluated Electron Data Library (EEDL), Z=1-100. DE92-007986, Lawrence Livermore National Laboratory, 1991.

NONLINEAR DYNAMICS OF SINGLE BUNCH INSTABILITY

G. V. Stupakov
Stanford Linear Accelerator Center, Stanford University, P.O. Box 4349, Stanford, CA 94309 USA,
B.N. Breizman and M.S. Pekker
Institute for Fusion Studies, The University of Texas, Austin TX, 78712, USA

Abstract

A nonlinear equation is derived that governs the evolution of the amplitude of unstable oscillations with account of quantum diffusion effects due to the synchrotron radiation. Numerical solutions to this equation predict a variety of possible scenarios of nonlinear evolution of the instability some of which are in good qualitative agreement with experimental observations.

1 INTRODUCTION

Microwave single bunch instability in circular accelerators has been observed in many machines. The instability usually arises when the number of particles in the bunch exceeds some critical value, N_c, which varies depending on the parameters of the accelerating regime.

Recent observations on the SLC damping rings at SLAC [1] with a new low-impedance vacuum chamber revealed new interesting features of the instability. In some cases, after initial exponential growth, the instability eventually saturated at a level that remained constant through the accumulation cycle. In other regimes, relaxation-type oscillations were measured in nonlinear phase of the instability. In many cases, the instability was characterized by a frequency close to the second harmonic of the synchrotron oscillations.

Several attempts have been made to address the nonlinear stage of the instability [2, 3, 4] based on either computer simulations or some specific assumptions regarding the structure of the unstable mode. An attempt of a more general consideration of the problem is carried out in this paper. We adopt an approach recently developed in plasma physics for analysis of nonlinear behavior of weakly unstable modes in dynamic systems [5]. Assuming that the growth rate of the instability is much smaller than its frequency, we find a time dependent solution to Vlasov equation and derive an equation for the complex amplitude of the oscillations valid in the nonlinear regime. Numerical solutions to this equation predict a variety of possible scenarios of nonlinear evolution of the instability some of which are in good qualitative agreement with experimental observations.

2 BASIC EQUATIONS

We start from the equations of motion in longitudinal direction (see, e.g., Ref. [6]):

$$\dot{z} = -c\eta\delta, \quad \dot{\delta} = K(z,t), \tag{1}$$

where z is the longitudinal coordinate, δ is the relative energy deviation, η is the slip factor, the dot indicates differentiation with respect to time t, and

$$K(z,t) = \frac{\omega_{s0}^2}{\eta c} z - \frac{r_e}{T_0\gamma} \int_z^\infty dz' n(z',t)\, w(z'-z). \tag{2}$$

In Eq. (2), ω_{s0} denotes the unperturbed synchrotron frequency, T_0 is the revolution period, r_e is the classical electron radius, γ is the relativistic factor, $n(z,t)$ is the longitudinal beam density, $\int_{-\infty}^{\infty} n(z,t)\, dz = N$, where N is the number of particles in the bunch, and $w(z)$ is the longitudinal wake function. The first term in Eq. (2) corresponds to the potential of the accelerating voltage, and the second term describes the wakefield generated by the bunch.

The distribution function $\psi(z,\delta,t)$ satisfies the Vlasov equation with a Fokker-Planck "collision" term on the right hand side,

$$\frac{\partial\psi}{\partial t} + \{H,\psi\} = R, \tag{3}$$

where we have the Poisson brackets on the left hand side, H is the Hamiltonian corresponding to the equations of motion Eq. (1), and R describes the effect of the synchrotron radiation,

$$R = \frac{\partial}{\partial\delta}\left(\gamma_D\psi\delta + \kappa\frac{\partial\psi}{\partial\delta}\right). \tag{4}$$

In Eq. (4), γ_D is the damping time for the amplitude of the synchrotron oscillations, and κ is the diffusion coefficient associated with the quantum nature of the radiation. In the equilibrium state, the distribution function ψ is given by Haissinski solution,

$$\psi(z,\delta) = \text{const} \times \exp\left(-H_0(z,-\delta)/c\eta\sigma_E^2\right), \tag{5}$$

where $\sigma_E = \sqrt{\kappa/\gamma_D}$ is the rms energy spread of the beam in the absence of the wake, and H_0 is the equilibrium Hamiltonian.

It is convenient to introduce dimensionless variables, $x = z/\sigma_z$, $p = -\delta/\sigma_E$, $\tau = t\omega_{s0}$, and $F = \sigma_z\psi$, where σ_z is the rms length of the beam without wake, $\sigma_z = \sigma_E|\eta|c/\omega_{s0}$. In these variables, the Hamiltonian H takes the form

$$H(x,p,\tau) = \frac{1}{2}p^2 + U(x,\tau), \tag{6}$$

where the "potential energy" U is

$$U = \frac{1}{2}x^2 - I\int_x^\infty dx' S(x'-x) \int_{-\infty}^{\infty} dp F(x',p,\tau), \tag{7}$$

0-7803-4376-X/98/$10.00 © 1998 IEEE

with

$$I = \frac{Nr_e}{T_0 \gamma \omega_{s0} \sigma_z \sigma_E}, \tag{8}$$

and $S(x) = \int_0^{x\sigma_s} dz w(z)$. Note that the function S is a dimensionless function of its argument.

Let us perform a canonical transform from x and p to action and angle variables J and θ, of the equilibrium Hamiltonian H_0, and denote by $\tilde{V}$ the deviation of the potential energy from the equilibrium, $\tilde{V} = U - U_0$. Since H_0 depends on J only, the total Hamiltonian $H(\theta, J, t)$ takes the form

$$H(\theta, J, \tau) = H_0(J) + \tilde{V}(\theta, J, \tau). \tag{9}$$

The Vlasov equation for F in terms of action-angle variables is

$$\frac{\partial F}{\partial \tau} + \omega_s \frac{\partial F}{\partial \theta} + \frac{\partial \tilde{V}}{\partial J}\frac{\partial F}{\partial \theta} - \frac{\partial \tilde{V}}{\partial \theta}\frac{\partial F}{\partial J} = R, \tag{10}$$

where $\omega_s = \omega_s(J)$ is the frequency of synchrotron oscillations with the wake taken into account, $\omega_s(J) = dH_0/dJ$.

3 LINEAR THEORY

Suppose that $F_0(J)$ is the equilibrium distribution function, and $\delta F(J, \theta, \tau) = F - F_0(J)$ is its deviation from the equilibrium. In linear theory, $\delta F = f_1(J, \theta) e^{-i\omega\tau} + \text{c.c.}$, where the notation " c.c." denotes a complex conjugate to the first term. The perturbation of the potential $\tilde{V}$ is $\tilde{V} = V_\omega e^{-i\omega\tau} + \text{c.c.}$. Since V_ω is a periodic function of θ, we can expand it in Fourier series, $V_\omega = \sum_{n=-\infty}^{\infty} v_n(J) e^{in\theta}$. For simplicity, we will neglect here the effect of the synchrotron damping in the linear theory by dropping the R-term in Eq. (10). This greatly simplifies the linear analysis and is usually assumed in the literature. However, it can be shown that the effect of the synchrotron damping is crucial for the nonlinear stage of the instability and will later be included in the derivation of the nonlinear equations.

Substituting the expressions for δF and $\tilde{V}$ into Eq. (10) gives in linear approximation

$$-i\omega f_1 + \omega_s \frac{\partial f_1}{\partial \theta} = F_0' \sum_{n=-\infty}^{\infty} inv_n(J) e^{in\theta}, \tag{11}$$

where $F_0' = \partial F_0/\partial J$. A solution to Eq. (11) is

$$f_1 = -F_0' \sum_{n=-\infty}^{\infty} \frac{nv_n(J)}{\omega - n\omega_s} e^{in\theta}. \tag{12}$$

Now, linearizing Eq. (7) and substituting Eq. (12) into it yields an infinite set of integral equations that determines eigenfrequencies and eigenfunctions for the collective oscillations of the bunch:

$$v_n(J) = I \sum_m m \int_0^\infty dJ_1 K_{nm}(J, J_1) \frac{F_0'(J_1) v_m(J_1)}{\omega - m\omega_s(J_1)}, \tag{13}$$

with the kernel given by

$$K_{nm} = \frac{1}{2\pi} \int_0^{2\pi}\int_0^{2\pi} d\theta d\theta_1 e^{i(m\theta_1 - n\theta)} K(J, \theta, J_1, \theta_1), \tag{14}$$

and $K(J, J_1, \theta, \theta_1) = S(x(J, \theta) - x(J_1, \theta_1))$. The integral on the right hand side of Eq. (13) defines an analytical function in the upper half plane of the complex variable ω; for $\text{Im}\omega \leq 0$ the integral must be analytically continued into the lower half plane.

4 NONLINEAR THEORY

Let us assume that the instability has a threshold corresponding to a critical value of the parameter $I = I_c$ with the frequency at the threshold $\omega = \omega_c$ ($\text{Im}\omega_c = 0$). We will be interested in the analysis of the nonlinear phase of the instability in the vicinity of the threshold when the growth rate of the instability, Γ, is much smaller than ω_c, $\Gamma \ll \omega_c$. It turns out that in this case one can separate a "slow" time scale on which the amplitude evolves from "fast" oscillations with the frequency ω_c and derive nonlinear equations for the evolution of the amplitude of the instability by averaging over ω_c [7].

First, we rewrite the result of the previous section in a concise form,

$$\hat{L}(\omega, I) V_\omega = 0, \tag{15}$$

where the linear operator $\hat{L}$ represents a set of integral equations (13). A particular form of the operator $\hat{L}$ is not essential for the analysis. The frequency of the oscillations ω_c at the threshold and the corresponding eigenfunction $V_{\omega_c} \equiv u_c$ are determined by the equation

$$\hat{L}(\omega_c, I_c) u_c = 0. \tag{16}$$

We now consider a situation when I slightly exceeds the threshold, $I = I_c + \Delta I$, with $\Delta I \ll I_c$, and denote the difference $\omega - \omega_c = \Omega + i\Gamma$ (ω is now the frequency of the unstable mode above the threshold), where Γ is the growth rate, and Ω is the coherent frequency shift. Following a general prescription of nonlinear theory of oscillations [8], we will assume the following type of solution (in time representation) for $\tilde{V}$,

$$\tilde{V} = \left[A(\tau) u_c e^{-i\omega_c\tau} + \text{c.c.}\right] + \Delta V(J, \theta, \tau), \tag{17}$$

where $|Au_c| \gg |\Delta V|$. The first term in Eq. (17) describes oscillations with the eigenfunction u_c, frequency ω_c and varying amplitude $A(\tau)$, and the second term is a correction due to the deviation of the exact eigenfunction from u_c. It is important to emphasize here that $A(\tau)$ is supposed to be a slow function of time, $|\partial \ln A/\partial\tau| \ll \omega_c$.

Solving the nonlinear Vlasov equation iteratively, after cumbersome calculations that we omit because of the lack of space (see details in Ref. [7]), one can obtain an equation for the complex amplitude A. This equation contains contributions from resonances characterized by different values of the action J_n, where $n\omega_s(J_n) = \omega_c$ with n being

and integer. In a typical situation, only one value of n contributes to the result due to a small synchrotron frequency spread within the bunch. Introducing scaled parameters: amplitude a, growth rate g, and time ξ according to equations $a = A\sqrt{\rho}/B_n^{5/6}e^{i\Omega\tau}$, $g = \Gamma/B_n^{1/3}$, $\xi = B_n^{1/3}\tau$, where $B_n = n^2\left(\omega_s'\right)^2 D\left(J_n\right)$, and ρ and ϕ are the absolute value and the phase of a matrix element of the kernel (see [7] for details) the equation for the amplitude takes the form

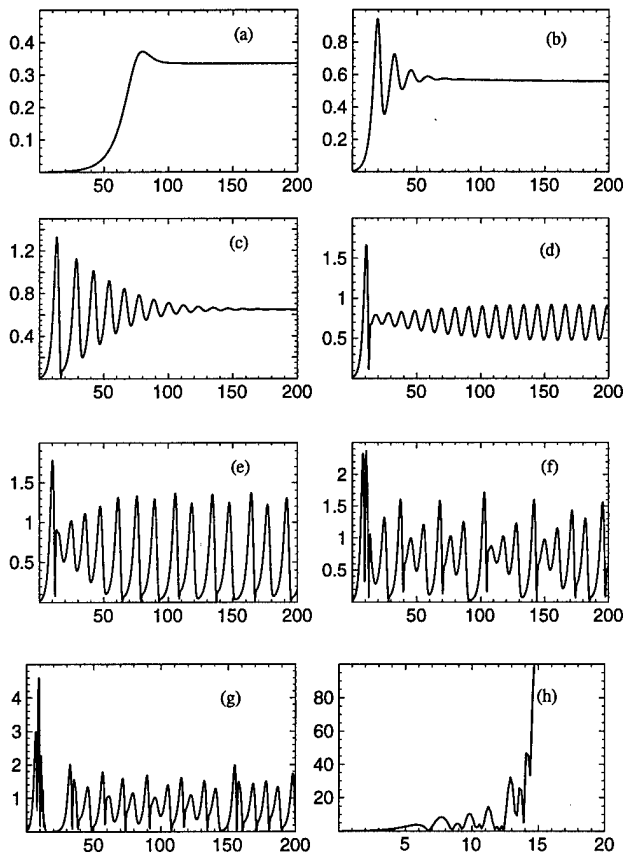

Figure 1: Plots of the absolute value of the amplitude, $|a|$, versus time ξ for $\phi = 0$. (a) – $g = 0.1$, (b) – $g = 0.3$, (c) – $g = 0.4$, (d) – $g = 0.48$, (e) – $g = 0.5$, (f) – $g = 0.6$, (g) – $g = 0.7$, (h) – $g = 0.8$.

$$\frac{\partial a}{\partial \xi} - ga = -e^{i\phi}\int_0^{\xi/2} d\zeta a\left(\xi-\zeta\right)\zeta^2$$

$$\times \int_0^{\xi-2\zeta} d\sigma a\left(\xi-\zeta-\sigma\right)a^*\left(\xi-2\zeta-\sigma\right)e^{-\zeta^2\left(\sigma+\frac{2}{3}\zeta\right)}. \quad (18)$$

The parameter g here plays a role of dimensionless growth rate of the instability that is measured in time units related to the synchrotron damping rate. Note that Eq. (18) contains only two real parameters, g and ϕ.

5 ANALYSIS

Equation (18) admits an asymptotic solution in the form of $a = \text{const} \times \exp\left(i\lambda\xi\right)$ that corresponds to oscillations with a constant amplitude and a coherent frequency shift λ. This solution is valid in the limit $\xi \to \infty$ and exists only if $|\phi| < \pi/2$. It is given by the following formula that can be easily verified by direct substitution, $a = 18^{1/6}g^{1/2}\left(\Gamma\left(\frac{1}{3}\right)\cos\phi\right)^{-1/2}e^{-i\xi\tan\phi}$, where $\Gamma\left(\frac{1}{3}\right)$ stands for the gamma function. According to this solution, the steady state amplitude $|a|$ increases in proportion to the square root of the dimensionless growth rate, $g^{1/2}$. It turns out however, that this solution is only stable for relatively small values of the parameter g.

We have solved Eq. (18) numerically for several sets of g and ϕ. The results for $\phi = 0$ are presented in Fig. 1.

Even visual comparison of the instability signal from Ref. [1] shows a clear resemblance to some of our curves. In one case (Fig. 5 of Ref. [1]), after injection in the ring, the amplitude of signal from spectrum analyzer tuned to a sideband frequency began to grow monotonically and after some time of the order of synchrotron damping time saturated at approximately constant level. This situation is very similar to our Fig. 1a. In another case (Fig. 4 of Ref. [1]), oscillations with decreasing amplitude were observed, which can be identified with Fig. 1b or 1c. In later measurements [9], amplitude oscillations with approximately constant modulation were measured. This situation reminds our Fig. 1e.

Further work is planned to make a more definite comparison of the theory with the experiment.

6 ACKNOWLEDGMENTS

This work was supported by the Department of Energy contracts DE-AC03-76SF00515 and DE-FG03-96ER-54346.

7 REFERENCES

[1] K. Bane et al., *Proceedings of the 1995 Particle Accelerator Conference on High-Energy Accelerators*, **5**, 3109 (1996).

[2] R. Baartman and M. D'yachkov, *Proceedings of the 1995 Particle Accelerator Conference on High-Energy Accelerators*, **5**, 3119 (1996).

[3] K.L.F. Bane and K. Oide, *Proceedings of the 1995 Particle Accelerator Conference on High-Energy Accelerators*, **5**, 3105 (1996).

[4] S.A. Heifets, Phys. Rev. E, **54**, 2889 (1996).

[5] H.L. Berk, B.N. Breizman and M. Pekker, Phys. Rev. Lett., **76**, 1256 (1996).

[6] A. W. Chao. *Physics of Collective Beam Instabilities in High Energy Accelerators* (Wiley, New York, 1993).

[7] G. V. Stupakov, B.N. Breizman and M.S. Pekker. Phys. Rev. E, **55**, No. 5, (1997).

[8] A.A. Galeev and R.Z. Sagdeev. *Reviews of Plasma Physics*, edited by M.A. Leontovich (Consultants Bureau, New York, 1979), **7**, p.3.

[9] B. Podobedov and R. Siemann, private communication.

STABILIZATION OF THE SPECTRAL INTENSITY FLUCTUATIONS WITH THE HIGHER ORDER MODE FREQUENCY TUNERS

Ch. Wang, L.H. Chang, S.S. Chang, Y.I Chang, C.C. Kuo, C.Y. Lai,
W.K. Lau, M.C. Lin, S.J. Lin, G.H. Luo, T.T. Yang
Synchrotron Radiation Research Center, Hsinchu 300, Taiwan

Abstract

A strong excitation of the longitudinal coupled-bunch instabilities, which is suspected to be driven by the TM_{011}-like mode of the DORIS-I cavities, was observed at the higher electron beam current in the storage ring of SRRC. Such instability leaded to heavy fluctuations of the photon beam intensity in the horizontal plane and therefore restricted the maximal useful beam current for the user experiments. This restriction has been released by replacing the damping antennae with the additional tuners. Here, we report our experiences after one-year routine operations of the main RF cavities with the second tuners at SRRC.

1 INTRODUCTION

After the SRRC storage ring was successful commissioning in 1993, a strong longitudinal coupled-bunch oscillation was observed from time to time. It started usually with the beam current of about 180 mA and disappeared when the current decayed. This strong beam-cavity interaction resulted in a blow up of the transverse beam size and leaded to heavy fluctuations of the spectral intensity. This restricted the maximal useful beam current. The TM_{011}-like mode of the DORIS-I cavity was suspected to be the driving source. In the spring shutdown of 1996, the damping antennae were replaced by the additional plunger tuners, i.e., the second tuners, to de-tune the exciting longitudinal cavity mode far away from the synchrotron oscillation sideband. After this re-arrangement, the strong beam-cavity interaction is successfully prevented and now the storage ring is routinely operated with the beam current up to 240 mA with spectral intensity fluctuation less than 0.5%. Here, we report our experience after one-year routine operation of the main RF cavities with the second tuners at SRRC.

2 HIGHER ORDER MODE FREQUENCY TUNER

Two DORIS-I cavities were installed in the storage ring of SRRC as main RF cavities to supply the beam energy loss due to the synchrotron radiation, etc. Each cavity has three main-ports: The first one was mounted with a plunger tuner to compensate for the drift of the fundamental mode frequency due to the fluctuations of the cavity cooling water temperature as well as the beam loading. The second port has been connected to the coaxial coupler for the input of the RF power from the klystron. The third port was originally equipped with a DESY-type damping antenna[1] to reduce the driving impedance of the cavity higher order modes by degradation of those quality factors.

With damping antenna, the ohmic quality factor of the TM_{011}-like mode can be dramatically reduced from 26000 to 2300. However, this might be still not lower enough to avoid excitation of strong longitudinal coupled-bunch oscillation at higher beam current.

As mentioned before, such exciting interaction resulted in a brow up of the transverse beam size, and leaded to heavy fluctuations of the photon beam intensity.

Therefore, the maximal useful stored beam current was restricted. Moreover, the damped cavity higher order modes have a wide resonance band, which enhances the interaction probability.

It is practically difficult to de-tune such resonance only by the adjustment of the cavity cooling water temperature. It has been shown that the TM_{011}-like mode can be de-tuned by the second tuner far away from the synchrotron side-band effectively, and the instability may then be avoided. Without damping antenna, the resonance band of the cavity higher order modes become narrow, and its resonance frequency can be easily manipulated by the variation of the cavity cooling water temperature. A combination of these two approaches enforces the possibility to avoid the instability driven by the cavity TM_{011}-like mode, and the temperature regulation capability of the cooling system can be relaxed. The resonance frequency of the TM_{011}-like mode of the DORIS-I cavity as a function of the second tuner position as well as the cavity cooling water temperature is shown in Fig. 1.

The replacement of the damping antennae by the second tuners was performed in the spring of 1996, following a half-year cold test on the DORIS-I cavity with two plunger tuners for the understanding of its effects on the higher-order modes. In our application, the second tuner works like a manipulator of the cavity higher-order mode (HOM) resonance frequencies. It is therefore named as HOM frequency tuner at SRRC. The first tuner was properly re-positioned such that the resonance frequency of the cavity fundamental mode to be of 499.666 MHz, the accelerating frequency of the SRRC storage ring.

If the electron beam is stored with a uniform filling pattern (and without any empty bucket) in the storage ring, the harmonics of the accelerating frequency (499.666 MHz for SRRC) will be the only spectral lines observable from the beam spectrum, providing that there is not any exciting instability. Obviously, this can be used to identify the existence of the coupled-bunch oscillations.

A beam spectrum of a quasi-uniform filling pattern (and no empty bucket) is shown in Fig. 2. In the meantime, the second tuners were adjusted to the so-called optimal

0-7803-4376-X/98/$10.00 © 1998 IEEE

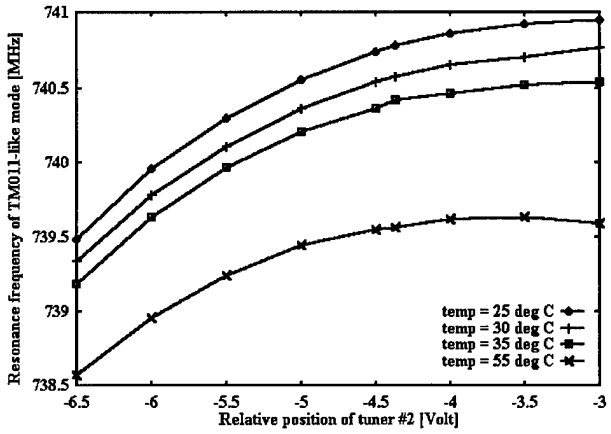

Figure 1: Resonance frequency of the TM_{011}-like mode of the DORIS-I cavity as a function of the second tuner position (measured in unit of volt) as well as the cavity cooling water temperature. The first tuner was properly repositioned such that the resonance frequency of the cavity fundamental mode was kept to be of 499.666 MHz, which was the accelerating frequency of the SRRC storage ring.

positions in both cavities with which the photon intensity fluctuations was minimal and less than 0.5%.

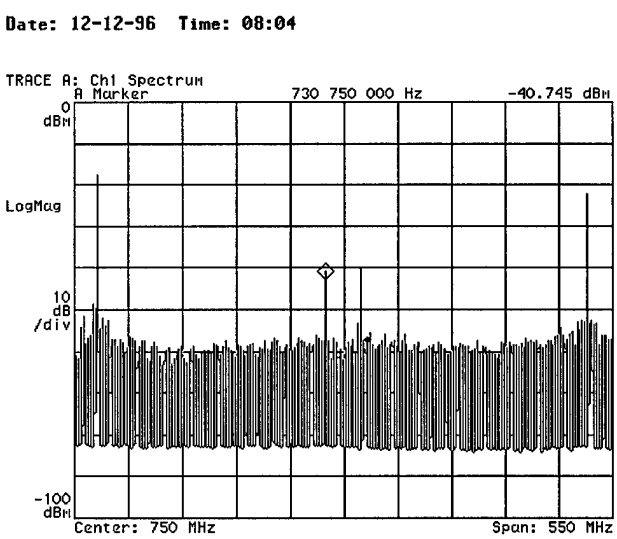

Figure 2: Beam spectrum for a quasi-uniform filling pattern. The second tuner is adjusted to an optimal position such that the spectral intensity fluctuations to be minimal.

The spectral lines had a frequency of 732.01MHz-28.750kHz (n=93) and its alias of 766.98625 MHz + 28.750 kHz (n=107), which were insensitive to the movement of the second tuner. The normalized oscillation amplitude was of about -20 dB or corresponding to 0.2^o phase jitters, which seemed to be driven by the cavity TM110-like mode (767-768MHz).

It has been verified to be insensitive to the tuner movement in our cold test.

3 OBSERVATION

In the operation of the cavity with the second tuner, this strong beam-cavity interaction can even be excited at lower beam current by tuning the resonance frequency of the driving mode closer to the synchrotron side-band.

This provides us a convenient and reproducible way to understand the instability mechanism in the linear and nonlinear regime by exciting the beam-cavity interaction with mechanically adjustable coupling strength/exciting level.

As shown in Fig. 3, the oscillation amplitude (in dB) for the synchrotron upper dipole mode of $n = 97$ (742.0035 MHz) is strongly dependent on the second tuner position (the tuner position is measured in Volt, and one volt drop is about 1 cm tuner movement).

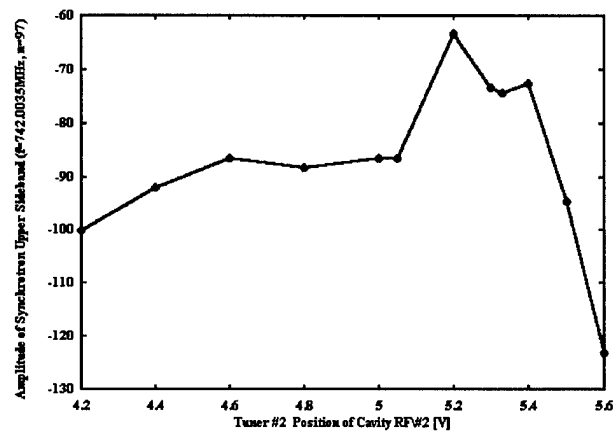

Figure 3: Oscillation amplitude (in dB) of the synchrotron upper dipole mode of $n = 97$ (742.0035 MHz) as a function of the second tuner position of cavity RF #1.

A strong beam-cavity interaction can be identified as the second tuner of the RF#1 cavity to be tuned close to the position of 5.2-5.4 Volt.

The corresponding beam spectrum is shown in Fig. 4 and 5. Obviously, the synchrotron tune spread is broadened, as shown in Fig. 5.

As shown in Fig. 6, the oscillation amplitude was quasi-periodically varied in the time domain, while its growth-rate remains almost the same.

From Fig. 6, the deduced growth rate was of about 0.35 msec, which is close to the theoretical value of 0.4 msec for the TM011-like mode[2].

4 DISCUSSION

In the operation of the SRRC main RF cavities with the second tuners, the strong beam-cavity interaction likely driving by the cavity TM_{011}-like mode was successfully prevented and the photon intensity fluctuations less than 0.5% have been achieved.

Through it may be practically difficult to prevent all of the longitudinal coupled-bunch instabilities only by the operation of the cavity with the second tuner, the maximal

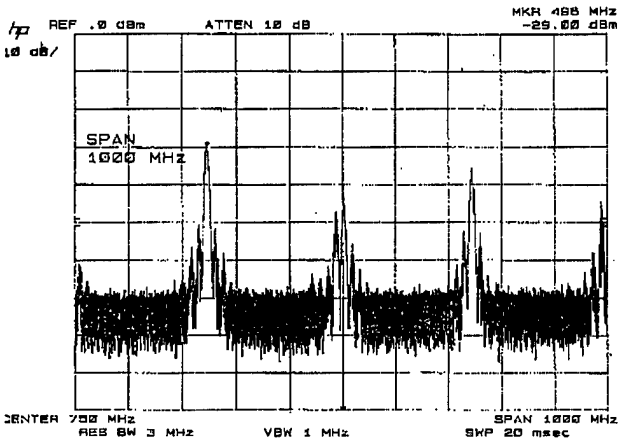

Figure 4: Beam spectrum when the second tuner of the cavity RF#1 was located close to the on-resonance position (tuner #2 position is 5.3 Volt).

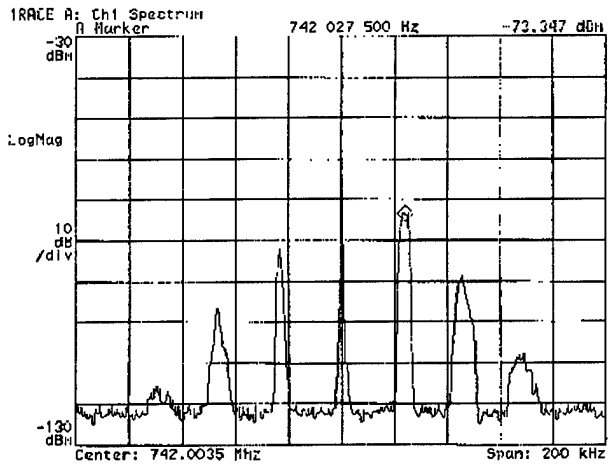

Figure 5: Zoom-in spectrum of Fig. 4.

coupling impedance of the storage ring can be effectively reduced by the optimization of the second tuners position.

Therefore, it will help to decrease the required operating gain of the wide-band high-power driver amplifier for the broad-band longitudinal feedback system. Moreover, such adjustable mechanism provides extra freedom for systematic study of the phenomena of the coupled-bunch instabilities. However, the possible damage of the second tuner due to the cavity HOM heating may be a critical issue and will be numerically studied in more detail in the future.

5 ACKNOWLEDGEMENTS

We benefits the discussions with Dr. E. Weihreter (BESSY II). This work was supported by the National Science Council of Taiwan under contract No. of NSC 86-2613-M-213-003.

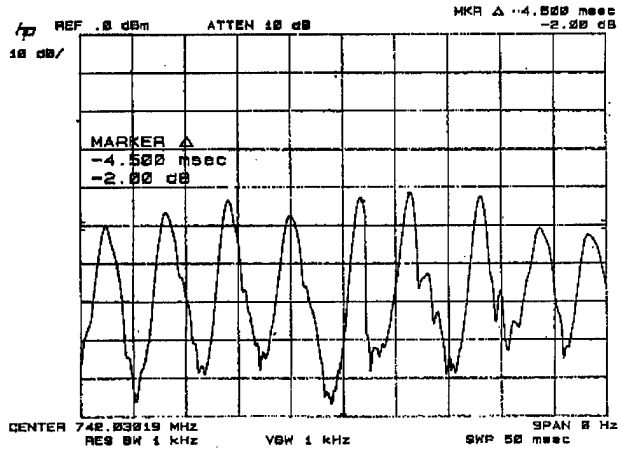

Figure 6: Quasi-periodical variation of the oscillation amplitude of the synchrotron upper dipole mode of $n = 97$ (742.03019 MHz) as a function of time.

6 REFERENCES

[1] N. Lehnart and H. Petersen, "Damping Antennae for Spurious RF-Modes in Electron-Positron Rings," Nucl. Instrum. & Mech. 153, pg. 51-52, 1978.

[2] J.M. Wang, "Symmetrical Coupled Bunch Modes in SRRC Storage Ring", SRRC technical note, 1992.

SHIELDED TRANSIENT SELF-INTERACTION OF A BUNCH ENTERING A CIRCLE FROM A STRAIGHT PATH

R. Li, C. L. Bohn, and J. J. Bisognano
Thomas Jefferson National Accelerator Facility, 12000 Jefferson Ave., Newport News, VA 23606

Abstract

When a short (mm-length) bunch with high (nC-regime) charge is transported through a magnetic bending system, self-interaction via coherent synchrotron radiation (CSR) and space charge may alter the bunch dynamics significantly. We consider a Gaussian rigid-line-charge bunch following a straight-path trajectory into a circle, with the trajectory centered between two infinite, parallel, perfectly conducting plates. Transients associated with CSR and space charge generated from source particles both on the straight path and the circle are calculated, and their net effect on the radiated power is contrasted with that of shielded steady-state CSR.

1 INTRODUCTION

When short (mm-length), high-charge (nC-regime) bunches are injected into magnetic bending systems, coherent synchrotron radiation (CSR) and space charge may cause serious degradation of beam quality. This possibility is a serious concern for various transport-lattice designs associated with, for example, free-electron lasers (FELs), including bunch-compressor chicanes preceding wigglers and recirculation loops associated with energy recovery. Almost all previous theoretical work on CSR has concerned its steady-state properties. Examples concerning steady-state CSR in free space include the frequency-domain [1] and time-domain analyses [2]. Examples concerning steady-state CSR with shielding, i.e., in the presence of conducting walls, also include frequency-domain [3, 4, 5] and time-domain [6] analyses. Only recently have transients in finite-length magnetic bends begun to be considered, the principal example being a time-domain analysis [7], concerning the transient interaction of a bunch with itself as it passes from a straight path into a circle in free space. These investigators showed that both space-charge forces originating from the straight path and CSR forces originating from the circle make important contributions to the transient self-interaction.

In this paper, we generalize the theory of transient self-interaction in a magnetic bend by incorporating conducting walls to introduce shielding of CSR. Working in the time domain, we consider an electron bunch with a rigid-line-charge Gaussian distribution orbiting in the center plane between two infinite, parallel conducting plates. The bunch moves from a straight path to a circular orbit and begins radiating. Transient forces arising from source particles on the straight path (space charge) and on the circle (space charge and CSR) are calculated, and their net effect is obtained. Parallel plates are incorporated by including forces originating from image charges.

2 ANALYSIS

The Hamiltonian for an electron with charge e is:

$$H = c\sqrt{(\mathbf{P} - e\mathbf{A}/c)^2 + m^2c^2} + e\Phi, \qquad (1)$$

where $\mathbf{P} - e\mathbf{A}/c = \gamma m\mathbf{v}$ is the kinetic momentum for the electron, in which $\mathbf{v}$ is its velocity, γ is the Lorentz factor; Φ and $\mathbf{A}$ are the scalar and vector electromagnetic potential on the electron, respectively, arising from the interaction of an external field and the rest of the charge distribution. Given a rigid-line-charge bunch entering a circle from a straight path, the rate of change of the kinetic energy for an "observer" electron S located on the bunch at the space-time coordinate $(\mathbf{r}, t)$ can be derived from the above Hamiltonian in terms of the potentials Φ_0 and $\mathbf{A}_0$ on S generated by a single "source" electron S':

$$\begin{aligned} mc^2\frac{d\gamma}{dt} &= \beta c F_\theta, \quad F_\theta = \int_{-\infty}^{\infty} ds' F_{\theta 0}(\mathbf{r}, t, s')\, n(s'), \\ F_{\theta 0}(\mathbf{r}, t, s') &= \frac{e}{\beta c}\left[-\frac{d\Phi_0}{dt} + \frac{\partial}{\partial t}(\Phi_0 - \boldsymbol{\beta}\cdot\mathbf{A}_0)\right], \\ (\Phi_0, \mathbf{A}_0) &= e\left[\frac{(1, \boldsymbol{\beta})}{(1 - \boldsymbol{\beta}\cdot\mathbf{n})R}\right]_{\text{ret}}, \end{aligned} \qquad (2)$$

where $F_{\theta 0}$ is the longitudinal electric force exerted by S' on S; $n(s')$ is the line-density of the bunch, with s' denoting the distance of electron S' from the bunch center in the bunch rest frame. The subscript "ret" in the single-electron potentials incorporates the retardation relation for a photon emitted by S' at $(\mathbf{r}', t')$ to reach S at $(\mathbf{r}, t)$: $c(t - t') = |\mathbf{R}|$, with $\mathbf{R} \equiv \mathbf{r}(t) - \mathbf{r}'(t')$. In addition, we have in Eq. (2) $\mathbf{n} = \mathbf{R}/|\mathbf{R}|$ and $\boldsymbol{\beta}_{\text{ret}} = \mathbf{v}_{\text{ret}}/c$. The force exerted on single particle by the whole bunch calculated by way of Eq. (2) forms the basis of our analysis. In what follows, we shall use the indices "(a)" and "(b)" to denote the case that at retarded times t' the source particle S' is located on the straight path and on the circle, respectively. To take into account of the interaction on S from image charges due to the presence of the parallel plates, the source particle S' is allowed to have an offset z' perpendicular to the plane of the orbit. This will correspondingly affect the retardation times associated with image charges.

2.1 *Case (a): S' on straight path at t', S on circle at t*

Fig. 1 depicts an observer electron S at angle θ on the circle of radius ρ at time t experiencing a force generated from a source electron S' (which, in Fig. 1, is an image charge) at coordinate $\mathbf{r}' = (-x', 0, z')$ at time t' ($x' \geq 0$). With $t = 0$

0-7803-4376-X/98/$10.00 © 1998 IEEE

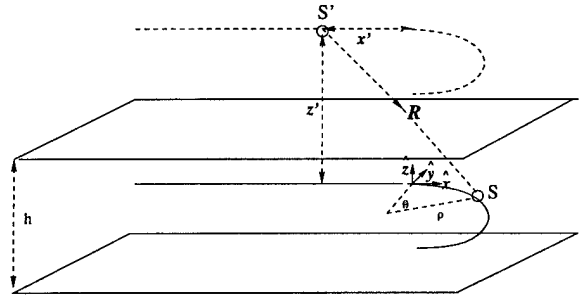

Figure 1: Interaction of S' on S, with S' on the straight path prior to the bend at the retarded time, and S on the circular orbit.

being the moment when the bunch center enters the circle, the trajectories of S and S' are respectively described by

$$S : \rho\theta = s + \beta ct, \qquad S' : -x' = s' + \beta ct'. \tag{3}$$

In the coordinate system $(\hat{\mathbf{x}}, \hat{\mathbf{y}}, \hat{\mathbf{z}})$, depicted in Fig. 1, the vector $\mathbf{R}$ from S' to S is $(R_x, R_y, R_z) = (\rho\sin\theta + x', \rho\cos\theta - \rho, z')$. According to Eq. (2), the longitudinal electric force exerted by S' on S can be obtained from

$$\begin{aligned}
&F_{\theta 0}^{(a)} = -e\partial V^{(a)}/\partial\Delta s, \;\; V^{(a)} = V_0^{(a)} + (\Phi_0 - \boldsymbol{\beta}\cdot\mathbf{A}_0)^{(a)},\\
&V_0^{(a)} = \mathcal{V}_0^{(a)}(\theta,\infty) - \mathcal{V}_0^{(a)}(\theta,\Delta s),\\
&\mathcal{V}_0^{(a)}(\theta,\Delta s) = e[(1-\cos\theta) - R_y R_x' \sin\theta/R_\perp^2]/R_1,\\
&(\Phi_0 - \boldsymbol{\beta}\cdot\mathbf{A}_0)^{(a)} = e(1-\beta^2\cos\theta)/R_1.
\end{aligned} \tag{4}$$

with $\partial V_0^{(a)}/\partial\Delta s = d\Phi_0^{(a)}/\beta c\,dt$. Here $R_1^2 = R_x'^2 + R_\perp^2/\gamma^2$, $R_\perp^2 = R_y^2 + R_z^2$, and $R_x' \equiv R_x - \beta R = \rho(\Delta\phi + \sin\theta - \theta)$ is the distance from S_p' to S projected on the $\hat{\mathbf{x}}$-direction, with S_p' denoting the position of S' at time t were it to continue executing uniform linear motion at all retarded times $t' \le t$. We are letting $\Delta s \equiv s - s'$ denote the distance between S' and S in the rest frame of the bunch, and we define $\Delta\phi = \Delta s/\rho$. We will show that when $R_x' = 0$, the straight path introduces transient space-charge forces on the bunch comparable to transient CSR forces from the circle.

2.2 *Case (b): S' on circle at t', S on circle at t*

The motions of S and S' are now described by

$$S : \rho\theta = s + \beta ct, \qquad S' : \rho\theta' = s' + \beta ct'. \tag{5}$$

Causality requires $\Delta\theta = \theta - \theta'$ to depend on $\Delta\phi = (s - s')/\rho$, the relative spacing of the two particles in the bunch rest frame, in the manner

$$\rho\Delta\theta = \rho\Delta\phi + \beta R, \qquad R = \sqrt{[2\rho\sin(\Delta\theta/2)]^2 + z'^2}. \tag{6}$$

Here only the forward radiation is considered in that $\Delta\theta \ge 0$. In free space, for which $z' \equiv 0$, the causality condition is $\Delta\theta = 4\mathrm{sh}[(1/3)\mathrm{sh}^{-1}(3\gamma^3\Delta\phi/2)]/\gamma$. For image charges, with $z' \ne 0$, $\sigma_s \ll h/\rho$, and $\Delta\theta \gg \gamma^{-1}$, one can approximate Eq. (6) by $\Delta\theta^4 - (24\Delta\phi)\Delta\theta - 12(z'/\rho)^2 = 0$, which has the solution

$$\Delta\theta = \frac{\Delta\theta_0}{3^{1/4}}\left[\sqrt{\sqrt{\frac{\mathrm{sh}\eta}{\mathrm{sh}(\eta/3)}} - \mathrm{sh}\frac{\eta}{3}} + \frac{\Delta\phi}{|\Delta\phi|}\sqrt{\mathrm{sh}\frac{\eta}{3}}\right], \tag{7}$$

where $\Delta\theta_0 \equiv (12)^{1/4}|z'/\rho|^{1/2}$ is the value of $\Delta\theta$ when $\Delta\phi = 0$, and $\eta \equiv \mathrm{sh}^{-1}[9\Delta\phi^2/2|z'/\rho|^3]$. Limiting cases include $\eta \ll 1$, for which $\Delta\theta \simeq \Delta\theta_0\left[1 + (3/4)^{1/4}\Delta\phi|z'/\rho|^{-3/2}\right]$, and $\eta \gg 1$, for which $\Delta\theta \simeq 2(3\Delta\phi)^{1/3}H(\Delta\phi)$, with $H(x)$ denoting the Heaviside step function.

It can be shown that $d\Phi_0^{(b)}/dt = 0$, and consequently

$$\begin{aligned}
&F_{\theta 0}^{(b)} = -e\partial V^{(b)}/\partial\Delta s, \qquad V^{(b)} = (\Phi_0 - \boldsymbol{\beta}\cdot\mathbf{A}_0)^{(b)},\\
&V^{(b)} = e\frac{\beta(1-\beta^2\cos\Delta\theta)}{\rho(\Delta\theta - \Delta\phi - \beta^2\sin\Delta\theta)},
\end{aligned} \tag{8}$$

where causality determines $\Delta\theta(\Delta\phi)$ per Eq. (6).

2.3 *Longitudinal Electric Force on S from Whole Bunch*

To remove the singularity due to the rigid-line-charge model when S and S' overlap, and to isolate the consequences of the circular motion of S, we now calculate the residual longitudinal electric force exerted by the whole bunch on S: $\hat{F}_\theta \equiv F_\theta - F_s$, where F_s is the integral of F_{s0} over the charge distribution, with $F_{s0} \equiv -e\partial V_s/\partial\Delta s$ being the space-charge force obtained when the bunch moves on a straight path with constant velocity $\mathbf{v}$, i.e., $V_s = e\gamma^{-2}(\Delta s^2 + z'^2/\gamma^2)^{-1/2}$. The corresponding residual potentials are $\hat{V}^{(a,b)} = V^{(a,b)} - V_s$.

To calculate $\hat{F}_\theta$, we let $\Delta s = \Delta s_t(\theta, z')$ when S' is at the entry to the circle $\theta' = x' = 0$, with $\Delta s_t(\theta, z') = \rho\theta - \beta\sqrt{[2\rho\sin(\theta/2)]^2 + z'^2}$. In applying Eq. (2), $F_{\theta 0}^{(a)}$ is used for $F_{\theta 0}$ if $\Delta s > \Delta s_t$ and $F_{\theta 0}^{(b)}$ is used if $\Delta s_0 < \Delta s \le \Delta s_t$, with $\Delta s_0(z') = -\beta|z'|$ designating the transition point between forward and backward radiation occurring at $\Delta\theta = 0$. Upon applying Eqs. (4) and (8) and integrating Eq. (2) by parts, noting that $\hat{V}^{(a)}(\theta,\infty) = \hat{V}^{(b)}(\Delta s_0) = 0$, we obtain the residual longitudinal electric force on S arising from the whole bunch:

$$\begin{aligned}
&\hat{F}_\theta(\theta, s, z') = F_0^{(a)} + F^{(a)} + F^{(b)};\\
&F_0^{(a)} = eV_0^{(a)}(\theta, \Delta s_t)n(s - \Delta s_t),\\
&F^{(a)} = e\int_{\Delta s_t(\theta,z')}^{\infty} d\Delta s\,\hat{V}^{(a)}(\theta, \Delta s, z')\frac{dn(s-\Delta s)}{d\Delta s},\\
&F^{(b)} = e\int_{\Delta s_0(z')}^{\Delta s_t(\theta,z')} d\Delta s\,\hat{V}^{(b)}(\Delta s, z')\frac{dn(s-\Delta s)}{d\Delta s},
\end{aligned} \tag{9}$$

where one has $V_0^{(a)}(\theta, \Delta s_t) = -e|R_y|/\rho(R + \rho\sin\theta)$ from Eq. (4). It turns out that $F_0^{(a)}$ is negligible compared to $F^{(a)}$ and $F^{(b)}$. Since the potentials are continuous at entry to the circle, $(\Phi_0 - \boldsymbol{\beta}\cdot\mathbf{A}_0)^{(a)}|_{\Delta s_t} = (\Phi_0 - \boldsymbol{\beta}\cdot\mathbf{A}_0)^{(b)}|_{\Delta s_t}$, a strong, energy-dependent, transient accelerating force arising from space charge generated on

the straight path cancels with a strong, energy-dependent, transient decelerating force arising from CSR on the circle.

From Eq. (4) one can show that in the high energy limit, $\hat{V}^{(a)}$ behaves like a step function which cuts off at $\Delta s = \Delta s_c = \rho(\theta - \sin\theta)$: $\hat{V}^{(a)} \simeq U^{(a)}(\theta, z')H(-R'_x)$, with $U^{(a)}(\theta, z') = 2e|R_y|\sin\theta/R_\perp^2$. This result can be traced to the impulse-like behavior of the single particle space-charge force $F_{\theta 0}^{(a)}$ in Eq. (4) on S from S' when $R'_x = 0$. For $\gamma\theta > 1$, the cutoff occurs on the straight path, $\Delta s_c > \Delta s_t$, leading to $F^{(a)} \simeq eU^{(a)}(\theta, z')[n(s - \Delta s_c) - n(s - \Delta s_t)]$, which is an energy-independent transient force with peak value comparable in magnitude with $F^{(b)}$.

It is now straightforward to incorporate two infinite parallel plates with spacing h, with the bunch moving on the plane centered between the plates, by considering the array of image charges that comove with the bunch in the planes $z' = \pm nh$. The total shielded longitudinal force $\hat{F}_\theta^{\rm sh}$ on the electron S from all the image bunches is thus obtained from the unshielded force $\hat{F}_\theta$ in Eq. (9),

$$\hat{F}_\theta^{\rm sh}(\theta_0, s) = \sum_{n=-\infty}^{\infty} (-)^n \hat{F}_\theta(\theta = \theta_0 + s/\rho, s, nh), \qquad (10)$$

in which $\theta_0 = \beta ct/\rho$ is the angular coordinate of the bunch center. Eq. (10) constitutes the starting point for calculating bend-induced energy spread, which in turn causes degradation in transverse emittance.

3 POWER LOSS

To look at the amplitudes and duration of the transients, we turn to a calculation of the shielded power loss $\hat{P}^{\rm sh}(\theta_0)$ of the bunch induced by its self-interaction. This is obtained by integrating the rate of kinetic energy loss of a single electron over the portion of the bunch on the circle:

$$\hat{P}^{\rm sh}(\theta_0) = \hat{P}(\theta_0, 0) + 2\sum_{n=1}^{\infty}(-)^n \hat{P}(\theta_0, nh),$$
$$\hat{P}(\theta_0, nh) = -\beta c \int_{-\theta_0}^{\infty} ds \hat{F}_\theta(\theta = \theta_0 + s/\rho, s, nh) n(s), \qquad (11)$$

where $\hat{P}(\theta_0, 0)$ is the power loss in free space, and $\hat{P}(\theta_0, nh)$ represents the bunch's power loss due to its interaction with the nth image bunch obtained from $\hat{F}_\theta$ given in Eq. (10). The integration spans $\theta \geq 0$, or $s \geq -\theta_0$. When the whole bunch is well into the bend, $\theta_0 \gg \sigma_s/\rho$, and the lower limit $-\theta_0$ effectively becomes $-\infty$. Denoting $\Delta s_t^{(n)}(\theta) = \Delta s_t(\theta_0, nh)$, we then have

$$\hat{P}(\theta_0, nh) \simeq \hat{P}_0^{(a)}(\theta_0, nh) + \hat{P}^{(a)}(\theta_0, nh) + \hat{P}^{(b)}(\theta_0, nh);$$
$$\hat{P}_0^{(a)}(\theta_0, nh) = -\beta c e V_0^{(a)}[\theta_0, \Delta s_t^{(n)}(\theta_0), nh] f[\Delta s_t^{(n)}(\theta_0)],$$
$$\hat{P}^{(a)}(\theta_0, nh) = -\beta c e U^{(a)}(\theta_0, nh)[f(\Delta s_c) - f(\Delta s_t^{(n)})]|_{\theta=\theta_0},$$
$$\hat{P}^{(b)}(\theta_0, nh) = -\beta c e \int_{\Delta s_0(nh)}^{\Delta s_t^{(n)}(\theta_0)} d\Delta s\, \hat{V}^{(b)}(\Delta s, nh) g(\Delta s). \qquad (12)$$

where

$$f(\Delta s) \equiv \int_{-\infty}^{\infty} n(s) n(s - \Delta s) ds, \;\; g(\Delta s) \equiv df(\Delta s)/d\Delta s, \qquad (13)$$

In steady-state cases one has $\hat{P}(\infty, nh) = \hat{P}^{(b)}(\infty, nh)$. In particular, one can show that the result of free-space power loss $\hat{P}(\infty, 0)$ agrees with that of Schiff [1].

The power loss obtained from Eq. (11) using numerical integration for Gaussian bunch distribution, $n(s) = e^{-s^2/2\sigma_s^2}/\sqrt{2\pi}\sigma_s$, is displayed in Fig. 2 for parameters $\rho = 1$ m and $\sigma_s = 1$ mm, typical values in the recirculating accelerator that will drive Jefferson Lab's infrared FEL (the IR Demo) [8]. The dotted curve is the transient power loss of the bunch in free space, $\hat{P}(\theta_0, 0)/\hat{P}(\infty, 0)$, which rises from zero loss and saturates to steady state. This free-space result agrees with that given in Ref.[7]. The other curves in Fig. 2 pertain to the presence of parallel conducting plates. The solid curve corresponds to $h = 5$ cm, a typical pipe size in the IR Demo. The spacing is relatively large to suppress beam loss, and it provides little shielding of the self-interaction. Stronger shielding can be obtained for narrower gap size with fixed bunch length, as indicated by the dashed curve corresponding to $h = 2$ cm. In this case the steady-state power loss is 25% of the free-space value, in agreement with results obtained by power-spectrum analysis as reflected in Fig. 2 of Ref. [9]. Many features of the transient power loss can be derived analytically and expressed in closed form, as we plan to show in a future, more comprehensive paper.

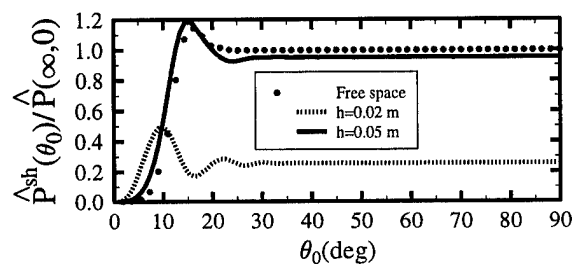

Figure 2: Transient power loss of a bunch, due to curvature-induced self-interaction in the presence of parallel plates, with $\rho = 1$ m, $\sigma_s = 1$ mm, $E = 40$MeV, and various plate spacings h. Here θ_0 is the angle of bunch center into the bend.

4 REFERENCES

[1] L. I. Schiff, Rev. Sci. Instr.17, 6-14, (1946).

[2] Ya. S. Derbenev, J. Rossbach, E. L. Saldin, and V. D. Shiltsev, DESY Report No. TESLA-FEL-95-05, 1995.

[3] J. S. Nodvick and D. S. Saxon, Phys. Rev., **96**, 180 (1954).

[4] R. L. Warnock and P. Morton, Part. Accel. **25**, 113 (1990).

[5] S. A. Kheifets and B. Zotter, CERN SL-95-92 (AP), 1995.

[6] B. Murphy, S. Krinsky, and R. L. Gluckstern, BNL-63090, (1996).

[7] E. L. Saldin, E. A. Schneidmiller, and M. V. Yurkov, DESY-TESLA-FEL-96-14, (1996).

[8] C. L. Bohn, these Proceedings.

[9] R. Li, C. L. Bohn, and J. J. Bisognano, these Proceedings.

ANALYSIS ON THE STEADY-STATE COHERENT SYNCHROTRON RADIATION WITH STRONG SHIELDING

R. Li, C. L. Bohn, and J. J. Bisognano
TJNAF, 12000 Jefferson Ave., Newport News, VA 23606

Abstract

There are several papers concerning shielding of coherent synchrotron radiation (CSR) emitted by a Gaussian line charge on a circular orbit centered between two parallel conducting plates. Previous asymptotic analyses in the frequency domain show that shielded steady-state CSR mainly arises from harmonics in the bunch frequency exceeding the threshold harmonic for satisfying the boundary conditions at the plates. In this paper we extend the frequency-domain analysis into the regime of strong shielding, in which the threshold harmonic exceeds the characteristic frequency of the bunch. The result is then compared to the shielded steady-state CSR power obtained using image charges.

1 INTRODUCTION

There have been several studies [1, 2, 3] concerning shielding of coherent synchrotron radiation (CSR) emitted by a Gaussian line charge on a circular orbit centered between two parallel conducting plates. Nodvick and Saxon [1] developed an exact expression for the power radiated by a bunch in steady state, written as a summation over all harmonics of the radiated power. Using the asymptotic behavior of the Bessel functions in these radiated-power harmonics, Kheifets and Zotter [2] recently developed a simple expression for the shielded CSR power as a function of beam and machine parameters. In an alternative derivation, Murphy, Krinsky, and Gluckstern [3] obtain the CSR power by including image charges from the parallel plates to calculate the CSR-induced steady-state longitudinal electric force across the bunch.

According to Ref. [2], shielded CSR is important for harmonic numbers n in the range $n_{th} < n < n_c$, where

$$n_{th} = \sqrt{2/3}(\pi\rho/h)^{3/2}, \qquad n_c = \rho/\sigma_s. \tag{1}$$

Here, ρ and h denote the radius of the circular orbit and the plate separation, respectively, σ_s denotes the root-mean-square bunch length, n_{th} is the threshold harmonic for satisfying the boundary conditions at the plates, and n_c is the characteristic harmonic number below which the radiation will be coherent. However, according to Fig. 9 of Ref. [3], which compares the shielded CSR power calculated using the image charge method with that given in Ref. [2], there is an evident discrepancy. For $n_{th} > n_c$, i.e., for strong shielding, the result given by Ref. [2] underestimates the shielded CSR power considerably.

In this paper, we modify the analysis of Ref. [2] using power harmonics in Ref. [1] to obtain a result for the steady-state CSR power in agreement with the exact result for $n_{th} > n_c$. We show that for this parameter range the shielded CSR power is not always negligibly small.

2 PREVIOUS RESULTS

We consider a line-charge bunch moving on a circular orbit of radius ρ with angular frequency ω_0 in the center plane between two perfectly conducting plates at $z = \pm h/2$. According to Kheifets and Zotter [2], based on the work of Nodvick and Saxon, the power radiated by a single relativistic electron in the nth harmonic is

$$P_n = \frac{4\pi n e^2\omega_0}{h}\sum_{p=1,3}^{p<nh/\pi\rho}\left[J_n'^2(\gamma_p\rho) + \frac{g_p^2}{n^2-g_p^2}J_n^2(\gamma_p\rho)\right] \tag{2}$$

where $\gamma_p\rho = \sqrt{n^2-g_p^2}$ with $g_p = p\pi\rho/h$, and p is the index of eigenfunctions satisfying the boundary condition at the plates. Only propagating modes, i.e., those satisfying $n > g_p$, contribute significantly to the power P_n; therefore, when $\pi\rho/h \gg 1$ it suffices to use asymptotic expressions of the Bessel functions for large n:

$$\begin{aligned} J_n(\gamma_p\rho) &\simeq \frac{1}{\sqrt{3}\pi}\left(\frac{g_p}{n}\right)K_{1/3}(g_p^3/3n^2), \\ J_n'(\gamma_p\rho) &\simeq \frac{1}{\sqrt{3}\pi}\left(\frac{g_p}{n}\right)^2K_{2/3}(g_p^3/3n^2). \end{aligned} \tag{3}$$

The modified Bessel functions are appreciable only when $n > g_p^{3/2} \gg g_p$. Consequently, for $\omega_0 = c/\rho$, the power harmonic of N electrons reduces to

$$P_n = \frac{4N^2e^2c}{3\pi\rho h}\sum_{p=1,3}^{p<nh/\pi\rho}A(n,p) \tag{4}$$

where

$$A(n,p) \equiv \frac{g_p^4}{n^3}\left[K_{1/3}^2\left(\frac{g_p^3}{3n^2}\right) + K_{2/3}^2\left(\frac{g_p^3}{3n^2}\right)\right]. \tag{5}$$

The CSR power generated by a relativistic Gaussian line charge with N electrons is

$$P_{coh} = \sum_{n=0}^{\infty}P_n e^{-(n\sigma_s/\rho)^2}. \tag{6}$$

In Ref. [2], it is assumed that the CSR power comprises mainly harmonics P_n for which $n > n_{th}$. Changing the summation over p into integration gives

$$P_n = \frac{C_0N^2e^2c}{\rho}n^{1/3} \qquad (n_{th} < n < n_c) \tag{7}$$

0-7803-4376-X/98/$10.00 © 1998 IEEE

where $C_0 = 2C/3^{1/3}\pi^2$, with $C \simeq 3.68$. The total CSR power is then obtained by replacing the summation over n by an integration over $x = (n\sigma_s/\rho)^2$,

$$P_{coh} \approx \frac{C_0 N^2 e^2 c}{2\rho}\left(\frac{\rho}{\sigma_s}\right)^{4/3} F(x_{th}),$$
$$F(x_{th}) = \int_{x_{th}}^{x_c} dx x^{-1/3} e^{-x} \approx \Gamma(2/3, x_{th}) \tag{8}$$

with $x_{th} = (n_{th}/n_c)^2$, $x_c = 4\pi$, and $\Gamma(\nu, x)$ denoting an incomplete gamma function.

The free space CSR power is obtained by setting x_{th} to 0,

$$P_{coh}^{(0)} = \frac{N^2 e^2 c}{(\rho^2\sigma_s^4)^{1/3}} \frac{F(0)C_0}{2} \tag{9}$$

where $F(0)C_0/2 \approx 0.35$. This result agrees with that obtained by Schiff [4],

$$P_{coh}^{(0)} = \frac{N^2 e^2 c}{(\rho^2\sigma_s^4)^{1/3}} \frac{3^{1/6}[\Gamma(2/3)]^2}{2\pi} \tag{10}$$

in that $3^{1/6}[\Gamma(2/3)]^2/2\pi \approx 0.35$. The formalism of Eq. (8) therefore sets the ratio of shielded CSR to that of free space as

$$P_{coh}/P_{coh}^{(0)} = F(x_{th})/\Gamma(2/3). \tag{11}$$

3 MODIFIED ANALYSIS

We will now show that the results of the previous section are applicable only for weak shielding, namely, $n_{th} \ll n_c$, due to the replacement of the sum over p by an integral and the discarding of the contribution of harmonics $n < n_{th}$. We do so by first showing that, for each pth mode satisfying the boundary conditions at the plates, there is a threshold harmonic $n_{th}^{(p)} = p^{3/2} n_{th}$, where n_{th} given in Eq. (1) is the threshold harmonic for $p = 1$, i.e., $n_{th} \equiv n_{th}^{(p=1)}$. The pth mode contributes significantly to the CSR power only when $n_{th}^{(p)} < n_c$, or $p < (n_c/n_{th})^{2/3}$. Using integration over p on the interval $[0, \infty)$ to derive Eq. (7) from Eq. (4) is valid only if $n_{th} \ll n_c$, which is the quasi-free-space, weak-shielding situation. However, if the parameters do not satisfy $n_{th} \ll n_c$, only the first few p modes contribute to P_{coh} in Eq. (6). In particular, when $n_{th} > n_c$, only the $p = 1$ mode contributes significantly to P_{coh}, and in this case Eq. (8) is manifestly inaccurate.

We begin our analysis by showing that it is permissible to exchange the order of the summations over p and n, which then allows an explicit calculation of the contribution of the pth mode to the CSR power. The asymptotic behaviors of the modified Bessel functions are

$$K_\nu(z) \sim \begin{cases} \sqrt{\frac{\pi}{2z}} e^{-z} & (\text{large } z) \\ \frac{1}{2}\Gamma[\nu](z/2)^{-\nu} & (z \to 0, \operatorname{Re}\nu \neq 0) \end{cases}. \tag{12}$$

Numerically one finds that the asymptotic behavior of $K_\nu(z)$ for large z is good to 10% at $z = 1/2$ for $\nu = 1/3, 2/3$. Therefore, the modified Bessel functions in Eq. (5) are exponentially small when $g_p^3/3n^2 \gg 1/2$ or $n \ll n_{th}^{(p)}$, and their contributions to P_n are then negligible. This typifies the nonpropagating modes, i.e., those for which $p \geq nh/\pi\rho$, because $g_p^3/3n^2 \geq n/3 \gg 1$ for large n. Consequently one can extend the summation over p to infinity in Eq. (4) without sacrificing accuracy, and therefore exchange the orders of summation for indices p and n in combining Eqs. (4) and (6) to obtain

$$P_{coh} = \frac{4N^2 e^2 c}{3\pi\rho h} \sum_{p=1,3}^{\infty} I(p), \tag{13}$$

with $I(p)$ denoting the contribution of the pth mode to the coherent radiated power:

$$I(p) = \sum_{n=0}^{\infty} A(n,p) e^{-(n/n_c)^2}. \tag{14}$$

To obtain a closed-form expression for P_{coh}, we first calculate the asymptotic form of $I(p)$. After defining

$$x_{th}^{(p)} = (n_{th}^{(p)}/n_c)^2, \quad x = (n/n_c)^2, \tag{15}$$

we note that, provided $n_c \gg 1$ and $n_{th}^{(p)} \gg 1$, the summation over n in Eq. (14) can be replaced by an integral:

$$I(p) \simeq \frac{3g_p}{4} \int_0^\infty f^{(p)}(x) dx, \tag{16}$$

with

$$f^{(p)}(x) = \left[K_{1/3}^2\left(\frac{x_{th}^{(p)}}{2x}\right) + K_{2/3}^2\left(\frac{x_{th}^{(p)}}{2x}\right)\right] \frac{x_{th}^{(p)} e^{-x}}{x^2}. \tag{17}$$

Applying the asymptotic form of the modified Bessel function in Eq. (12) for the frequency range $n < n_{th}^{(p)}$ gives

$$f^{(p)}(x) \simeq f_0^{(p)}(x) = \frac{2\pi}{x} \exp\left(-\frac{x_{th}^{(p)}}{x} - x\right) \quad (x < x_{th}^{(p)}). \tag{18}$$

Hence $I(p)$ in Eq. (16) is

$$I(p) \simeq I_0(p) + \Delta I(p);$$
$$I_0(p) = \frac{3g_p}{4} \int_0^\infty f_0^{(p)}(x)\, dx = 3\pi g_p K_0\left(2\sqrt{x_{th}^{(p)}}\right),$$
$$\Delta I(p) = \frac{3g_p}{4} \int_{x_{th}^{(p)}}^\infty [f^{(p)}(x) - f_0^{(p)}(x)]\, dx. \tag{19}$$

The relative error of estimating $I(p)$ using $I_0(p)$ is plotted in Fig. 1 as a function of $x_{th}^{(p)}$. The plot shows that when $x_{th}^{(p)} \geq 1$, $\Delta I(p)/I_0(p)$ is negligibly small, and in this limit $I(p) \simeq I_0(p)$. This circumstance arises because, in the integrand of $\Delta I(p)$, the error introduced by using the asymptotic form of $K_\mu(z)$ is suppressed by a factor e^{-x} for $x \geq x_{th}^{(p)} > 1$. Moreover, when $x_{th}^{(p)} > 1$, we can use Eq. (12) to

express $K_0\left(2\sqrt{x_{th}^{(p)}}\right)$ of Eq. (19) in its asymptotic form, after which we find $I_0(p) \propto p^{1/4}\exp[-2p^{3/2}(n_{th}/n_c)]$. This expression shows clearly that, when $n_{th} > n_c$, $I_0(p)$ rapidly decreases with increasing p, so in this strong-shielding limit, the CSR power

$$P_{coh} \simeq \frac{4N^2e^2c}{3\pi\rho h}\sum_{p=1,3}^{\infty} I_0(p) \qquad (n_{th} > n_c) \tag{20}$$

is dominated by $p = 1$ mode, and its ratio to the free-space steady-state CSR power in Eq. (10) gives

$$P_{coh}/P_{coh}^{(0)} \simeq C_0(n_{th}/n_c)^{5/6}\exp(-2n_{th}/n_c), \quad (n_{th} > n_c) \tag{21}$$

with $C_0 = 4\sqrt{3\pi}/2^{2/3}[\Gamma(2/3)]^2 \simeq 4.2$. This modified result for the shielded CSR power in the parameter regime $n_{th} > n_c$ differs markedly with the result in Eq. (11).

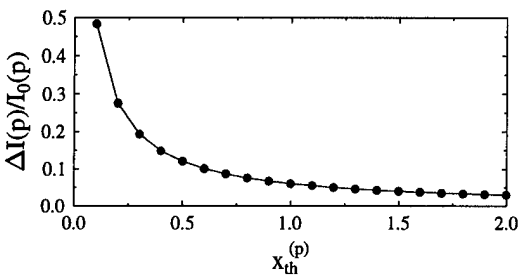

Figure 1: Relative error in using $I_0(p)$ to estimate $I(p)$ as a function of $x_{th}^{(p)}$, as obtained using Eq. (19).

To emphasize the importance of our findings, we compare the analytic results given in Eqs. (20) and (21) with the previous result in Eq. (11) by way of Figs. 2 and 3. The circular dots in Fig. 2 are obtained numerically from Eqs. (11) and (12) of Ref. [6] for the steady-state case, a result that derives from application of the image charge method. The crosses are obtained by direct summation of power harmonics in Eq. (6), in which the upper limit of the sum is chosen empirically by monitoring convergence of the result. It is clear that, for $n_{th} > n_c$, our simple result in Eq. (20) for $p = 1$ agrees well with exact calculations using the image charge method and superposition of power harmonics. It is also clear that a large number of p modes are needed only for the weak-shielding case when $n_{th}/n_c \ll 1$. An alternative way to view the results is provided in Fig. 3, in which the solid curve denotes the Kheifets-Zotter result, and the dashed curve denotes the result of Eq. (21) which is accurate for nearly the full range of values along the abscissa. Fig. 3 is to be compared with Fig. 9 in Ref. [3], in which our dashed curve is replaced by the exact results from the image-charge method. There is no discernible difference between the two figures. These comparisons show the validity of using Eq. (21) to describe $P_{coh}/P_{coh}^{(0)}$ when $n_{th} \geq n_c$, and they also underscore the validity of the image-charge method.

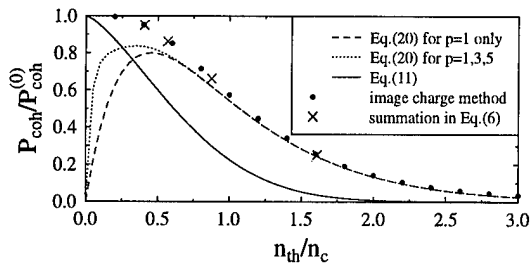

Figure 2: Comparison of P_{coh} in Eqs. (20) and (21) with results from the image-charge method and other approaches. Here n_{th}/n_c is varied by changing h with fixed values of ρ (= 1 m) and σ (=1 mm.)

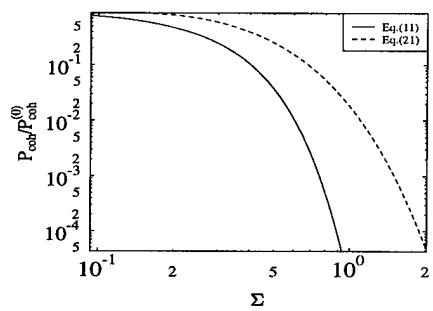

Figure 3: Plots of $P_{coh}/P_{coh}^{(0)}$ versus $\Sigma = \sigma/(2\rho\Delta^{3/2})$ with $\Delta \equiv h/(2\rho)$. This should be compared with Fig. 9 of Ref. [3].

4 DISCUSSION

According to Ref. [5], for the $p = 1$ mode, the radiation intensity in the nth harmonic falls off exponentially as n decreases from n_{th} to zero. This is seen in Eqs. (4), (5) and (12) for $p = 1$, where $K_\mu^2(g_1^3/3n^2) \propto e^{-n_{th}^2/n^2}$ for $n \leq n_{th}$. If $n_{th} \ll n_c$, then the contribution of the radiation intensity in the range $0 < n \leq n_{th}$ is negligible. However, for $n_{th} > n_c$, all the bunch frequencies lie inside the range $0 < n \leq n_{th}$, and thus those harmonics are the main contributor to P_{coh}. Discarding these harmonics results in a potentially considerable underestimation of the radiated power.

5 REFERENCES

[1] J. S. Nodvick and D. S. Saxon, Phys. Rev., **96**, 180 (1954).

[2] S. A. Kheifets and B. Zotter, CERN SL-95-92 (AP), 1995.

[3] B. Murphy, S. Krinsky, and R. L. Gluckstern, BNL-63090, (1996).

[4] L. I. Schiff, Rev. Sci. Instr.17, 6-14, (1946).

[5] S. Heifets and A. Michailichenko, SLAC/AP-83, 1991.

[6] R. Li, C. L. Bohn, and J. J. Bisognano, these proceedings.

LANDAU DAMPING OF THE WEAK HEAD–TAIL INSTABILITY FOR BEAMS WITH QUADRATIC AMPLITUDE–DEPENDENT BETATRON TUNES AND BINOMIAL AMPLITUDE DISTRIBUTIONS

H.J. Tran*, S.R. Koscielniak, TRIUMF, 4004 Wesbrook Mall, Vancouver, B.C., Canada V6T 2A3

Abstract

The simple theory of the weak head–tail instability does not exhibit a threshold current. Experimentally, the instability does not always appear, due to the readily available stabilizing mechanism known as Landau damping. Here we extend the theory to include Landau damping that arises from a quadratic dependence of betatron tune on amplitude, as occurs when octupoles are present in the synchrotron lattice. The binomial density distribution, which is appropriate for proton beams, is chosen as the steady–state for both the transverse and longitudinal phase–space distributions. Using Sacherer's formalism we look for solutions by expanding the perturbation in a set of basis functions. The method involves evaluating the dispersion integral, and finding the eigen–values of the interaction matrix. The results can be represented in a "stability diagram" with the standard interpretation but with the axes representing the real and imaginary parts of the eigen–values. As a numerical example, we determine the octupole strength needed to damp the reported high–order modes observed[1] in the CERN PS for bunches with "LHC characteristics".

1 INTRODUCTION

With ever increasing intensity, Landau damping of instabilities by the frequency spread produced by the residual nonlinearity in the transverse restoring force cannot be assumed to be sufficient, especially at high energies where the image charge force becomes negligible. This is clearly demonstrated by the observation of the high–order modes $l = 5, 6$, and 7 at the CERN PS [1].

The simple theory of the instability is formulated under the assumption that there is no intrinsic spread in the incoherent oscillation frequencies. With an intrinsic spread, coherent modes can exist only above a certain threshold and their frequencies are called Landau frequencies. We have extended the theory of Sacherer[2] to include Landau damping by a betatron frequency spread. We have derived an integral equation[3] which contains a dispersion integral due to the amplitude dependent betatron frequency; we call it the dispersive integral equation. The equation reduces to Sacherer's integral equation when there is no frequency spread, as expected.

In this report, we will consider a specific case in which the amplitude dependence is quadratic, as occurs when octupoles are present in the ring. The amplitude distributions of the transverse and longitudinal steady–state distributions are chosen to be the binomial distribution because its profile is sharp, which is appropriate for proton beams.

2 THE DISPERSION RELATION

The dispersive integral equation below is obtained from the linearized Vlasov equation where we have neglected transverse and longitudinal mode coupling and assumed that the transverse wake force does not affect the synchrotron motion,

$$\frac{R_l(r)}{f(\Lambda) + i\,g(\Lambda)} = W(r) \int_0^\infty r'\,dr' R_l(r') G_l(r, r'), \quad (1)$$

where $W(r)$ is the weight function, $R_l(r)$ the longitudinal radial density function of the lth head–tail mode, $G_l(r, r')$ the kernel function of the integral, and Λ the Landau mode frequency. The beam transfer response function (BTRF) $f(\Lambda) + i\,g(\Lambda)$ is obtained by evaluating the dispersion integral,

$$f(\Lambda) + ig(\Lambda) = \frac{1}{2} \int_0^\infty \frac{-f_0'(q) q^2\,dq}{\Lambda - \omega_\beta(q) - l\omega_s}, \quad (2)$$

where $f_0(q)$ is the binomial transverse amplitude (q) distribution and ω_s is the synchrotron frequency.

We followed Sacherer's formalism in transforming the integral equation into a set of linear equations by expanding $R_l(r)$ in terms of an appropriate set of basis functions with $W(r)$ as the weight,

$$\left[\frac{1}{f(\Lambda) + i\,g(\Lambda)}\right] a_k = \sum_{k'} M_{kk'} a_{k'}, \quad (3)$$

where k and k' are the index of the basis function $(f_k(r),\ k = 0, 1, 2, 3, \ldots)$, and $a_{k'}$ the coefficients of the expansion. The matrix elements $M_{kk'}$ are given by a summation of the total transverse impedance $Z_1(\omega')$ times the frequency spectra $h_{lk}(\omega')$ and $h_{lk'}(\omega')$ of the phase–space density functions formed by the kth and k'th basis functions times the phase density distribution,

$$M_{kk'} = -i \frac{\pi N r_0 c}{\gamma T_0^2 \omega_\beta} \sum_p Z_1(\omega') h_{lk}(\omega') h_{lk'}(\omega'), \quad (4)$$

where N is the number of particles in the bunch, r_0 the classical proton (electron) radius, T_0 the revolution period, ω_β the small amplitude betatron frequency, γ and c have the usual relativistic definitions. The summation is over the side bands of the revolution frequency ω_0; $\omega' = p\omega_0 + \Lambda$. For a nontrivial solution to exist, the reciprocal of the BTRF must satisfy

$$\det\left[\left(\frac{1}{f(\Lambda) + i\,g(\Lambda)}\right) \mathbf{I} - \mathbf{M}\right] = 0, \quad (5)$$

* Graduate student at the University of British Columbia, Vancouver, B.C., Canada.

0-7803-4376-X/98/$10.00 © 1998 IEEE

where $\mathbf{I}$ is the identify matrix and $\mathbf{M}$ is the interaction matrix defined above. This is true if and only if

$$\frac{1}{f(\Lambda) + i\,g(\Lambda)} = \lambda_n, \quad n = 0, 1, 2, 3 \ldots, \tag{6}$$

where λ_n is the nth eigen–value of $\mathbf{M}$. Thus, there are an infinite set of dispersion relations for each mode l, one for each eigen–value.

In the absence of an intrinsic frequency spread, the dispersion relation Eqn. 6 reduces to an expression which can be rearranged to give the Sacherer frequencies Ω of the lth mode,

$$\Omega = \lambda_n + l\omega_s + \omega_\beta. \tag{7}$$

The result above is obtained by evaluating the BTRF for the special case of no frequency frequency spread [3], that is, $\omega_\beta(q) = \omega_\beta$.

The dispersion relation Eqn. 6 has very limited usage. According to the standard interpretation of the dispersion relation, and using the definition of the Sacherer frequency (Eqn. 7), we can construct a complex map of the Landau frequency plane (Λ) into the Sacherer frequency plane (Ω) from the BTRF as follows,

$$\frac{1}{f(\Lambda) + i\,g(\Lambda)} = \Omega - l\omega_s - \omega_\beta. \tag{8}$$

This complex map allows one to obtain the stability boundary diagram in the familiar Sacherer plane by mapping contour lines of constant growth rates. The Landau damped (stable) region is free of contour lines and bounded by the line of zero growth and the horizontal axis. See Fig. 1. An unstable mode is Landau damped if its Sacherer frequency lies in this region. Ideally, one wants to obtain the stability diagram in the transverse impedance $Z_1(\omega)$ plane. However, it must be pointed out that the transverse impedance cannot be, at best, practically obtained from the Sacherer frequency.

3 THE BEAM TRANSFER RESPONSE FUNCTION

As an example, we will obtain the BTRF of a binomial amplitude distribution with quadratic amplitude dependent betatron frequency. The quadratic dependence can be written as

$$\omega_\beta(q) = \omega_\beta + Sq^2/\hat{q}^2, \tag{9}$$

where $0 \le q \le \hat{q}$, $\hat{q}$ is the maximum betatron amplitude, and S the width of the frequency spread. We use the binomial distribution of the form,

$$f_0(q) = \frac{\alpha(1+\alpha)}{2\hat{q}^2}\left(1 - \frac{q^2}{\hat{q}^2}\right)^\alpha, \tag{10}$$

where α is a parameter that determines the profile of the distribution. We cannot evaluate the dispersion integral for an unspecified value of α. We choose a specific value of 4 so we can use the result later. Substituting the binomial distribution and the quadratic dependence into the dispersion integral (Eqn. 2) and performing the integration, we obtain the BTRF,

$$\begin{aligned} f(\Lambda) &= \frac{20}{S^2}\left(\frac{\Delta\Lambda}{3} - \frac{3S}{4} + \frac{3S^2 - 3S\Delta\Lambda + \Delta\Lambda^2}{2S}\right. \\ &+ \frac{(\Delta\Lambda - S)^3}{S^2} + \frac{\Delta\Lambda(\Delta\Lambda - S)^3 \log|S - \Delta\Lambda|}{S^3} \\ &+ \left.\frac{(S - \Delta\Lambda)^3\Delta\Lambda \log|\Delta\Lambda|}{S^3}\right), \\ g(\Lambda) &= \frac{20\pi}{S^2}\left(\frac{\Delta\Lambda(\Delta\Lambda - S)^3}{S^3}\right), \end{aligned} \tag{11}$$

where $\Delta\Lambda = \Lambda - \omega_\beta - l\omega_s$.

4 THE HEAD–TAIL MODE SPECTRA

The mode spectra are required in the evaluation of the matrix elements of $\mathbf{M}$. In this section, we will outline the steps involved in obtaining the mode spectra $h_{lk}(\omega)$ of the longitudinal binomial amplitude distribution from the basis functions $f_k(r)$. The normalized longitudinal distribution $g_0(r)$ is

$$g_0(r) = \frac{(1+\alpha)}{\pi\hat{r}^2}\left(1 - \frac{r^2}{\hat{r}^2}\right)^\alpha, \tag{12}$$

where $\hat{r}$ is the maximum synchrotron amplitude, and the orthogonality condition that defines the basis functions is

$$\int_0^{\hat{r}} r\,dr\,g_0(r) f_k(r) f_{k'}(r) = \delta_{kk'}, \tag{13}$$

where $\delta_{kk'}$ is the Kroneker delta function. Looking up a standard list of weighted orthonormal functions we found the correct set and, after the normalization, we can write the basis functions as

$$\begin{aligned} f_k(r) &= \sqrt{\frac{2\pi(1+\alpha+2k+l)\Gamma(1+\alpha+k+l)\,k!}{(1+\alpha)\Gamma(1+k+l)\Gamma(1+\alpha+k)}} \\ &\times \left(\frac{r}{\hat{r}}\right)^l P_k^{l,\alpha}\left(1 - 2\frac{r^2}{\hat{r}^2}\right), \end{aligned} \tag{14}$$

where $\Gamma(x)$ is the gamma function and $P_k^{l,\alpha}(x)$ is the Jacobbi polynomial of order k with indices l and α. From the basis functions, we formed the corresponding phase–space density functions and took their Fourier transforms to obtain the spectra,

$$\begin{aligned} h_{lk}(\omega) &= 2^\alpha\sqrt{\frac{2}{\pi}\frac{(1+\alpha)(1+\alpha+2k+l)}{\Gamma(1+k+l)\,k!}} \\ &\times \sqrt{\Gamma(1+\alpha+k+l)\Gamma(1+\alpha+k)} \\ &\times J_{1+\alpha+2k+l}\left(\frac{\omega - \omega_\xi}{c}\hat{r}\right) \Big/ \left(\frac{\omega - \omega_\xi}{c}\hat{r}\right)^{1+\alpha}, \end{aligned} \tag{15}$$

for $\alpha > -1$, and where ω_ξ is the chromatic frequency shift, and $J_n(x)$ the nth order Bessel function of the first kind.

5 GROWTH RATES AND FREQUENCY SHIFTS OF THE "LHC" BUNCH

In this section, we will calculate, assuming the longitudinal amplitude distribution is binomial, and attempt to compare with the experimental observation. The approximate

l	2	3	4	5	6	7	8	10
k	-120	-45	-7	5	5.6	3.6	2.1	0.7
Δf	-160	-109	-67	-36	-18	-10	-6	-27

Table 1: Transverse head–tail frequency shifts and growth rates of the "LHC " bunch.

eigen–values can be found easily, if the cross–coupling terms, which are generally two orders of magnitude smaller than the diagonal terms, are neglected. This gives a simple expression for the frequencies,

$$\Omega_n = M_{nn} + l\omega_s + \omega_\beta. \tag{16}$$

The resistive wall impedance was identified as responsible. Using the beam parameters in [1] and also the impedance formula, we calculated Ω_0 for modes 2 to 10. For each mode, only the frequency with index n=0 was calculated, since this index value gives the largest frequency shift (Δf Hz) and growth rate (k s^{-1}), roughly two orders of magnitude larger than that of the next index value (n=1). We evaluated the matrix element M_{00} by broad–band approximating the summation with an integral, which is a good approximation since the resistive wall impedance is a smooth function without sharp peaks.

The results are shown in Table 1. We can see that modes 5,6, and 7 are unstable and they have the largest growth rates. The rise times of these three modes range from 200–285 ms, which are close to the observed[1] rise times 100–200 ms. However, we are not able to compare the frequency shifts with measurements as there are no data available. When we compared with the rise times obtained using the approximate mode spectra in Ref. [1], they differ by as much as a factor of two. This shows that the approximate spectra are inaccurate and the exact spectra $h_{lk}(\omega)$ should be used instead if a bunch has the binomial profile.

6 LANDAU DAMPING BY OCTUPOLES

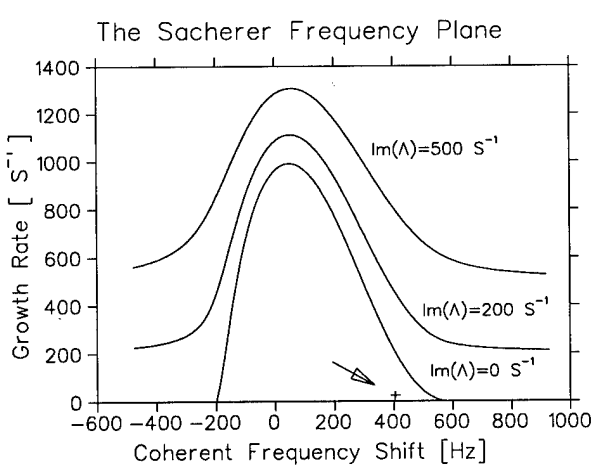

Figure 1: Contour lines and stability boundary diagram for the "LHC" bunch.

In this section, we will estimate the upper bound of the octupole strength required to Landau damp the instability as observed in [1]. Let us assume that the transverse amplitude distribution of the bunch is binomial with an α value of 4. This value gives the binomial distribution a profile that is similar to the Gaussian distribution but without the infinite tail. It is appropriate for bunches which do not have very sharp parabolic profiles. With octupoles installed in a ring, the time averaged betatron frequency depends quadratically on the amplitude. The BTRF for these conditions was evaluated as an example in Sec. 3 (Eqn. 11). The map can be obtained by taking the reciprocal of Eqn. 11 and equating it to the left hand side of Eqn. 6.

Given a frequency spread S, the contour lines are obtained by plotting the complex values of the map for different constant values of the growth rate [Im(Λ)], as the frequency shift [Re($\Delta\Lambda$)] is scanned from $-\infty$ to ∞. An upper bound on the octupole strength can be obtained from a minimum frequency spread required to put the point whose coordinates comprises the largest growth rate and coherent frequency shift in the stable area. As reported, the largest growth rate was 10 s^{-1}. The frequency shifts of the unstable modes are not available. Fortunately, that of the dipole mode (l=0) is given [1] and it is the upper limit, which would give a conservative estimate. Guided by the well–known rule of thumb for Landau damping, we found that a frequency spread of 1000 Hz is sufficient. Fig. 1 shows the location of the point and well inside the boundary. This frequency spread requires an integrated octupole strength of 63 m^{-3}.

7 CONCLUSIONS

We have derived the dispersion relations for the weak transverse head–tail modes of the binomial amplitude distribution, which also defines a complex map. When there is no intrinsic frequency spread, it reduces to an expression for the mode frequencies in terms of the eigen–values of the interaction. We have obtained an analytic expression for the mode spectra and calculated an example BTRF. As an application, we calculated the growth rates and coherent frequency shifts of the "LHC" bunch and estimated the octupole strength to promote Landau damping.

8 REFERENCES

[1] R. Cappi, *Observation of High–Order Head–Tail Instability at the CERN–PS*, Particle Accelerators, 1995, Vol. 50, pp. 117–124.

[2] F. Sacherer, *Methods for Computing Bunched–Beam Instabilities* CERN/SI–BR/72–5.

[3] H.J. Tran and S.R. Koscielniak, *Landau Damping of the Weak Head–Tail Instability*, Triumf Design Note in preparation.

PRELIMINARY MEASUREMENT OF ENERGY-SPREAD CHANGE RESULTING FROM THE RESISTIVE-WALL INSTABILITY*

H. Suk†, J.G. Wang, Y. Zou, S. Bernal, and M. Reiser
Institute for Plasma Research, University of Maryland, College Park, MD 20742, USA

Abstract

Experiments on the resistive-wall instability have been conducted. Electron beams with energies of 2.5 to 8.5 keV and currents of 30 to 135 mA are transported through a resistive glass tube for this experiment. The resistive tube is one-meter long and the resistance is 5.4 kΩ. The electron beams in the resistive tube are uniformly focused by a long solenoid. Localized space-charge waves are generated in the beams to investigate any energy spread change as a result of the resistive-wall instability. A longitudinal energy spread of the space-charge waves is measured at the entrance and the exit of the resistive channel for comparison. The preliminary experimental results are presented.

1 INTRODUCTION

The resistive-wall instability[1-3] is potentially dangerous for some accelerators with special experimental parameters. Especially it plays an important role in high current accelerators with space-charge-dominated beams[4]. According to the theory and simulation, the resistive-wall instability leads to amplitude growth of slow space-charge waves and damping of fast space-charge waves[5-7]. In addition to amplitude change, the instability may lead to an emittance growth and a longitudinal energy-spread increase. To answer these questions, small scale experiments with space-charge-dominated electron beams and a resistive glass tube have been conducted at the University of Maryland[8]. In this paper, preliminary experimental results on the energy-spread measurement are presented.

2 EXPERIMENTS

2.1 Experimental Setup

The experimental setup for energy spread measurement is shown in Fig. 1. The experimental system consists of an electron gun, solenoid matching lenses, a resistive tube, diagnostic tools, etc. Space-charge dominated electron beams with an energy of 2.5 to 8.5 keV and a current of 30 to 135 mA are generated from the gridded electron gun with a variable perveance. A single localized space-charge wave, i.e., a fast wave or a slow wave, is produced in the electron beam pulse to investigate the properties of the wave in a resistive environment. The electron beams are matched and injected into the resistive glass tube with the aid of three solenoid lenses. The resistive tube has a resistance of 5.4 kΩ, a length of 0.96 cm and a diameter of 3.8 cm. The resistive glass tube is located inside a long solenoid for uniform magnetic focusing. The magnetic field of the long solenoid is adjusted to confine the beams within the resistive tube. If the space-charge wave is a fast wave, its amplitude decreases as it propagates in the beam, while if the wave is a slow wave, its amplitude grows. The amplitudes of the space-charge waves are measured with two current monitors at the entrance and the exit of the resistive tube for comparison. To measure the energy of space-charge waves resulting from the resistive-wall instability, two retarding-field energy analyzers are placed at the entrance and the exit of the resistive transport channel, as shown in Fig. 1. The retarding-field energy analyzer[9,10] consists of two parallel conducting plates and a Faraday cup. Each plate has a hole with a diameter of 4.8 mm and both holes are covered with a fine stainless-steel mesh with a transmittance of 80 %. One plate is grounded and the other is charged with a negative high voltage, so that a uniform retarding electric field is produced between the two plates. With these energy analyzers, the energy spread is measured at both locations alternatively, and the results are compared.

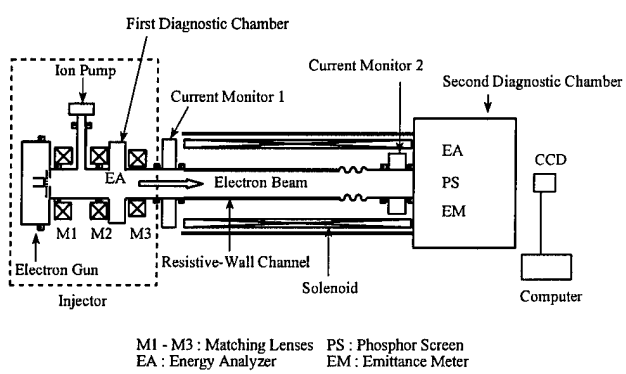

Figure 1: Experimental setup to measure an energy spread.

2.2 Energy Spread Measurements

Figure 2 shows a typical beam pulse with a localized fast wave. This beam pulse is measured with the Faraday cup of the first energy analyzer when the retarding high voltage is zero. In this case, the beams pass through the two plates without any retardation and arrive at the Faraday cup which is located just behind the two plates. As a result, the energy analyzer can measure the beam profile with space-charge waves.

The signal in Fig. 2 changes as the retarding voltage is increased. Figure 3 shows a fast wave on the beam for dif-

* This work was supported by the U.S. Department of Energy.
† Present address: Department of Physics and Astronomy, UCLA, Los Angeles, CA 90095, USA.

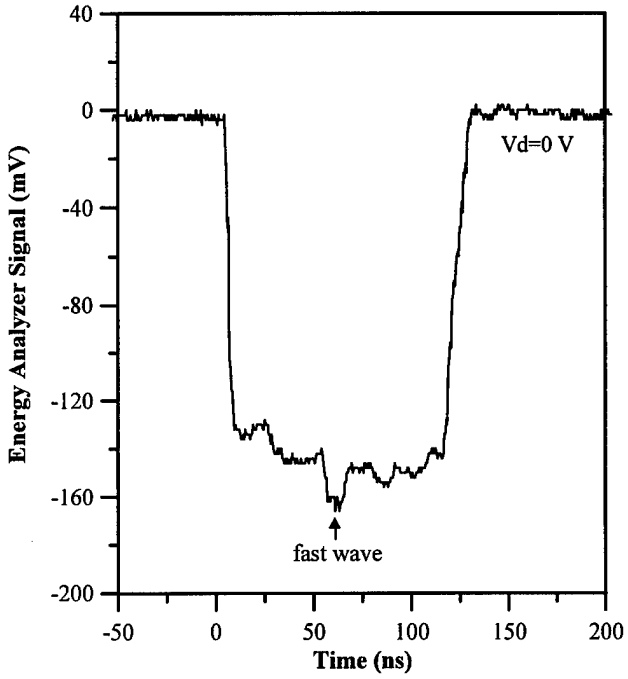

Figure 2: Typical electron beam pulse measured with a Faraday cup of the first energy analyzer at the entrance. The square-shaped localized wave in the central region of the pulse is a single fast space-charge wave.

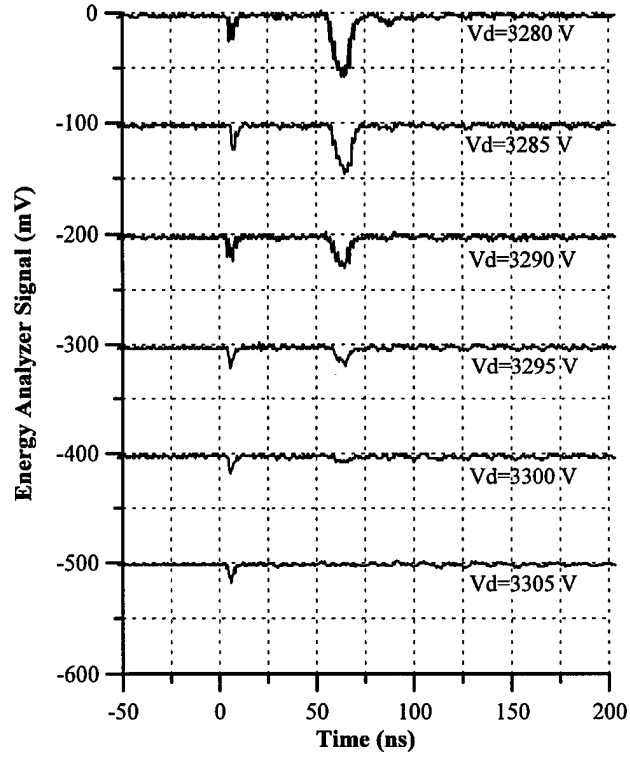

Figure 3: Fast wave signals from the Faraday cup of the first energy analyzer at different retarding voltages. The bump at t=64 ns is a localized fast wave and its amplitude decreases as the retarding voltage V_d increases.

ferent retarding voltages. The figure indicates that the flat part of the beam profile disappears when the retarding voltage V_d is 3,280 V, while two peaks are shown at t=5 ns and t=64 ns, respectively. Hence, the electrons at the two peaks have higher energies than those in the flat part of the beam pulse. Analysis in time scale indicates that the small peak at t=5 ns corresponds to the front edge of the beam pulse, where the electrons have a higher velocity, as a result of a strong nonlinear space-charge force in forward direction. The other peak at t=64 ns is the fast space-charge wave. The fast wave signal decreases as the retarding voltage V_d is increased gradually, and it disappears completely when V_d is 3,305 V. Therefore, the full energy width of the fast wave is 25 eV at the entrance of the resistive transport channel.

Similarly, a slow wave can be generated by adjusting electron gun conditions, and its energy spread can be measured. The wave is indentified as a fast wave or a slow wave by current monitor signals which are not shown here. Figure 4 shows a typical measurement result for a slow wave. The flat part of the beam pulse disappears at V_d=2,575 V and the slow wave disappears completely at V_d= 2,602 V. The full energy width of the slow wave is measured as 27 eV. The result implies that the electrons in the slow wave have higher energies than those in the flat part of the beam pulse. Hence, both fast and slow waves have higher energies, which is consistent with the previous measurement[11].

It should be noted that the above energy-width measurements of the space-charge waves are relative to the flat part of the beam pulse. In other words, the electrons in the flat beam pulse have a certain energy width and the space-charge waves have additional energy width above it. In this measurement, the additional energy width of the wave is measured. To verify this, the amplitude of a voltage perturbation which is added to the beam pulse for generation of the localized wave in the gun is measured. It turns out that the voltage perturbation is measured to be 27.2 V, and this is very close to the measured full energy width of 25 eV and 27 eV in Fig. 3 and Fig. 4, respectively. This fact implies that the above method employed to measure the net energy width of the localized space-charge wave is correct.

The same method is used to measure the energy spread of the space-charge waves at the exit of the resistive transport channel for comparison. Figure 5 shows the measurement result of the slow wave at the exit. In the figure, the flat part of the beam pulse disappears at V_d=2,565 V and the slow wave disappears completely when V_d is 2,607 V. Therefore, the energy width of the slow wave at the exit is 42 eV, which is 56 % larger than at the entrance of the resistive transport channel. This experimental result clearly demonstrates that the resistive wall instability leads to an increase in energy width of a slow space-charge wave. A similar measurement for a fast wave at the exit is in progress and will be reported in the near future.

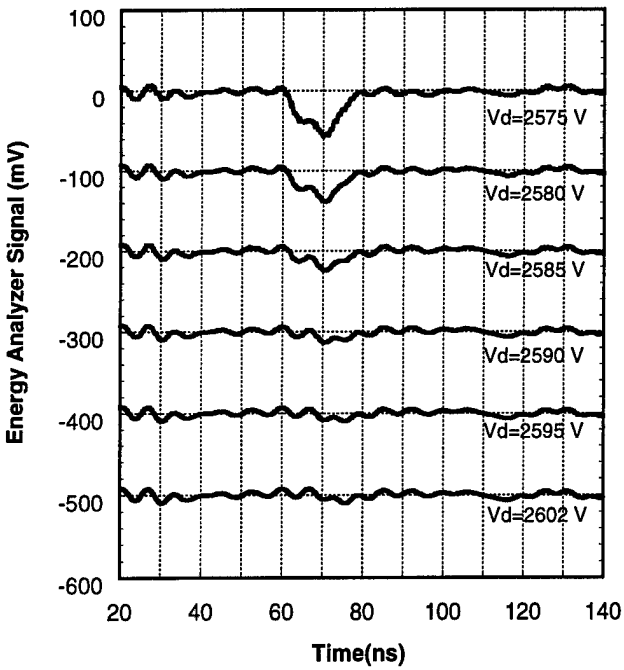

Figure 4: Slow wave signals from the Faraday cup of the first energy analyzer for different retarding voltages. In this figure, the full energy spread of the slow wave at the entrance of the resistive transport channel is measured as 27 eV.

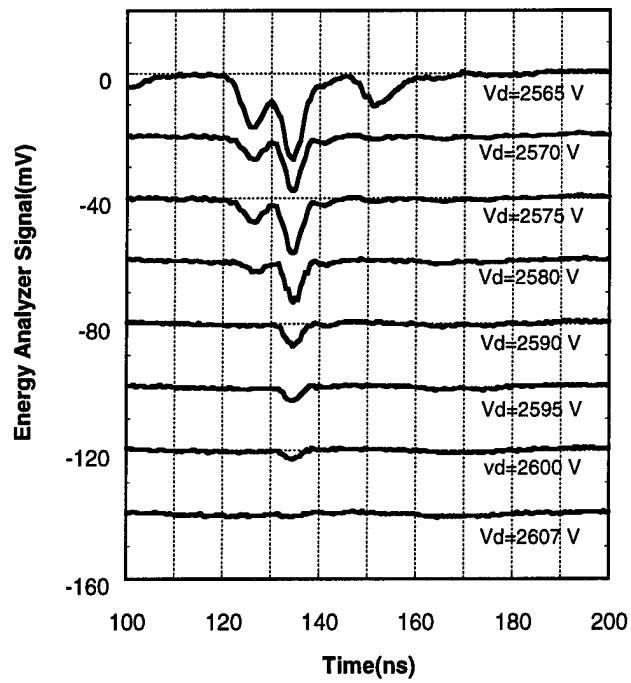

Figure 5: Slow wave signals from the Faraday cup of the second energy analyzer for different retarding voltages. The wave is shown to disappear completely at $V_d = 2,607$ V, so the full energy spread of the slow wave at the exit of the resistive transport is measured as 42 eV.

3 SUMMARY

Experiments have been conducted to investigate the energy spread change by the resistive-wall instability. The energy spread of a localized space-charge wave has been measured at the entrance and exit of the resistive transport channel for comparison. It was observed that a slow space-charge wave leads to an evident energy-width increase as a result of the resistive-wall instability. Experiments with a fast are underway.

4 REFERENCES

[1] C. K. Birdsall, G. R. Brewer, and A. V. Haeff, Proc. of I.R.E. **41**, July 1953.

[2] V. K. Neil and A. M. Sessler, Rev. Sci. Instr. **36**, 429 (1965).

[3] E. Lee, Nouvo Cimento **106A**, 1679 (1993).

[4] J. G. Wang and M. Reiser, Phys. Fluids **B5**, 2286 (1993).

[5] M. Reiser, *Theory and Design of Charged Particle Beams*(Wiley, New York, 1994), Sec. 6.3.2.

[6] J. G. Wang, H. Suk, and M. Reiser, submitted for publication to Phys. Rev. Lett.

[7] D. A. Callahan, Ph.D. Dissertation, Department of Applied Science, University of California, Davis, 1994.

[8] H. Suk, Ph.D. Dissertation, Department of Physics, University of Maryland, College Park, 1996.

[9] J. A. Simpson, Rev. Sci. Instrum. **32**, 1283 (1961).

[10] Y. Hamada, Y. Kawasumi, H. Iguchi, A. Fujisawa, Y. Abe, and M. Takahashi, Rev. Sci. Instrum. **65(5)**, 1994.

[11] J. G. Wang, D. X. Wang, D. Kehne, M. Reiser, and H. Suk, Il Nuovo Cimento, **106A**, 1745 (1993).

SPACE-CHARGE EFFECTS ON THE BEAM RESONANCE INSTABILITY

M. B. Ottinger, and T. Tajima,University of Texas, Austin, TX 78703 and
K. Hiramoto, Hitachi Research Lab, Hitachi Ltd. Hitachi-shi, Ibaraki-ken, 316, Japan

Abstract

We study the space-charge effects on the stability of low energy synchrotron accelerators with a Gaussian beam distribution. We show that the tune shift is not uniform throughout the beam, but decreases as a function of particle amplitude. The amplitude dependance leads to an equation for the region of beam instability due to integer resonance.

1 INTRODUCTION

One of the major concerns of beam dynamics and thus beam quality for a synchrotron in low energies (such as low energy injector/booster and medical proton therapy) is the space charge effect. In the non-relativistic, low energy regime the repulsive space charge electric force is not cancelled out by the magnetic force, thus yielding a substantial modification in beam dynamics, such as the tune shift [1]. In fact, it has been believed that the space charge effect increases the emittance. A rule of thumb on how to avoid or contain this deliterious effect is to avoid any conditions where the shifted tune might overlap integer (or other rational) resonances. Experimental observations, however, show that in many cases even though the beam has evidently crossed such a resonance, the beam is not destroyed. This has remained a mystery and some attempts at understanding the effects have been tried [2,3,4] but to no clear understanding to date. In this paper we address this problem by looking into the detailed kinetic radial distribution with the employment of our newly developed self-consistent space-charge PIC code [5].

In their 1958 paper on the theory of the alternating gradient synchrotron[6] E.D. Courant and H.S. Snyder show that magnet imperfections, and other non-linear effects, produce two classes of instabilities. The first occurs when either transverse beam tune (number of transverse oscillations the beam particles make around the design orbit per synchrotron revolution) is equal to a rational number (ν_0=n/m, where n and m are integers). The second class of instabilities occur when the sum of multiples of the transverse tunes is equal to an integer value ($n\nu_{x0} + m\nu_{y0} = p$). In their paper, Courant and Snyder used the machine tunes, or the number of transverse oscillations produced by a particle's interaction with only the synchrotron magnets. For low energy/high intensity beams the particle trajectory will also be influenced by the beam's self-fields, or space-charge. For a uniform density beam the space-charge produces a uniform shift in the beam tune. R.C. Davidson[7] calculates the average tune in a circular, uniform density beam with space-charge as

$$\nu = \left[\nu_o^2 + \left(\frac{KS}{2\varepsilon}\right)^2\right]^{\frac{1}{2}} - \frac{KS}{2\varepsilon}, \tag{1}$$

where S is the machine circumference, ε is the unnormalized beam emittance, and K is the self-field perveance ($K = 2Iem^{-1}[\gamma\beta c]^{-3}$).

For small K, the tune can be written in terms of the machine tune and a space-charge tune-shift,

$$\nu = \nu_o - \overline{\Delta\nu}, \quad \text{where } \overline{\Delta\nu} = \frac{1}{2}KS\varepsilon^{-1}. \tag{2}$$

Eqs. (1) and (2) were derived for a uniform density beam. To expand it to a Gaussian beam, the emittance is generally replaced by the rms emittance. Since the space-charge has been shown to produce a uniform shift in tune, it has been preported that the instabilities shown by Courant and Snyder occur at the new shifted tunes

$$\begin{gathered} \nu_o - \overline{\Delta\nu} = \frac{n}{m} \\ n\left(\nu_{xo} - \overline{\Delta\nu_x}\right) + m\left(\nu_{yo} - \overline{\Delta\nu_y}\right) = p. \end{gathered} \tag{3}$$

Baartman refutes this notion in his paper[3]. He proposes that the resonance is associated with the incoherent tune, which can be depressed beyond the integral value by a fractional amount determined by the machine design. The resonance occurs at

$$\nu_o - C_{mk}\overline{\Delta\nu} = n/m, \tag{4}$$

where C_{mk} is a function of the machine design.

In each of the prior studies the tune-shift is considered uniform over the beam. W.T. Weng[4] briefly shows that this is not the case, the tune-shift, for a non-uniform beam is dependent upon the individual particle amplitude.

2 AMPLITUDE DEPENDENCE OF TUNE SHIFT

Consider a long, circular proton beam with a Gaussian radial density profile, $\rho(r) = \rho_o e^{-\frac{r^2}{a^2}}$. From Maxwell's equations the electric and magnetic fields are:

$$\begin{gathered} \vec{E}(r) = E_r(r) = \frac{a^2\rho_o}{\varepsilon_o r}\left(1 - e^{-\frac{r^2}{a^2}}\right) \\ \vec{B}(r) = B_\theta(r) = \frac{\rho_o a^2\beta}{\varepsilon_o\gamma^2}\left(1 - e^{-\frac{r^2}{a^2}}\right), \end{gathered} \tag{6}$$

where β and γ are the relativistic factors, and ε_0 is the permittivity constant ($\varepsilon_0 = 8.8541\text{x}10^{-12}$ Fm^{-1}).

The Lorentz force will be radial with a magnitude

0-7803-4376-X/98/$10.00 © 1998 IEEE

$$F_r(r) = e\left(\vec{E} + c\vec{\beta} \times \vec{B}\right) = \frac{e\rho_o a^2 \beta}{\varepsilon_o \gamma^2 r}\left(1 - e^{-\frac{r^2}{a^2}}\right). \quad (7)$$

For a typical synchrotron this space-charge force is a perturbation to the force of the synchrotron magnets. The equation of motion for a beam particle can be written as

$$\frac{d^2 r}{ds^2} + [\kappa(s) + k(s)]r = 0, \quad (8)$$

where κ(s) is the synchrotron magnetic gradient and k(s) is the space-charge component given by

$$k(s) = \frac{1}{m\gamma\beta^2 c^2}\frac{dF_r}{dr} = \frac{e\rho_o a^2}{\varepsilon_o \gamma^3 \beta^2 c^2 m}\left[\frac{2r}{a^2} - \left(\frac{2r}{a^2} - \frac{1}{r^2}\right)\left(1 - e^{-\frac{r^2}{a^2}}\right)\right]. \quad (9)$$

The largest space-charge perturbation occurs for small amplitude particles (small average r) where k(s) is independant of r. The tuneshift in this region is [6]

$$\Delta\nu = \frac{1}{4\pi}\int_S k(s)\beta_{cs}(s)ds, \quad (10)$$

where β_{cs} is the Courant-Snyder amplitude function. Approximating the integral yields

$$\Delta\nu_{\max} = \frac{e\rho_o S\overline{\beta_{cs}}}{4\pi\varepsilon_o \gamma^3 \beta^2 c^2 m}, \quad (11)$$

where $\overline{\beta_{cs}}$ is the average Courant Snyder amplitude function around the synchrotron. Defining the beam current (I) and the normalized beam emittance(ε_n) as $I = \beta c \rho_o a^2 \pi$ and $\varepsilon_n = \frac{1}{4} a^2 \gamma\beta\, \overline{\beta_{cs}}^{-1}$, the maximum tune shift can be written as

$$\Delta\nu_{\max} = \frac{eIS}{16\pi^2 \varepsilon_o m c^3 \beta^2 \gamma^2 \varepsilon_n}. \quad (12)$$

Larger amplitude particles experience a smaller space charge force and therefore a smaller tuneshift. The general equation for the particle tuneshift as a function of particle amplitude (A) is found to be

$$\Delta\nu(A) = \Delta\nu_{\max}\frac{\left(1 - e^{-\eta A \varepsilon_n^{-1}}\right)}{\eta A \varepsilon_n^{-1}}, \quad (13)$$

where η is independent of A, ε_n, and I but is dependant on the synchrotron design and is proportional to βγ with a proportional constant of order unity. We note that since the beam will have a significant distribution in tune, it is not resonable to assume that the resonant instabilities are determined by the average beam tune, but by the tunes of the individual particles.

3 METHOD OF INVESTIGATION

To study the cause of instabilities we have developed a self-consistent computer model[5]. It tracks a set of macro-particles around the synchrotron lattice in full 6-dimensional phase space. For a long, lattice dominated beam with slowly varying radial profile the space-charge force has only a radial component and can be calculated using a two dimensional algorithm. The synchrotron magnets are applied as thin-elements as described by Schachinger and Talman[8]. The tracking method follows.

3.1 Regions without synchrotron magnets

Each particle is advanced in space a timestep dt, according to the equations

$$\begin{aligned} x^{n+1} &= x^n + \beta_x^n c\, dt \\ y^{n+1} &= y^n + \beta_y^n c\, dt \\ s^{n+1} &= s^n + \beta_s^n c\, dt, \end{aligned} \quad (14)$$

where x, y, and s are the horizontal, vertical, and longitudinal positions. The space-charge electric field at each particle is calculated using a standard 2-D PIC algorithm and the particle momentums are advanced as

$$\begin{aligned} \beta_x^{n+1} &= \beta_x^n + \frac{E_x}{\gamma^3}dt \\ \beta_y^{n+1} &= \beta_y^n + \frac{E_y}{\gamma^3}dt \\ \beta_s^{n+1} &= \beta_s^n + \frac{\beta_s^n}{\gamma^3}(\beta_x^n E_x + \beta_y^n E_y)dt. \end{aligned} \quad (15)$$

3.2 Regions with synchrotron magnets

When there is a thin element in a particle's path during the time step, the particle is advanced in time, dt_1, to the element and there the particle momentum receives its magnetic kick as

$$\begin{aligned} \beta_x^+ &= \beta_x^- - \frac{\beta_s}{1+\delta}\xi_y \\ \beta_y^+ &= \beta_y^- + \frac{\beta_x}{1+\delta}\xi_x \\ \beta_s^+ &= \sqrt{(\beta_s^-)^2 + (\beta_x^-)^2 + (\beta_y^-)^2 - (\beta_x^+)^2 - (\beta_y^+)^2}. \end{aligned} \quad (16)$$

The parameter δ is the particle's fractional deviation from the design momentum and ξ is calculated from the particle's position and the magnetic poles (a_n, b_n) as

$$\xi_x + i\xi_y = \sum_{n=0}^{n_{poles}}(b_n + a_n)(x + iy)^n. \quad (17)$$

Using the new momentum the particle is then advanced in space for the remainder of the timestep (dt_2=dt-dt_1).

4 SIMULATION RESULTS

For our simulations we have used a simple synchrotron lattice comprized of eight bending magnets and eight quadrupole magnets (four focusing and four defocusing). Unless otherwise stated the beam energy was set to 10 MeV, beam current 0.5 amps, and beam emittances (horizontal and vertical) 10π mm-mrad. The magnetic strengths were adjusted so the horizontal machine tune (ν_{xo}) was 1.75, while the vertical machine tune was adjusted to determine regions of instability.

Using the simulation with the vertical machine tune set to 0.85 (away from instabilities), we observed the amplitude dependence of the tune-shift for several

currents. Fig. 1 compares the computer results with Eq. (6) for currents of 0.1, 0.3, and 0.5 amps.

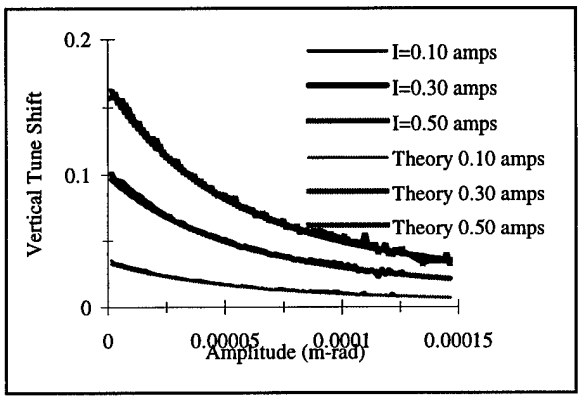

Fig. 1: Comparison of Theoretical Tune and Simulation

The region on integer instability was measured by scanning the vertical machine tune between 1.005 and 1.150. At each tune a simulation run was performed for up to 500 turns and the final saturation emittance was recorded. Fig. 2 shows that the maximum emittance growth is maximum at ν_{yo}=1.05 and ranges between 1.03 and 1.13.

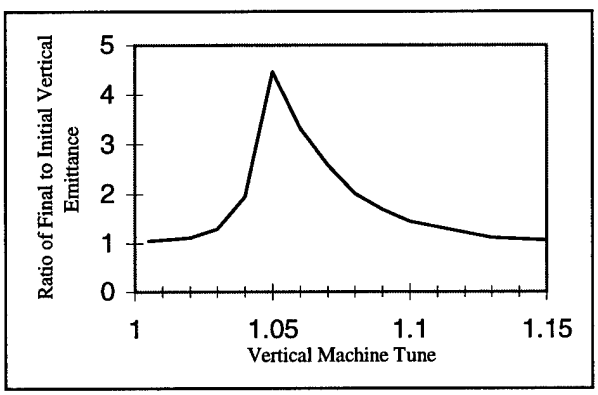

Fig. 2: Amplitude Growth as a function of machine tune

Fig. 3 shows the beam tune (ν_y) as a function of amplitude for five machine tunes(ν_{yo}=1.02, 1.05, 1.08, 1.10, and 1.15). Those beams whose tunes cross the integer are unstable, with the largest instability occuring when most of the beam lies slightly below the integer. As the resonant beam particles increase in amplitude the beam density decreases resulting in a lower overall tuneshift. This effect causes particles that had tunes slightly below resonance to become resonant. Typically the beam will be unstable when particles with amplitudes 1-20 times that of the beam emittance have integral tunes. The upper bound is set to be 20 by the scarcity of particles at such large amplitudes and the lower bound by the steep slope of the tune distribution at low amplitudes. The unstable band of machine tune in the vicinity of the integer resonance of n is

$$n+\frac{\Delta\nu_{\max}}{20\eta}(1-e^{-20\eta}) < \nu_o < n+\frac{\Delta\nu_{\max}}{\eta}(1-e^{-\eta}). \quad (18)$$

For our parameters, with η=0.32, $\Delta\nu_{\max}=0.165$, and n=1, the range of instability is $1.025<\nu_o<1.13$. This agrees with the region of instability from our simulation shown in Fig. (2).

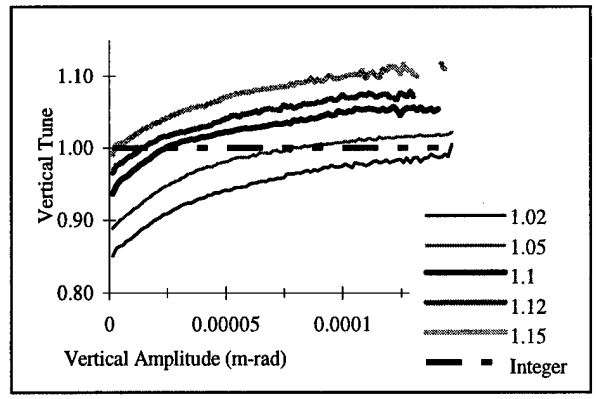

Fig. 3: Tune distribution as it crosses resonance

5 CONCLUSIONS

To understand the region of integral resonance, it is necessary to include the tune spread as a function of amplitude. A Gaussian beam will be unstable when particles with an amplitude greater than the rms emittance have integral tune. The resonance has the effect of increasing the beam emittance (which decreases the tune shift) until all of the individual particle tunes are above the resonant tune. The emittance growth is maximum when most, but not all, beam particles lie below the resonant tune. When all of the particles lie below the resonant tune, the beam is stable. Work supported by DOE and Hitachi.

REFERENCES

[1] A.W. Chao. *Physics of Collective Beam Instabilities in High Energy Accelerators* (John Wiley & Sons, New York, 1993).

[2] R. Baartman. *Proceedings of the International Workshop on Particle Dynamics in Accelerators,* edited by S. Machida and K. Hirata (1995) p. 273.

[3] S. Machida. *Nucl. Inst. & Methods.* **A309,** 43 (1991)

[4] W.T. Weng. *AIP Conference Proceedings* **153,** 349 (1987).

[5] M.B. Ottinger, T. Tajima, and K. Hiramoto. Submitted to *J. Comp. Phys.*, November 1996

[6] E.D. Courant and H.S. Snyder. *Annals of Physics,* **3,** 1 (1958).

[7] R.C. Davidson. *Physics of Nonneutral Plasmas* (Addison-Wesley Publishing, Redwood City, California, 1990).

[8] L. Schachinger and R. Talman. *Particle Accelerator* **22,** 35 (1987).

LONGITUDINAL COUPLED BUNCH INSTABILITIES IN THE JHF 50GeV MAIN RING

T. Uesugi, University of Tokyo, 3-2-1 Midori-cho, Tanashi, Tokyo 188, Japan
Y. Mori, S. Machida, C. Ohmori, KEK-Tanashi, 3-2-1 Midori-cho, Tanashi, Tokyo 188, Japan
and Y.H. Chin, KEK 1-1 Oho, Tsukuba, Ibaraki 305, Japan

Abstract

We have studied coupled bunch instabilities in the JHF proton synchrotron. We are particularly interested in the Q-dependence of the growth rate because we plan to have a newly developed broad band cavity. Results show that a lower growth rate can be achieved by broad band cavity.

1 INTRODUCTION

In the multi-bunch operation, each individual bunch can be coupled through RF cavities. This interaction causes the divergence of longitudinal and transverse bunch oscillations, called Coupled Bunch Instabilities (CBI). These instabilities are very serious problem for high intensity synchrotrons where the beam induced wake fields are large. We discuss CBI only in longitudinal motion because it is expected to be worse than the transverse counterpart.

The wake field which causes CBI comes from parasitic resonance at frequency larger than a few times of RF frequency. One way to avoid CBI is to use a feedback system and cancel the wake field.

Another possible way to avoid CBI is to use a broad band RF cavity (BBC), which is expected to damp out the wake field quickly. The BBC can be realized by using a magnetic core with a low Q (quality factor) value like FINEMET [3] whose Q is about 1. We have calculated the Q dependence of CBI to prove that the BBC is effective to CBI.

2 LINEAR THEORY OF COUPLED BUNCH INSTABILITIES

2.1 Pointlike bunch

Longitudinal coupled bunch motion can be represented by the superposition of N_B independent modes, where N_B is the number of bunches. If all bunches are equally populated in the ring, the longitudinal motion of N-th bunch in the μ-th mode can be written as

$$d\phi = \exp\left(i\Omega^{(\mu)}t + 2\pi i\mu\frac{N}{N_B}\right). \quad (1)$$

Here $d\phi$ is the displacement of bunch position in longitudinal direction, $\Omega^{(\mu)}$ the synchrotron frequency in the presence of coupling between bunches, -Im$\Omega^{(\mu)}$ the growth rate of CBI. We assumed that the amplitude of synchrotron oscillation is very small.

Equations of longitudinal bunch motion are

$$\frac{d\phi}{dt} = -\eta\omega_{rf}\frac{\delta P}{P_0} \quad (2)$$

$$\frac{dU}{dt} = \frac{\omega_{rf}}{2\pi h}(eV_{rf}\sin(\phi_0+\delta\phi)+U_{wake}) \quad (3)$$

which lead to the solution

$$-\mathrm{Im}\Omega^{(\mu)} = -\frac{e^2N\eta}{2\beta^2U_0\omega_sT_0^2}\times\mathrm{Re}\left\{\Delta\omega^{(\mu)}Z(\Delta\omega^{(\mu)})\right.$$

$$\left.+\sum_{k=1}^{+\infty}\left(\omega_k^{(\mu)+}Z(\omega_k^{(\mu)+})-\omega_k^{(\mu)-}Z(\omega_k^{(\mu)-})\right)\right\}. \quad (4)$$

Here $Z(\omega)$, the impedance, is the Fourier transformation of wake function $W(t)$, β the speed of particle, U_0 the synchronous energy, ω_s the synchrotron frequency, T_0 the revolution period, η the slippage factor, N the number of particles in the whole ring and $\omega_k^{(\mu)\pm}$ is the coupled bunch sideband at k times RF frequency, which is defined by

$$\begin{aligned}\omega_k^{(\mu)\pm} &= k\omega_{rf}\pm\Delta\omega^{(\mu)}\\ &= k\omega_{rf}\pm(\mu\omega_0+\omega_s)\end{aligned} \quad (5)$$

We will study the Q-dependence of growth rate with equation (4).

We assume the impedance of RF cavity to be that of LCR circuit, which is

$$Z_0(\omega) = \frac{R}{1+iQ(\omega_\mathrm{r}/\omega-\omega/\omega_\mathrm{r})}, \quad (6)$$

where ω_r is the resonant frequency and Q is quality factor. Then the wake field excited by a passage of pointlike charge at the light speed is

$$W_0(t) = 2e\alpha Re^{-\alpha t}\left(\cos\overline{\omega}t+\frac{\alpha}{\overline{\omega}}\sin\overline{\omega}t\right), \quad (7)$$

where e is the unit charge, $\overline{\omega}$ and α are real part and imaginary part of complex resonant frequency ω_r of the cavity, respectively.

2.2 Bunch with a Gaussian distribution

In previous subsection, we assumed the bunches as point charges. However, a real bunch has a finite length both in the longitudinal and transverse direction. If we take the longitudinal bunch length into account, we have to calculate the growth rate of CBI using effective impedance which is roughly obtained by the product $Z_0(\omega)\tilde{I}^2(\omega)$, where $\tilde{I}(\omega)$ is the bunch spectrum. For a Gaussian bunch, it is

$$Z(\omega) = Z_0(\omega)e^{-\omega^2\sigma^2}, \quad (8)$$

0-7803-4376-X/98 /$10.00 © 1998 IEEE

where σ is bunch length and

$$\omega_p = pM\omega_0 + \mu\omega_0 + \omega_s.$$

We assume that the bunching factor is 0.3, so that σ is about 35nsec. Figure 1 shows the real part of $\omega Z(\omega)$, for $Q = 1$ and $Q = 30$. The peak height of impedance is gradually falling down with ω. Thus, the parasitic resonance at sufficiently high frequency is not important.

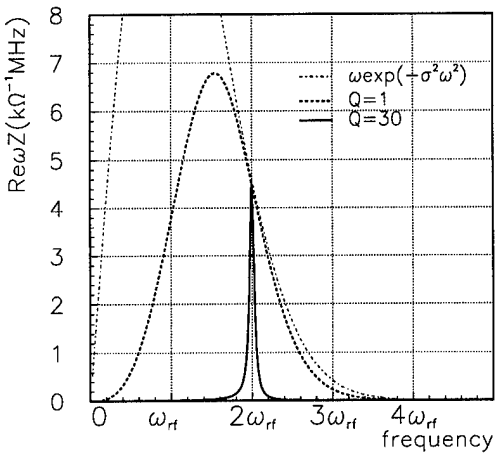

Figure 1: The real part of $\omega Z(\omega)$ for the parasitic resonance at two times of ω_{rf}, where Z is the effective impedance, calculated from Eq. (8). The bunching factor is 0.3.

kinetic energy	$K = U_0 - M = 3GeV$
number of particles	$N = 2 \times 10^{14} ppp$
harmonics	$h = 17$
RF voltage	$V_{RF} = 300kV$
RF frequency	$\omega_{rf}/2\pi = 3.43MHz$
slippage factor	$\eta = -0.0577$
synchrotron freq.	$\omega_s/2\pi = 717Hz$

Table 1: The parameters of JHF 50GeV ring at flat bottom.

3 RESULTS

First, we investigate the ω_r dependence of the growth rate of longitudinal CBI when $Q = 1$, 5 and 30 (Fig. 2) where the parameters of the JHF 50GeV ring at the injection energy as tabulated in Table 1 are used. We assumed the bunching factor to be 0.3. The figure shows, for example, the parasitic resonance with $R = 10k\Omega$ at about 3 times of RF frequency 'causes CBI with of 10sec^{-1} when $Q = 30$ and 0.1sec^{-1} when $Q = 1$, respectively.

Secondly, we investigate the Q-dependence. The maximum value among the growth rate for each region of ω_r is shown in Fig. 3. It is clear that the growth rate of the CBI is drastically reduced when the Q value of the parasitic resonance is less than 5.

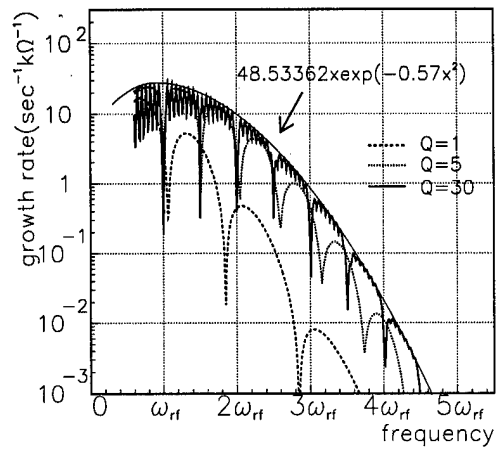

Figure 2: The growth rate of the longitudinal CBI vs frequency of parasitic resonance. ω_{rf} is the RF frequency.

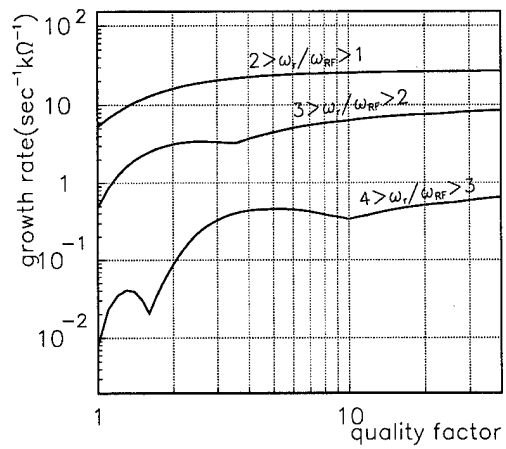

Figure 3: The growth rate of the longitudinal CBI as a function of quality factor. We assumed a parasitic resonance at each ω_r region and plotted the envelope.

4 CONCLUSION

We have calculated a growth rate of longitudinal coupled bunch instability for the JHF 50GeV proton synchrotron. It is found that in order to avoid CBI, the BBC is very useful. The BBC can be realized with FINEMET.

In the case of the flat bottom of JHF main ring, the growth rate becomes large and constant for the region $Q > 5$, but becomes lower quickly at $Q < 5$.

5 REFERENCES

[1] Y. Mori: The Japanese Hadron Facility, these proceedings.

[2] C. Ohmori *et al.*: A Wideband RF Cavity for JHF Synchrotrons, these proceedings.

[3] M. Fujieda *et al*: Studies of Magnetic Cores for JHF Synchrotorns, these proceedings.

COHERENT RADIATION OF AN ELECTRON BUNCH MOVING IN AN ARC OF A CIRCLE

E.L. Saldin, E.A. Schneidmiller
Automatic Systems Corporation, 443050 Samara, Russia
M.V. Yurkov
Joint Institute for Nuclear Research, 141980 Dubna, Moscow Region, Russia

Abstract

The paper presents some analytical results of the theory of coherent synchrotron radiation (CSR) describing the case of finite curved track length.

1 INTRODUCTION

Analysis of project parameters of linear colliders [1, 2] and short-wavelength FELs [1, 3, 4] shows that the effects of coherent synchrotron radiation of short electron bunches passing bending magnets influence significantly on the beam dynamics (see, e.g., [5, 6]). The first investigations in the theory of coherent synchrotron have been performed about fifty years ago [7, 8, 9]. In these papers the main emphasis was put on the calculations in far zone of CSR produced by a bunch of relativistic electrons moving on a circular orbit. Another part of the problem, namely that of the radiative interaction of the electrons inside a bunch has been studied for the first time in refs. [10, 11] and later in refs. [5, 12] where the energy loss along the bunch has been calculated. The results of the above mentioned CSR theories are valid for a model situation of the motion of an electron bunch on a circular orbit and do not describe the case of an isolated bending magnet. The first analytical results describing this case have been presented in ref. [13]. In particular, analytical expressions have been obtained for the radiative interaction force, for the energy loss distribution along the bunch and for the total energy loss of the bunch. The criterium for the applicability region of the previous theories to the case of a finite magnet length has been derived. In this report some analytical results of ref. [13] are presented.

2 RESULTS FOR A RECTANGULAR BUNCH

Let us consider a rectangular bunch of the length l_b passing a magnet with the bending angle ϕ_m and the bending radius R. We use the model of ultrarelativistic electron bunch with a linear distribution of the charge (zero transverse dimensions) and assume the bending angle to be small, $\phi_m \ll 1$. We neglect the interaction of the bunch with the chamber walls assuming the electrons to move in free space. The total number of particles in the bunch is equal to N and the linear density is equal to $\lambda = N/l_b$.

When the electron bunch passes the magnet, the electromagnetic field slips over the electrons due to the curvature and the difference between the electron's velocity and velocity of light c. The slippage length L_{sl} is given by the expression:

$$L_{sl} \simeq \frac{R\phi_m}{2\gamma^2} + \frac{R\phi_m^3}{24}\,, \tag{1}$$

where γ is relativistic factor. When applying the results of steady-state CSR theory (periodical circular motion) to the case of isolated magnet it is assumed usually that the bunch length is much shorter than the slippage length. To obtain more correct criterium for the applicability region one has to develop more general theory including transient effects when the bunch enters and leaves the magnet. Such an investigation has been performed in ref. [13]. In particular, it has been stressed that the radiation formation length of the order of $l_b\gamma^2$ before and after magnet plays an important role in CSR effects. In practically important case when the conditions $\gamma\phi_m \gg 1$ and $R/\gamma^3 \ll l_b < L_{sl}$ are satisfied, the expression for the total energy loss of the bunch can be written in the following form [13]:

$$\Delta\mathcal{E}_{tot} = -\left(\frac{3^{2/3}e^2N^2}{l_b^{4/3}R^{2/3}}\right)(R\phi_m) \times\left\{1+\frac{3^{1/3}4}{9}\frac{l_b^{1/3}}{R^{1/3}\phi_m}\left[\ln\left(\frac{l_b\gamma^3}{R}\right)+C\right]\right\} \tag{2}$$

where e is the charge of the particle and

$$C = 2\ln 2 - \frac{1}{2}\ln 3 - \frac{11}{2} \simeq -4\,.$$

The first term in eq. (2) is the solution obtained in the framework of steady-state approach (see, e.g., refs. [9, 11, 5]). Therefore, with logarithmical accuracy we can set the applicability region of the results of the steady-state theory for the case of a finite curved track length:

$$\frac{l_b^{1/3}}{R^{1/3}\phi_m}\ln\left(\frac{l_b\gamma^3}{R}\right) \ll 1\,. \tag{3}$$

In particular, the steady-state theory provides completely incorrect results for the case of the electron bunch much longer than the slippage length, $l_b \gg L_{sl}$. In this case the energy losses of the particles in the bunch due to CSR are proportional to the local linear density and take place mainly after the magnet [13]. For a "short" magnet, $\gamma\phi_m \ll 1$, the total energy loss of rectangular bunch is equal to

$$\Delta\mathcal{E}_{tot} = -\frac{2}{3}\frac{e^2N^2}{l_b}\gamma^2\phi_m^2\,. \tag{4}$$

0-7803-4376-X/98/$10.00 © 1998 IEEE

The energy loss of the rectangular bunch passing a "long" magnet, $\gamma\phi_m \gg 1$, is equal to:

$$\Delta\mathcal{E}_{tot} = -\frac{N^2e^2}{l_b}\left[4\ln(\gamma\phi_m) - 2\right] . \qquad (5)$$

These results has been obtained in ref. [13] by means of calculation the radiative interaction of the electrons in the bunch. It is interesting to compare the total energy loss of the bunch with the energy of coherent radiation in far zone. The radiation energy in far zone can be calculated as an integral over frequency of the spectral density of the radiation energy:

$$\frac{dW_{coh}}{d\omega} = N^2\eta(\omega)\frac{dW}{d\omega} , \qquad (6)$$

where $\eta(\omega)$ is the bunch form factor (squared module of the Fourier transform of the linear density distribution). The form factor for the rectangular bunch of the length l_b is given by the expression:

$$\eta(\omega) = \left(\sin\frac{\omega l_b}{2c}\right)^2\left(\frac{\omega l_b}{2c}\right)^{-2} . \qquad (7)$$

Function $dW/d\omega$ entering eq. (6) is the spectral density of the radiation energy of a single electron. The angular and the spectral characteristics of the radiation of an electron moving in an arc of a circle have been studied in ref. [14][1]. It has been shown that the spectrum of the radiation emitted by an electron moving in an arc of a circle differs significantly from that of conventional synchrotron radiation of an electron executing periodical circular motion. In the latter case the spectral density at low frequencies is proportional to $\omega^{1/3}$ [16]. In the case of a finite curved track length the spectral density is constant at $\omega \to 0$. When the bending angle is small, $\phi_m \ll 1$, the spectral density of the radiation energy emitted by ultrarelativistic electron is function of the only parameter $\gamma\phi_m$ [14]:

$$\frac{dW}{d\omega} = \frac{e^2}{\pi c}f_m , \qquad (8)$$

where

$$f_m = \left(\mu + \frac{1}{\mu}\right)\ln\frac{1+\mu}{1-\mu} - 2 ,$$

and

$$\mu = \frac{\gamma\phi_m/2}{\sqrt{1+(\gamma\phi_m/2)^2}} .$$

Formula (8) is valid in the frequency range $\omega \ll c/L_{sl}$. Taking into account formula (7) we can estimate that typical frequencies of the coherent radiation are below the frequency $\omega \sim c/l_b$. It means that we can use the asymptotical expression (8) in the case when $l_b \gg L_{sl}$. Integrating eq. (6) over the frequency, we obtain:

$$W_{coh} = \frac{e^2N^2}{l_b}f_m . \qquad (9)$$

[1]The same problem has been considered later in ref.[15], but the results of this paper are incorrect.

It is easy to obtain that in the case of a "long" magnet, $\gamma\phi_m \gg 1$, the energy of coherent radiation (9) coincides exactly with the bunch energy loss given by eq. (5) taken with opposite sign. In the limit of a "short" magnet, $\gamma\phi_m \ll 1$, there is also complete agreement between formulae (9) and (4).

3 BUNCH WITH AN ARBITRARY DENSITY PROFILE

The solutions obtained in ref. [13] for the rectangular bunch can be generalized for the case of an arbitrary linear charge density. We present here the results of the calculation of the transition process when the bunch enters the magnet. Let the bunch have the density distribution $\lambda(s)$ which satisfies the condition

$$\frac{R}{\gamma^3}\frac{d\lambda(s)}{ds} \ll \lambda(s) . \qquad (10)$$

Under this condition the rate of the energy change of an electron is given by the expression [13]:

$$\frac{d\mathcal{E}(s,\phi)}{d(ct)} = -\frac{2e^2}{3^{1/3}R^{2/3}}\left\{\left(\frac{24}{R\phi^3}\right)^{1/3}\left[\lambda\left(s-\frac{R\phi^3}{24}\right) - \lambda\left(s-\frac{R\phi^3}{6}\right)\right] + \int\limits_{s-R\phi^3/24}^{s}\frac{ds'}{(s-s')^{1/3}}\frac{d\lambda(s')}{ds'}\right\} , \qquad (11)$$

where s is the position of the electron in the bunch and ϕ is azimuthal angle.

For the Gaussian density distribution:

$$\lambda(s) = \frac{N}{(2\pi)^{1/2}\sigma}\,exp\left[-\frac{s^2}{2\sigma^2}\right] , \qquad (12)$$

expression (11) takes the form:

$$\frac{d\mathcal{E}}{d(ct)} = -\frac{2e^2N}{3^{1/3}(2\pi)^{1/2}R^{2/3}\sigma^{4/3}}G(\xi,\rho) , \qquad (13)$$

where function $G(\xi,\rho)$ is given by the expression:

$$G(\xi,\rho) = \rho^{-1/3}\left[e^{-(\xi-\rho)^2/2} - e^{-(\xi-4\rho)^2/2}\right] + \int\limits_{\xi-\rho}^{\xi}\frac{d\xi'}{(\xi-\xi')^{1/3}}\frac{d}{d\xi'}e^{-(\xi')^2/2} . \qquad (14)$$

Here $\xi = s/\sigma$ and $\rho = R\phi^3/24\sigma$. Function $G(\xi,\rho)$ reduces to

$$G(\xi,\rho) \simeq -\frac{9}{2}\xi\exp(-\xi^2/2)\rho^{2/3}$$

at $\rho \ll 1$. In the opposite case, at $\rho \to \infty$, expression (14) tends to the steady-state solution [11, 5, 12]. In Fig.1 we present the plot of function (13). One can see that there is excellent agreement of analytical results [13] and the results obtained by means of numerical simulation code [6].

4 ACKNOWLEDGMENTS

We wish to thank C.L. Bohn, R. Brinkmann, Ya.S. Derbenev, M. Dohlus, K. Floettmann, D. Jaroszynski, T. Limberg, H. Mais, A. Piwinski, J. Rossbach, V.D. Shiltsev and D. Trines for useful discussions.

5 REFERENCES

[1] "Conceptual Design of a 500 GeV e+e− Linear Collider with Integrated X-ray Laser Facility" (Editors R.Brinkmann, G. Materlik, J. Rossbach, A. Wagner), DESY 97-048, Hamburg, 1997.

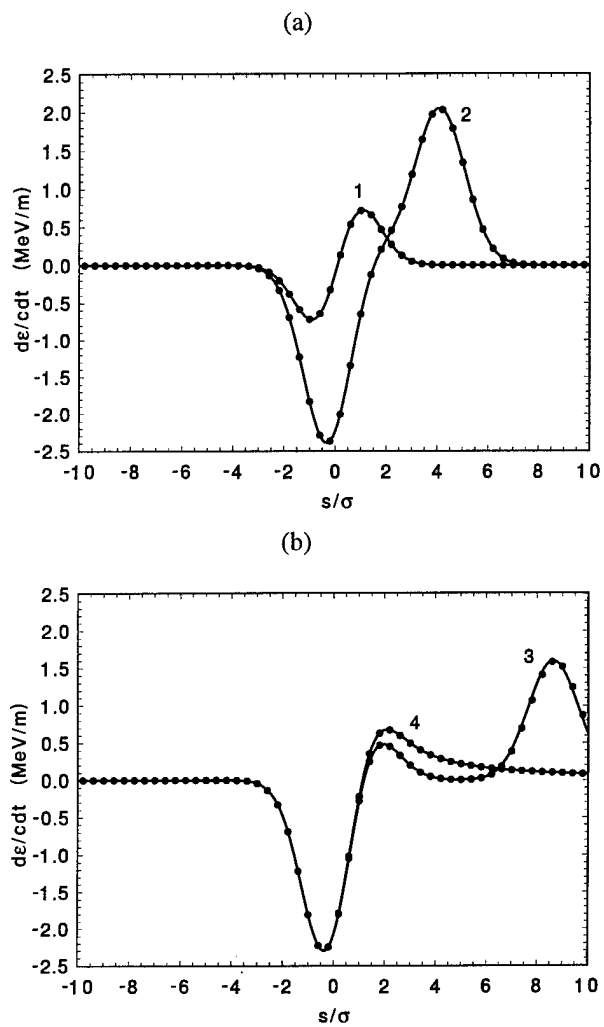

Figure 1: The rate of an electron energy change as a function of its position along the Gaussian bunch entering the magnet. Curve (1) in the graph (a): 5 cm after the begin of the magnet. Curve (2) in the graph (a): 14 cm after the begin of the magnet. Curve (3) in the graph (b): 18 cm after the begin of the magnet. Curve (4) in the graph (b): steady state. The curves are the results of calculations with formula (13) and the circles are the results of numerical simulations presented in ref. [6]. The parameters are as follows: $R = 1.5$ m, $\sigma = 50\ \mu$m, $q = 1$ nC.

[2] "Zeroth-Order Design Report for the Next Linear Collider", LBNL-PUB-5424,SLAC Report 474, UCRL-ID-124161 (May 1996).

[3] R. Tatchyn et al., Nucl. Instr. and Methods **A375**(1996)274.

[4] J. Rossbach, Nucl. Instr. and Methods **A375**(1996)269.

[5] Ya.S. Derbenev, J. Rossbach, E.L. Saldin, V.D. Shiltsev, "Microbunch Radiative Tail-Head Interaction", DESY Print, TESLA-FEL 95-05, Hamburg(1995).

[6] M. Dohlus, T. Limberg, "Emittance Growth due to Wake Fields on Curved Bunch Trajectories", presented at XVIII International Free Electron Laser Conference (Rome,1996); DESY print, TESLA-FEL 96-13 (1996).

[7] L.I. Schiff, Rev. Sci. Instr. **17**(1946)6.

[8] J. Schwinger, "On radiation by electrons in a betatron", 1945 (unpublished), see references in [9].

[9] J.S. Nodvick and D.S. Saxon, Phys. Rev. **96**(1954)180.

[10] I.E. Tamm, Report of the Institute of Physics, Acad. of Sciences, USSR, 1948 (in Russian).

[11] L.V. Iogansen and M.S. Rabinovich, Sov. Phys. JETP, vol.37(10), 1960, p.83.

[12] J.B. Murphy, S. Krinsky and R.L. Glukstern, "Longitudinal Wakefield for Synchrotron Radiation", Proc. of IEEE PAC 1995, Dallas(1995).

[13] E.L. Saldin, E.A. Schneidmiller, M.V. Yurkov, "On the Coherent Radiation of an Electron Bunch Moving in an Arc of a Circle", DESY Print, TESLA-FEL 96-14 (November 1996).

[14] V.G. Bagrov, I.M. Ternov and N.I. Fedosov, Sov. Phys. JETP, vol.55(5), 1982, p.835; Phys. Rev. **D28** (1983)2464.

[15] D.J. Wingham, Phys. Rev. **D35**(1987)2584.

[16] J. Schwinger, Phys. Rev. **75**(1949)1912.

WAKEFIELDS OF SHORT BUNCHES IN THE CANAL COVERED WITH THIN DIELECTRIC LAYER

A. Novokhatski* and A. Mosnier
CEA/DSM, CEA-Saclay, F-91191 Gif-sur-Yvette Cedex, France

Abstract

In new generation of accelerators shorter and shorter bunches are considered. In addition to the usual wakefields, excited in corrugated or resistive vacuum chambers, other harmful wakes can be excited in smooth beam tubes, covered by thin dielectric layer. Analytical approximation and results of computer simulations are presented for various bunchlengths and dielectric thickness. It is shown that a 50 μm long bunch, travelling through a tube with ceramic coating of only 0.1 μm gives rise to large amplitude wakefields, comparable to usual wakes in accelerating cavities. This effect can be dramatic for long transport lines. Dielectric coatings in the tubes can be of different types. A few examples, like oxide layer in aluminum tubes, are finally discussed. Derived estimations are also given for corrugated metallic surfaces, which can have similar behaviour to dielectric coated tubes.

1 INTRODUCTION

The wakefields, excited by intensive bunches in accelerating structures and transport lines, are of major concern in the design of future for Linear Colliders and X-ray Free Electron Laser, because they can give rise to large energy spreads and transverse instabilities. In new generation of accelerators, shorter and shorter bunches are considered. For example, bunches of 25 μ and less are foreseen in the SASE FEL of the TESLA facility [1]. In addition to the usual wakefields, excited in corrugated or resistive vacuum chambers, other harmful wakes can be excited in the beam pipes, which have not really "smooth" surface. In the range of high frequencies, the usual roughness of the surface can be sufficient to reduce the phase velocity down to the speed of the travelling particles, generally close to the speed of light.

2 SINGLE MODE WAKES

We consider bunches of finite length σ, travelling with a speed close to the speed of light, through round pipes of radius a, filled with dielectric material between a and $a+\delta$. Longitudinal and transverse wakefields will be induced, but we restrict to longitunal fields throughout this analysis. We assume that the higher order modes, of wave numbers k_n, are suppressed by the finite bunchlength σ

$$\exp[-\frac{1}{2}(\sigma k_n)^2] \ll 1 \tag{1}$$

but keeping, on the other hand, the lowest mode k_0, because of the non-zero thickness of the dielectric layer

$$\sigma k_0 \leq 1 \tag{2}$$

The wave number for main mode k_0 can be easily evaluated for the ultrarelativistic case. The longitudinal electric component E_z for the m-azimuthal mode is well known in the vacuum part $r < a$

$$E_z(r) = e(z-ct)(\frac{r}{a})^m \tag{3}$$

In the thin dielectric layer, E_z is decreasing rapidly and become zero at the metallic boundary. It can be approximated at first order in the dielectric canal vanishing on metallic part by

$$E_z(r) = E_z(a)(1-\frac{r-a}{\delta}) \tag{4}$$

The expression of the wave number can be established directly from Maxwell equations

$$k_0^2 = \frac{a\epsilon}{1-\epsilon}\frac{\frac{dE_z(r>a)}{dr}}{\int_0^a E_z(r)rdr} \tag{5}$$

where ϵ is the dielectric constant of the layer. Finally, we obtain simply

$$k_0^2 = \frac{2\epsilon}{a\delta(\epsilon-1)} \tag{6}$$

This derived formula is in quite agreement with ref. [3].

From the expressions 2 and 6 it is possible to give an estimation of the minimal thickness of the layer, which generate large wake amplitude :

$$\delta \geq \frac{2\epsilon\sigma^2}{a(\epsilon-1)} \tag{7}$$

We note that the dielectric constant dependance is very weak. Taking a dielectric constant of 2, the previous simply

$$\delta \geq \frac{4\sigma^2}{a} \tag{8}$$

Assuming for example a bunchlength of 25 μ and a pipe diameter of 20 mm, a dielectric coating of only 0.25 μ is very harmful. Numerical simulations, by means of the code already used in Ref.[2], were caried out to check this single mode regime. Fig.1 shows the wake potentials for a σ= 25 μ long bunch, moving in the pipe of radius a=50 mm for different thickness of dielectric layer (δ=0.0125, 0.05, 0.2, 0.8 and 3.2 μm). The amplitude of the induced fields habe been normalized by the quantity $Z_0c/\pi a^2$.

* Permanent address: Budker Institute of Nuclear Physics, 630090 Novosibirsk, Russia

0-7803-4376-X/98/$10.00 © 1998 IEEE

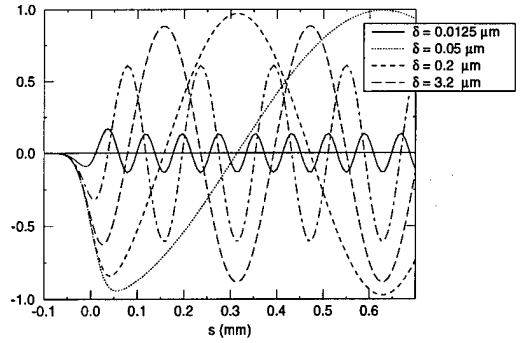

Figure 1: Wake potentials of a 25 μ bunch in .the tube of the radius a=50 mm for different thickness of dielectric layer δ=0.0125, 0.05, 0.2, 0.8 and 3.2 μ

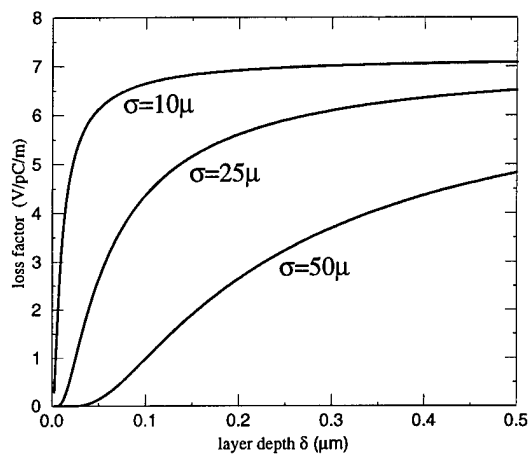

Figure 2: Loss factor (in V/pC/m) vs. layer thickness for different bunchlengths σ= 10, 25 and 50 μ

We note that the mode frequency scales with the square root of the layer thickness, as expected (see expression 6). Numerical results are in quite agreement with the description, given in Ref.[3], of the amplitude of the synchronous fields

$$E_z = \frac{Z_0 c}{\pi a^2} \exp[-\frac{1}{2}(K_0\sigma)^2] \qquad (9)$$

The loss factor per unit length, integral of the bunch wake potential with the charge distribution is given by

$$K_{loss} = \frac{Z_0 c}{2\pi a^2} \exp[-(K_0\sigma)^2] \qquad (10)$$

The dependence of the loss factor on the layer thickness is shown on Fig.2 for different bunchlengths.

3 CASE OF SLIGHTLY CORRUGATED PIPES

Some very small corrugations on beam pipes can behave like "ceramic" layers. The equivalent "dielectric" constant depends of course on the details of corrugation. However,

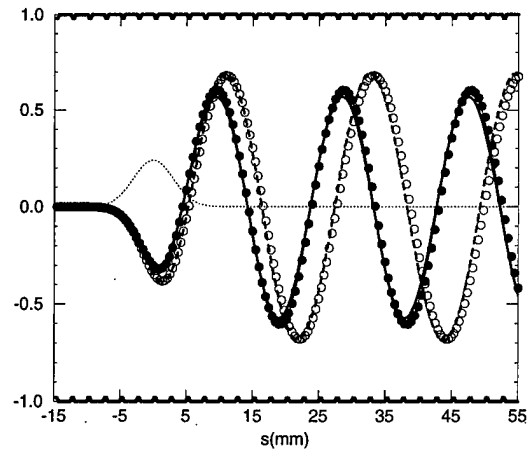

Figure 3: Normalized wake potentials (σ=3 mm) in slightly corrugated tube (dark lines) for periods 1.25 and 4.5 mm (solid lines) and 2.5 mm (dashed line) and in tubes covered with ceramic layer (same thickness as radial size of protuberances) of dielectric constant 2 (empty circles) and 1.6 (solid circles).

assuming that the sizes of the protuberances are not too much different, we can predict an equivalent "dielectric" constant in the range of 2. With the aim of comparing the wakefields induced in ceramic layer and in slightly corrugated tubes, calculations by means of the code NOVO for the latter case, and described in [4], were carried out. At first, a tube of radius $a = 50mm$ with small irises of 1 mm height and 0.5 mm width was chosen. A σ=3 mm bunch-length was selected in order to excite the same wave with k_0=0.28 mm^{-1} according to expression (6) for $\epsilon = 2$. The normalized wake potentials are shown on Fig.3 for different periods (1.25, 2.5 mm and 4.5 mm). We note that both 1.25 and 4.5 mm periods give the same wakes, up to several σs after the bunch. The wakes induced in tubes, coated with ceramic layers (dielectric constant 2 and 1.6) of the same thickness as radial size of the protuberances are also shown.

We observe very good agreements between both kinds of pertubated pipes. We conclude that the same wake formulae can be used. In the reality, the rough pipe surface has no perfect periodic corrugation, but exhibits random protusions. This random nature results in some decoherence of the induced fields, but only for the long-range wakefield, as it is shown on Fig.4, where the wakes are plotted for a 10 meters long tube, with a diameter of 100 mm, filled of 1 mm protusions, randomly spaced between 1 and 9 mm. A wake, excited by a 1 mm thich ceramic layer of dielectric constant 1.5 is also shown for comparison.

4 DISCUSSIONS

For short bunch acceleration and transportation, notice must be taken of the wakefields, which can be excited in

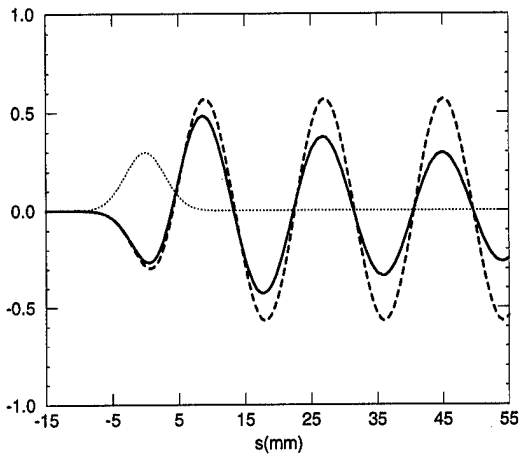

Figure 4: Normalized wake potentials (σ=3 mm) in a "real" tube, filled with randomly spaced protusions (solid line) and filled with dielectric material (dashed line).

beam tubes, covered by very tiny dielectric layers, or very slightly corrugated. The amplitudes of the wakes are comparable to those, induced in accelerating periodic structures. For aluminum vacuum chambers, the thickness of ceramic layer can vary in the range of a few nanometers, and can be harmful for very small bunches, in the range of 10 μ. Furthermore, the roughness of the surface can give a significant effect, and not only for very short bunches.

5 ACKNOWLEDGEMENT

The authors would like to thank Olivier Napoly for useful discussions, Reinhard Brinkmann and Jorg Rossbach for their interest to this work.

6 REFERENCES

[1] J.Rossbach, "New linac based FEL projects using bright electron beams", Proc. of 1996 Intern. Linac Conference, Geneva.

[2] A.V.Burov and A.V.Novokhatski "Wake potential of dielectric canal", Proc. of the XVth Int. Conf. on High Energy Accelerators, Hamburg, July 1992, p.537.

[3] King-Yuen Ng, "Wake fields in a dielectric-lined waveguide", Phys. Rev. D 42, 1819 (199).

[4] A.Novokhatski and A.Mosnier "Wakefield Dynamics in Quasi Periodical Structures", these proceedings.

MEASUREMENT OF THE LONGITUDINAL WAKE POTENTIAL IN THE PHOTON FACTORY ELECTRON STORAGE RING

Kazuhiro Tamura, SPring-8, Kamigori, Ako-gun 678-12, Japan
Toshio Kasuga, Makoto Tobiyama, Takashi Obina, High Energy Accelerator Research Organization, Tsukuba 305, Japan, Akira Mochihashi, University of Tsukuba, Tsukuba 305, Japan and Baogen Sun, University of Science and Technology of China, Hefei, Anhui 230029, China

Abstract

We tried to determine the longitudinal wake potential in the Photon Factory electron storage ring by measuring the longitudinal bunch structure with a photon counting method. A train of test bunches whose currents were small enough to neglect the interaction among them were injected behind a bunch with a large current. Deformation and the shift of the test bunches in the longitudinal direction due to the wake field generated by the large current bunch were measured, and the wake potential was estimated. We found the wake potential consists of two components: one is the short range wake which vanishes outside the bunch, and the other with the medium range of successive several bunches. The photon counting method is not always suitable for the multi-bunched beam. Development of a fast light shutter with a Pockels cell which enables us to measure the structure of a bunch in the multi-bunch mode is under way.

1 INTRODUCTION

According to the damping time of the wake field, we classified the wake into three types. The first is the short range wake which exists within a bunch only, the second is the medium range wake whose damping time is longer than the minimum bunch spacing but shorter than the revolution time of the bunch. The last is a long range wake which lasts longer than the revolution time. The short and medium range wakes are transient, but the long range wake is sometimes piled up and gives rise to beam instabilities. Although the long range wake has been widely studied theoretically and experimentaly, there are few experimental studies of the short and medium range wake so far. In this paper, we present the experimental results and discussion on the longitudinal wake of short and medium range.

We measured the longitudinal bunch structure with a single photon counting system[1] insalled in beamline 21 in the Photon Factory electron storage ring (PF-ring). Since the short range wake generated by a bunch affects only itself, we investigated the wake by measuring the longitudinal distribution of electrons in the bunch in the single-bunch mode as a function of the bunch current. In order to measure the medium range wake, we developed the test bunch method in which a main bunch with a large current and a train of small current test bunches as probes of the wake potential are stored simultaneously. The principle of the test bunch method is described in Sec.2. The short and medium range wakes are discussed in Sec.3.

We have been developing a fast light shutter with a Pockels cell which can select a light pulse out of successive light pulses radiated from the multi-bunched beam. A preliminary result of the beam test of the shutter is presented in Sec. 4.

2 PRINCIPLE OF TEST BUNCH METHOD

The test bunch method was developed for the measurement of the medium range wake. Making use of the wide dynamic range (>10^5) and the excellent time resolution (<10ps) of the photon counting method, we measured the change in bunch lengths and the longitudinal shifts of the test bunches following a large current main bunch, and estimated the longitudinal wake potential generated by the main bunch.

When the phase shift from the synchronous phase of the k-th test bunch in the presence of the wake potential $V_w(t)$ is ϕ_{sk}, the total acceleration voltage V_{tot} and its gradient $\dot{V}_{tot}$ are represented as

$$V_{tot}(t) = V_{RF}\sin(\omega_{RF}t + \phi_{sk}) + V_w(t) \quad (1)$$

and

$$\dot{V}_{tot}(t) = \omega_{RF}V_{RF}\cos(\omega_{RF}t + \phi_{sk}) + \dot{V}_w(t). \quad (2)$$

The bunch length is given by

$$\sigma_t = A\Big/\sqrt{\dot{V}_{tot}} \quad (3)$$

where A is a constant. Using eq. (2), the deviation of the bunch length $\Delta\sigma_t$ from its natural length is given by

$$\frac{\Delta\sigma_t}{\sigma_t} = -\frac{\dot{V}_w(t)}{2\dot{V}_{RF}(\phi_{sk})}.$$

When the wake potential and the radiation loss U_{rad} is small compared with the RF voltage, the deviation of the synchronous phase $\Delta\phi$, which corresponds to the shift of the bunch center Δt, is given by

$$\Delta\phi \cong \omega_{RF}\Delta t = \frac{V_w(t)}{V_{RF}}.$$

0-7803-4376-X/98/$10.00 © 1998 IEEE

The longitudinal shifts of the centers and the deviations of the lengths are proportional to the wake potential and its gradient, respectively. Therefore, by measuring the lengths and the centers of the test bunches, we can sample the wake potential and its gradient with the sampling period of the bunch spacing (2ns).

3 WAKE POTENTIAL IN PF-RING

3.1 Short range wake

We measured the dependece of the longitudinal distribution on the bunch current in the single-bunch operation with the photon counting method. The longitudinal distributions below the threshold current of the microwave instability are shown in Fig.1. The vertical bars in the figures show the statistical errors. The left hand side of the horizontal axis shows the head of the bunch. The distributions at the bunch current up to about 4 mA are nearly Gaussian, but those at larger currents become asymmetric due to the wake potential generated by the bunch itself.

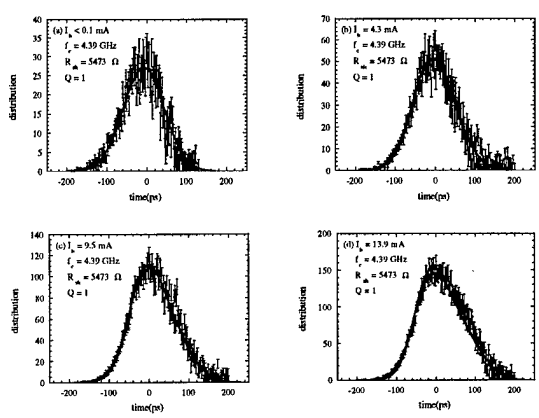

Fig. 1 : Longitudinal distribution of electrons in the bunch in single-bunch mode.

In order to explain the wake potential, we employed the broadband impedance model. The broadband impedance model is represented by a wideband resonator whose quality factor Q is unity. It contains the contribution of all the vacuum chamber components of the ring. We reconstructed the wake function of the broadband impedance and solved the Haissinski equation [2] iteratively. When we assume the shunt impedance and resonant frequency to be 5500Ω and 4.4GHz, respectively, which gives the coupling impedance |Z/n| of about 2Ω, the calculated distributions (solid lines in Figs. 1) are well fitted to the experimental distributions. These parameters are consistent with other studies [3,4].

3.2 Medium range wake

In order to investigate the medium range wake, we employed the test bunch method. Influence on the test bunches with a beam current of 1mA each was observed as a function of the beam current of the main bunch. If the wake fields produced by the main bunch excite longitudinal coherent oscillations of the bunches around the synchronous phases, the gross bunch lengths measured with the photon counting system become longer than the real lengths, because the system measures the averaged longitudinal distribution of the bunch. We determined amplitude of the longitudinal coherent oscillations of the test bunches, measuring a beam signal from a button-type pickup electrode with a histogram function of an oscilloscope (HP54121A and 54120B). The r.m.s. amplitudes of the oscillation were less than 10 ps. Since their contribution to the measurements of the bunch lengths are less than 1 ps, we concluded that the effect of the coherent oscillation is negligible in the test bunch method.

We stored the test bunches in one of regions listed below:

Region 1: just before the main bunch,
Region 2: just after the main bunch,
Region 3: opposite side of the ring with respect to the main bunch,

and estimated the damping time of the wake by measuring the length and the shift of the center of each test bunch. Considering the reproducibility of the bunch length measurement (±0.4ps) and that of the bunch center measurement (±5ps), the variation of the bunch lengths and the shifts of the bunch centers in Region 1 and 3 were meaningless. We therefore investigated the wake in Region 2 in detail. Examples of the variation of the bunch lengths and the shift of the bunch centers in Region 2 are shown in Figs. 2. The main bunch with a beam current of

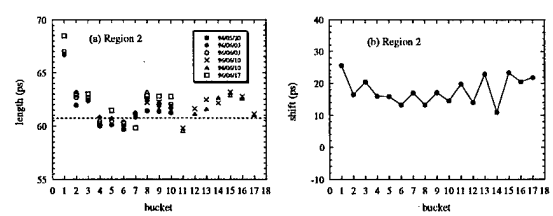

Fig. 2 :Results of the test bunch measurement. (a) variation of the lengths and (b) shifts of the centers of the test bunches stored just after the main bunch.

30mA was stored in 0th bucket. For the determination of the frequency components of the wake, we performed the discrete Fourier transform (DFT) on the data in Figs. 2. The results are shown in Figs. 3. Since the numbers of data are 17 and the sampling frequency is 500 MHz (RF frequnecy), the resolution of frequency is limited to ±15 MHz. According to the sampling theorem, the highest frequency we can identify is a half of the sampling frequency and the frequencies higher than that cause aliasing. Main components in Figs. 3 are

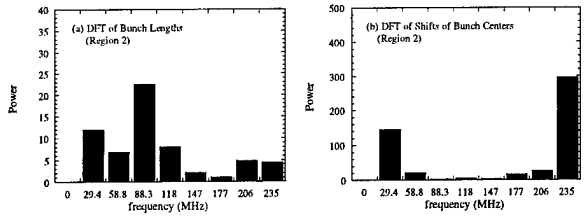

Fig. 3 : DFT's of (a) variation of the lengths and (b) shifts of the centers of the test bunches in Figs. 2

$$f_1 = n_1 \times f_{RF} + 88\text{MHz} \text{ or } -88\text{MHz}$$
$$f_2 = n_2 \times f_{RF} + 235\text{MHz} \text{ or } -235\text{MHz}.$$

RF cavities are often assumed as the impedance sources because they have many higher order mode (HOM) resonances. We calculated the wake potential in the RF cavities using the code ABCI [5,6], and calculated the lengths and the shift of the centers of the test bunches. This wake potential causes little change of the bunch lengths. On the other hand, it leads to the shifts of about 10ps of the bunch center. In Fig. 4, we show the DFT of

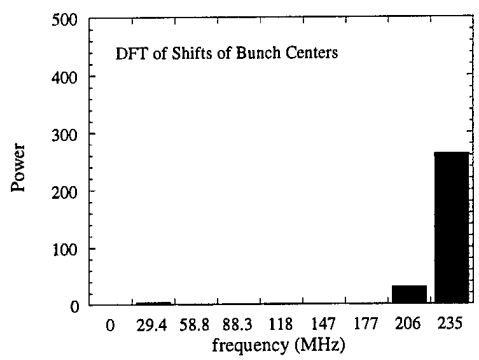

Fig. 4 DFT of the calculated shifts of the bunch centers due to the wake potential in the RF cavities.

the calculated shifts of the bunch centers due to the wake potential in the RF cavities. Although apparent pattern of the shift in the time domain differs from the experimental shifts, the power level of the frequency component of around 235 MHz in Fig. 4 is about the same as that of f_2 in Fig. 3 (b).

In order to explain the variation of the lengths of the test bunches phenomenologically, we intrduce an impedance of a resonator. Considering the cutoff frequency of the beam duct of the PF-ring and the damping pattern of variation of the bunch lengths, we set the resonant frequency and the quality factor to be 2575MHz and 120. Using these value, we determined the shunt impedance which can explain the experimental data to be about 80kΩ. The calculated lengths are shown in Fig. 5.

4. DEVELOPMENT OF FAST LIGHT SHUTTER

In the multi-bunch mode, speedy observation of a particular bunch using the photon counting system is

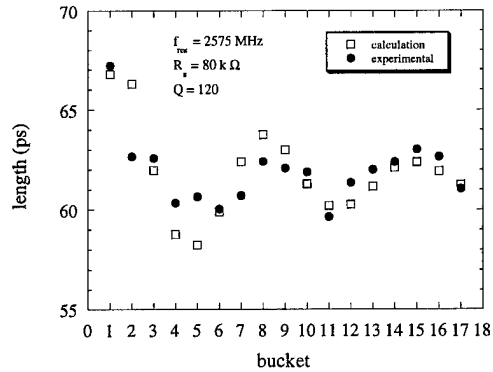

Fig. 5 : Variation of lengths of test bunches.

difficult because of a current limitation of the photomultiplier. A high speed shutter which can open or close within a time scale of the bunch spacing (2 ns in KEK-PF) enables us to observe one particular bunch: the time required to measure the single bunch impurity becomes short, and the longitudinal fine structure of the test bunches which emit less photons than the main bunch can be measured precisely.

The shutter system is composed of two polarizers and a Pockels-cell[7], which changes the polarization of penetrating light when a high voltage is applied. We succeeded to select photons from one particular bunch with the system. Some parameters of the shutter system are shown in Table 2.

We estimate that the extinction ratio makes the time required to measure the impurity down to about 1/100.

driving voltage	550 V
repetition rate	533 kHz
rise time (5 to 95 %)	1.5 ns
fall time (95 to 5 %)	1.6 ns
flat top	0.9 ns
extinction ratio	280

Table 2 : Parameters of the shutter system

K.Tamura would like to thank JSPS Research Fellowships for Young Scientists. This work wes partly supported by the Grant-in-Aid for Scientific Research from the Ministry of Education, Science and Culture.

REFERENCES

[1] T. Obina et. al., Nucl. Inst. and Meth. A 354 (1995) 204.
[2] J. Haissinski, IL NUOVO CIMENTO 18B, 72 (1973).
[3] M. Izawa et al., Rev. Sci. Instrum. 63, 363 (1992).
[4] N. Nakamura et al., in Proc of 1991 IEEE Part. Accel. Conf. (San Francisco) p.440.
[5] T. Weiland, Nucl. Instrum. Methods 212, 13 (1983)
[6] Y. H. Chin, CERN SL/94-92 (AP)
[7] A. Yariv, QUANTUM ELECTRONICS, third Ed., JOHN WILEY & SONS, Chap. 14.

WEAK-STRONG SIMULATION OF BEAM-PHOTOELECTRON INSTABILITY IN A POSITRON STORAGE RING

K. Ohmi, KEK-PF, Oho, Tsukuba, Ibaraki 305, Japan

Abstract

Growth of the photoelectron instability has been discussed by using a wake force occurred by electron cloud. Concept of the conventional wake force is available for the force which satisfies linearity and superposition for the coherent amplitude of bunches. Weak-strong simulation method for beam-photoelectron interactions is proposed to study the nonlinear wake effect. In the method, photoelectrons are expressed by macro-particles and the beam by a series of rigid Gaussian bunch. We can investigate by the method not only nonlinear wake effect but also instability for a bunch train and an arbitrary bunch filling.

1 INTRODUCTION

In positron storage rings, a huge number of photoelectrons are produced by the synchrotron radiation of the positron beam at the surface of the vacuum chamber. Positron bunches filled with a narrow spacing create photoelectrons successively, and attract them by coulomb force. Consequently the photoelectrons distributes near to the positron beam. It is presented that a coupled bunch instability may be caused by the interactions between the positron beam and the photoelectrons[1, 2]. In electron storage rings, ions are trapped by the attractive force due to the electron beam, and oscillate in the beam potential with a frequency. The oscillation induces the two beam instability. In the case of positron storage rings, the photoelectrons are not trapped and not oscillate a definite frequency in the beam potential. However in a sense that bunches leave an electric 'wake' field after their passage, both phenomena is the same, thus we can say that the photoelectron instability is a kind of two beam instability.

In the photoelectron issue, we used the idea of the wake force which was conventional in impedance issue. We assumed that the linearity and superposition rule of the wake force were satisfied in beam-photoelectron interactions. However the linearity and superposition may not be always guarantied. We now propose a simulation method which is based on the weak strong model. This method was available for studying the two beam instability due to the ion-beam interactions[3]. This method, which does not require linearity of the wake, can be solved nonlinear wake effects. In this method, a weak beam, which is photoelectrons here, is expressed by macro-particles, and the barycenter motion of a strong beam is taken into consideration.

In considering the simulation, the beam-photoelectron and beam-ion interactions are very similar. The differences between them only mass and initial condition of the mediated particle, i.e., photoelectrons or ions. Photoelectrons are produced at the surface of the beam chamber, though ions are at near to the beam. Production rates are extremely different, that is, those of photoelectrons and ions are $0.16m^{-1}$ and $3\times10^{-9}m^{-1}$ by a beam particle par meter in the case of KEK-PF, respectively. The difference is revealed in the neutralization factor $\eta = n_{e(i)}/n_{beam}$, where n_e, n_i and n_{beam} are number of photoelectrons, ions and beam particles in a unit length, respectively. η of photoelectrons will be about 1, but that of ions will be is much less than 1, maybe about a few % in trapped case, or 10^{-5} or less in bunch train case. It means that a space-charge force between the photoelectrons is important than that of ions. The distribution of them in the chamber will contrast with each other. The photoelectrons distribute in whole of the chamber, while ions are localized near to the beam. The distributions affect the characteristics of the interactions of the beam-photoelectron and the beam-ion. Beam-photoelectron force is nearly linear for the oscillation amplitude. Growth of the photoelectron instability is not saturated till the size of beam chamber. While beam-ion force is strongly nonlinear. Growth of the ion instability is reduced when the amplitude exceed the beam size. Landau damping for the beam oscillation due to the nonlinearity is strong.

From a view point of simulation technique, macro-photoelectrons are required more and more than macro-ion to avoid a statistical noise of mean amplitude of photoelectrons. Since Landau damping is expected to be small, weak-strong approximation is more reliable than ion case.

2 EQUATION OF MOTION

We now discuss equation of motion of positrons and photoelectrons. We consider only the transverse motion. The photoelectron distribution is assumed to be uniform in longitudinal direction. The equations of motion are expressed as

$$\frac{d^2\boldsymbol{x}_{p,a}}{ds^2} + K(s)\boldsymbol{x}_{p,a} = \frac{2r_e}{\gamma}\sum_{j=1}^{N_e}\boldsymbol{F}(\boldsymbol{x}_{p,a}-\boldsymbol{x}_{e,j}), \quad (1)$$

$$\frac{d^2\boldsymbol{x}_{e,j}}{dt^2} = 2r_ec^2\left[\sum_{a=1}^{N_p}\boldsymbol{F}(\boldsymbol{x}_{e,j}-\boldsymbol{x}_{p,a}) + \sum_{i\neq j}^{N_e}\boldsymbol{F}(\boldsymbol{x}_{e,j}-\boldsymbol{x}_{e,i})\right], \quad (2)$$

where suffices p and e denote the positron and photoelectron, respectively. N_p and N_e are the number of each and

0-7803-4376-X/98/$10.00 © 1998 IEEE

Table 1: Parameters of KEK Photon Factory

Energy (GeV)	2.5
Circumference (m)	187
Stored current (mA)	300
Number of bunch (=h)	312
Beam size (mm)	1.14/0.114

γ is the Lorenz factor of the beam. $\boldsymbol{F}(\boldsymbol{x})$ is the Coulomb force in two dimensional space. We should take into account the boundary condition to obtain $\boldsymbol{F}(\boldsymbol{x})$, since photoelectrons are not localized near to the center of the chamber. These consist of differential $N_e + N_i$ equations, where that of each positron couples to the motion of all photoelectrons, and that of each photoelectron couples to the motion of all positrons and other photoelectrons.

We now focus the dipole coupled bunch instability due to photoelectrons. Dipole moment of bunches $\bar{\boldsymbol{x}}_p$ is taken into considered in Eq.(1). By assuming Gaussian transverse distribution for positrons in a bunch, Eqs.(1) are reduced to one equation, and an averaged force $\boldsymbol{F}_G(\bar{\boldsymbol{x}}_p - \boldsymbol{x}_{e,j}; \boldsymbol{\sigma}(s)))$ is introduced, where $\boldsymbol{\sigma}$ is beam size. $\boldsymbol{F}_G$ is expressed by Bassetti-Erskine formula[4], if the vacuum chamber is cylindrical and the beam passes through the center of the chamber.

To simplify the second term of right hand side of Eq.(2), a mean field $\phi(\boldsymbol{x}_e)$ of photoelectrons are introduced. $\phi(\boldsymbol{x}_e)$ is obtained by solving the Poisson equation

$$\triangle\phi(\boldsymbol{x}) = \frac{e}{\epsilon_0}\sum_{i}^{N_e}\delta(\boldsymbol{x} - \boldsymbol{x}_i). \tag{3}$$

The equations of motion for a positron bunch and photoelectrons are expressed as

$$\frac{d^2\bar{\boldsymbol{x}}_p}{ds^2} + K(s)\bar{\boldsymbol{x}}_p = \frac{2r_e}{\gamma}\sum_{j=1}^{N_e}\boldsymbol{F}_G(\bar{\boldsymbol{x}}_p - \boldsymbol{x}_{e,j}; \boldsymbol{\sigma}(s)), \tag{4}$$

$$\frac{d^2\boldsymbol{x}_{e,j}}{dt^2} = 2N_p r_e c^2 \boldsymbol{F}_G(\boldsymbol{x}_{e,j} - \bar{\boldsymbol{x}}_p; \boldsymbol{\sigma}(s)) - \frac{e}{m_e}\frac{\partial\phi(\boldsymbol{x}_{e,j})}{\partial\boldsymbol{x}_{e,j}}. \tag{5}$$

We solve these equations by using macro-particles.

3 SIMULATION AND RESULTS

We show simulation results with an example of KEK-Photon Factory. Parameters of Photon Factory is shown in Table 1.

We consider cylindrical vacuum chamber with a radius of 5cm. Electric potential is easily obtained by Green function and mirror charge,

$$\boldsymbol{G}(\boldsymbol{x}) = -\frac{\boldsymbol{x}}{|\boldsymbol{x}|^2}\delta(s). \tag{6}$$

We used a mesh with $2mm$ spacing to obtain the electric potential. The size is insufficient for using dynamically because we consider beam motion with an amplitude less than it. To avoid the noise comes from the potential calculation, we assumed the electric potential was static. Since the photoelectron distribution become stationary after passage of several dozen bunches, this assumption will be reasonable. We neglected the potential disturbance due to beam motion.

Fig.1 shows the electric potential by the photoelectron distribution. The initial condition of photoelectrons is the same as that in Ref.[2], that is, we consider that the direct (primary) photoelectron production due to photon is dominant and magnetic field is negligible. 50,000 macro photoelectrons were produced for every bunch passage in the potential calculation. We assumed an actual photoelectron density is $6 \times 10^8 m^{-1}$ for one bunch passing. The density means that photoelectrons are produced in whole ring uniformly with the photon-photoelectron conversion efficiency of 0.1. The figure is the electric potential after passage of 100 bunches. In stationary distribution, there were 590,000 macro photoelectrons in the chamber. The neutralization factor was 1.1.

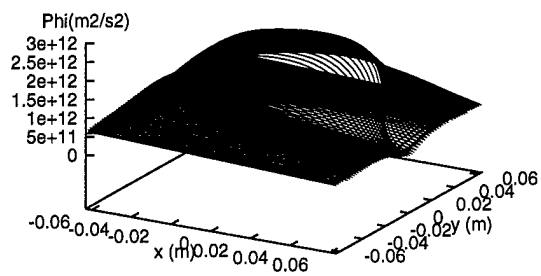

Figure 1: Electric potential created by photoelectron distribution.

In the weak-strong simulation, the electric potential, which is calculated with the high statistics (50,000), is treated as external field in the photoelectron motion. We solve Eqs.(4) and (5) by tracking the motion of macro-photoelctrons which feel the external field and beam force. Now 1000 macro-photoelectrons are produced in every bunch passage in the tracking. Fig.2 shows the growth of the maximum amplitude of all bunches. Growth of vertical oscillation dominate in this model. Growth time is estimated to be 700 turns from the figure. The growth was well fitted to exponential curve. Fig.3 shows transverse positions of all bunches after 3000 turns. It shows that a coupled bunch instability occurs. Since the bunch pattern had about 9 nodes, mode number $\sim$ 300 was dominant. These results were consistent with results obtained by wake method.

We now consider another model to study interactions in bending magnets. It is guessed that photon density is very

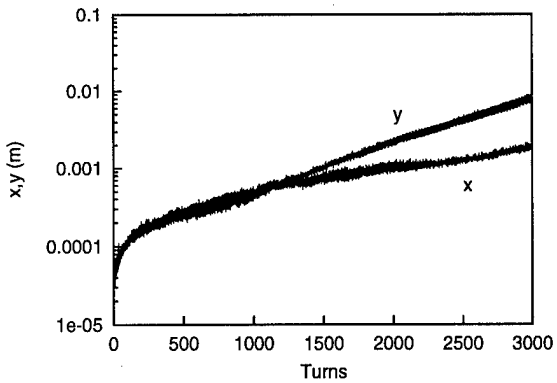

Figure 2: Growth of bunch amplitude. Primary photoelectrons which move in a region of no magnetic field are considered.

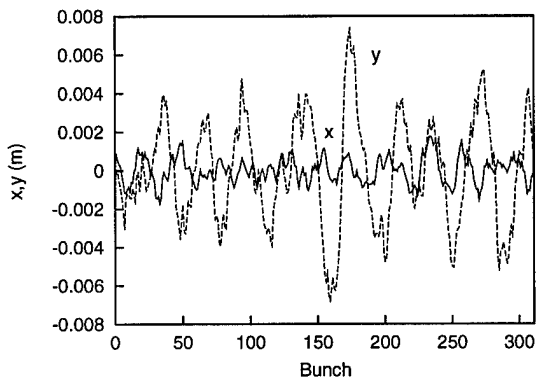

Figure 3: Transverse positions of all bunches after 3000 turns.

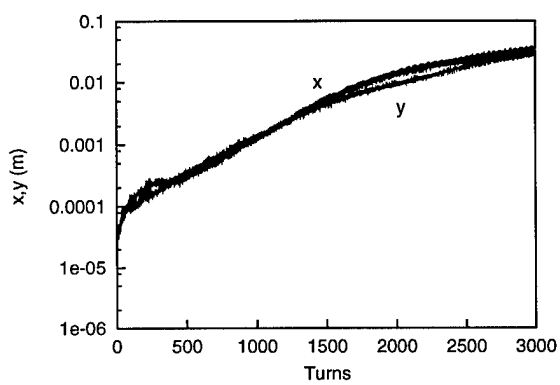

Figure 4: Growth of bunch amplitude. in bending magnet section. Photoelectrons move in a region of strong bending field.

high there. Reflected photon and secondary photoelectron production may be important. In strong vertical magnetic field $\sim T$, motion of photoelectrons is restricted along vertical direction. In the second model, photoelectrons are assumed to be created uniformly on the surface of the vacuum chamber. The photoelectron production rate is the same as the first model. In this production rate, since photoelectrons are accumulated till space charge limit, the detail of the production will not be important. Fig.4 shows a preliminary results for this model. Both of horizontal and vertical growth are seen. This figure is obtained for the case that whole ring is in bending magnet. Actual growth will be obtained by an adequate combination of these two model.

4 CONCLUSIONS

The weak strong based simulation is available for the beam-photoelectron instability. The simulation showed that coupled bunch instability was caused by photoelectron cloud.

These works are still in progress. Further study will be done.

5 REFERENCES

[1] M. Izawa, Y. Sato and T. Toyomasu, Phys. Rev. Lett. , 74, 5044 (1995).

[2] K. Ohmi, Phys. Rev. Lett. 75, 1526 (1995).

[3] K. Ohmi, to be published to Phys. Rev. E55 (1997).

[4] M. Bassetti and G. Erskine, CERN ISR TH/80-06 (1980).

[5] M. Furman and G. Lambertson, Proceedings of the EPAC96. F.Zimmermann, private comunications (1997).

EQUIVALENT CIRCUIT STUDY OF BEAM-LOADING USING A MOMENT METHOD*

T. F. Wang, Los Alamos National Laboratory, Los Alamos, New Mexico 87545, USA
S. Machida, Y. Mori, and C. Ohmori
Institute for Nuclear Study, University of Tokyo, Tanashi, Tokyo 188, Japan

Abstract

In this work, we present a formalism by considering the perturbations in the moments of a bunched beam for the equivalent circuit model to include all harmonics of the synchrotron oscillation in a beam-cavity interaction system. The linear coupling among all longitudinal modes under the influence of a narrow-band impedance can be naturally incorporated in this new approach. We used this method to re-examine the coupling between the dipole and the quadrupole modes. The dispersion relation obtained by this new method was compared with that derived from the linearized Vlasov equation up to the second harmonic of the synchrotron motion. We found excellent qualitative agreements between these two approaches.

1 INTRODUCTION

In designing the radio frequency (rf) system of an accelerator or storage ring, the interaction between the charged particle beam and the rf cavity is often modeled by an equivalent circuit. Because of its simplicity and its convenience to incorporate with engineering designs, the applications of this kind of modeling can range from a simple estimation of power requirement to complicated studies of system stability and control designs. In a more elaborated approach, a beam-cavity interaction system can also be studied by using Vlasov-Maxwell equations to include the dynamics of particles in the beam. For example, the Robinson instability in circular machines was initially investigated via an equivalent circuit model and later on studied by using Vlasov equations.[1-3] One of the advantages of using the kinetic theory approach over the equivalent circuit model is that the coupling among all synchrotron harmonics are covered in the formalism in a natural way. In all the equivalent circuit models utilized so far, only the dipole modes have been included. The reason is because a bunch of particles is modeled as a single macro-particle with no internal degree of freedom.

For narrow-band resonators, only those synchrotron sidebands near the resonant frequencies of the cavity contribute significantly to the beam-cavity interaction. It has been discussed previously, that for a tightly bunched beam interacting with a highly or moderately detuned narrow-band resonator, the neglect of higher synchrotron harmonics is a good approximation. However, for long beam bunches or small cavity detuning, higher synchrotron harmonics may affect the stability appreciably; therefore, at least a few of the higher synchrotron harmonics should be considered.[3] The purpose of this study is to formulate, at least in the linear regime, an approach in the equivalent circuit model that can take higher synchrotron harmonics into account. As will be discussed in the followings, one can incorporate any number of synchrotron harmonics in the equivalent circuit model by using the moment method.[4] A general moment method has been previously used to study transverse beam dynamics.[5,6] The "moment" we will study here is the moment in the configuration space of a bunched beam, it does not include all the moments in the phase space as some previous studies did. For simplicity, we shall concentrate on the case below transition, and we limit our study to the coherent mode, or the "0" mode, stability of a multi-bunch system, i.e., the coupled-bunch modes are not considered at here.

* Work partially supported by US Department of Energy

2 LINEARIZED EQUATIONS OF PARTICLE MOTION

The equation of synchrotron motion of a beam particle is

$$\frac{d^2\varphi}{dt^2} = \frac{\omega_s^2}{V_s\cos\psi_s}\left[V\sin\left(\psi_s+\phi_v-\varphi\right)-V_s\sin\psi_s\right], \quad (2.1)$$

where φ is the phase deviation of the particle's position with respect to the synchronous phase ψ_s, t is the time, $\omega_s = \left[-q\eta h V_s\cos\psi_s/(2\pi m_0\gamma R^2)\right]^{1/2}$, is the synchrotron frequency at equilibrium, q and m_0 are the charge and the rest mass of a beam particle, respectively, V_s is the maximum rf voltage on the cavity when the system is in steady state, V is the voltage on the cavity, ϕ_v is the deviation of the voltage phase from its equilibrium, γ is the ratio between the total energy and the rest mass of the synchronized beam particle, h is the rf harmonic number, $\eta = \gamma_t^{-2}-\gamma^{-2}$, is the momentum slip factor for a machine with transition gamma γ_t, and R is the effective machine radius. Assuming that φ and ϕ_v are small quantities, $V = V_s + \hat{V}$ with $\hat{V} << V_s$, Eq. (2.1) and its first order integral can be linearized to obtain

$$\frac{d^2\varphi}{dt^2}+\omega_s^2\varphi \approx \omega_s^2\left(\phi_v+\frac{\hat{V}}{V_s}\tan\psi_s\right), \quad (2.2)$$

and

$$\left(\frac{d\varphi}{dt}\right)^2 \approx -\omega_s^2\varphi^2-\omega_s^2\varphi^2\left(\frac{\hat{V}}{V_s}-\phi_v\tan\psi_s\right)+H_0\ , \quad (2.3)$$

where $H_0 = \omega_s^2\varphi_a^2$, and φ_a is the maximal excursion of the particle in the unperturbed rf potential well.

3 THE MOMENTS AND THEIR EQUATIONS OF MOTION

We assume that the phase space distribution of particles in a bunch, $f(z,v_z,t)$, is a steady part $f_0(z,v_z)$ plus a perturbation $f_1(z,v_z,t)$, i.e., $f=f_0+f_1$, where z is the coordinate along the bunch length, and v_z is the axial speed of a beam particle. The origin of the coordinate is chosen to coincide with the bunch center in the steady state which is synchronized with the rf phase. Assuming there are M identical bunches in the ring, the hth harmonic of the beam current I_h is then given by

$$I_h = I_h^{(0)} + I_{dc}\sum_{n=1}^{\infty}\frac{i^n}{n!}\left\langle\varphi^n\right\rangle_p , \tag{3.1}$$

where $I_{dc}=qMv_0N/(2\pi R)$, is the averaged (dc) beam current, v_0 is the average particle speed, $i=\sqrt{-1}$, N is the total number of particles in one bunch,

$$I_h^{(0)} = \frac{I_{dc}}{N}\int_{-\pi R}^{\pi R}\int_{-\infty}^{\infty} e^{ihz/R} f_0(z,v_z)dv_z dz , \tag{3.2}$$

$$\left\langle\varphi^n\right\rangle_p = \frac{R}{Nh}\int_{-\varphi_m}^{\varphi_m}\int_{-\infty}^{\infty}\varphi^n f_1(z,v_z,t)dv_z d\varphi , \tag{3.3}$$

is the nth moment due to the perturbation, φ_m is the half-length of the bunch in the rf phase, and use has been made of the relation $\varphi = hz/R$. The nth moment $\left\langle\varphi^n\right\rangle$ of the particle distribution is defined according to

$$\left\langle\varphi^n\right\rangle = \frac{R}{Nh}\int_{-\varphi_m}^{\varphi_m}\int_{-\infty}^{\infty}\varphi^n f(z,v_z,t)dv_z d\varphi , \tag{3.4}$$

Assuming that $\left\langle\varphi^n\right\rangle = \left\langle\varphi^n\right\rangle_0 + \left\langle\varphi^n\right\rangle_1$, i.e., $\left\langle\varphi^n\right\rangle$ consists of a steady part $\left\langle\varphi^n\right\rangle_0$ and a small perturbation part $\left\langle\varphi^n\right\rangle_1$; applying Eqs. (2.2) and (2.3), we can derive the following linearized equations for moments $\left\langle\varphi^n\right\rangle_1$:[4]

$$\frac{d^2\langle\varphi\rangle_1}{dt^2} + \omega_s^2\langle\varphi\rangle_1 = \omega_s^2\left(\phi_v + \frac{\hat{V}}{V_s}\tan\psi_s\right), \tag{3.5}$$

$$\frac{d^2\left\langle\varphi^2\right\rangle_1}{dt^2} + 4\omega_s^2\left\langle\varphi^2\right\rangle_1 = -2\omega_s^2\varphi_m^2\left(\frac{\hat{V}}{V_s} - \phi_v\tan\psi_s\right), \tag{3.6}$$

and

$$\begin{aligned}&\frac{d^2\left\langle\varphi^m\right\rangle_1}{dt^2} + m^2\omega_s^2\left\langle\varphi^m\right\rangle_1 = \\ &m(m-1)\left\langle H_0\varphi^{m-2}\right\rangle_0\left\langle\varphi^{m-2}\right\rangle_1\Big/\left\langle\varphi^{m-2}\right\rangle_0 \\ &+m\omega_s^2\left[\phi_v + \left(\hat{V}/V_s\right)\tan\psi_s\right]\left\langle\varphi^{m-1}\right\rangle_0 \\ &-m(m-1)\omega_s^2\varphi_m^2\left[\left(\hat{V}/V_s\right) - \phi_v\tan\psi_s\right]\left\langle\varphi^{m-2}\right\rangle_0 ,\end{aligned} \tag{3.7}$$

for $m=2,3\ldots$.

The analysis is then proceeded further by identifying the perturbed moment $\left\langle\varphi^n\right\rangle_1$ in Eqs. (3.5)-(3.7) with $\left\langle\varphi^n\right\rangle_p$ in Eq. (3.1). The hth harmonic of the beam current can be written in the polar coordinate notation as

$$I_h = I_b(t)e^{-i\phi_b(t)},$$

where $I_b(t) = I_{b0} + I_{b1}$, $I_{b0} = I_h^{(0)}$, $I_{b1} \approx \sum_{j=1}^{\infty} I_{h,2j}^{(1)}$,

$$\phi_b \approx -\sum_{j=0}^{\infty} I_{h,2j+1}^{(1)}\Big/I_h^{(0)},$$

$$I_{h,2j}^{(1)} = (-1)^j I_{dc}\left\langle\varphi^{2j}\right\rangle_1\Big/(2j)! ,$$

$$I_{h,2j+1}^{(1)} = (-1)^j I_{dc}\left\langle\varphi^{2j+1}\right\rangle_1\Big/(2j+1)! ,$$

and $I_{b1} << I_{b0}$. If only the first two lowest moments (the dipole and the quadrupole modes) are retained in the expansion of I_{b1} and ϕ_b, we have

$$I_{b1} \approx I_{h,2}^{(1)} = -I_{dc}\left\langle\varphi^2\right\rangle_1\Big/2, \tag{3.8}$$

and

$$\phi_b \approx -I_{h,1}^{(1)}\Big/I_h^{(0)} \approx -I_{dc}\langle\varphi\rangle_1\Big/I_h^{(0)} . \tag{3.9}$$

4 THE EQUIVALENT CIRCUIT MODEL

In the equivalent circuit model, an rf cavity is envisioned as a parallel RLC circuit; the applied rf power source and the circulating beam current are envisioned as currents i_g and i_b, respectively. Using Kirchhoff's law, one can derive that the total voltage on the cavity satisfies the differential equation

$$\frac{d^2v}{dt^2} + 2\alpha\frac{dv}{dt} + \omega_r^2 v = 2\alpha R_s\frac{d}{dt}\left(i_g + i_b\right), \tag{4.1}$$

where v is the total voltage, $\alpha = \omega_r/(2Q)$, Q is the quality factor of the cavity, ω_r is the resonant frequency of the cavity, and R_s is the shunt resistance. Substituting

$$i_g = I_g\exp\left\{-i\left(\omega_g + \psi_g\right)t\right\},$$

$$i_b = \left[I_{b0} + I_{b1}(t)\right]\exp\left\{-i\left[\omega_g + \phi_b(t)\right]t\right\},$$

and $$v = \left[V_s + \hat{V}(t)\right]\exp\left\{-i\left[\omega_g + \psi_v + \phi_v(t)\right]t\right\},$$

in Eq. (4.1), we can derive the following linearized equations for $\hat{V}$ and ϕ_v:

$$\frac{d\hat{V}}{dt} + \alpha\hat{V} = -\alpha R_s\left[I_{b1}\cos\psi_v + I_{b0}\left(\phi_b - \phi_v\right)\sin\psi_v\right], \tag{4.2}$$

and

$$\begin{aligned}\frac{d\phi_v}{dt} + \alpha\phi_v &= \frac{-\alpha R_s I_{b0}\cos\psi_v}{V_s} \\ &\times\left[\phi_b - \left(I_{b1}/I_{b0}\right)\tan\psi_v + \left(\hat{V}/V_s\right)\tan\psi_v\right],\end{aligned} \tag{4.3}$$

where ω_g is the frequency of the driving rf, ϕ_v and ϕ_b are the phase deviations of v and i_b from their steady states, respectively. In arriving at Eqs. (4.2) and (4.3), we have assumed that the system is in tune, i.e. $\psi_g = \psi_v$, and we have chosen a rotating polar coordinate system such that the steady state beam current I_{b0} is on the real axis. Also, in deriving Eqs. (4.2) and (4.3), we have assumed that for high-Q and high frequency resonators, $\alpha << \omega_g$, and that the derivatives of the quantities $d[v\exp(i\omega_g)]/dt$ and $i_b\exp(i\omega_g)$ are negligible when compared, respectively, with the products of these quantities with ω_g. Eqs. (3.5), (3.6), (4.2) and (43) are the basic equations for studying the beam-cavity interaction.

5 COMPARISON WITH KINETIC THEORY

We now compare the dispersion relation derived from the moment method with that obtained from the Vlasov equation. We shall study the dispersion relations up to the second moment, or to the second harmonic of the synchrotron oscillation.

The complete set of equations, up to the second moment, are Eqs. (3.5), (3.6), (3.8), (3.9), (4.2) and (4.3). Making Laplace transformations to Eqs. (3.5), (3.6), (4.2) and (4.3); using Eqs. (3.8) and (3.9), one can derive a set of simultaneous linear algebraic equations for the unknowns $\tilde{\tilde{V}}$, $\tilde{\phi}_v$, $\tilde{I}_{b1}$, and $\tilde{\phi}_b$, where the symbol ~ indicates the Laplace transformed quantities. Equating the determinant of the simultaneous algebraic equations to zero yields the dispersion relation:

$$s^6 + 2\alpha s^5 + \left(5\omega_s^2 + \alpha^2\sec^2\phi_y\right)s^4 + 10\alpha\omega_s^2 s^3 + a_2 s^2 + 8\alpha\omega_s^4 s + a_0 = 0 \ , \tag{5.1}$$

where s is the Laplace transformation variable,

$$a_0 = 4\omega_s^4\left[\alpha^2\sec^2\phi_y - \lambda^2\left(\mu_1 + \mu_2\right) + \lambda^2\mu_1\mu_2\sec^2\psi_s\right] \ , \tag{5.2}$$

$$a_2 = 4\omega_s^4 + 5\alpha^2\omega_s^2\sec^2\phi_y - \omega_s^2\lambda^2\left(\mu_1 + 4\mu_2\right), \tag{5.3}$$

$\lambda = \alpha R_s I_{b0}/V_s$, $\mu_1 = -I_{dc}/I_{b0}$, and $\mu_2 = I_{dc}\varphi_m^2/\left(4I_{b0}\right)$.

The derivation of the dispersion relation from the linearized Vlasov equation, including the second harmonic of the synchrotron frequency, has been presented in a previous work.[6] The result is quoted here in a slightly different notations:

$$s^6 + 2\alpha s^5 + \left(5\omega_s^2 + \alpha^2\sec^2\phi_y\right)s^4 + 10\alpha\omega_s^2 s^3 + b_2 s^2 + 8\alpha\omega_s^4 s + b_0 = 0 \ , \tag{5.4}$$

where

$$b_0 = 4\omega_s^4\left\{\alpha^2\sec^2\phi_y - \lambda^2\left[F_1\mu_1 + \left(4F_2/\varphi_m^2\right)\mu_2\right] + \left(4F_1F_2/\varphi_m^2\right)\lambda^2\mu_1\mu_2\sec^2\psi_s\right\} \ , \tag{5.5}$$

$$b_2 = 4\omega_s^4 + 5\alpha^2\omega_s^2\sec^2\phi_y - \omega_s^2\lambda^2\left[F_1\mu_1 + 4\left(4F_2/\varphi_m^2\right)\mu_2\right] \ , \tag{5.6}$$

$$F_m = 4\int_0^\infty\left[J_m\left(\frac{hr}{R}\right)\right]^2\frac{df_0}{dr}dr\Big/\left(\frac{h}{R}\right)^2\int_0^\infty f_0(r)rdr \ ,$$

is the *reduced form factor*[3], $r = \left[z^2 + (v_z/\omega_s)^2\right]^{1/2}$, and $J_l(x)$ is the Bessel Function of the lth order. The values of F_1 and F_2 have been calculated and charted for some different phase space distributions.[3] In general, the value of $F_1(F_2)$ decreases (increases) when the bunch length increases. For very short bunch lengths, F_1 and F_2 have values near 2.0 and 0, respectively. At the bunching factor of 0.5, most distributions have the values of F_1 near 1.3 and the values of F_2 near 0.17. For short bunch length, F_2 is roughly proportional to φ_m^2.

Thus, by comparing Eqs. (5.1)-(5.3) with Eqs. (5.4)-(5.6), we find that the dispersion relation derived from the equivalent circuit is the same as that inferred from the linearized Vlasov equation except for the factors F_1 and $4F_2/\varphi_m^2$ which depend on the detail of the perturbation in the phase space.

6 CONCLUSIONS

We have formulated an approach, in the regime of linear approximation, to incorporate all harmonics of synchrotron oscillation in the equivalent circuit model of beam-cavity interaction by considering the perturbed moments of a bunched beam. We found good qualitative agreements in comparing the dispersion relations obtained from this new approach with that derived from the linearized Vlasov equation up to the second synchrotron harmonic.

REFERENCES

[1] K. W. Robinson, Report No. CEA-11, Cambridge Electron Accelerator, Cambridge, Mass. (Sept. 1956).

[2] K. W. Robinson, Report No. CEAL-101, Cambridge Electron Accelerator, Cambridge, Mass. (Feb. 1964).

[3] See, for example, T. F. Wang, *Particle Accelerators*, **54**, pp. 105-126 (1990).

[4] T. F. Wang, Univ. of Tokyo, INS Report, INS-Rep.-1171, Nov. 1996.

[5] P. J. Channell, IEEE Trans. Nucl. Sci., **30** (4), Aug. 1983, p. 2607.

[6] W. P. Lysenko and M. Overley, *Accelerators and Beam Optics Codes*, AIP Conf. Proc. 177, ed. C. R. Eminhizer (AIP New York, 1988), p. 323.

COLLECTIVE CENTROID OSCILLATIONS AS AN EMITTANCE PRESERVATION DIAGNOSTIC IN LINEAR COLLIDER LINACS

C. E. Adolphsen, K. L. F. Bane, W. L. Spence * and M. D. Woodley
Stanford Linear Accelerator Center
Stanford University, Stanford, California 94305 USA

Abstract

Transverse bunch centroid oscillations, induced at operating beam currents at which transverse wakefields are substantial, and observed at Beam Position Monitors, are sensitive to the actual magnetic focusing, energy gain, and rf phase profiles in a linac, and are insensitive to misalignments and jitter sources. In the 'pulse-stealing' set-up implemented at the SLC, they thus allow the frequent monitoring of the stability of the in-place emittance growth inhibiting or mitigating measures—primarily the energy scaled magnetic lattice and the rf phases necessary for BNS damping—independent of the actual emittance growth as driven by misalignments and jitter. We have developed a physically based analysis technique to meaningfully reduce this data. Oscillation beta-beating is a primary indicator of beam energy errors; shifts in the 'invariant' amplitude reflect differential internal motion along the longitudinally extended bunch and thus are a sensitive indicator of the real rf phases in the machine; shifts in betatron phase advance contain corroborative information sensitive to both effects. Examples from initial SLC applications illustrate the method.

Differential internal motion due to intra-bunch energy or amplitude spread, or bunch spatial extension which makes collective or multiparticle interactions possible, causes striking differences between the behavior of the centroid of a bunched beam, which is measured by a beam position monitor, and a single particle. Bunch inhomogeneities that respond differentially to the beamline environment engender decoherence, and possibly recoherence and echo phenomena; current dependent collective effects can strongly excite novel patterns of centroid motion.

We first discuss general aspects of the difference between centroid and single particle mechanics in the context of developing a general parameterization scheme for the former, and then move to some more specific features of beam dynamics with transverse wakefields.

1 CENTROID KINEMATICS

To develop a useful description of centroid motion that provides more or less machine-error-specific indicators, we mimic to a large degree the familiar parameterization of single particle motion. The parameters acquire new meanings in the centroid context that fully incorporate its distinctive features, but recover their single particle significance in the limiting case in which the bunch as a whole moves rigidly. At every location in the beamline, every trajectory in the two dimensional phase space is mapped into a point on some unit circle, where it is located by a phase angle which can accordingly be taken to 'advance' from beamline location to location. Choosing the mapping to be linear makes families of trajectories comprising whole circles generically images of ellipses in the phase space observables. Both the ellipse and the phase angle contain non-redundant information about the motion, and are inextricably linked in that the phase angle and hence the phase advance is undefined without an associated ellipse. For linear motion choosing an ellipse at one beamline location determines an ellipse—its image under the transport map—at all other locations. It is usually especially useful to choose an initial family of geometrically similar ellipses whose shape has a conceptually or mnemonically useful property, like the same periodicity as the beamline itself, and/or, the distinction that it describes the bunch 'beam envelope'. Here the ellipse in phase space is a family of centroid trajectories, which could *e.g.*, correspond to the ensemble of trajectories generated by a specially distributed jitter source at the beginning of the beamline; it is emphatically not directly related to the family of collectively interacting single particle trajectories that constitute the beam envelope. The fact that linear transport maps ellipses into ellipses is all that we use; we do not assume the invariance of the ellipse area, even though it was this aspect of the single particle case that historically drew attention to ellipses in phase space. Phase advance is necessary to then fully describe the transport of the particular trajectories on the ellipse.

To be more explicit, the phase space centroid, or beam-average position $\langle x(s)\rangle$ and angle $\langle x'(s)\rangle$ coordinates at machine location s, is parameterized by the non-restrictive *ansatz*

$$\begin{bmatrix}\langle x(s)\rangle\\ \langle x'(s)\rangle\end{bmatrix} = \sqrt{2a(s)}\,A(s)\begin{bmatrix}\cos(\psi(s))\\ -\sin(\psi(s))\end{bmatrix} \qquad (1)$$

that linearly maps all trajectories into unit circles, on which they are located by an advancing phase $\psi(s)$. $A(s)$ is a 2×2 matrix; taking it to have unit determinant defines the numerical 'amplitude' factor $\sqrt{a(s)}$. Since circles are invariant under rotation the re-definition $A \rightarrow A\mathcal{O}$, where $\mathcal{O}$ is a rotation matrix, just re-defines the phase function; thus A has only two meaningful parameters. A set of trajectories at an 'initial' beamline location constructed to fill a unit circle and mapped in x, x' space into a fiducial ellipse that is geometrically characterized by the symmetric matrix $a_0A_0A_0^{\mathsf{T}}$, will be transported at each downstream location into a specific ellipse whose geometric form is given by aAA^{T}. By linearity the shape depends only on the initial shape parameters $A_0A_0^{\mathsf{T}}$ and the area scales like a_0, *i.e.*,

* present address: 320 Railroad Avenue, Ben Lomond, CA 95005 USA.

0-7803-4376-X/98/$10.00 © 1998 IEEE

only the ratio $a(s)/a_0$ is characteristic of the transport.

Since the circle that the ellipse is mapped to is invariant under rotations, to associate specific trajectories with phase angles $\psi(s)$, and hence be able to speak of a 'phase advance' requires a further but final convention. The historical choice made by Courant and Snyder for single particles assigns a 90° phase everywhere in the beamline to a trajectory on the x'-axis, or equivalently imposes $A_{12}(s) \equiv 0$. It has the unique property that zeros in x are 180° apart for any choice of the initial ellipse geometry.

The centroid transfer matrix R now satisfies $\sqrt{2a_0}RA_0 = \sqrt{2a}A\mathcal{O}(\Delta\psi)$, giving the representation

$$R = a_g\sqrt{\frac{E_0}{E}}A\mathcal{O}A_0^{-1} \tag{2}$$

where the *amplitude growth/damping factor* $a_g = \sqrt{aE/a_0E_0}$ parameterizes the *specific* amplitude shift (exclusive of 'adiabatic' damping due to acceleration).

In the single particle limit, where the bunch either is a single particle or behaves like one (*i.e.*, is rigid) $a_g \to 1$ and $A \to \frac{1}{\sqrt{\beta}}\begin{pmatrix}\beta & 0\\ -\alpha & 1\end{pmatrix}$, where β and α are the familiar functions describing pseudo-harmonic oscillations in the quadrupole magnetic focusing field for the initial condition A_0. In the single particle case A is *local*—it depends only on the beamline location at which the trajectory is observed and not on the oscillation's prior history, and the phase advance is *additive*, *i.e.*, the amount by which it increases as one moves along the beamline is independent of the initial location. Directly equivalent to these properties is the *factorization* of the R matrix: $R(a \to b) = R(c \to b)R(a \to c)$ for any intermediate point c. For generic centroid oscillations factorization/locality is not true, and caution should be applied to avoid being misled by the product decomposition in (2). Centroid transport depends on the detailed internal initial state of the bunch, something which is not completely specified by giving its centroid phase space coordinates alone; in fact without a specification of the suppressed internal variables, any centroid transfer map is seriously ill-defined. In the linear case it is convenient in practice to take all transfer matrices to correspond to rigid excitations (kicks or instantaneous displacements) of a homogeneous bunch (one whose internal transverse coordinates all line up with the centroid). Superpositions of appropriately distributed excitations then can describe any coherent β-tron oscillation. The set of centroid transfer maps in the space of centroid variables thus constitutes a complete physical description, at the price of tolerating hysteresis, or non-factorization/non-locality, at a basic level.

An instructive and practical application is to consider 'steering-out' a coherent oscillation by applying appropriate kicks in some neighborhood in the beamline. A rigidly excited oscillation (as with dipole magnets) can be superposed to precisely cancel an incoming oscillation at some point; however, since the internal bunch distribution in the incoming oscillation would generically differ from the homogeneous distribution associated with the excitation and accordingly transport differently, the cancellation will break down as the superposition propagates. An oscillation will grow 'spontaneously', a behavior impossible to achieve if the R matrix were to factorize.

It is frequently very useful to view the A matrix in terms of its deviation from a fiducial reference A_r, which in practice is usually chosen to be the single particle periodic lattice function already mentioned. The *oscillation* 'Bmag' $B = \frac{1}{2}\mathrm{tr}[A_r^{-1}A(A_r^{-1}A)^{\mathsf{T}}]$ is invariant downstream of an isolated discrepancy with respect to the reference, although the effective β and α functions continuously 'beat'; $\sqrt{B^2-1}$ is in fact the beat amplitude. B is equivalently the average of the squares of the semi-major and semi-minor axes of the ellipse corresponding to the transport of an initial unit circle of trajectories in the normal coordinates defined by A_r. The additional variable completing the description is the β-beat phase or orientation angle of the anomalous ellipse incorporated as Ψ in the parameterization $A_r^{-1}A(A_r^{-1}A)^{\mathsf{T}} = \begin{pmatrix}B+\sqrt{B^2-1}\cos\Psi & -\sqrt{B^2-1}\sin\Psi\\ -\sqrt{B^2-1}\sin\Psi & B-\sqrt{B^2-1}\cos\Psi\end{pmatrix}$. Collective and decoherence intrabunch effects produce a negligible deviation in $B-1$ in a lattice that is periodic and 'smooth' on the scale of the β-tron wavelength (*cf.* Section 2). Therefore when applied to data, *e.g.*, B serves as a useful indicator isolating effective magnetic strength errors. To the extent to which this is the case the beat phase in an error free region will advance according to $\Psi \to \Psi + 2\psi$, where ψ is the single particle phase shift, *i.e.*, is *exclusive* of any coherent phase shift. It is important not to ignore the β-beat phase since it is possible for a quadrupole strength error to be manifested as a rapid Ψ shift through $-2\times$ the prior Ψ at the error, while $B, > 1$ already due to an upstream error, accidentally does not change. Note again that the oscillation or coherent 'Bmag' is inequivalent to and has nothing direct to say about the beam envelope Bmag that expresses the possible elevation of the matched equivalent emittance.

An alternative representation is sometimes used, will be used in the next section, and is instructive to consider. Two orthogonal oscillations are treated as having individual *pseudo*-phase-advances $\Delta\psi_{1,2}$ and 'amplitudes' $\zeta_{1,2}$. The centroid 'normalized' transfer matrix

$$\sqrt{\frac{E}{E_0}}A_r^{-1}RA_{r\,0} = \begin{pmatrix}\zeta_2\cos(\Delta\psi_2) & \zeta_1\sin(\Delta\psi_1)\\ -\zeta_2\sin(\Delta\psi_2) & \zeta_1\cos(\Delta\psi_1)\end{pmatrix} \tag{3}$$

$$= \mathcal{O}(\Delta\psi_+)\begin{pmatrix}\zeta_2\cos(\Delta\psi_-) & \zeta_1\sin(\Delta\psi_-)\\ \zeta_2\sin(\Delta\psi_-) & \zeta_1\cos(\Delta\psi_-)\end{pmatrix} \tag{4}$$

where $\Delta\psi_\pm = \frac{1}{2}(\Delta\psi_1 \pm \Delta\psi_2)$ are the average and (half) difference pseudo-phase-advances. The term *pseudo*-phase advance is used to emphasize that even in the single particle case where the R matrix factorizes, these 'phase advance'-like parameters are not additive, in the sense described above. The phase independent amplitude growth $a_g = \sqrt{\zeta_1\zeta_2|\cos(2\Delta\psi_-)|}$. It is reduced by a *pseudo*-phase

advance difference for fixed $\zeta_{1,2}$. That $a_g \to 1$ in the single particle limit implies a constraint among the parameters in that case. $B = \frac{1}{2}\left[(\zeta_1/\zeta_2) + (\zeta_2/\zeta_1)\right] / |\cos(2\Delta\psi_-)|$. Thus $B > 1$ reflects disparate 'orthogonal amplitudes', and/or disparate pseudo-phase advances—this is perhaps the most useful way to conceptualize oscillation, as opposed to envelope, β-beating. Either condition $\zeta_2 \not\approx \zeta_1$ or $\Delta\psi_2 \not\approx \Delta\psi_1$ accordingly indicates a non-'smooth' lattice and significant collective effects (*cf.* above and Section 2), or the presence of effective magnetic field errors.

2 COLLECTIVE DYNAMICS

The beam dynamics of a longitudinally extended bunch in which transverse dipole wakefields are the dominant intra-bunch forces, reduces to the problem of the motion of a 'string' beam in which the variables are the centroid coordinates $x(s;\tau)$ and $x'(s;\tau)$, at longitudinal position τ. The restriction to a pure dipole wakefield makes an exact 'hydrodynamic' description possible; *i.e.*, the dynamics closes in terms of 'slice' first moments. Finite transverse emittance and energy spread within-a-slice effects can be recovered after this problem is solved.

As already discussed, the problem of interest here may be further reduced to a study of the transfer matrices for rigid excitations in terms of the whole bunch centroid, or the observable N particle slice average $\langle x(s)\rangle = \int dN(\tau)\, x(s;\tau)/N = \int d\tau\, (dN/d\tau)\, x(s;\tau)/N$, and similarly for $\langle x'(s)\rangle$. Each slice freely oscillates due to the initial dipole magnet impulse, to which is superposed free oscillations originating in deflections occurring along the entire length of accelerator through which the beam has moved, which are in turn proportional to the charge weighted accumulation of the instantaneous transverse offsets of the slices preceding it in the bunch, and the wakefield function of their longitudinal distance:

$$x(s;\tau) = R_{12}(s,s_0;\tau)\,\Delta x' + \int_{s_0}^{s} ds_1 R_{12}(s,s_1;\tau) \int dN(\tau_1)\, \frac{eW_\perp(\tau-\tau_1)}{E(s_1)}\, x(s_1;\tau_1) \quad (5)$$

and similarly with x'. $R(s,s_0;\tau)$ is the single particle transverse transfer matrix for longitudinal position τ, on which it depends significantly through the nominal energy spread arising from the accelerating rf waveform and the longitudinal wakefield. Since the slice centroid we are trying to find is related to the preceding slice centroids in the bunch, (5) is a linear integral equation to be solved. It is convenient to combine x and x' into a new complex variable by setting $x - i(\beta x' + \alpha x) = -i\sqrt{E_0/E}\,\beta\,\Delta x' \exp\big(i\Delta\psi(s,\tau)\big)\,\xi(s,\tau)$. It satisfies

$$\xi(s,\tau) = 1 - \frac{i}{2}\int_{s_0}^{s} ds_1 \frac{\beta}{E} \int dN(\tau_1)\, eW_\perp(\tau-\tau_1) \times \{\exp\left[-i\left(\psi(s_1,\tau) - \psi(s_1,\tau_1)\right)\right]\xi(s_1,\tau_1) + \exp\left[-i\left(\psi(s_1,\tau) + \psi(s_1,\tau_1)\right)\right]\xi^*(s_1,\tau_1)\} \quad (6)$$

$\psi(s,\tau)$ is the single particle phase, and the τ dependence of β has been suppressed on the grounds that it should be negligible in a viable, at least approximately periodic, lattice. The centroid $\xi(s) \equiv \exp\big(-i\psi(s,0)\big)\,\big\langle\exp\big(i\psi(s,\tau)\big)\xi(s,\tau)\big\rangle$ where $\tau = 0$ (the 'center' of the bunch, say) is chosen to define a reference single particle phase advance. The centroid transfer matrix in the 'two-phase' form (3) is then fixed since $\zeta_1 \exp[i(\Delta\psi_1 - \Delta\psi)] = \xi(s)$ for $\psi(s_0,\tau) = -90°$, and $\zeta_2 \exp[i(\Delta\psi_2 - \Delta\psi)] = \xi(s)$ for $\psi(s_0,\tau) = 0$.

The overall factor in the kernel in (6), $\int ds\,(\beta/E)NeW_\perp$, is $\sim$ the (Courant-Snyder) α-shift of the bunch tail due to the defocusing effect of the wakefield, and scales its excitatory strength.

The first term in the kernel has the factor $\exp\left[-i\left(\psi(s_1,\tau) - \psi(s_1,\tau_1)\right)\right]$, which oscillates with the 'tail-head' phase advance *difference*, and is independent of the absolute β-tron phase. It is the agent for BNS 'damping'.

The second term factor oscillates like the *sum* of 'tail' and 'head' phase advances and flips its sign for rigid excitations with a 90° initial phase difference. It is strongly suppressed relative to the first term if the lattice is periodic or 'smooth' over several cycles at twice the nominal β-tron phase advance, and may be neglected in the leading eikonal approximation. Thus the dominant wakefield effect is a phase independent phase shift $= \arg\xi(s)$, and amplitude growth/damping shift $a_g = |\xi(s)|$. To the extent this approximation is accurate $B = 1$.

Although interesting *gedankenphysik*, the asymptotic 'long' machine results that have also been obtained [1] are not quantitatively germane to any known extant or seriously contemplated machine. The perturbation series, in which distributed (non-macroparticle) $n+1$ particle-like contributions, each associated with an order n in the α-shift are superposed, is straightforward. Under SLC conditions ($N \approx 4\cdot 10^{10}$, $\tau_{\rm rms} \approx 1$ mm, $W'_\perp \cong 4.1$ GeV/(10^{10} mm-m^2)), $n_{\max} = 5$ suffices for $\sim 0.1\%$ accuracy in the centroid R-matrix.

A companion paper [2] provides details of the SLC "diagnostic pulse" implementation and examples of high bunch current centroid data. Another [3] is a case study in which the coherent oscillation physics discussed here contributed crucial diagnostic insight.

We thank Ralph Aßmann, Alex Chao, Franz-Josef Decker, Michiko Minty, Pantaleo Raimondi, Howard Smith, Tor Raubenheimer, and David Whittum for interest, discussions, and suggestions, and Fang Tian for participation in the early stages of the work. This work was supported by U. S. Department of Energy contract DE-AC03-76SF00515.

3 REFERENCES

[1] W. L. Spence, in *Emittance '93*, ed. J. Urakawa and K. Oide, KEK Proceedings 93-13, Tsukuba, Japan.

[2] R. W. Aßmann, *et. al.*, Paper 8W.24, these proceedings.

[3] F.-J. Decker, *et. al.*, Paper 8W.27, these proceedings.

BEAM LOADING COMPENSATION IN THE NLCTA*

C. Adolphsen, T. Lavine, C. Nantista, R. Ruth, J. Wang and D. Yeremian
Stanford Linear Accelerator Center, Stanford, CA 94309

Abstract

In the design of the Next Linear Collider (NLC), multi-bunch operation is employed to improve efficiency at the cost of substantial beam loading. The RF pulse that powers the accelerator structures will be shaped to compensate for the effect of the transient loading along the bunch train. This scheme has been implemented in the Next Linear Collider Test Accelerator (NLCTA), a facility built to test the key accelerator technology of the NLC. In this paper we describe the compensation method, the techniques used to measure the energy variation along the bunch train, and results from tests with NLC-like beam currents.

1 INTRODUCTION

In contrast to the single bunch operation of the SLAC Linear Collider, the Next Linear Collider (NLC) design has multiple bunches (90) being accelerated on each RF pulse. This improves the energy transfer efficiency to the beam but results in significant beam loading. In the zero'th order NLC design [1], the loading is about 25% of the unloaded gradient. That is, if the 126 ns long bunch train would pass through an accelerator structure filled with a constant amplitude RF pulse, the energy gain of the bunches would decrease along the train, reaching a steady-state value after one fill time (100 ns) that is smaller by about 25%. A more energy efficient parameter set is now being considered where the beam current, and thus loading, is halved while the bunch train length is doubled. In either case, one faces the challenge of compensating this loading to a level where the bunch energies are equal to a few tenths of a percent. This is required to preserve the small bunch emittances in the NLC linacs.

2 NLCTA ACCELERATION SYSTEM

The Next Linear Collider Test Accelerator was built at SLAC to test X-band (11.4 GHz) RF system and accelerator concepts for the NLC, in particular the ability to compensate beam loading [2]. Although the NLC design has a 1.4 ns spacing between bunches (2.8 ns in the latest version), the beam loading effects are essentially the same if the bunch spacing equals the X-band period (88 ps) and the bunch charge is reduced to yield the same average beam current. The NLCTA adopted this approach in its design which reduced costs and made the machine much simpler, in part, because only X-band RF components were used.

* Work supported by Department of Energy contract DE-AC03-76F00515.

In the injector of the NLCTA, an electron beam from a thermionic gun is bunched at X-band using two prebunchers followed by a capture section in the upstream end of the first accelerator structure [3]. This structure is a half-length version of the 1.8 m long detuned structure that was developed for the NLC. It is followed by a second half-length structure and then by a chicane-like layout of magnets and collimators which trim off the low energy tails of the beam that result from the bunching process. The beam then enters the linac which can accommodate up to six 1.8 m long structures. Currently it contains a detuned structure and the first prototype damped and detuned structure.

Two RF stations are currently in operation, one which powers the two injector structures and one which powers the two linac structures [4]. The key components of an RF station are shown in Fig. 1. The RF drive to the klystron is phase modulated as described below. The klystron is SLAC's model XL4 which nominally produces 50 MW of power. This power is roughly quadrupled in SLED II, a delay line version of the Stanford Linear Energy Doubler (SLED) [5]. The output SLED power is then split and feed to two accelerator structures (in the injector, part of the power also goes to the prebunchers). An unloaded gradient of 50 MeV/m, the initial NLC goal, is obtained with an input of 70 (90) MW to the injector (linac) structures. Our high power RF components are not yet fully processed which limits the power at which we can operate. We typically run with an unloaded gradient of 44 MeV/m in the linac and 47 MeV/m in the injector, although the unloaded beam energy gain in the injector is lower (36 MeV/m) due to the phase offset (40°) that results from the capture process.

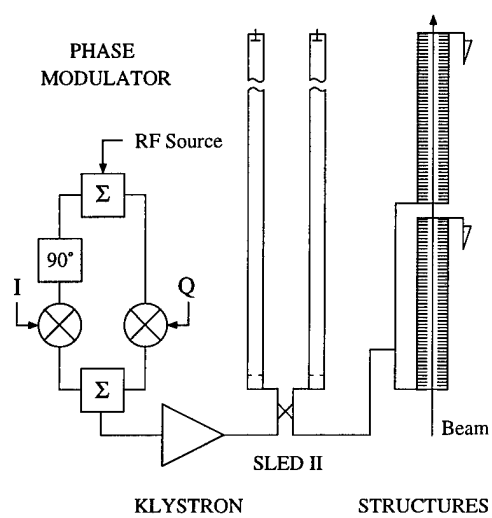

Fig. 1 Layout of an RF station.

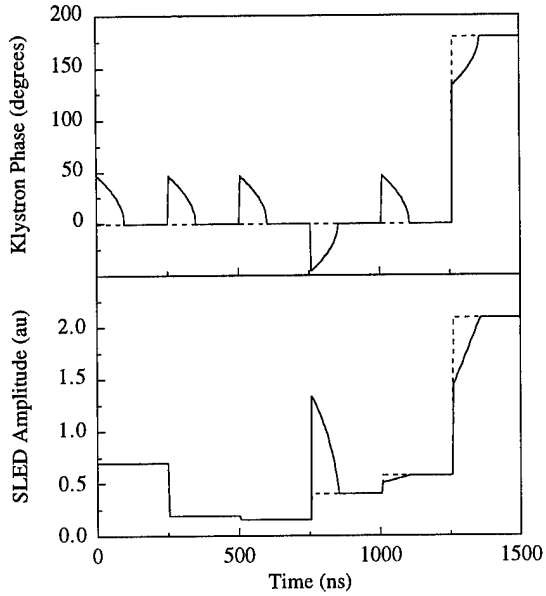

Fig. 2 Phase profile (upper plot) of the klystron drive RF and the predicted SLED output amplitude (lower plot) for 13% loading (solid line) and no loading (dashed line) in the linac.

3 LOADING COMPENSATION

To operate with NLC-like beam currents, we use a loading compensation scheme in which the RF waveform during the 100 (50) ns filling time of the linac (injector) structures is ramped. The ramp is shaped to produce a field profile in each structure equal to the steady-state profile for the operating current. The first bunch enters each structure just after the ramp, and thus witnesses the same fields that would be present if it were part of a long bunch train. The RF waveform remains constant after the ramp so subsequent bunches witness the same steady-state field profile.

Since it is preferable to run with the klystrons saturated, we do not vary the klystron drive amplitude to produce the waveform ramp but instead modulate the drive phase and use the ×6 folding of the RF in the SLED compression process to shape the final waveform while keeping the phase constant. The required drive phase profile and the resulting SLED waveform are shown in Fig. 2 for no loading and for 13% loading. For the loaded case, a 50° phase 'bump' is added to the no-load phase profile at the beginning of each folding, including the final 180° flip that produces the waveform used for acceleration. The shape of this bump was chosen to produce a linear ramp, which is very close to the optimal shape for compensation.

To vary the drive phase, an I/Q phase modulator is used as shown in Fig. 1 [6]. The I and Q signals, which amplitude modulate two out-of-phase components of the RF, are produced by two pulse generators that can be programmed to output any desired waveform. The signals are 'clocked-out' at 238 MHz, in synch with the beam timing system. Ideally, I and Q are proportional to the sine and cosine of the desired phase profile, such as that shown in Fig 2. In practice, the modulator is first calibrated against a phase demodulator, which does the inverse operation, producing I and Q signals whose arctangent and sum in quadrature are the phase and amplitude of the sampled RF. The demodulator itself is calibrated using an RF source with a frequency 10 MHz below the nominal X-band value. For both systems, six parameters (two amplitudes, two phases and two offsets) are derived and used to correct the I and Q values.

Figure 3 shows the results of using the phase profile in Fig 2. in the linac RF station to produce a ramped waveform with a peak power of 150 MW. The amplitude and phase of the ramped portion of the RF pulse are plotted. One sees some smoothing of the waveform as expected from the finite bandwidth of the system, as well as a few degree variation of the phase, which may be a related effect.

4 LOADING MEASUREMENTS

To verify that the loading compensation scheme works as predicted, the energy variation along the bunch train is measured in the spectrometer section of the NLCTA that follows the linac (see Fig. 4). It contains a SLC solid-epoxy-style kicker magnet [7] for this purpose. It is powered by a thyratron-switched capacitor bank which produces the current pulse shown in Fig. 4. The pulse is timed so the peak field occurs just before the beam arrives. This results in a nearly linearly variation of the kicker magnetic field during the pulse, which spreads the bunch train vertically by about 3 cm at the end of the spectrometer (a DC bend magnet just after the kicker is used to offset the average kick to the beam).

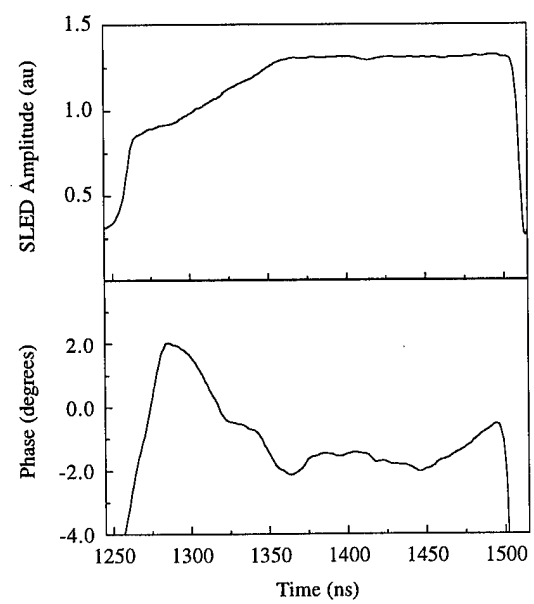

Fig. 3 Measured amplitude (top plot) and phase (bottom plot) of the SLED RF output in the linac for 13% beam loading compensation.

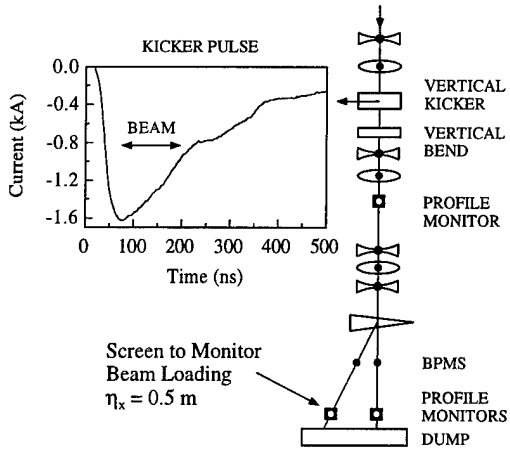

Fig. 4 Spectrometer layout and the kicker pulse shape.

For the energy measurement, a horizontal bend magnet steers the bunches into the off-axis beam line, which spreads the electrons horizontally in proportion to their energy. Thus, when viewing the beam on the off-axis profile monitor [8] with the kicker magnet on, one sees the variation of the bunch energy along the train. Figure 5 shows such images for a 120 ns bunch train with an average current of 0.50 A in the injector (12% loading) and 0.33 A in the linac (13% loading). The current profile along the train was fairly uniform as measured with our toroids [9]. To achieve the loading compensation, the phase profile for the two RF stations were configured based on the measured beam current and accelerator gradient. The timing of the RF pulse relative to the beam in each station was then adjusted to minimize the energy variation along the train. This yielded the image on the left: running with no RF waveform ramp in the linac yielded the image on the right.

Another measure of loading compensation comes from the RF that is monitored at the output couplers on the structures. An example is shown in Fig. 6. One sees that the RF output amplitude is constant during the passage of the beam, which is expected if the loading is properly compensated. At maximum, the loading reduces the output amplitude by 38%, making the phase shift between the beam on and beam off state a good measure of the bunch timing relative to the RF. Figure 6 shows the phase shifts from the two linac structures after the overall klystron drive phase was adjusted to minimize the bunch energy spread. The shifts are only a few degrees, indicting that the relative phasing of structures is good and that the bunches were near the crest of the net field from the two structures, as expected for minimum energy spread. For the NLC, this beam phasing technique could be very useful.

In summary, the beam loading compensation scheme purposed for the NLC has been demonstrated to work well in the NLCTA. We will add another RF station shortly and do further tests of loading compensation at higher currents.

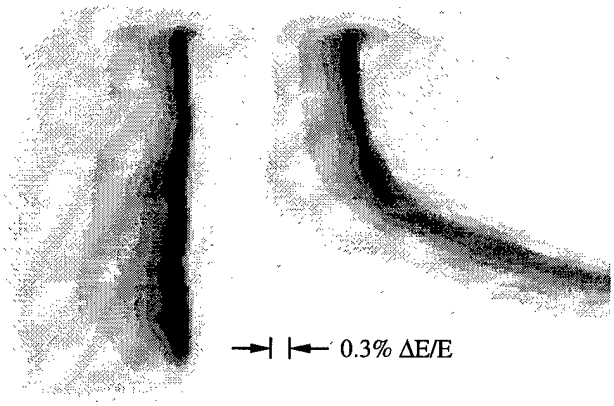

Fig. 5 Profile monitor images of the beam at the end of the spectrometer. The head of the bunch train is at the bottom and higher energy is toward the right (see text).

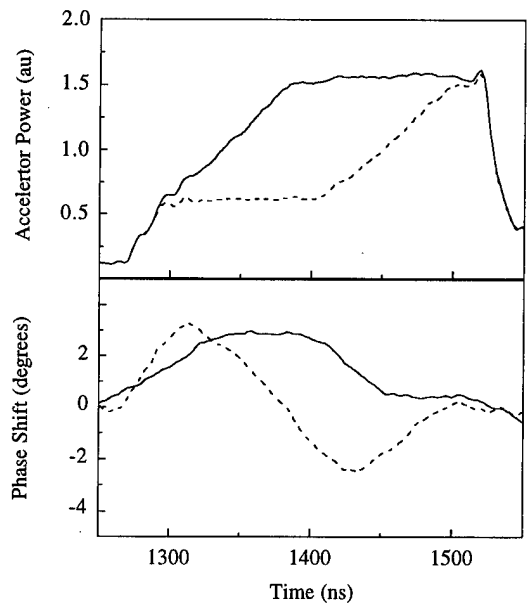

Fig. 6 Power output from a linac accelerator structure (top plot) with the beam off (solid line) and on (dashed line), and the beam on/off phase shift (bottom plot) for the two structures.

REFERENCES

[1] Zero'th-Order Design Report for the Next Linear Collider, SLAC Report 474, 1996.

[2] R. Ruth *et al.*, 'The Next Linear Collider Test Accelerator', SLAC-PUB-6293, and 'Results from the SLAC NLC Test Accelerator', these proceedings.

[3] A. Yeremian *et al.*, 'NLCTA Injector Experimental Results', these proceedings.

[4] J. Wang *et al.*, 'RF System for the NLCTA', these proceedings.

[5] S. Tantawi *et al.*, 'NLCTA's RF Pulse Compression and Transmission', these proceedings.

[6] Sharon Holmes *et al.*, 'Low Level RF Signal Processing for the NLCTA', these proceedings.

[7] T. Mattison *et al.*, 'Fast and Reliable Kicker Magnets for the SLC Damping Rings', SLAC-PUB-6892, (1995).

[8] C. Nantista *et al.*, 'Beam Profile Monitors in the NLCTA', these proceedings.

[9] C. Natista *et al.*, 'Beam Current Monitors in the NLCTA', these proceedings.

EMITTANCE DILUTION THROUGH COHERENT ENERGY SPREAD GENERATION IN BENDING SYSTEMS

P. Emma, *SLAC, Stanford, California,* USA*
R. Brinkmann, *DESY, 22603 Hamburg,* GERMANY

Abstract

For a bunched beam, coherent energy spread generated within a bending system may couple to the transverse (bending) plane coordinates through the chromatic transfer functions of the particular beamline—even an achromatic beamline. The resulting transverse emittance dilution is dependent on the magnitude of the energy spread, its generation rate along the beamline, and the beamline's chromatic transfer functions. The coherent energy spread may be due to resistive-wall wakefields or coherent synchrotron radiation. For specific beamlines, such as a periodic arc or wiggler, the longitudinal-to-transverse coupling is minimal and, in ideal cases, completely suppressed resulting in reduction or cancellation of all transverse emittance dilution effects. This is of particular interest for micro-bunch transport or compression systems such as exist in future FEL or linear collider projects.

1 INTRODUCTION

Many FEL and future linear collider projects utilize transport lines which bend high energy bunched electron beams—with bunch lengths in the sub-picosecond range—in order to achieve this bunch compression or, in some cases, simply to transport the micro-bunch [1,2,3]. Unfortunately, several processes exist which may generate significant energy spread as the bunch traverses this beamline, especially for a very short bunch. Along with the well known stochastic process of quantum fluctuations which produce an incoherent, random energy spread within the bunch, several mechanisms produce a coherent energy spread along the bunch such as resistive wall wakefields [4] or coherent synchrotron radiation [5,6,7].

An electron which, for example, looses energy, $\delta(s) \equiv \Delta E(s)/E_0$, at location s within this bending system will be transported to its end through the chromatic transfer functions, $\partial x/\partial\delta \equiv R_{16}(s)$ and $\partial x'/\partial\delta \equiv R_{26}(s)$, which map an off energy particle from the point of energy loss into transverse phase space at the end of the bending system. Since the energy loss can be different for different particles, the resulting energy spread can potentially dilute the transverse emittance in the bending plane depending on the coherence of the process. A random process results in an intrinsic emittance dilution which is not recoverable while a coherent energy spread generates a projected emittance dilution where correlations among the beam coordinates remain. The latter is therefore a reversible process. We present a few idealized bending systems which, depending on the details of the coherent energy spreading process, minimize or cancel this emittance dilution. We do *not* examine the actual energy spreading processes which lead to this dilution and in most cases we use an idealized or simplified model of the process.

2 EMITTANCE DILUTION

The bend plane phase space coordinates of a particle are expressed as the vector $\mathbf{x} = [x\ x']^{\mathrm{T}}$, and the rms emittance, ε, is then taken from the covariance of the particle ensemble.

$$\varepsilon^2 = \det\left\langle \mathbf{x}\cdot\mathbf{x}^{\mathrm{T}}\right\rangle \tag{1}$$

As defined in the previous section, when a particle looses (or gains) energy at a location s within a bending system (even an achromatic system) its final (bending-plane) phase space coordinates at the end of the system will be altered with respect to the on-energy particle as

$$\mathbf{x}_s = \mathbf{x}_0 + \Delta\mathbf{x}(s) = \mathbf{x}_0 + \begin{bmatrix} R_{16}(s) \\ R_{26}(s) \end{bmatrix}\delta(s)\ . \tag{2}$$

(For simplicity we define coordinates such that $\langle\mathbf{x}\rangle = \langle\Delta\mathbf{x}\rangle = 0 = \langle\delta\rangle$). From Eq. (1) and (2) and an input emittance ε_0, the final emittance at bend system end is

$$\begin{aligned}\varepsilon^2 = \varepsilon_0^2 + \varepsilon_0\left[\beta\left\langle\Delta x'^2\right\rangle + 2\alpha\left\langle\Delta x\Delta x'\right\rangle + \gamma\left\langle\Delta x^2\right\rangle\right] + \\ \left\langle\Delta x^2\right\rangle\left\langle\Delta x'^2\right\rangle - \left\langle\Delta x\Delta x'\right\rangle^2\end{aligned} \tag{3}$$

where β, α and γ are the nominal Twiss parameters at bend system end. The second line of Eq. (3) is an additive emittance even for a zero-emittance input beam.

For an incoherent energy loss process (i.e. δ is random with no correlation to other phase space coordinates) we first calculate the variance of $\Delta\mathbf{x}$ due to the incremental energy spread generated at each location s and sum these in quadrature over the beamline as uncorrelated quantities.

$$\left\langle\Delta x^2\right\rangle_{\mathrm{inc}} = \int R_{16}(s)^2 \frac{d}{ds}\sigma_\delta^2 ds \tag{4}$$

The square of the generated energy spread is represented by its rate along the beamline (similar relation for $\Delta x'$).

For a coherent process, where a particle's energy deviation is purely a function of its longitudinal position along the bunch, the transverse coordinate shifts, $\Delta\mathbf{x}(s)$, which originate at each s location add linearly, so we first sum $\Delta\mathbf{x}(s)$ over s and then find its total variance.

$$\left\langle\Delta x^2\right\rangle_{\mathrm{coh}} = \left(\int R_{16}(s)\frac{d\sigma_\delta}{ds}ds\right)^2 \tag{5}$$

* Work supported by Department of Energy contract DE-AC03-76SF00515

Here the incremental energy spread generation is expressed as a rate along the beamline (similar relation for $\Delta x'$).

The difference between the incoherent and the coherent process is now clear as Eq. (4), the incoherent process, represents a monotonically increasing summation of positive values, whereas Eq. (5), the coherent process, is a summation of signed quantities which may vanish.

The full emittance dilution for the coherent process is then written from Eq. (3) where, due to coherence, the correlation $\langle \Delta x \Delta x' \rangle^2 = \langle \Delta x^2 \rangle \langle \Delta x'^2 \rangle$, and so the second line (additive emittance) is zero.

$$\varepsilon^2 \approx \varepsilon_0^2 + \varepsilon_0 \frac{1}{\beta}\left[\left\langle \Delta x^2 \right\rangle + \left(\alpha \left\langle \Delta x^2 \right\rangle^{1/2} + \beta \left\langle \Delta x'^2 \right\rangle^{1/2}\right)^2\right] \quad (6)$$

The variances above are taken from Eq. (5). Here we assume full coherence so that, for example, a particle's energy deviation is solely a function of 1) its longitudinal position within the bunch and 2) a scalar which is equal for all particles at any particular location s along the beamline, but may vary with s (e.g. due to changing bunch length). This assumes particles do not shift with respect to each other in the bunch as will occur with a longitudinal phase space rotation of $>\pi/2$. We, therefore, only consider a functional energy dependence along the bunch whose shape does not vary significantly with s.

3 ARCS, WIGGLERS AND CHICANES

Several bending systems are of interest in future FEL and linear collider designs. We use as examples, a periodic FODO-cell arc, a simple wiggler and a magnetic chicane. There are two cases of interest for each. If we restrict ourselves to processes such as coherent synchrotron radiation (CSR) or resistive wall wakefields, which generate coherent energy spread of a magnitude which depends on the bunch length, then it is worth distinguishing between a simple transport line, where the bunch length is virtually constant, and a compressor, where the bunch length is reduced (or increased) along the beamline. We now describe how Eq.'s (5) and (6) apply to an arc, a wiggler and a chicane.

3.1 Arc

We restrict our analysis to an arc of constant bending radius constructed of FODO cells and which includes appropriate periodic dispersion matching and suppression sections prior to and following the FODO cells.

The chromatic transfer functions, $R_{16}(s)$ and $R_{26}(s)$, which map <u>from</u> locations s within an arc <u>to</u> just beyond the final dispersion suppression bend, can be shown to be periodic functions which oscillate about zero over the arc. Fig. 1 shows the dispersion function, η_x, and the transfer functions, as defined above, for a 36°-arc composed of 15 FODO cells of ψ_x = 108°/cell. Note, η_x maps δ (originating upstream of the first bend) to x at a location s in the arc, whereas the transfer functions map δ (originating at s) to x at a location beyond the last bend.

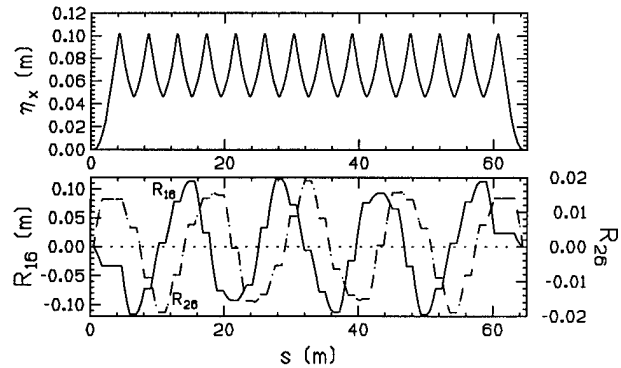

Figure 1. Dispersion function (top) and chromatic transfer functions (bot), for the example FODO-cell arc.

This arc has a 9π total phase advance and the dispersion function is matched to the periodic solution. In this case, the mean $R_{16}(s)$ and $R_{26}(s)$ are nearly zero. Therefore, a constant energy spread generation rate (e.g. constant bunch length) will generate almost no emittance increase. In Eq. (5) this implies extracting the constant energy spread rate from the integral leaving expressions for the mean R_{16} and R_{26}, both of which are nearly zero.

For a compressor-arc (changing bunch length), the energy spread generation rate must be included to evaluate the emittance growth. Fig. 2 shows the CSR emittance growth as a constant length bunch moves through the arc (a) and also for a compressing bunch (b).

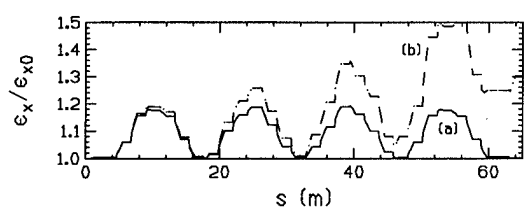

Figure 2. Fractional CSR emittance growth in arc for a constant 25-μm bunch (a) and a compressing bunch of 25-10 μm (b). The charge is 2 nC and input emittance is $\gamma\varepsilon_0 = 1$ μm.

In Fig. 2 the incremental rms coherent energy spread at each dipole magnet slice is generated as 'steady-state' CSR [7], ignoring vacuum chamber shielding, using

$$\Delta\sigma_\delta(s) \approx 0.22 \frac{r_e N \Delta L_B}{\gamma \rho^{2/3} \sigma_z^{4/3}}\ , \quad (7)$$

where N is the bunch population, ΔL_B is the dipole magnet slice length, ρ is the bend radius, σ_z is the bunch length, r_e is the classical electron radius and γ is the Lorentz energy factor. For a constant bunch length the net arc emittance growth is zero but oscillates by up to 20%. The compressing bunch destroys the symmetry and in this case produces a net 30% growth.

3.2 Wiggler

As an example of a wiggler system [8] we take the TESLA bunch compressor at DESY [9] which compresses a 9 mm rms bunch to 600 μm. The system is composed of eight 16° bends and two 8° bends to introduce an energy

dependent path length. The dispersion function and the transfer functions, as defined above, are shown in Fig. 3. As in the case of the arc, the transfer functions oscillate around zero.

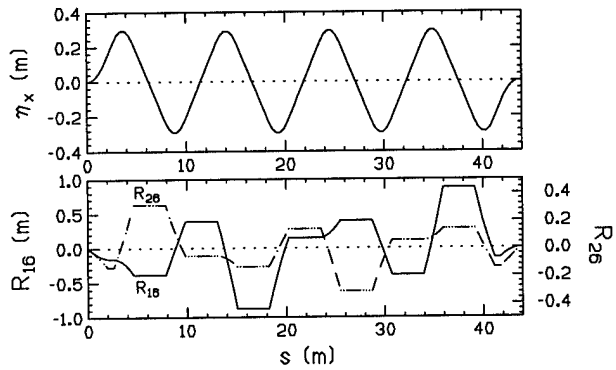

Figure 3. Dispersion function (top) and chromatic transfer functions (bot) of the TESLA bunch compressor wiggler.

The CSR emittance growth across this wiggler is shown in Fig. 4 for a 1-mm constant bunch length (a) and also a compressing bunch from 9 to 0.6 mm (b).

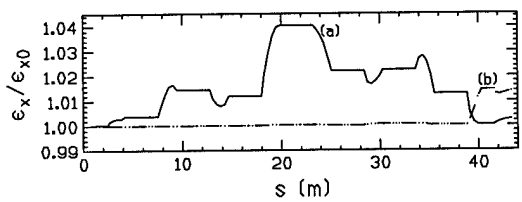

Figure 4. Fractional CSR emittance growth in wiggler of Fig. 3 for a constant 1-mm bunch length (a) and for a compressing bunch of 9-0.6 mm (b). The charge is 6 nC and input emittance is $\gamma\epsilon_{x0} = 8\ \mu$m.

Although the CSR effects are small, the constant bunch results in nearly full cancellation of emittance dilution whereas the compressing bunch results in a 1.5% dilution.

3.3 Chicane

As an example of a four-dipole magnetic bunch-compressor chicane we take the second compressor of the Linac Coherent Light Source (LCLS) [1] at SLAC. Its function is to compress a 390 μm rms bunch to 20 μm. This is in a regime of significant CSR and potential emittance dilution. A single 13.2-meter chicane with four 3.6°, 1.5-meter long bends can be used to make the compression but CSR calculations show the emittance more than doubles for a 1-nC beam and input emittance of 1 μm (the transfer functions do not oscillate about zero).

To compensate we form a double chicane of twice the length with separating optics (4 quadrupoles) to introduce a $-\mathbf{I}_{2\times2}$ bend plane transfer matrix between chicane centers. The first chicane bend angles are reduced (increasing the bunch length there which reduces the CSR energy spread) and the second chicane is set to complete the 20 μm final bunch compression such that dilution effects of the first chicane cancel with the second. The chicanes may also be empirically adjusted, if necessary, to minimize the observed dilution while maintaining final compression. The dispersion function, bunch length (σ_{z1}=single-chicane, σ_{z2}=double-chicane) and emittance growth are shown in Fig. 5 (top-dash is η_x of the single chicane).

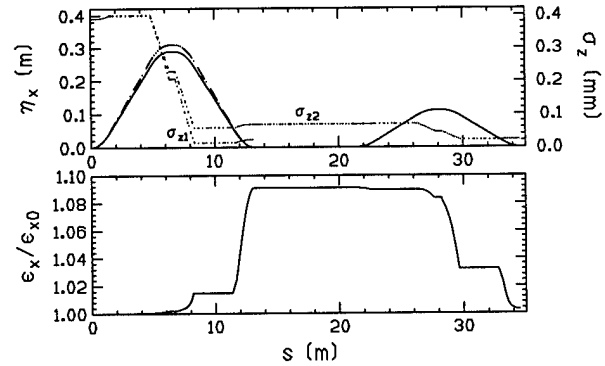

Figure 5. Dispersion (top-solid), bunch length (top-dots) and CSR emittance growth (bot) in single (σ_{z1}) and double (σ_{z2}) chicane for compressing bunch of 390-20 μm (top-dash is η_x of single chicane). The charge is 1 nC and $\gamma\epsilon_{x0} = 1\ \mu$m. Emittance growth of single-chicane ($\epsilon/\epsilon_0 \approx 2.3$) is not shown.

4 CONCLUSIONS

We have demonstrated that for a pure coherent energy spread generated within a bending beamline the resulting transverse emittance dilution can be minimized or canceled by a judicious choice of optics. The inherent periodicity of a FODO-cell arc and a wiggler generate cancellations which, for constant energy spread generation rate, can neutralize emittance growth. Variations on these basic bunch-compressor beamlines (e.g. the double chicane) can also be designed to compensate the emittance, even for a sharply compressing bunch. This compensation may prove useful in future FEL and linear collider projects which transport extremely short bunches.

5 REFERENCES

[1] V.K. Bharadwaj, et al., "Linac Design for the LCLS project at SLAC", these proceedings.

[2] "Zeroth-Order Design Report for the Next Linear Collider", SLAC Report 474, May 1996.

[3] "Conceptual Design of a 500 GeV e^+e^- Linear Collider with Integrated X-ray Laser Facility", DESY 97-048, 1997.

[4] O. Napoly and O. Henry, "The Resistive-Pipe Wake Potentials for Short Bunches", Part. Acc., Vol. 35, pp. 235-247, 1991.

[5] M. Dohlus and T. Limberg, "Wake Fields of a Bunch on a General Trajectory Due to Coherent Synchrotron Radiation", these proceedings.

[6] E.L. Saldin, et al., "On the Coherent Radiation of an Electron Bunch Moving in and Arc of a Circle", TESLA-FEL 96-14 (Nov. 1996).

[7] Ya. S. Derbenev, et al., "Microbunch Radiative Tail-Head Interaction", DESY, Sep. 1995.

[8] T.O. Raubenheimer, et al., "Chicane and Wiggler Based Bunch Compressors for Future Linear Colliders", SLAC-PUB-6119, May 1993.

[9] P. Emma, "Bunch Compressor Beamlines for the TESLA and S-band Linear Colliders", DESY-TESLA 95-17 (July 1995).

SINGLE BUNCH STABILITY IN PEP-II LER *

S. Heifets,
SLAC, Stanford, CA 94309, USA,
G. Sabbi,
Fermi National Laboratory, Batavia, Il.

Abstract

The note describes results of studies of the single bunch stability in the low energy ring (LER) of the PEP-II B-factory[?]. Simulations describe the potential well distortion (PWD) obtained by numerical solution of the Haiisinski equation[?] and results on the beam stability obtained with the code TRISIM[?]. Both longitudinal and transverse wake fields are taken into account.

1 INTRODUCTION

Preliminary estimates[?] indicate that single bunch in the LER of the PEP-II B-factory has to be stable, both longitudinally and transversely, at the maximum design bunch current 1.8 mA (beam current 3A). However, realistic wakes of the machine has been constructed only recently using results of the extensive numerical simulations of the vacuum components of the ring[?]. Additional to that, the code TRISIM[?], a simulation program for single-bunch collective effects written by one of the authors (G. S.), became recently available. This allows us to study beam stability in a more reliable way than it is possible analytically.

In the beginning, we discuss shortly how the wake fields responsible for the effects under consideration have been constructed. Then we present results on the PWD and, later, results on the beam stability obtained with the code TRISIM. The input parameters are based on the nominal parameters of the LER: energy 3.105 GeV, revolution period 7.336 μs, rf voltage 5.1 MeV, RF frequency 476 MHz, SR energy loss 0.75 MEV/turn, momentum compaction $\alpha = 1.23 \times 10^{-3}$, average beta function $\beta_y = 14.5$ m, betatron tune $\nu_y = 36.642$, horizontal emittance $\epsilon_x = 65.58$ nm, coupling $\epsilon_y/\epsilon_x = 0.03$, damping times $\tau_E = 30.2$ ms, $\tau_y = 61.1$ ms. The nominal bunch length of 33.1 ps and the rms energy spread of 2.394 MeV were used to generate the initial distribution of a bunch.

2 WAKE FIELDS

The longitudinal wake field of a point-like charge $W_l^\delta(z)$ was constructed[?] from the combination of a narrow-band impedances of the higher order modes of the RF cavities and 290 BPMs, and of the broad-band impedances of the resistive walls, high-frequency tail of the RF cavities impedance, and the impedance of the vacuum components of the ring. Parameters of the HOMs were taken from the results of the measurements[?]. The conservative scenario of 8 cavities in the ring was taken for calculations. Because of the large number of different vacuum components in the ring, the impedances of these components were calculated with the codes ABCI and MAFIA only for a Gaussian bunch with the nominal rms length $\sigma = 1$ cm. For such a bunch, the longitudinal components of the ring have mostly inductive impedances with the total inductance of all components $L = 87$ nH. However, the loss factor of these components is not zero, and the total loss factor was estimated $\kappa = 2.9$ V/pC at $\sigma = 1$ cm. (The loss κ is reduced here by the contribution of the high-frequency tail of the cavities).

To reconstruct the wake of a point-like charge, we use the modified inductive impedance (in CGS units, c_0 is the velocity of light)

$$Z(\omega) = -\frac{i\omega L}{c_0^2(1 - i\omega a/c_0)^{3/2}}. \qquad (1)$$

which is pure inductive at small frequencies $\omega a/c_0 << 1$ and rolls-off as $\omega^{-1/2}$ at high frequencies. The corresponding wake at $z > 0$ is

$$W_l^\delta(z) = \frac{L}{a\sqrt{\pi z a}}(1 - 2\frac{z}{a})e^{-z/a}, \qquad (2)$$

and is equal to zero at $z < 0$. In the limit $a \to 0$ it corresponds to the usual inductive wake $W_l^\delta(z) = L\partial\delta(z)/\partial z$. The roll-off parameter a defines the loss factor. Dependence of the loss factor on the rms σ of a collimator, with the wake of a typical component of the vaccum chamber, was compared with the numerical code ABCI. Dependence is in good agreement with that predicted by Eq. 1. Agreement is much better than that for $Q = 1$ model.

The transverse wake $W_\perp^\delta(z)$ was calculated from measured dipole modes of the RF cavities, impedance of the resistive walls, and the impedance of the vacuum components of the ring. The later was defined from the Wenzel-Panofsky theorem assuming that the dipole longitudinal wake $W_l^{m=1}(z)$ is related to the monopole longitudinal wake, $W_l^{m=1} \simeq 2W_l^{m=0}/b^2$ where b is the average beam pipe radius. This assumption was confirmed by ABCI.

The wake of the triangular bunch $W_l^\Delta(z)$, which is needed as input for TRISIM, was calculated then by convolution of the $W_l^\delta(z)$ with the density

3 POTENTIAL WELL DISTRORTION

The steady-state PWD is described by a solution of the Haiisinski equation[?] for the density of a bunch $\rho(x)$. Fig. 1 shows the dependence of the position of the bunch centroid $< x >$, the rms bunch length σ, and the energy spread $< \delta >$ in MeV vs bunch current in mA. Each point corresponds to one run of TRISIM. Fluctuations increase at large currents. The growth of the energy spread is noticable above 1 mA indicating onset of the microwave instability.

* Work supported by the Department of Energy, contract DE-AC03-76SF00515

The bunch lengthening is clear visible, but even in the last high current case (total current 6.2 A, bunch current 3.75 mA) the potential well does not show a second minimum. At the maximum nominal machine current of 3 A bunch lengthening is small, less than 10%.

Haiisinski solution defines the action variable $J = \int(dx/2\pi)\sqrt{2(H-U(x))}$ and the synchrotron frequency $\frac{\omega(I)=\partial H}{\partial I}$. Fig. 2 depicts the dependence of the synchrotron frequency on the action J of oscillations for various bunch currents. At small amplitudes, the frequency $\omega(0)$ decreases with N_B while the frequency spread increases and is about 20% at 3 A.

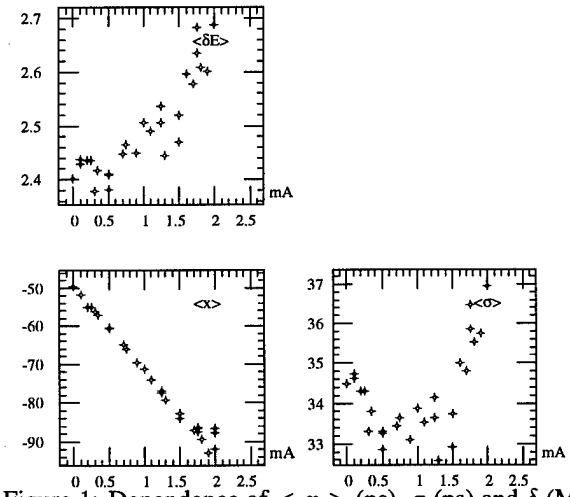

Figure 1: Dependence of $< x >$ (ps), σ (ps) and δ (MeV) on bunch current (mA).

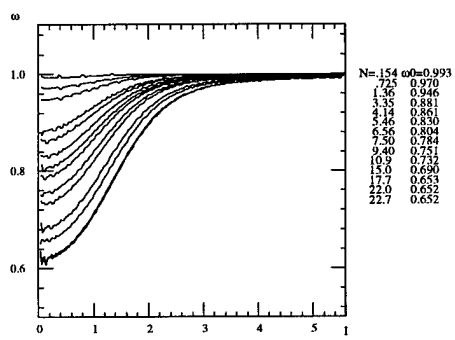

Figure 2: Dependence of the synchrotron frequency on action J .

4 BUNCH STABILITY

The bunch stability was studied with the code TRISIM. The typical results of TRISIM are shown in Fig. 3 at the bunch current $I_b = 1.8$ mA (total current 3 A). Both longitudinal and transverse wakes were taken into account. No feedback system was turned on. The chromaticity of the ring $\xi = (1/\nu_y)d\nu_y/d\delta$ was set to $\xi = 0.05$.

The bunch is stable: no particles were lost after 2×10^4 revolutions (about $5\tau_E$) but the bunch centroid oscillates with irregular and large amplitude variations which reaches

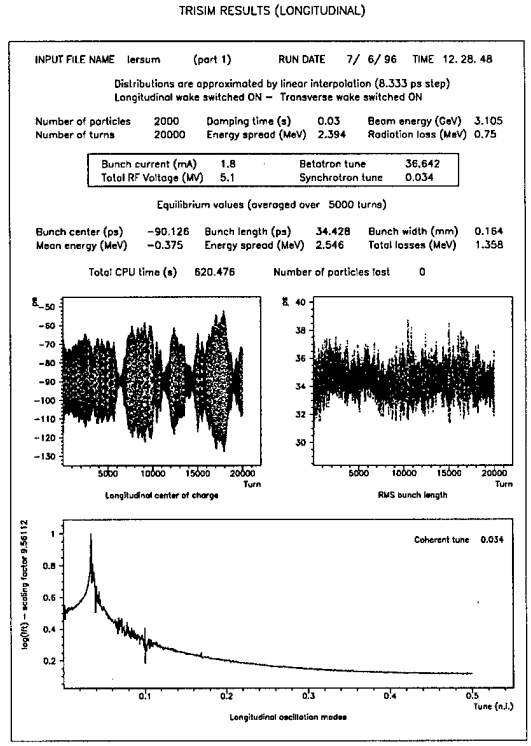

Figure 3: Typical output of TRISIM, $I_b = 1.8$ mA.

sometimes 40 ps. The rms bunch length increases at this current to 34.22 ± 1.0 ps, or by 8%, and the energy spread grows to 2.54 MeV. The spectrum of the longitudinal motion has a large peak at the synchrotron frequency $\nu_s = 0.034$ and a smaller peak at $2\nu_s$. The spectrum of the transverse motion indicates a large betatron peak at the fractional betatron tune $0.64 = 1 - 0.363$. At the positive chromaticity there are synchrotron sidebands with the amplitude strongly dependent on ξ.

Fig. 4 shows bunch profiles in (y,z) plane at each 5-th revolution after few damping times at 2 mA bunch current. The oscillations of the bunch centroid with synchrotron period are quite noticeable, but the distortion of the bunch remains relatively small.

These results has been checked and confirmed with the number of macro-particles increased up to 10^4. The instability occurs as a result of increasing longitudinal oscillations of the bunch centroid rather than due to oscillations of the bunch shape. Tracking with large apperture shows recurencies in the bunch blow-up: at the 2 mA bunch current, bunch slowly blows up during 8000-9000 turns, then shrinks in 100-200 turns to a small size, and blows up again. The process repeats itself several times during 40000 turns.

Bunch remains stable for positive chromaticity up to very high currents but, at 12.5 mA, becomes unstable indicating the onset of the (strong) head-tail instability. The situation is drastically different with a negative chromaticity. At the zero or negative chromaticity and $I_b = 1.8$ mA bunch is unstable.

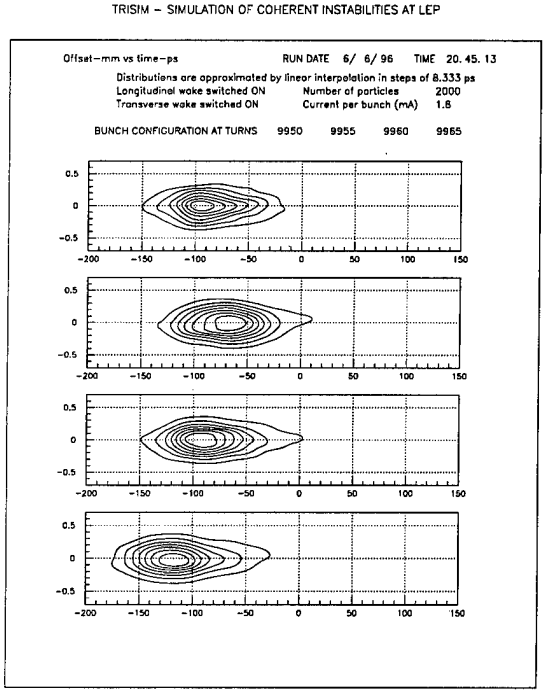

Figure 4: Oscillations of the bunch centroid, $I_b = 2.0$ mA.

5 DISCUSSION

The growth of the energy spread, indicating the onset of the microwave instability, is noticable at the bunch current above 1 mA. The growth of the energy spread and the rms bunch length is relatively small and not much different from the PWD results up to the bunch current 1.8 mA. However, the amplitude of the longitudinal bunch centroid oscillations increases and, at $I_b = 2.$ mA, bunch is already unstable, rms becomes very large, and particles get lost. It is interesting, that $\omega(I)$ dependence at this current becomes flat at small amplitudes I. This might indicate that microwave instability starts when $d\omega/dI = 0$. It would be interesting to understand whether the longitudinal feedback system can increase the threshold of the microwave instability. The bunch remains transversely stable up to the $I_b = 10$ mA at the zero or positive chromaticity. This corresponds to the previous estimates of the threshold of the head-tail instability. However, at the negative chromaticity the (weak) head-tail threshold is very low: bunch is unstable at $I_b = 1.8$ mA and $\xi = -0.05$.

6 REFERENCES

[1] PEP-II An Asymmetric B factory, Conceptual Design Report, LBL-PUB-5379, SLAC-418, (1993)

[2] J. Haissinski, Nuovo Cimento 18B, 72, (1973)

[3] G. Sabbi Simulation of single-bunch collective effect in LEP by linear expansion of the distribution moments, CERN SL/95-25 (AP) (1994),

[4] S. Heifets, et al, Impedance study for the PEP-II B-factory, SLAC/AP-99, (1995)

[5] S. Heifets,Wake Fields, PWD and Beam Stability in the LER PEP-II, PEP-II AP Note 96.08 (1996)

[6] R. Rimmer, unpublished

GEOMETRICAL WAKE OF A SMOOTH FLAT COLLIMATOR

G. V. Stupakov
Stanford Linear Accelerator Center, Stanford University, Stanford, CA 94309

Abstract

A transverse geometrical wake generated by a beam passing through a smooth flat collimator with a gradually varying gap between the upper and lower walls is considered. Based on generalization of the approach recently developed for a smooth circular taper [1] we reduce the electromagnetic problem of the impedance calculation to the solution of two much simpler static problems – a magnetostatic and an electrostatic ones. The solution shows that in the limit of not very large frequencies, the impedance increases with the ratio h/d where h is the width and d is the distance between the collimating jaws. Numerical results are presented for the NLC Post Linac collimator.

1 INTRODUCTION

In this paper we calculate the impedance of a flat smooth collimator schematically shown in Fig. 1. The collimator extends in the y direction from $y = -h$ to $y = h$ and is bounded by perfectly conducting walls. The beam propagates in the z direction. The collimator upper and lower walls are given by the equation $x = \pm b(z)$, where $b(z)$ is a smooth function such that $b'(z) \ll 1$. Throughout this paper we assume that $h \gg b(z)$.

For a smoothly varying wall and not very high frequency such that $kb^2 < l$, where $k = \omega/c \approx \sigma_z^{-1}$, and l is the length of the collimator, the energy loss of the beam due to the radiation in the collimator is small [1]. This results in the real part of the impedance being much smaller than its imaginary part, and, in the first approximation, the real part can be neglected. In this approximation, the transverse impedance is purely imaginary and does not depend on the frequency. The latter allows us to simplify its calculation considering only the limit $\omega \to 0$ [1]. In this limit, the electric field can be found as a solution to electrostatic equations, and magnetic field satisfies magnetostatic equations with proper boundary conditions. For the electrostatic problem, one has to find the electric field of a charged wire of unit charge density stretched along the beam trajectory $x = x_0$, $y = 0$. The magnetostatic problem requires finding the magnetic field generated by the same wire carrying a unit current. After the electric and magnetic fields are found, the transverse impedance in x direction can be calculated using the following formula

$$Z_x(x, y, x_0) = -\frac{i}{c}\int_{-\infty}^{\infty}(E_x - H_y)\,dz. \qquad (1)$$

This impedance has a dimension of Ohm and depends on the location of the driving particle x_0 and the coordinates of the test particle, x, y.

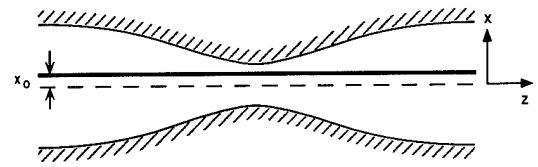

Figure 1: Sketch of a smooth flat collimator. The collimator extends from $y = -h$ to $y = h$ in the y direction. A heavy line shows the trajectory of a driving particle.

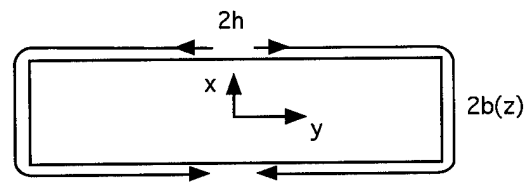

Figure 2: Cross section of the collimator by a plane $z =$ const and transverse currents flowing in the collimator walls.

The wake w corresponding to a purely imaginary transverse impedance (1) is $w(x, y, x_0, z) = icZ_x(x, y, x_0)\,\delta(z)$. After the passage of the collimator the bunch will be deflected in the x direction by an angle $Nr_e\kappa/\gamma$, where N is the number of particles in the bunch, r_e is the classical electron radius (for electron/positron beam), γ is the relativistic factor, and $\kappa = -c\mathrm{Im}Z_x/2\sqrt{\pi}\sigma_z$.

2 CALCULATION OF FIELDS

2.1 Electrostatic Problem

Since we assume that $h \gg b(z)$, for the electrostatic problem we set $h \to \infty$ and consider a collimator that extends infinitely in $\pm y$ directions. One can show that the effect of finite h in the electrostatic problem is exponentially small and can be neglected.

Let φ_e denotes the electrostatic potential such that $E_x = -\partial\varphi_e/\partial x$. It satisfies the Poisson equation with the right hand side representing a linear charge with a unit charge density,

$$\Delta\varphi_e = -4\pi\delta(x - x_0)\,\delta(y), \qquad (2)$$

with the boundary condition $\varphi_e|_{x=\pm b(z)} = 0$. Since the boundary $b(z)$ is a slow varying function of its argument, in the zero approximation, we can neglect the variation of the potential φ_e in the z direction. This assumption reduces

0-7803-4376-X/98 /$10.00 © 1998 IEEE

Eq. (2) to

$$\Delta_{x,y}\varphi_e^{(0)} = -4\pi\delta\left(x - x_0\right)\delta\left(y\right), \tag{3}$$

where $\Delta_{x,y} = \partial^2/\partial x^2 + \partial^2/\partial y^2$, and the superscript 0 indicates the zero approximation to the potential. The solution to Eq. (3) with the zero potential boundary condition is

$$\varphi_e^{(0)} = \ln\frac{\sinh^2\frac{\pi y}{4b(z)} + \cos^2\frac{\pi(x+x_0)}{4b(z)}}{\sinh^2\frac{\pi y}{4b(z)} + \sin^2\frac{\pi(x-x_0)}{4b(z)}}. \tag{4}$$

In the next approximation, the potential will be given by $\varphi_e = \varphi_e^{(0)} + \varphi_e^{(1)}$, where $\varphi_e^{(1)}$ is a first order correction that satisfies the following equation

$$\Delta_{x,y}\varphi_e^{(1)} = -\frac{\partial^2\varphi_e^{(0)}}{\partial^2 z^2}, \tag{5}$$

with the boundary condition $\varphi_e^{(1)}\Big|_{x=\pm b(z)} = 0$. The solution to Eq. (5) can be found explicitly using $\varphi_e^{(0)}$ as a Green's function,

$$\varphi_e^{(1)}\left(x, y, x_0, z\right) = -\frac{1}{4\pi}\int\limits_{-b(z)}^{b(z)} dx' \int\limits_{-\infty}^{\infty} dy'$$

$$\times\frac{\partial^2\varphi_e^{(0)}}{\partial z^2}\left(x', y', x_0; b\left(z\right)\right)\varphi_e^{(0)}\left(x, y - y', x'; b\left(z\right)\right). \tag{6}$$

It is easy to show that the integral over y' in Eq. (6) converges on a scale of the order of $|y'| \sim b$ which, by assumption, is much smaller than the half width of the collimator h. This observation justifies the limit $h \to \infty$ assumed above.

2.2 *Magnetostatic Problem*

A specific feature of the magnetostatic problem is that even though $h \gg b\left(z\right)$, one cannot set $h \to \infty$ and consider an infinitely wide collimator. As we will see below, the contribution of the magnetic field into impedance has a term that is directly proportional to the width of the collimator h, and hence diverges in the limit $h \to \infty$. The physical mechanism of this divergence is related to the currents generated in the walls of the collimator due to the variation of the image charges. This current flows around the collimator cross section, as shown in Fig. 2, and generates the magnetic field H_y which turns out to be proportional to h.

It follows from the Maxwell equations that the y component of the magnetic field, H_y, of an infinitely thin current wire between perfectly conducting walls satisfies the following equation

$$\Delta H_y = 4\pi\delta'\left(x - x_0\right)\delta\left(y\right), \tag{7}$$

with the Neumann boundary condition at the upper and lower walls, $\partial H_y/\partial n|_{x=\pm b(z)} = 0$, and the Dirichlet boundary condition $H_y = 0$ at the lateral walls $y = \pm h$. It is convenient to formulate the magnetic problem in a way analogous to the electric one by introducing the magnetic "potential" φ_m such that $H_y = -\partial\varphi_m/\partial x_0$. Note that the derivative in this equation is taken with respect to the location of the driving particle x_0, rather than x. The potential φ_m satisfies the Poisson equation

$$\Delta\varphi_m = 4\pi\delta\left(x - x_0\right)\delta\left(y\right), \tag{8}$$

with the boundary conditions

$$\frac{\partial\varphi_m}{\partial n}\bigg|_{x=\pm b(z)} = 0, \quad \varphi_m|_{y=\pm h} = 0. \tag{9}$$

Again, invoking a perturbation theory, in the zero approximation which neglects the z-dependence in the potential φ_m, we have

$$\Delta_{x,y}\varphi_m^{(0)} = 4\pi\delta\left(x - x_0\right)\delta\left(y\right). \tag{10}$$

The first of the boundary conditions (9) in this approximation takes the form

$$\frac{\partial\varphi_m^{(0)}}{\partial x}\bigg|_{x=\pm b} = 0. \tag{11}$$

The solution to this problem valid in the limit $h \gg b\left(z\right)$ is

$$\varphi_m^{(0)} = \ln\left[16\left(\sinh^2\frac{\pi y}{4b\left(z\right)} + \cos^2\frac{\pi\left(x + x_0\right)}{4b\left(z\right)}\right)\right.$$
$$\left.\times\left(\sinh^2\frac{\pi y}{4b\left(z\right)} + \sin^2\frac{\pi\left(x - x_0\right)}{4b\left(z\right)}\right)\right] - \frac{\pi h}{b\left(z\right)}. \tag{12}$$

This function satisfies Eqs. (10) and (11), and is exponentially small at $y = \pm h$, $\varphi_m|_{y=\pm h} \sim \exp\left(-\pi h/4b\right)$. For any practical purposes, the second of the boundary conditions (9) can be considered as satisfied as soon as $h > 4b$. Note that the presence of the second term on the right hand side of Eq. (12) does not allow us to consider the limit $h \to \infty$ in the magnetostatic problem.

In the next approximation, $\varphi_m = \varphi_m^{(0)} + \varphi_m^{(1)}$, where $\varphi_m^{(1)}$ satisfies

$$\Delta_{x,y}\varphi_m^{(1)} = -\frac{\partial^2\varphi_m^{(0)}}{\partial^2 z^2}. \tag{13}$$

However, the boundary condition for the function $\varphi_m^{(1)}$ differs from the zero approximation (9), because the normal to the wall $\mathbf{n}$ in the first approximation is equal to $\mathbf{n} = (\pm 1, 0, -b')$, yielding the boundary condition

$$\frac{\partial\varphi_m^{(1)}}{\partial x}\bigg|_{x=\pm b} = \pm b'\left(z\right)\frac{\partial\varphi_m^{(0)}}{\partial z}\bigg|_{x=\pm b}. \tag{14}$$

The solution of the inhomogeneous equation (13) with the Neumann boundary condition (14) can be explicitly expressed in terms of the Green's function $\varphi_m^{(0)}$ [2] similar to Eq. (6). The result can be found in Ref. ([3]).

3 IMPEDANCE

The impedance is given by Eq. (1),

$$Z_x = -\frac{i}{c}\int_{-\infty}^{\infty}\left(\frac{\partial\varphi_e^{(0)}}{\partial x}+\frac{\partial\varphi_e^{(1)}}{\partial x}-\frac{\partial\varphi_m^{(0)}}{\partial x_0}-\frac{\partial\varphi_m^{(1)}}{\partial x_0}\right)dz. \tag{15}$$

Note that from Eqs. (4) and (12) it follows that

$$\partial\varphi_e^{(0)}\Big/\partial x = \partial\varphi_m^{(0)}\Big/\partial x_0, \tag{16}$$

which means that the zero order terms do not contribute to the impedance. This fact can be easily explained by that in the zero order theory the geometry of the collimator reduces to the rectangular pipe of a constant cross section, in which the wake of an ultrarelativistic beam is known to be zero. In the first approximation we have,

$$\int_{-\infty}^{\infty}(E_x - H_y)\,dz = -\int_{-\infty}^{\infty}\left(\frac{\partial\varphi_e^{(1)}}{\partial x}-\frac{\partial\varphi_m^{(1)}}{\partial x_0}\right)dz. \tag{17}$$

Near the axis when $x, x_0 \ll b$ one can expand the general expressions for the impedance and carry out the integration over y. Omitting lengthy analytical calculations that were performed with the use of computer program Mathematica [4] we present here the result. We limit our consideration to the case $y = 0$ only, i.e. the case when both the driving and test particles are in the same vertical plane. In this case,

$$Z_x = \frac{-iZ_0}{4\pi}\left(Ax + Bx_0\right), \tag{18}$$

where

$$A = 2I_1, \quad B = -2I_1 + 2\pi h I_3, \tag{19}$$

and

$$I_1 = \int dz\frac{(b')^2}{b^2}, \; I_2 = \int dz\frac{(b')^2}{b^3}. \tag{20}$$

For $x = x_0$, for a conventional definition of the transverse impedance Z_t, we find

$$Z_t \equiv \frac{1}{x_0}\,Z_x\big|_{x=x_0} = \frac{-iZ_0}{2}hI_3. \tag{21}$$

Note that the integral I_1 also appears in Yokoya's theory of a smooth axisymmetric collimator [5], where $b(z)$ plays a role of the pipe radius. Comparison of our result with [5] shows that the impedance of a flat collimator is much larger (by factor of h/b) than the impedance of a cylindrical collimator of a radius $b(z)$.

4 NLC-TYPE COLLIMATOR

We apply the results obtained above to collimators considered in the design of the Next Linear Collider [6]. The geometry of a typical collimator is shown in Fig. 3 with the following parameters: $b = 0.5$ cm, $g = 0.1$ cm, $l = 40$ cm,

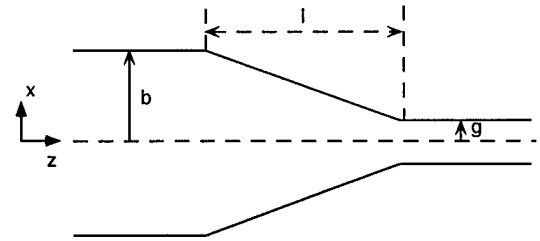

Figure 3: Schematic of the NLC collimator.

and the width of the collimator $h = 0.7$ cm. The applicability condition of the theory developed in the previous sections require the function $b(z)$ to be smooth together with its first two derivatives. Strictly speaking, this requirement does not hold for the profile shown in Fig. 3 where $b'(z)$ is not continuous at the entrance and the exit of the taper. In our calculations we assumed that in reality the angles of the collimator will be rounded in such a way that the smoothness condition is satisfied.

The integrals (20) for this collimator are equal: $I_1 = 0.08\ \mathrm{cm}^{-1}$ and $I_2 = 0.48\ \mathrm{cm}^{-2}$, which gives the transverse impedance near the axis,

$$-\mathrm{Im}Z_t = 6.3\times 10^3\ \mathrm{Ohm/m}. \tag{22}$$

5 ACKNOWLEDGMENT

I would like to thank K. Bane, A. Chao, S. Heifets, J. Irwin, and R. Warnock for useful discussions. This work was supported by Department of Energy contract DE-AC03-76SF00515.

6 REFERENCES

[1] G. V. Stupakov. Geometrical Wake of a Smooth Taper. *Particle Accelerators*, **56**, 83 (1996).

[2] P. M. Morse and H. Feshbach. *Methods of Theoretical Physics*. McGraw-Hill, Inc., Chapter 7.

[3] G. V. Stupakov. SLAC-PUB-7157, SLAC, 1996.

[4] S. Wolfram. Mathematica: a System for Doing Mathematics by Computer. Addison- Wesley, Redwood City CA, 1991.

[5] K. Yokoya. Impedance of Slowly Tapered Structures. CERN SL/90-88 (AP) (1990).

[6] Zero Design Report for the Next Linear Collider, SLAC-474, SLAC, 1996.

SYNCHROTRON RADIATION WAKE IN FREE SPACE

G. V. Stupakov
Stanford Linear Accelerator Center, Stanford University, Stanford, CA 94309

Abstract

A transverse force acting on particles of a short bunch coherently radiated in free space is derived.

1 INTRODUCTION

In this paper, we derive the transverse radiation force of a bunch of ultrarelativistic charged particles coherently radiating in free space assuming that the bending radius is much larger than the beam dimensions. In contrast to a similar recent study [1], where the authors decompose the total transverse force and find only a part that is responsible for the distortion of the beam orbit, we derive a full expression for the force and leave the issues of the beam dynamics for a separate consideration. Another approach to the calculation of the transverse force has been previously developed in [2].

In many cases considered in this paper, the calculations are extremely cumbersome; they were systematically performed with the use of symbolic engine of the computer program MATHEMATICA [3].

2 POTENTIALS AND FIELDS

Our approach is based on Taylor expansion of the electrostatic potential φ and the vector potential $\mathbf{A}$ in the vicinity of the particle. For a moving point charge, the potentials are given by the Lienard-Wiechert formula [4]

$$\varphi(\mathbf{r},t) = \frac{e}{(R-\boldsymbol{\beta}_{\rm ret}\mathbf{R})}, \quad \mathbf{A}(r,t) = \frac{e\boldsymbol{\beta}_{\rm ret}}{(R-\boldsymbol{\beta}_{\rm ret}\mathbf{R})}, \quad (1)$$

where $\mathbf{r}$ and t refer to the observation point and time, respectively, e is the particle charge, $\beta_{\rm ret}$ is the ratio $\mathbf{v}/c$ evaluated at the retarded time $t_{\rm ret}$, and $\mathbf{R} = \mathbf{r} - \mathbf{r}_{\rm ret}$, where $\mathbf{r}_{\rm ret}$ gives the location of the particle at the retarded time. The retarded time is determined by the equation $R = c(t - t_{\rm ret})$. The particle is considered to be extremely relativistic, so that the parameter $\delta \equiv \gamma^{-2} = 1 - \beta^2 \ll 1$.

We assume that the particle moves along a circular orbit of radius ρ, as shown in Fig. 1. The vector $\mathbf{r}_{\rm p}$ refers to the position of the particle at time t. We introduce the angle α between the vectors $\mathbf{r}_{\rm ret}$ and $\mathbf{r}_{\rm p}$, and the angle ψ between the vector $\mathbf{r}_{\rm p}$ and the projection of the vector $\mathbf{r}$ onto the plane of motion. The causality principle requires that $\alpha > 0$, i.e. the radiation observed at t is emitted by the particle prior to the observation time.

In a polar coordinate system $(r,\ \theta,\ y)$ with the origin located at the center of the orbit, the radius-vector $\mathbf{r}$ of the observation point is represented by $\mathbf{r} = (\rho + x, \theta_p + \psi, y)$, where $\theta_p = c\beta t/\rho$ is the angle corresponding to the position of the particle at time t. In this coordinate system, the equation $R^2 = c^2(t - t_{ret})^2$ which determines the angle α can be written as

$$\frac{\alpha^2}{\beta^2} = 1 + \left(1+\frac{x}{\rho}\right)^2 + \frac{y^2}{\rho^2} - 2\left(1+\frac{x}{\rho}\right)\cos(\psi+\alpha). \quad (2)$$

In terms of α, ψ and x, the denominator in Eq. (1) is

$$R - \boldsymbol{\beta}_{\rm ret}\mathbf{R} = \rho\frac{\alpha}{\beta} - \beta(\rho + x)\sin(\psi+\alpha), \quad (3)$$

and the polar components of the vector potential are

$$A_r = \frac{e\beta\sin(\alpha+\psi)}{R-\boldsymbol{\beta}_{\rm ret}\mathbf{R}}, \quad A_\theta = \frac{e\beta\cos(\alpha+\psi)}{R-\boldsymbol{\beta}_{\rm ret}\mathbf{R}}. \quad (4)$$

We expand the potentials in the Taylor series assuming

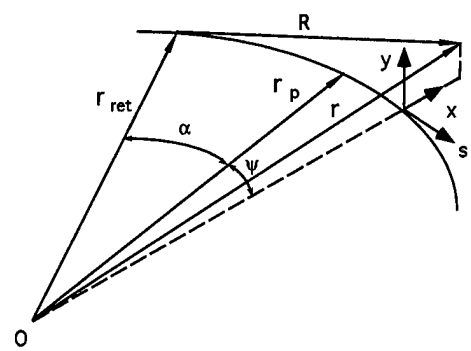

Figure 1: Particle trajectory and coordinate system.

that $\psi \ll 1$ and $x,\ y \ll \rho$. In order to perform Taylor expansions, we need to solve Eq. (2) for α and substitute the solution into Eqs. (3), (1) and (4). For given potentials, the electric field can be found by differentiating φ and $\mathbf{A}$:

$$\mathbf{E} = -\nabla\varphi - \frac{1}{c}\frac{\partial\mathbf{A}}{\partial t} = -\nabla\varphi + \frac{\beta}{\rho}\frac{\partial\mathbf{A}}{\partial\psi}, \quad \mathbf{H} = \mathbf{R}\times\frac{\mathbf{E}}{R}. \quad (5)$$

After finding $\mathbf{E}$ and $\mathbf{H}$, we calculate the Lorentz force $\mathbf{F}$ acting on a test particle located at point $\mathbf{r}$ such that $|\mathbf{r} - \mathbf{r}_{\rm p}| \ll \rho$, and moving with the velocity $\mathbf{v} = c\boldsymbol{\beta}$ along the circle in the same direction as the driving particle, $\boldsymbol{\beta} = (0, \beta, 0)$. Integration of this force with a Gaussian distribution function gives an expression for the radiation force acting on a Gaussian bunch due to the emission of the radiation in free space.

3 DERIVATION OF TRANSVERSE FORCE FOR A POINT CHARGE

For the sake of simplicity, we assume that the test particle trajectory lies in the plane $y = 0$. In addition, we also

0-7803-4376-X/98/$10.00 © 1998 IEEE

neglect the difference between the particle velocity and the speed of light and set $\delta = 0$.

In order to keep track of relative orders of different variables, it is convenient to assign to each variable a formal small parameter ε which will be set to unity in the final result. We choose ordering such that $\alpha \sim \varepsilon$, $\psi \sim \varepsilon^3$, $x/\rho \sim \varepsilon^2$, where ε is a small formal parameter. Expanding Eq. (2) and keeping terms up to fourth order of ε, yields a quartic equation for α,

$$-\frac{\alpha^4}{12} + 2\alpha\psi + \alpha^2\frac{x}{\rho} + \left(\frac{x}{\rho}\right)^2 = 0. \tag{6}$$

The real positive solution α to this equation as a function of ψ and x can be written in terms of a parametric dependence,

$$\alpha = \sqrt{q} f\left(\frac{x}{\rho q}\right), \quad \psi = q^{3/2} g\left(\frac{x}{\rho q}\right), \tag{7}$$

where q is a positive parameter varying from 0 to ∞, and the functions $f(\xi)$ and $g(\xi)$ are

$$\begin{aligned} f(\xi) &= \pm 1 + \left(-1 + 6\xi + 2\sqrt{1 - 6\xi + 12\xi^2}\right)^{1/2}, \\ g(\xi) &= \pm\frac{1}{3}\sqrt{1 - 6\xi + 12\xi^2}. \end{aligned} \tag{8}$$

The upper and lower signs in Eq. (8) correspond to the positive and negative values of ψ respectively. From Eq. (7) it follows that the product $\alpha\,|\rho/x|^{1/2}$ depends on the variable $\psi\,|\rho/x|^{3/2}$ only. In the limit $\psi \gg (x/\rho)^{3/2}$, approximately $\alpha \approx 2(3\psi)^{1/3}$. For large negative values of ψ, $|\psi| \gg (x/\rho)^{3/2}$, we find $\alpha \approx -x^2/2\psi\rho^2$. However, as a detailed analysis shows, the applicability of Eqs. (7) for negative ψ is limited by the condition $|x| \gg |\psi|$. Larger absolute values of (negative) ψ are considered below.

An important feature of our solution which follows from Eqs. (7) and (8) is that for each positive value of x the derivative of the function $\partial\alpha/\partial\psi$ becomes infinite at some point $\psi = \psi_0$. A simple calculation yields for ψ_0,

$$\psi_0 = -\frac{1}{3}\left(2\frac{x}{\rho}\right)^{3/2}, \quad \alpha(\psi_0, x) = \sqrt{2x}. \tag{9}$$

When x varies from 0 to ∞, the first of the equations (9) determines a curve in the $(x,\ \psi)$ plane which we will call a *singular line*, because both potentials and the fields will have a singularity here. It is important to emphasize that the singularity occurs only because we assume $\delta = 0$; for finite, though small δ, the fields would be limited everywhere as soon as $x \neq 0$. Note also that the parameter q on the singular line equals $2x$.

The origin of the singular line can be understood from the following geometrical consideration. If we draw wavefronts of the radiation emitted at different times by a particle moving with the speed of light around a circle, they will form a pattern shown schematically in Fig. 2. The wavefronts are condensed on the outer side of the circle forming a caustic which, as one can show, coincides with

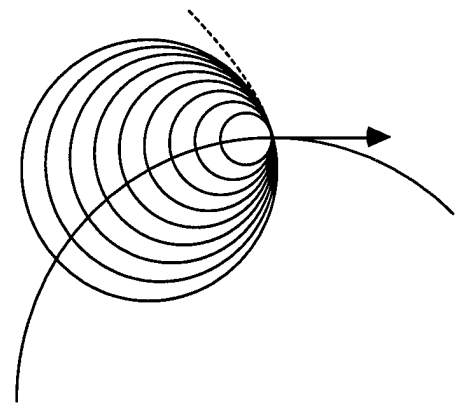

Figure 2: Formation of a singular line (dashed curve) due to radiation of ultrarelativistic particle moving around a circle. The circles show wavefronts emitted by the particle at different times.

the singular line found above and shown in Fig. 2 by the dashed curve. The superposition of multiple wavefronts on the caustic in the limit $v = c$ gives rise to the infinitely large fields on the singular line.

Expanding Eqs. (3) and (1) we find for the potential φ

$$\varphi = \frac{e}{\rho}\left(\frac{\alpha^3}{6} - \psi - \alpha\frac{x}{\rho}\right)^{-1}, \tag{10}$$

and for the components of the vector potential

$$\begin{aligned} A_r &= \frac{e}{\rho}\alpha\left(\frac{\alpha^3}{6} - \psi - \alpha\frac{x}{\rho}\right)^{-1}, \\ A_\theta &= \frac{e}{\rho}\left(1 - \frac{\alpha^2}{2}\right)\left(\frac{\alpha^3}{6} - \psi - \alpha\frac{x}{\rho}\right)^{-1}. \end{aligned} \tag{11}$$

The longitudinal electric field can be calculated using the formula

$$E_\theta = \frac{1}{\rho}\frac{\partial A_\theta}{\partial\psi} - \frac{1}{(\rho + x)}\frac{\partial\varphi}{\partial\psi} \approx \frac{x}{\rho^2}\frac{\partial\varphi}{\partial\psi} - \frac{1}{\rho}\frac{\partial(\varphi - A_\theta)}{\partial\psi}, \tag{12}$$

and for the transverse electric field we have

$$E_r = -\frac{\partial\varphi}{\partial x} + \frac{1}{\rho}\frac{\partial A_r}{\partial\psi}. \tag{13}$$

For the radial component of the transverse force we have

$$\begin{aligned} F_r &= E_r + (\boldsymbol{\beta} \times \mathbf{H})_r \\ &= E_r\left(1 - \beta\cos\left(\frac{\alpha + \psi}{2}\right)\right) + \frac{1}{2}E_\theta \sin\left(\frac{\alpha + \psi}{2}\right) \\ &\approx \frac{1}{8}\left(\alpha + \frac{2x}{\rho\alpha}\right)^2 E_r + \frac{1}{2}\left(\alpha + \frac{2x}{\rho\alpha}\right)E_\theta. \end{aligned} \tag{14}$$

After some algebra F_r can be written as

$$F_r = \frac{e}{\rho^2}\,|\rho/x|^{3/2}\,G\left(\psi\,|x/\rho|^{3/2}\right), \tag{15}$$

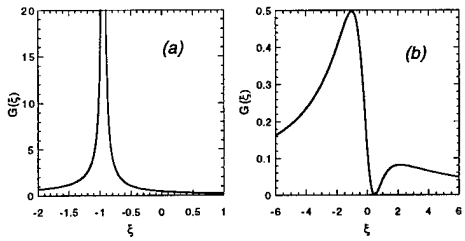

Figure 3: Function $G(\xi)$ for positive (a) and negative (b) values of x. For positive x, this function has a singularity at $\xi = -2^{3/2}/3 = -0.94$.

where the function G is different for positive and negative x. Plots of the function $G(\xi)$ are shown in Fig. 3. It is easy to check that the denominator in Eqs. (10) and (11) vanishes on the singular line and causes the potentials to diverge. Expansions of φ and A for small values of $|\psi - \psi_0|$ give the following singularity for F_r in the vicinity of the singular line:

$$F_r \approx \frac{e}{\rho^2} \frac{2^{1/6} x^{1/2}}{3^{4/3} (\psi - \psi_0)^{4/3}}. \tag{16}$$

To find the fields behind the particle ($\psi < 0$) we use the following ordering: $\alpha \sim \psi \sim x \sim \varepsilon$. Expansion of Eq. (2) up to the second order yields $2\alpha\psi + \psi^2 + x^2 = 0$ with the solution $\alpha = -\left[\psi^2 + (x/\rho)^2\right]/(2\psi)$. This solution leads to the following expressions for the potentials:

$$\begin{aligned} \varphi &= -\frac{e}{\rho\psi}, \quad A_r = -\frac{e}{\rho\psi}\left(\frac{\psi}{2} - \frac{x^2}{2\psi\rho^2}\right), \\ A_\theta &= -\frac{e}{\rho\psi}\left(1 - \frac{\psi^2}{8} + \frac{x^2}{4\rho^2} - \frac{x^4}{8\psi^2\rho^4}\right), \end{aligned} \tag{17}$$

and for the longitudinal and radial electric fields

$$E_\theta = \frac{e}{\rho^2}\left(\frac{x}{\rho^2\psi^2} + \frac{1}{8}\right), \; E_r = -\frac{e}{2\rho^2\psi}\left(1 - \frac{x^2}{\psi^2\rho^2}\right). \tag{18}$$

For the transverse force we find

$$F_r = -\frac{e}{\rho^2} \frac{x^2\left(x^2 + 3\rho^2\psi^2\right)}{\psi\left(x^2 + \rho^2\psi^2\right)^2}. \tag{19}$$

Examination of Eqs. (18) and (19) reveals that the electric field and the force F_r tend to infinity when $\psi \to 0$. These equations, however, are only valid if $|\psi| \gg (|x|/\rho)^{3/2}$; in the opposite limit Eq. (15) should be used.

Note also that immediately behind the particle on the orbit ($x = 0$) the longitudinal electric field is equal to $e/8\rho^2$.

We now want to calculate the transverse force f_r acting on a particle of unit charge in a bunch with a two-dimensional distribution function $g(x, s)$ normalized so that $\int g(x,s)dxds = 1$. Here we use the longitudinal coordinate s related to ψ by $s = \rho\psi$. By definition,

$$f_r(x', s') = N \int_{-\infty}^{\infty} dxdsg(x' - x, s' - \rho\psi) F_r(x, \psi) \tag{20}$$

The integration in Eq. (20) is not a simple task for two reasons. First, F_r has a peak in the region of small ψ, $|\psi| \sim (|x|/\rho)^{3/2}$, and one needs to accurately evaluate the contribution from this peak. Second, for positive x, the integrand exhibits a singularity (see Eq. (16)) which should be handled with caution. Tracing the origin of this singularity shows that it arises from the differentiation of the potentials which have an integrable singularity $\sim |\psi - \psi_0|^{-1/3}$. This prompts the technique that allows to evaluate the integral: representing F_r in terms of potentials and performing integration by parts over s. The resulting integral converges at $\psi = \psi_0$ and can be found with the help of numerical integration. This program is accomplished in Ref. [5]. To simplify the analysis we assume that the bunch length σ_s is such that

$$\sigma_s \gg \sigma_x \tag{21}$$

The result of the integration in Eq. (20) is

$$\begin{aligned} f_r(x', s') = -N\frac{e}{\rho}\Bigg[& 2\int_{-\infty}^{\infty} dxg(x' - x, s') \ln\left(1.1\frac{|x|}{\rho}\right) \\ & + \frac{1}{3}\int_{-\infty}^{\infty} dx \int_0^{\infty} ds \frac{\partial g(x' - x, s' - s)}{\partial s} \ln\left(\frac{s}{\rho}\right)\Bigg]. \end{aligned} \tag{22}$$

Note that for a two-dimensional Gaussian distribution,

$$g(x, s) = \frac{1}{2\pi\sigma_x\sigma_s} \exp\left(-\frac{x^2}{2\sigma_x^2} - \frac{s^2}{2\sigma_s^2}\right), \tag{23}$$

the second term in Eq. (22) reduces to a product of two one-dimensional integrals, and the force will be represented as a product of two functions one of which depends on s and the other depends on x only.

For illustration, we assume that $\sigma_x/\sigma_s = 0.1$ and $\sigma_s/\rho = 10^{-4}$, and calculate the force on the beam trajectory $x' = 0$. It turns out that, in this case, the first term in Eq. (22) dominates and $f_r(0, s)$ can be well approximated by a Gaussian:

$$f_r(x, s) = 8.4\frac{Ne}{\rho\sigma_s} \exp\left(-\frac{s^2}{2\sigma_s^2}\right). \tag{24}$$

4 ACKNOWLEDGMENTS

I would like to thank Ya. Derbenev and T. Raubenheimer for useful discussions. This work was supported by Department of Energy contract DE-AC03-76SF00515

5 REFERENCES

[1] Ya.S. Derbenev and V.D. Shiltsev. Preprint SLAC-PUB-7181, 1996.

[2] B.E. Carlsten and T.O. Raubenheimer. Phys. Rev. E, 51, 1453 (1995).

[3] S. Wolfram. Mathematica: A System for Doing Mathematics by Computer. Addison-Wesley, Redwood City, 1991.

[4] J.D. Jackson. Classical Electrodynamics. Wiley, New York, 1975.

[5] G. V. Stupakov, to be published.

EFFECTS OF THE LANDAU CAVITY ON THE ELECTRON BEAM

L.H. Chang, Ch. Wang, W.K. Lau, C.C. Kuo
Synchrotron Radiation Research Center, Hsinchu, Taiwan

Abstract

This paper presents the procedure and the formulas to analyze the effects of Landau cavity on the electron beam while the main RF system is operated on the compensated condition. It is shown that the maximal available current, determined by the phase instability limit, is reduced with Landau cavity. The model of " potential energy " [1] is used for the calculations of the bunch length and the synchrotron frequency of the storage ring with double RF system. It is shown that the bunch length can be manipulated by tuning the resonance frequency of the passive Landau cavity, and the spread of synchrotron frequency can be induced by the addition of a Landau cavity.

1 INTRODUCTION

The beam life-time is always the concern of synchrotron radiation users. Especially for the third generation storage ring , it is operated with low beam emittance and short bunch length. The Touschek scattering is usually a limit of the beam life-time for the low energy machine. It can be improved either by increasing the energy acceptance or by decreasing the charge density of a bunched beam. The Landau cavity is one of the solutions to decrease the charge density by increasing the bunch length.

The Landau cavity can be operated either in active mode or in passive mode. In active mode, the gap voltage and the RF phase are adjusted to manipulate the slop of the accelerating voltage, which affects the bunch length. The optimized conditions for bunch lengthening and the beam dynamic theory were discussed by Hofmann and S. Myers in 1980 [2]. In passive mode, the bunch length is current dependent, and is manipulated by adjustment of the tuning angle of the Landau cavity. The implementation of the Landau cavity enhances the phase instability [3], which reduces the maximal available beam current. Moreover, the RF power generated by beam current may be enough to cause the damage of the passive Landau cavity. It is important to estimate these effects in the design of the harmonic Landau cavity.

2 PHASE INSTABILITY LIMIT

In a double RF system composed of a main RF system with accelerating frequency ω_{RF} and a nth harmonic RF system, The total RF voltage V_T seen by the electron with time displacement τ can be written as

$$V_T(\tau) = V_M \cos(\phi_M + \omega_{RF}\tau) + V_L \cos(\phi_L + n\omega_{RF}\tau) \quad (1)$$

where V_M and ϕ_M are the total gap voltage and synchronous phase of the main RF system; V_L and ϕ_L are the total gap voltage and synchronous phase of the harmonic RF system. The accelerating voltage $V_T(0)$ is equal to the voltage for compensating the energy loss of the synchronous electron. Notice that the time displacement τ is defined to be positive if the electron lags behind the synchronous electron. In this paper, the subscript L, M represent the quantities related to the system of the harmonic Landau cavity and main RF system, respectively.

V_M in (1) is combined with the induced voltage V_b and the generated voltage V_g [4]. The relations between them can be expressed as

$$V_M \cos(\phi_M) = -V_b \cos(\psi) + V_g \cos(\phi_g) \quad (2)$$

where ϕ_g is the phase of generated voltage with reference to the synchronous electron, ψ is the tuning angle of the main RF cavity. Without beam current in cavity, ψ is equal to the tuning angle offset ψ_0, which is defined as

$$\tan(\psi_0) = 2Q_l \frac{\omega_r - \omega_{RF}}{\omega_r} \quad (3)$$

where Q_l is the loaded quality factor, ω_r is the resonance frequency of the cavity. By this definition, the positive tuning angle means that the resonance frequency ω_r is higher than the frequency of the electromagnetic field of the mode, ω_{RF}. Similarly, if the Landau cavity is operated in active mode, V_L can be expressed as

$$V_L \cos(\phi_L) = -V_{bL} \cos(\psi_L) + V_{gL} \cos(\phi_{gL}) \quad (4)$$

If the Landau cavity is operated in passive mode, ψ_L is not dependent on the beam current, and V_L is derived only from the induced voltage. Equation (4) needs to be modified as

$$V_L \cos(\phi_L) = -V_{bL} \cos(\psi_L) \quad (5)$$

where $\phi_L = \psi_L$. In (2), ψ is varied with the beam loading effect. The variation ψ_b is dependent on the operating condition. For our main RF system the feedback control always keeps the amplitude of V_M and the relative phase between V_M and V_{gr} constant. V_{gr} is the generated voltage at resonance frequency. On this condition, ψ_b can be obtained by the equation below [5].

$$\psi_b = -\tan^{-1}\left(\frac{V_{br}\sin(\phi_M - \psi_0)}{V_M/\cos(\psi_0) - \tan(\psi_0)V_{br}\sin(\phi_M - \psi_0)}\right) \quad (6)$$

where V_{br} is the induced voltage at the resonance frequency. With beam current in the cavity, ψ becomes

$$\psi = \psi_0 + \psi_b \quad (7)$$

The phase of V_g with reference to the synchronous electron becomes

$$\phi_g = \phi_M + \psi_b \quad (8)$$

0-7803-4376-X/98/$10.00 © 1998 IEEE

If we consider the main RF system with the couple coefficient β and ψ in (7) which are optimized for minimizing the reflected RF power from the cavity, the compensated condition [5]. And the bunch length is short enough to be ignored, in comparison with the cavity size. With these conditions, we can obtain V_{br} and V_b as follows:

$$V_{br} = 2I_a R_s \tag{9}$$

$$V_b = V_{br}\cos(\psi) \tag{10}$$

where R_s is the shunt impedance of the cavity, I_a is the average beam current. ϕ_g is decreasing with the increase of the beam current. As ϕ_g becomes zero, the phase is at the stability limit [4]. In passive Landau cavity, the interaction between the beam current and the RF field is stronger as ψ_L is getting close to zero. As shown in Fig. 1, the maximal available beam current is reduced from 512 mA to 153 mA as ψ_L is tuned from 90° to 0°. From the energy conservation law, we can obtain the RF power for the cavity to keep V_M constant

$$P_M = \frac{V_M^2}{2.0 \cdot R_s} + V_M \cdot \cos(\phi_M) \cdot I_a \tag{11}$$

The discussion above for the main RF system are still valid with the Landau cavity operated in active mode.

For the Landau cavity operated in passive mode, V_{brL} is given by

$$V_{brL} = \frac{2I_a R_{sL}}{1+\beta_L} \tag{12}$$

and the power loading of the Landau cavity is given by

$$P_L = \frac{[V_{brL} \cdot \cos(\psi_L)]^2}{2.0 \cdot R_{sL}} \tag{13}$$

P_L in equation (13) is dependent on the beam current and ψ_L. For the case in Fig. 2, P_L is obtained at the phase instability limit. The maximal P_L, at $\psi_L = 0$, is beyond 50 kW.

3 BUNCH LENGTH

If we neglect the radiation damping term, the time deviation in synchrotron oscillation can be described by the equation

$$\frac{d^2\tau}{dt^2} = \frac{\alpha}{E_0 T_0} \cdot \{e \cdot V_T(\tau) - U_0\} \tag{14}$$

where U_0 is the radiation loss of the electron with nominal energy in one revolution, E_0 is the nominal energy, T_0 is the revolution time, α is the momentum compaction. We define α as

$$\frac{d\tau}{dt} = \alpha\frac{\epsilon}{E_0} \tag{15}$$

where ϵ is the energy deviation from the nominal energy. Eq. (14) is similar to the equation of motion under the

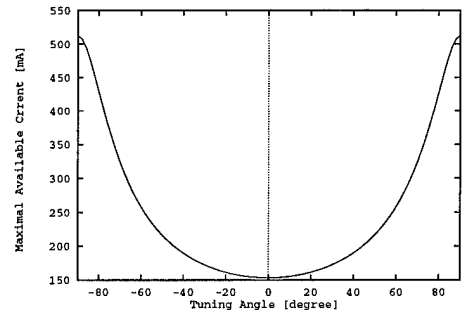

Figure 1: The beam current at phase instability limit versus the tuning angle of the passive Landau cavity. The machine parameters are listed as follows: nominal energy is 1.5 GeV, harmonic number of Landau cavity is 3.0, number of main cavities is 3, energy spread is 6.6×10^{-4}, accelerating frequency is 500 MHz, $R_s = 3.0M\Omega$, $R_{sL} = 1.2M\Omega$, $\alpha = 6.78\times10^{-3}$, $V_T = 157kV$, $V_M = 1200kV$.

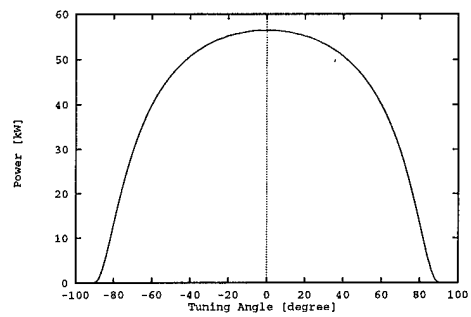

Figure 2: The power loading of the Landau cavity with maximal available beam current (at the phase stability limit). The machine parameters are the same as in Fig. 1.

conservative force ($d^2\tau/dt^2$). The " potential energy " can be obtained by integrating the "force" [Eq. (14)].

$$\phi(\tau) = -\frac{\alpha}{E_0 T_0}\int_0^{\tau}\{e \cdot V_T(t) - U_0\}dt \tag{16}$$

For the electron with peak energy deviation $\hat{\epsilon}$, the maximal potential energy, which is equal to the maximal kinetic energy $[1/2(d\tau/dt)^2]$, can be obtained from Eq. (15)

$$\hat{\phi} = \frac{1}{2}(\alpha\frac{\hat{\epsilon}}{E_0})^2 \tag{17}$$

The maximal time displacement is at the point where the potential energy is maximal.

$$\phi(\tau_p) = \phi(\tau_n) = \hat{\phi} \tag{18}$$

where τ_p (τ_n) is the maximal time displacement behind (ahead) the synchronous phase. The bunch length of the electrons with peak energy deviation $\hat{\epsilon}$ is then given by

$$\sigma_l(\hat{\epsilon}) = c \cdot (\tau_p - \tau_n) \tag{19}$$

where c is the velocity of the photon. For an electron beam with Gaussian spread in energy deviation, we may express the normalized electron density as

$$n(\hat{\epsilon}) = \sqrt{\frac{2}{\pi}} \cdot \epsilon_{rms} \cdot exp(-\hat{\epsilon}^2/2\epsilon_{rmx}^2) \qquad (20)$$

where ϵ_{rms} is the root-mean-square deviation of energy. The root-mean-square bunch length is given by

$$\sigma_{rms} = \sqrt{\int n(\hat{\epsilon})\sigma_l(\hat{\epsilon})^2 d\hat{\epsilon}} \qquad (21)$$

For the machine with a Landau cavity operated in passive mode, ψ_L is the parameter that we can use to manipulate the bunch length.

As shown in Fig. 3, the bunch is lengthened with the larger beam current if ψ_L is positive. In this case, the bunch is lengthened more than 70% with the beam current at 200 mA. But the power loading is beyond 45 kW (see Fig. 2).

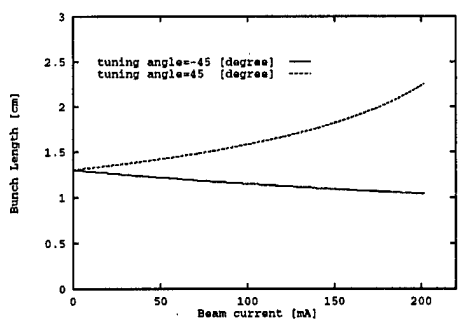

Figure 3: The bunch length versus the beam current for two different tuning angles. The parameters are the same as in Fig. 1.

4 SYNCHROTRON FREQUENCY

From energy conservation law, the " velocity" $(d\tau/dt)$ is given by

$$\frac{d\tau}{dt} = \sqrt{2}[\hat{\phi} - \phi(\tau)]^{1/2} \qquad (22)$$

From Eq.(22), we can obtain the time period of synchrotron oscillation.

$$t_\nu = 2.0 \int_{\tau_n}^{\tau_p} \frac{1.0}{\sqrt{2}[\hat{\phi} - \phi(\tau)]^{1/2}} d\tau \qquad (23)$$

The synchrotron frequency is obtained from the inverse of t_ν

$$f_\nu = \frac{1}{t_\nu} \qquad (24)$$

Fig. 4 shows that the shift of synchrotron frequency, introduced by the addition of a Landau cavity, is dependent on the peak energy deviation. It results in a synchrotron tune spread for a bunched beam, which will enhance the Landau damping against longitudinal coupled bunch instability.

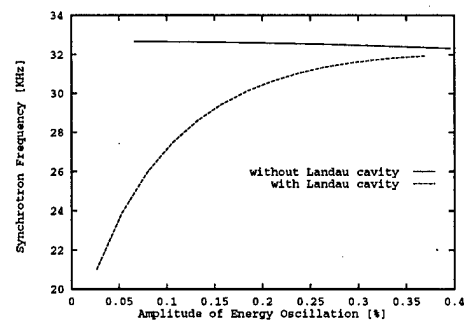

Figure 4: The synchrotron frequency versus the peak energy deviation. $I_a = 180mA$, $\psi_L = 45°$, and the other parameters are the same as in Fig. 1.

5 DISCUSSION

The Landau cavity proposes an approach to lengthen the bunch, and enhances the Landau damping against the longitudinal coupled bunch instability. But it also causes unwanted effects, such as the reduction of the available beam current. V_b in (10) is obtained assuming that the RF system is operated on the compensated condition. In reality, the compensated condition can be met only at a certain beam current. In our machine, the couple coefficient of the main RF cavity is 1.2. It means that without beam current, the ratio between the reflection power and the power loss in the cavity is about 0.84 %. With this mismatch, the error for V_b in (10) is about 1 % when beam current is very small. If the couple coefficient is getting larger, a further study is necessary. Moreover in passive mode, if R_{sL} is large enough and the beam current is above some threshold value, the "potential energy " may be deformed to two valleys. In such case, Eq.(19) is invalid for the bunch length calculation.

6 REFERENCES

[1] Matthew Sands "The Physics of Electron Storage Rings –An Introduction," SLAC-121, pp. 90-95.

[2] A. Hofmann and S. Myers "Beam Dynamics In A double RF System," International Conference on High Energy Accelerators –CERN 1980, pp. 610–614.

[3] Y. Miyahara, etc. " Equilibrium Phase Instability in the Double RF System for Landau Damping," Nuclear Instruments and Methods in Physics Research, 1987, PP. 518–528.

[4] Perry B. Wilson " High Energy Electron Linacs: Application to Storage Ring RF Systems and Linear Colliders," SLAC–PUB–284, 1982, pp. 20–24.

[5] Matthew Sands " Beam Cavity Interaction - I," technical report number 2 - 67 from LAL, Orsay, France, 1976, pp. 26-30.

BEAM BREAKUP IN A MICROTRON*

Byung C. Yunn and Lia Merminga
Thomas Jefferson National Accelerator Facility
12000 Jefferson Avenue, Newport News, VA 23606, USA

Abstract

In a microtron, the path length change from pass to pass is a fixed multiple of the RF wavelength, and the accelerating system can be reasonably well approximated as a single cavity. Under such circumstances it is possible to derive an analytical formula for the multipass beam breakup threshold current. The threshold current determined by numerical simulations agrees very well with the formula for a machine with a small number of passes. The analytic formula can serve as a useful guide in examining optics designs to improve the BBU threshold.

1 INTRODUCTION

Multipass beam breakup (BBU) is an important performance-limiting factor in microtrons. Extensive computer simulations are generally unavoidable to determine BBU thresholds since the tens of recirculations involved make analysis very difficult. When the betatron phase advance through the accelerating cavities is small, a good approximation is to replace the whole accelerating system by a single cavity. Furthermore, the total kick received passing through the cavity can be treated as if received by a point kick located at the middle of the cavity in describing beam motion. The resulting simplification allows an analytic treatment of the multipass BBU phenomenon without losing too much information.

We have developed an analytic formula for the BBU threshold current in this single cavity approximation. A benchmarking of the formula using a 25-pass racetrack microtron as an example has shown its potential as a design tool. Time-consuming computer simulations could be minimized at the early stage of design.

2 A MODEL OF BBU

We start by defining our model of BBU in a microtron under the assumption that a single cavity approximation can be made. For the convenience of readers, we will closely follow the notations of references [1] and [2], which represent previous study of an analytical model of multipass BBU in recirculating linacs.

Consider a bunch(say, the Nth one) entering a cavity at its pth pass through the linac with its motion represented by a two component column matrix, $U_p(N)$ of x and p_x. While traversing the cavity, the bunch will get a momentum kick due to transverse wakes excited in the cavity by preceding bunches in addition to gaining nominal energy. The bunch then recirculates and enters the cavity for the $(p+1)$th time. A dipole mode of frequency ω with a quality factor Q is assumed to be generated at the cavity for the following discussions. The equation of transverse bunch motion described in this physical picture is

$$U_{p+1}(N) = T^{p+1,p}U_p(N) + IT^{p+1,p}G\sum_{q=1}^{n_p}\sum_{M=1}^{N+S(p,q)} U_q(L)s^{pq}_{NM}(\omega,\tau)\,, \quad (1)$$

where

$$s^{pq}_{NM}(\omega,\tau) = (\frac{e}{2})\tau_{rf}(\frac{\omega}{c})^2 L(\frac{R_\perp}{Q})e^{-\frac{\omega}{2Q}((N-M)\tau+\tau_p-\tau_q)} \times \sin\omega((N-M)\tau+\tau_p-\tau_q),$$

and

$$S(p,q) = \begin{cases} \text{int.}(\frac{\tau_p-\tau_q}{\tau}), & \text{if } p \geq q \\ \text{int.}(\frac{\tau_p-\tau_q}{\tau})-1, & \text{otherwise} \end{cases}.$$

$T^{p,q}$ is the transfer matrix from the cavity at the qth pass to the cavity at the pth pass. I is the average current and G is a 2×2 matrix with all elements equal to zero except $G_{21}=1$. n_p is the number of passes and $R_\perp$ is the transverse shunt impedance per unit length of the higher order mode ω excited in the cavity, which is assumed to have an effective length of L. We also note that $R_\perp$ is related to other commonly used transverse shunt impedance Z'' as $R_\perp = \frac{c^2 Z''}{\omega^2}$. τ_p is the summation over recirculation times up to the pth pass, and $\tau_1 = 0$. In general, τ_p has to be an integer multiple of the RF period, τ_{rf}, if recirculations are all in the same direction. However, it is not necessary to be an integer multiple of the bunch spacing τ, when the beam is subharmonically bunched.

3 THRESHOLD CURRENT

As noted in [2], we must deal with an (n_p-1)-dimensional eigenvalue problem for the threshold current for multipass BBU in the most general circumstances even for a single cavity case. Deferring an analysis of general subharmonic bunching schemes until a later time, we restrict our attention to the case when every bucket of the accelerating mode of the cavity (i.e. $\tau = \tau_{rf}$) is filled. The model simplifies significantly in this situation and the eigenvalue problem reduces to

$$\frac{1}{I} = (\frac{e}{2})\tau(\frac{\omega}{c})^2 L(\frac{R_\perp}{Q})h(\Omega)\sum_{p=2}^{n_p}\sum_{q=1}^{p-1} T^{p,q}_{12}e^{-i\Omega(\tau_p-\tau_q)}, \quad (2)$$

*This work was supported by the U.S. Department of Energy, under contract No. DE-AC05-84ER40150.

where

$$h(\Omega) = \frac{H(\Omega)\sin\omega\tau}{1 + H^2(\Omega) - 2H(\Omega)\cos\omega\tau},$$

and

$$H(\Omega) = e^{-\frac{\omega\tau}{2Q}} e^{-i\Omega\tau}.$$

This still is a complicated nonlinear equation for Ω which requires a numerical approach to solution in general. Note that the imaginary part of Ω changes sign from plus to minus as we cross threshold current. Solving Eq.(2) to first order in current, we find the following expression for the BBU threshold current:

$$I_{\text{th}} = -\frac{2c^2}{e\omega L R_\perp M}, \tag{3}$$

where M is

$$M = \sum_{p=2}^{n_p} \sum_{q=1}^{p-1} T_{12}^{p,q} e^{\frac{\omega}{2Q}(\tau_p - \tau_q)} \sin\omega(\tau_p - \tau_q).$$

This is our central result. The important parameters determining the BBU threshold current are clearly spelled out.

4 APPLICATIONS

We have selected a 25-pass microtron essentially identical to the NIST RTM (racetrack microtron)[3] as our example to test the validity of Eq.(3) and have performed extensive simulations of the microtron BBU problem using the computer code TDBBU[4] developed at Jefferson Lab originally for the 5-pass nuclear physics CEBAF accelerator. Figure 1 summarizes results of a TDBBU threshold current scan of the microtron when limited to 1 to 3 recirculations. The parameters for simulation and analytic study are:

Injection Energy = 5 MeV

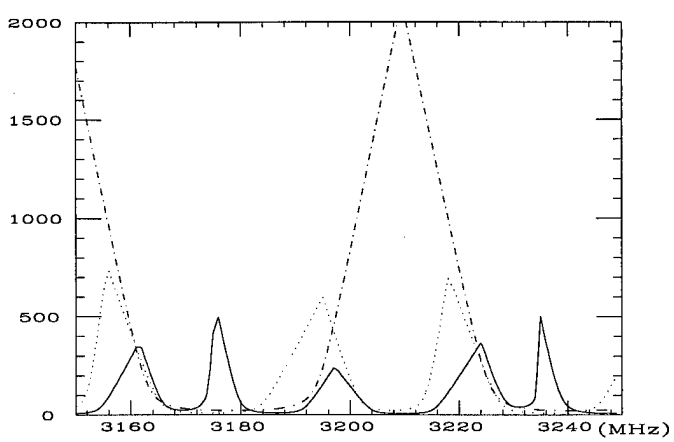

Figure 1: TDBBU scan of threshold current (mA) vs. HOM frequency (MHz). The dot-dashed line is for a two-pass machine, the dotted line for a 3-pass, and the solid line is for a 4-pass system.

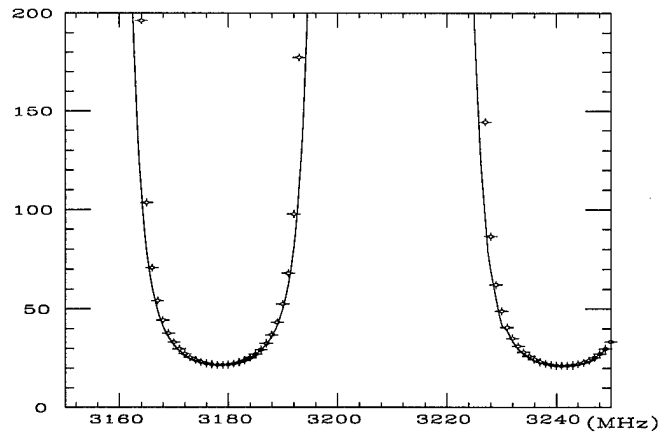

Figure 2: I_{th}(mA) vs. HOM frequency (MHz): Comparison of simulation results with I_{th} predicted with Eq.(4) for a 2-pass system.

Energy Gain per pass = 1.404 MeV
τ^{-1} = 2380 MHz
$(\frac{R_\perp}{Q})L = 250\ \Omega$
$\tau_2 = 38\tau$

and each subsequent path length is increased by one RF wavelength per pass. The HOM frequency is allowed to vary between 3150 MHz and 3250 MHz and Q of the mode is set to 10000.

Let us start with a 2-pass system. Since $n_p = 2$, we get

$$I_{\text{th}} = -\frac{2c^2}{e\omega L R_\perp T_{12}^{2,1} e^{\frac{\omega\tau_2}{2Q}} \sin\omega\tau_2}. \tag{4}$$

This is a threshold formula studied in detail by Sereno[5]. Clearly, the '12' element of transfer matrix and phase advance are the two most important parameters in designing a system like this as far as the BBU threshold is concerned. Regions of high threshold correspond to regions where $\sin\omega\tau_2$ term is positive. I_{th} is infinity at least in the first order approximation we make. As one can see from Figure 1, it is finite even though very high. We have compared I_{th} given by Eq.(4) with the TDBBU scan (dot-dashed line of Figure 1) in Figure 2. The minimal threshold current of this 2-pass machine is 21 mA.

For a 3-pass system, I_{th} is obtained from Eq.(3) with M replaced by

$$M = T_{12}^{2,1} e^{\frac{\omega\tau_2}{2Q}} \sin\omega\tau_2 + T_{12}^{3,1} e^{\frac{\omega\tau_3}{2Q}} \sin\omega\tau_3 + T_{12}^{3,2} e^{\frac{\omega}{2Q}(\tau_3 - \tau_2)} \sin\omega(\tau_3 - \tau_2). \tag{5}$$

Noting that $\tau_3 = 77\tau$ we find that the 38th, 39th and 77th subharmonics of the fundamental accelerating frequency appear in Eq.(5). As a result, the pattern of threshold current scan should be quasi-periodic with a period of approximately 62 ($\simeq \frac{2380}{38.5}$) MHz with two minima in the period. The minimum at 3175 MHz is due to all $T^{i,j}$ terms contributing coherently to their maximum values at the frequency. The second minima occurs when phase terms are such that $T^{3,1}$ and $T^{3,2}$ terms are maximally

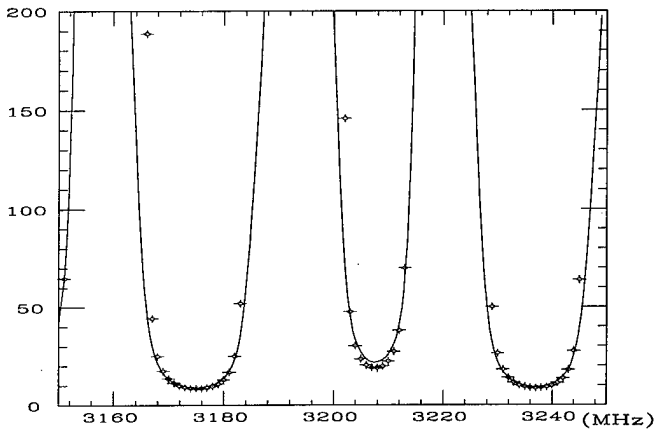

Figure 3: I_{th}(mA) vs. HOM frequency (MHz): Comparison of simulation results with I_{th} predicted with Eq.(5) for a 3-pass system.

adding with the $T^{2,1}$ term being 180 deg apart in phase. We also notice that the graph is truly periodic with the period of 2380 MHz, if the small perturbation in amplitudes due to exponential terms is neglected. We have compared analytic I_{th} with the TDBBU scan(dotted line of Figure 1) in Figure 3. The agreement is excellent and the lowest threshold current we found is 9 mA in this 3-pass operation.

The expression for the I_{th} of a 4-pass system is already too long to fit on one line. It involves 6 interpass transfer matrices $T^{2,1}, T^{3,1}, T^{3,2}, T^{4,1}, T^{4,2}$, and $T^{4,3}$ with associated sinusoidal terms resulting in a characteristic 3 minima threshold current pattern. This arises as a result of superposing terms which contain roughly 3 frequencies, the 39th, 78th and 117th subharmonics of 2380 MHz. Comparison of the TDBBU scan(solid line of Figure 1) with the analytically obtained I_{th} exhibits a good agreement as shown in Figure 4. The lowest threshold current is 6.4 mA, occurring at the HOM frequency of 3210 MHz.

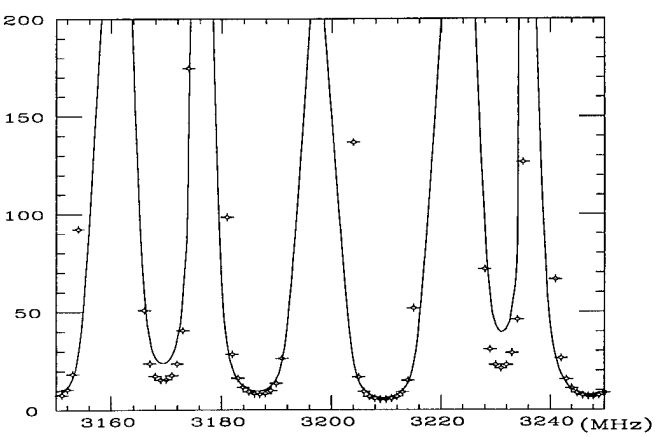

Figure 4: I_{th}(mA) vs. HOM frequency (MHz): Comparison of simulation results with analytic prediction of I_{th} for a 4-pass system.

Finally, in Figure 5 drawn in solid line we present a TDBBU scan for a of 25-pass microtron. The threshold current calculated from Eq.(3) is also plotted. It is encouraging to find that regions of low threshold current are accurately predicted.

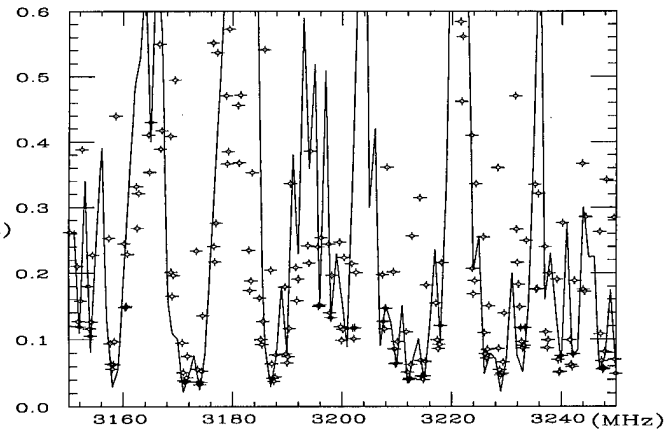

Figure 5: I_{th}(mA) vs. HOM frequency (MHz): Comparison of simulation results with I_{th} predicted with Eq.(3) for a 25-pass microtron.

5 CONCLUSION

The agreement between the approximate expression Eq.(3) and simulation is quite satisfactory even for a 25-pass machine which involves superposition and interference of 300 distinct frequencies and recirculation matrices. Our analytic formula is able to pinpoint regions of HOM frequency where one should look to find lower threshold current. Furthermore, it provides a qualitative understanding of the characteristic pattern of valleys and peaks in the threshold current scan of a typical multipass machine.

The analytic formula for BBU threshold current presented here in Eq.(3) makes various parameter interrelations clear and should serve as a useful guide in designing microtrons.

6 ACKNOWLEDGEMENTS

We are grateful to J. J. Bisognano and S. Corneliussen for reading the paper.

7 REFERENCES

[1] J. J. Bisognano and R. L. Gluckstern, *Proc. 1987 Particle Accelerator Conf.*, 1078 (1987).

[2] B. C. Yunn, *Proc. 1991 Particle Accelerator Conf.*, 1785 (1991).

[3] S. Penner *et al.*, *IEEE Transactions on Nuclear Science*, 2269 (1985).

[4] G. A. Krafft *et al.*, "Calculating Beam Breakup in Superconducting Linear Accelerators", CEBAF Publication (1991).

[5] N. Sereno, Ph.D. Dissertation, Univ. of Illinois, (1994).

BEAM LOADING OPTIMIZED FILLING PATTERNS FOR PARTIALLY FILLED STORAGE RINGS

S.A. Bogacz, Center for Advanced Accelerators, Physics Department, UCLA, 405 Hilgard Avenue, Los Angeles, CA 900095-1547

Abstract

A method of selecting a favorable, with respect of the beam loading effects, multi-bunch (M bunches) filling pattern for a partially filled ring (harmonic number N) is presented. Starting with a standard set of wake field-coupled equations of motion, the beam loading effects (higher order mode loss) are evaluated analytically (using contour integration technique) for a partially filled ring (M < N). Resulting analytic formula describe the mode loss experienced by a given bunch within a train, as a function of the resonant frequency and the quality factor of the coupling impedance, Q. The analytic formula reveals filling pattern dependent resonant frequency regions, where the beam loading effects are highly suppressed. A possible application of the presented formalism is that for a given configuration of cavity resonances one can design the optimum bunch filling pattern.

1 INTRODUCTION

While coupled multi-bunch motion for a symmetric configuration of populated buckets in a storage ring has been extensively studied and the stability problem has a closed analytic solution [1] for most standard wake fields a fully populated ring is rarely the case for any operational mode of a realistic synchrotron.

We present a rigorous treatment of the beam loading effects for a non symmetric configuration of populated buckets. The core of this paper is an analytic method, involving contour integration in complex frequency domain, which yields a closed expressions describing the mode loss due to a general resonant impedance, for the case of partially filled ring.

The parasitic mode loss is expressed explicitly in of: the bunch index, the resonance frequency and the quality factor of the impedance peak. Superimposing many parasitic cavity modes one can use the above formulas to choose appropriate tuning of existing configuration of parasitic modes to minimize mode loss effects, or to optimize the filling bunch pattern (number of bunches in a train) to suppress the beam loading effects.

2 COUPLED MULTI-BUNCH MOTION

We assume a storage ring of a harmonic number N populated by a train of M consecutive bunches ($M \le N$). For the dipole mode consideration, it will be sufficient to model each bunch as a macro particle combining intensity of the entire bunch. To describe a coupled motion of a system of M bunches we represent a state of the system at a given time by a vector. Its n-th component describes the longitudinal coordinate of the n-th bunch (y_n is the phase of the bunch with respect to the center of an unperturbed bucket).

Collective synchrotron motion of the system on M bunches coupled via wake fields can be described by the following set of equations of motion [1].

$$\frac{\partial^2}{\partial t^2} y_n(t) + \omega^2 y_n(t) = A \sum_{k=-\infty}^{\infty} \sum_{m=0}^{M-1} \Big\{ W'\Big(-(k + \tfrac{m-n}{N})T_0\Big) + \frac{1}{c} W''\Big(-(k + \tfrac{m-n}{N})T_0\Big)\Big[y_n(t) - y_m\Big(t - (k + \tfrac{m-n}{N})T_0\Big)\Big]\Big\} \tag{1}$$

$$A = \frac{N_0 r_0 \eta \omega_0}{2\pi\gamma} .$$

Here W' and W'' are the time derivatives of the wake function, ω is the unperturbed synchrotron frequency, η is the phase slip factor, c is the velocity of light, r_0 is the classical proton radius, ω_0 is the revolution frequency and T_0 is the revolution period. The index k gives the sum of the wake fields from all previous turns.

One can identify the first term in the right hand side of Eq.(1) with the mode loss [2]–[3] suffered by the n-th bunch. It explicitly depends on the bunch index n. One can notice in passing, that the mode loss can be viewed as a shift of the minimum of the potential well – the synchronous phase shift – f_n.

$$f_n = A \sum_{k=-\infty}^{\infty} \sum_{m=0}^{M-1} W'\Big(-(k + \tfrac{m-n}{N})T_0\Big) . \tag{2}$$

The term proportional to y_n in the right hand side of Eq.(1) can be absorbed by the synchrotron frequency. This is known as the synchrotron frequency shift, $\Delta\omega_n$, due to the potential well distortion [3]–[4] (change of its curvature) and it is given by the following formula

$$\Delta\omega_n^2 = A \frac{1}{c} \sum_{k=-\infty}^{\infty} \sum_{m=0}^{M-1} W''\Big(-(k + \tfrac{m-n}{N})T_0\Big) . \tag{3}$$

The resulting set of equations, Eqs.(1)–(3), along with a convenient representation of the wake field coupling, will be analyzed in the complex frequency domain later in the paper.

3 PARASITIC MODE LOSS – PARTIALLY FILLED RING

To evaluate the mode loss term (or the incoherent synchrotron tune shift) it is convenient to express it in terms of the longitudinal coupling impedance via the inverse Fourier transform. The resulting expression, Eq(2) is rewritten as follows

0-7803-4376-X/98 /$10.00 © 1998 IEEE

$$f_n = \frac{Ac}{2\pi} \sum_{k=-\infty}^{\infty} \sum_{m=0}^{M-1} \int_{-\infty}^{\infty} d\omega \, e^{-i\omega(k + \frac{m-n}{N})T_o} Z_{\|}(\omega) \, . \qquad (4)$$

Infinite summation over k can be carried out explicitly using a trivial version the Poisson sum identity. This yields the following expression

$$f_n = \omega_0 \frac{Ac}{2\pi} \sum_{p=-\infty}^{\infty} \sum_{m=0}^{M-1} Z_{\|}(p\omega_0) \, e^{2\pi i p \frac{n-m}{N}} \, . \qquad (5)$$

Applying a simple sum identity to Eq.(5) one can rewrite it in the following form

$$f_n = \omega_0 \frac{Ac}{2\pi} \sum_{q=-\infty}^{\infty} \sum_{l=0}^{N-1} e^{2\pi i l \frac{n}{N}} Z_{\|}((Nq+l)\omega_0) \sum_{m=0}^{M-1} e^{-2\pi i l \frac{m}{N}} \, . \qquad (6)$$

the last summation (over m) in Eq.(6) can be carried out explicitly. The resulting formula is written as follows

$$f_n = \omega_0 \frac{Ac}{2\pi} \sum_{p=-\infty}^{\infty} e^{2\pi i (p\omega_0)\frac{n}{N\omega_0}} Z_{\|}(p\omega_0) \times$$

$$\frac{1 - e^{-2\pi i (p\omega_0)\frac{M}{N\omega_0}}}{1 - e^{-2\pi i (p\omega_0)\frac{1}{N\omega_0}}} = \sum_{p=-\infty}^{\infty} F(p\omega_0) \, . \qquad (7)$$

The second equality in Eq.(7) highlights generic sampling structure of the above expression. Applying the Poisson sum identity to Eq.(7) yields the following expression

$$f_n = iAc \sum_{q=-\infty}^{\infty} \frac{1}{2\pi i} \int_{-\infty}^{\infty} d\omega \, Z_{\|}(\omega) \frac{e^{2\pi i (q + \frac{n}{N}) \frac{\omega}{\omega_0}} - e^{2\pi i (q - \frac{M-n}{N}) \frac{\omega}{\omega_0}}}{1 - e^{-2\pi i \frac{\omega}{N\omega_0}}} \, . \qquad (8)$$

Introducing two kinds of generic integrals, namely:

$$I^+(k) = \frac{1}{2\pi i} \int_{-\infty}^{\infty} d\omega \, Z_{\|}(\omega) \frac{e^{2\pi i k \frac{\omega}{N\omega_0}}}{1 - e^{-2\pi i \frac{\omega}{N\omega_0}}} \, , \quad k \geq 0$$

$$I^-(k) = \frac{1}{2\pi i} \int_{-\infty}^{\infty} d\omega \, Z_{\|}(\omega) \frac{e^{-2\pi i k \frac{\omega}{N\omega_0}}}{1 - e^{-2\pi i \frac{\omega}{N\omega_0}}} \, , \quad k \geq 0 \qquad (9)$$

one can express the mode loss term, Eq.(8), in the following compact form

$$f_n = iAc \left\{ I^+(n) - I^-(k) + \sum_{q=1}^{\infty} \left[I^+(Nq+n) + I^-(Nq-n) + \right.\right.$$

$$\left.\left. - I^+(Nq-(M-n)) - I^-(Nq+(M-n)) \right] \right\} \, . \qquad (10)$$

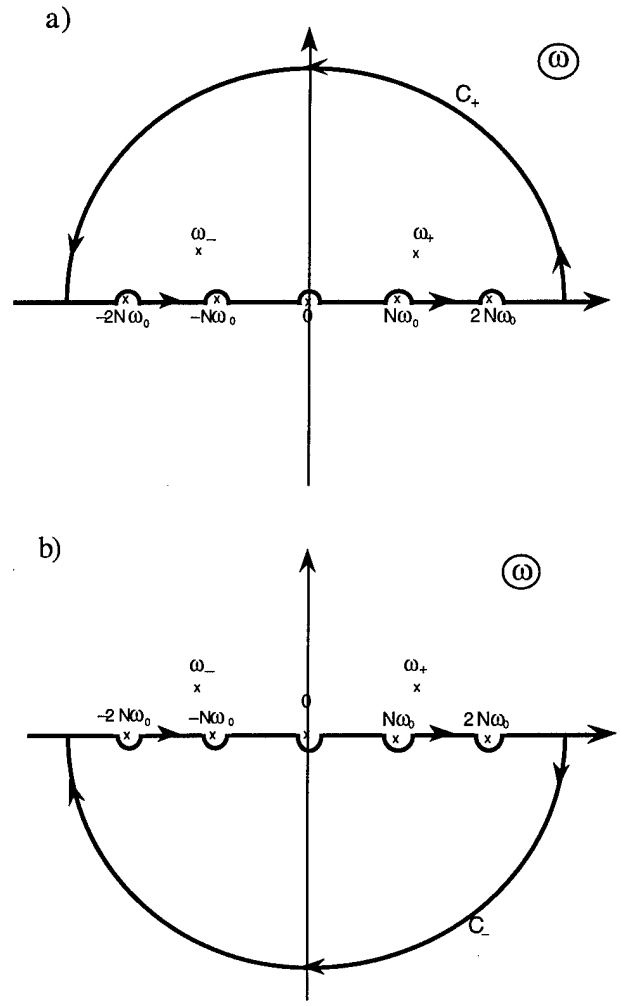

Figure: 1 Complete set of singularities along with the appropriate choice of integration contours for both $I^+(k)$ and $I^-(k)$ – C_+ and C_- respectively.

Assuming general form of the longitudinal impedance of a resonant structure, given by the following standard expression:

$$Z_{\|}(\omega) = \frac{R}{1 + iQ\left(\frac{\omega}{\omega_r} - \frac{\omega_r}{\omega}\right)} = -iR \frac{\omega_r}{Q} \frac{\omega}{(\omega - \omega_+)(\omega - \omega_-)} \, , \qquad (11)$$

where R is the shunt resistance, Q is the quality factor of the resonator and ω_r is its resonance frequency, the singularities of $Z_{\|}(\omega)$ are defined by the following pair of complex poles $\omega_\pm$ located in the upper half plane

$$\omega_{\pm} = \omega_r(\pm 1 + i\delta), \qquad \delta = \frac{1}{2Q} << 1 \quad . \tag{12}$$

The integrals, $I^{\pm}$, can be easily evaluated through contour integration via Cauchy's integral theorem. The choice if the integration contours is illustrated in Figure 1.

After evaluating the integrals, $I^{\pm}$, explicitly [4], one can rewrite Eq.(10) in the following closed form

$$f_n = \frac{AcR\omega_o}{\pi}\left\{\left(\frac{\pi\omega_r}{N\omega_o}\right)\delta^2 \frac{M\left(\frac{\pi\omega_r}{N\omega_o}\right) - \frac{1}{2}N\sin\left(\frac{2\pi\omega_r}{N\omega_o}\right)}{\sin^2\left(\frac{\pi\omega_r}{N\omega_o}\right) + \left(\frac{\pi\omega_r}{N\omega_o}\right)^2\delta^2} + \right. \tag{13}$$

$$\left. - \frac{\sin\left(\frac{\pi\omega_r}{N\omega_o}\right)\sin\left(\frac{\pi\omega_r}{N\omega_o}M\right)\cos\left(\frac{\pi\omega_r}{N\omega_o}(2n-M-1)\right)}{\sin^2\left(\frac{\pi\omega_r}{N\omega_o}\right) + \left(\frac{\pi\omega_r}{N\omega_o}\right)^2\delta^2}\right\}.$$

Denoting the expression in curly bracket by $\tilde{f}_n$, one can introduce a dimensionless mode loss. Figure 2 illustrates a family of curves for different values of n, calculated according to Eq.(13).

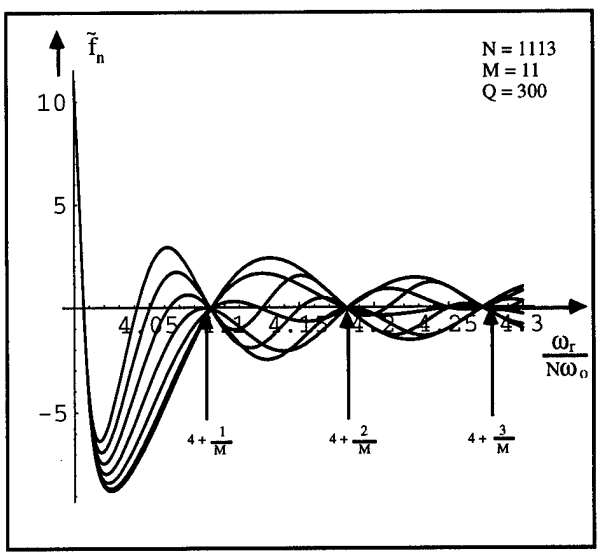

Figure: 2 Dimensionless mode loss, $\tilde{f}_n$, suffered by the n-th bunch – a discrete set of resonant frequencies, ω_r, defined by the fractional, $1/M$, multiples of $N\omega_o$.

As one can see Eq.(13) has a simple asymptotics for the resonance frequencies, ω_r, in the vicinity of the integer multiples of the r.f. frequency, $kN\omega_o$, and away from them. These two asymptotic regions are determined by the relative strength of the expressions appearing in the denominator of Eq.(13), namely: $\sin^2(\pi x)$ and $(\pi x)^2\,\delta^2$. One can notice, that for the resonance frequencies in 'the immediate vicinity of the integer multiple of the r.f. frequency' the resulting mode loss does not depend on the bunch index, n, and it is governed by the quality factor, Q. Conversely, for the resonance frequencies outside that region, the resulting mode loss does not depend on the quality factor, Q, and it is governed strictly by the bunch index, n, which explains why the so called 'de-Q-ing' of the modes does not have any effect on the beam loading effects for a partially filled ring.

Furthermore, the structure of Eq.(13) – zeros of $\sin(\pi x M)$ – reveal another finer level of symmetry defined by the fractional, $1/M$, multiples of $N\omega_o$. The mode loss vanishes up to terms of $O(\delta^2)$, for a discrete set of resonance frequencies marked in Figure 2 (arrows).

4 SUMMARY – OPTIMIZED FILLING PATTERN

The mode loss experienced by a given bunch within the train, were calculated analytically (using contour integration technique) for a partially filled ring. Resulting simple analytic formulas express both quantities, as a function of the resonance frequency, ω_r, and the quality factor of the coupling impedance, Q.

The formula reveals a set of characteristic resonant frequencies, spaced by the multiples of $N\omega_o/M$, at which the potential well distortion characteristics are not only bunch independent, but also considerably smaller (it scales as MQ^{-2}).

Finally, for a given configuration of cavity resonances one can get immediately a simple quantitative answer in terms of the mode loss and the synchrotron tune shift experienced by each bunch along the train [4]. These analytic expressions give one an insight into various optimizing schemes; e.g. to modify the existing configuration of parasitic cavity resonances (via frequency tuning), so that the resulting potential well distortion effects are minimized. One can also explore existence of the beam loading suppression frequencies, which depends on the bunch train index, M, to design an optimum filling pattern for a storage ring, e.g. a train of trains to maximize the net beam intensity, which is especially useful for a synchrotron light source to maximize its brightness and still avoid undesirable mode loss effects.

REFERENCES

[1] A.W. Chao, Physics of Collective Beam Instabilities in High Energy Accelerators, (John Wiley & Sons, Inc. 1993), Ch. IV.

[2] H.H. Umstätter, On the Distortion of the Center of Accelerating Bucket by Beam Loading Effects, CERN MPS/Int. RF 67-18 (1967).

[3] B. Zotter, Potential-well Bunch Lengthening, CERN SPS/81-14 (DI) (1981).

[4] S.A. Bogacz, Potential Well Distortion Effects for a Partially Filled Ring, Particle Accelerators, **48**, 19 (1994).

A POTPOURRI OF IMPEDANCE MEASUREMENTS AT THE ADVANCED PHOTON SOURCE STORAGE RING

N. S. Sereno, Y.-C. Chae, K. C. Harkay, A. H. Lumpkin, S. V. Milton B. X. Yang
Advanced Photon Source, Argonne National Laboratory
9700 South Cass Avenue, Argonne, Illinois 60439 USA

Abstract

Machine coupling impedances were determined in the APS storage ring from measurements of the bunch length, synchronous phase, and synchrotron and betatron tunes vs single-bunch current. The transverse measurements were performed for various numbers of small gap insertion device (ID) chambers installed in the ring. The transverse impedance is determined from measurements of the transverse tunes and bunch length as a function of single-bunch current. The shift in the synchrotron tune was measured as a function of bunch current from which the total cavity impedance was extracted. The loss factor was determined by measuring the relative synchronous phase as a function of bunch current. The longitudinal resistive impedance is calculated using the loss factor dependence on the bunch length. From these results, we can estimate what the impedance would be for a full set of ID chambers.

1 LONGITUDINAL

The longitudinal coupling impedance, $Z_{\|}(\omega)$, is responsible for a number of effects which potentially degrade the performance of an accelerator or storage ring. Discussion will be limited to single-bunch effects; these include bunch lengthening, microwave instabilities, and chamber heating, all of which can reduce the beam lifetime. In the 7-GeV APS positron storage ring, the main contributions to $Z_{\|}$ are the rf cavity higher-order modes (HOMs) and the broadband impedance due to vacuum chamber transitions, flanges, bellows, etc. A convenient quantity used as a measure of the total resistive impedance integrated over all frequencies is the loss factor, k. Loss factors may be associated with individual vacuum chamber components or with the entire accelerator as a whole. The reactive impedance, which changes the rf focusing and shifts the synchrotron frequency, will not be discussed.

One method of measuring the loss factor is to observe the shift in the synchronous phase of a bunch [1]. The resistive impedance causes the beam to lose energy, which must be compensated by shifting the bunch to a phase corresponding to a higher field in the rf cavities. The shift in synchronous phase of an intense test bunch was measured relative to a small bunch used as a time reference. The reference bunch phase is solely determined by the current-independent losses due to synchrotron radiation, U_{rad}, nominally 5.45 MeV/turn. The current of the reference bunch was 0.6 mA and spaced halfway around the ring at 1.8 μs relative to the test bunch, while the test bunch current was varied from 1.3 to 6.4 mA at a fixed rf voltage of 9 MV. A Hamamatsu C5680 dual-sweep streak camera was used to image the bunches using the optical synchrotron radiation from a bending magnet source. For each current value, 12 turns of data were acquired. The streak image intensity profiles for each bunch were averaged over the entire record, from which the centroids were computed.

The normalized intensity profiles for the test bunch are shown in Fig. 1. The time offset is measured relative to the reference bunch. As the bunch intensity increases, the energy loss increases, and the bunch centroid is observed to shift towards the head of the bunch (left in the figure). The centroid positions of each test bunch relative to the reference bunch are shown in Fig. 2. The shift is nearly linear with current. The energy loss is given by [1]

$$\Delta U = qV_{rf}\left|\sin\phi_s - \sin\phi_{s0}\right|, \qquad (1)$$

where q is the bunch charge, V_{rf} is the total rf voltage, ϕ_{s0} is the zero-current synchronous phase angle, and ϕ_s is the shifted phase. The loss factor, k_{TOT}, is defined as

$$k_{TOT} = \frac{\Delta U}{q^2} = \frac{1}{2\pi}\int_{-\infty}^{\infty} Z(\omega)e^{-\omega^2\sigma_\tau^2}d\omega\,, \qquad (2)$$

where I_0 is the average bunch current, and a gaussian charge density with rms bunch length σ_τ is assumed.

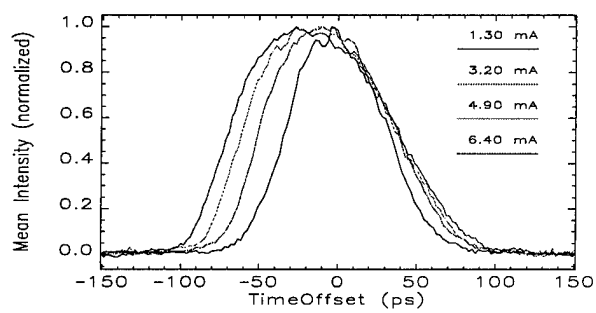

Figure 1: Normalized streak camera profiles for increasing test bunch current.

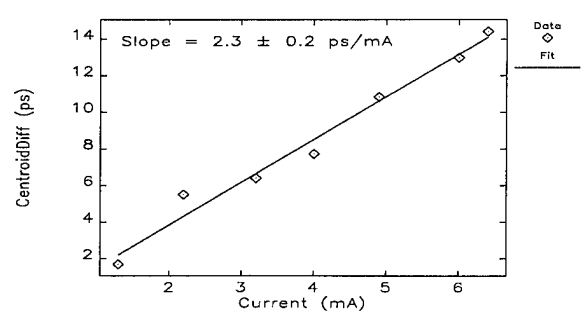

Figure 2: Centroid position shift of test bunch relative to reference bunch plotted vs. test bunch current.

0-7803-4376-X/98/$10.00 © 1998 IEEE

Using Eqs. (1) and (2), and assuming a small shift, $\Delta\phi_s = \phi_s - \phi_{s0}$, the loss factor is computed using

$$k_{TOT} = \mathrm{sign}(\eta) V_{rf} \cos\phi_{s0} \left(\frac{\Delta\phi_s}{q}\right) = 10 \text{ V/pC},$$

where η is the slip factor and $U_{rad} = V_{rf} \sin\phi_{s0}$. The slope in Fig. 2 is 1.4 μrad/pC and is derived using 2.84 nsec per rf wave and a revolution frequency of 271.55 kHz. This value of k_{TOT} may be compared to the loss factor estimated from the rf cavity higher-order modes (HOMs). The program ABCI [2] was used to estimate the loss factor per cavity. The loss calculated was 0.43 V/pC for an rms bunch length of 1 cm. For 16 cavities in the ring, the HOMs contribute about 70% of the total intensity dependent energy loss while about 30% can be attributed to other sources. The loss factor dependence on bunch length could not be determined because of the small bunch length variation over these data.

A measurement of the local loss factor around the ring was attempted by measuring the position offset of a BPM in the high dispersion (η = 0.4 m) positions in the ring. The measurement did not yield any systematic energy shift for single-bunch currents up to 5 mA. There are two reasons for this. First the magnitude of the effect is very small; at 5 mA, the expected position shift is only 10 μm assuming all the loss (10 V/pC) is located near a single high dispersion point. In reality, the loss is distributed around the ring so the position offsets expected are at least an order of magnitude less. Second and most important, the BPM offset intensity dependence is anywhere from 10 to 50 μm as the current is varied by 5 mA [3]. At this time, there is no independent way to measure this dependence with current so that it may be separated out from the losses due to the local impedance.

2 TRANSVERSE

The transverse impedance $Z_\perp(\omega)$ describes the influence of various beamline components on the transverse dynamics of the beam. An important consideration for the APS storage ring is the transverse impedance due to a series of small-gap (8-mm vertical aperture) insertion device (ID) chambers that the beam must traverse. The wakefields generated in each chamber are relatively short, and hence it is the broadband impedance that will increase as more chambers are installed in the ring. The objective is to obtain an experimental value for the impedance of a single small-gap chamber to compare with the expected ring impedance.

The impedance generates coherent oscillation modes of the particles within a bunch or coupled-bunch modes of several bunches. For the measurements described here, a single bunch was used so that modes of oscillation of the particles in the single bunch are considered. The complex frequency shift for mode m is given in terms of the effective transverse impedance by [4]

$$\frac{\delta\omega_m}{\omega_o} = j\left(\frac{I}{\sigma}\right)\left(\frac{1/(4\sqrt{\pi})}{1+m}\right)\left(\frac{\bar{\beta}R}{E/e}\right)\bar{Z}_\perp(\omega) \quad , \qquad (3)$$

$$\bar{Z}_\perp(\omega) \equiv \frac{\sum Z_\perp(\omega) h_m(\omega - \omega_\xi)}{\sum h_m(\omega - \omega_\xi)} \quad , \qquad (4)$$

where $\bar{\beta}$ is the average ring beta function, R is the ring radius, I is the average beam current, σ is the rms bunch length, E/e is the energy expressed as a voltage, ω_o is the angular revolution frequency, $h_m(\omega - \omega_\xi)$ is the single-bunch spectrum shifted by frequency ω_ξ, which depends on the chromaticity, and $\bar{Z}_\perp(\omega)$ is the effective transverse impedance due to all the ring components. The effective impedance is seen to be a convolution with the bunch power spectrum. Assuming the bunch spectrum is narrow, as is the case with long bunches in a proton ring, the impedance $Z_\perp(\omega)$ can be removed from the sum, and by varying the chromaticity the impedance can be determined as a function of frequency. This assumption is not valid for the short positron bunches in the APS ring which result in an rms spectral width (~10 GHz) on the same order as ω_ξ. Therefore it is only the effective transverse impedance that is obtained in this measurement.

The imaginary part of Eq. (3) gives the inverse growth rate of the particular mode m. The real part yields the frequency shift of mode m. The mode m = 0 is the mode that is most strongly driven by the impedance and represents the rigid oscillation of all particles within the bunch. As the bunch current is increased, this mode is detected by observing the tune shift. Referring to Eq. (3), the imaginary part of the effective transverse impedance can be deduced from a measurement of the tune shift. The tunes were observed by driving a pair of striplines using a network analyzer and detecting beam motion using a similar pair of striplines [5].

In addition to the tunes, the bunch length is measured using the streak camera. The rms bunch length in the APS ring is observed to increase on the order of 50 ps as the single-bunch current is varied on the order of 10 mA consistent with potential well distortion [1, 6]. The bunch length vs current data are well fit by a 3rd-order polynomial as predicted by the potential well model. This fit is interpolated and used to compute the quantity I/σ in Eq. (3).

Figures 3 and 4 show the effective impedance for the horizontal and vertical planes deduced from three measurements for different numbers of small gap chambers installed in the ring. The horizontal axis of the figures are in units of the the standard 8-mm gap, 5-m long chamber used for IDs in the APS ring. The relatively large error bars in both figures reflect the tune measurement uncertainty which is due to the slope error of the linear fit to the tune vs I/σ data. The effective impedance per chamber is derived from the slope of a linear fit to the three impedance values in each figure.

The effective horizontal transverse impedance per chamber is seen to have a very large uncertainty. This is

due to the fact that the horizontal tune shift was observed to be very small and difficult to measure as compared to the vertical tune shift vs I/σ. The horizontal data are consistent with the fact that the chamber is very wide horizontally as compared to the vertical dimension, and therefore one expects the horizontal impedance to be small.

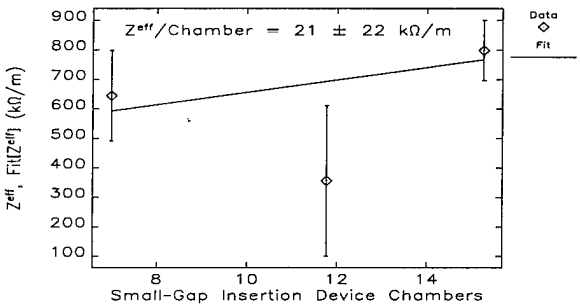

Figure 3: Horizontal transverse impedance as a function of the number of small-gap chambers in the ring.

The vertical data shown in figure 4 indicate a definite trend toward higher effective impedance as the number of chambers increases. The slope of the line indicates an effective transverse impedance of 53 kΩ/m per chamber which is much larger than the anticipated value of 1.76 kΩ/m [7]. The effective impedance is larger in part because it includes the resistive wall impedance. The anticipated value is computed neglecting the resistive wall part of the impedance. The large value is also due to the fact that the bunch spectrum for APS bunches is very wide and therefore the large broadband impedance at near $\omega = 0$ contributes substantially to the sum in Eq. (2). Using the computed value of the effective vertical impedance per chamber, one would expect 1.8 MΩ/m for the full complement of 34 chambers in the ring.

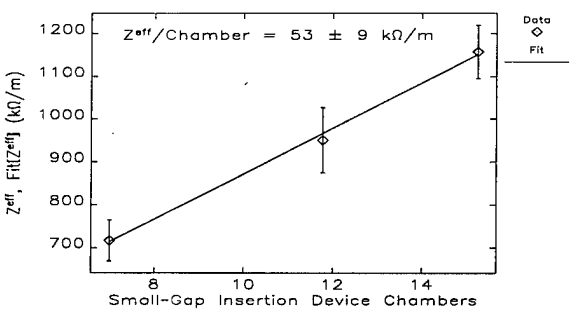

Figure 4: Vertical transverse impedance as a function of the number of small-gap chambers in the ring.

The local reactive component of the vacuum chamber transverse impedance was measured using a method first developed at CERN [8]. The BPM beam history modules were used to acquire vertical position data over 128 turns after the beam had been excited in the vertical plane using a kicker. This data was subsequently processed to determine the vertical betatron phase advance variation per mA as a function of position around the machine. Four positions in the machine were measured in this initial study.

The sum of the phase advance converted to tune units for all four positions results in -4.6/A. This value was found to be in agreement with measurements of the tune shift with current using the standard tune measurement technique [4]. The measured values reveal qualitatively that the region with the rf, injection elements, and ID chambers have a larger effect on the beam (larger tune shift with current) than a region with standard vacuum chamber components. More measurements will be made to determine in detail the transverse impedance around the ring at more than the four points done in this exploratory measurement.

3 CONCLUSIONS

The longitudinal loss factor was determined by measurement of the synchronous phase vs single-bunch current for the APS ring. The loss due to HOMs in the cavities was estimated by a calculation so that losses due to other sources around the ring could be estimated. An attempt was made to measure the local loss around the ring at high dispersion areas. This proved to be difficult primarily due to the relatively large BPM offset intensity dependence. The effective transverse impedance was determined for the 8-mm small-gap ID chambers by measuring the tune shift as a function of single-bunch current. The result was a large vertical transverse impedance relative to horizontal due to the small vertical aperture of the chambers. A measurement was made using the beam history modules to estimate the local effective transverse impedance around the ring. The data confirm qualitatively the high transverse impedance features of the APS ring.

4 ACKNOWLEDGEMENTS

The authors would like to thank M. Borland, G. Decker, L. Emery, and J. Galayda for useful comments and suggestions regarding this work. This work was supported by U.S. Department of Energy, Office of Basic Energy Sciences, under Contract No. W-31-109-ENG-38.

5 REFERENCES

[1] H. Wiedemann, *Particle Accelerator Physics II,* Springer-Verlag 207 (1995).

[2] Y. H. Chin, "Users Guide for New ABCI Version 6.1," CERN SL/92-49 (1992).

[3] L. Emery, M. Borland "Advances in Orbit Drift Correction in the Advanced Photon Source Storage Ring," these proceedings.

[4] F. Sacherer, B. Zotter, "Transverse Instabilities of Relativistic Particle Beams in Accelerators and Storage Rings," CERN 77-13 (1977).

[5] W. Sellyey, E. Kahana, and X. Wang, "Tune Measurement in the APS Rings," *Proceedings of the 1993 Particle Accelerator Conference,* Washington DC, 2237 (1993).

[6] A. H. Lumpkin, B. X. Yang, Y. C. Chae, "Observations of Bunch-Lengthening Effects in the APS 7-GeV Storage Ring," Proceedings of 1996 FEL Conf., NIM-A (1997) (in print).

[7] L. Emery, private communication.

[8] D. Brandt et al. "Measurements of Impedance Distributions and Instability Thresholds in LEP," *Proceedings of the 1995 Particle Accelerator Conference,* Dallas, TX, 570 (1995).

BEAM IMPEDANCE STUDY FOR THE BESSY-II STORAGE RING

S. Khan, BESSY-II, Rudower Chaussee 5, 12489 Berlin, Germany

Abstract

The longitudinal impedance of components of the BESSY-II storage ring is studied using the computer code MAFIA.

1 INTRODUCTION

BESSY-II is a high-brilliance synchrotron radiation source presently under construction at Berlin-Adlershof [1]. Since instabilities of the electron beam deteriorate the quality of the delivered synchrotron radiation, it is important to design the storage ring components such that wakefields excited by the beam at discontinuities are reduced as much as possible.

Section 2 summarizes the relations used in this study (see also [2] [3]). Section 3 describes the strategy followed here. The results are given in sections 4 and 5.

2 LONGITUDINAL WAKE AND IMPEDANCE

The longitudinal wake function for a pointlike unit charge $q_1(\vec{r}_1)$ is defined as the energy lost by a unit charge $q_2(\vec{r}_2)$ that follows q_1 with a time delay t:

$$w_z(\vec{r}_1, \vec{r}_2, t) \equiv \frac{U(\vec{r}_1, \vec{r}_2, t)}{q_1\, q_2}. \tag{1}$$

In the following, the transverse displacements $\vec{r}_{1,2}$ of the charges are neglected, and, assuming longitudinal quantities, the index z is dropped. A numerical time-domain integration of Maxwell's equations on a mesh can only yield the wake function for an extended charge distribution $i(t)$ normalized to q_1:

$$W(t) = \frac{1}{q_1} \int_{-\infty}^{\infty} i(t')\, w(t-t')\, dt'. \tag{2}$$

The coupling impedance $Z(\omega)$ i.e. the complex power spectrum of the wake function for a point charge is obtained by dividing the spectrum of $W(t)$ by the spectrum of the charge distribution $I(\omega)$:

$$Z(\omega) \equiv \int_{-\infty}^{\infty} w(t)\, e^{-i\omega t}\, dt = \frac{\int_{-\infty}^{\infty} W(t)\, e^{-i\omega t} dt}{I(\omega)}. \tag{3}$$

Figure 1 shows an example. Assuming a Gaussian particle bunch of rms duration τ, the charge distribution reads

$$i(t) = \frac{q_1}{\sqrt{2\pi}\tau} e^{-t^2/2\tau^2} \quad \text{or} \quad I(\omega) = q_1 e^{-\omega^2\tau^2/2}. \tag{4}$$

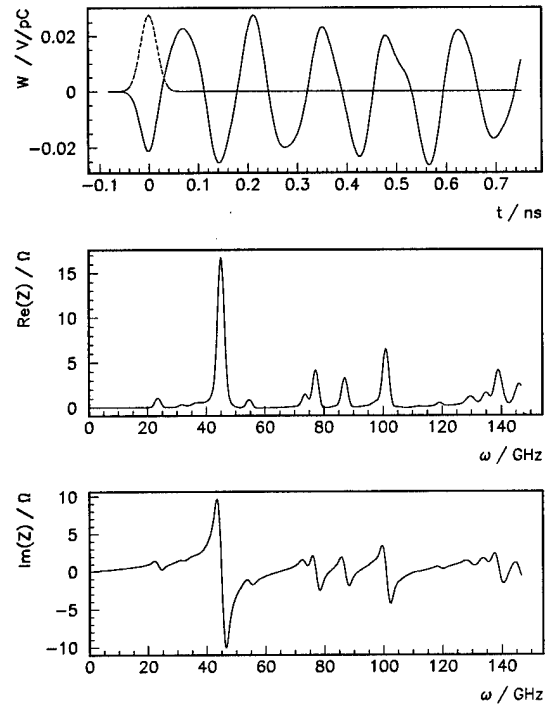

Figure 1: Wake function of a beam position monitor (top). Dividing the Fourier transform of the wake function by the bunch spectrum yields the corresponding impedance.

In order to optimize the design of a vacuum component, the loss factor may be used as a figure of merit. The longitudinal loss factor k is defined as the energy deposited by a charge distribution after its passage through the object under study and can be either computed from the wake function or from the impedance:

$$k = \frac{1}{q_1} \int_{-\infty}^{\infty} W(t)\, i(t) dt = \frac{1}{\pi q_1^2} \int_{0}^{\infty} \mathrm{Re}\,[Z(\omega)]\, |I(\omega)|^2\, d\omega. \tag{5}$$

The total impedance is usually quoted in terms of

$$|Z/n| \quad \text{with} \quad n \equiv \omega/\omega_o, \tag{6}$$

where ω_o is the revolution frequency. Since $Z(\omega)$ is in many cases inductive and linear in ω, this quantity is expected to be constant over a wide frequency range.

Traditionally, $|Z/n|$ is obtained by fitting a broadband model to the loss factor as function of the bunch length.

0-7803-4376-X/98 /$10.00 © 1998 IEEE

In the present case, however, such a fit was found to yield rather ambiguous results, and the total impedance was estimated as described in the next section.

3 NUMERICAL COMPUTATION

Using the time domain modules of the computer code MAFIA [4], the wake function $W(t)$ for the shortest applicable bunch length ($c\tau = 5$ mm in multibunch mode) was obtained. The mesh size was 1 mm or smaller. the wake function was monitored over a range of 3.3 ns. In most cases, the component under study required a 3-dimensional model (e.g. figure 2 and 3).

For each machine component, the design option with the lowest longitudinal loss factor was favored.

The impedance $Z(\omega)$ as function of frequency was computed by applying a Fast Fourier Transform to $W(t)$ and dividing the result by the bunch spectrum (equation 3). The mesh size in the time domain determines the frequency range, while the finite time range limits the frequency resolution. The time domain calculation does not resolve the higher order cavity modes (HOMs), which were studied in the frequency domain by [5].

In order to obtain a worst-case value for $|Z/n|$, the absolute values of the impedance of all individual components were summed up.

Component	quantity	total k [V/pC]
Rf cavities	4	4.57
insertion device chambers	13	1.30
beam position monitors	112	0.88
bellows, short	80	0.17
bellows, long	48	0.14
flanges, NW100	192	0.13
flanges, NW250	32	0.02
depolarization kicker	1	0.14
excitation striplines	4	0.11
current monitors	2	0.05
dipole chambers	32	0.05
pumping slots	96	0.03
septum chamber	1	0.02

Table 1: Longitudinal loss factors k for components of the BESSY-II storage ring. The value quoted for the rf cavities includes the fundamental mode.

4 RELEVANT STORAGE RING COMPONENTS

The longitudinal loss factors and the respective number of components in the storage ring are listed in table 1. Some comments on the individual components are in order.

The largest contribution comes from the rf cavities. The 2-d MAFIA model comprises four 500 MHz DORIS-type pillbox cavities connected by 400 mm long tubes of 146 mm diameter with pumping slots, and two 100 mm long end pieces tapered from 146 mm down to 35 mm.

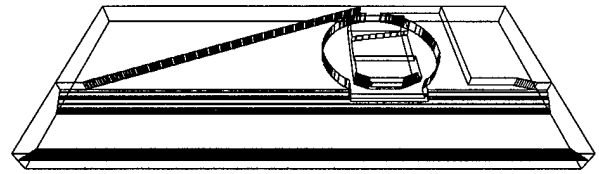

Figure 2: MAFIA 3-d model for the dipole chamber with a 15 mm wide slot for synchrotron radiation and a radiation absorber suspended in a cylindrical pumping port.

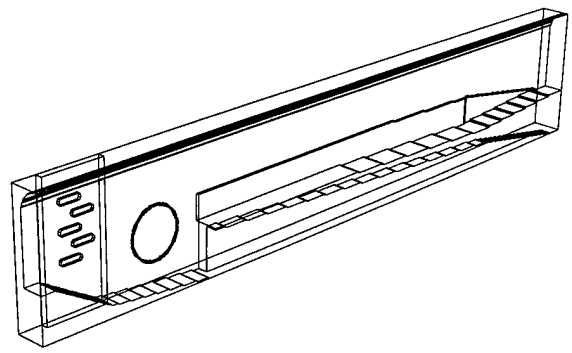

Figure 3: MAFIA 3-d model for the injection region. In this picture, the beam is injected from the right. The model includes the septum, a screen monitor and an array of pumping slots.

The elliptical insertion device chamber (60×18 mm) is connected to an ante-chamber by a 10 mm wide channel. The ante-chamber does not contribute significantly to the impedance budget, neither does the radiation absorber at the end of the chamber. The loss factor is essentially given by the tapers at both ends, where the vertical size of the chamber changes from 18 mm to 35 mm.

Another large contribution comes from the 112 beam position monitors with a button diameter of 15 mm. Their impedance shows a prominent resonance at $\omega = 45$ GHz (figure 1).

The discontinuities at bellows and flanges are shielded by sliding rf fingers. Their design was optimized using a 2-d model of 35 mm diameter, corresponding to the vertical chamber size.

A kicker close to the beam is required to depolarize the beam in order to measure the beam energy. A chamber with a vertical size of 18 mm and a stripline embedded in its wall yields a significantly lower loss factor compared to a wider chamber with a stripline protuding into it.

Each of the 32 dipole chambers a has 15 mm wide slot for synchrotron radiation. The main contribution of its impedance comes from the radiation absorber. The curvature of the beam had to be neglected in the MAFIA model

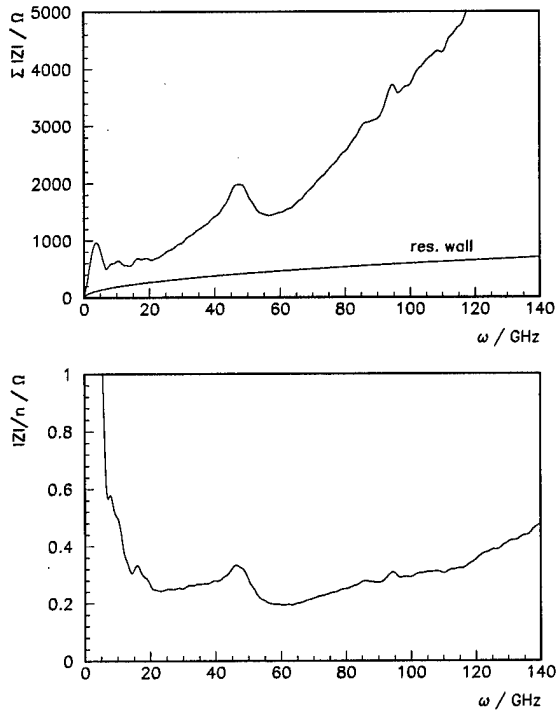

Figure 4: Summed longitudinal impedance of all components including the resistive wall impedance (top), and $|Z/n|$ as function of frequency.

(figure 2).

The 65×35 mm chamber in the region of the quadrupole and sextupole magnets has no ante-chamber. The only discontinuities are the pumping ports, where the compromise between impedance and pumping speed is an array of 96 mm long and 7 mm wide slots with semi-circular ends.

The model of the chamber in the injection region is shown in figure 3. The impedance contribution of the septum, the pumping slots and the screen monitor is negligible.

5 TOTAL STORAGE RING IMPEDANCE

The summed impedance of all components listed in table 1

$$|Z(\omega)| \equiv \sum_i |Z_i(\omega)| \tag{7}$$

is shown in the upper part of figure 4. As mentioned before, HOMs do not appear as prominent peaks due to the limited frequency resolution.

Also shown is the longitudinal resistive wall impedance given by

$$Z_{rw}(\omega) = \frac{(1-i)}{2\pi\, b\, \delta\sigma} L, \tag{8}$$

where b is the chamber radius, which was approximated by the smaller (vertical) semi-axis of the respective chamber. L is the chamber length, σ is the conductivity of the chamber material and

$$\delta = \frac{c}{\sqrt{2\pi\,\sigma\,\omega}} \tag{9}$$

is the skin depth. While most of the vacuum chambers are made of stainless steel ($\sigma = 1.4 \cdot 10^6\ 1/\Omega\mathrm{m}$, $b = 17.5$ mm), the narrow insertion device chambers are made of aluminium ($\sigma = 3.5 \cdot 10^7\ 1/\Omega\mathrm{m}$, $b = 9$ mm).

The lower part of the figure shows the quantity $|Z/n|$ which is nearly constant over the frequency range of $\omega = 20-120$ GHz. A value of $|Z/n| \approx 0.3\,\Omega$ can be concluded. This moderate broadband impedance may slightly increase when additional diagnostic elements or insertion devices with smaller gaps are introduced.

The transverse impedance was not considered in the context of optimizing the machine components. A discussion of the transverse resistive wall impedance of the BESSY-II storage ring can be found in [6].

6 ACKNOWLEDGEMENTS

This work is funded by the Bundesministerium für Bildung, Wissenschaft, Forschung und Technologie and by the Land Berlin. The help of K. Balewski (DESY, Hamburg), L. Palumbo (Universita di Roma "La Sapienza") and M. Zobov (INFN, Frascati) is gratefully acknowledged.

7 REFERENCES

[1] E. Jaeschke: 'Status of the High Brilliance Synchrotron Light Source BESSY-II', this conference.

[2] L. Palumbo, V.G. Vaccaro and M. Zobov: 'Wake Fields and Impedance', Proceedings of the CAS 5th Advanced Accelerator Physics Course, Rhodes, CERN 95-06, p.331.

[3] A. Chao: 'Physics of Collective Beam Instabilities in High Energy Accelerators', by A.W. Chao, published by John Wiley & Sons, New York, 1993.

[4] 'MAFIA User's Guide', CST, Darmstadt.

[5] F. Schönfeld and Bengt Littmann: 'Determination of Resonat Fequency and External Q Values for the BESSY-II HOM-Damped Cavity', Proceedings of the 1995 Particle Accelerator Conference, Dallas, May 1995, p.1711.

[6] S. Khan: 'Simulation of Transverse Coupled Bunch Instabilities', Proceedings of the 1995 Particle Accelerator Conference, Dallas, May 1995, p.2762.

THE COUPLING IMPEDANCE OF THE RHIC INJECTION KICKER SYSTEM

H. Hahn* and A. Ratti†, Brookhaven National Laboratory, Upton, New York 11973

Abstract

In this paper, results from impedance measurements on the RHIC injection kickers are reported. The kicker is configured as a "C" cross section magnet with interleaved ferrite and high-permittivity dielectric sections to achieve a travelling wave structure. The impedance was measured using the wire method in which a resistive match provides a smooth transition from the network analyzer to the reference line in the set-up. Accurate results are obtained by interpreting the forward scattering coefficient via the log-formula. The four kickers with their ceramic beam tubes contribute a $Z/n = 0.22\ \Omega$/ring in the interesting frequency range from 0.1 to 1 GHz, and less above. At frequencies above ~100 MHz, the impedance is ferrite dominated and not affected by the kicker terminations. Below 100 MHz, the Blumlein pulser with the ~75 m feeding cables is visible in the impedance but makes no significant contribution to the results. The measurements show that the kicker coupling impedance is tolerable without the need for impedance reducing measures.

1 INTRODUCTION

The RHIC injection kicker[1] is configured as "C" cross section magnet with interspersed ferrite[2] and dielectric[3] blocks as shown in Fig. 1 The deflection properties of the kicker are dominated by the magnetic field and thus by the ferrite properties and its geometrical configuration. The dielectric blocks provide the capacitance required to achieve a transmission line kicker and to reduce the charcteristic impedance so as to match the 25 Ω of the Blumlein pulser.

The longitudinal coupling impedance of a half-size kicker model was previously measured by Mane et al[4] with the results raising some concern due to the presence of sharp resonances in the GHz region. A more extensive study identified the origin of these resonances as local resonances in the dielectric blocks exposed to the beam.[5] In the modified kicker configuration, the resonances were completely suppressed by removing the dielectric blocks at the sides and replacing them by ferrite. The two kicker versions are shown in Fig. 1.

In this paper, measured results for the longitudinal coupling impedance of a half-size injection kicker model, both free-standing as well as part of the kicker system with Blumlein pulser, are presented.

* Work performed under the auspices of the U.S. Department of Energy
† Present address: LBNL, Berkeley, CA 94720

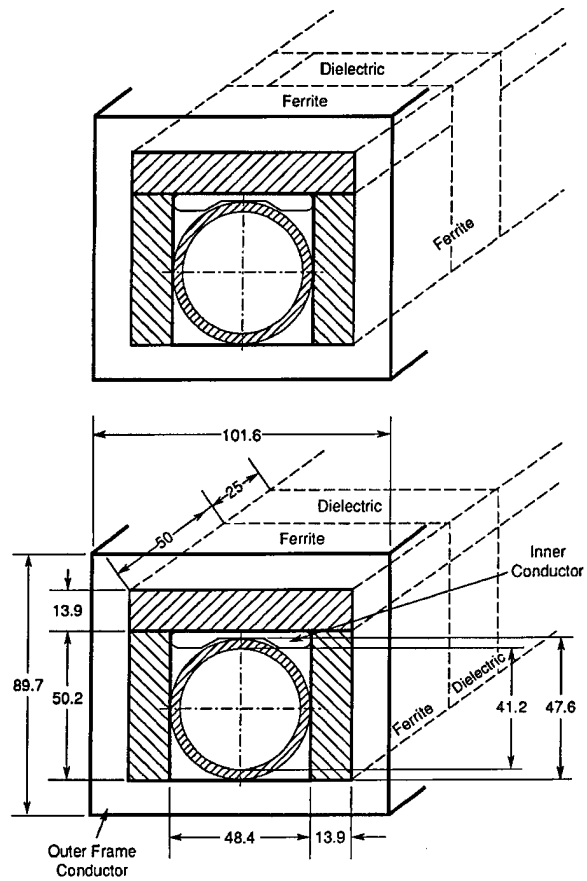

Figure 1: Geometry of original (bottom) and modified (top) RHIC injection kicker design.

2 WIRE MEASUREMENT OF THE COUPLING IMPEDANCE

The coupling impedance of the kicker system was measured with the existing bench setup for wire measurements previously used and described,[4] but now using the wire method in which a resistive match provides a smooth transition from the 50 Ω of the network analyzer to the characteristic impedance of the reference line in the setup.[6] The advantage of this method stems from the simplicity of its calibration procedure and the fact that a sufficient approximation of the results for the impedance in terms of real/imaginary or amplitude/phase is directly provided by the network analyzer and can be plotted without post processing. However the results quoted were obtained using the more accurate "log-formula" appropriate for distributed systems.

The measurements were performed with the Hewlett-Packard Network Analyzer 8753C connected to the S-Parameter Test Set 85078A. The characteristic impedance of the connecting reference waveguides was measured directly to be $Z_{ref} = 165\ \Omega$ by shorting the output port of a waveguide section, for which the input impedance becomes

$$Z_{in} = Z_{ref} \tan\left(\frac{\pi}{2}\frac{f}{f_{\lambda/4}}\right)$$

Matching the 50 Ω of the network analyzer to the 165 Ω of the reference line is achieved by adding at the input port, a parallel resistor of ~59.9 Ω and a series resistor of 137.7 Ω which provides forward and backward matching. At the output port, a series resistor of ~ 115 Ω provides forward matching. The frequency dependence of the carbon resistors and stray inductances/capapcitances destroys the match at higher frequencies, but is corrected by the calibration procedure.

The coupling impedance is obtained from the change in the forward scattering coefficient $S_{21\mathrm{DUT}}$ with respect to the reference system with $S_{21\mathrm{ref}} = 1$ if properly calibrated. In the case of a single lumped disturbance, the coupling impedance is obtained by the well known formula

$$Z_{hp} = 2Z_{ref}\frac{(1 - S_{21DUT}/S_{21ref})}{(S_{21DUT}/S_{21ref})}$$

which as a first approximation can also be used in the case of a distributed impedance such as the kicker.[7] This formula is used by the *hp* network analyzer and is quite useful in an exploratory study involving distributed impedances. However, if accurate results are required, at least the "log-formula"

$$Z_{\log} = -2Z_{ref}\ln\frac{S_{21DUT}}{S_{21ref}}$$

in which the scattering coefficients are complex quantities should be used; [8,9] although itself an approximation, it is extremely simple to use and sufficient in the present application.

3 THE KICKER SYSTEM WITH CERAMIC BEAM TUBE

The RHIC injection kicker system consists of four separate units, each 1.12 m long with separate pulser. The impedance measurements were performed in a half-length model with pulser and then extrapolated to the total system.[10] The kicker will operate in air and thus requires a ceramic beam tube, the dimensions of which are 47.6 mm o.d. and 41.3 mm i.d. Insertion of the ceramic beam tube into the kicker increases the capacity by ~2% and thus the impedance by only 1%. The coupling impedance of the kicker system, that is with the output port terminated and the input port connected to the pulser, has been measured with and without the ceramic beam tube. The hp impedance for both cases is compared in Fig. 2. Inspection of Fig. 2 shows an unphysical negative real part of the

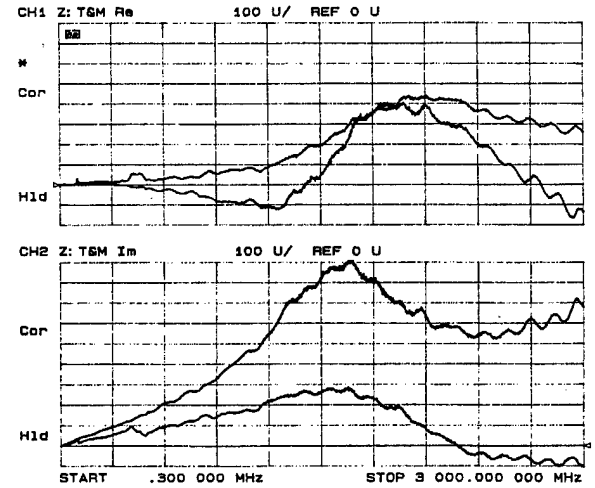

Figure 2: Comparison of impedance of kicker with and without beam tube.

impedance. It has been verified, that this problem is caused by the use of the hp formula and can be corrected via the log-formula.

The results for the kicker system impedance are at frequencies above ~100 MHz independent of the port terminations and can be summarized by the impedance values with beam tube of

$$|Z/n| = 0.22\ \Omega/\mathrm{ring}$$

and without beam tube of $|Z/n| = 0.14\ \Omega/\mathrm{ring}$, in the range up to ~1 GHz, but lower at higher frequencies. Note that the impedance is resonance free in the measured region up to 3 GHz. The low-frequency end is discussed in the next section.

Overall, one finds that the impedance contribution by the injection kicker is tolerable without the need for special impedance reduction measures such as a low-impedance (R-square, $R_{sq} \sim 1 - 10\ \Omega$) coating. A low-impedance coating can limit the rise time and cause arcing at higher fields. A high-resistance coating ($R_{sq} \sim 1\mathrm{M}\ \Omega$) will not reduce the coupling impedance but is required to prevent electrostatic charging of the beam tube, and will be provided in the RHIC kicker.

4 LOW FREQUENCY COUPLING IMPEDANCE

At frequencies below ~100 MHz the ferrites have low losses and the kicker acts as a transmission line magnetically coupled to the beam. As a result, the kicker terminations and in particular the pulser with the ~75 m long connecting cable become visible in the coupling impedance, as seen in Fig. 3.

Nassibian and Sacherer[11] have theoretically analyzed this situation, but their results were limited to fully terminated kickers and a later report by Nassibian[12] gave only

expressions for the real part of the impedance. A generalized derivation of the longitudinal coupling impedance valid at "low" frequencies, is presented in an internal report.[13] The kicker is still treated as a transformer-coupled uniform transmission line, but the constraints on the terminations are removed. The kicker is defined by its characteristic impedance Z_K and the wave number k_K, both beam-independent parameters measurable directly on the magnet. The generalized theory of the coupling impedance has two additional free parameters: (1) the mutual inductance M and (2) the "self"-inductance of the beam L_B. The values of these parameters are obtained from "wire"-measurements, using the theoretical expressions for their interpretation. As intuitively expected, the "self"-inductance of the beam follows from the results for the kicker open at both ports. The mutual inductance is expected to be

$$M = \frac{1}{2} L_K (1 + x/a)$$

with L_K the kicker inductance, a the kicker half-aperture and x the displacement from the center towards the bus bar. For a centered beam, one has $M = L_K/2$.

The general expression for the coupling impedance is best handled via the computer program MACSYMA. The case of one port terminated, $R_o = Z_K$, and the input port represented by the general impedance $R_i = R + jX$ is of practical importance, as it reflects the typical situation of the kicker system. Here one finds

$$\begin{aligned} Z = & \frac{1}{2} Z_K \left(\frac{M}{L_K}\right)^2 \{ Z_K^2 (1 - \cos 2\theta) \\ & + 4 Z_K R (1 - \cos\theta) \\ & + (R^2 + X^2)(3 - 4\cos\theta + \cos 2\theta) \\ & - 2 Z_K X (2\sin\theta - \sin 2\theta) \} / D \\ & + j Z_K \frac{L_B}{L_K} \theta - j \frac{1}{2} Z_K \left(\frac{M}{L_K}\right)^2 \{ Z_K^2 (2\theta - \sin 2\theta) \\ & + 4 Z_K R (\theta - \sin\theta) \\ & + (R^2 + X^2)(2\theta - 4\sin\theta + \sin 2\theta) \\ & - 2 Z_K X (1 - 2\cos\theta + \cos 2\theta \} / D \end{aligned}$$

with the denominator $D = (Z_K + R)^2 + X^2$,

$$Z_K = \sqrt{< L > / < C >}$$

and $\theta = \omega l \sqrt{(< L >< C >)} = 2\pi f / f_{2\pi}$ the electrical length of the kicker where $< L >$, $< C >$ are the quantitites per unit length. Theory and measured results for the coupling impedance are in reasonable agreement as long as the "electrical length" of the kicker is less than one free-space wavelength. At higher frequencies, the assumption of magnetic coupling is still valid, but the kicker is no longer the ideal lossless, uniform transmission line and a more general treatment, for example based on equivalent circuits, is required.[14]

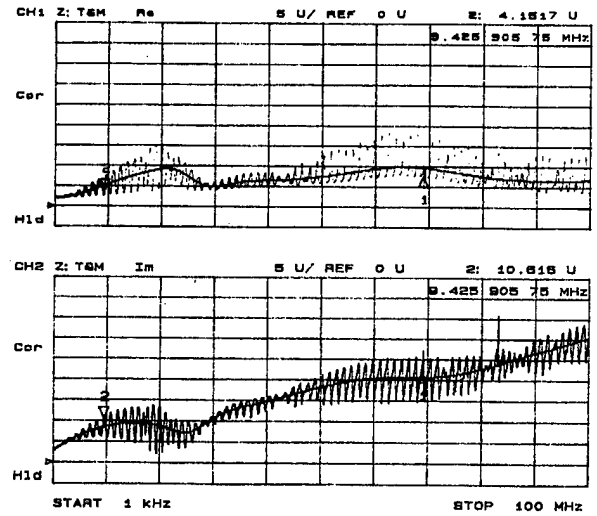

Figure 3: Low frequency coupling impedance of kicker system (rapid oscillation) and free standing kicker (smooth curve).

5 REFERENCES

[1] H. Hahn, et al, "The RHIC Injection Kicker," (these Proceedings).

[2] CMD-5005 by Ceramic Magnetics, Inc., Fairfield, NJ

[3] MCT-100 by Trans-Tech, Inc., Adamstown, MD.

[4] V. Mane, S. Peggs. D. Trbojevic, W. Zhang, Proc. 1995 PAC, Dallas, TX, p. 3134.

[5] H. Hahn, M. Morvillo, A. Ratti, BNL Report AD/RHIC/RD-95 (1995).

[6] A. Ratti, Fourth EPAC, London 1994, vol. 2, p. 1262.

[7] H. Hahn and F. Pedersen, Report BNL #50870 (1978).

[8] L. S. Walling, Nucl. Instr. Meth., A 281, p. 433 (1989).

[9] V. G. Vaccaro, et al, Proc. 1993 PAC, Washington, D.C., p. 2154 (1993).

[10] H. Hahn and A. Ratti, BNL Report AD/RHIC/RD-105 (1996).

[11] G. Nassibian and F. Sacherer, Nucl. Instr. & Meth., vol. 159, p. 21 (1979).

[12] G. Nassibian, Report CERN/PS 84-25(BR) (1984) and CERN/PS 85-68(BR) (1986).

[13] H. Hahn and A. Ratti, BNL Report AD/RHIC/RD-111 (1997).

[14] H. Hahn and A. Ratti, "Equivalent Circuit Analysis of the RHIC Injection Kicker," (these Proceedings); BNL Report AD/RHIC/RD-112 (1997).

DESIGN OF A HEAVILY DAMPED SUPERCONDUCTING CAVITY FOR SOLEIL

A. Mosnier, Projet SOLEIL, DRIF CNRS, Av. de La Terrasse, Bât. 5, 91198 Gif-sur-Yvette
S. Chel, X. Hanus, A. Novokhatski †, DSM/DAPNIA, CEA-Saclay, 91191 Gif-sur-Yvette
G. Flynn, LURE, Centre Universitaire Paris-Sud, Bât. 209A, 91405 Orsay, France

Abstract

To provide the necessary beam power and RF voltage, while coping with coupled bunch instabilities, a superconducting RF system is under study for the Synchrotron Light Source SOLEIL. A special arrangement combining a pair of single-cell cavities, strongly coupled through a large beam pipe, but ended with much smaller ones, and equipped with "classical" HOM dampers is investigated. Results of simulations, after optimization of the cavity shape, beam pipe opening and length, as well as the HOM-couplers design, are presented. Lastly, as beam power deposition and contribution to the overall ring impedance are of main concern, the short range wakefields of the overall cavity assembly have been also carefully studied.

1 INTRODUCTION

An R&D program, involving collaboration with other european laboratories, in particular CERN and ESRF, on a superconducting RF system for the 2.5 GeV storage ring of SOLEIL light source [1] has been set up. The relevant parameters are the total RF voltage of about 4 MV for an rf acceptance of ±6%, and the RF power of 400 kW, including the magnet and insertion losses, to transfer to the beam. The LEP cavity frequency, or more rigorously 353 Mhz, has been chosen. Two single-cell cavities can then be used, with a very moderate gradient (below 4 MV/m) and a power of 200 kW per coupler, which lies in the capability range of the existing LEP couplers. Coupled bunch instabilities is of major concern, because of the high design beam current of 500 mA, (with the total rf buckets filling by 396 bunches), needed for the high brilliance multibunch mode. The order of magnitude of the required damping of the longitudinal and transverse Higher Order Modes of the cavities is given by the well-known approximate formula (assuming short bunches and coincidence of HOM frequency with one single excitation spectral line)

$$f_r R_s < \frac{2E/eQ_s}{\alpha \tau_s I_o}, \quad f_o R_\perp < \frac{2E/e}{\beta_\perp \tau_\perp I_o}$$

with I_o the beam current, E the energy, Q_s the synchrotron tune, α the momentum compaction, $\beta_\perp$ the beta function at the cavity location, τ_s and $\tau_\perp$ the longitudinal and transverse radiation damping times, f_r and f_o the HOM resonance and revolution frequencies.

The harmful HOM impedances are of the order of 10 Ω for monopole and 100 Ω/m for dipole modes per cavity Taking the SOLEIL parameters and assuming that the cavities are installed in the short straight sections, where $\beta_\perp \leq 5$m, one obtains HOM damping requirements better than 2500 for longitudinal and 1250 for transverse planes.

2 CAVITY CALCULATIONS

For SC cavities, we refrain from mounting couplers along the cavity wall and two strategies can be prospected :

- either wide-open beam tubes, covered in rf lossy materials on the inner surface, form themselves coupling devices [2,3]; efficient damping can then be achieved but at the expense of large openings, risk of cavity pollution due to the proximity of the ferrite, and large overall lengths (one single cavity per cryostat).
- or a string of cavities, linked with large beam pipes in-between, but terminated on smaller outer pipes, form then resonant multi-cell structures, with strong coupling for the HOMs and very weak coupling for the accelerating mode [4]; "classical" HOM dampers can hence be mounted on the large pipes, where the standing wave HOM fields have large amplitude; several cavities can be housed in one cryostat and the end beam pipes have moderate opening.

Since first estimations look very promising, this latter solution has been chosen for the Soleil project. Intensive calculations have been carried out with the help of a self-acting code, which has been specially developed for the optimization of a 2-cavity system. The expected external Qs are computed, assuming magnetic or electric coupling (the maximal penetration depth of the coupler has been fixed to one quarter of the pipe radius. All geometric parameters have been varied, like the equator and iris radii of the cell, and in particular the beam tube diameters and the cavity spacing. At each step, after an automatic re-adjustment of the equator radius to get the right accelerating mode frequency (350 Mhz), the optimal location of the coupler, which minimizes the impedances, is sought by a scan all along the inner beam tube. At each location, the product $R/Q_n{*}Qex_n$ is computed for all the n modes below the cut-off frequency of the smaller end tubes and the maximal value $R_{max} = \mathrm{Max}\{R/Q_n{*}Qex_n\}$ of these n products is retained. The optimal coupler

† Permanent address: Budker Institute of Nuclear Physics, 630090 Novosibirsk Russia

0-7803-4376-X/98 /$10.00 © 1998 IEEE

location is of course the one which gives the minimal value of R_{max}. Fig.1 shows for example the maximal impedance - at optimal coupler location - for dipole (top) and monopole (bottom) modes, as a function of the inner tube length and for different tube radii, from 140 to 220 mm. The end pipes aperture has been fixed to R=130mm. The impedances decrease regularly when the inner pipe increases, but above a certain radius (about 20 cm), the situation reverses.

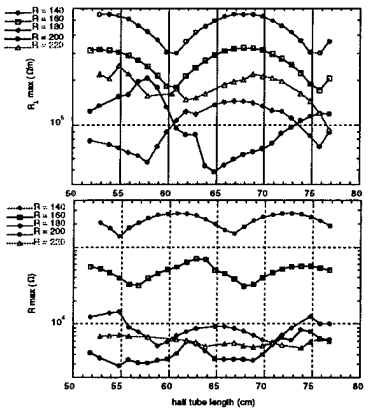

Figure 1: maximal impedances for dipole (top) and monopole (bottom) modes, as a function of the inner tube length & for different tube radii.

We conclude that a tube radius of 20 cm, with a cavity spacing of about 3 half wavelengths, is optimal for both transverse and longitudinal modes. Besides, the optimal locations of the dipole and monopole couplers are found very far from the iris of the cavities (21 and 53 cm), relaxing the power constraints on the fundamental mode rejection filter. The twenty dipole and monopole modes are listed on Table 1. Assuming magnetic coupling with a loop area of 20 cm^2, the predicted external Q is also given. Furthermore, we checked that the modes above cut-off, of much lower R/Q, can be easily damped by simple room-temperature couplers outside the cryostat, close to the conic transitions.

Freq (MHz)	R/Q (Ω/m)	Qex (10^3)	Freq (MHz)	R/Q (Ω)	Qex (10^3)
403	4.8	0.80	579	0.2	0.15
404	51.6	0.90	594	2.7	1.27
454	0.01	0.50	611	11.6	0.30
482	61.6	0.27	632	0.1	0.48
493	6.7	5.01	663	6.3	0.30
504	100.0	0.49	699	8.35	0.25
540	2.5	0.21	723	1.9	1.49
587	2.4	1.53	746	0.3	0.23
636	14.6	0.96	788	0.9	2.61
674	3.4	1.11	844	0.5	0.11

Table 1: Frequency, R/Q and predicted Qex for dipole (left) and monopole (right) modes below cut-off.

Electric field lines, calculated by URMEL, are plotted for example on Fig.2 for the fundamental mode (very weak cavity coupling) and the highest R/Q monopole HOM (strong cavity coupling). The main fundamental mode parameters are R/Q of 45 Ω per cavity, peak electric and magnetic surface fields of 2 and 4.5 mT/MV/m.

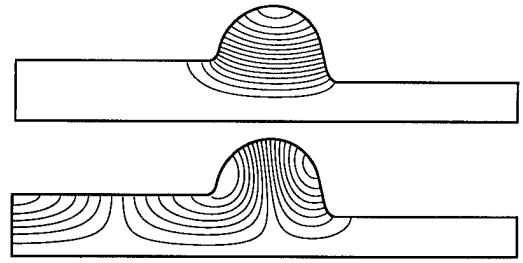

Figure 2: Electric field lines for the fundamental mode (top) and the highest R/Q monopole HOM (bottom)

3 HOM DAMPERS DEVELOPMENT

The specifications on the mode damping levels will be carefully checked in the near future through measurements on copper cavities and adjustable HOM couplers prototypes. Meanwhile, the performance of the couplers have been evaluated with the help of the "High Frequency Structure Simulator" (HFSS) code. These calculations intended first to insure the validity of the above Q predictions, but will also serve as a guide to the rf optimization of the couplers. Concerning the dipole mode damping, we adopted the SC loop coupler with the loop perpendicular to the beam axis, already used on Saclay, LEP or TESLA cavities (see [5] or [6] for example), which proved itself, but with a much higher coupling factor. Concerning the longitudinal mode damping, magnetic coupling with the loop parallel to the beam axis, much more efficient than electric coupling, has also been chosen, but with an additional sheet notch filter. The outer diameter (160 mm) of the HOM devices has been set to 40% of the bam pipe diameter, leading to a loop mean radius of almost 50 mm, whereas the inner conductor is between 20 and 30 mm. Once the coupling parameters are known, the rf elements, which are usually added to improve further the response of the coupler, especially in the vicinity of the HOM frequencies, can be determined by means of equivalent circuits. Though very similar to the longitudinal coupler, we present here only the method we folllowed for designing the dipole coupler.

The first step consists in evaluating the parameters related to the necessary notch filter centered on the fundamental mode. For the dipole coupler (loop perpendicular to the beam axis for Hz coupling), the filter is made of the loop inductance, in series with the capacitance formed by the loop end, facing the outer wall. We build HFSS models composed of a cylindrical waveguide (the beam pipe of diameter 400 mm), connected to the HOM port. Three modes are launched from the WG (the mode of interest, TM01, being the third one), and the notch frequency corresponds to a zero transmission. By varying the length of the capacitive line at the end of the loop, the parameters of the notch filter can be accurately determined from a linear fit (L=32 nH and C=6.4 pF).

We look now for 'universal' parameters, which characterize completely the coupling system, allowing to predict the damping for any mode and any resonator, assuming of course the same beam pipe stand. From an equivalent circuit [7], composed by a RLC circuit for the cavity mode, a transformer for the coupling factor, and a L_bC_b serie circuit for the loop, we deduce that 3 parameters, L_b, C_b and an equivalent coupling area S_b of the loop, are enough for the dipole coupler. These relevant parameters were determined with a HFSS model composed of a lossy cylindrical cavity (diameter 400 mm, the length fixing the resonance frequency) connected to the HOM coupler. Because of the strong coupling, the conductivity of the cavity has to be very low (around 10 $\Omega^{-1}m^{-1}$), in such a way that the reflection coefficient is closer to 0 rather than unity. The TEM mode is launched from the coupler end at frequencies around the resonance frequency of the TE_{113} mode, where the Hz component is maximum at the coupler location. Fig.3 shows for example the density plot of the magnetic field (Hϕ component maximal at the coupler location) for the TM_{012} mode, used for the design of the longitudinal coupler. From the S_{11} curves obtained for various cavity lengths, and with a least squares method, the values of the relevant 3 parameters are determined. For the dipole coupler, we find L_b=42 nH, C_b=4.9 pF and Qex=45 at 650 Mhz, corresponding to an equivalent loop area of 40 cm^2. The S_{11} curves, calculated from the above parameters and provided by HFSS for the TE_{113} mode of the pillbox cavity (the first resonance peak corresponds to the polarization with the electric field in the loop plane) are plotted on Fig.4. These coupler parameters should meet easily the damping requirements of the Soleil cavities.

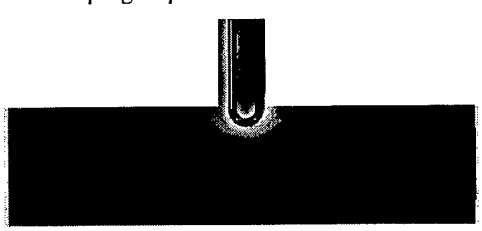

Figure 3: density plot of the magnetic field (Hϕ maximal at the coupler location) for the TM_{012} mode.

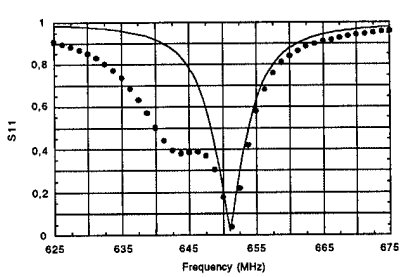

Figure 4: S_{11} curves, calculated from the equivalent circuit (solid line) and calculated by HFSS (circles) for the TE_{113} mode of the pillbox cavity

4 BUNCH WAKE AND HOM POWER

For the design short bunches (around 5 mm), the beam power deposition is of major importance, and must be, as much as possible, avoided at cryogenic temperature. If the loss factor coming from the cavities alone is rather small (about 0.75 V/pC for both cavities), the main contribution come from the two transition tapers between the cavity beam pipe and the tiny ring vacuum chamber of half height 12.5 mm, amounting to almost 3 V/pC in total, assuming conic 0.5 m long tapers. The bunch wake potentials (σ_z=5mm), computed by the code NOVO [8], are plotted on Fig.5, which shows also the individual contributions of the cavities and the tapers. The HOM power amounts to about 2 kW and 3 kW for the high flux (396 × 1.26 mA) and temporal structure (9 × 10 mA) modes, respectively. If it turns out that this HOM power gives too much trouble, the taper could be lengthened or the vacuum chamber could be enlarged in this region. Lastly, the wakefield has been computed for very short bunches (σ_z=1mm), is reproduced on Fig. 6 up to 150 mm behind the bunch center, will be very useful for bunch lengthening calculations. It exhibits resistive behaviour at low frequency , but also sharp resonances at higher frequency (around 10 GHz)

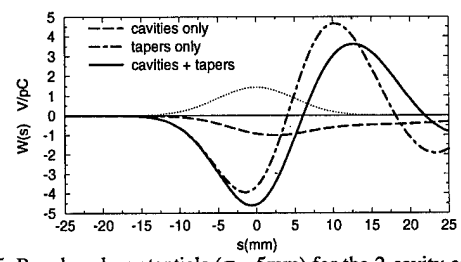

Figure 5: Bunch wake potentials (σ_z=5mm) for the 2-cavity assembly

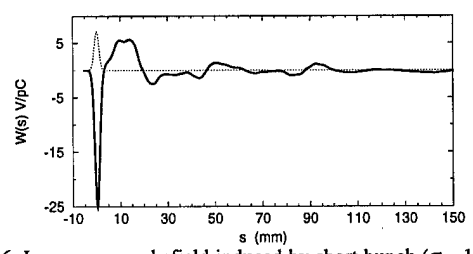

Figure 6: Long range wakefield induced by short bunch (σ_z=1mm) for the 2-cavity assembly.

5 REFERENCES

[1] 'Status of the SOLEIL Project', J.-L. Laclare and M.-P. Level, on behalf of the Soleil project team, these proceedings.

[2] 'Superconducting RF System for the CESR Luminosity Upgrade : Design, Status and Plans', Belomestnykh et al., Proc. of the 1996 European Part. Acc. Conf., Sitges.

[3] 'A Prototype Module of a Supercon. Damped Cavity for KEKB', T. Furuya et al., Proc. of the 1996 European Part. Acc. Conf., Sitges.

[4] 'Supercond. Cavities Calculations for a B-Factory', O. Henry, A. Mosnier, Proc. of the 1992 European Part. Acc. Conf., Berlin.

[5] 'Demountable E/H Field HOM Couplers for the Nb-Sputtered 4-cell LEP Cavity', Ph. Bernard et al., Proc. of the 5th Workshop on RF Superconductivity, Hamburg, 1991.

[6] 'Thermal Tests of HOM Couplers for SC Cavities', S. Chel et al., Proc. of the 1994 European Part. Acc. Conf., London.

[7] 'Couplers for Cavities', E. Haebel, CERN 96-03, May 1996.

[8] A.V. Novokhatski, to be published.

STABILITY DIAGRAMS FOR LANDAU DAMPING

J. Scott Berg and Francesco Ruggiero
European Laboratory for Particle Physics (CERN)

Abstract

Coherent modes which are present when there is no incoherent tune spread may be absent when such a spread exists. Such modes are "Landau damped." There is instead an incoherent spectrum, a continuum of an infinite number of frequencies, which will decohere (filament), thus not leading to collective instabilities. A stability diagram indicates when Landau damping will be effective. It divides the effective impedance plane, or equivalently the plane of coherent frequency in the absence of tune spread, into regions. The region which contains $+i\infty$ corresponds to instability. Thus, one can substitute a simpler computation (finding discrete eigenvalues) for a more complex computation (solving an eigenvalue system with both a discrete and a continuous eigenvalue spectrum). We present stability diagrams assuming a linear tune shift with amplitude, allowing tune spread in two transverse planes or in the longitudinal plane alone. When there is longitudinal tune spread, this can not be done exactly, and we describe approximations which make the computation tractable.

1 INTRODUCTION

This paper discusses stability diagrams for Landau damping in two situations: Landau damping of transverse oscillations when there is tune spread with transverse amplitude in *both* planes, and Landau damping of longitudinal or transverse oscillations when there is tune spread with longitudinal amplitude only, and when the relevant frequencies in the impedance are small compared to the frequencies in the bunch. The latter has been described by Wang and others [1, 2], however, only for Gaussian distributions. Here, we treat distributions other than Gaussian, and point out a caution for the use of these stability diagrams in the transverse case which was not addressed in [2]. These computations require one to ignore azimuthal mode coupling; however, they do demonstrate how to determine the effects of tune spread on mode coupling under some conditions.

First, assume that the coordinates in terms of action-angle variables are $\sqrt{2J_\alpha\beta_\alpha(s)}\cos[\theta_\alpha+\Delta\psi_\alpha(s)]$, and that the distribution about which one is analyzing perturbations is of the form

$$\Psi_0(\boldsymbol{J}) = (2\pi)^3\frac{1}{\epsilon_x\epsilon_y\epsilon_z}S(J_x/\epsilon_x, J_y/\epsilon_y)\lambda(J_z/\epsilon_z),$$

where the integrals of the functions λ and S are 1, as are their first moments. Then the following integrals, closely related to the beam transfer function, appear when performing a perturbation analysis to obtain the coherent modes (see, for example, [3]):

$$-\int\frac{J_y\,\partial\Psi_0/\partial J_y}{\Omega-\omega_y(J_x,J_y)-m\omega_z(J_x,J_y)}d^3\boldsymbol{J} \tag{1}$$

$$\int\frac{J_z^{|m|}\Psi_0(\boldsymbol{J})}{\Omega-\omega_y(J_z)-m\omega_z(J_z)}d^3\boldsymbol{J} \tag{2}$$

$$-\int\frac{J_z^{|m|}\,\partial\Psi_0/\partial J_z}{\Omega-m\omega_z(J_z)}d^3\boldsymbol{J}, \tag{3}$$

where m is the longitudinal azimuthal mode number. These are for the cases of transverse y modes for tune spread with two-plane transverse amplitude (Eq. (1)), transverse y modes for tune spread with longitudinal amplitude (Eq. (2)), and longitudinal modes for tune spread with longitudinal amplitude (Eq. (3)). There are similar terms with ω_y taking the opposite sign. Equations (2–3) are only correct under the assumption that the frequency of the impedance is small compared to the frequencies in the bunch spectrum. In the more general case these terms will depend on the frequency of the impedance. Also, Eqs. (1–2) ignore a term giving the longitudinal force due to the transverse wake, which is typically small.

If $\boldsymbol{\omega}(\boldsymbol{J})$ is a constant $\boldsymbol{\omega}_L$ ("linear lattice"), then the integrals (1–3) simplify greatly:

$$\frac{1}{\Omega-\omega_{Ly}-m\omega_{Lz}} \tag{4}$$

$$\frac{1}{\Omega-\omega_{Ly}-m\omega_{Lz}}\int J_z^{|m|}\Psi_0(\boldsymbol{J})d^3\boldsymbol{J} \tag{5}$$

$$-\frac{1}{\Omega-m\omega_{Lz}}\int J_z^{|m|}\frac{\partial\Psi_0}{\partial J_z}d^3\boldsymbol{J}. \tag{6}$$

When this is the case, the coherent frequencies Ω can be found by solving an eigenvalue problem. If one ignores azimuthal mode coupling, the problem for the nonlinear lattice can be solved in terms of the problem for the linear lattice: solve the eigenvalue system to find the value of the appropriate term from Eqs. (4–6), equate that to the corresponding term from Eqs. (1–3), and solve for the Ω appearing in the latter.

Equations (1–3) do not map the complex Ω plane completely onto itself; there are some points in the complex plane for which there is no Ω mapped onto that point. This is because the integrals (1–3) are bounded functions of Ω; in other words, for currents/impedances which are sufficiently small, even though there is a solution for the eigenvalue problem for a linear lattice, there is no corresponding solution for the problem for the nonlinear lattice. Such a solution is "Landau damped."

0-7803-4376-X/98/$10.00 © 1998 IEEE

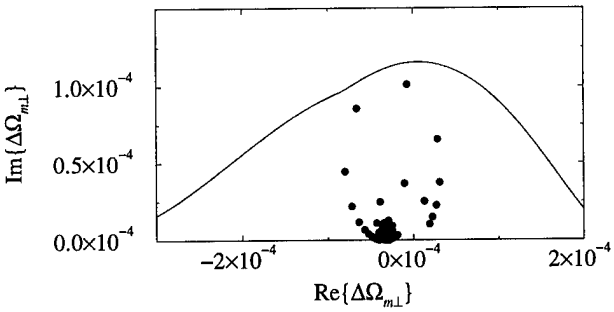

Figure 1: Example use of a stability diagram. The circles are the complex tune shifts of the transverse $m = 1$ multi-bunch modes computed for a linear lattice. The solid line is the stability diagram. In this case, all the modes are Landau damped since they all lie below the stability curve.

A stability diagram is simply a "stability curve" drawn in the plane of the complex coherent tune shifts for the linear problem which delimits the region for which solutions exist for the nonlinear problem. Figure 1 demonstrates how a stability diagram is used.

Formulas and example stability diagrams will be given here; derivations will be given in a forthcoming paper. Programs to produce the curves described here can be obtained from http://wwwslap.cern.ch/collective/jsberg/landau/.

We make the additional assumption that the incoherent tune, due to forces from magnets and potential well distortion, is linear in the action: $\boldsymbol{\omega} = \boldsymbol{\omega}_L + A\boldsymbol{J}$. A is a symmetric constant matrix, whose components are given by $A_{\alpha\beta} = a_{\alpha\beta}/\epsilon_\beta$, where the ϵ_β are the emittances. This is a good assumption in the transverse planes, but may not be as good in the longitudinal plane, mainly because of potential-well distortion.

2 TRANSVERSE TUNE SPREAD

For transverse tune spread only, begin by making a further assumption that $S(x, y) = \rho(x + y)$. The integral (1) is

$$-\int_0^\infty \int_0^\infty \frac{y\rho'(x+y)}{\Delta\Omega_{m\perp} - v_x x - v_y y} dx\, dy,$$

where $\Delta\Omega_{m\perp} = \Omega - \omega_{Ly} - m\omega_{Lz}$ and $v_\alpha = a_{y\alpha} + m a_{z\alpha}$. This integral can be written in the form

$$\frac{w_y f'(w_y) - v_x \dfrac{f(w_y) - f(w_x)}{v_y - v_x}}{v_y - v_x}, \qquad \text{for } v_x \neq v_y \quad (7)$$

$$-\frac{1}{2v_y}\frac{d}{dw_y}[w_y^2 f'(w_y)] \qquad \text{for } v_x = v_y$$

where $w_\alpha = v_\alpha/\Delta\Omega_{m\perp}$, and

$$f(z) = -\int_0^\infty \rho(u)\ln(1 - zu)\, du.$$

The asymptotic expansion of $f(z)$ as $z \to 0$ is $z + z^2 + O(z^3)$, making the expansion of the reciprocal of Eq. (7)

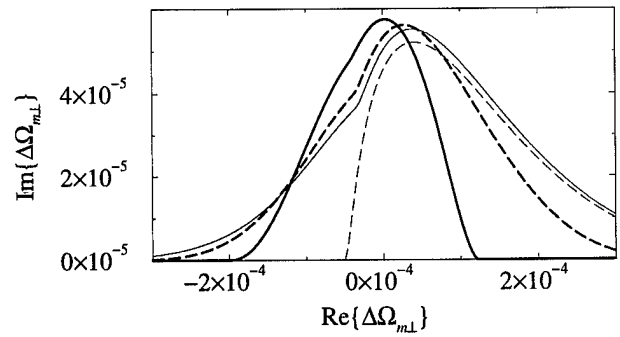

Figure 2: Stability curves for transverse tune spread, when $v_y = 5 \times 10^{-5}$. The thin lines are for the distribution (8), whereas the thick lines are for (9) ($\mu = 4.5$ for the solid, $\mu = 12.5$ for the dashed). All lines have $v_x = -3.58 \times 10^{-5}$, except for the thin dashed line, for which it is zero (one-dimensional).

for $\Delta\Omega_{m\perp}$ large $\Delta\Omega_{m\perp} - v_x - 2v_y + O(v_i/\Delta\Omega_{m\perp}^2)$. This asymptotic expansion allows one to compute the effects of tune spread when the mode one is examining has a coherent tune shift which is large compared to the tune spread. In such cases, one can compute the mode frequencies to second order in the ratio of the tune spread to the tune shift by replacing all the terms like Eq. (1) with the corresponding term (4), except that $\omega_{L\alpha} + a_{\alpha x} + 2a_{\alpha y}$ is used instead of $\omega_{L\alpha}$, expressing the fact that the average tune in the bunch is not the tune at zero amplitude. This allows one to perform a mode coupling analysis in cases where both modes have shifted by amounts large compared to the tune spread.

2.1 *Specific Distributions*

Consider two distributions

$$\rho(u) = e^{-u} \quad (8)$$

$$\rho(u) = \frac{(\mu-1)(\mu-2)}{\mu^2}\left(1 - \frac{u}{\mu}\right)^{\mu-3}, \quad 0 \le u \le \mu \quad (9)$$

which correspond to Gaussian and parabolic-like distributions in one transverse coordinate:

$$\frac{1}{\sqrt{2\pi}\sigma_y} e^{-y^2/2\sigma_y^2} \quad (10)$$

$$\frac{1}{\sqrt{2\pi\mu}\sigma_y}\frac{\Gamma(\mu)}{\Gamma(\mu - 1/2)}\left(1 - \frac{y^2}{2\mu\sigma_y^2}\right)^{\mu-3/2}. \quad |y| < \sqrt{2\mu}\sigma_y \quad (11)$$

The distribution (11) gives a good approximation for a beam which has been collimated at an amplitude $\sqrt{2\mu}\sigma_y$. The $f(z)$ for (8) and (9) respectively are $-e^{-z^{-1}}E_1(-z^{-1})$ and $zF(1, 1; \mu; z\mu)$, where E_1 is the exponential integral, and F is a hypergeometric function (which for 2μ an integer, is expressible in terms of elementary functions in this case and subsequent cases) [4].

Figure 2 demonstrates that including the tune spread in both planes can give substantial improvement over the case

where only one plane is considered. It also demonstrates that removing the high-amplitude tails from the distribution can substantially affect the amount of Landau damping one obtains.

3 LONGITUDINAL TUNE SPREAD

Next, consider Landau damping of either transverse or longitudinal oscillations due to longitudinal tune spread. In this case, one computes

$$\left[\int_0^\infty u^{|m|} f(u)\, du\right]^{-1} \int_0^\infty \frac{u^{|m|} f(u)\, du}{\Delta\Omega_m - v_z u}, \qquad (12)$$

where the symbols are defined as:

Symbol	Transverse	Longitudinal
$f(u)$	$\lambda(u)$	$d\lambda/du$
v_z	$a_{yz} + m a_{zz}$	$m a_{zz}$
$\Delta\Omega_m$	$\Omega - \omega_{Ly} - m\omega_{Lz}$	$\Omega - m\omega_{Lz}$

and compares the results to $1/\Delta\Omega_m$ for the linear lattice.

3.1 Specific Distributions

Expressions can be obtained in the cases when $\lambda(u)$ takes on one of the two forms

$$e^{-u} \qquad (13)$$

$$\frac{\mu - 1}{\mu}\left(1 - \frac{u}{\mu}\right)^{\mu-2}. \qquad (14)$$

These correspond to distributions in the longitudinal displacement given by Eqs. (10) and (11). For longitudinal oscillations, (12) is

$$\frac{-1}{\Delta\Omega_m}\left[\frac{z^{-|m|-1}}{|m|!} e^{-1/z} E_1(-1/z) + \sum_{k=1}^{|m|} \frac{(|m|-k)!}{|m|!} z^{-k}\right]$$

$$\frac{1}{\Delta\Omega_m} F(1, |m|+1; \mu + |m| - 1; \mu z)$$

for the two λ respectively, where $z = v_z/\Delta\Omega_m$. For the transverse case, the expression for the exponential distribution is the same, and for the other one obtains $F(1, |m| + 1; \mu + |m|; \mu z)$.

The asymptotic expansion of the reciprocal of (12) for large $\Delta\Omega_m$ is now given by

$$\Delta\Omega_m - v_z \frac{\int_0^\infty u^{|m|+1} f(u)\, du}{\int_0^\infty u^{|m|} f(u)\, du} + O\left(\frac{v_z^2}{\Delta\Omega_m}\right).$$

The coefficient of v_z is $|m| + 1$ for (13), and $\mu(|m| + 1)/(\mu + |m|)$ and $\mu(|m| + 1)/(\mu + |m| - 1)$ for (14) for transverse and longitudinal oscillations respectively. An argument for cases with large tune shifts similar to that which was made for the transverse case applies here as well.

The stability curves for this case look qualitatively similar to those for the transverse case with tune spread in only one plane. However, as $|m|$ increases, the size of the stability region increases rapidly (roughly linearly in $|m|$). Also, collimating the distribution gives a more drastic reduction of the stability region than in the transverse case.

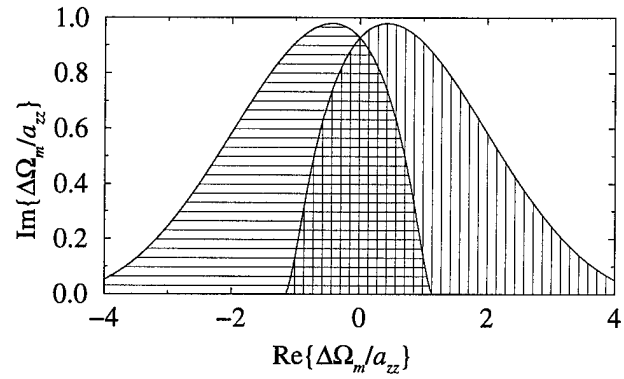

Figure 3: Stability curves for transverse oscillations when $a_{yz} = 0$. Vertical lines give the stable region for $m = +1$, and horizontal lines give the stable region for $m = -1$.

3.2 Other Points of Interest

To make the problem more tractable, it was assumed that the relevant frequencies in the impedance were small compared to the frequencies in the bunch spectrum. This results in the $J_z^{|m|}$ terms in Eqs. (1–6). In the more general case, this factor is replaced by a function which depends on the frequency of the impedance. This can significantly reduce the size of the stability region. Often one considers transverse oscillations with $a_{yz} = 0$. The coherent frequencies one finds are virtually identical for the modes with the same $|m|$ but different signs of m. However, the stability curves are mirror reflections of each other about the imaginary axis. Thus, the modes generally need to be within the intersection of the two stability regions, as shown in Fig. 3, often preventing Landau damping due to longitudinal tune spread when there are large real tune shifts in the transverse modes.

Combining these facts with the observation that the longitudinal tune shift with amplitude is often very nonlinear in action due to potential-well distortion, one should use a great deal of caution in relying on stability diagram based models for determining Landau damping due to longitudinal tune spread.

4 REFERENCES

[1] J. M. Wang, "Longitudinal Symmetric Coupled Bunch Modes," Brookhaven National Laboratory report BNL 51302, Upton, New York, 1980.

[2] M. S. Zisman, S. Chattopadhyay, and J. J. Bisognano, "ZAP User's Manual," Lawrence Berkeley Laboratory report LBL-21270, Berkeley, California, 1986.

[3] J. S. Berg, "Coherent Modes for Multiple Non-Rigid Bunches in a Storage Ring," Ph.D. thesis, Stanford University, 1996.

[4] M. Abramowitz and I. A. Stegun, *Handbook of Mathematical Functions* (Dover, New York, 1972).

AN IMPEDANCE DATA BASE PROGRAM FOR LEP2 AND THE LHC

O. Brüning, CERN, Geneva, Switzerland

Abstract

The development of an impedance data base program was motivated by the changing impedance budgets in the LEP and LHC machines and the resulting need to recalculate the instability thresholds for different parameters. For LEP, the changes are implied by the LEP2 upgrade and for the LHC, the impedance data for most items is still being calculated and continues to change as the geometries of the impedance components converge to a final design. In both cases, feedback from the impedance calculations is desirable. A central data base that allows a semi-automatic recalculation of the impedance data once the geometry of an item changes facilitates such a feedback. The development of the program was guided by four goals. First, the data base program should collect the impedance information in a central place and in a standard format allowing easy access. Second, it should provide procedures for estimating the impact of the impedance on the beam dynamics. Third, the program should provide a user friendly graphical interface to the data base and all external programs that are used for calculating the impedance data. Fourth, it should store the input files for the external programs allowing a semi-automatic recalculation of the impedance data once the geometry of an item changes.

1 INTRODUCTION

Collecting not only the impedance data but also the input files for the programs that were used for calculating it and all data necessary for calculating stability threshold currents, greatly facilitates the recalculation of the threshold currents if the parameters change. For LEPII, for example, the transverse mode coupling instability is expected to limit the maximum current in the machine. As the number of installed impedance components and the optics functions in the machine will change during the upgrade of LEP from 1996 to 1998 it is desirable to provide all the information required for estimating the instability threshold current in the data base and to provide an estimate for any stage of the upgrade. Furthermore, an interface of the data base to ABCI [2] allowed an automatic recalculation of all wake-potentials for different bunch length. The batch-job handling and the data acquisition of the final results is done automatically by the ZBASE program.

For the LHC, most of the impedance items are still in the design process and feedback from the impedance calculations is desirable at this stage. A central data base that allows a semi-automatic recalculation of the impedance data once the geometry of an item changes facilitates such a feedback. Having all the data and input files of the impedance items in a central place and in a standard format also facilitates the exchange of information between the different groups and laboratories who are involved in the design process.

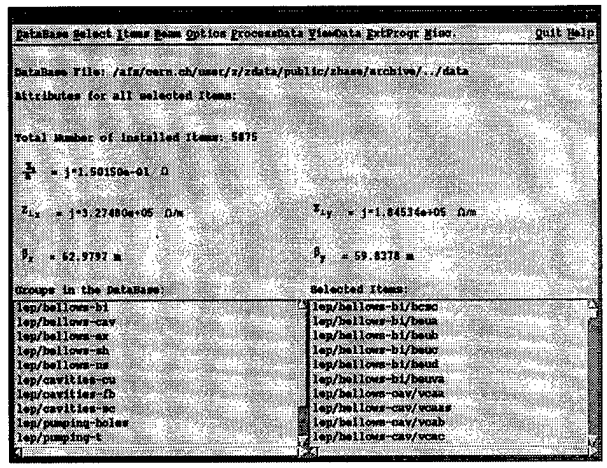

Figure 1: *The graphical user interface for the* **ZBASE** *program showing the net impedance attributes for all LEP* **items** *but the RF-cavities.*

2 REALIZATION OF THE DATA BASE

The data base program is written in the Tcl-Tk scripting language to provide portability between different Unix platforms and to facilitate the programming of a graphical user interface. The program, all sub-programs and all data reside on an afs-file system. In this way the data can be accessed from any machine with an afs-mount which facilitates the exchange of information between the different laboratories which participate in the design/analysis of the impedance components. Fig. 1 shows the main graphical user interface for the data base.

The interface allows the user to select different beam and optics parameters (e.q. LEP or LHC), to select different impedance items for further processing, to modify the number of installed items in the machine, or to change and add items to the data base. For example, Fig. 2 shows the interface for selecting and modifying the beam parameters.

3 ORGANISATION OF THE DATA BASE

All data resides on an afs-file system under one common directory. Directly under this directory is a log-file and a file containing the default beam properties. The impedance data is hierarchically organised in four different levels of

0-7803-4376-X/98/$10.00 © 1998 IEEE

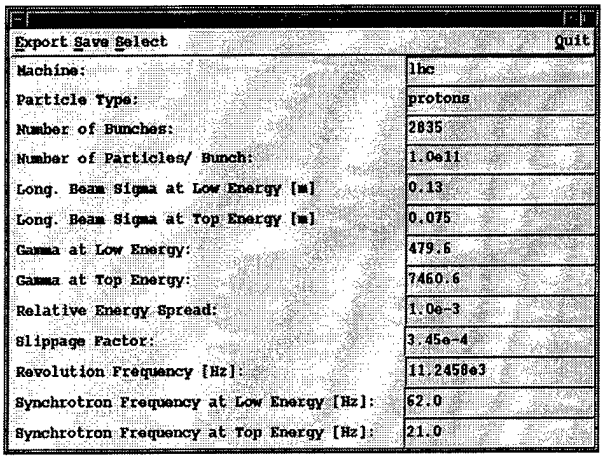

Export Save Select	Quit
Machine:	lhc
Particle Type:	protons
Number of Bunches:	2835
Number of Particles/ Bunch:	1.0e11
Long. Beam Sigma at Low Energy [m]	0.13
Long. Beam Sigma at Top Energy [m]	0.075
Gamma at Low Energy:	479.6
Gamma at Top Energy:	7460.6
Relative Energy Spread:	1.0e-3
Slippage Factor:	3.45e-4
Revolution Frequency [Hz]:	11.2458e3
Synchrotron Frequency at Low Energy [Hz]:	62.0
Synchrotron Frequency at Top Energy [Hz]:	21.0

Figure 2: *Listing of the default parameters for the LHC machine in the ZBASE data base.*

sub-directories:

$$data/machine/group/item/mode/data-files. \quad (1)$$

The machine sub-directory corresponds to a machine for which the data base contains entries. This directory also contains entries for the different optics and beam parameters which are available for the machine. Each group sub-directory contains a certain class of impedance items (e.q. bellows or cavities) and the third sub-directory specifies a single impedance item. Here, each item sub-directory in the ZBASE program corresponds to one element in the Oracle data base. This allows a straight forward link between the Oracle data base and the ZBASE program. Fig. 3 shows an example listing of the items in the data base. The fourth sub-directory specifies the mode, e.g. longitudinal or transverse, for which the impedance data entries are calculated. Such a hierarchical directory structure allows an access of the impedance data without the graphical user interface.

4 DATA TYPES

The impedance data entries consist of six different types of data:

- First, there is one file which contains some basic information on the impedance item (item attributes). It contains comments, the number of items in the machine, the average betatron function values at the location of the items in the machine and the low frequency inductance of the item.
- The second type of data are the higher-order-mode entries.
- The third data type are the loss factors related to an impedance item for different bunch lengths.
- Fourth, the data base program stores wake potentials.

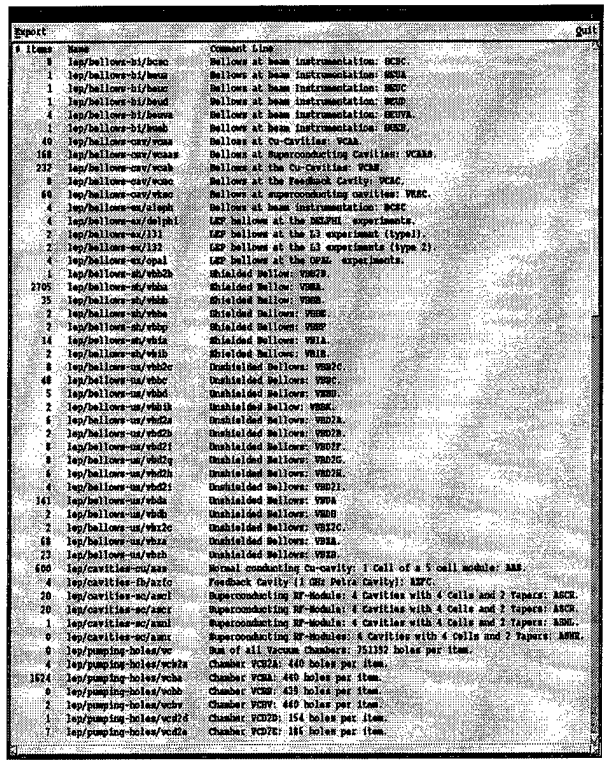

Export			Quit
# items	Name	Comment Line	
1	lep/bellows-bi/bcsc	Bellows at beam instrumentation: BCSC.	
1	lep/bellows-bi/bscu	Bellows at beam instrumentation: BSCU.	
1	lep/bellows-bi/bscc	Bellows at beam instrumentation: BSCC	
1	lep/bellows-bi/bscd	Bellows at beam instrumentation: BSCD	
4	lep/bellows-bi/bscva	Bellows at beam instrumentation: BSCVA.	
1	lep/bellows-bi/bscb	Bellows at beam instrumentation: BSCB.	
40	lep/bellows-cav/vcaa	Bellows at Cu-Cavities: VCAA.	
168	lep/bellows-cav/vcaas	Bellows at Superconducting Cavities: VCAAS.	
232	lep/bellows-cav/vcab	Bellows at the Cu-Cavities: VCAB.	
8	lep/bellows-cav/vcac	Bellows at the Feedback Cavity: VCAC.	
64	lep/bellows-cav/vtsc	Bellows at superconducting cavities: VTSC.	
4	lep/bellows-ex/alsph	Bellows at beam instrumentation: BCSC	
4	lep/bellows-ex/delphi	LEP bellows at the DELPHI experiments.	
2	lep/bellows-ex/l31	LEP bellows at the L3 experiment (type1).	
2	lep/bellows-ex/l32	LEP bellows at the L3 experiments (type 2).	
4	lep/bellows-ex/opal	LEP bellows at the OPAL experiments.	
1	lep/bellows-sh/vbb2h	shielded Bellow: VBB2H.	
2705	lep/bellows-sh/vbba	Shielded Bellow: VBBA.	
35	lep/bellows-sh/vbbb	Shielded Bellow: VBBB.	
2	lep/bellows-sh/vbbe	Shielded Bellows: VBBE.	
7	lep/bellows-sh/vbbp	Shielded Bellows: VBBP.	
14	lep/bellows-sh/vbia	Shielded Bellows: VBIA.	
2	lep/bellows-sh/vbib	Shielded Bellows: VBIB.	
8	lep/bellows-us/vbt2c	Unshielded Bellows: VBT2C.	
48	lep/bellows-us/vbbc	Unshielded Bellows: VBBC.	
5	lep/bellows-us/vbbd	Unshielded Bellows: VBBD.	
2	lep/bellows-us/vbb1k	Unshielded Bellow: VBBK.	
6	lep/bellows-us/vbd2a	Unshielded Bellows: VBD2A.	
2	lep/bellows-us/vbd2b	Unshielded Bellows: VBD2B.	
8	lep/bellows-us/vbd2f	Unshielded Bellows: VBD2F.	
8	lep/bellows-us/vbd2g	Unshielded Bellows: VBD2G.	
6	lep/bellows-us/vbd2h	Unshielded Bellows: VBD2H.	
4	lep/bellows-us/vbd2i	Unshielded Bellows: VBD2I.	
161	lep/bellows-us/vbda	Unshielded Bellows: VBDA	
2	lep/bellows-us/vbdb	Unshielded Bellows: VBDB	
2	lep/bellows-us/vbz2c	Unshielded Bellows: VBZ2C.	
68	lep/bellows-us/vbza	Unshielded Bellows: VBZA.	
23	lep/bellows-us/vbzb	Unshielded Bellows: VBZB.	
600	lep/cavities-cu/aaa	Normal conducting Cu-cavity: 1 Cell of a 5 cell module: AAA.	
4	lep/cavities-fb/arfc	Feedback Cavity:(1 GHz Petra Cavity): ARFC.	
20	lep/cavities-sc/ascl	Superconducting RF-Module: 4 Cavities with 4 Cells and 2 Tapers: ASCL.	
20	lep/cavities-sc/ascr	Superconducting RF-Module: 4 Cavities with 4 Cells and 2 tapers: ASCR.	
1	lep/cavities-sc/asnl	Superconducting RF-Module: 4 Cavities with 4 Cells and 2 Tapers: ASNL.	
6	lep/cavities-sc/asnr	Superconducting RF-Modules: 4 Cavities with 4 Cells and 2 Tapers: ASNR.	
0	lep/pumping-holes/vc	Sum of all Vacuum Chambers: 351192 holes per item.	
4	lep/pumping-holes/vcb2a	Chamber VCB2A: 440 holes per item.	
1624	lep/pumping-holes/vcba	Chamber VCBA: 440 holes per item.	
6	lep/pumping-holes/vcbb	Chamber VCBB: 435 holes per item.	
2	lep/pumping-holes/vcbv	Chamber VCBV: 440 holes per item.	
1	lep/pumping-holes/vcd2d	Chamber VCD2D: 154 holes per item.	
7	lep/pumping-holes/vcd2a	Chamber VCD2A: 186 holes per item.	

Figure 3: *Listing of the number of installed items in the* **ZBASE** *data base.*

- Fifth, the program stores the input files and some of the output files of the programs that were used for calculating the impedance data. All input and output files have a prefix that specifies the program that is associated with the files.
- Sixth, the program stores the location of the items in the machine.

5 PROCESSING DATA

One of the goals for the ZBASE data base program in addition to storing impedance information is evaluating the net effect of the impedance on the beam dynamics. For example, it provides not only the HOM parameters for the impedance items but also some estimates for the corresponding multi-bunch instability rise times. To this end, ZBASE distinguishes between primary and secondary data:

- The primary data describes all information directly associated with the geometry of an item. This would include the inductance, the loss factors and the HOM parameters for example.
- The secondary data describes all information not directly associated with an item. This includes for example the betatron functions and the beam parameters.

During startup the program searches the directories in the data base for secondary data and stores the values in internal arrays. The entries of these arrays can be modified

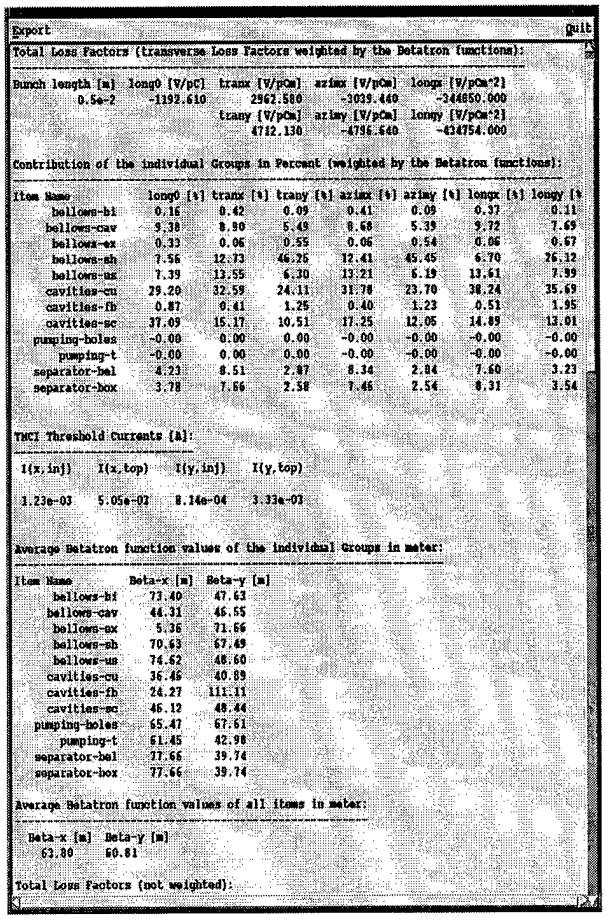

Export quit

Total Loss Factors (transverse Loss Factors weighted by the Betatron functions):

Bunch length [m]	long0 [V/pC]	tranx [V/pCm]	azimx [V/pCm]	longx [V/pCm^2]
0.5e-2	-1192.610	2962.580	-3039.440	-344850.000
		trany [V/pCm]	azimy [V/pCm]	longy [V/pCm^2]
		4712.130	-4796.640	-434754.000

Contribution of the individual Groups in Percent (weighted by the Betatron functions):

Item Name	long0 [%]	tranx [%]	trany [%]	azimx [%]	azimy [%]	longx [%]	longy [%
bellows-bi	0.16	0.42	0.09	0.41	0.09	0.37	0.11
bellows-cav	9.38	8.90	5.49	8.68	5.39	9.72	7.69
bellows-ex	0.33	0.06	0.55	0.06	0.54	0.06	0.67
bellows-sh	7.56	12.73	46.26	12.41	45.45	6.70	26.12
bellows-us	7.39	13.55	6.30	13.21	6.19	13.61	7.99
cavities-cu	29.20	32.58	24.11	31.78	23.70	38.24	35.69
cavities-fb	0.87	0.41	1.25	0.40	1.23	0.51	1.95
cavities-sc	37.09	15.17	10.51	17.25	12.05	14.89	13.01
pumping-holes	-0.00	0.00	0.00	-0.00	-0.00	-0.00	-0.00
pumping-t	-0.00	0.00	0.00	-0.00	-0.00	-0.00	-0.00
separator-bel	4.23	8.51	2.87	8.34	2.84	7.60	3.23
separator-box	3.78	7.66	2.58	7.46	2.54	8.31	3.54

TMCI Threshold Currents [A]:

I(x,inj)	I(x,top)	I(y,inj)	I(y,top)
1.23e-03	5.05e-02	8.14e-04	3.33e-03

Average Betatron function values of the individual Groups in meter:

Item Name	Beta-x [m]	Beta-y [m]
bellows-bi	73.40	47.63
bellows-cav	44.31	46.55
bellows-ex	5.36	71.66
bellows-sh	70.63	67.69
bellows-us	74.62	48.60
cavities-cu	36.46	40.89
cavities-fb	24.27	111.11
cavities-sc	46.12	48.44
pumping-holes	65.47	67.61
pumping-t	51.45	42.98
separator-bel	77.66	39.74
separator-box	77.66	39.74

Average Betatron function values of all items in meter:

Beta-x [m]	Beta-y [m]
63.80	60.81

Total Loss Factors (not weighted):

Figure 4: *The net lossfactors and estimates for the transverse-mode-coupling instability (tmci) threshold currents for the LEP impedance data.*

by any user. In order to process impedance data, the user must first select items from the data base. All selected item names are again stored in an array. When the program processes the impedance data it first goes through this name array and reads the required primary data for each item from the files in the data base. The required secondary data is read from the internal arrays. For example, the graphical user interface in Fig. 1 shows the processed attributes of all the LEP impedance items but the RF-cavities. Fig. 4 shows an example for the lossfactors with an estimate for the transverse mode coupling instability.

6 PROGRAM INTERFACES

Currently ZBASE offers graphical user interfaces and example input files to ABCI, URMEL, MAD and MAFIA [3][5][4]. The interfaces allow the user to select and modify input files from the data base or any other directory and manage the job handling on the CERN-SP batch computer system. For example, the ABCI interface of the ZBASE program can resubmit a selected range of items from the data base, automatically collect the final results of the calculations and update the data base accordingly. The job-submision and job-handling is done by the data base program. In this way it is easy to recalculate the loss factors and wakepotentials for different bunch length and mesh sizes for a large number of impedance items. The Tcl-Tk scripting language allows the creation of additional interfaces for any other program which is of interest for an impedance analysis.

7 SUMMARY

The main aim of the ZBASE impedance data base is to provide the impedance data of one or more machines in a standard format and in a central place which is accessible to everybody. The program is written in the Tcl-Tk scripting language to provide portability between different Unix platforms and to facilitate the installation of additional procedures and interfaces to external programs which evaluate the impact of the machine impedance on the beam dynamics. By collecting not only the impedance data but also the input files for the programs that were used for calculating the impedance data and providing graphical user interfaces for the programs that were used for the impedance calculations, greatly facilitates the recalculation of the impedance data if the parameters change. The current data base contains impedance data for LEP and LHC. However, the data base could easily be extended to other machines like the SPS for example.

8 REFERENCES

[1] John K. Ousterhout, 'Tcl and the Tk Toolkit' Addison-Wesley Professional Computing Series (1994).

[2] Y. H. Chin 'User's Guide for ABCI Version 8.7', CERN SL/94-02 (AP).

[3] C. Palm, U. van Rienen, T. Weiland 'URMEL and URMEL-T USER GUIDE', DESY M-85-11, December 1985

[4] R. Klatt, F. Krawczyk, W.R. Novender, C. Palm, T. Weiland (DESY), B. Steffen (Julich,Forschungszentrum), T. Barts, M.J. Browman, R. Cooper, C.T. Mottershead, G. Rodenz, S.G. Wipf 'MAFIA - A THREE-DIMENSIONAL ELECTROMAGNETIC CAD SYSTEM FOR MAGNETS, RF STRUCTURES, AND TRANSIENT WAKE FIELD CALCULATIONS', DESY M-86-07, August 1986

[5] H. Grote and F.C. Iselin, 'The MAD Program User's reference Manual', CERN SL/90-13 (AP).

[6] O.S. Bruning, 'ZBASE User's Guide Version 1.1 An Impedance Data Base Program', CERN SL 96-69 AP

THE HOM STUDY OF CESR RF CAVITIES USING SINGLE CIRCULATING BUNCH *

A. Temnykh[1], D. Hartill, S. Belomestnykh[1] and R. Kaplan
Laboratory of Nuclear Studies Cornell University, Ithaca NY 14953, USA

Abstract

The CESR RF system consists of four 5-cell RF cavities [1]. Each cell has a field probe sensitive to the voltage in the cell. We used a single bunch circulating in the ring as the driving current which gives a well known spectrum. The signals from the field probes were analyzed and we were able to identify the peaks seen in the spectra as higher-order modes (HOMs) that are excited by the beam in RF cavities. Analysis of the peak shapes and location gave us the Q factors of parasitic modes and their frequencies. The reliability of data was verified with direct measurement using a Network analyzer. The information about Qs and frequencies of the parasitic modes will be used for the multi-bunch beam stability analysis.

1 INTRODUCTION

It was found that the maximum beam current at CESR is limited by the muti-bunch beam instability. The appearance of this instability is seen as the self-excited lines in the spectra of the signals picked up from BPM buttons. To determine which of CESR elements are responsible for that we performed the following experiment. Keeping beam current constant we changed the temperature of one of the CESR RF cavities at a time and observed the amplitude of the self-excited line in the spectrum (see [2]). The cavity temperature variation causes the small profile distortion leading to the frequency shift of the cavity HOMs. The frequency of the fundamental mode is kept in place by the tuner, but the frequencies of all other modes can be shifted unpredictably. If the frequency of one of those HOMs will appear in the vicinity of the lines presented in the spectrum of the beam current, it may result in high parasitic voltage in cavity which may drive the beam instability. The mode voltage is proportional to the beam current and depends on the quality factor Q and the mode specific impedance R/Q. While R/Q for each mode can be calculated, the reliable value of Qs and frequencies can be obtained only from measurements. To obtain this information for the cavities presently installed in the ring we directed experiments described below. Obtained data will help us to analyze multi-bunch beam instability and make a proper choice for the beam current increase strategy.

2 HIGHER ORDER MODES IDENTIFICATION

The CESR RF system consists of four 5-cell RF cavities. Two of them, E1 and E2, are located in the east side of the ring and two others, W1 and W2, are in the west side. Each cell has a field probe sensitive to the voltage in the cell. We analyzed the signals from these probes in our experiments. To excite higher-order modes we used a single bunch circulating in the ring which gives us simple spectrum of driving current. This spectrum contains all harmonics of the revolution frequency, $f_0 = 390.13kHz$. The harmonic strength depends on its frequency, f, as $exp(-f^2/(2f_c^2))$, where $f_c \sim 3GHz$ is determined by the bunch length. Figure 1 shows spectra of a signal picked from the field probe of the E1 cavity cell number 4. The circulating current was 6 mA in a single positron bunch. The first plot, marked as

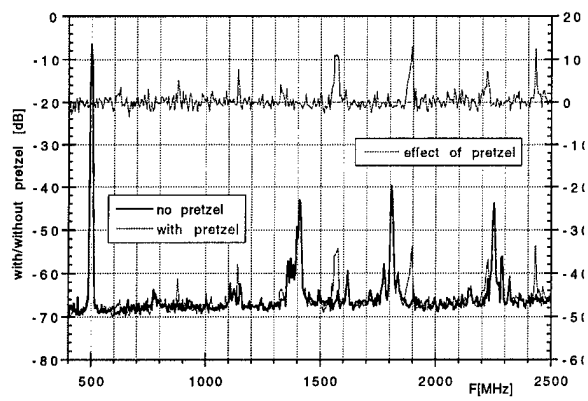

Figure 1: Spectra of signal from field probe of E1 cavity cell 4.

"no pretzel", is the spectra obtained with the beam orbit close to the cavity axis. We can expect excitation of only longitudinal HOMs in this case. The second spectrum, labeled as "with pretzel", is for the pretzelized orbit, i.e. the beam orbit was shifted by approximately 10 mm off the axis in horizontal plane. One can see that additional peaks appear which may be interpreted as the excitation of the dipole modes. The bottom plot, "effect of pretzel", is the result of subtraction of the first spectrum from the second one.

The next step was to identify peaks seen in spectrums with calculated higher-order modes. The URMEL calculations were done for the single-cell. Table 1 shows the calculated characteristics of longitudinal modes found by URMEL in the frequency range from $500MHz$ to $2.5GHz$. It contains frequencies and R/Qs. The measured spectrum for the on axis beam orbit is shown in figure 2. Dots represent calculated HOMs. We used the logarithm of the ratio of a mode R/Q to the fundamental mode R/Q

* Work supported by the National Science Foundation
[1]On leave from BINP, Novosibirsk

Num	Type	f [MHz]	$R/Q[\Omega]$	seen in spectra
1	TM0-Ex-1	498.16	132.47	yes
2	TM0-Mx-1	773.52	25.645	yes
3	TM0-Ex-2	1125.4	1.6010	yes
4	TM0-Ex-3	1351.4	6.0730	yes
5	TM0-Mx-2	1401.8	12.578	yes
6	TM0-Ex-4	1750.5	5.0770	yes
7	TM0-Mx-3	1791.5	4.9880	yes
8	TM0-Ex-5	1961.0	0.0170	no
9	TM0-Mx-4	2146.0	0.5930	?
10	TM0-Ex-6	2228.7	3.4640	yes
11	TM0-Mx-5	2274.2	1.2160	yes

Table 1: List of longitudinal modes found by URMEL between 500 MHz and 2.5 GHz.

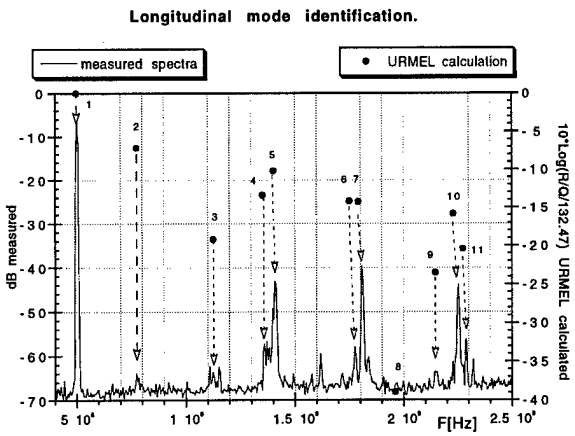

Figure 2: Longitudinal modes identification.

for the vertical positioning the dots. It gives us a sense of the relative mode strength.

There is no doubt that the peaks in the spectra are related to the higher-order modes and we can say with certain which mode is responsible for the appearance of which peak. Note that the field probe sensitivity is different for different modes. It depends on the probe location and on the mode field pattern. The mode with the higher voltage may give the peak with smaller amplitude than the other one with the lower voltage. So, it would be wrong to compare measured peaks amplitude with calculated R/Q.

The same procedure was done for the dipole modes. Figure 3 shows the difference between two spectra, with and without pretzel. Here, also, one can see correlation between peaks and dots representing calculated HOMs, (see Table 2). So we again are able to say which peak corresponds to which mode.

The next step was to study the characteristics of higher-order modes needed for multi-bunch beam stability analysis.

Num	Type	f [MHz]	$R/Q[\Omega]$ @4.4cm	seen in spectra
1	1-Mx-1	747.19	0.77700	
2	1-Ex-1	871.35	17.696	yes
3	1-Mx-2	1138.8	24.971	yes
4	1-Ex-2	1225.8	0.014000	
5	1-Mx-3	1327.6	0.91400	yes
6	1-Ex-3	1500.5	0.87600	
7	1-Mx-4	1562.2	19.187	yes
8	1-Ex-4	1621.8	0.57700	
9	1-Ex-5	1749.8	0.18100	
10	1-Mx-5	1879.8	6.5990	yes
11	1-Ex-6	1885.6	19.667	yes
12	1-Mx-6	1948.8	0.061000	
13	1-Mx-7	2046.4	0.91400	
14	1-Ex-7	2196.6	3.0320	yes
15	1-Mx-9	2223.9	2.7300	yes
16	1-Ex-8	2264.4	0.63000	

Table 2: List of dipol modes found by URMEL between 500 MHz and 2.5 GHz.

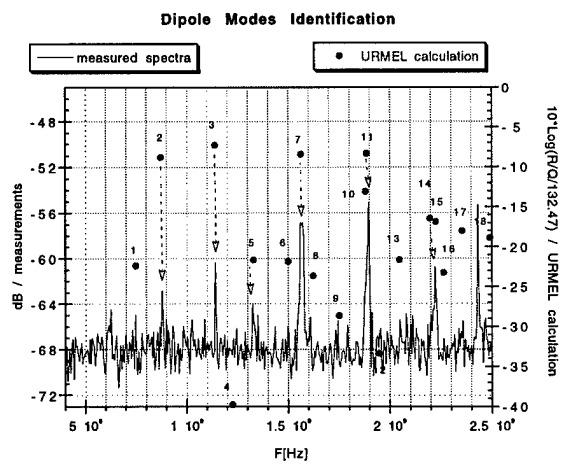

Figure 3: Dipol modes identification.

3 HOM CHARACTERISTICS STUDY

Figure 4 shows a spectrum of signal from the E1 cell 4 field probe in a $\pm 3.5\,MHz$ frequency range around 1801.5 MHz. We know from the previous measurements that here is a peak caused by the TM0-Mx-3 mode excitation. The form of the spectrum seen in figure 4 reflects the spectrum of driving current as well as shape of the resonance. As far as we used a single circulating bunch, its spectrum has lines at harmonics of the revolution frequency. The envelope of the spectrum is determined by the TM0-Mx-3 mode parameters. This envelope was fitted with the theoretical resonant function using the resonant frequency f_m and the quality factor Q as free parameters. The best fitting was obtained with $Q = 15,853 \pm 9,000$ and $f_m = 1801.4MHz$. One can see relatively large uncertainty in Q. It occurs because

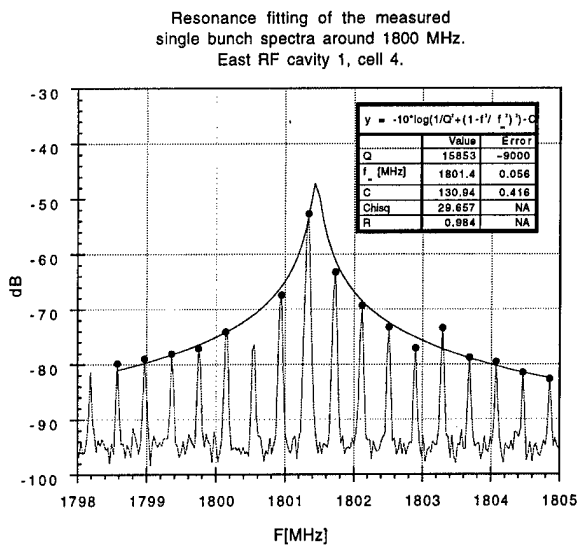

Figure 4: Resonance fitting of spectrum around TM0-ME-3 mode location. E1 cavity, cell 4.

the fitted points are sampled by the revolution frequency and in the case of high Q only few of them, which are close to the mode frequency, play role in the Q determination. In the case of low Q the number of points important for the Q determination is getting larger and the accuracy becomes better. The accuracy of the mode frequency fitting is always better than 0.1 MHz.

To verify these numbers we performed the direct measurements of the cell 4 of the E1 cavity using a Network analyzer. The higher-order mode probe [3] was used to drive field in the cell and field probe was used to pick up the signal. By measuring the S21 function we found the peak of the TM0-Mx-3 mode with $Q = 16,400$ and $f_m = 1801.563MHz$. These numbers are in a good agreement with numbers obtained from the beam measurement. The CESR RF system contains a total of 20 accelerating cells. All of them have slightly different spectra, i.e. slightly different peak amplitudes and positions. It may be easily explained by the their mechanical differences. For the purpose of the muti-bunch beam stability analysis it is necessary to know the mode frequency and Q variation among the cells. Table 3 shows the result of analysis of two longitudinal modes, TM0-Mx-2 and TM0-Mx-3, for 12 cells. One can see that the TM0-Mx-3 mode has average frequency of $1803.2MHz$ with $\pm 1.8MHz$ rms. spread among the cells. Its average Q is about 11,000 with $\pm 7,000$ rms. The TM0-Mx-2 mode characteristics are $1406.41 \pm 1.94MHz$ frequency and Q in a range from 400 to 3,000. Note that the TM0-Mx-2 modes have remarkably lower Qs than those of TM0-Mx-3.

4 CONCLUSION

Peaks seen in spectra of the signals from the RF field probes have been identified as higher-order modes exited by the beams. We measured Q factors and tunes of the TM0-Mx-2 and TM0-Mx-3 modes in 12 RF cells using a single circulating bunch as a driving current . This information will be used for multi-bunch beam stability analysis.

Cav/cell	TM0-Mx-2 mode		TM0-Mx-3 mode	
	$f_m[MHz]$	Q	$f_m[MHz]$	Q
E1/1	1405.3	485	1800.4	12300
E1/2	1409	507	1803.7	8922
E1/4	1404.9	1007	1801.4	24800
E1/5	1405.7	3168	1803	5302
E2/1	1404	506	1802	12484
E2/2	1410.2	2117.6	1806.5	5548
W1/1	1404.1	614	1801.3	9227
W1/2			1804.9	3535
W1/4	1406.1	613	1803.4	5736
W1/5	1407.3	1944	1804.2	3860
W2/1	1406.9	422	1803.8	18842
W2/2	1407	550	1803.5	20000
Average	1406.4	1085	1803.2	10879
RMS	1.9	914	1.7	7011

Table 3: Characteristics of the TM0-Mx-2 and TM0-Mx-3 modes.

5 ACKNOWLEDGMENT

We wish to thank all people of the CESR operating group who assisted us in our measurements.

6 REFERENCES

[1] *RF Cavity Design for High Current Operation of the Cornell Electron Storage Ring*, S. Greenwald, et al. Proceedings of the 1989 Particle Accelerator Conference, Chicago, IL, March 1989, Vol. 1, pp. 226-228

[2] *CESR Elog: Machine Studies, CESR Impedance and Instabilities, Sept 17 1996*

[3] *CESR RF System* , R. Sundelin, et al. IEEE Trans. on Nucl. Sci., Vol. NS-28, No. 3, Part 2 , pp. 2844-2846 (June 1981).

CONTROLLING THE RESISTIVE WALL INSTABILITY IN THE FERMILAB MAIN RING

D. Capista, D. McGinnis, J Steimel, I. Kourbanis, and D.Still
*Fermi National Accelerator Laboratory** P.O. box 500 Batavia, IL 60510

Abstract

The Fermilab Main Ring has a strong transverse instability identified as a resistive wall[1] . Previous methods of dealing with this problem have primarily been to find settings of tune, chromaticity, and octupole that result in stable operation. Controlling this instability in this manner has had limited success and reduces beam lifetime. A new damper system has been installed in the Main Ring to control this instability. This damper effectively provides a negative impedance to the accelerator to cancel the effects of the resistive wall. With this damper in operation we have been able to adjust the tune, chromaticity, and octupole settings to improve beam efficiency without becoming unstable due to the resistive wall of the accelerator.

INTRODUCTION

The transverse modes commonly referred to as the resistive wall, instability have previously been observed and measured in the Main Ring1. When running intensities above about 1 E13 in the machine it becomes necessary to make adjustments in the chromaticity and octupole circuits away from nominal settings to stabilize the beam. If adjustments are not made, the resistive wall will became strong enough to cause growth in the betatron oscillations until the beam hits the accelerator wall and is lost (fig 1 and 2). Notice that the growth rate in the vertical plane is significantly greater than that in the horizontal. This difference is due to the geometry of the rectangular beam pipe. In the Main Ring, on average, the horizontal aperture is about 2.7 times that of the vertical. Since the magnetic field produced from the wall currents changes as 1/r2, where r is the distance from the beam to the beam pipe, it is clear that the kick the beam receives will be much stronger in the vertical plane than it is in the horizontal. In the past there were two different damper systems built for the Main Ring. These systems are referred to as the Slow dampers and the Super damper. The Slow dampers operate in both planes and have bandwidth to damp first 40 modes. The super damper operates in the vertical plane only and can damp all 1113 modes. The main reason the slow dampers do not damp the resistive wall is that they are saturated by the revolution frequency of the beam. These dampers do not have any cancellation of the revolution frequency, or harmonics, and as a result are sensitive to the position of the beam through the beam position detector. The Super damper was built for the vertical plane because the resistive wall is so much stronger. This damper has the same problem with the revolution frequency as the Slow dampers but has more bandwidth to work on a bunch by bunch basis. This Super damper does provide some damping for the resistive wall but it turns out that the overall gain of the system may not be high enough and the result is that this damper is not sufficient for the resistive wall at high intensities. The horizontal plane was not addressed because it was thought that the resistive wall would not be an issue. As improvements to the upstream machines occurred, the beam emittance in all planes improved and the intensity threshold of the instability became lower. Consequently, the horizontal plane became the limiting factor on the intensity before the new dampers were implemented.

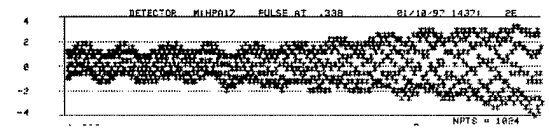

Fig 1. Turn by turn data from a BPM showing growth in horizontal betatron amplitude due to resistive wall. 1024 turns are displayed.

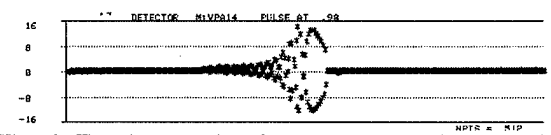

Fig 2. Turn by turn data from a BPM showing growth in vertical betatron amplitude due to resistive wall. 512 turns are displayed.

NEW DAMPER SYSTEM

The damper system consists of 4 beam position detectors, two for each plane, two kickers, low level electronics, and high level electronics. The beam position signals are detected at the RF frequency and down converted by mixing with the low level RF signal (LLRF). This process creates a phase synchronization problem between the LLRF and the beam due to the locations of the LLRF and the damper systems[3]. These two systems are separated by about 2 Km and the frequency shift during acceleration is about 291 khz.

The number of wavelengths that occur across this 2 Km distance changes as the LLRF frequency sweeps. This effect needs to be compensated in order for the damper to remain in phase with the beam. This compensation is accomplished with a phase unwinder and a phase locked loop. The phase unwinder monitors the LLRF frequency and makes course adjustments to the LLRF phase. The phase locked loop compares the phase of the beam and the phase of the LLRF signal and makes fine adjustments to the phase of the LLRF signal. Together these two phase corrections provide a stable, beam synchronous, LLRF signal for the damper

* Operated by Universities research Association Under contract with the U.S. department of energy.

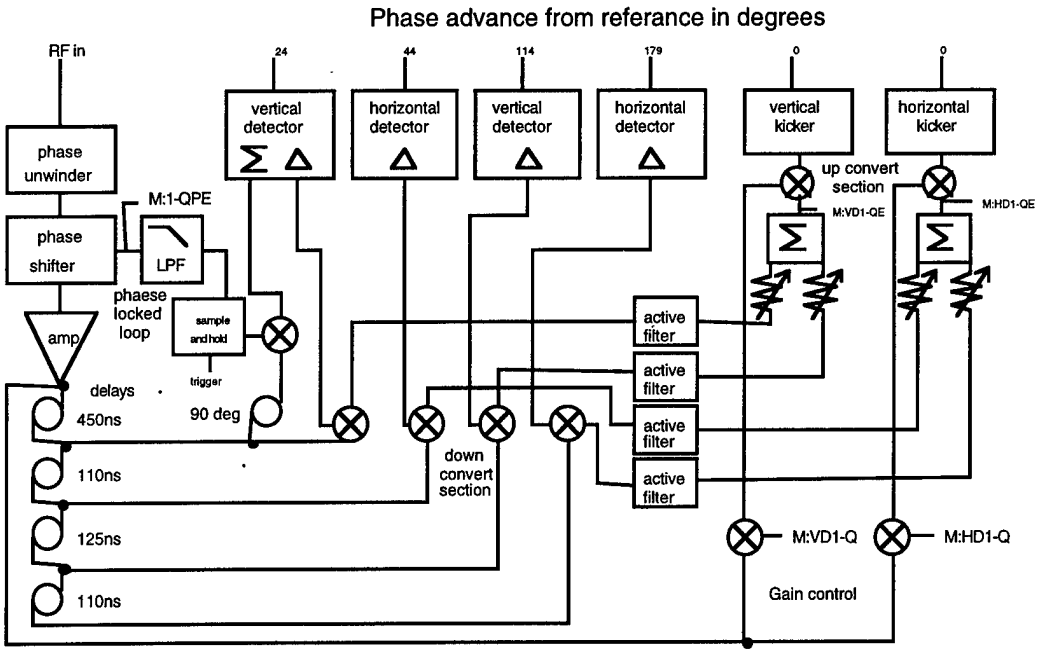

Fig 3. Block diagram of the damper system. M:1-QPE is the phase correction of the phase locked loop. M:HD1-QE and M:VD1-QE are horizontal and vertical corrections applied to the kickers. M:HD1-Q and M:VD1-Q are ramp generators which control the gain of the damper during the machine cycle.

system. This LLRF signal is sent through a series of delay elements which correct for cable length differences between detectors. The next stage of the damper is the down conversion section. In this section the difference signals from the beam detectors are mixed with the phase corrected LLRF signals. The reason this conversion is necessary is because the response of the beam detector is much greater at the RF frequency. The down converted beam signal is then sent through a series of filters to isolate the component due to the resistive wall instability. The frequency components induced on the beam from the resistive wall below the first revolution frequency are $\omega[1-f(\sqrt{\ })]$ and $\omega[f(\sqrt{\ })]$ .Where ω is the revolution frequency and $f(\sqrt{\ })$ is the fractional tune[2]. In the Main Ring the revolution frequency is 47 khz and the induced frequencies from the resistive wall are about 19 and 28 khz. There are actually three sections to these active filters: a high pass filter to eliminate the low frequency signals such as the synchrotron frequency, a low pass filter to eliminate the higher order modes and a sharp notch filter at the revolution frequency. These filters are tuned such that the phase shift is 0° at F_{rev} / 2. The filters are set in this manner is to provide an integer revolution period delay. Together these filters select the signal necessary to correct the instability from the resistive wall. In an ideal situation one would have one beam pickup with 90° of phase advance between the pickup and the kicker. A position error at the pickup would then be an angle correction at the kicker. Since ideal situations rarely exist in practice, two pickups are used with the signals summed to give the kick correction. The filtered signals are sent through variable attenuators and then summed together. This type of system is sensitive to the tune of the machine and these attenuators need to be adjusted if a different operating point is desired. After these signals are summed, they are up converted to the RF frequency of the accelerator. The gain of the damper is controlled by changing the level of the RF signal. The fundamental RF frequency is suppressed from this modulated signal leaving the two sidebands to be passed to the high level for final amplification. The high level final is a broad band solid state amplifier. This amplifier has a bandpass from 22 to 94 mhz and a power output of 1.6 Kw. There are two of these amplifiers for each plane, one for each plate. They are driven 180° out of phase with each other to provide the voltage at the kicker plates to deflect the beam. Diagnostics to aid in tuning the gain for optimal performance are also provided by this damper. The summed signals from the damper are fed into the accelerator control system and provide information as to the amplitude of the beam oscillations induced by the resistive wall.

MEASUREMENTS AND PERFORMANCE

Since the damper system provides a measurement of the strength of the resistive wall instability, it is a convenient way to measure the growth rate. By turning off all the dampers in the Main Ring and setting the chromaticity more positive at 8 Gev, it is easy to induce this instability. Figure 4 is an example of this situation.

Repeating this measurement for the horizontal plane and fitting to an exponential function will give a rough idea of the growth rates of the instabilities. In this case the growth rates came out to be 130/sec vertically and 23/sec horizontally[4]. The response of the damper's

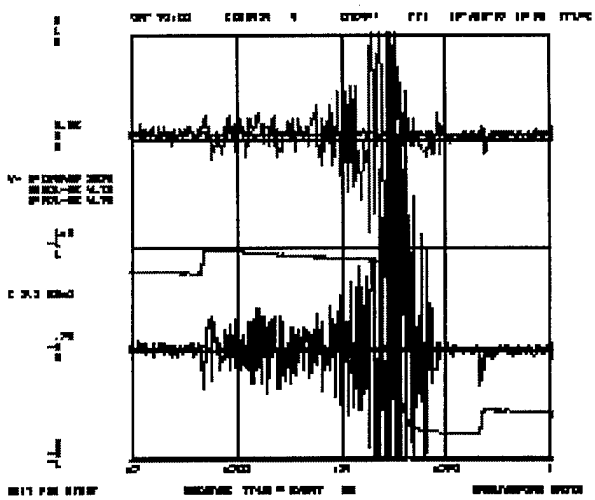

Fig. 4 Shows the growth rate of the instability in the vertical plane. Displayed is the beam current and the error signals from both damper planes. bottom trace is vertical error, center trace is beam current, top trace is horz error.

filters could effect this measurement. When analyzing the turn by turn data from fig. 2, the actual growth rate appears to be larger. Measurements of the damping rate can be found by measuring the open loop gain of the damper system and measuring the frequency spread of the betatron signal. This measurement gives a damping rate of about 10 turns and depends on the chromaticity. Another way to look at the damping rate is to look at the injection oscillations on the BPM turn by turn fig. 5.

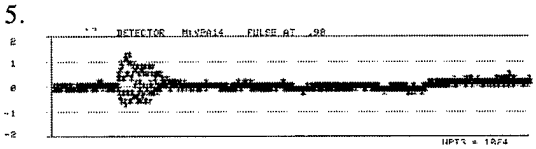

Fig. 5 injection oscillations and damping. 1024 points.

With this type of measurement it is difficult to obtain a valid number for the damping rate because the damper system saturates with vary small oscillations. This saturation causes linear damping until the oscillations become small enough for the damper to get out of saturation.

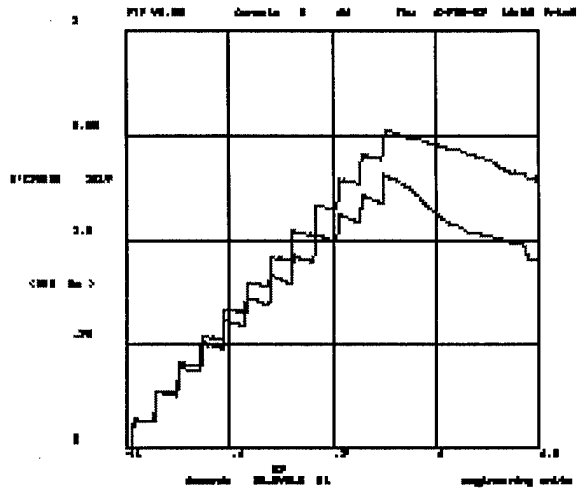

Fig.6 Multibatch injected beam. The two traces show the efficiency difference with the damper on and off. In both cases the accelerator was adjusted for maximum efficiency while avoiding the resistive wall instability.

CONCLUSION

The overall effectiveness of this damper system can be seen from fig. 6. Without the damper system it is necessary to introduce large chromaticities into the beam in order to avoid the resistive wall. This process causes the beam lifetime to suffer which results in poor efficiency. When this damper is in use, the impedance from the accelerator wall is effectively canceled. With this instability under control, adjustments to tune, chromaticity, and octupole can be made to optimize the efficiency of the accelerator.

With this damper in operation we have been able to obtain an intensity of 2.81 E13 ppp. Without this damper it would have been difficult to reach 2 E13ppp. In the era of the Main Injector, the damper system will be modified to operate over many modes. For this modification to work effectively, electronics will have to effectively cancel the revolution frequency.

REFERENCES

[1] G.Jackson, "Measurement of the Resistive Wall Instability in the Fermilab Main Ring" IEEE Part.Acc.Conf., Vol 3, (1991) p.1755.

[2] F. Sacherer. "Transverse Bunched Beam Instabilities-Theory", Proc. 9th Int.Conf. on High Energy Acc. (1974), P341.

[3] J. Steimel, "Trigger Delay Compensation for Beam Synchronous Sampling", Fermilab Beam Instrument. workshop. (1996).

[4] D.Capista "Transverse Dampers for the Main Ring Resistive Wall" Fermilab EXP-200. (1997)

IMPEDANCE SCALING AND IMPEDANCE CONTROL

W. Chou and J. Griffin, Fermilab,* P.O. Box 500, Batavia, IL 60510, USA

Abstract

When a machine becomes really large, such as the Very Large Hadron Collider (VLHC),[1] of which the circumference could reach the order of megameters, beam instability could be an essential bottleneck. This paper studies the scaling of the instability threshold *vs.* machine size when the coupling impedance scales in a "normal" way. It is shown that the beam would be intrinsically unstable for the VLHC. As a possible solution to this problem, it is proposed to introduce local impedance inserts for controlling the machine impedance. In the longitudinal plane, this could be done by using a heavily detuned rf cavity (*e.g.*, a biconical structure), which could provide large imaginary impedance with the right sign (*i.e.*, inductive or capacitive) while keeping the real part small. In the transverse direction, a carefully designed variation of the cross section of a beam pipe could generate negative impedance that would partially compensate the transverse impedance in one plane.

1 INTRODUCTION

In a recent workshop LHC96 at Montreux, Switzerland, a survey was conducted for the measured impedance of existing machines and expected impedance of some new machines.[2] It is interesting to note that the impedance, $Z_{\|}/n$, has been lowered by about an order of magnitude since 1980s, thanks to a number of low impedance design features in new machines (*e.g.*, a uniform beam pipe cross section, rf shielding of vacuum components, tapered transitions, *etc.*). Nowadays one believes that for high energy machines, in which space charge contribution is negligible, $Z_{\|}/n$ can be held at around 1 ohm or below, no matter how big the machine is. However, the transverse impedance $Z_{\perp}$ scales almost linearly with the machine size due to accumulation effects of discontinuities in the beam environment. This raises the question whether the beam could become intrinsically unstable in a large machine.

2 INSTABILITY SCALING

2.1 *The transverse mode coupling instability*

Although this type of instability has been well studied and clearly observed in electron machines, it has never been seen in any proton machine. But still, one always wants to keep the beam current below the threshold. The threshold current per bunch is:

$$I_{th} = \frac{2\nu_s(E/e)}{\beta_{av}(\mathrm{Im}Z_{\perp})} \cdot \frac{4\sigma_b}{R} \tag{1}$$

in which ν_s is the synchrotron tune, E the particle energy, e the electron charge, β_{av} the average β-function, $\mathrm{Im}Z_{\perp}$ the imaginary part of transverse impedance, σ_b the *rms* bunch length and R the machine radius. In a relativistic case, the following relations hold:

$$\nu_s\sigma_b = R\eta \cdot \left(\frac{\sigma_E}{E}\right) \tag{2}$$

$$\eta = \frac{1}{\gamma_t^2} \tag{3}$$

where σ_E/E is the relative *rms* energy spread, η the slip factor and γ_t the transition γ. Plugging into (1) one gets:

$$I_{th} \propto \frac{\frac{R}{\gamma_t^2} \cdot E}{\beta_{av}(ImZ_{\perp}) \cdot R} \cdot \left(\frac{\sigma_E}{E}\right) = \frac{E}{\beta_{av}(ImZ_{\perp}) \cdot \gamma_t^2} \cdot \left(\frac{\sigma_E}{E}\right)$$

A *large* machine means large R and high E. The scaling goes as:

$$\begin{aligned} E &\propto R \\ \gamma_t &\propto \sqrt{R} \\ \beta_{av} &\propto \sqrt{R} \\ \mathrm{Im}Z_{\perp} &\propto R \end{aligned}$$

Thus, the threshold bunch current decreases when the machine size increases:

$$I_{th} \propto R^{-3/2} \cdot \left(\frac{\sigma_E}{E}\right) \tag{4}$$

This scaling can also be expressed in terms of particle numbers. In view of

$$\begin{aligned} I_{th} &= N_b \cdot f_0 \cdot e = N_b \cdot \frac{c}{2\pi R} \cdot e \\ &\propto \frac{N_b}{R} \end{aligned}$$

in which N_b is the number of particles per bunch, f_0 the revolution frequency and c the velocity of light, the maximum N_b would be scaled as:

$$N_b \propto R^{-1/2} \cdot \left(\frac{\sigma_E}{E}\right) \tag{5}$$

Therefore, for large machines (*e.g.*, 10^6 meters in circumference), the transverse mode coupling could become an intrinsic bottleneck limiting the beam intensity and luminosity.

2.2 *The resistive wall instability*

The growth rate of resistive wall instability is:

$$\begin{aligned} \frac{1}{\tau_w} &= \frac{cr_pN_bM}{2\pi\gamma\nu_\beta b^3}\sqrt{\frac{2\rho}{\mu\omega}} \\ &\propto \frac{M}{E\nu_\beta} \cdot \sqrt{\frac{1}{\omega_0}} \cdot N_b \end{aligned} \tag{6}$$

* Operated by Universities Research Association Inc. under Contract No. DE-AC02-76CH03000 with the U.S. Department of Energy.

in which r_p is the classical radius of proton, M number of bunches, γ the relativistic energy of the particle, ν_β the betatron tune, b the beam tube radius, ρ the wall resistivity, μ the vacuum permeability and ω the angular frequency, which equals the product of fractional tune and angular revolution frequency ω_0. By using the following scaling:

$$\begin{aligned} M &\propto R \\ \nu_\beta &\propto \sqrt{R} \\ \omega_0 &\propto R^{-1} \end{aligned}$$

one gets:

$$\begin{aligned} \frac{1}{\tau_w} &\propto \frac{R}{R\sqrt{R}} \cdot \sqrt{R} \cdot N_b \\ &\propto N_b \end{aligned} \tag{7}$$

It is seen that the growth rate is *independent* (to the extent that the scaling holds) of machine size. In other words, for given bunch intensity, bunch spacing and beam pipe (material and cross section), large and small machines have more or less the *same* growth time of the resistive wall instability.

However, when expressing the growth time in terms of turn numbers:

$$n_w = f_0 \tau_w = \frac{c}{2\pi R} \tau_w$$

one obtains:

$$n_w \propto R^{-1} \cdot N_b^{-1} \tag{8}$$

Thus, large machines would require powerful feedback systems (*e.g.*, criss-crossing feedback and one-turn correction scheme).

2.3 *The longitudinal microwave instability*

The longitudinal impedance of a machine, $|Z_\parallel/n|$, is more or less independent of the machine size. So is the microwave instability threshold current:

$$I_{th}^{\text{peak}} = \frac{2\pi\eta}{|Z_\parallel/n|} \left(\frac{E}{e}\right) \left(\frac{\sigma_E}{E}\right)^2 \propto R^0 \tag{9}$$

3 IMPEDANCE CONTROL

3.1 *Longitudinal impedance*

There have been some discussions about using ferrite tori, which provides large inductive part of impedance, to compensate the capacitive part of impedance from, say, space charge. The problem is that the ferrite also introduces large additional real part of impedance, which may hurt the beam as well. Hence, the trick is how to get large reactance (either inductive or capacitive, whichever is needed) while keeping resistance under control. This can be achieved by using a heavily detuned rf cavity. When such a cavity is represented by a lumped RLC circuit, its impedance is:

$$Z(\omega) = R_s \cos\theta \exp(-j\theta) \tag{10}$$

$$\theta = 2Q\frac{\Delta\Omega}{\Omega_0} \tag{11}$$

where R_s is the shunt impedance, Q the quality factor, Ω_0 the resonance frequency, and $\Delta\Omega$ the amount of detuning. From Eq. (10), it is seen that, for any given ImZ, the ReZ is double valued: one for $\theta < 45°$, another for $\theta > 45°$. The ratio of the imaginary and real part of impedance is:

$$\frac{\text{Im}Z}{\text{Re}Z} = \tan\theta \tag{12}$$

For large θ, one gets large ImZ and small ReZ. For instance, when $\theta = 84.3°$, the ratio is 10. A special type of cavity, the biconical structure, is of particular interest for this application. This is because its fundamental and higher order modes (HOM) cover a unique spectrum: $f_0, 3f_0, 5f_0, 7f_0$, *etc.* The existence of a beam pipe attached to this structure will certainly skew the Slater plot slightly but not too much. Table 1 shows the URMEL simulation results of a biconical resonator (17 cm in radius) connected with a beam pipe (2 cm in radius). It is seen the Slater perturbation is small. This special spectrum of resonance modes in this beam-excited resonator indicates that, while the beam induced reactive voltage will offset the potential well (the slope of the rf voltage) and thereby the bunch length, the peak voltage can remain flat due to superposition of the HOMs. (All the HOMs are on the "right" frequencies.)

Table 1. Modes of a Biconical Resonator with Beam Pipe

Mode	Freqency (MHz)	R/Q (Ω)	Q
TM_{01}	487.48 ($1 \times f_0$)	131.8	23788
TM_{02}	1459.6 ($2.994 \times f_0$)	37.04	34204
TM_{03}	2422.9 ($4.970 \times f_0$)	15.53	43231
TM_{04}	3369.6 ($6.912 \times f_0$)	6.159	52383

3.2 *Transverse impedance*

The control of transverse impedance is based on the observation of the so-called negative transverse impedance.[3]-[4] For certain type of structure, *e.g.*, the CERN SPS adaptor, which has a circular cavity connected with rectangular beam pipes on both ends, the first peak of the transverse wakefield in one plane is negative. This means focusing in that direction, *i.e.*, any deflection of the beam from the axis will see a kick to force it back to the axis. Simulations and measurements both show the horizontal and vertical transverse impedance in the SPS are of opposite signs. Thus, one may design special vacuum ports as local impedance insert to control the total transverse machine impedance.

Negative transverse impedance means energy gain of a beam. From the viewpoint of energy conservation, one plane's gain must be another plane's loss. In other words, there would be more positive transverse impedance in the other plane. That plane should be chosen as a less critical one if both planes are not equivalent (which is usually the case in most machines). Furthermore, it will be interesting to see what would be the combined effect if a beam sees alternate focusing and defocusing transverse wakefield kicks.

4 ACKNOWLEDGEMENTS

The authors had interesting discussions on these subjects with B. Zotter, Y. Mori, A. Thiessen and R. Cappi.

5 REFERENCES

[1] G. W. Foster and E. Malamud, Fermilab-TM-1976 (June, 1996).

[2] W. Chou, 'Summary Report of the Intensity Limitations Working Group,' the 3rd International LHC Workshop, Montreux, Switzerland, October 13-18, 1996, to appear in Particle Accelerators (1997).

[3] W. Chou, 'Negative Transverse Impedance,' Light Source Note LS-140, Advanced Photon Source, Argonne National Laboratory (June 1989).

[4] D. Brandt *et al.*, 'Tune Shift Measurements in the SPS,' SPS/AMS/Note/88-14, CERN (December 14, 1988)

MEASUREMENT OF THE KICKER COUPLING IMPEDANCES IN THE SIS AND ESR AT GSI

Udo Blell
Gesellschaft für Schwerionenforschung (GSI)
Planckstr. 1, D-64291 Darmstadt, Germany

Abstract

At high particle intensities coherent transverse beam oscillations may be excited due to the coupling of the beam to individual accelerators components. The characteristic values to describe these beam instabilities are the longitudinal- and transverse coupling impedances. One reason for this beam instability is the inductive interaction between the beam and the lumped kicker magnets. The type of the magnet, e.g. window-frame magnet or C-magnet, and his external electric network are the most important quantities to identify the coupling impedances below the cut-off frequency (for wavegiude modes) of the beam pipe. For the kicker modules in the **SIS** and **ESR** accelerators at **GSI** theoretical calculations and measurement are presented.

1. COUPLING IMPEDANCES OF LUMPED KIKKER MAGNETS

A beam that oscillates with an amplitude $\pm x_0$ induces differential currents on the walls of the beam pipe. These currents produce a transverse magnetic field **B** and an electric field **E,** which deflect the beam. The threshold for beam instability and the growth rates depend on the coupling impedances.
The general definitions of the longitudinal and transverse coupling impedance $Z_\parallel$ and $Z_\perp$ are:

$$Z_\parallel(\omega) = -\frac{\oint E_\parallel(\omega, s)\cdot ds}{I_B} \quad (\Omega) \qquad (1)$$

$$Z_\perp(\omega) = \frac{j}{\beta}\cdot\frac{\oint\left[\vec{E}+\vec{v}\times\vec{B}\right]_\perp \cdot ds}{I_B\ x_0} \quad (\Omega/m) \qquad (2)$$

Where I_B is the beam current, $\vec{v}$ is the beam velocity, and $\beta = v/c$. As for a lumped kicker magnet the electric deflection can be neglected, only the magnetic contribution is considered.
As an approximation the longitudinal and transverse coupling impedances of a lumped and a window frame kicker magnet with the length **l** and a gap height of **2a** can be calculated with the following relations [1]:

Window frame magnet:

$$Z_\parallel(\omega) = \frac{\omega^2\ \mu_0^2\ x_0^2\ l^2}{4\ a^2\ Z_k} \quad (\Omega) \qquad (3)$$

$$Z_\perp(\omega) = \frac{c\ \omega\mu_0^2\ l^2}{4\ a^2\ Z_k} \quad (\Omega/m) \qquad (4)$$

C-magnet with a constant gap height:

$$Z_\parallel(\omega) = \frac{\omega^2\ \mu_0^2 (x_0+b)^2\ l^2}{4\ a^2\ Z_k} \quad (\Omega) \qquad (5)$$

$$Z_\perp(\omega) = \frac{c\ \omega\ \mu_0^2\ l^2}{4\ a^2\ Z_k} \quad (\Omega/m) \qquad (6)$$

with

$$Z_k = j\omega L + Z_g$$

where **L** is the magnet inductance and **Zg** is the contribution of the external circuit. Note that the longitudinal impedances strongly depend on the beam position x_0.In the relations 3-6 one effect is neglected:
There is a relatively large longitudinal impedance due to the induced flux that circulates within the core. It is mostly inductive, with a resistive component due to core losses. This flux does not link the magnet winding, and so is independent of the external electric network of the kicker.
At GSI both at the synchrotron SIS and the storage ring ESR lumped kicker magnets are in operation. Whereas at SIS window-frame modules are used, C-shaped modules are installed at the ESR. The electrical circuit of every modul is based on a 25 Ohm system and the maximum cable load voltage is 80 kV. Figure 1 shows the external electrical circuit part which gives a significant contribution to the coupling impedance. Only those parts of the electric circuit are included, that may be coupled to the circulating beam. For this circuit the impedance **Zg** is defined as:

$$Z_g = \frac{U_{V-Test}}{I_{V-Test}} \qquad (7)$$

0-7803-4376-X/98/$10.00 © 1998 IEEE

The parasitic capacites CD-1 and CD-2 of the HV-terminator in figure 1 are not negligible as they reduce the coupling impedances.

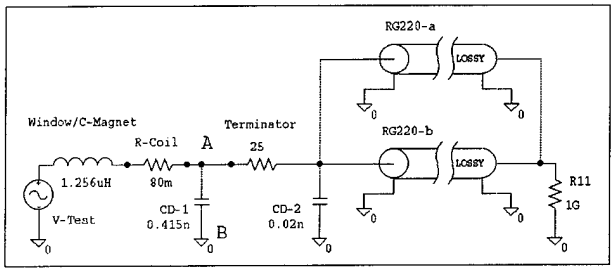

Figure 1: Equivalent electrical circuit for one kicker generator with a test voltage source.

2. MEASUREMENTS

For the calculation of the coupling impedances, based upon equal 3-6, the impedance **Zg** has been determined. As the magnet is installed in a vacuum tank, it is not easy to measure these impedances directly; the only electrical connection outside of the vacuum, is between the points A and B shown in figure 1. For additional measurements the 25 Ohm teminator resistor can be disconnected from the magnet and the cables (length 45m) from the terminator resistor.
To determine **Zg** two measurements of the S(1,1) parameter (reflection-factor) have been performed:

- with terminator and cables, but without the magnet (M1);
- with the magnet and terminator but without the cables (M2).

The correlation between **Z** and **r** is

$$\mathbf{Z} = \mathbf{Z}_0 \frac{\mathbf{1}+\mathbf{r}}{\mathbf{1}-\mathbf{r}} \qquad (8)$$

with $\mathbf{Z}_0 = \mathbf{50\ \Omega}$.

With the first measurement M1 the unknown capacites CD-1 and CD-2 (fig. 1) could be determined by a mathematical comparision with the replaced electrical circuit. With the measurement M2 the total network is determined and the unknown impedance **Zg** has been calculated. The longitudinal and transverse coupling impedances can be calculated with the equation 3-6. The results for the real part of the impedances up to 40 MHz are shown in the lower figures 2 und 3. The resistance of the magnet coil and the dispersion of the rf cables in this frequency range can be neglegted; the parasitic capacites CD-1 and CD-2 are replaced by a 100 pF capacity (voltage divider) between the points A and B (fig 1).
For this case the real part of calculated coupling impedances are shown in the upper figures 2 and 3. Note that the vertical scaling is different for the calculated and measured results.

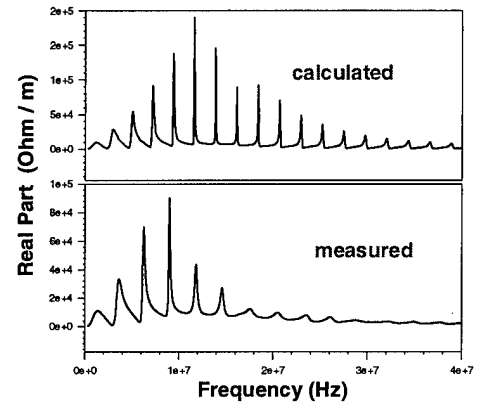

Figure 2: Calculated and measured transverse coupling impedance of one **ESR**-kicker modul.

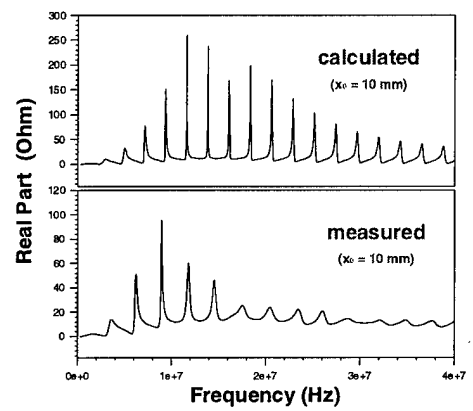

Figure 3: Calculated and measured longitudinal coupling impedance of one **ESR**-kicker module.

The measured coupling impedances are lower than calculated, especially above 15 MHz. The parasitic capacites CD-1 and CD-2 (fig. 1) reduce the influence of the cabels with increasing frequency, this positive effect is also observed in the imaginary part. Impedance measurements at a **SIS** kicker module (window frame) show the similar results.

3. CONCLUSIONS

A method has been described to determine the coupling impedances of the **SIS** and **ESR** kicker module by combining analytical formula and impedance measurements. The measured results are a good basic to calculate beam instabilites. An advantage of this procedure is, that all measurements could be performed at the installed kicker outside of the vacuum.

4. REFERENCES

[1] G. Nassibian, F. Sacherer, 'Methods for measureing transverse coupling impedances in circular accelerators', CERN / ISR-TH/77-61, 1977

IMPEDANCE STUDIES FOR BEPC

F.Zhou, Z.Y.Guo, S.H.Wang,
IHEP, Chinese Aacdemy of Sciences, P.O.Box 918(9),Beijing 100039,China
G.W.Wang, C.X.Tang
TsingHua University, Beijing, China

Abstract

This paper focuses on the impedances from various beamline elements in the BEPC with and without vacuum chamber upgrade. We also discuss their power depositions generated by a beam in the form of the High-Order-Mode(HOM) losses by interacting with its surroundings.

1 INTRODUCTION

The high luminosity is the destination of every electron-positron collider, due to which, one can reduce the β functions at the interaction point while shortening the bunch length, especially for the lower RF frequency like 200MHz in BEPC. Small coupling impedances is thus requested in order to shorten the bunch length. Due to this reason, in 1995 we made vacuum upgrade in BEPC while shielding 33 of 40 pairs of the 2-cm-long gaps on both sides of all bellows in the arcs. The impedance sources with and without upgrade in BEPC mainly come from the RF cavities, separators, injection kickers, bellow gaps, gate valves , flanges, all bellows and so on, which is shown in Fig.1, where the dashed line means the elements are completely or partly shielded after upgrade.

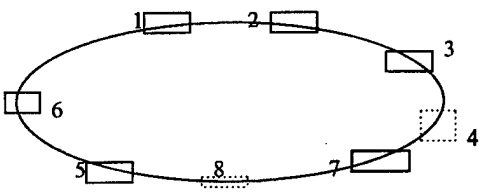

1-RF cavities, 2-Separators, 3-kickers, 4-Bellow gaps
5-Bellows, 6-Flanges, 7-Gate valves, 8-IR

Figure 1: Layout of BEPC Vacuum components

2 IMPEDANCES OF COMPONENTS

In this section, we summarize our estimates of impedances and loss factors of main beamlines in the BEPC, respectively.

RF Cavities

Through calculation, the wake of BEPC cavity almost characterizes in capactive, as shown in Fig.2, where we use the 4.2-cm-long bunch length. Using the wake Green functions of four cavities and one cavity respectively, and then solving their Haissinski equation we find that both of their bunch lengths are suppressed, as shown in Fig.3. After comparision, it is shown that the bunch length of four cavities is shortened more than that of one cavity. Next using the perturbation approach to solve the linearized, time independent Vlasov equation, which includes the potential well distortion as zero order effect, we find that there is no microwave instability. From the simulation results, it is shown that these cavities have no contribution to the bunch lengthening in BEPC. However, four cavities contribute to more loss factor, 0.2526V/pC per cavity at 4.2cm bunch length, which corresponds to the 250W HOM loss at I=35mA.

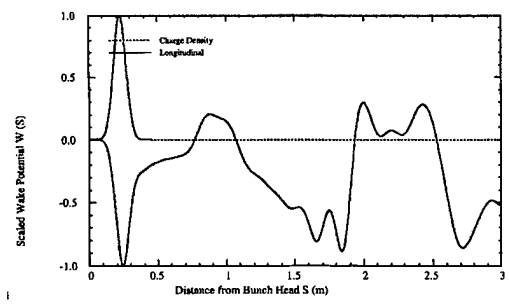

Figure 2: Wake potential of BEPC cavity

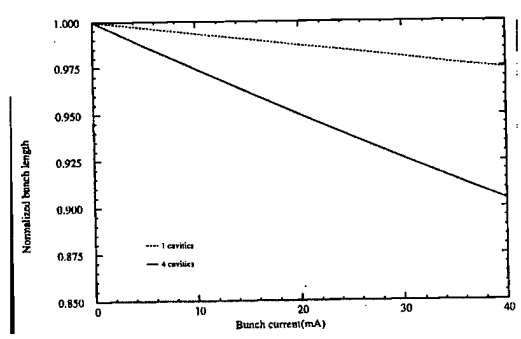

Figure 3: Bunch length with beam current

Bellow Gaps

Before vacuum chamber upgrade in BEPC, there exist 40 pairs of 2-cm-long gaps on both sides of bellows in the arcs as shown in Fig.4. Using the 3-D MAFIA, one can obtain its wakefield as shown in Fig.5. It is shown that its wakefield in inductive and its inductance per pair of gaps is 8.75nH. Its loss factor is 0.0425V/pC and corresponding HOM loss is 70W at 45mA. With the help of temperature probes, it is measured that the temperature rise is near 10 degrees while other temperature rises of other

0-7803-4376-X/98/$10.00 © 1998 IEEE

vacuum components are below 1 degree. In the view of frequency domain, there exists one trapped mode in the gap, whose frequency is 1.66 GHz through transmission measurements. During vacuum upgrade we shield 33 of 40 pairs of gaps, and then find the 1.6GHz trapped mode has disappeared and its HOM loss is also small, only 0.2 degree with almost the same condition as that of previous measurements. It is much clear that the impedance of bellow gaps are reduced greatly with vacuum chamber upgrade.

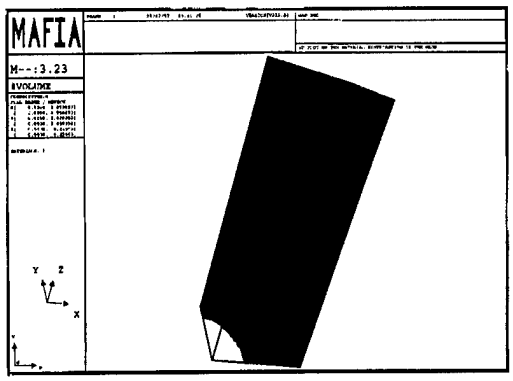

Figure 4: Sketchic map of bellow gaps

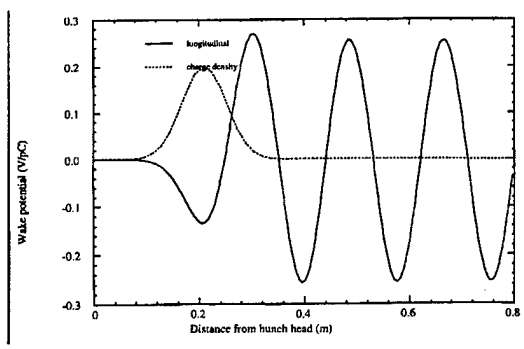

Figure 5: Wake potential of bellow gaps

Injection Kickers

BEPC has four injection kickers, which is the conventional air-coil magnet which has two metallic current plates surrounded by a large vacuum tank. Exprement shows that its impedance comes from the tapers and the two ends of metallic plates. Its wakefield is shown in Fig.6, from which one can obtain that the effective inductance is 10nH, and loss factor is 0.0365V/pC, corresponding to 36W HOM loss at 35mA current. In 1995, we fabricated one slotted-pipe type kicker model[1,2], which has low impedance in two magnitudes than that of the present kicker.The new slotted-pipe kicker model is principally based on the vacuum pipe itself with properly arranged slits as current conductors. Both ends of the vacuum pipe are directly connected with two ends of the external vacuum tank flanges, respectively. These two parallel conductors on both sides of the beam axis form an inductive loop, and the slits between

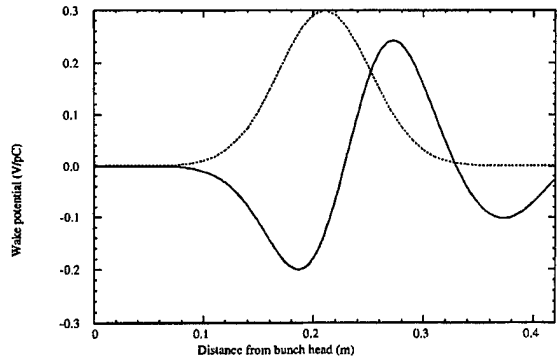

Figure 6: Wake potential of injection kicker

the conductors are connected to ground, which is one of the most important features different from the present one. Due to the racetrack beam pipe, the central metallic plates are the nearest to the moving beam and carry most of the image current. Thus, it is obvious that the impedance of BEPC will be further reduced if we apply the new type of kicker.

Separator

Using the transmission method, one can obtain its transmission spectrum as shown in Fig.7. It is observed that there exist some trapped modes below 1GHz, and their high-order-mode frequencies are intger multipoles of the lowest resonant frequency. In fact, one can consider the separator as the transmission line, where the parallel plates is considered as internal conductor, while external vacuum tank as external one. The relation between the loadings

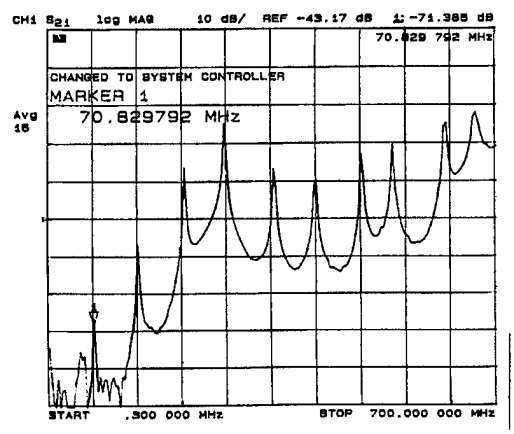

Figure 7: Transmission spectrum without loadings

of the plates and the trapped modes is studied. Results show that some modes are suppressed as shown in Fig.8, while the current plates are connected with the 5-cm-long cables. Analyzing both spectums, one can find that the odd modes are still trapped inside, but even modes are suppressed through the coupling between the cable and the fields of the modes. According to above two plots, one

can determine the field directions of the modes. The field distrdibutions of both odd and even modes are analyzed in detail in the thesis[3]. On the basis of the field distributions, one can determine its total shunt impedances of the modes, when the shunt impedances of two ends are measured.Uisng MAFIA, one can obtain that its inductance and loss factor are 9.6nH and 0.0375V/pC, respectively.

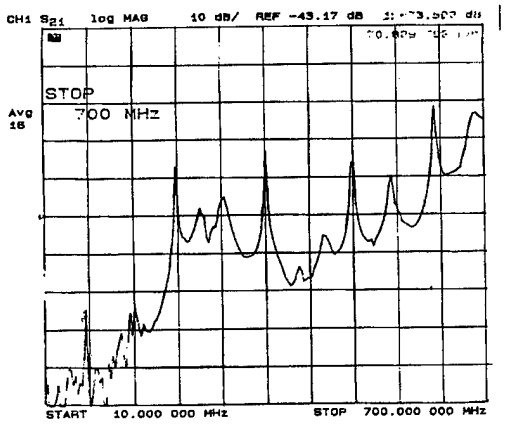

Figure 8: Transmission spectrum with loadings

Others

In addition to the components mentioned above, there are eight flanges, sixteen gate valves and sixty-four bellows in the BEPC. Their structures are small cavity-likes except bellows. The impedances of bellows is almost pure inductive.

3 IMPEDANCE BUDGET

The effective inductances and loss factors of the individual elements in the BEPC are tabulated in Table 1. The total longitudinal wake potentials for the BEPC with and without upgrade are plotted in Fig.9. Using the least-squares fit, the scaling laws of total loss factors of components without and with upgrade vs bunch length are obtained as followings:

$$k_l = 35.0(\sigma(cm))^{-1.45} V/pC, \quad (1)$$

$$k_l = 23.3(\sigma(cm))^{-1.51} V/pC, \quad (2)$$

where equation(1) and equation(2) are the cases without and with upgrade for BEPC vacuum chmabers, respectively. The impedance and loss factor budgets with and without vacuum chamber upgrade are shown in Table 1, where the values in the brackets are the ones with upgrade. From the above plots and data, it is shown that the whole impedance and HOM loss have been decreased greatly after vacuum chamber upgrade.

Table 1 Impedance and loss factor budgets

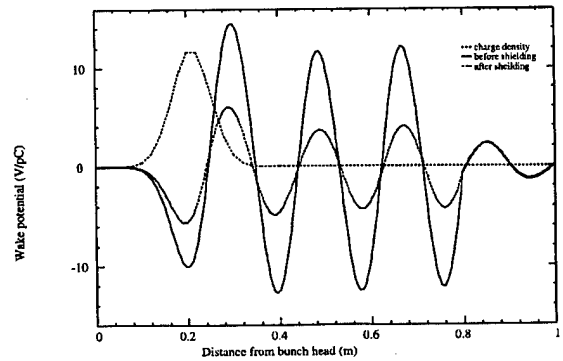

Figure 9: Total wake potential of BEPC

component	inductance(nH)	loss factor (V/pC)
RF cavities	-	1.01
Separators	38	0.15
Kickers	40	0.146
Bellow gaps	350(61.4)	1.7(0.34)
Bellows	63.7	0.019
Gate valve	50	0.218
Flange	31.8	0.205
IR	28.1(0)	0.14(0)
Total	602.5(313.9)	3.6(2.2)

4 REFERENCES

1. F. Zhou, Impedance study for a slotted-pipe kicker model, CEIBA'95 workshop, KEK, (1995).

2. F. Zhou, Impedance calculation of a slotted-pipe kicker, EPAC'96, Barcelona, (1996).

3. F. Zhou, The studies of the impedance theories and their applications, Ph.D thesis, IHEP, (1997).

BEAM COUPLING IMPEDANCES OF OBSTACLES PROTRUDING INTO BEAM PIPE

Sergey S. Kurennoy
LANSCE-1, Los Alamos National Laboratory, MS H808, Los Alamos, NM 87545, USA

Abstract

The beam coupling impedances of small obstacles protruding inside the vacuum chamber of an accelerator are calculated analytically at frequencies for which the wavelength is large compared to a typical size of the obstacle. Simple formulas for a few important particular cases, including both essentially three-dimensional objects like a post or a mask and axisymmetric irises, are presented. The analytical results are compared and agree with three-dimensional computer simulations. These results allow simple practical estimates of the broad-band impedance contributions from such discontinuities.

1 INTRODUCTION

Due to high currents in modern accelerators and colliders, even contributions from small discontinuities of the vacuum chamber to the impedance budget of the machine have to be accounted for. Numerous pumping holes — a few hundred per meter — in the vacuum screen of the Large Hadron Collider (LHC) can serve as an example. Their total contribution to the machine impedance in the initial design was calculated[1, 2] using the Bethe theory of diffraction of EM-waves by a small hole in a metal plane [3], and found to be dangerously large, close to the beam instability threshold. Proposed design changes reduced the impedance more than an order of magnitude[4]. The method's basic idea is that the hole, at frequencies where the wavelength is large compared to the typical hole size, can be replaced by two induced dipoles, an electric and a magnetic one. Using essentially the same idea, the method was extended for arbitrary-shaped small discontinuities on the pipe of an arbitrary-shaped cross section[5]. The impedance calculation for a given small discontinuity was therefore reduced to finding its electric and magnetic polarizabilities. Analytical results in this direction have been obtained for axisymmetric obstacles[6], as well as for holes and slots: circular[3] and elliptic[7] holes in a zero-thickness wall, circular[8] and elliptic[9] holes in a thick wall, various slots[10], and a ring-shaped cut[11].

In a recent paper[12] the method was applied to calculate the coupling impedances of obstacles protruding inside the beam pipe, like a narrow post or a mask intercepting synchrotron radiation. Formulas derived make practical estimates very simple. Numerical simulations required to obtain similar results are necessarily 3D ones, and therefore are rather involved. This statement is generally applicable for any small discontinuities, but especially for those protruding into the vacuum chamber. Below we list the analytical results[12] and compare them with simulations.

2 GENERAL SOLUTION

The longitudinal coupling impedance of a small discontinuity on the wall of a circular beam pipe of radius R is[1]

$$Z(k) = -iZ_0 k \frac{\alpha_e + \alpha_m}{4\pi^2 R^2}\,, \tag{1}$$

when the wavelength $2\pi/k$ is large compared to the obstacle size. Here $Z_0 = 120\pi\ \Omega$ is the impedance of free space, $k = \omega/c$ is the wave number, and α_e, α_m are the electric and magnetic polarizabilities of the discontinuity. The transverse impedance is proportional to the same combination of polarizabilities $\alpha_e + \alpha_m$, and the real part of the impedance is small at such frequencies (see[5, 4] for detail, as well as for other chamber cross sections). Let the obstacle shape be a half-ellipsoid with semiaxis a in the longitudinal direction (along the chamber axis), b in the radial direction, and c in the azimuthal one. When $a, b, c \ll R$, the obstacle is small and the Bethe approach can be applied. To find the polarizabilities, one needs to calculate the induced electric dipole moment P of the obstacle illuminated by a homogeneous radial electric field E_0, and the magnetic dipole moment M when it is illuminated by an azimuthal magnetic field H_0. This problem was reduced[12] to the well-known problem for an ellipsoid immersed in a homogeneous field, e.g.,[7]. Adding obvious symmetry considerations, we get

$$\alpha_e = \frac{P}{2\varepsilon_0 E_0} = \frac{2\pi abc}{3I_b}\,, \qquad \alpha_m = \frac{M}{2H_0} = \frac{2\pi abc}{3(I_c - 1)}\,, \tag{2}$$

where

$$I_b = \frac{abc}{2}\int_0^\infty \frac{ds}{(s+b^2)^{3/2}(s+a^2)^{1/2}(s+c^2)^{1/2}}\,, \tag{3}$$

and I_c is given by Eq. (3) with b and c interchanged.

3 POST AND MASK

In the case $a = c$, $b = h$ we have an ellipsoid of revolution, and the integral in Eq. (3) can be expressed in terms of the hypergeometric function ${}_2F_1$:

$$\alpha_e = \frac{2\pi a^2 h}{{}_2F_1(1,1;5/2;1-h^2/a^2)}\,, \tag{4}$$

and

$$\alpha_m = \frac{2\pi a^2 h}{3\left[{}_2F_1(1,1;5/2;1-a^2/h^2) - 1\right]}\,. \tag{5}$$

In the limit $a \ll h$, which corresponds to a pin-like obstacle, $\alpha_e \simeq (2\pi h^3/3)/\left[\ln(2h/a) - 1\right]$ is much larger than

0-7803-4376-X/98/$10.00 © 1998 IEEE

$\alpha_m \simeq -2\pi a^2 h/3$. Note that in this limit $\alpha_m \simeq -V$, where $V = 2\pi a^2 h/3$ is the volume occupied by the obstacle (and subtracted from that occupied by the beam magnetic field), similarly to the axisymmetric case[6]. These results give us a simple expression for the inductive impedance of an **narrow pin (post)** of height h and radius a, $a \ll h$, protruding radially into the beam pipe:[1]

$$Z(k) \simeq -ikZ_0 \frac{h^3}{6\pi R^2 \left(\ln\left(2h/a\right) - 1\right)} \,. \qquad (6)$$

One more particular case of interest here is $h = a$, i.e., a **semispherical obstacle** of radius a. From Eqs. (4)-(5) the impedance of such a discontinuity is

$$Z(k) = -ikZ_0 \frac{a^3}{4\pi R^2} \,, \qquad (7)$$

which is $3\pi/2$ times that for a circular hole of the same radius in a thin wall[1].

The MAFIA code package[14] was used to compute the impedances of various small protrusions for comparison with analytical results. Calculating wakes due to protrusions is a more difficult task for MAFIA than those due to cavities. One has to either use a long pipe (which leads to a huge mesh since it should be homogeneous along the beam path), or apply a trick with tapers on the pipe ends. The tapers make transitions to a new end pipe with radius $R_p \leq R - h$, so that the new structure looks like a shallow cavity. The difference of wakes computed with and without a protrusion gives us its contribution. We used the second approach with pipes from $4R$ to $8R$ long and meshes up to $2 \cdot 10^6$ points. Simulation results are usually higher than the analytical ones, but go down as a finer mesh is used. Figure 1 gives some comparison for a semisphere.

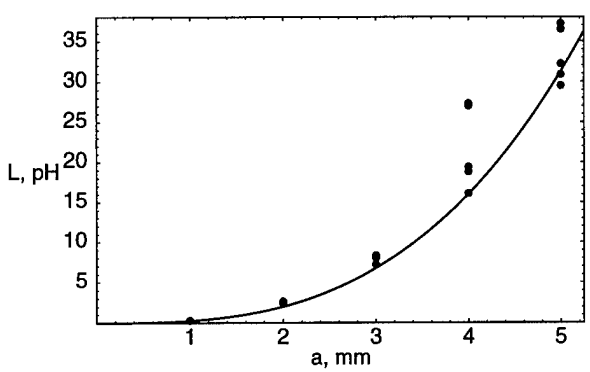

Figure 1: Comparison of MAFIA results (dots) for the inductance of a semispherical protrusion with the analytical ones (solid line) from Eq. (7), for different sphere radii. Pipe radius $R = 2$ cm.

Another practical result that can be derived from the general solution, Eqs. (2)-(3), is the impedance of a **mask** intended to intercept synchrotron radiation. We put $b = c = h$, so that our model mask has the semicircular shape with radius h in its largest transverse cross section. Then the integral in Eq. (3) is reduced to

$$I_b = I_c = {}_2F_1\left(1, 1/2; 5/2; 1 - h^2/a^2\right)/3 \,,$$

and we further simplify the result for two particular cases.

The first one is the **thin mask**, $a \ll h$, in which case $\alpha_e \simeq 8h^3/3$, and again it dominates the magnetic term, $\alpha_m \simeq -V = -2\pi a h^2/3$. The coupling impedance for such an obstacle — a half-disk of radius h and thickness $2a$, $a \ll h$, transverse to the chamber axis — is therefore

$$Z(k) = -ikZ_0 \frac{2h^3}{3\pi^2 R^2} \left[1 + \left(\frac{4}{\pi} - \frac{\pi}{4}\right)\frac{a}{h} + \ldots\right] \,, \qquad (8)$$

where the next-to-leading term is shown explicitly.

In the opposite limit, $h \ll a$, which corresponds to a **long** (along the beam) **mask**, the leading terms $\alpha_e \simeq -\alpha_m \simeq 4\pi a h^2/3$ cancel each other. As a result, the impedance of a long mask with length $l = 2a$ and height h, $h \ll l$, is

$$Z(k) \simeq -ikZ_0 \frac{4h^4}{3\pi R^2 l} \left(\ln\frac{l}{h} - 1\right) \,, \qquad (9)$$

which is relatively small due to the "aerodynamic" shape of this obstacle, in complete analogy with results for long elliptic slots[1, 2, 10]. Figure 2 shows the impedance of a mask with a semicircular transverse cross section of radius h versus its normalized half-length, a/h. The comparison with the asymptotic approximations Eqs. (8) and (9) is also shown. One can see that the asymptotic behavior (9) starts to work well only for very long masks, namely, when $l = 2a \geq 10h$. Figure 2 demonstrates that the mask impedance depends rather weakly on the length. Even a very thin mask ($a \ll h$) contributes as much as $8/(3\pi) \simeq 0.85$ times the semisphere ($a = h$) impedance, Eq. (7), while for long masks the impedance decreases slowly: at $l/h = 20$, it is still 0.54 of that for the semisphere.

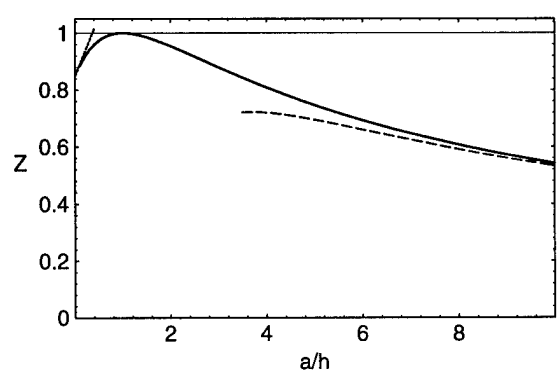

Figure 2: Mask impedance Z (in units of that for a semisphere with the same depth, Eq. (7) with $a = h$) versus its length. The narrow-mask approximation, Eq. (8), is short-dashed, and the long-mask one, Eq. (9), is long-dashed.

In practice, however, the mask has usually an abrupt cut toward the incident synchrotron radiation, so that it is rather

[1]One could use the known result for the induced electric dipole of a narrow cylinder parallel to the electric field [13]. It will only change $\ln(2h/a) - 1$ in Eq. (6) to $\ln(4h/a) - 7/3$.

one-half of a long mask. Numerical simulations show that the low-frequency impedances of a semisphere and a half-semisphere of the same depth — which is a relatively short mask — are almost equal (within the errors), and close to that for a longer half-mask. From these results one can conclude that a good estimate for the mask impedance is given simply by Eq. (7). One more interesting observation is that the inductances found numerically for two half-semispheres — one with a cut toward the incident beam and the other, mirrored $z \to -z$ — differ by 3%, while they have to be equal as was proven analytically[15].

4 AXISYMMETRIC IRIS

Following a similar procedure one can also easily obtain the results for axisymmetric irises having a semi-elliptic profile in the longitudinal chamber cross section, with depth $b = h$ and length $2a$ along the beam. For that purpose, one should consider the limit $c \to \infty$ in Eq. (3) to calculate polarizabilities $\tilde{\alpha}_e$ and $\tilde{\alpha}_m$ per unit length of the circumference of the chamber transverse cross section. The broad-band impedances of axisymmetric discontinuities have been studied in [6], and the longitudinal coupling impedance is given by

$$Z(k) = -iZ_0 k \frac{\tilde{\alpha}_e + \tilde{\alpha}_m}{2\pi R}\,, \qquad (10)$$

quite similar to Eq. (1). As $c \to \infty$, the integral $I_c \to 0$, and I_b is expressed in elementary functions as

$$I_b = \frac{1}{2}{}_2F_1\left(1, \frac{1}{2}; 2; 1 - \frac{h^2}{a^2}\right) = \frac{a}{a+h}\,.$$

It gives us immediately

$$\tilde{\alpha}_e = \pi h(h+a)/2\,; \qquad \tilde{\alpha}_m = -\pi a h/2\,, \qquad (11)$$

and the resulting impedance of the iris of depth h with the semielliptic profile is simply

$$Z(k) = -ikZ_0 \frac{h^2}{4R}\,, \qquad (12)$$

which proves to be independent of the iris thickness a. The same result has been recently obtained using another, direct method[16].

One should emphasize that $\tilde{\alpha}_m$ in Eq. (11) is just an iris cross-section area (with negative sign), which is correct for any small axisymmetric discontinuity, as was pointed out in [6]. However, calculating $\tilde{\alpha}_e$ in general is not easy: a conformal mapping was constructed for that purpose in [6] for irises (as well as for chamber enlargements) having a trapezoid (or rectangular, or triangular) profile. An interesting fact is that the leading behavior for thin irises of all shapes is exactly the same as Eq. (12).

In fact, the same approach can be applied here. The conformal mapping from the upper half-plane w into z with the boundary including the iris having a semielliptic profile is given by

$$z = aw + h\sqrt{w^2 - 1}\,.$$

We need an inverse mapping, but, fortunately, it is enough to find its asymptotic behavior at large z and w [6], which is

$$w = \frac{z}{a+h} + \frac{h}{2}\frac{1}{z} + \ldots$$

The ratio of the coefficients of the second and first terms on the RHS is $\tilde{\alpha}_e/\pi$, cf.[6], which leads us exactly to the result for $\tilde{\alpha}_e$ in Eq. (11). It is even easier for the particular case $h = a$, when the iris has a semicircular profile of radius a. The explicit conformal mapping for this case is very simple, $w = (z/a + a/z)/2$. The comparison of the second and first terms on the RHS gives us $\tilde{\alpha}_e = \pi a^2$, in agreement with Eq. (11).

5 SUMMARY

Analytical expressions of the impedances for both 3D and axisymmetric small obstacles protruding inside a beam pipe are obtained, and they agree well with numerical results. These formulas greatly simplify calculations of the broad-band contributions to the coupling impedances from such discontinuities, especially in the 3D case.

The present approach does not work for enlargements of the vacuum chamber. However, existing analytical results for holes and slots[1, 2, 4, 5], as well as for axisymmetric enlargements[6], cover this case quite well.

Stimulating discussions with Dr. R.L. Gluckstern and Dr. F.L. Krawczyk are gratefully acknowledged.

6 REFERENCES

[1] S.S. Kurennoy, Part. Acc. **39**, 1 (1992).

[2] R.L. Gluckstern, Phys. Rev. A **46**, 1106, 1110 (1992).

[3] H.A. Bethe, Phys. Rev. **66**, 163 (1944).

[4] S.S. Kurennoy, Part. Acc. **50**, 167 (1995).

[5] S.S. Kurennoy, R.L. Gluckstern, and G.V. Stupakov, Phys. Rev. E **52**, 4354 (1995).

[6] S.S. Kurennoy and G.V. Stupakov, Part. Acc. **45**, 95 (1994).

[7] R.E. Collin, *Field Theory of Guided Waves* (IEEE Press, NY, 1991).

[8] R.L. Gluckstern and J.A. Diamond, IEEE Trans. MTT **39**, 274 (1991).

[9] B. Radak and R.L. Gluckstern, *ibid.* **43**, 194 (1995).

[10] S.S. Kurennoy, Report SSCL-636, Dallas (1993).

[11] S.S. Kurennoy, IEEE Trans. MTT **44**, 1109 (1996).

[12] S.S. Kurennoy, Phys. Rev. E. **55**, 3529 (1997).

[13] L.D. Landau and I.M. Lifshitz, *Electrodynamics of Continuous Media* (Pergamon Press, Oxford, 1960), §3.

[14] M. Bartsch *et al.*, Computer Physics Comm. **72**, 22 (1992).

[15] R.L. Gluckstern and B. Zotter, CERN LEP-Note 613 (1988); S.A. Heifets, Report SLAC/AP-79 (1990).

[16] R.L. Gluckstern and S.S. Kurennoy, Phys. Rev. E. **55**, 3533 (1997).

IMPROVEMENTS IN CURING COUPLED BUNCH INSTABILITIES AT ELETTRA BY MODE SHIFTING AFTER THE INSTALLATION OF THE ADJUSTABLE HIGHER ORDER MODE FREQUENCY SHIFTER (HOMFS).

M.Svandrlik, A.Fabris, C.Pasotti, Sincrotrone Trieste, S.S. 14 km 163.5, Basovizza, Trieste, Italy

Abstract

Mode shifting is the technique used at the third generation synchrotron light source ELETTRA to cure Coupled Bunch Instabilities (CBI). Temperature tuning of the RF cavities, based on an analytical prediction algorithm, allows longitudinal stable operating conditions to be obtained. However, once longitudinal stability has been achieved transverse instabilities can be observed, particularly during the energy ramp from 1.0 to 2.0 GeV. There has therefore been the need to extend the flexibility of the mode shifting technique. This has been achieved by the installation of adjustable HOMFS on the storage ring RF cavities. The HOMFS is effective on those longitudinal and transverse cavity Higher Order Modes which are unstable over a wide temperature range, by shifting them out of the operating temperature interval of the cavity. The installation of the HOMFS has improved the reliability and reproducibility of machine operation, also in view of the beam current upgrade.

1 CURING CBI BY HOM SHIFTING

The technique of curing CBI by shifting the frequency of the Higher Order Modes (HOM) of the RF cavities can be an interesting solution, particularly for high energy and compact storage rings. At ELETTRA the distribution of the Coupled Bunch Modes (CBM) and their growth rates have been calculated as a function of cavity temperature [1], [2]. This allows a quite flexible operation of the storage ring, with the possibility of a lifetime increase by controlled use of CBI which lengthen the bunch [3]. Characterisation of the excitation of Low Frequency Oscillations for different levels of CBI has also been possible [4]. Secondary effects on the RF cavities like cross-talk between cavities, cavity temperature oscillation and spurious vacuum interlocks could be observed and understood [5].

1.1 Mode shifting by temperature tuning

Cavity temperature intervals where the growth rates of all CBM are below the radiation damping level, which is a conservative condition to achieve stability, are more easily available if :

- the radiation damping time is short;
- the width of the temperature interval where a cavity HOM doesn't drive any unstable CBM is large;
- the number of HOMs one has to deal with is small;
- the temperature tuning range of the cavity is wide

The first two conditions are more easily met by small, high energy rings. The RF cavities should not be provided with any HOM damping system, so that the HOM resonances are still sharp, high Q resonances. The experience at ELETTRA shows that the number of modes one has to deal with does not exceed about ten for the longitudinal case and ten for the transverse case (considering the double polarisation for the dipole modes). A cavity temperature tuning range of about 30 °C, as used in ELETTRA, is usually large enough to provide stable temperature windows. However, even a small bandwidth HOM can be unstable over a wide temperature range, if its temperature coefficient τ is low. Then the temperature tuning method can fail. This was the case for the first longitudinal mode, L1, of the ELETTRA cavity named S3. The solution was to shift L1 out from the temperature range, by installing a fixed HOMFS [2].

1.2 Need for a further degree of freedom

Following the installation of the fixed HOMFS, longitudinal stable intervals could be found. Transverse effects then became evident, particularly during the energy ramping from 1.0 to 2.0 GeV, when the beam begins to stabilize longitudinally, while it is still quite sensitive in the transverse plane, due to the lower natural damping available. The origin of these effects could be identified with the horizontal CBM 318, excited by the third dipole mode in cavity S9 [5]. At the same time there were still problems with cavity S3, where the largest stable longitudinal interval showed again a transverse CBM excited, as can be seen in fig. 1 and 2. The other stable interval, towards 70 °C, resulted smaller than expected in [2], due to difficulties in measuring the frequency of HOM L5, whose actual position in temperature was a couple of degrees lower than expected.

This shows the need for an additional degree of freedom to effectively cure CBI by mode shifting in ELETTRA. An adjustable HOMFS could give more flexibility in getting stable longitudinal working points, not affected by transverse effects, also in view of a beam current increase.

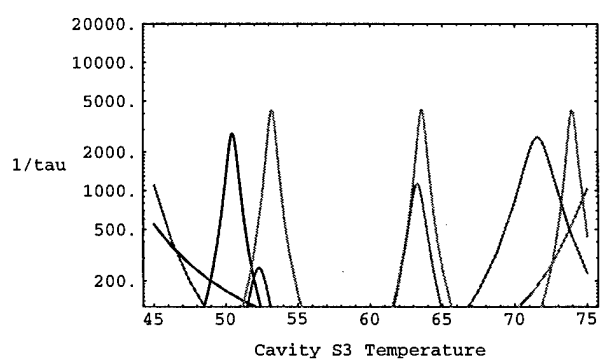

Fig. 1: Longitudinal CBMs, fixed HOMFS on S3, 2 GeV, 250 mA

0-7803-4376-X/98 /$10.00 © 1998 IEEE

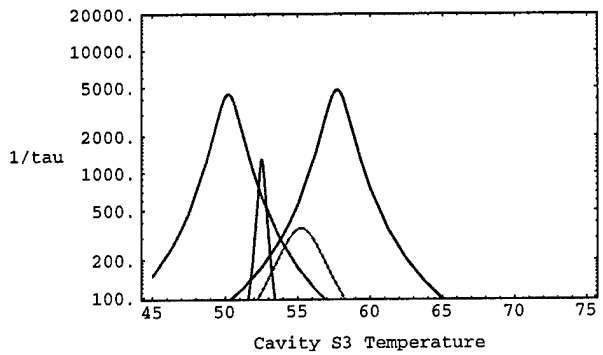

Fig. 2: Horizontal CBMs, fixed HOMFS on S3, 2 GeV, 250 mA

2 THE ADJUSTABLE HOMFS

2.1 Longitudinal modes

The adjustable HOMFS is installed on one of the three equatorial ports available on the ELETTRA cavity. It is a copper cylinder of 81 mm diameter, driven by a stepping motor. The range goes from 0 to 34 mm; at its deepest position, +34 mm, it enters 10 mm inside the cavity. The frequency shifts introduced by the HOMFS itself, Δf_{HFS}, depend on the intensity of the field of the specific HOM in the equatorial region of the cavity. For many of the considered HOMs, this field is quite low in that region, as it can be seen from a simulation with URMEL. The second column of table 1 lists the maximum obtained frequency shifts for the relevant longitudinal HOMs, as measured on cavity S3. Modes with stronger field in the HOMFS region like L2, L3, L5 and L6 show a maximum shift of more than 1000 kHz. The shift on mode L1, one of the modes for which the HOMFS is thought, is equal to - 428 kHz.

Table 1: Adjustable HOMFS effect on longitudinal HOM

HOM	Δf_{HFS} kHz	φ_K	Δf_{tot} kHz	τ_K kHz/°C	ΔT °C
L0	823	1.00	0		
L1	-428	0.63	-946	-11.5	82.3
L2	3459	-0.31	3714	-19.3	-192.4
L3	-1567	-2.16	211	-43.1	-4.9
L4	683	-0.31	938	-28.2	-33.3
L5	4529	-2.33	6447	-41.6	-155.0
L6	-1288	-0.14	-1173	-33.4	35.1
L7	-140	-2.30	1753	-51.2	-34.2
L9	0	-9.30	7654	-111.4	-68.7

There is however a second contribution to the frequency shift generated on the HOMs. This comes from the external tuning cage, acting on the axial length of the cavity to recover the frequency shift Δf_{HFSL_0} caused by the HOMFS on the fundamental mode, L0. The total frequency shift on the HOMs, Δf_{tot}, is therefore given by

$$\Delta f_{tot} = \Delta f_{HFS} - \varphi_k \, \Delta f_{HFSL_0} \; .$$

φ_k is the HOM frequency shift corresponding to a unitary frequency change of L0 by the axial tuning cage, as defined and listed in [5] for all HOMs. The third column in table 1 shows the total frequency shifts for the longitudinal modes when the HOMFS is at the +34 mm position. The mapping of the total frequency shifts versus the most significant range of the HOMFS is shown in fig. 3.

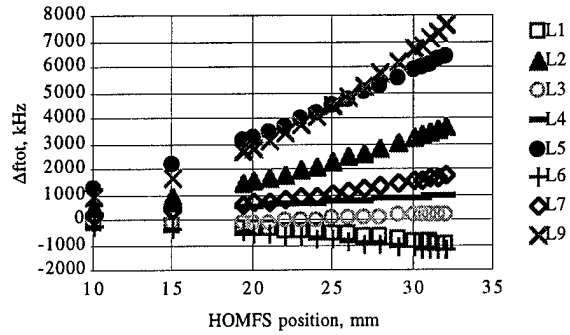

Fig. 3: Total frequency shift

If Δf_{HFS} and φ_k are opposite in sign, the corresponding mode shows an increased frequency shift. This is particularly important for mode L1, for which the frequency shift is now more than doubled. The shift on L9 becomes quite impressive due to the large value of φ_k. On the contrary the shift on L3 is now reduced, since the effect of the tuning cage is opposite to that of the HOMFS. Finally the effect which is of interest for the mode shifting technique is the equivalent shift in temperature for any CBM excited by one of the considered HOM. It can be calculated as

$$\Delta T = \frac{\Delta f_{tot}}{\tau_k}$$

Thanks to the lowest temperature coefficient τ_k, the effect on HOM L1 results fairly large in temperature. Any position beyond 20 mm is sufficient to shift out the mode L1 from the temperature range of the cavity.

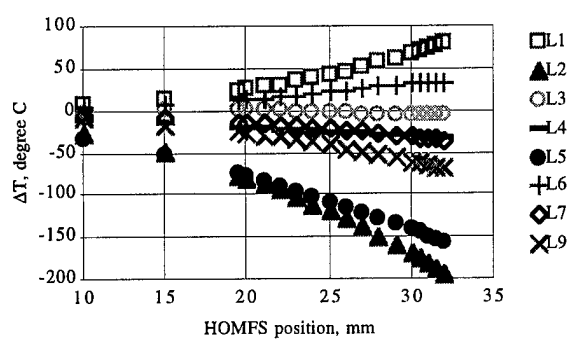

Fig. 4: Equivalent shift in temperature for the CBM excited by the longitudinal modes listed on the right.

Fig. 4 shows that only mode L3 is little affected by the HOMFS. This is not a problem since it is only unstable in a small temperature interval. Further this is the mode

which is used to introduce a reduced longitudinal excitation to increase the lifetime in the relaxed operation of the machine.

2.2 Transverse modes

For the transverse modes the installation of the adjustable HOMFS on cavity S3 results in the temperature shifts shown in fig. 5 for the relevant modes.

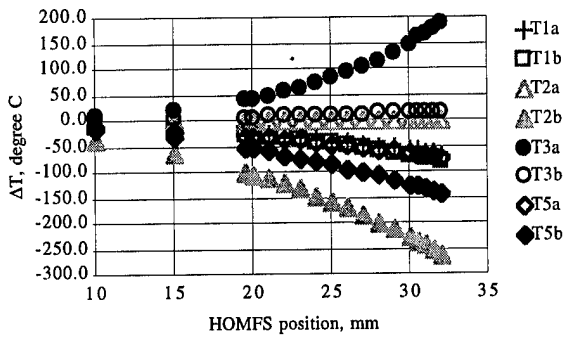

Fig. 5: Temperature shifts for the transverse CBMs

The transverse mode T2a results to be the only one which is almost untouched by the HOMFS, having almost zero field in the equatorial region and also $\varphi_{T2a} = 0.0$. Also T3b is little affected by the HOMFS. Both are strong impedance modes, but due to the low temperature coefficient (-13.5 kHz/°C for T2a, - 16.1 kHz/°C for T3b) the temperature interval between the interactions of those HOMs with two adjacent CBMs is large (60-70 °C).

3 IMPROVEMENTS ON THE MACHINE

The installation of the adjustable HOMFS on cavity S9 in September 96 eliminates the problems during energy ramping, as described in [6]. Furthermore, for users' operation, the controlled excitation of the longitudinal mode L3 can be done in a more selective way, without need of adjustments for different beam current intensities.
In February 97 the second adjustable HOMFS has been installed on cavity S3 to replace the fixed version. The improvement is clearly shown in fig. 6 and fig. 7, where the CBM excitation for the longitudinal and transverse horizontal case is drawn. They are computed for 2.0 GeV, 250 mA, with the present position of the HOMFS, +27 mm. Now a large stable window exists for longitudinal CBMs in the 70 °C temperature region of cavity S3 (fig. 6). At the same time fig. 7 shows that this temperature region is free of interactions with the horizontal spectrum ($Q_x = 14.300$).

4 CONCLUSIONS

A significant improvement in the mode shifting technique to cure CBIs has been obtained after installing two adjustable HOMFS. Transverse effects during the energy ramping are no more observed. Larger stable intervals in the longitudinal plane allow a more flexible and selective operation of the machine. Further installation of adjustable HOMFS on the other two cavities is foreseen in the near future, also in view of a beam current increase.

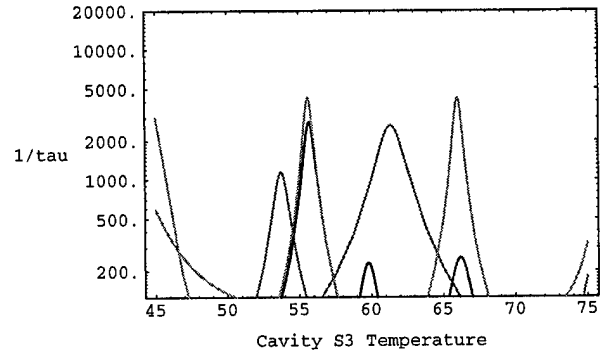

Fig. 6: Longitudinal CBMs, HOMFS + 27 mm.

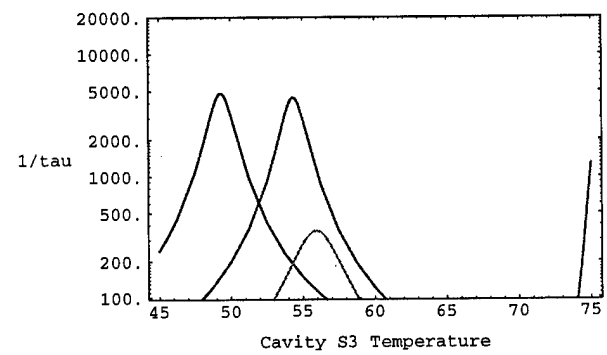

Fig. 7: Transverse Horizontal CBMs, HOMFS +27 mm.

REFERENCES

[1] M.Svandrlik et al., "The cure of Multibunch Instabilities in ELETTRA", in Proceedings of the 1995 Particle Accelerator Conference, Dallas, USA, May 1995, pp. 2762-2764.

[2] M.Svandrlik et al., "Improved Methods of Measuring and Curing Multibunch Instabilities in ELETTRA", in Proceedings of the 1996 European Particle Accelerator Conference, Sitges (Barcelona), Spain, June 1996, pp. 1144-1146.

[3] C.J.Bocchetta et al., "Operational Experience with ELETTRA", in Proceedings of the 1996 European Particle Accelerator Conference, Sitges (Barcelona), Spain, June 1996, pp. 76-80.

[4] A.Wrulich et al., "Observations of CBI in ELETTRA", in Proceedings of the 1996 European Particle Accelerator Conference, Sitges (Barcelona), Spain, June 1996, pp. 1108-1110.

[5] M.Svandrlik et al., "Simulations and Measurements of Higher Order Modes of the ELETTRA RF Cavities in view of Coupled Bunch Instability Compensation by Temperature Variation", in Proceedings of the 1996 European Particle Accelerator Conference, Sitges (Barcelona), Spain, June 1996, pp. 2053-2055.

[6] C.J.Bocchetta et al., "ELETTRA Performance and Upgrade", this conference.

ESTIMATE OF THE IMPEDANCE DUE TO WALL SURFACE ROUGHNESS *

K.L.F. Bane, C.K. Ng, and A.W. Chao
SLAC, Stanford, CA 94309, USA

1 INTRODUCTION

In the Next Linear Collider (NLC) after being accelerated the beam is collimated to remove tail particles. Wakefields generated in the collimator section, however, can significantly degrade the beam emittance[1]. The collimators are, therefore, carefully designed to balance and minimize the effects of the geometric and the resistive wall wakefields. Recent measurements of collimator wakefields in the Stanford Linear Collider (SLC) linac seem to confirm the geometric wakefield calculations but yield results for the resistive wall wakefield that are 3–4 times as large as expected[2]. One possibility is that this discrepancy is due to the roughness of the collimator surface. In this report we estimate this effect.

The longitudinal impedance of small perturbations on a vacuum chamber pipe is a well studied subject (see *e.g.*, Ref. [3, 4, 5]). Let us limit ourselves to perturbations in a round beam pipe with radius b. In Ref. [3], exact expressions are derived for the impedance of small elliptical holes on such a beam pipe. For the special case of a circular hole[3, 4]

$$Z^{\parallel}(\omega) = -i\frac{\omega}{c}Z_0\frac{a^3}{6\pi^2 b^2}f \quad , \tag{1}$$

with $Z_0 = 377\ \Omega$, $a \ll b$ the hole radius, and the form factor

$$f = \left\{\begin{matrix} 1 \\ 0.56 \end{matrix}\right\} \quad \text{[small hole with } \left\{\begin{matrix} \text{thin} \\ \text{thick} \end{matrix}\right\} \text{ wall]} \ . \tag{2}$$

In Ref. [5] exact expressions are derived for small ellipsoidal protrusions on the pipe wall. In the special case of a small hemispherical bump it is shown that Eq. 1 is still valid, if a is taken to represent the radius of the sphere and

$$f = \frac{3\pi}{2} \qquad \text{[small hemispherical bump]} \quad . \tag{3}$$

Note that Eq. 1 is an inductive impedance, *i.e.*, it can be written in the form $Z^{\parallel} = -i\omega L$, with L the inductance.

In a round beam tube the transverse impedance of a small perturbation is related to the longitudinal impedance by [6]

$$Z^{\perp}(\omega) = \frac{4c}{\omega b^2}Z^{\parallel}(\omega) = -iZ_0\frac{2a^3}{3\pi^2 b^4}f \quad . \tag{4}$$

This equation assumes a dipole beam on axis, with the dipole moment in the direction of the perturbation. Note that the transverse impedance is related to the same form factor f as in Eq. 1 and is independent of ω at low frequencies.

* Work supported by the Department of Energy, contract DE-AC03-76SF00515

Fourier transforming, we find that the transverse kick to the beam is proportional to its longitudinal charge distribution. For a Gaussian beam the average kick is given by

$$\langle \Delta y' \rangle = \frac{4}{3\pi^{\frac{3}{2}}}\frac{N r_0 y_0 a^3}{\gamma \sigma_z b^4}f \quad , \tag{5}$$

with N the number of electrons in the bunch, r_0 the electron classical radius ($= 2.8 \times 10^{-15}$ m), eNy_0 the dipole moment of the beam, γ the relativistic energy factor, and σ_z the rms bunch length. Note that if the directions of the dipole moment and the perturbation are not aligned, then Eqs. 4 and 5 need to be multiplied by $\cos\phi$, with ϕ the angle between the two directions, and the kick direction is toward the perturbation[6].

In Ref. [7] the low frequency impedance of narrow, longitudinal slots in a round chamber wall were studied numerically. It was shown, for example, that with square ends the impedance is 50% larger than with round ends. In this report, we perform similar calculations but applied to small protrusions of differing sizes and orientations, and find the effect on the form factor f. These results are then applied to estimate the importance of surface roughness to the transverse impedance of the collimators in the NLC and the SLC.

2 NUMERICAL RESULTS

We use the 3-dimensional, finite difference computer module of MAFIA, T3[8], to find the wakefield generated by an on-axis Gaussian bunch passing by a small protrusion in the beam tube wall. The geometries that we consider are right rectangular solids and wedges with 45° angles, objects that can be exactly represented by a cubic mesh. The low frequency impedance we are interested in can be obtained by using a relatively long Gaussian bunch in the simulation. We use $\sigma_z = 1$ cm, while the small perturbations we simulate are on the order of 1 mm in size. As beam tube radius we take $b = 1$ cm. A typical result, giving the longitudinal wakefield, is shown in Fig. 1. As expected, the wake is nearly exactly proportional the derivative of the bunch shape, implying that the impedance is inductive. From the MAFIA results we obtain the inductance L using

$$L \approx \hat{W}^{\parallel}\frac{\sqrt{2\pi}\sigma_z^2 e^{1/2}}{c^2} \quad , \tag{6}$$

with $\hat{W}^{\parallel}$ the peak of the longitudinal wake function. Alternatively, we can obtain the low frequency impedance from the transverse wake as obtained by MAFIA. For a small perturbation this function is proportional to the charge distribution itself. Comparing the two results is a consistency

0-7803-4376-X/98 /$10.00 © 1998 IEEE

check of the MAFIA results, as well as a validation of the applicability of Eq. 4. In all cases to be presented the results of the two methods agree to within 1–2%.

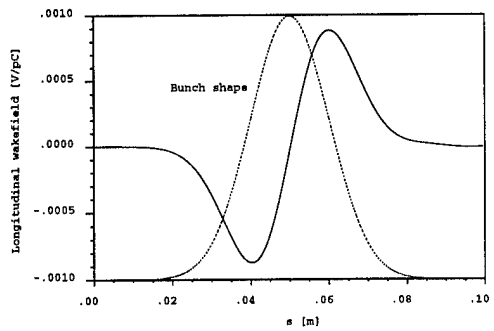

Figure 1: A typical MAFIA result. Plotted is the longitudinal wakefield excited by a gaussian bunch (the solid curve) and the bunch shape (the dots), with the head to the left.

In Fig. 2 we present results for a rectangular post in the beam tube wall, showing what happens when the height h (a), length l (b), and width w (c) are varied. In Fig. 2a, for comparison, the dashed curve gives the inductance of a half-ellipsoid of revolution[5], with radius $a = .5$ mm and height h; at $h = .5$ mm it becomes a hemispherical bump. The MAFIA results vary roughly as h^2. Note that the case with a square base (the $l = 1$ mm curve) has a result that is much larger than that of the half-ellipsoid of the same height, by a factor of 3.7 at $h = .5$ mm, by a factor of 2.5 at $h = 2$ mm. In Figs. 2b-c we note that the dependence of the impedance on l and w is much weaker than the dependence on h.

In Table 1 we present the inductance of 5 selected objects: (1) a hemisphere with radius $a = .5$ mm, (2) a half cube with $w = l = 1$ mm, $h = .5$ mm, (3) a post with $w = l = 1/\sqrt{2}$ mm and $h = .5$ mm, rotated by 45°, (4) a wedge with base dimensions $w = l = 1$ mm, depth $h = .5$ mm, and (5) a cube with $w = l = h = 1$ mm. Also given is the form factor f when comparing to a shallow hole with radius $a = .5$ mm. The longitudinal and transverse profiles are sketched below the table. We note by the first 4 examples that for object that look very similar, the form factor f can vary by a large factor, in this case by a factor 3–4. The fifth example again demonstrates the roughly quadratric dependence on height.

In Fig. 3 we plot the inductance of two cubes, 1 mm on a side, that are longitudinally aligned, as function of the space between them d, and note that when the distance is comparable to the length of a side the result is nearly the same as for two independent cubes. It has been suggested that there might be a partial cancellation of effect when there are many perturbations longitudinally aligned[10]. To test this question we ran an example with five 1-mm cubes, each separated by a distance of 2 mm. The resulting inductance was 5/2 times the corresponding two-cube result, consistent with there being no such cancellation.

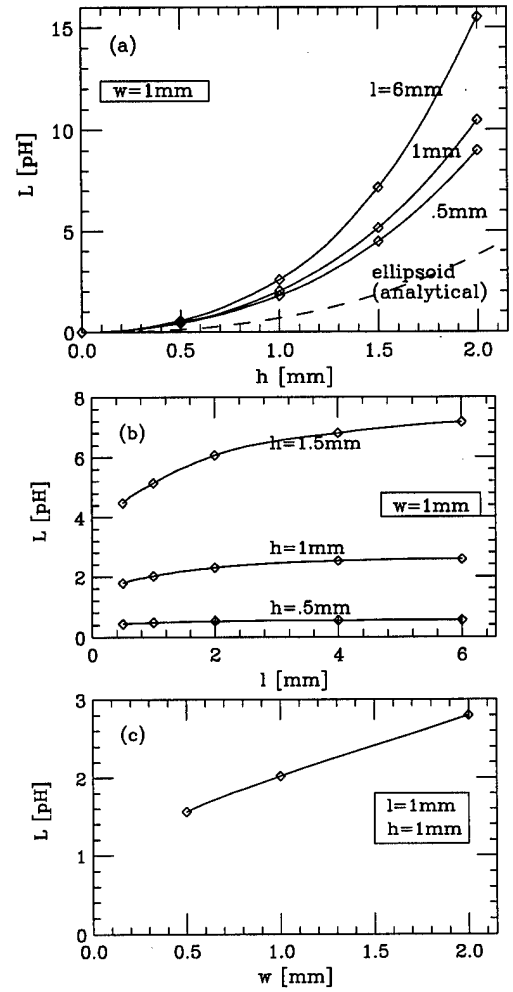

Figure 2: The inductance obtained for a single rectangular post when varying the height h (a), length l (b), and width w (c) (the plotting symbols). The dashed curve in (a) is the analytic result for a half-ellipsoid with radius $a = .5$ mm[5].

3 ROUGH SURFACES

The microstructure of a metallic surface depends on the manufacturing and machining method used to create the surface. For simplicity we here model a rough surface as a random distribution of small bumps and cavities of a certain size—the granularity size—on a smooth surface. Since the impedance of a bump seems to be significantly larger than that of a cavity of similar size, we will neglect the effect of the cavities. We begin with the transverse kick due to a single bump, Eq. 5, and average the effect over a random distribution of such bumps. Note that averaging over all azimuthal angles introduces a factor 1/2 in the amplitude, and the direction of the kick becomes the direction of the beam offset. The average kick to a Gaussian beam which is displaced by an amount y_0 in the y-direction is given by

$$\langle \Delta y' \rangle = \frac{4}{3\pi^{\frac{3}{2}}} \frac{N r_0 y_0 Z}{\gamma \sigma_z b^3} a f \alpha \quad , \tag{7}$$

Table 1: Results for 5 selected objects, whose longitudinal and transverse profile are sketched below. Given is the inductance L, and the form factor f when comparing to a shallow hole with radius $a = .5$ mm.

Case	L [pH]	f
Hemisphere (analytical)	0.13	4.7
Half Cube	0.48	17.4
Rotated Post	0.33	11.9
Wedge	0.21	7.6
Cube	2.02	73.0

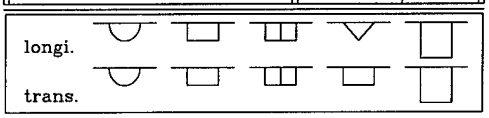

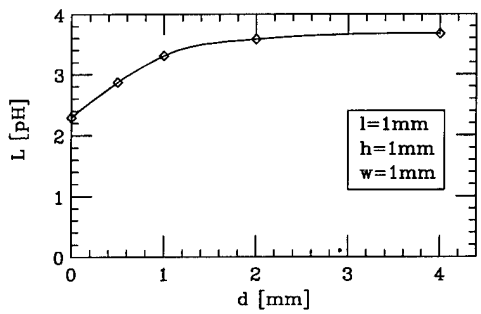

Figure 3: The inductance of two cubes, 1 mm on a side, that are longitudinally aligned, as function of the space between them d.

with Z the length of the beam pipe, a the typical size of the bumps, and α the surface filling factor of the bumps.

This kick should be compared to that due to the resistive wall wakefield of a smooth pipe of radius b

$$\langle \Delta y' \rangle_{rw} = (0.78)\sqrt{\frac{8}{\pi}}\frac{N r_0 y_0 Z}{\gamma \sigma_z b^3}\delta \quad , \qquad (8)$$

with δ the skin depth. For a Gaussian bunch we take $\delta = \sqrt{c\sigma_z/(2\pi\sigma)}$ with σ the conductivity of the metal. Eq. 7 is expected to be valid only if a is large compared to δ. If the two are comparable, and one wants an accurate result, a self-consistent calculation of the impedance, including both the geometric and resistive effects, is needed.

4 APPLICATION TO THE NLC AND THE SLC

For the case of the NLC collimators the surface is copper, for which $\sigma = 5.8 \times 10^{17}$ s^{-1}, and the linac bunch length $\sigma_z = 100$ μm; therefore, the effective skin depth $\delta = .1$ μm. If we assume $f\alpha = 10$, then for the kick due to wall roughness, Eq. 7, to be small compared to the resistive wall kick, Eq. 8, implies that the granularity at the surface of the collimators would need to be small compared to 50 nm.

For the case of the SLC linac collimators the surface is made of vanadium, for which $\sigma = 4 \times 10^{16}$ s^{-1}, or titanium nitride, for which $\sigma = 2 - 4 \times 10^{16}$ s^{-1}. The granularity is expected to be on the order of $a \sim 1$ μm[9]. We expect $f\alpha \sim 5 - 15$. The typical bunch length in the SLC linac is $\sigma_z = 1$ mm, and the corresponding skin depth $\delta = 1.1$ μm (for vanadium). With these parameters we find that the kick due to the bumps is 1–2.5 times as large as that due to the wall resistance. Although this calculation is rough the results suggest that surface roughness may conceivably explain the factor 3–4 discrepancy in the SLC collimator wakefield measurements. For a more quantative result, however, more study, particularly concerning the microstructure at the surface of the collimators, is needed.

5 ACKNOWLEDGEMENTS

The authors thank Dieter Walz for helpful discussion on the properties of metals.

6 REFERENCES

[1] "Zeroth-order Design Report for the Next Linear Collider," SLAC Report 474, Chapter 9, 1996.

[2] F.-J. Decker *et al.*, LINAC96, Geneva, Switzerland, p. 137.

[3] S. Kurennoy, *Part. Accel.* **39**, 1 (1992).

[4] R. Gluckstern, *Phys. Rev.* **A46**, 1106 (1992).

[5] S. Kurennoy, *Phys. Rev.* **E55**, 3529 (1997).

[6] S. Kurennoy, EPAC96, Sitges, Spain, p. 1449.

[7] K. Bane, C.-K. Ng, 1993 PAC, Washington, D.C., p. 3432.

[8] The MAFIA collaboration, "User Guide," CST GmbH, Darmstadt, Germany.

[9] D. Walz, private communication.

[10] G. Stupakov, private communication.

LONGITUDINAL BEAM-TRANSFER-FUNCTION MEASUREMENTS AT THE SLC DAMPING RINGS *

M.G. Minty and F. Zimmermann
SLAC, Stanford, CA 94309, USA

Abstract

A longitudinal single-bunch instability[1] in the damping rings at the Stanford Linear Collider (SLC) is thought to contribute to pulse-to-pulse orbit variations in downstream accelerator sections. To better understand this instability, we measured the beam phase and bunch length under harmonic modulations of the rf phase and rf voltage. For small phase-modulations the measured response can be explained by interaction of the beam with the cavity fundamental mode. For larger excitations, we observed bifurcation and hysteresis effects. The response to an rf voltage modulation revealed two peaks near the quadrupole-mode frequency, one of which appears to be related to the longitudinal instability. In this paper we present the experimental results.

parameter	symbol	value
circumference	C	35.27 m
momentum compaction	α	0.015
beam energy	E	1.19 GeV
rf frequency	f_{rf}	714 MHz
harmonic number	h	84
rf gap voltage	V_c	800–860 kV
synchrotron frequency	f_s	$\sim$ 100 kHz
long. rad. damping time [7]	τ_{rad}	1.55 ms
rms bunch length	σ_z	5.3–6.8 mm
relative energy spread	σ_δ	9×10^{-4}
bunch population	N_b	0–2.6$\times 10^{10}$
number of klystrons/cavities	N_k/N_c	1/2

Table 1: Damping ring parameters during measurement.

1 INTRODUCTION

Beam-transfer functions measurements (BTFs) were first suggested[2] as a technique by which to determine beam stability limits and the coupling impedance of the beam environment. Since then, measurements have revealed a rich spectrum of beam physics. For example, ring impedance studies were carried out using coasting beams by at the ISR in 1977[3], and for bunched beams at SPEAR in 1990[4]. In 1992, Byrd performed a comprehensive study of collective phenomena in CESR[5]. More recent measurements from the IUCF[6] have used BTF's in the study of nonlinear effects including the creation of resonance islands, beam splitting, chaos and bifurcations.

We here describe experimental studies at the SLC damping rings in which we externally modulated the phase or amplitude of the RF cavities. Typically, the beam was injected and stored, with the modulation turned on. The response was measured using a network analyzer (50 s sweep time, 1 kHz rbw, 401 discrete frequency steps). The parameters of the SLC Damping Rings are shown in Table 1. All measurements were performed with a single bunch.

2 PHASE MODULATION

Ignoring Landau damping, the synchrotron motion of the beam centroid is described by the same type of differential equation as the single-particle motion[8]. Representing an rf phase modulation as a harmonic perturbation, including the Robinson interaction, and linearizing the rf potential, the equation of motion is

$$\ddot{\psi} + 2\lambda\dot{\psi} + \omega_s^2\psi = \hat{\phi}\,\nu_m^2 e^{j\omega t}, \tag{1}$$

where ψ is the relative phase of the beam with respect to the modulated RF phase (which, at low current, equals the beam phase w.r.t. the cavity voltage); i.e.,

$$\psi \equiv \phi - \hat{\phi}\sin(\nu_m\theta + \chi), \tag{2}$$

In Eq. (1), $\lambda = 1/\tau$ is the Robinson damping rate, ω_s the angular synchrotron frequency, $\hat{\phi}$ the modulation amplitude, $\nu_m f_{rev}$ the modulation frequency, χ a constant phase factor, and for simplicity the synchronous phase angle has been set to zero. Defining[1] the complex beam transfer function BTF as the ratio of the beam centroid phase and the rf modulation amplitude $\hat{\phi}$,

$$\mathrm{BTF}(\omega_m) \equiv \frac{\bar{\phi}(\omega_m)}{\hat{\phi}}, \tag{3}$$

the amplitude of the BTF is a Lorentzian

$$A_{\mathrm{BTF}}(\omega_m) = \omega_m^2 \left(\frac{1}{(\omega_s^2 - \omega_m^2)^2 + 4\lambda^2\omega_m^2}\right)^{1/2} \tag{4}$$

and its phase is

$$\theta_{\mathrm{BTF}}(\omega_m) = \tan^{-1}(-\lambda/(\omega_s - \omega_m)). \tag{5}$$

Shown in Fig. 1 is a BTF measured in the positron damping ring (SDR) for a small phase-modulation depth ($\hat{\phi} \approx 0.006°$) and low beam current ($N_b \approx 7 \times 10^9$). The data were acquired by modulating the phase of the 714 MHz drive using a network analyzer which output an excitation

* Work supported by the Department of Energy, contract DE-AC03-76SF00515

[1] Note that this definition differs from that in Refs. ([4, 5], which both define the BTF as $\dot{\bar{\phi}}/(\hat{\phi}\omega_m^2)$.

of fixed amplitude and variable (swept) frequency to a fast phase shifter located upstream of a klystron. The phase of the beam with respect to the cavities was measured using a detector which mixed the signals from a cavity pickup and from a single stripline of a beam position monitor. The detector output was normalized to the modulation output. Figure 1 demonstrates that the measured response is well described by Eqs. (4) and (5) with a damping time $1/\lambda$ equal to the measured (coherent) oscillation decay time of ~3500 turns.

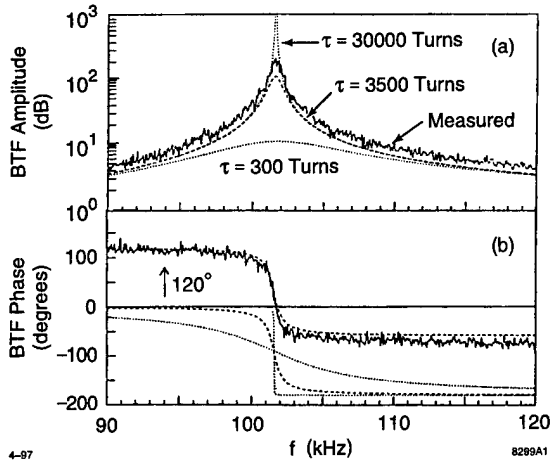

Figure 1: Comparison of measured BTF amplitude and phase with Eqs. (4) and (5) for a single-bunch population $N_b \approx 7 \times 10^9$ and small excitation, $\phi_{rms} \approx 0.004°$.

We also calculated the beam phase response that would be expected from Landau damping due to the nonlinearity of the RF voltage, in this case ignoring the Robinson damping. The calculated response agreed poorly with measurement which indicates that the single-bunch measurement was dominated by the Robinson interaction.

Figure 2 illustrates the dependence of the BTF on the excitation amplitude. For low excitation amplitudes the response is Lorentzian as in Fig. 1. With increasing modulation depth the response revealed an asymmetric behavior, characteristic of a driven nonlinear oscillator. In particular, a pronounced dip transition was observed at frequencies somewhat below the peak-response frequency.

An oscillatory solution of the nonlinear equation of motion (*i.e.*, for a sinusoidal rf potential) is [9] $\psi(\theta) = \alpha \sin(\nu_m \theta)$. The fixed-point amplitude α is approximately described by a cubic equation, which bifurcates at a modulation frequency $f_m = f_{rev}\nu'_m$:

$$\frac{\Delta\nu}{\nu_s} \equiv \frac{\nu_s - \nu'_m}{\nu_s} = \hat{\phi}^{2/3}\left(\frac{3}{8}2^{1/3}\right), \qquad (6)$$

At the bifurcation point, one of two stable fixed points vanishes. In Eq. (6), f_{rev} is the revolution frequency and $\nu_s \equiv \omega_s/(2\pi f_{rev})$ the synchrotron tune. Fitting a straight line to the measured data of $\log \Delta\nu/\nu_s$ versus $\log \hat{\phi}$, we find a slope of 0.637 ± 0.015 and an intercept of -0.875 ± 0.08. This is consistent with the expected slope ($\frac{2}{3}$) and intercept

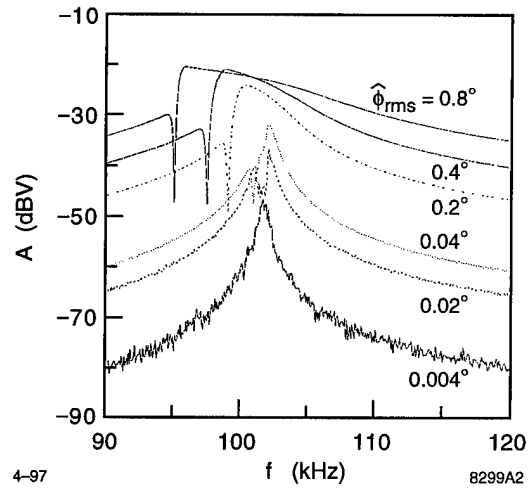

Figure 2: SDR beam-phase transfer function for various excitation amplitudes. The single-bunch population is about $N_b \approx 3\text{–}7 \times 10^9$.

(-0.76) from Eq. (6), which supports the assertion that the dip is related to a transition between the two fixed points. The origin of the dip has been studied in more detail recently at the ALS [10].

Because the beam response is strongly reminiscent of a driven nonlinear oscillator, we expect to see a different response curve when the frequency is swept downward. This is demonstrated in Fig. 3, which shows two beam-phase transfer functions for up- and downward frequency sweeps. At large excitation, we observe a clear hysteresis effect.

3 VOLTAGE MODULATION

Shown in Fig. 4 is the measured response of the beam peak current to an rf amplitude modulation in the SDR. The data were acquired by modulating the amplitude of the 714 MHz drive using an rf attenutator. The detected peak current signal is inversely proportional to the bunch length. As illustrated in Fig. 4, the response curve for the SDR revealed two peaks. In contrast, only a single peak was detected in the electron damping ring (NDR). Fig. 5 summarizes the current dependence of the response peaks in the two damping rings. The lower-frequency peak in the SDR and the peak in the NDR show a current-dependent frequency similar to that predicted for the longitudinal instability (7 kHz/10^{10}[11]). The higher-frequency peak of the SDR occurs almost exactly at $2\nu_s$. In the SDR, the beam response to a voltage modulation was largest when the two response peaks came close to each other. This happened both for large excitations ($\Delta V/V \geq 3\%$) and for low bunch intensities ($N_b \leq 10^{10}$). The peculiar shape of the phase response (bottom part of Fig. 4) may contain additional information about the instability.

4 OUTLOOK

The reasonably good agreement between the measured beam response and Eq. (4) suggests that, at low current

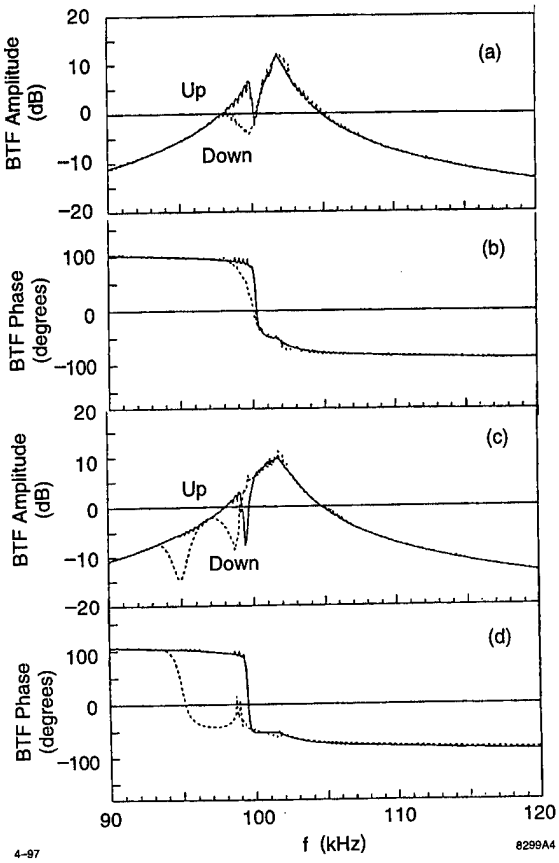

Figure 3: Comparison of SDR beam-phase transfer functions for upward and downward frequency sweeps at different excitation amplitudes.

and for low excitation, the response is dominated by the Robinson interaction with the fundamental cavity mode. It is difficult therefore to extract information about the beam distribution and/or the broad-band impedance. A more direct approach would be to excite an $l \neq 0$ multi-bunch mode[5], since this would suppress the effect of the fundamental mode. A measurement of the broadband impedance may improve our understanding of the longitudinal instability, and resolve the discrepancy between the inductive impedance calculated with MAFIA and that required to reproduce the observed instability in simulations[11].

5 ACKNOWLEDGEMENTS

We thank J. Byrd, R. Akre, M. Ross, R. Siemann, B. Podobedov, D. Pritzkau, R. Stege, and J. Turner for help with measurement setup, and K. Bane, P. Krejcik, B. Podobedov, and M. Seidel for useful discussions and contributions to the theoretical analysis. We are especially grateful to D. McCormick and S. Horton-Smith for their help with data acquisition and data recovery.

6 REFERENCES

[1] K. Bane *et al.*, Proc. *PAC95 and Int. Conf. on High-Energy Acc.*, Dallas, 1995, p. 3109, and SLAC-PUB-6894 (1995).

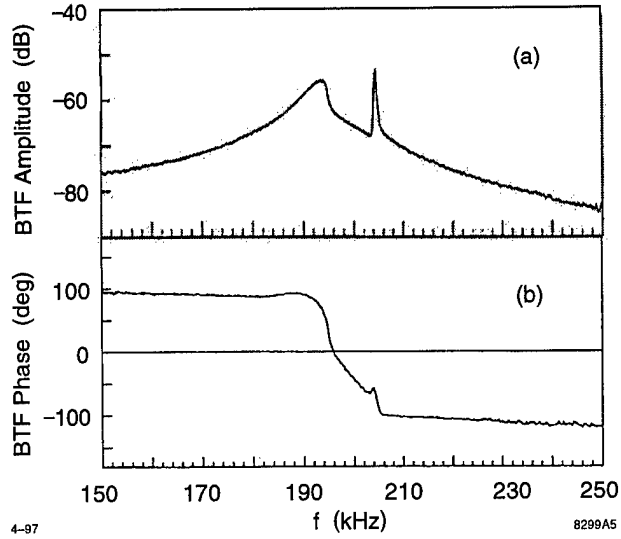

Figure 4: Voltage-modulation BTF in the SDR with $N_b = 1.6 \times 10^{10}$ and an rms gap voltage modulation of 2 kV.

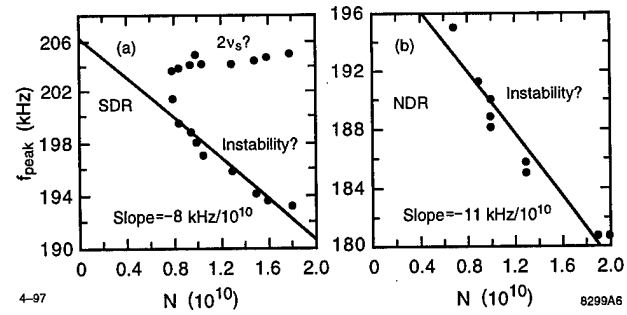

Figure 5: Peak response function of voltage-modulation BTF as a function of current.

[2] C.D. Curtis *et al.*, Proc. 5th Int. Conf., Dubna 63, p. 815 (1963); H. Grunder, G. Lambertson, Proc. 8th Int. Conf. on High-Energy Acc. CERN 71, p. 308 (1971); D. Möhl, A. Sessler, Proc. 8th Int. Conf. on High-En. Acc., CERN 71, p. 308 (1971).

[3] A. Hofmann, B. Zotter, IEEE Trans. N. S. 24, No. 3 (1977).

[4] J. Jowett, A. Hofmann, K.L.F. Bane, P.L. Morton, W. Spence, R. Stege, EPAC 90, Nice (1990).

[5] J. Byrd, Ph.D thesis Cornell University (1992).

[6] M. Ellison *et al.*, PRL 70, 5 p. 591 (1993); D.D. Caussyn et al, IEEE PAC 93 (1993); D. Li *et al.*, NIM A 364, p. 205 (1995).

[7] R. Holtzapple, Ph.D thesis, Stanford University (1996).

[8] See for instance A.W. Chao, "Physics of Collective Beam Instabilities in High Energy Accelerators", J. Wiley (1993).

[9] G. Tsironis, S. Peggs, and T. Chen, EPAC 1990, Nice, p. 1753.

[10] J. Byrd, W.-H. Cheng, F. Zimmermann, these proceedings.

[11] K.L.F. Bane and K. Oide, SLAC-PUB-95-6878 (1995).

ANALYTIC AND NUMERICAL ANALYSIS OF THE LONGITUDINAL COUPLING IMPEDANCE OF AN ANNULAR CUT IN A COAXIAL LINER

Alexei V. Fedotov, Robert L. Gluckstern
Physics Department, University of Maryland, College Park, Maryland 20742 USA

Abstract

Beam pipes of high-energy superconducting colliders require a shielding tube (liner) with pumping slots to screen cold chamber walls from synchrotron radiation. Pumping slots in the liner walls are required to keep high vacuum inside the beam pipe and provide for a long beam lifetime. As previously discussed [Fedotov and Gluckstern, Phys. Rev. E **54**, 1930 (1996)], for a long narrow slot whose length may be comparable with the wavelength, the usual static approximation for the polarizability and susceptibility which enter into the impedance is a poor one.[1] Our objective is eventually to analyze and obtain numerical values for a rectangular slot of arbitrary dimensions. In this paper we present an analysis, based on a variational formulation, for the impedance of an annular cut in the inner conductor, including both the realistic coaxial structure of the beam-pipe and the effect of finite wavelength. For low frequencies, the numerical results are checked against analytical results, with which they agree.

1 INTRODUCTION

The solution is based on the method of field matching at the liner radius, including the discontinuity. We construct a variational form for the impedance, which is stationary with respect to arbitrary small variations of the field about its true value. The variational approach ensures very good accuracy for the impedance, since the error will be proportional to the square of the error in the chosen trial fields.

We assume the liner thickness to be negligible and call the region inside the inner conductor the "pipe region" and the region outside the inner conductor the "coaxial region". The technique consists of expanding fields in both regions into a complete set of functions. At the common interface the fields have to be matched, yielding equations for the expansion coefficients.

Since the driving current on axis is proportional to $\exp(-jkz)$, the problem is simplified by obtaining $Z_{\|}(k)$ for an even driving current $\cos kz$ and an odd driving current $-j\sin kz$ separately and then taking their sum. We should note that the variational method becomes possible only when the problem is separated into an even and an odd part. In the even problem E_z is even in z, while in the odd problem E_z is odd in z (where $z=0$ is chosen to be the center of the cut). We use the superscript (e) for the even part and the superscript (o) for the odd part.

2 GENERAL ANALYSIS

In the pipe region the fields are given by the source fields plus a general solution of the Maxwell equations for the cylindrical waveguide. In the coaxial region we have the general solution of the Maxwell equations for the coaxial waveguide. Due to the symmetry of the problem we have no θ dependence, and therefore need to consider only the azimuthally symmetric TM modes. For the portion of the problem when $E_z^{(e)}$ is even in z we have

$$E_z^{(e)}(r,z) = \int dq \cos qz A^{(e)}(q) \left[\frac{J_0(\kappa r)}{J_0(\kappa a)}, \frac{F_0(\kappa r)}{F_0(\kappa a)}\right]. \quad (1)$$

Here we use the notation where the first part in square brackets corresponds to the pipe region $r \le a$, and the second part corresponds to the coaxial region $a \le r \le b$, with the function F_0 being the solution of the Maxwell equations for the coaxial region for the TM modes $[F_0(u) = Y_0(u)J_0(\kappa b) - J_0(u)Y_0(\kappa b)]$. Note that we consider the inside and outside surfaces of the liner both to be at $r=a$, since we neglect the thickness of the liner compared to the wavelength. Therefore, the coefficient $A^{(e)}(q)$ is the same for both $r<a$ and $r>a$, since $E_z^{(e)}$ is continuous at $r=a$ within the hole and on both sides of the liner surface, where $E_z^{(e)}=0$. The continuity of $H_\theta^{(e)}$ in the hole gives

$$\int dz' E_{z'}^{(e)}(a,z') K_{11}^{(e)}(z,z') = Z_0 I_0 \cos kz, \quad (2)$$

where

$$\begin{aligned} K_{11}^{(e)}(z,z') &= K_{11}^{(e)}(z',z) \\ &= a\int dq \cos qz \cos qz' k_{11}, \end{aligned} \quad (3)$$

with

$$k_{11} = jkaP(q), \quad (4)$$

and

$$P(q) = \left[\frac{J_0'(\kappa a)}{\kappa a J_0(\kappa a)} - \frac{F_0'(\kappa a)}{\kappa a F_0(\kappa a)}\right]. \quad (5)$$

We now treat $P(q)$ as a function of κa with $\kappa b = (b/a)\kappa a$ and express this function as a sum over the zeros of the respective denominators. The resulting expression for $K_{11}^{(e)}$, in Eq. (3), can then be integrated over q by means of the residue theorem. Using the definition of the impedance for the even part, we can rewrite Eq. (2) as

$$\frac{Z_0}{Z_{\|}^{(e)}} = -\frac{(\int\int dz' dz E_{z'}^{(e)}(a,z') E_z^{(e)}(a,z) K_{11}^{(e)}(z,z'))}{(\int dz E_z^{(e)}(a,z)\cos kz)^2}, \quad (6)$$

0-7803-4376-X/98/$10.00 © 1998 IEEE

which is easily seen to be a variational form for the impedance, with trial function $E_z^{(e)}(a,z)$. Expanding $E_z^{(e)}(a,z)$ into a complete set in $|z| < g/2$ and evaluating the integrals in Eq. (6), the solution for the even part of the impedance is obtained by finally truncating and inverting the resulting matrix equations.

For the portion of the problem when $E_z^{(o)}$ is odd in z we perfom similar analysis, and obtain the variational form for the odd part of the impedance

$$\frac{Z_0}{Z_{\|}^{(o)}} = -\frac{(\int\int dz' dz E_{z'}^{(o)}(a,z') E_z^{(o)}(a,z) K_{11}^{(o)}(z,z'))}{(\int dz E_z^{(o)}(a,z)\sin kz)^2}, \tag{7}$$

where

$$\begin{aligned} K_{11}^{(o)}(z,z') &= K_{11}^{(o)}(z',z) \\ &= a\int dq \sin qz \sin qz' k_{11}. \end{aligned} \tag{8}$$

3 ANALYTIC DERIVATION FOR LOW FREQUENCIES

In our particular case where the slot is a narrow annular cut, for low frequencies the leading non-vanishing term in the odd part is a factor of $(g/a)^2$ less than the same term in the even part. To present the analytic result for a narrow annular cut it is therefore sufficient to consider only the even part of the impedance.

For small ka and g/a, using the static approximation for $E_{z'}$, E_z, we evaluate Eq. (6) analytically and obtain

$$\begin{aligned} \frac{Z_{\|}}{Z_0} &= \frac{\ln(b/a)}{\pi}\left[1 + j\frac{4}{\pi^2}kag/a\right. \\ &- \left. 2jka\frac{\ln(b/a)}{\pi}\Big(C_1 + C_2 + 2\ln(4a/g)\Big)\right]. \end{aligned} \tag{9}$$

In this result we supressed the superscript (e), since the odd part of the impedance is negligible. Numerical study shows that $[C_1 + C_2]$ can be replaced by $[\ln(b/a - 1) - 1.78]$ for the range of b/a from 1 to 3.

4 NUMERICAL RESULTS AND DISCUSSION

The even part of the impedance is calculated using Eq. (6) and the odd part is calculated using Eq. (7). Finally, one sums together the even and the odd parts to obtain the coupling impedance. The general behavior of the real and imaginary parts with respect to frequency is presented in Figs. 1 and 2.

For low frequencies we obtain the leading terms for the real and imaginary parts analytically, according to Eq. (9). The agreement between the analytic and numerical results is very good. As an example, results for $b/a = 2$ are presented in Table 1. For other values of b/a, the analytic and numerical results are also in good agreement.

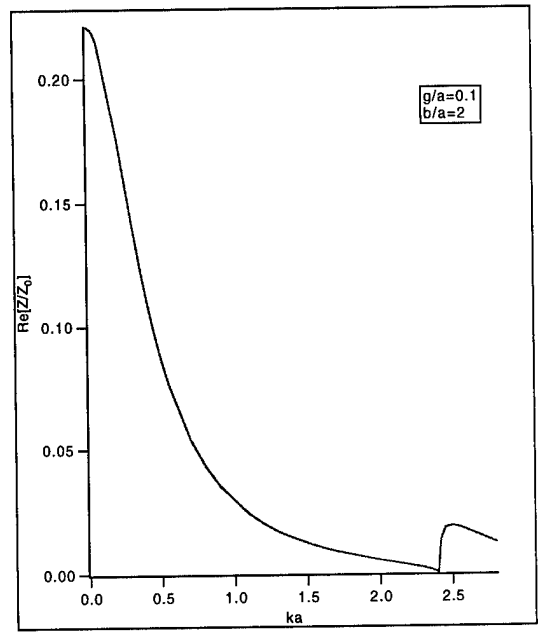

Figure 1: Real part of the coupling impedance of an annular cut in a coaxial liner.

	g/a	Analytic approximation	Numerical result
	0.01	0.02976	0.02907
b	0.03	0.02332	0.02308
	0.05	0.02025	0.02022
	0.07	0.01823	0.01830

Table 1: $Im[Z_{\|}/Z_0]$ for $b/a = 2$ at frequency $ka = 0.03$, $C_1 = -0.667, C_2 = -1.117$.

The real part of the impedance in the limit of zero frequency becomes finite, and is equal to $\ln(b/a)/\pi$, which agrees with the result obtained by Palumbo.[2] Its physical origin is the energy radiated in the TEM mode in the coaxial region.

For low frequencies, the coupling impedance of the narrow annular cut can be easily presented in terms of an equivalent circuit. Specifically, for $g \ll a$, we can write for the admittance

$$Y = R^{-1} + j\omega C, \tag{10}$$

where R is given by $Z_0 \ln(b/a)/\pi$, and C is given by $2a\epsilon_0(C_1 + C_2 + 2\ln(4a/g))$, corresponding to the parallel combination of the resistance R and the capacitance C. In Figs. 3 and 4 we present the real and imaginary parts of the admittance Y as a function of ka. As one can see, the real part of the admittance is purely $1/R$ until $ka = 2.405$, the cutoff of the TM_{01} mode. At this cutoff the singularity corresponds to the fact that power starts to dissipate not just in the coaxial region, but also in the pipe region.

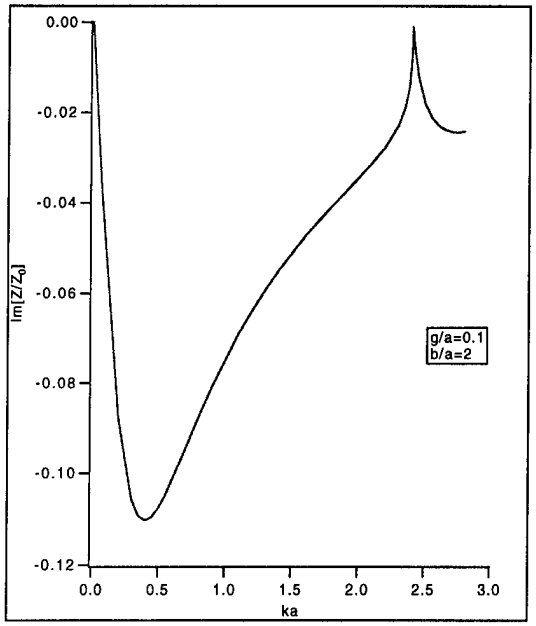

Figure 2: Imaginary part of the coupling impedance of an annular cut in a coaxial liner.

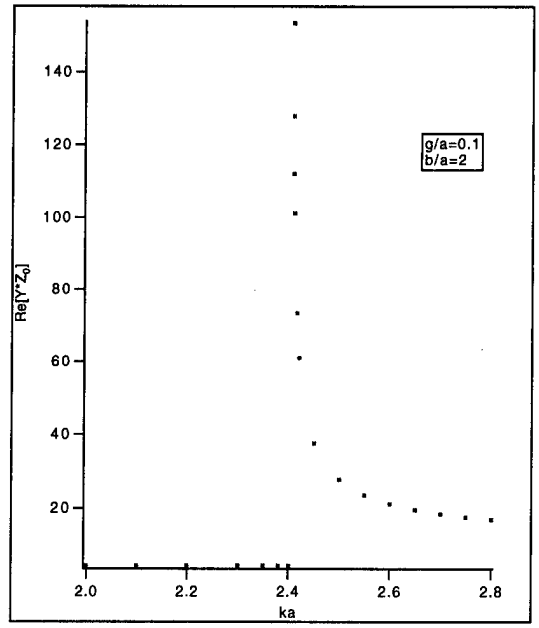

Figure 3: Real part of the admittance of an annular cut in a coaxial liner.

5 SUMMARY

The purpose of this paper is to present the analysis of the calculation of the coupling impedance of an annular cut in a coaxial liner of negligible wall thickness. We obtain equations for calculating the even and odd parts of the impedance, expressed in variational form. The use of the variational method makes numerical study fast and accurate. In order to check the developed technique, an analytic calculation is performed for low frequencies and compared with the numerical results. The agreement between the analytic and numerical results is very good. As previously mentioned, the present calculation is a first step in the development of an analysis for the coupling impedance of a rectangular slot with finite azimuthal length.[3]

6 ACKNOWLEDGMENTS

The authors wish to thank Dr. S. Kurennoy for helpful comments. This work was supported by the U.S. Department of Energy.

7 REFERENCES

[1] A.V. Fedotov and R.L. Gluckstern, Phys. Rev. E, **54**, 1930 (1996).

[2] L. Palumbo, Analytic Calculation of the Impedance of a Discontinuity, Particle Accelerators, 25, 1990.

[3] A.V. Fedotov and R.L. Gluckstern, General Analysis of the Longitudinal Coupling Impedance of a Rectangular Slot in a Thin Coaxial Liner, following paper.

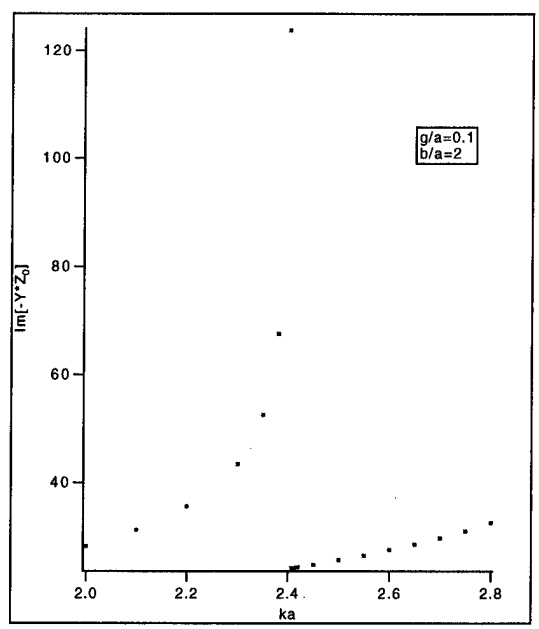

Figure 4: Imaginary part of the admittance of an annular cut in a coaxial liner.

GENERAL ANALYSIS OF THE LONGITUDINAL COUPLING IMPEDANCE OF A RECTANGULAR SLOT IN A THIN COAXIAL LINER

Alexei V. Fedotov, Robert L. Gluckstern
Physics Department, University of Maryland, College Park, Maryland 20742 USA

Abstract

As previously discussed [Fedotov and Gluckstern, Phys. Rev. E **54**, 1930 (1996)], for a long narrow slot whose length may be comparable with the wavelength, the usual static approximation for the polarizability and susceptibility which enter into the impedance is a poor one. Therefore, finding semi-analytic expressions for the impedance of a rectangular slot in a broad frequency range is highly desirable. We develop a general analysis based on a variational formulation, which includes both the realistic coaxial structure of the beam-pipe and the effect of finite wavelength in the calculation of the coupling impedance of a rectangular slot in a liner wall of zero thickness. We then present a numerical study of the frequency dependence of the coupling impedance of a transverse rectangular slot.

1 INTRODUCTION

We have earlier considered a liner with a symmetric annular slot.[1] This time we consider the azimuthally asymmetric problem of a single rectangular slot in an inner conductor (liner) of zero thickness.

We call the region inside the inner conductor $r \leq a$ the "pipe region" and the region outside the inner conductor $a \leq r \leq b$ the "coaxial region". The technique consists of expanding fields in both regions into a complete set of functions. At the common interface the fields have to be matched, yielding equations for the expansion coefficients. The solution is then obtained by finally truncating and inverting the resulting matrix equations.

The longitudinal coupling impedance can be written in the following form

$$\frac{Z_{\|}(k)}{Z_0} = -\frac{1}{2\pi a Z_0 I_0} \int dS E_z(a,\theta,z;k) e^{jkz}, \quad (1)$$

where the surface integral is only over the hole, since E_z vanishes on the liner wall. Since the driving current on axis is proportional to $\exp(-jkz)$, the problem is simplified by obtaining $Z_{\|}(k)$ for an even driving current $\cos kz$ and an odd driving current $-j\sin kz$ separately and then taking their sum. We should note that the variational method becomes possible only when the problem is separated into an even and an odd part. In the even problem E_z, H_r, H_θ are even in z, while in the odd problem E_z, H_r, H_θ are odd in z (where the center of the hole is chosen to be at $z = 0$, $\theta = 0$). In any case E_z, E_r, H_θ are always even in θ, and H_z, H_r, E_θ are always odd in θ. We use the superscript (e) for the even problem and the superscript (o) for the odd problem.

2 THE EVEN PART OF IMPEDANCE

Due to the asymmetry of the problem we now have θ dependence, and therefore need to use both TM and TE modes. For the TM portion of the modes we have

$$E_z^{(e)}(r,\theta,z) = \int dq \cos qz \phi^{(e)}(r,\theta), \quad (2)$$

where

$$\phi^{(e)}(r,\theta) = \sum_n \cos n\theta A_n^{(e)}(q) \left[\frac{J_n(\kappa r)}{J_n(\kappa a)}, \frac{F_n(\kappa r)}{F_n(\kappa a)}\right]. \quad (3)$$

Here we use the notation where the first part in square brackets corresponds to the pipe region $r \leq a$, and the second part corresponds to the coaxial region $a \leq r \leq b$, where F_n is the solution of the Maxwell equations for the coaxial region for the TM modes $[F_n(u) = Y_n(u)J_n(\kappa b) - J_n(u)Y_n(\kappa b)]$. The other TM field components can be obtained using Eq. (2).

For the TE portion of the modes we similarly have

$$Z_0 H_z^{(e)}(r,\theta,z) = \int dq \sin qz \psi^{(e)}(r,\theta), \quad (4)$$

where

$$\psi^{(e)}(r,\theta) = -\sum_n \sin n\theta B_n^{(e)} \left[\frac{J_n(\kappa r)}{J_n'(\kappa a)}, \frac{G_n(\kappa r)}{G_n'(\kappa a)}\right], \quad (5)$$

where $G_n(\kappa r)$ is the solution of the Maxwell equations for the coaxial region for the TE modes $[G_n(u) = Y_n(u)J_n'(\kappa b) - J_n(u)Y_n'(\kappa b)]$. The other TE field components can be obtained using Eq. (4).

For the general solution, we must include both TM and TE modes. The continuity of $H_z^{(e)}$ and $H_\theta^{(e)}$ in the hole at $r = a$ leads to

$$\int dS' E_{\theta'}^{(e)}(a,\theta',z') K_{22}^{(e)} + \int dS' E_{z'}^{(e)}(a,\theta',z') K_{21}^{(e)} = 0, \quad (6)$$

$$\int dS' E_{z'}^{(e)}(a,\theta',z') K_{11}^{(e)} + \int dS' E_{\theta'}^{(e)}(a,\theta',z') K_{12}^{(e)} = a Z_0 I_0 2\pi \cos kz, \quad (7)$$

0-7803-4376-X/98/$10.00 © 1998 IEEE

where

$$K_{11}^{(e)} = a\sum_n \int dq \cos qz \cos qz' \cos n\theta \cos n\theta' k_{11}, \quad (8)$$

$$K_{12}^{(e)} = K_{21}^{(e)} = a\sum_n \int dq \cos qz \sin qz' \sin n\theta' \cos n\theta k_{12}, \quad (9)$$

$$K_{22}^{(e)} = a\sum_n \int dq \sin qz \sin qz' \sin n\theta \sin n\theta' k_{22}, \quad (10)$$

with

$$k_{11} = jkaP_n(q) - j\frac{q^2n^2}{\kappa^2 ka}Q_n(q), \quad (11)$$

$$k_{12} = k_{21} = j\frac{qn}{k}Q_n(q), \quad (12)$$

$$k_{22} = -j\frac{\kappa^2 a}{k}Q_n(q). \quad (13)$$

Here the functions $P_n(q)$ and $Q_n(q)$ are given by the following expressions

$$P_n(q) = \left[\frac{J_n'(\kappa a)}{\kappa a J_n(\kappa a)} - \frac{F_n'(\kappa a)}{\kappa a F_n(\kappa a)}\right], \quad (14)$$

$$Q_n(q) = \left[\frac{J_n(\kappa a)}{\kappa a J_n'(\kappa a)} - \frac{G_n(\kappa a)}{\kappa a G_n'(\kappa a)}\right]. \quad (15)$$

We now treat P_n and Q_n as functions of κa with $\kappa b = (b/a)\kappa a$ and express these functions as a sum over the zeros of the respective denominators. The detailed expansion of functions P_n and Q_n in terms of algebraic series is given in [2]. The resulting expressions for $K_{11}^{(e)}$, $K_{12}^{(e)}$, $K_{21}^{(e)}$ and $K_{22}^{(e)}$, in Eqs. (8)-(10), can then be integrated over q by means of the residue theorem.

From Eq. (1) the even part of the impedance is

$$\frac{Z_{\parallel}^{(e)}}{Z_0} = \frac{-1}{2\pi a Z_0 I_0}\int dS E_z^{(e)}(a,\theta,z)\cos kz. \quad (16)$$

Using Eqs. (6) and (7) we can form

$$\begin{aligned} Z_0/Z_{\parallel}^{(e)} = & \\ - & \Big(\iint dS'dS[2E_{\theta'}^{(e)}(a,\theta',z')E_z^{(e)}(a,\theta,z)K_{12}^{(e)} \\ + & E_{z'}^{(e)}(a,\theta',z')E_z^{(e)}(a,\theta,z)K_{11}^{(e)} \\ + & E_{\theta'}^{(e)}(a,\theta',z')E_\theta^{(e)}(a,\theta,z)K_{22}^{(e)}]\Big) \\ / & \left(\int dS E_z^{(e)}(a,\theta,z)\cos kz\right)^2, \end{aligned} \quad (17)$$

a form independent of the normalization of the fields. If we ask that the numerator of Eq. (17) be a minimum with respect to the variations of $E_z^{(e)}$ and $E_\theta^{(e)}$, subject to the constraint $\int dS E_z^{(e)}(a,\theta,z)\cos kz = 1$, we confirm that Eq. (17) is a variational form for the impedance.

After evaluation of the integrals, we obtain the final form for the even part of the impedance.[2]

3 THE ODD PART OF IMPEDANCE

We now consider the portion of the problem where $E_z^{(o)}$ is odd in z. We perform field expansions similar to those for the even portion of the problem. The continuity of $H_z^{(o)}$ and $H_\theta^{(o)}$ in the hole at $r = a$ leads to the following integral equations

$$\int dS' E_{\theta'}^{(o)}(a,\theta',z')K_{22}^{(o)} + \int dS' E_{z'}^{(o)}(a,\theta',z')K_{21}^{(o)} = 0, \quad (18)$$

$$\int dS' E_{z'}^{(o)}(a,\theta',z')K_{11}^{(o)} + \int dS' E_{\theta'}^{(o)}(a,\theta',z')K_{12}^{(o)} = aZ_0 I_0 2\pi(-j\sin kz), \quad (19)$$

where

$$K_{11}^{(o)} = a\sum_n \int dq \sin qz \sin qz' \cos n\theta \cos n\theta' k_{11}, \quad (20)$$

$$K_{12}^{(o)} = K_{21}^{(o)} = - a\sum_n \int dq \sin qz \cos qz' \cos n\theta \sin n\theta' k_{12}, \quad (21)$$

$$K_{22}^{(o)} = a\sum_n \int dq \cos qz \cos qz' \sin n\theta \sin n\theta' k_{22}, \quad (22)$$

with k_{ij} given by Eqs. (11)-(13).

From Eq. (1) the odd part of the impedance is

$$\frac{Z_{\parallel}^{(o)}}{Z_0} = \frac{-j}{2\pi a Z_0 I_0}\int dS E_z^{(o)}(a,\theta,z)\sin kz. \quad (23)$$

Using Eqs. (18) and (19) we can form

$$\begin{aligned} Z_0/Z_{\parallel}^{(o)} = & \\ - & \Big(\iint dS'dS[2E_{\theta'}^{(o)}(a,\theta',z')E_z^{(o)}(a,\theta,z)K_{12}^{(o)} \\ + & E_{z'}^{(o)}(a,\theta',z')E_z^{(o)}(a,\theta,z)K_{11}^{(o)} \\ + & E_{\theta'}^{(o)}(a,\theta',z')E_\theta^{(o)}(a,\theta,z)K_{22}^{(o)}]\Big) \\ / & \left(\int dS E_z^{(o)}(a,\theta,z)\sin kz\right)^2, \end{aligned} \quad (24)$$

which is the variational form for the odd part of the impedance. After evaluation of the integrals, we obtain the final form for calculation of the odd part of the impedance [2].

4 NUMERICAL RESULTS AND DISCUSSIONS

Formulas for direct numerical computation of the impedance of a rectangular slot have been obtained.

As an example, and to test our formulas, we present here a numerical study of the impedance of rectangular slots of different azimuthal length. In order to compare our results with those presented by Filtz and Scholz[3] we also choose the parameters of the LHC design.

In Figs. 1 and 2, the frequency dependence of both the real and imaginary parts of the coupling impedance of the transverse rectangular slot is presented, with an angular length 180 and 350 degrees, respectively. As expected, the behavior with respect to frequency strongly differs from the one of slots with the small angular length, even for relatively low frequencies.

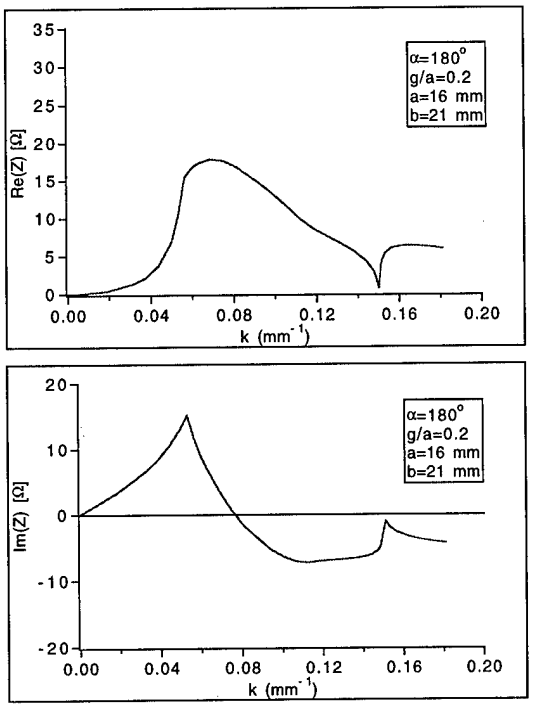

Figure 1: Real and imaginary parts of the coupling impedance of transverse rectangular slot with the azimuthal length 180 degrees.

The general behavior of the impedance agrees with the results of Filtz and Scholz, even though there is some shift between our results and theirs. They used a similar field matching technique, and their calculations of impedance were apparently performed without using a variational form, presumably requiring large matrices and considerable CPU time. Our approach, which uses a variational form, requires only modest size matrices.

5 SUMMARY

The main purpose of this paper is to present a detailed analysis of the calculation of the coupling impedance of a rectangular slot in a coaxial liner of negligible wall thickness over a wide frequency range. We obtain equations for calculating the even and odd parts of the impedance, expressed in variational form. The use of the variational method makes numerical study fast and accurate. The numerical results obtained for both the imaginary and the real part correspond to the expected ones for frequencies below and above cutoff.

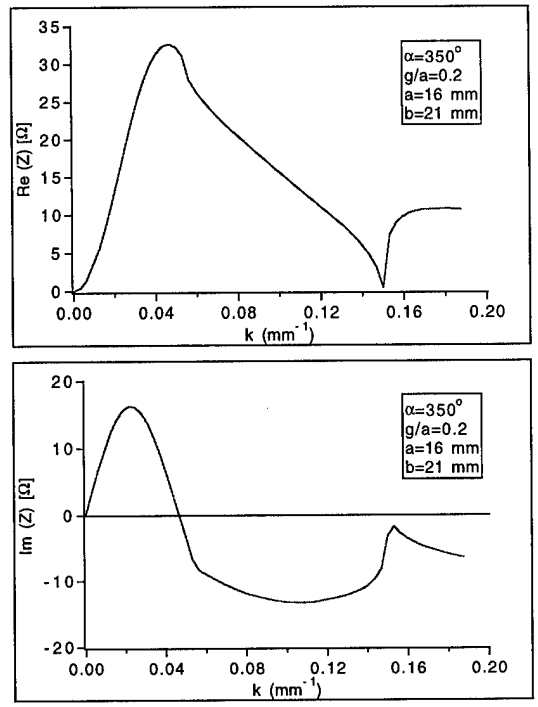

Figure 2: Real and imaginary parts of the coupling impedance of transverse rectangular slot with the azimuthal length 350 degrees.

6 ACKNOWLEDGMENTS

The authors wish to thank Dr. S. Kurennoy for helpful comments. This work was supported by the U.S. Department of Energy.

7 REFERENCES

[1] A.V. Fedotov and R.L. Gluckstern, Analytic and Numerical Analysis of the Coupling Impedance of an Annular Cut in a Coaxial Liner, preceding paper (submitted for publication).

[2] A.V. Fedotov and R.L. Gluckstern, Analysis of the Longitudinal Coupling Impedance of a Rectangular Slot in a Thin Coaxial Liner, Dept. of Phys., University of Maryland, College Park, 1997 (submitted for publication).

[3] M. Filtz, T. Scholz, Impedance Calculations for a Coaxial Liner, Proceeding of the EPAC-94, London, 1994.

RESONANT EFFECTS IN THE LONGITUDINAL COUPLING IMPEDANCE OF A RECTANGULAR SLOT IN A COAXIAL LINER

Alexei V. Fedotov, Robert L. Gluckstern
Physics Department, University of Maryland, College Park, Maryland 20742 USA

Abstract

We earlier developed a general analysis, based on a variational formulation, which includes both the realistic coaxial structure of the beam pipe and the effect of finite wavelength in the calculation of the coupling impedance of a rectangular slot in a liner wall of zero thickness. In the present paper we use this analysis to study the frequency dependence of the coupling impedance of a longitudinal rectangular slot. Resonant effects in the coupling impedance are discussed.

1 IMPEDANCE OF A SMALL SQUARE HOLE EFFECT OF THE OUTER WALL

We use expressions obtained earlier[1] to obtain numerical values for a small square hole with the edge length equal to $w = l = 0.25\ a$, where a is the radius of the liner, and $b/a = 1.3125$. For a=16 mm this corresponds to the parameters used in the calculation of Scholz.[2] The frequency dependence of both the real and imaginary parts of the coupling impedance are presented in Fig. 1. Plots similar to Fig. 1 were obtained by Scholz,[2] but the peaks he obtains for the cutoffs of the modes in the coaxial region are in error.[3]

1.1 Imaginary Part

Using the expressions for the magnetic susceptibility ψ and electric polarizability χ for the square hole in a plane metallic wall in the well known Bethe small hole approximation, for the frequency 1 GHz and dimensions of the square hole given above, one obtains

$$Z = j0.0073[\Omega]. \tag{1}$$

In the problem we consider, the wall of the outer pipe is at radius $b = 21$ [mm], with $b - a = 5$ [mm]. The result is expected to be influenced by the outer metallic wall, being less than the one given by Eq. (1), and to approach this result for large $(b - a)$. This behavior is consistant with the numerical results in Table 1. Results obtained by Scholz[2] for 1 GHz are a few percent higher, and at $b/a = 2$ the numerical value obtained by Scholz is already 10 percent above the static result in Eq. (1) for the hole in the pipe without an outer wall.

1.2 Real part

At the frequency 1 GHz ($ka = 0.3351$) with $a = 16$ [mm], our numerical results (Ref.[1]) and the results obtained by

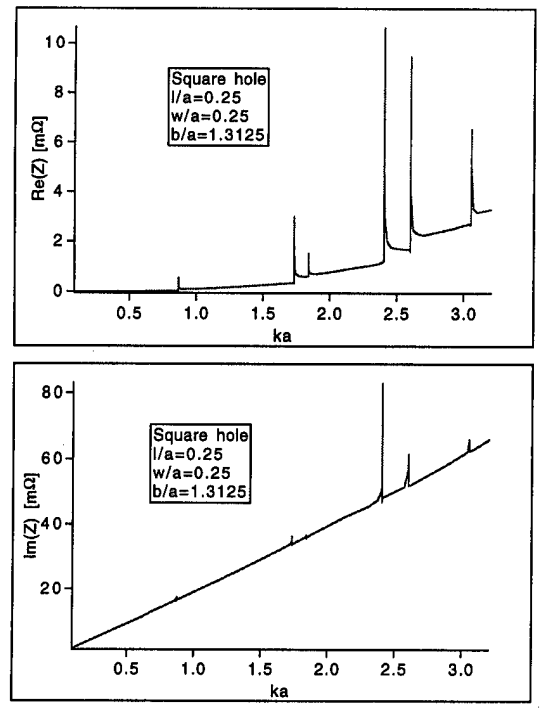

Figure 1: Real and imaginary parts of the impedance of a square hole (for a=16 mm, w=l=4 mm).

ka	$b/a = 1.2$	$b/a = 1.3125$	b/a=1.5
0.3351	6.46	6.57	6.60

Table 1: $Im(Z)$ $[m\Omega]$ for a square hole with 4 [mm] edge length at frequency 1 GHz.

Scholtz[2] in Table 2 are significantly larger than those obtained by using the formula of Palumbo *et al.*[4]

Based on our earlier analysis[1] we can examine the low frequency behavior analytically. For frequencies below all possible cutoffs, we obtain

$$Re\left(\frac{Z}{Z_0}\right) = \frac{k^2}{64\pi^3 a^4 ln(b/a)}(\psi^2 + \chi^2) \tag{2}$$

due to energy radiated in the TEM mode. The available static approximations for ψ and χ can be now used to estimate the real part of the impedance for holes of different shape. The value of the impedance obtained in this way will be a few percent higher than the real one due to the fact that expressions for ψ and χ are given in the literature

0-7803-4376-X/98 /$10.00 © 1998 IEEE

Ref.	$b/a = 1.2$	$b/a = 1.3125$	$b/a = 1.5$
[1]	7.54	5.21	3.53
[2]	≈ 7.7	≈ 5.3	≈ 3.8
[4]	1.64	1.1	0.74

Table 2: $Re(Z)$ $[\mu\Omega]$ for frequency 1 GHz.

b/a	1.2	1.3125	1.5	$\rightarrow \infty$
$\chi/(2w^3)$	0.0998	0.1010	0.1015	0.1082
$\psi/(2w^3)$	0.2305	0.2339	0.2351	0.2532

Table 3: The electric polarizabilty χ and magnetic susceptibility ψ of a square hole ($w = l$).

for a hole in a plane metallic wall (without the outer wall which is present in the coaxial structure). As an example, in Table 3 we present the b/a dependence of ψ and χ, which approach the results available for a square hole in a metallic plate when $b/a \rightarrow \infty$. For the circular hole, using Eq. (2) we obtain

$$Re\left(\frac{Z}{Z_0}\right) = \frac{5k^2r^6}{36\pi^3a^4ln(b/a)}, \qquad (3)$$

where r is the radius of the hole. The expression given in Eq. (3) is a factor of 5 larger than the one obtained by Palumbo *et al.*[4] The results obtained by using Eq. (3) are now in good agreement with the numerical calculations.

The real part of the impedance of a small hole in a coaxial structure varies as k^2 in contrast to the k^4 behavior for the radiation of a hole into free space and is now relatively more important.

2 IMPEDANCE OF A LONGITUDINAL SLOT

2.1 *Validity of the static approximation for low frequencies*

The frequency correction for the elliptical slot[5] suggests that the imaginary part of the impedance of a long elliptical slot should be strongly reduced at finite frequencies. Therefore, it is important to understand whether a similar effect is present for a rectangular slot at finite frequencies. Numerical study of this question for a long rectangular slot shows that the reduction in the imaginary part of the impedance at low frequencies is insignificant. The available static approximations for ψ and χ, give a reasonably good description for low frequencies even when the slot length is larger than the radius of the pipe, starting to lose its accuracy at large l/a (Fig. 2). For higher frequencies ($ka \geq 1$) the static approximation loses its accuracy at much smaller values of l/a (Fig. 3). However, the dependence of the imaginary part of the impedance on slot length is insignificant (Figs. 2 and 3).

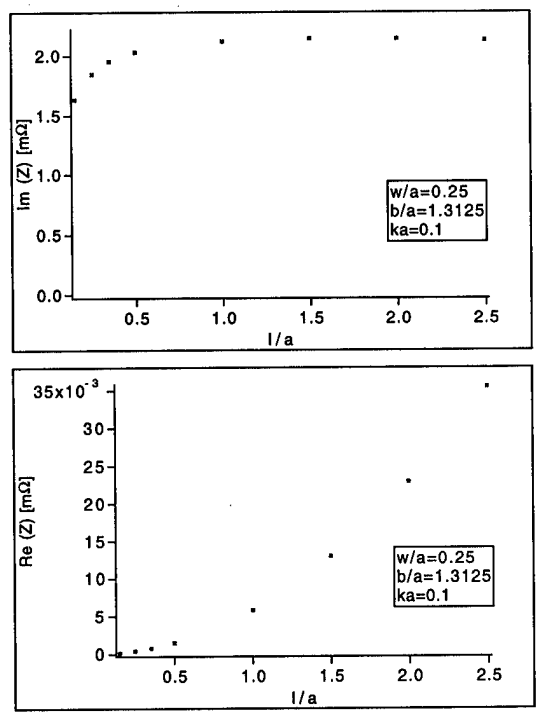

Figure 2: Real and imaginary parts of the impedance for low frequencies ($ka = 0.1$).

2.2 *Resonances*

One can see the appearance of resonant behavior for the real part of the impedance in Fig. 4. For the imaginary part we identify the resonances as the place where the impedance changes its sign. There appears to be resonant behavior for the odd and even parts of the impedance separately (Fig. 4), but due to the strong cancelation between the even and odd parts no resonant behavior is seen for the imaginary part of total impedance (Fig. 6). This makes it possible to design relatively long slots. The first two resonances can be seen in Fig. 5 for slot lengths $l/a = 3$ and $l/a = 5$. The frequency behavior of the real and imaginary parts of the total impedance for a very long rectangular slot ($l/a = 5$) is shown in Fig. 6.

3 REFERENCES

[1] A.V. Fedotov, R.L. Gluckstern, General Analysis of the Longitudinal Coupling Impedance of a Rectangular Slot in a Thin Coaxial Liner, preceding paper.

[2] T. Scholz, Impedance of rectangular slots in a round coaxial tube. Proceeding of the EPAC-96, Spain, 1996.

[3] T. Scholz, Private communication.

[4] S. De Santis, M. Migliorati, L. Palumbo and M. Zobov, Impedance of a hole in coaxial structures. Proceeding of the EPAC-96, Spain, 1996.

[5] A.V. Fedotov and R.L. Gluckstern, Phys. Rev. E, **54**,1930 (1996).

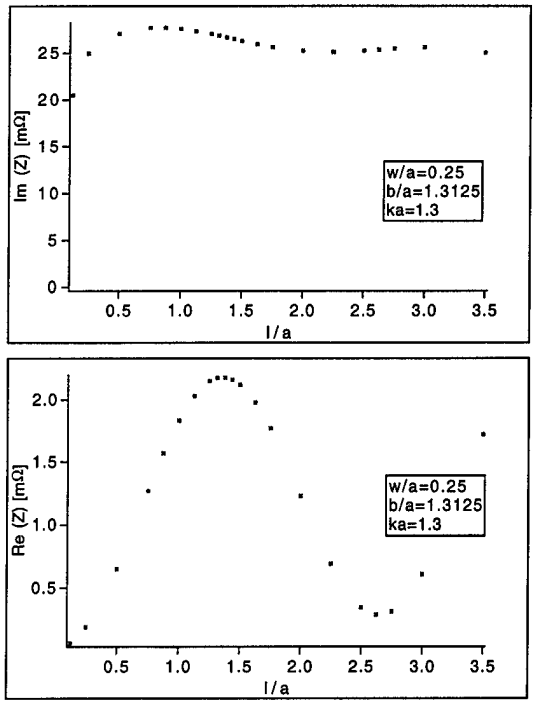

Figure 3: Real and imaginary parts of the impedance for high frequencies ($ka = 1.3$).

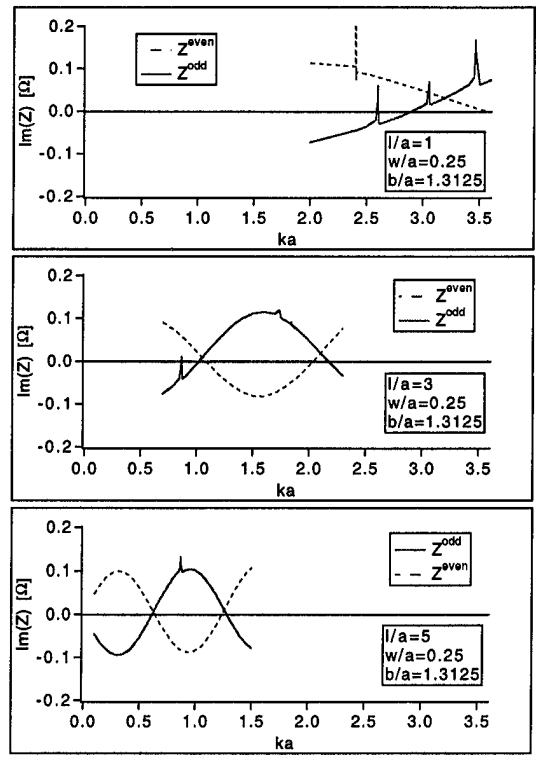

Figure 5: Resonant behavior of the imaginary part of the impedance for slots of different length.

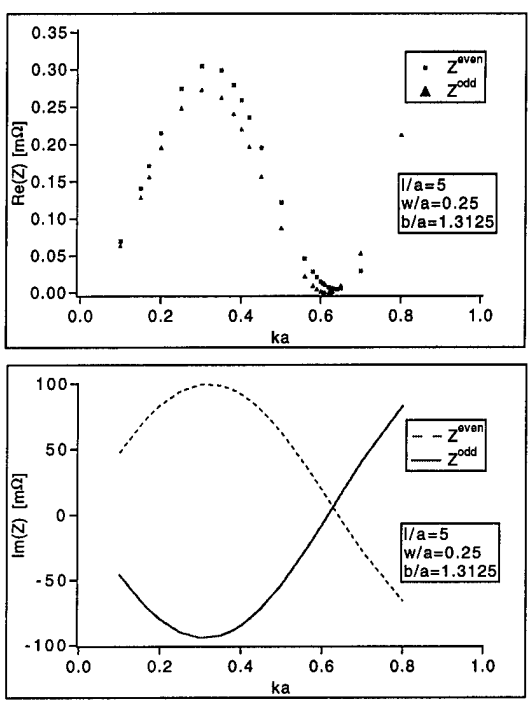

Figure 4: Resonant behavior in the even and odd parts of the impedance.

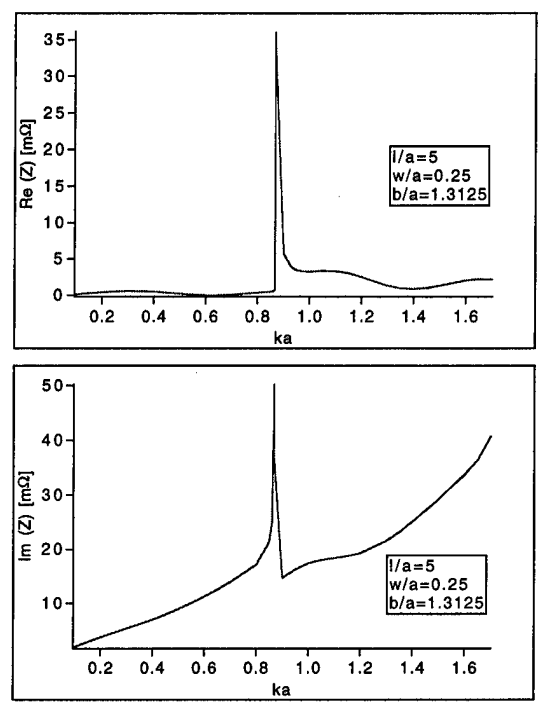

Figure 6: Real and imaginary parts of the impedance for a very long slot ($l/a = 5$).

PATH INTEGRAL COMPUTATION OF LASLETT COEFFICIENTS IN PIPES WITH ARBITRARY TRANSVERSE GEOMETRY

S. Petracca*, F. Ruggiero, CERN, SL/AP Group,
V. Galdi, I.M. Pinto, D.I.^{3}E., Univ. of Salerno, Italy

Abstract

An efficient (accurate and fast) numerical framework is introduced for computing the (incoherent) betatron normal mode Laslett coefficients for beam-liner with completely general transverse geometry.

1 INTRODUCTION

In previous papers[1][2] we introduced a general framework for computing the normal mode Laslett coefficients for beam liners in terms of the associated complex (2D) potential. In this communication we extend the previous result to the most general case where the (transverse) liner geometry is so complicated that the (2D) potential cannot be computed in analytic form. The extension is based on (a suitable generalization of) Cauchy integral formula for computing the Lasletts without using derivatives, and an application of Monte-Carlo Wiener-Ito stochastic integration for solving Poisson equation.

2 NORMAL MODE LASLETT COEFFICIENTS

The betatron normal mode incoherent[1] Laslett coefficients for beam liners possibly surrounded by a co-axial magnetic yoke can be conveniently computed from an auxiliary complex potential $\bar{\Psi}$:[1][2]

$$\phi^{(im.)} - \beta_0 A_z^{(im.)} = 2\Lambda \, Re \, \bar{\Psi}(\bar{z}, \bar{z}_b, \bar{z}_b^*), \qquad (1)$$

as:

$$\epsilon_{1,2}^{(inc.)} = \pm \frac{1}{2} \left| \ddot{\bar{\Psi}} \right|_{\bar{z}=\bar{z}_b=\bar{z}_{eq.}} . \qquad (2)$$

In (1) $\bar{z} = L^{-1}(x+iy)$ and $\bar{z}_b = L^{-1}(x_b+iy_b)$ denote the (complex, scaled) field-point and source-point transverse positions, $\bar{z}_{eq.} = L^{-1}(x_{eq.} + iy_{eq.})$ is the beam center of charge (complex, scaled) equilibrium position, L is a problem-dependent scaling length (e.g., the pipe diameter), and $\phi^{(im.)}$, $A_z^{(im.)}$ are the electric and magnetic *image potentials*, which are obtained by subctracting from the full potentials the free-space terms, and dots indicate derivation w.r.t. the argument.[2]

Unfortunately, Eq. (2) seems useless whenever explicit (analytic) solutions of Laplace equation are not available.

3 THE SCHWARTZ FORMULA

Whenever only a *numerical* solution for the (real valued) potential ϕ is possible *at a discrete set of points*, the Laslett coefficients can *still* be efficiently computed using (2) by numerical evaluation of Schwartz formulas[3][2]:

$$\ddot{\bar{\psi}}(z_0) = \frac{2}{\pi} \int_0^{2\pi} \frac{1}{(z-z_0)^2} \, \phi[Re(z), Im(z)] \, d\theta \qquad (3)$$

where $z = z_0 + Re^{i\theta}$ is any circle embracing z_0, and $f(z)$ is analytic within and on the aforementioned circle. Computing the Lasletts in terms of *integrals* instead of *derivatives* of $\bar{\Psi}$ is indeed nice, since, loosely speaking, for the same prescribed accuracy, this requires knowledge of *much fewer values* of the numerically evaluated potential. However, in order to use (3), one needs to know the potential at a suitable number of points *on a circle*, whereas *most* available numerical methods yield values of ϕ arranged on *noncircular* mesh grids. This suggests resorting to a numerical algorithm which *does not* rely to *any* prior meshing to find a numerical solution for ϕ.

4 POTENTIALS FROM WIENER INTEGRALS

The connection among Wiener processes, functional integrals and Poisson's equation is well known in probability theory.[4] Accordingly, the solution of the Dirichlet problem:

$$\begin{cases} \nabla_t^2 \Phi(x,y) = -g(x,y), & (x,y) \in \mathcal{D}, \\ \Phi(x,y) = 0, & (x,y) \in \partial\mathcal{D}. \end{cases} \qquad (4)$$

can be written[4][3]:

$$\Phi(x,y) = E\left[\int_0^\tau g\left[w_x(t), w_y(t)\right] dt \right], \qquad (5)$$

where $E[\cdot]$ represents an *expectation value* with respect to the probability measure associated to the Wiener processes (random walks) (w_x, w_y) starting at (x,y) at time $t=0$, and (first) crossing the boundary $\partial\mathcal{D}$ at $t=\tau$.

Monte Carlo Implementation

The expectation value in (5) is recognized to be a Wiener Integral, which can be computed using Monte Carlo

---

*On leave of absence from Dip. Scienze Fisiche "E.R. Caianiello", Univ. of Salerno, and I.N.F.N. Salerno, Italy

[1]For a strictly relativistic ($\beta_0 = 1$) beam, Eq. (2) also gives the coherent betatron normal mode Laslett coefficients in the non-penetrating magnetic-field regime.[2]

[2]Schwartz formulas can be derived from Cauchy integral theorem, by exploiting the well known fact that the analytic complex potential is uniquely determined, up to an irrelevant constant, from its real part alone.

[3]Equation (4) can be extended to the case where $g(x,y)$ is a line source by a suitable limiting process.

0-7803-4376-X/98/$10.00 © 1998 IEEE

methods.[5] Accordingly, we introduce a piecewise-linear, $\Delta-$time-step discretized *Euler approximation*[6] for the Wiener processes involved:[4]

$$\begin{cases} w_x(t_{k+1}) = w_x(t_k) + \sqrt{2}\,\delta_x \quad , \quad w_x(0) = x, \\ w_y(t_{k+1}) = w_y(t_k) + \sqrt{2}\,\delta_y \quad , \quad w_y(0) = y, \end{cases} \tag{6}$$

where $t_k = k\Delta$, and δ_x, δ_y are independent gaussian random variables with moments:

$$E(\delta_x) = E(\delta_y) = 0 \quad , \quad E[(\delta_x)^2] = E[(\delta_y)^2] = \Delta. \tag{7}$$

A random walk is created, using (6),(7), and evolved until, at $t = t_Q$, it has (first) gone beyond $\partial\mathcal{D}$, viz.:

$$(w_x(t_Q), w_y(t_Q)) \notin \mathcal{D},$$
$$(w_x(t_k), w_y(t_k)) \in \mathcal{D}, \;\; 0 \le k < Q. \tag{8}$$

The exit time τ is computed from:

$$\frac{\tau - t_{Q-1}}{\Delta} =$$
$$= \left\{ \frac{[x_e - w_x(t_{Q-1})]^2 + [y_e - w_y(t_{Q-1})]^2}{[w_x(t_Q) - w_x(t_{Q-1})]^2 + [w_y(t_Q) - w_y(t_{Q-1})]^2} \right\}^{-1/2} \tag{9}$$

where the coordinates of the *exit point* (x_e, y_e) are the (only) solution in $x_e \in [min\{w_x(t_{Q-1}), w_x(t_Q)\}, max\{w_x(t_{Q-1}), w_x(t_Q)\}]$ of the system between the (rectilinear) random walk between t_{Q-1} and t_Q:

$$y_e - w_y(t_{Q-1}) = \frac{w_y(t_Q) - w_y(t_{Q-1})}{w_x(t_Q) - w_x(t_{Q-1})}\,[x_e - w_x(t_{Q-1})], \tag{10}$$

and the equation describing (locally) the $\mathcal{D}-$domain boundary curve, $y_e = f(x_e)$. For each realization (labeled by a superfix j) of the random path we can compute the random variable:

$$\phi^{(j)}(x,y) = \Delta \sum_{k=0}^{Q_j - 1} g\left[w_x^{(j)}(t_k), w_y^{(j)}(t_k)\right] +$$
$$+ (\tau^{(j)} - t_{Q_j - 1})\; g\left[x_e^{(j)}, y_e^{(j)}\right], \tag{11}$$

and the associated first and second order moments $\mu_1(M,\Delta)$ and $\mu_2(M,\Delta)$ where M is the total number of paths.

The potential in (5) can be accordingly evaluated as a double limit:

$$\Phi(x,y) = \lim_{\Delta \longrightarrow 0} \lim_{M \longrightarrow \infty} \mu_1(M,\Delta). \tag{12}$$

Estimating $\Phi(x,y)$ by $\mu_1(M,\Delta)$ will produce, for any finite Δ and M, both *i)* a systematic error ϵ_{sys} due to discretization, for which:[6]

$$\epsilon_{sys}(\Delta) \sim \mathcal{O}(\Delta), \tag{13}$$

[4]In the following we refer to Wiener processes with diffusion coefficient $D = 1$, and use a dimensionless time variable.

and *ii)* a statistical error, ϵ_{stat} which in view of the central limit theorem is asymptotically gaussian, with zero average and r.m.s deviation:[6]

$$\epsilon_{stat}(M,\Delta) \sim M^{-1/2}\, var^{1/2}\left\{\phi^{(j)}\right\} \tag{14}$$

depending (weakly) on Δ, as well as (strongly) on M. The confidence interval of the estimated potential is thus:

$$\delta(M,\Delta) = \mu_1(M,\Delta) \pm \alpha[\mu_2(M,\Delta) - \mu_1^2(M,\Delta)]^{1/2}, \tag{15}$$

where α depends on the sought confidence level.

5 COMPARISON WITH OTHER METHODS AND CONCLUSIONS

The main merits and drawbacks of the above Wiener-integral+Monte Carlo-method (henceforth WIMC) as compared to more usual methods, including finite-elements and the method of moments (henceforth FEM and MoM, respectively) for solving (4) can be summarized as follows:

- WIMC does *not* require any prior mesh-algorithm, nor is restricted to compute the potential at predetermined grid points; it can be used to compute the potential only where needed;
- WIMC has extremely mild memory requirements. In contrast, MoM and FEM require the storage of *large* matrices;
- WIMC is intrinsecally parallelizzable;
- WIMC has a rather slow (statistical, $\propto M^{-1/2}$) convergency rate. By comparison with other methods, however, it is not significantly slower. Tight accuracy bounds are also easily obtained.

As a conclusion, WIMC should be seriously considered for complicated geometries, whenever fast (possibly parallel) computing engines and relatively little memory are at hand.

The above formalism has been applied to compute the Laslett coefficients for the proposed stadium-shaped LHC liner in [7]. More or less obvious generalizations, include computation of the coherent Laslett coefficients, dielectric insertions and more general boundary conditions. This work has been sponsored in part by INFN through the Salerno University group.

6 REFERENCES

[1] S. Petracca, CERN SL 93-13 (AP), 1993; Part. Acc., 48, p. 181, 1994; CERN SL 97-03 (AP), 1997.

[2] S. Petracca I.M. Pinto, F. Ruggiero, Proc. EPAC96, p. 1408, 1996.

[3] H.A. Schwartz, *Gesammelte Mathematische Abhandlungen*, vol II, p. 152.

[4] A.D. Ventsel, *Stochastic Processes*, MIR, Moscow, 1983.

[5] L.S. Schulman, *Techniques and Applications of Path Integration*, J. Wiley & Sons, New York, 1981.

[6] P.E. Kloeden, E. Platen, *Numerical Solution of Stochastic Differential Equations*, Springer, New York, 1991.

[7] S. Petracca, CERN SL/AP rept. XXX-1997, in print.

INFLUENCE OF RESISTIVE WALL IMPEDANCE ON THE VSX LIGHT SOURCE

N. Nakamura and T. Koseki
Synchrotron Radiation Laboratory, Institute for Solid State Physics(ISSP)
The University of Tokyo, Midori-cho 3-2-1, Tanashi, Tokyo 188, Japan

Abstract

We describe the calculated resistive wall impedance of the vacuum chamber and the corresponding growth rate of coupled-bunch instabilities for the VSX light source, a Japanese third generation VUV and soft X-ray source with a beam energy of 2 GeV. The impedance calculation was performed for the normal Al vacuum duct and the SiC duct, a higher-order mode (HOM) absorber of the damped RF cavity. The impedance of the Al vacuum duct with a narrow vertical aperture is sufficiently high at low frequencies for exciting a transverse coupled-bunch instability. On the other hand, the SiC duct does not cause a serious problem about coupled-bunch instabilities and it gives only a small contribution to the broad-band impedance related to single-bunch instabilities.

1 INTRODUCTION

The VSX light source [1] is a third generation synchrotron radiation source for producing a highly brilliant light in the VUV and soft X-ray region. It is designed to attain a low emittance of about 5 nmrad for DBA lattice [2] and 16 long straight sections (14.3m x 4, 7m x 12) for 14 insertion devices, injection magnets and RF cavities. Since small bore radii of the quadrupole and sextupole magnets and a narrow magnetic gap (less than 20 mm) of the insertion device are required, the vacuum chamber of the storage ring has a small aperture. As a result, the resistive wall impedance of the vacuum chamber become considerable. Furthermore, the circular SiC duct is installed on both ends of each RF cavity in order to damp the HOMs generated in the cavity [3]. The resistive wall impedance of the SiC duct should be estimated, because the resistivity of SiC, 0.2 Ωm, is higher in eight orders of magnitude than that of Al. In addition, the radiation damping force of the ring, a defense against instabilities, is not strong because of its low beam energy (E=2GeV). Therefore, coupled-bunch instabilities due to the resistive wall impedance may be occur below the design beam current of 400mA. In this paper, we report the influences of the normal Al vacuum duct and the SiC duct on the VSX storage ring in terms of beam instabilities.

2 RESISTIVE WALL IMPEDANCE

2.1 Al vacuum duct

Almost all vacuum ducts of the VSX storage ring will be made of Al alloy. Figure 1 shows the cross-sectional view of the vacuum duct for quadrupole and sextupole magnets. The vacuum duct for bending magnets has almost the same cross section. Here, we approximate all the ring vacuum ducts by a circular Al pipe with a length of the ring circumference C (=388.45m) and a pipe radius b (=1.8cm). The longitudinal and transverse resistive wall impedances of this circular pipe are given by

$$\frac{Z_l^{Al}(\omega)}{n} = (1-i)\frac{Z_0\delta_1}{2b}, \tag{1}$$

$$Z_t^{Al}(\omega) = (1-i)\frac{Z_0 R\delta_1}{b^3} \tag{2}$$

with

$$n = \omega/\omega_0, \quad \delta_1 = \sqrt{\frac{2\rho_1}{\omega\mu_0}}. \tag{3}$$

Here, Z_0, ω_0, $R(=C/2\pi)$, μ_0, ρ_1 and δ_1 are the characteristic impedance of vacuum, the angular revolution frequency, the average ring radius, the magnetic permeability of vacuum, the resistivity and skin depth of Al. Both impedances vary like $\omega^{-1/2}$ and increase at low frequencies. The transverse resistive wall impedance reaches to 0.38MΩ/m at the revolution frequency 771.8 kHz.

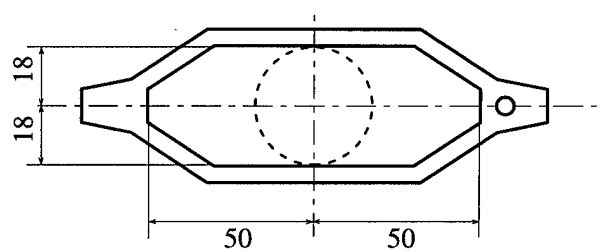

Figure: 1 Cross section of the Al vacuum duct for quadrupole and sextupole magnets. Dimensions are in unit of mm. A pipe indicated by a dotted circle was used in the impedance estimation.

0-7803-4376-X/98/$10.00 © 1998 IEEE

2.2 SiC duct

Figure 2 shows the cross section of the SiC duct. This duct consists of an inner SiC layer and an outer Al layer, which were joined by sintering. The total length of the SiC duct is 90 cm for three RF cavities.

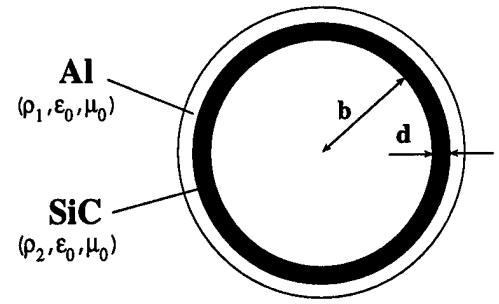

Figure: 2 Cross section of the SiC duct (b=7cm, d=1cm).

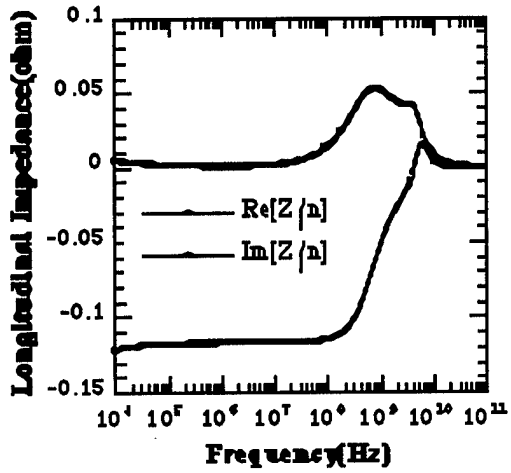

Figure: 3 Longitudinal resistive wall impedance of the SiC duct.

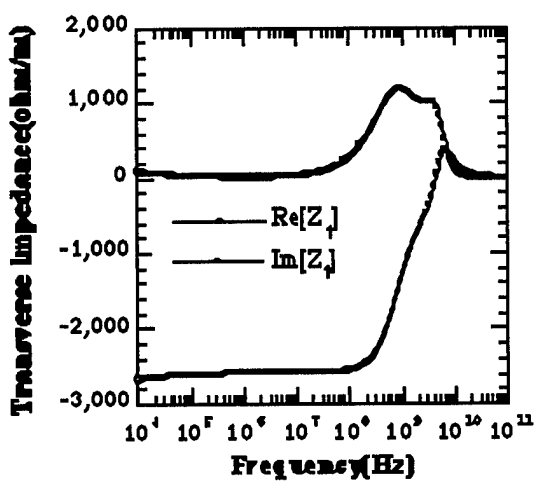

Figure: 4 Transverse resistive wall impedance of the SiC duct.

The resistive wall impedance of the SiC duct is obtained by solving the Maxwell equations analytically [4]. The longitudinal impedance of the SiC duct with a length of L is given by

$$Z_l^{SiC}(\omega) = \frac{L}{2\pi\varepsilon_0 bc\left\{\frac{ib\omega}{2c} - i\left\{\frac{\omega}{\lambda_{2c}} + \frac{\lambda_{2c}}{\omega}\right\}\frac{J_1(\lambda_2 b)+\kappa N_1(\lambda_2 b)}{J_0(\lambda_2 b)+\kappa N_0(\lambda_2 b)}\right\}} \quad (4)$$

where

$$\kappa = \frac{i\left(\frac{\omega}{\lambda_{2c}} + \frac{\lambda_{2c}}{\omega}\right)J_1(\lambda_2(b+d)) - \left(\frac{\omega}{\lambda_{1c}} + \frac{\lambda_{1c}}{\omega}\right)J_0(\lambda_2(b+d))}{\left(\frac{\omega}{\lambda_{1c}} + \frac{\lambda_{1c}}{\omega}\right)N_0(\lambda_2(b+d)) - i\left(\frac{\omega}{\lambda_{2c}} + \frac{\lambda_{2c}}{\omega}\right)N_1(\lambda_2(b+d))} \quad (5)$$

$$\lambda_{1,2} = \frac{1+i}{\delta_{1,2}} = \sqrt{\frac{\mu_0\omega}{2\rho_{1,2}}}\,(1+i) \quad (6)$$

Here, J_0, J_1, N_0, N_1 are the Bessel functions and b, d, c, ε_0, ρ_2 and δ_2 are the inside radius and thickness of the SiC layer, the speed of light, the permittivity of vacuum, the resistivity and skin depth of SiC. The transverse impedance is also given by an analytic expression [4]. However it is not shown here, because it is too long. The calculated longitudinal and transverse impedances of the SiC duct are shown in Figures 3 and 4. The real parts of these impedances are not remarkable at low frequencies, though they have a broad peak at high frequencies. Each impedance can be approximated by a broad-band resonator model with a Q-value of 0.3–0.6 and a resonant frequency of 4–5GHz. In addition, one can find a rough connection between the longitudinal and transverse impedances, $Z_t^{SiC} \sim (2c/b^2\omega_0)(Z_l^{SiC}/n)$.

3 COUPLED-BUNCH INSTABILITIES

3.1 Longitudinal growth rate

The growth rate of longitudinal symmetric coupled-bunch mode μ for a beam with the number of bunches k_b and the bunch current I_b is given by [5]

$$g_l^{\mu} = \frac{e\alpha k_b I_b}{4\pi E\omega_s}\sum_{p=-\infty}^{+\infty}\left\{\omega_p^l - \omega_s\right\}^2 e^{-\left\{\frac{\sigma_l^2\{\omega_p^l-\omega_s\}^2}{2c^2}\right\}}\cdot \mathrm{Re}\left[\frac{Z_l(\omega_p^l)}{n}\right] \quad (7)$$

$$\omega_p^l = (pk_b+\mu+\nu_s)\omega_0\,, \quad \omega_s = \nu_s\omega_0$$

α, ν_s, and σ_l are the momentum compaction factor, synchrotron tune and bunch length. The parameter values of the ring used for the calculation are summarized in reference [2]. For the beam current of 400mA (k_b=648, I_b =0.62mA), the calculated growth rates of the circular Al pipe and the SiC duct are less than 0.1 sec^{-1} and negligible as compared with the longitudinal radiation damping rate (81 sec^{-1}).

3.2 Transverse growth rate

The growth rate of transverse symmetric coupled-bunch mode μ is given by [5]

$$g_t^{\mu} = -\frac{ek_b I_b \omega_0 \beta_t}{4\pi E} \sum_{p=-\infty}^{+\infty} e^{-\left\{\frac{\sigma_l^2 (\omega_p^t - \omega_\xi)^2}{2c^2}\right\}} \cdot \mathrm{Re}\left[Z_t(\omega_p^t)\right]$$

$$\omega_p^t = (pk_b + \mu + \nu_t)\omega_0 , \quad \omega_\xi = (\xi_t/\alpha)\omega_0. \tag{8}$$

Here ξ_t, ν_t, and β_t are the chromaticity, betarton tune, and betatron function at the vacuum chamber.

From Eq. (8), we calculate the vertical growth rate of the Al pipe for $k_b I_b$=400mA. The maximum growth rate (μ=638) is estimated to be about 390 sec^{-1} at b=18mm and ξ_y=0, and it is much higher than the transverse radiation damping rate (41 sec^{-1}). Therefore the vertical coupled-bunch mode will be excited in the ring if no other damping mechanisms exist. In Figures 5 and 6, the dependences of the maximum growth rate on the betatron tune ν_y and the chromaticity ξ_y are shown. These figures suggest that the growth rate can be reduced by a smaller fraction of the betatron tune or a larger positive chromaticity.

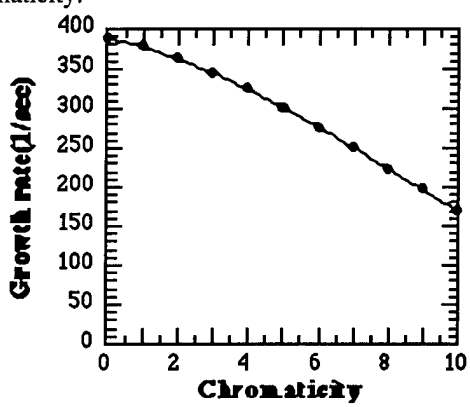

Figure: 5 Chromaticity dependence of the growth rate.

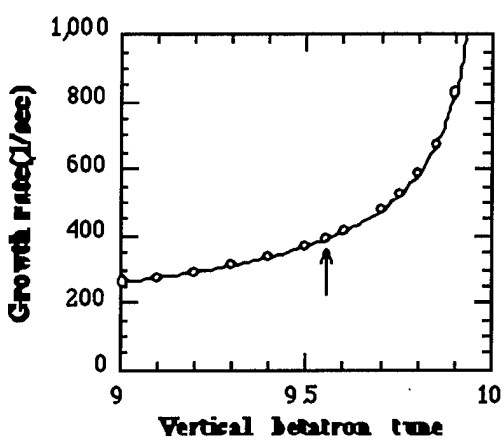

Figure: 6 Betatron-tune dependence of the growth rate. The arrow indicates the data point for the present design value of betaton tune (ν_v=9.55).

The transverse growth rate of the SiC duct is also calculated and found to be very low (< 0.1 sec^{-1}) like the longitudinal one because of its broad impedance spectrum. The SiC duct cause neither transverse coupled-bunch instabilities nor longitudinal ones.

4 SINGLE-BUNCH INSTABILITIES

The resistive wall impedance of the Al vacuum duct decreases with the frequency and it is not considerable at high frequencies. Thus the influence of the Al vacuum duct on single bunch instabilities is probably small. The longitudinal and transverse broad-band impedances of the SiC duct is estimated from the approximated broad band resonator model to be $|Z_l^{SiC}/n|^{BB}$~0.1Ω and $|Z_t^{SiC}|^{BB}$~ 3kΩ/m. Both of them are much smaller than the broad-band impedances of the ordinary storage rings, which are usually dominated by discontinuities of the vacuum chamber such as bellows and transitions.

5 CONCLUSIONS

The resistive wall impedance of the Al vacuum chamber in the VSX storage ring will excite a transverse coupled-bunch mode with a growth rate of about 390 sec^{-1}, while it never causes longitudinal coupled-bunch instabilities. We need to prepare a transverse feedback system with a damping rate of about 1000 sec^{-1}, taking account of the insertion device vacuum ducts which is not considered here. The calculated impedance of the SiC is completely negligible for coupled-bunch instabilities and it is not substantial for single-bunch instabilities.

6 ACKNOWLEDGEMENTS

The authors would like to thank Prof. Y. Kamiya and the other staff members of our laboratory for their continuous encouragement and support.

REFERENCES

[1] Y. Kamiya et. al, "A Future Project of VUV and Soft X-ray High-Brilliant Light Source in Japan", Proc. of the 4th EPAC, London, 1994, p639.

[2] H. Takaki, T. Koseki, N. Nakamura, Y. Kamiya, M. Yokoyama, Y. Kobayashi and T. Nagatsuka, These Proceedings.

[3] T. Koseki, M. Izawa, and Y. Kamiya, Rev. Sci. Instrum., 66 (1995) 1926.

[4] N. Nakamura, "Resistive wall impedance of the SiC duct", VSX Accelerator Design Note D-173/No.226, 1996.

[5] J. M. Wang, "Longitudinal Symmetric Coupled Bunch Modes", BNL 51302, 1980. ; M. S. Zisman et al., "ZAP User's Manual", LBL-21270, 1986.

TWO EXAMPLES OF INTEGRABLE SYSTEMS WITH ROUND COLLIDING BEAMS

V.V. Danilov and E.A. Perevedentsev
Budker Institute of Nuclear Physics, 630090, Novosibirsk, Russia

Abstract

The work is devoted to analytical study of application of integrable systems to round colliding beams, aiming at enhancement of the beam-beam limit. Two examples of "integrable" beam-beam forces are presented, relevant to round counter beams with special density distributions. In such systems all the resonances will vanish, hence the beam-beam effects can be suppressed, and the intensities of colliding beams may be strongly increased, at least in the "weak-strong" case.

1 INTRODUCTION

The concept of "Round Colliding Beams" (RCB) is considered as a possibility to reach higher luminosity and to improve beam stability in colliders ([1] and references therein). The essential conditions of the RCB are: equal horizontal and vertical emittances $\varepsilon_x = \varepsilon_y = \varepsilon$; equal horizontal and vertical beta-functions at the Interaction Point (IP) $\beta_x^* = \beta_y^* = \beta^*$; equal horizontal and vertical tunes $\nu_x = \nu_y = \nu$. The rotational symmetry of the kick from the round opposite beam, complemented with the $X - Y$ symmetry of the betatron transfer matrix between the collisions, result in an additional integral of motion $\mathcal{M} = xy' - yx'$, *i.e.* the longitudinal component of particle's angular momentum.

Thus, the transverse motion becomes equivalent to a one-dimensional (1D) motion [2]. Resulting elimination of all betatron coupling resonances is of crucial importance, since they are believed to cause the beam lifetime degradation and blow-up. Reduction to 1D motion makes impossible the diffusion through invariant circles. Although this 1D motion has more "regularity" in comparison with a general 2D motion, with the time-dependent Hamiltonian it is still stochastic in general. What we need here to make the motion regular, is *to construct one more integral of motion, valid for any value of the angular momentum* $\mathcal{M}$. At first glance, it is not evident, that we can find the needed forces (among those physically feasible), especially when we deal with the fields of the counter beam. But solutions exist [3], and we present two interesting examples, which may be already useful for practice.

2 EXAMPLE 1: INTEGRABLE BEAM-BEAM KICK

Let us take a drift space with the unity length (for simplicity) followed by an axially symmetric thin lens, as a representation of the angular-momentum-preserving linear optics in between the IPs, and the radial beam-beam kick. The 2D map for particle trajectory displacements x, y and slopes x', y' through such a period is:

$$\begin{aligned} \overline{x} &= x + x' \\ \overline{y} &= y + y' \\ \overline{x}' &= x' + \overline{k}_x \\ \overline{y}' &= y' + \overline{k}_y, \end{aligned} \tag{1}$$

where $k_x = \frac{x}{r}k(r)$, $k_y = \frac{y}{r}k(r)$, and $r = \sqrt{x^2 + y^2}$. Due to conservation of the angular momentum, the motion is reducible to 1D. Previously we reported on existence of invariants of this map in the particular case of 1D motion ([4] and referencs therein). This corresponds in (1) to $x = x' = 0$, or $y = y' = 0$, or generally, to any meridianal trajectory with $\mathcal{M} = xy' - yx' = 0$. With x, x' lying in the plane of such a trajectory, the desired integrals of motion may be sought among these invariants:

$$\begin{aligned} \mathcal{I}(x, x') = (a_2x^2 + a_1x + a_0)(x' + x)^2 \\ +(a_1x^2 + b_1x + b_0)(x' + x) + a_0x^2 + b_0x\,, \end{aligned} \tag{2}$$

and the kick function k must have the form:

$$k(x) = -2x - \frac{a_1x^2 + b_1x + b_0}{a_2x^2 + a_1x + a_0}\,. \tag{3}$$

Here the 5 coefficients are arbitrary parameters of the kick force.

Turning back to the general case $\mathcal{M} = M \neq 0$, we can use the generic form of 1D invariant (2) for construction of an axially symmetric invariant involving only r, r' as dynamic variables. The kick function (3) is now understood as a radial kick $k(r)$, and we observe that only the case $b_0 = a_1 = 0$ is practically interesting, otherwise $k(r)$ would have singularities at $r = 0$. The Courant–Snyder terms with a_0, b_1 in (2) give a clue to the form of the axially-symmetric invariant, to be tried for any value M of the angular momentum $\mathcal{M} = xy' - yx'$ (certainly valid at $M = 0$):

$$\begin{aligned} \mathcal{I}_M(r, r') = (a_2r^2 + a_1r + a_0)\Big((r' + r)^2 + \frac{M^2}{r^2}\Big) \\ +(a_1r^2 + b_1r + b_0)(r' + r) + a_0r^2 + b_0r. \end{aligned} \tag{4}$$

The variables here are changed to r, r', use has been made of the following relations: $r' = (xx' + yy')/r$, $x'^2 + y'^2 = \big((rr')^2 + (xy' - yx')^2\big)/r^2 = r'^2 + M^2/r^2$.

Rewriting accordingly the map (1) in terms of (r, r'):

$$\begin{aligned} \overline{r} &= \sqrt{r^2 + 2rr' + r'^2 + M^2/r^2}, \\ \overline{r}' &= \Big(r'(r' + r) + \frac{M^2}{r^2}\Big)\frac{1}{\overline{r}} + k(\overline{r}), \end{aligned} \tag{5}$$

we apply this transformation to (4). The invariance relation $\mathcal{I}_M(r,r') = \mathcal{I}_M(\bar{r},\bar{r}')$ then yields: $a_1 = b_0 = 0$. Thus we find the desired integral of motion which holds at any constant value M of $\mathcal{M}$:

$$\mathcal{I}_M(r,r') = (a_2r^2 + a_0)(r'+r)^2 + b_1r(r'+r) + a_0\Big(r^2 + \frac{M^2}{r^2}\Big). \quad (6)$$

The corresponding radial kick function

$$k(r) = -2r - \frac{b_1 r}{a_0 + a_2 r^2}. \quad (7)$$

has only 3 free parameters, just in accord with our assumption that the integrable systems for RCB form a subset of all 1D integrable systems.

In the present context we interpret the 2nd term in (7) as the beam-beam kick, while the 1st term together with the drift length form the linear optics in between the IPs. The optics appears to be a 90° lattice in both X and Y planes, with the matrix of the period:

$$T_x = T_y = \begin{pmatrix} 1 & 0 \\ -2 & 1 \end{pmatrix}\begin{pmatrix} 1 & 1 \\ 0 & 1 \end{pmatrix} = \begin{pmatrix} 0 & 1 \\ -1 & 0 \end{pmatrix} \quad (8)$$

In order to return to the physical units in the result one should replace 1 to β^*, and -1 to $-1/\beta^*$.

Relevance of the solution to the beam-beam kick force from a short (relativistic!) opposite bunch (practically, with the length $\ll \beta^*$), can be seen from the conformity of both $r \to 0$ and $r \to \infty$ limits of the fraction in (7) to the realistic beam-beam kick behaviour. We may put $a_0 = 1$, $a_2 > 0$, relate $a_2^{-1/2}$ to the radial beam size Δ, and express b_1 via the beam-beam parameter ξ: $b_1 = 4\pi\xi$. Specifically, the transverse density distribution in the counter bunch

$$\mathrm{d}n \propto N\frac{2\pi r \mathrm{d}r}{(1+(r/\Delta)^2)^2} \quad (9)$$

exactly corresponds to the kick (7).

In practice, implementation of this solution in a RCB scheme requires short colliding bunches with radial distributions close to (9), a linear optics with equal transfer matrices in x and y planes, and with equal betatron phase advances of 90° in between the IPs. Integrability of the resulting dynamics will show in regularity of motion which will be bounded by closed invariant curves $\mathcal{I}_M(r,r') = const$, and free from resonance islands throughout the linear stability range, *i.e.* for the beam-beam parameter $|\xi| < 1/2\pi$.

3 EXAMPLE 2: A SPECIAL LONGITUDINAL DISTRIBUTION

In the previous example we dealt with a short nonlinear kick, the time dependence was represented by the delta-function. Now we turn to a continuous-time dependence of the nonlinear force, and present a dynamical system with two invariants, which can be derived by means of usual accelerator theory tools. Let us take the 1D equation of particle's motion in an accelerator:

$$x'' + g(s)x = F(x,s), \quad (10)$$

where $g(s)$ is the focusing function and $F(x,s)$ is an arbitrary force. This equation can be simplified by using the betatron phase $\psi = \int ds/\beta(s)$ instead of s and changing the physical variable x to the normalized variable $X = x/\sqrt{\beta(s)}$:

$$X'' + X = \beta^{3/2}F(X\sqrt{\beta}, s(\psi)). \quad (11)$$

The force due to round counter beam with the transverse Gaussian distribution can be presented now in the factorized form, thus separating its dependence on the transverse and longitudinal coordinates:

$$F_{rb} = -\frac{2Ne^2}{\gamma mc^2}\frac{1-\exp(-r^2/2\beta\varepsilon)}{r/\sqrt{\beta}}\frac{f(\delta - 2s)}{\sqrt{\beta}}, \quad (12)$$

Here ε is the emittance of the opposite beam, f is the longitudinal distribution of counter beam ($\int f d\delta = 1$), δ is the longitudinal position of the test particle in the weak bunch with respect to the bunch center. The "time" $s = 0$ corresponds to the moment when the central test particle ($\delta = 0$) meets the center of the strong bunch.

The equation of particle motion in the interaction region in terms of $r = \sqrt{x^2+y^2}$ is:

$$r'' + g(s)r = F_{rb} + M^2/r^3, \quad (13)$$

where the last term means the "centrifugal" force.

Now let us consider a case when the weak bunch of the test particles is short with respect to the beta function at the IP and we can put $\delta = 0$, and at the same moment, the longitudinal charge distribution of the strong bunch is proportional to the inverse β-function: $f(2s) = C/\beta(s)$. For an interaction region which is free of focusing we have: $\beta(s) = \beta^* + s^2/\beta^*$, and the perfect distribution is:

$$f(s) = \frac{C}{1+(s/2\beta^*)^2}, \quad (14)$$

where C is a constant, β^* is the β-function value at the IP.

After substitution of the normalized variable $R = r/\sqrt{\beta(s)}$ and replacement of s by the phase ψ, one gets:

$$R'' + R = \frac{M^2}{R^3} - C\frac{2Ne^2}{\gamma mc^2}\frac{1-\exp(-R^2/2\varepsilon)}{R}. \quad (15)$$

One can see, that the force in this equation does not depend on time, and therefore, this 1D equation is integrable. The coordinate dependence on time can be found using conventional 1D formulas.

The trick with obtaining the time-independent force is related with the fact, that the 'centrifugal' force is invariant under substitution of new variables and changing 'time' to the betatron phase. It is easy to see, that the force in (15)

has one zero for a counter beam with opposite sign of electric charge.

If one wants to realize this strategy in practice, then one has to create the longitudinal distribution in the form of Eq.(14) over a wide range of s, and to make it zero outside. Next step is to make a linear transformation with the phase advance of $2\pi m$, m is an integer[1], to the next interaction region. Having reversed the sign of β-function derivative, we enter again in the interaction region and see the same counter beam with the same distribution (and so on periodically), we have a system with the needed equation of motion.

Of course, it is difficult to create a longitudinal distribution in accurate approximation to the perfect bunch shape over entire length of the strong bunch, including its tails. But apparently, small deviations of the distribution from the inverse β-function for $s \gg \beta^*$, will cause negligible perturbation. Approximation of the perfect longitudinal distribution (14) at small s by a Gaussian $\exp(-s^2/2\sigma^2) \approx 1 - s^2/2\sigma^2$, leads to a recipe for an optimum length of a longitudinally-Gaussian strong bunch: $\sigma = \sqrt{2}\beta^*$.

One can see, that the Gaussian shape of the betatron distribution is not important here; the distribution may be any smooth function of r, s, provided that its dependence on R and s can be factorized.

Another essential feature of this solution is that the working point of this system is near the half-integer resonance, when the number of interaction points is odd, and near the integer resonance, when this number is even. So, perturbations of the arcs of collider determine the permissible distance of the working point from the resonance, and consequently, determine the accuracy of the conservation of integrals (this situation is common for integrable systems: perturbations almost always lead to small stochasticity in nearly integrable systems, the point is in allowable values of perturbations).

One more remark is needed. The weak bunch has a small longitudinal size in our dynamical system (while the longitudinal distribution of the strong bunch is taken proportional to the inverse β-function). If its length is not small in comparison with the β-function, then the force becomes time-dependent for particles with large energy off-sets and deviations δ even in the normalized variables. Importance of this modulation was checked by simulation [5].

A formal construction of the integrable distribution for the above example can be found in [3].

4 CONCLUSION

The paper presents new ways to improve single particle stability in colliders. The essence of these ways is obtaining integrability of the particles' dynamics with proving additional integrals of the particle motion. For example, if the "round colliding beams" conditions are fulfilled then the longitudinal component of the angular momentum is the invariant for colliding beams. In some particular cases of the RCBs, additionally to the angular momentum $\mathcal{M}$, we can find one more invariant which is quadratic in momentum, and holds for any value of $\mathcal{M}$. These two integrals of motion suffice for a non-autonomous 2D dynamical system to be integrable.

The both RCB examples above deal with what is called a "weak-strong" beam-beam model: study of motion of a test particle affected by a strong nonlinear fields of a strong counter beam. In the both recipes the arc lattice in between the IPs must be perfectly linear. The 1st example with a short counter bunch requires a special transverse distribution in the strong bunch for integrability. In the 2nd example, the strong bunch length is of the order of β^*. Here, we can choose an "inverse β-function" longitudinal bunch profile for reduction of motion to a 1D autonomous dynamics.

The proposed integrable systems with globally regular motion and without any beam-beam blow-up threshold have strengthened the concept of round colliding beams. They were tested in simulations [1, 5] against perturbations inevitably present in a real machine. The beam emittance growth becomes mostly determined by the arc lattice nonlinearities and imperfections, so we believe that it will be possible to achieve a higher luminosity by reducing the impact of nonlinear lattice resonances.

5 REFERENCES

[1] V.V. Danilov et al., "The Concept of Round Colliding Beams", *Proc. EPAC'96*, Barcelona (1996), p.1149.

[2] A.G. Ruggiero, "Integrability of the Two-Dimensional Beam-Beam Interaction in a Special Case", *Particle Accelerators*, v.12 (1982), p.45.

[3] V.V. Danilov and E.A. Perevedentsev, "Invariants for Nonlinear Accelerator Optics and Round Colliding Beams", *Proc. of VII ICFA Beam Dynamics Workshop on Beam-Beam Issues for Multibunch, High Luminosity Circular Colliders*, Dubna, 18–20 May 1995, Dubna, Russia, (1996), p.167;
V.V. Danilov and E.A. Perevedentsev, "On Invariants and Integrability in Nonlinear Accelerator Optics", CERN SL/Note 94-74(AP).

[4] V.V. Danilov and E.A. Perevedentsev, "Analytical 1D Method of Increasing the Dynamic Aperture in Storage Rings", *Proc. EPAC'96*, Barcelona (1996), p.893;
V.V. Danilov and E.A. Perevedentsev, "Integrable Nonlinear Map of the Accelerator Lattice Type", CERN SL/Note 94-21(AP).

[5] V.V. Danilov and V.D. Shiltsev, "'Round Colliding Beams' as a Way to Integrability: Theory and Simulations for Tevatron", Preprint FERMILAB-FN-655, February 1997;
V.V. Danilov and V.D. Shiltsev, "Evaluation of Round Colliding Beams for Tevatron", poster paper 8V.10 at this Conference.

[1] Actually, the both x and y phase advances of π are also acceptable. We obtain the same motion for r, r' due to symmetry of potential of this motion. In this case we always stay near the integer resonance.

BEAM-BEAM EFFECTS SIMULATION FOR VEPP-2M WITH FLAT AND ROUND BEAMS

I. Nesterenko, D. Shatilov, E. Simonov
Budker Institute of Nuclear Physics, 630090, Novosibirsk, Russia

Abstract

Increasing of the luminosity is one of the main reasons of VEPP-2M optics modernization and transition from flat to round beams, which can be realized by a few optical schemes, including so-called Möbius lattice. The beam-beam simulations have been performed for the different schemes of VEPP-2M optics, such as Möbius, conventional round (equal betatron tunes), and flat beams. The main source of nonlinearities on the ring, sextupoles, have been accounted as well as nonlinear beam-beam kick. The simulations show an essential advantage of the round beams over the flat ones, but the Möbius scheme turns out to be more difficult for realization and in general worse than the conventional round beams.

1 INTRODUCTION

This work has been initiated with the plans of VEPP-2M optics modernization. In particular, a transition from the flat to round beams is expected to be useful and provide an essential increasing of the luminosity. In the proposed scheme [1] the changes in the VEPP-2M optics are reduced to the installation of the superconducting solenoids instead of the quadrupole lenses near the Interaction Points (see Fig. 1). On the other hand, such a scheme can be easily transformed to so-called Möbius lattice [2]. So, the study of beam dynamics with the purpose to compare these different optical schemes in the particular VEPP-2M case becomes very important and useful in order to make the best decision.

Beam-beam simulations, carried out for VEPP-2M collider, help us to clarify the situation, although there are some restrictions of the obtained results' validity, since the tracking model was not perfect.

2 TRACKING TECHNIQUE

The subjects of our study are the core region of the equilibrium distribution and r.m.s. beam sizes. A separate investigation of the lifetime problem also is necessary, since the dynamic aperture in the considering variants is about 13-15 sigmas only, but this work will be performed in future and it is not discussed in this paper. We used two tracking codes: TURN (author E. Simonov) and LIFETRAC (author D. Shatilov). Detailed comparison has been performed and a perfect agreement between them has been detected.

2.1 Data gathering

In our simulations both codes track a single test particle for a long time (over 500 damping times, i.e. more than 10^8 turns). Equilibrium phase volume and r.m.s. beam sizes are obtained by the averaging of the particle coordinates on each turn at the first IP. If the particle's coordinate exceeds the aperture, it is lost and then restarted again, so that the total tracking time remains unchanged. However, when the lifetime becomes comparable or less than the damping time, these restarts affect the obtained beam sizes, since the initial distribution for restarts (unperturbed Gaussian) differs from the true equilibrium one. On the other hand, there is no sense to care about correct beam sizes while the lifetime drops to a few milliseconds.

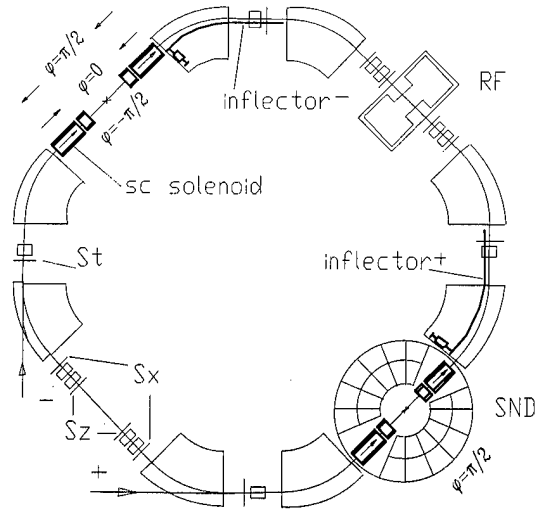

Figure 1: Layout of the VEPP-2M collider. Arrows inside solenoids indicate the direction of the longitudinal magnetic field.

2.2 Tracking through IP

The simulations are performed by a "weak - strong" model, with the strong bunch assumed Gaussian in all three directions, and longitudinally divided into 5 slices. A few working points have been also tested with the twice number of slices, and actually the same results have been obtained. The beam-beam kicks are calculated by means of 6-dimensionally symplectic formulas [3].

2.3 Transport map between IPs

The lattice of the collider is defined by the sequence of elements, such as bending magnets, lenses, solenoids, sextupoles, etc. We consider all the elements as linear, except the sextupoles. The linear elements are defined by their transport 4×4 matrixes, which may contain coupling. These matrixes are assumed do not depend on the particle's

0-7803-4376-X/98/$10.00 © 1998 IEEE

coordinates, that means in particular that the natural chromaticity is ignored, otherwise the tracking would be much more complicated and CPU consuming. The sextupoles are tracked by separate formulas as thin nonlinear lenses.

2.4 *Dispersion function*

The dispersion function is assumed equal to zero elsewhere on the ring. Although it seems strange and incorrect, this is the only way to include sextupoles in our consideration. The matter is that since the linear elements of the ring are simulated without natural chromaticity, sextupoles should also give no chromaticity, otherwise it will not be compensated and the beam will be damaged dramatically. On the other hand, since we know a priory that the natural chromaticity is compensated by sextupoles, we need not to care about it, but we still are interested in nonlinear dynamics which is affected by sextupoles significantly. So we try to account these nonlinear effects, although we realize that this approach cannot be considered as a completely correct.

2.5 *Next step*

In the nearest future we plan to develop tracking codes which will be able to track the particle through a real nonlinear lattice with account of the chromaticity, edge fields, etc. However, we believe that the present results also describe the situation, at least qualitatively.

3 MACHINE PARAMETERS AND SIMULATION RESULTS

The layout of VEPP-2M collider is shown on Fig. 1, the main working parameters are presented in the Table 1.

Parameter	R, M1, M2	M3	F
ε_x [cm · rad]	$1.7 \cdot 10^{-5}$	$1.4 \cdot 10^{-5}$	$1.1 \cdot 10^{-5}$
ε_y [cm · rad]	$1.7 \cdot 10^{-5}$	$1.4 \cdot 10^{-5}$	$1.3 \cdot 10^{-7}$
τ_x [turns]	$2.7 \cdot 10^5$	$2.6 \cdot 10^5$	$3.4 \cdot 10^5$
τ_y [turns]	$2.7 \cdot 10^5$	$2.6 \cdot 10^5$	$2.1 \cdot 10^5$
τ_z [turns]	$8.4 \cdot 10^4$	$8.7 \cdot 10^4$	$8.7 \cdot 10^4$
β_x^* [cm]	5.0	5.0	43.9
β_z^* [cm]	5.0	5.0	6.4
σ_z [cm]	3.3	2.9	2.8
σ_ε	$3.5 \cdot 10^{-4}$	$3.6 \cdot 10^{-4}$	$3.6 \cdot 10^{-4}$
ν_x	3.092	2.680	3.057
ν_y	3.092	3.680	3.097
ν_z	0.006	0.006	0.006

Table 1: The VEPP-2M parameters relevant for simulations. In fact, betatron tunes for M1 and M2 cases are shifted by ± 0.25 and ± 0.5 from the values shown in the table.

As is seen, there are two Interaction Points (IP) with the *different* transport maps between them. The round beams can be obtained from the existent scheme with the flat beams by replacing the nearest to the IPs Q-lenses by SC solenoids, as described in [1]. Each pair of solenoids rotates the plane of betatron oscillations on the angle $\phi = \pi/2$. In the base operating mode (R) these rotations compensate each other, so that we have a conventional round beams. Besides, the Möbius lattice can be also obtained easily by the change of polarity of one solenoid: in this case (M1) one pair of solenoids makes the rotation on $\pi/2$, but the second pair does not compensate it. Another possibility we have with the change of polarity of the whole solenoids pair: in these cases (M2, M3) both pairs make the rotations in the same direction on the same angle $\pi/2$. Here the differences between M2 and M3 are the only initial betatron tunes.

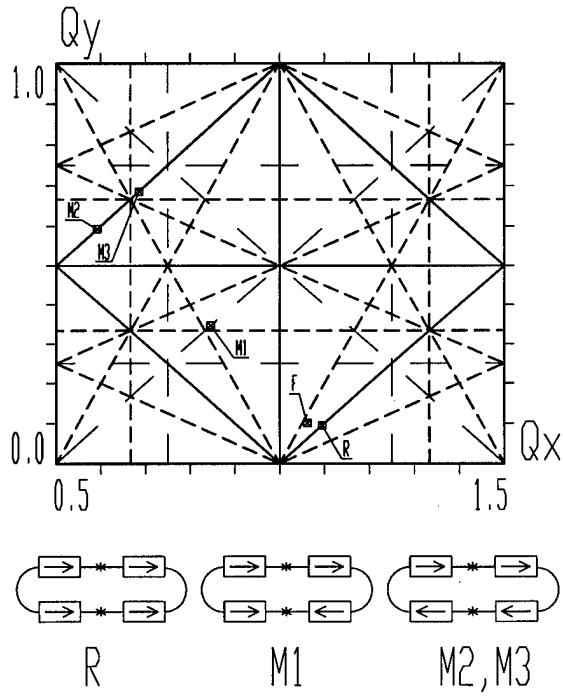

Figure 2: The grid of working resonances up to 4th order. Sextupole resonances are shown as bold dashed, betatron resonances of 4th order as long-dashed. For the Möbius cases Q_x and Q_y should be read as Q_+ and Q_- for "+" and "-" modes. At the very bottom the schemes of solenoids polarities are shown for the described cases.

An important peculiarity of the Möbius lattice is the betatron tunes splitting:

$$\mu_\pm = (\mu_x + \mu_y)/2 \pm \theta, \qquad (1)$$

where $\theta = \pi/2$ in the M1 case and $\theta = \pi$ in the M2, M3 cases. This jump from the main coupling resonance turns out to be the source of troubles. The main working resonances (without synchro-betatron ones) are shown on Fig. 2. It is clear from this plot that the base working point (conventional round beams, R) has the most room free of resonances. The M1 and especially M2 working points have not enough room for increasing ξ parameter. How-

ever, M2 case can be shifted (it is M3) in up-right direction to step over the crowd of sextupole resonances, but in any case the base working point just on the main coupling resonance is preferable. A further shift to step over 4th order resonances requires an additional increasing of the focussing lenses strength and, therefore, sextupoles strength to compensate natural chromaticity, that causes the problems with dynamical aperture.

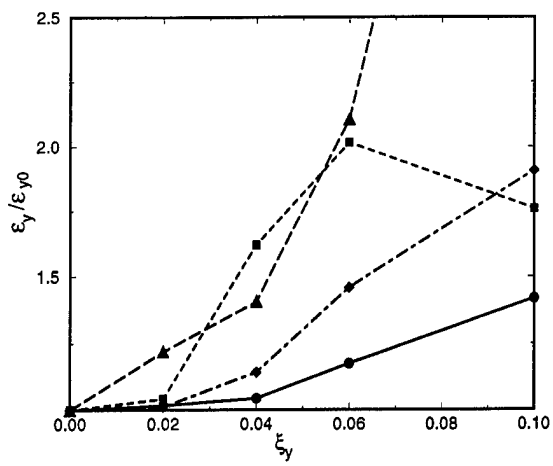

Figure 3: Equilibrium emittances for the different schemes: R (circles), M1 (squares), M3 (diamonds), and F (triangles).

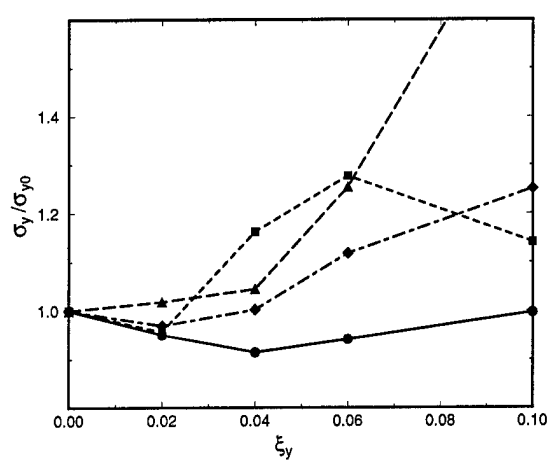

Figure 4: Equilibrium beam sizes for the different schemes: R (circles), M1 (squares), M3 (diamonds), and F (triangles). The decrease of the beam size for a small ξ occurs due to the dynamic beta effect.

The simulation results for all the described schemes except M2, which is the worst one, are presented on Figures 3 and 4. The only conventional round beams have a acceptable lifetime when $\xi = 0.1$. The corresponding points for the flat beams and Möbius cases are shown for the sake of completeness, but they are not very correct (see 2.1). The parameter ξ_x for the flat beams can be evaluated by the equation $\xi_x = 0.23 \cdot \xi_y$.

4 CONCLUSION

Our study demonstrated that the conventional round beams take an essential advantage over both the Möbius lattice and the flat beams for the VEPP-2M collider.

5 ACKNOWLEDGMENTS

Some part of our calculations has been performed on ACSAD1 computer (KEK, Japan) and we would like to thank KEK's computer center for the help.

6 REFERENCES

[1] I. Koop et al., 'Dynamic Aperture of the Storage Ring VEPP-2M in round beam mode', these proceedings.

[2] R. Talman, Phys. Rev. E 74, 1995, p. 1590.

[3] K. Hirata et al., Part. Acc. 40, 1993, p. 205.

A LUMINOSITY MONITOR USING THE COHERENT BEAM–BEAM INTERACTION

D. Sagan, J. Sikora and S. Henderson*
Laboratory of Nuclear Studies, Cornell University, Ithaca, NY 14853

Abstract

A new method of monitoring the luminosity has been developed at CESR. The method involves shaking one bunch at a specific frequency and observing the resulting oscillations of the corresponding opposing bunch. In initial tests, 1% accurate measurements have been obtained in 1 second. Measurements of different bunches in a train shows bunch to bunch differences with the optimum conditions for one bunch not coinciding with the optimum for another.

1 INTRODUCTION

In a colliding beam storage ring it is essential to be able to monitor the luminosity so as to be able to adjust machine elements (magnets, separators, etc.) to maximize the luminosity. Two methods that are used at the Cornell Electron/positron Storage Ring CESR involve measuring the vertical σ–π tune split and counting babas using the CLEO detector. The problem with the former method is that the π mode is not always cleanly visible. On the other hand, the latter method is slow since the counting rates are low—the characteristic time scale for a measurement being a minute.

With these problems in mind an alternative method has been developed[1] that uses the coherent beam–beam interaction: A given bunch of one beam is shaken vertically. This "shaker" bunch interacts with a bunch of the opposite beam (the "detected" bunch) at the interaction point (IP). The oscillations of the detected bunch are monitored and the amplitude of the oscillation is a measure of the luminosity. This Beam–Beam Interaction (BBI) luminosity monitor has proved to have several advantages: The hardware requirements are minimal and the response is fast—about a second. An added benefit is that with multiple bunches in each beam it is possible to individually monitor the luminosity of any given pair of bunches.

2 THEORY

The configuration of the BBI luminosity monitor is shown schematically in figure 1. The sinusoidal reference signal at frequency ω_s from a lock–in amplifier is used to vertically shake a given bunch of a given beam. This shaker bunch is given a kick $\Delta y'_s$ of

$$\Delta y'_s = A'_s(\mathrm{sh}) \cdot \cos \omega_s t \,. \tag{1}$$

At the IP the shaking translates into an oscillation of the shaker bunch with amplitude $A_s(\mathrm{ip})$ given by

$$A_s(\mathrm{ip}) = A'_s(\mathrm{sh}) \sqrt{\beta_y(\mathrm{sh})\, \beta_y(\mathrm{ip})}\, F_{sh} \,, \tag{2}$$

* Work supported by the National Science Foundation

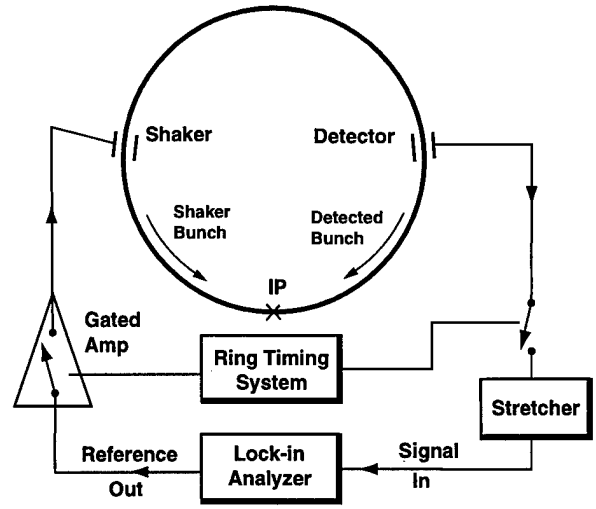

Figure 1: Schematic diagram of the BBI luminosity monitor configuration.

where F_{sh} is the transfer function from the shaker to the IP (cf. reference [1]).

At the IP the oscillations of the shaker bunch give a kick to the detected bunch. The amplitude of this kick, $A'_d(\mathrm{ip})$, is

$$A'_d(\mathrm{ip}) = \left| \frac{dy'}{dy} \right|_{y_{ds}} \cdot A_s(\mathrm{ip}) \,, \tag{3}$$

where dy'/dy is the derivative of the beam-beam kick which is evaluated at y_{ds} with y_{ds} being the vertical offset between the centers of the two bunches when there is no shaking. For head-on collisions

$$\left| \frac{dy'}{dy} \right|_0 = \frac{4\pi\kappa\xi_y}{\beta_y(\mathrm{ip})} \,, \tag{4}$$

where ξ_y is the beam–beam tune shift parameter. If we were only dealing with particles near the core of the bunches then the correction factor κ in Eq. (4) would be 1. However, since it is the centroid motion that is measured, and since particles away from the core receive less of a kick, κ is less than 1. Measurements and calculations[2] give $\kappa \approx 0.6$. ξ_y can be related to the beam sizes through the standard formula

$$\xi_y = \frac{N_p \beta_y(\mathrm{ip}) r_e}{2\pi\gamma\sigma_y(\sigma_x + \sigma_y)} \,, \tag{5}$$

with N_p being the number of particles in a bunch, γ is the standard relativistic factor, and r_e the classical electron radius. ξ_y can also be related to the luminosity by

$$\mathcal{L} = \frac{\gamma I \xi_y}{2 e r_e \beta_y(\mathrm{ip})} (1 + r) \,, \tag{6}$$

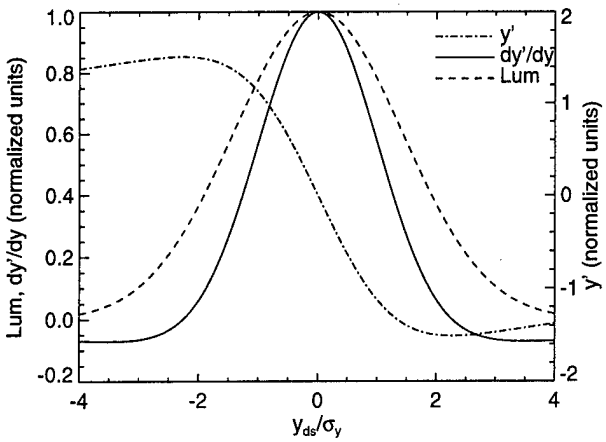

Figure 2: $\mathcal{L}$, dy'/dy, and y' as a function of y_{ds}/σ_y for $\sigma_y/\sigma_x = 0.1$. At $y_{ds} = 0$, $\mathcal{L}$ and dy'/dy are scaled to be 1.

where e is the electron charge, I the beam current, and $r \equiv \sigma_y/\sigma_x$.

Given $A'_d(\text{ip})$ the amplitude of oscillation $A_d(\text{det})$ of the detected bunch at the detector is

$$A_d(\text{det}) = A'_d(\text{ip})\sqrt{\beta_y(\text{ip})\beta_y(\text{det})}\,F_{det}\,, \qquad (7)$$

where F_{det} is the transfer function from the IP to the detector. Combining Eqs. (2), (3), (4), and (7) gives

$$A_d(\text{det}) = A'_s(\text{sh})\;\beta_y(\text{ip})\left|\frac{dy'}{dy}\right|_{y_{ds}} \sqrt{\beta_y(\text{sh})\beta_y(\text{det})}\,F_{sh}\,F_{det}\,. \qquad (8)$$

For head–on collisions

$$A_d(\text{det}) = 4\pi A'_s(\text{sh})\,\kappa\xi_y\sqrt{\beta_y(\text{sh})\beta_y(\text{det})}\,F_{sh}\,F_{det}\,. \qquad (9)$$

Eqs. (8) and (9) are not quite correct since the effect of the detected bunch upon the shaker bunch has been neglected. However, since this effect is small ($< 10\%$) for CESR it will be ignored.

The detector signal is stretched and held for a turn until the next signal is received. The stretched signal is measured by the lock–in amplifier (cf. figure 1). In order to prevent unwanted interference the shaker is gated so as to only kick the shaker bunch. Additionally, the signal from the BPM is gated to exclude the direct signal from the shaker bunch.

With multiple bunches in each beam the oscillations of the shaker bunch may also be transmitted to the detected bunch via intermediate bunches and the long range BBI at the parasitic crossing points. Since the long range tune shift ξ_y is an order of magnitude smaller than ξ_y at the IP this effect can be ignored.

From Eqs. (5), (6), and (9), for head–on collisions with flat beams

$$A_d(\text{det}) \propto \xi_y \propto \beta_y(\text{ip})\cdot\mathcal{L} \propto \frac{\beta_y(\text{ip})}{\sigma_x\sigma_y}\,. \qquad (10)$$

Parameter	Value	Parameter	Value
ω_s	$2\pi\cdot 100\,\text{kHz}$		
$A'_s(\text{sh})$	$0.5\,\mu\text{rad}$	ξ_y	0.03
$\beta_y(\text{ip})$	0.019 m	$\sigma_y(\text{ip})$	$7\,\mu\text{m}$
$\beta_y(\text{sh})$	21.5 m	$\beta_y(\text{det})$	32.3 m
F_{sh}	0.79	F_{det}	0.82

Table 1: CESR BBI luminosity monitor parameters.

Thus, the BBI luminosity monitor can be use to adjust skew quadrupoles to minimize σ_y and maximize $\mathcal{L}$. However, because of the factor of $\beta_y(\text{ip})$ in Eq. (10), the BBI luminosity monitor cannot be used to adjust $\beta_y(\text{ip})$ since it is possible to increase $A_d(\text{det})$ by increasing $\beta_y(\text{ip})$ while simultaneously decreasing $\mathcal{L}$. This drawback is also inherent with the σ–π tune split since the σ–π tune split also is essentially proportional to ξ_y.

Figure 2 shows y', dy'/dy, and $\mathcal{L}$ as a function of y_{ds}/σ_y with dy'/dy and $\mathcal{L}$ being normalized to 1 at $y_{ds} = 0$. The kick y' was calculated using the standard Bassetti and Erskine complex error function formula (cf Talman[2]). For $|y_{ds}| \lesssim 2\sigma_y$, dy'/dy tracks $\mathcal{L}$ with maximum $\mathcal{L}$ coinciding with maximum dy'/dy at $y_{ds} = 0$. The BBI luminosity monitor can thus be used to adjust machine elements to obtain head–on collisions.

3 CESR BBI LUMINOSITY MONITOR

"Typical" values for the parameters of the CESR BBI luminosity monitor are given in table 1. The choice of the shaking frequency is not too critical except that it should not be near a betatron resonance frequency so that changes in the betatron frequency do not produce large changes in the signal. From Eq. (2) $A_s(\text{ip})$ is given to be

$$A_s(\text{ip}) = 0.25\,\mu\text{m}\,. \qquad (11)$$

This is 4% of σ_y so the effect of the shaking on the luminosity is small. From Eq. (9) the signal at the detector is

$$A_d(\text{det}) = 1.9\,\mu\text{m}\,. \qquad (12)$$

The detector electronics is described in reference [1]. "Typical" measured signal levels (without any amplification) are $200\,\mu\text{V}$ with noise around $2\,\mu\text{V}/\sqrt{\text{hz}}$. This corresponds to a 1 second averaging time producing a measurement with noise–to–signal of 1%.

4 EXPERIMENTAL RESULTS

In CESR, the bunches in a beam are clustered in "trains." The bunches within a train are called "cars." The data shown was taken with 9 trains per beam and with two cars (numbered #2 and #5) per train. The spacing between the two cars was 42 nsec and the spacing between trains was either 280 or 294 nsec.

The vertical differential orbit through the IP was varied using an electrostatic bump. Figure 3 shows the monitor

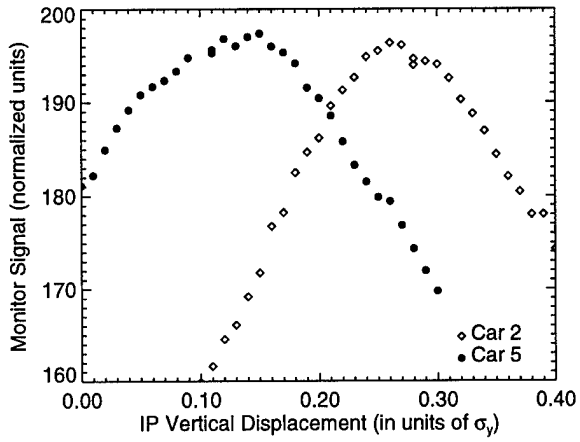

Figure 3: Monitor signals for car 2 and car 5 as a function of vertical displacement of the bunches.

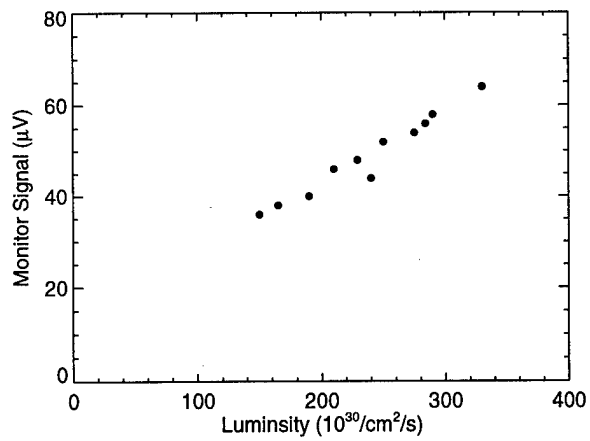

Figure 4: Car 2 monitor signal as a function of Cleo luminosity while varying y_{ds}.

signals from car 2 and car 5 of train 1 as a function of separation at the IP. The monitor signals have been normalized by the total beam current. The vertical separation is calibrated in units of the nominal σ_y (7 μm). Thus, from one end of the plot to the other, the change in y_{ds} is $0.4\sigma_y$. The fact that the peaks of the two signals do not coincide implies that the cars are not following the same vertical trajectory. This is probably due to the short range wake fields produced by the leading (#2) car.

The width of the monitor signal shown in figure 3 for car 2 or car 5 is substantially less than what one would expect from figure 2. This is not surprising since the curves in figure 2 were calculated assuming a constant beam size. However, with the beams colliding off–center, resonances will be excited through the beam–beam interaction. This will lead to beam blowup and hence greater sensitivity to y_{ds}. Indeed, a measurement of car 2 and the luminosity measured by the CLEO detector as a function of vertical displacement, as shown in figure 4, shows a linear relationship. This is appropriate for variations in σ_y (cf. Eq. (10)), but is not what would be predicted from figure 2.

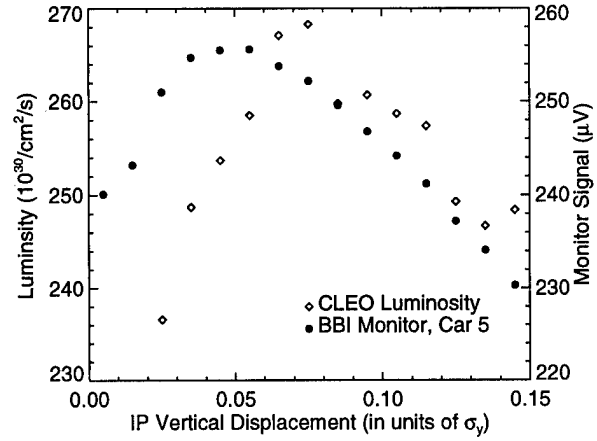

Figure 5: Monitor signal for car 5 and CLEO luminosity as a function of vertical displacement of the bunches.

Figure 5 shows the car 5 monitor signal and the CLEO luminosity as functions of the vertical displacement at the IP. Comparing with figure 3 the luminosity peak falls between the car 2 and car 5 peaks as expected. To obtain a usable signal for tuning all that is required is to simultaneously shake/detect a car 2 and a car 5 bunch to get an average signal.

5 CONCLUSION

Using the coherent beam-beam interaction to monitor the luminosity has several clear advantages: The system has a fast response time so tuning of machine elements can be done efficiently. The system is also easy to construct—the necessary shaker and detector hardware are typical of any storage ring and the external electronics is minimal. Additionally, bunch to bunch variations in the luminosity can be monitored. The one significant drawback is that it is not possible to use the BBI luminosity monitor to optimize the beta at the IP.

6 ACKNOWLEDGEMENTS

Our thanks to Bob Meller, Mike Billing, and Don Hartill for useful discussions, and to Gerry Codner for help with the electronics. Thanks also must be given Elizabeth Young and Richard Talman whose work on measuring the beam–beam kick was the inspiration for the present work.

7 REFERENCES

[1] For an expanded version of this paper see: D. Sagan, J. Sikora, and S. Henderson, "A Luminosity Monitor Using the Coherent Beam–Beam Interaction (Internal Report)," Cornell CBN 97–13 (1997). Available on the web from: http://www.lns.cornell.edu/

[2] R. Talman, "Multiparticle Phenomena and Landau Damping," in AIP Conf. Proc. **153** pp. 789–834, M. Month and M. Diens editors, American Institute of Physics, New York (1987). K. Yokoya and H. Koiso, "Tune Shift of Coherent Beam–Beam oscillations," Part. Acc. **27** pp. 181-86, (1990).

THE INCOHERENT LONG RANGE BEAM-BEAM INTERACTION IN CESR.*

Alexander Temnykh† and David Sagan
Cornell University, Ithaca NY

1 INTRODUCTION

CESR has reached the world's highest luminosity using mutibunch operation. The key to this operation is a horizontal 'pretzel' separation of the beams in the arcs and a crossing angle at the IP. The pretzel separation is needed since the counter rotating bunches share the same beam pipe and there is thus a long range beam–beam interaction (LRBBI) between the beams. The LRBBI involves individual particles of one beam (henceforth called the "probe" beam) interacting with the other "strong" beam. Particles of the probe beam are destabilized when their horizontal oscillation amplitude is large enough to pass near the strong beam. This sets the limit for the minimum practical pretzel separation between beams.

Future plans call for increases in current as well as the number of bunches. Since more current will mean a stronger beam-beam kick and more bunches will mean more parasitic crossing points, it is important to understand how the LRBBI destabilizes particles. Temnykh, Welch and Rice[2] have studied the LRBBI experimentally and have put forward phenomenological models to predict the minimum separation achievable for a 50 minute beam lifetime.

To go beyond these phenomenological models the way in which the LRBBI destabilizes particles must be understood. It is shown in this paper using a simple numerical simulation that, with CESR (Cornell Electron/positron Stroage Ring) conditions, and with the beams separated horizontally, the LRBBI leads to vertical beam tail growth and loss of particles in the vertical plane. Furthermore, the threshold of this instability depends on the vertical size of the opposite beam. An increase of the vertical size of the opposite beam leads to an increase of the allowed beam intensity for a given separation and for a given lifetime. These conclusions are shown to be supported experimentally.

2 TRACKING

Using a tracking simulation a previous study[2] found that the horizontal and synchrotron motion did not exhibit instabilities. Only the vertical motion was seriously affected by the LRBBI. At the time it was not clear why this was so. A simple explanation for this can be constructed as follows: Consider a simple particle tracking model where a particle is first transformed from a parasitic collision point back to the parasitic collision point using a linear matrix. After the 'arc' transport the LRBBI kick is given by

Parameter	Symbol	value
Horizontal beta	β_x	10 m
Vertical beta	β_y	20 m
Horizontal tune	Q_x	0.538
Vertical tune	Q_y	0.602
Horizontal sigma	σ_x	1.50 mm
Vertical sigma	σ_y	0.25 mm
Bunch-bunch offset	x_{sep}	9.3 mm
Strong bunch current	I	10.0 mA

Table 1: Parameters used in tracking.

$$(x', y') = (\mathcal{F}_x(x - x_{sep}, y), \mathcal{F}_y(x - x_{sep}, y)) \quad (1)$$

where the kick $\mathcal{F}$ is calculated from the standard Bassetti and Erskine formula[3] for a bi–Gaussian strong bunch and x_{sep} is the horizontal separation of the beams.

Figure 1 shows the results of tracking using parameters appropriate for minimum acceptable separation in CESR as given in table 1. The beams were separated by a distance $x_{sep} = 9.3\,\text{mm}$ ($6.3\sigma_x$) the tracked partical had initially $x = 5.5\sigma_x$ (corresponding to a 50 min lifetime) and $y = 1.0\sigma_y$. The particle was tracked for 1000 turns. As seen in the figure, the horizontal motion is stable and practically unperturbed. The vertical motion, on the other hand, looks chaotic. This simple simulation agrees well with previous results[2].

The vertical kick is strongly influenced by the horizontal oscillations. This coupling from horizontal to vertical makes the analysis of the vertical motion extremely complicated. With this being said, in order to try to understand the vertical motion consider the following numerical experiment: Consider the motion of a particle in vertical phase space due to the LRBBI assuming that the x–position of the particle is frozen at some constant value. For purposes of illustration consider the particle tracked in figure 1. On the first turn it had $x_{\text{off}} \equiv x - x_{sep} = 0.86\,\sigma_x$, on the second turn x_{off} was $9.90\,\sigma_x$. The vertical phase space with x_{off} fixed at these two values is shown in figures 2a and 2b respectively. With $x_{\text{off}} = 0.86\sigma_x$ the difference in vertical tune between small and large amplitudes is large enough such that two low order nonlinear resonances can be excited. Overlapping of these resonances results in the appearance of a stochastic region up to $15\sigma_y$. In this region there is strong diffusion and particles experience fast and unpredictable changes in amplitude. In figure 2*b* there are stable, practically unperturbed, trajectories.

If we now include the effect of the horizontal motion we see that a particle passes near the center of the opposite

* Work supported by the National Science Foundation
† On leave from BINP, Novisibirsk

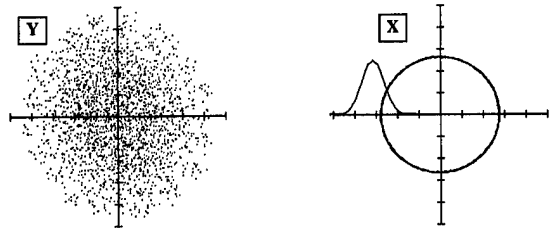

Figure 1: Tracking simulation in phase space using the parameters of table 1. The starting point was $(x, x', y, y') = (5.5\sigma_x, 01.0\sigma_y, 0)$ The scale is $2\sigma_{x,y}$ per division. The Gaussian curve in the X plot is the horizontal strong bunch profile.

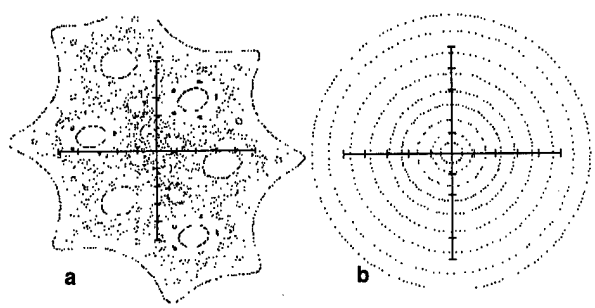

Figure 2: Vertical phase space for particles with fixed $x_{\text{off}} = x - x_{sep}$. (a) $x_{\text{off}} = 0.86\sigma_x$, (b) $x_{\text{off}} = 9.90\sigma_x$.

beam, due to the stochastic motion seen on figure $2a$ the vertical amplitude will be unpredictably changed. This will cause diffusion in vertical phase space as has been seen in figure 1. The condition for resonances overlapping, seen on figure $2a$, is affected by the vertical strong beam size and by the strong beam intensity. An increase of the vertical beam size for a given intensity reduces the strength of the resonance harmonics as well as the tune difference between large and small amplitude. This results in a reduction of the number of resonances between these amplitudes and the disappearance of the stochastic region. This will stabilize the vertical motion.

Figures 3 and 4 illustrate this. Figure 3 shows the vertical motion using the same parameters as used for figure $2a$ except with a strong beam vertical size of $\sigma_y = 0.75$ mm which is 3 times larger than what was used for figure $2a$. The figure shows regular trajectories with little sign of chaotic behavior. Figure 4 shows the 2 dimensional tracking and in contrast with figure 1 there is no hint of unstable motion. Thus, with an increase in vertical beam size we can expect that for a given separation it should be possible to reach higher beam current. This is indeed seen experimentally as discussed in the next section.

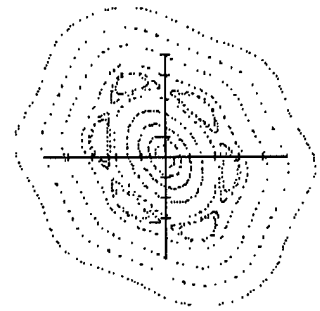

Figure 3: Vertical phase space for particles with the same the same conditions as in figure $2a$ except with a large strong beam sige of $\sigma_y = 0.75$ mm.

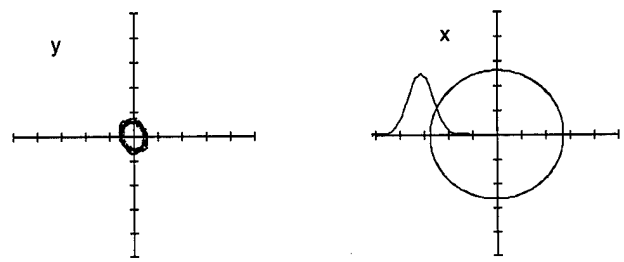

Figure 4: Tracking with a large strong beam size of $\sigma_y = 0.75\,mm$. Other parameters same as used in figure 1.

3 EXPERIMENTS AT CESR

The enlargement of the beam tails due to the LRBBI was measured experimentally by by monitoring beam lifetime versus the position of a scraper. One bunch per each beam were filled that the bunches did not collide at the IP but interacted at two opposing parasitic crossing points in the arcs. Table 2 gives parameters of the two crossing points.

Figures 5 and 6 show the loss rates (which in the tails are roughly proportional to the beam density at the scrapper tip) for horizontal and vertical scrapping as a function of scraper position with and without the strong bunch. For the horizontal, the presence of the strong bunch only enlarged the tails by 20% or so. For the vertical the enlargement of the tails was dramatic such that the size of the vertical tails became similar to that of the horizontal. This is in qualitative agreement with tracking and shows that the instability is indeed a vertical one.

Parameter	PC1	PC2
$\beta_x(m)$	9.30	10.30
$\beta_y(m)$	33.20	20.40
$\eta(m)$	0.10	1.19
$\sigma_x(mm)$	1.26	1.51
$x_{sep}(mm)$	9.16	9.78
x_{sep}/σ_x	7.26	6.47

Table 2: Parameters at the parasitic crossing points.

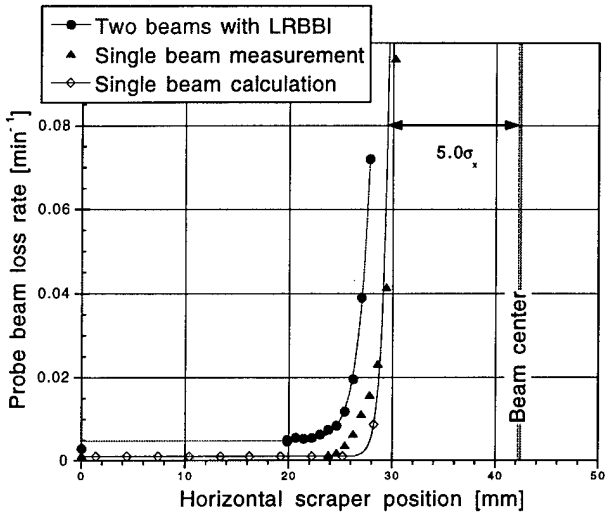

Figure 5: Weak beam loss rate versus horizontal scraper position.

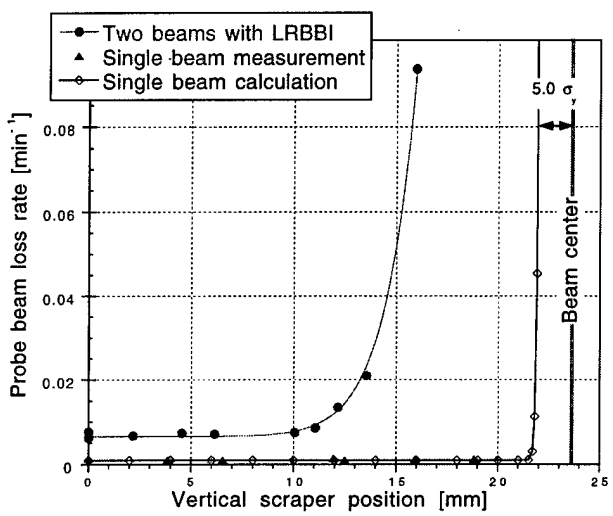

Figure 6: Weak beam loss rate versus vertical scraper position.

To observe the effect of vertical strong beam size on the LRBBI, experiments were preformed where the lifetime of a probe bunch was measured as a function of current for fixed vertical strong beam size. The vertical beam size of the strong bunch was varied without affecting the probe bunch by taking advantage of the fact that the beams follow different trajectories. It was thus possible to change the tune of one beam but not the other by using sextupole magnets. By tuning the strong bunch to be near the coupling resonance sideband $Q_x - Q_y + Q_s = n$ the strong bunch beam size could be increased without affecting the probe bunch. The conditions here are the same at with the first experiment.

The probe positron bunch had a current of 3 to 5 mA while the strong electron bunch had currents up to 18 mA. Care was taken to keep beam tunes, beam-beam separation,

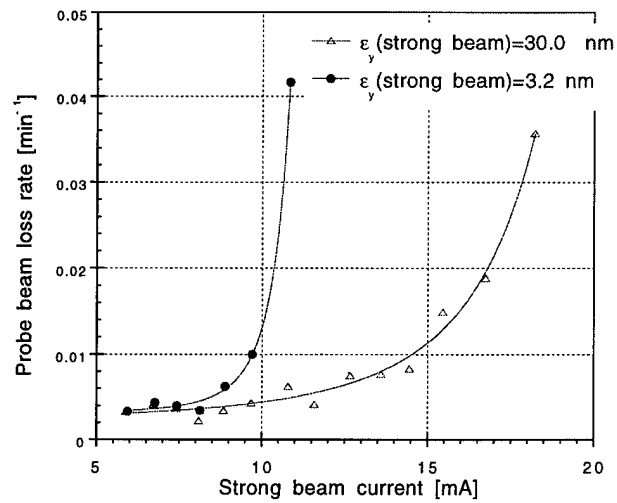

Figure 7: Probe beam loss rate versus strong beam current.

etc. constant. In particular the horizontal emittance of the strong beam was constant in spite of the presence of the coupling sideband resonance used to vary the vertical beam size.

Figure 7 shows the probe beam loss rate for two different strong beam sizes. As can be seen from the figure the loss rate of the probe beam is very dependent on the strong vertical size with the larger stron beam size giving a dramatically lower loss rate.

4 CONCLUSIONS

We have found good qualitative agreement between a simple simulation model and experiment which indicates that the incoherent LRBBI may be simply simulated with good reliability. In particular it is shown that there is diffusion in the vertical plane. It is also seen that a larger vertical beam size decreases the LRBBI which. This fact could possibly be used to achieve smaller separations at the parasitic crossing points.

5 ACKNOWLEDGMENTS

Thanks must be extended to J. Welch and D. Rubin for useful discussions, to John Hylas for useful remarks and to all the CESR operating group for their assistance.

6 REFERENCES

[1] D. Rubin, 1995 IEEE Particle Accelerator Conference.

[2] A. B. Temnykh, J. J. Welch and D. H. Rice, 1993 IEEE Particle Accelerator Conference, Vol 3, p.2007.

[3] M. Bassetti and G. Erskine, CERN-ISR-TH/80–06 (1970).

MEASUREMENT AND SIMULATION OF NONLINEAR BEAM-BEAM MODE COUPLING IN THE FERMILAB TEVATRON

S. Assadi and C.S. Mishra
Fermi National Accelerator Laboratory† P.O. Box 500, Batavia, IL 60510, USA

Abstract

The Tevatron beam dynamics has been studied from the "weak-strong" representation of the beam-beam effects for various octupole field settings. A single particle is tracked using TEAPOT in the presence of the other beam. The nonlinearities introduced by the beam-beam forces introduces two unwanted effects: (1) it excites nonlinear resonances; (2) it introduces dispersion of the tunes with amplitude. The strength of nonlinear three mode coupling satisfying the sum rules $\nu_3=\nu_1\pm\nu_2$ for various octupole settings are calculated. The higher order spectral analysis results are presented.

1. INTRODUCTION

The Fermilab Tevatron is a 1.8 Tev/c center of momentum proton-antiproton collider, delivering a peak luminosity greater than 2.E31 $cm^{-2}sec^{-1}$. Tevatron operating with six protons and six bunches colliding at CDF and D0 interaction points does not seem to be limited by beam-beam effects. Average intensity of proton and antiproton bunches are about 25E10 and 8E10 respectively. The Fermilab III accelerator complex upgrade, including the Main Injector will increase the peak luminosity to 10E32 $cm^{-2}sec^{-1}$. Higher luminosity will be achieved by injecting more proton and antiproton bunches with similar intensities. Number of bunches will increase from 6x6 to 36x36 and eventually to ~109x109, to keep the number of interactions per crossing at each high energy detectors at a manageable level.

The purpose of this paper is two folds: (i) to introduce higher order spectral analysis to visualizes turbulent or chaotic data to the accelerator physics community, (ii) to apply octupole field to reduce the beam-beam tune shift of high amplitude particles. We investigate the combined effect of long range interactions and higher order multipoles to calculate the nonlinearly generated frequency spectrum. In this paper we discuss three cases. First we restrict ourselves to syncro-betatron and betatron-betatron coupling of a single beam with betatron tunes close to the operating tunes at collision when higher order multipoles are present but no applied octupole field strength,(k_3l) Second, beam-beam with two positive settings of octupole field strength. Finally beam-beam with negative octupole field which results in resonance extraction are analyzed. A modified version of thin element tracking program TEAPOT has been used ro simulate the turn by turn data for Tevatron lattice.

2. ANALYSIS

Higher order spectral analysis has been used to calculate the bicoherence spectrum of the three-wave coupling contributing to he characteristics of beam-beam coupling in the Tevatron. The *bicoherency* is defined as

$$b^2(\nu_1,\nu_2)=\frac{B(\nu_1,\nu_2)^2}{\langle |X_{\nu 1}X_{\nu 2}|^2\rangle P(\nu)}$$

where B(ν1,ν2) is the bispectrum defined as $B(\nu 1,\nu 2)=\langle X_{\nu 1}X_{\nu 2}X_{\nu 3}^*\rangle$, the power spectrum is $P(\nu)=\langle X_{\nu 1}X_{\nu 2}^*\rangle$, and Xν is the Fourier transform of the turn by turn data X(t), and ⟨⟩ means ensemble averaging over many statistically similar realizations. The bicoherency measures the fraction of the fluctuating power at the frequency ν3 which is phase correlated with the spectral components at frequencies ν1 and ν2 obeying the summation rule $\nu_3=\nu_1\pm\nu_2$. The bicoherency thus qualifies the degree of coupling among three waves (modes). The bicoherency is bound between 0 and 1: when b^2 is equal to 1 then the oscillations at frequency ν3 are completely coupled with frequencies ν1 and ν2 and completely decoupled for the zero value. The use of the bicoherence as a measure of three wave coupling is independent of any closure assumption. The bicoherence is nonzero if there is a statistically significant phase relation between the three modes.

3. CALCULATIONS AND RESULTS

During Run II and TEV33 the Tevatron will be filled with three bunch trains each containing either 12 or 36 bunches respectively. The detector readout requires a gap between bunch trains of 2.5μsec. Due to this gap the bunches at the

† Operated by the University Research Assoc. Inc, under contract with the U.S. Department of Energy.

0-7803-4376-X/98/$10.00 © 1998 IEEE

two ends of each bunch train will encounter different amont of beam-beam kicks. During Run II and Tev-33 the antiproton beam will occupy a much larger tune space due to larger tune shift and uneven bunch tune shifts. This will require us to adjust the tune of the Tevatron during the opposing beam injection process. Fig.(1) is an example of dependencies of tunes on intensity with and without head-on collision.

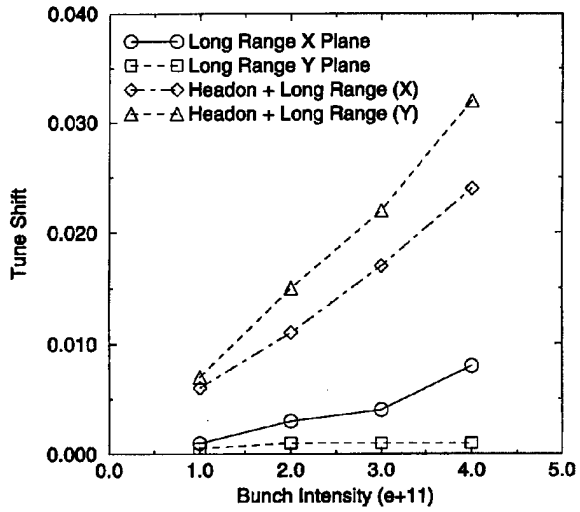

Fig.1) Betatron tune as a function of bunch intensity.

As expected the head-on tune shift is larger by about a factor of four at the bunch intensity of 3.0E11. In the Tev-33 operations the number of bunches are going to increase from 36 to 108, hence the number of long range beam-beam interactions will increase from 70 to 214. If we consider that the long range tune shift will increase linearly, the long range beam-beam tune shift will be approximately of the same size as head-on tune shift. Further due to higher number of closely placed bunches the number of near misses and reduced separations between the two beams will increase, contributing more to beam-beam tune shift. As

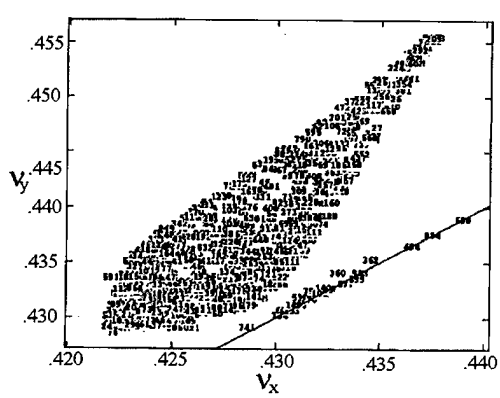

Fig.2) Tune-Tune Foot-print of the beam in presence of beam-beam effects.

such, we need to consider ways to reduce the beam-beam tune shift. Fig.2 shows a tune foot print of the beam in presence of the beam-beam effects for 36x1 case.

4. REDUCTION OF TUNE-TUNE FOOT PRINT

We are investigating several options to reduce the tune-tune foot print. The presence of the octupole component in the lattice causes an amplitude dependent tune shift. The octupoles can also be used to reduce the effect of beam-beam tune shift. The octupoles can also be used to reduce the effect of beam-beam tune shift by introducing the tune shift of opposite sign. We have used the octupole magnets present in the Tevatron to study this idea. Of course, distribution of the octupoles can be optimized. In a detail study, we will need to place more octupoles at different locations in the lattice. Figure 3 shows the tune of launched particles as a function of its amplitude.

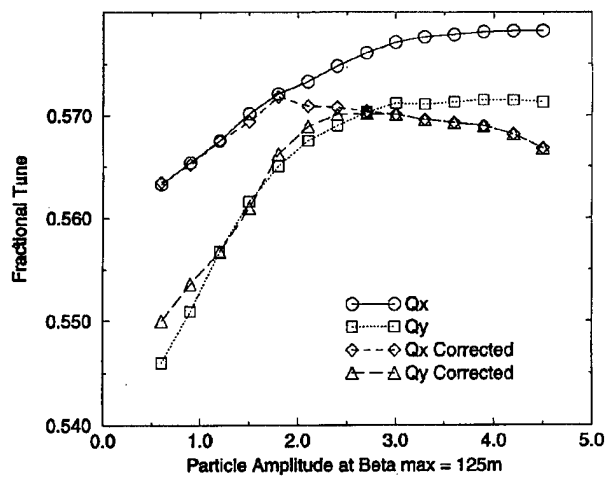

Fig.3) Tune-Tune footprint of the beam in presence of beam-beam effects with and without octupole fields.

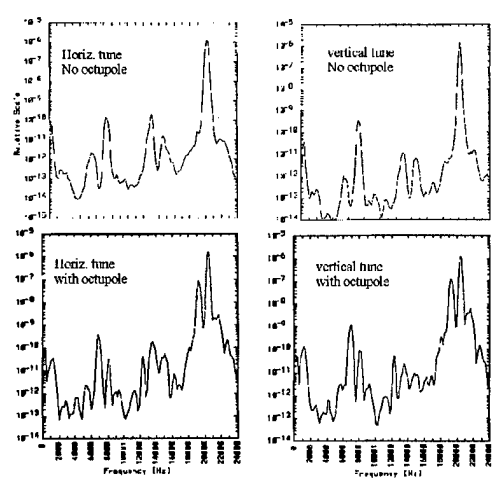

Fig.4) Effect of octupole field on tunes.

It is clear from these calculations that octupoles can be used to reduce the tune-tune foot print, but the details of number, strength and their placement in the lattice need more detailed simulations. From Fig. (4), it is clear that octupole fields introduce coupling and as such, the usual phase-space plots are not a reasonable representation of visualizing beam structures.

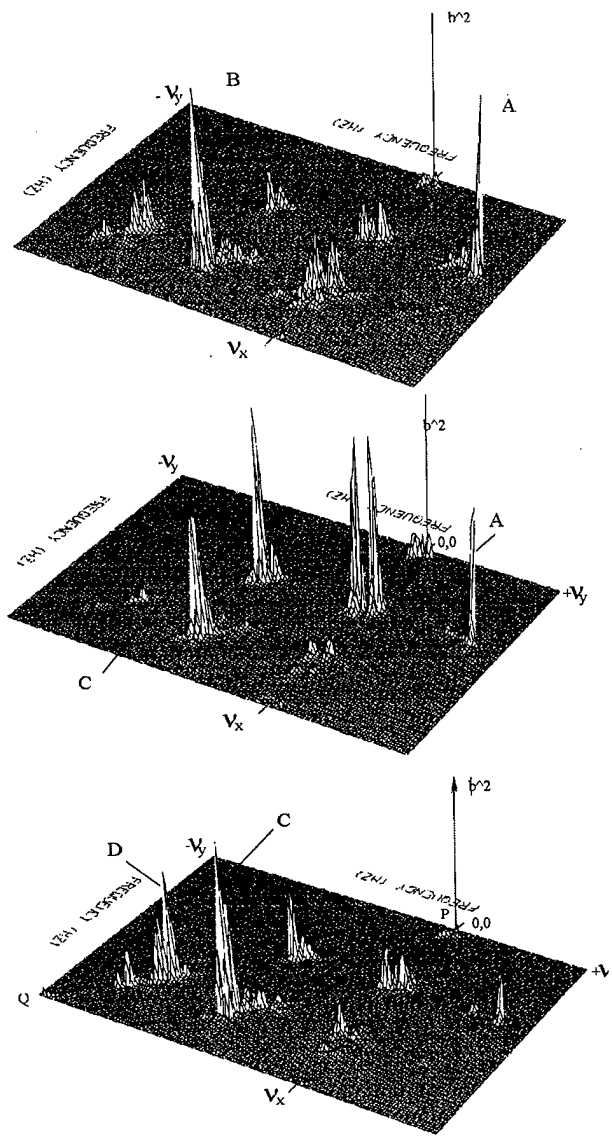

Fig.5) (Top) Horizontal self-coupling and synchro-betatron coupling, (middle) vertical self-coupling and synchro-betatron coupling, (bottom) cross-coupling of horizontal to vertical tune-tune coupling are shown.

In Figure 5, the octupole field strength is 15 units. This figure is composed of three parts, the top section is the representation of horizontal synchro-betatron coupling shown by Peak (A). Peak (B&C) shows the betatron-betatron coupling in horizontal plane due to beam-beam and the helical closed orbit (compare to Fig.6 which octupole fields are turned off). Peak (D) on the bottom section of figure 5 is due to the octupole field and arises at the difference vx-vy resonance line.

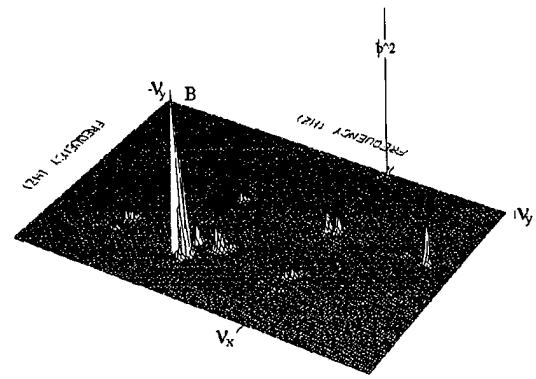

Fig.6) Bicoherence of beam-beam without any applied octupole field.

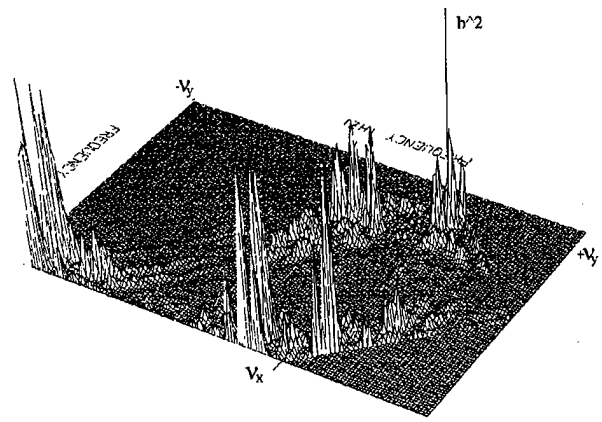

Fig. 7) Applied negative octupole field causes beam loss due to difference resonance and ½ integer extraction.

If we change the sign of the octupole field, we observe particle losses and the bicoherency shows the difference tune resonance and ½ integer extraction (Fig.7).

5. SUMMARY

In this paper we have presented the initial results from an study to understand and visualize the effect of beam-beam as octupole field strength is varied. A closer attention needs to be paid by changing the Tevatron operating procedures to overcome the effects of increasing beam-beam forces. We have introduced an idea to reduce he size of the tune foot-print.

6. ACKNOWLEDGMENTS

Particular thanks to Dr. P. Colestock, Dr. J. Marriner, and Dr. R. Talman.

BEAM-BEAM SIMULATIONS WITH CROSSING ANGLE IN TEV33

V. D. Shiltsev, FNAL*, M.S.345, P.O. Box 500, Batavia, IL 60510, USA

Abstract

We consider effects of finite crossing angle at collision point on beam dynamics in the Tevatron collider upgrade (TEV33). Impact of the beam-beam interaction on beam sizes, particles diffusion and luminosity is studied with use of computer simulations. Parameter space for better collider performance is proposed.

1 INTRODUCTION

The Tevatron collider upgrade (TEV33) [1] intends to operate with some hundred bunches in each beam. Large number of bunches N_b results in small bunch spacing of 132 ns and, therefore, collisions occur more frequently. The colliding beams share the same vacuum chamber that leads to $2(N_b-1)$ parasitic collisions besides specially designed interaction points (IPs). Detrimental effects of the parasitics collisions of high current beams can be reduced by separation of the orbits of p and $\bar{p}$ beams everywhere except the IPs. However, due to limited space available and limited strength of electrostatic separators several crossing points around the IPs can not be effectively treated in such a way. Collision with half-crossing angle of $\phi = 0.2$ mrad will allow to increase the separation up to a safe value of 3 rms beam size at the first parasitic crossing [2].

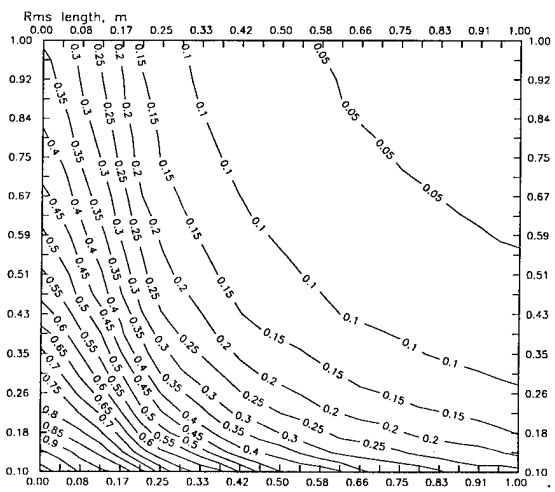

Figure 1: Contour plot of the geometrical luminosity reduction factor R due to tilt effect vs. bunch length σ_z and crossing half-angle ϕ, $\beta^* = 25$ cm.

Collisions with a crossing angle result in geometrical luminosity reduction. Then, in the case of strong electromagnetic interaction between beams, characterized by the beam-beam parameter $\xi = \frac{r_p N_p}{4\pi\varepsilon_n} N_{IP}$, (here $r_p = 1.53\cdot 10^{-18}$m is the classical proton radius, N_p is the number of particles in opposing bunch, ε_n is the transverse normalized emittance of round beam, and N_{IP} is the number of IPs), the harmful impact of non-linear force due to the opposing beam tends to enhance for particles off the bunch center (at the tail and head). Finally, there is a coupling between longitudinal and transverse degrees of particle motion that causes synchrobetatron (SB) resonances at frequencies of $n\nu_x + m\nu_y + l\nu_z =$ integer, where ν_x, ν_y, ν_z are horizontal, vertical and synchrotron tunes, respectively.

2 SIMULATIONS WITH CROSSING ANGLE

BBC code and beam parameters We employ the BBC code Ver. 3.3 developed by K.Hirata [3] for beam-beam simulations in "weak-strong regime" which is close to the TEV33 conditions where proton bunch population is about 6 times the antiproton one. The "weak" (antiproton) bunch is presented by number of test particles, while the "strong" (proton) bunch appeared as an external force of Gaussian bunch. Typically we tracked 100 (maximum 300) test particles through five slices of strong bunch for (10-50)$\cdot 10^3$ turns. Typical number of 30,000 turns corresponds to about 0.6 s in TeV'33, it is some 100 synchrotron oscillation periods. No damping due to radiation or cooling is assumed to play role in the beam dynamics. Further increase of the number of particles as well as number of slices gave almost identical results. The code assumes one-plane crossing angle (e.g. horizontal) and one IP.

The code outputs of greatest practical utility are luminosity, rms beam sizes and maximum betatron amplitudes which any of the test particles attained during tracking. These outputs are given with respect to unperturbed values, e.g. sizes and amplitudes are divided by their design rms values $\sigma_{x,y}/\sigma^0_{x,y}$ and $A^{max}_{x,y}/\sigma^0_{x,y}$, the luminosity is presented by the reduction factor of $R = L/L_0$ where the bare design luminosity $L_0 = f_0 N_p N_{\bar{p}}/(4\pi\sigma^0_x\sigma^0_y)$ and f_0 is the rate of collisions.

The relevant parameters of the simulations were chosen close to the TeV33 design ones, [1], namely: energy E=1000 GeV; $p, \bar{p}$/bunch $(N_p, N_{\bar{p}})$=(30, 6) $\cdot 10^{10}$; the rms energy spread of $\sigma_E = \Delta E/E$=2.2$\cdot 10^{-4}$ σ_z=15 cm rms bunch length; synchrotron tune ν_z=0.0045; rms transverse emittance $\varepsilon_{x,y}$=3 $\cdot 10^{-9}$ m·rad; beta-function at IP $\beta^*_{x,y}$=25 cm; nominal $\bar{p}$ beam-beam parameter ξ=0.025 (in TEV33 this tune shift is accumulated over two IPs). These parameters correspond to beginning of the collision store.

Results Luminosity reduction due to geometrical "hourglass" and beam tilt effects depends on two parameters: the bunch length to beta function ratio $S = \sigma_z/\beta^*$ and normalized angle $\Phi = \phi\sigma_z/\sigma^*$ (also known as Piwinski angle). For TeV'33 $S = 0.6$ at the injection and about 1.0 after 12 hours of beam life time; the normalized angle of

* Operated by Universities Research Association, Inc., contract with the US Department of Energy

$\Phi = 1.0$ corresponds to $\phi = 0.183$ mrad. The simulations of the geometrical luminosity reduction shows the R goes down with either decrease of S or increase of Φ as shown in Fig.1. The approximate formulae $R \approx 0.96/\sqrt{1+\Phi^2}$ can be used for the parameter of $S = 0.6$. At some particular tunes and the total luminosity degradation is about the pure geometrical one as in Fig.1, e.g. no signs of the degradation due to SBRs are seen after 30,000 turns with "good" tunes of $\nu_x = 0.57$, $\nu_y = 0.58$, $\xi = 0.025$ [4].

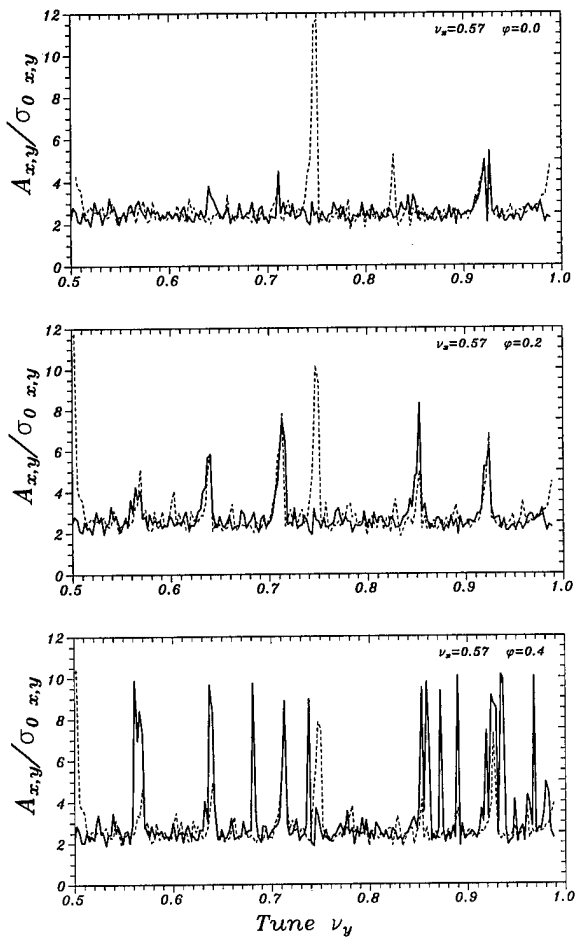

Figure 2: Maximum horizontal (A_x/σ_x^0 - solid) and vertical ($A_y\sigma_y^0$ - dashed) amplitudes vs. ν_y. $\nu_x = 0.57$, $\xi = 0.025$, $S = 0.6$, crossing angle $\phi = 0$ mrad (top), 0.2 mrad (center, $\Phi \simeq 1$), and 0.4 mrad (bottom).

Our simulations show that the resonances due to SB coupling distinctly manifest itself in the growth of the maximum betatron amplitude. The later is an indicator of transverse particle diffusion which forms a halo and concludes in particles losses. Performing scan over the vertical tune $\nu_y = 0.5....1.0$ with $\nu_x = 0.57$, we have found the resonance picture qualitatively changes with increase of the half-angle ϕ. Fig.2 presents the values of A_x/σ_x^0 (solid curves) and A_y/σ_y^0 (dashed curves) after 10,000 turns vs. ν_y without the crossing angle $\phi = 0$ (upper plot), and with crossing angle of $\phi = 0.2$ mrad (center plot) and $\phi = 0.4$ mrad (bottom plot). First of all, the number resonances grows with ϕ: five of them are seen without the angle, while

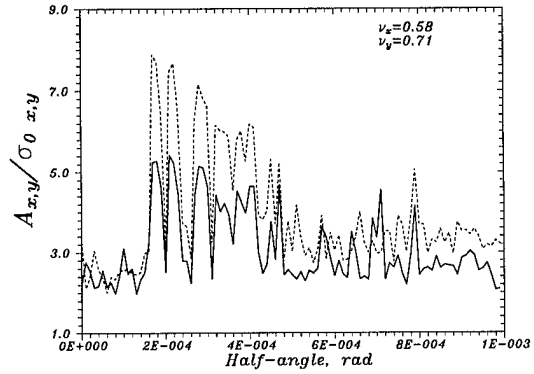

Figure 3: Maximum horizontal (A_x - solid) and vertical (A_y - dashed) amplitudes vs ϕ ($\nu_x = 0.58$, $\nu_y = 0.71$, $\xi = 0.025$, $\Phi = 0...5$, $S = 1$).

about ten and twenty at ϕ=0.2 mrad and 0.4 mrad, respectively, leaving not too much tune space for the collider operation. The synchrotron tune is comparatively small - at the particular case presented in Fig.2 $\nu_z = 0.0046$, therefore, the SBRs – at the tunes $\nu_{x,y,z}$ of $n\nu_x + m\nu_y + l\nu_z = q$, where (n, m, l) and q are integer – look like closely spaced sidebands of (n, m) resonances (line "splitting").

The major resonances at $\phi = 0$ are (4,-2); (2,4); (0,4); (0,6); (2,2); while a number of new SBRs appears at $\phi = 0.4$ mrad – split line of (1,-1,$\pm$1) at $\nu_y = 0.57$, (4,-2,0) and (4,-2,-2) at ν_y=0.64, (4,4,0) at 0.68, the line of (2,4) resonance becomes wider and lager; the (0,4,-2) sideband of the 3/4 resonance appears at 0.74; then one can see (2,1,0) at 0.86 and (2,1,2) at 0.87; split (2,2) lines at 0.93 and (1,-2,$\pm$1) at 0.97; higher order resonances are seen at ν_x =0.89 and 0.98. The degradation is also seen in the rms beam sizes but not as drastic as for the maximum amplitudes in Fig.2.

Finally, from Fig.2 one can conclude that at $\xi = 0.025$, $\nu_x = 0.57$, there are "windows" in ν_y without SB resonances at 0.51–0.56, 0.58–0.62 and 0.77–0.83. The first two are preferable from the point of larger luminosity [4]. This "off-resonant" case shows no meaningful changes in particles diffusion rates with increase of the angle, while at the "bad" operation point – see maximum amplitudes vs. the crossing angle with close to resonance tunes $\nu_x = 0.58$, $\nu_y = 0.71$ in Fig.3 – the amplitude does not grow until normalized angle of $\Phi \simeq 1$ ($\phi \simeq 0.2$ mrad), then rapidly increases and slowly decreases after $\Phi \geq 3$. That weakening of the SBR at $\Phi \sim 3-5$ is probably due to the fact that the effective beam-beam interaction becomes smaller due to the tilt effect.

In order to determine the tune space for better performance we made a 2-D scan over the tune space of ν_x, ν_y (0.55...0.65, 0.55...0.65). Without the crossing angle, betatron amplitude has no peculiarities. The resonance "hills" are clearly seen in the plots of maximum amplitudes of horizontal and vertical betatron oscillations – see top and bottom plots in Fig.4, respectively – if the crossing angle is equal to 0.2 mrad. After only 10,000 turns the ratio of $A_{x,y}/\sigma_{x,y}^0$ could reach values of the order of 5 at some res-

onance lines, while without the angle they do not exceed 2.7. One can recognize the most valuable resonances in the tune space – they are at $\nu_x \approx 0.59$ and $2\nu_x + \nu_y$ in horizontal dynamics, and at $\nu_x + 3\nu_y$ and $\nu_x + \nu_y$ in the vertical one. Note, that if both tunes are in the area of 0.55–0.59 then both amplitudes are small.

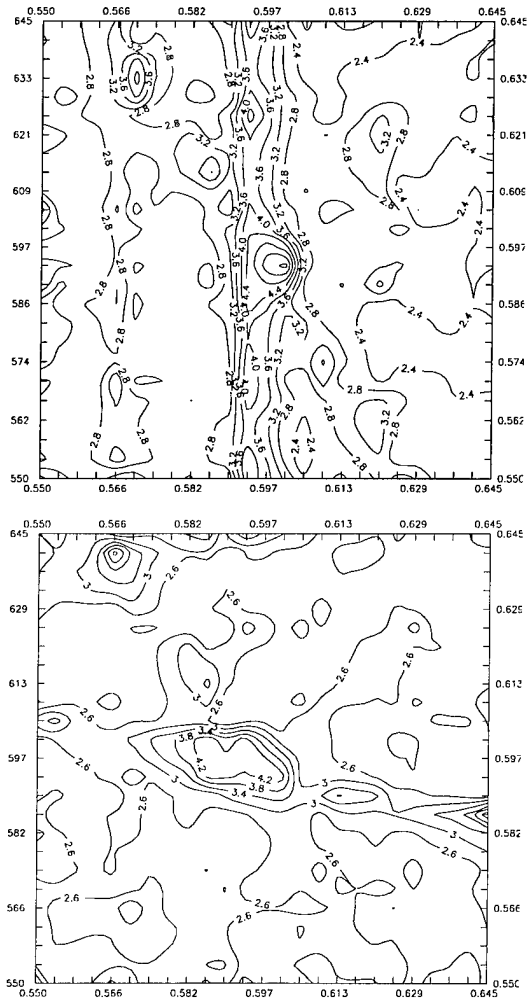

Figure 4: The A_x and A_y scan contour plots (upper and lower plots). The abscissa and ordinate are horizontal and vertical tunes, respectively;$\xi = 0.025$, $\Phi = 1$, $S = 0.6$

Fig.5 presents the luminosity reduction factor R contour plot in (ν_x, ν_y) plane. The darker areas correspond to the higher luminosities with maximum R of about 0.9. The contour spacing is 5% in luminosity reduction. One can see, that there several areas with small luminosity where the R is about 0.7. The lower left corner of the plot $0.55 < \nu_x < 0.59$, $0.55 < \nu_y < 0.59$ is rather dark, that means better luminosity conditions.

3 DISCUSSION AND CONCLUSIONS

We found that far of resonances only geometrical luminosity degradation due to "hour-glass" and tilt takes place. We observe no enhanced particle diffusion over the tune space of $0.55 < \nu_x, \nu_y < 0.59$ with crossing angle less than

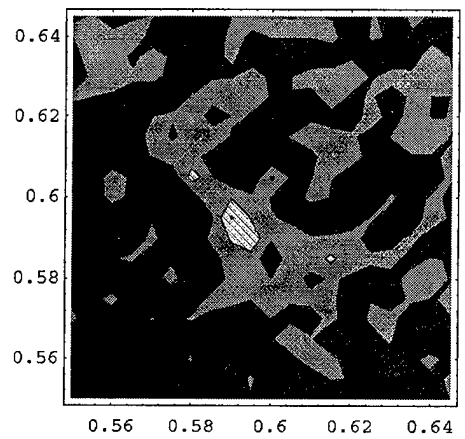

Figure 5: Luminosity contour plot (scan). The abscissa and ordinate are horizontal and vertical tunes, respectively;$\xi = 0.025$, $\Phi = 1$, $S = 0.6$.

0.2 mrad $\Phi < 1$, while other tune areas are influenced by synchrobetatron resonances, and dangerous increase of the loss rate occurs at $\Phi \geq 1$ ($\phi \geq 0.2$ mrad). The beam size or maximum betatron amplitudes do not grow monotonically with increase of Φ – instead, they rather be constant or even decrease slightly. The effects are found to be larger for larger beam-beam parameter ξ [4].

The experiments with crossing angle at the SPS(CERN) collider [6] shown no SB luminosity reduction and no substantial particle loss increase with parameters of $\Phi = 0.5$, ξ=0.02 and $\nu_z = 0.005$. We should emphasize that the TEV33 parameters are close to the SPS (except twice larger Φ), therefore, our "optimistic" conclusions about SB dynamics are consistent with the previous experience.

Nevertheless, the effects of tune ripple, coupling and sextupole fields in the rest of the lattice, two IPs instead of one, smaller synchrotron tune, beam separation at the IPs, and the crossings angle in two planes need further studies. The BBC code can also be used for investigation of the parasitic crossings effect.

Author thanks K. Hirata(KEK) for an opportunity to use his simulation code. Valuable comments and fruitful discussions with M.Zobov(Frascatti), A.Piwinski(DESY), V.Danilov(Budker INP), P.Bagley, J.Marriner, D.Finley and L.Michelotti(FNAL) are sincerely acknowledged. I am thankful to N.Gelfand and O.Krivosheev for their help with the BBC code compilation and launching.

4 REFERENCES

[1] J.P.Marriner, FERMILAB-Conf-96/391 (1996).

[2] P.P.Bagley, *et.al,*, FERMILAB-Conf-96/392 (1996).

[3] K.Hirata, *Phys. Rev. Lett., 74*, p.2228 (1995).

[4] V.Shiltsev, FERMILAB-FN-653 (1997).

[5] A.Piwinski, DESY Report 77-18 (1977).

[6] L.R.Evans, A.Faugier, R.Schmidt, IEEE Trans., NS-32, No.5 (1985), p.2209.

EVALUATON OF "ROUND COLLIDING BEAMS" FOR TEVATRON

V.V. Danilov, Budker Institute of Nuclear Physics, 630090, Novosibirsk, Russia,
V.D. Shiltsev, FNAL* ,P.O. Box 500, Batavia, Illinois 60510

Abstract

This paper presents investigation of the proposed use of round beams for increasing the luminosity in colliders. The main idea of round beams is briefly discussed. Numerical simulations of round colliding beams for the Tevatron are much in favor of round beams, because they provide reduction of harmful impact of beam-beam forces on beam sizes, particles diffusion and better stability with respect to errors and imperfections.

1 INTRODUCTION

The essential conditions of the round beams [1] are equality of horizontal and vertical emittances $\varepsilon_x = \varepsilon_y = \varepsilon$, beta functions at interaction point (IP) $\beta_x = \beta_y = \beta$, and tunes $\nu_x = \nu_y = \nu$. Consequently, the transformation matrix in between of IP's can be generally presented in the form of

$$R(\phi) \cdot \begin{pmatrix} T & 0 \\ 0 & T \end{pmatrix}$$

(where T is a 2×2 matrix with $detT = 1$ and R is the matrix of rotation over an angle ϕ), therefore, the rotational symmetry of the kick from the round opposite beam, complemented with the $X - Y$ symmetry of the betatron transfer matrix between the collisions, result in an additional integral of motion $\mathcal{M} = xy' - yx'$ that is longitudinal component of the angular momentum. Thus, the transverse motion becomes equivalent to a one dimensional (1D) motion. Resulting elimination of all betatron coupling resonances is of crucial importance, since they are believed to cause the beam-lifetime degradation and blow-up. The reduction to 1D motion makes impossible the diffusion through invariant circles. Moreover, the beam-beam parameter for the round beams $\xi_{x,y} = \frac{N r_0}{4\pi\gamma\varepsilon}$, does not depend on s because the emittance $\varepsilon = \sigma^2/\beta$ is independent of the longitudinal coordinate. This leads to suppression of synchrobetatron resonances (one can find more detailed discussion of these questions in [2]).

One can expect, that for hadron colliders, where the beams are almost round from the beginning, the most useful predicted properties of the Round Colliding Beams (RCBs) lead to their better stability, lower losses and longer beam lifetime.

* Operated by Universities Research Association, Inc., under Contract No. DE-AC02-76CH03000 with the US Department of Energy

2 BEAM-BEAM SIMULATIONS WITH ROUND BEAMS IN TEVATRON

2.1 *Beam-beam simulation code and parameters of the Tevatron upgrade*

We employ a recently developed beam-beam simulation code BBC Ver.3.3 [3] developed by K.Hirata for the beam-beam interaction in "weak-strong regime" which is close to conditions of the Tevatron collider upgrade named TEV33 [4] where proton bunch population is several times the antiproton one. The "weak" (antiproton) bunch was presented by number of test particles, while the "strong" (proton) bunch appeared as an external force of Gaussian bunch.

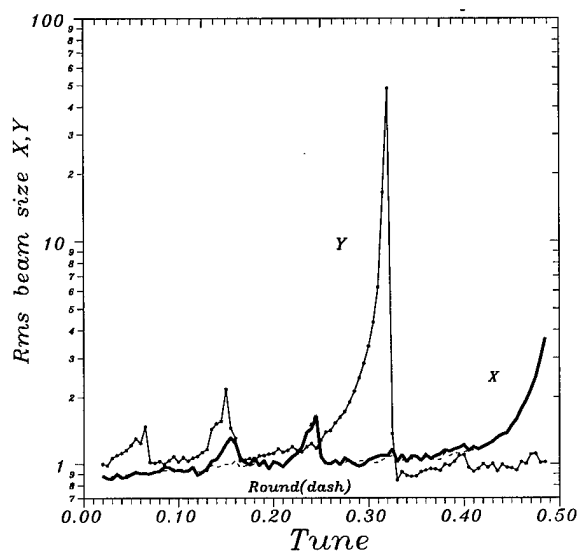

Figure 1: The rms beam size σ/σ_0 vs betatron tune $\nu_y = \nu_x = \nu$ for the round beams (dashed line), and the rms horizontal and vertical sizes $\sigma_{x,y}/\sigma_{0\,x,y}$ for non-round beams (solid and marked lines, respectively). ($\xi = 0.05$, $\Delta\vartheta = 0.002$, 50,000 turns).

Typically we tracked 100 (maximum 1000) test particles through five slices of strong bunch for (50-100)$\cdot 10^3$ turns. 50,000 turns in Tevatron correspond to about 1 s, some 200 synchrotron oscillation periods. No damping due to radiation or cooling is assumed to play role in the beam dynamics. Further increase of the number of particles or number of slices gave almost identical results.

The code outputs of greatest practical utility are luminosity, rms beam sizes and maximum betatron amplitudes which any of the test particles attained during tracking. These outputs are given with respect to unperturbed values, e.g. sizes and amplitudes are divided by their design rms values $\sigma_{x,y}/\sigma^0_{x,y}$ and $A^{max}_{x,y}/\sigma^0_{x,y}$, the luminosity is pre-

sented by the reduction factor of $R = L/L_0$ where the bare design luminosity $L_0 = f_0 N_p N_{\bar{p}}/(4\pi\sigma_x^0\sigma_y^0)$ and f_0 is the rate of collisions. The relevant parameters of the simulations were chosen close to the TEV33 design ones.

We present here the results for the RCB scheme without rotation of betatron oscillations axis, although other schemes proposed originally for electron damping rings require such rotation, i.e. strong $x - y$ coupling. The comparison of the different schemes is made partly in [2].

2.2 *Comparison of RBs and non-RBs. Random tune modulation.*

In order to make more realistic simulations we use noisy betatron phases jumps. The reason is that the weak resonances of high orders are usually not well seen after a small number of revolutions and in order to enhance them we used a method of the Ornstein-Uhlenbeck tune modulation (see, for example [5]) with correlation time of 100 turns.

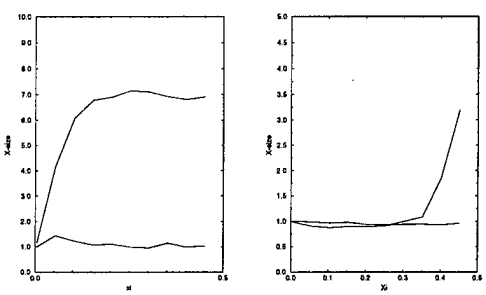

Figure 2: Beam size after 50,000 turns versus ξ. The upper curve corresponds to the short strong Gaussian bunch, the lower one — to the strong counter bunch with the "inverse beta-function" distribution. The beta-function at IP is 25 cm. **a** – left figure – tunes are equal to $\nu_x = \nu_y = -0.01$; **b** – right figure – tunes are equal to 0.05.

Now, with use of small noisy phase modulation (the parameter $\Delta\vartheta$ with the meaning of maximum changing of phase per turn in the Ornstein-Uhlenbeck process is equal to 0.002) , we compare the rms beam sizes after 50,000 turns for the round beams and the beams which are far from round. The colliding round beams satisfy to all the conditions:

$\varepsilon_x = \varepsilon_y = 3 \cdot 10^{-9}$ m· rad;

$\beta_x^* = \beta_y^* = 25$ cm; $\nu_x = \nu_y = \nu$,

while the "not-RBs" break them all:

$\varepsilon_x = 5/3\varepsilon_y = 5 \cdot 10^{-9}$ m· rad;

$\beta_x^* = 35/25\beta_y^* = 35$ cm; $\nu_x = \nu$; $\nu_y = \nu + 0.18 \neq \nu_x$.

As the result, the maximum X, Y betatron amplitudes (see Fig.1) for the non-round beams are larger than the amplitude at the RBs case. Several strong resonances are seen in the non-RB curves while the RBs perform only the size increase at $\nu = 0.25$.

2.3 *Simulations with "inverse beta function" charge distribution. Optimum bunch length.*

Everywhere above we deal with 2D motion, which can be reduced to 1D motion due to the angular momentum conservation. But 1D motion with the time-dependent Hamiltonian, generally speaking, is also stochastic, although it has more "regularity" in comparison with a general 2D motion. What we need to make the motion regular, is one more integral of motion for any value of the first one (angular momentum). It was proved in [6], that we obtain additional integral of motion if we take the betatron tunes near integer or half-integer resonance and the longitudinal charge distribution of the strong bunch (e.g. proton one in the Tevatron) proportional to the inverse β-function (one can find additional details of this system in [2]):

$$f(2s) = C/\beta(s) = C/(\beta^* + s^2/\beta^*), \qquad (1)$$

where C is a constant, β^* is the β-function value at the IP.

The beam-beam interaction of the bunches with the "inverse beta function" longitudinal charge distribution can provide integrable dynamics and better stability. We compare the behavior of such beams with the case of short round Gaussian colliding bunches at two working points. Note, that transverse sizes, bunch intensities, the weak bunch length of 15 cm and $\beta^* = 25$ cm are the same in both cases. Fig.2.2a presents the beam size growth vs. ξ after 50,000 turns for $\nu = -0.01$.

From the upper curve one can see significant growth of the beam sizes of the short bunches with increase of ξ, while there is almost no effect for the integrable case (in fact, we allowed about 10% deviation of the longitudinal charge distribution in the strong bunch from the exact $1/\beta(s)$ solution) – see the lower curve. There is only a small growth at $\xi \simeq 0.1$; if the charge distribution differs by about 1% from $1/\beta(s)$ then there are no peaks at all and the beam size is not changing in time (this trivial result is not presented).

The second working point of $\nu = 0.05$ looks better for the both cases and Fig.2.2b shows a significant difference between the two cases only for large ξ.

If it's difficult to make such a distribution function, one can choose the best ratio of the length of the Gaussian bunch and beta-function at IP (the previous results for the Gaussian bunch were obtained with a very short strong beam). This optimum length depends on the working point. For better understanding of this fact, one can imagine a simple model of the "flat-top" (or rectangular) charge distribution over the full length of l and with phase advance over half-turn equal to $d\psi = ds/\beta_0 = l/2\beta_0$, where β_0 is beta-function at IP. Let's assume, that the beta function is almost constant over the bunch length $\beta(s) \approx \beta_0$ and the longitudinal distribution is a constant within the coordinate interval of $\pm l/2$ and vanishes elsewhere (as well as the transverse kick) and in between of the tail of one bunch and the head of another we have the unity transformation I of the betatron variables , then one can leave out the arcs and connect kicks from all our bunches together. As here is no dependence of the force on time so this dynamical system is integrable and has no resonances, so we have an optimum in beam lifetime for presented above relation of the phase advance and bunch length.

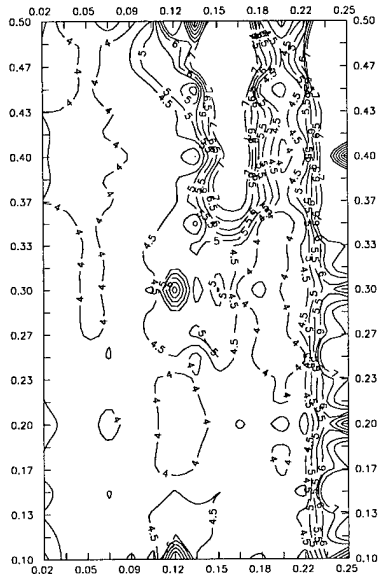

Figure 3: Contour plot of maximum betatron amplitude A_{max}/σ_0 vs rms bunch length σ_s and tune $\nu_y = \nu_x = \nu$, $\xi = 0.05$, $\Delta\vartheta = 0.002$, 75,000 turns.

We performed a search for optimal σ_s over tunes of $\nu_x = \nu_y = \nu = 0.02...0.25$ – see Fig.2.3 with the contour plot of the maximum betatron amplitude A/σ_0 vs. σ_s and ν (75, 000 turns, ξ =0.05, $\beta^* = 25$ cm, phase modulation of $\vartheta = 0.002$). The optimal bunch length (at which, say, $A/\sigma_0 \simeq 4$) depends on the tune and is about 30 cm for the tune around 0.2, about 20 cm for the tune around 0.12, and about 40 cm for the area of a good lifetime near the integer resonance. The last one corresponds to formula $\sigma \simeq \sqrt{2}\beta^*$. One of the probable explanations of that relation can be that the first terms in Taylor expansion of the Gaussian distribution $f(s) \propto \exp -s^2/2\sigma_s^2$ and the "inverse beta function" distribution $f(s) \propto 1/(1+(s/2\beta^*)^2)$ are equal if $\sigma_s = \sqrt{2}\beta^*$. It is interesting to note, that similar results on the optimum bunch length were observed in RCBs simulations for electron-positron colliders [7].

2.4 *Asymmetry between two IPs*

The degradation of the collider performance due to beam-beam effects is often thought to be more significant if there are several asymmetric interaction points. Fig.4 present results of the maximum amplitude simulations for the scheme with two IPs. If one denotes the phase advance between the first IP and the second one as ν and between the second one and the first one as $\nu + \Delta\nu_{1,2}$ then the horizontal axis is for ν and the vertical axis is for $\Delta\nu_{12}$. The lighter areas correspond to smaller maximum betatron amplitude after 10,000 turns, the contour spacing goes as follows: (A_{max}/σ_0)=4, 5, 7, 10, 15, 20, 25, 30, 40, 50.

It is interesting to note, that over large tune space the optimum in A_{max} lays out of the condition of symmetry, i.e. at $\Delta\nu_{12} \neq 0$.

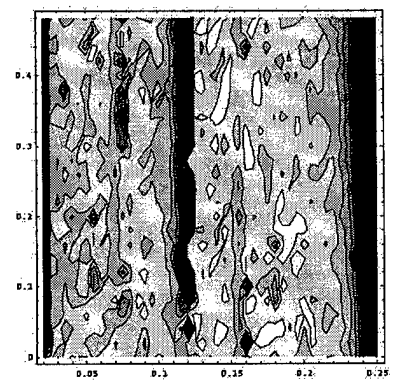

Figure 4: Contour plot of the maximum betatron amplitude vs. tune ν (horizontal axis and the tune difference between two IPs $\Delta\nu_{12}$ (vertical axis) for the round beams. $\Delta\vartheta$ = 0.002, 100,000 turns.

3 CONCLUSION

In this article we studied new ways to improve single particle stability in colliders. From the simulations we conclude that in the presence of the beam-beam interaction, the round beams show better particle stability and slower transverse diffusion rates than not-round beams. We also performed a search for optimum bunch length and investigated the "inverse beta-function" longitudinal distribution and found a qualitative agreement with theoretical predictions.

The model we used in our simulations is not quite adequate to the Tevatron due to some evident reasons, and for further investigations of beam-beam effects we plan to study the influence of non-linearities outside the IP, consequences of the RCBs implementation for intrabeam scattering issues and for the effects of the parasitic interactions.

Authors thank K. Hirata(KEK) for an opportunity to use his simulation code. We sincerely acknowledge numerous and fruitful discussions with E. Perevedentsev, I. Nesterenko, D. Shatilov, Yu. Shatunov and P. Ivanov (Novosibirsk INP), J. Marriner, D. Finley and L. Michelotti (FNAL), R. Talman and E. Young (Cornell), T. Sen (DESY), Ya. Derbenev (Michigan University, Ann-Arbor) and J. Cary (University of Colorado, Boulder). We are thankful to E. Perevedentsev for careful reading of the manuscript and numerous corrections.

4 REFERENCES

[1] V.V.Danilov, *et. al, Proc. EPAC'96*, Barcelona (1996), p.1149.

[2] V. Danilov, V. Shiltsev, FNAL FN-655 (1997).

[3] K.Hirata,*et. al, Part. Accel.*, v.40 (1993), p.205.

[4] J.P.Marriner, FERMILAB-Conf-96/391 (1996).

[5] T. Sen, J.A. Ellison, *Part. Acceler.*, v.55 (1996), p.[293]/47.

[6] V.V. Danilov, E.A. Perevedentsev. *Proc. ICFA Workshop on Beam-Beam Effects*, Dubna, Russia (1995).

[7] S. Krishnagopal, R. Siemann, *Proc. of 1989 IEEE PAC*, p.836.

A STUDY ON BEAM-BEAM INTERACTIONS FOR BTCF

C. Zhang, N. Huang, IHEP, Beijing, China
K. Hirata, KEK, Tsukuba, Japan

Abstract

A study on beam-beam interactions in the proposed Beijing Tau-Charm Factory (BTCF) is carried out. Various parameters of the collider, such as tunes, beam-beam parameters, bunch length, beta functions at the interaction point (IP), crossing angle and vertical dispersion at IP, are examined. It is concluded that with the optimized parameter set, the luminosity goal of BTCF is feasible.

1 MOTIVATION

BTCF is a double-ring electron-positron collider working in the τ lepton and charm meson energy region of 3~5 GeV [1]. The target peak luminosity is $1\times10^{33}cm^{-2}s^{-1}$. The parameters of BTCF closely related to the beam-beam effects are listed in Table 1.

Table 1: BTCF parameters related to beam-beam effects.

Parameter	Crossing Angle	Monochromator
E (GeV)	2.0	1.55
C (m)	385.447	
β_x/β_y (m)	0.65/0.01	0.01/0.15
D_y^* (m)	0	±0.35
$Q_x/Q_y/Q_s$	11.8/12.6/0.068	13.08/11.11/0.057
ϵ_x/ϵ_y $(nm\cdot rad)$	153/2.3	48/4
σ_e (10^{-4})	5.84	8.0
σ_z (cm)	0.76	1.0
$\tau_x/\tau_y/\tau_e$ (ms)	30/30/15	25/59/95
ξ_y	0.04	0.015
ϕ_c $(mrad)$	2.6	0
N_b	86	29
I_b (A)	0.57	0.2
L_0 $(10^{33}cm^{-2}s^{-1})$	1	0.1

It can be found from the Table 1 that the beam-beam interactions in BTCF have following features in comparison with other machines like B-factories [2]: (1) with lower beam energy and larger damping ratio $\tau_{x,y,e}/T_0$, T_0 being the revolution period, the beam-beam effects get stronger for the same ξ; (2) for the longer bunch ($\sigma_z/\beta^* \sim 1$) and higher synchrotron tune, the synchro-betatron coupling gets more important; (3) the variety of collision fashions with crossing angle and vertical dispersion at IP makes the beam-beam behavior in the BTCF varied and interesting.

2 ISSUES WITH BEAM-BEAM INTERACTIONS

The luminosity in a collider is expressed as

$$L(cm^{-2}s^{-1}) = 2.17\times10^{34}\frac{\xi_y(1+r)}{\beta_y^*(cm)}I_b(A)E(GeV), \quad (1)$$

where I_b is current per beam and $r = \sigma_y/\sigma_x$ defines the beam aspect ratio.

As the bunches have a finite length, the β functions at the positions where the different parts of the bunches meet are different ("hour glass" effect). Furthermore, crossing angle brings another geometrical effect to the luminosity reduction. The luminosity reduction due to the final bunch length and crossing angle is given by [3]

$$\frac{L_g}{L_0} = \sqrt{\frac{2}{\pi}}\, a\, e^b\, K_0(b), \quad (2)$$

where K_0 is the modified Bessel function, a and b are defined as

$$a = \frac{\beta_y^\star}{\sqrt{2}\sigma_z}\cos\phi_c, \quad (3)$$

and

$$b = a^2[1+(\frac{\sigma_z}{\sigma_x}\tan\phi_c)^2]. \quad (4)$$

The horizontal flat beam ($\sigma_y \ll \sigma_x$) is assumed in eq.(2). In the case of the vertical flat beam ($\sigma_x \ll \sigma_y$), the subscript "y" in eq.(3) should be replaced with "x". On the other hand, the eq.(4) is applied to horizontal crossing scheme, while in the case of vertical crossing, the subscript "x" should be replaces with "y".

Above discussion on the beam-beam issues is based on a simplified model and linear approximation. In reality, the beam-beam effects are much more complicated. The computer simulation is necessary in order to study the complexity of the nature for beam-beam interactions. The simulation is performed by taking advantage of the computer code BBC (Beam-Beam interaction with a Crossing angle) developed by K.Hirata.

The algorithm applied in the code is detailed in the reference [3]. The simulation takes the machine parameters listed in Table 1. In our weak-strong simulation, the distribution of weak beam changes due to the beam-beam interaction, while the strong beam remains Gaussian. The distribution of the weak beam is obtained by simulation as the sum of δ-functions, which represent the ensemble of particles. The simulated luminosity is computed as a convolution of the distribution function of both weak and strong beams.

3 BEAM-BEAM TUNE SCAN

The purpose of beam-beam tune scan is to examine the design luminosity and to optimize the tunes. Figure 1 gives the simulated luminosity scanned on the (fractional) tune plane $\delta Q_x \in (0,1)$, $\delta Q_y \in (0,1)$ for ϕ_c = 2.6 mrad. The mash size is 0.025, which is smaller than the synchrotron tune Q_s = 0.069. In the figure, the magnitude of luminosity is presented with the gray scale. The darker the gray

0-7803-4376-X/98 /$10.00 © 1998 IEEE

is, the higher the luminosity gets. The contour spacing is $5\times10^{31}cm^{-2}s^{-1}$. The luminosity reduction due to the beam-beam driven resonances of $\nu_x \pm \nu_s = k, 2\nu_x \pm \nu_s = k, \nu_y \pm \nu_s = k, 2\nu_y \pm \nu_s = k, 2\nu_x \pm 2\nu_y \pm \nu_s = k$, k being integer, is indicated in Figure 1. The simulation is also done when ϕ_c=0, and the results show that it is hard to find the difference between them. This means that the effect of the crossing angle of 2×2.6 mrad is small enough.

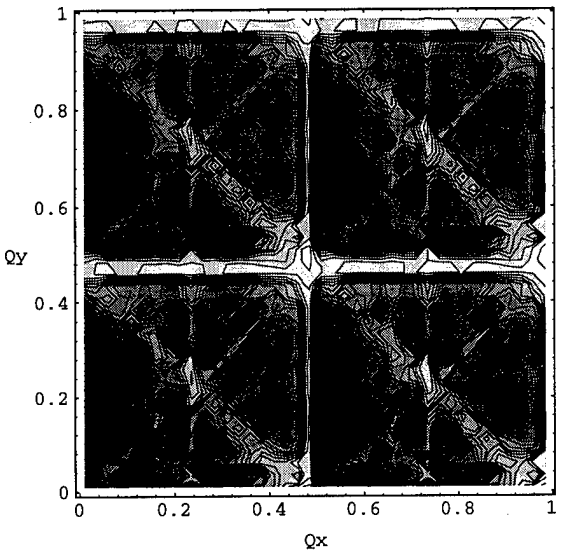

Figure 1: Tune scan for ϕ_c=2.6 mrad.

4 BEAM-BEAM PARAMETERIZATION

4.1 Beam-beam parameter

It can be found from eq.(1) that the larger the beam-beam parameter ξ_y reaches, the higher the luminosity can be obtained. However, the maximum value of ξ_y is limited by the beam-beam interaction. The simulation shows that the vertical beam blow-up takes place for ξ_y above 0.02. The blow-up factor is 1.1∼1.2 for the design value of ξ_y=0.04. The relative luminosity keeps above the analytic values of the luminosity for $\xi_y \in$ (0,0.05) at the tunes of δQ_x=0.53 and δQ_y=0.60. This is understood as the dynamic β effect. The simulation confirms the design value of ξ_y=0.04 is reasonable with certain safety margin.

4.2 Crossing angle

A crossing angle of 2×2.6 mrad is chosen for the BTCF in order to make it possible to increase the bunch number. However, the collision with the crossing angle will not only cause the geometric luminosity reduction, referring to eq.(2)-(4), but also influence on the synchro-betatron coupling. The question remains how large the crossing angle is acceptable. Figure 2 displays the simulated luminosity and vertical beam size as functions of crossing angle. It is revealed in Figure 2 that the vertical beam size increases rapidly when the crossing angle is larger than 4 mrad and the luminosity reduction occurs. However, the slope of the luminosity reduction is smaller than the beam blow-up rate. This is explained as the non-Gaussian tail, which may largely influence the rms beam size, while the luminosity is still dominated by the beam core. The simulation shows that for the design crossing angle ϕ_c=2×2.6 mrad the luminosity reduction is only a few percent.

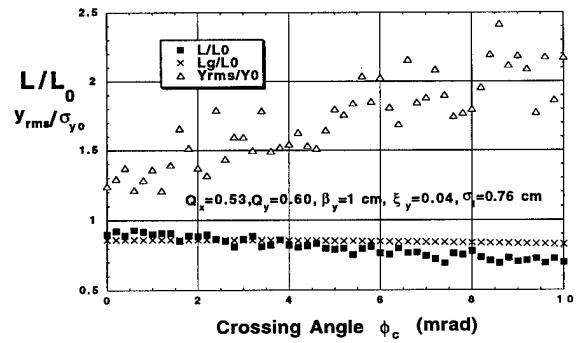

Figure 2: Luminosity and vertical beam size vs. ϕ_c.

4.3 Bunch length

The simulated luminosity as a function of bunch length is shown in Figure 3. It can be found from the figure that the simulated luminosity is close to the analytic values calculated with eq.(4) for $\beta_y^*/\sigma_z \approx 1$ (β_y^*=1 cm). At the design value of bunch length σ_z=0.76 cm, the luminosity $L \approx L_0$ is expected. However, if the bunch length gets to 1.25 cm, the luminosity reduces to $0.8L_0$ according to the simulation. In order to maintain the good luminosity, the bunch lengthening for various reasons should be avoided.

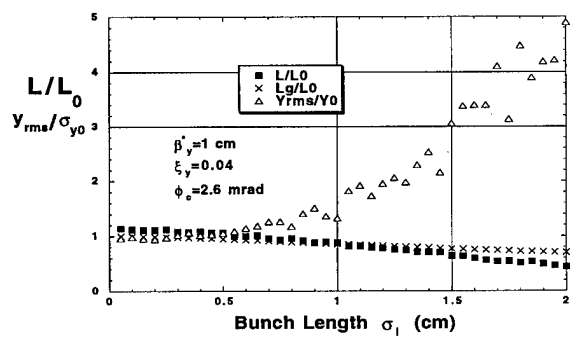

Figure 3: Luminosity and vertical beam size vs. σ_z.

5 MONOCHROMATOR

The monochromator mode provides a narrow center-of-mass energy spread in the collider. This is achieved by means of opposite orbit dispersion of electron and positron beams. The vertical dispersion functions at the IP is chosen as $D_y^{e+,e-}$ = 0.35 ,-0.35m for the BTCF monochromator. The large dispersion function makes the vertical beam size dominated by the orbit dispersion $\sigma_y/\sigma_{y\beta} \simeq 11$ and vertical flat beam $\sigma_y/\sigma_x \simeq 13$ in the monochromator. A particle with the betatron amplitude y and momentum error of δ receives a dipole kicker of -$4\pi\xi_y(y + D_y^*\delta)/\beta_y^*$ from the opposite beam. This momentum dependent beam-beam kick may drive the synchro-betatron resonance.

The tune scan is done based on the parameters listed in Table 1. The mesh size of 0.025 is smaller than Q_s = 0.057, the vertical beam-beam parameter is chosen as 0.015. Figure 4 pictures a 3-dimensional vertical betatron beam size

on the $Q_x - Q_y$ plane. The resonance lines of $Q_y \pm Q_s = k$, $2Q_y \pm Q_s = k, 3Q_y \pm Q_s = k, 4Q_y \pm Q_s = k$ are clearly seen in the figure, where k is integer.

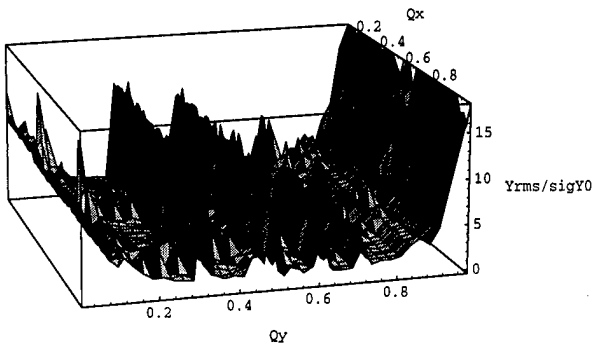

Figure 4: Vertical beam size scan on $Q_x - Q_y$ plane.

The beam size blow-up can be reduced by a careful choice of the tunes. As the design tunes are in the region of (0,0.5), we choose Q_x=0.08 and Q_y=0.11 for the further study.

Figure 5 displays the luminosity and beam size vs. the vertical beam-beam parameter. Although the vertical beam size increases about linearly with ξ_y, the luminosity does not reduce obviously at the chosen tunes of Q_x=0.08 and Q_y=0.11. The design beam-beam parameters ξ_y=0.015 and ξ_x=0.014 sit at a quite comfort region where no significant blow-up takes place and the luminosity is close to the analytic value.

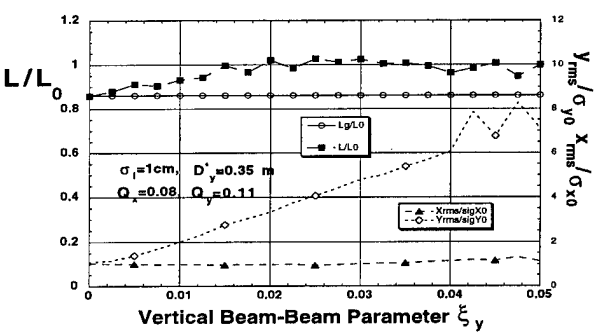

Figure 5: Luminosity and beam size vs. ξ_y for D_y^*=0.35m.

The luminosity and beam size as functions of vertical dispersion are shown in Figure 6. The simulation has shown a possibility to increase the vertical dispersion, say to 0.5 m, in the case of the optimized tunes and other parameters from the viewpoint of beam-beam interaction. The primary study on beam-beam effects shows that it is possible to get the goal luminosity of monochromator mode.

6 PARASITIC BEAM-BEAM EFFECTS

The multi-bunch collision will cause the parasitic beam-beam interaction. In the BTCF, there are seven and two parasitic crossings symmetrically located on either sides of the IP in the crossing angle scheme and monochromator respectively. The tune shift ΔQ_x, and ΔQ_y experienced by

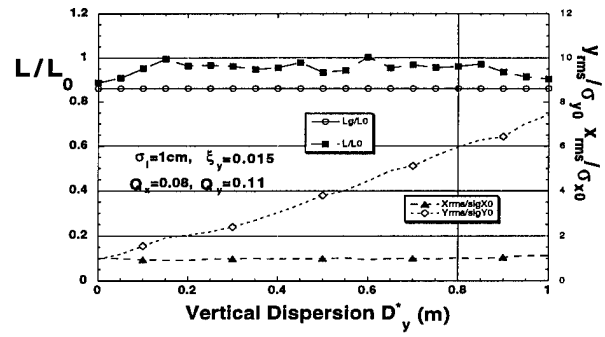

Figure 6: Luminosity and beam size vs. D_y^*.

a particle at the center of the bunch from a single parasitic IP are given by [4]:

$$|\Delta Q_{x,y}| = \frac{n_b r_e \beta_{x,y}^{pc}}{2\pi\gamma(2d)^2} \tag{5}$$

where n_b is particles per bunch, $d = (d_x^2 + d_y^2)^{1/2} \gg \sigma_{x,y}$, d_x and d_y being the half distances between two beams in the horizontal and vertical planes respectively. Parasitic beam-beam force may also disturb closed orbits. As a zeroth order evolution of the effect, the Temnykh parameter B is derived from the measurement at CESR [5] with some modifications.

$$B = \frac{10372}{\gamma} \frac{10 n_b}{1.6 \times 10^{11}} \sqrt{\sum_i^{n_{pc}} (\frac{\beta_y^{pc} \sigma^2}{(2d)^2})_i^2} \quad , \tag{6}$$

where σ is the relevant beam size.

The parasitic beam-beam parameters for the crossing angle scheme and monochromator are given in Table 2. According to the experience of CESR, $B \leq 10$ is considered to be safe. The parameters shown in Table 2 are believed to be conservative. However, there is only a little experience in this aspect, we intend to carry on relevant simulation and machine studies with BEPC.

Table 2: Parameters for the parasitic beam-beam interaction.

Parameter	Crossing Angle	Monochromator
E (GeV)	2.0	1.55
I_{bunch} (mA)	6.6	7.1
$N_b\ 10^{10}$	5.3	5.7
$2\phi_c$(mrad)	2×2.6	0
$\sum \Delta Q_x (10^{-3})$	-3.44	8.44
$\sum \Delta Q_y (10^{-3})$	-0.46	-10.8
B	7	6

7 REFERENCES

[1] BTCF, IHEP-BTCF Report-03 (1996).

[2] PEPII, SLAC-418, (1993); KEKB, KEK Report, 95-7 (1995).

[3] K.Hirata, Phys. Rev. Lett 74, 2228 (1995).

[4] J.L. Tenneson, ABC Note 28 (1991).

[5] A.Temnykh and J. Welch, Proc. PAC'95 (1995).

DISPERSION IN THE INTERACTION POINT

S. Petracca*, Dip. di Scienze Fisiche E.R. Caianiello, Univ. of Salerno and I.N.F.N. Salerno, Italy
and
K. Hirata†, KEK, High Energy Accelerator Research Organization, Tsukuba 305, Japan

Abstract

In the presence of a dispersion at the interaction point, the betatron and the synchrotron oscillations affect each other. Just as linear effects, the beam-beam kick modifies the synchrotron tune, the bunch length, the energy spread etc, as well as the betatron tune and the Twiss parameters. Dispersion is no longer enough to describe the coupled dynamics and we needs two more parameters.

1 INTRODUCTION

The dispersion is a dangerous concept. Usually [1, 2], it is defined in terms of the closed orbit ($\mathbf{x}_0$) in the betatron phase space of a fictitious particle with a constant energy ($D \equiv [\mathbf{x}_0(E)-\mathbf{x}_0(E_0)]/(E-E_0)$). Once upon a time, this was a good definition with a full physical meaning for the coasting beam accelerators. In modern accelerators with RF cavities, particularly in electron rings, however, no particle has a constant energy. The dispersion defined as above is a kind of a limiting concept which has a physical meaning only in the limit with a vanishing synchrotron tune: $\nu_s \to 0$. If it was a useful concept, why do not we define "bispersion" as a closed orbit difference in the synchrotron phase space for a particle with a fixed slope (y')?

To discuss the interaction between betatron and synchrotron motions, we should use concepts consistent with the synchrotron motions. Otherwise, our discussion will become quite complicated and we might need an acrobatic manipulation of logics to be accurate. (It is something like to discuss quantum mechanics using classical concepts).

The effects of dispersion at the interaction point (IP) has been studied for long time [3, 4]. The synchrotron motion was assumed to be unaffected and the interest was only on the effect of synchrotron motion on the betatron motion. There are several reasons to study it more carefully now. First of all, the monochromatic collision[5] became an important and practical issue for tau-charm factories. In addition, for future high performance colliders, we need more detailed controle of dispersion and a deeper knowledge of it.

This paper is organized as follows. In Sect. 2 we discuss the factorization of a general 4×4 symplectic matrix. Then in Sect. 3, the one-turn map is parametrized for the case with dispersion at the IP. Conclusions follow under Sect. 4.

* Also KEK as a Fellow of the Canon Foundation Europe.
† Also Univ. of Salerno as a Visiting Researcher.

2 GENERAL 4×4 SYMPLECTIC MATRIX AND ITS FACTORIZATION

It is well known that any stable symplectic 2×2 matrix m can be represented as[1]

$$m = t\begin{pmatrix} \cos\mu & \sin\mu \\ -\sin\mu & \cos\mu \end{pmatrix} t^{-1}, \tag{1}$$

where $\mu = 2\pi\nu$, ν being the tune. Here

$$t = \begin{pmatrix} \sqrt{\beta} & 0 \\ -\alpha/\sqrt{\beta} & 1/\sqrt{\beta} \end{pmatrix}.$$

In Ref. [6], it was shown that any stable symplectic 4×4 matrix M can be factorized as follows:

$$M = H\, diag(m_u, m_v)\, H^{-1}, \tag{2}$$

where

$$H = \begin{pmatrix} bI & h \\ \tilde{h} & bI \end{pmatrix}, \quad h = \begin{pmatrix} \zeta & \eta \\ \zeta' & \eta' \end{pmatrix}, \tag{3}$$

and $m_{u(v)}$ is m in Eq.(1) with suffices of $u(v)$ for μ, α and β. Here, h is a 2×2 matrix and

$$\tilde{h} = jh^t j = \begin{pmatrix} -\eta' & \eta \\ \zeta' & -\zeta \end{pmatrix}, \quad j = \begin{pmatrix} 0 & 1 \\ -1 & 0 \end{pmatrix}.$$

Here, $b = \sqrt{1-\det(h)}$ is a constant. Note that H, as well as M, is symplectic in 4-dim sense:

$$H^t J H = J, \quad J = diag(j, j).$$

The 4×4 symplectic matrix has 10 free parameters. The u and v modes have 3 parameters each (ν, α, β). We need 4 parameters, η, η', ζ, and ζ' to characterize the coupling between two degrees of freedom.

In Ref.[7], it was shown that when the dispersion D vanishes in cavities, then η is identical to D and ζ vanishes all over the ring. For more general cases, D and D' are not sufficient and we need h, in particular ζ and ζ'. To be precise,

$$\lim_{\nu_x\to0} h = \begin{pmatrix} 0 & D \\ 0 & D' \end{pmatrix}. \tag{4}$$

We thus call η the (generalized) dispersion.

The normal modes (u, u') and,(v, v') are defined as

$$(u, u', v, v')^t = diag(t_u^{-1}, t_v^{-1})\, H^{-1}\mathbf{x},$$

where $\mathbf{x}$ are 4-vectors (physical variable): $\mathbf{x}^t = (y, p, z, \delta)$. It seems convenient here to discuss the expressions of the

0-7803-4376-X/98 /$10.00 © 1998IEEE

beam sizes under the assumption that the beam envelope matrices for the normal modes are given as follows: $\langle u^2\rangle = \langle u'^2\rangle = \epsilon_u$, $\langle v^2\rangle = \langle v'^2\rangle = \epsilon_v$, and $\langle uu'\rangle = \langle vv'\rangle = \langle uv\rangle = \langle uv'\rangle = \langle vu'\rangle = \langle u'v'\rangle = 0$. At a glance, one can get, for example,

$$\begin{aligned}
\langle y^2\rangle &= b^2\beta_u\epsilon_u + \{\eta^2 + (\beta_v\zeta - \alpha_v\eta)^2\}\beta_v^{-1}\epsilon_v \\
\langle p^2\rangle &= b^2\gamma_u\epsilon_u + \{\eta'^2 + (\beta_v\zeta' - \alpha_v\eta')^2\}\beta_v^{-1}\epsilon_v, \\
\langle z^2\rangle &= \{\eta^2 + (\alpha_u\eta + \beta_u\eta')^2\}\beta_u^{-1}\epsilon_u + \beta_v b^2\epsilon_v \\
\langle \delta^2\rangle &= \{\zeta^2 + (\alpha_u\zeta + \beta_u\zeta')^2\}\beta_u^{-1}\epsilon_u + b^2\gamma_v\epsilon_v, \\
\langle yp\rangle &= -\alpha_u b^2\epsilon_u + \{\gamma_v\eta\eta' - \alpha_v(\eta\zeta' + \zeta\eta') + \beta_v\zeta\zeta'\}\epsilon_v, \\
\langle yz\rangle &= -b(\alpha_u\eta + \beta_u\eta')\epsilon_u - b(\alpha_v\eta - \beta_v\zeta)\epsilon_v, \\
\langle y\delta\rangle &= b\beta_u(\alpha_u\zeta + \beta_u\zeta')\epsilon_u + b(\gamma_v\eta - \zeta)\epsilon_v,
\end{aligned} \tag{5}$$

where $\gamma = (1+\alpha^2)/\beta$.

3 BEAM-BEAM COLLISION

We assume that there is a single IP in the ring and there is a dispersion η_0. The revolution matrix from the IP to IP without the beam-beam kick is

$$M_{arc} = H_0\, diag(m_y^0, m_z^0)\, H_0^{-1},$$

where H_0 is H, Eq.(3), with h being replaced by

$$h_0 = \begin{pmatrix} 0 & \eta_0 \\ 0 & 0 \end{pmatrix},$$

$$m_y^0 = \begin{pmatrix} \cos\mu_y^0 & \beta_y^0\sin\mu_y^0 \\ -1/\beta_y^0\sin\mu_y^0 & \cos\mu_y^0 \end{pmatrix},$$

and m_z^0 being m_y^0 with y replaced by z. Note that for usual electron rings, we have $\nu_z < 0$. In the weak-strong picture the dynamics of the single (test) particle in the weak beam is influenced by the strong beam, which is not affected at all. In the linear approximation the particle receives a kick at IP from the strong beam. This interaction is described by the matrix

$$M_{bb} = \begin{pmatrix} 1 & 0 & 0 & 0 \\ -4\pi\xi_0/\beta_y^0 & 1 & 0 & 0 \\ 0 & 0 & 1 & 0 \\ 0 & 0 & 0 & 1 \end{pmatrix}, \tag{6}$$

which contains the vertical (nominal) beam-beam parameter ξ_0, viz., for Gaussian bunches:

$$\xi_0 = \frac{r_e}{2\pi\gamma}\frac{N\beta_y^0}{\sigma_y^0(\sigma_x^0 + \sigma_y^0)}, \tag{7}$$

N being the number of particles in the strong beam, r_e the classical electron radius, γ the relativistic factor, σ_y^0 the vertical beam size.

$$\sigma_y^0 = \left[\beta_y^0\epsilon_y^0 + \eta_0^2\epsilon_z^0/\beta_z^0\right]^{1/2}, \tag{8}$$

ϵ_y^0 and ϵ_z^0 are the vertical and longitudinal emittances, and all quantities are evaluated at the IP.

Now, the complete revolution matrix with the beam-beam collision is:

$$M = M_{bb}^{1/2} M_{arc} M_{bb}^{1/2}. \tag{9}$$

4 CHANGE OF OPTICS

For the tunes, we can get the explicit form easily[7]

$$2\cos\bar{\mu}_\pm = \cos\mu_y^0 + \cos\mu_z^0 - 2\pi\xi_0(\sin\mu_y^0 + \chi\sin\mu_z^0) \pm \sqrt{D}, \tag{10}$$

where

$$D = (\cos\mu_y^0 - \cos\mu_z^0 - 2\pi\xi_0(\sin\mu_y^0 - \chi\sin\mu_z^0))^2 + 16\pi^2\xi_0^2\chi\sin\mu_y^0\sin\mu_z^0, \tag{11}$$

and

$$\chi = \frac{\eta_0^2}{\beta_z^0\beta_y^0} \simeq \frac{\eta_0^2\sigma_\delta}{\sigma_z^0\beta_y^0} \tag{12}$$

is the synchrotron tune shift factor. The motion is stable if and only if $|\cos\bar{\mu}_\pm| \le 1$ and $D \ge 0$.

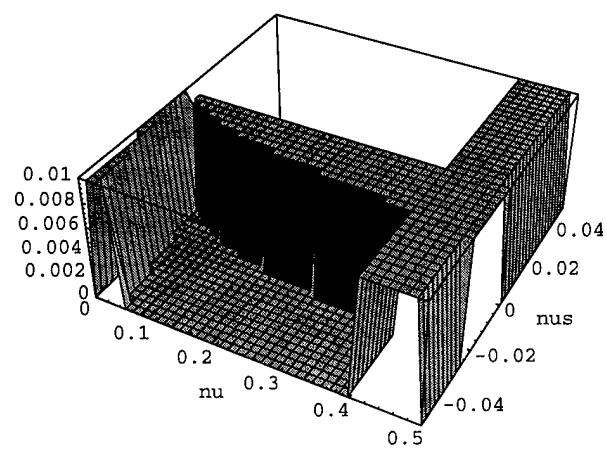

Figure 1: The (growthrate -1) at $\xi_0 = 0.05$, $\beta_y^0 = 0.1$m, $\beta_z^0 = 10$m and $\eta_0 = 0.5$m as a function of ν_y^0 and ν_z^0.

To lowest order in ξ_0, we get

$$\nu_y \to \nu_y + \xi_0, \quad \nu_z \to \nu_z + \xi_0\chi. \tag{13}$$

A synchrotron tune shift is thus predicted due to the combined effect of η_0 and ξ_0. The perturbative equation , Eq.(13), implies that the linear instability occurs for

- $\nu_y \lesssim$ half integers (betatron instability)
- $\nu_z \lesssim$ half integers (synchrotron instability).
- $\nu_z + \nu_y \lesssim$ integers (synchro-betatron instability).

The instability regions in the (ν_y^0, ν_z^0) plane is shown in Fig. 1, in terms of the growthrate. The three unstable regions stated above are clearly seen.

For other parameters, we get the exact values numerically. In particular, the change of η's and ζ's are of interest. At the middle of the IP, by symmetry reason, we have $\eta' = \zeta = 0$. In Fig.2, we show η as a function of ξ_0. (When $\nu_z^0 \lesssim 0$, M can become unstable and we do not get

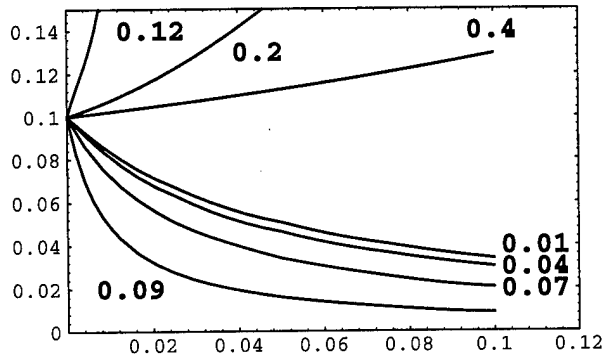

Figure 2: The dispersion η as a function of ξ_0 for several ν_z, with $\beta_y^0 = 0.1$m, $\beta_z^0 = 10$m, $\nu_y^0 = 0.1$, $\eta_0 = 0.1$m. For $0 \leq \nu_z^0 < 0.01$, the curve is almost identical with that for $\nu_z^0 = 0.01$.

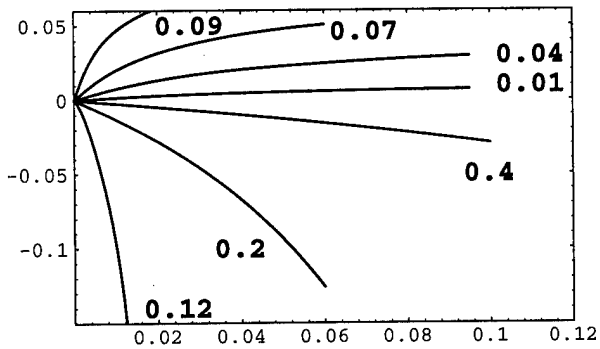

Figure 3: The ζ' as a function of ξ_0 for several $\nu_z^0 > 0$, all other parameters are the same as previous figure.

η. Outside the instability region, the $\eta(\nu_z^0)$ is the same as $\eta(-\nu_z^0)$.) Here, we see clearly, how the dispersion depends on ν_z. In Ref.[4], the evaluation of D at the IP was done as follows:

$$D(\xi_0) = D(0)/[1 + 2\pi\xi_0 \cot(\mu_y^0/2)].$$

This formula does not show the dependence on ν_z^0 and agrees only with the curve in Fig.2 for $\nu_z^0 = 0$. The deviation of η from D is remarkable for $\nu_z^0 \simeq \nu_y^0$.

For ζ', we show it in Fig.3 for $\nu_z^0 > 0$. We also see the remarkable growth of ζ' in particular for $\nu_z^0 \simeq \nu_y^0$. From Eq.(5), there seems to be a possibly dangereous growth of $\langle p^2 \rangle$ because of ζ'. Also from Eq.(5), the $\langle y\delta \rangle$ can be modified a lot which might affect the effective energy resolution of the monochromatic collision.

5 DISCUSSION AND CONCLUSION

Because of the synchrotron instability, $\nu_s = 0$ is one of the singular point of M. Thus, we should modify Eq.(4) as

$$\lim_{\nu_z \to 0_+} h = \begin{pmatrix} 0 & D \\ 0 & D' \end{pmatrix}.$$

The discussion based on D might be dangerous with synchrotron oscillations. As discussed in Ref.[7], D is a well defined concept even with the presence of the synchrotron oscillation as long as $D = D' = 0$ in cavities. By the beam-beam insertion, however, this condition can be violated even if it was so before the insertion. In such a case, if one insists D, (s)he might fall into an unsolvable confusion. The (generalized) dispersion η is a natural extension of D which (with ζ's) can work for general cases.

One might understand the change of ν_s as caused by the change of the momentum compaction factor α_m through the change of D all around the ring ($\alpha_m = \langle D/\rho \rangle$, ρ being the bending radius). It is similar to understanding the beam-beam tune shift ($\delta\nu_y$) as caused by the change of β_y all around the ring ($2\pi\nu = \int ds/\beta$), instead of looking at the eigenvalues. When the synchro-betatron coupling becomes large, in particular for the monochromatic collision, we can no longer use the traditional dispersion D which suited to the coasting beams and we should treat the optics more carefully and use more genaral formalism. There can be a factorization method of the the revolution matrix simpler and better than that discussed here. At least, however, it is unthinkable that we can treat coupled synchro-betatron oscillations with less parameters than the number of free parameters of the symplectic matrix (3,10, and 21 for 1d, 2d, and 3d problems).

6 ACKNOWLEDGEMENTS

The authors would like thank Dr. A. Piwinski for his kind communication to them and information on his early works on the dispersion effects. The Canon Foundation Europe is gracefully acknowledged for supporting S.P. during her stay at KEK as a Visiting Research Fellow. She also thanks the Members of the KEK Accelerator Theory Group for their hospitality and help. A part of this job was done when K.H. has been in the University of Salerno with the support of I.N.F.N. Salerno. He thanks I.N.F.N and the members of the "Dipartimento di Scienze Fisiche E.R. Caianiello" for hospitality.

7 REFERENCES

[1] E.D. Courant and H.S. Snyder, Ann. Phys. **3**, 1958, 1.
[2] M. Sands, SLAC-121(1970).
[3] A. Renieri, INF-75/6(R), February 1975.
[4] A. Piwinski, DESY 77/18, 1977; A. Piwinski, DESY Internal Bericht, DESY H1/71-1 (1971).
[5] J.M. Jowett, *Frontiers of Particle Beams: Factories with e+e- Rings*, eds. M. Denies, M. Month, B. Strasser, S. Turner, Springer Verlag, 1994; and references given in this paper.
[6] K. Ohmi, K. Hirata and K. Oide, Phys. Rev., **E-49**, 1994, 751.
[7] S.Petracca and K. Hirata, KEK Preprint 96-162 (1996). Wang, Part.Acc. **51**, 1995, 15.

EFFECT OF NOISE IN BEAM-BEAM INTERACTION

Yuri K. Batygin, The Institute of Physical and Chemical Research, Saitama, 351-01, Japan
Takeshi Katayama, Institute for Nuclear Study, University of Tokyo, Tokyo 188, Japan

Abstract

Beam-beam instability induced by random fluctuations in size of a strong beam has been studied both numerically and analytically. In contrast with stochastic particle motion due to overlapping of nonlinear beam-beam resonance islands, noise beam-beam instability exists at any value of beam-beam parameter. Two conditions are essential to initiate instability: beam-beam kick has to be a nonlinear function of coordinate and parameter of the kick has to be a subject of noise. Meanwhile, the value of beam emittance is conserved even in noise regime if beam-beam kick is a linear function of coordinate. It gives an idea to prevent beam-beam instability using linearization of beam-beam kick. Compensation scheme utilizing higher order component in field distribution of the focusing elements is suggested.

1 INTRODUCTION

One of the main problems in ion-ion circular colliders is a small value of achievable beam-beam tune shift ξ=0.005. Physical reason for beam-beam limitation is usually attributed to the excitation of a set of nonlinear resonances due to a periodic nonlinear kick in linear system. Overlapping of nonlinear resonances is an universal mechanism of stochastic particle instability in nonlinear systems [1]. Another mechanism of unstable particle motion is a diffusion, created by a noise [2-5]. This noise can exist, for example, due to mismatch of the beam with the channel. In this paper we study the noise which appears in an incoherent beam-beam interaction. As it is shown below, such a noise can induce beam-beam instability in much more simple conditions than the overlapping of nonlinear resonances. Due to the diffusion character, noisy beam-beam instability does not have a threshold character and can exists under any value of beam-beam tune shift.

2 NUMERICAL SIMULATION OF NOISE BEAM-BEAM INSTABILITY

Let us consider for simplicity a one-dimensional model, which is suitable to demonstrate main features of noise beam-beam instability. Results of this study are valid for a multi-dimensional problem as well. Particle motion is described in coordinates (x, p =β dx/dz), where β is a value of beta-function of collider. Between subsequent collisions particle experience linear matrix transformation with betatron angle $\theta = 2\pi Q$. Beam-beam interaction is treated as a thin lens with nonlinear beam-beam kick Δp_n:

$$\begin{pmatrix} x_{n+1} \\ p_{n+1} \end{pmatrix} = \begin{pmatrix} \cos\theta & \sin\theta \\ -\sin\theta & \cos\theta \end{pmatrix} \begin{pmatrix} x_n \\ p_n + \Delta p_n \end{pmatrix}. \qquad (1)$$

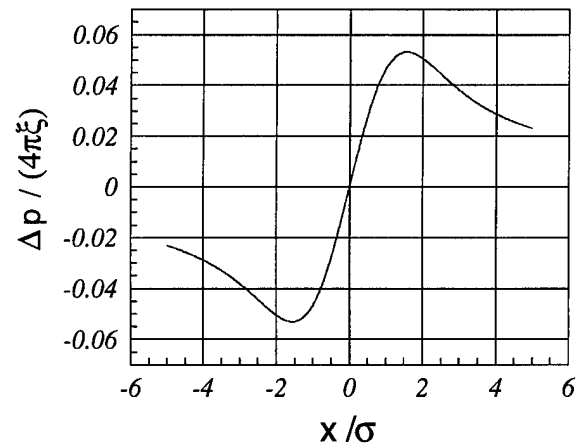

Fig. 1a

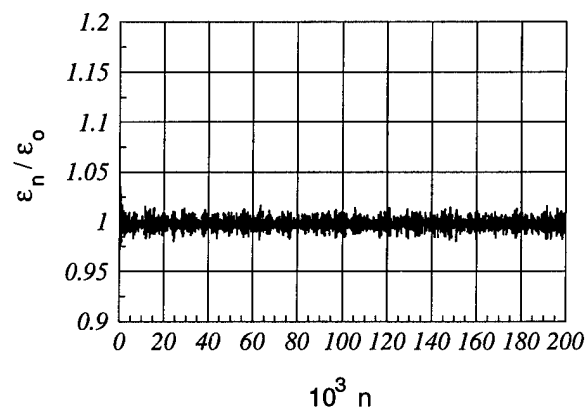

Fig. 1b

Fig. 1. Stable particle motion with the values of beam-beam tune shift ξ =0.005 and betatron tune Q=3.168: a) beam-beam kick, b) rms beam emittance.

Beam-beam kick Δp is expressed by a Gaussian function of coordinate x, beam-beam tune shift ξ, and size of the opposite beam σ:

$$\Delta p = -4\pi\xi x \frac{1 - \exp(-x^2/2\sigma^2)}{(x^2/2\sigma^2)}. \qquad (2)$$

Nonlinear kick (2) induces a set of nonlinear resonances, which are stable, until islands do not overlap each other. In Fig. 1 an example of stable beam-beam interaction in the vicinity of the 6th order resonance is presented. In simulations, one beam is presented as a collection of 3000 particles. Simulations are done for the value of betatron tune Q = 3.168, close to the 6th order resonance value 3.16666 (or 6Q=19). From the simulations it is clear that beam emittance is stable.

0-7803-4376-X/98 /$10.00 © 1998 IEEE

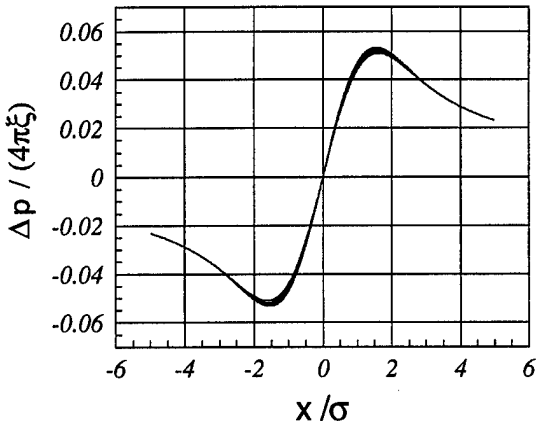

Fig. 2a

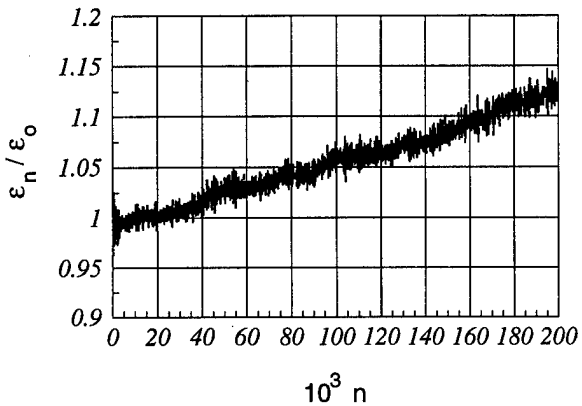

Fig. 2b

Fig.2. Beam-beam instability under 5% noise in the parameter σ during particle interaction with $\xi = 0.005$ and Q=3.168: a) beam-beam kick, b) rms beam emittance growth.

Another picture is observed if the parameter σ of beam-beam kick (2) is a subject of noise. In the calculations, presented in Fig. 2, parameters of the process are chosen to be the same as those in Fig.1, but standard deviation σ is changed from turn to turn according to the expression:

$$\sigma^{(n)} = \sigma^{(o)} \left(1 \pm \frac{u}{2} u_n\right) , \qquad (3)$$

where u is a noise amplitude and u_n is a random noise function within the interval (0,1). It corresponds to the noise in the size of the opposite beam, which can exist due to small beam mismatch with the channel. The value of noise amplitude u=0.05 is chosen arbitrary to demonstrate appearance of diffusion-type instability in the presence of small random perturbation of beam-beam kick. As shown in Fig. 2, this noise destroys the stability. In contrast with Fig. 1, beam emittance expand with time. Important feature of the noise regime is that this kind of instability can exist apart from the excitation of nonlinear resonances. Noise beam-beam instability appears if two conditions are met:

- beam-beam kick is a nonlinear function of coordinate
- parameter of beam-beam kick (beam standard deviation σ) is a subject of noise.

3 ANALYTICAL TREATMENT OF EFFECTIVE BEAM EMITTANCE GROWTH

Let us provide analytical estimations of emittance growth under noise beam-beam interaction. Transfer matrix after n turns with arbitrary momentum kick at every turn, Δp_i , is given by the expression [6]:

$$x_n = a \cos(n\theta + \Psi) + \sum_{i=0}^{n-1} \Delta p_i \sin(n-i)\theta ,$$
$$p_n = - a \sin(n\theta + \Psi) + \sum_{i=0}^{n-1} \Delta p_i \cos(n-i)\theta , \qquad (4)$$

where Ψ is the initial phase of oscillations. Random beam-beam kick (Δp_i) can be expressed as a function of unperturbed trajectory. It gives an approximate treatment of the problem, valid for small values of perturbation. Suppose that perturbation is a linear function of coordinate:

$$\Delta p_i = \delta_i x_i. \qquad (5)$$

We study evolution of the root-mean-square (rms) beam emittance $\varepsilon_n = 4\sqrt{\langle x_n^2\rangle \langle p_n^2\rangle - \langle x_n p_n\rangle^2}$, where brackets mean averaging on initial phases of particles. Calculation of beam emittance growth gives:

$$\frac{\varepsilon_n^2}{16} = \left[\frac{a^2}{2} + \frac{a^2}{4}\sum_{i=0}^{n-1}\delta_i^2\right]^2 -$$
$$- \left[\frac{a^2}{2}\sum_{i=0}^{n-1}\delta_i \sin(2n\theta-2i\theta) - \frac{a^2}{4}\sum_{i=0}^{n-1}\delta_i^2 \cos(2n\theta-2i\theta)\right]^2 -$$
$$- \left[\frac{a^2}{2}\sum_{i=0}^{n-1}\delta_i \cos(2n\theta-2i\theta) + \frac{a^2}{4}\sum_{i=0}^{n-1}\delta_i^2 \sin(2n\theta-2i\theta)\right]^2 . \qquad (6)$$

Analysis of the expression (6) shows that terms proportional to δ, δ^2, δ^3 are vanished. Rms beam emittance is conserved until high order of perturbation:

$$\frac{\varepsilon_n^2}{\varepsilon_o^2} = 1 + \varsigma(\delta^4), \quad \varsigma(\delta^4) = \frac{1}{4}\sum_{i=0}^{n-1}\sum_{k=0}^{n-1}\delta_i^2\delta_k^2 [1 - \cos(2i\theta - 2k\theta)]. \qquad (7)$$

Above derivations are approximate due to suggestion that linear beam-beam kick is proportional to the unperturbed trajectory. Numerical simulations exhibit exact conservation of rms beam emittance in the linear beam-beam kick regime. Preservation of beam emittance is explained by the fact that in case of linear kick a beam of particles experiences sequence of linear transformation, each of them conserves beam emittance.

Let us consider now the case when kick is a nonlinear function of unperturbed trajectory:

$$\Delta p_i = 4\ \delta_i x_i^3 . \qquad (8)$$

Calculation of rms beam emittance gives:

$$\frac{\varepsilon_n^2}{16} = [\frac{a^2}{2} + \frac{5}{2} a^6 \sum_{i=0}^{n-1} \delta_i^2]^2 -$$

$$- [\frac{3a^4}{2} \sum_{i=0}^{n-1} \delta_i \sin(2n\theta-2i\theta) - \frac{5a^6}{2} \sum_{i=0}^{n-1} \delta_i^2 \cos(2n\theta-2i\theta)]^2 -$$

$$- [\frac{3a^4}{2} \sum_{i=0}^{n-1} \delta_i \cos(2n\theta-2i\theta) + \frac{5a^6}{2} \sum_{i=0}^{n-1} \delta_i^2 \sin(2n\theta-2i\theta)]^2 . \quad (9)$$

In contrast with linear beam-beam kick the terms proportional to δ^2 in expression (9) do not vanish. Effective beam emittance growth is then as follows:

$$\frac{\varepsilon_n^2}{\varepsilon_o^2} = 1 + \delta^2 a^4 n + \zeta(\delta^4) , \quad (10)$$

$$\zeta(\delta^4) = 25 a^8 \sum_{i=0}^{n-1} \sum_{k=0}^{n-1} \delta_i^2 \delta_k^2 [1 - \cos(2i\theta - 2k\theta)] . \quad (11)$$

In the case of nonlinear kick, the beam emittance growth does not vanish in the first positive term δ^2, which indicates that nonlinearity is an essential point for expansion of emittance growth under noise conditions.
Comparison of eq.(10) with eq. (2) gives an expression for a diffusion coefficient D in beam emittance growth under noise regime $\varepsilon_n/\varepsilon_o = \sqrt{1 + D n}$:

$$D = \pi^2 (\xi u)^2 . \quad (12)$$

Diffusion coefficient exhibits quadratic dependence on noise amplitude and on value of beam-beam parameter, which is confirmed by computer simulations. It indicates, that noise instability in beam-beam interaction appears under arbitrary small values of u and ξ.

4 COMPENSATION OF BEAM-BEAM KICK

From results of previous section it follows, that the linear beam-beam kick preserves beam emittance even in the case of noise. Therefore linearization of the kick is expected to be a way to improve particle stability. A trivial approach assumes that the opposite beam is uniformly populated. Another method suggests utilization of high order components in focusing lenses.
In an axial -symmetric magnetic lens a particle with a larger radius experiences stronger focusing as compared with linear law:

$$\Delta r' = - \frac{r}{f} (1 + \frac{C_s}{f} \frac{r^2}{f^2}) , \quad (13)$$

where f is the focal length of the lens, and C_s is the spherical aberration coefficient. The dimensionless ratio C_s/f indicates significance of lens aberrations and is a figure of merit of the lens quality. The nonlinear term $\sim r^3$ can be used for compensation of the corresponding nonlinear term in the beam-beam collision. Magnetic lens

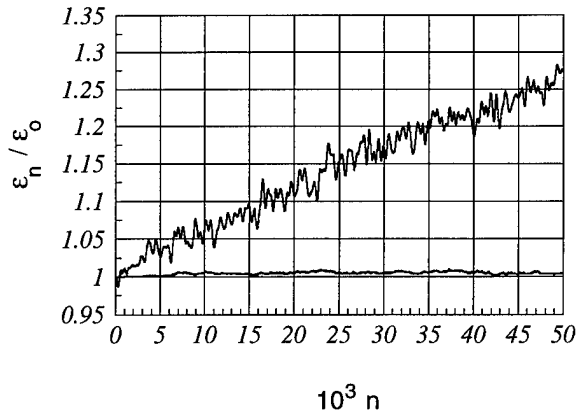

Fig.3. Beam emittance evolution in circular beam-beam interaction with kick (14), Qx = Qy =3.175 , ξ=0.015 and 5% noise in σ: (top) without compensation; (bottom) with compensation.

always focuses particles, therefore it can be used to compensate for beam-beam effect of colliding beams with opposite charge which also provides mutual focusing. Suppose beam-beam kick includes only the linear ~ r and first nonlinear ~ r^3 terms:

$$\Delta p = - 4\pi\xi r (1 - \frac{r^2}{4 \sigma^2}) . \quad (14)$$

Nonlinear terms of beam-beam kick and of aberration have to be equal each other. Taking into account that $p=\beta \cdot dr/dz$, the condition for compensation is :

$$(\frac{C_s}{f}) \frac{\beta}{f^3} = \frac{\pi\xi}{\sigma^2} . \quad (15)$$

Fig.3 illustrates the effect of compensation of the cubic term in beam-beam kick. As can be seen, beam emittance is kept constant if a compensation lens is applied. Nevertheless, the effect of compensation vanishes if beam-beam kick includes all higher order nonlinear terms of the Gaussian kick and the compensation kick is still proportional to r^3. Therefore, the suggested compensation by lens aberration can be applied only to a weakly nonlinear beam-beam kick.

REFERENCES

[1] B.Chirikov, Physical Reports, 52 , p. 263 (1979).
[2] K.Cornelis, In Proceedings of the Third Workshop on LEP Performance, CERN SL/93-19 (1993).
[3] J.K.Koga and T.Tajima, Physical Review Letters, Vol. 72, No. 13 , p.2025 (1994).
[4] T.Sen and J.A.Ellison, Physical Review Letters, Vol. 77, No. 6, p.1051 (1996).
[5] Y.Batygin and T.Katayama, Proceedings of the EPAC96, Barcelona, 1170, 1173 (1996).
[6] V.Lebedev et al., Particle Accelerators, Vol. 44, p.147, (1994).

BEAM-BEAM SIMULATIONS WITH NON-GAUSSIAN DISTRIBUTIONS FOR SLC AND SLC-2000*

K.L.F. Bane, P. Chen, F. Zimmermann
Stanford Linear Accelerator Center, Stanford University, CA 94309, USA

Abstract

Due to various upstream beam manipulations, the longitudinal bunch shape at the interaction point of the Stanford Linear Collider (SLC) is highly non-Gaussian. In this paper, we report beam-beam simulations with realistic longitudinal bunch shapes for the present SLC parameters and for the SLC-2000 luminosity upgrade. The simulation results allow us to estimate the luminosity enhancement due to the pinch effect and to find optimum parameter settings for the bunch compressor and the linac.

1 INTRODUCTION

Many linear-collider beam-beam simulations performed in the past have assumed simplified longitudinal beam distributions at the interaction point, usually a Gaussian and, sometimes, a uniform distribution. However, real bunch distributions are neither Gaussian nor uniform.

At the Stanford Linear Collider, the first and only linear collider in the world, the longitudinal distribution at the interaction point (IP) is clearly non-Gaussian. The longitudinal bunch shape at the SLC IP is determined by a variety of effects [1]: bunch-lengthening in the damping rings, (over)compression, rf curvature and second-order momentum compaction in the ring-to-linac transfer lines, rf curvature and longitudinal wake fields in the linac, and, finally, another bunch compression or expansion plus synchrotron radiation in the collider arcs. As a result of all these effects, the bunch distribution at the interaction point (IP) differs markedly from the idealized distributions usually considered. There is, in fact, some evidence that luminosity predictions derived from Gaussian-bunch simulations compare poorly with SLC observations [2].

A study of non-Gaussian beam-beam collisions is further motivated by the proposed luminosity upgrade SLC-2000 [3], for which, due to stronger bunch-length compression in the arcs (necessary to reduce the hourglass effect for the smaller $\beta_y^\star$), the distortion of the IP distribution will be even more pronounced.

In this paper, we report recent simulation results of beam-beam collisions, both for the present SLC and for the SLC-2000 upgrade. The simulations are based on realistic IP bunch distributions including all the effects in longitudinal phase space mentioned above, and starting with the potential-well distorted beams in the damping rings. The purpose of these simulations is: (1) to provide an estimate of the expected luminosity and of the pinch effect for real, non-Gaussian bunches, (2) to determine settings of compressor voltage and linac phase which are optimized for maximum luminosity, and (3) to provide guidance for the operation of two newly installed IP bunch-length monitors [7, 8]. Table 1 lists nominal IP beam parameters for the present SLC and for the SLC-2000 upgrade, which will be assumed in the remainder of this paper.

Table 1: Nominal IP beam parameters for the 1996 SLC and for the SLC-2000 upgrade.

parameter	SLC-1996	SLC-2000
$\gamma\epsilon_x$ (m)	5.9×10^{-5}	4.0×10^{-5}
$\gamma\epsilon_y$ (m)	1.9×10^{-5}	1.1×10^{-5}
$\theta_x^\star$	350 μrad	550 μrad
$\theta_y^\star$	350 μrad	500 μrad
$\beta_x^\star$	5.4 mm	1.47 mm
$\beta_y^\star$	1.7 mm	0.5 mm
δ_{rms}	0.1%	0.2 %
N	3.5×10^{10}	3.5×10^{10}
$\sigma_x^\star$	1.9 μm	810 nm
$\sigma_y^\star$	600 nm	250 nm

2 OPTIMUM BUNCH SHAPE FOR THE SLC

The longitudinal bunch distribution at the SLC IP is calculated with the program LITRACK [4], by which we model the longitudinal dynamics in the damping rings and in all downstream systems. This distribution is used as an input to the beam-beam program Guinea-pig [5]. Other input parameters, including the angular divergence and the spot size, are taken from Table 1. We have performed a series of simulations to study the dependence of the IP bunch shape and luminosity on the linac phase and bunch compressor voltage.

Figure 1 illustrates how a change of the average linac phase ϕ affects the IP bunch shape. Displayed is the longitudinal beam distribution for three different linac phases, with the center figure representing the nominal case. In this report, the phase ϕ is measured with respect to the crest of the linac rf, with $\phi < 0$ (or $z < 0$) to the front of the bunch.

In Fig. 2, the IP bunch length, energy spread and luminosity enhancement factor are shown as a function of the linac phase, for a constant compressor voltage V_c. The luminosity enhancement factor H_D is defined as the ratio of the effective luminosity L and the geometric luminosity L_0, where the latter is calculated from the IP beam size without collision. The enhancement factor can be larger than 1 due to the pinch effect (mutual focusing of the two beams

* Work supported by the U.S. Department of Energy under contract DE-AC03-76SF00515.

by each other) or smaller than 1 due to the hourglass effect (*i.e.*, the angular divergence of the two beams). During SLC operation, the injection time is continually adjusted in order to compensate for diurnal drifts of the linac-rf reference phases. Usually, this adjustment is done by minimizing the beam energy spread at the end of the linac. This is not necessarily the best choice in regard to the pinch effect, although Figs. 2 (a) and (d) suggest that it is not too far from the optimum. For comparison, the luminosity enhancement for a Gaussian bunch, one with the same rms length, is also shown in Fig. 2 (a), by the dotted line. In this particular case, the enhancement factors for Gaussian and real distributions are almost identical.

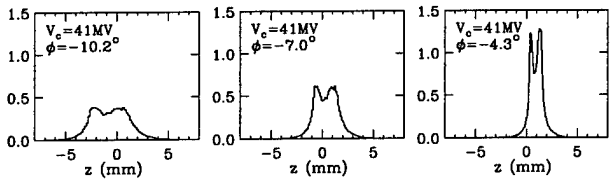

Figure 1: IP bunch shape for different linac phases. The vertical axis gives the instantaneous current in units of kA.

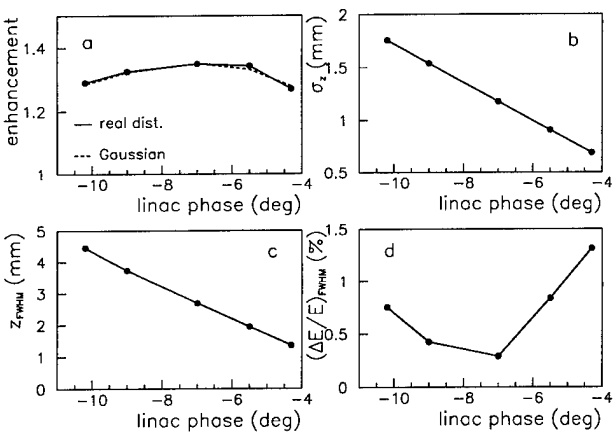

Figure 2: Luminosity enhancement (a), rms bunch length (b), FWHM bunch length (c) and FWHM energy spread (d) as a function of the linac phase, for the 1996 parameters.

The second parameter that can substantially affect the IP distribution is the voltage of the compressor rf. Examples of IP distributions for different compressor voltages are depicted in Fig. 3, where in each case the linac phase is adjusted to minimize the final energy spread. Figure 3 shows that a too small compressor voltage may result in a very spiky distribution, which is unlikely to show a large pinch effect. The nominal rf voltage is 41 MV (center case of Fig. 3), which yields an rms bunch length in the linac of about 1.2 mm. Figure 4 displays simulation results which illustrate how the IP bunch length, the energy spread and the luminosity vary with the compressor voltage, again minimizing the energy spread. For comparison, the dotted line in Fig. 4 (a) shows the luminosity enhancement for a Gaussian distribution of equal rms length. The clear difference between the dotted and solid lines demonstrates that a Gaussian is not always a good approximation.

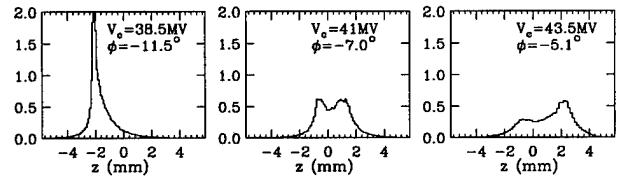

Figure 3: IP bunch shape for different compressor voltages. The vertical axis gives the instantaneous current in units of kA.

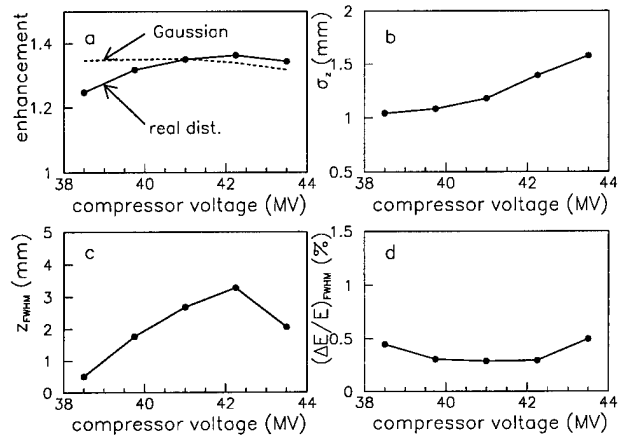

Figure 4: Luminosity enhancement (a), rms bunch length (b), FWHM bunch length (c) and FWHM energy spread (d) as a function of the compressor voltage for the 1996 parameters.

3 BUNCH LENGTH MONITORING

To optimize the luminosity enhancement, for the 1997 SLC run two novel bunch-length monitors have been installed in the SLC final focus: 1) a laser-heterodyne monitor based on the laser-wire system [8], which can be used to measure the entire Fourier transform of the beam profile; 2) a broadband rf monitor, which detects signals in 4 different frequency ranges (8–11.6 GHz, 11.6–19 GHz, 19–110 GHz, 59–110 GHz) and which will provide continuous information about the bunch length. Figure 5 displays the expected signals in the four channels of the rf monitor for various linac phases and compressor voltages equivalent to those considered in Figs. 2 and 4. The signals are calculated by performing a fast fourier transform of the bunch distribution and then integrating over the different frequency ranges. As expected, channel 4 is the most sensitive to the bunch length. In the 1997/98 SLC run, the signal of this channel will allow us to constantly monitor the IP bunch length of electron and positron beams, and, thus, to ascertain that the linac and compressor are set up properly for maximum pinch effect.

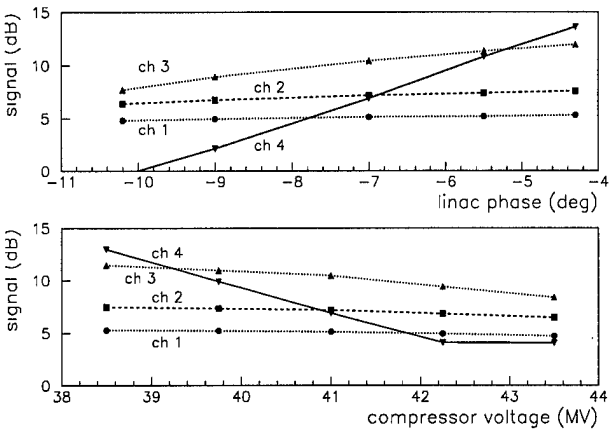

Figure 5: Predicted signal in the 4 channels of the newly installed RF bunch-length monitor [7], as a function of the linac phase and the compressor voltage (same horizontal scale as in Figs. 2 and 4, respectively).

4 LUMINOSITY ENHANCEMENT AT SLC-2000

In simulation studies for SLC-2000, we have used the parameters listed in the right-hand column of Table 1, and we have considered four different values of the compressor rf voltage. For each compressor voltage, we have varied the linac phase ϕ within a certain range constrained by the resulting energy spread (see Fig. 6). Given the present SLC-2000 final-focus energy acceptance of 0.6% [3], the optimal compressor voltage is $V_c \approx 40$ MV and the luminosity enhancement is 20–30%. However, if the energy acceptance can be increased to 1.4%, a shorter IP bunch length and an enhancement up to 60% would become possible, with a compressor voltage $V_c = 41$ MV. Our simulation results for the 1996 SLC and SLC-2000 are summarized in Table 2.

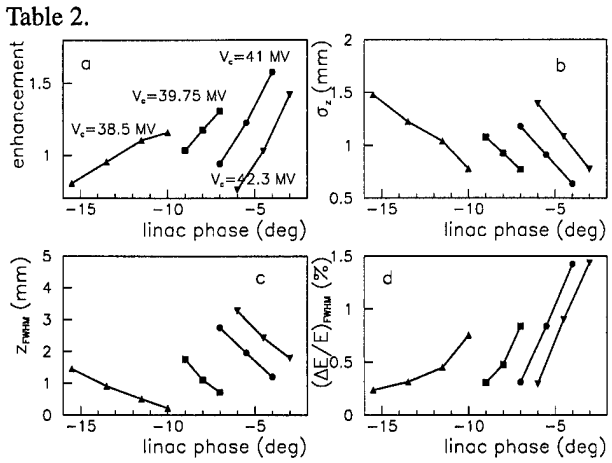

Figure 6: Luminosity enhancement (a), rms bunch length (b), FWHM bunch length (c) and FWHM energy spread (d), as a function of the linac phase for SLC-2000, considering four different compressor voltages: 38.5 MV (triangles), 39.75 MV (squares), 41 MV (rectangles), and 42.25 MV (inverse triangles).

Table 2: Predicted luminosity, spent-beam and photon-beam characteristics for the 1996 SLC and SLC-2000, obtained in beam-beam simulations with realistic distributions using the program Guinea-pig [5]. The symbol L_0 (L) denotes the luminosity without (with) pinch and hourglass effect, and H_D is the enhancement factor L/L_0, which, in the simulation, was optimized by adjusting the linac phase for a constant compressor voltage of 41 MV. The values given in parentheses are results for a Gaussian distribution (see also [6]). The last two rows refer to the beamstrahlung photons.

parameter	SLC-1996	SLC-2000
ϕ	$-7°$	$-4°$
V_c	41 MV	41 MV
σ_z	1.18 (1.0) mm	0.64 (0.5) mm
L_0	110 Zs/hr	640 Zs/hr
L	150 (149) Zs/hr	998 (1073) Zs/hr
H_D	1.35 (1.34)	1.56 (1.68)
θ_x	0.62 (0.62) mrad	1.18 (1.29) mrad
θ_y	509 (532) μrad	616 (661) μrad
$< \frac{dE}{E} >$	0.039 (0.042) %	0.53 (0.61) %
σ_E	49 (54) MeV	441 (482) MeV
N_γ/electron	0.68 (0.68)	1.77 (1.80)
$< E_\gamma >$	25 (26) MeV	141 (154) MeV

5 CONCLUSION

Using realistic longitudinal bunch distributions, we have determined the optimum compressor setting and the optimum linac phase for the 1996 SLC and for the SLC-2000 upgrade. We find that, in most cases, the Gaussian approximation to the bunch shape gives nearly the same luminosity enhancement factor as the actual bunch shape. For the 1996 SLC parameters, the maximum enhancement due to the pinch effect is about 30%, while for SLC-2000 an enhancement of 20–30% is expected for the present final-focus design optics, which may be increased to 60% with an improved final-focus energy bandwidth.

Acknowledgement
We thank O. Napoly for stimulating discussions.

6 REFERENCES

[1] K.L.F. Bane, SLAC/AP-80 (1990).

[2] T. Markiewicz, private communication (1997).

[3] M. Breidenbach et al., "SLC-2000: A luminosity upgrade for the SLC", LINAC 96, and SLAC-PUB-7268 (1996).

[4] K. Bane, unpublished.

[5] D. Schulte, private communication (1997).

[6] O. Napoly, SLAC CN-408 (1996).

[7] F. Zimmermann, G. Yocky, et al., "An RF bunch-length monitor for the SLC final focus", these proceedings (1997).

[8] T. Kotseroglou et al., "A laser-heterodyne bunch-length monitor for the SLC interaction point", these proceedings (1997).

HIGH CURRENT MAGNETIZED PLASMA DISCHARGES AND ELECTRON BEAMS FOR CAPTURE AND COOLING OF CHARGED LEPTONS AND HADRONS

Ady Hershcovitch
Brookhaven National Laboratory, Upton, N.Y. 11973, USA

Abstract

Nowadays most magnetic lenses used to capture and to focus pions and muons utilize azimuthal magnetic fields generated by large axial currents, like horns or lithium rods (or even a Z-pinch at GSI). Capture and focusing angle is proportional to the product of the current and length of the lens. State-of-the-art for these lenses is no more than 750 kA and 70 cm. A meter long, multi-MA, magnetized axial discharges were generated in the early days of fusion. Lenses based of such devices can increase the capture angle of pions, e.g., by more than a factor of 2. Electron beam cooling is presently achieved in storage rings by having charged particles interact with a co-moving electron beam. In these devices, typical parameters are electron beam currents of about 1 A, an interaction length of about 1 meter, and interaction time of about 30 msec. Multi-MA electron beams can be used for single-pass final stage cooling in a number of machines. Calculations for some applications, as well as other advantages indicate that these schemes deserve further more serious consideration.

1 INTRODUCTION

1.1 Focusing

In many areas of research involving charged particle beams, various methods of magnetic focusing have been employed to enhance the flux of charged particles from a divergent source such as a production target,[1] or to confine ions emerging from the crossover region of an ion diode to betatron oscillation for propagation to a small target a few meters away.[2] The method of choice for focusing of high energy charged particles, produced in nanosecond to microsecond bursts, that need to be transported for a distance of a meter or more has been the use of azimuthal magnetic fields that pull the particles radially inward as a consequence of the Lorentz force. These fields are usually generated by currents that are oriented along the desired flight path of the charged projectiles.

Lithium lenses[3,4] and focusing horns[1,5] have been used in high energy physics research, while various spark and Z channels were developed for fusion experiments.[2,6]

Although some features vary from experiment to experiment, there are a number of common requirements for all these lenses: 1). Very large axial currents must be generated and sustained. 2). The lens medium should have as low a density as possible to minimize particle absorption and scattering. 3). Due to large currents and high magnetic fields, the lens must withstand high mechanical and thermal stresses. 4). The lens must survive prolonged exposure to radiation.

1.2 Cooling

A low thermal spread electron beam moving at the same velocity with a hotter charged particle beam will have a cooling effect on that beam. Electron beams, and other discharges can be designed to have cold electrons moving at the same velocity as leptons and hadrons to cool them.

2 PLASMA DISCHARGES OPTIONS

Interest in charged particle focusing and/or cooling is varied and many of the broad number of applications require customized configurations. Evaluation of applicability of schemes, based on plasma devices, is done for the AGS muon g-2 experiment, a proposed AGS neutrino experiment, and the muon collider. These schemes do not have the drawbacks and limitation of presently used devices.

Requirements on horns to withstand very large thermal and mechanical stresses, and yet be fabricated from light elements to minimize particle losses, have limited their current to about 300 kA. The drawbacks of a lithium lens are due to the fact that lithium has very low mechanical strength, and it is very reactive chemically. Consequently, it must, however, be kept under high pressure in a strong container made of a chemically compatible material like titanium or stainless steel. Practical currents reached have been limited to about 500 kA.

Spark (or Z) channels are plasma transport channels, characterized by large currents (100's of kA), which have been developed to transport intense beams of light ions over distances of up to 5 meters.[7] These channels consist of two annular plates placed in a vacuum chamber usually filled to a pressure of about 10 Torr. Pulse lengths of 10's of nsec at a repetition rate of 500 Hz - 1 kHz have been generated, as well as three microseconds long pulses at lower repetition rates. Channel radii from 1 cm to more than 10 cm were reported.

Electron beam currents that are in the mega-Ampere range have been generated by diodes. Although most of these diodes operate with pulses that are in the nsec

0-7803-4376-X/98 /$10.00 © 1998 IEEE

range, some diodes have operated with pulse lengths of up to 2 microseconds. Hollow-beam electron guns are particularly attractive due to their larger perveance and enhanced stability in addition to the obvious advantage of their hollow structure.

Z pinches involve a sudden compression of a low-density plasma by means of a large discharge current that lasts usually for up to a few microseconds. Its fill pressure is below a milli-Torr. Discharge currents of 10 MA over a few centimeters have been reached. However, in the early days of fusion research with Z pinches, experiments were performed with magnetized Z pinches. In one device with an axial magnetic field of 1.5 tesla, 2 MA were reached in a length of 0.8 meters for 250 microseconds.[8] This approach failed for fusion, since in that device little pinching occurred (the ion temperature was only 50 eV). But, these early devices reached parameters which make them ideal candidates for lepton and hadron lenses.

3 NOVEL PION AND MUON LENSES

Requirements for first focusing lens of the neutrino oscillation experiment are a 0.2 meter long lens with a current of 2.8 MA pulsed at the AGS cycle for 2.5 microseconds, and a 10 cm diameter.[9] Similar requirements exist for the g-2 experiment with regard to the current and length combination of the lens, however, there is a preference for shorter pulse lengths (10's of nsec) at a higher repetition rate. A pion acceptance angle can be calculated from Danby's formula,

$$p \cdot \sin(\partial) = (B \cdot L)/1313.22 \qquad (1)$$

Where p is particle momentum in GeV/c, B is magnetic field in kG, and length L in inches.
The magnetic field is determined from Ampere's Law which for uniform current distribution at a radial distance r yields

$$B = 0.2 \cdot I/r \qquad (2)$$

Where the units for B, I, and r are Gauss, Amperes, and centimeters, respectively.

A wall-stabilized Z pinch with a magnetic field reached the following parameters 40 years ago [8]: 0.8 meter long discharge with a current of 2 MA for a duration of 250 μsec was achieved. The axial magnetic field was 1.5 Tesla and the discharge radius was about 6 cm. A lens based on such a discharge yields, from equations (1) and (2), an acceptance angle of at least 0.263 radians (the axial magnetic field enhances the acceptance). Tapering the discharge can further enhance pion focusing for these experiments.

For the muon collider, a magnetized Z pinch with a current of 10 MA was considered. A preliminary computation[10] for the focusing capability of a lens based on a series of 10 MA Z pinches, which were equivalent in size and length to conventional lenses, was performed with a computer code that was developed by J. Gallardo and R. Palmer. The production target was bombarded by 10 GeV protons yielding pions with energies of 1.2 GeV ± 0.98 GeV, which later decay into 0.8 GeV ± 0.73 GeV muons. The muon-to-proton ratio for this system of lenses is $\mu/p = 0.38$. This represents a 50% enhancement in muon capture when compared to two other scenarios that utilize similar configurations. For example, lithium lenses yielded $\mu/p = 0.23$

4 SINGLE PASS ELECTRON COOLING

At first glance, this idea does not seem feasible with untrapped particles. However, if the parameters from LEAR are scaled up, this idea seems more interesting. At LEAR,[11] a 1 Ampere electron beam will cool antiprotons in 0.03 seconds if exposed continuously to the electron beam. Thermal equilibration time is

$$\tau = 5.56 \; x \; 10^{18} \; \frac{(m_h T_c + m_c T_h)^{3/2}}{(m_c m_h)^{1/2} Z_h^2 Z_c^2 \lambda \; n_c} \text{ sec} \qquad (3)$$

given by (eV, cgs units)[12]
Where subscripts c and h refer to cold and hot particles, respectively. It is clear from Equation 3 that equilibration time is proportional to the density of the lower temperature particles and for electron beams with equal cross section (and velocity), the electron density is proportional to the current. To scale up from LEAR, equation 3 indicates that a 3 meter long 1 MA electron beam can cool a muon in its transit time of about 10 nsec.

If pions or muons are initially cooled by other means, electron cooling can provide final stage cooling for the muon collider, e.g., a muon beam, that was cooled and slowed down to a momentum P = 300 MeV/c and a momentum spread of $\Delta p/p = 4\%$, can be further cooled by a 10 MA, 1.68 m. long, 1 cm. radius electron beam (with 0.516 MeV electrons) to $\Delta p/p = 2.86 \times 10^{-3}$. A second stage of 10 MA, 56 cm. long electron beam reduces $\Delta p/p$ to 1.53×10^{-5}.[13]

In cooling $\mu-$, the magnetic field generated by the co-moving electrons focuses $\mu-$. But, such a magnetic field defocuses μ^+. To cool μ^+ particles, no net axial current should exist in a channel. One possibility is to shoot the 10 MA electron beam through a 10 MA Z pinch such that the two currents cancel each other.[13]

5 CONCLUSIONS

Evaluation of pion and muon capturing and focusing capability of a lens, based on parameters which were achieved in a magnetized Z pinch 40 years ago (2 MA, 0.8 m. long, 6 cm. radius), indicates that this lens performance can far exceed that of presently used lenses. Additionally, particles focused in a spark channel or a Z pinch lens travel in what is essentially vacuum, hence

there is indeed negligible absorption and scattering of pions or muons. By comparison, state-of-the-art performance for a horn is 300 kA, while peak performance of a typical lithium lens is at about 500 kA. Since a lithium lens has a radius of 1 cm or smaller, the magnetic field at a distance of about 10 cm from the lens axis (where it is most important for focusing) is too low to be of interest for the AGS neutrino oscillation experiment and the g-2 experiments, for example. Thirty years ago, a very modest version of such a lens was used in an AGS experiment. This lens performed well until a ceramic liner broke and was not replaced since the experiment was close to its conclusion.[14] Similarly, a series of lenses based on magnetized Z pinches could greatly improve pion capture and focusing, for the muon collider, over presently pursued schemes.

Single pass final stage cooling with very intense electron beams, suitable for the muon collider or between accelerators and storage rings, does not seem unreasonable. However, there is no data base which suggests that generating the needed electron beams is straight forward.

Multi-Mega-Ampere Z pinches deserve a further, more serious consideration for possible use as lenses in various experiments, and in the muon collider. State-of-the-art Z pinches have reached 10 MA with vastly improved capacitor technology. Extending a Z pinch type discharge length and radius with wall and axial magnetic field stabilization is possible. This will result in a larger current as well. Consequently, pursuing this approach can result in a formidable pion capturing and focusing lens.

6 ACKNOWLEDGMENTS

Work performed under the auspices of the U.S. Department of Energy. The author is grateful to J. Gallardo, R. Palmer, J. Phillips, and A. Bogacz for many useful discussions. Computer calculation performed by J. Gallardo is gratefully acknowledged.

REFERENCES

[1] M. Giesch, et al., NIM 20, 58 (1963).
[2] C.L. Olson, J. Fusion Energy 1, 309 (1982).
[3] G. Dugan, et al., IEEE Trans. Nucl. Sci. NS-30, 4, 3660 (1983).
[4] A. Ijspeert and P. Sievers, CERN SPS/86-18 (ABT).
[5] A. Carroll, et al., Proceedings of IEEE Particle Accelerator Conf. 1987, p. 1731.
[6] J. Olsen and R. Leeper, J. Appl. Phys. 53, 3397 (1982).
[7] P. Ottinger, et al., Proceedings of IEEE, 80, 1010 (1992).
[8] A series of papers (by Golovin, et al., Komelkov, et al., and Andrianov, et al.), presented at the second U.N. Conf. on Peaceful Uses of Atomic Energy, Vol. 31 and 32, Geneva, 1958.
[9] A. Carroll, private communication, 1994; G. Bunce, private communication, 1994.
[10] A. Hershcovitch, Some Options for Pion and Muon Focusing in the AGS g-2 and Neutrino Oscillation Experiments (and Possible New Focusing and Cooling Schemes for a Muon Collider), AGS/AD Tech.Note 413 (1995).
[11] H. Poth, CERN-EP/90-04; H. Poth, et al., NIM A287, 328 (1990).
[12] B.A. Trubnikov, Particle Interactions in a Fully Ionized Plasma, Rev. of Plasma Phys., 1 (Consultants Bureau, N.Y.) 105 (1965).
[13] Muon Muon Collider: Feasibility Study, BNL - 52503, FNL - Conf. 96/092. LBNL - 38946, July 1996, Ch. 12.
[14] E.B. Forsyth, L. Lederman, and J. Sunderland, IEEE Trans. Nucl. Sci., p. 872 (June, 1965); E.B. Forsyth, private communication, 1995.

LARGE LINAC-BASED ELECTRON COOLING DEVICE

N.S.Dikansky, V.V.Parkhomchuk, V.M.Petrov, V.G.Shamovsky,
A.N.Smirnov, P.D.Vobly, V.N.Volkov.
Budker Institute of Nuclear Physics, 630090, Novosibirsk, Russia

The electron beam for electron cooling is traditionally obtained by direct electrostatic acceleration. But for the higher electron energies (above 5 MV), the difficulties in implementing sharply increase and set natural limits for such method in use.

That is why it is interesting to consider alternative ways for obtaining a high energy electron beam applicable for the electron cooling. Thus, to obtain the electron cooling at the collider ENC for GSI storage ring, it is necessary to have an electron beam with an energy of 15 MV, a current of up to 1A, an energy spread of $\frac{\Delta\gamma}{\gamma} \sim 10^{-4}$, and $\frac{\Delta P_\perp}{P_\parallel} \sim 10^{-4}$ spread in a transverse momentum.

As the ion beams cooled at GSI are bunched with a σ_z of 10 cm, and the bunches follow each other at a 60 MHz frequency, the cooling electron beam can be bunched as well.

The usual source of bunched electron beam of such energy and intensity is a linear accelerator. The main problem for using the linear accelerator for our purposes is a way to meet high precision requirements to the energy and momentum spreads of beam.

For the sake of definiteness, let us consider a device, one of possible rough drawing of which is given in Fig.1. The version of linear accelerator under consideration consists of six identical units, each unit consists of four 60 MHz frequency resonant cavities with a 700 KV voltage, one 180 MHz frequency resonant cavity, and one 300 MHz frequency resonant cavity (2 of these 6 units are shown in the figure). A rough drawing of the main 60 MHz resonant cavity is given in Fig.2. The supposed characteristics of the resonant cavities are given in Table 1.

Table 1.

N	1	2	3
Frequency of a cavity (MHz)	60.0	180.0	300.0
Voltage at a gap (kV)	700.0	466.0	56.0
Amount of cavities	24	6	6
Shunt resistance (ohm)	$2.4 \cdot 10^6$	$3.5 \cdot 10^6$	$15 \cdot 10^3$
Q-factor	$15.5 \cdot 10^3$	$33 \cdot 10^3$	$14 \cdot 10^3$
Power dissipated by (kW) one cavity	104.0	31.0	1.5
Total power dissipated by all the cavities (kW)	2500	181	9
Power consumed by electron beam in one cavity (kW)	70.0	-47.0	5.6
Total power consumed by electron beam in all the cavities (kW)	1680	-287	34

The bunched electron beam of 0.5 - 1 MV energy is injected to the linear accelerator from an electrostatic preinjector. The whole cavity system as well as the preinjector is immersed in a longitudinal 0.5 T magnetic field, created by a superconducting solenoid.

The main factors, affecting the energy and momentum spreads of the electron beam in this linear accelerator, are the following:

1. The time dependence of the accelerating RF voltage in the accelerating gap during the passage of a short electron bunch.

2. The influence of a space charge field on the energy spread of particles.

3. The influence of inhomogeneity of the longitudinal magnetic field and of the electric field transverse components of the cavity on an increment in transverse momentum of particles.

4. The influence of the wake field upper harmonic of the cavity on the motion of particles.

We shall briefly consider each of these factors.

1. The way to obtain the rather constant RF voltage in a cavity during the passage of a short bunch through the accelerating gap is well known. For this one needs only to add the required quantity of upper harmonics of a necessary amplitude to the main RF harmonic. In order to meet a requirement of $(\frac{\Delta\gamma}{\gamma})_{gap} \sim 10^{-4}$ for every section of the accelerator, one need only to add both the third harmonic with a relative amplitude of 0.167 and the 5th one with a relative amplitude of 0.02 to the leading harmonic. The additional correcting cavities of 180 and 300 MHz frequencies, shown in Fig.1, are used for this purpose.

2. When the short bunch passes through, the particles which are at a distance s from its center are affected by the longitudinal component of the space charge force. Let us suppose that the density distribution of bunch particles is parabolic in form.

$$n(s) = \frac{3}{4} \cdot \frac{N}{\sigma_x} \cdot (1 - \frac{s^2}{{\sigma_x}^2})$$

Then once the bunch passed the distance l, the particle being at a distance s from the bunch center has an additional longitudinal momentum.

$$\frac{\Delta P_\parallel}{P} = \frac{3}{2} \cdot \frac{N r_e g}{{\sigma_x}^3 \gamma^3 \beta^2} \cdot ls$$

Here: $g = 1 + 2ln(\frac{a}{b})$,

N is the number of the electrons in the bunch

a is the radius of the beam

b is the radius if a vacuum chamber

r_e is the classical electron radius of 2.810^{-13} cm.

At high energies ($\gamma \sim 10$) this value is negligibly small ($\sim 10^{-5}$) when the bunch passes the distance of 100 m. But at low energies ($\gamma \geq 1$) the value $\frac{\Delta P_{\parallel}}{P}$ will be equal to 10^{-3} just after the bunch passes 1 m. But, as the phase dependence of the longitudinal momentum increment is a linear one at a chosen special form of the density distribution of bunch space charge, this effect can be easily corrected.

Here it is pertinent to note the following. At a first glance it would seem that the accelerator operating in a range of rather short wave lengths of about $1 \div 10$ cm is more attractive, as its overall dimensions are relatively small as well as its cost. But as $\frac{\Delta P_{\parallel}}{P} \sim {\sigma_z}^3 \sim {\omega_0}^3$, where ω_0 is a main frequency, it is obvious that the difficulties, related to the effect of space charge on the accelerator particle dynamics, sharply increase with an increase in the accelerator working frequency and become insuperable. Besides, there are much more problems connected with the necessity to obtain super short electron bunches at a stage of their injection to accelerator and to significantly elongate the accelerated bunch. In this connection it is seen that we should use the minimum RF frequency. So the accelerator working frequency is chosen considering the reasons just listed.

3. The particle can acquire an additional transverse momentum, when it moves in the inhomogeneous electrical field of the cavity, and effected by small inhomogeneities of the longitudinal magnetic field.

It can be shown that in the case of small disturbances the transverse momentum increment of a particle can be compensated by a special correcting magnetic lens. This lens creates an additional disturbance of longitudinal magnetic field of the required amplitude. It should be located at a point determined by a phase of a Larmour motion. Fig. 3 shows the possibilities to compensate the transverse momentum increment of a particle moving in the inhomogeneous electrical field of the cavity. There are shown trajectories of particle motion in the transverse momentum space for the case of absence of such compensation (b) and for the case of presence of a correcting lens (c). Fig.3(a) presents strength component distributions of the cavity electrical RF field and of the leading magnetic field along the direction of particles movement.

The precise adjustment of all the correcting lenses positioned after every resonant cavity is a delicate and labour-consuming work. Besides, errors in production and alignment of the cavities lead to an increase in the transverse momentum of particles. This casts some doubt upon the real ability to obtain the accelerated electron beam of required characteristics and hence upon the serviceability of the proposed device. But there is one rather elegant way to avoid these difficulties. Let us assume the bunch moves along the system of cavities, acquiring the transverse momentum component increment at the accelerating gaps for some reasons. Assume there is a special correcting lens at the accelerator outlet (for some cases, when the total value of transverse momentum is sufficiently small, its role is played by the electrical field inhomogeneity of the last cavity).

Let us consider an ideal case, when the particle motion disturbances caused by cavity fields are in one plane, for example X-Z (Z is the direction of the particle motion). Here we can always eliminate the increment of particle transverse momentum, acquired during the acceleration. For this we need to properly choose the value and phase of the disturbance created by the correcting lens.

Obviously for the case of one-dimensional disturbances, we can always eliminate the residual increments of particle transverse momentum, acquired during the acceleration, by a proper choice of these two parameters. To show the efficiency of the described method we have simulated the simplest model. We supposed that the disturbance in the transverse motion of particles was due to a random error in the cavity angle alignment in a plane (X–Z) (Z is the direction of particles motion; the value of a standard deviation in our calculations was adopted as 0.01). We calculated the particle transverse momentum (at the accelerator outlet) depending on the value of the leading longitudinal magnetic field. The results are presented in Fig.4(a) and Fig. 4(b). It is seen that this value is close to zero at a specific b. The extension of the described method to the case of non-one-dimensional disturbances of the particle transverse motion is obviously out of principal difficulties. This correction method was successfully used for electron cooling at INP.

4. The wake fields of upper harmonics for the current with a peak amplitude of 1A, and a bunch length of 10 cm following each other at a frequency of 60 MHz were calculated for the main 60 MHz resonant cavity. Relatively small dimensions of the cavity provide a low beam–imposed voltage at an accelerating interval. Fig.4(a) shows the spectrum of upper axial symmetrical modes in the cavity, which are excited by the beam. The values of both active and reactive components of the imposed RF voltage are given in Fig. 4(b) and 4(c), respectively. As is evident, the imposed voltage values are small. Moreover, the reactive component of the imposed voltage, contributing significantly to the amplitude, linearly depends on phase, and this value can be easily corrected when needed.

So, the results of the above estimations show, that there are reasons to hope to obtain the electron beam parameters required for electron cooling. This will enable to extend the use of electron cooling of heavy particles in a several GeV range energies per nucleon.

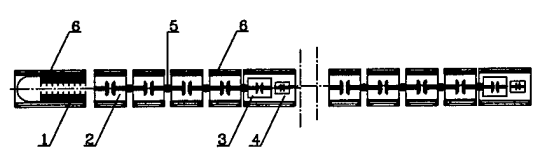

Fig.1 General view of LINAC

1–preinjector,
2–main cavity (F=60MHz),
3–correcting cavity (F=180MHz),
4–correcting cavity (F=300MHz),
5–correcting magnet lens,
6–superconducting solenoid

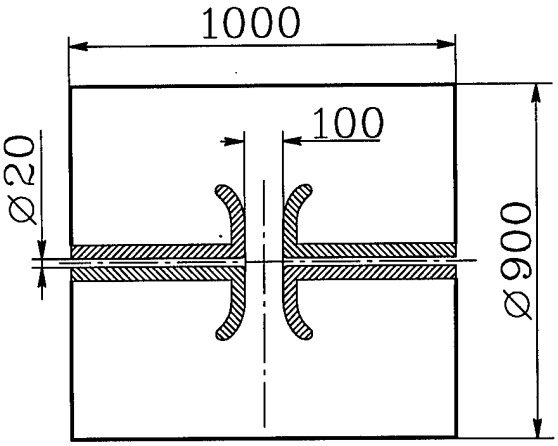

Fig.2 General view of main cavity,
(F=60MHz, U=700kV)

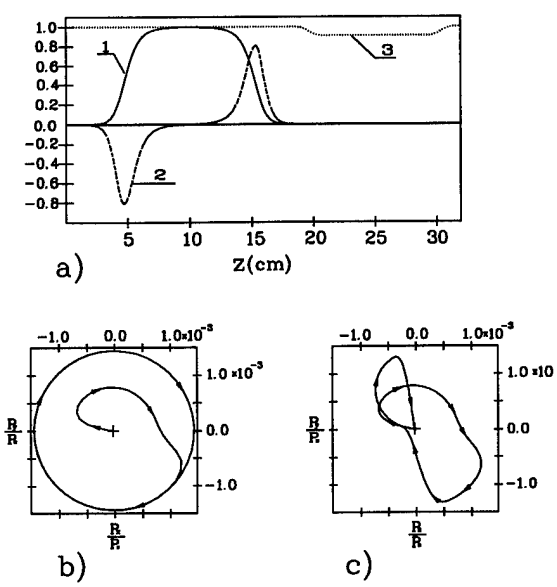

Fig.3 Correction ot the influence of inhomogenity in cavity electric field on the transverce motion of electron.

a) distribution of fields
   1–longitudinal electric field of cavity
   2–radial electric field of cavity
   3–longitudinal magnetic field
b) trajectory of the particle motion in a transverse momentum spase (correcting lens is absetnt)
c) trajectory of the particle motion in a transverse momentum space (correcting lens is present)

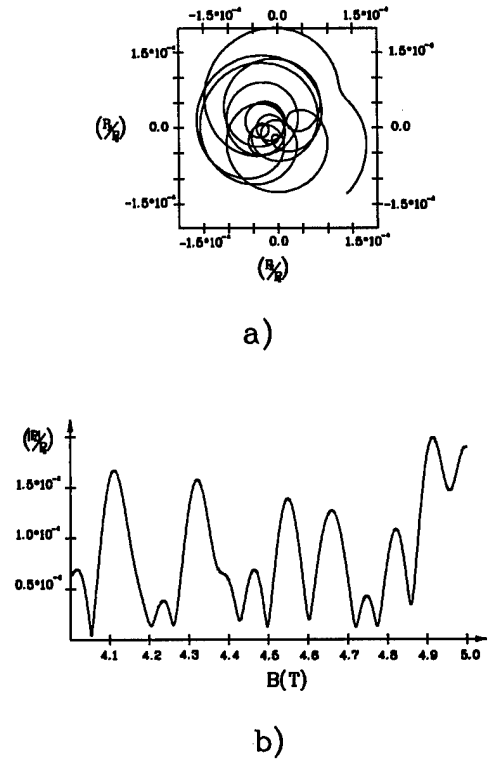

Fig. 4

a) position of a particle in its transverse momentum space at accelerator outlet, depending on the longitudinal magnetic field.
b) dependence of transverce momentum, aquired by particle after its passage througtout the accelerator on the longitudinal magnetic field

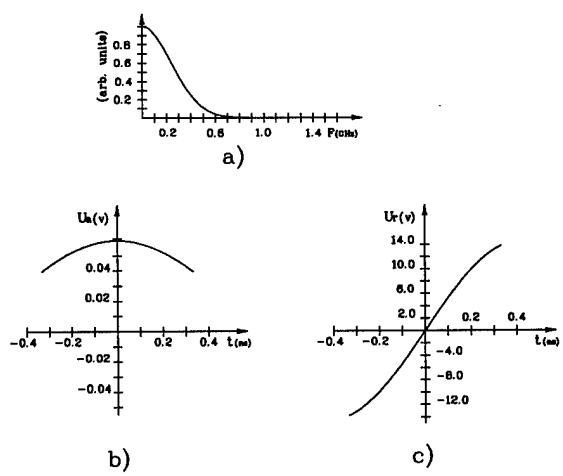

Fig.5 Cavity fields awaked by accelerated electron beam.(peak electron current is 1 A electron banch duration is 60 MHz, length of bunch 20cm).

a) wake field spectrum
b) active component of wake field volage
c) reactive component of wake field voltage

THE COUPLING-CAVITY SCHEME FOR THREE-DIMENSIONAL LASER COOLING

T. Kihara, H. Okamoto, Y. Iwashita,
NSRF, Institute for Chemical Research, Kyoto University,
Gokanoshou, Uji, Kyoto 611, Japan,
K. Oide, KEK, Oho 1-1, Tsukuba, Ibaraki 305, Japan

Abstract

We study three-dimensional laser cooling of fast circulating beams, employing the tracking code SAD. As an example, the lattice parameters of the storage ring ASTRID in Denmark are taken to figure out the efficiency of transverse cooling by synchrobetatron coupling. In this paper, the stress is put upon the so-called coupling-cavity scheme of laser cooling[1]. A possible design of the coupling cavity is also presented.

1 INTRODUCTION

The high potential of laser cooling in a storage ring has been demonstrated during the last several years through extensive experimental efforts by the TSR group of MPI and by the ASTRID group of Aarhus University[2]. The longitudinal temperature of $\sim$1 mK has already been achieved for low-energy heavy ion beams. However, concerning the transverse degrees of freedom, laser cooling of fast circulating beams is not particularly efficient although natural Coulomb coupling reduces the transverse temperatures to the level achievable with the electron cooling technique[3].

In order to obtain the transverse cooling rates comparable to the longitudinal rate, we studied, in the previous publications, the effect of dynamical coupling due either to a coupling cavity[1] or to dispersion at an ordinary rf cavity[4]. It was then shown that the transverse cooling rates could considerably be enhanced under the linear resonance conditions; namely,

$$\nu_x - \nu_L = \text{integer and } \nu_x - \nu_y = \text{integer}, \qquad (1)$$

where ν_x, ν_y, and ν_L are, respectively, the horizontal, vertical, and longitudinal tune of a storage ring.

In the present paper, we compare the cooling properties of the two coupling schemes, giving some simulation results obtained with the tracking code SAD[5].

2 DISPERSIVE COUPLING

In the dispersive coupling scheme, we need nothing new to develop transverse-longitudinal coupling; namely, it is only necessary to put an ordinary rf cavity at a location with a finite dispersion while a skew quadrupole magnet must be introduced in order to couple the two transverse degrees of freedom.

Fig.1 shows a simulation result obtained with SAD, where the lattice parameters of the ASTRID ring have been taken into account. A skew quadrupole magnet is installed, for horizontal-vertical coupling, at the opposite side of the laser cooling section, and the field gradient optimized to realize the largest transverse cooling rates is $(L/B\rho)\cdot(\partial B/\partial y) = 0.06\,\mathrm{m}^{-1}$ where L is the axial length of the magnet. The stored beam assumed here is 100 keV $^{24}Mg^+$ which has been employed in recent laser-cooling expriments in ASTRID. To approximately meet the resonance requirement in Eq.(1), the horizontal and vertical tunes have been adjusted to be 3.11 and 3.09 respectively. The longitudinal tune should then be set at around 0.1. This high value of longitudinal tune can easily be achieved with a low rf voltage because of the very low beam energy. In fact, adopting the harmonic number of 260, the rf gap voltage of only 34 volts is needed to have $\nu_L = 0.1$. To adiabatically capture the initial continuous Mg-beam into the rf bucket, the rf voltage is linearly increased from 0 to 34 volts within the first 0.022 seconds in this simulation. Then, the upper half of the longitudinal phase space of the beam is scanned with a cooling laser in the next 0.45 seconds. It is evident, from Fig.1, that all three degrees of freedom have efficiently been cooled.

Needless to say, beam density becomes higher as the cooling process advances. Consequently, the tunes should be depressed by strong Coulomb repulsive forces, leading to the breakdown of the resonance conditions. It might thus be important to know how strongly this coupling scheme

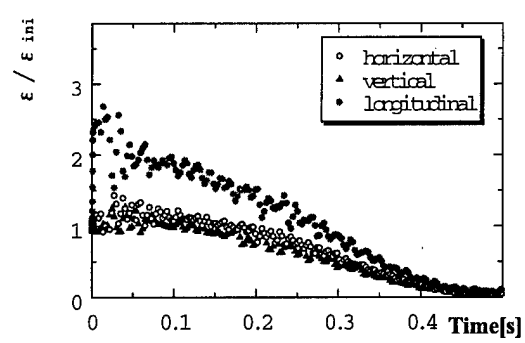

Figure 1: Time evolution of root-mean-squared(rms) emittances of a laser-cooled $^{24}Mg^+$-beam. ε_{ini} denotes the initial value of the rms emittance. An ordinary rf cavity has been set 10 meters away from the cooling section where the size of dispersion is 2.15 meters.

0-7803-4376-X/98 /$10.00 © 1998 IEEE

depends on the resonance conditions. Fig.2 shows the ratio of the rms emittances after cooling to the initial values. We see that the transverse cooling efficiency gets worse rapidly as the longitudinal tune is deviated from the resonant value.

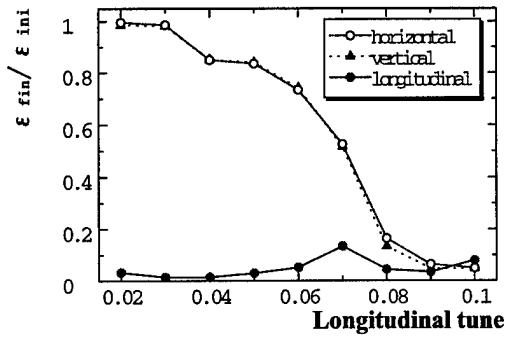

Figure 2: The rms-emittance ratio $\varepsilon_{fin}/\varepsilon_{ini}$ vs. longitudinal tune in the dispersive coupling scheme. ε_{fin} stands for rms emittance after laser scan is completed.

3 THE COUPLING CAVITY

3.1 A possible conceptual design

Let us now explore the cooling properties of the coupling-cavity scheme. The vector potential of an ideal coupling cavity can be given by

$$\boldsymbol{A} = (0, 0, Vx \sin \omega t) \tag{2}$$

where ω is the rf frequency, V is the constant proportional to the gap voltage, and x is the horizontal coordinate measured from the closed orbit. Apparently, this potential yields a longitudinal electric field linearly dependent on the transverse coordinate, which enables us to have a transverse-longitudinal coupling. Note here that, in the coupling-cavity scheme, we additionally need an ordinary rf cavity to provide a finite longitudinal tune such that the resonance condition in Eq.(1) is satisfied. The coupling-cavity frequency ω should then be taken roughly the same as the operation frequency of the ordinary cavity.

The easiest way to approximately obtain the potential in Eq.(2) is to excite TM_{210} mode in a simple rectangular pill-box cavity. This is, however, impractical in our case since ω is usually not high enough; namely, ω should be of the order of a few tens of MHz or less. In this frequency region, the cavity dimension becomes huge as far as a simple pill-box is used as a resonator. Therefore, we propose here a lumped circuit as illustrated in Fig.3. The approximate electric field distribution is shown in Fig.4. In order to verify that the coupling cavity in Fig.3 can roughly generate the vector potential proportional to the horizontal coordinate x, we evaluated the integrated effect of the longitudinal electric field in the cavity. The result is given in Fig.5 which actually demonstrates a good linearity with respect to x.

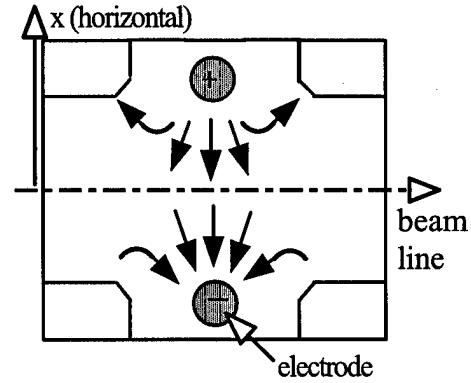

Figure 3: A possible geometry of coupling cavity.

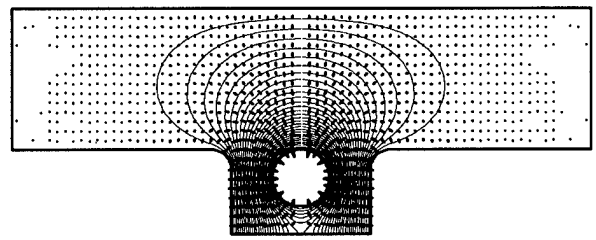

Figure 4: The approximate electric field and equipotential line of the coupling cavity. Only the lower half of Fig.3 has been shown.

3.2 Simulation results

To simulate the motion of laser-cooled beams under the influence of a coupling cavity, we have added a new subroutine to SAD. In the subroutine, the effect of a coupling cavity is analyzed, based on the electric-field data as shown in Fig.5. The field distribution is fitted with power series. Since the field linearity is sufficiently good, we have neglected the terms of higher than third order.

We have performed simulations again with the ASTRID lattice, modifying some fundamental parameters. The rf frequency of the coupling cavity has been fixed at about 5.8 MHz corresponding to the harmonic number of 260. This frequency is the same as that of the ordinary rf cavity. The peak voltage applied to the two electrodes of the coupling cavity is 487.1 volts. It has been confirmed, as anticipated, that the coupling cavity scheme works excellently under

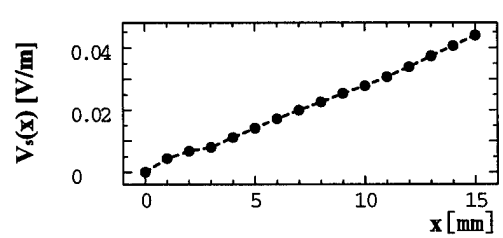

Figure 5: The dependence of the effective longitudinal electric field strength on the transverse coordinate. The absolute value of the electrode voltage has been set at 1 volt.

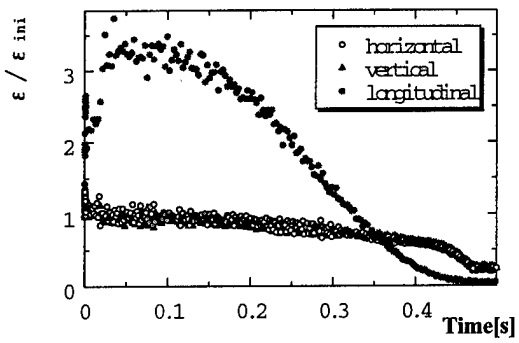

Figure 6: Time evolution of rms emittances of a laser-cooled $^{24}Mg^{+}$-beam under the influence of a coupling cavity. The longitudinal tune has been set at 0.04 while the two transverse tunes are roughly equal to 3.1. Note that an ordinary rf cavity is sitting at a dispersive position. We thus have synchrobetatron coupling not only by a coupling cavity but also by dispersion at the ordinary cavity.

the resonance conditions satisfied. Furthermore, we have found that this scheme is less sensitive to the longitudinal-transverse resonance condition, compared to the dispersive coupling scheme. As an example, we show, in Fig.6, a simulation result in which off-resonant value of the longitudinal tune has been assumed; namely, the longitudinal tune is 0.04 while the transverse tunes are identical to those employed in Fig.1. We see that both transverse rms emittances have been reduced to about 20% of the initial values after the laser scan is completed. The sensitivity to the resonance condition is given in Fig.7 which exhibits much better cooling properties than the dispersive coupling cases.

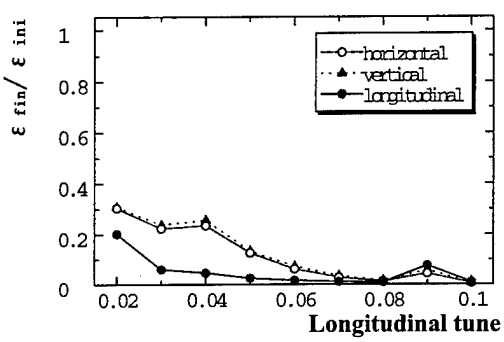

Figure 7: The rms-emittance ratio $\varepsilon_{fin}/\varepsilon_{ini}$ vs. longitudinal tune in the coupling-cavity scheme.

4 CONCLUSION

Two different schemes, i.e. dispersive coupling scheme and coupling-cavity scheme, have been considered to accomplish three-dimensional laser cooling of stored and circulating ion beams in a storage ring. We have confirmed that the transverse cooling rates can considerably be enhanced through dynamical coupling under the linear resonance conditions.

A possible design of a coupling cavity has been presented. Although the coupling-cavity scheme seems a bit more complicated than the dispersive coupling scheme, it might deserve further study because it is much less sensitive to the resonance conditions.

5 ACKNOWLEDGEMENTS

One of the authors (HO) would like to thank Dr. A.M. Sessler and Dr. D. Möhl for illuminating discussions throughout the work.

6 REFERENCES

[1] H.Okamoto, A.M.Sessler, and D.Möhl, Phys. Rev. Lett. **72** (1994) 3977.

[2] *See, e.g., Proc. of the Workshop on Beam Cooling and Related Topics,* CERN94-03 (1994).

[3] H.-J. Miesner et al., Phys. Rev. Lett. **77** (1996) 623.

[4] H. Okamoto, Phys. Rev. **E50** (1994) 4982.

[5] *See,*e.g.,http://www-acc-theory.kek.jp/SAD/sad.html.

DESIGN AND ANALYSIS OF A COOLING INSERTION LATTICE FOR OPTICAL STOCHASTIC COOLING*

A. Zholents and M. Zolotorev
Accelerator and Fusion Research Division,
E.O. Lawrence Berkeley National Laboratory, Berkeley, CA 94720
W. Wan
University of Colorado, Boulder, CO 80309

1 INTRODUCTION

In this paper we consider an example of a highly isochronous beam line that can be used in the Optical Stochastic Cooling method [1], [2] to bypass an optical amplifier. As it is stated in [1], there are stringent requirements on the time-of-flight properties of the bypass lattice employed in a cooling scheme. Namely, it is necessary to preserve relative longitudinal positions of particles inside the bunch from the beginning to the end of the bypass with the accuracy of $\lambda/2\pi$, where $\lambda \simeq 0.6\,\mu$m is a carrying (optical) wavelength. At first glance, $\lambda/2\pi$ is such a small value that reaching this accuracy looks nearly impossible. However, simulations show that a carefully designed bypass can meet all the requirements even with rather conservative tolerance to errors. Currently, we are planing to build a highly isochronous beam line where we can learn how to handle a difficult problem of time-of-flight operation at record accuracy. Preparations for this experiment are described in the accompany paper at this conference [3].

2 BYPASS LATTICE

The isochronicity of the bypass requires that the bypass be an achromat; and the dependence of the path lengths of electrons from energy, coordinate and angular deviations vanish. Theoretically, an achromat of the second order and higher can be made [4]. In practice, this has been proven to be impossible due to the tight space constraint in the planned experimental area. Therefore, in this design we aimed at finding a first-order achromat with weak second and higher order aberrations and large tolerance to errors.

As shown in Figure (1), the bypass lattice is mirror symmetric about the center. It contains one combined function magnet in the center, two approximately parallel faced dipole magnets, eight quadrupoles and six sextupoles.

After a careful selection of the first-order solution, aberrations above the second order become negligible and the second-order aberrations become weak. To minimize the remaining second-order aberrations, six sextupoles are placed in the bypass. The three independent sextupole strengths are fitted to minimize nine second-order time-of-flight matrix elements: T_{511}, T_{512}, T_{522}, T_{533}, T_{534}, T_{544}, T_{516}, T_{526}, T_{566} (in TRANSPORT notation). Each matrix element was considered to be small if the path length deviation associated with this coefficient at the end of fitting procedure fell below 0.1 μm. As a result, the ideal lattice, i.e. the lattice without errors, met all the constraints.

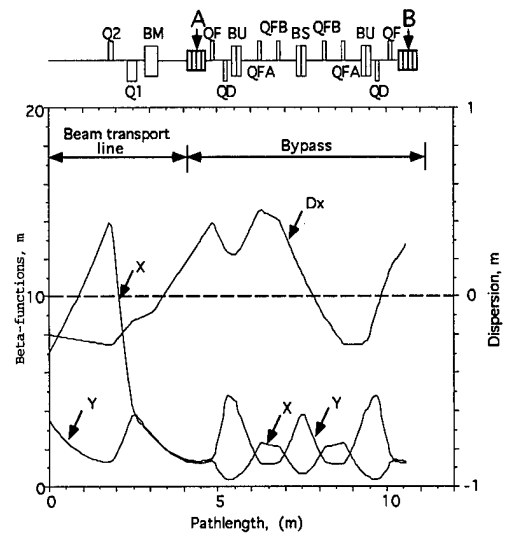

Figure 1: The beta-functions and the dispersion function of the bypass. Magnet locations, except sextupoles, are shown in the top.

3 SIMULATION RESULTS

In order to have a detailed check of the isochronicity of the bypass lattice with errors, we performed a 'brute-force' particle tracking using code COSY INFINITY[5]. In all simulations we looked at the spread of the longitudinal coordinates of 10^4 electrons after their passage through the bypass. The electrons entered the lattice at the same time, but had distributions in energy, transverse coordinates and angles. We assumed that all beam distributions were Gaussian with the horizontal emittance $\epsilon_x = 1.1 \times 10^{-7}$ m·rad, the vertical emittance $\epsilon_y = 6 \times 10^{-8}$ m·rad and the relative energy spread $\sigma_{\Delta E/E} = 7 \times 10^{-4}$, as measured in [3].

At the beginning, we calculated the spread of path lengths for an ideal lattice without errors. The result of simulations with and without sextupoles correcting second order aberrations is shown in Figure (2). Without sextupoles, the spread of path lengths is not acceptable.

Then, we included static errors, i.e. errors due to manufacturing, assembly and calibration of the magnets, misalignment errors and tilt errors. Error specifications are given in Table I. (We assumed all errors having Gaussian

* Work supported by DOE under Contracts DE-AC03-76SF00098 and DE-FG03-95ER40926.

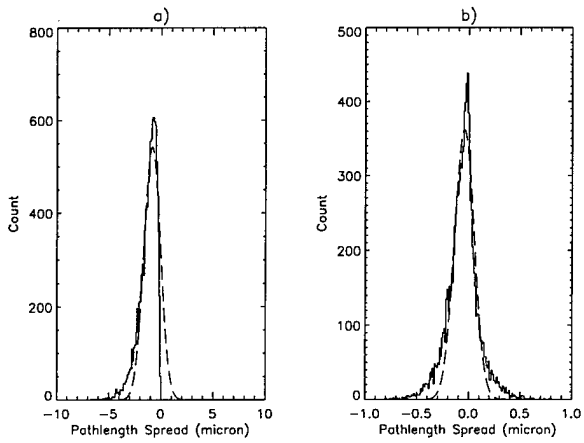

Figure 2: Histograms showing a spread of the pathlengths for the ideal lattice: a) without sextupole correction ($\sigma = 0.74$ μm), b) with sextupole correction ($\sigma = 0.09$ μm). Here and in subsequent similar pictures all sigmas are given for a fitted Gaussian distribution, which is shown by the dashed line. Note that the scale of the horizontal axis is ten times larger for the first histogram.

Table I: The specification of the errors.

	Static errors
Setting errors	$\sigma(\frac{\Delta B}{B}, \frac{\Delta G}{G}, \frac{\Delta S}{S}) = 1 \times 10^{-3}$
Tilt errors, [mrad]	$\sigma(\Delta\psi) = 0.2$
Misalignment errors in x, y, z [mm]	0.15, 0.03, 1
Multipole error [a)]	
dipoles	$\sigma(\frac{b_3}{b_1}) = 1 \times 10^{-4}$ at $r = 3$cm
quadrupoles	$\sigma(\frac{b_3}{b_2}) = 5 \times 10^{-4}$ at $r = 5$cm
	Dynamic errors
Jitter in x, y	0.15 mm, 0.04 mm
Jitter in x′, y′	0.10 mrad, 0.03 mrad
Energy jitter	0.5%
Power supply ripple	1×10^{-4}

[a)] b_1, b_2 and b_3 are the dipole, quadrupole and sextupole components of the magnetic field.

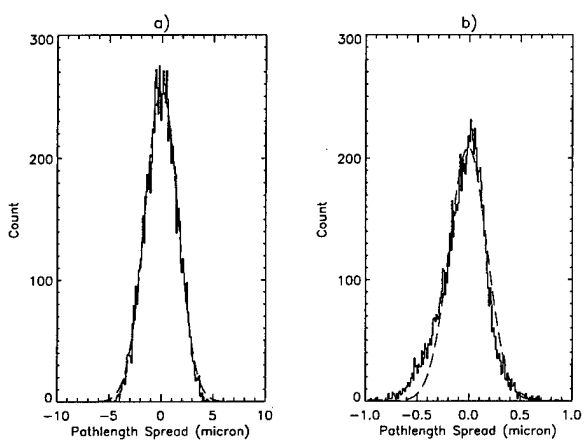

Figure 3: Histograms showing a spread of the pathlengths due to the static errors: a) before correction ($\sigma = 1.57\mu$m), b) after correction ($\sigma = 0.181\mu$m). Note that the scale of the horizontal axis is ten times larger for the first histogram.

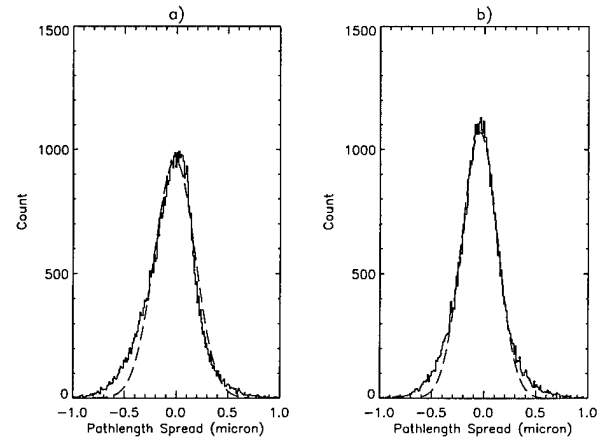

Figure 4: Histograms showing a combined effect of all static errors and all dynamic errors: a) first seed ($\sigma = 0.194$ μm), b) second seed ($\sigma = 0.169$ μm).

distribution truncated at $\pm 2.5\sigma$, where σ is the standard deviation of the distribution).

The static errors can be corrected to a certain extent using a beam-based correction technique. For example, as soon as static errors were added to the bypass lattice, the path length spread rose to about 1 μm (see the histogram in Figure 3a). This growth was mainly due to the setting errors leading to the linear distortions to the lattice. Tuning two families of quadrupoles, excited symmetrically (QF) and asymmetrically (QD), allowed us to reduce the spread to ~ 0.2 μm (see, the histogram in Figure 3b).

There are also dynamic errors, i.e. errors that change each time the beam passes the bypass. They are smaller than static errors, but cannot be fixed with beam-based technique. Figure (4) shows the combined effect of all static and dynamic errors found in two seeds.

4 ANALYSIS

In this section we perform a quantitative analysis of the effect of time-of-flight errors. For this purpose we calculate the degree of coherence between the radiation fields of two undulators, which can be characterized by a dimensionless correlation function [6]:

$$\gamma(\tau) = \frac{\langle E_1(t) E_2^*(t+\tau)\rangle}{[\langle |E_1(t)|^2\rangle \langle |E_2(t)|^2\rangle]^{1/2}} \simeq \exp\left\{-\frac{k^2\Delta\ell^2}{2}\right\} \exp\left\{-\frac{\Delta\omega^2\tau^2}{2}\right\} \exp\{i\omega_0\tau\}, \quad (1)$$

where $E_1(t)$ and $E_2(t)$ is the far field beam radiation in the first and second undulators, respectively, $\Delta\omega$ is the bandwidth of the radiation field, $k = \omega_o/c$ is the wave number, c is the speed of light and ω_0 is the central frequency of the radiation field. Averaging, denoted by the brackets $\langle ... \rangle$, involves integration over a large time interval.

The second exponent in Eq.(1) shows that the coherence drops with the characteristic time scale $1/\Delta\omega$. The first exponent in Eq.(1) shows the effect of imperfections. It shows that the coherence drops with increasing particle longitudi-

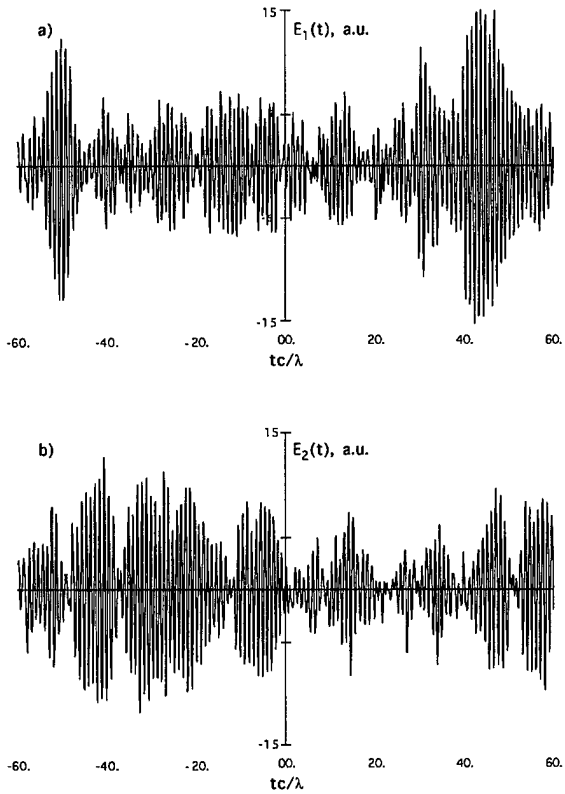

Figure 5: The field of beam radiation in the undulator with ten periods: a) the radiation field $E_1(t)$, b) the radiation field $E_2(t)$. Only a short pattern of the field near the center of the radiation pulse is shown.

nal mixing, $\Delta\ell$, during the beam passage between the two undulators.

We performed the simulation of the coherence of the fields of electron bunch radiation in the first and the second undulators with a 'brute-force' technique. In these simulations we assumed that the two undulators are identical and each undulator has ten undulator periods. The central wavelength of the radiation spectrum is $0.6\,\mu$m. First, we model the field $E_1(t)$ by taking a sum of the radiation fields of 10^4 electrons randomly distributed along the bunch with uniform average longitudinal density. An example of such a field is shown in Figure (5a). Then, we reproduce the actual mixing of the longitudinal coordinates of electrons within the bunch that occurs during the bunch passage through the bypass lattice and model the field $E_2(t)$. An example of this field is shown in Figure (5b). In this example we consider a case when all kind of errors are present (see histogram in Figure 4b).

Finally, we calculate the correlation function of two radiation fields and plotted it in Figure (6a). The maximum of the correlation function characterizes the degree of coherence between the radiation fields E_1 and E_2. It should be 1 if no mixing is present, but here it is dropped to 0.21. According to Eq.(1), this degree of coherence corresponds to $\Delta\ell = 0.171\,\mu$m (recalling that $\lambda = 0.6\,\mu$m), which is in

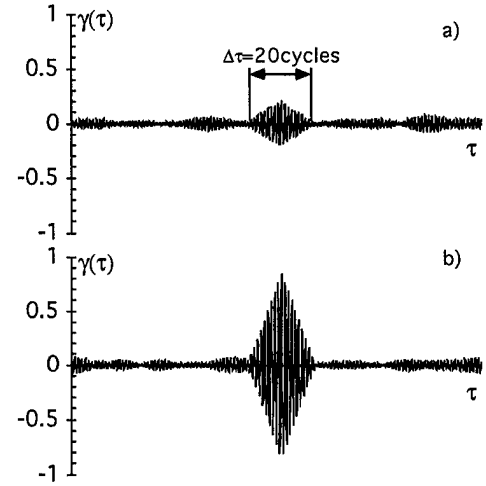

Figure 6: The correlation function of two radiation fields for a beam with the following parameters: a) $\epsilon_x = 1.1 \times 10^{-7}$ m·rad, $\epsilon_y = 6 \times 10^{-8}$ m·rad, $\sigma_{\Delta E/E} = 7 \times 10^{-4}$; b) $\epsilon_x = \epsilon_y = 10^{-8}$ m·rad and $\sigma_{\Delta E/E} = 3 \times 10^{-4}$.

good agreement with the spread of the pathlengths of 0.169 μm in Figure (4b). The degree of the coherence let us also conclude how machine imperfections and beam parameters effect damping time in Optical Stochastic Cooling. In the above example, we should expect approximately 5 times longer damping time, than in the ideal case.

Figure (6b) shows the correlation function calculated for the same lattice and with the same errors, but for $\epsilon_x = \epsilon_y = 10^{-8}$ m·rad and for $\sigma_{\Delta E/E} = 3 \times 10^{-4}$, i.e. for a beam parameters similar to the beams in the TEVATRON collider. The degree of coherence rose to 0.85. Thus, only 15% increase in the damping time is projected in this case.

5 CONCLUSION

We have designed a demonstration beam line to bypass the amplifier and to provide a necessary time delay in the method of Optical Stochastic Cooling. This involved designing a first-order achromat with corrections of the second-order geometrical and chromatic aberrations affecting the time-of-flight properties of the beam line. We have shown, by doing various simulations, that this beam line can meet design requirements with rather conservative tolerance to the errors.

6 REFERENCES

[1] A. Mikhalichenko and M. Zolotorev, Phys. Rev. Lett., v.71, 25, (1993)4146.

[2] M. Zolotorev and A. Zholents, Phys. Rev. E, v.50, N4, (1994)3087.

[3] A. Zholents et.al., this conf., Abstr. Log Number 5799.

[4] W. Wan and M. Berz, Phys. Rev. E, v.54, (1996)2870.

[5] M. Berz, Technical Report MSUCL-977, Michigan State University, (1995).

[6] S. Chattopadhyay et. al., Preprint LBNL-39788,(1997).

AN AMPLIFIER FOR OPTICAL STOCHASTIC COOLING*

A. Zholents and M. Zolotorev
Accelerator and Fusion Research Division,
E.O. Lawrence Berkeley National Laboratory, Berkeley, CA 94720

1 INTRODUCTION

A method of Optical Stochastic Cooling (OSC) of protons/antiprotons and heavy ions in high energy colliders has been recently proposed [1], [2] to achieve much shorter damping time than in conventional microwave stochastic cooling. According to [2], (see also [3] for details on the method of stochastic cooling), stochastic cooling damping time can be written as:

$$\tau \simeq N_b \frac{\Pi}{\Delta f \sigma_z}, \qquad (1)$$

where N_b is the number of particles in the bunch, Π is the circumference of the ring (we assume one cooling system), σ_z is the rms bunch length, and Δf is the bandwidth of the amplifier.[1] Clearly, for a fast cooling it is crucial to have a maximum possible Δf. Remarkably, currently available mediums for optical amplification possess bandwidths up to 10^{14} Hz [4], which is superior to any other amplifier.

Recall that cooling insertion into a storage ring consists of a pick-up undulator, bypass lattice, and kicker undulator. Relativistic beam particles radiate a light signal in a pick-up

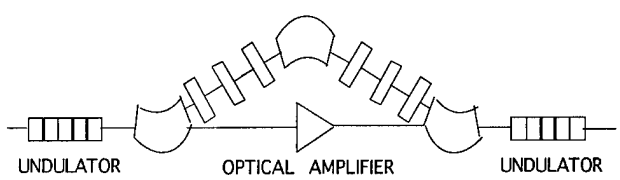

Figure 1: A schematic drawing of the cooling insertion into a storage ring for OSC.

undulator and proceed into the bypass which has a proper path length to provide the time delay needed for light amplification. Then, particles meet their own amplified radiation in the kicker undulator where they receive a correcting kick. The optical amplifier is located between the undulators. In practice, achieving a large difference (say, more than several tens of centimeters) between beam and light paths is difficult and time spent in the amplifier should be minimized. Therefore, we consider a single pass amplifier consisting of few high gain amplification stages.

The intent of this paper is to study specific features of application of the optical amplifier in stochastic cooling. We have found that this is convenient to do using practical examples, and for them we choose cooling of antiprotons in the TEVATRON collider[5] and cooling of electrons in the electron storage ring DELTA[6], although, there are no known for us plans to use OSC on these machines. Table (1) contains lists of parameters for both rings.

Table 1: Beam and ring parameters.

Storage ring	TEVATRON[5]	DELTA[6]
Type of particles	$\bar{p}$	e
Revolution frequency, f_0 [kHz]	49.5	2604
Number of bunches, m	36	1
Number of particles per bunch	1×10^{10}	1×10^{9}
Beam energy, E [GeV]	1000	0.3
Energy spread, σ_e	3×10^{-4}	8×10^{-4}
Bunch length, σ_z [cm]	45	2

2 AMPLIFIER FOR COOLING OF ANTIPROTONS

Damping time calculated for the TEVATRON using Eq.(1) is $\sim$ 3 sec, but an amplifier with the average power $P \simeq 4 \times 10^5$ W would be required for such a fast damping. In this paper we consider much modest (and feasible with the current technology) amplifier with $P \simeq 2$ W. Then, instead of 3 sec, damping time becomes $\sim$23 min. (Damping time scales with the amplifier power as $P^{-1/2}$ [2]).

Table (2) contains optical properties of Ti:sapphire. We choose this material as the amplifier medium because of its wide bandwidth (one of the best among optical amplifiers) and because of its relatively long flourescense lifetime.

Table 2: Optical properties of Ti:sapphire at 300 K.

Property	Value	Ref.
Refractive index, n	1.76	[4]
Temp. coefficient [a)], dn/dT	1.3×10^{-5} K^{-1}	[7]
	1.4×10^{-6} K^{-1}	[8]
Saturation intensity, I_s	2.4×10^5 W/cm^2	[4]
Quantum efficiency, η	0.9	[4]
Flourescence peak, λ_f	780 nm	[4]
Flourescence lifetime, τ_f	3.2 μs	[4]
Bandwidth, FWHM, $\Delta\omega_a/2\pi$	10^{14} Hz	[4]

a) There is a discrepancy in the data cited in Ref. [7] and Ref. [8].

As a pump source for Ti:sapphire, we consider a cw argon-ion laser with 15 W of power operated at $\lambda_{Ar} = 514$ nm. This laser will produce $\sim$ 10 W of the available power in Ti:sapphire at $\lambda_f = 780$ nm. (The remaining 5 W, which accounts for a difference between absorption photon energy and flourescence photon energy and quantum

* Work supported by DOE under Contract DE-AC03-76SF00098.

[1] In a general case Δf is the bandwidth of a whole system that includes pick-up, amplifier and kicker, but in OSC it is the amplifier that determines the overall bandwidth.

efficiency of Ti:sapphire, will go into heat.) From 10 W of available power in the last amplification stage we are going to use approximately 2 W for output signal. The remaining 8 W are continuously drained by the flourescence emission.

A schematic of an amplifier based on Ti:sapphire is shown in Figure (2). The amplifier has four identical stages with a total gain of $G_{dB} = 44$ db. The corresponding bandwidth of the amplifier, defined as the distance between two frequency points at which the amplitude gain has fallen to half the peak, is calculated [9]:

$$\Delta f = \frac{\Delta\omega_a}{2\pi}\sqrt{\frac{3}{G_{dB}/2-3}} \simeq 4\times 10^{13}\text{Hz}. \qquad (2)$$

A small signal gain of the amplifier stage is equal [9]:

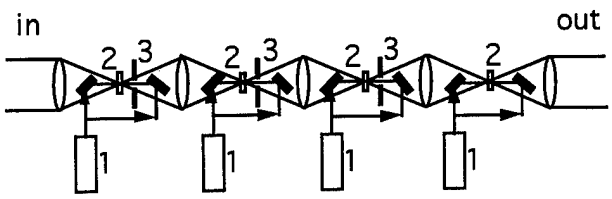

Figure 2: A schematic of the amplifier: (1) is the argon-ion laser, (2) is the Ti:sapphire crystal and (3) is the aperture. Arrows show pumping from two directions.

$$G_0 = \exp\left\{\eta\frac{I_p\lambda_{Ar}}{I_s\lambda_f}\right\}, \qquad (3)$$

where I_p is the pump laser intensity. Using $I_s = 2.4\times 10^5$ W/cm^2, $\lambda_f/\lambda_{Ar} \simeq 1.5$, $\eta = 0.9$ and $G_0 = 12.5$, we get $I_p \simeq 10^6$ W/cm^2. This intensity can be achieved by focusing a 15 W argon-ion laser into an area of $A = 1.5\times 10^{-5}$ cm^2. Assuming a Gaussian beam, we find $\sigma_w \simeq 1.5\times 10^{-3}$ cm in a waist and $Z_R = 2.5$ mm for the Rayleigh length. Therefore, a Ti:sapphire crystal with an absorption length of approximately $\ell = 5$ mm is required. According to [10], this can be made from a sapphire with a dopping of $N_{Ti} \sim 5\times 10^{19}$ Ti^{3+} ions/cm^3 (crystal orientation: c-axis normal to the rod axis).

The value of I_p, calculated above, is ~ 15 times higher than that in commercial Ti:sapphire lasers, which operate not too far from the damage threshold for a Ti:sapphire crystal due to the effect of thermal lensing [11]:

$$\frac{1}{F} \simeq \frac{1}{2\lambda_T}\frac{dn}{dT}\frac{P_T}{A}. \qquad (4)$$

Here F is the focal length of the thermo lens, P_T is the heating power, and λ_T is the thermal conductivity (for sapphire $\lambda_T = 0.33$W/(cm K) at 300 K, and $\lambda_T = 10$W/(cm K) at 77 K [12]). One solution of the thermo lensing problem is cooling the Ti:sapphire crystal to the liquid nitrogen temperature [7]. Then, a sharp rise in the thermo conductivity[2] will overpass the increase of I_p.

Let us consider now how the pulse of beam radiation in the undulator is distorted by the amplification medium. There could be the phase and the amplitude distortions, but only the phase distortions possess a threat for cooling, since the amplitude distortions average out during the damping time which consists of many thousands beam passes through a cooling system.

The phase distortions in the amplified signal appeared as a combination of the phase shifts caused by the depletion of the population inversion density in the medium, plus phase shifts caused by the beam energy spread. In the first case the leading part of the pulse changes the population inversion density of the medium, which will then act in a different manner at the trailing part. This means that different pulse parts will 'see' different optical path lengths, resulting in a time dependent phase change (chirp). To estimate this effect, let us calculate first the available energy in the Ti:sapphire crystal. It is 26 μJ for the above parameters (8W of spontaneous emission and 3.2 μs of a flourescence lifetime). The energy consumed by the amplified pulse is 2W$\times$0.55μs=1.1 μJ, where 0.55 μs is a time interval between bunches in the TEVATRON ($1/mf_0$). Therefore, the change of the population inversion density in Ti:sapphire of the last amplification stage constitutes only 4.3% over the entire pulse length. A corresponding change in the refractive index is $\Delta n = 0.043\beta N_{Ti}$, where the coefficient β was measured to be $\sim 10^{-24}$cm^3 at 300 K [13]. Therefore, a change in the phase from the head to the tail of the pulse is $\Delta nk\ell \simeq \pm 0.4$ rad ($k = 2\pi/\lambda_f$). A reduction in the cooling rate associated with this phase distortion is 8%.

The second effect (that is phase distortions induced by the beam energy spread) develops when a carrying frequency of the light pulse, ω_p, is near the resonance frequency of atomic transitions in the medium. For an estimation of the magnitude of the phase shifts we approximate the complex gain coefficient α_m [9] with the Lorentzian:

$$\alpha_m(\omega) = \alpha_m(\omega_a)\frac{1 - i\frac{\omega-\omega_a}{\Delta\omega_a/2}}{1+\left(\frac{\omega-\omega_a}{\Delta\omega_a/2}\right)^2}, \qquad (5)$$

where ω_a is the central resonance frequency and $\Delta\omega_a$ is the resonance bandwidth. Assuming the input signal in the form:

$$E_{in} = a(t)\,e^{i\omega_p t},\ a(t) = \begin{cases} a_0 & \text{if } -\tau_u/2 < t < \tau_u/2, \\ 0 & \text{otherwise,} \end{cases} \qquad (6)$$

where a_0 is the amplitude, $\tau_u = 2\pi p/\omega_p$ is the duration of the pulse of the undulator radiation of a single particle and p is the number of undulator periods, we get for the amplified signal:

$$E_{out} = a_0 e^{i\omega_p t}\int_{-\infty}^{\infty}\frac{\sin\pi p\frac{\omega-\omega_p}{\omega_p}}{\pi p\frac{\omega-\omega_p}{\omega_p}}e^{4\ell\alpha_m(\omega)+i(\omega-\omega_p)t}d(\omega-\omega_p). \qquad (7)$$

The evaluation of the integral in Eq.(7) for different ω_p allows the finding of the phase shift as a function of ω_p. A corresponding plot is shown in Figure (3). In this calculations we assumed $4\ell\alpha_m(\omega_a) \simeq 5$, which gives a required G_{db}.

[2]There is indication that dn/dT also drops with temperature [7].

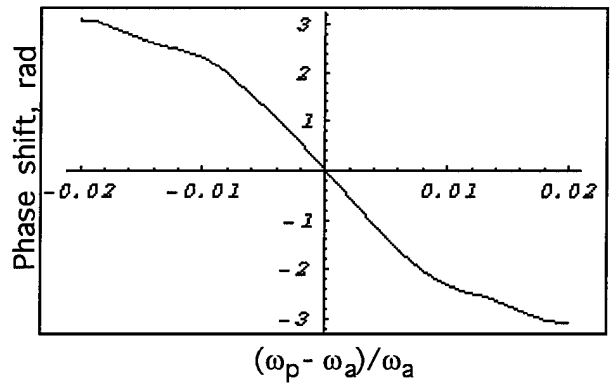

Figure 3: Phase shift of the amplifier output signal versus detuning from the resonance frequency of the atomic transition in Ti:sapphire crystal.

Recall, that the beam energy spread induces the spread of frequencies of the undulator radiation:

$$\omega_p - \omega_0 = 2\omega_0 \frac{\Delta\gamma}{\gamma}, \tag{8}$$

where ω_0 is the frequency of the undulator radiation of the equilibrium particle and $\Delta\gamma/\gamma$ is the relative energy deviation. If $\omega_0 = \omega_a$, i.e. the central frequency of the beam radiation in the undulator is matched to the resonance frequency of the medium, then there are no phase distortions in the amplified signals from the equilibrium particles, and phase distortions in the amplified signals from the non equilibrium particles are kept at a minimum. In this case, the phase shift in the signal for a particle with the energy deviation equal to the r.m.s. energy deviation in the TEVATRON is $\sim$ 0.2 rad. Obviously, it has a negligible effect on the damping time.

Let us now consider two effects related to spontaneous emission. First of all, the spontaneous emission in one stage can reach the neighboring stages and get amplification there. Then, this amplified radiation reaches the next stage and so on. As a result, this process drains the inversion population of the medium. However, draining can be reduced to a minimum, specified below, by installing the aperture near the waist points of the light beam (see Figure 2). Then, only photons of the spontaneous emission emitted in the same mode as signal photons can propagate through the amplifier. The number of such photons is roughly equivalent to the one photon per second per Hz of the bandwidth[3] at the input of the amplifier [9]. It gives us $n_{sp} \simeq 3 \times 10^{13}$photons/sec at the input and $\sim 7 \times 10^{17}$photons/sec at the output, which is equivalent to 0.2 W of the power. Clearly, it is small compared with the 10 W of the available power.

The second effect, related to the spontaneous emission, is the noise that the amplifier adds to the signal. Here we have to compare $\sim 10^5$ photons at the amplifier input that we get by multiplying n_{sp} by the bunch length ($\sim$ 3.3 ns) with the number of photons coming from the signal:

$$n_{ph} = \pi\alpha N_b \simeq 2 \times 10^8, \tag{9}$$

where $\alpha = 1/137$ is the fine structure constant.

[3]Here it is the amplifier power gain bandwidth.

3 AMPLIFIER FOR COOLING OF ELECTRONS

A demonstration experiment for OSC can be performed on electrons. As an example, we consider the storage ring DELTA [6]. Damping time given by Eq.(1) for this ring with beam parameters listed in Table (1) is 0.15 sec. At the same time, the synchrotron radiation damping at the energy of 300 MeV is 0.7 sec. Cooling would require the amplifier with $G_{dB} = 27$ and $P = 1.6$ mW. Such an amplifier is much simpler than the above-considered amplifier and can be made from two or three amplification stages, depending on the difficulty of the thermo lensing problem. Besides that, we do not expect to have any other problem with the amplifier for this machine.

4 CONCLUSION

By considering the optical amplifiers for OSC of antiprotons in the TEVATRON collider with the damping time of 23 min and cooling of electrons in the DELTA storage ring with the damping time of 0.15 sec, we come to the conclusion that, among the various effects known to us, related to optical amplification no one seems capable of having any noticeable impact on the cooling efficiency in OSC.

5 REFERENCES

[1] A. Mikhalichenko and M. Zolotorev, Phys. Review Letters, v.71, No.25, (1993), p.4146.

[2] M. Zolotorev and A. Zholents, Phys. Review E, v.50, No.4, (1994), p.3087.

[3] D. Möhl, CERN Accelerator School Report, CERN 87-03, (1987), p.453.

[4] W. Koechner, Solid-State Laser Engineering, Springer-Verlag, New York, (1992).

[5] G. Jackson, G.W. Foster, Particle Acc. Conf. PAC95, Dallas, v.1., (1995), p.428.

[6] K. Wille, European Particle Acc. Conf. EPAC96, Barcelona, v.1, (1996), p.95.

[7] P.A. Schultz, IEEE Journal of Quantum Electronics, v.27, No.4, (1991), p.1039.

[8] A. Penzkofer, Progress in Quantum Electronics, v.12, No.4 (1988).

[9] A.E. Siegman, *Lasers*, University Science Books, Mill Valley, California, (1986)

[10] Technical specifications for Ti:sapphire crystal. Union Crabide Inc., (1994).

[11] X.G. Huang et. al., Journal Opt. Soc. America B, v.13, No.12, (1996), p.2863.

[12] M.G. Holland, Journal of Appl. Phys., v.33, (1962), p.2910.

[13] K.F. Wall et al., Opt. Lett., v.14, (1989), p.180.

SIMULATION OF BEAM BUNCHING WITH ELECTRON COOLING FOR THE ION STORAGE RING OF RIKEN RI-BEAM FACTORY PROJECT

M. Takanaka and T. Katayama*
Cyclotron Laboratory, RIKEN, 2-1 Hirosawa, Wako-shi, 351-01 Japan
*Center for Nuclear Study, School of Science, University of Tokyo,
3-2-1 Midoricho, Tanashi-shi, 188 Japan

Abstract

Beam bunching with electron cooling can be carried out under the control which keeps the momentum spread constant. Simulation of the bunching for a 150 MeV/u U^{92+}_{238} beam in DSR has been done in which space charge effects and a transverse nonlinear effect are taken into account. Results of the simulation are presented about the transition of the bunching and the longitudinal and transverse behavior of the beam near the equilibrium.

1 INTRODUCTION

Collision experiments are planned with ion-ion or ion-electron beams in Double Storage Rings (DSR). Coasting ion beams are supplied from the cooler storage ring (ACR) or the booster synchrotron (BSR). The luminosity of the beams can become high by bunching them. The longitudinal space charge force is dominant over the longitudinal forces induced through the coupling impedances between beams and the vacuum chamber in the energy region 100 MeV/u to 1.5 GeV/u of the ring. As the currently-designed ion storage ring runs below the transition energy [1], the space charge force makes the bunch long. Electron cooling force can make the bunch short under an RF-voltage application. The bunching with electron cooling has been carried out at IUCF [2] and GSI [3] focusing on study of the longitudinal behavior of beams at the equilibrium, and on study of the longitudinal and transverse ones at the equilibrium, respectively.

The previous simulation of beam bunching under the momentum-spread control showed effectiveness of the cooling in the bunching, but whether the bunching process is stable or not was left to be answered [4]. The question is answered here. The simulation has been improved not only in taking into account more force elements, but also in the following;

- representation of a bunch of beam line density, which is used for evaluation of the longitudinal space charge force, by Fourier series expansion up to seventieth series,
- evaluation of the space charge forces every one-eightieth revolution.

2 BUNCHING PROCEDURE

A beam is injected to DSR, after it is accumulated as a coasting beam and cooled down to a given momentum spread and to such a transverse emittance in ACR that it does not meet resonances. The beam is cooled again there by electron cooling while RF is applied under the momentum spread control which increases the RF voltage so that the momentum spread stays constant. The beam becomes bunched as RF voltage. The larger the spread is, the higher can be the threshold of the beam line density due to the microwave instability [5]. The momentum-spread control is necessary to a high line-density beam. The bunching makes the space charge effects strong. The betatron tune shift due to the effects is dependent on the transverse amplitude, when the transverse charge distribution is not flat. Resonances make the transverse amplitude of ions large. So, the ions become off resonance. The longitudinal oscillation simultaneously makes crossings of resonances. The ions can have small amplitude due to the electron cooling again. Therefore, the beam can be expected to eventually dodge resonances. It is, however, dependent on the strength of the nonlinearity whether the ions have small amplitude again or not. The simulation has been done just for beams in DSR.

3 FORCE ELEMENTS

In the simulation, the following forces have been taken into account as forces acting on ions:

- the RF force,
- the longitudinal electron cooling force and the transverse one [6],
- the transverse linear force coming from the ring lattice and nonlinear one,
- the longitudinal space charge force and the transverse one.

The other collective forces induced through the vacuum chamber or RF cavities have been neglected because of, except for the resistive-wall force, their smallness by comparison with the space charge forces in the DSR energy region [7] and because the instability up to the fifth synchrotron mode due to the transverse resistive-wall force can be damped even at the chromaticity of -30 near the vertical natural one for the full bunch length of 1 m [8]. The space charge effects due to a colliding electron beam are left to be

0-7803-4376-X/98/$10.00 © 1998 IEEE

considered. The above electron cooling force does not include the component which induces betatron tune shifts of 0.02 for the flat transverse distribution of the electron beam at the cooling section. The component has been neglected because of the smallness by comparison with the shift due to ion-beam's own space charge.

4 SIMPLIFICATION

The following simplification has been done in the simulation mainly in order that one reduces CPU-time load and keeps statistic accuracy.

i) Except for the Twiss parameters during the cooling section, β function along the ring has been equal to the average one $\overline{\beta} = r/\nu$ where r is the mean radius of the ring and ν the betatron tune. α function has been 0.

ii) The longitudinal space charge force is induced by beam's space charge through a perfectly conducting vacuum chamber of the inner radius b. The ions of charge qe on the central orbit get the energy ΔE_{sp} from the force during time Δt, when the transverse charge distribution is round and Gaussian with one-dimensional standard deviation σ which is much smaller than the radius b [5];

$$\Delta E_{sp} = iqe \left[\frac{Z_\parallel}{n}\right]_{sp} \frac{v}{2\pi}\frac{dI}{ds}\Delta t,$$

$$\left[\frac{Z_\parallel}{n}\right]_{sp} = i\frac{g_0}{2\beta\gamma^2}Z_0, \quad g_0 \approx 0.577 + 2\log\left(\frac{b}{\sqrt{2}\sigma}\right),$$

where the beam of velocity v has current distribution I along the longitudinal direction s, and β and γ are the relativistic constants of v, and Z_0 impedance of free space. Longitudinal variation of the transverse charge distribution has been neglected. The deviation σ has been replaced by the r.m.s. of the transverse charge distribution. All ions at the position s have been made to get the same energy ΔE_{sp}, with the transverse distribution neglected.

iii) To estimate the transverse component of the electric field due to the space charge, the field has been treated the same as the field from a point charge in free space points strictly radially outward in the ultra-relativistic case. The field is not dependent on the structure of the chamber.

iv) The chromaticity has been set zero for both transverse directions. This simplification is just for clearly looking into the betatron tune distribution without noise due to the momentum spread.

5 PARAMETERS OF THE RING AND A BEAM

The simulation has been done just for a 150 MeV/u U^{92+}_{238} beam of current 3.4 mA. In Table 1, are shown parameters of the ring, a coasting beam, and the electron cooling, which have been used as input data of the simulation. The initial distribution of a coasting beam of 10^4 particles for the simulation has been flat along the RF phase axis, and Gaussian along the momentum axis, in the horizontal phase space and in the vertical one, respectively.

Table 1: Parameters of the ring, a coasting beam, and the electron cooling.

Ring	
Circumference	260 m
Momentum compaction factor	0.03772
Betatron tune (ν_x /ν_y)	7.38/5.8
Twiss parameters at the cooling section	
$\alpha_x^{ec} = \alpha_y^{ec}$	0
$\beta_x^{ec} = \beta_y^{ec}$	7 m
RF harmonics	87
Inner radius of the vacuum chamber b	4 cm
Coasting beam	
Momentum spread (6×rms)	10^{-3}
Rms transverse emittance ($\epsilon_x = \epsilon_y$)	$10^{-6}\pi$ mrad
Electron cooling	
Electron current	5 A
Cathode temperature kT_c	0.1 eV
Length of the cooling section	3 m
Electron-beam radius at the section	25 mm
Longitudinal magnetic field at the section	1 kG

6 RESULTS

Here are presented results of two simulated cases, the one being without nonlinear force and the other with it. In the latter case, as a source of nonlinear force a sextupole field has been numerically located at the cooling section with the field strength $B''\ell\beta^{ec}/2B\rho$ of 0.3 m^{-1} , β^{ec} being the beta function at the section. The strength is equal to about one-tenth to one-thirtieth of effective strengths used for beam extractions. The field induces the resonances $3\nu_x = 22$, $-\nu_x + 2\nu_y = 4$, and $\nu_x = 7$ near the working point, whose stop bandwidths are estimated to be about 0.0001, 0.0002, and 0.0004 for the rms emittance of $10^{-6}\pi$ mrad, respectively [9]. Figure 1 shows the transition of the bunching and no remarkable difference between the cases. The fluctuation of the momentum spread stays within ± 2 %, and that of the transverse emittance within ± 1 %. The bunching process is seen to be stable. After 30 ms on, the bunch length decreases slowly still, while the transverse emittance, that is, the mean of the horizontal one and the vertical one turns to increase. The rms transverse emittance is seen not to become so small as $5 \times 10^{-7}\pi$ mrad due to the space charge effects. The bunching factor, or the ratio of the full bunch length to the bunch separation becomes 0.34 at 50 ms, and the maximum peak current becomes 32 mA. It remains to be answered how long it takes to arrive at the equilibrium.

Figure 2 shows the ion distribution in the longitudinal phase space at 50 ms. The ions are classified roughly into two groups. The one locate densely and narrowly in the center, and the other thinly around the one. The distributions projected to each axis can be approximately represented with a broad Gaussian curve and a narrow one. The ion-population ratio of the central narrow group to the whole is estimated to be about 28 %, which includes 10 %

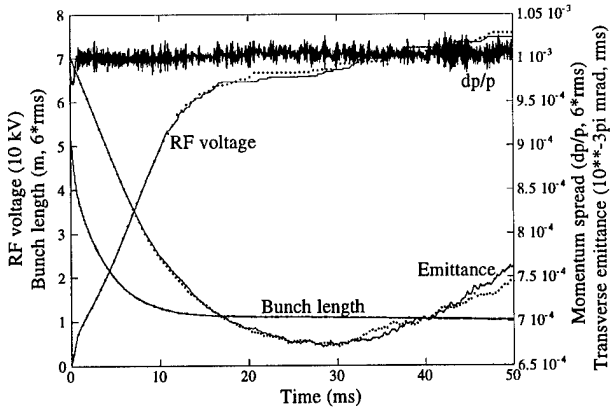

Figure 1: Transition of the bunching. The solid lines are for the case without the nolinearity, and the dotted lines for the case with it.

of the part under the narrow structure, by using the representation. The central group rotate at the synchrotron tune near zero in the longitudinal phase space because of the distortion of RF wave form due to the space charge effects, and the other near the tune corresponding to no distortion, as shown in Fig. 3. The transverse profile at 50 ms is seen to be more centralized than a Gaussian distribution, as shown in Fig. 4. The incoherent betatron tune shift due to the space charge effects reaches -0.5, as shown in Fig. 3, which means that the beam can meet major resonances. The effect of the resonaces at least due to the above sextupole has been already described to be negligibly small.

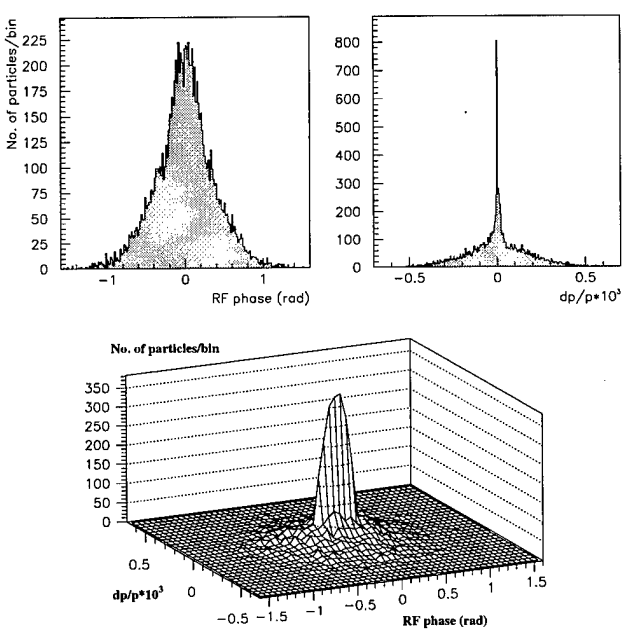

Figure 2: Longitudinal phase space distribution after 50 ms bunching.

7 CONCLUSION

The simulation of the bunching of a 150 MeV/u U^{92+}_{238} beam of 3.4 mA under the momentum-spread control at the electron density of 2.5 kA/m^2 at the cooling section has shown the following characteristic of the bunching.

- The process of the bunching is stable.
- The full bunch length becomes1.03 m after 50 ms bunching. The bunching factor is 0.34.
- The rms transverse emittance can not become so small as $5 \times 10^{-7}\pi$ mrad due to the space charge effects even without the effect of the intrabeam scattering.
- The sextupole field of the strength of 0.3 m^{-1} induces negligibly small effects of resonance, although the incoherent betatron tune spread due to the space charge effects reaches 0.5.

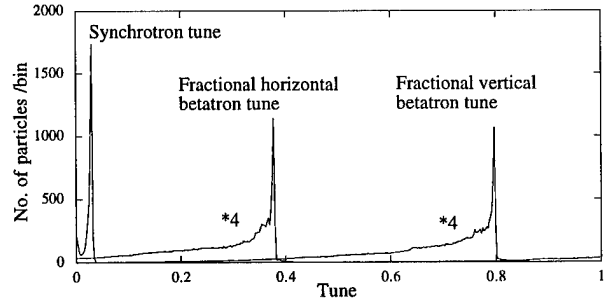

Figure 3: Tune distribution for 5000 particles after 50 ms bunching. The distributions of betatron tune are magnified vertically four times.

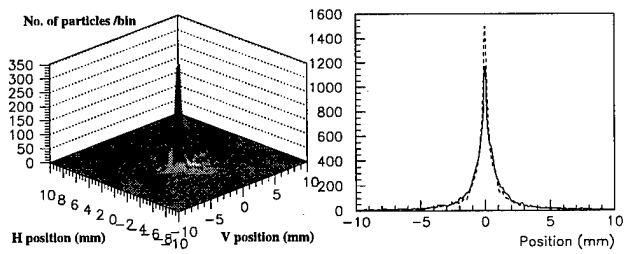

Figure 4: Transverse profile at the cooling section after 50 ms bunching. The solid line shows the vertical profile, and the broken line the horizontal one.

8 REFERENCES

[1] N.Inabe, T.Katayama, in these proceedings.

[2] T.J.P.Ellison *et al.*, Phys. Rev. Lett. 70, 790 (1993). S.S.Nagaitsev *et al.*, CERN 94-03, 405 (1994).

[3] I.Hofmann, Proc. of EPAC 94, 218 (1994). I.Hofmann *et al.*, Phys. Rev. Lett. 75, 3842 (1995).

[4] M.Takanaka, T.Katayama, Proc. of EPAC 96, 1991 (1996).

[5] A.Hofmann, CERN 77-13, 139 (1977).

[6] I.N.Meshkov, Phys. Part. Nucl. 25 (6), 631 (1994).

[7] M.Takanaka, T.Katayama, Proc. of EPAC 96, 1138 (1996).

[8] B.Zotter, F.Sacherer, CERN 77-13, 175 (1977).

[9] L.R.Evans, CERN 84-15, 319 (1984).

GENERATION OF SUB-PICOSECOND X-RAY PULSES AT BESSY-II

S. Khan, BESSY-II, Rudower Chaussee 5, 12489 Berlin, Germany

Abstract

Two methods to generate sub-picosecond x-ray pulses using the electron beam of the BESSY-II storage ring in combination with a femtosecond laser are discussed:

(1) Thomson scattering of laser pulses crossing electron bunches at a small angle.

(2) Energy-modulation of a short region within an electron bunch interacting with the laser in an undulator, and subsequent emission of synchrotron radiation.

1 INTRODUCTION

The technology of visible laser pulses below 100 fs duration is well established, whereas pulses produced by VUV and x-ray sources are in general much longer than 1 ps.

This paper describes two methods to generate sub-picosecond x-ray pulses using the electron beam of a third-generation synchrotron light source in combination with a femtosecond laser.

A suitable laser is a Ti:sapphire system based on chirped pulse amplification (CPA) with a wavelength of 800 nm, a typical pulse duration of 100 fs FWHM (43 fs rms) and an average power of a few Watt.

All estimates are based on the storage ring parameters of the high-brilliance synchrotron light source BESSY-II currently under construction at Berlin-Adlershof [1]. The following modes of operation are considered:

- A beam energy of 1700 MeV or 900 MeV.
- 100 mA in 320 bunches or 10 mA in a single bunch.

2 THOMSON SCATTERING

The generation of sub-picosecond x-ray pulses by crossing a femtosecond laser at a right angle with a 50 MeV electron beam has been successfully demonstrated at the Advanced Light Source (ALS) at Berkeley [2]. An analogous experiment at BESSY-II using the 50 MeV injection microtron is presently not considered because of the comparatively low beam current from this machine.

Generating x-ray photons using the BESSY-II storage ring beam at higher energy requires small crossing angles (10-50 mrad). Although the scattering rate is strongly reduced at small angles, there are several advantages to this configuration:

- Extremely short x-ray pulses ($\approx$ laser pulse length).
- Small source point (high brilliance).
- Small divergence of the x-ray beam (high brilliance).
- Small electron divergence (little spectral broadening).

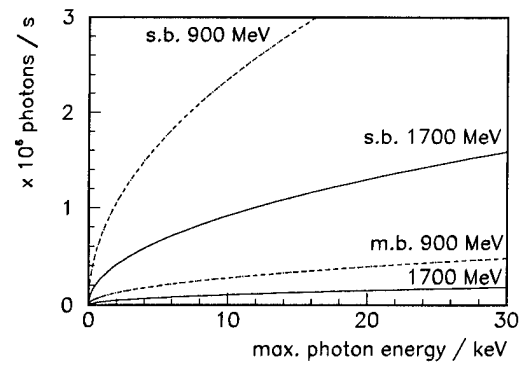

Figure 1: Scattering rate as function of the endpoint of the scattered photon spectrum for singlebunch (s.b.) and multibunch (m.b.) operation of the BESSY-II storage ring at 900 MeV and at 1700 MeV.

2.1 *Properties of Thomson Scattered Photons*

In a right-angle geometry, the transit time of the laser pulse through the electron bunch adds to the duration of the scattered photon pulse. When the laser and the electron beam are almost parallel, the x-ray pulse duration is essentially given by the laser pulse length.

The endpoint of the scattered photon spectrum is

$$E'_{\max} = 2\gamma^2 E(1 - \cos\alpha), \tag{1}$$

where E is the laser photon energy, α is the crossing angle, and γ is the electron Lorentz factor. For a laser pulse with N_γ photons crossing a bunch with N_e electrons, an upper limit for the scattering rate is

$$N = \frac{N_\gamma N_e \sigma_{\mathrm{Th}}}{2\pi\,\sigma_y\,\sigma_z} \cdot \frac{1-\cos\alpha}{\sin\alpha} \quad (\text{for } \sigma_x \ll \sigma_z,\ \beta = 1). \tag{2}$$

Here, $\sigma_{\mathrm{Th}} = 6.7 \cdot 10^{-29}$ m^2 is the Thomson cross section, σ_z is the rms bunch length, σ_x is the bunch size in the crossing plane, and σ_y is the bunch size perpendicular to it. Equation 2 holds for a transverse laser size being small compared to bunch dimensions. Half of the N photons are scattered into a cone of opening angle $2/\gamma$.

The photon scattering rate N as function of the endpoint energy E' is shown in figure 1 for different modes of operation. Singlebunch mode at a low beam energy is clearly favorable.

0-7803-4376-X/98 /$10.00 © 1998 IEEE

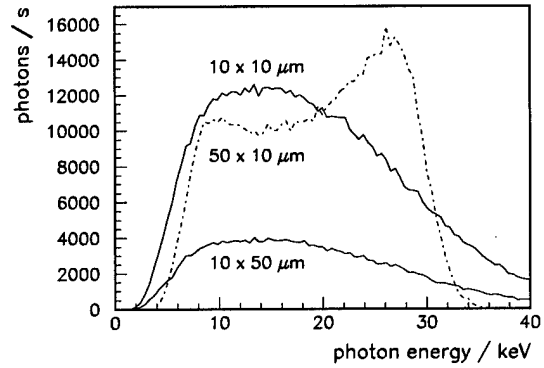

Figure 2: Spectra of Thomson scattered photons for different laser waists (horizontal × vertical rms size).

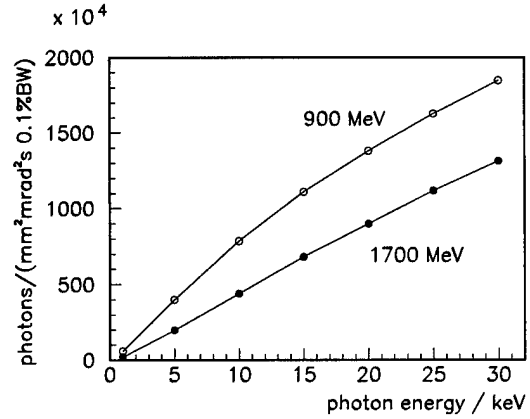

Figure 3: Brilliance of Thomson scattered photons as defined in equation 3 for single-bunch mode.

2.2 *Simulation of the Thomson Scattering Process*

In order to study the Thomson scattering process in more detail, a Monte Carlo simulation was performed. Event by event, the spatial and angular photon coordinates within a Gaussian laser pulse, the location of the interaction within the electron bunch, the angular electron coordinates, the polar and the azimuthal scattering angle were randomly chosen. For horizontal crossing, the following observations were made:

A small laser waist (e.g. 10×10 μm, figure 2) yields a large scattering rate, but the spectrum is broadened due to the angular divergence of the laser. Increasing the vertical waist size only reduces the rate, whereas increasing the horizontal waist reduces the broadening effect without affecting the rate.

Taking 85-100% of the endpoint energy into account, the scattered photon brilliance defined as

$$B = \frac{\text{photons}/(15\%\text{bw s})}{150 \cdot 2\sigma_x 2\sigma_y 2\sigma'_x 2\sigma'_y} \left[\frac{\text{photons}}{0.1\%\text{bw mm}^2\text{mrad}^2\text{s}}\right] \quad (3)$$

is shown in figure 3 for singlebunch operation. Here, $\sigma_{x,y}$ is the electron beam size, while $\sigma'_{x,y}$ is the observed rms angular spread of photons within a 15% bandwidth.

3 LASER-ELECTRON INTERACTION

The second method discussed in this paper and proposed by [3] is based on a short laser pulse of wavelength λ_L travelling together with an electron bunch of Lorentz factor γ through an undulator of period length λ_u. If the undulator parameter K satisfies the resonance condition

$$(1 + K^2/2)\lambda_u = 2\gamma^2\lambda_L, \quad (4)$$

the laser produces a short region within the bunch, where electrons have gained or lost energy, depending on their phase relative to the laser field. A transverse displacement of these energy-modulated electrons by dispersion in the next bending magnet or undulator allows to extract a short synchrotron radiation pulse.

3.1 *Estimates*

Among the to-date specified insertion devices for BESSY-II, only the W/U-125 with $N_u = 32$ periods of length $\lambda_u = 125$ mm and $K \leq 12.8$ satisties equation 4, provided a Ti:Sa CPA laser with second harmonic generation is employed i.e. $\lambda_L = 400$ nm, which leads to $K = 11.8$.

Following [3], the amplitude for an energy-modulation ΔE is given by

$$(\Delta E)^2 = 4\pi\alpha E_L A_L \frac{K^2/2}{1 + K^2/2} \cdot \frac{\Delta\omega_L}{\Delta\omega_u}, \quad (5)$$

where $E_L = 3.1$ eV is the laser photon energy and A_L is the energy per laser pulse. For a typical laser pulse length of 100 fs FWHM (or $\tau_L = 43$ fs rms), the laser/undulator bandwidth ratio is $\Delta\omega_L/\Delta\omega_u \approx 0.3$. Demanding a modulation amplitude of 2% of the beam energy, equation 5 leads to $A_L = 2.2$ mJ for a beam energy of 1700 MeV. Consequently, the repetition rate f is 0.45 kHz for an average laser power of 1 W.

The number of energy-modulated electrons per second is

$$N = f\,\eta\,N_e\,\tau_L/\tau_e, \quad (6)$$

where $\eta \approx 0.2$ [3] accounts for the fact that only a fraction of the electrons acquire a sufficiently large energy deviation. Table 1 summarizes the result for multibunch mode ($N_e = 1.6 \cdot 10^9$ electrons/bunch and rms bunch length $\tau_e = 17$ ps) at 1900 MeV and at 900 MeV. Singlebunch mode is not considered, because the background from previous interactions would limit f to the radiation damping rate (120 Hz at 1700 MeV, 20 Hz at 900 MeV).

E / MeV	A_L / mJ	f / kHz	N / s^{-1}
1700	2.2	0.45	$3.6 \cdot 10^8$
900	0.6	1.6	$1.3 \cdot 10^9$

Table 1: Estimates on energy modulation for multibunch mode at a beam energy of $E = 1700$ MeV and 900 MeV.

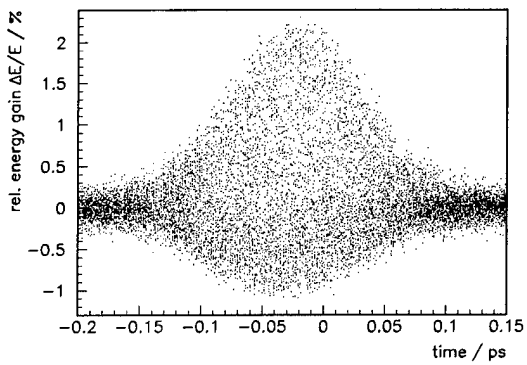

Figure 4: Distribution of electrons in time and energy after interacting with a laser pulse.

3.2 *Simulation of the Laser-Electron Interaction*

A numerical integration of the energy

$$\Delta E = -e\,c \int_{t_-}^{t_+} x'(t)\,\mathcal{E}(t)\,\sin\left[2\pi\,z(t)/\lambda_L\right]\,dt \qquad (7)$$

gained or lost between the two ends of the undulator at time $t_\pm$ was performed. $\mathcal{E}(t)$ is the electric field at the time-dependent electron position, and $x'(t)$ is the horizontally transverse electron velocity.

Figure 4 shows the distribution of 10^4 macro-particles in time and energy after interacting with a 400 nm laser pulse of 43 fs rms length. The following parameters were optimized numerically:

- The largest modulation amplitude was obtained for a transverse laser waist of 150 μm rms in both dimensions, given an electron waist size of 290×14 μm rms.
- Detuning the undulator parameter by 1% away from the resonance value K yields the asymmetric energy distribution shown in the figure.
- The energy per laser pulse was adjusted such that a peak modulation of 2% of the beam energy was obtained.

The results for multibunch operation at 1700 MeV and at 900 MeV are shown in table 2. The repetition rate is lower than estimated before, but detuning K allows to use a larger fraction of modulated electrons. The table lists the number of electrons with $\Delta E/E > 0.5\%$. Their originally 50 fs long distribution is stretched to 170 fs rms, if the radiating device is placed 15 m away in the next straight section, assuming the present momentum compaction of $7 \cdot 10^{-4}$.

The final task is to demonstrate that synchrotron radiation from the energy-modulated electrons can be separated from the large background created by the other electrons.

E / MeV	A_L / mJ	f / kHz	N (>0.5%) / s^{-1}
1700	4.0	0.25	$4.0 \cdot 10^8$
900	1.1	0.90	$1.7 \cdot 10^9$

Table 2: Simulation results for multibunch mode.

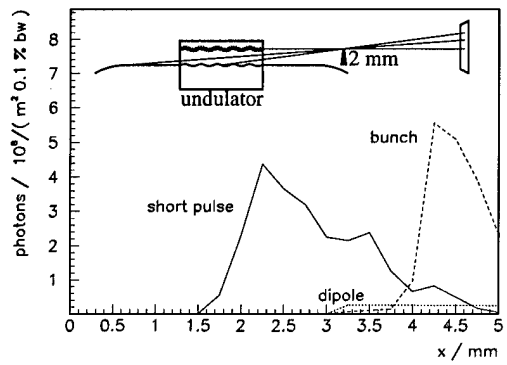

Figure 5: Radiation from energy-modulated electrons and from the other electrons of the bunch after passing a collimator edge at $x = 2$ mm, as scetched in the figure.

3.3 *Simulation of the Short Pulse Extraction*

In a simulation, radiation from macro-particles randomly chosen within the distribution of figure 4 was calculated numerically, assuming a dispersion of 0.2 m at the position of a U-49 undulator ($N_u = 84$, $\lambda_u = 49$ mm, $K = 1$).

A collimator edge was introduced 6 m downstream of the undulator center at a transverse position of 2 mm with respect to the undulator axis. The radiation hitting a screen 12 m from the undulator center is shown in figure 5. The short pulse is sufficiently separated from the bulk of radiation from other electrons. Also shown is a negligible amount of radiation from the dipole upstream of the U-49.

1-2% of backgrond radiation are expected from off-energy electrons due to Bremsstrahlung and Touschek scattering and from non-Gaussian beam tails due to Coulomb scattering. The amount of photons from Compton scattering and fluorescence at the collimator tip is negligible. Energy-modulated electrons from previous interaction cause no background after 1-2 radiation damping times.

4 ACKNOWLEDGEMENTS

This work is funded by the Bundesministerium für Bildung, Wissenschaft, Forschung und Technologie and by the Land Berlin. Useful discussions with M. Scheer, G. Wüstefeld (BESSY-II, Berlin), W. Becker, I. Will (MBI, Berlin), B. Keil, N. Marquardt (DELTA, Dortmund), A. Zholents, M. Zoloterev (LBL, Berkeley) are gratefully acknowledged.

5 REFERENCES

[1] E. Jaeschke: 'Status of the High Brilliance Synchrotron Light Source BESSY-II', this conference.

[2] R.W. Schoenlein et. al.: 'Femtosecond X-ray Pulses at 0.4 Å Generated by 90° Thomson Scattering', Science Vol.274 (1996), p.236.

[3] A.A. Zholents and M.S. Zoloterev: 'Femtosecond X-ray Pulses of Synchrotron Radiation', Phys. Rev. Lett. Vol.76, No.6 (1996), p.912.

ENERGY LOSS OF PROTON AND LEAD BEAMS IN THE CERN-SPS

J. Arnold, T. Bohl, H. Burkhardt, R. Cornali, K. Cornelis, G. Engelmann,
R. Giachino, A. Hofmann, M. Jonker, T. Linnecar, M. Meddahi, L. Normann,
E. Shaposhnikova, A. Wagner and B. Zotter, CERN, 1211 Geneva 23, Switzerland

Abstract

The energy loss of an unbunched beam circulating in the CERN-SPS has been obtained from the observed frequency change of a longitudinal Schottky signal. This experiment was carried out for protons at 14, 120 and 270 GeV/c and for lead ions Pb^{82}_{208} at $Z \cdot 270$ GeV/c momentum. The dominant effects which determine the energy loss are synchrotron radiation, ionization of the residual gas and parasitic mode loss in the resistive longitudinal impedance. Since all the protons in a lead nucleus radiate coherently the synchrotron radiation is proportional to Z^2 like the other effects. The experimental results are analyzed and the contributions of the individual effects determined. Using an impedance of $|Z/n| \approx 12\,\Omega$ gives the best fit through the experimental data.

1 INTRODUCTION

This experiment was carried out to measure the energy loss due to the synchrotron radiation emitted by protons and lead ions and due to the resistive wall impedance but also the energy loss due to ionization of the rest gas had to be considered.

The synchrotron radiation of a radially accelerated charge in free space is well known. For the fully stripped lead ions Pb^{82}_{208} it has to be considered that the charge is $q = Ze$ and all the 82 protons radiate coherently resulting in a emitted power being proportional to Z^2. Furthermore the shielding effect by the vacuum chamber has to be taken into account. For the energy loss caused by the impedance of the beam surroundings we have to consider that the unbunched beam consists of point charges without any phase relation between them. Each charge produces an electric field concentrated in the transverse direction with an opening angle of about $\pm 1/\gamma$ which induces on the wall a short current pulse of length proportional to $1/\gamma$. By measuring the loss for different beam energies some information about the resistive wall impedance can be obtained. In the following we will discuss the different effects leading to an energy loss and calculate the expected magnitude for the conditions used in the experiment. We make some estimates of the impedance based on earlier measurements done in the SPS and similar machines and we will use the actual measured pressures of the residual gas to estimate the loss due to ionization. The expected effects are presented and compared with the experimental results.

circumference	$2\pi R$	m	6912
bending radius	ρ	m	741.3
revolution freq.	ω_0	s^{-1}	2π 43400
mom. compaction	α_c		0.0018
chamber height	h_{MBA}	mm	24
"	h_{MBB}	mm	41
eff. chamber radius	b	mm	35

Table 1: Relevant SPS parameters

2 KINEMATICS

A particle with charge q, rest mass m_0 and momentum p circulates in a transverse magnetic field B on an orbit with radius of curvature ρ given by

$$\frac{1}{\rho} = \frac{qB}{p} = \frac{qB}{m_0 c \beta \gamma}. \tag{1}$$

Since the bending radius and the field are the same for protons ($q = e$, $m_0 = m_p$) and lead ions ($q = Zq$, $m_0 = m_{Pb}$) we have the relation

$$p_{Pb} = m_{Pb}\, c\, \beta_{Pb}\, \gamma_{Pb} = Z\, p_p = Z\, m_p\, c\, \beta_p\, \gamma_p. \tag{2}$$

As approximations we take for the mass of the lead isotope Pb^{82}_{208} ion $m_{Pb} = Am_p$ and set $\beta = 1$ except where it is subtracted from a quantity close to unity. With this we get for the two particles circulating on the same orbit in the same magnetic field

$$\frac{\gamma_{Pb}}{\gamma_p} \approx \frac{Z}{A} = \frac{82}{208} = 0.394. \tag{3}$$

In the experiment the energy loss has been determined by observing the change of the frequency $\omega_s = 2\pi f_s = k\omega_0$ of a Schottky signal being a harmonic of the revolution frequency ω_0 which depends on the momentum

$$\frac{d\omega_0}{\omega_0} = -\eta \frac{dp}{p} \approx -\eta \frac{dE}{E} \quad \text{with} \quad \eta = \alpha_c - \frac{1}{\gamma^2} \tag{4}$$

where α_c is the momentum compaction. The relative energy loss per unit time or the energy loss U per turn is obtained from the observed time variation of the Schottky signal frequency

$$\frac{1}{E}\frac{dE}{dt} = -\frac{1}{\eta f_S}\frac{df_S}{dt} \quad \text{and} \quad U = \frac{E}{\eta f_0 f_S}\frac{df_S}{dt}. \tag{5}$$

Table 1 lists the relevant parameters of the SPS.

0-7803-4376-X/98/$10.00 © 1998 IEEE

3 SYNCHROTRON RADIATION

For the calculation of the energy loss due to synchrotron radiation we use the equation

$$U_s = \frac{q^2\beta^3\gamma^4}{3\epsilon_0\rho} \approx \frac{q^2\gamma^4}{3\epsilon_0\rho}. \quad (6)$$

Here q is the charge of the circulating particle. For the proton it is just the elementary charge $q = e$. However, for the lead ion we have $q = Ze$ since the nucleus containing Z protons can be considered as a point charge within the scale of the wavelength of the emitted radiation, in other words, all the protons of the lead nucleus radiate coherently. Using the ratio between the Lorentz factors for protons and the lead ions (3) we get for the energy loss ratio

$$\frac{U_{Pb}}{U_P} = \left(\frac{\gamma_{Pb}}{\gamma_P}\right)^4 Z_{Pb}^2 = \frac{Z_{Pb}^6}{A_{Pb}^4} = \frac{82^6}{208^4} = 162.4. \quad (7)$$

The relative energy loss per unit time

$$-\frac{1}{E}\frac{dE}{dt} = f_0\frac{U_s}{E} = \frac{e^2Z^2f_0\gamma^3}{3\epsilon_0 A m_P c^2\rho} = \frac{1}{2}\frac{1}{\tau_{\rm rad}}, \quad (8)$$

is half the total radiation damping rate $1/\tau_{\rm rad}$ and has the ratio

$$\frac{\left(\frac{1}{E}\frac{dE}{dt}\right)_{Pb}}{\left(\frac{1}{E}\frac{dE}{dt}\right)_P} = \frac{Z^5}{A^4} = 1.98. \quad (9)$$

We arrive at this somewhat surprising result that the lead ions have a larger damping rate and move faster to the inside than the protons. But this is true only in free space and the radiation from lead, being at lower frequencies, is reduced by the vacuum chamber more than the one from protons. The spectrum of the emitted radiation is characterized by the critical frequency ω_c of wavelength λ_c which divides it into two parts of equal power

$$\omega_{crit} = \frac{3c\gamma^3}{2\rho}\ ,\ \lambda_c = \frac{4\pi\rho}{\gamma^3}. \quad (10)$$

So far the synchrotron radiation has been calculated for the case of free space. The presence of the conducting vacuum chamber may reduce the emitted radiation because the lower frequencies cannot propagate. The calculation of this suppression is quite complicated. We use here an equation from [1, 2] which gives the frequency ω_{th} above which radiation is possible

$$\frac{\omega_{th}}{\omega_0} = \sqrt{\frac{2}{3}}\left(\frac{\pi\rho}{h}\right)^{3/2}. \quad (11)$$

Here, h is the full height of the chamber listed in table 1. The emitted power is calculated for the two types of magnet chambers using the simplifying assumption that the synchrotron radiation spectrum lying above ω_{th} is not changed while the part below is completely suppressed.

4 IONIZATION OF THE RESIDUAL GAS

The energy loss due to ionization of the residual is [3]

$$\frac{dE}{dX} = -K\frac{Z^2}{\beta^2}\frac{Z^*}{A^*}\left[\frac{1}{2}\ln\left(\frac{2m_ec^2\beta^2\gamma^2T}{I^2}\right) - \beta^2 - \frac{\delta}{2}\right] \quad (12)$$

$$\text{with } T = \frac{2m_ec^2\beta^2\gamma^2}{1 + 2\gamma m_e/M + (m_e/M)^2}. \quad (13)$$

Here, X is the mass per unit cross section (usually given in [gr/cm^2]), A^* and Z^* are atomic weight and number of the residual gas, $K = 4\pi N_A r_e m_e c^2 = 0.307$ g^{-1} cm^2 and M the mass of the nucleus. For our application we can neglect the density effect $\delta/2$ and set $\beta = 1$. The quantity I is the mean excitation energy which is about 19.2 eV for H_2, 82 eV for N_2 and 95.1 eV for O_2, [3].

Based on earlier measurements the relative partial pressures of the residual gas were estimated to be about 52% H_2, 30% H_2O and 18% N_2. For our calculation we split the water molecule and get for the partitions of the partial densities 11% for H, 66% for N and 23% for O. The pressure has been measured with about 70 gauges around the ring and averaged taking the distance between the measurement points and the pressure bumps in between into account. These values are listed in table 2. For three of the experiments a lower pressure was obtained by using the sublimation pumps.

5 PARASITIC MODE LOSS

The resistive impedance of the vacuum chamber leads to an energy loss of the particles in the coasting (unbunched) beam. Each charge produces an electric field which is by the relativistic contraction concentrated in the transverse direction with a typical opening angle of $\pm 1/\gamma$. It induces on the conducting wall surface a current pulse of rms length [4] $\sigma_t = b/(\sqrt{2}c\gamma)$ where b is the radius of a circular cylinder which approximates the different cross sections of the vacuum chamber. The energy loss is proportional to an integral over the product of resistive impedance times the Fourier transformation of wall pulse. By measuring this loss for different energies and hence, for different pulse lengths σ_t, we get some information about the impedance. At high frequencies the impedance is mainly due to diffraction on the aperture changes which decreases like $1/\sqrt{\omega}$ and, to a lesser extent, due to the smooth resistive wall which increases like $\sqrt{\omega}$. For the diffraction contribution we assume that the impedance has a maximum around 1.3 GHz similar to the PS and ISR rings. Based on various SPS measurements we take for the characteristic impedance at low frequencies $|Z/n| = 10\,\Omega$. The resistive wall effect is calculated for a stainless steel chamber with radius b. The estimated parasitic mode loss factor k_{pm} are listed in table 2 for both contributions. This quantity is related to the energy loss by $U = q^2k_{pm}$.

parameters	particle		proton	proton		proton		lead
	p/Z	GeV/c	14	120		270		270
	γ		14.96	127.9		287.8		113.4
	η		-0.00267	0.00174		0.00179		0.00172
Synch. rad.	$\lambda_{crit.}$	mm	94	1.5		0.13		2.1
(free space)	U_s/Z^2	m eV	0.0	2.2		55.8		1.3
reduced	U_s/Z^2	m eV	0.0	0.3		50.3		0.1
Impedance	σ	mm	1.65	0.194		0.086		0.217
	k_{pm}/-diff.	V/pC	3560	10 470		15 610		9 826
	k_{pm}-res. w.	V/pC	40	940		3 200		800
	U_{pm}/Z^2	m eV	0.6	1.8		3.0		1.7
Ionization	P	nTorr	4.6	9.35	4.6	9.35	4.6	7.7
	density	μg/m^3	0.031	0.063	0.031	0.063	0.031	0.052
	U_i/Z^2	m eV	5.1	13.7	6.8	14.9	7.3	12.1
Total estimated	U	m eV	5.7	15.8	8.9	68.2	60.6	13.9
	$U - U_s$	m eV	5.7	15.5	8.6	17.9	10.3	13.8
Measured	U/Z^2	m eV	9.7	20.7	16.3	74.7	62.5	16.3
	$(U - U_s)/Z^2$	m eV	9.1	20.4	16.0	20.4	12.2	16.2

Table 2: Top:Estimated energy losses of protons and Pb^{82}_{208} due to synchrotron radiation, due to parasitic modes (using $|Z/n| = 10\Omega$) and due to ionization (taking for the partial pressures 52% H_2, 30% H_2O and 18% N_2). Bottom: Results of the measurements and their correction for synchrotron radiation.

6 EXPERIMENTS AND RESULTS

In the experiments a beam was accelerated to the desired energy where it was debunched and left coasting. A longitudinal Schottky signal around $\omega_S = 2\pi\, 10^9 s^{-1}$ was observed and its central frequency measured as a function of time for about 3 hours. From this the energy loss U per turn was obtained using (5). For the case of 14 GeV protons the life time was only about an hour which made the measurement less accurate. All other cases had a long life time. The variation of the dipole magnet field was checked and found to be negligible. The results are listed at the lower part of table 2.

The measured energy losses are corrected for synchrotron radiation $U - U_s$ and listed in table 2. In order to determine the contributions of the impedance and of the ionization to the energy loss we use the calculated values of the corresponding energy losses and calculate the factors by which they have to be multiplied in order to get the best agreement with the measurements. This procedure was carried out for all proton measurements and for the case which also included the lead measurements. The two approaches resulted in differences of about 30% for the impedance and 10% for the pressure. Taking both with the appropriate weight we find for the impedance and the ionization loss which give the best fit through the measured data

$$\left|\frac{Z}{n}\right| \approx 12 \pm 4\Omega \text{ and } U_i(\text{meas.}) \approx 1.4\, U_i(\text{exp.}). \quad (14)$$

The result for the impedance is good agreement with other measurements done at the SPS [5]. The obtained ionization loss could be explained by a slightly higher pressure or a different gas composition. In fact a distribution of 52% H_2, 30% H_2, 4% N_2, 10% CO and 4% of other gases like Argon could be more realistic. In any case the measurements have errors large enough to explain differences with expectations.

7 ACKNOWLEDGEMENTS

We thank the LEP-SPS operation group for setting up the coasting beams for this experiments. We also thank U. Wehrle for his help to obtain the Schottky signal and H. Jacob for measuring the beam life time.

8 REFERENCES

[1] S. Heifets, A. Michailichenko: Poc. of the 1991 Part. Accel. Conference, p. 458.

[2] S.A. Kheifets, B. Zotter; CERN SL-95/92 (AP), 1995.

[3] Review of Part. Phy.; Phys. Rev. D, Vol 54, 1996.

[4] A. Hofmann, T. Risselada; IEEE-NS 30 (1983), p. 2400.

[5] L. Vos; CERN SPS/86-21(MS), 1996.

BEAM ECHOES IN THE CERN SPS

O. Brüning, T. Linnecar, F. Ruggiero,
W. Scandale, E. Shaposhnikova, D. Stellfeld, CERN, Geneva, Switzerland

Abstract

Longitudinal echo signals have been produced in the CERN SPS by exciting a proton beam at 120 GeV/c with two short RF pulses separated by a suitable time-delay. The aim of the experiments was to confirm the analytical predictions for beam echoes in the SPS and to probe the applicability of beam echoes for a measurement of the energy distribution and diffusion coefficients in the accelerator. We summarise here the results obtained with bunched and un-bunched beams. For an un-bunched beam, the excitation frequencies are at different harmonics of the revolution frequency and result in an echo response at the difference frequency of the two RF kicks. For the case of a bunched beam, the RF kicks are adjusted to excite the quadrupole mode of the bunch motion and the beam echo response can also be observed as a quadrupole mode.

1 INTRODUCTION

Echo phenomena have been well known in plasma physics for many years [1]. However, the effect has only been recently introduced to accelerator physics and first measurements of the echo signal in a storage ring suggest the possibility of using echo techniques in the beam diagnosis [2][3]. This paper summarises the echo measurements in the CERN SPS with bunched and un-bunched beams.

The echo signal is an interference pattern of two consecutive short RF-pulses. In the case of an un-bunched beam, the echo signals in the CERN-SPS were generated by exciting a coasting proton beam at 120 GeV/c with two short RF pulses using the 200 MHz travelling wave RF system. Without diffusion, one can find an exact solution for the echo response in a coasting beam and one can show that the beam echo appears at a time

$$t^* = \frac{h_1}{h_2 - h_1} \cdot \Delta t \tag{1}$$

after the second RF-kick, where Δt is the time separation of the two RF-kicks. For a non-vanishing diffusion term the echo response in the beam current is given by [4][5]

$$\begin{aligned} I_{echo}(t) \approx\ & 2e\omega_0 \cdot J_1(\epsilon_1\tau) \cdot J_1(x + \epsilon_2\tau) \\ \times\ & \tau \cdot \int \rho(p) \cdot e^{-ip\tau}\ dp \\ \times\ & e^{-Dk_0^2\left[h_1^2(\Delta t)^3 + (h_2-h_1)^2 \cdot t^3\right]/3}, \end{aligned} \tag{2}$$

where D is the diffusion coefficient, $\rho(p)$ the initial energy distribution with $p = \Delta E/E_0$, τ the time measured relative to the centre of the echo response,

$$\tau = k_0(h_2 - h_1) \cdot (t - t^*) \tag{3}$$

and t the time measured from the second RF kick. $J_n(x)$ are Bessel functions of the first kind with

$$x = h_1\epsilon_2 k_0 \Delta t \tag{4}$$

and

$$k_0 = \frac{\omega_0\eta}{\beta^2}; \qquad \eta = \frac{1}{\gamma_t^2} - \frac{1}{\gamma^2}. \tag{5}$$

ϵ_1 and ϵ_2 are perturbation parameters

$$\epsilon_i = \frac{\omega_0 T_i}{2\pi} \cdot \frac{eV_i}{E_0}; \qquad i = 1, 2 \tag{6}$$

where $\omega_0 = 2\pi f_0$ is the revolution frequency, T_1 and T_2 the kick lengths and V_1 and V_2 the kick amplitudes of the first and second RF kick respectively. ϵ_1 and ϵ_2 are the relative energy gains during the first and second RF-kick respectively. In the following we will assume that the relative energy gain during the two RF-kicks are small compared to the initial energy spread in the distribution.

The first line in Equation (2) implies that the leading term of the echo response varies with the time separation of the two RF-kicks like a Bessel function of the first kind $J_1(x)$. The integral in Equation (2) indicates a strong influence of the energy distribution on the shape of the echo signal. In the following we will call it the form factor $F(\tau)$ of the echo response. The strong cubic dependence of the damping term on time suggests the possibility of measuring even very small diffusion coefficients within a reasonably short time interval.

In the case of a bunched beam, the echo signals in the CERN SPS were generated by applying two short amplitude reductions to the nominal RF voltage of the 200 MHz travelling wave RF system which provides the RF buckets for the proton beam at 120 GeV/c.

2 EXPERIMENTAL SETUP

Fig. 1 shows the experimental setup for the echo measurement and Table 1 lists the relevant parameters for the CERN SPS.

f_0 [kHz]	$\lvert\eta\rvert$	E_0 [GeV]	f_{RF} [MHz]
43.23	$1.8 \cdot 10^{-3}$	120	200

Table 1: *Machine parameters of the SPS.*

3 EXPERIMENTAL DATA FOR AN UNBUNCHED BEAM

We presented first results of un-bunched beam echo measurements already in [6]. Here, we will only briefly illustrate the effect and demonstrate how the echo measurement

0-7803-4376-X/98/$10.00 © 1998 IEEE

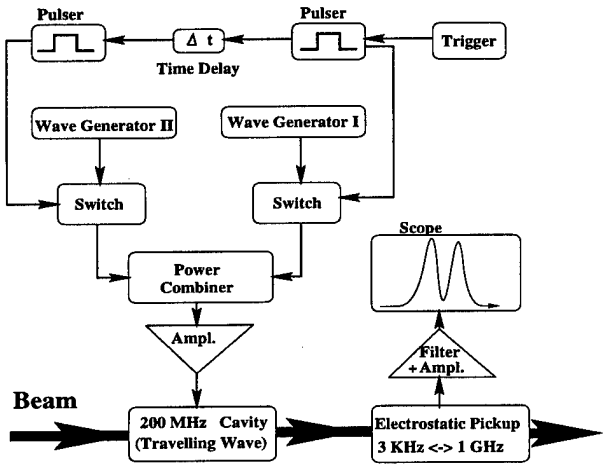

Figure 1: *Schematic setup for the echo measurements.*

can be used for measuring the diffusion coefficient. Fig. 2 shows a typical echo measurement for a kick amplitude of 500 kV. Each kick lasted for 92 μ s (4 turns) and the two kick have a time separation of 45 ms. Fig. 3 shows the super-imposition of 25 such measurements, each having a different time separation between the first and the second RF-kick. The time separation varies from 45 ms to 230 ms. Note that for a time separation of 230 ms the echo response occurs only 2 minutes after the second RF-kick. The enve-

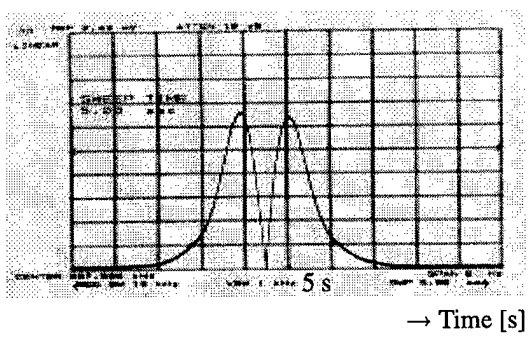

Figure 2: *The measured echo signal on a linear scale. The measured echo response corresponds to an approximately Gaussian energy distribution. The horizontal scale is 0.5 s per division.*

lope of the echo signals in Fig. 3 agrees qualitatively with the expected Bessel function dependence indicated in the first line of Equation (2). However, the later the echo signal appears after the second RF-kick, the larger the divergence of the measured signal from the pure Bessel function envelope in the first line of Equation (2) indicating a non-vanishing diffusion coefficient in (2). For $D \approx 10^{-13} \cdot s^{-1}$ the measured data agrees very well with the expected behaviour in (2) and corresponds to an emittance growth of

$$\Delta\sigma_{\Delta p/p_0} = 10^{-3} \tag{7}$$

in 115 days.

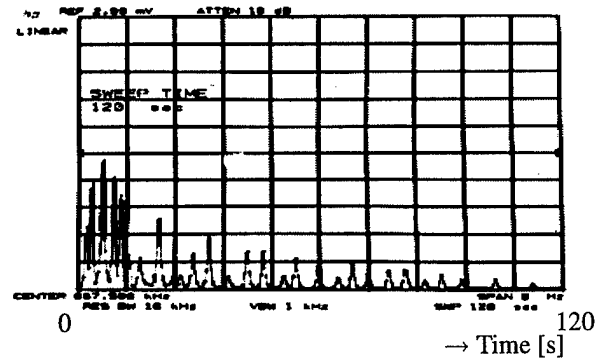

Figure 3: *The picture shows the superposition of 22 beam echos for different separation times Δt as a function of time after the second RF kick. The time separation of the two RF kicks varies between 5 ms and 220 ms, resulting in an echo response up to two minutes after the second RF-kick.*

In [6] it was shows that the echo signal can also be used for measuring the energy distribution function and the energy spread in the beam.

4 MEASURING DIFFUSION COEFFICIENTS

The results of the previous Section indicated the possibility of measuring even very small diffusion coefficients with echo signals. This aspect was analysed in more detail by deliberately applying a noise signal to the 800MHz cavity in the SPS. The noise signal was calibrated by measuring the growth of the energy spread in the beam for different noise amplitudes from the longitudinal Schottky signal [7]. Over a time interval of 100 s, the Schottky signal was sensitive to noise signals which correspond to Once the noise signal was calibrated the noise amplitude was reduced to values where we could no longer observe a growth of the energy spread in the longitudinal Schottky signal. The beam echo could be successfully used to measure noise amplitudes which were at least two orders of magnitude smaller. Fig. 4 shows the measured diffusion coefficients versus the applied noise amplitude in dB. The points with noise amplitudes larger than -45 dB are calculated from measurements using a Schottky signal [7]. All other points are calculated from echo measurements. All data points agree with the analytical estimates and lie on a straight line with slope 1/10 in the double logarithmic plot.

5 BUNCHED BEAM ECHOES

Recent experiments in the CERN SPS extended the echo measurements to the case of a bunched beam. Fig. 5 and Fig. 6 show typical measurements, where the beam was excited with two consecutive quadrupole kicks. Each kick lasted approximately 200 μ s. Both kicks in Fig. 5 had an amplitude of -500 kV compared to a nominal RF-voltage of 5.1 MV and were separated by $\Delta t = 90$ ms. The first kick in in Fig. 6 had also an amplitude of -500 kV but the second kick was approximately four times smaller than

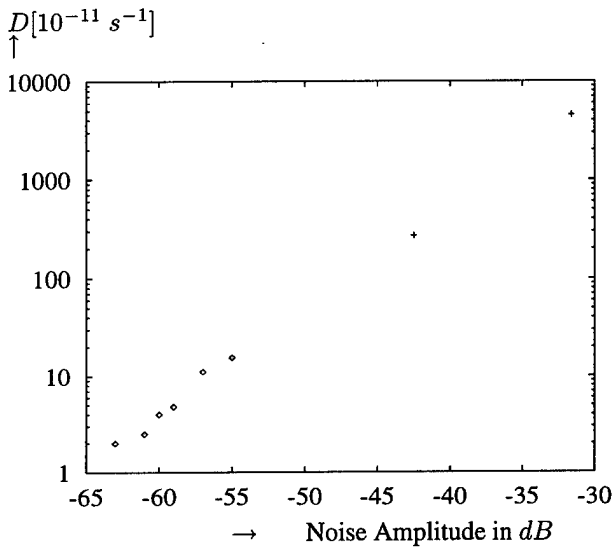

Figure 4: *Infered diffusion coefficients. The vertical axis shows the diffusion coefficients on a logarithmic scale in units of* $10^{-11}\ s^{-1}$ *and the horizontal axis the noise amplitude in dB. Assuming a diffusion process with white noise, one expects a straight line with slope 0.1 in this representation. The points with a noise amplitude larger than* $-45\ dB$ *are calculated from measurements using the Schottky signal. All other points are calculated from echo measurements.*

the first kick. Nevertheless the echo response in this case is more pronounced than in Fig. 5. The two kicks in Fig. 6 were separated by $\Delta t = 200\ ms$. A detailed study of the bunched beam echo is still in progress and we summarise here only the main features observed in the measurements:

- The echo signal could only be observed if the bunch filled almost the whole RF-bucket.
- The measured echo response was larger if the second RF-kick was smaller than the first kick.

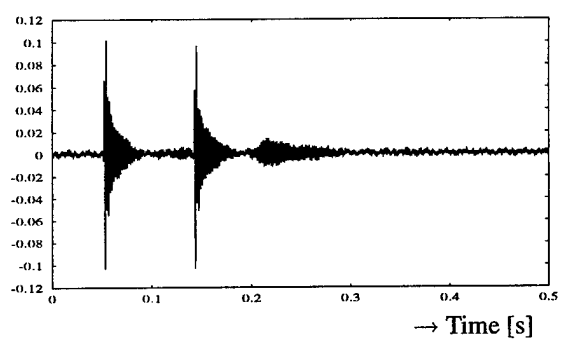

Figure 5: *The measured echo signal in a bunched beam on a linear scale for a time separation of* $\Delta t = 90\ ms$ *between the two RF-kicks. The horizontal scale is 0.5 s.*

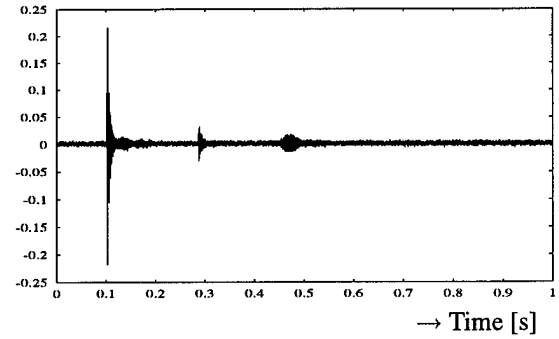

Figure 6: *The measured echo signal in a bunched beam on a linear scale for a time separation of* $\Delta t = 200\ ms$ *between the two RF-kicks. The second RF-kick is approximately four times smaller than the first RF-kick. The horizontal scale is 0.5 s.*

6 SUMMARY

The un-bunched beam echo measurements in the CERN SPS agree well with the analytical expectations and show that echo signals can be used for measuring beam distributions and diffusion coefficients. Measurements of bunched beam echoes are just starting and a detailed study of this effect is still in progress.

7 REFERENCES

[1] T.M. O'Neil and R.W. Gould, Phys. Fluids **11**, 1 (1968)

[2] L.K. Spenzouris, J.-F. Ostigy, P.L. Colestock, Phys. Rev. Letters **76**, 620, 1996.

[3] O. Brüning, T. Linnecar, F. Ruggiero, W. Scandale, E. Shaposhnikova, D. Stellfeld, AIP Conf. Proc., Arcidosso, Italy 1996

[4] O. Brüning, CERN SL/95-83 (AP), 1995.

[5] E. Shaposhnikova, CERN SL-Note/96-03 (RF), 1996.

[6] O. Bruning, T. Linnecar, F. Ruggiero, W. Scandale, E. Shaposhnikova, D. Stellfeld, EPAC'96, 1996.

[7] T. Linnecar and W. Scandale, PAC'91, 2147, Wash D.C., 1981.

OBSERVATION AND SIMULATION OF BEAM TAILS IN LEP

I. Reichel RWTH Aachen, Germany and CERN, SL Division
H. Burkhardt, G. Roy, CERN, SL Division, Geneva, Switzerland

Abstract

Transverse beam tails have been measured in LEP using scraping collimators and loss monitors. Very significant non-Gaussian tails are present for colliding beams and high beam-beam tune shift. On a lower but still significant level, non-Gaussian tails are also present in the horizontal plane for a single beam. Comparison of measurements with detailed simulations allowed us to identify off-momentum particles produced by scattering processes as a source of significant transverse tails.

1 TAIL SCANS

1.1 Technique

Transverse beam tails are measured at LEP using scraping collimators. The loss rate is measured with loss monitors installed close to some collimators [1]. The loss rates are directly converted into beam lifetime due to scraping. The calibration in lifetime is done for high loss rates, such that the beam lifetime is dominated by scraping and easily measurable as reduction of beam current with time.

1.2 Results

Tail measurements have been done in LEP on many occasions in recent years [1]. The main conclusions from these measurements were:

1. At 45 GeV strong vertical tails were observed with colliding beams.
2. In the horizontal plane on a lower but still significant level, non-Gaussian tails were observed which were present for a single beam and colliding beams.

2 TAIL PRODUCTION DUE TO OFF-MOMENTUM PARTICLES

2.1 Production Mechanism

The results in the horizontal plane pointed to a mechanism other than the beam-beam interaction for the production of tails. Scattering processes were proposed as a source of these tails [1], and have now been studied through detailed simulations and dedicated measurements in LEP where the scattering process with the highest probability is Compton-scattering on thermal photons [2] (photons from the black body radiation of the beam pipe). In this process the scattered electron (or positron) loses some of its energy. If this happens in a region where the dispersion is nonzero, the particle will start betatron oscillations, with an amplitude depending on the energy loss and on the dispersion. This is shown schematically in Fig. 1. The relative energy loss increases with beam energy and reaches about 2 % on average at the present LEP beam energies (around 90 GeV).

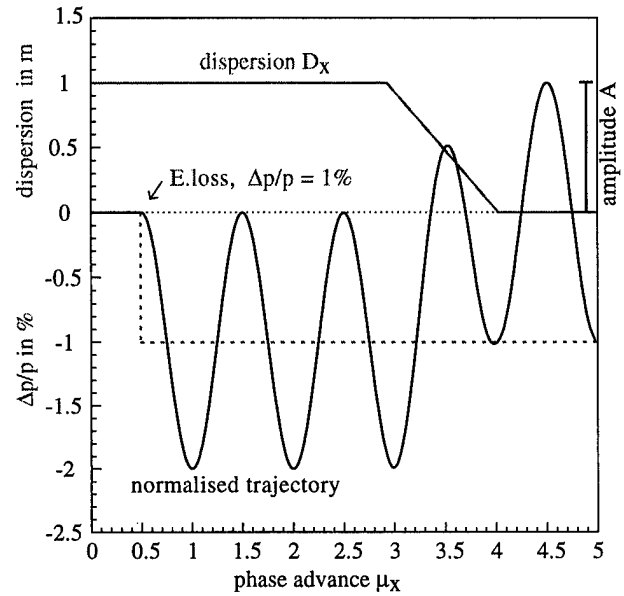

Figure 1: Transverse tail production mechanism: A particle loses some energy due to a scattering process in a region with dispersion. Due to the energy loss it starts betatron oscillations.

If the energy loss is more than 3 %, the electrons are lost locally. For an energy loss between 1 and 3 %, the scattered electrons have very large oscillation amplitudes and are lost within a couple of turns. These electrons contribute to the very far tails. Even if the energy loss is less than the RF bucket height or energy acceptance (about 1 %), the scattered electrons remain at large amplitudes within a damping time (less than 100 turns at 90 GeV).

2.2 Tracking Scattered Particles with DIMAD

To study the tail production due to scattering processes in detail, we started to implement a simulation of these processes in the tracking code DIMAD [3].

The tracking of particles in DIMAD is based on a matrix formalism at first or second order and is done element by element. In addition DIMAD offers the possibility to include other processes such as synchrotron radiation in the tracking. DIMAD can simulate the effects of synchrotron radiation in bending magnets and quadrupoles, for both the systematic part, considering the average energy loss, and the stochastic part by individual photon emission accord-

0-7803-4376-X/98/$10.00 © 1998 IEEE

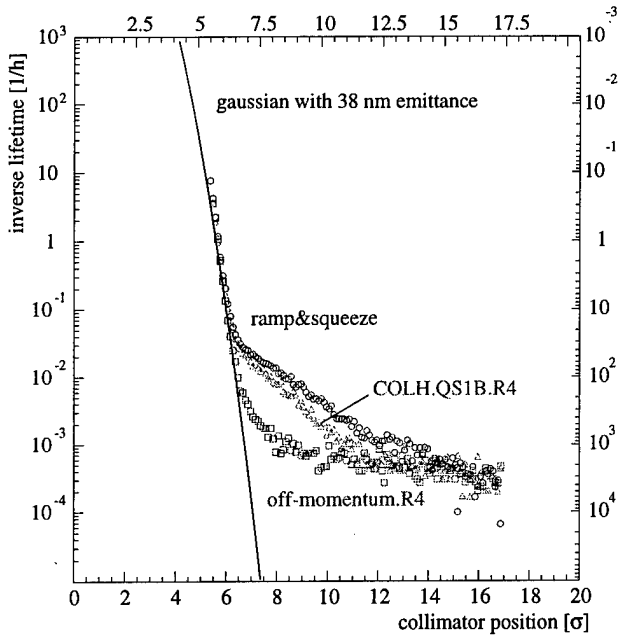

Figure 2: Horizontal tail measurements at 80.5 GeV with different collimator settings. The collimators were moved to a position corresponding to 8.6 on the lower scale of the x-axis, which is in units of 'nominal' σ_{nom} corresponding to 40 nm emittance (used to calculate collimator settings). The top scale is in σ_{meas} corresponding to the measured emittance (38 nm).

ing to different distributions.

For the thermal photon simulation the scattering occurs at random places around the ring. The scattered particles are tracked for several damping times and their maximum excursions at the scraping collimators are stored. Knowing the cross-section for the Compton-scattering, one can then convert the number of particles which would hit the collimator at a certain position to an inverse lifetime and compare the results to the measured tails.

2.3 *Horizontal Single Beam Tails*

To demonstrate that the horizontal tails consist mainly of off-momentum particles, some measurements were made with different collimator settings. One measurement was done with all collimators at the nominal 'RAMP&SQUEEZE' settings (corresponding to 17 σ for collimators in regions without dispersion and more than 20 σ in regions with high dispersion; σ being the standard deviation of the transverse particle distribution in the beam). Then one collimator in a region without dispersion (COLH.QS1B.R4) was moved close to the beam and the tail scan repeated. This reduced the tails noticeably but not significantly. Moving the off-momentum collimators, which are at a position with high dispersion, to an equivalent position in beam size reduced the tails significantly as shown in Fig. 2.

If the collimator jaw is moved to closer than about 6 σ one reaches the Gaussian core of the beam for which the

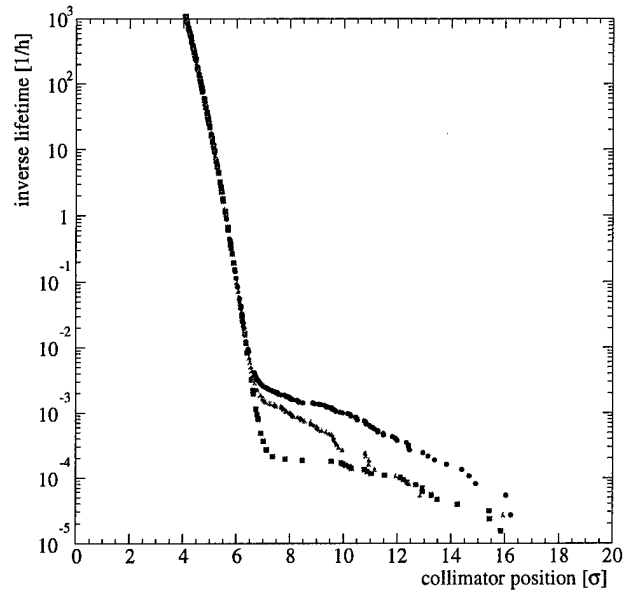

Figure 3: Horizontal tail simulations at 80.5 GeV with the same collimator settings as in Fig. 2.

lifetime due to scraping can be calculated [4]. From this one can deduce the emittance at a 5 to 6 σ level. For the measurements shown in Fig. 2 we found 38 nm. This method can be used to cross-check emittance measurements from other instruments. As it uses the region between about 5 and 6 σ whereas the other instruments typically use the first 2 σ, it can provide additional information on the beam profile. This proved to be helpful in understanding some problems due to resonances in a low-emittance lattice which was tried in LEP in 1996 [5].

Simulations with the same collimator settings as shown in Fig. 2 were done by tracking particles which undergo Compton-scattering on thermal photons using DIMAD. The results are shown in Fig. 3.

The results from the tracking are in good agreement with the measurements taking into account errors due to the calibration and contributions to the tails due to Bremsstrahlung on the residual gas which was included in a rough estimate but is not yet included in the full simulation.

2.4 *Horizontal vs. Vertical Tails*

The betatron oscillation amplitude of a particle, in number of σ, after the scattering depends on the energy loss $\Delta p/p$ and the dispersion D_x:

$$N_x[\sigma] = \frac{D_x \cdot \frac{\Delta p}{p}}{\sqrt{\beta_x \cdot \varepsilon_x}} \tag{1}$$

The horizontal dispersion in LEP is about 1 m and the average β-function in the arcs is 81 m. For a horizontal emittance of 40 nm we expect from Eq. (1) that a scattering process resulting in $\Delta p/p = 1$ % will launch the particle to an amplitude corresponding to 5.6 σ.

The same effect also exists in the vertical plane. For most of the ring, the vertical and horizontal β-functions are comparable. The residual vertical dispersion in LEP ($D_y = 0$ by design) is on average about 30 times less than the nominal horizontal dispersion in the arcs. Even if we take into account the emittance ratio $\varepsilon_y/\varepsilon_x = 0.5$ % we expect from Eq. (1) that tail production in terms of σ will be smaller in the vertical plane by a factor of $30\sqrt{0.005} \approx 2$.

2.5 *Vertical Tails due to Beam-Beam Bremsstrahlung*

We have also started to investigate the effect of energy loss in scattering processes at the interaction point, where the β-function in the vertical plane is very small. The main process to consider is the nearly zero angle radiative Bhabha scattering (also called beam-beam Bremsstrahlung) due to its large cross section and energy loss. For $\beta^* = 5$ cm, a vertical emittance of 0.5 nm and a residual vertical dispersion of typically 3 mm at the interaction point we find that a scattering process with $\Delta p/p = 1$ % would launch particles to 6 σ. We have started to implement a simulation of the energy loss due to beam-beam Bremsstrahlung in DIMAD. First results of the tracking are shown in Fig. 4. They indicated, that some particles can be launched up to the dynamic aperture and then drift even further out into very far non-Gaussian tails, until they hit a physical aperture.

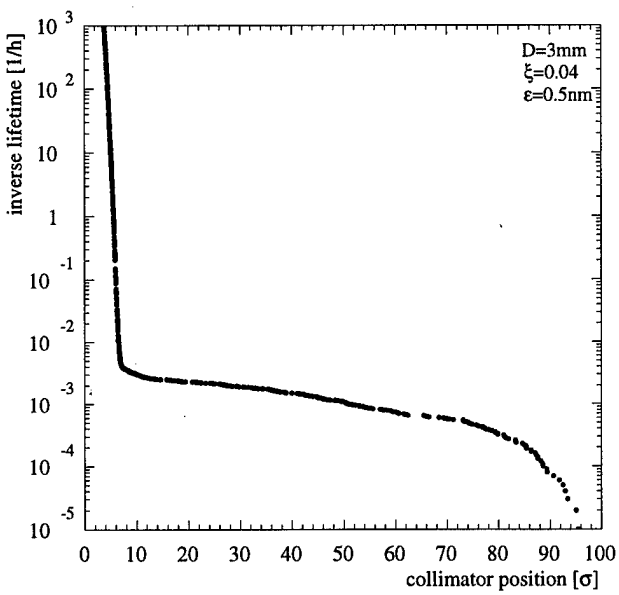

Figure 4: Simulation of vertical tails due to beam-beam Bremsstrahlung for 45.6 GeV, a beam-beam tune shift of $\xi_y = 0.04$ and an emittance of 0.5 nm. The x-axis is in units of σ corresponding to the emittance of 0.5 nm. The physical aperture of LEP is around 90 σ in this units.

3 SUMMARY

Measurements and simulations have shown that the transverse non-Gaussian tails in LEP consist partially of off-momentum particles. Many of these particles are lost from the beam within a few turns. We have identified the production mechanism as energy loss from scattering processes in dispersive regions. The particles are not lost immediately after the scattering, but they continue to travel for typically up to 10 turns at very large amplitudes, often outside the dynamic aperture, which increases their amplitudes even further.

We have started to implement the detailed scattering processes in the tracking code DIMAD. The tracking confirmed that horizontal tails are already present without colliding beams and that the main process in the case of LEP is Compton-scattering on thermal photons. In the vertical plane, tail production can be initiated by residual vertical dispersion at the interaction point and beam-beam Bremsstrahlung.

4 REFERENCES

[1] H.Burkhardt et al. Beam Tails in LEP. In V. Suller and Ch. Petit-Jean-Genaz, editors, *Proceedings of the 5th European Particle Accelerator Conference*, volume 2, pages 1152–1154, 1996.

[2] H. Burkhardt. Beam-Beam and Lifetime. In J. Poole, editor, *Proceedings of the 3rd Workshop on LEP Performance*, pages 117–122, 1993.

[3] R. V. Servranckx, K. L. Brown, L. Schachinger, and D. Douglas. Users Guide to the Program DIMAD. SLAC REPORT 285 UC-28 (A), SLAC, May 1985.

[4] M. Sands. The Physics of Electron Storage Rings. SLAC REPORT 121, SLAC, 1970.

[5] I. Reichel. Dynamic Aperture and Tail Scans. In J. Poole, editor, *Proceedings of the 7th Workshop on LEP Performance*, pages 67–71, 1997.

SYNCHROTRON OSCILLATION DRIVEN BY RF PHASE NOISE

Kern W. Ormond and Joseph T. Rogers
Cornell University, Laboratory of Nuclear Studies, Ithaca, NY, USA 14853*

Abstract

We report results of calculations and measurements relating RF phase noise to longitudinal motion of a stored beam. Treating the beam as a noise driven coupled oscillator system, we have made calculations to determine what coupled bunch synchrotron oscillation amplitudes result from RF phase noise. Measurements have also been carried out at CESR of phase noise in the RF system and coupled bunch synchrotron oscillation amplitudes. We also consider the impact of this noise on the dynamic range of a longitudinal feedback system.

1 UNCOUPLED SINGLE BUNCH RESPONSE

The equation of motion for small phase oscillations ϕ in an accelerator is given by [1]

$$\ddot{\phi} + 2\alpha_s\dot{\phi} + \Omega_s^2\phi = 0, \tag{1}$$

where α_s is the damping decrement given by

$$\alpha_s = -\frac{1}{2T_0}\left.\frac{dU}{dE}\right|_{E_0} \tag{2}$$

and Ω_s is the synchrotron frequency given by

$$\Omega_s^2 = \frac{-h\omega_0\eta e}{cp_0T_0}\left.\frac{dV}{d\psi}\right|_{\psi_s}, \tag{3}$$

where T_0 is the revolution time, ω_0 is the revolution frequency with $h\omega_0 = \omega_{RF}$, and η is the momentum compaction. For a sinusoidal driving potential,

$$V(\psi) = V_0 \sin\psi = V_0 \sin(\psi_s + \phi), \tag{4}$$

where V_0 is the amplitude of the driving potential and ψ_s is the synchronous phase, Eq. 3 becomes

$$\Omega_s^2 = \frac{-h\omega_0\eta}{cp_0T_0} eV_0 \cos\psi_s. \tag{5}$$

1.1 Noise response

An RF noise error, δV, can add either a noise forcing term (additive noise) or frequency fluctuations (multiplicative noise) or both in Eq. 1. For amplitude noise,

$$\delta V = v(t)\sin(\psi), \tag{6}$$

where $v(t)$ is a stochastic amplitude error. For phase noise,

$$\delta V = V_0(\sin(\psi + \theta(t)) - \sin(\psi)), \tag{7}$$

where $\theta(t)$ is a stochastic phase error. For small $\theta(t)$ this can be approximated by

$$\delta V \approx V_0\,\theta(t)\cos\psi. \tag{8}$$

The equation of motion including both additive and multiplicative noise is

$$\ddot{\phi} + 2\alpha_s\dot{\phi} + (\Omega_s^2 + g(t))\phi = f(t), \tag{9}$$

where $f(t)$ is the additive noise term and $g(t)$ is the multiplicative noise term. For amplitude noise

$$f_A(t) = \frac{h\omega_0\eta}{cp_0T_0} e\,v(t)\sin\psi_s \tag{10}$$

$$g_A(t) = \frac{h\omega_0\eta}{cp_0T_0} e\,v(t)\cos\psi_s, \tag{11}$$

and for phase noise

$$f_\phi(t) = \frac{h\omega_0\eta}{cp_0T_0} eV_0\,\theta(t)\cos\psi_s \tag{12}$$

$$g_\phi(t) = \frac{h\omega_0\eta}{cp_0T_0} eV_0\,\theta(t)\sin\psi_s. \tag{13}$$

Either RF amplitude noise or phase noise can produce both additive and multiplicative noise in the equation of motion for ϕ. Though in general amplitude noise will contribute more to multiplicative noise, and phase noise will contribute more to additive noise.

1.1.1 Additive noise

The complex frequency response, $H(\omega)$, to a noise driving force (additive noise only) can be found by making the substitution $\phi(t) = H(\omega)\exp(-i\omega t)$ and $f(t) = \exp(-i\omega t)$ in the equation of motion to obtain [2]

$$H(\omega) = \frac{-1}{\omega^2 - \Omega_s^2 + 2i\alpha_s\omega}. \tag{14}$$

The mean square response is then given by

$$\begin{aligned}\langle\phi^2\rangle &= \int_{-\infty}^{\infty} |H(\omega)|^2 S_f(\omega)d\omega \\ &= \int_{-\infty}^{\infty} \frac{S_f(\omega)}{(\Omega_s^2 - \omega^2)^2 + 4\alpha_s^2\omega^2} d\omega\end{aligned} \tag{15}$$

where $S_f(\omega)$ is the mean square spectral density of the excitation (noise). The spectral density is the Fourier transform of the autocorrelation function of the excitation, $R_f(\tau)$, i.e.

$$S_f(\omega) = \frac{1}{2\pi}\int_{-\infty}^{\infty} R(\tau)e^{-i\omega\tau}d\tau \tag{16}$$

* Work supported by the National Science Foundation

where

$$R(t-t') = \langle f(t)f(t')\rangle \tag{17}$$

where the brackets denote an average over the ensemble of realizations of f. For white noise, $S_f(\omega) = S_f =$ constant,

$$\langle\phi^2\rangle = \frac{\pi S_f}{2\alpha_s\Omega_s^2}. \tag{18}$$

1.1.2 Multiplicative noise

The derivation of the response for a combination of additive and multiplicative noise is a bit more involved. The result given is only good for zero-centered, delta-correlated white noise where the spectral density of $f(g)$ is $S_{f(g)}(\omega) = S_{f(g)} =$ constant. From references [3, 4] the mean square response is given by

$$\langle\phi^2\rangle = \frac{\pi S_f}{2\alpha_s\Omega_s^2 - \pi S_g}. \tag{19}$$

Comparing this to Eq. 18 one can see that the frequency fluctuations act to increase the the mean square phase oscillations. This can be interpreted as an effective increase of the spectral density of the additive fluctuations, $S_f \rightarrow S_f/(1-\pi S_g/2\alpha_s\Omega_s^2)$. Also note that Eq. 19 only makes sense for $S_g < \pi\alpha_s\Omega_s^2$. For $S_g > \pi\alpha_s\Omega_s^2$, large frequency fluctuations produce an energy instability that grows exponentially in time.

2 COUPLED BUNCH RESPONSE

For a single bunch of charge Ne in a circular accelerator, the equation of motion for small phase oscillations including coupling due to wake fields is [5]

$$\ddot{\phi} + 2\alpha_s\dot{\phi} + \Omega_s^2\phi = \frac{Nr_0c\eta}{\gamma T_0}\sum_{k=0}^{\infty} W_0''(-kC)(\phi(t) - \phi(t-kT_0)). \tag{20}$$

For additive noise forcing we can solve this in the same manner as in Sec. 1.1.1 for the spectral response. In terms of the longitudinal impedance, the spectral response is given by

$$H(\omega) = -\left[\omega^2 - \Omega_s^2 + 2i\alpha_s\omega + \left(\frac{iNr_0\eta}{\gamma T_0^2}\right)\Xi\right]^{-1} \tag{21}$$

where

$$\Xi = \sum_{p=-\infty}^{\infty}[p\omega_0 Z_0^{\parallel}(p\omega_0) - (p\omega_0+\omega)Z_0^{\parallel}(p\omega_0+\omega)]. \tag{22}$$

3 RF CAVITY COUPLING

The cavity itself is also coupled to a generator that drives the voltage in the cavity. It was convenient to measure the noise of the generator rather than the noise in the RF cavities. Therefore it was important to know how the noise in the generator is transferred to the beam via the RF cavities. We can treat this as a system comprised of two coupled oscillators, the cavity and the beam. Consider two oscillators cascaded where one is driven and there is no feedback from the second oscillator to the first, having equations of motion

$$\ddot{x} + 2\alpha_x\dot{x} + \Omega_x^2 x = f(t) \tag{23}$$

$$\ddot{y} + 2\alpha_y\dot{y} + \Omega_y^2 y = x(t) \tag{24}$$

It is easy to show that in this case the spectral response of the second oscillator is

$$H_y(\omega) = -\frac{H_x(\omega)}{\omega^2 - \Omega_y^2 + 2i\alpha_y\omega} = H_{x_0}(\omega)H_{y_0}(\omega) \tag{25}$$

where H_{x_0} and H_{y_0} denote the spectral response functions for the uncoupled oscillators. The mean square response is then just the combination of the uncoupled response functions with the spectral density of the excitation

$$\langle y^2\rangle = \int_{-\infty}^{\infty}|H_{x_0}(\omega)H_{y_0}(\omega)|^2 S_f(\omega)\,d\omega. \tag{26}$$

A similar case arises for the system we are considering when there is little beam loading on the RF cavities; the motion of the beam is driven purely by the voltage in the RF cavity. The spectral response of the RF cavity is given by the impedance of the cavity and the spectral response of the beam is given in Eq. 14. In this case, the total response of the beam is given by

$$H(\omega) = -\frac{Nr_0\eta}{\gamma T_0^2}\frac{(\omega_{RF}+\omega)Z_0^{\parallel}(\omega_{RF}+\omega)}{\omega^2 - \Omega_s^2 + 2i\alpha_s\omega}. \tag{27}$$

For an RF cavity impedance

$$Z_0^{\parallel}(\omega) = \frac{R_s}{1 + iQ\left(\frac{\omega_r}{\omega} - \frac{\omega}{\omega_r}\right)}, \tag{28}$$

where ω_r is the cavity resonant frequency, Eq. 15 gives the mean square response as

$$\langle\phi^2\rangle \approx \left(\frac{Nr_0\eta}{\gamma T_0^2}\right)^2\frac{\pi S_f}{4\alpha_s\Omega_s^2}Z^2, \tag{29}$$

where $Z^2 = |Z_0^{\parallel}(\omega_{RF}+\Omega_s)|^2 + |Z_0^{\parallel}(\omega_{RF}-\Omega_s)|^2$ is approximately given by

$$Z^2 \approx \omega_{RF}^2 R_s^2\left(\frac{1}{1+4\frac{Q^2}{\omega_r^2}(\Omega_s-\Delta\omega)^2} + \frac{1}{1+4\frac{Q^2}{\omega_r^2}(\Omega_s+\Delta\omega)^2}\right), \tag{30}$$

where $\Delta\omega = \omega_{RF} - \omega_r$.

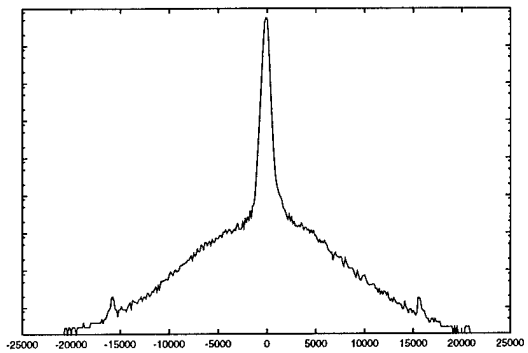

Figure 1: The RF generator spectrum about ω_{RF} = 499.765 MHz.

4 RESULTS

4.1 Measurements

At CESR, measurements were made of the noise spectrum of the RF generator and of the synchrotron oscillation amplitude. The measured synchrotron oscillation amplitude was 2.7 mrad. The noise spectral density of the RF generator at the synchrotron frequency was measured to be 1.7×10^{-11} rad^{2}Hz^{-1}. From Eq. 29, this would correspond to a synchrotron oscillation amplitude of 1.9 mrad. Improvements were then made to reduce the noise in the RF generator. After the improvements were made the measured noise spectral density was 6.3×10^{-12} rad^{2}Hz^{-1}. This would correspond to a predicted synchrotron oscillation amplitude of 1.1 mrad compared to a measured amplitude of 1.2 mrad.

CESR Parameters	
E_0	5.3 GeV
T_0	2.56 μs
γ	10370
η	0.01
α	1160 s^{-1}
Ω_s	20 kHz
ω_{RF}	499.765 MHz
ω_r	499.750 MHz
R_s	140 MΩ
Q	6275
N	10^{11}

Table 1: The CESR parameters used for the calculations of synchrotron oscillation amplitudes.

4.2 Longitudinal feedback

A receiver for a longitudinal feedback system might compare the phase of the beam to a reference oscillator. The resulting error signal would then be sent to a power amplifier which would apply a voltage to the beam. The damping rate of a such a feedback system is

$$\alpha_E < \frac{\delta E \eta}{2\pi E_0 Q_s \sigma_\tau} \tag{31}$$

where σ_τ is the rms phase fluctuation divided by the RF frequency, and δE is the average voltage applied to the beam, equal to half the maximum voltage for a linear feedback system.

The phase fluctuation in this case can come from either the beam motion or the reference oscillator. We have found that the reference oscillator phase fluctuations are much larger than the beam phase fluctuations, so σ_τ=2.5 ps. We are constructing a feedback system for CESR with a maximum voltage of 1.5 kV, so the maximum damping rate α_E is 1730 s^{-1}.

5 ACKNOWLEDGEMENTS

We would like to thank Mark Brathwaite for his help in performing noise measurements and also Cheng-Yang Tan for many helpful discussions.

6 REFERENCES

[1] Helmut Wiedemann, *Particle Accelerator Physics*, (Springer-Verlag, 1993).

[2] Stephen H. Crandall and William D. Mark, *Random Vibration in Mechanical Systems*, (Academic Press, 1963).

[3] Katya Lindenberg, V. Seshadri, K. E. Shuler, and Bruce J. West, *J. Stat. Phys.* **23**, 755 (1980).

[4] Katya Lindenberg, V. Seshadri, and Bruce J. West, *Phys. Rev. A* **22**, 2171 (1980).

[5] Alexander Wu Chao, *Physics of Collective Beam Instabilities in High Energy Accelerators*, (John Wiley & Sons, Inc., 1993).

NUMERICAL SOLUTION FOR FOKKER-PLANCK EQUATIONS IN ACCELERATORS

M.P. Zorzano, H. Mais, DESY, D-22607 Hamburg, Germany and
L. Vazquez, Universidad Complutense, 28040 Madrid, Spain

Abstract

A finite difference scheme is presented to solve the Fokker-Planck equation in (2+1) variables numerically. This scheme is applied to study stochastic beam dynamics in two-dimensional phase space.

1 INTRODUCTION

One important problem of accelerator physics is to investigate the particle motion under the influence of noise [1]. There are various sources of noise: rf noise, random power supply ripple, random ground motion, restgas scattering, and quantum fluctuations due to radiation. The physical questions one wants to answer are: what is the longtime behaviour of the dynamics, what is the probability for the particle to hit the vacuum chamber (and then be lost) (mean first passage time), what are the average fluctuations of the particle around the periodic design orbit of the accelerator (moments), and what is the time evolution of the probability density (transient and stationary behaviour).

Mathematically stochastic systems can be modelled by stochastic maps (in the time discrete case) and by stochastic differential equations (s.d.e.) in the time continuous case. In the following we will restrict our considerations to s.d.e. with Gaussian white noise. Gaussian white noise is a very good approximation in many accelerator problems [1]. The solution of these s.d.e. are Markovian diffusion processes which can be described by the Fokker-Planck equation [2]. The Fokker-Planck equation is a partial differential equation for the probability density and the transition probability of these stochastic processes.

In general, the stochastic equations of motion of a particle in an accelerator are very complicated and can not be solved analytically, therefore one has to use numerical schemes. One way is to consider the s.d.e. directly. An alternative way is to investigate and solve the Fokker-Planck equation.

In this paper we study stochastic beam dynamics in two-dimensional phase space. We describe a finite difference scheme to solve the corresponding Fokker-Planck equation with two phase space variables plus time. Extensive numerical simulations for this kind of problem have been performed in [3] using finite elements for the partial differential equation and Monte Carlo simulations for the s.d.e.. Here we concentrate on the finite difference scheme because of its simple implementation, its flexibility with respect to different boundary conditions, the straightforward extension to higher dimensional problems, its efficiency concerning CPU time and because it is easy to understand the physical meaning of each term in the scheme.

The paper is organized as follows: in section 2 we present the numerical scheme for solving the Fokker-Planck equation in (2+1) variables and in section 3 we present some examples and applications to accelerator physics. Section 4 summarizes the main results and gives a list of open questions for future studies.

2 NUMERICAL SCHEME FOR SOLVING THE FOKKER-PLANCK EQUATION

We restrict our investigation to stochastic dynamics in two-dimensional phase space. The general equations of motion we want to study are of the form

$$\frac{d}{ds}x_1 = x_2 \tag{1}$$

$$\frac{d}{ds}x_2 = -a_1(x_1) - a_2(x_1,x_2) + a_3(x_1)\eta_1 + a_4\eta_2 \tag{2}$$

with η_1, η_2 a Gaussian white noise vector process. $a_1(x_1)$ can be an arbitrary nonlinear potential (field), $a_2(x_1,x_2)$ can include van der Pol-like damping terms, $a_3(x_1)\eta_1$ describes random parameters and $a_4\eta_2$ represents an additive noise term. The corresponding (Ito) Fokker-Planck equation for the probability density reads [2]

$$\begin{aligned}\frac{\partial}{\partial s}p(x_1,x_2,s) &= \\ &= -\frac{\partial}{\partial x_1}[x_2 \cdot p(x_1,x_2,s)] + \\ &+\frac{\partial}{\partial x_2}[(a_1(x_1)+a_2(x_1,x_2)) \cdot p(x_1,x_2,s)] + \\ &+\frac{1}{2}\frac{\partial^2}{\partial x_2^2}[(a_3^2(x_1)+a_4^2) \cdot p(x_1,x_2,s)]\,.\end{aligned} \tag{3}$$

Equation (3) can be written in the form of two fluxes, one in x_1 and one in x_2 such that

$$\frac{\partial p}{\partial s} = \frac{\partial A}{\partial x_1} + \frac{\partial B}{\partial x_2} \tag{4}$$

a form which suggests to use an operator splitting method [4]. First we evaluate implicitly the x_2 derivative and then - also implicitly - the x_1 derivative with a tridiagonal scheme

$$\frac{p_{i,j}^{n+\frac{1}{2}} - p_{i,j}^{n}}{\Delta s} = \frac{F_{i,j+\frac{1}{2}}^{n+\frac{1}{2}} - F_{i,j-\frac{1}{2}}^{n+\frac{1}{2}}}{\Delta x_2} \tag{5}$$

$$\frac{p_{i,j}^{n+1} - p_{i,j}^{n+\frac{1}{2}}}{\Delta s} = -x_2\,\frac{p_{i+1,j}^{n+1} - p_{i-1,j}^{n+1}}{2\Delta x_1} \tag{6}$$

0-7803-4376-X/98/$10.00 © 1998 IEEE

with

$$F_{i,j+\frac{1}{2}} = D\ \frac{p_{i,j+1} - p_{i,j}}{\Delta x_2} + \\ +[a_1(x_1) + a_2(x_1, x_2 + \Delta x_2)]\frac{p_{i,j+1} - p_{i,j}}{2} \quad (7)$$

where we have set $2D = [a_3^2(x_1) + a_4^2]$. Making the von Neumann analysis of stability it turns out that the scheme is unconditionally stable. For more information see [5],[6].

3 RESULTS AND EXAMPLES

3.1 *Harmonic oscillator*

The first example we have studied is the damped harmonic oscillator with strong diffusion i.e. $a_1(x_1) = Kx_1$, $a_2(x_1, x_2) = \gamma x_2$, $a_3(x_1) = 0$ and $a_4 = \sigma$. K, γ, σ are constants. Since this problem can be studied analytically [7] it served to check our numerical scheme. With the parameter set $K = 1$, $\gamma = 2.1$, $\sigma = 0.8$, a 80×80 grid, $\Delta x_1 = \Delta x_2 = 0.1$, $\Delta s = \pi/1000$ and the exact solution at $s = 0.95$ as initial condition we obtained the time evolution of the probability density depicted in figure 1.

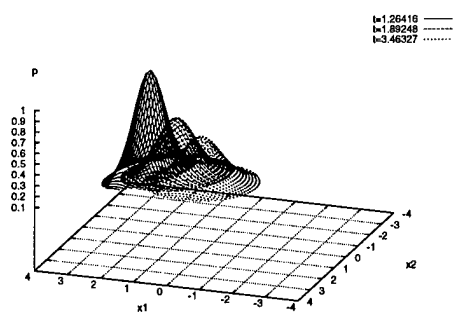

Figure 1: Density evolution in the damped linear harmonic oscillator equation, drift and diffusion resulting from the stochastic excitation.

3.2 *Duffing oscillator*

As a second example we have investigated the Duffing oscillator with damping, multiplicative and additive Gaussian white noise. In this case $a_1(x_1) = \omega^2[\alpha x_1 + \epsilon x_1^3]$, $a_2(x_1, x_2) = 2\tau\omega x_2$, $a_3(x_1) = -\omega^2\sqrt{2D_{11}}x_1$, and $a_4 = \sqrt{2D_{22}}$. $\omega = 1, \alpha = -1, \tau = 0.2, \epsilon = 0.1$ are constants. For two different sets of noise intensities D_{11}, D_{22} we obtained the results shown in figure 2 and figure 3.

In this nonlinear system with multiplicative noise one can observe a noise induced transition [8]. In the additive noise case the system has two stable points just like the deterministic system. Under the influence of multiplicative noise the probability density at the origin grows. Further increasing of the strength of the multiplicative noise changes the stability of the origin - the origin becomes a stable point.

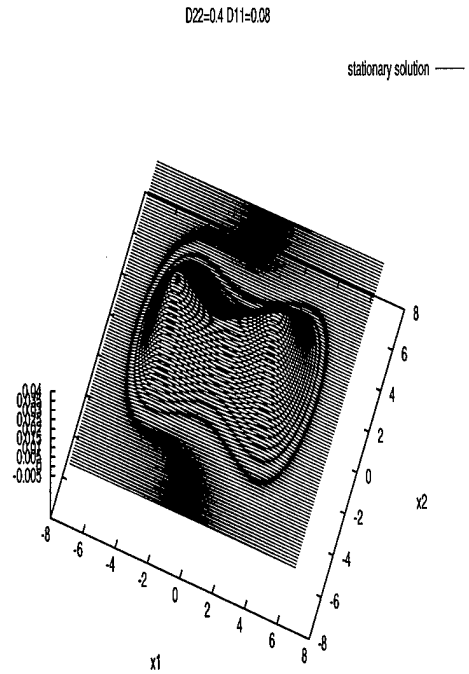

Figure 2: $D_{22} = 0.4$, D_{11}=0.08, view of the stationary density in phase space. dt=π/1000 Finite difference integration.

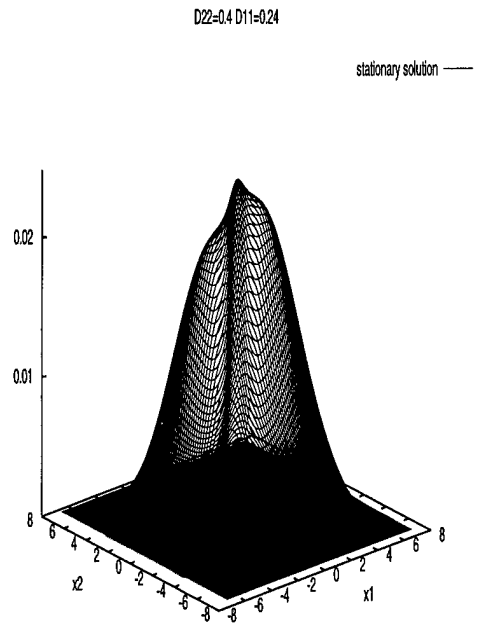

Figure 3: $D_{22} = 0.4$, D_{11}=0.24, view of the stationary density in phase space. dt=π/1000 Finite difference integration.

3.3 *Beam-beam interaction in storage rings under the influence of noise*

We have made a preliminary study of the the beam-beam interaction in storage rings under the influence of noise.

The model we have chosen was defined by

$$\frac{\partial p}{\partial s} = -\frac{\partial(x_2 p)}{\partial x_1} + \frac{\partial}{\partial x_2}[(\alpha x_2 + w^2 x_1 + f(x_1, s))p] + \frac{1}{2}\frac{\partial^2}{\partial x_2^2}(dp). \quad (8)$$

with $f(x_1, s) = \sum_{n=1} -8\pi\xi_{bb}(\frac{1-e^{-\frac{1}{2}x_1^2}}{x_1})\delta_(s = nL)$. We set the parameters to $\frac{d}{2} = 0.000147, \tau = 0.0000310, w = 0.7, \xi_{bb} = 0.07$ (see figure 4).

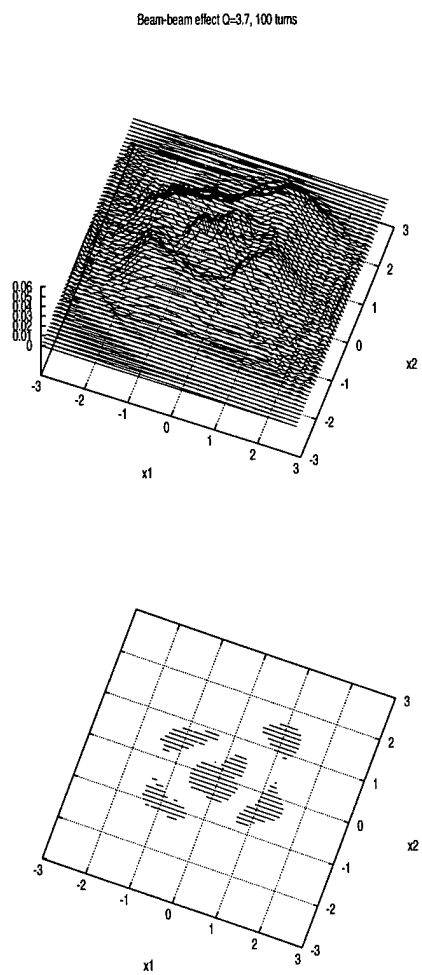

Figure 4: Electron case. Density for the beam-beam effect with Q=3.7, $\xi = 0.07$, damping time 250 turns. The lower figure is the projection onto the phase space of the areas of highest probability.

4 SUMMARY AND CONCLUSIONS

In this paper we have presented a robust finite difference scheme for the numerical solution of the Fokker-Planck equation in (2+1) variables. The scheme has been checked with finite element calculations and with direct numerical simulations of the underlying s.d.e. It seems to be a good candidate for solving more complicated and more realistic accelerator models such as higher dimensional problems (coupled betatron motion), non- Gaussian white noise perturbations of Ornstein-Uhlenbeck type and explicitly time dependent coefficients $a_i(..., s)$.

5 ACKNOWLEDGEMENT

This research was partly supported by the EC Human Capital and Mobility grant no: ERBCHRXCT940480, and by a DESY PhD scholarship. L.V. thanks the support of the Comision Interministerial de Ciencia y Tecnologia of Spain under grant PB95-0426. The authors want to thank L.A. Bergman, B.F. Spencer, S.F. Wojtkiewicz, E. Johnson for information about their work.

6 REFERENCES

[1] A. Pauluhn. Thesis: *Stochastic Beam Dynamics in Storage Rings* DESY 93-198 December 1993

[2] H. Risken. *The Fokker-Planck Equation,Methods of Solutions and Applications.* Springer-Verlag, 1984.

[3] B.F. Spencer, L.A. Bergman. Nonlinear Dynamics, 4 (1993) 357-372.

[4] W. Press, S. Teukolsky, W. Vetterling, B. Flannery. *Numerical Recipes in C* Cambridge University Press, 1994.

[5] R.D. Richtmyer, K.W. Morton. *Difference Methods for Initial-Value Problems.* Interscience Publishers, 1967.

[6] M.P. Zorzano, H. Mais, L. Vazquez. *"Numerical solution of two dimensional Fokker-Planck equations"* to be published.

[7] S. Chandrashekar. *Stochastic Problems in Physics and Astronomy.* Reviews of Modern Physics. Vol. 15. (1943) 1-44.

[8] W. Horsthemke, R. Lefever. *Noise-Induced Transitions* Theory and Applications in Physics, Chemistry, and Biology. Springer-Verlag Heidelberg New York Tokyo, 1984.

MULTIBUNCH COLLISION SCHEME IN BEPC

L.F.Wang, C.Zhang, Z.Y.Guo and S.H.Wang
Institute of High Energy Physics
Chinese Academy of Sciences, P.O. Box 918, Beijing, P.R.China

Abstract

The multibunch collision by means of pretzel scheme to enhance the luminosity in BEPC have been studied. The modification of the lattice is carried out, the solenoid compensation and chromaticity correction are studied, the physical aperture is examined, the long range beam-beam interaction and coupled bunch instabilities are investigated. The results show that the pretzel scheme with six bunches per beam is feasible.

1 LATTICE MODIFICATION

The purpose of pretzel scheme is to enhance luminosity by increasing the number of bunches N_b beyond the present N_b=1. Since N_b evenly spaced bunches encounter each other in 2 N_b points around the ring and collision is desired only at the south interaction point (IP) in BEPC. Multibunch collision can give rise to unwanted destructive beam-beam interactions at parasitic encounters unless something can be done to separate the beams there. As the operating betatron tunes are ν_x=5.84 and ν_y=6.76, six bunches are allowed with the pretzel, which is generated in horizontal direction by three separators. Two separators are placed on each side of south IP, and the third one is placed at the north IP. Only one separator, i.e. the north one is used when beams are injected to generate the pretzel orbits, (see Figure 1). As shown in Figure 2, three separators are applied when two beams are brought onto collision. The main parameters of multibunch collision scheme are list in Table 1. The results presented in the following sections are based on these data.

Table 1 The parameters of multibunch collision in BEPC

Energy	E(GeV)	2.0
Betatron function at IP	β_x(m)	1.2
	β_y(m)	0.05
Betatron tune	ν_x	5.84
	ν_y	6.76
Natural emittance	ε_0(rad·m)	3.23×10^{-7}
Bunch number per beam	N_b	6
Natural Bunch length	σ_l(cm)	5
Bunch current	I_b(mA)	25.3
Luminosity	L($cm^{-2}s^{-1}$)	5.5×10^{31}

The superperiodicity number of pretzel scheme lattice is one with mirror symmetry in comparison with the superperiodicity number of two in the present lattice. Additional twenty quadrupole and fourteen sextupole power supplies are required.

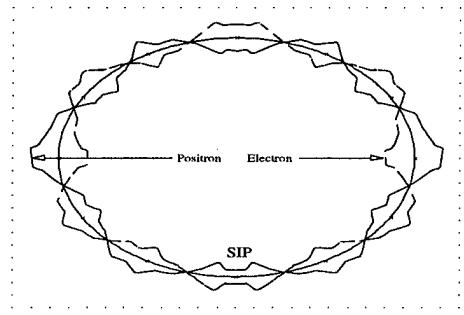

Figure 1: Pretzel orbit of injection mode

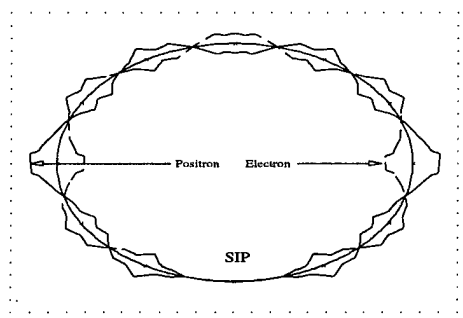

Figure 2: Pretzel orbits of Collision Mode

2 SOLENOID COMPENSATION

Global correction for detector solenoid field with skew quadrupole applied in BEPC now is not suitable for the pretzel scheme. The skew quadrupole where electron and positron beams have no-zero horizontal pretzel orbits of opposite sign can produce vertical orbit separation with opposite sign for two beams. Furthermore, the vertical orbits $y_c^{\pm}$ in the sextupole then give rise to an equivalent skew quadrupole components of opposite sign for the two beams:

$$(\tilde{k_1})_{eff} = k_2 y_c^{\pm}, \tag{1}$$

where k_2 is the sextupole strength. The different equivalent skew quadrupole components will make two beam have different coupling, so the simultaneous coupling compensation for both beams gets difficult.

The rotating frame method is adopted in our pretzel scheme. Two quadrupoles on each side of south IP are rotated by 3.0825°, following by one compensator solenoid. The coupling is compensated locally in the interaction region where is no pretzel orbit.

Figure 3 gives vertical orbit and vertical dispersion function along the ring. It can be seen from Figure 3 that the

0-7803-4376-X/98/$10.00 © 1998 IEEE

vertical orbit and vertical dispersion function are negligible.

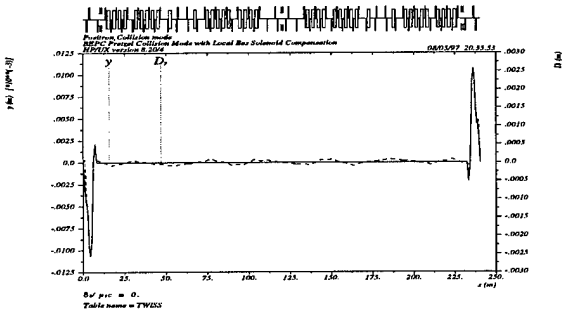

Figure 3: vertical orbit and dispersion function

3 CHROMATICITY CORRECTION

Pretzel orbits pass off-center horizontally in sextupoles, and then an effective normal quadrupole of opposite sign for two beams is generated:

$$(k_1)_{eff} = k_2 x_c^{\pm} \tag{2}$$

where $x_c^{\pm}$ are the horizontal orbits of two beams. The equivalent quadrupoles will disturb the betatron motion, the betatron function, betatron tune and other parameters get different for two beams. As there is only one interaction point with head-on collision in the pretzel scheme, this leads to the conditions for a symmetric pretzel scheme (see figure 1 and 2) in which the effects of sextupole perturbation do not cancel. All sextupoles are adjusted to make betatron tune, chromaticity and betatron function at south IP independent of pretzel amplitude (and therefore the same for electron and positron). Eighteen independent sextupoles are needed in the pretzel scheme. Code PCCC(pretzel chromaticity correction code)[2] will be used to compensate the chromaticity. PCCC code also gives the analysis of the resonance excited by sextupoles. Figure 4 shows the particle tracking spectrum given by PCCC. Figure 5 and 6 show the dynamic aperture of positron and electron beams respectively.

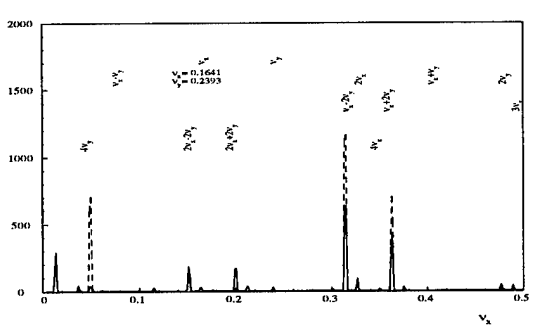

Figure 4: tracking FFT spectrum

4 PHYSICAL APERTURE

The beam stay clear region in pretzel scheme is defined as:

$$\mathrm{BSC}_x = x_c \pm 10\sigma_x \pm 10\mathrm{mm} \quad \mathrm{BSC}_y = \pm 10\sigma_y \pm 5\mathrm{mm}$$

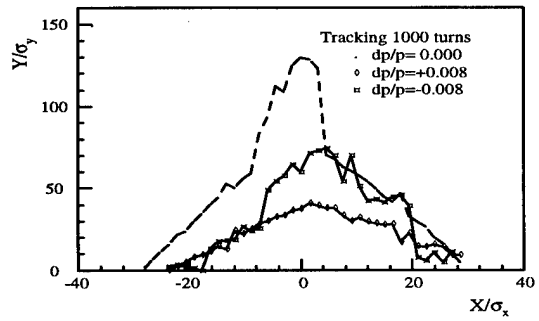

Figure 5: Dynamic aperture of positron

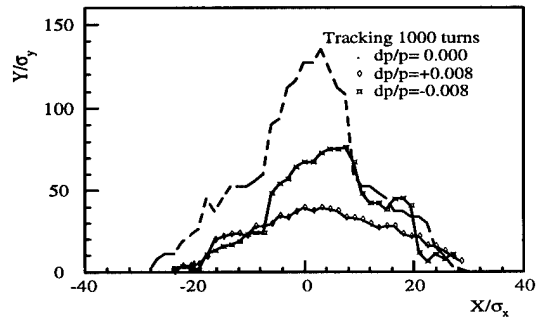

Figure 6: Dynamic aperture of electron

here, x_c is the horizontal pretzel orbit. The investigation shows that there are enough vertical physical aperture for both electron and positron beams. Figure 7 and Figure 8 display the horizontal physical aperture of positron and electron beams respectively. It can be seen from these figures that the positron beam has enough horizontal physical aperture, but it is not satisfied for electron beam in the injection region, which needs to be improved.

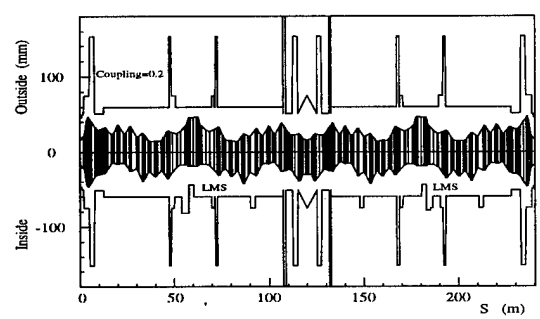

Figure 7: Horizontal physical aperture of positron beam

5 LONG RANGE BEAM-BEAM INTERACTION

The strength of the parasitic beam-beam effects are characterized by the equivalent linear tune shift

$$\xi_x = \frac{N\beta_x r_e}{2\pi\gamma}\int_0^{\infty} dt\left(1 - \frac{2X^2}{2\sigma_x^2 + t}\right)$$

$$\frac{exp(-X^2/(2\sigma_x^2+t) - Y^2/(2\sigma_y^2+t))}{(2\sigma_x^2+t)^{3/2}(2\sigma_y^2+t)^{1/2}}, \tag{3}$$

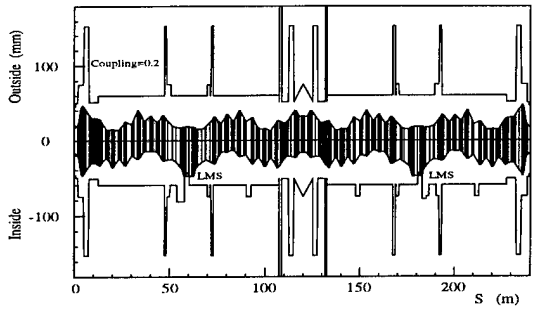

Figure 8: Horizontal physical aperture of electron beam

where X and Y are horizontal and vertical separations respectively. The formula for ξ_y is similar. Figure 9 gives the parasitic beam-beam parameters versus horizontal separation calculated with eq.(3). The Figure 9 indicates that the horizontal parasitic beam-beam parameter is negative when horizontal separation is larger than about σ_x. The parasitic beam-beam parameters of collision mode in the parasitic IPs are given in Table 2.

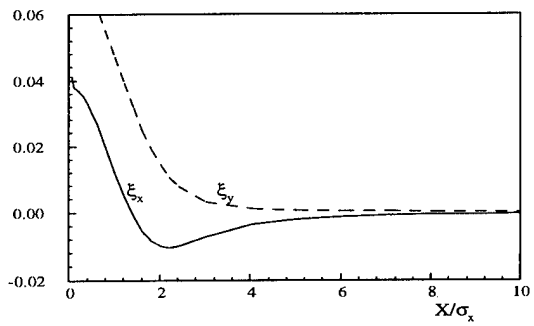

Figure 9: parasitic beam-beam parameters vs. separation

Table 2 : Long range b-b parameter of collision mode

X(mm) min	X/σ_x min	$\lvert\xi_x{}^j\rvert$ max	$\xi_y{}^j$ max	$\sum \xi_x^j$	$\sum \xi_\nu^j$
15.0	10.4	3.92×10^{-4}	8.95×10^{-4}	-0.0018	0.0017

In each parasitic interaction point, the bunches receive a kick. In the case of X¿¿σ_x, the beam-beam kick can be expressed as

$$x' = -\frac{2Nr_e}{\gamma X}, \tag{4}$$

where N is the bunch population, r_e is the classical electron radius and γ is the relativistic energy. The closed orbit distortion at south IP caused by all parasitic beam-beam kicks is calculated as 0.25 mm which is about half of the horizontal beam size. This current dependent horizontal orbit at IP should be adjusted during collision. The long range beam-beam interaction will reduce the stable tune space and cause betatron tune split. In the case of horizontal separation, the injection on the horizontal plane will make a larger tune spread due to long range beam-beam interaction, and therefore vertical injection is preferred.

6 COUPLED BUNCH INSTABILITIES

The transverse growth time due to HOMs[3] is estimated as 2.0 second which is longer than transverse radiation damping time 22 ms, the longitudinal growth time due to HOMs[3] is as 0.20 ms, which is shorter than the its radiation damping time of 11 ms.

As the two beams are stored in the same vacuum chamber in BEPC, the wake field excited by one beam will disturb the motion of another beam. The shunt impedance $\tilde{R}$ seen by the counter-moving bunches becomes complex in the general case. For a symmetric cavity,

$$\tilde{R} = \pm R, \tag{5}$$

where R is the shunt impedance seen by the co-moving bunches, the "+" ("-") sign applies to the symmetric (antisymmetric) mode. The longitudinal growth time is calculated as 0.11 ms when the counter-moving bunches is considered[2]. Figure 10 gives the transverse growth rate versus transverse tune due to resistive wall effect. Therefore the feedback system is needed for pretzel scheme.

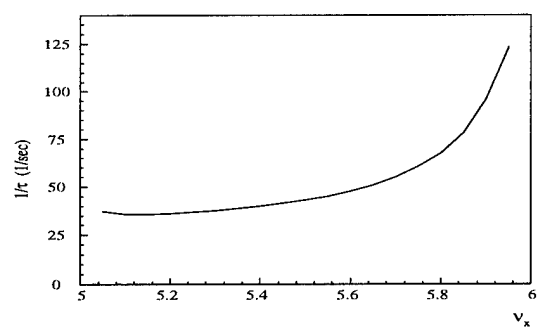

Figure 10: transverse resistive wall growth rate vs. tune

7 SUMMARY

The pretzel scheme is one of the feasible methods for BEPC to increase the luminosity. The solenoid can be locally compensated. The chromaticity can be compensated by adding more independent sextupole power supplies. The long range beam-beam effect is tolerable. However, the longitudinal coupled bunch instability may limit the multibunch performance and feedback system is needed.

8 REFERENCES

1. H. Grote and F. .C Iselin, CERN/SL/90-13(AP), 1996.
2. F.L.Wang, Ph.D. thesis, 1997.
3. J.Qin, Private communication.

EMITTANCE MEASUREMENT FROM THE DECAY RATE OF COHERENT OSCILLATION THROUGH NONLINEAR FILAMENTATION

S. Kamada, N. Akasaka and K. Ohmi
KEK, 1-1 Oho, Tsukuba-shi, Ibaraki-ken, 305 Japan

Abstract

A completely new approach to measure beam emittance is examined. It is based on measuring the decay rate of coherent betatron-oscillation through nonlinear filamentation caused by lattice nonlinearity. Experimental results, computer simulations and analytic approach using differential algebra (DA) [1] [2] are presented. This method may provide useful tools in measuring emittance at high brightness light sources, high luminosity particle factories and damping rings for linear colliders where emittance and coupling are expected to be very small.

1 INTRODUCTION

Emittance measurement is an essential issue for tuning performance of accelerators, but it can not be done easily in case of very low emittance.

In these days, it has become an established technique that coherent oscillation of beam excited by a kicker magnet is detected using a single passage beam position monitor and recorded turn by turn for studies of beam dynamics.[3]

A beam consisting of many particles with slightly different betatron tune shows decay of coherent oscillation through nonlinear filamentation, in which the motion of beam mass center damps while oscillation amplitude of each particle remains constant.[3][4]

Amplitude dependence of the decay rate through nonlinear filamentation has been observed experimentally at the TRISTAN main ring as shown in Fig. 1. In section 2, the decay rate will be derived analytically from Hamiltonian whose nonlinear coefficients should be calculated by DA. The decay rate depends on initial beam emittance before kick and lattice nonlinearity as well as amplitude of the kick.

To simulate emittance measurement from the decay rate, multi-particle tracking by the SAD code [7] was conducted using interleaved and non-interleaved optics of the TRISTAN main ring and optic for the low energy ring of KEK B-factory (KEKB-LER). Each of these optics has unique character of lattice nonlinearity. It will be introduced in section 3.

Results of the simulation and the analytic treatment will be presented in section 4. They will be compared and discussed.

2 THEORY

2.1 Hamiltonian and tune

Applying the canonical perturbation, one turn Hamiltonian for a particle in a circular accelerator is given as (1) in action-angle form up to the 2-nd order.

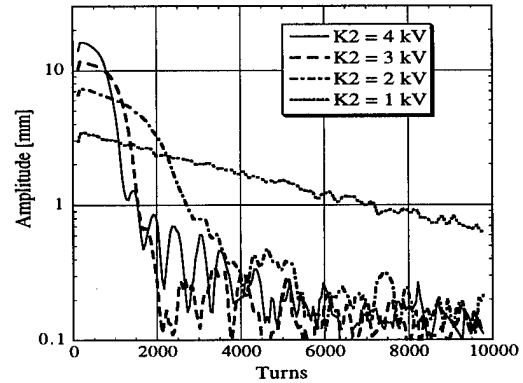

Figure 1: Decay of vertical oscillation through nonlinear filamentation. The data were taken at various kicker voltages $K2$ in non-interleaved sextupoles optic of the TRISTAN main ring. The decay curve is characterized by parabola and the decay rate grows at the larger amplitude oscillation. The beam current was kept around $30\mu A$ to reduce damping by head-tail effect.

$$\mathcal{H} = \sum_{w\in(x,y,z)} \{2\pi\nu_w^0 J_w + a_{ww} J_w^2\} + \frac{1}{2} \sum_{u,v\in(x,y,z)}^{u\neq v} a_{uv} J_u J_v \tag{1}$$

where x, y and z represent horizontal, vertical and longitudinal coordinates, respectively and a_{uv} describes the lowest order nonlinearity of the system.

Tune of a particle in w-coordinate is obtained by differentiating the Hamiltonian by action J_w partially,

$$\nu_w \equiv \frac{1}{2\pi}\frac{\partial\psi_w}{\partial n} = \frac{1}{2\pi}\frac{\partial\mathcal{H}}{\partial J_w} \tag{2}$$

A beam, a set of many particles of different actions, looses coherence of oscillation phase because of the tune-spread caused by (2), that is called nonlinear filamentation.

2.2 Distribution of action

Before a coherent kick or displacement, particles' distribution in a beam is assumed to be Gaussian in phase space of coordinate-momentum form and described by the distribution function of action as

$$f_w(J_w) = \frac{1}{\varepsilon_w} e^{-J_w/\varepsilon_w}, \tag{3}$$

where ε_w represents beam emittance in w-coordinate.

0-7803-4376-X/98/$10.00 © 1998 IEEE

By coherent vertical displacement of the beam, the distribution function of J_y becomes,

$$f_y(J_y) = \frac{1}{\varepsilon_y} e^{-\{J_y + \frac{1}{2}(\frac{\Delta_y}{\sqrt{\beta_y}})^2\}/\varepsilon_y} I_0(\frac{\Delta_y}{\sqrt{\beta_y}} \frac{\sqrt{2J_y}}{\varepsilon_y}), \quad (4)$$

where Δ_y, β_y and I_0 stand for amount of displacement, β-function at the displacement place and the modified Bessel function of 0-th order, respectively.

2.3 Distribution of tune

Standard deviation of tune in y-coordinate just after the coherent displacement is obtained by taking the following ensemble mean using the distribution functions given by (3) and (4).

$$\sigma_{\nu_y} = \sqrt{\langle \nu_y^2 \rangle - \langle \nu_y \rangle^2} \quad (5)$$

This gives,

$$\sigma_{\nu_y} = \frac{1}{2\pi} \sqrt{a_{xy}^2 \varepsilon_x^2 + a_{yz}^2 \varepsilon_z^2 + 4a_{yy}^2 \varepsilon_y^2 \{1 + (\frac{\Delta_y}{\sqrt{\varepsilon_y \beta_y}})^2\}}. \quad (6)$$

When coherent displacement is much larger than initial emittances, (6) the following approximation is valid.

$$\sigma_{\nu_y} = \frac{1}{\pi} |a_{yy}| \sqrt{\frac{\varepsilon_y}{\beta_y}} \Delta_y \quad (7)$$

2.4 Decay rate of coherent oscillation

Assuming that particles in a beam have same radial amplitude $\sqrt{2J_y(0)}$ and azimuthally allocate in Gaussian distribution of standard deviation σ_θ. Then the radial amplitude of mass center motion becomes smaller than $\sqrt{2J_y(0)}$ by factor $e^{-\sigma_\theta^2/2}$.

n-turns after coherent displacement of a beam, tune-spread of the beam given by (6) causes azimuthal distribution of particles and reduces the radial amplitude of mass center motion as in the following.

$$\sqrt{\frac{J_y(n)}{J_y(0)}} = e^{-\sigma_\theta^2/2} = e^{-(2\pi\sigma_{\nu_y} n)^2/2} \equiv e^{-(n/n_{NF})^2} \quad (8)$$

where $J_y(n)$ stands for action of mass center motion n-turns after the coherent displacement. Eq. (8) also defines n_{NF}, damping time of coherent oscillation through nonlinear filamentation. In experimental measurements, n_{NF} is observable and gives tune-spread of the beam.

$$\sigma_{\nu_y} = \frac{1}{\sqrt{2}\pi n_{NF}} \quad (9)$$

3 TRACKING SIMULATION

3.1 Method of simulation

Multi-particle tracking was conducted by SAD code, typically with 300 particles for 1000 turns. Radiation damping and quantum fluctuation were included.

Tracking result, a series of mass center position, was treated in the same way made in the experiments.[4] The instantaneous spectrum is calculated with a series of data which corresponds to N_{bin} turns. The Hanning window is adopted as a weight function. In order to find the frequency and amplitude of the peak precisely, the true continuous spectrum around the peak is approximated by a parabola fitted to the largest three points. The time variation of the spectrum is obtained by shifting the data by N_{step} turns. We adopted $N_{bin} = 64$ and $N_{step} = 16$.

This treatment is essential for getting smooth time variation of amplitude and tune from the simulation as well as experiments. Fig. 2 (a) is a decay plot of Courant-Snyder invariant obtained from the tracking. The plot shows certain roughness which is not suitable in finding the decay constants. Fig. 2 (b) and (c) show tune and amplitude decay plots, respectively, they were treated by the explained method.

Amplitude decay plots in various conditions were fitted with the function $\alpha_0 e^{-(\alpha_1 n + \alpha_2 n^2)}$, where α_0, α_1 and α_2 are fitting variables and α_2 gives tune-spread using (8) and (9). An example of fitting is shown in Fig. 2 (c).

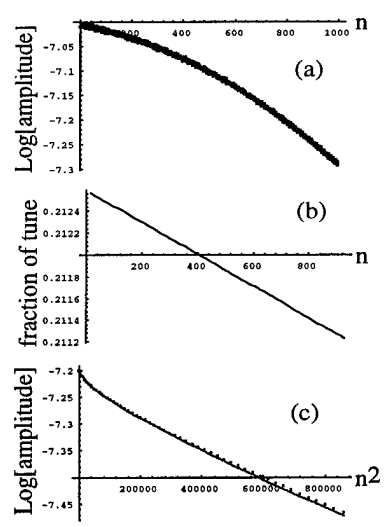

Figure 2: Example of the simulation. (a) decay plot of Courant-Snyder invariant. Position and angle information by the tracking and Twiss parameters are used. (b) decay plot of tune. (c) decay plot of oscillation amplitude and a fitted curve

3.2 Optics for the simulation

Nonlinear coefficients introduced by (1) were calculated using DA-package incorporated to SAD code [6] and listed in Table 1 for the three optics used in the simulation.

Table 1: Nonlinear coefficients of optics for the simulation. Natural emittances and radiation damping rates are also given.

	TRISTAN Interleaved	TRISTAN Non-interleaved	KEKB-LER Non-interleaved
a_{xx} $[m^{-1}]$	5356.91	52.28	5998.13
a_{xy} $[m^{-1}]$	-9299.00	44.493	13178.38
a_{xz} $[m^{-1}]$	88.86	728.87	87.86
a_{yy} $[m^{-1}]$	47106.96	-59.76	29273.20
a_{yz} $[m^{-1}]$	152.134	323.14	-16.45
a_{zz} $[m^{-1}]$	16.28	19.46	3.85
ε_x $[nm]$	4.66	4.77	19.04
ε_z $[nm]$	957.87	599.36	2431.12
$\alpha_{x,y}$	0.91×10^{-4}	0.91×10^{-4}	1.29×10^{-4}

Two of TRISTAN optics are almost same in linear optics, but nonlinear effect by sextupoles was canceled out very well in the non-interleaved one and nonlinear coefficients are much smaller than in the interleaved one.

In KEKB-LER optic where sextupoles are also non-interleaved, edge effect of the nearest quadrupoles to IP contributes to the nonlinear coefficient a_{yy} largely. [5]

4 RESULTS AND DISCUSSION

4.1 Simulation result the analytic treatment

Results of the simulation are presented in Fig.3 together with results of the analytic calculation by (6).

A good agreement between the simulation and the analytic treatment is found in Fig. 3 (a) for the interleaved TRISTAN optic. Also tune-spread depends on coherent-amplitude linearly as expected by (4).

On the other hand, the non-interleaved optic of TRISTAN in Fig. 3 (b) gives completely different answer between the simulation and the analytic results. Tune-spread does not depend on amplitude linearly and suggests non-linear terms higher than included in (1). The simulation could not explain the experimental results and confess that the simulation model is far from reality.

KEKB-LER optic shows a fairly good agreement between the simulation and the analytic results especially in case of small coherent-amplitude.

4.2 Discussion

The possibility of emittance measurement by nonlinear filamentation is demonstrated in optics where nonlinear coefficients of the lowest order are dominant. However when the lowest nonlinear coefficients are very small, nonlinear optics depend highly on errors and it becomes difficult to measure emittance by the proposed method.

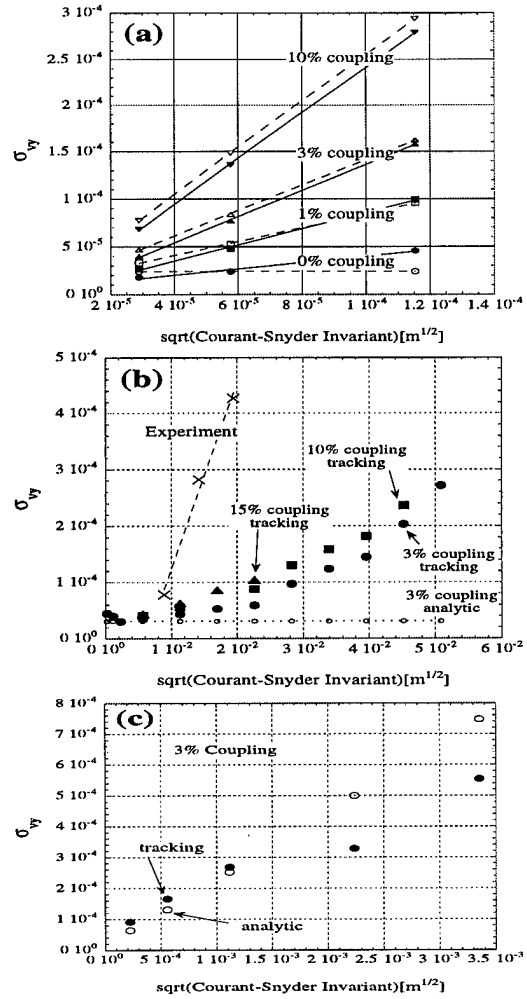

Figure 3: Tune-spread vs. Coherent-amplitude. Be aware large difference of horizontal scale between interleaved and non-interleaved optics. (a) Interleaved optic of TRISTAN. The simulation and the analytic results are indicated solid and broken lines, respectively. By increasing coupling, tune-spread becomes larger as expected from (7). (b) Non-interleaved optic of TRISTAN. Experimental data are calculated from Fig. 1. (c) KEKB-LER optic.

5 ACKNOWLEDGMENTS

One of the authors (S. K.) enjoyed fruitful discussions with Prof. K. Yokoya on the distribution function.

6 REFERENCES

[1] M. Berz, SSC-166 (Part I), (1988).

[2] E. Forest, Particle Accelerators,24,91 (1989).

[3] S. Kamada, AIP Conference Proceedings 344, 1 (1995).

[4] N. Akasaka and S. Kamada, proc. of EPAC'96, 1141 (1996).

[5] K. Oide and H. Koiso, Phys. Rev. E47, 2010 (1993).

[6] K. Oide, H. Koiso and K. Ohmi, KEK Preprint 96-130 (1996).

[7] http://www-acc-theory.kek.jp/SAD/sad.html.

EFFECT OF DIFFUSION ON BUNCHED BEAM ECHO

G. V. Stupakov and A. W. Chao
Stanford Linear Accelerator Center, Stanford University, Stanford, CA 94309

Abstract

When a beam receives a dipole kick, its centroid signal decoheres due to the betatron tune spread in the beam. Long after the signal has decohered, however, a follow-up quadrupole kick to the beam brings a pronounced echo back to the centroid signal. This echo effect has been analyzed for the case of a bunched beam in Ref. [1]. In this work, the perturbation calculation of Ref. [1] is extended to include a diffusion in betatron amplitude. The effect of diffusion on the magnitude of the echo is then parameterized and studied.

1 INTRODUCTION

The echo effect has been known in plasma physics for many years (see, e.g., [2]). Relatively recently a concept of echo has been introduced into accelerator physics [1, 3]. For a bunched beam, the echo in a circular accelerator can be observed when the beam is kicked off-center at time $t = 0$ causing its centroid to undergo betatron oscillations. After these oscillations completely damped out due to beam decoherence, the beam is excited by a quadrupole kick at time $t = \tau$. This kick does not produce any visible beam centroid displacement at that time, but it turns out that close to time $t = 2\tau$ the beam centroid undergoes transient betatron oscillations with an amplitude that is a fraction of the initial beam offset. The echo can also be observed in the longitudinal direction [4] in which case RF phase shift and RF amplitude jump play a role of the dipole and quadrupole kicks, respectively.

Experimentally, longitudinal echo has been observed in the anti-proton accumulator ring at FNAL [5] and in the CERN SPS [6] for coasting beams. Those experiments demonstrated that echo can be effectively used for measuring an extremely weak diffusion inside the beam.

For a longitudinal echo in a coasting beam, the theory of echo effect taking into account the diffusion has been developed in Refs. [5, 7]. In the present paper we extend the theory of transverse echo to include the diffusion effects in a bunched beam.

2 THEORY

Following approach of Ref. [1] we will use the action - angle variables, J and ϕ, for description of transverse dynamics of a bunched beam. With diffusion, we need to solve the Fokker-Planck equation

$$\frac{\partial\psi}{\partial t} + \omega_\beta(J)\frac{\partial\psi}{\partial\phi} = \frac{\partial}{\partial J}(D(J)J\frac{\partial\psi}{\partial J}), \qquad (1)$$

where $\psi(J,\phi)$ is the beam distribution function, $\omega_\beta(J)$ is the betatron frequency as a function of the amplitude of the betatron oscillations, and $D(J)$ is the diffusion coefficient.

We will solve Eq. (1) in the limit of weak diffusion. Specifically, we assume that the diffusion has a small effect on a time scale during which the beam decoheres. The decoherence time, τ_{decoh}, can be estimated as $\tau_{decoh} \sim 1/\omega'_\beta J$, and the diffusion time, τ_{dif}, is roughly equal to $\tau_{dif} \sim J/D$. Requiring $\tau_{dif} \gg \tau_{decoh}$ we get

$$D \ll \omega'_\beta J^2. \qquad (2)$$

In the limit of very strong diffusion (typical for electron accelerators where diffusion is caused by quantum fluctuations of the synchrotron radiation), when the inequality opposite to (2) holds, the diffusion completely suppresses the echo effect.

For $t < 0$, we assume an initial distribution function,

$$\psi = \psi_0(J). \qquad (3)$$

At time $t = 0$, the beam receives a small dipole kick such that the amplitude of the dipole oscillation is much smaller than the beam size. Immediately after the kick we have from Ref. [1] that the perturbation ψ_1 of the distribution function is

$$\psi_1(J,u) = \epsilon\sqrt{2J}\psi'_0(J)\sin u, \qquad (4)$$

where ϵ gives the strength of the kick, $\epsilon \ll 1$, and $u = \phi - \omega_\beta(J)t$.

In the period $0 < t < \tau$, changing variable from (J,ϕ,t) to (J,u,t) in Eq. (1) gives for ψ_1

$$\begin{aligned}\frac{\partial\psi_1}{\partial t} &= (\frac{\partial}{\partial J} - \omega'_\beta(J)t\frac{\partial}{\partial u}) \\ &\times \left[D(J)J\left(\frac{\partial\psi_1}{\partial J} - \omega'_\beta(J)t\frac{\partial\psi_1}{\partial u}\right)\right]. \qquad (5)\end{aligned}$$

When $|\omega'_\beta|tJ \gg 1$, Eq. (5) becomes

$$\frac{\partial\psi_1}{\partial t} \approx [\omega'_\beta(J)t]^2 D(J)J\frac{\partial^2\psi_1}{\partial u^2}. \qquad (6)$$

With initial condition (4), the solution of (6) for $0 < t < \tau$ is

$$\psi_1(J,u,t) = \epsilon\sqrt{2J}\psi'_0(J)\, e^{-\frac{1}{3}D(J)J(\omega'_\beta(J))^2t^3}\sin u. \qquad (7)$$

At $t = \tau$, the beam receives a quadrupole kick, after which the perturbation ψ_2 is (see Ref. [1])

$$\begin{aligned}\psi_2(J,u) &= \sqrt{2}q\epsilon\omega'_\beta(J)\tau J^{3/2}\psi'_0(J) \qquad (8)\\ &\times \exp\left[-\frac{1}{3}D(J)J(\omega'_\beta(J))^2\tau^3\right]\sin(2u + 2\omega_\beta(J)\tau)\\ &\times \cos u,\end{aligned}$$

0-7803-4376-X/98/$10.00 © 1998 IEEE

where q gives the strength of the quadrupole kick. Using a trigonometric identity, we can expand the product $\sin(2u+2\omega_\beta(J)\tau)\cos u$ into a sum of the first ($\frac{1}{2}\sin(u+2\omega_\beta(J)\tau)$) and the third ($\frac{1}{2}\sin(3u+2\omega_\beta(J)\tau)$) harmonics with respect to the variable u. From these two terms only the first harmonic is responsible for the dipole echo; the second term gives rise to a sextupole echo which we omit in what follows.

In the period $t > \tau$, we make a change of variable from (J,ϕ,t) to (J,u_1,t) where $u_1 = \phi - \omega_\beta(J)(t-2\tau)$ in Eq. (1) to obtain for ψ_2

$$\frac{\partial\psi_2}{\partial t} = \left(\frac{\partial}{\partial J} - \omega'_\beta(J)(t-2\tau)\frac{\partial}{\partial u_1}\right) \times \left[D(J)J\left(\frac{\partial\psi_2}{\partial J} - \omega'_\beta(J)(t-2\tau)\frac{\partial\psi_2}{\partial u_1}\right)\right]. \quad (9)$$

When $|\omega'_\beta(t-2\tau)|J \gg 1$, we have

$$\frac{\partial\psi_2}{\partial t} \approx [\omega'_\beta(J)(t-2\tau)]^2 D(J)J\frac{\partial^2\psi_2}{\partial u_1^2}. \quad (10)$$

The solution with the initial condition (8) (keeping only the term $\propto \sin(u+2\omega_\beta(J)\tau)$) is

$$\begin{aligned}\psi &= \frac{1}{\sqrt{2}}q\epsilon\omega'_\beta(J)\tau J^{3/2}\psi'_0(J) \\ &\times \sin(\phi - \omega_\beta(J)t + 2\omega_\beta(J)\tau) \quad (11)\\ &\times \exp\left[-\frac{1}{3}D(J)J(\omega'_\beta(J))^2((t-2\tau)^3 + 2\tau^3)\right].\end{aligned}$$

Now, we have to note that although Eq. (10) is not valid in the vicinity of $t = 2\tau$ due to the approximation made in Eq. (10), the solution (11) turns out to be approximately valid for all times. The reason for that is that duration of the period when $|(t-2\tau)| < 1/\omega'_\beta J$ is of the order of the decoherence time, and according to our assumption (2) the diffusion is negligible during that period. Formally, the right hand side of Eq. (10) becomes small when $|(t-2\tau)|$ approaches zero, and we can neglect it putting $\partial\psi_2/\partial t \approx 0$ during that period, from which is follows that $\psi_2 \approx$ const. On the other hand, we find that solution (11) indeed does not change noticeably during this interval.

The centroid offset of the bunch is given by

$$\bar{\eta}(t) = \int_0^\infty dJ\sqrt{2J}\int_0^{2\pi} d\phi\cos\phi\,\psi(J,\phi,t). \quad (12)$$

Substituting (11) into (12) gives for the echo signal

$$\begin{aligned}\bar{\eta}^{\text{echo}}(t) &= -\pi q\epsilon\tau\int_0^\infty dJ\,\omega'_\beta(J)J^2\psi'_0(J) \\ &\times \sin[\omega_\beta(J)(t-2\tau)] \quad (13)\\ &\times e^{-\frac{1}{3}D(J)J(\omega'_\beta(J))^2(2\tau^3+(t-2\tau)^3)}.\end{aligned}$$

Eq. (13) can be cast into a complex form by substituting $\sin[\omega_\beta(J)(t-2\tau)]$ by $\exp[i\omega_\beta(J)(t-2\tau)]$ that defines a complex echo signal of which the real echo is its imaginary part,

$$\bar{\eta}^{\text{echo}}(t) = -\pi q\epsilon\tau\int_0^\infty dJ\,\omega'_\beta(J)J^2\psi'_0(J) \quad (14)$$
$$\times e^{i\omega_\beta(J)(t-2\tau)}e^{-\frac{1}{3}D(J)J(\omega'_\beta(J))^2(2\tau^3+(t-2\tau)^3)}.$$

Note that the echo appears when the argument of the first exponent in the integrand of Eq. (14) approaches zero, $t \approx 2\tau$. Since we assume that diffusion is small (see Eq. (2)), the second exponent is a slow function of time, and we can put $t = 2\tau$ in it,

$$\begin{aligned}\bar{\eta}^{\text{echo}}(t) &\approx -\pi q\epsilon\tau\int_0^\infty dJ\,\omega'_\beta(J)J^2\psi'_0(J) \quad (15)\\ &\times e^{i\omega_\beta(J)(t-2\tau)}e^{-\frac{2}{3}D(J)J(\omega'_\beta(J))^2\tau^3}.\end{aligned}$$

Assuming that $\psi'_0(J)$ is a monotonous function of its argument and using Schwarz's inequality, one can conclude that the maximum amplitude of echo occurs at $t = 2\tau$, and is equal to the following expression

$$\begin{aligned}&|\bar{\eta}^{\text{max echo ampl}}| = |\bar{\eta}^{\text{echo}}(2\tau)| \quad (16)\\ &= -\pi q\epsilon\tau\int_0^\infty dJ\,\omega'_\beta(J)J^2\psi'_0(J)e^{-\frac{2}{3}D(J)J(\omega'_\beta(J))^2\tau^3}.\end{aligned}$$

Eq. (15) is our main result. Given $\omega_\beta(J)$, $\psi_0(J)$ and $D(J)$, it gives the echo response as a function of time. In the special case when

$$\begin{aligned}\omega_\beta(J) &= \omega_0 + \omega' J,\\ \psi_0(J) &= \frac{1}{2\pi J_0}e^{-J/J_0}, \quad (17)\end{aligned}$$

and assuming a constant diffusion coefficient, $D(J) = D_0$, the integration in (15) can be performed explicitly. The result is

$$\bar{\eta}^{\text{echo}}(t) = \frac{q\epsilon\omega'\tau J_0}{(\beta - i\xi)^3}e^{i\Phi}, \quad (18)$$

where

$$\begin{aligned}\xi &= \omega' J_0(t-2\tau),\\ \beta &= 1 + \frac{2}{3}D_0(\omega')^2 J_0\tau^3,\\ \Phi &= \omega_0(t-2\tau). \quad (19)\end{aligned}$$

When $D_0 = 0$, this reduces to Ref. [1].

One may calculate the amplitude of the dipole echo,

$$|\bar{\eta}^{\text{echo ampl}}(t)| = \frac{q\epsilon\omega' J_0\tau}{(\beta^2+\xi^2)^{3/2}}. \quad (20)$$

The plot of this function is shown in Fig. 1. As mentioned above, the maximum value of the echo is achieved at time $t = 2\tau$, and the amplitude of the echo rolls off as $1/|t-2\tau|^3$ for large values of $|t-2\tau|$. For small values of τ such that $\beta \approx 1$, the width of the echo pulse is of the order of the decoherence time τ_{decoh}; it increases for larger τ.

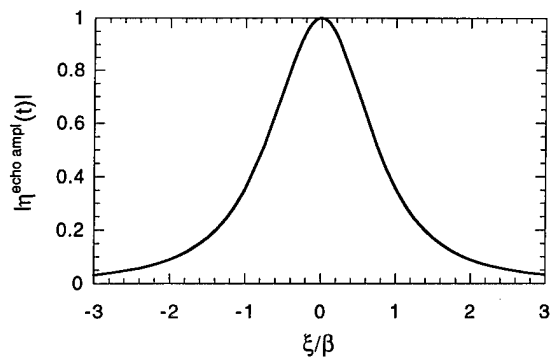

Figure 1: Echo signal as a function of the variable ξ normalized to its maximum value.

Fig. 2 shows the maximum value of the echo amplitude as a function of the time τ between the dipole and quadrupole kicks. The maximum value of the echo amplitude is achieved at $\tau = \tau_{\max} = 0.91\,(D_0(\omega_0')^2 J_0)^{-1/3}$. In terms of decoherence and diffusion times, the maximum is achieved at $\tau_{\max} \sim (\tau_{\text{dif}}\tau_{\text{decoh}}^2)^{1/3}$.

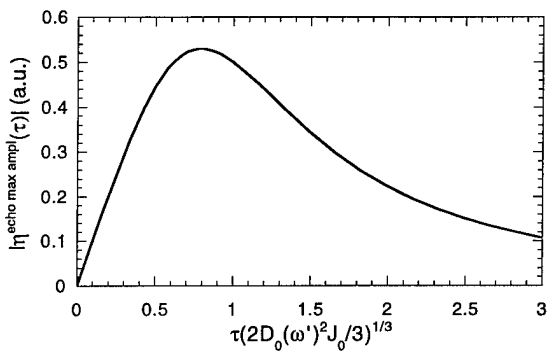

Figure 2: The maximum amplitude value of the echo as a function of the kick time τ.

Experimentally, both quantities ω' and D_0 can be found from the echo measurements. The full width at half maximum of the echo signal in the limit of small τ (when $\beta \approx 1$) is equal to $1.53 J_0\omega'$. If beam emittance J_0 is known, this allows to determine ω'. After that D_0 can be found as $D_0 = 0.75\,\tau_{\max}^3/(\omega_0')^2 J_0$.

More complex dependences of the diffusion coefficient $D(J)$ can also be treated. We consider here the maximum echo amplitude for the case when $D(J)$ can be approximated by a power function,

$$D(J) = D_n J^n, \tag{21}$$

and still assuming Eq. (17). From Eq. (16) we have

$$|\bar{\eta}^{\text{max echo ampl}}| = \frac{1}{2}\pi q\epsilon\omega' J_0 \tau_n F_n(\frac{\tau}{\tau_n}), \tag{22}$$

where

$$\tau_n = (\frac{2}{3}(\omega')^2 D_n J_0^{n+1})^{-1/3} \tag{23}$$

and

$$F_n(\zeta) = \zeta \int_0^\infty dx\, x^2 \exp\left(-x - x^{n+1}\zeta^3\right). \tag{24}$$

Fig. 3 shows the plots of the functions F_n for n=1,2 and 3.

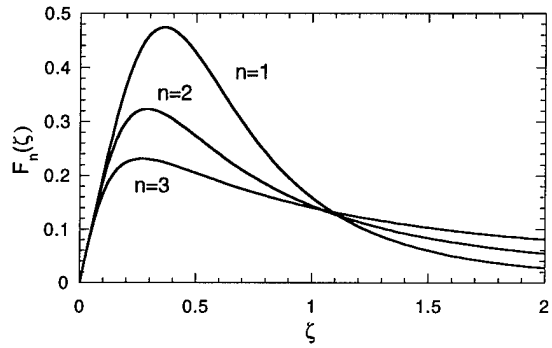

Figure 3: Plot of functions F_n for n=1,2 and 3.

3 CONCLUSION

We extended the perturbation theory of the transverse echo effect in a bunched beam to include the diffusion. Without diffusion, the perturbation theory predicts a linear growth of the echo signal with the delay time τ (which is only true if the the echo signal is small; see nonperturbative approach in Ref. [3]). With diffusion, we find that the echo signal reaches maximum at $\tau_{\max} \sim (\tau_{\text{dif}}\tau_{\text{decoh}}^2)^{1/3}$, and vanishes when $\tau \gg \tau_{\max}$. The exact value of $\tau_{\max}$ depends on the functional form of the diffusion coefficient and is calculated above for several simple power dependences. Experimentally, transverse echo gives a possibility not only to measure the diffusion coefficient within the bunch, but also to distinguish between different dependences $D(J)$.

4 ACKNOWLEDGMENT

This work was supported by Department of Energy contract DE-AC03-76SF00515.

5 REFERENCES

[1] G. Stupakov. "Echo Effect in Hadron Colliders", SSCL Report 579 (1992).

[2] T.M. Malmberg, Phys. Rev. Letters, **19**, 219 (1967).

[3] G. Stupakov and S. Kauffmann, "Echo Effect in Accelerators", SSCL Report 587 (1992).

[4] N. Mahale et al. SSCL Report No. SSCL-N-817, 1993.

[5] L.K. Spenzouris, J.-F. Ostigy, P.L. Colestock, Phys. Rev. Letters **76**, 620 (1996).

[6] O. Bruning et al. "Longitudinal Beam Echo in the CERN SPS", EPAC 96.

[7] O. Bruning. "On the Possibility of Measuring Longitudinal Echos in the SPS", CERN SL/95-83 (AP), 1995.

ADVANCES IN 3D ELECTROMAGNETIC FINITE ELEMENT MODELING

E. M. Nelson*, Los Alamos National Laboratory, Los Alamos, NM 87545

Abstract

Numerous advances in electromagnetic finite element analysis (FEA) have been made in recent years. The maturity of frequency domain and eigenmode calculations, and the growth of time domain applications is briefly reviewed.

A high accuracy 3D electromagnetic finite element field solver employing quadratic hexahedral elements and quadratic mixed-order one-form basis functions will also be described. The solver is based on an object-oriented C++ class library. Test cases demonstrate that frequency errors less than 10 ppm can be achieved using modest workstations, and that the solutions have no contamination from spurious modes. The role of differential geometry and geometrical physics in finite element analysis is also discussed.

1 INTRODUCTION

Electromagnetic finite element analysis (FEA) is becoming more popular as the accuracy and reliability of FEA codes improve. Accurate models of complicated structures have long been sought, and FEA with warped and/or unstructured meshes has been perceived as one path to achieve this accuracy. Thermal and mechanical FEA has met great success, but electromagnetic FEA has traditionally been plagued with reliability problems. Usually these reliability problems take the form of spurious modes (see [4] for many references). Fortunately, numerous workers have made steady progress in the past decade to eliminate these problems.

I will start by briefly reviewing the current state of the art in electromagnetic FEA. The state of the art is being advanced by the accelerator physics community as well as the RF, microwave, radar and antenna communities.

The remainder of this paper is a review of my own work. I will (1) describe an electromagnetic FEA code similar to [6] which I've written, (2) describe what I've learned about electromagnetic FEA from studying differential geometry, and (3) demonstrate the accuracy and reliability of this FEA code.

2 THE STATE OF THE ART

A recent special issue [1] focused on numerical electromagnetic modeling, including electromagnetic FEA. It shows that the techniques for good finite element frequency domain and eigenmode calculations are well established. Edge elements are used to avoid problems with spurious modes. Some reliable 3D electromagnetic FEA codes have existed for some time (see [3] and [6] for example). A number of commercial codes [5] using edge elements are now available. Edge elements with arbitrarily high order basis functions have been described [8] as well.

Applications of electromagnetic FEA in accelerator physics are widespread. In addition to modest work at LANL, there are significant efforts at SLAC and LAL. Adaptive mesh refinement [17] and parallel processing techniques [12, 17] have been applied to accelerator structures. The effect different sets of basis functions have on frequency accuracy has also been studied [9].

Time domain applications of electromagnetic FEA are rapidly maturing. A number of methods for the discretization in time have been described [11]. Some of these methods give explicit time domain formulations which have many similarities to finite difference time domain (FDTD) formulations. Advances are also being made in perfectly matched layers (PMLs) and absorbing boundary conditions (ABCs) for open boundaries for time domain problems [10, 16]. Such boundaries can effectively model ports in accelerator cavities, even when they experience broad spectrum excitations. However, despite dramatic advances in time domain electromagnetic FEA, there is still much work necessary before it is considered competitive with FDTD calculations.

3 A FINITE ELEMENT FORMULATION

In vector calculus notation, this FEA code is based on the following weak formulation of the eigenmode problem for electric fields: find eigenvalues ω^2/c^2 and the corresponding eigenmode fields $\mathbf{E} \in \mathcal{U}_E$ such that $\forall \mathbf{F} \in \mathcal{U}_E$,

$$\int_\Omega (\nabla\times\mathbf{F}) \cdot \boldsymbol{\mu}^{-1}(\nabla\times\mathbf{E}) - \frac{\omega^2}{c^2}\mathbf{F}\cdot\boldsymbol{\epsilon}\mathbf{E}\, d\Omega = 0, \qquad (1)$$

where Ω is the cavity interior and the space $\mathcal{U}_E$ of test functions $\mathbf{F}$ and trial functions $\mathbf{E}$ is

$$\mathcal{U}_E = \{\mathbf{E} \in \mathcal{H}_{\text{curl}}(\Omega) : \hat{\mathbf{n}}\times\mathbf{E} = 0 \text{ on } d\Omega\}, \qquad (2)$$

and $\mathcal{H}_{\text{curl}}(\Omega)$ is the space of vector fields on Ω which are square integrable in the following sense,

$$\mathcal{H}_{\text{curl}}(\Omega) = \{\mathbf{E} : \int_\Omega |\nabla\times\mathbf{E}|^2 + |\mathbf{E}|^2\, d\Omega \text{ exists}\}. \qquad (3)$$

A similar formulation is based on the magnetic fields: find eigenvalues ω^2/c^2 and the corresponding eigenmode fields $\mathbf{H} \in \mathcal{U}_H$ such that $\forall \mathbf{G} \in \mathcal{U}_H$,

$$\int_\Omega (\nabla\times\mathbf{G}) \cdot \boldsymbol{\epsilon}^{-1}(\nabla\times\mathbf{H}) - \frac{\omega^2}{c^2}\mathbf{G}\cdot\boldsymbol{\mu}\mathbf{H}\, d\Omega = 0, \qquad (4)$$

where the space $\mathcal{U}_H = \mathcal{H}_{\text{curl}}(\Omega)$.

* Work supported by DOE, contract W-7405-ENG-36.

0-7803-4376-X/98/$10.00 © 1998 IEEE

The cavity interior Ω is partitioned into quadratic hexahedral (27-node) elements. Curved edges and faces allows these elements to closely follow curved boundaries. On each element there are 54 quadratic mixed-order 1-form basis functions, which are described in more detail below.

Numerical integration is used to compute the matrix components, and a simple subspace iteration scheme with a conjugate gradient solver is used to solve the sparse algebraic eigenvalue problem. A C++ class library handles matrices and bookkeeping of elements, faces, edges, nodes and basis functions.

4 LESSONS FROM GEOMETRICAL PHYSICS

Differential geometry has been mentioned a few times [2, 4] in the electromagnetic FEA literature. It is an excellent tool for understanding electromagnetic FEA. Unfortunately, most of the current literature continues to use vector calculus notation, thus obscuring the simple nature of electromagnetic FEA. In this section I discuss some things I've learned about electromagnetic FEA from applying a little differential geometry.

In the finite element method, the problem domain Ω is divided into elements with simple shapes like tetrahedra and hexahedra. Each element Ω_e has a local coordinate system (i.e., a master element) and a map x_e from local to global coordinates. This map is typically only used to define basis functions and to change variables to numerically integrate equation (1) over Ω_e.

There is a close parallel between FEA and differential geometry. In differential geometry one considers a manifold (the problem domain Ω) which is covered by coordinate patches (the elements). Where the coordinate patches overlap, the coordinate system of one patch is a differentiable function of the coordinates in the other patch. Differential geometry does not demand that a global coordinate system exist, but it accomodates one very well.

What does one learn from this comparison? First, the local coordinates of an element are a valid coordinate system. The physical equations can be expressed in local coordinates just like they are expressed in global coordinates.

Consider a vector basis function. There is no conceptual difference between a vector in global coordinates and a vector in local coordinates. The two are related by the transformation rule for vectors,

$$v^i = \sum_{j=1}^{3} \frac{\partial x_e^i}{\partial u^j} \bar{v}^j, \tag{5}$$

where v^i and $\bar{v}^j$ are the components of the vector in the global and local coordinate basis, respectively, and $x_e^i(u^j)$ is the map from local coordinates u^j ($j = 1, 2, 3$) to global coordinates x^i ($i = 1, 2, 3$). Note that early attempts at 3D electromagnetic FEA violated this transformation rule. They would use scalar basis functions for the vector components, and simply map these components from local to global coordinates, $v^i = \bar{v}^i$. This procedure is geometrically incorrect, and thus the results of these FEA codes were usually flawed.

Table 1: Quadratic 1-form basis functions for hex elements.

$a_1 = (1-v)(1-w)\,du$	$a_7 = (1-u)v\,dw$
$a_2 = (1-u)(1-w)\,dv$	$a_8 = uv\,dw$
$a_3 = u(1-w)\,dv$	$a_9 = (1-v)w\,du$
$a_4 = v(1-w)\,du$	$a_{10} = (1-u)w\,dv$
$a_5 = (1-u)(1-v)\,dw$	$a_{11} = uw\,dv$
$a_6 = u(1-v)\,dw$	$a_{12} = vw\,du$
$a_{13} = (2u-1)a_1$	$a_{19} = (2w-1)a_7$
$a_{14} = (2v-1)a_2$	$a_{20} = (2w-1)a_8$
$a_{15} = (2v-1)a_3$	$a_{21} = (2u-1)a_9$
$a_{16} = (2u-1)a_4$	$a_{22} = (2v-1)a_{10}$
$a_{17} = (2w-1)a_5$	$a_{23} = (2v-1)a_{11}$
$a_{18} = (2w-1)a_6$	$a_{24} = (2u-1)a_{12}$
$a_{25} = 4u(1-u)(1-w)\,dv$	$a_{31} = u\,4w(1-w)\,dv$
$a_{26} = 4v(1-v)\,(1-w)\,du$	$a_{32} = u\,4v(1-v)\,dw$
$a_{27} = (1-v)\,4w(1-w)\,du$	$a_{33} = 4u(1-u)\,v\,dw$
$a_{28} = 4u(1-u)\,(1-v)\,dw$	$a_{34} = v\,4w(1-w)\,du$
$a_{29} = (1-u)\,4v(1-v)\,dw$	$a_{35} = 4v(1-v)\,w\,du$
$a_{30} = (1-u)\,4w(1-w)\,dv$	$a_{36} = 4u(1-u)\,w\,dv$
$a_{37} = (2v-1)a_{25}$	$a_{43} = (2v-1)a_{31}$
$a_{38} = (2u-1)a_{26}$	$a_{44} = (2w-1)a_{32}$
$a_{39} = (2u-1)a_{27}$	$a_{45} = (2w-1)a_{33}$
$a_{40} = (2w-1)a_{28}$	$a_{46} = (2u-1)a_{34}$
$a_{41} = (2w-1)a_{29}$	$a_{47} = (2u-1)a_{35}$
$a_{42} = (2v-1)a_{30}$	$a_{48} = (2v-1)a_{36}$
$a_{49} = 4v(1-v)\,4w(1-w)\,du$	$a_{52} = (2u-1)a_{49}$
$a_{50} = 4u(1-u)\,4w(1-w)\,dv$	$a_{53} = (2v-1)a_{50}$
$a_{51} = 4u(1-u)\,4v(1-v)\,dw$	$a_{54} = (2w-1)a_{51}$

Now consider which basis functions are appropriate for electromagnetic FEA. In [7], Maxwell's equations are described in terms of differential geometry and geometrical physics. In particular, it is pointed out that the electric field is most naturally expressed as a 1-form, or covariant vector. Hence the appropriate basis functions for electric fields is most easily expressed as 1-forms, not vectors. Recent literature typically shows complicated constructions for these basis functions (see [4], [8] and [15] for examples), but if one writes the basis functions as 1-forms in local coordinates (u, v and w), they are simple polynomials. This is the spirit of FEA—the field is a linear combination of simple basis functions on simple elements.

The choice of basis functions is important, as described in [13] and [14]. The basis functions should be mixed-order, with the basis for the field along a coordinate direction, say E_u, being complete to order p in v and w, but only $p-1$ in u. The basis functions employed in this FEA are listed in table 1. The local coordinates of the hexahedra are $0 \le u \le 1$, $0 \le v \le 1$ and $0 \le w \le 1$, and the coordinate basis for 1-forms is du, dv and dw.

The basis functions are assembled so that the tangential component of the field at an interface between elements

is continuous. Thinking of the basis functions as 1-forms makes it easy to verify that the assembly process works. The basis functions are characterized by their non-zero tangential field on an edge or face. The first 12 basis functions have constant tangential field along one edge. These basis functions, by themselves, are appropriate for a linear mixed-order approximation to the fields. The next 12 basis functions (a_{13} to a_{24}) have linear tangential field along one edge. The next 24 basis functions (a_{25} to a_{48}) have non-zero tangential field on one face but no edges. Finally, the last 6 basis functions (a_{49} to a_{54}) have no tangential field on the element boundary.

To assemble global basis functions, the first 24 basis functions must coordinate with all elements which share their one edge. The second 24 basis functions must coordinate with the element which shares their one face. The last 6 basis functions are valid global basis functions by themselves, and need not coordinate with any neighboring elements.

In terms of exterior products ($\wedge$) and exterior derivatives (d), equation (1) can be expressed as

$$\int_\Omega dF \wedge \boldsymbol{\mu}^{-1} dE - \frac{\omega^2}{c^2} \mathbf{F} \wedge \boldsymbol{\epsilon} E = 0, \qquad (6)$$

where $\boldsymbol{\mu}$ and $\boldsymbol{\epsilon}$ are now Hodge-star operators which convert 1-forms (e.g., E and H) to 2-forms (e.g., D and B) using some tensor (i.e., the permittivity and permeability tensors). Differential geometry reminds us that we can differentiate in local coordinates (where the basis and their derivatives are simple) and transform the result to global coordinates (where the permittivity, permeability and metric tensors are usually simple). This avoids messy applications of the chain rule and extra calculation. In some cases it may be cost-effective to transform the tensors to local coordinates and perform all of the computations in local coordinates.

5 TESTS OF THE FEA CODE

This FEA code was tested on 3 geometries: a $3 \times 2 \times 1$ rectangular cavity; a pillbox cavity with radius $\rho = 1$ and height $l = 1$; and a $\rho = 1$ spherical cavity. The mesh was refined in a regular manner from a coarse mesh to a fine mesh. The relative error of the computed eigenvalues for both electric and magnetic field calculations is shown in Fig. 1. Excellent accuracies (less than 10ppm error) are achieved on a modest workstation. The error is proportional to h^4, where h is the element size. The numerical eigenvalue of the spurious modes is less than 10^{-12}, so spurious modes are well separated from the physical modes.

Test cases with inhomogeneously filled cavities show similar results. The spurious modes still have zero eigenvalue, even when the dielectric properties change within an element. The accuracy is excellent, with the caveat that sharp corners cause a significant reduction in accuracy, so the mesh needs to be refined in these locations.

The execution times are reasonable when compared with MAFIA. Fig. 2 compares this FEA code (named YAP) with

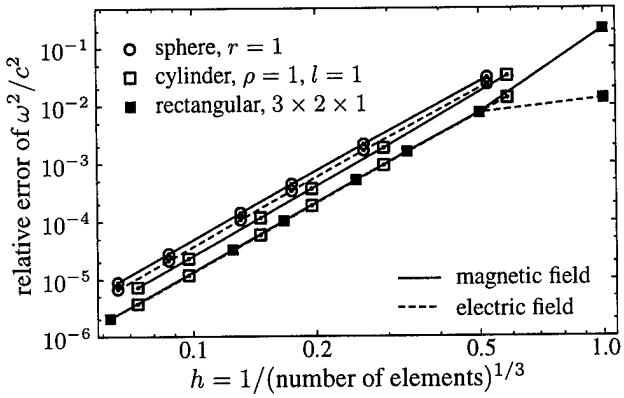

Figure 1: Relative eigenvalue error versus element size h for three test cavities.

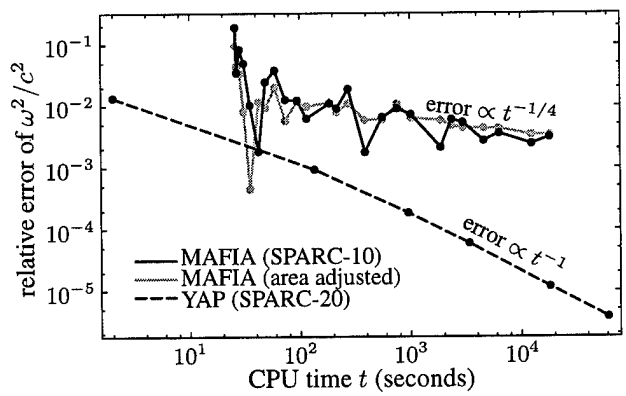

Figure 2: Relative eigenvalue error versus CPU time for MAFIA and the FEA code YAP. The test structure is a pillbox cavity with radius $\rho = 1$ and height $l = 1$. The YAP results are electric field calculations. The MAFIA results employed a uniform grid.

MAFIA on a pillbox test cavity. A uniform grid was employed in the MAFIA calculations in order to produce the typical accuracy achieved by MAFIA in a more complicated structure. This FEA excels when good accuracy is desired since the FEA error scales as t^{-1} instead of $t^{-1/4}$. This difference is due to the discretization error (proportional to h^4 for this FEA code, and h for MAFIA).

The new subgrid features of MAFIA remain to be investigated. However, the error in MAFIA is at best $t^{-1/2}$, even with subgrids. Hence this FEA code remains competitive with MAFIA when accuracy is desired.

6 CONCLUSION

Electromagnetic FEA technology continues to improve. A 3D electromagnetic FEA code with high accuracy and with no contamination from spurious modes has been demonstrated. Such codes are competitive with FDTD codes like MAFIA. Differential geometry and geometrical physics is useful for understanding the features of electromagnetic FEA codes and why they work.

7 REFERENCES

[1] *IEEE Trans. Antennas and Propagation* **45** 313–572 (1997).

[2] Bossavit, A., *IEE Proc.* **135**, 493–500 (1988).

[3] Barton, M. L. and Cendes, Z. J., *J. Appl. Phys.* **61**, 3919–3921 (1987).

[4] Cendes, Z. J., *IEEE Trans. Magnetics* **27**, 3958–3966 (1991).

[5] SOPRANO/EV from Vector Fields Ltd., MicroWaveLab from MSC and MICAV from SRAC are a few examples.

[6] Crowley, C. W. *et. al.*, *IEEE Trans. Magnetics* **24**, 397–400 (1988).

[7] Deschamps, G. A., *Proc. IEEE* **69**, 676–696 (1981).

[8] Graglia, R. D., *et. al.*, *IEEE Trans. Antennas and Propagation* **45**, 329–342 (1997).

[9] Iwashita, Y., COMPUMAG '97, to be published in *IEEE Trans. Magnetics.*

[10] Kuzuoglu, M. and Mittra, R., *IEEE Trans. Antennas and Propagation* **45**, 474–486 (1997).

[11] Lee, J.-F., *et. al.*, *IEEE Trans. Antennas and Propagation* **45**, 430–442 (1997).

[12] Le Meur, G. and Touze, F., *AIP Conf. Proc.* **391**, 113–118 (1996).

[13] Nédélec, J. C., *Numer. Math.* **35**, 315–341 (1980).

[14] Nédélec, J. C., *Numer. Math.* **50**, 57–81 (1986).

[15] Nelson, E. M., Ph.D. thesis, Stanford University (1993); also SLAC-431.

[16] Volakis J. L., *et. al.*, *IEEE Trans. Antennas and Propagation* **45**, 493–507 (1997).

[17] Zhan, X. and Ko, K., *AIP Conf. Proc.* **391**, 389–394 (1996).

EXPERIMENTAL RESULTS ON BEAM HALO

G. Haouat, Commissariat à l'Energie Atomique, BP-12, 91680 Bruyères-le-Châtel, France.

Abstract

The increasing interest for high-intensity, high-energy linear accelerators has induced the scientific community to consider a phenomenon whose effects are worrying: the beam losses. Lost particles can, indeed, produce enough radioactivation in the accelerator structures to considerably complicate operation and maintenance of the machine. They originate in a low-density halo which can extend far from the beam core. Theoretical and experimental studies have been undertaken in order to understand the physics of halo production and to develop methods to limit and control beam losses. The present work reviews efforts and advances in beam-halo and emittance-growth experiments. Experimental techniques, used in different laboratories, are described and measurement results are presented and commented. Experiments on the transport of space-charge dominated beams through periodic focusing channels are considered with particular emphasis.

1 INTRODUCTION

Advances achieved this last decade in the physics and technology of high-intensity, high-power linear accelerators have brought the scientific community to consider their use in a variety of applications. In many projects, examined in recent review papers, large proton (or H^-) linacs are proposed as drivers of intense spallation-neutron sources for transmutation of radioactive nuclear wastes [1], safe production of tritium [2], burning of defense and commercial plutonium inventories [3], energy production in hybrid reactors [3] and for basic research [4]. In these accelerators, with up to 200 mA CW beam current and 200 MW beam power, beam losses are a major concern, since they will cause unacceptably large activation of the structures. Therefore, accelerator designs have to account for this worrying phenomenon. For example, to ensure hands-on maintenance of a 100-mA linac, estimates of the allowed relative losses range from ~10^{-6}/m at 10 MeV to ~10^{-9}/m at 1 GeV [5].

Beam losses are attributed to the particular behavior of a small fraction of beam particles surrounding a dense core and called the halo. The term "halo" has been proposed for the first time at the outset of the seventies by LAMPF physicists to designate tails in the beam transverse distribution they observed in the early experiments on the 1-mA, 800-MeV proton beam [6].

The projects of new accelerators, with beam currents 100 times (or more) larger than at LAMPF, have led up to a major challenge: understanding the mechanisms involved in beam-halo production in order to elaborate methods to limit and control beam spill. The efforts include essentially theoretical studies with model developments and extensive numerical simulations. Several scenarios for the formation and development of halos have been proposed:

- Incoherent effects of space-charge and focusing forces on a matched beam which can, via resonant interactions [7] and/or chaotic processes [5,8], expel particles from the beam core toward the periphery.
- Transverse mismatch and misalignment effects on a space-charge dominated beam [9].
- Incomplete longitudinal capture and longitudinal mismatch [10].
- Longitudinal and transverse space-charge waves generated in a beam bunch which can, during their relaxation toward an equilibrium state, generate particle ejection [8].
- Effects of the transverse-longitudinal coupling force which can, via space-charge forces and non-linear accelerating RF fields, communicate transverse energy to some particles [11].
- Coulomb elastic scattering of beam particles on residual gas which modify particle trajectories [12].

This non-exhaustive list of mechanisms calls for a question: what is the criterion for defining the halo? Brown and Reiser [13] define the "halo" as the ensemble of non-thermalized particles of a beam having betatron oscillation amplitudes larger than the maximum extent of the beam core. They make the difference between the halo and the "tail", which is the part of the thermal equilibrium distribution that extends beyond the beam core. Tail and halo particles are, however, unfavorable with regard to beam loss.

The halo appears to experimentalists essentially in the transverse plane, as a collection of particles, of any origin and behavior, which lie in the low-density region of the beam transverse distribution far from the core, beyond a given number n of rms core radii (say $n \approx 3$). It is so tenuous that its observation is difficult. Halo can be more precisely defined as the ensemble of particles having radial position greater than $n\sigma_r$ or trajectory slope greater than $n\sigma_{r'}$, σ_r and $\sigma_{r'}$ being the second order moments of the phase-space beam distribution. The halo formed around the dense core results in emittance growth, a quantity which is accessible to measurement.

In the present paper, we survey recent and prominent experimental studies of beam halo formation and emittance growth. The experimental techniques developed in different laboratories are described. Periodic focusing channels are considered with special emphasis since they constitute excellent tools for studying the development of instabilities in space-charged dominated beams. Measurement results and proposed interpretations are presented.

0-7803-4376-X/98/$10.00 © 1998 IEEE

2 EMITTANCE GROWTH AND FIELD ENERGY

Emittance growth of low-energy, intense ion beams, induced by space-charge effects through the nonlinear field energy [14], has been investigated in two laboratories. Palkovic [15] reports on emittance measurements in a drifting, decompensated proton beam, at energies between 19 and 45 keV and currents between 9 and 39 mA. They were made at three different positions along the beam axis using a moving-slit emittance probe. Analysis of the results, which are in good agreement with simulations, shows that almost all of the emittance growth is due to a halo containing ~10% of the beam particles. These halo particles are found to be located near the edge of the distribution in phase space.

In a study of the influence of partial space-charge compensation on the transverse emittance of space-charge dominated beams, the University of Frankfurt group observes a severe emittance growth in a 10-keV, 2.5-mA, He^+ beam transported through a magnetic transfer line [16]. Emittance measurements were performed at different locations in the beam line with an electric sweep scanner. They attribute this emittance growth to charge-redistribution and beam-instability effects dominating lens aberrations. This group observes also halo formation in He^+ and Ar^+ beams caused by solenoids, Gabor plasma lenses and radio-frequency quadrupoles [17].

3 HEAVY-ION BEAM TRANSPORT IN A FODO CHANNEL

Heavy-ion drivers for inertial confinement fusion depend crucially on the capability to produce high-intensity, high-quality beams. Emittance growth and beam loss are the primary issues in designing the various components of a heavy-ion fusion accelerator. Of particular concern are the low-energy, multi-beam, electrostatic-focusing induction linacs and the beam-combining devices [18]. Since no comprehensive self-consistent analytical theory for high-current dynamics in such accelerators is so far available, experimental and simulation works are needed to clarify design issues.

3.1 The Lawrence Berkeley Laboratory experiments

As part of the Heavy Ion Fusion Program at Lawrence Berkeley Laboratory [18], a Single Beam Transport Experiment (SBTE) and a Multiple Beam Experiment (MBE) have been set up, more than 10 years ago, to investigate the stability limits for a highly space-charge dominated ion beam in a long alternating-gradient transport channel. Experiments, surveyed here, have been performed on the SBTE [19-22]. The experimental apparatus is composed of an ion gun, a matching section and a transport section, with 82 electrostatic quadrupoles arranged in a FODO lattice, and diagnostic instrumentation. The ranges of beam parameters are: Cs^+ beam, kinetic energy 120-160 keV, beam current 0.7-23 mA, normalized beam emittance 0.08-5 π mm.mrad. Beam emittance is measured at four locations in the FODO channel with the conventional two-slit scan method [19].

Halo formation has been demonstrated in several experiments. In a first one [20], a well-matched beam is provided for injection in the FODO channel. The single-particle betatron phase advance per period without space charge σ_0 is varied in the range 45°-150° to determine the stability limits for the space-charge depressed phase advance σ. The beam transport is defined as stable if both the emittance and current remain unchanged from the entrance to the exit of the channel, and unstable if either the emittance grows or the current decreases because of collective effects. Data analysis indicates that beam transport is always stable below $\sigma_0 = 90°$, within the limits of current and emittance accessible to measurement. It is unstable above $\sigma_0 = 90°$ if sufficiently high current is injected, leading to emittance growth and beam loss. Stable transport conditions can seemingly be met in this region, at low beam currents (See Fig. 4 in Ref. 20).

In a combined experimental and simulation study, the effects on transverse beam dynamics of charge induced on focusing electrodes are analyzed [21]. For misaligned highly space-charge-dominated beams ($\sigma/\sigma_0 \sim 0.1$), a large oscillation of the rms emittance appears, in a beat pattern, along the FODO channel, and can result in beam instability.

In another experiment, emittance growth in mismatched intense beams is investigated [22]. It is found that in the transport of a mismatched beam in both horizontal and vertical directions, with mismatches of the same amplitude but of opposite sign, the emittance grows by as much as a factor of four over that of the matched beam. Observation of the phase space shows a very extensive, but low-level, halo which has formed around the beam core and contains 2 to 3% of the beam particles.

3.2 The experiments at GSI

An experimental program has been undertaken at GSI to explore stability thresholds and instability modes of a high-current ion beam in a transport channel of a few periods [23]. Computer simulation studies have shown, indeed, that many space-charge effects should be observable in such a transport channel [24].

The experimental set-up consists of a 190-keV Ar^+ beam injected, through a matching section, into a six-period magnetic-quadrupole FODO channel. Injected beam current can be varied from 0.1 to 6 mA, and unnormalized emittance from 2 to 30 π mm.mrad. Emittance measurements are made with a conventional slit-collector system positioned at the entrance and exit of the channel. Measurements can be performed on unneutralized and partially space-charge compensated beams.

Analysis of the data shows an enormous deterioration of beam emittance depending on the tune σ_0 and the beam current [23]. Emittance growth is observed, not only above $\sigma_0 = 90°$, where envelope instabilities develop as predicted by theory and computer simulations, but also below $\sigma_0 = 90°$. Emittance growth occurs at high intensities even when the beam passes through only one FODO period. The

source of this emittance increase is attributed to homogenization of the particle distribution at least in cases where no instabilities occur [25].

4 THE MARYLAND TRANSPORT EXPERIMENT

The University of Maryland has carried on, for more than 15 years, an active research program on the fundamental physics of space-charge-dominated beams. A remarkable feature of this program is the tight connection between experiment, theory and simulation.

The Maryland Transport Experiment (MTE) has been originally designed to study the causes of emittance growth and instabilities that limit beam current and brightness in a periodic-focusing transport channel. The experimental setup consists of a thermionic gun delivering a 5-keV electron beam, a transport channel with 36 periodically spaced solenoids and a two-solenoid matching section between the gun and the channel [26]. The full 240-mA solid beam produced by the gun can be masked to form a 5-beamlet configuration of 44 mA total current. Beam emittance is measured at the end of the channel using a slit/pinhole device. A movable phosphor screen is used to observe the beam profile anywhere along the channel.

In earlier experiments made with the solid beam and only 12 lenses [27], it is shown that beam transport with essentially no particle losses and with very little emittance growth (~30%) can be achieved over a range of $40° \leq \sigma_0 \leq 110°$ at large tune depression of $\sigma/\sigma_0 \sim 0.1$. On the other end, the rapid current drop above $\sigma_0 = 110°$ is due to halo formation which results in beam loss to the wall of the tube. It has been proposed that this beam loss could result from envelope instabilities.

Subsequent experiments in the full 36-lens channel indicate considerable beam loss occurring in the longer system, which is explained by misalignment effects and injection errors. Simulations performed with the expected misalignment from mechanical tolerances reproduce an emittance growth comparable to the measured one. Further measurements with the realigned system show a dramatic improvement of beam transmission efficiency [28].

Recent experiments have been conducted on the MTE with a 44-mA beam, divided into five separate beamlets, to study the effects on the transverse dynamics in intense beams of nonuniformity as well as mismatch and misalignment [29]. This beamlet combination is also of interest for investigating merging of several beams for heavy-ion-fusion purpose. The use of a movable fluorescent screen in these experiments is of great importance since it allows to examine beam-profile evolution as the beam propagates down the transport channel.

Experimental observations of a nonuniform, matched beam indicate charge homogenization in the transverse space and emittance growth, which occur not only in a focusing channel, but also in a drift space [30]. These trends are theoretically predicted to be due to conversion of free energy, associated with a nonuniform rms-matched charge distribution, into random transverse kinetic energy. There is, however, no evidence of halo formation and misalignment is believed to contribute negligibly to emittance growth.

On the contrary, for a nonuniform mismatched beam, experiment and simulation reveal a strong halo at the channel end [29]. This can be seen on images from the movable fluorescent screen. Comparison of these images to those produced by the numerical simulations shows excellent qualitative agreement in the beam profile throughout the channel (See, for example, Fig. 3 in Ref. 29). On the other hand, the measured beam emittance is much smaller (about half) than that predicted by theory and simulation. This difference is attributed to the lack of sensitivity of the profile and emittance detectors for the very diffuse halo surrounding the mismatched beam core [29].

Analysis of measurement and simulation results indicates that *i)* most of the energy associated with the mismatch goes into the halo, *ii)* the halo is responsible for most of the emittance growth predicted by theory and *iii)* the beam core thermalizes much faster than the surrounding halo [31]. It has also been found that many of the particles that form the halo are determined by their position in the initial distribution.

5 THE BRUYERES-SACLAY HALO PROGRAM

The Bruyères-Saclay halo program is associated with the TRISPAL project of a high-intensity, high-power proton linac [2]. Its objective is the study of halo-producing mechanisms in two different scenarios: the generation and transport of a very intense, very bright electron beam [32] and the transport of a high-current proton beam through a periodic magnetic-quadrupole FODO channel [33]. For these purposes, sophisticated experimental techniques have been developed for measuring transverse profile and emittance of the beams over a large dynamic range, and for analyzing the very low density regions constituting the halo. They are described below and measurement results are presented.

5.1 Measurement techniques

Beam transverse distribution is measured using either of two experimental procedures, established on the corona observation: the hole-drilled screen method and the neutral-density filter method. They both ensure a correct measurement of the low-density outer part of the beam profile. They are based on an imaging technique in which the light emitted from a charged-particle/photon conversion screen, is analyzed by an intensified video camera. The converter is an optical-transition-radiation screen in the electron experiments and a phosphor screen in the proton experiments.

In the hole-drilled screen method, a hole is bored in the center of the conversion screen. The beam being slightly off-center with respect to the hole in the disk, the beam core is first observed. The beam is then steered toward the hole through which most of the core particles pass. Then, the halo can be properly observed by increasing amplification

of the light intensifier. This method is very powerful since background light originating from the core is eliminated [32].

Another way to observe the beam corona is to use the neutral-density filter method in which the light corresponding to the beam, and provided by a conversion screen without hole, is attenuated only for the core by a circular filter. Images of the halo and the attenuated core are then observed on the same picture [34].

Beam emittance is measured using the quad-scan technique for the electron beam, and the pepper-pot or pinhole/profile-harp techniques for the proton beam.

5.2 Transverse dynamics in an electron photo-injector

In an experiment, performed at Bruyères-le-Châtel, on the electron beam from the ELSA photo-injector, the effect of focusing strength of the photo-injector anode coil on the beam transverse dynamics has been analyzed for various electron-bunch charges [35]. The focusing anode coil is of particular importance since it counteracts the space-charge defocusing force, which is important at low electron energy.

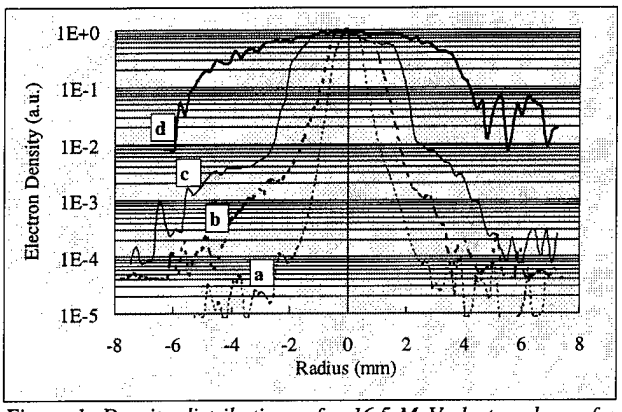

Figure 1: Density distributions of a 16.5-MeV electron beam for four settings of the parameters Q (Bunch charge), B (Anode-coil current) which are:

a) Q = 0.5 nC, B = 16.0 A; b) Q = 0.9 nC, B = 17.5 A
a) Q = 1.8 nC, B = 19.0 A; b) Q = 2.8 nC, B = 19.7 A

The results show different beam behaviors as illustrated on Fig. 1: *i)* At low charge and coil current, the density profile decreases rapidly from the center of the beam toward the outside (curve a), *ii)* At mid current, the density profile seems to be composed of two different shapes, as if two beams, with different transport properties, were traveling together. The more dense beam could be called the "core", the other one, the "halo". Curves b and c of Fig. 1 exhibit this particular pattern, *iii)* At high current, the core and the halo seem to be completely mixed (curve d).

Processing of the density profiles yields an estimate of the fraction of the beam that extends beyond a given distance from the beam center. Beam radii enclosing 90%, 99%, 99.9% and 99.99% of the particles have been deduced for each measurement. Variations of the beam radius enclosing 99% of the particles in the bunch-charge/coil-current space are displayed in Fig. 2 as a 3D contour plot labeled as "EXPERIMENT".

The experiment has been simulated using the code PARMELA. Because of the limited numerical capabilities of the code, contour plots could not be obtained for beam radii enclosing more than 99% of the particles. Data corresponding to this value are presented as "PARMELA" in Fig. 2. Comparison of contour plots for measured data and simulation results shows good qualitative agreement, in spite of some discrepancies in the magnitude of beam radii [35]. In particular, the valley in the contour plot is nicely reproduced by the simulation.

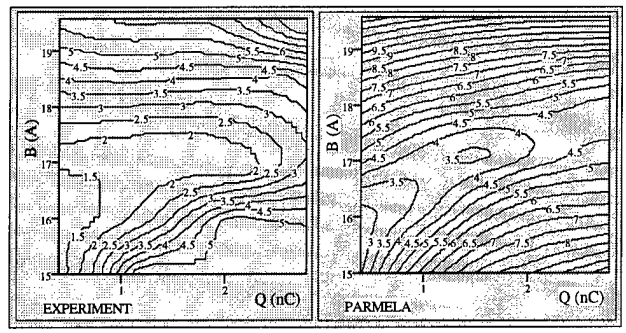

Figure 2: Contour plot of the 99% beam-radius variations with charge Q and anode-coil current B for a 16.5-MeV electron beam..

Experiment and simulation indicate that the anode-coil current should be higher if the objective is to optimize the transport of the beam core only, and relatively lower if the objective is to optimize the transport of the whole beam, core and halo.

5.3 The FODO experiment at Saclay

An experimental study of halo formation in a space-charge-dominated proton beam transported through a periodic FODO channel is in progress at Saclay. It is based on a proposal consisting of using the 29-periods magnetic-quadrupole FODO channel of the Saturne 20-MeV Alvarez linac (not powered with RF) as a transport line for the proton beam of the injector Amalthée (See Ref. 33). Because of the Alvarez-linac structure, the period length of the FODO channel is not constant, but increases gradually from the entrance to the exit.

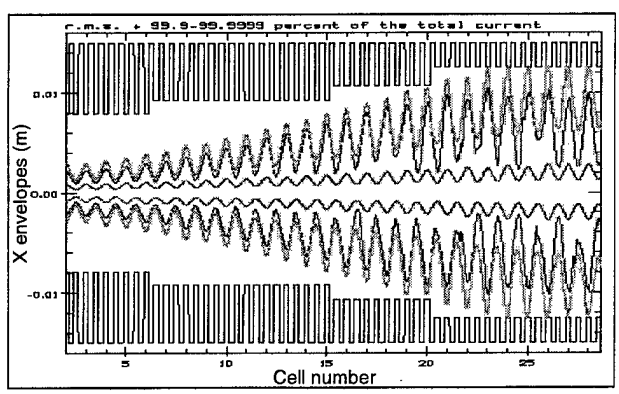

Figure 3: Beam envelopes in the x-direction along the FODO channel from the RENOIR-code simulation for σ_0 = 100° and I = 30 mA. The most inward envelope correspond to the rms beam radius and the most outward envelope to 99.9999% of the particles.

The experimental set-up is composed of the proton source, a low-energy matching section with diagnostic equipment, the FODO channel and a diagnostic chamber at the end of the channel. The source produces a proton beam of 300 to 750 keV energy, 5 to 50 mA intensity, in 0.5-ms bunches.

Beam-halo formation appreciably depends on the initial beam conditions, in particular the emittance. Precise measurements of this parameter have been performed at the front end of the FODO channel using both the pepper-pot mask with fluorescent screen and the pinhole/profile-harp system [36].

The emittance data have been introduced in the Particle-in-Cell code RENOIR [8], based on a self consistent model, to simulate beam transport through the FODO channel. The simulation yields beam distribution over a wide dynamic range including core and halo particles, and allows to find transport conditions for an rms-matched beam (Fig. 3). Using these transport conditions, emittance and halo measurements will be performed soon at the end of the FODO channel. However, a coherent interpretation of halo measurements implies to consider not only halo formation from space-charge effects but also halo production by beam-particle Coulomb scattering on the residual gas [37], and neutralization effects on the propagating beam [38].

6 CONCLUSION

Progresses in the reviewed experimental studies of halo formation and emittance growth contribute greatly to improve our understanding of the fundamental physics of space-charge-dominated beams. Close coordination between experimental works and numerical simulations, based on theoretical models, is essential and stimulates advances in each of the domains. However, the studies apply essentially to the transverse dynamics of intense beams.

Efforts remain to be done to experimentally study halo formation induced by the longitudinal effects, including incomplete capture, mismatch and longitudinal/transverse coupling. These effects are believed to be important sources of halo. Also, the effects of transverse and longitudinal space-charge waves have to be considered.

7 ACKNOWLEDGEMENTS

I express my sincere gratitude to N. Pichoff for support and great help in preparing this paper, and to A. Piquemal who kindly provided useful information and results from the code RENOIR.

REFERENCES

[1] M. Mizumoto, "Accelerators for nuclear wiste transmutation", LINAC 94, p.317.
[2] M. Promé, "Major projects for the use of high power linacs", LINAC 96, p.9.
[3] G. Lawrence, "Transmutation and energy production with high power accelerators", PAC 95, p.35.
[4] H. Klein, "Spallation Neutron Sources", LINAC 94, p.322.
[5] J.M. Lagniel, "Halos and chaos in space-charge dominated beams", EPAC 96, p.163.
[6] R. A. Jameson, "Beam halo from collective-core/single-particle interactions" Los Alamos Report LA-UR-93-1209, March 1993.
[7] R. L. Gluckstern, LINAC 94, p.333; Phys. Rev. Letters, **73**, 1247 (1994).
[8] J.M. Lagniel, A. Piquemal, "On the dynamics of space-charge dominated beams", LINAC 94, p.529.
[9] D. Kehne, M. Reiser and H. Rudd, Proc. 1991 Part. Acc. Conf., San Francisco, CA, p.248 (1991); A. Cucchetti, M. Reiser and T. Wangler, *ibid.* p.251.
[10] R. Garnett, E. Gray, L. Rybarcyk and T. Wangler "Simulation studies of the LAMPF proton linac", PAC95, p.3185.
[11] M. Pabst and K. Bongardt, "Halo simulation in a realistic proton linac", LINAC 96 p.27.
[12] J.M. de Conto, "Emittance growth and beam halo due to incoherent random phenomenons", EPAC94, p.1362.
[13] N. Brown and M. Reiser, Phys. Plasmas **2**, 965 (1995).
[14] T. Wangler, K. Crandall, R. Mills and M. Reiser, IEEE Trans. Nucl. Sci. NS **32**, 2196 (1985).
[15] J. Palkovic, "Emittance growth in a low-energy proton beam", PAC93, p.21.
J. Palkovic, "Gabor lens focusing and emittance growth in a low-energy proton beam", Thesis, the University of Wisconsin - Madison, 1991.
[16] P. Gross, J. Pozimski, R. Dölling, T. Weiss and H. Klein, LINAC94, p.520.
[17] G. Riehl, Pozimski and W. Barth, Proc. 1990 Lin. Acc. Conf., LA-12004-C, UC-910/UC-414, 755 (1991).
[18] P. Seidl, "Beam dynamics in heavy ion fusion", PAC95, p.3159.
[19] A. Feltens, D. Keefe, C. Kim, S. Rosenblum, M. Tiefenback and A. Warwick, Proc. 1984 Lin. Acc. Conf., Seeheim, GSI-84-11, 312 (1984).
[20] M. Tiefenback and D. Keefe, IEEE Trans. on Nucl. Sci. NS **32**, 2483 (1985).
[21] C.M. Celata, Proc. 1987 Patr. Acc. Conf., 996 (1987).
[22] M.G. Tiefenback, Proc. 1987 Patr. Acc. Conf., 1046 (1987).
[23] J. Klabunde, A. Schönlein, R. Keller, T. Kroll, P. Spädtke and J. Struckmeir, Proc. 1984 Lin. Acc. Conf., Seeheim, GSI-84-11, 315 (1984).
[24] J. Struckmeir and M. Reiser, Part. Acc. **14**, 227 (1984); J. Struckmeir, J. Klabunde and M. Reiser, Part. Acc. **15**, 47 (1984).
[25] J. Klabunde, P. Spädtke and A. Schönlein, IEEE Trans. on Nucl. Sci. NS **32**, 2462 (1985).
[26] J. Haber, D. Kehne, M. Reiser and H. Rudd, Phys. Rev. A **44**, 5194 (1991).
[27] M. Reiser, E. Chojnacki, P. Loschialpo, W. Namkung, J. Lawson, C. Prior and G. Warner, Proc. Proc. 1984 Lin. Acc. Conf., Seeheim, GSI-84-11, 309 (1984).
[28] M. Reiser, J. McAdoo, K. Low, D. Kehne and T. Shea, Proc. 1987 Patr. Acc. Conf., 1135 (1987).
[29] D. Kehne, M. Reiser and H. Rudd, AIP Conf. Proc. **253**, 47 (1991).
[30] M. Reiser, C. Chang, D. Kehne, K. Low, T. Shea, H. Rudd and J. Haber, Phys. Rev. Lett. **61**, 2933 (1988).
[31] D. Kehne, M. Reiser and H. Rudd, PAC93 p.65.
[32] G. Haouat, N. Pichoff, C. Couillaud, J. Di Crescenzo, S. Joly, S. Seguin and S. Striby, AIP Conf. Proc. **333**, 245 (1995).
[33] P.Y. Beauvais, D. Bogard, P. Chamouard, R. Ferdinand, G. Haouat, J.M. Lagniel, J.L. Lemaire, N. Pichoff and C. Ruiz, PAC95, p.3173.
[34] N. Pichoff, G. Haouat, C. Couillaud, J. Di Crescenzo, S. Joly, C. Ruiz, S. Seguin and S. Striby, DIPAC95, Travemünde, Germany, 28-31 May 1995, Conf. Proc. p.63.
[35] G. Haouat, N. Pichoff, C. Couillaud, J. P. De Brion, J. Di Crescenzo, S. Joly, A. Loulergue, C. Ruiz, S. Seguin and S. Striby, PAC95, p.3170.
[36] G. Haouat, N. Pichoff, P.Y. Beauvais and R. Ferdinand, EPAC96, p.1206.
[37] N. Pichoff, G. Haouat and P.Y. Beauvais, EPAC96, p. 1209.
[38] P.Y. Beauvais, J.M. Lagniel, N. Pichoff, G. Haouat and P. Chaix, LINAC96, p.202.

CORE AND HALO PARTICLE DYNAMICS OF HIGH INTENSITY PROTON BEAMS

M. Pabst and K. Bongardt, Forschungszentrum Jülich GmbH, 52425 Jülich, Germany
A. P. Letchford, Rutherford Appleton Laboratory, Chilton, Didcot, UK

Abstract

A very critical design issue for a high intensity proton linac is to keep particle losses below 1 W/m at the high energy end allowing unconstrained hands-on maintenance. For the ESS linac, with it's 214 mA peak current, Monte Carlo simulations with up to one million particles are performed. Single particle trajectories are shown along the linac demonstrating the existence of a space charge potential with non-linear terms and transverse-longitudinal coupling.

Radial halo particles at the final energy of 1.334 GeV start at 70 MeV at the boundary of the longitudinal phase space and also transversely close to a boundary of a 4D waterbag distribution. The single particle motion of these halo particles is characterised, on the average, by conservation of the sum of all three emittances. Trajectories are presented for both horizontal-vertical coupling and also transverse-longitudinal coupling. Core particles have a very different behaviour. For core particles, located around the rms emittances at 70 MeV, the single particle emittances can be either increased or decreased.

1 INTRODUCTION

High intensity proton linacs can be either pulsed H^- – accelerators up to 5 MW average beam power or cw H^+ – accelerators up to 130 MW beam power. The major design problem is to reduce the particle loss along the linac down to 1 W/m which corresponds to a loss rate below 10^{-7}/m. Losses above this limit prevent hands-on maintenance. Particle loss is caused by a small number of particles outside the dense beam core, called the beam halo. The origin and formation of the halo and it's dynamics are important issues for understanding the particle loss.

For this investigation of halo properties the underlying realistic high current linac design is the linac of the European Spallation Source (ESS) [1][2]. The main part of the 5 MW ESS linac is a coupled cavity linac (CCL) at 700 MHz with an effective bunch current of 214 mA which accelerates the beam from 70 MeV up to 1.334 GeV. The CCL is designed to have a tune depression of about 0.8 in all three planes. This non space charge dominated design results in less than 10% RMS emittance increase, preserves the cylindrical bunch shape and reduces the sensitivity to mismatch and tolerances [3]. At the end of the linac at 1.334 GeV, a beam halo can be recognised which contains less than 10^{-3} of the particles. To understand the properties and dynamics of these halo particles, single particle trajectories have been examined.

2 PROPERTIES OF THE HALO

Results from Monte Carlo simulations with 200 000 particles are presented for the realistically designed ESS CCL. The output distribution of a preceding DTL was transferred into the CCL. No effect can be associated with the frequency jump and the change from a singlet to a doublet focussing system. Space charge calculations are fully three dimensional and no symmetries are assumed. At the input to the DTL at 5 MeV, the transverse and longitudinal phase spaces are filled independently with waterbag distributions. The space charge forces in such a distribution can be calculated analytically [4].

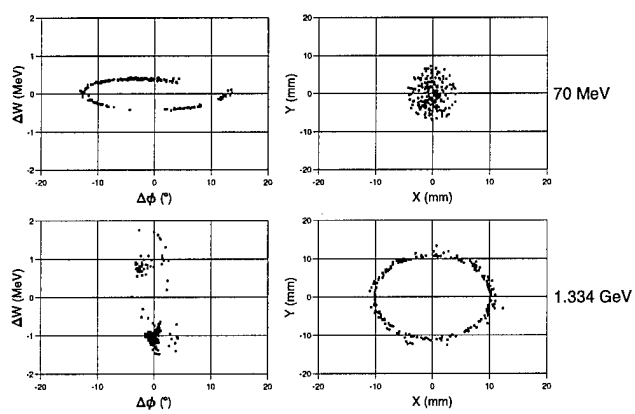

Figure 1: Longitudinal phase space ($\Delta W, \Delta\phi$) and real space (X,Y) projections at input (70 MeV) and at output (1.334 GeV) for the 200 outermost particles in (X,Y) space (halo particles) at the linac end.

In Figure 1, the 200 outermost radial halo particles are shown together with their position in the longitudinal phase space at 1.334 GeV. Also shown are the corresponding real space and longitudinal phase space positions at 70 MeV. There is obviously a strong transverse-longitudinal coupling because all the radial halo particles at 1.334 GeV start at the boundary of the longitudinal phase space at 70 MeV. Please note that the chosen 200 halo particles are not the outermost ones in real space at all energies. These particles are oscillating through the core. Also, they are not necessarily the outermost ones in either the horizontal or vertical phase space

In Figure 2, the same particles are shown in the transverse phase space at 70 MeV. All of the particles start from close to the boundary of the four dimensional transverse hyper-ellipsoid. The η's and the ζ's corresponds to the standard circle transformation of single particle coordinates and velocities. In Figure 2c the absolute value

0-7803-4376-X/98 /$10.00 © 1998 IEEE

of the transformed transverse velocity is plotted against the transformed transverse radius. Areas inside circles of Figure 2c are proportional to the sum of the transverse emittance. The inner line in Figure 2c is the boundary for a 4D waterbag distribution (total emittance = 6 x rms emittance) with the same rms emittances as the beam. The dashed line corresponds to the boundary for the actual distribution where the total emittance = 7.68 x rms emittance.

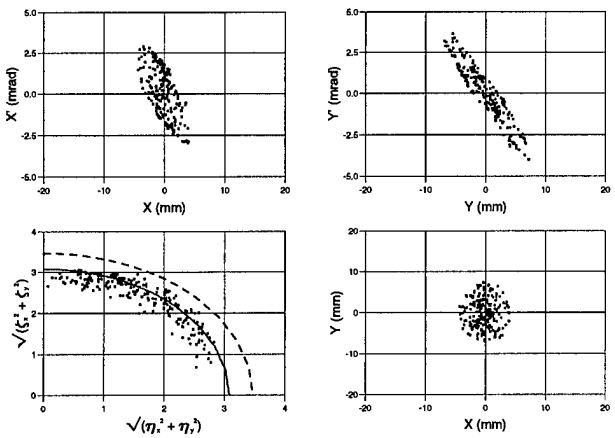

Figure 2: Transverse phase space projections of the halo particles at 70 MeV.

This strong horizontal-vertical correlation and the coupling to the longitudinal plane is also apparent at 1.334 GeV as shown in Figure 3a. Here the sum of the normalised single particle emittances Ex + Ey + Ez is plotted against the sum of the normalised transverse emittances Ex + Ey, at 70 MeV and 1.334 GeV respectively, for the 200 radial halo particles. Evident is an increase in the sum of the transverse emittances, whereas the total sum stays constant on average, indicating a decrease in the longitudinal emittance on average. Figure 1 and Figure 3 are both a consequence of a transverse - longitudinal coupling term in the space charge potential. As a result radial core particles at 70 MeV become the outermost radial particles at the linac end. This process goes together with the exchange of emittances between the longitudinal and transverse directions.

For comparison, in Figure 3b the same parameters are plotted for particles in the beam core at 70 MeV. 200 particles are chosen which have single particle emittances in a range of 80% - 120% of the rms emittance in all three planes at 70 MeV. These core particles show completely different behaviour than the particles which become the radial halo at 1.334 GeV. Their total transverse emittance as well as their longitudinal emittance can either increase or decrease. Note that these core particles would be located in the lower left corner of Figure 3a.

Figures 4 and 5 show two typical halo particle single particle trajectories. Figure 4 depicts a particle with strong horizontal-vertical coupling. This leads to a rosette form in the radial plane as the elliptical path precesses. The longitudinal emittance is large but conserved in this case.

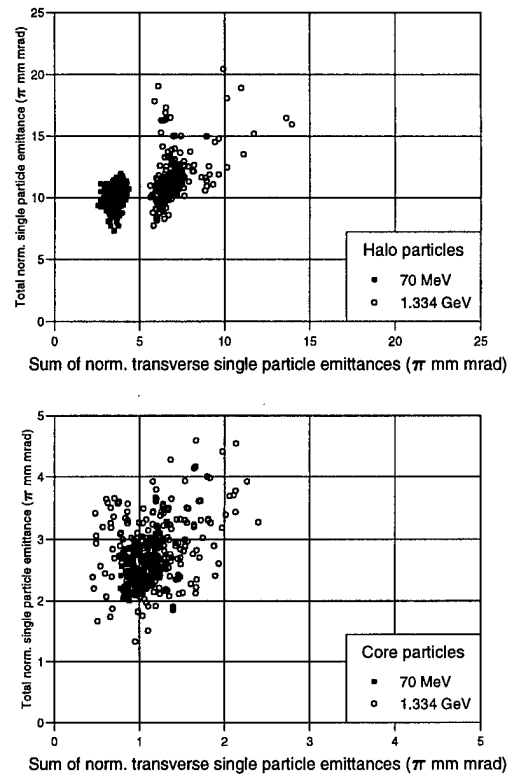

Figure 3: Plot of total normalized single particle emittance (Ex+Ey+Ez) as a function of the transverse single particle emittance (Ex+Ey) for the halo particles (upper graph) and some 200 selected core particles (lower graph)

Figure 5 represents a longitudinal-vertical coupling. The horizontal emittance is much smaller than the vertical one here. The longitudinal emittance decreases as the vertical emittance increases, the sum remaining more or less constant. The rosette form in the (Y, $\Delta\phi$) plane is not as evident as in Figure 4. One reason may be the presence of non-linear external forces at the bunch head and tail. Also the difference in the transverse and longitudinal phase advance prevents a regular form, as in Figure 4, from appearing.

This analysis of halo particle properties is somewhat different to results obtained by the particle-core model [6]. Normally, an unbunched space charge dominated beam with tune depressions below 0.5 is considered The space charge forces are assumed to be linear inside the core. Test particles are positioned outside the core. Their motion, caused by strong mismatch, is studied. Chaotic behaviour can be seen. This model cannot describe how core particles can become halo particles. However, phase space boundaries can be obtained.

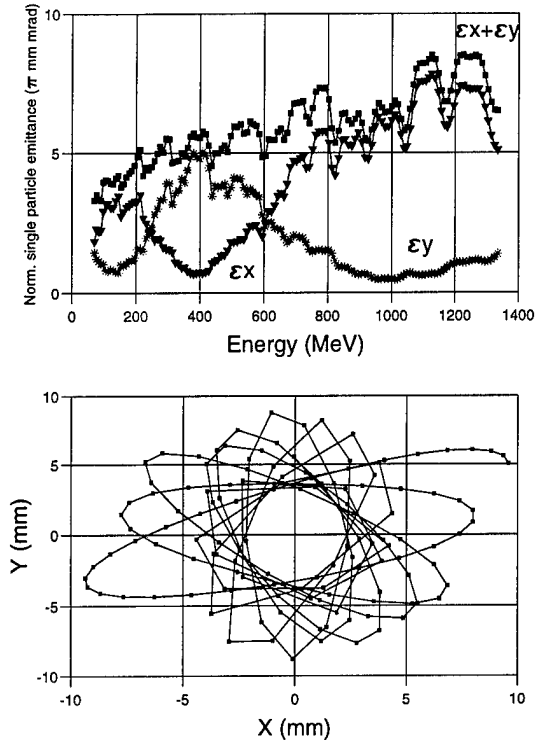

Figure 4: Single particle emittances and trajectories along the ESS CCL of a selected halo particle.

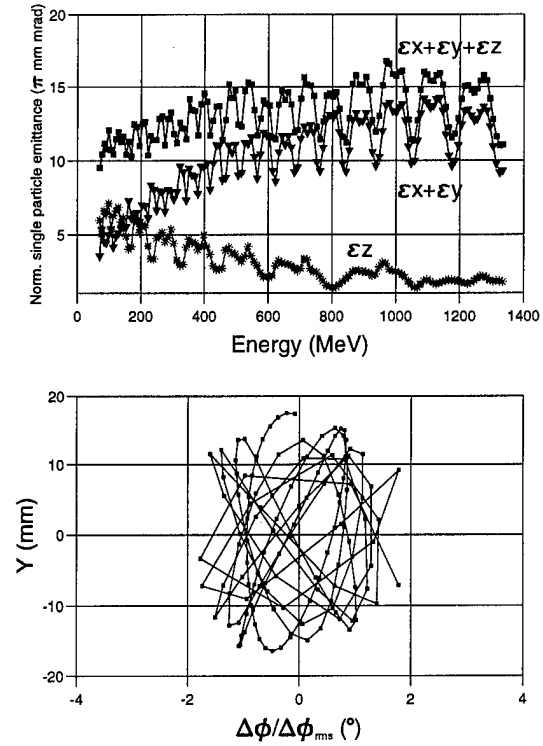

Figure 5: Single particle emittances and trajectories along the ESS CCL of another selected halo particle.

3 HALO PRODUCTION RATE

As has been recognised before from investigations of dc beams [5], halo production in a bunched beam is increased due to mismatch [3]. In the results presented above, there is about 60% change in the matched transverse beam radii, due mainly to the change in the number of accelerating cells per focusing period. In addition, the 20% longitudinal dc emittance growth which occurs in the preceding DTL has not been corrected for at the CCL input. By injecting a longitudinally matched beam, the longitudinal halo, which is not shown here, is substantially decreased. The driving force for the halo production is the non-linear space charge potential, associated with the non-self consistent distribution of a cylindrical bunch. Even for a perfectly rms matched beam there will be halo production. Mismatch, tolerances and errors then enhance the halo production rate.

This is somewhat different from the situation for a dc beam. Here, self consistent particle distributions are known which result in a zero halo production rate for a matched beam. Mismatch is then the driving term for halo production, not only an enhancement factor. More realistic unbunched distributions are associated with non-linear space charge forces with an elliptical boundary in real space. It appears to be difficult to scale the halo production rate from a dc beam to a bunched beam as in the latter case the transverse-longitudinal coupling cannot be ignored.

In order to estimate a particle loss rate at the beam pipe, Monte Carlo simulations with one million particles have been carried out for the first third of the CCL. From these on-going studies it is hoped to extrapolate, using data for 200 000 and 1 000 000 particles, the particle distribution at the pipe radius. Quadrupole displacement errors have also been included in some simulations. As expected, even for beam displacements of up to 4 mm, the particle distribution is only weakly effected. More dramatic changes are expected when sextupole errors are included.

4 REFERENCES

[1] ESS A Next Generation Neutron Source for Europe, Volume 3, The ESS Feasibility Study, March 1997.

[2] I. S. K. Gardner et al., these proceedings.

[3] M. Pabst et al., LINAC 96, Geneva, p27.

[4] M. de Magistris, V. G. Vaccaro, L. Verolino, "Bunched Beams in Axisymmetric Systems", submitted to: Il Nuovo Cimento.

[5] C. Chan, R. A. Jameson, Phys. Rev. E, vol. 52, p. 3074, 1995.

[6] Contributions to the 8th ICFA Advanced Beam Dynamics Workshop, Bloomington, USA, Oct. 1195, AIP conf. proc. 377, ed. S. Y. Lee.

THE FINE STRUCTURE OF THE LONGITUDINAL MACHINE IMPEDANCE OBSERVED WITH SINGLE BUNCHES

T. Bohl, T. Linnecar, E. Shaposhnikova
CERN, SL Division, 1211 Geneva 23, Switzerland

Abstract

Using a beam spectrum measurement the detailed structure of the CERN SPS longitudinal machine impedance has been observed over a wide frequency range. Single high intensity proton bunches were injected into the machine with RF off. The spectrum of the unstable bunch modes, produced by the different resonant impedances in the ring, was measured during slow debunching. The maximum mode amplitude as a function of frequency was recorded for many injected bunches. The central frequency of each bunch mode is close to the resonant frequency of the impedance and the width depends upon the bunch length. Using sufficiently long bunches allowed the machine impedance to be seen in detail in the frequency range 100MHz to 4GHz. The low frequency of this range is defined by the initial stable bunch spectrum, and the high frequency by the vacuum chamber cut-off frequency. The dominant peaks in the spectrum have been identified with different impedance sources in the machine - some previously unknown.

1 INTRODUCTION

When trying to understand or predict the behaviour of intense beams in particle accelerators, accurate knowledge of the machine coupling impedance is essential. The design of new accelerators profits from an estimation of the impedance by powerful numerical codes. Older machines which have not been able to benefit as much from these calculations usually have significantly larger and less well known impedance.

The SPS, built in the 70's, has a non-smooth vacuum chamber with many cross section changes around its circumference. The SPS has exceeded its initial design intensity many times over, but must now be upgraded to be the injector for the new LHC machine. One of the critical beam parameters for this mode of operation is the longitudinal emittance. The emittance at extraction at 450GeV must be kept between 0.5eVs and 1eVs with a preference from LHC for the lower value defined by dynamic aperture [1]. In addition if the emittance turns out to be higher than 0.6eVs, clean injection into the LHC would require a new additional RF system in the SPS. The emittance at injection at 26GeV is foreseen as 0.35eVs which will increase to ~0.5eVs after the matching process [2]. Consequently great care must be taken to control emittance blow up and therefore both single and coupled bunch instabilities during the cycle. Note that the beam of 243 bunches, intensity 10^{11} per bunch, filling 3/11 of the machine circumference, combines the high single bunch intensities obtained during collider operation in the past, where the microwave instability was a limitation [3], with the large total intensities achieved in fixed target operation, where coupled bunch instabilities are seen.

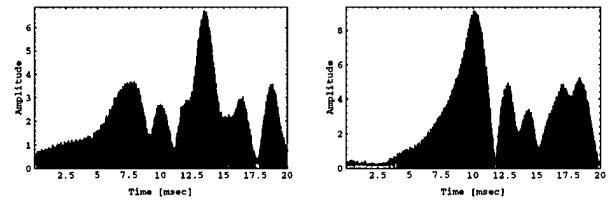

Figure 1: Examples of beam signals at 1.56GHz.

The microwave instability, first observed in the SPS in 1976 [4], is not harmful for present operation, but it limits the single bunch intensity of the LHC beam. A new measurement technique [5], used last year and described below, has allowed us to determine the dominant sources of longitudinal impedance in the SPS responsible for this instability.

2 SPECTRUM MEASUREMENT

2.1 *Method of measurement and results*

The method was first found experimentally and then justified from linear theory and simulation. This is the "recipe" we followed in our measurements.

- Inject long single bunches above the instability threshold, (in our case at 26GeV, bunch length τ = 25-50ns, emittance $\varepsilon \sim$ 0.2-0.3eVs and intensity $N = 1 - 5 \times 10^{10}$ particles per bunch). RF is off.
- Observe the signals growing after injection as a function of time, (wideband longitudinal pickup with spectrum analyser, bandwidth 3MHz, used as a receiver). See examples in Fig.1. Record the maximum amplitude at each frequency, (centre frequency varied over from 100MHz to 4GHz).
- Take data at each frequency from a large number of bunches (at least 10).
- The bunch should debunch very slowly (length changes $< 50\%$ during the observation time $\sim$ 100ms).

The result of this method applied to the SPS in two different sets of measurements is shown in Fig.2. The fine structure of the beam spectrum, which was very reproducible, is clearly seen.

2.2 *Justification for method from linear theory*

We measured the peak mode amplitude of the instability and used simulation to confirm our interpretation of the re-

0-7803-4376-X/98/$10.00 © 1998 IEEE

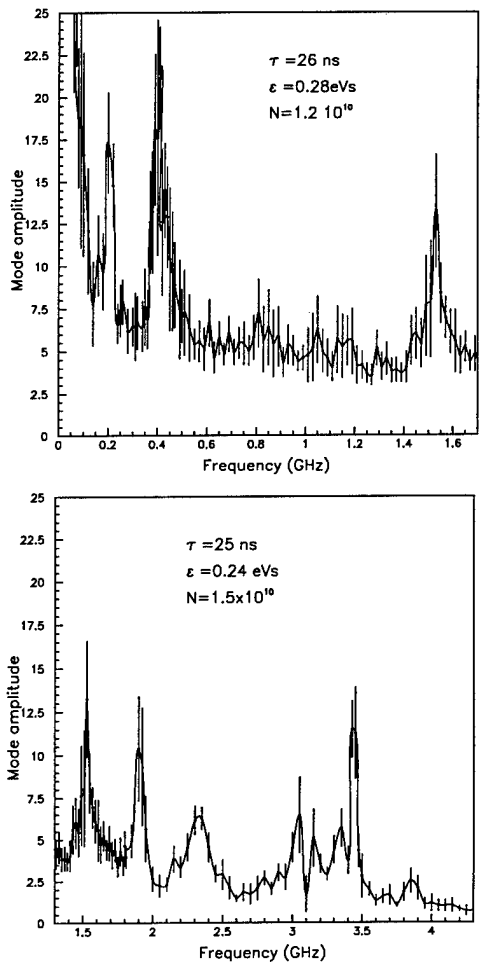

Figure 2: Structure from 0.1GHz to 4.0GHz.

sults for this non-linear regime. However it is possible to gain some information from the theory for the linear regime of a fast microwave instability. We assume: (a) the instability growth rate is much faster than the debunching time defined as the time when the bunch length increases by $\sqrt{2}$; (b) $\omega_r \tau \gg 1$, where ω_r is the centre frequency of the impedance, (many wavelengths cover the bunch); (c) the impedance bandwidth is less than the bunch spectrum bandwidth $\sim 1/\tau$, (narrowband impedance regime), but not so low as to provoke strong coupled bunch phenomena. Then from linear theory the spectrum of the unstable bunch mode at azimuthal harmonic n is,

$$\Delta\rho_n \sim n \int_{-\pi}^{\pi} \rho_0(\theta) e^{-i(n-n_r)\theta} d\theta, \qquad (1)$$

where θ is the azimuthal coordinate, $\rho_0(\theta)$ is the bunch line density, $n_r = \omega_r/\omega_0$, and ω_0 is the revolution frequency.

We see that the spectrum shape is given by the Fourier Transform (FT) of the stable bunch, shifted to the resonant frequency of the impedance. As an example Fig.3 shows this solution in space and frequency domain for a parabolic bunch. Longer bunches have narrower spectral bandwidth giving finer resolution, (recipe item 1). This can be seen in reality in measurements on the SPS. In Fig.4 the bunch pro-

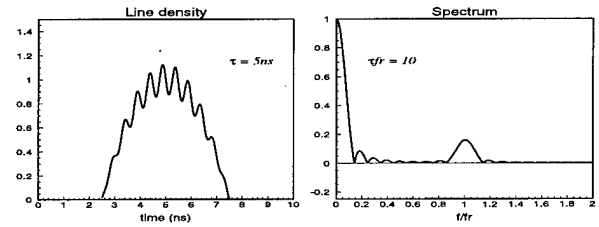

Figure 3: Profile and spectrum of unstable bunches.

file measured every 100 turns from injection is presented in the first plot as a mountain range display. The unstable modes grow on the bunch and by taking the FT of each profile we see clearly in the second plot the increase of signals with definite width at each frequency corresponding to the different impedance sources. The projection of the spectra from Fig.4 averaged over many bunches would give similar results to Fig.2. Peaks appearing at different times explains why taking the maximum amplitude, (recipe item 2), reproduces many unstable modes. Note also the slow debunching.

The initial perturbation grows as $\Delta\rho_n(t) \propto e^{-i\Omega t}$, with instability for $\mathrm{Im}\Omega > 0$. For a resonator with shunt impedance R_{sh} and quality factor Q the instability growth rate is given by

$$\mathrm{Im}\Omega \simeq \omega_r \left(\frac{N e^2 \omega_0 |\eta|}{16\pi E_0} \frac{R_{sh}}{Q} \right)^{\frac{1}{2}}, \qquad (2)$$

where η is the slip factor and E_0 is the synchronous energy.

In this approximation the growth rate is independent of the initial bunch distribution and proportional to $(R_{sh}/Q)^{1/2}$. The same formula can be applied when RF is on if the growth rate is much larger than the synchrotron frequency. It was first conjectured in [6] that for a single bunch instability due to a narrow band impedance, the instability threshold should depend on R_{sh}/Q and average current, in contrast to the broad band impedance case ($1/\tau \ll \omega_r/2Q$) where Z/n and peak current are important.

From Eq.2 we draw the important conclusion that although damping resonators (reducing R_{sh} but $R_{sh}/Q = const$) can always help cure coupled bunch instabilities, this does not apply to the single bunch case until the broadband impedance regime is reached.

3 IMPEDANCE SOURCES

Using the results of the measurements shown in Fig.2, it was possible to determine the sources of the dominant impedances in the SPS. The peaks at 200MHz and 800MHz are from the fundamental mode of the two travelling wave (TW) RF systems which have high R_{sh}/Q and low Q ($\sim$ 130). Small peaks from 0.4GHz to 1.4GHz can be identified with the HOM modes of the six RF systems in the SPS [7]. However the sources of peaks at 400MHz and above 1.4GHz were not obvious.

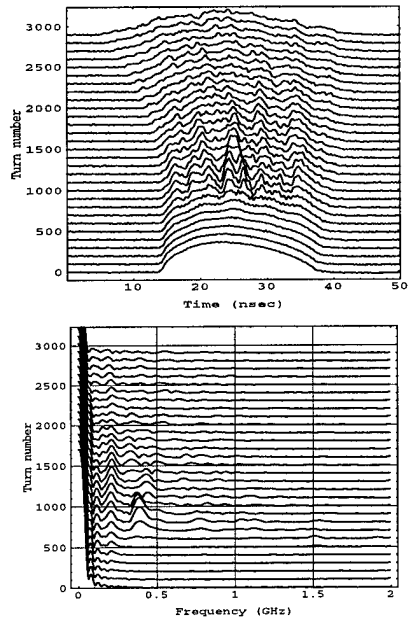

Figure 4: Fourier analysis of longitudinal bunch profiles.

Frequencies above 1.4GHz suggest cavity-like devices with a radius r of around 8cm. In the SPS there are about 800 pumping ports which fit this criterion and can explain all high frequency resonances. It is interesting that the simple formula for the resonant frequency for the TM_{mnl} modes of a cylindrical cavity

$$f_r = \frac{c}{2}\sqrt{\left(\frac{l}{z}\right)^2 + \left(\frac{u_{m,n}}{\pi r}\right)^2} \qquad (3)$$

is in good agreement with the frequencies observed. Here z is the cavity length, l is the axial mode number and $u_{m,n}$ is the n-th root of equation $J_m(u) = 0$, $J_m(x)$ being the Bessel function. For an axial longitudinal electric field, TM_{0nl} modes, u_{01} = 2.405 and u_{02} = 5.52.

The lowest frequencies of the TM_{01l} and TM_{02l} modes (l = 0,1,2...) from Eq.3 for r = 8.2cm and z = 24.0cm, are 1.4, 1.53, 1.88, 2.34, 2.87, 3.2, 3.42, 3.7 and 4.0GHz. They can all be seen in Fig.2 at close frequencies. Simulation shows a frequency shift between ω_r and the mode centre frequency increasing with intensity. The code MAFIA was used [8] for a more precise 3-D geometrical representation. It also gives an estimation of R_{sh}/Q. The 1st mode has low $R_{sh}/Q = 3.9\Omega$ (one cavity) and is hardly visible in the spectrum whereas the 2nd has 27.8Ω and gives a large peak. These accidental cavities were always damped by ceramic resistors - laboratory measurements give a $Q \sim 70$. This Q is quite low but due to the wide spectrum of the LHC bunches ($\tau < 5$ns) this case corresponds to the narrowband impedance regime. We believe that the pumping ports are the main cause of microwave instability in the SPS.

A search for the source of the unknown peak at 400MHz led finally to the identification of the magnetic extraction septa as the guilty elements.

4 GROWTH RATE MEASUREMENTS

The measured spectrum in Fig.2 suggests the frequencies of the various sources. The amplitude of the peaks already gives some indication of R_{sh}/Q. For a further estimation we have tried to use growth rate measurements. Indeed, from Eq.2, $R_{sh}/Q \propto (\mathrm{Im}\Omega/\omega_r)^2$. However these measurements are difficult for the following reasons. First the stable bunch spectrum moves with debunching. Second, all frequencies within the unstable bunch spectrum grow simultaneously. This means that sources close together can contaminate each other, see Fig.1 (left). This leads to a huge scatter in the measurements. However in some cases the signal is relatively clean, see Fig.1 (right). This signal, at 1.56GHz, has an average growth time of 2ms for N = 4 $\times 10^{10}$. This gives R_{sh}/Q = 11.5kΩ which should be compared with the value of 21.7kΩ given by MAFIA. We also used threshold measurements at given frequencies, observing the maximum amplitude as a function of intensity to estimate this impedance [9], and obtained the same results.

5 CONCLUSIONS

Our present SPS impedance model to describe single bunch phenomena consists of the 12 dominant resonant impedances whose frequencies were found from measurements with the beam. R_{sh}/Q and Q values were obtained from MAFIA calculations and laboratory measurements, respectively. These impedances correspond to four main sources: two TW RF systems, extraction septa and vacuum ports. Using this model for the LHC beam in the SPS suggests that the beam with nominal intensity, 10^{11} protons per bunch, will be at the limit of instability. Knowing the guilty elements in the machine measures will be taken to reduce their impedance in readiness for the SPS as LHC injector.

Finally we believe that this method of impedance measurement could be applied to other accelerators.

We thank R. Cappi, D. Manglunki and the CERN PS and SPS operations groups for their help. We are grateful to D. Boussard for useful discussions.

6 REFERENCES

[1] J. Gareyte, Proceedings of the LHC96 Workshop, Montreux, to be published in Particle Acc.

[2] R. Garoby, CERN PS/RF/Note 93-17, 1993.

[3] L.R. Evans, J. Gareyte, CERN SPS/85-15 (DI-MST), 1985.

[4] D. Boussard, G. Dome, T. Linnecar, A. Millich, IEEE Trans. on Nucl. Science, Vol.NS-24, No.3, 1977, p.1399.

[5] T. Bohl, T. Linnecar, E. Shaposhnikova, Phys. Rev. Lett., 21st April 1997, p.3109.

[6] K.Y. Ng, Proc. 1986 Summer Study on Phys. of SSC, 1986, p.590.

[7] T. Linnecar, E. Shaposhnikova, CERN SL-Note 96-49 (RF), 1996.

[8] W. Hofle, SL/Note 96-40 (RF), 1996.

[9] T. Linnecar, E. Shaposhnikova, Proceedings of the LHC96 Workshop, Montreux, to be published in Particle Acc.

EQUIPARTITIONING AND HALO DUE TO ANISOTROPY

Ingo Hofmann, GSI, Planckstr. 1, 64291 Darmstadt, Germany

Abstract

Equipartitioning and certain aspects of halo formation in high-current linac beams are explained in terms of collective multipole oscillations in x-y geometry. For strong space charge tune depression and anisotropy (emittance and/or focusing strength) some eigenmodes can - in principle - become unstable leading to emittance exchange. It is shown that for parameters of practical interest in linac design beams can be un-equipartitioned without risk of instability. The effect of (stable) mismatch core oscillations on the halo is briefly discussed.

1 INTRODUCTION

Anisotropy in conjunction with space charge effects has its most important potential application in high-current linear accelerators for protons or ions (spallation neutron sources, radioactive waste transmutation linacs, heavy ion fusion linacs etc.). In such linac bunches one of the crucial beam dynamics issues is to what extent deviations from "equipartitioning" can be tolerated without risk of emittance growth (for more recent discussions see Refs. [1, 2].

Coupling resonances leading to amplitude exchange are a familiar subject in circular accelerators, where they are driven by deviations from ideal focusing. It will be shown here that beam self-fields in the space-charge-dominated regime can play a similar role in an ideal linear lattice: in the presence of internal energy anisotropy between different degrees of freedom initially small space charge coupling terms can grow exponentially due to collective instability. Although our theory is derived for cylindrical x-y geometry we assume that the basic arguments also hold for all three degrees of freedom in a bunched beam.

Our analysis contains as a special case the KV-"breathing" ("fourth-order") mode of round isotropic beams in constant focusing, which has recently been suggested as a driving mechanism for halo [3]. This isotropic "breathing" mode is, however, known to vanish if the KV δ-function distribution is slightly broadened [4]. We assume that anisotropy as a driving mechanism is much more robust with respect to the detailed form of the distribution function. While results for the isotropic case can be expressed in terms of one dimensionless parameter, ν/ν_0, anisotropy requires two further dimensionless parameters.

2 ANALYTICAL MODEL

Basic assumptions of the model are summarized in the following, whereas details of the analytical theory are presented elsewhere [5] (see also Ref. [6] for an earlier reference to certain aspects of this work). The unperturbed equilibrium beam is assumed to have uniform density within an elliptic cross section defined by $\left(\frac{x}{a}\right)^2 + \left(\frac{y}{b}\right)^2 \leq 1$, with a, b the semi-axis of the boundary ellipse. Assuming linear and time-independent external focusing forces for the equilibrium beam ("smooth approximation") we can write separate Hamiltonians for the x- and y- motion:

$$\begin{aligned} H_{0x} &= (p_x^2 + m^2\gamma^2\nu_x^2 x^2)/(2m\gamma) \\ H_{0y} &= (p_y^2 + m^2\gamma^2\nu_y^2 y^2)/(2m\gamma) \end{aligned} \tag{1}$$

and define a generalized anisotropic Kapchinskij-Vladimirskij distribution as δ-function of a linear combination of the two separate Hamiltonians:

$$f_0(x, y, p_x, p_y) = \frac{NT\nu_y/\nu_x}{2\pi^2 m\gamma a^2}\,\delta\left(H_{0x} + TH_{0y} - m\gamma\nu_x^2\frac{a^2}{2}\right) \tag{2}$$

Here T is the ratio of oscillation energies in the x and y directions which can be readily written for harmonic oscillators as $T = (a^2\nu_x^2)/(b^2\nu_y^2)$. The ratio of emittances is given by $\epsilon_x/\epsilon_y = (a^2\nu_x)/(b^2\nu_y)$. The time-independent f_0 in Eq. 2 is a solution of Vlasov's equation since H_{0x}, H_{0y} are constants of the motion. For the perturbed distribution function $f \equiv f_0(H_{0x}, H_{0y}) + f_1(x, y, p_x, p_y)e^{-i\omega t}$ we linearize Vlasov's equation keeping only first order terms in f_1 and in the perturbed electrostatic potential Φ, which is expanded as polynomial in x, y in the interior of the beam. The order l of this polynomial is related to the spatial profile of the density perturbation as is shown in Fig. 1. It is

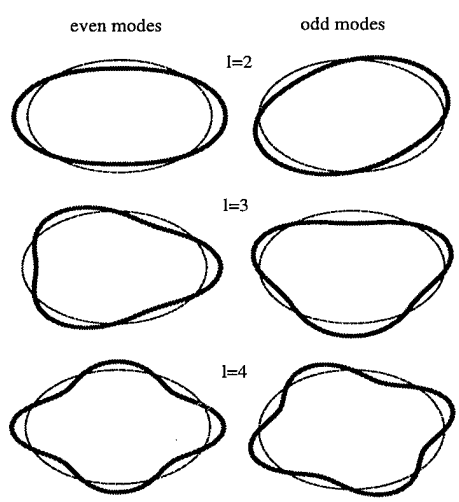

Figure 1: Beam cross sections for second , third and fourth order even and odd modes (schematic).

noted that the even modes are symmetric with respect to the horizontal (here $x-$) axis. The odd modes lack this

symmetry; in 3-d these modes correspond to a lack of rotational symmetry around the longitudinal axis, hence they are suppressed in $r-z$ simulation codes.

The assumption of vanishing perturbed potential at infinity leads to a dispersion relation for the coherent frequency ω in the form of an algebraic expression depending on the three variables to describe the equilibrium beam. For this purpose we use ν_y/ν_{y0}, $\alpha \equiv \nu_y/\nu_x$ and $\eta \equiv a/b$ (≥ 1) and characterize the eigenfrequency by the dimensionless coherent frequency ω/ν_{y0}. The energy anisotropy is then given by η^2/α^2 and the ratio of emittances by η^2/α.

3 EIGENFREQUENCIES

Starting with second order modes the simplest modes are the well-known envelope oscillations. In addition, our analysis yields odd ("tilting") modes (see also Ref. [7] where a matrix formalism is used for the second order modes) which lead to a linear coupling between x and y and can become unstable for sufficiently large anisotropy. The coupling is caused by the space charge force corresponding to that of skew quadrupoles. The number of eigenfrequencies increases considerably with order l due to the anisotropy. In Fig. 2 this is shown for the $l = 3$ odd mode and $\nu_x/\nu_y = 0.8$, $a/b = 1.94$ ($\epsilon_x/\epsilon_y = 3$ and $T = 2.4$). It indicates transition to an unstable solution ($Im\omega > 0$ with $Re\omega = 0$) for $\nu_y/\nu_{y0} < 0.39$ with a maximum growth rate of about 10% of the betatron frequency; note that there exists simultaneously a damped solution with $Im\omega < 0$ not shown here. The isotropic case is completely stable. We note that for the same parameters $l = 4$ yields already 16 different frequencies. For different values of α, η the thresholds for onset of instability may vary considerably.

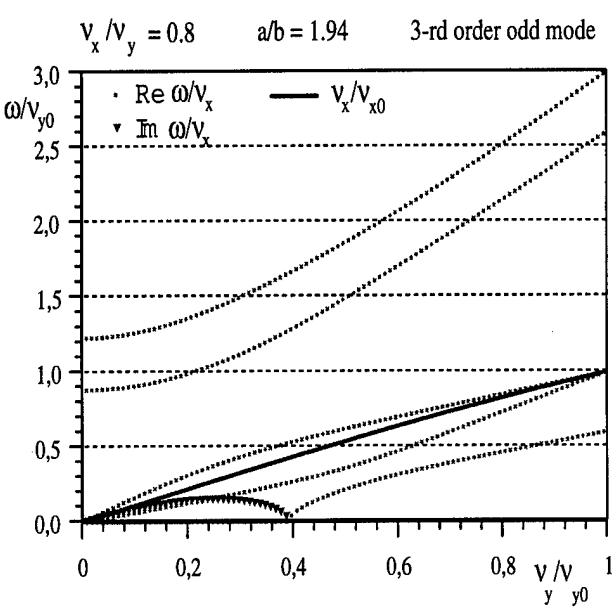

Figure 2: Example of frequencies for third order odd mode with $T = 2.4$ anisotropy.

4 LINAC DESIGN STABILITY CHARTS

For the design of high-current linacs it is desirable to identify regions in parameter space where growth rates leading to emittance exchange might occur. For this purpose we have created charts (see Fig. 3) which show the tune

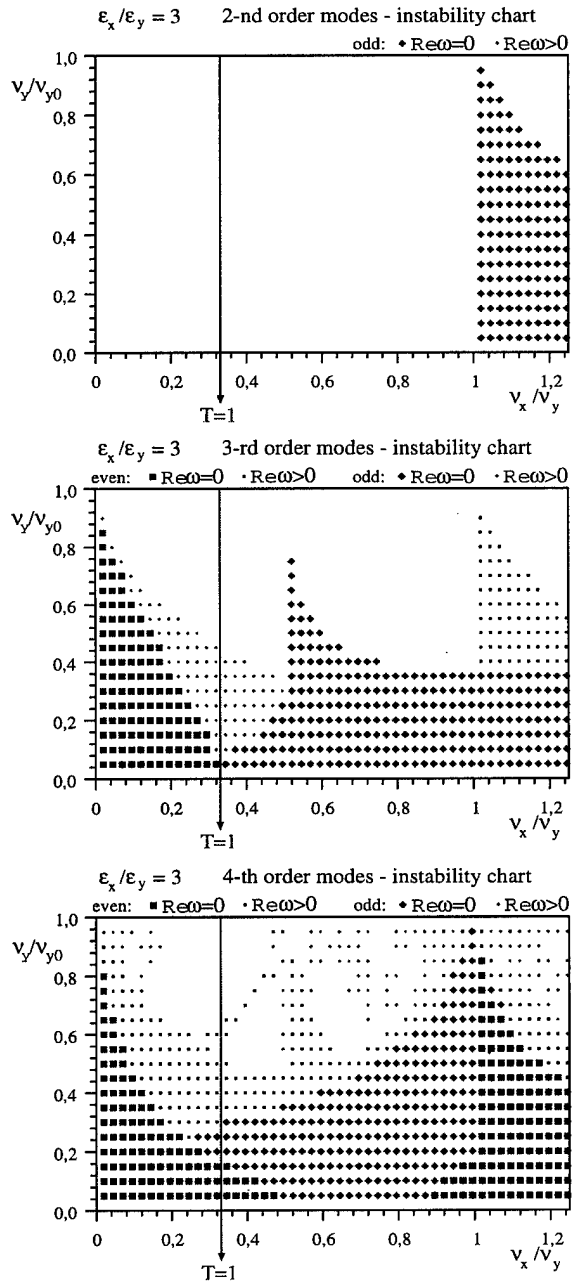

Figure 3: Stability charts for second, third and fourth order modes assuming $\epsilon_x/\epsilon_y = 3$.

depression ν_y/ν_{y0} versus tune ratio for a given ratio of emittances, and corresponding marks whenever an eigenfrequency indicates instability. Hence, at the boundaries of the marked regions growth rates vanish. The temperature anisotropy T is given by the product of tune ratio and emittance ratio and can be larger or smaller than unity. In

Fig. 3 we have assumed $\epsilon_x/\epsilon_y = 3$. We note that for different values of the emittance ratio ($>> 1$) the charts are qualitatively similar. ν_x/ν_{x0} is determined by these three parameters: one finds that for $T < 1$ it is the more strongly depressed one of the two tunes (assuming $\epsilon_x/\epsilon_y >> 1$), and the less depressed for $T >> 1$. Seriously large growth rates are found only for the non-oscillatory instabilities with $Re\omega = 0$; for completeness we also show in Fig. 3 the oscillatory instabilities with $Re\omega > 0$ (small marks)). We find that for $T = 1$ none of the modes are of concern; for $T > 1$ first the odd modes grow unstable, whereas for $T < 1$ only the even mode seems of concerns.

Linac Design: We suggest that the charts presented above give a useful orientation not only for the x-y coupling case but also for the longitudinal-transverse coupling (z-y or z-x), which is of real interest in linac bunches. If $\epsilon_l/\epsilon_t > 1$ we identify l with x and t with y in Fig. 3. We find that there is sufficient space free of instabilities right and left of the equipartitioning line $T = 1$. For $T = 1/3$ (3 times higher transverse oscillation energy), for instance, the transverse tune depression must be below 0.6 to enter into the unstable region of the third order even mode (and even lower for the fourth order even mode). We find that the odd mode instabilities come into play only for T sufficiently larger than unity. Hence we conclude that linac beams can be moderately "un-equipartitioned" without risk of emittance transfer, even for relatively strong tune depression.

In computer simulation of infinitely long coasting beams it was recently observed that a transverse to longitudinal temperature equilibration occurs, presumably driven by a similar mechanism [8].

5 COUPLING EFFECT ON HALO

While the above theory describes collective behaviour driven by the core of the beam we also expect that excitation of some of these eigenmodes causes a coupling in the halo. It is thus appropriate to extend the core/test-particle halo studies developped originally for round, isotropic beams [9] to anisotropic situations.

As a first step in this direction we have examined a particular case by exciting the second order odd mode at the level of 20% mismatch for different parameters ($a/b = 1.414$ fixed), where this mode is stable. We have traced 2 halo test particles with initial $x = 0.9a$ (crosses) and $x = 1.9a$ (triangles) assuming $a = 1.414$, and set initially p_x, y, p_y equal to zero. We have integrated their motion by a symplectic integrator (leap-frog) in the presence of the space charge field of the periodically oscillating core over 30 betatron periods. Fig. 4 shows the full time history of these 2 particles. While for $\nu_y/\nu_{y0} = 0.99$ we find practically no coupling into the $y-$plane, a significant effect occurs for stronger tune depression ($\nu_y/\nu_{y0} = 0.5$) due to the coupling space charge force, which compares with a skew quadrupole force. For the small amplitude particle the weakly anisotropic beam case (top, with $T = 2$) shows a stronger excursion in the x-direction, whereas the strongly anisotropic case (bottom, with $T = 8$) shows an enhanced y-amplitude. The coupling does, however, not lead to a full exchange of "temperatures". Hence, this example demonstrates that anisotropy in the halo is only partially removed by the effect of the space charge force. Obviously a more extensive exploration of the three-dimensional parameter space is required to establish decisively to what extent mismatch oscillations lead to equipartitioning in the halo.

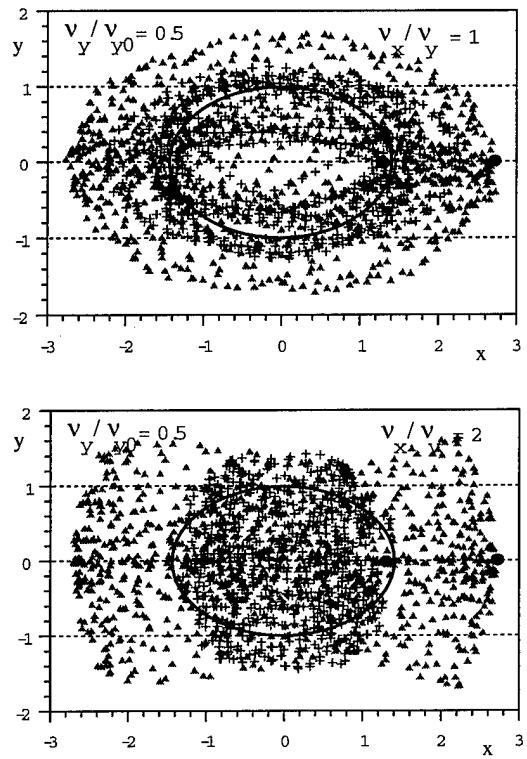

Figure 4: Halo development driven by second order odd (tilting) mode for different anisotropy ($\nu_x/\nu_y = 1, 2$) and tune depression.

6 REFERENCES

[1] R.A. Jameson, *Fusion Eng. Des.* **32-33**, 149 (1996)

[2] N. Brown and M. Reiser, *Phys. Plasmas* **2**, 965 (1995)

[3] R.L. Gluckstern, *Phys. Rev. Lett.*, **73**, 1247 (1994)

[4] I. Hofmann, *Phys. Fluids* **23**, 196 (1980)

[5] I. Hofmann, *GSI-Preprint* **97-27** (1997)

[6] I. Hofmann, IEEE Trans. Nucl. Sci. **NS-28**, 2399 (1981).

[7] D. Chernin, Part. Accel. **24**, 29 (1988).

[8] I. Haber, D.A. Callahan, A. Friedman, D.P. Grote and A.B. Langdon,*Fusion Eng. Des.* **32-33**, 169 (1996)

[9] J.S. O'Connell, T.P. Wangler, R.S. Mills and K.R. Crandall, Proc. 1993 Part.Accel.Conf., Washington DC, 3651 (1993)

DESIGN AND DEVELOPMENT OF AN ELECTRON RECIRCULATOR FOR STUDY OF HIGH-CURRENT BEAM DYNAMICS†

J.G. Wang, S. Bernal, P. Chin, J.J. Deng [a], Y. Li, M. Reiser, H. Suk [b], M. Venturini, Y. Zou,
Institute for Plasma Research, University of Maryland, College Park, MD 20742
T. Godlove, FM Technologies, Inc.
R. C. York, NSCL, Michigan State University

Abstract

An electron recirculator is being developed at the University of Maryland for studying the physics of space-charge dominated beams in circular systems. The E-ring has been designed to transport an electron beam of 10 keV, 100 mA, 50 ns in a smooth circular lattice of 11.5 m in circumference, focused by 72 printed-circuit (PC) quadrupole FODO elecments, and deflected by 36 PC dipoles. This paper reports the progress and status of the E-ring project.

I. INTRODUCTION

Rapid-cycling rings and other recirculator systems operating with intense beams beyond the conventional space-charge limit are of great interest for applications in high-energy physics accelerators such as high-intensity booster synchrotrons and muon colliders, heavy-ion inertial fusion drivers, spallation neutron sources, and other fields. There is very little theoretical or experimental knowledge that would allow us to make any predictions on the beam behavior in such novel systems.

The history of high currents in conventional synchrotrons has been dominated by the necessity for a very large number of revolutions of the beam and the danger of crossing ring resonances slowly. Previous studies [1, 2] have shown that it may be possible to exceed the limiting beam current - the Laslett tune shift limit - by a large factor, provided the number of turns is limited to perhaps 100. The natural solution is then a rapid cycling ring or recirculator.

We have been developing a small electron ring at the University of Maryland for studying the evolution of a space-charge dominated beam in a circular lattice [3]. The important physics issues to be addressed by the E-ring are limits on the number of turns, resonance traversal, maximum transport current, thermal equilibrium and equipartitioning, bending of space-charge dominated beams and dispersion [4] in circular lattices, space-charge waves and longitudinal instabilities, etc. The E-ring will also provide a longer path for the experimental study of the physics of space-charge dominated beams than is available in our existing 5-m long transport channel.

† Research supported by the US Department of Energy.

II. DESIGN CONSIDERATIONS

The schematic of the E-ring layout is shown in Fig. 1. A 10 keV, 100 mA, 30-75 ns electron beam with a normalized effective emittance of 10 mm-mrad from our existing electron gun is injected into the ring with the aid of a pulsed, Panofsky-type quadrupole, and a fast deflecting dipole. The ring design is based on a "wound-up" linear channel. Transverse focusing is provided by 70 printed-circuit quadrupoles (plus two Panofsky quads of special design). Three induction gaps are employed for longitudinal focusing of both parabolic and rectangular bunches. The diagnostics along the E-ring include three resistive beam position monitors, three capacitive BPMs, three retarding field beam energy analyzers, and three phosphor screen beam image viewers. A pulsed extraction system similar to the injector is included for beam analysis in the end chamber housing an emittance meter and an energy analyzer.

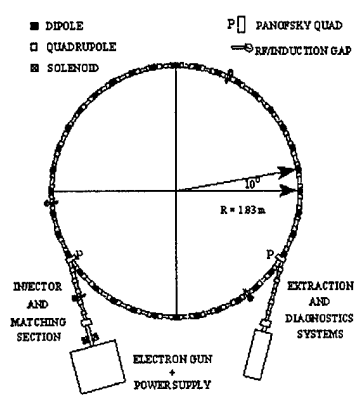

Fig. 1 Layout of the E-ring design.

A distinct feature in the transport of space-charge dominated beams is that the focusing elements have to be packed very densely along the channel. In the E-ring design, the PC quadrupole length is 4.4 cm, while the half-lattice length is 16 cm. For a focusing strength which corresponds to the phase advance σ_o=76° without space-charge, the mean beam radius is 1.04 cm and the ripple factor is 0.7, according to the smooth approximation theory [5]. The bore diameter of the

transport channel is chosen to be 4.90 cm. The space-charge depresses the tune by a factor of more than 5. The lap time is 197 ns which is sufficient to allow for pulsing of injector elements, and extraction into a diagnostic chamber after any given number of turns.

The ring would initially operate in a transport mode, with single-bunch injection, minimum dispersion. The future acceleration of beams up to 50 keV through the induction gaps is also considered in the design. The wall thickness is chosen to be 0.5 mm and the dipole mandrels are designed with non-metallic material, so that the magnetic field can penetrate fast enough into the pipe during acceleration.

The ring main parameters are summarized in Table I.

TABLE I Design Parameters for the E-Ring

Injection Energy	10 keV
Injection Current	100 mA
Generalized Perveance	0.0015
Initial Emittance	10 mm-mrad
Mean Beam Radius	1.04 cm
Vacuum Tube Bore Diameter	4.90 cm
Circumference	11.5 m
Lap Time	197 ns
Lattice Periods	36
Half-Lattice Length	16 cm
Quadrupole Length	4.4 cm
Quadrupole Diameter	5.3 cm
Gradient	8.1 G/cm
Tune υ_0	7.6
Phase advance w/o space charge σ_0	76°
Phase advance w/ space charge σ	9° - 25°

III. MAGNET DESIGN

Due to the low energy of electron beams in the E-ring the magnetic field strength required to focus the beams in a FODO lattice and to bend the beams in a small angle is very moderate. We have decided to employ short magnetic quadrupoles and dipoles made of current loops on flexible printed circuits. This approach not only can meet satisfactory performance for beam dynamics in the E-ring, but also can achieve substantial economic savings.

The design of a model PC quadrupole was reported in the 1995 PAC conference [6]. Some revisions have been made ever since. The new PC quadrupoles have an aspect ratio of 0.83 as indicated in Table I. The calculated radial linearity of the axially-integrated field is satisfactory. For radii through 0.7R, where R is the quadrupole radius, the largest deviation is 0.13%. The required current to produce the focusing field is 1.7 A.

The PC dipole design is based on the same method as for the PC quadrupoles, except that the number of current loops is only half of that for the quadrupoles. The calculated maximum deviation from linearity is found to be 0.35% at 0.7R. The aspect ratio has been chosen to be unity.

IV. SINGLE-PARTICLE DYNAMICS

The lattice of the E-ring employs short magnetic elements. Since this introduces nonlinearities in the transverse dynamics of the charged particles, transfer maps have been constructed to take this effect into account. These maps have been used to simulate single-particle motion and determine the dynamic aperture of the E-ring by using MaryLie 3.0, a particle code based on Lie algebraic methods.

The single-particle study has investigated the effects of those nonlinearities in terms of dynamic aperture. For the stability studies, the linear fields of the E-ring quadrupoles and dipoles are used and then compared to the results when non-linear fringe fields are included. The simulation has showed the satisfactory dynamic aperture of the E-ring design. The stability domain in the transverse plane (controlled by the nonlinearities arising from extended fringe fields) is large enough to include the physical aperture of the vacuum pipe [7].

We have also extended the simulation studies of single-particle dynamics to include the effects of random errors in the magnetic fields due to magnet mispowering or misplacement and an imperfectly compensated earth's magnetic field. The results in the case of mispowered magnets show only a modest erosion of the dynamic aperture. This study has provided acceptable tolerances on the mechanical design.

V. INJECTION AND EXTRACTION

The E-ring is designed to have a single bunch injection and to operate in a transport mode. The injector consists of a gridded electron gun, a straight matching section, a Panofsky quadrupole, and a fast deflecting dipole. The straight matching section contains a short solenoidal lens and two periods of the PC FODO quadrupoles. The Panofsky quadrupole, chosen to handle the special geometric problem in that region, is a regular focusing element on the ring. Its magnetic field should be off during injection, and well established before the beam comes back after one turn, i.e., after 197 ns. Thus, this quadrupole should be a special design, not only for its elongated shape but also for its fast rising time. The fast deflecting dipole performs two functions: it deflects beams by 10° counter-clockwise during injection, and afterwards, it should change its field polarity within the 197 ns lap time and deflect the beam 10° clockwise during the beam life time. This dipole should also have very fast rise time.

The design of the injection/extraction, as well as the fast defecting dipole and the Panofsky quadrupole is detailed in an accompanying paper in these Proceedings [8]. We also have an experimental program in progress to study beam transport in two periods of a PC

quadrupole lattice, and bending [9]. This experiment will include bending of beams, and will provide necessary information to validate the injection design.

VI. LONGITUDINAL FOCUSING

The longitudinal bunch profiles envisioned in the electron recirculator include parabolic bunches and rectangular bunches. For focusing parabolic bunches, an external linear field along the bunch is required. On the other hand, focusing rectangular bunches requires so-called "ear" field. We have designed longitudinal focusing elements for controlling of bunch profiles in the electron ring. Three induction modules with different gap-voltage waveforms will be placed 120° apart along the ring to fulfill this task.

The longitudinal dynamics of the E-ring, the requirement for focusing both parabolic and rectangular bunches, the design and development of the induction module and its modulators are described in another paper in these Proceedings [10].

VII. DIAGNOSTICS

The diagnostics along the electron ring include three resistive beam position/current monitors, three capacitive beam pick-ups, three retarding field energy analyzers, and three phosphor screens for beam viewing. In addition, a diagnostic chamber at the end of the extraction line will also be installed. The BPMs should provide a sensitivity of better than 10 mV for the beam current and a rise time of less than 1 ns. The development of the resistive BPMs is described in another paper in these Proceedings [11].

In addition, three capacitive beam position monitors (BPM) will also be employed. Capacitive pick-ups do not require magnetic ferrite for insulation, thus, they can be put in vacuum with little out-gassing. Capacitive probes have the advantage of higher sensitivity, hence better signal-to-noise ratio. They may in fact be the only way to diagnose small beam currents, e.g., beams required for initial tune-up free from space-charge effects. On the other hand they have poorer frequency response. Thus we propose that it is wise to have both resistive and capacitive BPMs available.

The design of the energy analyzers and phosphor image viewers is straight-forward following the design of our existing devices.

VIII. MECHANICAL DESIGN

Mechanically, the ring consists of 18 sections plus the injection and extraction. Each section contains two 10° bends and two periods of FODO elements. Nine sections contain vacuum/diagnostic chambers each, to obtain a vacuum in the range of 10^{-10} torr. The vacuum/diagnostic chambers also house the diagnostics such as three capacitive pick-ups, three energy analyzers, and three phosphor screen image viewers. A major advantage of the vacuum/diagnostic chambers is their flexibility. The BPMs and energy analyzers can be modified and reinstalled without major disruption to the E-ring. Other nine sections contain three induction gaps, three resistive BPMs, and two locations for the injection and extraction. The main consideration for two different kinds of sections is that the induction gaps and resistive BPMs require magnetic cores and other components, so that it would be difficult to install them inside the vacuum/diagnostic chambers.

IX. EARTH MAGNETIC FIELD

An important problem in our ring design is the effect of the earth's magnetic field due to the relatively low beam energy and hence the low focusing and bending field. Under the action of the vertical component of the earth's field alone, a 10 keV electron is deflected by about 2 mm in a half-lattice distance. This problem has been considered seriously since the start of this project. The remedy includes cancellation by external current-carrying wires, compensation by steering magnets, and/or shielding by mu-metals. We intend to orient the direction of orbital motion so that the earth's field assists in the bending. The dipoles themselves will also be used for further orbit control.

REFERENCES

[1] M. Month and W.T. Weng, 12th Int-l Accel. Conf., 324 (1983); see also review article by W.T. Weng, AIP Conf. Proc. 153, 349 (1987).

[2] I. Hofmann and K. Beckert, IEEE Trans. Nucl. Sci. NS-32, 2264 (1985).

[3] M. Reiser, S. Bernal, A. Dragt, M. Venturini, J. G. Wang, H. Onishi, and T. F. Godlove, Fusion Engineering and Design **32-33**, 293 (1996).

[4] M. Venturini and M. Reiser, in these Proceedings.

[5] M. Reiser, Theory and Design of Charged Particle Beams (John Wiley, New York, 1994).

[6] T.F. Godlove, S. Bernal, M. Reiser, in the Proc. of Part. Accel. Conf., 2117 (1995).

[7] M. Venturini, S. Bernal, A. Dragt, M. Reiser, J.G. Wang and T.F. Godlove, Fusion Engineering and Design **32-33**, 283 (1996).

[8] T. Godlove, S. Bernal, J. J. Deng, Y. Li, M. Reiser, J. G. Wang, and Y. Zou, in these Proceedings.

[9] S. Bernal, A. Dragt, M. Reiser, M. Venturini, J. G. Wang, and T. F. Godlove, Fusion Engineering and Design **32-33**, 277 (1996).

[10] J. J. Deng, J. G. Wang, M. Reiser, and T. Godlove, in these Proceedings.

[11] H. Suk, J. G. Wang, S. Bernal, and M. Reiser, in these Proceedings.

---

a. Permanent Address: PO.Box 523-56, Cheng-Du, China.

b. Present Address: Dept. of Physics, UCLA.

PARASITIC ENERGY LOSS IN THE LEP SUPERCONDUCTING CAVITIES

G. Arduini, O. Brüning, G. Cavallari, P. Gayet, G. Geschonke, E. Häbel, A. Hofmann, M. Jimenez, O. Meincke, G. Morpurgo, G. Roy, H. Schmickler, J. Uythoven, A. Wagner, B. Zotter,
CERN, 1211 Geneva 23, Switzerland

Abstract

The energy loss of bunches in the LEP superconducting (SC) cavities has been determined by measuring the closed orbit as a function of current with the beam position monitors located at finite dispersion. This method has already been used in earlier experiments to determine the distribution of the longitudinal impedance of different parts of LEP. In the present experiment the energy loss in two straight sections, containing only SC cavities, was compared with that in sections having both copper cavities and SC cavities. The results confirm the impedance calculations for the two types of cavities. The accuracy of the measurements was considerably improved by determining simultaneously the orbits of bunches with different currents. At the same time with these beam-based impedance measurements, the power dissipation was observed directly by local temperature monitors in different elements: the inter-cavity bellows inside the cryostat, the warm intermodule bellows, and Ferrite absorbers which were installed in two places to reduce the energy leaking out of cavities. These observations were correlated with the change of cryogenics power consumption, and showed an unexpected dependence of energy loss on beam energy.

1 INTRODUCTION

The total energy loss of the beam in a storage ring can be determined by measuring the change of the synchronous phase as function of bunch current. This was done in LEP by comparing the output from a fast intensity monitor with the signal from an RF cavity. In a second method, the longitudinal bunch position was measured with a streak camera triggered by the RF-voltage [1]. Since the loss factor is expected to be a strong function of bunch length, all these measurements were carried out for a number of different RF voltages which changes this length.

The spatial distribution of energy loss in LEP has been determined by measuring the change of the closed orbit as function of bunch current, using beam position monitors in dispersive regions [2]. A similar method has also recently been used for energy loss measurements at KEK [3]. These measurements permit independent determination of the impedances of RF-cavities and of distributed elements in the arcs. By measuring simultaneously orbits of bunches with different currents, rather than measuring the same bunch after changing its current, errors due to fast orbit drifts could be avoided - and the accuracy of the measurements was thereby improved considerably.

During the last few years, a large number of SC cavities - grouped in "modules" of four four-cell cavities - has been installed in LEP, in addition to the already existing five-cell copper cavities. Due to their large beam hole diameter, as well as their smooth shape, their impedance was expected to be lower than that of the copper cavities with smaller openings and re-entrant nose cones. Since the bunch current in LEP is often limited by collective effects, it was important to measure the impedances of these cavities to verify these calculations. Furthermore, the energy lost in the SC cavities can lead to an excessive heat load of the cryogenic system, and it is hence desirable to reduce it as much as possible by the higher-order-mode (HOM) couplers in each cavity. Also two Ferrite absorbers were recently installed tentatively near two SC cavity modules, in order to reduce the energy leaking into neighbouring cavities.

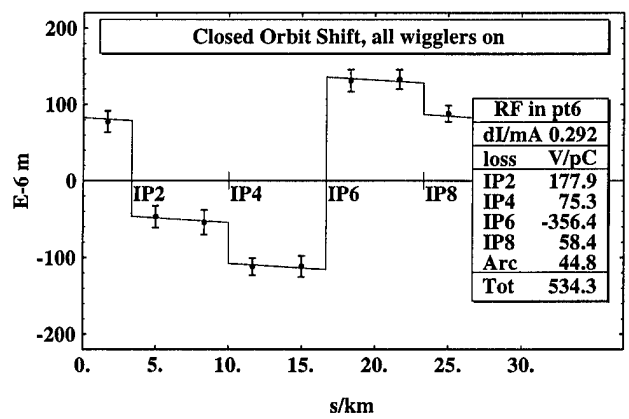

Figure 1: Closed orbit shift as function of position.

2 THE CALCULATED MODE LOSS PARAMETERS OF THE CAVITIES

The impedances of the copper and SC cavities, as well as that of inter-cavity and inter-module bellows, have been calculated extensively using a variety of computer programs such as ABCI[5]. The results are usually expressed by the "longitudinal loss factor" $k_{||}(\sigma)$ which is given by the integral over the product of the impedance and the power spectrum of the bunch current. It is therefore a function of the bunch shape - which is well approximated by a Gaussian in LEP - and of its rms length σ. For a typical bunch length of $\sigma = 10$ mm, one SC cavity has a loss factor of $k_{||} = 1.21$ V/pC, while a Cu cavity has $k_{||} = 2.86$ V/pC. The loss factors are plotted in figure 2 as a function of bunch length. The loss factor of all other elements are much smaller and can be found in the LEP Design Report [6] as well as in a data base which is updated whenever the

0-7803-4376-X/98/$10.00 © 1998 IEEE

cavity type	Point 2	Point 4	Point 6	Point 8
Cu	60	–	60	–
Nb	16	–	–	–
Nb-Cu	16	56	32	56

Table 1: Distribution of the cavities in LEP.

number of installed cavities changes [4]. At the time of the experiment (November 1996), a total of 120 Cu-cavities, with a beam hole of 50 mm radius, and 176 SC cavities with a beam hole of 120 mm radius were installed in LEP. Among the SC cavities, the majority (160) are of the Nb-Cu type, and 16 of the full Nb type (in Point 2), but their geometries - and hence their loss factors - are essentially the same. All these cavities are located in dispersion-free straight sections, at both sides of the even numbered interaction points. Their distribution is shown in table 2.

3 THE EXPERIMENT

3.1 The beam measurement

The energy loss of a bunch along the circumference of LEP was determined by measuring the closed orbits for different bunch currents with the beam position monitors (BPMs) at locations of finite dispersion. In the LEP lattice, only the (eight) arcs have nonzero dispersion, and BPMs are installed at each D-quad where for the present optics $D_x = 0.597$ m. The deviation of a bunch from the nominal energy can be obtained from the measured orbit change Δx_{co} through the relation $\Delta x_{co} = D_x \Delta E/E$. This measurement depends critically on the stability of the closed orbit, and one therefore loses accuracy when measuring only after changing the current in a bunch which takes time. Therefore a method has been developed which simultaneously measures the orbits of up to four bunches with different currents. Then the orbits are subtracted from each other in order to calculate the loss factors. However, the difference orbits show some distortion due to small betatron oscillations, which may be excited by energy losses at finite dispersion. Also the rather strong tune dependence on current could lead to a distortion [7]. To minimize the influence of these effects, the measurements in each arc - extending over several betatron wave lengths - were averaged individually.

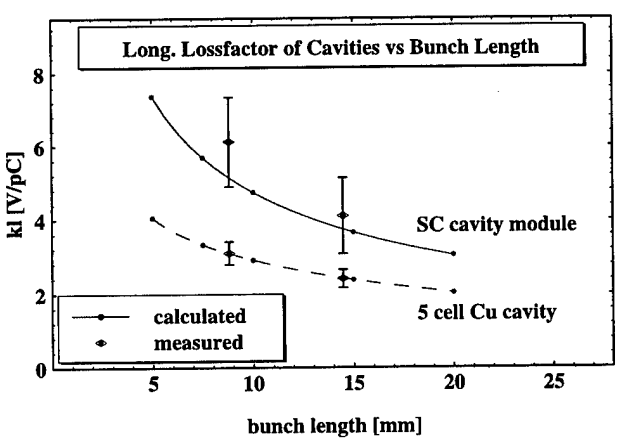

Figure 2: Calculated and measured loss factors versus bunch length for Cu and SC cavities in LEP.

The bunch lengths were adjusted with two sets of wiggler magnets, which are called "damping wigglers" and "polarization wigglers". The measurements were performed for $\sigma = 14.5$, 8.8 and 2.7 mm. For the two cases of long bunches with one or both wigglers excited, bunch lengthening by collective effects is expected to be negligible up to a bunch current of 0.45 mA. The shortest bunches are obtained without wigglers, but then the maximum current which could be stored was limited to 0.1 mA. For this case, some bunch lengthening is expected already at that value. Such low currents reduce the accuracy of the measurements - fortunately, they are not important for LEP operation.

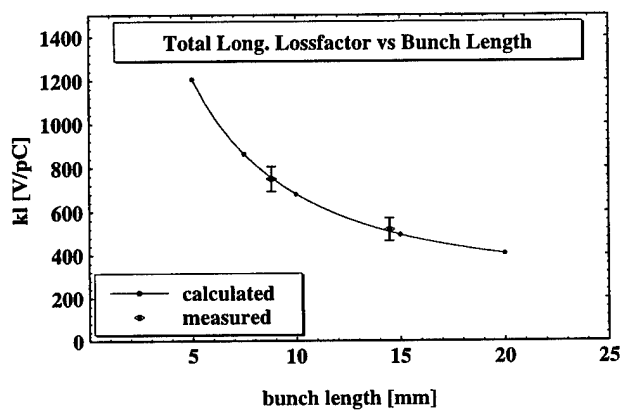

Figure 3: Calculated and measured total loss factor versus bunch length.

The RF cavities were powered only in point 2 or in point 6, which allows measuring the energy losses in the three other points where RF cavities are installed. The passive SC cavities were detuned in order to avoid a large energy loss due to excitation of the fundamental mode ("beam loading") - which is normally compensated by increased RF power when the cavities are excited. Then the beam induced voltage is sufficiently small to be neglected.

3.2 Temperature measurements at the cavities

The energy lost by the beam, which is not eliminated by the HOM couplers or travelling down the beam tube, appears as a heat load in the module[8]. The calorimetric measurements of the heat load correspond to only about 1% of the total beam losses. The dynamic load dependence of beam induced heating for a module can be described as an impedance, which surprisingly depends on beam energy. The power loss is 0.9 MW at the injection energy of 22 GeV

σ	arcs	pt.2	pt.4	pt.6	pt.8	total
mm	V/pC	V/pC	V/pC	V/pC	V/pC	V/pC
14.5	26.2	178.9	69.5	186.8	56.1	**517.6**
8.8	68.5	241.8	95.1	248.1	96.1	**749.2**
2.7	113.6	-485.9	54.9	257.0	60.5	742.9

Table 2: Measured longitudinal loss factors for arcs, RF-sections and the whole machine for different bunch lengths.

and 4.2 MW at the operating energy of 86 GeV. Temperature measurements of the cold inter-cavity bellows and of the warm intermodule bellows have been made. The power loss in the warm, 100 mm diameter bellows is 0.08 MW at 22 GeV, 0.17 MW at 45 GeV, and 0.35 MW at 86 GeV. For the cold bellows with 200 mm diameter we found 0.13 MW at 46 GeV and 0.18 MW at 86 GeV. The bellows temperature along a straight section shows an exponential decrease with distance from the modules.

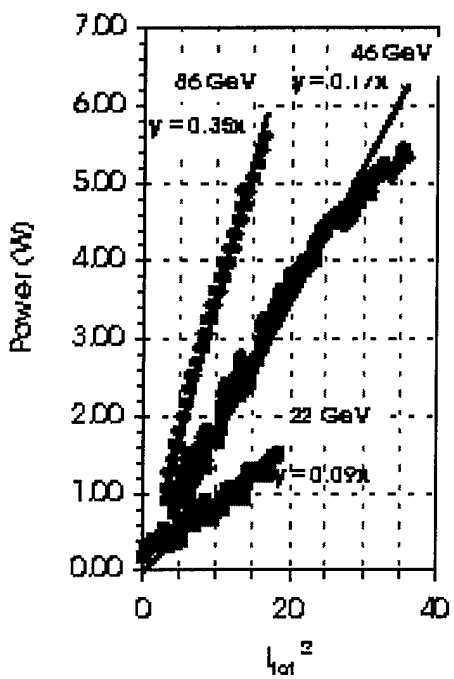

Figure 4: Dissipated power in intermodule bellows.

4 RESULTS

The results of the orbit measurements as function of current are shown in figure 1 for the case of $\sigma = 14.5$ mm and for powering the cavities in point 6. The sudden drop of the orbit displacement caused by the loss in the cavities in points 2, 4 and 8, is clearly visible. Since the dispersion is close to zero in the long straight sections where the cavities are located, the orbit change can only be observed in the adjacent arcs. In the 8 arcs, one can see a small drift of the orbit towards the inside, which allows estimating the distributed impedance. This is mainly caused by the shielded bellows, of which there are a large number (2800) in the arcs, and to a lesser degree by the larger unshielded bellows, the holes to the pumping chamber, and by the nonzero wall resistivity. The cavities in point 6 replace the energy lost in the rest of the ring and makes a jump to the outside.

From this and other measurements we get the orbit change per unit bunch current dx_{co}/dI_bThen the longitudinal loss factors of all 4 cavity sections and of the arcs can be obtained from the expression

$$k_{\|} = \frac{f_0 E}{e D_x} \frac{\Delta x_{co}}{\Delta I_b} \tag{1}$$

with f_0 is the revolution frequency, E the beam energy, and D_x the horizontal dispersion. The loss factors for the arcs, the four RF-sections and the complete machine for different bunch lengths (obtained by different wiggler settings) are listed in table 2.

These loss factors contain not only the effect of all the cavities in one long strait section but also the one of the bellows located there. The factors of the latter were subtracted to obtain the ones of the Cu and superconducting cavities alone. These measurement are show in figure 2 together with the calculations. The agreement is very good. Finally the measured total loss factor of LEP is plotted in figure 4 showing also good agreement.

5 REFERENCES

[1] D. Brandt, P. Castro,K. Cornelis, A. Hofmann, G. Morpurgo, G.L. Sabbi, J. Wenninger, B. Zotter; Proceedings of the 1995 Particle Accelerator Conference.

[2] D. Brandt, K. Cornelis, V. Danilov, A. Hofmann, J.C. Juillard, E. Perevedentsev, E. Peschardt, E. Rossa, F. Tecker, D. Wang, B. Zotter; Proceedings of the 1993 Particle Accelerator Conference, p 3429

[3] C. Zhang; KEK Preprint 96-88.

[4] O. Brüning;"An Impedance Data Base for LEP and LHC", contribution to this conference.

[5] Y. Chin: User's Guide for ABCI, CERN SL/94-02 (1994).

[6] LEP Design Report, Vol. III LEP 2, ed. C. Wyss, CERN-AC/96-01 (1996).

[7] S. Heifets; private communication.

[8] G. Cavallari, P. Gayet, G. Geschonke, M. Jimenez, S. Myers: CERN LEP2 note 97-40 (1997).

TRANSMISSION LINE ANALYSIS OF BEAM DEFLECTION IN A BPM STRIPLINE KICKER

George J. Caporaso, Yu Ju Chen and Brian Poole, Lawrence Livermore National Laboratory, Livermore, California 94550 USA

Abstract

In the usual treatment of impedances of beamline structures the electromagnetic response is computed under the assumption that the source charge trajectory is parallel to the propagation axis and is unaffected by the wake of the structure. For high energy beams of relatively low current this is generally a valid assumption. Under certain conditions the assumption of a parallel source charge trajectory is no longer valid and the effects of the changing trajectory must be included in the analysis. Here the usual transmission line analysis [1] that has been applied to BPM type transverse kickers is extended to include the self-consistent motion of the beam in the structure.

1 INTRODUCTION

The desire to use one induction accelerator to provide multiple lines of sight for advanced radiography [2] has stimulated work in the use of cylindrical stripline kickers to deflect kiloampere electron beams. We consider a cylindrical stripline kicker as shown in Fig. 1 consisting of four electrodes. Two of the electrodes are grounded while the remaining two are driven from the downstream end by opposite polarity cable signals. For simplicity, we will assume that the kicker impedance is matched to that of the drive cables but that the upstream termination cables have an arbitrary impedance Z_t.

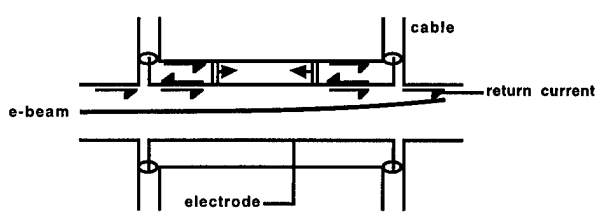

Fig. 1 Schematic of return currents in the stripline kicker

2 TRANSMISSION LINE EQUATIONS

The transmission line model of the kicker structure is shown in Fig. 2. The quantity I_r represents the beam return current which is introduced into the transmission lines formed by the electrodes and the outer vacuum housing at the gaps at either end of the striplines. These are the usual sources used in the analysis of reference [1]. Also shown is the voltage source representing the pulser. The schematic is shown only for one of the driven plates and Ir is interpreted as the dipole return current flowing on that strip (since the monopole return current will not generate a net deflecting force). To these sources we must add distributed shunt current sources to account for the fact that the beam is changing its transverse position within the structure. If we follow a given "slice" of the beam as it enters the kicker imagine that it enters on axis so that there is no dipole return current at z=0. We now allow the beam slice to deflect due to the action of, say, an external bias coil. That slice will then generate a dipole return current on the strip. Since the current on the strip must be conserved, an equal and opposite current must be induced on the other side of the strip, i.e., in the transmission line. This can be represented by the distributed shunt current source $g(z,\tau)$ given by

$$g(z,\tau) = -\frac{\partial}{\partial z}\left[I_r(z,\tau) - I_r(0,\tau)\right] . \qquad (1)$$

Here the variable τ is the slice label given by $\tau \equiv t - L/c - z/c$. We will assume that the axial velocity is c, vacuum light speed and L is the length of the kicker. We will solve the transmission line equations in the variables z and t so that we will need to convert g to the proper form. The transmission line equations become

$$\frac{\partial V}{\partial t} = -L\frac{\partial i}{\partial t} \qquad (2)$$

and

$$\frac{\partial i}{\partial t} = -C\frac{\partial V}{\partial t} + g(z,t) \qquad (3)$$

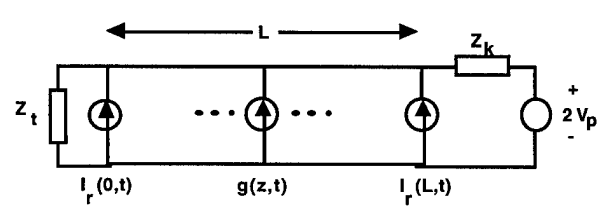

Fig. 2 Transmission line circuit showing distributed sources

where C is the capacitance per unit length of the line and L in the inductance per unit length of the line. We take $Z_k = \sqrt{L/C}$ and $c = 1/\sqrt{LC}$ vacuum light speed which

is also the propagation speed on the line. We have two boundary conditions for the problem. At $z=0$ we have that

$$V(0,t) = -Z_t\big(i(0,t) - I_r(0,t)\big) \tag{4}$$

and

$$V(L,t) = 2V_p + Z_k\big(i(L,t) + I_r(L,t)\big). \tag{5}$$

We will also need to compute the total Lorentz force on an electron passing through the structure. It can be shown that $\vec{E} + \vec{v} \times \vec{B}$ is proportional to the quantity V* defined as

$$V^* = V - Z_k i \quad . \tag{6}$$

We solve these equations by Laplace transforming in t to s. By using the method of variation of parameters we find that

$$\begin{aligned}\tilde{V}^*(z,s) = &\left[2\tilde{V}_p(s) + \tilde{I}_r(L,s)Z_k e^{-\frac{2sL}{c}}\right] e^{-\frac{s}{c}(L-z)} \\ &+ Z_k \int_z^L dz'\, \tilde{g}(z',s) e^{-\frac{s}{c}(L+z') + \frac{s}{c}(z-z')}\end{aligned} \tag{7}$$

Note that the force does not depend on the upstream termination impedance. This is due to the fact that waves moving in the positive z direction have the magnetic force canceling the electric force. Only waves moving upstream will exert a force on the beam. Since the downstream termination is matched to the line any waves reflecting off the upstream termination exert no force and leave the problem when they arrive at the downstream termination.

3 BEAM DYNAMICS

In order to compute the behavior of a slice of the beam we need $V^*(z,\tau)$. We can invert equation (7) and use the definition of τ to obtain

$$\begin{aligned}V^*(z,\tau) = &2V_p\left(\tau + \frac{2z}{c}\right) + I_r\left(L, \tau - \frac{2L}{c} + \frac{2z}{c}\right) Z_k \\ &+ Z_k \int_z^L dz'\, g\left(z', \tau + \frac{2z}{c} - \frac{2z'}{c}\right)\end{aligned} \tag{8}$$

Let us examine the consequences of equation (8) for the usual case. We set $V_p=0$ and take a parallel beam trajectory for the source charge so that g vanishes and

$$I_r = \frac{Q\eta x_0}{b}\delta(\tau) \tag{9}$$

where x_0 is the particle offset, Q is it's charge, b is the kicker electrode radius and η is a geometric factor. We thus find that V^* is given by

$$V^*(z,\tau) = \frac{Q\eta x_0 Z_k}{b}\delta\left(\tau - \frac{2L}{c} + \frac{2z}{c}\right) \quad . \tag{10}$$

We can integrate the transverse force over the length of the kicker to obtain the wake function as

$$W(\tau) = \frac{\alpha Q\eta x_0 c}{2b}\left[\theta(\tau) - \theta\left(\tau - \frac{2L}{c}\right)\right] \tag{11}$$

where α is another geometric factor. We can now find the transverse impedance by taking the Fourier transform of the wake function.

$$Z_\perp(\omega) = \frac{i}{Qx_0}\int_{-\infty}^{\infty} W(\tau) e^{-i\omega\tau} d\tau \tag{12}$$

to obtain

$$Z_\perp(\omega) = \frac{\alpha\eta Z_k L}{2b}\left[\frac{1 - e^{-\frac{2i\omega L}{c}}}{\frac{\omega L}{c}}\right] \tag{13}$$

the normalized real and imaginary parts of which are plotted in Fig. 3 and 4 respectively as a function of $x \equiv \omega L / c$. These forms match those found previously [1].

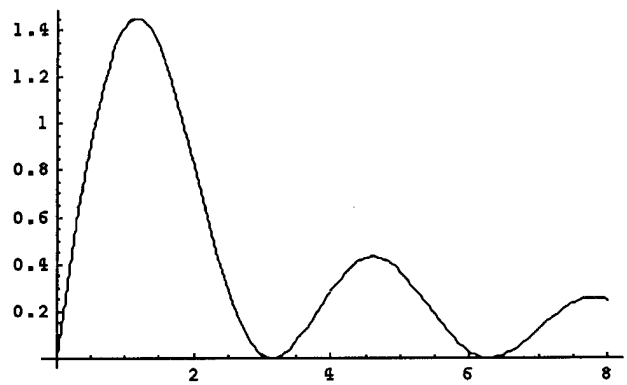

Fig. 3 Plot of normalized real part of the impedance vs. $\omega L / c$

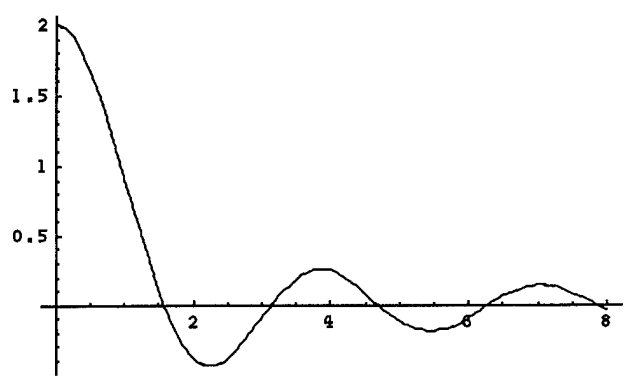

Fig. 4 Normalized plot of the imaginary part of the impedance vs. $\omega L / c$

4 ASYMPTOTIC DEFLECTION

We may use the expression for V^* to find the self-consistent displacement of the beam inside the kicker due to the action of the wakefields. Let us consider the case of a continuous beam with no applied voltage. The dipole return current is given by

$$I_r = -\frac{2I_b(\tau)x(z,\tau)}{\pi b}\sin\left(\frac{\phi_0}{2}\right) \tag{14}$$

where I_b is the beam current (I_b is <0 for electrons) and where ϕ_O is the angle subtended by the driven stripline. Let us consider the case of a long electron beam and put I_b=-I_B where I_B is a positive constant. Inserting the appropriate geometric factors we may write the differential equation of motion for a slice of the beam as

$$\frac{\partial^2 x(z,\tau)}{\partial z^2} = \frac{2I_B}{I_c L^2}\left[x\left(L,\tau-\frac{2L}{c}+\frac{2z}{c}\right) - \int_z^L \frac{\partial}{\partial z'}x\left(z',\tau+\frac{2z}{c}-\frac{2z'}{c}\right)dz'\right] \tag{15}$$

Let us now Laplace transform this equation in τ to s.

$$\frac{\partial^2 \tilde{x}}{\partial z^2} = \frac{2I_B}{I_c L^2}\left[\tilde{x}(L,s)e^{-\frac{2sL}{c}+\frac{2sz}{c}} - \int_z^L \frac{\partial}{\partial z'}\left[\tilde{x}(z',s)e^{\frac{2sz}{c}-\frac{2sz'}{c}}\right]dz'\right] \tag{16}$$

The quantity I_C is the "critical current" and is given by

$$I_c \equiv \frac{\pi}{16}\frac{Z_0}{Z_k}\frac{b^2}{L^2}\frac{\gamma\beta^2 I_0}{\sin^2\left(\frac{\phi_0}{2}\right)} \tag{17}$$

where Z_O is the impedance of free space (377 ohms) and I_O is approximately 17kA.

Upon integrating (16) by parts we obtain

$$\frac{\partial^2 \tilde{x}(z,s)}{\partial z^2} = \frac{2I_B}{I_c L^2}[\tilde{x}(z,s) - \frac{2}{c}\int_z^L s\tilde{x}(z',s)e^{\frac{2sz}{c}-\frac{2sz'}{c}}dz'] \tag{18}$$

which can be solved in the asymptotic limit for large τ. This limit corresponds to the limit s->0. Therefore, in the limit τ->∞ we have

$$\frac{\partial^2 x(z,\tau)}{\partial z^2} = \frac{2I_B}{I_c L^2}x(z,\tau) \tag{19}$$

which can be solved to yield

$$x(z,\tau) = x(0,\tau)\cosh\left(\sqrt{\frac{2I_B}{I_c}}\frac{z}{L}\right) + \frac{x'(0,\tau)L}{\sqrt{\frac{2I_B}{I_c}}}\sinh\left(\sqrt{\frac{2I_B}{I_c}}\frac{z}{L}\right) \tag{20}$$

Thus the input position and angle are both amplified by the factor $\cosh\left(\sqrt{2I_B/I_c}\right)$ at the exit of the kicker.

5 CONCLUSIONS

We have studied the deflection due to beam induced voltages in a stripline transverse kicker. The asymptotic displacement of the beam position at the kicker output is predicted as a function of the beam current, kicker impedance and dimensions of the structure. In the limit of infinitely stiff beams the usual result is recovered for the transverse impedance.

6 ACKNOWLEDGMENTS

The work was performed under the auspices of the U.S. Department of Energy by LLNL under contract W-7405-ENG-48.

REFERENCES

[1] K-Y. Ng, Particle Accelerators, 23, 93-102 (1988).
[2] G. Caporaso, "Linear Induction Accelerator Approach for Advanced Radiography", this conference.
[3] B. Poole, G. Caporaso and W. Ng, "Wake Properties of Stripline Beam Kicker ", this conference.

SPACE-CHARGE FORCES OF A DC BEAM IN A CONTINUOUS BEND

Yu-Jiuan Chen, Lawrence Livermore National Laboratory, Livermore, California 94550, USA

Abstract

It has been shown that the net space-charge forces for a dc beam with space-charge potential depression in a bend have the usual inverse energy square dependence to the first order in the beam radius a over the bend radius R. We extend the analysis to the second order in a/R and allow the beam to have a small transverse displacement. The net space-charge forces are no longer cancelled to inverse energy square factor. The non-cancelled part of self-induced magnetic forces are at the second order in a/R and independent of the beam energy. The nonlinear parts of these forces are much larger than that of the usual inverse energy square forces. Scaling laws for emittance growth caused by the curvature of the beam and a transverse beam displacement, respectively, are presented.

1 INTRODUCTION

The recent trend in radiography machines is to provide multiple lines of sight for a dynamic radiography. The most straightforward approach to obtain multiple lines of sight is to provide each line with its own driver that is costly. The more economic approach is to generate either a long pulse beam or a train of several pulses in one accelerator [1]. Then the pulse (or pulses) will go through kickers and several large angle bends in order to arrive at the x-ray targets simultaneously. The x-ray brightness depends on the electron beam's final spot size and divergence angle, and hence on its emittance. Performance of radiographic machines using a single accelerator as a driver depends on whether beam quality can be preserved in these bends. Lee [2] showed that the net space-charge forces for a dc beam with space-charge potential depression in a bend have the usual inverse energy square dependence ($1/\gamma^2$) to the first order in the beam radius a over the bend radius R. Hence, sending beams through bends does not degrade the beam quality. Later, Carlsten and Raubenheimer [3] discussed an additional space-charge force term which arises when the beam bunch length is short in comparison to the beam pipe size. This term is not cancelled by the potential depression effect. A typical beam in radiography machines is generally more than 10 m long. The space-charge effects studied in Ref. 2 do not exist for such beams. In this paper, we discuss other additional terms which also do not exhibit the usual relativistic cancellation. An analytic model to study emittance growth caused by these force terms is presented. The dc beam is treated as a uniform density ring in a continuous bend. The beam pipe's cross section is round. In general, the Lorentz factor γ of the beam is comparable to R/a for a radiography machine. To compare these terms with the usual space-charge force term in $1/\gamma^2$, we extend the analysis to the second order in a/R and find that the nonlinear parts of these non-canceled forces are in general much larger than that of the usual inverse energy square forces. To obtain a scaling law for emittance growth, we ignore the effects of charge redistribution and betatron motion of particles. By fixing the bending magnet's length, we obtain that the emittance growth is proportional to square of the bend angle and square of the beam radius. We also study the additional space-charge forces due to a small beam transverse displacement Δ such that $\Delta << a$. There is a nonlinear force component in the first order of Δ/a. However, we find that the emittance growth caused by the beam displacement does not appear in the first order of Δ/a.

2 EQUATIONS OF MOTION

The equations of motion for a charge q are

$$\gamma\dot{v}_r = \gamma\frac{v_\varphi^2}{r} - \dot{\gamma}v_r + \frac{F_r}{m} \quad , \tag{1}$$

$$\gamma\dot{v}_\varphi = -\gamma\frac{v_r v_\varphi}{r} - \dot{\gamma}v_\varphi + \frac{F_\varphi}{m} \quad , \tag{2}$$

and

$$\gamma\dot{v}_z = -\dot{\gamma}v_z + \frac{F_z}{m} \quad , \tag{3}$$

where

$$\vec{F} = q\vec{v}\times\frac{B_b\vec{z}}{c} - q\nabla\Phi + q\frac{\vec{v}}{c}\times\left(\nabla\times\vec{A}\right) \quad , \tag{4}$$

$$\dot{\gamma} = -\frac{q}{mc^2}\vec{v}\cdot\nabla\Phi \quad , \tag{5}$$

$B_b\vec{z}$ is the external bending magnetic field, and Φ and $\vec{A}$ are the electric and vector potential arising from the space charges of the beam. We assume that the beam is symmetric about the major radius, i.e., $\partial/\partial\varphi = 0$. The space charge potential depression $\Phi(r,z)$ and magnetic potential $\vec{A}(r,z) = A_\varphi(r,z)\hat{\varphi}$ are obtained by solving

$$\nabla^2\Phi = -4\pi\rho \quad , \tag{6}$$

and

$$\nabla^2 A_\phi - \frac{A_\phi}{r^2} = -4\pi\rho\beta_\phi \quad . \tag{7}$$

0-7803-4376-X/98/$10.00 © 1998 IEEE

Variation of the particle velocity β_φ in (r,z) is negligible. The electron beam pulses for radiography machines are normally in the range of tens to hundreds of nanoseconds long. Assume that the electric field along the beam pipe wall remains zero during the entire beam pulse duration. Hence, both of Φ and A_φ vanish on the wall. Set

$$A_\phi(r,z) = \beta_\phi \Phi(r,z) + \delta A_\phi(r,z) \quad . \tag{8}$$

By substituting Eq. (3) into Eq. (2), we obtain an equation for $\delta A_\phi(r,z)$ as

$$\nabla^2 \delta A_\phi = \frac{\beta_\phi \Phi}{r^2} \quad , \tag{9}$$

and δA_φ vanishes on the wall. Equation (9) indicates that δA_ϕ is in the second order of a/R compared to Φ.

Substituting Eqs. (4), (5) and (8) into Eqs. (1) to (3), we obtain

$$\begin{aligned}\gamma \dot{v}_r = {} & \beta_\varphi \left(\frac{\gamma_w v_\varphi c}{r} + \frac{qB_b}{m} \right) \\ & - \frac{q}{\gamma^2 m} \frac{\partial \Phi}{\partial r} + \frac{q\beta_\varphi}{m} \left(\frac{\partial \delta A_\varphi}{\partial r} + \frac{\delta A_\varphi}{r} \right) \\ & + \frac{q\beta_z}{m} \left(\beta_r \frac{\partial \Phi}{\partial z} - \beta_z \frac{\partial \Phi}{\partial r} \right) \quad ,\end{aligned} \tag{10}$$

$$\begin{aligned}\gamma \dot{v}_\varphi = {} & -\beta_r \left(\frac{\gamma_w v_\varphi c}{r} + \frac{qB_b}{m} \right) \\ & - \frac{q}{m} \left(\beta_r \frac{\partial \delta A_\varphi}{\partial r} + \beta_z \frac{\partial \delta A_\varphi}{\partial z} \right) - \frac{q\beta_r \beta_\varphi}{m} \frac{\delta A_\varphi}{r} \quad ,\end{aligned} \tag{11}$$

$$\gamma \dot{v}_z = -\frac{q}{\gamma^2 m} \frac{\partial \Phi}{\partial z} + \frac{q\beta_\varphi}{m} \frac{\partial \delta A_\varphi}{\partial z} \quad , \tag{12}$$

where γ_w is the Lorentz factor for a beam without space-charge potential depression. Assuming that the ideal orbit for the beam is to along the bend's minor axis, i.e., $r = R$, we obtain

$$0 = \frac{\gamma_w v_\varphi c}{R} + \frac{qB_b}{m} \quad . \tag{13}$$

Then, the first terms in Eqs. (10) and (11) give the usual radial betatron oscillations that will not lead to an emittance growth. We can therefore ignore these terms. The last term in Eq. (10) and the remaining terms in Eq. (11) are negligible compared with the usual space-charge force term, i.e., the second term in Eq. (10). We also ignore the terms containing $\delta A_\varphi / r$ since they are smaller than $\partial \delta A_\varphi / \partial r$ by an order of a/R. We now rewrite Eqs. (10) to (12) as

$$\dot{v}_r \cong \frac{\gamma_w v_\varphi^2}{\gamma R} \left(\frac{1}{r/R} - 1 \right) - \frac{q}{\gamma^3 m} \frac{\partial \Phi}{\partial r} + \frac{q\beta_\varphi}{\gamma m} \frac{\partial \delta A_\varphi}{\partial r} \quad , \tag{13}$$

$$\dot{v}_\varphi \cong 0 \quad , \tag{14}$$

$$\dot{v}_z \cong -\frac{q}{\gamma^3 m} \frac{\partial \Phi}{\partial z} + \frac{q\beta_\varphi}{\gamma m} \frac{\partial \delta A_\varphi}{\partial z} \quad , \tag{15}$$

Note that, in general, the Lorentz factor γ of the beam in a radiography machine is comparable to R/a. The usual space-charge force terms with $1/\gamma^2$ reduction factor are comparable to the additional space-charge terms containing $\partial \delta A_\varphi / \partial r$.

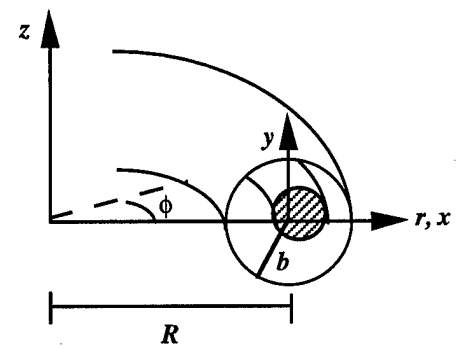

Fig. 1 A displaced round beam in a continuous bend

3 SPACE CHARGE FIELD CALCULATION

Let us consider a round beam in a continuous bend as shown in Fig. 1. Assume that the beam pipe's minor radius b is much less than its major radius R such that $\lambda = b/R << 1$. The space-charge potential depression can now be presented as

$$\Phi = \Phi_0 + \lambda \Phi_1 + \lambda^2 \Phi_2 + O(\lambda^3) \quad ,$$

where Φ_0 is the potential depression in a straight beam. We further assume $O(\lambda) \approx O(1/\gamma)$. Then, only the straight beam's potential depression Φ_0 and the second order magnetostatic potential δA_ϕ are needed to calculate the forces in Eqs. (13) and (15). Let us assume that the beam with a constant current density $I/\pi a^2$ is transversely displaced with $\Delta\cos\alpha$ and $\Delta\sin\alpha$ in the x and y direction, respectively, and $\Delta << a$. We solve Eqs. (6) and (9) in the local cylindrical coordinates (μ, θ, ζ). The space-charge potential depression Φ_0 and the second order magnetostatic potential δA_ϕ are given as

$$\begin{bmatrix} \Phi_0(\mu,\theta) \\ \delta A_\varphi(\mu,\theta) \end{bmatrix} = \begin{bmatrix} \Phi_{00}(\mu) \\ \delta A_{\varphi 0}(\mu) \end{bmatrix} + \begin{bmatrix} \Phi_{01}(\mu) \\ \delta A_{\varphi 1}(\mu) \end{bmatrix} \cos(\theta - \alpha) + O\left(\frac{\Delta^2}{a^2}\right) , \quad (18)$$

and for $r \le a + \Delta$,

$$\Phi_{00}(\mu) = \frac{I}{\beta_\varphi c}\left[1 + 2\ln\left(\frac{b}{a}\right) - \left(\frac{\mu}{a}\right)^2\right] , \quad (19)$$

$$\Phi_{01}(\mu) = -\frac{I}{\beta_\varphi c}\left(\frac{\Delta}{a}\right)\left(\frac{a^2}{b^2} - 1\right)\left(\frac{\mu}{a}\right) , \quad (20)$$

$$\delta A_{\varphi 0}(\mu) = -\frac{I}{8c}\left(\frac{a}{R}\right)^2 \left\{\frac{b^2}{a^2} - \frac{5}{8} - \frac{a^2}{2}\ln\left(\frac{b}{a}\right) - \left[\frac{1}{2} + \ln\left(\frac{b}{a}\right)\right]\frac{\mu^2}{a^2} + \frac{\mu^4}{8a^4}\right\} , \quad (21)$$

$$\delta A_{\varphi 1}(\mu) = \frac{I}{4c}\left(\frac{a}{R}\right)^2 \left(\frac{\Delta}{a}\right)\left\{\left[1 - \frac{a}{b} + \frac{a^3}{b^3} + \frac{a^4}{b^4} + 4\ln\left(\frac{b}{a}\right)\right]\left(\frac{\mu}{a}\right) + \left(\frac{a^2}{b^2} - 1\right)\left(\frac{\mu}{a}\right)^3\right\} . \quad (22)$$

4 EMITTANCE GROWTH

Equations (19) to (22) indicate that a uniformly distributed ring beam in a bend will experience non-cancelled, nonlinear magnetic forces due to the curvature of the beam. To obtain a scaling law for emittance growth caused by these nonlinear forces, we ignore the effects of charge redistribution and betatron motion of particles. We assume that the nonlinear forces only add angle kicks in particles' transverse velocities, and the changes in their transverse positions due to these kicks are negligible. We find the emittance growth arise from the space-charge forces as

$$\begin{aligned} \Delta\varepsilon_{n,x} &= \Delta\varepsilon_{n,y} \\ &= 4\gamma\beta x_{rms}\Delta x'_{rms} \\ &\cong \frac{\sqrt{2}}{8}\frac{I}{\beta_\varphi I_o}\frac{a}{R} a\,\alpha_b + O\left(\left(\frac{a}{R}\right)^3, \left(\frac{\Delta}{a}\right)^2\right) , \end{aligned} \quad (23)$$

and this beam emittance growth is added in quadrature to the initial beam emittance. In Eq. (23), α_b is the bend angle, and $I_o = q/mc^3$ is the Alfven current. According to Eq. (22), there is a nonlinear force component in the first order of Δ/a. However, we find that the emittance growth caused by the beam displacement does not appear in the first order of Δ/a. DARHT-2 may use a chicane combined with a septum as one of chopper options. In this case, beams will be bent 180° four times, and the bend radius is about 25 cm [4]. The estimated emittance growth is 52.3 mm-mrad for each 180° bend, and the final emittance specification is 1200 mm-mrad.

In many cases, the lengths of the bending magnets on a given beam line are the same. The emittance growth for each bend with a bending magnet length ℓ is proportional to square of the bend angle as given by

$$\Delta\varepsilon_{n,x} \cong \frac{\sqrt{2}}{8}\frac{I}{\beta_\varphi I_o}\frac{a^2}{\ell}\alpha_b^2 . \quad (24)$$

Assume that we need to bend the beam N times to reach a total bend angle $\alpha_{b,tot} = N\alpha_b$. The total emittance growth is then given as

$$\Delta\varepsilon_{n,x} \cong \frac{\sqrt{2}}{8N^{3/2}}\frac{I}{\beta_\varphi I_o}\frac{a^2}{\ell}\alpha_{b,tot}^2 . \quad (25)$$

It is obvious that bending beams gently is more desirable in terms of emittance preservation if we can afford the lab space for a longer beam line. Let us consider an AHF beam (1-cm radius beam, 4.5 kA, and 20 MeV [1]) making a 360° turn by traveling through sixteen 22.5^o bends. Each bend is 20 cm long. The normalized emittance growth is about 3.6 mm-mrad for one bend, and the total normalized emittance growth is 9.2 mm-mrad.

5 CONCLUSIONS

We have studied the emittance growth of a long dc beam in bends caused by the curvature of the beam. By ignoring the effects of charge redistribution and betatron motion of particles, we find the emittance growth is proportional to square of the beam radius and square of the bend angle. A small beam transverse displacement is included in our beam model. Our analysis shows that the transverse displacement does not contribute to the emittance growth, at least to the first order of the transverse displacement divided by the beam radius. For a typical radiography machine's beam parameters, the emittance growth caused by traveling through a bend is very small.

6 ACKNOWLEDGMENTS

The work was performed under the auspices of the U.S. Department of Energy by LLNL under contract W-7405-ENG-48.

REFERENCES

[1] G. Caporaso, "Linear Induction Accelerator Approach for Advanced Radiography", this conference.
[2] E. P. Lee, Part Accel. **25**, 241 (1990).
[3] B. R. Carlsten and T. O. Raubenheimer, Phys. Rev. Lett. **51**, 1453 (1995).
[4] E. P. Lee, private communication.

DIODE AND FINAL-FOCUS SIMULATIONS FOR DARHT

Thomas P. Hughes and Dale R. Welch
Mission Research Corporation, Albuquerque, NM 87106
Randolph L. Carlson
Los Alamos National Laboratory, Los Alamos, NM 87545

Abstract

Beam dynamics calculations for the injector and final-focus region of a 4 kA, 20 MeV linear induction accelerator are presented. The injector is a low-emittance 4 MeV thermionic or photocathode diode designed to produce four 70 ns pulses over 2 μsec. Due to the long total pulse length, we have kept the field stress to < 200 kV/cm over the cathode electrode, and to ≈ 50 kV/cm on the radial insulator stacks. The normalized edge emittance produced by the diode is only ≈ 0.019 cm-rad. In the final-focus region, we have modelled the effect of ion emission from the target. The intense electric field of the beam at the 1-mm-diameter focal spot produces substantial ion velocities, and, if the space-charge-limited current density can be supplied, significant focal spot degradation may occur due to ion space-charge. Calculations for the existing Integrated Test Stand, which has a larger focal spot, show that the effect should be observable for H^+ and C^+ ion species. The effect is lessened if there is insufficient ion density on the target to supply the space-charge-limited current density, or if the ion charge-to-mass ratio is sufficiently small.

1 INTRODUCTION

The Dual-Axis Radiographic Hydrodynamics Test Facility (DARHT) will use tightly-focused electron beams to create large X-ray doses with a time-integrated spot-size on the order of 1 mm [1, 2]. The first axis of DARHT, currently under construction at Los Alamos National Laboratory, is a nominally 20 MeV, 4 kA linear induction accelerator providing a single pulse with a 60 ns flat-top. One proposal for the second axis of the facility is to generate up to four pulses over a period of 2 μsec [3]. We have designed a low-emittance thermionic injector, described in Sec. 2, for the second axis. The diode provides 4 kA at 4 MeV. The beam has been transported through the first 8 induction accelerating gaps, demonstrating that the low emittance is preserved over that distance.

At the other end of the accelerator, the beam is focused onto an X-ray converter to produce a spot with a diameter of about 1 mm. Numerical simulations presented in Sec. 3 show that if the target becomes a space-charge-limited source of light ions, then significant disruption of the focal spot is possible as the ions move upstream. We have calculated the effect for an existing 3.85 kA, 5.5 MeV prototype for DARHT, the Integrated Test Stand (ITS) [1, 2], and find that the effect should be observable.

2 LOW-EMITTANCE 4 KA INJECTOR

The injector we have designed to produce four discrete pulses for DARHT is based on the present ITS injector [4, 5]. The latter is a 4 MeV, 4 kA diode with a flat velvet cathode set in a flat electrode. The pulse has excellent voltage and current flatness, and reproducibility. The beam emittance is dominated by the thermal emittance introduced at the emission surface, and has been measured to be ≈ 0.16 cm-rad (normalized Lapostolle edge emittance). For the 4-pulse injector, we have modified the design in order to reduce electrode field stresses (since the stresses are applied for a longer time), and also to take advantage of a low-emittance thermionic- or photo-cathode. The injector layout is shown in Fig. 1. Metglas cores, 10 on one side and

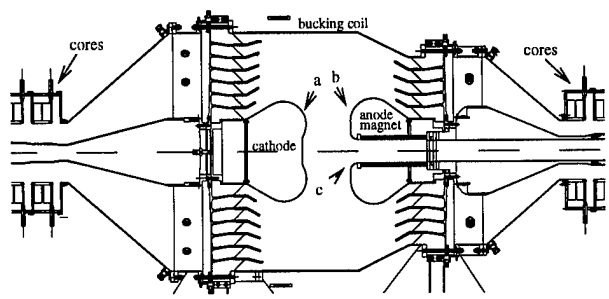

Figure 1: Layout of 4-pulse injector. The field stresses (kV/cm) with (without) the beam at the points marked are: (a) 184 (187), (b) 161 (157) (c) 185 (159).

6 on the other, each provide about 0.25 MeV of inductive voltage, summing to 4 MeV across the AK gap. A Pierce-like electrode surrounding the emission area replaces the flat electrode on the ITS injector because (a) it keeps the current density at the cathode surface below 20 A/cm^2 (a reasonable number for a thermionic emitter) and (b) edge effects which contribute to the beam emittance in the ITS are reduced. The AK gap, defined as the distance from the emission surface to the nearest plane intersecting the anode, is 33.7 cm. The emission-surface radius is 8.9 cm and the radius-of-curvature of the cathode shroud is 16.25 cm.

Using the PBGUNS [6] code, we calculated the field stresses along the cathode and anode electrodes. The maximum values are given in Fig. 1. These values are lower than those for the ITS injector by factors of 0.6–0.7 and are in line with commonly used scaling laws for breakdown as a function of pulse length.

To model the detailed optics of the diode, we used the particle-in-cell code IVORY. Results are shown in Fig. 2.

The simulation is carried out with a mesh size $(\Delta z, \Delta r)$

0-7803-4376-X/98 /$10.00 © 1998 IEEE

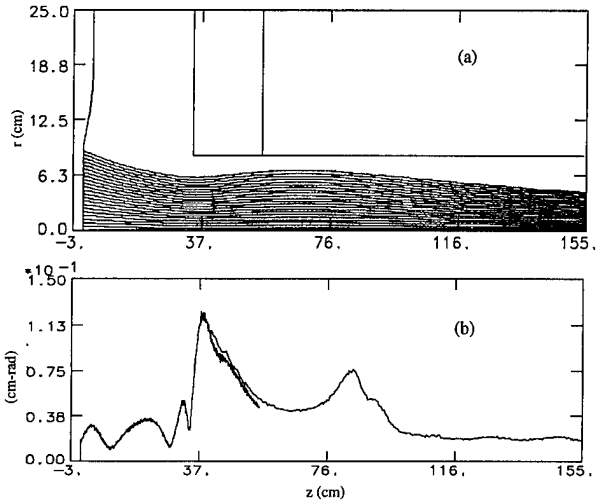

Figure 2: Simulation of 4 MeV, 4 kA diode in Fig. 2 using IVORY showing (a) particle positions and (b) normalized edge emittance vs. z.

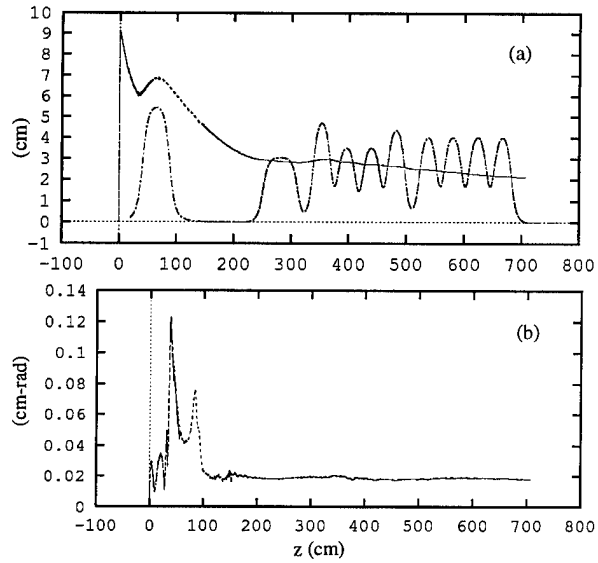

Figure 3: (a) Beam edge radius with overlay of axial magnetic field and (b) normalized emittance from the injector through the first eight cell magnets.
vspace-2mm

of (1 mm, 1 mm) in the AK gap region, transitioning to (4 mm, 2 mm) downstream. A cathode temperature of 0.1 eV, typical of thermionic emitters, is assumed. The normalized edge emittance as a function of z is shown in Fig. 2(b). The variation of emittance through the AK gap and focusing magnet due to nonlinear self and external fields, has previously been studied [7]. The emittance settles to a reasonably constant value of 0.019 cm-rad downstream of the anode magnet. Unlike the ITS beam, this value is dominated by optical effects rather than by the cathode temperature.

To transport the beam further downstream, we use the single-slice code SPROP. This code solves Maxwell's equations on a radial mesh assuming $\partial/\partial z \equiv 0$. It includes the diamagnetic field generated by beam rotation, and the inductive axial self-electric field gives the correct kinetic-energy variation of a converging or diverging beam. SPROP is initialized at $z = 145.2$ cm with a slice of beam particles from IVORY. To control the beam between the anode magnet and the first cell, we have placed two solenoids between the anode magnet and the first induction-cell magnet. Adjusting these magnets and the first eight cell magnets gives us the beam edge radius and emittance shown in Fig. 3,

where we have plotted both the IVORY diode results and the SPROP downstream results. We see that the emittance remains reasonably constant at about 0.019 cm-rad over the $\approx$ 7 meter distance.

3 EFFECT OF ION EMISSION FROM TARGET

The high space-charge density at the DARHT X-ray converter target gives rise to a large axial electric field (on the order of 4 MeV/cm). There is strong experimental evidence [8, 9] that anode plasmas are formed when loosely-bound surface layers (typically hydrocarbons) are heated to on the order of 400^0 C. The layers evaporate off the surface and are ionized by the electron beam, providing a source of positive ions which are accelerated into the beam by the axial electric field. Sanford *et al.* [8] found evidence of several A/Z (atomic weight/charge state) ratios in the measured ion flux.

To study the effect of ion emission, we carried out simulations with the IPROP code using typical DARHT parameters: $\gamma = 40$ ($\approx$ 20 MeV), a current of 4 kA, and a normalized edge emittance of 0.1 cm-rad. As shown in Fig. 4, the beam is injected from the open left boundary with a radially inward velocity such that it focuses to a minimum at the conducting right boundary. We assume a space-charge-limited source of a given ion species from regions of the right boundary which are heated to 400^0 C.

For the case of protons, the beam radius near the target surface is plotted as a function of time in Fig. 5. The run was stopped soon after ions reached the left boundary. We see that there is a large effect after just a few nanoseconds. The electron and ion positions after 6.7 ns are shown in Fig. 4. At this time the protons are moving upstream with a velocity on the order of $0.03c$ (0.9 cm/ns). The line charge-density of the ions is on the order of 10% of the beam line density, which produces a large radial focusing force on the beam. Initially, the ions cause a decrease in the focal spot, but as they move upstream against the beam, they cause the beam to overfocus.

The calculation was repeated with space-charge-limited emission of singly-ionized tungsten ($A/Z = 184$), giving the *RMS* radius shown in Fig. 5. The timescale for devel-

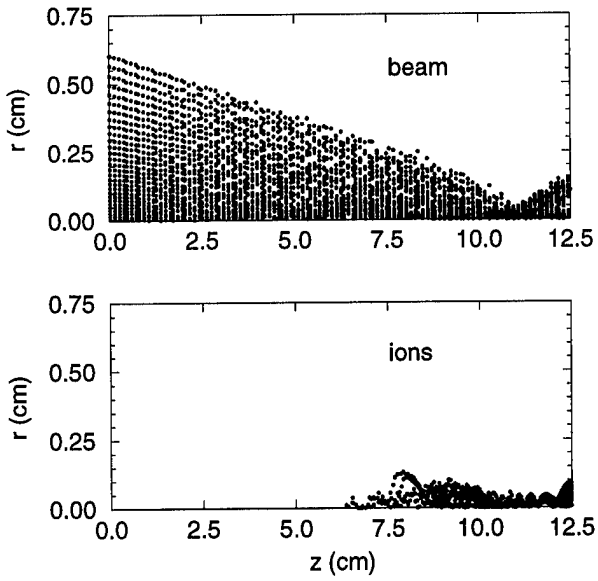

Figure 4: Simulation of space-charge-limited proton emission from target using IPROP. Beam and proton positions are shown after 6.7 ns.

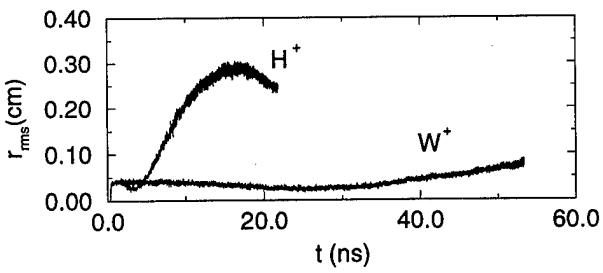

Figure 5: Beam *RMS* radius near target surface as a function of time for nominal DARHT parameters, with space-charge-limited emission of H^+ and W^+ (singly-ionized tungsten) from target.

opment of beam pinching increases roughly as the square root of the mass ratio, i.e., a factor ≈ 13.

The ITS prototype for DARHT [1, 2] may allow the effects of target ions to be studied before the DARHT beam is available. The 3.85 kA, 5.5 MeV beam has a normalized edge emittance of ≈ 0.16 cm-rad. We have carried out simulations with typical ITS final-focus parameters for two species: H^+ and C^+. The focal spot behavior is shown in Fig. 6. Comparing the H^+ case with that for DARHT parameters (Fig. 5), we see that because the beam is larger, it takes considerably longer for the ions to have an effect on the beam spot. Nevertheless for both H^+ and C^+ there is a large change in the focal spot during a 60 ns pulse which should be observable with streak-camera diagnostics.

The principal uncertainty in applying these results to experiments is due to the fact that it is difficult to predict the type and abundance of ions produced at the target. Existing streak-camera data [10] from ITS with parameters comparable to those used to obtain Fig. 6 show considerably less

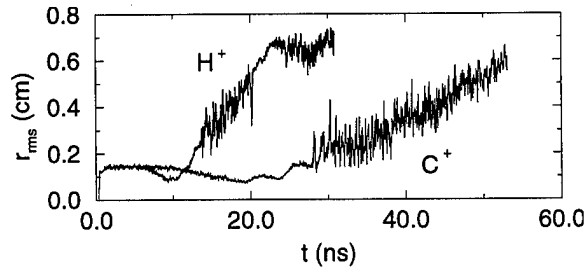

Figure 6: Beam RMS radius near target for ITS parameters with space-charge-limited emission of H^+ and C^+ ions from the target.

variation in radius. Further experiments are currently underway at the ITS and other machines to study the phenomenon in detail [10, 11].

Several schemes have been proposed to mitigate the effects of ion emission, including cleaning to remove surface deposits, placing the target in a low-pressure gas cell, and electrically biasing the target. We will await the results of target experiments currently under way before carrying out detailed evaluation of these options.

4 ACKNOWLEDGMENTS

This work was carried out under the auspices of the U.S. Department of Energy. We have had useful discussions with Craig Olson (SNL), Dave Moir (LANL), and Dan Prono (LANL) concerning target plasma effects.

5 REFERENCES

[1] M. Burns, P. Allison, R. Carlson, J. Downing, D. Moir, and R. Shurter, *Proc. XVIII International LINAC Conference*, Geneva, 1996. (LA-UR-96-2946).

[2] M. Burns, P. Allison, J. Downing, D. Moir, G. Caporaso, Y. J. Chen, *Proc. 9th International Conference on High Power Beams*, Washington, May 1992, p. 283.

[3] R. Carlson, J. Downing, J. Melton (LANL) and J. Fockler (PSI), private communication.

[4] T. P. Hughes, D. C. Moir, and P. W. Allison, *Proc. 1995 Particle Accelerator Conference*, p. 1207.

[5] J. Fockler *et al.*, *Proc. 8th International Pulsed Power Conference*, San Diego, 1996, p. 177.

[6] J. E. Boers, *Proc. 1995 Particle Accelerator Conference*, p. 2312.

[7] T. P. Hughes, R. L. Carlson, and D. C. Moir, J. Appl. Phys. **68**, 2562 (1990).

[8] T. W. L. Sanford, J. A. Halbleib, J. W. Poukey, A. L. Pregenzer, R. C. Pate, C. E. Heath, R. Mock, G. A. Mastin, and D. C. Ghiglia, J. Appl. Phys. **66**, 10 (1989).

[9] D. R. Welch, M. E. Cuneo, C. L. Olson, and T. A. Melhorn, Phys. Plasmas **3**, 2113 (1996).

[10] D. Moir (LANL), private communication.

[11] D. Prono (LANL), private communication.

INFLUENCE OF ION CHANNEL ON ELECTRON BEAM PROPAGATION*

Han S. Uhm, Naval Surface Warfare Center, West Bethesda, MD 20817-5700
E. H. Choi, J. J. Ko and H. M. Shin, Kwangwoon University, Seoul 139-701, Korea

The electron beam propagation from a gas-filled diode is investigated. The beginning portion of the electron beam pulse creates an ion channel not only inside the diode but also the region beyond the anode. A theoretical model is developed for a space-charge limited current of a relativistic electron beam propagating through an ion channel. A simple analytical expression of the space-charge limited current is obtained within the context of a thin beam approximation, where the conducting tube radius is much larger than the beam radius. Beam current propagating through an ion channel is measured experimentally for a mildly relativistic electron beam. Whenever the ion density inside a diode is the same as the beam electron density, the diode is short-circuited. The ion channel density at the short-circuiting time is numerically calculated and is used to estimate the space-charge limited current. It is shown that experimental data agree well with analytical results predicted by the theoretical model.

1. INTRODUCTION

There is a strong renewed interest[1-6] in theoretical and experimental studies of the space-charge limited current for relativistic electron beams propagating through a grounded cylindrical conducting tube. As the charged beam current in a drift tube increases to a limiting value, electrostatic potential builds up due to the beam's self-space charge field and as a result, the beam cannot propagate, creating a virtual cathode in the drift tube. This limiting current is the ultimate restriction on power increase in various electron beam applications. Therefore, a correct estimation of the limiting current is one of the important tasks in these applications. The limiting current I_L of a unneutral solid beam has been derived empirically for a uniform density and is expressed as[1]

$$I_L = \frac{I_A(\gamma_z^{2/3} - 1)^{3/2}}{1 + 2\ln(R_c/R_b)}, \qquad (1)$$

where $I_A = mc^3/e = 17$ kA is the Alfven current, -e and m are charge and rest-mass of electrons, respectively, c is the speed of light in vacuum, γ_z is the relativistic mass ratio due to the axial motion of beam electrons, and R_c and R_b are radii of drift tube and beam, respectively. The limiting current in Eq. (1) represents an approximation that the beam is thin in comparison with the drift tube. We develop a theoretical model of the space-charge limited current for a relativistic electron beam propagation, including an ion channel, which will partially neutralize the space-charge field created by beam electrons.

2 SPACE-CHARGE LIMITING CURRENT IN AN ION CHANNEL

The relativistic mass ratio γ associated with axial motion of electrons at the axis is expressed as

$$\gamma = \gamma_T - \frac{I}{I_A}\left[1 + 2\ln\left(\frac{R_c}{R_b}\right)\right]\frac{\gamma}{\sqrt{\gamma^2 - 1}}, \qquad (2)$$

where the total mass ratio γ_T is defined by

$$\gamma_T = \gamma_z + \delta\gamma = \gamma_z + \frac{\pi R_b^2 n_i c e}{I_A}\left[1 + 2\ln\left(\frac{R_c}{R_b}\right)\right], \qquad (3)$$

and use has been made of the definition $\beta = (\gamma^2 - 1)^{1/2}/\gamma$.

Equation (1) is equivalently expressed as

$$\frac{I}{I_A} = \frac{(\gamma_T - \gamma)\sqrt{\gamma^2 - 1}/\gamma}{1 + 2\ln(R_c/R_b)}, \qquad (4)$$

which has its maximum value at the relativistic mass ratio

$$\gamma = \gamma_T^{1/3}. \qquad (5)$$

Substituting Eq. (5) into Eq. (4), the space-charge limited current I_L of a relativistic electron beam propagating through a ion channel is given by

$$I_L = \frac{I_A(\gamma_T^{2/3} - 1)^{3/2}}{1 + 2\ln(R_c/R_b)}, \qquad (6)$$

where $I_A = 17$ kA is the Alfven current. Equation (6) with Eq. (3) is one of the main results of this article and can be used to investigate the space-charge limited current of an electron beam propagating through an ion channel. We remind the reader that the space-charge limited current in Eq. (6) recovers the previous result in Eq. (1) when the channel ion density approaches zero. The total relativistic mass ratio γ_T in Eq. (3) is linearly increasing function of the ion density n_i. On the other hand, the limiting current I_L in Eq. (6) is nonlinearly increasing function of the mass ratio γ_T. Therefore, the limiting current is nonlinearly increasing

*This work was supported by IR Fund at NSWC and by KSEF

function of the ion density when beam's axial motion is not ultra-relativistic. The limiting current in the ion channel increases drastically, whenever intensity of the ion channel increases.

3 ELECTRON BEAM PROPAGATION THROUGH A GAS CELL

An experiment has been carried out for a relativistic electron beam propagating through a gas-filled chamber with radius of 5 cm. The electron beam is obtained from an accelerator which is a high-voltage Marx generator consisting of 12 capacitors. Each capacitor has 0.2 μF. The total stored energy of the accelerator with maximum charging voltage of ± 50kV can be raised to 3 kJ. A relativistic electron beam with 600 kV, 88 kA and 60 nsec pulse length can be generated if the water-filled pulse forming line with characteristic impedance of 6.8 Ω is impedance-matched to a field emission diode. However, in this experiment, we used the electron beams with 300 kV, 33 kA in a gas-filled diode. The tungsten tip cathode in the diode has a 4-mm diameter and the stainless steel anode has a 20-mm aperture. The cathode and anode gap is kept to 3 mm throughout whole experiment. An aluminum foil with 15-μm thickness is installed at 20-cm downstream from the anode plane to separate the gas-filled region from propagation zone. More than 100 shots were made before replacing the aluminum foil. The diode pressure has been varied from 10 mTorr to 100 mTorr. The gas used in this experiment is air. To measure electron beam signals, a Faraday cup is located just behind the aluminum foil, where the pressure is kept to be 10^{-4} Torr. The electron beam current is measured by a Faraday cup. The B-dot probe at the diode chamber is used to measure diode current. The C-dot probe installed in the isolator section of the pulse forming line is used to measure diode voltage signal. These probes are connected to a four-channel digital oscilloscope with 2 GHz sampling rate. Diagnostic coaxial cables are adjusted so that all the signals are triggered synchronously on the oscillograph.

Although the electron beam current inside the diode is more than 30 kA, the beam current beyond the anode is about 6 kA or less due to a finite size of the anode aperture. Current measured at the Faraday cup is the beam current that propagates through the gas cell and penetrates through the aluminum foil. Stopping power of this foil is about 30 keV. The peak beam current has been measured in terms of the chamber pressure and is shown in Fig. 1. The closed dots represent experimental data and dotted curve is an approximate trace of the data. We believe that the majority of beam electrons may have much less than 300 keV, which is the peak diode energy. The space-charge limited current associated with zero chamber pressure must be far less than the propagation currents shown in Fig. 1. Therefore, we believe that the beginning part of the beam pulse creates an ion channel through which the later portion of the beam pulse can propagate.

Ions are created from neutral particles by the electron impact ionization. The ion production rate dn_i/dt inside the diode by the electron impact ionization is given[2,7]

$$\frac{d}{dt}n_i(t)=\frac{J_d(t)\,n_g\,\sigma(t)}{e}, \tag{7}$$

where $J_d(t)$ is the beam current density at the diode, $\sigma(t)$ is the ionization cross section and n_g is the neutral number density. Secondary electrons, generated by the ionization, are assumed to instantaneously leave region of the diode electrons, being radially expelled by the large space-charge field of electrons accelerated by the diode voltage. Integrating Eq. (15) over time t, the ion density is expressed as

$$n_i(t) = \frac{n_g}{e}\int_0^t d\,t'\,J_d(t')\,\sigma(t'), \tag{8}$$

where the current density $J_d(t)$ in the gas-filled diode is given by

$$J_d(t)=\frac{I_d(t)}{\pi R_b^2}, \tag{9}$$

and $I_d(t)$ is the diode current. The empirical cross section $\sigma(t)$ of neutral gases[8] by the electron impact ionization is given by

$$\sigma(t)=1.874\times 10^{-24}(M^2 x_1 + C x_2) \quad (m^2), \tag{10}$$

where $M^2 = 3.83$, $C= 35.6$ for air, $x_1 = 2\beta(t)^2 \ln[\gamma^2(t) -1]-1$, $x_2 = \beta(t)^{-2}$, and $\gamma(t)$ and $\beta(t)c$ are the relativistic mass ratio and velocity, respectively of beam electrons.

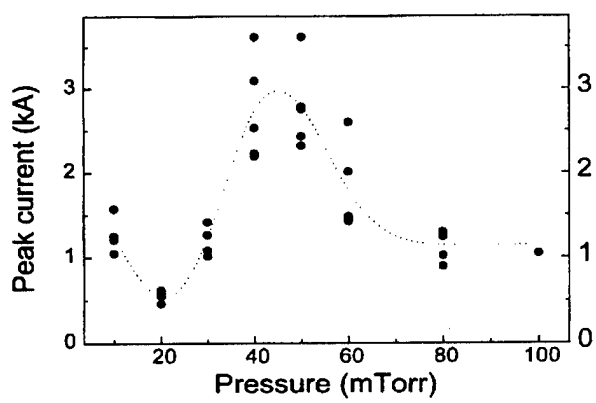

Fig. 1. Plot of the peak beam current propagated through gas cell versus the chamber pressure. Closed dots represents experimental data and dotted curve is an approximate trace of data.

A typical voltage pulse in the diode consists of three parts. They are the leading portion, main pulse and the tail. The leading portion, which is the first part of the diode

pulse, is a low voltage portion accompanied by a small diode current. The main pulse, which is the 300 kV and 30 kA current, is followed by a low-voltage, low-current tail. Typical experimental data indicates that the current levels of the leading portion and tail are one order in magnitude less than that of the main pulse. Therefore, the diode beam current $I_d(t)$ typically starts from a small beam current, increases to a peak value, and then decreases to a small tail current, as time goes by. Detailed features of the diode current must be experimentally obtained for individual pulse device, which has its unique machine and diode impedances. The ion density $n_i(t)$ inside the diode can be numerically calculated by substituting Eqs. (9) and (10) into Eq. (8) after digitizing experimental data of the diode beam current $I_d(t)$ and voltage $V_d(t)$. Here the beam radius R_b is assumed to be 1 cm. The ion density $n_i(t)$ is numerically calculated as a function of time for various gas pressures.

It is required to consider the electron beam current inside a high-power diode with the presence of ions. Particularly when the ion density is the same as the beam electron density inside a diode, the diode may be short-circuited. Since the cathode plasma can be considered as a metal surface whose work function is effectively zero, the cathode electron current supply is essentially unlimited. In this case the current that flows in the diode is determined by the modification of the equipotential contours in the diode due to the space charge of the electron current. Thus, the electron current in the diode must be the space-charge limited current,[2] which originates from a zero electric field at the cathode even for a large voltage difference between the anode and cathode. The zero electric field at the cathode is the outcome of the potential modification due to the space-charge field of the negatively-charged electron current. The zero electric field regulates injection of electrons abundantly available at the cathode surface, essentially controlling the diode current. If the ion density inside the diode is the same as the beam electron density, there will be no space-charge field and no potential modification. The electric field at the cathode in this case will be a non-zero value, which forces all electrons at the cathode to flow to the anode instantaneously, short-circuiting the diode. Thus, the ion density increases from zero to the value of the beam electron density as time goes by. When the ion density is the same as the beam electron density, the voltage and current pulses drop to zero and remain to be zero after this time. Therefore, the highest ion density attainable is the ion density the same as the beam electron density at the time. The ion density in a low pressure diode builds up very slowly for the pressure of 10 mTorr. The ion density in this low pressure diode increases to be the same as the beam electron density in the tail portion of the beam pulse, where the diode beam current is low. The ion density increases more rapidly as the diode pressure increases. This means that the time at which the ion density is the same as the beam electron density occurs at the earlier portion of the beam, where the diode beam current and beam electron density are high. The peak ion density at a certain optimum pressure will coincide the highest beam electron density corresponding to the peak value of diode current. The ion density in a very high pressure diode builds up too quickly and reaches the same value of the beam electron density at the beginning portion of the diode pulse. The highest ion density attainable in this high pressure diode is therefore low. We summarize that the maximum ion density inside the diode increases from a small value to a peak and then decreases to a small value again, as the diode pressure increases from 10 mTorr to 100 mTorr.

Figure 2 shows the ion density n_i inside the diode at the diode shorting time, when the ion density is the same as the beam electron density. In obtaining the numerical results in Fig. 5, we have used the digitizing experimental data of the diode beam current $I_d(t)$. As expected, the ion density in Fig. 2 increases to a peak value and decreases, as the diode pressure increases from 20 mTorr to 60 mTorr. However, this numerical calculation indicates more diversified detailed structures than the general description mentioned above. These minor structures may be caused by the ion density calculation including the highly-fluctuating experimental data of the beam current. We found that the profile of the ion density n_i at the diode shorting time in Fig. 2 is very similar to that of peak propagation current in Fig. 1 measured by the Faraday cup. However, we remind the reader that the peak propagation current in Fig. 1 is enhanced considerably more than the peak ion density in Fig. 2.

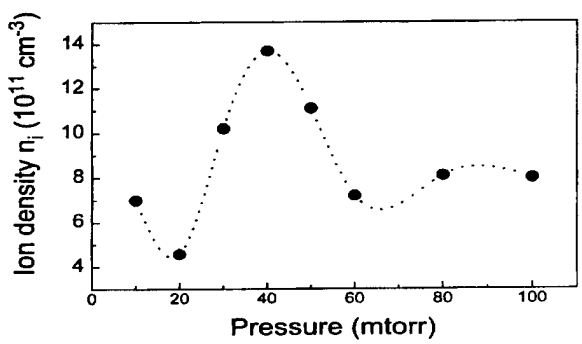

Fig. 2. Plot of ion density at the time of peak current propagation versus the chamber pressure obtained numerically from Eq. (8).

REFERENCES

[1] L.S. Bogdankevich and A. A. Rukhadze, Sov. Phys. Usp. **14**, 163 (1971).

[2] R.B. Miller, *An Introduction to the physics of Intense Charged Particle Beam* (Plenum, New York, 1982), Chaps.2, 3 and 5.

[3] R.C. Davidson, *Physics of Nonneutral Plasmas* (Addison-Wesley, Reading, MA, 1990), Chap. 9.

[4] C. Grebogi and H. S. Uhm, Phys. Fluids **31**, 1277 (1988).

[5] M. Reiser, Phys. Fluids **20**, 477 (1977).

[6] H.S. Uhm, Phys. Fluids B **5**, 1919 (1993).

[7] C.L. Olson, Phys. Rev. A **11**, 288 (1975).

[8] F.F. Rieke, W. Prepejchal, Phys. Rev. A. **6**, 1507 (1972).

SIMULATION OF BUNCH PRECOMPRESSION AT HIGH CURRENTS IN THE SLC DAMPING RINGS *

K.L.F. Bane, M.G. Minty, A.W. Chao, SLAC, Stanford, CA 94309, USA

Abstract

In the Stanford Linear Collider (SLC) each beam, after leaving a damping ring, is compressed in the Ring-to-Linac (RTL) transfer line before entering the linear accelerator. At a bunch population of 4.0×10^{10} particles, due to the limited energy acceptance of the RTL, approximately 15% of the beam has normally been lost. During the 1996 run, however, to eliminate this loss the bunch was partially precompressed in the damping ring, just before extraction; the beam loss in the RTL was reduced to almost zero. In Ref. [1] the operation and performance of precompression are presented. Also given is an analysis which, however, does not include the effects of the longitudinal wakefield on the beam dynamics. In this report we extend that analysis to include these effects.

1 INTRODUCTION

In bunch precompression in the SLC damping rings[1, 2] the amplitude of the rf cavity voltage V_{rf} is varied over a time interval of about one synchrotron period before extraction. The beam is given two (longitudinal) kicks that generate and cancel an oscillation in the bunch centroid while, at the same time, constructively drive an oscillation in bunch length. The beam is then extracted at a minimum in bunch length. Fig. 1 displays a simulated voltage profile for bunch precompression in the SLC, one which takes into account the response time of the rf system and results in a 25% reduction in bunch length at extraction[1]. Note that k_0 in the plot is the nominal (initial) synchrotron wave number and s/c is the elapsed time, with c the speed of light; therefore, the abscissa is in units of the nominal synchrotron period.

In this report we begin by using multi-particle tracking to study the effects of short-range wakefields on the development of longitudinal phase space parameters, assuming the voltage profile of Fig. 1. The wakefield used in the simulations[3] has been shown to give results that are in reasonably good agreement with measurements[4, 5]. We then apply a moment analysis to the problem—something that was also done in Ref. [1]—but now including wakefields. In this report we focus on two questions: (i) What is the validity of the moment approach in the presence of wakefields? To better explore this we will allow the beam to continue to oscillate beyond the extraction time, and compare the moment results with those obtained by tracking. (ii) How do the wakefields affect the properties of the extracted beam in the SLC?

* Work supported by the Department of Energy, contract DE-AC03-76SF00515

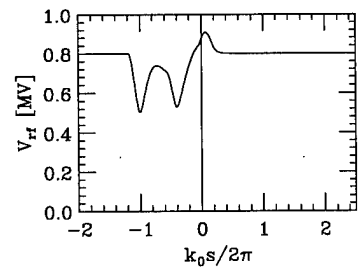

Figure 1: Cavity voltage amplitude in the SLC damping rings for bunch precompression with $N = 4 \times 10^{10}$ particles per bunch[1]. The bunch is extracted at $s = 0$.

2 MULTI-PARTICLE TRACKING

Consider an electron bunch in a storage ring. Each bunch particle i has relative position and energy coordinates (z_i, ε_i), with $z = 0$ at the rf zero crossing ($z < 0$ is to the front) and $\varepsilon = 0$ for an on–energy particle. On each turn the coordinates advance by

$$\begin{aligned} \Delta\varepsilon_i &= eV'_{rf} z_i - U_0 + eV_{ind}(z_i) \\ \Delta z_i &= \frac{\alpha c T_0}{E_0}(\varepsilon_i + \Delta\varepsilon_i) \end{aligned} \qquad (1)$$

with V'_{rf} the slope of the cavity voltage (a negative quantity), U_0 the per turn synchrotron radiation loss, T_0 the revolution period, α the momentum compaction factor, and E_0 the nominal beam energy; the beam induced voltage

$$V_{ind}(z) = -eN \int_{-\infty}^{z} W(z - z')\lambda_z(z')\, dz' \quad , \qquad (2)$$

with N the bunch population, $W(z)$ the Green function wakefield, and $\lambda_z(z)$ the longitudinal charge distribution, normalized so that its area is 1.

Following Eqs. 1, with V_{rf} varied according to the profile of Fig. 1, we track the phase space coordinates of 85,000 macro-particles numerically. We include also, however, the effects of radiation damping and quantum excitation[6]. The wakefield used is that given in Ref. [3]. As machine parameters we take: $\alpha = 0.01469$, nominal (initial) cavity voltage $V_{rf0} = 0.8$ MV, rf frequency is 714 MHz, $cT_0 = 35.3$ m, $E_0 = 1.19$ GeV, $U_0 = 79.8$ keV. Note that a synchrotron period is 87 turns and a damping time is 15,000 turns.

The bunch population $N = 4 \times 10^{10}$, initial rms energy spread $\sigma_{\delta 0} = 7.7 \times 10^{-4}$, and initial unperturbed bunch length $\sigma_{z00} = 5.5$ mm. Solving the Haissinski Equation[7] we obtain the initial bunch shape and induced voltage (see Fig. 2). The rms length of this distribution $\sigma_{z0} = 6.7$ mm; the higher mode losses $U_{hml} = -e^2 N \langle V_{ind} \rangle = 76.8$ keV.

0-7803-4376-X/98 /$10.00 © 1998 IEEE

This bunch shape agrees well with measurements[8]. Note that the SLC damping ring impedance can be characterized as a resistive impedance, *i.e.* one for which

$$V_{ind} \approx -ceNR\lambda_z \qquad \text{[a resistive impedance]}, \quad (3)$$

with resistance $R = 880\ \Omega$[3] (the dashed curve in Fig. 2). Eq. 3 is not used in the tracking simulations.

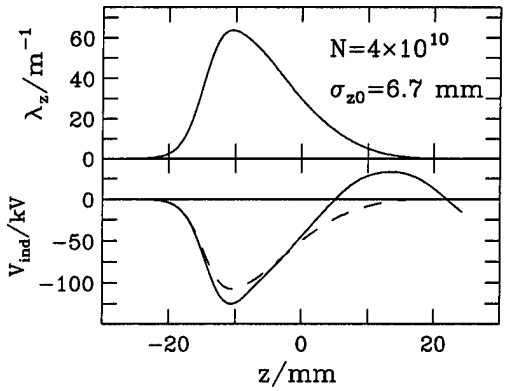

Figure 2: The initial bunch distribution used in the simulations, and the induced voltage. Also shown is Eq. 3 with $R = 880\ \Omega$ (the dashes).

Note that the beam current is 2.5 times the threshold to the microwave instability. We have two remarks: (i) The microwave instability in the SLC is a weak instability, with a growth time much larger than a synchrotron period[9]. Since precompression requires about a synchrotron period, the behavior of the instability is not significantly affected by bunch precompression. (ii) A time dependent feature of the observed instability, the so-called "saw-tooth" behavior, which involves the movement of a few percent of the beam[9], is not reliably seen in our simulations, and will not be addressed in this report.

3 MOMENT EQUATIONS

We can write second order differential equations for the moments in position and energy of the bunch distribution[1, 10]. Each moment equation, however, contains as driving terms moments of $V_{ind}(z)$, terms which themselves depend on higher moments of the distribution, and the system does not close. It will be shown, however, that since precompression occurs rather quickly, before higher order distortions become significant, and since the damping ring impedance is largely resistive, approximate solutions to the first and second moment equations can be obtained which agree quite well with tracking results.

Eqs. 1 can be written as two coupled, first-order differential equations:

$$z' = \alpha\delta \quad , \quad \delta' = [-k^2(s)z - u_0 + v(z,s)]/\alpha \quad , \quad (4)$$

with the relative energy deviation $\delta = \varepsilon/E_0$, the square of the synchrotron wave number $k^2 = -\alpha e V'_{rf}/(cT_0E_0)$, the normalized synchrotron radiation loss $u_0 = \alpha U_0/(cT_0E_0)$, and normalized induced voltage $v = \alpha e V_{ind}/(cT_0E_0)$. Note that k and v depend explicitly on s: the former due to the fact that the applied rf voltage changes with time, the latter because v depends on λ_z, which also changes with time. The moment equations given below are based on Eqs. 4.

3.1 First Moments

The first moments are given by

$$\langle z\rangle'' + k^2\langle z\rangle = -u_0 + \langle v\rangle \quad , \quad \langle\delta\rangle = \langle z\rangle'/\alpha \quad , \quad (5)$$

where the brackets signify taking the average over all particles in the bunch. Note that $\langle v\rangle = -\alpha U_{hml}/(cT_0E_0)$; therefore, in the initial, steady state the centroid is given by $\langle z\rangle = (U_0 + U_{hml})/(eV'_{rf})$. For the special case of a resistive wake at steady state it can be shown that

$$\langle v\rangle \approx -\frac{\alpha e^2 NR}{2\sqrt{\pi}T_0E_0\sigma_z} \qquad \text{[a resistive impedance]}, \quad (6)$$

with σ_z the rms bunch length (discussed below).

We expect Eq. 6 to continue to be valid away from steady state, early in the precompression process. To confirm this we plot in Fig. 3a the development of $\langle v\rangle\sigma_z$ during precompression as obtained by tracking, and note that it deviates only gradually from its initial value. In our moment calculations we will take Eq. 6 to be valid throughout. To obtain $\langle z\rangle$ we first find σ_z (as described below), then substitute Eq. 6 into Eq. 5, and solve.

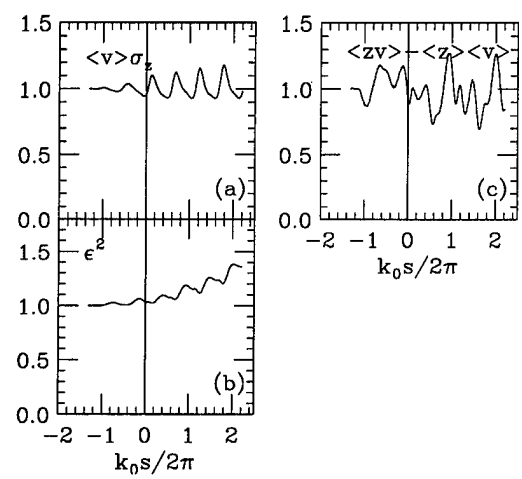

Figure 3: The evolution of three bunch parameters during precompression, as obtained by tracking [(b),(c) are discussed below]. All plots are normalized to begin with 1.

3.2 Second Moments

The rms bunch length is given by

$$\sigma_z'' + k^2\sigma_z = \frac{\epsilon^2}{\sigma_z^3} + \frac{\langle zv\rangle - \langle z\rangle\langle v\rangle}{\sigma_z} \quad , \quad (7)$$

with the emittance defined as

$$\epsilon = \alpha\sqrt{\sigma_z^2\sigma_\delta^2 - \sigma_{z\delta}^2} \quad , \quad (8)$$

where σ_δ and $\sigma_{z\delta}$ are the second moments in δ and $z\delta$ with respect to the centroid. Note, however, that with wakefields ϵ is not a constant of motion whenever $v(z)$ depends nonlinearly on z, which is the case here. In Fig. 3b we plot the development of ϵ^2 during precompression as obtained by tracking; we note that it changes only gradually, and at extraction has hardly changed at all. In the moment calculations we will take ϵ to remain fixed at its initial value.

The development of the term $\langle zv\rangle - \langle z\rangle\langle v\rangle$ in Eq. 7 during precompression, as obtained by tracking, is shown in Fig. 3c. The relative size of this term compared to ϵ^2/σ_z^2 is $(40 \pm 25)\%$. For the steady state bunch distribution with a resistive impedance $\langle zv\rangle - \langle z\rangle\langle v\rangle$ depends linearly on the skew of the distribution S_z, and we might expect this to continue to be approximately true during precompression. The tracking results, however, do not give such a simple result. In solving Eq. 7 to find σ_z we will simply approximate this term to be constant. For the initial conditions to be steady-state requires that constant to be

$$\langle zv\rangle - \langle z\rangle\langle v\rangle = \alpha^2\sigma_{\delta 0}^2(\sigma_{z0}^2/\sigma_{z00}^2 - 1) \quad . \qquad (9)$$

4 RESULTS

We begin by plotting in Fig. 4 the development of $\langle z\rangle$ and σ_z during precompression assuming no wakefields, obtained by tracking (the solid curves) and by the moment approach (the dashes). Note that the plot of σ_z is normalized to the nominal (no potential well distortion) bunch length σ_{z00}. Note also that at extraction ($s = 0$) the slopes of both $\langle z\rangle$ and σ_z are zero by design.

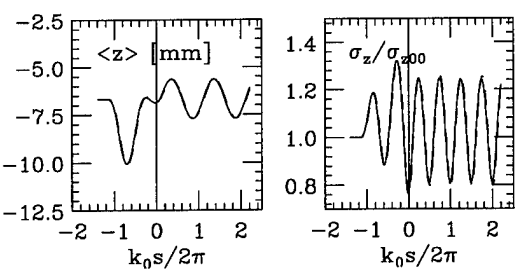

Figure 4: The development of $\langle z\rangle$ and σ_z during precompression assuming no wakefields, as obtained by tracking (solid curves) and by the moment calculations (the dashes).

In Fig. 5 we plot the results when wakefields are included. In the upper part the first 2 moments in z and δ, as obtained by the two methods, are given. Note that the plot of σ_z is normalized to the initial bunch length σ_{z0}. The results of the two methods agree quite well. In the bottom frames of Fig. 5 we plot the skew moments as obtained by tracking. Note, for example, that due to the wakefields the skew in z, S_z, a parameter which is important in linac dynamics, does not change sign during phase space rotation.

Comparing to the earlier, no-wakefield results (Fig. 4) we find that with wakefields $\langle z\rangle$ begins more offset from 0 (due to the higher mode losses), has larger excursions, and, beyond $s = 0$, has more irregular motion. As for σ_z the

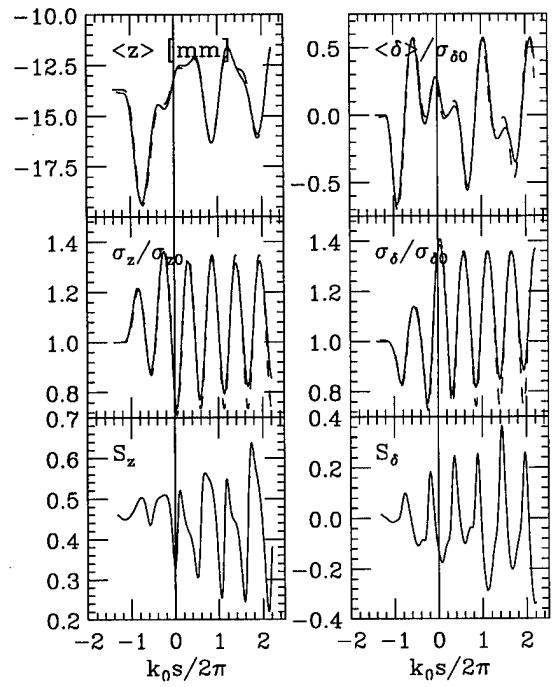

Figure 5: The development of the first 3 moments of the distribution during precompression when wakefields are included, as obtained by tracking(solid curves) and by the moment equations (the dashes). Extraction occurs at $s = 0$.

relative oscillation amplitude is similar to before but the phase advance lags—at $k_0 s = 4\pi$ by 65°. At extraction we find that with wakefields the minimum position of σ_z has moved by $k_0\Delta s = 0.3$ and the slope of $\langle z\rangle$ is 3 μr. This effect, however, is not important for the SLC since the rf timing can be kept steady to 0.5 ns, and a 0.5 ns drift results in a centroid shift of only 0.5 μm.

Finally, the implications of bunch precompression on machine stability are studied in detail in Ref. [1]. There it is pointed out, for example, that a tolerance arises from current fluctuations leading to centroid motion. Here we merely point out that at $N = 4\times 10^{10}$ a 10% change in current leads to a 0.6 mm change in $\langle z\rangle$ at extraction, whereas with precompression the effect is nearly twice as large.

5 REFERENCES

[1] M. Minty, *et al*, "Operation and Performance of Bunch Precompression at the SLC," these proceedings.

[2] F.-J. Decker, *et al*, HEEAC, Hamburg, Germany, 1992, p. 148.

[3] K. Bane, C.-K. Ng, 1993 PAC, Washington, D.C., p. 3432.

[4] K. Bane, *et al*, 1995 PAC, Dallas, TX., p. 3109.

[5] K. Bane and K. Oide, 1995 PAC, Dallas, TX., p. 3105.

[6] See *e.g.* R. Siemann, *Nucl. Instr. Meth.*, **203**, 57 (1982).

[7] J. Haissinski, *Il Nuovo Cimento*, **18B**, No.1, 72 (1973).

[8] R. Holtzapple, SLAC-REPORT-487, PhD thesis, June 1996.

[9] B. Podobodev, private communication.

[10] A. Chao, *Physics of Collective Beam Instabilities in High Energy Accelerators*, (J. Wiley & Sons, New York, 1993).

MEASUREMENT OF THE LONGITUDINAL WAKEFIELD AND THE BUNCH SHAPE IN THE SLAC LINAC*

K.L.F. Bane, F.-J. Decker, J.T. Seeman, F. Zimmermann
Stanford Linear Accelerator Center, Stanford University, CA 94309, USA

Abstract

We report on measurements of the bunch energy spectrum at the end of the SLAC linac. Using the spectra obtained for two different linac rf phases we obtain both the bunch induced voltage and the longitudinal distribution of the bunch. The measurement results are compared with theoretical predictions. In particular, the induced voltage is in good agreement with that obtained using the calculated wake function for the SLAC linac. This measurement technique may be useful for monitoring changes of the linac bunch shape in the SLC.

1 INTRODUCTION

In a linear accelerator the final energy spectrum of a bunch depends on the applied rf voltage, the bunch length, and the wakefield. If the beam phase is chosen sufficiently far off crest so that (1) there exists a 1-to-1 correspondence between the longitudinal position within the bunch and the final energy, and (2) the wakefield effect can be ignored, then a single measurement of the beam energy spectrum at the end of the linac suffices to reconstruct the bunch shape. Normally there are practical limitations as to how far off crest one can go and it may be the case that condition (1) can be satisfied but condition (2) cannot. In such a case a single measurement of the energy spectrum does not suffice for obtaining the bunch shape. However, if the energy spectrum is measured for at least two different beam phases, both of which are far enough off crest to satisfy condition (1), then both the bunch shape and the bunch wake (the induced voltage) can be reconstructed[1].

Estimating the bunch length from spectrum measurements in the SLAC linac has been done before[2, 3]; in both cases, however, wakefield effects were ignored. In addition, the parasitic mode losses—the average of the induced voltage—have been measured as a function of current[3]. In this report, we describe the first measurement of both the induced voltage and the bunch shape in the SLAC linac, using the technique mentioned above. This method is straightforward, and possibly a simpler alternative to bunch length measurements using a streak camera. A quick measurement of the electron or positron bunch shapes in the SLAC linac can be of great help in adjusting the rf parameters of the bunch compressors, which are located between the damping rings and the linac, so as to optimize the luminosity at the interaction point of the Stanford Linear Collider (SLC) [4].

* Work supported by the U.S. Department of Energy under contract DE-AC03-76SF00515.

2 THEORY[1]

Consider a bunch of charged particles that pass through the linac. The peak energy gain of the rf in the linac is E_a; the bunch phase with respect to the crest is ϕ, with a more negative value of phase a position more forward on the rf wave. Let us assume that $E_f/E_0 \gg 1$, with E_f and E_0, respectively, the final and the initial energy of the beam, so that we can ignore the component of energy variation that is uncorrelated with longitudinal position. Then the relative energy of a particle at position z within the bunch becomes

$$\delta(z) = [E_0 + E_a \cos(k_{rf} z + \phi) + eV_{ind}(z)]/E_f - 1 \,, \quad (1)$$

with k_{rf} the rf wave number and $V_{ind}(z)$ the induced voltage, given by

$$V_{ind}(z) = -eN \int_0^\infty W_z(z')\lambda_z(z - z')\, dz' \quad , \quad (2)$$

with N the bunch population, W_z the Green function wakefield, and λ_z the normalized longitudinal charge distribution.

By knowing both $\lambda_z(z)$ and $\delta(z)$ over the bunch length we can compute the energy distribution $\lambda_\delta(\delta)$. Conversely, if we know $\lambda_\delta(\delta)$ and $\delta(z)$, we can calculate $\lambda_z(z)$, provided $\delta(z)$ is monotonic over the bunch. Let us assume that this is the case. Then

$$\lambda_z(z) = \lambda_\delta(\delta(z))\, |\delta'(z)| \quad . \quad (3)$$

Suppose now that we know E_0, E_a, E_f, k_{rf}, and ϕ. Without knowing the induced voltage we cannot, in general, obtain λ_z from λ_δ, since δ depends also on V_{ind}. Only if eV'_{ind} is small compared to $\delta' E_f$ over the bunch does a single measurement of λ_δ suffice to give λ_z.

Suppose we measure the bunch spectrum twice: with the beam at phase ϕ^a we obtain λ_δ^a, and then with the beam at ϕ^b we obtain λ_δ^b. We assume the phases are chosen so that $\delta(z)$ is monotonic for both measurements. For the first measurement Eq. (3) becomes

$$\lambda_z(z) = \lambda_\delta^a \left| E_a k_{rf} \sin(kz + \phi^a) - eV'_{ind}(z) \right| / E_f \,, \quad (4)$$

and a similar equation, with superscript b replacing superscript a, holds for the second measurement. Combining these two equations we obtain

$$V'_{ind}(z) = \frac{E_a k_{rf}}{\lambda_\delta^a \pm \lambda_\delta^b} \left[\lambda_\delta^a \sin(kz + \phi^a) \pm \lambda_\delta^b \sin(kz + \phi^b)\right] . \quad (5)$$

In Eq. (5) (and below) the upper symbol of $\pm$ applies if the sign of $\delta'(z)$ is different for the two measurements, otherwise the lower symbol applies. The right hand side of Eq. (5) is a function both of z and—through the argument of λ_δ—of $V_{ind}(z)$. Eq. (5) is therefore a first order nonlinear differential equation which we can solve numerically for the unknown $V_{ind}(z)$. As initial condition we take V_{ind} at the front of the bunch to be zero. Once V_{ind} is known we obtain λ_z using

$$\lambda_z(z) = \frac{E_a k_{rf} \lambda_\delta^a \lambda_\delta^b}{E_f |\lambda_\delta^a \pm \lambda_\delta^b|} \left|\sin(kz + \phi^a) - \sin(kz + \phi^b)\right| . \tag{6}$$

3 ENERGY SPECTRA

The measurements were performed with the machine in a Final Focus Test Beam (FFTB) configuration. The number of particles per bunch was relatively small $N = 7.5 \times 10^9$; $E_0 = 1.19$ GeV, $E_f = 46$ GeV, $k_{rf} = 60$ m^{-1}. The peak rf voltage of the damping ring was 800 kV. The bunch compressor voltage was set to $V_c = 32.4$ MV. (However, there was circumstantial evidence that the actual compressor voltage was substantially lower, a suspicion, as we shall see, that is supported by our analysis.) For these conditions, the expected rms bunch length in the linac was about 0.5 mm. The FFTB final focus lattice was modified to give a large dispersion ($\eta = 60$ cm) and a small beta function (corresponding to a beam size of 150 μm) at the wire monitor in the FFTB dump line that was used for the measurements. The wire size is 75 μm, corresponding to an energy resolution of about 0.01%.

Our first measurement was to check that the calibration of the phase shifter was correct, and to find the phase corresponding to the top of the rf crest (which we designate as $\phi = 0$). For this measurement a beam-position monitor (BPM) at a high dispersion point was used to record the average beam energy as the phase knob was varied. The results are shown in Fig. 1, with the phase shifted to fit the expected dependence (the curve). The deviation seen for phases below $-5°$ is likely due to spraying of the BPM by beam particles.

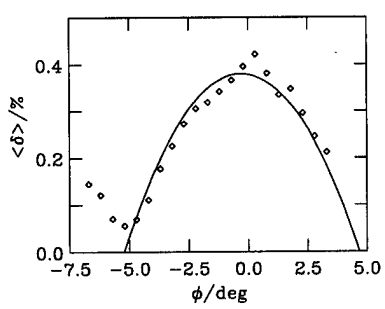

Figure 1: A calibration measurement.

We then performed a series of energy spectrum measurements using the wire monitor, for different linac phases, first without and then with the beam energy feedback activated. When turned on, this feedback tries to maintain a constant average beam energy in the FFTB line without changing ϕ. We were not successful in obtaining good data for $\phi < -6.7°$ or $\phi > 2.3°$. Figure 2 displays 6 representative spectra, all of which were measured with the energy feedback on. For comparison, Fig. 3 presents two simulated spectra, with phases corresponding to those of Fig. 2a and f, but with V_c reduced to 30.4 MV. The agreement with the measurements is quite good. In the bottom frames of Fig. 3 contours of phase space are also shown.

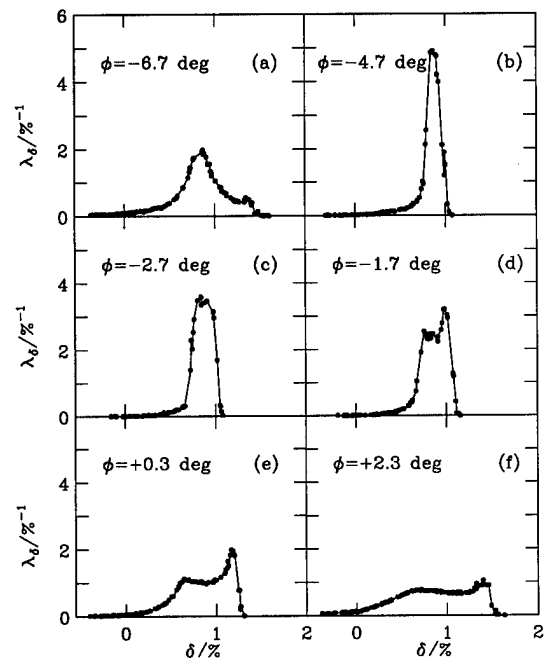

Figure 2: Six representative measurements of the energy spectrum. For all cases shown the energy feedback is on.

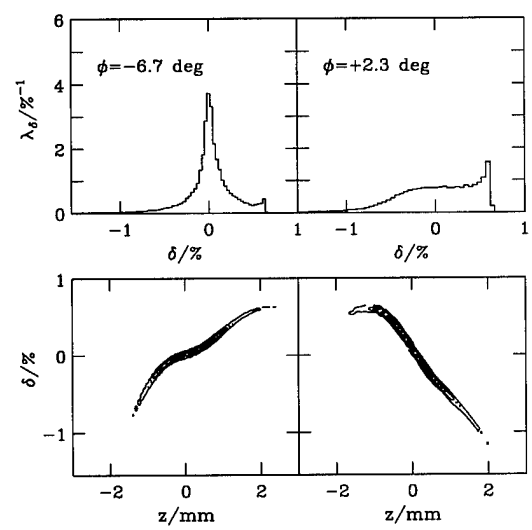

Figure 3: Two simulated spectra and the corresponding contours in phase space, assuming $V_c = 30.4$ MV.

The spectral measurements are summarized in Fig. 4. In Fig. 4a the area under the spectrum curve is plotted; we see

that it deviates by no more than 10%. Figure 4b shows the centroid energy. The curve gives the expected behavior (up to an arbitrary amount of shift) when the feedback is off. With feedback on $\langle\delta\rangle$ remains fairly constant. With feedback off, however, the data points do not exactly follow the expected behavior, which may be due to klystrons cycling on or off. In Figs. 4c-d we plot the rms and the FWHM width of the spectra. We note that the minimum in both plots occurs when the beam is 4–5° in front of the rf crest. The curves in Figs. 4c–d give results obtained from simulations, for the nominal compressor setting $V_c = 32.4$ MV (solid), and for $V_c = 30.4$ MV (dashes). The latter curves agree much better to the measurements, adding support to the belief that the compressor voltage was low.

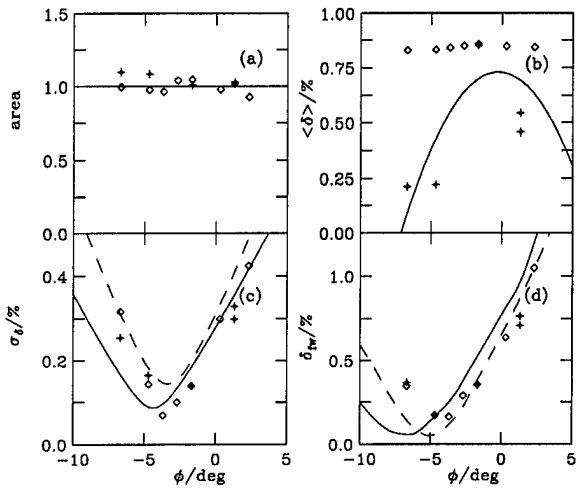

Figure 4: The area (a), the centroid position $\langle\delta\rangle$ (b), the rms length σ_δ (c), and the FWHM δ_{fw} (d) of the measured spectra as functions of phase ϕ. The diamonds signify measurements with energy feedback, the crosses, without. The curves are described in the text.

4 BUNCH SHAPE AND WAKEFIELD

First, as an example, let us neglect the effect of the wakefield (let $V_{ind}(z) = 0$) and invert Eq. 4 using the spectrum of Fig. 2a. Figure 5 shows the result. The FWHM width $z_{fw} = 0.53$ mm, which is smaller than is theoretically possible. This demonstrates that even at this low current the wakefields can be important for this measurement.

For our two-phase calculations we would like the phases to be at opposite sides of $\phi = 0$ [otherwise the terms in the denominators of Eqs. (5),(6) subtract], and as far apart as possible. We choose the spectra shown in Fig. 2a and f. We see from the contour plots of Fig. 3 that for the $\phi = 2.3°$ case we expect that $\delta(z)$ is not monotonic at the head of the bunch, for $z < -1$ mm. So we begin our solution at $z = -1$ mm at which point we set $V_{ind} = -40$ MV. The results are shown in Fig. 6.

Shown in Fig. 6a is the bunch shape; the gaussian fit (the dashes) has $z_{fw} = 1.50$ mm, which is similar to our expectations when $V_c = 30.4$ MV (at $V_c = 32.4$ MV we expect $z_{fw} = 1.2$ mm). Note that the area under the

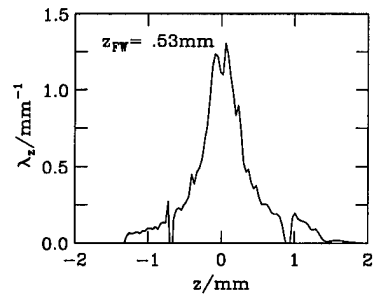

Figure 5: Result of the inversion using the spectrum of Fig. 2a when the effect of the wakefield is neglected.

curve equals 0.82, and not 1, probably due to the non-monotonicity problem discussed above. In Fig. 6b we show V_{ind}; it is smooth because it is the result of an integration. As a check we convolve the gaussian fit bunch shape with the calculated SLAC wake function[5] according to Eq. (2) and obtain the dashed curve. The agreement over the core of the bunch is good. Finally, we should point out that although the details may change, the basic features of our results do not seem to be very sensitive to exactly how we begin the calculation at the head of the bunch.

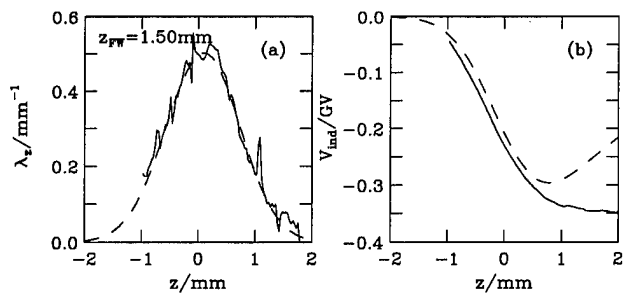

Figure 6: Result of the inversion using the spectra of Figs. 2a and f: (a) the bunch shape and (b) the measured induced voltage (the solid curves). The dashed curves are discussed in the text.

5 ACKNOWLEDGEMENTS

The authors thank P. Tenenbaum for setting up the FFTB optics for this measurement, and K.B. thanks R. Warnock for a helpful discussion on this topic many years ago.

6 REFERENCES

[1] K.L.F. Bane, SLAC/AP–80 (1990).

[2] J. Seeman, Proc. of the 1988 Linear Acc. Conf., CEBAF, 1988, p. 487.

[3] K. Bane *et al.*, Proc. of the 2nd European Particle Acc. Conf., Nice, France, 1990, p. 1762.

[4] K.L.F. Bane, P. Chen, F. Zimmermann, "Beam-beam simulations with non-Gaussian distributions for SLC and SLC-2000", these proceedings (1997).

[5] K. Bane and P. Wilson, Proc. of the 11th Int. Conf. on High-Energy Acc., CERN, 1980, p. 592.

ANALYTIC EXPRESSIONS FOR LONGITUDINAL SCHOTTKY SIGNALS FROM BEAMS WITH GAUSSIAN MOMENTUM DISTRIBUTION

V. Ziemann, The Svedberg Laboratory, S-75121 Uppsala, Sweden

Abstract

We calculate closed analytic expressions for the longitudinal Schottky Signals from beams with gaussian momentum distribution. All dispersion integrals can be evaluated in terms of complex error functions. Using a Padé approximation for the error functions allows very rapid evaluation of the Schottky spectra.

1 INTRODUCTION

In ref. 1 and 2 expression are deduced for the longitudinal Schottky spectrum at the $p-$th harmonic for a beam under the influence of cooling, characterized by the cooling rate ν and a longitudinal impedance $Z_{\|}$

$$P(\Omega) = 2I_0^2 \frac{N}{p} \left| \frac{1 + i\nu I(\Omega)}{\varepsilon(\Omega)} \right|^2 \psi(\Omega/p) \qquad (1)$$

where the dielectric function $\varepsilon(\Omega)$ is given by

$$\varepsilon(\Omega) = 1 - iJ(\Omega) \frac{q\eta}{\gamma_0 \beta_0^2} \frac{\omega^2}{2\pi} \frac{I_0 Z_{\|}}{mc^2} + i\nu I(\Omega) \,. \qquad (2)$$

The gaussian distribution function $\psi(\omega)$ is defined by

$$\psi(\omega) = \frac{1}{\sqrt{2\pi}\sigma} e^{-\frac{(\omega-\omega_0)^2}{2\sigma^2}} \,. \qquad (3)$$

The dispersion integrals $I(\Omega)$ and $J(\Omega)$ can be evaluated analytically in terms of the complex error function $w(z)$ [3] which is shown in the appendix and are given by

$$\begin{aligned} iI(\Omega) &= i \int_{-\infty}^{+\infty} d\omega \frac{\psi(\omega)}{\Omega - p\omega - i\nu} = -\sqrt{\frac{\pi}{2}} \frac{1}{p\sigma} w(z) \qquad (4) \\ iJ(\Omega) &= i \int_{-\infty}^{+\infty} d\omega \frac{\partial\psi(\omega)/\partial\omega}{\Omega - p\omega - i\nu} = \frac{1}{p\sigma^2}(i - \sqrt{\pi} z w(z)) \end{aligned}$$

with

$$z = -\frac{\Omega - p\omega_0 - i\nu}{\sqrt{2}p\sigma} \qquad (5)$$

Having calculated the dispersion integrals in closed form allows us to directly fit eq. 1 to data and extract physical parameters such as frequency spread σ or the damping rate ν from measured schottky spectra. We propose to use the following fitting function

$$\begin{aligned} P(\Omega) &= A + Be^{-\frac{(\Omega-D)^2}{2C^2}} \qquad (6) \\ &\times \left| \frac{1 - \sqrt{\frac{\pi}{2}} E w(z)}{1 - (F + iG)\,(i - \sqrt{\pi} z w(z)) - \sqrt{\frac{\pi}{2}} E w(z)} \right|^2 \end{aligned}$$

with

$$z = -\frac{\Omega - D}{\sqrt{2}C} + \frac{i}{\sqrt{2}} E \,. \qquad (7)$$

The fitting parameters $A, B, \ldots, F$ have the following interpretation

A	=	offset or base line
B	=	amplitude of the signal
C	=	frequency spread $p\sigma = p\omega_0 \eta \sigma_p$
D	=	center frequency of $p-$th harmonic $p\omega_0$
E	=	scaled damping rate $= \nu/p\sigma$
$F + iG$	=	scaled impedance $= \frac{1}{2\pi} \frac{q\eta}{\gamma_0 \beta_0^2} \frac{I_0 Z_{\|}/p}{m_0 c^2} \frac{\omega_0^2}{\sigma^2}$

Note that in this representation the fit-parameter E alone describes the effect of damping and that $F + iG \propto \eta Z_{\|} I_0$ alone describes the effect of the impedance. [1]

2 QUALITATIVE FEATURES

In this section we will exploit eq. 6 and generate longitudinal Schottky spectra that allow us to deduce the beam's properties directly from the shape of spectra similarly to the discussion in ref. 1.

- In the absence of damping ($E = 0$) and collective effects ($F + iG = 0$) the schottky spectrum is given by the momentum distribution $\psi(\Omega/p)$.
- In the absence of impedance ($F + iG = 0$) the cooling rate does not affect the schottky power spectrum as can be seen from eq. 6, where the entire term in absolute values vanishes. Note that the damping rate still enters indirectly, because it affects the equilibrium energy spread and consequently the frequency spread σ as well.
- The effect of cooling is most pronounced at low harmonics as can be seen from the definition of the fit-parameter $E = \nu/p\sigma$.
- A large capacitive impedance ($G > 1$ below transition) causes the Schottky spectrum to exhibt double peaks as can be seen in Fig. 1.
- Adding a resistive impedance ($F < 0$ below transition) causes the low frequency peak to be higher at the expense of the high frequency peak.
- Adding damping, e.g. due to electron cooling, will cause to smooth out the effect of the impedance and

[1] Obviously the same type of parametrisation can also be done for beam transfer functions.

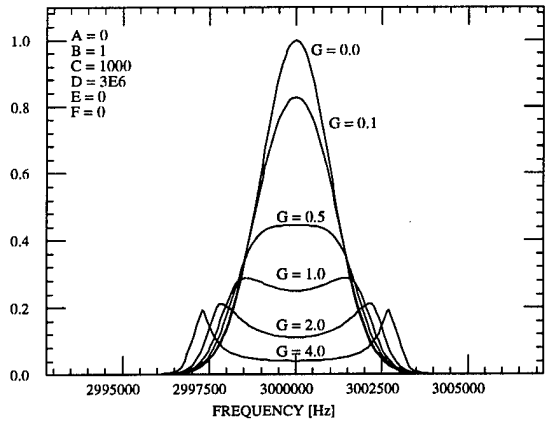

Figure 1: *The effect of a finite capacitive impedance on the longitudinal Schottky spectrum.*

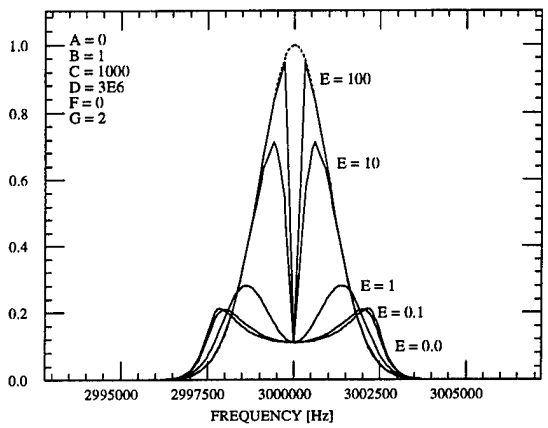

Figure 2: *The effect of damping or cooling on the longitudinal Schottky spectrum in the presence of a finite capacitive impedance ($G = 2$). Note that the damping counter-acts the collective effects.*

will make the spectrum more similar to an unperturbed gaussian with a narrow valley in the center. This is illustrated in Fig. 2.

After having discussed the qualitative features of longitudinal Schottky spectra we will discuss the feasability of fitting measured spectra to eq. 6.

3 FITTING SCHOTTKY SPECTRA

In order to test the feasability of determining the seven parameters $A, B, \ldots, G$ from directly fitting eq. 6 to data we generate a longitudinal Schottky spectrum with $A = 0, B = 1, C = 1000, D = 3\,10^6, E = 0, F = -0.1$, and $G = 1$. We then fit eq. 6 to the data by minimizing the cost function

$$\chi^2 = \sum_{\text{data}} (y - P(\Omega; A, B, \ldots, G))^2 \qquad (8)$$

with respect to the parameters $A, B, \ldots, G$. For the minimization a Nelder-Mead Simplex minimizer is used [4].

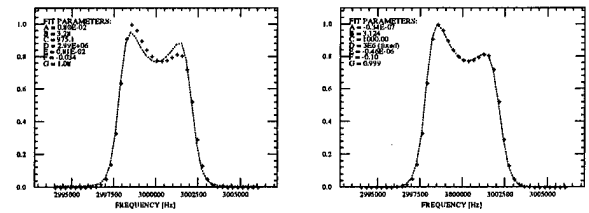

Figure 3: *Fitting a longitudinal Schottky spectrum with $A = 0, B = 1, C = 1000, D = 3\,10^6, E = 0, F = -0.1, G = 1$. In the left graph all seven parameters are fitted which results in a rather poor fit and in the right graph the center frequency D is fixed at $3\,10^6$.*

In the evaluation of eq. 6 we use a Padé approximation $w(-iz) = P(z)/Q(z)$ for which the coefficients of the polynomial P, Q (of order 10 and 11) are all real [5].

The left graph in Fig. 3 shows the result from fitting all seven parameters simultaneously. Clearly the result is rather poor. In the right graph we fit the same data but fixing the central frequency to its correct value $D = 3\,10^6$ and then fit the remaining six parameters which results in much more accurate results. In practice the central frequency is always known before-hand, because it is a harmonic of the revolution frequency. We presume that the inaccuracy shown in fitting all parameters simultaneously is caused by a correlation between finding the resistive part of the impedance F which causes the asymmetry and the central frequency D.

Finally we analyze Schottky spectra from 2 mA cooled 436 MeV deuterons stored in CELSIUS [6], observed at the 32nd revolution harmonic. From the fit shown in Fig. 4 we deduce a frequency spread of about 1.2 kHz which translates to a momentum spread of $3.5\,10^{-5}$. From the fit parameters F and G we deduce an impedance of $Z_{\|}/p = (0.2 - 2.3i)\,\text{k}\Omega$ which is consistent with earlier measurements. The fitted damping coefficient E, however is much too large and would imply a damping time on the order of ms which is orders of magnitude smaller than expected.

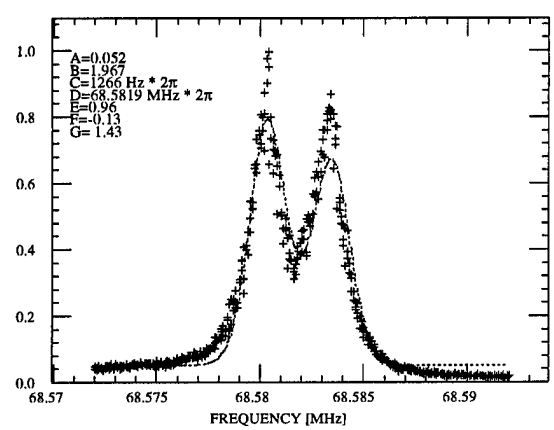

Figure 4: *Schottky spectrum from 436 MeV deuterons.*

Qualitatively, however, the deep narrow valley in spectrum indicates strong damping.This is currently an unresolved problem, which may e.g. be due to a non-gaussian beam or finite reolution bandwidth of the spectrum analyzer.

4 ACKNOWLEDGMENTS

The author wishes to thank D. Reistad, TSL for fruitful discussions.

5 REFERENCES

1. S. Cocher, *Effets collectifs d'un faiseau refroidii d'ions lourds dans un anneau de stockage,* These soutenue a l'universite de Paris XI le 19 mai 1989.
2. S. Cocher, I. Hofmann, *On the stability and diagnostics of heavy ions in storage rings with high phase space density,* Part. Acc. **34**, 189, 1990.
3. M. Abramowitz, I. Stegun, *Handbook of Mathematical Functions,* Dover Publications, 1970, chapter 7.
4. W. Press, et al., *Numerical Recipes,* Cambridge University Press, Cambridge, 1986.
5. V. Ziemann, *The Interaction of Free Electron Lasers and Storage Rings, analyzed with a Mapping Algorithm for Distribution Functions,* Thesis, Universität Dortmund, 1990, unpublished.
6. T. Bergmark et al., *Recent Activities at CELSIUS,* contributed to the 1996 European Particle Accelerator Conference, Barcelona, Spain.

A EVALUATION OF $I(\Omega)$

In this appendix we will evaluate the first the dispersion integrals given by eq. 4. If the damping rate ν is positive, we can represent the denominator by

$$\frac{1}{x} = i \int_0^{+\infty} d\alpha \, e^{-i\alpha x} \tag{9}$$

where $\nu > 0$ implies $\operatorname{Im} x < 0$ which makes the integral convergent. In the limit $\operatorname{Im} x \to 0$ we revover the well known principal value relation

$$\lim \frac{1}{y + i\varepsilon} = \mathrm{PP}\frac{1}{y} - i\pi\delta(y) \, . \tag{10}$$

This trick we use to turn the denominator of eq. 4 into an exponential. Exchanging the order if integration, performing the gaussian integral over ω, and introducing auxiliary variables $x = \omega/\sigma$ and $x_0 = \omega_0/\sigma$ we arrive at

$$iI(\Omega) = -\int_0^{+\infty} d\alpha \, e^{-\alpha^2 p^2 \sigma^2/2 - i\alpha(\Omega - p\omega_0 - i\nu)} \, . \tag{11}$$

Substituting $\beta = \alpha p \sigma/\sqrt{2}$ we obtain

$$iI(\Omega) = -\frac{\sqrt{2}}{p\sigma} \int_0^{+\infty} d\beta \, e^{-\beta^2 + 2i\beta z} \tag{12}$$

with z given by eq. 5 in the main text. The integral appearing in eq. ? is a representation of the complex error function $w(z)$ [3]

$$w(z) = \frac{2}{\sqrt{\pi}} \int_0^{+\infty} d\beta \, e^{-\beta^2 + 2i\beta z} \, . \tag{13}$$

Inserting in eq. ? we finally get the second half the first of eq. 4.

B EVALUATION OF $J(\Omega)$

In this appendix we will evaluate the second dispersion integral in eq. 4 for which we need the derivative of the gaussian distribution function

$$\frac{\partial \psi(\omega)}{\partial \omega} = -\frac{1}{\sqrt{2\pi}\sigma} \frac{\omega - \omega_0}{\sigma^2} e^{-(\omega-\omega_0)^2/2\sigma^2} \tag{14}$$

Inserting in eq. 4 and again turning the denominator into an exponential with the aid of eq. ? we can exchange the order of integration and get

$$\begin{aligned} iJ(\Omega) &= \frac{1}{\sqrt{2\pi}\sigma^3} \int_0^{+\infty} d\alpha \, e^{-i\alpha(\Omega - i\nu)} \\ &\times \int_{-\infty}^{+\infty} d\omega \, (\omega - \omega_0) e^{-(\omega-\omega_0)^2/2\sigma^2 + i\alpha p\omega} \, . \end{aligned} \tag{15}$$

The ω appears linearly in the integral and is taken care of by parametric differentiation which can be pulled out of the $d\omega$ integral. Remembering that the $\partial/\partial\alpha$ operator acts to the right hand side only we rewrite the previous equation

$$\begin{aligned} iJ(\Omega) &= \frac{1}{\sqrt{2\pi}\sigma^3} \int_0^{+\infty} d\alpha \, e^{-i\alpha(\Omega - i\nu)} \\ &\times \left(\frac{1}{ip} \frac{\partial}{\partial \alpha} - \omega_0 \right) \int_{-\infty}^{+\infty} d\omega \, e^{-(\omega-\omega_0)^2/2\sigma^2 + i\alpha p\omega} \end{aligned} \tag{16}$$

which leaves a gaussian integral over $d\omega$ that can be easily evaluated. After performing the differentiation with respect to α we arrive at

$$iJ(\Omega) = ip \int_0^{+\infty} d\alpha \, \alpha e^{-\alpha^2 p^2 \sigma^2/2 - i\alpha(\Omega - p\omega_0 - i\nu)} \tag{17}$$

which upon substituting $\beta = \alpha p \sigma/\sqrt{2}$ transforms to

$$iJ(\Omega) = \frac{2i}{p\sigma^2} \int_0^{+\infty} d\beta \, \beta e^{-\beta^2 + 2iz\beta} \tag{18}$$

with z defined in eq. ?. The β linear in the integral can be treated again by parametric differentiation with the result

$$iJ(\Omega) = \frac{1}{p\sigma^2} \frac{\partial}{\partial z} \int_0^{+\infty} d\beta \, e^{-\beta^2 + 2iz\beta} = \frac{\sqrt{\pi}}{2p\sigma^2} w'(z) \tag{19}$$

where we use the integral representation of the error function given in eq. ?. Note that $w'(z)$ is the derivative of the complex error function which can be evaluated [3] as

$$w'(z) = \frac{2i}{\sqrt{\pi}} - 2zw(z) \, . \tag{20}$$

Thus it suffices to know the complex error function at z in order to calculate its derivative. Utilizing this we arrive at the expression stated in the main part of the text.

PROTON INJECTION AND RF CAPTURE IN THE NATIONAL SPALLATION NEUTRON SOURCE

A.U. Luccio * , J. Beebe-Wang, D.Maletic, Brookhaven National Laboratory, Upton, NY 11973
F.W. Jones, TRIUMF, 4004 Wesbrook Mall, Vancouver, B.C. Canada

Abstract

The accelerator system for the 1 to 5 MW National Spallation Neutron Source (NSNS) consists of a linac followed by a 1 GeV proton accumulator ring. Since the ring is a very high current machine, the injection and rf capture of the protons is deeply affected by transverse and longitudinal space charge effects. Results of numerical simulation of the process are presented together with considerations on methods and results of space charge treatment in high intensity proton storage rings.

1 INTRODUCTION

The injection and RF capture processes in the accumulator ring is being studied with the code *Accsim*[1]. The simulation is 6-dimensional, with tracking of a number of representative macro particles through the lattice, in the presence of space charge forces and beam to wall interaction.

A 1 GeV H^- beam is injected from the linac, stripped to H^+ and moved to the equilibrium orbit. *Accsim* calculates the scattering in the stripping foil, that is traversed a few times by the beam during the first turns. Losses arise from two main sources: H^- ions missing the foil, or not being converted to protons, and protons hitting the walls during the accumulation process. *Accsim* counts lost particles and takes them off the tracking cycle. A general strategy is to limit the losses to a specific region of the ring (controlled losses). To decrease the beam diffusion, we plan to extract the beam immediately after the injection is completed. To study losses to the level of 10^{-4}, the number of macro particles in the simulation is chosen between 10^4 and 10^6, with a limit set only by computing time.

2 MACHINE LATTICE. INJECTION

The lattice of the accumulator ring, with super symmetry 4 [2], consists of an array of FODO cells with four straights, for injection, collimation, to accommodate the RF, and extraction, respectively. The lattice is optimized with *Mad* [4], that produces the 51 matrices used in tracking. In the simulation, to account for wall beam losses, a set of collimating apertures were placed at various points around the circumference.

During injection [3], the H^- are converted to H^+ in a $400\mu g/cm^2$ carbon stripping foil. A plural tabulated scattering distribution [7] is used to generate scattering angles in the foil. Nuclear scattering is not currently simulated in *Accsim*.

Table 1: Parameters of the injected beam.

	α	β [m]	ϵ [mm-mrad]
radial:	0.0014	19.140	0.35
vertical:	0.	4.150	0.35
longitudinal: $\Delta\phi = 240^0$, dE/E=0.001			

The injected number of protons in the accumulator ring is 1.042×10^{14}, for a 1 MW machine. The injection takes about 1 msec, or 1,200 turns This number of turns and the longitudinal phase bite injected, 240^0 or 2/3 of the bucket, were chosen to best match the linac beam structure.

At injection, the ring equilibrium orbit is distorted with a radial and a vertical bump. Initially, the beam is directed to the foil in correspondence with the center of the phase space acceptance ellipse of the ring, both radially and vertically. The bumps collapse in time, so that at the end of injection the beam sits on a less bumped radial orbit in the horizontal plane.

The injection line dispersion was matched to the ring dispersion at the foil. Among the other twiss functions, only α was matched, while we tried several radial and vertical β values. Typical injection parameters are given in Table 1.

The distribution of macro particles at injection is taken as random gaussian in the radial and vertical phase space, and flat in the longitudinal phase. The values for the transverse emittance shown in the Table are for 2σ.

3 RF CAPTURE. BEAM LOSSES

Since the beam will be extracted soon after the 1,200 turn injection process is completed, long term beam accumulation and RF capture beyond 1 msec are of no concern. For such a high intensity beam, its size and stability during injection and RF capture are strongly affected by space charge. Tune shifts and tune spread are indicative of transverse space charge effects and should be kept small. A design limit for transverse tune shift is $\Delta\nu = -0.2$. Space charge issues will be discussed in more detail in Sec.4.

Following our experience with AGS operation, and in agreement with previous calculations [5], we also studied the performance of vertically hollow, or "smoke ring" beam, that seems to reduce the tune shift. To obtain a (vertical) smoke ring, during injection we turned off the vertical bump. Beam stacking was studied with two different RF systems [6]: (i) employing the 1.st (or fundamental) harmonic, and (ii) adding a 2.nd harmonic to the fundamental.

* Work sponsored by the Division of Material Sciences, U.S. Department of Energy, under contract DE-AC05-96OR22464 with Lockheed Martin Energy Research Corp. for Oak Ridge National Laboratory

0-7803-4376-X/98/$10.00 © 1998 IEEE

Both RF waveforms are shown in Figure 1.

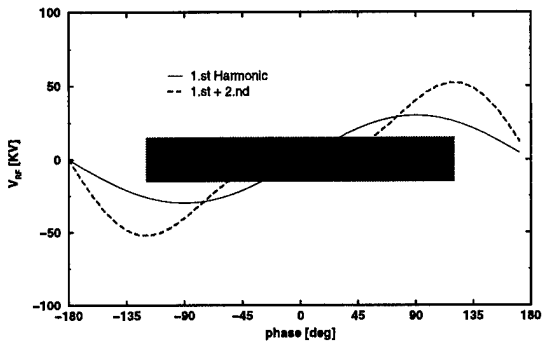

Figure 1: 1.st harmonic (solid line), and 1.st + 2.nd harmonic cavity voltage (dashed line). A 240^0 beam bunch is also diagrammatically shown.

Case (i). With the orbit bump, we found a solution with no beam losses in excess of 10^{-4} during the 1,200 turns of injection and capture, at a peak accelerating voltage of 40 KV. The resulting bucket area was 6.67 eV-sec. Transverse emittance tune shifts in the center of the beam were well contained within the design limits of -0.2.

Case (ii). A good solution, shown in Figure 2, with losses $< 10^{-4}$ was also found, at a peak accelerating voltage of 40 KV ($h = 1$) and 20 KV ($h = 2$). Adding a 2.nd harmonic to the RF system improves the longitudinal phase space and the transverse tune shift [6] and creates a more compact beam. The bucket is less than 2 eV-sec (plus halo). Figure 3 shows the emittance and tune shifts for this case.

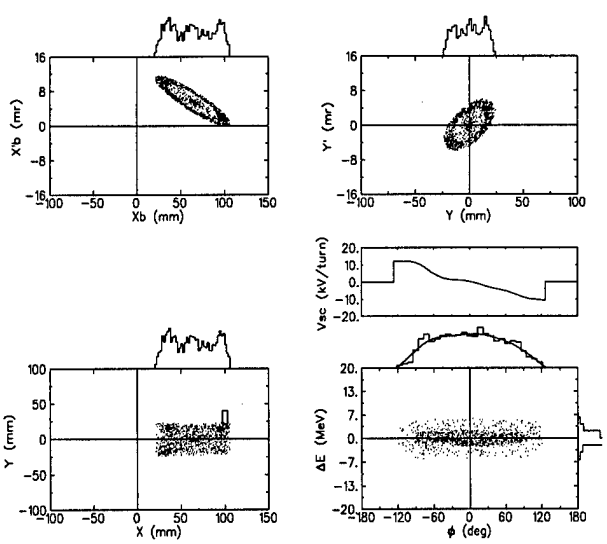

Figure 2: *Accsim* snapshots at 1,200 turns. 1.st + 2.nd harmonics RF. 1MW accumulator.

Calculations were repeated for a vertical smoke ring in the conditions of case (ii) above. Losses and foil traversals for the 3 scenarios are are given in Table. 2

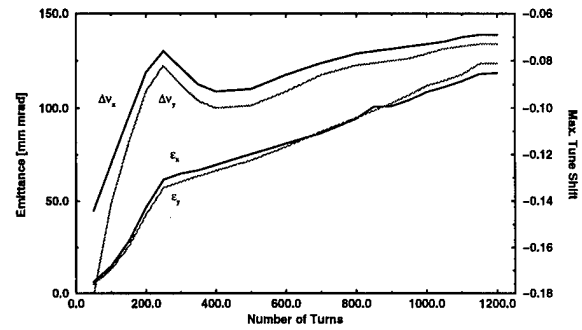

Figure 3: Transverse emittance and tune shift. 1.st + 2.nd harmonics RF. 1 MW accumulator.

Table 2: Losses and foil hits. 1 MW accumulator.

Macroparticles = 120,000, Total charge = 1.042×10^{14}			
lost[%]	at foil	elsewhere	ave. foil hits
1.st harm. RF:	1.962	$< 8 \times 10^{-5}$	3.612
1.st + 2.nd:	1.867	$< 8 \times 10^{-5}$	3.592
smoke ring:	1.867	$< 8 \times 10^{-5}$	3.592

4 SPACE CHARGE TUNE SPREAD

The transverse tune shift is calculated in *Accsim* for each macro particle with a formalism which computes the amplitude dependent tune shift due to the space charge forces of the instantaneous 2-dimensional betatron amplitude distribution, with walls removed. Individual particles are assumed to perform prescribed oscillations within the beam [8].

In the longitudinal dynamics *Accsim* includes space charge with perfectly conducting smooth walls. The additional space charge voltage induced on the beam is calculated with [10]

$$V_{sc} = -\frac{Z_0 c}{4\pi}\left(1 + 2\ln\frac{b}{a}\right)\frac{d\lambda}{ds}$$

with Z_0 is the impedance of free space, $d\lambda/ds$ the longitudinal gradient of the particle distribution in the beam, and b/a the ratio between beam and chamber radii ($b/a = 3$ in our simulation). At the present, no detailed longitudinal impedance budget is included in *Accsim*.

A general expression for the (maximum) transverse tune shift induced by space charge in the center of a beam is [9]

$$\Delta\nu = -r_0 \frac{\lambda}{\beta^2\gamma^3\nu}\frac{g}{r}$$

with r_0 the classical proton radius, λ the longitudinal linear charge density, β and γ the relativistic velocity and energy, ν the bare tune, and g/r a form factor that describes the distribution of particles in the beam. *Accsim* agrees with the above expression when the beam transverse profile has only one peak (pseudo gaussian distribution), but the algorithm that evaluates the tune distribution in the beam (i.e. the tune spread $\Delta\nu$), does not provide good accuracy for the general

case (say, a smoke ring). Work is in progress to calculate space charge forces in a more complete way[11].

In dealing with space charge, the immediate problem is that the on line calculation can be very time consuming and therefore impractical when a very large number of representative particles are used. The evolving charge distribution should be continuously updated to calculate transverse kicks and the tune associated with each particle, in order to evaluate the diffusion of the beam and the growth rate of possible destructive resonances.

Far from walls, the transverse space charge forces on a particle at P can be calculated by an integration on the actual charge distribution (it is $\xi = x$, or y)

$$F_\xi(P) = \frac{\mu_0 e^2 c^2 n}{4\pi\gamma^2} \int \frac{\rho(Q)}{r^3} \xi \, dQ,$$

with ne the charge contained in a beam volume V. Taking into account the relativistic longitudinal compression of the field, the preceding integral describes the interaction between filaments of current for not too high energies (our case) and point interaction for extreme energies.

The space charge force produces a tune shift $\Delta\nu$ at each macro particle location. To calculate the tune at P, consider the betatron equation in r (either x or y):

$$\frac{d^2\xi}{dz^2} + K_\xi \xi = f(\xi, z) = \frac{F_\xi}{m_0 \gamma \beta^2 c^2}.$$

The space charge force is zero in the center of the beam and is anti symmetric in ξ, because the net force is repulsive on both sides. The tune shift near the center will be represented by the radial derivative of f. We deal in general with a non linear equation that generates oscillations with a variety of frequencies. The r.h.s. contains both x and y and generates also coupling beat frequencies. With numerical integration followed by a FFT analysis we could calculate the tune distribution in the beam and the coupling frequencies. The calculated radial component of the space charge force for a pseudo gaussian and for a smoke ring is shown in Figure 4. The figures show how the force derivative in the center can be much smaller for a smoke ring. Results of the FFT analysis shows that the tune shift and tune spread are smaller for a smoke ring, also when averaged over all particles in the beam. The FFT shows also the coupling beats.

An example of "necktie" diagrams, taken every 135 turns during beam stacking, for a 2 MW machine, are in Figure 5. The figure clearly shows that the necktie area increases very fast when the total beam charge is approaching its upper limit. .

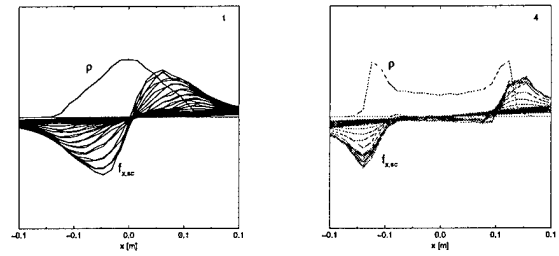

Figure 4: Pseudo Gaussian vs. Smoke Ring. Density and Space charge force vs. x for various y.

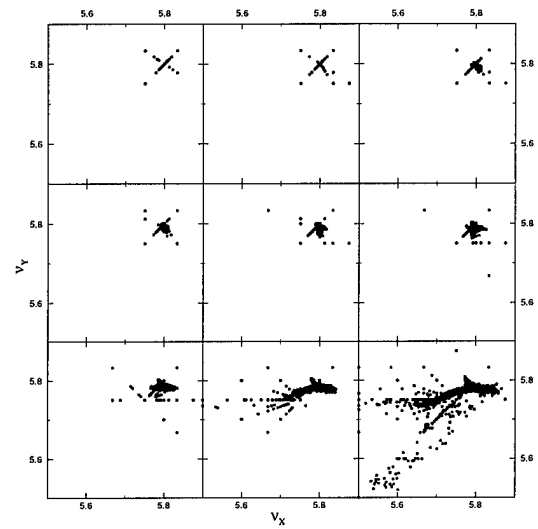

Figure 5: Distribution of peaks in the tune chart. 256 particles. Pseudo Gaussian population.

5 REFERENCES

[1] F.W.Jones: "User's Guide to Accsim". TRIUMF Design Note TRI-DN-90-17, June 1990 (and later additions).

[2] Y.Y.Lee: Proceedings of this Conference.

[3] L.Blumberg: Proceedings of this Conference.

[4] F.Ch. Iselin and J. Niederer. "The Mad Program. User's Reference Manual". CERN/LEP-TH/88, July 13, 1988 (and later additions).

[5] L.N. Blumberg, A.U. Luccio, A. VanSteenbergen, F.W. Jones. BNL-62391, UC-414, AGS/AD/96-2, Upton, 1995.

[6] M. Blaskiewicz, J.M. Brennan and Y.Y.Lee. Proceedings this Conference

[7] E. Keil, E. Zeitler and W. Zinn. Z. Naturf. 15a,1031,1960.

[8] H. Schönauer. TRIUMF Design Note TRI-DN-89-K50, August 1989.

[9] A.W. Chao: 'Physics of Collective Beam Instabilities in High Energy Accelerators', Wiley, New York 1993

[10] A. Hoffman, CERN 77-13,1977.

[11] A.U. Luccio, BNL/NSNS Tech. Note No.023, Upton, 1997.

TRANSVERSE INSTABILITY IN HIGH INTENSITY PROTON RINGS*

S.Y. Zhang and W.T. Weng
Brookhaven National Laboratory, Upton, NY 11973, USA

Abstract

Most high intensity proton rings are at low energy below transition. Several aspects of the beam dynamics of this kind of rings are different from the electron or high energy rings. The transverse microwave instabilities will be discussed in this article.

1 INTRODUCTION

In recent years, many applications are being considered for low energy high intensity proton synchrotrons, see for example[1]. This kind of rings are different from the electron or high energy proton rings in several aspects of beam dynamics. The transverse microwave instability is the subject to be discussed in this report.

The transverse beam dynamic equation will be presented, where it is indicated that among several factors responsible for the instabilities, the most concerned issue is the impedance, especially the transverse space charge impedance.

It will be shown that the conventional transverse space charge impedance is related to the difference of the space charge coherent and incoherent tune shifts. The space charge incoherent tune spread is an important stabilizing force for the transverse microwave instabilities. Thus, the transverse space charge impedance is relevant to both coherent motion and the tune spread for the Landau damping.

This scenario dominates the transverse beam dynamics for the low energy proton rings. Many important issues in the beam dynamics for the electron and high energy machines become secondary or even negligible effects. On the other hand, for high intensity rings, the space charge incoherent tune spread has to be limited, which is likely to affect the stability margin.

2 BEAM DYNAMIC EQUATION

Consider the transverse bunched beam dynamic equation with the azimuthal mode $m = 0$[2],

$$\omega - \omega_\beta = \frac{j\beta e I_0}{2Rm_0\gamma\nu_0\omega_0}\sum_{n=-\infty}^{\infty} Z_T(n)\Lambda_0^2(n') \qquad (1)$$

where ω_β and ω_0 are the betatron and revolution frequencies, respectively, I_0 is the average beam current, R is the machine average radius, and m_0 is the rest mass of proton. Z_T is the transverse impedance, and Λ_0 is the spectrum of the beam line density for $m = 0$ mode. The notation n' denotes the beam spectrum frequency shift due to the chromatic effect.

In (1), the beam line density spectrum, the effective spectrum lines, the impedance, and the chromatic effect for bunched beams are relevant to the beam instabilities.

For high intensity proton rings, the bunch has to be long to reduce the space charge effect. Therefore, the beam line density spectrum will be narrow, approaching the situation of coasting beams. The effective spectrum lines will be few. In other words, the coasting beam criterion will be more relevant to the transverse instabilities. Now it appears that the most concerned issue in the beam instabilities is the impedance, especially the transverse space charge impedance.

3 TRANSVERSE SPACE CHARGE IMPEDANCE

The transverse space charge impedance is conventionally defined as[3],

$$Z_{TSC} = j\frac{RZ_0}{\beta^2\gamma^2}\left(\frac{1}{b^2} - \frac{1}{a^2}\right) \qquad (2)$$

where Z_0 is the impedance of free space, a and b are the average radius of the beam and the average half chamber height, respectively.

For coasting symmetric beam with non-penetrating fields, the space charge incoherent and coherent tune shifts are defined as[4],

$$\Delta\nu_{inc} = \frac{-NRr_0}{\pi\nu_0\beta^2\gamma}\left(\frac{\epsilon_1}{b^2} + \beta^2\frac{\epsilon_2}{g^2} + \frac{1}{2a^2\gamma^2}\right) \qquad (3)$$

and

$$\Delta\nu_{coh} = \frac{-NRr_0}{\pi\nu_0\beta^2\gamma}\left(\beta^2\frac{\epsilon_1}{b^2} + \beta^2\frac{\epsilon_2}{g^2} + \frac{\xi_1}{b^2\gamma^2}\right) \qquad (4)$$

where N is the total number of particles, r_0 is the classical radius of proton, ν_0 is the betatron tune with zero beam current, g is the half pole gap, and ϵ_1 and ϵ_2 are the Laslett incoherent electric and magnetic coefficients, respectively. The coefficient ξ_1 is the Laslett coherent electric coefficient.

For the simplified model, we consider circular chamber, which gives rise to,

$$\epsilon_1 = \epsilon_2 = 0,\ \xi_1 = 0.5 \qquad (5)$$

then the incoherent and coherent tune shifts become,

$$\Delta\nu_{inc} = \frac{-NRr_0}{2\pi\nu_0\beta^2\gamma^3a^2} \qquad (6)$$

* Work performed under the auspices of the U.S. Dept. of Energy

and

$$\Delta\nu_{coh} = \frac{-NRr_0}{2\pi\nu_0\beta^2\gamma^3 b^2} \tag{7}$$

For low energy synchrotrons, since γ is small, the simplification (5) is approximately right even the chamber is not circular, see (3) or (4). For bunched beams, we take a simplified approach, by adding the bunching factor B_f to the denominators of Eqs. (6) and (7).

In the following, we show that,

- The tune shifts shown in (6) and (7) can be obtained by substituting a proper part of the space charge impedance into the dynamic equation (1).
- The transverse space charge impedance represents the difference between the coherent and incoherent tune shifts.
- The incoherent tune shift will be cancelled in the dynamic equation, and therefore, it pays no role in the coherent motion.

3.1 *Impedance and dynamic equation*

First, we take the chamber part of the impedance (2),

$$Z_T = j\frac{RZ_0}{\beta^2\gamma^2}\frac{1}{b^2} \tag{8}$$

For coasting beams, the beam power spectrum is a delta function, with the amplitude $1/2\pi$ [2],

$$\Lambda_0^2(n) = \frac{1}{2\pi}\delta(n) \tag{9}$$

Thus, the summation in (1) is removed.

Now we use $I_0 = Ne\omega_0/2\pi$, and $Z_0 = 1/\epsilon_0 c$, where ϵ_0 is the permittivity in free space. Also using

$$r_0 = \frac{1}{4\pi\epsilon_0}\frac{e^2}{m_0c^2} \tag{10}$$

and $\omega_0 = \beta c/R$, then substituting (8) into (1), we get exactly the space charge coherent tune shift shown in (7). In other words, the impedance of (8) represents the space charge coherent tune shift. Similarly, the beam part of the impedance (2) is relevant to the space charge incoherent tune shift.

3.2 *Transverse space charge impedance*

Now substituting the transverse space charge impedance (2) into the dynamic Eq. (1), we have,

$$\omega - \omega_\beta = \Delta\nu_{coh}\omega_0 - \Delta\nu_{inc}\omega_0 \tag{11}$$

i.e., the transverse space charge impedance represents the difference between the coherent and incoherent tune shifts.

The impedance (2) is defined based on the deflecting electromagnetic fields distributed between the beam and the perfectly conducting wall[5]. Exactly what it means to the beam motion has to come from the Eq. (11).

Specifically, the transverse space charge impedance represents neither coherent nor incoherent tune shift. In the case that $a \ll b$, the implied tune shift will be approximately equal to the incoherent tune shift. However, this tune shift is increased, while the space charge incoherent tune shift should be decreased.

3.3 *Incoherent tune shift and coherent motion*

Writing on the left side of the Eq. (1) by the following convention ,

$$\omega_\beta = \omega_{\beta 0} + \Delta\nu_{inc}\omega_0 \tag{12}$$

and also using (11), the Eq. (1) becomes,

$$\omega - \omega_{\beta 0} - \Delta\nu_{inc}\omega_0 = \Delta\nu_{coh}\omega_0 - \Delta\nu_{inc}\omega_0 \tag{13}$$

where the incoherent tune shift is cancelled. This shows that the incoherent tune shift plays no role in the transverse coherent motion. Therefore, the beam part of the transverse space charge impedance, i.e., the contribution of $1/a^2$, is a redundancy in the dynamic equation.

The writing of (12) is following the longitudinal case, where one has to write the synchrotron oscillation frequency in the way of $\omega_S = \omega_{S0} + \Delta\nu_{S,inc}\omega_0$, because the incoherent frequency shift affects the longitudinal focusing, which is often called the potential well effect. In the transverse case, the similar effect is negligible. This is one of the fundamental differences between the transverse and longitudinal beam dynamics.

4 TRANSVERSE LANDAU DAMPING

For long bunches, the power spectrum of the perturbation can be a delta function $\delta(n - n_1)/2\pi$, where the spectrum line n_1 represents the frequency $(n_1 + \nu_0)\omega_0$, because only the perturbation at these frequencies has a chance to grow.

Also substituting the beam peak current I_p for the average current I_0, the Eq. (1) becomes,

$$\omega - \omega_\beta = \frac{j\beta e I_p}{4\pi R m_0\gamma\nu_0\omega_0} Z_T(n_1) \tag{14}$$

To proceed further, we write the left side of the Eq. (14) as the frequency spread $\Delta\omega = \Delta\nu\omega_0$, which will be responsible for the Landau damping.

Note that the Landau damping has two implications.

- If the impedance is real and positive, the system is stable and the Landau damping is not needed. If it is negative, then the frequency spread must be larger than the growth rate to suppress the instability.
- If the impedance is imaginary, then the frequency spread on the left side must be larger than the coherent frequency shift on the right side of (14). Otherwise, an infinitesimal perturbation may cause instability.

The microwave instability criterion is, therefore, obtained as follows,

$$\Delta\nu > \frac{\beta e I_p}{4\pi R m_0\gamma\omega_\beta\omega_0}|Z_T(n_1)| \tag{15}$$

It remains to clarify the sources responsible for the incoherent and coherent tune shifts.

4.1 *Incoherent tune spread*

For the incoherent tune spread, we consider the following sources.

- Space charge incoherent tune spread, which is the largest stabilizing force for the low energy proton synchrotrons. For the high energy machine, the tune spread is decreased, and its contribution diminishes. This is one of the reasons that the transverse instabilities is more critical for the high energy machines.
- Chromatic tune spread. For bunched beams, the chromatic tune spread is not effective for the weak instabilities with the growth rate comparable to the synchrotron frequency. It is, however, effective for the strong instabilities.
- Frequency slippage. This tune spread could be cancelled by the chromatic tune spread, then the trick is to let the cancellation happen at a stable frequency region.
- Octupolar tune spread. This tune spread is betatron oscillation amplitude dependent.
- Finally, the synchrotron oscillation may help. Conventionally, this contribution is estimated as $\Delta\omega \approx \omega_S = \Delta\nu_S\omega_0$.

The combined tune spread can, therefore, be written for the effective frequency $(n_1 + \nu_0)\omega_0$ as,

$$\Delta\omega = ((n_1+\nu_0)\eta - \xi\nu_0)\frac{\Delta p}{p} + \Delta\nu_{inc} + \Delta\nu_{oct} + \Delta\nu_S)\omega_0 \tag{16}$$

where $\Delta p/p$ is the beam momentum spread.

4.2 *Coherent tune shift*

The coherent tune shifts simply come from mainly two sources.

- Space charge coherent tune shift.
- Broad band impedance induced tune shift.

It can be observed that if the conventional transverse space charge impedance (2) is used, then it is relevant to both incoherent and coherent tune shifts, and it takes effect on both sides of the Eq. (15).

However, the transverse microwave instability can be estimated by taking the sum of the transverse space charge impedance with the broad band impedances, such as in[6]. If the sum is negative, then the incoherent tune spread is dominant, and the system is stable. Otherwise, the space charge incoherent tune spread is not large enough to stabilize the system by itself. It has been shown that this approach is valid for low energy rings. For high energy rings, the image effect is often stronger than the direct effect, however, the image incoherent effect is approximately cancelled with the coherent effect. Therefore, the approach is also valid.

5 HIGH INTENSITY PROTON RINGS

Most high intensity proton rings are at low energy below the transition. At low energy, the space charge incoherent tune spread is relatively large. At high intensity, the bunch has to be long to reduce the space charge tune spread. Also to eliminate the longitudinal microwave instability, the beam momentum spread will be relatively large. Thus, the chromaticity has to be corrected, and the machine is likely to work at a region with a slightly negative chromaticity. Therefore, the high intensity synchrotrons are different from the electron or high energy proton machines in terms of beam instabilities.

The issues relevant to the transverse instability of high intensity proton rings are summarized as follows.

- The space charge incoherent tune spread is an important stabilizing force for the transverse microwave instabilities. The transverse mode coupling will not happen for the low energy machines, because the space charge incoherent tune spread will be larger than the synchrotron tune.
- The coherent tune shift comes from the broad band impedance and the chamber part of the space charge impedance, both of which are small for low energy rings, because of the large chamber height and the small ring radius. On the other hand, for high intensity rings, the space charge tune spread has to be reduced as much as one can, therefore, the stability margin will be affected.
- The chromatic tune spread and the frequency slippage effect are relatively small. The cancellation of these effects, of interest for high energy machines, is not much concerned. Also the higher order mode, such as $m = 1$ mode, is not important.
- The synchrotron oscillation can eliminate the damping effect of the space charge incoherent tune spread for the transverse rigid bunch instabilities, such as the resistive wall instability. Careful study, or correction, will be needed.

6 REFERENCES

[1] W.T. Weng, these proceedings.

[2] S.Y. Zhang, BNL-63799 (Dec. 1996).

[3] B. Zotter, CERN 85-19, p. 253 (1985).

[4] P.J. Bryant, CERN 87-10, p. 62 (1987).

[5] D. Möhl and A. Sessler, Univ. California Report, LBL-42 (1971).

[6] F. Ruggiero, CERN SL/95-09 (AP), LHC Note 313 (1995).

COMPENSATION OF BEND-PLANE EMITTANCE GROWTH IN A 180 DEGREE BEND*

David H. Dowell, Boeing Free Electron Laser Program, Seattle, WA, 98124-2499

Abstract

Emittance preservation in beam bending systems is vitally important in the production of bright, high-current electron microbunches. Generally, the emittance increase occurs in the bend plane and results from changes in the microbunch energy distribution as the beam transits the bend. This redistribution of electron energies increases the beam's divergence, and hence the emittance, by spoiling the achromatic transport of the bending system. In this paper we investigate the correlated emittance growth in a 180 degree isochronous bend due to coherent synchrotron radiation (CSR). Introducing sextupole fields in the high dispersion region of the bend partially cancels the CSR-induced correlation thereby reducing the bend plane emittance growth. The generalization of this emittance compensation scheme is discussed.

1 INTRODUCTION

Emittance growth in beam transport sytems typically occurs in the plane of the bend and is due to changes in the beam microbunch energy distribution. While there are many effects capable of producing this redistribution, the most common is the space charge force which tends to increase the microbunch head and tail energies relative to that of the center, thereby correlating an angle change with longitudinal position in the microbunch. The other mechanisms which can redistribute the electron energies are wake fields and CSR. In a sense, these three phenomena are similar in their effects upon the beam in a bend. They all change the energy distribution of the microbunch, which leads to a combination of both correlated and uncorrelated emittance growth. This work concentrates upon CSR-induced emittance, but the basic principles can be applied to any combination of these three effects.

2 COHERENT SYNCHROTRON RADIATION INDUCED EMITTANCE GROWTH

CSR occurs when the bending of a relativistic electron beam allows the synchrotron radiation emitted by the tail of the microbunch to "catch up" with the head electrons. If the arc length of the bend is long enough, this radiation sweeps along the entire length of the microbunch and transfers energy from the tail to the head. Therefore CSR tends to increase the energy of the head while lowering that of the tail[1].

The transport of the microbunch through a multi-magnet bending system is computed using ray tracing with the first order matrix formalism of TRANSPORT [2] in combination with an energy redistribution using CSR formulae. In this procedure, one defines an initial four dimensional phase space distribution consisting of the bend-plane transverse coordinates, x and θ, and the longitudinal coordinates, z and ΔE/E. The non-bend plane degrees of freedom are ignored. Each macroparticle is incremented through the bending system with each step from location 0 to location 1 consisting of first the linear matrix transformation,

$$\begin{pmatrix} x_i(1) \\ \theta_i(1) \\ z_i(1) \\ \frac{\Delta E}{E}_i(1) \end{pmatrix} = R(\text{stepsize}) \begin{pmatrix} x_i(0) \\ \theta_i(0) \\ z_i(0) \\ \frac{\Delta E}{E}_i(0) \end{pmatrix}, \qquad [1]$$

followed by the CSR-produced change in the energy of the i-th macroparticle as given by,

$$\left.\frac{\Delta E}{E}\right|_i (1) = \left.\frac{dE(z_i(0))}{cdt}\right|_{CSR} * \text{stepsize} * \frac{1}{E_{beam}} + \left.\frac{\Delta E}{E}\right|_i (0). \qquad [2]$$

Here R(stepsize) is the 4x4 TRANSPORT transformation matrix which propagates the electrons the distance equal to stepsize through the bend. The CSR energy change of each macroparticle, $\left.\frac{dE(z_i(0))}{cdt}\right|_{CSR}$, is evaluated at the z-location of the i-th macroparticle and the fractional energy change added to its current energy fraction. The details for computing CSR energy loss gradient are given in Reference [3].

3 THE REDUCTION OF CSR-INDUCED, CORRELATED EMITTANCE

The energy redistribution impressed upon the microbunch by phenomena such as CSR, leads to a transverse angle vs longitudinal position (θ-z) correlation at the end of the bending system[3]. In order to understand the emittance compensation process, consider an effect similar to CSR, but which increases quadratically both the head and tail energies relative to the microbunch center. Such an effect leads to an final angle change along the microbunch given by,

$$\theta(z) = B(E(z) - E(z=0))^2 \qquad [3]$$

Here B includes all the details of the bending system as well as the strength of the hypothetical quadratic force.

* Work supported by USA/SSDC contract DASG60-90-C-0106.

Introducing a sextupole field in the bend where the energy dispersion is a maximum adds a second term to the equation

$$\theta(z) = B(E(z) - E(z=0))^2 + T_{211}(x(z) - x(z=0))^2 \quad [4]$$

Given that the transverse position of the each electron is well-correlated with the energy deviation impressed upon it by the quadratic force, then it is possible to cancel any correlated emittance growth with a sextupole field. In principle, it should be possible to compensate for more complicated correlations by introducing octupole and higher-order fields.

4 EMITTANCE GROWTH AND COMPENSATION IN AN ISOCHRONOUS 180 DEGREE BEND

4.1 Description of the Dundee Bend

As an example for emittance compensation we choose the 180 degree bend capable of adjustable non-isochronism proposed by Gillespie [4], hereafter referred to as the Dundee bend. An isochronous version of the bend is shown in Figure 1, and consists of three pairs of quadrupoles and sextupoles. The quadrupole strengths and magnet spacings are adjusted to obtain a nearly diagonal first-order unity matrix with the exception of R_{12} which is 96.3 cm/mrad for the entire bending system. The transverse dispersion term, R_{16}, peaks at the Q2 quadrupoles and the S2 sextupoles. In Gillespie's orginal design, the sextupoles are used to minimize second-order chromatic terms such as T_{516} and T_{566} which distort the longitudinal shape of the microbunch. Here the S2 sextupole pair are used for emittance compensation.

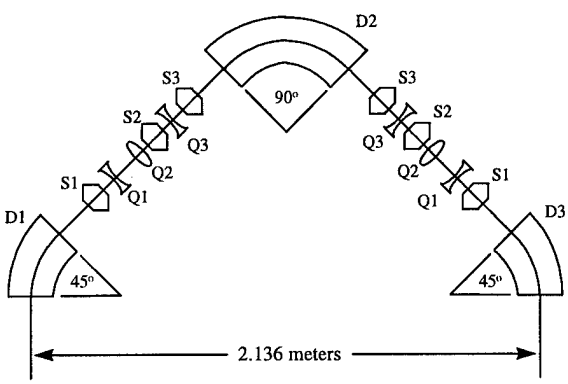

Figure 1. The isochronous 180 degree Dundee bend used to compute CSR emittance growth and emittance compensation.

4.2 Emittance Growth in the Dundee Bend Due to CSR.

The calculation assumes the beam is initially at 100 MeV with a rms emittance of 1 π mm-mrad, a rms microbunch length of 1.4 mm, negligible energy spread and a microbunch charge of 5 nC. This corresponds to a peak current of approximately 500 amperes. The final, CSR-induced emittance is 8 π mm-mrad. Figure 2 gives the transverse phase space and Figure 3 shows the θ-z correlation at the exit of D3 for these conditions.

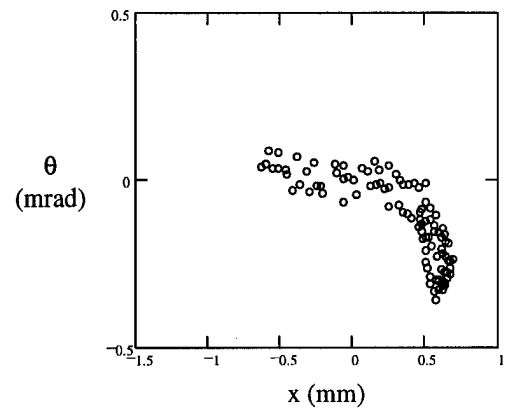

Figure 2. The transverse phase space at the exit of the Dundee bend for sextupoles $S2_{tip}$ =0 KG.

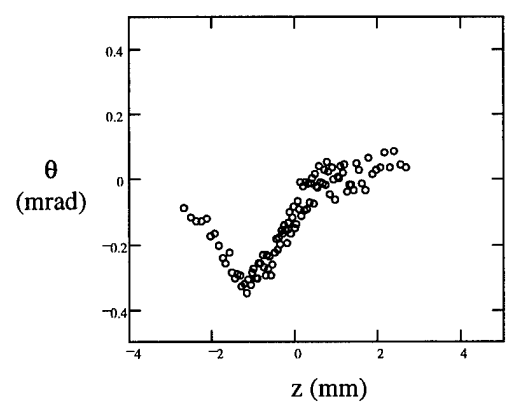

Figure 3. The correlation between beam divergence and longitudinal position in the microbunch for sextupoles $S2_{tip}$ =0 KG.

A comparison of these two figures shows that a significant portion of the emittance growth is correlated. That is, the tail electrons which are at lower energies exit the bend at smaller angles compared to those at the head. The electrons near z = -1 mm are approximately 0.5% lower in energy than the head electrons.

4.3 Compensated Emittance in the Dundee Bend

The final emittance as a function of S2 sextupole tip field from 0 to 8 KG upon is shown in Figure 4. The minimum emittance of 4.5 π mm-mrad occurs at 4 KG (aperture diameter = 25 mm and effective length = 5 cm).

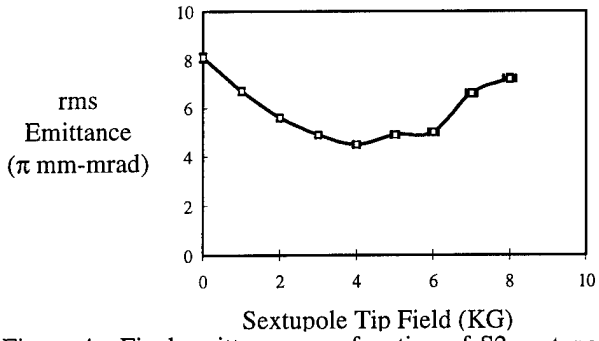

Figure 4. Final emittance as a function of S2 sextupole field.

The microbunch transverse phase space and θ-z correlation are plotted in Figures 5 and 6 for $S2_{tip} = 4$ KG. The sextupole removes the half of the CSR-induced correlated emittance growth associated with the quadratic correlation. The remaining portion appears to include higher-order correlations which may require the addition of octupole fields. However, the reduction of the emittance growth by a factor of two illustrates the benefit of this correction scheme.

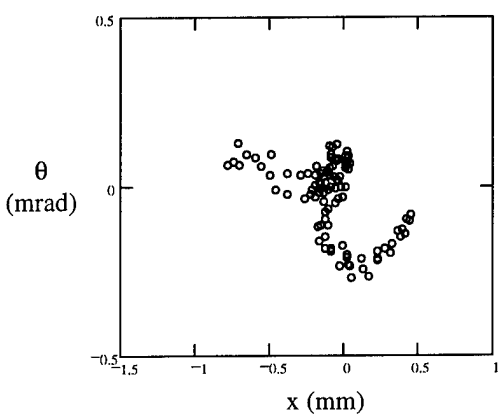

Figure 5. Transverse phase space at the exit of the bend for a S2 sextupole tip field of 4 KG.

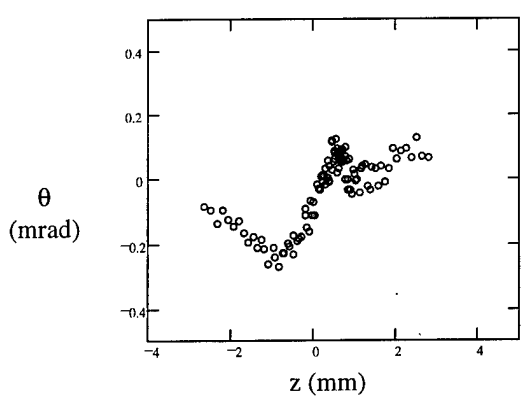

Figure 6. The correlation between beam divergence and longitudinal position in the microbunch for S2 at 4 KG.

5 DISCUSSION

The energy distributions produced by space charge forces, wakefields and CSR in a bending system typically lead to correlations between electron angle and longitudinal position in the microbunch. The result is a component of the emittance growth in bends which is correlated to various orders of the z-position in the microbunch. This work shows it is possible to cancel the quadratic piece of the correlation by introducing a sextupole field in a high dispersion section of the bend. In the case considered here, the CSR-induced emittance growth is reduced by a factor of two.

The next step involves generalizing Equation [4] to include higher-order correlations, i.e.,

$$\theta(z) = \sum_{j=2}^{n} [B_j (E(z) - E(z=0))^j - S_j (x(z) - x(z=0))^j]$$

where B_j result from the distorting forces and the bend transport, and S_j are the strengths of the multipole fields introduced in the high-dispersion section of the bend. As long as there is a strong correlation between the energy and beam size, it should be possible to cancel any correlated emittance growth term by term.

A final comment: while in these calculations the pair of S2 sextupoles were coupled and varied together, only the one in the last half of the bend affected the emittance. This is because there is significantly less CSR-induced energy spread at the first S2 location compared to the second S2. Therefore additional flexibility in this compensation scheme is possible by deliberately programming an energy slew along the length of the microbunch. This energy-z correlation can then be used by multipoles at the high dispersion position in the first half of the bend to correct for θ-z correlations induced later in the bend by phenomena such as CSR. This should be most useful in microbunch compressors where there is already an energy slew present to bunch the beam.

6 ACKNOWLEDGEMENTS

The author is grateful to T. Hayward, P.G. O'Shea, C. Parazzoli and A. Vetter for stimulating discussions on this and other topics concerning emittance growth in bends. This work was motivated in part by a workshop on CSR-induced emittance growth held March 6, 1997 at NPGS, Monterey, CA by W. Colson.

REFERENCES

1. Y.S. Derbenev et al. DESY TESLA-FEL Technical note 95-05 (1995).
2. D.C. Carey, K.L. Brown and F. Rothacker, SLAC-R-95-462.
3. D.H. Dowell and P.G. O'Shea, "Coherent Synchrotron Induced Emittance Growth in a Chicane Buncher", Contribution to these proceedings.
4. W.A. Gillespie, NIM **A374**(1996)395-400.

COHERENT SYNCHROTRON RADIATION INDUCED EMITTANCE GROWTH IN A CHICANE BUNCHER *

David H. Dowell, Boeing Free Electron Laser Program, Seattle, WA, 98124-2499 and
Patrick G. O'Shea, Duke University, Durham, N.C. 27708-0319

Abstract
Short high-current microbunches are of considerable importance for future linear colliders and electron beam sources of coherent radiation such as x-ray free-electron lasers. There is recent interest in beam degradation associated with the transport of short high-current electron beams in magnetic bends and bunchers. We compare the observed emittance growth in an existing magnetic buncher system at Boeing with that calculated when coherent synchrotron radiation (CSR) effects are included, and conclude that the CSR effects are significant.

1 INTRODUCTION

Though long anticipated [1], CSR from short electron bunches was not observed until 1989 [2]. Recently, there has been concern that CSR might contribute to significant emittance growth of high brightness beams in bends and magnetic bunch compressors. [3]

The emittance growth in a bend of angle α, of a beam with rms radius <x>, with induced energy spread $\Delta E/E$ is given approximately by $\Delta\varepsilon \approx \langle x\rangle\alpha\Delta E/E$. Energy spread can be induced by conventional and non-inertial space charge forces [4], wakefields and CSR. A discussion of the space-charge induced emittance growth is beyond the scope of this paper. In this paper we evaluate the CSR induced emittance growth a three-dipole chicane buncher used at the Boeing Free Electron Laser Laboratory

It is useful to compare conventional wakefields and CSR. Wakefields, generated by the interaction of the fields of the bunch with the boundary conditions, trail behind the bunch and can cause the disruption of the tail of the bunch. CSR fields are generated in bends, and can propagate toward the head of the bunch by traveling along a chord, resulting in a disruption of the head of the bunch. In a qualitative sense the wake potential and the CSR potential functions look similar, except that the wake potential has its peak toward the tail and the CSR potential toward the head of the bunch. Both effects can also result in bunch lengthening. In practice, the two effects may combine so as to be indistinguishable by time integrated diagnostics. It should be possible, however, to distinguish between the wakefield and CSR effects by using time-resolved emittance measuring techniques.

2 SUMMARY OF CSR PHENOMENA

It is well known that a bunch of length σ_z will radiate coherently at wavelengths $\lambda \geq 2\pi\sigma_z$. We estimate the distance required for the CSR from the tail of the bunch to catch up with the front of the bunch and reach a steady state to be $L_o \approx 5(\rho^2\sigma_z)^{1/3}$ [somewhat greater than found in ref. 5]. Boundary conditions imposed by the vacuum chamber result in three modes of CSR propagation: Free space, diffraction limited propagation for a >> λ; guided wave propagation where $\lambda \leq 2a\sqrt{\frac{a}{\rho}}$ [6]; and waveguide cut off for $\lambda > 2a\sqrt{\frac{a}{\rho}}$. (a = vacuum chamber height, ρ = bend radius)

For the free-space propagation case, we consider CSR in the long-wavelength limit of $\omega << \omega_c$, where $\omega_c = \frac{3\gamma^3 c}{2\rho}$. The characteristic angle of emission of the CSR $\theta = \frac{1}{\gamma}\left(\frac{\omega_c}{\omega}\right)^{\frac{1}{3}}$ is > $1/\gamma$. The effective source length (L_s), or formation length, is the distance the electrons must travel in the bend so as to produce a coherent free-space wavefront, $L_s \approx \rho\theta$. The diffraction-limited effective source transverse rms size is $\sigma_s = (\sigma_x^2 + \sigma_r^2)^{0.5}$ where σ_x is the rms electron beam radius and $\sigma_r = \sqrt{\frac{\lambda L_s}{\pi}} = \sqrt{\frac{\lambda\rho}{\pi}\left(\frac{3\lambda}{4\pi\rho}\right)^{\frac{1}{3}}}$. The characteristic distance for propagation is the Rayleigh range $Z_R = 4\pi\sigma_s^2/\lambda$.

The worst possible CSR case, i.e. where guided propagation is optimized, occurs when over the approximate range $\lambda_{max}/20 < \sigma_z < \lambda_{max}/6$. For longer bunch lengths the CSR is cut off by the vacuum chamber, and for shorter the CSR spreads because of diffraction.

Consider the case of the Boeing three-dipole chicane with ρ = 0.6 m; a ≈ 7 cm; γ = 35, and bunch compression from σ_z = 7 mm to 1.1 mm [7]. The cut-off wavelength λ_{max} = 48 mm. Therefore the CSR propagation begins as a guided wave and transitions to a quasi-free-space mode as the bunching progresses. The catch-up length L_o goes from 71 cm in the guided mode to 38 cm at the end of the buncher. At the end of the bunching process Z_R = 33 cm.

* Boeing work supported by USA/SSDC contract DASG60-90-C-0106, Duke work supported by SDC contract DASG60-84-C-0028.

3 COHERENT SYNCHROTRON RADIATION INDUCED EMITTANCE GROWTH

The microbunch loses energy due to CSR in two ways: as an average energy loss of all the electrons, and as a differential or gradient energy loss along the length of the microbunch. The average energy loss results in a change in the average bend angle, and results in little emittance growth for a properly designed bend. However, an energy loss gradient can significantly increase both the transverse and longitudinal emittances. In particular, an energy gradient increases the beam divergence, which in its early stages is correlated with position along the microbunch.

In this work we modify the coherent synchrotron radiation overtake potential function given by Derbenev et al. [5] and describe how it is applied to calculate the emittance growth for specific bend designs. The overtake potential function for the linear charge distribution, $\lambda(s)$, is,

$$F_0(x) = \int_{-\infty}^{x} \frac{dx'}{(x-x')^{1/3}} \frac{\partial \lambda(x')}{\partial x'} \qquad [1]$$

resulting in

$$\frac{dE}{cdt} = -\frac{2Ne^2}{\sqrt{2\pi}\, 3^{1/3} \rho^{2/3} \sigma_z^{4/3}} F_0(s/\sigma_z) \qquad [2]$$

for the energy loss gradient along the microbunch per unit distance traveled in the bend. ρ is the bend radius of curvature, σ_z is the rms microbunch length and N is the number of electrons in the microbunch.

The overtake potential function given in Equation [1] applies to the equilibrium situation where the tail radiation has overtaken the head, and radiation emitted by the electrons continually washes over those ahead of them in the microbunch. This radiation field moves energy from the rear to the front of the microbunch at the rate given in Equation [2]. However, at the beginning of the curved trajectory, the tail radiation has not yet caught up with the head electrons, and the overtake potential function is in transition from zero to its equilibrium form while traveling the catchup length, L_0 from the start of the bend.

We account for this startup of CSR at the beginning of the bend by modifying the above definition of the overtake potential function,

$$F_1(sb, x) = \int_{x-sb}^{x} \frac{dx'}{(x-x')^{1/3}} \frac{\partial \lambda(x')}{\partial x'} \qquad [3]$$

Changing the lower integration limit allows only the radiation a distance sb behind electrons at position x to reach them.

The energy loss gradient is shown in Figure 1 for the gaussian linear charge distribution,

$$\lambda(s) = \frac{1}{\sqrt{2\pi}\,\sigma_z} e^{-s^2/2\sigma_z^2}. \qquad [4]$$

The energy loss gradient is given in keV/meter for a 1 nC microbunch in a bend with a 1 meter radius, and is plotted for sb/σ_z from 0.25 to 15.

Figure 1 indicates that the Equation [3] startup prescription reaches the equilibrium form for $sb/\sigma_z > 6$. Therefore our transport calculations use Equation [3] and linearly increases sb/σ_z from zero to 6 to compute the overtake potential function while the microbunch travels its first characteristic overtake length in the bend.

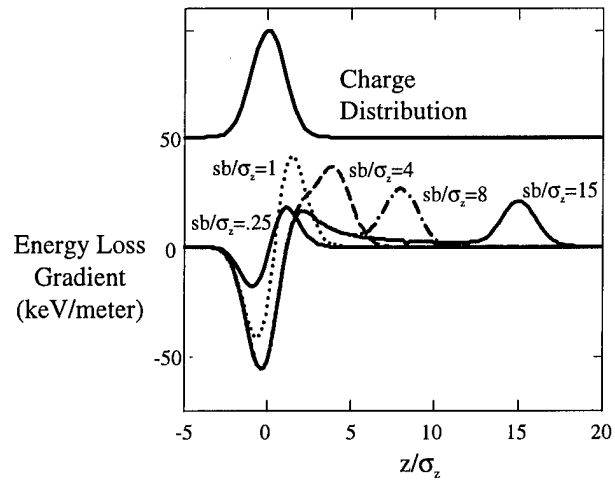

Figure 1. Evolution of the energy loss gradient along the microbunch for 1 nC and a bend radius of one meter. The CSR-induced gradient reaches equilibrium for $sb/\sigma_z > 6$. The transient radiation produced when the bunch enters the bend is seen propagating to the right for $sb/\sigma_z > 4$.

The transport of the microbunch through a multi-magnet bending system is computed using the first order matrix formalism of TRANSPORT [8] along with basic ray tracing to account for any non-linear CSR effects. In our procedure we define an initial four dimensional phase space distribution consisting of the bend plane transverse coordinates x and θ, and the longitudinal coordinates z and $\Delta E/E$. The non-bend plane degrees of freedom are ignored. Each macroparticle is stepped through the bending system with each step consisting of first the matrix transformation followed by a change in energy as given by Equation [2].

4. THE BOEING THREE-DIPOLE CHICANE.

Our example for computing CSR-induced emittance growth in a system of magnets is the Boeing three-dipole chicane. This magnet system is shown in Figure 2 and consists of three n=1/2 dipoles: the outer two being sector magnets, i.e. no pole face rotations, while the center dipole has -19.5 degree rotations on both the entrance and exit pole faces. These rotations on the center dipole make the chicane doubly achromatic. The chicane is non-isochronous with R_{56} = 3 mm/%.

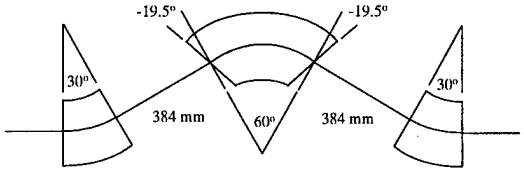

Figure 2. Boeing chicane composed of three n=1/2 dipoles.

For comparison with experiment, we compute the microbunch phase space distributions in the absence of CSR and correlate the z-ΔE/E distribution to compress a 2.7 nC microbunch from 7.0 mm to 1.0 mm (rms). The initial normalized transverse rms emittance is 8.8 π mm-mrad. These are the measured data from a bunch compression experiment recently performed with this chicane [9]. In this matrix model, the beam emittance is unchanged in the absence of CSR when the microbunch is transported around the bend. When CSR is included, the transverse phase space distribution increases in divergence as expected. In this case, the rms emittance increases 11 π mm-mrad due to CSR. The initial and final phase space distributions are shown in Figure 3.

The correlation of the macroparticles with their longitudinal position on the microbunch is shown in Figure 4. There is a clustering of the electrons toward the tail and the spread in divergence is considerably larger than in the front half of the microbunch. Some of the CSR induced emittance growth is correlated, therefore it could be removed using additional beam transport. [10].

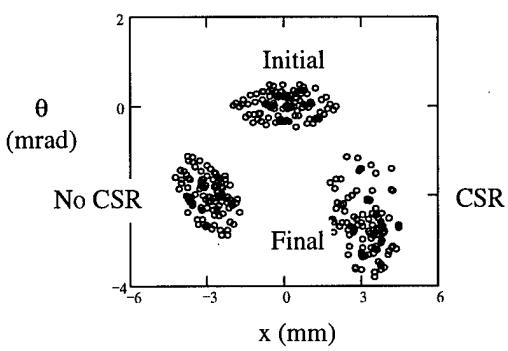

Figure 3. The initial and final transverse phase space distributions, with and without CSR, when the microbunch is compressed. The distributions are offset for display only.

A comparison of these emittance calculations with experimental data [9] is shown in Figure 5. The effect of space charge emittance growth is obtained using PARMELA with its starting emittance normalized to the uncompressed peak current of 50 amperes. The PARMELA calculation of the emittance growth during compression falls short of the compressed data point. However, adding the computed CSR emittance growth in quadrature with the PARMELA calculation results in good agreement with the data.

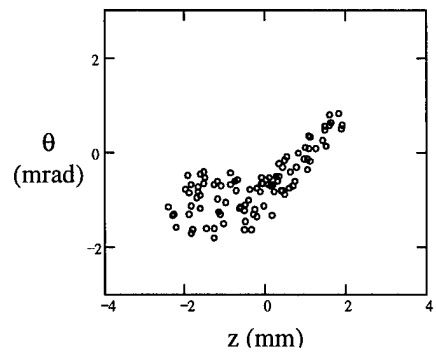

Figure 4. The correlation of divergence with longitudinal position at the exit of the chicane due to CSR.

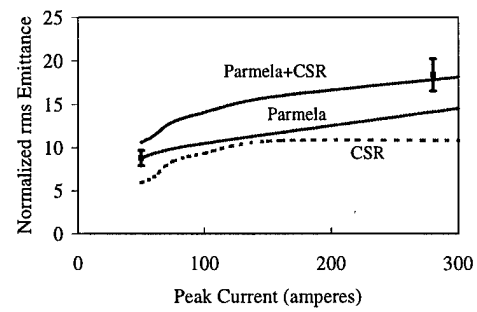

Figure 5. Comparison of experiment with PARMELA and CSR emittance growth calculations.

5 ACKNOWLEDGEMENTS

The authors thank C. Parazzoli at Boeing for the PARMELA calculations.

REFERENCES

[1] J.S. Nodvick and D.S. Saxon, Phys. Rev. 96, 180 (1954).

[2] T. Nakazato et al. Phys. Rev. Lett. **63**, 1245 (1989).

[3] Microbunches Workshop, E.B. Blum, M Deines and J.B. Murphy, AIP Conf. Proc. No. 367 (1996).

[4] B.E. Carlsten and T.O. Raubenheimer, Phys. Rev. E, **51**, 1453 (1995).

[5] Y.S. Derbenev et al. DESY TESLA-FEL Technical note 95-05 (1995).

[6] R.L.Warnock and P.Morton, Part. Accel. **25**, 113 (1990).

[7] D.H. Dowell et al, Proc. 1995 IEEE Particle Accelerator Conf. P. 992.

[8] D.C. Carey, K.L. Brown and F. Rothacker, SLAC-R-95-462.

[9] D.H. Dowell et al., "Results of the Boeing Pulse Compression and Energy Recovery Experiments", To be published in Nuclear Instr and Meth.

[10] D.H. Dowell et al. "Compensation of Bend-Plane Emittance Growth in Pulse Compressors", Contribution to these proceedings.

FREE ENERGY RELAXATION IN A DRIFT-TUBE LINAC

Nathan A. Brown, George H. Gillespie and Barrey W. Hill
G. H. Gillespie Associates, Inc., PO Box 2961, Del Mar, CA 92014

Abstract

A beam that is injected in a state that is not in equilibrium has free energy that can be thermalized as the density profile relaxes. Relaxation will also occur as the beam evolves through a channel with changes in energy, size and shape, and this relaxation will affect the subsequent beam behavior in the channel. PARMILA is used to simulate various input distributions for beams in a drift-tube linear accelerator. Properties of the final beam state, including size, shape, emittance and the presence of halo particles, are found for each of the initial phase space distributions.

1 INTRODUCTION

Charged particle beams are normally injected into focusing and accelerating channels with distributions in phase space that are not in thermal equilibrium [1, 2]. Any beam that is not in equilibrium has free energy that can be thermalized as relaxation occurs. Mismatch, misalignments and nonequilibrium density profiles are well-known sources of free energy that can be thermalized during relaxation [3]. The changes in the external forces that a beam experiences as it evolves through a series of lenses and accelerating sections also affect the relaxation process and can prevent the phase space distribution from coming close to equilibrium. Knowledge of the emittance growth resulting from the relaxation of free energy, and the rate at which it occurs, is important for applications requiring high intensity, low emittance beams, such as high energy colliders, spallation neutron sources, tritium production, radioactive waste transmutation, free electron lasers, and heavy ion inertial fusion.

Emittance growth resulting from space charge forces has been found analytically and with simulations for continuous beams [3-5] and for bunched beams [6]. Measurements of emittance growth from free energy have also been found to agree with simulations for a continuous beam in a periodic solenoid channel [7]. All of these cases considered beams with continuous focusing or with smooth periodic focusing.

PARMILA is used here to simulate a bunched proton beam through the first few cells of a drift-tube linear accelerator (DTL). Comparison is made between the final beam properties, including size, shape, emittance and the presence of a halo, for different initial distributions. The beam in each case experiences variations in eccentricity and size by factors of approximately two, so that in each case the relaxation of free energy, which affects the beam size and emittance, has subsequent effect on the evolution of the beam through the channel. Similar initial distributions, therefore, can have significantly different final beam sizes, shapes, density profiles and emittances.

The beam distributions are presented here with a new analysis tool in the graphic user interface (GUI) for PARMILA. This tool and the GUI are described in Section 2. In Section 3, variations in the final beam properties found with PARMILA are compared for several initial distributions, and comparison is made with previous results.

2 THE GRAPHIC USER INTERFACE

A graphic user interface has been developed for use with PARMILA in the Shell for Particle Accelerator Related Codes (S.P.A.R.C.) [8, 9]. Graphical icons represent beamline elements, and channel setup is accomplished by selecting and dragging the icons from a palette bar. Beam and channel parameters are controlled in an intuitive way through multi-pane windows connected with each element, so that a beamline can be set up and run with no knowledge of how to write a PARMILA input file.

As part of this GUI, we are developing an analysis tool that shows three-dimensional color plots of the particle distributions at any point along the channel. Each particle is represented by a point or a small sphere. These distributions can be rotated freely to allow the user to visually analyze the particle distributions in three dimensions. Figure 1 shows the final distribution for a bunched beam simulated with PARMILA through ten cells of a DTL. Changes in the density profiles, the shape and size of the beam, and the evolution of halo particles can be easily seen with this tool in conjunction with the GUI.

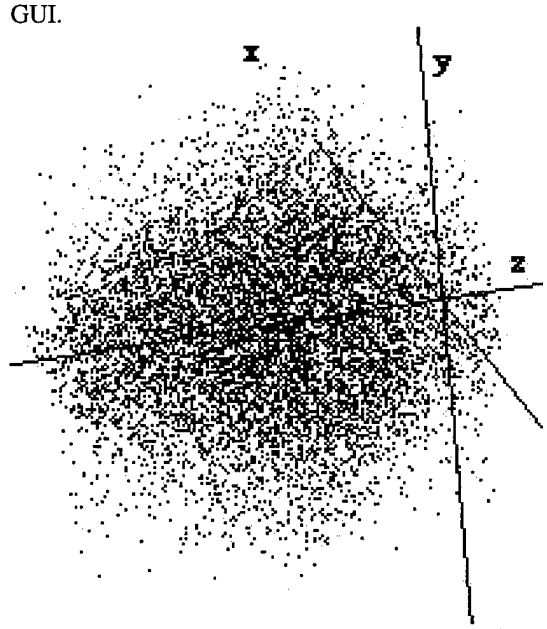

Figure 1: Final distribution of an initially uniform (ellipsoidal) beam after passing through ten cells of a DTL. Transverse halo particles are distributed approximately uniformly along the longitudinal direction.

0-7803-4376-X/98/$10.00 © 1998 IEEE

3 SIMULATION RESULTS

Six different initial density profiles were simulated with PARMILA in a 200 MHz DTL. The initial matched beam state has an average radius of 2.7 mm and a half-length of 5.4 mm. The initial beam was matched into the first lens of the DTL with variations in the transverse envelopes of +20% from the average in x and -20% from the average in y. The phase angle was -40° in the rf wave, and the initial beam had a phase half-width of about 20°. At the position of the final distribution, the beam has traveled through ten cells of the DTL from 2 MeV to 3 MeV, in a time of about one plasma period. In this distance, significant density profile relaxation and emittance growth has occurred in every case.

The six initial distributions were uniform ellipsoidal, Gaussian truncated at three standard deviations, Gaussian truncated at four standard deviations, parabolic, conical and a grid distribution. All of these distributions will experience different changes in self-potential energy and thermal energy if they are allowed to relax towards a thermal equilibrium density profile; in this channel, they experienced changes in shape and size along each dimension by factors of approximately two as the relaxation of free energy occurred. As a result of this, the beam evolution through the channel is different in every case. The final beam states have different density profiles, and they also developed different sizes and shapes as they reacted to the external focusing forces of the DTL. Three final beam profiles are shown in Figures 1, 2 and 3. All six initial distributions are included in Tables 1 and 2, which show the fractional changes in the emittance and rms size for each beam in the x, y and z directions.

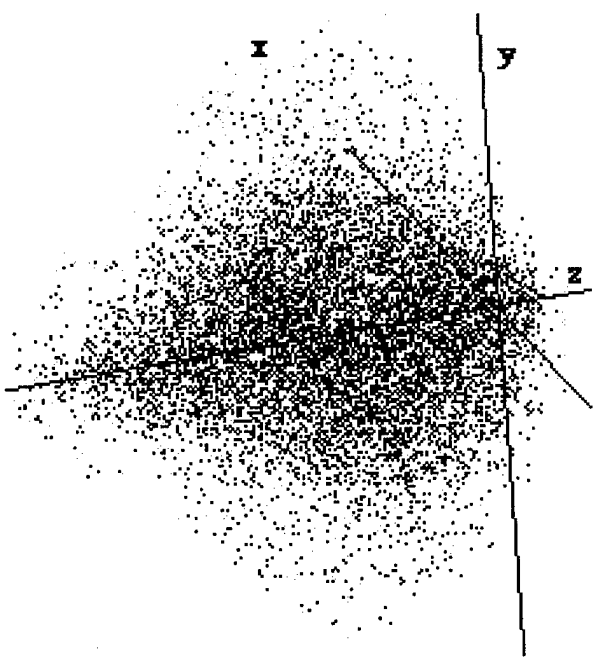

Figure 2: Final distribution of an initially Gaussian beam after passing through ten cells of a DTL. The halo particles are separated along the three focusing directions.

Figures 1, 2 and 3 show the final distributions in three dimensions for three different initial beam distributions in the same channel. In Figure 1 the initial density profile is uniform. Figure 2 shows a distribution for a beam that initially has a Gaussian density profile that is truncated at four rms radii, and Figure 3 corresponds to an initially parabolic profile.

The three-dimensional beam distribution in Figure 1 has a slight longitudinal tail in the trailing end of the bunch. This is also present in the profiles of Figures 2 and 3. This feature is also present in the thermal equilibrium distribution for a bunched beam with external focusing that is linear in the transverse direction and nonlinear in the longitudinal direction due to the shape of the effective focusing potential of the rf bucket [10]. The beams that start with a longitudinal tail (the initially Gaussian and parabolic profiles of Figures 2 and 3) have a more pronounced longitudinal tail in the trailing end than the initially uniform ellipsoidal beam.

The distribution shown in Figure 2 has a separation of the halo particles along the three focusing axes, and also has the largest emittance growth of the three shown, probably due to the initial state with particles at large distances from the beam center. The largest relative transverse halo of the three initial distributions shown is in the initially parabolic beam in Figure 3.

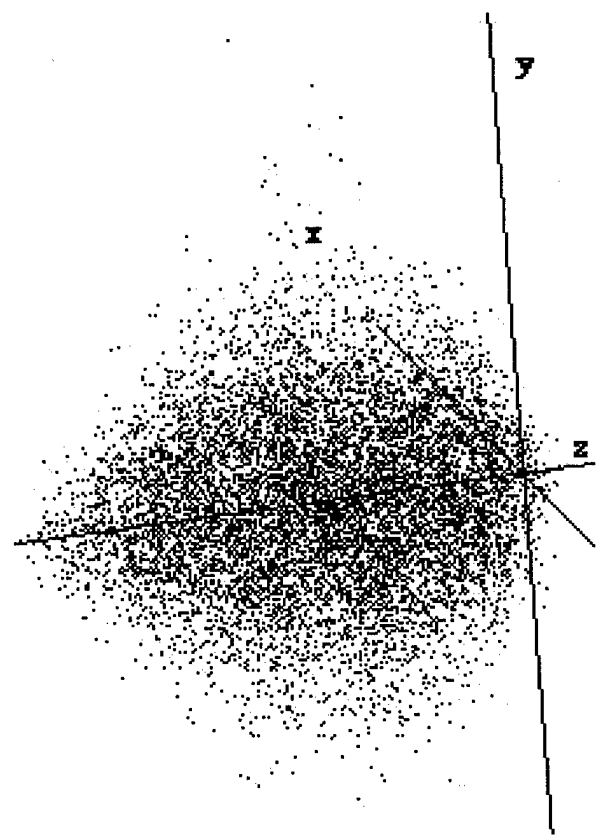

Figure 3: Final distribution of an initially parabolic beam after passing through ten cells of a DTL. The transverse halo near the longitudinal center of the beam is the largest of the three distributions shown, in comparison with the extent of the beam core.

Table 1: Ratios of final to initial rms emittance in the x, y, z directions at the end of ten cells in the DTL.

Initial State	$\varepsilon_{xf}/\varepsilon_{xi}$	$\varepsilon_{yf}/\varepsilon_{yi}$	$\varepsilon_{zf}/\varepsilon_{zi}$
Uniform	1.3	1.3	2.9
Gaussian3	2.2	2.4	4.1
Gaussian4	3.5	1.7	5.3
Parabolic	1.2	1.6	3.3
Conical	1.7	1.7	2.8
Grid	1.4	1.7	3.6

Table 1 shows the fractional changes in emittance for each of six initial distributions. The largest emittance increase in every case occurred along the longitudinal direction. This was probably due to nonlinearities in the longitudinal focusing, which are evident from the three-dimensional particle distributions of Figures 1, 2 and 3.

Table 2 shows the fractional changes in rms beam size for each of the six initial distributions. The initial beam entered the first quadrupole lens of the DTL with 20% variations in the x and y beam envelopes from the average beam envelope. The beam in each case was rms-matched into the DTL, and the relaxation of free energy then led to variations in the size of the oscillations in every direction and also to mismatch. The final beam state in every case had a larger fractional difference between the x and y rms sizes after traveling through ten cells. The largest fractional transverse emittance increases, however, varied in direction from one initial distribution to the other. Only for the intially Gaussian beam truncated at four standard deviations was the fractional x emittance increase larger than in y; for the others either the fractional y emittance increase was larger or there was not a significant difference.

4 CONCLUSION

Six different initial beam distributions were simulated with PARMILA through ten cells of a DTL. A significant amount of emittance growth from free energy was found to occur in the time of about one plasma period in all six cases. Variations in the final beam size between the different initial distributions were also found, showing the effects of the conversion of free energy on the evolution of the beam through the periodic channel.

In each of six cases, fractional changes in the rms emittance and beam size were shown in x, y and z. Although each beam started rms-matched in the same channel, the relaxation of free energy from the initial distributions affected the subsequent evolution so that there were large variations in the final rms beam properties.

The final three-dimensional beam distributions were shown for three cases, revealing variations in the beam distribution, including the presence of longitudinal tails and the extent and positions of halo particles.

Table 2: Ratios of final to initial rms beam size in x, y and z directions at the end of ten cells in the DTL. The initial beam size was about 45% larger in x than in the y direction for matching into the first lens of the DTL.

Initial State	x_{mf}/x_{mi}	y_{mf}/y_{mi}	z_{mf}/z_{mi}
Uniform	1.2	1.1	1.5
Gaussian3	1.7	1.2	1.8
Gaussian4	2.2	1.0	1.6
Parabolic	1.5	1.1	1.7
Conical	1.7	1.3	1.8
Grid	0.9	0.7	3.5

A new graphical visualization tool for the PARMILA GUI has been described and used, and it has proven valuable in analyzing the beam distributions.

5 REFERENCES

[1] M. Reiser and N. Brown, "Thermal Distribution of Relativistic Particle Beams with Space Charge," Phys. Rev. Lett. 71, 18, p2911 (1993).

[2] N. Brown and M. Reiser, "Thermal Equilibrium of Bunched Charged Particle Beams," Phys. Plasmas 2, 3, p965 (1995).

[3] M. Reiser, "Free energy and emittance growth in nonstationary charged particle beams," J. Appl. Phys. 70, 4, 1919 (1991).

[4] P. Lapostolle, "Possible Emittance Increase Through Filimentation due to Space Charge in Continuous Beams," IEEE Transactions on Nuclear Science, NS 18, p1101.

[5] T. Wangler, "Emittance Growth from Space Charge Forces," in High Brightness Beams for Advanced Accelerator Applications, College Park, MD, p21 (1991).

[6] I. Hofmann and J. Struckmeier, "Generalized Three Dimensional Equations for the Emittance and Field Energy of High-Current Beams in Periodic Focusing Structures," Part. Accel. 21, p69 (1987).

[7] I. Haber, D. Kehne, M. Reiser and H. Rudd, "Experimental, theoretical, and numerical investigation of the homogenization of density nonuniformities in the periodic transport if a space- charge dominated beam," Phys. Rev. A44, p5194 (1991).

[8] G. Gillespie, B. Hill and J. Gillespie, "Making PARMILA Easy to use - *Really Easy to Use!*," Proceedings of the 10th International Conference on High Power Particle Beams, San Diego, 1994, p626.

[9] G. Gillespie and B. Hill, "An Interactive Graphical User Interface for the Linac Beam Dynamics Code PARMILA," Proceedings of the 1994 International Linac Conference, Tsukuba, Japan, p517.

[10] N. Brown and M. Reiser, "Longitudinal current losses in rf linear accelerators," Phys. Rev. E54, p4188 (1996).

HIGH CURRENT BEAM DYNAMICS FOR THE UPGRADED UNILAC

W. Barth, L. Dahl, J. Glatz, J. Klabunde, U. Ratzinger, GSI Darmstadt, Germany and
A. Schempp, University of Frankfurt, Germany

Abstract

The performance of the UNILAC as a high cur-rent, heavy ion injector into the SIS has been in-vestigated including the future RFQ-IH-type pre-stripper accelerator. The beam dynamics are in-fluenced by space charge forces in all sections of the accelerator, most severely after the the strippers at 1.4 MeV/u and 11.4 Mev/u. In previous studies a strong dependence of emittance growth on the initial intensity distribution and the envelope forming of the beam had been found. In order to obtain reliable beam parameters and to determine the consequences for the injection into the SIS, the beam behaviour was simulated through the complete system down to the SIS starting with Gaussian particle distributions after the ion source.

1 INTRODUCTION

Within the GSI high intensity progamme [1] the present Wideroe-DTL will be replaced by an RFQ [2] and two IH-structures [3] designed for the acceleration of high current, low charge state beams.

In Fig. 1 the future structure of the UNILAC is shown with some of the design parameters. The space charge forces, indicated by normalized numbers, are high in all sections due to the charge state jumps in the two strippers. The Alvarez DTL and the transfer channel to the SIS were originally not intended for high current operation. Previous studies of beam behaviour in the individual sections using artificial particle distributions have indicated tolerable emittance growth; however, the realistic transformation of a beam through the complete system could be done only recently.

2 UNILAC AND BEAM TRANSPORT LINES

It is under discussion to replace the existing LEBT line, equipped with a 77.5° bending magnet for mass analysis, by an alternative [4] which uses two 60° magnets with intermediate focus and dispersion compensation. These beam lines are

BEAM TRANSPORT SYSTEM BEFORE RFQ Dipole Magnets	Existing LEBT 77.5°	Optional LEBT 2 x 60°	Without LEBT
ION SOURCE			
Current	32 mA	20 mA	
90% rms-Emittance (norm)	0.010μm	0.010μm	
LEBT			
Space Charge Compensation	> 97%	> 70%	
SC-compensated Current	1 mA	6 mA	
RFQ INPUT			
Current	28 mA	20 mA	17 mA
90% rms-Emittance (norm)	0.11μm	0.043μm	0.03μm
Beam in RFQ-Acceptance	47%	75%	88%
RFQ OUTPUT (15mA)			
90% rms-Emittance (norm)	0.11μm	0.08μm	.056μm

Table 1: High current parameters for LEBT lines used in the simulations with uranium ions

very different in emittance growth, current limit and beam loss (Table 1). In order to achieve the design RFQ output current of 15emA U^{4+} also different requirements must be imposed on ion source current and space charge compensation.

The high current beam transport through the gas stripper section was investigated [5] with respect to various types of particle distributions; the advantage of

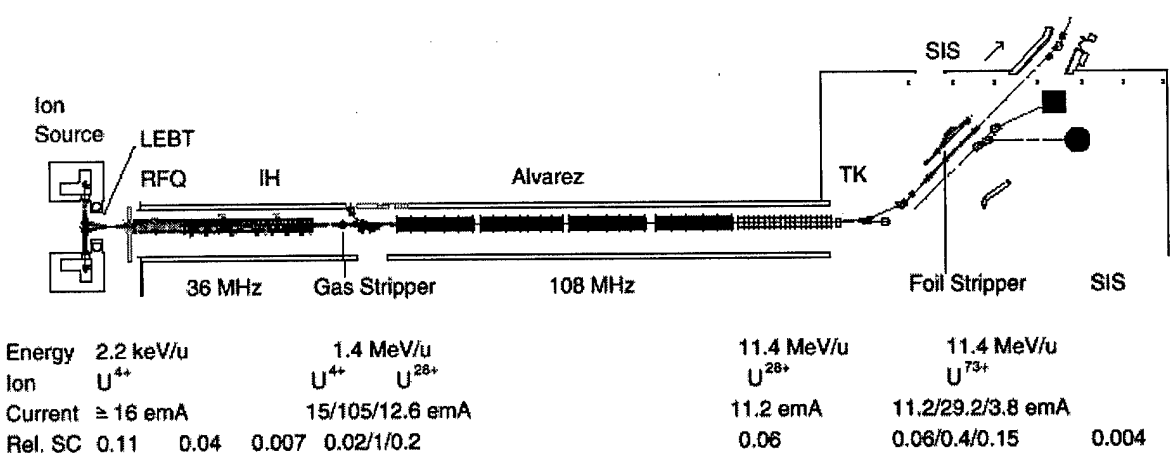

Figure 1: Unilac plan view and high current beam parameters (SC: space charge force)

flat distributions was shown. It was found that even small changes of the beam envelopes may affect the emittance growth in the transverse phase planes. This section will be modified in order to improve the longitudinal matching to the Alvarez Linac.

In the Alvarez DTL the large transverse accep-tance of up to 10μm permits the low current operation at phase advances between 10° and 100° in a time share mode for different ions [6]. An already expanded beam with an rms emittance of 0.2μm may fill the drift tube aperture even at 50°. The possibilities of time share operation will be restricted.

A foil stripper in the transfer line is used to achieve high SIS output energies. In high current operation the foil must be protected against dam-age and the beam should be saved from emittance growth by angular scattering and energy stragg-ling. The fast beam deflection system [7], now combined with a vertical charge separator, is included in the beam simulations. With a narrow upright beam spot on the foil the emittance growth in the horizontal plane will be minimized, while an increase of the vertical emittance is tolerated in view of the acceptance of the synchrotron.

3 BEAM DYNAMICS SIMULATION

3.1 Simulation Procedure

For the simulation of beam dynamics in the different accelerator sections the PIC-codes PARMT, PARMTEQ, PARMILA, LORAS were used; the particle transfers between the codes had to be established. Extensions to the codes were implemented to treat stripper effects, multi-charge beam dynamics and emittance evaluations. The ion optical parameters were determined in advance using an envelope code (MIRKO); even so, iterative readjustments of matching lenses had to be made.

3.2 Input Beams

Three particle simulation runs will be compared. Basis of comparison are beams of 15emA U^{4+} behind the RFQ. They were obtained from a Gaussian particle distribution which was either injected directly into the RFQ or was first transformed through the existing or the optional LEBT lines using the parameters of Table 1. From the entrance of the RFQ on, the beams were transformed through the UNILAC and transfer line without any adjustments.

3.3 Emittance Growth

The development of 90% rms emittances is shown in Fig. 2. Emittance growth is obvious in the IH-DTL in both transverse planes, between gas stripper and charge separation predominantly horizontally - resulting from specific beam envel-opes, in the foil stripper only in the vertical plane. Disregarding the foil stripper, only slight emittance growth is seen after the gas stripper section. Growth factors from RFQ to SIS are about 6.5 in the horizontal and 9 in the vertical plane.

The longitudinal emittance, though growing by a factor of 15 can be shaped to satisfy the require-ment of $dp/p<10^{-3}$ at the SIS.

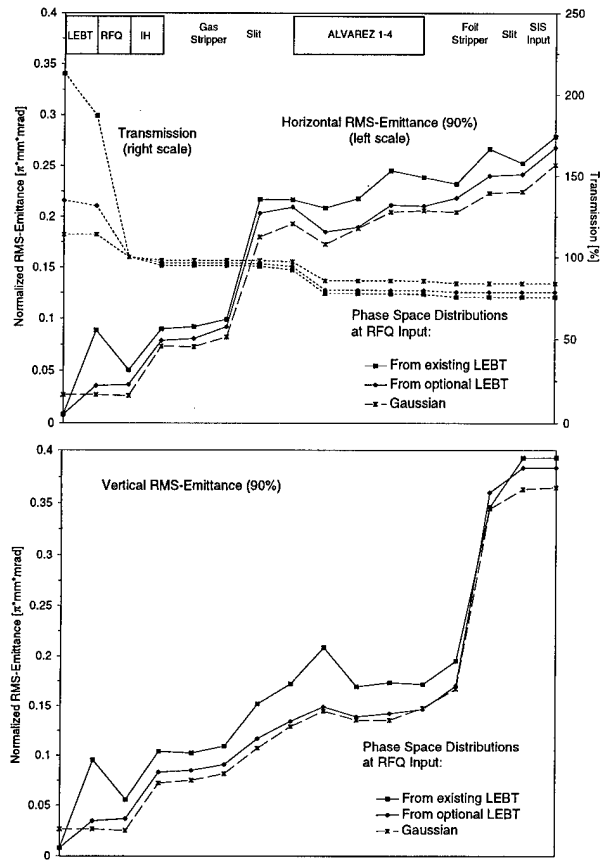

Figure: 2 Transverse rms emittances along the UNILAC for different input beams; Transmission (normalized to 100% at the RFQ exit)

3.4 Acceptance of SIS

The final full beam emittances do not fit into the acceptance of the SIS. The curves of Fig. 3 show the relations between partial beam intensity and occupied emittance. The vertical acceptance of the SIS (2.4μm) corresponds to the 70%-level of the design intensity and the horizontal one (0.8μm) to the 55%-level. The final acceptance numbers from the beam simulations are, referring to the design beam of 3.8emA U^{73+}:

beam from existing LEBT 44%
beam from optional LEBT 47%
beam from RFQ input 52%

Due to the emittance growth experienced by the beams the results do not depend significantly on the input particle distribution.

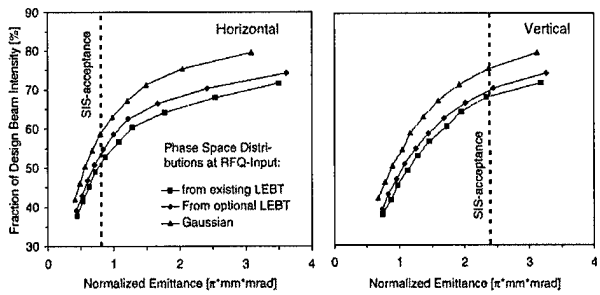

Figure: 3 Beam intensity within partial tansverse emittance at injection into the SIS. Intensity is normalized to the design current of 3.8emA U^{73+}

4 CONCLUSION

In the upgraded UNILAC the intended high currents will be delivered by the RFQ even from realistic, distorted input distributions, if the input current density is sufficiently increased. The required (LEBT-dependent) ion source currents are in a realistic regime (and have been produced with uranium).

The particle distributions obtained after the RFQ may be considered as realistic: after having lost their initially very different properties in the course of space charge dominated transformation through the RFQ they behave nearly identically furtheron.

From the consistent dynamics simulation of such a realistic particle ensemble over 250m of accel-eration and transport can be concluded that the transformation of the real beam through the UNILAC and transfer line will be possible without prohibiting beam losses.

However, emittance growth by space charge forces is of concern in all sections and emittance growth arising in the foil stripper can be minimized only in one phase space plane.

The final transverse emittances exceed the acceptance of the SIS. About 50% of the design beam intensity can be injected into 25 turns during 100μs, giving $2 \cdot 10^{10}$ particles of U^{73+} per pulse in the ring. This number corresponds to the space charge limit obtained from recent machine studies.

For ions lighter than uranium the space charge conditions are relaxed and a higher fraction of the beam intensity will be acceptable.

Some reduction of emittance growth may be expected from a redesign of the gas stripper section.

REFERENCES

[1] `Beam Intensity Upgrade of the SIS Accelerator Facility´, GSI Report, GSI - 95 - 05, 1995

[2] A.Schempp, `Design of Compact RFQs´, Proc. of the 18th Intern. Linac Conf., p. 53, Geneva, 1996

[3] U. Ratzinger, `The New GSI Prestripper Linac for High Current Heavy Ion Beams´, Proc. of the 18th Intern. Linac Conf., p. 288, Geneva, 1996

[4] W. Barth, L. Dahl, J. Klabunde, C. Muehle, P. Spaedtke, `High - Intensity Low Energy Beam Transport Design Studies for the New Linac of the UNILAC´, Proc. of the 18th Intern. Linac Conf., p. 134, Geneva, 1996

[5] W. Barth, J. Glatz, J. Klabunde, U. Ratzinger, `Space Charge Dominated Beam Transport in the 1.4 MeV/u - UNILAC - Stripper Section´, Proc. of the 18th Intern. Linac Conf., p. 131, Geneva, 1996

[6] N. Angert, J. Glatz, L. Dahl, J. Klabunde, H. Schulte, P. Spaedtke, `Two Ion Time Share Operation of the UNILAC´, Proc. of the 1994 Intern. Linac Conf., p. 707, Tsukuba, 1994

[7] J. Glatz, B. Langenbeck,`A High Duty Foil Stripper System in the Injection Line to the SIS´, Proc. of the 5th Europ. Particle Accelerator Conf., p. 2406, Sitges,1996

CONSIDERATIONS ON PARTICLE DYNAMICS IN A HEAVY ION DTL*

Horst Deitinghoff and Giovanni Parisi
Institut für Angewandte Physik, Frankfurt University, Robert-Mayer-Str. 2-4, D-60054 Frankfurt

Abstract

In heavy ion inertial fusion scenarios presently discussed, a long linac is proposed for the acceleration of intense beams of singly charged heavy ions, e.g. Bi^+ or Pt^+. A particle dynamics layout of a conventional DTL has been attempted with respect to low emittance growth at high transmission for beam currents up to 400 mA. Design aspects and first results of single particle beam dynamics calculations will be presented.

1 LAYOUT OF THE LINAC

In the HIDIF (Heavy Ion Driven Ignition Facility) scenario [1] the formation and acceleration of an intense $^{209}Bi^+$ ion beam (400 mA current) with a transverse emittance of 1.2 π mm mrad (full, normalized) is required for injection into some following storage rings at an energy of 50 MeV/u. The beams from 8 or 16 identical ion sources have to be captured, accelerated and merged together in successive funnelling steps, to produce such a high current.

The beam behaviour has been investigated in a 200 MHz Alvarez DTL taking some advantage from a preliminary study performed in Frankfurt in the framework of INTAS 94-1713 [2].

The same focusing scheme of Ref. [3] was adopted: each period is formed by five quadrupoles of the same sign followed by five quadrupoles of the opposite one (FFFFFDDDDD) in order to limit the maximum magnetic gradient required and to get a smoother focusing. The strength of the quadrupoles decreases linearly with the distance, while their length increases, the product being kept constant. The maximum pole tip field is 1.15 Tesla at a bore hole radius of 1.6 cm.

The electrical field amplitude was set to 3.0 MV/m, leading to a calculated shunt impedance of 26 MΩ/m, which is a reasonable value. The input synchronous phase, its slope along the linac and the injection energy have been varied to study their influence on the beam behaviour. The generation of the linac for the particle dynamics calculations was done with the computer programs CLAS and GENLIN; beam dynamics calculations were done with MAPRO.

2 RESULTS

At first, an injection energy of 4.73 MeV/u was chosen (β= 10%), with an injection synchronous phase linearly decreasing from –40° to –21° The input emittance was set to 0.5 π mm mrad (full, normalized) in both transverse planes.

The transverse input parameters were chosen in the middle of the third quadrupole of a same sign, for better matching conditions ($\alpha_x = \alpha_y = 0$); betatron amplitudes are β_x= 13.0 m, β_y= 6.5 m. The bunch full length is 54°; the momentum spread is dp/p= 0.23%. From the above parameters, input emittances were generated using a waterbag random distribution.

For a first check, due to limited storage capacity, only 1000 particles were tracked on the first 900 cells of the linac. Especially in the longitudinal phase space, filamentation occurred rather soon, resulting in a not acceptable emittance growth. Keeping the beam input parameters, the electrical field strength and phase fixed, only the choice of a higher input energy was possible to enlarge the longitudinal acceptance.

In a next step, the injection energy was increased to 10 MeV/u, and synchronous phase is now decreasing exponentially rather than linearly to gain acceleration rate. The input transverse emittance was raised to 0.75 π mm mrad, giving still some space for emittance increase due to errors and misalignments.

The linac is made of 9260 cells (14.5% < β < 31.4%), corresponding to a length of about 3 km. A first check with 1000 particles, tracked all along the linac, gave less filamentation and better symmetry, with rms emittance growth at the output of $\Delta\varepsilon_x/\varepsilon_x$= 4%, $\Delta\varepsilon_y/\varepsilon_y$= 8%, $\Delta\varepsilon_z/\varepsilon_z$= 15%.

The following table summarizes the linac and the beam parameters.

Table 1

Mass number	209 (Bi^+)
Frequency	200.0 MHz
Mode	2π
Current	400 mA
Injection energy	10.0 MeV/u
Electric field	3.0 MV/m
Initial phase	–40.0°
Final phase	–21.0°
Final energy	50.0 MeV/u
Number of cells	9260
Total length	3192 m
Total energy gain	40.0 MeV/u
Shunt impedance	26 MΩ/m

* Work supported by BMBF.

Then the number of particles was increased to 5000, to improve space charge calculations; unfortunately this is quite time consuming. Figure 1 shows the development of the emittance along the first half of the DTL for 5000 particles (—), compared to the case of 1000 particles (- - -). Figure 2 shows a good emittance shape but also indicates some halo formation.

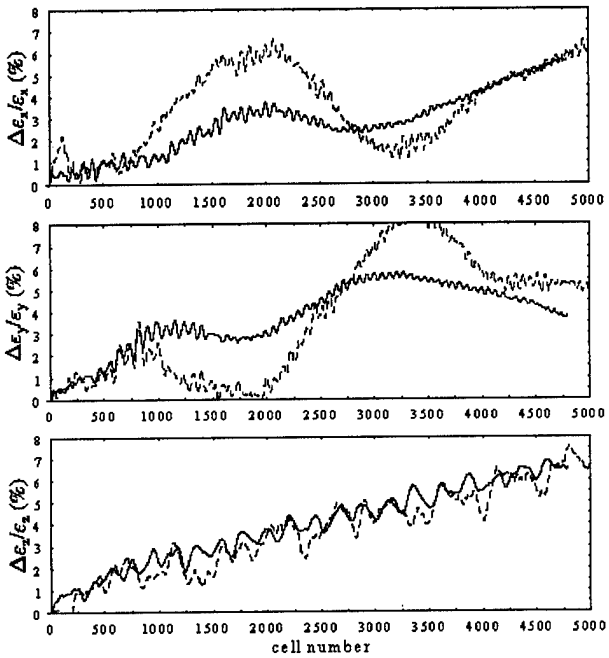

Figure 1: rms emittance along the linac (1000/5000 particles).

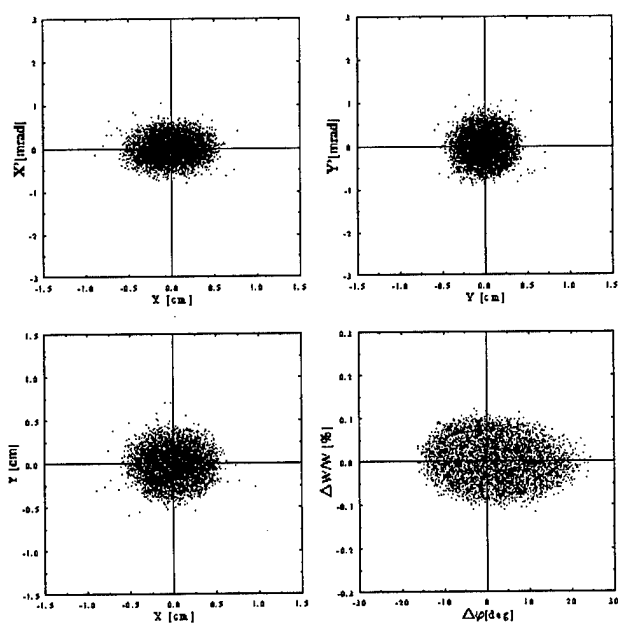

Figure 2: output emittances after 4800 cells (5000 particles)

This can also be seen in Figure 3, in which the total emittance is plotted for 100%, 99.9%, 99% and 95% of the particles, for 5000 particles, for the section from cell number 2000 to cell number 2400, as an example.

Only a few particles contribute to the emittance growth: the emittances for 99% are already rather smooth. A big contribution comes from only a small fraction of the beam. The ratio between full and rms emittance is always smaller than 10.

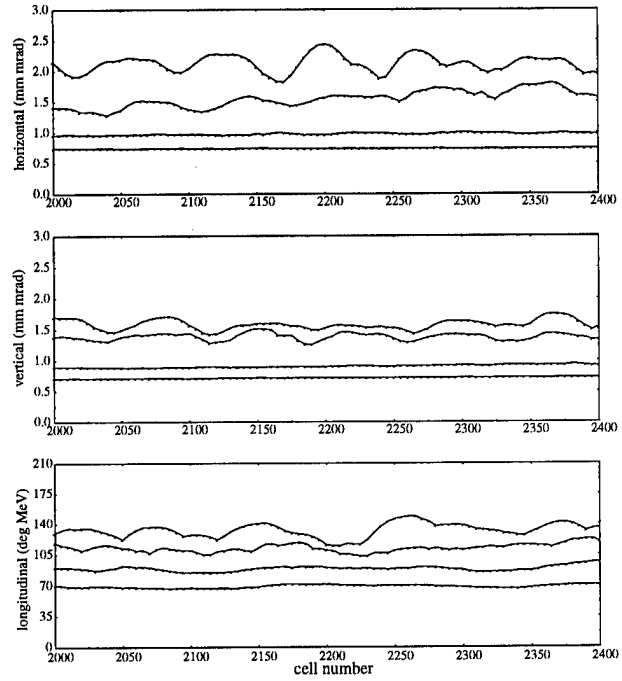

Figure 3: total emittance on a part of linac (5000 particles).

3 CONCLUSIONS

Preliminary results show that a 400 mA DTL, accelerating heavy ions from 10 to 50 MeV/u is feasible, with 100% transmission and a small rms emittance growth. The calculated shunt impedance is 26 MΩ/m; the total length is about 3 km.

These results can be considered as a starting point for further optimization (e.g. fine tuning of the quadrupole gradients) and for the design of a realistic structure.

4 ACKNOWLEDGEMENTS

The authors want to thank M. Pabst (FZ-Jülich) for his tutorial in using the computer codes CLAS, GENLIN and MAPRO, and K. Bongardt (FZ-Jülich) for valuable discussions on beam dynamics design aspects.

The computations were done at the Hochschulrechenzentrum of the University of Frankfurt am Main.

5 REFERENCES

[1] I. Hofmann, Proc. EPAC'96, Sitges, Spain, June 1996, Inst. of Physics, p. 255.

[2] D.G. Koshkarev, I.L. Korenev, L.A. Yudin, Proc. Linac'96, CERN 96-07 Geneva, August 1996, p. 423.

[3] H. Deitinghoff, M. Pabst, G. Parisi, A. Sauer, Proc. Linac'96, CERN 96-07 Geneva, August 1996, p. 62.

BUNCH SPACE CHARGE LIMITS IN AN RTM*

V.I. Shvedunov
Institute of Nuclear Physics, Moscow State University, R-119899 Moscow, Russia
H. Euteneuer, K.-H. Kaiser
Institut fur Kernphysik, J.-Gutenberg Universitaet, D-55099 Mainz, Germany

Abstract

We consider analytically and by computer simulation the limits imposed by space charge forces on the charge per bunch, which can be accelerated in an RTM. For this we took into account ordinary space charge forces and coherent synchrotron radiation forces. We present numbers for space charge limit estimations especially for the MAMI-RTMs.

1 INTRODUCTION

CW RaceTrack Microtrons (RTMs) offer the possibility to get a very low transverse and longitudinal emittance beam with an average current appropriate for nuclear physics experiments. At the same time the peak current at CW operation, even for picosecond bunches, is too low for applications of these machines e.g. as an FEL-driver. Subharmonic, or as an extreme, single bunch RTM operation is a way to get high peak current. However, different instabilities, caused by space charge forces, transient beam loading of the accelerating structure and excitation of transverse parasitic modes can lead to emittance growth and beam blowup. Here we consider analytically and by computer simulation the limits for the charge which can be accelerated in an RTM, imposed by the space charge forces. We present space charge limit estimations especially for the Mainz Microtron (MAMI) RTMs.

2 MANIFESTATION OF THE SPACE CHARGE FORCES IN AN RTM

The cascade of MAMI CW RTMs consists of a 3.5 MeV injector linac and three RTMs, with output energies of 14, 180 and 855 MeV respectively [1,2]. Because of the low accelerating gradient in normal conducting CW linacs and the large number of orbits, the total path length in these accelerators is about, respectively, 90 m, 745 m and 2700 m. So, ordinary space charge forces, decreasing as a square of beam energy, should be taken into account when considering a high bunch charge especially for RTM1 and RTM2. These space charge forces do not change the bunch energy, but lead to an effective emittance growth: directly, owing to their nonlinear character and indirectly by the introduced energy spread. In the latter case a horizontal (bending plane) emittance growth takes place because of the energy change inside and between the 180° end magnets, and a longitudinal effective emittance growth because of the strong nonlinearity of phase oscillations in the RTM. Building a new injection system with appropriate beam energy, specially designed for high space charge operation, it is possible to make the role of ordinary space charge forces negligible, but other types of space charge forces, nearly independent of beam energy, come into play.

These forces are connected with the transverse particle acceleration when moving along the circular orbit in bending magnets. We consider here only the better studied and indirectly experimentally verified [3] longitudinal coherent synchrotron radiation (CSR) [4] force. The RTM with its short electron bunches, small bending radii and large number of orbits presents good conditions for a manifestation of this force. CSR forces change the average bunch energy and introduce a strong nonlinear bunch energy modulation. The average energy change leads to phase oscillations of the bunch as a whole, and energy change within it to a horizontal and effective longitudinal emittance growth.

Estimations based on the formulas given in [5] show, that for RTMs the transverse "centripetal and collective focusing" forces can also play a definite role in emittance growth, but less than the longitudinal CSR force.

3 SPACE CHARGE LIMITS FOR THE ORDINARY SPACE CHARGE FORCES

A rough limit for the bunch charge can be obtained from the consideration of longitudinal phase oscillations in an RTM, mostly sensitive to repulsive space charge forces [6]. The synchronous particle at the center of a longitudinally symmetric bunch is not influenced by these forces. Later particles at the rear of the bunch decrease their energy while those at the head increase it. In this respect space charge forces act on nonsynchronous particles similar to the RTM linac field. To estimate the energy change δE_{sc} per orbit by space charge forces, of a particle with phase deviation $\delta\phi$ from synchronous, we use as a model of the bunch a uniformly charged ellipsoid. In the MAMI RTMs transverse and longitudinal bunch dimensions are close to each other. So for a relativistic beam we have:

$$\delta E_{sc} \approx \frac{3 q_b \pi L_{orb}\, \delta\phi}{\varepsilon_0 \gamma^2 \lambda^2 \delta\phi_{max}^3} [\ln 2\gamma - 1] \ , \qquad (1)$$

* Work supported by DFG (SFB 201)

where q_b - bunch charge, L_{orb} - orbit length, γ - mid of linac relative beam energy, λ - rf wavelength, $\delta\phi_{max}$ - maximum bunch halflength, defining a longitudinal parabolic charge distribution: $\psi_p(\delta\phi)=3[1-(\delta\phi/\delta\phi_{max})^2]/(4\delta\phi_{max})$. Formula (1) is valid under the assumption: $\gamma\lambda\delta\phi_{max}/2\pi\approx\gamma\sigma >> \sigma$, where σ - average beam radius, which is always fulfilled in the cases considered below.

Phase oscillations in the RTM, changing particles position within the bunch, decrease the energy spread caused by space charge forces. In linear approximation these oscillations are stable for the bunch charge less then [6]:

$$q_b^{\lim} \approx \frac{4\varepsilon_0\lambda^2\gamma^2\delta\phi_{max}^3\Delta E_s}{3\pi e L_{orb}\left[\ln 2\gamma - 1\right]}\xi \text{ , with} \tag{2}$$

$$\xi = \frac{1}{2\pi\nu}\left(1 - \frac{\pi\nu\tan\phi_s}{2} + \sqrt{1 + \frac{(\pi\nu\tan\phi_s)^2}{2}}\right) \tag{2a}$$

where ΔE_s - synchronous energy gain per orbit, ϕ_s - synchronous phase and ν - increase of orbit length per turn in number of wavelengths (for MAMI $\phi_s=16^0$, $\nu=1$).

In estimations for $q_b^{\lim}$ the parameters of the first orbit should be used, as the influence of space charge forces decreases as $1/\gamma^2$. As can be seen from (2), the most essential factors which can be adjusted for a given RTM-design to increase the charge are bunch length and injection energy.

To get a more accurate estimation for charge per bunch limits and also an estimation of transverse emittance growth due to energy change in the 180^0-magnets, we introduced into the RTMTRACE code [7] space charge calculations based on the model of the uniformely charged 3-D ellipsoid, and made beam dynamics calculations for the injector linac, RTM1 and RTM2. We should stress, that in this model space charge forces are proportional to the particle deviation from the bunch center, and thus directly do not contribute to the effective emittance growth. Effective emittance growth due to nonlinearity of space charge forces depends essentially on the details of the real charge distribution and can be estimated separately [8]. Table I presents limits for the bunch charge estimated with formulas (2,2a) and those calculated with RTMTRACE. In both cases the results were obtained for $\delta\phi_{max}=0.035$ rad$\approx 2^0$. The injector linac was also calculated with the PARMELA code.

As criterion of the limit for bunch charge we considered an abrupt growth of the longitudinal emittance caused by nonlinear oscillations. Below this limit the transverse emittance growth is negligible, though just at the threshold the horizontal emittance grows by a factor of 2-4. Estimations of transverse emittance growth $\Delta\varepsilon_{tr}$ due to the nonlinearity of space charge forces, based on [8], for the first orbits are also given at Table I.

Thus, to avoid effects of ordinary space charge forces at MAMI for a reasonable charge per bunch, say about 100 pC, a new injection system should be built with an energy of at least 30 MeV.

Table I. Injected beam normalized rms transverse and longitudinal emittances used in calculations, transverse emittance growth and limits in pC for bunch charge imposed by ordinary space charge forces.

	ILAC	RTM1	RTM2[c]	RTM2[d]	RTM3
ε_x,μm	0.08	1	1	1.4	-
ε_y,μm	0.08	1	1	1.4	-
ε_L,kV•deg	0.5	0.7	12.5	12.5	-
$\Delta\varepsilon_{tr}$, μm	0.4-1[e]	3	0.8	0.2	
$q_b^{\lim\ a}$	-	2.7	43	150	4000
$q_b^{\lim\ b}$	0.4-1.3	3-4	30-40	100-140	-

[a]Calculated with formulas (2,2a), [b]RTMTRACE
[c),d)] 14 resp. 30 MeV injection, [e]PARMELA

4 EFFECTS OF THE CSR FORCES

The spectrum of synchrotron radiation, including the coherent part, for a bunch of N particles with Gaussian longitudinal distribution, moving in free space in a uniform magnetic field is given by [9,10]:

$$\frac{dW}{dy} = \frac{Nce^2}{6\pi\varepsilon_0 R^2}\gamma^4\varphi(y)\left(1 + (N-1)e^{-\frac{9}{4}(y\frac{\delta_z}{R}\gamma^3)^2}\right) \tag{3}$$

$$\varphi(y) = \frac{9\sqrt{3}}{8\pi}y\int_y^\infty K_{5/3}(x)dx, \quad y = \frac{4\pi R}{3\lambda_r\gamma^3}$$

Here δ_z - ½ rms bunch length, R - bending radius, $K_{5/3}$ - modified Bessel function, λ_r - wavelength of radiation; and as bunch distribution function is supposed:

$$\psi(z) = \frac{1}{\sqrt{2\pi}\delta_z}e^{-\frac{1}{2}\left(\frac{z}{\delta_z}\right)^2} \tag{4}$$

Fig. 1 shows examples of synchrotron radiation spectra calculated for different orbits in RTM2. To have correspondence in bunch length with the ordinary space charge calculations, the parameter δ_z in (4) here and further was chosen such, that parabolic and Gaussian distributions have equal height ($\delta\phi_{max}=2^0$, i.e. $\delta_z\approx 0.36$ mm).

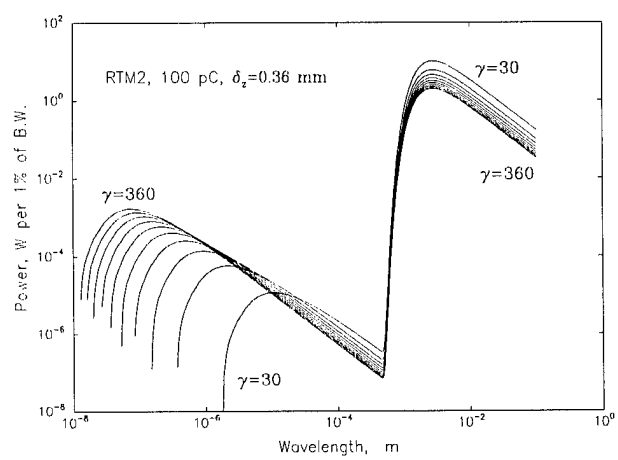

Fig. 1. Spectra of synchrotron radiation for MAMI RTM2 (100 pC, δ_z=0.36 mm bunches).

The approximation of free space, used in (3), is valid for less than 1 mm long bunches moving in a vacuum

chamber with several cm height and several m width at the MAMI RTMs. The position of the maximum of CSR is beam energy independent and determined by bunch length, $\lambda_r \approx 2\pi\delta_z$. The total power radiated by the bunch (4) due to this coherent effect is also energy independent for constant bending radius and is given by [11]:

$$W_{coh} = \frac{\Gamma(5/3) q_b^2 c}{\Gamma(4/3) 8\sqrt[3]{3}\pi\varepsilon_0 \delta_z^{4/3} R^{2/3}} \qquad (5)$$

Because the RTM magnet field is the same for all orbits, the radiated power decreases as $1/\gamma^{2/3}$. For the first orbit of RTM2 with bunch parameters as in Fig.1, $W_{coh} \approx$ 1770 W, while the power of incoherent radiation, $W_{inc} \approx c q_b e \gamma^4 / (6\pi\, \varepsilon_0 R^2)$ is only 2.7 mW. Average particle energy losses by synchrotron radiation per one 180° - magnet, calculated with the relation $\delta E_{sr} = W\pi / fNc$ are shown at Fig. 2 for RTM2 and RTM3.

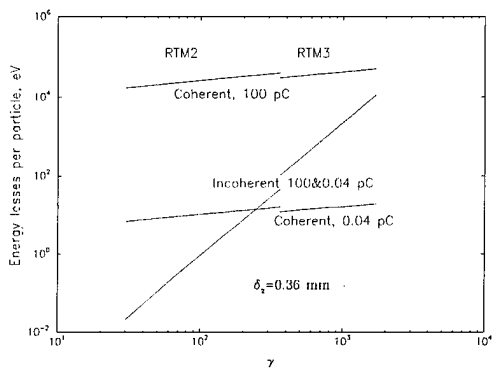

Fig. 2. Average particle energy losses due to coherent and incoherent synchrotron radiation for RTM2 and 3.

The average CSR energy losses are growing as $\gamma^{1/3}$, with a jump from RTM2 to RTM3 because of the magnet field change. These losses for 100 pC charge change from 17 to 40 KeV for RTM2 and from 30 to 50 keV for RTM3, as compared with maximum incoherent radiation losses of about 11 keV. The CSR losses will lead to bunch phase oscillations, which however can be partially compensated by RTM tuning.

More important is the fact that, in contrast to incoherent radiation, CSR energy losses strongly depend on particle position within the bunch. The longitudinal force acting on a particle at position z with respect to the center of a Gaussian bunch is [12]:

$$F_L = \frac{q_b e \chi(p)}{2^{5/3} 3^{1/3} \pi^{3/2} \varepsilon_0 \delta_z^{4/3} R^{2/3}}, \quad p = \frac{z}{\sqrt{2}\delta_z} \qquad (6)$$

$$\chi(p) = \frac{e^{-p^2}}{6} \sum_{n=0}^{\infty} \frac{\Gamma(n/2 - 1/6)}{n!} (2p)^n$$

Fig. 3 shows a comparison of the particle energy change by CSR forces and by ordinary space charge forces for RTM2. Results are given per one orbit: two 180°-magnets + two drifts between them. The distance between RTM2 end magnets is about 5 m, first and last orbit bending radii are about 0.09 m and 1.1 m. One can see, that the maximum energy change by ordinary space charge forces for the existing injection energy (14 MeV, $\gamma \approx 30$) exceed that by CSR forces for all orbits, but for energies above 70 MeV ($\gamma \geq 140$) the CSR forces will play a major role.

The change of the particle energy within the bunch will modify RTM phase oscillations, but now a linear approximation cannot be used to get limits for the bunch charge; this can only be done with a computer simulation which is in progress by introducing into the RTMTRACE code both longitudinal CSR forces and the transverse space charge forces arising in bends.

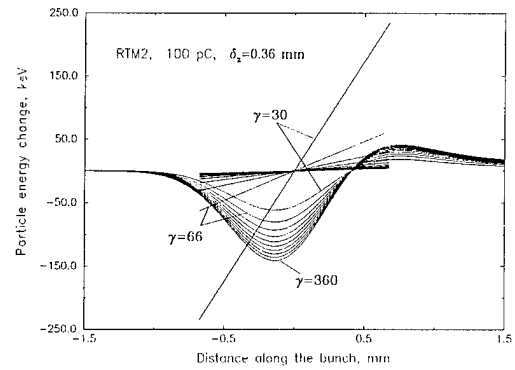

Fig. 3. Particle energy change within bunch, per one RTM2 orbit. Straight lines - ordinary space charge forces, curved - CSR forces.

To get crude numbers for charge per bunch limits by CSR forces we can compare the energy spread introduced by them with that by ordinary forces. The CSR-spread is maximal for the last orbit of RTM3, and is about 1.5 times higher than that from ordinary forces at the first RTM2-orbit with 30 MeV injection. Thus the limit for charge per bunch can be at least 1.5 times lower. - In principle the influence of CSR forces can be essentially reduced by decreasing the vacuum chamber height to the order of the bunch size.

REFERENCES

[1] H. Herminghaus, Proc. LINAC '88, p. 247 (1988)
[2] H. Euteneuer et al., Proc. EPAC '94, p.506 (1994)
[3] T. Nakazato et al, Phys. Rev. Lett.63, p. 1245 (1989
[4] L.I. Shiff, Rev. Sci. Instr.,17, p. 6 (1946)
[5] Ya.S. Derbenev et al, Proc. EPAC '96, p.1347 (1996)
[6] V.I. Shvedunov, Internal Notes MAMI 13/94, 1/95
[7] V.I. Shvedunov, Internal Note MAMI 7/94
[8] M.E. Jones, B.E. Carlsten, Proc. PAC '87, p.1319 (1987)
[9] E.B. Blum et al, NIM A307, p. 569 (1991)
[10] N.P. Klepikov, I.M. Ternov, NIM A308, p. 113 (1991)
[11] J.S. Nodvick, D.S. Saxon, Phys.Rev., 96, p. 180 (1954)
[12] L.V. Iogansen, M.S. Rabinovich, J. Exptl. Theoret. Phys. (USSR) 37, p. 83 (1960)

COMPARATIVE STUDY OF ACCELERATING STRUCTURES PROPOSED FOR HIGH POWER LINAC

A. Kolomiets, S. Yaramishev
Institute for Theoretical and Experimental Physics, Moscow, Russia

Abstract

The basic problems for design of high intensity linear accelerator are providing of high efficiency, reliability and reduction of induced radioactivity in its parts. In spite of very wide studies of processes leading to beam halo formation, there are no reliable methods to evaluate the small particle losses. The possible method based on analysis of beam dynamics simulations are discussed. The particle coordinates stored in output file and representing particle trajectories are considered as sequences of random points and spectral density of correlation function for each sequence is calculated. It allows to study spectral properties of the particle trajectories as well as growth of their amplitudes.

The method has been applied for analysis of beam dynamics simulation carried out for test accelerating - focusing structures which represent a intermediate part of hypothetical high power linac. The obtained results are discussed.

1 INTRODUCTION

The projects of the high power proton linacs have been offered in various laboratories. They are designed practically under the same block scheme with very similar parameters of the beam. The value of the beam current 100 mA and output beam energy ≈1000 MeV are chosen. The proposed projects are the realistic solution of a high power accelerator design. However to build the linac with high average beam power it is necessary to solve a critical problem of the accelerator parts activation. The permissible value of particle losses under conditions of hand - operated service of installation is equal ≈0.2 nA/m and depends on energy of the beam [1]. It means, that in the powerful linac constructed in accordance with the proposed schemes and with the parameters mentioned above, the level of relative losses should be reduced in two order of the magnitude in comparison with achieved in LAMPF linac level.

2 SIMULATION OF BEAM DYNAMICS

Beam of charged particles in accelerating focusing structure in presence of space charge is very complicated system. The numerous analytical and computer investigations have been carried out to study beam dynamics, especially beam halo formation processes [2]. Computer simulations used very widely for study of evolution of charged particle beam taking into account space charge forces. The goal of such simulations is usually determination of beam emittance growth in dependence on beam current and parameters of focusing channel. The evaluation of small particle losses for high power linac requires, however, study of the beam with parameters which do not lead to remarkable emittance growth. In this case calculation of rms emittances do not lead to any reliable methods for quantitative evaluation of halo formation and consequently of particle losses. It is mainly due to limited number of particles used in simulations and absence of suitable methods for analysis of simulation results.

Recently made simulations as well as analytical works showed the great importance of stochastic component of charged particle beam dynamics. According to the general nonlinear mechanics the main mechanism of appearance of stochastic dynamics is local instability of particle motion when it is in vicinity of separatrix of nonlinear resonance [3].

The result of simulation of particles motion is usually file containing their coordinates and velocities, recorded at some discrete time moments. It means that each trajectory is represented in simulation output file as a discrete sequence of the points. It is well known that in the case of linear motion transverse coordinates of the particle determined at the same cross section of focusing periods belongs to sinusoid

$$x_k = A\sin(\mu_0 \tau_k + \theta_0) \qquad (1)$$

here μ_0 is transverse phase advance at absence of space charge, τ - dimensionless time, θ_0 - initial phase.

The appearance of stochastic component of particle motion means that sequence of coordinate calculated for each focusing period can be written as

$$x_k = A\sin[\mu(I)\cdot\tau_k + \theta_0] \pm \Delta x_k \qquad (2)$$

where $\mu(I)$ is depressed phase advance at beam current I and Δx_k is some random value. It can be assumed that local instabilities can be the main source for occurrence of random component in particle trajectory.

The consideration of some specific spectral properties of dynamic system in the transition region from order to chaos is given in [3]. It is based on the study of the spectral densities of the correlation function $R_N(\omega_m)$ calculated for sequence of particle coordinates x_k stored at certain cross section in every cell during the simulation. The spectral density of correlation function is:

0-7803-4376-X/98/$10.00 © 1998 IEEE

$$R_N(\omega_m) = \frac{1}{N} \sum_{-\frac{1}{2}N \le k \le \frac{1}{2}N} R_N(k) e^{-ik\omega_m}$$

$$R_N(k) = \frac{1}{N} \sum_{-\frac{1}{2}N \le j \le \frac{1}{2}N} x_j x_{j+k} \qquad \omega_m = 2\pi \frac{m}{N} \tag{3}$$

In this expression N determines the number of stored points for every particle trajectory.

3 IMPLEMENTATION OF CORRELATION FUNCTION TO SIMULATION

This discussed method was used to analyze simulation results, obtained in ITEP in framework of feasibility study of high power linac. The spectral densities in terms of phase advances were calculated for transverse coordinates of particles obtained in numerous beam dynamics simulations under different conditions. The results of the work contains in [4].

It is follow from [3] that the appearance in the spectra well marked peak $R_N(\omega_m = 0)$ (so called "central peak") is universal spectral property of nonlinear system. It is due to some trajectories pass the vicinity of hyperbolic points of the separatrix for a very long time. It means the appearance of constant term in the correlation function. It is clear that for stable motion of particle in quadrupole channel there is no permanent displacement of the trajectory, so we can consider this effect as jump of particle oscillation amplitude due to local instability occurred during its movement in the focusing structure.

The values $R_N(\omega_m = 0)$ have been calculated for proton trajectories obtained by beam dynamics simulations in two test accelerating structures with different numbers of accelerating gaps per focusing period. Lengths of focusing periods were $2\beta\lambda$ and $4\beta\lambda$. The channels have the parameters given in Table 1.

Table 1

Parameter	$2\beta\lambda$	$4\beta\lambda$
Focusing lattice	FODO	FODO
Number of RF gaps in period	2	4
Number of focusing periods	382	382
Transverse phase advance	60°	60°
Synchronous phase	-90°	-90°
Relative velocity of protons	0.4282	0.4282
RF wave length (m)	1	1

The parameters of the channels have been chosen to model structures proposed for intermediate parts of high power linac. Structure with $2\beta\lambda$ corresponds to conventional DTL, period with $4\beta\lambda$ was chosen to represent structure similar to CCDTL. The synchronous phase -90^0 allows to keep constant average particle energy taking into account defocusing action of RF gaps.

Simulations were carried out in two steps. The truncated gauss distribution with parameters for best matching was used for first run. The output particle distribution was considered as fully matched with channel and has been used as initial for second run. The simulation results obtained by second step have been used for further analysis.

The results of the analysis of these simulation are shown in Fig.1, Fig. 2 and Table 2. In figures are presented distributions of particles on their mean value of displacement from axis. These histograms are plotted for both simulated structures and for beam currents 10, 20, 40 and 100 mA. The distributions can be described by function:

$$f(x) = 4 \cdot \frac{x^2}{\sqrt{\pi}\xi^3} e^{(-\frac{x}{\xi})^2} \tag{4}$$

Distributions of particles on transverse coordinate in our simulation can be approximated by function:

$$g(x) = \frac{2}{\sigma\sqrt{2\pi}} e^{-\frac{1}{2}(\frac{x}{\sigma})^2} \tag{5}$$

It is clear that particle with transverse coordinate x which have got on some focusing period additional random impulse and increased its transverse amplitude on Δx will be lost if

$$x + \Delta x \ge a, \tag{6}$$

where a is focusing channel aperture. Therefore losses of particles per focusing period can be expressed by

$$\int_0^a g(x) \int_{a-x}^a f(z)\, dz\, dx \tag{7}$$

Parameters of particle distributions σ and ξ calculated from simulation results as well as space charge parameter $h \approx 1 - \mu/\mu_0$ are given in Table 2. These parameters have been used to evaluate the relative particle losses per meter for both considered structures. The losses in dependence of channel aperture are given in Fig.3 and Fig.4. As it follows from the figures the particle losses less then 10^{-7} per meter for 100 mA of beam current can be achieved in structure with length of focusing period $2\beta\lambda$ at aperture 0.8 cm. Aperture 1.2 cm is required for the same beam current if focusing period is $4\beta\lambda$.

4 CONCLUSION

The method for evaluation of small particle losses in linac using spectral densities of correlation function is proposed. It has been applied to comparison of structures with different focusing periods, proposed as intermediate part of high power linac. The first results show that the method can be useful for calculation of small particle losses taking into account different perturbation factors.

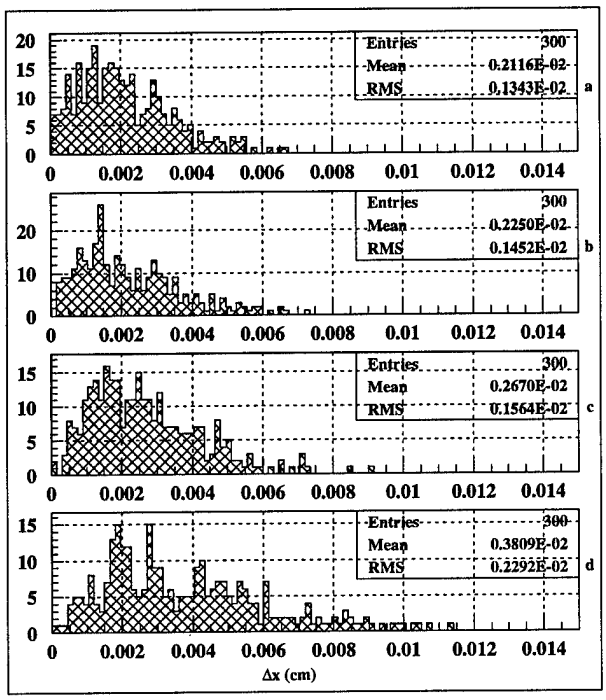

Fig. 1. Particle distributions on Δx for structure with focusing period $2\beta\lambda$. Beam currents 10 mA (a), 20 mA (b), 40 mA (c), 100 mA (d).

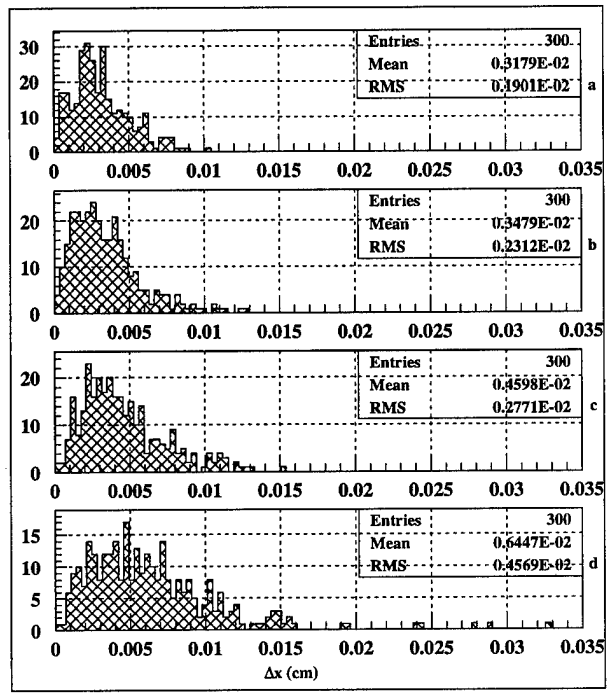

Fig. 2. Particle distributions on Δx for structure with focusing period $4\beta\lambda$. Beam currents 10 mA (a), 20 mA (b), 40 mA (c), 100 mA (d).

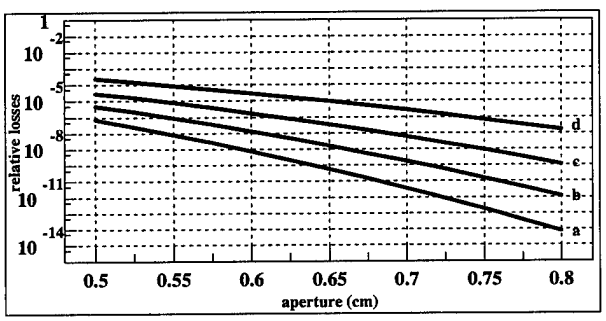

Fig. 3. Relative particle losses in $2\beta\lambda$ structure in dependance of aperture. Beam currents 10 mA (a), 20 mA (b), 40 mA (c), 100 mA (d).

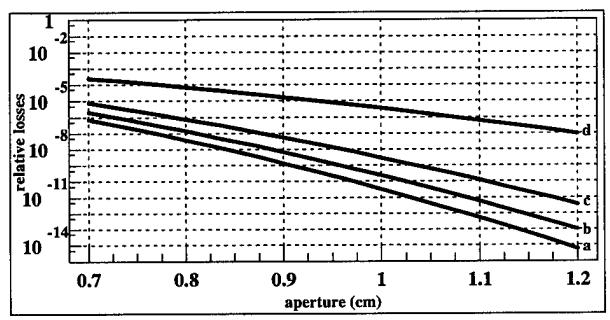

Fig. 4. Relative particle losses in $4\beta\lambda$ structure in dependance of aperture. Beam currents 10 mA (a), 20 mA (b), 40 mA (c), 100 mA (d).

Table 2

I (mA)	h	σ (cm)	$\xi\ 10^{-3}$(cm)
		$2\beta\lambda$	
10	0.0052	0.11	2.12
20	0.0101	0.12	2.25
40	0.0183	0.14	2.67
100	0.0461	0.16	3.81
		$4\beta\lambda$	
10	0.0101	0.16	3.20
20	0.0182	0.17	3.48
40	0.0370	0.18	4.60
100	0.0520	0.25	6.45

REFERENCES

[1] V.A. Andreev et al., "Engineering design of ITEP Proton Linac for Nuclear Waste Transmutation". Proc. of Linac 96 Conf., Geneva, 1996, p. 252.

[2] R.A. Jameson, "Self-Consistent Beam Halo Studies & Halo Diagnostic Development in a Continuous Linear Focusing Channel", Los-Alamos Report LA-UR-94-3753.

[3] G.M. Zaslavskii, R.Z. Sagdeev, " Introduction to Nonlinear Physics", "Nauka", Moscow, 1988.

[4] A.Kolomiets et al, "The Study of Nonlinear Effects Influenced by Space Charge in High Intensity Linac", Proc., of Particle Acc. Conf., Dallas, 1995.

INTENSITY DEPENDENCE OF BETATRON RESONANCES OBSERVED AT THE KEK-PS

Y. Shoji*, D. Arakawa, J. Kishiro, K. Koba†, S. Machida, K. Marutsuka, Y. Mori, C. Ohmori, H. Sato, M. Shirakata, H. Takagi, K. Takayama, T. Toyama and M. Yoshii
KEK, Oho 1-1, Tsukuba-shi, Ibaraki-ken, 305 JAPAN

Abstract

An intensity dependent betatron resonance in the tune diagram was observed at the KEK-PS. The strong imperfection resonances were corrected by correction magnets. However with high intensity beam we still observed a big structure of beam loss in the tune diagram. One of possible explanations was a space-charge induced nonstructure resonance.

1 INTRODUCTION

A trial to extend a working area in the tune diagram was performed at the KEK-PS. This study is a part of the intensity up-grading program[1] for the neutrino oscillation experiment combined with Super-KAMIOKANDE. The goal of the program is to double the beam intensity in daily operation, which was 4×10^{12}ppp at that present. The parameters of the KEK-PS is listed in Table 1. A single bunched beam from the 500 MeV Booster synchrotron is injected into the Main Ring (MR) 9 times during the injection period. It takes more than 400 ms because the repetition rate of the Booster is 20 Hz. The beam is accelerated to 12 GeV and is slowly extracted for fixed target experiments or will be extracted in one turn for the neutrino oscillation experiment.

Among the intensity limiting phenomenon in the MR the space charge tune spread was thought to be responsible for a beam loss at the injection porch. It amounted to about 15% for the injection of 5.5×10^{12}ppp and its rate increased rapidly with the beam intensity. According to the tune diagram survey, the working area in the tune space was believed to be limited by three betatron resonance lines: $2Q_x = 14$, $2Q_x - 2Q_y = 0$ and $4Q_y = 29$. Here Q_x and Q_y are horizontal and vertical betatron tunes. The allowed maximum tune spread was $\Delta Q_y = 0.25$. The best operation point (a set of measured coherent tunes) had been $(Q_x, Q_y) = (7.12, 7.21)$. Our initial plan was to apply resonance corrections and double the working area. However after a careful resonance correction observing low intensity beam, the working area still remained the same for the beam intensity of the daily operation. What we observed was a intensity dependenct structure in the tune diagram. It became clear that the resonance, which we had thought was $4Q_y = 29$, could not be explained by a conventional simple model.

One of our speculations to this resonance was a *space charge induced nonstructure resonance*, which had never been considered in any other synchrotrons. Space charge induced structure resonancs had been pointed out first by B. Montague[3] and later by G. Parzen[4] and S. Machida[5]. Those were resonances in the absence of magnetic field errors. Since the space charge force is modulated according to the beam envelope, it has harmonic components of the superperiod times an integer. Especially when the harmonic number is identical to the periodicity of a focusing function, the resonance becomes very strong and is called a *superstructure resonance*[6, 7]. However in some high intensity proton synchrotrons which take some hundreds of milliseconds for a multi-step injection, much weaker *space charge induced nonstructure resonances* become effective. Quadrupole imperfections modulate the beam envelope function, then to produce other harmonic field components other than the structure number. This effect was analyzed numerically by S. Machida[7] and analytically by Y. Shoji and H. Sato[8]. They calculated the stop-band width of $4Q_y = 29$ of the KEK-PS using experimental data of the magnetic field imperfections. The width of $4Q_y = 29$ was about 40 times that driven by the octupole magnetic field imperfections for the beam intensity of 1×10^{12}ppp = 1TP per bunch. The calculations also predicted that the width of $4Q_y = 21$ was about 30% of that of $4Q_y = 29$. In this report we show some experimental data on this resonance.

Table 1: Parameters of the KEK-PS

circumference	340 m
lattice type	FODO
periodicity	28
injection energy	500 MeV
harmonic number	9
horizontal physical aperture	80πmm · mrad.
vertical physical aperture	25πmm · mrad.

2 EXPERIMENTS

The study started from the correction of normal sextupole resonance $Q_x + 2Q_y = 22$ and two normal octupole resonances: $4Q_y = 29$ and $2Q_x + 2Q_y = 29$. We let the low intensity beam cross a resonance, energized the harmonic correction magnets and optimized them to minimize the beam loss by the crossing. The correction was not applied to skew sextupole and skew octupole resonances, but the beam loss by crossing them was very small compared to those of the normal multipole field resonances.

* Present address: Laboratory of Advanced Science and Technology for Industry (LASTI), Himeji Institute of Technology
† Permanent address: Miyazaki University

0-7803-4376-X/98/$10.00 © 1998 IEEE

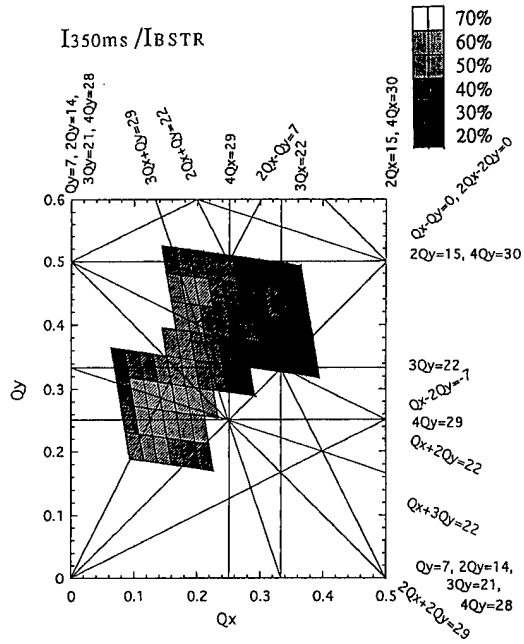

Figure 1: Two dimensional tune diagram survey for high intensity beam of 1.3TP. The frame was a bare tune diagram.

Figure 1 shows the two dimensional tune diagram survey. A single bunched beam of 1.3TP was injected into the ring and stored for longer than 350 ms. The beam survival ratio to the bare machine tune was measured. Here the bare machine tune means the betatron tune with no space charge tune shift. The best operating point (bare machine tune) was $(7.12, 7.25)$. Below that point (lower Q_y) the beam was lost rapidly by the integer coupling $Q_x - Q_y = 0$ or $2Q_x - 2Q_y = 0$ (Montague resonance). On the left of that point (lower Q_x) the beam was lost by $2Q_x = 14$ or $4Q_x = 28$ (superstructure resonance). Above that point the beam was lost slowly by the unknown resonance.

Figure 2 shows the intensity dependence of the beam survival ratio measured along the line in the tune diagram.

With low intensity beam (0.1TP) there was no serious structure in the tune diagram. However with higher intensity (0.3TP) a dip of the beam loss appeared where the space charge shifted tune would be on the resonance $4Q_y = 29$. With higher intensity than the daily operation (more than 0.6TP) the dip became broader and deeper then merged to be a step.

This kind of a dip could be produced intentionally either by a quadrupole perturbation or an octupole perturbation as shown in Fig. 3. Figure 4 showed that for a higher intensity a weaker quadruple perturbation worked. The expected half-integer stop-band width by the quadrupole imperfection was 0.04. The quadrupole magnet (EQ) could excite the same width at 15 A in horizontal and 50 A in vertical.

We tried to optimize the quadrupole perturbations and minimize the beam loss dip. Two quadrupole magnets:

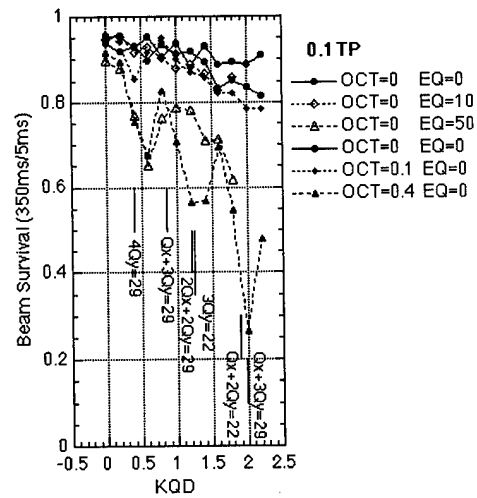

Figure 3: The beam loss dip intentionally produced by an octupole or quadrupole perturbations. As an perturbation quadrupole, a quadrupole for magnet the resonant beam extraction was temporary used.

EQ1 and EQ2 were originally set for the half-integer resonant extraction. It was fortunate that they were roughly in diagonal positions in $29th$ harmonic phase. However we observed only a tiny improvement by the optimization of two quadrupoles (Fig. 5). The optimized quadrupoles were very much weaker than the expected imperfection.

The other prediction from our speculation was the dependence on the integer part of the tune. Figure 6 shows the beam survival ratio around $4Q_y = 29$ and $4Q_y = 21$. Our speculation was a good explanation of the difference between two at the sub-integer part from 0.23 to 0.35.

3 SUMMARY

We observed the intensity dependent resonance at the injection porch of the KEK-PS. It was possible that this resonance was a space charge induced nonstructure octupole resonance produced by quadrupole imperfections. However we could not prove it by applying the quadrupole correction. The correction scheme could be bad, because it has only one quadrupole magnet for each of sine and cosine component. Different explanations would be possible, such as a mirror charge field induced resonance[8].

4 REFERENCES

[1] H. Sato, Proc. of the 10th Symp. on Accelerator Science and Technology, Hitachinaka, Japan (Oct. 1995) p. 11.

[2] G. Guinard, CERN 76-06 (1976); CERN 78-11 (1978).

[3] B.W. Montague, CERN 68-38 (1968).

[4] G. Parzen, Nucl. Instr. & Meth. A281 (1989) 413-425.

[5] S. Machida, Nucl. Instr. & Meth. A309 (1991) 43-59.

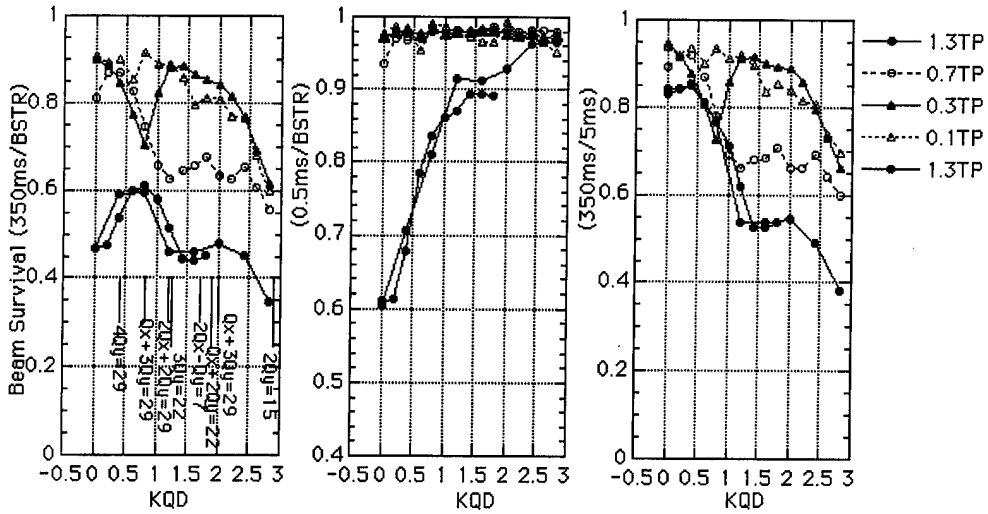

Figure 2: Intensity dependence of the beam survival ratio. The horizontal axis is the strength of the lattice focusing quadrupoles. The plots are the total loss, the initial fast loss and the slow loss, respectively from the left. The positions of the resonances in the figure were calculated from the bare tunes. The surveyed line started from (7.12, 7.21) and ended at (7.23, 7.49) in the tune diagram.

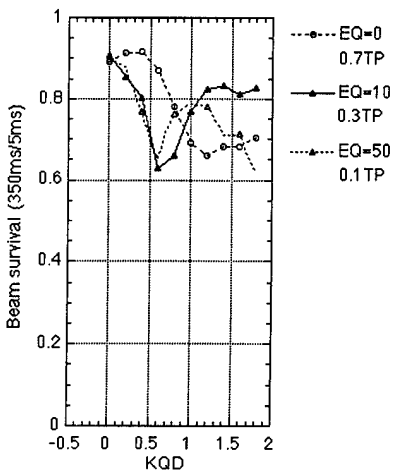

Figure 4: The beam loss dip intentionally produced by the quadrupole perturbations. The shift of the dip was thought to be came from the space charge tune shift.

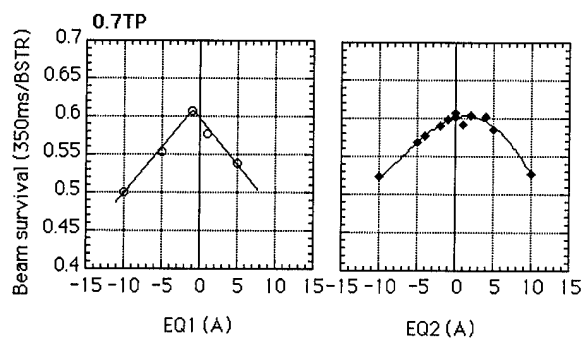

Figure 5: The dip depth vs. quadrupole perturbations.

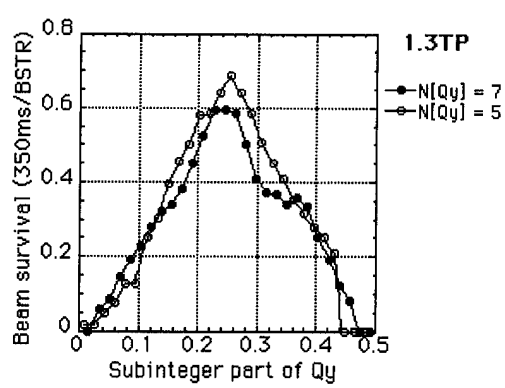

Figure 6: The tune surveys along lines for two different integer part of vertical tunes; 5 and 7. The horizontal tune was fixed to 7.13.

[6] S. Machida and Y. Shoji, Workshop on Space Charge Dominated Beams, Bloomington, Indiana (Sept. 1995) AIP Conference proceedings 377, pp. 160-168.

[7] S. Machida, Nucl. Instr. & Meth. A384 (1997) 316-321.

[8] Y. Shoji and H. Sato, 'An analytical formula for the bandwidth of a strong nonstructure octupole resonance induced by a space charge', to be published in Nucl. Instr. & Meth.

HALO FORMATION FROM AXISYMMETRIC BREATHING BEAMS

Masanori Ikegami and Hiromi Okamoto
Nuclear Science Research Facility, Institute for Chemical Research, Kyoto University
Gokanosho, Uji, Kyoto 611, JAPAN

Abstract

We study halo formation from mismatched axisymmetric beams propagating in a periodic solenoidal channel as well as in a uniform channel. Some fundamental properties of halos are self-consistently explored with a one-dimensional space-charge code designed particularly for breathing-mode study. We apply the code to three different types of phase-space distributions, i.e., Gaussian, waterbag and parabolic distribution. A possibility of removing halo particles is also discussed.

1 INTRODUCTION

In designing a linac system for intense beam acceleration, it is extremely important to have a clear understanding of space-charge-induced phenomena since the beam quality can easily be deteriorated by them. The halo formation is one such phenomenon which must be investigated in more detail. In fact, recent interest in using high-current ion linacs for the production of tritium, the transmutation of nuclear waste, etc. has greatly enhanced the activity of halo study, because these machines must operate with a extremely low beam loss to avoid serious radio-activation.

According to recent work on halos[1-4], beam mismatch is understood to be the primary factor of halo formation. In particular, it is speculated that the breathing mode-oscillations excited by a beam-size mismatch might have the most dominant effect in causing halos. Following this viewpoint, we develop, in the present paper, an essentially one-dimensional space-charge routine dedicated to breathing-mode study. Self-consistent simulation results are given to deepen our current understanding of halo formation in a periodic focusing channel as well as in a uniform channel. Finally, we try to figure out whether a halo may be scraped off, as pointed out in the previous work[5], by means of a multi-collimator system.

2 UNIFORM FOCUSING CHANNEL

First of all, we examine breathing-beam properties in a uniform focusing channel. In this case, the beam motion is governed by the Hamiltonian

$$H=\frac{1}{2}\left(p_r^{\,2}+\frac{p_\theta^{\,2}}{r^2}\right)+\frac{1}{2}\kappa^2 r^2+\frac{q}{mu^2}V(r;s), \qquad (1)$$

where m, u and q are, respectively, the mass, speed and charge state of an ion, κ is a constant corresponding to the external focusing-field strength, and the independent variable s is the distance measured along the transport line. Note here that, because of the symmetry of breathing modes, the space-charge potential $V(r;s)$ is independent of the azimuthal coordinate θ, which enables us to put $p_\theta=L$=const. Scaling the variables, we reach the equation of motion

$$\frac{d^2\tilde{r}}{d\tilde{s}^2}+\tilde{r}=\frac{\tilde{L}^2}{\tilde{r}^3}+\tilde{K}\frac{\xi(\tilde{r};\tilde{s})}{\tilde{r}}, \qquad (2)$$

where $\tilde{r}=\sqrt{\kappa/\varepsilon}\,r$ with ε being the initial rms emittance, $\tilde{K}=K/\kappa\varepsilon$ with K being the generalized perviance, $\tilde{s}=\kappa s$, and $\xi(\tilde{r};\tilde{s})$ is the number of ions contained in the circular region of the radius $\tilde{r}$ relative to the total ion number. The parameter $\tilde{K}$ can be related to the tune depression η as $\tilde{K}=(1-\eta^2)/\eta$, where η has been defined as the ratio of the space-charge depressed betatron frequency to the zero-current frequency. The angular momentum $\tilde{L}=(xp_y-yp_x)/\varepsilon$ is a particle-dependent constant, and can be determined from an initial beam distribution generated in four-dimensional phase space (x, y, p_x, p_y). In this work, three types of realistic beam distribution, i.e., Gaussian-, waterbag-, and parabolic-type distribution, are adopted as the initial distribution. Once L and the initial shape of the function $\xi(\tilde{r};\tilde{s})$ are determined, we then integrate Eq. (2) fixing $\xi(\tilde{r};\tilde{s})$ within every time step. Since most beams come to roughly saturated state before arriving at $\tilde{s}=20\lambda_p$, where λ_p is the scaled plasma wave length, we consider a uniform focusing channel of $20\lambda_p$ long.

Fig. 1 shows the maximum extent of halos plotted as a function of tune depression η. The parameter μ is the mismatch factor defined as the ratio of the initial rms beam radius to the matched rms radius ρ_0[6]. The matched rms radius can be evaluated from

$$\rho_0^{\,2}=\left(\tilde{K}+\sqrt{\tilde{K}^2+4}\right)\Big/4. \qquad (3)$$

It is evident from Fig. 1 that the halo extent divided by $R_0\equiv\sqrt{2}\rho_0$ is almost independent of η. The same tendency

0-7803-4376-X/98 /$10.00 © 1998 IEEE

as shown in Fig. 1 has been confirmed with different values of μ unless μ is too close to one.

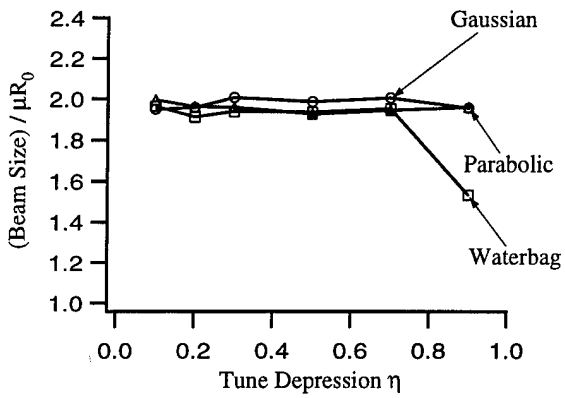

Figure 1: Maximum halo extent vs. tune depression η. The abscissa is the maximum halo size scaled with μR_0 where $R_0 = \sqrt{2}\rho_0$. We have here assumed the mismatch factor of 1.3. We find that the results are quite insensitive to both η and initial distribution type.

3 PERIODIC FOCUSING CHANNEL

Let us now proceed to a periodic focusing situation, generalizing the code. We here consider a periodic solenoidal channel consisting of 150 focusing cells, each having 50% filling factor. The equation of motion is

$$\frac{d^2\hat{r}}{d\hat{s}^2} + \vartheta(\hat{s})\hat{r} = \frac{\hat{L}^2}{\hat{r}^3} + \hat{K}\frac{\xi(\hat{r};\hat{s})}{\hat{r}}, \tag{4}$$

where $\hat{r} = r/\sqrt{\varepsilon s_f}$ with s_f being the length of a focusing period, $\hat{K} = Ks_f/\varepsilon$, $\hat{s} = s/s_f$ and $\hat{L} = L/\varepsilon$. The periodic step function $\vartheta(\hat{s})$ has the periodicity of one, and its step size corresponds to the focusing-field strength. In the same scaling as employed in Eq. (4), the envelope equation is written as

$$\frac{d^2\hat{\rho}}{d\hat{s}^2} + \vartheta(\hat{s})\hat{\rho} = \frac{\hat{K}}{2\hat{\rho}} + \frac{1}{4\hat{\rho}^3}, \tag{5}$$

from which the time evolution of the matched rms beam radius $\rho_0(\hat{s})$ is numerically evaluated.

The density-dependence of maximum halo extent is shown in Fig. 2 where we have considered mismatched Gaussian beams with μ=1.3. The definition of the mismatch factor μ is $\mu \equiv \rho_{in}/\rho_0^{\max}$ where ρ_{in} denotes the initial rms beam radius, and $\rho_0^{\max} \equiv \rho_0(0)$. Note here that $\rho_0(0)$ corresponds to the maximum rms radius of a matched beam since the origin of the coordinate s has been set at the middle of a focusing magnet. Similar to the result in Fig. 1, the maximum extents of halos are insensitive not only to the tune depression η but also to the zero-current phase advance σ_0.

When σ_0 exceeds 90°, we may encounter the strong instability caused by the periodic nature of the focusing force. Emittance growth rate is plotted in Fig.3 as a function of tune depression, where matched Gaussian beams with σ_0=105° have been considered. In waterbag and parabolic beams, some additional weak instabilities caused by higher-order resonances are observed in the region σ_0>60°, while no such instability has so far been identified in the region σ_0<90° for Gaussian beams.

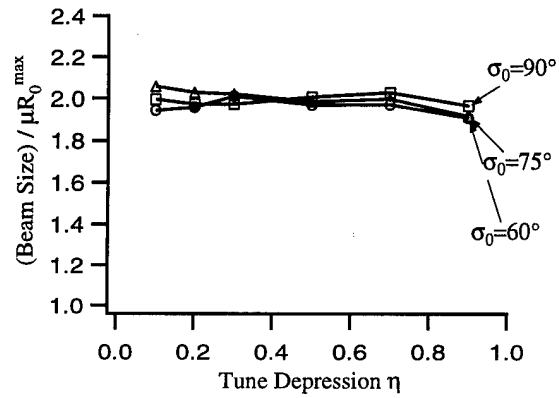

Figure 2: Maximum halo extent vs. tune depression η. The abscissa is the maximum halo size scaled by $\mu R_0^{\max}$ where $R_0^{\max} = \sqrt{2}\rho_0^{\max}$. Gaussian beams with the initial mismatch factor of 1.3 have been assumed. Three different values of zero-current phase advance, i.e., σ_0=60°, σ_0=75° and σ_0=90°, have been considered.

4 A POSSIBILITY OF HALO SCRAPING

In a previous work[5], we found that a halo was formed largely by the particles initially located around the tail portion of a phase-space distribution. This suggests that the beam core may roughly be stable and, accordingly, there is a possibility to efficiently reduce the halo intensity. In this section, we consider a simple halo-scraping system consisting of several collimators with a circular hole of the radius r_s. Each collimator is installed in the middle of drift space. For simplicity, we assume that both the geometrical and resistive-wall wake fields induced by the collimators are negligible.

As an example, let us take a Gaussian distribution which initially satisfies the conditions σ_0=60°, η=0.3 and μ=1.3. As shown in Fig. 4(a), a clear halo ring is formed around the central core region after the beam traverses 150 focusing periods. The beam is then delivered into a multi-collimator system of 14-cell long to scrape the halo. We have here set the radius of the collimator hole to be

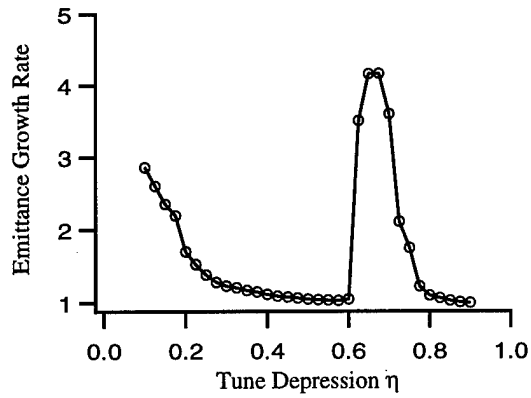

Figure 3: Emittance growth rate vs. tune depression η at σ_0=105°. Matched Gaussian beams have been considered.

$r_s/\mu R_0^{max}$=1. It is demonstrated, in Fig. 4(b), that the halo has been successfully removed by the collimators, although the beam intensity is reduced by 9.3% compared to the original intensity. The collimated beam in Fig. 4(b) further travels through a 150-cell transport channel to reach the final state in Fig. 4(c). We now recognize that the regeneration of halo has been completely suppressed while the core beam still has a mismatch executing a significant breathing oscillation.

5 SUMMARY

We have explored some characteristics of halo formation from axisymmetric mismatched beams propagating in a periodic solenoidal channel as well as in a uniform focusing channel, developing a 1D space-charge code for breathing-mode study. It has been shown that the maximum halo extent divided by the matched rms radius ρ_0^{max} is quite insensitive to the tune depression η. In particular, it always takes the value around $2\sqrt{2}$ times the size of initial mismatch regardless of the shape of distribution function, when the beam is subjected to a sufficiently large mismatch. It may thus be said that the minimum aperture size of a high-power linac should be well above $2\sqrt{2}\,\mu_{max}\,\rho_0^{max}$ when we expect the possible maximum mismatch factor to be μ_{max}.

It has been demonstrated that halo intensity may significantly be reduced by the multiple halo-scraping scheme, provided that the wake fields generated by the collimators are negligible. It, however, seems that the practicability of such a collimator system depends on how much we could minimize the effect of wake fields neglected here. In addition, it is indeed necessary to include multi-dimensional effects to draw more definitive conclusions on this subject.

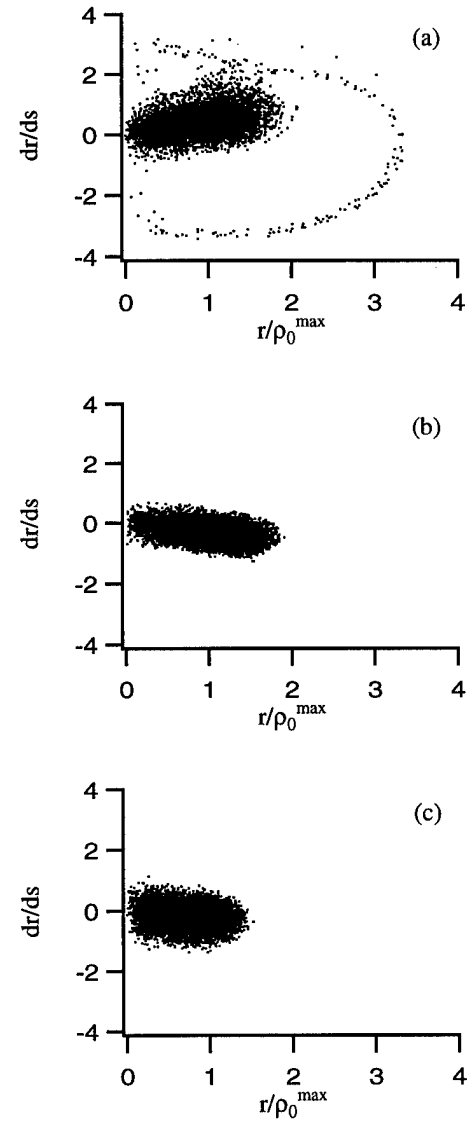

Figure 4: Phase-space configurations of a mismatched Gaussian beam initially with η=0.3 and μ=1.3. The zero-current phase advance has been set to be 60°. (a): the distribution after traveling through 150 focusing periods. (b): the beam collimated with a 14-cell halo scraper. (c): the collimated beam after traveling through another 150-cell focusing channel.

6 REFERENCES

[1]. R. A. Jameson, Los Alamos Report LA-UR-93-1029 (1993).

[2]. R. L. Gluckstern, Phys. Rev. Lett. **73**, 1247 (1994).

[3]. J. S. O'Connell, T. P. Wangler, R. S. Mills and K. R. Crandall, in Proceedings of the Particle Accelerator Conference, Washington DC, 3657 (1993).

[4]. J. M. Lagniel, Nucl. Inst. Meth. A345, 46 (1994).

[5] H. Okamoto and M. Ikegami, Phys. Rev. E. **55**, 4694 (1997).

[6]. In this paper, μ is always taken to be larger than one.

EMITTANCE GROWTH OF AN INTENSE ELECTRON BEAM IN A FOCUSING CHANNEL

B. E. Carlsten, Los Alamos National Laboratory, Los Alamos, NM 87545 USA

Abstract

We use the single-particle radial equation of motion to identify nonlinear forces which lead to an emittance growth in a focusing channel consisting of solenoids. For a uniform density beam, the two dominant effects are the axial velocity variations within a solenoid due to the particles' azimuthal velocity and changes in the particle's energy due to radial motion and the radial electric space-charge field. We derive estimates for the emittance growth for a space-charge dominated beam due to these effects, both for the case of a hard focus to a small beam waist and for the case where there is gentle beam scalloping. We also briefly catalog less important emittance growth mechanisms.

1 INTRODUCTION

In this paper, we will analyze the emittance growth of a continuous, intense electron beam in a transport channel made up of short discrete solenoids. Our goal is to derive formulas for the emittance growth for the case that the beam is focused to a small waist and for the case the beam is radially oscillating (either due to a mismatch or the discreteness of the focusing solenoids). By far, the most important effect is due to beam-density nonuniformities, and there is a mistaken tendency to assume that there is no emittance growth if the density is uniform. However, we will show that particles in a uniform-density beam still have a nonlinear radial equation of motion. We will estimate the emittance growth for these cases for a uniform-density beam, which would be then useful for evaluating beamline designs. These estimates are also valid if the beam is in the emittance-dominated regime. We will assume that the electron beam does not reach an equilibrium or periodic phase-space distribution. For simplicity, we will assume that all elements are perfectly aligned and that the focusing elements are perfect with no fringe fields. The emittance growth will be dominated by effects arising from axial velocity variations within the soleniods (due to a radius-dependent azimuthal velocity, and which leads to particles at larger radii spending more time within the solenoid and thus being overfocused) and from changes in the particles' energy (due to the coupling between the radial space-charge force and a particle's radial velocity). For a nominal 4-kA, 6-MeV electron beam, the normalized emittance growths from these mechanism can easily exceed 200 mm mrad.

2 RADIAL EQUATION OF MOTION

The radial equation of motion for a particle within the beam within the central part of a solenoid (where the applied magnetic field from the solenoid is purely axial) is given by

$$m\frac{d(\gamma\dot{r})}{dt} = eE_r + e(v_\theta B_{dia} - v_z B_\theta) + ev_\theta B_{ext} + \frac{\gamma m v_\theta^2}{r}, \quad (1)$$

where γ is the relativistic mass factor, B_{ext} is the total external axial magnetic field (from both the solenoid and the diamagnetic effect from the image currents in the beampipe), B_{dia} is the diamagnetic axial magnetic field induced from the beam current opposing the solenoidal field, B_θ is the azimuthal magnetic field from the space charge, and E_r is the radial electric field from the space charge, all at the position of the particle, and e and m are the electronic charge and mass, respectively. For balanced flow, the solenoid strength is adjusted such that the linear part of the combination of $ev_\theta B_{ext}$ and the centrifugal force will cancel the linear part of the resulting space-charge force. There is also a potential depression within the beam (a variation of γ that is a function of radius). Our approach will be to expand the radial equation of motion in terms of the variation of γ, to lowest order, which we will then use to estimate the emittance growth for the two cases.

We will assume that the particles have no intrinsic angular momentum (there is no axial magnetic field at the location of the cathode) and that the external magnetic field is radially constant. Thus, the azimuthal velocity can found by application of Busch's Theorem [1] (the conservation of angular momentum):

$$v_\theta = -\frac{e}{2\gamma m}\int_0^r (B_{ext} + B_{dia})\nu\, d\nu \quad , \qquad (2)$$

where ν is a dummy variable for the radial integration. We will use Gauss' Law to find the radial electric field,

$$E_r(r) = \int_0^r \frac{\rho(\nu)\nu}{\varepsilon r} d\nu \quad , \qquad (3)$$

where ρ is the charge density. The diamagnetic field is given by

$$B_{dia} = \int_r^{r_b} \mu v_\theta(\nu)\rho(\nu)\, d\nu \qquad (4)$$

0-7803-4376-X/98/$10.00 © 1998 IEEE

where r_b is the radial edge of the beam. The diamagnetic field is small, and, to first order, only the azimuthal velocity depending on the externally applied solenoidal field needs to be considered in Eqn. (4). We can write the relativistic mass factor as $\gamma(r) = \gamma_a + \gamma_1(r)$, where γ_a is the mass factor along the axis ($r=0$). Let us assume that the space-charge density is of the form $\rho = \rho_o r^n$. Explicit evaluation of the above integrals for this charge density profile gives [2]

$$B = B_a\left(1+\frac{\gamma_1}{\gamma_a}\frac{n+2}{2}\right) \tag{5}$$

where B is the total axial magnetic field and B_a is the field on axis. The azimuthal velocity in terms of the field and relativistic mass factor on axis is given by

$$v_\theta = -\frac{eB_a r}{2\gamma_a m}\left(\frac{1+\frac{\gamma_1}{\gamma_a}\frac{n+2}{n+4}}{1+\frac{\gamma_1}{\gamma_a}}\right) \quad . \tag{6}$$

The beam-induced azimuthal magnetic field in Eqn. (1) is given in terms of the vector potential by

$$B_\theta = \frac{\partial}{\partial z}A_r + \frac{1}{r}\frac{\partial}{\partial r}rA_z \quad . \tag{7}$$

If the beam is converging or diverging, there is a nonzero radial vector potential, and if the beam is being focused in a solenoid, the axial derivative of the radial vector potential is nonzero [3]. In that case, the azimuthal magnetic field is approximated by

$$B_\theta = -\frac{\beta}{c}\frac{1}{r}\frac{\partial}{\partial r}(r\phi) + \frac{\beta}{c}\left(\frac{13-8r/r_b}{10}\right)\frac{d^2r}{dz^2}\phi_b \quad , \tag{8}$$

where the scalar potential at the beam radius is $\phi_b = \gamma_b mc^2/e$, and where γ_b is the difference in the relativistic mass factor between the center and radial edge of the beam.

Using dots to refer to time derivatives and primes to refer to axial derivatives, we have

$$\frac{d}{dt}\gamma\dot{r} = \dot{r}\frac{d\gamma}{dt} + \gamma\ddot{r} = \frac{eE_r}{mc^2}\dot{r}^2 + \gamma\ddot{r} \tag{9}$$

and

$$\begin{aligned} \dot{r} &= r'v_a\left(1+\frac{v(r)}{v_a}\right) \\ \ddot{r} &= r''v_z^2(r) = r''v_a^2\left(1+2\frac{v(r)}{v_a}\right) \end{aligned} \tag{10}$$

where we are defining v_a to be the axial velocity at the axis and v to be the relative axial velocity, $v_z(r) = v_a + v(r)$. After combining the focusing term and the centrifugal acceleration term, and combining the r'' terms and dividing through by a factor of γ, Eqn. (1) becomes

$$\begin{aligned} r''mv_a^2\left(1+2\frac{v}{v_a}-\frac{\gamma_b}{\gamma_a}\chi\right) &= \frac{eE_r}{\gamma\gamma^*(r)^2} + \\ \frac{1}{\gamma}\left(ev_\theta\left(B_{ext}+B_{dia}\right)+\frac{\gamma mv_\theta^2}{r}\right) &- \frac{e}{c^2\gamma}v_o^2E_r r'^2 \end{aligned} \tag{11}$$

where $\chi = 8r/10r_b - 13/10$ and γ^* is an effective relativistic mass factor. To lowest order in the small quantities, the radial force equation becomes in terms of the parameters evaluated on axis

$$\begin{aligned} \dot{r}'' &= \left(1-2\frac{v}{v_a}+\frac{\gamma_b}{\gamma_a}\chi\right)\times \\ &\left[\frac{eE_r}{mv_a^2\gamma_a\gamma^*(r)^2}\left(1-\frac{\gamma_1}{\gamma_a}\right)-\frac{e^2B_a^2r}{4\gamma_a^2m^2v_a^2}\left(1+n\frac{\gamma_1}{\gamma_a}\right)-\frac{eE_r r'^2}{\gamma_a mc^2}\right]. \end{aligned} \tag{12}$$

For a uniform density beam after a drift of length l, we find that the integrated radial divergence is given by

$$\begin{aligned} r' &= \left(1-2\frac{v}{v_a}+\frac{\gamma_b}{\gamma_a}\chi\right)\times \\ &\left[\frac{leE_r}{mv_a^2\gamma_a\gamma^*(r)^2}\left(1-\frac{\gamma_1}{\gamma_a}\right)-\frac{r}{f}-\frac{le}{\gamma_a mc^2}E_r r_o'^2\right] \end{aligned} \tag{13}$$

where r_o' is the initial radial divergence and where we are using the definition of the focal length of a solenoid, $f = 4\gamma_a^2m^2v_a^2/le^2B_a^2$. Note that the effect of the potential depression of the beam exactly cancels the effect of the diamagnetic field, leading to a purely linear focusing force and no emittance growth. However, there are four terms present that lead to an emittance growth, even for a uniform density beam. These are: (1) the axial velocity shear (which will arise from the conservation of energy and the particles' azimuthal velocity), (2) the chi term (which is from the axial derivative of the radial vector potential), (3) the radial space-charge term (for balanced flow, γ^* is independent of radius, and the nonlinear term scales as I^2/I_A^2), and (4) the radial velocity term (which arises from the divergence of the beam leading to energy variations). For most cases of interest, terms 2 and 3 are small, and we will only consider terms 1 and 4 in the next section.

Nonlinear space-charge forces arising from a nonuniform charge density can easily dominate these effects; special care must be made to ensure the beam density is uniform.

3 EMITTANCE GROWTH ESTIMATES

3.1 Emittance growth in the hard focusing case

There are two effects worth considering when the beam is focused to a tight waist. First, inside the solenoid itself there is an axial velocity shear. Second, there is a significant convergence of the beam as it travels to the waist. We will assue as nominal parameters $\gamma_a = 12.74$, $l = 0.1$ m, $f = 0.6$ m, and the beam radius in the final focus solenoid is $r_b = 0.03$ m.

Inside the solenoid, the variation in the axial velocity ($v_z = v_a + v$) is given by

$$v = -\frac{c^2}{2v_a}\beta_\theta^2 = -\frac{e^2 B_a^2 r^2}{8\gamma_a^2 m^2 v_a} \qquad (14)$$

The divergence in the beam introduced by the solenoid is then (ignoring all terms except for the terms depending on the solenoid's focal length)

$$r' = -\frac{r}{f}\left(1 - 2\frac{v}{v_a}\right) = -\frac{r}{f}\left(1 - \frac{r^2}{lf}\right) \quad . \qquad (15)$$

The normalized, 90% emittance growth from the nonlinear part of this divergence is

$$\varepsilon = \frac{1}{3\sqrt{2}}\gamma_a \frac{r_b^4}{lf^2} \quad . \qquad (16)$$

For the nominal parameters given, the emittance growth is about 70 mm mrad.

After the solenoid, the divergence term in Eqn. (13) dominates. We need to be a little careful because the beam radius is changing over the axial range we are interested in. The growth of the radial divergence is given by

$$dr' = \frac{eE_r}{\gamma_a mc^2}\frac{r^2}{\zeta^2}d\zeta \qquad (17)$$

where ζ is the distance from the beam waist. The differential emittance growth is

$$d\varepsilon = d\zeta \frac{\sqrt{2}}{3}\frac{r_b^2}{\zeta^2}\frac{I}{I_A} \quad , \qquad (18)$$

where $I_A = 4\pi\varepsilon mc^3 / e$. This expression is easy to integrate, using $r_b = \zeta r_{lens} / L$, where r_{lens} is the beam radius at the solenoid and L is the total separation between the solenoid and beam waist. We find the total accumulated emittance growth at the final focus to be

$$\varepsilon = \frac{\sqrt{2}}{3}\frac{r_{lens}^2}{L}\frac{I}{I_A} \quad . \qquad (19)$$

For the previous parameters and a final focus length L of 60 cm, the emittance growth is about 180 mm mrad.

3.2 Emittance growth for a scalloping beam

In general, the beam is not in completely balanced, uniform flow or being focused hard to a waist. The solenoids are discrete, and the beam-edge radius gently undulates down the beamline. We can estimate the emittance growth for a length l of scalloping motion, by using the divergence term in Eqn. (13) while assuming that the beam radius is a constant.

In this case, the accumulated nonlinear divergence after a length l is given by

$$r' = l\frac{eE_r}{\gamma_a mc^2}\frac{r^2}{r_b^2}\overline{\alpha}^2 = 2\frac{I}{\gamma_a \beta I_A}\frac{lr^3}{r_b^4}\overline{\alpha}^2 \qquad (20)$$

where now $\overline{\alpha}$ is the rms divergence of the scalloping of the radial beam edge (let us say it is on the order of 20 mrad). For this case, the normalized, 90% emittance growth is given by

$$\varepsilon = \frac{\sqrt{2}}{3} l \frac{I}{I_A}\overline{\alpha}^2 \quad . \qquad (21)$$

Note that neither the beam radius nor the beam energy enters this equation. For the other parameters used in the previous example, the normalized, 90% emittance growth is about $6(10^{-5})l$. This emittance growth will tend to accumulate, and can become very large over long beamlines of several tens of meters.

4 ACKNOWLEDGEMENTS

This work was supported by funds from the Laboratory-Directed Research and Development program at Los Alamos National Laboratory, operated by the University of California for the US Department of Energy.

REFERENCES

[1] J. F. Gittens, Power travelling-wave tubes, American Elsevier Publishing Company, Inc., New York, 1965.
[2] B. E. Carlsten, "Emittance growth mechanisms of a nonequilibrium intense electron beam in a transport channel with discrete focusing ," submitted to *Nucl. Instrum. Meth. Phys. Res, A.*
[3] B. E. Carlsten, "Centrifugal space-charge force of an electron beam in a focusing element," *Phys. Rev. E.*, May (1997).

BEAM MATCHING AND HALO CONTROL

W. Lysenko, Los Alamos National Laboratory, MS H808, Los Alamos, NM 87545, USA, and
Z. Parsa, Brookhaven National Laboratory, 901A Physics Dept., Upton, NY 11973-5000, USA

Abstract

We present an overview of the status of ongoing work on physics models describing beam matching and halo control for particle accelerators, particularly high power ion linacs. We consider moments and various new variables that more naturally describe beam halo evolution. We compute matched beams and "mode invariants" (analogs of moment invariants) using primarily symbolic techniques.

1 INTRODUCTION

Future intense ion linacs will require good control of beam halo. To understand halo production, we consider the evolution of the phase-space distribution in the Vlasov regime. Since this is a non-imaging application, single-particle motion and its associated concepts such as aberrations are not as relevant. What is important is matching the beam to high order, taking into account nonlinearities such as those that arise from space charge.

Moments are an example of coordinates for the phase-space distribution. We can compute the values of the moments at any time from their initial values by solving the moment-evolution equations. The idea here is that we directly solve for the quantities of interest (properties of the distribution) rather than looking at the single-particle motion. Our goal is to extend this idea to computing the evolution of the halo, i.e., we are seeking "halo variables."

2 MATCHING

A matched beam is one whose distribution function $f(x,p,t)$ is a function of single-particle invariants. For a linear periodic lattice, for example, f is matched if it is an arbitrary function of the Courant-Snyder invariant ellipse

$$f(x,p,t) = F(\gamma x^2 + 2\alpha xp + \beta p^2). \tag{1}$$

Any matched f will be periodic in time, as will be its moments. If we see that a moment does not have the same value at times one lattice period apart, we know the beam is not matched. This is not true for the single-particle motion, which always contains a betatron-frequency component, even for a matched beam. This is the advantage of using moments or other coordinates of the distribution. For nonlinear motion, we still have periodic moments, even though the single-particle motion is more complicated.

3 HALO VARIABLES

An ideal set of variables would be one that includes a variable that describes the fraction of the beam outside a given radius. Knowing the evolution equation for such a variable would allow us to compute and be able to control particle loss. How close can we come to this goal?

Here, we will begin to answer this question by considering several different descriptions of beam distributions. We will compute matched beams for a simple nonlinear example and, where possible, mode invariants (the analog of moment invariants) in the new variables. One question we would like to answer is why we have not been able to determine the moment invariants for nonlinear motion.

4 LIE-POISSON FORMULATION

We can maintain Hamiltonian structure in distribution coordinates as follows.[1] Suppose we describe the solution to the Vlasov equation with some dynamical variables G_i. Think of the G_i as functionals that map the phase-space distribution function $f(x,p,t)$ to numbers (the moments, e.g., in a moments description). The variables G_i will form a Lie algebra if we define a Lie-Poisson (LP) bracket in terms of the ordinary Poisson bracket by

$$[G_i, G_j]_{\text{LP}} = \iint dx\, dp\, f(x,p,t)[\frac{\delta G_i}{\delta f}, \frac{\delta G_j}{\delta f}], \tag{2}$$

where $\delta G/\delta f$ is the variational derivative of G with respect to f. The dynamics (evolution of the variables) is given by

$$\frac{d}{dt}G = [G, H_{\text{LP}}]_{\text{LP}}. \tag{3}$$

The LP Hamiltonian H_{LP} is derived from the usual single-particle Hamiltonian H by

$$\frac{\delta H_{\text{LP}}}{\delta f} = H. \tag{4}$$

If the functional G is an integral over phase space involving f, x, p, and t, then the variational derivative is the partial derivative of the integrand with respect to f. In this case,

$$H_{\text{LP}} = \iint dx\, dp\, f(x,p,t)H(x,p,t). \tag{5}$$

5 EXAMPLES OF NEW VARIABLES IN LIE-POISSON FORMULATION

We compute matched beams and mode invariants symbolically using *Mathematica*[1] for three kinds of variables: moments, Fourier modes, and what we call histogram modes. We define the properties of the LP bracket and compute a LP Hamiltonian, which then allows us to compute the time derivatives of a quantity by taking the

[1] We thank D. Holm for pointing out this approach (private communication, 1989).

0-7803-4376-X/98/$10.00 © 1998 IEEE

bracket of the quantity with the $H_{\rm LP}$. In these examples, we consider the following single-particle Hamiltonian

$$H(x,p) = \frac{p^2}{2} + k\frac{x^2}{2} + k_2\frac{x^3}{3}. \tag{6}$$

We assume the force constants k and k_2 are time-independent, which means matched beams are those whose distributions are constant in time. We compute matches by requiring the LP bracket of all variables with $H_{\rm LP}$ to be zero. To compute mode invariants, we assume a function of the variables and solve for parameters of the function that result in making the function time independent.

5.1 Moments

Moments are averages of monomials in phase space over the phase-space distribution. For example, $<x^2>$ is defined for continuous and discrete distributions by

$$<x^2> = \int\int dx\, dp\, f(x,p,t)\, x^2 = \frac{1}{N}\sum_{i=1}^{N} x_i^2. \tag{7}$$

The LP bracket for moments is given by

$$[<x^i p^j>, <x^m p^n>]_{\rm LP} = (in - jm)<x^{i+m-1}p^{j+n-1}>. \tag{8}$$

We achieve closure for finite order by replacing the above right hand side with zero if it involves moments of orders greater than the cutoff value. Note that is hard to reconstruct f from the moments. Fortunately, this is not necessary to compute the LP Hamiltonian, which is simply

$$H_{LP} = \frac{<p^2>}{2} + k\frac{<x^2>}{2} + k_2\frac{<x^3>}{3}. \tag{9}$$

5.1.1 Matched moments

A matched beam satisfies the following relations.

$$\begin{array}{ll}
<p^2> = k<x^2> - \frac{5k_2^2}{k^2}<x^2p^2> & <p^3> = 0 \\
<xp> = 0 & <x^4> = \frac{3<x^2p^2>}{k} \\
<x^3> = -\frac{5k_2}{k^2}<x^2p^2> & <x^3p> = 0 \\
<x^2p> = 0 & <xp^3> = 0 \\
<xp^2> = -\frac{k_2}{k}<x^2p^2> & <p^4> = 3k<x^2p^2>
\end{array} \tag{10}$$

Any set of moments related this way will be constant in time. The non-linearity give rises to a nonzero value of some moments that are of odd degree in x. The matched distribution does not have elliptical symmetry if $k_2 \neq 0$.

5.1.2 Moment invariants

Moment invariants are functions of moments that are conserved. With the nonlinearity turned off ($k_2 = 0$), we find the invariant $I_{22} = <x^2><p^2> - <xp>^2$, which is just the square of the rms emittance, and higher-order invariants like $I_{44} = <x^4><p^4> - 4<x^3p><xp^3> + 3<x^2p^2>^2$, which we already know about (see the review in Ref.[2]). Our code finds the complete set of functionally-independent invariants, including those of mixed order (e.g., containing both second and fourth moments). Moment invariants for nonlinear motion are still unknown.

5.2 Fourier Modes

Define Fourier modes on a finite region of phase space by

$$f_{mn} = \frac{1}{(2\pi)^2}\int_{-\pi}^{\pi} dx \int_{-\pi}^{\pi} dp\, f(x,p)\, e^{-i(mx+np)} \tag{11}$$

The LP bracket of two of these quantities is

$$[f_{ij}, f_{mn}]_{\rm LP} = -\frac{1}{(2\pi)^2}(in - jm)\, f_{i+m,j+n}. \tag{12}$$

We attempt closure by zeroing higher modes. Unlike the situation for moments, this does not preserve all the properties of a Lie algebra for the truncated system, but we proceed anyway, in the hope it will lead to something useful. The LP Hamiltonian is expressed in terms of the modes by

$$f(x,p,t) = \sum_{m,m=-N}^{N} f_{mn}\, e^{i(mx+np)}. \tag{13}$$

5.2.1 Matched Fourier modes

For a cutoff of $N = 1$, the matched modes satisfy

$$\begin{array}{ll}
f_{-1,0} = (k+\bar{k})f_{0,-1} & f_{-1,-1} = \frac{k+\bar{k}}{k-\bar{k}}f_{1,1} \\
f_{1,0} = (k-\bar{k})f_{0,-1} & f_{-1,1} = \frac{k+\bar{k}}{k-\bar{k}}f_{1,1} \\
f_{0,1} = f_{0,-1} & f_{1,-1} = f_{1,1}
\end{array} \tag{14}$$

where $\bar{k} = ik_2(\pi^2 - 6)/3$. There are nine modes at this order, so there are three free modes for a matched beam.

5.2.2 Fourier mode invariants

For $k_2 = 0$, some invariants (truncated at order 1) are

$$\begin{array}{l}
f_{0,0} = \text{const.} \\
f_{-1,-1} + f_{-1,1} + f_{1,-1} + f_{1,1} = \text{const.}
\end{array} \tag{15}$$

The first of these is just the conservation of particles and is equivalent to <1>=const. for moments.

5.3 Histogram Variables

Let us divide phase space into rectangular bins labeled by the indices m in the x-direction and n in the y-direction. Let both indices range from $-N$ to N ($4N^2$ bins total). Let the mode f_{mn} describe the density in phase space at the bin specified by the indices m and n. The following LP bracket will approximate the correct physics (again, the truncated system is not exactly Hamiltonian).

$$[f_{ij}, f_{mn}]_{\rm LP} = \begin{cases} (m-i)(n-j)(f_{in} - f_{mj}), & \\ \qquad |m-i| = 1 \text{ and } |n-j| = 1 \\ 0, \qquad \text{otherwise.} \end{cases} \tag{16}$$

Note that closure for these variables is a boundary problem. If the beam is localized (as are real beams) then closure is automatic and involves no additional physics approximations. The LP Hamiltonian is

$$H_{\text{LP}} = \sum_{m,n=-N}^{N} f_{mn} <H>_{mn}, \tag{17}$$

where $<H>_{mn}$ is the average of $H(x,p)$ over the bin.

5.3.1 Matched histogram modes

In the continuous case, a matched beam would be elliptical for $k_2 = 0$. We find N independent modes (bin values) in a matched beam. Figure 1 shows an example with and without the nonlinearity. Equal densities in phase space are depicted by equal gray levels.

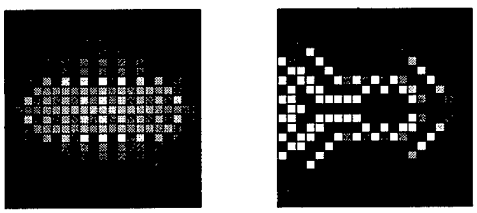

Figure 1: Matched histogram without nonlinearity (left) and with nonlinearity (right).

5.3.2 Histogram mode invariants

For general k and k_2, we found one invariant of degree 1 in the modes. For N odd it consists of the sum of all modes having odd indices and for N even, it consists of the sum of all modes having even indices. For $k_2 = 0$, the mode $f_{0,0}$ is separately conserved.

6 WEIGHTED MOMENTS

Consider generalizing the moments, not by using a new set of basis functions, but by changing the weights. Define "weighted moments" by

$$\begin{aligned} <g(x,p)>_n &= \frac{\iint dx\,dp\,[f(x,p,t)]^{n+1}\,g(x,p)}{\iint dx\,dp\,[f(x,p,t)]^{n+1}} \\ &= \frac{\sum_{i=1}^{N}[f(x_i,p_i,t)]^n\,g(x_i,p_i)}{\sum_{i=1}^{N}[f(x_i,p_i,t)]^n}, \end{aligned} \tag{18}$$

where the basis functions $g(x,p)$ are monomials in x and p. The usual moments result when the weight index is $n = 0$. For negative values of n, the halo is emphasized. Numerical experiments indicate that it is possible to get the Courant-Snyder parameters for the halo by using weighted moments with weight indices of about $n = -2$. A LP formulation of weighted moments is difficult (part of the problem is that they are defined by a nonlinear functional) and will not be done here. A nice feature of the weighted moments is that we already know the dynamics of these objects. Since the distribution function is constant on phase-space trajectories, so is any function of it. Thus

$$\frac{d}{dt}<g(x,p)>_n = <\frac{d}{dt}g(x,p)>_n, \tag{19}$$

just as for regular moments. So, we already know the linear invariants. For example, we have

$$<x^2>_n <p^2>_n - <xp>_n^2 = \text{const.}, \tag{20}$$

which is the weighted-moment analog of rms emittance.

Instead of using higher-order moments to achieve a more accurate beam description, we can combine second-order moments of various weights. In the absence of space charge, moments of different weights do not interact; core and halo evolve independently. Space charge introduces coupling through the force constants, which depend on the spatial moments of all weights.

7 DISCUSSION

Histogram variables are probably not the correct approach but could be usefully further studied because they so completely separate the halo and core of the beam. Weighted moments appear promising because they factor the core and halo motion in a very desirable way. They can give us the evolution of the Courant-Snyder parameters for the core and halo separately; there is no need to go to higher moments to see the halo. We need not consider higher moments unless the additional physics they represent is actually involved in halo generation. Another advantage of this approach is that it could be used to extend existing codes like TRACE 3-D[3] to include nonlinear effects.

8 ACKNOWLEDGEMENTS

We thank Paul Channell for helpful comments. This work was partially carried out at the Institute for Theoretical Physics, University of California, Santa Barbara, as part of the New Ideas for Particle Accelerators Program with partial support by the U.S. Department of Energy and the National Science Foundation.

9 REFERENCES

[1] Stephen Wolfram, *The Mathematica Book*, 3rd ed., Wolfram Media/Cambridge University Press (1996).

[2] W.P. Lysenko, "The moment approach to high-order accelerator beam optics," Nucl. Instr. and Meth. in Phys. Res. A 363 (1995) 90-99.

[3] D.P. Rusthoi, W.P. Lysenko, and K.R. Crandall, "Further improvements in TRACE 3-D," (this conference).

EQUIPARTITIONING IN A HIGH CURRENT PROTON LINAC*

Lloyd M. Young
Los Alamos National Laboratory, MS H817, Los Alamos, NM 87545, USA

Abstract

The code PARMILA simulates the beam transmission through the Accelerator for the Production of Tritium (APT) linac. The beam is equipartitioned when the longitudinal and transverse temperatures are equal. This paper explores the consequence of equipartitioning in the APT linac. The simulations begin with a beam that starts at the ion-source plasma surface. PARMILA tracks the particles from the RFQ exit through the 1.7-GeV linac. This paper compares two focusing schemes. One scheme uses mostly equal strength quadrupoles. The equipartitioning scheme uses weaker focusing in the high-energy portion of the linac. The RMS beam size with the equipartitioning scheme is larger, but the relative size of the halo is less than in the equal-strength design.

INTRODUCTION

R. Jameson and Martin Reiser recommend tailoring the transverse focusing in high-current linacs to equipartition [1,2] the beam. To explore the merits of equipartitioning I compare simulations of the beam distributions through two linacs, one with equipartitioning and one without equipartitioning. The two linacs are identical up to 25 MeV. In both cases the simulations follow the same particle collection to the end of the linac at 1.7 GeV. The code PARMELA [3] simulates the transport of the beam through the ion source extractor and the low-energy beam-transport line (LEBT) to the radio frequency quadrupole (RFQ) [4]. PARMELA uses electrons to simulate space charge neutralization in the first 40 cm of the LEBT. For the remainder of the LEBT, PARMELA simulates space charge neutralization by reducing the effective charge to 4% of the proton-beam charge. The input distribution to the RFQ obtained this way is quite different from the "type 6" distribution normally used in the code PARMTEQM [5]. This beam is rotating in real space because it is "born" in the longitudinal magnetic field of the ion source. It also has a hole in the center. The code PARMTEQM generates the "type 6" distribution by placing the particles randomly in a four-dimensional transverse hyperspace with uniform phase and no energy spread. The beam current after the RFQ was 100 mA. PARMELA, PARMTEQM, and PARMILA[6] performed all of the simulations shown in this paper with 100,000 macro particles.

THE EQUIPARTITIONING CONCEPT

Equipartitioning implies: $\varepsilon_x^2/x_{rms}^2 = \varepsilon_y^2/y_{rms}^2 = \varepsilon_z^2/(\gamma \cdot z_{rms})^2$, where γ is the relativistic ratio of total energy to rest mass, ε_x, ε_y, and ε_z are the normalized emittances for the transverse and longitudinal coordinates respectively. The respective RMS beam sizes are x_{rms}, y_{rms}, and z_{rms}. The RFQ, the coupled-cavity drift-tube linac (CCDTL), the coupled-cavity linac (CCL), and the superconducting (SC) linac have alternating gradient quadrupole focusing channels. These focusing channels cause the x_{rms} and y_{rms} values to oscillate about the equilibrium value $\sim\sqrt{x_{rms} \cdot y_{rms}}$. Therefore, averaging over these oscillations the partitioning ratios Ax and Ay are defined as:

$$Ax = \gamma^2 \left(\frac{\varepsilon_x^2}{x_{rms} \cdot y_{rms}} \right) \cdot \left(\frac{z_{rms}^2}{\varepsilon_z^2} \right), \quad Ay = \gamma^2 \left(\frac{\varepsilon_y^2}{x_{rms} \cdot y_{rms}} \right) \cdot \left(\frac{z_{rms}^2}{\varepsilon_z^2} \right).$$

Because the transverse emittances ε_x and ε_y are nearly equal, Ax and Ay will fall on top of each other when plotted.

THE RADIAL DISTRIBUTION

Comparison of Figures 1 and 2 shows that the particle distribution at the exit of the linac has no halo from the equipartitioned linac and a large halo from the nonequipartitioned linac.

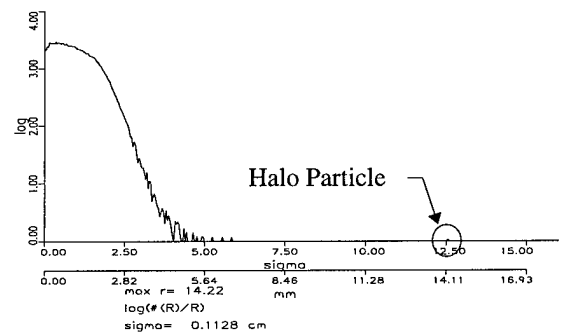

Figure 1. The logarithm of particle density versus radius in the nonequipartitioned linac.

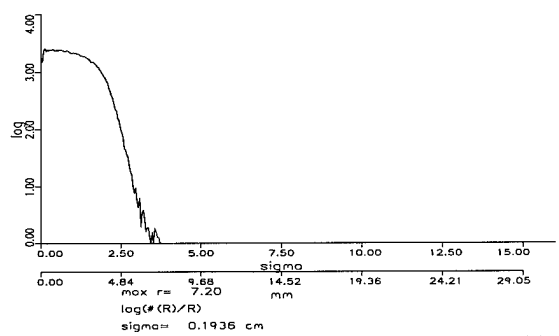

Figure 2. The distribution at the end of the equipartitioned linac.

These figures show the transverse distributions and the extent of the tail. The plots of the radial distribution are generated by populating the elements of an array

*Work supported by the US Department of Energy.

according to each particles' radial position **r**. The beam distribution is first normalized to circular symmetry. For example, if x_{rms} is smaller than y_{rms} all the x coordinates are multiplied by y_{rms}/x_{rms} then $r=\sqrt{y^2+\left(x\cdot y_{rms}/x_{rms}\right)^2}$. To plot the logarithm of this array we initialize the array elements to 1. Each element, which corresponds to a small range of r values, is increased by 1/r for each particle so that the final array gives the distribution of local particle density. The plots show the radial density distribution versus distance from the center of the beam. The upper abscissa on these plot has units of σ, the standard deviation, where σ is the larger of x_{rms} and y_{rms}. The lower abscissa is in mm.

The distribution in Figure 1 extends beyond 12 σ, while the largest particle radius occurs at 14.2 mm. In Figure 2 (the equipartitioned case) the distribution extends only to ~4 σ, and the largest radius is 7.2 mm. The beam expander and target designers prefer the distribution from the equipartitioned linac because the tails of the beam do not extend as far.

Figure 3 shows the zero-current phase advance in the nonequipartitioned linac from 100 keV to 1.7 GeV. Note that σ_{0l}/σ_{0t}, the ratio of the longitudinal phase advance to the transverse phase advance, increases beyond 25 MeV. Figure 4 shows the zero-current phase advance in the equipartitioned linac, where σ_{0l}/σ_{0t} is nearly constant throughout the linac. **Equipartitioning requires only this slight difference in the transverse focusing strength above 25 MeV.** The quadrupole strength at the end of the equipartitioned linac is 55% of the strength in the nonequipartitioned linac.

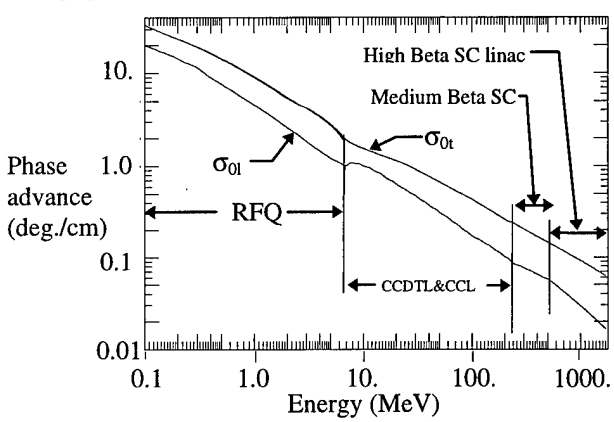

Figure 3. The zero-current phase advance σ_x, σ_y, and σ_l per unit length in the nonequipartitioned linac.

The APT linac uses normal conducting (NC) structures up to 217 MeV, and SC cavities from 217 MeV to 1.7 GeV. The NC linac consists of a 6.7-MeV RFQ, a CCDTL to 100 MeV, and a CCL to 217 MeV. PARMILA calculates the phase advance in the SC linac by averaging over one period of the lattice consisting of accelerating cavities and quadrupole magnets. The period in the SC linac is much longer than in the NC linac where the period spans two quadrupoles. A cryomodule has three SC cavities in the medium-β section (217 MeV to 469 MeV) and four SC cavities in the high-β section (469 MeV to the end). If the space between cryomodules contained an accelerating cavity the two-quadrupole period of the magnetic lattice would have been preserved. However, this warm space between the cryomodules is used by the valves and beam diagnostics. Therefore, the period in the medium-β section now spans four quadrupoles instead of two. In the high-β SC linac the period spans 10 quadrupoles.

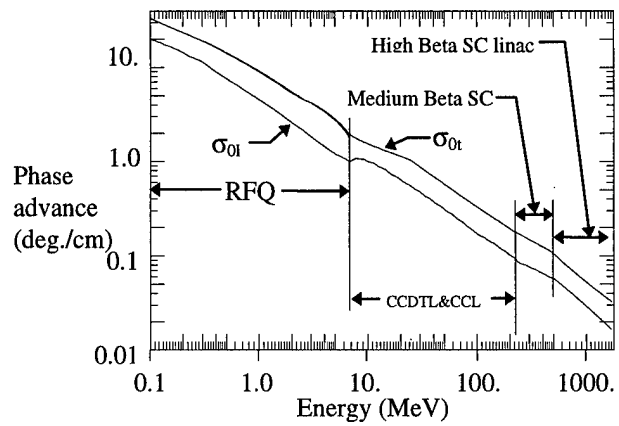

Figure 4. The zero-current phase advance σ_x, σ_y, and σ_l per unit length in the equipartitioned linac.

Figures 5 and 6 show the partitioning ratios Ax and Ay through the RFQ to the end of the linac. The slight excess of the longitudinal focusing between 7 and 20 MeV does not appear to cause any problems. The transverse focusing is as strong as the 8 $\beta\lambda$ period allows in this region. The only way to correct the equipartitioning ratio in this region is the use of a more gradual increase in the accelerating gradient.

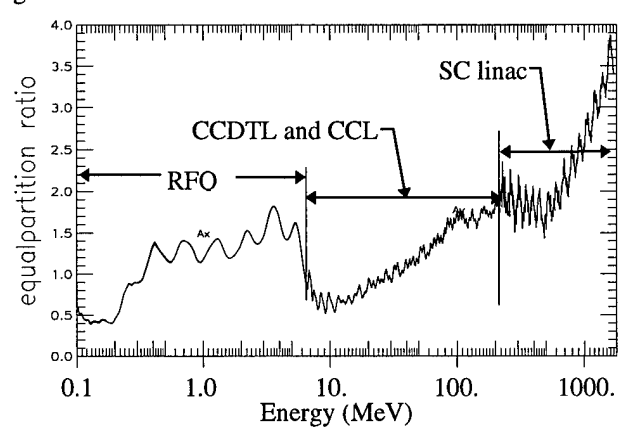

Figure 5. The partitioning ratio Ax and Ay in the nonequipartitioned linac.

Although it is desirable to have these ratios near unity, they are extremely sensitive to mismatch. A slight mismatch at the entrance to the RFQ and CCDTL causes the oscillations of *Ax* and *Ay* in these figures. A larger mismatch between the CCL and the SC linac causes the large oscillations starting at 217 MeV.

The partitioning ratios are greater than 1.0 in most of the RFQ. In this structure we deliberately use strong transverse focusing relative to the longitudinal focusing to minimize the beam loss. Any halo that develops in the RFQ is scraped off on the RFQ vanes. The smaller longitudinal acceptance of the 700-MHz CCDTL

compared to the 350-MHz RFQ required relatively stronger longitudinal focusing. This bias toward reducing beam loss in designing the APT front end resulted in partitioning ratios greater than 1 in the RFQ and less then 1 near the end of the RFQ and in the low-energy portion of the CCDTL. For higher beam energy, the longitudinal focusing weakens faster than the transverse focusing does. Thus, for fixed accelerating gradient, the partitioning ratios tend to grow at high energy without a reduction in the transverse focusing. (The accelerating gradient is limited by power loss considerations in the NC linac and by peak electric field in the SC linac.)

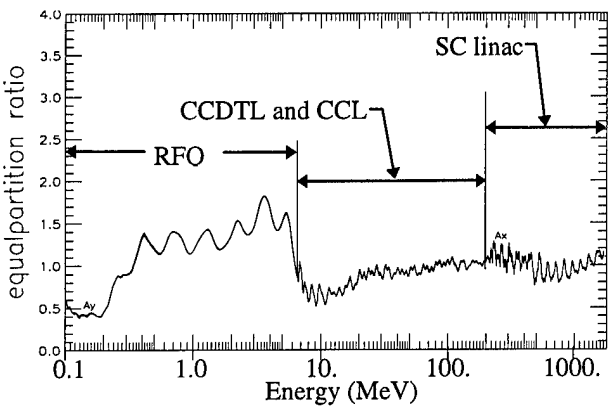

Figure 6. The partitioning ratio Ax and Ay in the equipartitioned linac.

In the equipartitioned linac the quadrupole strength tapers off slowly with increasing energy from the 25-MeV point to the end of the linac. Figure 6 shows the ratios Ax and Ay in the equipartitioned linac. To match the transverse focusing in the CCL to the SC linac, the quadrupole strength in the nonequipartitioned linac is also reduced with increasing energy from 100 MeV to 217 MeV. This reduction smoothly matches the transverse focusing in the CCL to the transverse focusing in the SC linac, which has a longer period.

From 217 MeV to 469 MeV, in both the equipartitioned linac and the nonequipartitioned linac the synchronous phase slowly increases from −25° to −35°, while the strength of the quadrupoles remains constant. This phase ramp matches the longitudinal focusing of the CCL to the medium-β SC section and the medium-β to the high-β SC section. The high-β SC section has a higher average accelerating gradient than the medium-β SC section. The CCL and the high-β SC section both have a synchronous phase of −30°. Coincidentally in the equipartitioned linac, this phase ramp tailors the longitudinal focusing sufficiently to maintain the partitioning ratio close to 1.

Comparison of the beam size shown in Figs. 7 and 8 for the two designs shows that a halo develops in the nonequipartitioned linac, but not in the equipartitioned linac. This halo extends to about 12 times the RMS beam size. In the beam-dynamics simulations the halo develops in the NC accelerator between 50 and 100 MeV. In both simulations, the beam is matched in exactly the same.

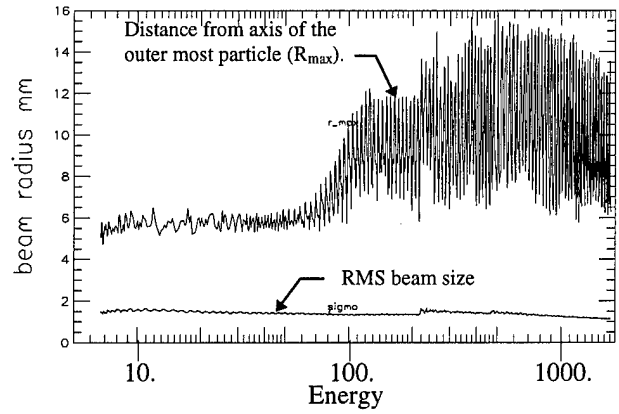

Figure 7. Beam size in the nonequipartitioned linac.

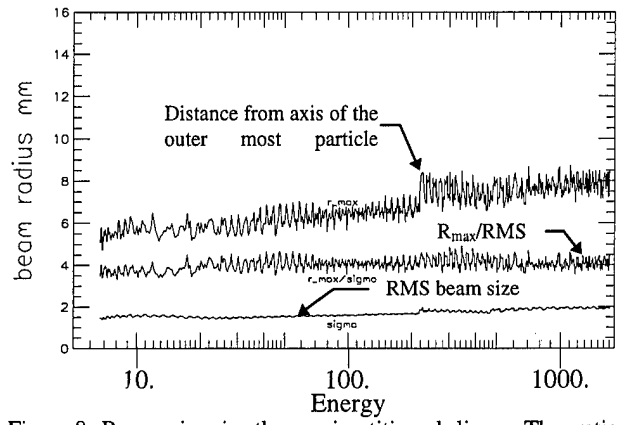

Figure 8. Beam size in the equipartitioned linac. The ratio R_{max}/(RMS beam size) is also plotted.

CONCLUSIONS

Virtually no halo developed in the equipartitioned linac with some mismatch while a substantial halo developed in the nonequipartitioned linac. Other simulations, not presented here, show that a large mismatch will cause halo to develop in an equipartitioned linac, but to less extent relative to the rms beam size than in a nonequipartitioned linac.

REFERENCES

[1] R. A. Jameson, "On Scaling & Optimization of High Intensity, Low-Beam-Loss RF Linacs for Neutron Source Drivers", AIP Conf. Proc. 279, ISBN 1-56396-191-1, DOE Conf-9206193 (1992) 969-998, Proc. Third Workshop on Advanced Accelerator Concepts, 14-20 June 1992, Port Jefferson, Long Island, NY, (LA-UR-92-2474, Los Alamos National Laboratory).

[2] Martin Reiser, "Theory and Design of Charged Particle Beams," John Wiley & Sons, Inc., p. 573 (1994).

[3] L. M. Young and J. H. Billen, "PARMELA," Los Alamos National Laboratory report LA-UR-96-1835 (revision March 14, 1997).

[4] L. M. Young, "Simulations of the LEDA RFQ 6.7 MeV Accelerator", this conference.

[5] Kenneth R. Crandall, et al., "RFQ Design Codes," Los Alamos National Laboratory report LA-UR-96-1836 (revision February 12, 1997).

[6] H. Takeda and J. E. Stovall, "Modified PARMILA Code for New Accelerating Structures," Proc. of the 1995 Particle Accelerator Conf, p. 2364 (May 1-5, 1995, Dallas, Texas).

NUMERICAL SIMULATION STUDIES OF THE LBNL HEAVY-ION BEAM COMBINER EXPERIMENT

W.M. Fawley and P. Seidl, Lawrence Berkeley National Laboratory, Berkeley, CA 94720
I. Haber, Naval Research Laboratory, Washington, D.C. 20375
A. Friedman and D.P. Grote, Lawrence Livermore National Laboratory, Livermore, CA 94550

Abstract

Transverse beam combining is a cost-saving option employed in many designs for heavy-ion inertial fusion energy[1] drivers. A major area of interest, both theoretically and experimentally, is the resultant transverse phase space dilution during the beam merging process. Currently, a prototype combining experiment is underway at LBNL and we have employed a variety of numerical descriptions to aid in both the initial design of the experiment as well as in the interpretation of the experimental data. These range from simple envelope codes to detailed 2- and 3-D PIC simulations. We compare the predictions of the different numerical models to each other and to experimental data at different longitudinal positions.

1 INTRODUCTION

In the heavy-ion approach to inertial fusion energy(IFE), transverse beam combining is an attractive, cost-savings option in many designs based on the induction linac approach. The basic reason for this is that in the low energy end of the accelerator near the injector, it is generally most cost-effective to employ electrostatic, quadrupole focusing. Due to electrical breakdown constraints, one is then forced to use subdivide the current into a large number of beamlets. As the beams accelerate to higher energies, eventually magnetic quadrupoles become more attractive for transverse focusing , in part because they more efficiently transport higher currents per beamlet. Hence, transverse beam-combining is seen as a useful (although not necessarily essential) transition from electrostatic to magnetostatic focusing.

Presently at LBNL, a prototype combining experiment employing the MBE-4 injector at 160 keV and four new Cs^+, 5 mA sources is underway. The actual beam combining/merging region is composed of a number of electrostatic quadrupoles (labeled Q1-4) and a combined function elements (QD5) whose purpose is to first bring the four individual beamlets close together in a "Stonehenge" configuration, and then merge them into one large beam with (hopefully) minimal current loss and transverse phase space dilution. Details concerning the actual beamline layout of MBE-4 combiner experiment may be found in the accompanying paper Seidl *et al.*[1]. In support of the experiment, we have conducted a relatively extensive set of numerical simulations, employing a variety of codes ranging from simple envelope models to 2- and 3-D PIC simulations which include detailed modeling of the complex geometry of the focusing elements. Our basic concerns include obtaining good agreement with the measured beamlet properties both in the upstream (of QD5) transport region (where nonlinear effects are generally small) and the downstream region (where the merged beamlets have encountered strong nonlinear space charge fields and is undergoing mismatch oscillations). The remainder of this paper first discusses the simulation tools used in our study and then several comparisons between simulation and experimental data.

[1]see the U.S. HIF WWW site http://fusion.lbl.gov/

2 SIMULATION CODE DESCRIPTIONS

The **HIBEAM** 2D, electrostatic code was originally written by K. Hahn of LBNL and closely follows the structure of its forerunner, the venerable SHIFT-XY[2]. HIBEAM has recently been ported to Fortran90 which has aided considerably in its maintainability and extendibility. The field solver employs an FFT together with a capacity matrix for inclusion of conducting electrodes (and image charges thereon). At present, the code does not include a fringe field model.

Our most comprehensive simulation tool for modeling the combiner experiment is the 3D, electrostatic PIC code **WARP3D**[3]. Via an FFT or SOR field solver, the code models the full 3D fields of both the heavy-ion beam and of conducting electrodes, including fringe and image charge components. Unfortunately, we were unable to complete the necessary coding in WARP3D to model the QD5 "squirrel cage" combined function element. Consequently, the WARP3D simulations stop just upstream at the M2 diagnostic. For computational efficiency, the simulations model the time-steady transport of the longitudinal beam center. This is done by continuously injecting beam at the upstream entry plane and, once a time-steady state is evident throughout the simulation grid, stopping the simulation and diagnosing beam properties as a function of z.

3 BEAM BEHAVIOR FROM THE SOURCE TO THE M2 DIAGNOSTIC PLANE

We began the numerical simulations at an entry plane just beyond the cathode plate which terminates the diode. These simulations model the "unapertured" beamlets with initial currents of 4.8 mA and normalized "edge" emittances of 2.0×10^{-8} m-rad. Since there was no phase space diagnostics at the entry plane, it was necessary to infer the initial beam conditions by using experimental data for

0-7803-4376-X/98/$10.00 © 1998 IEEE

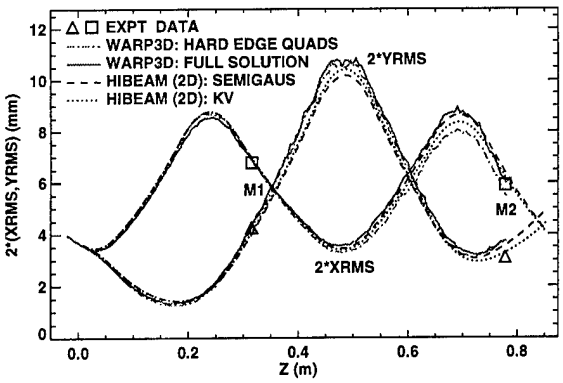

Figure 1: Predicted x and y beam envelope extents plotted versus z from both HIBEAM and WARP3D simulation code results. The open triangles and squares refer to experimental data taken at the M1 and M2 diagnostic planes.

(a, b, a', b') at the M1 diagnostic location 0.315 m downstream and then integrating the envelope equation backwards. Figure 1 displays the HIBEAM and WARP3D predictions for the beamlet envelope (defined to be twice the RMS radius) in each plane together with experimental measurements at M1 and M2. Two sets of WARP3D results are shown: one corresponding to a full field solution and a second set ("HARD EDGE QUADS") in which the voltages on the quadrupole electrodes were set exactly to zero and an external, linear focusing field was applied at those z-locations corresponding to the quadrupole rods. This field solution thus ignores higher order multipoles and fringe field terms but does include the effects of image charges. The two HIBEAM runs differ only in the initial phase space distributions, one employing a semi-Gaussian and the other a K-V distribution. One sees that, not surprisingly, there is good agreement between experiment and simulation for beam envelope sizes at M1 and fair agreement at the M2 diagnostic location.

We believe that the discrepancies between the experimental data and simulation results at M2 arise for a number of reasons. First, the large excursions (see Fig. 1) in the envelope radii in both planes (especially the tight focus of $\approx$1.5 mm at z=0.18 m near Q2) cause the beam behavior downstream of Q2 to be quite sensitive to the transport system parameters. For example a change of only a few percent in the quadrupole gradients of one of the lenses can result in a substantial movement of the longitudinal position of a downstream beam waist which occurs quite close to the M2 diagnostic plane. Such movement can significantly modify the predicted beam divergence/convergence angles a',b' at M2. Similarly, small differences between the numerical code representation and the actual physical structures, such as might arise from numerical algorithm inaccuracies or alignment errors, can also be magnified by this effect. Second, an additional source of uncertainty results from the use of the backward integration of envelope equation from M1 to infer beam parameters at the entry plane. If the beam phase space deviates in any significant fashion from the presumed K-V distribution of the envelope solution, this produces an additional inconsistency between the assumed entry condition and the actual experiment. Since the HIBEAM K-V simulation shows the best agreement at M2 for beam envelope size, we suspect that a more direct measurement of beam phase space properties near the entrance plane would produce much better agreement between the semi-Gaussian runs of both WARP and HIBEAM.

One of the more gratifying comparisons to come out so far between experiment and simulation is the actual phase space shape at the M2 diagnostic location. In the $y - y'$ projection (where the beamlet is just beyond a waist and diverging), both HIBEAM (Fig. 2) and WARP3D (not shown) predict a pronounced "S"-ing. This is also seen clearly in the experimental measurements (Fig. 3). Surprisingly, this shape is *not* due to focusing nonlinearities but rather to the strong compression of the initially semi-Gaussian phase space distribution near Q2. If a K-V initial distribution is chosen for the simulation, no such "S" develops. It appears that the semi-Gaussian's thermal spread in velocity space is rotated into a "halo" in configuration space at the beam waist, which is accompanied by a strong nonlinear space charge force in the outer portions of the beam. This nonlinearity then results in the outermost particles having a smaller tune depression and thus rotating more rapidly in phase space with z. The commonality of 2- and 3-D simulation results has been extremely useful in delineating the physics underlying the phase space distortion.

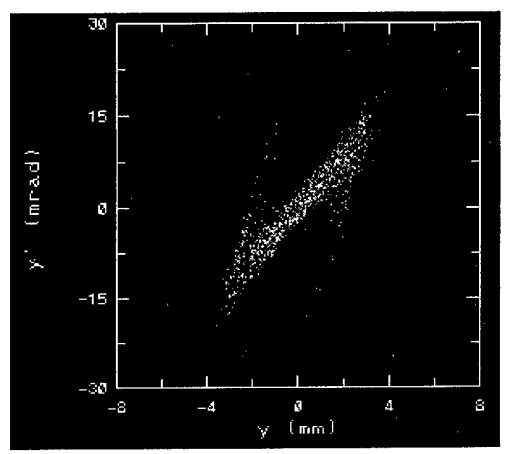

Figure 2: HIBEAM-predicted $y - y'$ phase space at the M2 diagnostic location. This run was initialized with a semi-Gaussian phase space distribution.

4 BEAM BEHAVIOR IN THE QD5 "SQUIRREL CAGE"

The last focusing element before the beamlet merge point is the combined function (dipole/quadrupole) electrostatic element QD5 commonly referred to as the "squirrel cage". Approximately 70 separate, cantilevered tungsten rods sur-

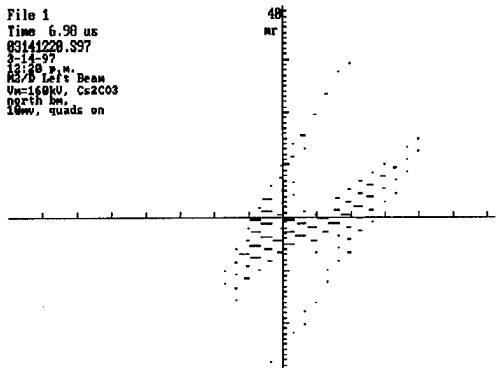

Figure 3: Experimental phase space data at the M2 diagnostic location for the left beamlet. The length of the horizontal bars indicate the signal amplitude. The major tick marks on the abscissa correspond to 1 mm intervals.

round four separate openings arranged in a tapered (with z) "Stonehenge" geometry for the individual beamlets. The beamlets enter the cage at a six degree angle relative to the downstream central axis with a converging focus in the transverse plane parallel to their offset. The individual voltages on the tungsten rods are designed to remove both the six degree angle (via the dipole component) and the convergence (via the quadrupole component) by the exit point from the cage.

Utilizing a 3D capacity matrix in order to take into account the effects of the taper, fringe fields, and the discrete azimuthal nature of the rods (but not image charge forces), we performed detailed calculations[4] during the design stage to determine an optimum set of individual voltages for the squirrel cage rods. In Fig. 4 we plot the predicted beam offsets versus z from both the full 3D calculation (which uses the values of the z-varying line charges on the discrete tungsten rods) and the HIBEAM code results (whose 2D solution includes the local effect of the taper but not fringe fields). In this figure, the cage extends longitudinally from -40 to +40 mm. In order to remove (empirically) the full six degree offset by cage exit, it was necessary in the HIBEAM calculation to increase the cage voltages a uniform 14% from their nominal values. This correction was *not* necessary for the 3D solution - examination of $y'(z)$ for the top cage and $x'(z)$ for the side cage respectively shows that both the upstream and downstream fringe fields remove approximately 6 mrad from the input 105 mrad angle which we believe is the major difference between the 2- and 3-D calculations. Experimentally, it appears (as of May 1997) that the nominal cage voltages may be slightly (of order a few percent) *too high*. If so, this may be related to details of the exact geometry that the wire leads in the individual rods follow of the MACOR plate supporting the cage assembly (A. Faltens, private communication). Any "energy effect" (which is not modeled in HIBEAM) would be in the opposite direction because each beam accelerates a couple percent as it enters the cage.

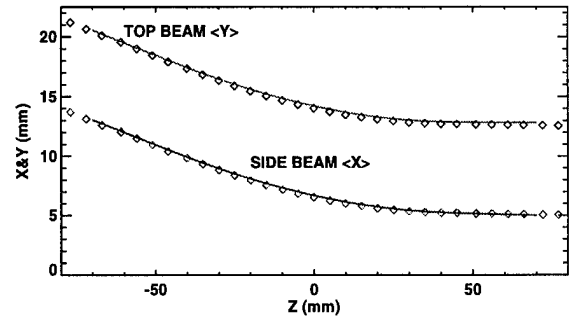

Figure 4: Top and side beam offsets in the squirrel cage (relative to the downstream central axis). The solid lines are predictions using the "exact" 3D capacity matrix solution whereas the open triangles are HIBEAM simulation results.

5 MERGED BEAM BEHAVIOR BEYOND THE SQUIRREL CAGE

With the cage exit at 0.96 m downstream of the entry plane, the first diagnostic location beyond the merge point is M4 at 1.33 m, by which point the beamlets have passed the Q6 and Q7 quadrupoles. Although the predicted nonlinear curvature for each beamlet is small (see Fig. 3 of Ref .[1]) one notices that divergence angles of the outboard beamlets visibly differ from that of inboard beamlets. This undesirable feature arose from upstream lattice modifications necessary both because of the larger current of the unapertured beamlets and an accompanying increase in their convergence angles at the diode exit relative to the original the original design values. After eventual downstrwam phase mixing, this produces a greater final emittance than would be true otherwise.

Preliminary M4 experimental data is in good agreement with both the beam sizes and the overall convergence/divergence angles but is insufficiently detailed to make fine comparisons on the sub-10-mrad scale.

6 ACKNOWLEDGEMENTS

This work was supported by the U.S. Department of Energy under Contracts No. DE-AC03-76SF00098 (LBNL), DE-AI02-94ER54232 (NRL), and W-7405-ENG-48 (LLNL), and used computational resources of the DOE NERSC.

7 REFERENCES

[1] P.A. Seidl *et al.*, "A Scaled Beam-Combining Experiment for Heavy Ion Inertial Fusion", these proceedings, Paper 8V46.

[2] I. Haber, in *High Current, High Brightness, High Duty Factor Ion Injectors*, **AIP Conf. Proc. 139**, Ed. G.H. Gillespie, (Amer. Inst. Physics, New York, 1986), p. 107 (1986).

[3] A. Friedman, D.P. Grote, D.A. Callahan, A.B. Langdon, and I. Haber, *Part. Accel.*, **37-38**, 131 (1992).

[4] W.M. Fawley: "Life on the Edge: Squirrel-Cage Fringe Fields and Their Effects in the MBE-4 Combiner Experiment", LBNL report *LBL-38399* (1996).

A SCALED BEAM-COMBINING EXPERIMENT FOR HEAVY ION INERTIAL FUSION

P. A. Seidl, C. M. Celata, W.W. Chupp, A. Faltens, W. M. Fawley, W. Ghiorso, K. Hahn, E. Henestroza, S. MacLaren, C. Peters, Lawrence Berkeley National Laboratory, Berkeley, CA 94720

Abstract

Transverse beam combining is a cost-saving option employed in many designs for induction linac heavy ion fusion drivers. The resultant transverse emittance increase, due predominantly to anharmonic space charge forces, must be kept minimal so that the beam remains focusable at the target. A prototype combining experiment has been built and preliminary results are presented. Four sources each produce up to 4.8 mA Cs^+ beams at 160 keV. Focusing upstream of the merge consists of four quadrupoles and a final combined-function element (quadrupole & dipole). All lattice elements of the prototype are electrostatic. Due to the small distance between beams near the merge (~ 3-4 mm), the electrodes here are a cage of small rods, each at different voltage.

1 MOTIVATION

Transverse beam combining is an important cost-saving feature of standard driver designs for heavy ion fusion. At the low-energy end of a driver, electrostatic quadrupoles are used to focus each beam of the multiple-beam array. Voltage breakdown and economic considerations dictate a small aperture for these quadrupoles, and thus a large number of beams. At higher energies it is more economical to accelerate fewer fatter beams through large-aperture magnetic quadrupoles. Thus, transverse beam combining should be implemented at about 100 MeV.

Since space charge contributes significantly to the beam dynamics for these intense beams, the interactions between particles during merging serve as a source of emittance growth, along with the usual "phase space filling" seen, for instance, in beam stacking in storage rings. As shown in previous work[1], transverse emittance growth is minimized by packing the beams as tightly as possible. The experimental challenge is to position the beams with sufficient accuracy to allow tight packing, and to keep them focused as their centroids converge while preserving low emittance.

2 DESCRIPTION OF THE EXPERIMENT

At Lawrence Berkeley National Laboratory an experiment to demonstrate 4-to-1 transverse beam combining has been built on the old MBE-4 accelerator[2]. The MBE-4 apparatus is used mainly to provide a long transport channel; the "beam combiner" is new. The combiner, consisting of a Cs^+ source, 160 keV diode, and focusing transport channel for each of the four beams, replaces the old MBE-4 diode and matching system. The beamlines (including the sources and diodes) converge with angle of 6° relative to the combiner centerline. A computer-aided design (CAD) view of one of the combiner elements is shown in Fig. 1. Four electrostatic quadrupoles, followed by an electrostatic combined-function (quadrupole and dipole) element, are used to focus each beam and straighten its trajectory so that the beams emerge from the combiner almost parallel to the centerline of the MBE-4 transport channel. The design configuration for the beam cross sections as they emerge from the combiner is shown in Fig. 2. As can be seen, the cross section is x-y asymmetric to allow for good packing of the elliptical beams. After the combiner the merged beam is transported (without acceleration) and diagnosed in the remaining 30 lattice periods of one channel of MBE-4. Further description of the experimental setup is found in ref. [3] and [4].

Quadrupole and dipole fields in QD5 are produced by surrounding the beams with a "wire cage" of 71 1-mm diameter tungsten rods at a spacing of ~1 mm, approximately parallel to the beam path. The voltage on each rod is set according to the desired Dirichlet boundary condition, resulting in voltage differences of up to 1.5 kV from rod to rod.

Beam steering is accomplished with sources mounted on gimbals which allow them to rotate about their centers, followed by articulation in x and y of Q2. Both operations can be done in vacuum. Since the beams emerge from the combiner separated by about 4 mm, their clearance from the rods within the wire cage is only about a millimeter near the exit of the cage. Thus, steering must be correct to the sub-millimeter level.

3 PRELIMINARY RESULTS AND FUTURE PLANS

The combiner focusing elements have been fabricated and are operational. Most of the ions is transmitted through the wire cage with no evidence of voltage breakdown.

The experiment has begun to produce results, and this first round of measurements are providing guidance for beam steering adjustments and other modifications that are underway. What follows is a description of what we have measured to date and implications for future measurements.

The beam current from the four diodes has been measured with Faraday cups in place of the Q2 quadrupole array. Each beam is within ±2% of the design value of

0-7803-4376-X/98/$10.00 © 1998 IEEE

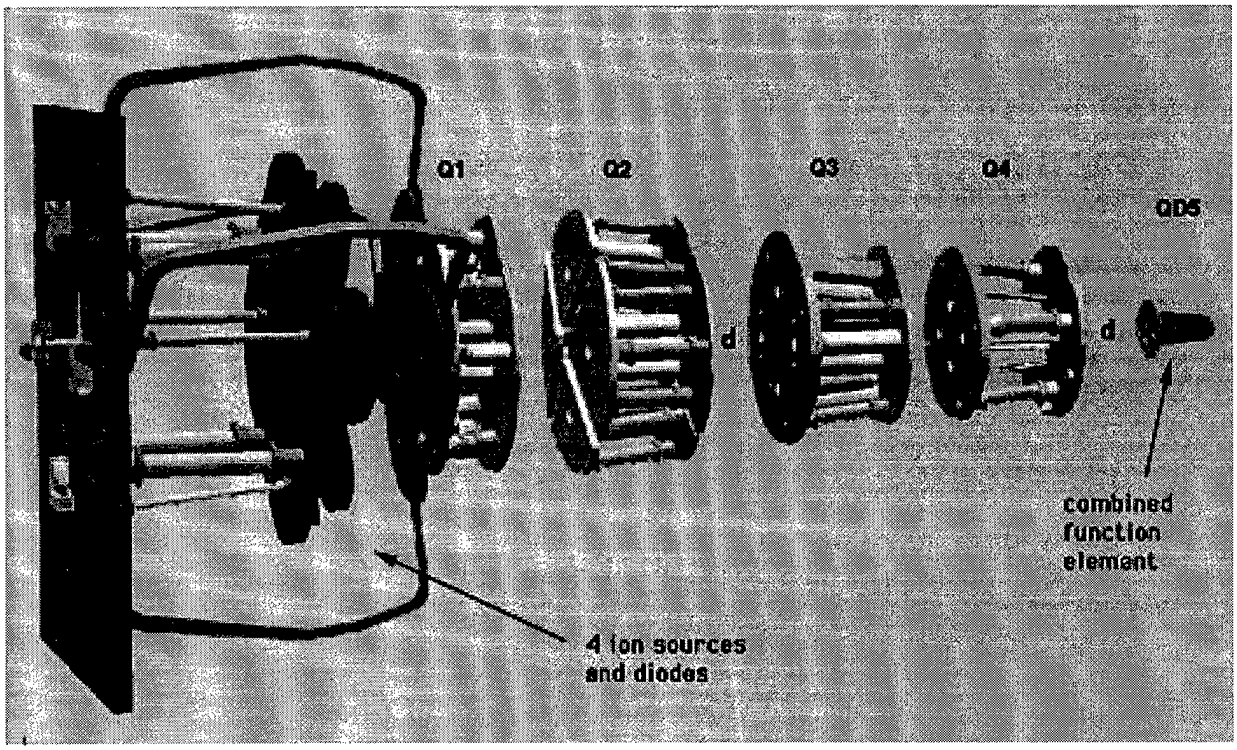

Figure 1. A CAD view of the lattice elements of the combiner apparatus. Diagnostics are at locations marked "d". The first four elements (Q1-Q4) are electrostatic quadrupoles. Each of the quadrupoles of Q2 are separately articulable. QD5 is the combined-function dipole and quadrupole. The distance from the source emitting surfaces to the end of the wire cage is ~108 cm. Downstream of QD5 the beams emerge into a 31 period transport lattice (Q7 - Q67).

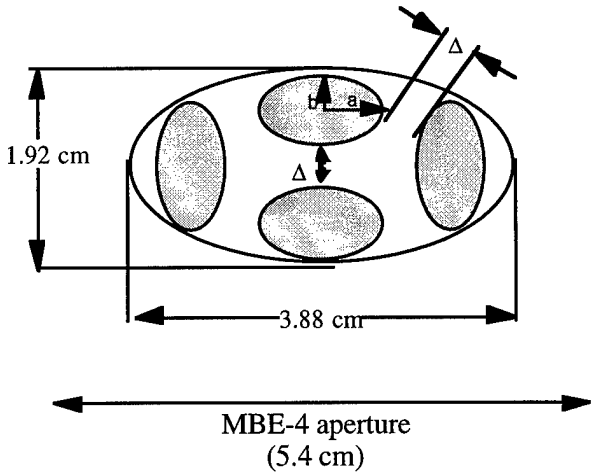

Figure 2: Design configuration of four beams as they emerge from the combiner. Beam semimajor and semiminor axes are 6.5 and 3.7 mm. Δ=4 mm.

4.75mA. This spread is consistent with the fabrication tolerances of the diode.

An aperturing mask between each diode exit and Q1 is designed to vary the current of the beams, allowing the study of merged beam phase space as a function of initial current. Phase space measurements show an unexpected, large convergence angle and a non-uniform beam profile, precluding properly matching the beam downstream. It appears that this problem is associated with secondary electron production and consequent perturbation of the ion beam properties due to the space charge of the electrons. Calculations are underway that will aid the design of a modified aperturing mask -- possibly incorporating added electric or magnetic fields -- to satisfactorily reduce the influence of secondary electrons on the ion beams.

2D and 3D particle-in-cell (PIC) simulations are used to help interpret the data. The simulations are described elsewhere in these proceedings [5]. The phase space measured at the first diagnostic station is in good agreement with the 2D PIC. Data at the second diagnostic location, just upstream of the wire cage, shows distortions in phase space that are also well reproduced by the 2D (and 3D) PIC simulation. This level of agreement lends confidence to the accuracy of the PIC simulation of this experiment and validates its use as an interpretive tool.

The third diagnostic station is located one quadrupole doublet downstream (after Q7) of the wire cage. Measurements of the merged beam current there indicate that most of the ions are transported through the wire cage (~70%). A phase space measurement of the merged beams at that location is compared to the 2D PIC simulation in Figure 3. There is rough agreement, and indications of misalignments of individual beams whose corrections are now being undertaken using the remotely articulable sources and Q2 array. Figure 3 also shows that the beams are relatively distinct and separated in phase space at this location, and are expected to remain so for several more lattice periods before the phase space

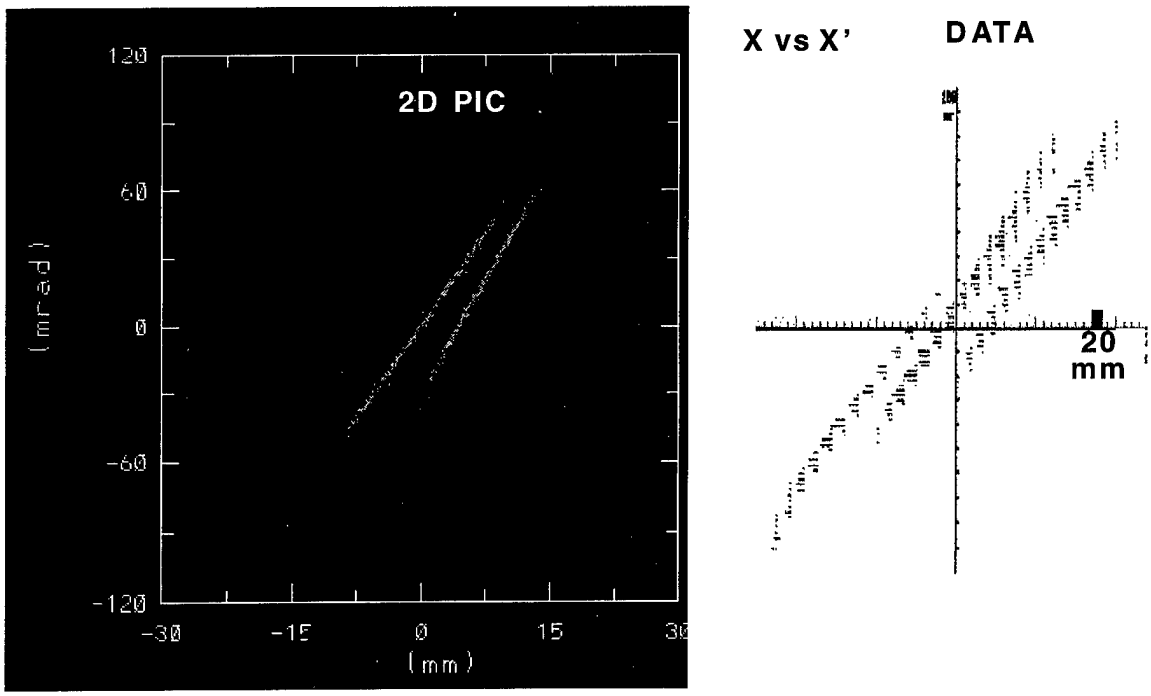

Figure 3: 2D PIC simulation of the merged beams compared to the phase space measured in the experiment at the third diagnostic location, or one quad doublet downstream of the wire cage. In this horizontal phase space, two of the four beams are at the middle. For the data, the length of the horizontal bars indicates the signal amplitude at the right edge of each bar. Table 1 shows the experimental parameters for the measurements and simulation.

TABLE 1: Experimental parameters for the data presented in this paper.

Initial current, one beam	4.8 mA
Ion kinetic energy	160 keV
beam edge radius (diode exit)	3.7 mm
beam edge convergence angle	-12 mr
Voltage of Q1	-5.032 kV
Voltage of Q2	-4.747 kV
Voltage of Q3	-4.867 kV
Voltage of Q4	-3.075 kV
Voltage of QD5	±3.800 kV
Voltage of Q6	-11.976 kV
Voltage of Q7	-17.361 kV
Voltage of Q8	-16.026 kV
Voltage of Q9	-14.207 kV
Voltages of Q10-67	-14.600 kV
Pressure in combiner	$<4\times10^{-6}$ Torr

becomes thoroughly mixed. This makes matching the beams to the downstream lattice a complicated function of the properties of each beam at the merge point and thus requires tight coupling of the experiment to simulation tools. Faraday cup measurements after Q17 show further beam loss. Along with capacitively coupled signals from electrostatic quadrupoles (sensitive to beam ions striking the quadrupole electrodes) the measurements are consistent with beam loss locations predicted by the 2D simulation.

The distinctness of the beams over several lattice periods downstream of the merge point leaves open the possibility of reducing the empty space between beams with non-linear correction elements.

Upcoming experimental efforts will include steering the beams and correcting the observed misalignments. The matching solution to the downstream lattice will be refined. Following the modification of the aperturing system, merging measurements with lower initial currents will be carried out.

4 ACKNOWLEDGEMENTS

The authors gratefully acknowledge the outstanding support of the LBNL technical staff led by Mr. R. Hipple and Mr. W. Strelo.

This work was supported by the Director, Office of Energy Research, Office of Fusion Energy, U.S. Dept. of Energy, under Contract No. DE-AC03-76SF00098.

REFERENCES

[1] C.M. Celata et al., Proc. of 1987 Part. Acc. Conf., Washington, D.C., 2 (1987), 1167.

[2] Thomas J. Fessenden, et al., Proc. of the 1987 Part. Acc. Conf., Washington, D.C., 2 (1987), 898.

[3] C.M. Celata et al., Proceedings of the 1995 Part. Acc. Conf., p. 3220.

[4] C.M. Celata et al., Fusion Eng. and Design, V32-33 (1996) 219.

[5] W.M. Fawley et al., "Numerical Simulation Studies of the LBNL Heavy-Ion Beam Combiner Experiment", these proceedings.

THEORY OF LONGITUDINAL BEAM HALO IN RF LINACS: I. CORE/TEST-PARTICLE FORMULATION*

John J. Barnard and Steven M. Lund
Lawrence Livermore National Laboratory, L-440, Livermore, CA 94550

Abstract

For intense beams, the analysis of tenuous halo components of the particle distribution that surround the main core of the beam can be challenging. So-called core/test-particle models in which a test-particle is evolved in the applied and space-charge forces of the beam core have been instrumental in understanding the structure and extent of transverse beam halo produced by resonant particle interactions with the oscillating space-charge forces of a mismatched beam core. Here we present a core/test-particle model developed for the analysis of longitudinal beam halo in intense, ion-beam rf linacs. Equations of motion are derived for a test-particle moving interior to, and exterior to, a uniform density ellipsoidal beam bunch. Coupled transverse-longitudinal mismatch modes of the ellipsoidal beam envelope are analyzed. Typical parameters suggest the possibility of a low-order resonant interaction between longitudinal particle oscillations and a low-frequency envelope mode. Properties of this resonance are analyzed in an accompanying paper by the authors in these proceedings[1].

1 INTRODUCTION

Ion linacs with high average current are being considered for applications such as the production of tritium and the transmutation of radioactive wastes. In such applications, beam halo can lead to a degradation of beam quality and/or particle losses resulting in activation of the accelerator. Therefore, the structure and control of halo components of the particle distribution is a critical issue. Recently, the understanding of transverse ($\perp$) beam halo has been advanced through analytic theory and numerical simulations[2–6]. In this and an accompanying article[1], we present theoretical and numerical work on longitudinal ($\|$) beam halo. Longitudinal halo particles are an issue of concern because such particles can have large-amplitude $\|$ oscillations about the synchronous particle, causing a degradation of $\|$ beam quality and possibly particle loss should the oscillation result in a loss of particle synchronisim with the rf fields. Moreover, the control of such halo losses could be challenging since the phase width of a beam bunch in the rf bucket cannot be made small in most intense-beam applications. In contrast, loss of $\perp$ halo particles can be mitigated, though with increased cost, through the use of large-aperture structures.

The core/test-particle model developed applies to a coasting ellipsoidal beam bunch that is continuously focused and has azimuthal symmetry. The space-charge of the bunch is assumed to remain uniformly distributed while undergoing coupled $\perp$ and $\|$ envelope mismatch oscillations, and details of the bunch velocity distribution are left unspecified. Self-field forces associated with the bunch are analytically calculated to obtain coupled equations of motion of a general test-particle undergoing both $\perp$ and $\|$ oscillations. These equations are employed to analyze $\|$ halo of on-axis particles (no $\perp$ motion) both with linear and nonlinear rf focusing, and to analyze effects of $\perp/\|$ coupling on halo particles (both $\perp$ and $\|$ motion).

To illustrate results, we employ the beam and accelerator parameters summarized in the Table. These parameters represent the 100 MeV and 1.2 GeV points of a conceptual coupled-cavity proton linac (normal conducting design) for the Accelerator Production of Tritium (APT) project[6]. In this design, an intense proton beam is accelerated from 100 MeV to 1.3 GeV over 1060 meters, and beam halo is an issue of concern.

Proton Energy, $\mathcal{E}_s$	GeV	0.1	1.0
Bunch Current, I	mA	200	200
Sync. Particle Phase, ϕ_s	degrees	-30	-30
rf Frequency, ν	MHz	700	700
Betatron "Freq.", $k_{\beta 0}$	rad/m	1.04	0.204
Synchrotron "Freq.", k_{s0}	rad/m	0.30	0.041
$\perp$ Norm. Emit., $\gamma_s\beta_s\epsilon_{x,rms}$	mm-mr	0.24	0.24
$\|$ Norm. Emit., $\gamma_s\beta_s\epsilon_{z,rms}$	mm-mr	0.58	0.62

Table 1: APT parameters in coupled cavity linac.

2 THEORETICAL MODEL

We consider an isolated ellipsoidal beam bunch composed of a single species of ion of charge q and mass m. The bunch is centered about a synchronous particle with phase $\phi = \phi_s$ relative to the peak of the synchronous space harmonic of the full rf wave. Acceleration is neglected, and the synchronous particle has $\|$ kinetic energy $\mathcal{E}_s$ =const. Beam focusing is provided transversely by a constant, linear applied field that represents the average effect of an alternating gradient focusing lattice, and longitudinally by a continuous sinusoidal wave that represents the average effect of the synchronous rf space harmonic. The bunch is taken to be azimuthally symmetric ($\partial/\partial\theta = 0$) and to have uniformly distributed charge-density $\bar{\rho}$ = const interior to a sharp ellipsoidal envelope specified by $(\mathbf{x}_\perp/r_\perp)^2 + (\Delta z/r_z)^2 = 1$, and zero charge-density exterior to the envelope. Here, $\mathbf{x}_\perp$ and Δz are the $\perp$ and $\|$ coordinates relative to the synchronous particle, and $r_\perp$ and r_z are the $\perp$ and $\|$ radii of the ellipsoidal beam enve-

* Work performed under the auspices of the U.S. D.O.E. by LLNL under contract W-7405-ENG-48

0-7803-4376-X/98/$10.00 © 1998 IEEE

lope. The $\parallel$ coordinate Δz is related to the rf phase ϕ by $\Delta z = -(\beta_s\lambda/2\pi)\Delta\phi$, where $\Delta\phi \equiv \phi - \phi_s$, λ is the vacuum wavelength of the rf wave ($\lambda = c/\nu$, where c is the speed of light in vacuo and ν is the rf frequency), and β_s and $\gamma_s = 1/\sqrt{1-\beta_s^2}$ denote the usual synchronous particle relativistic factors. Denoting the time average current of the bunch over an rf period by I, the charge-density in the bunch is $\bar{\rho} = 3I\lambda/4\pi r_\perp^2 r_z c$.

The $\perp$ and $\parallel$ forces acting on a particle due to electrostatic and leading-order self-magnetic fields can be calculated in the absence of material boundaries as[7]

$$\begin{aligned} F_\perp &= \tfrac{q\bar{\rho}}{2\epsilon_0\gamma_s^2}\left[\tfrac{\alpha^2}{(\alpha^2+\chi)(1+\chi)^{1/2}} - F(\chi,\alpha)\right]\mathbf{x}_\perp, \\ \Delta F_z &= \tfrac{q\bar{\rho}}{\epsilon_0}F(\chi,\alpha)\Delta z. \end{aligned} \tag{1}$$

Here, ϵ_0 is the permittivity of free-space,

$$F(\chi,\alpha) \equiv \tag{2}$$

$$\begin{cases} \frac{\alpha^2}{1-\alpha^2}\left[\frac{1}{\sqrt{1-\alpha^2}}\tanh^{-1}\left(\frac{\sqrt{1-\alpha^2}}{\sqrt{1+\chi}}\right) - \frac{1}{\sqrt{1+\chi}}\right], & \alpha < 1, \\ \frac{1}{3(1+\chi)^{3/2}}, & \alpha = 1, \\ \frac{\alpha^2}{\alpha^2-1}\left[\frac{1}{\sqrt{1+\chi}} - \frac{1}{\sqrt{\alpha^2-1}}\tan^{-1}\left(\frac{\sqrt{\alpha^2-1}}{\sqrt{1+\chi}}\right)\right], & \alpha > 1, \end{cases}$$

$\alpha = r_\perp/\gamma_s r_z$ is the aspect ratio of the ellipsoidal beam as measured in the synchronous-particle frame, and χ is the positive root of the equation

$$\frac{\alpha^2(\mathbf{x}_\perp/r_z)^2}{\alpha^2+\chi} + \frac{(\Delta z/r_z)^2}{1+\chi} = 1 \tag{3}$$

for a particle exterior to the bunch envelope [i.e., $(\mathbf{x}_\perp/r_z)^2 + (\Delta z/r_z)^2 > 1$], and $\chi = 0$ for a particle interior to the bunch [i.e., $(\mathbf{x}_\perp/r_z)^2 + (\Delta z/r_z)^2 < 1$]. For the special cases of a particle in the beam, $\chi = 0$, and the self-field forces (1) reduce to the familiar linear expressions[8,9], and for a spherical bunch in the beam frame ($r_\perp = \gamma_s r_z$), the forces fall off with the required inverse-square form exterior to the bunch.

Within the paraxial approximation, the $\perp$ and $\parallel$ equations of motion of a single test-particle moving in the applied focusing fields and self-field defocusing forces (1) of the bunch can be expressed as

$$\begin{aligned} &\tfrac{d}{ds}\mathbf{x}_\perp = \mathbf{x}'_\perp, \qquad \tfrac{d}{ds}\Delta\phi = -\tfrac{2\pi}{\gamma_s^3\beta_s^3\lambda}\tfrac{\Delta\mathcal{E}}{mc^2}, \\ &\tfrac{d}{ds}\mathbf{x}'_\perp = -k_{\beta 0}^2\mathbf{x}_\perp + \tfrac{K_{3D}}{2r_\perp^2 r_z}\left[\tfrac{\alpha^2}{(\alpha^2+\chi)(1+\chi)^{1/2}} - F(\chi,\alpha)\right]\mathbf{x}_\perp, \\ &\tfrac{d}{ds}\left(\tfrac{\Delta\mathcal{E}}{mc^2}\right) = \tfrac{qE_0}{mc^2}\left[\cos(\Delta\phi+\phi_s) - \cos\phi_s\right] \\ &\qquad - \tfrac{\beta_s^3\gamma_s^3}{2\pi}\tfrac{\lambda K_{3D}}{r_\perp^2 r_z}F(\chi,\alpha)\Delta\phi. \end{aligned} \tag{4}$$

Here, s is the axial distance the beam has propagated, $\mathbf{x}_\perp$ and $\mathbf{x}'_\perp$ are the $\perp$ coordinate and convergence angle of the particle, $\Delta\phi$ and $\Delta\mathcal{E} = \mathcal{E} - \mathcal{E}_s$ are the $\parallel$ particle phase and kinetic energy relative to the synchronous particle, $k_{\beta 0}$ =const is the undepressed ($I = 0$) betatron wavenumber of $\perp$ particle oscillations, E_0 ($E_0 \to E_0 T$ for a standing-wave structure, with T the transit-time factor) is the peak, on-axis ($\mathbf{x}_\perp = 0$) field value of rf wave, and $K_{3D} \equiv 3qI\lambda/4\pi\epsilon_0\gamma_s^3\beta_s^2 mc^3$ is a three-dimensional space-charge parameter of dimension length. In general, note that the $\perp$ and $\parallel$ Eqs. (4) are coupled due to the coordinate dependence in χ. However, for a particle moving within the bunch (i.e., $\chi = 0$) or along the axes of symmetry of the bunch (i.e., $\mathbf{x}_\perp = 0$ or $\Delta\phi = 0 = \Delta z$), the equations are uncoupled. Finally, for small $\parallel$ particle excursions from the synchronous particle with $2\pi|\Delta z|/\beta_s\lambda \ll 1$, the $\parallel$ rf focusing force becomes linear, i.e.,

$$\tfrac{qE_0}{\beta_s^2\gamma_s^3 mc^2}\left[\cos(\Delta\phi+\phi_s) - \cos\phi_s\right] \longrightarrow k_{s0}^2\Delta z, \tag{5}$$

where $k_{s0} \equiv \sqrt{2\pi qE_0\sin(-\phi_s)/\gamma_s^3\beta_s^3\lambda mc^2}$ is the wavenumber of undepressed "synchrotron" oscillations about the synchronous particle. In the presence of space-charge ($I \neq 0$) and within the bunch, it follows from Eqs. (4) that the characteristic $\perp$ and $\parallel$ spatial frequencies of undepressed particle oscillations $k_{\beta 0}$ and k_{s0} are depressed to

$$\begin{aligned} k_\beta^2 &= k_{\beta 0}^2 - \tfrac{K_{3D}}{2r_\perp^2 r_z}[1 - f(\alpha)], \\ k_s^2 &= k_{s0}^2 - \tfrac{K_{3D}}{r_\perp^2 r_z}f(\alpha), \end{aligned} \tag{6}$$

where $f(\alpha) \equiv F(\chi = 0, \alpha)$ is a beam aspect ratio form factor [corresponding to f in Ref. 8].

3 ENVELOPE EQUATIONS

To consistently determine the ellipsoidal bunch radii $r_\perp$ and r_z in terms of beam and accelerator parameters, it is necessary to derive so-called "envelope equations" for the evolution of $r_\perp$ and r_z. For a uniform density distribution, $r_\perp^2 = (5/2)\langle r^2\rangle$ and $r_z^2 = 5\langle\Delta z^2\rangle$, where $\langle\rangle$ indicates an average over the entire 3D distribution function. By taking derivatives of these relations and using the equations of motion (4), the envelope equations

$$\begin{aligned} \tfrac{d^2 r_\perp}{ds^2} &= -k_{\beta 0}^2 r_\perp + \tfrac{K_{3D}[1-f(\alpha)]}{2r_\perp r_z} + \tfrac{\epsilon_x^2}{r_\perp^3} \\ \tfrac{d^2 r_z}{ds^2} &= -f_{rf}(\zeta)\, k_{s0}^2 r_z + \tfrac{K_{3D}f(\alpha)}{r_\perp^2} + \tfrac{\epsilon_z^2}{r_z^3} \end{aligned} \tag{7}$$

are obtained[8,9]. Here, $f(\alpha) = F(\chi = 0, \alpha)$, $\epsilon_x^2 \equiv 25[\langle x^2\rangle\langle x'^2\rangle - \langle xx'\rangle^2] = 25\epsilon_{x,rms}^2$ and $\epsilon_z^2 \equiv 25[\langle\Delta z^2\rangle\langle\Delta z'^2\rangle - \langle\Delta z\Delta z'\rangle^2] = 25\epsilon_{z,rms}^2$ are the squares of the unnormalized $\perp$ and $\parallel$ 3D bunch emittances, and

$$f_{rf}(\zeta) = \tfrac{15}{\zeta^5}[(3-\zeta^2)\sin\zeta - 3\zeta\cos\zeta] \tag{8}$$

with $\zeta \equiv (2\pi/\beta_s\lambda)r_z$ is a nonlinear rf focusing factor.

Note that Eqs. (7) differs from those in Refs. 8 and 9 by the inclusion of a multiplicative factor $f_{rf}(\zeta)$, which arises when the external rf force is included in an average over the $\parallel$ coordinate. This factor approaches unity as $\zeta \to 0$, corresponding to small $\parallel$ beam extent r_z relative to the rf wavelength λ. Note that Eqs. (7) are not self-consistent in that the distribution function is *assumed* to evolve such that its density remains uniform within an ellipsoid, whereas in general, such evolution does not occur. It is hoped that, since the extent of the distribution is not constrained (though the form of the distribution is), the evolution of these envelopes is close to the actual evolution of rms measures of the radii, thereby providing halo particles with approximately correct space-charge impulses.

4 LINEAR ENVELOPE MODES

Denote stationary ($d/ds = 0$) equilibrium (subscript 0) solutions to the envelope equations (7) by $r_{\perp 0}$ and r_{z0}, and assume coupled, sinusoidally varying perturbations about the equilibrium radii of the form $r_\perp = r_{\perp 0} + \delta r_\perp e^{iks}$ and $r_z = r_{z0} + \delta r_z e^{iks}$ with constant amplitudes $\delta r_\perp$ and δr_z. For $|\delta r_{\perp,z}|/r_{\perp 0,z0} \ll 1$ these perturbations can be expanded to leading order in Eq. (7) to obtain the dispersion relation

$$k^4 - (K_{11} + K_{22})k^2 + K_{11}K_{22} - K_{12}K_{21} = 0 \quad (9)$$

for the mode wavenumber or spatial frequency k. Here,

$$\begin{aligned} K_{11} &= 4k_{\beta 0}^2 - \frac{K_{3D}}{r_{\perp 0}^2 r_{z0}}\left[1 - f(\alpha_0) - \frac{\alpha_0}{2}\frac{df(\alpha_0)}{d\alpha_0}\right], \\ K_{22} &= 4k_{s0}^2\left[f_{rf}(\zeta_0) + \frac{\zeta_0}{4}\frac{df_{rf}(\zeta_0)}{d\zeta_0}\right] \\ &\quad - \frac{3K_{3D}}{r_{\perp 0}^2 r_{z0}}\left[f(\alpha_0) - \frac{\alpha_0}{3}\frac{df(\alpha_0)}{d\alpha_0}\right], \qquad (10) \\ K_{12} &= \frac{K_{3D}}{2r_{\perp 0}^2 r_{z0}}\left[1 - f(\alpha_0) - \alpha_0\frac{df(\alpha_0)}{d\alpha_0}\right], \\ K_{21} &= \frac{K_{3D}}{r_{\perp 0}^2 r_{z0}}\left[2f(\alpha_0) - \alpha_0\frac{df(\alpha_0)}{d\alpha_0}\right], \end{aligned}$$

are equilibrium parameters. Since Eq. (9) is quadratic in k^2, two modes are present, a high frequency (HFM, $k \equiv k_H$) and low frequency mode (LFM, $k \equiv k_L$), each with a relative amplitude of $\perp$ to $\|$ oscillation given by

$$R \equiv \frac{\delta r_\perp / r_{\perp 0}}{\delta r_z / r_{z0}} = \frac{K_{12}}{k^2 - K_{11}}. \quad (11)$$

In the Figure, equilibrium and mode properties are presented as a function of bunch current I assuming fixed $\perp$ and $\|$ beam emittances ϵ_x and ϵ_z. Parameters correspond to the 100 MeV linac presented in the Table with I varied about the nominal 200 mA value.

5 CONCLUSIONS

From Figure a and c, it is apparent that for beams in which the $\perp$ / $\|$ applied focusing and equilibrium radii ratios $k_{\beta 0}/k_{s0}$ and $r_{z0}/r_{\perp 0}$ are of order a few, the frequencies of the HFM (k_H) and LFM (k_L) are well separated. (However, for the more recent superconducting design of APT, the ratio $r_{z0}/r_{\perp 0}$ is closer to unity[10] implying less separation of the oscillation frequencies.) From Figure c, note that the LFM is antisymmetric, with $\perp$ envelope excursions much smaller than $\|$ excursions, and 180 degrees out of phase. In contrast, the HFM is symmetric, with $\|$ excursions much smaller than $\perp$ excursions and in-phase. The frequency of the LFM falls between twice the $\|$ particle frequency within the beam ($\sim 2k_s$), and twice the undepressed frequency ($\sim 2k_{s0}$, i.e. twice the $\|$ particle frequency at large $|\Delta z|$ in the linear rf focusing approximation). Particles outside the beam envelope longitudinally will have an oscillation frequency between k_s and k_{s0}, suggesting a possible low-order (2:1) resonant interaction between $\|$ particle and envelope motion. This situation is analogous to the transverse case[2-5] and has analogous implications for longitudinal beam halo. This longitudinal resonance is analyzed in an accompanying paper[1].

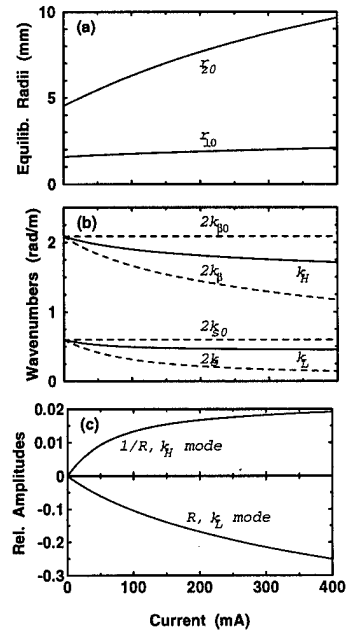

Figure 1: Ellipsoidal beam equilibrium and mode properties as a function of current. **a.** Equilibrium beam radii $r_{\perp 0}$ and r_{z0}. **b.** Wavenumbers for high (k_H) and low (k_L) frequency envelope modes (solid curves), and two times the undepressed and depressed frequencies of $\perp$ ($k_{\beta 0}$, k_β) and $\|$ (k_{s0}, k_s) particle oscillations (dashed curves). **c.** Ratio R of $\perp$ to $\|$ mode amplitude for the high and low frequency envelope modes.

6 ACKNOWLEDGMENTS

The authors wish to thank Rob Ryne, Tom Wangler, and Bob Gluckstern for many valuable discussions on beam halo and their support of this project.

7 REFERENCES

[1] S.M. Lund and J.J. Barnard, "Theory of Longitudinal Beam Halo in RF Linacs: II. Envelope/Particle Resonances," these proceedings.

[2] J.S. O'Connell, T.P. Wangler, K.R. Krandall, Proc. 1993 Part. Accel. Conf., Washington DC, p. 3657.

[3] R.A. Jameson, loc. sit. 2, p. 3926.

[4] R.L. Gluckstern, Phys. Rev. Letters, **73**, 1247, (1994).

[5] R.D. Ryne, T.P. Wangler, Proc. Accel. Driven Transmutation Tech. Conf., Las Vegas, NV, July 1994.

[6] J. Stovall et al., APT Design Review Presentation, Los Alamos National Laboratory, Oct., 1996.

[7] J.J. Barnard and S.M. Lund, "Theory of Longitudinal Beam Halo in High Current Ion RF Linacs," in prep.

[8] T.P. Wangler, "Introduction to Linear Accelerators," Los Alamos Report, LA-UR-94-125 (1994).

[9] M. Reiser, "Theory and Design of Charged Particle Beams," (Wiley & Sons, New York, 1994).

[10] T.P. Wangler, private communication (1997).

THEORY OF LONGITUDINAL BEAM HALO IN RF LINACS: II. ENVELOPE-PARTICLE RESONANCES*

Steven M. Lund and John J. Barnard
Lawrence Livermore National Laboratory, L-440, Livermore, CA 94550

Abstract

Using the core/test-particle model described in a companion paper in these proceedings[1] ("Theory of Longitudinal Halo in rf Linacs: I. Core/Test-Particle Formulation," by J. J. Barnard and S. M. Lund), we analyze longitudinal beam halo produced by resonant self-field interactions in intense, ion-beam rf linacs. It is shown that particles moving in the presence of the space-charge forces of an oscillating, mismatched ellipsoidal beam bunch can be resonantly driven to large longitudinal amplitude. This resonantly produced halo is first analyzed in a limit where it is most simply understood, with particles moving purely longitudinally and with linear rf focusing. Then modifications of the resonance induced by nonlinear rf and transverse-longitudinal coupling are explored.

1 INTRODUCTION

Resonant interactions between particle orbits and oscillating space-charge forces associated with a mismatched beam core are known to be a significant cause of transverse ($\perp$) beam halo[I2-I5,2-4]. Recently, simulation work using idealized core/test-particle models has suggested that analogous, resonantly produced halo may occur longitudinally and be an issue of concern in intense-beam applications[2]. Here, we examine resonantly produced longitudinal ($\|$) halo using a more detailed core/test-particle model developed in an accompanying paper (Ref. 1, hereafter referred to as Paper I). In Paper I it was shown that a low-frequency mode (LFM) of a mismatched ellipsoidal beam bunch with uniform space-charge can drive a low-order longitudinal resonance (LR). This LR leads to $\|$ beam halo with analogous properties to that of resonantly produced $\perp$ halo[I2-I5]. To understand the essential physics that determines the structure of the resulting $\|$ halo, the LR is numerically and analytically analyzed under increasingly realistic conditions in Secs. II-IV. The notation employed in this paper is developed in Paper I. Specific references to citations and equations from Paper I will be denoted by the prefix I. All model results are illustrated using the parameters of the 100 MeV point of an intense proton-beam linac presented in the Table of Paper I. This linac is the normal conducting design originally considered for the Accelerator Production of Tritium (APT) project.

2 LINEAR RF FOCUSING

To simply elucidate the essential features of the LR, a linear rf approximation is taken [see Eq. (I-5)] where the $\|$ focusing force is linear about displacements from the synchronous particle, envelope motion is assumed to be in a pure linear LFM (as opposed to a general linear mode superposition of a LFM and HFM, or a finite amplitude solution to the full nonlinear envelope equations), and only on-axis particles (i.e., $\mathbf{x}_\perp = 0$) are considered. To visualize the structure of the LR in $\Delta\phi - \Delta\mathcal{E}$ phase-space, particles are initialized with $\Delta\mathcal{E} = 0$ and $\Delta\phi$ uniformly distributed over half the phase-width of the rf bucket and Poincaré plot images of the particle phase-space are formed by numerically integrating Eqs. (I-4) with respect to s and superimposing strobed snapshots of the $\|$ phase-space accumulated at s where the $\|$ envelope radius r_z is minimum (at s-increments of $2\pi/k_L$). A typical Poincaré plot produced by accumulating long enough to clearly visualize the LR is presented in Fig. 1(a) for 20 particles and an envelope mode amplitude of $\delta r_z/r_{z0} = 0.1$. The solid vertical lines indicate the phase width of the equilibrium beam radius r_{z0} and the dashed vertical lines indicate the phase extent of the envelope oscillations. Particles deep within and far outside the core of the beam undergo simple depressed and undepressed synchrotron oscillations, respectively. At intermediate particle oscillation amplitudes there is a strongly expressed resonant structure in which particles

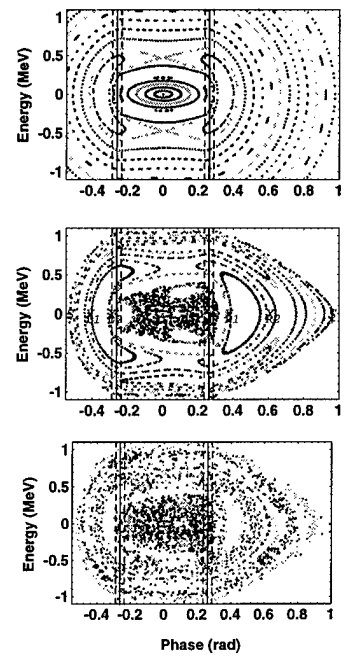

Figure 1: Poincaré plots of energy ($\Delta\mathcal{E}$) and phase ($\Delta\phi$) phase-space for $\delta r_z/r_{z0} = 0.1$, $I = 200$ mA, and: **a.** (top) Linear rf and $\mathbf{x}_\perp = 0$. **b.** (middle) Nonlinear rf and $\mathbf{x}_\perp = 0$. **c.** (bottom) Nonlinear rf and $\mathbf{x}_\perp \neq 0$.

* Work performed under the auspices of the U.S. D.O.E. by LLNL under contract W-7405-ENG-48

undergo approximately two oscillation periods over a LFM envelope period, thereby identifying the LR suggested in Paper I. Higher-order resonances with smaller particle oscillation amplitudes also appear. Such resonances become stronger and interact with the LR with increasing space-charge forces (i.e., increasing I).

In analogy to Gluckstern's analysis of transverse beam halo[I4], the LR can be analyzed analytically if, in addition to the assumptions above, a limit of a spherical bunch in the beam frame (i.e., $\gamma_s r_{z0} = r_{\perp 0}$) is taken. In this case, the space-charge force exterior to the bunch [see Eq. (I-1)] has a simple inverse-square fall-off $\sim \Delta z/|\Delta z|^3$ exterior to the bunch, and the equations of motion (I-4) can be expressed in a phase-amplitude form and with all non-resonant phases averaged over to derive a phase-averaged constant of the motion[I7]. This constant can be interpreted as a resonant particle Hamiltonian given by (1)

$$H = -(2k_s - k_L)w - \frac{k_{sc}^2}{\pi k_s}\left\{(w-6)\left[\pi - 2\sin^{-1}\left(\frac{1}{\sqrt{w}}\right)\right] + 2\sqrt{w-1} + \frac{8}{\sqrt{w}}\ln\left(\sqrt{w}+\sqrt{w-1}\right)\right\}\Theta(w-1) - \frac{3k_{sc}^2}{k_s}\left(\frac{\delta r_z}{r_{z0}}\right)\left\{\frac{1}{2} + \frac{1}{\pi}\left[\sin^{-1}\left(\frac{1}{\sqrt{w}}\right) - \frac{\pi}{2} - \frac{\sqrt{w-1}(w-2)}{w^2}\right]\Theta(w-1)\right\} w\cos\Psi,$$

where $k_{sc} = \sqrt{K_{3D}/3\gamma_s^2 r_{z0}^3}$ is a space-charge wavenumber, $\Theta(w-1)$ is a Θ-function with $\Theta(w-1) = 1$ for $w > 1$ and $\Theta(w-1) = 0$ for $w < 1$, and (w, Ψ) are coordinates related to the $(\Delta\phi, \Delta\mathcal{E})$ coordinates as

$$w = \left(\frac{\Delta\mathcal{E}}{\Delta\mathcal{E}_b}\right)^2 + \left(\frac{\Delta\phi}{\Delta\phi_b}\right)^2, \qquad (2)$$

$$w\cos\Psi = \left(\frac{\Delta\mathcal{E}^2}{\Delta\mathcal{E}_b^2} - \frac{\Delta\phi^2}{\Delta\phi_b^2}\right)\cos k_L s - 2\frac{\Delta\phi}{\Delta\phi_b}\frac{\Delta\mathcal{E}}{\Delta\mathcal{E}_b}\sin k_L s.$$

Here, $\Delta\phi_b \equiv 2\pi r_{z0}/\beta_s\lambda$ and $\Delta\mathcal{E}_b \equiv mc^2\gamma_s^3\beta_s^2 k_s r_{z0}$ are the equilibrium bunch radii in phase and energy, and envelope oscillations with $r_z = r_{z0} - \delta r_z\cos(k_L s)$ are assumed. The LR phase-space determined by the $H =$ const. surfaces of this *spherical* bunch conservation constraint is plotted in Fig. 2 for $I = 50$ mA (other parameters fixed) and with the characteristic frequencies k_s, k_{sc} and k_L, equilibrium radius r_{z0}, and mode amplitude $\delta r_z/r_{z0}$ taken from the *ellipsoidal* bunch problem. The corresponding numerically calculated Poincaré plot of the ellipsoidal bunch is shown in overlay. The rough agreement between these solutions is due to an insensitivity of the LR structure with respect to the precise nature of the $\parallel$ space-charge force. For example, if the inverse-square fall-off in the exterior space-charge force law is replaced by one with a more rapid falloff, similar conservation constraints can be derived and little change is observed in the LR structure. However, this agreement appears to break down at higher bunch currents I, suggesting a limit to this argument that has yet to be quantified in detail.

3 NON-LINEAR RF FOCUSING

The linear rf approximation fails as distance from the synchronous particle is increased. Moreover, even the equilibrium bunch can occupy a significant fraction of the rf

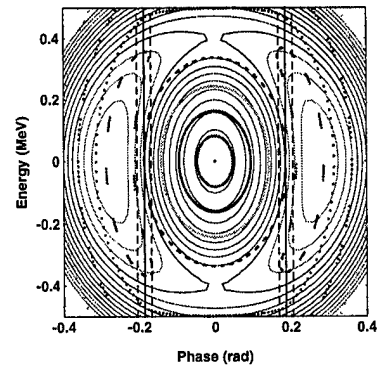

Figure 2: Overlay of theoretical (spherical bunch) and simulated (elliptical bunch) LR energy ($\Delta\mathcal{E}$) and phase ($\Delta\phi$) phase-space for linear rf, $\mathbf{x}_\perp = 0$, $I = 50$ mA.

wavelength. In this section, modifications of the LR induced by the sinusoidal nature of the applied rf focusing are analyzed numerically. For simplicity, all assumptions outside of the linear rf focusing limit of the ellipsoidal beam analysis in Sec. II are maintained (i.e., on-axis particles and a linear LFM envelope mode). The phase space obtained is presented in Fig. 1(b) for the same parameters as Fig. 1(a). Note that the LR structure now has a left-right asymmetry associated with the anharmonic nature of the rf focusing and is well confined within the separatrix of particle loss for the rf bucket. At larger mismatch amplitudes $\delta r_z/r_{z0}$ the structure becomes broader and moves closer to bucket seperatrix, but for $|\delta r_z|/r_{z0} < 0.5$ does not lead to particle loss from the bucket. This result is illustrated in Fig. 3, where the phase-variation (in $\Delta\phi$) of labeled structure features is plotted as a function of mismatch amplitude $|\delta r_z|/r_{z0}$. Note that the width of the LR structure (as measured by the phase widths of X_{L1} to X_{L2} and X_{R1} to X_{R2}) increases with amplitude and approaches the beam core, while the structure O-point varies little with amplitude. At large amplitudes, the close proximity of the LR structure to the core ($\pm\Delta\phi_{eq}$ = phase edges of core) suggests that it will be easily populated, potentially degrading beam quality. However, as a consequence of the nonlinear field structure, halo extent appears to remain confined within the extent of the rf bucket (indicated with $S_\pm$ markers).

When the bunch current I is varied with nonlinear rf focusing, an interesting bifurcation of the LR is observed. Namely, at low- ($I < 22.1$ mA) and high-currents ($I > 284$ mA), the low-order LR disappears. Furthermore, at high-currents, higher-order resonances with smaller particle oscillation amplitude appear to dominate. This situation can be understood with reference to Fig. 4. Here, the maximum particle frequency k_M, which generally occurs exterior to the beam core, is numerically calculated as a function of I (with other parameters fixed). Note that for low and high currents, half the LFM frequency ($k_L/2$) falls above the maximum frequency k_M, thereby precluding the LR (see arguments in Paper I). Note that higher-order resonances are still possible for $I > 283$ mA as demonstrated by the

$k_L/3$ curve falling between k_M and the depressed core frequency k_s. Consistent with Fig. 4, no resonances are observed for $I < 22.1$ mA.

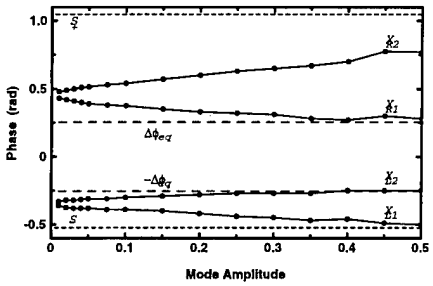

Figure 3: Phase ($\Delta\phi$) measures of LR features versus mode amplitude ($|\delta r_z|/r_{z0}$) for nonlinear rf, $\mathbf{x}_\perp = 0$, $I = 200$ mA.

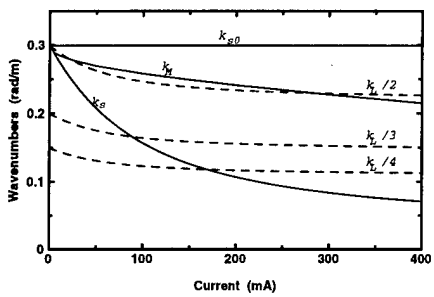

Figure 4: Maximum particle (k_M), depressed and undepressed synchrotron (k_s and k_{s0}), and subharmonic LFM envelope mode ($k_L/2$, $k_L/3$, and $k_L/4$) frequencies versus bunch current I with nonlinear rf.

4 EFFECTS OF $\perp$ / $\|$ COUPLING

Since the accelerator beams have finite $\perp$ emittance, particles will, in general, have finite $\perp$ betatron oscillations ($\mathbf{x}_\perp \neq 0$) and, outside the bunch, this motion will introduce $\perp/\|$ coupling in the particle equations of motion. This coupling is included in the core/
test-particle model derived in Paper I. In this section, we analyze the effects of this $\perp/\|$ coupling on the LR. In Fig. 1(c), we show a Poincaré phase space plot for the same parameters as Fig. 1(b), with the exception that all particles are initialized at $x = 0.6r_{\perp 0}$ instead of $\mathbf{x}_\perp = 0$. Notice that the LR structure persists, although it is somewhat smeared.

It has been noted[3] that under some circumstances $\|$ particle oscillation amplitude can be converted into larger $\perp$ oscillation amplitude. We confirm the qualitative observation that such conversion occurs, but fail to confirm the magnitude of the effect. To investigate this we simulated four particles, all with identical initial $\perp$ coordinates $x = 0.6r_{\perp 0} = 1.1$ mm and varying initial $\|$ Δz (three with $\Delta z/r_{z0} = 0.4$, 0.94, and 2.5, and a fourth at 0.80 of the maximum $\|$ phase of the stable rf bucket at $\Delta z/r_{z0} = 3.0$). These scaled parameters were similar to those employed in Ref. 3, although the overall beam and accelerator parameters were different. As in Ref. 3, we initialized the LFM and HFM envelope mismatch modes consistent with total amplitudes of $\delta r_z/r_{z0} = 0.1$ and $\delta r_\perp/r_{\perp 0} = 0.1$, and numerically integrated the equations of motion (I-4) for the four particles under the approximation of linear rf focusing. In Fig. 5 we present a Poincaré plot of the transverse ($x - x'$) phase-space obtained while strobing at the frequency of the HFM. The two particles with the large initial $\|$ amplitudes increased their $\perp$ amplitudes by a factor of approximately 1.8, reaching amplitudes slightly exterior to the $\perp$ beam extent. This is in contrast to factors of up to 30 seen in Ref. 3. For these parameters, a factor of 1.8 is consistent with particle motion bounded by the equipotential corresponding to the total energy of a particle moving in the potential well of a *matched* beam[17]. The main effect of the coupling appears to allow the particles to access a larger fraction of the available phase-space bounded by the total potential in the absence of mismatch.

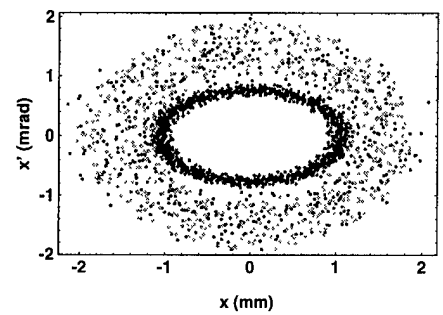

Figure 5: Poincaré plot of $\perp$ phase-space of four particles with identical initial $x = 0.6r_{\perp 0} = 1.1$ mm and varying initial Δz interior and exterior to the core.

5 CONCLUSIONS

A core/test-particle model developed in Ref. 1 has been employed to explore $\|$ beam halo due to resonant interactions with envelope oscillations. Characteristic frequencies of particle and envelope oscillations play a critical role in determining the extent and structure of the halo. Model predictions of halo extent are shown to persist under increasingly realistic conditions.

6 ACKNOWLEDGMENTS

The authors wish to again thank R. Ryne, T. Wangler, and R. Gluckstern and in addition note helpful discussions with D. Bruhwiler ($\perp$ / $\|$ coupling) and C. Chen, A. Friedman, and I. Hofmann.

7 REFERENCES

[1] J.J. Barnard and S.M. Lund, "Theory of Longitudinal Beam Halo in RF Linacs: I. Core/Test-Particle Formulation," these proceedings.

[2] T.P. Wangler, R.W. Garnett, E.R. Gray, R.D. Ryne, and T.S. Wang, Proc. of the XVIII Int. Linear Accel. Conf., Geneva, 1996, p. 372.

[3] D.L. Bruhwiler, loc. cit. 2.

[4] M. Pabst and K. Bongardt, loc. cit. 2.

SELF-PINCHED TRANSPORT THEORY FOR THE SABRE ION DIODE

Dale R. Welch
Mission Research Corporation, Albuquerque, NM 87106
C. L. Olson and D. L. Hanson
Sandia National Laboratories, Albuquerque, NM 87185

Abstract

The efficiency of delivering an ion beam to an inertial confinement fusion target depends on the ability to control the breakdown of the gas in the transport region. The gas in the reactor vessel must provide excellent charge neutralization and specified current neutralization to permit the beam transport and focusing to a < 1 cm radius, spherical target. An interesting scheme for transport, using residual effective (or net) current for confinement, is the "self-pinch" mode. Here, we present recent self-pinch theory results and ideas for beam conditioning, focusing and transport in the self-pinch mode for the SABRE experiment. Results from the IPROP hybrid code are discussed.

1 INTRODUCTION

For ion-driven inertial confinement fusion (ICF), an ion beam must be transported several meters. A sizable transport distance prevents damage to the accelerator from the target explosion and permits voltage-ramped beam bunching. The transport method is determined by the degree of ion charge and current neutralization in the ionizing gas. Complete neutralization permits ballistic transport. Self-pinched transport is possible for nearly complete charge neutralization and only partial current neutralization, yielding a net confining force. In the self-pinched transport for light-ion beams, the ion beam is focused to a small radius and confined as it propagates to the target. Previous simulations with the hybrid electromagnetic particle-in-cell code IPROP [1] have calculated that, in argon, a pressure of 5-100 mtorr permits a sufficient net force to confine even a hot ion beam.[2] [3]

In anticipation of a self-pinched experiment on the 4-MV (90 kA of Li^{+3}) SABRE diode at Sandia National Laboratories and the 2-MV (150 kA of protons) GAMBLE II diode at the Naval Research Laboratory, we have been examining the practical application of self-pinched transport. We are developing an analytic theory of self pinch that has provided insight into the physical mechanism of the low-pressure neutralization. We are also simulating the transport and propagation to examine equilibrium and stability issues. Focusing ion-diode experiments envisioned on SABRE and GAMBLE II involve non-ideal effects, including large beam divergence, large focusing angle and beam annularity. To address these problems, we have been studying the benefits of beam conditioning in the focus region between the diode and the self-pinched region after the beam has reached a small radius. We have found some benefit from including a passive conical structure and a low-pressure gas in the focusing region.

To illustrate the concept of self-pinched transport of light ions, we examine a high quality Li^{+3} beam with 32 MeV energy and 1-MA current (10-ns rise time). As seen in Fig. 1, the beam is extracted from a 8-12 cm radius annular diode with an RMS divergence of 6 mrad and a 100 mrad focusing angle. The beam is ballistically focused to a 0.75-cm aperture 1-m downstream. Due to the high energy tail of the transverse energy distribution, we only transport 83% of the beam through the aperture. At this point, we use IPROP's magneto/electrostatic field solver, assuming an ambient plasma provides 100% charge neutralization and 87% current neutralization in the self-pinch region ($z > 1$ m as in Fig. 1) which yields a 105-kA effective current. The beam then confines itself for 2 meters.

Except for the low-current early-time portion of the beam (near z =300), the beam RMS radius remains at 0.4 cm to the endplate. Roughly 95% of the beam remains within a 0.7-cm radius with few ions extending to 1.2 cm. The beam RMS transverse velocity $\beta_\perp$ is 0.01 in the pinch region. A simple energy balance for a Bennett radial profile beam yields the matched effective current (units of 17 kA) $I_{eff} = (m_i/Zm_e)\beta_\perp^2/\beta_i$. Thus, the above I_{eff} exceeds that necessary for confinement (72 kA), accounting for the excellent beam confinement.

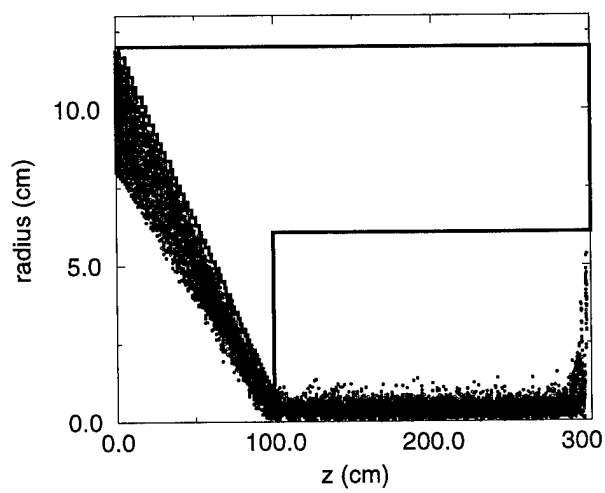

Figure 1: The 32-MeV 1-MA Li^{+3} beam is plotted 100 ns into a static field IPROP simulation. A uniform-density beam is extracted from a 8-12 cm radius annular diode with 6-mrad RMS divergence and a 100-mrad focusing angle.

0-7803-4376-X/98 /$10.00 © 1998IEEE

2 SELF-PINCHED TRANSPORT THEORY

The neutralization of an ion beam requires that electrons be drawn from outside the beam, either radially or axially. In a low pressure gas, neutralizing electrons are transported via $E \times B$ drift. In the beam body or late in time at a given axial position, z, electrons move forward axially due to the residual radial electric and azimuthal magnetic fields with $\beta_z = E_r/B_\theta$. A simple equilibrium theory,[3] that predicts $\beta_z(z)$ as a function of the gas ionization rate due to beam impact, has shown that $\beta_z(z)$ approaches the ion velocity β_i in the beam nose (as the beam first reaches a given z). The theory calculates E_r and B_θ as a function of the charge and current neutralization for a trumpet shaped beam temporal profile (large beam radius at $t = 0$, pinching down to smaller radius). A free parameter in this theory is the radius of the plasma electron envelope, r_e. In the absence of inductive electric fields, we assumed that the electrons are drawn into the beam and $r_e = r_b$. This theory predicted large effective pinch currents are possible in the 5-100 mtorr pressure range. The optimal pressure occurs when the mean-free path for beam ionization of the gas is $\lambda_{mfp} = \tau\beta_i c/4Z$, where τ is time for the beam to reach its minimum radius. Thus, more efficient ionizing beams have large pinch currents at smaller pressures.

Radial neutralization by plasma electrons, when the Larmor radius $\ll r_b$, is accomplished through an $E_z \times B_\theta$ drift. The inward current is driven by unneutralized beam space charge in the beam nose. This process continues until an axial inductive field is produced which negates the electrostatic field. A deficiency in the earlier theory is that it neglected inductive fields that inhibit the rise of I_{eff}, $I_{eff} = 0.5r_b(B_\theta(r_b) - E_r(r_b)/\beta_i)$. To include inductive effects, we assume that the axial inductive field is given by $E_{ind} = \partial I_{eff}/\partial t$ and the axial electrostatic field is equal to the radial electrostatic field, E_{es}, which scales strongly with beam radius. E_{es} is calculated as before except that r_e is constrained. At each time in the beam frame, r_e is chosen such that $E_{ind} \leq E_{es}$. If the inductive fields are sufficiently weak, the r_e is, as before, set equal to the beam radius.

The inductive effects included in the new theory limit I_{eff} for beam with large radii and small β_i. The scaling of I_{eff} with energy in an Ar gas is shown in Fig. 2 for a 50-ns Li^{+3} beam with 1.5-cm radius, 1-ns current rise and a 10-ns trumpet radial shape. We see that the maximum fraction of I_{eff}/I_b is largest (nearly 0.9 at 10 mtorr Ar) for the fusion quality 32-MeV beam. As the beam energy is reduced to 4 MeV, the optimal Ar pressure decreases to 1-mtorr and the fraction falls to 0.1. As in the earlier theory, the results are independent of beam current, suggesting the pinch current available for ICF quality beams is well beyond that required (1-10%). However, near term experiments at lower voltages may not generate sufficient current to observe a tightly pinched beam.

We simulate the breakdown of a gas in the presence of an ion beam using the hybrid simulation code IPROP.[1] IPROP

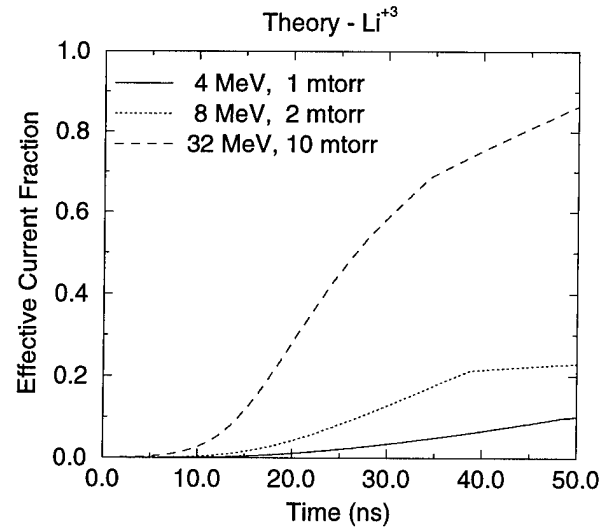

Figure 2: The fraction of I_{eff} to beam current for a Li^{+3} beam with 4, 8 and 32 MeV energy (1-ns current rise time) is plotted versus time into the beam pulse. The beam radius was initially 3-cm pinching to 1.5 cm with a 10-ns gaussian "trumpet" shape.

has shown good agreement with GAMBLE II experiments in which net currents were measured outside a nominal 10 kA, 1-MeV proton beam.[4] We have calculated fractional effective currents of up to 0.5 for beams with $\beta_i \geq 0.1$.[2] The optimal pressures are consistent with the above theory. We have just begun to look at the slow beams $\beta_i \approx 0.03 - 0.05$ expected in the near term experiments.

To speed up the simulations, we examine a 50-kA Li^{+3} beam with 32 MeV energy ($\beta_i = 0.1$). From the above theory, we can expect roughly a 0.2 fractional effective current. This 10-kA effective current matches a 50-mrad divergence with which we initialize the beam. The beam is injected into a 8-cm radius, 50-cm long conducting tube filled with 20-mtorr argon. We see in Fig. 3 that the beam core remains well pinched with some hotter particles escaping to larger radius. A trumpet developed with a characteristic time $\tau \approx 5$ ns (15 cm in z) and the maximum effective current reached 9 kA. IPROP calculates an optimal pressure near 5 mtorr for this beam with a 15-kA effective current in rough agreement with the theory. We have also looked at lithium beams in the focusing geometry (see Fig. 1). We find that, unlike the thermal transverse energy beams discussed above, these beams are more difficult to contain because all the beam ions have large transverse energy. Thus, we have been examining methods for beam conditioning which maximize the beam transport to small radius and ways to thermalize the beam transverse energy by removing the macro focusing angle.

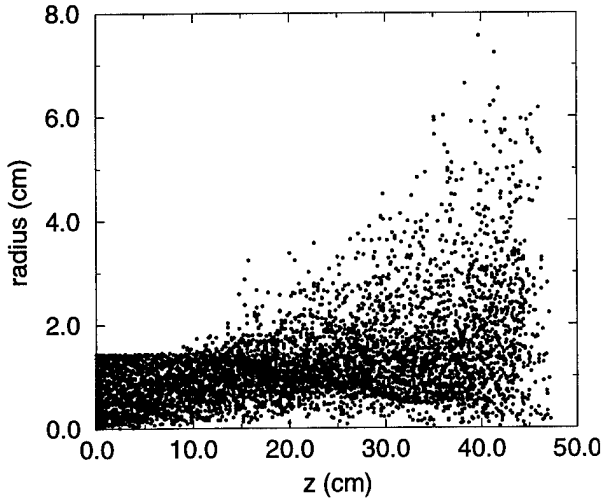

Figure 3: The 32-MeV, 50-kA (3-ns rise time) Li^{+3} beam is plotted 15 ns into a electromagnetic IPROP simulation. A uniform 50-mrad divergence beam is injected normally into a 8-cm radius tube filled with 20-mtorr argon gas.

3 BEAM CONDITIONING FOR THE SABRE EXPERIMENT

In the SABRE experiment, we plan to focus a lithium ion beam to small radius and propagate the beam in the self pinch mode as illustrated in Section 1. The Li^{+3} beam will exit the diode with a $\approx$ 40 mrad divergence and a shallow focusing angle of roughly 75 mrad. The beam is annular with an 4.6-cm inner radius and a 6.6-cm outer radius. The above theory predicts a small radius ($\leq$ 3 cm) is required to optimize beam self pinch. Therefore, we have been considering ways to efficiently transport this beam through a 3-cm radius aperture from the 4.6-6.6-cm annular SABRE diode. With ballistic transport of the focusing beam 75-cm downstream and a 3-cm aperture, we will lose roughly 50% of the current given a 40-mrad divergence (a conservative estimate based on Li divergence measurements).

If we can generate a $>$ 20 kA effective current within a concentric conical structure, the beam ions can be kept off the cone and redirected through the aperture. With an inner conductor, the self-fields act to preserve the annulus. Using the IPROP, we simulated a 75-kA (10-ns rise), 32 MeV Li^{+3} in the geometry described above. The inner cone had a 4-cm radius at the diode exit (z=0) and reached the axis at z= 75 cm. The outer cone had an inner radius of 7.2 cm at z=0 reaching a 3-cm radius (the aperture) at 75 cm. The 40-mrad divergence beam injected into 10 and 20-mtorr Ar is efficiently guided to the aperture at 75 cm. The transport efficiency was considerably better than that for ballistic transport with 85% and 72% of the beam maximum current transported for the 10 and 20-mtorr pressures, respectively. The beam self fields direct the beam to the center of the cone with peak fields near the axis reaching 7 and 4 kG for the two pressures. While improving overall transport efficiency, one drawback is that the beam is somewhat hollow at the start of the self-pinch region which may not be desired for self pinch.

A second, similar method is to inject the beam into the above geometry cone but in vacuum. In this case, electrons emitted from the metal structure $E \times B$ drift in the self fields. The beam is initially well neutralized in charge and current, however, the current neutralization at the far wall degrades in time as the neutralizing electrons pile up at the endplate where the radial electric fields are shorted and the drift slows. The neutralizing electrons carry sufficient charge forward to neutralize the beam column and move with velocity β_i. As these electrons stagnate, they carry sufficient charge to neutralize the beam space charge in a wave moving backwards at roughly the beam velocity. Because their forward velocity drops to 0, there is no current neutralization. Thus, we have a time-dependent lens effect with focusing or defocusing magnetic fields depending on if an inner metal cone exists. The inner cone carries return current which results in a defocusing magnetic field. If none exists, the magnetic fields are positive and radially focusing. IPROP calculates strong pinch forces moving back from the endplate with this method.

4 CONCLUSIONS

The self-pinched transport mode for ion ICF provides standoff from the target explosion. We are developing a physics understanding of this mode leading up to experiments on SABRE and GAMBLE II. Theory and simulation predict large effective currents that can confine the transverse beam momentum. The self pinch theory has been improved to include inductive effects that tend to limit the effective currents for lower energy and larger radius beams. Optimal argon pressures of 1-10 mtorr, independent of current, are calculated for a Li^{+3} beam with 4-32 MeV energy. We are continueing to explore methods for beam conditioning that facilitate the transition from the beam focusing region into the self pinch region. Future work will involve three-dimensional IPROP simulations to examine stability issues.

5 ACKNOWLEDGMENTS

This work is supported by Sandia National Laboratories.

6 REFERENCES

[1] D. R. Welch, C. L. Olson and T. W. L. Sanford, Phys. Plasmas **1**, 764 (1994).

[2] D. R. Welch, M. E. Cuneo, C. L. Olson and T. A. Mehlhorn, Phys. Plasmas **3**, 2113 (1996).

[3] D. R. Welch and C. L. Olson, Fusion Engineering and Design **32-33**, 477 (1996).

[4] F. C. Young, D. D. Hinshelwood, R. F. Hubbard, M. Lampe, J. M. Neri, C. L. Olson, P. F. Ottinger, D. V. Rose, S. P. Slinker, S. J. Stephanankis and D. R. Welch, Phys. Rev. Lett. **70**, 2573 (1993).

EMITTANCE GROWTH AND PARTICLE DIFFUSION INDUCED BY DISCRETE-PARTICLE EFFECTS IN INTENSE BEAMS

Renato Pakter and Chiping Chen
MIT Plasma Science and Fusion Center, Cambridge, Massachusetts 02139

Abstract

We analyze particle diffusion and emittance growth induced by discrete-particle effects in two-dimensional self-consistent numerical simulation studies of beam dynamics. In particular, an analytical model is presented which describes the slow time-scale variation of edge emittance for a perfectly matched beam in a periodic solenoidal magnetic focusing field. A scaling law for edge emittance growth is obtained.

1 DISCUSSION

There has been a growing interest in the study of high-current electron and ion accelerators for a variety of applications. An important issue in the development of such advanced accelerators is to avoid beam halos and associated beam losses [1]. While modern accelerator design relies heavily on self-consistent computer simulations, accurate predictions of the processes of beam halo formation and beam losses have not been accessible in the simulations because of discrete-particle effects [2]. In this paper, we derive a scaling law which governs the processes of edge emittance growth and particle diffusion induced by discrete-particle effects in self-consistent simulations of periodically focused intense charged-particle beams.

Let us consider a thin, continuous charged-particle beam which propagates with average axial velocity $\beta_b c\vec{e}_z$ through an axisymmetric linear focusing channel provided by a periodic solenoidal magnetic field

$$\vec{B}_0(x,y,s) = B_z(s)\,\vec{e}_z - [B_z'(s)/2]\,(x\vec{e}_x + y\vec{e}_y). \quad (1)$$

In Eq. (1) $s = z = \beta_b ct$ is the axial coordinate, $B_z(s+S) = B_z(s)$ is the axial component of the applied magnetic field, S is the fundamental periodicity length of the focusing field, c is the speed of light in *vacuo*, and the "prime" denotes derivative with respect to s.

In the present two-dimensional macroparticle model, the beam density is given by

$$n(x,y,s) = \frac{N}{N_p}\sum_{i=1}^{N_p}\delta[x - x_i(s)]\,\delta[y - y_i(s)], \quad (2)$$

where N and N_p are the number of microparticles and macroparticles per unit axial length of the beam, respectively, and (x_i, y_i) is the transverse displacement of the ith macroparticle from the beam axis at $(x,y) = (0,0)$. Under the paraxial approximation, we can express the transverse equations of motion for the ith macroparticle of the beam in the Larmor frame as [1]

$$\frac{d^2\tilde{x}_i}{ds^2} + \kappa_z(s)\,\tilde{x}_i = -\frac{q}{\gamma_b^3\beta_b^2 mc^2}\frac{\partial}{\partial\tilde{x}_i}\Phi^{(s)}(\tilde{x}_i,\tilde{y}_i,s), \quad (3)$$

$$\frac{d^2\tilde{y}_i}{ds^2} + \kappa_z(s)\,\tilde{y}_i = -\frac{q}{\gamma_b^3\beta_b^2 mc^2}\frac{\partial}{\partial\tilde{y}_i}\Phi^{(s)}(\tilde{x}_i,\tilde{y}_i,s). \quad (4)$$

In Eqs. (3) and (4), $i = 1,2,...,N_p$, $\gamma_b = (1-\beta_b^2)^{-1/2}$ is the relativistic mass factor, m and q are the particle rest mass and charge, respectively, $\kappa_z(s) = [qB_z(s)/2\gamma_b\beta_b mc^2]^2$ is a measure of the strength of the focusing field, and

$$\Phi^{(s)}(\tilde{x}_i,\tilde{y}_i,s) = -\frac{qN}{N_p}\sum_{j=1(j\neq i)}^{N_p}\ln[(\tilde{x}_i-\tilde{x}_j)^2+(\tilde{y}_i-\tilde{y}_j)^2] \quad (5)$$

is the self-field scalar potential associated with the beam space-charge.

In order to develop an analytical model to describe diffusive behavior induced by discrete-particle effects in beam dynamics, we first consider the limit of a smooth equilibrium distribution of particles corresponding to the Kapchinskij-Vladimirskij (KV) equilibrium function [1]. In the KV equilibrium, the beam density is given by

$$n_{KV}(\tilde{x},\tilde{y},s) = \begin{cases} N/\pi r_b^2(s), & 0 \le r \le r_b(s), \\ 0, & r > r_b(s), \end{cases} \quad (6)$$

where $r \equiv (x^2+y^2)^{1/2} = (\tilde{x}^2+\tilde{y}^2)^{1/2}$ is the radial coordinate, and $r_b = r_b(s)$ is the beam radius. The scalar potential for the self-electric field is given by

$$\Phi_{KV}^{(s)}(\tilde{x},\tilde{y},s) = -qNr^2/r_b^2(s) \quad (7)$$

in the beam interior ($r < r_b$). Substituting $\Phi^{(s)}(\tilde{x}_i,\tilde{y}_i,s) = \Phi_{KV}^{(s)}(\tilde{x}_i,\tilde{y}_i,s)$ into Eqs. (3) and (4), the equilibrium particle orbits $\tilde{x}_i(s)$ and $\tilde{y}_i(s)$ can be expressed as

$$\tilde{x}_i(s) = A_{xi}\,r_b(s)\cos[\psi(s)+\phi_{xi}], \quad (8)$$

$$\tilde{y}_i(s) = A_{yi}\,r_b(s)\sin[\psi(s)+\phi_{yi}], \quad (9)$$

where A_{xi}, $A_{yi} = (1-A_{xi}^2)^{1/2}$, ϕ_{xi} and ϕ_{yi} are constants determined by the initial conditions, $\psi(s) = 4\epsilon\int_0^s ds/r_b^2(s)$ is the accumulated phase of the betatron oscillations, and $r_b(s) = r_b(s+S)$ solves the beam envelope equation

$$r_b'' + \kappa_z(s)\,r_b - K/r_b - (4\epsilon)^2/r_b^3 = 0, \quad (10)$$

0-7803-4376-X/98/$10.00 © 1998 IEEE

with ϵ being the unnormalized rms emittance of the beam, and $K \equiv 2q^2N/\gamma_b^3\beta_b^2mc^2$, the normalized perveance of the beam. The particle distribution function for the KV equilibrium can be expressed as $f_{KV}(\tilde{x},\tilde{y},\tilde{x}',\tilde{y}',s) = (N/16\epsilon^2\pi^2)\,\delta(A_x^2+A_y^2-1)$, where $\delta(x)$ is the Dirac δ-function. Because the four-dimensional phase-space volume element is given by $d\tilde{x}d\tilde{y}d\tilde{x}'d\tilde{y}' = 16\epsilon^2 A_x\,A_y\,dA_x dA_y d\phi_x d\phi_y$, integrating f_{KV} over A_y, ϕ_x and ϕ_y yields the distribution function for A_x over a KV beam

$$F_{KV}(A_x) = \begin{cases} 2NA_x, & 0 \le A_x \le 1, \\ 0, & A_x > 1, \end{cases} \tag{11}$$

where $\int_0^\infty F_{KV}(A_x)dA_x = N$. Note from Eq. (11) that the largest concentration of particles occurs at $A_x = 1$. Note also from Eq. (8) that particles with $A_{xi} = 1$ reach the edge of the beam with $x_i = r_b$, as they execute betatron oscillations. Therefore, they are most likely to leave the beam core under the perturbations induced by discrete-particle effects.

In numerical simulations as well as in experiments, the beam density deviates from the smooth beam density $n_{KV}(\tilde{x},\tilde{y},s)$ of the KV equilibrium. For a coarse-grained uniform density distribution, the deviation is small when there is a large number of particles. Such small deviation will induce slow-time-scale evolution of $A_{xi}(s)$, $A_{yi}(s)$, $\phi_{xi}(s)$ and $\phi_{yi}(s)$ in the particle orbit given in Eqs. (8) and (9). In the remainder of this paper, we analyze the dynamics of edge particles initially with $A_{xi}(s=0) = 1$ and $A_{yi}(s=0) = [1-A_{xi}^2(s=0)]^{1/2} = 0$, because they are most likely to diffuse away from the beam core as discussed previously. We disregard dynamical couplings between $(A_{xi};\phi_{xi})$ and $(A_{yi};\phi_{yi})$ because $A_{yi}(s) \approx 0$, and introduce the dimensionless variables and parameters defined by $s/S \to s$, $\tilde{x}/(4\epsilon S)^{1/2} \to \tilde{x}$, $\tilde{y}/(4\epsilon S)^{1/2} \to \tilde{y}$, $r_b/(4\epsilon S)^{1/2} \to r_b$, $S^2\kappa_z \to \kappa_z$ and $SK/4\epsilon \to K$. Substituting Eq. (8) into Eq. (3), and taking into account the *slow* dependence of A_{xi} and ϕ_{xi}, we find that

$$\begin{aligned} &\left[A'_{xi}\,r'_b - \frac{A_{xi}\,\phi'_{xi}}{r_b}\right]\cos(\psi+\phi_{xi}) \\ &-\left[\frac{A'_{xi}}{r_b} + A_{xi}\,\phi'_{xi}\,r'_b\right]\sin(\psi+\phi_{xi}) = \\ &\qquad -\frac{K}{4qN}\frac{\partial}{\partial x_i}[\phi^{(s)} - \phi^{(s)}_{KV}], \end{aligned} \tag{12}$$

where use has been made of Eq. (10). It is evident in Eq. (12) that $A'_{xi} = 0 = \phi'_{xi}$ for $\phi^{(s)} = \phi^{(s)}_{KV}$.

To derive a closed set of equations for the slowly varying variables A_{xi} and ϕ_{xi}, we average Eq. (12) over fast oscillations pertaining to the focusing field and the betatron oscillations. Making use of Eqs. (5), and (7)-(9), we can express Eq. (12) as

$$\frac{dA_{xi}}{ds} = -\frac{K}{N_p}\sum_{j=1(j\neq i)}^{N_p}\frac{B_jb_j + C_jc_j}{b_j^2+c_j^2}, \tag{13}$$

$$\frac{d\phi_{xi}}{ds} = \frac{K}{2} - \frac{K}{A_{xi}N_p}\sum_{j=1(j\neq i)}^{N_p}\frac{C_jb_j - B_jc_j}{b_j^2+c_j^2}, \tag{14}$$

where

$$B_j = -(A_{xj}/2)\sin\Delta_{xj},\ C_j = (A_{xi} - A_{xj}\cos\Delta_{xj})/2,$$

$$\begin{aligned} b_j = [(A_{xi} - A_{xj}\cos\Delta_{xj})^2 - A_{xj}^2\sin^2\Delta_{xj} \\ -A_{yj}^2\cos(2\Delta_{yj})]/2, \end{aligned} \tag{15}$$

$$c_j = (A_{xi} - A_{xj}\cos\Delta_{xj})A_{xj}\sin\Delta_{xj} + \frac{1}{2}A_{yj}^2\sin(2\Delta_{yj}),$$

with $\Delta_{xj} \equiv \phi_{xj} - \phi_{xi}$ and $\Delta_{yj} \equiv \phi_{yj} - \phi_{xi}$. Since the derivation of Eqs. (13) and (14) does not require the explicit form of the focusing magnetic field $B_z(s)$, Eqs. (13) and (14) are valid for an arbitrary periodic focusing channel.

In principle, detailed dynamics of edge particles initially with $A_{xi} = 1$ and $A_{yi} = 0$ can be analyzed using Eqs. (13) and (14). In this paper, however, we examine particle diffusion induced by discrete-particle effects. To describe the diffusion process quantitatively, we introduce the quantities $\mu(s) = \langle A_{xi}\rangle$ and $\sigma^2(s) = \langle(A_{xi}-\mu)^2\rangle$, where $\langle\ \rangle$ stands for the average over particles that are initially located at $A_{xi} = 1$. We compute the expectation values of $d\mu/ds = \langle A'_{xi}\rangle$ and $d^2\sigma^2/ds^2 = \langle(A'_{xi}-\mu')^2\rangle$ by ensemble averaging over all possible beam distributions which approach the KV distribution when $N_p \to \infty$. The results are $\mu(s) = \mu(0) = 1$, and

$$\sigma^2(s) = D\,s^2, \tag{16}$$

where the 'diffusion' coefficient is given by

$$D(K,N_p) = \overline{\xi}\,K^2/N_p, \tag{17}$$

$\overline{\xi} = (1/N)\int \xi_j f_{KV}(\tilde{x}_j,\tilde{y}_j,\tilde{x}'_j,\tilde{y}'_j,s)d\tilde{x}_j d\tilde{y}_j d\tilde{x}'_j d\tilde{y}'_j$, $\xi_j = [(B_jb_j + C_jc_j)/(b_j^2+c_j^2)]^2$. It should be stressed that unlike usual diffusive processes, the variance σ^2 here is proportional to s^2. Due to the highly oscillatory nature of ξ_j, our best estimate of the value of $\overline{\xi}$ is $\overline{\xi} = 0.7 \pm 0.3$. In dimensional units, it follows from Eq. (16) that the edge emittance 4ϵ evolves according to

$$\langle 4\epsilon(s)\rangle = 4\epsilon(0)[1 + \overline{\xi}K^2s^2/16\epsilon^2(0)N_p]. \tag{18}$$

To verify the scaling law in Eqs. (16) and (17), we carry out self-consistent simulations by integrating Eqs. (3) and (4) numerically for various particle distributions. We adopt the following procedure to calculate the diffusion about $A_{xi} = 1$. In such a self-consistent, a first set of N_p macroparticles is loaded corresponding to a KV distribution, a second set of N_t test particles is loaded at $A_{xi} = 1$ with a uniform distribution of ϕ_{xi} in the range from 0 to 2π. As the beam propagates through the focusing channel, the particles in the first set interact with each other self-consistently, whereas the test particles experience the electric and magnetic forces imposed by the particles in the first

set. Integrating Eq. (10) concurrently in the simulation and using the relation $A_{xi} = [(\tilde{x}_i/r_b)^2 + (\tilde{x}_i\, r_b' - \tilde{x}_i'\, r_b)^2]^{1/2}$, the expectation values of $\mu(s)$ and $\sigma^2(s)$ over the test distribution are readily computed. Results are summarized in Figs. 1-3.

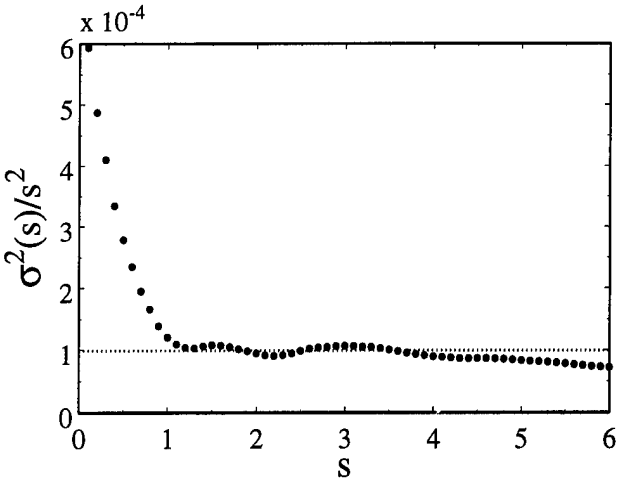

Figure 1: Plot of σ^2/s^2 as function of s.

Figure 1 shows plots of σ^2/s^2 versus the propagation distance s obtained from a self-consistent simulation of intense beam propagation through a sinusoidal periodic focusing channel. The choice of system parameters in Fig. 1 corresponding to $N_p = 1024$, $N_t = 512$, $K = 0.5$, and $\kappa_z(s) = [a_0 + a_1 \cos(2\pi s)]^2$, where $a_0 = a_1 = 0.648$. Due to small residual correlation in the initial distributions of test particles and background macroparticles, the value of σ^2/s^2 is large for $s \ll 1$. As the beam propagates, the residual correlation decays rapidly, and the value of σ^2/s^2 approaches a plateau for $s > 1$, where the diffusion coefficient is calculated to be $D = 1.0 \times 10^{-4}$ ($\bar{\xi} = 0.4$), as indicated by the dashed line. As the beam propagates further through the focusing channel, the plateau levels off because the test particles become widely spread about $A_{xi} = 1$.

The scaling law is verified by self-consistent simulations. Figure 2 shows a logarithmic plot of D versus K obtained from self-consistent simulations for beam propagation through the same periodic focusing channel as in Fig. 1. In Fig. 2, the number of background macroparticles is kept at a constant value of $N_p = 1024$. The dotted curve is from the self-consistent simulations, whereas the solid line is the analytical result given by $D = \alpha K^2$, where $\alpha = \bar{\xi}/N_p = 3.5\times10^{-4}$ ($\bar{\xi} = 0.35$). In Fig. 3, the diffusion coefficient D is plotted versus N_p, as obtained from self-consistent simulations of beam propagation through the same periodic focusing channel in Fig. 1 for a fixed value of $K = 0.5$. The dotted curve is from the self-consistent simulations, whereas the solid line is the analytical result given by $D = \beta K^2$, where $\beta = \bar{\xi} K^2 = 0.12$ ($\bar{\xi} = 0.48$). In comparison with Fig. 2, data fluctuations in Fig. 3 are larger because the initial distribution changes as N_p is varied. Nevertheless, it is evident in Fig. 2 and 3 that simulation results are in good agreement with the analytically predicted scaling law.

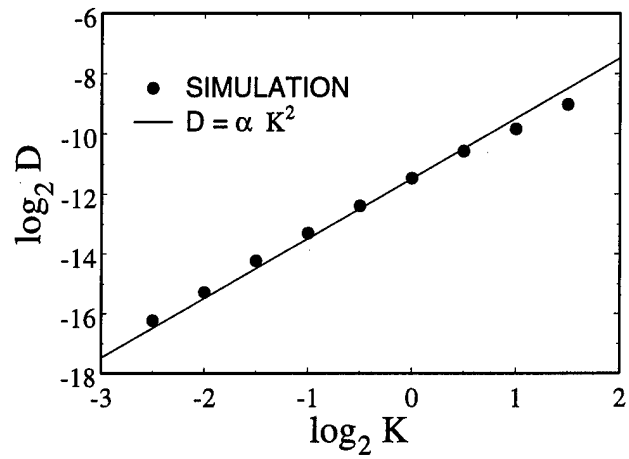

Figure 2: Log-log plot of D versus K.

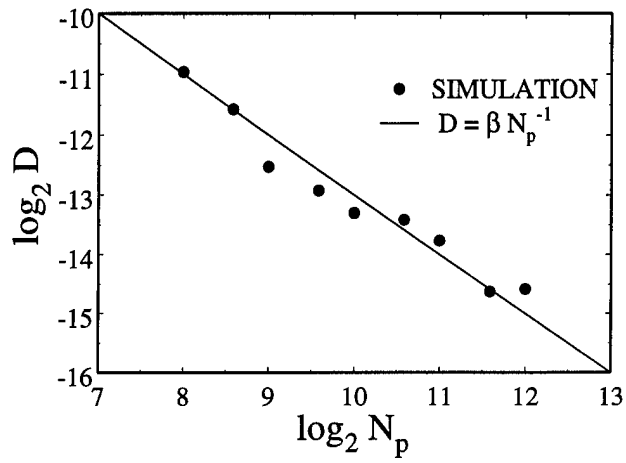

Figure 3: Log-log plot of D versus N_p.

To conclude, we have obtained a scaling law for edge emittance growth induced by discrete-particle effects in two dimensional self-consistent simulations of intense charged-particle beams in a periodic solenoidal focusing field. The scaling law may be applied to establish criteria for accurate simulation studies of the process of beam halo formation and beam losses.

Work supported by DOE Grant No. DE-FG02-95ER-40919 and AFOSR Grant No. F49620-94-1-0374. R. Pakter also supported by CAPES, Brazil.

2 REFERENCES

[1] C. Chen and R. A. Jameson, Phys. Rev. **E52**, 3074 (1995) and references therein.

[2] R. W. Garnett, *et al.*, AIP Conf. Proc. No. **377**, p. 60 (1996).

PREVENTION OF HALO FORMATION IN HIGH BRIGHTNESS BEAMS

Yuri K. Batygin,
The Institute of Physical and Chemical Research (RIKEN), Saitama, 351-01, Japan

Abstract
Four vanes quadrupole structure with duodecapole field component is analyzed to suppress emittance growth and halo formation in high brightness beams. Beam profile in such a structure has to be close to square instead of conventional circle cross section. Adiabatic change of electrode shapes along the channel results in transformation of initially nonuniform beam into the beam, matched with the channel with pure quadrupole field. Results of prevention of halo formation in the bright beam with phase space density of 1.5 A/(π cm mrad) are given.

1 INTRODUCTION

Emittance conservation of a high brightness particle beam is an issue for existing and future high intensity accelerator projects. Nonuniform space charge dominated beam is mismatched with linear focusing channel. It results in beam emittance growth and halo formation (see Fig.1). In Refs. [1, 2] it was shown that incorporation of a duodecapole component in pure quadrupole alternating-gradient structure provides better matching of the beam with the transport channel. Special case is a four-vanes structure, where shape of electrodes is modified to create multipole field distribution [3]. Potential of an uniform four vanes structure is given by

$$U(r,\varphi,t) = \left(\frac{G_2}{2} r^2 \cos 2\varphi + \frac{G_6}{6} r^6 \cos 6\varphi \right) \sin \omega_o t , \quad (1)$$

where G_2 is a quadrupole gradient, G_6 is a duodecapole component and $\omega_o = 2\pi c/\lambda$ is an operational frequency. Averaging of equations of motion of particle with mass m_o, charge q and energy γ gives an effective scalar potential of the structure, which describes smoothed particle trajectories [2, 3]:

$$U_{ext}(r,\varphi) = \frac{m_o c^2}{q} \frac{\mu_o^2}{\lambda^2} \left[\frac{r^2}{2} + \zeta r^6 \cos 4\varphi + \frac{\zeta^2}{2} r^{10} \right], \quad (2)$$

where μ_o is a smoothed transverse oscillation frequency and ζ is a ratio of field components:

$$\mu_o = \frac{q\, G_2 \lambda^2}{\sqrt{8\,\gamma}\, \pi\, m_o c^2}, \qquad \zeta = \frac{G_6}{G_2} . \quad (3)$$

The effective potential (2) is an axial - nonsymmetrtic and a highly nonlinear radius function. Equipotential lines $U_{ext}(r,\varphi) = C$ are circles near axis and are transformed to a 45° skewed square far from the axis [2].

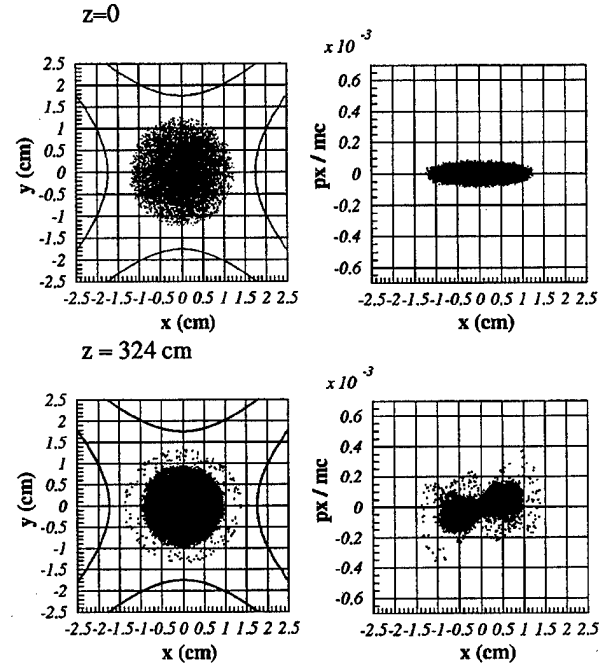

Fig. 1. Emittance growth and halo formation of the 150 keV, 100 mA, 0.06 π cm mrad nonuniform proton beam in a four vanes quadrupole structure.

Beam emittance is conserved, if beam is matched with the channel. Finding matched conditions for the beam requires solution of self-consistent problem for beam distribution function in phase space. Self consistent particle distribution creates potential, in which particle motion maintains this distribution.

2 SELF-CONSISTENT PARTICLE DISTRIBUTION IN A CONTINUOUS FOCUSING CHANNEL

General approach to find a self-consistent distribution function in uniform focusing channel is to represent it as a function of Hamiltonian [4]

$$f = f(H), \qquad H = \frac{p_x^2 + p_y^2}{2\, m_o\, \gamma} + q\, U_{ext} + q\, \frac{U_b}{\gamma^2}, \quad (4)$$

where U_b is a space charge potential of the beam. Convenient way is to use an exponential function $f = f_o \exp(-H/H_o)$. Distribution function contains two unknown constants H_o, f_o, which can be expressed through beam parameters. Root-mean-square (rms) beam emittance ε is defined via beam radius $R = 2\sqrt{<x^2>}$ and rms beam size in phase space $p_o = 2\sqrt{<p_x^2>}$:

$$\varepsilon = \frac{4}{m_o c} \sqrt{<x^2><p_x^2>} = \frac{R\, p_o}{m_o c} . \quad (5)$$

Comparing definition of distribution function and eqs.(4), (5), the value of H_o is given by:

$$H_o = \frac{p_o^2}{4m_o\gamma} = \frac{m_o c^2}{4\gamma}\left(\frac{\varepsilon}{R}\right)^2 . \qquad (6)$$

Space charge density of the beam is expressed through beam distribution function after integration over particle momentum:

$$\rho = q\int_{-\infty}^{\infty}\int_{-\infty}^{\infty} f\, dp_x dp_y = \rho_o \exp\left(-q\,\frac{U_{ext} + \gamma^{-2} U_b}{H_o}\right), \qquad (7)$$

where $\rho_o = 2\pi\, q\, \gamma\, m_o\, f_o\, H_o$ is a value of space charge particle density in the center of the beam. Value of ρ_o is unknown at this point due to unknown self potential of the beam U_b. Typical particle distribution of a laboratory beam has a maximum density in the center of the beam, which drops toward beam periphery. Let us introduce an average value of space charge density of the beam $\bar{\rho} = I/(\beta c\pi R^2)$, where I is a beam current and β is a particle velocity. In general case space charge density in the center of the beam ρ_o differs from the average value of space charge density $\bar{\rho}$ as a factor of k, where parameter k=1 for uniform distribution $\rho(r) = \rho_o$ and k=2 for Gaussian distribution $\rho(r) = \rho_o \exp(-2r^2/R^2)$. Taking into account adopted relationship $\rho_o = k\,\bar{\rho}$, the value of f_o is expressed as follow:

$$f_o = k\,\frac{2I}{\pi^2\,\beta\, q\, m_o^2\, c^3\, \varepsilon^2} . \qquad (8)$$

Substitution of the distribution function into Poisson's equation gives a nonlinear equation for unknown space charge potential of the beam U_b. After solution of the Poisson's equation, one can find the self-consistent particle distribution, which will be maintained in the focusing channel. Let us introduce dimensionless variables:

$$V_{ext} = \frac{q\,U_{ext}}{H_o}, \quad V_b = \frac{q\,U_b}{H_o}, \quad \xi = \frac{r}{a}, \qquad (9)$$

where a is a channel radius. In new variables, Poisson's equation in cylindrical polar coordinates is

$$\frac{1}{\xi}\frac{\partial}{\partial\xi}\left(\xi\frac{\partial V_b}{\partial\xi}\right) + \frac{\partial^2 V_b}{\xi^2\partial\varphi^2} = -\,8kb\left(\gamma\frac{a}{R}\right)^2 \exp\left(-V_{ext} - \frac{V_b}{\gamma^2}\right), \qquad (10)$$

where b is a dimensionless value of beam brightness:

$$b = \frac{2}{\beta\gamma}\,\frac{I}{I_c}\left(\frac{R}{\varepsilon}\right)^2 , \qquad (11)$$

and $I_c = 4\pi\varepsilon_o m_o c^3/q = 3.13\cdot 10^7 (A/Z)$ Amp is a characteristic value of beam current.

Unknown space charge potential of the beam can be expressed as Fourier-Bessel series

$$V_b = V_o + \sum_{n=0}^{\infty}\sum_{m=1}^{\infty} J_n(\upsilon_{nm}\xi)(A_{nm}\cos n\varphi + B_{nm}\sin n\varphi) , \qquad (12)$$

where $J_n(x)$ is a Bessel function and υ_{nm} is a m-th root of the equation $J_n(x) = 0$. Constant $V_o = -\,bk\gamma^2$ is defined in such a way, that total potential of the structure vanishes at the axis $V_{ext}(0,\varphi) + V_b(0,\varphi)\,\gamma^{-2} = 0$.

To find an approximate solution of Poisson's equation, let us take the first term in the near-axis expansion of exponential function $\exp(-V_{ext} - V_b\gamma^{-2}) \approx 1 - V_{ext} - V_b\gamma^{-2}$. Poisson's equation becomes:

$$\sum_{n=0}^{\infty}\sum_{m=1}^{\infty}\left[1 + \frac{\upsilon_{nm}^2}{8kb}\left(\frac{R}{a}\right)^2\right] J_n(\upsilon_{nm}\xi)(A_{nm}\cos n\varphi + B_{nm}\sin n\varphi) =$$

$$= (1 - V_{ext})\,\gamma^2 - V_o . \qquad (13)$$

Space charge dominated beam transport is achieved, if b >> 1. It gives the possibility to simplify approximation of Poisson's equation (13). Expression in square brackets in equation (13) can be taken as a constant, close to unit:

$$1 + \frac{\upsilon_{nm}^2}{8kb}\left(\frac{R}{a}\right)^2 \approx 1 + \delta, \quad \delta = \frac{1}{bk} << 1 . \qquad (14)$$

With that approximation, self-consistent space charge dominated beam potential is:

$$V_b = -\,\frac{\gamma^2}{1+\delta}\,V_{ext} . \qquad (15)$$

Second approximation to the self-consistent potential is given by holing one more term in expansion of exponential function $\exp(-V_{ext} - V_b\gamma^{-2}) \approx 1 - V_{ext} - V_b\gamma^{-2} + 0.5\,(V_{ext} - V_b\gamma^{-2})^2$:

$$V_b = \gamma^2\left[1 + \delta - V_{ext} - \sqrt{(1+\delta - V_{ext})^2 - V_{ext}(V_{ext} - 2)}\right]. \qquad (16)$$

From eqs. (15), (16) it follows, that space charge potential of a high brightness matched beam always tends to the same distribution as an external focusing potential with opposite sign, regardless the focusing field is applied. With increasing of beam brightness, exact solution of eq. (10) becomes close to eq.(15). In the extreme case of infinitely high bright beam, space charge potential of the beam completely compensates for focusing field $V_b = -\,\gamma^2 V_{ext}$.

Self consistent space charge distribution of matched beam in the channel with potential (2) is given by

$$\rho_b = \frac{\varepsilon_o}{1+\delta}\gamma^2\,\Delta U_{ext} = \rho_o\,(1 + 10\zeta r^4\cos 4\varphi + 25\zeta^2 r^8) . \qquad (17)$$

In the limit of very high brightness beam $\delta \to 0$ space charge density of the matched beam (17) does not depend on beam brightness. Particle distribution (17) has a 4-folded symmetry. Every 45° variation of azimuth angle results in change of particle distribution from decreasing to increasing function of radius and vice versa.

Realistic beam distribution has monotonically decreasing density function of radius. Good approximation to realistic beam is a parabolic distribution

in phase space [2, 3], which gives projection in real space as $\rho(r) = \rho_o [1 - 0.5 (r/R)^2]^2$, close to truncated Gaussian distribution . In Refs. [2,3] expressions for required values of quadrupole gradient and duodecapole components to provide approximate matching of such a beam with the channel were found:

$$G_2 = \frac{\sqrt{8}\,\pi\, m_o\, c^2}{q\,\lambda\, R} \sqrt{\frac{\varepsilon^2}{R^2} + \frac{3\,I}{I_c\,\beta\gamma}}, \qquad (18)$$

$$G_6 = -\frac{G_2}{12\,\beta\,\gamma\,R^4}\frac{I}{I_c}\left(\frac{\varepsilon^2}{R^2} + \frac{3\,I}{I_c\,\beta\,\gamma}\right)^{-1}. \qquad (19)$$

To make the realistic beam distribution as close to matched beam distribution as possible, beam has to be truncated along equipotential lines. Therefore, beam boundaries have to be 45° skewed square.

3 RESULTS OF PARTICLE-IN-CELL SIMULATION

Computer simulations using particle-in-cell code BEAMPATH [5] were done to verify the derived matched conditions of the beam. Nonlinear transformer with adiabatic change of duodecapole component was tested. If parameters of the structure are changed adiabatically, beam emittance is a constant of motion. One can expect modification of a nonuniform particle distribution into more uniform distribution in the structure, where higher order focusing field components drops gradually.

In Fig. 2 results of beam dynamics in quadrupole channel with gradual variation of a duodecapole component are presented. The value of quadrupole gradient G_2 = 50 kV/cm^2 was kept constant along the channel. The duodecapole component was adiabatically changed from the value G_6 = -1.9 kV/cm^6 as required by matched conditions, to zero for the distance L = 100 cm utilizing linear law $G_6(z) = G_6(1 - z/L)$. After nonlinear matching section z > L, the channel was a pure quadrupole and the beam was transported 224 cm more to check the results of transformation. As seen, beam profile in real space is modified from a square to a circular shape. Rms beam emittance growth in simulations, presented in Fig. 2 is 15%, which is substantially smaller, than 50% emittance growth in a pure quadrupole channel, presented in Fig. 1. The final beam emittance and beam profile are matched without serious phase space portrait distortion. After transformation, the beam can be transported in a conventional structure with a linear focusing field.

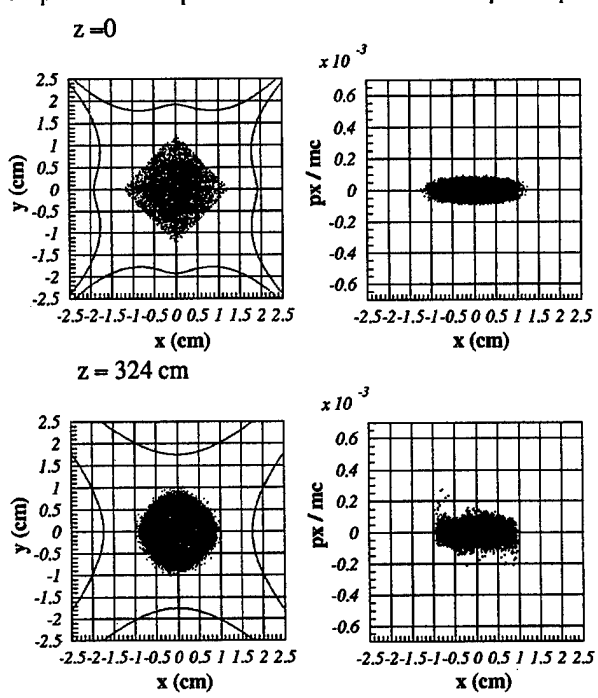

Fig. 2. Adiabatic matching avoiding halo formation of 150 keV, 100 mA, 0.06 π cm mrad proton beam in a nonlinear matching section.

4 CONCLUSIONS

Self consistent space charge potential of a high brightness beam is derived in case of arbitrary potential of continuos focusing channel. It is shown, that matched beam always tends to compensate for applied potential. Simple formula is given, which demonstrates the effect of shielding in case of arbitrary focusing potential. Four vanes quadrupole structure with a multipole component of the 6th order is analyzed to prevent space charge dominated beam emittance growth. In such a structure, the matched beam profile has to be close to square, instead of the conventional circle beam cross section. The adiabatic change of a nonlinear focusing field along a structure results in gradual transformation of an initially nonuniform beam distribution into a distribution matched with the linear focusing channel. Given analysis provides matched conditions for a non-uniform high brightness particle beam transport without beam halo formation.

REFERENCES

[1] Y. Batygin, Phys. Review E, 53, 5358, (1996).

[2] Y.Batygin, Phys. Review E, 54, 5673, (1996).

[3] Y.Batygin, A.Goto and Y.Yano, Proceedings of the 5th Europ. Part. Acc. Conference (EPAC96), Barcelona, 1236 (1996).

[4] I.M.Kapchinsky, Theory of Resonance Linear Accelerators, Harwood, Chur, 1986.

[5] Y. Batygin, Proceedings of the 3rd European Part. Acc. Conference (EPAC92), Berlin, 822 (1992).

NEW CLASSES OF UNIFORM DISTRIBUTIONS FOR CHARGED PARTICLES IN LONGITUDINAL MAGNETIC FIELD

O.I.Drivotin, D.A.Ovsyannikov
St.-Petersburg State University, St.-Petersburg, Russia

Abstract

The problem of stationary self-consistent distributions for charged particles beam in longitudinal magnetic field was considered in various works. The simplest known distribution is Brillouin flow. Another simple case is Kapchinskij-Vladimirskij distribution [1]. The supporters of these distributions in the phase space of transverse configurations and velocities have zero volume. The distributions with non-zero phase volume for beams with constant cross-section radius were also obtained previously [2] – [6].

In the present report more general case is investigated when radius of beam cross-section, longitudinal velocity, and magnetic field change along the longitudinal axis. Wide classes of new stationary axially symmetric self-consistent distributions are found. New distributions have uniform charge density in the beam cross-section and, generally speaking, nonzero phase volume in the phase space of transverse motion.

In particular case of longitudinal uniformity they coincide with known ones. Such distributions can be applied for modelling of the beam in nonuniform along its axis magnetic field with particles moving with different velocities in various cross-sections. [1]

1 DYNAMICS EQUATIONS

Consider axially-symmetric stationary charged particles beam in longitudinal magnetic field. We will look for such particle distributions that particle density in configuration space $\rho(r,z)$ is constant throughout the beam cross-section:

$$\rho(r,z) = \begin{cases} \rho_0(z), r \le R(z), \\ 0, \qquad r > R(z) \end{cases}$$

where r, φ, z are cylindrical coordinates, axis z coincides with the beam axis.

Suppose that R essentially changes only at the distances which are sufficiently greater then R. Then the equation of radial motion of particles will be

$$\ddot{r} = -\omega^2 r + M^2/r^3 \tag{1}$$

where $\omega^2 = \omega_0^2 - \lambda/R^2$, $\omega_0^2 = eB_z/2m_0\gamma$, $\lambda = eJ/2\pi\varepsilon_0 m_0\gamma^3\dot{z}$, J is beam current, ε_0 is electric constant, $\dot{z}$ is longitudinal velocity of particles supposed to be equal for all particles in given cross-section, but depended on z, $M = r^2(\dot{\varphi} + \omega_0)$, e and m_0 are charge and rest mass of particle, B_z is z-component of applied magnetic field, γ is reduced particle energy, $\gamma = (1-\beta^2)^{-1/2}$, $\beta = \dot{z}/c$, dot means differentiating on independent variable t, $t \ge t_0$.

It can be shown that the equation for beam envelope $R(z)$ can be written in the form

$$\ddot{R} = -\omega^2 R + \frac{a_0^2 c_0^2}{R^3}. \tag{2}$$

The system of equation (1) and (2) can be reduced to known Ermakov system [7] if the variable ω, which depends on t and R, is regarded as function of t.

Using the known expression for the integral of the Ermakov system [8] we obtain that the value

$$I = (R\dot{r} - r\dot{R})^2 + \frac{M^2R^2}{r^2} + \frac{a_0^2c_0^2r^2}{R^2} =$$

$$(\frac{dq}{d\tau})^2 + \frac{M^2}{q^2} + a_0^2c_0^2q^2 \tag{3}$$

is integral of motion. Here $q = r/R$, $d\tau = dt/R^2$. Another integral of motion is

$$M = q^2(\frac{d\varphi}{d\tau} + R^2\omega_0). \tag{4}$$

Let find such set Ω in the space of variables I, M that the condition $q \le 1, \forall t \ge t_0$ is satisfied for all particles. It follows from (3) that

$$I \le M^2 + a_0^2c_0^2. \tag{5}$$

Also $I \ge \min_q(\frac{M^2}{q^2} + a_0^2c_0^2q^2) = 2|M|a_0c_0$. Excluding the particles on the low boundary of the set we obtained that

$$I > 2|M|a_0c_0. \tag{6}$$

The set Ω defined by the conditions (5),(6) is shown on fig.1. Analogous set for beam, uniform along its longitudinal axis, was considered in works [5], [6].

Let consider also the set Ω_q of such I and M that particle possessing these I and M passes through a point with coordinate q. First, we note that

$$I \ge \frac{M^2}{q^2} + a_0^2c_0^2q^2. \tag{7}$$

Besides that, we have the inequality (5) limiting the value of I at a given value of M. So, the set Ω_q is defined by (7), (5).

[1] This work is supported by Russian Foundation for Fundamental Researches 96-01-00926a

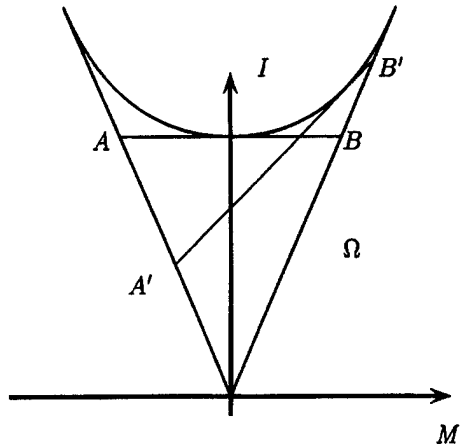

Figure 1: the set Ω.

2 DISTRIBUTION IN THE SPACE OF INTEGRALS

Further we consider the phase distribution of particles of some infinitely thin layer moving along the axis z with the velocity $\dot{z}$. We suppose that this layer is limited by two parallel infinitely closed planes moving along the axis z with the same velocity. Taking into account velocity variation along the axis and corresponding variation of the thickness of the layer we normalize all densities dividing them by the $dz/\dot{z}$.

Let us denote the particles distribution density on the variables $a, b, \ldots$ by $DN/D(a, b, \ldots)$. Consider the phase density in the four-dimensional phase space of transverse configurations and velocities $n = DN/D(x, y, \dot{x}, \dot{y})$. Here x, y are transverse Cartesian coordinates.

We assume that phase density n depends only on I and M: $n = n(I(r, \dot{r}, \dot{\varphi}), M(r, \dot{\varphi}))$ where $n(I, M)$ denotes some function of I and M. Independence from the variable φ means axially symmetry of the beam. Independence from the variable r narrows the class of admissible distribution, but sufficiently simplifies the further analysis because in that case the conservation of phase density along particles trajectories means conservation $n(I, M)$ along z-axis.

Then we have

$$\frac{DN}{D(q, I, M)} = \int_0^{2\pi} d\varphi \frac{DN}{D(q, \varphi, I, M)} = \frac{2\pi}{q^2|q'|} \times$$

$$\frac{DN}{D(q, \varphi, q', \varphi')} = \frac{2\pi}{q^2|q'|R^4} \frac{DN}{D(q, \varphi, \dot{q}, \dot{\varphi})} = \frac{2\pi n(I, M)}{|q'|}$$

(stroke denotes differentiating on variable τ).

Let introduce the distribution density of the particles in the space of integrals I and M : $f(I, M)$. Taking into account previous equality we get

$$f(I, M) = \int_{q_{min}(I,M)}^{q_{max}(I,M)} \frac{DN}{D(q, I, M)} dq = \frac{\pi^2 n(I, M)}{a_0 c_0},$$

as

$$\int_{q_{min}(I,M)}^{q_{max}(I,M)} dq/|q'| = \pi/2a_0c_0.$$

Expressing the particles density in configuration space $\rho(r)$ through $f(I, M)$ we get

$$\rho(r) = \int_{\Omega_q} \frac{DN}{D(r, I, M)} \frac{dI\, dM}{2\pi r} = \frac{1}{rR} \int_{\Omega_q} \frac{n(I, M)\, dI\, dM}{|q'|}.$$

Concerning the particle density in the space with the coordinates x/R, y/R denoted by $\tilde{\rho}$ we will obtain

$$\tilde{\rho}(q) = \frac{a_0 c_0}{\pi^2 q} \int_{\Omega_q} \frac{f(I, M)\, dI\, dM}{|q'|}. \tag{8}$$

In the expression (8) we exclude the particles for which $q' \equiv 0$ in accordance with (6). Accounting of these particles requires an additional term in the expression (8).

The expressions (5),(6),(8) are analogous to the expressions obtained in the work [6], where the beam with constant radius R was considered. So, results of that work can be extended to the present case.

For example, if $f(I, M)$ is the density of a simple layer[2] on the segment A'B' which is tangent to the upper boundary of the set Ω, then

$$f(I, M) = f_0 \delta_{I = I_0(k) + kM}, \; f_0 > 0, \; (I, M) \in \Omega \tag{9}$$

where $I_0(k) = a_0^2 c_0^2 - k^2/4$. Substituting (9) to (8) we have

$$\tilde{\rho}(q) = \frac{a_0 c_0 f_0}{\pi^2 q} \int_{\Omega_q} \frac{\delta_{I = I_0(k) + kM}\, dI\, dM}{(I - M^2/q^2 - a_0^2 c_0^2 q^2)^{1/2}} =$$

$$\frac{a_0 c_0 f_0 \sqrt{1 + k^2}}{\pi} \quad \text{as}$$

$$\int \delta_s\, dI\, dM = \int \left(\int \frac{\delta(I - I(M))}{|\cos\varphi|} dI \right) dM$$

where $|\cos\varphi| = (1 + k^2)^{-1/2}$. Hence, particles density throughout the beam cross-section is constant for distribution (9) and, therefore, it is solution of the problem.

Normalizing as pointed out above we have $\tilde{\rho}_0 = J/\pi$, so $f_0 = J/a_0 c_0 (1 + k^2)^{1/2}$. Here J is beam current supposed to be not depended on t.

As it is shown in the work [6], the supporter of the distribution density (9) is segment of straight line which is tangent to the upper boundary of the set Ω. The segment is

[2]The density of the simple layer is surface density of the distribution which supporter is some surface.

bounded by the lines $I = \pm 2a_0c_0M$ (the segment A'B' on the figure). When $k = 0$, this segment is parallel to the axis M (segment AB on the figure). If R is constant

$$R^2 = (\lambda + \sqrt{\lambda^2 + 4\omega_0^2 a_0^2 c_0^2})/2\omega_0^2, \quad \lambda, \omega_0 = const,$$

then the distribution (9) at $k = 0$ coincides with the Kapchinskij-Vladimirskij distribution for the beam with constant R (see [1]), and the distributions with $k \neq 0$ coincide with distributions described in [2] for beam with constant R (equilibrium of rigid rotator type).

3 LINEAR COMBINATIONS OF PARTICLES DISTRIBUTIONS

Besides that, every linear combination of the distributions (9) also will be uniform in the beam cross section:

$$f(I, M) = \sum_{k \in K} \alpha_k \delta_{I = I_0(k) + kM}$$

where $K \subset (-2a_0c_0, 2a_0c_0)$ is some set of real numbers or

$$f(I, M) = \int_{-2a_0c_0}^{2a_0c_0} \alpha(k) \delta_{I = I_0(k) + kM} \, dk.$$

For these cases we have

$$\rho = \frac{a_0c_0}{\pi R^2} \sum_{k \in K} \alpha_k \, (1 + k^2)^{1/2} \qquad \text{and}$$

$$\rho = \frac{a_0c_0}{\pi R^2} \int_{-2a_0c_0}^{2a_0c_0} \alpha(k) \, (1 + k^2)^{1/2} \, dk$$

correspondingly.

4 INTEGRAL EQUATION FOR DISTRIBUTION DENSITY

Another way to search the uniform distributions is to consider the equality (8) as integral equation for distribution density. Transposing the equation (8) we get

$$\frac{a_0^2c_0^2}{2\pi} \int_0^{2\pi} \int_0^1 \frac{F(y\cos(\psi - \vartheta), y\cos(\psi + \vartheta))}{(1 - y^2)^{1/2}} y \, dy \, d\psi = J.$$

Here

$$F(k_1, k_2) = \begin{cases} f(I, M)(M^2 - I + a_0^2c_0^2)^{1/2}, k_1 \geq k_2, \\ F(k_2, k_1), k_1 < k_2 \end{cases},$$

$k_{1,2} = 2(M \pm (M^2 - I + a_0^2c_0^2)^{1/2})$, $\vartheta = \arccos q$. This is the integral equation for the function of two arguments $F(k_1, k_2)$. Both arguments depend on q. The problem is to find such $F(k_1, k_2)$ that result of integration doesn't depend on q. Any nonnegative symmetric solution corresponds to some self-consistent particle distribution.

The simplest solution $F(k_1, k_2) = g_0$ corresponds to

$$f(I, M) = g_0(M^2 - I + a_0^2c_0^2)^{-1/2}, \quad g_0 > 0. \qquad (10)$$

Here g_0 is constant. This distribution doesn't reduce to any distributions obtained before. Another simple case is $F(k_1, k_2) = g(k_1) + g(k_2)$ corresponding to

$$f(I, M) = \frac{g(k_1) + g(k_2)}{(M^2 - I + a_0^2c_0^2)^{1/2}}, \quad g(k) \geq 0.$$

Other solutions can be sought in the form of a series or a polynomials. For example, the distribution

$$f(I, M) = \frac{-c\,(I - a_0^2c_0^2)(10M^2 - 5I + 2a_0^2c_0^2) + g_0}{(M^2 - I + a_0^2c_0^2)^{1/2}}$$

corresponds to the polynomial of third degree. The constant values c and g_0 must be taken so that $f(I, M) \geq 0$ for all $(I, M) \in \Omega$.

Thus, wide classes of new stationary self-consistent nonuniform along z-axis distributions are obtained. These distributions can be used for the solution of various problems of calculation and optimization of accelerating structures.

5 REFERENCES

[1] I.M.Kapchinskij, "Particles Dynamics in Linear Resonance Accelerators", Atomizdat, Moscow, 1966.

[2] R.C.Davidson, "Theory of Nonneutral Plasmas", Benjamin, Reading, Massachusetts, 1974.

[3] I.Hoffmann, "Transport and Focusing of High Intensity Unneutralised Beams", in: Applied Charged Particle Optics, ed. by A.Septier, part C, Academic Press, New York, 1983, pp.49-140.

[4] A.D.Vlasov, "Self-Consistent Cylindrical Beams with Uniform Density", Zh.Tekhn.Fiz.(USSR), **49** (9), 1821-1826 (1979).

[5] O.I.Drivotin, D.A.Ovsyannikov, "Constructing Stationary Solutions of the Vlasov Equation for an Axially-Symmetrical Flow of Charged Particles in a Longitudinal Magnetic Field", Zh.Vychisl.Mat.Mat.Fiz.(USSR), **27** (3), 416-427 (1987). In Russian. English translation in USSR Comput.Math.Math.Phys.(UK).

[6] O.I.Drivotin, D.A.Ovsyannikov, "New Classes of Stationary Solutions to the Vlasov Equation for an Axially-Symmetrical Beam of Charged Particles with Uniform Density", Zh.Vychisl.Mat.Mat.Fiz.(USSR), **29** (8), 1245-1250 (1989). In Russian. English translation in USSR Comput.Math.Math.Phys.(UK).

[7] V.P.Ermakov, Univ.Izv.(Kiev), **20** (9), 1-25 (1880).

[8] J.R.Ray," N-dimensional Nonlinear Systems with Exact Invariants", Adv.Nonlinear Waves, **1**, 230-233 (1984).

THE CALCULATION, SIMULATION, AND MEASUREMENT OF LONGITUDINAL BEAM DYNAMICS IN ELECTRON INJECTORS

B. Dunham, H. Liu and R. Kazimi
Thomas Jefferson National Accelerator Facility
12000 Jefferson Ave., Newport News, VA 23606

Abstract

Polarized electrons are a valuable commodity for nuclear physics research and every effort must be made to preserve them during transport. Measurements of the beam emitted from the polarized source at the Thomas Jefferson National Accelerator Facility (Jefferson Lab) have shown a considerable bunch lengthening with increasing beam current. This lengthening leads to unacceptable loss as the beam passes through the injector chopping system. We present an application of the longitudinal envelope equation to describe the bunch lengthening and compare the results to measurements and simulations using PARMELA. In addition, a possible solution to the problem by adding a low power buncher to the beamline is described and initial results are shown.

1 INTRODUCTION

Polarized electrons are a very valuable commodity for nuclear physics research, and every effort must be made to preserve them during transport through the accelerator. A typical thermionic injector discards 5/6th of the DC beam during the initial chopping process to prepare the beam for bunching and capture before injection into the main accelerator: this is clearly not the preferred method for polarized electrons. In addition, throwing away part of the charge during the chopping process will effectively lower the useful lifetime of the cathode.

To overcome this problem, the beam from the photocathode must either be prechopped at the cathode using a laser (as is done in RF guns), or adiabatically bunched with minimal beam loss (as is done for protons and ions using an RFQ). As no reliable adiabatic bunching scheme exists for electrons, and prechopping with a laser is straightforward, this is the method chosen for the polarized source at the Jefferson Lab. The present laser has a pulse width of 54 ps (FWHM) [1] which matches the 60° (110 ps) total RF phase acceptance (at 1497 MHz) used in the chopping system.

Initial measurements of the bunch length after the beam has traversed approximately 10 meters through the injector show that bunch length is much longer than the initial laser pulse width and also depends on current. In this report, the longitudinal envelope equation will be reviewed and applied to the observed bunch lengthening. In addition, a corrective action using a buncher is discussed.

2 DESCRIPTION OF THE SYSTEM

In the calculation of the longitudinal properties of the beam (see section 3), the longitudinal envelope equation assumes that the beam has a constant transverse dimension. While this is certainly not the case, the mean beam size can be used as an estimate for the longitudinal calculations. Thus, the sketch below only includes the location of elements that effect the longitudinal properties of the beam, and not focusing elements such as solenoids. Details of the polarized beam transport system and the chopping system can be found elsewhere (see [2] and [3] respectively).

The beam is accelerated to 100 kV in a photocathode gun and then deflected from vertical to horizontal using a dipole (see figure 1). It then passes through a 'Z' shaped spin manipulation system consisting of two electrostatic bends plus a number of solenoids. After leaving the 'Z' the beam continues on and enters the regular thermionic injector beamline where it is chopped, bunched and accelerated before injection into the main machine.

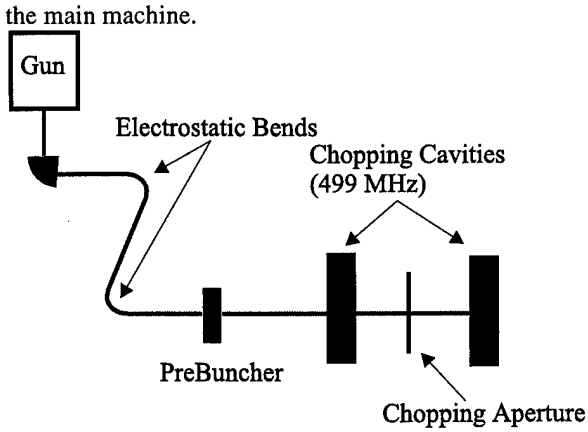

Figure 1 Schematic of the injector beamline

To measure the bunch length, the first chopping cavity deflects the beam and sweeps it into a 3 cm diameter circle at the chopping aperture. The chopping aperture is then set to transmit a 10° slice from the circle incident on it, and the transmitted current is measured as a function of the laser phase in a downstream faraday cup. A plot of the transmitted current versus the laser phase gives a direct measure (after correcting for the

0-7803-4376-X/98 /$10.00 © 1998 IEEE

finite size of the slit) of the bunch length at the chopping aperture.

3 LONGITUDINAL ENVELOPE EQUATION

Many are familiar with the calculation of the transverse envelope behavior of a beam using the envelope equation, but not with the calculation of the longitudinal envelope properties (bunch length and energy spread). The longitudinal envelope equation [4,5] represents the ideal situation of a beam with a parabolic charge distribution with no transverse variations. The parabolic distribution leads to a self-consistent solution with linear space charge forces. It is also is correct relativistically and includes the effects of acceleration. Experimental verification of the equation at low energies using a beam with a parabolic distribution have been carried out [5].

The longitudinal envelope equation can be written (ignoring acceleration) as [4]

$$\frac{d^2z}{ds^2} - \frac{2gz_{init}I_{peak}}{\beta^3\gamma^5 I_0}\frac{1}{z^2} - \frac{\varepsilon_L^2}{z^3} - K(s)z = 0$$

where z is the half bunch length, K is the focusing term, ε_L is longitudinal emittance, I_0 is a constant equal to 17 kA, and g is the geometry factor $1+2\ln(R/r)$, where R is the pipe radius and r is the average beam radius. For now, we will assume that the emittance is negligible and that there is no external focusing. The equation can then be written in the simplified form

$$\frac{d^2z}{ds^2} = \frac{a^2 z_{init}}{2z^2} \quad \text{where} \quad a^2 = \frac{4gz_{init}}{\beta^3\gamma^5 I_o}.$$

This equation can be integrated to give $\eta'^2 = \frac{a^2}{z_{init}^2}\left(b - \frac{1}{\eta}\right)$ with $b = 1 + z_{init}'^2 / a^2$ and $\eta = z / z_{init}$. Integrating once more gives (for $z_{init}' > 0$)

$$\frac{sab^{3/2}}{z_{init}} = \log\left(\sqrt{\eta b} + \sqrt{\eta b - 1}\right) + \sqrt{\eta b}\sqrt{\eta b - 1} - \log\left(\sqrt{b} + \sqrt{b-1}\right) - \sqrt{b}\sqrt{b-1}$$

and

(for $z_{init}' < 0$)

$$\frac{sab^{3/2}}{z_{init}} = \pm\left[\log\left(\sqrt{\eta b} + \sqrt{\eta b - 1}\right) + \sqrt{\eta b}\sqrt{\eta b - 1}\right] + \log\left(\sqrt{b} + \sqrt{b-1}\right) + \sqrt{b}\sqrt{b-1}$$

where the + sign is for positions before the waist and the - sign is for positions after the waist.

4 CALCULATIONS AND RESULTS

The longitudinal envelope equation requires that the initial particle distribution be parabolic in order for the self-consistency condition to be satisfied. The laser beam profile for the polarized source is roughly Gaussian with a FWHM of 54 ps [1]. For the first step in the bunch lengthening calculations, we will assume that the initial electron distribution follows the laser beam distribution, and that the Gaussian can be approximated by a parabolic distribution with the same rms width and area. Then, assuming that the beamline is a 10.0 meter drift (s=10 m, the distance from the gun to the chopping aperture) the final bunch length can be calculated using the equations in section 3 with the initial conditions given by parameters a and b. The geometry factor 'g' is calculated using PARMELA to be 4.84 (σ_r = 0.4 mm) including all of the transverse focusing elements. Figure 2 shows the results of the calculations as a function of average current and several geometry factors (g) along with the measured bunch length. The numbers are all in terms of the parameters of the parabolic distribution (i.e. the plotted bunch length (2z) corresponds to the parabolic distribution, not the actual number). A comparison to the PARMELA simulations is also shown.

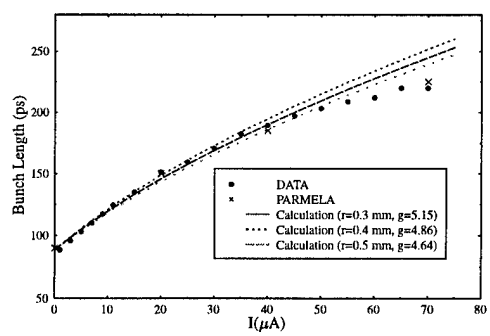

Figure 2 Bunch lengthening calculations compared to measurements and PARMELA simulations.

The calculations agree well for currents up to about 40 μA. For higher currents, beam loss occurs during the last meter of travel as the beam passes through two small emittance defining apertures. This reduces the bunch lengthening and distorts the longitudinal profile, making comparisons more difficult. The apertures, which are necessary only for operation of the thermionic gun, have since been enlarged to allow nearly complete transmission of the beam from the photocathode gun.

5 ADDITION OF A BUNCHER

A buncher located after the Z spin manipulator can provide a longitudinal kick to compensate for the debunching during transport through the injector. Instead of solving the envelope equation including the force term, the kick can be treated by matching boundary conditions

at the location of the buncher. To solve the problem the slope ($z' = dz / ds$) and bunch length (z) at the entrance to the buncher are calculated, then the change in the slope at the buncher necessary to reduce the bunch length to the nominal ±30° at the chopping aperture is determined.

To find the relationship between the change in slope and the buncher amplitude, note that $z' = \Delta\beta/\beta$ where the difference is between the center of the bunch and the head (or tail) of the bunch. The energy gain is $\Delta E = mc^2\Delta\gamma = eV\sin\varphi$ where φ is the phase of the electron with respect to the center of the bunch. Using the relation $\beta\,\Delta\beta = \Delta\gamma / \gamma^3$, this can be rearranged to find the peak buncher voltage for an ideal, zero-length buncher (see figure 3)

$$eV = \frac{mc^2\beta\Delta\beta\gamma^3}{\sin\varphi} = \frac{z'mc^2\beta^2\gamma^3}{\sin\varphi}$$

Making the small angle approximation and substituting $\varphi = \omega z / \beta c = \omega\eta z_{init} / \beta c$ gives

$$eV = \frac{\gamma\beta c(\gamma^2 - 1)z'mc^2}{\omega\eta z_{init}}.$$

A low power buncher has been constructed and installed in the beamline. Figure 4 shows pictures of a viewer at the chopping aperture. The upper left picture shows the nominal beam (no buncher): three beams are present as the choppers operate at 499 MHz while the gun fills every bucket at 1497 MHz. The upper right picture displays the beam with the buncher on and at zero crossing phase. A buncher power of 1.5 W is sufficient to compress the 30 μA (average current) beam to pass through the chopping system loss-free.

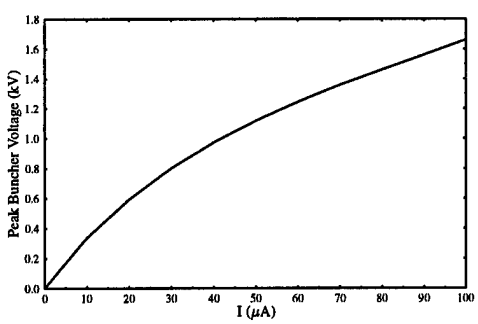

Figure 3 Calculated buncher voltage as a function of current (for an ideal, zero-length buncher).

4 CONCLUSION

Polarized electrons are a very valuable commodity for nuclear physics research, and every effort must be made to preserve them during transport through the accelerator. Initial measurements of the bunch length of the beam emitted from the polarized source have shown that the beam cannot pass loss free through the injector chopping system. We present an application of the longitudinal envelope equation to describe the measured bunch lengthening and find very good agreement between the prediction and the measurements. A solution to the problem of bunch lengthening using a buncher cavity has also been demonstrated.

5 ACKNOWLEDGEMENTS

This work was supported by the U.S. DOE under contract number DE-AC05-84ER40150. Thanks to M. Poelker for helping to obtain the data and to C. Sinclair for motivating this work. Also, thanks to C. Piller and C. Hovater for quickly designing and building the prebuncher.

REFERENCES

[1] M. Poelker, private communication.
[2] D. Engwall., B. Dunham, L.S. Cardman, D.P. Heddle and C.K. Sinclair, Nucl. Instr. Methods **A324**, 409 (1993).
[3] M.G. Tiefenback and G.A. Krafft, 1993 Part. Accel. Conf, 426 (1993).
[4] D. Neuffer, IEEE Trans. Nucl. Sci., **26**, 3031 (1979).
[5] D.X. Wang, J.G. Wang, D. Kehne, and M. Reiser, Appl. Phys. Lett. **95** (25), 3232 (1993).

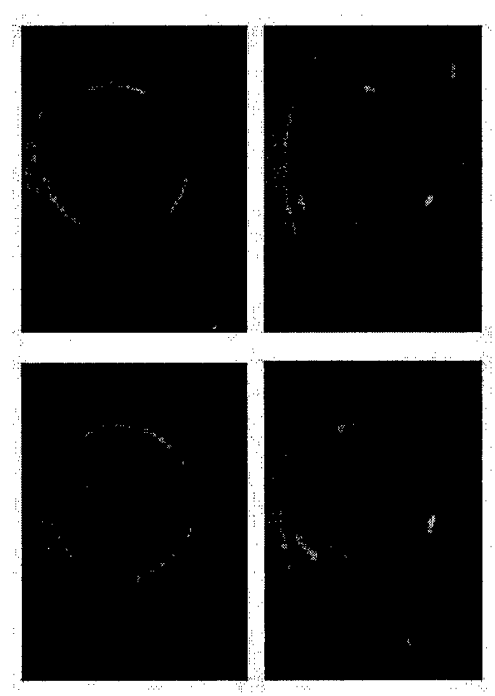

Figure 4 Clockwise from upper left: 1) buncher off with 30 μA of average current; 2) buncher on at zero crossing; 3) buncher on 30° off zero crossing; and 4) buncher on with the phase set to the wrong zero crossing.

STABILITY AND HALO FORMATION IN AXISYMMETRIC INTENSE BEAMS

Robert L. Gluckstern, University of Maryland, College Park, MD 20742, and
Sergey S. Kurennoy, LANSCE-1, LANL, MS H808, Los Alamos, NM 87545

Abstract

Beam stability and halo formation in high-intensity axisymmetric 2D beams in a uniform focusing channel are analyzed using particle-in-cell simulations. The tune depression - mismatch space is explored for the uniform (KV) distribution of the particle transverse-phase-space density, as well as for more realistic ones (in particular, the waterbag distribution), to determine the stability limits and halo parameters. The numerical results show an agreement with predictions of the analytical model for halo formation [1].

1 INTRODUCTION

There is an increasing interest in high-current applications of ion linacs, such as the transformation of radioactive waste, the production of tritium, and fusion drivers. High currents of the order of 100 mA restrict beam losses below 1 ppm. Thorough studies are necessary to understand mechanisms of intense-beam losses, in particular, beam instabilities and halo formation.

Most of the theoretical efforts so far have concentrated on the Kapchinsky-Vladimirsky (KV) distribution of particles in transverse phase space [2]. The KV beam density is uniform so that space-charge forces inside the beam are linear. It allows an analytical investigation and results are used to predict the behavior of real beams. On the other hand, it is recognized that the KV model, in which all particles have the same transverse energy, is not a realistic beam distribution, e.g. [3]. The present paper compares the KV beam with other, nonlinear particle-density distributions, which can serve as better models for real beams.

2 ANALYTICAL CONSIDERATION

We study a continuous axisymmetric ion beam in a uniform focusing channel, with longitudinal velocity $v_z = \beta c$. The Hamiltonian of the transverse motion ($v_\perp \ll v_z$) is

$$H(r,s) = s^2/2 + k_0^2 r^2/2 + q\Phi(r)/(m\gamma^3\beta^2c^2)\,, \quad (1)$$

where m and q are ion mass and charge, k_0 is the focusing strength of the channel, $\gamma = (1-\beta^2)^{-1/2}$, $r = \sqrt{x^2+y^2}$ is the distance from the z-axis in the transverse plane, and $s = \sqrt{x'^2+y'^2}$ ($x' = \dot{x}/\beta c$, $y' = \dot{y}/\beta c$) is the dimensionless transverse velocity. The electric potential $\Phi(r)$ must satisfy the Poisson equation

$$\nabla^2\Phi(r) = -(q/\varepsilon_0)\iint d\vec{s} f(r,s)\,, \quad (2)$$

where $f(x,y,x',y') = f(r,s)$ is the distribution function in the transverse non-relativistic 4-D phase space. The integral on the RHS is the particle density $d(r)$.

Since the Hamiltonian (1) is an integral of motion, any distribution function of the form $f(r,s) = f(H(r,s))$ is a stationary distribution. We consider a specific set of stationary distributions for which the beam has a sharp edge (for all ions $r \le r_{max} = a$), namely,

$$f_n(H) = \begin{cases} N_n n(H_0 - H)^{n-1} & \text{for } H \le H_0\,, \\ 0 & \text{for } H > H_0\,. \end{cases} \quad (3)$$

The normalization constants N_n are chosen to satisfy $2\pi\int_0^a r dr d(r) = I$, where $d(r)$ is the particle density, and I is the beam current. The set includes the KV distribution, $f_0 = N_0\delta(H_0 - H)$, as a formal limit of $n \to 0$, as well as the waterbag (WB) distribution, $f_1 = N_1\theta(H_0 - H)$, where $\theta(x)$ is the step-function. For a detailed discussion of these two specific examples see [4].

We introduce the function $G(r) = H_0 - H(r,s) + s^2/2$, because the density can be expressed from (3) as $d(r) = 2\pi N_n G^n(r)$. Physically, this function gives the maximal transverse velocity for a given radius, $s_{max}(r) = \sqrt{2G(r)}$, and defines the boundary in the phase space (r,s). It allows us to rewrite Eq. (2) as

$$[rG'(r)]'/r - \lambda^2 G^n(r) = -2k_0^2\,, \quad (4)$$

with boundary conditions $G(a) = 0$, and $G(0) \equiv G_0$ is finite. Here the parameter $\lambda^2 = K/\left[\int_0^a r dr G^n(r)\right]$, where $K = 2I/\left(I_0\beta^3\gamma^3\right)$ is the beam perveance, and $I_0 = 4\pi\varepsilon_0 mc^3/q$ is a constant. Particular solutions to (4) are easy to find for $n = 0$ (KV) and $n = 1$ (WB) [4]. For $n \ge 2$ a numerical solution is required.

To compare different transverse distributions on a common basis, we consider rms-equivalent beams which have the same perveance K, rms radius, and rms emittance $\tilde{\mathcal{E}}$. To characterize the space-charge strength, one introduces an equivalent (or rms) tune depression

$$\eta = \sqrt{1 - K/(4k_0^2 x_{rms}^2)}\,, \quad (5)$$

which reduces to the usual one for the KV beam. For numerical simulations we use dimensionless variables: $\hat{z} = k_0 z$, and $\hat{x} = x\sqrt{k_0/\mathcal{E}}$, where $\mathcal{E} = a'a$. In normalized variables the beam matched radius is $\hat{a} = \sqrt{(C_\mathcal{E}/C_2)/\eta}$, where $C_\mathcal{E} = \tilde{\mathcal{E}}/\mathcal{E}$ and $C_2 = x_{rms}^2/a^2$. For the KV case, $C_\mathcal{E} = C_2 = 1/4$, so that $\hat{a} = 1/\sqrt{\eta}$. The "hats" are omitted below to simplify notation.

3 NUMERICAL SIMULATIONS

We use particle-in-cell simulations to study beam stability and halo formation in the presence of instabilities. A leap-frog integration is applied to trace the time evolution for

0-7803-4376-X/98/$10.00 © 1998 IEEE

a given initial phase-space distribution. The space-charge radial electric field of an axisymmetric beam can be found from Gauss' law by counting the numbers of particles in cells of a finite radial grid, which extends up to four times the beam matched radius. The initial phase-space state is populated randomly but in accordance with (3) for a chosen n. The matched distributions remain stable except for a minor dilution related to numerical errors. However, even the matched KV beam is unstable for $\eta \leq 0.4$, in agreement with existing theory [5] and earlier simulations [6].

The beam breathing oscillations are excited by loading a mismatched initial distribution $r_i = \mu\tilde{r}_i$, $r'_i = \tilde{r}'_i/\mu$, where $\tilde{r}_i, \tilde{r}'_i$ correspond to the matched one, and the mismatch parameter $\mu \leq 1$. A typical range of the simulation parameters: time step $\Delta t = T/100$, where T is the period of breathing oscillations, total number of particles $N_{par} = 16K$ to $4096K$, where $K = 1024$, and radial mesh size $\Delta r = a/128$ to $a/16$. The code performs simulations of about 100 breathing oscillations per CPU hour for $N_{par} = 256K$ on Sun UltraSparc 1/170.

The beam behavior is studied as a function of tune depression η and mismatch μ. Due to a discrete filling of a mismatched beam distribution in simulations and, for $n \geq 1$, due to non-linear space-charge forces, higher modes are excited in addition to the breathing mode. Some of them can be unstable depending on values of η and μ. A detailed numerical study of stability and halo formation for the KV beam and its comparison with the theory predictions [5, 1] have already been reported in [7, 8]. Here we compare results for different transverse distributions. In Figs. 1-2 the maximal radius of the whole ensemble of particles is plotted versus the number of breathing oscillations for the KV and WB beams, for the particular case of $\eta = 0.7$ and $\mu = 0.8$ ($N_{par} = 256K$, $\Delta r = a/64$).

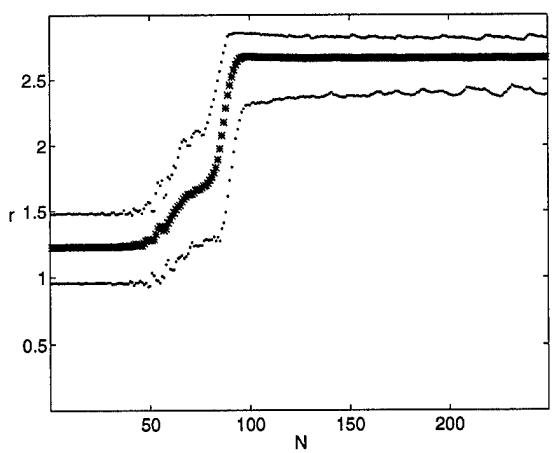

Figure 1: KV beam radius versus the number of breathing periods for $\eta = 0.7$ and $\mu = 0.8$. Stars are for period averages, dots show minimum and maximum during a period.

Comparison of Figs. 1 and 2 shows that for these parameters the WB beam remains stable much longer than the KV one, but eventually it also blows up and some particles form a halo far from the beam core. Results for the $n = 2$

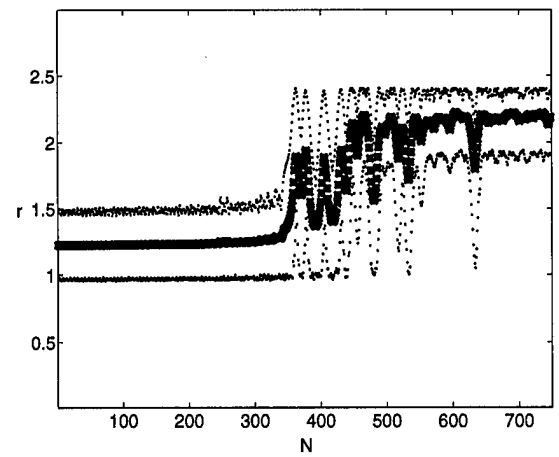

Figure 2: The same as Fig. 1, but for the WB beam.

distribution are similar to those for WB. Some results depend on simulation parameters; e.g., it takes a smaller number of the breathing periods for a beam to blow up if N_{par} is smaller (i.e., higher noise). However, the maximum radius, as well as the fraction of particles outside the core, are practically independent of N_{par}. The number of particles which go into the halo and produce jumps of r_{max} seen in Figs. 1-2, might be rather small. We define the halo intensity h as the number of particles outside the boundary $r_b = 1.75a$ divided by N_{par}. Such a definition is arbitrary, but convenient to compare beam halos over a wide range of tune depressions. While the beam behavior in Figs. 1 and 2 seems qualitatively similar, the halos for these two cases are very different: $h \simeq 3.5 \cdot 10^{-3}$ for KV, and about 100 times less for the WB, with only a few particles in the halo (less than 10 of 256K). That is the reason for oscillations of r_{max} in Fig. 2: these few halo particles can initially all come back to the core simultaneously.

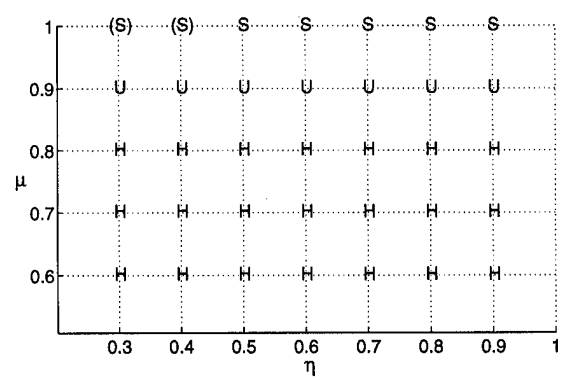

Figure 3: Beam behavior (qualitatively) versus tune depression η and mismatch μ.

A qualitative picture of the beam behavior for various values of the tune depression and mismatch is shown in Fig. 3, and is practically the same for all distributions studied. 'H' corresponds to beam instability with halo formation, usually with a noticeable emittance growth, 'U' means that the beam is unstable but a halo is not observed in our simulations, and 'S' indicates beam stability. The most sur-

prising feature of the diagram is the lack of any significant dependence on η for mismatched beams; on the contrary, the qualitative changes depend primarily on μ. When μ changes from 0.6 to 0.8, the ratio $\tilde{\mathcal{E}}_{fin}/\tilde{\mathcal{E}}_{ini}$ decreases from 1.7–2 to 1.03–1.07 for the KV beam, and from 1.4–1.5 to 1.00–1.01 for the WB and $n = 2$. The number of breathing periods after which the beam radius starts to grow noticeably and the halo forms, has some dependence on η; it is smaller for small η.

We performed a systematic study of the KV, WB, and $n = 2$ distributions for tunes η from 0.1 to 0.9 and mismatches μ from 0.6 to 1.0. Figure 4 shows the ratios of the halo radius to that of the matched beam for the KV and WB beams with three different mismatches, $\mu = 0.6$, 0.7, and 0.8. Results for $n = 2$ beam are not shown; they are slightly lower than those for the WB beam. The KV halo has a larger radius, especially with small space charge (large η), but for space-charge dominated beams, at very small η, the ratios converge for all distributions. The analytical model for the KV halo formation [1] predicts finite values of r_{max}/a between 2 and 2.5 depending on η and μ. One can see from simulations that it works well also for WB and $n = 2$ beams.

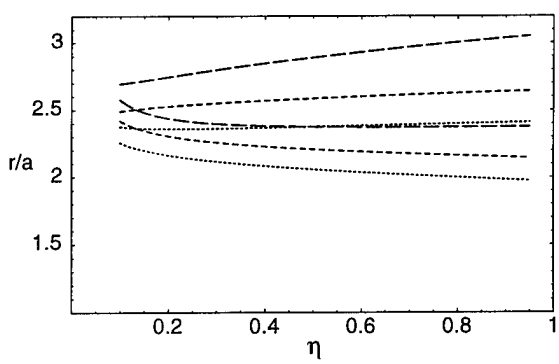

Figure 4: Ratio of halo radius to that of the matched beam for KV (top curves) and WB (bottom curves) beams versus tune depression η for different mismatches: $\mu = 0.6$ long-dashed, $\mu = 0.7$ short-dashed, $\mu = 0.8$ dotted.

Simulation results for halo intensity h are shown in Fig. 5 for KV and WB distributions. Again, results for $n = 2$ are just slightly lower than for the WB beam, and not shown. The intensity depends essentially on the mismatch, and decreases quickly as the mismatch decreases. The WB halo is about 2–3 times less intense than the KV halo for small space charge and large mismatch (0.6 and 0.7) but, for space-charge dominated beams, the intensities are about the same. For $\mu = 0.8$, however, the WB halo is at least an order of magnitude less intense than the KV one; it is not even included in Fig. 5. An apparent decrease of h as η decreases is due to the definition used: the halo boundary radius $r_b = 1.75a$ increases as $1/\sqrt{\eta}$. If a fixed boundary is used instead, the same for all tunes, the halo intensity would be larger for larger space charge.

One more interesting feature is how fast the halo develops. For the KV beam, the process is usually rather fast,

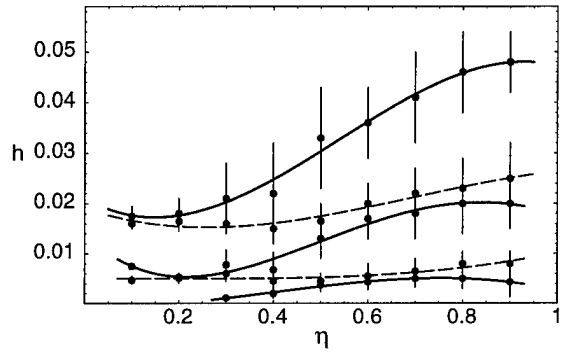

Figure 5: Halo intensity for KV (solid) and WB beams (dashed) vs tune depression η for mismatches $\mu = 0.6$ (top pair), $\mu = 0.7$ (middle pair), $\mu = 0.8$ (bottom, KV only).

and the halo saturates after a few hundred breathing periods. For the WB and $n = 2$ distributions, it continues to grow rather slowly, and asymptotic values are usually reached after a few thousand breathing oscillations; it takes especially long for $\eta \leq 0.3$. Data plotted in Fig. 5 correspond to the asymptotic values, after N=5000 breathing periods for WB and after N=600 for KV (except $\eta \leq 0.2$, where KV results are also for N=5000). These 5000 breathing oscillations correspond to 5–10 km of the length for a typical machine, much longer than existing proton linacs.

4 CONCLUSIONS

Our simulations show the qualitative similarity of the beam behavior for all transverse distributions studied. The KV beam can be considered as an extreme case compared to the WB and $n = 2$ distributions which are closer to real beams. The halo intensity is a few times higher and saturates faster for the KV distribution than for the other two.

An interesting new observation is that for axisymmetric beams under consideration the beam stability and halo formation depend primarily on the mismatch, not on the tune shift. The halo was clearly observed only for large mismatches, at least 20%, and its radius is in agreement with the analytical model [1] for halo formation.

5 REFERENCES

[1] R.L. Gluckstern, Phys. Rev. Letters **73**, 1247 (1994).

[2] I.M. Kapchinsky and V.V. Vladimirsky, in *Proceed. Int. Conf. on High Energy Accelerators* (CERN, Geneva, 1959), p. 274.

[3] H. Okamoto and M. Ikegami, Phys. Rev. E **55**, 4694 (1997).

[4] M. Reiser, *Theory and Design of Charged Particle Beams* (Wiley, New York, 1993).

[5] R.L. Gluckstern, in *Proceed. of the Linac Conference* (Fermilab, 1970), p. 811.

[6] I. Hofmann, L.J. Laslett, L. Smith and I. Haber, Particle Accelerators **13**, 145 (1983).

[7] R.L. Gluckstern, W.-H. Cheng and H. Ye, Phys. Rev. Letters **75**, 2835 (1995).

[8] R.L. Gluckstern, W.-H. Cheng, S.S. Kurennoy and H. Ye, Phys. Rev. E **54**, 6788 (1996).

KV-BEAM IN A DISPERSIVE CHANNEL

M. Venturini, Dept. of Physics, University of Maryland, College Park MD 20742 USA, and
M.Reiser, Institute for Plasma Research, University of Maryland, College Park MD 20742 USA

Abstract

The interplay between dispersion and space charge in circular accelerators or storage rings is investigated by looking for self-consistent solutions of the Vlasov-Poisson equation that generalize the KV-distribution to the case where dispersion is present. The results show a growth of the rms quantities describing the beam distribution with the momentum deviation and tune depression. The growth, however, is modest for realistic values of these parameters.

1 INTRODUCTION

The combined effect of space charge and dispersion is one of the issues to be investigated in the Electron Ring at the University of Maryland [1]. The goal is to produce, maintain and study a beam with a depressed-tune factor in the range $0.2 \div 0.4$. In this range of highly space charge dominated beams the answer to the question of whether the usual single-particle treatment of dispersion is still justified is not obvious and very little can be found in accelerator physics literature on this topic [2]. In order to get an insight into the scale of the problem, we studied a simplified model of the Electron Ring dynamics. In the model we assume the smooth approximation in which the external focusing functions and the radius of curvature are constant. Moreover, all the nonlinearities due to the external focusing are neglected. The study has been carried out by looking for self-consistent solutions of the Vlasov-Poisson equations.

2 DISPERSION

Dispersion is usually characterized in terms of the dispersion function $D(z)$, solution of the equation (see e.g. [3]):

$$D(z)'' + k(z)D(z) = \frac{1}{\rho(z)}.$$

where $\rho(z)$ is the local radius of curvature and $\delta = \frac{\Delta p}{p_0}$ describes the relative deviation from the designed momentum p_0.

In a multi-particle perspective we are interested in describing how the beam distribution is affected by the presence of dispersion. Consider a beam of non-interacting particles with a gaussian distribution in both the transverse variables and the longitudinal momentum. In other words, let the beam be described by the following distribution function:

$$f(x, p_x, y, p_y, \delta) = \frac{f_o}{\delta_o\sqrt{\pi}} e^{-\frac{\delta^2}{\delta_o^2}} \exp(-\frac{I}{T}),$$

where I is an invariant for the system and T a constant. An obvious choice for I is

$$I = \frac{1}{2}(p_x - \delta D(z)')^2 + \frac{1}{2}k(x - \delta D(z))^2 + \frac{1}{2}p_y^2 + \frac{1}{2}ky^2,$$

where, for semplicity, we have supposed that the focusing function k is constant. The second moment of the distribution can be easily seen to be:

$$< x^2 >_{\delta_o} = \frac{< x^2 >_o}{1 - \frac{\delta_o^2 D(z)^2}{2 < x^2 >_o}} \simeq < x^2 >_o + D(z)^2 < \delta^2 > . \tag{1}$$

Here we wrote $< x^2 >_o$ to indicate the second moment of the distribution when $\delta_o \to 0$ and the last equality holds for small δ_o. We see that if we neglect the mutual interaction among the particles, the dispersion function turns out to be a measure of the second moment of the distribution.

One of the questions we want to address in this paper is how the relation (1) changes when we allow space charge effects to enter the picture. A consequence of the presence of space charge is to modify the strength of the effective focusing forces acting on the particles and therefore to *depress* the tune ν_o. In the smooth approximation and absence of space charge $D = \rho_o/\nu_o^2$. We can question whether in presence of space charge the expression for the second moment of the distribution can be recovered from (1) by the change $\nu \leftrightarrow \nu_o$ in the expression for the dispersion (ν_o is the undepressed tune, ν is the depressed tune as calculated for an equivalent KV-beam in absence of dispersion). As we will see, the estimate we get in this way, while working for a moderate space charge, fails for higher tune depression giving a very high upper limit.

Finally, notice that (1) provides the natural generalization for the definition of dispersion in the presence of space charge.

3 THE VLASOV-POISSON EQUATIONS

Our model is described by a Hamiltonian [3] $H = H_\perp + H_\parallel$, where $H_\parallel = \frac{m^2c^4}{E_o^2}\delta^2$ is a purely longitudinal term and

$$H_\perp = \frac{1}{2}(p_x^2 + p_y^2) + \frac{k}{2}(x^2 + y^2) - \frac{x}{\rho_o}\delta + g_o\psi,$$

(with $g_o = q/mv_z^2\gamma^3$).

The Hamiltonian refers to a beam of particles of charge q and mass m in a smooth circular channel. The self-force is described by the potential ψ. The designed momentum, longitudinal velocity, and the corresponding relativistic factor are p_o, v_z, and γ.

0-7803-4376-X/98 /$10.00 © 1998 IEEE

Since the Hamiltonian is time independent the momentum deviation δ is a constant of the motion. Clearly $H_\perp$ is also an integral of the motion.

We want to search for self-consistent solutions of the Vlasov-Poisson equation associated with H:

$$\frac{\partial f}{\partial z} + \{f, H\} = 0, \qquad \nabla^2\psi = -\frac{q}{\epsilon_0} n(x,y),$$

where

$$n(x,y) = \int\int\int d\delta dp_x dp_y f(x, p_x, y, p_y, \delta). \quad (2)$$

In particular, we want to look for a stationary solution $\frac{\partial f}{\partial z} = 0$. We recall that any function of integrals of motion of an Hamiltonian system is a stationary solution of the corresponding Vlasov equation. Therefore, a particular stationary solution of the Vlasov equation associated with the Hamiltonian H is given by:

$$f(x, p_x, y, p_y, \delta) = f_\parallel(\delta) f_\perp(H_\perp).$$

4 GENERALIZED KV BEAM

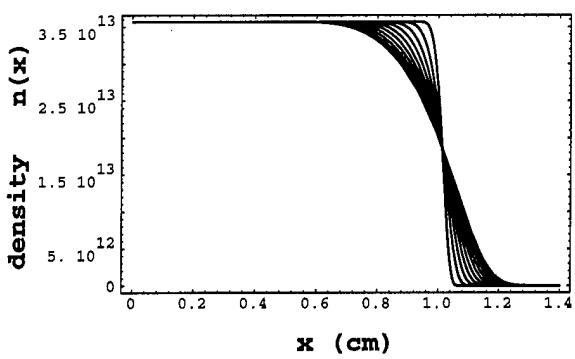

Figure 1: Section of $n(x,y)$ at $y = 0$ for different values of δ_o, ranging from .001 to .01, (I = .105 A, ν/ν_o =0.317).

We look for solutions of the Poisson-Vlasov equation describing a beam with a gaussian distribution of the longitudinal momentum and a KV-beam like distribution in the transverse plane:

$$\begin{aligned} f_\parallel(\delta) &= \frac{1}{\delta_o\sqrt{\pi}} e^{-\frac{\delta^2}{\delta_o^2}}, \\ f_\perp(H_\perp) &= f_0 \delta(H_\perp - H_0). \end{aligned}$$

In the limit $\delta_o \to 0$, we recover the usual KV distribution. The corresponding space density (see eq. 2) can be expressed in terms of the Gauss error function:

$$n(x,y) = \pi f_o [erf\left(\frac{\lambda(x,y)\rho_o}{\delta_o|x|}\right) + 1]. \quad (3)$$

with

$$\lambda(x,y) = H_o - \frac{k_x}{2}x^2 - \frac{k_y}{2}y^2 - g_o\psi(x,y).$$

Therefore the Poisson equation then reads:

$$\nabla^2\psi = -\frac{q}{\epsilon_o}\pi f_o [erf\left(\frac{\lambda(x,y)\rho_o}{\delta_o|x|}\right) + 1]. \quad (4)$$

The two parameters f_o and H_o are related respectively to the density of the beam and its size. They depend on each other through the normalization equation

$$\begin{aligned} N_L &= \int\int n(x,y)dxdy \\ &= \pi f_o \int\int [erf\left(\tfrac{\lambda(x,y)\rho_o}{\delta_o|x|}\right) + 1]dxdy, \end{aligned} \quad (5)$$

where N_L is the linear density of the beam, which is related to the current I by the relation $N_L = I/(qv_z)$. When we solve equation (4) for different values of the parameter δ_o we will be interested in comparing solutions corresponding to beams that carry the same current (i.e. same N_L). After setting f_o to a fixed value, we shall use equation (5) to determine H_o.

4.1 Emittance Calculation

The beam distribution can be charcaterized in terms of the emittance and related rms quantities. The rms emittance in the horizontal plane is:

$$\epsilon_x = (< x^2 >< p_x^2 > - < xp_x >^2)^{1/2}.$$

For a KV round beam of radius a in absence of dispersion $\epsilon_{xo} = a\sqrt{H_o/8}$. When dispersion is present it is possible to reduce the expression for the rms quantities to the calculation of double integrals over x and y. Although these integrals cannot be carried out analytically, it is possible to find out the scaling with respect to δ_o using simple arguments. It turns out that

$$(\epsilon_x - \epsilon_{xo}) \propto \delta_o^2. \quad (6)$$

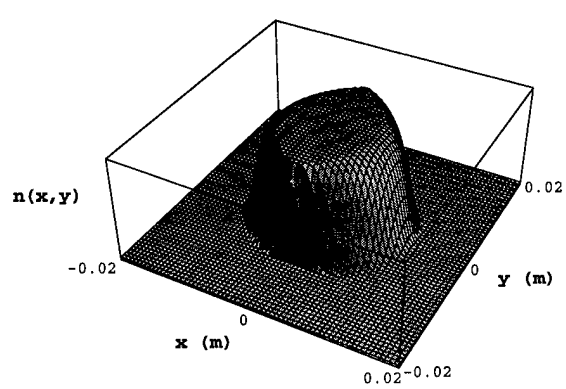

Figure 2: Density distribution $n(x,y)$ for I = .105 A, ν/ν_o =0.317, δ_o = .01.

4.2 *The Numerical Solution*

Beam Energy E_o	10 keV
Tune ν_o	7.6
Focusing func. k	17.437 m^{-2}
Radius of curv. ρ_o	1.82 m

In solving numerically equation (4) we have used the Succesive Overrelaxation Method (SOR) [4].

We show two sets of solutions. The first set of solutions describes beams carrying the same current (I=.105 A, corresponding to a tune depression factor $\nu/\nu_o = .317$. [1]) for various values of the rms momentum spread. In particular, δ_o ranges between 10^{-2} and 10^{-3}. The results, in terms of the horizontal profile ($y = 0$) of the beam density $n(x, y)$, see (3), are shown in Fig. 1.

Fig. 2 shows the full density function in the (x, y) plane for $\delta_o = .01$. The scaling of the emittance with respect to δ_o (6) has also been checked and is shown in Fig. 3. The curve in the picture is a parabola obtained by numerical fitting of the first four points.

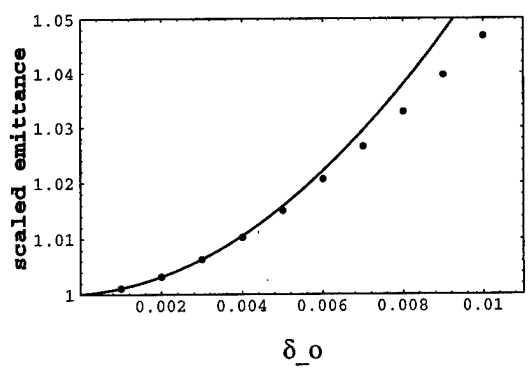

Figure 3: Scaled horizontal emittance (ϵ_x/ϵ_{xo}) as a function of δ_o, (I= .105 A, ν/ν_o =0.317).

In the second set of solutions the parameter δ_o is kept fixed ($\delta_o = .01$), while the value of the beam currents is being varied. Ten different currents have been considered, ranging from $I = .02$ to $I = .112$ A, and corresponding to tune depression factors ranging from $\nu/\nu_o = .91$ to $\nu/\nu_o = .20$. In each case the scaled rms values of the horizontal size of the beam $(< x^2 >_{\delta_o} / < x^2 >_o)^{\frac{1}{2}}$ have been calculated and are shown in Fig. 4. The gray curve in the picture is described by eq. (1) with $D = \rho_o/\nu^2$, (ν replacing ν_o). Although eq. (1) was derived for a gaussian beam we can see that it gives a good approximation also for a KV distribution if the ratio ν/ν_o is sufficiently high. However, it gives increasingly and excessively larger values as ν/ν_o decreases.

5 CONCLUSIONS

As expected the presence of dispersion increases the emittance in the horizontal plane. However, for a tune depression factor of $\nu/\nu_o \sim .3$ and $\delta_o = .01$ the growth in emittance, relative to the case where no dispersion is present, remains below 5%.

[1]The tune depression is evaluated for the KV-beam in the limit $\delta_o \rightarrow 0$. Only in this limit the tune depression is a well defined quantity.

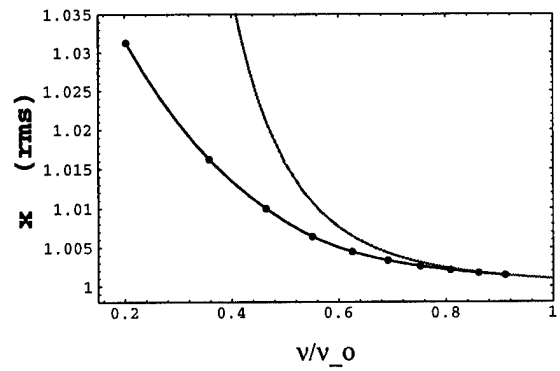

Figure 4: $(< x^2 >_{\delta_o} / < x^2 >_o)^{\frac{1}{2}}$ as a function of ν/ν_o, ($\delta_o = .01$).

6 ACKNOWLEDGMENTS

We thank N. Brown and S. Bernal for useful discussions. The work was supported by the US Department of Energy.

7 REFERENCES

[1] M. Reiser, S. Bernal, A. Dragt, M. Venturini, J.G. Wang, H. Onishi, and T.F. Godlove, Design Features of a Small Electron ring for Study of Recirculating Space-Charge Dominated Beams, 'Fusion Engineering and Design', 32-33, 293-298 (1996); J.G. Wang et al, Design and Developement of an Electron Recirculator for Study of High-Current Beam Dynamics, at this Conference.

[2] A. Garren, Proc. Heavy Ion Fusion Workshop, 1979 Reports LBL-10301/SLAC-PUB 2575, UC-28, p.397 ; J.J. Barnard et al., Emittance growth in Heavy ion Recirculators, 1992 Linear Accelerator Conference Proc. AECL-10728 Vol. 1, p.229.

[3] M. Reiser, Theory and Design of Charged Beams, Wiley & Son (1994).

[4] R.L. Spencer, S.N.Rasband, R.R. Vanfleet, Numerical Calculation of Axisymmetric Non-neutral Plasma Equilibria, Phys. Fluids B 5 (12), December 1993.

LONGITUDINAL FOCUSING OF SPACE-CHARGE DOMINATED BEAMS IN THE UMD ELECTRON RING*

J.J. Deng†, J.G. Wang, M. Reiser, Institute for Plasma Research, University of Maryland at College Park,MD 20742

T. Godlove, FM Technologies,Inc.

Abstract

Longitudinal focusing is of great importance in space-charge-dominated bunched beams. The bunches lengthen rapidly due to the strong space-charge forces during transport. The UMD electron ring[1] is designed to operate with bunches having rectangular and parabolic profiles. Three induction cavities along the ring will be employed for longitudinal focusing. In this paper, we first briefly review the longitudinal dynamics of parabolic and rectangular bunches. The design of the induction cavities with their high repetition rate modulators is then presented. The preliminary test results of lower voltage and repetition rate version of two different modulators and the SPICE simulation results show that modulators work well.

1. INTRODUCTION

The longitudinal focusing of space-charge dominated beam is of great interest in recirculator systems for applications in high energy physics, heavy ion inertial fusion, spallation neutron sources and so on. Longitudinal expansion due to the strong space-charge force will result in rapid change in the beam profile. An initially rectangular profile of a drifting beam does not remain rectangular, thus, so-called "ear-field" must be applied to the edges of the beam to focus the expanded beam back to the rectangular shape. A linear force should also be applied to focus a parabolic beam. Three induction modules will be employed for longitudinal focusing in order to maintain a proper beam profile in the UMD electron ring. The focusing voltages for beams with rectangular and parabolic profiles are given in section 2. The design of the induction cavity and its pulse modulators, as well as preliminary results of low voltage version test are presented in this paper. More details on the development of a full-voltage, MHz-repetition-rate modulator will described elsewhere later.

2. LONGITUDINAL EXPANSION OF BUNCHED BEAMS WITH RECTANGULAR AND PARABOLIC LINE CHARGE DENSITY DISTRIBUTIONS

The particles in the leading edge of bunched beams will be accelerated, and particles in the trailing edge will be decelerated due to the space-charge force. The line charge density and the velocity distributions along the bunches will change with drifting distance S.

For an initial rectangular beam with a uniform velocity, the line charge density and velocity in the beam frame can be obtained from the solution of one-dimension cold-fluid equations[2,3,4] in the simple wave region,

$$\frac{\lambda}{\lambda_0}=\begin{cases} 1 & |t|<t_1 \\ \left[\frac{2}{3}+\frac{S_{cusp}}{3S}\left(1-\frac{2|t|}{\tau_0}\right)\right]^2 & t_1\le|t|\le t_2 \\ 0 & |t|>t_2 \end{cases} \qquad (1)$$

$$\frac{v}{C_s}=\begin{cases} -\frac{2}{3}\frac{|t|}{t}\left[1-\frac{S_{cusp}}{S}\left(1-\frac{2|t|}{\tau_0}\right)\right] & t_1\le|t|\le t_2 \\ 0 & t_2<|t|<t_1 \end{cases} \qquad (2)$$

$$t_1=\left(\frac{1}{2}-\frac{S}{2S_{cusp}}\right)\tau_0,\quad t_2=\left(\frac{1}{2}+\frac{S}{S_{cusp}}\right)\tau_0,$$

$$S_{cusp}=v_0^2\tau_0/2C_s,\qquad C_s=\sqrt{\frac{egI_i}{4\pi\varepsilon_0 m v_0\gamma^5}}$$

where λ is the line charge density, v is the velocity in the beam frame, ε_0 the permittivity of free space, e/m is the ratio of charge to mass of the particles, γ is the Lorenz factor, g is a geometry factor in the order of unity. I_i is the initial beam current, v_0 is the beam velocity, τ_0 is pulse width of beam.

According to Eq. (1), a 10 keV, 0.1A, 50ns rectangular beam in the UMD ring will reach the "cusp" point after about three turns[4]. In order to maintain a good beam profile during transportation, an external force must be applied to the beam before the "cusp" point.

For a parabolic bunch, the line charge density and velocity distributions can be expressed as follows[5] if $z_m - z_i << z_i$

$$\lambda(z,S)=\frac{I_i z_i}{\beta c z_m}\left(1-\frac{z^2}{z_m^2}\right) \qquad (3)$$

$$v \approx E_i\frac{4\alpha g S}{I_0\beta^4 m v_0 c}t \qquad (4)$$

where

---

* Work supported by U.S. Department of Energy.

†Permanent Address: Institute of Fluid Physics,CAEP,P.O.Box 523-56,Chengdu,610003,China

$$\alpha = \frac{4gI_i}{\beta_0^3 I_0 \gamma^5} \qquad z_m \approx \frac{gI_i}{I_0 \beta^3 Z_i}\frac{C}{N_g} + z_i$$

z_i is the initial bunch length, E_i is the beam energy.

3. DESIGN OF LONGITUDINAL FOCUSING IN THE UMD RING

3.1 Voltages for longitudinal focusing in the UMD ring

Because the equations of motion are time reversible[3], we could restore the beam profile by tilting the beam velocity distribution in the beam frame properly in very short time. This can be realized by applying a voltage pulse from a small induction gap, during which the transition time of the particles could be negligible.

From Eq. (2), we can derive the voltage for restoring the rectangular bunch

$$V(t) = \frac{4t}{3e|t|} m v_0 C_s [1 - \frac{S_{cusp}}{S}(1 - \frac{2|t|}{\tau_0})] \qquad t_1 < |t| < t_2$$

$$0 \qquad , \quad t_2 < |t| < t_1$$

In the UMD ring design, three induction modules will be employed for longitudinal focusing for good beam profiles. In this case, the expansion distance S is 1.92 m. For an initial rectangular beam of 10keV, 0.1A, 50 ns, the voltage waveform for restoring the beam after the expansion distance S is plotted in Fig. 1

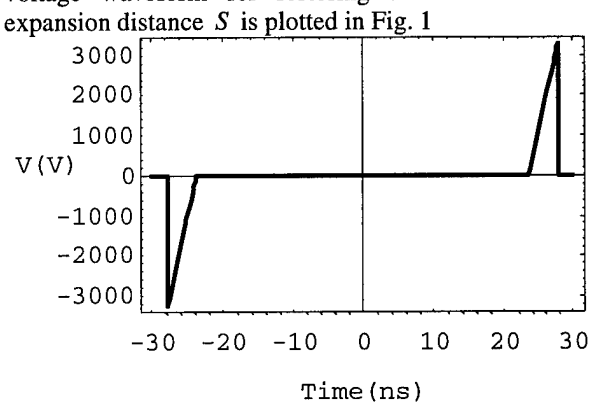

Fig. 1 "Ear-field' for focusing rectangular bunch

This is the so-called "ear-field". The particles in the leading edge will be decelerated by the negative "ear",while the particles in the trailing edge will be accelerated by the positive "ear". The beam profile will be restored after another distance of S. This process repeats periodically, so that the longitudinal beam envelope will oscillates along the ring.

For a matched space-charge dominated beam bunch with a parabolic profile, we get the voltage for restoring the beam profile from the equation of longitudinal beam envelope [6],

$$V(t) = \frac{2cgI_i}{I_0 N_g \gamma^2 (z_m / Z_i)^3}\frac{C}{}\frac{mc^2}{q} t \qquad (5)$$

Where C is the circumference of the UMD ring. N_g is the number of the induction gaps along the ring. To focus the parabolic bunch, the voltage waveform is as the follows:

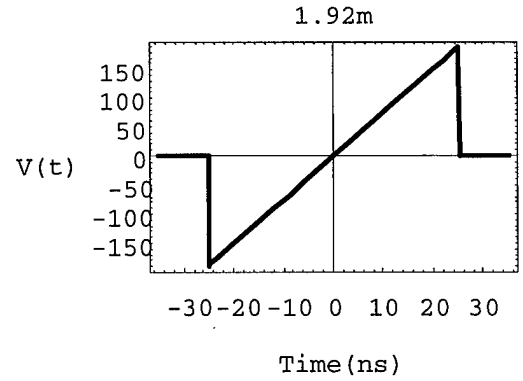

Fig. 2 Voltage for focusing parabolic bunch

Due to the short revolution time of the UMD ring, the repetition rate of both voltage pulses should be 5.08 MHz. This is very tough for the pulse switch technology, especially for the fast rise/fall time "ear-field".

3.2 Longitudinal matching

Longitudinal matching is also important in longitudinal focsing. In order to match the beams between the injection and the ring, the distance between the electron gun and the first focusing cavity should be 1.92 m.

4. DESIGN AND DEVELOPMENT OF COMPACT INDUCTION MODULE

The principle of induction cavities has been described in many places[7,8]. Here we just describe some special requirements on the induction cavity design for the UMD ring.

4.1 Special requirements on the cavity design

4.1.1 High frequency response

Due to the high rep-rate and the fast rise/fall time of the ear field, most magnetic materials cannot be used. A special Nickel-Zinc ferrite toroid of material CMD5005 ,which can run in frequency range up to more than 100 MHz with low core loss and high permeability, has been chosen for the cavity design. The initial permeability of the ferrite is 1600 and the maximum flux density is 3200 Gauss. The dimensions of the ferrite toroids are 6" OD, 2.1" ID, 1.3" Height.

4.1.2 High vacuum and bakable

The ring must be capable of vacuum as low as 10^{-10} Torr and must be bakable. To meet these requirements, a glass-metal seal has been designed for the induction gap, so the cavity is outside the vacuum. This not only avoids the possible problems which could occur if the ferrite be put in vacuum, but also makes the special mechanical design possible which makes a cavity bakable by splitting the ferrite toroid and its housing (see Fig . 3)

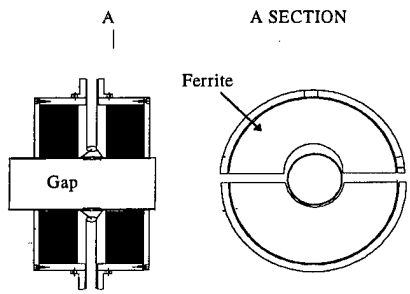

Fig. 3 Mechanical design of the compact cavity

The C-type toroids can be taken out before the system is baked.

4.1.3 The transverse focusing due to the gap voltages

The induction gap voltage plays a role in transverse focusing[6]. The focusing length depends on the gap voltage[9]. In the case of the "ear-field", the focus length varies from infinite to 25 m with the "ear" from 0V to V_{peak},. The minimum focus length is about 1500 m[10] for parabolic bunch. So the effects on transverse focusing in both cases are negligible.

4.2 Modulator design for driving the cavity

A circuit that generates the "ear-field" has been designed for the rectangular bunch. A triangular pulses have been generated to focus the parabolic bunch. PSPICE simulations and low voltage tests of the circuits have been carried out. Preliminary results show that the circuits work well. More details about developments of the full high voltage, MHz-rep-rate modulators will be described elsewhere.

5. CONCLUSIONS

The line charge density and velocity distributions of both rectangular and parabolic bunches after expansion have been given. The voltages for focusing the rectangular and parabolic bunches have also been derived individually. A compact, bakable induction module for high frequency response, has been designed and developed.

REFERENCES

[1] J.G. Wang, S. Bernal, J.J. Deng, Y. Li, M. Reiser, H. Suk, M. Venturini, T. Godlove, Design and Development of an Electron Recirculator, in this proceeding.
[2] A. Faltens, E.P. Lee, and S.S. Rosenblum, Beam end erosion, J. Appl. Phys. 61(12)(1987)5219-5221.
[3] D.D. Ho, S.T. Brandon,and E.P. Lee, Part. Accel. 35,15(1991).
[4] D.X. Wang, J.G. Wang, M. Reiser, Phys. Rev. Vol. 73, No.166-69(1994).
[5] D.X. Wang, J.G. Wang, D. Kehne, M. Reiser,Appl. Phys. Lett. 62(25),1993
[6] M. Reiser, Theory and Design of Charged Particle Beams, Wiley, New York, 1994.
[7] R. J. Briggs, Linear Induction Accelerator, LINAC'86 (1986), 10-13
[8] J.G. Wang, D.X. Wang, E. Boggasch, D. Kehne, M. Reiser, T. Shea, Nucl. Instru. Meth. in Phys. Res. A301(1991) ,19-26.
[9] Y.B. Chen, M. Reiser, J. Appl. Phys. 65(9)(1989), 3324-3328.
[10] J.J. Deng, Technical note, E-Ring-96-18

INJECTOR DESIGN FOR A MODEL ELECTRON RING AT THE UNIVERSITY OF MARYLAND*

T.F. Godlove, FM Technologies, Inc., Fairfax, VA
S. Bernal, J.J. Deng[a], Y. Li, M. Reiser, J.G. Wang and Y. Zou, Institute for Plasma Research, University of Maryland, College Park, MD

Abstract

A model electron recirculator is being developed at the University of Maryland. It employs a 10-keV, space-charge-dominated beam injected into a 1.8-m radius ring equipped with a strong-focused lattice based on printed-circuit quadrupoles and dipoles. The motivation and general features are described in separate papers. Here we describe the design for injecting a single-turn bunch into the ring. The system includes a low-emittance e-gun, matching section, pulsed dipole and Panofsky quadrupole. The dipole at the injection point must deflect the beam -10° during entry and +10° after entry, with about 25 ns transition time. The Panofsky quadrupole must be off during entry and on for subsequent laps, with a similar rise time.

I. INTRODUCTION

During the last decade increasing attention has been given to issues related to achieving higher intensity in particle accelerators. Applications include synchrotrons and storage rings for colliders, spallation neutron sources, free electron lasers and heavy-ion inertial fusion. Many of these applications either require or can make good use of intense beam pulses if they were available. A recirculating linac is an attractive new approach to achieve high intensity beam pulses. The idea is to use space-charge-dominated beam currents appropriate to a linac but limit the number of turns to achieve stable operation.

A project to develop and build a small electron ring to study the evolution of a space-charge-dominated beam in a circular lattice is in progress at the University of Maryland's Institute for Plasma Research (IPR). The general features of the ring have been described, including an accompanying paper at this conference [1,2]. Briefly, a 1.8-m radius ring is designed for a 100 mA, 10-keV e-beam using a FODO lattice with 72 quadrupoles and 36 dipoles, all based on a printed circuit design [3].

* Research supported by the US Department of Energy.

Major issues include resonance crossing, bunch profiles, longitudinal-transverse coupling, space-charge waves and instabilities.

In this paper we describe the planned injector system including the special components required and some of the calculations pertaining to the injector.

II. INJECTOR

Figure 1 shows the injector system. Q1 is a Panofsky-type pulsed quadrupole. It replaces one of the ring quadrupoles. Since it is centered on the main ring it must be turned on after the beam bunch enters and remain on for subsequent laps. D1 is a pulsed dipole, replacing one of the 36 ring dipoles. It must deflect the beam -10° during entry and +10° after entry.

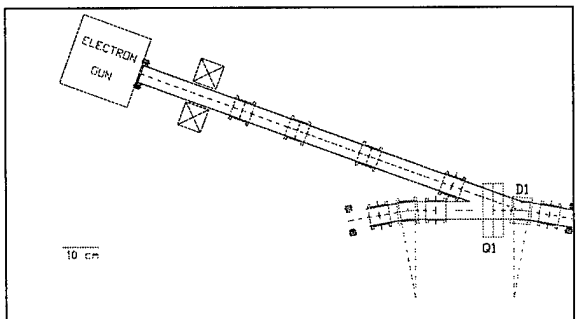

Fig. 1. Injector layout.

This arrangement allows the angle between the injector and the adjacent straight section to be 20°. Considering a lap time of 200 ns, a switching time of about 25 ns is acceptable for the pulsed elements.

The system includes a matching section which consists of a solenoid and four quadrupoles. This system has been assembled with one of the two e-guns available in the IPR laboratory in order to evaluate the beam performance with the new printed-circuit quadrupoles. The e-gun operates at 4 kV. An aperture of 3.18 mm radius was added, yielding a beam current of 18 mA. The generalized perveance, $2I/(I_0\beta^3\gamma^3)$, is 0.0011, i.e., a space-charge-dominated beam. Here I_o is 17 kA and β, γ, are the usual normalized velocity and total energy of the electrons.

III. SIMULATION

Several codes have been used to design the injector beam line, to predict the performance, and most important, to compare with the experiments. We report here on calculations using an envelope code due to C.K. Allen [4] and the particle-in-cell code WARP3d developed at the Lawrence Livermore National Laboratory [5]. Figure 2 shows an envelope code result and Fig. 3a shows the corresponding WARP3d result.

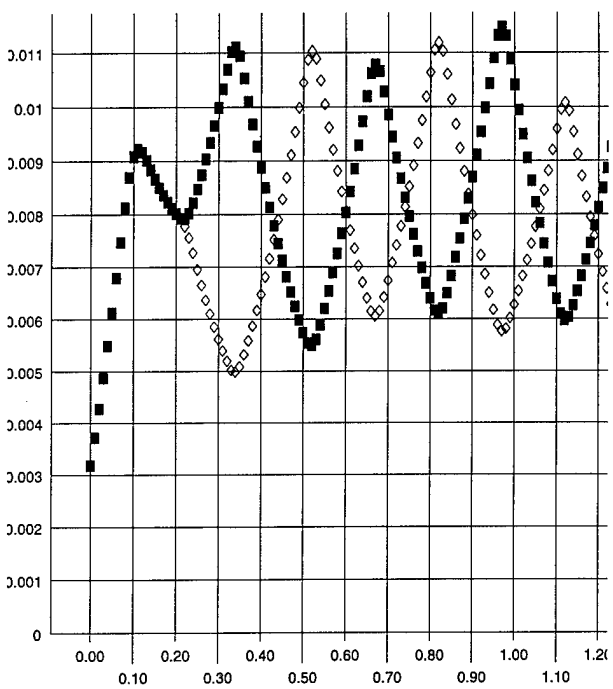

Fig. 2. Envelope code.

The beam radii in the two transverse dimensions are plotted vs. z (m). For WARP, twice the rms radii are plotted. Table I gives the parameters used.

Table I. Parameters for Fig's 2 and 3.

	Solenoid	Q1	Q2	Q3	Q4	Q5
Location (cm)	10	22.4	34	52	67	82
B_0 (G) Envelope	73	5.6	-11.7	13.1	-13.1	13.1
B_0 (G) WARP3d	72	5.3	-11.7	13.1	-13.1	13.1

The peak field for the quadrupoles refers to a radius of 2.20 cm; the gradient, for example, is 5.95 G/cm from Q3 on. z = 0 at the aperture.

Other parameters are emittance (unnormalized, effective) = 50 mm-mrad; and aperture x' = y' = 54 mrad, in rough agreement with previous experiments.

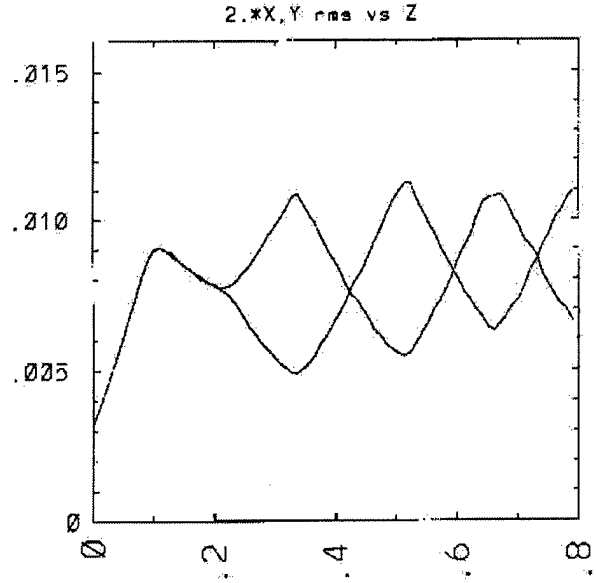

Fig. 3a. WARP3d simulation.

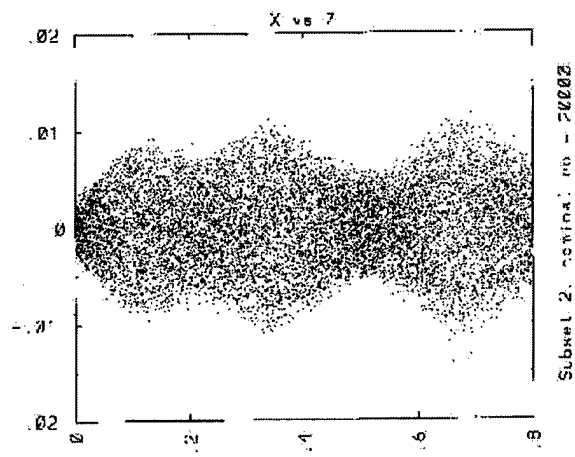

Fig. 3b. WARP3d, x vs. z.

The envelope code and WARP agree quite well, with the exception that the parameters in the envelope code had to be modified slightly for the peak field in the solenoid and Q1, as given in Table I. Without this small change the agreement was poor. We ascribe this to the fact that the envelope code treats the solenoid as a linear element, whereas WARP includes the nonlinear fields to fourth order.

A separate question involves the quadrupole fields. We currently use an empirically fit formula in WARP. In the near future we plan to use the exact field array

derived from a 3-D magnetics program. Since the quad's are "thin" we do not expect a significant change in the result, but it remains to be tested. Also, we plan to compare these calculations with the experiments as soon as reliable data are available.

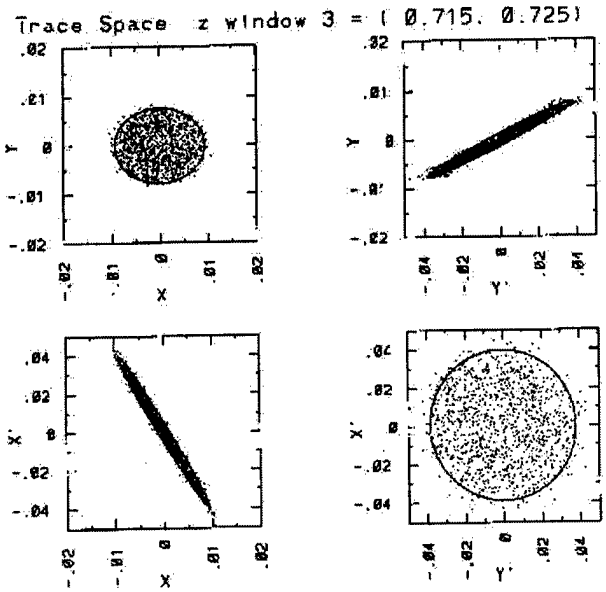

Fig. 3c. WARP3d phase-space plots, at 0.72 m, with $\Delta z = 1$ cm.

IV. PANOFSKY QUADRUPOLE

Figure 4 shows a sketch of a proposed geometry for the conductors of a pulsed Panofsky-type quadrupole. As with the cylindrical quad's, the conductor location is determined using a 3-D magnetics program to optimize the linearity. Conductors are paired to reduce the stray fields from the "twisted-pair" external connections. The peak current required in each conductor is ~40 A. An alternative geometry using loops analogous to the ring quad's would require less current, but would have higher inductance, hence longer switching time.

A detailed design is in progress. Currently, the linearity is of the order of 1% to 3%, depending on the number of conductors and the details of conductor placement. Linearity is based on the integral of Bdz, as it is for the ring quadrupoles.

A number of electronic switch circuits will be required, the number depending on the final number of required parallel circuits. Precision resistors will guarantee equal currents in parallel conductors.

The vacuum chamber at the injection point must be glass or ceramic to allow field penetration on a 25-ns time scale. We currently favor glass in view of the skills available at the IPR. It should have a thin inner conducting coating to avoid charge buildup.

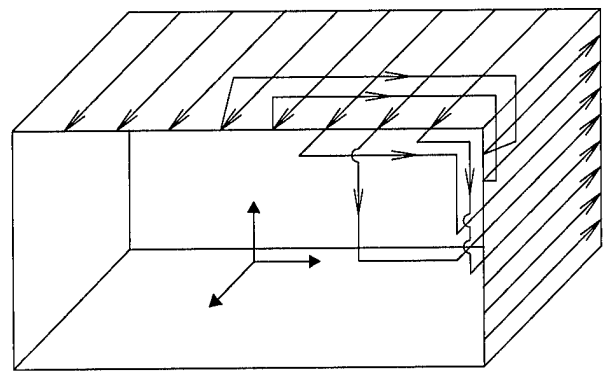

Fig. 4. A proposed conductor geometry for the Panofsky quadrupole.

V. ACKNOWLEDGMENTS

We are grateful to A. Friedman and D. Grote of LLNL for the use of the WARP3d code. In this connection, TFG acknowledges invaluable assistance from Irving Haber at the Naval Research Laboratory in the use of the code.

VI. REFERENCES

[1] M. Reiser, S. Bernal, A. Dragt, M. Venturini, J. G. Wang, H. Onishi and T. F. Godlove, Fusion Engr. and Design **32-33**, 293 (1996).

[2] J.G Wang, S. Bernal, P. Chin, J.J. Deng, Y. Li, M. Reiser, H. Suk, M. Venturini, Y. Zou, T. Godlove and R.C. York, "Design and Development of an Electron Recirculator for Study of High-Current Beam Dynamics" in these Proceedings.

[3] T.F. Godlove, S. Bernal and M. Reiser, IEEE Cat. 95CH35843, 2117 (1996).

[4] Christopher K. Allen, Samar K. Guharay and Martin Reiser, IEEE Cat. 95CH35843, 2324 (1996).

[5] A. Friedman, D.P. Grote and I. Haber, Phys. Fluids **B4**, 2203 (1992); D.P. Grote, A. Friedman and I. Haber, IEEE Cat. 93CH3279-7, 727 (1993); D.P. Grote, A. Friedman and I. Haber, IEEE Cat. 95CH35843, 831 (1996).

---

a. Permanent address: PO Box 523-56, Cheng-Du, China.

HIGH BEAM CURRENT HANDLING IN THE JHF MAIN RING

S. Machida, Y. Mori, C. Ohmori, Y. Ishi, S. Shibuya, and M. Tomizawa
KEK-Tanashi, 3-2-1 Midori-cho, Tanashi-shi, Tokyo, 188 JAPAN

Abstract

The Japan Hadron Facility (JHF) synchrotrons are expected to store and accelerate ten times larger number of protons than that of the machines under operation ($2x10^{14}$ protons in the 50GeV main ring and $5x10^{13}$ protons in the 3GeV booster). A stable operation with a very small beam loss is essential. Beam dynamics not only of the beam core but of the tail and halo should be considered. More specifically, transverse space charge effects have to be taken into account from the design stage of the lattice. In that sense, a conventional way of the lattice optimization, such as maximizing dynamic aperture and minimizing smear, may not be applicable. We have started to simulate commissioning of a high intensity machine. As a first attempt, the tune survey with space charge effects is simulated. Beam loss and emittance growth are examined in the wide range of tune space. Those results are compared with dynamic aperture without space charge effects.

1 INTRODUCTION

The synchrotrons of the Japan Hadron Facility (JHF) are expected to deliver high energy and high intensity beams [1]. To obtain the average current of 10 μA in the 50 GeV main ring and 200 μA in the 3 GeV booster, the total number of particles in the rings becomes $2x10^{14}$ and $5x10^{13}$, respectively. That is more than ten times higher intensity than that of now available.

The total number of particles in a proton synchrotron is normaly limited by transverse space charge effects at the injection energy. Where the incoherent tune shift makes the tune of individual particle spread out in the large area of the tune space. The maximum allowable tune spread is around -0.2 to -0.7 depending on other machine parameters. For example, a slow cycling synchrotron such as the main ring, whose repetition rate is 0.3 Hz, forces the beams to stay at the injection energy for considerable time, say 1 s, and the allowable tune shift seems smaller than that of a fast cycling synchrotron such as the booster, whose repetition rate is 25 Hz.

Although one knows that space charge effects have to be taken into account to design a high intensity proton synchrotron, it is not clear how to incorporate the effects in designing a synchrotron. The best one can do is to calculate tune shift. A lattice and its operating point are determined almost independently of the effects.

Instead, one usually examine linear and nonlinear resonance structure in the tune space, and calculate dynamic aperture. Those procedures in most cases do not include space charge effects. One tries to find larger resonance free area in the tune space and enlarge dynamic aperture in a given lattice design by playing with phase advance of a unit cell, position of sextupole magnets, and so on. If it does not satisfy some requirements, one modifies the lattice or designs it from the scratch.

It is plausible that the optimized lattice and the best operating point without space charge effects should give reasonably stable operation even with strong space charge effects in reality. If necessary, further fine tuning can be done when the machine is constructed and commissioning is started. It is one of the reasons to leave a number of knobs available and makes the flexible lattice for the beam commissioning.

Recent progress of the beam tracking technique, however, makes it possible to simulate some of the commissioning procedures in a very realistic manner. Let us say ten years ago, most of them have been thought unrealistic even though not impossible. Nowadays, so called "dry run" of the machine has been tried extensitively everywhere a new machine is designed.

We study a possible way to visualize the commissioning of the JHF 50 GeV main ring and to incorporate the space charge effects from the design stage. We survery tune space and examine "dynamic aperture", emittance growth, and beam loss with space charge effects included. Comparison of those results with conventional dynamic aperture survey without space charge effects is made.

2 JHF 50 GEV SYNCHROTRON

The main ring of the JHF is a 50 GeV synchrotron. In order to minimize beam loss, the lattice has been designed with imaginary transition energy. When we fixed the injection energy of 3 GeV and the extraction energy of 50 GeV, transition energy crossing during a ramping is inevitable unless the dispersion function is modulated and the momentum compaction factor is forced to be far from the nominal value. In our design, two missing bend magnets every three FODO cells introduce dispersion wave. The beta functions (βs) and dispersion function (η) of one quarter of the ring are depicted in Fig. 1. The whole ring makes four-fold symmetry.

The tune of the whole ring is adjusted in the following way. First, the arc of a superperiod is tuned to obtain a negative momentum compaction factor. Its nominal value is -0.001 and 31.6i in term of the Lorentz factor at the transition. At the same time, the phase

0-7803-4376-X/98/$10.00 © 1998 IEEE

advance of the arc is fixed to be 2π times [(total tune)/4-1] for the horizontal plane and 2π times [(total tune)/4-0.5] for the vertical. Secondly, the long straight insertion next to the arc is adjusted to connect βs, its derivative αs and η smoothly with the fixed phase advance of 2π for horizontal and π for vertical. In that way, lattice functions in the arc are not be altered by the long straight insertion. The momentum compaction factor is simply scaled with a ratio of the path length with and without the insertion.

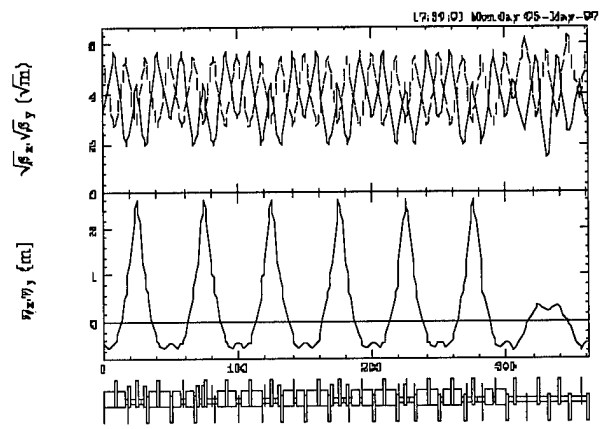

Figure 1: Lattice functions of one quarter of the 50 GeV main ring. Solid line on the top is the horizontal beta function and dashed line is the vertical one.

3 SPACE CHARGE MODELLING

Multi-particle tracking code has been employed to include space charge effects self-consistently. Based on the 3-D tracking code "Simpsons" [2], the algorism of the space charge calculation is simplified to gain the computational speed. It can be summarized as follows.

First, only 2-D transverse space charge effects are included. Beams are modelled as a cylindrical tube. The line density is fixed to the peak density of the actual bunched beam. The bunching factor is 0.3.

Secondly, in order to calculate the electric force, the particle distribution n and the electric potential ϕ are decomposed in the azimuthal direction [3],

$$n = \sum_m n_m \exp(im\theta)$$
$$\phi = \sum_m \phi_m \exp(im\theta)$$

where m is the mode number. The solution can be obtained from the equation,

$$\frac{1}{r}\frac{\partial}{\partial r}\left(r\frac{\partial \phi_m}{\partial r}\right) - \frac{m^2}{r^2}\phi_m = -4\pi n_m$$

A test shows that simulation results does not change much if we take m up to 2 (quadrupole mode). Another test shows that simulation results does not change much if we take more than 10^4 macro particles.

Finally, space charge force is applied as a kick every 10 ns in the actual time scale. It corresponds to several kicks per a quadrupole focusing unit.

4 DYNAMIC APERTURE

Before simulating tune survey with space charge effects, we measure dynamic aperture in the same range of the transverse tune space without space charge effects. There is no misalignment errors or fabrication errors. Only nonlinearity comes from the chromaticity correction sextupoles. These sextupoles are excited to make the chromaticity zero in both planes. Twenty two circles in Fig. 2 indicate the tune points we measure the dynamic aperture. The fractional part of the tune is either 0.3 or 0.8 for the horizontal tune and 0.4 or 0.9 for the vertical one. All the circles together make a triangle area where the momentum compaction factor becomes negative with reasonable β maximum, around 35 m. Higher tunes in both horizontal and vertical can be obtained on paper with reasonable lattice functions. They are, however, not practical because of the strong quadrupole strength, more than 20 T/m, which is out of our specifications of the magnet.

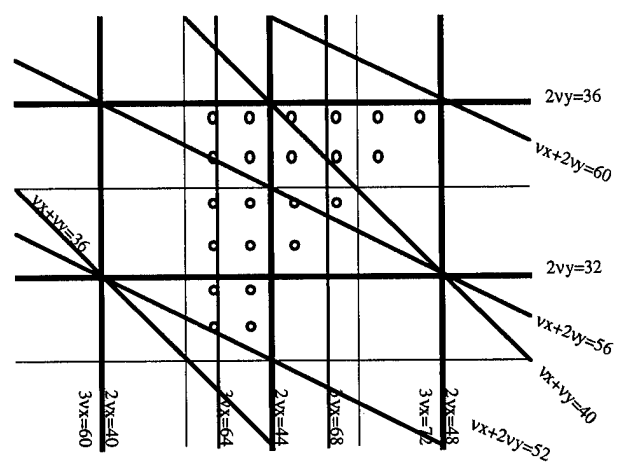

Figure 2: Tune space with the possible operating point of the 50 GeV main ring. Twenty two circles indicate the tune points we measure the dynamic aperture and survey emittance growth, beam loss, and "dynamic aperture" with space charge effects. Some systematic resonance lines are drawn with its order and harmonics.

Dynamic aperture is defined as the maximum amplitude of tracking particles survived for 1,000 turns. Table 1 lists it in the unit of a beam size whose emittance is 54 πmmmrad. Less than 1 means the dynamic aperture is smaller than the physical acceptance.

It is noticeable that the operating points along by the sextupole coupling resonance, $\nu x+2\nu y=56$, have small dynamic aperture, even smaller than the physical acceptance. On average, the dynamic aperture at the tune above the sextupole coupling resonance is larger than that below the resonance.

Table 1: Dynamic aperture at the tune points indicated in Fig. 2. The unit is a beam size whose emittance is 54 πmmmrad.

	21.30	21.80	22.30	22.80	23.30	23.80 (hor.)
17.90	4.0	3.1	3.5	3.6	3.1	3.7
17.40	0.3	1.8	4.0	3.8	3.7	
16.90	1.2	0.6	0.4	3.9		
16.40	1.9	1.7	1.4			
15.90	2.0	2.0				
15.40	2.9	2.1				
(ver.)						

5 TUNE SURVEY WITH SPACE CHARGE

We track 10,000 macro-particles for 64 turns at the injection energy of the 50 GeV main ring at the same operating points above.

Table 2: Survival rate (%) at each operating point. Beam intensity is 6.9 A.

	21.30	21.80	22.30	22.80	23.30	23.80 (hor.)
17.90	100.	100.	100.	100.	100.	100.
17.40	1.	99.	98.	100.	100.	
16.90	95.	100.	2.	92.		
16.40	100.	100.	94.			
15.90	100.	100.				
15.40	100.	100.				
(ver.)						

Table 3: Final rms emittance at each operating point. Beam intensity is 6.9 A.

	21.30	21.80	22.30	22.80	23.30	23.80 (hor.)
17.90	14.0	14.2	13.3	13.9	13.9	14.5
17.40	N/A	24.7	13.1	15.5	13.8	
16.90	13.2	15.9	29.5	28.6		
16.40	13.4	14.0	12.5			
15.90	13.3	14.1				
15.40	13.3	13.8				
(ver.)						

The transverse particle distribution is gaussian. With the nominal intensity of 6.9 A and the initial rms emittance of 13.2 πmmmrad, the rms tune shift becomes -0.17. Table 2 and 3 show the survival rate in % and the final rms emittance in πmmmrad, respectively. We consider a particle is lost when its amplitude is more than 0.1 m. The final emittance is either horizontal or vertical whichever the larger one.

Both tables show that, in principle, where the dynamic aperture is small, beam loss occurs. The loss is accompanied by the emittance growth at the points above the sextupole coupling resonance, but that is not the case below the resonance. In addition, because of the space charge tune shift, an operating point with large dynamic aperture such as (22.80, 16.90) also suffers.

Table 4: Survival rate (%) when the intensity is doubled.

	21.30	21.80	22.30	22.80	23.30	23.80 (hor.)
17.90	100.	100.	100.	100.	100.	100.
17.40	89.	70.	100.	99.	100.	
16.90	100.	96.	94.	60.		
16.40	100.	100.	100.			
15.90	100.	100.				
15.40	100.	100.				
(ver.)						

Table 5: Final emittance when the intensity is doubled.

	21.30	21.80	22.30	22.80	23.30	23.80 (hor.)
17.90	20.8	16.0	16.2	14.0	17.8	15.2
17.40	15.0	51.0	18.5	19.2	18.9	
16.90	17.5	16.7	15.2	43.9		
16.40	16.8	13.8	15.8			
15.90	16.1	16.1				
15.40	15.7	14.0				
(ver.)						

Now the intensity is doubled and Table 4 and 5 show the results. Because of the tune spread, the beam loss is smoothed out. The emittance growth occurs at almost all the points. As far as the table shows, the operating point with the minimum emittance growth (21.80, 16.40) does not necessarily corresponds to the point with large dynamic aperture.

REFERENCES

[1] Y. Mori, `Japan Hadron Facility', these proceedings.
[2] S. Machida, 'The Simpsons Program', AIP Conference Proceedings 297, p.459, 1993.
[3] M. L. Sloan, private communications.

SPACE CHARGE DOMINATED ENVELOPE DYNAMICS OF ASYMMETRIC BEAMS IN RF PHOTOINJECTORS

J. B. Rosenzweig, S. Anderson, and Luca Serafini*
Department of Physics and Astronomy, University of California, Los Angeles
405 Hilgard Avenue, Los Angeles, CA 90095-1547

While it has been proposed for several years that strongly asymmetric $(\sigma_x >> \sigma_y)$ beams can be employed in rf photoinjectors to obtain asymmetric emittances for linear collider applications[1,2], it is known that the emittances obtained directly from rf photocathode guns are not suitably small for this purpose. Because of this, simulational work has been performed in an attempt to apply the principle of emittance compensation to recover the small and asymmetric emittances after suitable focusing and acceleration of photoinjector beams. In order to guide this difficult three-dimensional analysis, we present here an extension of a previous theoretical model of the emittance compensation process in axisymmetric photoinjectors. In the extended model, we first analyze the general quadrupolar oscillations in a symmetric accelerating system, and then proceed to examine a propagation mode under asymmetric focusing. This mode is a generalization of the previously analyzed axisymmetric invariant envelope, allowing an optimization of the compensation process. Design philosophies, including rf cavity considerations, are included in the discussion.

I. INTRODUCTION

The envelope equation for an axisymmetric beam is

$$\sigma'' + \sigma'\frac{\gamma'}{\gamma} + \Omega^2\left(\frac{\gamma'}{\gamma}\right)^2\sigma = \frac{\kappa_s(\zeta)}{\sigma\ \gamma^3} + \frac{\varepsilon_{n,th}^2}{\sigma^3\ \gamma^2} \qquad (1.1)$$

where the perveance $\kappa_S(\zeta)$ explicitly keeps a dependence on the longitudinal position ζ of the particular slice, so that $\kappa_S(\zeta) = I(\zeta)/2I_0$ ($I_0 = 17$ kA), and $\Omega^2 = \eta/8 + b^2$. The *invariant envelope* solution $\hat{\sigma}$ reads[3],

$$\hat{\sigma} = \frac{1}{\gamma'}\sqrt{\frac{2I}{I_0\gamma\left(1+4\Omega^2\right)}} \qquad (1.2)$$

which is an exact solution of Eq. 1.1 in the laminar flow regime (*i.e.* $\varepsilon_{n,th} << \sigma^2\kappa_s/\gamma$).

For an asymmetric beam the two envelope equations for σ_x and σ_y become (Eqs. 1.3-4)

$$\sigma_x'' + \sigma_x'\frac{\gamma'}{\gamma} + \Omega_x^2\left(\frac{\gamma'}{\gamma}\right)^2\sigma_x = \frac{I}{I_0\left(\sigma_x+\sigma_y\right)\gamma^3} + \frac{\varepsilon_{nx}^2}{\sigma_x^3\ \gamma^2}$$

$$\sigma_y'' + \sigma_y'\frac{\gamma'}{\gamma} + \Omega_y^2\left(\frac{\gamma'}{\gamma}\right)^2\sigma_y = \frac{I}{I_0\left(\sigma_x+\sigma_y\right)\gamma^3} + \frac{\varepsilon_{ny}^2}{\sigma_y^3\ \gamma^2}.$$

II. ACCELERATING ASYMMETRIC BEAMS WITH SYMMETRIC FOCUSING

We again assume laminar flow, and proceed by ignoring the thermal emittance contributions to Eqs. 1.3-4. Let us define now the two quantities $\Delta \equiv \sigma_x - \sigma_y$ and $\Sigma \equiv \sigma_x + \sigma_y$. By linear combinations of Eq. 1.3 and 1.4 we obtain, in case of symmetric rf focusing $\Omega_x = \Omega_y = \Omega$ (solenoidal focusing is not relevant, as it introduces an unwanted beam rotation), the following:

$$\Delta'' + \frac{\gamma'}{\gamma}\Delta' + \Omega^2\left(\frac{\gamma'}{\gamma}\right)^2\Delta = 0, \qquad \text{and} \qquad (2.1)$$

$$\Sigma'' + \Sigma'\frac{\gamma'}{\gamma} + \Omega^2\left(\frac{\gamma'}{\gamma}\right)^2\Sigma = \frac{2I}{I_0\gamma^3\Sigma}. \qquad (2.2)$$

The forms of Eqs. 2.1-2 are gratifyingly simple; Eq. 2.1 is identical to that of single particle motion (no space-charge, $I = 0$) in this system[4], while Eq. 2.2 is formally identical to Eq. 1.1 in the case of laminar flow. Thus we immed-iately have, by analogy to previous work[4], the solution of Eq. 2.1 in terms of the initial conditions on the envelopes,

$$\Delta(z) = \Delta(0)\cos[\alpha(z)] + \Delta'(0)\frac{\sqrt{8}}{\gamma'}\sin[\alpha(z)], \qquad (2.3)$$

where $\alpha(z) = \frac{1}{\sqrt{8}}\ln\left(\frac{\gamma(z)}{\gamma(0)}\right)$. Likewise, the particular solution for Eq. 2.2 becomes (*a la* Ref. 3)

$$\hat{\Sigma} = \frac{2}{\gamma'}\sqrt{\frac{2I}{I_0\gamma\left(1+4\Omega^2\right)}}\ , \qquad (2.4)$$

which has the expected invariant envelope property that the phase space angle $\hat{\Sigma}'/\hat{\Sigma} = -\gamma'/2\gamma$, independent of current.

As Eq. 1.7 is purely oscillatory, it is clear that the sum invariant envelope given by Eq. 1.8 cannot be composed of invariant envelopes in both x and y. To illustrate this point, we assume the system is launched at $z = 0$ in a nominally invariant envelope configuration, with $\Sigma = \hat{\Sigma}$, and $\Delta'/\Delta = \sigma_x'/\sigma_x = \sigma_y'/\sigma_y = -\gamma'/2\gamma$, then the beam envelopes are given by

$$\sigma_x(z) = \frac{\hat{\Sigma}(0)}{2}\left[\sqrt{\frac{\gamma(0)}{\gamma(z)}} + \frac{A-1}{A+1}\left(\cos[\alpha] - \sqrt{2}\sin[\alpha]\right)\right] \qquad (2.5)$$

and

Work supported by U.S. DOE grants DE-FG03-90ER40796 and DE-FG03-92ER40693, DOE SBIR program and Sloan Foundation grant BR-3225. *Perm. address: INFN-Milano, Via Celoria 16, Milan, Italy.

$$\sigma_y(z) = \frac{\hat{\Sigma}(0)}{2}\left[\sqrt{\frac{\gamma(0)}{\gamma(z)}} - \frac{A-1}{A+1}\left(\cos[\alpha] - \sqrt{2}\sin[\alpha]\right)\right]. \quad 2.6)$$

where $A = \sigma_x(0)/\sigma_y(0)$.

It should be noted that Eqns. 2.5-6 describe, in all generality, quadrupolar oscillations of intense, laminar relat-ivistic beams in an accelerating system with axisymmetric applied forces. These systems include standing wave ($\eta \cong 1$) and travelling wave ($\eta < 1$) rf linacs, and electrostatic accelerating systems with solenoid focusing (in the rotating Larmor frame, $b^2 > 0$, $\eta = 0$).

These solutions, because of there oscillatory character, obviously do not correspond to an invariant envelope condition, which is characterized by monotonically decreasing, well controlled size under acceleration. In fact, the small envelope is characterized by a cross-over (nonlaminar) trajectory for large enough A and/or γ, which violates the assumptions leading to Eqs. 2.1 and 2.2. We thus must look further, to asymmetric focusing systems, to find invariant envelope-like behavior for asymmetric beams.

III. ACCELERATING BEAMS WITH ASYMMETRIC FOCUSING: ASYMMETRIC INVARIANT ENVELOPES

We consider now the case of a flat beam, for which we assume that the horizontal size σ_x is always much larger that the vertical size σ_y, *i.e.* $\sigma_x >> \sigma_y$, and that the ratio of these beam sizes is constant for some values of external focusing strength. In this case Eqs. 1.3 and 1.4 become, in the laminar flow regime

$$\sigma_x'' + \sigma_x'\frac{\gamma'}{\gamma} + \Omega_x^2\left(\frac{\gamma'}{\gamma}\right)^2\sigma_x = \frac{I}{I_0\sigma_x\gamma^3} \quad \text{and} \quad (3.1)$$

$$\sigma_y'' + \sigma_y'\frac{\gamma'}{\gamma} + \Omega_y^2\left(\frac{\gamma'}{\gamma}\right)^2\sigma_y = \frac{I}{I_0\sigma_x\gamma^3}, \quad (3.2)$$

where $\Omega_{x,y}^2 = \eta/8 \mp g$, with $g = \left(B'\gamma^2/B\rho\gamma'^2\right)$ the normalized vertical focusing gradient, assumed to arise from an applied quadrupole field. Note that the space charge term on the right hand side of Eqs. 3.1-2 ignores the (assumed small) contribution to the sum of the beam sizes from σ_y.

Under this approximation, these two coupled equations have exact particular invariant envelope solutions for $\hat{\sigma}_x$ and $\hat{\sigma}_y$, as follows,

$$\hat{\sigma}_x = \frac{2}{\gamma'}\sqrt{\frac{I}{I_0\gamma\left(1+4\Omega_x^2\right)}}, \quad \text{and} \quad (3.3)$$

$$\hat{\sigma}_y = \frac{2}{\gamma'\left(1+4\Omega_y^2\right)}\sqrt{\frac{I\left(1+4\Omega_x^2\right)}{I_0\gamma}}. \quad (3.4)$$

To be consistent with the assumption of flat beam, the asymmetry ratio, which is dependent only on the external focusing, must satisfy

$$\hat{A} \equiv \hat{\sigma}_x/\hat{\sigma}_y = 1+4\Omega_y^2/1+4\Omega_x^2 >> 1 \quad (3.5)$$

In order to achieve high asymmetry ratios one has to apply some a second order (*i.e.* scaling as $(\gamma'/\gamma)^2$) defocusing force to the horizontal plane, so that $\Omega_x^2 \to -1/4$. This limiting condition is in fact the strength of the space charge defocusing in the cylindrically symmetric case; the invariant envelope is always a defocusing (hyperbolic) trajectory, which is monotonically decreasing only by virtue of adiabatic damping present during acceleration. The limit on horizontal defocusing is therefore also a limit on vertical focusing, in that the beam must not be so strongly focused in the vertical plane to overcome the defocusing of space charge — this produces a nonlaminar condition.

Eqs. 3.3-4 obey $\hat{\sigma}_x'/\hat{\sigma}_x = \hat{\sigma}_y'/\hat{\sigma}_y = -\gamma'/2\gamma$, implying an angle in both x- and y- phase space which is independent of current. This condition, should it be achieved for all longitudinal slices in the beam, would freeze all emittance oscillations. In practice, however, one typically matches the beam in an rms sense to the invariant envelopes, and so oscillations are performed around the invariant envelopes. These oscillations are described by a set of equations of the same form and solution type as Eq. 2.1

$$\delta\sigma_x'' + \delta\sigma_x'\frac{\gamma'}{\gamma} + \left[2\Omega_x^2 + \frac{1}{4}\right]\left(\frac{\gamma'}{\gamma}\right)^2\delta\sigma_x = 0, \text{ and} \quad (3.6)$$

$$\delta\sigma_y'' + \delta\sigma_y'\frac{\gamma'}{\gamma} + \left[\Omega_y^2\left(1+\frac{1}{\hat{A}^2}\right) + \frac{1}{4\hat{A}^2}\right]\left(\frac{\gamma'}{\gamma}\right)^2\delta\sigma_y = 0, \quad (3.7)$$

giving oscillation frequencies again independent of current, which allows the entire ensemble of slices to perform coherent oscillations in phase space. This coherent phase space motion is a characteristic of emittance compensation, but in the highly asymmetric ($\hat{A} >> 1$) case it can be seen that the two oscillation frequencies are quite different, $\alpha_y \propto \Omega_y$,, $\alpha_x \propto i|\Omega_x|$, and unstable small amplitude motion is found in the horizontal deviations. This implies that simultaneous compensation in both transverse phase planes is not possible in this mode, with the horizontal emittance left uncompensated.

Another characteristic is the secular diminishing of the phase space, and therefore emittance, oscillations. The trace space oscillations described by Eqs. 3.6 and 3.7 are Liou-villian, in the sense that a constant normalized emittance can be associated with this (offset from the origin) area. But, since this area is constantly moving towards the origin as the invariant envelope damps secularly as $\gamma^{-1/2}$, the projected normalized emittance damps by approximately this factor[3]. It should also be noted that the emittance ratio predicted by this model of compensation is $\varepsilon_x/\varepsilon_y \cong \sigma_x/\sigma_y = \hat{A}$.

IV. ASYMMETRIC ACCELERATING STRUCTURES

In order to implement this compensation scheme in an rf photoinjector we must specify the low energy section which precedes matching to the invariant envelopes. This

process begins with the rf structure. We note that in a split photoinjector (gun plus linac[5]) that the for a highly asymmetric beam, the rf emittance associated with the exit electromagnetic kick from a cylindrically symmetric structure would be prohibitive. Therefore, we have designed an asymmetric structure, which from the point of view of the beam region has no dependence of the longitudinal electric field on x, and therefore has a transverse fields only in y. This is accomplished by use of an H-shaped structure, in which the central region is essentially a waveguide operated at cut-off, with slit regions ($L_x >> L_y$) for the beam holes.

This structure has been simulated using the 3-D electro-magnetic solver code GDFDIL[6], with the results of an S-band (2856 MHz) 1.5 cell gun modeling shown in Fig. 1. The field is balanced in both cells, and has only a 0.3% variation of E_z over 4 cm in x in the x-z symmetry plane.

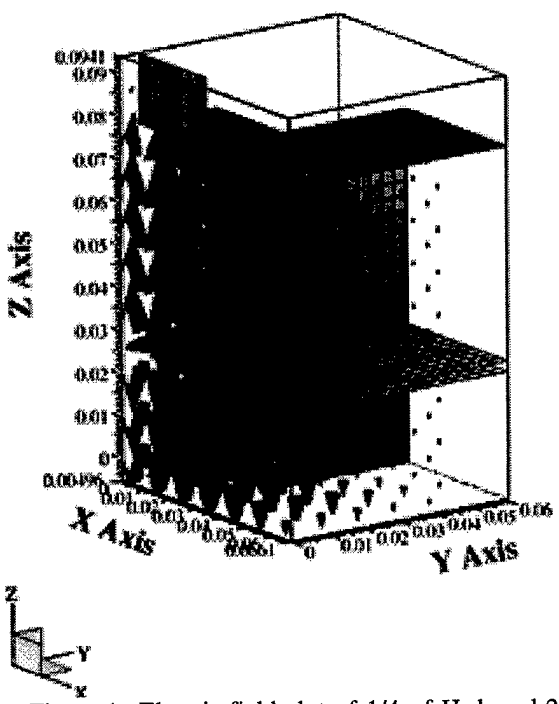

Figure 1. Electric field plot of 1/4 of H-shaped 2856 MHz rf gun structure π-mode with slit-shaped beam holes, obtained from GDFIDL simulation.

V. SYMMETRIC STRUCTURE OPTION

The original proposal for an asymmetric beam and emit-tance photoinjector was stimulated by the prospect of eliminating the electron damping ring for TESLA superconducting (SC) linear collider (LC). This motivation is strong because the emittances are not as small as for normal conducting (NC) linear collider designs. On the other hand, the duty cycle is very high, and so to save on rf power, only NC guns with SC linacs (split photoinjector configuration) have been considered.

If one is willing to look beyond the near term TESLA Test Facility demands and technical limitations (*e.g.* limits on rf power), this restriction is perhaps unnecessary, however. If it is relaxed, one can conceive of a more elegant solution to the asymmetric beam and emittance problem. The main problem which is ameliorated in this case is the large vertical kick at the gun exit, which is twice as large as in the symmetric gun, because the field fringes only in one direction. In the case of a long injector, one does not encounter an rf emittance problem, however, because the beam leaves the structure on the invariant envelope and with a small beam size. Thus there is no need of rf asymmetries, and no large asymmetric kick for the external quadrupole focusing to overcome (solenoids are forbidden because of a shearing due to differential $\vec{E}\times\vec{B}$ rotation, but quadrupoles are more difficult to work with in a compact space). Preliminary calculations indicate that asymmetric beam handling problems (*e.g.* preservation of small vertical beam size without introducing large horizontal angles) are indeed mitigated in this type of device.

Long photoinjectors have been developed by LANL[7], and are now undergoing further development, using the plane-wave transformer[8] (PWT) concept, at UCLA in collaboration with DULY Research[9]. Whether we choose to investigate asymmetric beam rf photoinjectors in the split (asymmetric rf gun) or integrated long photoinjector geometry depends on detailed simulation work. The simulation of 3D self-consistent, space-charge dominated, trans-relativistic beam dynamics is difficult, but we are now pursuing two new methods of attack: 3-D particle in cell codes (e.g. extending GDFIDL), and 3-D Lienard-Wiechert mesh calculators[10]. Both promise great improvements in performance over the point-by-point PARMELA simulations we have previously pursued[11].

REFERENCES

[1] J.B. Rosenzweig, *Proc. 1991 IEEE Part. Accel. Conf.* **1**, 1987 (IEEE, New York, 1991).

[2] J.B. Rosenzweig, *et al, Proc. 1992 Adv. Accel. Workshop*, 684 (AIP, 1993).

[3] L. Serafini and J.B. Rosenzweig, to appear in *Phys.Rev.E* (June 1997).

[4] [4]J.Rosenzweig and L.Serafini, *Phys. Rev. E* **49**, 1599(1994)

[5] L. Serafini and J.B. Rosenzweig, these proceedings.

[6] W. Bruns, GDFDIL Users Manual (TU-Berlin, 1996).

[7] D.C.Nguyen *et al.*, *NIM A* **341**, 29 (1994).

[8] R.Zhang, *et.al., Proc.1995 Part. Accel. Conf.* , 1102 (IEEE)

[9] J.B. Rosenzweig *et.al.*, and D.U.L.Yu, *et al.*, these proceedings.

[10] L. Giannessi, private communication.

[11] E. Colby, *et. al,* in *Advanced Accelerator Concepts* **335**, 708 (AIP, 1995).

BEAM DYNAMICS IN AN INTEGRATED PLANE WAVE TRANSFORMER PHOTOINJECTOR AT S- AND X-BAND

J.B. Rosenzweig, X. Ding, D.T. Palmer+, C. Pellegrini, L. Serafini* and D. Yu❖
Department of Physics and Astronomy, UCLA, Los Angeles, CA 90095

The beam dynamics of an integrated S-band rf photo-injector based on the plane wave transformer (PWT) concept, proposed as part of an SBIR collaboration between UCLA and DULY Research, are studied. The design, which calls for an 11.5 cell structure run at a peak accelerating field of 60 MV/m and uses a compact solenoid around the initial 2.5 cells, is based on a recently developed theory of emittance compensation[1]. It calls for matching the beam onto a generalized equilibrium envelope, which produces a beam which diminishes in transverse size monotonically with acceleration. This condition minimizes the emittance, which is 1 mm-rad at Q=1 nC. This design is also scaled to produce nearly identical performance at X-band, giving an injector appropriate to running an FEL at the SLAC NLCTA. These designs are insensitive to rf emittance increase, allowing a wide choice of injection phase, and the option to compress the emitted pulse.

I. INTRODUCTION

An integrated rf photoinjector, in which the rf gun and post-acceleration linac are joined, is attractive for several reasons. Perhaps the primary motivation for this geometry is to allow emittance compensation with a smaller acceleration gradient in the cathode region, ameliorating power demand (a larger total energy is obtained for constant power use) and handling problems, as well as dark current emission levels. This advantage is obtained in the integrated geometry because the beam does not encounter a large exit kick after the final iris (typically second) in the gun structure. This exit kick causes outward motion which must be controlled by a powerful solenoid, and which interferes with the emittance compensation process. The use of lower accelerating gradient in an integrated injector further admits use of a lower launch phase, which allows for pulse compression.

These advantages have been obtained to some degree by the LANL injectors, typified by AFEL[2], which has produced the lowest emittance to charge ratios of any photoinjector. The performance of the PWT integrated photoinjector at both S- and X-band, are discussed below. The S-band device is now being constructed by a collaboration between UCLA and DULY Research. The X-band case represents simple scaling[3] of the S-band device to deliver FEL quality beams to the NLCTA at SLAC.

II. S-BAND PWT INJECTOR RF DESIGN

The rf structure of the S-band PWT[4] injector has been specified in a two-stage process: initial optimization of the field profile for acceleration by SUPERFISH, followed by a three-dimensional analysis using MAFIA (see Ref. 5). In the first stage, we make an initial specification of the fields to provide a baseline geometry and the nominally axisymmetric fields in the beam channel, which are used in PARMELA simulations. This exercise is subject to the following constraints: (1) high shunt impedance (2) low higher spatial harmonic content (3) cell number and gradient yielding 20 MeV beam (4) good coupling, mode separation (5) relatively low Q_0 to allow fast structure (6) minimizing of outer diameter to allow compact focusing solenoid.

The first two constraints can be partially satisfied by using the disk and iris geometry of the present UCLA PWT linac, which has, relative to 1.5-1.625 cell S-band rf gun designs, a thinner disk and smaller iris[4]. This naturally leads to a high shunt impedance, with moderate spatial harmonic content. The near-axis fields are in any case of high enough quality to produce a very high brightness beam, because the beam sizes are controlled to be a fraction of the iris size. All compact guns are coupled cell-to-cell on axis, but this is not possible here due to the small iris size. Fortunately, the PWT structure has very high coupling, allowing a standing-wave, π-mode, multi-cell design with excellent mode separation. The reason for this high level of coupling is the large volume between the outer wall and the disks. This volume, because of its large stored energy, also serves to raise the Q_0 of the device. This high Q_0 makes it is difficult to fill a PWT structure, and thus we choose a smaller outer wall radius than is presently employed at UCLA. This choice is reinforced by the need to have a solenoidal focusing field, which must be localized within the first few cells of the photoinjector.

Given all of these constraints, we have chosen an inner radius of the cavity wall to be 5.5 cm, and proceeded to analyze the detailed performance of the device. According to the recent analytical theory of emittance compensation[1] by Serafini and Rosenzweig (SR), the solenoidal field must begin to assert focusing within the first cells of the device for optimum performance. In addition, the somewhat anti-intuitive result is obtained that for an integrated photoinjector, emittance compensation is not possible for high gradients, in that the parameter $\alpha = eE_0/k_{RF}m_ec^2$ (E_0 is the on-axis field amplitude, and $k_{RF} = 2\pi/\lambda_{RF}$) must be less than approximately one. We have $\lambda_{rf} = 10.49$ cm, and E_0 =60 MV/m. With such a modest gradient, we must employ an 11+1/2 cell (60.3 cm) structure to obtain 20 MeV electrons. Using the shunt impedance calculated from MAFIA[4] for the four-rod disk-support design we plan to use ($Z'T^2 = 55$ MΩ/m), for the maximum available power input of 24 MW we obtain E_0 =90 MV/m.

Work supported by U.S. DOE grants DE-FG03 90ER4-0796 and DE-FG03-92ER40693, and Sloan Found. grant BR-3225. +SLAC, *also INFN-Milan, ❖DULY Research.

While the shunt impedance in the PWT is mainly dictated by the iris geometry, the cell-to-cell coupling is a function of the distance from the inner radius of the outer wall to the outside of the disks. Here we have chosen the wall radius to be 5.5 cm, while the disk outer radius is 4.07 cm. For these parameters, the coupling is enormous — the width of the lowest pass band is over 900 MHz. The mode separation between the π and the $11\pi/12$ is 16 MHz, which is many times the mode width due to finite Q_0. This separation compares favorably with the 0-π mode separation in the current UCLA 1.5 cell 2856 MHz gun (<2 MHz), and is comparable to the separation of the next generation 1.625 cell guns developed by the BNL-SLAC-UCLA collaboration[6].

The 3-D modeling of structure performance has been studied with MAFIA, as the introduction of 4 support/cooling rods at the nominal on-disc field null significantly perturbs the mode profile[]. It has been found, however, that this perturbation has a negligible effect on the beam dynamics.

III. S-BAND BEAM OPTICS

The design of beam optics in an rf photoinjector is intimately related to the rf design of the injector structure, as well as the design of the focusing solenoid, in sometimes subtle ways. The fundamental mode for obtaining the lowest emittance and highest beam brightness is termed *emittance compensation,* in which the emittance increase due to space charge effects is reversed, leaving a minimized emittance beam for applications such as FELs, wake-field accelerators and precision test beams for advanced accelerators.

Recent work by Serafini and Rosenzweig (SR) has developed both a physical and an analytical understanding of the process[1]. The physical model for the emittance growth and subsequent diminishing (one cycle of an emittance oscillation) is that of transverse plasma oscillations about a generalized equilibrium in an accelerating system. Because the beam has a finite length and non-uniform current profile, these oscillations have amplitudes which are dependent on the longitudinal slice of the beam under consideration. On the other hand, under proper conditions, the frequency of the slice envelope oscillation is not strongly dependent on the current, and the phase space, which after the initial beam expansion has a fanned-out appearance, recoheres after one envelope oscillation. When the proper conditions prevail for emittance minimization (compensation), the beam envelope in the accelerating structure must be focused, after its initial expansion, onto a generalized equilibrium trajectory designated as the *invariant envelope,* which has the form $\sigma_x(z) = \frac{2m_e c^2}{E_{acc}} \sqrt{\frac{I}{3I_0\gamma(z)}}$,

where for a standing wave structure the average gradient $E_{acc} \cong E_0/2$, I is the rms current, and $I_0 = ec/r_e \cong 17\text{kA}$.

This equation displays a diminishing beam size during acceleration which gives a secular damping of the emittance upon which the emittance oscillations are superimposed. In a long photoinjector structure, damping of the beam size at high energy has the additional advantage of mitigating the emittance increase arising from the time dependent rf kick imparted at the structure exit. This allows for freedom in the choice of launch phase, and the possibility to run forward of the rf crest, allowing for longitudinal pulse compression.

The analytical theory developed by SR also allows the beam parameters which give emittance compensation to be specified. This theory predicts that, in order to not let the beam expand much in the initial few cells, that the peak in the focusing field of the solenoid be placed as close to the cathode as possible. This has been done for our design, as the POISSON flux map shown in Fig. 1. The theory also gives $\alpha \leq 1$, setting $E_0 = 60$ MV/m and the nominal launch phase $\phi_0 = 32°$. The low gradient can be explained as follows: for higher gradients, the invariant envelope is smaller, and thus the launched beam must be radially smaller in order to match to the invariant envelope well after the solenoid. In this case, the beam is too dense (the beam plasma frequency is too high) and expands excessively in the first half-cell, thus denying the possibility of invariant envelope matching.

In addition to these considerations, we work with the following constraints: (1) The charge, set by the nominal desired for FEL experiments, is 1 nC, and (2) the laser pulse length, set by the available PBPL/Neptune uv (262 nm) system, is 7.5 psec FWHM. Given these constraints, we find that the beam should be launched with an rms radius of 1.1 mm. The theory also predicts that the solenoid field be a rather small $B_0 = 1.8$ kG at the peak, occurring at $z = 7$ cm, or just before the second iris of the structure. The field is roughly 1/2 that used presently at the UCLA photoinjector, where the solenoid must overcome the exit kick of the gun's rf field. In the case of a long photoinjector the beam is small at the gun exit, and if the beam is directly on the invariant envelope, it exits the structure on a parallel trajectory after the exit kick.

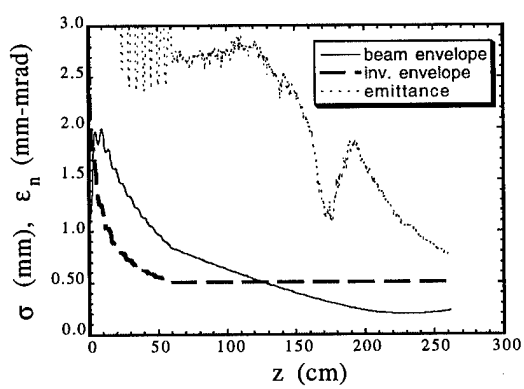

Figure 1. Evolution of the rms beam envelope, emittance in S-band PWT; invariant envelope shown for comparison.

These phenomena are illustrated by the PARMELA simulations of the beam dynamics we have performed. Figure 7 displays the evolution of the rms beam sizes along the photoinjector, along with the invariant

envelope for these conditions ($I = 120$A), shown for reference. It can seen that the beam begins larger, but ends focusing slightly smaller than the invariant envelope. This behavior is in fact typical of emittance compensated photoinjector designs, as one tends to drive the beam a bit smaller, to speed up the compensation process, and make it more effective — the final emittance is roughly proportional to the beam size. There is a limit to how much one can violate the invariant envelope condition, however, dictated by the need to avoid a "cross-over" waist, in which the previously nearly laminar, space-charge dominated beam comes to a nonlaminar, emittance dominated minimum, causing irreversible emittance growth. Our design comfortably avoids this situation, and a beam waist and emittance minimum occur roughly 1.5 m after the end of the PWT. This additional drift is needed because the phase advance of the emittance oscillation, should it all occur inside of the rf structure, would imply accelerating the beam to roughly 200 MeV in a structure 10 times as long.

This injector is also designed to produce low charge (15 pC) ultra-low emittance beams for use in plasma beatwave acceleration experiments[7]. Scaling the charge in the device requires that the beam plasma frequency, and thus the beam density, be kept constant[3]. Using this guide, we have simulated a 16 pC case with the bunch length 1.9 psec FWHM corresponding to the 266 nmlaser system now in use at UCLA. In this case we obtain extremely small emittance, $\varepsilon_n = 0.06$ mm-mrad. We have also performed simulations of pulse compression of the beam using a chicane after the compensation point. We were able to compress the beam by a factor of 3.5 while running at the nominal injection phase. This illustrates the flexibility of the long photoinjector with respect to choice of ϕ_0.

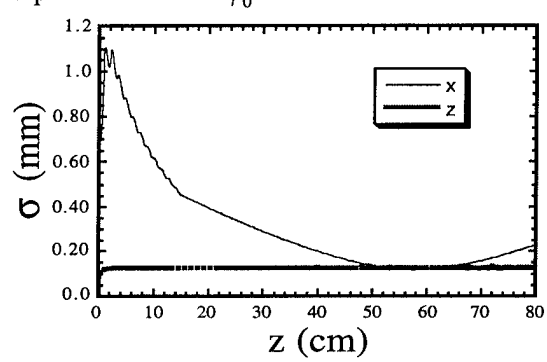

Figure 2. Beam size evolution in the scaled X-band photoinjector (Q=1 nC).

III. X-BAND INJECTOR

In order to have the option of running a SASE FEL at the SLAC NLCTA, a high quality ($\varepsilon_n = 2$ mm-rad, Q=1 nC, with $\sigma_z = 120\ \mu$m) injector beam must be made available. The desire for short bunch length at high charge, plus the availability of the 11.4 GHz (4 x 2.856 GHz) power at the NLCTA[8], make an X-band injector attractive for this application. Happily, the design techniques developed in Ref. 3 include the scaling of designs with respect to λ_{rf}. This technique is based on the appropriate scaling of all frequencies (rf, focusing, plasma) in the problem, and requires

$$E_0, B_0 \propto \lambda_{rf}^{-1},\ \ \sigma_i \propto \lambda_{rf},\ \text{and}\ \ Q \propto \lambda_{rf},$$

to give $\varepsilon_n \propto \lambda_{rf}$ and $\sigma_z \propto \lambda_{rf}^{2/3}$ (at constant Q). Again the bunch dimension scaling is somewhat flexible, especially since we "lost" a factor of 4 in charge in the λ_{rf}-scaling, we must rescale with respect to charge by a factor of 4 to obtain a 1 nC design. As we must choose a 1 psec FWHM laser pulse, we then must have $\sigma_r = 700$ μm. The peak accelerating field E_0=240 MV/m, which is reasonable for this rf frequency, and the peak solenoid field B_0 =7.2 kG, which can be obtained by straightforward water-cooled design. The results of PARMELA simulation of this design is shown in Figs. 2 and 3. It can be seen that the beam envelopes are nearly identical in form to the S-band case, with the desired $\sigma_z = 120$ μm. The emittance performance is also better demanded by the FEL application, which is not surprising - we expect ε_n to diminish by 1/4 in the λ_{rf}-scaling, and grow by ~4 in the charge scaling.

It should be noted that it is unlikely to obtain a good design for the X-band photoinjector with a split photo-injector because of several reasons: (1) the scaling of the fields make the design impractical (an X-band version of the 1.625 cell gun would require E_0 = 480 MV/m), (2) the beam debunches in the drift between gun and linac. The PWT is a good candidate for this structure, because it is straightforward to obtain a high shunt impedance with good mode separation and ease of manufacture.

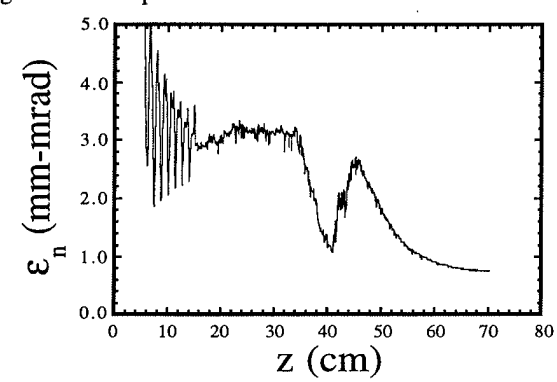

Figure 3. Emittance evolution in scaled X-band photoinjector (Q=1 nC).

REFERENCES

[1] L. Serafini and J.B. Rosenzweig, to appear in *Phys.Rev.E.* [2] D.C.Nguyen *et al.*, *Nucl. Instr. Meth. A* **341**, 29 (1994).

[3] J.B. Rosenzweig and E. Colby, in *Advanced Accelerator Concepts*, **335**, 724 (AIP, 1995).

[4] R. Zhang, *et. al., Proc. of the 1995 Part. Accel. Conf.*, 1102 (IEEE, 1995).

[5] D. Yu, *et al.*, these proceedings.

[6] D.T. Palmer, *et al.* in *Proc. 1995 IEEE Particle Accel. Conf.* 2432 (IEEE, 1996).

[7] C. Clayton, *et al.*, these proceedings.

[8] R. Miller and D. Yeremian, private communication.

PICOSECOND-RESOLUTION 'SLICE' EMITTANCE MEASUREMENT OF ELECTRON-BUNCHES*

Ilan Ben-Zvi, Joe X. Qiu and Xijie Wang, National Synchrotron Light Source 725C,
Brookhaven National Laboratory, Upton NY 11973-500 USA

Abstract

The Slice Emittance diagnostic is applicable to particle bunches in a linac that are of the order of a few degrees of phase long. In this technique, the transverse phase space of a longitudinal slice about one degree long is measured. The Slice Emittance diagnostic has been demonstrated on an electron bunch produced by a laser-photocathode RF gun. We measured the transverse beam matrix of one picosecond slices out of a 10 picosecond long bunch (about 10 degrees at the RF frequency of 2856 MHz).

To implement this diagnostic one needs a phase shifter on part of the linac, a momentum analyzer (a dipole magnet followed by a slit) and a transverse emittance measuring system following the analyzer. By dephasing the last section (or sections) of the linac, longitudinal position in the bunch is correlated with energy. The momentum analyzer selects a short longitudinal slice by discriminating on energy and the transverse phase space of this slice is measured downstream of the analyzer.

The Slice Emittance diagnostic, particularly in conjunction with tomographic analysis of the transverse phase space of the slices, provides significant new information about the 6-D phase space distribution of the beam. The experimental work done with this diagnostic has been used to study the details of the important emittance compensation method that is in wide use in photoinjectors. This diagnostic makes it possible to take the emittance compensation method a step further and apply non-linear emittance compensation for higher brightness beams.

1 THE SLICE EMITTANCE TECHNIQUE

High brightness particle beams are an important frontier in accelerator physics. Our ability to measure beams in the greatest detail possible is the key for future progress. There is need for diagnostics to study in detail the phase space of the beam and provide guidance for multi-parameter adjustment of the beam source and transport. The 6-D phase space distribution of a short longitudinal slice of a beam of electrons or other particles is particularly important. The slice-emittance technique [1] is such a diagnostic. In this technique, a short slice is selected out of an energy chirped beam by a slit in a dispersive region. The emittance of this slice is measured downstream of the slit using the quadrupole scan technique (or any other method). The measurement is repeated for different slices and for different beam conditions, like a new value for the current in the emittance compensating solenoid. We can also apply tomographic analysis techniques to the data taken in the quadrupole scan. Then we extract the density distribution in the transverse phase space slice by slice. This procedure provides us with a nearly complete characterization of the density distribution in the 6-D phase space of the beam.

1.1 Description of the set-up and the measurement method

Figure 1 shows the schematic layout of the slice-emittance measurement diagnostic at the BNL Accelerator Test Facility. The beam is generated at the photocathode by a 10 ps long UV laser pulse. The electron bunch, in the measurement described below, has a charge of 0.4 nC. The gun output energy is 4 MeV (corresponding to a 89 MV/m peak electrical field on the cathode). The beam emerging from the gun is focused by a solenoid magnet and injected into a 2856 MHz linear accelerator (linac). A laminar-flow beam waist is formed in the linac, during acceleration. The acceleration continues until the space charge forces become negligibly small, freezing the resultant phase space distribution.

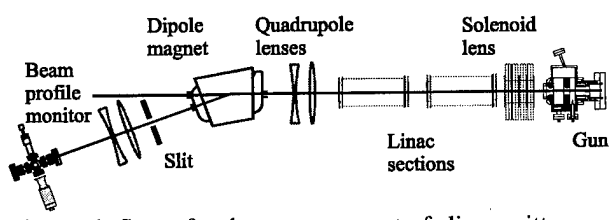

Figure: 1 Setup for the measurement of slice emittance at the BNL Accelerator Test Facility.

The linac consists of two sections. The phase of the second section is controlled independently by a motor controlled phase shifter. The high energy beam is bent horizontally by a 20 degrees dipole magnet and a small slice in energy is selected by a slit. A quadrupole magnet following the slit is scanned in current and the vertical beam size is measured on a Beam Profile Monitor (BPM). The BPM comprises a phosphorous screen to form a luminous image of the beam intensity profile and a CCD camera to record it. The distance from the quadrupole to the BPM is 8.96 m. For clarity we omit from the figure

* Work supported by the US Department of Energy under contract No. DE-AC02-76CH00016.

various beam transport quadrupole lenses in the high energy beam line.

The second linac section, dipole and slit form a filter that passes only a short slice of the beam pulse downstream of the slit. The quadrupole lenses and beam profile monitor downstream of the filter form an analyzer to measure the beam matrix of the slice. The filter is tuned to a given slice by changing the phase of the second linac section. Since the dipole current is constant, the energy of a selected slice is constant regardless of its position along the bunch, and the optics of the selected slices in the filter (and before it) are identical. However, under regular operation of the machine the slices enter the second linac section at slightly different phases around the crest of the accelerating wave-form. Thus they will experience a slightly different focusing. The maximum relative defocusing kick along a 10 ps long bunch positioned at the crest is of the order of half a micro-radian. This is two orders of magnitude smaller than the angular spread in the approximately one millimeter diameter beam as it enters the second linac section and thus negligible.

The horizontal spot size on the slit is determined by the beta function at that point and by the energy spread.. The measured horizontal spot size was equivalent to an energy spread of 0.5 % FWHM with the known 5.3 mm/% dispersion at the slit.. The slit opening was adjusted to an opening of 2.6 mm equivalent to an energy bite of about 0.5%. Next, the second linac section was dephased by 29.8 degrees to produce a nearly linear energy chirp of 0.439 % per picosecond. Due to this chirp, the slit opening corresponded to 1.1 ps.

The experimental data was obtained by the BPM. The image of the beam is captured by a CCD camera (Pulnix model 745E) with a frame grabber (Spiricon model LBA-100A). The CCD camera has pixel size of 11 by 13 microns and the number of pixels is 512 by 480. A remotely controlled iris is used to avoid saturation in the 8 bit dynamic range of the frame grabber. The Gd_2O_2S:Tb phosphor is linear in light per charge output under our beam energy and charge conditions. The spatial resolution of the light emanating from the phosphor is better than 100 microns, thus our resolution is determined by a combination of the pixel size and the phosphor resolution. This resolution is the basis for the error estimate in the emittance measurements. The digitized image from the frame grabber was written onto a diskette to be analyzed off-line. The analysis consists of integrating over the horizontal direction and obtaining the rms beam size for the vertical direction. Each vertical rms size corresponds to one point in a quadrupole scan. The beam size as a function of the quadrupole strength is used in a best-fit analysis to extract the beam matrix just upstream of the quadrupole. In this analysis we make the usual assumption that the transverse phase space distribution is an ellipse.

1.2 Results of the ATF slice emittance measurement

One application of this powerful technique is a study of emittance compensation in electron photoinjectors.. In the emittance compensation technique, suggested by Bruce Carlsten [2], the observed emittance growth due to linear components of space charge forces in the photoinjector is compensated by passing the electron beam through a laminar-flow beam-waist. The space charge interaction in this beam waist results in a differential rotation of the slice ellipses to bring them into alignment at some point downstream of this waist. To understand this emittance growth and compensation, one has to look at the slice emittance of a number of slices as they evolve. To go beyond this correction that is characterized by a single variable (the solenoid current), it is necessary to monitor the slice by slice emittance of the beam and deduce a non-linear (multi-parameter) correction.

The beam matrix provides us with the emittance of the measured slice and the orientation of the phase-space ellipse. The measured normalized rms emittances of the three slices are 3.5 ±1.1 , 2.8 ±1.1 and 2.3 ±1.1 for the front, center and end of the bunch slices, respectively.

To illustrate the relative orientation between the slice ellipses, they were rotated with a known transfer matrix so that the phase space ellipse of the end slice is an erect ellipse and has a fixed beam size in each of the plots. Figure 2 shows only the relative rotation of the slice ellipses and a reversal in this differential rotation at some solenoid field does not imply an absolute reversal. The best emittance compensation is achieved when all the slice ellipses line up. This will reduce the emittance of the whole electron bunch by producing the smallest projected area, with summation weighted by the charge in each slice.

As the beam passes through the waist created by the solenoid, the ellipses of the slices rotate relative to each other since the space-charge force is not uniform along the bunch. According to Carlsten's theory, the angle of rotation is a function of the solenoid field and the charge distribution. We name the slices after their relative position in the electron bunch: front, middle and end. The front slice has the largest charge, the middle the second largest and the end the smallest relative charge.

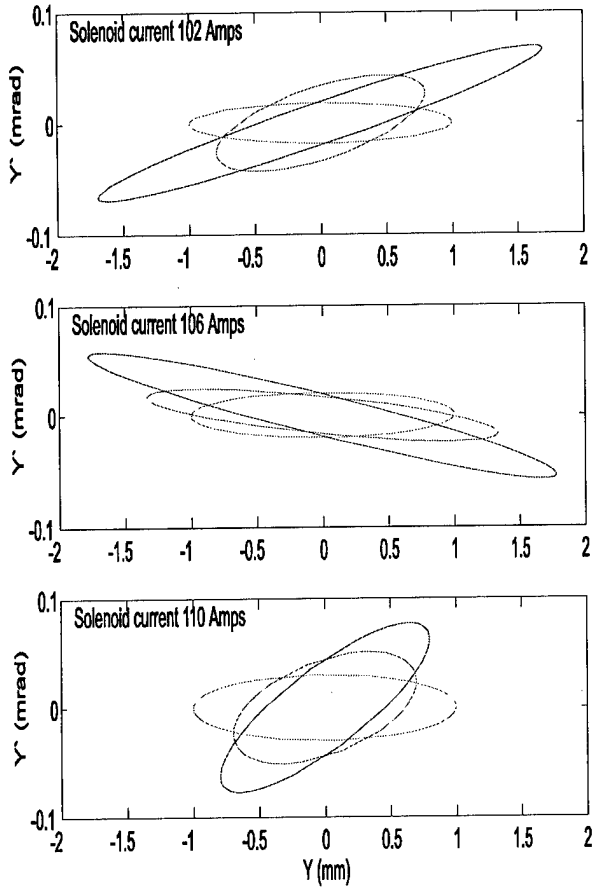

Figure: 2 The fitted beam ellipses for the slice emittance measurement for three solenoid currents. Top: 102 A. Center: 106 A. Bottom: 110 A.The slice at the end of the beam bunch is taken as a beam waist, showing the relative rotation of the front and middle slices as the solenoid current is increased.

Comparing Figs. 2-top and 2-center we notice that the larger charge slices rotates through the larger angle, as expected. While Fig. 2-top (at 102 A) represents an under-rotation, Fig. 2-center. (at 106 A) represents an over-rotation (a point of near alignment was passed). As we continue to increase the solenoid current to 110 ampere, seen in Fig. 2-bottom., the relative rotation reverses itself, passing through near alignment once again. We expect that the closest alignment of the slice ellipses is attained at two solenoid currents, one between 102 and 106 A, the other between 106 and 110 A.

2 THE FORMATION OF BEAM HALOS IN EMITTANCE COMPENSATION

Emittance measurement, in particular that of a very small emittance, is difficult. One problem is the handling of beam halo. The process of emittance compensation can lead to a formation of a beam halo. The Carlsten model of emittance compensation uses a constant space charge force and thus predicts that compensation will apply to all longitudinal slices regardless of their current. A more detailed model, based on the envelope equation, shows that slices with a local current larger or smaller that some critical values will not fall into the compensation range and will form a beam halo. This will increase the integrated rms emittance, but due to the limited dynamic range of the frame grabber the measured value may be smaller since a diffuse halo may be missed.

As an example, consider the quad scan measurement of the total emittance as a function of solenoid current. As seen in Figure 3, the emittance initially decreases as expected as a result of emittance compensation. However, the increase in emittance is not as rapid as one would expect. This is the result of a cross over (non-laminar) of some part of the beam. A cross over results a large divergence and the creation of a low intensity beam halo that is not registered by a low dynamic range camera and frame-grabber system. The loss of the halo electrons due to the dynamic range results in a better emittance than should be observed otherwise.

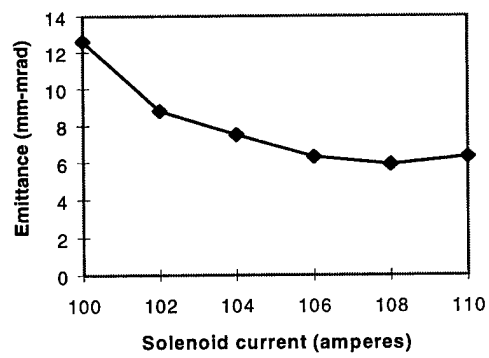

Figure: 3 Normalized total vertical emittance measured as a function of solenoid current.

The reason for the cross-over on some low current slices at a large solenoid field and the resultant beam halo can be shown by integrating the envelope equation of the beam in the linac. The relativistic envelope equation of a beam with space charge and emittance is given by:

$$R''+R'\frac{\gamma'}{\gamma}=\frac{2I}{\gamma^3 I_A}\frac{1}{R}+\frac{\varepsilon_n^{\,2}}{\gamma^2}\frac{1}{R^3}$$

R is the local envelope, γ is the energy, I_A is the van Alfven current, I is the local current and ε_N is the normalized local emittance.

The emittance correction relies on a laminar flow beam waist, which is described by the envelope equation without the emittance term. We can define a critical beam waist envelope size, R_c by equating the two terms on the right hand side, resulting in:

$$R_c = \sqrt{\frac{\gamma \varepsilon_n^2 I_A}{2I}}$$

A beam waist that is larger (smaller) than the critical size, R_c, is dominated by space charge (emittance). The emittance dominated beam waist leads to a cross over of electrons at that particular slice. Since R_c is a function of the current, the low current slices will cross over while high current ones will maintain a laminar flow.

This is not the problem with beam slices that have too little (or too much) current. The slope of the beam ellipse in phase space, given by R'/R, can be tracked by integrating the envelope equation without the emittance term [3]. Plotting the slope at a point downstream of the solenoid lens as a function of beam current and various focusing powers of the lens, one learns the following:

- There are a few values of the focusing strength that result compensated beams.
- A lower limit and an upper limit slice current exist for each solution such that the slices with a current lower than the lower limit or higher than the upper limit will not align their slope with the compensated slices.
- The range of current for which the slope is constant (an emittance compensated range) depends on various parameters: initial conditions, position of the lens, position of the observation point, position and gradient of the accelerator (if there is one) and so on.
- The best solution is the first one (the lower lens power).

A Gaussian photocathode laser longitudinal distribution is thus bad for emittance compensation since it will result low current slices at the head and the tail of the electron bunch. The laser distribution may be modified on a sub-picosecond scale by known optical techniques. Using a slice-emittance measurement one may observe the results of the laser profile modification and tune the beam for a better emittance.

3 TOMOGRAPHIC MEASUREMENT OF SLICE EMITTANCE

By discussing beam ellipses or by making a-priory assumptions concerning the distribution of the beam in phase space in order to fit a quadrupole scan data (or other measurement techniques) to some beam parameters we are loosing a lot of information. As has been shown by McKee, O'Shea and Madey [4], one can apply tomographic techniques to a quadrupole scan and derive the full phase space distribution. This is a powerful technique that, together with the slice emittance measurement technique can provide a greater understanding of the beams of photoinjectors and help improve the performance.

Figure 4 shows the measured phase space density distribution of the total beam (not just one slice). The horizontal axis is a transverse coordinate (horizontal, in this case) in mm, and the vertical axis is the divergence in mrad. This is an emittance compensated beam from the ATF photoinjector. It is possible to see the typical beam halo that shows up in measurements even with the limitted dynamic range (8 bits) of our frame grabber. The measured quadrupole-scan rms normalized emittance is about 4.5 mm mrad. However, as discussed above, the large halo causes an underestimation of the emittance.

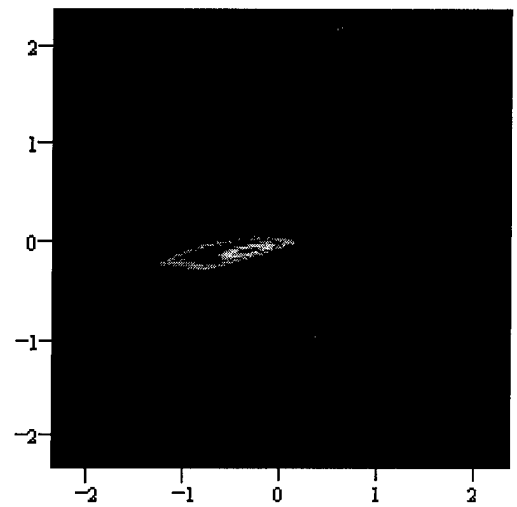

Figure: 4 Tomographic reconstruction of the horizontal non-normalized phase space of the total bunch of an emittance compensated beam. The horizontal axis is in milimeters, the vertical axis is in miliradians.

Figures 5,6 and 7 show the (transverse-vertical) phase space distribution of a beam slice of 50, 100 and 200 pC, respectively. (Please notice the change of scale from Figure 4, but the units are still mm and mrad). Some of the 'splatter' in figures 6 and, in particular 7, is due to the fact that the measurement was not designed originaly as a tomographic measurement but as a plain quadrupole scan emittance measurement. Nevertheless, the significant features of the distribution are clear enough. The measured quadrupole-scan rms normalized emittances are 2.5, 2.9 and 3.7 mm mrad, respectively. Most of the halo seen in the full beam measurement is gone, since it is formed by low current slices that are cut out by the slice-emittance filter. As a result the emittance measured by a quadrupole scan technique is more believable. As we increase the charge, we see that most of the emittance increase is through spreading of the core and some distortion. This is a new information that may be used now for a better understanding of the emittance growth mechanism and, hopefully, to improvement of the brightness of the beam.

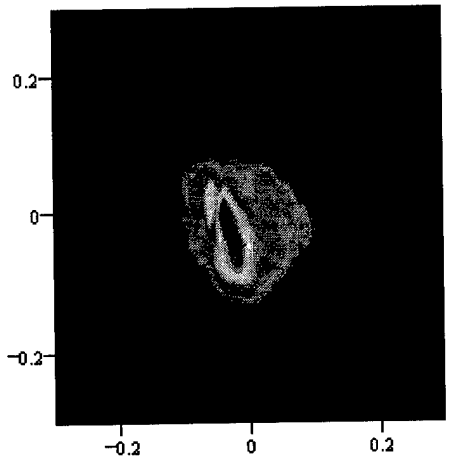

Figure: 5 Tomographic reconstruction of the vertical non-normalized phase space of a slice. The horizontal axis is in mm, the vertical axis is in mrad. The total charge is 50 pC.

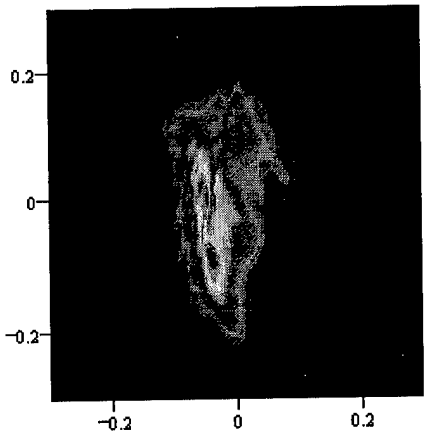

Figure: 6 Tomographic reconstruction of the vertical non-normalized phase space of a slice. The horizontal axis is in mm, the vertical axis is in mrad. The total charge is 100 pC.

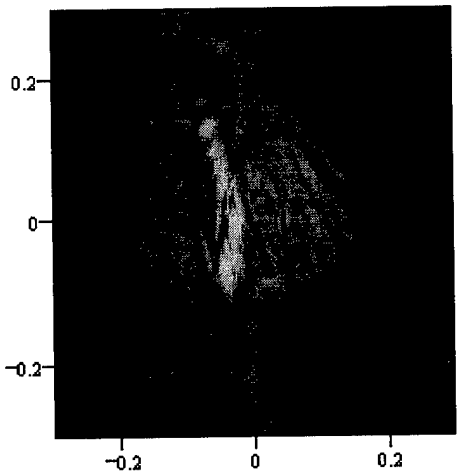

Figure: 7 Tomographic reconstruction of the vertical non-normalized phase space of a slice. The horizontal axis is in mm, the vertical axis is in mrad. The total charge is 200 pC.

REFERENCES

[1] 'Demonstration of emittance compensation through the measurement of the slice emittance of a 10 picosecond electron bunch', X. Qiu, K. Batchelor, I. Ben-Zvi and X.J. Wang, Phys. Rev. Let. 76 No. 20, 3723, (1996)

[2] 'New Photoelectric Injector Design for the LANL XUV FEL Accelerator', B.E. Carlsten, Nucl. Instr. And Meth. In Phys. Res. **A285**, 313 (1989)

[3] Ph.D. dissertation, J.X. Qiu, The University at Stony Brook, ny 1997 (unpublished)

[4] 'Phase Space Tomography of Relativistic Electron beams', C.B. McKee, P.G. O'Shea and J.M.J. Madey, Nucl. Inst. And Meth. In Phys. Res. **A358**, 264 (1995).

ELECTRON BEAM INSTRUMENTATION TECHNIQUES USING COHERENT RADIATION

D. X. Wang, Thomas Jefferson National Accelerator Facility
12000 Jefferson Avenue, Newport News, VA

Abstract

Much progress has been made on coherent radiation research since coherent synchrotron radiation was first observed in 1989. The use of coherent radiation as a bunch length diagnostic tool has been studied by several groups. In this paper, brief introductions to coherent radiation and far-infrared measurement are given, the progress and status of their beam diagnostic application are reviewed, different techniques are described, and their advantages and limitations are discussed.

1 INTRODUCTION

In recent years, there has been increasing interest in short electron bunches for different applications such as short wavelength FELs, linear colliders, advanced accelerators, e.g. laser or plasma wakefield accelerators, and Compton backscattering X-ray sources [1-3]. Meanwhile, much progress has been made on photoinjectors and different magnetic and RF bunching schemes to produce very short bunches [4-7]. Measuring short bunches becomes essential for developing, characterizing, and operating such machines.

Conventionally, the longitudinal distribution and bunch duration of short electron bunches can be measured by streak cameras or transverse RF deflecting cavities [6, 8]. However, with such devices it becomes very challenging to measure bunch lengths down to a few hundred femtoseconds. Another technique is the RF zero-phasing method with the use of RF cavities and a spectrometer [9-12]. Using such a technique, bunch lengths as short as 84 fs (rms) have been measured and the longitudinal distribution function has been retrieved. However, the measurement is destructive. Recently, frequency domain techniques have been developed, based on a relation between the bunch profile and the coherent radiation spectrum. This paper will focus on the progress and status of such frequency domain measurements.

2 COHERENT RADIATION

Coherent synchrotron radiation was theoretically studied by Nodvick and Saxon in 1954 and later by Michel in 1982 [13-14]. It was first observed by Nakazato and his colleagues at Tohoku University in 1989 [15]. Since then, extensive experimental studies have been carried out by several groups to characterize the coherent radiation of various radiation mechanisms and to explore their applications [16-19]. If a single electron radiates under certain conditions, the total radiated electromagnetic field from an electron bunch is the superposition of that of each individual electron with phase factors. Therefore, the radiation power at a measurement point can expressed as [20]

$$P_{\text{total}}(\lambda) = P_{\text{ind}}(\lambda)\left|\sum_{i=1}^{N} e^{j2\pi z\cos\theta/\lambda}\right|^2$$
$$= P_{\text{ind}}(\lambda)[N + N(N-1)F(\lambda)] \qquad (1)$$

where $P_{\text{ind}}(\lambda)$ and $P_{\text{total}}(\lambda)$ are the radiation power of individual electron and all electrons in the bunch, respectively, N is the number of electrons in the bunch, λ is the radiation wavelength, z is the longitudinal position of electrons, θ is the angle between the longitudinal direction and the observation direction, and $F(\lambda)$ is the so-called form factor given by

$$F(\lambda) = \left|\int_{-\infty}^{+\infty} dz S(z) e^{j2\pi z\cos\theta/\lambda}\right|^2 \qquad (2)$$

where $S(z)$ is the normalized longitudinal distribution function. The first term on the right side of Eq. (1) is the incoherent part proportional to N. The second term is the coherent part proportional to the square of N. $P_{\text{ind}}(\lambda)$ is usually well characterized and N can be known from current measurement. The form factor is of real interest from the beam diagnostic point of view. When the radiation wavelength is much shorter than the bunch size, electrons radiate out of phase, the form factor becomes zero, and the coherent effect diminishes. When the wavelength is much longer than the bunch length, the electrons radiate in phase, the form factor approaches one, and the radiation power is enhanced coherently by a factor of N, which is typically in the range of 10^6 to 10^{10} for most accelerators. In between, there is a transition regime where the wavelength is comparable to the bunch size. The shape of the form factor and the location of the transition region are completely determined by the distribution function, i.e. both the bunch shape and size. A plot of the numerical calculation of Eq. (1) is shown in Fig. 1, where the solid curves are the coherent synchrotron radiation power versus wavelength for different bunch lengths of Gaussian profile bunches, while the dashed curve is the incoherent part.

It is very important to bear in mind that the form factor is derived from the power spectrum, i.e. it is a real and positive quantity. All the phase information of the Fourier transformation of the distribution function is lost,

0-7803-4376-X/98/$10.00 © 1998 IEEE

as shown in Eq. (2). It is unfortunate that in general, the distribution function can not be uniquely determined by the measured form factor.

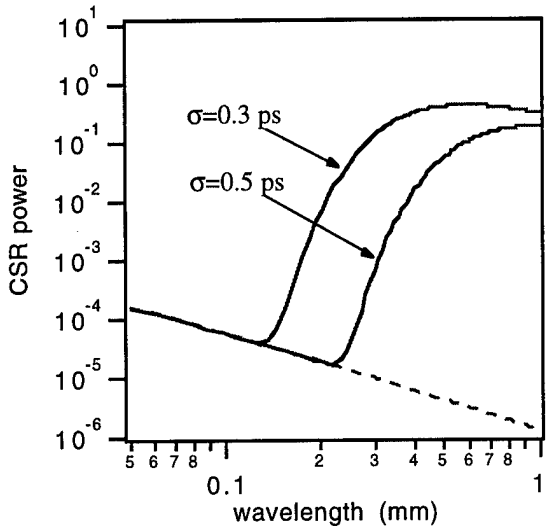

Fig. 1 Calculated CSR power spectrum with 20% flat bandwidth for Gaussian beams with different bunch length.

The above equations are derived for the one dimensional case, i.e. all the phase differences between electrons are due to their longitudinal position differences. In practice, when bunches are short, their application to certain experimental conditions needs to be evaluated. They may become inaccurate if the phase differences due to the transverse beam size or the finite acceptance angle are not negligibly small, compared to the phase differences due to the longitudinal position. It is also assumed that the longitudinal distribution function remains unchanged during radiation formation. This may not be a good approximation for synchrotron radiation if the path length difference introduced by the bending magnetic field is significant compared to the bunch length, particularly for very short bunches.

Since coherent radiation is a result of the superposition of electromagnetic waves, coherent enhancement exists for all electromagnetic radiation mechanisms such as synchrotron radiation, transition radiation, diffraction radiation, Cherenkov radiation, Smith-Purcell radiation, and even wakefield effects. However, the radiation at long wavelengths may be suppressed by boundary conditions, noting the equations are valid only for free space. Coherent synchrotron radiation has been widely used for beam diagnostic purposes due to its noninvasive nature, while transition radiation has been favored for the flatness of its emission spectrum. Recent studies on diffraction radiation make it another potential noninvasive alternative, especially for high energy beams [18].

3 FAR-INFRARED RADIATION MEASUREMENT

Most broadband spectrum measurements are performed with thermal detectors because of their flat frequency response [21]. The radiation is absorbed by the bulk of the material, which changes its physical properties due to the temperature change. Helium-cooled bolometers are the most sensitive thermal detectors. Their superb performance comes at the expense of higher cost and complicated operations. The Golay cell is one of the most widely used room temperature far-infrared detectors. It has flat frequency response well into the millimeter region. Even though its detectivity is much less than that of helium-cooled bolometers, it is adequate for most high charge, short bunch applications. Unfortunately, reliable vendors are becoming difficult to find. Another room temperature detector is the pyroelectric detector. Its responsitivity can be comparable to the Golay cell and its time response is faster than other thermal detectors. It is commercially available and relatively inexpensive. However, its frequency response, especially at long wavelengths, is not readily available from the vendor.

Another type of far-infrared bandpass detector is the Schottky whisker diode, which has been used in bandpass measurement of coherent synchrotron radiation [22-25]. It has adequate sensitivity for most short bunch applications and is also relatively inexpensive. Although it is quite fragile to electrical and mechanical shocks, it has been used in a typical accelerator environment.

To obtain spectral information, either a grating monochromator or an interferometer is needed [21]. The typical example of the former is the conventional echelette grating type. The radiation power at a specific wavelength is enhanced by the diffraction effect and collected at a corresponding angle of the grating plane. The radiation power spectrum is measured by scanning the angle. To avoid higher diffraction orders, prefiltering of the radiation is required. An interferometer uses the interference between two beams split from the incident radiation beam. The radiation power is measured versus the path differences, yielding a so-called interferogram. The radiation spectrum can be computed from the Fourier transform of the interferogram. Another wavelength selecting device is the bandpass mesh filter with a typical bandwidth of 20%. Such a filter combined with a broadband thermal detector is also suitable for the bandpass measurement [26].

Mirrors, focusing parabolic reflectors, and cone shaped light pipes are the most widely used optical components. One of the difficulties for the spectral measurement is that the absorption and refractive indexes of many non-metal materials are strongly frequency dependent. The frequency properties of the vacuum windows, beam splitter, and the effect of water absorption need to be evaluated at the design stage for the wavelength region of interest.

4 COHERENT RADIATION SPECTRAL MEASUREMENT

It is clear that in order to obtain the longitudinal distribution, namely the bunch shape and length, the spectrum of the coherent radiation needs to be measured over the wavelength span of the transition region. Many spectrum measurements of coherent radiation have been successfully performed. Only a few representative examples are discussed here to illustrate the principles.

In 1991, Ishi and his colleagues at Tohoku University reported their spectral measurement results of coherent synchrotron radiation in the far-infrared region [27]. The spectrum was measured by a far-infrared spectrometer consisting of a Helium-cooled bolometer, five echelette gratings, and long-wavelength-pass and short-wavelength-pass filters. All optical components were enclosed in vacuum to eliminate water absorption. Radiation intensity was monitored by another detector during the grating rotation scan to correct beam induced fluctuations. The system was calibrated with a blackbody radiator to within a factor of 1.5. The coherent enhancement was comparable with the number of electrons in the bunch, 3.6×10^6. A spectrum from wavelengths of 0.16 to 3.5 mm was obtained with a resolution of 0.1 cm^{-1} at wavelength of 1 mm, and the bunch form factor was derived accordingly.

A cosine transformation of the square root of the form factor was applied to estimate the distribution function. Though such an approximation ensured the resulting distribution function to be real and positive, it also artificially forced the resulting distribution function to be symmetric and peaked at the center. The result shows a Gaussian like shape with a full width at half maximum of 0.25 mm, which is much shorter than the 2 mm length estimated. One of the simulated results indicated that the bunch shape is about 1.3 mm with three spikes of about 0.1 mm in width at the ends. It was then believed that these spikes might contribute to the measured fall-off at short wavelength, resulting in the computed narrow bunch length.

In 1991, using a polarizing interferometer with a resolution of 0.09 cm^{-1}, Shibata and the Tohoku group observed a bunch-to-bunch interference pattern, i.e. RF sidebands on the coherent synchrotron radiation spectrum derived from a measured interferogram [28]. In 1994, the first cross-comparison was made by the same group between a streak camera measurement of the bunch shape and a spectrum measurement of the coherent transition radiation [29]. Instead of using a cosine transformation, a triangular distribution function with a width of 8.5 mm was found. The measured form factor matched the envelope of its calculated oscillatory closely. A streak camera measurement revealed that the bunch shape could be fitted very well by a Gaussian function with a width of 7.2 mm. Though these two distributions are rather close in the time domain, but clearly distinguishable, the corresponding form factors differed significantly in the frequency domain.

In 1994, another interferogram measurement of the coherent transition radiation was reported by Kung of Stanford University, and later the refined results were given by Lihn [5, 31]. Such a measurement was proposed by Barry of CEBAF in 1991 [32]. A pyroelectric detector and a Michelson interferometer with a resolution of 0.5 cm^{-1} were used to obtain the interferogram. The spectrum computed from the interferogram was contaminated by water vapor absorption and the interference pattern of the beam-splitter. Based on the assumption of uniform charge distribution, the bunch length was estimated to be 50 fs (rms) using a thin mylar beam-splitter of 12.7 μm. This value was later revised to 142 fs (rms) still based on the uniform distribution assumption, after a careful analysis of the effect of the thickness of the beam-splitter on the width of the measured interferogram. The difficulties of obtaining the distribution function were discussed. Similar measurements were also performed by other group [33]. No longitudinal distribution function was reconstructed due to the bandwidth limitation of the measurement.

Using the Kramers-Kronig relation was first proposed by Lai of Cornell University in 1994, to compute phase information from the measured spectrum under a minimal phase condition [34]. The method is able to generate asymmetric distribution functions from an inverse Fourier transform. The technique was applied to spectral measurement results of both coherent synchrotron and transition radiation [35]. Artificial asymptotic attachment to both ends of the measured spectrum was discussed, given that the bandwidth of the measurement is limited in practice. Unfortunately, due to practical limitations, the results were not verified by an independent bunch distribution measurement. Numerical studies with distributions which are a superposition of three Gaussian components revealed that the sequential order of the Gaussian peaks could not be uniquely determined [36]. In some cases, the calculated minimal phase significantly differed from the actual phase. Therefore, the minimal phase assumption is not always valid. In practice, the minimal phase assumption is difficult to validate because the bunch distribution is generally unknown.

5 COHERENT RADIATION BANDPASS MEASUREMENT

Despite the difficulties of reconstructing the distribution function, the strong dependence of radiation power on bunch distribution and bunch length were observed in experiments. As can be seen in Fig. 1, the radiation power within a certain bandwidth in the transition region changes rapidly as bunch length varies. Therefore, an appropriate bandpass detector can be employed as a bunch length monitor to detect relative bunch length and shape changes.

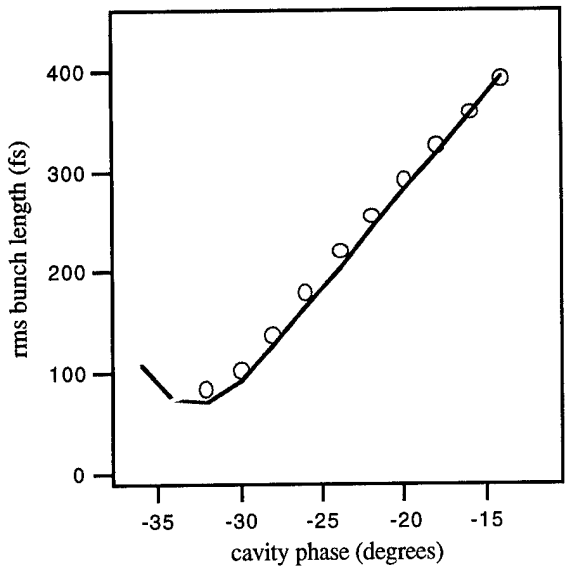

Fig. 2 Bunch lengths versus phase change of the bunching cavity, where the circles are from measurement while the solid curve is from simulation.

A very stringent demand on final energy spread, with a design goal of 2.5×10^{-5} (rms), requires short bunches at the Continuous Electron Beam Accelerator Facility (CEBAF) of Jefferson Lab. CEBAF is routinely operated within its bunch length specification of 0.5 ps (rms). A different approach was taken. Instead of trying to obtain absolute longitudinal distributions by measuring the spectrum of the coherent radiation, relative distribution changes were measured by detecting integrated coherent radiation power within the transition region. Such a noninvasive coherent synchrotron radiation bunch length monitor has been developed at Jefferson Lab to detect bunch length changes resulting from RF phase drifts in the bunch forming region during CW beam delivery [25]. Schottky whisker diodes were used as far infrared detectors. The bunching process, and bunch shape and length were systematically studied by measurement using an RF zero-phasing technique and by numerical simulation [37, 12]. Bunch lengths were varied as the RF phase of a bunching cavity was changed. The measurements are in excellent agreement with simulation, as shown in Fig. 2 where the circles are from measurement while the solid curve is from simulation. The monitor was calibrated by an RF zero-phasing measurement. The results are shown in Fig. 3. The minimum bunch length of 84 fs (rms) was actually found by maximizing the output signal from the diode, which is proportional to the detected radiation power, as shown in Fig. 4. The monitor was able to detect a few femtosecond bunch length change for a 0.5 ps (rms) Gaussian bunch containing 3×10^5 electrons, and still better for shorter bunches. An optical chopper was installed to enable the monitor to operate for both pulsed and CW beam delivery. It is worth mentioning that since the bandpass measurement is a relative measurement of only the changes, it is much less sensitive to errors introduced by finite transverse beam size, radiation acceptance angle of the detector, and path difference due to dispersion. The monitor signal changes result from not only the bunch length changes but also the bunch shape in general.

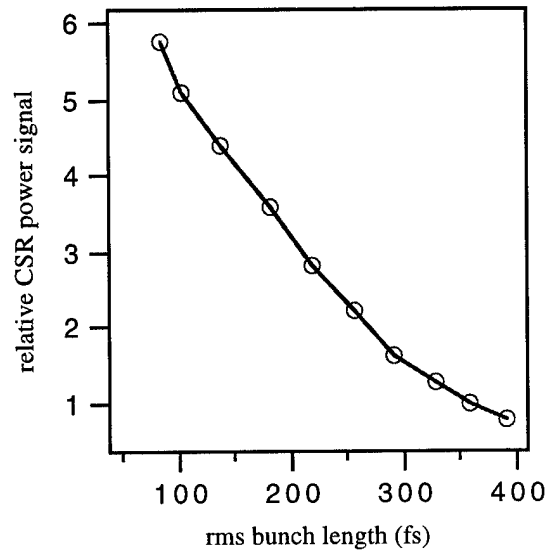

Fig. 3 Experiment result of CSR power versus rms bunch length where CSR power was measured by the Schottky diode and bunch lengths were measured by the zero-phasing technique.

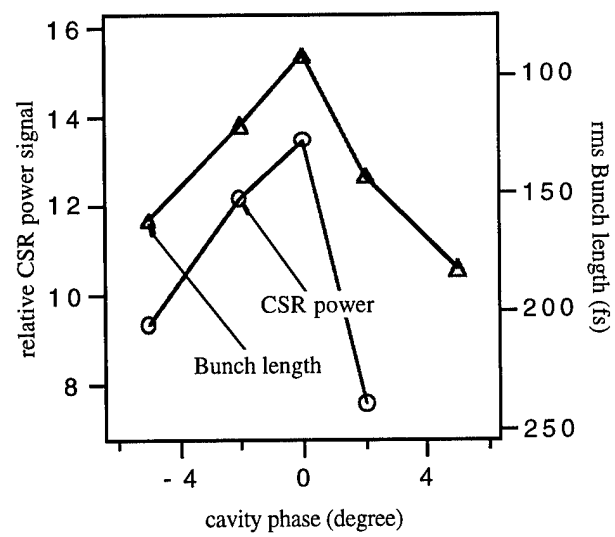

Fig. 4 Measurement results of CSR power and bunch lengths versus relative SRF phase changes. The maximum CSR power signal yields the shortest bunch length

The strategy for bunch length control at Jefferson Lab is: (1) use zero-phasing measurements as the primary standard to characterize the longitudinal beam dynamics and to calibrate the coherent synchrotron radiation monitor, assisted by PARMELA simulations as cross-checks; (2) use noninvasive monitoring to detect bunch length change during beam delivery, and when the

monitor signal varies outside of acceptable bounds indicating the bunch length has changed; (3) use a phase transfer function measurement to correct the RF phase drifts that have occurred [38].

From a single monitor signal, it is difficult to determine which RF phase has drifted among multiple RF bunching phases. However, a multi-frequency monitor, such as the one developed at Tohoku University, may be able to provide patterns or signatures to identify certain phase drifts [39]. One can also use either a multiple bandpass detector or a broadband detector plus rotation filters or gratings.

5 SUMMARY

Extensive work has been done to use coherent radiation as a tool to diagnose bunch shape and length. Many spectrum measurements have been carried out by various groups. Different techniques have been employed to derive the bunch distribution function from the measured spectrum, such as using cosine transformations, envelope matching, and the Kramers-Kronig relation. Due to the lack of phase information, a general procedure has not yet been established to obtain the actual bunch distribution and length. In order to advance the technique and to verify measurement results, it is essential and invaluable to employ an independent method, such as RF zero-phasing or a streak camera, just like every development of a new diagnostic technique. A well-tested particle simulation code can also provide very helpful insights on the bunching process and parameter dependence.

Despite difficulties in obtaining bunch shapes and lengths, bunch length monitors have been developed. They can be built with either bandpass detectors or broadband detectors plus frequency selection devices such as bandpass filters or gratings. These monitors are very sensitive to bunch length and longitudinal distribution variations. They are primarily used as diagnostic tools during beam delivery, rather than for beam characterization. To be useful, they need to be calibrated.

In short, the coherent radiation technique has not yet reached a stage at which it can be employed as the sole means of characterizing longitudinal distributions of short electron bunches. Therefore, it is essential to use an accurate longitudinal distribution measurement with the verification of simulations for characterizing bunching processes. Then, both bandpass and spectral measurements can be highly valuable in routine optimization of machine performance, in a noninvasive fashion if desired.

6 ACKNOWLEDGMENT

This work was supported by the U.S. DOE under contract number DE-AC05-84ER40150.

REFERENCES

[1] H. Winick, et al., NIM, A**347** (1994), 199.
[2] R. H. Siemann, Proc. of 1993 PAC Conf., 532.
[3] W. B. Mori, et at., AIP Conf. Proc. **335**, 112 (1994).
[4] T. Raubenheimer, et al., Proc. of 1993 PAC Conf., 635.
[5] P. Kung, et al., Phys. Rev. Lett. **73**, 967 (1994).
[6] B. Carlsten, AIP Conf. Proc. **367**, 21 (1995).
[7] G. A. Krafft, AIP Conf. Proc. **367**, 46 (1995).
[8] A. H. Lumpkin, AIP Conf. **367**, 327 (1995).
[9] L. Rivkin et al., Proc. of 1st EPAC (1988), 634.
[10] J. Seeman et al., Proc. of 1988 LINAC Conf., 441.
[11] K. Bane et al., Proc. of 2nd EPAC (1990), 1762.
[12] D. X. Wang, et al. "Measuring Longitudinal Distribution and Bunch Length of Femtosecond Bunches with RF Zero-phasing Method", these proceedings.
[13] J. S. Nodvick, et al., Phys. Rev. **96**, 180 (1954).
[14] F. C. Michel, Phys. Rev. Lett. **48**, 580 (1982).
[15] T. Nakazato, et al.., Phys. Rev. Lett. **63**, 1245 (1989).
[16] U. Happek, et al., Phys. Rev. Lett., **67**, 2962 (1991).
[17] Y. Shibata, et al., Phys. Rev. **A44**, R3449 (1991).
[18] Y. Shibata, et al., Phys. Rev. E52, 6787 (1995).
[19] Y. Shibata, et al., AIP Conf. **367**, 473 (1995).
[20] C. J. Hirschmugl, et al., Phys. Rev. **A 44**, 1316 (1991).
[21] M. F. Kimmitt, Far-Infrared Techniques, (Pion Limited, London, 1970).
[22] T. W. Crowe, et al., Proc. IEEE, **80**, 11 (1992).
[23] W. Peatman, et al., Int. J. of Infrared and Millimeter Waves, **11** (3), 355 (1990).
[24] P. Wood, PhD Thesis, University of Virginia (1994).
[25] D. X. Wang, et al., Appl. Phys. Lett. **70** (4), 529 (1997).
[26] D. Porterfield, et al., Appl. Optics, **33** (25), 6046 (1994).
[27] K. Ishi, et al., Phys. Rev. A**43**, 5597 (1991).
[28] Y. Shibata, et al., Phys. Rev. **A44**, R3445 (1991).
[29] Y. Shibata, et al., Phys. Rev. **A44**, R3445 (1991).
[30] Y. Shibata, et al., Phys. Rev. **E50**, 1479 (1994).
[31] H. C. Lihn, et al., Phys. Rev. **E53**, 6413 (1996).
[32] W. Barry, et al., Proc. of Workshop on Advanced Beam Instrumentation, KEK, Tsukuba, Japan (1991).
[33] V. Schlott, et al., Particle Accelerators, **52**, 45 (1996).
[34] R. Lai, et al., Phys. Rev. E **50**, 3342 (1994).
[35] R. Lai, et al., Phys. Rev. E **50**, 4294 (1994).
[36] R. Lai, et al., Phys. Rev. E **52**, 6787 (1995).
[37] D. X. Wang, Proc. of 1996 LINAC Conf., 303.
[38] G. A. Krafft, et al., Proc. of 1995 PAC Conf., 2601.
[39] T. Nakazato, et al., Proc. of 1994 LINAC Conf., 890.

A LASER-HETERODYNE BUNCH-LENGTH MONITOR FOR THE SLC INTERACTION POINT*

T. Kotseroglou, R. Alley, D. McCormick, S. Horton-Smith, K. Jobe,
P. Raimondi, M.C. Ross, T. Shintake ‡, F. Zimmermann
Stanford Linear Accelerator Center, Stanford University, CA 94309, USA
‡ *KEK, 1-1 Oho, Tsukuba-shi, Ibaraki-ken 305, Japan*

Abstract

Since 1996, the transverse beam sizes at the SLC interaction point (IP) can be determined with a 'laser wire', by detecting the rate of Compton-scattered photons as a function of the beam-laser separation in space. Nominal laser parameters are: 350 nm wavelength, 2 mJ energy per pulse, 40 Hz repetition rate, and 150 ps FWHM pulse length. The laser system is presently being modified to enable measurements of the longitudinal beam profile. For this purpose, two laser pulses of slightly different frequency are superimposed, which creates a travelling fringe pattern and, thereby, introduces a bunch-to-bunch variation of the Compton rate. The magnitude of this variation depends on the beat wavelength and on the Fourier transform of the longitudinal distribution. This laser heterodyne technique is implemented by adding a 1-km long optical fibre at the laser oscillator output, which produces a linearly chirped laser pulse with 4.5-A linewidth and 60-ps FWHM pulse length. Also, the pulse is amplified in a regenerative amplifier and tripled with two nonlinear crystals. Then a Michelson interferometer spatially overlaps two split chirped pulses, which are temporally shifted with respect to each other, generating a quasi-sinusoidal adjustable fringe pattern. This laser pulse is then transported to the Interaction Point.

1 INTRODUCTION

At the interaction-point (IP) of the Stanford Linear Collider (SLC), the bunch length has long been one of the least controlled beam parameters. Due to a variety of effects, the IP bunch length can easily vary between about 0.4 and 1.5 mm rms. For example, the bunch length is sensitive to changes of the linac rf phase due to bunch compression (or anticompression) in the collider arcs (the transport lines connecting linac and IP), to steering in the bunch compressor (RTL) and to longitudinal instabilities in the damping rings [3]. A diagnostic for monitoring the IP bunch length is desirable, since there is circumstantial evidence for a correlation of bunch length and luminosity, and since the predicted luminosity enhancement due to disruption [2] and the effect of longitudinal wake fields are both strongly bunch-length dependent.

One promising scheme to measure the bunch length utilizes the IP 'laser wire' [1]. So far the laser wire is being used only to determine the transverse single-beam sizes, which are inferred from the variation of the Compton-scattering rate as the electron or positron beams are moved across the laser beam. In this paper, we describe a modification of the laser system which will allow us to also measure the (average) longitudinal beam profile.

2 MEASUREMENT PRINCIPLE

The method of choice was first proposed in Ref. [4]: Two collinear laser pulses of slightly different frequency are superimposed to generate a non-stationary fringe pattern. For a sufficiently small beat frequency, the spacing between fringe maxima and minima is comparable to, or larger than, the bunch length. Assuming the phase between fringe pattern and beam is random, the Compton rate will vary from pulse to pulse. The depth of this variation, M, is proportional to the Fourier transform of the longitudinal profile $f(t)$ [4]:

$$M \equiv \frac{N_{\gamma,\max} - N_{\gamma,\min}}{N_{\gamma,\max} + N_{\gamma,\min}} = \frac{F_\omega}{F_0} \qquad (1)$$

where $F_0 = \int_{-\infty}^{\infty} f(t)\, dt$, $N_{\gamma,\max\,(\min)}$ the maximum (minimum) Compton signal, and

$$F_\omega^2 = \left(\int f(t)\cos\omega_b t\, dt\right)^2 + \left(\int f(t)\sin\omega_b t\, dt\right)^2 \qquad (2)$$

and $\omega_b = \omega_1 - \omega_2 = \omega/\lambda\ (\Delta\lambda)$. Here ω_1, ω_2 are the frequencies of the two overlaping laser pulses, while λ the average wavelength and $(\Delta\lambda)$ the difference in wavelength between the two pulses. By measuring the variation depth M at different beat frequencies ω_b, the entire Fourier transform of the bunch spectrum can be obtained. Ref. [4] also introduces a dilution factor caused by the finite transverse sizes of electron and laser beams. Due to the smallness of the SLC IP beam sizes, this factor is not relevant for our application here.

3 LASER SYSTEM

The first stage of the existing laser is a mode-locked Nd:YLF oscillator, that produces 150 ps pulses, with 2 nJ of energy at 119 MHz repetition rate and is phase locked to the accelerator rf frequency. Subsequently, some of these laser pulses are amplified in a Nd:YLF regenerative amplifier (RA), where in approximately 10 roundtrips they reach an energy of 9 mJ, each at a repetition rate of 40 Hz. In order to achieve the smaller possible laser spot size in the IP, the laser pulse frequency is tripled using a doubling CD^*A and a tripling KD^*P crystal. Laser parameters are: $\lambda = 350$ nm, 150 ps FWHM, 2 mJ pulse energy,

* Work supported by the U.S. Department of Energy under contract DE-AC03-76SF00515.

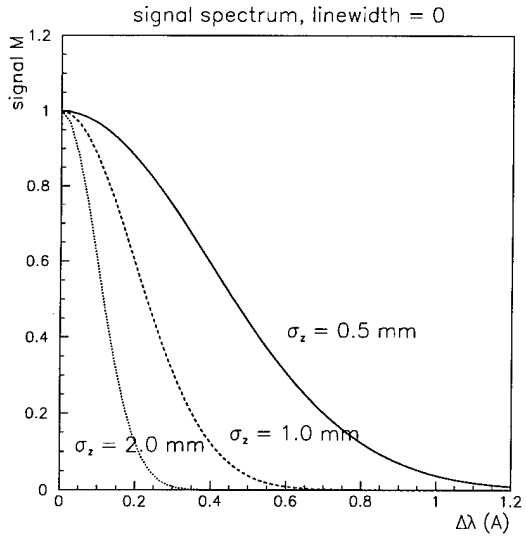

Figure 1: Modulation depth for Gaussian bunches of different rms bunch lengths versus wavelength difference $\Delta\lambda$.

and 40 Hz repetition rate [1]. The system is converted into a bunch-length monitor by adding a 1-km long optical fiber between oscillator and RA, and a Michelson interferometer after the harmonic generation, while also taking into account the effect of gain narrowing in the RA and of the nonlinear crystals on the bandwidth of the laser pulse [5]. A rough schematic of the original and upgraded laser systems is shown in Fig. 2

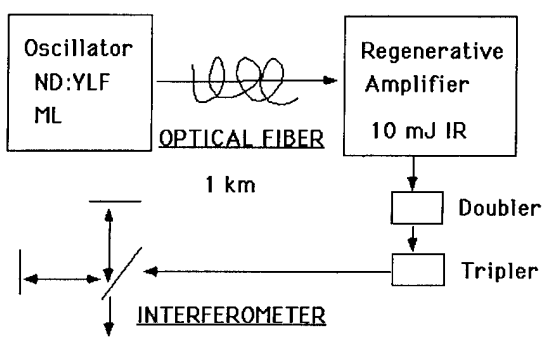

Figure 2: Schematic of the SLC IP laser system; elements added for the heterodyne bunch-length monitor are shown underlined.

The initial laser pulse produced by the mode-locked oscillator is 150 ps long and has a linewidth of 0.1 A. Self-phase modulation (SPM) in the optical fiber increases the linewidth to about 4.5 A and group-velocity dispersion (GVD) lengthens the pulse to 210 ps. The intensity of the input and output pulses in the fiber and the chirping introduced on the output pulse is shown in Fig. 3.

In the RA, the length of this 'chirped' pulse is reduced to 60 ps and the linewidth is decreased to about 3.5 A, due to 'gain-narrowing' as shown in Fig. 4.

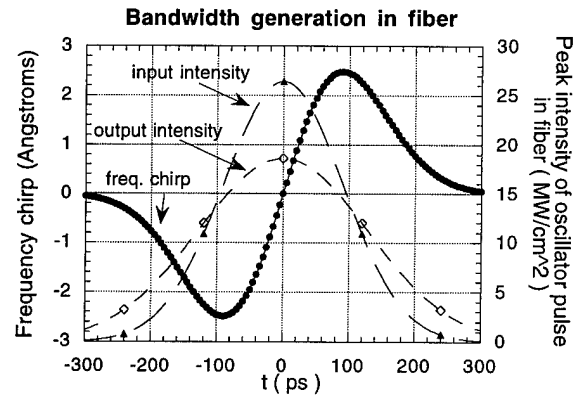

Figure 3: Intensity of input and output laser pulse and chirping introduced on the output pulse due to SPM and GVD from the fiber.

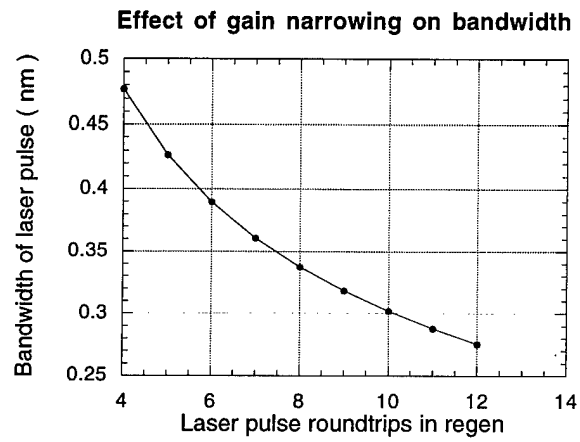

Figure 4: Effect of the amplification process in the regenerative amplifier (RA) on the bandwidth of the oscillator laser pulse as a function of the number of roundtrips in the RA.

In the frequency doubler and tripler, the linewidth increases again, by about a factor $\sqrt{2}$. Finally, the electric field of the pulse that enters the Michelson interferometer is

$$E(t) \approx \hat{E}_0\, e^{-\alpha_0 t^2} e^{i(\omega_0 t + b t^2)} \tag{3}$$

with $\alpha_0 \approx 3.85 \times 10^{20}\ \mathrm{s}^{-1}$, $\omega_0 \approx 5.39 \times 10^{15}\ \mathrm{s}^{-1}$, and $b_0 \approx 5.8 \times 10^{22}\ \mathrm{s}^{-1}$. If the path length in the two interferometer arms is different, there is a time delay $\Delta t = 2\Delta x/c$ between the two split light pulses ($2\Delta x$ is the pathlength difference, controlled by a movable mirror), and the intensity of the final recombined pulse is

$$\begin{aligned} I(t) &= I_0 \left(e^{-2\alpha_0 t^2} + e^{-2\alpha_0 (t+\Delta t)^2} + \right. \\ &+ \left. 2 e^{-2\alpha_0 (t+\Delta t) t} \cos(b_0 2 t \Delta t) \right) / 4 \end{aligned} \tag{4}$$

which represents a quasi-sinusoidal fringe pattern with an effective wavelength difference of $\Delta\lambda = \lambda^2 2 b_0 (\Delta x)/(\pi c^2)$; I_0 is the peak intensity of

the original pulse. As an example, $\Delta x = 0.9$ mm corresponds to $\Delta\lambda = 0.5$ A. Figure 5 shows an exemplary fringe pattern according to Eq. (4).

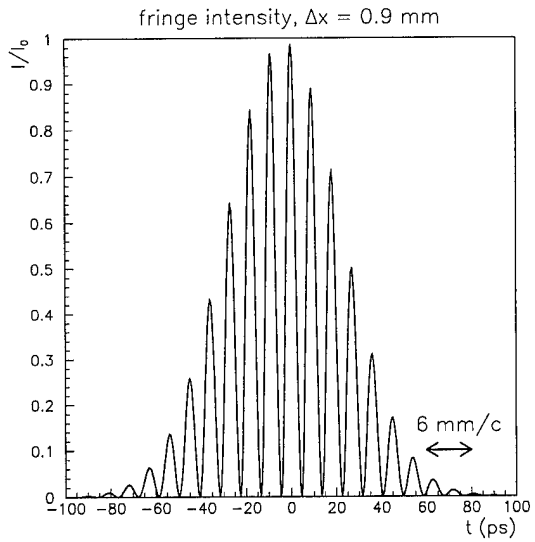

Figure 5: Intensity fringe pattern for a mirror displacement Δx ~0.9 mm.

The fringe pattern will be monitored by converting the laser beat wave into infrared (IR) radiation using a photoconducting GaAs antenna. This radiation in turn is characterized with a (second) Michelson interferometer operating in the IR, that is followed by a Si-based bolometer [6, 7].

4 RESOLUTION

For SLC bunch lengths, highest sensitivity is achieved when the wavelength difference $\Delta\lambda$ is chosen as about 0.3 A (see Fig. 1). For this value of $\Delta\lambda$ and assuming $\sigma_z \approx 1$ mm, the relative change of the signal M is approximately equal to that of the bunch length: $\Delta M/M \approx \Delta\sigma_z/\sigma_z$.

Several effects determine the achievable bunch-length resolution.

- Beam-orbit jitter: the horizontal beam orbit varies randomly by about $0.3\sigma_x$, from pulse to pulse. For a horizontal collision offset of Δx, the signal M decreases roughly as $\exp(-(\Delta x)^2/(4\sigma_x)^2)$, if the laser-beam diameter approximately equals that of the particle beam. Hence, a $0.3\sigma_x$ orbit variation changes the signal by about 2%.

- Laser-intensity imbalance: denoting the intensity ratio of the two split pulses by x, the maximum signal M is given by $2x/(x^2+1)$. If the imbalance $(1-x)$ is smaller than 10%, the resulting error of the measurement will be less than 1%.

- Laser-intensity variation: pulse-to-pulse variation of the laser intensity, which should be smaller than 5%, introduces a measurement error of similar magnitude.

During the last SLC run, a larger IP beam-orbit variation than that quoted above was observed over a time period of a few minutes. The reason was that the IP beam-orbit feedback is not active when one of the colliding beams is dumped while measuring the size of the other. This problem can be avoided by intermittently reestablishing the collisions, between laser-wire scans.

In conclusion, we expect to measure the bunch length and bunch profile with a relative accuracy better than 10%.

5 OUTLOOK

The laser-heterodyne bunch-length monitor at the SLC interaction point will be commissioned in the summer of 1997. The monitor is expected to prove a valuable diagnostic tool for SLC operation. Specifically, it should facilitate linac RF phasing and RTL tuning, support studies of final-focus wakefields and disruption luminosity enhancement, and be used as a calibration for a multi-channel RF bunch-length monitor which has recently been installed in the SLC South Final Focus [8].

6 REFERENCES

[1] M.C. Ross et al., "A High Performance Spot Size Monitor", Proceedings, International Linear Accelerator Conference, Geneva, Switzerland, July 1996.

[2] P. Chen and K. Yokoya, Lecture at 1990 US-CERN School on Particle Accelerators, Hilton Head Isl., So. Carolina, Nov 7-14, 1990.

[3] K. Bane et al., Proc. of IEEE PAC95 Dallas, p. 3109 (1995).

[4] T. Shintake, "Beam-Profile Monitors for Very Small Transverse and Longitudinal Dimensions using Laser Interferometer and Heterodyne Techniques", *Invited Talk at 1996 Beam Instrumentation Workshop, ANL, Argonne*, KEK 96-81 (1996).

[5] A.E. Siegman, "Lasers", University Science Books (1986).

[6] A.W. Weling, B.B. Hu, N.M. Froberg, D.H. Auston, "Generation of Tunable Narrow-Band Free-Space Terahertz Radiation", Springer Series in Chem. Physics, Vol. 60, p. 405 (1994).

[7] B.I. Greene, J.F. Federici, D.R. Dykaar, "Interferometric characterization of 160 fs far-infrared light pulses", Appl. Phys. Lett. 59 (8) p. 893 (1991).

[8] F. Zimmermann et al., "An RF Bunch-Length Monitor for the SLC Final Focus", these proceedings (1997).

LASER BASED SUB-PICOSECOND ELECTRON BUNCH CHARACTERIZATION USING 90° THOMSON SCATTERING*

W. P. Leemans, P. Volfbeyn, M. Zolotorev, K-J. Kim, S. Chattopadhyay, R. W. Schoenlein, A.H. Chin, T.E. Glover, P. Balling, and C. V. Shank, LBL, Berkeley, CA 94720 USA

X-rays produced by 90° Thomson scattering of a femtosecond, near infrared, terawatt laser pulse off a 50 MeV electron beam are shown to be an effective diagnostic to measure transverse and longitudinal density distributions of an electron beam (e-beam) with subpicosecond time resolution. The laser beam was focused onto the e-beam waist, generating 30 keV x-rays in the forward direction. The transverse and longitudinal e-beam structure have been obtained by measuring the intensity of the x-ray beam, while scanning the laser beam across the e-beam in space and time. The e-beam divergence has been obtained through measurement of spatial and spectral characteristics of the scattered x-ray beam.

1 INTRODUCTION

Measurement of the transverse and longitudinal phase space properties of electron bunches produced with high performance linear accelerators, requires development of beam diagnostics with high spatial (micron or sub-micron) and temporal (femtosecond) resolution requirements. A laser based beam diagnostic [1] has been developed and used at the Beam Test Facility (BTF) [2] of the Center for Beam Physics at Lawrence Berkeley National Laboratory (LBNL).

2 EXPERIMENT

A. Electron Transport Line and Laser Beam Parameters

The experiment[1,3] was conducted at the BTF and used the linear accelerator (linac) injector of the Advanced Light Source in conjunction with a terawatt short pulse laser system. The lay-out of the experiment is shown in Fig. 1.

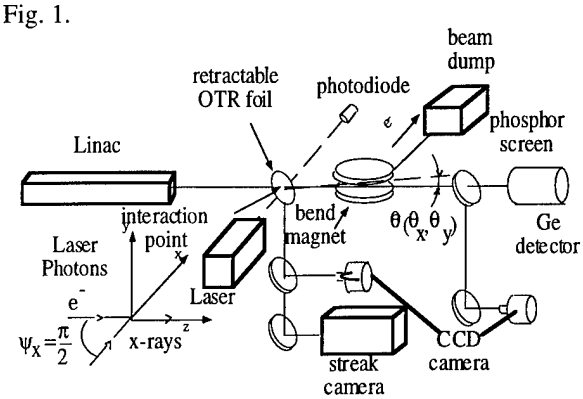

Figure 1: Lay-out of the laser probe experiment.

Electron bunches were transported using bend magnets and quadrupoles to an interaction chamber where they were focused and scattered against the laser beam. After the interaction chamber, a 60° bend magnet deflected the electron beam onto a beam dump, away from the forward scattered x-rays. The measured electron beam parameters are given in Table 1.

Maximum Energy	50 MeV
Charge	1.3 -1 .5 nC/bunch
Bunch Length (σ_z)	10-15 ps
Emittance rms (unnorm)	0.3 mm-mrad
# bunches/macropulse @ 125 MHz	1 - 10 (max 100)
Macropulse rep. rate	1 - 5 Hz

Table 1: ALS Linac parameters

The terawatt laser system, with center wavelength at 800 nm, was based on chirped pulse amplification in Ti:Al_2O_3 [4]. The laser system parameters are shown in Table 2. A 75 cm radius of curvature mirror was used to focus the S-polarized amplified laser pulses to about a 30 μm diameter spot at the IP (measured by a charge coupled device (CCD) camera at an equivalent image plane outside the vacuum chamber).

Wavelength	0.8 μm
Energy/pulse	50 mJ
Pulse length	50 - 200 fs
Repetition rate	10 Hz
Timing jitter with e-beam	< 2 ps

Table 2: Laser system parameters

To measure the spot size (and position) of the electron beam at the interaction point (IP), an image of the electron beam was obtained by relaying optical transition radiation (OTR) [5] from a foil onto a 16 bit CCD camera or optical streak camera using a small f-number telescope. Electron beam spot sizes as small as 35 μm rms have been measured.

Synchronization between the laser oscillator and linac was accomplished by using a phase-locked loop which dynamically adjusts the oscillator cavity length [6]. Timing jitter measurements (using a streak camera with an instrument response of 1.5 - 2 ps) which simultaneously detected a laser pulse and OTR from the electron bunch indicated an rms jitter of 1-2 ps.

During the interaction of an electron beam and laser beam, scattered x-ray photons are produced with energy U_x, given by (for $\gamma >> 1$)

$$U_x = \frac{2\gamma^2 \hbar\omega_0}{1+\gamma^2\theta^2}(1-\cos\psi) \qquad (1),$$

where ω_0 is the frequency of the incident photons, ψ is the interaction angle between the electron and laser beam ($\psi=\pi/2$ in our experiments) , and θ is the angle at which the radiation is observed and assumed to satisfy $\theta << 1$ (see Fig. 1). When the 50 MeV electron beam ($\gamma = 98$) collides at 90° with the laser pulse (center wavelength =

* This work was supported by DOE under contract No. DE-AC03-76SF00098.

800 nm), x-rays with a maximum energy of 30 keV (0.4 Å) are generated. The x-ray beam parameters are shown in Table 3.

Wavelength (Å)	0.4
Pulse length (fs)	200
# photons (10 % bandwidth)	1×10^5
Full angle cone (mrad)	10
Bandwidth (%)	10-15%

Table 3: x-ray source parameters.

B. Electron beam characterization

To measure the transverse electron beam distribution for a given slice of the electron beam, we scanned the laser beam transversely across the electron beam in steps of 10 μm, by changing the tilt of the focusing mirror. and monitored the x-ray yield on the phosphor screen. It was found (Fig. 2) that the laser based technique and the results from OTR were in good agreement and give a half-width half maximum (HWHM) vertical size of 66 μm. However, whereas the beam core overlaps, the tails are different and both non-Gaussian. From the OTR data an HWHM horizontal size of 47 μm was obtained.

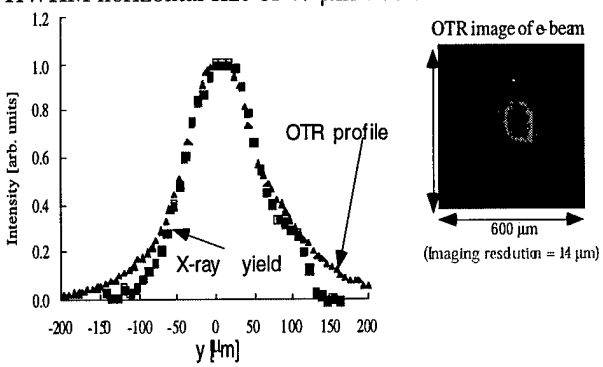

Figure 2: a) OTR image of the focused electron beam and b) s (triangle) - vertical line-profile through the OTR image of the electron beam; ˛ (square)- x-ray yield vs. vertical laser beam position.

Measurement of the electron beam divergence for a fixed longitudinal location (i.e. fixed delay time between the laser and electron beam) of a time slice of the electron beam, with a duration equal to the convolution of the transit time of the laser pulse and the laser pulse duration, was done by monitoring the spatial x-ray beam profile on the phosphor screen using the CCD camera (see Fig.(3)). The scattered x-ray energy flux contains information of the angular distribution of the electron beam. By convoluting the single electron spectrum [7] with a Gaussian distribution for the horizontal and vertical angles ($\sigma_{\theta x}$ and $\sigma_{\theta y}$ are the rms. widths of the angular distribution of the electron beam in the horizontal and vertical direction respectively) and integrating over all energies and solid angle[1] the energy flux can be written as:

$$\frac{dP}{d\theta_x d\theta_y} \propto \int_0^{2\pi} d\phi \int_0^1 d\kappa F(\kappa)\kappa\left[1-4\kappa(1-\kappa)\cos^2\phi\right] \exp\left[-\frac{(\theta_x-\gamma^{-1}\sqrt{\frac{1}{\kappa}-1}\cos\phi)^2}{2\sigma_{\theta x}^2}\right] \exp\left[-\frac{(\theta_y+\gamma^{-1}\sqrt{\frac{1}{\kappa}-1}\sin\phi)^2}{2\sigma_{\theta y}^2}\right] \quad (2).$$

Here dP is the radiated x-rays intensity in a solid angle $d\theta_x d\theta_y$, ϕ is the azimuthal angle and $F(\kappa)$ is an x-ray energy dependent function which takes into account overall detector sensitivity and x-ray vacuum window transmission, $\kappa = U/U_{max} = (1+\gamma^2\theta^2)^{-1}$ with $U_{max} = 2\gamma^2\hbar\omega$ and we have assumed a single incident laser frequency.

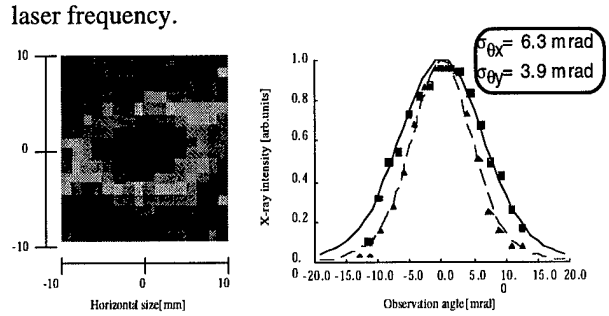

Figure 3. a) False color CCD image of the spatial profile of a 30 keV x-ray pulse on the phosphor screen, which is located 80 cm from the IP; b) ˛ (square)- horizontal line-profile and fitting curve (solid line), s (triangle) -vertical line-profile and fitting curve (dashed line) from Fig. 3 (a). The scale has been converted into angular units.

By fitting the data (see Fig. 3) using Eq.(2), an electron beam divergence of $\sigma_{\theta x}$ ($\sigma_{\theta y}$) = 6.3 ± 0.2 (3.9 ± 0.2) mrad was found. $F(\kappa)$ was adjusted to account for the spectral dependence of the x-ray window transmission. The difference between $\sigma_{\theta x}$ and $\sigma_{\theta y}$, is due to a combination of, the electron beam being focused astigmatically at the IP, resulting in a tilted phase space ellipse (y, y′), and a laser spot size much smaller than the vertical electron beam size. As the laser beam crosses the focal volume of the electron beam, the complete horizontal (direction of propagation of the laser) phase space (x, x′) is sampled by the laser beam. However, only electrons occupying the region in the vertical phase space defined by the spatial overlap with the laser beam will contribute to the x-ray flux. As opposed to the transition radiation based detector, the laser beam therefore acts as an optical microprobe of a finite region of the transverse phase space. This value of the electron beam divergence is also consistent with an effective angular divergence of the electron beam of 3.5 - 4 mrad obtained from analyzing the x-ray spectra. Of course, the main difference is that measurement of the spatial profile is a single shot technique as opposed to measuring the x-ray spectra which requires accumulation of thousands of shots.

The spot size measurements and beam divergence measurements imply a horizontal geometric slice emittance $\sigma_x \sigma_{\theta x}$ for the electron beam of 0.25±0.03 mm-mrad. A linac beam emittance of 0.32±0.02 mm-mrad was measured using a quadrupole scan technique [8], which is in reasonable agreement with the x-ray slice measurements.

Finally, since the x-ray yield is sensitive to both the longitudinal bunch profile and the degree of transverse overlap between the laser and electron beam, time-correlated phase space properties of the electron beam can be studied. When an electron bunch, which exhibits a finite time-correlated energy spread (chirp), is focused at the IP with a magnetic lattice which has large chromatic aberrations, different temporal slices of the bunch will be focused at different longitudinal locations. The transverse overlap between e-beam and laser will therefore strongly depend on which time slice the laser interacts with. This in turn will lead to a time dependence of the x-ray yield varying faster than the actual longitudinal charge distribution. To illustrate this, the x-ray flux was measured as a function of the delay between laser and e-beam, for two different magnetic transport lattices. In both lattices, the magnet settings were optimized to obtain a minimum electron beam spot size in the horizontal and vertical plane (as well as zero dispersion at the IP), but chromatic aberrations were about 5 times larger in the second lattice. Result of a 60 ps long scan (time step of 1 ps) and time-resolved OTR from the streak camera for the lattice with low and high chromatic aberrations is shown in Fig. 4(a, b).

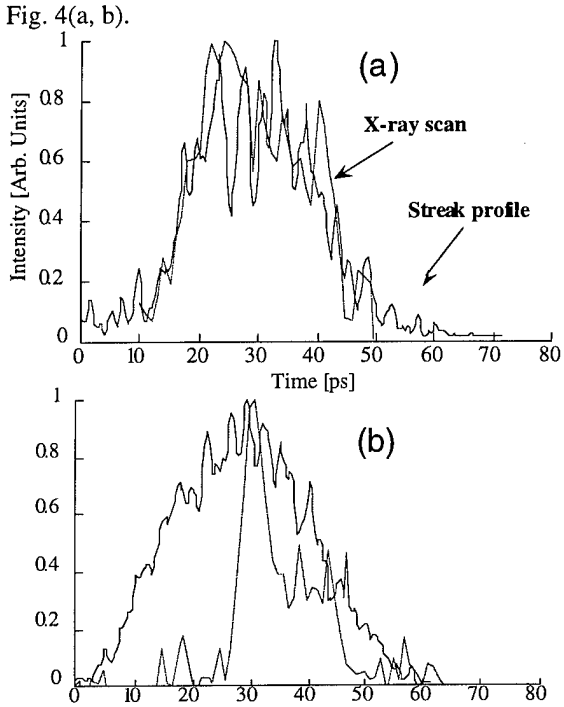

Figure 4: x-ray yield vs. delay time between laser and electron beam and profile of time resolved OTR image from a streak camera for a lattice with a) small and b) large chromatic aberrations.

Whereas the temporal scan for the lattice with low chromatic aberrations (Fig.4a) is in good agreement with the time-resolved OTR measured with a visible streak camera, the scans taken for the second configuration (Fig.4b) typically showed a 2-3 times larger amplitude 5 ps wide peak sitting on a 20 ps wide pedestal. This is to be compared to the time resolved OTR from the streak camera which typically showed a 25-30 ps wide electron beam without any sharp time structure. Lattice calculations for our experiment with MAD [9] indicated that an energy change of 0.25 % would increase the vertical spot size by a factor two at the IP, compared to best focus, resulting in a proportional reduction in vertical overlap between the laser and electron beam, and hence in x-ray yield. The measurements indicate the potential of the laser based Thomson diagnostic to measure time-correlated energy changes of less than a percent, with sub-picosecond time resolution.

3 SUMMARY

Laser based probing of electron beams has been used for measurement of longitudinal and transverse bunch distributions of picosecond and sub-picosecond slices. From a study of x-ray beam images and total flux, the transverse electron beam phase space distribution of essentially a 300 fs slice of the electron beam was obtained. By scanning the laser beam in time along the electron bunch, not only the longitudinal density distribution was measured, but it was also found that the Thomson scattering technique can become a powerful and sensitive tool to measure detailed longitudinal phase space properties. The main limitation on the slice duration arose from the finite transit time of the laser pulse across the electron beam. Shorter slices and higher photon yields are expected when using RF photocathode guns which produce beams with normalized emittance on the order of a few π mm-mrad. Synchronization jitter between the laser and the linac were experimentally found to be on the order of a picosecond. The laser based method is best suited for photocathode driven RF guns, where lower jitter between laser and electron beam is expected.

4 ACKNOWLEDGEMENTS

The authors wish to thank the ALS personnel for their help in the operation of the BTF, in particular Terry Byrne. We would also like to thank Leon Archambault and Jim Dougherty for engineering and technical support.

5 REFERENCES

[1] W.P. Leemans et al., Phys. Rev. Lett.**77**, pp. 4182 (1996).
[2] W. P. Leemans et al., Proc. 1993 Part. Accel. Conf, 83 (1993).
[3] R.W. Schoenlein et al., Science **274**, pp.236-238(1996)
[4] D. Strickland and G. Mourou, Opt. Comm. **56**, 219 (1985); C. LeBlanc, et al., Opt. Lett. **18**, 140 (1993).
[5]L. Wartski, J. Marcou and S. Roland, IEEE Trans. in Nucl. Science, vol. 20, pp. 544 (1973).
[6]M.J.W. Rodwell, D.M. bloom, K.J. Weingarten, IEEE J. Quant. Electron. **25**, 817 (1989).
[7] K.- J. Kim, S. Chattopadhyay and C.V. Shank., NIMA 341, 351 (1994).
[8] J. Bengtson, W. Leemans, and T. Byrne, Proc. 1993 Particle Accelerator Conf., pp. 567(1993).
[9] H. Groter and F. Iselin, "The MAD program", CERN/SL/90-13 (1993).

SYNCHROTRON RADIATION INTERFERENCES BETWEEN SMALL DIPOLES AT LEP

C. Bovet, A. Burns, F. Méot*, M. Placidi, E. Rossa, J. de Vries

CERN, Geneva, Switzerland.

Abstract

Synchrotron Radiation interferences between small dipoles in the very low (visible) frequency range have been studied at the LEP diagnostic mini-wiggler. Their understanding allowed a substantial brightness gain by adequate layout modifications. The phenomenon is described analytically in terms of time coherence effects. This serves as a basis for further detailed numerical simulations of the experiment by means of stepwise ray-tracing, and allows precise interpretation of the spectral, polarization and intensity measurements collected at LEP. It also provides guidelines for SR diagnostic at injection energy in LHC.

1 INTRODUCTION

Two identical devices (**mini-wigglers**) [1] provide dedicated SR for transverse and longitudinal bunch profile measurements on e^+ and e^- beams in LEP with a streak camera sensitive in the near-UV to visible range [2]. They are located at $\sim$ 67 m on either side of IP1 where the light beams are extracted by plane mirrors.

A first configuration exploited until 1993 (Fig. 1) involved a $\sim$ 3 m long localised closed orbit bump. It was subject to harmful multiple image formation and interference effects which received theoretical interpretation [3]. This led to the design of a new configuration (Fig.2) now operational and compatible with bunch train operation at LEP2 energies [4].

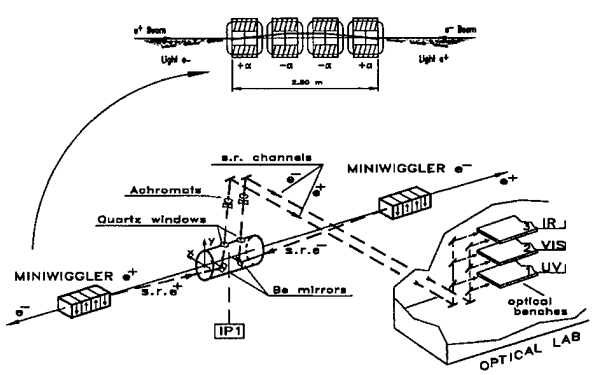

Figure 1: The first mini-wiggler set-up in the LSS1 LEP straight section. e^+e^- synchrotron light beams extracted at IP1 are focused in the optical laboratory.

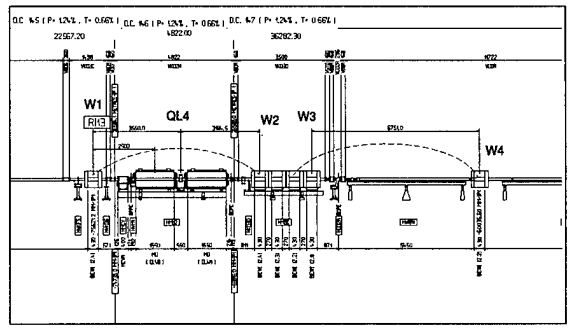

Figure 2: The new mini-wiggler layout at the left side of IP1 for diagnostics on the e^+ beam. The closed orbit bump now extends over 15.6 m from W1 to W4. A similar set up is installed symmetrically to IP1 for the e^- beam. SR sources from both dipoles W3 and W4, now 6.75 m away, fall within the acceptance of the imaging optics (Fig. 1) which focuses on W4 and the effect of W3 is reduced to $\simeq$ 10% parasitic blurring while W1, W2 are not seen.

2 EXPERIMENTAL RESULTS

The first comparative measurements between the original mini-wiggler set-up and a configuration where the SR emission from a single dipole could be observed were performed in 1993 [5]. In the former case the light intensity was comparable to that from the parasitic sources (e.g. the quadrupole QL4) while in the latter case about 2 orders of magnitude intensity were gained (Fig. 3). This result suggested that the interference effects could be cured on the basis of the theoretical investigations [3]. Experiments have been performed using this new configuration the main results can be summarised as follows.

The intensity from the W3–W4 pair agreed, well with SR froma single dipole confirming the remaining factor of $\sim$ 2 in the interference intensity loss predicted from the numerical simulations for the case of a pair of dipoles 6 m apart. It is worth to mention that following the improvements in the production of visible light a series of accelerator physics experiments requiring the use of the streak camera were performed with a very low current (4μA single bunch).

Intensity measurements as a function of the deflection α in W3 and W4 were performed making use of polarising filters to separate the σ- and the π-components of the radiation (Table 1) [6]. The two vertical lobes of the π-component were clearly observed on a screen positioned slightly out of focus. This method was adopted to precisely determine the longitudinal position of the image plane defined by the superposition of the two π-lobes.

* BD/Physics, FNAL, Batavia, IL, USA. On leave from CEA/DSM, Saclay, France

0-7803-4376-X/98 /$10.00 © 1998 IEEE

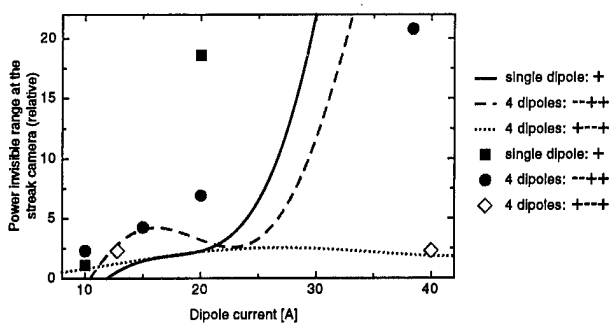

Figure 3: Comparison of the experimental data [4,5] with numerical simulations (continuous curves [3]) performed in 1993 and 1994. The radiated power at the streak camera is shown as a function of the dipole excitation for two different 4-dipole configurations and for the single-dipole case. The + and − are deflection signs in the dipoles W1-W4 juxtaposed as in Fig. 1. Note a remarkable result in the +− − + configuration: due to the interference, the SR intensity stays constant within the 10–40A current range.

Table 1: Integrated (relative) intensities of the light spots at the image plane. (Beam energy $E = 20$ GeV). In the case of the images corresponding to 40A excitation it was possible to measure the W4 and W3 light spots separately. The integrals obtained for the other images correspond to a combination of the light from the 2 sources. These values compare fairly well with the theoretical predictions as shown on Fig. 5.

Source	I (A)	α (mrad)	Intensity in σ-	Intensity in π-	$\sigma+\pi$	$\frac{\sigma}{\sigma+\pi}$	$\frac{\pi}{\sigma+\pi}$
W3	40	1.40	0.80	0.13	0.93	0.86	0.14
W4	40	1.40	0.86	0.20	1.06	0.81	0.19
W3+W4	25	0.88	2.39	1.71	4.10	0.58	0.42
W3+W4	12	0.42	1.53	0.85	2.38	0.64	0.36

3 THEORETICAL INTERPRETATION

3.1 *Interference*

Numerical simulations of interference [3] by ray-tracing [7] in the first 4-dipole configurations (Fig. 1) are reported in Fig. 3. Interference consists of time coherence effects which can be summarized as follows. An electron traversing a pair of dipoles (for simplification) delivers a double electric field impulse (Fig. 4) which can be written

$$E(t) = e(t)\left[\delta\left(t - \frac{T}{2}\right) - \delta(t + \frac{T}{2})\right]$$

where $e(t)$ is the single dipole impulse, δ is the Dirac distribution, t is the observer time, $T = d(1 + \gamma^2\Psi^2 + K^2/2)/(2\gamma^2 c)$ is the time delay between the two impulses (γ= relativistic Lorentz factor, Ψ = observation angle, $K = \alpha\gamma$, c= light velocity, d=magnet separation).

The squared Fourier transform of $E(t)$ is homogeneous to the SR brightness at the observer and is written

$$|\tilde{E}(\omega)|^2 = 4\sin^2\frac{\omega T}{2}|\tilde{e}(\omega)|^2$$

where $|\tilde{e}(\omega)|^2$ describes the brightness due to one dipole, homogeneous to the $K_{1/3}$ or $K_{2/3}$ Bessel functions in regular SR. For dipoles which are $d \simeq$ metres apart (Fig. 2), and $\omega \simeq 0.5$ eV (visible light, left end of the spectrum in Fig. 4), one gets $\omega T/2 \ll 1$ and the attenuation due to the interference amounts to $\sin^2(\omega T/2) \simeq (\omega T/2)^2$.

Pulling the two dipoles 6.75 m apart (W3–W4 in Fig. 2) leads to an increase in $\sin^2(\omega T/2)$ by a factor $(6.75/0.76)^2 \simeq 80$, consistent with the measured intensity gain obtained by going from the first miniwiggler configuration to the second one.

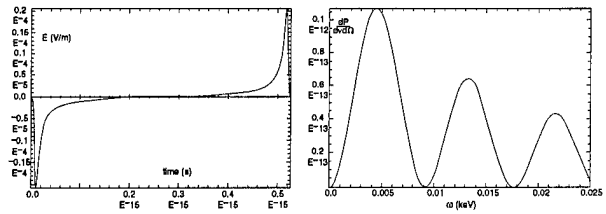

Figure 4: Double electric field impulse $E_\sigma(t)$ emitted by a 45GeV electron undergoing a $\alpha = 0.43$ mrad deflection in W3 and W4 d = 0.76 m apart, and the corresponding brightness $dP_\sigma/d\nu d\Omega$ (normalized to 1mA circulating beam current) in the direction $\varphi = \alpha/2$, $\Psi = 0$.

3.2 *Single dipole*

Figure 5 presents a comparison between intensity measurements in the new configuration (Fig. 2) and the theoretical predictions schemed in Fig. 6 which displays the shape of the σ- and π- components of the visible SR due an electron traversing a single dipole, as observed at the surface of the extraction mirrors at IP1 (Fig. 1).

It can be shown (Fig. 5 and Table 1) that the P_σ/P_π ratio varies strongly from one dipole excitation to another, but is very different from the usually assumed (2/3)/(1/3) ratio of the low frequency SR approximation [9]. It can be verified that $dP_\sigma/d\varphi$ is zero for $\varphi = \alpha$ (Fig. 6); this is due to $\int E_\sigma dt = 0$ for that particular direction of radiation [3].

An important feature of these simulations is that they involve the single SR source W4, thus neglecting any residual interference effects due to W3. Such interference would result in a distortion of the SR spectrum by a partial sine-modulation (Fig. 4) which in turn would translate into non-linear effects in Fig. 5, where the light power as a function of the dipole excitation is implicitely correlated to the overlapping of the two sources W3 and W4.

The intensity measurements do not prove the existence of such residual interference. Nevertheless the slight discrepancies between the measurements and the simulations (Fig. 5) might reveal it. This point would deserve deeper experimental and theoretical investigations. It might for instance explain the fringes that appear in the π-spot of the W3–W4 image observed at 12A [4].

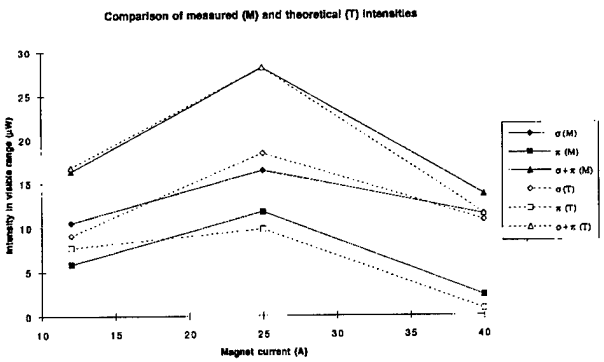

Figure 5: Comparison between the measured intensities (Table 1, M curves) and numerical simulations for a 20 GeV electron, normalised to 1 m A beam (T curves), in the 400–800 nm spectral range (data normalised to the calculated $\sigma + \pi$ intensity at 25A).

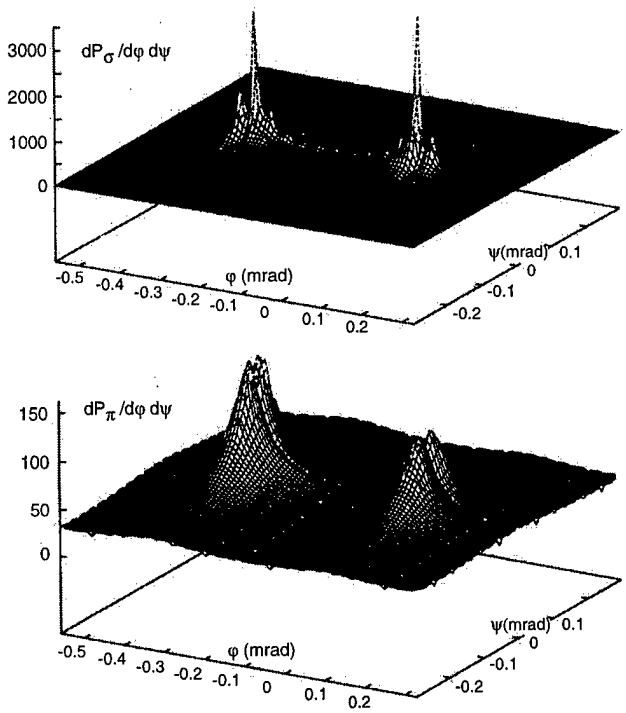

Figure 6: 3-D plot of the σ- and π-components of the visible light intensity (400–800 nm) from W4 ($\alpha = -0.43$ mrad), at large distance, obtained by ray-tracing of a single 20 GeV electron [7]. The transverse axes are the angles φ (horizontal) and ψ (vertical). The end intensity peaks are due to the edge radiation [3], [8]. It can be observed that $dP_\sigma/d\varphi d\psi \simeq 0$ at $\varphi = \alpha = -0.43$ mrad (upper plot).

As well, special properties apparent in Fig. 6 (such as $\int E_\sigma dt \neq 0$ at $\omega \simeq 0$, consistent with the concept of 'strange electromagnetic waves' as developped in Ref. [10]), deserve finer experimental investigation. The edge effect might explain the double spot shape of the π-image of W4 at 40A [4] namely the two spots corresponding to the two end peaks of W4 (Fig. 6). Works relevant with this issue have been accomplished recently [11].

4 CONCLUSIONS

A new configuration of the dedicated SR source (mini-wiggler) compatible with LEP2 energies and the bunch train scheme is now in operation. Pulling the last two dipoles 6.75 m apart considerably reduces the destructive interference and improves the light intensity by a factor of 30 compared to the previous configuration.

These experimental results confirm the theoretical investigations and provide a deeper insight into interference issue in connection with the emission of synchrotron radiation from small dipoles. This might be of particular importance for the optimisation of LHC beam diagnostics [12] where the same ray-tracing methods and codes are used to investigate the brightness of a short dipole in the spectral range beyond the critical energy.

5 REFERENCES

[1] C. Bovet, M. Placidi, A dedicated synchrotron radiation source for LEP beam diagnostics, LEP Note 532, CERN, 11/4/85.

[2] E. Rossa, F. Tecker, J.C. Mathae, Performance limits of a streak camera in real time three-dimensional measurement of bunch oscillation in LEP, Preprint of 1993 PAC, May 17–20, Washington, D.C.

[3] F. Méot, Synchrotron radiation interferences at the LEP mini-wiggler, CERN SL/94-22 (AP), CERN, 28/06/94.

[4] C. Bovet, A. Burns, F. Méot, M. Placidi, E. Rossa, I. de Vries, The new configuration of the synchrotron radiation service for beam diagnostics in LEP Report SL/BI, CERN, to be published.

[5] K. Hanke, Measurements of the bunch length of LEP with a streak camera and comparison with results from LEP experiments, CERN SL/Note 95–65 (BI), CERN, 13/06/95.

[6] A.J. Burns, Measurement of intensity of synchrotron light spots for different mini-wiggler currents, CERN SL/Note 96–53 (BI), CERN, 21/08/96.

[7] F. Méot and S. Valéro, ZGOUBI users' guide, Report LNS/GT/93–12, CEA, Saclay, 1993.

[8] O. Chubar, Measurement of effective electron beam emittance using edge radiation, Kurtchatov Institute, preprint AE–5698/14 (1994).

[9] A. Hofmann, Theory of synchrotron radiation, SLAC report, SSRL–ACD Note 38, Sept. 1986, p. 32.

[10] E.G. Bessonov, On a class of electromagnetic waves, Sov. Phys. JETP53(3), March 1981.

[11] C. Denise, Ph.D. Thesis, ESRF, Grenoble, (1997).

[12] J. Bosser, C. Bovet, R. Jung, LHC Note 192, CERN, 17/6/92.

ELECTRON BUNCH LENGTH DIAGNOSTIC WITH COHERENT SMITH-PURCELL RADIATION

D. C. Nguyen
MS H851, Los Alamos National Laboratory, Los Alamos, NM 87545

Abstract

We have designed a new technique for measuring subpicosecond electron bunch lengths using coherent Smith-Purcell radiation. This new diagnostic technique involves passing the electron beam in close proximity of a grating with period comparable to the electron bunch length. The emitted Smith-Purcell radiation will have a coherent component whose angular position and distribution are directly related to the electron bunch length and longitudinal profile, respectively. This new diagnostic technique is inherently simple, inexpensive and non-intercepting. We show that the new technique is also scaleable to femtosecond regime.

1 INTRODUCTION

Many advanced concepts such as the fourth generation light sources and plasma wakefield accelerators depend on the ability to generate a high-brightness electron beam with high peak current. The latter has been obtained via bunch compression in a magnetic chicane.[1] Equally important is the ability to characterize the longitudinal profile of the subpicosecond electron bunches. Streak cameras with sub-picosecond resolution are not only expensive and difficult to operate, they are not scaleable to the femtosecond regime. Alternative methods involve generating coherent transition radiation, coherent undulator radiation or coherent synchrotron radiation.[2] From the measured spectra or autocorrelation curves, information about the electron longitudinal profiles is deduced. In this paper, we discuss the use of coherent Smith-Purcell radiation as a technique for diagnosing electron bunch longitudinal profiles.

Smith-Purcell radiation (SPR) has been studied extensively in the past three decades, mainly as a means of generating short-wavelength radiation from low-energy electron beams.[3] Recently, Ishi et al. reported the first observation of coherent SPR from 50 picosecond electron bunches.[4] Independently, Lampel and Nguyen[5] came up with the idea of using coherent SPR as a diagnostic technique for subpicosecond electron bunches. They predicted the coherent SPR would appear at large angles with respect to the beam propagation, and its intensity would be much higher than the incoherent SPR. This paper explores the capabilities of coherent SPR in measuring femtosecond electron bunches and in detecting microscopic longitudinal density fluctuations.

The schematic of the beam diagnostic module for coherent SPR bunch length measurement is shown in Figure 1. The electron beam coming in from the left is focused to a ribbon beam with a vertical waist at the grating. A collimator is used to confine the beam to a well-defined height above the grating. Two mirrors, one cylindrical and one spherical, act like a 90° paraboloid and focus the coherent SPR to a spot at the detector located outside the diagnostic module. The coherent SPR signals at different angles, provided they are within the acceptance angle of the two curved mirrors, are focused to different positions at the focal plane. A detector array located at the focal plane of the curved mirrors is used to cover a range of observation angles at any given time. Alternatively, the two curved mirrors can be rotated together with the pivot at the grating to cover a larger range of angles.

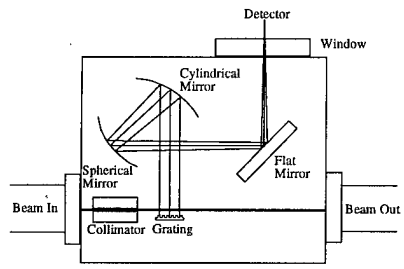

Figure 1. Schematic of the coherent Smith-Purcell radiation bunch length diagnostic module. The detector is at the focal plane of the two curved mirrors.

2 THEORY

When an electron beam passes close to the surface of a metallic diffraction grating, it emits Smith-Purcell radiation (SPR). The SPR wavelength depends on the angle of observation, as given by the well-known dispersion relation,

$$\lambda = \frac{d}{n\beta}(1 - \beta\cos\theta)$$

where d is the grating period, n is the diffraction order (in this paper, we will use n=1 order as the higher orders only shift the short-wavelength incoherent SPR to larger angles), β is the usual beam velocity normalized to the speed of light, and θ is the angle of the emitted SPR with respect to the beam propagation direction. When the electron bunch length is less than the SPR wavelength, the radiation emitted by different parts of the bunch add, and the resulting SPR becomes coherent, i.e. its power scales with N^2. Since long wavelengths occur at large angles, the degree of coherent enhancement increases with the angle of observation. The plot of SPR power versus angle thus exhibits high-intensity peaks at large

0-7803-4376-X/98 /$10.00 © 1998 IEEE

angles. If the electron profile has density modulations at high frequencies, we expect additional coherent SPR peaks to appear at smaller angles but at much higher intensity than the incoherent SPR.

The SPR angular distribution is given by

$$\frac{dP}{d\Omega} = KN(1 + f(k)N)\frac{\sin^2\theta}{(1-\beta\cos\theta)^3}e^{-\frac{2\pi h}{\gamma\lambda}}$$

where K is a proportionality constant that includes the electron charge, grating period, order, reflectivity, etc., N is the number of electrons in the bunch, θ is the azimuthal angle of observation, h is the height of the electron beam above the grating, and $f(k)$ is the form factor defined by the square of the Fourier transform of the longitudinal density function, $S(z)$

$$f(k) = \left|\int S(z)e^{-ikz\cos\theta}dz\right|^2$$

where $k = 2\pi/\lambda$.

Typical $S(z)$ functions like the gaussian and square distributions have been studied [5]. The corresponding form factors are gaussian and sinc square functions, respectively. Another longitudinal distribution of interest is that of electron beams exiting a wiggler in a free-electron laser (FEL). This distribution is expected to have modulations at the fundamental and odd harmonics of the FEL frequencies.

$$S(z) = \frac{e^{-z^2/2\sigma^2}}{\sigma\sqrt{2\pi}}\left(1 + \sum_{n=1}^{\infty} b_n e^{ink_0\sigma}\right)$$

where σ is the longitudinal rms bunch length. The corresponding form factor is obtained via Fourier transform of the above equation,

$$f(k) \approx e^{-k^2\sigma^2\cos^2\theta} + \sum_{n=1}^{\infty} b_n^2 e^{-(k-nk_0)^2\sigma^2}$$

where b_n is the bunching factor of the nth harmonic and k_0 is the modulation wavenumber. This expression suggests that with sufficient bunching, e.g. b_n approaching 1, there should be strong coherent SPR signals at the fundamental and odd harmonics of the modulation frequency.

3 CALCULATIONS

To evaluate the temporal resolution of the coherent SPR technique, we performed calculations for a 20-MeV electron beam with 3 different rms bunch lengths, e.g. 40, 60 and 80 microns, corresponding to approximately 120, 180 and 240 femtoseconds. The grating period is 0.8 mm and the beam is a one-dimensional line passing over the grating at a fixed height of 0.1 mm. The number of particles in a bunch is 10^8 (charge ~ 16 pC). The calculated SPR power versus angle is plotted in Fig. 2. As evidenced by these plots, the 60-fs change in the electron bunch length translates into an easily measurable 5° change in the peak location. The calculated coherent SPR angular distributions are, to a good approximation, independent of the electron beam height above the grating.

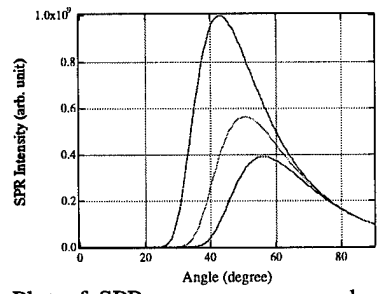

Figure 2. Plot of SPR power versus angle for different bunch lengths. The bunch lengths are 40, 60 and 80 microns from left to right.

Another feature of the coherent Smith-Purcell radiation is its ability to enhance the harmonics. The form factor of a square pulse is the square of a sinc function which contains many harmonics. As the radiation pattern shifts toward smaller angles at higher beam energy, the harmonics, occurring at small angles, are strongly enhanced in intensity. Consequently, the coherent SPR distribution of a square bunch changes drastically as the beam energy increases (Fig. 3).

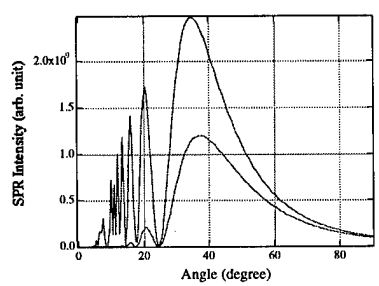

Figure 3. Dependence of coherent SPR pattern of a square pulse on beam energy. The top curve is for 100 MeV beam, the bottom 10 MeV.

Our last calculation involves a gaussian electron bunch with microscopic density modulations, such as those exiting an FEL. For this case, we use a 100-μm rms bunch length and a 30-μm modulation period. The bunching factor for the fundamental is 0.32 and the third harmonic is 0.1. The calculated SPR distribution exhibits, in addition to the coherent SPR of the bunch envelope, two narrow peaks at small angles corresponding to the fundamental and third harmonic, on top of the incoherent SPR background (Fig. 4).

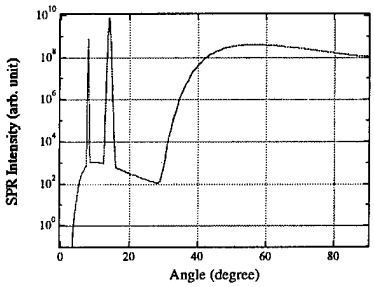

Figure 4. Semi-log plot of SPR power versus angle for an electron bunch with a 100-μm rms bunch length and 30-μm density modulations.

4 CONCLUSIONS

We have shown that coherent Smith-Purcell radiation is potentially a sensitive diagnostic technique for measuring sub-picosecond electron bunches. This new method is also capable of detecting microbunch structures, on the scale of microns (femtoseconds). The new diagnostic technique is simple to implement, does not require any spectrometer or interferometer, and can potentially be used as a non-intercepting, single bunch measurement.

5 ACKNOWLEDGMENTS

This work was conducted under the auspices of the US Department of Energy and supported by the Laboratory Directed Research and Development funds at LANL. The author thanks James Rosenzweig for helpful discussion.

REFERENCES

[1] B. E. Carlsten and S. J. Russell, *Phys. Rev. E.* **53**, R2072 (1996).
[2] H. Wiedemann, *Particle Accelerator Physics, Springer Verlag*, Heidelberg 1993; R. Lai, et al., *Phys. Rev. E.* **50**, R4294 (1994).
[3] G. Doucas, et al., *Phys. Rev. Lett.* **69**, 1761 (1992).
[4] K. Ishi, et al., *Phys. Rev. E.* **51**, R5212 (1995).
[5] M. C. Lampel, *Nucl. Instr. and Meth. A* **385** 19 (1997); D. C. Nguyen, accepted for publication in *Nucl. Instr. and Meth. A*

A HIGH RESOLUTION ELECTRON BEAM PROFILE MONITOR

W.S. Graves, E.D. Johnson
NSLS, Brookhaven National Laboratory, Upton, NY 11973 USA
P.G. O'Shea, Duke University, Durham, NC USA

Abstract

A new beam diagnostic to measure transverse profiles of electron beams is described. This profile monitor uses a Yttrium:Aluminum:Garnet (YAG) crystal doped with a visible-light scintillator to produce an image of the tranverse beam distribution. The advantage of this material over traditional fluorescent screens is that it is formed from a single crystal, and therefore has improved spatial resolution. The current system is limited to a resolution of about 10 microns. Improvements in the optical transport will enable measurements of RMS beam sizes of less than 1 micron. The total cost of the system is modest.

1 INTRODUCTION

Fluorescent screens are widely used to measure the transverse profiles of electron beams at high-energy accelerator facilities. Traditional fluorescent screens[1], such as ZnS, have an individual grain size of 50 – 100 microns. This limits the image resolution to the same scale. The high brightness electron beams now being produced for short wavelength FELs and high energy colliders have focused sizes of a few microns in diameter. Resolution below this is necessary for accurate reproduction of the transverse profiles. We have tested a profile monitor that meets this requirement by employing a single crystal scintillator. The material is doped so that it fluoresces in the visible.The crystal is uniform at the molecular level, which provides very high resolution by removing individual grain size as the limiting factor in measuring very small beams.

2 MEASUREMENTS

Measurements of electron beam sizes and of the crystal's properties were performed at both the Accelerator Test Facility (ATF) [2] at BNL and at Duke University's Free Electron Laser Laboratory [3]. At Duke the brightness, linearity, damage resistance, and time structure of the fluorescence were made while the measurements at the ATF were devoted to spatial resolution limits. The actual configurations of the two experiments differ somewhat, but they share several common elements, most notably the scintillator crystals.

The YAG crystals are supplied as disks 10 mm in diameter and 0.5 mm thick. We were concerned that these nominally insulating materials might develop potentially damaging electrostatic charge on their surfaces in the electron beam. To address this issue we used a standard electron microscopy sample preparation technique and evaporated an approximately 14 nm thick coating of 60% Au / 40% Pd on both faces of the crystal. We have not run any experiments with uncoated crystals.

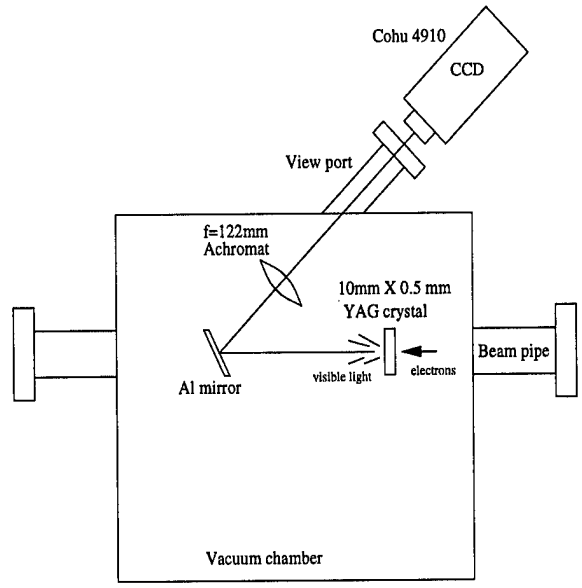

Figure 1: Optical layout of profile monitor at ATF.

For these experiments the duration of the optical pulse is less than 100 ns, therefore a camera that simultaneously exposes both interlaced video fields is necessary. For this reason, each measurement was recorded with a Cohu 4910 video camera. To provide the best image fidelity, the monitors are all arranged with the crystal at normal incidence to the electron beam. An aluminum mirror is placed downstream of the crystal to deflect the fluorescence light out to the camera. We made preliminary measurements on airports at the Duke FEL linac at 36 and 264 MeV to make sure that the crystals were robust, and then made in-vacuum measurements at the high energy port (264 MeV). In this configuration, the light from the crystal is brought out at 90 degrees from the electron beam, deviated and inverted by a rooftop (Amici) prism, and focused to the CCD camera by a 55 mm focal length telecentric lens with a 2X adapter. In this arrangement the field of view of the screen was 11.6 by 9.46 mm (h x v) corresponding to a pixel resolution of 15.5 by 16.3 microns.

To test damage resistance the YAG was inserted for an extended period in the beam, and its performance monitored. It was then removed and examined for surface damage. After 2 hours and approximately 1200 nC of charge, no loss of intensity was observed, and no visible damage was apparent on the crystal. A PMT was used to measure the time duration of the YAG flourescence. The pulse duration was measured to be about 80 ns FWHM. Figure 2

0-7803-4376-X/98/$10.00 © 1998 IEEE

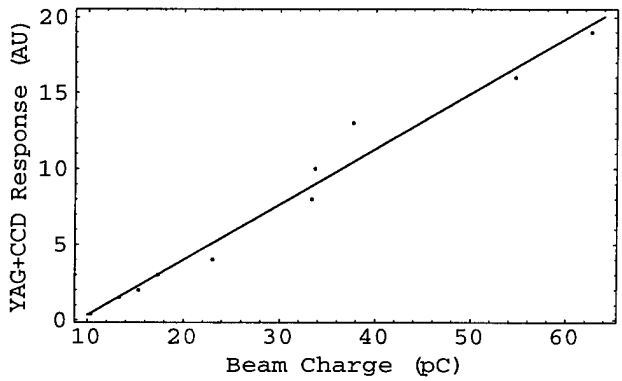

Figure 2: Linearity of YAG/CCD response. Charge variation estimated at 10% at each point.

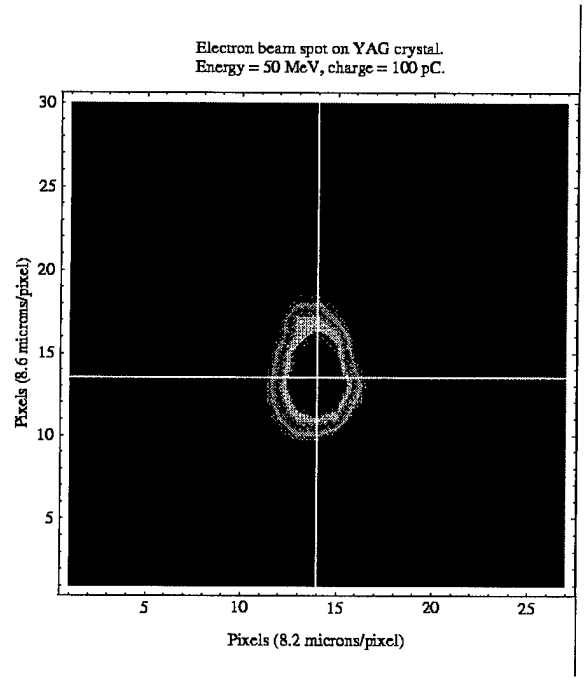

Figure 3: Smallest beam spot observed at ATF.

shows a plot of light energy recorded by the CCD vs beam charge. The crystal exhibits good linearity for this range of charge. The brightness of the spot produced on the YAG was compared to similar beam spots on a ZnS screen. The intensity of the YAG matched that of the ZnS.

The smallest spot sizes were produced by the high brightness electron beam at the ATF. Figure 1 shows the layout of the optical system used to measure the small beams. The system is installed as part of the Smith–Purcell experiment [4] located on beamline 1. In this case the available ports on the vacuum chamber dictated that the optical beam be taken out at an angle of 45 degrees with respect to the electron beam axis. To improve the resolution of the experiment we also removed the telecentric lens from the camera and substituted for it a diffraction-limited achromat of 122 mm focal length located inside the vacuum chamber. It is positioned to produce a 1 to 1 image of the YAG outside the chamber on the CCD camera. The optical focus and magnification were calibrated by placing a metal plug with 100 micron hole at the YAG position and recording the image. After the components are locked in place, no adjustments are available. In this case, the field of view is equal to the CCD chip size, 6.4 mm X 4.8 mm corresponding to 8.3 by 8.6 micron pixels.

The minimum electron beam size measured had a RMS radius of 10.7 μm at 50 MeV and approximately 100 pC of charge (Fig. 4). This is consistent with normalized emittance of 0.5 πmm-mrad and a beta function of 2 cm. These values are in reasonable agreement with TRANSPORT calculations.

3 RESOLUTION LIMITS

The ultimate resolution is set by both the minimum object size that can be produced by the crystal and by the diffraction of visible light. The minimum object size for high energy electrons is limited by multiple Coulomb scattering of the beam through the crystal and by the generation of bremsstralung. The multiple scattering angle through the material is given approximately by [5]:

$$\theta_{ms}(z) = \frac{13.6\text{MeV}}{pc}\sqrt{z/Z_0}\,[1 + 0.20\ln(z/Z_0)] \quad (1)$$

where z/Z_0 is the material thickness in radiation lengths and pc is the electron momentum. The radiation length for YAG is 5.2 cm. For a 50 MeV beam traveling through a 0.5 mm thick crystal, $\theta_{ms} = 1.9$ mrad, yielding a minimum possible spot size of

$$x_{ms} = \int_0^{0.5\text{mm}} \theta_{ms}(z)dz = 0.6\ \mu\text{m} \quad (2)$$

The critical energy, where energy losses due to ionization and radiation of bremsstrahlung are equal, is about 50 MeV. Above this energy the xrays generated by electrons passing through the material will also cause scintillation, limiting the minimum measureable beam size. The characteristic emission angle of the xrays is $1/\gamma = 10$ mrad at 50 MeV. Thus $x_{brem} = 2.5\ \mu$m at 50 MeV.

The minimum spot size limits due to either multiple scattering or bremsstrahlung are both dependent on the electron beam energy. The limits are reduced at higher energies (Fig. 5).

The diffraction limited diameter of a lens focus is $d_0 = 2.44\lambda(f/D)$, where the wavelength, λ, of the light is 550nm, f is the lens focal length, and D is the lens diameter. This is the diameter of the zeroes of the Airy disk. For reasonable working distances of a few centimeters, the lowest diffraction-limited f/D that can be achieved is about

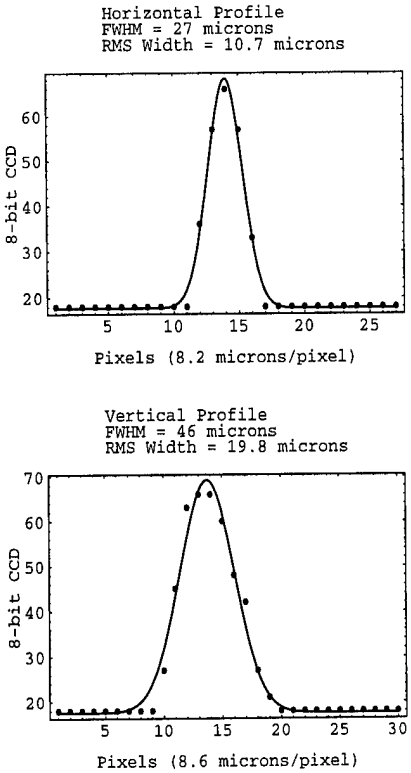

Figure 4: Smallest measured electron beam profiles.

3. Therefore the optics of visible light limit our resolution to beam spots of 4 microns diameter, or 0.7 microns RMS size. Figure 5 summarizes the RMS spot size limits due to multiple scattering, bremsstrahlung, and diffraction. The optics installed on our system have a magnification of unity and diffraction limited resolution of 6 microns. The camera pixel size is 8.5 microns. This pixel size currently sets the resolution limit.

Diffraction-limited resolution may be achieved by using two achromats to produce a 1 to 1 relay image outside of the vacuum chamber. Assuming that resolution of approximately 1 micron is required, the intermediate image may be magnified by a factor of 10 using a flat-field microscope objective. A CCD camera with 6–10 micron pixels would then provide the required resolution.

4 CONCLUSIONS

RMS beam sizes as small as 10.7 microns have been measured using a new flourescent screen based on a YAG crystal. This beam size is at the limit of the current optical resolution. The resolution may be improved by using more lens elements with greater magnification. Diffraction of visible light limits the resolution to 0.7 micron RMS beam sizes. The crystal has been shown to be sensitive to small beam charges, to have a linear response, and to be damage resistant.

One of the important features of this profile monitor is its

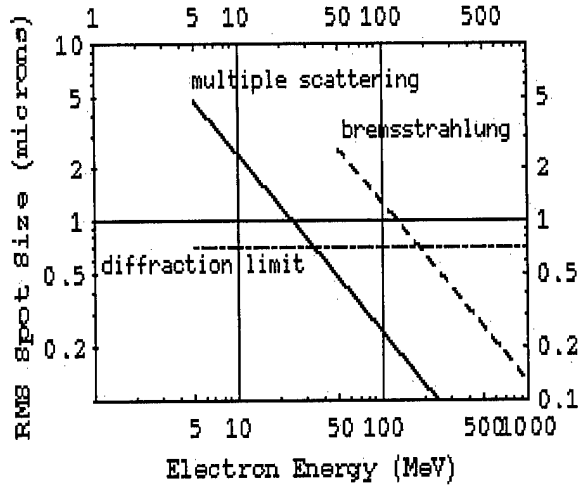

Figure 5: Effects that limit minimum spot size that may be measured as a function of electron beam energy for a 0.5 mm thick crystal.

low cost. The system described here, including achromat, YAG crystal, CCD camera, and mounting hardware can be purchased for under $1500 US.

5 ACKNOWLEDGEMENTS

We are grateful to the accelerator operators at the Duke FEL facility, to Vitaly Yakimenko of the ATF for producing the very small measured beams, and to Harold Kirk of the Physics Dept at BNL for assistance with installation and mounting of the profile monitor at the ATF. This work performed under the auspices of the U.S. Department of Energy Contract DE-AC02-76CH00016. The work at Duke University supported by USASDC Contract DASG-60-84-C-0028.

6 REFERENCES

[1] J.T. Seeman, V. Luth, M. Ross, J. Sheppard. Beam tests of phosphorescent screens. Technical report, SLAC, 1985. Single Pass Collider Memo CN-290.

[2] I. Ben-Zvi et al. The Accelerator Test Facility at BNL. *Nuc. Inst. and Meth.*, A296:348–350, 1990.

[3] P.G. O'Shea et al. Single bunch injection system for storage ring FEL using an rf photoinjector. *These proceedings*

[4] K.Woods, J. Walsh, R. Stoner, H. Kirk, R. Fernow. The Smith Purcell experiment. *Phys. Rev. Lett.*, 74:3808–3811, 1995.

[5] Particle Data Group, editors. *Particle Properties Data Booklet.* North-Holland, 1990.

THE ARGONNE WAKEFIELD ACCELERATOR: DIAGNOSTICS AND BEAM CHARACTERIZATION

M. Conde, W. Gai, R. Konecny, X. Li, J. Power, P. Schoessow
Argonne National Laboratory, Argonne, IL 60439, USA
and N. Barov
UCLA, Los Angeles, CA 90024, USA

Abstract

The Argonne Wakefield Accelerator is comprised of two L-band photocathode RF guns and standing wave linac structures. The high charge bunches (20 - 100 nC) produced by the main gun (drive gun) allow us to study the generation of wakefields in dielectric lined structures and plasmas. The secondary gun (witness gun) generates low charge bunches (80 - 300 pC) that are used to probe the wakefields excited by the drive bunches. We use insertable phosphor screens for beam position monitoring. Beam intensity is measured with Faraday cups and integrating current transformers. Quartz or aerogel Cerenkov radiators are used in conjunction with a Hamamatsu streak-camera for bunch length measurements. The beam emittance is measured with a pepper-pot plate and also by quadrupole scan techniques. We present a description of the various diagnostics and the results of the measurements. These measurements are of particular interest for the high current (drive) linac, which operates in a much higher charge regime than other photoinjector-based linacs.

1 EXPERIMENTAL SETUP

The Argonne Wakefield Accelerator (AWA) group operates two photocathode-based RF guns. One of them was designed to produce electron bunches of very high charge (up to 100 nC) and short bunch length (25 – 50 ps FWHM). The high intensity beam from this gun is used to excite wakefields in dielectric-loaded waveguides and also in pre-formed plasma columns. For this reason this gun is referred to as the "drive gun" (which generates the drive beam). The second RF gun generates electron bunches of lower charge (typically 300 pC) that are used to probe the wakefields generated by the drive beam. This gun is then appropriately called the "witness gun".

Figure 1 shows a schematic of the experimental setup [1]. The half-cell drive gun was designed to have a high accelerating field (92 MV/m at the photocathode surface) to allow the extraction of high charge bunches, and to produce a 2 MeV beam with the limited RF power available at the design time (1.5 MW at 1.3 GHz). Magnesium was chosen for the photocathode material for its ruggedness and quantum efficiency (5×10^{-4}). The 2 MeV bunches generated by the drive gun subsequently go through two standing-wave, $\pi/2$ mode linac tanks, increasing the beam energy to about 14 MeV. The beam is then focused by quadrupoles and bent by three dipoles to allow for the injection of both the drive beam and the witness beam into the wakefield experimental section. The witness gun [2] is a 6-cell standing-wave $\pi/2$ mode structure that generates 4 MeV bunches of 300 pC. Its photocathode material is presently copper, but a change to magnesium will occur soon. The witness beam goes through combining optics and then through the dielectric-loaded structure trailing the drive beam, thereby probing the wakefields excited by the drive bunches. Energy changes of the witness beam are measured by a spectrometer located downstream of the wakefield experimental section.

The two RF guns and the two linac structures are powered by a single klystron (Thomson TH2022D; 20 MW, 4 μs pulses), via necessary power spliters and phase shifters. The laser system is comprised of a dye oscillator (496 nm) pumped by a tripled YAG, which is then followed by a dye amplifier, a doubling crystal and finally an excimer amplifier. We thus obtain laser pulses of up to 8 mJ with 6 ps FWHM at 248 nm. The laser beam is then split and a small fraction of it (~ 15%) sent to the witness gun. There is an adjustable delay between the drive gun and the witness gun laser beams. This allows us to vary the delay between the drive and the witness electron bunches (obviously the RF phases have to be adjusted accordingly, in order to maintain the same launching phase).

The AWA control software was developed in house and is based on the Tcl/Tk scripting language. At the core of the control system is an HP-750 RISC workstation which is interfaced to VMEbus. The 68060 CPU board on the VMEbus handles command requests from the workstation and provides auxiliary processing capabilities. Most of the control and monitoring functions are handled through a VME-CAMAC parallel bus interface. VME boards are used to acquire images and oscilloscope traces.

0-7803-4376-X/98/$10.00 © 1998 IEEE

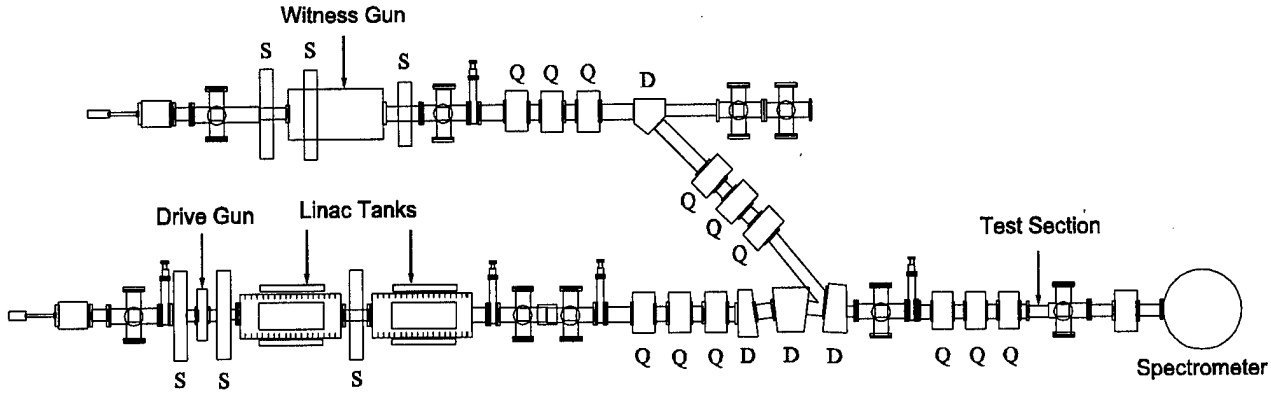

Figure 1: Schematic of the AWA experimental setup; S, Q, and D indicate solenoids, quadrupoles and dipoles, respectively.

2 DIAGNOSTICS

There are four integrating current transformers (Bergoz ICT - 082-070-20:1) installed on the beamlines to measure bunch charge at various locations. Alternatively, we can use insertable Faraday-cups at diagnostic ports along the beamlines and also at the beam-dumps. The ICTs appear to be more reliable, since they are easier to calibrate, while the Faraday-cups suffer from secondary electron emission and electric breakdown due to the high peak voltages generated.

Cerenkov light generated by the electron beams is sent to a Hamamatsu M1952/C1587 streak camera for bunch length measurements. Insertable quartz or aerogel plates are used as Cerenkov radiators. The aerogels require a more elaborate holder, but offer several advantages over the quartz plates. The aerogels need to be in a vacuum-tight holder which is inserted in the beam path. The electron beam enters our holder through a thin aluminum window (0.15 mm). It then traverses the aerogel (under atmospheric pressure) and emits Cerenkov radiation, which leaves the aerogel holder through a quartz window. Our aerogels [3] have an index of refraction of 1.009, therefore the Cerenkov light is emitted at an angle of 7.4° with respect to the direction of propagation of the 14 MeV electrons. The light is then reflected by a mirror and leaves the vacuum chamber through a diagnostic view port.

Contrary to the aerogels, quartz plates are compatible with the vacuum of the accelerator and can be easily inserted in the beam path. However, due to their higher index of refraction (1.54), their Cerenkov light is emitted at an angle of 49.5°, making it difficult to collect more than a small fraction of the total cone of radiation. Multiple reflections within the quartz plate are also a problem to be considered. They can be minimized by placing the plate such that the radially polarized Cerenkov light leaves the plate at the Brewster angle. In practice, because emission in quartz occurs at large angles, it is harder to achieve good alignment of the associated optics to transport the light to the streak camera.

A pepper-pot plate is used for emittance measurements. It consists of a 1.5 mm thick tungsten plate with 0.3 mm diameter holes spaced by 3 mm. A phosphor screen 75 cm downstream of the pepper-pot plate is used to image the resulting beamlets.

3 EXPERIMENTAL RESULTS

We have measured the bunch length of the drive beam as a function of the RF launching phase, for several values of the laser beam energy. By varying the laser energy we change the amount of charge emitted by the photocathode, and thus the influence of the space-charge force in the dynamics of the electron bunches. Figure 2 shows RF phase scans for two different laser beam energies. In these plots the relative RF phase between the drive gun and the linac tanks was kept constant, and only the phase of the klystron power with respect to the laser pulses was changed. The plots show how the bunch length and the extracted charge vary as a function of the launching RF phase. We notice that the dependencies on the RF phase are stronger in the higher charge case, since in that case the space-charge forces are stronger and it becomes more critical to optimize the RF fields. It is also important to optimize the focusing solenoidal fields, otherwise the bunch length may become much longer and even show a bimodal temporal distribution of charge.

Figure 3 shows bunch length as a function of bunch charge. In this plot the RF phases have been set to their optimum values. We have plotted the 95% RMS value of the bunch lengths and also the corresponding FWHM. The ratio between the 95% RMS and the FWHM values shows that the pulses are not gaussian. The large fluctuation in the FWHM of the pulses also shows that the detailed shape of the temporal profile

varies considerably from pulse to pulse. In Fig. 3, the data points represented by circles correspond to the optimum points observed in five RF phase scans (two of which are shown on Fig. 2). The points represented by squares and triangles were measured when the input RF power into the drive gun was at a higher level. We notice that the points represented by the triangular symbols indicate remarkably shorter bunches; this is our most recent data and we are presently performing a more comprehensive study of operation near these settings.

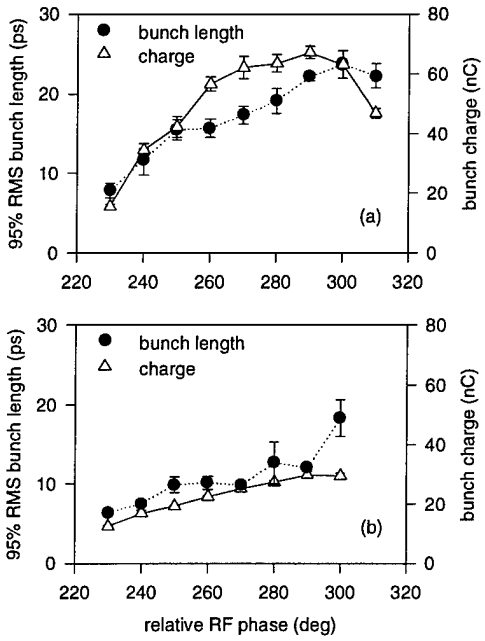

Figure 2: Bunch length and charge as a function of the RF phase: (a) high charge case; (b) low charge case. The error bars represent the standard deviation calculated by averaging three shots.

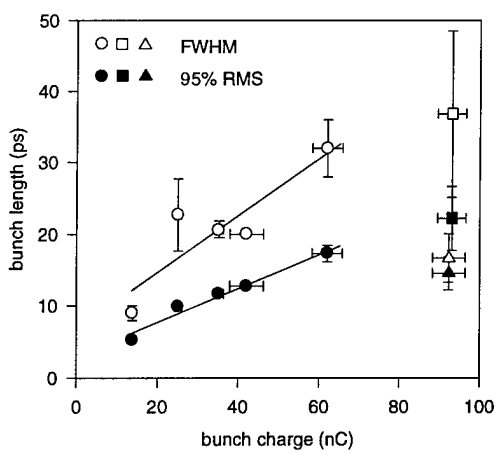

Figure 3: Measurements of electron bunch length as a function of bunch charge. The points represented by circles correspond to the average of three pulses. The squares and triangles correspond to the average of ten and sixteen pulses, respectively.

Emittance measurements of high charge electron beams are quite difficult. We attempted to measure the emittance of the drive beam with a pepper-pot plate. Unfortunately, the resulting images are rather irregular. We are now trying to determine if that is caused by scattering on the holes, by nonlinear response of the phosphor screen, or simply by a very irregular distribution of particles in the phase space.

We have measured the normalized emittance of the witness beam by quadrupole scan techniques (3.5 π mm mrad). This procedure could be applied to the drive beam, even with its high charge, since we have developed a quadrupole scan model that includes space-charge forces. However, our phosphor screens currently cannot withstand a focused 100 nC electron bunch.

4 DISCUSSION

We are approaching the design goals of the AWA facility (100 nC, 25 ps FWHM). There are still many aspects of the generation of these unprecedented high charge, short electron bunches that call for more detailed studies. While this constitutes an interesting and challenging research program in itself, we are concomitantly proceeding with experiments on plasmas and dielectric wakefields [4,5].

5 ACKNOWLEDGMENTS

We would like to thank L. Balka, A. Caired, C. Keyser, R. Taylor and K. Wood for their technical support.

This work is supported by the Department of Energy, Division of High Energy Physics, under contract No. W-31-109-ENG-38.

REFERENCES

[1] P. Schoessow et al., "The Argonne Wakefield Accelerator High Current Photocathode Gun and Drive Linac", Proc. 1995 Particle Accelerator Conf., pp. 976 - 978.

[2] J. Power et al., "Measurements of the Argonne Wakefield Accelerator's Low Charge, 4 MeV RF Photocathode Witness Beam", Proc. 1996 Advanced Accelerator Concepts Workshop.

[3] We thank J. Rosenzweig for initiating us in the use of aerogel radiators, and J. Oyang and P. Tsou for making them available to us.

[4] P. Schoessow et al., "High Gradient Dielectric Wakefield Device Measurements at the Argonne Wakefield Accelerator", These Proceedings.

[5] N. Barov et al., "Results of Blowout Regime Propagation of an Electron Beam in a Plasma", These Proceedings.

TIME-RESOLVED IMAGING OF ELECTRON AND POSITRON BEAMS AT APS

A. H. Lumpkin and B. X. Yang
Advanced Photon Source, Argonne National Laboratory
9700 South Cass Avenue, Argonne, Illinois 60439 USA

Abstract

Characterizations of stored electron beams and more recently positron beams circulating in the Advanced Photon Source (APS) 7-GeV storage ring have been done using optical synchrotron radiation (OSR) and x-ray synchrotron radiation (XSR) imaging techniques. Results include the measurement of the bunch length and horizontal beam size versus single-bunch current for both electron and positron beams, observations of multibunch bunch length effects near 100 mA stored beam current, and initial diagnostics of a coupled-bunch instability with 15-minute period. Both the Hamamatsu C5680 dual-sweep streak camera using OSR and a pinhole camera using XSR from a bending magnet source point were utilized. Proposed enhancements to the beamline will also be presented.

1 INTRODUCTION

The transition of the Advanced Photon Source (APS) 7-GeV storage ring from the commissioning phase with electrons to the operations phase with positrons [1] has been supported by the use of time-resolved imaging techniques based on synchrotron radiation. Characterizations of the stored beams' bunch length and transverse size have been done using both optical synchrotron radiation (OSR) and x-ray synchrotron radiation (XSR) from a bending magnet (BM) source point. As part of the program to evaluate the impedance of the ring, single-bunch studies of these parameters as a function of single-bunch current have been performed. Bunch lengthening effects have been observed to be more significant than energy spread growth with an increase in current. These results have been compared to predictions of a potential well distortion (PWD) model and a microwave instability calculation, and the data are found to be more consistent with the PWD calculations [2]. Additionally, apparent coupled-bunch instabilities have been diagnosed via the increase in observed horizontal beam size at this dispersive point in the lattice as well as a separate bunch length measurement. The techniques will be briefly described followed by examples of results.

2 EXPERIMENTAL BACKGROUND

As described elsewhere [3], the APS storage ring diagnostics include a bending magnet source dedicated to beam characterizations. The source point at about the one-eighth length of the dipole also is at a dispersive point in the lattice which allows access to the energy spread of the beam. Both optical synchrotron radiation (OSR) and XSR-based techniques are used. Initially, a split, water-cooled pickoff mirror was used to direct the OSR out of a window and into an optical transport while allowing the high power, lower-divergence x-ray beam to pass on to an in-air pinhole aperture. At present the front-end vacuum transport line includes a mask that separates the BM radiation into three pieces. One part continues to an in-vacuum 4-jaw aperture that acts as the pinhole aperture, and a second part strikes a single mirror that is shadowed from x-rays by a horizontally on-axis, cylindrical rod.

The x-ray images are converted to visible light at a $CdWO_4$ converter and viewed by a Questar telemicroscope with a charge-coupled-device (CCD) camera. The visible, OSR is transported out of the tunnel to an optics lab which has a C5680 dual-sweep streak camera for bunch length measurements.

3 EXAMPLES OF EXPERIMENTAL RESULTS

3.1 Transverse Beam Size

Measurements of the transverse beam size have been done within machine studies periods and the routine observation plans for beam quality with 100-mA stored beam. The observed beam sizes have been consistent with the baseline design of 8.2 nm-rad natural emittance and better than the 10% vertical coupling design in almost all instances of user runs. In Fig. 1 an example of the x-ray pinhole image in a recent run is shown. The values of the total observed size, $\sigma_{xT} \approx 160$ μm and $\sigma_{yT} \approx 90$ μm, are

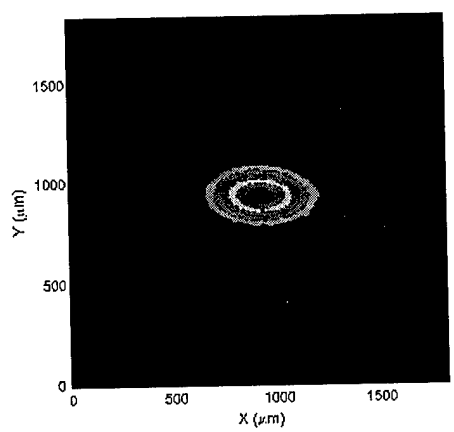

Figure 1: Example of an x-ray pinhole image of the APS stored positron beam at about 100 mA. The horizontal ($\sigma_x \sim 160$ μm) and vertical sizes ($\sigma_y \sim 90$ μm) are consistent with the baseline design but with vertical coupling less than 10%.

0-7803-4376-X/98 /$10.00 © 1998IEEE

representative of the runs in recent months with both the 6 + 200 bunch pattern and the 6 + 17 triplets bunch pattern. Using the calculated $\beta_x = 1.8$ m and $\beta_y = 18.4$ m, the measured dispersion $\eta_x = 85$ mm, and the estimated system resolutions of $\sigma_{xres} = 60$ μm and $\sigma_{yres} = 40$ μm, a vertical coupling of about 4-5% is indicated. These patterns involve a trade on beam lifetime and compatibility with time-resolved user experiments.

In the fall of 1996, a different fill pattern was employed involving four trains of 12-bunches positioned at 90° intervals around the ring. Each 12-bunch set was initially filled to 25 mA (~2 mA/bunch) average current. An unanticipated phenomenon occurred as exhibited by the significant increase in horizontal beam size. This was observed to have about a 15-min period which persisted from 100 mA down to 60 mA early on a user run. Figure 2 shows the plot of horizontal size (FWHM) measured in pixels or channels of the video processing system. The normal value of ~12 ch at 28 μm/ch corresponds to $\Delta x =$ 336 μm (FWHM) or 143 μm (σ). The maximum of the size increase is almost twice as large as the baseline value. There was very little change in the vertical size. Since this source point is at a dispersive point in the lattice, a longitudinal instability effect was likely involved. The 15-min time scales were traced to oscillations of the rf cavity temperatures as the cooling water regulator valves opened and closed. As shown in Fig. 3, the S37 cavity temperatures display a less than 1-degree oscillation at the 15 min period. EPICS [4] allowed the tracking of the temperature process variable and the beam size process variable together. Since it was determined that the instability was worse at the cavity temperature minima, the set points for the rf cavity temperatures were raised, and the instability was suppressed. Further details on the rf side are given by Harkay et al. [5].

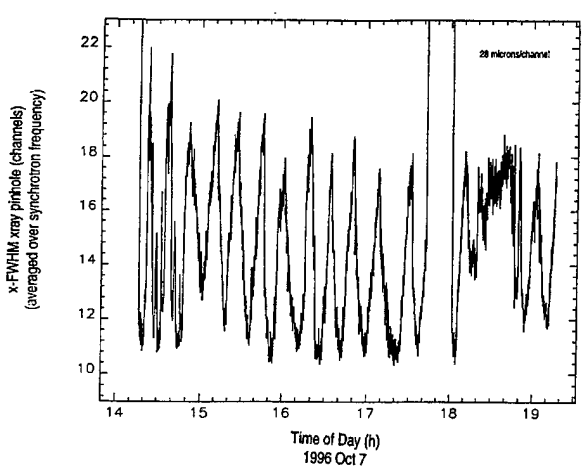

Figure 2: Plot of the variation of the horizontal beam size (positrons) in channels (FWHM) versus time. A significant size growth is seen with a 15-min period.

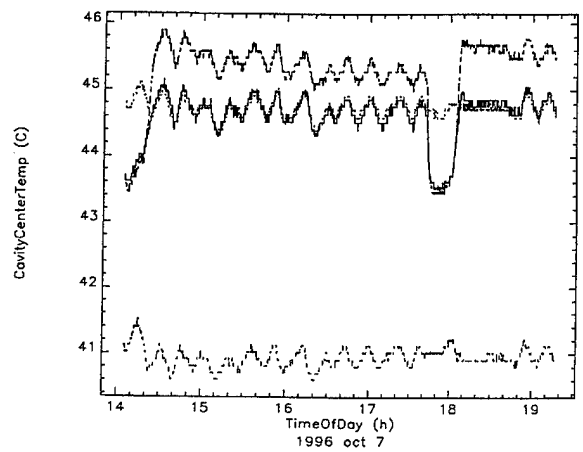

Figure 3: Plot of the variation of the sector 37 rf cavity temperature probe versus the same time as Fig. 2. The maxima in Fig. 2 align with the temperature minima for this set of cavities.

3.2 Longitudinal Phase-Space Effects

Previously, we reported measurements in single-bunch studies which involved lower rf gap voltages and synchrotron frequencies [2]. A more extensive set of data were obtained in June 1996 with electrons that addressed both the observed horizontal beam size at the energy dispersive source point and the longitudinal bunch profile and duration. Figure 4 shows the beam size and bunch length versus single-bunch currents up to 18 mA on the upper half and lower half of the figure, respectively. The bunch length (triangles) clearly more than doubles and could be fit to the $I^{1/3}$ dependence. The horizontal beam size (circles), and hence the effective energy spread, does not show any significant increase up to 12 mA, but there does seem to be some increase after that. These combined effects are consistent with calculations done using the potential well distortion (PWD) model rather than the predicted 2 1/2 times energy spread increase from a microwave instability-based scenario [2]. It is also noted that the peak current attained was about 400 A. Subsequently, bunch length measurements have been taken for stored positron beams up to 7.5 mA. These data show a similar bunch current dependency as the electron beam data.

An additional phenomena was observed in multibunch mode in dual-sweep streak images taken near 100 mA, the baseline stored beam current. At 101 mA the observed bunch lengths were almost 190 ps (FWHM) (Fig. 5) versus 70 ps (FWHM) shortly thereafter when the current was 99 mA. This appears to be an alternative measurement of the signature of a coupled-bunch instability which was related to the rf cavity higher-order modes (HOMs) at that time. These particular data were taken during our first attainment of 100 mA on January 12, 1996 and are likely related to the complementary type measurement shown in Fig. 2.

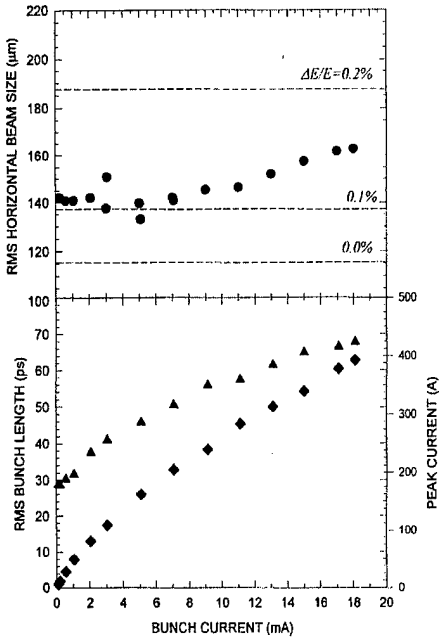

Figure 4: Plot of the rms beam size and bunch length versus single bunch current (electrons) taken on June 30, 1996. Significant bunch lengthening is observed but without comparable energy spread growth. The dashed lines in the upper figure show the 0.0, 0.1, and 0.2% ΔE/E calculated sizes. In the lower half of the figure, the trianges (left-hand axis) are bunch length values and the diamonds are the peak current values (right-hand axis).

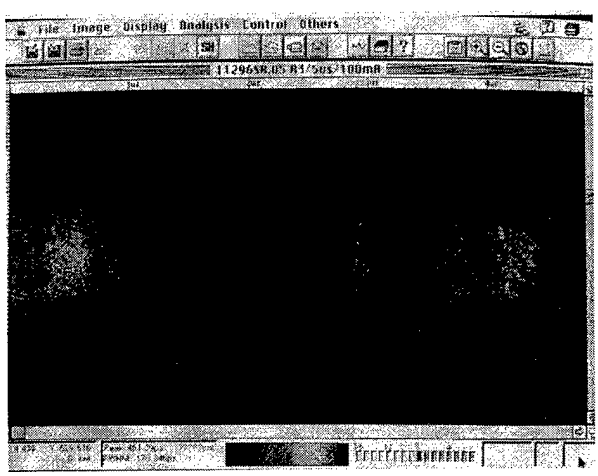

Figure 5: Dual sweep streak images of the stored beam at 101 mA. The bunch length changed from 170 ps (FWHM) in this image to 70 ps (FWHM) at I_B = 99 mA. The vertical scale is 800 ps and the horizontal scale is 5 μs The vertical white lines denote the region-of-interest for the time profile of the multi-bunch train. Individual micropulses are <u>not</u> seen on this time scale. The next pass of the pulse train is seen at the left of the image where the vertical profile is displayed.

4 SUMMARY

In summary, we have used the time-resolved imaging techniques to monitor the APS storage-ring beams under a variety of conditions. The transverse beam size measurements are now on-line and archived in data loggers with EPICS tools. Additionally, longitudinal effects as revealed in energy spread or bunch length have also been tracked. These techniques are now being complemented by a diagnostics undulator which can directly address beam divergence [6].

5 ACKNOWLEDGMENTS

The authors acknowledge the APS/ASD support of John Galayda and Glenn Decker as well as the assistance in the main control room of Louis Emery, Mike Borland, and Nick Sereno. APS work was supported by the U.S. Department of Energy, Office of Basic Energy Sciences, under Contract No. W-31-109-ENG-38.

6 REFERENCES

[1] Glenn Decker, "Performance of the Advanced Photon Source," these proceedings.

[2] A. H. Lumpkin, B. X. Yang, and Y. C. Chae, "Observations of Bunch Lengthening Effects in the APS 7-GeV Storage Ring," *Nucl. Instrum. Methods*, in press.

[3] B. X. Yang and A. H. Lumpkin, "Particle Beam Profiling Techniques on the APS Storage Ring: Commissioning Results," AIP Conf. Proc. 390, p. 491 (1997).

[4] EPICS or Experimental Physics and Industrial Control System, e.g., K. Sidorowicz and W. P. McDowell, "The APS Control System Network," Proceedings of ICALEPCS, Oct. 30-Nov. 3, 1995, Chicago, IL, p. 68.

[5] K. Harkay et al., "Compensation of Longitudinal Coupled-Bunch Instability in the APS Storage Ring," these proceedings.

[6] B. X. Yang et al., "Status of the APS Diagnostics Undulator Beamline," these proceedings.

OPTICAL TRANSITION RADIATION MEASUREMENTS ON THE ELETTRA LINAC

D. Giove[(1)], C. De Martinis[(1)], G. D'Auria[(2)], M. Ferianis[(2)], C. Rossi[(2)], A. Variola[(3)]
[(1)]INFN and University of Milano, Via F.lli Cervi 201, Segrate (Mi), Italy;
[(2)] Sincrotrone Trieste, Padriciano 99, 34012 Trieste Italy;
[(3)] LAL IN2P3 - CNRS, Orsay France

Abstract

An experimental apparatus has been developed and installed on the Elettra Linac in Trieste in order to measure OTR spectra at energies below 100 MeV.
In this paper we report the results so far obtained at electron energies between 30 and 100 MeV. Beam diagnostics obtained from OTR data will be discussed

INTRODUCTION

Beam monitors using electromagnetic waves, especially visible light radiated by charged particles, have several excellent and unique features for beam diagnostics: they are free from environmental electromagnetic noise and are characterized by high-speed response time. OTR based beam diagnostics are beginning to be used more and more at accelerator facilities around the world. They are one of the most promising monitors concerning position, size, emittance, energy and time structures of bunches of electron beams.
OTR was first predicted by Ginzburg and Frank[(1)] in 1946, but its practical usefulness as an e-beam diagnostic was not explored until 1975 by Wartski[(2)]. During the 1980s further developments were carried out working with beam energies of the order of 100 MeV or higher[(3)].
OTR is generated when a charged particle beam crosses the interface between two media of different dielectric constants. For beam diagnostics it is usually used the radiation emitted from a vacuum-metal boundary. In practice a thin metal foil is inserted into the beam line at an oblique angle to the beam direction of motion. OTR is emitted in both forward and backward emisphere.
The fundamental characteristics of the transition radiation emission shows both a rather complicated relation between many different parameters and the coexistence of different regimes. This latter feature is mainly related to the dependence of the emission from the energy of the charged particles. The boundary between the so called "low-energy" and "high-energy" regimes may be found at a value of γ around 20[(4)]. In the following we are going to discuss and analyze the properties of electron beams in the high energy regime.
OTR main features are the large emission spectrum, the absence of an energy threshold, the polarization of the emitted radiation and a high directivity which increases with energy. Measurements have shown that no intrinsic limits are present in OTR that is resolved limited only by diffraction and optical setup[(5)]. This gives a beam diagnostic tool to measure beam profiles with an improved spatial resolution. The surface nature of the OTR allows to use very thin targets which gives reduction in beam scattering and bremsstrahlung radiation. OTR screens may work inserted on the beam line during beam transport to give on line monitoring of beam parameters.
The OTR angular distribution pattern can be exploited to measure beam divergence and energy. The distance of the two peaks (Δ) in the spectra is proportional to $1/\gamma$ and they present a 10% of unsimmetry along the observation angle. The minimum in the emission distribution overlaps with the beam reflection direction, so that a foil at 45° to the beam emits at 90°, the standard port geometry for accelerator lines.

THE EXPERIMENTAL SET-UP

The OTR measurement facility installed at Elettra Linac has been conceived to quantitatively study the dependence of OTR properties from:

- beam energy (in the range 30-100 MeV)
- beam intensity and distribution
- beam divergence
- screen materials and thickness
- beam incidence angle.

The measurement station is located at the end of the Linac preinjector where the electron beam has energies ranging from 30 to 100 MeV. A spectrometer positioned just before the OTR station provides a reference measurement for beam energies.
The diagnostic box (shown in fig. 1) has been specially designed with the following characteristics :

- the box has been machined in a way such that its mechanical alignment with respect to the beam line structure will guarantee the geometric relations between the beam direction and the OTR screen
- the pneumatic actuator which holds the OTR screen can be remotely moved under vacuum according to two degrees of freedom. The first allows to put at the beam intersection point two different screen types (OTR or alumina screen) or a free position for non perturbed beam transport. The second possible movement is a rotation of the full actuator in order to change the incidence angle of the beam on the screen.
- the viewing angle of the OTR window (assuming to collect backward radiation) is 900 mrad and it has

0-7803-4376-X/98 /$10.00 © 1998 IEEE

been maximized in order to collect as much light as possible and to avoid the cut of the tails in angular distribution spectra.

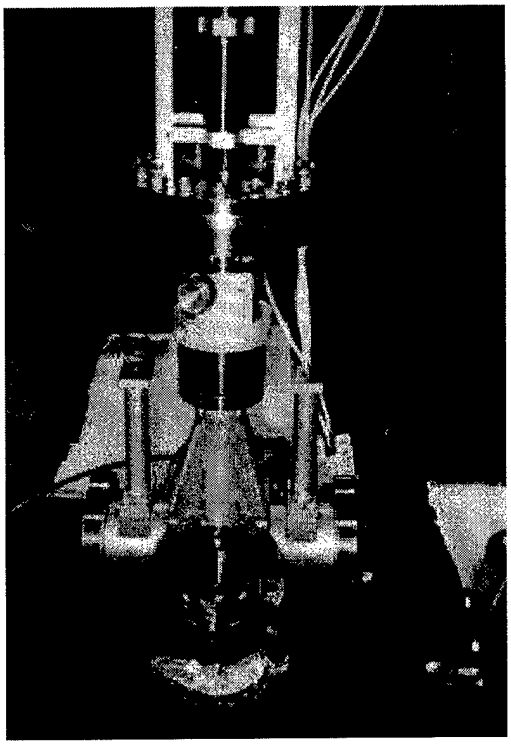

Fig. 1 OTR diagnostic box

The optical elements for light collection and transport from the radiator up to the detector have been assembled on an optical rail to guarantee the proper alignment characteristics (fig. 2). The rail has been positioned perpendicular to the beam direction within an accuracy of 0.1 mrad and each element has been assembled on the rail using linear translators (hand driven or remotely controlled) to adjust their final position.

The optical system was designed to have an angular field of view of about two times the peak angle of the OTR pattern at the lower energy used. The limiting aperture of the system is set by the detector size.

The system has been designed to allow simultaneous monitoring of the beam image and angular distribution pattern. Radiation coming from the radiator can be splitted into two different orthogonal paths, one for each measure, by means of a conventional beam splitter, as far as optical radiation is concerned. This configuration has not been used in the preliminary measures since we had no experimental knowledge on photons budget and background noise. Therefore the measure of the beam image and the angular pattern have been performed in separate sessions and with different configurations.

To ensure the proper alignment of the optical elements with respect to the beam direction, the light coming from the thermoionic cathode and reflected from the metal foil was used to define the axis of the optical path. The beam has been then steered to intersect the light spot on the foil. The alignment accuracy is of the order of 0.1 mrad. The image of the cathode has been removed from the radiation measures along with the background noise.

Two detectors has been used according to the expected and measured light level. Beam image acquisition has been accomplished using a conventional CCD monochrome camera with a sensitivity of 0.3 lux coupled to a 50 mm objective. The angular distribution pattern has been measured using an intensified camera with a sensitivity lower than 3 order of magnitude with respect to a conventional camera.

The spatial limit resolution of these detectors has been measured on a test bench in term of Modulation Transfer Function. A value of 12 line pairs for mm has been found which gives a limit resolution of the order of 80 μm.

Both camera types transfer frames according to the RS-170 standard. A workstation based on an NT PC acquires images using a frame grabber and allow the storage and the real time analysis of the main characteristics of the beam. A LabVIEW based application has been developed for this purpose.

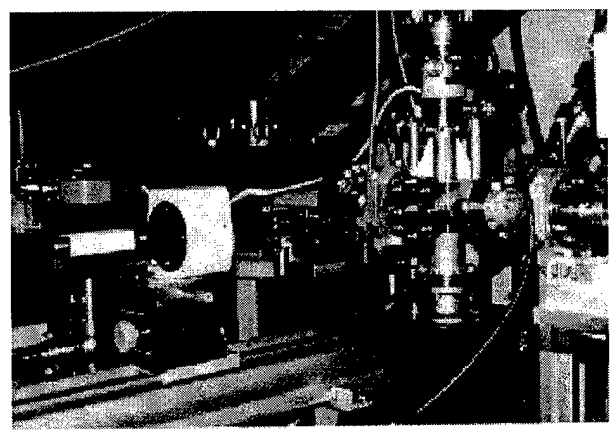

Fig. 2 Experimental set-up

MEASUREMENTS

The system so far described has been used during two shifts in September 1996 and March 1997. The first set of measurements has been devoted to the set up of the whole optical chain and to the measure of the light budgets. OTR beam images has been taken over the whole range of energies with bunches of 16 nC and 70 ns length. Conventional CCD camera sensitivity have been showed adequate to ensure beam profiles with an overall resolution of 0.1 mm, which is close to the intrinsic detector limit. OTR images are better defined than Chromox 6 images taken for comparison purpose at the same point and on the same beam as the difference at FWHM is of the order of 20%. This is due mainly to the lack of light contribution due to volume effects which take place in alumina or fused silica screens. Fig. 3 shows an OTR beam image at 50 MeV.

Fig. 3 OTR beam image at 50 MeV

Measurements of the angular distribution pattern have been done using both a conventional camera and an intensified camera at 100 MeV using a C-mount 50 mm objective. The sensitivity provided by the conventional camera has been satisfactory due to the small aperture of the angular pattern. Nevertheless the use of the 50 mm objective gives poor spatial resolution in the image and a real infinite focusing condition may not be achieved.

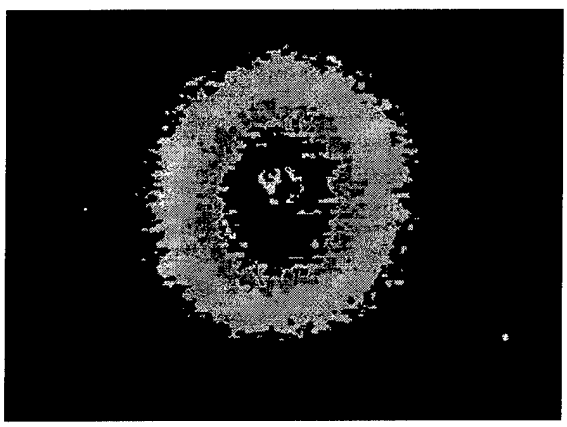

Fig.4 OTR angular pattern at 60 MeV

The second shift has been devoted to a deep study of the relations between peak distance and energy. The optical arrangement has been based on a movable lens of 125 mm focal length and 40 mm diameter and the intensified camera has been used as the detector. The magnification factor provided by the optics has been chosen so that this arrangement allows to make measurements over the whole energy range with the same ratio pixel/mm. This allows a comparison between patterns referred to different energies. Infinite focusing has been defined as the position of the lens relative to the camera CCD which focuses the reflected image of the thermoionic cathode on the radiator (this distance is of the order of 25 meters). Particular care has been devoted to the choice of the camera gain in order to work in linear gain region.

Fig. 4 shows OTR pattern at lens focal plane. The electron energies was 60 MeV. The OTR pattern is ideally a cone with the peak intensity at an angle of approximately 1/c about the direction of specular reflection. The low divergence of the electron beam results in the well defined central null intensity, which gives the "doughnut" shaped pattern observed.

Fig. 5 shows the measured values of the peak distances as function of $1/\gamma$. The relation is linear as expected.

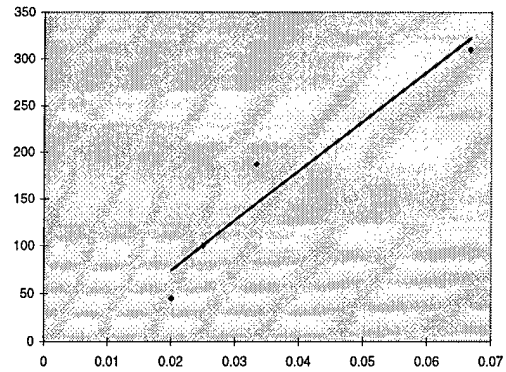

Fig. 5 OTR Peaks Distances vs. $1/\gamma$

CONCLUSIONS

The preliminary measurements above discussed have shown that the experimental setup installed at the Elettra Linac would provide extensive data on OTR emission. Measurements of beam divergence from OTR angular pattern and analysis of the behaviour of different screen materials and thickness will be carried out during 1997.

REFERENCES

1. V. L. Ginzburg, I.M. Frank - JETP 16 (1946) 15
2. L. Wartski - Thesis- Univ. Paris Sud Centre D'Orsay (1976)
3. R.B. Fiorito, D.W. Rule , OTR Beam Emittance Diagnostics - 1993 Faraday Cup Invited Paper
4. D. Giove et al., Low Energy Regime for Optical Transition Radiation Emission, 1995 PAC
5. D. Giove et al., NIM to be published

MEASURING THE RMS LENGTH OF SHORT ELECTRON PULSES WITH AN RF CAVITY AND A BEAM POSITION MONITOR

Steven J. Russell, MS H851, Los Alamos National Laboratory, Los Alamos NM 87545

Abstract

The Sub-picosecond Accelerator at Los Alamos National Laboratory is a 1300 MHz, 8 MeV photoinjector. Its beam can be bunched to sub-picosecond lengths using a magnetic chicane. To observe this, we use an rf cavity operating in a TM_{110} mode to generate a transverse magnetic dipole field that "streaks' each bunch as it passes. Inserting a screen downstream, we determine the pulse length by measuring the increase in the beam spot width. To achieve sufficient resolution two things must happen: first, the unstreaked beam must be well focused at the screen, and, second, the drift after the cavity must be long enough. At high charge and short pulse lengths, these goals become mutually exclusive. To eliminate this problem, we propose using a beam position monitor instead of a screen. The second moment of the beam position monitor signals determines the difference between the x and y rms widths of the beam. With a properly orientated cavity, the resulting change in this quantity also gives the pulse length. However, the BPM does not require a well focused beam at its position, eliminating that constraint on resolution.

1 INTRODUCTION

The Sub-picosecond Accelerator (SPA) has compressed electron bunches containing 1 nC of charge to sub-picosecond lengths[1]. However, in those experiments the length of the electron bunch was inferred by measuring the increase in the beam energy spread after it had drifted some distance[1]. Although effective, this technique is not particularly satisfying because it is not a direct measurement of the bunch length.

For low charge beams, 0.1 nC per beam bunch, we found that a very effective technique for measuring the pulse length was to utilize a simple cylindrical cavity like that shown in Figure 1[1]. By operating the cavity in its TM_{110} mode, the dominate field in the region defined by the 1 inch aperture is a time varying magnetic dipole field. When the timing between the beam pulse and the cavity fields is correct, the head and tail of the pulse are directed in opposite directions, streaking the beam. (Figure 2) Measuring the increase in beam width due to the fast deflector determines the beam bunch length.

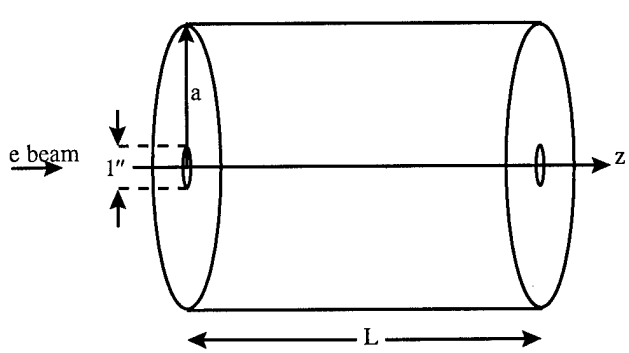

Figure 1: Schematic of fast deflector cavity.

The change in the beam spot width that results from the action of the fast deflector cavity depends upon how far the beam drifts after being streaked. For very short bunch lengths, the drift must be quite long to achieve sufficient resolution. However, the beam must also be focused tightly to get a good image for the camera. At low charge (0.1 nC) we found no conflict between these two requirements. However, at high charge (1 nC) we found that the defocusing due to space charge and the higher beam emittance limited this measurement to resolutions that were not adequate for our purposes[1].

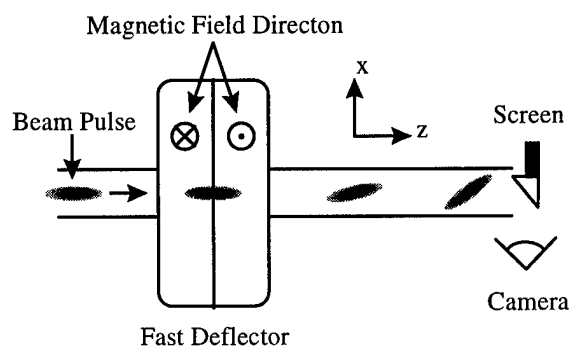

Figure 2: Illustration of fast deflector streaking beam bunch with screen.

To avoid the resolution problem, we intend to replace the screen with a beam position monitor (BPM). (Figure 3) With the fast deflector off, the second moment of the BPM signal determines $\langle x^2\rangle - \langle y^2\rangle$ at the BPM location[2], [3], [4]. The angled brackets indicate an ensemble average. What I will show is that, when the fast deflector is on, this quantity will change to $\langle x^2\rangle - \langle y^2\rangle + a_1^2\langle \phi_z^2\rangle$, where a_1^2 is a constant and $\langle \phi_z^2\rangle$ is the ensemble average of the beam bunch length referenced to the phase of the rf. Therefore, the change in the second moment of the BPM signal determines the rms length of the beam. Unlike the screen, however, the BPM does not require a focus at its position. Therefore, as long as the beam does not intercept the pipe walls, the

0-7803-4376-X/98 /$10.00 © 1998 IEEE

drift length after the fast deflector can be any desired length.

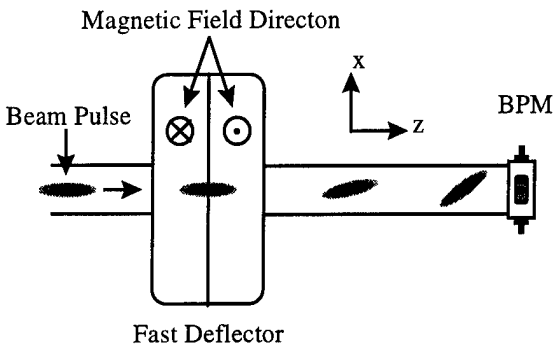

Figure 3: Illustration of fast deflector streaking beam bunch with beam position monitor (BPM).

2 CAVITY FIELDS

In this section, I start with the ideal electric and magnetic fields for a cylindrical cavity operating in its TM_{110} mode. I then change to Cartesian coordinates and make a first order approximation so that the calculation of the motion of an electron through the fast deflector cavity is more manageable.

2.1 Ideal fields

The ideal fields for a cylindrical cavity operating in its TM_{110} mode are

$$E_z = E_0 J_1(k_{11} r)\cos\theta\cos(\omega t + \phi), \tag{1}$$

$$B_r = \omega \frac{a^2}{x_{11}^2 r c^2} E_0 J_1(k_{11} r)\sin\theta\sin(\omega t + \phi) \tag{2}$$

and

$$B_\theta = \omega \frac{a}{x_{11} c^2} E_0 J_1'(k_{11} r)\cos\theta\sin(\omega t + \phi). \tag{3}$$

All other field components are zero. The angular frequency is $\omega = 2\pi f$ where f is 1300 MHz. The constant k_{11} is defined as

$$k_{11} \equiv \frac{x_{11}}{a}$$

where x_{11}, equal to 3.8317, is the first zero of the first Bessel function. The radius of the cavity, a, is 14 cm. The length of the cavity, L, is 14.48 cm. The maximum value of the electric field, E_0, is 24 MV/m, from measurement. The kinetic energy of the electrons as they enter the cavity will be on the order of 8 MeV. The aperture of the cavity, the opening that the beam travels through, is one inch in diameter, or 1.27 cm in radius.

2.2 First order approximation in Cartesian coordinates

Using the relationships

$$\hat{r} = \hat{x}\cos\theta + \hat{y}\sin\theta$$

and

$$\hat{\theta} = -\hat{x}\sin\theta + \hat{y}\cos\theta,$$

I can convert (1), (2) and (3) to Cartesian coordinates. Then, in the 1.27 cm radius aperture region, I can show that the cavity fields are well approximated by

$$E_z \cong E_0 \frac{k_{11}}{2} x\cos(\omega t + \phi), \tag{4}$$

$$B_x \cong \frac{\omega x_{11}}{4ac^2} E_0 xy\sin(\omega t + \phi) \tag{5}$$

and

$$B_y \cong \frac{\omega a}{2x_{11}c^2} E_0 \sin(\omega t + \phi). \tag{6}$$

The magnitude of the ratio of B_x to B_y is

$$\left|\frac{B_x}{B_y}\right| \le \frac{x_{11}^2 r_{max}^2}{2a^2} = 0.03.$$

It can be shown that the electric field will produce a relative change in an 8 MeV electron's energy of less than four percent. In most cases it will be much smaller than this. Therefore, the only significant field in the aperture region is given by equation (6).

3 SOLUTION TO EQUATIONS OF MOTION

In this section, the change in trajectory of a single electron due to the fast deflector is derived. This result is then extended to show the effect of the fast deflector on the value of $\langle x^2\rangle - \langle y^2\rangle$ at the BPM position.

3.1 Trajectory change of single electron

Using equation (6), the equation of motion for an electron through the fast deflector is

$$x'' = \frac{e}{\beta\gamma mc}\frac{\omega a}{2x_{11}c^2} E_0 \sin\left(\frac{\omega z}{\beta c} + \phi\right)$$

where $z = 0$ is defined as the beginning of the cavity. This equation is easily integrated, resulting in

$$x_L \equiv x(L) = -\frac{e}{\gamma m}\frac{a}{2x_{11}c^2} E_0 \frac{\beta c}{\omega}\sin\left(\frac{\omega L}{\beta c} + \phi\right) + c_1 L + c_2 \tag{7}$$

and

$$x_L' \equiv x'(L) = -\frac{e}{\gamma m}\frac{a}{2x_{11}c^2} E_0 \cos\left(\frac{\omega L}{\beta c} + \phi\right) + c_1 \tag{8}$$

where

$$c_1 = x_i' + \frac{e}{\gamma m}\frac{a}{2x_{11}c^2} E_0 \cos\phi \tag{9}$$

and

$$c_2 = x_i + \frac{e}{\gamma m}\frac{a}{2x_{11}c^2} E_0 \frac{\beta c}{\omega}\sin\phi. \tag{10}$$

The initial values of x and x' at the entrance to the fast deflector are x_i and x_i', respectively. The values of x and x' at the fast deflector exit are x_L and x_L'.

3.2 *Effect of fast deflector on* $\langle x^2\rangle - \langle y^2\rangle$

When the fast deflector is off, the second moment of the BPM signal determines the value of $\langle x^2\rangle - \langle y^2\rangle$ for the beam at the position of the BPM. So, we can define this measurement as

$$M_{FD\,Off} \equiv \langle x^2\rangle - \langle y^2\rangle .$$

When the fast deflector is on, the value of $\langle x^2\rangle - \langle y^2\rangle$ changes because the fast deflector is now streaking the beam. The goal is to calculate this change using (7), (8), (9) and (10).

When considering a beam and not a single electron, it is convenient to write the phase angle, ϕ, as

$$\phi = \phi_0 + \Delta\phi + \phi_z .$$

The angle $\phi_0 + \Delta\phi$ is the phase of the beam bunch center with respect to the rf. $\Delta\phi$ is defined as much less than one and is included for calibration purposes. The angle ϕ_z is defined as the phase of a particular electron in the bunch with respect to $\phi_0 + \Delta\phi$.

If the electron beam bunches are short, as is true for the SPA beam, then

$$|\Delta\phi + \phi_z| << 1 .$$

If we assume that the beam line between the fast deflector cavity and the BPM is linear, with the transfer matrix

$$\bar{\bar{R}} = \begin{bmatrix} R_{11} & R_{12} & 0 & 0 \\ R_{21} & R_{22} & 0 & 0 \\ 0 & 0 & R_{33} & R_{34} \\ 0 & 0 & R_{43} & R_{44} \end{bmatrix},$$

then it can be shown that $\langle x^2\rangle - \langle y^2\rangle$ changes to

$$\langle x^2\rangle - \langle y^2\rangle + a_1^2\langle \phi_z^2\rangle$$

where

$$a_1 = \frac{e}{\gamma m}\frac{a}{2x_{11}c^2}E_0\left\{R_{11}\frac{\beta c}{\omega}\left[\cos\phi_0 - \frac{\omega L}{\beta c}\sin\phi_0 - \cos\left(\frac{\omega L}{\beta c} + \phi_0\right)\right] + R_{12}\left[\sin\left(\frac{\omega L}{\beta c} + \phi_0\right) - \sin\phi_0\right]\right\}. \quad (11)$$

Therefore, the measurement with the fast deflector is on is

$$M_{FD\,On} \equiv \langle x^2\rangle - \langle y^2\rangle + a_1^2\langle \phi_z^2\rangle = M_{FD\,Off} + a_1^2\langle \phi_z^2\rangle .$$

So,

$$\langle \phi_z^2\rangle = \frac{M_{FD\,On} - M_{FD\,Off}}{a_1^2} .$$

4 ESTIMATE OF MEASUREMENT RESOLUTION

Assume that the beam line between the fast deflector and the BPM is a drift of length d. The value of a_1 can be calculated from (11). Assuming that the longitudinal distribution of the beam is Gaussian, the value of $a_1^2\langle \phi_z^2\rangle$ can be estimated for different drift lengths and different pulse lengths. The results are shown in Table 1.

It is expected that we will be able to measure the value of $M_{FD\,Off}$ and $M_{FD\,On}$ to ± 0.5 mm^2. Therefore, with a drift length of 2 meters, it is not unreasonable to expect a resolution of 1 picosecond.

	FWHM of Beam Bunch (picoseconds)			
d	20 ps	10 ps	1 ps	0.1 ps
0.5 m	13.65	3.41	0.03	0.000341
1.0 m	52.67	13.17	0.1317	0.001317
1.5 m	117.1	29.28	0.2928	0.002928
2.0 m	206.9	51.73	0.5173	0.005173

Table 1: Value of $a_1^2\langle \phi_z^2\rangle$ (in mm^2) versus drift length, d (in meters), and the full width at half maximum (FWHM) pulse length of the beam.

5 ACKNOWLEDGEMENTS

Work supported by Los Alamos National Laboratory under the auspices of the US Department of Energy.

REFERENCES

[1] B. E. Carlsten and S. J. Russell, "Subpicosecond Compression of 0.1-1 nC Electron Bunches with a Magnetic Chicane at 8 MeV," *Physical Review E*, Volume 53, Number 3, p. 2072-2075.

[2] R. H. Miller et al., "Non-intercepting Emittance Monitor," Proc. 12th Int. Conf. On High Energy Accelerators, (Fermilab, 1983), p. 602 (1983).

[3] S. J. Russell and B. E. Carlsten, "Measuring Emittance Using Beam Position Monitors," Proc. of the 1993 Part. Accel. Conf., p. 2537, IEEE 93CH3279-7.

[4] S. J. Russell, "Preliminary Results of RMS Emittance Measurements Performed on the Sub-picosecond Accelerator using Beam Position Monitors," (these proceedings.)

DEVICE FOR THE ELECTRON BUNCH LENGTH MEASUREMENT OF 1-5 MM RMS

V.E.Kaljuzhny, D.V.Kostin, N.P.Sobenin, S.N.Yarigin,
Moscow Engineering Physics Institute, Russia,
A.A.Zavadtsev, Moscow Radiotechnical Institute of Russian Academy of Sciences, Russia,
M.Dohlus, N.Holtkamp, Deutsches Electronen Synchrotron, Germany.

Abstract

Two variants of bunch length monitor (BLM) for the measurement of 1-5 mm rms bunch length (σ_z) are offered. The first one was designed for the measurement of a single bunch rms. It consists of two cavities, each of them operates at two modes, E_{010} and E_{110}. The second variant of BLM was designed for the measurement of a rms of the bunches with repetition period less then 16 ns (series of identical bunches). There are two cavities in the BLM too. Loop coupling is used for the cavities and cavity-filters.

1 INTRODUCTION

There are some methods of electron bunch length measurement with unknown charge distribution in the bunch. One of them is based on the measurement of the amplitudes of oscillations excited by the bunch in the two cavities with various frequencies [1]. The ratio of these amplitudes permit to determine σ_z. This work is devoted to development of the BLM for the measurement of σ_z in a range from 0.5 to 1 mm. Additional work is devoted to development of BLM for the measurement of a single bunch length and of the identical bunches in the series in the range of σ_z from 1 to 5 mm.

2 THEORETICAL SUBSTANTIATION

Let us consider the bunch with the charge distribution, given by:

$$\xi(z_1) = qF(z_1) \tag{1}$$

where q is bunch charge, $F_G(z_1)$ and $F_R(z_1)$ are Gaussian and rectangular charge distribution:

$$F_G(z_1) = \frac{1}{\sqrt{2\pi}\sigma_z}\exp\left(-\frac{z_1^2}{2\sigma_z^2}\right);\ F_R(z_1) = \begin{cases}\left[2\sqrt{3}\sigma\right]^{-1} & \text{if } |z_1| \le \sqrt{3}\sigma_z \\ 0 & \text{if } |z_1| > \sqrt{3}\sigma_z\end{cases} \tag{2}$$

The electromagnetic field components of the bunch may be represented as

$$E_Z(r,t) = -\frac{Z_0 cq}{4\pi r^2}\int_{-Z_{11}}^{Z_{11}} F(z_1)\gamma\frac{z_1+\beta ct}{r}\left[1+\left(\gamma\frac{z_1+\beta ct}{r}\right)^2\right]^{-3/2} dz_1$$

$$E_r(r,t) = \frac{Z_0 cq}{4\pi r^2}\gamma\int_{-Z_{11}}^{Z_{11}} F(z_1)\left[1+\left(\gamma\frac{z_1+\beta ct}{r}\right)^2\right]^{-3/2} dz_1 \tag{3}$$

$$H_\varphi(r,t) = \frac{\beta}{Z_0}E_r(r,t)$$

where γ is relativistic factor of the bunch, Z_0 is a free space impedance, Z_{11} can be equaled to $5\sigma_Z$ for the Gaussion distribution and $\sqrt{3}\,\sigma_Z$ for the rectangular distribution, $\beta=\gamma^{-1}(\gamma^2-1)^{1/2}$, r is a distance from the bunch axis.

Let's represent the cavity excited by the bunch as two port junction with own frequency f_{res}, loaded Q-factor Q_L, input coupling coefficient with free space χ_1 and output coupling coefficient with waveguide χ_2 (its wave impedance Z_{02}). The e.m.f. exciting the cavity has the same time dependence as $E_r(t)$ or $H_\varphi(t)$ in expressions (3). Using superposition principle one can get the expression for the output voltage $U_2(t)$ after excitation by N bunches as follows

$$\begin{aligned} U_2(t) \propto\ & 3\frac{\gamma^2 Z_0 cq}{4\pi r^3}\sqrt{\frac{Z_{02}}{Z_0}}\frac{\sqrt{\chi_1\chi_2}}{1+\chi_1+\chi_2}\times \\ & \times\frac{\sqrt{A^2+B^2}}{Q_L\sqrt{1-(1/2Q_L)^2}}\times \\ & \times\left|\frac{\exp(-N\Delta Z_b/\beta c\tau_c)\exp(j\omega N\Delta Z_b/\beta c)-1}{\exp(-\Delta Z_b/\beta c\tau_c)\exp(j\omega\Delta Z_b/\beta c)-1}\right|\times \\ & \times\exp\left(-\frac{z-(N-1)\Delta Z_b+Z_{22}}{\beta c\tau_c}\right)\times \\ & \times\cos\left\{\frac{\omega}{\beta c}\left[z-(N-1)\Delta Z_b+Z_{22}\right]+\varphi+\alpha\right\} \end{aligned} \tag{4}$$

where $\omega=\omega_{res}[1-(1/2Q_L)^2]^{1/2}$, $\omega_{res}=2\pi f_{res}$, $\tau_c=2Q_L/\omega_{res}$, $\Delta Z_b=\beta c/f_b$, f_b is repetition frequency of the bunches, $z=\beta ct \ge (N-1)\Delta Z_b+Z_{11}$, Z_{22} can be equaled to $10r/\gamma$,

$$A+jB = \int_{-Z_{11}}^{Z_{11}}\int_{-Z_{22}-Z_{11}}^{Z_{22}+Z_{11}} F(z_1)\gamma\frac{z_1+z_2}{r}\left[1+\left(\gamma\frac{z_1+z_2}{r}\right)^2\right]^{-5/2}\times$$

$$\times\exp\left[\frac{z_2}{\beta c\tau_c}+j\left(\frac{\pi}{2}-\frac{\omega}{\beta c}z_2\right)\right]dz_1dz_2$$

$$\varphi = \arg(A+jB)$$

$$\alpha = \arg\left[\frac{\exp(-N\Delta Z_b/\beta c\tau_c)\exp(j\omega N\Delta Z_b/\beta c)-1}{\exp(-\Delta Z_b/\beta c\tau_c)\exp(j\omega\Delta Z_b/\beta c)-1}\right]$$

Spectra of H_φ (r is vary small) for rectangular and Gaussian distributions and bunch lengths of 1 and 5 mm are shown in Fig.1. For a measurement of σ_z it is necessary to choose frequencies of cavities in a such way that Gaussian and rectangular distributions are close to each other and steepness of characteristic is satisfactory.

0-7803-4376-X/98 /$10.00 © 1998 IEEE

3 SINGLE BUNCH σ_Z MEASUREMENT

BLM shown in Fig.2 includes two cylindrical cavities. Each cavity operates at frequencies of two modes E_{010} and E_{110} (frequencies of the first cavity are 4.5 and 7.2 GHz, frequencies of the second cavity are 11.3 and 18.0 GHz).

Each cavity (1 and 2) has input slot (3 and 4), two output slots for the coupling of E_{010} mode with waveguide (5 and 7) and one output slot for the coupling of E_{110} mode with waveguide (6 and 8).

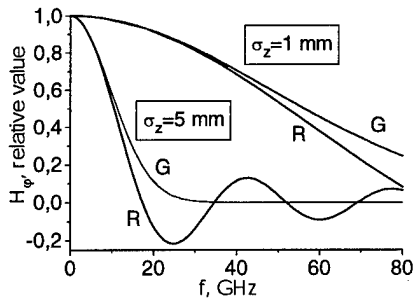

Figure: 1 The spectra of magnetic field H_φ at σ_z=1 and 5 mm for rectangular (R) and Gaussian (G) distributions.

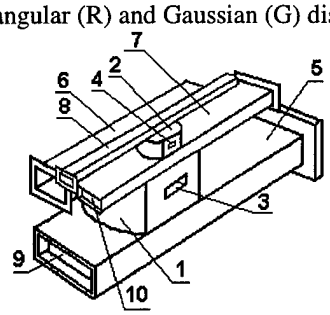

Figure: 2 Single bunch BLM.

One end of each waveguide is connected to a recording equipment. Movable plunger (9 and 10) is located in other end for regulation of output coupling coefficient χ_2.

The signal excited by bunch through input slot is extracted from the cavity through output slots, and comes through the waveguides to the recording equipment.

The time constants τ_c of cavities at these four frequencies should be equal each other and $\tau_c < T/3$, where T is bunch period (T=16 ns in this case). Let's assume τ_c = 5 ns. The values of own Q-factor Q_0, χ_1 and χ_2 are shown in Table 1.

The results of measurements of coupling coefficients χ_1 of the E_{010} and E_{110} cavity modes with free space are shown in Fig.3 (l_{s1} is slot length, cavity diameter D=82.9 mm, cavity length L=29.4 mm, slot width h_{s1}=4 mm).

The possibility of output coupling coefficient regulation by plungers displacement is shown on Fig.4 (D=51 mm, L=16 mm; E_{010} - 4,5 GHz, two slots, l_{s2}=23 mm, h_{s2}=3 mm; E_{110} - 7.2 GHz, one slot, l_{s2}=8 mm, h_{s2}=2 mm. Λ - wave length in the waveguide).

Parameters of BLM got on the basis of calculations and measurements are summarized in Tab.1.

Calculations executed with use of the above-mentioned method allow to get the form of the signal in output waveguide (see Fig.5).

Table 1

D, mm	51		20	
L, mm	8.0		6.8	
l_{s1}, mm	16.0		5.4	
h_{s1}, mm	2.4		1.0	
f_{res}, GHz	4.5	7.2	11.3	18.0
l_{s2}, mm	23	8	5	2.5
h_{s2}, mm	3	2	2	1
a, mm	35	23	16	11
b, mm	15	10	8	5.3
Q_0	7860	10240	4960	6460
χ_1	5	85	1	18
χ_2	105	5	28	4
σ_Z, mm	-	5-4	4-2.5	2.5-1
$\Delta\sigma_z/\sigma_z$, %	-	15-21	6-16	6-29

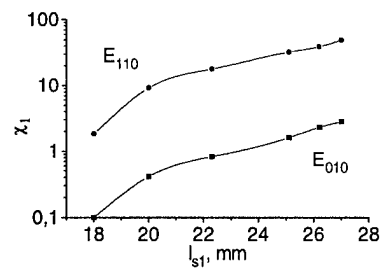

Figure: 3 Input coupling coefficients as function of coupling slot length.

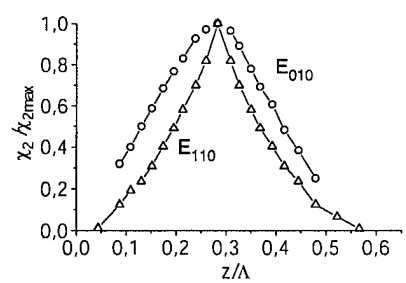

Figure: 4 The output coupling coefficients χ_2 as function of plunger position.

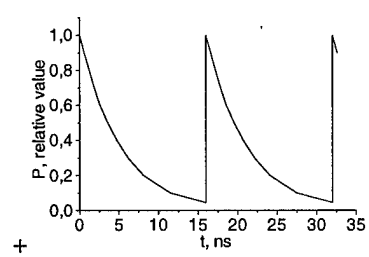

Fig.5. Time dependence of RF power in the output waveguide (T=16 ns).

The calibration diagram is shown in Fig.6, where P_i (i=1, 2, 3, 4) are peak power in waveguides (see Fig.5)

with sides a and b at frequencies 4.5, 7.2, 11.3 and 18.0 GHz correspondingly.

The error of σ_z measurement is determined by recording equipment error (3%), errors of χ_1, χ_2, Q_0 measurements (3%), and by steepness of calibration diagram $\sigma_z(P_i/P_1)$ in the point of interest.

4 σ_Z MEASUREMENT WITH A SERIES OF BUNCHES

Series of bunches have following parameters: the bunch length σ_z=1-5 mm, the frequency of an accelerating field f_0=2998 MHz, the bunch repetition rate $f_b=f_0/48$-$f_0/18$ (bunch spacing T=6-16 ns), the current pulse length τ_p=2 μs. The BLM must satisfy the following conditions.

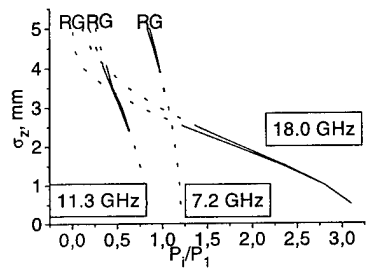

Figure: 6 Calibration diagram.

The own frequencies of BLM cavities should be divisible by f_0. The values of operational frequencies of the BLM are f_0, $3f_0$, $5f_0$ (see Tab.2). The time constants of cavities should be equal to each other and should satisfy to following condition $T<\tau_c<\tau_p/3$. χ_1 and χ_2 decrease with increasing of τ_c, with results in a decrease of the transmission factor of the BLM. At low τ_c the envelope of the RF oscillations becomes more sawtooth, but simultaneously the cavity frequency tuning tolerance increases. We take τ_c =50 ns.

Table 2.

Cavity	1	2	
D, mm	76	25	
L, mm	4	9	
l_{s1}, mm	17.5	5	
h_{s1}, mm	4	2	
f, MHz	2998	8994	14990
Q_0	2400	5560	7240
χ_1	2.5	0.1	2
χ_2	1.6	2.8	0.1
σ_Z, mm	-	5-2.5	2.5-1
$\Delta\sigma_z/\sigma_z$, %	-	6-22	10-40

BLM includes two cavities. The first cavity has an operational mode E_{010} and resonant frequency $f_{res1}= f_0$, the second one has two operational modes E_{010} and E_{110} with frequencies $f_{res2}=3f_0$ and $f_{res3}=5f_0$.

The second cavity represented in Fig.7 includes input slot 1, output E_{010} mode pin coupler 2 with the RF connector 4, output E_{110} mode loop coupler 5 with the RF connector 3, tuning elements 6, 7, 8. The ring ledges 9 near the cavity axis allow to ensure $f_{res2}/f_{res3}=3/5$. The first cavity includes an input slot, output pin coupler and axial tuning element. The parameters of BLM are summarized in Table 2. The calculated voltage pulses in output line for T=6 ns and T=16 ns are shown in Fig.8. The calibration diagram calculated with expression (3) is shown in Fig.9.

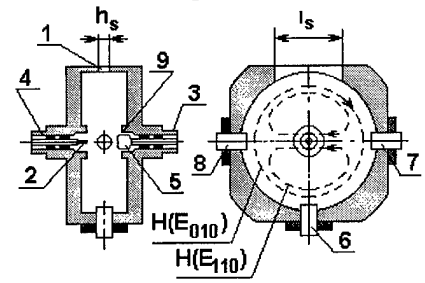

Figure: 7 The cavity with frequencies $3f_0$ and $5f_0$.

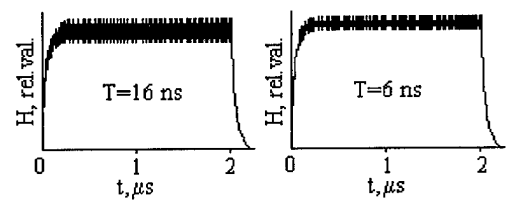

Figure: 8 The voltage pulses in output line.

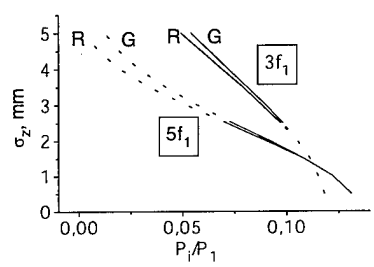

Figure: 9 The calibration diagram.

5 HIGH FREQUENCY FILTERS

Fig.1 shows the bunches generate frequencies up to tens GHz. RF signal at frequencies of higher non-operational modes of BLM cavities can pass through BLM to the recording equipment and produce an additional error of the measurement. The cavity-filters are used to eliminate this influence. The lowest own frequency of the cavity-filter is equal to operational frequency f_0.

These cavity-filters are necessary for both BLM modifications.

REFERENCES

1. E.Babenko, R.K.Jobe at. all. Length Monitor for 1 mm SLC Buncher, Proc. of the 1993 Particle Accelerator Conference, 1993, V.3, p.2423-2426.

A NEW FREQUENCY-DOMAIN METHOD FOR BUNCH LENGTH MEASUREMENT

M. Ferianis, M. Pros, Sincrotrone Trieste, Italy and A. Boscolo, Università di Trieste-DEEI, Italy

Abstract

A new method for bunch length measurement has been developed at ELETTRA. It is based on a spectral observation of the synchrotron radiation light pulses. The single pulse spectrum is shaped by means of an optical process which gives the method an increased sensitivity compared to the usual spectral observations.
Some simulations have been carried out to check the method in non-ideal conditions. The results of the first measurements are also presented.

1 INTRODUCTION

ELETTRA is a third generation synchrotron light source in operation in Trieste since 1993. In the ELETTRA storage ring electrons with energies from 1 GeV to 2 GeV are routinely accumulated, both in Multi Bunch (MB) and in Single Bunch (SB) mode.

The length of the electron bunches in Storage Rings is an important parameter to measure, both for machine Physicists and for Synchrotron Light Users. In fact, the bunch length vs. current curve is necessary when the broadband impedance of the vacuum chamber is evaluated [1]. Similarly, when Users are doing fast time dependent experiments, they need to know the bunch length in order to have an indication of the time resolution of their experiment [2].

2 METHOD DESCRIPTION

2.1 Bunch Length measurements

In third generation synchrotrons, the measurement of the bunch length is not a straightforward task due to the extremely short stored bunches (in the mm range).

For these measurements, optical methods [3] have many advantages over purely electrical ones, particularly in Storage Rings. In these machines, the temporal profile of the intensity of the synchrotron radiation from a bending magnet is an exact replica of the electron longitudinal distribution within the bunch. This train of very short light pulses can be optically transported up to the acquisition point without appreciable distorsion. As a direct consequence, the length of the cable connecting the sensor to the acquisition instrument is reduced to a minimum and so is the Rise Time of the system. At ELETTRA, the synchrotron light of a storage ring bending magnet, already used for other diagnostic purposes [4] [5], has been therefore chosen as the source point for this measurement. The work and the results here reported are part of an Electronic Engineering degree thesis [6] at the Trieste University.

2.2 Method general features

This new method thoroughly exploits the information buried in the short light pulse without using dedicated instruments, like the Streak Camera; it has been developed under the assumption of gaussian light pulses.

This new technique is based on the Frequency-Domain analysis of a fast photodiode response to an optically processed version of the beam produced light pulse. This technique, which makes use of standard laboratory instrumentation, like the Spectrum Analyser (SA), offers an enhanced resolution if compared to usual spectral observations (see next paragraph).

Using a SA for the acquisition, this method does not provide a Single Shot measurement of the bunch length. This feature is not of big concern when dealing with stable beams and triggers. At ELETTRA, this operating condition has been recently checked out in SB mode [7].

Moreover, the input extended dynamic range of the SA [8] could eliminate the need for an amplifier: this is also a major advantage as any element between the source and the acquisition point deteriorates the measurement quality.

2.3 The optical signal processing

The optical signal processing used in this method creates a delayed replica of the original pulse. It is obtained by means of multiple reflections between parallel mirrors. A similar optical arrangement has been used at CERN, by E. Rossa, to perform "Real Time Slice Tomography" [9]. The original pulse, along with its delayed replica, are summed up by means of an ultra-fast photodiode [10], [11]; the output from the photodiode is then sent to the SA.

This "slice and sum" technique generates a modified version of the original pulse spectrum, the modification depending on the introduced optical delay. As a consequence, the SA is not used for an absolute amplitude measurement of the spectral lines, but rather it is used to find a threshold, defined in par. 3, by means of a relative measurement on the whole spectrum envelope. This threshold is searched by varying the optical delay. The bunch length is then computed from the value of the introduced optical delay. This, in turn, can be either directly measured (time observation of the processed signal) or estimated (from the mirror distance).

3 THEORY AND SIMULATIONS

3.1 Theoretical background

The spectrum (see Fig. 1) of the sum of two gaussian time-delayed pulses is given by:

$$H(\omega) = \left|\cos\left(\frac{\omega d}{2}\right)\right| e^{-\frac{\omega^2\sigma^2}{2}}$$

0-7803-4376-X/98 /$10.00 © 1998IEEE

where:

- $H(\omega)$ normalised amplitude of $F(\omega)$
- σ variance of a single gaussian pulse
- d delay between pulses
- $F(\omega)$ Fourier transform of the sum of two pulses

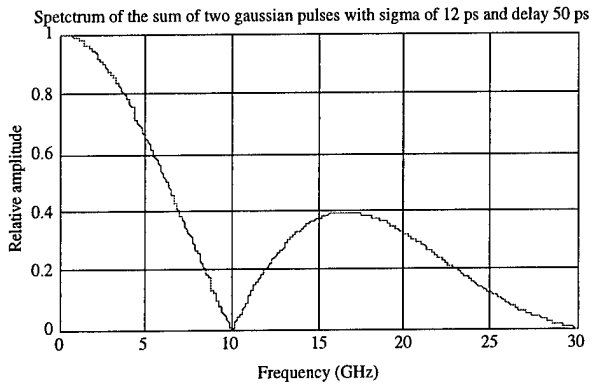

Figure : 1 Theoretical spectrum of the sum of two delayed gaussian pulses (σ=12 ps) with a delay of 50 ps.

The left-hand factor of $H(\omega)$ depends both on frequency and on the delay; it does not depend on σ. The right-hand factor of $H(\omega)$ is the spectrum of a single gaussian pulse; it is independent on the delay. Therefore, by varying the delay d, the second peak of the spectrum moves along the spectrum of the single gaussian pulse.

It has been computed a maximum of sensitivity for $d = 0.4428*\sigma$; in that situation the second maximum of the envelope is 43.27% of H(0).

3.2 Simulation set-up overview

Since the stored beam generates a pulse train whose periodicity reflects the machine circumference and its filling mode, simulations have been carried out to evaluate the perfomance of the method when applied to a not purely gaussian pulse.

At first, a model of the MB (80% filling) time structure, normally used at ELETTRA, has been created and its spectrum computed (see fig.2) by means of an FFT algorithm [12].

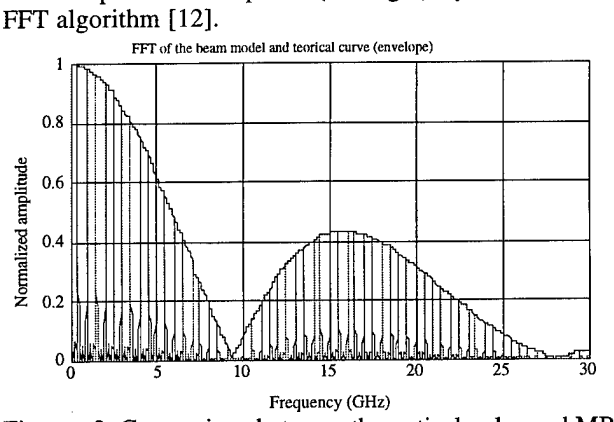

Figure : 2 Comparison between theoretical pulse and MB periodic structure pulses spectra.

Then, distorsions which can be found in real beams, have been introduced into the model, like pulse-to-pulse amplitude and σ variations, longitudinal oscillations, single pulse waveform distorsions from purely gaussian (ringing, tails). The effects of these distorsions on the computed spectrum amplitudes and, therefore, the errors introduced in the bunch length evaluation, were found to be of few percent.

Simulations have also been performed to estimate the spectrum distorsion introduced when using the actual photodiode [11]. A delayed and summed up gaussian pulse has been convoluted with the pulse response of the photodetector. By doing so, the waveform available at the Spectrum Analyser input has been simulated. Then, the spectrum has been computed and the threshold condition searched. The σ obtained in this way has been compared to the σ of the original gaussian pulse. A maximum error of 11 % has been found out, for a range of σ from 12 to 70 ps.

4 FIRST MEASUREMENTS

4.1 Measurement set-up

As already mentioned, the optical delay line has been implemented by means of two square mirrors (see Fig. 3). The first one has been mounted on a motorised translation stage and reflects backwards half of the beam radiation. The second mirror, placed at a fixed location, reflects forwards the radiation from the first mirror. As a result, two parallel beams are created and summed up by the photodiode. The delay between the two pulses is proportional to the distance between the mirrors and can be varied in steps much smaller than a pico-second (Δt=13.3 fs for a 2 μm stepping motor).

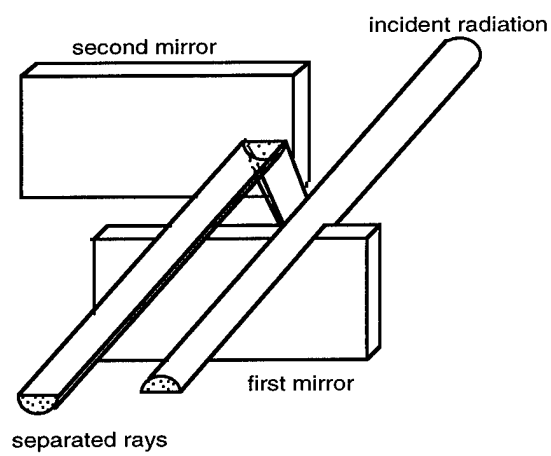

Figure : 3 Schematic of the double mirrors assembly.

A grin lens is used to focus both rays on the active area of the photodiode (25<D<400 μm). The signal from the photo-diode is sent to the Spectrum Analyser with no amplifier in between.

4.2 First results: time-domain observation

Some preliminary observations have been carried out with a 1.5 GHz bandwidth photodiode [10]. The correctness of the method and its practical feasibility have been checked with this component.

The set-up of the optical delay line has been carried out observing in time-domain the photodiode output signal. A Tektronix TDR 7S12 sampling scope, equipped with a 12.4 GHz sampling head, has beeen used. In order to achieve two pulses (see Fig. 4) of the same amplitude the photodiode has been carefully aligned. The 2-ns period of our MB filling is visible as well as the introduced 650 ps delay between pulses.

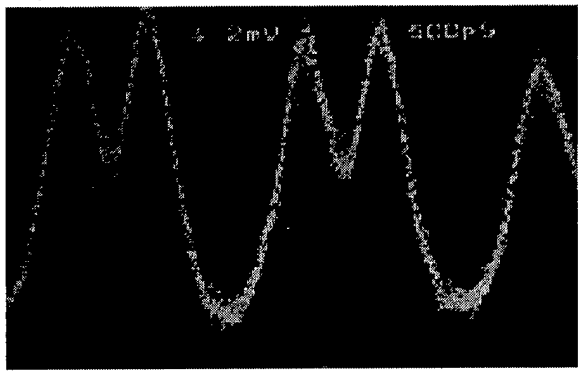

Figure : 4 original pulse and delayed replica relative to two MB pulses (delay 650 ps).

The 650 ps delay is compatible with the slow pulse response of the photodiode (bandwidth limited to 1.5 GHz). To allow an easier time-domain observation the photodiode signal has been amplified by means of an in-house made amplifier with a cut-off frequency of 2 GHz (MAR7 monolitic amplifier from Minicircuit).

4.3 Frequency-domain observations

Some preliminary spectral observations have been performed matching the photodetector directly to a Rhode & Schwarz Spectrum Analyser (model FSMS). The spectral lines from 500 MHz to 3.5 GHz have been measured.

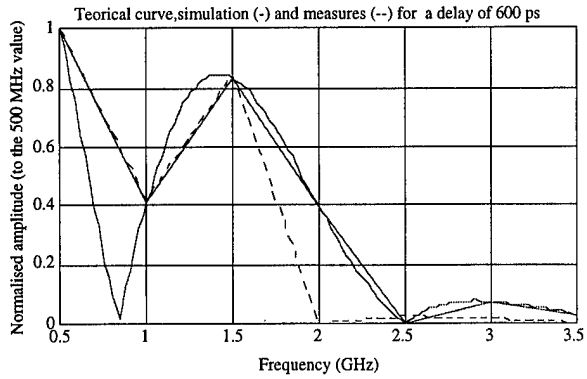

Figure : 5 Comparison between theoretical, simulated and measured spectral line amplitudes.

In Figure 5 these values are compared both with the values obtained in the previously described beam simulation and with the values of the theoretical spectrum of two gaussian pulses. In this simulation, the pulses have been considered gaussian, matching in duration the photodiode pulse response which has been measured with the sampling scope. In the theoretical computation two gaussian pulses with the same σ and delay as in the simulation have been used. The comparison has been made normalising the data to the 500 MHz peak value: a good agreement with the theoretical and calculated values within the band of the photodiode. At 2 GHz the photodiode cut-off is dominant.

5 CONCLUSIONS

A new method for bunch length measurement has been studied at ELETTRA. The theoretical studies have been checked with an extended numerical simulation to analyse the effects on the method due to the actual acquired signal. Preliminary tests has been carried out with a 1.5 GHz photodiode: the results are in good agreement both with the theory and the numerical model.

One major advantage of this method consists in that it uses ordinary laboratory instrumentation, like the Spectrum Analyser.

Future work include extended tests with a wide bandwidth photo-diode to perform a true bunch length measurement in order to fully confirm the validity of the method.

6 ACKNOWLEDGMENTS

The Authors wish to thank the whole Instrumentation Group of ELETTRA Accelerator Division for the very valuable assistance during the measurements: in particular, R. De Monte for his support in the wide-band amplifier design and implementation.

7 REFERENCES

[1] J. A. Clarke et al., "Revised SRS Impedance Estimates" in EPAC '94 London, June 1994
[2] G. Margaritondo, "Synchrotron Light and Free-Electron Lasers", Il nuovo cimento, 1995
[3] E. Rossa, "Picosecond Diagnostics", Optical Engineering, August 1995, Vol.34 No. 8, pp.2353-2360
[4] M. Ferianis et al., "The Optics of the ELETTRA Transverse Profile Monitor" in EPAC '94 London, June 1994
[5] M. Ferianis et al., "An Optical System for the observation of Transverse Beam Motion" in EPAC '96 Barcelona, June 1996
[6] M. Pros, "Misura del Profilo Longitudinale del Fascio di Elettroni di ELETTRA", Degree Thesis at:"Universita' degli Studi di Trieste", 1996
[7] M. Ferianis et al., "Bunch Length Measurements at ELETTRA" Sincrotrone Trieste Technical Note, April 1997
[8] "FSMS Spectrum Analyser", Rohde & Schwarz
[9] E. Rossa at al., "Real Time Measurement of Bunch Instabilities in LEP in three Dimensions using Streak Camera", EPAC '92 Nice 1992
[10] "S 4753, High-speed PIN silicon Photodiode, Technical Data, Hamamatsu Photonics
[11] "High speed Photodetectors", New Focus inc.
[12] "MATLAB User Manual", The Mathworks inc.

MECHANICAL DESIGN OF THE HER SYNCHROTRON LIGHT MONITOR PRIMARY MIRROR FOR THE PEP-II B-FACTORY*

Edward F. Daly, Alan S. Fisher, Nadine R. Kurita and J Brian Langton,
Stanford Linear Accelerator Center, Stanford CA USA

Abstract

This paper describes the mechanical design of the primary mirror that images the visible portion of the synchrotron radiation (SR) extracted from the High Energy Ring (HER) of the PEP-II B-Factory. During off-axis operation, the water-cooled GlidCop mirror is subjected to a heat flux in excess of 2000 W/cm^2. When on-axis imaging occurs, the heat flux due to scattered SR, resistive wall losses and Higher-Order-Mode (HOM) heating is estimated at 1 W/cm^2. The imaging surface is plated with Electroless Nickel to improve its optical characteristics. The design requirements for the primary mirror are listed and discussed. Calculated mechanical distortions and stresses experienced by the mirror during on-axis and off-axis operation will be presented.

1 INTRODUCTION

The design approach for the SR Light Monitor System has been described in detail[1] and is based on standard design parameters for the HER Arc Vacuum System[2]. The 3 A, 9 GeV electron beam is circulated around the HER through 192 dipole magnets with bend radii of 165m that each emit 55 kW of radiation. The SR is widely distributed in the arcs; the copper vacuum chamber outer wall intercepts up to 102 W/cm.

The shallow angle of SR incidence on the chamber wall, stringent impedance requirements and the magnet packing factor in the arcs lead to complicated design solutions. These factors adversely impact any designs that employ relatively large source-to-optic distances, crotch-style absorbers and "Y"- chambers such as those implemented by APS[3] and others. At SLAC, PEP had originally implemented a system that reflected the light back across the beam axis to optics on the inside of the ring perimeter. The system for PEP-II is similar in concept, but manages the SR heat loads in a slightly different fashion.

A GlidCop mirror and photon absorber replace a 190mm (7.5") section of the outer wall of the dipole vacuum chamber. During on-axis operation, the hot portion of the SR fan, estimated at 1 mm in height, passes through a shallow slot in the mirror imaging face and is intercepted in the GlidCop photon absorber. The heat load during imaging due to scattered SR, resistive wall losses and HOM heating is estimated at 1 W/cm^2. During off-axis imaging, the SR is incident on the mirror at nominally 4° to grazing, depositing up to 200 W/cm along the mirror face for 3 A, 9 GeV operation. This lineal power deposition corresponds to a heat flux of 2000W/cm^2. This power deposition may occur as high as 5 mm from the nominal HER beam axis.

2 MIRROR DESIGN DESCRIPTION

2.1 General Requirements

The GlidCop mirror and absorber combination have the following design criteria:

- Reliable on-axis imaging
- Withstand off-axis thermal loading
- In-situ adjustment and replacement capability
- Integrate into existing dipole chamber design
- Compatible with 10 nTorr UHV System
- Minimal impedance
- Provide SR masking

The general requirements cover three basic categories: optical, vacuum and mechanical requirements.

2.2 Optical Design Requirements

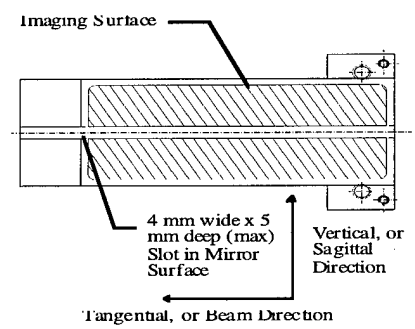

Figure 1 Optical Surface of the Primary Mirror

The imaging surface of the mirror is plated with Electroless Nickel (9% Sulphur, 180°C bath) to a maximum of 0.1 mm thick. Reliable imaging dictates fairly stringent surface quality including figure, slope error and surface roughness. The figure of the mirror after polishing is specified to be flat to $\lambda/40$ rms measured by He-Ne laser interferometry at 632.8 nm over the 81.2 mm x 34.9 mm (3.198" x 1.375") optical surface. The required slope error is specified not to exceed 5 μrad rms,

* Work supported by the U.S. Department of Energy under contract number DE-AC03-768F00515

corresponding to an rms slope of λ/5 over a 25 mm distance. The mirror roughness after polishing is acceptable if less than 10 Å rms.

Image quality near the slot is important to minimize the effects of edge scattering. Therefore, the specifications above apply up to 0.2 mm from the edge of the slot. This surface adjacent to the slot as well as a 2-mm-wide area along the outer perimeter of the imaging surface are not required to meet the surface quality specifications.

2.3 Vacuum Requirements

For 10 nTorr UHV systems, SLAC requires certified materials, cleanliness consistent with 100K class clean rooms, and no direct water-to-vacuum joints. These requirements are implemented to improve vacuum system reliability. In particular, welded or brazed joints that carry cooling water are air-guarded from the vacuum system.

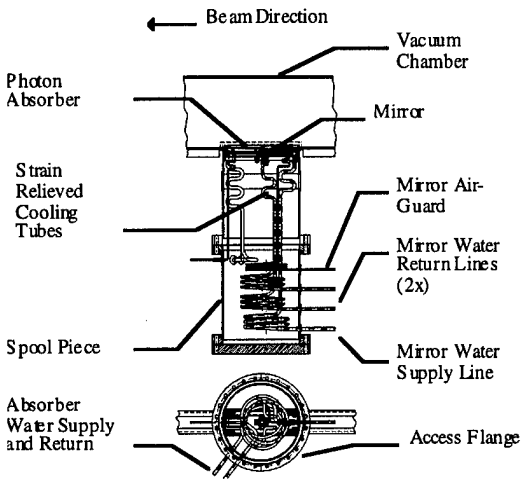

Figure 2 Mirror and Absorber Assembly

2.4 Mechanical Design Requirements

The key elements of the mechanical design consist of managing the thermal loads to facilitate reliable imaging, packaging the assembly in the dipole chamber geometry, providing in-situ alignment and repair or replacement.

For thermally loaded mirrors, substrate selection is dependent on three material properties: thermal conductivity, thermal expansion and yield strength. Manufacturing considerations such as metals joining, machining and optical preparation also drive material selection.

GlidCop , Molybdenum, Beryllium and Copper have been considered. While Molybdenum has very high yield strength and low thermal expansion, it is difficult to machine and join. Beryllium has relatively high thermal expansion but low yield strength. It too requires special care during machining. Copper has better thermal conductivity than even the best GlidCop, but has very low yield strength after brazing compared with GlidCop. GlidCop is chosen for its relatively high thermal conductivity, yield strength and relative ease of manufacture.

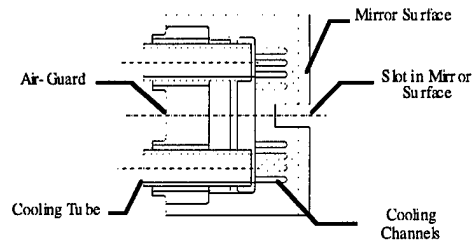

Figure 3 Section of Mirror at Cooling Outlets

Thermal distortion is minimized on the substrate by employing a cooling scheme similar to those implemented by DiGennarro et al[4]. The cooling passages are within 2.5 mm of the imaging surface and are evenly spaced in the sagittal direction. A flexible mount allows the mirror to expand 0.2 mm during off-axis operation.

Masking is required to avoid SR striking any surfaces at more than grazing incidence angles. During on-axis imaging, the chamber opening masks the upstream end of the mirror and absorber simultaneously. During off-axis imaging, the chamber masks the mirror and the mirror masks the absorber. Three RF seals, each masked by their immediate upstream components, bridge gaps between the chamber, mirror and absorber. By design, the leading edge of the mirror cannot inadvertently be moved beyond its masking point into the SR fan.

The mirror and absorber are attached with adjustable fasteners to a mounting plate. Yaw and roll of the mirror can be set to within ±1 mrad and ± 3 mrad respectively. Strain-relieved cooling tubes are routed from the back of the subassembly to a spool piece. The spool piece provides external water supply to the mirror and absorber. The air-guard, which eliminates water-to-vacuum braze and weld joints, has a small tube routed through the spool to the tunnel atmosphere. The assembly is inserted through a flange-to-rectangular-tube brazement that is electron-beam welded to the modified dipole chamber.

3 ANALYSIS

Modulus of Elasticity	131 GPa (19E6 psi)
Yield Strength (1 hr @ 1000°C)	303 MPa (44E3 psi)
Thermal Conductivity	365 W/m-°C
Thermal Expansion	16.6E-06/°C

Table 1 Mechanical Properties of GLidCop AL-15

The mirror must function reliably at low heat loads, 1 W/cm^2, and withstand high thermal stresses while intercepting the off-axis SR fan, 2000 W/cm^2. A 2D triaxial stress finite element model has been developed using ANSYS to help determine the optimum cooling

geometry. Strategic water routing can markedly improve mirror performance. To provide symmetry during on-axis operation, all cooling channels are plumbed in parallel. A flow rate of 1 gal/min, corresponding to a heat transfer coefficient of 2 W/cm^2-°C, yields almost no bulk temperature rise during imaging for a ~35W total heat load. A conservative value of 0.8 W/cm^2-°C is used for the analyses, along with a bulk water temperature of 35°C.

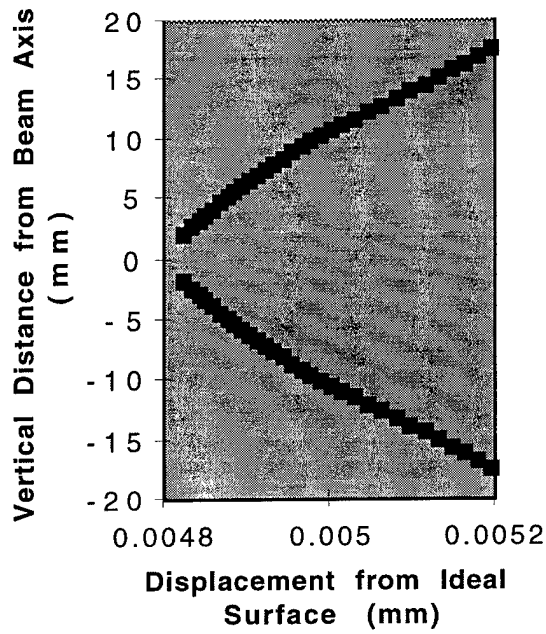

Figure 4 Distortions from Ideal Surface for 2.5 mm Deep Slot

The water passages are machined inward from the backside of the mirror. A cover is then brazed on to seal the passages. It is assumed that the cover is not thermally connected to each web between water passages, but only in the thick middle portion as well as the outer edges. This is a conservative assumption since the added thermal conduction and subsequent convection would lower the peak temperatures of the mirror for both loading cases. Also, hydraulic pressure has almost no effect on mirror surface figure or slope error.

3.1 On-Axis Imaging

The water passage number, height, width and depth (below the optical surface) directly affect the optical characteristics. Deeper slots reduce the mirror temperature during imaging but increase the estimated sagittal slope errors. The added surface area cools the backside and increases angular errors on the mirror face. Shallower slots raise the bulk temperature of the mirror adversely affecting the mirror figure, and produce higher peak compressive stresses during off-axis operation.

3.2 Off-Axis Durability

Peak compressive stresses due to the SR strike during off-axis imaging are estimated at 267 MPa (39 ksi). The hot-spot peak temperature is 196°C. This peak value is relative insensitive to the depth of the cooling passages. For 3A, 9 GeV operation, the peak stress is 89% of the quoted yield strength.

3.3 Three-Dimensional Effects

The sagittal slope error calculated is ~23 μrad for a 2.5mm deep slot. For reference, the installed mirror system must limit the tangential and sagittal slope errors to 15 μrad and 35 μrad respectively. The 2D analysis shows that increasing the depth of the slot markedly increases the sagittal slope error. At 5 mm deep, the slope error is more than an order of magnitude larger. A slope error of this size is clearly unacceptable for proper imaging.

The slot varies in depth from 0.5 mm at the leading edge of the mirror to 5 mm at its deepest. This axial slot depth variation requires three dimesional modeling to fully determine the mirror figure and slope errors. The operational stresses predicted by the 2D analysis will be comparable to the 3D calculations.

4 PLATING AND POLISHING RESULTS

The mirror has been plated and polished by SESO in France. The results of the plating and polishing are quite good, and the mirror finish and quality will be acceptable for use in the HER.

Optical Feature	Specified	Reported
Figure, rms (λ=632.8 nm)	λ/40	λ/30
Tangential Slope Error, rms	<5 μrad	<4 μrad
Sagittal Slope Error, rms	<5 μrad	<3 μrad
Roughness (Å rms)	< 10	7 to 8

Table 2 Specified and Reported Optical Characteristics After Plating and Final Polishing

5 CONCLUSIONS

The mechanical design of the SR Primary Mirror is capable of withstanding an off-axis hit of 2000 W/cm^2 at 3 A at 9 GeV. The reported optical quality of the mirror component is acceptable for operation. The operational optical quality of the mirror varies along the mirror surface with the depth of the slot. Further 3D analyses should be conducted and compared with operational results to determine overall mirror performance.

REFERENCES

[1] A. S. Fisher et al., 'Design and Initial Commissioning of Beam Diagnostics for the PEP-II B-Factory', Proceedings from this Conference.

[2] 'Vacuum System Design for the PEP-II B-Factory High Energy Ring', C. Perkins et al., EPAC94, London, England, June 27 - July 1, 1994.

[3] H. A. Winick,ed., *Synchrotron Radiation Sources - A Primer*, (World Scientific 1994), p.203.

[4] R. DiGennaro and T. Swain, Nucl. Instr. and Meth.A291 (1990) 305-312.

SUB-PICOSECOND ELECTRON BUNCH LENGTH MEASUREMENT

Chitrlada Settakorn, Michael Hernandez, and Helmut Wiedemann
Applied PhysicsDepartment, Physics Department and SLAC
Stanford University, Stanford, California 94309*

Abstract

A subpicosecond electron bunch length measuring system has been developed at the SUNSHINE facility. The method is based on an autocorrelation technique in the frequency domain utilizing the coherent radiation emitted from the electron bunch at wavelengths equal and longer than the bunch length. The radiation spectrum is the Fourier transform of the electron bunch distribution and measuring this spectrum in a far-infrared Michelson interferometer allows the determination of the bunch length down to the femto-second regime. The experimental setup and measurement of subpicosecond electron pulses including possible improvements to maximize the bunch information available from an interferogram will be described.

1 INTRODUCTION

The ability to measure sub-picosecond electron bunches greatly determines the progress to produce ultra short electron and radiation pulses as desired for future linear colliders, x-ray FEL's or the development of far infrared(FIR) coherent radiation of very high intensity. At the SUNSHINE facility sub picosecond electron bunches can be generated down to 100 f-sec rms[1]. To aid this development a FIR Michelson interferometer has been developed for bunch length measurement[2] which is based on a frequency-resolved autocorrelation technique [3] utilizing coherent transition radiation emitted at wave lengths equal to or longer than the bunch length while the electron beam passes through a thin Al-foil. This FIR Michelson interferometer works in such a way that the primary signal is the Fourier transform of the radiation spectrum which is exactly what is desired to obtain information about the bunch length[2,4]. Unlike time-resolved technigues which suffer from technical limitations and high cost, this method allows to determine the electron bunch length in the subpicosecond range without complicated hardwares.

2 PRINCIPLE OF THE TECHNIQUE

Transition radiation (TR) can be generated when the electron beam passes throught a thin metalic foil. At wave lengths longer than the bunch length the radiation is coherent and the intensity of the radiation is proprotional to the square of the number of electrons per bunch. The intensity is therefore very high such that room temperature radiation detectors can be used and its spectrum includes information about the particle distribution in the bunch. The coherent power spectrum of TR from an electron bunch can be written like

$$P_{tot}(\lambda) = P_e(\lambda)\,[N + N(N-1)\,f(\lambda)],$$

where $P_e(\lambda)$ is the spectral radiation power from a single electron and N is the number of electrons per bunch. The form factor $f(\lambda)$ is defined by

$$f(\lambda) = \left|\int dz\, e^{i2\pi z/\lambda}\, S(z)\right|^2,$$

and is the Fourier transform of the longitudinal particle distribution S(z) normalized to unity.

The frequency information can be extracted from a FIR Michelson interferometer in the from of a power spectrum. Radiation entering the Michelson interferometer is split into two parts by a polyethylene beam splitter and directed into two different directions to be reflected back by mirrors. One mirror is fixed in position while the other mirror can be moved to change the path length. After reflection the beams are combined again and sent to a bolometer to measure the intensity. In this arrangement one can use one part of the coherent radiation pulse as a scale to scan the other part. While the two path lengths are different by more than the bunch length both pulses arrive at the bolometer at different times and generate a signal independent of the path length difference. As, however, the path length difference becomes comparable to the bunch length both radiation pulses overlap and the coherent fields add up thus generating an increase in intensity and signal at the bolometer. Energy conservation is met if all radiation in the Michelson interferometer is considered [2]. The bolometer signal recorded as a function of the path length difference is called the interferogram and is the Fourier transform of the radiation spectrum. By observing the autocorrelation interferogram of coherent TR one can derive the bunch length. Since this method is based on optical principles it works for any short bunchlength provided that optical elements are avaialble and used for the frequency range corresponding to the Fourier transform of the particle distribution.

To generate TR we use an Al foil which is tilted by 45° with respect to the electron path and the backward TR is then emitted at 90° with respect to the beam axis. The radiation exits through a polyethylene window from the beam pipe and enters the FIR Michelson interferometer.

In the analysis of the interferogram one must eliminate all effects which alter the radiation spectrum and may therefore lead to erroneous bunch length

0-7803-4376-X/98 /$10.00 © 1998 IEEE

measurements. Specifically, the beam splitter has a particular spectral response which comes from the interference of reflections from the front and back of the beam splitter. These effects can be calculated from material constants and thus, in principle, be eliminated. The detailed analysis and formalism for this has been reported in [2]. A similar concern relates to water absorption for a Michelson interferometer set up in air. The water absorption lines are very narrow and therefore do not affect the overall radiation spectrum as the beam splitter does. In first approximation, we can therefore neglect water absorption effects. However, more than just a measure for the bunch length can be obtained from the exact form of the interferogram if we eliminate water absorption as well.

A typical autocorrelation interferogram from the SUNSHINE facility is is shown in Fig.1(a) and the corresponding radiation spectrum in Fig.1(b). Many water absorption lines are clearly visible.

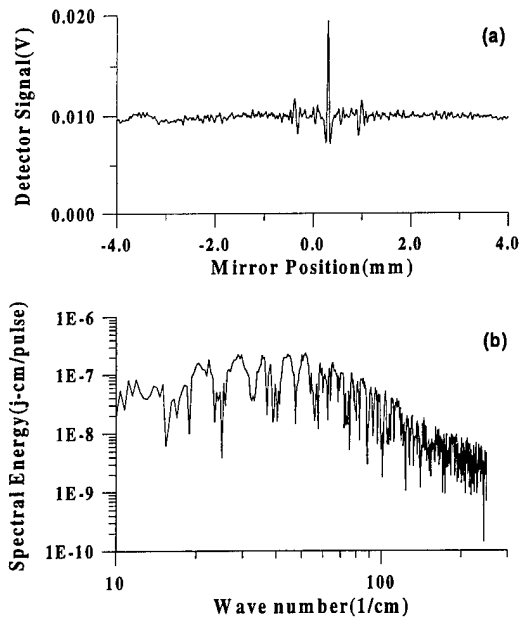

Figure:1 A typical interferogram for f-sec electron bunches at SUNSHINE.with 12.7μm thick beam splitter(a) and the Fourier transform of the interferogram(b)

Numerical elimination of beam splitter effects requires the knowledge or assumption of the actual electron distribution because the spectral modification is different for a gaussian or uniform particle distribution. The required correction is minimized if one uses a beam splitter which is thicker than about half the equivalent bunch length[2]. We define an equivalent bunch length as the length of a uniform bunch or equal to $\sqrt{2\pi}\sigma$ for a Gaussian bunch. With a thick beamsplitter the equivalent bunch length is then equal to or 75% of the FWHM of the interferogram for a uniform or Gaussian distribution, respectively.

Generally the equivalent bunch length can be derived from the interferogram for an arbitrary beam splitter thickness utilizing the graph in Fig.2.

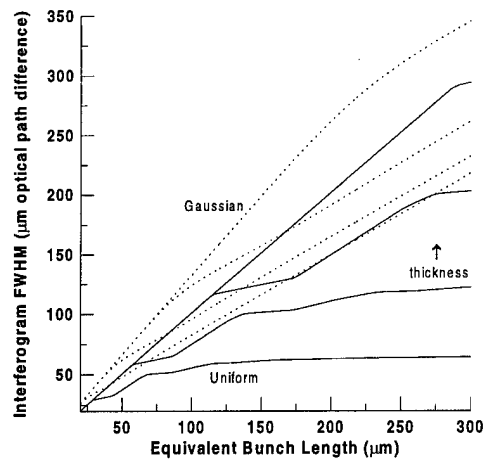

Figure:2 Equivalent bunch length as a function of the interferogram FWHM assuming a Gaussian (dotted line) or a uniform (solid line) bunch distribution for a 12.7, 25.4, 50.8, 127 μm thick Mylar beamsplitter[2].

From Fig.2 it is clear that a significant uncertainty about the bunch length exists if the general form of the particle distribution is unknown. For too thin a beam splitter and a uniform distribution no bunch length can be derived. Some knowledge of the bunch distribution is highly desirable to obtain the actual bunch length. In principle this information is lost in frequency domain measurements. However, from the form of the interferogram and spectrum some of this information can be recovered.

3 THE POWER SPECTRUM

Most realistic particle distributions can be assumed to be somewhere between a gaussian and uniform distribution. For each of these extremes we calculate the interferogram and radiation spectrum assuming the same equivalent bunch length. Both interferograms are shown in Fig 3(a). The difference is noticable in case of negligible extraneous spectral modifications. In case of real measured interferograms, however, the difference can be obscured by beam splitter effects and water absorption lines. At SUNSHINE an in-vacuum Michelson interferometer has been assembled which is expected to produce interferograms which can be interpreted in more detail as to the character of distribution.

The spectrum, on the other hand, shows significant diference between both distributions as evident form Fig.3(b). The uniform distribution spectrum extends to greater frequencies compared to that for a Gaussian bunch. The measurements should be sufficiently accurate to allow the distinction between both distribution or at least to conclude which distribution the

real bunch is closer to. With this information a more precise determination of the bunch length becomes possible.

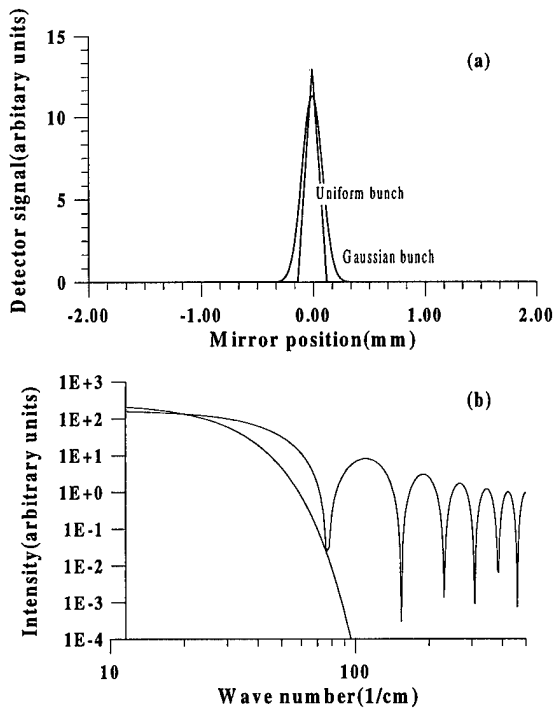

Figure:3 Calculated interferograms(a) and power spectrum(b) for a gaussian and uniform particle distribution of the same equivalent bunch length l = 160μm.

To obtain more information on the bunch distribution, we compare the measured power spectrum of Fig.1(b) with calculated spectrum of uniform and Gaussian distributions including beam splitter effects. This comparison is shown in Fig 4. To generate the appropriate spectra the actual equivalent bunch length must be known. Obviously, we must apply an iteration process. First we assume a bunch length, then we determine the closest particle distribution and determine from that the bunch length, etc.

The roll-off of the measured power spectrum at high frequencies looks more like that of a uniform than that of a Gaussian distribution which has a much faster drop-off of the spectrum.

The comparison would be greatly improved with the elimination of the multitude of water absorption lines in the measured spectrum. For the new in-vacuum Michelson interferometer at SUNSHINE, it is expected

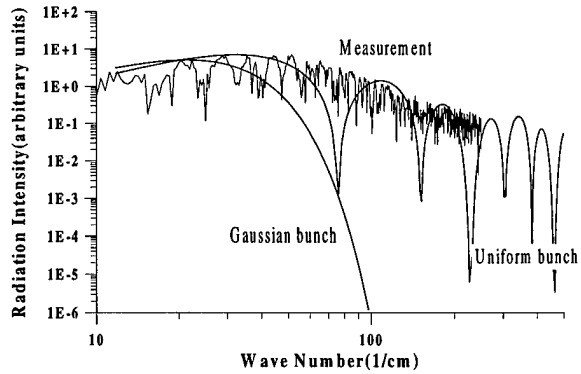

Figure:4 The power spectrum for a uniform and Gaussian distribution including 12.7 μm thick beam splitter effect in comparison with measurement.

that all water apsorption lines in the power spectrum will disappear and the cleaner power spectrum is expected to reveal more detail of the bunch distribution.

4 CONCLUSION

A bunch length measurement method using an autocorrelation of the coherent transition radiation is capable to measure electron bunch lengths in the femtosecond range. The approximated bunch length is obtained directly from the autocorrelation scan. To obtain more detail of the bunch length, the power spectrum need to be considered including the frequency effect from beam splitter and water absorption lines. An in-vacuum system is expected to improve the frequncy information from the measurement.

REFERENCES

[1] P. Kung, D. Bocek, H. Lihn, H. Wiedemann, Phys. Rev. Lett. **73**(1994)967

[2] H.C.Lihn, D. Bocek, P. Kung, C. Settakorn, H. Wiedemann. Phys.Rev.E **53**(1996)6413

[1] W. Barry, *An autocorrelation technique for measuring subpicosecond bunch length using coherent transition radiation*, Proc. of Workshop on Adv. Beam Instr. **1**, KEK, Tsukuba, Japan,(1991); CEBEF preprint PR-91-012 (1991).

[4] H.-C. Lihn, *Stimulated Coherent Transition Radiation* PH.D thesis (Stanford University, Stanford, CA, 1996).

* work supported by DOE Contract No. DE-AC03-76F00515

MEASURING LONGITUDINAL DISTRIBUTION AND BUNCH LENGTH OF FEMTOSECOND BUNCHES WITH RF ZERO-PHASING METHOD

D. X. Wang, and G. A. Krafft, Thomas Jefferson National Accelerator Facility
12000 Jefferson Avenue, Newport News, VA

Abstract

Recently there has been increasing interest in applications of very short electron bunches. Accurately measuring bunch length and profiles becomes essential for characterizing, commissioning, and operating such short bunch machines. The RF zero-phasing method is the only technique that is able to measure bunch length and longitudinal density distribution in the femtosecond regime. In this paper, analytical formulas for calculating longitudinal profile and bunch length are given. Using a such technique, bunch lengths as short as 84 fs rms have been measured.

1 INTRODUCTION

In recent years, there has been increasing interest in the use of very short electron bunches [1-3]. The shortest bunch for proposed and existing accelerators is around 100 fs (rms). Bunch length measurement is essential to develop and operate such accelerators. Such measurement also plays a crucial role in developing and advancing new techniques such as the coherent radiation method [4].

It becomes very challenging for conventional techniques such as streak cameras to resolve bunch lengths of a few hundred femtoseconds [5]. Recently developed frequency domain techniques measuring coherent radiation spectra are not able to uniquely determine bunch shape and length [4, 6-9]. The RF zero-phasing technique has been used to measure longitudinal distributions and bunch lengths of picosecond bunches. Good consistency was found between measurement and simulations [10-14]. However, the longitudinal profiles reported in Ref. 10 and 12 were obtained where the transverse beam sizes can be neglected, while the formula used in Ref. 11 to calculate bunch lengths is only valid for Gaussian distributions. There is no general method to determine bunch shape and length. Furthermore, it is not clear if this technique can be applied to the femtosecond regime. In this paper, analytical formulas are given for computing the longitudinal distribution function and bunch length for arbitrary longitudinal and transverse distributions. Applicability of the technique to femtosecond bunches is demonstrated and confirmed by numerical simulations.

2 RF ZERO-PHASING METHOD

The zero-phasing measurement utilizes several RF accelerating cavities (the zero-phasing cavities), a spectrometer, and a horizontal profile measuring device. The zero-phasing cavities operate at the zero-crossing of the accelerating wave and impart a time-correlated momentum deviation along the beam bunch. Then a spectrometer translates the longitudinal momentum spread into a horizontal position spread. Based on measurement of the horizontal profiles, the bunch length and longitudinal distribution function can be determined.

With the following two assumptions, an analytical expression for the longitudinal distribution function can be derived as a function of the horizontal distribution function and horizontal profile measured at the spectrometer with the zero-phasing cavities on. First, it is assumed that the distribution function in the longitudinal and transverse directions can be separated, i.e.

$$f(x,x',z,z') = f_x(x,x')f_z(z,z'), \tag{1}$$

where f, f_x, and f_z are the total, longitudinal, and horizontal normalized distribution functions, respectively. Second, it is assumed that the longitudinal phase space can be treated as an ellipse, and that the intrinsic energy spread or the width of the ellipse can be neglected.

The horizontal position of an electron at the spectrometer can be then written as $X = x + Cz$,where x is the nondispersive part,

$$\begin{aligned} C &= C_0 + C_1 \\ &= (2\pi \cdot eV_{\mathrm{rf}} / \lambda_{\mathrm{rf}} + dE/dz) \cdot \eta / E_0, \end{aligned} \tag{2}$$

η is dispersion of the spectrometer, E_0 is average beam energy, λ_{rf} is the RF wavelength, V_{rf} is the summed accelerating voltage of the zero-phasing cavities, and dE/dz is the slope of the longitudinal phase space ellipse. The linear slope of the accelerating voltage of the zero-phasing cavities, i.e. $2\pi \cdot eV_{\mathrm{rf}} / \lambda_{\mathrm{rf}}$, is used under the approximation that the RF wavelength is much longer than the bunch length. The horizontal profile measured at the spectrometer with the zero-phasing cavities on is then found to be

$$\begin{aligned} F(x) &= \iiint f_x(x,x')dx' f_z(z,z')dzdz' \\ &= \int f_x(x+Cz)f_z(z)dz, \end{aligned} \tag{3}$$

where $\int f_x(x,x')dx' = f_x(x)$ and $\int f_z(z,z')dz' = f_z(z)$ are used by definition. Therefore, the measured horizontal profile is simply a convolution of the longitudinal distribution function and the horizontal distribution function. The longitudinal distribution function can be deconvolved as

0-7803-4376-X/98/$10.00 © 1998 IEEE

$$f_z(z) = \frac{C}{2\pi}\int\left[\frac{\int F(x)e^{ikx}dx}{\int f_x(x)e^{ikx}dx}\right]e^{iCzk}dk. \quad (4)$$

Now $f_x(x)$ may be directly measured or it may be approximated by the horizontal profile measured at the spectrometer with the zero-phasing cavities off, if the dispersive part of the initial energy spread is small compared to the horizontal beam size. Such an approximation was made for the following measurement. It can be shown from Eq. (4) that if the horizontal distribution function and the measured horizontal profiles are Gaussian, the longitudinal distribution function is also Gaussian. The longitudinal bunch length is given to

$$\sigma_z = (\Omega^2 - \sigma_x^2)^{1/2} / C, \quad (5)$$

where σ_z, Ω, and σ_x are corresponding widths of the Gaussian profiles, as used in Ref. 11. If $f_x(x)$ is negligibly small compared to $F(x)$ and can be replaced by a delta function, the longitudinal distribution function equals the measured profile, i.e. $f_z(z = x/C) = F(x)/C$ as used in ref. 10 and 12, with a scale conversion factor C between the horizontal and longitudinal dimensions. Usually, C_0 can be experimentally determined, but dE/dz or C_1 is unknown. To overcome this problem, the horizontal profiles are measured at both zero-crossing points of the RF waves, which alters the sign of C_0. It is noticed that using C_0 instead of C in Eq. (4) is equivalent to compressing the z axis by a factor of C/C_0. Therefore, the longitudinal rms length is

$$\begin{aligned} z_{\rm rms} &= z^+_{\rm rms} \cdot C_0 / (C_0 + C_1) \\ &= z^-_{\rm rms} \cdot C_0 / (C_0 - C_1), \end{aligned} \quad (6)$$

where $z^+_{\rm rms}$ and z^-_{rms} are the rms lengths with the zero-phasing cavity at +90 $^{\circ}$ and -90° off crest, respectively, using C_0. Then the rms length and initial phase space slope normalized by the RF slope are given by

$$z_{\rm rms} = (z^+_{\rm rms} + z^-_{\rm rms})/2 \quad (7)$$

and

$$\begin{aligned} C_1/C_0 &= (dE/dz)/(2\pi \cdot eV_{\rm rf}/\lambda_{\rm rf}) \\ &= (z^+_{\rm rms} - z_{\rm rms})/z_{\rm rms}. \end{aligned} \quad (8)$$

Accordingly, the z axis for both measured profiles needs to be corrected by the corresponding factor of C_0/C. The difference between the two resulting distribution functions indicates the validation of the assumptions.

3 MEASUREMENT AND SIMULATION RESULTS

The formula and measurement procedure were tested using PARMELA simulation, which has been used extensively during CEBAF commissioning to verify experimental results. Very good agreement has been found between various measurements and simulation results in the past. The zero-phasing measurement was performed numerically and compared to the actual bunch length in the simulation. The test case showed good agreement over bunch lengths in the range of 100 to 400 fs, with a 10 fs systematic offset, indicating that the assumptions are good approximations.

The measurement was carried out at the CEBAF injector [15-16]. A 500 keV bunched electron beam is further bunched and accelerated to 5 MeV by the two superconducting RF (SRF) cavities. Following acceleration to the final injection energy of 45 MeV by 16 SRF cavities, little additional bunching occurs, due to the relativistic effects. Nominally, 16 SRF cavities run on crest. During the measurement of the shortest bunches, the last 8 SRF cavities are phased to plus and minus 90° off crest. A wire scanner is used to measure the horizontal profile at the spectrometer. Three typical profiles are shown in Fig. 1 and can be fit closely to Gaussian distributions. Both zero phases of each individual zero-phasing cavity are determined by finding the phase that yields zero transverse movement at the spectrometer viewer when the cavity is turned on and off. The beam energy and summation of the zero-phasing cavity gradient were measured by the spectrometer Hall probe. The experimental parameters in this measurement are: $\lambda_{\rm rf}$ of 20 cm, η of 1.52 m, $V_{\rm rf}$ of about 20 MV, and E_0 of

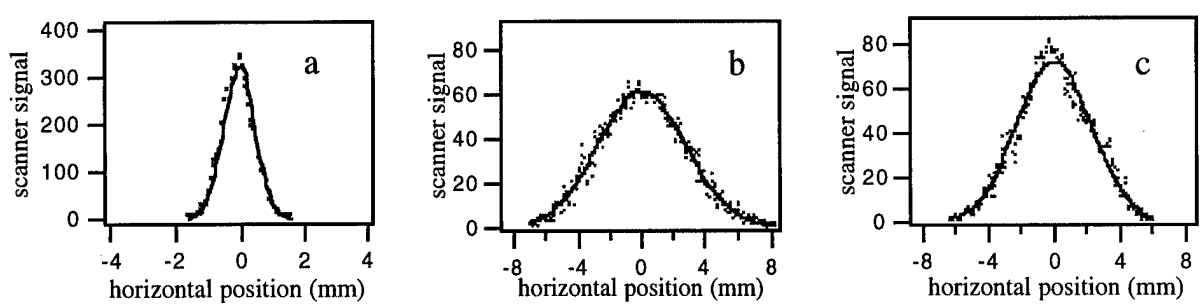

Fig. 1 Horizontal profile measured by the wire scanner at the spectrometer, where the scanner signal is proportional to the charge density and the circles are from measurement and the solid curves are Gaussian fittings. Profile (a) was measured with the zero-phasing cavities off while profiles (b) and (c) were measured with the zero-phasing cavities at +90 $^{\circ}$ and -90° off the crest, respectively.

about 25 MeV. The bunch length was systematically changed by varying the second SRF cavity phase, resulting in a series of longitudinal phase space rotations. Excellent agreement has been achieved between the measurement and simulation, shown in Fig. 2. In addition, the measurement results are consistent with a power measurement of the coherent synchrotron radiation (CSR) [17]. As expected, CSR power increased when the bunch length became shorter, and minimum bunch length yielded maximum CSR power. The left side of Eq. (8) is plotted from simulation in the solid line while the right side is displayed from measurement in the circles of Fig. 3, as the phase of the second SRF bunching cavity is varied as in Fig. 2. Measurements and simulation results agree well. It is noted that the zero value point represents the upright position of the ellipse in the longitudinal phase space, where the shortest bunch was obtained in both experiment and simulation, i.e. the minimum point in Fig. 3. There is a steep slope around the zero point where the slope of the ellipse changes sign, corresponding to the transition from under-compression to over-compression. Therefore, the maximum slope of the ellipse dE / dz is about a factor of seven smaller than the RF slope, $2\pi \cdot eV_{rf} / \lambda_{rf}$ of 720 MeV/m.

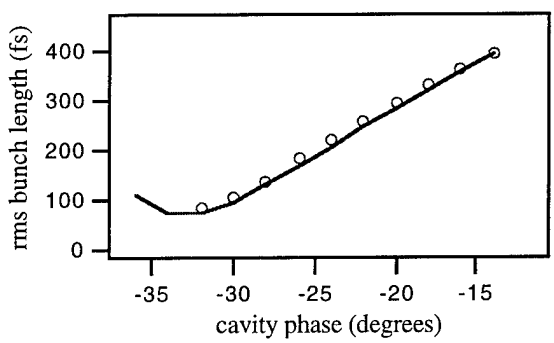

Fig. 2 The bunch length versus the second SRF cavity phase, where the circles are from measurement and the solid curve is from simulation.

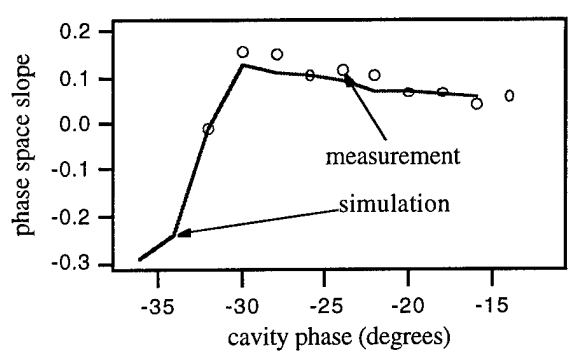

Fig. 3 The normalized longitudinal phase space slopes. The circles are the measurement of the right-hand side of Eq. 8, $(z^{+}_{rms} - z_{rms}) / z_{rms}$, while the solid curve is the left-hand side, $(dE / dz) / (2\pi \cdot eV_{rf} / \lambda_{rf})$, from simulation.

The zero-phasing technique provides a means of measuring the longitudinal density distribution function and the bunch length of femtosecond bunches. Its resolution is mainly limited by the constraints of the specific machine configuration. In practice the following considerations may be given to better interpret the measurement results: (1) measure the horizontal distribution function at the straight-ahead location and the horizontal profile at the spectrometer with the zero-phasing cavities off, which provides information about the longitudinal phase space ellipse, with orientation information obtained from Eq. (8); (2) focus the beam spot tightly in the horizontal direction; (3) increase the energy spread produced by the zero-phasing cavities; (4) the errors due to RF amplitude and phase stability can be estimated from horizontal beam jitters at the spectrometer viewer, which result in a longer measured bunch length. The zero-phasing technique has been proven to be crucial at CEBAF for characterizing the bunching process and calibrating a noninvasive CSR bunch length monitor that is an invaluable tool for machine operations.

4 CONCLUSION

In summary, analytical formulas for calculating the longitudinal distribution function and bunch length are derived. An electron bunch length as short as 84 fs (rms) has been measured. This is the first accurate bunch length measurement in the regime of less than 100 fs, and the zero-phasing is the only technique that has demonstrated such a capability. Numerical simulation provides validation of the assumptions of the technique. The systematic measurement results are in excellent agreement with the simulation and consistent with CSR power measurements.

5 ACKNOWLEDGMENT

The authors acknowledge C. K. Sinclair for his guidance and support, and also thank B. Dunham and H. Liu for help running the PARMELA code and CEBAF operations personnel for their help. This work was supported by U.S. DOE under contract number DE-AC05-84ER40150.

REFERENCES

[1] H. Winick, et al., NIM, A**347** (1994), 199.
[2] R. H. Siemann, Proc. of 1993 PAC Conf., 532.
[3] W. B. Mori, et at., AIP Conf. Proc. **335**, 112 (1994).
[4] D. X. Wang, "Electron Beam Instrumentation Techniques Using Coherent Radiation", these proceedings.
[5] A. H. Lumpkin, AIP Conf. **367**, 327 (1995).
[6] K. Ishi, et al., Phys. Rev. A**43**, 5597 (1991).
[7] Y. Shibata, et al., Phys. Rev. **E50**, 1479 (1994).
[8] R. Lai, et al., Phys. Rev. E **52**, 6787 (1995).
[9] H. C. Lihn, et al., Phys. Rev. **E53**, 6413 (1996).
[10] L. Rivkin et al., Proc. of 1st EPAC (1988), 634.
[11] J. Seeman et al., Proc. of 1988 LINAC Conf., 441.
[12] K. Bane, SLAC-PUB-5177, Feb. 1990 (A).
[13] K. Bane et al., Proc. of 2nd EPAC (1990), 1762.
[14] K. Bane et al., SLAC/AP-80, Sept. 1990 (AP).
[15] G. A. Krafft, Proc. of 1994 LINAC Conf., 9.
[16] D. X. Wang, Proc. of 1996 LINAC Conf., 303.
[17] D. X. Wang, et al., Appl. Phys. Lett. **70** (4), 529 (1997).

THE ALGEBRAIC RECONSTRUCTION TECHNIQUE (ART)*

D.Raparia, J.Alessi, and A.Kponou
AGS Department, Brookhaven National Lab, Upton, NY 11973, USA

Abstract

Projections of charged particle beam current density (profiles) are frequently used as a measure of beam position and size. In conventional practice only two projections, usually horizontal and vertical, are measured. This puts a severe limit on the detail of information that can be achieved. A third projection provides a significant improvement. The Algebraic Reconstruction Technique (ART) uses three or more projections to reconstruct 3-dimensional density profiles. At the 200 MeV H- linac, we have used this technique to measure beam density, and it has proved very helpful, especially in helping determine if there is any coupling present in x-y phase space. We will present examples of measurements of current densities using this technique.

1 INTRODUCTION

In Computed Tomography (CT), three dimensional reconstruction techniques from projection have been used for many years in radiology. The two dimensional Fourier transform is the most commonly used algorithm in radiology. In this technique a large number of projections at uniformly distributed angles around the subject are required for reconstruction of the image. In the field of accelerator physics, one expects that the relatively simple charged particle beam distributions can be reconstructed from a small number of projections. In conventional practice only two projections, usually horizontal and vertical, are measured. This puts a severe limit on the level of detail that can be achieved. The Algebraic Reconstruction Technique (ART) introduced by Gordan, Bender and Herman[1] uses three or more projections to reconstruct the 2-dimensional beam density distribution. They have shown that the improvement in the quality of the reconstruction is pronounced when a third projection is added, but additional projections add much less to the reconstruction quality.

2 ALGEBRAIC RECONSTRUCTION TECHNIQUE (ART)

The ART algorithms have a simple intuitive basis. Each projected density is thrown back across the reconstruction space in which the densities are iteratively modified to bring each reconstructed projection into agreement with the measured projection. Assuming that the pattern being reconstructed is enclosed in a square space of n x n array of small pixels, ρ_j $(j = 1, \ldots, n^2)$ is grayness or density number, which is uniform within the pixel but different from other pixels. A "ray" is a region of the square space which lies between two parallel lines. The weighted ray sum is the total grayness of the reconstruction figure within the ray. The projection at a given angle is then the sum of non-overlapping, equally wide rays covering the figure. The ART algorithm consists of altering the grayness of each pixel intersected by the ray in such a way as to make the ray sum agree with the corresponding element of the measured projection. Assume **P** is a matrix of m x n^2 and the m component column vector **R.** Let $p_{i,j}$ denote the (i,j)th element of **P** , and R_i denote the ith ray of the reconstructed projection vector **R**. For $1 \leq i \leq m$, N_i is number of pixels under projection ray R_i, defined as $N_i = \sum_{j=1}^{n^2} p_{i,j}^2$. ART is an iterative method. The density number ρ_j^q denotes the value of ρ_j after q iterations. After q iterations the intensity of the ith reconstructed projection ray is

$$R_i^q = \sum_{j=1}^{n^2} p_{i,j}\rho_j^q,$$

and the density in each pixel is

$$\rho_j^{\sim q+1} = \rho_j^q + p_{i,j}\frac{R_i - R_i^q}{N_i} \quad \text{with starting value } \rho_j^{\sim 0} = 0$$

where R_i is the measured projection ray and,

$$i = \begin{cases} \text{m, if (q+1) is divisible m} \\ \text{the remainder of dividing (q+1)by m, otherwise} \end{cases}$$

and,

$$\rho_j^q = \begin{cases} 0, & \text{if } \rho^{\sim q} \leq 0 \\ \rho_j^{\sim q}, & \text{if } 0 \leq \rho_j^{\sim q} \leq 1 \\ 1, & \text{if } \rho_j^{\sim q} \geq 1 \end{cases}$$

This algorithm is known as fully constrained ART.

It is necessary to determine when an iterative algorithm has converged to a solution which is optimal according to some criterion. Various criteria for convergence have been devised. The discrepancy between the measured and calculated projection elements is

$$D^q \equiv \left\{ \frac{1}{m} \sum_{i=1}^{m} \frac{(R_i - R_i^q)^2}{N_i} \right\}^{\frac{1}{2}},$$

and the nonuniformity or variance of constructed figure is

$$V^q \equiv \sum_j \left(\rho_j^q - \overline{\rho}\right)^2,$$

and the entropy constructed figure is

$$E^q \equiv \frac{-1}{2\log n} \sum_j \left(\frac{\rho_j^q}{\overline{\rho}}\right) \log\left(\frac{\rho_j^q}{\overline{\rho}}\right).$$

* Work performed under the auspices of the U. S. Department of Energy.

D^q tends to zero, V^q to a minimum and S^q to a maximum with increasing q. For a known test pattern ($\rho^t_{i,j}$), the Euclidean Distance is define as

$$s^q \equiv \sqrt{\frac{1}{n^2}\sum_j \left(\rho^q_j - \rho^t_j\right)^2}.$$

3 TEST FIGURE

It is instructive to test the reconstruction capabilities of ART with two to four views by using projections from a known test figure. In the following example, we have used an x-y coupled (about 18°)two-dimensional gaussian enclosed in a square space of 100 x 100 array with $\sigma_x = 5$ and $\sigma_y = 20$. We have used a ray width in the 45° and 135° projection as $\sqrt{2}$ times of ray width in x or y projection, making number of ray in each projection same namely 100. Figure 1 shows the test figure and reconstructed test figure from two projections. Figure 2 shows reconstructed test figure from three and four projections.

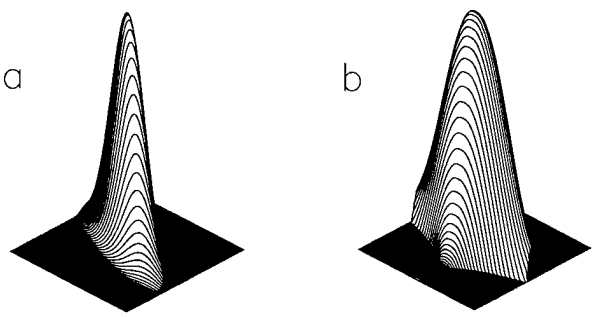

Figure 1: (a) Original test figure and (b) reconstructed test figure from two projections.

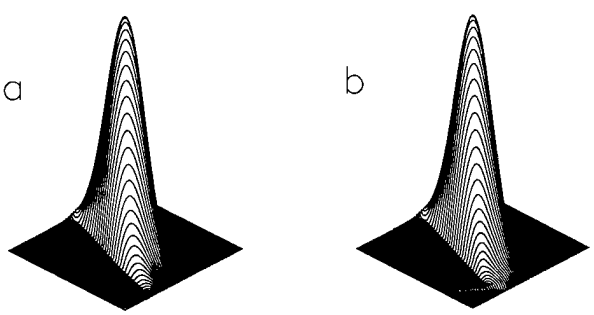

Figure 2: Reconstructed test figures from (a) three and (b) four projections.

Figure 3 shows the contours of Figs. 1 and 2. It is clear from Fig. 3 that two projections are not enough for catching the coupling. The accuracy of the reconstructed figure from four projection is slightly better than three projections. Figure 4 shows the discrepancy (D), variance (V), the entropy (E) and the Euclidean Distance (s) as a function of iteration number for case of three projections. The convergence criteria was if discrepancy is less than 10^{-6}. Table 1 shows the numerical values of discrepancy (D), variance (V), the entropy (E) and the Euclidean Distance (s) for two, three and four projections.

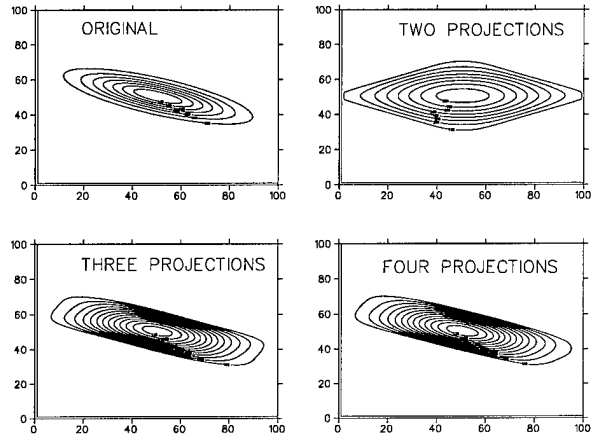

Figure 3: Contour plots of test figure and reconstructed figures with two, three and four projections.

Table 1: The convergence criteria discrepancy (D), variance (V), the entropy (E) and the Euclidean Distance (s) for two, three and four projections.

	2 Proj.	3 Proj.	4 Proj.
Iteration No	67	1426	1083
Time (sec)	201	6393	6534
Discrepancy	$1.0\ 10^{-6}$	$1.0\ 10^{-6}$	$1.0\ 10^{-6}$
Variance	$4.8\ 10^{-8}$	$1.3\ 10^{-8}$	$1.3\ 10^{-8}$
Entropy	$1.9\ 10^{+3}$	$2.3\ 10^{+3}$	$2.4\ 10^{+3}$
E. Distance	$1.5\ 10^{-4}$	$4.6\ 10^{-5}$	$4.6\ 10^{-5}$

4 BEAM DENSITY MEASUREMENT

There are stepping wire profile scanners at 13 locations throughout the 200 MeV linac and transport lines. These scanners are mounted at a 45° angle with respect to horizontal, and single horizontal and vertical wires are stepped through the bea We have added a third wire at 45° to horizontal in two of the scanners, one in the 750 keV line[2] and one in the 200 MeV BLIP [3] transport line. Figure 5 shows a schematic of the scanner with three wires. Figure 6 shows the reconstructed density distributions at 750 keV line. There is no x-y coupling in the 750 keV line. Figure 7 shows beam density contour plots in the BLIP line. The x-y coupling is clearly seen. This coupling could come from one or more rotated quadrupoles or vertical beam offset in a dipole. In the presence of x-y coupling, the usual technique of emittance measurement from profiles at three or more locations will not work. Figure 8 compares the measured and reconstructed projections in the BLIP line.

5 REFERENCES

[1] R. Gordon *et al.*, "Three-Dimensional Reconstruction from Projections: A Review of Algorithms", International Review of Cytology, Vol. 38, p. 111 (1974).

[2] J. G. Alessi *et al.*, " Upgrade of the Brookhaven 200 MeV Linac", Proceedings of the XVII International Linear Accel-

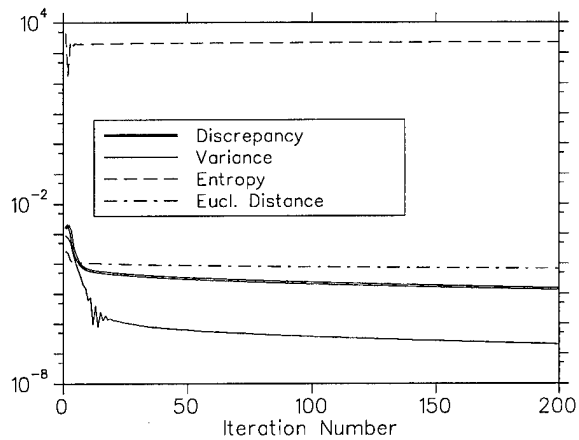

Figure 4: The discrepancy (D), variance (V), entropy (E) and the Euclidean Distance (s) as a function of iteration number for case of three projections. The convergence criteria was if discrepancy is less the 10^{-6}.

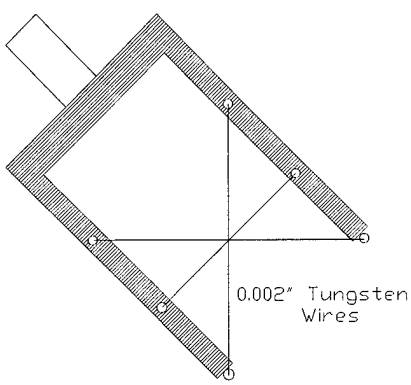

Figure 5: Schematic of the scanner with three wires.

erator Conference, Geneva, Switzerland, 26-30 August 1996, p. 773.

[3] A. Kponou *et al.*, " A New Optical Design for the BNL Isotope Production Transport Line", Proceedings of the XVII International Linear Accelerator Conference, Geneva, Switzerland, 26-30 August 1996, p. 770.

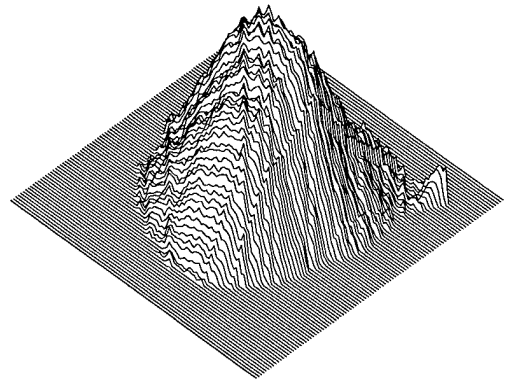

Figure 6: Reconstructed 3D density distribution in the 750 keV line using ART.

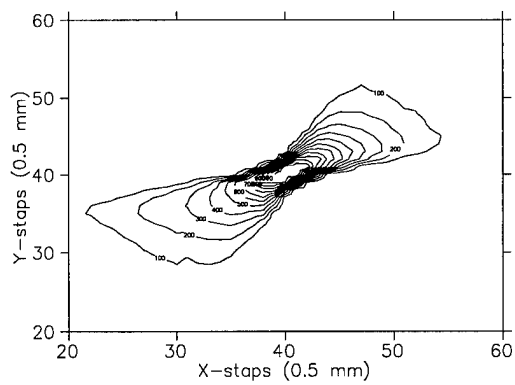

Figure 7: Reconstructed contour plot using ART in the BLIP line, showing x-y coupling.

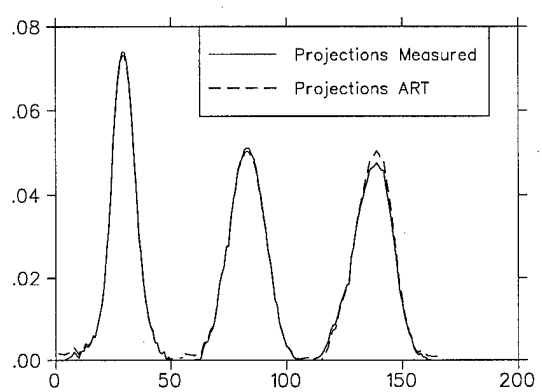

Figure 8: Beam projection measured and reconstructed on X, Y, and 45° planes at BLIP line.

NOISE REDUCTION ON THE LEP BUNCH CURRENT MEASUREMENT SYSTEM

A. Burns, B. Halvarsson, H. Jakob, H. Schmickler
CERN, CH–1211 Geneva 23, Switzerland

Abstract

The lifetimes of coasting beams in LEP are computed from the difference of the bunch currents measured during a time interval of a few seconds. The quality of these measurements is presently limited by the noise figure of the bunch to bunch aquistion system. This paper decribes comparative studies on the aquistion system in order to improve the noise figure by one order of magnitude. For this purpose three different principles, i.e., integrating measurements, peak hold circuits with internal timing (autotrigger) or peak hold circuits with external timing were studied. The paper describes the results of these studies.

1 INTRODUCTION

The LEP bunch current monitoring system has been described in previous publications[1, 2, 3]. The system is used for daily LEP operation and an online display of the measured bunch currents and computed beam lifetimes is available in the main control room. Figure 1 shows a screen dump of the online display for the positron bunches during a LEP physics coast with four bunchtrains of four bunches in each train. In addition to the bunch currents the lifetime averaged over all bunches is displayed (56.4 hours in Fig. 1) and the time evolution of the lifetime is shown as the yellow trace. Although the beam conditions had not changed a significant variation of the measured lifetime is visible in the graph. This variation is linked to noise contributions in the individual current measurements and will be discussed in the following section.

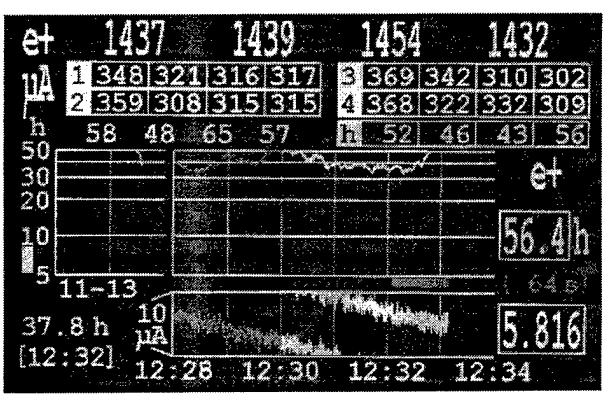

Figure 1: Online Display in the main control room of the LEP-BCT.

Figure 2 illustrates how the lifetime is computed from two consecutive bunch current measurements, which themselves are averages of many beam revolutions during a time interval Δt. Error propagation yields for the measurement error on the lifetimes:

$$\frac{\sigma_\tau}{\tau} = \frac{\tau \cdot \sigma_{\Delta I}}{I \cdot \Delta t^{3/2}} \tag{1}$$

where $\sigma_{\Delta I}$ is the variance of the measured current difference, which can be evaluated as $\sqrt{2}$ times the variance of indivudual current measurements. The above equation shows the strong influence of the integration time interval Δt. In the present LEP system this is exploited by having a dynamic adjustment of the integration time. For long lifetimes the integration time is increased up to 128 seconds, and only for short lifetimes integration times of 1 second are used (see details in[4]).

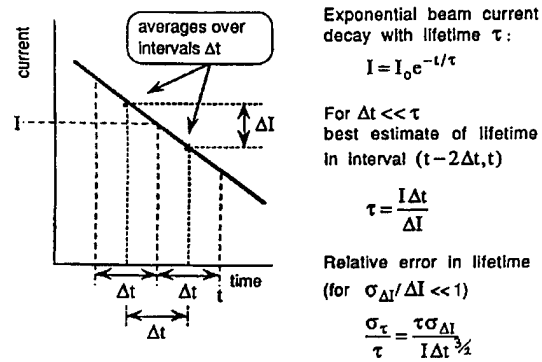

Figure 2: Illustration of lifetime calculation from two consecutive beam current measurements.

Of course a better solution to the problem would be to reduce drastically the variance of individual current measurements, such that the system could be operated with a fixed integration time of 1 or 2 seconds. This is very convinient for operators, as the recovery time of the instrument after sudden lifetime changes is much quicker.

Using Eq. 1 with an integration time of 2 seconds and asking for 5% of measurement error on lifetimes of about 20 hours requires a current measurement noise of about 20 ppm. This has to be compared with the value of the present BCT system of 100–200 ppm.

The following chapters describe measurement results on different acquistion systems in order to obtain the required factor 10 improvement in noise performance.

2 ACQUISITION ELECTRONICS

2.1 Signal Integration

This circuit is used in the present BCT system and its design was aimed at obtaining maximum absolute precision. The bunch signal (1) is measured as difference between the integrated beam signal and an integration of the baseline

0-7803-4376-X/98/$10.00 © 1998 IEEE

(pedestal) of the detector. The subtraction is done as analog circuit. Two "Integrate and Hold" Circuits, which are controlled by two timing gates (2) & (3) of equal length, are used for the integration.

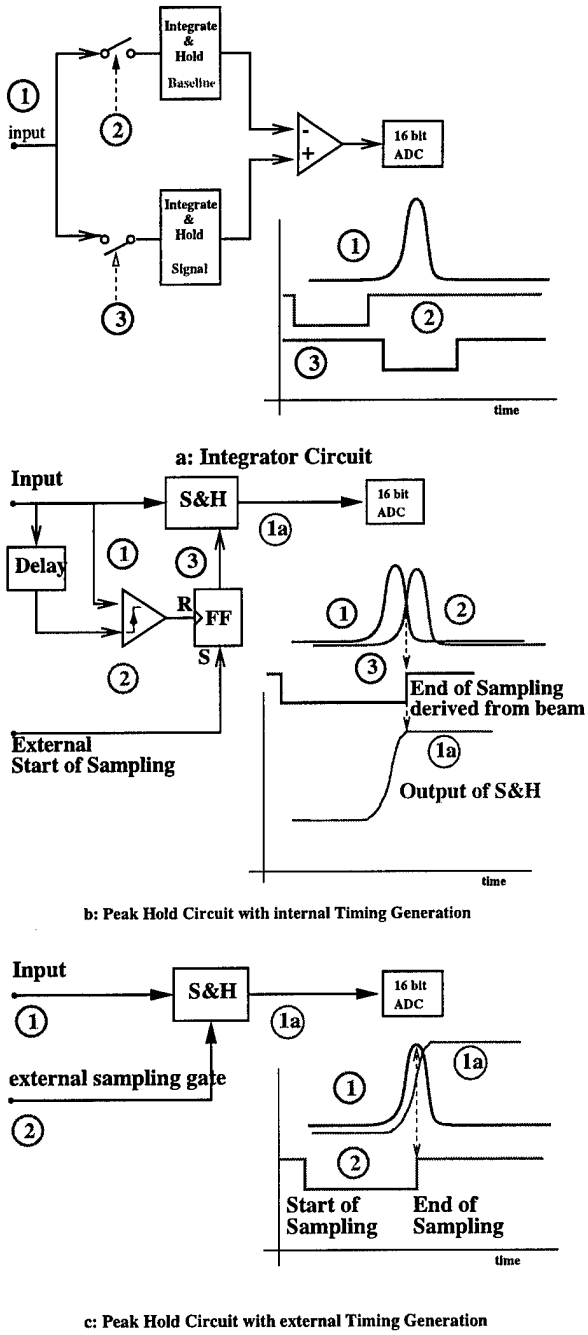

Figure 3: Block Diagram and Timing Sequence of the three different electronics circuits, top: integrator, middle: peak hold with internal timing, bottom: peak hold with external timing.

2.2 *Peak Hold Circuits*

Compared to the previous circuit a peak hold circuit is not optimum in terms of absolute precision as the baseline of the signal is neglected, on the contrary the circuit can be optimized for best noise performance. The signal to noise ratio depends largely on the bandwidth of the input signal and the jitter on the sampling gate. In bunch train operation the spacing between two bunches of the same polarity is 335 nsec. In order to have less than 1% crosstalk between bunches the transformer signal was filtered with a lowpass of 12 MHz corner frequency. The noise requirements of 20 ppm translate into the specification of having a jitter on the sampling gate of less than 3 nsec rms.

Two circuits with a different circuit for the sampling gate were tested. All tests were done by using modified digitizing cards of the BOSC system[5], which is presently used for the SPS tune measurements.

2.2.1 Internal timing

The objective of this design was to render the system almost independent of the LEP filling scheme as the sampling gate is derived from the beam signal itself. The signal is split into a direct path (1) and into a delayed pass (2). A comparator circuit detects the cross over between direct and delayed signal. By adjusting the amplitude of the delayed signal the cross over point can be set such that the end of the sampling gate coincides with the crest of the input signal at the S& H circuit.

2.2.2 External Timing

In this case the "end of sampling gate" is applied from the outside to the circuit. For the tests a signal directly derived from the Rf-system was used. This signal had a timing jitter below 3 nsec rms.

3 RESULTS

Figure 4 shows measurements of the the bunch currents using the three different electronics as described in the previous chapter. Each point in the graphs corresponds to the average of 5622 machine turns, i.e., the equivalent of 0.5 seconds of data. A straight line fit is applied to the data and the rms spread around the fitted curve is displayed in the measurement graph. The obtained rms values depend on the selection of the input data, as the straight line fit implies a constant life time during the measurements. With different data sets the following range for the noise figures were obtained: integrator: 120-300 ppm, peak hold internal timing: 80-140 ppm, peak hold external timing: 19-37 ppm.

4 DISCUSSION

The above results show clearly that both peak hold circuits give better noise performance than the present integrator circuit. Since the prototype design in 1989 the present BCT system has the integrator circuits and the digitizing electronics in separate chassis making it very difficult to avoid ground loops or other noise sources. A modern and more compact circuit design would probably give also better results.

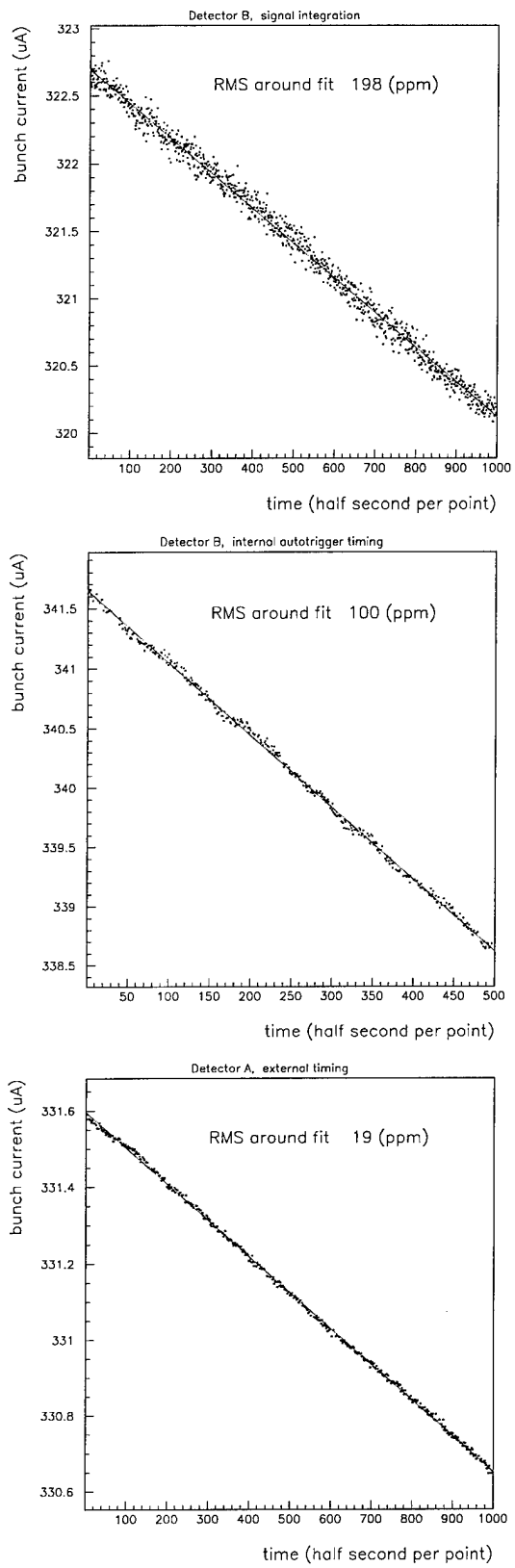

Figure 4: Noise measurements on the three different electronic circuits: top: integrator, middle: peak hold with internal timing, bottom: peak hold with external timing reference.

The choice between the two peak hold circuits is almost evident. Only the external timing circuit yields the required performance in terms of rms noise. Another argument in favour of the external timing circuit is the required dynamic range. LEP is filled with bunches between 1 μA bunch current in special machine experiments up to 1 mA bunch currents in high intensity operation. In case of an internal autotrigger circuit this dynamic range of 60 dB can not be realized without switching the gain of an preamplifier. The best result for the dynamic range of the autotrigger, which we achieved in the laboratory was 42 dB (for the bandwidth considerations as described in the previous chapter).

So in conclusion the new LEP BCT system scheduled for 1997 operation will make use of peak hold circuits with external timing reference. With a short integration window of 2 seconds on the bunch current measurements (see Fig. 1) and 20 ppm rms noise lifetimes of 20 hours will be measured with a precision of 5% rms.

5 REFERENCES

[1] K.B. Unser, *Measuring bunch intensity, beam loss and bunch lifetime in LEP*", Proceedings of the 2nd European Particle Accelerator Conference, Nice, France (June 1990) pp. 786-788.

[2] G. Burtin *et al.*, "*Mechanical Design, Signal Processing and Operator Interface of the LEP beam current transformers*", Proceedings of the 2nd European Particle Accelerator Conference, Nice, France (June 1990) pp. 794-796.

[3] L. Vos, "*The LEP monitor for the measurement of bunch intensity*", CERN SL/94-18 (BI) (May 1994).

[4] A.J. Burns *et al.*,"*Real Time Monitoring of LEP Beam Currents and Lifetimes* Proceedings of the 4th European Particle Accelerator Conference, London, Great Britain (June 1994) pp. 1716-1718.

[5] A.J. Burns *et al.*, "*The BOSC project*", CERN Divisional Note, SL 90-68(AP)

A BEAMLOSS DIAGNOSTIC SYSTEM FOR CESR

S. Henderson*, Laboratory of Nuclear Studies, Cornell University, Ithaca, NY 14853

Abstract

A diagnostic system utilizing commercially available fast analog digitizers has been developed at the Cornell Electron Storage Ring (CESR) for capturing and analyzing transient beam behaviour preceding rapid beamloss. The diagnostic system is based on a turn-by-turn data acquisition system which records beam position information from individual bunches in CESR, as well as RF system diagnostic signals. An accompanying display and analysis package has been developed to aid in diagnosing the causes of beamloss events. Examples of beamloss mechanisms are described.

1 INTRODUCTION

Loss of all or a portion of the stored beam current at a collider facility represents a substantial penalty in operational efficiency. The cost in time to refill the storage ring and collide the beams can become significant if beamlosses are frequent. Furthermore, as the stored beam current in CESR is increased, high-current phenomena may manifest themselves most noticeably as the causes of rapid beamloss. Therefore, understanding the causes of beamloss is central to identifying current limiting phenomena, and constitutes an important aspect of the ongoing program of addressing beam current limits in CESR.

By continuously recording beam position information for a selection of bunches in CESR, it is possible to observe the behaviour of the beam prior to beamloss. In addition to the beam position information, we have found it particularly useful to record fast diagnostic signals from the RF system as well, in order to better understand the interaction between the beam and RF system. The turn-by-turn diagnostic system described in this paper is part of a set of diagnostic tools in use at CESR for evaluating beamlosses.

2 INSTRUMENTATION

2.1 COMET^{TM} Digitizers

The turn-by-turn data acquisition system is shown in figure 1. The heart of the system is a set of COMET^{TM} VME multichannel analog digitizer boards manufactured by Omnibyte, Inc.[1] Four input channels per board are digitized with individual 12-bit ADCs at rates up to 5 MHz. Digitized data from each channel is sequentially stored in its own 128 kbyte buffer (for a total of 512 kbyte of on-board memory). Since each data word is 16 bits, each channel has a buffer depth of 64 k samples.

* Work supported by the National Science Foundation

[1]Omnibyte, 245 West Roosevelt Road, West Chicago, Illinois, 60185

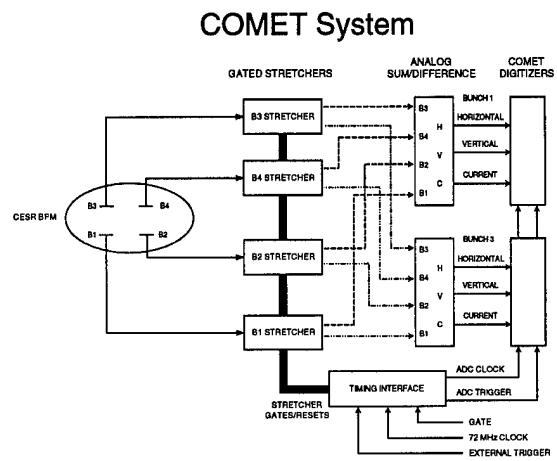

Figure 1: The turn-by-turn data acquisition system. Four beam position monitor signals are gated, stretched, and combined to provide bunch-by-bunch horizontal, vertical, and current signals. The system shown provides signals for one beam species. Another identical system provides signals for the other species.

The digitizer boards support several operating modes. In the "one-shot" mode, a specified number of samples is recorded and sequentially written in local memory *following* a trigger. In the "circular buffer mode," the inputs are continuously sampled and written to on-board RAM, "wrapping-around" to the beginning of the buffer when the end of buffer is reached. In this mode, data-taking is initiated via a software enable, and stopped with a hardware trigger. The number of samples acquired after the "stop" trigger is programmable in software. The turn-by-turn data acquisition system operates in the "circular-buffer-mode" for beamloss monitoring.

The COMET^{TM} on-board RAM is a dual port data buffer that is accessible from the host CPU (a CESR control system VAX) as VME address space through a TurboChannel to VME adapter. The address space is mapped to VAX/VMS global sections so that access to the on-board RAM is accomplished with a read or write operation to an address within the global section.

2.2 CESR BPM Processing

CESR presently collides trains of closely spaced bunches. Each beam consists of 9 trains with 2 bunches per train, spaced by 42 nsec. The CESR Phase II design calls for 3 bunches per train, and an upgrade (CESR Phase III) will allow operation with 5 bunches per train. The minimum

0-7803-4376-X/98/$10.00 © 1998 IEEE

bunch spacing within a train is 14 nsec, and the spacing between trains is ~280 nsec. Due to the closely spaced bunches, narrow gating of beam position monitor signals is necessary to retreive information from a single bunch.

Signals from four individual beam buttons of a standard CESR BPM are brought from the tunnel to the control room for processing. The receiver is a gated stretcher module developed for CESR's digital transverse feedback system[1]. The receiver uses GaAs fast gates to shunt the beam signal into one of five parallel stretcher channels, one for each 14 nsec "bucket" in a train providing individual stretched output for each bunch in a train. The stretcher diode is reset before the next train passage. Two sets of gated stretchers are required to provide positron and electron signals.

The set of four stretched outputs (one for each beam button) for each bunch in a train is then combined in an analog sum/difference board to provide a horizontal position error signal, a vertical position error signal and a bunch current signal. Sets of these signals are available for all bunches in CESR.

Local timing signals are generated by a timing interface card, one for positron timing and another for electron timing. These cards generate gates and reset signals for operation of the stretcher modules, and ADC clock signals used by the COMET cards. In addition, the timing interface card synchronizes an external trigger to local timing.

In order to obtain a beamloss trigger, a single beam button signal is stretched and then differentiated. A threshold is set on the differentiated output to provide a beamloss trigger. During normal CESR operation with ~300 mA of stored beam current, the threshold corresponds to loss of approximately ~150 mA.

In addition to beam position and intensity signals, we have found it valuable to record a set of diagnostic signals obtained from the four CESR RF cavities on a turn-by-turn basis. These include RF-enable signals, forward power, reflected power, tuning angle, and cavity phase.

At present, the beamloss diagnostic system uses 5 COMET^{TM} ADC boards to digitize a total of 20 beam position and RF system signals. We plan to increase the capacity of the system to 40 channels.

3 SOFTWARE

The beamloss diagnostic system runs continuously during CESR operation. When a beamloss is detected, a subset of the total information available (the total RAM is ~2.5 Mbytes) is written out in three data files. One data file contains 2048 turns (a CESR turn is 2.56 μsec) of BPM data for one bunch in all 9 trains of electrons and positrons. A second data file contains 2048 turns of BPM data for a single e^+ bunch and a single e^- bunch and 2048 samples of RF system data. A third data file contains RF system data sampled at the train spacing frequency (~280 nsec). When a beamloss is detected, data is made available on a control-room screen for diagnosis.

The beamloss data is stored on disk and is available for viewing and analysis. An X-windows based data viewer and analysis package has been developed for studying and analyzing beamloss data.

4 BEAMLOSS ANALYSIS

Although we have seen a wide variety of beamloss mechanisms at work in CESR, most beamlosses in the past year may be placed into one of three categories: i) RF system trips; ii) beam instabilities; and iii) electrostatic separator action.

4.1 RF System Trips

The CESR RF system protection circuits may trip for a variety of reasons. Common occurances are unacceptably high vacuum conditions or high reflected power (VSWR trips).

One such particularly interesting high reflected power event is shown in Fig. 2. The figure shows the reflected power of three CESR RF cavities together with the stored e^- beam current for the final 128 turns bracketing the beamloss. The e^- current begins to decrease near turn -65 (less current *increases* in the raw units) and has completely disappeared ~20 turns later. The cause of the beamloss is the E2 cavity VSWR occuring near turn -70 which initiates removal of the forward power. The striking feature shown in this data is the lack of a beam signal in the E2 cavity. After the forward power is removed, the W1 and W2 cavities extract power from the beam, as seen by the increasing reflected power near turn -63. The E2 cavity, however, is incapable of being driven by the beam, as if the cavity were "shorted" for a period of time. It has the behaviour of an arc which takes some time to recover.

We have found that by processing the RF at high pulsed power we have been able to reduce the RF system trips substantially, and to increase the stored beam current in CESR.

4.2 Beam Instabilities

The total beam current in CESR is presently limited by a longitudinal dipole coupled bunch instability[2]. Figure 3 shows the horizontal position of a positron bunch for 2048 turns prior to beamloss. The lower figure is the corresponding frequency spectrum (shown as a function of fractional tune), showing a peak at the synchrotron tune $Q_s = 0.05$ and higher harmonics. The longitudinal oscillation frequency is readily seen in the horizontal signal because of dispersion at the BPM. The longitudinal oscillation grows without bound, eventually causing loss of beam near turn -100. A longitudinal feedback system is under development.

4.3 Electrostatic Separator Action

CESR has four horizontal and two vertical electrostatic separators. As beam currents in CESR have increased, we have observed increased photocurrents on the separator plates. In the case of the vertical separators, this increased current has led to instabilities, sparks, trips, and

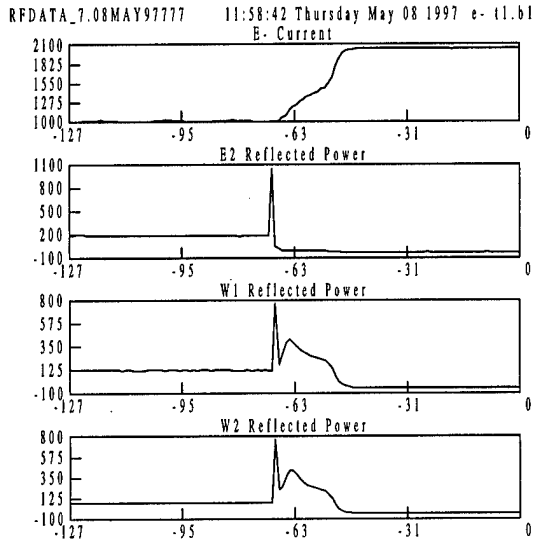

Figure 2: Beamloss due to an E2 RF cavity reflected power trip. The e^- current (decreasing upward) and RF cavity reflected power signals are shown for 128 turns bracketing the beamloss.

loss of beam. Figure 4 shows the vertical position signal of a positron bunch for 1024 turns prior to beamloss. the vertical separator sparks near turn -255, and the beam is lost near turn -80. The lower curve is the corresponding frequency spectrum, showing a peak at the vertical tune q_v = 0.41. The photocurrents in the vertical separators have been reduced by installing permanent magnets to act as electron traps, and by biasing the separator plate voltages[3]

5 ACKNOWLEDGEMENTS

The author gratefully acknowledges Mike Billing, Charlie Strohman and Donna Kubik for their contributions to the work reported here.

6 REFERENCES

[1] J.T. Rogers *et al.*, "Operation of a Fast Digital Transverse Feedback System in CESR," Proc. 1995 Part. Acc. Conf, 2426 (1995).

[2] M. Billing, "Observation of a Longitudinal Coupled Bunch Instability with Trains of Bunches in CESR", these proceedings.

[3] S. Greenwald, "Photocurrents in Electrostatic Separators at CESR", these proceedings.

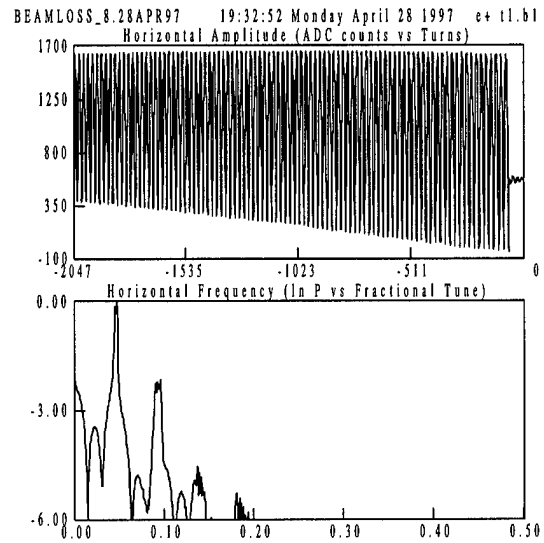

Figure 3: Beamloss due to a longitudinal coupled bunch instability. The horizontal position and frequency spectrum of a single bunch for 2048 turns prior to beamloss are shown.

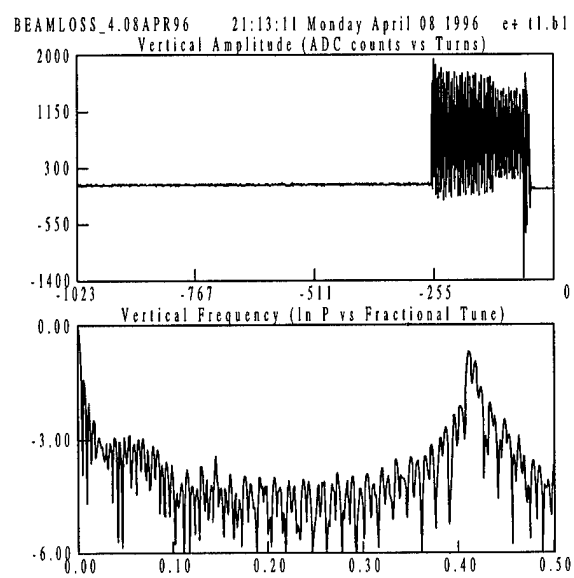

Figure 4: Beamloss due to a vertical electrostatic separator spark. The vertical position and frequency spectrum for 1024 turns prior to beamloss are shown.

A NEW FLYING WIRE SYSTEM FOR THE TEVATRON

W. Blokland, G. Vogel, and J. Dey, Fermi National Accelerator Laboratory[1†], Batavia, IL, USA

Abstract

A new flying wire system replaces an older system to enhance the analysis of beam emittance, improve reliability, and support future upgrades to the Tevatron. New VME data acquisition and timing modules allow for more bunches to be sampled more precisely. A LabVIEW application, running on a Macintosh computer, controls the data acquisition and wire motion. The application also analyzes and stores the data as well as handles local and remote commands. The new system flies three wires and fits profiles of 72 bunches to a gaussian function in a total of three seconds. A new console application allows remote operator control and display from any control console. This paper discusses the hardware and software setup, capabilities, and measurement results of the new flying wire system.

1 INTRODUCTION

The flying wire system measures the transverse beam size by moving a wire through the beam. The collision of the beam particles with the wire generates a spray of secondary particles with an intensity proportional to the number of beam particles present at the position of the wire. A portion of the secondary particles hits a nearby scintillator paddle to produce light. The light is converted into an electrical signal by a photo multiplier tube. This signal is plotted versus the position of the wire to obtain the profile of the beam. A gaussian function is fitted to the profile and its sigma represents the transverse beam size.

1.1 Problems with the old system

The old system, described in [1] and [2], suffered from reliability problems and a lack of an upgrade path. The VME hardware often generated bus errors resulting in an aborted fly or corrupted data. The optical encoder module that measured the position of the wire was sensitive to radiation and needed to be replaced every month. Sometimes the damage to the encoder would halt the wire in the middle of the beam, destroying the wire. The old hardware would also not be able to measure the additional beam bunches for the planned Tevatron upgrade. The results, sigma and mean, were not consistent. Each counterclockwise fly was followed with a clockwise fly but the results were often more than ten percent apart. The profile could also contain bad points due to, as later diagnosed, a vibration from the drive belt and the use of a soft coupler between the encoder and fork. The analysis itself was very sensitive to noise if the beam intensity was low. The software for the system was written in C and Assembly, and no one with knowledge of the programs was available to update it. The old system used two different embedded processors with slightly different programs to control the three wires. The difference in programs turned out rather tedious to maintain.

As the Instrumentation Group had good prior experience with LabVIEW based systems, it was decided to use LabVIEW on a single Macintosh computer along with commercial motion control and digitizers.

2 HARDWARE CONFIGURATION

In the new configuration, the integrator, position FIFO, and timer modules are all new or upgraded in-house designs. In addition, we switched from the optical encoders to resolvers to minimize radiation induced failures. A direct drive replaced the belt drive of the earlier system and the resolver was hard coupled to the fork shaft, with a floating mount to prevent binding.

The wire can has a diameter of 21 centimeters, the fork has a radius of 10 centimeters and holds a 33 micron carbon filament that flies at a speed of about 5 m/s. The position is measured with a resolver and 14-bit R/D converter, providing an angular resolution of 0.022 degrees. To reduce the number of samples, the R/D converter implements programmable aperture gates to turn sampling on during that part of the fly path where beam might be present. The beamloss signal from the phototube is first integrated by an in-house fast integrator VME board and then A/D converted by a 12-bit Omnibyte Comet 2MS/s VME digitizer. The high voltage to the phototube can be adjusted for low and high intensity beam by using a Vero model VME48240 4-channel D/A converter module card that controls a rack-mounted high voltage power supply. Beam synchronous timing is provided by standard in-house VME timing cards. A Macintosh computer using a National Instruments NB-MXI interface controls the VME crate. The Macintosh computer also has a Nulogic motion control board that is connected to a drive amp to provide motor control.

The fly path of the wires is a total 540 degrees. The wire first accelerates, then passes through beam twice, and then decelerates. The resulting rest position is different from the start position, but by flying in the opposite direction for the next fly, the next rest position will be the original start position while giving us extra length to accelerate and decelerate. A simplified configuration with only one wire, instead of two horizontal and one vertical wire, is shown in figure 1.

[1†] Operated by Universities Research Association

0-7803-4376-X/98 /$10.00 © 1998 IEEE

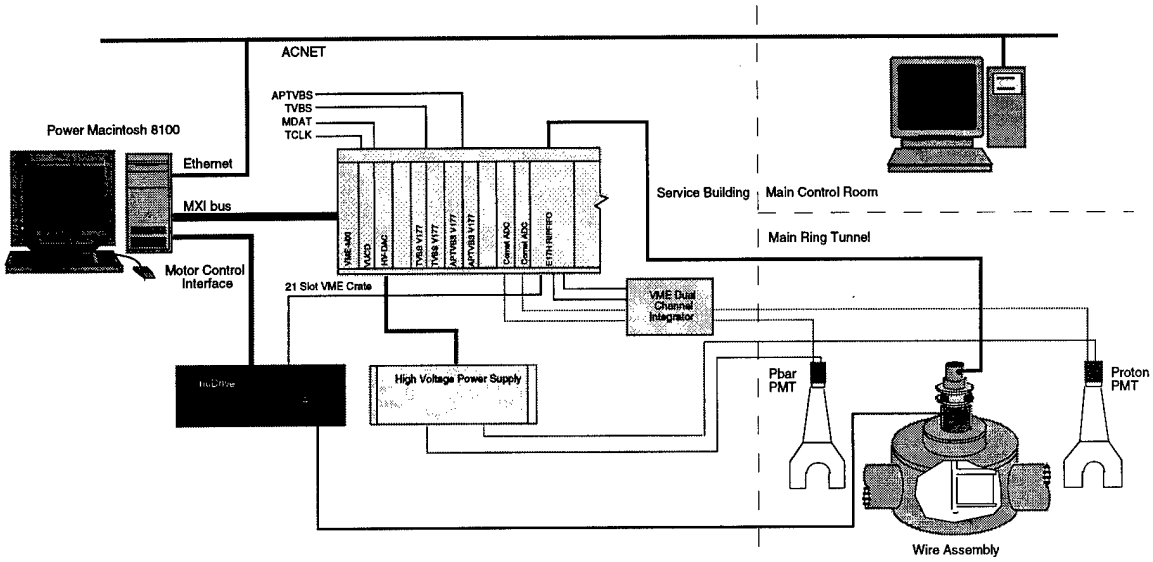

Figure 1. Single Wire Configuration.

3 SOFTWARE SETUP

3.1 User-interface

The local graphical user interface (GUI), see figure 2, can display current or saved profiles, manually control the wires, and, using menus, modify all hardware settings and analysis parameters on-line or in the default setting files. The local GUI can also be remotely controlled using an utility like Timbuktu. Each fly must use one out of 40 user-defined specifications. These specifications include which bunches are sampled at what multiple of beam turns, the integration time, when to fly, whether the data is to be saved or not, the type of analysis (full or quick), the next fly specification, the aperture, and the high voltage.

The console application Tevatron Flying Wires T46, provides remote control for operators and experimenters from any standard X Windows based console located anywhere in the lab. The consoles use the ACNET communication protocol which is supported by the LabVIEW application, see[3]. All of the programming for the console application was done in C. The two main menu items to the program are Fly Spec and Plot Six. Under Fly Spec one is able to modify the fly specifications just as under the local GUI. The menu item Plot Six allows one to view new ACNET data or saved disk data from a given fly. The plots generated under Plot Six very closely resemble the ones shown in figure 2.

3.2 Analysis algorithm

The old system's analysis routine first did a background subtraction and then did a second moment calculation to estimate the sigma. As it turned out this calculation was very sensitive to noise during low beam intensity and could not handle a slope in the background noise. Knowing this, the new system's analysis is made more robust for background noise and poor signals. Using

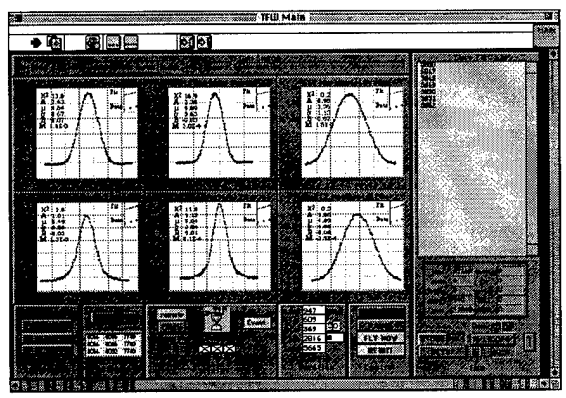

Figure 2. The local GUI.

LabVIEW, we could select from a library of filter and fitting routines and check the processing by plotting the data at different stages.

The new analysis has two parts: the first part performs a quick analysis of the data to serve as an estimate for the second optional part, a least-squares fit. The quick analysis starts by cutting out data acquired while the wire moves within the aperture gates but doesn't intercept any of the particle beam. Next, it will do a quick estimate by smoothing the data, finding the peak with a quadratic peak finder, estimating the background noise using data right before and after the profile, determining the slope of the background noise, and estimating the sigma from the half peak value.

The new system flies the wire through the beam twice, once upstream and once downstream, producing two peak locations. Knowing that the beam travels straight and given the locations of the peaks, we calculate and correct for any rotational misalignment of the resolver. The resolver counts can now be properly mapped into millimeters perpendicular to the beam. The estimates are also corrected, given the rotation and mapping.

The second part of the analysis uses the estimates as an initial guess to fit the rotated and mapped profile with a non-linear Levenberg-Marquardt method to the function:

$$a \cdot e^{\left(\frac{-(x-\mu)^2}{2\sigma^2}\right)} + b \cdot x + c \qquad (1)$$

The Levenberg-Marquardt method that came with the LabVIEW libraries has been optimized to obtain a ten-fold increase in speed. This particular routine is also used in other instrumentation systems that also deal with beam parameters, see [4].

4 PERFORMANCE

4.1 Speed

Using a PowerMac 8100 at 110 MHz, the system acquires data and fits profiles of three wires for a beam of six proton and six pbar bunches and two passes within 3 seconds (total of 72 fits) with 80 points per profile. Faster than 2 seconds speeds but with reduced accuracy are obtained by reducing the number of points of the profile or by completely turning the fit off and using the estimates as final results.

4.2 Repeatability

We looked at RMS (Root Mean Square) values of the measurements to quantify the repeatability. Figure 3 shows the sigma for the first proton bunch. The first part of the graph shows results from measurements taken at 149 GeV. As bunches are injected into the Tevatron, first proton than pbar, the emittance is changing. Once the ring accelerates to 900 GeV and the collision is turned on, we have measured an average of about 1% RMS with a worst case of 2% RMS around a logarithmic growing sigma. The error in the emittance is twice that of the sigma. RMS percentages of the other parameters have similar values.

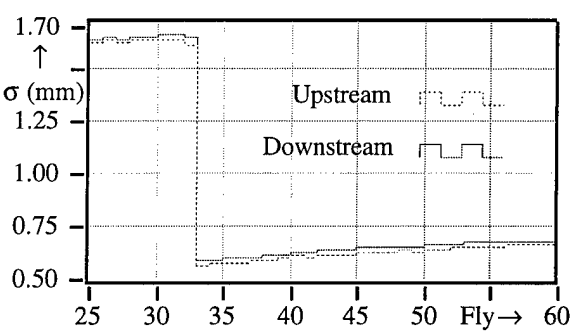

Figure 3. The sigma of bunch #1 in store 5905.

4.3 Reliability

The number of failures has been drastically reduced. We have not lost a wire since commissioning the new system. Some crashes have occurred, but after completing modifications to the program, the system has stabilized.

5 CONCLUSION AND FUTURE

The new system delivers a big improvement in reliability and gives more consistent results with a typical repeatability of around 1% RMS.

We will further investigate the accuracy of the flying wire data. We found a consistent difference for one of the wires in the upstream and downstream sigma, much larger than would be expected, due to emittance growth from the wire colliding with the beam. We plan to find out if this is related to phototube saturation by reducing light coming from the paddles or to the position of the beam/wire interaction by varying the position of the paddles.

The Tevatron will be upgraded to hold 36 proton and 36 pbar bunches instead of 6 each. A test setup supporting this upgrade has been made and is currently being tested. This setup will also be used for the Main Ring (and later Main injector) flying wires, which has a cycle of 3 to 5 seconds. To perform multiple flies during this cycle, the program is structured into different tasks with different priorities. The acquisition task runs under the highest priority and can be retriggered independently from the analysis task that runs at a lower priority. Thus, the wires can fly again before all data has been fully analyzed. The analysis can take part during the following flying of a wire and after the Main Ring cycle has been completed. Retrigger rates of almost 2 Hz are possible.

As the number of bunches increases six fold, we must also process six times as much data. We plan to upgrade the 8100 with a newer model. As three times faster models are already available, we expect that future Macintoshes will give us close to a six times speed increase compared to the current system.

6 ACKNOWLEDGEMENTS

Many people other than the authors have helped develop the new system. Special thanks go to Dong Chen for his early work, Alan Hahn for the analysis optimization, Jim Crisp for his work on the vibration of the old wire system, Jim Zagel and Brian Chase for their experience with the old system and suggestions, and Shoua Moua and Brian Fellenz for the technical support and hardware design.

REFERENCES

[1] J. Gannon et al., 'Flying Wires at Fermilab', Proc. of the 1989 IEEE PAC, pp. 68-70, March 20-23, 1989.

[2] J. Zagel et al., 'Upgrades to the Fermilab Flying Wires Systems', Proc. of the 1991 IEEE PAC, pp. 1174-6, May 6-9, San Francisco, USA 1991.

[3] W. Blokland, 'Integrating the commercial software package LabVIEW with Fermilab's Accelerator Control NETwork', ICALEPS 95, pp. 226-234, Oct. 29 - Nov. 3, Chicago, USA.

[4] A.A. Hahn, 'A Levenberg-Marquardt Least Squares Fit Algorithm Optimized for LabVIEW', Technical Note, 1997.

A HIGH SPEED, MULTI-SAMPLING DATA ACQUISITION FOR BEAM DIAGNOSTICS

Ming-Jen Yang, Fermi National Accelerator Laboratory, Batavia, IL 60510 USA

Abstract

A program is developed to collect accelerator data using a high speed digitizer and to display data for beam diagnostics. The digitizer has speed up to 2 Gs/s and is multiply retriggerable up to 1024 traces. The signal can be from either wall current monitor for longitudinal dynamics or the strip-line detector for transverse dynamics. The FFT spectral analysis of individual data trace gives the frequency composition of the signal from a train of beam bunches. The FFT analysis of transposed data gives the spectral composition down to sub-synchrotron frequencies. The data is displayed as a plot of single trace, mountain ranges, or 2-dimensional contours to give different perspectives. The physics examples are given.

1 INTRODUCTION

This write-up is about an effort at Fermilab to have a computer program that will serve as a user interface to a TEKTRONIX RTD720 fast digitizing oscilloscope for the purpose of control, readback, and display data. This fast digitizing scope is currently used at Fermilab for beam diagnostics in Tevatron and in Main Ring. The signal comes either from a strip-line beam position detector for observing the head-tail instability or from the wall-current monitor for studying the longitudinal beam dynamics. In either case the digitizer is sufficiently fast for the signal that carries a fundamental frequency of 53 MHz RF.

Most of the reasons for having such a computer program are obvious, not counting the fact that a scope usually sits in a noisy place with cables running everywhere. A computer has large amount data storage space, can make data available to anybody any time and almost any where. It provides much better graphical capability than a simple scope. It allows user to manipulation data numerically rather than mentally, things like re-calibrating, corrections with special algorithm, fitting, or applying analysis tools such as FFT. A program also has the ability to present data in a way that gives evolutionary perspective of signal being observed, not just individual traces. This program is written to be part of the Fermilab Accelerator Control software and can be used readily for studies.

2 DIGITIZER DATA

Data acquisition

The RTD720 is a 2 Gs/s, multiply retriggerable digitizing scope. It has a memory of 0.5 Mbyte and can be partitioned in may ways for the combination of record length and number of records up to 1024. Once armed, it will respond to the external triggers as many times as was requested. Trigger signals are synchronized with the beam revolution such that the digitization starts always at the same place along the beam bunch train. Successive triggers are usually an integral number of beam revolutions apart, depending on the objective of study.

The digitizer is linked to the Fermilab Accelerator Control NETwork (ACNET) via GPIB interface. All the control knobs pertaining to the operation of an oscilloscope can be done through this link, as well as the return of error messages. It takes about 15 seconds to read off half MByte of data which can be saved to file to be retrieved later.

Data display

With the amount of data available the only way to view and understand it at a reasonable amount of time is through graphical display. A 3-dimensional display requires porting data over to other graphical programs and is not covered here. Three basic types of display are implemented and described here.

i. Trace by trace

A trace display is basically reproducing what one normally sees on a scope with the added advantage that many traces are available. This is where one looks for basic characteristics of the signal, such as bunch spacing and signal magnitude. Figure 1 shows a single trace of Tevatron wall current monitor signal.

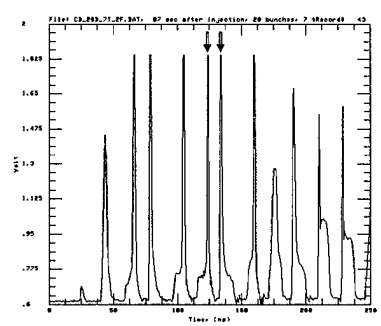

Figure 1: Fermilab Tevatron wall-current monitor signal as digitized in one single trace.

ii. Mountain range

This is a display that has kind of 3-D look, could be kind of messy, and may not always give accurate perspective. A traditional Mountain Range display was implemented through the use of scope and TV camera and is available only as images from TV display. With RTD720 the mountain range display can be replayed forward, backward, and with as many traces as

0-7803-4376-X/98 /$10.00 © 1998 IEEE

reasonable on the computer screen. Figure-2 is a good example of a mountain range display showing the process of beam bunch coalescing within the Main Ring operation.

iii. Contours

Short of doing 3-D graphics contour plot is the next best thing for viewing two dimensional array of data. Figure-3 is an example with data on two individual bunches plotted in the time/trace space. There are 30 sets of the same kind of data as that of Figure 1 but taken successively in time. The horizontal array index is the digitizer sample number at an interval of 0.5 ns, and the vertical array index is the trace number, at an interval of 1.36 ms. Depending on the data being plotted the interpretation of the array index will be different. From the contour the relative magnitude of data within the array can be visualized.

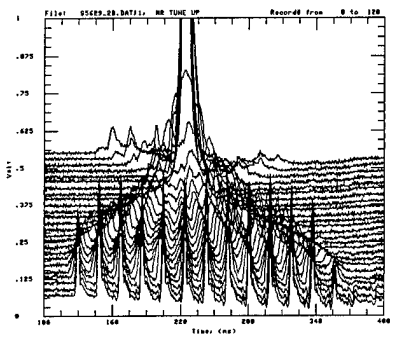

Figure 2: Mountain range plot of Fermilab Main Ring wall-current monitor signal. Data was captured during a collider run setup, at the time 13 proton bunches were being coalesced.

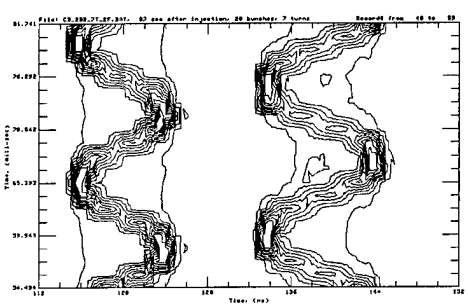

Figure 3: Contour plot of a Tevatron wall-current monitor signal. Only two of the bunches are shown in this plot for a duration of about 27 ms.

Data manipulation

The advantage of having the digitized data is that it can be retrieved, re-scaled, added to other data from other signal, arithmetically. It can also be ported over to specialized program for specific type of analysis. Listed below are functionalities already implemented.

i. FFT

This is probably the most common thing to be done to the digitizer data to obtain frequency composition of the signal, making the digitizer work like a spectrum analyzer. To use this feature effectively one has to plan ahead and partition data such that a longer stretch of data can be used for analysis.

ii. Transposed data

The digitizer data is organized in a trace by trace sequence for each trigger given. It is sometimes useful to see the data from all the consecutive traces but of same location within a trace. Such transposed data therefore allows a view of the signal evolution.

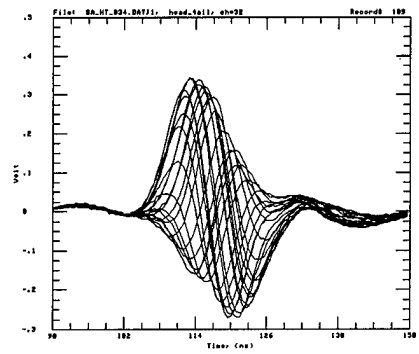

Figure 4: Difference signal of a strip-line BPM detector as was digitized. The effect of reflection can be seen to have distorted the actual signal.

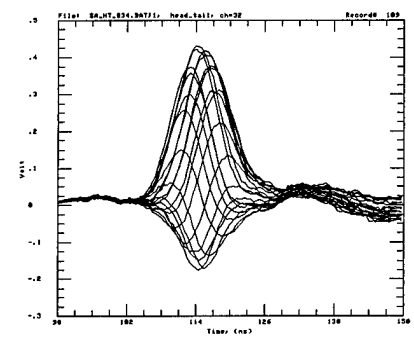

Figure 5: The same strip-line BPM detector signal as in last figure except that the effect of reflection is removed.

iii. Reflection correction

For signals from strip line BPM detector the reflection is inevitable. A common practice would be to used a longer, Quarter-Wave type, detector such that the reflected signal does not overlap the actual beam signal. In real life the beam bunch length could be quite a bit longer or such detector may not be available. The effect of reflection, in principle, can be unfolded to show the actual signal, limited only by the noise level and the resolution of digitizer.

3 APPLICATION EXAMPLES

Clearly, program like this could be useful to other types of beam studies. It could be used for the longitudinal injection matching study. With possibly even higher sampling rate in the future the transition crossing could also be a good application. Given below are the background information relevant to the examples already given so that reader may feel free to draw their conclusion.

Head-tail instability

The head-tail instability has been observed both in Fermilab Tevatron [1] and Main Ring [2]. Figure 4 shows the signal as was digitized with distortion caused by reflection and Figure 5 shows the edited signal with the effect of reflection removed. Removing reflection requires that the reflection coefficient and reflection delay time be matched. Some thing that could also be of interest. While procedure clearly is not perfect the signature of head-tail mode Ø can readily be identified [3].

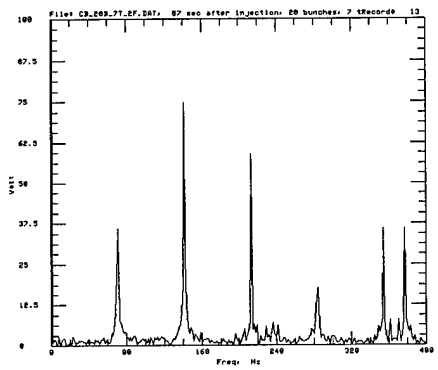

Figure 6: The FFT spectrum of the transposed data for trace position at 118.5 nano-seconds.

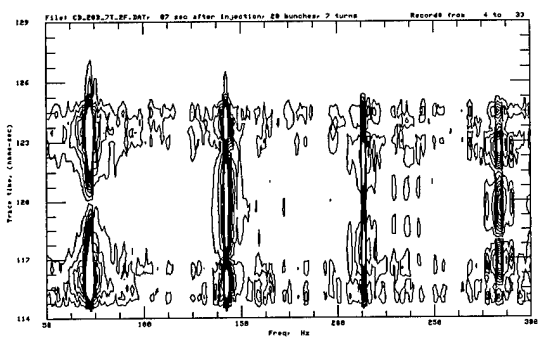

Figure 7: Contour plot of FFT spectrum of transposed data at trace locations from 114 to 129 nano-seconds.

Coupled bunch instability

Figure 1, 3, 6, and 7 are all from the same set of data which contains 1024 traces [4]. The uneven spacing between bunches seen in Figure 1 is indicative of instability effect. The two bunches marked by the arrow heads are also contour plotted in Figure 3, which shows the synchrotron motion of the beam bunch longitudinally. A FFT spectrum of transposed data, at 118.5 ns of each trace, is shown in Figure 6. The 70 Hz synchrotron frequency and its higher harmonics are visible. The spectrum is symmetric around the cut-off frequency of 367 Hz, due to the fact that traces were taken at 1.36 ms apart. In Figure 7 is the contour plot of a collection of spectrum as shown in Figure 6, except that each is at different trace time. It covers the entire left beam bunch shown in Figure 3, and indicated by the vertical axis. It is apparent that the spectral sensitivity depends greatly on the trace time.

Beam coalescing

During the Fermilab collider mode operation up to 13 proton bunches are coalesced to increase single bunch intensity. This coalescing process was done at the Main Ring before transferring the beam to Tevatron. Shown in Figure 1 is the mountain range plot of data taken at the setup time of collider run 5629, July 1995. Only every five traces, or approximately 5 ms apart, are displayed. For comparison, the same data is displayed in Figure 8 as contour plot, with 125 traces of data at 1 ms apart. In both figure the process start at the bottom of plot with 13 proton bunches clearly visible. The bunches diffused and finally came together and were captured as a single bunch at the top of plot. A small portion of the beam was not recapture by the RF bucket and started to wonder away.

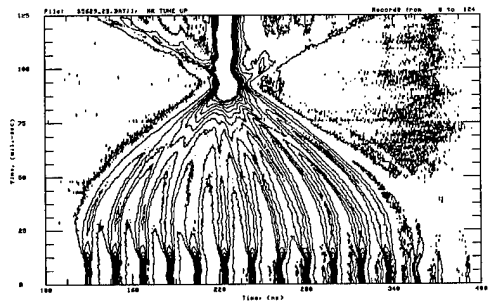

Figure 8: Contour plot of Main Ring wall-current monitor signal during proton beam bunch coalescing. A total of 125 traces of data at about 1 ms apart are included in this plot.

4 CONCLUSION

It is hoped that the effort presented here will result in more than just pretty pictures, that it will promote faster understanding in diagnosing and identifying problems, and that the advantage of this remarkable digitizer be fully utilized. Most of the functionalities implemented are quite basic. It is assumed that more elaborated analysis of the beam data, such as looking for the position, intensity, and the length of each individual bunches, will be done by porting data over to specialized programs.

5 ACKNOWLEDGMENT

I would like to thank Dr. S. Assadi for his generous offer of his study data as examples and many conversations on this subject.

[1] S. Assadi, private communication.

[2] J. Chou and G. Jackson, "Experimental Studies of Transverse Beam Instabilities at Injection in the Fermilab Main Ring", Proceedings of 1995 IEEE Particle Accelerator Conference, Vol. 5, p.3091.

[3] Garett, "Beam Observation and the Nature of Instabilities", CERN SPS/87-18 (AMS)

[4] Assadi, private communication.

LOW INTENSITY BEAM DIAGNOSTICS WITH MICROCHANNEL PLATE DETECTORS

G. Cuttone*, C. De Martinis**, P. Finocchiaro*, D. Giove**, G. Raia*, A. Rovelli*
*INFN-LNS, Via Santa Sofia, Catania - Italy
**INFN-LASA and University of Milan, Via Flli Cervi 201, Segrate(MI)- Italy

Abstract

A non destructive low intensity ion beam profile monitor has been designed and tested. The system is based on a MCP that detects the residual gas ionization produced by the ion beam. The detector is coupled to a phosphorous screen for the readout of the vertical and horizontal density profiles. Experimental results have shown that the system is able to detect beam intensities as low as 10^8 pps with a local vacuum in the measuring box of the order of $8x10^{-6}$ mbar. In the paper we report the results so far obtained in beam sensitivity and measure precision as a function of the residual pressure and in different regimes of the detector.

INTRODUCTION

The measurement of low intensity beam profiles is of great interest for the design of accelerator based medical and radioactive beam facilities[1]. The typical electrical and optical devices used in beam diagnostic can hardly operate below 10^8 pps. At this end a research program is underway at our laboratory for the development of detectors which sensitivity range could span from 10^{10} pps to at least 10^5 pps, and which have no interference with the beam[2]. In this paper we present the results so far obtained in the development of detectors based on microchannel plate coupled to a phosphorous screen that gives a one dimensional optical image of the ionization track in the residual gas. The design of a beam imaging device that allows to produce a 2D transverse beam profile with a higher sensitivity with respect to the residual gas is also presented. It is still based on a MCP coupled with a scintillating screen, but in this case we collect the secondary electrons produced in the interaction of the beam with a thin carbon foil.

EXPERIMENTAL SET-UP

A non destructive profile monitor has been designed to quantitatively study the beam transversal distributions and dimensions versus the total current. The experimental set-up has been improved also including a Faraday cup for the total beam current measurement before the MCP station and a Chromox 6 alumina screen used as a reference device for the transversal beam dimension determination. The measurement point has been fixed along a beam transport line at LNS (Catania) where Tandem and Cyclotron beams are available.

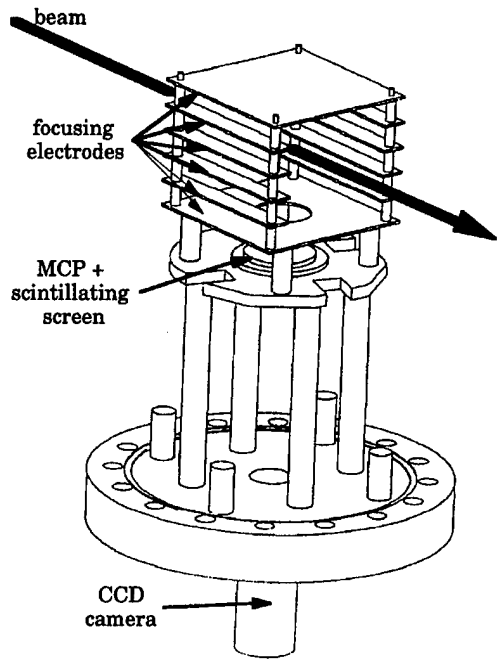

Fig. 1 Sketch of the residual gas beam monitor

A significant limitation of this set-up is represented by the lack of a precise residual pressure control due to the large volumes involved in the detector area. Two different configurations of the beam profile monitor based on microchannel plates coupled to a phosphorous screen have been built. The first one detects the ionization track of the beam on the residual gas. Fig. 1 shows a schematic of this set-up. The electrons or the ions produced on the residual gas are driven to the MCP input by a transverse electric field. The MCP amplified electrons impinging on a phosphorous screen produce an optical image which is strictly correlated with the projection of the beam track on the MCP plane, so providing a one dimension position information. The MCP we used is the F2222-P21 type from Hamamatsu and has an useful dimension of 20 mm diameter. The readout system is a thin scintillating screen, viewed through a vacuum glass window by a CCD camera. The acquisition of video signals is performed by means of a frame grabber board installed inside a Windows 95 driven PC. The board is a Neotech ISA PC plug-in board with 1 Mbyte of on board memory and the capability to handle timing and trigger information along with video frames. Data acquisition, storage and analysis

0-7803-4376-X/98 /$10.00 © 1998 IEEE

are performed by a LabVIEW based application developed according to the typical requirements for a beam diagnostic tool. The software consists of different modules providing functionality like acquisition and handling of single frames or sequences, image averaging, automatic measurements of beam FWHM. The same analysis software has been used for the management of the images produced by the Chromox 6 screens.

The system previously described has been extensively tested with C and Ni beams at 6 MeV/n and 30 MeV/n respectively and results are presented in the following.

A second apparatus has been built and it is based on secondary electron emission by thin metallic foils (carbon or aluminium with thickness down to 30 •g/cm^2). This should enhance by order of magnitude the sensitivity of the system due to the higher yield of electrons produced in comparison with residual gas ionization. Fig. 2 shows a sketch of the system.

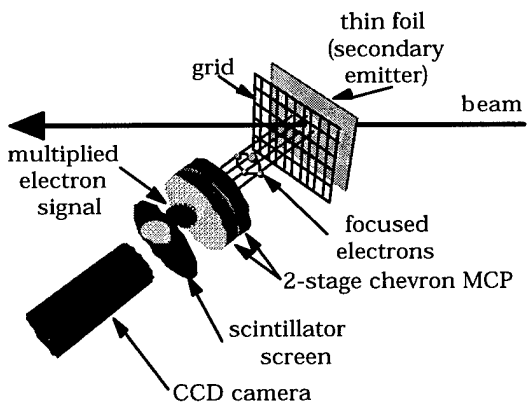

Fig. 2 Secondary electrons emission beam monitor sketch

The secondary electrons produced by the beam interaction are suddenly accelerated to a few keV of energy by the grid and then driven to the MCP input which is screened from the beam path. In this way the lateral diffusion of the electrons is prevented and in our configuration we calculated that it is less than 0.3 mm. The MCP readout system and image analysis are identical to the one discussed above. We have to point out that this type of detectors can not be considered completely non interfering with respect to the beam because of the stripping action of the foil, unless we do not consider only fully stripped ions.

MEASUREMENTS AND DISCUSSION

The residual gas beam profile monitor has been extensively tested using a C^{5+} beam at 6 MeV /n and a Ni^{16+} beam at 30 MeV/n. Preliminary measurements have shown that collecting the positive ions at the MCP we have a more defined image in comparison to the electrons collection mode. This behaviour should be due to the lower signal to noise ratio and to a lower lateral diffusion of the ions with respect to the electrons. All the results reported in the following refer to the ion collection mode. Measuring a Carbon beam of 10^{10} pps in a operating vacuum of about 10^{-6} mbar we get the image shown in fig.3.

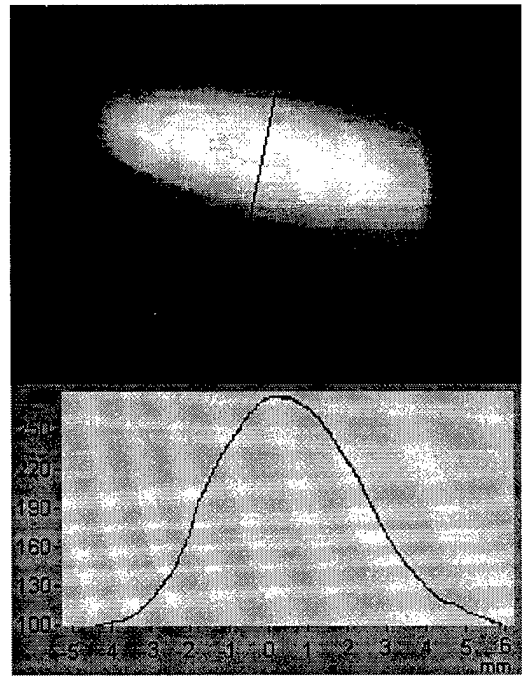

Fig. 3 Trace and horizontal profile with 10 enA of C^{+5}

The measured beam size is about 5 mm FWHM and the estimated resolution is of 0.3 mm taking into account the calibration error and the broadening of the ions. The quality of the image is very good and assuming that we have a significant picture if the ratio of the peak value to the background is at least a factor two, we can deduce that the sensitivity of the system is at least of 10^9 pps. This means that if the expected electron-ion production yield[3] is of the order of $2x10^{10}$ pairs/mm/mbar/pnA, neglecting the collection losses we get a production of $3.2x10^{-6}$ pair/particle/mm. Assuming that the sensitivity of the system is 10^9 pps, we deduce that the limit to the detection of the ionization track is of 3.2 10^3 pairs/mm/s.

More systematic measurements have been done with a Ni^{16+} beam at 30 MeV/n. In this case the beam was 5 mm wide (measured also with a Chromox 6 alumina) with intensities of 1 enA and 0.5 enA. The nominal pressure in the beam line was $8x10^{-6}$ mbar. As shown in fig. 4 the image is clear and the limit of detection is near to 0.3 enA, which corresponds to 10^8 pps. Applying the same considerations done for the carbon beam about the ion-electron pair production, we have, assuming a yield of $9x10^{10}$ pairs/mm/mbar/pnA, that the production rate is 10^{-4} pairs/mm/particle. In the limit case of 0.3 enA, i.e. 10^8 pps, we have a system sensitivity of 10^4 pairs/mm/s, a

value which is very similar to that one obtained for the carbon (3.2 10^3 pairs/mm/s), as we expected.

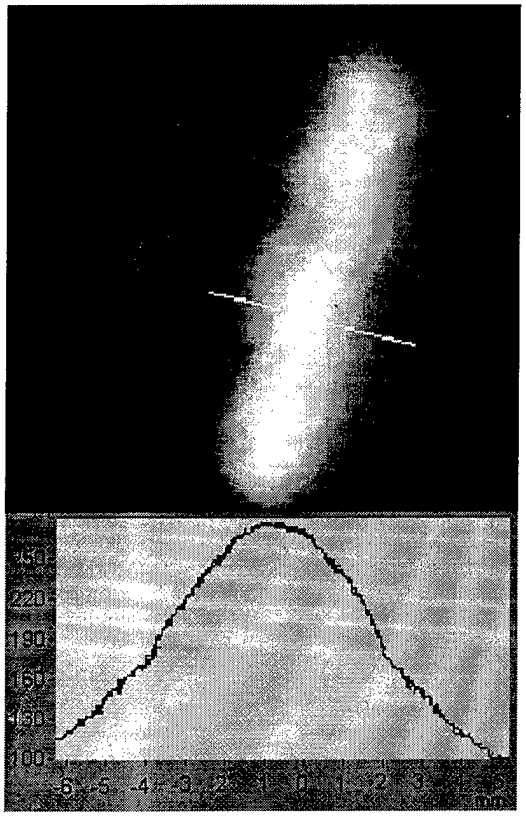

Fig. 4 Trace and horizontal profile with 1 nA of Ni^{+16}

Within a factor three, given by the uncertainties in the knowledge of the true value of the pressure on the MCP region and by the error in the production yield calculation of the electron-ion pairs number in the residual gas, we can assume that the detection limit of our system is given by a production rate of 10^3 ~ 10^4 pair/mm/s for a beam which is a few millimeters wide.

A preliminary test has also been performed with the secondary electron emission device with a Ni beam at 30 MeV/n. A clear beam image was obtained at a very low amplification level of the MCP but, unfortunately, we were not able to continue the measurements for a failure of the MCP.

CONCLUSIONS

We have constructed two non intercepting beam profile monitors based on the use of MCP. The first one detects the ionization track in the residual gas and has been extensively tested with C and Ni beams. The results obtained are interesting and a few comments are in order:

- the technique has proved to be an efficient on line monitor for position, size and beam distribution with beams producing a minimum ionization track in the 10^3 ~ 10^4 pairs/mm/s range and for a few millimeters diameter spot (with the beams used in our test this means a limit of 10^9 pps for Carbon and 10^8 pps for Nickel);
- an increase in the pressure results in a better signal, but the region of 10^{-5} mbar the gain in sensitivity is modest because the noise increases and the MCP is at the limit of its working pressure;
- spatial resolution of 0.3 mm are obtainable and are well within the requirements for the characterization of the beam.

To increase the detector sensitivity up to 10^5 pps or less we have realized a second device based on the secondary electron emission by thin metallic foil, but we had no chance to make quantitative measurements with the beam. We plan to do this in the near future and we expect to decrease the lower limit of detection of about two order of magnitude with the same overall performances of the residual gas monitor.

ACKNOWLEDGMENTS

We should thank Mr. A. Amato for his help in electronics development, Mr. V. Campagna, Mr. C. Marchetta and Mr. S. Salomone for their help in the measurement point assembling.

REFERENCES

[1] R. Alba et al., Radioactive Ion Beam Facilities at LNS, Proc. RNB III, p. 31, Ed. Frontieres, 1993.

[2] A. Rovelli et al., Low Intensity Beam Diagnostics With Particle Detectors, presented at BIW 96, Argonne.

[3] W. R. Leo, Techniques For Nuclear And Particle Physics Experiments, Springer-Verlag 1987.

DESIGN OF A VXI MODULE FOR BEAM PHASE AND ENERGY MEASUREMENTS FOR LEDA*

J. F. Power, J. D. Gilpatrick, and M. W. Stettler

Los Alamos National Laboratory, Los Alamos, NM, 87545, USA

Abstract

Beam diagnostics systems being designed for the Low Energy Demonstrator Accelerator (LEDA) at Los Alamos include beam synchronous-phase and beam energy measurements[1]. The LEDA machine will utilize an RFQ front end operating at 350 MHz, followed by several 700-MHz DTL accelerating structures. Signals from cavity-field probes and beam image-current probes will be down-converted to 2 MHz for phase measurement in VXI modules. Each 2-MHz signal is sampled at 8 MHz with a 12-bit ADC and the resultant data stream is converted into I and Q components which update at a 2-MHz rate. The I and Q signals are then converted to a relative phase measurement. Each VXI module will contain four channels of phase measurement hardware which allow for two channels of differential-phase measurement. Low-noise AGC circuits will accommodate signal variations over a 64 dB dynamic range. An on-board calibration system provides a system absolute accuracy of ±1 degree. DSP filtering allows 200-kHz bandwidth measurements to be made with a resolution of <0.1 degrees over a dynamic range of 46 dB.

1 INTRODUCTION

The energy and synchronous phase of the LEDA beam will be determined via a time-of-flight measurement system. Capacitive pick-up probes, as shown in Fig.1 will be placed along the beam line to sample the 350-MHz component of the beam current. The probes consist of a cylindrical electrode of 5-mm length, suspended by two SMA vacuum feedthrough connectors. Three of these probes will be installed on the beamline during the first testing period of the LEDA RFQ. At the nominal accelerator current of 100 mA, over 25 dBm of signal power at 350 MHz is available. These beam signals will be down-converted to 2-MHz IF signals in VXI modules located in the diagnostics equipment racks which are about 60 m from the beamline. In a similar fashion, the cavity field probes will produce high-level signals which are also down-converted.

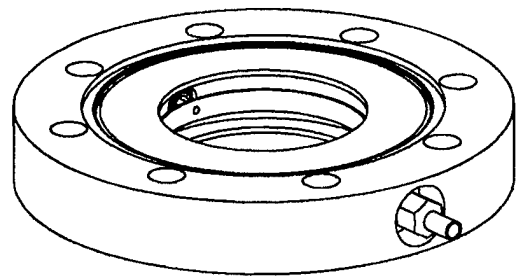

Figure 1 The capacitive probes are designed as integral parts of standard 4.5 in. Dia. Conflat vacuum flanges. Two SMA vacuum-feedthrough connectors support the pick-up electrode.

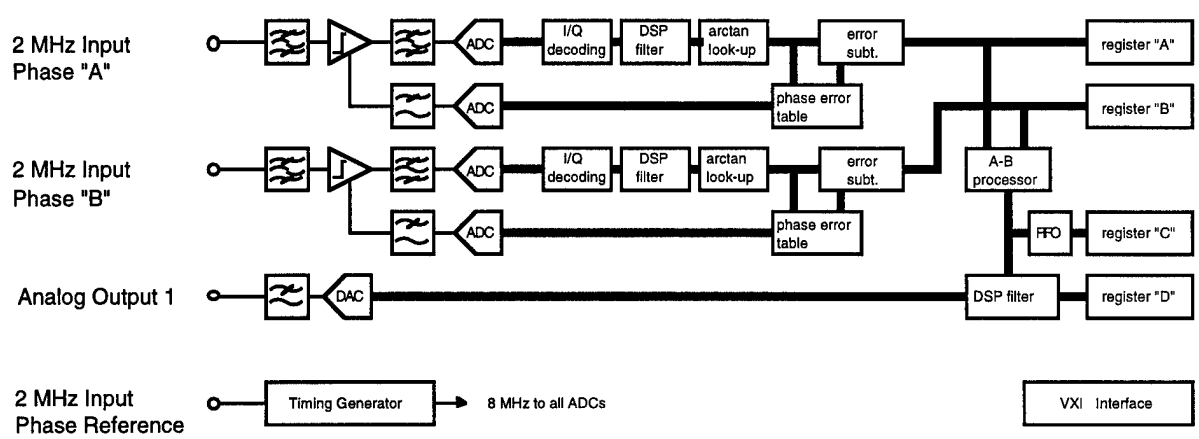

Figure 2 A block diagram of the digital processor. The phase of the analog input is measured and output as a 12-bit word. One LSB corresponds to 0.0879 degrees.

*Work supported by the US Department of Energy

Two types of down-converters are required as the DTL cavities operate at twice the frequency of the RFQ. The 700-MHz cavity-field signals must be down-converted to 2 MHz for comparison with the beam. This requires the generation of two local oscillator frequencies (348 and 698 MHz) from a common 2-MHz reference.

The outputs of the down-converter module mate with a second VXI-based module being designed to measure the phase relationship of the 2-MHz IF signals. This module must have a dynamic range of at least 46 dB (+6 to -40 dBm) and a phase resolution of 0.1 degrees. This phase measurement will have a bandwidth of from dc to 200 kHz, which is greater than the frequency response of the accelerator rf system.

A third module will generate constant-phase 350- and 700-MHz signals for calibration of each phase-measurement channel. The amplitude of the calibration signals will be variable over a 64-dB range.

In this article we describe the salient features of the design of the VXI module which performs the phase-measurement. These features include the digital filtering and I/Q process, the analog AGC front end, and the calibration and error correction technique.

2 I/Q PROCESS

The phase of a sinusoidal signal is readily available from its in-phase and quadrature-phase (I&Q) components. The arctangent of the ratio of I and Q gives the angle of the signal relative to the phase of the sampling clock used to define I and Q.

To get the I and Q components, a signal is sampled at four times its frequency , or once every 90 degrees. This results in a repeating pattern of I, Q, -I and -Q values. These values are subtracted appropriately to produce 2I and 2Q. All common-mode errors are consequentially eliminated and low frequency noise (relative to one half the sampling frequency) is attenuated.

We have chosen 2 MHz as our IF which requires a 8-MHz sampling clock. Since our measurement bandwidth is only 200 kHz, we can apply some FIR filtering to the 2-MHz I and Q data streams to reduce the noise by about 50% before the arctangent is calculated. The arctangent function is calculated by a Plessey PDSP16330 Pythagorus processor[2]. This chip uses a look-up table technique to provide a 12-bit 360-degree range with no ambiguity of quadrant. A block diagram of the digital processor is shown in Fig. 2.

In the final design the FIR filter between the I/Q process and the arctangent process to reduces the measurement bandwidth and noise. Unfortunately the PDSP16330 has a fixed 12-bit output, so this filtering will not enhance the measurements ultimate resolution. For this reason an additional programmable FIR filter will follow the arctangent process to be used in cases in which increased resolution is desired. In this case it will be important to guarantee that the phase noise is sufficiently low relative to the average value, so that the averaging is not done over the inherent discontinuity that occurs at zero and 360 degrees. In other words, the phase of the input signal as seen by the Phythagorus chip should be adjusted to be near 180 degrees at the nominal beam energy.

3 THE ANALOG FRONT END

The digital process, which calculates the signal phase, is inherently normalized in amplitude by taking the ratio of I to Q. To maintain the optimum phase resolution, however, it is necessary to use most of the range of the ADC which is 12 bits in our case. We use an AGC circuit to provide a nearly constant output amplitude over a 75 dB dynamic range. This circuit presents the 2-MHz signal to the ADC at a level which is always near its full scale range. Figure 3 shows a diagram of the analog front end (AFE).

The AGC circuit is based on an Analog Devices AD600 part which has an electronically-controlled variable attenuator followed by a 40-dB, fixed-gain amplifier[3]. One of the interesting features of this chip is that the output noise is independent of the gain of the circuit when a single stage is used. Since we require a 46-dB dynamic range we have cascaded two stages of gain control (the AD600 has two stages per package).

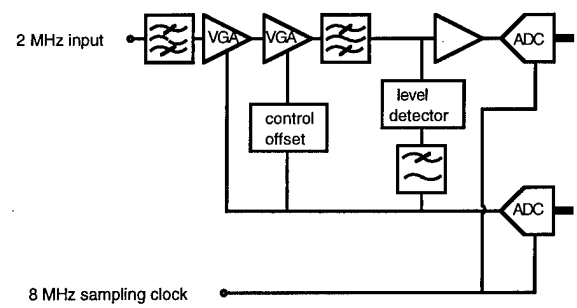

Figure 3 A diagram of the analog front end which includes an AGC circuit with a 75-dB dynamic range.

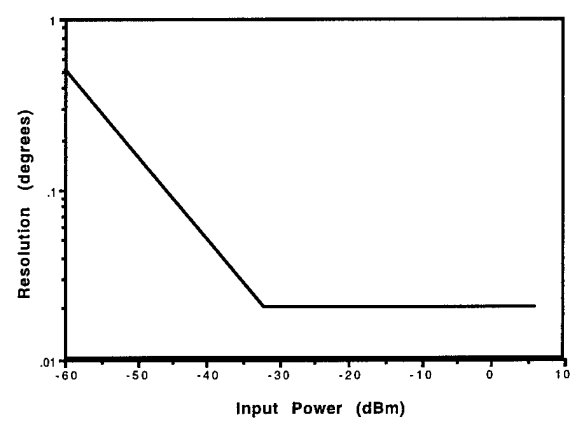

Figure 4 The theoretical phase resolution of the analog front end circuit as a function of signal amplitude for a 400-kHz bandwidth.

The two AGC stages are configured to always use the maximum gain in the first stage and minimum (unity) gain on the second stage, thereby keeping the output noise to a minimum. For signals which are large enough to not require the additional gain of the second stage, the noise level is fixed as a function of amplitude. As the input signal decreases and more gain is required, the noise from the first stage is amplified, along with the signal, by the second stage. A graph of the phase resolution of the AFE as a function of signal amplitude is shown in Figure 4.

The signal that is used to control the gain of the AGC is linear in dB of relative magnitude of the input signal, and is presented to an ADC in addition to the leveled output. This feature will be used to facilitate the phase error correction.

4 CALIBRATION AND ERROR CORRECTION

In order to achieve the desired ±1-degree absolute accuracy it will be necessary to correct for the phase shift of the AGC circuit as a function of input signal level as well as provide a periodic calibration of the system to correct for thermal drifts and aging effects. A separate VXI module will generate multiple pairs of constant-phase, 350-MHz and 700-MHz signals whose amplitudes can be programmed over a 64-dB range. These signals will be connected to the beam-phase and cavity-phase probes on the accelerator beamline via phase-stabilized Heliax® cables.

The calibration signals will be stepped through their 64-dB dynamic range while the phase of each digital channel and the associated AGC-control level are logged. The control system will interpolate this data to create an array of phase correction data vs. control level which will then be down-loaded into the phase measurement module. Subsequent phase measurements will then use this correction table to correct the phase data from the Pythagorus processor in real time. A default data set will be stored in ROM to improve the measurement accuracy prior to, or in lieu of, the on-line calibration.

5 ADDITIONAL FEATURES

There may be times when it is desirable to analyze a large array of phase data taken just prior to an event such as a fast-protect or beam-abort trigger. A large FIFO memory will be incorporated with each differential-phase channel (two per VXI module) which will store the most recent 200,000 measurements at the full 2-MHz rate (100-ms worth). This data will also be useful for "off-line" FFT analysis, where it is undesirable to take data over the VXI bus at the full 2-MHz rate on multiple channels, simultaneously.

A 12-bit DAC will provide an analog representation of each of the two differential-phase measurements to the front panel. These outputs will be useful during the installation and commissioning of the measurement system. They may also prove to be useful for some beam measurements using analog test instrumentation.

6 PROTOTYPE TESTING

A prototype circuit was fabricated which includes the AGC circuits and ADCs for testing. In addition, the digital processor circuits were fabricated using a programmable gate array for decoding the I/Q data stream and interfacing to the Plessey Pythagorus chip. Testing of these two circuits has just begun.

The initial results indicate that the phase resolution of the single-channel system is about 0.035 degrees for a 0-dBm input level versus a theoretical value of 0.02 degrees (defined as one standard deviation). This corresponds to a differential-measurement resolution of about 0.05 degrees which is well within our requirements. A single measurement at an input level of -40 dBm showed a resolution of only 0.2 degrees which is four times higher than the theory predicts. This discrepancy needs further study.

Noise immunity problems with interfacing the two separate analog front end and the digital circuits, combined with some test instrumentation limitations, have prevented us from finishing the characterization of the response over the full dynamic range at this time. A second prototype board which combines all of the required circuitry on a single board is in the process of being fabricated. This is expected to eliminate the interface problems we experienced, and allow us to finish the characterization of the analog and digital front end of the VXI phase measurement system.

7 CONCLUSION

The design of a prototype VXI-based beam energy and synchronous-phase measurement system is underway. Low-noise AGC circuits will accommodate signal variations over a 64-dB dynamic range. An on-board calibration system provides a system absolute accuracy of ±1 degree. DSP filtering allows 200-kHz bandwidth measurements to be made with a resolution of <0.1 degrees over a dynamic range of 46 dB. The analog and digital front-end circuitry of the phase-measuring module has been designed and testing is underway. The initial testing indicates that the phase resolution of the module will easily meet the specification at the higher signal levels. Additional testing is underway.

REFERENCES

[1] J. D. Gilpatrick, T. Hodapp, K. F. Johnson, D. G. Martinez, R. P. Martinez, J. F. Power, C. R. Rose, R. E. Shafer, R. B. Shurter, M. Stettler,"LEDA and APT Beam Diagnostics Instrumentation", these proceedings

[2] "PDSP16330/A/B Pythagorus Processor", Plessey Semiconductors data sheet, (408) 438-2900, 1995.

[3] "Dual, Low Noise, Wideband Variable Gain Amplifiers, AD600/AD602", Rev. A, Analog Devices data sheet, (617) 329-4700, 1996.

DESCRIPTION AND OPERATION OF THE LEDA BEAM-POSITION / INTENSITY MEASUREMENT MODULE*

C. R. Rose, and M. W. Stettler
Los Alamos National Laboratory, Los Alamos, NM 87545

Abstract

This paper describes the specification, design and preliminary operation of the beam-position/intensity measurement module being built for the Low Energy Demonstration Accelerator (LEDA) and Accelerator Production of Tritium (APT) projects at Los Alamos National Laboratory. The module, based on the VXI footprint, is divided into three sections: first, the analog front-end which consists of logarithmic amplifiers, anti-alias filters, and digitizers; second, the digital-to-analog section for monitoring signals on the front panel; and third, the DSP, error correction, and VXI-interface section. Beam position is calculated based on the log-ratio transfer function.. The module has four, 2-MHz, IF inputs suitable for two-axis position measurements. It has outputs in both digital and analog format for x- and y-position and beam intensity. Real-time error-correction is performed on the four input signals after they are digitized and before calculating the beam position to compensate for drift, offsets, gain non-linearities, and other systematic errors. This paper also describes how the on-line error-correction is implemented digitally and algorithmically.

1 INTRODUCTION

This paper describes the specification, design and preliminary operation of the beam-position/intensity measurement module for the LEDA and APT projects at Los Alamos National Laboratory. It is one sub-system of the entire beam-position measurement system described more fully in references [1] and [2]. Related parts of the system include the down-converter module and the error-correction reference chassis. A block diagram of the position/intensity measurement module is shown in Fig. 1. The measurement technique is based on the log-ratio transfer function which has been described by several authors [3,4,5]. The log-ratio technique is defined as

$$V_{\log ratio} = \log(T) - \log(B) \qquad (2)$$

where T and B represent the intermediate-frequency signals for opposite top and bottom lobes of a beam-line probe. Subtraction is easier to perform than division and can be done either by digital or analog techniques.

The module is divided into three sections: first, the analog front-end; second, the digital-to-analog section; and third, the DSP, error-correction, and VXI-interface section. Some of the important specifications of this module are listed in Table 1.

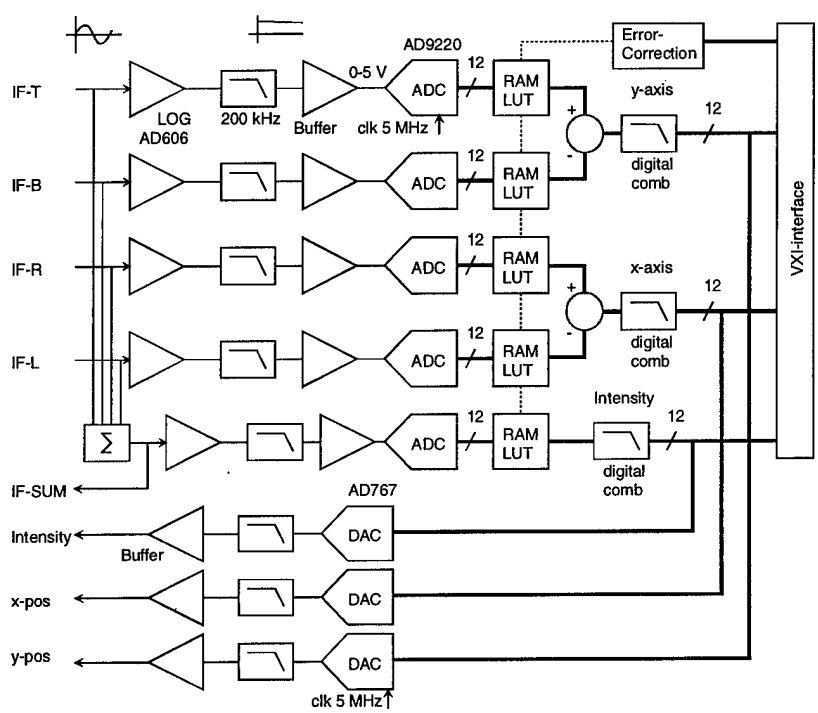

Fig. 1 Block diagram of the position/intensity module.

* Work supported by the US Department of Energy.

Table 1. Requirements for the LEDA/APT Beam Position/Intensity Module.

Item	Value	Units
Frequency input (IF input)	2.00	MHz
Maximum input signal power	15	dBm
Input impedance	50	Ω
# of IF inputs	4	each
# of axis measurements/module	2	each
Range, x-, y-axis outputs	±10	V
Range, intensity output	0-10	V
Measurement bandwidth	≥ 180	kHz
Measurement resolution	0.03	dB
ADC Resolution	12	bits
ADC sampling rate	5	MHz

2 ANALOG FRONT-END

Referring to Fig. 1, the analog section is comprised of the AD606 log amplifiers, the 200-kHz anti-alias filters, the IF summer, and the ADCs. The log amplifiers are rated to 50 MHz with usable dynamic range in excess of 80 dB [6]. A typical curve for the AD606 is shown in Fig. 2. The data were taken from -80 dBm to +20 dBm. There is some distortion at the

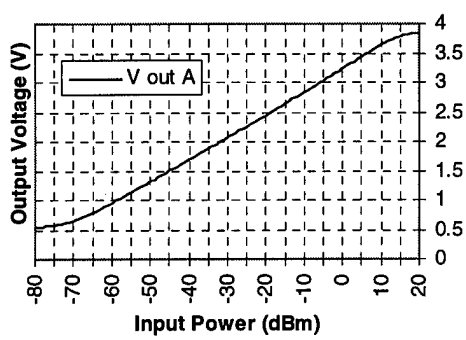

Fig. 2 Vout vs. input power for a typcial AD606 log amp operating at 2 MHz.

upper end starting at an input power of about 15 dBm due to saturation and also at the lower end of the input range where the log amp approaches the reference level. The ideal response for this log amp is

$$V_{out} = K \log\left(\frac{v_{in}}{v_{ref}}\right) \tag{3}$$

where v_{in} is the rms amplitude of the input signal , v_{ref} is 8.60 μVrms (corresponding to -88.3 dBm reference level), and K=0.75 [7]. Since the log amp is non-ideal, there are small perturbations in its transfer function and distortion effects at the upper and lower ends of the dynamic range. By using digital error-correction, non-ideal performance in the log amps and other system non-linearities can be taken out of the overall transfer function of the system.

The output of each log amp is filtered with a 200-kHz anti-alias low-pass filter. After the low-pass filters, each signal is over sampled at 5 MHz by an AD9220 12-bit ADC. The signal-level range at the input of the ADCs is 0-5 V. The voltage resolution using 12 bits and 5 V is ±0.61 mV which corresponds to a probe dB offset resolution of ±0.0163 dB. The resolution in mm depends on the specific probe sensitivity.

The four IF-inputs are combined in the IF-SUM circuit to be used to measure beam intensity by a fifth log amp channel. This IF-SUM signal is also available to other accelerator systems via the module's front panel. Even though the sum of the four signals is a non-linear response to beam intensity if the beam is off center, knowing beam position in x-and y-space, and measured intensity, the real beam intensity can be calculated. This calculation is done in the main control system and not in the module.

3 DSP AND ERROR-CORRECTION SECTION

The DSP and error-correction section consists of the 12-bit RAM look-up tables (LUTs), the digital comb filters, and the VXI-interface circuitry. To perform the on-line error-correction process, a known power level is input to the four IF-inputs, the digital data is allowed to bypass the RAM look-up tables. This "actual" data is then compared to the theoretical values that would be obtained at the end of the electronics chain with the known-input power levels. Correct values are calculated and uploaded to the respective RAM look-up tables. The ADC outputs are addresses for the LUTs. Thus when "real" IF signals are input to the module, the log amplifiers attempt to convert the signals according to eqn. 3, the ADCs sample these now-converted dc signals, and the ADC outputs address the LUTs and output the "correct" data to the bus for processing. The "known" power levels are supplied by an Error-Correction Reference chassis described in more detail in reference [8].

Each digital subtractor and comb-filter pair are implemented in a single 12000-gate FPGA which can operate up to 20 MHz. The comb filters are eight-point moving-average filters with a -3 dB cutoff frequency of about 215 kHz assuming a data flow rate of 5 MHz. The input data is 12 bit, and after the subtraction and filtering, 15-bit data is available. The moving average division is implemented by ignoring the bottom three bits and using the upper 12.

The register-based VXI-interface chip-set takes care of essential bus functions and facilitates bi-directional data flow to the module including uploading the corrected data for the LUTs. This part of the module

also provides all of the necessary 5-MHz clock signals to the ADCs, the necessary clock signals to the subtractors, and the clocks for the comb filters.

4 DAC SECTION

The digital-to-analog-converter (DAC) section converts the 12-bit x- and y-axis, and intensity data to analog signals for monitoring at the module's front panel. The x- and y-axis signals' range is ±10 V. The intensity channel is converted to a 0-10 VDC signal. Analog Devices AD767 12-bit DACs are used to perform the conversions. The digital section of the module supplies the proper clock signals and data stream to the DACs. The DAC outputs pass through 200-kHz low-pass filters and buffers before being available at the front panel.

5 TESTING

Preliminary testing of the error-correction technique has been done. These tests used prototype printed-circuit boards and crudely taken data but proved the concept. Uncorrected-position data is shown in Fig. 3. The vertical scale is in dB, and the horizontal scale is in

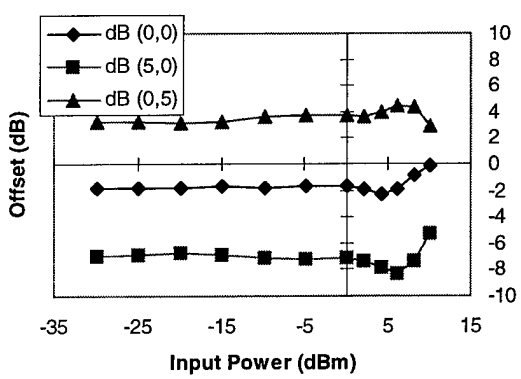

Fig. 4 Graph of uncorrected single-axis position data.

dBm. The input rf signals were offset by 0-dB, 5-dB, and -5 dB. An offset in one of the log amps shifted the curves downward. Important characteristics to note in the graph of Fig. 3 are that the curves exhibit significant distortion and offset over the measured dynamic range of the test. For a properly performing log-ratio system, the lines will be centered about zero offset and be flat. Assuming these errors are caused in general by anomalies such as log amps with differing gains and offsets, dc offsets in the buffers, and ADC non-linearities, error-correcting LUTs will correct the response.

Preliminary error-correction LUTs have been calculated and put into EPROMs. The same system was then tested again and curves plotted in Fig. 3. The dc offset has been removed, and the distortion in the curves of Fig. 4 have been significantly removed. The top curve is +5-dB offset, and the bottom curve is -5 dB offset.

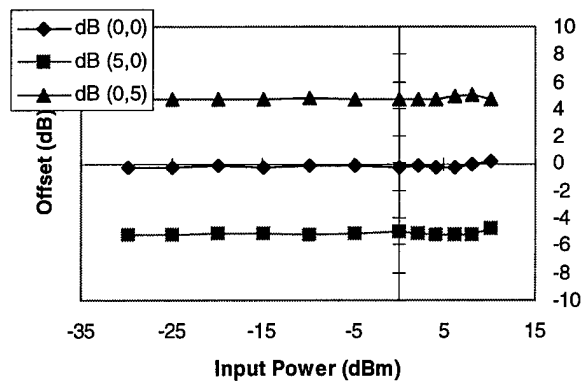

Fig. 3 Graph of error-corrected single-axis position data.

REFERENCES

[1] Rose, C. R. *et. al.*, "The LEDA Beam-Position Measurement System," these proceedings.

[2] Gilpatrick, J. D., *et al.*, "LEDA and APT Beam Diagnostics Instrumentation," these proceedings.

[3] Gilpatrick, J. D., "Comparison of Beam-Position-Transfer Functions Using Circular Beam-Position Monitors," these proceedings.

[4] Wells, F. D., *et al.*, "Log-Ratio Circuit for Beam Position Monitoring," American Institute of Physics, Accelerator Instrumentation, Second Annual Workshop, Batavia, Illinois, 1990.

[5] Aiello, G. R., and M. R. Mills, "Log-Ratio Technique for Beam Position Monitor Systems," Nuclear Instruments and Methods in Physics Research, 1994.

[6] "AD606 50 MHz, 80 dB Demodulating Logarithmic Amplifier with Limiter Output," Analog Devices, One Technology Way, PO Box 9106, Norwood, MA 02062, USA.

[7] *Ibid.*

[8] Rose, C. R. *et. al.*, "The LEDA Beam-Position Measurement System," these proceedings.

DESIGN STUDY FOR AN UNDULATOR PHOTON BEAM POSITION AND PROFILE MONITOR

Ian C. Hsu, C.-T. Wang, and P.-C. Lai
Department of Nuclear Science, National Tsing Hua University and SRRC, TAIWAN

Abstract

This paper we presented part of the design study for building a semi-nondestructive undulator photon beam position and profile monitor. It is a mesh wire monitor. However, in order to be classified as a semi-nondestructive monitor, the destruction to the undulator photon beam have to be minimized under the constrains of the required position resolution. The destruction considered should include the flux reduction and the beam size blowup due to diffraction (the later part are not presented in this paper). The variation parameters are the wire diameter and the wire spacing. The resolutions of the position and the profile measurements as function of the variation parameters are simulated.

1 INTRODUCTION

The photon beam line having an extremely high resolution is one of the primary characteristics of a third generation synchrotron radiation light source. Such characteristic has caused the photon beam lines' optical systems to become quite sensitive to their photon sources' position and angle, i.e. the electron beam orbit. A fundamental issue of all of these light sources, the photon beam line's flux fluctuates due to instabilities of the electron beam position and angle. To resolve this problem, at the first, the sources of the orbit instabilities have to find out and remove as clear as we can. The second step will be to build all kinds of the orbit stabilization feedback loops.

For the purpose of stabilizing a certain beam line, the local orbit feedback loop are usually applied. To stabilize a beam up to a few micrometers range, the resolution of the detecting system of the loop has to be no worse than a few micrometers. To accomplish this requirement, photon monitors are used for their high resolution character. However, the feedback system for the undulator beam line has an extra complication. Because, the synchrotron radiation from up-stream and down-stream bending magnets will unavoidable add to the photon monitor of the undulator light, this will confuse the beam position signal when adjusting the gap of the undualtor.[1] In most of application of undulator light, gap adjusting is a necessary while doing the experiment. This difficulty force people to think other monitor system, e.g. high resolution electronics BPM.

This paper we proposed and presented part of the design study for building a semi-nondestructive undulator photon beam position and profile monitor. It is a mesh wire monitor. However, in order to be classified as a semi-nondestructive monitor, the destruction to the undulator photon beam have to be minimized under the constrains of the required position resolution. The destruction considered should include the flux reduction and the beam size blowup due to diffraction (the latter part are not presented in this paper). The variation parameters are the wire diameter and the wire spacing. The resolutions of the position and the profile measurements as function of the variation parameters are simulated. Later, the estimated measurement and electronics errors should be included.

One of the advantage of this method is that by fitting the measurement results to the known photon beam profile functions, we can subtract the light contribution from the up-stream and the down-stream bending magnets. Thus, over come the difficulty, we mentioned earlier in this section. Also, besides knowing the beam position, we have the beam profile information.

2 SIMULATIONS

We first used a gaussian beam to simulate the undulator light. That just for simplicity. Later, we should used the known photon beam profiles (both the undulator light and the bending synchrotron light). By using gaussian beam, we can also experimentally exam our simulation results in bench and using handy Laser beam.

Figure 1 depicts the photon beam and wires parameters used in the simulations.

0-7803-4376-X/98 /$10.00 © 1998 IEEE

Where **S**: the photon beam size (±2 sigma), **M**: the center wire spacing, **a**: normal (beside center) wire spacing, and **da**: the wire diameter.

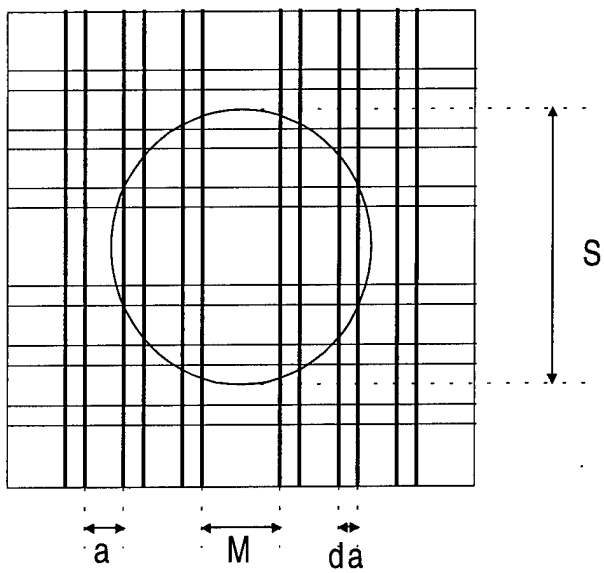

Fig. 1 The photon beam and wires parameters used in the simulations

Figure 2 shows the relative photon flux for different wire number and different wire diameter with the same beam size and the same center spacing.

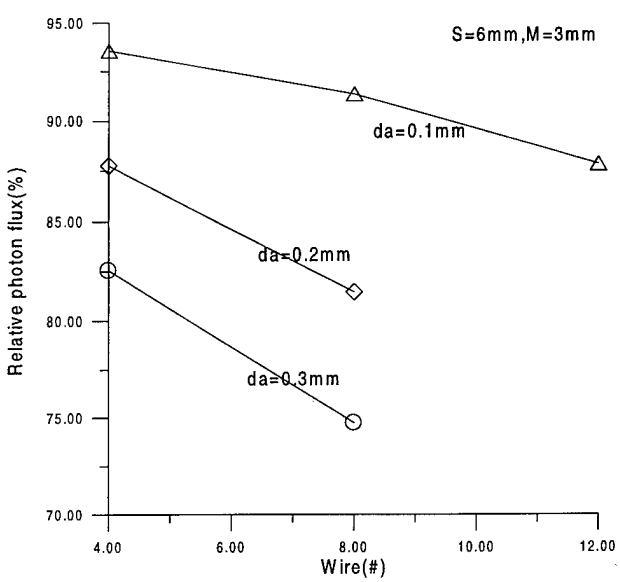

Figure 2 shows the relative photon flux for different wire number and different wire diameter

For different wire diameter, we will gain different photon electrons and thus different measurement uncertainties. For different wire number (wire spacing), we will get different amount of information and thus different fitting errors. Figure 3 shown a 6 mm (±2 sigma) gaussian beam measured by different wire spacing and added the measurement uncertainties, then fitted by gaussian function. We can see that for wire spacing larger than 0.6 mm the fitting error become very large.

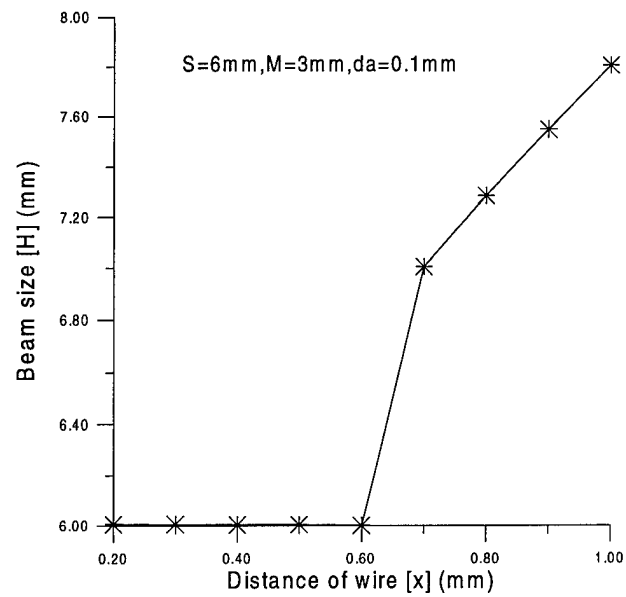

Fig. 3 A 6 mm (±2 sigma) gaussian beam measured by different wire spacing and added the measurement uncertainties, then fitted by gaussian function

3 DISCUSSIONS

This very preliminary study shown that the error analysis can play an important role for designing the mesh wire photon monitor. Lots of further studies have to be carry on.

ACKNOWLEDGEMENTS

This work was supported by the NSC of Taiwan, under contract NSC 85-2112-M-007-019.

REFERENCES

[1] J. N. Galayd, Y. Chung and R. O. Hettel, in *Synchrotron Radiation Source - A Primer*, edited by H. Winick (World Scientific, Singapore, 1994) 352

AN RF SIGNAL PROCESSING MODULE FOR THE SPS ORBIT OBSERVATION SYSTEM UPGRADE

W.R. Rawnsley, K. Fong, S. Fang
TRIUMF, 4004 Wesbrook Mall, Vancouver, B.C., Canada V6T 2A3 and
J-P. Papis, CERN, CH-1211 Geneva 23, Switzerland

Abstract

CERN will replace the 200 MHz electronic calibrator and filter modules used in the SPS Orbit Observation System as part of an ongoing upgrade. TRIUMF is designing the new modules and will supervise the manufacture of 300 modules as part of Canada's contribution to the LHC. Six prototype modules were also provided for additional diagnostics with injected long ion bunches in Fall 1996. The SPS accelerated fully stripped Pb ions and the modules operated at 47.5 MHz, the fifth harmonic of the bunch spacing. The beam position was measured during the first few turns following injection before the beam was captured by the 200 MHz RF. The modules process the RF sum and difference signals from the beam position monitors. They allow for compensation of phase drift in the cables from the monitors, provide for calibration of the electronics system and house pairs of bandpass filters.

1 SYSTEM DESCRIPTION

Fig. 1 is a block diagram of a SPS beam position monitor and its front end electronics. A beam of charged particles, which can be electrons, positrons, protons or lead ions, induces signals in the monitor electrodes by its passage. 50 Ω cable matching networks on the air side of the vacuum feedthroughs were designed for 200 MHz and are not ideal for 47.5 MHz. For 200 MHz operation, each monitor has a ring hybrid constructed of lengths of coaxial cable near the monitor to form the sum and difference of the electrode signals. Anzac H9 wideband hybrids are used for the 47.5 MHz monitors. The beam position is determined by the ratio of the amplitudes of the sum and difference signals.

The signals are carried by coaxial cables from the beamline area to the electronics area. The losses in these cables are equalized to 25 dB. Each segment of the ring also has 6 long cables with 32 dB attenuation but these particular monitors are not used at 47.5 MHz. Pre-amps with a gain of 30 dB are switched into the signal path when accelerating lead ions or switched out for other species.

A manually adjustable phase shifter in the difference path allows for compensation of drift in the cables from the beamline. It is anticipated that this adjustment will only be made about once a year. A phase shifter in the sum channel has a fixed value at the midrange of the variable phase shifter. This combination allows for positive or negative phase compensation. A splitter and RF switches facilitate compensation for errors in the gain and phase matching of the system. The signals pass through the bandpass filters to remove all but the 47.5 or 200 MHz component.

The gains of the variable amplifiers which follow the calibrator module may be set from 0 to 60 dB in 10 dB steps. The amplified sum signal is passed through a limiter and used to homodyne itself and the difference signal via a pair of mixers. The outputs from the mixers pass through low pass filters finally yielding the envelopes of the two signals. These signals are sampled for continuous beams or peak detected for single bunches and then digitized.

2 CALIBRATOR MODULE COMPONENTS

The description that follows refers mainly to the 47.5 MHz modules [1][2]. Many modifications in the design will be incorporated in the 200 MHz units.

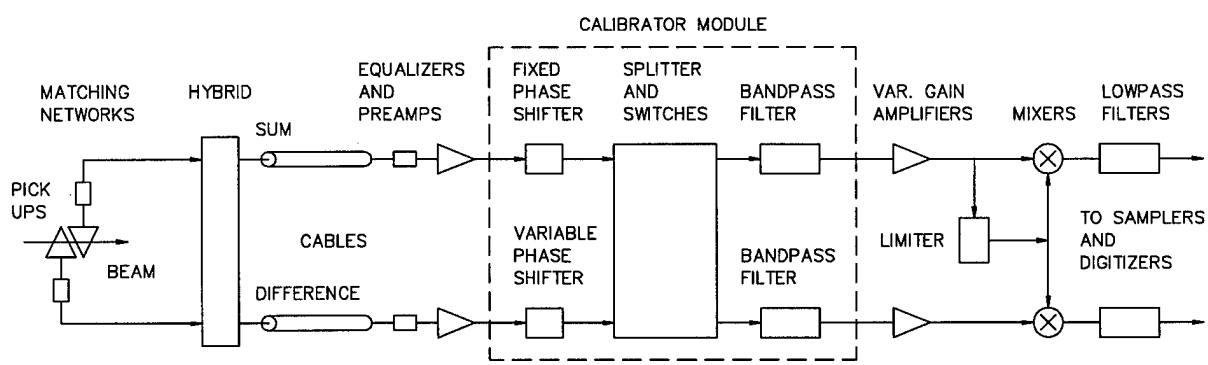

Figure 1. A block diagram of the system.

0-7803-4376-X/98/$10.00 © 1998 IEEE

2.1 *Module Layout*

The module is a double height Eurocard (VME) 233.35 mm high, 39.2 mm wide and 220 mm deep. Ten modules fit in a Eurocrate. Signals enter the module via SMA jacks which project through the front panel. Coplanar microstrip carries the signals to OCX connectors on the motherboard. These connectors mate with a daughter board which supports the surface mount phase shifters and RF switching network. The control signals and power are carried to the daughter board by pin headers. Coaxial cables with Teflon dielectric take the signals to the bandpass filters. The outputs from the filters are available on N connectors which project through the front panel. The daughter card is contained inside an RF shield and can be unplugged from the main card for service.

2.2 *Phase Shifters*

The variable phase shifter consists of a quadrature hybrid with its 0° and -90° ports terminated by variable capacitance diodes (varicaps). The output is taken from the normally isolated port. The phase shift through the network is $\phi=\arctan((1-\omega^2 C^2 Z_c^2)/(2\,\omega C Z_c))-180°$ where ω is the angular frequency, C is the capacitance of the varicaps (assumed equal) and Z_c is the characteristic impedance of the hybrid, 50Ω. The capacitance of the Motorola MMBV109LT1 varicap diodes as a function of their reverse bias voltage can be approximated as $C=C_0/(1+V/V_0)^{GAMMA}$ where C_0=52.8, V_0=10.2 and GAMMA=2.36 at 1 MHz. In fig. 2 the measured phase shift at 47.5 MHz is shown as a function of the varicap reverse bias voltage using a test fixture incorporating a M/A-Com JHS-115 quadrature hybrid.

The diode reverse bias available in the module is variable from 3 to 13 V corresponding to a measured phase shift from -131.44° to -100.27°, a range of 31.17 °. This is a little less than the calculated range of 32.7°. The smallest range measured for the actual modules as delivered was 31.1°. The worst input VSWR of the phase shifter over its range and over the 7 modules delivered was 1.18. To maintain equal delays the phase shifter in the sum channel uses a similar quadrature hybrid circuit but with fixed capacitors.

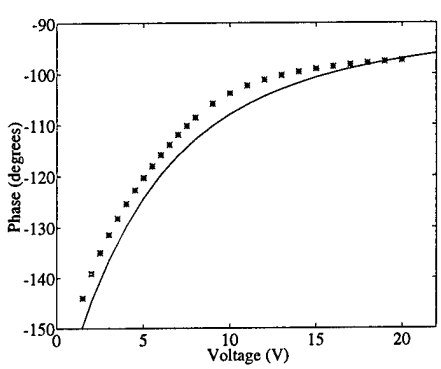

Figure 2. The measured (points) and calculated phase shift versus the varicap reverse bias voltage.

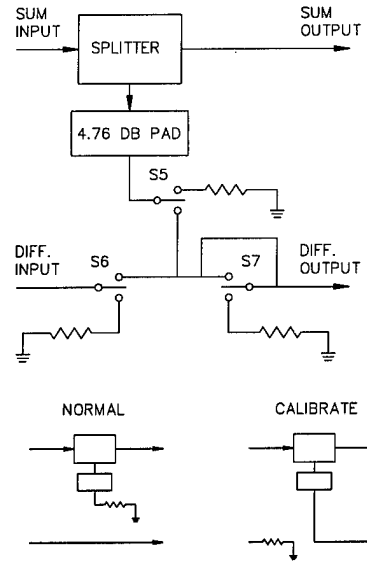

MODE	RF SWITCHES S5	S6	S7
NORMAL	0	1	1
CALIBRATION	1	0	1
OFFSET	0	0	0

0 = OPEN (TERMINATED) 1 = CLOSED (THROUGH)

Figure 3. Calibration modes.

2.3 *RF Switching*

The calibrators have three operating modes which are illustrated in fig. 3. Beam position measurement occurs in the Normal mode. The Calibrate mode is used to measure the gain balance of the amplifiers that follow the module. In this mode, the sum input is split between the sum and difference outputs. The 4.76 dB pad following the splitter insures that the sum channel output will be 6 dB greater than the difference channel output. The splitter is a wideband transformer and provides lower loss, 3.75 dB, and better isolation, 25 dB, between its outputs than a simple resistive splitter. The Offset mode is used to measure the position offset error of the system by zeroing the difference channel output.

The mode switches will be operated frequently, once each cycle (16 s) or few cycles, to measure the offset. Calibration mode will be used less frequently. Solid state switches were chosen for reliability. CERN has had problems with mechanical switches and limited their use to occasional calibrations done by experts. GaAs FET switches allow the 60 dB isolation specification for the module to be met. The M/A-Com SW-221 switches have built in 50 Ω termination resistors. Their guaranteed isolation at 500 MHz is 60 dB and is typically 75 dB at 47.5 MHz. Their guaranteed insertion loss is 0.9 dB but is typically 0.7 dB. A 16L8 Programmable Array Logic (PAL) chip is used to convert the control signals to the patterns required by the RF switches. The TTL level signals from the PAL control Harris CMOS dual switches which act as level converters. These devices pass ground to one of the controls lines of a GaAs switch and -8 V to the other. The control line voltages are reversed to change the state of the GaAs switch.

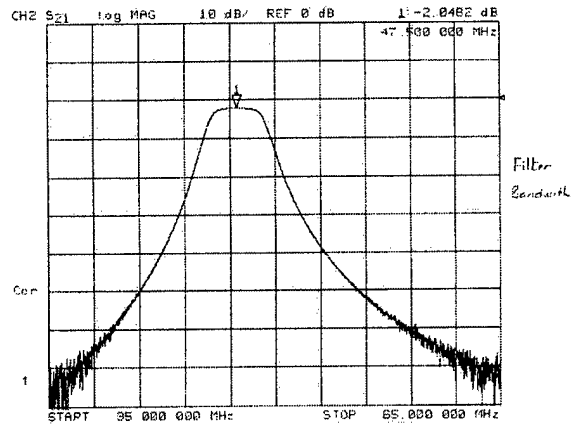

Figure 4. The frequency response of a 47.5 MHz filter.

2.4 Filters

The 47.5 MHz filters are Bessel type and were made at CERN. They are an adaptation of the 200 MHz filters developed by the LTT company and are housed in the same type of aluminum cases. They are constructed using hand wound inductors, air trimmers, and ceramic capacitors. The bandwidth is 4 MHz and the insertion loss is 2 dB, fig. 4. The beam position can be measured in two modes. In continuous mode the filters remove all but the 47.5 MHz component of the signals. In single bunch mode the filters ring at 47.5 MHz. The envelope of the ringing response builds quickly to a well defined peak at 250 ns whose amplitude is measured by a peak detector. The ringing duration is about 600 ns, fig. 5.

200 MHz combline filters, with 4.4 MHz bandwidth, will be purchased from the Microwave Filter Co. A filter consists of 4 copper rods shorted to the case at one end and loaded by paralleled porcelain capacitors and piston tuning capacitors at the other ends. The input and output coupling loops are adjustable. It is a 4 pole, 0.1 dB ripple Chebychev design with 2.7 dB insertion loss. The $\lambda/26$ resonators give ≥80 dB harmonic rejection to 2.5 GHz.

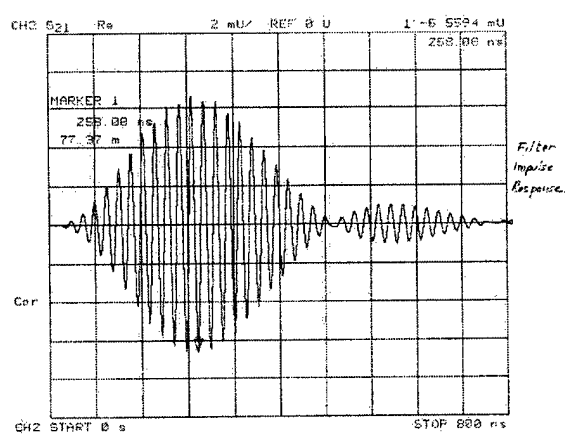

Figure 5. The time response of a 47.5 MHz filter to an impulse.

The phase shifts through the sum and difference channels of a module, of which the filters are the major contributors, should track within 3° over a temperature range of 15°C to 30°C. The error in the amplitude measurement of the signals in the synchronous detection system is 1-cosϕ where ϕ is the phase error between the sum and difference signals. A phase error of 3° gives an amplitude error of 0.14%. The requirement that the phase shift through a filter pair track within 3° at 200 MHz is equivalent to their centre frequencies tracking within 33 kHz. The requirement that their ringing responses track within 3° at the peak of the envelope is equivalent to their centre frequencies tracking within 39 kHz.

3 BEAM TESTS

The six modules installed for the Fall run operated satisfactorily. Fig. 6 shows the growth of 200 MHz on a pair of bunches of Pb ions injected 105 ns apart. A spare module was also supplied and four more modules for additional monitors have been built.

4 ACKNOWLEDGEMENTS

We wish to thank D. Smith, G. Dennison and R. Barton for their assistance.

REFERENCES

[1] 'A 47.5 MHz Calibrator Module for the CERN SPS Orbit Observation System', W.R. Rawnsley, S. Fang, K. Fong, J-P Papis, TRIUMF Design Note TRI-DN-97-9

[2] 'Documentation for 47.5 MHz Calibrator Module of CERN SPS Orbit System', S. Fang, TRIUMF, 1997

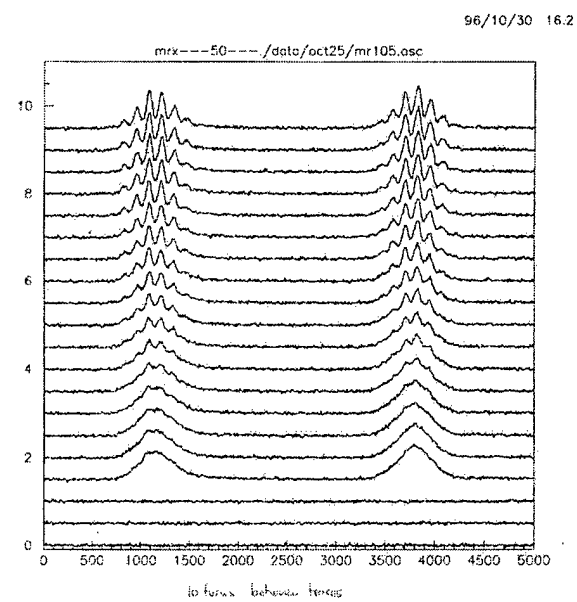

Figure 6. The growth of the 200 MHz component on a pair of bunches spaced by 105 ns. The horizontal scale is in arbitrary units. The traces were taken 10 turns apart.

CHARACTERIZATION OF BEAM DYNAMICS IN THE APS INJECTOR RINGS USING TIME-RESOLVED IMAGING TECHNIQUES

B. X. Yang, A. H. Lumpkin, M. Borland, K. Harkay, A. Nassiri
Argonne National Lab, 9700 South Cass Avenue, Argonne, IL 60439, USA

Abstract

Images taken with streak cameras and gated intensified cameras with both time (longitudinal) and spatial (transverse) resolution reveal a wealth of information about circular accelerators. We illustrate a novel technique by a sequence of dual-sweep streak camera images taken at a high dispersion location in the booster synchrotron, where the horizontal coordinate is strongly correlated with the particle energy and the "top-view" of the beam gives a good approximation to the particle density distribution in the longitudinal phase space. A sequence of top-view images taken right after injection clearly shows the beam dynamics in the phase space. We report another example from the positron accumulator ring for the characterization of its beam compression bunching with the 12th harmonic rf.

1 INTRODUCTION

The time-resolved imaging techniques using gated cameras and dual-sweep streak cameras have been applied to linac-based free-electron lasers and large accelerators [1, 2]. In this work, we will show that by viewing the optical synchrotron radiation from a high dispersion area with a streak camera, one can directly visualize particle motion in the longitudinal phase space. In another case, we report studies of longitudinal damping and bucket impurity in the APS positron accumulator ring (PAR).

2 VISUALIZING THE LONGITUDINAL PHASE SPACE IN THE APS BOOSTER SYNCHROTRON

2.1 Conditions in the APS Booster Synchrotron

Three synchrotron radiation ports have been installed in the Advanced Photon Source (APS) booster synchrotron; this experiment was performed at the third port, which has the highest dispersion. Table 1 lists values of relevant parameters for the accelerator and fully damped beam at this location. While the size of the beam is dominated by the emittance effect for fully damped beams, any momentum offset (from the nominal value) due to injection or ramping phase/energy mismatch will cause beam motions in the longitudinal phase space. This is particularly true in the first half of the ramp (acceleration) where the damping by synchrotron radiation is weak.

Table 1 APS Booster Synchrotron Parameter at Photon Port No. 3 (horizontal beta function = 10.65 m)

Particle energy (GeV)	0.375 (inject)	7.0 (extract)
Design emittance (mm·mrad)	0.25	0.13
Horizontal size due to emittance (mm)	1.632	1.181
Horizontal size due to energy spread(mm)	0.683	0.683

2.2 Experimental Setup [3]

The visible synchrotron radiation light was collected by a molybdenum mirror, relayed by an achromatic lens, and focused onto the streak camera slits by a second lens. The part of the slits being illuminated is thus a true image of the horizontal profile of the particle beam.

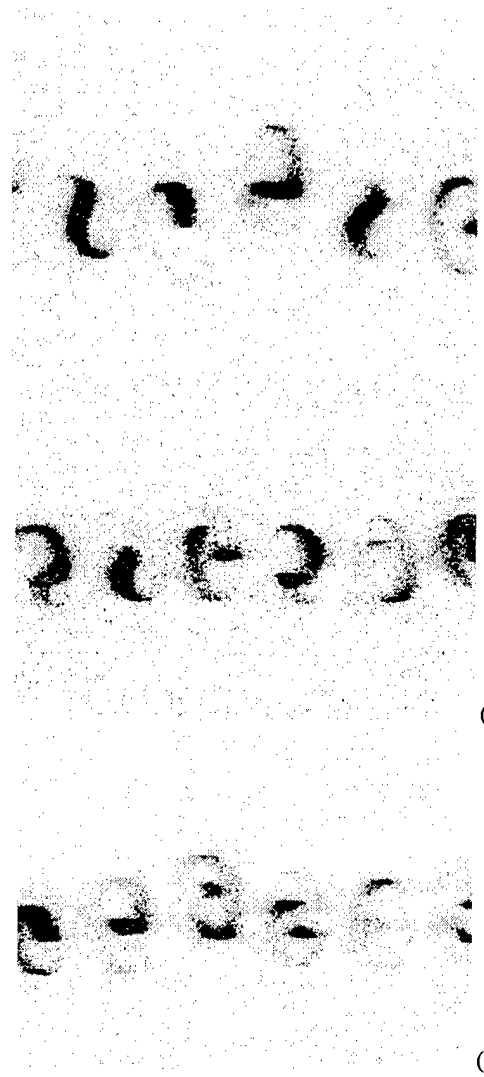

Figure 1: Top view of the positron bunch in the APS booster synchrotron at a high dispersion area. All pictures are taken with vertical full scale of 5 ns and horizontal 50 μs. (a) the first 50 μs after injection, (b) after 50 μs delay from the injection; (c) after 100 μs delay.

A dual-sweep streak camera (Hamamatsu C5680 with M5677 slow-sweep unit and M5679 dual-time base extender unit) was used to record the images. A DG535 delay

0-7803-4376-X/98/$10.00 © 1998 IEEE

generator (from Stanford Research), triggered by the booster injection timing pulse, was used to generate the trigger for the horizontal scan unit M5679.

The positron revolution time in the booster is 1.228 μs. The turn signal was used to trigger a second delay generator which generated a vertical trigger pulse for the vertical scan unit M5677 in multiples of the revolution time. The frequency of the vertical trigger pulse was chosen to be about 6 - 10 times that of the horizontal scan time of the camera since only 6 - 10 beam images could fit in the same screen without interfering with each other.

2.3 Results and Discussion

Figure 1 shows three frames taken after the injection, 50 μs (40 turns) apart in their delay time. The interval between each beam image is seven turns. The vertical axis corresponds to time or particle phase, and the horizontal motion is the combination of the particle's betatron motion and energy offset. The pictures show that the synchrotron motion is the dominant component. After injection, the captured bunch tumbles (clockwise in the picture) in the phase space with a period ~ 25 μs, which roughly correlates to the measured synchrotron frequency of 30 kHz about 1 ms into the ramp. The motion of the particle immediately starts to decohere due to nonlinearity of the effective potential, decohering almost completely into a "doughnut" shape within the first 150 μs (125 turns).

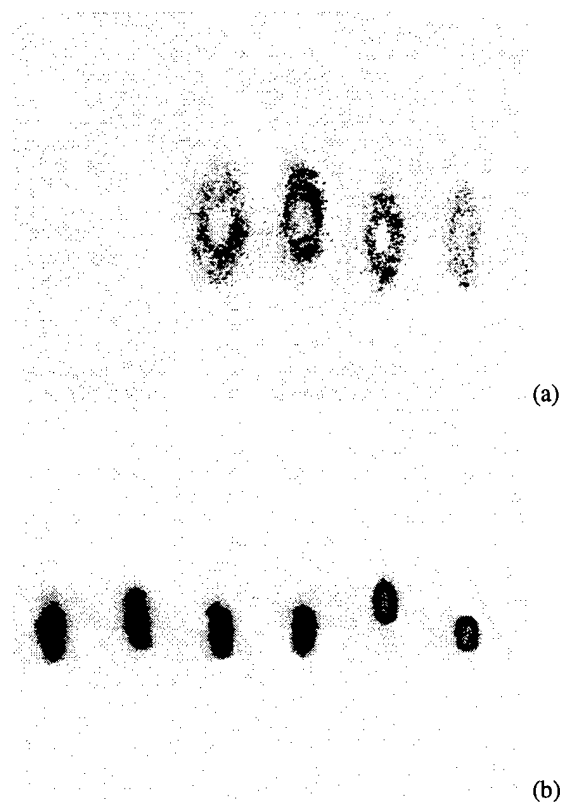

Figure 2: Top view of the positron bunch in the APS booster synchrotron at a high dispersion area. Both pictures were taken with vertical full scale of 5 ns and horizontal 50 ms. (a) the first 50 ms after injection and (b) after 50 ms delay from the injection.

Figure 2 shows two frames taken in the same experiment but using a larger time scale: the horizontal extent is now 50 ms, and the frames are 50 ms apart in delay time. The size of the "doughnuts" shrinks down with the ramping, since increased particle energy results in increased synchrotron radiation and enhanced longitudinal damping. The emittance effect finally dominates the beam size at ~100 ms into the ramp or when the positron energy reaches ~3 GeV.

2 GATED CAMERA MEASUREMENT OF APS BOOSTER SYNCHROTRON BEAM EMITTANCE

Due to continued energy change of the particle beam during the ramp in the booster, the beam profile imaging is best performed with only a single pass to avoid blurring due to beam motion. We used an intensified gated camera (Quik 05 from Stanford Computer Optics) to acquire the image. The camera was triggered by a delayed pulse from the injection timing, and its exposure time was set to be less than the revolution time. Figure 3 shows a typical image taken about five turns before the extraction. Using the design lattice functions, we deduced from the beam profile (σ_x=0.80mm, σ_y=0.17mm) that the emittance at extraction was ε=0.125mm·mrad, with a vertical coupling of χ=0.02, matching the design goal of ε=0.131mm·mrad, and χ<0.1.

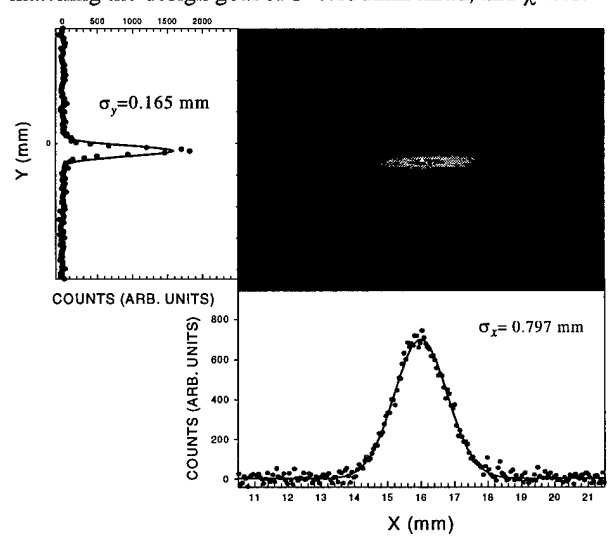

Figure 3: The front view of the positron bunch in the APS booster synchrotron at the extraction, a snapshot taken in a single pass.

3 STUDIES OF BEAM DAMPING IN THE PAR

In the APS positron accumulator ring (PAR), the bunch length is compressed before the extraction by turning on a twelfth harmonic rf cavity (RF-12, 117.3 MHz) for about 100 ms to match the booster capture requirement. The phase of the harmonic relative to the fundamental is crucial to the compression.

We used a streak camera to study the beam dynamics during the compression. The optical transport [4] here is similar to that in the booster, except that a short focal length lens was used to condense the photons so that the spatial information was lost. Figure 4 shows a streak image taken

with 50 ns full scale in the vertical direction, and 50 ms in the horizontal. The vertical scan is triggered every 2 ms. The RF-12 cavity was turned on about 7 ms after the start of the horizontal scan in this picture. By carefully examining this picture one can extract much information about the compression process.

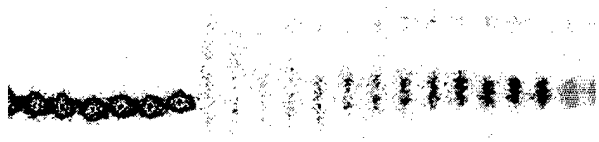

Figure 4: A dual-sweep image of the APS PAR beam during bunch compression by the 12th harmonics rf (117.3 MHz).

3.1 Bunch Length and Longitudinal Damping

The bunch length can be obtained by fitting the integrated vertical intensity profile of any of the beam images. The bunch with RF-12 off was found to be 0.84 ns long, which compares with a theoretical value of 0.88 ns for the operating condition during the experiment. Figure 5 plots the bunch length as a function of time after RF-12 was turned on. From this plot, we deduced the longitudinal damping time to be 24.1 ms, which may be compared with its design value of 25.4 ms. The bunch length at the end of the compression was measured in a similar manner and found to be 0.22 ns, which may be compared with its design value of 0.21 ns.

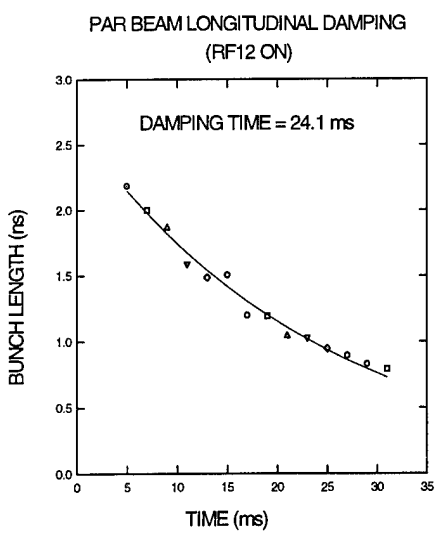

Figure 5: Bunch length of the PAR as a function of time after the 12th harmonic is turned on.

3.2 Bunch Purity and Compressor Phase

It can also be seen from Fig. 4 that the phase of the harmonic cavity was mismatched when this image was taken. The mismatch caused the bunch to lengthen significantly after turning on RF-12. In fact, some particles were spilled over to the adjacent bucket and captured. This satellite bunch propagated through the booster synchrotron into the storage ring (known as bucket impurity), where it became quite a nuisance for nuclear resonance experiments.

Figure 6 shows the fraction of the integrated intensity of the main and satellite peaks as a function of RF-12 phase. By varying the phase, one can minimize the satellite bunch intensity to a level acceptable to the users.

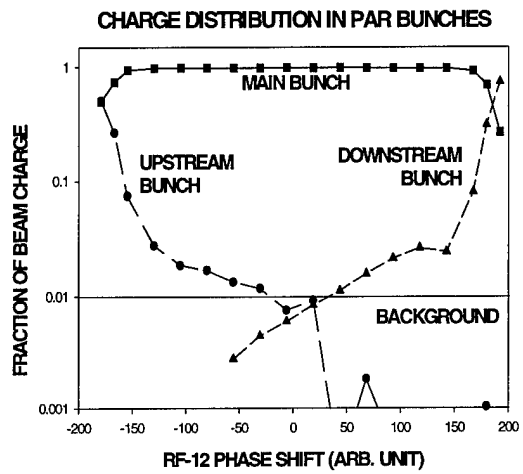

Figure 6: Intensity of bunches as a function of the RF-12 phase. The optimal operating phase shift is near zero.

4 SUMMARY

The time-resolved imaging techniques have been used successfully to study the beam dynamics in the APS injector accelerator. A novel technique was used to visualize the evolution of particle bunches in the longitudinal phase space. The technique is useful in optimizing injection phase/energy match for circular machines. It will also be useful in studying bunch compression dynamics for the fourth-generation light sources.

5 ACKNOWLEDGEMENTS

This work was supported by U. S. Department of Energy, Office of Basic Energy Sciences, under Contract No. W-31-109-ENG-38.

REFERENCES

[1] A. H. Lumpkin, "Advanced, time-resolved imaging techniques for electron-beam characterizations," AIP Conf. Proc. 229, 1991.
[2] E. Rossa, "Real time single shot three-dimensional measurement of the picosecond photon bunches," AIP Conf. Proc. 333, 1995.
[3] A. H. Lumpkin and B. Yang, "Status of the radiation monitors for the APS facility rings," Proc. of the 1995 PAC, 1995.
[4] W. Berg, B. Yang, A. Lumpkin and J. Jones, "Design and commissioning of the photon monitors and optical transport lines for the Advanced Photon Source positron accumulator ring," AIP Conf. Proc. 333, 1995.

LATTICE FUNCTION MEASUREMENTS IN THE FERMILAB ACCUMULATOR RING

M. Church, Fermilab*, PO Box 500 Batavia, IL, 60510

Abstract

The betatron phase advance between two points in a storage ring can be very accurately determined from a transverse beam transfer function measurement with DC beam. The phase advance can be determined from the difference in the phase response between an upper betatron sideband (N+Q line) and a lower betatron sideband (N-Q line) in an open loop network analyzer measurement between a kicker and a pickup. The beta functions can then be extracted from these phase measurements. This method has the advantage that it does not depend on the amplitude response of the pickup, kicker, or electronics. This technique is applied to the Fermilab Accumulator Ring to measure the betatron phase advance at 90 points around the ring, and these measurements are compared to a MAD[1] model.

1 INTRODUCTION

The Accumulator was designed to accumulate and store antiprotons for use in Fermilab's Collider program[2]. Relevant machine parameters are listed in Table 1.

central momentum	8820 MeV/c
revolution period	628820. Hz
circumference	474 meters
gammaT	5.45
horizontal tune	6.609
vertical tune	8.607
symmetry	3-fold symmetric; each section mirror symmetric

Table 1: Accumulator parameters

It has been in operation since 1985 and there has never been an accurate experimental determination of the lattice parameters. Recent phasing measurements with the ring's stochastic cooling systems indicate there is a discrepancy between the design lattice and the actual lattice. It is difficult to fully characterize the lattice from the standard technique of adjusting a quadrupole strength and observing the subsequent tune shift because only 9 of the 84 quadrupoles are instrumented with separately controllable shunt circuits. Measuring the beta functions by the method of "1-bumps" is limited by the uncertainty in the BPM calibration (greater than 10%). In addition, measuring phase advance via turn-by-turn oscillations from a one-pass kick is only possible on the injection/extraction orbit of the machine and is limited by signal/noise in the BPM's. In the Accumulator, measuring the phase advance by comparing phase response difference between upper and lower Schottky sidebands offers the greatest potential for accurately determining the lattice.

The amplitude response of a beam to a transverse excitation at frequency ω has been calculated by several authors[3][4]. It is given by:

$$\frac{V_{out}(\omega)}{V_{in}(\omega)} = -iP(\omega)\int \Psi(\omega')\frac{\sqrt{\beta_{PU}\beta_K}}{4}e^{i2\pi\alpha\omega(\frac{1}{\omega'}-\frac{1}{\omega_c})} \left[e^{i2\pi\alpha_2 Q}\left(1+\frac{i}{\tan(\frac{\pi\omega}{\omega'}+\pi Q)}\right) - e^{-i2\pi\alpha_2 Q}\left(1+\frac{i}{\tan(\frac{\pi\omega}{\omega'}-\pi Q)}\right)\right] d\omega' \quad (1)$$

where ω is the frequency of excitation, $P(\omega)$ contains the pickup, kicker, and electronic response functions, $\Psi(\omega')$ is the beam distribution, β are the beta functions at the pickup and kicker, Q is the tune, α is the fractional distance from pickup to kicker, α_2 is the fractional phase advance from pickup to kicker, and ω_c is the frequency at which the cable delay is matched to the beam delay. At harmonics with no Schottky band overlap, the terms in brackets in eq. (1) separate into a single pole at each sideband. For the case of a symmetric beam distribution, 0 chromaticity, ω_c set to the central beam frequency, no Schottky band overlap, and if $P(\omega)$ has a linear phase slope, the response at the center of the sidebands is dominated by the residue term in the integral. The difference in phase between the upper sideband (USB) response and the lower sideband (LSB) response reduces to

$$\phi_{USB} - \phi_{LSB} = 2\left((2n+1)\tfrac{\pi}{2} - \phi_{PU-K}\right)$$

where n is an integer and ϕ_{PU-K} is the betatron phase advance from the pickup to the kicker.

*Operated by Universities Research Association, Inc. under contract with the U.S Department of Energy.

0-7803-4376-X/98/$10.00 © 1998 IEEE

2 MEASUREMENT

The measurement setup is shown in Figure 1. The pickups used were the Accumulator BPM pickups[5], which are split plate capacitive pickups. The kickers used were the Accumulator damper kickers[6], which are stripline kickers terminated in 50Ω. Cables used were 3/8" and 1/2" heliax (1500-2400 nsec) and RG58 (40-400 nsec). Additional electrical delay was added in the network analyzer to make the total electrical delay equal to the beam delay to within a few 10's of nsec in order to avoid any confusion with 360 degree phase wrap. The deviation

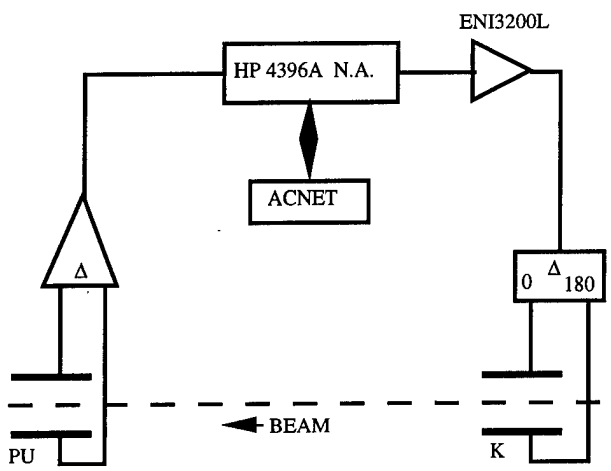

Figure 1: Measurement setup

of the electronic phase slope from linear was determined to be less than 1 degree over the ranges of interest by making S_{21} measurements of the input and output sections of the loop using the damper kicker fanback signal and the BPM test signal cable. An application program was written to interface the accelerator controls system to the network analyzer and to record data to disk for later analysis.

For the measurement 3×10^{10} antiprotons were stored on the "core" orbit of the Accumulator and stochastically cooled in all 3 dimensions to transverse emittances of about 1 π-mm-mrad and a momentum full width of 4 MeV/c. Tunes were separated slightly to .610 and .604 to avoid confusion between horizontal and vertical measurements. The chromaticity was measured to be ≤ .5 in both dimensions, and the momentum distribution was recorded periodically to assure that it remained symmetric (and gaussian). The USB and LSB phase and amplitude responses were measured at the N=16,17,18,19 harmonics (9.6 - 12.4 MHz) and an average $\phi_{USB} - \phi_{LSB}$ was used in the analysis. The phase differences between adjacent USB's and adjacent LSB's was used to calculate and correct for any additional local electronic phase slope (set $\omega_c = \omega_0$). A typical measurement of a single sideband is shown in Figure 2. The phase advance to 48 horizontal pickups and 42 vertical pickups was measured.

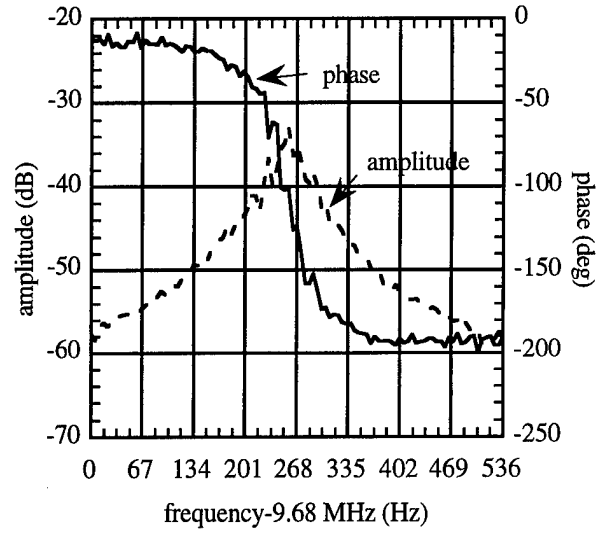

Figure 2: Typical sideband measurement. Network analyzer parameters were: ResBW=10Hz, Power=-26dB, sweep=20 sec, #pts=101, #avg=1.

3 ANALYSIS

Figure 3 is a plot of the difference between the measured phase advance from location A1Q1 to each pickup and the calculated phase advance based on the TevI design. A1Q1 is 7m from the center of a zero dispersion straight section which is a point of symmetry in the ring. There are several sources of error in the phase measurements. 1) The error due to the finite signal/noise ratio is approximately 2 degrees, as determined by observation of repeated measurements.

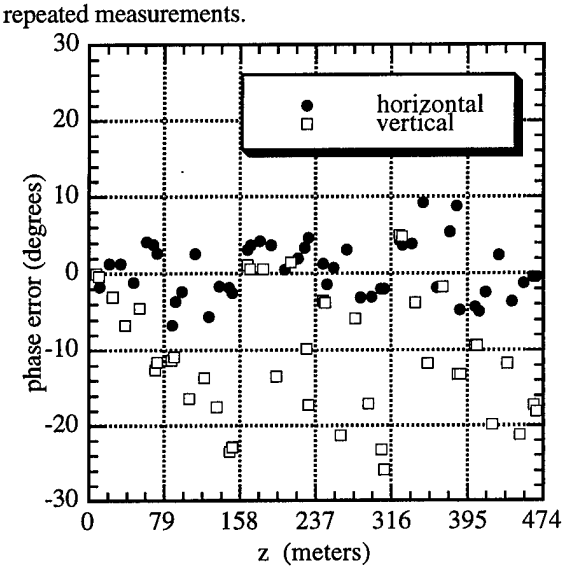

Figure 3: Difference between measured phase advance and phase advance calculated from TevI model.

2) The error due to the nonlinearity of the electronic phase slope is measured to be ≤ 1 degree. 3) The error due to the excitation disturbing the beam and distorting the theoretical response was kept to ≤ 2 degrees by keeping the excitation amplitude as small as possible. The errors due to an asymmetry in the beam distribution and finite chromaticity were calculated from eq (1) and found to be negligible in this case.

Quadrupole, sextupole, and octupole gradients were adjusted in the model in an attempt to bring the model into agreement with the measurements. Three techniques were used: 1) Individual quadrupole strengths were adjusted one-by-one to minimize the sum of the squares of the phase deviations. Seven quadrupoles were adjusted by .1% - .5%, introducing a slight asymmetry into the lattice. 2) The four major quadrupole busses were varied, and the average strength of each quadrupole type was adjusted by .0% - .2%. 3) A global linear least square fit was done for the 12 quadrupole gradients and bus currents to minimize the sum of the squares of the phase deviations. This last method was found to be ineffective. The phase deviations between measurement and model, after these adjustments, is shown in Figure 4. The vertical phase deviations have shifted to be approximately symmetric about 0 degrees, and the maximum swing has been reduced by about 20%. However, there is still a systematic difference between measurement and model for the vertical measurements. Figure 5 shows the vertical beta function in 1/3 of the ring as predicted by the adjusted model.

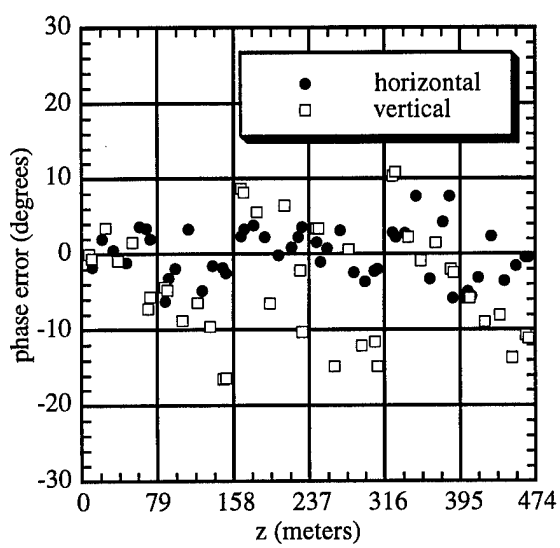

Figure 4: Difference between measured phase advance and phase advance calculated from adjusted model.

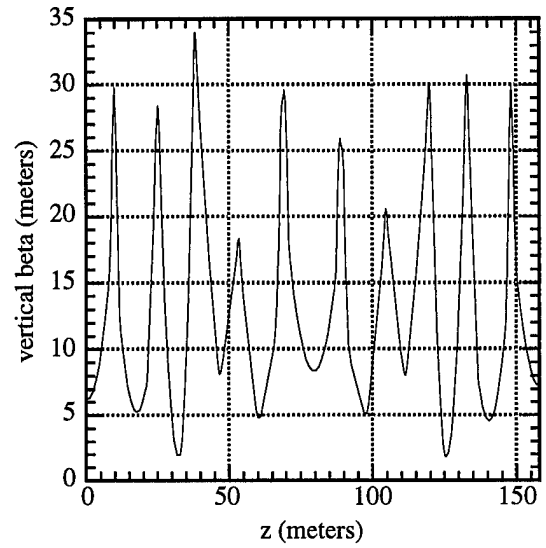

Figure 5: Vertical beta function of adjusted model. Asymmetries and differences from TevI model are approximately 5%.

4 CONCLUSIONS

The measurements made here have some agreement with the model, although there is clearly a discrepancy in the vertical case. The source of this discrepancy is unknown. The type of measurement described here requires that cables be run from pickups and kickers back to a single network analyzer, so it is practically limited to storage rings of small to modest size. In addition, an approximate model of the lattice is required at the outset in order to make some sense of the data. This technique offers an alternative to the more usual technique of measuring the phase advance by turn-by-turn oscillations due to a one-pass kick to the beam. The two techniques are in many ways equivalent, although this author has not fully investigated this equivalence.

5 REFERENCES

[1] "Methodical Accelerator Design,"Version 8.13/8 CERN/SL/90-13(AP) (1990)

[2] Design Report for the Tevatron I Project, Fermilab (1984)

[3] S van der Meer, "A Different Formulation of the Longitudinal and Transverse Beam Response", CERN/PS/AA/80-4, (1980)

[4] J Marriner, D McGinnis, "An Introduction to Stochastic Cooling", in AIP Conference Proceedings #249, ed. M Month, M Dienes, New York (1992)

[5] S Holmes, et al, "The Tev1 Beam Position Monitor System" IEEE Trans. Nucl. Sci. NS-28 #3, p2323 (1981)

[6] J Petter, et al, "Transverse Beam Dampers for the FNAL Antiproton Rings", in IEEE 1987 Part. Acc. Conf. V2, p791, Washington DC (1987)

REALTIME TUNE MEASUREMENTS IN SLOW-CYCLING ACCELERATORS

D. Herrup*, Fermi National Accelerator Laboratory, P.O. Box 500, Batavia, Illinois, 60510

Abstract

Measurement and control of the tunes, coupling, and chromaticities in storage rings is essential to efficient operation of these accelerators. Yet it has been very difficult to make reliable realtime measurements of these quantities. We have built and commissioned the microprocessor-based Generic Finite State Data Acquisition (GFSDA) system. GFSDA provides turn-by-turn data acquisition and analysis of accelerator signals in a way that can be easily related to accelerator operations. The microprocessor is capable of calculating FFTs and correlations in real time. Both the Fermilab Main Ring and Tevatron use open loop tune, chromaticity, and coupling control, and the GFSDA measurements can easily be used to improve the open loop tables. We can add realtime feedback control with simple extensions of the system. We have used this system to make tune measurements closely spaced in time over an entire Tevatron ramp cycle.

1 INTRODUCTION

Accurate and synchronized control of many magnetic and other elements in hadron synchrotrons is one of the major operational problems associated with these accelerators [1]. The Fermilab Tevatron illustrates these issues [2]. The Tevatron operates in two modes - in a fixed target mode in which p's are accelerated to 800 GeV in about 15 sec. and are then extracted for experimental use over a 20 sec. period, and in a collider mode in which it accelerates both p's and $\overline{p}$'s to 900 GeV in 80 sec., undergoes lattice modifications (the low-β squeeze) and stores the beams for up to 12 hours in collisions. Fixed target operation is relatively straightforward since the tune spreads are small and one can tolerate "slightly" inaccurate tune and chromaticity settings. However, in collider running the tune spreads are large due to the full RF buckets and the beam-beam interaction. In addition, time-dependent persistent current effects modify the sextupole moment in the dipole magnets, creating a time-dependent chromaticity even when the Tevatron is not ramping [3].

Maintaining the desired operating point has been difficult because the control is entirely open loop, the basic phenomena causing changes with time are not completely understood (ie., persistent current effects in the superconducting filaments of the Tevatron dipoles), and measurement of the relevant physical quantities (tunes, coupling, chromaticity) has been very difficult. In the Tevatron, measurements have been made with commercially available spectrum analyzers whose output is viewed manually. The spectrum analyzer traces must be correlated in time with the accelerator process. Corrections to the magnetic circuits can then be inserted into the open loop tables for the "next time." This system has clear drawbacks: it follows changes in the accelerator with a time lag, resulting in non-optimal operation, it is extremely labor-intensive, and the open loop tables do not necessarily have breakpoints at the needed times. Additional breakpoints can be added, but the result will be a set of very long tables which require much effort to tune properly.

A more satisfactory approach to this control problem is to build a data acquisition system that is intimately tied into the accelerator control system and mirrors the accelerator cycles. In this way data acquisition and analysis can be handled automatically, and the relationship between a measurement and the state of the accelerator is evident. One can then easily close the loop to the open loop tables or construct slow, realtime control loops. The Generic Finite State Data Acquisition (GFSDA) system was designed to simplify all these tasks.

2 THE GFSDA SYSTEM

Our goal in designing GFSDA was to design a flexible system that fit naturally into the Tevatron accelerator and Fermilab controls environment [4], allows realtime data processing so that control loops can be implemented if desired, and stores data in a way that allows for easy acces by a user at the Fermilab console system.

GFSDA is primarily a tune measurement system, although it can be used on any accelerator signals. The initial implementation in the Tevatron uses as inputs horizontal and vertical Schottky detectors which measure the transverse beam position oscillations. When fourier analyzed, these signals provide measurements of the betatron tunes. The Tevatron has two horizontal and two vertical detector separated by $\lambda/4$ at the 21.4 MHz resonance frequency. The horizontal and vertical signals are combined in hardware to provide about 20 db of directional rejection, providing as outputs horizontal and vertical p and $\overline{p}$ signals [5] which are digitized by GFSDA. Betatron oscillations in the Tevatron are driven coherently through an un-understood mechanism, and as a result we do not need external excitation to measure the tune. The signals shown in this paper are not Schottky signals but are the driven betatron oscillations.

Currently in the Beams Division at Fermilab, low-level systems such as GFSDA are implemented using embedded microprocessors. A GFSDA system is a VME crate running VxWorks using a 68060 processor with 32 MBytes

* Operated by the Universities Research Association under contract with the U. S.

0-7803-4376-X/98/$10.00 © 1998 IEEE

of on-board memory, an 8-channel, 16 bit ADC with on-board memory for 500,000 digitizations per channel, and 128 MBytes of additional memory for data storage. The crate also contains cards necessary for network communications and the receipt of timing and other realtime accelerator data. All microcode is written in C using the MOOC protocol [6].

The software is based around a set of FSMs with a group of states corresponding to different accelerator operations. Each system can be programmed with up to 25 FSMs and 50 states. The FSM is responsible for controlling transitions between its assigned states. The transitions arise either on accelerator timing signals (or a signal plus a time delay), at a fixed time into the state, or by software triggers generated in Fermilab console software. Up to 8 transitions can be specified for a state. Several FSMs can be active simultaneously as long as they are not using the same ADC channels.

Data acquisition, analysis, and storage for user access are handled by the states. States are specified with the transition table discussed in the previous paragraph and data acquisition event rules. The event rules specify the event records used, for instance, to calculate the tune at a given time. Data are collected either on the occurrence of an accelerator timing event (which may occur many times during an instance of a state), at a specified time after the transition into the state, or at a frequency. The data collected are specified by a list of ADC channels, a number of digitizations and the digitization rate, either a fixed frequency or the beam revolution frequency. One can also specify that the microprocessor calculate FFTs in real time on a fraction of the digitizer data, and store in memory only the FFT output from the frequencies of interest. Windowing algorithms can be applied to the raw data and a primitive peak-finding routine can be run on the on the FFT data.

Event records can be spaced very closely in time, with the requirement that data collection for one event end before the next event occurs. This time is a few hundredths of a second. However, the fastest periodic interrupt allowed is 15 Hz, so if event records at a faster rate are desired, they must be specified individually rather than through a single frequency.

The lengths of the event records are determined by the processes being measured. Measurements with 8192 digitizations give a frequency resolution of about 3 Hz. (the revolution frequency is about 47700 Hz.). These long event records must be stored in a manner which permits easy, labelled access to high-level users at the Fermilab console system.

We have solved this problem by associating with each state three circular buffers of sub-buffers, one each for the event rule ADC and FFT data, and one for a Time of Day Stamp (TODS). For each instance of a state, the next available TODS, FFT, and data sub-buffers in their respective circular buffers are chosen. The TODS sub-buffer is filled with a 28 byte string which has the ACNET time of day at which the state was entered. The data and FFT sub-buffers are filled sequentially with the ADC and FFT data from the various event records. When the exit from a state occurs, the two sub-buffers are closed. Upon the next instance of the state, the next available sub-buffers in the circular buffers are chosen. Once all sub-buffers have been filled, they are overwritten in order. This buffering system has several convenient features: the TODS buffer ensure that a console user can easily correlate an instance of a state with other time-stamped accelerator data, the relationship between the three buffers is maintained until they are overwritten in concert, and the circular buffers can be deep enough so that needed data will not be overwritten before it is transferred to the console system and analyzed by the user.

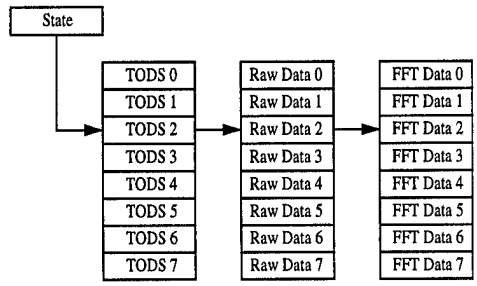

Figure 1: Buffer structure for a state with 8 sub-buffers.

3 HIGH-LEVEL SOFTWARE SUPPORT

In the previous section I described the GFSDA hardware and related microcode. A system as complicated as GFSDA requires significant high level software support to be useable. Also, there are many accelerator applications which require substantial accelerator control, data analysis and display features which at Fermilab only exist at the console level. In this section we will describe the additional software support for GFSDA.

3.1 FSM Specification

The FSMs and states are complicated software objects. Full specification of a single state or FSM requires over 1 KByte of data, and a single system can contain 50 states and 25 FSMs. We have written a single application to handle all aspects of the FSM programming. This application allows the user to select any of the 25 FSMs in a system, assign the states, and program the data acquisition and transition rules for each state. The programmer also specifies the depth of the circular buffers for TODS and data (raw and FFT) storage. The program also performs various error and consistency checks before loading the microprocessor.

3.2 Analysis Applications

GFSDA itself has only limited data analysis capabilities. Currently these include the ability to calculate a windowed FFT on any fraction of a single event record and a peak-finding algorithm. The real physics analysis of the data

must take place at the console level. In addition, through the consoles one has access to all devices in the Fermilab accelerator complex, enabling one to create complete applications for control and measurement.

GFSDA can be used to make a digital spectrum analyzer. An example is the Tevatron Acceleration state within the FSM for fixed target operation. During this state, event interrupts occur at 8 Hz. and we digitize the Schottky signals for 2048 turns. The application to display the data queries GFSDA to determine how many data collection events occurred and how much data are in each event, then reads the data and either displays the FFT or the discrete correlation of the two signals for each event as a function of time through the state. Figure 2a shows a typical example of the tune spectra through the Acceleration state after the correlation analysis has been performed. Two clear tune lines are visible through most of the cycle (The color spectrogram is considerably more informative as it shows the fine structure within a trace. Figure 2b shows the correlation for a single event record.).

[Correlation spectrogram of tunes during the Tevatron ramp.]

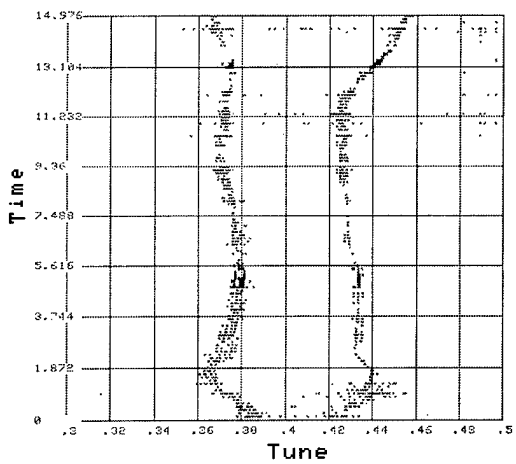

[Correlation plot of tunes from a single event record during the Tevatron ramp.]

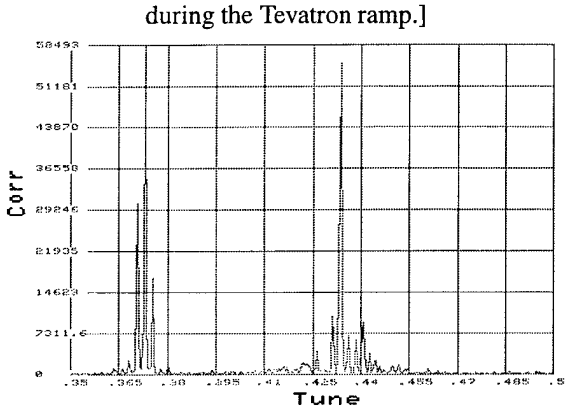

Figure 2: Tune data taken during the Tevatron Energy ramp.

Library routines for GFSDA data retrieval exist, so designing an application to perform a specific analysis function is not difficult. As an example, it would be straightforward to develop a single application to measure chromaticities on the front and back porches. The application would control the RF frequency, data acquisition, tune-finding and the actual calculation of the chromaticities. Measurements could be made at 0.5 Hz., which is adequate for the porches.

4 FEEDBACK

The GFSDA system can easily be the principle component of a slow, realtime control loop. The most logical use for such loops would for tune and coupling control. GFSDA would continue its current functions but with the addition of real pattern recognition to determine the tunes and coupling. The microprocessor analysis would also include a model of the Tevatron consisting of a matrix relating tune and coupling changes with changes in magnetic circuits and a table of "desired" tunes (downloaded from the console system). For each event record, GFSDA would calculate the desired current changes in the circuits, and then output the corrections onto an existing realtime link which communicates with the power supply controllers. Several years ago we built a much simpler system with fewer capabilities using this architecture to do closed loop tune control [7].

5 CONCLUSIONS

We have simplified the problems of tune and chromaticity control in hadron synchrotrons by building a data acquisition system matched to the accelerator operations. The data can easily be correlated with accelerator operations and corrections made either to open loop control tables or through realtime control loops. We have described only the system operating in the Fermilab Tevatron, but an identical system is operating in the Main Ring [8].

6 ACKNOWLEDGEMENTS

I'd like to thank John Marriner, Boris Lublinsky, Jerry Firebaugh, Junye Wang, and Brian Hendricks for help and support with this project.

7 REFERENCES

[1] See the Proceedings of the LHC Workshop on Dynamic Effects and their Control, CERN, Geneva, 5-7 February 1997.

[2] G. Dugan, Part. Accel. 26 (1990) 12.

[3] D. Herrup et. al., Phys. Rev. E 49, 5660 (1994).

[4] D. Bogert, Nucl. Instr. and Meth. A247, 231 (1986).

[5] D. Martin et. al., Proc. 1989 IEEE Part. Accel Conf., March 20-23, 1989, (Chicago, IL), 1486.

[6] B. Lublinsky, Nucl. Instr. and Meth. A352, 403 (1994).

[7] D. Herrup et. al., Nucl. Instr. and Meth. A329, 470 (1993).

[8] D. Still et. al., Tune Measurement Methods in the Fermilab Main Ring, Proceedings of this Conference.

TUNE MEASUREMENT METHODS IN THE FERMILAB MAIN RING

D. Still, I. Kourbanis, D. Capista
Fermi National Accelerator Laboratory*, P.O. Box 500 Batavia, IL, 60510 USA

Abstract

The Fermilab Main Ring has three different systems for measuring the betatron tune. The three systems are designed around a resonant beam pickup which interfaces to independent data collecting hardware. The data collecting hardware systems consist of a Hewlett Packard 35665A Dynamic Signal Analyzer, a Tektronix 3052 DSP and a Generic Finite State Data Acquisition (GFSDA) microprocessor system. This paper will describe the systems and the methods for measuring the betatron tune and chromaticity in the Fermilab Main Ring.

1 TUNE MEASURING SYSTEMS

The tune measurement systems for the Fermilab Main Ring provide data for operations that allow the betatron tune and chromaticties to be measured to improve machine efficiencies and troubleshoot machine problems. The three tune measuring systems used provide different analysis of the tune measurement data to provide a quick and clear tune or chromaticity measurement.

1.1 Beam Excitation for Tune Measurements

Most transverse tune measurements require that the beam be excited transversely by a kicker magnet referred to as a "pinger" or random noise that is applied to the low level input of the transverse beam damper system in order to enhance the betatron tune signal. The excitation for both systems can be applied in the horizontal or vertical plane. The pinger is most often used for tune measurements made at a specific time in an acceleration cycle since it can only be fired a few times within the cycle due to its slow charge/recovery time. The excitation from the noise source of the damper can be used to make tune measurements for the complete acceleration cycle. More details of the damper system can be found in [1].

1.2 Tune measurement overview

Data collection for the three tune monitors centers around a resonant capacitive pickup located at A17 in the Main Ring. The signal from the pickup then passes through a receiver that references the pickup frequency to the revolution frequency of the beam. The output of the receiver is sent 500 ft through heliax to the Main Control Room where it interfaces to a unity buffer amplifier and the signal is then distributed to the three different tune monitors. Details on the resonant beam pickup can be found in [2].

Beam sync triggers are used to trigger each monitor independently. Data collection is accomplished through dedicated software applications for each tune monitor system. Figure 1 depicts a block diagram of the three Main Ring tune monitors. A software sequencing application provides control over setting up timing and reference of beam sync triggers and also control over the use of the pinger or noise source to excited the beam. Gathering tune data using the sequencer application allows for the beam excitation with the pinger or noise source to be accomplished in a single Main Ring acceleration cycle. A detailed description of the sequencer software can be found in [3]. Use of the pinger and noise source are destructive to the beam when used to help measure the tunes and are minimized during high energy physics operations.

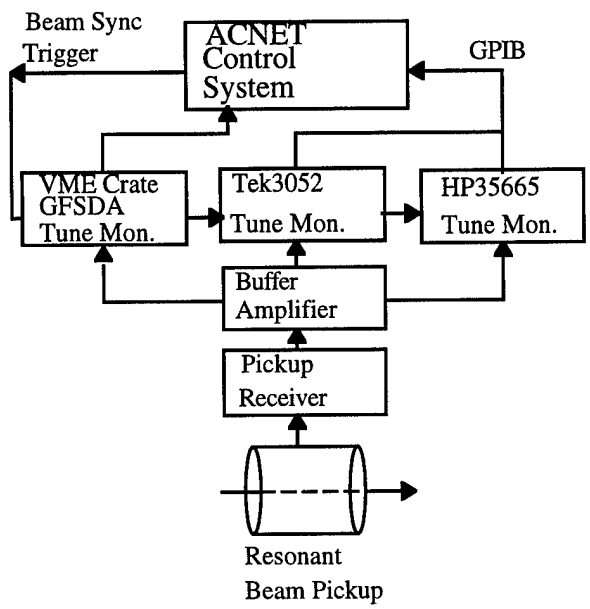

Figure 1: The block diagram of the betatron tune measuring system used in the Main Ring.

1.3 *Operational machine modes for tune measurements*

The machine conditions for operational tune measurements follow two fundamental cycles. Cycles used for Tevatron injection are 3.3 seconds long and for colliding beams 10 seconds long. These cycles accelerate protons from 8 to 150 Gev with a revolution frequency of 47417 and 47746 Hz respectively. The tune is typically horizontally 19.44 and vertically 19.42. Fixed target intensities for multibatched beam are typically 1 E12 to 2.81 E13 protons/pulse where collider intensities are 2.5 E12 protons/bunch. Antiproton production cycles

* Operated by Universities Research Association Inc., under contract with the U.S. Departement of Energy.

accelerate protons from 8 to 120 Gev and have a minimum cycle time of 2.4 seconds.. These are single batch cycles with typical intensities of 2-3 E12 protons/pulse.

2 METHOD USING THE TEK3052

The Tektronix 3052 Digital Signal Processing instrument is used to capture the resonant pickup signal of the beam to gather the betatron tune. This instrument is a VME based microcomputer that uses a UNIX operating system controller. It can acquire data with updates rates up to 200 µsec per frame with four slower frame modes to optimize viewing and processing functions. It has a 25.6 M sample/sec D/A converter in a bandwidth of 0-10MHz. This instrument provides a color spectrogram (frequency vs. time with amplitude color coded) that allows the tune over the entire Main Ring acceleration cycle to be captured and viewed. Tune data is acquired by initiating a tune measurement sequence from the sequencer application mentioned earlier and waiting for the completion of the acceleration cycle. The tune data is then transferred from the TEK3052 to the ACNET control system over a General Purpose Instrumentation Bus (GPIB) by a separate application program. The application then is used to analyze the betatron tune as a function of time of the Main Ring acceleration cycle. The application also provides a graphical interface that allows easy and detailed analysis of each tune spectrum as a function of time. Figure 2 is a plot a tune vs. time of a 120 Gev Main Ring antiproton production cycle acquired by using the TEK3052 tune monitor.

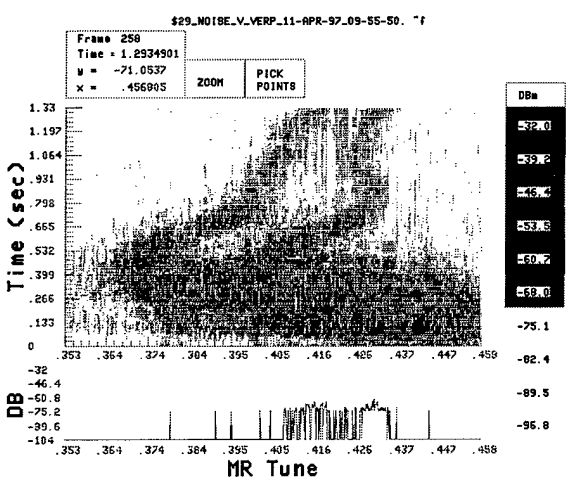

Figure 2: Tune data for a Main Ring acceleration cycle using the TEK3052.

3 METHOD USING THE HP35665A

This tune monitor uses the Hewlett Packard 35665A Digital Signal processor to process the betatron tune data of the resonant beam pickup. A specific software application is used to control tune measurement setups and acquisition. This does not use the general sequencer application for setting up tune measurements like the TEK3052. The time of tune measurements in the acceleration cycle are input as a table into the application. There can be multiple requests for different times in the cycle but it requires a complete acceleration cycle to acquire a single requested time. Once the data for a cycle is obtained from the HP35665A is then transferred by GPIB to the ACNET control system where each cycles time request is saved in a file. The application uses a fitting algorithm to calculate the horizontal and vertical betatron tune from the fast fourier data of the HP35665A. The application also provides a calculation of the coupling. Figure 3 shows the betatron tune results taken with the HP35665A tune monitor.

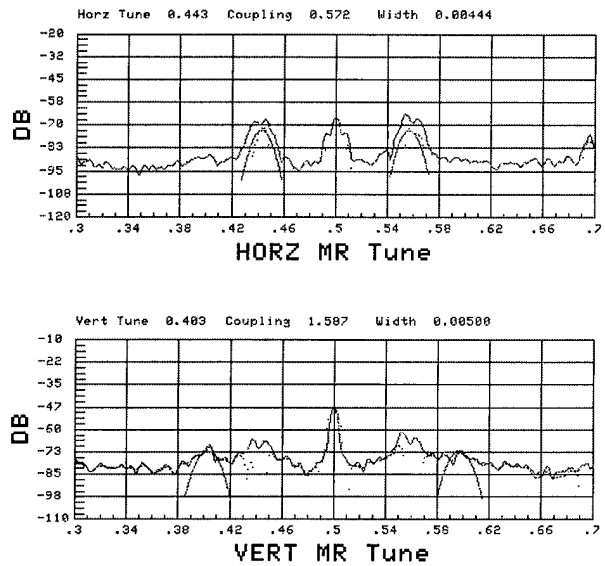

Figure 3: Tune measurement made with the HP35665A tune monitor showing the horizontal and vertical tunes.

4 METHOD USING THE GFSDA

The GFSDA tune monitor hardware consists of a VME crate with a 68060 processor. The crate contains an 8 channel, 16 bit ADC with on-board memory for 5000,000 digitizations per channel and houses extra memory for data storage. The crate also contains necessary cards for network communications and timing for other accelerator data. The GFSDA digitizes horizontal and vertical Main Ring resonant beam pickup signals and completes a fast fourier analysis on board the VME microprocessor for faster and more efficient data retrieval. There are two software applications associated with the GFSDA. One application is dedicated to controlling the GFSDA microprocessor and digitizer as a finite state machine. As a finite state machine flexability is gained in allocating times for consecutive sets of tune data. The maximum rate at which consecutive tune data can be taken is 15 Hz. The second software applications associated with the GFSDA allows tune data to be retrieved from the VME processor and analyzed at the ACNET controls console. Operationally, tune measurements are made with the sequencer software similar to the TEK3052 monitor to coordinate beam excitations with the pinger or damper noise source. It also coordinates timing as to the acceleration cycle to take

data. Once the sequence is completed, tune data is retrieved from the software application where it can be analyzed. The analysis software provides a colorspectrogram for viewing the tune as a function of time and also provides a data correlation analysis between the horizontal and vertical beam pickup signals to enhance the tune measurement. Figure 4 is a plot of tune versus time using the GFSDA tune monitor to acquire the betatron tune for 120 Gev antiproton production cycle. More details on the GFSDA can be found in [4].

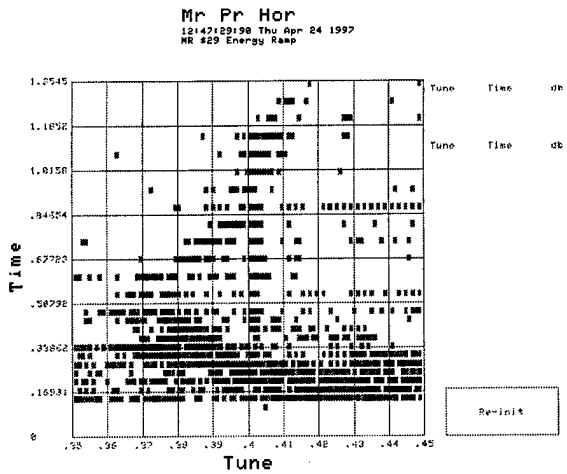

Figure 4: Horizontal tune measurement of the Main Ring antiproton production cycle using the GFSDA tune monitor.

5 CHROMATICITY MEASUREMENTS

Chromaticity measurements are made with the same hardware and software application that is used to measure the tune using the HP35665A. The chromaticity can be determined by:

$$\delta\upsilon = \zeta \, dp/p$$

where $\delta\upsilon$ is the change in tune, ζ is the chromaticity and dp/p is the deviation of ideal momentum. The method of measuring the chromaticity is done by moving the beam radialy to different positions using the low level radio frequency (RF) and the horizontal and vertical tune are measured as a function of position at a specific energy in the acceleration cycle. The data is then fit to a polynomial to calculate the chromaticity. The chromaticity is then plotted as a function of time in the acceleration cycle. Figure 5 is a plot of the chromaticity vs. time of a 120 Gev antiproton production cycle.

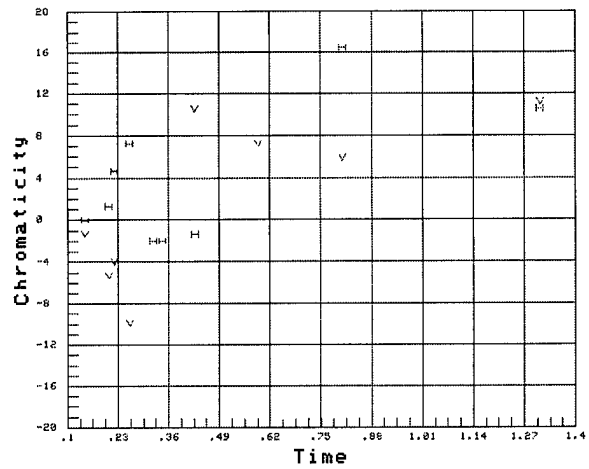

Figure 5: Chromaticity measurement made in the Main Ring using the HP35665A.

6 DISCUSSION

In the past, most tune measurements in the Main Ring were made at a single time in the acceleration cycle. If the tunes were measured over the entire acceleration cycle, it would require many beam cycles and was usually destructive to the high energy physics program and laborious to acquire data. The TEK3052 and GFSDA now can retrieve tune data for the complete acceleration cycle in one cycle. It also has been difficult to measure the tunes from 9 to 20 Gev in the acceleration cycle without exciting the beam transversely. The HP35665A and the GFSDA can passively average tune data for consecutive acceleration cycles to enhance the betatron tune. The GFSDA can also enhance these tune measurements by correlating tune data between the horizontal and vertical beam pickup plates. Current chromaticity measurements in the Main Ring are time intensive which takes many cycles to complete a single energy measurement. When the Main Ring is replaced by the Main Injector, it will be easier to make specifications for the hardware and software for tune and chromaticity measurements. The Main Injector will most likely adopt a version of the GFSDA which will also include software upgrades for making chromaticity measurements.

REFERENCES

[1] J. Crisp, "Main Ring Slow Damper Noise Gates",, Fermilab Operations Bulletin #1204.

[2] P.J. Chou et. al., "A Transverse Tune Monitor for the Fermilab Main Ring", Proc. PAC95, pg. 2479, 1995.

[3] J. Annala and A. Braun, "The New Colliding Beams Sequencer", Fermilab Operations Bulletin #1234.

[4] D. Herrup, "Realtime Tune Measurements in Slow-Cycling Accelerators", Proceedings of this Conference.

AUTOMATIC BEAM POSITION CONTROL AT LASREF

M. Oothoudt, C. Pillai and M. Zumbro
Los Alamos National Laboratory, Los Alamos, NM 8754

Abstract

Historically the Los Alamos Spallation Radiation Effects Facility (LASREF) has used manual methods to control the position of the 800 kW, 800 MeV proton beam on targets. New experiments, however, require more stringent position control more frequently than can be done manually for long periods of time. Data from an existing harp is used to automatically adjust steering magnets to maintain beam position to required tolerances.

1 INTRODUCTION

The LASREF uses the 800 MeV, 1000 μA proton beam from the Los Alamos Neutron Science Center (LANSCE, formerly known as LAMPF) to irradiate samples with protons and neutrons. Samples in the direct proton beam require control of the beam position; in past years these samples were large enough compared to the 30 mm beam diameter (Gaussian two sigma) that precise, continuous position control was not necessary. Operators checked beam position as infrequently as a few times per day to catch occasional beam lurches that could shift the beam far enough to cause cooling water leaks on some of the samples.

Beginning in 1996 and continuing through 1997, new samples consisting of 19 mm bundles of 3 mm diameter tungsten rods required much finer control of beam position. For comparison with calculations of radiation damage effects, it is important to maintain beam position to approximately ±1 mm. Typical uncontrolled beam motion is considerably larger than this, so a full-time operator would have been required to hold the beam position. Tight position control is also required to avoid water leaks from other samples, since the tungsten rods are sensitive to even small water leaks.

2 IMPLEMENTATION

Both budget and a short lead time limited the solutions that were feasible. An existing steering magnet and multi-wire harp were used. Software used to display harp spectra was modified to add control functions.

In the harp read-out system, charge accumulated on harp wires was digitized and read by a remote computer on demand from the main control computer. The main control computer provided an interactive user interface to allow selecting data acquisition parameters and to display the data. Hardware for controlling the steering magnet is not directly accessible from the remote computer, so implementation of automatic control in the remote computer was not considered.

The interactive harp display program on the main control computer was modified to produce a "harp watcher" program running as a detached background job that would not interfere with the interactive version. Code was added to the harp watcher to periodically read the beam position and resteer the beam. There was considerable concern that an error in the steering algorithm could cause the beam either to drill a hole through the beam line vacuum window between the harp and the samples or to steer the beam grossly off position, rupturing vacuum or water o-ring seals. Since there was little time to validate a steering algorithm, a minimalist approach was taken and a very simple algorithm was used. Since the simple algorithm proved good enough to meet the experiment's needs, only minor changes have been made since the initial use.

```
DO (forever)
  sleep 10 seconds
  read harp x and y spectra
  calculate x and y centroids
  DO (x,y)
    IF (data is valid) THEN
      Δposition = desired_position - centroid
      IF (abs(Δposition) > tolerance) THEN
        IF (abs(Δposition) > max_change) THEN
          warn operators  !don't risk oversteering beam
        ELSE
          IF (steering_enabled) THEN
            ΔI = κ*Δposition
            change steering magnet current by ΔI
          ENDIF
        ENDIF
      ENDIF
    ENDIF
  ENDDO ! x,y
ENDDO ! infinite loop
```

Figure: 1 Algorithm initially used for controlling beam position. Error handling is shown only in one case.

The steering algorithm initially used is shown in Figure 1. To keep the algorithm simple, it makes no attempt to perform error recovery. Instead operators are informed of the problem by blowing a horn in the control room. The incidence of false alarms (a few a day) was felt preferable to a more complicated algorithm that might mis-steer the beam.

0-7803-4376-X/98/$10.00 © 1998 IEEE

An interactive interface was provided to set the parameters *desired_position*, *tolerance*, *max_change*, *steering_enabled* and κ (conversion between position change and steering magnet current change). Harp spectrum centroids and widths and steering magnet currents were archived by the harp watcher for later analysis.

3 RESULTS AND CONCLUSIONS

Figure 2 shows harp centroids and steering magnet values over a two hour period for the Y direction. Data was recorded every 10 seconds by the harp watcher. The positions plotted are those before any attempt at steering was made. Some apparently out of tolerance positions do not result in magnet steering because a second data-take showed the first point was erroneous.

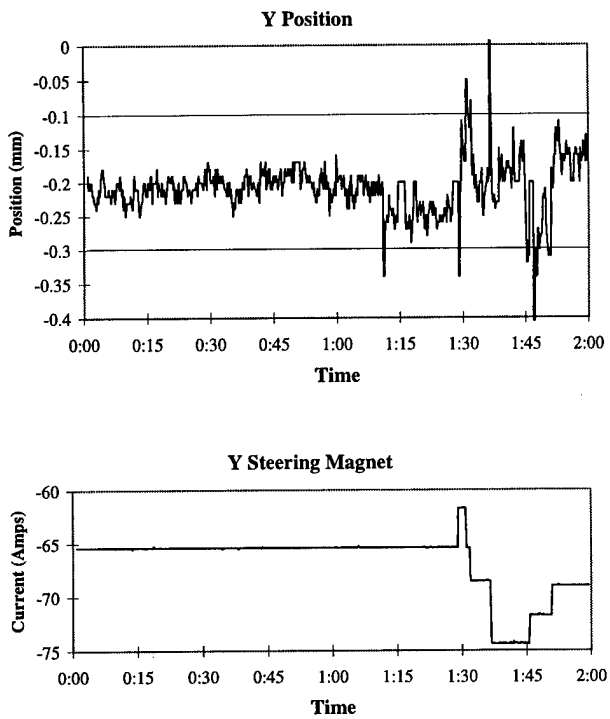

Figure: 2 Beam position and steering magnet current for Y direction. The ±1 mm tolerance band is -0.3 to -0.1 mm.

An early concern was that continuous steering of the beam would damage stepper motors used to control the steering magnet currents. As can be seen in Figure 2, the number of changes in current per hour is small and no problems with the stepper motors have been observed.

Figure 3 shows histograms of beam positions over a 24 hour period recorded every 10 seconds. The vertical bars indicate the tolerances requested by the experiment. The beam is held within tolerance 94% of the time for X and 99% for Y, meeting the beam stability needs of the experiment.

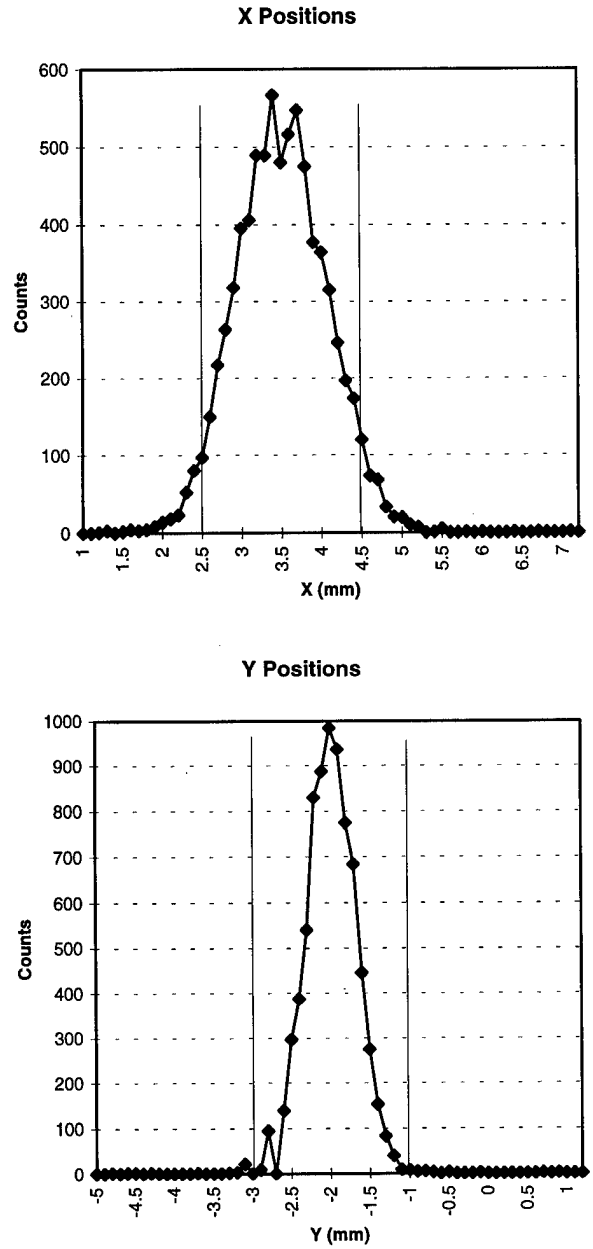

Figure: 3 Histograms of beam position over a 24 hour period. The vertical lines indicate the ±1 mm tolerance requested by the experiment.

The beam shows significantly more jitter in X than in Y. It is believed a small "pendulum" motion of the drift tubes in the front end of the accelerator are responsible for this jitter.

The only significant problem found with the algorithm after several months of use was a tendency to steer the beam in one direction followed ten seconds later by steering in the opposite direction. This was caused by short term beam lurches. The algorithm was modified to

re-take the harp data after a delay of several seconds if the first harp spectrum indicated the need for steering. Steering was done only if both spectra indicated need for a similar change. This greatly reduced the frequency of the problem.

It was expected at the start of the project that the position control would need to be re-implemented in the remote computer to get adequate control without overloading the main control computer. The data acquisition and control functions proved to take 0.2% of the main control computer's cpu (a VAX 4000/500) and required about two input/output operations per second. Since Figure 3 shows the position control meets the needs of the experiment, this simple control system running on the main computer has been retained.

4 ACKNOWLEDGEMENTS

The authors wish to thank Walter F. Sommer and Richard D. Werbeck for their input on this project.

This work was performed under the auspices the U.S. Department of Energy under contract W-7405-ENG-36.

MECHANICAL DESIGN OF A PINGER SYSTEM FOR THE LBNL ADVANCED LIGHT SOURCE ACCELERATOR

W. Thur, J. Akre, A. Gavidia and J. Guigli, Lawrence Berkeley National Laboratory

Abstract

A fast magnet "Pinger System" has been designed for the Advanced Light Source 1.9 GEV electron Storage Ring. Intended for beam dynamics studies, its purpose is to provide a fast (< 600 ns) transverse magnetic field pulse to perturb the orbit of an electron bunch in a single turn. A key component is the special resistive-coated ceramic beam tube which is needed for fast magnetic field penetration. The evolution of the design concept is described, with emphasis on simplifications to provide an economical and mechanically robust device.

1 INTRODUCTION

The Advanced Light Source at Lawrence Berkeley National Laboratory is a third generation synchrotron radiation source. The ALS storage ring circulates bunched electrons at energies of 1.0 to 1.9 Gev, at currents up to 400 mA. Bend magnets, undulators, and wigglers produce intense photon beams with energies from 10 ev to 10 kev for a wide variety of experiments.

As more photon beamlines are added to the ALS, tuning the storage ring for precise electron beam position and stability at all beamlines becomes increasingly difficult. To meet this challenge, ALS accelerator physicists are working to improve their understanding of the complex electron beam dynamics of the storage ring. The new "Pinger System" is currently being installed, and will be an important tool in this effort.

2 THE PINGER SYSTEM - SPECIFICATIONS

The new Pinger system will provide a pair of very fast dipole magnets to intentionally perturb the orbit of a single electron bunch in a single pass. The effects of this controlled transverse "kick" will be monitored by an existing system of beam position monitors for validation and improvement of beam dynamics models. In order to accomplish this, the Pinger system must deliver calibrated vertical and/or horizontal dipole fields of up to 315 Gauss in a pulse which lasts no longer than 650 nanoseconds. This will require single turn dipole magnets, discharging 10 kilovolts to ground. A special ceramic beam tube section is needed so that induced eddy currents will not retard the penetration of the magnetic field.

3 ENGINEERING

As is often the case, the initial intention for this project was to closely duplicate an existing design. The beam kickers in the ALS injection straight perform a similar function, and we hoped to save on engineering costs. However, a closer study of the injection straight revealed many reasons not to do this. The following is a brief summary of the design evolution of the Pinger system. As you will see, considerable effort has gone into creating a cost effective, reliable design, with many well-motivated departures from the original concept.

3.1 Simplifications

Our reference design, the ALS injection straight, has a rectangular vacuum aperture of 83 x 38 mm. Its ceramic vacuum tube was expensive, difficult to manufacture, difficult to align, and the unbalanced vacuum forces stressing the ceramic are high. For the Pinger, an 88 mm ID round ceramic beam tube was chosen to be much stronger, easier to fabricate, and its "square" aperture allows the horizontal and vertical kick magnets to be essentially identical. A further advantage emerged: in the round geometry, beam image currents can be handled by a uniform resistive coating on the tube ID, with no need for the difficult patterned resistive coating used with the rectangular aperture. The optimum coating resistance is a trade-off between minimizing the eddy current induced field penetration delay, and living with the steady state I^2R heating of the ceramic tube caused by beam image currents of up to 400 mA. An experimental mock-up indicates that a 2.0 ohm per square coating of titanium will allow acceptable field penetration times with a maximum steady state image current heat load of about 100 watts, which will be cooled with an air flow system.

3.2 RF Concerns

The original electrical joint design used to connect the injection straight resistive coating to the conventional metal beam tube has caused some concern at the ALS. Beam current induced heating at or very near these joints has necessitated forced air cooling. Although the cause of this problem has not been resolved, a leading theory is that small cavities in the electrical joint design may be coupling with RF energy, resulting in local heating. In the Pinger design, only a single, round fingerstock joint is used, with a minimum cavity.

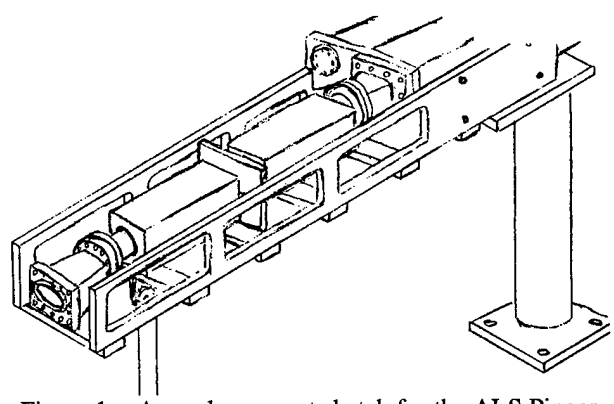

Figure 1 - An early concept sketch for the ALS Pinger

0-7803-4376-X/98/$10.00 © 1998 IEEE

3.3 A Single Ceramic Tube

The various risks and expense of the ceramic tube end electrical and vacuum connections motivated a further simplification: - a single long ceramic tube threaded through both the horizontal and the vertical kick magnets. A 54 inch tube length is required, with only two end connections, rather than the four which would have been needed with separate tubes for each magnet.

3.4 Support and Vacuum Loads

The support and alignment of the ceramic tubes in the injection straight had also been a problem, due to variations in ceramic wall thickness. For the Pinger, we will avoid this by not doing it! We plan to rely only on the engagement of the electrical contact sleeve in the neighboring transition piece to flexibly support the 25 lb. weight of the ceramic tube.

Axial vacuum loads were considerable in the injection straight design because of the difference in cross section between the large round bellows and the "racetrack" ceramic tube aperture it encloses. (The collapsing load of the bellows exerts a sizable tension load on the ceramic tube.) Since the Pinger ceramic tube is round, it is possible to use a bellows of only slightly larger area than the tube itself. The calculated vacuum load tension in the Pinger ceramic tube is much reduced; - only 102 lbs. This load is taken in tension by the Kovar fittings brazed to the ends of the ceramic beam tube. The maximum stress in the critical braze joint was further reduced by making the O.D. of the ceramic backing ring 1.8 mm larger than the ceramic tube. A finite element analysis shows that this small change will reduce the maximum stress in the braze joint by a factor of six. These increased safety margins all work to improve the vacuum integrity of the ALS storage ring.

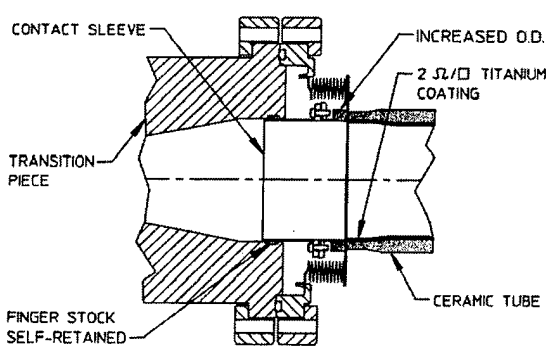

Figure 2 - Ceramic Tube End Joint Design

3.5 System Layout

The Pinger system will be installed in ALS straight section 2. The one-piece ceramic tube allows the Pinger to be short enough to occupy only the upstream half of the straight section, reserving the downstream half for future diagostic instruments, or possibly even an insertion device. In this location, photon masking had to be carefully considered; that is, the synchrotron radiation from the bend magnet immediately upsteam had to be absorbed by a water cooled photon stop incorporated in the Pinger transition piece. In the course of studying these layouts, a further simplification emerged: There is no need for the electron beam to be perfectly centered in the ceramic beam tube. By introducing an intentional offset of 10 mm, we were able to reduce the tube inner diameter from 88 mm to only 74 mm. This resulted in a reduced magnet aperture and a reduced pulsed power requirement to drive the magnets.

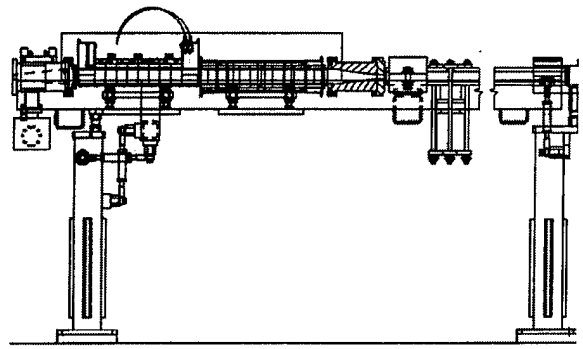

Figure 3 - The ALS Pinger system

4 FABRICATION AND INSTALLATION

With a robust, conservative design in hand, we confronted the realities of component procurement. The ceramic tube with its brazed Kovar metal end fittings turned out to be an exceedingly involved fabrication. Over 20 different ceramic, metalization, and brazing vendors were contacted, revealing a wide variety of capabilities and limitations. Ultimately, the 1.35 meter long 99.5% alumina tubes were pressed, fired, and metalized in 0.68 meter long halves by WesGo, Inc. of Belmont, Ca., and these were subsequently brazed together and to their Kovar metal end fittings by Alpha Braze of Fremont, Ca.

Other design involvements include the "transition pieces" which are EDM'd (Electric Discharge Machined) from solid metal blocks to provide a smooth vacuum chamber transition from the eliptical section of the storage ring to the round ceramic tube, and a carefully thought out support system designed to protect the ceramic beam tube from mechanical stress, especially in torsion. As this is written in May 1997, we are in the midst of the May 1997 shutdown of the ALS, and the vacuum related components of the Pinger system are being installed, with the fast magnets to follow at a later date.

Like many accelerator upgrade projects, an idea which initially sounded fairly straightforward has spawned a rich mix of engineering complications and challenges. If we succeed in delivering a working ALS Pinger system sometime this summer, it will be cause for a celebration!

REFERENCES

[1] D.E. Anderson, G. Stover and W. Thur, Design of Quasi-Traveling Wave Pinger Magnet for Beam Diagnostics on the Advanced Light Source, Particle Accelerator Conference, 1997

PERFORMANCE OF THE UPGRADED NSLS BEAM POSITION MONITORS

R.J. Nawrocky and J. Keane

National Synchrotron Light Source, Brookhaven National Laboratory, Upton, NY 11973

Abstract

The design and initial performance of the original NSLS beam position monitor (BPM, also referred to as the "rf receiver") were described by J. Bittner and R. Biscardi in 1989 [1]. The receiver, which processes signals from four button type pick-up electrodes by time-division multiplexing, operates at the third harmonic of the ring rf frequency (158.66 MHz). It has an output bandwidth of about 2 kHz and a dynamic signal range of approximately 36 dB. A total of 92 receivers have been installed in the NSLS X-ray and VUV storage rings for orbit monitoring and for real time feedback.

As part of a continuous effort to improve the NSLS storage ring performance, the BPMs as well as other instrumentation systems have also been undergoing upgrades over the past two years to improve their performance. In the BPM, the front end has been modified to prevent saturation of the rf multiplexing switch, the detector operating point was changed to improve output signal linearity, the dynamic range was increased to over 60 dB, and the gain calibration was standardized to 0.5 volts/mm (i.e. 2 μm/mV). This paper describes the BPM modifications and presents some performance data and measurements on stored beam.

1 INTRODUCTION

The NSLS storage rings operate with many different fill patterns – from one to nine bunches in the VUV ring (normal operation is with seven bunches), and from one to thirty bunches in the X-Ray ring (normal operation is with 25 bunches). The harmonic numbers of the VUV and X-ray rings are 9 and 30, respectively. Initially, the X-Ray ring stored current in the multi-bunch mode was limited to 250 mA due to heating of the beam-line front ends and in the single bunch mode it was limited to 100 mA due to heating of the inflector chamber.

In the VUV ring, on the other hand, the maximum stored current in multi-bunch mode could be as high as 1000 mA while single bunch intensity was limited to 400 mA. The Bittner-Biscardi receivers, which were intended for use in both storage rings, had sufficient sensitivity to measure beam position at an intensity level of 0.16 mA/bunch (i.e. 4 mA in 25 bunches) but had a dynamic range of only 36 dB. Accordingly, the range of the X-Ray ring receivers was set to 4-250 mA, while that of the VUV ring receivers was set to 16-1000 mA. At high beam intensities (near 100 mA/bunch), however, the PUE peak signal levels were approaching the saturation level of the front end rf switch, even with the 300 MHz input low pass filters ahead of the switch. In addition to saturation of the multiplexing switch and limited range of the AGC, a disadvantage of the original design was the fact that the setting of the detector operating point was directly affecting the gain calibration of the output channels and that the gains of the two output channels could not be set independently. Thus, each receiver had somewhat different gain coefficients which complicated record keeping as well as troubleshooting. Once the front-end heating problems in the X-Ray ring are solved, the stored multi-bunch beam intensity will be increased to the design value of 500 mA. The single bunch limit has already been increased to over 200 mA. Since the X-Ray ring active interlock system is routinely tested at about 6 mA (any bunch pattern), the receivers must now operate over an intensity range from labout 0.16 mA/bunch to greater than 100 mA/bunch, i.e. over a range of about 60 dB.

The original NSLS BPM design proved to be quite reliable and the receivers performed well over a period of nearly seven years. With ninety-two BPMs installed and in continuous operation, the failure rate has been less than one per month. Improvements in machine operation, i.e. a wider range of stored beam current and demand for higher intensity single bunch runs, called for the enhancement of BPM capability which resulted in the design upgrade effort described in this report. Presently, all of the 48 X-ray ring orbit BPMs have been upgraded and work on the X-ray ring active interlock system BPMs and VUV ring orbit BPMs is underway.

2 BPM UPGRADE

A block diagram of the upgraded BPM is shown in Fig.1. As mentioned earlier, the following changes were made to the original design:

0-7803-4376-X/98/$10.00 © 1998 IEEE

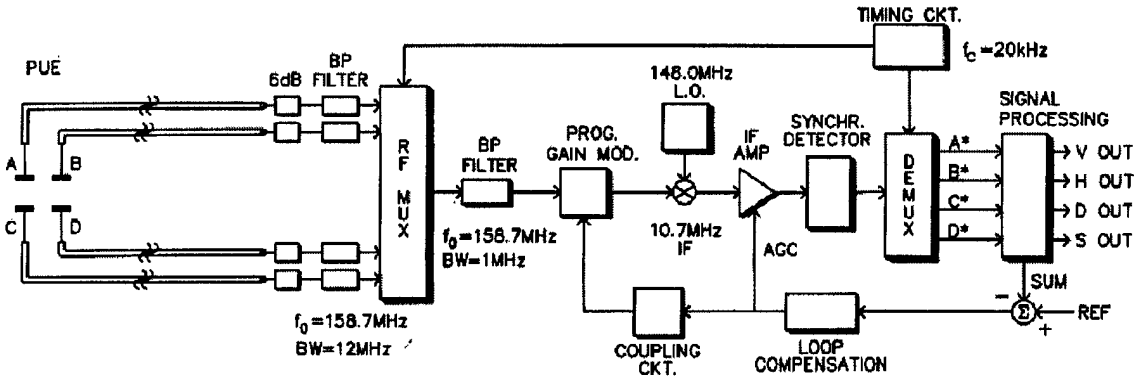

Fig.1. Block diagram of the upgraded BPM

Front End – In the original design, the PUE signal pulses were first processed by a 300 MHz low-pass filter (to limit peak amplitude) and then applied to the GaAs 4PST rf multiplexing switch. In single bunch high current mode, the peak signal voltages were approaching the saturation level of the switch. Attenuating the PUE signals with broadband attenuators would avoid switch saturation, however, it would also reduce the BPM sensitivity by attenuating the 158.66 MHz component processed by the receiver.

This problem was solved by adding a low-cost 12 MHz band-pass (BP) filter to each BPM input. These filters are used in addition to the costly and bulky 1 MHz band-pass tuned cavity filter which is needed to reject the revolution harmonics. A 6 dB attenuator pad was added ahead of each filter to help damp out reflections of the out-of-band components at the filter end as well as any re-reflection at the "open" PUE button electrode end.

Dynamic Range – To increase the dynamic range of the BPM, a wideband programmable gain stage (PGM) was added ahead of the IF mixer (see Fig. 1). This stage consists of a voltage controlled attenuator module (Watkins-Johnson, G-2, 3-31 dB range) followed by a 22 dB low noise amplifier (WJ-A81-2). The addition of the amplifier in the PGM resulted in an increase in the level of the rf switch noise at the input to the IF mixer at low input signal levels. This problem was solved by decreasing the clock frequency from 40 kHz to 20 kHz and delaying the 4 μs de-multiplexing pulse to the end of the overall 12.5 μs PUE button sampling period. The 20 kHz clock frequency is just over a factor of two higher than the VUV ring synchrotron oscillation frequency (VUV ν_s = 9 kHz, X-ray ν_s = 4 kHz).

Detector Operating Point – The output dc operating point of the video detector (Motorola MC1330) was moved down to 5.0 volts to improve the linearity of the BPM output signals over the full ±10 mm range of beam displacements.

Gain Calibration – Gain potentiometers were added to the signal processing board to permit the setting of the vertical and horizontal gains independently of each other and of the detector operating point.

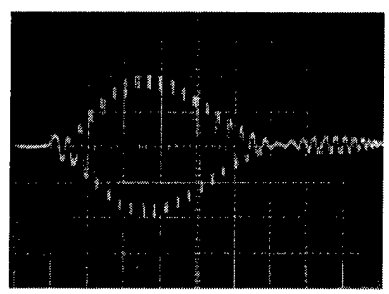

Fig. 2. Response of the 12 MHz BP filter to a 6V, 2ns-wide input pulse (10 mV/div, 10 ns/div).

3 PERFORMANCE OF THE UPGRADED BPM

Referring to Fig.1, the 12 MHz input BP filters reduce the peak signal amplitude by approximately 50 dB. This is illustrated in fig. 2 which shows the filter response to a 6V peak, 2 ns-wide input pulse.

The minimum detectable signal (MDS) was measured in the laboratory for the original and the upgraded receivers using an amplitude-modulated rf signal source and a four-way hybrid splitter. In each case, a 158.66 MHz rf signal modulated with a 1 kHz sinewave was applied to the input and the detected signal approximately 6 dB above the "noise floor" was observed at the BPM sum signal output. The measured data for the two cases is given in Table 1.

Table I.

BPM Configuration	RF Input (dBm)	Noise Floor (dBVrms)
Original	-80	-65
Upgraded	-100	- 62

The above data shows that, as expected, the PGM improves the MDS by 20 dB while increasing the noise floor only by about 3 dB. Figure 3 shows the error in the overall response for centered as well as off-center beams. Fig.3 data was generated using an rf signal source, a four-way splitter and fixed attenuators and does not include nonlinearities due to electric field distribution within the actual PUE assembly. Thus, the output error of the upgraded receiver is under ± 10 μm for beam displacements up to ± 10 mm over a dynamic range greater than 60 dB.

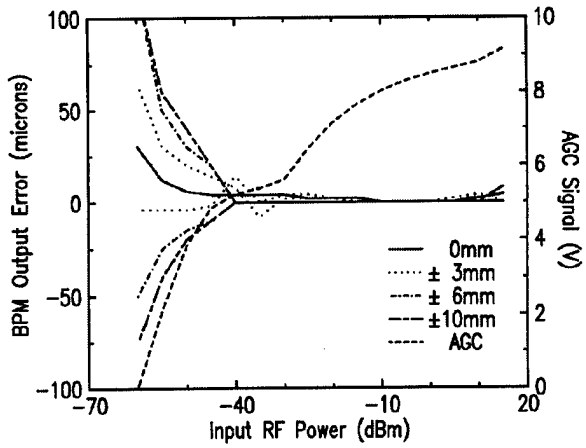

Fig. 3. Error in BPM output signal as a function of input rf power for simulated beam displacements up to ± 10 mm.

The noise level in the BPM output corrupting the beam position signal varies inversely with the input signal strength, while its bandwidth is limited to 2 kHz by low-pass output filters, as shown in the spectrumm of the noise in fig. 4. Note that the -60 dBV level corresponds to 1 mV rms which is equivalent to 2 μm rms of beam motion. As an illustration of BPM operation with stored beam, fig.5 shows the vertical beam position output signal and the AGC voltage of one of the ring monitors during a typical injection cycle into the X-ray ring. Data in figures 4 and 5 can be related in terms of the AGC signal, i.e. the two figures permit a translation from rf signal power in dBm to stored beam current in mA and vice versa. The small variations in beam position signal during injection (Figure 5) indicate normal beam motion when orbit feedback is switched off. During stored beam operation, closed orbit feedback reduces the motion to a few microns.

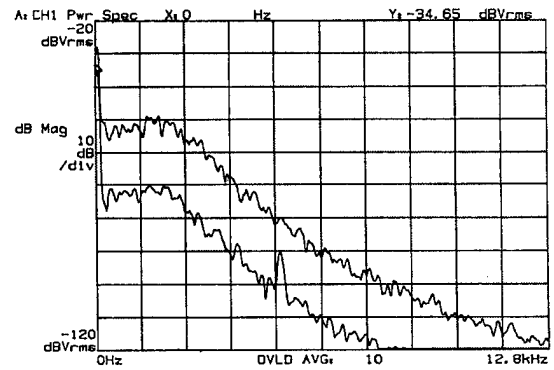

Fig. 4. BPM output noise spectrum with no input signal (upper trace) and with input power = 0 dBm (lower trace).

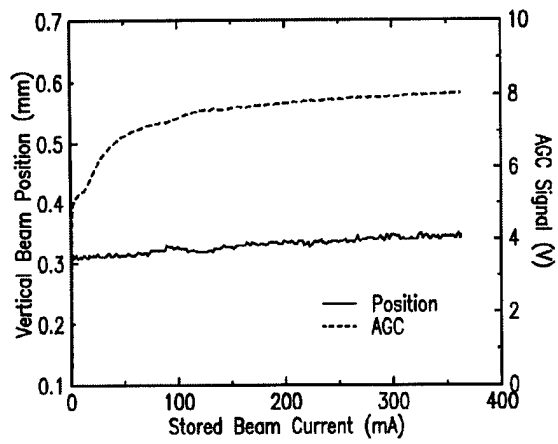

Fig. 5. BPM vertical output signal and AGC voltage during injection into the X-ray storage ring.

ACKNOWLEDGEMENTS

The following individuals contributed to the design and implementation of the BPM upgrade as described: M. Bordoley, A. Borelli, J. Tallent and O. Singh. This work was performed under the auspices of the U.S. Department of Energy under contract number DE-AC02-76CH00016.

REFERENCES

[1] R. Biscardi and J. Bittner, "Switched Detector for Beam Position Monitor", Proc. Of 1989 IEEE PAC, pg. 1516.

A COMPACT BPM FOR THE FERMILAB MAIN INJECTOR

J. Fitzgerald, J. Crisp
FNAL* Batavia, IL, USA 60510

Abstract

The Main Injector will use Beam Position Monitors (BPM) located inside the downstream end of every quadruple magnet. These magnets are reused (or derivatives of) Main Ring quads with existing beam tube still in place. The limited space available, and the desire to maintain the beam pipe aperture, required an unusual shaped BPM with innovative design and production techniques. Information on the various stages of the design, assembly, testing, calibration, and installation of the BPMs is presented.

1 INTRODUCTION

The design of the Fermilab* Main Injector (MI) reuses much of the Fermilab Main Ring (MR) equipment, including the quadrupole magnets (1). New quadrupole magnets were also fabricated baised on the original Main Ring design. These magnets have an beam pipe permanently fixed in place. The Main Injector elliptical shaped beam pipe telescopes inside the MR pipe, leaving a small space between them.

In order to conserve tunnel space and reduce beam impedance, the MI design uses these areas for the Beam Position Monitors (BPM). A total of 203 BPMs are required. The Main Injector tunnel cost approximately $2400 per foot. By conserving one foot per BPM, $487K is saved.

The MI beam pipe aperture must be maintained through the BPM. The available area consists of two small crescent shaped regions on the vertical axis. Elsewhere there is only space for the BPM housing. Fig.1 shows cross sections of the MI beam pipe, the BPM and the magnet beam pipe. Space limitations caused considerable restrictions on the BPM design, requiring compromises to be made.

1.1 Previous Work

The physical limitations on the BPM have driven the design, leaving few options in their configuration. Preliminary design work identified the basic layout available (2). The BPM would have four strip line electrodes, with the resulting signals combined externally to produce either vertical or horizontal positions. All connections must be made at the portion protruding from the magnet. To produce a non-directional BPM the electrodes were terminated with a ground connection at the opposite end. The MR BPM electronics will be reused. This electronics uses AM to PM conversion to obtain position information from signals between -38 dBm and +22 dBm.

Software from Artech House "Matrix Parameters for multiconductor Transmission Lines" was used to analyze the electrical characteristics of various combinations of the striplines electrodes (3). This program produces the 2D transmission line matrices and electrostatic charge distributions for user defined geometry's. It was determined that an electrode width of .5 inch by 20 cm would provide -24dBm at the beam intensity of 1E9 particles per bunch at the 53 Mhz RF frequency.

Two prototypes were designed and fabricated to test construction techniques and to verify the electrical characteristics. The first design attempted to "EDM" wire cut the electrodes directly into a section of MI beam pipe. The second design used separate electrodes weleded into a slot cut into the MI beam pipe (2). These designs proved to be impractical because the residual stresses in the formed elliptical shaped beam pipe are relaxed when it is cut or welded. In addition, the MI pipe did not have sufficiant strength to maintain an accurate geometry under vacuum

2 CONTINUING DESIGN

In an effort to overcome the problems, and reduce the amount of assembly work required, a new design was sought out. New mechanical problems also became apparent.

After available Quad magnets were measured, the aperture was found to have large variations in size from the design nominal. The standard deviation (σ) was over .060 mills. To insure that all the BPMs would fit, the outside dimension was choosen to be 3σ less than the mean reducing the already small vertical space available.

As the BPMs will be placed inside the magnet field, all components had to be non magnetic. Magnetic material would distort the field, causing undesirable higher order fields. The ramping magnet could exert force on components causing position measurement errors.

The limited space available required a thin housing, however it had to maintain shape under vacuum. A related issue of concern was differential thermal expansion between the housing and electrode.

2.1 Mechanical

In the final design, the BPM housing is formed by joining two identical stamped half shells. Finate elenent Analysis of the proposed shape indicated that 12 ga (.105) stainless steel would give adequate strength. Testing of completed housings under vacuum has shown -5 mills of vertical and + 5 mills of horizontal deflection. An electrode section, forming two striplines and a ground plane is stamped from 20 ga stainless steel. A channel shape is used to increase stiffness. The stampings

* Operated by Universities Research Association under contract with the U. S. Department of Energy.

incorporate intregal mounting provisions for the electrodes and alignment holes for assembly. The electrodes are grounded at one end, and attached directly to an SMA coaxial connector pin at the other end. Feedthrus with flexable pins are used to accomodate the differental thermal expansion expected. Including the ceramic feedthrus and an external protection and locating plate the assembly uses only four different parts. Shown below in Fig.1 are superimposed cross sections of the MR and MI beampipes. Fig. 2 a photo of the final BPM. Fig 3 is a photo of a BPM installation in the Mi beam line.

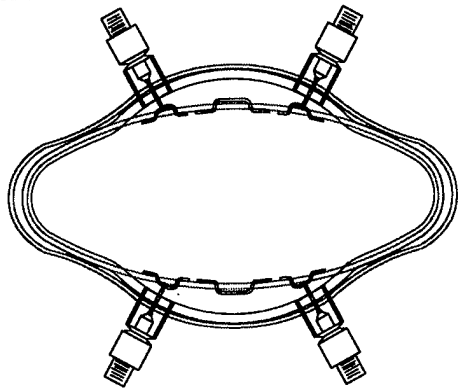

Fig 1: Sections of the BPM, MR, and MI beam pipe.

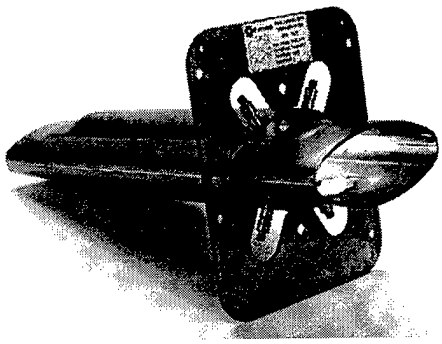

Fig 2: Photo of a complete MI BPM Assembly.

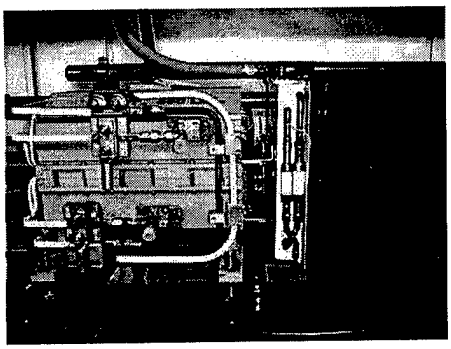

Fig 3: Photo of BPM installed between magnets.

The magnetic material issue was solved by using 316L (low carbon) stainless steel. All major welding including the feedthrus was done with a CNC controlled laser welder, resulting in high quality with minimun weld beads. The magnetic permeability was checked with a commercial gauge, and is less than 1.05 along the weld, and equal or less than 1.01 elsewhere. The small weld beads produced with laser welding also reduced distortion. During final assembly only one of 250 housings and 10 of 1000 feedthru welds leaked.

Since the stripline electrodes are attached directly to the pin it was necessary for the pin itself to be somewhat flexible. Several coaxial Feedthrus were tested to determine their electrical characteristics, resistance to damage, and pin felxability. A semicustom feedthru from Ceramaseal Inc. proved to be rugged and inexpensive at $28 each. The Feedthru was manufactured with a longer housing, to allow for a longer and more flexable pin. A flat plate attached to the exterior of the BPM provides protection for the feedthrus, cable mounting and alignment holes.

2.2 Electrical

The "Artech House" software was used to select electrode spacing and shape to optimize response linearity. The channel shaped electrode has a more uniform electric charge distribution and is less sensitive to dimensional variations at edges near the ground plane. The electrodes are placed at the maximum horizontal spacing, while maintaining 50 ohm impedance. The electrode is .5 in wide by 11 in length. The length is aproximately 1.3 wavelengths at 2 Ghz., chosen to avoid resonance with the feedthru. Although the feedthru is not designed to be a 50 ohms connector, it is electrically idnetical to a 2.9 pf capacitor and is 1/4 wavelength long at 2 Ghz. The beam pipe cut off frequency is 1.5 Ghz.

2.3 Measurements

All BPMs were measured on a stretched wire xy positioning stand, controlled by Labview software. A HP 8753B network analyzer drives 30 mill wire at 53 Mhz. and measures the four output amplitudes. Forty Nine positions spaced on a 5mm qrid are measured for each BPM. This data along with beamline survey data will be used to make offset and linearity corrections. Shown below (Fig. 3) is a plot of measured wire positions.

The "pin cushion" shaped response is a result of the restricted electrode location. The accuracy can be improved by using curve fitting algorithms to partically linearize the output. Shown below (Fig. 3) is the error remaining after a correction doing a LSF on vertical 5 mm measurements. Shown below (Fig 4) is the error remaining after doing a LSF on average of the vertical positions of +5, 0, and, -5 mm.

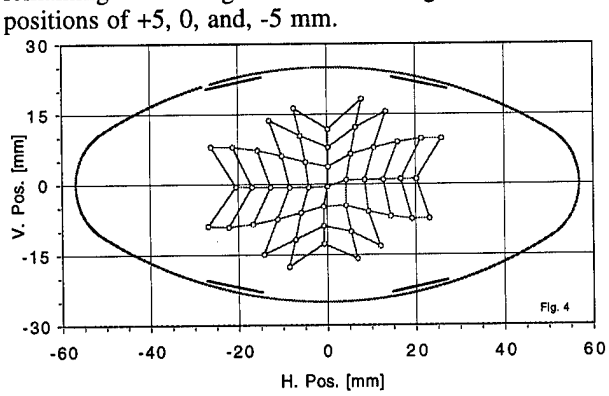

Fig 4: Typical plot of measured position vs wire position.

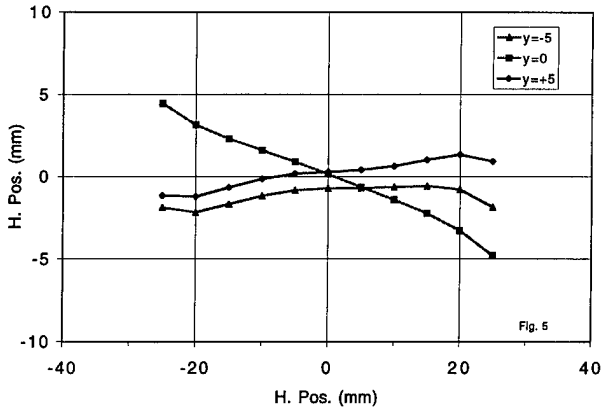

Fig 5: Horizontal fit (on y=5), error vs. xy position.

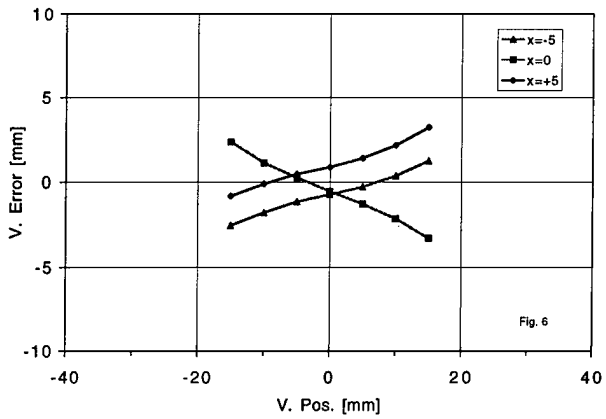

Fig 6: Horizontal fit (on ave.), error vs. xy position.

3 SUMMARY

The MI design saved some money by placing the BPMs inside the Quad Magnets, however, the linearity and the resolution of the BPMs is compromised. The limitation on the location of the electrodes forces the BPM output to have interdependent vertical and horizontal responses. The non lineraity and variations between BPMs makes this difficult to correct.

This design demonstrated new fabrication and assembly techniques and has produced usable BPMs that fit into a very limited space.

4 REFERENCES

[1] 'The Fermilab Main Injector Technical Design Handbook' 1994.

[2] E Barsotti: 'Preliminary design of the Beam Position Detectors for the Fermilab Main Injector'. Procedings of the Particle Accelerator Conference, IEEE, 1993

[3] A. Djordevic et al., 'Matrix Parameters for Multiconductor Transmission Lines' Artech House, Norwood, MS, 1989

[4] P.J. Chou: 'Theoretical Study of Stripline Beam Position monitors''

[5] E Barsotti: `Calculation of Linearity vs Strip position in Mi BPM Detectors' Fermilab,unpublished.

UPGRADE OF THE BPM SYSTEM FOR THE BEPC STORAGE RING

Li Ma and Ping Shi
Institute of High Energy Physics, Beijing 100039, China

Abstract

The Beijing Electron Positron Collider (BEPC) is a machine with a designing energy up to 2.8 GeV. Thirty-two button-type beam position monitors (BPMs) are used for the position measurement of the colliding e^+ e^- beams in the storage ring. In order to improve the measurement resolution and reduce the measurement time, the hardware and the software of the BPM system have been partially modified at last year and have been tested with beams. The BPM processing electronics and the measurement behavior can be fully controlled by a personal computer (PC) in the local control room. The measured beam position data are stored in the memory on another PC, which serves as a communication server. These data can be accessed by the main computer in the central control room through the network. The short-term reproducibility of the measurement is better than 10 microns. The measurement time for scanning all 32 BPMs is about 11 seconds. The reliability of the measurement is assured by the self-consistency check. The dynamic rang of the system is over 81 dB and the minimum measurable beam intensity is less than 0.5 mA. This paper will describe the hardware and the software of our upgraded BPM system. The performances of the BPM system are also given in the paper.

1 GENERAL DESCRIPTION

The BEPC currently has 32 BPMs spaced around the ring. Each BPM consists of four button-type electrodes, labeled A, B, C and D. The button mounted on a BNC-type feedthrough has a 20-mm diameter. The structures of all BPMs can be divided into two types as shown in Figure 1. The type with a race track cross-section (Figure 1-(a)) is used in the bending sections of the storage ring and their pick-up connectors are directly welded on to the aluminum beam duck. The number of BPMs of this type is 24. The another type with a circular cross-section (Figure 1-(b)) is used in two long straight sections close to IPs of the ring. The four buttons with their feedthough connectors are mounted on a section of the circular stainless steel beam pipe with flanges for the button or the feedthough exchange. The number of this type BPMs is 8.

A set of four RG223/U coaxial cables bring up pick-up signals of each monitor to the local control room where the signal processing electronics is located. So, for 32 BPMs with 4 buttons each we have 128 cables. The lengths of cables vary from 60 to 90 meters depending on locations of monitors in the ring.

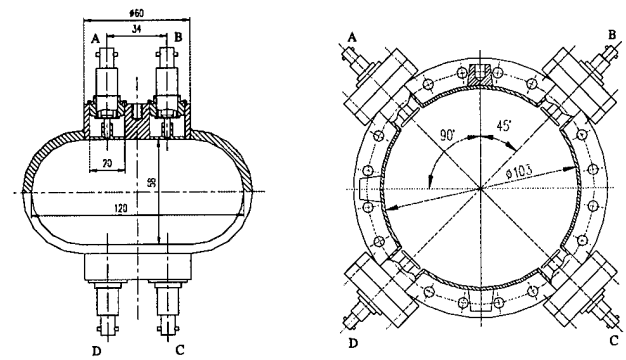

(a) (b)

Figure 1: BPM structures for the BEPC storage ring

2 SIGNAL PROCESSING

Before upgrading, the short-term reproducibility of the BPM system for the BEPC storage ring is larger than 20 μm (average), mainly due to the noise of the wide-band processing electronics. The purpose of the upgrade is to improve the reproducibility of the measurement without increasing the measurement time. To attain this purpose, the simplest way is to increase the number of ADC readings per button with high speed ADC modules, and then average the readings to improve the S/N ratio. Reference [1] can be referred for the more detailed description about the hardware and the software of our upgraded BPM system.

2.1 Hardware Electronics

Figure 2 shows a schematic block diagram of the BPM signal processing electronics. There are several modifications in the hardware electronics.

First of all, two 25-μs ADC (12 bits) modules are used to replace the original 120-ms ADC (14 bits) module. The measurement time can be reduced from 50 seconds to 11 seconds while the number of ADC readings per button increases from 1 to 500 (default value).

Secondly, the CAMAC serial crate controller (SCC), which was designed especially for the SLC control system by SLAC people, is replaced by the parallel crate controller Model CCU-2-80B with a PC interface card developed by the Electronics Division of our institute. All 21 BPM modules in two CAMAC crates then can be controlled by a PC or compatible processors as the host.

0-7803-4376-X/98 /$10.00 © 1998 IEEE

Finally, the computer network is used for data communications between PCs and the BEPC main control computer, VAX4500A.

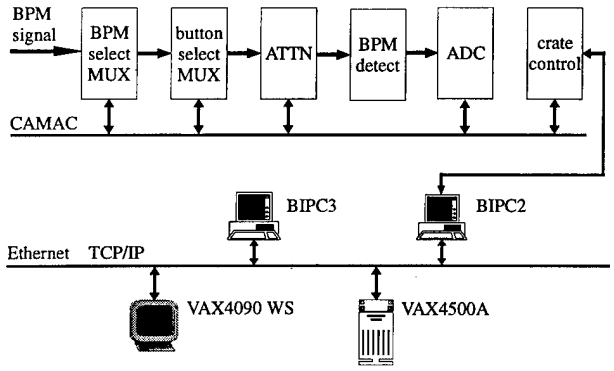

Figure 2: The BPM signal processing electronics after upgrading

2.2 *Software Program*

The graphical user interface panel on the VAX4090 workstation is kept the same after and before upgrading. Only the data acquisition program was modified and moved from VAX4500A to the PC named BIPC2. The program on BIPC2 was developed on the platform of the Microsoft Windows 95 and the Microsoft Visual C/C++ 2.0. The measurement control parameters, such as the number of ADC readings per button, and the measured beam position data are stored in the server, BIPC3.

When the BPM measurement program "WINBPM" on BIPC2 starts, it firstly initializes the electronics hardware of the system. Then the C function "BPMSCAN" of "WINBPM" begins to loop forever. In each loop, the function performs the following procedure: read the user specified measurement control parameters from BIPC3; adjust attenuation automatically according to the beam intensity; read the raw button voltage value of each button for *N* times, average them, and then compute x and y positions for each BPM; write button voltage values and positions to the database of BIPC3.

Operators can send the new measurement control parameters to and receive the latest measured beam position data from BIPC3 through the network, and to display the closed orbit distortion (COD) on the VAX4090 workstation. Communications between the main computer and PCs are based on the client/server model by using the TCP/IP protocol.

3 SYSTEM PERFORMANCE

3.1 *Closed Orbit Measurement*

The CODs can be measured simultaneously for e^+ and e^- beams. Though the scan time of the measurement for all 32 BPMs is about 11 seconds, the system response time to operators is much faster because the beam position data of the last measurement are always available in the memory of BIPC3 and can be accessed from the control console within a second through the network.

Figure 3 shows typical measured CODs for both e^+ and e^- beams. The horizontal COD is 2.2 mm rms while the vertical COD is 1.5 mm rms. The maximum measured position difference between the e^+ and e^- beams is around 0.5 mm and always appears with a few fixed monitors, such as BPM1. The reason is not yet very clear to us.

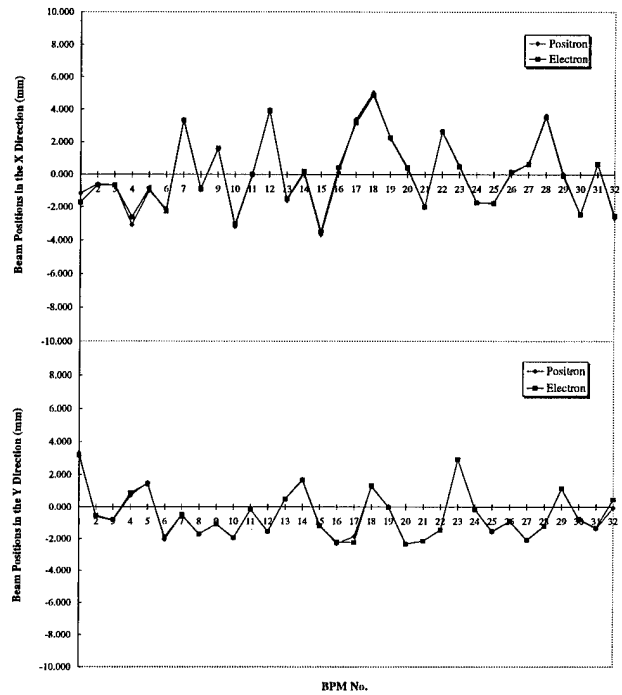

Figure 3: The closed orbit distortions for e^+ e^- beams

3.2 *Short-Term Reproducibility*

Ten-time consecutive measurements of the COD were performed during the beam storage to check the short-term reproducibility of the system. Table 1 lists the statistics of the standard deviation of measurements for all 32 monitors. The averaged standard deviations are 31(x)/21 (y) μm and 7(x)/8(y) μm before and after upgrading respectively. BPMs with the standard deviation being larger than 10 μm after upgrading basically belong to the type shown in Figure 1-(b). This type of monitor has a lower sensitivity due to the larger distance from the button to the axis of the monitor.

Table 1: A comparison of the standard deviation in 10 consecutive COD measurements before and after upgrading

	before upgrading			after upgrading		
σ (μm)	≤10	≤20	>20	≤10	≤20	>20
number (x)	5	13	14	27	3	2
number (y)	16	11	5	25	5	2

3.3 *Beam Intensity Dependence*

Figure 4 shows the beam intensity and the beam position measured at a test monitor during the beam storage in 8 hours. When the beam intensity changes, the measurement program automatically adjusts the setting values of programmable attenuators to keep the output level of the BPM detector in the useful range of the ADC. To prevent the BPM electronics from damage at high beam intensities, the minimum attenuation value is set at 5 dB when the measurable beam current is about 0.5 mA. The maximum attenuation is 81 dB in steps of 1 dB so that the dynamic range of the system is at least 81 dB without considering a 20-dB linear range of the BPM detector itself.

The peak-to-peak beam position drifts shown in Figure 4 are less than 50 μm in the horizontal direction and less than 40 μm in the vertical direction.

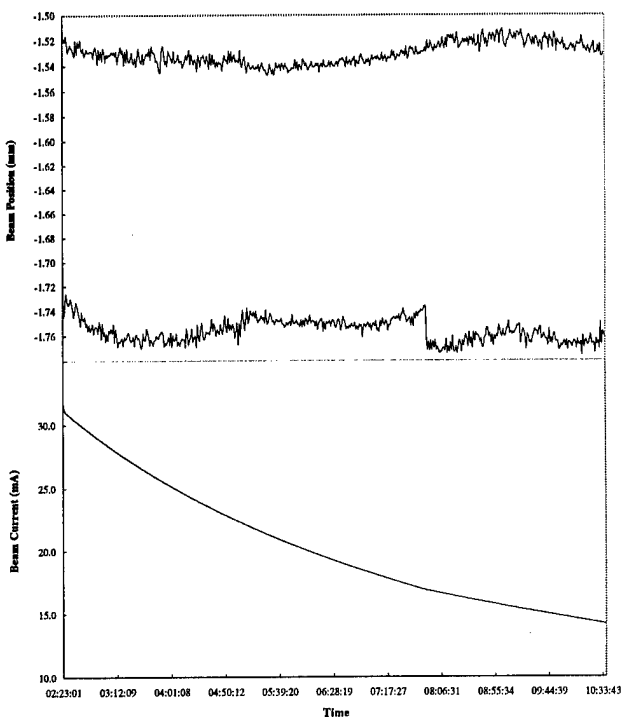

Figure 4: The long-term beam position drifts during the beam storage in 8 hours

3.4 *Self-Consistency Check*

As we know, the beam position at a BPM location can be computed by using any one of four 3-electrode normalizations and the 4-electrode normalization as well. Whenever we measure the COD, we will compare those five position values. If the maximum difference among those values for a BPM is larger than a small value δ in either x or y plane, we will mark the position of that BPM as a bad reading. Figure 5 shows the ratio of the number of bad readings to the total number of measurements performed in the period from November 1996 to April 1997 for all 32 BPMs. The total number of the measurements is about 9000.

When we began to use this self-consistency method to check the reliability of the beam position measurement, many of 32 monitors have higher bad reading ratios. Some of ratios even reach to 90%. We found that it is mainly caused by the relative attenuation change of the signal transmission cables and the channel to channel offset change of the PIN diode multiplexer. We remeasured these parameters carefully and replaced old parameters in the computer. At present, the differences between positions obtained from the 4-electrode normalization and other 3-electrode normalizations are usually less than 0.2 mm for most BPMs.

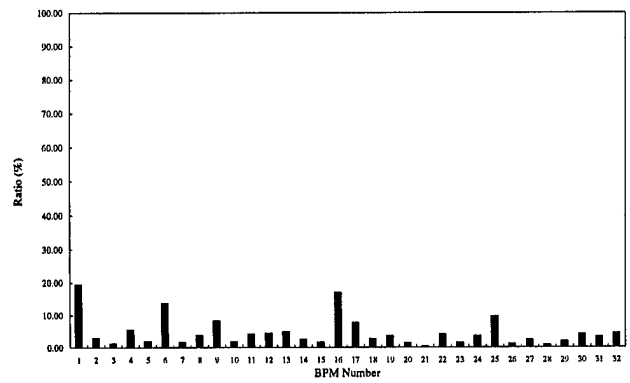

Figure 5: The ratio of the number of bad readings to the total number of measurements

4 SUMMARY

The beam position monitoring system of the BEPC storage ring basically satisfies the requirements for the machine operation and machine studies after upgrading. The short-term reproducibility of measurements is improved from over 20 μm to less than 10 μm. The measurement time for scanning all 32 BPMs is reduced from 50 seconds to 11 seconds with the default 500 ADC readings per button. The dynamic range of the system is over 81 dB and the minimum measurable beam intensity is less than 0.5 mA. The reliability of the measurement is guaranteed by the self-consistency check.

5 ACKNOWLEDGMENTS

We would like to thank many colleagues in the Beam Instrumentation Group and the Control Group who made contributions to this work. The authors would also like to thank our colleagues at SLAC for their helps and suggestions on building the BPM processing electronics.

REFERENCES

[1] L.Ma, P.Shi, K.Ye and X.Geng, "Beam Position Monitoring System for the BEPC Storage Ring", Proceedings of EPAC'96, Sitges, Spain, June 1996.

BUNCH SHAPE MONITORS FOR THE DESY H⁻ LINAC

A.V.Feschenko, A.V.Liiou, A.N.Mirzojan, A.A.Menshov, P.N.Ostroumov
Institute for Nuclear Research, Moscow 117312, Russia
N.Holtkamp, C.Kleffner, M.Nagl, I.Peperkorn
Deutsches Electronen Synchrotron, DESY
Notkestrasse 85, 22603 Hamburg, Germany

Abstract

For better tuning and control of the longitudinal beam parameters two Bunch Shape Monitors (BSM) and one Bunch Length and Velocity Detector (BLVD) have been developed and installed in the DESY H^- linac (Linac-III). The BSMs have a standard function to measure the longitudinal distribution of particles in bunches and the mechanical layout has been optimized in order to fit the extremely narrow space between the DTL tanks. The BLVD has an additional feature to measure the beam absolute energy and is installed downstream of the Linac. Due to the use of a thin wire as a source of secondary electrons the devices can be used as a non-destructive beam diagnostic tool during Linac operation. The performance of the BSMs as well as the results of the Linac-III beam studies using the new devices are presented.

1. INTRODUCTION

A longitudinal distribution of the charge in the bunches (a bunch shape) is one of the most important parameters of a beam in an ion linear accelerator. This characteristic can be used both for beam dynamics studies and for precise tuning of the accelerator. Information about a bunch shape in the DESY Linac-III allows to improve quality of the accelerated beam. The design of the BSMs was based on the long term experience of the Institute for Nuclear Research of Russian Academy of Sciences [1,2,3]. The principle of operation of the BSMs is based on the coherent transformation of longitudinal distribution of charge of the analyzed beam into a spatial distribution of low energy secondary electrons through transverse RF modulation. Though this principle was directly used in the BSMs for the DESY Linac-III much work has been done to satisfy mechanical requirements thus resulting in rather intricate and precise design of the detectors.

The measurement of the average energy is based on the time of flight method. The initial idea to use precise longitudinal mechanical translation of the BSM for energy measurements [4] was firstly implemented in the Bunch Length and Velocity Detector (BLVD) for the CERN Linac-III [5]. The subsequent analysis of measurement errors enabled us to find solutions to improve the accuracy which then have been applied in the BLVD for the DESY Linac-III.

2. GENERAL DESIGN OF THE DETECTORS

The BSMs are installed in the intertank sections between the Alvarez tanks. The simplified general assembly drawing of the BSM is presented in fig. 1. The BSM consists of the two assembly units: the main unit (1) containing the rf deflector combined with the electrostatic lens and the detector of electrons and the target actuator (2) with the target unit. The target actuator and the main unit are installed in the intertank sections using the existing spare flanges. Due to different diameters of the intertank sections the lengths of the actuators (2) for the BSM-1 and BSM-2 are different. The main units (1) are identical for the two BSMs. The difference of the diameters of the intertank sections is compensated by using the additional spacer (3) between the flange of the intertank section and the flange of the main unit.

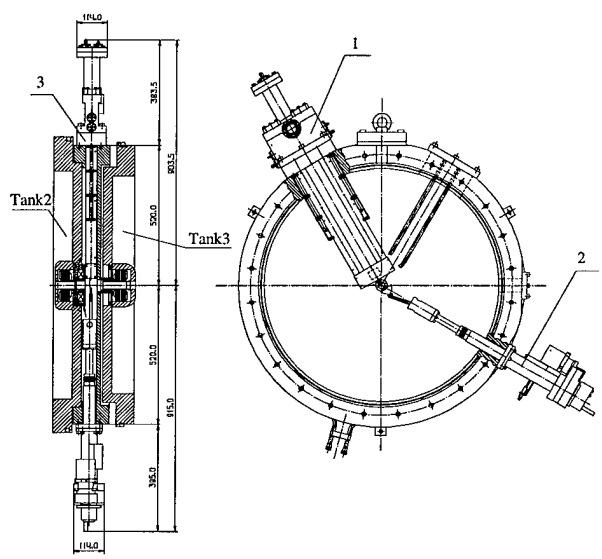

Fig. 1 General assembly drawing of the BSM

A three dimensional view of the BLVD is presented in fig. 2. The BLVD consists of the following main elements: body of the detector (1), target actuator (2) with the target unit, rf deflector combined with

electrostatic lens (3), registration unit (4), permanent adjustable magnet (5) to steer the electrons vertically, glider (6) with the actuator (7) to provide longitudinal translation of the detector, bellows (8,9) and support 10.

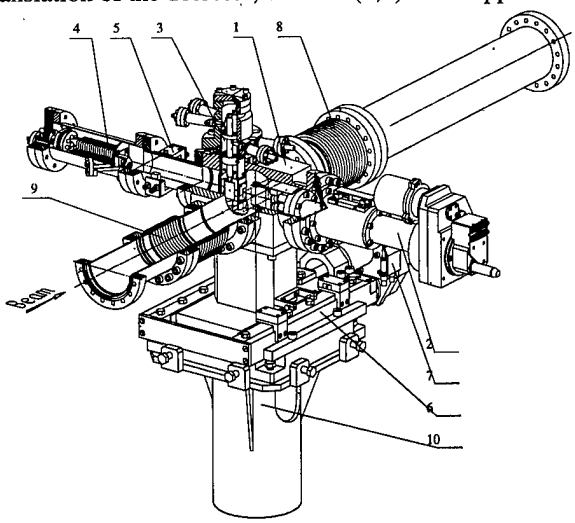

Fig. 2 Three dimensional view of the BLVD

3. SIGNAL DETECTION, RF AND CONTROL SYSTEMS OF THE DETECTORS

To detect the secondary electrons secondary electron multiplier tubes (type: Hamamatsu R596) are used. The gain of the tube can be varied within 4-5 orders of magnitude by changing the supplied high voltage thus eliminating the problem to precisely know the intensity of the electrons. The signal from the SEM tube is amplified by the fixed gain (0.5 V/μA) signal preamplifier and is digitized with 1 μsec time intervals providing information on a behavior of the measured distributions in time at a typical beam pulse length of 30 μsec.

The three detectors have a common independent control system using an IBM PC and one CAMAC crate. Special electronic modules (HV, rf, interface, stepper motor drivers) are housed in three additional CAMAC crates.

The software includes three programs. Two of them are used for signal observation, adjustment of the parameters of the detectors and tuning of the detectors. The measurements and the initial data processing are made with the third program.

The RF reference signal is taken from the reference line of the accelerator (f=202.56 MHz). The deflector of the BSM operates at the fundamental harmonic while the forth harmonic (810.24 MHz) is used for the BLVD.

During the measurements a phase of the deflecting field and the steering voltage are varied between the beam pulses. Total time required for the bunch shape measurement depends mainly on the number of the measuring points in phase. For the energy measurements this time increases due to two or four measurements of the bunch shape, double adjustment of the steering voltage and translation of the detector.

4. SOME EXPERIMENTAL RESULTS

Typical longitudinal profiles at the exits of Tank 1, Tank 2 and Tank 3 for normal mode of Linac-III operation are presented in fig. 3. One can see that the bunch widths are less than 20° at the base line for all the three energies: 10, 30 and 50 MeV.

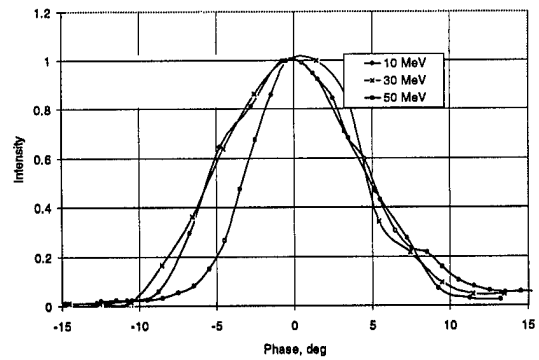

Fig. 3 Typical longitudinal profiles for normal mode of Linac-III operation

Fig. 4 shows the bunch shape evolution along the beam pulse at the exit of the Tank 1.

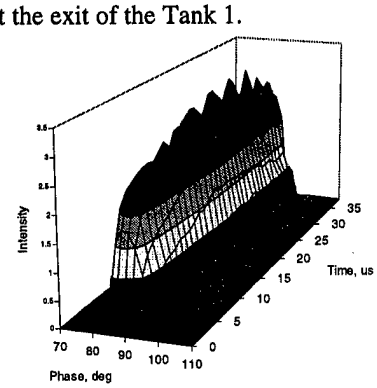

Fig. 4 Bunch shape evolution along the beam pulse at the exit of the Tank 1.

Fig. 5 shows the bunch shape and bunch center evolution as the phase of Tank 3 is varied. One can observe essential variation of both bunch shape and bunch phase position. This is just a result of longitudinal motion of particles. The behavior of the bunch center as a function of tank phase can be used as a good characteristic to set the rf amplitude in the tank. Fig. 6 presents the experimental results for the exit of the Tank 3 along with the three theoretical curves: for the nominal field $E = E_0$, $E = 0.95E_0$ and $E = 1.05E_0$. One can see the field level to be close to the nominal value. (In general these curves must be analyzed taking into account the input energy of beam).

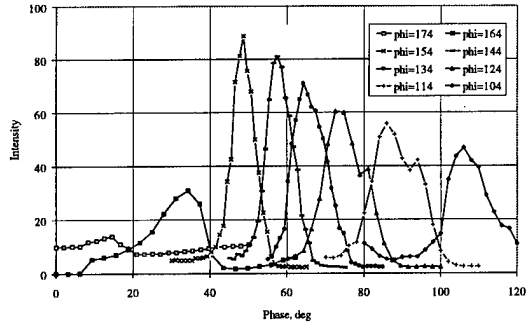

Fig. 5 Bunches for different phases of the Tank 3.

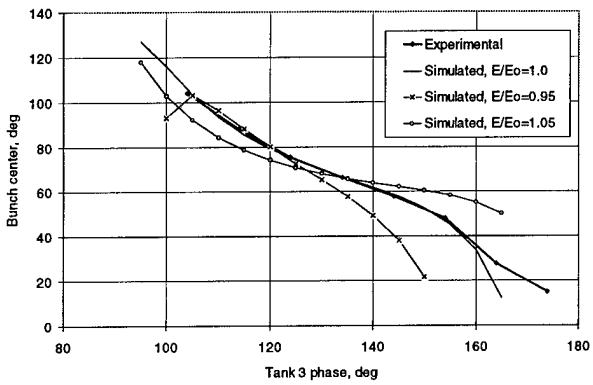

Fig. 6 Experimental and theoretical behavior of the bunch centers at the exit of the Tank 3.

The procedure of energy measurements [5] was modernized to improve the accuracy [6]. To avoid influence of errors of phase adjustment the value of the detector translation was selected to be close to $\beta\lambda/2$, where λ is a wavelength of the deflecting field. To decrease the value of the translation the forth harmonic of the fundamental bunch array frequency was taken as the frequency of the deflecting field. To compensate the influence of external magnetic fields on the electron trajectories adjustment of the steering voltage between the deflector plates is foreseen for both positions of the detector. Measurements are made for two phase ranges shifted by 180° thus enabling to remove errors of measurements arising from non symmetry of the

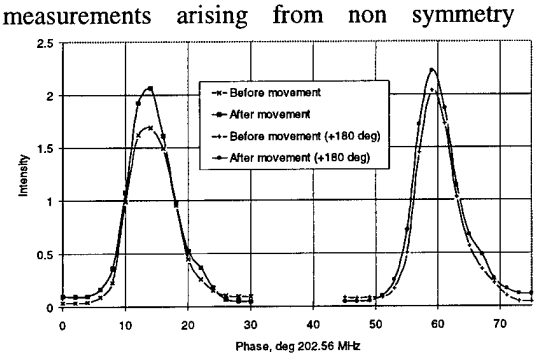

Fig. 7 Results of energy measurements.

deflecting field. The average value of the two measurements is taken as the correct one. The above measures along with the precise calibration of the detector translation gave the possibility to minimize systematic errors down to ±0.1%. The total error including both systematic and random components is equal to ±0.35%. The value of energy found from the data shown in fig. 7 is equal to (50.04±0.175) MeV.

5. PROBLEMS AND CONCERNS

In case of H^- ions, besides the low energy secondary electrons, higher energy electrons detached from the ions and scattered at the target are observed. This effect can be seen as a lower intensity maximum in front of the measured bunch. Though the distortions in our case can be neglected, the effect is of importance for precise measurements especially for longitudinal halo observations and is under study now.

6. CONCLUSION

The detectors of longitudinal beam characteristics installed and successfully commissioned in the Linac-III provide qualitatively new information about beam behavior. Information obtained with the detectors enable to reliably set both phases and amplitudes of the accelerating fields in the tanks especially during set up and commissioning. Bunch shape and average energy at the exit of the Tank 3 serve as a good criteria for normal operation of the accelerator. Further matching of the energy spread for the synchrotron can be made with the debuncher installed after the linac.

7. ACKNOWLEDGMENT

The authors are grateful to Dr. D.Trines, Dr. S.Esin and Dr. L.Kravchuk for the support of this work.

REFERENCES

[1] Feschenko A.V., Ostroumov P.N. Bunch Shape Measuring Technique and Its Application For an Ion Linac Tuning, Proc. of the 1986 Linear Accelerator Conference, Stanford, 2-6 June, 1986, pp. 323-327.

[2] Hurd J.W. et al. Bunch Shape Monitor for SSCL Linac. Proc of the 1993 Particle Acc. Conf., Washington, May 17-20, 1993, V.3, pp. 2426-2428.

[3] S.K.Esin, A.V.Feschenko, P.N. Ostroumov. INR Activity in Development And Production of Bunch Shape Monitors, Proc. of the 1995 PAC and Int. Conf. on High-Energy Accelerators, Dallas, 1-5 May, 1995, V.4, pp. 2408-2410.

[4] Ostroumov P.N. Average Velocity Measurement of Accelerated Beam by Means of an Upgraded Bunch Length Detector. INR Preprint - 812/93, May 1993.

[5] Bylinsky Yu.V. et al. Bunch Length and Velocity Detector and its Application in the CERN Heavy Ion Linac. Proc. of the EPAC-94, London, June 27-July 1, 1994, pp. 1702-1704.

[6] A.V.Feschenko, P.N.Ostroumov. Velocity Measurement by Means of Mechanical Movement of a Detector, AIP Conference Proceedings 333. Beam Instrumentation Workshop, Vancouver, B.C. Canada, October, 1994, pp. 478-484.

DESIGN AND COMMISSIONING OF BEAM POSITION MONITORS IN THE IUCF COOLER INJECTOR SYNCHROTRON

M. S. Ball, B. J Hamilton, D. Bilodeau,
Indiana University Cyclotron Facility, Bloomington, IN. 47408

Abstract

IUCF is completing construction of the cooler injector synchrotron (CIS). A secondary emission profile monitor system (harp) is used for beam profile and emittance measurement. The harp design was patterned after a design used for many years at Fermilab [1]. Two, non-interceptive, beam position monitor (BPM) systems have been built to facilitate and enable commissioning and operation. In the 7 MeV injection beamline, high input impedance front-end amps are used to detect the signal from 4-quadrant, electrostatic pickups. The beam in this area will average 200 μA peak, with a pulse width of 100 - 200 μs and repetition rate of up to 5 Hz . In the CIS ring, 4-quadrant, elliptically shaped electrostatic pickups are used for impedance matching to the beamline. An electric field modeling program was used to determine the parameters of the plates in the pickup. Logarithmic amplifiers are used to detect the beam in the CIS ring, providing a linear output and an extended range. A time of flight system is also discussed.

1 BEAM PROFILE MONITOR

1.1 Electronics

The harp uses a 5 printed circuit board stack, with 24 wires on each of the horizontal and vertical detector boards, spaced 1 mm apart. The first, third, and fifth board have 6 wires, spaced 4 mm apart, and are biased with a small voltage to collect scattered electrons. A large range of bias voltages were tried, finding 90 volts to be optimum. The signal is carried from the vacuum chamber on a ribbon cable and through a vacuum connector designed and built in house. A 100 ft. folded and shielded ribbon cable is then used to send the currents to the electronics board which is housed in a NIM crate. The circuit board front-end electronics have 5 MΩ resistors to ground in parallel with 0.01 μF capacitors providing a time constant of 50 ms. The signals are then sequentially multiplexed and integrated. The integrator uses a low bias current op-amp with a shorting switch in parallel with the feedback resistor, which is activated after each channel is read from the multiplexer, zeroing the amp before the next multiplexed channel is read. After a buffer amp, the signal goes to a fast ADC with FIFO memory. This type of ADC allows the user to acquire data at a fast rate and display it whenever it is desired. The timing for the harp electronics is incorporated on the circuit board, using a programmable array logic chip (PAL). A trigger from the master timing clock initiates the PAL, which sends out the appropriate pulses to the devices on the board and provides the ADC clock. The data acquisition parameters can changed by reprogramming the PAL. During commissioning, a stand-alone display system is used, incorporating a PC and graphical programming package, HP VEE, from Hewlett-Packard [2]. In the operational system the signals will be displayed at the operations console through the controls computer.

1.2 Operation

The harp has been the primary diagnostic during commissioning of the CIS ring. Two harps have been placed in the ring injection beamline and one in the ring. The first harp is mounted in front of a stop, allowing one to monitor intensity while adjusting the profile. The harps are moved in and out of the beam path using air actuated insertion devices. The flexibility of this setup, allows an operator to observe a harp display of first turn beam in the CIS ring along with multi-turns (Fig. 1) and also accumulate maximum intensity with the harp out of the beam path.

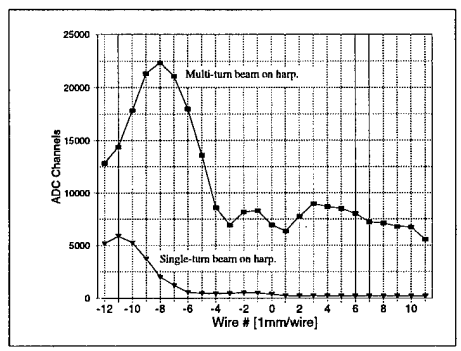

Figure 1: Horizontal harp display. The lower trace is first turn beam in the CIS ring. The upper trace is multiple turns.

2 BEAM POSITION MONITORS

2.1 Injection Beamline

The 7 MeV injection beamline and the CIS ring have a non-interceptive BPM systems designed into them. The injection BPMs have not been useful because of electron stripping from the H- beam. When electrons are stripped from the beam their flight angle can change so that they strike the electrostatic pickup, saturating the electronics. A biased guard electrode has been tried but has had little beneficial effect. The system should be useful when proton beams are accelerated.

0-7803-4376-X/98/$10.00 © 1998 IEEE

2.2 *Accelerator Ring Pickups*

When a beam pipe with circular cross-section is divided into four segments as electrodes to measure beam position (upper and lower segments for vertical position and right and left segments for horizontal position), it is obvious by symmetry that all four segments should be cut with the same arc length to get equal responses (equal induced currents) to a beam pulse traveling along the centerline of the pipe. An elliptical cross-section will behave very differently, since some points on the pipe are significantly farther from the centerline than others. If the long axis of the ellipse is horizontal, then the upper and lower segments will have to be much smaller than the right and left segments to get the same response. It is necessary, then, to be able to calculate where to cut the pipe to get segments of the appropriate size.

Past experience indicated that to a good approximation the charge induced on the beam position segments could be computed electrostatically, i.e. electrodynamic (radio frequency) corrections were apparently small. Therefore the relative responses of a set of segments of any given size were calculated as a two-dimensional electrostatic problem with the segments held at ground and with a point charge (actually a line charge in three dimensions) at the desired beam position. The system was enclosed in a rectangular boundary also held at ground. The relative responses of the segments should then be proportional to the total charge induced on the surface of each segment. By Gauss' Law, the surface charge density on a conductor is proportional to the magnitude of the electric field strength just outside the surface.

Calculations were done with the electro/magnetostatic program MagNet by Infolytica Corp. This program includes the capability of defining a curve as a succession of line segments by manually selecting end point locations with a cursor. The program can then generate a graph of electric field strength magnitude vs. position along the curve. Graphs of this type were produced for each segment and then integrated by finding the area under the graph line to get a number for each segment which should be proportional to the total charge. Calculations of this type were done both to determine the segment sizes which should be cut and to predict the relative responses of the four electrodes to various beam positions.

2.3 *BPM Electronics*

The CIS ring uses elliptically shaped 4 quadrant electrostatic pickups. They are positioned at the entrance and exit of each of 4 bending magnets. Each pickup has a dedicated set of electronics attached to it. The detectors used are Analog Device, AD640 logarithmic amplifiers [3]. The log amp detector design [4] was selected for it's wide dynamic range, 65 dB, and ease of use, requiring no local oscillators or mixers. The log amps are followed by low noise op-amps with 30 kHz active filters. The difference of the log amps, L-R, and U-D, gives the normalized position in the horizontal and vertical planes. The sum of the two horizontal signals provide the intensity. The signals go to dedicated high speed ADC modules with on board memory. This type of signal buffering allows the operator to view the position and intensity history of the beam during injection, and ramping in great detail.

2.4 *BPM Operation*

The log amp detector has been very useful during commissioning. The intensity output from the amp can be displayed on an oscilloscope (Fig. 2) showing the lifetime of the injected beam in log scale. Intensity was detected even when the rf buncher was turned off, because of the beam self bunching in the high "Q" cavity. The high bandwidth of the detector gave a very accurate position measurement during the short time the beam was in the ring between injections. One can imagine tracking the position, in a 100 microsecond scale if need be, during the ramping, acceleration process, correcting ramp parameters.

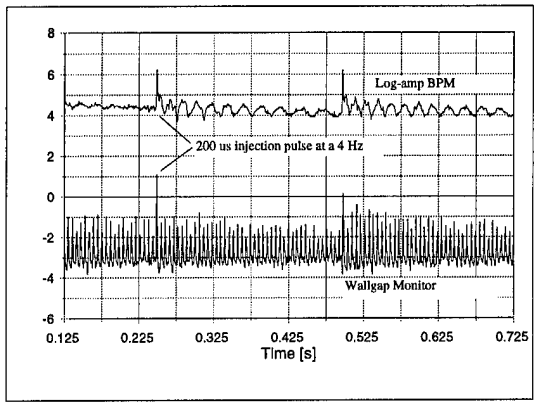

Figure 2: Injected and stored beam in the CIS ring. The top trace is the DC output of the log-amp BPM intensity. The lower trace is the WGM RF output.

Two, more conventional BPMs, are used in the ring for beam feed-forward. The system uses diagonally cut pickups, a 10.7 MHz intermediate frequency (IF), and AM to PM convertors to measure the position of the beam in the horizontal plane. The system has yet to be tested with beam.

3 TIME OF FLIGHT

A time of flight system (ToF) is being used in the 7 MeV injection beamline to detect changes in the beam energy from the RFQ/DTL. The system is similar to the one used at TRIUMF [5], where as, a change in energy is measured as a change in phase between two pickups of a fixed, known distance apart.

3.1 *Electronics*

The 200 us, pulsed, beam is accelerated through the RFQ/DTL, using a 425 MHz RF amp. The non-

interceptive, resonant, beam pickups are immediately down stream of the accelerator, 2.5 meters apart. A beam signal is detected, buffered and sent to the ToF electronics. An Analog Device AD607 [6] is used as an RF to IF, 10.7 MHz, convertor.

The AD607 is normally used in wireless communications as a down-convertor amplifier. It has a mixer and log amp with AGC, as well as, an I & Q demodulator, all in a 20 pin surface mount chip. It has been tested in the lab as an AGC beam position detector with a 75 dB range.

The output of the AD607 is a constant 300 mV signal, which is fed into limiting amps and then a type II phase detector. The output is filtered to a DC level and amplified, sample/held, and buffered. The signal then goes to an ADC, to be displayed on a controls computer electronic strip chart, a constant monitor of the 7 MeV energy.

3.2 Operation

The theoretical resolution of the ToF was calculated as 1.5 keV/degree. In preliminary testing with beam, the resolution was 3.8 keV/ degree when calibrated against a down stream bending magnet, this disparity has yet to be solved.

4 ACKNOWLEDGMENTS

We would like to thank Jim Lacky, and Keith Solberg and the wire chamber group for their help in developing the Harp system, also the operations group for their support and patience while helping us build and test the new systems. The CIS project is supported by a grant from the National Science Foundation, Grant No. NSF PHY 93-147-83.

5 REFERENCES

[1] Jim Lacky, private communication.

[2] Hewlett-Packard "Test and Measurement Catalog" pp. 47-49, 1996.

[3] Analog Devices "Linear Products Data Book", pp. 7.7-22,1990/91.

[4] F.D. Wells, J. D. Gilpatrick, R. E. Shafer, and R.B. Shurer "Log-ratio Circuit For Beam Position Monitoring" IEEE PAC, San Francisco, CA, May 6-9, 1991, pp. 1139-1141.

[5] Yan Yin, Robert E. Laxdal, Anotoli Zelenski, Peter Ostroumov, 'A Very Sensitive Non-Intercepting Beam Average Velocity Monitoring System for the TRIUMF 300-keV Injection Line', Beam Instrumentation Workshop, Argonne, IL, May, 1996.

[6] Analog Device, Preliminary Technical Information Rev. 4.0, "Low-Power Mixer/AGC/RSSI 3V Receiver IF Subsystem"

MEASUREMENT OF INJECTION ORBIT USING A SINGLE PASS BPM SYSTEM AT THE PF RING

T. Honda, M. Katoh, A. Ueda, M. Tadano, Y. Kobayashi and T. Mitsuhashi, Photon Factory, KEK, High Energy Accelerator Research Organization, 1-1 Oho, Tsukuba, Ibaraki, 305 Japan

Abstract

A single-pass beam-position monitor (BPM) system for the injection beam was developed. The injection orbit during the 1st turn to the 4th turn could be measured with a single injection pulse. The resolution of the measurement was estimated to 0.15 mm for the electron beam. The injection orbit at the usual operation condition was measured and was confirmed to coincide with the design orbit. A trial of the on-axis injection with a dc bump was performed. The orbit correction based on the single-pass measurement was attempted by using the best corrector method.

1 INTRODUCTION

The Photon Factory (PF ring) is a 2.5-GeV electron storage ring dedicated to a synchrotron-radiation source. At present, large reconstruction for a lower emittance lattice is in progress. [1] The reduced emittance is to be achieved by replacing the quadrupoles and sextupoles in the FODO cells. In the normal-cell sections, vacuum ducts are to be replaced by new ones; the number of quadrupole magnets and BPMs will be doubled.

The purpose of the single-pass BPM system is the correction of the injection orbit error in advance of the beam storage at the commissioning of the new lattice. In the low-emittance configuration, there is a weak point of a small dynamic aperture. This small aperture would demand a strict correction of the injection beam orbit in the storage ring. So a COD correction in advance of the beam storage will be inevitable.

In the following sections we report on the signal processing method for the single-pass measurement and some injection orbits measured at various conditions.

2 SIGNAL PROCESSING METHOD

The signal processing scheme to obtain the beam position was shown in figure 1. The outline of the processing was same as that of the previously reported. [2][3] Bipolar bunch signals extracted through button electrodes were recorded in real time using a high-speed waveform digitizer compatible with the VXI bus. The digitizer has four channels with four analog-to-digital converter (ADC). Each channel is an 8-bit ADC which has a maximum sampling rate of $5X10^9$ samples/s and an analog bandwidth of 1 GHz. The duration of the bipolar bunch signals of the injection beam was 3 or 4 ns, so the sampling rate was fast enough to store the waveform. The intensity of the specific button signal was determined as a peak-to-peak amplitude of the bipolar shape, and the beam position was calculated from the peak-height ratios.

The signals from 8 BPMs were combined by the aid of RF power combiners and were measured with one waveform digitizer. The button signals made discrete pulse trains, and were well resolved on the time axis. The record length of the digitizer was $1.5x10^4$ words for each channel. On the other hand the revolution period of the ring was 625 ns. When the signal is digitized at the maximum sampling rate, about 4 turns of bunch signals could be stored in the memory. We used two waveform

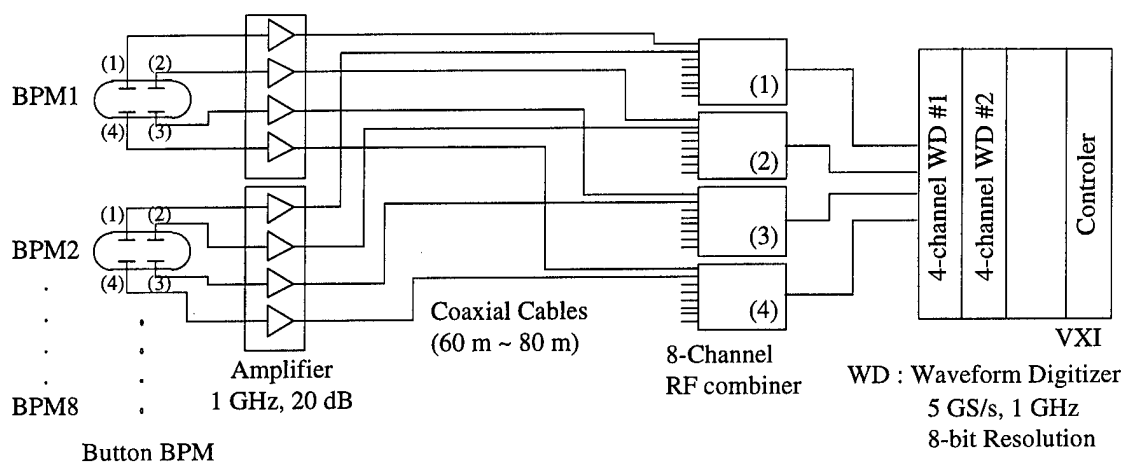

Figure 1 : Signal processing scheme of the single-pass BPM system.

digitizers and the beam position of 16 BPMs could be measured with a single injection pulse.

The dispersion of the measurement was estimated to be 0.6 % as the voltage ratio for the typical electron beam of about 2×10^{-10} C supplied from the 2.5 GeV linac injector. As the relative resolution of the beam position, that value corresponded to $\Delta X = 0.13$ mm and $\Delta Y = 0.39$ mm according to the conversion factor of the BPM.

3 MEASUREMENT RESULTS

3.1 Injection Orbit of the PF ring

Figure 2 is the measured injection orbit at the usual operation condition of the PF ring. In this report, all the measurements were performed without the RF acceleration power and the average values of 20 injection pulses were plotted. Horizontal axis of each graph is the distance along the beam orbit. The origin of the horizontal axis corresponds to the injection point of the storage ring. And the full scale corresponds to the 4 turns just after the injection.

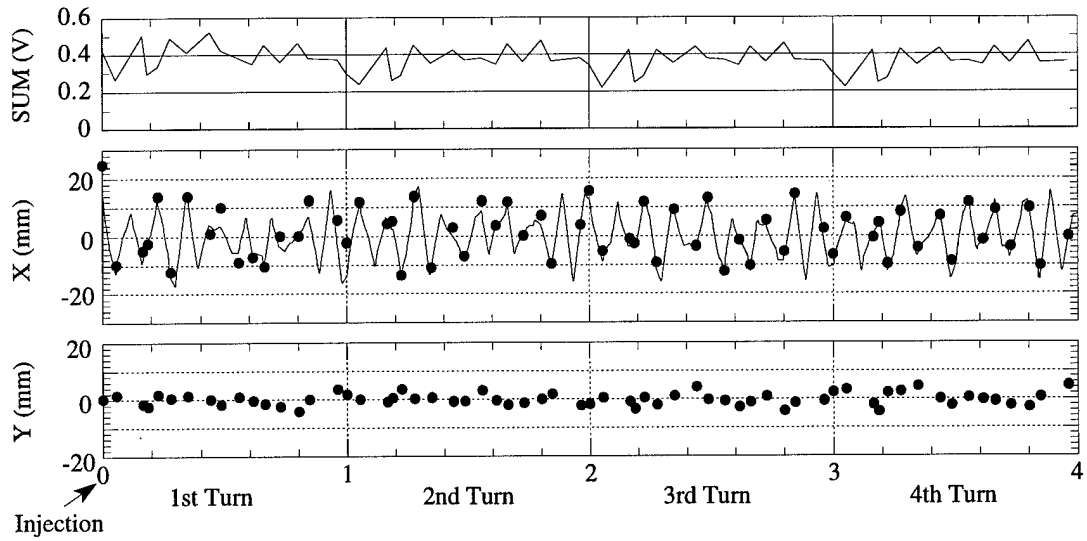

Figure 2 : Measurement of the regular injection orbit.

The topmost graph shows the summation of the four button signals as a measure of beam loss. Because this was the measurement at the normal injection condition, any beam loss was not observed in the four turns. The horizontal (X) and the vertical (Y) beam positions were shown as solid circles in the 2nd and 3rd graphs, respectively. 16 data points were plotted in a single turn. The solid line of the 2nd graph is the injection orbit calculated based on the design parameters of the ring, not including the injection bump. The measurement points well lie on the calculated line except for the first data point. The first point of each turn was the position of the BPM in the kicker bump. The kicker bump falls completely within 4 turns after the injection. The data points of the vertical direction were distributed in the range of 2 or 3 mm. The vertical orbit error should be

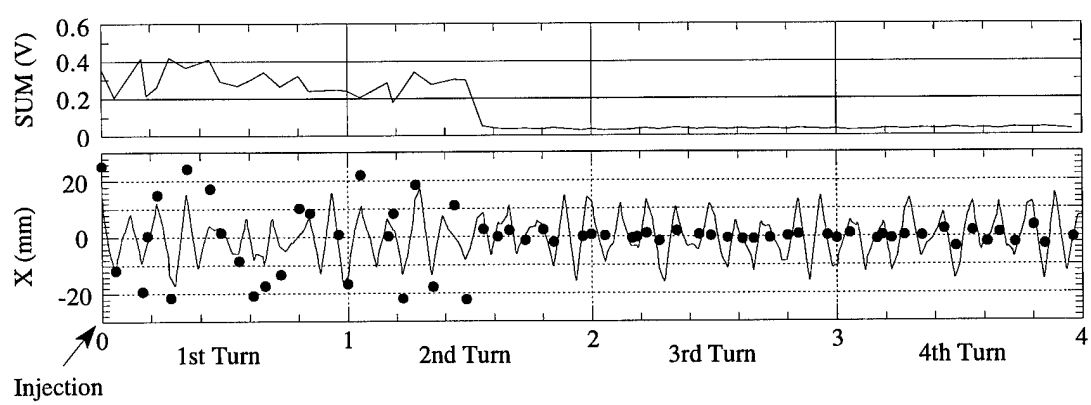

Figure 3 : Example of an irregular injection orbit.

zero ideally. These distribution contained not only the injection orbit errors but also the offsets of the single-pass measurement.

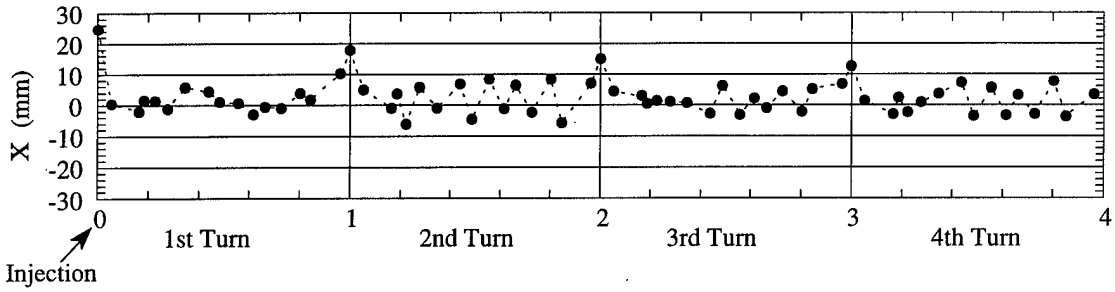

Figure 4 : Trial of the on-axis injection with a DC bump.

An example of the irregular injection orbit is shown in figure 3. One of the horizontal steering magnets located between the second BPM and the third BPM was abnormally excited. At that condition, any beam storage was impossible. The data points after the 3rd BPM oscillate with a large amplitude compared to the normal orbit (the solid line). In the halfway of the second turn, the beam disappeared suddenly. The beam loss point could be fixed between the 9th BPM and 10th BPM. We have the super conducting vertical wiggler at that location, where the horizontal aperture of the ring take a local minimum.

3.2 Trial of on-axis injection

On-axis injection mode was attempted by the aid of a local dc bump at the injection point, which was formed using auxiliary windings of the four bending magnets. The horizontal injection orbit at that condition was shown in figure 4. The betatron oscillation in the first turn was well suppressed within a small value. If the ideal on-axis injection would realized, the beam should be hit the septum wall at the beginning of the second turn, because the present kicker bump dose not yet fall within one revolution period. The setting up of the dc bump should have some errors.

In the low-emittance reconstruction, the kicker magnets are upgraded, and the pulsed bump will complete within a single turn. [4] This will enable the beam storage with the on-axis injection, that would be useful for the commissioning of the new lattice with small dynamic aperture.

3.3 Orbit correction by the best corrector method

Correction of the injection orbit using the best corrector method was attempted. Firstly, all vertical steering magnets were deexcited and the vertical injection orbit was measured. In figure 5, differences from the orbit at the normal condition were plotted as open circles. Then the correction was performed using two steering magnets based on the best corrector method. The solid circles are the beam position after the correction. The orbit error was well reduced in spite of a simple correction method. More sophisticated method, such as the singular value decomposition, would be used for more precise correction.

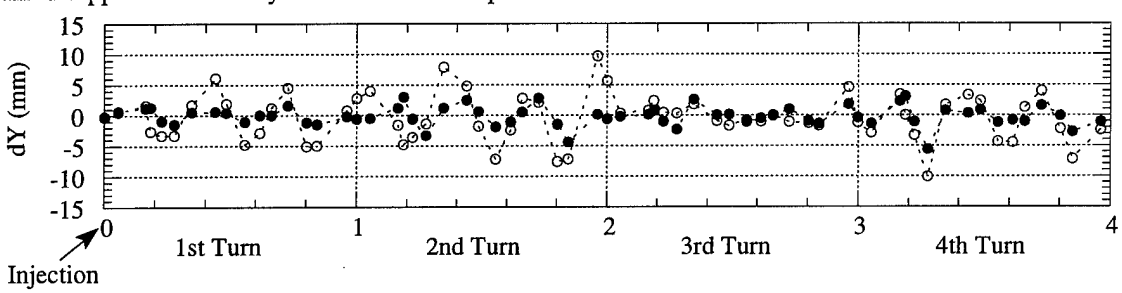

Figure 5 : Correctoin of the injection orbit by the best corrector method using two steering magnets.

REFERENCES

[1] M. Katoh and Y. Hori, "Status of the emittance upgrade project at the Photon Factory storage ring", EPAC'96.

[2] T. Honda and M. Katoh, "A single-pass beam position monitor for the injection beam at the Photon Factory storage ring", EPAC'96.

[3] T. Honda, "Single-pass measurements of the injection-beam position at the Photon Factory storage ring", KEK Preprint 95-128, 1995.

[4] Photon Factory Activity Report #13, A-13, 1995.

CALIBRATION OF KEKB BEAM POSITION MONITORS

Kotaro Satoh and Masaki Tejima
KEK, High Energy Accelerator Research Organization
Oho 1-1, Tsukuba, Ibaraki 305 Japan

Abstract

This paper first proposes a practical model for output signals of BPM electrodes. The model is based on a definition of the geometric center of a BPM head, and on the assumption that the character of the head can be specified only by a small number of parameters, the relative gains of electrodes. On the basis of the model, calibration was done to find the relative gains of all KEKB LER BPM heads. The paper reports and discusses the calibration results.

1 INTRODUCTION

Stability of the closed orbit is essential for stable operations of rings, particularly of those requiring strong sextupole magnets. To stabilize the beam orbit, the first step would be to measure the beam position with respect to the design orbit, or to measure the absolute beam position. On installation of a BPM head its mechanical reference axis is alligned to the ideal orbit. For the absolute position measurement, therefore, location of the electric center, relative to the reference frame, of each BPM head must be known. This is the main reason why we need calibration of BPM heads. Here we apply a signal wire method to the calibration.

This paper first proposes a practical model for output signals of BPM electrodes, and define a geometric monitor center by assuming that each electrode has its ideal position-response function. This model also assumes that the real output signal from an electrode is proportional to its response function multiplied by a constant factor, called its gain, and that the gain is independent of the beam position [1]. We would say here that character of each head can be specified only by a small number of gains.

In a real BPM head, variation of the gains from their ideal values displaces its electric center from the ideal one. Following the present model, the calibration is to know the relative gains among electrodes of each BPM head. A least-square method estimates the gains from many output data with various wire positions. After the calibration the electric center is expected to coincide with the geometric one.

With this method the calibration of KEKB LER BPM heads is in progress. The present paper reports and discusses the results.

2 MODELING OF OUTPUT DATA

2.1 Dependence of fields on the beam position

Consider electromagnetic fields produced by a point charge moving inside a perfectly conducting uniform pipe. The point charge is moving with the light velocity along an orbit, parallel to the axis, displaced by $\mathbf{R}(X = R\cos\theta, Y = R\sin\theta)$ shown in Fig.1.

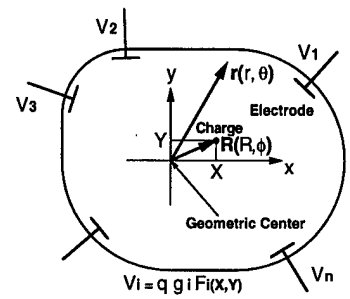

Figure 1: Coordinate system and an image of the model monitor.

The moving charge couples only to TEM fields, whose potential is governed by a two-dimensional Laplace's equation. We consider a Green function $G_2(\mathbf{r}, \mathbf{r}')$

$$G_2(\mathbf{r}, \mathbf{r}') = -\frac{1}{2\pi}\log|\mathbf{r} - \mathbf{r}'|, \tag{1}$$

which satisfies

$$\Delta_2 G_2(\mathbf{r}, \mathbf{r}') = -\delta_2(\mathbf{r} - \mathbf{r}'), \tag{2}$$

where Δ_2 and $\delta_2(\mathbf{r})$ are the two-dimensional Laplacian operator and δ-function.

Then the field potential $\Phi(\mathbf{r})$ is a sum of the direct field given by the Green function, and fields $\Phi_{imag}(\mathbf{r})$ produced by the image charge on the pipe surface. With a constant K we can write

$$\Phi(\mathbf{r}) = K\log|\mathbf{r} - \mathbf{R}| + \Phi_{imag}(\mathbf{r}). \tag{3}$$

The direct field depends on $\mathbf{R}$ as $\log|\mathbf{r} - \mathbf{R}|$, which can be expanded into a series

$$\log|\mathbf{r} - \mathbf{R}| = \log r - \sum_{k=1}\frac{1}{k}(\frac{R}{r})^k\cos k(\phi - \theta). \tag{4}$$

Finally we have

$$\begin{aligned}\Phi(\mathbf{r}) \;=\; & K[(\log r - C_0(\mathbf{r})) \\ & -\sum_{k=1}\frac{1}{k}R^k\cos k\theta(\frac{\cos k\phi}{r^k} + C_k(\mathbf{r})) \\ & -\sum_{k=1}\frac{1}{k}R^k\sin k\theta(\frac{\sin k\phi}{r^k} + S_k(\mathbf{r}))],\end{aligned} \tag{5}$$

where $C_k(\mathbf{r})$ and $S_k(\mathbf{r})$ corespond to the fields by the image charge.

0-7803-4376-X/98/$10.00 © 1998 IEEE

Now we find that the field must be expressed as a superposition of components each of which is derived from the k-th moments of charge distribution, $R^k \cos k\theta$ and $R^k \sin k\theta$, and hence depends on the beam position (X, Y) through a special manner only with the k-th harmonic functions of X and Y.

2.2 *Output signal of BPM*

Electrodes of a BPM head are nothing but antennas probing the field inside the chamber, as shown in Fig.1. The output of the electrode is determined by the field strength at its location, or more precisely, the averaged field strength, with a weight function, over the electrode port. The relation between the averaged field strength and the beam position is called a position-response function. For an ideal BPM head the output of each electrode is determined only by the response function. For a real BPM, however, the output of an electrode is differed from the ideal repsonse function mainly due to stray capacitance and impedance of the vacuum feedthrough. Now we are in a position to write down a model for the output signal from the i-th electrode,

$$V_i = q g_i F_i(X, Y), \tag{6}$$

where $F_i(X, Y)$ is the ideal position response function and is normalized by $F_i(0, 0) = 1$. The parameter q measures the strength of simulating current on the wire. The factors g_i are gains representing the signal imbalance among the electrodes. By giving each electrode its ideal response function we have just defined a geometric center so that equations (6) hold simultaneously.

We have known that $F_i(X, Y)$ can be always expanded into a series of harmonic functions of X and Y,

$$\begin{aligned} F_i(X,Y) &= 1 + \sum_{k=1} R^k (a_i(k) \cos k\theta + b_i(k) \sin k\theta) \\ &= 1 + a_i(1)X + b_i(1)Y \\ &+ a_i(2)(X^2 - Y^2) + b_i(2)(2XY) \\ &+ a_i(3)(X^3 - 3XY^2) + b_i(3)(3X^2Y - Y^3) \\ &+ \ldots \end{aligned} \tag{7}$$

Coefficients $a_i(k)$ and $b_i(k)$ are determined by the cross-section of the BPM head and geometry of the electrode, and can be calculated with numerical methods.

Variation of performance of BPM heads is introduced not only by the impedance imbalance but also by mechanical fabrication errors. These errors produce a responce function different from the ideal one with the result of a slightly wrong position sensitivity. What we want to measure, howevere, with the BPM system is the absolute positions with respect to the ideal orbit, rather than precise position movements. This is the reason why we have adopted the present modeling of a BPM head. Even with the mechanical errors, we can define the geometric center and find its absolute position relative to the reference frame by the calibration. Moreover, considering recent mechanical fabrication technique we expect that the variation of the response function would be sufficiently small.

3 GAIN ESTIMATION

How to estimate the gains has been reported before [1]. Only a brief description for calibrating the gains is presented here. Let the number of electrode be n and the total number of the measurement be m. At each measurement the wire position is changed and the output signal of each electrode is measured. At the j-th measurement the output signal from the i-th electrode V_{ij} can be written as

$$V_{ij} = g_i q_j F_i(X_j, Y_j), \tag{8}$$

where q_j is the signal strength of the wire, normalized by g_1=1, and X_j and Y_j are the wire position at the j-th measurement relative to the unknown geometric center. Notice that the wire impedance is dependent on its position and that the strength q_j may change at each measurement. After the m-th measurement the unknown parameters are $g_2, g_3, \ldots, g_n$, and $(q_1, X_1, Y_1), \ldots, (q_m, X_m, Y_m)$ with the total number of $3m + n - 1$. On the other hand the data are $(V_{11}, V_{21}, \ldots, V_{n1}), \ldots, (V_{1m}, V_{2m}, \ldots, V_{nm})$ with the total number of $4m$. If the number of the data is larger than that of the unknown parameters, we can estimate the unknown parameters with a least square method.

4 CALIBRATION RESULTS AND DISCUSSION

We have finished the calibration of two types of circular symmetric BPM heads for the KEKB LER. One is 94 mm in diameter, and the other is 150 mm. Each BPM has 4 output ports. Signals were measured with a narrow-band detector with a center frequency of 1.018 GHz, two times the acceleration frequency.

Measurements were done with a 1mm step both in the horizontal and vertical directions, within a rectangular area of $\pm$ 10 mm(H) by $\pm$ 6 mm(V). The total number of measurement points for each BPM head is 21×13. The present analysis, however, uses only 25 data, which are sampled within the same area by 5 and 3 mm steps in the horizontal and vertical directions, respectively. The number of unknown parameters is 78 whereas that of the data is 100.

Table I shows an example of fitting results. In the analysis all the data are divided by a common factor so that V_{ij} and q_j are close to unity. The coordinates of the wire position are fixed on the reference frame of each BPM head, and the wire is set at the reference center at j=13 in Table I. We can, therefore, estimate displacements of the geometric center from the reference axis by reading X_{13} and Y_{13}.

Fig.2 displays the estimated gain g_2 of all circular BPMs of 94mm in diameter. Fig.3 shows the displacement of the geometric center from the reference axis of the BPM head. Systematic displacements of the center are explained by the fact that some heads have had their reference frames trimmed two times. The rms difference between the output and the expected output from the estimated parameters,

$$\sqrt{\sum_{i,j} (V_{ij} - g_i q_j F_i(X_j, Y_j))^2 / 4m},$$

Table 1: An example of data analysis
[A:LER001.data/Fri-20/Sep/1996@16:37]

g_1	g_2	g_3	g_4
1	.962	.970	.952
j	q_j	X_j(mm)	Y_j(mm)
1	.992	10.120	5.917
2	1.000	10.115	2.971
3	1.006	10.100	-.004
4	.999	10.123	-2.991
5	.994	10.168	-5.995
6	1.010	5.136	6.033
7	1.019	5.096	2.999
8	1.025	5.127	-.015
9	1.017	5.123	-3.025
10	1.018	5.118	-6.030
11	1.016	.099	5.981
12	1.027	.055	3.030
13	1.030	.107	.006
14	1.027	.074	-3.016
15	1.027	.105	-6.017
16	1.012	-4.929	5.997
17	1.022	-4.956	3.027
18	1.025	-4.942	.014
19	1.021	-4.967	-3.003
20	1.021	-4.921	-6.018
21	.995	-9.983	5.968
22	1.004	-9.941	3.017
23	1.005	-9.951	.046
24	1.004	-9.979	-2.959
25	1.001	-9.978	-5.990

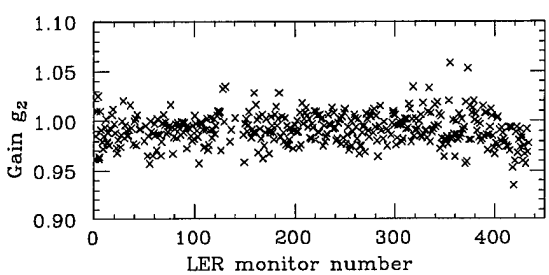

Figure 2: Estimated g_2 of all LER arc BPMs.

is summarized in Fig.4.

The rms difference, which is introduced by imperfection of the model and measurement errors, is satisfactorily small. This fact demonstrates validity of the present model and reliability of the calibration system. By analyzing the covariant matrix associated with a least square fitting we can know confidence limits of estimated parameters. Assuming that the measurement error is at most a typical rms difference of 4×10^{-4}, typical confidence limits of g_i, q_j, X_j and Y_j would be 1×10^{-3}, 5×10^{-4}, 17 μm and 11 μm, respectively.

To find X_j and Y_j we have used only ideal response functions, but have not used any information of the absolute wire positions on the calibration bed. It is, therefore, a good examination for verifying the scale of the model response function to compare the estimated wire positions and the calibrated ones. After subtracting the displacement of the geometric center, we found that the rms difference between the two sets of positions was as small as 34 μm

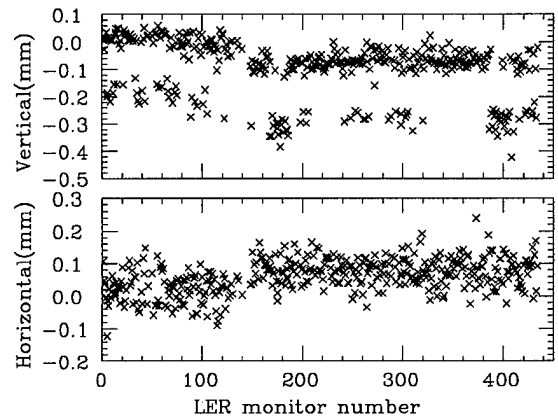

Figure 3: Displacements of the geometric center in the horizontal and vertical directions.

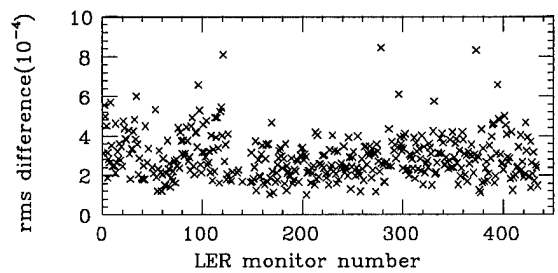

Figure 4: The rms difference of all LER arc BPMs.

for the case in Table I.

Finally we close the paper with adding a comment to the geometric monitor center. In beam operations the signals from each BPM head must travel through cables, connectors, switches and so on, before reaching detectors. It is afraid that initial and long-term variations of performance of these elements break the balance of the output of each head and make its electric center wander. Fortunately enough, however, we can apply eq.(6) also to signals measured at detectors, and can expect that the performance variations contribute only to changing the gains. This observation leads an idea that the overall gains at detectors can be estimated by changing beam orbits as in the wire calibration method. We are now in a position to emphasize that the geometic center defined here is stable with respect to the reference frame of each head, and that the center position can be searched by re-calibration with beams [1].

5 REFERENCES

[1] K. Satoh and M. Tejima, Recalibration of position monitors with beams, Proceedings of 1995 Particle Accelerator Conference, Dallas, Texas.

COMPARISON OF BEAM-POSITION-TRANSFER FUNCTIONS USING CIRCULAR BEAM-POSITION MONITORS *

J. D. Gilpatrick
Los Alamos National Laboratory, Los Alamos, NM, 87545, USA

Abstract
A cylindrical beam-position monitor (BPM) used in many accelerator facilities has four electrodes on which beam-image currents induce bunched-beam signals. These probe-electrode signals are geometrically configured to provide beam-position information about two orthogonal axes. An electronic processor performs a mathematical transfer function (TF) on these BPM-electrode signals to produce output signals whose time-varying amplitude is proportional to the beam's vertical and horizontal position. This paper will compare various beam-position TFs using both pencil beams and will further discuss how diffuse beams interact with some of these TFs.

1 BPM SENSITIVITY

BPMs typically have four electrodes on which beam image currents induce bunched-beam signals. These probe signals are initially processed or naturally configured to provide information about the horizontal and vertical axes that describes the beam's position. BPMs may have a variety of cross-sectional shapes, such as circular, rectangular, elliptical, etc. For the circular-cross-section BPM detecting thin beams, sufficient beam position information is contained within $R_{\bar{y}}$. Specifically,

$$R_y = |I_T|/|I_B| \tag{1}$$

where I_T and I_B are the top and bottom BPM-electrode signal amplitudes. I_T and I_B are defined as

$$I_T = \frac{\hat{i}_0}{2\pi R_p}\left[\frac{\theta_0 \mathrm{I}_0\left(g\frac{r_0}{R_p}\right)}{\mathrm{I}_0(g)} + \sum_{m=1}^{\infty}\frac{4\mathrm{I}_m\left(g\frac{r_0}{R_p}\right)}{m\mathrm{I}_m(g)}\sin\left(\frac{m\theta_0}{2}\right)\cos(m\phi_0)\right], \tag{2}$$

and

$$I_B = \frac{\hat{i}_0}{2\pi R_p}\left[\frac{\theta_0 \mathrm{I}_0\left(g\frac{r_0}{R_p}\right)}{\mathrm{I}_0(g)} + \sum_{m=1}^{\infty}\frac{4\mathrm{I}_m\left(g\frac{r_0}{R_p}\right)}{m\mathrm{I}_m(g)}\sin\left(m\left(\pi+\frac{\theta_0}{2}\right)\right)\cos(m\phi_0)\right], \tag{3}$$

where $\hat{i}_0$ is the Fourier component of the beam current, θ_0 is the electrode subtended angle, and r_0 and ϕ_0 are the polar coordinates of the beam position, and R_p is the BPM-probe-electrode radius[1]. The functions I_0 and I_m are the zeroth and mth order-modified-Bessel functions, respectively[1,2]. The term "g" includes the effects of the relative beam velocity, β, and is calculated to be

$$g = 2\pi R_p/\beta\gamma\lambda \tag{4}$$

where γ is the Lorentz factor, $\gamma = \left(1-\beta^2\right)^{-1/2}$.

References 3, 4, and 5 show that Eq. (1) may be described with the less complicated 2-D polynomial equation

$$R_{\bar{y}} = y_0 + S_y\bar{y} + S_{y^3}\bar{y}^3 + S_{yx^2}\bar{y}\bar{x}^2 \tag{5}$$

where y_0 and S_y is the manufactured probe offset and sensitivity, S_{y^3} and S_{yx^2} are third-order nonlinear coefficients, and $\bar{x}$ and $\bar{y}$ is the horizontal and vertical beam position[3,4,5]. While the original equation does not have an analytically expressible inverse function, Eq. (5) does by performing a least-squares inverse fit to the original equation or set of measured BPM data. The resulting equation from this inverse fit procedure may be written as a function of $R_{\bar{x}}$ and $R_{\bar{y}}$.

2 PROCESSOR TRANSFER FUNCTIONS

The electronic BPM processor performs a mathematical TF using the four BPM signals to produce output signals whose time-varying values are proportional to the beam's horizontal and vertical position. Mathematically, a position-processor's TF accepts $R_{\bar{y}}$ as an input and its output signal must be proportional to the beam position. However, in practice, the two output signals from the probe's opposite electrodes are cabled to two processor-input connectors.

To be an effective position measurement TF, the mathematical functions describing the combined BPM and processor TF have several characteristics. First, the effective combined TF output signal, V_{Proc}, must satisfy the odd symmetry equation of

$$V_{Proc}(\bar{y}) = f(\bar{y}) = -f(-\bar{y}) \tag{6}$$

where f is a particular mathematical function. Note that if the beam is centered (i.e., $\bar{y}=0$), then the processor's output signal is zero. Eq. (5) may also be expressed as a function of $R_{\bar{y}}[dB]$ as

$$V_{Proc}\left(R_y[dB]\right) = f\left(R_y[dB]\right) = -f\left(-R_y[dB]\right), \tag{7}$$

* Work supported by the US Department of Energy

where $R_y[dB] = 20\log(R_y)$, therefore, fulfilling the odd symmetry criterion.

Second, it is preferred, but not necessary, that the combined BPM and processor TF be linear or very nearly linear. If this combined function is highly non-linear, then the sensitivity or gain will vary with beam position and either the range or the precision of the overall position measurement will be adversely affected.

Third, it is preferred, but not necessary, that the combined BPM and processor TF have a single-variable analytically expressible inverse function. The existence of an analytic inverse function allows an accelerator control system to easily recalculate the beam position from the processors output signal amplitude. If the TF has an inverse function that is not analytically expressible with specific variables (e.g., R_x and R_y), the control system may still translate the processors output signal into a beam position by using look-up tables stored in the accelerator-control system's memory. However, to meet the required measurement resolution, these look-up tables are often very large.

There are many hardware-realizable mathematical functions for a beam position processor. Some of the more common functions are the difference over sum (Δ/Σ), arctan (AT), log ratio (LR), and normalized power difference (NPD) functions[6]. The forward and analytically expressible inverse TFs for each of these mathematical functions are shown in Table 1. $K_{\Delta/\Sigma}$, K_{AT}, K_{LR}, and K_{NPD} are the processor TF sensitivity or gain constants. Note that for centered beams, the AT function reduces to the Δ/Σ function[7].

Table 1: Processor transfer functions

	Forward TF $V_{Proc}[v] =$	Analytic Inverse TF $R_y[dB] =$
Δ/Σ	$K_{\Delta/\Sigma}\dfrac{R_y - 1}{R_y + 1}$	$20\log\left(\dfrac{K_{\Delta/\Sigma} + V_{Proc}}{K_{\Delta/\Sigma} - V_{Proc}}\right)$
AT	$K_{AT}\left[\tan^{-1}(R_y) - \dfrac{\pi}{4}\right]$	$20\log\left[\tan\left(\dfrac{V_{Proc}}{K_{AT}} + \dfrac{\pi}{4}\right)\right]$
LR	$K_{LR}\log(R_y)$	$20\dfrac{V_{Proc}}{K_{LR}}$
NPD	$K_{NPD}(R_y - R_y^{-1})$	Does Not Exist

3 FUNCTION COMPARISON

Fig. 1 displays the combined BPM and processor TFs using a linear BPM response whose sensitivity is 1.11 mm^{-1} or 0.87 dB/mm. This linear BPM position response allows for a true and direct comparison of the individual processor TFs. Under centered beam conditions, the "K" sensitivity constants were normalized, resulting in processor TFs sensitivities $K_{\Delta/\Sigma}$, K_{AT}, K_{LR}, and K_{NPD} equaling 17.4-, 17.4-, 20-, 4.3-v, respectively. The LR function has a slightly larger gain constant than the Δ/Σ and AT function and the NPD's gain constant is significantly smaller. However, having a low gain constant is not advantageous if the function is highly nonlinear.

As displayed in Fig. 2, the Δ/Σ processor TF is the only function whose sensitivity is linear with beam position. The AT function is the least non-linear function and the only nonlinear function whose sensitivity reduces with increased displacement from the BPM's center. The NPD function is highly non-linear. This non-linearity either will limit the processor's bandwidth from beam-position-dependent gain switching, will have too large of a digital word for control system digitizers, or will provide inadequate beam position resolution for centered-beam conditions.

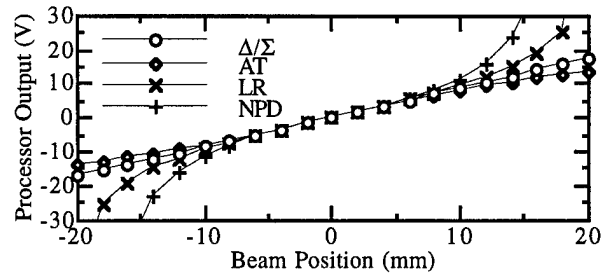

Figure 1. Processor output signal versus beam position for Δ/Σ, AT, LR, and NPD transfer functions. A linear 0.87-dB/mm BPM response was used and all processors were normalized to have the same centered beam response.

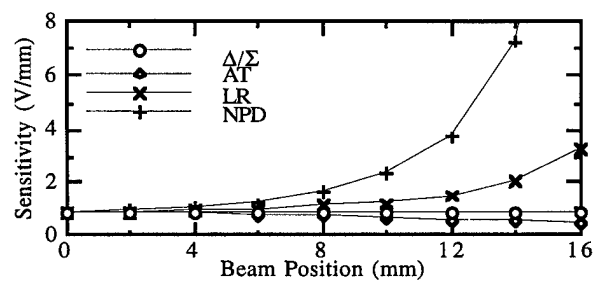

Figure 2. Combined sensitivities versus beam position for Δ/Σ, AT, LR, and NPD processor transfer functions using a linear 0.87-dB/mm-sensitivity BPM.

The cylindrical-geometry BPM changes the combined BPM and processor TF. Fig. 3 shows the processor TFs' sensitivities for a 6.7-MeV proton beam drifting through a BPM described by Eq. (1) with θ_0 and R_p equal to 45° and 25 mm, respectively. This particular BPM's sensitivity is 1.6 dB/mm. The added nonlinear position sensitivity of the BPM changes the shape of the combined position-sensitivity response. All of the TFs are nonlinear and the LR function is the least nonlinear. Both the AT and Δ/Σ position sensitivities approach zero as the beam displacement from the BPM's center is increased. Finally note that the NPD function continues to be highly nonlinear.

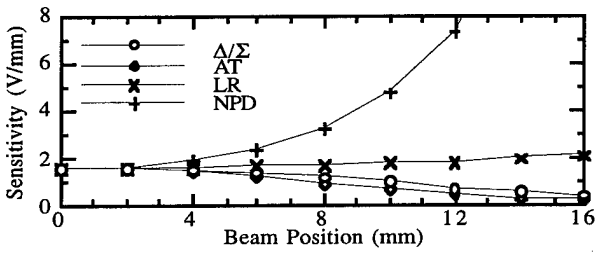

Figure 3. Combined sensitivities versus beam position for Δ/Σ, AT, LR, and NPD processor transfer functions using a cylindrical 1.6-dB/mm-sensitive BPM.

4 BPM RESPONSE TO DIFFUSE BEAMS

The calculation of a BPM's sensitivity, Eqs. (1), (2), and (3) assume the beam rms width is a significant portion of the BPM electrode radius, R_p. In most applications, this thin-beam assumption is adequate. However, in some low energy linacs, it is necessary to keep the beam pipe radius small. Because the particle beam has a finite size, the resultant beam-pipe radius to rms beam width ratio can be approximately 7:1. If the beam widths are sufficiently wide and these pipe-to-beam-width ratios are sufficient small, the BPM's position sensitivity diverges from the nominal thin-beam position sensitivity. This diffuse beam effect was experimentally observed in Fig. 6 of Reference 1.

To initially explore these diffuse-beam effects, the BPM electrode currents, as defined in Eqs. (2) and (3), were redefined as diffuse beams using a superposition of multiple thin beamlets whose beam currents were distributed in a two-dimensional gaussian distribution. Eq. (2) then becomes

$$I_T = \sum_{n=-3\sigma}^{+3\sigma} \sum_{m=-3\sigma}^{+3\sigma} \hat{I}_T a_n b_m \, e^{\frac{-(x_n^2-\bar{x}^2)}{2\sigma^2}} \, e^{\frac{-(y_m^2-\bar{y}^2)}{2\sigma^2}} , \qquad (8)$$

where $\hat{I}_T$ is the original top electrode current as defined in Eq. (2), σ is the round-beam rms width, and a_n and b_m are normalization constants. A similar equation was redefined for Eq. (3). The width for each of the bins in the diffuse beam distribution was $1\,\sigma$. Fig. 4 displays the diffuse-beam effects to a BPM sensitivity using two rms beam widths of 2.85 mm and 0.01 mm and BPM electrode θ_0 and R_p of 45° and 7 mm, respectively. For the 2.85-mm diffuse beam, the BPM position sensitivity increases more than the thin-beam BPM sensitivity as the beam displacement from the BPM center is increased. However, beam pipe radius to rms beam-width ratios of 3:1, as shown in this example, are rare. Further calculations have shown that the sum of beam displacement and rms beam width must be greater than approximately 65 % of the BPM electrode radius for the BPM's response to significantly diverge from a BPM's thin-beam response.

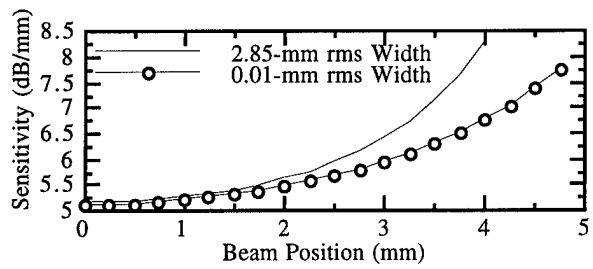

Figure 4. Diffuse- and thin-beam BPM sensitivity versus beam displacement from a BPM center. The BPM's radius and subtended angle were 7.0 mm and 45°, respectively.

5 CONCLUSION

All of the combined circular-cross-section BPM and processor TFs described in this note have odd symmetry and are nonlinear. The LR function is the least nonlinear, and therefore, the optimum choice. All of the processor functions have a single-value analytically expressible inverse function except for the normalized power-difference function. Finally, displaced diffuse-beam effects to BPM sensitivities were initially explored. It has been observed that sum of the rms beam width and displacement from BPM center must be >65% of the BPM radius for the diffuse beam effects to be significant.

REFERENCES

[1] J. D. Gilpatrick, et. al., "Experience with the Ground Test Accelerator Beam-Measurement Instrumentation," (AIP Conference Proceedings 319), Beam Instrumentation Workshop, pp. 154-169, 1993.

[2] J. H. Cuperous, et. al., "Monitoring of Particle beam sat High Frequencies," **NIM**, 145, pp. 219-231, 1977.

[3] J. Power, et. al., "Characteristics of Beam Position Monitors in Two-Dimensions," 1992 Linear Accelerator Conference Proceedings, Ottawa, August 1992, pp.362-364.

[4] John D. Gilpatrick and Tom Hardek, "Known Problems and Solutions of the RI Beam Position Measurement Systems," AOT-1 Technical Note No. 95-98, May 10, 1995.

[5] J. D. Gilpatrick, Derivation of the LANSCE BPM Nonlinear Beam Position Response," AOT Division Technical Note, LA-CP-97-21, February 13, 1997.

[6] R. E. Shafer, "Beam Position Monitoring," (AIP Conference Proceedings 212), Beam Instrumentation Workshop, pp. 27-58, 1989.

[7] J. D. Gilpatrick, "Phase and Synchronous Detector Theory as Applied to Beam Position and Intensity Measurements," 1995 IEEE Particle Accelerator Conference and International Conference on High-Energy Accelerators, pp.2563-2565.

THE LEDA BEAM-POSITION MEASUREMENT SYSTEM*

C. R. Rose, J. D. Gilpatrick, and M. W. Stettler
Los Alamos National Laboratory, Los Alamos, NM 87545

Abstract

This paper describes the beam-position measurement system being developed for the Low Energy Demonstration Accelerator (LEDA) and the Accelerator Production of Tritium (APT) projects at Los Alamos National Laboratory. The system consists of a beam-position monitor (BPM) probe, cabling, down-converter module, position/intensity module, on-line error-correction system, and the necessary control system interfaces. The modules are built on the VXI-interface standard and are capable of duplex data transfer with the control system. Some of the key, system parameters are: position-measurement bandwidth of at least 180 kHz, the ability to measure beam intensity, a beam-position measurement accuracy of less than 1.25 percent of the bore radius, a beam-current dynamic range of 46 dB, a total system dynamic range in excess of 75 dB, and built-in on-line digital-system-error correction.

1 INTRODUCTION

A key part of the APT project is to demonstrate the technical feasibility of the front end of the accelerator. This proof-of-concept machine, called the Low Energy Demonstration Accelerator (LEDA), will operate in both pulsed and cw modes using a 100-mA proton injector, a 6.7-MeV RFQ, a high-energy-beam-transport (HEBT), and a beamstop. This paper describes the beam-position measurement system being designed for the LEDA experiment keeping in mind that the measurement system implemented for LEDA will likely need to be scaled to accommodate a much larger APT facility [1].

Some of the important technical requirements of the LEDA beam-measurement system are shown in Table 1.

Table 1: LEDA Beam-Position Requirements.

Item	Value	Units
Beam Frequency	350.0	MHz
Beam current range	0.5-100	mA
Beam Dynamic range	46	dB
Max. signal dynamic range	75	dB
Req'd # of 20.5 mm diameter probes (1")	1	each
Req'd # of 47.5 mm diameter probes (2")	3	each
Req'd # of 175.3 mm diameter probes (6.9")	1	each
Sensitivity, 20.5 mm probe (at center)	3.38	dB/mm
Sensitivity, of 47.5 mm probe (at center)	1.63	dB/mm
Sensitivity, 175.3 mm diameter probe (at center)	4.22	dB/mm
Measurement Accuracy, each probe (≤ 50% of radius)	≤ 1.25%	of radius
Measurement Accuracy, 20.5 mm probe (≤ 50% of radius)	≤ ±0.13	mm
Measurement Accuracy, 47.5 mm probe (≤ 50% of radius)	≤ ±0.30	mm
Measurement Accuracy, 175.3 mm probe (≤ 50% of radius)	≤ ±1.1	mm
Measurement Resolution (≤ 50% of radius)	≤ 0.2%	of radius
Processing Intermediate Frequency (IF)	2.00	MHz
Position-Measurement bandwidth	≥ 180	kHz

The beam-position-monitor (BPM) probes have inside diameters ranging from 20.5 to 175.3 mm and are the four-lobe type. Image currents from the beam induce voltages on the four lobes proportional to beam position with respect to the lobes and beam intensity.

An additional requirement of the system is to employ real-time error correction to compensate for cable mismatches, probe variations, and processing-electronics offset and gain non-linearities.

There are several common implementations of beam-position-measurement systems: amplitude-to-phase, difference-over-sum, and log ratio [2]. The chosen system uses log ratio. One advantage of the log-ratio transfer function is its improved sensitivity and linearity over that of the other methods. Its main drawback is logarithmic ripple errors in the log amplifiers because they don't strictly follow a true log-transfer function.

Each beam-position measurement system consists of a probe (three probe diameters will be used in LEDA), cabling, a down-converter module, and a position/intensity module. The Error-Correction Reference Chassis provides reference/calibration signals

* Work supported by the US Department of Energy.

to the various systems. A block diagram of one beam-measurement system is shown in Fig. 1.

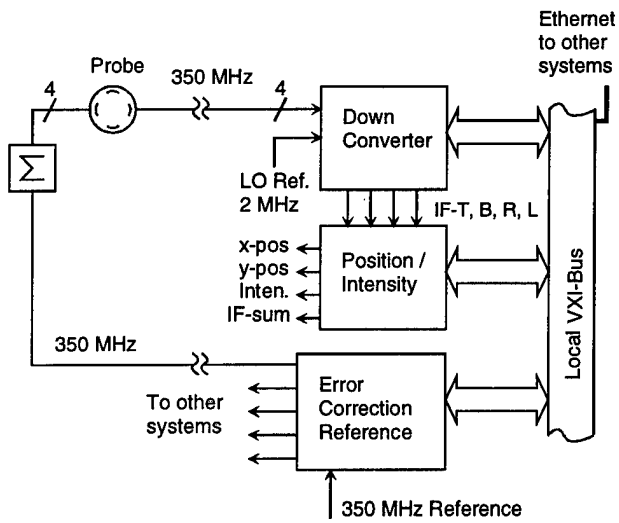

Fig. 1 Block diagram of one beam-position/intensity system.

Signals from each beam-line probe are fed to a down-converter module in which they are converted to an intermediate frequency (IF). These IF signals, labeled IF-T, B, R, and L in the figure, are then sent to the position/intensity module for beam-position and intensity processing. A 2-MHz local-oscillator reference signal is provided to each down-converter module to be used in deriving the 348 MHz. Digital data and control signals are fed to the modules via the VXI-bus. The error-correction reference chassis can accommodate up to six BPM systems. It provides 350-MHz error-correction signals to each system one at a time. An internal multiplexer in the chassis is used to select and switch the signals.

2 DOWN-CONVERTER MODULE

The down-converter module is used to convert the 350-MHz rf signals down to the intermediate frequency (IF) of 2 MHz. It has four rf inputs, one LO reference input (2 MHz), and four IF outputs. Some of its requirements are listed in Table 2.

Table 2: Down-Converter Requirements.

Item	Value	Units
RF input frequency	350	MHz
IF output frequency	2.00	MHz
# of rf inputs	4	each
Input Impedance	50	Ω
Input VSWR	≤ 1.2:1	
# of IF outputs	4	each
LO reference frequency	2.00	MHz
Max. rf input power	0	dBm
Max. IF output power (P_{1dB})	15	dBm
Channel Insertion Gain	15	dB
Max. noise figure	16	dB
Dynamic range	≥ 75	dB
Channel-to-channel amplitude tracking error	≤ 0.5	dB
Channel-to-channel phase tracking error	≤ 3	deg.

3 POSITION / INTENSITY MODULE

The position/intensity module processes the IF signals according to the log-ratio transfer function. This processing technique is explained in detail in several papers including reference [3]. The module uses AD606 logarithmic-amplifiers with usable dynamic range exceeding 80 dB at the 2-MHz IF. Some of the position/intensity module's requirements are listed in Table 3.

Table 3: Position/Intensity Module Requirements.

Item	Value	Units
Number of IF inputs	4	each
Input Impedance	50	Ω
Number of measurement axes	2	each
Range, x-, y-axis (into 1 MΩ)	± 10	V
Range, intensity (into 1 MΩ)	0-10	V
Max. input power	15	dBm
Digitizer Resolution	12	bits

Additionally, this module incorporates digital error-correction circuitry to compensate for non-linearities in the system such as from the cabling, probe effects, and the processing electronics. This module is described in detail in reference [4].

4 ERROR-CORRECTION SUBSYSTEM

The design of the entire beam-position measurement system is built around the central requirement of using real-time error correction. The log-ratio technique provides a good foundation for such a system and was one of the main reasons for its selection. The error-correction process is implemented in the following fashion. The slot-zero controller in the VXI chassis selects the BPM system to correct. It does this by selecting the desired Position/Intensity module. It then addresses the Error-Correction Reference Chassis and outputs a known power level to the pre-selected measurement system. When the cable attenuation, the splitter losses, and the probe parameters are already known and accounted for, the actual power at the input of the down-converter module can be calculated based on the known output power level from the Error-

Correction Reference Chassis. The selected channels on the Position/Intensity module are then read by the control system and compared with the expected value based on known system parameters. The error is then subtracted from the ideal to obtain a corrected value. This error-correction process begins at the largest input-power level and proceeds in 1-dB steps to the lowest expected level. In doing so, an 12-bit array is constructed of expected values and actual values. A linear interpolation routine fills in the corrected table values between the 1-dB sampled steps. Once the tables are computed, the slot-zero controller uploads the correct lookup table values to RAM lookup tables in the selected Position/Intensity module. The process is the same for each of the measurement systems.

After these lookup tables are computed and uploaded to the respective modules, then in real-time, 12-bit sampled data from the log amps in each module is corrected before the algebraic difference is taken. It should be noted that the generation of reference signals, recording these data, and computing the LUT values does not occur in real time.

5 CONCLUSIONS

The beam-position measurement system has been fully specified and work begun on each of the subsystems or modules.

REFERENCES

[1] Gilpatrick, J. D., et. al., "LEDA and APT Beam Diagnostics Instrumentation," IEEE 1997 Particle Accelerator Conference, Vancouver, B. C., Canada.

[2] Gilpatrick, J. D., et. al., "Comparison of Beam-Position-Transfer Functions using Circular Beam-Position Monitors," IEEE 1997 Particle Accelerator Conference, Vancouver, B. C., Canada.

[3] Aiello, G. R., and M. R. Mills, "Log-Ratio Technique for Beam Position Monitor Systems," Nuclear Instruments and Methods in Physics Research, 1994.

[4] Rose, C. R., and M. W. Stettler, "Description and Operation of the LEDA Beam-Position Measurement Module," IEEE 1997 Particle Accelerator Conference, Vancouver, B. C., Canada.

ORBIT MEASUREMENT AND CORRECTION IN THE LNLS SYNCHROTRON LIGHT SOURCE

R.H.A. Farias, L.C. Jahnel, Liu Lin, D. Macedo, F.S. Rafael, A.R.D. Rodrigues and P.F. Tavares

Laboratório Nacional de Luz Síncrotron - LNLS/CNPq
Caixa Postal 6192 - 13081-970 Campinas - SP - Brazil.

Abstract

The orbit measurement and correction system of the LNLS synchrotron light source is presented. Measurements of the correction matrix, orbit stability and reproducibility are presented and discussed.

1 INTRODUCTION

The LNLS Synchrotron Light Source consists of the 1.37 GeV electron storage ring UVX and a 120 MeV injector LINAC. Commissioning of the ring started in May 1996 and users have had access to the machine since November 1996. It became clear from the early stages of beam line commissioning that orbit reproducibility from fill to fill as well as orbit stability over long periods (several hours) are critical performance figures of the light source from the user's point of view. In this report, we describe the main parts of the correction system, including the BPM's and their calibration procedures, the control system facilities for orbit measurement and manipulation and present results of measurements of orbit stability and reproducibility.

2 HARDWARE

The UVX storage ring has 24 beam position monitors (striplines) distributed along its six superperiods. The stripline signals are read by 6 commercial electronic readout modules (manufactured by BERGOZ, France). Since there is only one read-out module per superperiod, each module must read four different BPM's. This is accomplished by multiplexing those signals via a computer controlled RF switch-board, which allows the four monitors to be read in any order set by the high level control system. The total time for a complete scan of all four BPMS in a superperiod is dominated by the time needed by the RF switches to stabilise their output signal and it is 400 ms.

The BPM's were calibrated in a characterisation bench with a stretched wire to simulate the beam. A 476 MHz signal was applied to the stretched wire and the signals induced in the stripline were measured with a spectrum analyser. The bench was computer controlled so that the wire could be moved automatically in order to obtain a two dimensional map of the response of the striplines to the excitation by the wire. The resulting data were used to derive an offset of the electrical centre of the monitors with respect to the geometrical centre and a gain factor. The offset and gain for each BPM characterise the geometry of the BPM as far as the linear response to beam position is concerned.

An off-set and gain were also determined for the BPM electronics (in fact, this offset and gain includes the effects not only of the electronics, but also of the cables, RF switches and connectors). The offset was determined with a calibrated four-way splitter fed by a 476 MHz signal and connected to the same cables, RF switches, connectors that take signals from the BPM's to their electronics (this measurement takes place in the machine). The measured dc voltages (horizontal and vertical) at the output of the BPM electronics give directly the off-set. The gain was determined by adding attenuators to two of the output ports of the four-way splitter and again measuring the voltages delivered by the BPM electronics. The calibration parameters for each BPM (geometrical) as well as those of the BPM electronics were organised in databases for the control system allowing the conversion of the voltages read by the control system to beam position in mm.

The BPM absolute accuracy is determined by the alignment procedure and is better than 0.2 mm. The BPM resolution is determined by the electronic noise and by the resolution of the AD converters used to read the BPM output voltages. The noise level in the electronics has been measured prior to installation with an RF generator substituting the beam and, without any averaging, was found to be $\pm$ 4 μm (at an equivalent beam intensity of about 5 mA). The resolution of the AD converters is $\pm$ 8 μm. The overall resolution can be reduced to $\pm$2 μm by averaging the signal over 10 seconds.

The orbit correctors are 10 cm long C-type (vertical) and H-type (horizontal) magnets. There are 11 vertical and 18 horizontal correctors. They are capable of producing up to 70 gauss.m of integrated field, corresponding to 1.5 mrad deflection at 1.37 GeV.

3 SOFTWARE

It is possible to observe and store orbits as well as to perform simple arithmetic with stored orbits and newly acquired data. The acquisition cycle is fast enough that on-line observation of the orbits is possible and has proved useful in commissioning the energy ramp.

Orbit correction can be performed via three different methods: matrix, best correctors and harmonic. In all

0-7803-4376-X/98 /$10.00 © 1998 IEEE

methods, specific corrector and monitors can be excluded from the correction procedure by pointing and clicking, e.g., in order to eliminate known erroneous data. The proposed corrections may be examined before implementation in the machine and it is possible to implement a fraction of the correction. All calculations are performed in a remote Unix workstation where a model of the machine optics may be established either from the quadrupole and sextupole strengths as implemented in the machine (and derived from the measured excitation curves of the storage ring magnets) or by fitting the quadrupole strengths to the measured machine tunes. Both models are found to work equally well at the operating energy (1.37 GeV), but at injection energy it is mandatory to use the fitted model to get efficient correction. This is due to remnant field effects which make the quadrupole calibration curves less reliable at low energies as well as the spread between calibration curves of different quadrupoles connected to the same power supply larger.

During commissioning (and even in some user shifts) we often had the need to produce localised orbit bumps, eg. in order to look for vacuum chamber obstructions or produce special conditions for a beam line with minimal disturbance to the others. This can be accomplished easily once an optical model has been generated for the machine via a point and click interface.

4 MEASUREMENT RESULTS

4.1 Correction Matrix

In various correction methods one needs to know the *correction matrix* that relates changes in corrector strengths to changes in beam position within linear approximation. Figure 1 shows a comparison between calculated (from a fitted model of the machine optics) and measured correction matrix elements for two different horizontal correctors. The calculation is performed according to the well-known formula

$$x(s) = \frac{\sqrt{\beta(s)\beta(0)}}{2\sin(\pi\upsilon)}\cos(\varphi(s) - \varphi(0) - \pi\nu) \qquad (1)$$

One of the correctors (ACH04) is located in a dispersive straight section while the other (ACH01A) is located in a non-dispersive straight section. The discrepancies between theory and experiment may be ascribed partly to non-linearities in BPM response (for the larger orbit deviations, such as in BPM's AMP07A and AMP07B for corrector ACH01A) and partly to the fact that orbit perturbations produce energy changes which result in the addition of a periodic perturbation to the closed orbit proportional to the dispersion function and to the magnitude of the energy change. This can be more easily seen in the implementation of horizontal localized bumps and will be discussed further below. Note however in figure 2 that the difference between theory and experiment closely resembles the machine dispersion function (being non-zero in even, i.e., dispersive sections) for corrector ACH04, except in section 9 where the orbit distortion is largest and the non-linearity effects are correspondingly more important. The inclusion of the energy change correction to the correction matrix elements was found to be essential to correct the horizontal orbit when the average uncorrected orbit is different from zero. Although this can in principle be dealt with by changing the RF frequency, in the particular case of the LNLS machine there is an appreciable change of the dipole magnets effective length as the energy is ramped, and the ability to correct orbits with non-zero average is needed in order to avoid changing the RF frequency during the ramp.

4.2 Orbit correction and reproducibility

We have found it necessary to apply the correction procedure iteratively (often beginning with a few iterations of the best correctors method and then turning to the matrix method as the orbit distortion gets smaller). The horizontal rms orbit deviation is reduced from 2 to 0.3 mm whereas the vertical rms orbit deviation is reduced from 2 to 0.4 mm (Figure 3).

More important than the orbit itself however, is the ability to reobtain the same orbit after each injection and energy ramping cycle. Figure 4 shows that simply ramping to a previously corrected configuration reproduces the orbit to within about 0.8 mm. We have therefore adopted the strategy of correcting the orbit towards a *standard* orbit previously considered as the best possible orbit we can get and with respect to which users align their beam lines. We have found (Figure 4) that we can reobtain this same orbit to within ± 60 μm at every injection by recorrecting the orbit before delivering the beam to users.

4.3 Orbit stability

The stability of the orbit has been analysed in two different temporal regimes: fast (few second) orbit fluctuations and long term (several hours) orbit drifts. Fast fluctuations are compatible with the BPM resolution.

Long term drifts (particularly of the vertical orbit) have been correlated to drifts in magnet temperatures, which has led us to include a temperature stabilisation system for the cooling water of the main ring magnets. Although this has decreased the orbit drift, we have found it necessary to implement an automatic orbit correction system that periodically (every few minutes) recorrects the orbit. With this system on, the vertical orbit is kept to within ± 30 μm of the initial orbit over 3-4 hours of a user run. Figure 5 shows the time evolution of the orbit envelope (maximum absolute orbit deviation along the machine) with the correction system on and off.

4.4 Orbit Manipulation

Figure 6 shows a measured localized horizontal bump as well as the calculated bump. The presence of *anti-bumps* in the dispersive sections of the lattice is a result of the change in energy of the beam due to the orbit distortion, as can be seen from the calculations that include this longitudinal-transverse coupling effect as well as the conventional orbit distortion formula above (Eq. 1).

5 CONCLUSIONS

The orbit measurement and correction system of the LNLS UVX electron storage ring has proved to be versatile during commissioning and up to specifications for user runs. Orbit reproducibility from fill to fill is better than 60 μm, long term orbit drifts can be kept below ± 30 μm by means of an automatic periodic correction. The effect of energy changes due to corrector kicks can be clearly seen in the correction matrix as well as in orbit bumps.

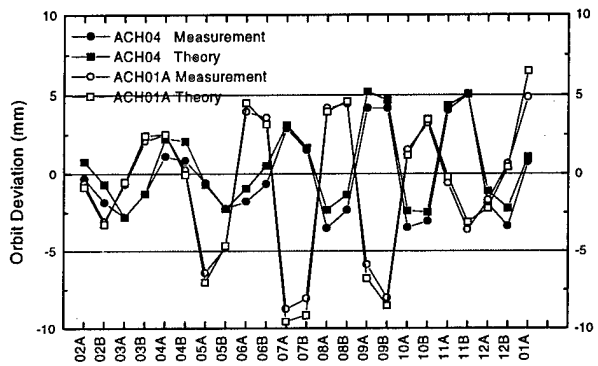

Figure 1: Calculated and measured orbit distortions for correctors located in non-dispersive (ACH01A) and dispersive (ACH04) straight sections.

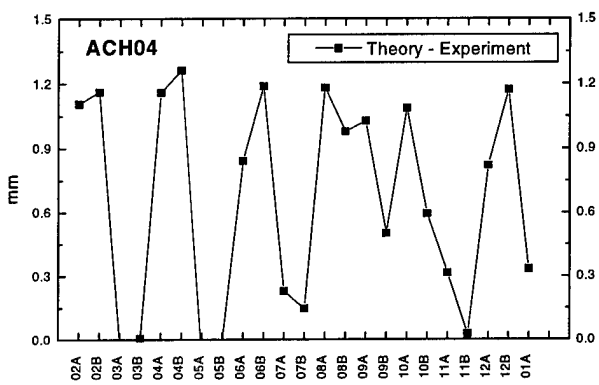

Figure 2: Difference between theoretical prediction and measurement for the orbit distortion produced by corrector magnet ACH04.

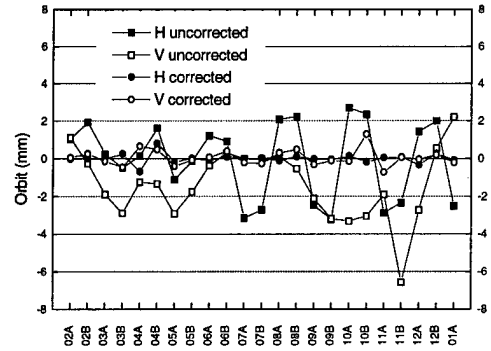

Figure 3: Uncorrected and corrected orbits at 1.37 GeV.

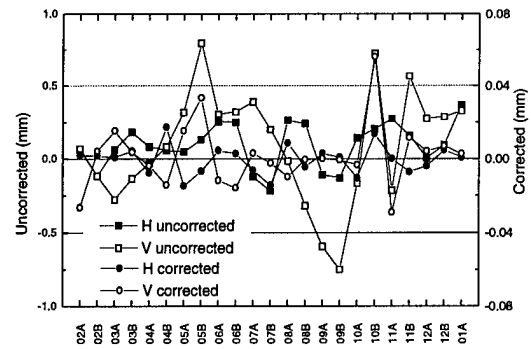

Figure 4: Orbit deviations with respect to the standard orbit. The *uncorrected* curves refer to the orbits obtained right after ramping to full energy.

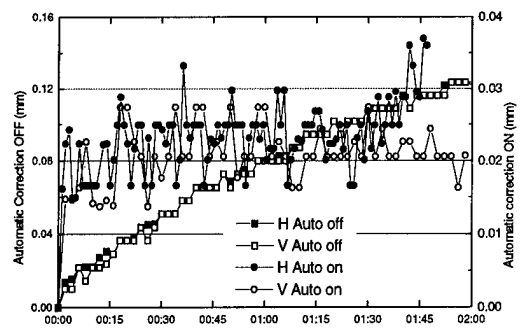

Figure 5: Variation of orbit envelopes as a function of time with the automatic correction system on and off.

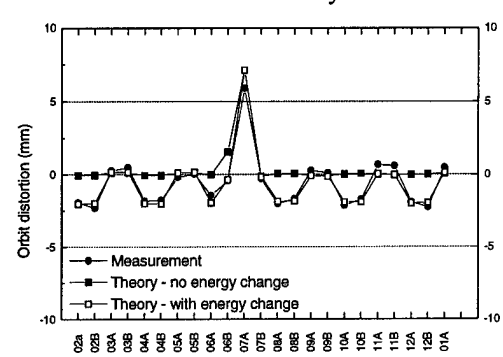

Figure 6: Measured and calculated horizontal localised orbit bumps. The calculations are done either with the correction matrix (Eq. 1) or with the inclusion of an energy change term.

REAL TIME DISPERSION MEASUREMENTS AT THE MIT BATES LINAC*

K. Jacobs, S. Bradley, A. Carter, B. McAllister,
C. Sibley, F. Wang
MIT-Bates Linear Accelerator Center

Abstract

The MIT-Bates Linear Accelerator Center comprises a 1GeV electron linac/recirculator system, beam lines to two main experimental halls, and a pulse stretcher/storage ring. Proper tuning of the beam requires the transverse dispersion to be zero, or some specified non-zero value, at all locations along the beam lines. Dispersion measurements are made by correlating beam positions measured by BPMs, with energy measurements made using a BPM in a region of known non-zero dispersion. Data are acquired continuously from the BPMs and displayed on a graphical user interface in real time. This allows the accelerator operators to set dispersion quadrupoles and sextupoles so that the first and second order position and angle dispersions have their correct values at all points along the beam line. Details of the system design and operation are presented.

1. INTRODUCTION

The proper setup of any beamline requires that a number of conditions be satisfied. These include making sure the beam is on the correct trajectory, that the focussing and optics are as desired, and that chromatic terms are set to the specified values. To help the accelerator operators efficiently set the elements affecting the transverse dispersion, we have implemented a system for making real-time dispersion measurements. The system consists of appropriately located beam position monitors, a data acquisition system, and a graphical user interface to display the data, analyze it, and display the results.

The following describes details of the implementation of the dispersion measuring system, along with operational results.

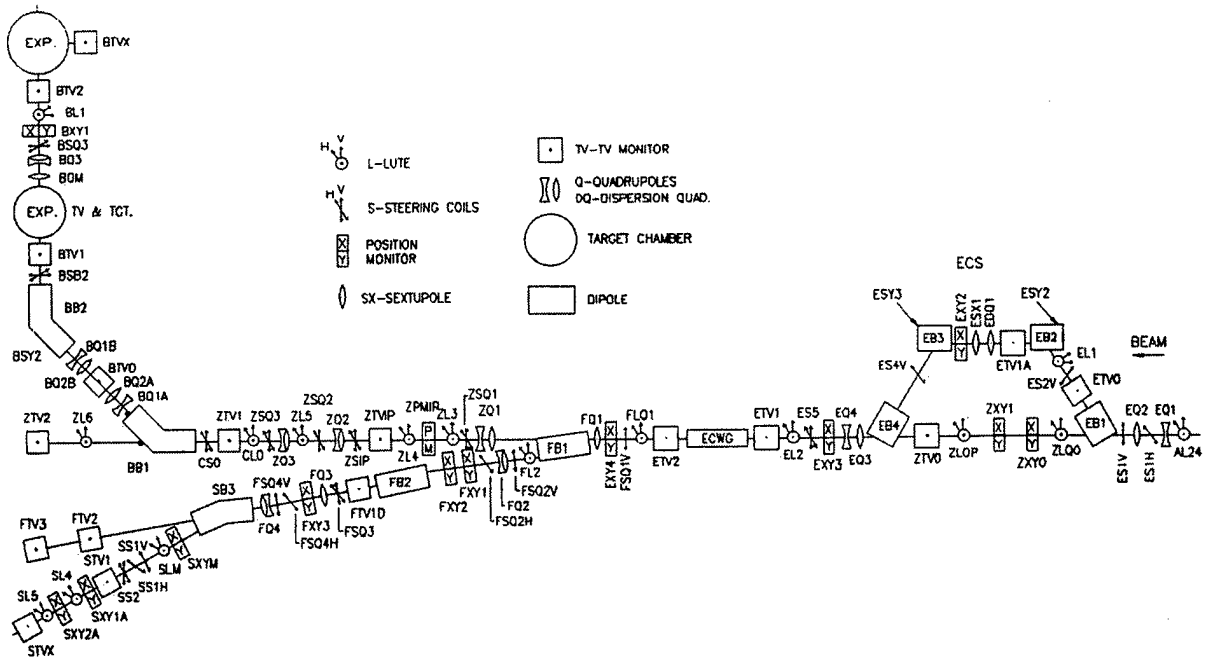

Fig. 1 Layout of the Bates beam switchyard showing the elements used to measure the dispersion

* Work supported by U.S. Department of Energy

2. SYSTEM DESCRIPTION

The key elements of the dispersion measuring system are several beam position monitors (BPMs), located in the beam switchyard. One of these monitors is located in a region of known dispersion, and is used to determine the deviation of the beam energy with respect to the nominal energy. Two additional BPMs are situated at or near the location where we wish to measure the dispersion. By measuring the beam position at these monitors, as a function of energy, we can determine how the beam position and angle vary with energy.

The layout of the Bates switchyard beamlines is shown in Figure 1. In the offset leg of the Energy Compression System (ECS) chicane, the horizontal dispersion x/δ = 33 mm/%. A BPM, designated EXY2, is situated in this position, and used for the energy determination. Other BPMs are placed at various locations in the switchyard, allowing us to measure the dispersion at these locations. For example, the BPMs designated EXY3 and EXY4, located just past the ECS chicane, allow us to measure the dispersion at that location.

In typical operation, the beam is delivered from the linac in 16 μs pulses. Data is acquired from the BPMs on a pulse-by-pulse basis, with a maximum acquisition rate of 4 Hz. The analog-to-digital converters for all the BPMs used in the measurement are read by the same Local Area Computer on the Bates control system. By monitoring the sequence number associated with the digitization process, it is possible to guarantee that all BPMs have acquired data during the same beam pulse. This removes the effects of pulse-to-pulse energy variations from the data analysis. The data is broadcast over the control system network, making it available at any computer on the network.

The dispersion measuring system is controlled from a graphical user interface, written in C, using X-windows and Motif, and run on DEC Ultrix workstations. When the program is first started, it prompts for the location at which the dispersion is to be measured, then sets the appropriate BPMs to the correct data acquisition mode, and begins acquiring data. At any time, the operator may request an analysis of the data. This involves fitting a parabola to the position data as a function of energy, and the angle data as a function of energy. The results are the first and second order dispersion elements, x/δ, x/δ^2, θ/δ, and θ/δ^2. Other program options include switching between measuring the dispersion in the horizontal and vertical dimensions, clearing the data and restarting acquisition, stopping data acquisition, restarting acquisition after stopping, making a hardcopy of the measurements and analysis, or exiting the program.

3. OPERATIONAL RESULTS

To make a dispersion measurement, the accelerator operator starts up the dispersion program. In order to accurately determine the dependence of the beam position or angle on the energy, it is necessary to scan the beam energy over some range, typically 0.5%.

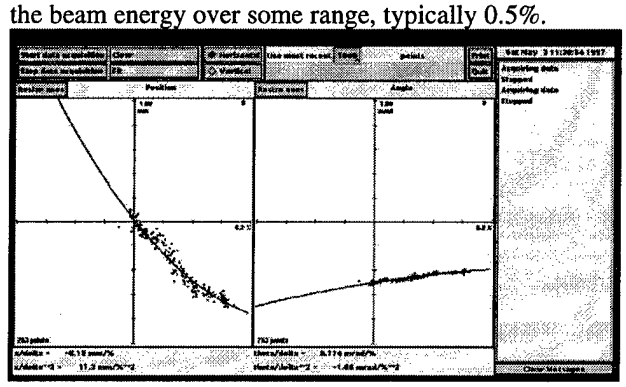

Fig. 2 Measured horizontal dispersion after the ECS chicane with the sextupole ESX1 set to -3.00 A

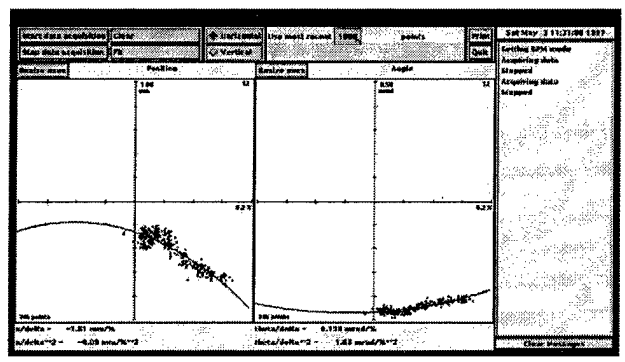

Fig. 3 Measured horizontal disperion after the ECS chicane with the sextupole ESX1 set to +0.155A

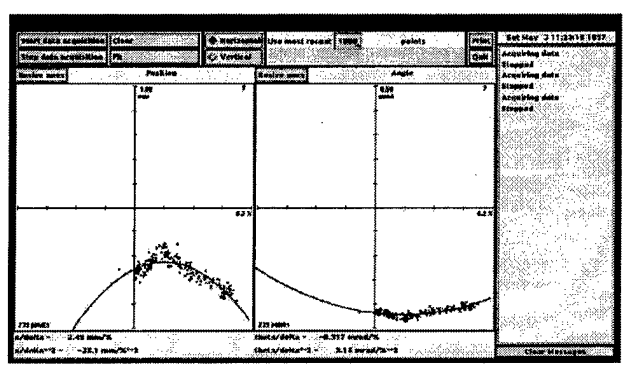

Fig. 4 Measured horizontal dispersions after the ECS chicane with the sextupole ESX1 set to +3.00 A

This is accomplished by varying the phase of the RF from one of the klystrons powering the latter part of the linac. As the energy is varied, and data acquired, the points are plotted in real-time on graphs of position versus energy and angle versus energy. Once the operator feels he has data over a large enough range of energy, and of sufficient quality, he can fit a parabola (or optionally a straight line) to the data. If the dispersion is out of spec, upstream dispersion quads or sextupoles are adjusted, until the desired values are achieved.

Measurements of the horizontal dispersion after the ECS chicane are shown in Figures 2-4, for different settings of a sextupole located in the chicane. The effect of the sextupole on the second order dispersion is clearly shown in the figures. This is an example of how the dispersion program can be used to set elements which control the chromatic aspects of a beamline tune.

The BPMs are calibrated with an RF source, and the calibration is then verified using the beam and a well known beam position measuring device, such as a wire scanner or a calibrated steering coil. The BPMs are capable of ±0.1 mm resolution, with a usable range of ±10mm. For a typical measurement of x/δ at a BPM, this gives a precision of 0.3 mm/%.

Using transport theory, the results of the measurement can be propagated to any desired location. This is done in situations where the BPMs are not located at the point at which we are trying to achieve the desired dispersion. For example, setting x/δ and θ/δ to zero at an experimental target is done using two BPMs upstream from the target, and propagating the measured results to the target.

4. SUMMARY

We have implemented a system for making beamline dispersion measurements in a convenient and efficient manner. It makes use of three beam position monitors. One of the BPMs is in a region of finite, known, dispersion, to act as an energy monitor. Data is acquired through the accelerator control system, and then displayed and analyzed in real time through a graphical user interface. The system allows the accelerator operators to readily achieve the specified values for the dispersion (zero or otherwise) by adjusting the appropriate beamline components. It is now in routine use.

BEAM SIZE EFFECTS ON BEAM POSITION MEASUREMENTS IN PROTON SYNCHROTRON

T. Nakagawa, Advanced Technology R&D Center, Mitsubishi Electric Corp., Hyogo, Japan

Abstract

Three-dimensional surface electric charge method has been applied to calculate the effects of the beam size on the beam position measurements. We confirmed that the change of the beam size led to beam position errors. The calculated results were compared with experimental data, indicating the validity of the simulation. The output signal ratio of beam position monitor was smaller when the beam size was large in the horizontal direction. The proposed method can estimate the effects of the beam size when a beam cross section is given.

1 INTRODUCTION

The electrostatic beam position monitor (BPM) is used to measure a closed orbit distortion (COD) produced by the misalignment of magnets in accelerators. BPM is usually calibrated using a straight wire antenna that models an accelerated pencil beam. The relationship between the antenna position and an output signal ratio of the electrodes of BPM is measured[1]. The beam position is estimated using the above relationship. However, the measured data contains significant errors when the cross section of a real proton beam is much larger than that of the calibration antenna; and therefore, it is important to estimate the effects of the beam size on the measurement beforehand.

The author estimated the influence of the beam size in case of a button type BPM for an electron synchrotron using two-dimensional boundary element method, and showed that the measurement error was produced by a large-sized beam[2]. However, a three-dimensional analysis is required for the BPM in a proton synchrotron because of its complicated geometry. We compare the calculated results with experimental results to confirm the validity of the proposed method.

2 BEAM POSITION MONITOR

Figure 1 shows the schematic drawing of the structure of the BPM that is used in the proton synchrotron having a low accelerated current.

The BPM consists of two separated triangular electrodes that are closely located with each other. The electrode size is 190 mm wide and 200 mm long. They are surrounded with the ground board. When the beam deviates from the center of the BPM, the distance from the center is given as a function of an output signal ratio, $(V_L - V_R)/(V_L + V_R)$, where V_L and V_R are output voltages on the two electrodes. The relationship between the output signal ratio and the horizontal beam position is usually measured using the antenna in advance. An actual beam's position is determined using the calibration curve.

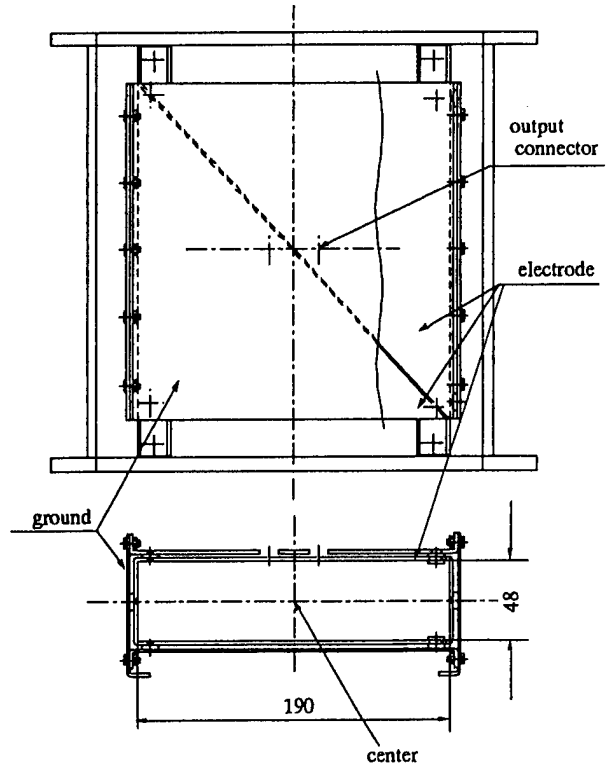

Figure 1: Schematic drawing of the structure of a BPM.

3 NUMERICAL CALCULATION

3.1 Method

The potentials generated by the beam on the electrode is calculated using the three dimensional surface electric charge method. The potential, V_p, at an observation point is given by the following equation:

$$V_p = \sum_{k=1}^{n} \frac{1}{4\pi\epsilon_0} \int_{S_k} \frac{\sigma_k}{r}\, dS \tag{1}$$

where σ is the surface electric charge density on a triangular element, r represents the distance between the center of the triangular element and the observation point, n denotes the total number of triangular elements. The boundary condition, total charges become zero on the conductor surface, is required because the electrodes are isolated from the ground shown in Figure 1. After discretization, the resulting equations are given as follows:

$$\sum_{i=1}^{n} P_{ij}\, \sigma_j = V_c \tag{2}$$

$$\sum_{j=1}^{n} C_{n+1,j}\, \sigma_j = 0 \tag{3}$$

0-7803-4376-X/98/$10.00 © 1998 IEEE

where V_c is the known potential on the electrode and P_{ij} represents the integration in equation (1). The unknown electric potentials on the two electrodes are calculated when the electric potential on the beam is given. The change of the output signal ratio is calculated with the obtained voltages, V_L and V_R.

3.2 *Calculation*

The effects of the beam size is calculated for two different beam models. One is a pencil beam having a diameter of 2 mm. The other is a rectangular beam having a cross section of 70 mm × 9 mm. The pencil beam models the calibration antenna and the rectangular beam shows the multiturn injection beam having the large beam size horizontally. The beam length is much longer than the BPM length. The ground position is adjusted so that the calculated output signal ratio equals to the measured one using the pencil beam model. We calculated the output signal ratio for the rectangular beam model with the same condition. The calculation is done with an upper half model for the fast calculation.

4 RESULTS AND DISCUSSION

Figures 2 shows the upper half model with the rectangular beam, its surface being subdivided into small triangular elements.

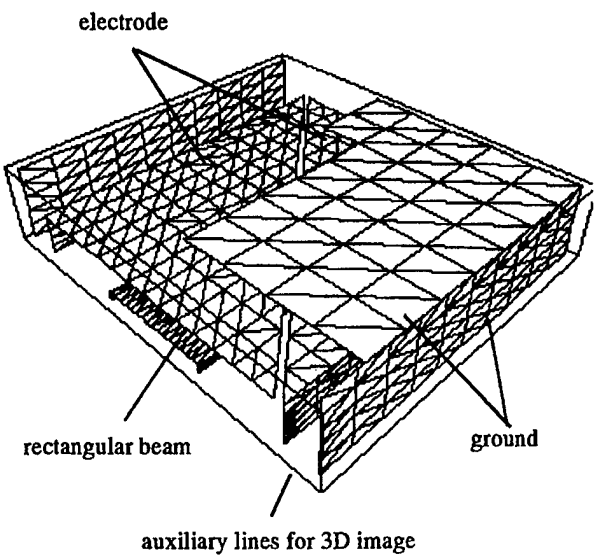

Figure 2: Upper half model subdivided on the surface of BPM with a rectangular beam.

The calculated and measured relationship between the positions and the output signal ratios are shown in Figure 3. The solid line refers to the pencil beam calculation, while the dashed line shows the rectangular beam calculation. The open circles indicate measured values for the pencil beam model, and the dots show those for the rectangular beam model. The wire with 2 mm diameter and an aluminum block with a cross section of 70 mm × 9 mm are used as the beam models in the measurement.

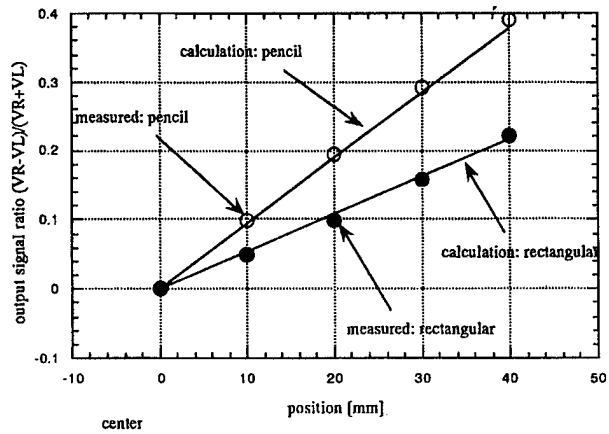

Figure 3: The calculated and measured relationship between the positions and the output signal ratio.

The calculated values for the rectangular beam agree well with the measured one. The figure also suggests a larger-sized beam results in a smaller difference signal-to-sum signal ratio. The reason is that the surface electric charge on the two electrodes is not changed significantly according to the displacement of the beam when the beam size becomes large. Therefore, the estimated deviation is smaller than the true position when the beam size is large in the horizontal direction, indicating that the beam cross section should be evaluated for a precious position measurement.

5 CONCLUSION

Three-dimensional surface electric charge method was applied to calculate the effects of the beam size on the beam position measurements. We have confirmed that the change of the beam size led to beam position errors. It is found that the output signal ratio decreases and the measurement errors increases when the beam cross section became large horizontally. The proposed method can estimate the effects of the beam size when a beam cross section is given.

The relationship between the beam cross section and the beam sized effect will be studied in detail including the vertical displacement of the beam.

6 ACKNOWLEDGEMENTS

I am thankful to Dr H. Harada at Mitsubishi Electric Corporation for many useful discussions.

7 REFERENCES

[1] M. Tejima, H. Ishii, T. Shintake, J. Kishiro, A. Ogata, T. Ieiri and Y. Mizumachi: IEEE Trans. Nucl. Sci. NS-32, 1947 (1985).

[2] T. Nakagawa and S. Nakata: Jpn. J. Appl. Phys., Vol. 132, 325 (1993).

TWO FREQUENCIES CAVITIES FOR BEAM POSITION MONITOR

V.E.Kaljuzhny, D.V.Kostin, M.W.Lalayan, O.S.Milovanov, N.P.Sobenin, S.N.Yarigin,
Moscow Engineering Physics Institute, Russia.,
N.Holtkamp, M.Dohlus, Deutsches Elektronen Synchrotron, Germany.

Abstract

Use of the symmetrical SBLC section coupler (hybrid coupler) as well as one of the section cell (BPM cell) for the beam position monitor (BPM) was studied. In both cases the requirements were the high order mode (HOM) power withdrawal of two polarization without changing frequencies at operational mode and HOM. In case of hybrid coupler the protrusions inside the cavity were used. In case of the BPM cell in 15-th cell of SBLC disk loaded waveguide (DLW) four cut-off waveguides at operating frequency were used. Calculations and measurements with initial 30 cells of SBLC DLW results are presented.

1. INTRODUCTION

The trapped modes in initial 30 cells of the SBLC DLW with the symmetric coupler matched with the structure at the operational mode were studied[1]. The first trapped mode (f=4130 MHz) occupies five initial cells, but the field was absent in the coupler cavity. The last mode fully trapped in the structure has the frequency f=4161 MHz and at this frequency the field in the input coupler is just beginning to show up. Hence, it is clear that the coupler frequency on the HOM differs from that of SBLC DLW first cell and supposedly lies at the frequency more than 4161 MHz. The influence of the coupler frequency on the HOM field distribution was studied with the structure having the coupler, which allowed to vary this frequency [2]. By means of changing of the movable plunger (3 at Fig.1) and using the tuning pins 1 and matched loads 2 the coupler frequency was reduced by 30MHz and the Q-factor value was reduced from 8000 to 2000-4000 over the frequency band about 20 MHz.

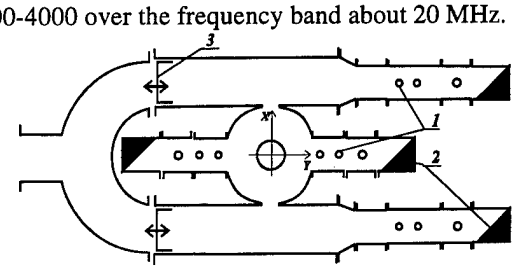

Fig.1 Sketch of the hybrid coupler

2. HYBRID COUPLER

The difference between the coupler frequencies at the operational and first dipole modes in case of SBLC DLW should be in the range of 1150-1230 MHz. The influence of some elements (the choke type grove and the circular protrusions), inserted inside symmetrical coupler on the values of corresponding coupler frequencies was investigated using the method of resonator-analogue [3] and with MAFIA code 3.20 for the coupler with height d_c=28.33mm and variable other dimensions ($2b_c$, $2a_1$, $2a_2$, t_1, t_2). The dimensions of rectangular waveguides (RW) were: A_1=72mm, B_1=28.3mm, A_2=48mm, B_2=24mm. At first, the coupler cell was terminated at both sides by drift tubes with length l_c=100mm and diameter 31.02mm. The calculations were carried out not only for infinite RW, but also for RW1 with movable plunger (m.p.) at one end of every waveguide. The frequencies, calculated using resonator-analogue method and MAFIA code for the coupler with $2b_c$=74mm, $2a_1$=34.8mm, t_1=8.5mm, $2a_2$=27mm, t_2=3.6mm, z=24mm and two ring-type protrusions with diameter 45x55mm and height 2x2mm (1 at Fig.2) are shown in Table1. The influence of movable plunger position z (from 24 mm to 60mm) on the frequencies was about 30MHz at E_{01} mode and 60MHz at E_{11} mode.

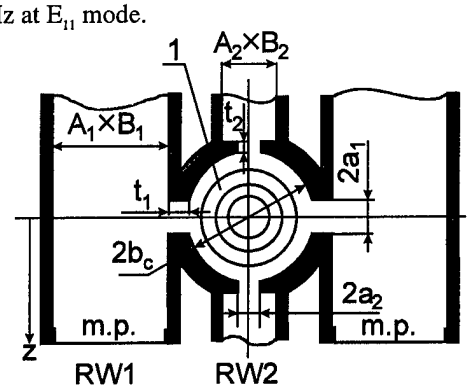

Fig.2. Cross-section of the coupler cells with four RW.

Table 1. The frequencies (in MHz) .

	Resonator-analogue	MAFIA
E_{01} mode	2885	2930
E_{11} mode in RW1	4228	4250-4300
E_{11} mode in RW2	4286	4270-4300

Table.2. The frequencies (in MHz)

	$2b_c$=72mm, h=2x2mm.	$2b_c$=72mm, h=3x3mm.	$\Delta f=f_1-f_2$
E_{01}	2992	2940	52
E_{11} in RW1	4367	4254	113
E_{11} in RW2	4410	4297	113

More substantial changing in frequencies may be obtained, if the cavity diameter and protrusions height were changed (Table2). Obviously, the influence of protrusion height h at the operational frequency is two times more than at the hybrid mode. Using this situation

0-7803-4376-X/98 /$10.00 © 1998 IEEE

and the possibility of changing the dimensions $2b_c$, a_1, a_2, t_1 and t_2 one can obtaine the necessary frequencies for the coupler with four RW and with two drift tubes.

These results would be changed in case when one drift tube is replaced by DLW cells. Some calculations were carried out for the coupler with $2b_c$=74mm, two circular protrusions 45x55mm with height h=2mm, $2a_1$=34.8mm, t_1=8.5mm, $2a_2$=27mm, t_2=3.6mm, z=24mm and two DLW cells with 2b=82.664mm, 2a=30.68mm. With magnetic wall in symmetrical plain the power was observed at the frequencies 2945MHz and 2998MHz at E_{01} mode in DLW and at H_{10} in RW1. In this case we also observed the power at the frequencies 4120MHz and 4153MHz at E_{11} mode in DLW and at H_{10} in RW2. In case with electric wall we had the power at the frequencies 4140MHz at E_{11} mode in DLW and at H_{10} (H_{20}) modes in RW1. The electromagnetic field was calculated only at the pointed out frequencies. At these frequencies we had the maximum signal. But the power was observed in wider frequency band. Hence the hybrid coupler with these dimensions may be used for BPM.

Another scheme for the withdrawal of two polarization hybrid modes may be realized by means of using RW1 of the coupler for one polarization and first DLW cell with RW2 for the second polarization. In this case we may tune the hybrid coupler easier at the operational and hybrid modes. In Table3 one can see the calculation results with MAFIA code for the case of the coupler with $2b_c$=76mm and only RW1 with two protrusions h=2x2mm and without them. Similar coupler with two DLW cells (cell N1 of SBLC DLW) was calculated too and the power in RW1 was observed at frequency 4130-4140MHz.

Table.3. The frequencies (in MHz)

	With protrusions	Without protrusions
E_{01} mode	2915	2975
E_{11} mode	4410	4550

3. BPM CELL

The possibility of restoring the preliminary frequencies at the operational and hybrid modes in the BPM cell was tested with the constant impedance structure having dimensions of the last cell of SBLC DLW. The tuning of the cell at the operational mode was made by means of cell diameter changing and also by means of tuning pins, inserted into the cell. The changing of the HOM frequency of this cell was realised by introducing the reactive conductivity in the cell, using the RW with movable plungers or mismatched loads. As the dimensions of RW were chosen as cut-off for fundamental mode we may neglect their influence at these frequencies. The equivalent circuit of the device, consisting of some cells is presented in Fig.3. L,C,G are the parameters of equivalent circuit at some mode, l is the rectangular waveguide length, G_a is conductance of theload. There is the following expression for the n mode frequency

$$f_n = f_{0n}\left[1-\frac{\sin\frac{4\pi l}{\lambda_w}}{2Q_{ext}\left(\cos\frac{4\pi l}{\lambda_w}+\frac{1+\Gamma^2}{2\Gamma}\right)}\right]$$

where f_{0n} is the own frequency at n mode, Q_{ext} is the external Q-factor being determined by the coupling between the cell at n mode and waveguide with load, Γ is the load reflection coefficient.

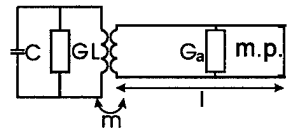

Fig.3 Equivalent circle.

The frequencies versus the movable plunge position l were measured the structure, consisting of one cell (0-mode), three and six cells (modes 0,π/3 and 2π/3). The BPM cell dimension wasn't equal that of to last cell, because there was two slots in the cell and therefore it was corrected. The experiments were carried out with two movable plungers and with the mismatched load with standing wave ratio (SWR) of 5.6. The BPM cell was tuned at the calculated frequency of the operation 0 mode using four tuning screws 4 (see Fig.4). It is clear from these experiments that with increasing of cell number in the stock under investigations (in 6 times) the frequency change decreases (about in 6-7 times).

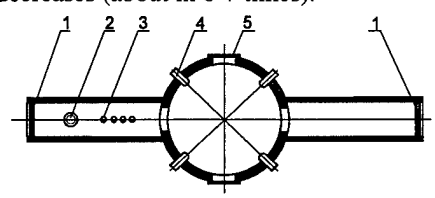

Fig.4. BPM cell

The next experiments were performed with the device where the matched load was connected to one slot and the movable plunger to another one (see Fig.4.). The matched load was made on the basis of RW with cross section dimensions 37.5x5 mm and had the movable plunger (1), some tuning screws (3) and coaxial output with the absorbing load (2). SWR was achieved less than 1.1 in the frequency range 4130-4175 MHz. Using four tuning screws in a cell we have obtained the 0-mode frequency equal to the calculated one 2965MHz. Then the frequencies $0, \pi/3$ and $2\pi/3$ modes in the resonant stock consisting of tree cells were measured and their values appeared to be equal to the calculated values: 2965, 2975 and 2998 MHz correspondingly. In Table 4 one can see the hybrid mode frequencies(f_1) measured after tuning by means of the movable plunger and calculated one (f_2) for the structure consisting of six cells. From these data and the similar data with three cells we may conclude that with increased number of cells in the

resonant structure after tuning the BPM cell by means of movable plunger the hybrid frequencies became close to calculated values. At the setup consisting from six cells the transmission coefficient K_{tr} at HOM from DLW into RW was measured. The cell with input loop and screws was tuned at the frequency of $2\pi/3$ mode with SWR 1.05. The transmission coefficient was equal 3dB.

The longitudial electric field distributions were measured with this structure with and without the BPM cell by means of the small needle with 0.05 mm radius and 12 mm length. It is being placed 3mm of axis. The formfactor of this bead was equal $2.5\times10^{-19}m^2/c\cdot Ohm$ and direction coefficient was equal 16. It was shown, that the longitudinal electric field distribution depends on resonant structure length, frequency and slot sizes.

Table 4. The frequencies (in MHz).

MODE	f_1, MHz	f_2, MHz	Q-factor
0	4597	4600	1840
$\pi/6$	4580	4583	1650
$\pi/3$	4546	4546	5600
$\pi/2$	4507	4508	1500
$2\pi/3$	4580	4479	1000
$5\pi/6$	4462	4462	1600

The investigations of the initial part of SBLC DLW consisting of 30 cells were carried out with the BPM cell instead of cell #15. This BPM cell has two pairs of narrow slots with dimensions $2\times15mm^2$, $2x25mm^2$ or $2x37mm^2$. The BPM cell was connected with RW through these coupling slots. Rectangular wavequides were ended by the loads having SWR less than 1.2 in investigating frequency band. At first the BPM cell was tuned with the resonant structure, consisting of cells #14, #15, #16. Dimension 2b of the BPM cell was less than 2b of real 15-th cell in order to compensate the influence of four coupling slots with connected RW and matched loads at the operational frequency. The radial electric field component distribution versus longitudinal coordinate was measured by mean of the perturbating shim having the diameter 6mm and the thickness 0.3mm being moved along the structure axis (formfactor was equal $6.05\times10^{-19}m^2/c\cdot Ohm$ and direction coefficient was equal 25). The measurements were performed in the frequency range 4135MHz-4171MHz. The upper frequency value was chosen from condition RF power filling of all section 30 cells. In Fig.5 one can see the frequency changes for structure without the BPM cell and with the BPM cell at different slot sizes. The position z of the first cell at these pictures is equal to 1000mm. The analysis of these experimental results show that the BPM cell influences on the field structure. At some frequencies and slot dimensions the resonant structure seems to be divided into two slightly coupled parts, the field excitement in one part is being smaller than in the other one. This effect is the result of the difference between BPM cell impedance and that of other cells. Using these data it is possible to calculate the transverse shunt impedance function structure length for different frequencies and slot sizes compare it with that of the structure without the BPM cell. The necessary slot size of the BPM cell is to be chosen with accounting for small influence of these slots at the transverse shunt impedance over the frequency range and the required the transmission coefficient between DLW and RW. The measured transmission coefficient versus slot length (the height 2mm) is shown in Fig.6. The data for every slot length were averaged over the frequency range 4131-4171MHz.

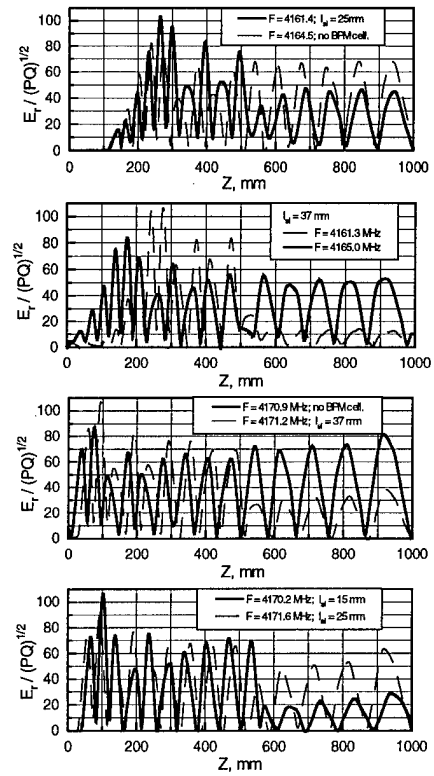

Fig.5. Radial electric field on the DLW axis with cell number

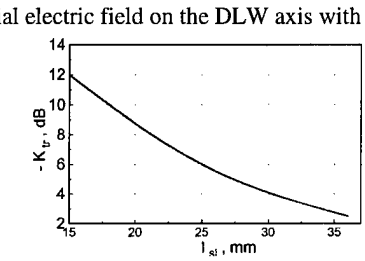

Fig.6. Transmission coefficient at HOM depends on slot length.

REFERENCES

[1] V.E.Kaljuzhny, D.V.Kostin, O.S.Milovanov. and N.P.Sobenin in *Proc. 5-th European Particle Accelerator Conf.*, Ch.Petit-Jean-Genaz ed. (World Scientific, Singapore,1996) vol.3,p.2041.

[2] V.E.Kaljuzhny, D.V.Kostin, O.S.Milovanov, N.P.Sobenin, N.Holtkamp,and M.Dohlus, in *Proc. 18-th Intl. Linac Conf. (LINAC-96)* 1996, vol.2,p.824.

[3] V.E.Kaljuzhny, D.V.Kostin, O.S.Milovanov, N.P.Sobenin, N.Holtkamp, and M.Dohlus, "Investigation of a Hybrid Coupler for a 6 Meter S-band Linear Collider Accelerating Structure", *Internal report DESY M 96-05,* April 1996.

BEAM-BASED OFFSET CALIBRATION OF THE PLS BPM

J. Y. Huang, D. H. Jung, K. H. Kim, S. H. Nam, M. Yoon and I. S. Ko
Pohang Accelerator Laboratory, POSTECH
Pohang 790-784, Korea

Abstract

There are 108 beam position monitors in the PLS for the orbit measurement and closed orbit correction. As the BPM pickup electrodes are assembled directly on the 10m-long vacuum chamber, calibration of the electrical center of BPMs have been done with the external rf transmission-reflection method. Since the closed orbit distortion is still larger than 500 μm rms, we are developing the beam-based calibration method for the BPMs in PLS to improve the accuracy of the absolute position reading. In this report we present the method of beam-based calibration of BPMs and its experimental results.

1 INTRODUCTION

The Pohang Light Source (PLS) is a dedicated third generation synchrotron light source with nominal beam energy of 2 GeV. In the low emittance storage ring like PLS, minimization of the closed orbit distortion is a necessary condition for the optimum performance of the machine. To minimize the closed orbit distortion, the alignment accuracy of the accelerator component has to be within 150 μm. Novel opto-mechanical methods have been used for the survey and alignment of the lattice magnets and BPMs in the PLS. Local alignment accuracy is less than 100 μm rms [1]. Among the accelerator components, BPMs and magnets are particular ones which have magnetic or electrical center different from the mechanical center. In view of the charged particles circulating in the storage ring, the true centers of the lattice components are magnetic or electrical centers, not the mechanical ones. The magnetic center of each magnet was precisely measured within 20 μm on the magnetic field measurement table before the installation. However, BPMs could not be calibrated individually in the PLS, because the BPMs are plugged into the 10m-long single piece vacuum chamber. Instead, we have measured all the coupling coefficients between the pickup electrodes using a network analyzer and a 48dB gain power amplifier to find the relative gains of the pickup electrodes and the electrical centers of the BPM.

However, since the coupling coefficients are very sensitive to the chamber structure, it seems that this method is not as accurate as done on the test bench [2]. Indeed, the closed orbit distortion after the closed orbit correction is no better than 500μm in the PLS. Therefore, we believe the rms error of the electrical offset measurement of the BPMs should be larger than 500μm.

Recently, beam-based alignment (BBA) techniques by using quadrupole magnets are tried in several laboratories [3,4,5]. In the PLS, we are also developing the beam-based alignment technique for the calibration of electrical offsets of selected BPMs. In particular, we try to do a beam-based alignment which is rather geometrical method derived from simple beam dynamics. For the preliminary test, we installed 14 quadrupole magnet current shunt circuits in one cell of the storage ring [6]. In this paper, we describe on the preliminary tests and results of the BBA experiments.

2 BEAM BASED ALIGNMENT

The purpose of the BBA is the measurement of the offset of electrical center of the BPM from an ideal reference orbit or the magnetic center of the nearest quadrupole magnet. If the BPM is located at the center of the quadrupole magnet, or even when the BPM is located very close to the quadrupole magnet as shown in Fig. 1, the deviation $d\theta_Q$ between the reference orbit and the beam trajectory is very small or even eliminated by taking average over the many beam trajectories passing through the center of the quadrupole magnet. In this case, the offset Δx_{PM} is just the average of the beam position $\langle x_{PM}\rangle$ read by the BPM when the orbit passes through the center of the quadrupole magnet.

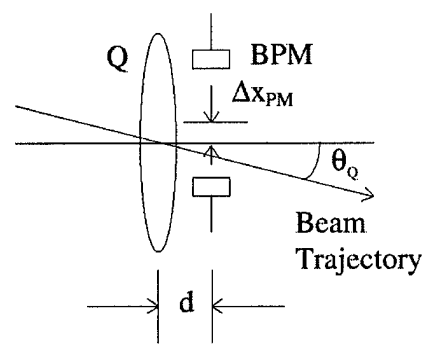

Figure 1: When the distance d between quadrupole magnet and BPM is small compared to the betatron wavelength or the crossing angle θ_Q is negligible by taking average over many beam trajectories ($\langle d\theta_Q\rangle \sim 0$), the BPM offset Δx_{PM} is equivalent to the average of beam position $\langle x_{PM}\rangle$.

For the test, we consider that the initial beam position is x_Q at the quadrupole magnet, and x_{PM} at the BPM. A corrector magnet and another BPM2 are also selected. These are well apart from the quadrupole magnet. By changing the corrector magnet current, the beam position x_Q at the quadrupole magnet can be controlled. When the quadrupole magnet strength is changed by δk_Q, the beam experiences the change of kick angle $\delta\theta_Q$ such as

$$\delta\theta_Q = \delta k_Q x_Q l_Q. \quad (1)$$

Consequently, the closed orbit change δx_{PM2} at BPM2 is

$$\delta x_{PM2}=\delta\theta_Q(\beta_Q\beta_{PM2})^{1/2}\cos(\varphi_Q-\varphi_{PM2}+\pi\nu)/2\sin(\pi\nu), \quad (2)$$

where l_Q is the effective length of the quadrupole magnet and β_Q is the betatron function at the quadrupole magnet. If the orbit passes through the center of the quadrupole magnet, $x_Q = 0$ and, accordingly, $\delta x_{PM2} = 0$. The offset Δx_{PM} of the BPM is then equivalent to the average of the beam position reading $\langle x_{PM}\rangle$.

In some accelerators like the PLS, however, BPMs are not located close to the quadrupole magnets. The average $\langle d\theta_Q\rangle$ is not negligible if the distance from the quadrupole magnet d is large. Then we need a reference orbit or a reference trajectory, instead of a closed orbit, to measure the absolute BPM offsets. The closed orbit is not uniquely defined in a storage ring, because it changes with the change of lattice parameters, such as tunes. We will here define a unique reference trajectory by connecting the centers of the quadrupole magnets piecewise as shown in Fig. 2. The offset of the BPM is then defined as the offset from the reference trajectory. In the practical sense, the reference trajectory defined as above may be almost the same to the design orbit or the closed orbit, because the overall alignment accuracy of the storage ring components are less than 150 μm rms.

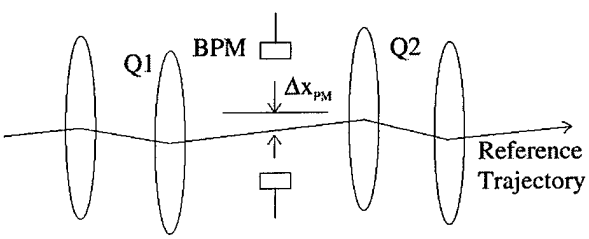

Figure 2: A reference trajectory is defined as the piecewise straight lines connecting the centers of the quadrupole magnets.

Measurement of the absolute offset of BPMs can be realized using two quadrupole magnets. First, we find the orbit which passes through the center of the quadrupole magnet Q1 near the BPM. Beam position x_{PM} measured by BPM is not the offset of the BPM in this case, because the beam will cross the quadrupole magnet center with an angle θ_{Q1}

$$\theta_{Q1} = x_{PM}/d_1 = x_{Q2}/d \quad (3)$$

where x_{Q2} is the beam position at Q2 and d is the distance between two quadrupole magnets Q1 and Q2. To measure θ_{Q1}, x_{Q2} should be measured first. It can be done by measuring the change of beam position δx_{PM} at the BPM with respect to the change of the focusing strength δk_{Q2} of Q2. Then x_{Q2} can be obtained from Eq. (2) as

$$x_{Q2} = 2\delta x_{PM}\sin(\pi\nu)/[\delta k_{Q2}l_{Q2}(\beta_{Q2}\beta_{PM})^{1/2} \times\cos(\varphi_{PM}-\varphi_{Q2}+\pi\nu)]. \quad (4)$$

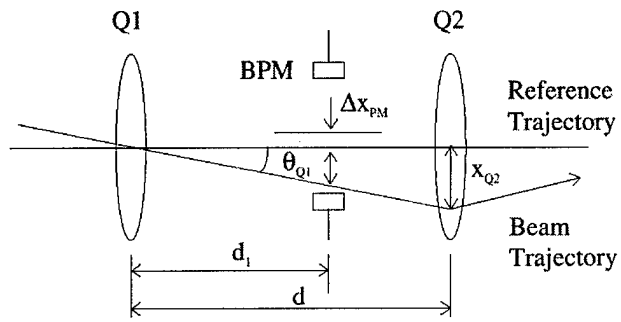

Figure 3: Difference of the beam trajectory and the reference trajectory, $d_1\theta_{Q1}$, can be measured with two quadrupole magnets Q1 and Q2.

In Fig. 3, the offset Δx_{PM} of the BPM from the reference trajectory is finally

$$\begin{aligned}\Delta x_{PM} &= x_{PM} - d_1\theta_{Q1}\\ &= x_{PM} - d_1 x_{Q2}/d\\ &= 2d_1\delta x_{PM}\sin(\pi\nu)/[\delta k_{Q2}dl_{Q2}(\beta_{Q2}\beta_{PM})^{1/2}\\ &\quad\times\cos(\varphi_Q-\varphi_{PM}+\pi\nu)]. \end{aligned} \quad (5)$$

We again take the average over the many beam trajectories passing through the center of the quadrupole magnet using the selected corrector magnets. In these analysis, the tune shift by the change of quadrupole magnet strength is neglected.

3 EXPERIMENTS

We have done an experiment as a preliminary test for the application of BBA to the PLS storage ring. Two focusing quadrupole magnets, P05Q1D and P06Q1U, at both sides of the BPM 6PM2, and a corrector magnet P05CH6 are used for the experiment. A bending magnet located in between two quadrupole magnets is regarded as the free drift space. Two corrector magnets, P06CH1 and P06CH2, located in between two quadrupole magnets are turned off. Fig. 3 is, therefore, equivalent to our experimental setup.

Current shunt circuits for 14 quadrupole magnets of one lattice period of the storage ring are installed for the experiment. It is controlled linearly within 10% of the quadrupole magnet strength. Since the data acquisition and control system is not completed yet, each shunt circuit is manually controlled for this experiment.

The closed orbit is changed by the corrector magnet P05CH6 to change the beam position at the quadrupole magnet Q1 (P05Q1D). Changes of the beam position δx_{PM}, between the shunt current on and off, are measured and plotted with respect to the beam position x_{PM}. By fitting the data, the closed orbit passing through the center of Q1 is found. In Fig. 4, $x_{PM} = 2.5843$ mm with the fitting accuracy better than 170 μm rms. To find beam position x_{Q2} at Q2 when the beam passes through the center of Q1, the change of beam position δx_{PM} at the BPM is measured by changing the focusing strength δk_{Q2} of Q2. In Fig. 5, we get $\delta x_{PM}/\delta k_{Q2} = -1.775$, and x_{Q2} is calculated from Eq. (3) as 1.637 mm. The linearity of the quadrupole magnet current shunt circuit, tested with the beam, is sufficiently

good as shown in Fig. 5. Finally, the true offset of the BPM can be calculated from Eq. (4). With d_1=6.813 m and d=7.04 m, we obtain Δx_{PM} = 0.947 mm.

4 CONCLUSION

We have done an experiment as a preliminary test for the application of BBA to the PLS storage ring. Two defocusing quadrupole magnets P05Q1D, P06Q1U and a BPM 6PM2 are used for the experiment.

Results of this experiments are shown in Figs. 4 and 5, where Δx_{PM} = 0.947 mm with the fitting accuracy 170 μ m rms. The linearity of the shunt circuit is sufficiently good for the purpose of beam-based alignment. As we expected before the test, the electrical offset of the BPM seems to be large.

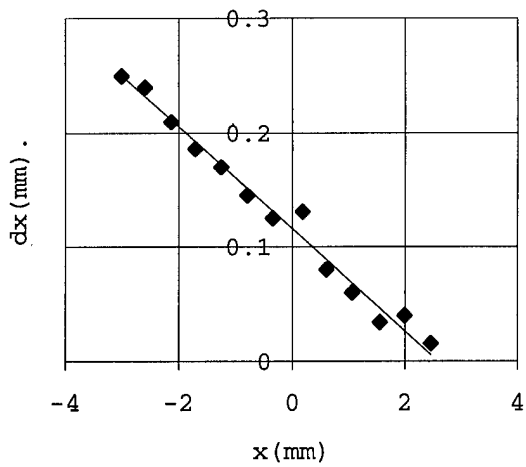

Figure 4: Plot of beam positions at the BPM and change of beam position by turn on and off the quadrupole magnet shunt current.

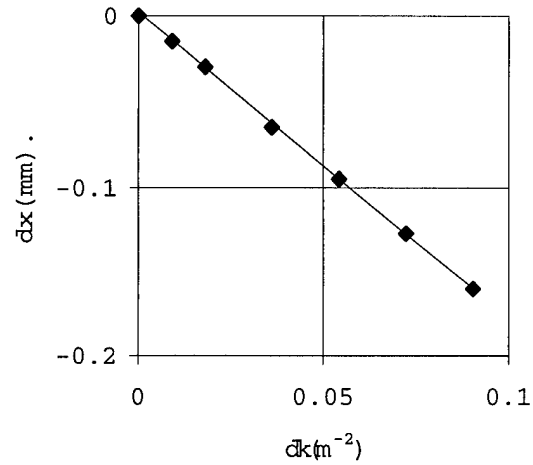

Figure 5: Change of beam position vs change of quadrupole magnet strength. Nominal focusing strength of the quadrupole magnet k_0 is -0.64178m^{-2}

Since the shunt circuits were controlled manually, sufficient averaging of the data was not taken. To verify the consistency of the BBA technique in the PLS, we have to do the same experiment in the reverse direction. The same offset values should be obtained for the same BPM.

All the new current shunt circuits are completed and are being installed now [6]. The shunt current is linearly variable up to 10% of the quadrupole magnet current. By the end of this year, all the current shunt circuits will be controlled with RS232 from the local VME-bus MIU (machine interface unit). Each MIUs will be controlled offline from the main PLS control system via the independent Ethernet which has been installed for the development of the low level MIU program. Control software for the system is now under developing. Several precision BPMs are also prepared for the test. When all these are installed, more precise BBA will be possible.

5 REFERENCES

[1] K. W. Seo et. al., "Precision Surveying and Smoothing Analysis for Pohang Light Source," in this proceedings.
[2] J. M. Hinkson, ALS, private communications.
[3] Barnett et. al., "Dynamic Beam Based Alignment," 2nd European Workshop on Beam Diagnostics and Instrumentation for Particle Accelerators, DESY M-95-07 (1995).
[4] K. Endo et. al., "Preliminary Orbit Measurement for Beam-Based Alignment," Proc. of 1996 EPAC, Sitges (1996).
[5] P. Tenenbaum et. al., "Beam-Based Magnetic Alignment of the Final Focus Test Beam," Proc. of 1995 PAC, Dallas (1996).
[6] S. H. Nam et. al., "A High Current Shunt Regulator for Quadrupole Magnets in PLS 2GeV Storage Ring," in this proceedings.

CALIBRATION OF THE BEAM-POSITION MONITOR SYSTEM FOR THE SLAC PEP-II B FACTORY

R. Johnson, S. Smith, N. Kurita, SLAC, Stanford, CA 94309; K. Kishiyama, LLNL, Livermore, CA 94550; and J. Hinkson, LBNL, Berkeley, CA 94720

Abstract

The Beam-Position Monitors (BPM) for the PEP-II B Factory consist of four 1.5-cm diameter button style pickups mounted on the diagonals of the quadrupole vacuum chambers. Before installation of the vacuum chambers in the quadrupole assemblies, the electrical center of the BPMs is measured with respect to the mechanical center in a calibration test stand. In this paper the calibrations test stand is described and the precision and accuracy of the calibrations are presented. After installation of the quadrupole assemblies in the PEP-II tunnel, the passive attenuation for each channel of the system is measured to preserve the accuracy of the calibration. Finally, the active electronics includes an on-board calibrator. Results for these portions of the calibration are presented.

1 INTRODUCTION

The Beam-Position Monitors (BPM) for the PEP-II storage rings are monunted in vacuum chambers which are part of the quadrupole assemblies. The BPMs consist of four 1.5-cm diameter button style pickups mounted on the diagonals of the vacuum chambers. In general there are three types of chambers, *i.e.*, for the high-energy ring (HER) arcs, the low-energy ring (LER) arcs, and the HER and LER straights. Each of the three systems is the responsibility of a collaborator in the PEP-II project, SLAC for the HER arcs, LBNL for the LER arcs, and LLNL for the HER and LER straights.

An absolute calibration of the BPM system requires several steps. This calibration is defined relative to an ideal orbit, which is determined by a global survey. The steps required to relate the measured positions with respect to this ideal orbit are:

- Establish the electrical center of the BPMs with respect to defined mechanical center of the vacuum chambers. (Section 2)
- Measure and correct for the attenuation of the signals through cables and the passive electronics. (Section 3)
- Measure and correct for the offset of the active electronics. (Section 4)
- Establish the offset from the mechanical center of the chambers to the ideal orbit. (Section 5)

In this paper calibration for the HER BPMs will be discussed. This system is complete and installed. Calibration for the LER BPMs is underway; but, will not be described.

2 CALIBRATION TEST STAND

The BPMs and vacuum chambers require calibration to determine the electrical and mechanical centers before they are installed in a quadrupole assembly.

Various methods have been used for electrical calibration of BPMs. These include sending a short pulse or a continuous rf signal down a stretched wire or rod which is terminated in the characteristic impedance. The method selected here is to launch a travelling wave using a short antenna centered in the vacuum chamber. Signals induced on the BPM buttons are measured with a power meter. To reduce systematic errors, measurement channels are swapped and averaged.

The mechanical design of the calibration test stand used at SLAC is shown in Figure 1.

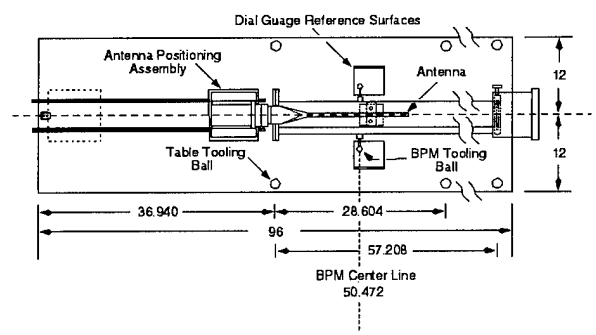

Figure 1. BPM Calibration Test Stand (SLAC).Dimensions in inches.

The quadrupole chambers are located by a pin and reference plate located at the BPM position. At the other end of the chamber a mounting surface positions the chamber in the test stand. Tooling balls (fiducials) mounted at the sides of the chamber (at the BPM position) are measured with respect to reference surfaces using precision dial guages.

2.1 Electrical Calibration

The antenna is designed to launch a TEM wave (at 952 Mhz) from a point beyond the buttons to the near end of the quadrupole chamber where it is absorbed in an electrical lossy material (ECHOSORB). The length of the antenna is specified by balancing the requirements of mehanical stability and starting the traveling wave at a point sufficiently beyond the buttons so that higher order modes damp out. A distance of 25 cm is sufficient for 40 dB of damping for the next higher mode. The diameter of the rod, 1.59 cm, is selected for mechanical stability. The antenna can be moved in the xy plane by the precision

0-7803-4376-X/98/$10.00 © 1998 IEEE

stage and the assembly is mounted on rails to facilitate installation and removal of quadrupole chambers.

Power at 952 Mhz is delivered to the antenna from a supply that consists of a phase-locked oscillator, an amplifier, and a narrow band filter. The rf signal is delivered to an open stub at the end of the antenna through semi-ridged coaxial cable. The coupling stub is simply 2.86 cm of the center conductor of the coax. A 1.59-cm diameter cylinder of nylon both protects the stub and increases the efficiency of the antenna through dielectric loading.

The travelling wave created by the antenna induces signals on the four buttons of the BPM. Each button is connected to a 4P1T rf switch and the common terminal of the switch is connected to a power meter. The rf switch and power meter are controlled by a MacIntosh IIci running LabView.

A position measurement is made by measuring the power on each button sequentially. Then the cables at the buttons are diagonally swapped and the measurement is repeated. Calculation of the position can then be made [1]. An average of the measurements helps to eliminate systematic errors while the difference in the measurements represents the systematic error.

2.2 Mechanical Calibration

The calibration test stand was measured and aligned by a survey. In particular the primary requirements are the accurate centering of the antenna in the quadrupole chamber and accurate knowledge of the reference surfaces with respect to the locating pin and surface. The surveys were repeated several times over the period in which the quadrupole chambers were calibrated.

Measurement of the position of the tooling balls are made at each calibration. The x and y positions of the tooling balls are entered into the LabView program and become part of the calibration database.

The description on the calibration test stand as described applies to the setup at SLAC. At LLNL the mechanical system was somewhat different. There the system was based on a CCMM.

2.3 Calibration Test Stand Results

In commissioning the calibration test stand extensive test were performed. These include tests for electrical reproducibility, mechanical reproducibility, response mapping, and survey errors. Also a standard chamber was checked periodically during calibrations. The standard errors for electrical and mechanical reproducibility totaled about 15 μm while the survey errors were about 25 μm.

The mapping of the chamber out to a radius of 8.13 mm from the center was done to estimate the accuracy of the calculated calibration factors. The precision of these factors was determined to be 0.5% and 1.3% in the x and y directions, respectively.

3 ATTENUATION OF PASSIVE ELECTRONICS

A block diagram of the electronics for the BPM system [2] is shown in Figure 2.

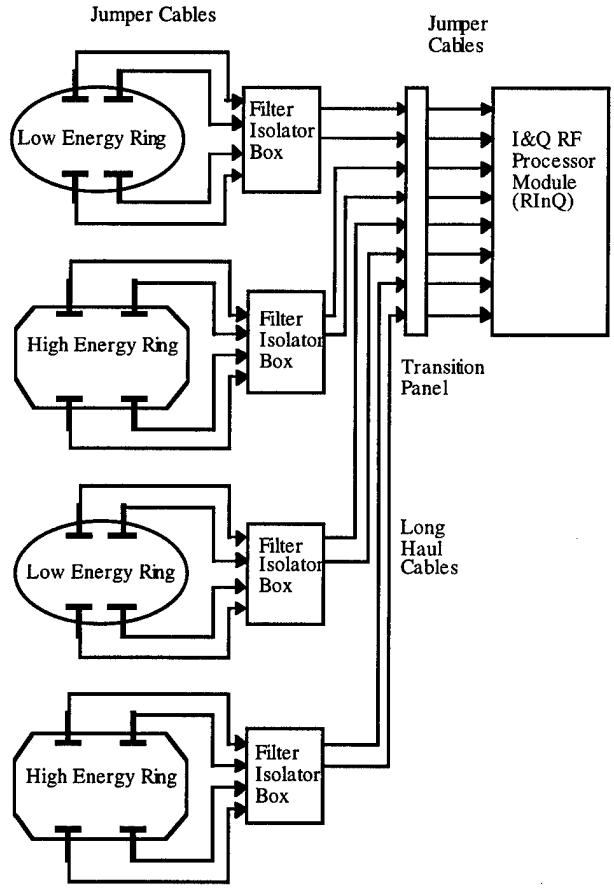

Figure 2. BPM System Block Diagram

The components that contribute to the passive attenuation are the button to Filter Isolator Box (FIB) jumper cables, the FIB, the long haul cables from the FIB to the transition panel, and the transition panel to processor module (RInQ) jumper cables.

Attenuation of the button to FIB jumper cables were measured before being installed. The attenuation of the long haul cables and the transition panel to RInQ module jumper cables were measured together following installation. The system was designed to have an attenuation of at least 8 dB in order to reduce the effect of reflections. Here the concern is in the difference in attenuation from channel to channel. The average difference in attenuation leads to an offset of about 130 μm. The measurement error is approximately 15 μm.

4 CALIBRATION OF ACTIVE ELECTRONICS

The active electronics [I&Q RF Processor (RInQ) Module] processes signals using baseband conversion by in-phase and quadrature demodulators. The signals are then digitized and the position calculated. The RInQ module also contains an on board calibrator. The calibrator injects rf signals (near 952 Mhz) through a 10-dB coupler at the

input of each channel. Using this calibrator several sources of error can be reduced. These errors include channel gain mismatch, channel offset, and amplitude and phase unbalance. The total offset due to these sources was specified to be less than 0.12 dB. Production modules have measured offsets of less than 0.04 dB or 30 μm with an error of approximately 10 μm.

A part of the channel offset is not measured through these calibration procedures. An offset can be present from the input circuit through the coupler. This offset is measured during the acceptance testing of the modules. A single source is used to drive a splitter and the split signal is sent to the module and the position offset measured. To help eliminate systematic errors the cables to the input channels are swapped and the offset measured again. The average of these measurements is then used.

The average offset measured through this procedure is about 30 μm with an error of approximately 10 μm.

5 GLOBAL ALIGNMENT

For the puposes of this paper the global alignment is a process in which the idealized beam transport and the placement of the beam line structures as determined by their fiducials results in a set of ideal coordinates [3]. Even more specific to the BPM system the required information is the offsets between the ideal beam position and the BPM mechanical center (defined as the position of the antenna at calibration).

The errors involved in this process are primarily the survey errors, *i.e.*, determination of the position of the fiducials on the magnet to the fiducials on the vacuum chamber and determination of the position of the fiducials on the magnet with respect to the magnetic center. These errors have not been fully analyzed at this time; however, they do not exceed the requirements, 60 μm and 45 μm, respectively .

6 SUMMARY AND CONCLUSIONS

As part of the planning for the PEP-II BPM system the precision or accuracy requirements were specified. In the following table the actual results are compared to the requirements. The errors listed in the table represent one standard deviation.

Table 1. BPM System Requirements and Performance

Calibration Element	Required (μm)	Actual (μm)
Calibration of electrical center to fiducials on chamber	90	
Electrical center to antenna		15
Antenna to fiducials		25
Fiducials on chamber to fiducials on magnet	60	60
Fiducials on magnet to magnetic center	45	45
Electronics and cables	175	
Passive attenuation		15
External calibration of RInQ		10
Internal calibration of RInQ		10
Mechanical stability of electrical with respect to magnetic centers	60	40
Total (quadrature)	220	90

The calibration of the BPM system has been shown to be better than the requirements. Offsets for each of the effects discussed in this paper will be entered in the on-line data base and will help in the tuning of the PEP-II beams.

7 ACKNOWLEDGEMENTS

Work supported by the U.S. Department of Energy contracts DE-AC03-76SF00515 (SLAC), W-7405-Eng-48 (LLNL), and DE-AC03-76SF00098 (LBNL). The authors wish to thank Wendy Sibbring, Brooks Collins, Robert Noriega, and Vernon Smith for their technical support and Matthew Pietryka for discussions on survey issues.

REFERENCES

[1] R.E. Shafer, Beam Position Monitoring, Proc. Accelerator Instrumentation 1989, eds. E.R. Beadle and V.J. Castillo, AIP Conf. Proc. 212 (AIP, New York, 1990) pp. 26-55.

[2] G.R. Aiello, *et al.*, Beam Position Monitor System for PEP-II, Beam Instrumentation, Proc. of the Seventh Workshop, 1996, eds. A.H. Lumkin and C.E. Eyberger, AIP Conf. Proc. 390 (AIP, Woodbury, NY, 1997) pp. 341-349.

[3] Ideal Layout Coordinate Calculation, SLAC Internal Publication.

A TWO-BUNCH BEAM POSITION MONITOR

E. Medvedko , R. Aiello, S. Smith
Stanford Linear Accelerator Center, Stanford, CA 94309, USA

Abstract

A new beam position monitor digitizer module has been designed, tested and tuned at SLAC. This module, the electron-positron beam position monitor (epBPM), measures position of single electron and positron bunches for the SLC, LINAC, PEPII injections lines and final focus. The epBPM has been designed to improve resolution of beam position measurements with respect to existing module and to speed feedback correction [1]. The required dynamic range is from 5×10^8 to 10^{11} particles per bunch (46dB). The epBPM input signal range is from ±2.5 mV to ±500 mV. The pulse-to-pulse resolution is less than 2 μm for 5×10^{10} particles per bunch for the 12 cm long striplines, covering 30° at 9 mm radius. The epBPM module has been made in CAMAC standard, single width slot, with SLAC type timing connector. 45 modules have been fabricated.

1 INTRODUCTION

The epBPM module has four input channels X+, X-, Y+, Y- (Fig. 1), named to correspond with coordinates of four striplines - two in horizontal and two in vertical planes, processing signals to the epBPM inputs. The epBPM inputs are split for eight signal processing channels to catch two bunches, first - the positron, then the electron bunch in one cycle of measurements. The epBPM has internal and external trigger modes of operations. The internal mode has two options - with or without external timing, catching only first bunch in the untimed mode. The epBPM has an on board calibration circuit for measuring gain of the signal processing channels and for timing scan of programmable digital delays to synchronize the trigger and the epBPM input signal's peak. There is a mode for pedestal measurements. The epBPM has 3.6 μs conversion time.

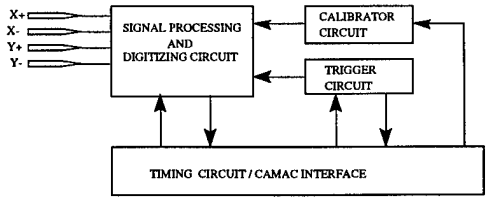

Figure 1. The epBPM module block diagram.

2. THE SIGNAL PROCESSING AND DIGITIZING CIRCUIT

The input signal from the stripline electrode "X+" propagates through the Splitter/Combiner S/C1 (5MHz - 500MHz bandwidth) and Bessel Lowpass Filter (40 MHz bandwidth) (Fig. 2). This signal goes to the Signal Amplifier (OA1, gain 5) and to the Trigger Amplifier (OA2, gain 2). The S/C2 accepts the calibration signal, S/C3 assepts signal from the stripline electrode "X-".

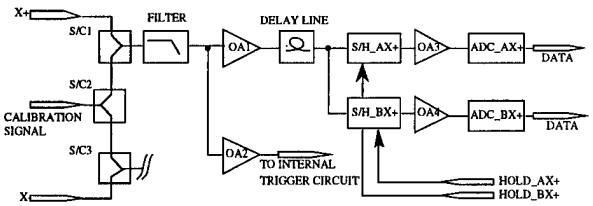

Figure 2. The Signal Processing and Digitizing Circuit - X+ channel.

The Signal Amplifier feeds a 27 ns delay line (74 MHz bandwidth). Delayed signal goes to two fast sample-and-hold amplifiers analog inputs S/H_AX+ and S/H_BX+ (14-bits accuracy, 30 ns acquisition time, ±2 mV/μs droop rate). The delay line compensates propagation delay of the S/H triggering pulse through the Trigger Circuit in order to hold the S/H input signal peak. The "A" and "B" sample-and-hold output signals go to amplifier OA3 and OA4 (gain 2), respectively. Those amplifiers narrow signal bandwidth to 4 MHz to meet ADC bandwidth (1.5 MHz). The ADC has 14 bit resolution (13 bits plus sign), 400 ns acquisition time, 2.9 μs convertion time, serial data output.

3. CALIBRATOR CIRCUIT

The Calibration Circuit generates bipolar pulses like positron or electron signals from the stipline electrode. The Calibrator is used for the signal processing channels gain measurements and for the calibration of the programmable digital delays in the trigger pulse chain.

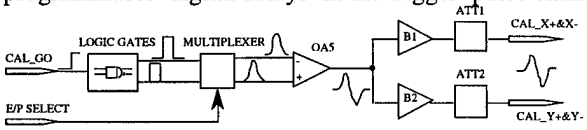

Figure 3. The Calibrator Circuit.

The calibration start pulse (CAL_GO) propagates through gates and generates two short pulses, one delayed from the other by 4 ns (Fig. 3). The multiplexer selects which pulse will be first at the differential amplifier OA5 (gain 2) inputs. If the first pulse goes to positive input and the delayed pulse goes to negative input - the OA5 output pulse will be positron-like, if the first pulse goes

0-7803-4376-X/98/$10.00 © 1998 IEEE

to the negative input and the delayed one - to the positive, it will be electron-like pulse. OA5 output signal feeds two buffers. The buffers output signals drive programmable attenuators, 30 dB dynamic range, both attenuators have the same input data. The Calibrator's attenuated signal supplies two S/C (channels X+, X- and Y+, Y-). The Calibrator's output signal maximum amplitude is ±1.5 Vpk-pk, 4 ns between peaks.

4. TRIGGER CIRCUIT

4.1 Trigger mode selection and timing adjustment circit

The epBPM module has three options for triggering the S/H amplifier synchronous with the epBPM input signal peak. The sources of triggering pulses are - external gates, coming from the SLAC timing distribution system, internal trigger pulse or combination of the external gate and the internal trigger pulse. Those triggering modes are called - External Trigger, Gated and No Timing. In the External trigger mode there is an option to fire a pedestal trigger pulse calibrating the zero offset of the signal processing and digitizing channels.

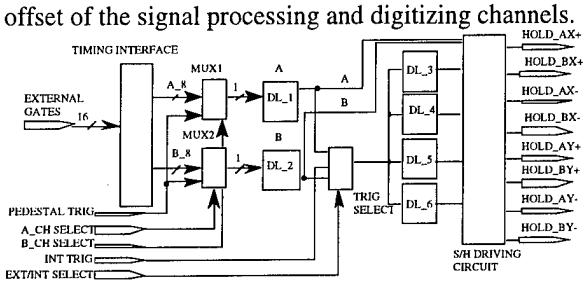

Figure 4. Trigger Circuit block diagram.

Timing interface is a 16-channels bus. The first signal (A) gate channels are 0 to 7 and the second signal (B) gate channels are 8 to 15 (Fig. 4). Multiplexers MUX1 and MUX2 select specific A and B channels respectively. MUX1 and MUX2 outputs go to trigger inputs of the programmable delays DL_1 and DL_2. The purpose of those delays is to compensate external gate cables mismatch.

DL_1 and DL_2 output signals (gate "A" and gate "B" respectively) and the internal trigger pulse go to trigger mode select gate (TRIG SELECT). The TRIG SELECT output pulse is gate "A" or gate "B" in the External Trigger mode, or internal trigger pulse in Gated or No Timing mode. The selected signal comes to the input of programmable delays DL_3 to DL_6. Delays DL_1 - DL_6 feed the S/H driving circuit, distributing inputs signals according to the selected mode of operation.

In the External Trigger mode the S/H "Hold" clock is synchronized with the external gate, in the Gated mode - with the internal trigger within the external gate, in the No Timing mode - with the internal trigger.

The signals from the Calibrator come to the S/H_A and the S/H_B at the same time. In the beam measurements the second bunch can be delayed from the first by time delays between 60 ns (minimum) and 400 ns (maximum), so the S/H_A starts to hold signal earlier, than the S/H_B. The ADCs start convertion signals for channels A and B is held off until 400 ns (ADC aquisition time) after the B channels are held. This prevents the noise due to start convertion and data clocking out pulses from corrupting the B channels data being held. After the signals convertion, all ADCs data are clock out (16 pulses, 5 MHz frequency) to the CAMAC interface registers, then the S/H driving circuit resets and the S/H amplifiers switch to sample mode.

The programmable delays DL_3 to DL_6 are used for the epBPM internal timing adjustment - to match S/H "Hold" pulse and S/H input signal peak. An individual delay is used for each signal processing channel. Calibrated delay data is stored in programmable read only memory (EPLD). Every module has individually burned EPLD. Delay data loads automatically at power on or at module reset.

The delays DL_1 to DL_6 output signal duration is 50 ns, programmable delay value could vary from 0 to 9.8 ns with 38 ps step, digital data 0 to 255 respectively.

4.2 Pedesta l trigger processing circuit

Timing channel 15 is reserved for pedestal measurements. Pedestal trigger follows the same chain as external gate. Synchronous with pedestal trigger the S/H stores the input signal value with no beam or calibrator pulse present. The ADC returns this value, which is the zero offset of the signal processing and digitizing channel.

4.3 Internal trigger circuit

The internal trigger pulse is the reference for the S/H "Hold" pulse in Gating and No Timing modes of operation. The Internal Trigger Circuit derives a trigger pulse from the zero crossing of the epBPM input signals.

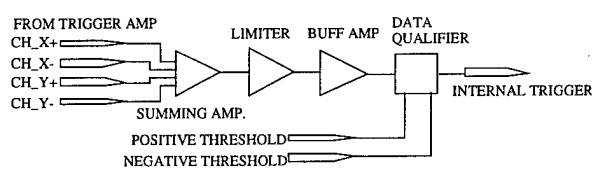

Figure 5. Internal Trigger Circuit

The Summing Amplifier (gain 1/2 - one channel) (Fig. 5) output signal is the sum of the signals from four trigger amplifiers (Fig. 2). Its output feeds the Limiter input. The limiter amplifier output signal range is limited to ±1V. This increases the dynamic range of the internal trigger circuit. Limiter output goes through the Buffering Amplifier (gain 2) to the Data Qualifier. The Data Qualifier consists of two threshold comparators and one zero crossing comparator. The thresholds levels determine

the level of the lowest signal which could be "seen" by the Data Qualifier. Potentiometers are used to adjust threshold level. The Data Qualifier generates a single trigger pulse synchronous with zero crossing event, 30 ns duration time. After generation of one pulse the Data Qualifier is ready for the next zero crossing event.

5. TIMING CIRCUIT AND CAMAC INTERFACE

CAMAC instruction decoding, timing distribution and data conversion are performed in a Field-Programmable Gate Array (FPGA). The following blocks are programmed in the FPGA: CAMAC instruction decoding; power startup (to load calibrated delay data); Calibrator control - to send CAL_GO pulse, to set attenuators values and to select pulse polarity; ADC control - to read data from the ADC, to reset the S/H driving circuit; Pedestal Trigger control - to start pedestal calibration; Trigger Modes control- to select trigger mode; Delay control - to load data to delay DL_1 - DL_6. Data and timing signal are distributed over the epBPM module via 8-bits local bus or individual traces. A crystal oscillator, 30 MHz ferquency, is used as reference for the internal clock.

6. MODULE SPECIFICATION AND BENCH TESTS RESULTS

The estimations of the epBPM module resolution and dynamic range are based on accurate calculations of the circuit noise level. The ADC signal-to-noise plus distortion ratio (SINAD) is 78 dB using a 50kHz input signal, 300 kHz sampling rate. The effective number of bits (N_{eff}) from the SINAD:

$$N_{eff} = \frac{SINAD - 1.76}{6.02} \approx 12.7$$

So the quantization error σ is:

$$\sigma = \frac{q}{\sqrt{12}} \cdot 2^{(N_{id} - N_{eff})} \approx 0.7 \cdot q,$$

where q is the ADC quanta's size, N_{id} - ideal ADC number of bits. Thus $\sigma \approx 610$ µV, or 434 µV rms. The OA3 (Fig. 2) input noise in 4 MHz bandwidth is 22 µV rms, the S/H noise is specified as 65 µV rms, OA1 input noise in 100Mhz bandwidth is 25 µV rms. Total noise value at the input of OA1, including 14 µV rms noise, generated by resistors, is 54 µV rms or 15.4 dB, refered to 50 Ohms resistance noise value in 100 MHz band. The signal processing channel gain is 10, so the equivalent ADC input noise is 540 µV rms [2].

The dynamic range is 6.5×10^3 or 76 dB (the ratio between the ADC maximum input signal and circuit noise at the ADC input). Resolution (Δx) is [3]:

$$\Delta x = \frac{a}{2\sqrt{2}} \cdot \frac{V_N}{V_0},$$

where V_N - is the rms noise value at the OA1 input, V_0 - is the bunch peak voltage for the beam in the center, a - is the half of beam pipe aperture (9 mm).

The measured bunch peak voltage from the Linac stipline electrode, connected in series with the S/C and Filter is 200 mV at 3.8×10^{10} particles per bunch (ppb) for the beam in the center. For this number of particles per bunch the resolution is ≈0.9 µm. The required resolution, specified at 5×10^{10} ppb is the 5 µm, the calculation gives 0.7 µm. The calculated resolution for PEPII 5×10^8 ppb (minimum) is 65 µm and for 10^{11} ppb (maximum)it is 0.5 µm.

Bench tests give less than 3.5 µm resolution of the beam position with the Calibrator pulse, corresponding to 1.52×10^{10} ppb. This is worse than the 2 µm estimated for this value, but better than 16 µm, derived from the required 5 µm. The resolution limiting factor is the difference of the propagation delay between peak and zero crossing for electron and positron- like pulses in the Internal Trigger circuit. The result is - different programmable delays values for the pulses with different polarity of the first peak. To achieve the best resolution for both pulses, an average delay value is used.

The measured dynamic range in the External Trigger mode with external pulser is 68 dB (pulser dynamic range), in the Internal Trigger it is 48 dB. In the Internal Trigger and Gated mode dynamic range is limited by noise, coming from the digital part of the epBPM board and from external sources.

7. SUMMARY

The Two-Bunch Beam Position Monitor design and specifications have been discussed. The bench tests results have been described. Comissioning of the epBPM modules has been planned for May, 1997, so the tests results may be available at conference time.

8. ACKNOWLEDGEMENTS

We would like to thank Ron Johnson, Jeff Olsen, Brooks Collins, Bob Noriega, Bob Traller, Ray Larsen, Tom Himel, Alan Fisher, Vern Smith for fruitful discussions, useful advices, help in prototypes debugging and modules tune up.

Work supported by U.S. Department of Energy, contract DE-AC03-76SF00515.

REFERENCES

[1] "epBPM Manual", Roberto Aiello, work note, SLAC, 1995

[2] "epBPM Noise, Dynamic Range, Resolution Estimates", Evgeny Medvedko, work note, SLAC, 1996

[3] "Beam Position Monitoring", Robert E. Shafer, AIP conference proceedings 212, Accelerator Instrumentation, Upton, NY 1989

EFFECT OF TE MODE POWER ON THE PEP-II LER BPM SYSTEM*

J. Corlett[1], C.-K. Ng[2] and S. R. Smith[2]
[1] Lawrence Berkeley National Laboratory, 1 Cyclotron Road, Berkeley, CA 94720, USA
[2] Stanford Linear Accelerator Center, Stanford University, Stanford, CA 94309, USA

Abstract

The beam chamber of the PEP-II B-Factory Low Energy Ring (LER) arc sections is connected to an antechamber for the absorption of synchrotron radiation on discrete photon stops. The presence of the antechamber substantially reduces the cutoff frequency of the vacuum chamber and, in particular, allows the propagation of higher-order-mode (HOM) TE power generated by beamline components at the BPM signal processing frequency. Calculations of the transmission properties of the TE mode in different sections of the vacuum chamber show that the power is trapped between widely separated bellows in the arc sections. Because of the narrow signal bandwidth and weak coupling of the TE mode to the BPM buttons, the noise contributed by the HOM TE power will not produce a noticeable effect on the BPM position signal voltage.

1 INTRODUCTION

The LER arc vacuum chamber employs an antechamber with a discrete photon stop for absorption of synchrotron radiation and with pumps for maintaining pressure below 10 nTorr [1]. The horizontal dimensions of the antechambers at the pumping chamber section and the magnet chamber section are larger or comparable to that of the beam chamber. Because of the increase in the horizontal dimension, the cutoff frequency of the TE_{10}-like mode (in rectangular coordinates) of the vacuum chamber is considerably reduced and, in particular, is less than the BPM signal processing frequency at 952 MHz. TE power propagating in the vacuum chamber will penetrate through the BPM buttons and will affect the pickup signal if its magnitude is not properly controlled. It is the purpose of this note to clarify various issues pertaining to this problem.

TE power is generated when the beam passes a non-cylindrically symmetric beamline component such as the RF cavity, the injection region, the IR crotch and the IP region. The beampipes connected to these components have TE cutoff frequencies greater than 952 MHz (for example, the TE cutoff frequency of the RF cavity beampipe is 1.8 GHz), and hence no TE power at this frequency propagates from the component. TE power can also be generated by the scattering of TM power through these beamline components. Since the cutoff frequency of the TM mode is in general higher than that of the TE mode, this mechanism is not pertinent to the problem related to the BPM signal. Consequently, the TE power that needs to be considered is mainly generated by components of the LER arc vacuum chamber, where the TE cutoff frequency is less than the BPM processing frequency.

* Work supported by the Department of Energy, contracts DE-AC03-76SF00515 and DE-AC03-76SF00098.

2 TE POWER GENERATION

The discontinuities in the arc chamber are the transitions between the pumping chamber and the magnet chamber, the BPM button gaps, the flange tapers and steps, and the transitions between the straight and the arc sections. In the following, we calculate the loss parameters of these components using MAFIA [2] and estimate the TE power generated by them.

(a) Pumping-to-magnet chamber transition The anamorphic schematic layout of the LER arc vacuum chamber is shown in Fig. 1. The magnet chamber is connected to the pumping chamber, which joins another magnet chamber at the downstream after a bellows. The cross sections of the magnet chamber, the pumping chamber and the bellows chamber are shown in Fig. 2. While the beam chamber cross section is the same at different sections, the antechamber geometry varies considerably. The pumping chamber contains a photon stop and pumps, and the magnet chamber and the bellows chamber each has a clearance slot of different horizontal dimension. The slot height (1.8 cm) is the same for all the chamber sections.

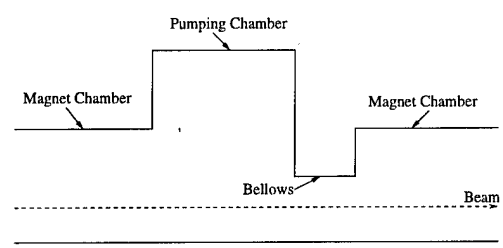

Figure 1: Schematic layout of LER arc vacuum chamber.

Wakefields are generated when a beam passes through discontinuities of a vacuum chamber. The slot of the LER arc vacuum chamber appears as a long continuous groove with discontinuities at the junctions of different chamber sections hidden inside. This is similar to the hidden slots structure introduced in Ref. [3] and follows the design of the ALS vacuum chambers. The beam electromagnetic fields seen by the hidden discontinuities are suppressed because of the exponential drop-off of the fields into the groove, and consequently the wakefield excitation is also reduced exponentially. Thus when the depth of the groove is larger than its height, the vacuum chamber produces very low impedance. This kind of slot structure has been used in the High Energy Ring (HER) arc vacuum chamber, and it was found to have very small impedance [4]. The lon-

gitudinal wakefield for one section of the LER arc vacuum chamber (see Fig. 1) when the beam is on axis is shown in Fig. 3. The wakefield is inductive in nature, and the loss parameter is found to be 1.14×10^{-8} V/pC, which corresponds to 0.41 mW for 3 A current and 4.2 ns bunch spacing. The TE power that can propagate at 952 MHz is generated when the beam is offset vertically. Since the loss parameter varies slowly with the beam offset, the generation of TE power at this frequency is expected to be negligible.

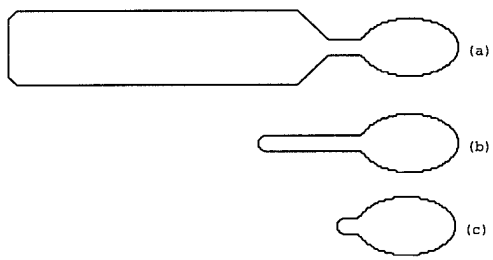

Figure 2: Cross sections of (a) the pumping chamber; (b) the magnet chamber; and (c) the bellows chamber.

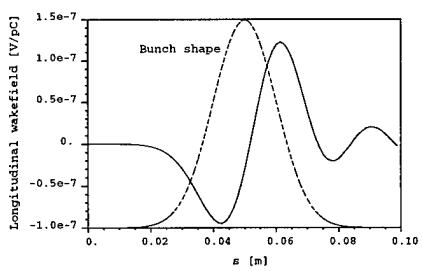

Figure 3: Longitudinal wakefield of the LER arc vacuum chamber. $\sigma_z = 1$ cm.

(b) BPM

The BPM button gaps will produce a larger loss parameter than that from the hidden discontinuities of the arc vacuum chamber. The loss parameter of the BPM in the HER arc vacuum chamber has been calculated before [5]; here we calculate the loss parameter in the LER arc vacuum chamber with the consideration of the side slot of the magnet chamber. The loss parameter is found to be 2.14×10^{-3} V/pC, which is much bigger than the contribution from the chamber discontinuities discussed above. Hence, the TE power generated by the BPM when the beam is off axis may not be negligible.

The TE power generated by the BPM can be evaluated using MAFIA by driving the beam off axis. The electromagnetic fields excited by the beam when it traverses the BPM will propagate along the vacuum chamber or into the BPM button. The fields propagating in the vacuum chamber can be decomposed into the waveguide eigenmodes of the chamber. In particular, we monitor the amplitude of the TE_{10} mode as a function of time. From the Fourier transform of the time variation, we obtain the spectral amplitude $\tilde{a}(\omega)$ of the TE power. The spectral amplitude for 1 cm beam offset is shown in Fig. 4. Since the BPM processes the signal at 952 MHz with a bandwidth of 20 MHz, we need to integrate the TE spectrum within this frequency range to obtain the power, which is given by

$$P = \frac{1}{2\pi}\Delta\omega|\tilde{a}(\omega_o)|^2\frac{q^2}{t_b},$$

where q is the bunch charge, and t_b is the bunch spacing in time. For a current of 3A, $q = 8.3\times10^{10}\,e$, and $t_b = 4.2$ ns, the TE power generated within the bandwidth $\Delta\omega/2\pi = 20$ MHz at $\omega_o/2\pi = 952$ MHz is found to be 3.78 μW.

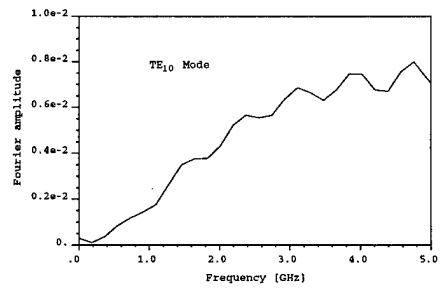

Figure 4: Fourier transform of the TE_{10} mode amplitude generated by the BPM.

(c) Other components

The other components that can generate TE power at around 952 MHz are the arc-to-straight transitions and the flange tapers and steps in the arc vacuum chamber. Since the transition is smooth, the flange taper has a small angle of 20 mrad maximum and the flange step is 0.3 mm or less, the loss parameters generated by these components are expected to be small. We approximate the discontinuities of these components by 2D models. The loss parameters of the arc-to-straight transition and the flange are found to be 6.80×10^{-4} V/pC and 2.38×10^{-4} V/pC, respectively. These are smaller than the loss parameter of the BPM. The TE power generated by these components are expected to be smaller also as the chamber cross sections have similar symmetry to that of the magnet chamber where the BPM is located.

3 TE POWER TRANSMISSION

TE power propagating in the LER arc vacuum chamber has different transmission properties at different sections due to the change in chamber cross sections. For the TE_{10} mode, the electromagnetic field is high in the slot region. The transmission properties of this mode are essentially governed by the slot region at the transition. At the pumping-to-magnet chamber transition, the clearance slot of the magnet chamber matches well with the slot region of the pumping chamber; and therefore the TE power can transmit through this transition with relatively little reflection. At the bellows transition region, the depth of the clearance slot of the bellows chamber is small compared with those of the magnet chamber and the pumping chamber at opposite ends; and thus a substantial amount of TE power will be reflected at this transition. In the following, we calculate the S-parameters for the TE_{10} mode at the pumping-to-magnet chamber transition and the bellows transition. With reference to the signal processing frequency of the BPM, the TE mode frequency is chosen to be 952 MHz.

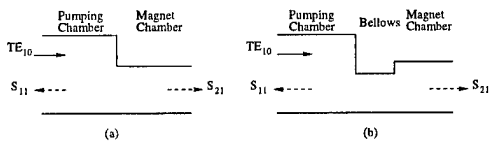

Figure 5: Schematics for S-parameter calculations at (a) the pumping-to-magnet chamber transition; (b) the bellows transition.

(a) Pumping-to-magnet chamber transition

The schematic for the S-parameter calculation at the pumping-to-magnet chamber transition is shown in Fig. 5(a). The cutoff frequencies of the TE_{10} mode of the pumping and magnet chambers are 324 MHz and 748 MHz, respectively, and hence TE power at 952 MHz can propagate through this transition. We drive the TE_{10} mode from the pumping chamber. The transmission coefficient, S_{21} is found to be 0.83. In other words, more than 50% of the power transmits to the BPM region in the magnet chamber.

(b) Bellows transition

The schematic for the S-parameter calculation at the bellows transition is shown in Fig. 5(b). The cutoff frequency of the TE_{10} mode of the bellows chamber is 1662 MHz, and hence TE power at 952 MHz is evanescent in the bellows chamber. The reflection coefficient, S_{11}, is found to be 0.99 at 952 MHz, and most of the power is reflected at this transition. Therefore, the bellows is expected to be shielded from TE power propagating in the vacuum chamber, and to isolate following sections of vacuum chambers from TE power generated prior to the bellows.

4 TE POWER PENETRATION IN BPM

The BPM is located either at the upstream or downstream end of the magnet chamber. The TE_{10} mode couples with opposite sign to the two buttons located at the top and at the bottom of the vacuum chamber as does the beam displacement signal. The vertical position measurement is obtained by the difference of the sum of the two top buttons signals and the sum of the two bottom buttons signals, while the horizontal position measurement by the difference of the sum of the two left buttons signal and the sum of the two right buttons signal. Therefore the coupled TE mode appears predominantly as a displacement error in the vertical direction and does not affect the horizontal measurement.

We carry out an S-parameter calculation to determine the transmission coefficients at the coaxial cables connected to the BPM buttons by driving at 952 MHz the TE_{10} mode of the magnet chamber. Fig. 6 shows the electric field pattern at the steady state of the calculation. It can be seen that the field concentrates in the slot, and hence the coupling of the TE mode to the BPM is small. The transmission coefficients at the left and the right buttons are found to be 1.56×10^{-2} and 7.81×10^{-3}, which correspond to power transmissions of 0.024% and 0.006%, respectively. The left button has a larger transmission coefficient than the right one because of the closer proximity of the left button to the high electromagnetic fields in the slot.

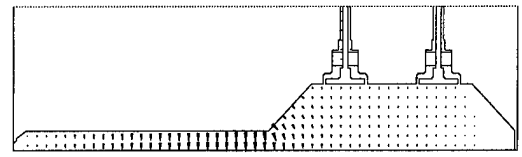

Figure 6: Electric field pattern at the BPM for the TE_{10} mode propagating in the magnet chamber.

As shown in section II(b), the dominant TE power at 952 MHz is generated by the BPM when the beam is off axis; a 3A beam vertically offset by 1 cm induces a TE power of about 4 μW within a 20 MHz bandwidth in the LER arc section. Some of this power couples to the BPM buttons causing an apparent vertical beam offset. A TE mode propagating past the BPM couples 0.03% of the mode power out the top two buttons in the bandwidth of the BPM processor. The attenuation length of the mode in the elliptical beampipe is about 250 m. Because of the large reflection coefficient at the bellows found in the last section, the power is trapped between two bellows 7 m apart, so the TE mode power passes the BPM approximately 35 times before being absorbed by the walls. This means that the buttons absorb approximately 1% (40 nW) of the TE power, which corresponds to a noise signal on the buttons of amplitude $\sim$ 1.4 mV. Comparing with the position signal voltage of 0.7 V at this current times displacement, the TE mode power represents a position error of 20 μm. However, this is a systematic effect; it is a transverse scale error equivalent to an error in pipe radius of two parts in 10^3. Our tolerances in transverse scale are at least 10 times larger.

5 SUMMARY

The LER arc vacuum chamber allows TE power propagating at the BPM signal processing frequency at 952 MHz. We have evaluated the TE power generated by different components of the vacuum chamber and the transmission properties of the TE power at different chamber transitions at this frequency. By calculating the coupling coefficients of the TE mode to the BPM buttons, the noise signal contributed by the TE power within the bandwidth of the BPM processor is small compared with the normal position signal voltage and is within the tolerances of the BPM system.

6 REFERENCES

[1] M. S. Zisman et. al., Design of the PEP-II Low-Energy Ring, Proc. of PAC95, p533, Dallas, May 1995.

[2] MAFIA User's guide Version 3.20, CST GmbH, Germany.

[3] T. Weiland, Low Impedance Vacuum Chambers, PEP-II Technical Note No. 59,1994.

[4] C.-K. Ng and T. Weiland, Impedance of the PEP-II DIP Screen, SLAC-PUB-95-7005.

[5] N. Kurita et. al., Simulation of PEP-II Beam Position Monitors, PEP-II Technical Note No. 87, 1995.

DETECTION OF BEAM INDUCED DIPOLE-MODE SIGNALS IN THE SLC S-BAND STRUCTURES

M. Seidel, C. Adolphsen, R. Assmann, D.H. Whittum
Stanford Linear Accelerator Center, Stanford University, CA 94309

Abstract

Beam emittance dilution caused by wakefield effects is one of the important issues in the SLC linac. The detection of beam induced dipole mode signals in the C-band range could provide a direct measure of the strength of transverse wakefield kicks the beam experiences in the accelerating structures. We investigate the applicability of these microwave signals for beam steering purposes. The RF distribution system in the linac sectors 2, 6 and 29 has been equipped with a simple experimental setup to observe the beam induced dipole mode signals. The paper discusses the setup, the mode-structure of the observed signals as well as experimental results from beam steering scans, obtained during the 95/96 SLC runs.

1 INTRODUCTION

The SLC main linac consists of roughly 900 ten foot long accelerator sections which are operated at 2.856 GHz (S-Band) in $2\pi/3$ mode. The linac accelerates positron and electron beams, delivered by damping rings, from 1.2 GeV injection energy to 47 GeV final energy. The injected beams are naturally flat with normalized emittances of $\gamma\varepsilon_x = 30$ mm mrad, $\gamma\varepsilon_y = 3$ mm mrad. During the acceleration process the vertical emittance grows typically by $100\ldots200\,\%$ due to wakefield effects. The head of the bunch excites asymmetric fields in the accelerating structures, to lowest order dipole modes, that consequently deflect the tail of the bunch. Energy variations along the bunch lead to a chromatic filamentation of this $y-z$ correlated distribution and an increased projected emittance. This type of emittance growth can be avoided in principle if the beam could be precisely centered in the structures to prevent the excitation of Higher Order Modes (HOM's). For centering of the beam orbit one relies in the SLC on beam position monitor (BPM) information and on a good alignment of the BPM's with respect to the structures. A better way for beam steering is therefore to measure the beam induced dipole mode signals directly in the structures and to minimize them to reduce the wakefields. Such a *structure BPM* would measure an absolute beam position in the only relevant reference frame, namely with respect to the electrical center of the structure itself. The whole scheme is possible because the dipole mode signals occur at higher frequencies than the much stronger accelerating mode, which then can be suppressed by appropriate filtering.

It can be expected that the application of structure BPM's to the SLC would improve the performance of the machine as well as the efficiency of orbit steering procedures.

2 SIGNAL ACQUISITION AND PROPERTIES

Beam induced dipole mode signals can be observed at the standard high power input and output couplers of the SLC structures. In our experiments we accessed the signals using a Bethe Hole coupler in the waveguide network that distributes the RF power from the klystron to two or four structures in the SLC tunnel [1], with the consequence that we observe in general the superposition of signals from several structures. The very strong accelerating mode component in the waveguide network is suppressed by a WR187 waveguide filter with a cutoff frequency of 3.16 GHz. The second harmonic is removed by an additional lowpass filter at 4.5 GHz. The bandpass-filtered signal is then analyzed either with a crystal detector, or a spectrum analyzer. Fig. 1 shows the time domain signal, obtained from the crystal after the passage of a single bunch at station 20-3c. This station differs from all others in that only one structure is connected to the klystron. From an estimated $Q \approx 7000$ one expects a ringing time of the signal of 1 μs, however, there are likely several reflections in the network which is not well matched at 4 GHz.

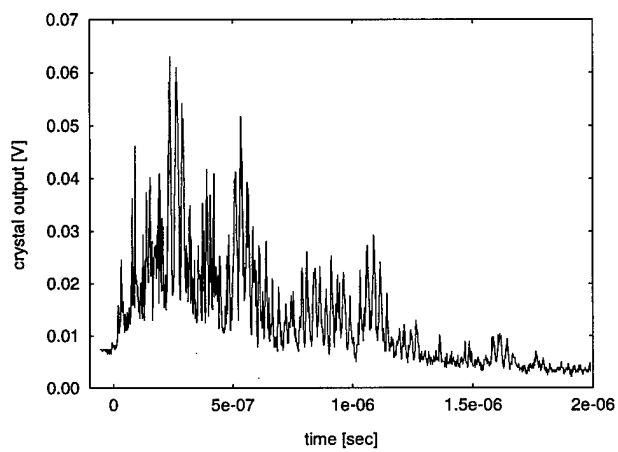

Figure 1: Crystal detector output signal showing signals in the frequency range $\approx 4-4.5$ GHz. The bunch enters the structure at $t=0$.

The dipole mode spectrum extends from 4.14 GHz to roughly 4.35 GHz. A trace of the peak-power vs. frequency that was recorded with a spectrum analyzer is shown in Fig. 2. The shown spectrum is typical for all stations that have been measured. It exhibits some features that are not expected - the signals extend in frequency below the lowest dipole mode at 4.140 GHz, and for no obvious reason we find a very strong signal around 4.210 GHz. All signals are seen to vary linearly with the beam position, i.e. they are

0-7803-4376-X/98 /$10.00 © 1998 IEEE

indeed dipole modes. We performed bench-measurements on a standard ten foot structure to investigate the mode-spectrum. Fig. 3 shows VSWR measurements of the structure from both ports, demonstrating that roughly 50 modes (out of 86) can be accessed from the input coupler. Here the lowest mode was observed at 4.143 GHz and no unusual structure was found around 4.210 GHz.

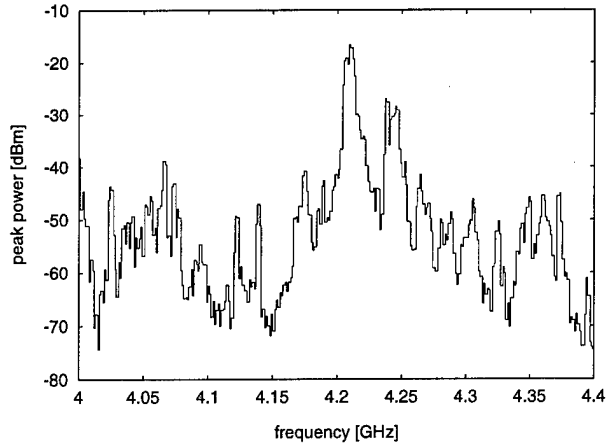

Figure 2: Typical beam excited dipole mode spectrum measured at a single structure (20-3c).

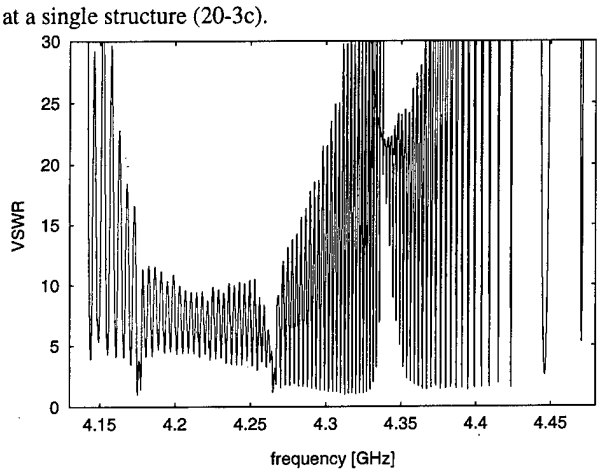

Figure 3: Standing wave ratio measurement on a ten foot structure. Left side from input end, right side output end.

3 BEAM STEERING EXPERIMENTS

In the simplest case we used gated ADC's to digitize the crystal detector video signals. The beam was steered in both planes to minimize the signals and to find the structure electrical center where minimal wakefield deflection should occur. This scheme was tried in sector 29 of the SLC linac were all klystron stations have been equipped with bandpass filters and crystal detectors. In this sector each klystron feeds four structures. In Fig. 4 we show the vertical beam positions at which the crystal detector signal was minimal, measured with BPM's. The data points exhibit a mostly positive offset of the order of 1 mm which is far outside the alignment tolerance of structures and BPM's. One possible explanation is that the signals are biased by x-polarized fields, although this would unlikely shift all measurements to one side.

More information on beam-to-structure alignment can be extracted by a spectral analysis of the dipole mode signals. The beam is swept in steps transversely across the structure and a complete spectrum is recorded at each step. The resulting two-dimensional power spectrum as a function of frequency and position is then fit slicewise to a parabolic parametrization with respect to the position. As one of the fit-parameters we obtain the minimum power position of the beam as a function of frequency. Because of the detuning of the structure the frequency of the signal provides a measure of the longitudinal position in the structure were it originated. The result of such a measurement is shown in Fig. 5. We find a smooth variation of $x_{\min}$ as a function of frequency. This method has been applied later successfully to perform a beam-based straightness measurement of an X-band structure [4].

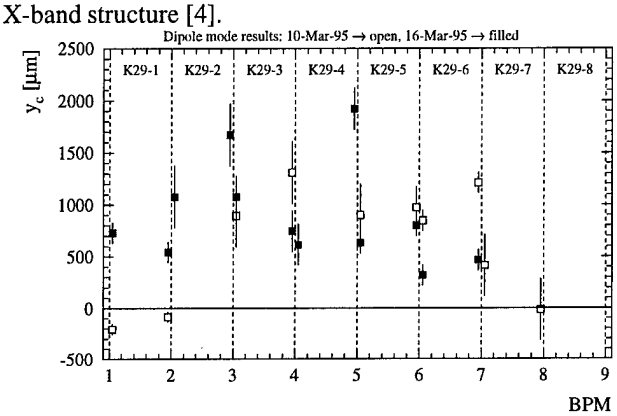

Figure 4: Measured vertical beam positions at 8 stations in sector 29 for minimum excitation of dipole modes in the corresponding structures.

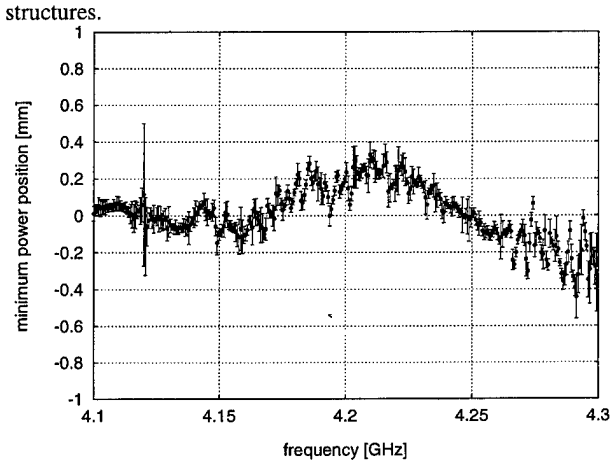

Figure 5: Minumum power positions in the horizontal plane as a function of frequency, obtained from a parallel beam scan at station 2-2.

Finally, the most precise way to measure the beam position locally in a structure is to detect both amplitude and phase with respect to beam arrival time of the dipole mode signal at a certain frequency. This was achieved in our setup by using the spectrum analyzer as a receiver at

a fixed frequency and analyzing the first stage IF signal ($f_{\mathrm{IF}} = 310\,\mathrm{MHz}$). For the phase measurement a broad band BPM signal was filtered around 4 GHz and mixed with the spectrum analyzer LO signal as well. The resulting two IF signals were then digitized in a fast scope and their amplitudes and relative phases determined by fitting sine functions to them.

The measured signal can be interpreted as a superposition of a component that scales linearly with the beam position and another component at some arbitrary phase that stays constant. The position independent component originates from coupling to fields polarized in the other plane, or from another structure that is connected to the same waveguide network.

$$
\begin{aligned}
U(x,t) &= A(x-x_0)\cos(\omega t) + B\cos(\omega t - \Delta\phi) \\
&= \hat{U}(x)\sin\left(\omega t + \phi(x)\right) \\
\hat{U}(x) &= \Big(A^2(x-x_0)^2 + \\
&\quad + 2AB(x-x_0)\cos(\Delta\phi) + B^2\Big)^{1/2} \\
\phi(x) &= \arctan\left(\frac{A(x-x_0)}{B\sin(\Delta\phi)} + \cot(\Delta\phi)\right)
\end{aligned}
$$

When the beam is moved transversely across the structure the amplitude $\hat{U}(x)$ reaches some minimum value, determined by the size of the *out-of-phase* component and grows again afterwards. In the same course the phase of the signal $\phi(x)$ shifts by 180°. A linearized beam position measurement can thus be obtained from the measured phase and amplitude by computing

$$\hat{U}(x)\sin\left(\phi(x)\right) = A(x-x_0) + B\cos(\Delta\phi)$$

Note that the position independent signal component shifts the minimum power position by $-B\cos(\Delta\phi)/A$.

The linearized result of such a beam scan in the horizontal plane is shown in Fig. 6. This measurement has been performed at station 2-2 that feeds two structures. An orbit fit from fifteen BPM's has been used to determine the real beam position at the location of the two structures. From a correlation analysis of the linearized dipole mode signal with the BPM data we obtain a resolution of 12 μm for our structure BPM.

4 SUMMARY

In summary we were able to detect beam induced microwave signals in the lowest dipole mode band in the SLC S-Band structures. Beam-to-structure alignment information was extracted in several ways. Using amplitude and phase detection a position measurement resolution of 12 μm was demonstrated. However, there is a much larger uncertainty in the determination of the absolute center position in the structure. This uncertainty is believed to be caused by mainly two reasons:

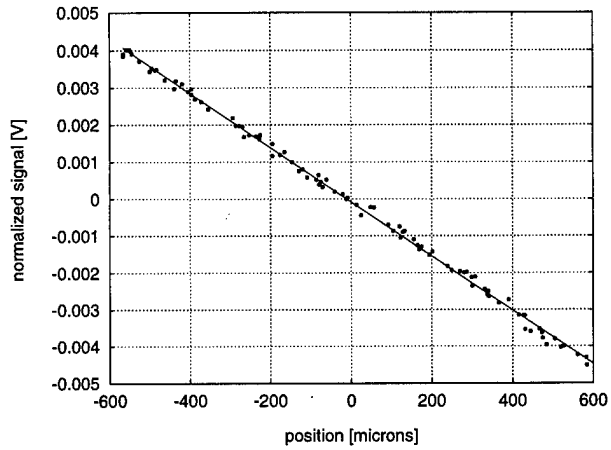

Figure 6: Linearized and signed amplitude of the dipole mode signal at station 2-2, frequency 4.139 GHz, as a function of the horizontal beam position determined with BPM's. The solid line is a linear fit.

1. The SLC structures have no dedicated HOM couplers that would allow one to separate horizontally and vertically polarized fields. Using the standard input coupler we measure a mixture of both signals which couples the response to offsets in both planes. Furthermore the input and output couplers introduce intrinsic asymmetries in the horizontal plane of the structure that might shift the electrical center for certain modes.

2. The detected dipole mode signals are a superposition from several structures which could introduce interference effects.

Despite the described problems, dipole mode detection can be useful if the signal is carefully minimized in multi-dimensional beam position/angle scans in both planes. The signal amplitude at the minimum of a one-dimensional scan can be used to assess the quality of the beam-to-structure alignment. As a first step the goal in the SLC is to identify badly misaligned structures which can be accomplished with the described methods. This work was supported by the Department of Energy, contract DE-AC03-76SF00515.

5 REFERENCES

[1] R.B. Neal *et al.*, The Stanford Two-Mile Accelerator, W.A.Benjamin Inc. (1968)

[2] A.M. Vetter, J.L. Adamski, W.J. Gallagher, IEEE Trans. Nucl. Sci. NS-32, 2329 (1983)

[3] C. Peschke *et al.*, in Proceedings 5th European Particle Accelerator Conference, Sitges, Spain (1996)

[4] M. Seidel, these proceedings

BEAM POSITION MONITOR SYSTEM FOR PEP-II

Stephen R. Smith, G. Roberto Aiello, Linda J. Hendrickson, Ronald G. Johnson, Mark R. Mills, and Jeff J. Olsen, Stanford Linear Accelerator Center, Stanford, CA 94309, USA

Abstract

We describe the beam position monitor system built for PEP-II, the B-factory at SLAC. The system reports beam position for bunches of between 5×10^8 and 8×10^{10} electron charges, either singly or as continuous streams of bunches every 4.2 ns. Resolution at full charge is to be better than 10 microns in a single turn. Higher resolution is available via on-board multi-turn averaging. The position signal is processed in a 20 MHz bandwidth around 952 MHz. This bandwidth, rather broader than that typical of RF position monitors, allows good resolution for low charge single bunches. Additional novel features include stringent control of return losses in order to minimize cross-talk between nearby bunches which may contain very different charges. The digitizing electronics is multiplexed between the two PEP-II storage rings. Design, construction, and installation experience, as well as first results with beam are presented.

1 PEP-II

The PEP-II B-Factory[1] is based on colliding e+ and e- beams stored in two rings operating at different energies. Currently the high energy ring is nearly complete; the low energy ring will be installed later this year. Both rings will contain up to 1658 bunches of electrons or positrons. The high energy ring will store currents up to 1 Amp, while the low energy ring, to be installed later this year, will operate to 3 Amps. The machine is to operate as a factory, meaning that the machine is expected to be colliding efficiently a large fraction of the time; sufficient diagnostics must be available to keep it running optimally.

Parameter	Value
Position Monitors	608 in two rings
RF frequency	476 MHz
Bunch spacing	238 MHz
Filled bunches	1658
Revolution Frequency	136 kHz
BPM Processors	170
Processing frequency	952 MHz
Time resolution	~ 5 bunches
Measurement rate	136 kHz
New measurement every	120 Hz

Table 1. PEP-II and beam position monitor system parameters.

Challenging aspects for the BPM system are the need for high dynamic range, from 8×10^{10} e^+ per bunch at a 238 MHz rate, down to a single bunch of 5×10^8 e^-. Good resolution and stability are required, as is the ability to measure even low-charge single bunches injected into an 80 ns gap in an otherwise filled storage ring.

Measurement Mode	Required Resolution (σ)
Single bunch, single turn	1 mm @ 5×10^8 e^-
	and 100 μm @ 1×10^{10} e^-
Single bunch, 10^3 turns	15 μm @ 1×10^{10} e^-
Multi-bunch, single turn	< 10 μm @ 1×10^{10} e^-

Table 2. BPM resolution requirements.

2 BEAM POSITION TRANSDUCERS

Each monitor consists of four buttons welded into the beam duct walls. Most BPM's have their button signals added pairwise so they read out either horizontal or vertical position. Buttons are 1.5 cm diameter in beam ducts with radii from 3.3 cm in the arc chambers to 4.5 cm in the straight sections. PEP-II RF is at 476 MHz. The first harmonic, 952 MHz was chosen for the BPM processing frequency. The button transfer impedance was calulated with MAFIA, as were wake-field impedances due to the buttons. The latter led to slight redesign of the buttons to meet the wake-field budget consistant with providing sufficient signal to meet BPM resolution requirements at low current.

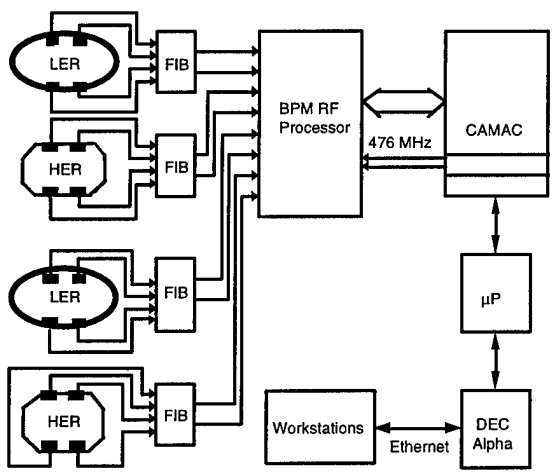

Figure 1. Diagram of BPM system, showing beam pickups, filter-isolator boxes, BPM processor, CAMAC, and control system.

0-7803-4376-X/98/$10.00 © 1998 IEEE

3 FRONT-END ELECTRONICS

Button signals are preprocessed in a "filter-isolator box" (FIB) mounted within a few feet of the buttons. This device is a constant input impedance 952 MHz band-pass filter with an RF isolator on each output so that its outputs are well-matched to the 50 Ω long-haul cables. Low S_{22} is needed to suppress round-trip reflections on the long-haul cable plant which would otherwise contaminate measurements of small single-bunches injected into a short gap in the high-current stored beam. The FIB sums the buttons pairwise for those BPM's where only a single coordinate is measured. It also provides a DC block and HV bias capability should we decide to place an ion-clearing field at the button locations.

4 DIGITIZING ELECTRONICS

The choice of 952 MHz as the processing frequency constrains the digitizing electronics to be located in the tunnel. Signal loss and cable costs prohibit bringing the signals out of the tunnel except for the BPM's closest to the centers of the straight sections. The processors are in CAMAC crates underneath the high energy ring bend magnets, which provide some shielding from synchrotron radiation.

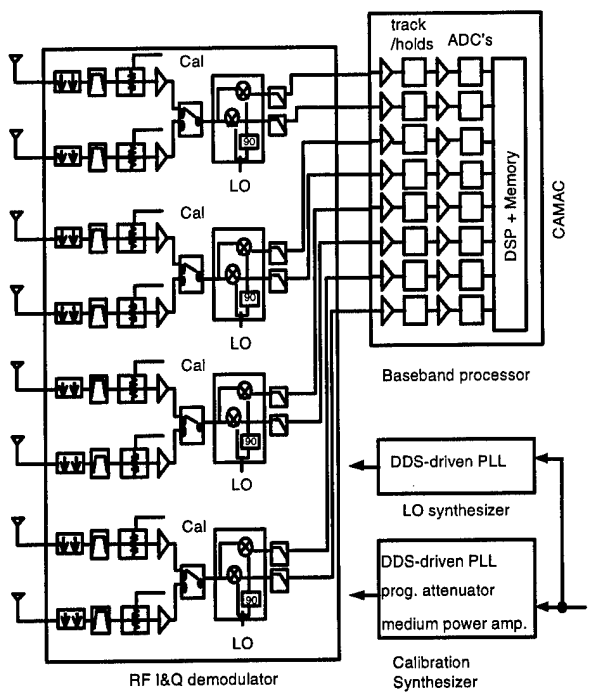

Figure 2. Ring I&Q BPM Processor block diagram. Each measures an X and Y BPM for each of two rings.

Signal processing is based on direct quadrature (I&Q) down-conversion of the 952 MHz bunch harmonic pesent in the button spectrum. A 20 MHz bandwidth was chosen to provide adequate signal-to-noise in the measurement of low-charge single bunches. The ratio of bandwidth to center frequency swayed the decision toward direct down-conversion rather than the more conventional dual conversion via an intemediate frequency. Quadrature demodulation was chosen to elimate the need for either a stable phase reference or a PLL locked to the beam which might prove troublesome at low currents absent stored beam.

Each processor module handles BPM's from both storage rings, selectable by a programmable high-isolation switch. The processor signal path includes a calibration coupler, a band-pass filter, programmable attenuator, and low-noise preamplifier in front of the switch. The ring-selection switch is followed by a quadrature demodulator which downconverts the 952 MHz signal directly to baseband. Both the in-phase and quadrature components are low-pass-filtered, sampled, and digitized at the ring revolution frequency. A DSP converts eight digitized vector components to the four button amplitudes. Position is calculated from the ratios of the differences of the amplitudes divided by their sums. The DSP also computes multi-turn averages, if requested.

5 CALIBRATION SCHEME

Each measurement of an X,Y position requires accurate measurement of the I and Q components of the signals on four buttons. Thus there are 8 voltages measured. Assuming linear response of the system, this requires knowledge of 18 calibration parameters: 8 pedestals (or ADC zero offsets), 4 ratios of the gains of in-phase channels to their respective quadrature channels, 4 I-to-Q phase angle errors, and the two ratios A_{up}/A_{down} and A_{left}/A_{right} which give the position offsets of a centered beam. These calibration parameters can be expected to drift with time and temperature and, in a factory machine which can't shut down to re-calibrate, must be measurable in the presence of stored beam.

Calibration tones, synthesised by an on-board DDS-driven PLL, are injected into the processor signal path upstream of the initial band-pass filter. Gain differences upstream of this point are expected to be static, and measured in the lab. The downconverted I & Q components are digitzed at the ring-turn rate of 136 kHz and fitted to a sine wave at the difference frequency between the local oscillator and the calibration tone. Calibration data is acquired during the ion-clearing gap. Beam-induced signal is further rejected by the fitting process when the the L.O. and calibration frequencies are chosen to be different from each other and from the 952 MHz harmonic of the bunch frequency. The amplitude, offset, and phase angles of the fitted sine curves provide all the needed calibration data.

A train of bunches at 4.2 ns spacing produces a line spectrum at the button, while a single bunch passing the button gives a spectrum broad compared to the band-width of the electronics. For bunch-train measurements

the processor is calibrated at 952 MHZ, while for single-bunch measurements gains are averaged over the channel bandwidth.

6 STATUS

Checkout of the processing electronics in the tunnel indicate the resolution and accuracy requirements are met. Measurements of simulated beam show 10^3 turn resolution $\sigma < 1$ μm at moderate currents.

All high-energy ring BPM's are installed, except for those in the interaction region. First beam was injected into the high energy ring and transported to a temporary beam dump upstream of the interaction region on May 10. The beam was seen on BPM's, but neither the beam nor the response of the position monitors to it are well-characterized at this time.

11 ACKNOWLEDGEMENTS

Work supported by the Department of Energy, contract DE-AC03-76SF00515.

REFERENCES

[1] PEP-II, An Asymmetric B Factory, Conceptual Design Report, SLAC-418, June 1993.

OPTICS MEASUREMENT RESOLUTION AND BPM ERRORS

Yu-Chiu Chao, Thomas Jefferson National Accelerator Facility

Abstract

We study the impact of BPM resolution on optics measurements at various levels of complexity: (1) Formula linking a given distribution of BPM resolutions to the degree of precision to which any beam trajectory can be determined based on these BPM's. (2). Formula for the precision achievable in a generalized experimental scheme measuring transfer matrices in the presence of (potentially coupled) orbit errors. (3) Formula constructed from results of (1) and (2) to relate the precision of the transfer matrix measurement to the signal-to-noise ratio of the BPM system. (4) Criterion defined to summarize how well the overall optical behavior of a large modular beam transport system can be quantified. The results from (1), (2) and (3) are used to arrive at the final analytical expression providing a generic criterion on BPM resolution for such systems. Realistic examples are discussed.

1 INTRODUCTION

The purpose of this report is to present a highly accurate formulation of the criterion for BPM resolution under various optics measurement schemes.[1]

Besides monitoring the beam orbit, BPM's are collectively used in trajectory determination for feedback systems or correction programs in the control system. The trajectories in turn can be collectively used to determine the transfer matrices across a section of the beam line. This is illustrated in Figure 1. The symbol $\mathbf{m}^{\mathbf{ab}}{}_{\mathbf{ij}}$ stands for the ij-th transfer matrix element from point **a** to **b**, while $x^{\mathbf{p}}$ stands for the orbit vector (x,x') at the point **p**.

2 PULSE-TO-PULSE TRAJECTORY MEASUREMENT

Using the notation of Fig. 1, we study the achievable precision in determining the pulse-to-pulse trajectory at point **p** using the BPM's in beam line section **A** upstream of the unknown section. The difference between two orbits can be determined by fitting the difference in the BPM data to the known optical model of **A**:

$$\mathbf{x^B} = \begin{pmatrix} x_1^1 \\ x_1^2 \\ \vdots \\ x_1^{N_B} \end{pmatrix} = \begin{pmatrix} m_{11}^{p1} & m_{12}^{p1} \\ m_{11}^{p2} & m_{12}^{p2} \\ \vdots & \vdots \\ m_{11}^{pN_B} & m_{12}^{pN_B} \end{pmatrix} \bullet \begin{pmatrix} x_1^p \\ x_2^p \end{pmatrix} = \mathbf{m} \bullet \mathbf{x^p},$$

$$\mathbf{x^p} = \mathbf{m}^{-1} \bullet \mathbf{x^B} \qquad (1.1)$$

where N_B is the number of BPM's used. The matrix inverse represents the least square fit. The covariance error matrix for the fitted orbit vector at **p**, $\langle \delta_x^{pi} \delta_x^{pj} \rangle$, can be derived, using symplectic conditions, as a function of the optics and the resolution $\sigma_B{}^q$ for the BPM's, with q indexing the BPM:

$$\sigma_X^{p1\,2} = \left\langle \delta_X^{p1} \cdot \delta_X^{p1} \right\rangle = \frac{2}{N_B} \cdot \frac{\left\langle m_{12}^{pa} \right\rangle_s^2}{\left\langle m_{12}^{aa} \right\rangle_s^2},$$

$$\sigma_X^{p2\,2} = \left\langle \delta_X^{p2} \cdot \delta_X^{p2} \right\rangle = \frac{2}{N_B} \cdot \frac{\left\langle m_{11}^{pa} \right\rangle_s^2}{\left\langle m_{12}^{aa} \right\rangle_s^2},$$

$$S^{p12} = \left\langle \delta_X^{p1} \cdot \delta_X^{p2} \right\rangle = \frac{-2}{N_B} \cdot \frac{\left\langle m_{11}^{pa} \cdot m_{12}^{pa} \right\rangle_s}{\left\langle m_{12}^{aa} \right\rangle_s^2},$$

$$\left\langle m_{12}^{aa} \right\rangle_s^2 = \sum_{a^i=1}^{N_B} \sum_{a^j=1}^{N_B} \left(\frac{m_{12}^{ai\,aj}}{\sigma_B^{ai} \sigma_B^{aj}} \right)^2,$$

$$\left\langle m_{12}^{pa} \right\rangle_s^2 = \sum_{a^j=1}^{N_B} \left(\frac{m_{12}^{paj}}{\sigma_B^{aj}} \right)^2,$$

$$\left\langle m_{11}^{pa} \cdot m_{12}^{pa} \right\rangle_s = \sum_{a^j=1}^{N_B} \left(\frac{m_{11}^{paj} m_{12}^{paj}}{\sigma_B^{aj} \sigma_B^{aj}} \right),$$

$$\left\langle m_{11}^{pa} \right\rangle_s^2 = \sum_{a^j=1}^{N_B} \left(\frac{m_{11}^{paj}}{\sigma_B^{aj}} \right)^2. \qquad (1.2)$$

This result can be used in feedback systems or other control program designs.

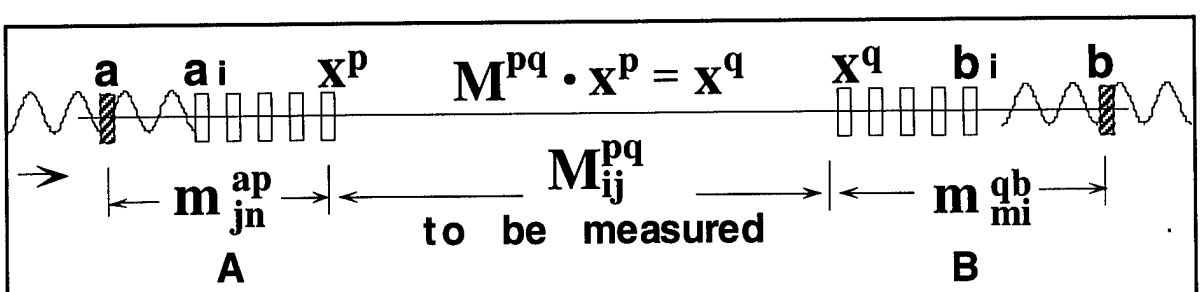

FIGURE 1

Partitioning the Double Sum

In many cases discussed below we can partition the BPM's into subgroups and simplify the double sum in Eqn. 1.3. These subgroups can be identical cells or all the BPM's identically located in each cell. The double sum then is reduced to

$$\frac{1}{G^2}\cdot\left\langle m_{12}^{aa}\right\rangle^2 = \sum_{k=1}^{G}\left\langle m_{12}^{aa}\right\rangle_k^{\,2} + \sum_{\substack{m>n\\ m=1,n=1}}^{G}\sum_{a=1}^{N_m}\sum_{b=1}^{N_n}2\left(m_{12}^{ab}\right)^2. \tag{1.4}$$

G above is the total number of subgroups, indexed by m and n. The subscript k indicates double sum only within a subgroup.

Simple Rule of Thumb

The sums in Eqn. 1.3 are actually very easy to calculate.[1] If one wants even more immediate estimates, the following rules of thumb can be a substitute. Notice that the last three equalities break down for small number of BPM's.

$$\begin{aligned}
&\left\langle m_{12}^{aa}\right\rangle^2 = \left\langle\beta\beta\right\rangle_{\sin}^2 = \frac{1}{2N^2}\sum_{i=1}^{N}\sum_{j=1}^{N}\beta^i\cdot\beta^j\cdot\sin^2\left(\varphi^i-\varphi^j\right),\\
&\left\langle m_{11}^{pa}\right\rangle^2 \xrightarrow{N>>1} \frac{\gamma_p\left\langle\beta\right\rangle}{2} = \frac{\gamma_p}{2N}\sum_{j=1}^{N}\beta^j,\\
&\left\langle m_{12}^{pa}\right\rangle^2 \xrightarrow{N>>1} \frac{\beta_p\left\langle\beta\right\rangle}{2} = \frac{\beta_p}{2N}\sum_{j=1}^{N}\beta^j,\\
&\left\langle m_{11}^{pa}\cdot m_{12}^{pa}\right\rangle \xrightarrow{N>>1} \frac{-\alpha_p\left\langle\beta\right\rangle}{2} = \frac{-\alpha_p}{2N}\sum_{j=1}^{N}\beta^j.
\end{aligned} \tag{1.5}$$

The subscript p labels the observation point **p**.

3 TRANSFER MATRIX MEASUREMENT

A scheme for measuring the unknown transfer matrix M^{pq}_{ij} is devised in Fig. 1. A total of N_O trajectories are sent through beam line sections **A** and **B**, where the orbit vectors are determined in the fashion discussed above at observation points **p** and **q**. These two sets of orbit vectors are sufficient for unfolding the unknown M^{pq}_{ij}. This scheme is better than the commonly adopted method relying only on knowledge of upstream kickers, in that it is immune to kicker errors and incoming orbit/energy jitters, that the beam line structure affords more exact error analysis, and that the flexibility in expanding the upstream section frees us from the limit on overall precision occurring otherwise[1]. The fitting problem now takes on the form

$$\begin{aligned}
&\left(M_{11}^{pq}\quad M_{12}^{pq}\right)\bullet\begin{pmatrix} x_1^{p1} & x_1^{p2} & \dots & \dots & x_1^{pNo}\\ x_2^{p1} & x_2^{p2} & \dots & \dots & x_2^{pNo}\end{pmatrix}\\
&\qquad = \left(x_1^{q1}\quad x_1^{q2}\quad \dots\quad \dots\quad x_1^{qNo}\right),\\
&\left(M_{21}^{pq}\quad M_{22}^{pq}\right)\bullet\begin{pmatrix} x_1^{p1} & x_1^{p2} & \dots & \dots & x_1^{pNo}\\ x_2^{p1} & x_2^{p2} & \dots & \dots & x_2^{pNo}\end{pmatrix}\\
&\qquad = \left(x_2^{q1}\quad x_2^{q2}\quad \dots\quad \dots\quad x_2^{qNo}\right).
\end{aligned} \tag{2.1}$$

Fitting for M^{pq}_{ij} is more involved now that the orbit vectors on both sides of Eqn. 2.1 have random errors, most likely coupled in the manner of Eqn. 1.2. Similar problem involving <u>uncorrelated</u> orbit errors in normalized coordinates has been addressed[2]. They correspond to eigenvectors of the covariance matrix constructed as follows:

$$\mathbf{C}_{ij} = \sum_{k=1}^{N_o} z_i^k\cdot z_j^k,\quad \mathbf{C}_{ij}\cdot\mathbf{N}_j = \lambda\mathbf{N}_i,$$

$$\mathbf{u_1} = \frac{\mathbf{N}}{|\mathbf{N}|},\quad |\mathbf{u_r}| = 1,\ r = 2,\dots.n. \tag{2.2}$$

The z^k_i's are the orbit vectors normalized by the uncoupled errors. The eigenvectors $\mathbf{N}_i$ contain the fitted transfer matrix elements, which are then normalized to $\mathbf{u}_i$'s. The error covariance for the $\mathbf{u}_i$'s is given by

$$\left\langle(\delta\mathbf{u_1})_i(\delta\mathbf{u_1})_j\right\rangle = \sum_{r=2}^{n}\frac{\lambda_r+\lambda}{(\lambda_r-\lambda)^2}(\mathbf{u_r})_i(\mathbf{u_r})_j. \tag{2.3}$$

To make Eqn. 2.3 applicable, we need to take the following steps.

- <u>Diagonalization</u>: We find the transformations diagonalizing the orbit error covariance matrices in <u>both</u> upstream and downstream sections. This is accomplished with symplectic matrices of the form

$$O_{p,q} = \frac{1}{\sqrt{2}}\begin{pmatrix} 1 & m\sqrt{\dfrac{A_{p,q}}{D_{p,q}}}\\ \pm\sqrt{\dfrac{D_{p,q}}{A_{p,q}}} & 1\end{pmatrix}, \tag{2.4}$$

$$\begin{aligned}
A_{p,q} &= \left\langle\delta x_1^{p,q}.\delta x_1^{p,q}\right\rangle,\\
B_{p,q} &= \left\langle\delta x_1^{p,q}.\delta x_2^{p,q}\right\rangle,\\
D_{p,q} &= \left\langle\delta x_2^{p,q}.\delta x_2^{p,q}\right\rangle.
\end{aligned}$$

In doing this we introduce extra couplings among the orbit vectors at **p** and **q**.

- <u>Application of Eqn. 2.3</u>: This gives the error covariance between the fitted matrix elements in the diagonalized coordinates.
- <u>Cross coupling between rows:</u> The two equations of Eqn. 2.1 appear uncorrelated. They nonetheless are coupled through sharing the same set of incoming orbits. This coupling has nontrivial effects when we restore to the undiagonalized coordinates. This effect, not addressed by Eqn. 2.3, has to be calculated.
- <u>Un-normalizing the unit vectors $\mathbf{u}_i$</u>: This gives the covariance in $\mathbf{N}_i$'s.
- <u>Un-diagonalization</u>: This gives the final error covariance in the physical coordinates, summarized as follows:

$$\left\langle {}^{\delta}M_{ij}^{pq} \cdot {}^{\delta}M_{kl}^{pq} \right\rangle = \sum_m \sum_n \sum_r \sum_s T^{mnrs}$$

$$T^{mnrs} = \left(O_q\right)_{im}^{-1} \cdot \left(O_q\right)_{kr}^{-1} \cdot \left\langle \delta M'^{pq}_{mn} \cdot \delta M'^{pq}_{rs} \right\rangle \cdot \left(O_p\right)_{nj} \cdot \left(O_p\right)_{sl} . \tag{2.5}$$

One quantity δ^{qi}_{Em}, defined by

$$\delta^{q1}_{Em} = M^{pq}_{11} \cdot \delta^{p1}_{Xm} + M^{pq}_{12} \cdot \delta^{p2}_{Xm} - \delta^{q1}_{Xm} ,$$

$$\delta^{q2}_{Em} = M^{pq}_{21} \cdot \delta^{p1}_{Xm} + M^{pq}_{22} \cdot \delta^{p2}_{Xm} - \delta^{q2}_{Xm} ,$$

$$m = 1,2,\ldots N_O, \tag{2.6}$$

stands out in the final expression. Notice that δ^{qi}_{Em} has an index m for the trajectory number. It represents the error at the exit point **q** when the difference between the exit orbit and the properly propagated entrance orbit from **p** is calculated. The error covariance in the fitted matrix elements then takes on an intuitive form:

$$\left\langle \delta M_{ij}^{pq} . \delta M_{km}^{pq} \right\rangle = \frac{1}{N_O} \cdot \frac{\left\langle \delta_E^{qi} \cdot \delta_E^{qk} \right\rangle}{\left\langle x_j^p \cdot x_m^p \right\rangle_{(d)}} , \quad i,j,k,m = 1,2.$$

$$\left\langle x_j^p \cdot x_m^p \right\rangle_{(d)} = \begin{cases} \left\langle x_j^p \cdot x_m^p \right\rangle \cdot \left(1 - R_p^2\right), & j = m \\ \left\langle x_j^p \cdot x_m^p \right\rangle \cdot \left(1 - R_p^{-2}\right), & j \neq m \end{cases} ,$$

$$R_p^2 = \frac{\left\langle x_1^p \cdot x_2^p \right\rangle^2}{\left\langle x_1^p \cdot x_1^p \right\rangle \cdot \left\langle x_2^p \cdot x_2^p \right\rangle} . \tag{2.7}$$

4 OVERALL FORM FACTOR

Combining Eqns. 1.3 and 2.7, we can calculate the overall error covariance in the fitted matrix elements in terms of the signal-to-noise ratio of the BPM's. We need to use the generalized symplectic condition:

$$m_{12}^{p\,ai} = -\frac{P_p}{P_{ai}} \left(m^{p\,ai}\right)_{12}^{-1} = -\frac{P_p}{P_{ai}} m_{12}^{ai\,p},$$

$$m_{11}^{p\,ai} = -\frac{P_p}{P_{ai}} \left(m^{p\,ai}\right)_{22}^{-1} = -\frac{P_p}{P_{ai}} m_{22}^{ai\,p}, \tag{3.1}$$

in case the momenta are different at **p** and **q**. This allows us to propagate all the orbits from **p** to **q**. The overall error covariance is then given by

$$\left\langle \delta M_{ij}^{pq} \cdot \delta M_{km}^{pq} \right\rangle =$$

$$2 \cdot \frac{1}{N_O} \cdot S_B^{jm} \cdot \frac{1}{T_{(d)}^{jm}} \cdot \left[\frac{1}{N_{B_q}} \cdot M_b^i \cdot M_b^k + \frac{1}{N_{B_p}} \cdot M_a^i \cdot M_a^k \cdot \left(\frac{P_p}{P_q}\right) \right], \quad i,j,k,m = 1,2.$$

$$R_p^2 = \frac{\left\langle x_1^p \cdot x_2^p \right\rangle^2}{\left\langle x_1^p \cdot x_1^p \right\rangle \cdot \left\langle x_2^p \cdot x_2^p \right\rangle} ,$$

$$S_B^{jm} = \frac{\sigma_B^2}{\sigma_O^{pj} \cdot \sigma_O^{pm}} , \quad T_{(d)}^{jm} = \begin{cases} \left(1 - R_p^2\right), & j = m \\ \left(1 - R_p^{-2}\right), & j \neq m \end{cases} ,$$

$$M_a^1 = \frac{\left\langle m_{12}^{qa} \right\rangle}{\left\langle m_{12}^{aa} \right\rangle} , \quad M_a^2 = \frac{\left\langle m_{11}^{qa} \right\rangle}{\left\langle m_{12}^{aa} \right\rangle} ,$$

$$M_b^1 = \frac{\left\langle m_{12}^{qb} \right\rangle}{\left\langle m_{12}^{bb} \right\rangle} , \quad M_b^2 = \frac{-\left\langle m_{11}^{qb} \right\rangle}{\left\langle m_{12}^{bb} \right\rangle} . \tag{3.2}$$

The physical significance of these quantities deserves some elaboration:

1. Factors determined by experimental parameters:

- S_B^{jm} is the generalized signal to noise ratio. It may take on a dimension of meter or meter^2 in some cases.
- $T_{(d)}^{jm}$ characterizes the position-angle coupling at the observation point **p**, nearly inevitable in real experiments. When R_p=0, this term makes some of the correlation terms disappear.
- N_O is the sample size, i.e., the number of orbits used.

2. Factors determined by machine parameters:

- $N_{p,q}$ are the number of BPM's used to determine each trajectory at the observation points **p** and **q** respectively. It's evident by Eqn. 3.1 that the overall precision can not be improved indefinitely by increasing the number of BPM's <u>only</u> on one side of the measured section.
- $P_{p,q}$ are the momentum values at the observation points **p** and **q**.
- $M_{a,b}^{1,2}$ are the RMS ratios defined in Eqn. 1.3. Their evaluation is easier than appears.(1) Notice the minus sign in the last equation.

For a BPM system designer, these quantities translate into other machine specifications and have to be taken into account in optimizing the performance. For example, N_O is limited by the speed of the BPM electronics and operation/control interface, S_B^{jm} is limited by the beam pipe radius and transfer properties all around the machine, $M_{a,b}^{1,2}$ are bound by optical or experimental conditions, while everything else has to conform to cost restrictions. But Eqn. 3.2 does take the guesswork out of the design so far as optical requirements are concerned. All analytic formulas presented above have been numerically verified.

ACKNOWLEDGMENTS

This work was supported by the U.S. DOE under contract number DE-AC05-84ER40150.

REFERENCES

[1] Complete detail, more specific formulas and numerical examples can be found in 'Optics-Driven Design Criteria for BPM's', Y. Chao CEBAF TN-93-073 (1993).

[2] Lohse, T. and Emma, P., "Linear Fitting of Beam Orbits and Lattice Parameters," SLAC-CN-371 (1989).

LINEAR OPTICS CORRECTION IN THE CEBAF ACCELERATOR*

V. A. Lebedev, M. Bickley, J. Bisognano, S. Schaffner, J. van Zeijts, G. A. Krafft, M. Tiefenback, W. A. Watson III, B. Yunn, Thomas Jefferson National Accelerator Facility, 12000 Jefferson Ave., Newport News, VA 23606 USA

Abstract

During commissioning of the CEBAF accelerator, correcting dispersion, momentum compaction and betatron beam envelopes was essential for robust operation. To speed the diagnostic process we developed a method which allows one to track and correct the machine optics on-line. The method is based on measuring the propagation of 30 Hz modulated betatron oscillations. The beam optics of the accelerator was altered to decrease lattice sensitivity at critical points and to simplify control of the betatron function match. The calculation of the Courant-Snyder invariant from signals of each pair of beam position monitors was used for a correction of the betatron functions. The experience of optics correction and the study of long and short term machine reproducibility obtained during 1996 and early 1997 are also discussed. With minor modifications this method can also be used for on-line optics measurement and correction in circular accelerators.

1 INTRODUCTION

The CEBAF accelerator[1,2] is a five pass CW recirculator with beam power up to 800 kW. It consists of a 45 MeV injector, two superconducting (SC) linacs of 400 MeV ener-gy gain, and nine arcs which connect the linacs for beam recirculation for total beam energy of 4.045 GeV. Logically the machine is separated into the following regions: injec-tor, north and south linacs, nine 180^0 bend recirculation arcs with associated entrance and exit matching regions, and the spreader and recombiner regions at the ends of each linac which separate particles of different energies or merge them for reinjection into the succeeding linac. After acceleration to the desired energy, the beam can be split and directed to three experimental halls for nuclear physics experiments. The path traversed to full energy is more than 6 km in length, over which the beam is focused by about 700 quadrupoles. Each quadrupole is independently powered, which creates many possibilities for machine optics but also complicates the machine tuning and operation.

During machine commissioning in early 1995, the betatron functions were found to be seriously degraded with beam acceleration and local dispersion correction was not reliably stable over time spans of days. Machine operation was overly sensitive to small energy and steering fluctua-tions. Periodic arc-by-arc dispersion correction allowed ma-chine operation with the full energy CW beam at the end of 1995, but severe betatron mismatch still remained. Initially, corrections were done using measurements of differential orbits generated by DC changes in steering magnet settings. The combination of poor machine reproducibility and limited tuning time made it difficult to accomplish optics diagnostics and correction with existing instrumentation.

2 INSTRUMENTATION FOR OPTICS STUDY

To accelerate the measurements[3], we added an ability for the BPMs to detect beam displacements excited by an AC external perturbation. Because line-synched 60 Hz pulsed beam has been the main mode for machine tuning, we chose the modulation frequency of 30 Hz. This choice automatically suppresses both power line electromagnetic interference and the deleterious effects of slow beam drifts. The 30 Hz modulation is generated by a function generator that resides in the machine control center and is phase locked to the beam pulses. The modulation is delivered to one of the modulation devices by computer controlled switches, depending on the type of measurement to be accomplished. Presently, there are two types of modulation used: beam energy modulation performed by changing the accelerating gradient of the superconducting cavities, and transverse beam modulation performed by air core dipole correctors. Both types of the modulation can be applied at the end of the injector at an energy of 45 MeV, and at the beginning of ARC1 at an energy of 445 MeV, providing optics measurements of the entire machine. Beam energy modulation is achieved by switching the modulating voltage to an analog input of the gradient feedback loop of the eight RF control modules. The modulation voltage is adjusted for a relative energy change of about $(1\div2)\cdot10^{-3}$. The eight se-lectable correctors (two vertical and two horizontal in each of the 45 and 445 MeV energy regions) allow for excitation of a betatron motion with different betatron phases. Usually we excite beam motion with an initial amplitude of about 3 mm, which after acceleration by a factor of ten dies down to about 1 mm due to adiabatic damping.

The beam position measurement system includes approximately 500 BPMs distributed across a network of 20 input-output controllers (IOC). Data for the BPM measurements are acquired at a 60 Hz rate and stored in IOC memory for processing. The mean value of the beam

* This work was supported by U.S. D.O.E. contract #DE-AC05-84ER40150.

position and the amplitude of the 30 Hz beam motion are calculated from each 12-sample buffer of successive hardware readings. Because the modulating voltage is locked to the beam pulses, the ADC measurements of the BPM signals are automatically synchronized to the modulation. The synchronization of readings for different IOCs is accomplished by broadcasting a sign bit of the 30 Hz modulation. One of the IOCs, called the master IOC, measures the sign of the 30 Hz signal and sends synchronization messages through the network.

3 ALTERNATE OPTICS

The large scale of the accelerator requires high field accuracy of the magnets. The design specifications for the quadrupoles ($\sim 1 \cdot 10^{-3}$) have not been met in the real machine, and, consequently, that required an intensive study how to tune the accelerator optics to provide high quality beam transport. These matters were complicated by frequent adjustments of the accelerating profile along the linacs and the machine path length, and by overall deficiencies in machine reproducibility.

Adjustment of the accelerating profile is caused by changes of state of the accelerating cavities as they are taken off- or on-line for maintenance reasons. The accelera-ting profile is always non-uniform and changes from day to day. Such changes are accounted for in the focusing of the first-pass beam at the time of accelerating gradient adjust-ment, but the higher passes are subjected to the betatron mismatch. Path length adjustments are necessary to keep higher passes on the crest of the accelerating wave. The desired path length accuracy of about 0.25 mm (~0.5 deg.) results in frequent path length adjustment to track seasonal and weather variations. The large vertical beta-function in the path length correction chicane (dogleg) magnets (located in the spreaders) results in a significant change of the vertical focusing in the course of correction. The largest effect has been found in the first two arcs where the beta-functions deviate from the design values by more than a factor of two over the nominal adjustment span of one path length chicane.

The following requirements have guided the redesign of the optics: decreasing beta-functions at linacs and doglegs, creating a set of orthogonal knobs for global betatron match, and adjusting functions to satisfy the requirements of beam-based feedback systems used for suppressing beam drifts[4]. To satisfy these requirements, the quadrupoles in the spreaders and recombiners were adjusted, changing the machine functions in the spreaders, recombiners, and linacs while leaving them unchanged in the arcs. The vertical beta functions inside the doglegs were decreased by about a factor of three. The largest improvement in the beta functions of the linacs was for the last two passes. In particular, for the fifth pass, the decrease of the beta functions was about 30% for the north linac and more than a factor of two for the south linac.

The orthogonal knobs for optics correction, have been a main feature of the new optics. Eighteen regions, one in each spreader and recombiner, allow one to do a smooth match throughout the entire machine. Each region has four quadrupoles assigned for correction of the beta-function and its derivative, for both the horizontal and vertical planes. To decouple the horizontal and vertical corrections there is a large difference in the horizontal and vertical beta-functions inside these quadrupoles. Because a mismatch of the beam envelope oscillates at twice the betatron frequency, the two quadrupoles of each correction set, horizontal or vertical, are shifted by $(45+n\times 90)$ deg. in betatron phase. This orthogonality of their effects results in minimal changes of their gradients to perform a betatron match.

4 PERFORMING OPTICS CORRECTION

Dispersion correction requires a modulation of the beam energy. The horizontal and vertical differential beam positions will be proportional to the horizontal and vertical dispersions. Adjustment of assigned quads allows on-line cancellation of the cumulative dispersion downstream from each dispersive section of the machine for both the horizontal and vertical planes.

Performing the betatron match is more complicated. It is based on the fact that if the machine lattice matches the design lattice the Courant-Snyder invariant remains constant. The general idea is to excite the betatron motion and observe how the invariant changes during beam transport. The changes occur at elements which have incorrect focusing. The perturbation depends both on the focusing error and the betatron phase. Thus measurements with different betatron phases are performed to obtain complete information on the betatron match.

For performing the betatron match, in addition to the differential BPM screens, we built a program which calculates (x, x', y, y') from pairs of adjacent BPMs. Using design beta-function information, this program plots the effective betatron motion amplitude for the entire machine. This amplitude is proportional to the square root of the Courant-Snyder invariant and has an additional beam energy normalization so that the amplitude remains constant with beam acceleration.

As in the case of dispersion correction, the correction of betatron functions is performed arc-by-arc. To match beta-functions of two sequential regions of the machine an operator must adjust four corresponding quadrupoles (two for each plane) assigned for betatron match between these regions so that the normalized amplitudes for all four correctors are unchanged throughout the accelerator.

Figure 1 shows the behavior of normalized amplitudes for a horizontal perturbation after correction of the betatron match. Note that the normalized amplitude does

not change significantly in one arc and errors are not accumulated along the machine. Without this tuning the normalized betatron amplitude usually grows by a factor of from three to ten. The occasional large spikes on the curves are associated with BPMs that are not functioning properly.

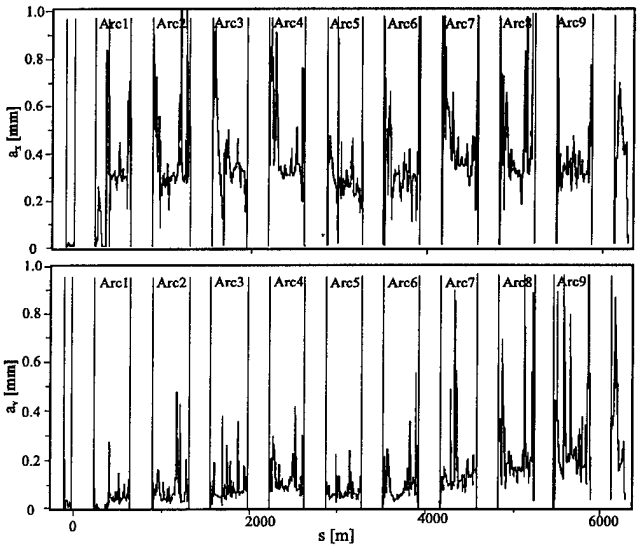

Figure 1. Normalized betatron amplitude for horizontal and vertical beam motion throughout the accelerator in the case of horizontal kick at the beginning of ARC1.

Usually an operator watches screens for horizontal and vertical normalized amplitudes simultaneously and can see an effect of the horizontal-vertical coupling in the process of correcting the betatron functions. This coupling originating from skew-quadrupole fields of the SC-cavity couplers[5] is adjusted during and at the end of the betatron match by skew-quadrupole correctors located near each cryomodule. The effect of the coupling is seen in Figure 1 where the amplitude of the vertical motion is slowly growing along the machine for an initial horizontal perturbation. Although one can still see a residual coupling, its size is significantly reduced compared to the case without corrections.

5 DISCUSSION AND CURRENT STATE

These improvements in instrumentation, software, and procedures provide fast on-line ability to carry out tests of the beam optics and to perform any necessary corrections. The ability to tune the machine quickly has been crucially important in conditions of poor machine reproducibility. After the machine was tuned it has been much easier to study the causes of irreproducibility. As a result one of the first actions taken was zeroing of all machine sextupoles. The sextupoles were installed to perform chromatic correction of the machine functions and, consequently, to increase energy aperture. Unfortunately they make the optics orbit dependent, so that in the real machine a change of vertical orbit in the arcs causes a strong mismatch in both vertical and horizontal dispersions and a decrease of the energy aperture.

The main issue for study over the past year, after correction of a serious problem with the magnet power supplies, was machine reproducibility. This study showed that the major remaining problem occurs during hysteresis cycling of the quadrupoles and correctors. Each of these magnets (about 1600 in number) has its own power supply. The high inductance of the highest-energy quadrupoles (the largest quadrupole family) was not properly considered in the selection of tuning parameters for the power supply regulation circuits. As a result the power supplies are under-damped when used with these magnets, which makes a cur-rent overshot at the cycle end. The IOC-based control used to ramp the magnet setpoints then introduces a timing de-pendence upon network and IOC load. That causes a varia-ble result of hysteresis cycle. A second problem is hard-ware errors in the digital communication path, which causes incorrect setpoints to be written to the power supply a few times per million writes. These points are being corrected.

In spite of the fact that during dispersion and betatron function matching we did not directly monitor the beam sizes, performing the match resulted in a small beam size throughout the machine. Measurement shows that there is practically no emittance growth during beam transport, which yields average rms beam sizes of about 50 μm at full beam energy. Although we already achieved the design quality of the beam transport, we still need to understand better the reasons of the machine optics deviations from the design, such as too large field correction in quads responsible for vertical dispersion correction, and the origin of x-y coupling in spreaders and recombiners.

We would like to thank A. Hutton, C. Sinclair, and D. Douglas for fruitful discussions and support of this work. We greatly appreciate the help of the whole operations department, which helped us by their continuous efforts.

REFERENCES

[1] Douglas, *et al.*, CEBAF-PR-89-008; *Proc. of the 1989 Particle Accelerator Conference*, pp. 557-559 (1989)
[2] Bowling, *et al.*, *Proc. of the 1991 Particle Accelerator Conference*, pp. 446-448 (1991).
[3] Correction of Dispersion and the Betatron Functions in the CEBAF Accelerator, V. A. Lebedev, *et al.*, *submitted for publication in NIM.*
[4] Development of Digital Feedback Systems for Beam Position and Energy at the Thomas Jefferson National Accelerator Facility, J. Karn, *et al.*, *this conference.*
[5] Li, Zenghai, *Proc.of the 1993 Particle Accelerator Conference*, pp. 179-181 (1993)

1 nA BEAM POSITION MONITORING SYSTEM

Rok Ursic, Roger Flood, Chip Piller and Edward Strong, Larry Turlington
Thomas Jefferson National Accelerator Facility, Newport News, VA 23693 USA

Abstract

A system has been developed at Jefferson Lab for measuring transverse position of very low current beams delivered to the Experimental Hall B of the Continuous Electron Beam Accelerator Facility (CEBAF). At the heart of the system is a position sensitive cavity operating at 1497 MHz. The cavity utilizes a unique design which achieves a high sensitivity to beam position at a relatively low cavity Q. The cavity output RF signal is processed using a down-converter and a commercial lock-in amplifier operating at 100 kHz. The system interfaces with a VME based EPICS control system using the IEEE 488 bus. The main features of the system are simple and robust design, and wide dynamic range capable of handling beam currents from 1 nA to 1000 nA with an expected resolution better than 100 μm. This paper outlines the design of the system.

1 INTRODUCTION

The Thomas Jefferson National Accelerator Facility, or Jefferson Lab, is a basic research laboratory built to probe the nucleus of the atom to learn more about the quark structure of matter. The underground recirculating accelerator uses superconducting radio-frequency technology to drive electrons to energies between 800 MeV and 4 GeV. The electron beam can be split for use by three simultaneous experiments in the end stations.

The middle one of the three experimental stations, hall B, requires beam currents in the range from 1 nA to 1000 nA. A new BPM system was needed to accommodate beam position measurements at such low currents. We selected a system using position sensitive resonant cavities as pickups and phase-sensitive synchronous demodulators. The project started in January 1996.

2 SYSTEM OVERVIEW

Number of BPMs	3
Beam Energy	800 MeV - 4 GeV
Operating Range	1 nA - 1000 nA
Parameters to be Measured	x and y positions, current
Nominal Measuring Rate out of control system	1 orbit/s
Position Measuring Range	$\lvert x\rvert, \lvert y\rvert \leq 5$ mm
Absolute Accuracy	≤ 1 mm
Resolution	≤ 100 μm @ 1 nA CW
Linearity Within	$\partial x/x \leq 10$ %
Measuring Range	$\partial y/y \leq 10$ %
Current Dependence	≤ 50 μm peak-peak @ required current ±50 %
Stability, Drift	≤ 25 μm rms in 8 hours

Table 1: System specifications.

Concept selection was the most difficult part of this project. We searched at Jefferson Lab as well as at other laboratories and industry for alternative concepts that would give us a good starting point.

At the time the project started, CEBAF was equipped with a Switched Electrode Electronics BPM system (SEE) covering dynamic range from 1 μA to 1000 μA [1]. We initially hoped to increase the sensitivity of the beam-pickups and the electronics each by factor of thirty to make a BPM system that works down to 1 nA. However, we soon realized that we could increase the SEE electronics sensitivity by no more than factor of five. The key limitation of the system was a quasi-synchronous demodulator around which the electronics was built. The problem does not lie in the particular circuit that we use, but in the quasi-synchronous demodulation concept, where signal to be demodulated is also used to generate a demodulation carrier. A phase-sensitive demodulation scheme appeared to be the only feasible solution for electronics. A similar system that uses phase-sensitive synchronous demodulation is operational at Mainz Microtron in Germany [2]

A position sensitive resonant cavity came at the top of our list among alternatives for beam pick-ups. It was the only type of pick-up that promised an increase in position sensitivity by factor of approximately 30 with respect to the wireline BPMs used at CEBAF accelerator [3]. We evaluated different resonant cavity configurations: circular, rectangular, off-centered TM010. We selected a design that is conceptually similar to the RF separator cavity design used at CEBAF to split electron beam to three experimental halls [4]. This position sensitive cavity, explained in detail below, gives approximately 10 dB greater position sensitivity than a circular TM110 cavity.

Figure 1 shows a system block diagram. A position measurement is done by taking the signal from a position sensitive cavity (x or y) and normalize it with the one from a current cavity. To get x, y positions and beam current we need three dedicated electronic channels.

0-7803-4376-X/98/$10.00 © 1998 IEEE

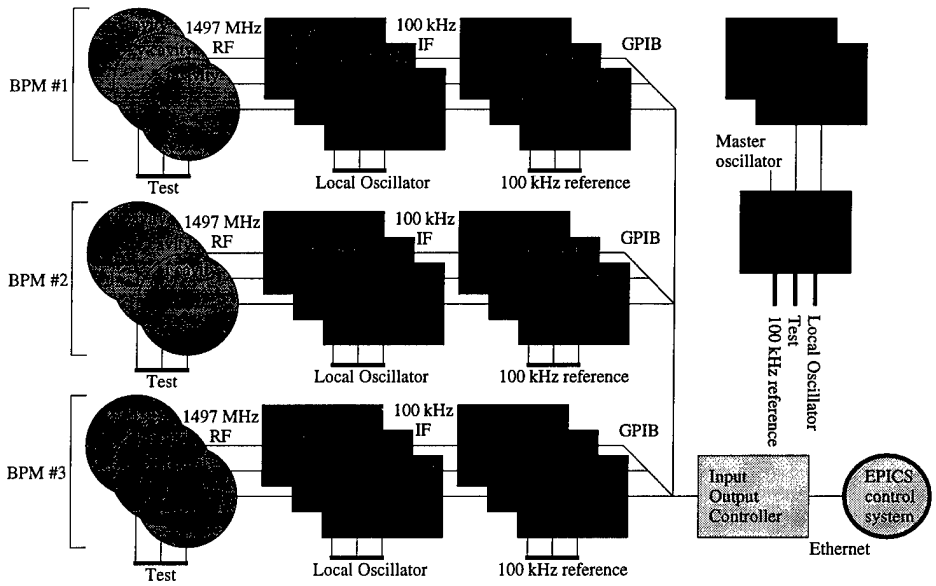

Figure 1: 1 nA BPM system block diagram.

3 POSITION CAVITY

Information about the beam is provided to the electronics by three room temperature RF cavities operating at the third harmonic of the 499 MHz bunch frequency. Two of the cavities are position monitors with one producing an X position x current signal and the other a Y position x current signal. The third cavity is a CEBAF Beam Current Monitor [5] that provides beam current and phase information necessary for position signal amplitude scaling and sign correction.

Bunching Frequency	499 MHz
Beam Line Aperture Restriction	3.0 cm diameter minimum
BPM Resolution	70 pV/μm (-150 dBm @ 100 μm)@1nA
Longitudinal Beam Line Space	90 cm maximum
Position measuring range	$\lvert x\rvert, \lvert y\rvert \leq 5$ mm
Resonant Frequency	1497 MHz
Loaded Q	3500
Diameter	19.0 cm
Depth	9.5 cm
Rod Gap	3.0 cm
Material	Copper Plated Stainless Steel

Table 2. Position cavity specifications.

The position cavity is a new design that offers excellent stability and transverse sensitivity and mode isolation. The cavity is a pillbox with field perturbing rods operating in a dipole type mode (see figure 2). Resolution is defined here as the ratio of the change in the cavity output signal voltage divided by the change in the beam position for a given current. The longitudinal electric field of the mode goes through a null point (and sign reversal) in the center of the cavity resulting in a shunt impedance of zero and no output signal for a centered beam. The position cavity is designed to measure accurately beams that travel through a one centimeter square window centered on the cavity axis. Inside this window the electric field amplitude changes linearly with position and the resolution is at its highest value.

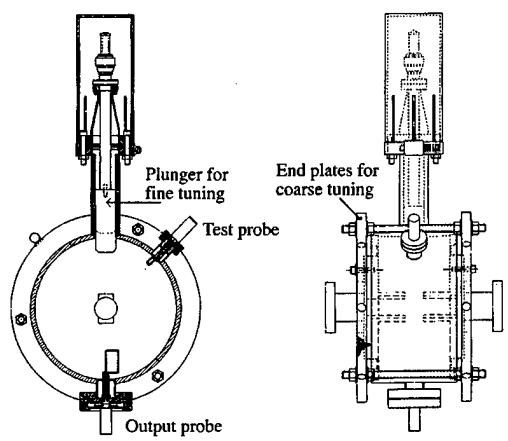

Figure 2. Position cavity front and side view.

Placing rods within the cavity draws the electric field maxima locations of the mode closer to the cavity axis. This field redistribution increases the resolution by a factor of 2.5 compared to a cavity with no rods (see figure 2). The rods also have a polarizing effect in the cavity, locking the orientation of the fields and eliminating the transverse mode. This improves the x-y isolation and permits greater overall system accuracy. The rods also

introduce loss and the Q of the mode is reduced by half. The resulting broader resonance is then beneficial in reducing drifts for improved long term measurement stability.

4 ELECTRONICS

A separate electronics package processes the 1497 MHz radio frequency (RF) signal coming from each cavity. Nine equivalent electronic channels use phase-sensitive demodulators to digitize and extract amplitude and phase of the signals.

Operating Frequency	1497 MHz
Dynamic Range	-156 dBm to - 40 dBm
Demodulation scheme	IF sampling, digital I-Q
Dynamic reserve	100 dB
Stability, Drift	≤ 0.5 % rms in 8 hours
Channel-channel isolation	55 dB
Baseband time constant	10 μs - 10 s
Testing capabilities	Frequency sweep ± 1 MHz

Table 3: Electronics specifications.

The 1497 MHz signal from each cavity is first amplified in a low noise amplifier, mixed with a 1497.1 MHz local oscillator (LO) signal in a dual-balanced mixer and then low pass filtered. This yields an IF frequency signal of 100 kHz that can be processed by a lock-in amplifier; the latter sets the limit on to how high the IF frequency can be. The lock-in amplifier is a commercial off-the-shelf model 7200 available form AG&G. This DSP based instrument samples 100 kHz signal and demodulates it in a numerical (DSP) I-Q demodulator using an externally supplied 100 kHz reference. Use of the digital demodulator significantly improves the accuracy, stability and flexibility of the system.

The 100 kHz reference, LO and 1497 MHz test signals are generated by a reference frequency module. Figure 3 shows a simplified block diagram of the module. The 100 kHz reference is generated by mixing 1497.1 MHz signal form the LO frequency source with a 1497 MHz RF signal received from the CEBAF machine master oscillator. It was a design challenge to generate a 1497.1 MHz LO signal with minimum content of 1497 MHz RF signal. It turns out that 1497 MHz signal in the LO channel limits system performance at the lower signal levels; a weak 1497 MHz signal in the LO path enters the mixer in a downconverter module, where it couples to the RF port of the mixer and gets reflected back to the RF port. This process generates an unwanted 100 kHz signal. This phenomenon can be easily observed by terminating the downconverter input to 50 Ω and taking a reading from the lock-in amplifier. This explains use of isolators in LO and RF signal paths.

The connection to the CEBAF EPICS [6] control system is a dedicated input output controller (IOC). Each lock-in amplifier communicates with and is controlled by that IOC via a GPIB bus. Our estimate is that bandwidth of the GPIB bus will permit obtaining 10 readings of all lock-in amplifiers per second which is 10 times faster than is required.

The system is to be installed in the transport line tunnel close to the cavities to minimize signal loss due to cable attenuation. A modular design was chosen to facilitate maintenance and minimize time to repair in case of a failure. The modules conform to 3U, 220 mm Eurocard standard and use DIN type M connectors with RF inserts.

5 SUMMARY

The system is to be installed in September 1997. Cavities are under construction. We have tested electronics in our laboratory. The measured sensitivity of the system is -156 dBm and the worst case channel to channel isolation greater than 55 dB. We now plan to install the system in the tunnel and repeat the measurements to check performance in situ since a system with such a high sensitivity is more susceptible to any externally generated interference.

6 ACKNOWLEDGMENTS

Jean-Claude Denard helped us identify customer needs and provided encouragement and technical support. Ronalald Lorenz helped us kick-off this project by providing valuable input. Ron Sundelin was the ultimate source of the suggestion to consider a design similar to the separator cavity. This work was supported by the U.S. DOE under contract number DE-AC05-84ER40150.

REFERENCES

[1] T. Powers et al.: 'Design, Commissioning, and Operational Results of Wide Dynamic Range BPM Switched Electrode Electronics', Proceedings of the Seventh Beam Instrumentation Workshop, Argonne IL, (AIP conference proceeding 390)

[2] H. Euteneuer: 'Beam Monitors at the Mainz Microtron', reprinted paper

[3] W. Barry: 'A General Analysis of Thin Wire Pickups for High Frequency Beam Position Monitors', Jefferson Lab PR 90-024, October 1990.

[4] C. Hovater et al.: 'The CEBAF RF Separator System', Proceedings of the XVIII International Linear Accelerator Conference, 26-30 August 1996, Geneva, Switzerland

[5] R. Ursic et al.: 'CEBAF Beam Loss Accounting' Proceedings of the 1995 Particle Accelerator Conference, Dallas, TX

[6] http://www.cebaf.gov/accel/documents/epics_doc.html

BEAM POSITION MONITORS INSIDE THE FEL-UNDULATOR AT THE TESLA TEST FACILITY LINAC

R. Lorenz, H. Henke, TU Berlin, Einsteinufer 17, D-10587 Berlin
T. Kamps, DESY-IfH Zeuthen, Platanenallee 6, D-15738 Zeuthen
U. Hahn, HASYLAB at DESY, M. Wendt, DESY Hamburg, Notkestrasse 85, D-22607 Hamburg

Abstract

Beam-based alignment is essential for the operation of a SASE-FEL at the TESLA Test Facility Linac. It requires the transverse beam position to be measured at several points inside and between the undulator modules with a resolution of better than 5 μm. Between the undulator modules cylindrical cavities will be used, excited in the TM_{110}-mode by an off-center beam. The amplitude of this mode is detected in a homodyne receiver by mixing the cavity output and a 12 GHz reference signal. For monitors inside the undulator modules the realization of two different concepts is under way. The first one is a button-type monitor using very small feedthroughs. The second one is a structure consisting of four ridged waveguides oppositely arranged around the chamber, where the averaged position of a single bunch train will be measured in a narrowband X-band receiver. The fabrication and test of prototypes is under way. This paper summarizes the designs and some preliminary results.

1 INTRODUCTION

The construction of a free-electron laser (FEL) is under way at DESY yielding a coherent, very bright beam of photons with wavelengths tunable between 6 and 20 nm [2]. The electron beam of high intensity to drive the undulator will be delivered by the TESLA Test Facility Linac (TTFL) [1]; some parameters are listed in Table 1.

Bunch train length	800 μs
Number of bunches	max. 7200
Repetition rate	10 Hz
Bunch charge	1 nC
Bunch length (FWHM) Phase I / II	250 μm / 50 μm

Table 1: Parameters for the FEL, at the end of the TTFL

The operation of this FEL is based on the the self-amplified spontaneous emission mechanism (SASE). Inside the undulator the electron beam performs a snake-like motion due to the alternating magnetic field of the dipoles. Synchrotron radiation is emitted because of this motion, a density modulation takes place and the electron beam is micro-bunched. In order to focus the beam along the undulator beamline, a FODO structure is superimposed.

The position of the electron beam might vary, mainly because of field imperfections in the dipole and quadrupole magnets. Since the overlap between the electron beam and the photon beam is essential for the operation of the FEL, the position of the electron beam has to be measured and corrected along the undulator beamline. Beam position monitors (BPM) are to be installed within and between the modules, and steering coils are located inside each undulator module. In Phase I the 15 m long undulator consists of three identical modules and the bunch length is a factor of 5 larger than it will be for Phase II. The beam pipe having a radius of 5 mm will be made of aluminium.

2 BETWEEN UNDULATOR MODULES

The transverse beam position has to be measured with a resolution of about 1 μm between two undulator modules. These monitors have to fit in a block of stainless steel, housing two wire scanners (see Fig. 1). Circular cavities excited in the first dipole-mode by an off-axis beam were chosen because of the desired resolution and the transverse space available. The amplitude of this TM_{110}-mode yields a signal proportional to beam displacement and bunch charge, its phase relative to an external reference gives the sign of the displacement. The signal amplitude is much higher than the signal given by other monitors and is a linear function of the beam displacement. Both TM_{110}-polarizations have to be measured to obtain the displacements in x and y.

2.1 *Cavity Design and Signals*

For a cavity without beam pipes, the voltage of the TM_{110} excited by a single bunch of charge q at a position δx can be estimated using the following relation:

$$V_{110}(\delta x) = \delta x \cdot q \cdot \frac{l}{{R_{\mathrm{res}}}^3} \cdot {T_{tr}}^2 \cdot \frac{J_1^{\max}}{J_0^2(a_{11})} \frac{a_{11}}{2\pi\varepsilon_0} \qquad (1)$$

a_{11} is the first root of J_1, T_{tr} the transit time factor. Since the resolution is proportional to the cavity size, a resonant frequency (TM_{110}-mode) of 12 GHz was chosen, limited by the beam pipe diameter. In the preliminary design of the block which has to be inserted between two modules (Fig. 1) one clearly sees the two cavities and their coupling to WR-90 waveguides. Table 2 summarizes some important parameters. The temperature of all cavities made of aluminium will be stabilized. The dimensions of the coupling iris to the waveguide were designed following a method described in [4], resulting in a coupling factor of about 2.5.

Since the field maximum of the common modes is on the cavity axis, they will be excited much stronger than the

0-7803-4376-X/98/$10.00 © 1998 IEEE

Cavity radius R_{res} / length l	14.6 mm / 8.4 mm
Loss factor k_{110}	0.2 V/pC
Unloaded and loaded Q_{110}	about 6000 / 1000
Frequency f_{110}	12.0 GHz

Table 2: Design parameters for the cavity monitor

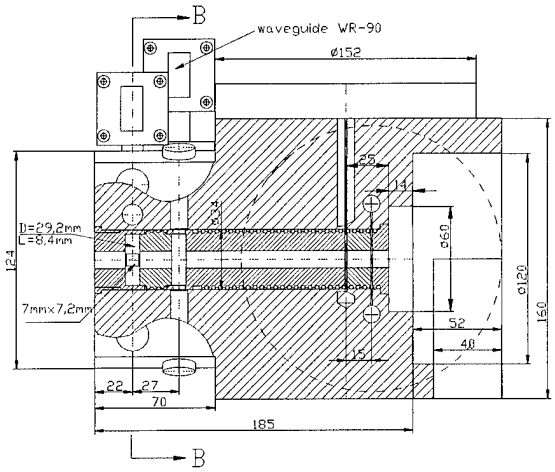

Figure 1: Block to be inserted between two modules

TM_{110} by a beam near the axis. Due to their finite Q, all modes have field components even at the TM_{110}-mode frequency. The excitation of the dominant TM_{010}-mode with respect to the one of the TM_{110}-mode and their spectral densities can be estimated following [3]. Two opposite cavity signals will be combined in a hybrid to reach the desired resolution. A frequency sensitive common-mode rejection of about 73 dB is necessary to detect this displacement [5].

2.2 *Electronics*

The TM_{110}-amplitude is detected in a homodyne receiver by mixing the cavity output and a reference signal down to DC in two stages [6]. First the 12 GHz-signals from the BPM and a reference cavity will be converted down to 1.517 GHz, using a reference signal from a common oscillator. In the second stage these signals will be mixed down to DC, using components developed for the TTFL-monitors [5]. The beam position can be calculated from the resulting I- and Q-signals, digitized by 12-bit ADCs. Near the electrical center of the cavity the resolution is also limited by the thermal noise of the electronics.

3 INSIDE UNDULATOR MODULES

The block to be inserted into an undulator module and containing the beam pipe will be made of aluminium having a rectangular profile (12 mm in height). A first prototype section of about 4 m length will be equipped with an alternating arrangement of 10 correction coils and monitors. The requirements on the monitors are listed below:

- A resolution of less than 5 μm around the center is necessary to realize the overlap between the electron and the photon beam.
- All mechanical parts of the pickup have to fit inside the undulator gap of 12 mm; the magnets allow only a horizontal access.
- The effect on the impedance of the vacuum chamber has to be minimized (large number of BPM).

The realization of two different monitor concepts is under way. Both types are described in the following.

3.1 *Broadband Electrostatic Pickup*

3.1.1 Design and First Tests

The pickup mechanics of this BPM concept is intended to be "as simple as possible". It seems feasible to use it with the longer bunches of Phase I, and it might be operated even with shorter bunches (Phase II, see Table 1).

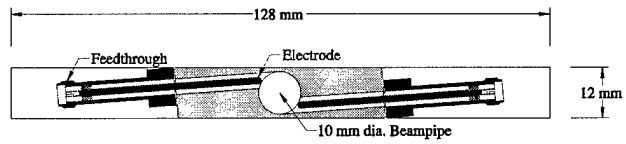

Figure 2: Cross-section of the electrostatic pickup.

Figure 2 shows a sketch of this "degenerated button" pickup. Because of the small beam pipe diameter the center-pin (.8 mm radius) of a coaxial vacuum feedthrough is used as an electrostatic "button"-electrode. It couples to the electromagnetic field of the electron beam; the level of the induced signal depends on the beam intensity and the transverse beam position. Four symmetrically arranged electrodes are used to measure the beam position with respect to the center of the beam pipe. Due to the space limitations, we had to split them longitudinally by 41 mm $\equiv$ 3/2 of the betatron wavelength. Each couple of two opposite electrodes is rotated by 30^0 from the horizontal plane, so the horizontal and vertical position characteristics of the BPM differ. 50 Ω coaxial cables will be used for the signal transmission from the electrodes to the readout-electronics, where the levels of all four signals are detected to compute the horizontal and vertical beam displacement.

The vacuum feedthroughs used are commercial SMA types from KAMAN Corp. having an increased center-pin length and modified for flange-mounting. Each pin-end is shaped spherically in order to reduce the local electric field strength (protection of sparks, induced by the fields of very short electron bunches).

First tests were made by measuring a simplified 'electrical' model (brass, silver/gold plated) with the network-analyzer. Figure 3 shows the transfer characteristics between this simulated 'beam' - a rod placed in the beam pipe center, giving a coaxial system with a 50 Ω characteristic impedance - and one pickup electrode (output). The useful frequency response range is 4 . . . 12 GHz: at 4 Ghz

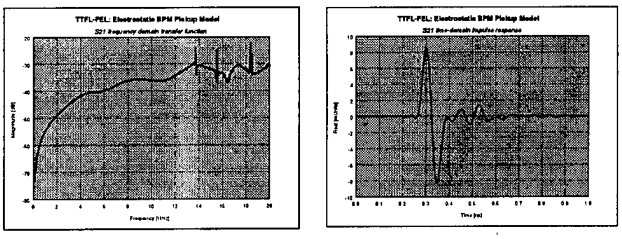

Figure 3: Measurements on the electrostatic pickup model.

the highpass-like roll-off frequency was found, and above 13 Ghz unwanted, but weak resonances were observed. A differentiated signal appears as a time-domain impulse response. Taking into account the 20% reduced feedthrough pin-diameter of the model, the beam-to-electrode coupling estimated from these measurements is about 1%.

3.1.2 Signal Detection

The electronics will be realized as a single broadband channel, aquiring the levels of the four electrode signals in consecutive time steps of 25 ns. Therefore, three of the four pickup signals will be delayed by 25 ns, 50 ns and 75 ns, and all of them will be combined in one transmission line. The signal processing includes low-pass filtering which has to be effective at very high frequencies, probably realized with help of lossy coaxial cables and attenuators.

3.2 Waveguide Monitors

3.2.1 Design

Because of the required compact size and extremely short bunches in Phase II, microwave concepts were used for the realization of a second pick-up structure. In this case the magnetic field of the electron beam couples to a waveguide through a slot in the beam pipe. Four coupling slots and waveguides are positioned 90 degrees apart in azimuth, similar to standard electrode-type monitors. The coupling factor of each slot is about 1% at 12 GHz according to MAFIA-calculations. Rigded waveguides of a special shape were designed to reduce their size and to realize the coupling. At the end of each waveguide, a coaxial adapter with a vacuum feedthrough is flange-mounted. Its cross-section is shown in Fig. 4. The fabrication of a prototype is under way (see Fig. 5).

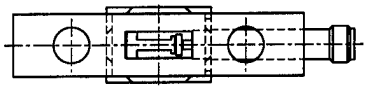

Figure 4: Cross-section of the coaxial adapter including the waveguide (center) and the feedthrough (to the right)

3.2.2 Electronics

The $\frac{\Delta}{\Sigma}$-signal of two opposite waveguides yields the normalized beam position, similar to the formalism used for electrode monitors. A narrowband receiver will be used to

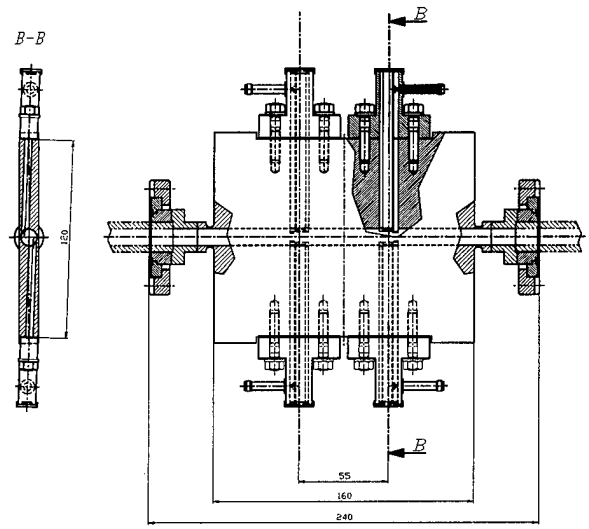

Figure 5: Prototype-Design of the waveguide monitor

detect the rf-signals of all individual waveguides. The filtered 12 GHz-signal will be amplified in a low-noise amplifier (LNA) and down-converted to 1.9 GHz. In the second stage this signal will be further down-converted, to about 50 MHz, and the $\frac{\Delta}{\Sigma}$-ratio of two channels will be detected using the amplitude-to-phase conversion scheme.

In the near future prototypes of both monitors will be tested at the CLIC Test Facility at CERN [7], where the bunchlength is close to the one planned for Phase I.

4 ACKNOWLEDGEMENTS

The authors would like to thank J. Rossbach, J. Pflueger and J. Schreiber from DESY for many helpful discussions and for pushing this work. Special thanks are extended to H. Thom from IPEA Berlin for his help in the mechanical design of the cavity monitor.

5 REFERENCES

[1] *TESLA TEST FACILITY LINAC - Design Report*, edited by D.A. Edwards, DESY Hamburg, TESLA-Note 95-01, March 1995

[2] *A VUV Free Electron Laser at the TESLA Test Facility Linac - Conceptual Design Report*, DESY Hamburg, TESLA-FEL 95-03, 1995

[3] W. Schnell, "Common-mode rejection in resonant microwave position monitors for linear colliders", CLIC Note 70, 1988

[4] N. M. Kroll, D. Yu, "Computer Determination of the External Q and Resonant Frequency of Waveguide Loaded Cavities", in *Particle Accelerators*, 1990, Vol.34, pp.231-250

[5] R. Lorenz et.al., "First Operating Experiences of Beam Position Monitors in the TTF Linac", this Conference

[6] R. Lorenz et.al., "Study of Orbit Feedback Systems for the TESLA Linear Collider", this Conference

[7] H.H. Braun et.al., "Results from the CLIC Test Facility", in Conference Proc. of the EPAC94, London, 1994, pp.42-46

FIRST OPERATING EXPERIENCES OF BEAM POSITION MONITORS IN THE TESLA TEST FACILITY LINAC

R. Lorenz, TU Berlin, Einsteinufer 17, 10587 Berlin, Germany
M. Sachwitz, H.J. Schreiber, F. Tonisch, DESY-IfH, Platanenallee 6, 15738 Zeuthen, Germany
M. Castellano, P. Patteri, F. Tazzioli, INFN-LNF, Via E. Fermi 40, I-00044 Frascati, Italy
L. Catani, INFN-ROMA2, Via Ricerca Scientifica 1, I-00133 Roma, Italy

Abstract

Different types of monitors were installed in the TESLA Test Facility Linac to measure the beam position. At each superconducting quadrupole, the transverse beam position will be measured with a resolution of better than 10 μm, using a cylindrical cavity excited in the TM_{110}-mode by an off-center beam. In addition, two 'warm' cavities working at room temperature were built for the Injector I and the Bunch Compressor. The amplitude of the TM_{110}-mode and its phase are measured in a homodyne receiver. For the experimental area, stripline monitors having a resolution of better than 100 μm were built, tested and installed. The averaged position of the whole bunch train of Injector I is measured in a narrowband receiver using the amplitude-to-phase conversion. This paper summarizes the designs, cold tests and first operating experiences of both monitor types.

1 INTRODUCTION

In order to establish a technical basis for a superconducting Linear Collider, the TESLA Test Facility is an essential part of the development of injectors, accelerating structures, cryostats and diagnostic techniques [1].

Because of special requirements at different locations three types of beam position monitors were installed in the TTF Linac [2]. The purpose of this note is to discuss the cavities attached to cold quadrupoles and at two warm locations close to the Injector, and the striplines, installed in the temporary beamline and in the experimental area. Results of first beam tests are presented.

2 CAVITY-MONITORS

For the alignment of the quadrupoles a single circular cavity was designed because of the limited longitudinal space and the desired resolution of 10 μm in a cold environment. The amplitude of the TM_{110}-mode excited by the beam in the cavity yields a signal proportional to the beam displacement and the bunch charge, its phase relative to an external reference gives the sign (up/down, left/right). Both TM_{110}-polarizations have to be measured to get the x- and y-offset.

2.1 Monitor Design and Signal Processing

After cooling down, the seventh harmonic of 216.7 MHz has to be within the TM_{110}-bandwidth for the cold monitors to avoid an active tuning system inside the cryostat. A pre-tuning before cooling down can be realized by adjusting the coupling of each antennae. The temperature of the 'warm' cavities is stabilized in a thermostat and can be changed to tune the monitor slightly (about 20 kHz/K).

In both cases CrNi was chosen as the cavity material to measure individual bunches spaced at 1 μs (Injector II). Most of the parameters given in Table I were calculated, whereas the resonant frequencies and the coupling factors were measured at room temperature.

Parameter	'Cold' cavity	'Warm' cavity
Cavity radius R_0	115.2 mm	117.6 mm
Cavity length l	52.0 mm	52.5 mm
Beam pipe radius	39.0 mm	29.75 mm
Loss factor k_{110}	0.24 V/pC	0.23 V/pC
Unloaded Q_{110}	2965	3025
Frequency f_{110}	1.513 GHz	1.517 GHz
Coupling β_{110}	1.31	0.95

Table 1: Design and measured parameters (at 25 ^{0}C)

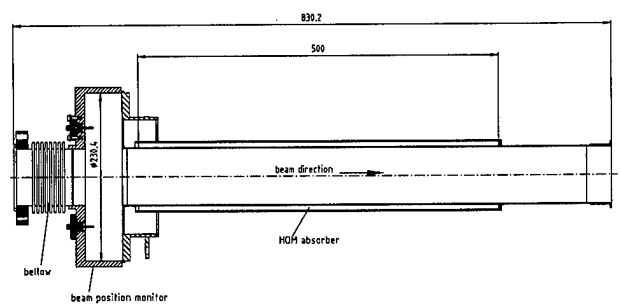

Figure 1: Cold cavity BPM with HOM absorber

Since the field maximum of the common modes is on the cavity axis, they will be excited much stronger than the TM_{110} by a beam near the axis. The estimated resolution near the electrical center is only 60 μm for a single cavity output, due to residual signals even at f_{110}. This can be reduced by combining two opposite outputs in a field selective filter [2]. Because of the limited space inside the cryostat, a stripline hybrid was used outside. The rejection of common field components is limited by its finite isolation between the Σ- and the Δ-port; an isolation of 20 dB brings the theoretical resolution down to less than 6 μm. In addition, a frequency sensitive TM_{010}-rejection of about 69 dB is required to detect a beam displacement of 10 μm. The resolution near the electrical center of the cavity is also limited by the thermal noise of the electronics [2].

0-7803-4376-X/98/$10.00 © 1998 IEEE

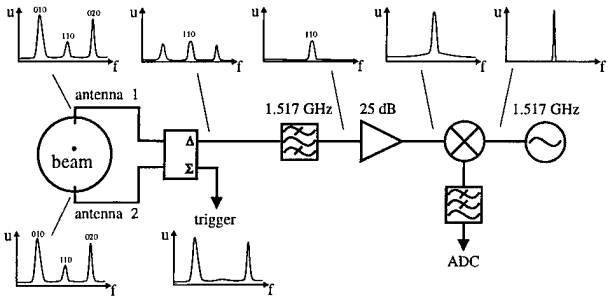

Figure 2: Signal processing scheme for a cavity BPM

The TM_{110}-amplitude is detected in a homodyne receiver by mixing the cavity output and a reference signal down to DC (Fig.2). A frequency sensitive TM_{010}-rejection of more than 100 dB is realized by the coupling factors of the antennae, the hybrid and the stopband attenuation of the bandpass filter. No additional phase stabilization for the reference is needed by using a I/Q-mixer scheme (*In-phase/quadrature*), providing two equal amplitude IF outputs that are in phase quadrature. Two narrowband devices were realized with different types of mixers, one using the MD-164 of M/A-COM, Inc., and the other one the M2G of W.-Johnson Company. Both mixers shown in Fig.3 contain the same components (from right to left): a hybrid, two mixers, a power divider and two IF-amplifiers. In addition, an error-correction scheme was developed for calibration. After passing a low-pass filter and a bipolar video amplifier, the signal may be either viewed directly on an oscilloscope or digitized by 12-bit ADCs [3].

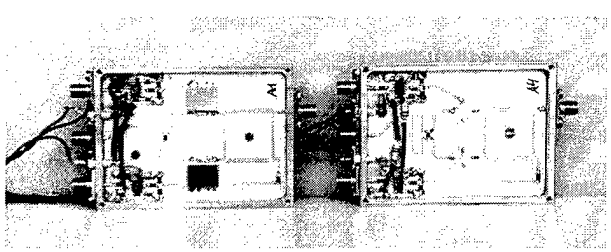

Figure 3: Realized I/Q-mixers: MD-164 (left) and M2G

2.2 *Test Results*

Bench tests were carried out on a stainless steel prototype to determine the resolution near the center and to test the electronics. Therefore, the cavity was excited by an antenna, fed by a network analyzer. A resolution of about 5 μm was measured in the frequency domain [2].

Another prototype was tested at the CLIC Test Facility (CERN) to demonstrate the principle single bunch response and to measure the TM_{110}-amplitude as a function of the relative beam displacement. The BPM was installed in the spectrometer arm and the beam was moved vertically by changing the current of the steering coil. Due to the measurement position, the mechanical setup and some machine parameters it was not possible to measure the minimum detectable signal. For a single scan, the output of the electronics vs. the relative beam position is shown in Fig. 4. More details are given in [2].

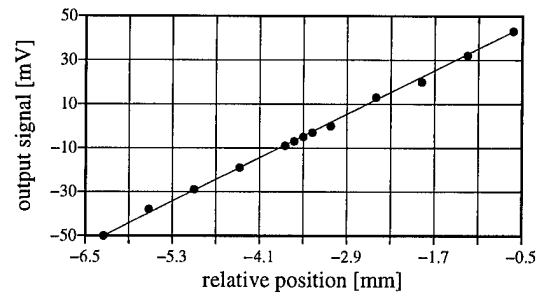

Figure 4: Test at CTF - output versus rel. position

3 STRIPLINE-MONITORS

3.1 *Monitor Design*

Stripline monitors were built for the experimental area and a temporary beamline because of the relaxed requirements - 100 μm resolution around the center - and the warm location. All monitors consist of four 50 Ω coaxial striplines, positioned 90 degrees apart in azimuth [2].

The BPM body is machined from a single block of stainless steel, four holes and the beam aperture are drilled. Each electrode is 175 mm long and shorted at the end; the geometrical coupling is about 3 %. The main distortion in the transition from the electrode into the cable is caused by the feedthrough, selected for mechanical reasons. All 9 monitors were built and tested at DESY-IfH Zeuthen.

3.2 *Signal Processing*

The electronics to detect the $\frac{\Delta}{\Sigma}$-signal of two opposite electrodes were built and tested by INFN-LNF [4]. Signal processing is done in the frequency domain by using the amplitude-to-phase conversion scheme together with heterodyning (intermediate frequency of 50 MHz). A normalized output over a wide dynamic range is the main advantage of this system. Furthermore, it is relatively insensitive to electromagnetic noise.

During electronics tests, a peak-to-peak noise of less than 4 mV was measured, corresponding to a position resolution of about 40 μm. This agrees very well with bench test results, where the position of a thin wire was changed until the first 'significant' readout of the electronics was detected. The whole system (monitor and electronics) gives a linear response for off-center positions of up to 5 mm.

4 BEAM TESTS

After the installation of all stripline monitors and the 'warm' cavities in the TTFL beamline, a first test was performed with a 10 MeV beam from Injector I. The beam pulse duration was about 30 μs. For both types of monitors the beam current was varied and the current of a steering

coil close to a BPM position was changed. Due to the limited time and some problems with beam parameters it was not possible to get a full scan.

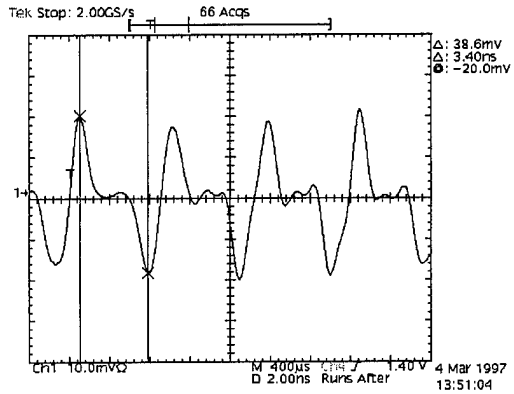

Figure 5: Measured signal for a stripline BPM

Figure 5 shows the output signal of a single stripline monitor channel after 25 m long cables, measured on a fast Tektronix-scope. One clearly sees the expected waveform for 4 bunches. The analog waveform from the detection circuit (prop. to the beam displacement, Fig. 6) shows an initial transient fluctuation of about 10 μs. It seems to be attributable to the beam because the electronics time constant is less than 1 μs. The dynamic range of the circuits has been checked by verifying that the steady state value of this waveform did not change for beam currents of .5 mA $\cdots$ 5 mA.

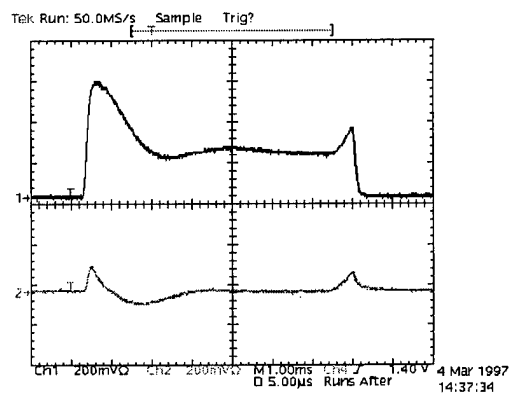

Figure 6: Measured signal of the detection circuit

As a simple check of macroscopic mistakes in scale and offset settings, a cross comparison of the readings of a stripline monitor and a close-by viewscreen has been performed. Some results for the horizontal signals are shown in Fig.7. The discrepancies betweeen the two curves are due to partial misalignment of the target and to a slight change of shape of the image when the beam is steered. This measurement has to be repeated after the installation of the first 100 MeV accelerating module, with a finer beam steering to determine the resolution.

In addition, the readout of a stripline BPM and a 'warm' cavity were compared. Both curves shown in Fig.8-a have the same time structure. The ordinate is given in arbitrary

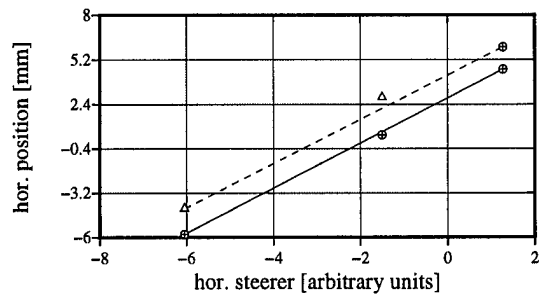

Figure 7: Beam deflection vs. steering - Full line (circles) = stripline readout; dashed line (triangles) = image center.

units since all calibration constants are not included yet. Figure 8-b shows the measured signal for three different levels of beam currents.

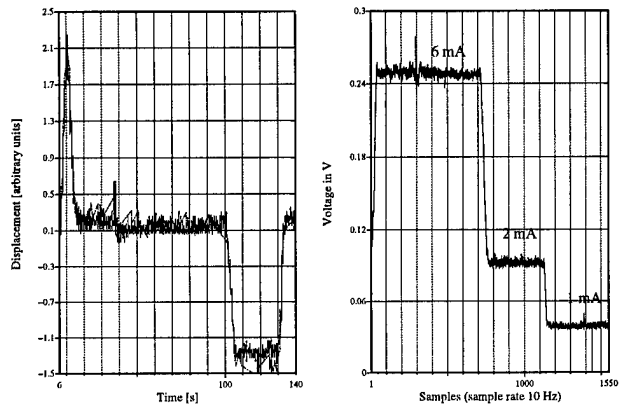

a) b)

Figure 8: a) Cavity signal (full line) and stripline signal b) Cavity signal for different beam currents

5 ACKNOWLEDGEMENTS

The authors would like to thank all people from the TTFL-group for their help in realizing the measurements. Special thanks are extended to Kay Rehlich and his group at DESY Hamburg for integrating the ADCs into the control system and for the software interfaces and drivers.

6 REFERENCES

[1] *TESLA TEST FACILITY LINAC - Design Report*, edited by D.A. Edwards, DESY Hamburg, TESLA-Note 95-01, March 1995

[2] R. Lorenz et.al., "Measurement of the Beam Position in the TESLA Test Facility", in Conference Proceedings of the LINAC96, Geneva, August 1996, pp. 527-529

[3] *COMET - VMEbus I/O Board, Reference Manual*, Omnibyte Corporation, 245 West Roosevelt Road, West Chicago, Illinois, Feb. 1994

[4] M. Castellano et.al., "TESLA Test Facility Stripline Readout System", in Conference Proceedings of the EPAC 96, Barcelona, June 1996, pp. 1633-1635

THE CLOSED ORBIT MEASURING SYSTEM AT THE DELTA SYNCHROTRON RADIATION FACILITY

A. Jankowiak, K. Wille, University of Dortmund, Institute for Accelerator Physics and Synchrotron Radiation, Emil Figge Straße 74B, 44221 Dortmund, Germany

Abstract

This paper presents the closed orbit measuring system of the DELTA SR Facility, concerning the hardware set-up, data processing and the calibration methods. The results of the calibration measurements and the recent operating experiences will be discussed. These results show, that the BPM offsets with respect to the magnetic centre of the quadrupole magnets turn out to be not acceptable. Therefore it was decided to install a beam based BPM calibration system in the near future.

1 INTRODUCTION

At DELTA (**D**ortmund **E**lectron **T**est **A**ccelerator) [1] we installed a total number of 58 identical BPM heads, 44 in the main storage ring and 14 in the synchrotron (**Bo**oster **D**ortmund). The main design parameters of the BPM electronics are:

resolution:	< 10μm
long-term stability (12h)	< 50μm
absolute accuracy (in relation to quadrupole axis)	< 100μm
measuring frequency	10Hz
dynamic range	-60dbm – 0dbm (0.5mA – 500mA)

2 HARDWARE SET-UP

2.1 BPM Head

The BPM heads (see Fig.1) are made of blocks of stainless steel with an inner geometry identical to the vacuum chamber. 4 capacitive pick-up electrodes (ESRF type) are mounted into the BPM. Due to the minimum wall thickness of 20mm the change of the geometry forced by air pressure is negligible. All BPMs are mounted in quadrupole magnets without mechanical fixing. The pick-ups are connected to the BPM-electronics with double shielded RG223U cables via SMA connectors.

2.2 BPM Electronics

For cost reasons we used a simple design [2] without First Turn capability. One basic unit consist of two electronic boards (16cm×10cm). The measuring frequency is set to the accelerating frequency of 499.790MHz for both machines. On the mixer board all 4 signals of one BPM pass through 600MHz low pass filters. The subsequent multiplexing is performed by a PIN switch using a 400Hz clock signal. The output signal is mixed to the intermediate frequency of 10.7MHz. The local oscillator for down converting the signal is of the PLL type, consisting of a crystal reference oscillator, a VCO, a 1:256 divider and a phase comparator. One local oscillator board supplies four mixer boards. The second board is the IF amplifier board. It consists of two gain controlled video amplifiers followed by a 10.7MHz band pass filter (100KHz bandwidth), a fixed gain amplifier and a fast rectifier. The output signal is demultiplexed to four output channels, each averaged with a time constant of 100ms. The gain control of the two leading amplifiers is done in that way that the average output voltage is equal to a reference voltage U_r (U_r=4V).

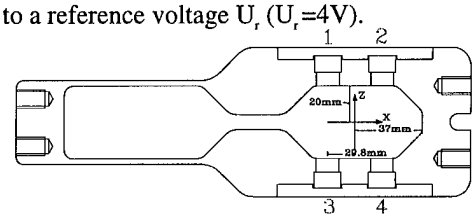

Fig.1 General layout of the DELTA BPM.

Four of these basic units together with one oscillator and two CAN modules with 16 0-10V input channels with 12 bit resolution are housed in one 19″ rack. 12 of these racks are placed around the storage ring and 4 BPMs each are connected to one of these racks.

3 DATA PROCESSING

From the control system we have access to the 4 pick-up signals from each BPM. This gives us flexibility for the calculation of the beam position. The calculation is done in linear approximation by using the BPM calibration factors of the centre of the BPM (c_x=15.9mm/%, c_z=19.6mm/%).

This leads to an absolute position error of 0.5mm for an offset of 5mm in x-direction of the centre of the BPM.

If a more accurate absolute determination of the beam position for greater offsets is necessary we can perform the calculation by an algorithm of iteration and polynomial fit. For this algorithm we are using signal functions of the BPMs calculated by MAFIA resulting in an absolute accuracy of 10μm for offsets of ± 10mm.

4 TEST MEASUREMENTS

The test measurements were done in two steps. First we made basic laboratory measurements using a signal

0-7803-4376-X/98/$10.00 © 1998 IEEE

source and a calibrated 4 way power splitter. Subsequent beam tests were done at ELSA (ELectron Stretcher Accelerator), University of Bonn.

4.1 BPM test with signal source and power divider

The tests of the dynamic range of several BPM electronics showed that the electronics work as specified in the range of –60dBm to –5dBm input power (this is comparable to a average beam current of 0.5mA to 280mA). The virtual orbit drift in the x-direction is in the order of 20μm, the resolution is smaller than 10μm. The long-term stability test over 16h with constant power level of –40dBm showed an orbit drift of 20μm.

4.2 BPM test with beam at ELSA

The measurements were done during normal synchrotron radiation runs (40 minutes duration, current between 60mA to 12mA). During a single run we saw an orbit drift of about 30μm in x- and 20μm in the z-direction. During 17 runs we could detect an additional drift from 20μm in the x-direction. These drifts are most likely caused by thermal movements of the BPM or influences on the pick-ups and cables. The resolution was tested by making slightly variations of the rf-frequency.

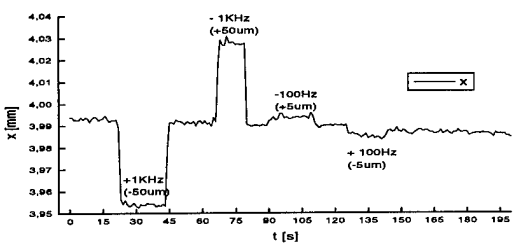

Fig.2. Variation of the rf frequency (500MHz) of ELSA (dispersion=1.63m, momentum compaction = 0.0615).

These measurements showed that the BPM electronics fulfill the requirements listed above.

5 CALIBRATION

The first step of the calibration procedure is to perform a calibration of the system with respect to the centre of the BPM.

5.1 BPM Head

Due to the manufacturing process of the DELTA vacuum chamber it was not possible to calibrate each BPM individually on a test bench with an antenna simulating the beam. Therefore we developed a method (pick-up method) to calibrate the BPMs by applying and measuring signals from the 4 pick-ups. The goal of this method is to determine 4 factors describing the individual attenuation of the pick-ups (coming from the pick-up itself and a displacement of the pick-up in the z-direction). These factors equalise the measured signals for a centred beam

To perform this calibration for one BPM we measure the signal received by three pick-ups if the fourth pick-up is connected to a signal-source. This results in 12 measured signals $S_{i,j}$ (= signal received from pick-up i when pick-up j is transmitting) and allow for the calculation of calibration factors a_i for each pick-up [3]:

$$a_1 = 1 \; ; \; a_2 = \sqrt{\frac{S_{1,4} \cdot S_{1,3}}{S_{2,4} \cdot S_{2,3}}} \; ; a_3 = \sqrt{\frac{S_{1,4} \cdot S_{1,2}}{S_{3,4} \cdot S_{3,2}}} \; ; a_4 = \sqrt{\frac{S_{1,2} \cdot S_{1,3}}{S_{4,2} \cdot S_{4,3}}}$$

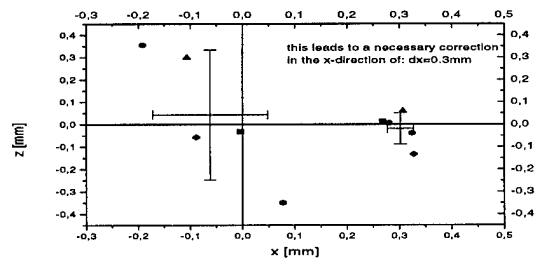

Fig.3 Calculated beam positions of a centred beam before and after pick-up calibration for 5 different BPM.

The offset in the x-direction is caused by the influence of the asymmetry of the vacuum chamber.

Measurements performed with all 14 BoDo BPMs showed an average variation of the relative pick-up sensitivity of ±2%.

5.2 Electronics

The calibration of the electronics (BoDo and DELTA) were done after installation. We used a signal source with calibrated power divider and measured the output signals obtaining a calibration of the whole data acquisition system. The relative deviation between the sensitivity of the 4 input channel is ±3%

5.3 Measuring Cables

The calibration of the cables together with the BPM head by the pick-up method was only possible in a rough manner. The necessary input signal of 40dBm to get output signals of –45dBm led to a not vanishing cross talk between the cables and an uncertainty in the calibration in the order of 0.5mm.

5.4 Overall Calibration

Performing the whole calibration procedure of pick-ups, cables and electronics it is possible to guarantee an absolute accuracy of the determination of beam position with respect to the BPMs of better than 100μm. Up to now this has been done for BoDo only. So for DELTA just a rough test of cables and pick-ups were made. Interpolating the calibration results from BoDo this leads to an uncertainty in the beam position of ±0.3mm.

On the other hand it is quite clear that we need a calibration with respect to the magnetic centre of the

quadrupoles. The BPMs are mounted into the quadrupoles in two different ways. 50% of the BPMs fit to the aperture of the quadrupole magnets with an accuracy of 100μm. The other has no mechanical connection to the quadrupole and can move to avoid any stress on the quadrupole due to thermal movements. The resulting uncertainty of the position of the BPM centre in relation to the quadrupole is in the order of 1mm. A system for beam based BPM calibration is therefore absolutely necessary to reach the desired accuracy.

6 EXPERIENCES DURING COMMISSIONING

During the first period of operating BoDo the commissioning of the BPM system suffered from low beam current (< 0.5mA) and high noise level from the accelerating RF. The installation of an additional amplifier on the mixer board and the change of the measuring frequency to the next harmonic of the revolution frequency have solved these problems and allow sufficient orbit measurements in single bunch train mode (5-8 buckets filled). For DELTA operation with different filling patterns however the frequency change is not acceptable and the RF noise problem must be solved.

During the commissioning of DELTA we detect a very strong dependence of the measured orbit from the stored beam current. Some BPMs showed a virtual orbit drift of 9mm. The problem was solved for most of the electronics by removing the additional amplifier. Some BPMs shows furthermore a small but not negligible dependence of the orbit measurement from the beam current.

First measurements with 24 BPM electronics installed allow for a reduction of the average absolute orbit deviation in the x-direction from 3.9mm to 1.4mm and an increase of the average stored beam current from 20mA to 50mA.

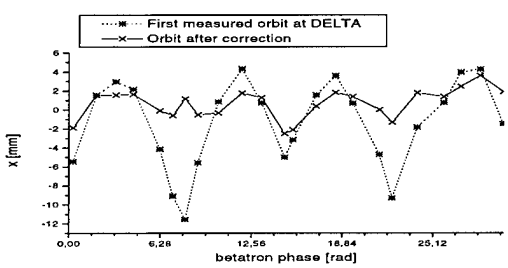

Fig.3 Measured orbit (horizontal plane) before and after first correction.

7 FUTURE PLANS

As described in section 4 DELTA needs a beam based BPM calibration system. The basic idea is to change slightly the k-value (quadrupole strength) of a quadrupole magnet and to detect the resulting orbit deviation. By steering the beam in the selected quadrupole and minimising the orbit deviation the magnetic centre of the quadrupole can be determined.

Because no DELTA quadrupole has a separate power supply we will install additional cables for all quadrupoles and a relay cascade to select each quadrupole individually. The k-value of the selected quadrupole will be changeable in a static way by shunting the quadrupole with a variable resistor or in a dynamic way with a dedicated power supply and frequencies between 1Hz and 40Hz.

To measure the dynamic orbit deviation at 2 BPMs (approximately 90° spaced in betatron phase), we will install a dedicated electronic to detect the amplitude modulation of the stored beam. This electronic consists of a AM demodulator followed by an FFT analyser.

With this system it is possible to determine at any time the offset between the BPM centre and the magnetic axis of the quadrupoles. Also a determination of the offset between any given orbit and the magnetic centres of all quadrupoles is possible. This allows a beam based alignment of the quadrupoles.

Furthermore we want to answer all questions concerning possible thermal movements of the BPMs. Additional it is possible to perform measurements concerning the optic of the machine. The beta functions of each quadrupole can be measured individually by measuring the tune shift caused by the variation of the k-value of the quadrupole.

A important step in the near future is to equip the remaining 20 DELTA BPMs with electronics to allow orbit corrections for the low emittance optics with higher tune values.

8 ACKNOWLEDGEMENTS

Many thanks to Prof. Dr. D. Husmann, J. Keil and M. Gentner, Accelerator Group of Physics Institute at Bonn University, for carrying out the test measurements at ELSA.

REFERENCES

[1] J. Friedl, DELTA group, 'Recent Results of the Commissioning of the DELTA Facility', PAC97, Vancouver, Canada, 1997

[2] S. Brinker, 'DELTA Beam Position Monitor', IEEE Particle Accelerator Conference Volume2, San Francisco, USA, 1991

[3] A. Jankowiak, 'Kalibration der DELTA Strahllage-monitore', Diploma Thesis, Department of Physics, University of Dortmund, Germany.

DEVELOPMENT OF A RESISTIVE BEAM POSITION/CURRENT MONITOR FOR THE UMD ELECTRON RING*

H. Suk†, J.G. Wang, S. Bernal, and M. Reiser
Institute for Plasma Research, University of Maryland, College Park, MD 20742, USA

Abstract

A prototype resistive beam position/current monitor has been developed for the proposed small electron ring at the University of Maryland. It consists of 32 low-inductance resistors which are uniformly distributed around a ceramic gap between two conducting pipes. The resistors are divided into four quadrants and each quadrant has a total resistance of 0.625 Ω. The beam image currents are measured in the four quadrants and the measurement leads to the information about beam position and total beam current. A bench test has been done for the prototype beam position/current monitor. The result shows that the beam position/current monitor gives an accurate total beam current with an error of 2% and satisfactory position information in both radial and azimuthal directions. The rise time of the monitor is measured as about 1 ns.

1 INTRODUCTION

A small electron ring is being developed at the University of Maryland[1, 2]. In this machine, space-charge dominated electron beams with an energy of 10 keV and a current of 100 mA are designed to recirculate in the ring with a circumference of 11.5 m. The beams easily tend to be off-centered in this ring because of misalignment, earth magnetic field, etc. Therefore, it is necessary to detect the beam position and to restore the beams to the axis. Furthermore, one needs to measure the total beam current. For these purposes, a prototype resistive beam position/current monitor was designed and built[3]. In this paper, the design and the bench test results of the prototype beam position/current monitor are presented.

2 BASIC PRINCIPLE

The basic principle of a resistive beam position/current monitor is quite simple. When a charged particle beam propagates in a conducting tube, an image current is induced on the inner surface of the tube. If the current is a little off-centered from the geometrical axis, the image current is induced nonuniformly in the azimuthal direction. The azimuthal current distribution is determined by the position of the beam. Therefore, the position can be determined by measurement of the azimuthal current distribution. Figure 1 shows a schematic diagram to explain the basic principle. As shown in the figure, the conducting tube is divided into four quadrants. Suppose that a thin current flow is at the position of (r, ϕ) in the polar coordinate system, as shown in the figure. In this case, the current distribution $J(\theta)$ on the conducting tube is given by[4]

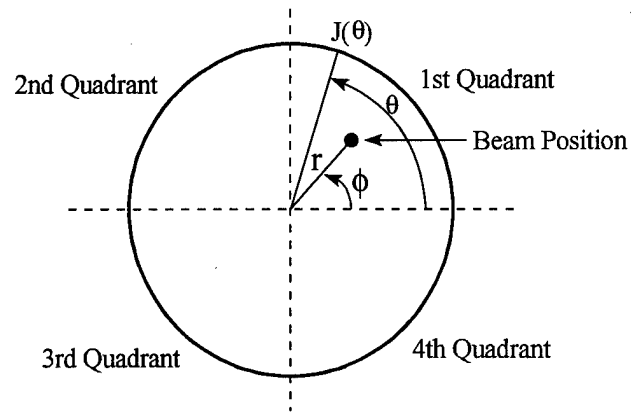

Figure 1: Schematic diagram of an off-centered beam in a conducting tube. As shown in this figure, the nonuniform image current $J(\theta)$ is induced when the thin beam is positioned at (r, ϕ).

$$J(\theta) = \frac{I_t}{2\pi R}\frac{1-(r/R)^2}{1+(r/R)^2-2(r/R)\cos(\theta-\phi)}, \quad (1)$$

where R is the diameter of a conducting tube and I_t is the total current. Hence, I_t is a sum of the currents in the four quadrants, i.e., $I_t = I_1 + I_2 + I_3 + I_4$, where I_1 through I_4 are the currents flowing in the four quadrants, respectively. Instead of measuring an exact current distribution as a function of θ, the beam position (r, ϕ) can be determined by measurement of I_1 through I_4, based on the following two equations:

$$\frac{2(r/R)\cos(\phi)}{1-(r/R)^2} = \tan\left[\frac{\pi}{2}\left(\frac{I_1+I_4-I_2-I_3}{I_1+I_2+I_3+I_4}\right)\right], \quad (2)$$

$$\frac{2(r/R)\sin(\phi)}{1-(r/R)^2} = \tan\left[\frac{\pi}{2}\left(\frac{I_1+I_2-I_3-I_4}{I_1+I_2+I_3+I_4}\right)\right]. \quad (3)$$

To measure the current in each quadrant, there are two ways, i.e., a capacitive method[5] and a resistive method. For faster response, the resistive method is employed in our case. In other words, the conducting tube is split into two pieces and resistors are uniformly distributed around the gap between the two conducting tubes. Resistors in each quadrant are electrically connected in parallel, and the current in each quadrant is measured to determine the position

* This work was supported by the U.S. Department of Energy.
† Present address: Department of Physics and Astronomy, UCLA, Los Angeles, CA 90095, USA.

and total current. In the next section, the detailed design parameters and the bench test results of a prototype are presented.

3 DESIGN AND BENCH TEST OF A PROTOTYPE POSITION/CURRENT MONITOR

3.1 Design

A prototype resistive position/current monitor was designed and built, based on the principle given in Section 2. It consists of two stainless-steel tubes with an inner diameter of 30.5 mm and a ceramic insulator of 6.4 mm in width. The two conducting tubes are brazed with the ceramic insulator for high vacuum sealing. The total length of the monitor is 6.1 cm, including two flanges at both ends. 32 low-inductance carbon resistors are uniformly distributed around the ceramic insulator and 8 resistors in each quadrant are connected to a common BNC cable. Each resistor has 20 Ω, so each quadrant has 2.5 Ω. With these parameters, a voltage drop from each quadrant is expected to be 62.5 mV if the beam current is 100 mA. The expected voltage 62.5 mV is large enough to measure with high accuracy.

3.2 Bench Test Results

Figure 2 shows the experimental setup to test the prototype beam position/current monitor. As shown in the figure, the position/current monitor is connected with two additional conducting tubes at both ends, and a current in a conducting rod is used to simulate a beam current. The conducting rod has a diameter of 12.7 mm so that the coaxial structure has an approximate transmission impedance of 50 Ω. A square pulse with a voltage of 5 V and a duration of 50 ns is sent to the setup for test of the monitor. In this case, the current in the conducting rod is 100 mA. To avoid a reflection from the end of the system, a 50 Ω terminator is connected at the end, as shown in the figure.

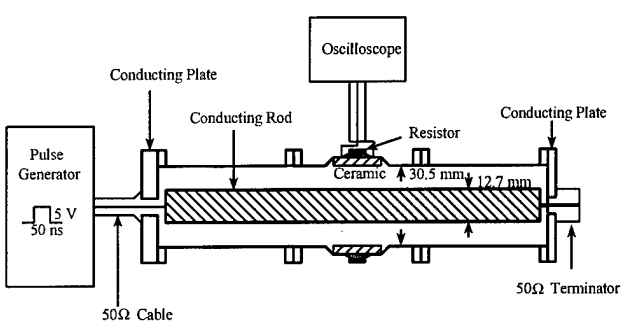

Figure 2: Bench-test setup of the resistive position/current monitor.

If the conducting rod is exactly on the axis, signals from the four quadrants yield almost the same square pulses. However, if the conducting rod is a little off-centered towards the first quadrant, for example, the signals from the four quadrants are different. The signal from the first quadrant will be larger than signals from other quadrants, according to Eq. (1). Figure 3 shows the measured signals from the first quadrant when the conducting rod is at r = 0 mm, r = 1.43 mm, r = 2.63 mm, and r = 4.75 mm, respectively, with a constant angle of $\phi = 45°$. As expected, the top trace is almost flat, but other traces show larger overshoots as the rod is moved away from the axis in the first quadrant. The large overshoots decay to flat signals after about 15 ns. The reason for this is that the resistors with a finite resistance are distributed around the conducting pipes so that an initial nonuniform potential around the circumference of the conducting tube becomes uniform after some time. Therefore, the four signals in Figure 3 have almost the same amplitude of about 63.5 mV after about 15 ns, which is close to the expected value of 62.5 mV. If these voltages are converted into currents, the current in the conducting rod is calculated as 101.6 mA, which is very close to the setup current 100 mA. Hence, this device gives an accurate total current.

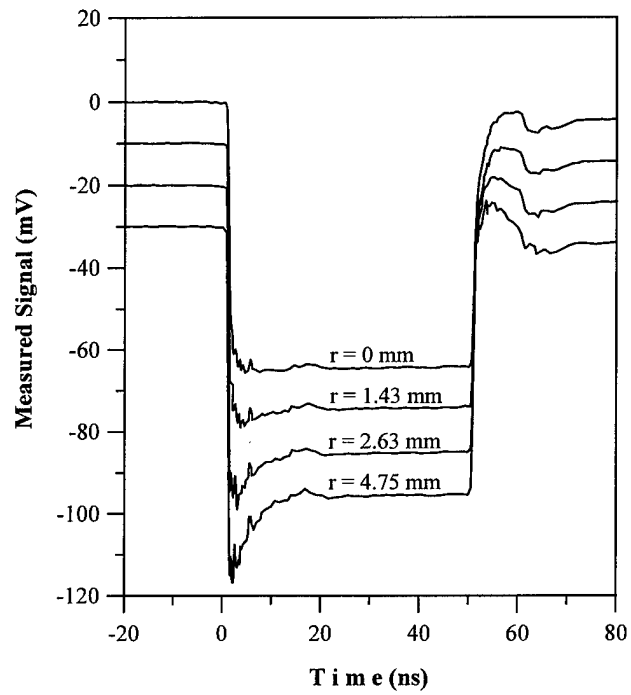

Figure 3: Signals from the first quadrant when the conducting rod is positioned at r = 0, 1.43, 2.63, 4.75 mm, respectively for a fixed azimuthal angle $\phi = 45°$.

The signals obtained from the four quadrants are analyzed to yield the information about the conducting rod position. Figure 4 shows the measurement result for a fixed $\phi = 45°$. In this case, the conducting rod is positioned at r = 0 mm, 1.43 mm, 2.63 mm, and 4.75 mm, respectively. Figure 4(a) shows a comparison between the setup radii and the measured radii. Deviation from the straight dotted line implies the difference between setup and measurement. According to the graph, their difference is equal to or less than 0.46 mm. Figure 4(b) shows a comparison between the setup azimuthal angle $\phi = 45°$ and the measured angles.

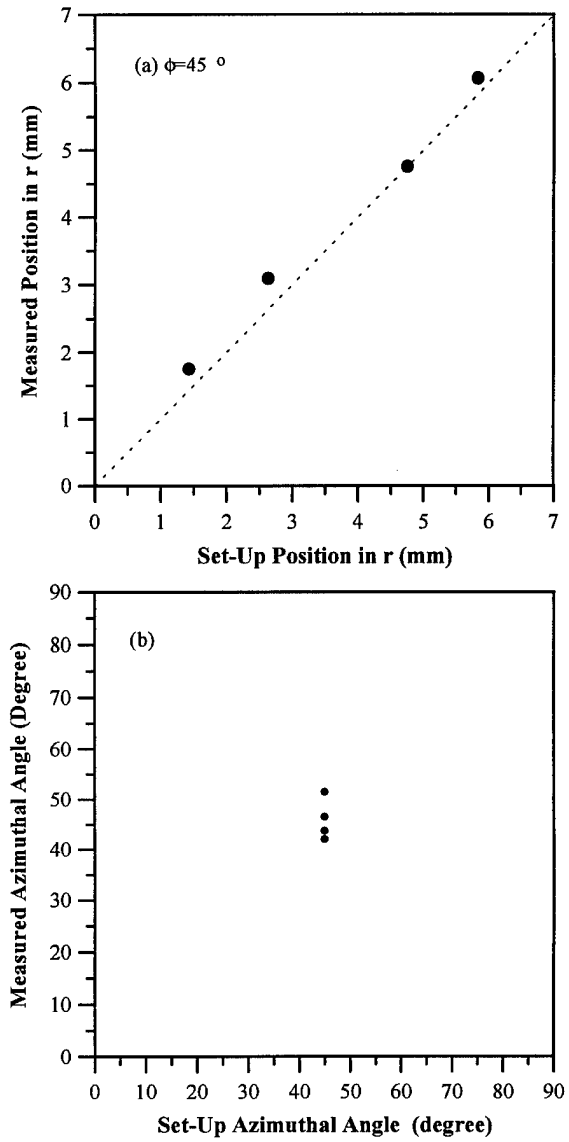

Figure 4: (a) Comparison of measured radii with setup radii for fixed $\phi = 45°$. (b) Comparison of azimuthal angle measurement with a setup angle for different radii in Fig. 4(a).

Similar comparisons are done for different angles. The case for $\phi = 90°$ is shown in Figure 5. Figure 5(a) shows that all data points are distributed close to the straight dotted line within 0.35 mm in radial direction. An angular comparison is shown in Figure 5(b), where the data points are distributed from 85° to 90°.

4 CONCLUSIONS

The small scale prototype of a resistive beam position/current monitor was designed and tested. The bench test shows that it yields satisfactory results in position, total current, and response time. Thus, a full-size beam position/current monitor will be built and tested for the electron ring.

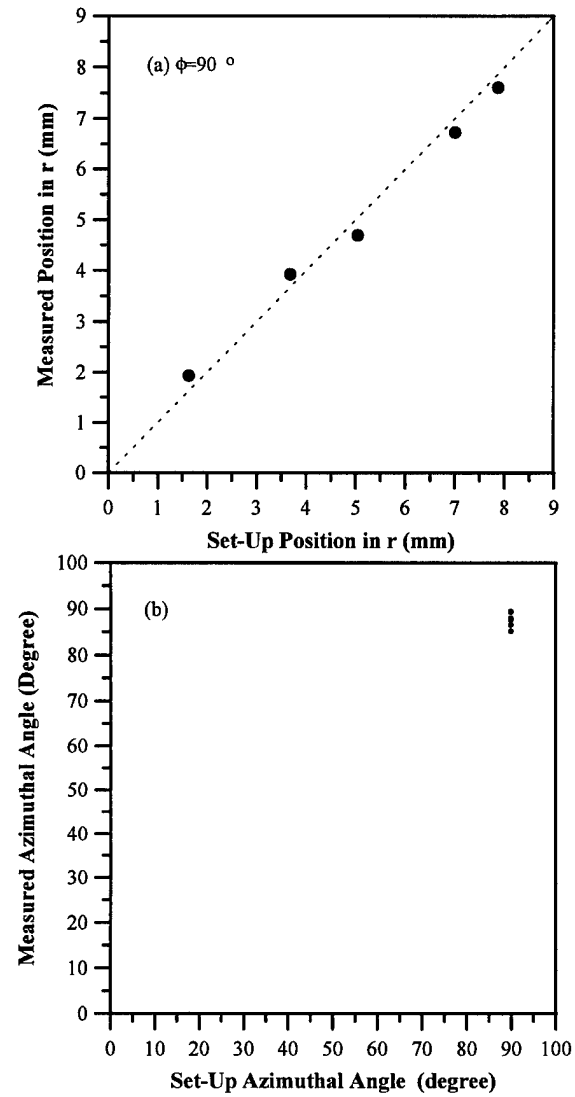

Figure 5: (a) Comparison of measured radii with setup radii for fixed $\phi = 90°$. (b) Comparison of azimuthal angle measurement with a setup angle for different radii in Fig. 5(a).

5 REFERENCES

[1] M. Reiser, S. Bernal, A. Dragt, M. Venturini, J. G. Wang, H. Onishi, and T. F. Godlove, Fusion Engineering and Design **32-33**, 293 (1996).

[2] J. G. Wang *et al.*, in these proceedings.

[3] H. Suk, Ph.D. Dissertation, Dept. of Physics, Univ. of Maryland, College Park, 1996.

[4] T. J. Fessenden, B. W. Stallard, and G. G. Berg, Rev. Sci. Instrum. **43**, 1789 (1972).

[5] F. J. Deadrick, J. J. Barnard, T. J. Fessenden, J. W. Meridith, and J. Rintamaki, Proc. IEEE 1995 Particle Accelerator Conference, Dallas, Texas, 1995, Vol. 4, p. 2557.

PERFORMANCE OF THE SINGLE-PASS POSITION MONITOR AT SOR-RING

Hirofumi Kudo, Kenji Shinoe, Hiroyuki Takaki, Tadashi Koseki,
Norio Nakamura, Yukihide Kamiya
Synchrotron Radiation Laboratory, Institute for Solid State Physics (ISSP),
The University of Tokyo, Tanashi, Tokyo 188, Japan

Tohru Honda
Photon Factory, High Energy Accelerator Research Organization (KEK),
Tsukuba, Ibaraki 305, Japan

Abstract

The R&D of single-pass beam position monitor is being carried out at SOR-RING, a 500-MeV electron storage ring. The bunch signals from four button electrodes are directly fed into a 4-channel digital oscilloscope through semi-rigid cables. The digitized data are sent to a workstation for the beam position calculation. The relative accuracy much less than 0.1 mm has been obtained with this system.

1 INTRODUCTION

The project for constructing a third-generation vacuum ultraviolet and soft X-ray synchrotron radiation source, VSX Light Source, is being planned by the University of Tokyo. In the fiscal year 1997, a budget for preliminary study of the facility has been appropriated by the government. The accelerator scheme consists of a 300-MeV linac, a 2.0-GeV booster synchrotron and a 2.0-GeV storage ring. The storage ring has a circumference of about 390 m and an emittance of 5 nm·rad [1].

Single-pass measurement of beam position are expected to play an important role in commissioning and tuning of the accelerator facility. A program to develop a single-pass monitor system using a fast digitizing oscilloscope is under way at 500-MeV electron storage ring, SOR-RING, in collaboration with the Photon Factory (KEK-PF) [2]. In this paper, we report the signal processing of the single-pass measurement and some recent results of the position measurement at SOR-RING.

2 BPM SYSTEM

SOR-RING is the first storage ring in Japan and also the first light source in the world for the dedicated use of synchrotron radiation from the beginning. Its construction was completed in 1974. The operation for synchrotron radiation experiment has been terminated at the end of the fiscal year 1996, and it is now operated only for the accelerator study and R&D's of the VSX facility.

Figure 1 shows a schematic view of SOR-RING. It is 17.4 m in circumference and consists of eight bending magnet (B1-B8) and four quadrupole triplets (Q1-Q4). The RF frequency is about 120.9 MHz and the harmonic number 7. Electron beam of 308 MeV is injected into the ring from the Electron Synchrotron (ES) which belongs to the Tanashi branch of KEK. The injected beam is accelerated up to 500 MeV and then stored.

SOR-RING has four BPM's (BPM1 - BPM4) fixed on vacuum chambers of quadrupole triplets [3]. BPM consists of four pickup electrodes of a button type. The BPM system is usually used for C.O.D. measurement [4].

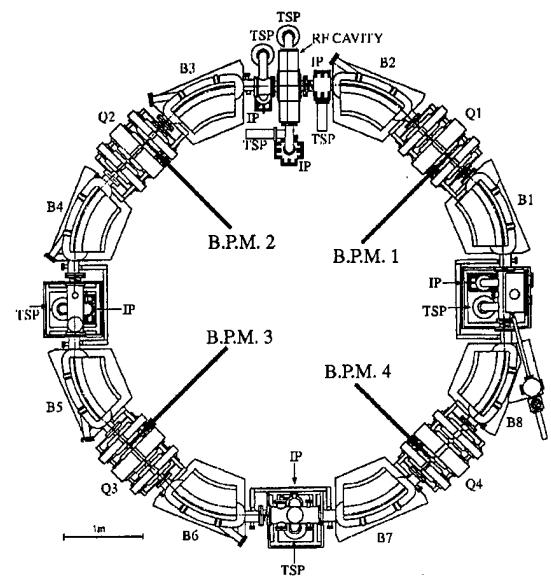

Figure 1: Plan view of SOR-RING.

In the beam transport (BT) line between ES and SOR-RING, there are three BPM's of a button type. The detailed description of the BPM's at BT appears in Ref. [2].

3 PERFORMANCE

For the single-pass monitoring, the bunch signals from four button electrodes are directly fed into a high-speed digitizing oscilloscope through semi-rigid coaxial cables (The cable for the ring is 2 m long and that for the BT line is 20 m long). The cable attenuation is 30

0-7803-4376-X/98 /$10.00 © 1998 IEEE

dB/100m at 100 MHz. The digitizing oscilloscope (Digital Real-time Oscilloscope, TDS684A by Tektronix) has four independent inputs. Each channel has a 8-bit digitizer with a maximum sampling rate of 5G samples/s and an analog bandwidth of 1 GHz. A maximum record length is 15000 points per channel. The digitized data are sent to a workstation (HP715) by GP-IB interface bus, and the beam position is calculated from the intensities of four button signals. The time duration of the button signal by a beam bunch at SOR-RING is about 3 ns, so that the sampling rate is fast enough to measure the waveform of the signal.

To calculate the beam position, the following two methods of data processing were adopted. The intensities of the button signals were obtained from (1) peak heights of the signals (The peak height method) or (2) peak height of an integrated waveform of the button signal (The integration method). Time span of the oscilloscope was set to 10 ns and the number of sampling data points N_s in the span was varied from 50 to 2500.

The relative accuracy of beam positions were estimated at a low beam current less than 5 mA in the single bunch operation of SOR-RING. Figure 2 shows the measured accuracy for the integration method; horizontal and vertical deviations from the average values are plotted. The number of sampling data points N_s is 500. Standard deviations σ less than 0.1 mm has been obtained.

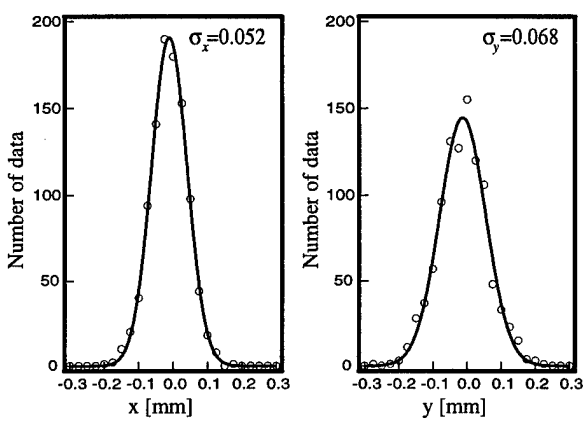

Figure 2: An example of relative accuracy.

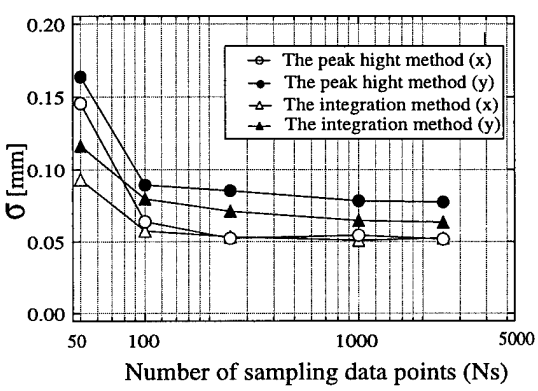

Figure 3: A comparison of relative accuracy between two data processing methods.

Figure 3 shows a comparison of relative accuracy σ between two methods. The abscissa is the number of data points N_s. Since the time span is 10ns and maximum sampling rate of the digitizer is 5 G samples/s, the data with N_s more than 50 were interpolated in the oscilloscope. The relative accuracy becomes almost constant more than N_s =250. In this measurement, it is confirmed that the integration method gives higher accuracy than the peak-height methods. The accuracy of the integration method more than N_s =500 seems to be limited by the 8-bit resolution of the digitizer.

4 BEAM POSITION MEASUREMENTS

4.1 Measurement using RF combiners

We measured the beam position at four BPM's of SOR-RING using RF power combiners. Figure 4 shows the schematic of the single-pass monitoring system with the RF combiners. The four button signals of the four BPM's were combined and then recorded in four channels of the oscilloscope. The same method is also adopted in the PF ring [5]. In the case of N_s =500, the digitizer can store a time range of 0.3 μs in maximum. As the revolution time of the SOR-RING is 57.8 ns, about 5 turns of bunch signals can be stored in the digitizer memory.

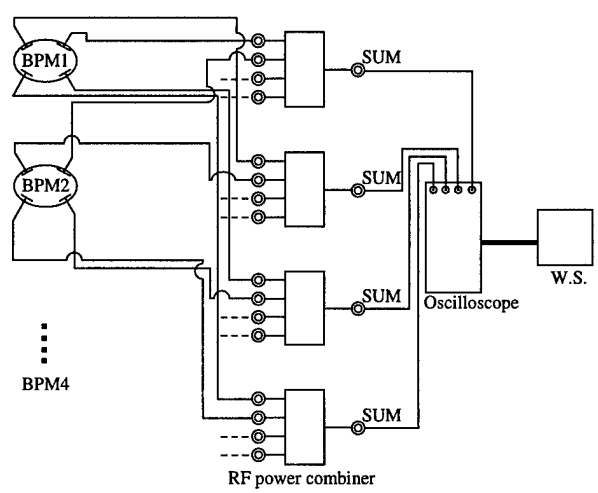

Figure 4: Schematic of single-pass monitoring system with RF power combiner.

Figure 5 shows the measured button signals of 5 turns in the single bunch operation of SOR-RING. A beam current was less than 5 mA for this measurement. The distance between two adjacent BPM's is 4.35 m and the time interval between two signals from adjacent BPM's is about 14.5 ns. As the time duration of a button signal is a few ns, the signals from the different BPM's were well separated each other. The calculated beam positions are

shown in Fig. 6. The dotted lines are measured beam positions and the solid lines are the deviations from the average of 5 turns. The accuracy using RF combiners is well agree with the results of Fig. 3.

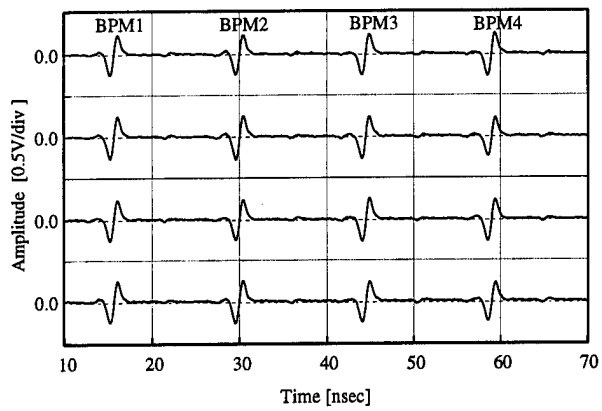

Figure 5: The measured button signals of 5 turns in the single bunch operation.

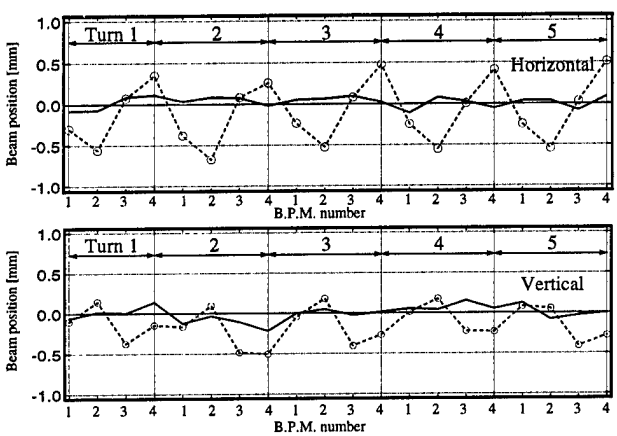

Figure 6: The measured beam positions of 5 turns in the single bunch operation.

4.2 Beam position of the BT bunch train

308-MeV electron beam extracted from ES is injected into SOR-RING with a repetition of 1 Hz. The beam positions at the BT line were measured by the single-pass monitor system. Figure 7 shows an example of the measured bunch train at one of the three BPM's of the BT line. 12 bunches were extracted from ES by the fast kicker magnet.

5 SUMMARY

The single-pass monitoring system using high-speed digitizing oscilloscope has been tested at SOR-RING. We have obtained the relative accuracy less than 0.1 mm. The system must be useful enough for the commissioning and tuning of the VSX accelerator facility. In the VSX storage ring, in which 128 BPM's will be installed, at least 8 BPM's will be used as the single-pass monitoring system with RF power combiner.

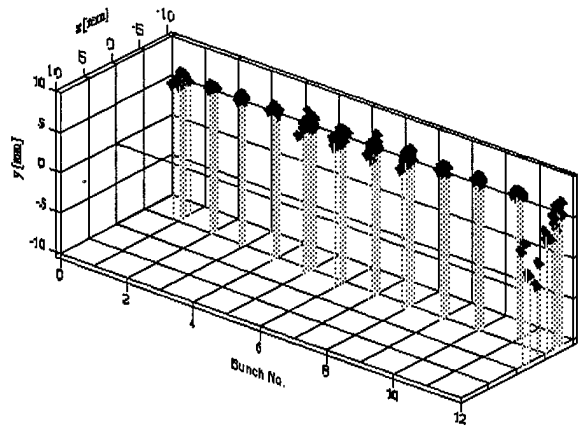

Figure 7: An example of the measured positions of bunch train at the BT line.

6 REFERENCES

[1] H. Takaki *et al.*, "A Lattice for the Future Project of VUV and Soft X-ray High Brilliant Light Source" in these proceedings.

[2] H. Kudo *et al.*, Proc. 5th European Particle Accelerator Conference, Barcelona, 1996, p. 1651.

[3] K. Shinoe *et al.*, Proc. 1993 PAC, Washington, D.C., 1993, p. 2337.

[4] K. Shinoe *et al.*, Proc. 1993 PAC, Washington, D.C., 1993, p. 2295.

[5] T. Honda *et al.*, Proc. 5th European Particle Accelerator Conference, Barcelona, 1996, p. 1660.

A SCANNING TARGET PROFILE MONITOR FOR THE SLOW EXTRACTED BEAM AT THE AGS*

K.A. Brown, I.H. Chiang, D. Gassner, J. Geller, J.W. Glenn, J. Hock
G.A. Smith, J. Tuozzolo, R. Witkover, E. Zitvogel
Brookhaven National Laboratory, Upton, NY 11973

1 INTRODUCTION

The purpose of this new instrument is for probing beam halo and obtaining beam profiles of the resonant extracted beam at the AGS. The device described here is a prototype version, to obtain data and prepare for a more permanent device. The goals of the permanent device are to allow emittances of low current, but high intensity slowly extracted beams to be accurately measured and to have a diagnostic for probing the wings of the beam distribution. The device works on secondary emission from thin targets as well as scattering into two scintillator telescopes. The targets are movable over the entire aperture at the device.

We were motivated to build a new device by the very high intensity beams now routinely being extracted from the AGS. We typically run at intensities that are as high as 6×10^{13} protons per AGS pulse. The AGS Switchyard was originally designed to operate at 1×10^{13}. The central core emittance of the beam does not change too greatly with beam intensity.[1] With the increased AGS injection energy, that came with the AGS Booster, it has been found that to reach these high intensities, the full acceptance of the AGS was being used at injection. This implies that the normalized emittance is increased. Measurements of the emittance, last year and again this year, show that the emittance of the resonant extracted beam is more than twice as big as it was in the pre-Booster era. What is more significant, though, is the twiss parameters were significantly changed. In effect the orientation of the phase space had not changed, but we now were extracting a beam which was fatter.[2] Modeling simulations agreed with the measured results.[3] The measurement results are shown in table 1.

Table 1: Summary of emittance measurement results.

(note: β and α are referred to start of SEB line)

	$\epsilon_x^{95\%,N}$	β_x (m)	α_x	$\epsilon_y^{95\%,N}$	β_y (m)	α_y
FY82	31.9	57.6	-6.6	38.8	3.25	0.87
FY96	64.4± 9.60	8.8± 1.4	−0.9± 0.2	54.7± 5.0	4.2± 0.4	1.0± 0.09

The performance of this new device has exceeded our expectations. We were very concerned about singles rates in the area, since the telescopes were located inside the beam enclosure and had effectively no sheilding. The singles rates were not insignificant, as high as 1 MHz, but the triple coincidence circuitry had no problems contending with these rates.

2 DISCUSSION

The device consists of two 2.5 mm tungsten targets, one which scans accross the beam horizontally and the other scans vertically. It is located at the beginning of the AGS Switchyard, before the electrostatic splitters. The vacuum at this location is in the range of 10^{-7} torr, making it very good for looking at secondary emission. For the secondary emission to be seen we apply a voltage to the wires, to repel any stray electrons that may wish to collect back onto the targets. Good signals were obtained at voltages down to about 20 volts. Above that we saw little change in the signal. Since the majority of the electrons knocked out of the target have energies in the range of less than 10 eV, it isn't suprising that we didn't need very much voltage.

The scintillator telescopes consisted of three EMI 9813 photomultiplier tubes, covered with mu-metal shielding and steel pipe shielding. The stray magnetic fields at the photomultiplier tubes were estimated to be in the range of a few gauss to at most 10 gauss. There are two telescopes, one in the vertical plane and the other in the horizontal plane, each at 90 degrees in the lab frame. The first detector is located 1 meter from the target and the detectors are seperated by 10 cm. The solid angle acceptance of each telescope is about 10^{-4} steradian.

We were initially concerned about temperature problems with the targets, since they were to be electrically isolated and they were relatively massive. Initial calculations, a small amount of simulation, and tests made with an electron-beam welder (in a 10^{-3} torr vacuum), all showed that the targets and holder assembly would be very stable and temperatures would not reach any significant levels.

One unique concern we had was with the significant change in solid angle seen by the telescopes due to the movement of the targets. In order to cope with this we designed the sizes of the scintillators such that they accepted the same solid angle and could accept a source changing in angle relative to the alignment of the scintillators. The area of the scintillators increase much more than just the linear change in distance from the target. This allowed the horizontally moving target to be viewed with the vertically mounted telescope, and give very little change in observed solid angle over the range of movement of the target.

* Work performed under the auspices of the U.S. Dept. of Energy

3 RESULTS

These results are very preliminary, the data only taken recently. We have had no time to carefully go over the data, so it is certainly possible that systematic errors may exist. Figures 1 - 4 demonstrate some of the data taken with the scanning target. The beam at this time had a definite momentum tail on it, which is most easily seen in figure 2. Figure 1 shows that for a normal plot the two telescopes basically give the same curve. But in figure 2 it is seen that the Horizontal telescope shows a wider beam, more clearly, than the vertical telescope.

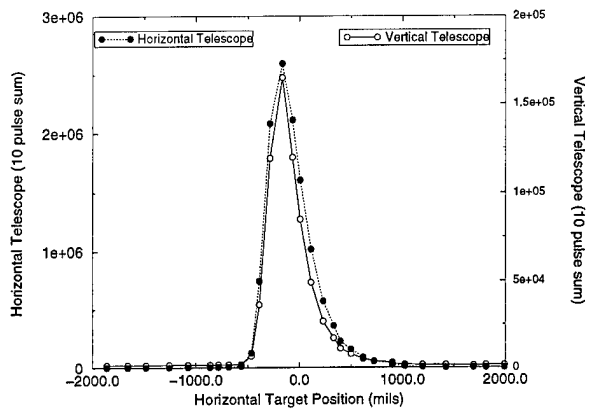

Figure 1: Horiz. and Vert. Telescope triples for Horz. scan

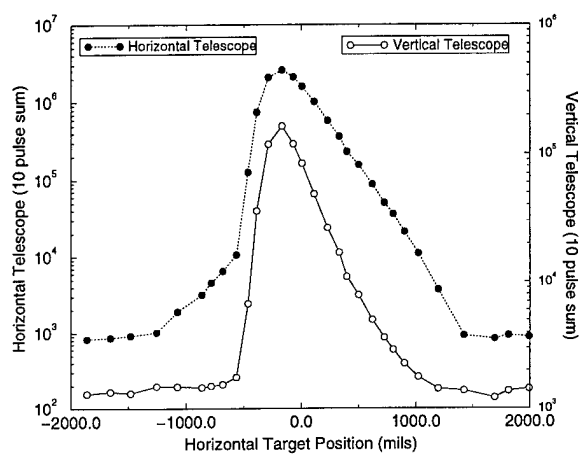

Figure 2: Horz. and Verti. Telescope triples for Horz. Scan

This is the effect of the solid angle changing more for the horizontal telescope than for the vertical, which has much less change in solid angle over the same range. Figure 3 shows the curves for the secondary emission from the target, on linear and on logrithmic scales. The secondary emission curve closely follows the vertical telescope. Figure 4 demonstates the ratio of telescope counts to secondary emission counts for each. Again the vertical telescope has much less variation than the horizontal.

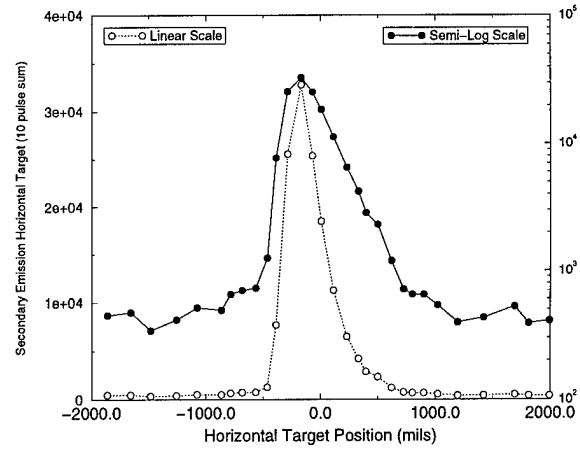

Figure 3: Secondary Emission from target for Horz. Scan

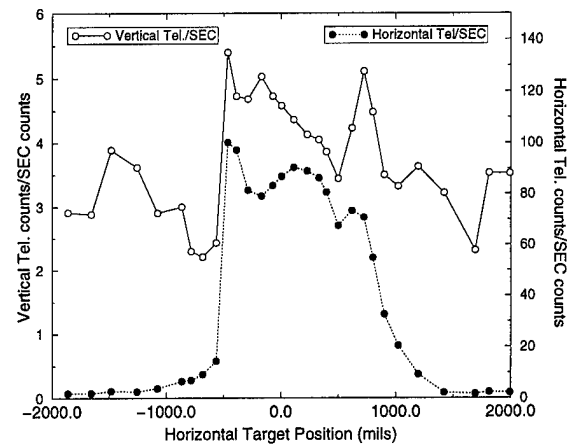

Figure 4: Ratio of Telescope Counts to SEC Emission

4 CONCLUSIONS

The performance of the device has exceeded our expectations. We see a clean dynamic range of over 5 orders of magnitude giving significant resolution of the wings of the beam distribution. Unfortunately the device does not perform well at the higher beam intensities. Background singles rates are larger than we anticipated and at high intensities become a serious problem. But we are actually encouraged, since this is at least a parameter we have control over. We could reduce the mass of our targets without effecting the performance, and reduce the solid angle acceptance of the telescope without greatly effecting the dynamic range. The effort that went into considering the solid angle effects for the telescope produced a fairly flat response for the vertical telescope when moving the horizontal target. The same compensations done for the horizontal telescope yields a similarly flat response when targeting on the vertical target.

5 ACKNOWLEDGEMENTS

The AGS instrumentation group, supervised by T. Curcio, along with the excellent mechanical skills of the AGS Beam Components group, supervised by D.Lehn, did a tremendous job putting together this entire system in less than 6 months.

6 REFERENCES

[1] K.A.Brown and R.Thern, 1995 IEEE Particle Accelerator Conference, Dallas, TX, p. 3212

[2] AGS/AD/Tech.Note 445; FY96 SEB Emittance Measurements, K.Brown, M.Blaskiewicz, H.Brown, K.Reece, Oct. 1996

[3] AGS/AD/Tech.Note 447; Mad Simulation: HEP/SEB Extraction (FY1996), M.(Sanki) Tanaka, Oct. 1996

A PROTOTYPE IONIZATION PROFILE MONITOR FOR RHIC

R. Connolly, P. Cameron, W. Ryan, T.J. Shea, R. Sikora, and N. Tsoupas
Brookhaven National Lab, Upton, New York 11973

Abstract

Transverse beam profiles in the Relativistic Heavy-Ion Collider (RHIC) will be measured with ionization profile monitors (IPM's). Each IPM collects and measures the distribution of electrons in the beamline resulting from residual gas ionization during bunch passage. The electrons are swept transversely from the beamline and collected on strip anodes oriented parallel to the beam axis. At each bunch passage the charge pulses are amplified, integrated, and digitized for display as a profile histogram. A prototype detector was tested in the injection line during the RHIC Sextant Test. This paper describes the detector and gives results from the beam tests.

1 INTRODUCTION

The Relativistic Heavy Ion Collider (RHIC) at Brookhaven National Lab will accelerate and store beams of ions ranging from protons to gold nuclei [1]. Transverse beam profiles will be obtained by measuring the distribution of free electrons formed by beam ionization of the residual gas [2,3]. The electrons are swept from the beamline by a transverse electric field, amplified by a microchannel plate (MCP), and collected on a circuit board with strip anodes oriented parallel to the beam axis. A uniform magnetic field, parallel to the sweep electric field, counters the defocusing effects of space charge and recoil momentum [4].

A prototype IPM was installed near the end of the AGS-to-RHIC transfer line (ATR) and tested during the sextant commissioning run [5]. It measured vertical profiles of single bunches of Au nuclei containing 0.6-1.0 x 10^8 particles. These profiles are compared to profiles on a fluorescent screen (WF3) located 2m downstream from the IPM [6]. Here we describe the detector and give results from the beam test.

2 ELECTRON KINEMATICS

The transverse density of ionization events in the residual gas is a map of the transverse beam distribution. To obtain a vertical beam profile it is necessary to extract each electron from the beamline at the Y coordinate where it was formed. However, the ionizing events impart momenta to the electrons, and the electrons are formed in the space-charge electric field of the beam. The impulse from the collision and the transverse component of the space-charge electric field can move the electrons perpendicular to the sweep direction resulting in a measured profile which is wider than the beam. To counter these effects the detector is placed in a magnetic field parallel to the electric field which sweeps the electrons from the beamline.

Consider the defocusing effect of the space-charge electric field of the beam bunch. This is a radial field whose strength increases with radius to a maximum near the beam's edge. At each point in the beamline the space-charge field has a component which is parallel to the desired drift direction and one that is perpendicular to it. Only the perpendicular component, $E_\perp$, has a defocusing effect.

An electron subjected to perpendicular electric and magnetic fields will drift with a cycloidal motion in the direction defined by the vector product **E** x **B** with a velocity of,

$$\mathbf{v} = (\mathbf{E} \times \mathbf{B})/B^2 \qquad (1)$$

and a gyration radius of,

$$R = Em/qB^2. \qquad (2)$$

During bunch passage there is a transverse electric field which would broaden the profile without the magnet. With the magnet the electron responds to this field by moving with a cycloidal pattern parallel to the collector anodes.

The maximum space-charge field in RHIC will be about 10^5 V/m. With a magnetic field of 0.2 T, the gyration radius will be <20 μm everywhere in the beamline and electrons will drift parallel to the anode by <0.2mm. Therefore profile broadening by the space-charge field is eliminated. Also, by the same mechanism, potential profile distortions from errors in the sweep electric field are eliminated.

The second defocusing effect is the momentum impulse from the ionizing collision. The energy spectrum of recoil electrons extends to 64 GeV in RHIC but over 95% of them have energies <500 eV. In a magnetic field the electron trajectory is a helix whose radius depends inversely on the transverse component of momentum. A 0.2T field confines a 500 eV electron to a Larmor radius of <0.4 mm which is less than the spacing between collector anodes. By placing the detector in a field of ~0.2T most of the electrons are collected on the anodes over which they are formed.

0-7803-4376-X/98/$10.00 © 1998 IEEE

3 DETECTOR DESIGN

The detector is shown in fig. 1. The vacuum chamber is made from a 38-cm long piece of 10 x 15 cm rectangular Al tubing with a 4.5-cm long piece of tubing welded into the side, forming a 'T'. This is placed between the poles of a 'C' magnet which produces fields of up to 0.5 T. Shims on the magnet poles make the field lines parallel within the active area of the detector. All of the detector parts and electrical feedthroughs are mounted on a 10" conflat flange which mounts on the side flange of the 'T'.

Two rectangular brackets hold the collector board and chevron MCP amplifier on one side of the beam and a sweep-field electrode and secondary electron suppression grid on the other side. The collector board is 0.625 mm-thick alumina, plated with gold, and etched with 48 collection anodes. The anodes are 10-cm long and spaced 0.5 mm center-to-center. At one end of each anode a plated through hole conducts the charge to a trace on the back which takes the signal to the edge of the board. A wire connects each trace to a pin on a D-connector vacuum feedthrough.

Figure 2 shows the circuit. The collector anodes are at ground potential to eliminate leakage currents. A Galileo 3810 chevron MCP amplifier [7] is attached to the circuit board and insulated from the ground plane by 0.125 mm Kapton. The MCP has an 8x10 cm collection area and a maximum gain of 10^7 when biased at 2.0 kV. In this experiment a bias of 1.2 kV gave almost full-scale reading from the digitizers. A sweep field is generated by biasing the opposing electrode at -6.5 kV. This gives electrons about 2.5 keV which is the peak of the detection efficiency for MCP's.

A 30-cm long cable connects the signal feedthrough to the front-end electronics. The charge collected on each channel is integrated by one channel of a LeCroy HQV810 8-channel charge-sensitive preamplifier ($C=2pF, \tau=4\mu s$) [8]. The integrator outputs are connected to AD783 track-and-hold amplifiers with a common gating signal. The AD783's are connected to AD846 amplifiers [9] set to a gain of 2, giving a charge sensitivity of 1V/pC. Each signal is carried out of the tunnel on a 100 Ω shielded twisted-pair cable. The signals are digitized by 24-channel A/D boards in VXI which were built for the BPM system [10]. The VXI cards are read by a Labview [11] program.

4 TEST RESULTS

Beam profiles were taken with a very broad beam ($\sigma \approx 8$ mm) and a narrower beam ($\sigma \approx 4.5$ mm). In these measurements the magnetic field was 0.2 T. Figure 3 shows the IPM beam-profile data overlaid with a Gaussian fit to the screen profile (WF3) for one of the narrow-beam bunches.

Gaussian profiles were fit to the IPM data. A comparison between the beam widths measured with the IPM and WF3 is shown in fig. 4. A line with unity slope is drawn to aid in comparison. The profiles of the narrow beam fit entirely on the detector so the gaussian fits were much better. These ten profiles averaged widths of 0.91 of the screen profiles. Because the beam is diverging and the screen is downstream the WF3 profile should be wider than the IPM.

Later, twelve beam profiles were measured with the IPM while the magnetic field was changed in 0.1-T steps from 0 to 0.5 T. Corresponding flag profiles were not measured for these data. Figure 5 shows the profile

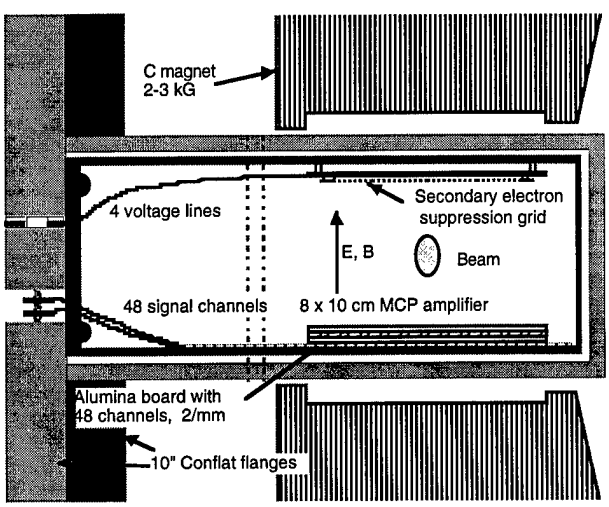

Figure 1. Cross section of IPM. View is looking down the beamline. In this experiment the orientation was rotated 90° CW so the detector mounting flange was horizontal.

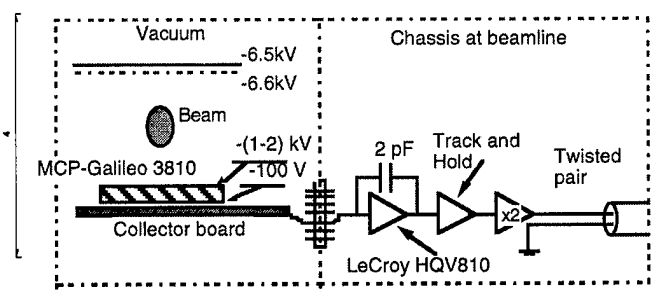

Figure 2. Schematic of the electronics in the tunnel. The trigger signal for the track-and-hold is generated by a digital delay generator in the instrument racks.

widths vs. magnetic field. Without the magnetic field the measured profiles are several millimeters too wide. In this case a field of 0.1 T seems to give adequate electron focusing.

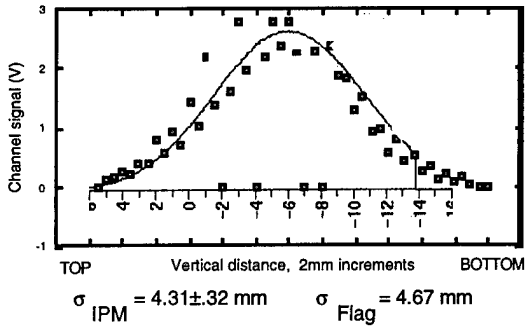

Figure 3. A Gaussian fit to the fluorescent screen profile, solid curve, overlaid the data collected from the IPM. The screen was located 2m downstream and the beam was diverging.

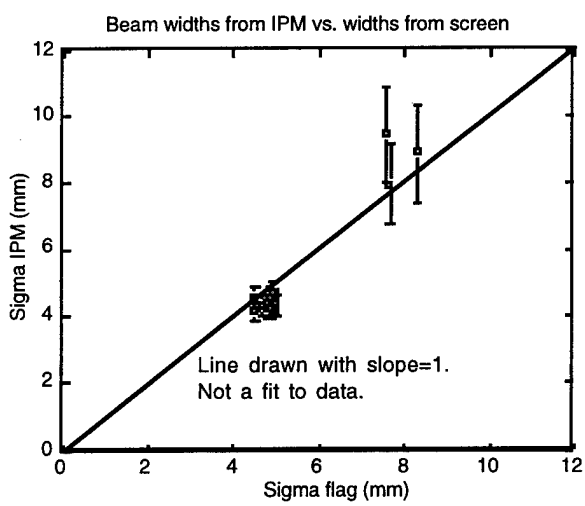

Figure 4. Gaussian profiles were fit to both the IPM data and the fluorescent screen data. Here sigma(IPM) is plotted vs. sigma (screen).

5 CONCLUSION

The prototype IPM produced accurate profiles of single bunches with intensities of 5-10% of the RHIC design intensity. From the signals and the measured bunch intensities the ionization cross section is estimated to be 1.2×10^{-15} cm^2, which is approximately the cross section that is expected [12]. Large backgrounds swamped the beam signal when the beam did not pass cleanly through the section of beamline containing the IPM. RHIC will have collimators so this should not be a problem.

The electrons fall out of the beamline in ~2 ns and the MCP is capable of time resolution of <100 ps so the speed of this detector is limited only by the signal size and the digitizing electronics. It should be possible to measure a single bunch on a turn-by-turn basis.

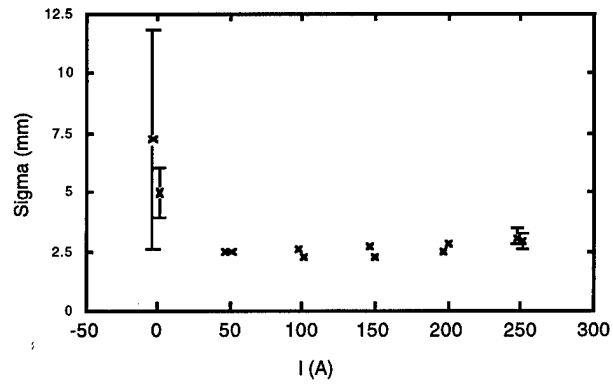

Figure 5. Beam width (sigma) from Gaussian fit to IPM data plotted vs. magnet current. Field is about 0.1T/50A.

6 ACKNOWLEDGMENTS

We thank Phil Cerniglia, John Cupola, and Chris Degen for their help in assembling hardware and writing software. Arnie Stillman and Dick Witkover provided valuable advice based on the IPM they built for the AGS Booster. Also Jim Zagel from Fermilab was extremely helpful. Finally we give special thanks to Brien Connolly and Wendy Connolly for their timely help in stuffing the last circuit board. This work was done under the auspices of the U.S. Department of Energy.

7 REFERENCES

1. "RHIC Design Manual" ,http://www.rhichome.bnl.gov /NT-share/rhicdm/00_toc1d.pdf
2. W.H. DeLuca, "Beam Detection Using Residual Gas Ionization", IEEE Trans. Nucl. Sci., NS-16, 813 (1969).
3. A.N. Stillman, et. al., "An Ultrahigh Vacuum Beam Profile Monitor", Rev. Sci. Instrum., 63 (6) (1992).
4. P. Zhou did the initial conceptual design which included magnetic focusing.
5. S. Peggs, "RHIC Status," these proceedings.
6. R.L. Witkover, "Design of the Beam Profile Monitor System for the RHIC Injection Line", Proceedings of the 1995 Particle Accelerator Conf., Dallas, TX.
7. Galileo Electro-Optics Corp., Sturbridge, MA 01566.
8. LeCroy Research Systems, Chestnut Ridge, NY 10977-6499.
9. Analog Devices, Norwood, MA 02062-9106.
10. "ATR Injection Line BPM Block Diagram," http://iguana. rhic.bnl.gov/Systems/BPMElec.
11. Labview, National Instruments, Austin, TX 78730-5039.
12. F. Sauli, "Principles of Operation of Multiwire Proportional and Drift Chambers," CERN 77-09 (1977).

A MULTI-WIRE BEAM PROFILE MONITOR IN THE AGS*

H. Huang , W. Buxton, V. Castillo, J.W.Glenn,
G. Mahler, M. Syphers, W. van Asselt, R.L. Witkover, S.Y. Zhang
Brookhaven National Laboratory, Upton, NY 11973, USA

Abstract

A multi-wire beam profile monitor which can be used to directly monitor and control the optical matching between the Booster and AGS rings has been installed and tested in the AGS. Placement of a multi-wire monitor directly in the AGS provides profile measurements taken upon injection and the first two or more revolutions of the beam. The data from such measurements can be used to determine the optical properties of the beam transport line leading into the AGS.

1 INTRODUCTION

As the AGS prepares to serve as the injector for RHIC, monitoring and control of the beam transverse emittances will become a major and important topic. Before installing the multi-wire beam profile monitor, there was no device for directly measuring the optical matching between the Booster and AGS rings. Previously the only beam profile measurement device in the AGS was the Ionization Profile Monitor (IPM) [1]. However, the IPM measurement is integrated over a finite time interval and therefore can provide only the average profile over a great many number of turns. Hence, at injection, the profile obtained with the IPM is the profile after dilution has occured, instead of the profile as delivered by the Booster and BTA (Booster to AGS) beamline. Placement of a multi-wire monitor in the AGS can provide profile measurements taken upon injection and the first two or more revolutions of the beam. The data from such measurements can be used to determine the optical properties of the beam transport line leading into the AGS.

2 HARDWARE AND ELECTRONICS

Multi-wire profile monitors (harps) have been used in the HITL (Heavy Ion Transfer Line) [2], the LTB (Linac to Booster) line and the BTA line [3]. These are commercially produced devices which have proven to be very reliable. The newly installed harp built for the AGS is similar to existing units and is located in the A20 straight section which is close to the injection into the AGS.

Fig. 1 shows the arrangement of the harp wires. Horizontal beam-profile information is derived from the 64 wires that run vertically and the vertical beam-profile information is derived from the 32 wires that run horizontally. The 0.1 mm diameter tungsten wires are separated by 2 mm spacing to cover an area of 13.2 cm× 6.4 cm. The horizontal and vertical wires are mounted on the same plane. The harp is pneumatically inserted to a fixed position in the beam pipe. To insert, a 3-way solenoid valve on the harp is powered allowing 60 psi air to move a plunger which, in turn, moves the harp into the beam path; to extract, power is taken off the solenoid and the air moves the plunger in the opposite direction (out of the beam path). Microswitches close when the plunger reaches the end of its travel and readbacks indicating position are relayed to the control system.

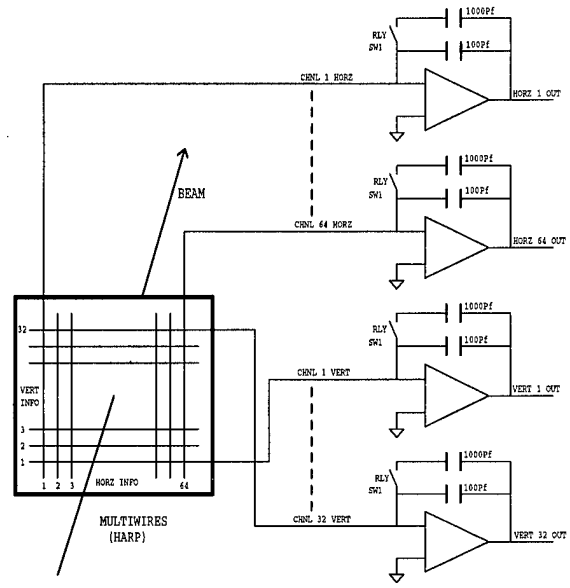

Figure 1: The A20 harp wires and corresponding integrator channels. The Reset, Integrate, and Hold switches are not shown for simplicity.

In the A20 harp electronic system, charge from the multi-wires goes to individual gated integrator channels producing an output voltage. These voltages, 64 for horizontal information and 32 for vertical, go to 96 MUX (sample and hold) channels which are read out sequentially, and fed to the control system which produces both transverse beam profiles displayed in the AGS main control room.

There are two main processes going on: the integration process during which the charge is collected from the wires in the beam path and the integrating capacitor is charged to a proportional voltage which is directly coupled to a MUX channel; and the scan process during which the voltages on the 96 MUX channels are sequentially read out to the control system.

When the A20 harp is inserted in the beam path the charge on the wires bleed off to the integrating capacitor. The integrating op-amp presents a high impedance input and in balancing the charge on the integrating capacitor

* Work performed under the auspices of the U.S. Dept. of Energy

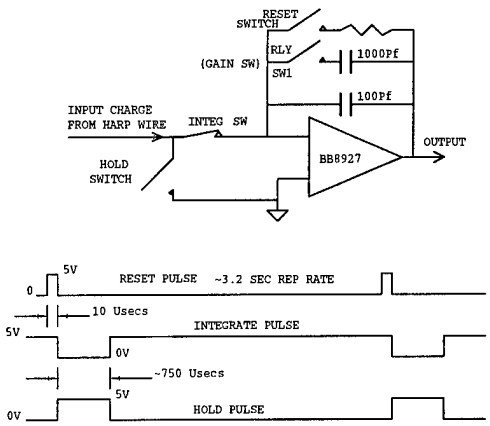

Figure 2: a) Integrator channel showing Reset, Integrate and Hold switches during the integration process. b) Timing signals that control the Reset, Integrate and Hold switches.

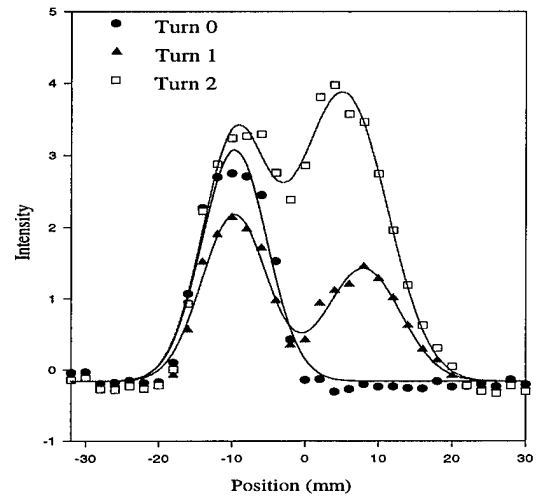

Figure 3: Vertical beam profile taken consecutively in the first three turns with the A20 harp. The lines are Gaussian fits. High sensitivity gain was used.

produces an output voltage. There are two available capacitor values: 100 pF used as a high sensitivity range and 1100 pF, obtained by remotely closing the relay, used as a low sensitivity range.

The integration process is regulated by the Reset, Start Integrate and Hold (Stop integrate) timing pulses. An integrate channel is shown in Fig. 2 with the switches (FETs) that allow the regulation process. Also shown in Fig. 2 is the timing arrangement that controls these switches. The cycle starts with the Reset pulse shorting the integrating capacitor and thus zeroing the output voltage. Next, incoming Integrate and Hold pulses simultaneously close the Integrator switch and open the Hold switch allowing charge to get to the op-amp. After the integrate time, the process is reversed: the Hold switch closes and the Integrate switch opens simultaneously, shorting the incoming charge to ground. At this point, the integrator channels all have voltages on their outputs thus marking the end of the integrate process. These voltages are directly coupled to their respective MUX channels and the read-out process commences. To read out the MUX channels sequentially, each MUX chip is selected and its 16 channels are sequentially selected for readout by a group of 16 channel advance pulses. The sequence is continued for the 64 channels in the horizontal plane and 32 channels in the vertical plane, to complete the readout process and end the cycle. The next reset signal shorts the integrating capacitor, thus zeroing the output voltage and the cycle proceeds with incoming integrate and hold pulses.

3 TESTS WITH HEAVY ION BEAM

In determining the optical set-up of the beam transport system, it is relatively straightforward to measure the trajectory of the beam at the injection to the AGS and to measure how well it is matched to the closed orbit. This is performed by looking at a beam position monitor to see the residual betatron oscillation after injection. A similarly straightforward process is a measurement of the dispersion function being delivered by the beamline. This can be performed by looking at motion on position monitors as the energy of the Booster is varied slightly. Previously, the difficult measurement in the AGS was the amplitude function being delivered by the beamline. The multi-wire profile monitor performs this measurement in the AGS.

A series of tests with Gold beam were conducted during the last heavy ion run. The tests have demonstrated that the A20 harp is capable of directly measuring beam profiles in the AGS as delivered from the Booster and through the BTA beamline. The A20 harp is also effective in capturing profiles of consecutive turns about the AGS. Vertical steering magnet DV120, located in the BTA line, was used to mis-steer the beam. The beam current was monitored during this operation to assure minimal beam loss due to the beam mis-steering. The AGS vertical tunemeter kicker was timed to drive the beam into a beam scraper after the desired number of turns. The beam profile of injection turn, after one-turn revolution and after two-turn revolution were obtained by turning on the kicker in the first three consecutive turns. These three profiles are shown in Fig. 3. By fitting these three beam profiles to separated Gaussian distributions, the beam widths of these three consecutive turns were given as $\sigma_0 = 4.4$ mm, $\sigma_1 = 5.0$ mm, $\sigma_2 = 5.2$ mm, respectively.

At the given position of the lattice, the beam profile is determined by three parameters: ϵ, α, β. The AGS ring parameters α, β and betatron tunes are known fairly well, therefore a one turn transfer matrix can be easily generated. These three parameters of the beam can be solved using the width measurements in three turns, therefore determining the three unknowns ϵ, α and β of the incoming beam.

Assuming the emittance does not change in the first three

turns, by definition,

$$\epsilon = \pi\frac{\sigma_0^2}{\beta_0} = \pi\frac{\sigma_1^2}{\beta_1} = \pi\frac{\sigma_2^2}{\beta_2}, \tag{1}$$

where σ is the beam width, β is the beta functions of the beam, and subscripts 0, 1, and 2 stand for injection turn, first turn and second turn, respectively. The single particle emittance can be written in the phase space coordinates y, y',

$$\begin{aligned} \epsilon &= \gamma_0 y_0^2 + 2\alpha_0 y_0 y_0' + \beta_0 y_0'^2 \\ &= \gamma_1 y_1^2 + 2\alpha_1 y_1 y_1' + \beta_1 y_1'^2, \\ &= \gamma_2 y_2^2 + 2\alpha_2 y_2 y_2' + \beta_2 y_2'^2 \end{aligned} \tag{2}$$

where y_0, y_0'; y_1, y_1' and y_2, y_2' are phase space coordinates of the injection turn, the first turn and the second turn, respectively. Using a one turn mapping matrix M, we have

$$\begin{pmatrix} y_1 \\ y_1' \end{pmatrix} = M \begin{pmatrix} y_0 \\ y_0' \end{pmatrix} = \begin{pmatrix} C_1 & S_1 \\ C_1' & S_1' \end{pmatrix} \begin{pmatrix} y_0 \\ y_0' \end{pmatrix}, \tag{3}$$

with

$$M = \begin{pmatrix} \cos 2\pi\nu + \alpha_r \sin 2\pi\nu & \beta_r \sin 2\pi\nu \\ -\gamma_r \sin 2\pi\nu & \cos 2\pi\nu - \alpha_r \sin 2\pi\nu \end{pmatrix}$$

where the subscript r corresponds to the parameters at the harp location in the AGS ring. These parameters can be determined fairly well using MAD calculation. Similarly,

$$\begin{pmatrix} y_2 \\ y_2' \end{pmatrix} = M \begin{pmatrix} y_1 \\ y_1' \end{pmatrix} = \begin{pmatrix} C_1 & S_1 \\ C_1' & S_1' \end{pmatrix} \begin{pmatrix} y_1 \\ y_1' \end{pmatrix}. \tag{4}$$

After some algebra, the injected beam parameters can be written as

$$\begin{aligned} \beta_0 &= \frac{1}{\sqrt{(\frac{\sigma_1^2}{\sigma_0^2})(\frac{1}{S_1^2}) - (\frac{C_1}{S_1})^2 + \frac{C_1}{S_1}A - \frac{1}{4}A^2}}, \\ \alpha_0 &= \frac{1}{2}\beta_0 A, \\ \epsilon_0 &= \pi\frac{\sigma_0^2}{\beta_0}, \end{aligned} \tag{5}$$

where

$$A = \frac{(\frac{\sigma_1}{\sigma_0})^2 \frac{1}{S_1^2} - (\frac{\sigma_2}{\sigma_0})^2 \frac{1}{S_2^2} - (\frac{C_1}{S_1})^2 + (\frac{C_2}{S_2})^2}{(\frac{C_2}{S_2}) - (\frac{C_1}{S_1})}. \tag{6}$$

With measured betatron tune and beam widths σ_0, σ_1 and σ_2, the injected beam parameters α, β and ϵ can be determined uniquely. The vertical betatron tune was measured as 8.66. The ring parameters at the multi-wire location as calculated using MAD are $\alpha_r = -1.25; \beta_r = 14.25$ m. Substituting the beam size values

$$\sigma_0 = 4.4 \text{ mm}, \sigma_1 = 5.0 \text{ mm}, \sigma_2 = 5.2 \text{ mm} \tag{7}$$

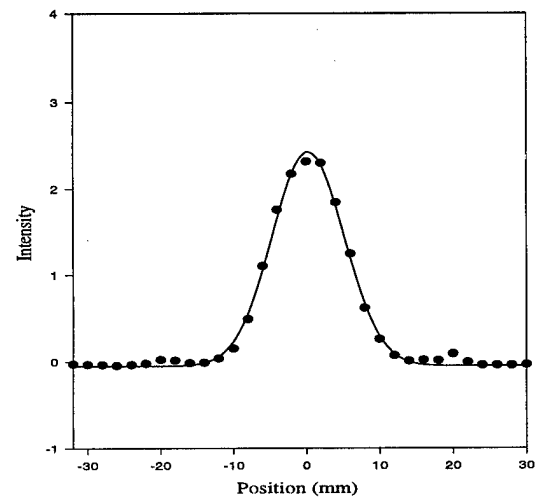

Figure 4: The multi-turn vertical beam profile taken by the A20 harp. Solid points are the experimental data and the solid curve is Gaussian fit. Low sensitivity gain was used.

into Eq.(6), the injected beam parameters are

$$\alpha_0 = -1.09; \beta_0 = 11.95 \text{ m}, \epsilon_0 = 1.67\pi \text{ mm-mrad}. \tag{8}$$

Thus the normalized 95% vertical beam emittance is $\epsilon_{95\%}^v = 6\beta\gamma\epsilon_0 = 4.3\pi$ mm-mrad. The measured emittance at the injection of the AGS using IPM is 5π mm-mrad. Further experiment is needed to understand the emittance growth mechanism.

A multi-turn profile measurement was also performed without mis-steering of DV120, resulting in the diluted vertical beam profile. Beam loss associated with the scattering between the beam and multi-wire monitor limits beam survival to less than 100 turns. A profile is shown in Fig. 4 where the beam width is $\sigma_0 = 5.5$ mm and the corresponding beam emittance is $\epsilon_{95\%}^v = 5.3\pi$ mm-mrad, which is slightly larger than the value measured by the AGS IPM and is due to the scattering between the beam and the wires.

4 CONCLUSION

A multi-wire beam profile monitor has been installed and tested in the Brookhaven AGS. It can be used to directly measure the beam profile being delivered from the Booster through the BTA beamline, and the evolution of this profile in consecutive turns about the AGS. The system can also be used to simply tune injection, if an optical match to the AGS lattice is desired. As the AGS prepares to serve as the injector for RHIC, it will justify its importance in transverse emittance control.

5 REFERENCES

[1] H. Weisberg, et al., *Proc. IEEE Particle Accelerator Conference, 1983*, p.2179.

[2] R.L. Witkover, et al., *Proc. IEEE Particle Accelerator Conference, 1987*, p.567.

[3] G.A. Smith, et al., *Proc. IEEE Particle Accelerator Conference, 1991*, p.1264.

RADON RECONSTRUCTION IN LONGITUDINAL PHASE SPACE

V. Mane, S. Peggs, J. Wei*
Brookhaven National Laboratory, Upton, New York 11973, USA

Abstract

Longitudinal particle motion in circular accelerators is typically monitored by one dimensional (1-D) profiles. Adiabatic particle motion in two dimensional (2-D) phase space can be reconstructed with tomographic techniques, using 1-D profiles. A computer program RADON has been developed in C++ to process digitized mountain range data and perform the phase space reconstruction for the AGS, and later for Relativistic Heavy Ion Collider (RHIC).

1 INTRODUCTION

The mathematical problem of 2D image reconstruction from an infinite number of 1D projections was formulated and solved by J. Radon in 1917 [1]. In practical algorithms, now in use in computerized tomography, the image is reconstructed on a 2D grid from a finite number of projections. These algorithms can be broadly classified into Fourier convolution algorithms and iterative algorithms. The Algebraic Reconstruction Technique (ART) is a commonly used iterative technique and is described by Gordon [2]. The Fourier convolution algorithm is based on papers by Bracewell and Riddle [3] and Ramachandran and Lakshminarayanan [4]. These algorithms are also presented in texts on computerized tomography [5], [6], [7].

Beam tomography in accelerators for longitudinal and transverse phase space has been used by several authors [8], [9], [10], using the ART algorithm. In longitudinal phase space, the synchrotron osillation period is typically several hundred turns and many bunch profiles are available over half a period. Therefore the Fourier convolution techniques are adequate. In this paper, we present reconstruction for mountain range data shown in Figure 1 and discuss a filtered backprojection algorithm for phase space reconstruction. During the Sextant test of RHIC in early 1997, this program was employed to reconstruct the motion of Au^{77+} beam in the AGS.

2 RADON TRANSFORM AND RECONSTRUCTION

Let $f(x,y)$ represent a 2D object (Figure 2). Let (x_r, y_r) be the coordinate system rotated by angle θ with respect to the (x,y) coordinate system, where $x_r = x\cos\theta + y\sin\theta$ and $y_r = -x\sin\theta + y\cos\theta$. The projections $P(x_r,\theta)$ obtained by integrating $f(x,y)$ along all lines of constant

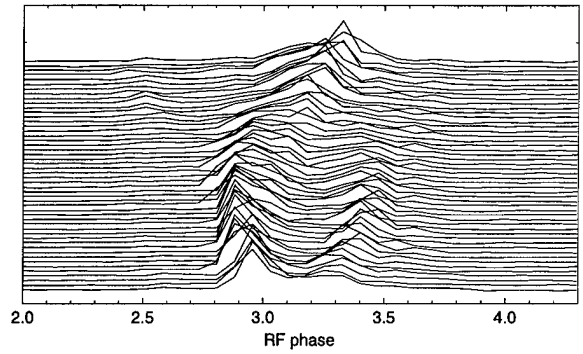

Figure 1: Mountain Range Data from the AGS, used for reconstruction in figure 5.

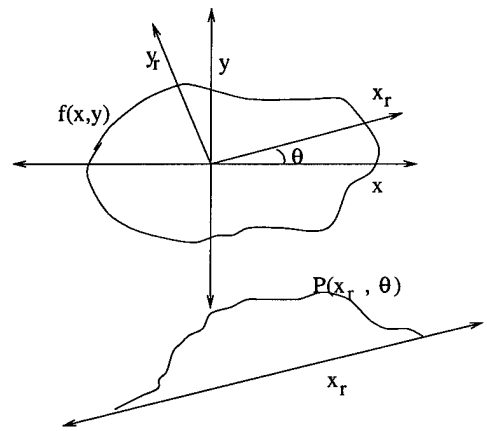

Figure 2: The profile $P(x_r,\theta)$ is the Radon Transform of the two dimensional function $f(x,y)$.

x_r in the plane is the Radon transform of f(x,y)

$$P(x_r,\theta) = \int_{-\infty}^{\infty} f(x_r, y_r)dy_r \qquad (1)$$

The filtered backprojection algorithm, a form of Fourier convolution algorithm, is employed in the program RADON. In this algorithm, each projection $P(x_r,\theta)$ is Fourier transformed, multiplied by a high pass filter, inverse Fourier transformed, backprojected, and all the backprojections are summed up. Note that backprojection is not the inverse of projection, and hence the high pass filter.

Let $F(u,v)$ be the 2D Fourier Transform of $f(x,y)$ and let (w,θ) represent the polar coordinates in the frequency

* Work performed under the auspices of the U.S. Department of Energy.

space, with $u = w\cos\theta$ and $v = w\sin\theta$

$$f(x,y) = \int_{-\infty}^{\infty}\int_{-\infty}^{\infty} F(u,v)e^{i2\pi(ux+vy)}dudv$$
$$= \int_{0}^{2\pi}\int_{0}^{\infty} F(w,\theta)e^{i2\pi w(x\cos\theta+y\sin\theta)}wdwd\theta \quad (2)$$

Since $x_r = x\cos\theta + y\sin\theta$ and $F(w,\theta+\pi) = F(-w,\theta)$, the above equation can be written as

$$f(x,y) = \int_{0}^{\pi}\int_{-\infty}^{\infty} F(w,\theta) \mid w \mid e^{i2\pi w x_r}dwd\theta \quad (3)$$

The Fourier Transform of a projection at angle θ with respect to x gives a slice of the 2D Fourier Transform F(u,v) at angle θ wrt u. Therefore, $F(w,\theta)$ is the Fourier Transform of $P(x_r,\theta)$ and

$$Q(x_r,\theta) = \int_{-\infty}^{\infty} F(w,\theta) \mid w \mid e^{i2\pi w x_r}dw \quad (4)$$

gives the filtered projection, where the frequency response of the filter is given by $|w|$. The reconstructed image can be obtained by integrating over the filtered backprojections

$$f(x,y) = \int_{0}^{\pi} Q(x_r,\theta)d\theta \quad (5)$$

The following two filters are defined in RADON [6]
Ramp Filter

$$H(f) = \begin{cases} \mid f \mid & \text{if} \mid f \mid \leq f_c \\ 0 & \text{otherwise} \end{cases}$$

where f_c is the cutoff frequency
Hann Filter

$$H(f) = \begin{cases} 0.5 \mid f \mid (1+\cos(\pi f/f_c)) & \text{if} \mid f \mid \leq f_c \\ 0 & \text{otherwise} \end{cases}$$

3 RECONSTRUCTION EXAMPLES

The program RADON, written in C++ generates simulation profiles, reconstructs images, and displays them graphically. The program also reads mountain range data, reconstructs in longitudinal phase space, and calculates the longitudinal emittance. This section gives an example of image reconstruction from simulation and compares it with the original image. Reconstruction with data acquired from AGS is described in next section. The signal and background errors, as described below, compare the original image with the reconstruction.

3.1 Signal Error

Let I_{ij} and X_{ij} be the intensity of the original image and the reconstructed image, respectively, in cell (i,j). Let I_{max} be the maximum intensity of the original image. Define the cutoff intensity I_c to be 10% of the maximum intensity, that is $I_c = 0.1I_{max}$. Define the signal region S such that $I_{ij} > I_c$. Signal Error is defined by

$$E_s = \frac{1}{I_{max} - I_{min}}\sqrt{\frac{1}{\alpha_s}\sum_{i,j\in S}(I_{ij} - X_{ij})^2} \quad (6)$$

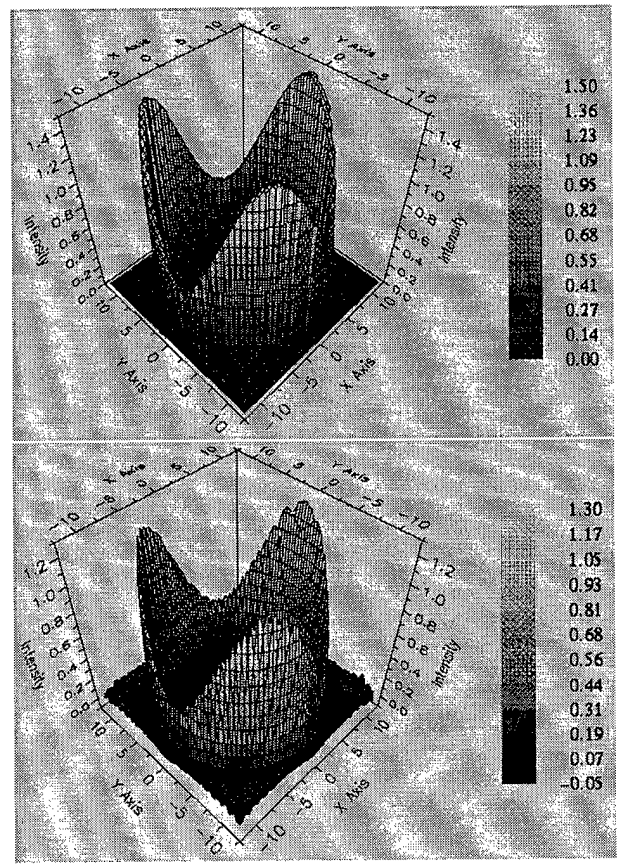

Figure 3: Original image (top) and reconstructed image using RADON (bottom). A total of 30 profiles with 64 samples per profile are used for reconstruction.

where $\alpha_s = \sum_{i,j\in S} 1$

3.2 Background Error

Define the background region B consisting of all the cells (i,j) that are not in S. Background Error is defined by

$$E_b = \frac{1}{I_{max} - I_{min}}\sqrt{\frac{1}{\alpha_b}\sum_{i,j\in B}(I_{ij} - X_{ij})^2} \quad (7)$$

where $\alpha_b = \sum_{i,j\in B} 1$.

3.3 Example

Figure 3 compares the reconstructed image with the original image for an annular distribution, modulated in the azimuthal direction. A total of 30 profiles equally spaced between 0 and π, with 64 samples per profile are used for the reconstruction. The signal and background errors are 0.21 and 0.07, respectively. In this case, the signal error is due to the difference in amplitude of the reconstruction. Sensitivity analysis were performed to determine the error in reconstruction due to insufficient profiles, samples and the error in synchrotron period. Figure 4 gives the signal and the background errors, for a gaussian distribution due to the error in synchrotron period. Several examples of re-

construction with gaussian and annular distribution, and the associated errors are given in [11].

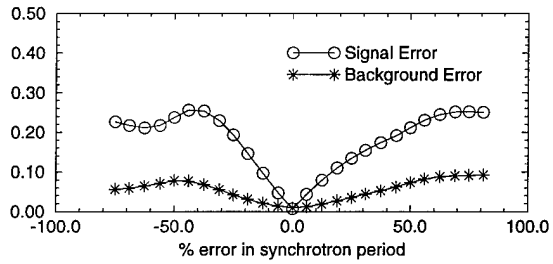

Figure 4: Signal and Background error vs. error in synchrotron period, for a gauss beam.

4 APPLICATION IN RHIC SEXTANT TEST

RADON application was successfully used during the Spring 1997 RHIC Sextant Test [12] for longitudinal phase-space reconstruction of Au^{77+} beams in AGS. Mountain-range beam profile data from the Wall Current Monitor taken at AGS exrtraction flattop was captured into a fast scope, LeCroy Model 9354TM, with a rearm time of 100 μs. The data was transfered to a computer via GPIB using a LabVIEW program.

Particle motion was reconstructed from a set of profiles recorded over half a synchrotron period (Figure 1), along with basic parameters of the machine and the rf system. Since the bunch only occupied a small fraction of the rf bucket, synchrotron motion was linearized. The rf voltage was calibrated by observing the synchronous phase difference as transition was crossed at a known ramp rate. Signal width broadening caused by finite cable bandwidth [12] was taken into account.

Figure 5 shows the reconstructed phase space diagram at an early stage of the test after two bunches were coalesced to increase the beam intensity. The bunch rotated by 110° in synchrotron motion, from the top figure to the bottom figure. The calibrated rf voltage was 254 kV, the harmonic number was 8, the rf frequency was 2.96 MHz, the relativistic γ was 12.1, transition γ_t was 8.49, and the synchrotron period was 9.6 ms. Totally, 49 profiles with 100 μs separation sampled at 4 ns were used for the reconstruction.

5 CONCLUSIONS

A program RADON has been developed to reconstruct 2D longitudinal phase space plot of the beam from 1D profiles. During the Sextant test of RHIC in early 1997, this program has been successfully employed to reconstruct the motion of Au^{77+} beam in the AGS. In the future, we plan to generalize the application for both longitudinal and transverse phase space, including nonlinear motion.

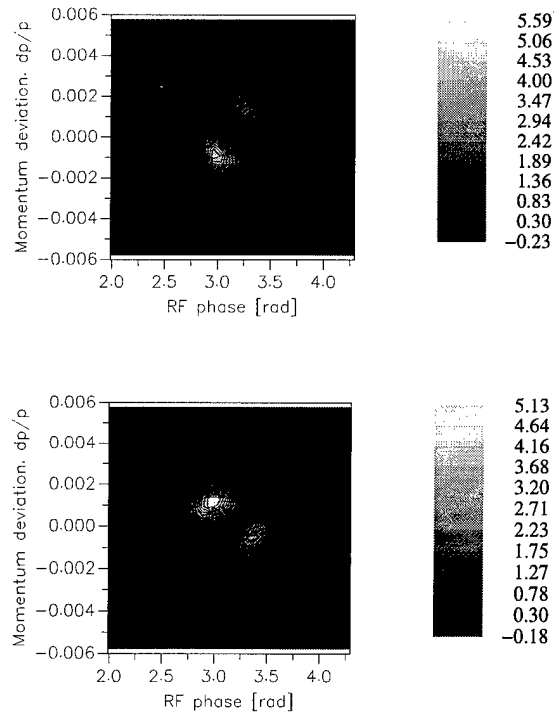

Figure 5: This figure shows two distinct globs of charge of Au^{77+} rotating in an AGS rf bucket, with the bottom frame rotated by 110 degree wrt the top frame.

6 ACKNOWLEDGEMENTS

We would like to thank W. VanAsselt for the LabVIEW MountainRange program, and for his help with obtaining data. We would also like to thank S. Tepikian for the XRT graphics display program, B. Andrews, K. Brown and the AGS Main Control Room crew for their help and support.

7 REFERENCES

[1] Johann Radon, Ber. Verh. Sächs. Akad. Wiss. Leipzig, Math. Phys. Kl. 69, 262-277 (1917).
[2] R. Gordon, R. Bender, G. T. Herman, J. Theor. Biol., (1970), 29, pp 471-481.
[3] R. N. Bracewell, A. C. Riddle, Astrophys. J. 150 (2), pp 427-434 (1967).
[4] G. N. Ramachandran, A. V. Lakshminarayanan, Proc. Natl. Acad. Sci. 68 (9), pp 2236-2240 (1971).
[5] Stanley R. Deans, The Radon Transform and some of its applications, J. Wiley, 1983.
[6] G. T. Herman, Image Reconstruction from Projections, Springer-Verlag, 1979.
[7] A. Kak, M. Slaney, Computerized Tomographic Imaging, IEEE Press, 1988.
[8] J. S. Fraser, IEEE Trans. Nucl. Sci., Vol. NS-26, Feb 1979, pp 1641-1646.
[9] O. R. Sander et al., BNL-51134 (1980), 314.
[10] G. Jackson, IEEE PAC, Washington D. C. (1993), 2418.
[11] V. Mane, RHIC/AP/96, June 1996.
[12] J. Wei et al., "RHIC Sextant Test – Accelerator Systems and Performance", these proceedings.

ORBIT COMPENSATION FOR THE TIME-VARYING ELLIPTICALLY POLARIZED WIGGLER WITH SWITCHING FREQUENCY AT 100 HZ

O. Singh and S. Krinsky
NSLS, Brookhaven National Laboratory

Abstract

In October 1996, the elliptically polarized wiggler, installed in the X13 straight section of the NSLS X- ray ring, was commissioned at an operating frequency of 100 hz. This wiggler generates circularly polarized photons in the energy range of 0.1 to 10 keV with AC modulation of polarization helicity. The vertical magnetic field is produced by a hybrid permanent magnet structure, and the horizontal magnetic field is generated by an electromagnet capable of switching at frequencies up to 100 hz. Here, we discuss the compensation of the residual vertical and horizontal orbit motion utilizing a time-domain algorithm employing a function generator to drive trim coils at the wiggler ends, and the wideband high precision orbit mesurement system of the X-ray ring. The residual orbit motion has been reduced to a level below 1 micron, and the device has been run in regular operations with no negative effect on other users.

1 INTRODUCTION

The time-varying elliptically polarized wiggler [1, 2, 3] was installed in the X13 straight section of the NSLS X-ray ring in December 1994. This device produces variable polarized x-rays, with the right- /left- handedness of polarization switchable at up to 100Hz, making possible the use of gating or lock-in amplifier techniques to detect the very weak signatures of circular dichroism and other effects associated with right- vs. left- handedness of some physical and biological systems. The DC vertical magnetic field is produced by a hybrid permanent magnet wiggler, and the time-varying horizontal magnetic field is generated by an AC electromagnet wiggler. Critical to the successful operation of the AC electromagnet wiggler is the maintenance of the high degree of orbit stability required by the many experimental beamlines on the X-ray ring. Orbit compensation of the time-varying elliptically polarized wiggler operating at 2Hz was described in ref. 4. Here, we discuss the compensation of the residual orbit motion for 100Hz operation, utilizing a time-domain algorithm employing a function generator to drive the trim coils at the wiggler ends.

2 COMPENSATION METHOD

Our approach for 100 hz compensation consists of several steps: 1) measure orbit distortion in time-domain at two pick-up electrodes (pues) with electromagnet switching at 100 hz, 2) process these waveforms to remove offsets and add gains, 3) load processed waveforms into function generators which produce correction signals in synchronism to switching frequency, 4) apply correction signals to end trims and observe the frequency spectrum of residual distortion at the switching frequency and its harmonics. Fig.1 shows the block diagram for the dynamic compensation system

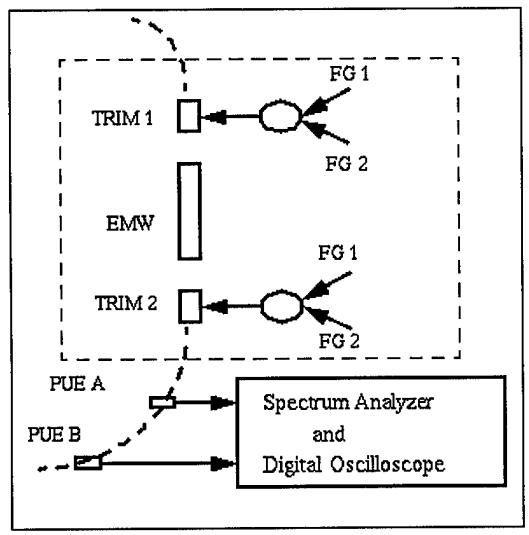

Figure 1: Dynamic Compensation System.

2.1 *Time-domain orbit distortion measurement*

A fast digital oscilloscope (LeCroy 9354) is used to measure orbit distortion. This oscilloscope is set up to sample at 1 Mhz and to collect 10,000 data points for every frame of 10 msec. Each frame's data is averaged point-to-point over several hundred frames. The averaging is critical to obtain an accurate time-domain orbit distortion because it removes ambient background motion. The dominant spectral content of the ambient orbit motion lies in the frequency range of 8 hz to 60 hz [4] and is cancelled by averaging. Figs. 2b and 2c show the uncompensated orbit distortion in the vertical and horizontal planes produced by the wiggler, in relationship to the driving wiggler current waveform shown in Fig. 2a. The level of distortions are 30 and 60 microns peak to peak in vertical and horizontal planes, respectively.

2.2 *Signal processing*

The measured average orbit distortion waveforms are transferred (off-line) to a PC based computer. The computer processes these waveforms to null for the offset in the orbit and to amplify the orbit waveform amplitude to provide sufficient correction trim signal level.

0-7803-4376-X/98/$10.00 © 1998 IEEE

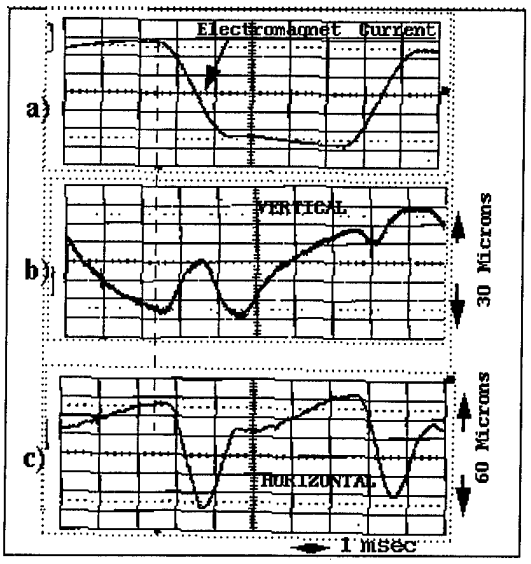

Figure 2: Waveforms with EPW (uncompensated) switching at 100 hz with 400 amperes amplitude; (a) Current waveform (b) Vertical orbit distortion at pue A and (c) Horizontal orbit distortion at pue A.

2.3 *Function generators*

The output waveforms are loaded into function generators (Fluke 5150). These function generators provide 10 msec long correction signals at every 100 hz trigger. Fig. 3 shows a set-up diagram utilizing four function generators, two for each plane. Note that the phase of each waveform can be adjusted by varying 100 hz trigger delays (D1 to D4) to the function generators.

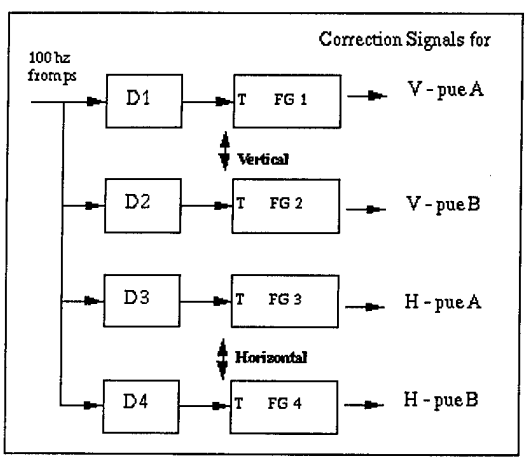

Figure 3: Function generators set-up with trigger delay units

2.4 *Compensation*

The spectrum analyzer was set to observe peaks at 100 hz and harmonics. Each correction signal, which corresponds to a given pue, is applied to the end trims in a linear combination to correct orbit at that pue while leaving other pue unchanged. While minimizing 100 hz line spectral amplitude, we noticed that harmonic line spectra amplitudes did not reduce. In fact, there was an increase in amplitude of some harmonics. This is due to the fact that the trim-to-pue response is not flat, see Fig. 4.

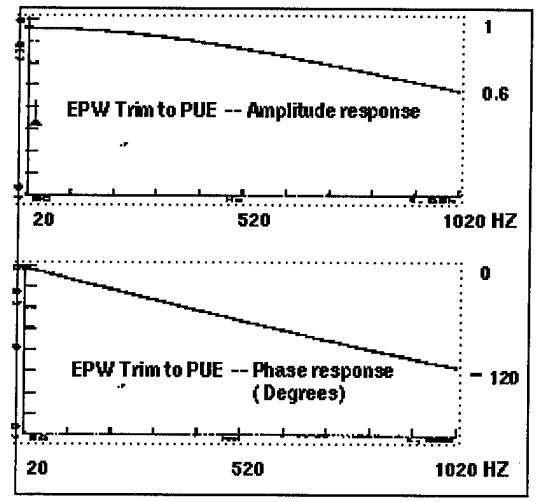

Figure 4: EPW trims to pues response.

For proper compensation, a new time-domain correction signal must be determined which takes into account the trim-to-pue response. In our approach, we determined this waveform by iteration, where each iteration minimizes the amplitude of only a few harmonics. Two iterations were sufficient to reduce the orbit distortion to a satisfactory level. The steps involved for compensation are discussed below. Let the first correction waveform be denoted by F_1, shown in Fig. 5a, which is a measured distortion waveform. During the 1st iteration, this waveform is loaded into the function generator and the line spectra's magnitude at 100 and 200 hz are minimized by adjusting amplitude and phase of the correction waveform. The optimized correction amplitude and phase are denoted by A_1 and P_1. So, the optimized waveform is given by (A_1F_1 with phase delay P_1).

With this correction, the residual orbit distortion F_2 is measured (Fig. 5b), and F_2 is now the new function for the 2nd iteration correction. In this iteration, the magnitude of the spectral lines at 300 to 600 hz are minimized and the optimized correction amplitude is A_2 and phase delay is P_2. The two optimized correction waveforms are combined in the computer to generate the final correction wave form (A_1F_1 with phase delay P_1) + (A_2F_2 with phase delay P_2). Fig. 5c shows the final residual orbit. No further iteration was necessary. The orbit distortion in frequency domain without compensation is shown in Fig. 6a; the distortion after 1st iteration is shown in Fig. 6b (note 100 and 200 hz peaks are reduced); and the distortion after 2nd iteration is shown in Fig. 6c (note all peaks are minimized). In time-domain, as shown in Fig 5, the vertical orbit distortion was reduced from 30 to 4 microns peak to peak (compare Figs. 5a to 5c). In frequency domain, 100 hz ver-

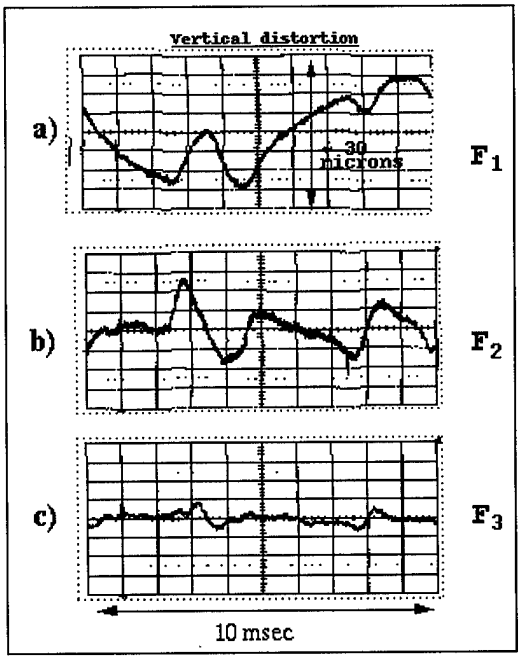

Figure 5: Time domain vertical orbit distortion when EPW switching at 100 hz: (a) no compensation (b) 1st iteration compensation and (c) 1st and 2nd iteration compensations.

tical distortion is reduced from 18 to 1.2 microns peak to peak (compare Figs. 6a and 6c). Compensation results for horizontal plane are shown in Figs. 7a and 7b without and with compensation, respectively.

3 ACKNOWLEDGEMENTS

We would like to acknowledge work done by H. Link and G. Frisbie for evaluating and programming efforts in the function generators. We would also like to acknowledge the collaboration with P.M. Ivanov and E.A. Medvedko in the early stages of this work. Work performed under the auspices of the U.S. Department of energy undercontract DE-AC02-76CH00016.

4 REFERENCES

[1] A. Friedman, S. Krinsky, and E. Blum, " Polarized Wiggler for NSLS X-Ray Ring: Design Consideration," Informal Report BNL - 47317, March, 1992.

[2] A. Freidman, X. Zhang, S. Krinsky, E. Blum and K. Halbach, "Polarized Wiggler for NSLS X-ray Ring", Proc. 1993 Part. Accel. Conf., Washington, D.C., May, 1993, p. 1599.

[3] E. Gluskin, D. Frachon, P.M. Ivanov, J. Maines, E. A. Medvedko, E. Trakhtenberg, L. R. Turner, I. Vasserman, G. I. Erg, Yu. A. Evtushenko, N. G. Gavrilov, G.N. Kulipanov, A. S. Medvedko, S. P. Petrov, N. A. Vinokurov, A. Friedman, S. Krinsky, G. Rakowsky, O. Singh, " The Elliptical Multipole Wiggler Project," Proc. 1995 Part. Accel. Conf., Dallas, Tx, May, 1995.

[4] O. Singh, S. Krinsky, P.M. Ivanov, and E. A. Medvedko," Orbit Compensation for the Time Varying Elliptically Polarized wiggler," Rev. Sci. Instrum. 67(9), September 1996.

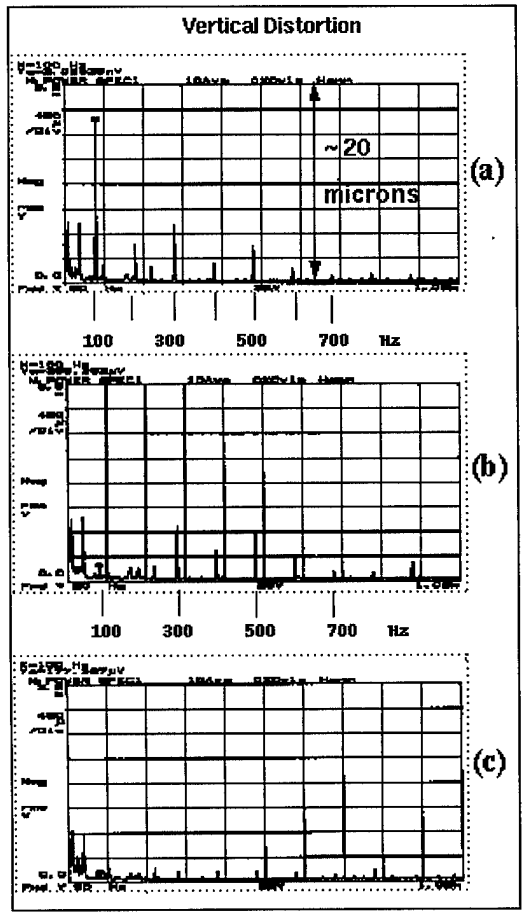

Figure 6: Fourier spectrum of vertical orbit when EPW switching at 100 hz: (a) no compensation (b) 1st iteration compensation and (c) 1st and 2nd iteration compensations.

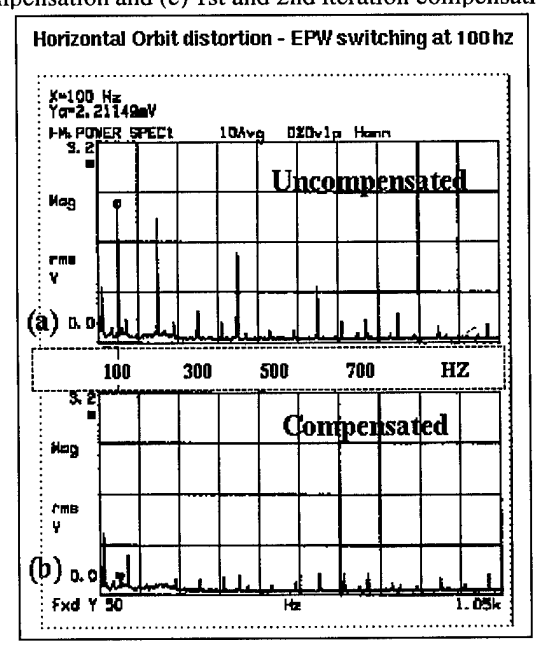

Figure 7: Fourier spectrum of horizontal orbit when EPW switching at 100 hz: (a) no compensation and (b) with full compensation.

A TURN-BY-TURN VERTICAL PROFILE MONITOR

R. Scott Smith, Stuart Henderson, D. Hartill, Laboratory of Nuclear Studies, Cornell University and Tong Chen, R.H.Siemann, Stanford Linear Accelerator Center, Stanford University

Abstract

A turn-by-turn vertical beam profile monitor has been developed at the Cornell Electron Storage Ring (CESR). The instrument optically images the vertical beam distribution with an array of optical fibers that transport visible synchrotron radiation to an array of photo-multiplier tubes. Each PMT signal is recorded by a turn-by-turn data acquisition system. With this instrument, we compare profiles of colliding and non-colliding electron bunches, from which we calculate an upper limit on the coherent beam-beam effect.

1 INTRODUCTION

The beam-beam interaction is thought to significantly limit luminosity in lepton (e+e-) storage rings; yet, experimental data is lacking. We know that the beam-beam force focuses in both transverse planes and that it may lead to a multi-turn oscillation in transverse beam size [1]. At the Cornell Electron Storage ring (CESR), we have developed a turn-by-turn vertical profile monitor suitable for observing synchrotron radiation at optical wavelengths. The monitor is compact, unimodular, and portable. We can distinguish bunches spaced at least fourteen nanoseconds apart and observe, in principle, beam density out to 5σ. Our real limitation in the out lying region is noise from photon-statistics.

2 DEVICE CHARACTERISTICS

The vertical profile monitor is basically a 10x2 array of optical fibers where each row transports visible light to a photo-multiplier tube. The optical fiber has a core diameter of 100 microns, sub-sampling the optical resolution of the beam telescope (174 microns). The total array size is approximately 1750x250 square microns, compared to the vertical Gaussian beam width of 200 microns. The ratio of the horizontal to vertical beam size is 10 at the point of observation. We may rotate the array about the image centroid and vertically translate it.

The Hamamatsu TO-8 PMT, used in our instrument, is small and compact – having a total volume of 1760 mm^3. The small size has allowed us to install the set of PMTs atop the fiber array assembly and, thereby, make a compact portable instrument. The TO-8 PMT is most sensitive to the shorter wavelengths of the visible spectrum, peaking at $\approx$450 nm. We digitize signals with a fast ADC system, recording the size of one bunch of one train with each run. The ADC full range input is ± 1 V, corresponding to ± 2000 ADC counts [2]. We sample at the rotation frequency of CESR (390.6 kHz).

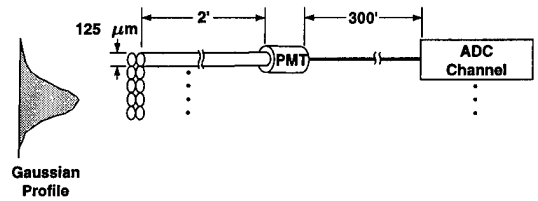

Figure 1: An image of the beam magnified by approximately unity is focussed onto a 10x2 array of fiber optics, where each row supplies a single PMT with light. The PMT signals are amplified and recorded on individual ADC channels.

3 CALIBRATION

We are interested in observing variations in the beam intensity distribution. Our linear CCD provides a time average picture for comparison, which is reliably Gaussian. A little reflection reveals that the area under the Gaussian curve should be constant for short time scales– typically a few thousand revolutions. Accordingly, we describe the intensity distribution by

$$\varrho(y,\sigma,\mu) = \frac{A}{\sqrt{\pi}\sigma} \exp\left(\frac{-(y-\mu)^2}{2\sigma^2}\right) \qquad (1)$$

The Gaussian width displayed by the CCD is in principle, if not measurably, larger than the Gaussian width in Eq(1). On a turn-by-turn basis, variations in the intensity distribution may be attributed to changes in σ and Schottky noise within the beam. The dipole contribution from Schottky noise is 10^{-3} smaller than the betatron amplitude of a few to several microns. Photon-statistics will prevent us from observing Schottky noise. In fact, photon-statistics will place a limit on all of our observations.

The fiber array performs a discrete sample of the image intensity. From this sample, we have two methods of reconstructing the profile behavior. The first method is a least squares fit. Although the best method for quantifying the density distribution, we will not be using it. We will use a simpler method. Before discussing changes in the Gaussian width, we need to know the device resolution. Stimulating vertical betatron motion is simple; and by shaking the beam at several intensities and measuring the beam position and distribution at the synch-light observation point, we directly calibrate the detector. The figure below depicts the FFT amplitude of a single channel as a measure of oscillation amplitude. The signal falls into the noise region near five microns.

0-7803-4376-X/98/$10.00 © 1998 IEEE

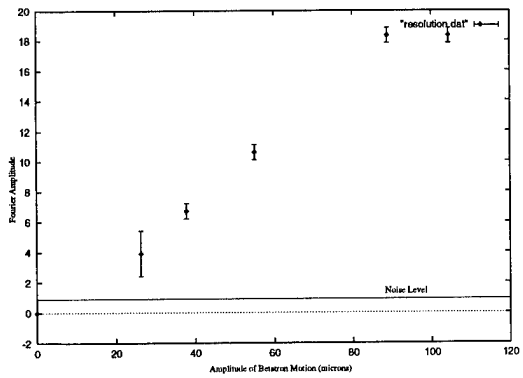

Figure 2: The response of a channel to centroid motion is measured. The channel lies one σ away from the centroid equilibrium position and has a resoluton of five microns.

4 MEASUREMENTS

We measure the device resolution by taking the difference of channel signals that flank the centroid. Below, we present the spectrum from a stimulated oscillation of 33 microns ± 10 microns.

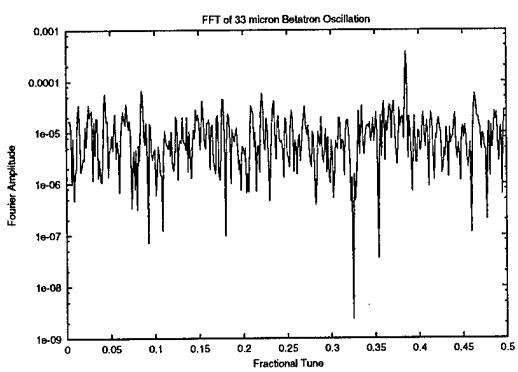

Figure 3: A FFT of a stimulated betatron oscillation of 33 μm. The signal was constructed by taking the difference of channel signals on either side of the centroid.

The signal to noise ratio is 7.91, indicating a resolution of four microns. Why did we not see a significant improvement? The derivative of Eq(1) with respect to the centroid position is

$$\frac{\partial \varrho}{\partial \mu} = \frac{(y-\mu)}{\sigma^2}\varrho \tag{2}$$

The extrema of Eq(2) lie at $\pm\sigma$ and imply that we do not gain much signal strength elsewhere.

A similar analysis is performed to investigate variation in the beam width. Strictly speaking, Eq(1) is non-analytic with respect to σ; but sufficiently far from the origin, we may make a first order expansion.

$$\frac{\partial \varrho}{\partial \sigma} = \left(\frac{(y-\mu)^2}{\sigma^3} - \frac{1}{\sigma}\right)\varrho. \tag{3}$$

The difference of channel signals lying within $\pm\sigma$ and those outside this region will increase the signal to noise ratio.

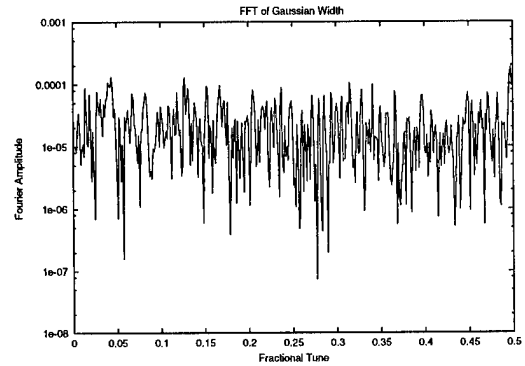

Figure 4: The difference in channel signals within $\pm\sigma$ of the centroid and those outside this range will measure the device response to oscillations in the Gaussian width of the beam. The response is flat.

We have performed this analysis on colliding beam data where the bunch currents were 7 mA and the vertical tune 9.61. The spectra is flat, implying that a more elaborate method of least squares fitting is not required. We can say that any oscillation in beam size is less than four microns. A four micron oscillation in beam size corresponds to a 4% change in emittance.

5 REFERENCES

[1] Siemann, R. H. 'The Beam-Beam Interaction ins e+e- Storage Rings.' Frontiers of Particle Beams: Factories with e+e- Rings. eds. M. Dienes, M. Month, B. Strasser and S. Turner. Springer-Verlag. (1992)

[2] Henderson, Stuart. 'A Beam Loss Diagnostic System for CESR.' These Proceedings.

FERMILAB MAIN RING ION PROFILE MONITOR SYSTEM

J. R. Zagel, J. L. Crisp, A.A. Hahn, P. G. Hurh, Fermilab†, Batavia, IL 60510

Abstract

An Ion Profile Monitor System is now in operation in the Fermilab Main Ring. This system captures up to 64K samples of both horizontal and vertical profiles in Main Ring at a turn by turn sample rate. The hardware and software of the system is described. Some early results are presented.

1 INTRODUCTION

Three Ion Profile Monitor (IPM) systems have been developed and installed in the Fermilab Main Ring. These systems incorporate many improvements but are based on the design installed in the Booster[1]. The monitors have been improved in mechanical design for better vacuum, ease of installation and maintenance, and utilize an increased clearing field of up to 30 kVolts to accommodate the increased intensity and beam energy of the Main Ring.

Operation of the monitor relies on residual gas molecules in the vacuum being ionized by the charged particle beam. The ions are accelerated toward a microchannel plate (MCP) by the applied clearing field. The MCP provides many electrons for each incident ion which are collected on anode strips running longitudinally with the proton beam. The charge on each strip is amplified, digitized, and saved in memory to produce single pass profiles.

1.1 Location

The horizontal monitors are located at A17 and F48; F25 is the vertical profile monitor.

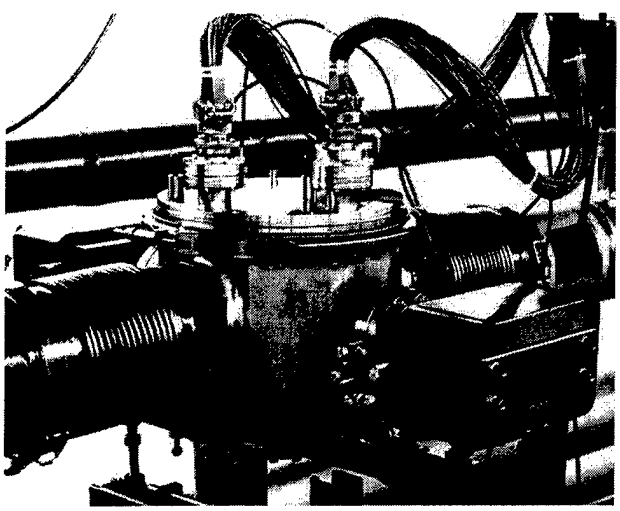

Figure 1. F48 Horizontal tunnel installation.

1.2 Components

The tunnel portion of the system consists of the vacuum housing containing a high voltage clearing field and field shaping components, MCP, and an anode strip circuit board. The circuit board contains a series of 120 signal anode strips on 0.5 mm centers, located below the plate, to collect the resulting electron charge.

Upstairs the raw signals are fed into an amplifier assembly and then to 12 bit, 4 channel Omnibyte™ Comet 2 MS/s VME digitizers. A total of 64 channels are digitized at a turn by turn sample rate to collect 64 k profiles. The data is read from the digitizers and analyzed by a MacIntosh™ 9500/150 using National Instruments™ PCI-MXI interface and LabVIEW® Software.

The instruments are remotely located in service buildings with no keyboard or monitor. Control of the measurement and the resulting data are made available via ethernet to the Fermilab ACNET Control System or accessed through the use of commercial communication packages such as Farallon™ Timbuktu.

The high voltage supplies for both the clearing field and MCP bias are controlled via PCI-GPIB interfaces. Immediately following a measurement, MCP voltage is turned off to conserve the lifetime of the plate.

2 PROFILE SIGNAL GENERATION

The quality of the image depends on many variables: the number of residual gas molecules, beam intensity, clearing field, and MCP gain. Noise pickup in the long signal cables contributes significant degradation to the signal to noise ratio.

2.1 Residual Gas

The Main Ring vacuum was analyzed to determine the nature of residual molecules in the vacuum pipe. The principal gasses found, (their associated atomic mass units), and partial pressure in Torr, were Hydrogen (2) $2.2*10^{-7}$ Torr, water (18) $1.8*10^{-7}$, water (17) at $5.1*10^{-8}$, Nitrogen, CO, and Ethane (28) at $4.5*10^{-8}$, Carbon Dioxide (44) at $1.5*10^{-8}$, and Oxygen (32) at $7.3*10^{-9}$.

2.2 Ion Production for IPM

Sauli [2] gives the ion production for minimum ionizing particles in O_2 and CO_2 as 22 and 34 primary ions/cm of gas at STP (1 atm, and 293° K respectively). If we take the average of these two gases (28 ions/cm) as

† Operated by Universities Research Association Inc. under contract with the U.S. Department of Energy

0-7803-4376-X/98/$10.00 © 1998 IEEE

a starting point, we can calculate the ion production (IP) at 10^{-8} Torr by:

IP = 28 ions/cm (10^{-8} Torr/(760 Torr/atm)) = 3.7 $*10^{-10}$ ions/cm.

This is the ion production of a single relativistic particle in a vacuum of 10^{-8} Torr. If we assume that the particle beam (with N protons or antiprotons) has a circular Gaussian shape, then the number of beam particles in a strip dx is

$$N(x)dx = \frac{N}{\sigma\sqrt{2\pi}} e^{-\frac{1}{2}(\frac{x}{\sigma})^2} dx$$

For a beam of N= 10^{11}, σ = 2 mm , and a strip at x = 0 with width = 0.5 mm, the number of beam particles is $2.0 *10^{10}$.

Multiplying the expression for the number of ions by this gives a total ion production of 7.4 ions/cm. If the strip is 10 cm long, we will collect 74 ions in the central part of the profile. This number can be scaled up by beam intensity and vacuum.

For example, a "typical" 2B cycle had a proton intensity (in Main Ring) of 30 $*10^{11}$ p. If the vacuum was 10^{-8} Torr, we would produce 2200 ions on the center strip of the IPM.

If the MCP has a gain of 5k, then the output charge onto the strip is $5 *10^{3} * 2.2*10^{3}*1.6*10^{-19}$ C/e = 1.8 pC.

3 ELECTRONIC DESIGN

The amplifier was designed with a 100 ohm input impedance which together with the capacitance of 30 meters of cable forms a 300 kHz low pass filter providing sufficient rise time for the 1.6 usec beam length. A current feedback amplifier, an AD844, was chosen for the first stage because of its ability to deal with high frequency noise. The second stage consists of both an OP37 and LH0002 in a single feedback loop configured to take advantage of the OP37 bandwidth and the power driving ability of the LH0002.

3.1 Amplifier Gain And Noise

The amplifiers have an overall voltage gain of 1500 and an input impedance of 100 ohms that together form a transimpedance of 150 kohm. The measured noise levels agree with specifications and correspond to an input current of 23 nA, the input noise of the AD844 amplifier. Sixty-four channels are placed on a single board, and two boards are combined in a single chassis to provide 128 independent channels. Coupling between channels has been measured to be less than -46db.

The high impedance and thin conductive coating of the MCP allows electromagnetic fields generated by the beam to pass through and induce currents directly in the electron collecting anode strips. These signals consist of the bunch frequency and several harmonics, much higher in frequency than the desired signals. This high frequency noise can be rectified in the first amplifier stage producing offsets that change with intensity and bunch length and can be seen with no voltage on the MCP. To combat this problem, the wires inside the detector leading to the strips are shielded, a second order low pass filter is placed in front of the amplifier, and a current feedback amplifier is used. These steps greatly reduce but do not eliminate the problem. Current feedback amplifiers have high bandwidths and fast slew rates which reduce the effect but they have poor temperature stability and drift. However, these errors change slowly and are corrected in software by measuring the offsets without beam.

3.2 Measured Signals and Noise

For $1*10^{12}$ protons, the strip with the largest signal at the amplifier is about 670 nA through the 1.6 μsec batch. Common operating levels of 810 volts provide an unsaturated gain of 3800 indicating about 1800 ions strike the MCP. The signal to noise ratio of the MCP is the square root of this number or 42. The signal to noise ratio of the amplifier is 29. The impedance across the MCP is 10 Mohms and the bias current is 510 nA for each strip. The manufacturer recommends signal currents be less than 10% of the bias current. We have been running well into saturation in an effort to overcome noise picked up in the 30 to 150 meter signal cables between the detectors located in the tunnel and the amplifiers located in the equipment gallery.

Noise induced on the signal cables is currently limiting performance of the system. It consists of short pulses of a volt or less in amplitude having duration of a few μsec. They are locked to the power line frequency and are believed to originate from SCR firing pulses controlling the main bus power supplies. They are separated in time by a few msec making the duty cycle low. Data is collected every turn and about one turn in 100 is corrupted with noise and is unusable. The strips which collect charge from the MCP are electrically open, making the source impedance very high which reduces noise currents. To overcome noise induced in signal cables, it is planned to place the amplifiers in the tunnel closer to the detector.

DATA HANDLING

A measurement is started by specifying the clock event on which to capture data. The MCP voltage is adjusted based on the anticipated intensity for the selected event. The data is captured using a beam synchronous clock system and is digitized once per turn until the entire 64 ksample/channel memory is full. Then 8.5 Mbytes of data is read out of the VME chassis, background and offsets subtracted, display of charge and intensity vs turn, and a multicolor intensity plot (figure 2) is created in 4.5 seconds. The data can then also be displayed as a single profile, or sigma and position plot using a nonlinear fit.

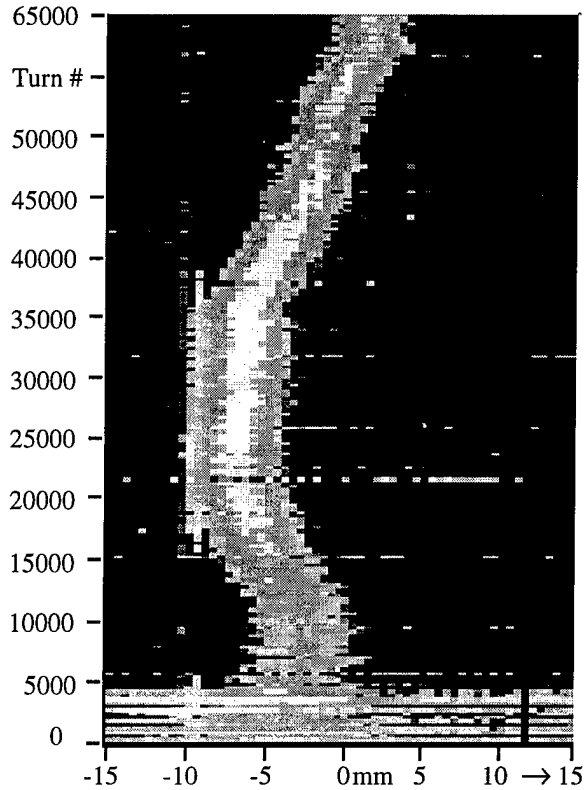

Figure 2. Multicolor Intensity Plot

The data analysis uses an optimized non-linear Levenberg-Marquardt algorithm. The system selects 200 profiles from the range specified, fits the data, and generates a display in 3.2 sec. This particular routine is also used in other instrumentation systems that deal with beam parameters [3].

4 MECHANICAL DESIGN

The mechanical design of the Main Ring Ion Profile Monitor includes several improvements over previous devices: higher clearing field voltage, higher vacuum compatibility, better sensor mounting mechanisms, and precise alignment features. These improvements also contribute to ease of maintenance.

The clearing field assembly is comprised of two 15 cm diameter stainless steel discs spaced 10.2 cm apart by two rectangular ceramic plates. Each ceramic plate is outfitted with five copper bars and six voltage dividing resistors to ensure a uniform clearing field across the gap. The lower potential electrode disc has a 8 x 10 cm rectangular opening in which the MCP is located.

The sensor assembly consists of a rectangular 8 x 10 cm MCP and an electron collecting signal anode strip circuit board. The MCP is delicately held into a precisely machined polystyrene mount by BeCu finger springs. The anode strip board is mounted 3.2 mm below the MCP on two aluminum mounting blocks. The mounting blocks feature small alignment pins which enable replacement of the anode strip board without requiring re-alignment. Signal connections to the board are made via custom designed polystyrene connectors. The connectors are designed to allow easy replacement. Nickel signal wires coated with poly-(amide-imide) insulation are used to bring the anode strip signals out to two commercial hermetic feed through connectors.

Ease of maintenance and precise alignment of internal components are further facilitated by mounting all the internal monitor parts to an easily removable end flange. This end flange has an outer diameter of 32 cm and has piloting pins to ensure proper and repeatable alignment in the monitor's vacuum housing. This allows work to be done on the interior components and then be replaced without requiring re-surveying.

Clearing field high voltage is fed into the vacuum housing through a 30 kV commercial feed through mounted opposite the end flange. A stainless steel disc mounted on a ceramic standoff tube transfers the high voltage to the high potential electrode disc (mounted on the end flange structure) via several BeCu spring fingers.

All internal components of the monitor were tested for vacuum compatibility. Where possible, machinable ceramic material is utilized rather than water absorbent organic materials. However, the anode strip board is constructed from an epoxy-glass laminate (G-10) which is notorious for its outgassing characteristics. Future boards will be made using a Teflon®-glass laminate material which has a much lower outgassing rate.

5 ACKNOWLEDGMENTS

The authors heavily relied on the following individuals for initial construction, system installation, and continuing calibration of the systems. Jeff Arthur was responsible for the assembly, calibration, and installation of the amplifiers, and provided oversight of the entire installation process. Brian Fellenz designed and built the high voltage interface. Shoua Moua and Mike Frett accomplished the vacuum vessel internal assemblies. Shoua and Jeff did most of the huge amount of cable termination. Thanks to Reidar Hahn and Jennifer Mullins for the photographic work to support the poster and publication. And finally to Greg Vogel for his assistance with the poster graphics. This debt is gratefully acknowledged.

REFERENCES

[1] Zagel, J. R., Chen, D., Crisp, J.L., "Fermilab Booster Ion Profile Monitor System Using LabVIEW", 1994 Beam Instrumentation Workshop, AIP Conference Proceedings 333, pp384-390.

[2] Sauli, F., "Principles of Operation of Multiwire Proportional and Drift Chambers", CERN 77-09, 3/5/77

[3] Hahn, A.A., "A Levenberg-Marquardt Least Squares Fit Algorithm Optimized for LabVIEW", Technical Note, 1997.

FIRST TEST RESULTS FOR A RESIDUAL GAS BEAM PROFILE MONITOR

V. Variale, N. Ceci, V. Valentino, G. V. Lamanna, INFN-sez. Bari
T. Clauser, V. Stagno, Dipartimento di fisica di Bari
A. Dainelli, M. Poggi, INFN-LNL

Abstract

A Residual Gas Beam Profile Monitor (RG-BPM) has been designed to study the cooling process of an ion beam circulating in a storage ring where the residual gas has a very low pressure. In this case the residual gas ion rate is very low and a single ion counting technique is required to reconstruct the beam profile. The peculiar feature of this device is the read-out system that can lead to a sensitive improvement of the spatial resolution. The same device can work also in analog mode at higher residual gas pressure and, then, it can be used also for other kind of accelerators. The test of the RG-BPM on an ion beam from an electrostatic accelerator is here given. The preliminary test arrangement for the ion single counting mode is also presented.

1 INTRODUCTION

Powerful non-destructive diagnostic methods based on the residual gas ionization produced by the ion beam has been developed and used on several accelerators [1,2]. In these devices the residual gas ions produced by the beam are collected, detected and spatially resolved in certain point of the accelerator by applying a transverse electric field plus a position sensitive detector. This kind of device is very helpful for any type of accelarator but it is of great importance for studing beam cooling in ion storage ring. However the high vacuum needed (< 10^{-11} mbar) for the storage ring operation leads to a very low residual gas ion production rate. This drawback has been overcome by using a vapor target to increase, locally, the background gas density. However, this technique perturbs the beam and if high quality beams are wanted it is no more useful.

Recently a new type of Residual Gas Beam Profile Monitor (RG-BPM) has been designed and constructed [3]. The device can employ a single-particle counting technique (counting mode) to increase the sensitivity of the detection in case of ultra high vacuum, as in the ion storage rings. The analog mode of operation is usually employed in single pass beams where the pressure of beam lines are of the order of 10^{-6}-10^{-8} mbar.

In this work the first test result of this device used in analog mode on the Legnaro Tandem accelerator ion beam is presented. Furtermore the experimental set-up of the counting mode test, where an alfa particle radioactive source will be used, is also shown.

2 THE RG-BPM

The working principle of a RG-BPM and its detailed design has been already presented in ref.3. For sake of clearness we present here, again, the operation scheme and shortly recall the main features of the device. The operation scheme, with its electric connections, is shown in fig. 1. PS1, PS2, PS3, PS4 are the Power supplies. The transverse electric field needed to accelerate the residual gas ion toward the MCP is given by the high voltage generator PS1 (16 kV) and PS2 (-4kV). The lower face voltage of MCP is given by PS3 and the upper face by PS4. The four power supplies allow of changing the voltage between the MCP faces and with respect to the phosphor screen in an independent way. In this way one can increase or decrease the voltage difference between the two stage MCP and then change the MCP gain. In this way, a suitable output signal for very different residual gas ion production rates can be obtained allowing the detector to be active in a wide range of beam currents.

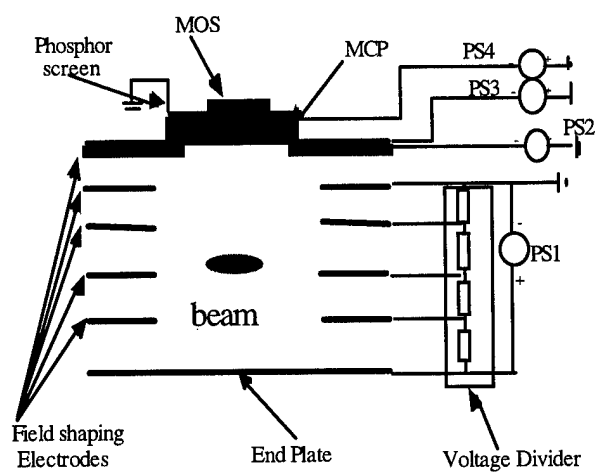

Fig.1 Operation scheme of RG-BPM.

The transvere electric field conveys the residual gas ions towards the lower face of MCP. At the exit of the two MCP stages a current of electrons proportional to the number of collected ions is produced. The electrons are accelerated towards the phosphor screen that emits a light spot which is detected by the MOS sensor. The MOS and the Phosphor screen are coupled by a Fiber Optic Plates (FOP). Compared to the lens coupling, this tecnique offers advantages such as high light transmission efficiency and compactness.

The MOS linear image sensor is a self-scanning linear photodiode array with a single video output line [4]. These kinds of sensors have a wide photosensitive area with a pixel height of 2.5 mm, a pixel pitch of 25 μm and a number of pixel of 1024. It has a high sensitivity in the range 500-800 nm, which is close to the spectral emission of the P-20 phosphor peaked at about 550 nm.

0-7803-4376-X/98 /$10.00 © 1998 IEEE

The ion production rate depends on the product of the vacuum pressure and beam current. Since on the test beam line the vacuum pressure is about 10^{-7} mbar and the ion beam current is of some particle-nano-Amperes, then a residual gas ion production rate sufficient to an analog mode operation is expected [5]. In this mode of operation typical MCP multiplication factor is kept in the approximate range of 10^2 to 10^4 to prevent charge saturation in the MCP channels.

Fig.2 shows the profile of a Au ion beam from the LNL tandem (230 MeV, 3 p-nA) obtained with the RG-BPM under test in analog mode.

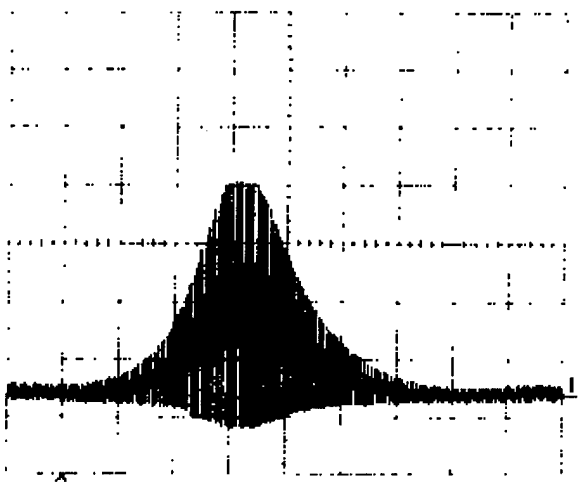

Fig.2. Ion beam profile given by the RG-BPM as seen on an oscilloscope screen; electronic noise: 500 mV.
(2 V/div, 1 ms/div equivalent to 3 mm/div in transverse space).

Just in front to the lower face of the MCP, two calibration wires were placed at a distance of 3 mm each others. The two wire shadows were visible by eyes trough the FOP, but, as it can be seen in the fig.2, they are not visible on the oscilloscope screen. The reason of this could be related to an insufficient optical coupling between the exit of the FOP and the entrance of the MOS sensor. Actually there is still a distance of about 1 mm between the FOP plane and the MOS face, causing a widining of the spot light. In this conditions the light exiting from the FOP has enough space to spread on the MOS and then the wire shadows on the MOS pixels are cancelled. To improve the coupling between the FOP and the MOS pixels the distance between them have to be reduced to less than 100 μm. The above considerations can suggest that the output shown in fig. 2 can suffer from this widening.

3 COUNTING MODE OPERATION

With very low ion production (very low currents or vacuum pressure below 10^{-9} mbar), a single particle detection is nedeed.

When at the MCP faces a voltage difference of 1.8 kV is applied, the MCP gain reach a value of 10^6. In this conditon a single particle impinging onto the lower face of MCP gives on the phosphor screen a light spot representing individual ion that can be detected by the MOS sensor [4].

Since, under these conditions, the MCP multiplication is saturated, these light spots have uniform intensity. Therefore the amplitude of the output signal is constant and not correlated to the density in transverse space. This mode of operation is called "counting mode". The transverse beam profile, is reconstructed recording in a frame memory the number of hits vs position of the light spots.

In fig.3 the block diagram of the experimental set-up to test the RG-BPM in counting mode is shown.

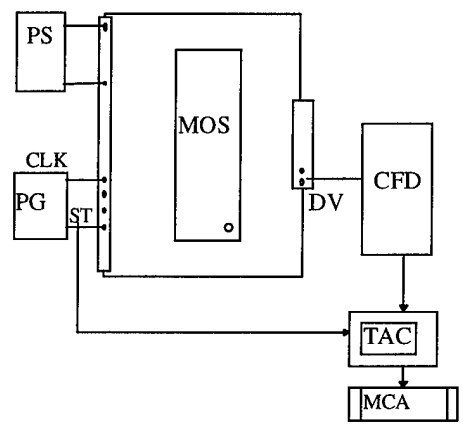

Fig.3 Block diagram of the experimental set-up for the counting mode operation of the RG-BPM: (PS) Power Supply, (PG) Pulse Generator, (CFD) Constant Fraction Discriminator, (TAC) Time to Amplitude Converter, (MCA), Multi-Channel Analyser.

DV (Data Video) is the MOS output signal generated by the self scanning shift-register, composed by the succession of the signals of each pixel [4].

The CFD is a level discriminator with a threshold set slightly above the noise signal, the logical output is used as the stop signal on a Time to Amplitude Converter module. CLK and ST are, respectively, the clock and the start signal needed to drive the MOS sensor. The ST signal is also used as start for the TAC.

The output signals of the TAC are collected and recorded on a Multi Channel Analyzer

REFERENCES

[1] W. H. DeLuca, IEEE Trans. Ncl. Sci. Ns-16 (1969)
[2] H.Weisberg et al., IEEE Trans. Ncl. Sci. Ns-30 (1983) 2179.
[3] B. Hochadel et al., Nucl. Instr. and Meth. in Phys. Res. A 343(1994) 401.
[4] "Hamamatsu Photonic" S3904 MOS Linear image sensors", Hamamatsu Photonic Catalog
[5] F.Hornstra DESY HERA-Report 87-25 (1987)

A LONGITUDINAL PHASE SPACE MONITOR AT THE PHOTON FACTORY STORAGE RING

Y. Kobayashi and M. Izawa, Photon Factory, KEK
Oho 1-1, Tsukuba, Ibaraki 305, Japan

Abstract

A phase detection circuit was developed to observe a synchrotron oscillation of the beam turn-by-turn at the Photon Factory Storage Ring (PF ring). A phase deviation from RF frequency was measured using the circuit connected to one of the button-type electrodes of the beam position monitor (BPM). A momentum deviation of the beam was simultaneously measured using a transverse beam position circuit of BPM placed on the dispersion section of the ring. These circuits were controlled with the on-line computer through GP-IB interface. Experimental data were taken in a stored single-bunch beam at a current of 10 mA. The resolution and the dynamic range of the phase detection circuit were less than 0.136 deg and over 8 deg, respectively. Then the tracking of the large coherent synchrotron oscillation caused by an RF phase modulation and a longitudinal single-bunch instability was displayed with a good accuracy on the longitudinal phase space.

1 INTRODUCTION

The PF ring, which is a dedicated synchrotron light source, has been stably operated for more than ten years. The high-brilliance project of the ring is now in progress [1]. By doubling the number of quadrupole and sextupole magnets in the normal cell sections, the beam emittance will be reduced to 27 nm•rad. The other accelerator components are also upgraded with the project. Especially a new RF-acceleration cavity has been developed [2]. The cavity is a higher-order-mode (HOM) damped type, which was designed to reduce the impedances due to HOM resonances. Consequently some coupled-bunch instabilities will be cured. So the existing four cavities are going to be replaced by the HOM-damped ones. It is very important to cure the coupled-bunch instabilities in order to store the higher current beam in the multi-bunch operation [3]. Because the coupled-bunch instabilities occur the beam size increases and then the brilliance of the synchrotron radiation decreases. The problem of the single-bunch

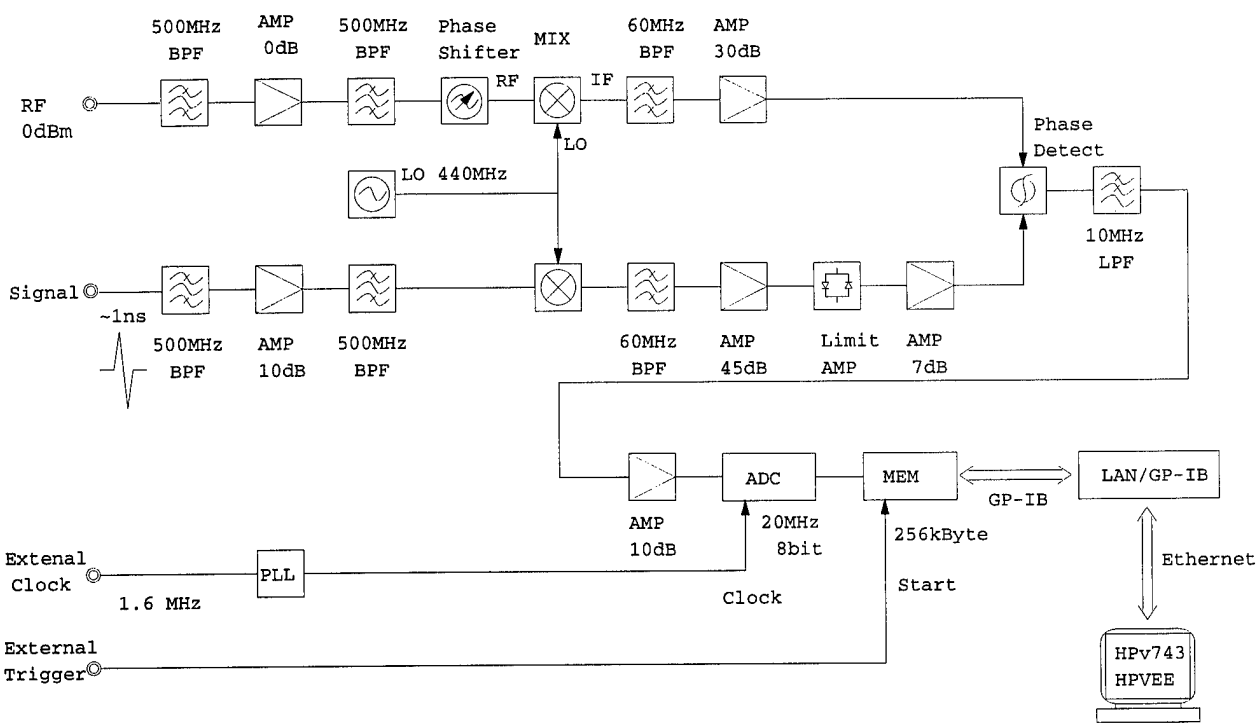

Figure 1: A block diagram of the phase detection circuit

instabilities is also important. For the FEL experiment the longitudinal feedback system was constructed to cure the single-bunch instability in the low-energy operation at the PF ring [4]. Much effort was also devoted to investigate the bunch-lengthening mechanism by measuring the bunch shape [5]. Recently the interesting experiments for a longitudinal nonlinear beam dynamics have been performed using a longitudinal phase space monitor at IUCF [6]. The transverse phase space monitor was already developed at the PF ring [7]. So we developed a phase detection circuit as a diagnostic tool for the longitudinal nonlinear beam dynamics study.

2 ELECTRONICS

The phase deviation ϕ of the synchrotron motion was determined by measuring the phase difference between the signals from BPM (SIG) and the RF master oscillator as a reference (REF), whose frequency is near 500.1 MHz. A block diagram of the phase detection circuit is shown in Fig.1. At first both of SIG and REF signals were passed through 500 MHz band-pass filter (BPF). They are converted to IF signals of 60 MHz using mixers and a 440 MHz local oscillator. In the REF line a phase shifter is added for the phase adjustment. For avoiding the current dependence a limiting amplifier is implemented in the SIG line after IF conversion. Then the phase difference between the SIG and the REF is made using a phase detection circuit. The output signal is digitized with 20 MHz 8 bit flash ADC after it is passed through 10 MHz low pass filter (LPF) to remove any RF components. It is immediately sent to the stored memory. The external clock signal (1.6 MHz: a revolution frequency of the PF ring) is made from dividing the signal of RF oscillator. It is employed for a start timing of ADC and a memory control after the phase is adjusted with a phase lock loop circuit (PLL). The accumulated data in the memory are transferred to the on-line computer through GP-IB interface.

On the other hand, the momentum deviation δ is easily found using a transverse beam position circuit of the BPM placed on the dispersion section. The monitor measures the horizontal position of the beam Δx. Then the momentum deviation can be obtained from $\delta = \Delta x / \eta$, where η is a value of dispersion.

3 EXPERIMENT

The experiment was performed in the single-bunch operation mode. The orbit and RF related parameters are shown in Table 1. The beam was stored at a current of 10 mA during this experiment. As a performance check of the phase detection the response of the beam to RF phase modulation was first measured. The phase modulation was achieved by modulating the RF control signal using a phase shifter whose control voltage was

Table 1: Orbit and RF related parameters of the PF ring

Beam Energy	E (GeV)	2.5
Betatron tune	ν_x / ν_y	8.45/3.30
RF frequency	f_{RF} (MHz)	500.1
RF voltage	V_{RF}(MV)	1.7
Harmonic number	H	312
Revolution frequency	f_{rev} (MHz)	1.6029
Energy Spread	σ_ε	0.00073
Synchrotron tune	ν_s	0.023

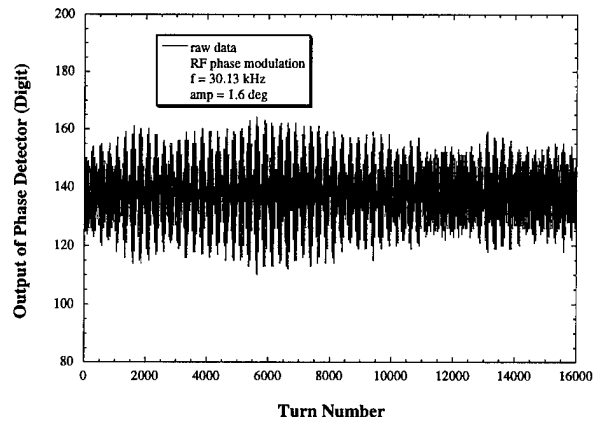

Figure 2: Digitized output data of 16000 turns

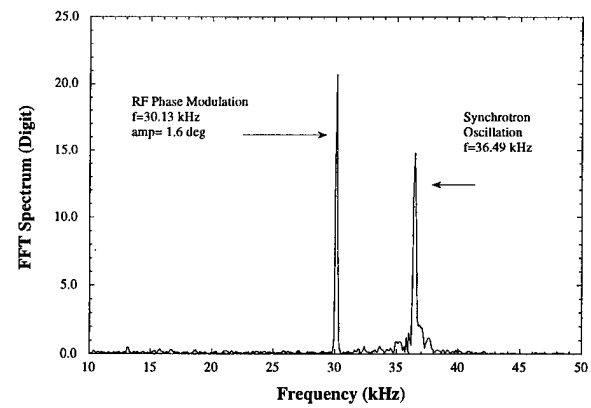

Figure 3: FFT spectrum of the data

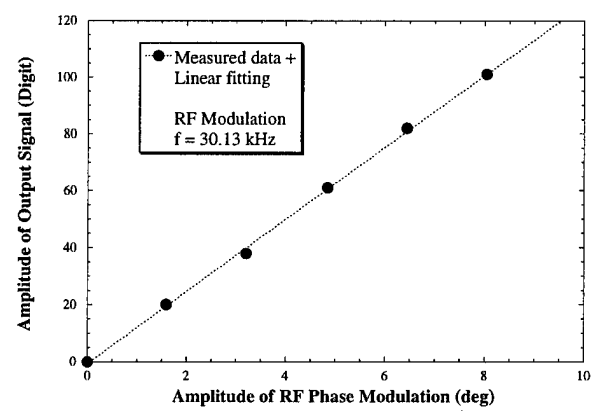

Figure 4: Calibration for converting the output digital data to the phase value

supplied by a function generator. The relationship between the voltage and the phase shift was already calibrated in the other experiment. The frequency and amplitude of the phase modulation are set to be 30.13 kHz and 1.6 deg, respectively. Figure 2 shows the digitized output data of 16000 turns. The FFT spectrum of the data is displayed in Fig. 3, but frequency range is set to be from 10 to 50 kHz. Two peaks were observed in this range; the first peak of 30.13 kHz is due to the RF phase modulation and the second one of 36.49 kHz is due to the coherent synchrotron oscillation caused by a longitudinal single-bunch instability. The calibration for converting the output digital data to the phase value was done with changing the modulation amplitude. Figure 4 shows the amplitude of the RF phase modulation versus the amplitude of the output digital data from the FFT spectrum. The figure shows a good linearity of the phase detection circuit over 8 deg. The phase resolution is about 0.136 deg, whose value was deduced after some signal processing.

As shown in Fig. 3, measured data includes the contributions from the RF phase modulation and the longitudinal single-bunch instability. Since the instability is so strong, we could not remove it in the experiment. So they were distinguished using a conventional signal processing method on the off-line computer. The momentum deviation was also deduced using the same method. Then, the longitudinal phase space plots of the oscillation caused by the RF phase modulation (a) and the single-bunch instability (b) are displayed in Figs. 5, respectively. Data of 16000 turns are plotted in the figures.

4 SUMMARY

The phase detection circuit was developed at PF ring. The good performance was obtained in the experiment. The momentum deviation was also measured using a transverse beam position circuit. Then the tracking of the large coherent synchrotron oscillation caused by an RF phase modulation and a longitudinal single-bunch instability was displayed with a good accuracy on the longitudinal phase space.

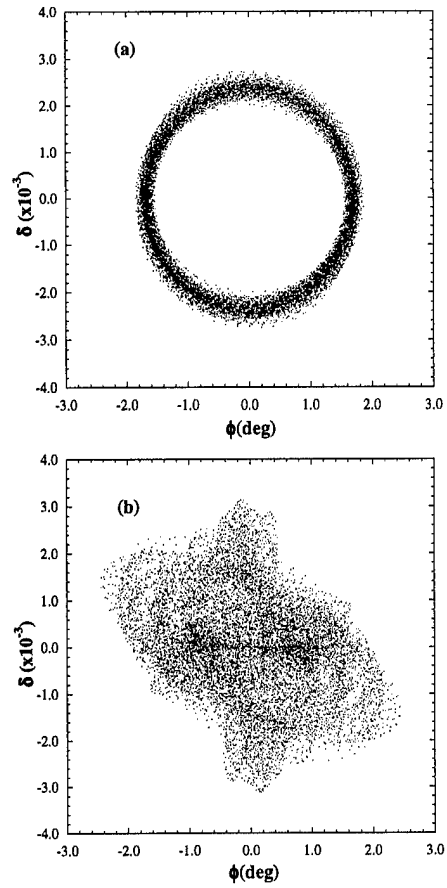

Figures 5: Longitudinal phase space plots of the oscillation caused by the RF phase modulation (a) and the single-bunch instability (b).

5 ACKNOWLEDGEMENTS

The authors wish to thank Prof. Kobayakawa for his good support, who was the director of the Light Source Division of the Photon Factory when the experiment was done. They also thank other staff for their help of the ring operation and Mr. Matsushita of Asahi Engineering & Trade Co., Ltd. for the cooperation in the design and production of the phase detection circuit.

REFERENCES

[1] M. Katoh et al., Proc. of the 5th EPAC, 650 (1996)
[2] M. Izawa et al., Rev. Sci. Instrum. **66**, 1910 (1995)
[3] H. Kobayakawa et al., Rev. Sci. Instrum. **60**, 1732 (1989)
[4] S. Sakanaka et al., Proc. of the 9th Sym. Acc. Sci. & Tech., 395 (1993)
[5] T. Obina et al., Nucl. Instr. & Meth. **A354**, 204 (1995)
[6] M. Ellison et al., Phys. Rev. Lett. **70**, 591 (1993)
[7] Y. Kobayashi et al., Proc. of the 5th EPAC, 1666 (1996)

STUDY OF A NON-INTRUSIVE ELECTRON BEAM RADIUS DIAGNOSTIC

Thomas J. T. Kwan, Barbara G. DeVolder, John C. Goldstein, and Charles M. Snell
Los Alamos National Laboratory, Los Alamos, NM 87545

Abstract

We have evaluated the usefulness and limitation of a non-intrusive beam radius diagnostic which is based on the measurement of the magnetic moment of a high-current electron beam in an axisymmetric focusing magnetic field, and relates the beam root-mean-square (RMS) radius to the change in magnetic flux through a diamagnetic loop encircling the beam. An analytic formula that gives the RMS radius of the electron beam at a given axial position and a given time is derived and compared with results from a 2-D particle-in-cell code. Our study has established criteria for its validity and optimal applications.

1. INTRODUCTION

In radiography, the x-rays are generated by an electron beam impacting a target of optimum thickness. The spot size of the electron beam before impact is an important factor in the resolution of radiography. It is therefore highly desirable to use a non-intrusive technique to measure the radius of the electron beam during its transport to obtain valuable information about the beam size on target.

2. CRITERIA OF APPLICABILITY

For the electron beam in the Integrated Test Stand (ITS) at Los Alamos National Laboratory, we have evaluated the usefulness and accuracy of the non-intrusive beam radius diagnostic proposed by W.E. Nexsen[1]. This diagnostic is based on the measurement of the magnetic moment of a high current electron beam in an axisymmetric focusing magnetic field, and relates the beam root-mean-square (RMS) radius to the change in magnetic flux through a diamagnetic loop that encircles the beam. The formula that gives the RMS radius R at a given axial position z and a given time t is[1]

$$R = \left[\frac{C|\Delta\Phi|}{B_z(0)|I_z|} \right]^{1/2} \tag{1}$$

where $\Delta\Phi \equiv \Phi(t) - \Phi(0)$, $\Phi(t)$ is the axial magnetic flux through the loop at time t, $B_z(0)$ is the external axial magnetic field at the z position of the loop, I_z is the axial particle current at z and t, and $C = 4mc\beta\gamma/\mu_o e$ is a constant in MKS units. The RMS radius R is defined by

$$R^2 I_z = \int r^2 dI_z \tag{2}$$

Using the particle-in-cell (PIC) code MERLIN, we can compare the RMS radius calculated from Eq. 1 with a code-calculated definition of R given by Eq. 2 to quantitatively evaluate the accuracy of Nexsen's diagnostic for the ITS beam. Some cautions are warranted in using this diagnostic. Nexsen's analysis is applicable to a steady-state electron beam born in a field-free region and injected into an axisymmetric magnetic field in a region with no boundaries. In applying this diagnostic to the ITS beam, we seek to use Nexsen's formula for a pinched beam with a finite risetime propagating in a drift tube. This diagnostic should be applied only after the beam current is fully risen to its peak (steady state) value and it cannot be used to measure the RMS radius of a beam immersed in a constant external magnetic field.

Equation 1 applies to unbounded systems, however, in the realistic (bounded) problem, the magnetic flux diffusion time is nonzero across boundary materials. On the time scales set by the ITS beam, flux displaced from the initial configuration (external magnetic field only), due to the presence of the propagating beam, cannot penetrate the drift tube wall. That is, for a beam propagating inside a drift tube and in an external solenoidal field, the total flux within the drift tube is conserved. For a diamagnetic beam, the total magnetic field inside the beam decreases below the value of the external field, and this is compensated by an increase in the field in the vacuum region between the beam and the drift tube wall. The complex dynamics of the beam propagating in the external and self fields may also produce regions in space where the field inside the beam exceeds the external field there, so that the beam is non-diamagnetic. In either case, the total flux is conserved within the drift tube. The presence of the flux-conserving wall modifies the flux change $\Delta\Phi$ in Eq. 1, which is applicable to an unbounded system. To use Nexsen's diagnostic in the case of a beam propagating inside a drift tube, we must adjust the code-calculated flux change for a bounded system in order to use Eq. 1. By inserting a flux-adjustment-factor (FAF) that depends on the loop and drift tube radii, we increase the magnetic flux $|\Delta\Phi|$ change to correspond to that which is appropriate to an unbounded system. This factor can be approximately derived[2] to be

$$FAF = \left[1 - \frac{A(loop}{A(drift)} \right]^{-1/2} \tag{3}$$

where A(loop) is the area of the diamagnetic loop and A(drift) is the area of the drift tube. This geometric flux-

adjustment-factor (Eq. 3) must be applied to Eq. 1 in order to use the diagnostic for a beam propagating in a drift tube. The flux change $\Delta\Phi$ in Eq. 1 varies with the axial location of the loop in the external magnetic field. When the loop is located in a region of small external field (say, near the ends of the solenoidal coils), the value of $\Delta\Phi$ is a small number (being the difference of two nearly equal numbers). The code-calculated flux is noisy, and the noise reduction procedure used to calculate a value for $\Phi(t)$ is somewhat arbitrary and may therefore produce non-unique values for $\Delta\Phi$. Such values of $\Delta\Phi$ could therefore be uncertain by 25% or more, and this fact will introduce uncertainties in the RMS radius calculated from Eq. 1. Locating the diamagnetic loop in a region of peak external magnetic field ensures larger flux and flux change $\Delta\Phi$, often larger by an order of magnitude or more. These larger values reduce the uncertainty in the calculated RMS radius. Therefore, the diamagnetic loop should be placed in a region of maximum external magnetic field. The flux change $\Delta\Phi$ in Eq. 1 also varies with loop radius, being largest when the loop radius approaches the beam radius. Because of the arbitrariness and uncertainty introduced in calculating $\Delta\Phi$ as the small difference of two nearly equal numbers, better accuracy for R is ensured for larger values of $\Delta\Phi$. In the limit that the loop radius approaches the drift tube radius, the flux change is zero because the total flux enclosed by such a loop is conserved. Furthermore, the FAF is a maximum (namely, infinity) as A(loop) approaches A(drift), but is a minimum as A(loop) approaches its minimum allowed value of A(beam), where A(beam) is the cross-sectional area of the beam at the axial location of the loop. The nature of the FAF is that of a back-of-the-envelope calculation, in that time and space variations of the fields and the particle positions are not taken into account. Hence, situations where the FAF is a minimum (i.e., the adjustment necessary to apply code-calculated quantities to Nexsen's formula for an unbounded system is a minimum) are more appropriate. For a given diamagnetic loop, the difference between the loop radius and the beam radius is largest at the pinch, and the corresponding $\Delta\Phi$ will be small and highly uncertain. In addition, the strongly two-dimensional behavior of the pinched electron beam casts doubt on the validity of Eq. 1 in this region. Therefore, the diamagnetic loop radius should be close to (but greater than) the beam radius. The diagnostic is not suited for measuring the RMS radius at or near the pinch.

The simulations described in the following section help to quantify the term "close" for the ITS beam. Accuracy to within a few percent can be achieved when the loop radius is within a couple of centimeters of (and larger than) the beam radius. When the loop radius is more than a couple of centimeters larger than the beam radius, such as when the loop is located close to the drift tube wall, then errors may be greater than 10%.

In summary, Nexsen's analysis is based on a steady state, unbounded system, and the formula in Eq. 1 must be applied to a bounded, flux-conserving experiment (and simulation). To accomplish this with reasonable confidence in the diagnostic, the loop should be placed far from the pinch, in a region of maximum external magnetic field, and should use a diamagnetic loop that is within a couple of centimeters of the beam radius (and encircles the entire beam). Because the location of the pinch is a priori unknown and depends on the initial beam radius and on the initial angle of the beam envelope, the simulations can play a crucial role in evaluating the accuracy of the diagnostic data. Moreover, since the experimentalist is limited to locating the diagnostic loop close to the drift tube wall, in order to ensure that the loop surrounds the entire beam, the code can serve as an essential benchmarking tool to correlate the RMS radius determined from the (experimental) large-radius loop with that determined from simulation loops whose radii are closer to the beam radius.

3. MERLIN SIMULATIONS

The ITS beam was modeled using the 2-1/2-dimensional PIC code MERLIN. The typical geometry used in the simulations, assumed axisymmetric, is depicted in the Fig. 1.

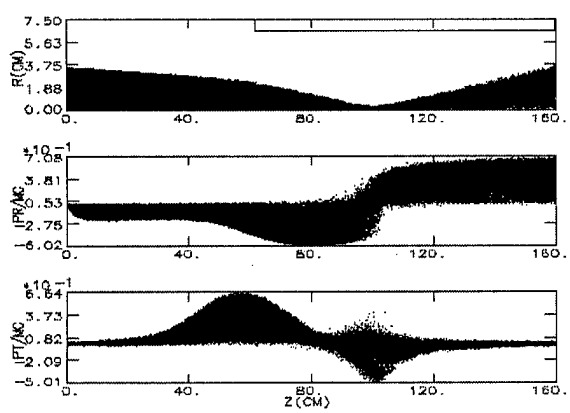

Figure 1. Configuration and phase space plots of a typical simulation at 16.7ns.

The drift tube radius is 7.5 cm, and the axial extent is 160 cm. A solenoid of length 13.125 inches is energized to produce a peak axial magnetic field of approximately 1 kG. This field was generated with the code BFIELD, which links to MERLIN, by specifying 35 current loops approximately uniformly distributed between z = 45.33 cm and z = 78.67 cm. positions. The magnetic field varies slightly with r in the vicinity of the maximum field, which is the location of diagnostic probes in both simulation and experiment. This small variation violates the assumption in the previous analysis and may introduce slight errors.

The electron beam has uniform initial density for $r \leq r_b$, the beam radius. The peak current is about 3 kA, with a 3-ns risetime and a flat top: the functional dependence used in MERLIN is $I(t) = I_0 [1-\exp(-0.5(t/\tau)^2]$ where τ is the 3-ns risetime. The electrons' initial kinetic energy is 5.31 Mev, which corresponds to a γ of 11.39. In ITS, a metal annular sleeve of thickness about 1 cm fits tightly into the drift tube and holds the diamagnetic loop, which is embedded in plastic. This sleeve is simulated as a 1-cm-thick conductor that extends from the position of maximum external magnetic field (z = 61.8 cm) to the downstream boundary at z = 160 cm as shown in Fig. 1. The numerical probes in the simulations to calculate the RMS radius are located at the z-position of maximum external field and at two different radial positions, 4.0 and 6.0 cm. Two radial locations were chosen, because the larger radius corresponds to the experiment and because the smaller-radius loop will allow us to quantify the improved accuracy of the calculated RMS radius resulting from the loop radius being closer to the beam radius.

We set up our simulations according to experimental observation that the range of initial beam radius is 2.5 - 4.0 cm, and the range of initial angle of the beam envelope (dr/dz) is ± 60 milliradians. In addition, we imposed an arbitrary initial Gaussian scatter of 1 milliradian on the beam for all cases.

Application of Eq. 1 requires the difference in magnetic flux at two times, t = 0 and some t > 0 at which the RMS radius of the beam is being calculated. Even in the region of maximum external magnetic field, the flux difference is a small number, typically for ITS parameters only a fraction of a percent of the absolute value of the flux. Although the flux at t = 0 can be determined exactly from the simulations, the flux at t > 0 is more uncertain and must be carefully processed to minimize numerical flux noise resulting from the simulations. Figure 2 is an example of the magnetic flux in one of the simulations.

Table 1 summarizes the results of nine simulations with various initial beam radii and angles of the injected beam envelope. It compares the RMS radius using Eq. (1) and the definition Eq. (2) for the nine simulations. The probes were placed at the axial position corresponding to maximum external magnetic field (z = 61.8 cm) and radial positions r = 4.0 cm (smaller diamagnetic loop to demonstrate increased accuracy) and r = 6.0 cm (larger diamagnetic loop typically used in experiments). The RMS radius is calculated at 16.2 ns, which is in the steady-state regime.

Except in cases where the particles' large radial positions render the diagnostic meaningless (a and b), we calculate three values of the RMS radius for each simulation: the definition and the Nexsen values at r = 4.0 and 6.0 cm. Error bars for the Nexsen RMS radii in Table 1 are certainly nonzero, but cannot be accurately quantified because the errors associated with the calculation of the flux change can only be roughly estimated. Better agreement is obtained when the loop radius is closer to the beam radius.

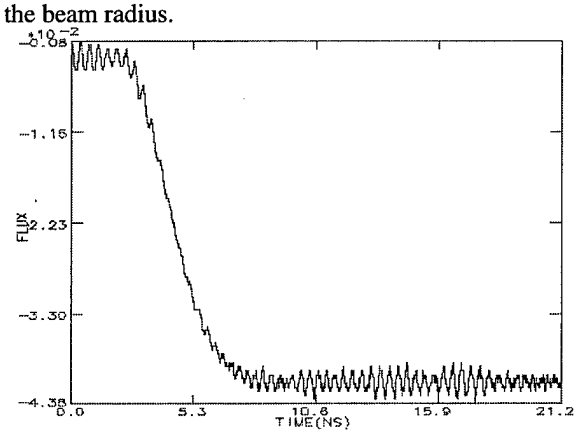

Figure 2. Example of magnetic flux, as a function of time, through a 4.0-cm loop located at the axial position of peak external magnetic field.

Table 1

r_0(cm)/θ_0(mrad)	RMS Radius (cm)		
	Definition	4.0 cm loop	6.0 cm loop
3.5	1.46	1.46	1.46
3.5/-60	1.18	1.21	1.35
3.5/63	4.00	a	3.12
4.0/0	1.80	1.79	1.68
2.5/0	0.79	0.90	1.19
4.0/-69	1.21	1.22	1.34
2.5/-42	1.11	1.18	1.30
4.0/71	4.66	b	b
2.5/45	2.58	2.52	2.16

4. CONCLUSIONS

In our study, we find that the accuracy of the RMS radius probe increases when the diamagnetic loop is far from the metal wall (close to the beam radius). A convenient rule-of-thumb, based on this limited set of data, is that placing the diamagnetic loop within a couple of centimeters of the beam radius is sufficient to ensure reasonable accuracy.

5. ACKNOWLEDGMENTS

We wish to acknowledge Dave Moir and Evan Rose for many useful discussions throughout this work.

6. REFERENCES

[1] W. W. Nexen, "A Non-Interfering Beam Radius Diagnostic," draft paper dated August 19, 1991.

[2] W. E. Nexsen, "Beam Brightness from Beam Diamagnetism," unpublished LLNL research memo 87-27, August 7, 1987.

PRELIMINARY RESULTS OF RMS EMITTANCE MEASUREMENTS PERFORMED ON THE SUB-PICOSECOND ACCELERATOR USING BEAM POSITION MONITORS

Steven J. Russell, MS H851, Los Alamos National Laboratory, Los Alamos NM 87545

Abstract

The Sub-picosecond Accelerator at Los Alamos National Laboratory is a 1300 MHz, 8 MeV photoinjector. Concerned mainly with the exploration of bunched electron beams, the Sub-picosecond Accelerator facility is also used for a variety of other research. One ongoing task is the exploitation of the second moment properties of beam position monitor signals to measure the rms emittance. The unique properties of photoinjector beams make Gaussian assumptions about their distribution inaccurate and traditional methods of measuring the rms emittance fail. Using beam position monitors to measure the emittance, however, requires no beam distribution assumptions. Presented here are our first emittance measurements with this method on the Sub-picosecond Accelerator.

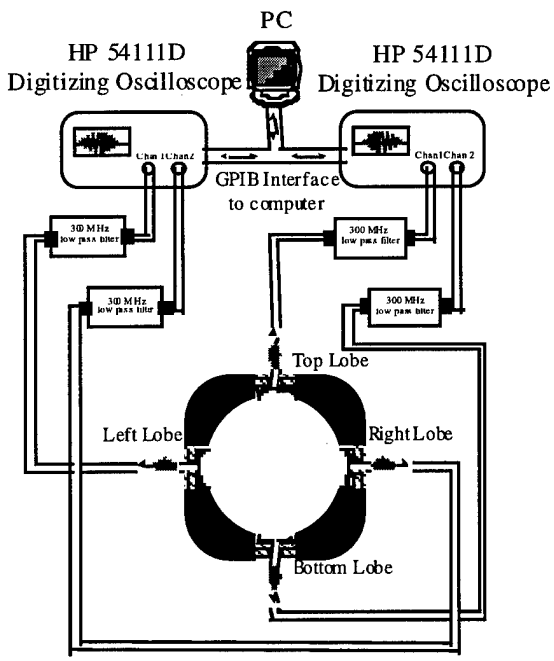

Figure 1: Schematic of data acquisition system.

1 INTRODUCTION

The primary mission of the Sub-Picosecond Accelerator facility (SPA)[1] is to explore the uses and dynamics of bunched electron beams. State of the art in its field, SPA has compressed electron pulses containing 1 nC of charge to sub-picosecond lengths[4].

Using a photoinjector as the source for the electron beam gives us the ability to dictate the shape of the initial electron pulse. In turn, this enables efficient bunching of the beam[4]. However, the attributes that make the photoinjector ideal for compression experiments also create problems for the electron beam diagnostics. A photoinjector accelerates the electrons to relativistic velocities very quickly. As a result, the beam does not have time to come to equilibrium. Its spatial distribution will be unknown and cannot be well approximated by a Gaussian[3], [5]. Therefore, when measuring the rms emittance of the beam, the diagnostic technique can make no assumptions about its spatial distribution.

Roger Miller et. al. first proposed using beam position monitors (BPMs) in a non-intercepting emittance probe[2]. Later, it was demonstrated that this technique measures the rms emittance without reference to the spatial distribution of the beam [6], making it ideal for SPA. What is presented here are the preliminary results of rms emittance measurements of the SPA beam using Miller's technique.

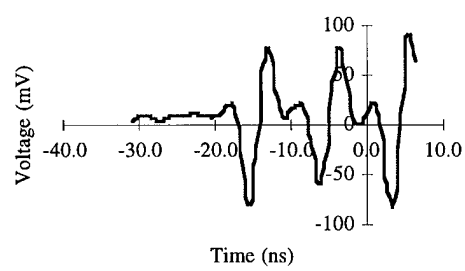

Figure 2: Typical voltage signal from a BPM electrode for two beam bunches.

2 DATA ACQUISITION

The BPMs used in this experiment are dual-axis, capacitive probes[7]. The signals generated in the four electrodes of the BPM are transported down a transmission line where they are filtered by 300 MHz, low-pass filters, digitized by two, dual channel 54111D Hp™ Oscilloscopes and captured by a PC running LabView®. (Figure 1) The oscilloscopes operate at 1 giga-sample per second. The digitized signals are filtered again by a one half Nyquist digital filter and then interpolated utilizing the well known sampling theorem. A typical result is shown in Figure 2.

0-7803-4376-X/98 /$10.00 © 1998 IEEE

After the four signals are interpolated, the peak-to-peak voltages of each micropulse is determined. Then, using the BPM calibration that has previously been determined[8], [9], the beam center, $(\bar{x},\bar{y})$, and second moment, $\langle x^2\rangle - \langle y^2\rangle + \bar{x}^2 - \bar{y}^2$, are calculated. $\langle x^2\rangle - \langle y^2\rangle$ is the difference in the rms widths of the beam.

3 MEASUREMENTS

I have performed two types of measurements. The first is a check of the BPM calibration. The second is the emittance measurement itself.

3.1 Calibration check

To check the calibration, I first transport the beam to the BPM location. Then, without changing the upstream focusing, I move the beam center to several positions in the BPM aperture with a simple steering coil. Since the beam focusing is constant, $\langle x^2\rangle - \langle y^2\rangle$ is constant. Therefore, if the calibration is correct, a plot of the second moment versus $\bar{x}^2 - \bar{y}^2$ should be a straight line with slope equal to one. Figure 3 is a typical result. Each point represents averages of approximately 99 beam shots. I do this because the SPA electron beam is unstable shot-to-shot but reasonably stable when averaged.

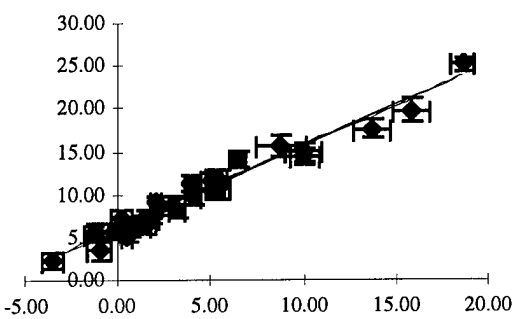

Figure 3: Second moment (mm^2) versus $\bar{x}^2 - \bar{y}^2$ (mm^2). The slope is equal to 0.95 ± 0.036.

Since the values of $\bar{x}^2 - \bar{y}^2$ and the second moment are both determined by the BPM signals, this is not an absolute check on the accuracy of the BPM calibration. However, it does provide a check on its consistency.

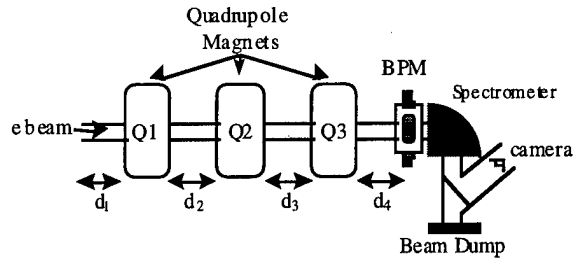

Figure 4: Schematic of beam line section used for emittance measurements.

3.2 Emittance measurement

To measure the emittance, we use a section of beam line like that shown in Figure 4. The quadrupole magnets are set to a number focusing strengths, each one carefully chosen to avoid numerical instabilities in the final result[10]. At each setting, 99 beam shots are grabbed and the average value of $\langle x^2\rangle - \langle y^2\rangle$ is determined.

Since the section of beam line in Figure 4 is linear, it is represented by a linear transfer matrix for each setting of the quadrupoles. Then, it can be shown that the value of $\langle x^2\rangle - \langle y^2\rangle$ at the BPM position is linearly related to the rms beam parameters, $\langle x^2\rangle$, $\langle xx'\rangle$, $\langle x'^2\rangle$, $\langle y^2\rangle$, $\langle yy'\rangle$ and $\langle y'^2\rangle$, at the entrance to the first quadrupole[2]. Changing the focusing of the quadrupoles at least six times results in a set of linear equations that can be solved to obtain the rms beam parameters at the entrance to the first quadrupole. Then, the rms emittances are given by

$$\varepsilon_x = \sqrt{\langle x^2\rangle\langle x'^2\rangle - \langle xx'\rangle^2},$$

and

$$\varepsilon_y = \sqrt{\langle y^2\rangle\langle y'^2\rangle - \langle yy'\rangle^2}.$$

I have performed several emittance measurements on the SPA beam using this technique. For a 1 nC per bunch beam, a typical result is

$$\varepsilon_x = 5.3\,\pi \text{ mm mrad} \pm 0.27\,\pi \text{ mm mrad}$$

and

$$\varepsilon_y = 4.3\,\pi \text{ mm mrad} \pm 0.34\,\pi \text{ mm mrad}.$$

Expressing these as normalized emittances gives

$$\varepsilon_{xn} = \beta\gamma\varepsilon_x = 94\,\pi \text{ mm mrad} \pm 4.8\,\pi \text{ mm mrad}$$

and

$$\varepsilon_{yn} = \beta\gamma\varepsilon_y = 76\,\pi \text{ mm mrad} \pm 6.0\,\pi \text{ mm mrad}.$$

The errors are estimated according to [2].

4 CONCLUSIONS

Overall, our progress to this point is promising. We are getting reasonable results using Miller's technique.

From simulation, we anticipated that the rms normalized emittances should be a factor of 10 lower than what we measure. However, we have inadvertently been operating with a sizable magnetic field in the region of the photo-cathode, increasing the emittance.

A second issue is the accuracy of the measurement, which is not as good as we hoped. This can be attributed to two factors: the limited accuracy of the digitizing oscilloscopes and the shot-to-shot instability of the electron beam.

At a 1 giga-sample per second digitizing rate, the Hp™ 54111D oscilloscopes are effectively limited to six bit accuracy. Experimenting with an oscilloscope that has 8 bit accuracy and a 500 mega-sample per second digitizing rate has shown marked improvement.

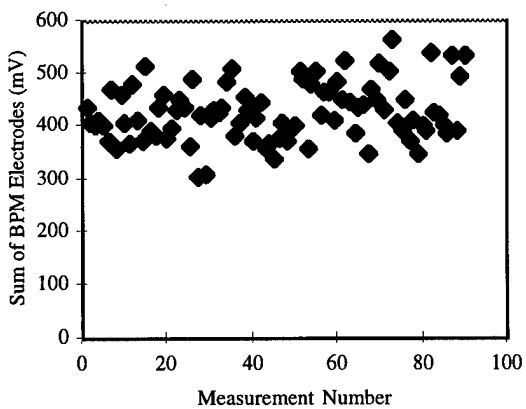

Figure 5: Sum of BPM Electrodes (beam intensity) versus measurement number for 90 beam shots.

As mentioned, SPA's shot-to-shot stability is poor. Figures 5 and 6 demonstrate this. Figure 5 shows a plot if beam intensity (sum of the BPM's four electrodes) versus measurement number for 90 beam shots. Figure 6 shows a plot of $\langle x^2 \rangle - \langle y^2 \rangle$ versus measurement number for the same 90 beam shots. We hope to improve the stability in the next few months.

5 ACKNOWLEDGEMENTS

Work supported by Los Alamos National Laboratory under the auspices of the US Department of Energy.

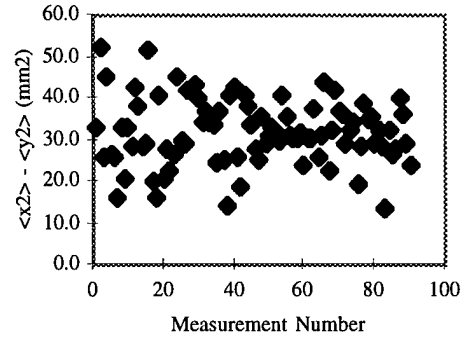

Figure 6: $\langle x^2 \rangle - \langle y^2 \rangle$ (mm^2) versus measurement number for 90 beam shots.

REFERENCES

[1] B. E. Carlsten et. al., "Subpicosecond Compression Experiments at Los Alamos National Laboratory," Micro Bunches Workshop, Upton, NY, September 1995.

[2] R. H. Miller et al., "Non-intercepting Emittance Monitor," Proc. 12th Int. Conf. On High Energy Accelerators, (Fermilab, 1983), p. 602 (1983).

[3] B. E. Carlsten, et. al., "Measuring Emittance of Non-thermalized Electron Beams From Photoinjectors," 14th International Free Electron Laser Conference, Kobe, Japan, August 23-28, 1992, Los Alamos National Laboratory document LA-UR 92 2561.

[4] B. E. Carlsten and S. J. Russell, "Subpicosecond Compression of 0.1-1 nC Electron Bunches with a Magnetic Chicane at 8 MeV," Physical Review E, Volume 53, Number 3, p. 2072-2075.

[5] K. Kim, "RF and Space Charge Effects in Laser-driven RF Electron Guns, " Nucl. Instrum Methods Phys. Res., vol. A275, p. 201, 1989.

[6] S. J. Russell and B. E. Carlsten, "Measuring Emittance Using Beam Position Monitors," Proc. of the 1993 Part. Accel. Conf., p. 2537, IEEE 93CH3279-7.

[7] J. D. Gilpatrick, et. al., "Design and Operation of Button-Probe, Beam-Position Monitors," Proc. of the 1993 Part. Accel. Conf., p. 2334, IEEE 93CH3279-7

[8] J. F. Power, et. al., "Characterization of Beam Position Monitors in Two-Dimensions," 16th International LINAC Conf., Ottawa Ontario, CANADA, 1992.

[9] S. J. Russell, et. al., "Characterization of Beam Position Monitors for Measurement of the Second Moment," Proc. of the 1995 Part. Accel. Conf., p. 2580, IEEE 95CH35843

[10] S. J. Russell, "Unstable Matrix Equations and Their Relationship to Measuring the Emittance of an Electron Beam Using Beam Position Monitors," (private communication).

SPECTRAL FLUCTUATIONS OF INCOHERENT RADIATION AND MEASUREMENT OF LONGITUDINAL BUNCH PROFILE

M. S. Zolotorev
Center for Beam Physics, Accelerator and Fusion Research Division
Lawrence Berkeley National Laboratory, University of California, Berkeley, CA 94720
and G. V. Stupakov
Stanford Linear Accelerator Center Stanford University, Stanford, CA 94309

Abstract

A method for measurement of ultrashort beam current profile $I_b(t)$ is proposed that is based on detecting fluctuations of the spectral intensity $P(\omega)$ of single bunch incoherent radiation. We show that the variance of the Fourier transform of the spectrum is proportional to the convolution function of the beam current. After the convolution function is found, using phase retrieval technique one can restore the shape of the pulse in many practical cases.

1 INTRODUCTION

Measurements of the longitudinal beam profile of a relativistic electron or positron beam is an important diagnostic tool in modern accelerators that is used both for routine monitoring and dedicated studies of beam physics. For bunch lengths in the range of picoseconds, such measurements can be performed by means of a streak camera. Shorter bunches usually require some kind of special techniques. Several methods have been proposed which have a potential of measuring ultrashort bunches. In Ref. [1], a coherent transition radiation emitted at wavelengths longer than or equal to the bunch length was used for analysis of subpicosecond electron pulses. In Ref. [2], Compton scattering of photons on interferometric pattern generated by two laser beams was proposed as a beam-profile monitor.

Recently, we have proposed a novel technique for measuring short bunches [3]. The method is based on the observation of the interferometric fringes produced by *incoherent radiation* of single bunch in a two beam interferometer. It was shown that fluctuations of the interferometric signal of a single bunch carry the information about the convolution function of the bunch current and allow to ascertain the bunch profile from analysis of the statistical properties of the fluctuations. In the present paper, we describe a new modification of the original idea that significantly simplifies the experimental apparatus and opens a possibility for designing a low-cost, easy-to-operate bunch length monitor.

2 SETUP AND MEASUREMENT

The schematic of the experimental setup of the measurement is shown in Fig. 1. Synchrotron light emitted by a bunch in a bend magnet passes through the spectrometer (S) and is measured by the CCD detector (D). The CCD selects a spectral range $\Delta\omega$ around the frequency ω_0 in the interval $(\omega_0 - \Delta\omega/2, \omega_0 + \Delta\omega/2)$. Assuming that CCD has N_{ch} channels, the frequency difference between the adjacent channels is $\Delta\omega/N_{ch}$. In order to be able to measure a bunch of length σ_b , the spectral resolution of the spectrometer should be better than τ_b^{-1}, where $\tau_b = \sigma_b/c$. Also, the spectral width $\Delta\omega$ must be much larger than the inverse bunch length τ_b, $\Delta\omega \gg \tau_b^{-1}$. Note that for the optimal performance the number of channels should be such that $\Delta\omega/N_{ch}$ is smaller the spectrometer resolution.

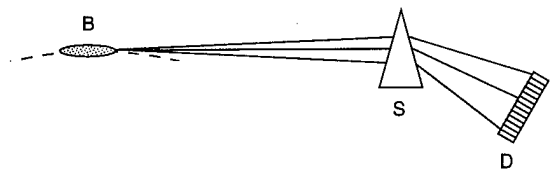

Figure 1: Schematic of the experimental setup. Synchrotron radiation of the beam (B) passes through the spectrometer (S) and is detected by the array of CCD (D).

Let us denote the the detector signal in channel m, $(1 < m < N_{ch})$ as P_m. This signal is Fourier transformed,

$$\Gamma_k = \sum_{m=1}^{N_{ch}} P_m e^{2\pi i m k}, \tag{1}$$

and the quantity Γ_k is stored. In case of a high repetition rate, one will have to use a fast shutter to prevent the exposure of the CCD by the light of the next bunch before the readout is completed. After accumulation of N_p number of pulses, large enough for statistical analysis, the following quantity is computed

$$d_k = \sum_{\alpha=1}^{N_p} \left| \Gamma_k^{(\alpha)} - \frac{1}{N_p} \sum_{\beta=1}^{N_p} \Gamma_k^{(\beta)} \right|^2, \tag{2}$$

where the superscripts α and β indicate the pulse number. As we will show in the next section, the quantities d_k give the convolution function of the particle density in the bunch (averaged over N_p bunches), and, with some additional assumptions, allow to find the bunch profile.

3 THEORY

We assume that the emitted radiation can be described in terms of the classical field, which is true if the number of photons in the coherence volume is much greater than one.

0-7803-4376-X/98/$10.00 © 1998 IEEE

Let $E(t)$ be the electric field of the radiation of a single bunch. The spectrometer decomposes this field into Fourier harmonics and the detector measures the absolute value of the spectral intensity $P(\omega)$,

$$P(\omega) \propto \left| \int_{-\infty}^{\infty} E(t) e^{i\omega t} dt \right|^2 . \quad (3)$$

Due to the incoherent nature of the radiation, the result of each measurement fluctuates from channel to channel and from bunch to bunch. An example of a simulation of one measurement of the spectrum is shown in Fig. 2, (see details below).

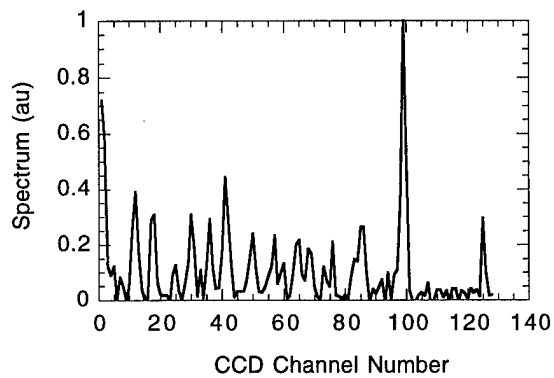

Figure 2: Simulation of a spectrum of a single bunch (in arbitrary units). The total number of channels N_{ch} is 128.

The quantity that carries information about the bunch profile is the Fourier transform of the measured spectrum which we denote by $\Gamma(\tau)$,

$$\Gamma(\tau) = \int_{-\infty}^{\infty} P(\omega) e^{-i\omega\tau} d\omega. \quad (4)$$

In reality, this Fourier transform will be performed in discreet form as given by Eq. (1) after digitizing the signal from the CCD. Since $P(\omega)$ is a fluctuating function of the frequency, the function $\Gamma(\tau)$ will also exhibit random fluctuations.

To relate the statistics of the fluctuations of $\Gamma(\tau)$ to the pulse parameters, we represent the electric field of the pulse in the detector $E(t)$ as a product of two functions,

$$E(t) = A(t) e(t), \quad (5)$$

where $e(t)$ is a stationary complex-valued stochastic process [4], and $A(t)$ denotes a (deterministic) complex amplitude of the pulse, $A(t) = \sqrt{I(t)} e^{-i\varphi(t)}$, where $I(t)$ is the instantaneous radiation intensity and $\varphi(t)$ is the phase of the pulse envelope. The characteristic time of the variation of both functions $A(t)$ and $\varphi(t)$ is of the order of the pulse duration τ_b. Related to the fluctuational part of the field $e(t)$ is a correlation function $K(\tau)$,

$$K(\tau) = \langle e(t) e^*(t-\tau) \rangle, \quad (6)$$

where the angular brackets denote ensemble average. The function $K(\tau)$ oscillates with the frequency ω_0 and falls off on the scale of the coherence time $\tau_{coh} \approx \pi/\Delta\omega \ll \tau_b$ associated with the spectral width $\Delta\omega$. The function $\Gamma(\tau)$ is then equal,

$$\Gamma(\tau) = \int_{-\infty}^{\infty} A(t) A^*(t-\tau) e(t) e^*(t-\tau) dt. \quad (7)$$

Using Eq. (6), we can easily find the average value of $\Gamma(\tau)$,

$$\langle \Gamma(\tau) \rangle = \mathrm{K}(\tau) \int_{-\infty}^{\infty} A(t) A^*(t-\tau) dt$$

$$\approx \mathrm{K}(\tau) \int_{-\infty}^{\infty} I(t) dt. \quad (8)$$

The quantity $\langle \Gamma(t) \rangle$ is proportional to the total charge of the bunch and does not contain information about the bunch profile.

Now, we want to show that the fluctuations of $\Gamma(\tau)$ around its average value indeed carry the information about $I(t)$. To this end, we calculate the absolute value of the variance $d_\Gamma(\tau)$ of the fluctuations of $\Gamma(t)$. For $d_\Gamma(\tau)$ we have

$$\begin{aligned} d_\Gamma(\tau) &= \left\langle |\Gamma(\tau)|^2 \right\rangle - |\langle \Gamma(\tau) \rangle|^2 \\ &= \int_{-\infty}^{\infty}\int_{-\infty}^{\infty} dt dt' A(t) A^*(t-\tau) A^*(t') A(t'-\tau) \\ &\times \langle e(t) e^*(t-\tau) e^*(t') e(t'-\tau) \rangle - |K(\tau)|^2 \\ &\times \int_{-\infty}^{\infty}\int_{-\infty}^{\infty} dt dt' A(t) A^*(t-\tau) A^*(t') A(t'-\tau). \end{aligned}$$

For a normal stochastic process, the fourth order correlators are reduced to the sum of the products of the second order correlators, yielding

$$\begin{aligned} &\langle e(t) e^*(t-\tau) e^*(t') e(t'-\tau) \rangle \\ &= \langle e(t) e^*(t-\tau) \rangle \langle e^*(t') e(t'-\tau) \rangle \\ &+ \langle e(t) e^*(t') \rangle \langle e^*(t-\tau) e(t'-\tau) \rangle \\ &= |K(\tau)|^2 + |K(t-t')|^2 . \end{aligned} \quad (9)$$

The first term on the right hand side of Eq. (9) appears in the theory of Hunbury Brown – Twiss interferometry [6], however, it does not contain information about the pulse shape. It will be canceled by the last term on the right hand side of Eq. (9). From Eqs. (9) and (9) on can find

$$d_\Gamma(\tau) = \int_{-\infty}^{\infty} |K(\xi)|^2 d\xi \times \int_{-\infty}^{\infty} dt I(t) I(t-\tau). \quad (10)$$

Note that $d_\Gamma(\tau)$ is proportional to the convolution of the intensity $I(t)$. For the discrete Fourier transformation,

d_k given by Eq. (2) represent the function $d_\Gamma(\tau)$, $d_k = d_\Gamma(k/\delta\omega)$.

Strictly speaking, knowledge of the convolution function does not allow a unique restoration of $I(t)$. However, as was shown in Ref. [7], using a phase retrieval technique allows to restore the beam profile in many practical cases.

The above consideration assumed that the quantum fluctuations of the number of photons in the detector are negligible. We can easily derive the condition for the beam intensity when this is requirement is met. The number of synchrotron photons, n_{ph} that reach the detector (they are radiated from $(1/\gamma)(\omega_c/\omega_0)^{1/3}$ radians of the beam trajectory, where ω_c is the critical frequency for the synchrotron radiation) is equal [5]

$$\langle n_{ph} \rangle \approx \alpha N_e \delta\omega/\omega_0, \tag{11}$$

where α is the fine structure constant, N_e is the number of electrons in the bunch, and $\delta\omega$ is the spectral width per one channel, $\delta\omega = \Delta\omega/N_{ch}$. The condition $\langle n_{ph} \rangle \gg 1$ gives a limitation on N_e from below. Note, that in this estimate we assumed that the beam radiation is coherent in the transverse direction, otherwise an additional factor would appear in Eq. (11).

If condition $\langle n_{ph} \rangle \gg 1$ is not met, quantum fluctuations superimpose on the random fluctuations described above. However, the information about the pulse shape is still present in the measured signal, although a larger statistics would be needed to suppress the additional noise introduced by the quantum fluctuations.

4 COMPUTER SIMULATIONS

We have performed computer simulation of the measurement of fluctuating spectra. The code simulates incoherent radiation of a large number N_e of independent sources (electrons) that are distributed according Gaussian function with the rms value τ_b. The average intensity of incoherent radiation is given by $I(t) = I_0 \exp\left(-t^2/2\tau_p^2\right)$.

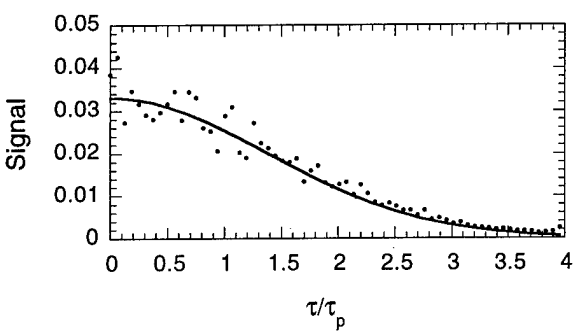

Figure 3: Simulation of a measurement averaged over 100 bunches. Dots represent simulated values of d_k, and the curve is a theoretical convolution function for the beam density.

The parameters for this particular example are: $\tau_b = 17$ps (rms bunch length $\sigma_b = 0.5$ cm), the wavelength of the central frequency $\lambda = 2\pi c/\omega_0 = 6300$Å. We assume a standard spectrometer with dispersion of about 10Å/mm and a CCD with 128 channels with a pixel size of 10 μm. A spectrum of a single bunch is shown in Fig. 2, and the result of the simulation of the measurement of $d_\Gamma(\tau)$ using averaging over 100 pulses is shown in Fig. 3 with a solid line showing theoretical prediction for a Gaussian beam, $d_\Gamma^{(th)}(\tau) = \text{const} \exp\left(-t^2/4\tau_b^2\right)$. A Gaussian fit to the measurement gives for $d_\Gamma(\tau)$ the rms width of 1.38 (instead of the theoretical value of $\sqrt{2}$) which translates into the measurement error of about 2%.

Note that Eq. (11) gives for the parameters cited above the following limitation for the number of particles in the bunch, $N_e \gg 5 \times 10^7$.

5 CONCLUSION

In summary, a technique is proposed, capable of measuring short pulses of incoherent radiation. It is based on the observation and statistical analysis of the bunch spectrum fluctuations. Although we assumed synchrotron radiation above, the nature of the radiation is not important, and, for example, transition radiation can be used as well. Typically, averaging over fluctuations requires accumulation of many (on the order of 10^2) pulses for a singe measurement, however, a modification of the method is possible in which one can perform averaging over different spectral intervals in a single pulse.

An important feature of the method is that it can be used for bunches with the lengths ranging from a centimeter to tens of microns.

Experimental verification of the method is under way at the synchrotron source ALS at the Lawrence Berkeley Laboratory.

6 ACKNOWLEDGMENTS

The authors are thankful to W. Leemans, K.-J. Kim and A. Zholents for useful discussions. This work was supported by Department of Energy contracts DE-AC03-76SF00515 and DE-AC03-76SF00098.

7 REFERENCES

[1] P. Kung *et al.*, Phys. Rev. Lett., **73**, 967 (1994).

[2] T. Shintake. KEK-PREPRINT-96-81, Jul 1996. 20pp. Invited talk at 7th Beam Instrumentation Workshop (BIW 96), Argonne, IL, 6-9 May 1996.

[3] M.S. Zolotorev and G.V. Stupakov. SLAC Preprint SLAC-PUB-7132. March, 1996.

[4] D. R. Cox and H. D. Miller, *The Theory of Stochastic Processes*, (John Wiley Inc., New-York, 1965).

[5] M. Sands. Preprint SLAC-121, p.117, (1970).

[6] W. Lauterborn, T. Kurz and M. Wiesenfeldt. *Coherent Optics*, (Springer, 1995).

[7] R. Lai, A.J. Sievers. *Micro Bunches Workshop*, AIP Conference Proceedings 367 (NY), p. 312 (1995).

A TURN BY TURN PHOTON BEAM PROFILE OBSERVATION BY A LASER BEAM SATURATED PHOTODIODE

Ian C. Hsu, C.-H. Lee, and G.-T. Cheng
Department of Nuclear Science, National Tsing Hua University and SRRC, TAIWAN

Abstract

A fast photodiode was demonstrated to be able to extract the turn by turn photon beam profile information of electron storage rings if the photodiode was operated at the saturated region. When applied this method to a 1.3 GeV synchrotron light source with 200 mA beam current, the synchrotron radiation intensity is not intense enough to saturate the photodiode. To apply this method to the type of light source as previously mentioned, a flat-top laser beam was constructed to saturate the photodiode. The theory and the preliminary experimental results are presented and discussed.

1 INTRODUCTION

In many accelerator physics experiments, e.g., the coherent damping time measurement and the dynamic aperture study experiments, we like to know the turn by turn variations of the beam positions. Usually, it is accomplished by the button type or the strip line type electrode beam position monitors (BPM). However, the measurements done by these types of BPM only gave us the information of the position of the beam centroid. If the beam centroid motion combined with the decoherence mechanism, the BPM would not be able to distinguish them. This means that by using the BPM, we can not distinguish the coherence damping or the decoherence. In order to distinguish them, we need to monitor the beam profile simultaneously. For lepton machines, the synchrotron radiation provides a very useful beam profile information. However, to perform a turn by turn beam profile monitor, we need a very fast detecting system. For the speed requirement we need, the commercial photodiode array and the following up electronic system is not available neither a cost reasonable approach. A method has been proposed, to monitor the beam profile by using a fast single photo diode.[1] The idea has been examined by using a modulated He-Ne laser to simulate the synchrotron radiation light. The results agree with computer simulation results. When applied this method to a 1.3 GeV synchrotron light source with 200 mA beam current, the synchrotron radiation intensity is not intense enough to saturate the photodiode. To apply this method to the type of light source as previously mentioned, a flat-top laser beam was constructed to saturate the photodiode. The theory and the preliminary experimental results are presented and discussed.

2 THEORY

Most P-N silicon photodiodes are linear (better than *1%*) over a wide range of magnitude of the incident power. In linear region, the total photocurrent is independent of the incident photon beam size as long as the total power is the same. At high photon intensity, however, nonlinearity is introduced due to the device saturation. Total photocurrent in nonlinearity region now is not only dependent on the incident total photon power but also dependent upon the photon beam size. This means that in the nonlinearity region, we can get the photon beam profile information by means of measuring the total photocurrent. More detailed discussions and computer simulations can be found in a previous paper.[1] However, we were not able to use the system to measure the beam size variation of the type of light source as previously mentioned. It was due to that the intensity of the synchrotron light is 10 to 100 times lower than that of the laser which we used in the experiments. To solve this problem, we can build a flat-top beam as a saturating beam. With the saturating beam, we can force the photodiode operated in the non-linear region. In this way, for either the case of a weak synchrotron light or the case of a larger beam size variation range i.e. larger photon intensity variation range, the detector system can detect the beam size variations. That means that we enlarge the dynamic range of the system. If the saturating beam is a gaussian beam (TEMoo mode), then, if the detected beam has a position variation but not the beam size variation, the detector system will still give us changing output signal which will cause confuse. That is reason why we need a flat-top beam as a saturating beam.

3 CONSTRUCTION OF FLAT TOP LASER BEAMS

Absorption method was used for this purpose. We photograph the expended gaussian beam. If we can manipulate the Gamma value of the film to be 1, when the expended gaussian beam passed the developed film, a flat-top beam can be obtained.

Figure 1 shown a theoretical Hurter-Driffield curve[2]. The curve describes the general relation between the Exposure (E) of the film to the light source and the photographic Density (D) after the film was developed. There is a linear region in the curve. The

0-7803-4376-X/98/$10.00 © 1998 IEEE

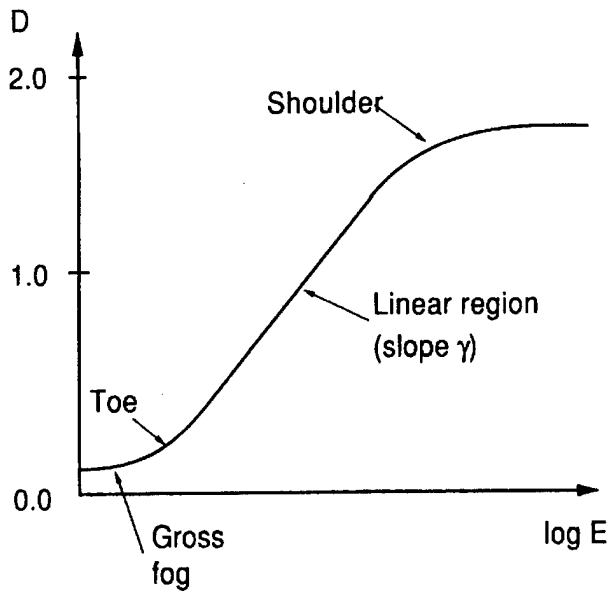

Fig. 1 The theoretical Hurter-Driffield curve

slope of the linear part is define to be the Gamma value of the film. It was shown[3] that if the exposure of the whole Gaussian beam as well as the development process was controlled such that the whole exposure area was remained inside the linear region and with the slop equals to 1, we can produce a flat-top beam by sending a gaussian beam with the same beam size through the film. Figure 2 is the Hurter-Driffield curve of one of the film which we produced. The horizontal axis is the photon flux (P) times the exposure time (t) which is proportional to the Exposure. The Gamma value equals to 1.072. Figure 3 is the flat-top gaussian beam produced by the same film which the Fig. 2 was measured from.

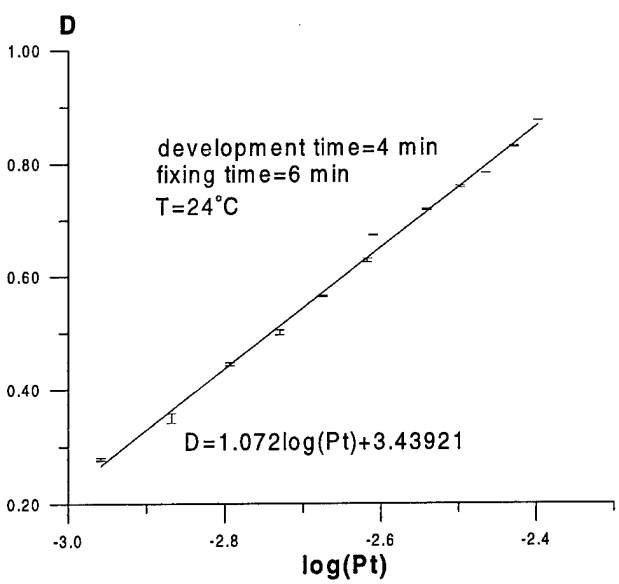

Fig. 2 The Hurter-Driffield curve of one of the film with Gamma value equals to 1.072

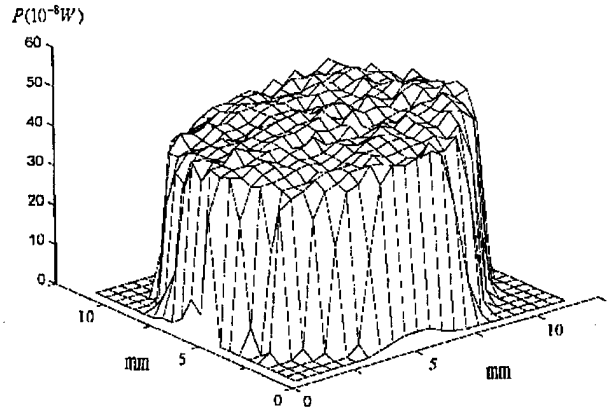

Fig. 3 The measurement results of the flat-top beam

4 EXPERIMENTS

The schematic drawing of the experimental setup was shown in Fig. 4.

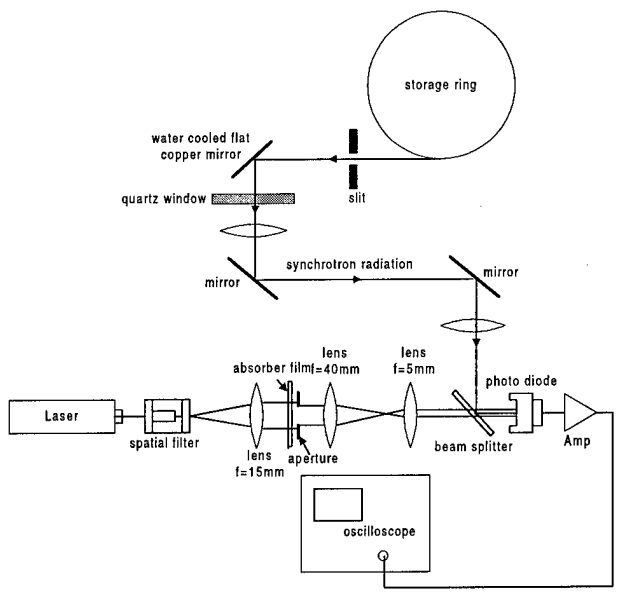

Fig.4 The schematic drawing of the experimental setup

To observe a predictable fast beam size varation, we fire one of the injection kickers. Due to the energy spread and the no-zero chromaticity value, the betatron oscillation of electrons inside the bunch will start to dechroherent, and increase the beam size. After one synchrotron oscillation period the bunch will recoherence again and the beam size shrank to the original one.[4] Then the process repeat itself again. The larger the value of the chromaticity the deeper the beam size variation will be.

Figures 5, 6 and 7 are the photodiode measurement results for different sextupole values. We see the beam size variation with a period of 30 microsecond, which is the synchrotron oscillation period of the storage ring under the experiment.

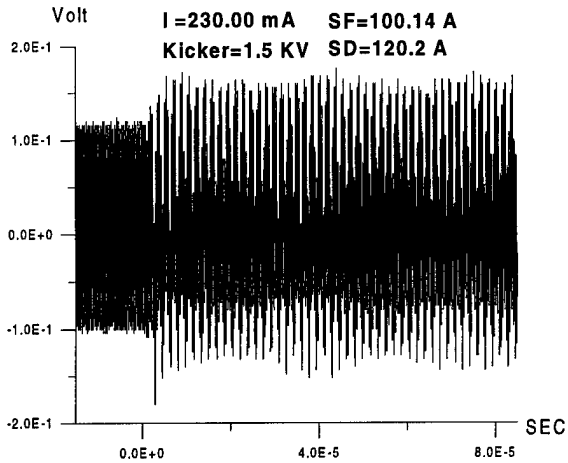

Fig. 5 Photodiode measurement results for smaller chromaticity value

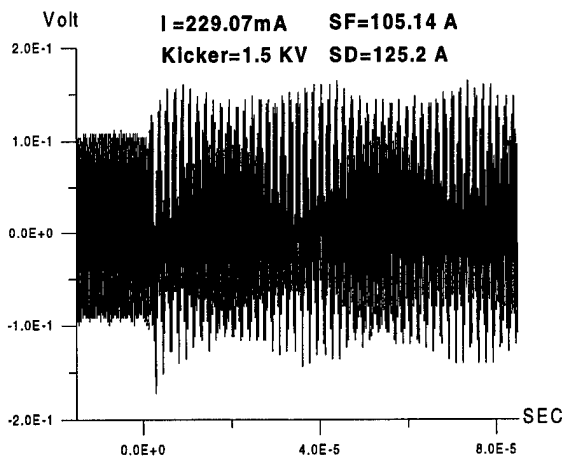

Fig. 6 Photodiode measurement results for medium chromaticity value

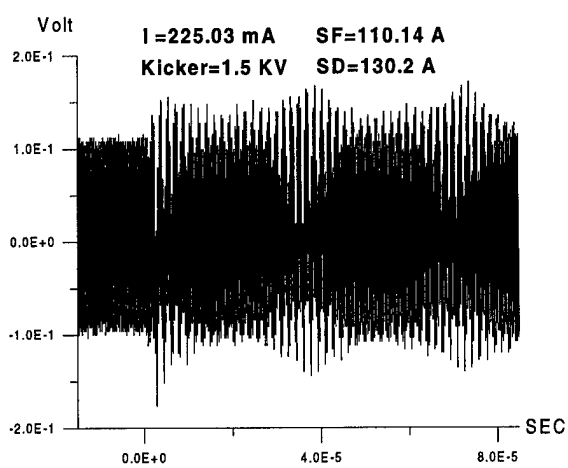

Fig. 7 Photodiode measurement results for larger chromaticity value

5 DISCUSSION AND CONCLUSSION

From the preliminary experiment results, it does show that the fast photodiode can provide turn by turn beam size information, if the photodiode operated in the nonlinear region. However, in this preliminary test, instead of using single bunch beam, we have used multibunch beam. The reason is that the efficiency of the production of flat-top beam is too low (12%, in our case), therefore, it is not strong enough to saturate the photodiode in the single bunch beam (typical beam current is 20 mA). The different method of producing flat-top beam is under study which should overcome this weak point.

ACKNOWLEDGEMENTS

We would like to thank Dr. K.-T. Hsu of SRRC, Taiwan, for his help in providing the BPM signal and the optics system of the synchrotron radiation monitor. This work was supported by the NSC of Taiwan, under contract NSC 85-2112-M-007-019.

REFERENCES

[1] Ian C. Hsu et al., in *Proceeding of the 1995 Particle Accelerator Conference* (Dallas, Texas, USA, 1995), pp. 2515-2517.
[2] J.W.Goodman,*Introduction to Fourier Optics* (McGraw-Hill,New York,1996),Chap.7,p. 176.
[3] Ian and C.-H. Lee, to be published.
[4] Ian C. Hsu, *Particle Accelerators* **34**(12) (1990) 43.

BEAM PROFILE MONITORS IN THE NLCTA*

C. Nantista, C. Adolphsen, R.L. Brown, R. Fuller and J. Rifkin
Stanford Linear Accelerator Center, P.O. Box 4349, Stanford, California 94309, USA

Abstract

The transverse current profile in the Next Linear Collider Test Accelerator (NLCTA) electron beam can be monitored at several locations along the beam line by means of profile monitors. These consist of insertable phosphor screens, light collection and transport systems, CID cameras, a frame-grabber, and PC and VAX based image analysis software. In addition to their usefulness in tuning and steering the accelerator, the profile monitors are utilized for emittance measurement. A description of these systems and their performance is presented.

I. INTRODUCTION

Among the devices which comprise the beam instrumentation system of the Next Linear Collider Test Accelerator [1] at SLAC are eight beam profile monitors: one near the gun, one between the injector sections, one each before, in the middle of, and after the chicane, one after the main accelerator, and one at each of the two dumps. Along with four wire scanners, these profile monitors allow us to view the transverse charge distribution of the electron beam at various positions along the beam line. They are of great utility for monitoring beam shape, verifying transmission, and, in the high dispersion region of the chicane and spectrometer, measuring energy spread in the long bunch train [2],[3]. In addition, they are employed in data acquisition for beam emittance and TWISS parameter measurement.

II. SCREEN

The screens used in our profile monitors are of the same type used in the SLC [4]. They are fabricated from aluminum, to which is bound a fine-grained surface layer of $Gd_2O_2S:Tb$. This coating phosphoresces with a decay time of about a millisecond where the incident electron beam deposits energy. The light emitted per unit area is proportional to the charge passing through the screen. They are supported on pneumatic vacuum feedthroughs which allow them to be retracted from the beam pipe volume when not in use.

When a screen is inserted, its surface makes an angle of 45° with the beam line axis so that it can be viewed through a vertical view port. A pattern of holes drilled in the screen allows for image dimensions to be calibrated. For most screens, this is a rectangular frame with seven holes horizontally and five vertically. The horizontal and projected vertical hole spacing is 1.5 mm. The last three profile monitors have larger screens with a different hole pattern.

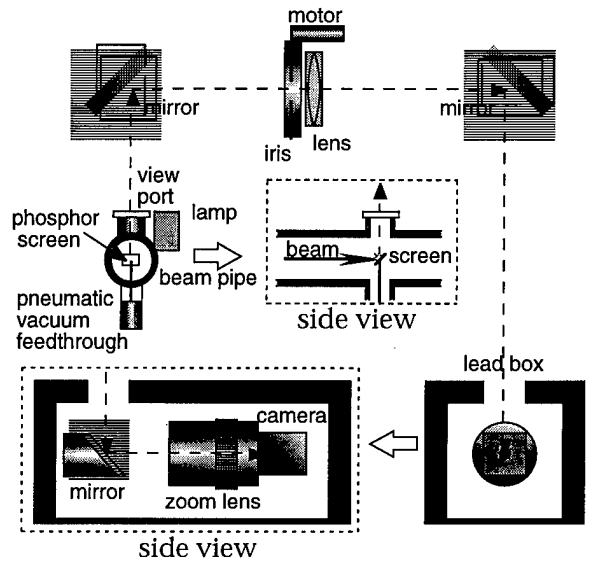

Figure 1. Profile monitor optics diagram.

III. OPTICS

An optical system is employed to distance the camera from the high radiation levels produced by the beam, particularly when incident on the screen. The layout of our optical elements is illustrated in Figure 1. They include three flat optical mirrors, an adjustable iris, and a three-inch, 350 mm focal length imaging lens. The image magnification is set close to unity to minimize aberration. The camera is placed a couple of feet off to the side of and below the beamline and is shielded by an enclosure of lead bricks supported by a steel frame. The amount of light entering the camera is adjusted by means of a remotely controlled motor connected to the iris. Also remotely controllable is a lamp aimed through a second window in the vacuum chamber. This allows us to illuminate the screen in order to view the hole pattern and calibrate the x and y scales of the received image. Illumination is also needed while manually aligning the optical elements and focusing the image.

IV. CAMERA

The camera used in our profile monitors is the CID2250D manufactured by CIDTEC, a 30 Hz, solid state, CID (charge injection device), monochrome video camera. The designation "CID" refers to the fact that

* Work supported by Department of Energy contract DE-AC03-76SF00515.

after each frame is read out from the sensor, the charge on its MOS capacitor array is injected into a substrate. It is rated for fifty times longer life than CCD (charge coupled device) cameras in an ionizing radiation environment and is much more "neutron-hard". The sensor is a 59 square millimeter surface containing 512×512 pixel capacitors with 0.015 mm spacing. Its sensitivity and range can be adjusted by setting the gain and offset voltage.

The camera is fitted with a close-up zoom lens which is focused on the screen image formed several centimeters away. A long, special cable connects the palm-sized camera body to a camera control unit (CCU) outside of the shielded accelerator housing.

V. FRAME-GRABBER / TIMING SIGNALS

Each of the eight CCU's is connected via two coaxial cables through a multiplexer and some electronics into a frame-grabber in the NLCTA control room. For the latter we employ Data Translation's Fidelity 200 Flexible Frame Processor board installed in an Industrial Computer Source 90 MHz PC. Figure 2 shows a diagram of our profile monitor signal processing system.

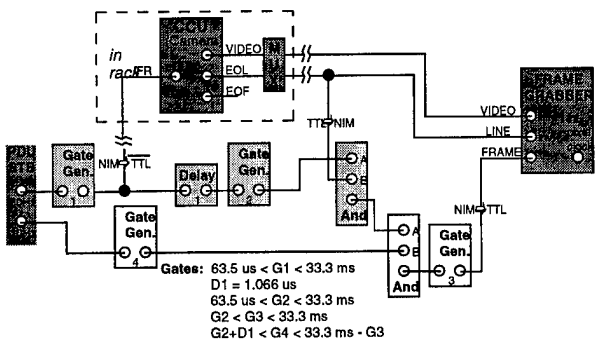

Figure 2. Timing signal electronics.

The frame-grabber operates on three timing signals: pixel clock, end-of-line, and end-of-frame. Using the board's internal oscillator for the pixel clock was found to eliminate a line-to-line image jitter problem. The end-of-line signal, output by the camera control units, is brought in through one of the coax cables. The other cable carries the raw video signal. To avoid stringing more cables than necessary, and because our multiplexer only switches two signals, we worked out a way to run without bringing the CCU's end-of-frame (EOF) signal into the frame-grabber, as described below.

A third coax cable, daisy chained to all of the CCU's from the control room, carries to them a 30 Hz frame-reset signal to synchronize the cameras with the accelerator timing system. The CCU's output end-of-frame signal is locked to its first end-of-line pulse after the leading edge of the frame reset. We can produce the same signal in the control room by combining the frame reset and incoming end-of-line signals in a NIM logic unit. This process is illustrated in Figure 3. A time delay reflectometer was used to determine the round-trip travel time between the control room and the CCU, so that the delayed frame reset pulse would select the proper end-of-line pulse. The necessary components are shown in light gray in the diagram of Figure 2.

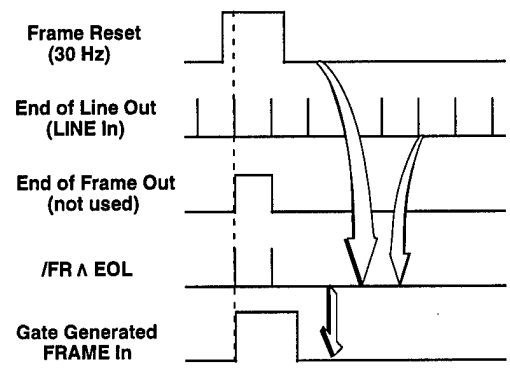

Figure 3. Generation of end-of-frame signal.

The cameras must operate at 30 Hz. However, in NLCTA operation, the beam repetition rate is generally 10 Hz. The resulting strobe effect in the video image can be annoying and gives one only a one third probability of capturing a beam image on each try. The following procedure was therefore incorporated. We take a 10 Hz trigger identical to that driving the electron gun from the same PDU (Programmable Delay Unit) that gives us our 30 Hz trigger. We expand this with a gate generator and combine it in a logic unit with our constructed end-of-frame signal. Since the latter has been slightly delayed, the effect is to pass every third end-of-frame pulse, as illustrated in Figure 4. When the frame-grabber is then given this signal and told to expect 10 Hz video, this is all that it digitizes, despite the fact that the camera is sending thirty frames per second. This is accomplished by the unshaded components in Figure 2.

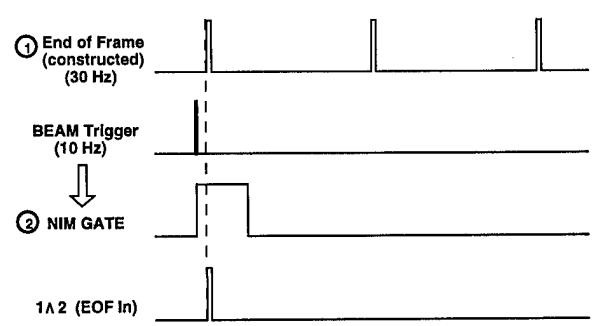

Figure 4. Reduction of end-of-frame frequency to 10 Hz.

VI. SOFTWARE

In conjunction with the Fidelity 200 frame-grabber card, we use Data Translation's GLOBAL LAB Image

software, running in Microsoft Windows for Workgroups. This image processing and analysis package has many features. It configures the frame-grabber for our camera model. It displays live video or captures single frames, which can be saved as TIFF format image files. It can plot the pixel values along any slice of an image selected by dragging a line. It also allows the user to program scripts to perform desired sequences of operations.

Unfortunately, GLOBAL LAB Image seems not to have been designed with beam physicists in mind. It cannot readily do such things as projections, curve fits, and contour plots. One can expand its capabilities by writing additional C-code. However, for our purposes, it was preferable to FTP beam images to the SLC VAX and analyze them there, when desired, with our own code written in MATLAB. This code subtracts the baseline from the image array, displays 2-D contour plots, projects the pixel values onto the x and/or y axis, and fits gaussian curves to determine the beam sigmas. An example beam spot is shown in Figure 5. Its projections, along with gaussian fits, are shown in Figure 6.

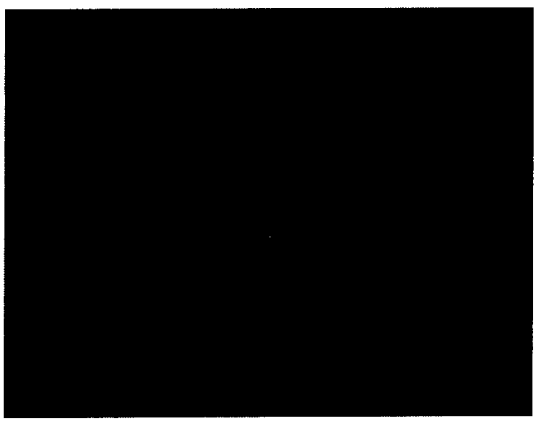

Figure 5. Beamspot image.

VII. EMITTANCE MEASUREMENT

The beam physics program of the NLCTA makes it desireable to be able to measure the beam emittance, as well as how well matched the beam is to the lattice. This is done with our profile monitors using to the general procedure described by Ross, *et al.* [5].

To measure horizontal beam phase space, for example, the CORRELATIONS PLOT program in our controls software is used to step a horizontally focusing quadrupole magnet upstream of the chosen profile monitor through seven field strengths about the nominal value. At each step, a trigger is sent to our frame-grabber, and GLOBAL LAB Image stores the beam image to disk.

These images are then transfered from PC to VAX, and their gaussian spacial distribution sigmas in the relevant dimension are determined. These are related to the beam sigma matrix at the screen by $\sigma_{11} = \sigma_x^2$. MATLAB

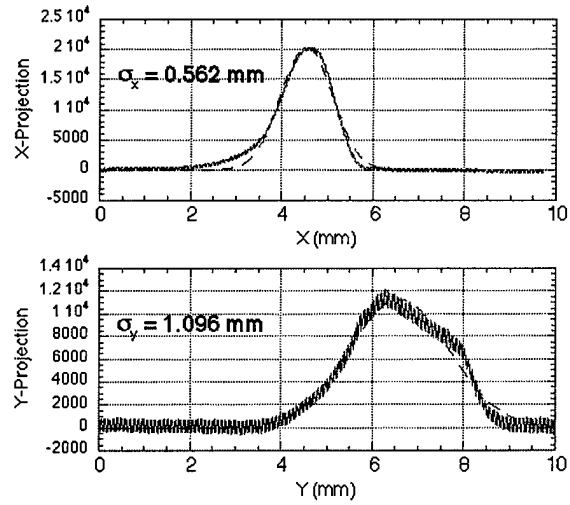

Figure 6. Projections and gaussian fits (dashed).

then reads in the quadrupole name and field values from the CORRELATIONS PLOT output and gets the tranfer matrix between the quadrupole and the profile monitor from the online database, as well as the beam energy. A parabola is fit to a plot of σ_x^2 vs. quadrupole strength. From its three coefficients and the transfer matrix, we can determine the 2×2 sigma matrix at the quadrupole. The emittance and TWISS parameters then follow from $\varepsilon = \sqrt{\det \sigma}$, $\beta = \sigma_{11}/\sqrt{\det \sigma}$, and $\alpha = -\sigma_{12}/\sqrt{\det \sigma}$. Using further transfer matrix information from our model, we can "swim" this beam ellipse upstream and calculate the mismatch at the accelerator input, characterized by

$$B_{\text{mag}} = \frac{1}{2}\left[\frac{\beta^*}{\beta} + \frac{\beta}{\beta^*} + \left(\alpha\sqrt{\frac{\beta^*}{\beta}} - \alpha^*\sqrt{\frac{\beta}{\beta^*}}\right)^2\right],$$

where the asterisked parameters are the measured values and the others the design values.

REFERENCES

[1] Ronald D. Ruth, "Results From the NLC Test Accelerator," these proceedings.

[2] A. Yeremian, *et al.*, "NLCTA Injector Experimental Results," these proceedings.

[3] C. Adolphsen, *et al.*, "Beam Loading Compensation in the NLCTA," these proceedings.

[4] M.C. Ross, *et al.*, "High Resolution Beam Profile Monitors in the SLC," proceedings of the 1985 Particle Accelerator Conference, Vancouver, B.C., Canada, May 13-16, 1985; SLAC-PUB-3640.

[5] M.C. Ross, *et al.*, "Automated Emittance Measurements in the SLC," proceedings of the 1987 Particle Accelerator Conference, Washington, D.C., March 16-19, 1987; SLAC-PUB-4278.

AN RF BUNCH-LENGTH MONITOR FOR THE SLC FINAL FOCUS*

F. Zimmermann, G. Yocky, D. Whittum, M. Seidel, P. Raimondi, C.K. Ng, D. McCormick, K. Bane
Stanford Linear Accelerator Center, Stanford University, CA 94309, USA

Abstract

In preparation for the 1997 SLC run, a novel RF bunch-length monitor has been installed in the SLC South Final Focus. The monitor consists of a ceramic gap in the beam pipe, a 160-ft long X-band waveguide (WR90), and a set of dividers, tapers and microwave detectors. Electromagnetic fields radiated through the ceramic gap excite modes in the nearby open-ended X-band waveguide, which transmits the beam-induced signal to a radiation-free shack outside of the beamline vault. There, a combination of power dividers, tapers, waveguides, and crystal detectors is used to measure the signal power in 4 separate frequency channels between 7 and 110 GHz. For typical rms bunch lengths of 0.5–2 mm in the SLC, the bunch frequency spectrum can extend up to 100 GHz. In this paper, we present the overall monitor layout, describe MAFIA calculations of the signal coupled into the waveguide based on a detailed model of the complex beam-pipe geometry, estimate the final power level at the RF conversion points, and report the measured transmission properties of the installed waveguide system.

1 INTRODUCTION

During the 1996/97 downtime of the Stanford Linear Collider (SLC), a novel RF bunch length monitor was installed in the South Final Focus, about 45 m away from the interaction point (IP). The monitor can detect the longitudinal distribution of both electron and positron bunches, which pass this point with a time separation of roughly 300 ns. It will permit control of the bunch length at the IP, which, due to bunch compression in the 1.2-km long collider arcs, can be very different from the bunch length that is measured in the SLAC linac, and may have a significant impact on the luminosity.

Previous attempts to commission a bunch-length monitor based on an RF cavity [1] at the same location failed, presumably because the crystal rectifiers used for converting the RF signal could not withstand the high radiation and electromagnetic noise level in the final-focus tunnel.

The suspected noise problem is overcome, if the RF signal conversion is performed outside of the beamline vault. For this purpose, we recently installed a 160-ft long section of WR90 (brass) waveguide, extending from the South final-focus tunnel through a 60-ft deep penetration to the Compton-laser shack South of the collider hall. As illustrated in Fig. 1, using waveguide filters and couplers, the RF signal is split into 4 different channels, which span the 4 frequency ranges 8–11.6 GHz, 11.6–19 GHz, 19–110 GHz and 59–110 GHz. The RF power in each channel is measured with crystal rectifiers connected to gated ADCs, and the 8 signals so obtained (4 each for both the electron and the positron beam) are continually read out by the SLC control system. Figure 2 shows a photograph of the signal-processing unit being assembled.

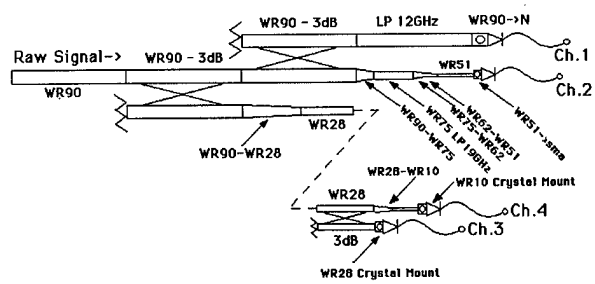

Figure 1: Schematic of RF signal processing.

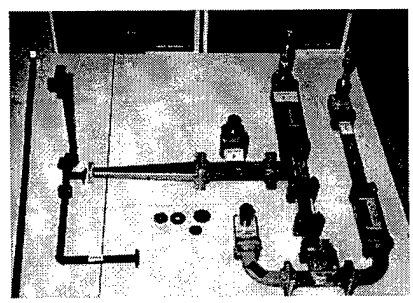

Figure 2: Assembly of signal-processing unit.

The signal detected in the different channels allows us to distinguish favorable and unfavorable bunch distributions at the interaction point. Beam-beam simulations with the code Guinea-Pig [2] were performed for different longitudinal distributions, as expected for small changes in the bunch-compressor (behind the damping rings) and linac set-ups [3]. Other beam parameters were assumed to be the same as in 1996. The simulations show that for bunches of rms length $\sigma_z \geq 1$ mm the luminosity is 30% higher than for 0.5 mm long bunches, due to the pinch effect (mutual focusing of the two beams during collision) [3]. The higher-frequency channels of our monitor are very sensitive to the bunch length: When the bunch length increases from 0.5 to 1 mm, the channel-4 signal is reduced by about 20 dB. For higher current and/or smaller horizontal IP spot size in 1997, the luminosity gain from bunch-length adjustment could approach 50–80%.

2 BEAM-WAVEGUIDE COUPLING

In the final-focus tunnel, the open-ended WR90 waveguide is pointed at a ceramic gap in the beam pipe; see photo-

* Work supported by the U.S. Department of Energy under contract DE-AC03-76SF00515.

graph in Fig. 3. This broadband pickup will be more versatile than a narrow-band cavity. Inner and outer radius of the ceramic are 1.5 cm and 1.9 cm, respectively. The total gap length is 4 cm, three quarters of which are occupied by a toroid. The waveguide is situated at the last free quarter of the gap and ends about 0.5 cm above the ceramic.

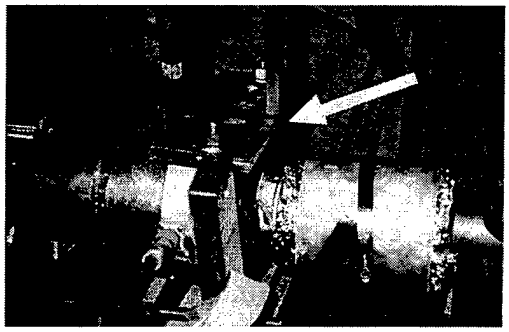

Figure 3: Waveguide pickup (arrow), toroid (left from waveguide), ceramic gap (below waveguide) and bellows (left and right), in the SLC South Final-Focus beam pipe.

The coupling of the radiated field into the waveguide was calculated for Gaussian bunches of different rms lengths, with the code MAFIA [4]. Figure 4 depicts the model of the beam-pipe geometry used in these calculations: The 0.5-cm wide gap between waveguide and ceramic is neglected, and the waveguide directly borders on the ceramic. The toroid is treated as a conducting boundary.

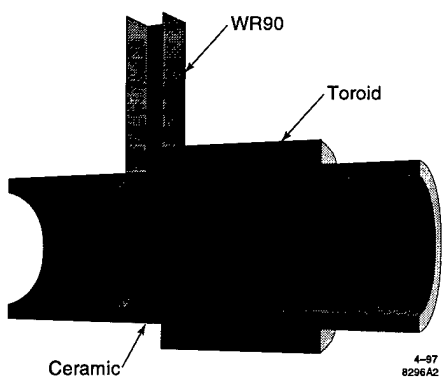

Figure 4: Model for the numerical calculation of beam-waveguide coupling using MAFIA [4].

The calculations show that the energy coupled into the TE_{10} mode is at least 2 times larger than that transmitted into the next important mode. Figure 5 illustrates the excitation of the TE_{10} mode by a 2-mm long Gaussian bunch as a function of frequency. Integration over time (or frequency) relates the signal a (or its Fourier transform $\tilde{a}$), that is computed by MAFIA, to the mode energy:

$$E_{TE_{10}} = \int |a(t)|^2 \, dt = \frac{1}{2\pi} \int |\tilde{a}(\omega)|^2 d\omega \qquad (1)$$

Dividing the energy by the excitation time yields the RF power coupled into the TE_{10} mode. This is listed in the center column of Table 1.

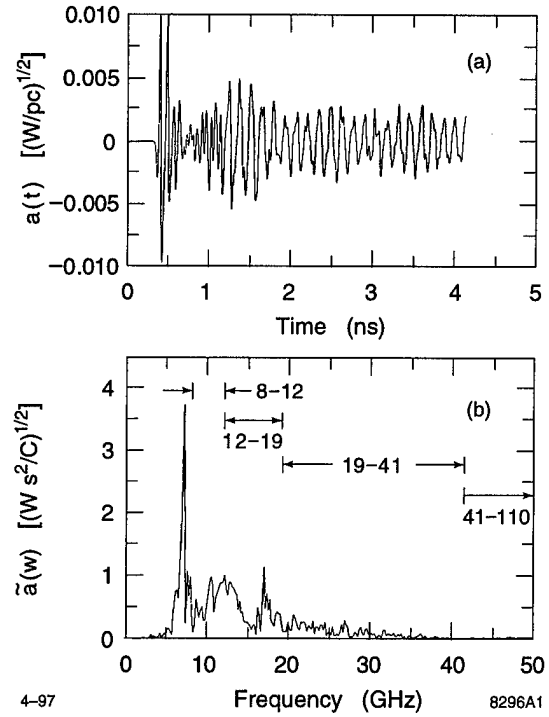

Figure 5: Signal $a(t)$ (in units of $W^{1/2}$) coupled into TE_{10} waveguide mode as a function of time, and its Fourier transform $\tilde{a}(\omega)$ (in units of $W^{1/2}s$) as a function of frequency, for a Gaussian bunch with 2 mm rms length.

3 WAVEGUIDE PROPERTIES

The interior broad dimension of the WR90 waveguide is $a = 2.286$ cm, which corresponds to a cutoff frequency $f_c = c/(2a) = 6.6$ GHz for the lowest (TE_{10}) mode. Using the skin depth $\delta_s \approx (2/(\omega\mu\sigma))^{1/2} \approx 4\mu/\sqrt{f(\mathrm{GHz})}$, where σ denotes the conductivity and the numerical value applies to brass, the surface resistance is given by $R_s = 1/(\sigma\delta_s) \approx 15\ \mathrm{m}\Omega\ \sqrt{f(\mathrm{GHz})}$.

As the RF wave propagates through the waveguide, the power decreases exponentially from its initial value $P(0)$. After a distance s, the power in the TE_{10} mode is $P(s) = P(0)\exp(-2\alpha s)$, with an attenuation coefficient [5]

$$\alpha = \frac{R_s}{Z_0} \frac{(2b\beta_c^2 + a\beta_0^2)}{ab\beta_0\beta_z}, \qquad (2)$$

where $Z_0 = 377\ \Omega$, $b \approx a/2$ the small waveguide dimension, $\beta_c = \pi/a$, $\beta_0 = \omega/c$, and $\beta_z = (\beta_0^2 - \beta_c^2)^{1/2}$. Expressed in decibels the attentuation can also be written

$$A(s)\ [\mathrm{dB}] = 8.686\ \alpha\ s \qquad (3)$$

At frequencies where the skin depth becomes comparable to the (unknown) surface roughness these formulae are no longer valid [5].

Figure 6 compares the measured attentuation of a signal reflected at the end of the 50-m long waveguide with the theoretical prediction of Eq. (3). At 10 GHz, the attenuation is about 7 dB for a wave propagating twice through the

entire waveguide, or about 0.2 dB per meter. This agrees well with the attenuation measured on a 12-ft long sample waveguide.

There are about 41 waveguide modes with a cutoff frequency below 50 GHz. The waveguide contains 11 H and E bends, at which part of the higher-frequency RF energy in the TE_{10} mode will be converted into other modes as the RF wave travels through the waveguide. In Fig. 6, the slight increase of the attenuation above 13 GHz may be due to excitation of the TE_{20} mode, whose cutoff frequency is 13.1 GHz.

Using the waveguide attentuation due to surface resistivity, given by Eqs. (2) and (3), assuming up to 10 dB additional attenuation due to conversion into other waveguide modes, and also including the two 3-dB couplers in the processing unit, we can roughly estimate the signal level at the crystal rectifiers, based on the power originally coupled into the TE_{10} mode. This estimate, shown in the right column of Table 1, is many 10's of dB above the noise.

Δf	init. power	est. signal
8–12 GHz	44 dBm	31 dBm
12 – 19 GHz	45 dBm	31 dBm
19 – 41 GHz	38 dBm	9 dBm
41 – 110 GHz	17 dBm	−22 dBm

Table 1: Power initially coupled into the TE_{10} waveguide mode and the estimated signal level, for a Gaussian bunch of rms length 2 mm, a bunch population of $N \approx 3 \times 10^{10}$ particles, and 4 different frequency ranges.

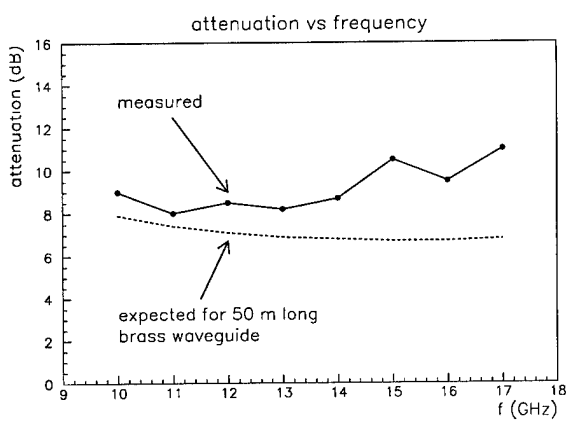

Figure 6: Measured attenuation of TE_{10} mode.

The group velocity in the waveguide is given by $v_g = c(1 - \beta_c^2/\beta_0^2)^{1/2}$ [5], and the propagation time over the distance $2L$ is simply $t_d = 2L/v_g$. Fig. 7 shows that, in the frequency range 7–12 GHz, the measured propagation times agree well with analytical expectation for a waveguide length L of about 50 m. For this measurement, the end of the WR90 waveguide was terminated with a reflecting plate.

The phase variation of the reflected RF wave as a function of frequency, $\Delta\phi(\omega)$, was measured with a mixer circuit combining the reflected and the drive signal. From this, and using the relation $L \approx c^2\beta_a/\omega(\Delta\phi/\Delta\omega)$, the electrical length of the waveguide was determined as $L \approx 49.24 \pm 0.03$ m, where the systematic error is probably much larger than the quoted statistical one.

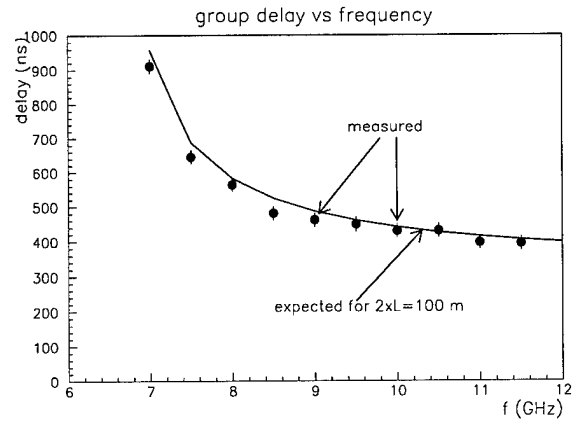

Figure 7: Measured and expected group delay for reflected TE_{10} mode in the ~130-ft long WR90 waveguide, as a function of frequency.

Assuming power-detecting diodes, the crystal detectors mounted at the end of the waveguide measure the square of the electric field, and, hence, their output voltage will be proportional to $V_{cr} \propto \sum_{k,l} E_k E_l^* e^{i(\phi_k - \phi_l)}$ where the sum is over all the modes above cutoff. If the length of the waveguide changes, *e.g.*, due to temperature variation, the relative phase of two modes changes as well (in case of a temperature change ΔT, the phase of the ith mode changes by $\Delta\phi_i/\Delta T \approx (\beta_{ci}^2/\beta_{zi}^2 + 1)\beta_{zi}L\alpha \geq 0.2$ K^{-1} where $\alpha \approx 2 \times 10^{-5}$ K^{-1} is the thermal expansion coefficient of brass, β_{ci} the cutoff frequency, and β_{zi} the propagation constant of the ith mode) and, as a consequence, so does the output signal. Since there are many modes, and since we average over wide frequency ranges, the sensitivity to length variation should be greatly reduced. More importantly, diurnal variations do not bar short scans of signal vs. compressor voltage or linac phasing, nor do they impede the continual comparison of electron and positron bunch lengths.

Acknowledgements

We thank M. Ross, M. Breidenbach and N. Phinney for support, A. Menegat, S. Tantawi and S. Hanna for helpful advice, and M. Woods for sharing the laser shack with us.

4 REFERENCES

[1] E. Babenko et al., PAC93, Washington, p. 2423 (1993).

[2] D. Schulte, private communication (1997).

[3] K.L.F. Bane, P. Chen and F. Zimmermann, these proceedings (1997).

[4] MAFIA RELEASE 3, DESY M-90-05K (1990).

[5] R.E. Collin, Foundations for Microwave Engineering, McGraw-Hill, Singapore (1966).

ANALYSIS OF A NOVEL DIFFRACTIVE SCANNING-WIRE BEAM POSITION MONITOR (BPM) FOR DISCRIMINATIVE PROFILING OF ELECTRON VS. X-RAY BEAMS*

R. Tatchyn
Stanford Synchrotron Radiation Laboratory, Stanford Linear Accelerator Center, Stanford, CA 94309 , USA

Abstract

Recent numerical studies of Free Electron Lasers (FELs) operating in the Self Amplified Spontaneous Emission (SASE) regime indicate a large sensitivity of the gain to the degree of transverse overlap (and associated phase coherence) between the electron and photon beams traveling down the insertion device. Simulations of actual systems imply that accurate detection and correction for this relative loss of overlap, rather than correction for the absolute departure of the electron beam from a fixed axis, is the preferred function of an FEL amplifier's Beam Position Monitor (BPM) and corrector systems. In this note we propose a novel diffractive BPM with the capability of simultaneously detecting and resolving the absolute (and relative) transverse positions and profiles of electron and x-ray beams co-propagating through an undulator. We derive the equations governing the performance of the BPM and examine its predicted performance for the SLAC Linac Coherent Light Source (LCLS), viz., for profiling multi-GeV electron bunches co-propagating with one-to-several-hundred keV x-ray beams. Selected research and development (r&d) tasks for fabricating and testing the proposed BPM are discussed.

I. INTRODUCTION

Beam Position Monitors (BPMs) that operate on the principle of direct scattering are widely employed for characterizing the phase space parameters of particle beams on present-day particle accelerators. One example of this type of diagnostic is the scanning carbon wire [1]. For diagnosing high energy particle beams with small divergences, the wire is typically used to generate bremsstrahlung radiation which is then monitored with an on-axis gamma-ray Position Sensitive Detector (PSD) well downstream of the BPM location. In principle, the directly-scattered beam particle distribution can also be analyzed to extract position-sensitive information.

In contrast to prior art, the recent advent of Å-wavelength Linac Coherent Light Source (LCLS) technology has placed novel and ever more stringent requirements on particle beam phase space diagnostics [2,3,4]. First, due to the sensitivity of the Free Electron Laser (FEL amplifier gain to the beam's emittance parameters along the photon/e-beam interaction region (viz., the undulator), the beam parameters require monitoring over increments on the order of the FEL gain length, i.e., at intervals of approximately 5% of the undulator length. The second, perhaps even more onerous, requirement is for the **simultaneous** characterization of both the electron beam **and** the x-ray beam co-propagating with it along the insertion device axis.

In this presentation we describe and analyze a novel low-Z-wire based BPM structure with the capability of accomplishing both these goals.

II. A NOVEL DIFFRACTIVE WIRE BPM

The configuration for the proposed structure was developed based on earlier investigations of diffractive BPMs [5] coupled with a systematic assessment of those properties of the charged-particle and radiation beams in the LCLS that allow for maximal discrimination. Referring to Table 1, we note that the properties offering the possibility of maximal discrimination are 1), 2), 3), and 5), implying the development of some sort of spectral/angular filter [5]. The structure of the resulting BPM [6] is schematized in Fig. 1.

Table 1. Selected properties of electron and x-ray beams inside a 1.5 Å LCLS undulator with Nu periods.

		e-Beam	X-Ray Beam
1)	Wavelength	1 μÅ	1.5 Å
2)	**Long. Coherence**	negligible	quasi-coherent ($1/N_u$)
3)	**Bandwidth**	0.02%	Broadband[b]
4)	**Photoemission yield**[c]	~η	~η
5)	**Scattering angle**	1/γ	large[d]

[a]negligible collective phase coherence. Each individual particle, however, can interfere with itself.

[b]In any paraxial direction, the bandwidth is $\sim 1/N_u$, and the angular width orthogonal to this direction is also $\sim 1/N_u$. The wavelength itself, however, increases rapidly with increasing angles away from the axis.

[c]total e-beasm vs. x-ray yields comparable for a 25μ diameter carbon wire

[d]Dipole scattering from an individual molecule is into ~4π steradians. Preferred scattering directions arise from collective effects and scattering from periodic distributions of matter.

* Work supported in part by the Department of Energy Offices of Basic Energy Sciences and High Energy and Nuclear Physics, and Department of Energy Contract DE-AC03-76SF00515. Other portions of this work were supported by Department of Energy CRADA SLAC-9302.

The basic (and major) component is seen to be, just as in a conventional BPM, a carbon (or an alternative low-Z material) wire, but with a rectangular cross section. In practice, this shape could be micro-machined from a round carbon wire, cut from a substrate on which the multilayer is deposited, or prepared *ab initio* as a carbon "micro-ribbon." This shape is required to allow the deposition of multilayers, composed of layer-pairs of alternating-Z materials, on the top and bottom facets, which, in the application, are oriented parallel to the undulator axis. In operation, the electrons scatter and induce bremsstrahlung off the wire and multilayers (as in an ordinary carbon wire BPM), while the x-ray beam diffracts in transmission through the multilayers. The period, a, of the multilayer, adjustable over a broad range (e.g., easily from 10Å-5000Å) is set to optimize the x-ray diffraction angle, while the number of periods, N, and the dimension d are set to: a) produce a thickness much smaller than the carbon wire's, and 2) optimize the spectral/angular filtering properties of the BPM for diagnostic purposes.

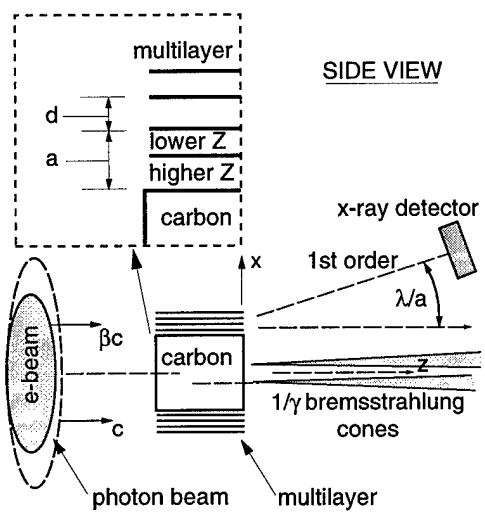

Figure 1. Diffractive wire-BPM structure.

III. ANALYSIS AND MODELED X-RAY PERFORMANCE

The analysis of diffraction induced by the structure in Fig. 1 is straightforward. The electric field distribution at the downstream side of the multilayer is the sum of the electric fields on the downstream facets of the high-Z (A(x/λ)) and low-Z (M(x/λ)) materials. This sum, and the fields, are expressed, with all *constant* dimensions in units of "# of wavelengths," as:

$$Ap\left(\frac{x}{\lambda}\right) = \left[M\left(\frac{x}{\lambda}\right) * \frac{1}{a}\sum_{j=-\frac{N}{2}}^{\frac{N}{2}-1} \delta\left(\frac{1}{a}\left(\frac{x}{\lambda} + \frac{d+a}{2} + ja\right)\right)\right] + \left[A\left(\frac{x}{\lambda}\right) * \frac{1}{a}\sum_{j=-\frac{N}{2}}^{\frac{N}{2}-1} \delta\left(\frac{1}{a}\left(\frac{x}{\lambda} + \frac{d}{2} + ja\right)\right)\right].$$

The far-field diffracted amplitude is the Fourier Transform of the field distribution, and is given by:

$$\bar{A}p(s) = e^{-\pi isd}\left\{\bar{M}(s)\sum_{j=-\frac{N}{2}}^{\frac{N}{2}-1} e^{2\pi is(\frac{a}{2}+ja)} + \bar{A}(s)\sum_{j=-\frac{N}{2}}^{\frac{N}{2}-1} e^{-2\pi isja}\right\} = e^{-\pi isd}\left(\frac{\sin\pi sNa}{\sin\pi sa}\right)\left[\bar{M}(s) + e^{\pi isa}\bar{A}(s)\right],$$

with

$$\bar{M} = \sqrt{I_0}(a-d)\left(\sin c((a-d)s)\right)e^{-2\pi iW(\delta_1 - ik_1)},$$

and

$$\bar{A} = \sqrt{I_0}(d)\left(\sin c(ds)\right)e^{-2\pi iW(\delta_2 - ik_2)}.$$

This yields

$$\bar{A}p(s) = e^{-\pi isd}\left(\frac{\sin\pi sNa}{\sin\pi sa}\right)\frac{\sqrt{I_0}}{\pi s}e^{-2\pi iW\delta_2}e^{-2\pi Wk_2} \times \left[\sin(\pi(a-d)s)e^{-2\pi W(k_1-k_2)}e^{-2\pi iW(\delta_1-\delta_2)} + e^{\pi isa}\sin(\pi ds)\right]. \quad (1)$$

As is known, the absolute value squared of the factor containing the sine ratio describes the lineshape of the diffracted beam as a function of angle (s). At the non-zero orders peaks (s=m/a), the intensity assumes the value:

$$I^{(1)} = \left|\bar{A}p\left(\frac{m}{a}\right)\right|^2 = I_0 N^2 (d)^2 \operatorname{sinc}^2\left(\frac{md}{a}\right)e^{-4\pi Wk_2} \times \left\{1 - 2e^{-2\pi W(k_1-k_2)}\cos(2\pi W(\delta_1-\delta_2)) + e^{-4\pi W(k_1-k_2)}\right\} \quad (2)$$

Equ's. (1-2), describing the distribution of the diffracted x-rays in the far field, now exhibit all the terms necessary to assess the x-ray performance of the BPM. First, we note the overall efficiency of the structure is determined by the material with the lower Z, via the exponential factor $\exp(-4\pi Wk_2)$. This means that for a typical carbon wire diameter of ~25μ, the structure will operate with adequate efficiency over the full spectral range of the LCLS (900 eV(1st harmonic) - 25 keV (3rd harmonic)) [4] as long as at least one of the materials has a Z of less than 20 or so. Second, further spectral/angular filtering action is possible via the dimension d in the sinc^2 factor, which can be set to suppress, for example, all the even angular harmonics, or selected odd angular harmonics. Third, by using one high-Z material, the multilayer can act as a vital "Soller Slit" spectral-angular filter for the impinging undulator light. Fourth, we note that as the BPM is scanned through the radiation, the number N will vary from 1 to its maximum value, allowing the changing angular width of the 1st order to be used as a fine measure of the BPM's location with regard to the desired x-ray beam. Finally, for favorable values of δ_1 and δ_2, we note that the factor in square brackets can significantly enhance the efficiency of the diffraction into the 1st and higher orders vs. the 0th order.

In Fig. 3 we graph the calculated efficiency of 5 different multilayer structures, all featuring a=400Å/λ, d=200Å/λ, N=25, and W=25000Å/λ. It is seen that the predicted performance is excellent for most of the high-Z/low-Z systems over the full operating range of the LCLS. The poorest performing systems, Cr/Ni, and B/C, feature materials with nearly identical Zs, resulting in overly slow development of a transverse phase difference in the transmitted wavefront. For B/C the performance for harder x-rays will significantly improve with increased BPM thickness.

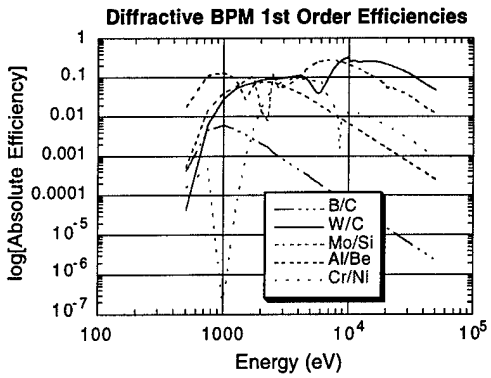

Figure 2. Modeled absolute BPM x-ray diffraction efficiencies.

In Fig. 4 we graph the corresponding ratios of the 1st diffracted order intensity to the 0th, illustrating the effectiveness of 1st order enhancement due to interference effects.

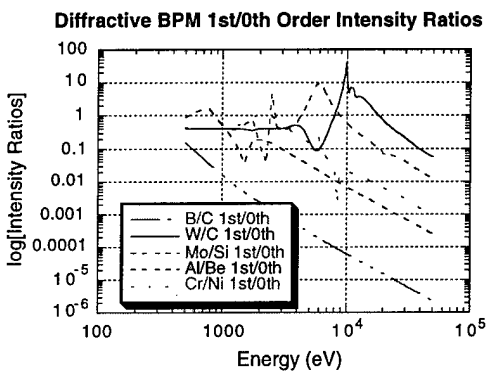

Figure 3. Modeled 1st/0th order diffracted intensity ratios.

For typical LCLS parameters [4], it is easy to calculate that 2 meters of undulator will generate on the order of 10^8 photons/pulse within a 1% BW, in the central cone of the spontaneous radiation's 1st harmonic. At 2 meters, the spatial extent of this central cone will be roughly 25μ. Given the assumed multilayer dimensions, approximately 4% of the light will be subtended by the multilayers, which, for the higher calculated efficiencies in Fig. 2, implies between 10^3-10^6 photons/pulse transmitted to a detector placed at the 1st diffracted order location. Further downstream, the diffracted spontaneous flux will increase roughly proportionally to undulator length, while the coherent FEL flux will peak at 2-3 orders of magnitude higher than the spontaneous.

V. DISCUSSION

The calculations reported here indicate that the proposed BPM structure appears adequate to characterize x-rays vs. e-beams from a 2m -100+m LCLS undulator section. Due to the possibility of lineshape monitoring (e.g., with a CCD), the resolution of the BPM (for x-rays) will be of the order of size of one period (a). Even finer resolution may be attainable by utilizing the relative interference between the two multilayers. Regarding multilayer performance, we note that the relatively large period not only desensitizes their structural quality to substrate imperfections, but to certain radiation-induced damage effects as well, such as accelerated interdiffusion at the interfaces. An expected difficulty, both in fabrication and operation, will be the rather tight requirements for angular orientation of the structure with respect to the beam axis. This may be exacerbated by thermally or mechanically induced distortions in the carbon (or other low-Z) wire, but can be mitigated in part by increasing a. These and other issues are expected to be addressed in a three-phase r&d program. The first phase will investigate the physical realizability and quality of the BPM. The second phase will test the BPMs survivability and performance in e-beams on linacs, and the third phase, if warranted, will focus on developing a working BPM system. Finally, alternative geometries and structures based on multilayer reflection may also be assessed.

V. REFERENCES

[1] X. Q. Wang, T. Groves, A. A. Hahn, G. Jackson, J. Marriner, K. Martin, J. Misek, "Design and Commissioning of Flying Wires in the Fermilab Accelerator," Proc. PAC91 Conference, IEEE Catalog No. 91CH3038-7, pp. 1180-1182.

[2] R. Tatchyn et al, "Research and development toward a 4.5-1.5 å Linac Coherent Light Source (LCLS) at SLAC," NIM A 375, 274(1996).

[3] J. Rossbach, "A VUV free electron laser at the TESLA test facility at DESY," NIM A 375, 268(1996).

[4] M. Cornacchia et al, "Performance and design concepts of a free-electron laser operating in the x-ray region," SPIE Proceedings 2988, 1997, paper 2988-01.

[5] R. Tatchyn and I. Lindau, "Transmission Grating Goniometer Elements for Use at Synchrotron Facilities," Nucl. Instrum. Meth. 195, 419(1982).

[6] R. Tatchyn, "Analysis of a Novel Diffractive Scanning-Wire Beam Position Monitor (BPM) for Discriminative Profiling of Electron vs. X-Ray Beams," SLAC-PUB 7438, March 1997.

ANALYSIS OF A SINGLE-SHOT LONGITUDINAL BUNCH PROFILING SYSTEM BASED ON AN ULTRA-SHORT PULSE Ti:SAPPHIRE LASER*

R. Tatchyn
Stanford Synchrotron Radiation Laboratory, SLAC, Stanford, CA 94309 USA

Abstract

Recent advances in ultra-short pulse high-power laser technology include the generation of <10 fs pulses at 1 μ wavelengths in the multi-terawatt regime. These parameters, coupled with the high per-pulse energy of the new sources, make possible the consideration of longitudinal bunch profiling schemes capable of accurately registering the longitudinal bunch density in a single shot. In this paper we assess the performance and advantages of a longitudinal bunch profiling system based on multi-photon absorption and fluorescence stimulated by the combined bunch and laser fields in a gaseous medium.

1 INTRODUCTION

A number of diagnostic techniques for measuring the longitudinal density profiles of single-pass or recirculating particle bunches are employed on present-day particle accelerators and storage rings. Examples include: 1) electronic spectral analysis of the outputs of distributed inductive or capacitive pickups placed in proximity to the beam [1,2], 2) streak camera or fast photodiode sampling of the spontaneous radiation emitted by the particle bunch [3,4], and 3) Michelson (autocorrelation) interferometry applied to quasi-coherent transition or synchrotron radiation emitted by the bunch [5]. Potential drawbacks of 1) and 2) for very short bunches include the limited angular or spectral bandwidths of conventional electronic deflection systems and instrumentation. Another drawback is the relatively weak signal induced or emitted by the bunch in a single pass, which usually necessitates sampling a large number of pulses to obtain acceptable statistics. These drawbacks can be expected to limit, and in some cases obviate, the applicability of the cited techniques, especially as particle bunch lengths decrease down to below 100 μ, a trend exemplified by the bunch parameters of the Ångstrom-wavelength Linac Coherent Light Source (LCLS) [6]. Needless to say, a diagnostic tool with the capability of accurately profiling a particle bunch in a single pass would contribute greatly to our ability to study and control systems (such as the LCLS) whose performance is stringently determined by the longitudinal distribution of electrons.

*Work supported in part by the Department of Energy Offices of Basic Energy Sciences and High Energy and Nuclear Physics, and Department of Energy Contract DE-AC03-76SF00515.

In this paper we describe an extension of a previously-proposed method [7,8] with the capability of accurately characterizing the longitudinal profiles, in a single shot, of high energy charged-particle bunches down to lengths of 10μ and beyond. It is based on the availability of IR/visible/UV terawatt laser pulses with temporal lengths of 10fs [9] or less and the following three principles: 1) the reduction in the group velocity of the laser pulse traveling through a gas; 2) the high compaction of an ultrarelativistic particle's transverse electric and magnetic fields; and 3) the nonlinear modulation of multiple-photon absorption in a gas by the combined laser and electron bunch fields. As will be seen, it is the shortness of the laser pulse in comparison to the bunch that enables it to be used as temporal probe, while the large amount of energy it contains is the key to generating a signal strong enough for reliable single-shot diagnostics.

2 REVIEW OF BASIC REQUIREMENTS

The following definitions are employed:

E[GeV]	≡ average energy of a charged-particle beam
I[mA]	≡ average current of a particle beam
q	≡ magnitude of the CGS unit of charge
me[g]c2	≡ electron (positron) rest energy in ergs
$m_p[g]c^2$	≡ proton (antiproton) rest energy in ergs
β_c	≡ speed of a relativistic particle
$\gamma = \sqrt{1-\beta^2}$	≡ relativistic contraction factor
ρ(z)[#/cm]	≡ number density of a particle bunch vs. z
N_C	≡ total number of particles in a bunch
$g(z)= \rho(z)/N_C$	≡ (normalized) Gaussian particle density
$\sigma_x,\sigma_y,\sigma_z$,	≡ standard deviations of random distributions of particle positions vs. x, y, and z
N_B	≡ total number of bunches in a storage ring

Consider a charged particle bunch traveling, on the average, along a locally rectilinear trajectory. Referring to Fig.1, we take the axis of this trajectory to be coincident with the symmetry axis (z-axis) of a cylindrical (rectangular) duct of radius (half-width) H. For normally distributed particle positions, we will associate the main bunch dimensions with the quantities $2\sigma_x$, $2\sigma_y$ and $2\sigma_y$. For our present analysis we will take $\sigma_x,\sigma_y \ll$ H. This restriction, valid

whenever the maximum transverse radius of the bunch is much smaller than the duct diameter, allows the representation of the bunch by a filamentary distribution of charge. Of central importance is the instantaneous peak transverse field generated at the location (x=H,z) by an electron j located at point (s_j, s'_j, z), where s'_j is its displacement vs. y. Under the assumed restriction, the transverse field magnitude at H can be expressed as

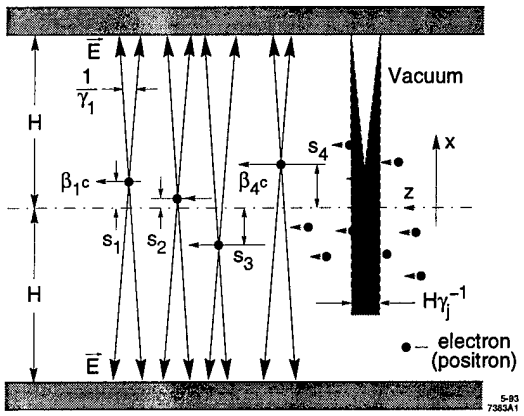

Fig. 1. Parameters of particle bunch in vacuum.

$$\left|\vec{E}(x=H,z)\right|_e\left[\frac{KV}{cm}\right]=\frac{0.3\gamma_j q}{\left(H-s_j\right)^2+\left(s'_j\right)^2}\cong\frac{0.3\gamma_j q}{H^2}. \tag{1}$$

Corresponding to the relativistic enhancement of the transverse field strength is a corresponding attenuation of the forward component by the amount γ_j^{-}. Assuming , then, that most of the electron's field is concentrated within the angle $\gamma_j^{\cdot}$, it follows that the limiting resolution of its instantaneous z-position at x=H is given by

$$\Delta z_e = H/\gamma_j. \tag{2}$$

An important quantity is the number of particles in the vicinity of electron j that also contribute significantly to the field at (x=H,z). Assuming a minimal energy spread, we can drop the index and define the designated group of electrons by projecting the resolution segment H/γ from the point (x=H,z) back toward the z axis. This yields

$$N_{1/\gamma}(z) = H\rho(z)/\gamma = \Delta z_e \rho(z). \tag{3}$$

For γ^{1} sufficiently small, the magnitude of the total field at (x=H,z) is given approximately by

$$\left|\vec{E}(x=H,z)\right|[KV/cm] = N_{1/\gamma}\left|\vec{E}\right|_e \approx \frac{0.3q\rho(z)}{H}. \tag{4}$$

For the case of a Gaussian $\rho(z)$, designated by $N_C(g(z))$, the instantaneous transverse field profile can be re-expressed in terms of the total number of particles in the bunch by

$$\left|\vec{E}(x=H,z)\right|[KV/cm] \cong \frac{0.3N_C q g(z)}{H}. \tag{5}$$

A graph displaying practical parameter ranges and attainable field strengths from charged-particle bunches in linacs or storage rings is shown in Fig. 2. First, we note, in passing, the high energies required for the method to be considered applicable to proton (antiproton) beams. Second, in order to obtain useful fields, there must be a sufficient quantity of particles within one electronic resolution length

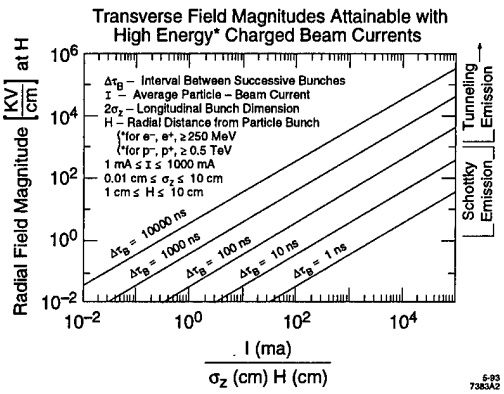

Fig. 2. Field magnitudes and corresponding surface-emission phenomena obtainable from charged- particle bunches.

(H/γ) along the beam. This quantity, which should ideally be present in the sparsest region of the bunch to be measured, can be used to establish the minimum current levels at which the profiling technique can be applied. In applying the graph, different storage rings (or linear machines) are identified not by their species of particle or energy (which is assumed to exceed a well-defined minimal value), but by their average currents and interbunch intervals. For example, taking the average current in the LCLS to be approximately $0.15\,\mu$A, with an interbunch interval of 10^7ns and a $60\,\mu$ full bunch length, extrapolation of the curves in the graph indicates that field strengths in excess of 2.5×10^3 kV/cm could be attained at a distances of a few mm from the bunch axis.

3 OUTLINE OF EXTENDED METHOD

As schematized in Fig. 3, an essential mechanism of the profiling method is the interaction of a probe photon pulse of full temporal length $(2(\pi)^{0.5}\sigma_{ph}$ with the particle bunch field as they both traverse a suitable medium at a relative lateral displacement H. Whereas in the cited prior work [7,8] surface and bulk interactions with various types of solid-state media were considered, in the present paper we consider the use of a gas. If we assume the group velocity, v_g, of the photon pulse to be different from βc, the particle bunch velocity, and $c\sigma_{ph} << \sigma_B (= \sigma_z)$, it is evident that the photon pulse will "scan" the electron field profile in a time equal to the temporal length of the bunch dilated by the factor $1/(\beta-(v_g/c))$. The function of the gaseous

medium is three-fold. First, its pressure and temperature are adjusted to set the group velocity of the probe pule almost equal to the bunch velocity to permit a sufficiently long scanning duration. Second, the pressure and temperature are both

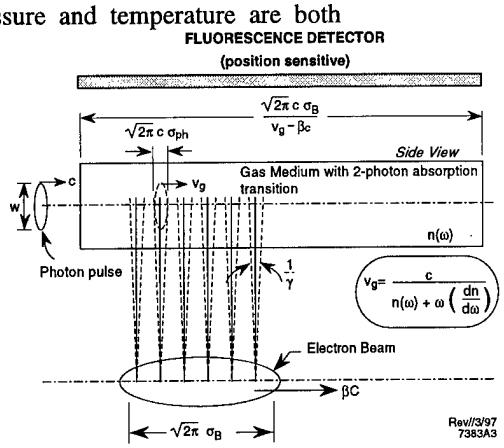

Fig. 3. Interaction of probe laser pulse and electron bunch field in passage through a gas medium

optimized to allow transit of the laser pulse through the interaction length in a "self-focusing" mode [10], which helps the pulse maintain a relatively constant cross section. Third, the gas is chosen to have a resonant or near-resonant two-photon transition corresponding to the laser wavelength. With reference to the above calculations, the strength of the combined fields is sufficient to modulate the two-photon absorption cross sections of the gas [11] via the Stark effect, resulting in a correlation between the absorption at any point in the medium and the strength of the bunch field. Due to parity, the excited atoms will have relatively long fluorescence lifetimes, allowing a conventional position-sensitive detector, installed over the interaction region, to register the intensity of the fluorescence trace. We note that if the use of a gas cell in proximity to the e-beam axis is found to be problematical due to the required dielectric interface to the vacuum, for diagnostic purposes the beam could be deflected into an off-axis gas cell isolated from the vacuum by differential pumping sections.

Table 1. Profiler system parameters. H=2 mm. E=15 GeV, $N_c=10^{10}$. Beam waist w=10 μ.

	Ti:sapphire Pulse	e-beam	Gas Cell (NO_2)
Power[a,b] [W]	10^{10}	7.5×10^{12}	-
Field [V/m]	2.7×10^{11}	10^7	-
Pulse Length [μ]	3	100	-
Bandwidth [%]	33	0.02	-
Group Vel.. Diff. [m/s]	-	-	1.53×10^4
Gas Press.[mTorr]	-	-	75
Interaction Length [m]	-	-	2
2-Photon Cross Sect.[b] [bn]	-	-	10^5
Fluoresc.Yield[b] [Phot./m]	-	-	10^{10}

[a]Critical power for self-focusing;
[b]order-of-magnitude estimate

In Table 1 we present a list of nominal operating parameters and performance estimates for a candidate system based on NO_2 [12,13,14]. The figures represent cell performance for the laser pulse only, since the Stark effects on the 2-photon cross sections of NO_2 have not, as yet, been assessed.

4 DISCUSSION

We have presented the analysis of a modulation scheme for the single-shot longitudinal profiling of ultra-short electron or positron bunches based on two-photon absorption induced by an IR femtosecond probe pulse. Figures for a commercially available Ti:sapphire laser and an NO_2 gas medium reveal acceptable performance parameters. Further work is required to quantify Stark modulation effects of the combined laser and electron beams and to investigate other material systems in other wavelength regimes.

5 REFERENCES

[1] C.-R. Carman and J.-L. Pellegrin, "The Beam Positions of the SPEAR Storage Ring, " NIM 113, 423(1973).

[2] T. Katsura, Y. Kamiya, K. Haga, and T.Mitsuhashi, "A Beam Position Feedback System for Beam Lines at the Photon Factory," in Proceedings of the 1987 IEEE Particle Accelerator Conference, IEEE Catalog No. 87CH2387-9, p. 538.

[3] I. Munro and A. Sabersky, "Synchrotron Radiation as a Modulated Source for Fluorescence Lifetime Measurements and for Time-Resolved Spectroscopy," in Synchrotron Radiation Research, H. Winick and S. Doniach, eds., Plenum Press, New York, 1980, p. 323 ff..

[4] D.R. Kania, R.J. Bartlett, and P.Pianetta, "Subnanosecond time resolved measurements of synchrotron x-ray pulses using photoconductive detectors," NIM A246, 534(1986).

[5] D. Bocek, P. Kung, H.-C. Lihn, C. Settakorn, H. Wiedemann, "Observation of SASE at 47 mm," - NIM A375, 13(1996).

[6] R. Tatchyn et al, "Research and development toward a 4.5-1.5 Å Linac Coherent Light Source (LCLS) at SLAC," NIM A 375, 274(1996).

[7] R. Tatchyn, "Field-Based Longitudinal Profiling Schemes for Short Charged-particle Bunches in High Energy Storage Rings, "in Proc. Workshop on 4th Generation Light Sources, M. Cornacchia and H. Winick, eds., SSRL, Feb. 1992, p.229 ff..

[8] R. Tatchyn, "A Field-Based Technique for the Longitudinal Profiling of Ultrarelativistic Electron or Positron Bunches Down to Lengths of $\lesssim$ 10 Microns," in Proceedings of the 1993 IEEE Particle Accelerator Conference, IEEE Catalog No. 93CH3279-7, p. 2429.

[9] C. P. J. Barty, T. Guo, C. LeBlanc, F. Raksi, C. Rose-Petruck, J. A. Squier, K. R. Wilson, V. V. Yakovlev, K. Yamakama, "Ultrashort pulse, ultrahigh peak power Ti:sapphire lasers," SPIE Proceedings 2701, 84(1996).

[10] J. F. Reintjes, "Nonlinear Optical Processes," in Encyclopedia of Physical Science and Technology, Vol. II, pp. 49-102, Academic Press, Inc., New York, 1992.

[11] R. H. Pantell and H. E. Puthoff, Fundamentals of Quantum Electronics, Wiley, New York, 1969.

[12] G. Herzberg, Molecular Spectra and Molecular Structure, Vol. III, D. Van Nostrand, New Jersey, 1966, p. 488 et ff.

[13] E. W. Washburn et al, eds., International Critical Tables, v. VII, McGraw-Hill, New York, 1930, p.8.

[14] K. Abe et al, "Resonance fluorescence spectrum of nitrogen dioxide," Jour. Mol. Spectr., 38(3), 552(1971).

HIGH POWER BEAM PROFILE MONITOR WITH OPTICAL TRANSITION RADIATION

J.-C. Denard, P. Piot, K. Capek, E. Feldl, Thomas Jefferson National Accelerator Facility, 12000 Jefferson Avenue, Newport News, VA 23606

Abstract

A simple monitor has been built to measure the profile of the high power beam (800 kW) delivered by the CEBAF accelerator at Jefferson Lab. The monitor uses the optical part of the forward transition radiation emitted from a thin carbon foil. The small beam size to be measured, about 100 μm, is challenging not only for the power density involved but also for the resolution the instrument must achieve. An important part of the beam instrumentation community believes the radiation being emitted into a cone of characteristic angle $1/\gamma$ is originated from a region of transverse dimension roughly $\lambda\gamma$; thus the apparent size of the source of transition radiation would become very large for highly relativistic particles. Our monitor measures 100 μm beam sizes that are much smaller than the 3.2 mm $\lambda\gamma$ limit; it confirms the statement of Rule and Fiorito that optical transition radiation can be used to image small beams at high energy. The present paper describes the instrument and its performance. We tested the foil in, up to 180 μA of CW beam without causing noticeable beam loss, even at 800 MeV, the lowest CEBAF energy.

1 SUMMARY

The CEBAF accelerator at Jefferson Lab delivers up to 200 μA of continuous electron beam in the 0.8 to 4 GeV energy range. The low emittance, 5×10^{-10} m–rad rms, constrains the beam to transverse dimensions smaller than 100 μm rms and may increase the power density to about 100 MW/mm^2.

Existing wire scanners measure profiles of only pulsed or low-current-CW beams to avoid melting their wire and also to prevent the beam loss monitors from triggering the machine protection system.

We present an operational prototype of a profile monitor that uses the optical part of the forward transition radiation emitted from a thin carbon foil when the beam passes through it. Previous studies [1, 2] indicated the heat the beam deposits on the foil should not damage it and also that the beam scattering through 0.25 μm of carbon should not deteriorate the beam characteristics down to 800 MeV. Here, we report on the successful operation of the instrument at 180 μA without damaging the foil and without any detectable beam loss in the range of CEBAF energy delivery.

An important issue for measuring small beam profiles is the resolution of the instrument. A relativistic particle beam yields a forward Optical Transition Radiation (OTR) with a peak intensity on a cone of characteristic angle $1/\gamma$. The thinking has been that there is an uncertainty $\approx \lambda\gamma$ in position of the OTR photon emission. Rule and Fiorito have challenged this concept [3]. We prove them to be right, after measuring a 100 μm rms size of a 3.2 GeV beam in the optical domain ($\lambda\gamma \approx 3.2$ mm).

In the near future, we are going to monitor the energy spread in the experimental beam lines with the same kind of profile monitor installed in a dispersive region. We mention a few improvements that will make these instruments better than the prototype from the operational point of view.

2 DESIGN CONSIDERATIONS

2.1 Forward versus Backward OTR

Transition radiation is generated on both sides of a conductive or dielectric foil when relativistic charged particles go through it, as shown in Figure 1. Backward OTR comes at specular angle, the foil behaving like a mirror [4]. The quantity of light is proportional to the reflection coefficient at the point of penetration. Very thin foils get wrinkles and local reflection defects. Using the thinnest foils is important to minimize beam scattering; therefore, we chose forward OTR to benefit from its advantages of not depending on either the beam's angle of incidence or the reflection coefficient.

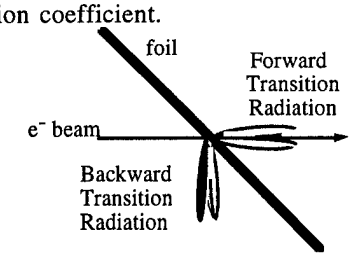

Figure 1: Direction of emission for backward and forward transition radiation.

2.2 Monitor

A simplified drawing of the monitor is shown in Figure 2. The electron beam passes near normal incidence through the 0.25 μm carbon foil. The foil is held on three sides of a square-hole support. The fourth side is open; in this way, one can insert or remove the foil without interrupting the beam delivery. A mirror sends the light outside the beam pipe through a vacuum optical window; the mirror and the foil support are mounted on a common assembly moved in or out of its operational position by a pneumatic actuator. The mirror has its edge 4 mm away from the beam trajectory when in working position. Two lenses focus the beam image on a Charge Injection Device (CID)

0-7803-4376-X/98/$10.00 © 1998 IEEE

camera specified up to 100 kRad of radiation dose. The video signal is sent to a monitor in the control room via the existing fiber optic network. It can also be switched to a video digitizer and processed to compute the beam size. The latter is still an off line process not yet available to the operators.

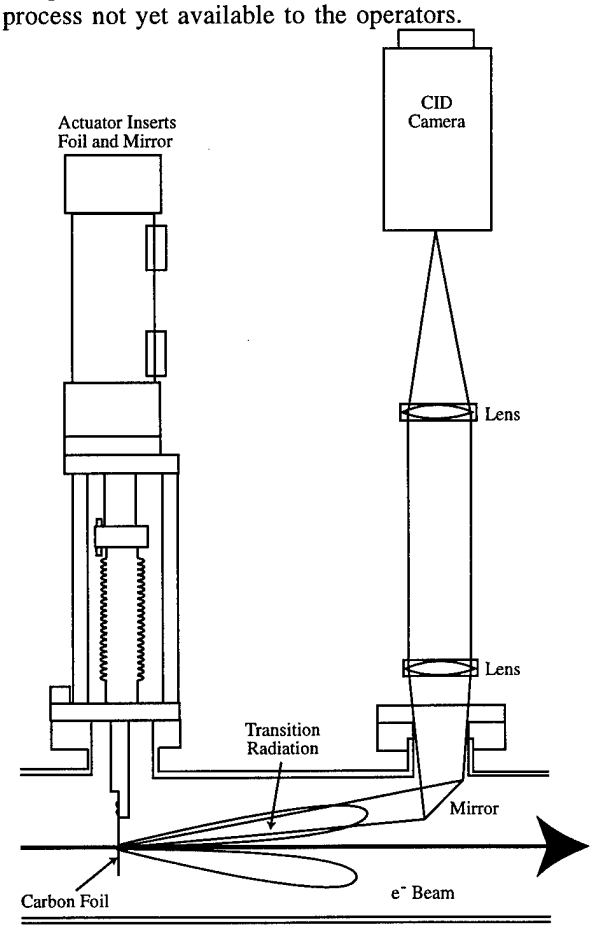

Figure 2: OTR profile monitor, top view.

2.3 The Resolution Issue

A low-emittance and high-energy linac like CEBAF is ideal to check whether the OTR phenomenon presents an intrinsic resolution limit of order $\lambda\gamma$. Figure 3 shows the vertical profile of a 3.345 GeV beam measured with the forward OTR monitor. With measurements at resolutions almost 40 times less than $\lambda\gamma$, it becomes clear that, as Rule and Fiorito stated a few years ago, there is no $\lambda\gamma$ limit and no uncertainty about the point of emission. The intrinsic resolution limit is that of the standard diffraction theory taking into account the specific distribution of the OTR (Figure 4) and the aperture shape. In our case, the first lens limits the vertical aperture, and the mirror the horizontal one. For the sake of simplicity, we considered only the first lens aperture : 50 mrad half-angle cone, 70 mrad off center in the horizontal plane. The numerical computation of the Fraunhoffer diffraction pattern along the horizontal axis (direction of aperture offset) and along the vertical one is shown in Figure 5. There is little difference with the Airy pattern $[J_1(x) / x]^2$ of an omnidirectional source of light.

Looking at the directivity curves (Figure 4), we can see that the light distribution in the aperture does not change significantly above 100 MeV; thus, the resolution will not worsen at higher energy. An infinitely small beam would have an apparent FWHM value of the Airy variable x equal to 4.8. Thus, in the central part of the CID spectral response, at λ=500 nm, the resolution is that of a Gaussian beam 3.2 μm in rms size.

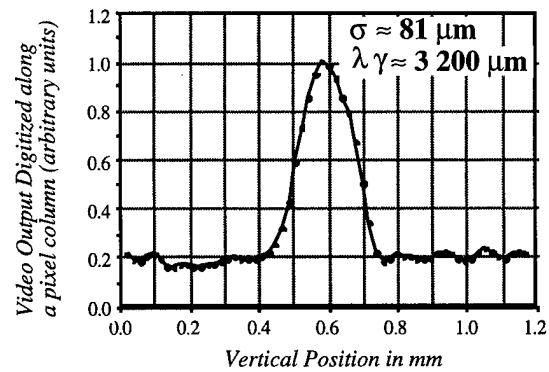

Figure 3: Vertical profile of a 3.245 GeV and 3 μA continuous beam.

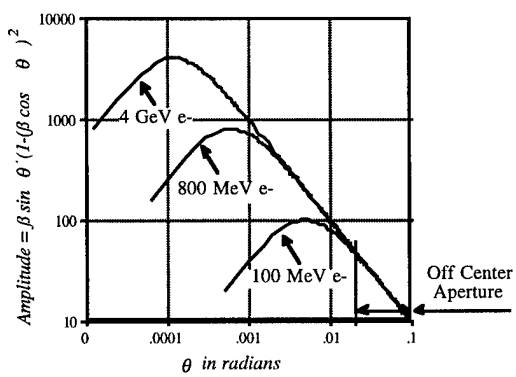

Figure 4: OTR Directivity versus spacial angle θ.

In practice, we do not need such a good resolution. We need to cover a field of 8 by 8 mm to calibrate the pixel size against the foil square holder. The pixel size and Modulation Transfer Function (MTF) of the camera contribute to a global resolution of about 50 μm rms.

3 OPERATIONAL CONSIDERATIONS

After a year of service, the CID camera failed once for reasons unrelated to radiation. Another failure occurred when the foil broke open after a vacuum opening and subsequent pumping in the vicinity of the monitor. The standard valve is now replaced by a restrictor valve that limits the pumping speed when recovering the vacuum after opening.

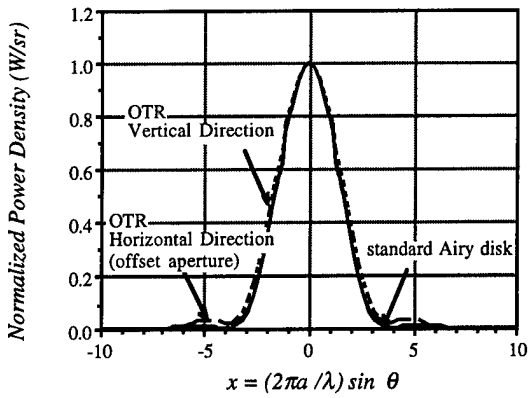

Figure 5: Diffraction patterns for standard Airy disk and for OTR through a 50 mrad half-angle aperture that is off-centered by 70 mrad. Both horizontal and vertical patterns are almost identical to the Airy disk.

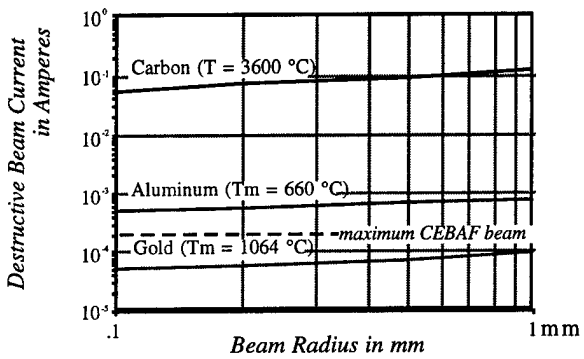

Figure 6: Computation of (destructive) beam currents that would bring Al and Au to their melting point and Carbon up to 3600 °C.

The instrument is only 50 m upstream of the experimental hall and has had no adverse influence on physics experiments. It can be inserted most of the time, even during end-station data acquisition. Two new instruments are going to be built for two of the experimental halls. A first improvement on these will consist of a better illumination of the foil support that will be implemented through a window opposite from the foil actuator. A second improvement will be to enhance the resolution down to 25 μm, adding a more powerful magnification to be switched after the calibration process. A third improvement pertains to measuring beam profiles at high currents: an automatic attenuator will prevent saturation of the camera. A simple software interlock will authorize the foil insertion only if the beam is centered well enough for not hitting the foil support or the mirror.

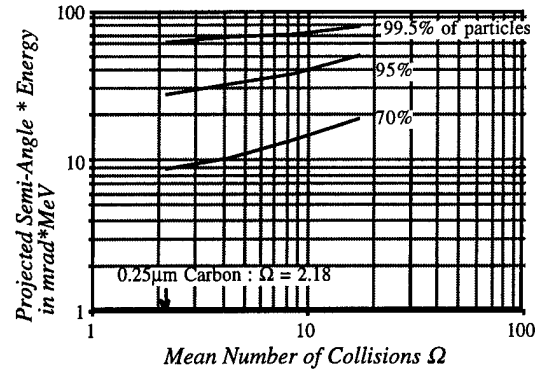

Figure 7: Plural beam scattering of highly relativistic electrons into thin materials. The number of collisions Ω is equal to $0.78\ \rho t[(Z+1)Z^{1/3})/A$ where ρ is the density in g/cm^3, t the beam path length in the material in μm, Z the atomic number, and A the atomic weight.

4 CONCLUSION

The size of the OTR source is much smaller than $\lambda\gamma$. There should be no problem measuring a beam of a few μm at the present and future highest energy with a simple and low cost OTR profile monitor. A carbon foil 1/4 μm thick is used in daily operation to measure the CEBAF high-power-density beam up to 180 μA without affecting noticeably the beam or damaging the foil. Two new profile monitors are being built to measure the beam-energy spread in the experimental beam line during beam delivery.

5 ACKOWLEDGEMENTS

We are grateful to Paul Guèye and other Hall C physicists who helped characterize the sensitivity of the experimental detectors in presence of the foil. This work was supported by the Department of Energy under the contract number DE-AC05-84ER40150

6 REFERENCES

[1] P. Piot, et. al., "High Current CW Beam Profile Monitors Using Transition Radiation at CEBAF", Beam Instrumentation Workshop 1996, *AIP Conference Proceedings 390,* 298-305 (1997).

[2] J.-C. Denard, et. al., "Experimental Diagnostics Using Optical Transition Radiation at CEBAF", Beam Instrumentation Workshop 1994, *AIP Conference Proceedings 333,* 224-237 (1995).

[3] D. W. Rule and R. B. Fiorito, "Imaging Micron-sized Beams with Optical Transition Radiation", Accelerator Instrumentation, 2nd Annual Workshop, Batavia, IL, 1990, *A.I.P. Conference Proceedings 229,* 315-321 (1991).

[4] L. Wartski, Doctoral Thesis, Université de Paris-Sud, Centre d'Orsay (1976).

AN EMITTANCE MEASUREMENT SYSTEM FOR A WIDE RANGE OF BUNCH CHARGES

B. Dunham, D. Engwall, A. Hofler, M. Keesee, and R. Legg
Thomas Jefferson National Accelerator Facility
12000 Jefferson Ave., Newport News, VA 23606

Abstract

As a part of the emittance measurements planned for the FEL injector at the Thomas Jefferson National Accelerator Facility (Jefferson Lab), we have developed an emittance measurement system that covers the wide dynamic range of bunch charges necessary to fully characterize the high-DC-voltage photocathode gun. The measurements are carried out with a variant of the classical two-slit method using a slit to sample the beam in conjunction with a wire scanner to measure the transmitted beam profile. The use of commercial, ultra-low noise picoammeters makes it possible to cover the wide range of desired bunch charges, with the actual measurements made over the range of 0.25 pC to 125 pC. The entire system, including its integration into the EPICS control system, is discussed.

1 INTRODUCTION

To fully characterize the high-DC-voltage photocathode gun [1] for the FEL injector at the Jefferson Lab, transverse emittance measurements covering a wide range of bunch charges are planned. Such measurements are necessary both to verify that the gun meets the specifications as well as to quantify agreement between the measurements and particle simulations using PARMELA [2]. In this paper we will describe the emittance measurement system and its performance, while the data is described in another paper [1].

2 DESCRIPTION OF THE SYSTEM

The emittance measurements are performed using a variant of the two slit method. Here, we sample the beam using a movable copper disk with a ~50 μm rectangular slot cut in it. The sampled portion of the beam traverses a drift distance L until it reaches a scanning wire device (see figures 1 and 2; see [1] for more details). The wire scanner (or harp) is the standard design used at the Jefferson Lab consisting of a 50 μm tungsten wire supported on a light-weight fork which is attached to a stepper motor through a bellows. For this application, we use one vertical wire instead of the usual three (vertical, horizontal, and 45 degree) wires to accommodate a large variation in beam diameter. The sampling slit and the vertical wire are aligned parallel to better than 1°.

The stepper motor (200 steps per revolution) is driven by an Oregon Micro Systems stepper motor controller in a VME crate (as opposed to the CAMAC based system used on the main accelerator). The data acquisition system (see figure 2) has been designed to provide extremely low noise and a large dynamic range for the beam signal, and low noise and high accuracy for the position readback (for both the slit and the harp position).

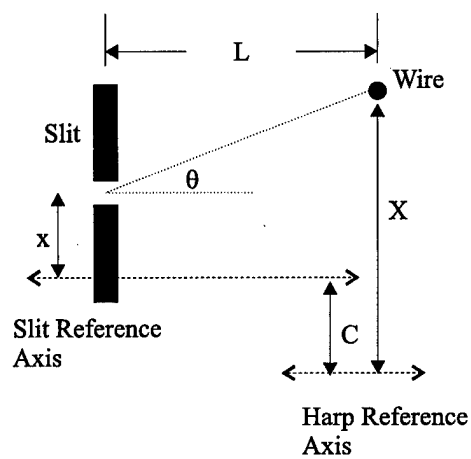

Figure 1 Layout of the emittance measurement system. The beam enters from the left and the transmitted slice hits the wire after drifting a distance L.

We have chosen to use commercial data acquisition devices whenever possible to improve reliability and lower cost. The isolated signal wire from the harp is connected directly to a Keithley 485 picoammeter using a short length of low triboelectric noise coax cable (Belden 9223). The picoammeter has several nice features including autoranging to cover a wide dynamic range, low noise (less than 100 fA), and good linearity over different ranges. The good linearity even applies to pulsed current which allows the emittance measurement to be done with CW or pulsed beam. By connecting the signal wire to the picoammeter with a short length of low noise cable, the opportunity to pick up noise is reduced, and the special cable reduces currents generated while the cable flexes during motion.

The position of the slit and harp wire are measured using a linear potentiometer. We require that the voltage readback be stable enough to resolve positions which are 10% of the wire diameter, or 5 μm. Over the 2.5 inch

0-7803-4376-X/98/$10.00 © 1998 IEEE

stroke of the harp there is a voltage change across the potentiometer of about 8 volts. Including the correction for the 45° tilt of the harp this gives a conversion factor of 5.6 μm per 1 mV.

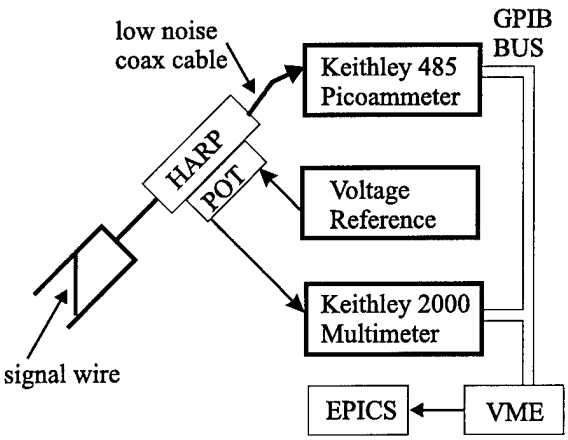

Figure 2 The data acquisition system for the emittance measurement system.

To obtain the desired accuracy in position the voltage readback must be good to within 1 mV. We use a programmable power supply (American Reliance LPS-305) with a measured long term stability (over 8 hours) of ±0.1 mV. A Keithley 2000 multimeter is used to monitor the voltage across the potentiometer. It has numerous acquisition modes, with the best compromise between accuracy and speed being the 'medium speed' mode which averages over one power line cycle, thus reducing pickup from the cables. This position measurement system provides an accuracy over a scan of less than ±1 μm which is better than the stated requirement.

The final component of the system is the EPICS software. It consists of three parts: the GPIB software; a sequence to move the slit or harp and collect and store the data; and a high-level application to organize the emittance measurement and perform preliminary analysis. The GPIB communication is accomplished by using an IP-488 chip (Industry Pack by Green Springs, Co.) on a mv162 board located in a VME crate. The system presently controls 4 picoammeters and 3 multimeters with an update rate of 2 to 3 Hz.

The low-level sequencer software controls the movement of the stepper motors and the readout of the position and current information. It moves the device (harp or slit) from a given initial position to a final position by a certain step size and stops for a delay time at each step before taking a data point. The position and current information are stored during the scan and written out to a file upon completion.

The high-level program overseeing the emittance measurement sequence is written using the Tcl/Tk language [4]. The program takes the user through a number of steps to set up the limits for the scans, performs the emittance measurement (displaying the data as it comes in), does a preliminary analysis of the data, and displays a 3 dimensional plot of the phase space.

3 EMITTANCE CALCULATION

The preliminary calculation of the emittance (and α and β) uses the usual rms definitions

$$\tilde{\varepsilon} = \sqrt{\langle x^2\rangle\langle\theta^2\rangle - \langle x\theta\rangle^2}, \quad \alpha = \langle x\theta\rangle / \tilde{\varepsilon}, \quad \beta = \langle x^2\rangle / \tilde{\varepsilon}$$

where x and θ are defined in figure 1. At this point, no correction for background or finite slit (wire) effects are included. Since the slit and the harp have different reference axes, the calculation of the angle must include the offset 'C', which can drift with time. Fortunately, this constant cancels out of the equations as seen below. The angle from the slit to the harp is given by $\theta \cong (X - x - C)/L$. Now, define a new quantity z, where $z = L\theta = X - x - C$. The rms quantities for z become

$$\langle xz\rangle = \frac{\sum w_i (x_i - \bar{x})(z_i - \bar{z})}{\sum w_i} = -\langle x^2\rangle + \langle xX\rangle$$

$$\langle z^2\rangle = \frac{\sum w_i z_i^2}{\sum w_i} - \bar{z}^2 = \langle x^2\rangle - 2\langle xX\rangle + \langle X^2\rangle$$

where w is the current on the wire. The offset 'C' cancels out everywhere in the calculation. Substituting the new rms quantities into the original emittance equation gives

$$\tilde{\varepsilon}^2 L^2 = \langle x^2\rangle\langle z^2\rangle - \langle xz\rangle^2 = \langle x^2\rangle\langle X^2\rangle - \langle xX\rangle^2$$

and similarly

$$\alpha = \frac{\langle xX\rangle - \langle x^2\rangle}{\tilde{\varepsilon}\, L} \quad \beta = \langle x^2\rangle / \tilde{\varepsilon}\ .$$

These calculations are implemented as follows. The slit position is represented by x_j where j ranges from 1 to M (the number of trials). For each trial, the harp position and harp signal are represented by $X_{i,j}$ and $w_{i,j}$ where i ranges from 1 to N(j). Using these definitions we can find the quantities necessary to calculate the emittance, alpha and beta. For example,

$$\langle xX\rangle = \frac{\sum_{j=1}^{M}\sum_{i=1}^{N(j)} w_{i,j} x_j X_{i,j}}{\sum_{j=1}^{M}\sum_{i=1}^{N(j)} w_{i,j}} - \bar{x}\,\bar{X}$$

with similar definitions for $\langle x^2\rangle$ and $\langle X^2\rangle$.

4 RESULTS

The emittance measurement system has been used to characterize the photocathode gun for the FEL injector over a wide range of bunch charges, with actual measurements taken from 0.25 pC to 125 pC. Figure 3 shows a single harp scan for an average beam current of 310 pA (as measured in a faraday cup), with a noise level below 100 fA, the stated noise level for the picoammeter. To obtain such a low noise floor, a delay time of 1 second was introduced after the wire stopped before taking data to allow the wire and cabling motion to damp out [3].

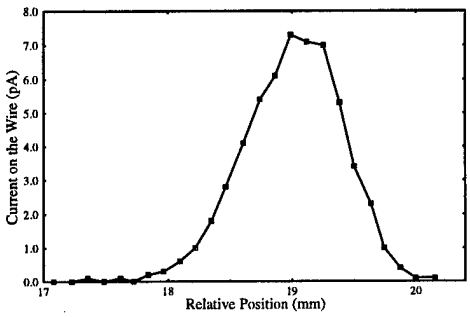

Figure 3 A typical harp scan - the average beam current is 310 pA with noise of less than 0.1 pA.

From the plot, one can estimate that the electronics are sensitive enough to measure currents roughly a factor of 10 lower than this. On the high end, the picoammeter can read to 2 mA, so the measurements could be extended by at least a factor of 100 to over 10 nC per bunch.

Figure 4 shows a three dimensional pseudo-phase space plot of the data. For each slit position (x) a harp scan is performed and plotted (X). The beam parameters can be calculated directly from the raw data as described in section 3.

The emittance measurement system has a number of good features: extremely low noise (< 100 fA); accurate position readback (±1 μm over a scan); a wide dynamic range (< 1 pC to over 10 nC); and it can operate in pulsed or CW mode. On the other hand, the low noise and high accuracy lead to fairly long data taking times: a full measurement including automatic limit determination can exceed 45 minutes. If the scan limits are known, the time for a measurement is reduced to 30 minutes. The low noise and wide dynamic range come at the expense of extended data taking times.

For higher currents where the noise due to cable and wire motion are less important, the measurement process could be speeded up considerably. By setting the delay time from when the wire reaches its position to when the data is acquired to zero and storing the data in the internal memory of the Keithley meters, the total time would be reduced by more than half.

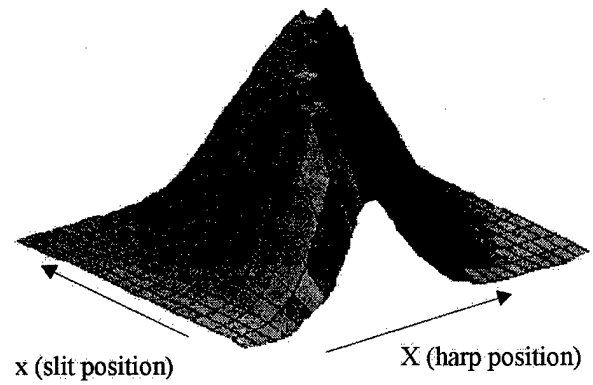

Figure 4 A pseudo-phase space representation of the data. Harp scans for 13 sequential slit positions are shown from front to back

5 CONCLUSIONS

We have developed an emittance measurement system to fully characterize the high-DC-voltage photocathode gun for the FEL injector at the Jefferson Lab. The system allows measurements to be carried out from the emittance dominated to the space charge dominated regimes, with actual measurements performed from 0.25 pC to 125 pC per bunch. The use of commercial low noise, high accuracy measurement devices allows for the required wide dynamic range as well as for reducing costs and development time and increasing reliability.

6 ACKNOWLEDGEMENTS

This work was supported by the U.S. DOE under contract number DE-AC05-84ER40150. Thanks to R. Hill for fixing the holding current problem on the stepper motors. Also, thanks to Brian Gold for helping with the Tcl programming.

REFERENCES

[1] D. Engwall, *et al.*, *A High-DC-Voltage GaAs Photoemission Gun: Transverse Emittance and Momentum Spread Measurements,* these proceedings.

[2] H. Liu, *et al.*, Nucl. Instr. And Meth., **A358** 475 (1995).

[3] B. Dunham, D. Engwall, A. Hofler, M. Keesee, and R. Legg, *Measuring Profiles of Beams with Extremely Low Average Current,* CEBAF-TN-96-058.

[4] J.K. OusterHout, *Tcl and the Tk Toolkit*, Addison-Wesley Publishing Co, 1992.

A MULTISLIT TRANSVERSE-EMITTANCE DIAGNOSTIC FOR SPACE-CHARGE-DOMINATED ELECTRON BEAMS

P. Piot, J. Song, R. Li, G.A. Krafft, D. Kehne, K. Jordan, E. Feldl, and J.-C. Denard,
Thomas Jefferson National Accelerator Facility, Newport News, VA 23606, USA

Abstract

Jefferson Lab is developing a 10 MeV injector to provide an electron beam for a high-power free-electron laser (FEL). To characterize the transverse phase space of the space-charged-dominated beam produced by this injector, we designed an interceptive multislit emittance diagnostic. It incorporates an algorithm for phase-space reconstruction and subsequent calculation of the Twiss parameters and emittance for both transverse directions at an update rate exceeding 1 Hz, a speed that will facilitate the transverse-phase-space matching between the injector and the FEL's accelerator that is critical for proper operation. This paper describes issues pertaining to the diagnostic's design. It also discusses the acquisition system, as well as the software algorithm and its implementation in the FEL control system. First results obtained from testing this diagnostic in Jefferson Lab's Injector Test Stand are also included.

1 INTRODUCTION

Jefferson Lab is building a tunable high-power free-electron laser operating in the mid-infrared to study technologies required for high-average-power operation [1]. This FEL incorporates a 350 keV photocathode gun capable of generating a charge-per-bunch beam of typically 135 pC. After acceleration with two CEBAF five-cell superconducting cavities the beam is at 10 MeV and injected via an achromatic bending system into the driver linac that accelerates the electrons up to about 42 MeV prior to the wiggler interaction. The transverse emittances at the wiggler location are required to be small (less than 13 mm-mrad) to operate the laser with a high gain and high extraction efficiency at full power. The specified transverse beam parameters at the wiggler constrain the emittance in the injector to be likewise small (Fig. 1). Therefore, in order to verify the emittance from the injector for operations, two multislit transverse-emittance diagnostics are going to be installed (Fig. 1) in the injector. A first monitor, located at the cryounit exit, will provide the necessary information to set the four matching quadrupoles of the downstream telescope. The second device allows beam parameters at the injection point in order to check the injector and linac are properly matched.

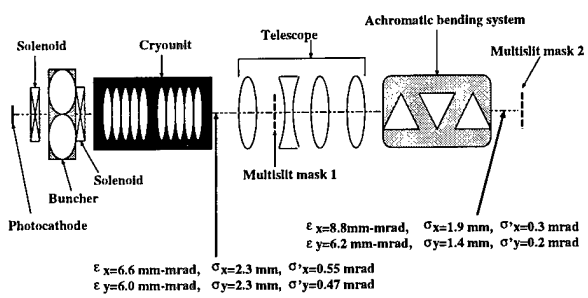

Figure 1: Schematic of the FEL injector. Normalized emittance, beam size and beam divergence at 135 pC bunch charge are given at the cryounit exit and the injection point according to PARMELA.

2 MULTISLIT TECHNIQUE

Techniques of phase-space sampling for emittance measurement are widely used for space-charge-dominated beams. The idea is to select one or several sample beamlets, at specific positions, by means of an intercepting mask in which small apertures have been machined. The beamlets retain the transverse temperature of the original beam at such low charge that space charge forces do not contribute significantly to the transverse momentum. The beamlets drift through a length long enough to allow the transverse momentum to impart a measurable contribution to the transverse position. The phase-space parameters can then be computed using the second-order moments ($\langle x^2 \rangle$, $\langle x'^2 \rangle$, $\langle xx' \rangle$) of the beamlet profiles [2]. There are several types of emittance monitors reported in the literature whose differences are essentially in the type of selecting apertures (pepper pot, slit,...) and the profile monitor used (wire-scanner, fluorescent screen, ...). Among the different methods we choose to intercept the beam with a multislit mask [3,4] since it provides the fast and precise measurement we need during the commissionning and operation of our injector. The multislit assembly consists of a series of slits which collimate the space-charge-dominated incoming beam into the emittance-dominated beamlets that drift up to a profile monitor, an optical transition radiation (OTR) viewer in our case. The principal drawback of this diagnostic is its narrow emittance acceptance compared with other methods [5]. Therefore we optimized the slit design for a specific charge per bunch that we have chosen to be the full operating charge: 135 pC.

3 DESIGN CONSIDERATION

3.1 Analytic Conditions

Due to mechanical constraints, a drift distance (L) was chosen to be 620 mm. The choice of the geometric parameters

0-7803-4376-X/98/$10.00 © 1998 IEEE

$\epsilon_{PARMELA}$ (mm-mrad)	$\epsilon_{RETRIEVED}$ (mm-mrad)
8.094	8.077
3.947	4.014
24.282	23.016

Table 1: Typical retrieved value for the normalized emittance obtained simulating the multislit mask using a phase-space distribution predicted by PARMELA

(slit width w and spacing d) are then imposed by three conditions.

(i) The beamlets must be emittance-dominated since space-charge expansion would cause appreciable broadening of the angular spread over the drift. We calculate the space-charge-over-emittance ratio defined from the transverse K-V equation to be about $R \simeq 11.75$ using the beam parameters predicted with PARMELA. After the multislit mask the value of the ratio, R', for one beamlet is scaled accordingly to: $R' = R/12 \times (w/\sigma)^2$, σ being the rms beam size. Setting w to 100 μm yields a ratio R'=2.8 $\times$ 10^{-3}. This guarantees the space-charge force contribution to transverse momentum is insignificant.

(ii) The beamlet profiles must not overlap on the screen, which implies the drift length (L) and the inter-slits distance (d) are related by: $4\sigma' L < d$. σ' is the rms beam divergence.

(iii) Finally, the resolution in position and in divergence should be comparable, i.e. $\sigma/d = L\sigma'/\rho$, where ρ is the resolution of the detector.

The two latter conditions yield a slits spacing of about 1.1 mm. The values determined for w and d have been used as a starting point for accurate numerical simulation of the slits with PARMELA.

3.2 *Optimization with Numerical Simulations*

We developed a MATLAB-based program to retrieve the phase-space parameters and distribution from a simulated OTR image. The image is generated from the distribution predicted by PARMELA, retracing each electron from before the slits up to the OTR screen. We optimized the design, after many iterative runs, changing the slit width and spacing, to try to minimize the error in the retrieved parameters over the required emittance range (normalized rms emittance between 4 and 20 mm-mrad). The values we finally found reasonable are: w=75 μm and d=1.5 mm. According to our simulation results for different emittances (by scaling the nominal one) we are confident in achieving a relative error on emittance and Twiss parameters of the order of 10%. Table 1 compares the nominal emittance with the one computed from the beamlet's OTR image.

3.3 *Some Mechanical Considerations*

In order to avoid using any cooling system, we have opted to make the slits out of copper and have a thermal bridge that quickly dissipates the heat toward the exterior of the vacuum chamber. In order to reduce the deposited power below the damage threshold of 3 W we will use a low duty factor beam mode for emittance measurement, which is possible since the physics of our beam is only dominated by single-bunch effects (bunch spacing is 8.02 m). The multislit mask thickness is a compromise between noise and angular acceptance: if the mask is not thick enough, electrons that go through copper can contribute to the OTR pattern. On the other hand, increasing the thickness would imply more stringent tolerance on the slit alignment with respect to the beam axis. After estimating multiple scattering, which is the dominant process for 10 MeV electrons, we set the thickness to 5 mm, which yields an angular acceptance of approximately 10 mrad. For this angle 10% of the electrons are lost because of edge scattering. The final design of the multislit assembly has two sets of thirteen slits that allow x and y transverse-emittance measurement. When the slits are removed from the beam path, a high-frequency shield insures beam-pipe continuity to minimize the wakefield impedance.

4 CONTROL AND ACQUISITION SYSTEM

The beamlet's OTR pattern is monitored with a charge-coupled-device camera whose analog video signal is digitized and processed using a DATACUBE VME-based frame grabber operating with its own VME input-output controller (IOC). In addition to digitizing, the CPU of the video board performs elementary image-processing functions such as background subtraction, projection along an axis, etc. The output of the DATACUBE, in our case a projection that contains the beamlet profiles, is transferred to the IOC on which we have implemented VxWorks routines. After identifying each beamlet profile and the slit it comes from, the code computes the emittance and Twiss parameters. The results can then be accessed from any X-station via the EPICS channel-access protocol. We developed X-window based screens that display emittance, Twiss parameters and possibly phase-space isocontours. The achieved speeds are, respectively, about 1 and 2 sec for updating parameters and plot refresh, a speed that allows observing the phase space parameters in real time while tuning the injector. Storing raw data and projections is also possible at each stage of the process for more detailed off-line analysis, e.g. using (time and CPU consuming) powerful image processing tools.

5 FIRST RESULTS

Since the 10 MeV energy region of the injector was not yet available, we chose to conduct the preliminary tests on the Jefferson Lab Injector Test Stand at 250 keV. The configuration is similar to that described elsewhere [5], consisting of a photocathode gun, a solenoid, and a diagnostic beamline. The charge-per-bunch was set to approximately 5 pC so that the achieved emittance is within the multislit assembly acceptance. Also, because of the low energy, we had to use a fluorescent viewer instead of an OTR viewer.

On Figure 2 we present an example beamlet profile. Depending on the solenoid setup, we were able to illuminate up to 8 slits, a very good number for emittance measurement with a 10% level accuracy. Unfortunately, we were not able to perform our measurement with such high number of peaks because of the reduced available area on the fluorescent viewer. Several cross-checks have been made

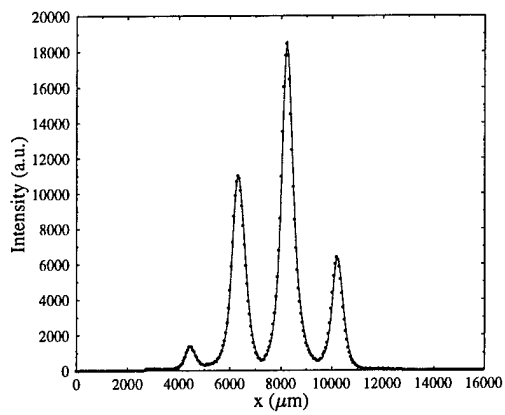

Figure 2: Typical beamlet profile obtained on a fluorescent screen at 250 keV with a charge-per-bunch of 5 pC.

with the single-slit-wire emittance diagnostic used in Reference [5] and both methods agreed within 10-15% for the emittance and the β-function. However, there is still substantial disagreement concerning the α-parameter, probably due to a not precise enough scale calibration of our fluorescent screen. This problem should be solved on the final version of the diagnostic where we plan to have precise calibration lines on the OTR screen.

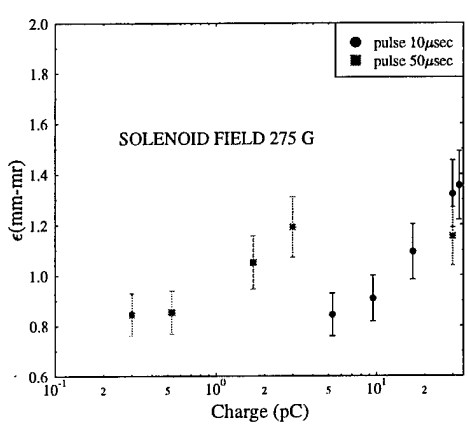

Figure 3: Unnormalized emittance versus charge for two different macropulse widths. Error bars of 15% have been considered after comparison with the single-slit-wire method.

We also measured the emittance versus the charge per bunch, for two macropulse width, as depicted in Figure 3, keeping the solenoid field value constant. The discrepancies between the two sets of data at low charge are probably due to low charge ghost pulses that are created as a consequence of laser light leaks between two consecutive micropulses. Therefore the wider the macropulse, the larger the ghost pulse contribution to emittance is.

Further studies and quantitative comparison of the multi-slit mask, with the single-slit-wire technique in the Injector Test Stand and with the one-quadrupole-OTR method in the FEL injector, will be forthcoming.

6 ACKNOWLEDGMENTS

The authors would like to thank S. Benson, C. L. Bohn, and G. Neil for useful discussions, and H. Liu and B. Yunn for their help with PARMELA. We are indebted to R. Legg and M. Shinn for setting up the beam during our experiment. This work was funded by the U.S. DOE contract DE-AC05-84ER-401 and the Office of Naval Research.

7 REFERENCES

[1] C. L. Bohn, "Recirculating Accelerator Driver for a High-Power Free-Electron-Laser: A Design Overview", these proceedings.

[2] P. Lapostolle, "Quelques effets essentiels de la charge d'espace dans les faisceaux continus", Rep. CERN/DI-70-36 (1970).

[3] S. C. Hartman, "The UCLA High-Brightness RF Photo-Injector", PhD thesis, University of California, Los Angeles (unpublished) and J. Rosenzweig and G. Travish, "Design Considerations for the UCLA PBPL Slit-Based Phase Space Measurement Systems", PBPL Internal (Feb 1994).

[4] M. Crescenti, U. Raich, "A Single Pulse Beam Emittance Measurement for the CERN Heavy Ion Linac", U. Raich, private communication.

[5] D. Engwall et al., "A High-Voltage-DC GaAs Photoemission Gun: Transverse Emittance and Momentum Spread Measurement", these proceedings.

STATUS OF THE APS DIAGNOSTICS UNDULATOR BEAMLINE

B. X. Yang, A. H. Lumpkin, G. A. Goeppner, S. Sharma, E. Rotela, I. C. Sheng, E. Moog
Argonne National Lab, 9700 South Cass Avenue, Argonne, IL 60439, USA

Abstract

We report the status of the diagnostics undulator beamline for the Advanced Photon Source (APS) storage ring. The beamline was designed for the characterization of the 7-GeV, low-emittance positron beam at high resolution. The special diagnostics undulator has been manufactured by STI Optronics. The device exhibits very low magnetic field errors at closed gap of 10.5 mm: first field integral less than 15 gauss·cm, and optical phase error less than 1.5°. The front end of the beamline and a monochromator are installed and tested for use on divergence and directional stability measurements with a target resolution of 3 μrad utilizing the first harmonic radiation of 25 keV. Initial results for the divergence measurement show that the storage ring is operating well within its design goals.

1 INTRODUCTION

For the high energy third-generation synchrotron radiation sources where the particle beam emittance still determines the x-ray beam brilliance, the narrow cone of undulator radiation provides an efficient method to characterize the particle beam divergence and directional stability [1,2].

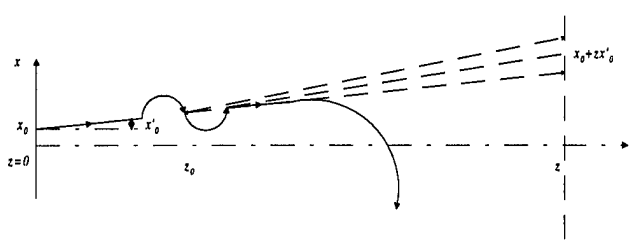

Figure 1: Schematics showing the undulator radiation cone from an off-axis particle: solid line is the particle trajectory and dashed line is the cone of undulator radiation.

Figure 1 illustrates the basic principle for an undulator to be used for particle beam divergence measurements. The undulator is located z_0 from the particle beam waist. A monochromator/detector combination is used at z to measure the x-ray beam profile. If we set the monochromator to select only the photons slightly above the harmonic energy, the observed profile of the x-ray beam generated by a particle with phase space coordinates (x_0, x_0') can then be approximated by a Gaussian function centered at $x_0 + zx_0'$, with a width of $(z - z_0)\sigma_{p0}$, where the natural undulator beam divergence is approximately

$$\sigma_{p0} \cong \sqrt{\frac{\lambda}{2L}}\,. \tag{1}$$

Summing over all particles in the Gaussian beam with widths of (σ_x, σ_x'), the total rms width of the (monochromatic) x-ray beam cross section is given by the quadrature sum,

$$\Sigma_x^{\,2} = \sigma_x^2 + z^2\sigma_x'^2 + (z - z_0)^2\sigma_{p0}^{\,2}\,. \tag{2}$$

The size and the divergence at the beam waist is further related to the emittance ε_x and the beta function β_x,

$$\sigma_x = \sqrt{\beta_x\varepsilon_x} \text{ and } \sigma_x' = \sqrt{\frac{\varepsilon_x}{\beta_x}}\,. \tag{3}$$

Hence we have

$$\varepsilon_x = \beta_x \frac{\Sigma_x^{\,2} - (z - z_0)^2\sigma_{p0}^{\,2}}{\beta_x^{\,2} + z^2}\,. \tag{4}$$

When $z=z_0$, this formula takes the form given in Ref. 1. Table 1 shows the design parameters of the APS storage ring insertion straight section. While the 10% vertical coupling was the baseline design goal, 1% and 0.1% coupling represents the upgrade path of the APS towards higher brilliance.

Table 1: APS Storage Ring Parameters in the Straight Section (for natural emittance ε = 8.2 nm·rad)

Function	Coupling	horizontal	vertical
β (m)		14.2	10.1
σ (μm)	10%	325	87
σ′ (μrad)	10%	23	8.6
σ (μm)	1%	340	29
σ′ (μrad)	1%	24	2.8
σ (μm)	0.1%	341	9
σ′ (μrad)	0.1%	24	0.90

2 DIAGNOSTIC UNDULATOR

The undulator used in the APS diagnostics beamline was specially designed for divergence measurements [3] and has a narrow central cone of radiation and tight field tolerances.

2.1 Undulator Design

Table 2 lists the design parameters of the APS diagnostics undulator. It can be seen that the central cone of the first harmonic (2.6 μrad) provides adequate resolution for

0-7803-4376-X/98 /$10.00 © 1998 IEEE

measuring the baseline beam (8.6 μrad at 10% vertical coupling) and the third harmonic (1.6 μrad) for the case of 1% coupling (2.8 μrad).

Table 2: APS Diagnostics Undulator Design Parameters

Period	18 mm
Number of periods	198
Total length	3.56 m
Center coordinate from beam waist, z_0	0.57 m
Minimum gap	10.5 mm
Maximum peak magnetic field	0.27 T
Maximum K-value	0.46
First harmonic photon energy ω_1	23.4 - 25.5 keV
Radiation cone angle at ω_1	2.7 - 2.6 μrad
Third harmonic photon energy ω_3	70.2 - 75 keV
Radiation cone angle at ω_3	1.6 μrad
Maximum peak power density	116 kW/mr^2
Maximum total power	0.83 kW
Storage ring operation condition	7 GeV / 100 mA

2.2 Magnetic Field Measurements

The undulator was manufactured by STI Optronics. In order to realize the narrow radiation cone for beam diagnostics, the undulator's field errors were specified to be below those of other APS undulators. Table 3 summarizes the design specification for the field errors and the actually measured values at STI [4]. The field was also measured at the APS magnetic field measurement facility [5], with similar results.

Table 3: APS Diagnostics Undulator Field Errors

Function	Spec	Actual
First horizontal field integral [g·cm]	50	25
First vertical field integral [g·cm]	50	5.3
Second horizontal field integral [g·cm^2]	10^5	0.12×10^5
Second vertical field integral [g·cm^2]	10^5	0.06×10^5
Integrated quadrupole field [g]	50	38
Integrated skew quadrupole field [g]	50	-16
Integrated sextupole field [g/cm]	200	-17
Integrated skew sextupole field [g/cm]	100	3
Integrated octupole field [g/ cm^2]	300	-7
Integrated skew octupole field [g/ cm^2]	50	14
Relative transverse field roll-off	0.1%	0.02%
Magnetic field quality (fit residuals)	0.5%	0.4%
Rms phase error	6°	1.2°
RMS trajectory angle error		
Horizontal [μrad]	1.0	0.9
Vertical [μrad]	1.0	0.3
RMS trajectory straightness		
Horizontal [μm]	1.0	0.1
Vertical [μm]	1.0	0.1

3 FRONT END

The front end of the diagnostics undulator beamline uses most components from the standard APS ID front ends [6]. However a number of special features were added to optimize the front end for beam diagnostics.

3.1 Beam Splitting Fixed Mask (FM1)

In addition to the undulator beam, the beamline is also designed to make use of the radiation from the bending magnet (designated as AM magnet in the APS nomenclature) just downstream of the insertion device to image the particle beam at the low dispersion region. The first fixed mask of the front end splits the beamline, and protects the downstream components from the missteered undulator beam. The design of the fixed mask utilizes grazing incidence in both horizontal and vertical planes to reduce the power density on the divider between the ID and AM beams. The aperture for the ID beam is 25 mm × 6 mm. The aperture for the AM beam is 0.4 mm × 0.4 mm, and is adjustable vertically.

3.2 Adjustable Pinhole Aperture for AM Source

An adjustable aperture formed by four independent blades is used as a pinhole for imaging the AM source. All blades are made of tungsten and controlled remotely via EPICS. The small aperture of the first fixed mask for the AM beam allows only 1 W of bending magnet radiation to pass through under normal operating conditions, which ensures the stable operation of the pinhole camera. It also allows only about 50 W of undulator beam to pass through when missteering occurs. This ensures the safety of the pinhole in such conditions.

3.3 Beryllium Windows

A pair of beryllium windows is used to separate the beamline from the storage ring vacuum, conforming to the APS vacuum policy. The window for the undulator beam employs a novel double concave shape for improved thermal conduction and higher flexural stiffness. A detailed thermal analysis is presented separately [7].

4 OPTICS AND DETECTOR

The divergence measurement was performed with a single crystal monochromator and an imaging detector using $CdWO_4$ scintillation crystal as a converter screen. Figure 2 shows the experimental setup.

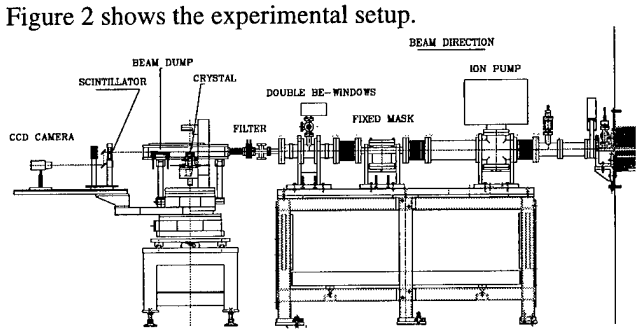

Figure 2: Schematics of the experimental setup for beam divergence measurement.

4.1 Monochromator

A Huber Goniometer is used as the base for the single crystal monochromator. The monochromator crystal, Ge(220), is clamped on a water-cooled copper block. The beam dump is made of GlidCop and is also enclosed in the monochromator chamber which is filled with helium. The monochromatic x-ray goes through an 80-μm aluminum window to reach the imaging detector located in the open air. Such an arrangement significantly reduces ozone generation by the white undulator beam.

4.2 Imaging Detector

The cross section of the monochromatic x-ray beam is imaged with a 0.3-mm-thick $CdWO_4$ scintillation crystal. A CCD camera with a C-mount photographic lens ($f = 75$ mm) is used for the image acquisition. The pixel scale of the camera is calibrated with a grid pattern mounted on the background of the scintillator crystal. A Spiricon digitizer (120×120 pixels with 35 μm/pixel) is used to record the image.

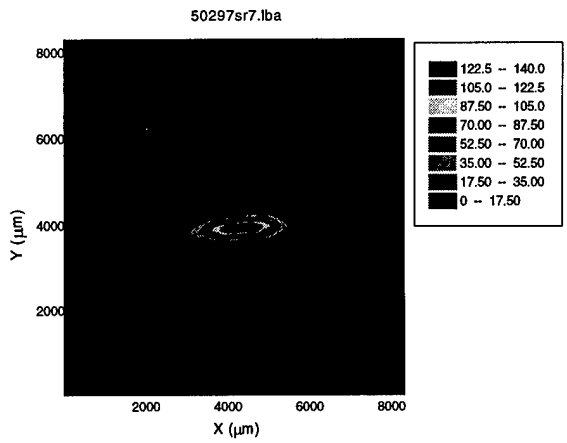

Figure 3: First image from the APS diagnostics undulator.

5 RESULTS

In the first experiment performed at the beamline on May 3, 1997, the undulator gap was set at 16.0 mm, with the first harmonic at 25.5 keV. The monochromator crystal angle was scanned to pass the maximum intensity point and to reach a minimum x-ray beam cross section. The photon energy was estimated to be around 25.7 keV. To simulate users' running conditions, the images of the x-ray beam were averaged every 8 frames (over 0.5 second) in the Spiricon, and five averaged images were recorded and examined to evaluate data consistency

A typical beam image taken at a stored beam current of 65 mA is shown in Fig. 3. Table 4 shows the beam cross section and the inferred particle beam properties based on the design lattice functions. In these calculations, we have not considered the contribution of the imaging detector resolution, and its subtraction would likely further reduce the measured beam emittance. The large error bars assigned to the beam parameters reflect largely the uncertainty of our knowledge about the lattice functions.

Table 4: APS Diagnostics Undulator Divergence Measurement (65 mA stored current)

X-ray beam size ($\Sigma_x \times \Sigma_y$)	674×164 (μm)^2
Partial emittance ($\varepsilon_x \times \varepsilon y_y$)	6.4×0.24 (nm·rad)
Total emittance (ε)	6.6 ± 0.6 (nm·rad)
Vertical coupling (χ)	0.037 ± 0.004
e-beam size ($\sigma_x \times \sigma_y$)	300×50 (μm)^2
e-beam divergence ($\sigma'_x \times \sigma'_y$)	21×4.9 (μrad)^2

6 SUMMARY

The APS diagnostics undulator has been commissioned and first results are used to characterize the storage ring beam. Using the design lattice functions, the measured particle beam size, divergence, and emittance are all within design specifications, which in turn translates to higher x-ray beam brilliance than the APS design goal.

7 ACKNOWLEDGEMENTS

We wish to thank I. Vasserman for his assistance in undulator field measurements; P. Den Hartog and E. Gluskin for their help in the undulator installation; M. Ramanathan, A. R. Passi, R. W. Nielsen, T. L. Kruy, J. Hawkins and N. Friedman for their help in the front end installation; and G. A. Decker and J. N. Galayda for their continued support for the project. This work was supported by U. S. Department of Energy, Office of Basic Energy Sciences under Contract No. W-31-109-ENG-38.

REFERENCES

[1] E. Tarazona and P. Elleaume, "Emittance measurements at ESRF," *Rev. Sci. Instrum.* 66, 1995.

[2] Z. Cai, R. J. Dejus, P. Den Hartog, Y. Feng, E. Gluskin, D. Haeffner, P. Illinski, B. Lai, D. Legnini, E. R. Moog, S. Shastri, E. Trakhtenberg, I. Vasserman, and W. Yun, "APS Undulator Radiation - First Results," *Rev. Sci. Instrum.* 67, (1996) CD ROM.

[3] B. Yang and A. H. Lumpkin, "The Planned Photon Diagnostics Beamlines at the Advanced Photon Source," BIW94, AIP Conf. Proc. 333, Oct. 1994.

[4] STI Optronics, "Magnetic Certification Data for U18, #14," 1996, unpublished.

[5] L. Burkel, R. Dejus, J. Maines, J. O'Brien, J. Pflueger, and I. Vasserman, "The Insertion Device Magnetic Measurement Facility: Prototype and Operational Procedures," ANL/APS/TB-12, 1993.

[6] D. Shu, and T. M. Kuzay, "General Layout Design for the Advanced Photon Source Beamline Front Ends," *Nucl. Instrum. Meth.* A 347, 1994.

[7] I. C. Sheng, B. X. Yang, and S. Sharma, "Design and analysis of a Be window for the APS diagnostics undulator beamline," these proceedings.

TESTS OF THE APS X-RAY TRANSMITTING BEAM POSITION MONITORS AT ESRF

Deming Shu, Juan Barraza, Tuncer M. Kuzay, Advanced Photon Source, Argonne National Laboratory, 9700 S. Cass Av. Argonne, IL 60439, U.S.A. and
Graham Naylor, Pascal Elleaume, European Synchrotron Radiation Facility, BP 220, F-38043 Grenoble, Cedek, France

Abstract

Two different types of synthetic diamond-based X-ray transmitting beam position monitor (XBPM) prototypes have been studied with an undulator white beam at the European Synchrotron Radiation Facility (ESRF) ID-6 beamline. Of particular interest was the possibility of designing an integral window and filter/photon beam position monitor for the Advanced Photon Source (APS) high heat flux insertion device beamlines.

The photoelectron-emission type transmitting XBPM prototype uses a 25-mm-diameter, 175-micron-thick CVD-diamond disk with 0.2-micron-thick electrically isolated patterns of aluminum coating on one side of the diamond disk. The photoelectron emission signal was collected from the aluminum-coat surface to provide the beam position information.

A novel photoconductive-type transmitting XBPM prototype uses the same CVD-diamond disk, but patterns of aluminum coating were applied on both sides of the diamond disk. A DC bias voltage was used to generate the current signal, which is based on photoconductive properties of the CVD-diamond. Test results are presented in the paper.

1 INTRODUCTION

There are many challenging tasks in the design of insertion device (ID) beamline instrumentation that relate to high heat load and high heat flux problems. One such component is the X-ray beam position monitor (XBPM) for the ID beamlines.

Synthetic diamond has been proposed for use as an XBPM blade material for the ID front end of the APS project [1]. Synthetic diamond, such as CVD diamond, offers superior thermal-physical properties, such as high thermal conductivity, low thermal expansion coefficient, and good mechanical strength and stiffness under heat. In the classic photoelectron emission-type XBPM, the monitor blade is mounted parallel to the radiation beam direction to eliminate the total thermal power absorbed by the blade. To reduce the heat power density on the blade edge surface, inclined edge geometry is usually utilized.

A photoelectron emission-type X-ray transmitting beam position monitor (TBPM) has been proposed for combining filter/window and XBPM functions [2]. The basic concept of the TBPM is to mount the monitor blade perpendicular to the synchrotron radiation beam and to design the blade and its sensor coating in such a way that most of the x-ray beam will be transmitted through the blade. Thus, the total absorbed photon power cannot cause thermal damage to the blade. Earlier a sample monitor was tested at NSLS on the X-25 wiggler beamline for proof of the principle [3]. Based on the success of this preliminary test with a focused wiggler beam, a compact filter/mask/window assembly was designed for undulator beamline commissioning activity at the APS beamlines [4].

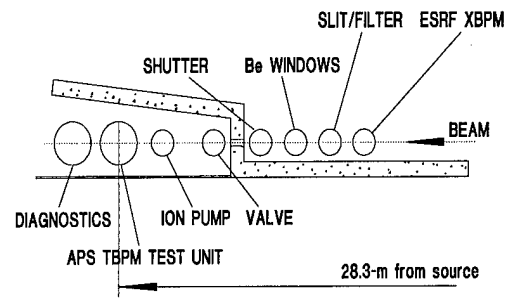

Fig. 1. Schematic layout of the ESRF ID-6 beamline.

Similar to the photoelectron emission-type TBPM, a novel photoconductive-type TBPM has also been proposed [5]. To test this design with a full power undulator beam, a prototype TBPM test base has been built. Two different types of synthetic-diamond-based TBPM test samples were prepared at the APS. The test plan at the ESRF beamline ID-6 was part of the Tripartite Joint Research Agreement Protocol among the APS, ESRF and SPring-8 synchrotron radiation facilities.

2 BEAMLINE TEST SETUP

The ID-6 beamline at the ESRF has a 46-mm-period, 1.66-meter-long undulator source. During the time we were doing our experiments, the ESRF storage ring was running in hybrid mode with a maximum of 140 mA current. The undulator was operating at a gap in the 21 mm to 41 mm range.

Fig. 1 shows a schematic of the ID-6 layout. During the test, an APS TBPM test unit was installed in the first optics enclosure (FOE). Upstream of the APS TBPM test-unit, a 500-micron-thick pyrolitic graphite filter and two 250-micron-thick Beryllium windows cut off most of the soft X-ray from the source. Downstream of the test

0-7803-4376-X/98/$10.00 © 1998 IEEE

unit, a fluorescent screen with a graduated aluminum filter and a CCD camera provides the capability to monitoring the beam profile and helps in the system alignment.

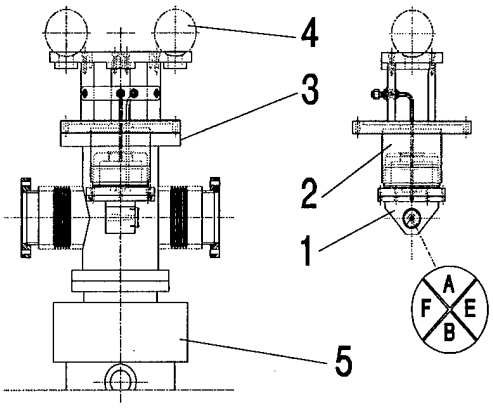

Fig. 2. The APS TBPM test-unit (1)sample mounting block ; (2) water-cooling base; (3) vacuum chamber; (4) survey-mark; (5) stepping-motor-driven stage.

The TBPM test unit was designed to be compatible with the ESRF XBPM vacuum chamber and its supporting stages. As shown in Fig. 2, the APS TBPM test unit consists of six components. The TBPM sample is assembled on a sample mounting block (1), which is cooled by a water-cooling base (2). The water-cooling base is mounted on the top of the ESRF XBPM vacuum chamber (3). There are two survey marks (4) on the mounting flange for alignment purpose. The vacuum chamber is supported by a set of stepping-motor-driven stages (5), which provide precise horizontal and vertical motions for fine alignment and scan motion for the TBPM test. An optical encoder with 0.1 micron resolution was added to the stage to verify the motion accuracy.

3 TESTS OF THE PHOTOEMISSION-TYPE XBPM

The test sample for photoelectron emission-type TBPM uses a 25-mm-diameter, 175-micron-thick CVD-diamond disk with 0.2-micron-thick electrically isolated quadrant patterns of an aluminum coating on one side of the diamond disk. Fig. 4 shows the CVD-diamond disk and its clamping and cooling structure. The photoelectron emission signal was collected from the aluminum-coated surface to provide the beam position information.

Three different sample setups were arranged for the experiments as shown in Fig. 3. In configuration (a), we used same clamping and cooling structure as we did in the NSLS X-25 test. The aluminum-sensor coating was facing the X-ray beam, and an alumina insulator was applied to isolate the sensor from the cooling base electrically but retain reasonable thermal conduction for cooling.

Configuration (b) was designed to test whether we can use the CVD-diamond as an electric insulator for the aluminum sensor coating to improve the disk cooling efficiency. So that, in configuration (b), the aluminum coating on the CVD-diamond disk was mounted facing downstream to the beam direction and no insulator applied between the copper cooling base and the CVD-diamond disk.

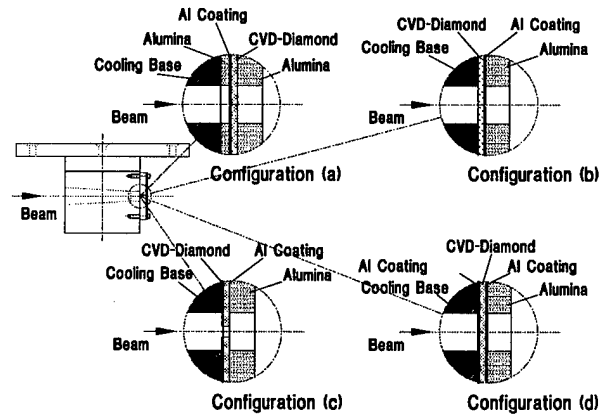

Fig. 3. Sample set-up configurations for the TBPM test.

The test configuration (c) was similar to (a), except a 1.5 mm through hole was made in the center of the CVD-diamond disk to allow a clear X-ray beam path.

The test results show that all of these three configurations provide good beam position sensitivity. Fig. 4 shows the output signal from the TBPM test sample in configuration (c) as a function of the stage vertical motion.

4 TESTS OF THE PHOTOCONDUCTIVE-TYPE XBPM

Since 1975, many researchers have explored the photoconductive properties of natural diamond with X-rays and gamma rays [6]. The photoconductive properties of CVD diamond have also been exploited [7]. A test sample for a novel photoconductive-type TBPM was designed and prepared at the APS as shown in Fig. 3 configuration (d). The sample was made from the same type of CVD-diamond disk as was used in the photoemission-type TBPM. But, the quadrant patterns of the aluminum coating were applied on both sides of the diamond disk. A DC bias voltage was used to generate the current signal, which is based on photoconductive properties of the CVD- diamond.

Fig. 5 shows the output signal from the photoconductive TBPM test sample in configuration (d) as a function of the stage vertical motion. During this test, the bias voltage applied to the CVD-diamond disk was 1.5-volts.

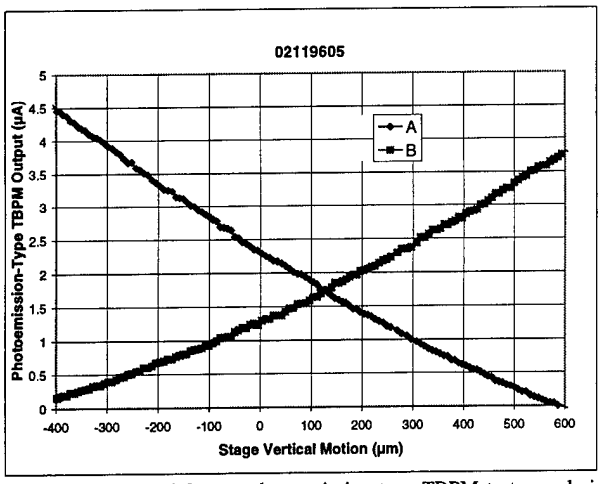

Fig. 4. Output signal from a photoemission-type TBPM test sample in configuration (c) as a function of the stage vertical motion. ID-6 undulator gap was 28.2-mm. ESRF storage ring current was 121-mA

5 DISCUSSION

According to the experiences obtained with the XBPMs in many synchrotron radiation laboratories, contamination signals caused by the bending-magnet (BM) emitted radiation become a major problem. Problems are exacerbated for the XBPM when the insertion devices (IDs) operate with different magnet gaps, because the percentage level of the contamination will be a variable.

From the test results, we have learned that, compared to a photoemmision-type TBPM, the beam position signal from a photoconductive-type TBPM has less ID gap dependence. This maybe caused by the higher sensitivity of the photoconductive type TBPM to the hard X-ray radiation.

6 ACKNOWLEDGEMENTS

This work was supported by the U.S. Department of Energy, BES-Materials Science, under contract W-31-109-Eng-38.

REFERENCES

[1] D. Shu, B. Rodricks, T. Sanchez, and T.M. Kuzay, "The APS X-ray undulator photon beam position monitor and tests at CHESS and NSLS", Nucl. Instru. and Meth. A319(1992)56-62.

[2] U.S. patent 5,404,014 (Feb. 1994)

[3] D. Shu, J.T. Collins, J. Barraza, and T.M. Kuzay, "The APS X-ray transmitting beam-position-monitor tests at the NSLS X-25 beamline", Nucl. Instru. and Meth. A347(1994)577-580.

[4] D. Shu, and T.M. Kuzay, "Design of the commissioning filter/mask/window assembly for undulator beamline front ends at the Advanced Photon Source", Rev. Sci. Instrum. 67(9), Sept. 1996.

[5] D. Shu, T.M. Kuzay, Y. Fang, J. Barraza, and T. Cundiff, "Synthetic diamond-based position-sensitive photoconductive detector development for the APS", to be submitted for the 6th International Conference on Synchrotron Radiation Instrumentation, Japan, Aug. 1997.

[6] D.R. Kania, L.S. Pan, P. Bell, O.L. Landen, H. Kornblum, P. Pianetta, and M. D. Perry, "Absolute x-ray power measurements with subnanosecond time resolution using type Iia diamond photoconductors", J. Appl. Phys. 68(1), July 1990.

[7] R.J. Keddy, T.L. Nam, and R.C. Burns, "Synthetic diamonds as ionisation chamber radiation detectors in biological environments", Phys. Med. Biol., Vol.32(6)751-759, 1987.

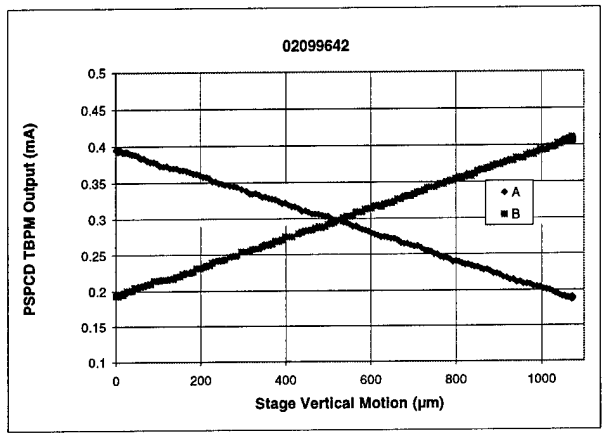

Fig. 5. Output signal from a photoconductive-type TBPM test sample in configuration (d) as a function of the stage vertical motion. ID-6 undulator gap was 29-mm. ESRF storage ring current was 110-mA.

OBSERVATIONS OF SECONDARY EMISSION CHAMBER DEGRADATION FROM VERY HIGH INTENSITY PROTON BEAMS AT THE AGS *

K.A. Brown, I.H. Chiang, A. Pendzick, T. Tallerico
Brookhaven National Laboratory, Upton, NY 11973

1 INTRODUCTION

Degradation of Secondary Emission Chamber (SEC) efficiencies has been seen in the past.[1] As a result, instruments in use today are built to minimize any such effects. With beam intensities as high as 6×10^{13} *protons per pulse* incident on these devices we are again observing significant degradation in SEC efficiencies. In this report we will present observations of these effects and methods we have developed to cope with them.

2 DISCUSSION

The AGS uses SEC's to monitor beam intensity of the slow extracted beam and at experimenter targets. Beam currents for these beams vary from less than $\frac{1}{2}$ μamp to over 2 μamp. Typically beam is 1.2 to 1.6 seconds in length with intensities of 15×10^{12} (on target SEC's) to over 60×10^{12} (just after extraction point), protons per 3.2 to 3.6 sec pulse rate.

Each SEC contains 5 successive parallel 1 mil silver plated aluminum plates. Three of the plates (#1,#3, & #5) are connected to a high voltage power supply and typically operate at 750 volts. A small titanium sputter ion pump (8L/sec) located on top of the SEC box keeps each SEC at a vacuum of 10^{-9} to 10^{-8} torr. Two of the plates (#2 & #4) are summed and the output goes into an I/F module which is adjusted to count 6500 counts per sec for 524 nA.

The principles behind how SEC's work have been described completely as long ago as the mid-1960's. [1][2] In general the foil surfaces can be considered as electron emitters. The emission is independent of foil thickness, being a surface phenomena. For the most part low energy electrons are collected, although for high energy proton beams, other effects, such as Rutherford scattering contribute to the signal. The SEC efficiency is defined to be

$$\rho_c = \frac{number\ of\ emitted\ electrons}{number\ of\ incident\ charged\ particles} \times 100\%$$

This is a function of foil material, surface conditions, chamber pressure, properties of incident particles, and incident angle of the incident particles. For thin low mass foils, the efficiency is a linear function of the energy lost by the incident proton beam.[2]

$$\rho = k \cdot \frac{dE}{dx}$$

For 24 GeV/c protons on aluminum, $\frac{dE}{dx}$ is about 1.8 MeV g^{-1} cm^2. [6] Typical efficiencies are of the order of 2.2 % per emitting surface. [2] The degree of degradation we have observed is or the order of 20 to 30 %, which implies the efficiency, or number of emitted electrons, has decreased by at least the same amount.

In order to study this phenomena, we installed an X-Y movable table at one of the target stations in the AGS Slow Extracted Beam Lines. The SEC was located about three feet in front of the target. It was driven remotely and the position control was calibrated. We monitored the change in SEC counts versus total intensity on target, from a 90 degree target monitor telescope. We then would move the table and compare the efficiency from a fresh area of the SEC surfaces to the normal operating position. Since the beam was targeted for an experiments use, the position of the beam on the SEC was fairly stable over the period of the run, although some changes were made in order to satisfy the experimenter needs.

The total beam that was put on target was more than 2×10^{19} protons at an energy of about 25.2 GeV/c.

We also did a very simple modeling exercise, to provide a picture of what the surface efficiency may look like. In this exercise a two dimensional gaussian beam was scanned accross a two dimensional gaussian "efficiency hole" each of the same widths. This simulated the moving of the table with the beam position held constant.

3 RESULTS

Figure 1 shows the efficiency versus horizontal position of the table, for the clean, new SEC and after it had been irradiated by 4×10^{19} integrated proton flux on the SEC.

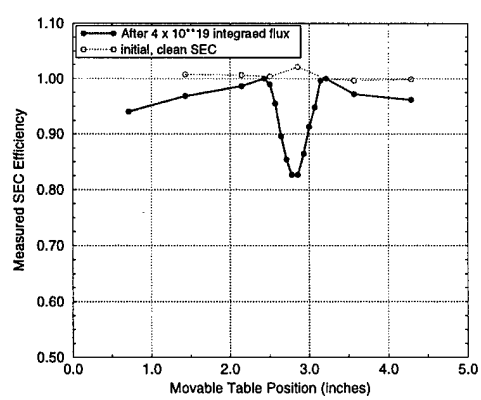

Figure 1: Horizontal Scan of SEC Efficiency.

Figure 2 shows the efficiency versus vertical position of the table, for the clean, new SEC and after it had been ir-

* Work performed under the auspices of the U.S. Dept. of Energy

radiated by 4×10^{19} integrated proton flux on the SEC. In Figure 3 the efficiency is shown degrading over time. This data is from a different SEC located just after the extraction channel in the AGS. This SEC shows efficiency dropping by about 0.2 to 0.3 % for every 10^{18} protons/cm^2, in which the total flux to this device was a little over 10^{20} protons/cm^2. The degradation of the SEC on the table after an integrated flux of 4×10^{19} corresponds to about 18 %. This means there was about a 0.4 % drop in efficiency for every 10^{18} protons/cm^2. We have done simple simulations of these scans of the SEC. From these, which simply moved a 2-dimensional Gaussian beam over a 2-dimensional Gaussian hole, we find the degradation at the core of the beam is significantly greater. A measured response of 75 % corresponds to the central part of the degradation being at a response of more like 40 %.

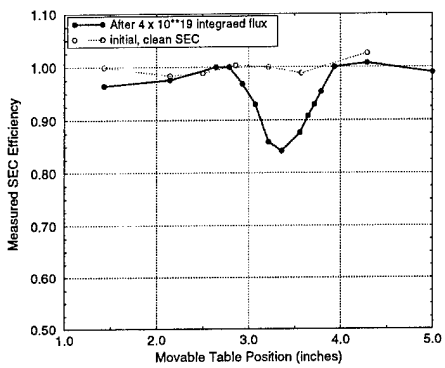

Figure 2: Vertical Scan of SEC Efficiency.

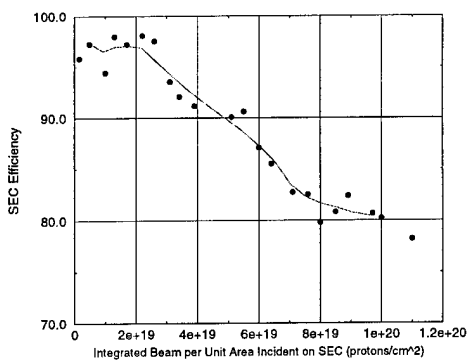

Figure 3: SEC Efficiency vs integrated incident beam flux.

4 CONCLUSIONS

With the AGS now reaching intensities of 6×10^{13} protons per AGS period, we are again seeing the effects of deteriorated SEC efficiency. Yamin and Repeta reported in 1979 that the newly designed SEC could expect to see a 1% change in efficiency for 10^{18} incident protons/cm^2. [7] What we have observed are rates of deterioration of 0.2 to 0.5 % per 10^{18} protons/cm^2. [3] [4] [5]

We do not think it is pratical to try to make a better SEC. The methods used to keep the surfaces clean are very good. We find, since only a small portion of the SEC surface is being hit with beam, that it is better to understand the degradation and have a movable SEC, which can be placed to a fresh location periodically. This extends the life of the SEC, provides us with reliable intensity monitoring, and allows us to preserve the methods we use to build these devices (which makes them more cost effective).

5 REFERENCES

[1] V.Agoritsas,CERN and R.L.Witkover,BNL, IEEE Transactions on Nuclear Science, Vol.NS-26,No.3. June 1979.

[2] V.Agoritsas, CERN/MPS/Int.CO66-30 (unpublished report). June 1966.

[3] K.A.Brown, AGS Studies Report No.319. January 1995.

[4] K.A.Brown, AGS Studies Report No.329. May 1995.

[5] I.H.Chiang, AGS Studies Report No.346. June 1996.

[6] Review of Particle Proterties, Physical Review D, Particles and Fields v.50 No. 3, August 1994.

[7] P.Yamin, L. Repeta, BNL, IEEE Transactions of Nuclear Science, Vol. NS-26, No. 3, p.3415, June 1979.

PERFORMANCE OF THE RHIC INJECTION LINE INSTRUMENTATION SYSTEMS*

T. J. Shea, R. L. Witkover, P. Cameron, R. Connolly, W. A. Ryan, G. A. Smith, E. Zitvogel
Brookhaven National Laboratory, Upton, NY 11973

Abstract

The beam injection line from the Alternating Gradient Synchrotron (AGS) to the Relativistic Heavy Ion Collider (RHIC) transports proton and heavy ion bunches. This line and the RHIC first sextant currently contain the following complement of beam instrumentation: stripline position monitors, ionization loss monitors, video profile monitors, and commercial current transformers. Over several years, these systems have been designed and bench tested to assure a desired performance level. Using data from laboratory tests and the recent single pass beam tests, attained performance will be reported. Finally, experience from the beam based tests will be applied to the design criteria for the future collider ring instrumentation.

1 BEAM PARAMETERS

The beams delivered by the AGS to RHIC (AtR) transfer line will include 10^{10} polarized protons and 10^{11} non-polarized protons (28 GeV/c) as well as 10^9 fully stripped gold (Au^{+79}) ions at 10.8 GeV/u, extracted as individual bunches at a 30 Hz rate[1]. The nominal bunch length is 20 nsec. Normalized emittance is 10 pi-mm-mrad. The AtR line is divided into sections starting with "U", which leads into "W" where it switches to the "X" or "Y" arcs to either of the 2 RHIC rings. The upstream part of the U-line branches off to the "V" line in which up to 5 x 10^{12} protons per bunch are brought to the "g-2" experiment.

2 BEAM POSITION MONITORS

The AtR position monitor system consists of shorted stripline electrodes[2] and gated, self triggering samplers[3]. This system was designed to measure the position of individual bunches injected into RHIC. Because the transfer line provided a convenient test bed, the injection electronics was based on a prototype of the collider ring implementation.

2.1 Accuracy and Stability

Installation of the electronics for transfer line and first sextant commissioning has provided opportunity to monitor stability in the real accelerator environment. The most recent results are shown in Figure 1. Each point is the mean vertical position of 100 single bunch samples. The position is calculated relative to an arbitrary orbit. The bunch contains about $8*10^{11}$ protons within a 30 ns length while the simultaneous reference pulse (measured on a different position channel) simulates a centered bunch of similar intensity. As shown, the vertical drift of the extracted bunches is less than ±30 microns while the drift of the electronics is less than ±6 microns. The physical aperture of the electrode is about 69 mm and the typical position of the measured bunch was about 2 mm from center.

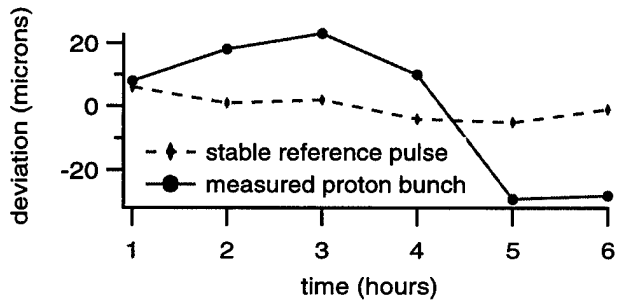

Figure 1: Average vertical position vs. time.

2.2 Noise

The noise performance of the sampling electronics has been characterized in the accelerator environment by measuring the distribution of simulated, single bunch acquisitions. With signal amplitudes near full scale, this distribution is gaussian with a width <5 microns rms. When measuring the collider's closed orbit, a sampler of this type will average the turn-by-turn data to provide a 100 Hz update rate with a noise floor of <200 nm. Early in the 1997 proton run, we measured the vertical position of several hundred bunches extracted from the AGS. The resulting histogram is shown in Figure 2. The 20 micron rms width of this measured distribution is comparable to that due to electronic noise at these signal amplitudes (about one fifth of full scale). This

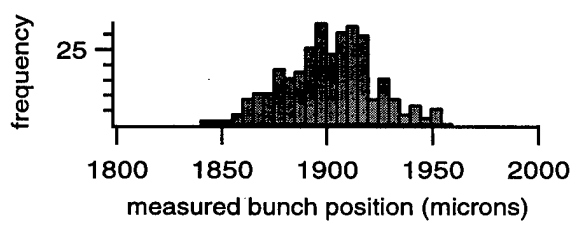

Figure 2: Histogram of vertical positions.

* Work supported by the U.S. Department of Energy

leads us to believe that the short term vertical extraction jitter of the AGS is less than 20 microns.

2.3 Future Work

In order to set the interval between calibrations, long term stability must be characterized. This will be done during the 1997 proton run at the AGS. Late in the AtR commissioning, a significant number of mistriggers were observed. During the 1997 sextant test, it was confirmed that the sampler's 70 MHz bandwidth was too wide to smooth the complex structure of coalesced bunches. Initial results show that the problem has been resolved by reducing the bandwidth to 20 MHz, but further optimization of the trigger circuit is desired.

3 BEAM LOSS MONITORS

Beam loss monitoring is one of the most important diagnostic tools in setting up the AtR transfer line. The loss monitors were designed to be sensitive at least one decade below nominal for low intensity studies. During the AtR commissioning in November 1995, the actual beam intensity varied from 10^6 to 2 x 10^7 Au^{79} ions, well below the design range, yet the system was able to monitor the losses. Modified Tevatron ion chambers[4] are mounted on the vacuum flanges downstream of each magnetic element. To limit the number of electronic channels while providing complete coverage, signals from the 120 detectors were grouped into 56 outputs. A number of ion chambers are mounted on movable stands to allow locating them where special attention was required.

The ion chamber consists of a 113 cc glass bulb filled with argon at about 725 milli-Torr. Each chamber is calibrated using a cesium-137 source. The mean sensitivity in the middle of the plateau for the AtR chambers was found to be 19.6 pA/R/hr at the nominal operating voltage of 1450 Volts. Ninety-five percent were within (1.5 pA/R/hr of the mean. The ionization current from the detector is fed to a low leakage gated integrator and read out using the standard RHIC MADC[5]. Non-tribo-electric cable was used to reduce noise due to mechanical motion. The circuit input is designed to pre-integrate the electron signal so that its rise time is in the millisecond range, (comparable to the ion collection time) greatly reducing noise from the kicker magnets which are time coincident with the beam. An isolated signal connector prevents a ground loop with the HV connector shield. These features resulted in the noise level of about 10 pA observed during the AtR commissioning.

4 VIDEO PROFILE MONITORS

The Video Profile Monitor[6] (VPM) consists of a high resolution video camera observing the light emitted by the beam hitting a phosphor screen. A VME-based frame grabber-image processing system acquires and processes the data from any 4 of the 12 cameras in the system. VPMs were used because multiwires were too expensive and would not meet the spatial resolution requirement and scanning wires cannot acquire the data on a single bunch. By using low mass phosphor screens to minimize scattering, profiles have been simultaneously measured at 4 locations for the single bunches. All of the 12 camera outputs are brought to a central processing location over wideband analog fiber-optic links to preserve resolution, since coax cable would degrade the high frequencies over the 1700-foot length of the furthest runs. For the initial AtR commissioning 8 VPMs were installed. For the RHIC First Sextant test in December 1996 the Y-line VPMs and a temporary unit at the end of the sextant were also used.

The .002" thick phosphor screen (Gadolinium Oxy-sulfide doped with Terbium Gd2O2S:Tb, deposited on an aluminum substrate) is mounted at 45° and inserted by a pneumatic drive. The drive, a 4" viewing window, and 2 lamp ports are mounted on the same 8" conflat flange, eliminating alignment errors. The flange is mounted on a vacuum tee with the window facing the floor. A first surface mirror mounted at 45° transfers the image to the camera. Typical optical path length is 3 meters. The phosphor has been tested and shown to fully decay within the 33 ms camera frame period. The batch of screens made for the AtR tests were found to "orange peel" when put under vacuum. This was traced to a change in the concentration of the potassium silicate which allowed water vapor to be trapped under the phosphor. While no quantitative problems resulted from this effect, the original recipe was used in later screens. The running period with the gold beam did not produce any damage to the screens but none was expected for the low intensity and short duration of the run.

All of the VPMs used Pulnix TM-7cn CCD cameras except UF1 which was in the AGS ring tunnel and exposed to much higher radiation. Typical CCD camera lifetime is 100 to 700 Rad. Cidtek manufactures a charge injection device (CID) based camera which typically can tolerate 20 kRad., which was used for UF1. During the high intensity running for the g-2 experiment the Cidtek camera (3710D) failed after 1 week, even though it was behind 0.5 m of heavy concrete, which appears to have been consistent with the rated dose. A newer model Cidtek camera rated at a mega-rad is now available and will be considered along with a Dage radiation hardened vidicon model. The cameras in the transfer line are typically mounted in 14-inch diameter holes bored into the tunnel wall to provide shielding in the lower radiation environment.

Since the light is emitted in a <2 msec pulse, the camera must either acquire the full frame at once as in the Cidtek, or have a period in which the odd and even fields overlap as in the Pulnix. The camera must be synchronized to start the scan just after the screen has decayed. By mis-timing the camera, a picket-fence like image appeared on the vertical display as every other line was blank. Because of the 3 decade range of intensity in the expected beams, a means of adjusting the light into the camera was required. A typical lens will only adjust over a range of about 40:1. A simple device was built using small solenoids to flip 4 neutral density filters into the light path between the camera and the lens, providing a range of 20,000:1. This worked very well over the wide range of studies, shapes, and intensities.

Most VPMs use a 500 mm f/5.6 Maksutov-Cassegranian reflector lens except for a 1000 mm f8 reflector lens at UF1, a 400 mm f5.6 refractor at UF2 and a 300 mm f5.6 refractor at WF2. About half of the cameras were rotated 90° to match the beam aspect ratio. The actual beam orientation was reestablished in the computer generated display. The lens, camera, and filter array are mounted using commercial optical hardware on a precision rail, allowing rapid replacement.

The overall resolution is limited by depth of field, camera resolution, and lens resolution. Phosphor screen grain size, air waves, and mechanical vibrations are not significant for the AtR beam sizes. Depth of field is a factor because the screen is tilted at 45° and can be significant if the beam is well off center or large vertically. Camera resolution is limited by the number of pixels, by fiber transmission system bandwidth, and by electronics bandwidth. The resolution was calculated to be better than 0.25 mm using measurements and manufacturer's data for the cameras and lenses.

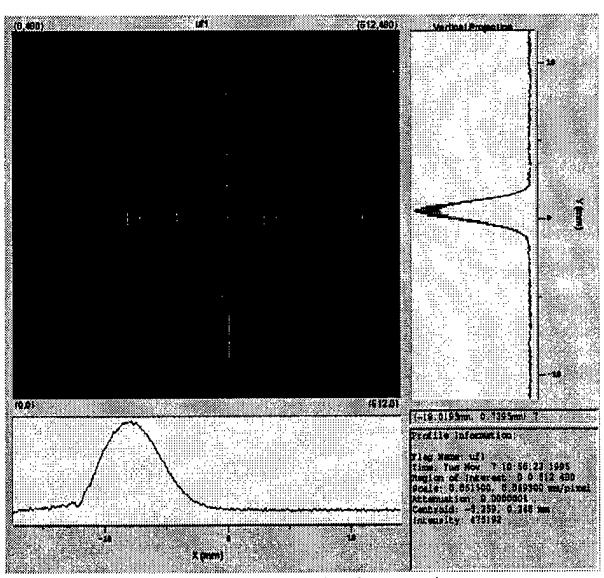

Figure 3: Beam on UF1. Scale tics are in mm.

Measurements of the fine fiducial marks on the screen were consistent with the estimate.

The acquisition and processing of the video data is done using 4 Imaging Technology Inc. IMA-VME-4.0 boards with 4 AMVS-HS acquisition modules, 2 CMCLU-HS Convolver arithmetic modules, and 2 CMHF-H histogram/feature extractor modules. The system is run under VxWorks. Forty-eight 512x512 pixel frames, plus base frames for subtraction and computational results can be stored on board. A 128x128 subset of the can be generated from a 4x4 convolution of the full frame or a region-of-interest (ROI). The computations available include: Pixel-by-pixel base frame subtraction of full frame data, centroid of the full frame, H and V projections, and sum of all pixels. The AtR data only used the full 512x512 frames for a single bunch. Figure 3 shows one set of results from the AtR tests.

5 BEAM CURRENT MONITORS

Beam current was monitored used the commercial Integrating Current Transformers (ICT) manufactured by Bergoz[7]. Three of the 5 units were installed for the AtR test with the Y-line unit added for the First Sextant Test. The X-line unit was temporarily installed at the end of the sextant. These devices use passive integration to filter a fast current pulse before it enters the core, reducing the effect of core losses and simplifying the electronics design. Initially, noise from the extraction kicker pulser interfered, but by passing the signal cable through a ferrite core (multiple turns) reliable signals were obtained even for 10^7 gold ions.

6 REFERENCES

[1] S. Peggs, "RHIC Status", these proceedings.

[2] P. R. Cameron, et. al, "RHIC Beam Position Monitor Characterization", Proc. 1995 Particle Accel. Conf. 95CH35843.

[3] W. A. Ryan and T. J. Shea, "A Sampling Detector for RHIC Position Monitor Electronics", Proc. 1995 Particle Accel. Conf. 95CH35843.

[4] R. E. Shafer, et al, "The Tevatron Beam Position and Beam Loss Monitoring Systems", Proc. 12th Int'l Conf on High-Energy Accel., Aug 1983, p609

[5] R. Michnoff, "The RHIC General Purpose Multiplexed Analog-to-Digital Converter System", Proc. 1995 Particle Accel. Conf. 95CH35843, p2229

[6] R. Witkover, "Design of the Beam Profile Monitor System for the RHIC Injection Line", Proc. 1995 Particle Accel. Conf. 95CH35843, p2589

[7] Bergoz Precision Beam Instrumentation, 01170 Crozet, France

RHIC BEAM LOSS MONITOR SYSTEM DESIGN

R. Witkover, E. Zitvogel, R. Michnoff
Brookhaven National Laboratory
Upton, NY, USA 11973

Abstract
The Beam Loss Monitor (BLM) System is designed to prevent the quenching of RHIC magnets due to beam loss, provide quantitative loss data, and the loss history in the event of a beam abort. The system uses 400 ion chambers of a modified Tevatron design. To satisfy fast (single turn) and slow (100 msec) loss beam criteria and provide sensitivity for studies measurements, a range of over 8 decades is needed. An RC pre- integrator reduces the dynamic range for a low current amplifier. This is digitized for data logging.. The output is also applied to an analog multiplier which compensates the energy dependence, extending the range of the abort comparators. High and low pass filters separate the signal to dual comparators with independent programmable trip levels. Up to 64 channels, on 8 VME boards, are controlled by a micro-controller based VME module, decoupling it from the front-end computer (FEC) for real-time operation. Results with the detectors in the RHIC Sextant Test and the electronics in the AGS-to-RHIC (AtR) transfer line will be presented.

SYSTEM DESIGN

It has been estimated that the RHIC superconducting magnets will quench for a fast loss > 2 mJ/g or a slow loss > 8 mW/g. This is equivalent to 78.3 krad/s at injection (49.3 krad/s at 100 GeV/c) for uniform loss over a single turn and 0.25 rad/s at injection (4.07 rad/s at 100 GeV/c) for slow losses. An input RC matched to the magnet thermal time constant compresses this range in a meaningful way. The amplified signal is digitized at 720 Hz by a standard RHIC VME multiplexed ADC (MADC) [1. The analog signal is also applied to high and low-pass filters preceding respective fast and slow loss comparators with independent programmable references. These can pull down the Beam Permit Link dumping the beam and halting data acquisition by the MADC. This provides a 10 second loss history preceding the abort.

Since RHIC is an accelerator storage collider some BLM parameters must be adjusted during the injection and acceleration phases. The BLM system uses predefined write lists to set gains, fast and slow loss thresholds and abort mask bits when specific RHIC Event Codes are detected.

*Work performed under the auspices of the U. S. Department of energy

The electronics, including the analog signal circuitry is packaged in VME format. A BNL designed micro-controller board manages all digital functions of the analog board independent of the crate CPU once the write list values have been set through the high level code. This insulates the real-time operations from the control system I/O functions even allowing the BLM system to continue operating during a FEC hangup. Sixty-four BLM channels will be serviced from each crate. Electronics will be located in 7 service buildings (2,4,5,7,8 10 and 12 o'clock) allowing access while beam is on.

THE DETECTOR

Ion chambers were chosen as the detectors in RHIC because they are economical, reproducible, require low maintenance and are well matched to the expected dose rates. The units were originally designed by R. Shafer for the Tevatron at FNAL [2] . For RHIC the packaging was modified, eliminating PTFE in the BNC and SHV connectors, using dual connectors to allow daisy-chaining, and isolating the BNCs to break the ground loops caused by the HV and signal cables. The ion chamber consists of a 113 cc glass tube containing argon at 725 mm Hg. The inner and outer electrodes are 0.25" and 1.5" diameter, 4" long, nickel cylinders. For the first 100 detectors the mean sensitivity was 19.6 pA/R/hr with 95% within ±1.5 pA/R/hr at 1450 V, roughly the plateau mid-point.

There are 120 detectors installed in the AGS-to-RHIC (AtR) transfer line which are independent of the RHIC Ring BLM system.[3] A total of 400 BLMs will be installed in the RHIC ring: 198 at standard quadrupoles (midway between rings), 96 at insertion region quads and dipoles, 68 at specific components in the warm regions and 38 relocatable units in the warm and insertion regions. BLMs located at cryostats are secured using 1.5"-wide stainless steel "belly-bands" to which an insulated mount is attached. In the warm regions the BLMs are typically secured to the vacuum flanges with hose clamps and similar insulated mounts.

Alternate detectors, daisy chained on two cables, each with its own HV bias supply provide redundancy. Since the electronics are accessible during operation, circuit modules or high voltage bias supplies can be readily replaced. Because the system will be used only for magnet protection and not personnel safety, higher levels of redundancy are not required.

0-7803-4376-X/98/$10.00 © 1998 IEEE

ANALOG FRONT END

The V119 Loss Monitor Analog Module contains 8 analog channels, all the data registers and the digital interface to the V118 Control Module. Mostly surface mount components were used because of the limited space. Figure 1 is a simplified schematic diagram showing one analog channel.

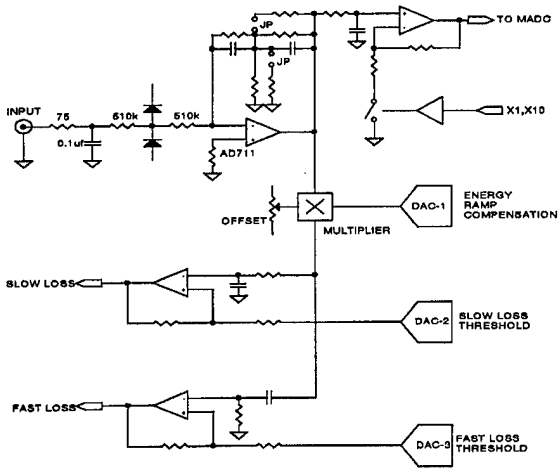

Figure 1. Simplified analog schematic.

The fast loss threshold at injection is equivalent to 5.5 mA from the detector, while the full energy , slow loss threshold corresponds to only 17.6 nA.. This wide range is reduced by pre-integrating with a 0.1 μF capacitor at the input. A low triboelectric cable, Belden 9504 was used to minimize noise. A 75Ω cable matching resistor prevents ringing while the back-to-back diodes protect the input. The capacitor rapidly charges for a fast loss. The charge is bled off through the 1.2 MΩ, matching the RHIC magnet thermal time constant. The circuit is a voltage amplifier for a fast loss, but behaves like a current amplifier for a slow loss. A "tee" configuration is used for the AD711 feedback to allow low valued resistors with reasonable roll off capacitors and to reduce thermal noise and parasitic capacitance. Two jumpers allow gains of one-tenth or 2 times greater than for the typical installation at a superconducting magnet since some monitors are not shielded by the cryostat and require less gain. Individual channel gains are recorded in the system data base. Data logging is via the MADC at 720 Hz through a programmable x1, x10 amplifier and a 360 Hz anti-aliasing filter. The slow and fast loss signals are separated by filters prior to the comparators. Each comparator derives an abort threshold reference from an associated programable 8-bit DAC. This provides sufficient settability for the storage mode, but not for the change in quench sensitivity during the magnet ramp. To compensate for this the signals to the comparators are processed by an AD734 analog multiplier which adjusts the gain as a function of magnet current in response to an event driven DAC, common to all channels on the board. The comparators incorporate hysteresis to eliminate spurious trips due to noise. All logic on the board is incorporated into an on-board ALTERA chip.

CONTROL SYSTEM INTERFACE

At each location the Loss Monitor System is housed in a standard RHIC VME chassis, including the Motorola 162 Front End Computer (FEC). Commercial digital I/O and DAC modules will be used. The standard RHIC MADC set consisting of a V113 Controller and V114 Analog Module will be housed in this chassis, along with up to 8 V119 RHIC Loss Monitor Analog Modules. The BNL designed V119 modules condition the detector outputs to 0-10 V signals for digitization and storage by the MADC for later analysis. These modules do not provide a standard VME interface: only the power pins on the VME bus are used. Registers totaling 256 bytes on the V119's are controlled by the V118 through user defined pins on the P2 connector. This P2 interface includes an 8-biy I/O bus to allow either the V118 on-board Microchip PIC16C64 microcontroller or the FEC to access the following registers on each V119 module:

- Enable/Disable Slow Loss Detection (1 bit/chan)
- Enable/Disable Fast Loss Detection (1 bit/chan)
- Slow Loss Threshold Setting (8-bit register/chan)
- Fast Loss Threshold Setting (8-bit register/chan)
- MADC Input Gain Setting (1-bit/chan)
- Loss Threshold Gain Setting (8-bit register/module)
- Slow Loss Status Latch (read only) (1-bit/chan)
- Fast Loss Status Latch (read only) (1-bit/chan)

The V118 module provides a 64k x 16 bit memory mapped to the VME space for I/O bus write lists of up to 255 address/data values for each of the 256 RHIC event codes. For each event the on-board microcontroller sequences through the associated write list, sending each data value to the specified address. This allows modification of all registers for each occurrence of a RHIC event code. An important feature of the V118 Control module is that a VME reset or FEC reboot will not affect operation of the I/O bus write list sequencing.The P2 interface includes a loss bit for each V119 module. When a trip occurs on an enabled channel, the V118 latches the loss status registers on all analog modules, allowing determination of the first loss channel. The FEC then resets the status registers allowing further trips to be detected.

TEST RESULTS

In addition to the BLMs in the AtR, 52 detectors were installed for first RHIC Sextant Test. Since the beam would make only a single pass the integrator electronics were used. The insitu noise observed was of the order of an MADC LSB (13-bit plus sign). Figure 2 shows the signal from a channel with the detector mounted in the AGS ring observing losses from the circulating gold beam with the MADC read at 100 μsec intervals.

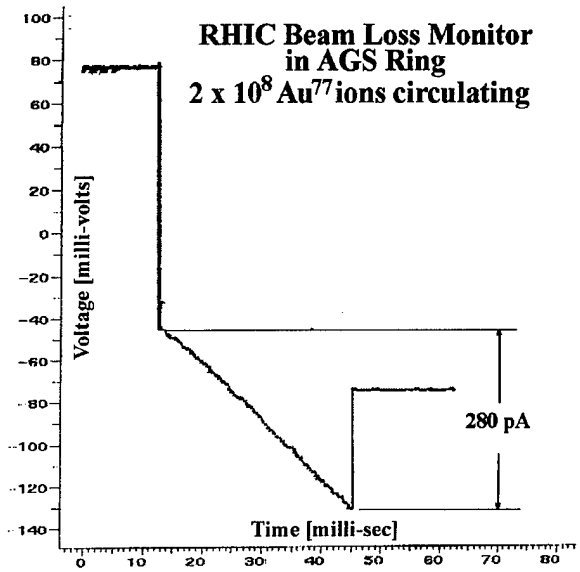

Figure 2.

During the Sextant Test the beam was purposely steered to produce losses along the RHIC magnet string. Figure 3 shows the results of the average of 2 runs normalized to 10^8 Au^{79}. The data spans the full range of the MADC. The beam direction can be determined from the asymmetry in the up and downstream loss patterns even though most detectors are mounted midway between the rings.

A VME crate containing the prototype Micro-controller, 8-channel analog module and an MADC was installed in the upstream AtR line allowing observation of slow losses due to the circulating beam in the AGS and fast extracted bunches down the AtR line. Measurements made with the low intensity gold beam verified the design bandwidth and sensitivity. Excessive noise was found to be coming from the 12 V crate switcher power supply, but chokes on the power supply lines reduced this considerably. The signals observed on the analog output were consistent with an LSB of the MADC. Noise at the input to the Slow Trip comparator circuit was also within an LSB of the threshold DAC, however, the Fast Trip circuit 30 kHz bandpass filter allowed noise equivalent to several LSBs to come through. This included residual switcher noise of the same order as thermal noise from the first stage

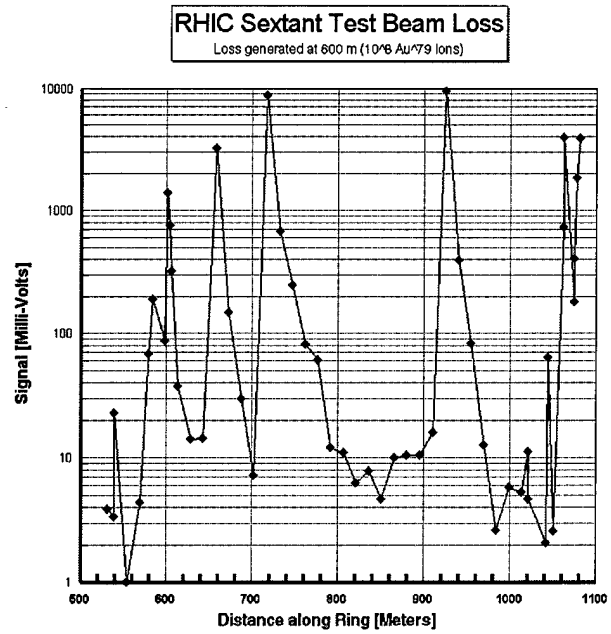

Figure 3.

resistors. The circuit will be redesigned using smaller resistor values to decrease the thermal noise to meet the 1 LSB requirement. Better power supply filtering or on-board DC-DC converters are being studied to eliminate the observed power supply noise.

ACKNOWLEDGEMENTS

The high level coding for the workstations and system commissioning was done by Dejan Trbojevic for the AtR tests and Pat Thompson for the First Sextant test. Barry Clay was a major contributor to the analog design and testing. Paul Ziminski did most of the detector testing.

REFERENCES

[1] R. Michnoff, "The RHIC General Purpose Multiplexed Analog-to-Digital Converter System ", Proc. 1995 Particle Accel. Conf. 95CH35843, p2229

[2] R. E. Shafer, et al, "The Tevatron Beam Position and Beam Loss Monitoring Systems", Proc. 12th Int'l Conf on High-Energy Accel., Aug 1983, p609

[3] T. Shea, R. Witkover, R. Connelly, P. Cameron, W. Ryan, G. Smith, E. Zitvogel," Performance of the RHIC Injection Line Instrumentation Systems", These procedings.

INSTRUMENTATION FOR LOW ENERGY ELECTRON MEASUREMENTS

C.Y. Tan*, Wilson Synchrotron Laboratory, Cornell University, Ithaca, NY 14853

Abstract

We report on the implementation of a beam charge, transverse beam position and bunch length measurement system for low energy electrons in the CESR injector. The core of the instrument is a piece of scintillating ceramic made from chromium doped alumina with a 200Å gold layer. Charge and current are measured when the beam is dumped onto the ceramic. Absolute beam position measurement is made by digitizing the image of the beam on the ceramic.

1 INTRODUCTION

The overall layout of the CESR injector is shown in Figure 1.[1] In the summer of 1995 when linac section 1 was removed to be replaced by a new SLAC section, we had the opportunity to install a package of instruments that enabled us to measure beam charge, transverse beam position and bunch length for low energy electrons (150 – 200 keV) in the CESR injector.

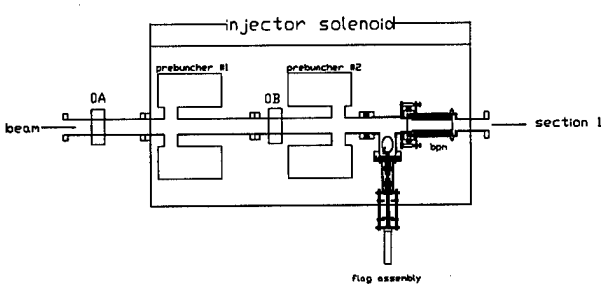

Figure 1: This is the overall layout of the injector. There are steerings in both the vertical and horizontal direction. By varying the phase and field strength of prebuncher 1 and 2, the amount of bunching and acceleration of the beam can be changed.

Central to the instrument package is a new flag made from chromium doped alumina with a 200Å thick layer. By dumping the bunches onto the flag, charge, bunch length and transverse position of the beam can be directly measured. Upstream from the flag is a stripline beam position monitor (BPM) which is used for non-destructive measurement of the charge and transverse position of the beam. To accurately measure the charge dumped on the flag, a temporary Faraday cup was also installed further downstream from the flag. After the flag was cross calibrated with the Faraday cup, the Faraday cup was removed for the installation of the new SLAC section.

* email: cytan@lns62.lns.cornell.edu

2 CHARGE MEASUREMENT WITH FLAG

Two methods of measurement were used to calibrate the flag with the Faraday cup

- Alternating current (AC) method where we numerically integrate the gun pulse on a digitizing oscilloscope.
- Direct current (DC) method where we directly integrate the current using an electronic integrator. See Figure 2 for the essential differences of the two methods.

The AC method allows us to bias the flag so that backscattering from the electrons is minimized.

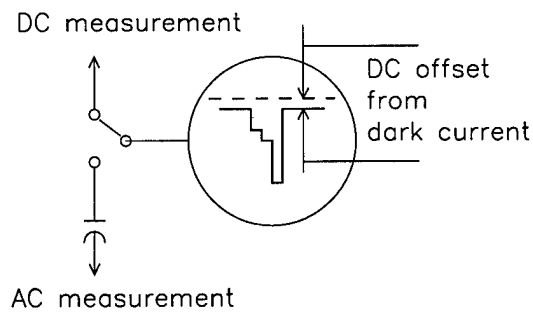

Figure 2: The essential difference between the AC and DC method is the capacitor which removes the dark current d.c. component in the AC method.

2.1 *Dark Current*

The main errors in the charge measurement comes from the large dark current component. Dark current is the DC current that is present when the gun is not pulsed and the gun grid is held at a bias of 300 V. The dark current comes from grid contamination of the gun. Figure 3 shows the dark current as seen on the flag.

2.2 *Results*

The graphs showing the cross-calibration curves are shown in Figure 4. The large error bars for the low current measurements come from the dark current component in the measurement. Since the flag is upstream from the Faraday cup, it intercepts more charge.

3 BUNCH LENGTH MEASUREMENT

By dumping the bunches onto the flag, we can measure the bunch length. Figure 5 shows the result after numerical filtering. The bandwidth of the system is such that we can clearly see bunches separated by 28 ns.

0-7803-4376-X/98/$10.00 © 1998 IEEE

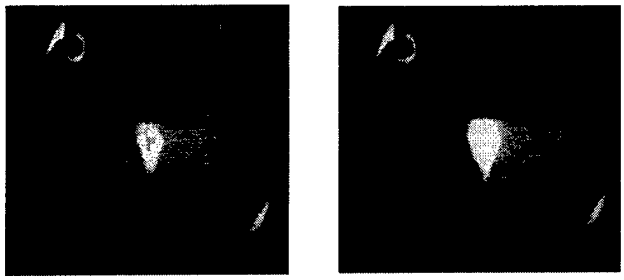

Figure 3: These photographs show how the structure of the dark current sources evolves through time. These photographs were taken 5 hours apart with the earlier photograph the left. Clear structural changes took place during the intervening period. These structural changes come from cycling the beam on and off during the 5 hours.

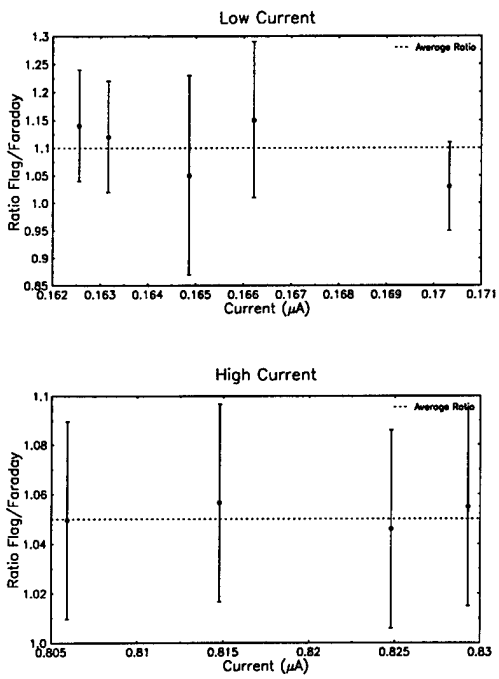

Figure 4: These two figures show the comparison between the flag and Faraday cup measurements using high current and low current conditions with the DC method. The flag intercepts more charge than the Faraday cup because the flag is upstream w.r.t. Faraday cup.

4 TRANSVERSE POSITION MEASUREMENT

The transverse position of the beam can be measured by measuring the centroid of the beam on the flag. Unfortunately, the large dark current component necessitated some simple graphics manipulation. The procedure for obtaining the centroid is shown in Figure 6. The BPM is then calibrated with the transverse position obtained from the flag and then beam-transported to the BPM.

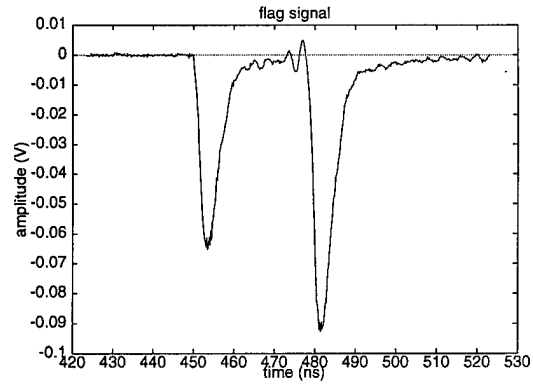

Figure 5: Bunch trains 28 ns apart as seen by the flag.

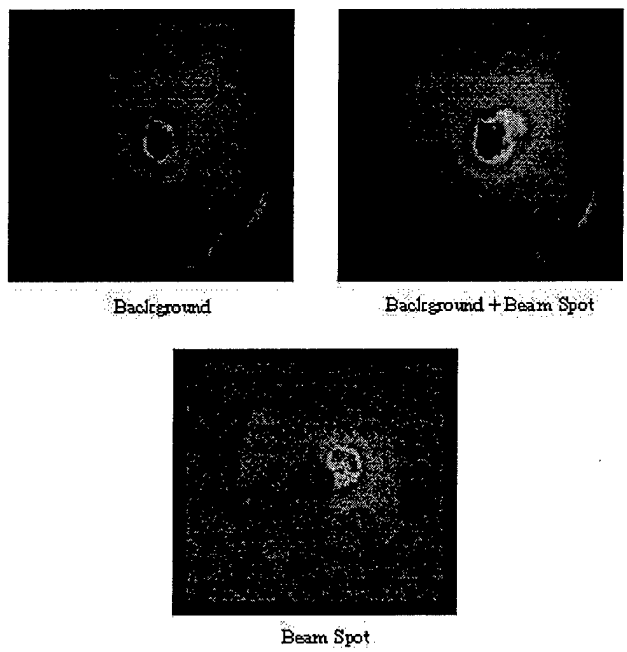

Figure 6: We show the process of digitization and image manipulation here: (i) background image is taken with the dark current, (ii) an image with both the dark current and the beam is taken, (iii) finally an image difference reveal the beam spot.

5 CONCLUSION

We have described an instrument package that is able to measure charge to better than 10% and differentiate bunches that are spaced 28 ns apart. Transverse position of the beam can either be measured with the flag or the BPM.

6 ACKNOWLEDGEMENTS

The author wishes to thank his advisor Prof. L.N. Hand and the CESR group for the help and advice which led to the successful completion of this project.

7 REFERENCES

[1] The CESR Injector, C.Y. Tan, thesis 1997.

A PROPOSED NEW HOM MONITORING SYSTEM FOR THE SRS

P. A. McIntosh, CLRC Daresbury Laboratory, Warrington, WA4 4AD, UK.

Abstract

A programme of work has recently been completed on the SRS, whereby a longitudinal coupled bunch (LCB) instability which was being driven in one of the RF cavities[1], was eliminated at high currents by adjustment of the cavity water temperature[2]. The technique for identifying irregularities in the action of particularly the RF cavities, has now been well established at Daresbury, and certain aspects of the identification process and even necessary corrective measures can be automated. This paper outlines a proposed new diagnostic system on the SRS which identifies when a HOM is resonated within a cavity and provides compensation by automated adjustment of its operating temperature.

1 INTRODUCTION

Since the upgrade of the beam steering control system on the SRS to allow global servoing (GS) of the electron beam and local vertical servoing (LVS) of the photon beam down individual beam lines, the control of the circulating electron beam has been greatly improved. Measures that have been implemented include the installation of highly accurate electron beam position monitors (BPM) giving 1μm resolution, plus improved photon tungsten vane monitors (TVM) providing sub-μm resolution. The stringent requirements of maintaining the electron beam orbit, and consequently the photon beam position, to these tolerances impacts on all components of the storage ring.

The RF system plays an important role and should be efficient in its operation and not cause the beam to deviate beyond the limits of the servoing systems. Instabilities introduced from the RF system are common place in circulating storage rings, and generally require some intervention from auxiliary control systems to minimise their effect. This paper outlines a control system adopted for use on the SRS which detects possible RF instability interaction with the electron beam and predicts, by way of a compensating shift in cavity operating temperature, a mechanism to avoid these instabilities.

2 THE MONITORING SYSTEM

Other laboratories around the world, such as SRRC[3], ALS[4] and PEP II[5] use active feedback systems, which detect the deviation from the required orbit due to cavity HOM interaction, and compensate by applying corrective kicks to the circulating beam in both the transverse and longitudinal planes. The real estate requirements for such a system on the space limited storage ring of the SRS makes this approach impractical. Hence the diagnostic and corrective systems must occupy a minimum of space when installed and if possible use existing diagnostic equipment.

The system that has been adopted uses existing stripline monitors to detect, from the beam spectrum, any contribution from the RF cavities; additional monitors on both the cavity and its associated waveguide system identify which cavity the instability originates from, and from precise knowledge of each cavity HOM spectrum, a magnitude of temperature variation can be calculated to shift the HOM in frequency away from coinciding beam resonances.

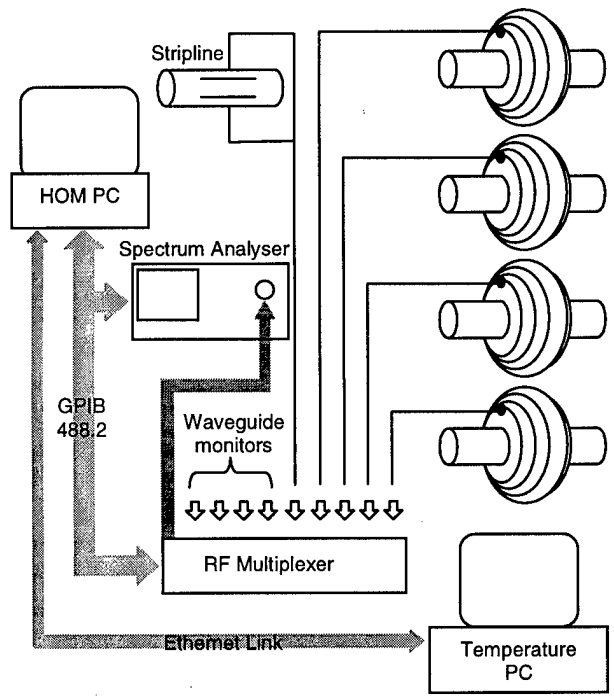

Figure 1. HOM Monitoring System layout

The monitoring system is controlled by an industrial PC via the data acquisition software LabVIEW. Through automatic control of the High Frequency Spectrum Analyser (HFSA), resonances about the beam orbit harmonics can be analysed.

2.1 Instability Identification.

For a uniform fill in the storage ring, ie. each circulating electron bunch containing approximately the same current, then the beam spectrum will only contain components n of Bf_{rev}, where B is the number of bunches and f_{rev} is the revolution frequency. Peaks at other frequencies indicate a non-uniform fill or that the beam

0-7803-4376-X/98 /$10.00 © 1998 IEEE

exhibits some coherent oscillation. Providing these oscillations cause the beam to move in a coherent way, the beam spectra will contain components:

$$f^{\pm}_{\mu,n} = nBf_{rev} \pm (\mu f_{rev} + f_{osc}) \qquad \text{Eqtn. 1}$$

where:

μ = integer corresponding to the CB mode number
f_{osc} = product of the fractional tune by f_{rev}

The $f_{\mu,n}$ peaks are observed as side bands of the main frequency components nBf_{rev}. Modulation of the beam with a frequency (μf_{rev}+f_{osc}) gives rise to these side bands and this modulation component exists if the beam contains a coherent oscillation with frequency f_{osc} (or f_{osc}+mf_{rev})[6]. For instability identification on the SRS, eqtn 1 holds true and can be used as the basis for an algorithm to detect spurious resonances from the electron beam itself. Knowing the synchrotron and betatron fractional tunes of the machine, evidence of the longitudinal CB (LCB) and transverse CB (TCB) instabilities can be located. Once a resonance has been detected, it is then necessary to determine whether the frequency is emanating from within the RF cavities.

2.2 HOM Determination

The HOM properties of each of the installed cavities are known and are extensively documented. More recent investigations have enabled the HOM's to be characterised in terms of both cavity temperature and tuner position[7]. The results of these characterisations have shown that for the strong monopole and dipole modes the variation in temperature has a linear effect, whereas changing tuner position introduces a more non-linear response in terms of the HOM frequency. The combined effect on HOM frequency can therefore be seen as a large non-linear frequency dependence on cavity tuner position, with a much smaller linear dependence on operating temperature.

The cavity monitor points are selective in their HOM identification. The cavity probe monitor is a magnetic probe which is sensitive to accelerating modes and will therefore only (to any certain degree) allow monopole HOM detection. The waveguide monitors chosen are E or H plane filter monitors which detect HOM resonances that exit the RF cavity via the coupling port. The restriction on the modes available to be detected at this point depends on the frequency of the HOM being sufficiently above the port cut-off to allow propagation.

The possible number of HOM's that can be excited in the SRS cavities are limited to 4 monopole, 6 dipole, 4 quadrupole and 2 sextupole. For the investigation for an automated monitoring and corrective control system, only algorithms for the monopole and dipole modes are to be included.

2.3 Correction Assessment

Having established that the observed instability is due to a HOM being resonated within one of the cavities, and having identified in which cavity the instability source is originating, some form of correction may then be implemented. The mechanism that has been chosen to move the HOM frequency spectrum to a region that is less susceptible to excitation from the beam is cavity temperature adjustment.

The SRS already has installed a diagnostic system which monitors all the critical power levels in the RF system of the storage ring, and in addition monitors both the temperature and water flow systems for the klystron and RF cavities[8]. The monitoring system also allows control of certain parameters including cavity temperature.

The assessment of required temperature change on a specific RF cavity to aid non-excitation of a HOM is complex. Not only does the adjustment of cavity temperature affect the mode under investigation, but also all other HOM's as well as the fundamental accelerating mode. By compensation using the cavity plunger tuner, the accelerating mode frequency can be maintained, whilst shifting the troublesome HOM away from any natural beam resonance and also not introducing any other HOM into a region of frequency space that could again allow HOM excitation.

3 PRELIMINARY RESULTS

The data acquisition software LabVIEW is used to compare the beam spectrum when beam instabilities are evident with that of a stable beam spectrum, in both the vertical and horizontal planes. This allows a localisation in frequency space as to where particular cavity instabilities appear when folded down to the base-band. Figure 2 shows the spectrum difference when a 1390MHz longitudinal HOM is excited.

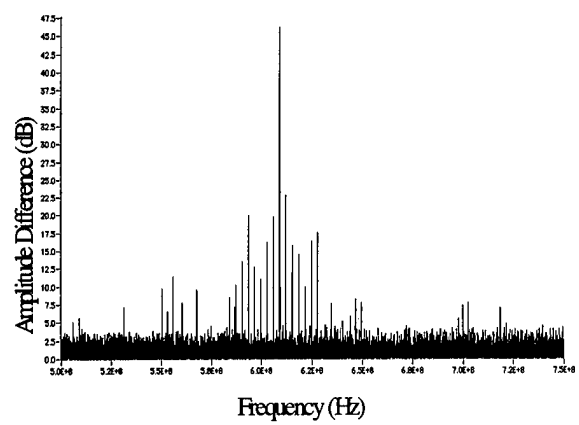

Figure 2. Instability Beam Spectrum Difference.

The maximum difference occurs at $-f_s$ from the 35th orbit harmonic, which when folded back into the natural frequency band, gives:

$$f^{\pm}_{125,n} = 2Bf_{rev} \pm (125f_{rev} + f_s) = 608.91 \text{ or } 1389.9\text{MHz}$$

The cavity probe monitor point provided a good diagnostic for this mode, showing a large response at 1389.9MHz. The signal amplitude was approximately 10dB larger for cavity 2 than any of the other cavity signals (see Figure 3).

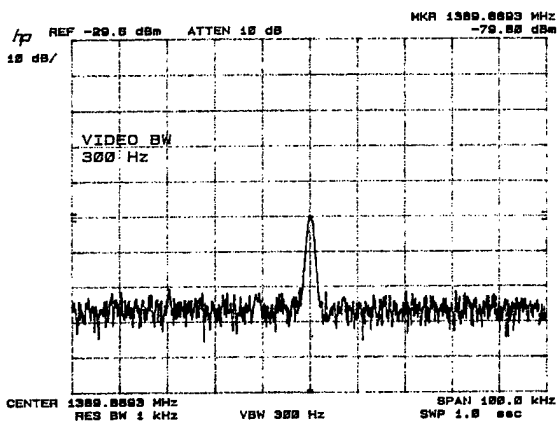

Figure 3. Cavity 2 Probe Signal.

Knowing the response of this mode to both cavity temperature and tuner position, a prediction for the change in cavity operating temperature could be made. An increase in cavity 2 temperature from 50°C to 52°C had the effect of shifting the mode frequency sufficiently away from any beam resonance, such that excitation of the 1390MHz mode could not occur at currents below 260mA.

4 FURTHER WORK

Although the HOM monitoring system is not yet fully completed, the instability identification process using the beam spectrum works well and allows accurate pin-pointing of any instability in the orbiting electron beam, whether due to the RF system or not. Having detected an instability resonance, the process of identifying a cavity HOM as the probable cause has also been proved using the LabVIEW control software. The required correction by temperature adjustment is however not yet implemented into the main control program, and correction thus far has been done manually. It is hoped that the 3 stages of instability identification, HOM determination and temperature compensation can be combined in the near future, to enable fully automated HOM monitoring.

The interface to the temperature control PC has not yet been implemented and should be relatively straightforward using the TCP/IP utilities within LabVIEW to allow the HOM monitoring PC to activate a control on the temperature control PC and therefore implement a change in cavity temperature.

5 CONCLUSIONS

The benefits of such a system for the SRS are great, particularly in terms of the SRS user requirements whereby they require strict control of the photon beam position. To date the diagnostic system has proved invaluable in determining where in frequency space to start looking for potential cavity HOM's. The ability of the system to then track an identified cavity instability and assess any changes as a function of cavity temperature and consequently cavity tuner position, has also proved very useful.

It is clear that there is still a lot of development work to be completed to allow the system to be fully integrated into the main SRS control system. The benefits of such a system would inevitably mean a more efficient RF system providing a stable electron beam orbit and consequently a more reliable photon beam for users.

REFERENCES

[1] 'Cavity-Beam Instabilities on the SRS at Daresbury', P A McIntosh and D M Dykes, Proc. PAC, 1995, Dallas, pp3125-3127.

[2] 'Higher Order Mode (HOM) Induced Longitudinal Coupled Bunch (LCB) Instabilities at the SRS', P A McIntosh and D M Dykes, Proc. EPAC 1996, Sitges, pp1135-1137.

[3] 'Performance of the Transverse Coupled-Bunch feedback System in the SRRC', K T Hsu et al, SRRC, Taiwan, Proc. EPAC 1996, Sitges, pp1920-1922.

[4] 'Longitudinal and Transverse feedback Kickers for the ALS', J N Corlett et al, Proc. EPAC 1994, London, pp1625-1627.

[5] 'Bunch-by-Bunch Longitudinal Feedback System for PEP-II', G Oxoby et al, Proc. EPAC 1994 , London, pp1616-1618.

[6] 'Critical Test of Coupled-Bunch Instability Theory', H Kobayakawa et al, Jap. Journal of App. Phys., vol25 No6, June 1986, pp864-874.

[7] 'Temperature Dependent HOM's in the SRS Cavities', P A McIntosh, Proc. EPAC 1996, Sitges, pp1961-1963.

[8] 'Implementation of a New RF Monitoring System for the SRS Using LabVIEW', M J Pugh and A R MacDonald, these Proceedings.

ONLINE CALCULATION OF TEVATRON COLLIDER LUMINOSITY USING ACCELERATOR INSTRUMENTATION

A.A.Hahn, Fermi National Accelerator Laboratory† , Batavia , Illinois, USA 60510

Abstract

The luminosity of a collision region may be calculated if one understands the lattice parameters and measures the beam intensities, the transverse and longitudinal emittances, and the individual proton and antiproton beam trajectories (space and time) through the collision region. This paper explores an attempt to make this calculation using beam instrumentation during Run 1b of the Tevatron. The instrumentation used is briefly described. The calculations and their uncertainties are compared to luminosities calculated independently by the Collider Experiments (CDF and D0).

1 INTRODUCTION

The primary focus of accelerator instrumentation is on diagnostics in order to identify problems in machine operations. However this same instrumentation may be used to calculate the luminosity of the collision regions assuming that one has knowledge of the lattice. Run 1 of the Tevatron Collider Program and the availability of online analysis tools provided the opportunity to attempt this measurement. Some initial uncertainty regarding the calculation of luminosity by the two Collider Detectors (CDF and D0 at the B0 and D0 collision regions respectively) provided the motivation.

1.1 Assumptions

The only assumption about the beam is that both proton and antiproton bunches can be described as three dimensional gaussian distributions,

$$\rho^{\kappa}(x,y,s,ct) = \frac{N^{\kappa} e^{-\frac{1}{2}\left(\left(\frac{x-x^{\kappa}(s)}{\sigma_x^{\kappa}(s)}\right)^2+\left(\frac{y-y^{\kappa}(s)}{\sigma_y^{\kappa}(s)}\right)^2+\left(\frac{s-ct+\phi^{\kappa}}{\sigma_l^{\kappa}}\right)^2\right)}}{\sqrt{(2\pi)^3}\sigma_x^{\kappa}(s)\sigma_y^{\kappa}(s)\sigma_l^{\kappa}},$$

where N^{κ} is the bunch intensity, $\sigma_x^{\kappa}(s), \sigma_y^{\kappa}(s), \sigma_l^{\kappa}$, are the transverse and longitudinal bunch sizes, $x^{\kappa}(s), y^{\kappa}(s)$, are the closed horizontal and vertical orbits, ϕ^{κ} is the cogging offset (collision offset with respect to s=0), and x, y, s, and ct are the independent transverse, longitudinal and time coordinates (in meters) of the bunch. The superscript $^{\kappa}$ signifies the type beam (p for proton, a for antiproton). Since the proton crossing at s=0 defines ct= 0, ϕ^{p} =0. The gaussian assumption is borne out by measurements from our transverse and longitudinal profile monitors.

1.2 Luminosity

With this form of the beam distribution, the luminosity (with units = $(\mathrm{m}^2\ \mathrm{s})^{-1}$) may be written as

$$L = h\nu \int_{x,y,s,ct} dx\, dy\, ds\,(2cdt)\, \rho^{p}(x,y,s,ct)\rho^{a}(x,y,s,-ct),$$

with h the rf harmonic number and ν the rf frequency. Integrating over x, y, and ct gives the longitudinal luminosity profile,

$$l(s) = \frac{h\nu N^{p}N^{a}\, e^{-\frac{1}{2}\left(\frac{\left(x^{p}(s)-x^{a}(s)\right)^2}{\sigma_x^{p}(s)^2+\sigma_x^{a}(s)^2}+\frac{\left(y^{p}(s)-y^{a}(s)\right)^2}{\sigma_y^{p}(s)^2+\sigma_y^{a}(s)^2}+4\frac{\left(\phi^{a}+s\right)^2}{\sigma_l^{p\,2}+\sigma_l^{a\,2}}\right)}}{\sqrt{2\pi^3\left(\sigma_x^{p}(s)^2+\sigma_x^{a}(s)^2\right)\left(\sigma_y^{p}(s)^2+\sigma_y^{a}(s)^2\right)\left(\sigma_l^{p\,2}+\sigma_l^{a\,2}\right)}} \quad (1)$$

with $l(s)$ having dimensions of $(\mathrm{m}^3\mathrm{s})^{-1}$. This quantity needs to be summed over the number of colliding bunches.

The transverse beam size σ_t may be written as functions of the lattice parameters β and D (dispersion), the measured values of emittance ε_t (in rms and unnormalized form), and fractional momentum spread $\Delta p/p$,

$$\sigma_t(\varepsilon_t, \Delta p/p, s) = \sqrt{\beta_t(s)\varepsilon_t + \left(D_t(s)\,\Delta p/p\right)^2}. \quad (2)$$

Usually the vertical dispersion is so small that it is neglected. Since the collision point is in a drift region,

$$\beta(s) = \beta_{\min} + \left(s - s_{\beta\min}\right)^2 / \beta_{\min},$$

and $D(s) = D'(s - s_{D\min}) + D_{\min}$ with D' the derivative of the dispersion. $\Delta p/p$ for a relativistic beam can be related to the longitudinal beam size σ_l by

$$\Delta p/p = \sqrt{2eV/\gamma_t h E_s}\,\sin(\pi\nu\sigma_l), \quad (3)$$

where V is the voltage of the rf, γ_t is the transition γ, and E_s is the synchronous energy.

Since the transverse beam monitors are (usually) not located within the collision region, it is necessary to know the lattice well enough to calculate the ratio of $\sqrt{\beta_{\min}/\beta_{monitor}}$ in order to use the measured bunch

† Work supported by the U.S. Deptartment of Energy under contract No. DE-AC02-76CH03000

sizes. In addition the location of $\beta_{\min}$ as well as the dispersion must be determined.

In order to minimize the beam-beam tune shift in Run 1, electrostatic separators were installed in the Tevatron. These separators give rise to separated helical orbits for the proton and antiproton beams. Another set of electrostatic separators near the collision regions are adjusted to bring the beams into collision once low beta is achieved. If this adjustment is incorrect, the trajectories of the proton and antiproton closed orbits in the collision region may not coincide and thus should be measured. In this region, the closed orbits are simply $x(s)=m_x\ s+b_x$, and $y(s)=m_y\ s+b_y$,with different slopes and offsets for proton and antiproton beams.

2 INSTRUMENTATION

The measurements described in this paper all took place at the end of Run 1B (1994-1996).The instrumentation platform in each of the following cases was a commercial Apple Macintosh® computer running National Instruments' LabVIEW® which was interfaced [1] to the Accelerator Divisions Control System ACNET via Token Ring or Ethernet. This front-end platform and software gave us a powerful data acquisition/analysis tool which allowed on-line analysis of copious amounts of data. The summary results were then available to ACNET. In addition another software interface TCPort allowed the front end to request data from any ACNET device in the accelerator. This last feature was used by the another front-end (the "Luminometer") to acquire the measured data from the other front-ends and make the luminosity calculations for each bunch and collision region. This was done by numerically integrating equation (*1*) over the variable "s". The update times (for 12 different collisions) was typically less than a few seconds and primarily was limited by the update times of the actual instrumentation.

The following sections provide brief details of the Instrumentation Front-Ends.

2.1 SBD - Beam Intensities and σ_l.

The Sample Bunch Display (SBD) [2] is composed of a front-end interfaced via GPIB to a Tektronix® 620 Oscilloscope. The oscilloscope was connected to a high bandwidth (3kHz to 6GHz) wall current monitor. The front end sequenced the oscilloscope through each individual proton and antiproton bunch, calculating the intensity, centroid, and rms of the central bunch as well as any satellite bunches (up to ± 5 rf buckets away). The system of oscilloscope, cabling, and wall current monitor were characterized *a priori* to better than 1% absolute intensity. During the a store the total summed intensity of all the bunches could be compared to a DCCT monitor, which had been calibrated to better than 1% by a current source. The two results agreed within the 1% error margin. The rms calculation precision was limited by the sampling rate of the scope (2Gsa/s), but was estimated to be accurate at the 5% level (the rms beam size varied from 2-3 ns during a store).

2.2 Flying Wires and Sync Lite - transverse σ_t.

The Flying Wire System [3] is composed of 3 Flying Wires, all controlled by the same front-end through a VME interface (for the loss monitor data) and a commercial (nuLogic®) NuBus® plug-in for the closed loop motion control. The wires are 30 micron diameter carbon filament which are "flown" through the beam at speeds of 5 m/s. The losses, primarily pions, are detected 1 m upstream (antiprotons) and downstream (protons) by two loss monitors (plastic scintillators). The loss profiles as a function of wire position are fitted to a gaussian profile with a sloping background using a non-linear Levenberg-Marquardt algorithm [4]. There are two horizontal Flying Wires, and one vertical. The two horizontal wires are used to measure both ε_x and $\Delta p/p$ by solving Eq. 2 for the two unknowns. Since the vertical dispersion is negligible and we ignore any coupling effects, the single vertical wire suffices for ε_y. During a store, the Flying Wires are flown every 30 minutes. The error in the Flying Wire measurement is 5% in emittance, ignoring the lattice uncertainties.

The Synchrotron Light Monitor (Sync Lite) [5] consists of two optical telescopes (one proton and one antiproton) which image the beam using the synchrotron light (at 400 nm) which is produced from the upstream edge of an upstream dipole(protons) and downstream edge of a downstream dipole (antiproton). Each telescope is equipped with a high-speed gated-Intensifier coupled to a CIDTech® CID camera. The cameras are multiplexed into a single Nubus® framegrabber. The analysis sequences through each proton and antiproton bunch with a complete cycle taking less than 12 seconds. The "normal" analysis consists of a pixel by pixel gain normalization and then the projection of the two dimensional image into horizontal and vertical profiles, These profiles are fitted with a similar algorithm as mentioned above. Since there is only one horizontal profile, it is impossible to unfold ε_x and $\Delta p/p$. However the SBD bunch length can be used as in Eq.3 to calculate $\Delta p/p$ and thus ε_x can be unfolded from σ_x.

During this measurement , the Flying Wires and the Sync Lite measurements were consistent with each other at the 5% level.

2.3 CPM - ϕ and closed orbit trajectories.

A Collision Point Monitor (CPM) [6] is located at the B0 and D0 Collision regions. Each system includes the standard front end interfaced to a Tektronix® 520 Oscilloscope. The two channels of the oscilloscope are connected through a multiplexer to two pairs (horizontal and vertical) Beam Position Monitors (BPM's). These BPM pairs are located on the drift region end of the low beta quad-

rupoles, one pair on the upstream side, the other on the downstream side. The function of the system is to calculate straight line beam trajectories (we ignore beam-beam steering) through the collision region. We have shorted the downstream end of the Upstream plates (and shorted the upstream end of the Downstream plates) in order to force the raw proton and antiproton BPM plate signals through the same analysis path (the two plates of each BPM are fed into the two scope channels). The analysis involves a digital rectification of the BPM signals, and the calculation of proton and antiproton trajectories. Since according to Eq.1 we are only interested in the difference between the proton and antiproton orbits, the absolute systematics should tend to cancel. Unfortunately, the system suffered from proton feed-through into the antiproton signal, thus spoiling the calculation. We plan to add an active feedthrough subtraction in a future update.

In addition the proton and antiproton doublet signals are captured on a single oscilloscope trace for each BPM plate. By determining the zero crossing point for each beam and subtracting, we can calculate the cogging offset. The result of this calculation was a measurement of the offset to better than 1.5 cm (50 ps).

3 RESULTS

The program "Luminometer" was written to acquire the instrumentation data every 20 seconds. In addition it read out the luminosities calculated by the Collider detectors from their luminosity monitors. Since the CPM position data was suspect, it was (arbitrarily) assumed that we had head-on collisions, but the cogging offset ϕ was used. The Flying Wire data were combined with the Sync Lite data and the SBD bunch length to obtain the transverse beam sizes. The lattice parameters were those which were considered as the best estimates (10%). The results are shown in the Figure. This particular store was a 6 (proton) on 1 (antiproton) store. Production luminosity begins at the rise of the D0 Detector plot. This where the beam has already been taken to low beta and scraped in order to lower the detector background. (A programming error in Luminometer prevented the acquisition of CDF data).

The most striking result is that the calculation predicts higher luminosity (50% more) than the detectors observe. The error in the detector luminosity is 5%. The suspicion is that the lattice values are incorrect, although the magnitude of the error seems to be outside the suspected theoretical bounds. We are exploring systematic errors in the Flying Wires and Sync Lite. It is also possible that the beams were not making head-on collisions, but this possibility seems remote since the beams are empirically adjusted to maximize luminosity. The "microstructure" in the calculated plots is due both to the statistical noise in the Sync Lite calculations (every 12 s), and the effect of a simplistic averaging of the current Sync Lite results with older Flying Wire results (flown only every 30 minutes). This gives rise to a step feature whenever fresh Flying Wire data became available. This will be changed in a future version which will weight the Flying Wire data as a function of elapsed time.

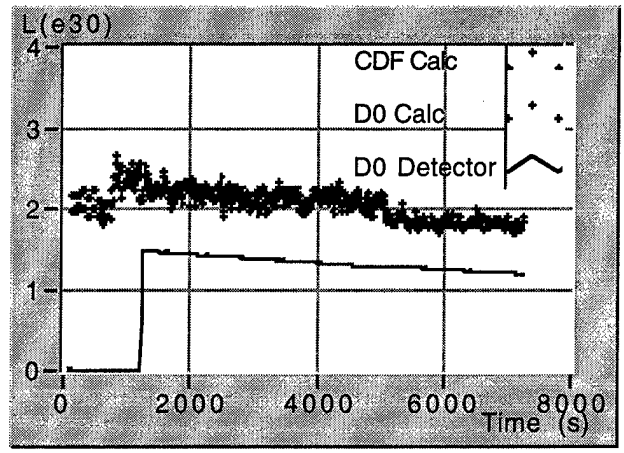

Figure: Operation of Luminometer. The upper traces are those calculated by the on-line program "Luminometer". The lower trace is the D0 Detector Luminosity . See text for more details.

4 CONCLUSIONS

The results from the Luminometer show much work remains to be done, if we are to achieve the goal of measuring luminosity with accelerator instrumentation. We hope to improve the software algorithms (CPM) and actual hardware (Flying Wires and Sync Lite) to give us more confidence in the results. Finally we need to spend a major effort on the attempt to measure the lattice, especially to correlate beam sizes from the measuring instruments to the collision regions. We may install a test Flying Wire system in a collision region (before the detectors are installed in Run 2) in order to compare the beam size there and that measured simultaneously at the normal Flying Wire and Sync Lite locations.

REFERENCES

[1] W. Blokland, "Integrating the Commercial Software package LabVIEW with Fermilab's Accelerator Control NETwork", ICALEPCS, Chicago, 1995.

[2] E.L. Barsotti, Jr., "A Longitudinal Bunch Monitoring System Using LabVIEW and High-speed Oscilloscopes", 1994 Accelerator Instrumentation Workshop, Vancouver, Canada, 1994, pp. 466-472.

[3] W.Blokland, G.Vogel, J.Dey, "A New Flying Wire System for the Tevatron", this conference (PAC 97).

[4] A.A.Hahn, " A Levenberg-Marquardt Least Squares Fit Algorithm Optimized for LabVIEW". Technical Note, 1997.

[5] A.A.Hahn, "Results from an Imaging Beam Monitor in the Tevatron using Synchrotron Light", HEACC'92, pp. 248-250 Int. J. Mod. Phys. A (Proc.Suppl.) 2B (1993).

[6] M.Olson, A.A.Hahn, "Position and Collision Point Measurement System for Fermilab's Interaction Regions", Seventh Beam Instrumentation Workshop 1996, Argonne, Il. pp. 468-475.

A BEAM MONITORING & CALIBRATION SYSTEM FOR HIGH-POWER ELECTRON LINACS

V.L.Uvarov, S.P.Karasyov, S.V.Maryokhin, R.I.Pomatsalyuk, S.Yu.Prokopenko, I.N.Shlakhov, A.Eh.Tenishev

National Science Center "Kharkov Institute of Physics & Technology" (KIPT), 310108, Kharkov, Ukraine

Abstract

Electron beams application in research and technology requires a strict control of main irradiation parameters: electrons energy, beam amplitude and power, as well as absorbed dose in a worked-up material. To provide a certification of accelerators and technologies using electron or bremsstrahlung irradiation a beam-calibration system is elaborated. It consists of a number of primary transducers (combined calorimeter - Faradey cup, Rogovski coils, full-absorption calorimeter for a scanned electron beam, ionization chambers, radiation-acoustic line etc.) provided with suitable electronic setups. PC is used for a data processing. The report describes a method of irradiation-transducer-interaction computer modeling as well.

INTRODUCTION

An "Accelerator" scientific research establishment, affiliated with the National Science Center KIPT, is a leading organization in Ukraine for electron linacs development and construction, including technologies on their base [1]. The establishment also has a number of radiation technology dedicated facilities based on utilization of electron and bremsstrahlung radiation fluxes [2]. Several measurement channels have been developed to exercise control over output radiation parameters. "Accelerator" Establishment, jointly with Kharkov Metrology Institute and Mendeleev Metrology Institute (St.Peterburg, Russia), have developed a reference measurement complex to be need for determination of basic parameters of electron and bremsstrahlung radiation in the electron energy range 5...50 MeV. This energy range choice warranted by the promise of advanced applications (sterilization, semiconductor- and polymeric materials modification, including production items on their base, rubber waste utilization, nuclear medicine radionuclide production, activation analysis, non-destructive testing, etc.). This communication describes measurement instruments for irradiation monitoring & calibration and their performances.

1 BASIC MEASUREMENT DEVICES

A list of main measurement instruments, used for calibration of technological measurement channels is given in Table 1. Below, one can find more detailed of the measurement instruments and results of their metrological studies.

Table 1. Basic Measurement Instruments & their Characteristics

Item No	Measurement instrument	Physics-quantity unit of measurement	Metrological value	Note
1	2	3	4	5
1.	Integrated calorimeter- Faraday cup ICFC-2	Energy flux, W	$10^2..10^4$	Unswept electron beam
		Energy flux density, W/m^2	$10^5..10^9$	
		Electron flux, s^{-1}	$10^{12}..10^{15}$	
		Electron flux density, $m^{-2}s^{-1}$	$10^{15}..10^{18}$	
		Mean electron energy, MeV	5...30	
2.	Electron radiation calorimeter ERC-1	Electron radiation energy flow, W	$5\cdot10^2..10^5$ $E_e = 4..12$ MeV	Swept (scanned) beam
3.	Magnetic analyzer	Electron radiation energy spectrum in the electron energy range, MeV	6...20	

0-7803-4376-X/98/$10.00 © 1998 IEEE

Table 1(continuation)

1	2	3	4	5
4.	Pulsed current precision reference coil	Pulsed current, A at pulse width	0.25...2.0 τ=4 μs	
5.	e^--radiation calorimeter of absorb. dose - ERC-2	Absorbed dose value, Gy/s	$2\cdot10^1$.$2.5\cdot10^4$	
6.	Thick wall ionization chamber ICV-6	Energy flux, W Energy flux density, W/m^2 of photon incident irradiation with photon energy, MeV	10^{-4}...20 $5\cdot10^{-2}$ .10^6 1...50	

1.1 Integrated calorimeter - Faraday cup

The transducer ICFC-2 is a vacuum pumped Faraday cup with an optimized content and geometry of the active volume in order to decrease the leakage of charge and energy by secondary emission out of the active volume in the incident electron beam energy range 5...30 MeV.

At present, R&D is being carried on to optimize further its geometry with the aim of decreasing its charge dissipation and beam energy losses for E_e up to 50 MeV without deterioration of weight-size characteristics of the active volume.

1.2 Beam energy spectrum magnetic analyzer

A general type of automatic beam energy spectrum analyzer (see fig.1) has been developed for measurement - taking of beam energy characteristics, based on electromagnet **M**, at the exit of which a slit collimator **K** and the Faraday cup are placed, and a magnetoinductive beam current transducer (**MIT** - Rogovski coil), positioned in front of the electromagnet.

By external command IBM PC assigns to the digital-analog converter (**DAC**) a digital code, using which at the exit of the latter there is formed a code-assigned voltage, converted into magnetizing coil current by the V-I converter (**V-IC**). The current value is monitored by the resistor **R1,** and via the normalizing amplifier (**NA**) NA1 and the analog-digital converter (**ADC**) ADC1 it enters PC as a digital code. Simultaneously, a digitized Faraday cup (**FC**) current pulse is fed from FC to PC via NA2 and ADC2,corresponding to the given current value, flowing through magnet winding **M** (to which, in turn, corresponds the given energy value of beam electrons hitting the FC) together with the digitized beam current pulse, obtained from MIT via NA3 and ADC3. Processing the incoming signals according to the assigned program, PC yields, wherever necessary, either a 3-D beam spectrum $I(E_e,\tau)$, where τ is the time space within beam pulse duration, or a $I(E_e)$ spectrum integrated over τ.

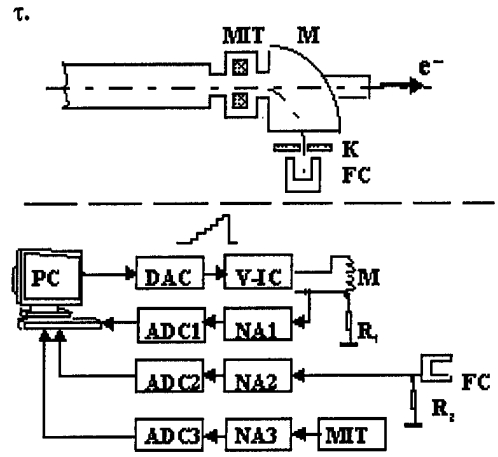

Fig. 1. Magnetic analyzer schematic

1.3 Total absorption calorimeter ERC-1

In order to measure the energy flux (power) of the scanned electron beam a transducer has been developed and constructed as a distilled water-cooled total absorption calorimeter ERC-1 [3].

The calorimeter ERC-1 measurement array includes a built-in turbine transformer of cooling water consumption and two platinum heat resistors, used to measure its temperature at the entrance and exit of the absorber, respectively. Determination of these parameters allows to measure the scanned electron beam energy flow.

This calorimeter ensures beam power measurements with the error, not exceeding 3%.

1.4 Calibration system of the magnetoinductive transducers (MIT) for pulsed beam current

As known, many accelerators have a built-in transducer of the Rogovski coil type, used to take beam current measurements in the beam continuous diagnostic set. For their calibration a system had been developed. The basic constituents of the system are a precision amplitude generator (**PAG**), a two-channel linear switch (**LS**), an ADC and a PC. The PC assigns to PAG the pulse repetition rate and amplitude (at 8 levels). Using LS, the ADC records the PAG pulse shape in sequence, employing a two-page memory, as well as a shape of the pulse at the MIT exit, measured from the load resister $\mathbf{R}_L$. The PC, than, performs their correlation analysis and yields the transducer calibration results. It takes not more then 10 s to run the entire procedure.

1.5 Absorbed dose calorimeter

By implementation of radiation technology processes, involving electron and bremsstrahlung radiation as working devices for measuring the absorbed dose in the range 4...150 kGy, usually requires employment of solid optical dosimeters, ensuring operation with an-error ±15%. To calibrate them the reference absorbed dose calorimeter ERC-3 was developed and constructed in 1994. Its operation principle is based on measurements of the radiation absorbed energy in the active volume, (a graphite pellet, 20 mm in diameter and 2 mm thick under the conditions of electron equilibrium). This accomplished, irradiation of the calibrated dosimeters is performed in the same conditions. As metrological studies showed, the calorimeter ERC-3 ensures measurement of the electron radiation absorbed dose in the dose power range $2\cdot10^1$- $2.5\cdot10^4$ Gy/s with the error not more than 5%.

1.6 Ionization chambers

Calibration of bremsstrahlung radiation measurement instruments over energy flux (power) is performed, using the reference thick-wall ionization chamber ICV-6, developed and constructed by Mendeleev Metrology Institute. The chamber ensures measurement accuracy, not worse then 10%. For metrological monitoring of radiation processes in the narrow bremsstrahlung radiation beams the above Institute has built a thin-wall ionization chamber-observer IC-O.

2 TECHNOLOGICAL RADIATION - CONTROL CHANNELS

A predominant part of the existing radiation technologies call for continuous control to be exercised over basic radiation parameters. In principle, it is achievable using either transparent transducers of the MIT-type, or radiation flux weakly perturbing transducer. The latter implies low energy losses by a particle during its interaction with the transducer. Preferable, as well, are measurement instruments allowing to use one transducer to obtain date on various radiation parameters. This approach has been implemented by us while developing radiation measurement sets for different applied technologies.

2.1 Electron radiation monitoring

For continuous non-perturbing control of the high-power (≥10kW) scanned electron beam main parameters, "Accelerator" R&D Establishment has developed a measurement channel, employing a phenomenon acoustic signal excitation in a thin magnetostrictive line. The primary transducer is a **FeCo 50%** tape, 0.3 mm wide and 50 μm thick, strung along the scanning line. Relying upon a special electric circuitry and a computer, this instrument provides a real-time control over such beam parameters as scanning area length, most probable electron energy value, transverse dimensions and energy spectrum width. Developed, as well, is a scheme of the instrument remote testing [4].

2.2 Bremsstrahlung monitoring

A number of radiation technologies employ HP (≥1kW) bremsstahlung radiation fluxes with the transverse cross-section up to 500 mm and more, obtainable, as a rule, by way conversion of HP scanned electron beams. For control over such radiation, "Accelerator" Establishment has developed and constructed a measurement channel in which the primary transducer is a wide aperture ionization chamber. It allows to take real-time energy flux measurements.

CONCLUSIONS

Described in this report, the reference measurement complex is used for metrological support of scientific and applied radiation physics programs and custom technological processing, performed by NSC-KIPT "Accelerator" R&D Establishment. A member of measurement sets find their applications for certification of some radiation technology facilities of Russia and Ukraine, as well.

REFERENCES

[1] A.N.Dovbnya et al.: Ukr. Phys.Jorn. vol.40, p.p.909-912 (1995).
[2] A.N.Dovbnya et al.: This Conference.
[3] V.L.Uvarov et al.: Proc. of the XIV Particle Accelerators Workshop. Protvino, 1994, v.2, p.p.117-120 (1994).
[4] S.P.Karasyov et al.: Proc. of the V Europ. Particle Accelerators Conf. EPAC-96. Sitges (Barcelona), v.2, p.p.1678-1679. (1996)

LEDA AND APT BEAM DIAGNOSTICS INSTRUMENTATION*

J. D. Gilpatrick, T. R. Hodapp†, K. F. Johnson, D. G. Martinez†, R. P. Martinez†, J. F. Power, C. R. Rose, R. E. Shafer, R. B. Shurter, M. Stettler
Los Alamos National Laboratory, Los Alamos, NM, 87505, USA

Abstract

A 20-MeV 100-mA-cw proton-accelerator, Low Energy Demonstration Accelerator (LEDA), is presently being developed, fabricated, and tested at Los Alamos National Laboratory (LANL). The beam diagnostic instrumentation for LEDA and the final 1700-GeV Accelerator Production of Tritium (APT) are classified into two categories: operation and characterization instrumentation. The operational instrumentation does not intercept or minimally-intercepts the beam and are sufficiently prompt and robust to provide accurate information to the operators and commissioners during full-current cw beam operation. The characterization instrumentation, primarily utilized during commissioning project-phases, operates under more traditional 100-mA-peak and approximately 0.1-mA-average beam-current conditions. This paper will review some of the LEDA and APT operational beam diagnostic instrumentation.

1 INTRODUCTION

1.1 Accelerator Description

To provide a reliable supply of tritium, a proton linear accelerator will be built as a part of a tritium production plant to be located at the Department of Energy Savannah River Site[1,2]. The APT facility will accelerate 100-mA cw protons from 75 keV to 1700 MeV using both normal-conducting (NC) and superconducting (SC) accelerating structures. The high energy beam is further transported and expanded onto target/blanket assemblies in a 16-cm by 160-cm rectangular distribution[3].

LEDA, the facility that will verify operation of the initial 20-Mev portion of APT, consists of an 75-keV 100-mA cw injector, an 6.7-MeV radio-frequency quadrupole (RFQ), a portion of the coupled-cavity drift-tube linac (CCDTL), and a small high energy beam transport (HEBT) that transports the beam to a 2 MW beamstop[4]. LEDA will be assembled so that the accelerator components are tested in a series of staged experiments. Experiment 1 has already tested the injector, Experiment 2 will integrate the RFQ and injector and will verify the RFQ operation, and Experiment 3 will verify the CCDTL operation.

1.2 Beam Diagnostics Instrumentation Goal

The beam-diagnostic-measurement goal is to provide sufficient and necessary beam information to the accelerator commissioners and facility operators to operate the machine under normal and expected off-normal conditions[5]. The measurement requirements for much of the beam diagnostics instrumentation are given in Table 1. Characterization diagnostics more fully measure the six dimensions of beam phase space, but typically at the cost of intercepting the beam. These beam characterization measurements are most useful at key locations throughout the accelerator and at the end of each staged-commissioning-experiment.

Table 1: Beam diagnostics measurement requirements

Beam Parameter	Range	Accuracy	rms Precision	Bandwidth (kHz)
Current:				
cw	0.5-100 mA	0.5 mA	<0.3 mA	dc-0.5
Pulsed	0.5-100 mA	0.5 mA	<0.3 mA	<0.02-200
Bunched	0.5-100 mA	<5 mA	<0.3 mA	<0.02-200
Loss (Fast Protect)	10000:1	few mA	≈50 pA (≈ 1 μA)	<0.005 (40)
Position	± 0.8 radius	1% radius	<0.5% radius	200
Traj. Angle	<±20 mrad	<1 mrad	<30 μrad	200
Phase	±180°	±3°	0.1°	200
Energy	±20% nom. W	±0.2% nom. W	0.01% nom. W	200
Trns. Prof.	± 3 σ	250 μm, 5 μA	100 μm, 2 μA	0.01
Energy Spread	± 3 σ	<0.3% ΔW/W	<0.1% ΔW/W	< 0.0005
Phase Spread	5-40°	<5°	<1°	<0.0005
Trns. Halo	10^6- ≈30 pA	>100 pA	20 pA	<0.0005

The operational (permanent) diagnostics provide beam information using non-interceptive or minimally interceptive techniques. The permanent diagnostic's non-interceptive or minimally interceptive nature allow them to operate under a variety of cw and pulsed beam conditions.

* Work supported by the US Department of Energy
† Employed by General Atomics Corporation

Each of the beam diagnostic measurements will have an integral error-correction subsystem that corrects for most absolute instrumentation errors. These error corrections are either implemented with digital signal processing in the electronics processors or are added software algorithms in the EPICS computer control system[6].

2 TYPES OF MEASUREMENTS

2.1 Beam Current Measurement

LEDA and APT will use three types of current measurements: dc- or average-beam, pulsed-beam, and bunched-beam current measurement[7,8]. Average current measurements are most useful during normal facility operation. Pulsed or transient beam-current measurements provide transient-current information during startup, off-normal-event recover, and pulsed-beam commissioning. Average beam currents will be acquired with a dc-current transformer that consists of a multiple saturable-core beamline device and an electronics processor. Pulsed- or transient-beam-current measurements consist of a single, high-permeability core with one multi-turn winding that acts as the secondary winding of a transformer with the beam acting as the primary winding. Bunched-beam-current measurements are proportional to the peak bunched-beam current and sum the 350-MHz bunched-beam induced signals from the four-electrode beam position monitors (BPM).

2.2 Beam Loss Measurements

Beam-loss measurement systems have a twofold purpose: to act as an input to the fast protect system that protects beamline hardware in case a catastrophic equipment failure should cause the beam to impinge on a beamline component, and to sense for slightly off-normal accelerator conditions such as beam mismatches[7,9]. Beam loss will be measured by using an argon- or nitrogen-filled ionization chambers to sense the ionizing radiation associated with lost beam. With typical sensitivity to ionizing radiation of 50-70 nC/rad and transient response to radiation-generated events of ten's of ms, the beam loss monitors (BLM) can easily sense a large unexpected radiation transient or a continuing excessive beam loss.

2.3 Transverse Centroids (Position and Angle)

The beam-position measurements consist of four components: a beam-position monitor (BPM) and its associated cabling, an electronic processor, an on-line calibrator, and algorithms in the computer control system that convert the processor signals into beam positions[7,10,11,12,13,14]. The BPM, designed to measure both transverse planes, has four micro-stripline transmission lines terminated in their characteristic impedance. As the 350-MHz bunched beam passes by the BPM electrodes, the beam image currents induce a current on these electrodes. The electrode signals are then fed to the processing electronics via high-quality rf coaxial cables. Typical BPM electrode 5-cm-lengths, 38°-subtended angles, and 1- to 10-cm radii, provide centered-beam signal powers of -3 to +12 dBm with 3.3- to 0.3-dB-per-mm probe sensitivities.

The electronics processor down converts the electrode signals to 2-MHz sinusoidal signals whose relative amplitudes are equal to the original probe 350-MHz Fourier component. The log ratio process on opposite-electrode 2-MHz signals is then performed using an analog logarithmic amplifier and a simple digital summing process. The processor's digital-output signal provides data to the software correction algorithms that compensates for the nonlinear BPM transfer function and the irregularities of the complete measurement system.

2.4 Longitudinal Centurions (Phase and Energy)

To properly set the CCDTL and CCL accelerating-cavity-fields' phases and amplitudes, the beam energy and phase must be measured at many locations throughout the accelerator[7,15]. The energy measurement is accomplished by performing a time of flight (TOF) measurement of the beam's relative velocity. This TOF technique uses signals from two cylindrically symmetric capacitive probes separated by a known drift distance. The TOF measurement system determines the time a particular bunch takes to travel this drift distance, and therefore the velocity, by measuring the phase difference between the 350-MHz probe signals. The energy is then calculated from the measured beam velocity.

The beam phase is the other required beam parameter necessary for proper cavity tuning. This measurement is performed by measuring the phase difference between the cavity accelerating field and the bunch. To provide an accurate measure of the beam phase, the phase-delay errors due to the energy-dependent drift times between the cavity and capacitive probes are subtracted from the actual measured phase. For both the phase and energy measurements, phase-measurement precisions of 0.1° at 350 MHz with the required overall bandwidths are typical.

2.5 Transverse Profiles

The primary goal for transverse profile measurements is to measure the cw full-current transverse profiles, the rms emittance and match parameters, and to verify that the beam is matched to its magnetic transport[7,16,17]. To acquire these rms match parameters, approximately 10 profile measurements will be placed within an approximate 2π range of phase advance. For the bulk of the profile measurements, two measurement techniques will be used to measure the beam profiles.

For beam energies below 200 MeV, the beam energy that is deposited in the background residual gas near the beam region fluoresces. The fluorescent-light flux density

is dependent on the local residual-gas partial pressure, the beam velocity, and the beam-current density. To acquire sufficiently precise profile information, the combined camera signal-to-noise (S:N) and light-to-background ratios must be >90:1 at the beam distribution peak. At beam energies >100 MeV, these S:N ratios drop below 100:1 with gas pressures of 10-6 Torr, 100-mA cw-beam currents, and 2-mm rms widths. Also, since APT will be required to operate under pulse beam conditions, many of the cameras viewing beam profiles will require either a light intensifier or increased light-integration times.

For beam energies above 200 MeV, a flying-wire will acquire beam profiles. The expected precision of the profile measurement is ~10 pC (or 2 μA) of beam charge (current) by 100 μm of relative wire position. For a wire made of SiC or C both having specific heats of approximately 1.2 joules per gram-K, the wire-temperature rise during a single sweep is about 320 K based on a 10-m/s wire velocity. For 1700-MeV protons, this temperature rise is also based on an energy-loss per unit length in these materials of 2 MeV-cm^2/g and 1.8 MeV-cm^2/g, respectively. The profile will either be measured by collecting the secondary electrons from the wire/beam interaction, measuring the moving-wire charge depletion (secondary electrons leaving the wire), or measuring the ionizing radiation produced by scattered protons interacting with the accelerator structures. The wire position will be measured by recording and integrating an attached tachometer signal.

To measure the expanded beams near either the final beamstop or target/blanket assemblies for LEDA or APT, expanded beam profile measurements are required. These expanded beam measurements use a multi-wire harp to acquire the horizontal, vertical, and two 45° projections. The wire composition may either be SiC, Ta or C. The 100-μm diameter SiC and Ta wires will operate at about 1200 K and 1600 K, respectively. Two focal-plane-array IR cameras will view the hot-wire thermal image through front-surface cylindrical mirror optics. The optics path to the cameras, which will be outside the radiation area, will be a labyrinth to attenuate neutrons.

2.6 Longitudinal Profiles (Phase and Energy Spread)

Beam-momentum spread and space-charge forces cause the beam-bunch length to rapidly increase after leaving the linac[7,18]. Multiple bunch-length or phase-spread measurements close to and in the linac can provide useful information on the linac operation and the momentum spread of the beam. Specifically designed image-current probes with bandwidths >4 GHz will be used to measure the Fourier-harmonic content of the microbunch-produced wall image currents. The phase spread or bunch length is acquired by measuring the ratio of the fundamental and higher harmonics of a beam-induced signal from these image-current probes. The linac-beam energy spread is acquired by measuring the beam's transverse profile in a dispersive region of the beam transport, such as in the bends of the APT HEBT.

2.7 Beam Halo Measurements

As with beam loss, existence of beam halo will be another sensitive measure of beam mismatch. The halo measurement relies on intercepting a protion of the beam outside ± two rms-widths of the beam tranverse profile. The halo-monitor jaw or plate, constructed of graphite or tantalum, will intercept the beam for a short period of time. A nearby BLM integrates the induced gamma radiation, which is proportional to the intercepted beam. Downstream collimators will intercept and localize the scattered radiation from these scrapers and localize the resultant activation.

3 SUMMARY

This paper discussed the requirements and measurement techniques necessary to measure the APT and LEDA accelerator-beam parameters. The topics included were the operational beam diagnostic instruments to measure beam current, loss, position, angle, phase, energy, transverse and longitudinal profiles, and halo.

REFERENCES

[1] P. W. Lisowski, "The Accelerator Production of Tritium (APT) Project," these proceedings.

[2] G. P. Lawrence, T. Wangler, "Integrated Normal-conducting/Superconducting High Power Proton Linac for APT," these proceedings.

[3] R. E. Shafer, et. al., "Overview of the APT High-Energy Beam Transport and Beam Expanders," these proceedings.

[4] J. D. Schneider, et. al., "Progress Update on the Low-Energy Demonstration Accelerator (LEDA)," these proceedings.

[5] D. C. Chan, et. al., "Commissioning Plan for A High-Current Proton Linac," these proceedings.

[6] M. E. Thuot, et. al., "The Success and Future of EPICS," Proceedings of the XVIII International Linear Accelerator Conference (Linac96), 26-30 August 1996, Geneva, Switzerland. p 611.

[7] J. D. Gilpatrick, et. al., "Experience with the Ground Test Accelerator Beam Measurement Instrumentation," in AIP Conference Proceedings 319, (Santa Fe, NM, August, 1993), p. 154.

[8] K. Unser, "The Parametric Current Transformer, A Beam Current Monitor Developed for LEP," in AIP Conference Proceedings 252, 1991, p. 266.

[9] C. R. Rose, et. al., "GTA Beamloss Monitor System," in 1992 Linear Accelerator Conference proceedings (Ottawa, Canada, August, 1992), g. 365.

[11] C. R. Rose, et. al., "Description And Operation Of The LEDA Beam Position Measurement Module," these proceedings.

[12] J. D. Gilpatrick, et. al., "Measurements and Performance of the Microstrip Beam Probe System," in 1991 IEEE Particle Accelerator Conference Proceedings, p. 1136.

[13] J. H. Cuperous. "Monitoring of Particle beam at High Frequencies," NIM, 145, (1977), 219.

[14] R. E. Shafer, "Characteristics of Directional Coupler Position Monitors," IEEE Transaction of Nuclear Science 32, No. 5 (1933).

[15] J. Power, et. al., "Design of a VXI Module for Beam Phase and Energy," these proceedings

[16] M. Wilke, et. al., "Status and Test Report of the LANL-Boeing APLE/HPO Flying-Wire Beam-Profile Monitor," LANL Report LA-12732-2180.

[17] D. P. Sandoval, et. al., "Fluorescence-Based Video Profile Beam Diagnostics: Theory and Experience," in AIP Conference Proceedings 319, (Santa Fe, NM, August, 1993), p. 273.

[18] J. D. Gilpatrick, et. al., "Design and Operation of a Bunched-Beam Phase-Spread Measurement," in 1992 Linear Accelerator Conference proceedings (Ottawa, Canada, August, 1992), g. 359.

PEP-II BUNCH-BY-BUNCH CURRENT MONITOR*

M.J. Chin, J.A. Hinkson

Lawrence Berkeley National Laboratory, University of California, Berkeley, California, 94720, U.S.A

Abstract

PEP-II is an asymmetric B-Factory that will have 2200 meter rings storing 9 GeV electrons and 3.1 GeV positrons, each with as many as 3492 beam bunches. To minimize beam-beam instabilities it is important to have equal bunch charge in each ring. This is accomplished by measuring the relative bunch charge and controlling injection timing and intensity. Because there may be a variety of bunch patterns, the bunch monitors are designed to measure beam in every possible bucket. Results of bunch amplitude measurements with a resolution of >9 bits are available to the injection control system at rates up to 66 Hz.

The bunch monitor hardware consists of beam pickups, front end filter/combiners, 1428 MHz down-converters, 1 GHz video detectors, and two VXI systems. In this paper we report on the bunch monitor design .

1 FRONT END ELECTRONICS

Fig. 1 is a block diagram of the Bunch Monitor system.

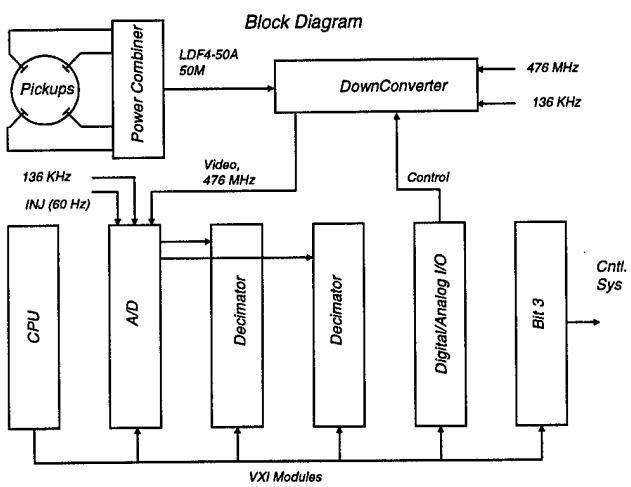

Figure 1 Bunch Monitor block diagram

In both rings the beam bunches are sensed by standard PEP-II BPM buttons, 15 mm in diameter. Bunch signals from these buttons are connected to a nearby filter/combiner chassis. This device consists of four microstrip directional couplers on a common substrate designed for 1428 MHz center frequency (three times the ring cavity RF). The four couplers filter and combine the button signals. Coaxial cables in the chassis are trimmed to eliminate time delay between signals. The pulse doublets occurring 700 ps apart are sent to the Down Converter via 50 meters of ½ inch Heliax™ cable.

1.1 Down Converter

The function of the Down Converter is to heterodyne the 1428 MHz beam signals down to base band video in a bandwidth of DC to approximately 1 GHz. Video output pulses representing the amplitude of individual beam bunches from this module are sent to the VXI electronics A/D converter module. Bunches will normally be 4.2 ns apart, but bucket spacing is 2.1 ns. The video bandwidth must be wide enough to detect the closest bunches.

To maintain phase coherence with the beam signals, it is necessary to synchronously detect the beam signals with 1428 MHz derived from the cavity reference RF. This is accomplished with a 3X frequency multiplier and a high-level doubly balanced mixer. The RF input to the multiplier is phase-adjustable to compensate signal path delay and changes in beam synchronous phase. A 1428 MHz monocycle generator triggered at the ring revolution frequency (136 kHz) is used to simulate a single bunch and is switched into the signal path during setup and testing. The mixer multiplies 1428 MHz against the beam signals. The DC to 1 GHz IF output of the mixer is lowpass filtered to remove high order mixing products. The filter has good pulse response with little ringing.

Charge in a single bunch may vary over 60 dB. A programmable attenuator in the Down Converter is used to adjust bunch signal levels for optimum detection. The A/D converter module input is about ±250 mV full scale. A video amplifier (DC to 1.1 GHz) is used to raise signal levels to the proper level for the digitizer and to provide a video monitor signal for an oscilloscope.

The 1428 MHz center frequency was chosen because of beam pipe size (90 mm). The RF sixth harmonic (2856 MHz) would be preferable because of the required wide video bandwidth, but the pipe diameter permits waveguide propagation of 2856 MHz beam signals unrelated to bunch charge.

*This work was supported by the Director, Office of Energy Research, Office of Basic Energy Sciences, Materials Sciences Division, of the U.S. Department of Energy, under Contract No. DE-AC03-76SF00098.

0-7803-4376-X/98/$10.00 © 1998 IEEE

2 VXI ELECTRONICS

An HP E1401B VXI mainframe powers the Bunch Monitor modules. These include a 500 MHz A/D Module, two Decimator Modules, and a commercial low-speed digital/analog I/O Module for range setting and status monitoring. All of the VXI modules are register-based, and are controlled by a 100 MHz Pentium embedded controller running the WinNT 3.51 operating system.

The 1 ns video pulses from the RF Down Converter along with PEP-II timing signals feed into the A/D module. It generates two streams of 8 bit data words at 238 MHz for the Decimators. The Decimators use Field Programmable Gate Arrays (FPGAs) to hardware-sum each bunch 255 times to improve resolution.

The CPU receives a VXI interrupt from the Decimators when the 255 hardware sum is complete. It then copies 3492 x 16-bit data words from the Decimators into local RAM, performs additional sums in software, and then sends the ~8 kbyte results to the PEP-II Control System via a Bit3 VME-VME interface card.

2.1 A/D Module

This module uses the Maxim 101, an 8-bit 500 MHz A/D with a built-in 1.2 GHz sample/hold; this chip is also used on the damping systems at the ALS, PEP-II and the KEK B-factory. The absolute accuracy of this chip is only 6-bits at full speed, but our goal is increased resolution, which is accomplished by summing multiple samples for each bunch. At a 60 Hz injection rate, there is enough time to sum every 2.1 ns bunch 255 times (resulting in a 16-bit sum) and still "decimate" by a factor of 8. Figure 2 is a subsection of a plot showing that, with 256 averages, the effective resolution increases from 2 mV/count to <1 mV/count. With 0 volts input to the A/D Module, the maximum noise peak is also at the 9 bit level .

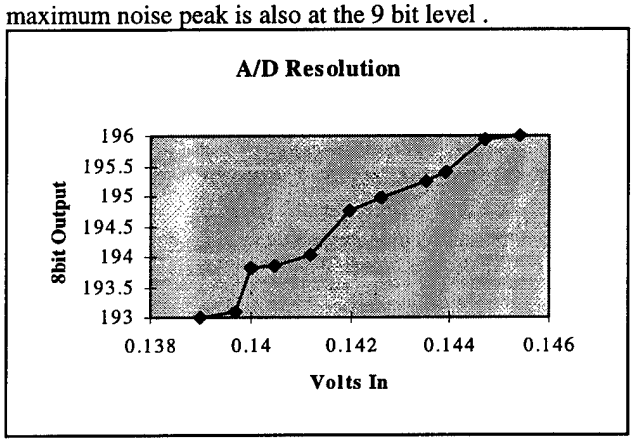

Figure 2 A/D resolution near full scale

The MAX101 continuously outputs two 8-bit output data busses on alternate 476 MHz clock cycles. The VXI A/D module contains a MAX101 evaluation printed circuit board (PCB) (fitted with connectors for clock, data and signal) mounted on a VXI PCB which uses 1 GHz ECL logic (ECLinPS™) circuitry to synchronize the two 238 MHz data streams with SLAC Timing System signals for clock, bunch #0, and injection. The outputs from the A/D module are two 8-bit data streams, the 238 MHz data clock, and a synchronizing pulse. Each stream is sent to a Decimator Module using ELCinPS differential driver/receivers via a custom parallel QuietZone™ cable from Gore Technology.

2.2 Decimator Module

Commercial VME digital signal processor (DSP) alternatives were considered for the Decimator Modules, but no single board could keep up with a 238 MHz data rate; providing synched and decimated data would have required additional design work anyway. Furthermore, we wanted the Decimator to double-buffer each 60 Hz data frame in onboard RAM so that the VXI CPU would have an entire 16 ms to extract the 3492 x 16-bit data across the VXI bus.

Each Decimator uses ECLinPS to split its 238 MHz data stream into 6 separate phased data streams running at ~50 MHz, each stream being responsible for a 291 bunch section of the 1746 total. The number of data streams was chosen based on available Xilinx FPGAs, their speed capabilities, and how many of the appropriate speed-package could be reasonably laid out on a single side of a VXI PCB. Also, 1746 is an even multiple of 6, which makes decimation easier.

The FPGA design would have been much simpler without decimation, but that would have required that read/modify/write (RMW) operations into dual-port RAM be performed in a single cycle. The new XC4000E™ FPGAs have on-chip synchronous dual-port RAM, which would have been perfect for a RMW. Unfortunately, we found no package/speed combination with sufficient RAM to hold the 291x16 bit values required, so we used Integrated Device Technology asynchronous dual-port RAM, which require multiple FPGA clock cycles to do the RMW. We chose 8 FPGA cycles to perform the RMW because it supplied clean control edges for the dual-port RAMs, and [8 x 256 orbits x 7 us/orbit] fits into the 16 ms period. We've also created single-shot FPGA designs that simply write consecutive 8 bit A/D values into the dual-port RAM as a diagnostic test.

A synchronization pulse from the A/D module starts the 6 FPGAs on the accumulation cycle. Each first zeros out 291 dual-port RAM locations, and then performs 291 x 255 RMW operations to this RAM. Upon completion, they toggle the level of an upper bit of the RAM address line; this performs the bank-selection process so that the data from the previous accumulation may be read out from the VXI bus while another accumulation cycle begins.

We investigated commercial VXI interface chips, but they seemed to have more capability (and complexity) than we required, and they are geared towards interfacing Motorola 68xxx processors rather than a slave board. In the end, we built our own VXI interface using a 168-pin

XC4013. It supports the usual register protocol, and also provides two features: first an interrupt service when the accumulator FPGAs signal the completion of an accumulation cycle, and secondly, a register-based address to map the dual-port RAMS into VXI memory space.

Both Decimator and A/D Module VXI PCBs use enclosures from ICS Electronics (Milpitas, CA), which have an elastomeric conductive gasket for EMI shielding.

2.3 CPU and Software

The VXI Pentium embedded CPU was about 6 months away from availability from National Instruments (Austin, TX) when we began software development. In the interim, we used an AT-MXI interface from National Instruments that allowed a desktop PC running WinNT™ to function as the controller. It was extremely gratifying that when the VXI controller did arrive (with WinNT preinstalled, no less), we had it booted and connected to our file server in an afternoon, and the next day it was running the exact same diagnostic LabVIEW™ software to control the Decimators. We did find a difference between the AT-MXI interface and the VXI CPU; the AT-MXI can perform only D16 transfers because of the AT bus width. For full compatibility, it would be better to get the PCI-MXI.

To simplify the VXI interface FPGA, the Decimator design allows access to the dual-port RAM from only A16/D16 space (instead of the more efficient A24/D32 space). Although we realized at the time that this would double the amount of time the VXI CPU would require to move data from the decimator to its local RAM, the CPU specifications suggested this would be small part of the overall time budget. Upon test, we discovered that not only would we have to make twice as many data accesses, but that A16/D16 operations are especially slow for this CPU. In order to keep up with 60 Hz operation, we recoded from LabVIEW™ VIs to MSVC++™ and achieved about twice the speed. The current 100MHz CPU takes about 12.5 ms to perform the data frame tasks, with about 8 ms of this time taken in moving the data across the VXI bus.

3 STATUS

A Down Converter and an HP E1401B VXI mainframe holding the A/D Module, two Decimator Modules, and a commercial low-speed digital/analog I/O Module for range setting and status monitoring has been tested in the lab and installed for the PEP-II High Energy Ring; an identical system will be fabricated for the Low Energy Ring. This system provides a measure of all 3492 bunch amplitudes at rates up to 66 Hz with >±9 bit resolution and noise levels.

OPTICAL BEAM DIAGNOSTICS FOR THE LNLS SYNCHROTRON LIGHT SOURCE*

R.H.A. Farias, L.C. Jahnel, Liu Lin and P.F. Tavares
Laboratório Nacional de Luz Síncrotron - Caixa Postal 6192 - 13083-970 Campinas SP - Brazil

Abstract
An optical characterization bench for the electron beam in the LNLS storage ring using visible synchrotron radiation is described. Preliminary measurements at injection energy (120 MeV) and at operation energy (1.37 GeV) are presented. The system includes a high frame rate (up to 400 Hz) CCD camera and a fast photodiode (7 ps FWHM) for longitudinal measurements.

1 INTRODUCTION

The Brazilian Synchrotron Light Source (LNLS) is based on a 1.37 GeV electron storage ring with a 120 MeV injector Linac. Commissioning of the storage ring [1] at low energy started on May 1996 and presently, an year later, we can store 120 mA at 120 MeV and ramp more than 75 mA to 1.37 GeV. The availability of a real time image of the beam in the control room proved to be very useful both during commissioning and normal operation of the ring. In addition, measurements of the stored electron beam transverse and longitudinal profiles yield information about the beam emittance and bunch length. Both quantities are affected to first order by lattice functions, and to higher order by current dependent collective effects. The ability to measure these quantities accurately is, thus, a very important tool to asses both the lattice focusing properties and the effects of collective phenomena, such as ion trapping and beam instabilities.

Several means of producing an image are described in the literature, including pinholes to collimate X-rays [2,3] or lenses to focus the visible part of the spectrum [4,5,6]. The LNLS UVX storage ring operating at injection energy (120 MeV) does not produce detectable X-ray intensities and the present beam characterization bench is set for visible light observation. The achieved resolution of about 70 μm, limited by diffraction due to the natural radiation opening angle, is well suited for the injection energy, where the large beam size is dominated by intra-beam scattering effects. At high energy, however, we expect difficulties to measure the small vertical beam size as well as the vertical emittance, since the latter is calculated from the beam size and the knowledge of the beta functions. In our case, the vertical emittance resolution is about 0.26 nm.rad.

2 THE OPTICAL BEAM DIAGNOSTICS BEAMLINE

The UVX optical electron beam characterization bench uses visible radiation produced at dipole ADI01 at a 4 degree low dispersion port. A schematic layout is shown in Figure 1. The high energy synchrotron radiation power is absorbed by a sapphire filter attached to a water cooled copper radiation mask. The visible light is then extracted into air through a sapphire vacuum window and guided by two mirrors (86 and 90 degree deflection) to the experimental hall. Two borosilicate plano-convex lenses form an image of the electron beam on the surface of a CCD sensor. A variable aperture is placed in front of the radiation exit port to define the horizontal-vertical optical acceptance of the line and consequently control diffraction and geometrical curvature effects. The visible radiation is monochromatized by a 10 nm bandpass interference filter to reduce chromatic aberrations. A set of two polarization filters is used to polarize and control beam intensity on the CCD sensor. The filters are placed near the detector to minimize potential errors due to their surface irregularities. The first mirror, located behind the shielding wall, is mounted on a platform which allows remote angular adjustments about the horizontal and vertical axes. The polarization filters can be commanded from the control room in order to adjust the beam intensity level at the CCD.

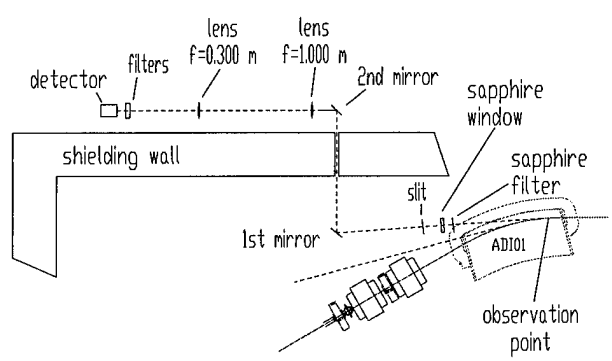

Figure 1: The LNLS UVX optical characterization bench.

The main line CCD camera (EEVCAM17-46), with 512x512 square pixels 15x15 μm in size, will be able to operate up to 400 Hz frame rate, allowing measurements of phenomena which occur in time scales as short as 10 ms such as beam damping at high energy. Meantime,

* This work is partially supported by 'Fundação de Amparo à Pesquisa do Estado de São Paulo'.

while the EEV camera is not operational, we have installed a common CCD video camera to perform the preliminary measurements.

A broadband dielectric beamsplitter divides a fraction of the light to a second branch of the characterization bench where a calibrated photodiode is used to monitor beam current and beam current decay variations for lifetime measurement purposes.

A second beamsplitter separates a fraction of light from the second branch to a third one. Here an ultrafast commercial photodetector (Picometrix PX-D7) with 7 ps FWHM response time will be used to measure single shot bunch length.

2.1 Optical resolution

The synchrotron light accepted by the aperture of the optical bench comes from an arc along the electron orbit. The longer the arc the greater the apparent transverse and longitudinal sizes of the source. If the aperture is made smaller, the limit to resolution from diffraction becomes worst. The optimum aperture is thus a compromise between these effects. In the case of visible synchrotron radiation, the natural diffraction limit imposed by the angular width of the emitted radiation is usually dominant. The optimum aperture should, thus, be approximately equal to the natural radiation opening angle as the diffraction limit will not improve by increasing the aperture but the apparent source size will. For UVX running at 1.37 GeV, the width of the radiation cone for 550 nm is ±3.6 mrad. The calculated resolution of 70 μm is dominated by diffraction, as expected. A bandpass filter with 10 nm FWHM is used to eliminate the long wavelength light which would degrade the diffraction limited resolution. The calculated parameters for UVX standard operation mode are given in Table I. The large value for the natural emittance at 120 MeV is due to intra-beam scattering effects. The transverse spatial resolution of 70 μm corresponds to emittance resolutions of 0.26 nm.rad and 3.5 nm.rad for the vertical and horizontal planes respectively. The principal limitations are expected in the vertical plane at 1.37 GeV whenever coupling coefficients are less than approximately 0.3%.

Table I: Parameters at the UVX beam diagnostics line.

Injection energy	120	MeV
Operation energy	1.37	GeV
Horizontal beta	1.4	m
Vertical beta	18.9	m
Natural emittance		
at 1.37 GeV	99.8	nm.rad
at 120 MeV	≈ 900	nm.rad

3 EXPERIMENTAL RESULTS

3.1 Emittance Measurements

A conventional CCD video camera has been installed at the main beam line to perform static beam emittance measurements. The beam image is captured using a frame grabber and the beam sizes are calculated by fitting gaussian functions to the horizontal and vertical beam profiles.

Beam transverse profiles have been measured as a function of current for the injection and operation energies. Figure 2 shows the beam image seen at the monitor in the control room.

Figure 2: Beam images from dipole ADI01 4 degree exit port corresponding to E=120 MeV (left) and E=1.37 GeV (right).

Figure 3 shows the fitted gaussian curves for an horizontal and a vertical beam profile. Figures 4a and 4b show the beam sizes (one standard deviation) measured as a function of beam current for 1.37 GeV and 120 MeV. Figures 5a and 5b show the natural emittance and coupling factor for both energies. The vertical emittance and coupling at 1.37 GeV are lower than 0.3 nm.rad and 0.3 %, respectively, and are limited by the measurement resolution. The measured natural emittance is in good agreement with the theoretical value at 1.37 GeV indicating that the linear optics of the machine is close to the calculated one. The slight increase in vertical beam size for low currents is probably due to a slow drift in the electron beam orbit which defocus the image on the CCD sensor, since the automatic orbit correction system was not activated during the measurements. At 120 MeV, the measured emittance at low currents is close to the value predicted from intra-beam scattering calculations. For higher currents we have measured an enormous increase in beam emittance. This is probably due to the fact that high current measurements need to be performed right after injection, when the beam is not yet damped (the damping time is 10 s).

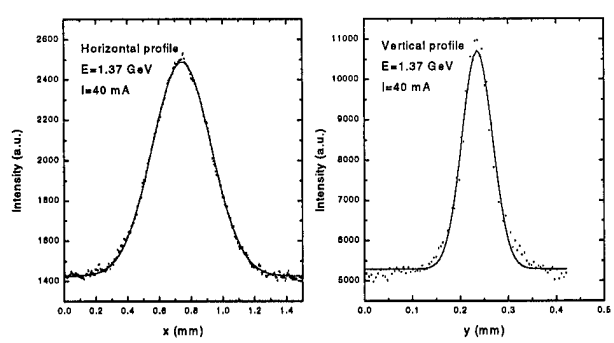

Figure 3: Horizontal (left) and vertical (right) beam profiles for E=1.37 GeV and I=40 mA. The solid curve is a gaussian fitted to the experimental data (dots).

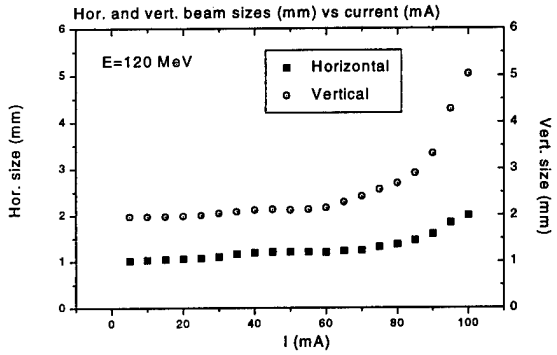

Figure 4a: Horizontal and vertical r.m.s. beam size as a function of beam current for E=120 MeV.

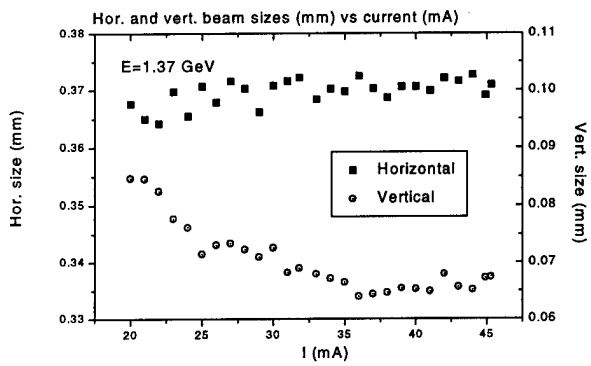

Figure 4b: Horizontal and vertical r.m.s. beam size as a function of beam current for E=1.37 GeV.

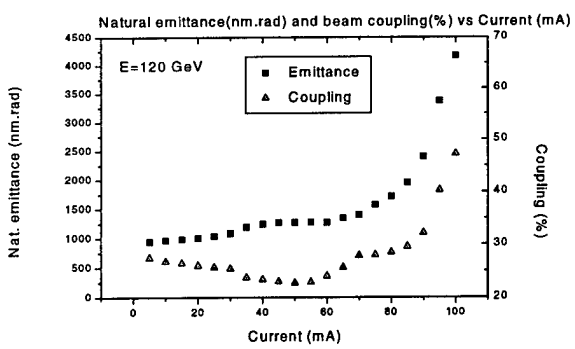

Figure 5a: Natural emittance and coupling as a function of beam current for E=120 MeV.

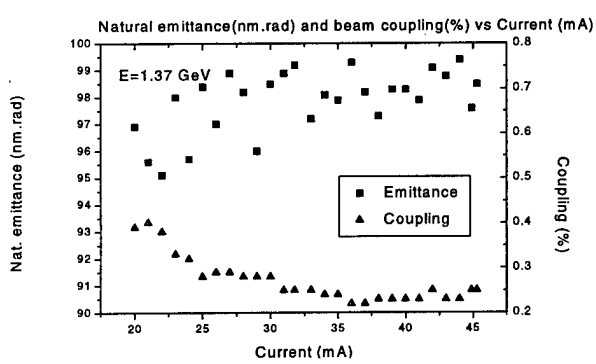

Figure 5b: Natural emittance and coupling as a function of beam current for E=1.37 GeV.

3.2 Observation of ion trapping

Effects of ion trapping have been observed in the storage ring at the synchrotron light monitor in the control room. Ion effects have been detected as a vertical expansion of the beam when a kicker is excited. The vertical enlargement of the beam persists even when the excitation is turned off. The beam can be made flat again by applying appropriate voltages to the clearing electrodes. Figure 6 shows two images of the beam at 900 MeV corresponding to the cases before and after a kicker excitation.

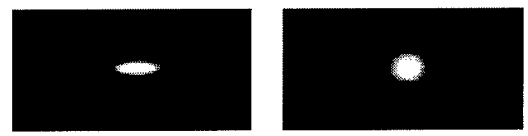

Figure 6: Images showing a vertical enlargement of the beam after excitation with a kicker.

4 CONCLUSIONS

The LNLS optical beam diagnostic line using visible synchrotron radiation has been described. Although not fully operational, some transverse beam size and emittance measurements have been carried out. The installation of the fast photodetector and the high frame rate CCD camera will allow measurements in the longitudinal plane as well as analysis of damping in the transverse plane.

The emittance measurements show that the system resolution is adequate for analysis at injection energy but is limited for measurements in the vertical plane at nominal operation energy. The results show, however, a vertical emittance lower than 0.3 nm.rad at 1.37 GeV, or coupling coefficient lower than 0.3 %, indicating a careful alignment of the magnets.

Some improvements in the beamline are in progress including a system for remote focusing of the beam image and modification of the beam extraction scheme. The new scheme will use a refrigerated mirror in the vacuum chamber in place of the sapphire filter, which has become darkened by radiation.

The limitation to resolution comes from inherent diffraction effects, so resolution improvement imply decreasing the wavelength towards X-rays. The idea of a new line using X-ray imaging is also being considered.

REFERENCES

[1] A.R.D.Rodrigues et al, 'Commissioning and Operation of the Brazilian Synchrotron Light Source', these proceedings.

[2] C.Bovet and E.Rosa, Workshop on Advanced Beam Instrumentation, KEK, 1991.

[3] E.Tarazona and P.Elleaume, Rev Sci.Inst. 66, Feb 95.

[4] A.Hofmann, IEEE Tran.Nuc.Sci., NS-28,No.3, 1981.

[5] Åke Andersson, Juri Tagger, Nuclear Instruments and Methods, A 364 (1995) 4-12.

[6] R.J.Nawrocky, J.Galayda, L.H.Yu and D.M.Shu, IEEE Trans. Nuc. Sci., NS-32, No. 5, 1985.

VIBRATION MEASUREMENT FOR INSTRUMENTATION AND DIAGNOSTICS

S. Sarkar, E. Ilhoff, C. Sibley, S.B. Soong, S. Wells, E. Tsentalovich, T. Zwart
MIT Bates Linear Accelerator Center, Middleton, MA 01949

J. Shaw
University of Massachusetts, Amherst, MA 01003

Abstract

Experimental requirements at Bates place stringent excursion limits on some beam parameters and on measurements of beam properties such as position and charge. Steering elements and measuring devices may be affected by vibrations transmitted along the beam pipe from vacuum pumps and turbulent cooling water flows. A vibration measurement setup, capable of generating displacement spectra and detecting displacements of less than 100nm at 20Hz, has been used in detecting and correcting vibration induced beam parameter deterioration and measurement error. The measurement setup, plans for improvements and vibration monitoring on site are described.

1 INTRODUCTION

Two of the major ongoing experiments at Bates have extreme stability requirements. The parity violation experiment requires the electron beam intensity to be stable such that the centroid can be accurately measured for the two opposing polarization states of the beam. Feedback correction is then applied to balance the charge delivered to the experiment, between both states, to an accuracy of one part per million, over the course of each half hour run. This translates to an instantaneous beam intensity stability requirement of less than 1%. In the experiment to measure the interference response functions in the (e,e'p) reactions, even small systematic uncertainties may result in large errors in the extracted response function due to the small cross sections involved. The total error budget for this experiment is 1% of which 0.1% is allocated to errors in the measurement of total charge. This then sets the differential pulse to pulse accuracy limits for the data taking toroids. Clearly any interference, electrical or mechanical, which adds jitter to the intensity distribution of the beam or causes measurement errors must be located and minimized.

Common causes of errors such as EMI, power line pickup, improper signal grounding and marginal electronics were first identified and corrected. Differential signals and solid copper shielded cables were used as required. With each step measurement errors and beam quality improved but did not fully meet requirements for either experiment. The isolation of a mechanical chopper wheel from the laser table reduced vibration induced jitter and improved beam intensity stability. The addition of bellows for the isolation of turbo pumps and the bracing of beampipe sections near susceptible toroids reduced measurement noise. These fixes were just adequate but the effect of minor mechanical changes, such as changes to brace or support locations, were difficult to predict and often caused stability and measurement errors to deteriorate out of limit.

It became increasingly apparent that some of the remaining source of noise was vibration induced and that a system to detect and correct vibration induced errors was needed.

2 MEASUREMENT SETUP

The vibration measurement setup consists of An ADXL05[1] acceleration transducer and associated electronics connected to a HP 35670A[2] dynamic signal analyzer.

The ADXL05's sensing element is a micromachined polysilicon capacitive acceleration transducer. The chip contains signal conditioning circuitry and can be used for vibration (AC coupled) and inertial force or gravity (DC coupled), measurements. A few external components are required to set the signal scaling factor and the output signal bandwidth. Transducer calibration is done in the DC coupled mode by using the Earths gravity. The maximum transducer bandwidth of ~4 khz is adequate to cover the high frequency vibration from turbo-mechanical pumps and turbulent cooling water flows. Component values were selected to set the gain and bandwidth at 400mV/g and 1.6khz respectively.

The HP 35670A dynamic signal analyzer can be programmed for transducer sensitivity and can generate fourier analyzed displays of the acceleration and the computed displacement signal. The transducer, electronics and signal analyzer noise floors, the selected FFT resolution and the signal averaging used comfortably allow the measurement of displacements of less than 100nm at 20 hz with changes of 20nm being discernible as seen from measurements. This, however, requires that the signals be repetitive but stationary in time over the duration of signal acquisition and averaging and sets a bound on the achievable measurement resolution.

0-7803-4376-X/98 /$10.00 © 1998 IEEE

3 APPLICATION EXAMPLES

1.1 The Polarized Injector Laser Transport

Laser spot size and position variations on the GaAs photocathode of the Bates polarized injector can cause beam intensity variations due to quantum photo efficiency gradients across the crystal. Beam intensity stabilization is done to first order by Laser intensity feedback modulation. Initial beam intensity noise was traced to chopper wheel vibrations and to inband electrical noise causing errors in the feedback. These were corrected as described above. Beam intensity stability deteriorated and 28.5 hz intensity modulation was seen after a routine shutdown. This was traced to 28.5 hz vibrations (figure 1) on `mirror 3' which is the

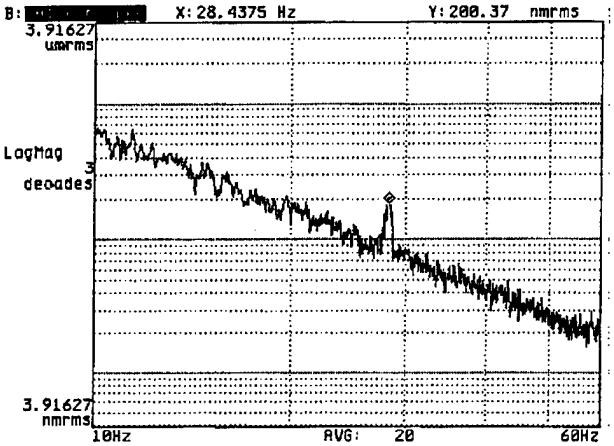

Figure 1: Mirror 3 Vibration

final mirror deflecting the injector laser beam onto the GaAs crystal. Resonance changes were probably caused by mechanical work done near the mirror box. Source of vibration was the cooling water flow in a nearby buncher cavity (figure 2) which is transmitted along the beam support

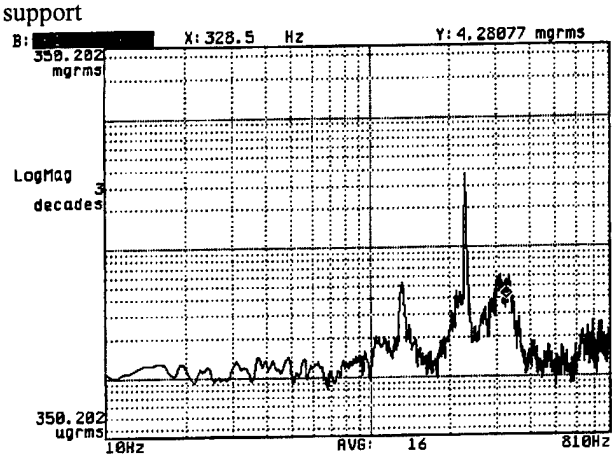

Figure 2: Buncher Cooling Water Flow Vibration

girder to `mirror box 3' support (figure 3). Damping had unpredictable effects, a lead shot filled bean bag did not eliminate the problem (figure 4), whereas two lead bricks in a particular position did (figure 5).

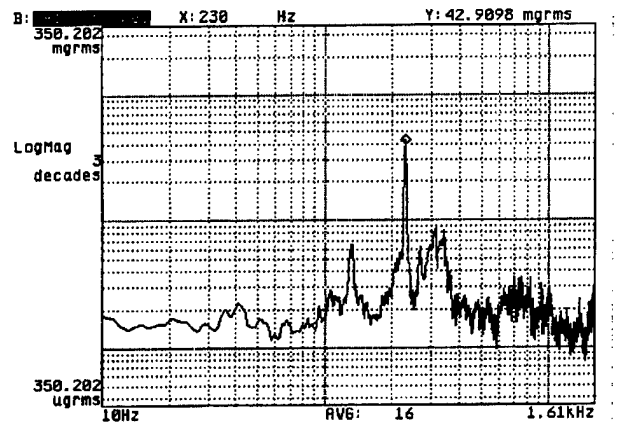

Figure 3: Vibration at Mirror Box 3 Girder

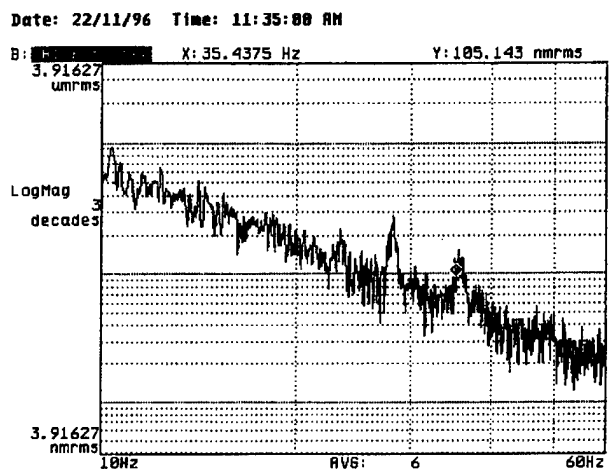

Figure 4: Effect of Lead Shot Filled Bean Bag

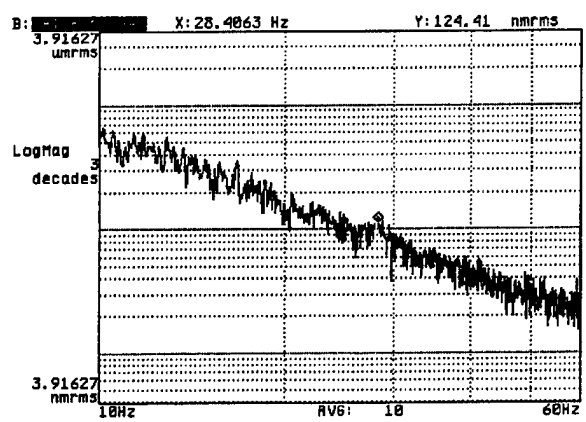

Figure 5: Damping from two Lead Bricks

1.2 The South Hall Datataking Toroids

The SH datataking toroids noise was reduced when turbo pumps were moved upstream, bellows isolated from the beampipe, water flow pipes were cushioned from common beam pipe support stands and the toroids were clamped. The pulse to pulse diferential error was reduced to less than the required 0.1% for a while for one of the two datataking

toroids in close proximity to each other. However when braces were adjusted to try to reduce the noise for the second toroid the figure deteriorated to slightly above the required 0.1% for both of them and has never gone down. Due to running schedules adjustments to the braces using the vibration measurement setup have yet to be done. Another line of attack has been to measure the sensitivity of the toroids to vibration. Figure 6 shows a Pearson toroid subject to floor

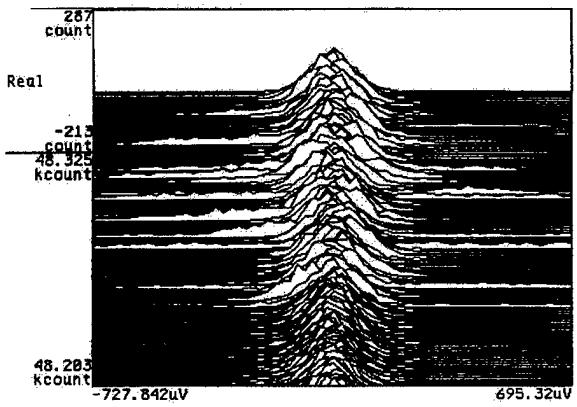

Figure 6: Unmodified Toroid Vibration Response

vibration, while figure 7 shows a modified pearson made to our requirement of potted core showing almost no sensitivity even with direct taps on the body of the toroid.

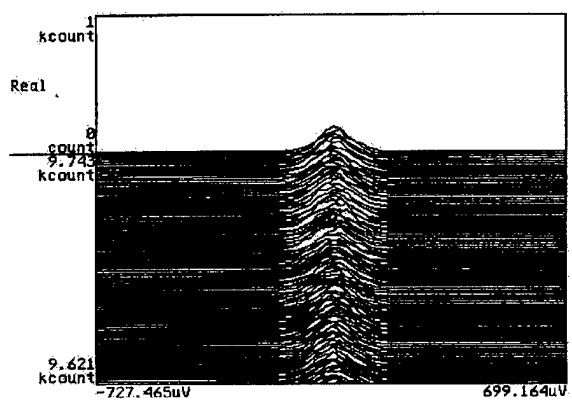

Figure 7: Potted Core Toroid Vibration Response

4 CONCLUSION

Vibration of position and intensity sensors such as beam position monitors and toroids can be interpreted falsely as position or intensity variations and data from these sensors used for feedback corrections can lead to errors deteriorating beam position or intensity stability.

Additions or modifications to beam line elements can cause changes in mechanical resonance characteristics of beam pipe sections causing the induced noise pickup of nearby transducers to change. Similarly physical routing of instrumentation analog signals, done by hand during installation of new systems or during the maintenance and upgrade of existing systems are prone to errors. Inadvertent routing or grounding errors or the incorrect setting of buffer gains offsets etc., which are measured and set to specifications by hand, may alter the path characteristics of the (re)routed signals and can change the electrical characteristics of signal provided to users.

We intend to put vibration transducers at selected locations along the Accelerator and experimental beamlines. Periodic or ongoing monitoring of vibration spectra at these locations along with information obtained using tuned magnetic field search coils when compared to signal spectra of interest can allow pinpointing and flagging of problems as they occur.

5 ACKNOWLEDGEMENTS

The authors would like to sincerely acknowledge the guidance and support received from Dr. Stanley Kowalski and the help of Tom Ferrari in the construction of the prototypes.

6 REFERENCES

[1] `Design-In Reference Manual', Analog Devices, one technology way, PO Box 9106, Norwood MA. 1994.

[2] `HP 35670A Operator's Guide', Hewlett Packard Company, 8600 Soper Hill Road, Everett, WA. 1994.

OPTION OF METHOD FOR ELECTRON BUNCH PHASE DISTRIBUTION MONITORING

A.Tron, I.Merinov, V.Smirnov,
MEPhI, Kashirskoe sh. 31, 115409 Moscow, Russia

Abstract

Methods for longitudinal bunch charge distribution monitoring can be divided onto two groups: the usings of coherent or incoherent radiation of the bunch electrons. The former can be used for estimation of the rms bunch length, and the latter - for the bunch charge distribution measurements. Methods of the bunch distribution monitoring with subpicosecond resolution based on use of secondary electrons, transition, Cherenkov or bremsstrahlung radiation are considered.

1 INTRODUCTION

Increasing interest in short electron bunches for different applications such as a linear collider, FEL, plasma or laser wakefield accelerators demands further development and creation of bunch length (BL) or bunch phase distribution (BPD) monitoring systems with subpicosecond and far better resolution.

All known methods for these measurements can be divided onto two groups: the usings of a coherent or incoherent radiation of the bunch electrons, i.e. the radiation on the wave lengths compared with the bunch length or considerably less than the BL.

It is known the former can be adopted for estimations of the rms BL [1,2,3,4,5,6]. The latter is for measuring the BPD without any model approach of the bunch distribution, and the beam instrumentation from this group form the metrological background for the BL or BPD monitoring. As to the tools of the first group they have to be simple and serve for fast operating control of the BL changes during the linac tuning. The instrumentation from both groups could complement to each other to obtain the complete monitoring system for a specific machine.

The principle of the BPD monitoring is based on the temporal analysis of the incoherent radiation including transition, Cherenkov, bramsstrahlung radiation and also secondary electron one.

The use of incoherent radiation, for example, on a scheme: Cherenkov radiator plus a streak camera [7,8,9], is mainly limited due to the longitudinal chromatic aberration of the camera gap (photocathode - mesh distance) caused by initial velocity spread of hpotoelectrons. To minimize this aberration in several tens times it was proposed [10] instead of a plane-parallel geometry of the gap to use emitter with a small radius of its surface.

The promising method for the BPD monitoring is the secondary electron one [10,11] allowing us to create the selfcalibrating monitor with resolution in the fs-range. This technique is simpler significantly than a streak camera because its rf-feed is taken from appropriate system of a linac. The rf-feed is locked in phase with the bunches, and in the case the time jitter (trigger jitter [12]) can be negligible.

2 SECONDARY ELECTRON MONITOR

One of scheme of secondary electron monitor for BPD measurements is shown in Fig.1.

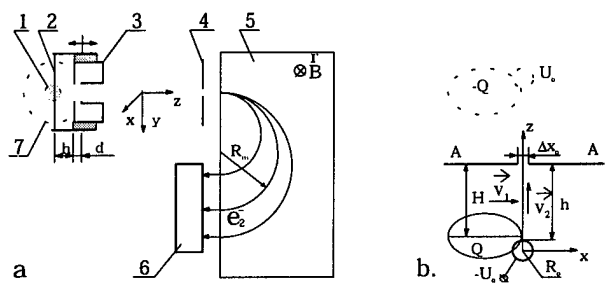

Figure 1: Layout of BPD monitor (a) and geometry of its primary converter (b).

Here BPD of a primary beam (1) in a result of the beam interaction with a wire emitter (2) being under negative potential (U_0) is isohronously transferred into the same distribution of secondary electrons which, then, is coherently transformed into transverse one in the plane of multichannel collector (6) through rf-modulation in the gap of toroidal resonator (3) and magnet (5) allowing direct presentation the BPD on a low frequency display. Taking into account that the beam diameter is rather small (of 1...2 mm), and the smaller h-distance the less transit time spread, the emitter was placed from the resonator at the small fixed distance h = 5 mm, and this monitor unit is moved in the beam for a time of measurement only.

The monitor phase resolution is mainly defined by the transit time spread of the electrons on the h-distance from the emitter with the R_0-radius to the conducting wall (A-A) of the resonator (3), the shutter phase resolution and additional phase dilution due to the beam space charge effect, considered in [13]. Restrictions on the limiting resolution of the shutter, as a rule, lay lower than it can be for the transit time spread, and we shall consider the latter more in detail.

0-7803-4376-X/98/$10.00 © 1998 IEEE

3 TRANSIT TIME SPREAD

Omitting the space charge effect the estimation of the transit time spread of the electrons in the accelerating gap can be done through the chromatic aberration of the gap and the aberration of diaphragm installed in its exit plane.

The chromatic aberration of the h-distance gap (being under the U_0-accelerating voltage) caused by initial electron kinetic energy spread, for example, from W_1 to W_2 can be determined from the expression

$$\Delta t = \frac{h}{c}\sqrt{\frac{W_0}{2U_0}}\left(\frac{2}{E_m/E_0}\frac{\sqrt{W_2}-\sqrt{W_1}}{\sqrt{U_0}}+\frac{W_2-W_1}{2U_0}\right), \qquad (1)$$

where U_0 - in an electron energy units(eV), c is the speed of light, W_0 is the electron rest energy, E_m/E_0 is the retio of the maximum electric field strength on the emitter surface to the strength in the case of the uniform field, i.e., when the plane-parallel geometry of the gap is used.

Denoting $h/R_0 \equiv m$ the E_m/E_0-ratio is given by

$$E_m/E_0 = \sqrt{(m+1)^2-1}\Big/\ln\left(m+1+\sqrt{(m+1)^2-1}\right)$$

values of which as a function of m is represented in Fig.2.

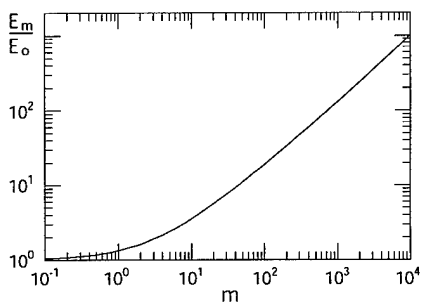

Figure 2: Maximum electric field strength on the emitter surface vs. the ration $m = h/R_0$.

Taking $m = 10^3$ one can increase the electric strength E_m by a factor of 10^2 and, as a consequence, minimize the longitudinal chromatic aberration significantly, that is show in Fig.3.

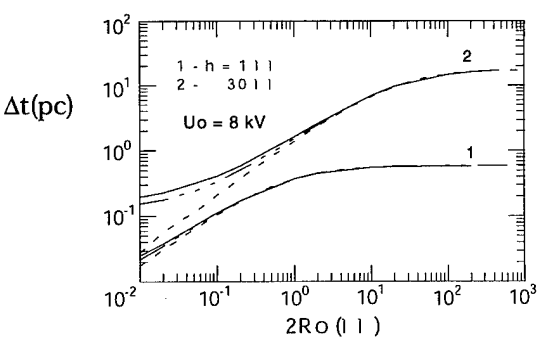

Figure 3: Longitudinal chromatic aberration of the gap vs. the emitter diameter for different distances h at $U_0 = 8$ kV.

The solid lines in Fig.3 are the dependencies taken from [10], the dotted lines represent the calculation results on the formula (1), but the dotted line coming from the upper curve to the bottom one is obtained without the second term in the circular bracket of the formula (1). One can see that with decreasing R_0 and h the longitudinal chromatic aberration of the gap can reach several tens fs.

It should be noted that with decreasing of h we will have to decrease, for example, the radius of the circular hole in the exit plane of the gap or increase the h-distance at the same output diaphragm so that the perturbation effect of the electric field, caused by this diaphragm, would be negligible.

Universal dependence of the transit time spread caused by the diaphragm with infinitesimal thickness in the case of plane-parallel gap vs. the ratio of the h-distance to the exit hole radius is represented in Fig.4, where $t_0 = (2h/c)(W_0/2U_0)^{1/2}$ is the transit time in the gap without the hole. Magnitude of $\bullet t_D$ is defined as the FWHM of the transit time distribution of the electrons started with the 1eV energy perpendicular to the emitter surface and with uniform density of escaping.

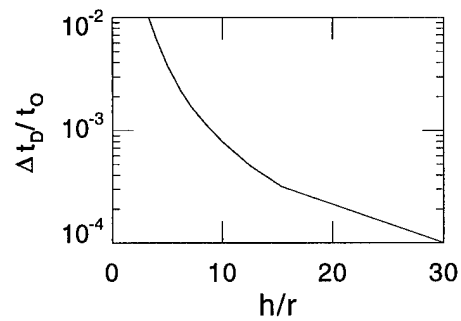

Figure 4: Transit time spread of electrons in the plane-parallel gap vs. its h-distance in units of the hole radius.

As an example, consider the gap of 1 mm with the 4 kV accelerating voltage, then the transit time of t_0 will be 53 ps, and to get the spread not more than 0.05 ps the hole radius of about 0.1 mm has to be taken. Another words, in some cases the account of the diaphragm aberration can decrease the device capacity significantly.

4 RF GAP

To minimize the space charge effect of the relativistic electron beam with the bunch population of $5\cdot10^{10}$ and more one can place the rf-gap of the monitor resonator in the beam [13] so that the directions of moving both the primary beam and the secondary one are coincided in the accelerating and rf-modulating gaps. It is permissible, for example, when the frequency of the bunches is rather low. In the case the rf-gap in the form of two plane-parallel strips from thin foil is placed in the beam so that their planes are perpendicular to the beam axis, and the inductance part of the resonator is outside of the beam pipe. As an example, in Fig.5 is shown the phase resolution of the 1 mm rf-gap with 3 kV amplitude of rf-voltage on the 3 GHz frequency vs. input secondary

electron phase for two cases: when initial electron energy is 4 keV (2) and when the electron is accelerated till this energy in the uniform static field in the rf-gap (1). Hence, at the same electrical and geometrical parameters of the monitor the second case is far more effective.

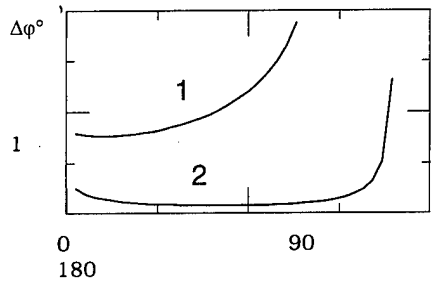

Figure 5: Phase resolution of the 1 mm rf-gap.

5 DELTA-RAYS

One of the way of the BPD monitoring with resolution in the fs-range is the use of the delta-electrons [11]. In Fig.6 the time distribution of the delta-electrons with energies of 10 and 50 keV scattered by the 10 MeV electrons in the carbon fibre of the 8 μm diameter is shown. Probability of escaping of the delta-electron captured by the 1 mm diameter collimator hole, spaced from the target on 5 mm so that the axes of the primary and secondary beams are perpendicular, is about $2 \cdot 10^{-8}$ per an electron of the primary beam with uniform current density distribution within its radius of 1 mm and at analysis of the delta-electrons within energy range of (10±0.05) keV. At the target from the tungsten the probability will be by an order of magnitude greater.

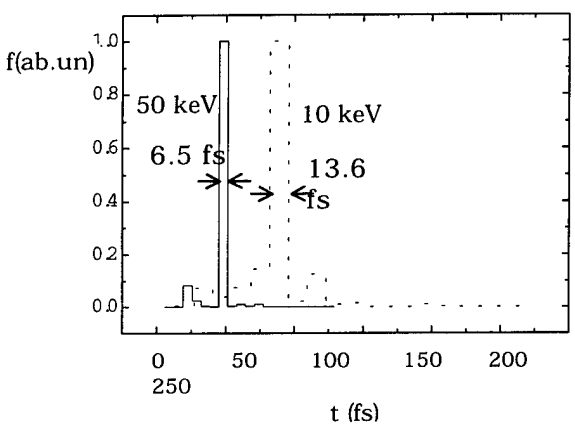

Figure 6: Time distribution of the delta-electrons with energy 10 and 50 keV scattered by the 10 MeV electrons in the carbon fibre of the 8 μm diameter.

6 X-RAYS

At present the x-ray streak camera resolution is limited by 1 ps [14] due to the chromatic aberration of the gap. Improving this resolution by the way mentioned above we have to estimate the efficiency of the x-ray use in our case. Dependence of the x-ray yield per an electron scattered in the tungsten wire of the 0.1 mm diameter (at the same geometry similar to the case of the delta-electron use) vs. the electron energy is shown in Fig.7 where the yield has been defined for the x-ray energy within the range of 1-10 keV. At the calculation the cross sections from [15,16] have been used.

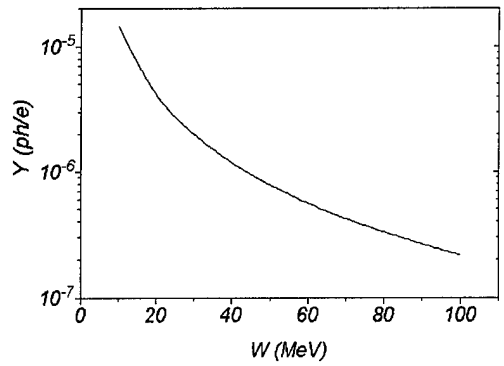

Figure 7: X-rays yield per scattered electron vs. the electron energy.

7 CONCLUSIONS

As it was shown there exist several methods for the BPD measurements with high resolution, and its option depends on the terms in a specific machine .

8 ACKNOWLEDGMENTS

The researches were supported by the Russian Fund for Fundamental Investigations.

REFERENCES

[1] R.H.Miller, et al., IEEE Trans.Nucl.Sci., NS-12, 804 (1965).
[2] E.Babenko, et al., SLAC-PUB-6203 (1993).
[3] A.V.Aleksandrov, et al., AIP Conf. Proc.333, 452 (1994).
[4] T.Nakazato, et al., Proc. of the LINAC94 Conf., 890 (1994).
[5] H.Linh, et al., SLAC-PUB-95-6958 (1995).
[6] D.X.Wang, Proc. of the LINAC96 Conf., 303 (1996).
[7] Y.C.Sheppard, et al., IEEE Trans.Nucl.Sci., NS-32, 2006 (1985).
[8] M.Uesaka, et al., Proc. of the LINAC94 Conf., 804 (1994).
[9] E.K.Zavoysky, S.D.Funchenko, Dok.Akad.Nauk, 226, 1062 (1976).
[10] A.Tron, et al., Proc. of the LINAC96 Conf., 514 (1996).
[11] A.Tron, et al., Proc. of the LINAC96 Conf., 517 (1996).
[12] Guide to Streak Cameras. 1994 Hamamatsu Photonics K.K.
[13] A.Tron, I.Merinov, "Space Charge Effect in Secondary Electron Monitors", this Conf.
[14] R.Shepherd, et al., Rev.Sci.Instrum. 66 (1), 719 (1995).
[15] H.W.Koch, et al., Rew.Mod.Phys., 31 (4), 920 (1959).
[16] S.M.Seltzer, et al., NIM, Phys.Res., B12, 95 (1985).

SPACE CHARGE EFFECT IN SECONDARY ELECTRON MONITORS

A.Tron, I.Merinov
MEPhI, Kashirskoe sh.31, 115409 Moscow, Russia

Abstract

Phase or spatial resolution of secondary electron monitors for, respectively, longitudinal or transverse bunch charge distribution measurements are restricted by the space charge effect of both a primary beam and secondary electron one. Simulation results of the effect in the monitors in an approach of ellipsoidal bunches of the primary beam with uniform charge density and taking into account the field of charges induced by the beam will be presented.

1 INTRODUCTION

Secondary electron monitors [1,2,3] for longitudinal bunch charge distribution measurement (BPD monitor) is the only tool at present for the measurement of short ion bunches with resolution up to 10 ps. This technique is the promising one for the bunch phase distribution monitoring of electron bunches with subpicosecond and far better resolution [4,5].

The space charge effect of the beam bunches is a main one restricting the monitor resolution [6,7,8].

Using, as an example, the beam parameters of the specific ion linac at CERN (Linac 2), IHEP (URAL 60) and also the electron linac beam with the bunch population of $5 \cdot 10^{10}$ this effect is considered.

In the paper the same definitions and symbols as in [2,4,5,6,8] are used.

In order to simplify the problem a two-dimensional charge distribution for the ellipsoidal ion bunches with uniform density and the circular cylinder with uniform charge distribution in the case of the electron beam have been taken. For these cases the expressions for the bunch field calculations were obtained on the base of the appropriate expressions published in [9,10].

2 GEOMETRY

The following geometry of the primary converters of the considered secondary electron monitors, where the perturbation of the secondary electron is occurred, is shown in Fig.1.

The geometry shown in Fig.1a was used in the case of the ion beams, so named geometry 1, and geometry 2 in Fig. 1b - for the case of the electron beam will be taken.

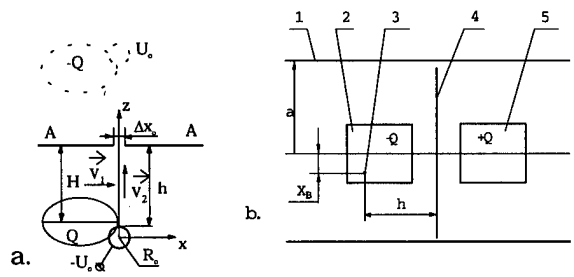

Figure 1: Geometry of primary converter with crossed (a) and coincident (b) beams.

In Fig. 1a the ion beam with charge Q places from the conducting wall (A-A) of the monitor resonator on a distance H. The secondary electron emitter with the R radius being under negative voltage U_o is apart of the wall on the h-distance. The ion bunch moves in the x-direction. Charges induced by the beam on the wall was taken into account through its image.

In Fig.1b the bunch (2) and its image (5) move in the circular conducting cylinder (1) with the a-radius crossing the wire emitter (with radius R_o) being apart from the beam axis and the conducting wall (4) of the monitor resonator on X_B and h distances respectively.

Everywhere below the following beam parameters are used: W - kinetic energy of the beam particle; f - frequency of the bunch accelerating field; I - the beam current; N - the bunch population; R - the beam radius; $\Delta\Phi$ - the bunch phase length on the f-frequency.

The perturbations of the secondary electron are described by the following parameters: $\Delta\varphi_q$- transit time spread (in unit of phase of the f-frequency) of the electrons reached the wall and started for a time of the bunch crossing by the emitter; δq - electron relative momentum spread at the wall caused by the bunch space charge effect; $\Delta x'_q$ - broadening of the electron beam divergence at the wall.

It should be noted that for reaching high resolution about 1° and less the above mentioned parameters, namely: $\Delta\varphi_q$, δq, $\Delta x'_q$ do not have to be in excess of 0.5°, 0.5...1 %, 10...20 mrad respectively.

3 PROTON LINAC BEAM

3.1 URAL 60 Linac

In Fig.2 one can see the dependencies of $\Delta\varphi_q$, δq, $\Delta x'_q$ vs. the emitter position relative to the beam axis for the beam

of the URAL linac: W = 62 MeV; I = 0.12 A; R = 5 mm; $\Delta\Phi = 12°$; f = 148.5 MHz, and for two emitters: the dotted lines - for $2R_o = 0.1$ mm; $U_o = 8$ kV, and the solid line - for uniform emitter field. The H-distance has been fixed at H = 15 mm.

The behavior of the $\Delta\varphi_q$ -curves at different R_o can be explained through Fig.3, where the E_z-component of the bunch electric field strength vs. the z-coordinate is shown. If we take the point A as the electron start, then, taking into account that the more emitter electric field strength the more electron path for a time of the bunch crossing by the emitter, the electron will reach the point B or C for the appropriate magnitude of the E_z-strength. On the AB path the sum effect of the bunch field is close to zero, and we have the another case for the AC path. In our case the AC path corresponds $2R_o = 0.1$ mm, and the AB path - for the emitter with large radius, i.e. when the emitter like a strip.

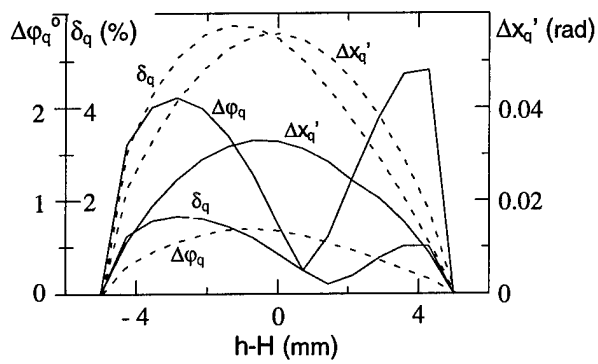

Figure 2: Space charge effect in the PC geometry 1 (see Fig.1a) for the URAL 60 linac beam vs. the emitter position.

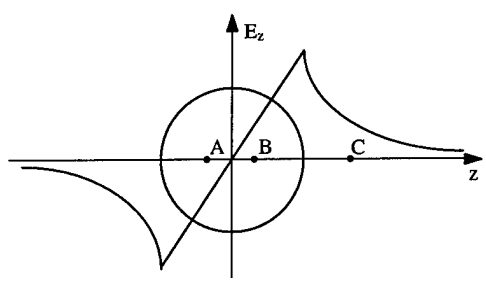

Figure 3: Electric field strength distribution.

In Fig.4 and Fig.5 the dependencies of the same parameters vs. the U_o-voltage or the bunch phase length ($2R_o = 0.1$ mm) at the emitter position being coincident with the beam axis are shown respectively.

One can see the strong dependence of these parameters in the case of the small radius of the emitter.

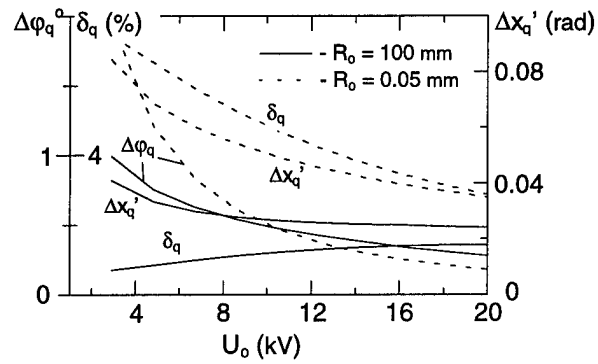

Figure 4: Space charge effect of the URAL 60 beam vs. the emitter voltage.

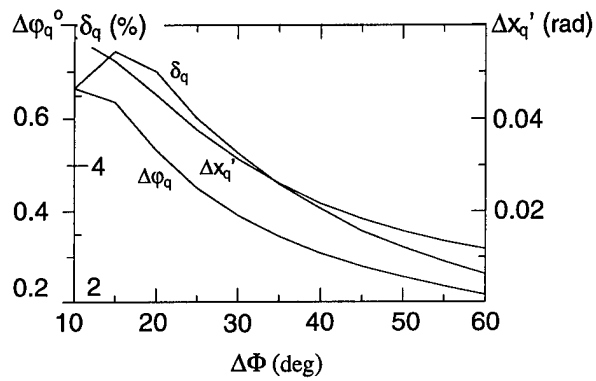

Figure 5: Space charge effect of the URAL 60 beam vs. its bunch length.

3.2 CERN Linac 2

Figure 6 represents the above mentioned dependencies for 3D-monitor [3] installed in the channel of the CERN Linac 2 for two proton energies, when the emitter of the 0.1 mm diameter under 10 kV is used.

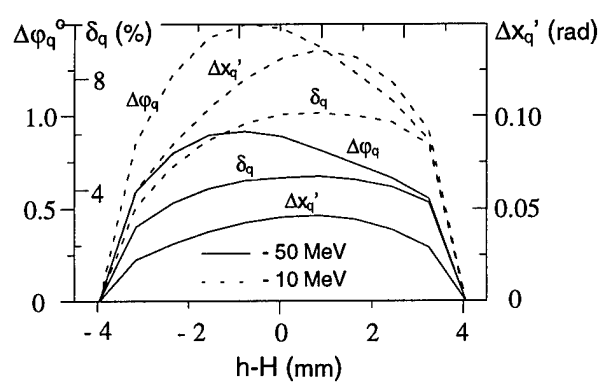

Figure 6: Space charge effect in the PC geometry 1 (see Fig.1a) for the CERN linac 2 beam vs. the emitter position.

The following beam parameters for these calculations have been taken: I = 0.15 A; f = 202 MHz; $\Delta\Phi = 30°$; R = 4 mm. These dependencies have been

obtained for the fixed h-distance of 20 mm. Getting the high resolution at these parameters both the beam and the monitor is a problem.

In Fig.7 for the same case the perturbations in the vertical plane are shown, where: 1 - the beam cross section; 2 - the emitter; 3 - the plane of the y-collimator; 4 - the plane of multichannel collector. All sizes are given in mm. Displacement of the electron in the collimator plane can reach about 0.8 mm. Below, the curves of the equal electron displacement in mm (a) in the plane of the collimator and their additional divergence in mrad (b) at the same plane vs. the points of the electron start within the beam cross section are shown.

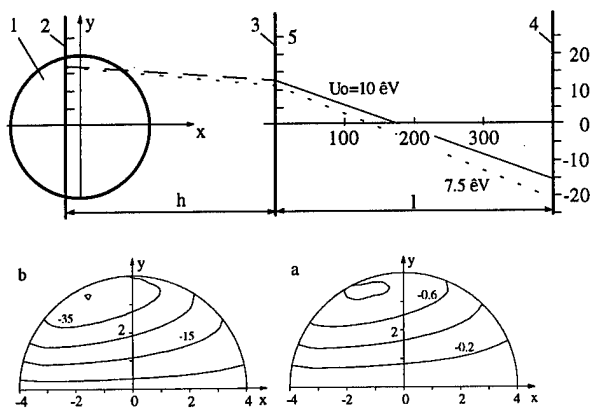

Figure 7: Electron trajectory perturbation in the 3D-monitor (CERN linac 2) vs. initial secondary electron position.

4 ELECTRON LINAC BEAM

The perturbation of the secondary electrons in the monitor [11] with geometry 2 (see Fig.1b) caused by space charge effect of the electron beam are shown in Fig.8.

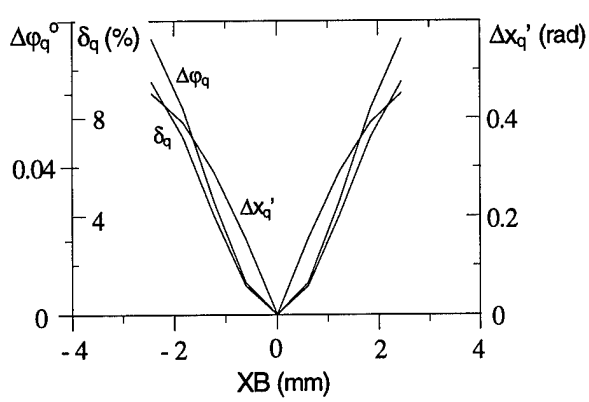

Figure 8: Space charge effect in the PC geometry 2 (see Fig.1b) vs. the emitter position.

The following beam parameters have been taken for these calculations: W = 500 MeV; $N = 5 \cdot 10^{10}$ el.; $\Delta\Phi = 30°$; f = 2.856 MHz; R = 2.5 mm. The parameters of the monitor were: $R_o = 0.025$ mm; $U_o = 4$ kV; h = 0.5 mm.

From these dependencies one can conclude that the bunch phase distribution monitoring with resolution in subpicosecond range can be reached within the beam area of the 0.5 mm radius near the beam axis.

5 CONCLUSIONS

Represented dependencies of the secondary electron perturbations in the primary converter allow to determine the phase resolution of the monitor on the base of simple algorithm for the monitor resolution calculation represented in detail in the paper [6] both for the monitor with longitudinal and transverse rf-modulation of the secondaries, the definitions and symbols used there are the same as in this paper.

By choosing the optimal values of the monitor's parameters we can reach the high resolution for any rf-linac beam, in particular, near the beam axis where for a rotationally symmetrical bunch its length and longitudinal emittance are maximum.

As to the 2D- beam current distribution measurement in the 3D-monitor [3] it should be noted that in the monitor there is no focusing in the y-direction, and the beam size measured in the y-direction (see Fig.7) will be smaller than it can be watched in the x-direction up to 1 mm from both its sides. The alternative methods and devices have been proposed for the 2D- and 3D-distribution measurements [12,13.14] in the case of the considerable space charge effect where the focusing in each direction are used.

6 ACKNOWLEDGMENTS

The research was supported by the Russian Fund for Fundamental Investigations.

REFERENCES

[1] R.L.Witkover, NIM 137, 203 (1976).
[2] A.Tron, Proc. of the LINAC90 Conf., 477 (1990).
[3] S.K.Esin,et al., Proc. of the LINAC96 Conf.,193 (1996).
[4] A.Tron, et al., Proc. of the LINAC96 Conf., 514 (1996).
[5] A.Tron, et al., Proc. of the LINAC96 Conf., 517 (1996).
[6] A.Tron, Proc. of the DIPAC95 Conf., 60 (1995).
[7] A.Tron, V.Vorontsov, Proc. of the 10th All-Un. PAC, Dubna, 452 (1986).
[8] A.Tron, V.Shako, Proc. of the PAC93 Conf., 1216 (1993).
[9] R.S.Muratov,"Potentials of Allipsoid", Moscow, Atom Pub., 1976.
[10] W.R.Smythe,"Static and Dynamic Electricity", New York, 1950.
[11] A.Tron, I.Merinov, V.Smirnov, "Option of Method for Electron Bunch Phase Distribution Monitoring", this Conf.
[12] A.Tron, et al., Abstracts of the 12th All-Un. PAC, Moscow, 213 (1990).
[13] A.Tron, Proc. of the LINAC94 Conf., 917 (1994).
[14] A.Tron, AIP Conf. Proc. 333, 438 (1994).

EQUIPMENT FOR BEAM CURRENT AND ELECTRON ENERGY MONITORING DURING INDUSTRY IRRADIATION

A.A. Zavadtsev, Moscow Radiotechnical Institute of Russian Academy of Sciences
132 Warshavskoe Road, Moscow, 113519 Russia

Abstract

The electron beam irradiation sterilization is placed first among all types of medical items sterilization. The quality of sterilization is determined by value of dose, which is in one's turn determined by beam current, electron energy and beam scanning system parameters. Therefore these parameters have to be controlled during the irradiation process. The equipment for beam current and electron energy monitoring allows to control beam current, electron energy spectrum and nominal deflection of electron beam when scanning during the irradiation process each scanning period or, for example, each tenth scanning period by request. The equipment consists of induction beam current sensor with registration equipment and two grounded electron collectors. The simplicity of this equipment allows to use it for irradiation quality monitoring practically in all electron beam irradiation technology processes.

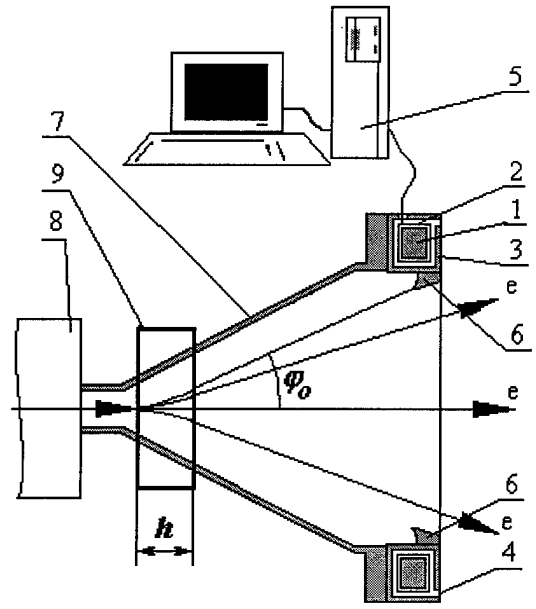

Figure: 1 Fan scanning beam monitoring.

1 INTRODUCTION

One of wide used and perspective methods of sterilization of medical items and materials, such as syringes, blood transfusion packages, various electrodes, dressing and surgical packages, is accelerated electron beam irradiation. The quality of sterilization is determined by the dose absorbed by all parts of sterilized object. In one's turn the dose is determined by beam current I, accelerated electron energy W, electron beam scanning on the object surface and the product of thickness τ and density ρ of irradiated object. The effective value $\tau\rho$ is constant for the same objects at conveyor irradiation. Therefore it is necessary to control values W, I and normal operation of the scanning system.

2 MONITORING SCHEME

2.1 Fan scanning beam monitoring

The accelerated electron beam scanning systems are used in modern facilities for commercial irradiation [1]. The object moves perpendicular to the scanning plane. The monitoring scheme, which may be used in fan beam scanning irradiation, is shown in Fig.1.

The electron beam, accelerated by LINAC 8, is shaped to fan beam by scanning system 7. The fan beam excites the alternating magnetic field in the magnetic core 1, surrounding the electron beam and correspondingly the electromotive force in the winding 2 on the core 1. The core 1 and winding 2 are placed into the body 3 with the slot 4. The electromotive force creates the voltage proportional to the beam current I on the resistor. This voltage is passes to the registration equipment (5) and analyzed by computer. This is well known induction beam current sensor [2].

Two grounded beam collectors 6 are placed in the scanning system. The beam passes out the scanning system and is not collected by collectors in the usual scanning regime. Let's increase the amplitude of saw-toothed magnetic field in the scanning system and correspondingly increase the maximum deflection of the beam so as to collect beam by collector at maximum deflection. If magnetic induction of deflecting field depends on time as $B(t)$ that the deflection angle $\varphi(t)$ for electrons with energy W and for poles shape shown in Fig.1 depends on time as

$$\varphi(t) = \arcsin\frac{echB(t)}{W} \qquad (1)$$

where e is electron charge, c is light velocity.

The accelerated electron beam has typical energy spectrum shown in Fig.2.

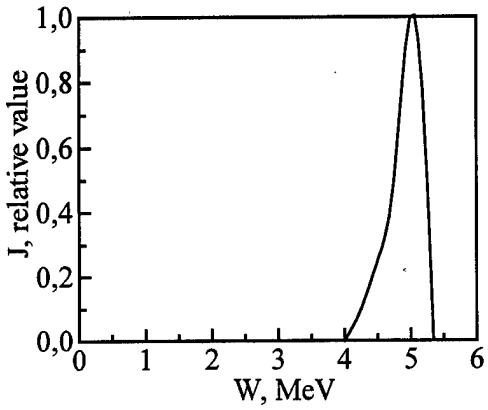

Figure: 2 Accelerated electron beam energy spectrum.

At changing $B(t)$ in time the energy $W(t)$ of electrons getting to the collector edge is changed too:

$$W(t) = \frac{echB(t)}{\sin\varphi_0} \qquad (2)$$

The electrons with energies $W \le W(t)$ are collected by collector.

Thus the registration equipment measures the current

$$I_m(t) = I - \int_0^W J(W)dW = \\ = I - \frac{ech}{\sin\varphi_0}\int_0^t J(W(t))\frac{dB(t)}{dt}dt \qquad (3)$$

The energy spectrum is determined by expression (2) and following parametric expression

$$J(W(t)) = -\frac{\sin\varphi_0}{ech}\frac{dI_m(t)}{dt}\left(\frac{dB(t)}{dt}\right)^{-1} \qquad (4)$$

Thus there is the possibility of the measurement of beam current I, beam energy spectrum $J(W)$ and the control of operation regime of the scanning system during each scanning period.

2.2 Belt scanning beam monitoring

The belt scanning beam monitoring system is shown in Fig.3.

The collectors 6 are placed between first and second bending magnets. On the whole the poles of bending magnets have arbitrary profile and the dependence of energy $W(t)$ of electrons getting to the collector edge is determined by (2), where value h is clear from Fig.3. The energy spectrum may be found using expression (4).

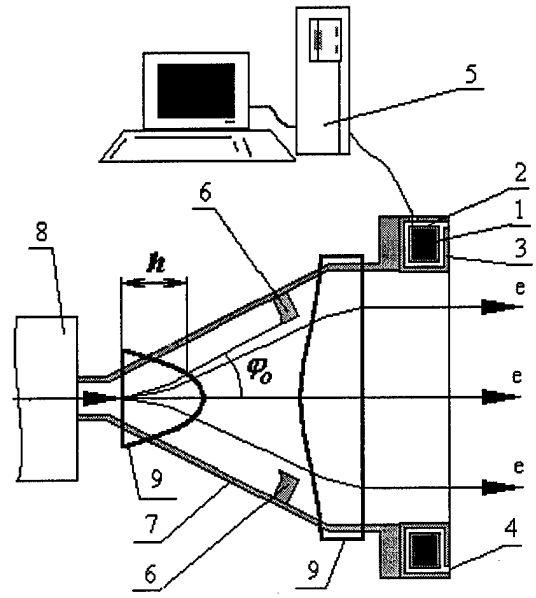

Figure: 3 Belt scanning beam monitoring.

3 DEVELOPMENT OF FULL-SCALE MODEL MONITORING SYSTEM

The beam parameters monitoring system was developed for medical items industry sterilization facility. This facility consists of 5 MeV standing wave electron LINAC and the belt beam scanning system analogous to one shown in Fig.3. The accelerating section, the scanning system with horn and two bending magnets and the beam parameters monitoring system are shown in Fig.4. The cardboard boxes with medical items are moved by means of rectilinear conveyor under the output foil window of scanning system horn. The box sizes are 49.5õ41õ27 cm. The belt scanning beam width is 43 cm.

The wire winding is winded up on the magnetic core with cross-section 2x2 cm and is loaded by 50 Ohm resistor. The voltage on this resistor is $U=kI$, where k = 1.25 Â/À.

The accelerator operates in the pulse mode with beam duration 6-12 μs and pulse beam current I=0.2 A. The voltage pulse form coincides with electron beam pulse form very well in case of axis pass of the beam. The pulse voltage amplitude on the resistor changes in the range from 0 to 0.625 V during beam scanning with full collecting. This pulse voltage may be looked at the oscilloscope in case of need or in the operating mode it is passes to the registration equipment and analyzed by computer to get the beam current and the average electron energy. The beam current, the electron energy and known pulse repetition rate and conveyor velocity allow to control the dose and thus to control the sterilization quality of each box.

The conveyor operates in the continue mode. The sterilization quality may be controlled during all

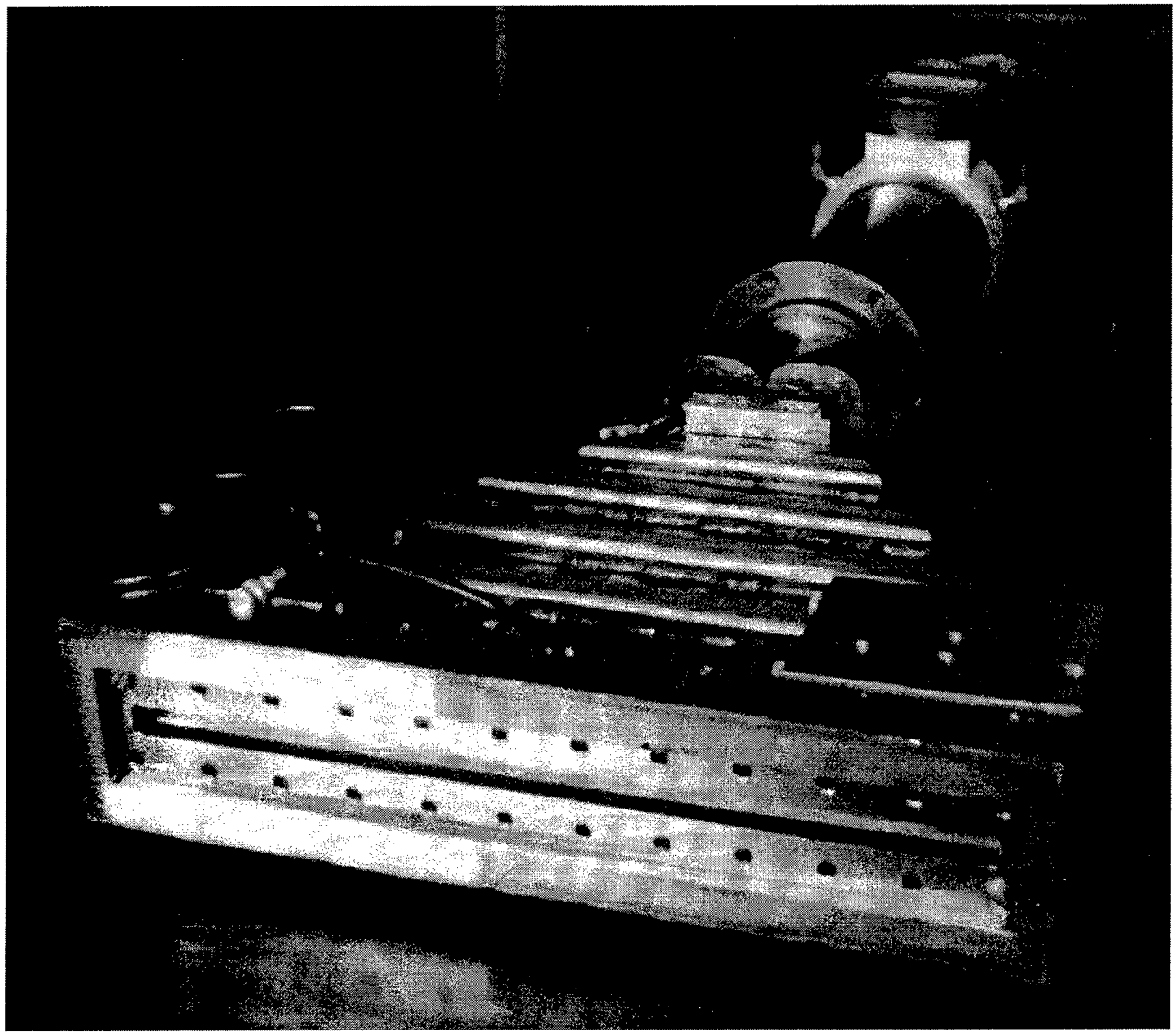

Figure:4 Full scale model monitoring system.

sterilization time each scanning half-period or more seldom. For example the scanning angle for measuring of electron energy is increased, when beam is between boxes. It allows to control the electron energy without decreasing of irradiation dose. The beam current is measured continuously.

The number and the dose of each box and the sterilization date may be marked on the box surface by means of laser marker or bar-code marker coupled with the control computer. The computer may store an information of the dose got by each box and give signals to operator about defective sterilization.

4 CONCLUSION

The described equipment allows to have accelerated electron beam parameters monitoring and therefore the necessary dose monitoring during the irradiation process. This monitoring may be carried out ones or twice every day, every tenth scanning period or every scanning period by request without interruption of the irradiation process.

5 ACKNOWLEDGEMENTS

The author wishes to thank S.N.Puchkov for help in manufacturing and testing of the core and winding of full-scale model monitoring system.

REFERENCES

[1] A.A.Zavadtsev, Electron Beam Scanning Systems, Proceeding of this conference.

[2] V.A.Moskalov, V.G.Shestakov and G.I.Sergeev, The Measurement of Charged Particles Beams Parameters, M.: Atomizdat, 1980. (in Russian).

DESIGN AND INITIAL COMMISSIONING OF BEAM DIAGNOSTICS FOR THE PEP-II *B* FACTORY

A.S. Fisher*, D. Alzofon*, D. Arnett*, E.L. Bong*, B. Brugnoletti*, B. Collins*, E. Daly*, A. Gioumousis*, R, Johnson*, A. Kulikov*, N. Kurita*, J. Langton*, D. McCormick*, R. Noriega*, S. Smith*, V. Smith*, R. Stege*, M. Bjork†, M. Chin†, J. Hinkson†, R. McGill†, T. Suwada**

* Stanford Linear Accelerator Center, Stanford University, Stanford, California 94309
† Lawrence Berkeley National Laboratory, University of California, Berkeley, California 94720
** National Laboratory for High-Energy Physics (KEK), Oho, Tsukuba, Ibaraki, 305 Japan

Abstract

PEP II is a 2.2-km-circumference collider with a 2.1-A, 3.1-GeV positron ring (the Low-Energy Ring) 1 m above a 1-A, 9-GeV electron ring (the High-Energy Ring); both are designed for 3 A maximum. We describe the beam diagnostics for HER commissioning, starting in May 1997. LER commissioning will follow in 1998. The beam size and pulse duration are measured using near-UV synchrotron light extracted by grazing-incidence mirrors that must withstand 200 W/cm. To measure the charge in every bucket at 60 Hz with an accuracy of •0.5%, the sum signal from a set of 4 pickup buttons is digitized and averaged over 256 samples per bucket. The sum is normalized to the ring current, measured by a DC current transformer. The 300 beam-position monitors per ring are multiplexed to share 171 processor modules, which use DSPs for recording positions over 1024 turns and for calibration. For diagnostics and machine protection, 100 photomultiplier-based Cherenkov detectors measure beam losses and abort the beam in case of high loss.

1 INTRODUCTION

The PEP-II *B* Factory [1], an electron-positron collider under construction [2] at the Stanford Linear Accelerator Center in collaboration with the Lawrence Berkeley and Lawrence Livermore National Laboratories, involves two rings at different energies; both rings require large currents for high luminosity (see Table 1). Because the HER reuses the PEP-I magnets (although with a new, low-impedance, vacuum chamber), its commissioning is beginning at the time of this conference (May 1997), while the LER, with similar diagnostics, will start in early 1998. The BaBar detector will be installed in 1999.

Parameter	HER	LER
Circumference [m]	2199.318	
Revolution time [μs]	7.336	
RF frequency [MHz]	476	
Harmonic number	3492	
Number of full buckets	1658	
Bunch separation [ns]	4.20	
Nominal current [A]	0.99	2.16
Maximum current [A]	3	3
Nominal energy [GeV]	9.01	3.10
Maximum energy [GeV]	12 (at 1 A)	3.5
Bend radius in arc dipoles [m]	165	13.75
Critical energy in dipoles [keV]	9.80	4.83

Table 1. PEP-II Parameters.

2 SYNCHROTRON-LIGHT MONITOR

Synchrotron radiation (SR) in the visible and near ultraviolet (600–200 nm) will be used to measure the beam's transverse profile and, with a streak camera, in the longitudinal direction. Both rings will be measured at the location shown in Fig. 1. The design must cope with high SR power on the first mirror, low-impedance vacuum chambers, limited access to the beam, and a narrow tunnel.

HER arcs are almost entirely occupied by dipoles, with a quadrupole, corrector and sextupole taking up much of the rest of each half cell (see Fig. 1). The intense SR fan strikes the water-cooled outer wall of the chamber. The mirror (Fig. 2), mounted in the vacuum chamber on the arc's outer wall, reflects the light horizontally across the chamber to the downstream inner corner. The arrangement shades both the mirror's upstream edge and the leading edge of the chamber at the downstream end from receiving power at normal incidence. The beam is incident on each mirror at 4• to grazing, giving a maximum power along the SR stripe of 200 W/cm.

The HER mirror cannot be cooled sufficiently at this power to obtain adequate flatness for good imaging. Instead, we make use of the fact that the SR fan at the critical energy is 15 times narrower than the visible fan we image. When the electrons travel on axis, a narrow slot along the mirror's mid-plane passes the x-ray fan, while the visible beam reflects from the surfaces above and below. Because of grazing incidence, the x rays never reach the bottom of the slot, but travel past the mirror to dump their heat into a thermally separate absorber (Fig. 2). When the electrons are off center, we demand only that the mirror not exceed its yield strength while the orbit is corrected and the mirror cools, as discussed in [3].

After this first mirror, two 45° mirrors and a fused-silica window bring the light to imaging optics in a nitrogen-filled enclosure on an optical table below the HER dipole, in order to get good resolution from a short, stable optical path. The beam is split, with half used for this local imaging and half sent upwards through a 10-m

0-7803-4376-X/98 /$10.00 © 1998 IEEE

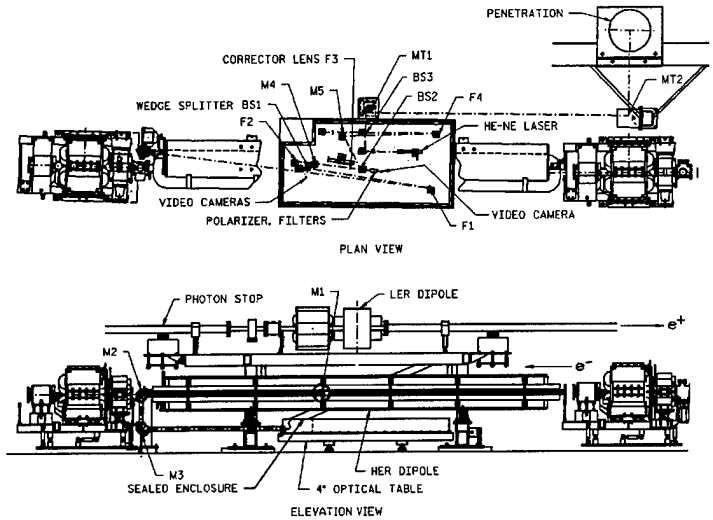

Figure 1. HER and LER beamlines in mid-arc, showing path of the HER synchrotron light and the optical table under the HER dipole.

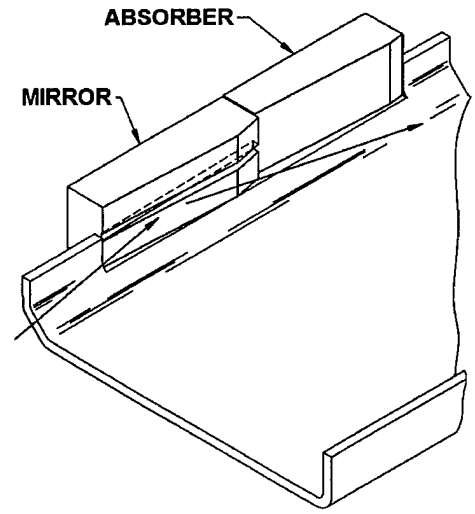

Figure 2. The slotted first mirror and the x-ray absorber, both mounted in the wall

penetration to an optics room at ground level, to keep equipment like the streak camera away from radiation.

In the LER, the SR diverging from the beam at each dipole enters an antechamber; 2/3 of these photons strike a water-cooled photon stop 6 m beyond the bend (Figs. 1 and 3), while the remainder hit the next photon stop downstream. We pass light from the closer dipole (to avoid clipping in the narrow antechamber of the intervening magnets) through a 15-mm-wide vertical slice in the photon stop. The light then strikes a slotted mirror similar to that of the HER but inclined at 9° to grazing. The maximum SR power density is 110 W/cm—half that of the HER. The light is deflected horizontally away from the positron orbit, since the slit in the photon stop shades the leading edge of the mirror. Two mirrors then send the beam down to the common optical table under the HER dipole.

3 BEAM-POSITION MONITORS

Beam position measurements use four 15-mm-diameter pickup buttons, arranged near ±45° to horizontal at each quadrupole, for a total of ≈300 sets per ring. Most

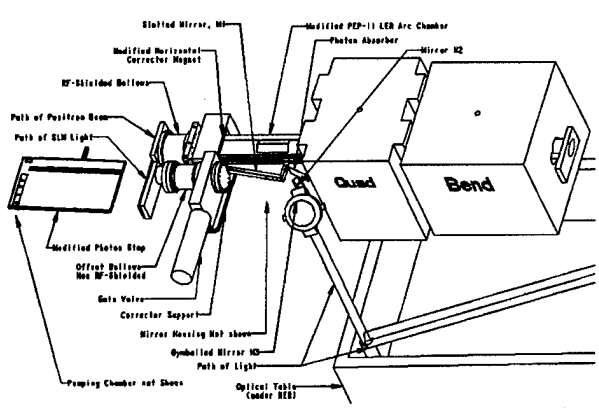

Figure 3. The LER synchrotron-light monitor, showing the modified photon stop and the slotted first mirror.

measurements are single plane (x only at QFs, y at QDs), except near the interaction and injection points, with pairs of buttons summed next to the quad. The CAMAC processor modules, multiplexed between HER and LER, use I&Q (in-phase and quadrature) detectors and digital signal processor (DSP) chips that record 1024 turns and can provide single-turn or averaged positions, with resolutions (measured in the lab) of 100 μm and 1 μm respectively. A detailed description and preliminary commissioning data are presented in other papers at this conference [4].

4 TUNE MONITOR

The tune of each ring will be monitored with a spectrum analyzer processing the signal from dedicated BPM-type pickup buttons. The analyzer includes a tracking generator to excite the beam with a swept sine or broadband noise. Instead of using separate excitation structures, the drive signal can be summed with the input to the power amplifiers for transverse [5] and longitudinal [6] feedback.

The button signals are combined with 180° hybrids to form a sum signal, and horizontal and vertical difference signals. Two of these are switched into two channels, then attenuated or amplified to cover a broad dynamic range, from one bunch of 5×10^8 electrons or positrons to 1658 bunches of 8×10^{10}, 4.2 ns apart. Broadband components are used up to this point to keep the pulses narrow, so that a 2-ns GaAs switch can gate the signal for measurements of specific bunches or pass the signal from the entire ring. The gate also allows us to measure the tune while turning off feedback for a specific bunch.

The two-channel spectrum analyzer uses DSPs and a fast Fourier transform (FFT) to compute spectra from 0 to 10 MHz. To bring the signals into range, the front end

includes mixers at $2f_{RF}$ (952 MHz). The analyzer incorporates both GPIB and an ethernet interface for control by an X terminal, using a functional image of the front panel. It has peak tracking to automatically follow the tune and runs user programs, allowing control, for example, of the beam-excitation signal to measure the peak with the minimum drive.

Other systems will be available to follow the beam's response. Each ring has a second dedicated set of buttons reserved for special measurements, such as high-frequency spectra to examine bunch dynamics. Also, the DSP on each BPM processor card can record signals from 1024 turns and calculate an FFT. Using all the BPMs, we can follow oscillations of a bunch around 1024 turns.

5 CURRENT MONITORS

The current in each ring is measured by a commercial [7] DC current transformer (DCCT) with a 5-μA resolution over a 1-s integration time and a full-scale value of 5 A. For comparison, a 1-A current with a 3-hour lifetime drops by 93 μA/s, and injecting 5×10^8 $e^{\pm}$ adds 11 μA. Our DCCT housing places it outside the vacuum envelope, provides an electrical gap directing DC wall currents around the transformer core, and capacitively bypasses the gap for higher frequencies to provide a low impedance to the beam.

A second system (detailed at this conference [8]) measures the charge in each of the 3492 RF buckets. In a normal fill (see Table 1), 1658 buckets, 4.2 ns apart (two RF periods), will be filled equally within ±2%, up to 8×10^{10} $e^{\pm}$ for a 3-A beam. With 0.5% accuracy, the bunch-current monitor must update measurements of each ring at 60-Hz to control the fill. To find the lifetimes of individual bunches, we need an accuracy of 0.05% in 1 s, allowing quick adjustments of a lossy bunch.

In each ring we sum and filter the signals from a set of four BPM-type buttons, then mix the signals at $3f_{RF}$. An 8-bit ADC in a VXI crate digitizes the signal at f_{RF} (476 MHz). The data stream is downsampled and divided among 12 logic arrays, to sample all buckets every 8 turns, and the data is averaged over 256 measurements in each 60-Hz interval. The averages are written into a table in a reflected (dual-port) memory. The VXI processor maintains a second table with sums over 1-s intervals.

Another VXI-based system, the bunch-injection controller, reads this memory and the DCCT. It normalizes the individual bunch currents, performs lifetime calculations, and communicates with the control system. The bunch-injection controller determines the injection sequence for a third system, the master pattern generator, which controls the timing of the injector linac to fill the appropriate buckets in the rings.

6 BEAM-LOSS MONITORS

A network of 100 beam-loss monitors (BLMs) detects beam losses at collimators, septa, and selected quadrupoles around the rings. The output will be used for machine tuning, for loss histories, and for the rapid detection of high losses requiring a beam abort. We have chosen a Cherenkov detector, using a small (16 mm diameter), fast (2-ns-wide pulses) photomultiplier, with a 10-mm-long, fused-silica cylindrical Cherenkov radiator over the fused-silica PMT window. The assembly is enclosed in 1 cm of lead to reduce synchrotron background, but still remains small enough to be moved around for commissioning and troubleshooting. Using the ring magnets as shielding, the BLMs can have preferential sensitivity to HER or LER. All are now being placed around the HER and have detected losses from the first injection.

Ten-channel CAMAC modules in crates around the rings process each BLM signal through two paths that together provide a wide dynamic range. For low losses, PMT pulses are sent through a discriminator and counted over 1-s or 8-ms intervals. At higher loss rates, the signal goes through a 10-μs *RC* filter; this integrated signal is used twice. First, it passes through a peak detector and is digitized every 8 ms for output to the control system. Second, if the 10-μs signal exceeds a programmable threshold, then one or both rings may be aborted. The processor records the channel that triggered the abort, and all BLMs around the rings freeze their most recent readings. For 100 μs after injection into a ring, the BLM network is inhibited from aborting the stored beam, since faulty injection is a more likely source of high loss rates. To measure injection loss, the output of the peak detector is digitized at the end of this inhibit interval.

REFERENCES

[1] *PEP-II: An Asymmetric* B *Factory*, Conceptual Design Report, LBL-PUB-5379, SLAC-418, CALT-68-1869, UCRL-ID-114055, UC-IIRPA-93-01, June 1993.

[2] U.S. Dept. of Energy contracts DE-AC03-76SF00515 (SLAC), DE-AC03-76SF00098 (LBNL), and W-7405-Eng-48 (LLNL).

[3] E.F. Daly, A.S. Fisher, N.R. Kurita, J Langton, "Mechanical Design of the HER Synchrotron-Light-Monitor Primary Mirror," in these Proceedings.

[4] S.R. Smith, G.R. Aiello, L.J. Hendrickson, R.G. Johnson, M.R. Mills, J.J. Olsen, "Beam Position Monitor System for PEP-II"; R. Johnson, S. Smith, N. Kurita, K. Kishiyama, J. Hinkson, "Calibration of the Beam-Position-Monitor System for the SLAC PEP-II *B* Factory," in these Proceedings.

[5] Barry, W., Byrd, J., Corlett, J., Fahmie, M., Johnson, J., Lambertson, G., Nyman, M., Fox, J., and Teytelman, D., "Design of the PEP-II Transverse Coupled-Bunch Feedback System," in *Proc. IEEE Particle Accelerator Conf.*, Dallas, TX, May 1995 (IEEE, Piscataway, NJ) in press.

[6] Oxoby, G., et al, "Bunch-by-Bunch Longitudinal Feedback System for PEP-II," in *Proc. European Particle Accelerator Conf.*, London, 27 June–1 July 1994 (World Scientific, Singapore, 1994) pp. 1616–1618; Teytelman, D., et al, "Feedback Control and Beam-Diagnostic Algorithms for a Multi-Processor DSP System," in these Proceedings.

[7] Parametric Current Transformer, Bergoz Precision Beam Instrumentation, Crozet, France.

[8] M.J. Chin, J.A. Hinkson, "PEP-II Bunch-by-Bunch Current Monitor," in these Proceedings.

BEAM CURRENT MONITORS IN THE NLCTA*

Christopher Nantista and Chris Adolphsen
Stanford Linear Accelerator Center, P.O. Box 4349, Stanford, California 94309, USA

Abstract

The current profile along the 126 ns, multi-bunch beam pulse in the Next Linear Collider Test Accelerator (NLCTA) is monitored with fast toroids (rise time ~1 ns). Inserted at several positions along the beam line, they allow us to track current transmission as a function of position along the bunch train. Various measurements, such as rise time, current, width, and slope, are made on the digitized signals, which can be corrected in software by means of stored frequency response files. The design and implementation of these devices is described.

I. INTRODUCTION

The Next Linear Collider Test Accelerator [1] at SLAC runs with an electron beam bunched at the X-band frequency of 11.424 GHz. A single pulse of ~126 ns duration contains a train of over 1400 bunches. This bunch train must be brought intact through the injector [2], a phase space tailoring chicane, and the accelerator proper, into a spectrometer and beam dump. A beam loading compensation scheme [3] is used to achieve uniform acceleration in the structures, minimizing energy variation along the pulse as it travels through the steering and focusing lattice.

As part of the beam instrumentation system of the NLCTA, six current monitoring toroids are incorporated at various locations along the beam line. These supplement the current information available from an insertable faraday cup and a series of beam position monitors.

While the latter are more numerous, the current transmission data acquired from them consists of a scalar value reflecting only the charge density at the leading edge of the long beam pulse. The toroid pickups allow us to view the temporal structure of the beam current (above the bunching scale). By comparing signals at different locations, for example before and after the chicane, we can determine not only where we might be losing current but also from which part of the bunch train it is being lost. This is crucial as we test our beam loading compensation scheme.

II. TRANSFORMER

The heart of our beam current monitoring system is the toroidal Fast Current Transformer manufactured by Bergoz (01170 Crozet, France). Developed in collaboration with Klaus Unser at CERN, this device was designed specifically for viewing charged particle bunches in accelerators. The "rad-hard" model we use has an inner diameter of 1.1", slightly larger than our beam pipe. The azimuthal magnetic induction of the beam current links a twenty-turn coil around the toroid core, giving a 1:20 transformer ratio. The core of cobalt/molybdenum amorphous alloy ribbon interleaved with nickel/iron crystalline alloy was designed to optimize frequency response (~1ns rise time) and suppress ringing. Fifty ohms of resistance is embedded within the toroid and an SMA connector on the outer wall allows for signal pick-up. The basic circuit is illustrated in Figure 1 below. When connected to an oscilloscope with 50Ω impedance, the transformer yields a nominal signal amplitude of

$$V_{\text{sig}} = \frac{I_{\text{beam}}}{20\ \text{turns}} \times \left(\frac{1}{50\Omega} + \frac{1}{50\Omega} \right)^{-1} = 1.25\Omega \times I_{\text{beam}}.$$

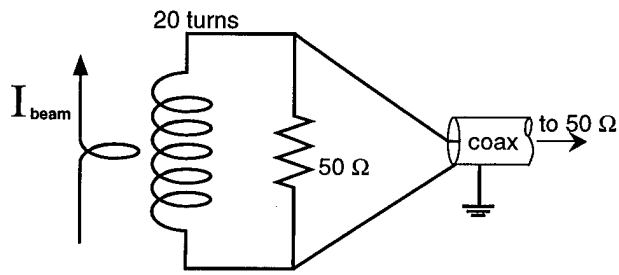

Figure 1. Circuit diagram for fast toroid current monitor.

III. HOUSING

In order for the transformer to "see" a net current passing through its center, the wall current imaging the charged particle beam must be diverted around the outside of the device. The beam pipe section and aluminum housing on which and in which the toroid is installed to achieve this end are shown in Figure 2 in a partly disassembled view.

The electrical continuity of the beam pipe is thus interrupted by an inch-long insulating ceramic gap. A thin coating of kovar deposited on the inner surface of the ceramic provides a finite conductivity to bleed off any build-up of charge deposited by the beam. The edges of the ceramic are metalized and brazed to the beam pipe to maintain vacuum integrity, and a small bellows is included to either side of the gap to relieve stress.

Around this structure, a mechanically engineered aluminum shell is assembled which supports the toroid and provides a conducting path for the wall current. The housing clamps to the steel beam pipe just beyond each bellows. An inner cylinder is brought into contact around the toroid, and an outer cylinder encloses some cabling, supports two cable connectors, and provides rigidity. Spring-loaded pins suspend the toroid around the ceramic.

0-7803-4376-X/98 /$10.00 © 1998 IEEE

The transformer signal is brought through the inner cylinder to an SMA-to-type N adapter in the outer shell. To the other type N connector is soldered a flat wire looping beween the toroid and the vacuum chamber. This can be pulsed to verify the operability of the current monitor.

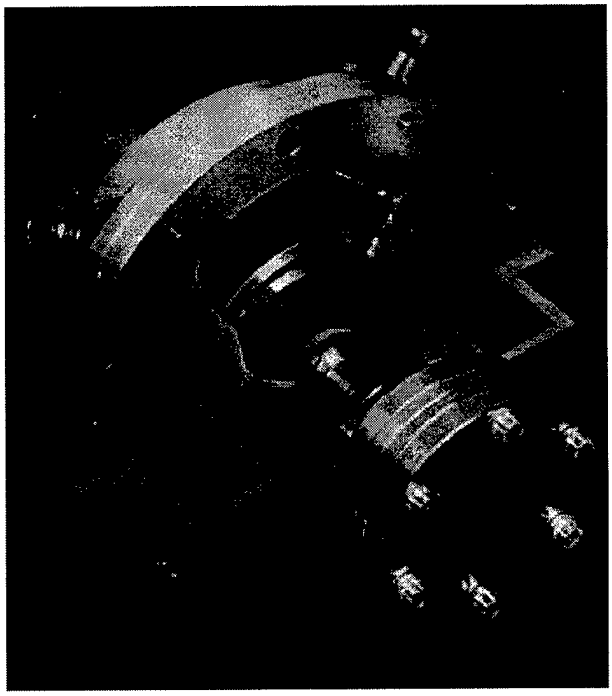

Figure 2. Toroid and housing installed on a beam pipe section with one quadrant of the housing removed.

IV. READOUT

The fast toroid signals are carried by low-loss heliax cables out from the accelerator enclosure to a rack near the klystron gallery. There they are fed through a high bandwidth multiplexer into a 250 MHz (1 gigasample/second) Hewlett Packard 1428a Digitizing Oscilloscope in a VXI crate. These instruments are controlled with an embedded, HPUX, multi-user processor, which is networked to a terminal in the NLCTA control room. The scope is run using an external trigger synched with the beam. Software routines written with HP VEE (Visual Engineering Environment) graphical programming language are used for sending commands, receiving digitized data, signal processing and display.

V. CALIBRATION

In an initial test of our toroid assembly in the SLC linac, the signal displayed significant ringing. This seems to have been due to capacitance and inductance in the circuit formed by our housing. To further study its response and try to ameliorate this effect, we fitted the current monitor with an aluminum rod center conductor supported between specially designed coaxial cable adapters, as shown in Figure 3.

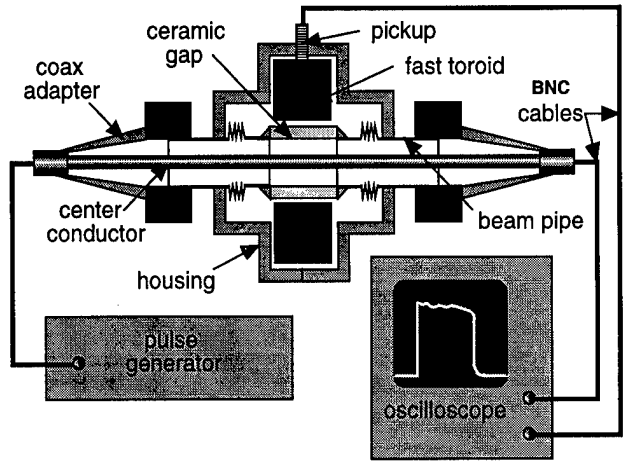

Figure 3. Beam current monitor test and calibration setup.

An HP 8510C Network Analyzer connected between one port and the pickup, with a load on the other port, showed the response function of the current transformer to be fairly flat out to about 1.3 GHz, where it drops off 15 dB. This is consistent with the manufacturer's rise time specification.

A variable width pulse generator and an oscilloscope were also used to study the device. Filling the cavity formed around the bellows with microwave absorber reduced the ringing from sharp pulses, but it was not considered suitable for permanent inclusion in a high radiation environment. What was found to improve the worst of our current monitors was the sanding down of spacers and application of silver paint to the edges of the inner cylinder halves to assure good electrical contact between them.

To remove, as far as possible, any remaining imperfection in their response, each of our beam current monitors was calibrated in the following way.

Electrical pulses were sent along the center conductor to simulate an electron beam. The transmitted pulses (essentially identical to the input pulses) and toroid pickup signals were recorded simultaneously with our two-channel digitizing scope. The Fourier transform of the latter waveform could then be divided by that of the former to give us the effect of the device on the true signal.

Because the Fourier transform of a square pulse has nodes at intervals of the inverse width, a response function generated from a single such pulse yields spurious noise (division by nearly zero) at these frequencies. Attempts to correct a pulse of a different width with such a function causes gross distortions. It was thus necessary to use many pulses of various widths for each calibration, generally about fifteen ranging from 1 ns to greater than a microsecond. The digitized waveforms were eight microseconds long, yielding a spacing of 0.125 MHz in our frequency spectra. The FFT's of the through signals and those of the toroid signals were added before dividing the two sums.

The resulting response functions were then stored in files. For any signal $h(t)$ recorded by the beam current monitor, a corrected signal $f(t)$ could thereafter be obtained with the stored file $G(\omega)$ from the relationship

$$f(t) = IFFT\left\{\frac{FFT\{h(t)\}}{G(\omega)}\right\}.$$

For greater speed, it is sometimes preferable to run our current monitors without implementing this correction. A scalar factor, also determined with our coaxial setup, is then used to convert output voltage to axial current. A typical effect of using the fast Fourier transform correction is to decrease a ~7 ns rise time to ~6 ns. Signal droop is not significant for our pulse length. We measured the L/R time constant of the toroid to be as large as 35 microseconds.

It should be noted that the performance of these current transformers deteriorates drastically in high magnetic fields (>~500 guass). In our injector, where the focusing solenoid field reaches two kilogauss, we had to substitute a homemade, 100 turn toroid on a G-10 core.

VI. MEASUREMENTS

As previously mentioned, the HP VEE programming software is used with our beam current monitoring system. Through its direct I/O capability, we select the desired current monitor or monitors from the multiplexer, set up the digitizing scope, and acquire waveforms. The signal processing we've encoded not only allows for the above FFT correction to be applied, but also performs a number of useful measurements on the pulses. These include beam current amplitude, pulse width, rise time, fall time, slope of the pulse top, rms variation across the pulse top from a linear fit, and integrated charge in the pulse. These measurements can be sent to the CORRELATIONS PLOT program in our control system and correlated with other variables.

The waveforms and measurement results are displayed on a convenient user interface panel. We can run in one-shot or "live" mode. In the latter mode, the screen is updated automatically every few seconds (including time for data processing). A feedback loop adjusts the oscilloscope range according to the measured signal amplitude, and the two scope channels allow us to monitor two beam current signals simultaneously on the same display. Figure 4 shows our display panel with toroids before and after the chicane indicating about 77% beam transmission.

VIII. REFERENCES

[1] Ronald D. Ruth, "Results from the NLC Test Accelerator," these proceedings.

[2] A. Yeremian, *et al.*, "NLCTA Injector Experimental Results," these proceedings.

[3] C. Adolphsen, *et al.*, "Beam Loading Compensation in the NLCTA," these proceedings.

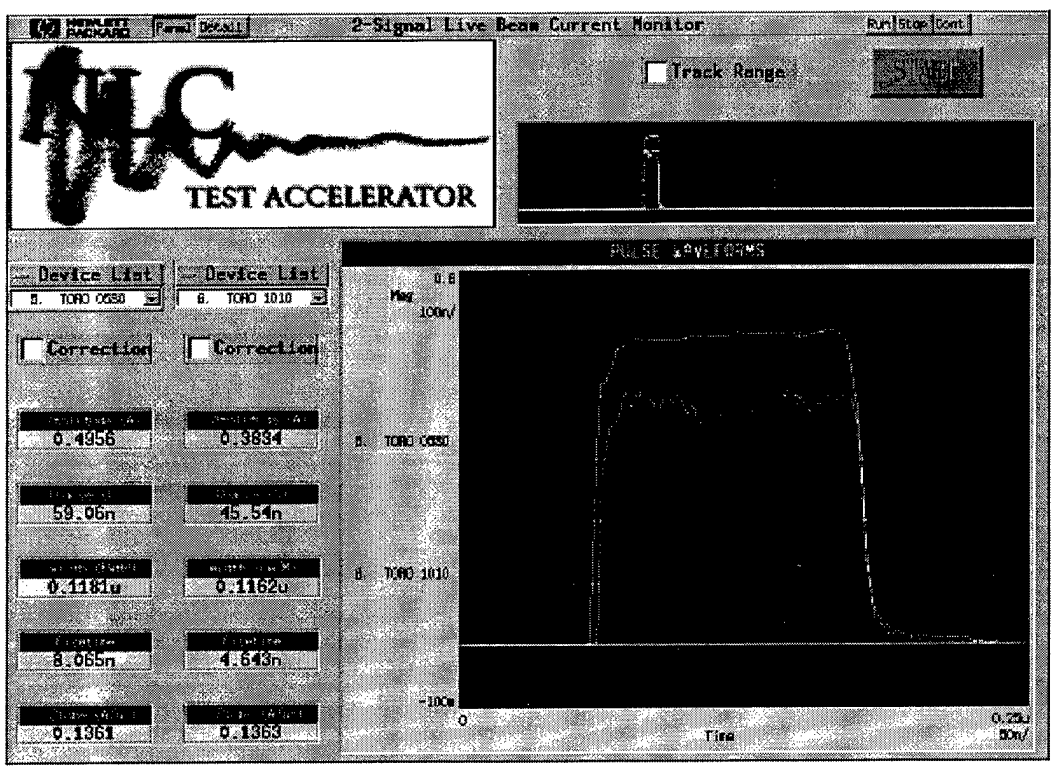

Figure 4. Current monitor two-signal live display panel.

REAL-TIME BEAM LOSS MONITORING SYSTEM AND ITS APPLICATIONS IN SRRC

K. T. Hsu, K. K. Lin, C. H. Kuo, and Y. C. Liu
Synchrotron Radiation Research Center
No. 1 R&D Road VI, Hsinchu Science-Based Industrial Park, Hsinchu 300, Taiwan, R.O.C.

Abstract

A new approach to measure and locate beam losses in the SRRC storage ring (Taiwan Light Source, TLS) by using semiconductor beam loss monitor (BLM) is presented in this report. Small size and low unit cost make it possible to be placed around the machine for amount of 50 in 120 meters storage ring. Beam loss counts is collected by multi-channel scalers on VME crate and is updated to database on workstation dynamically. Loss count information is updated into archive file for retrieval purpose. Two types of real-time display are supported by the graphical user interface on workstation: (1) Bar chart; (2) Loss counts display superimpose with storage ring layout. The first type is routinely used. The other type helps to identify beam loss with ease. During lattice change or operation of insertion devices, resonance lines crossing was observed by use of this beam loss monitoring system. Application to the tune space exploration indicates that this beam loss monitoring is a more efficient and sensitive devices in comparison with using beam size and beam lifetime estimation.

1. INTRODUCTION

With the information provided by the BLM placing around the ring, beam loss distribution pattern can then be directly monitored [1]. With the fast response nature provided by BLM, it is very helpful in studying the trapping phenomenon of dust or ions. The working principle of the BLM is described as follow. Two PIN-photodiodes mounted face-to-face can detect charged particles. It is becaused of the coincidence technique applied in the circuit, which makes it insensitive to synchrotron radiation. The BLMs produce voltage pulses when the active area of a PIN-diodes is struck by minimum ionizing particle (MIP), which causes a coincident. Installed BLM system distributes around 120 m TLS plays as a convenient and powerful diagnostic tool. Its real-time nature and integration with the control system making BLM system helpful for machine trouble shooting and routine operation.

2. TLS BEAM LOSS MONITORING SYSTEM

About 50 Bergoz's type BLMs have been installed around the storage ring in early of 1996 as shown in figure 1. The storage ring has six superperiods. Eight BLMs are installed per superperiod. Two additional BLMs are installed near by injection septum and scraper. This system has been operating for about one year. Beam loss counts are collected by multi-channel scalers on VME crate and updated to database on workstation dynamically. Time frame generator is planned to be included in the BLM upgrade version in order to provide useful information for studying dynamic phenomena. Loss counts is updated into archive file system for retrieval. Two types of real-time display mode are supported by the graphic user interface on workstation. The first type is a bar chart display which is routinely used by the operator and for radiation survey. The second type is a loss counts display superimpose with layout of the storage ring, as shown in figure 2, which helps to localize the beam loss spots.

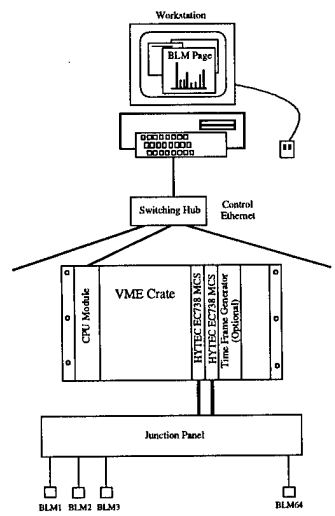

Figure 1. Functional block diagram of beam loss monitoring system

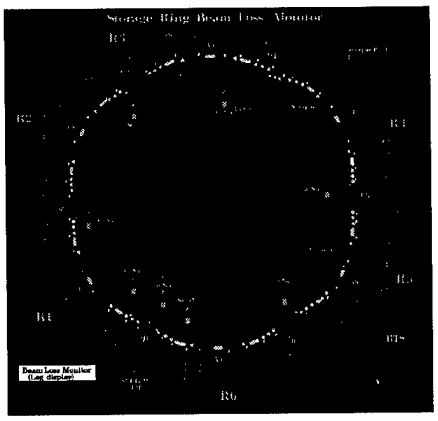

Figure 2. Loss counts display with the storage ring layout.

During recent shutdown in February-March 1997, independent quadrupole power supplies, undulator U5, and undulator U10 prototype were installed to be incorporated with storage ring operation. Commissioning of these newly installed devices started in April. Loss counts at the early stage of the commissioning is shown in figure 3. The peaks at BPM index 10 and 17 are the BLMs situated just at downstream of U10P and U5 with narrow gap vacuum chambers of 18 mm. Peak near BLM index 20 is located at the downstream of scraper and RF cavities. Effort has been made to reduce the losses by changinf orbit around these region. And the BLM system has demostrated that is is a very handy tool in monitoring the orbit response in terms of localized beam loss radiation.

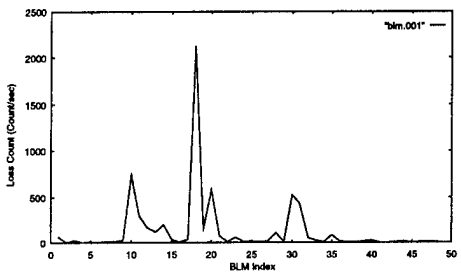

Figure 3. Beam loss distribution of first beam store on April 10, 1997 (beam current 16 mA). The ordinate shows the location of the monitor, and the abscissa shows the count rate.

3. BLM SYSTEM APPLICATIONS

BLM system is used in routine operation as well as some particular purposed machine study. From the operation experience gained in the passed few years, its has shown that the BLM system plays an improtant role on various topics study. Details of a few BLMs related activities in SRRC are describe as follows:

3.1 Beam loss pattern during injection

High injection efficient is desired from the radiation safety as well as operation point of view. BLM system provides an alternate tool for injection study. Figure 4(a) shows a typical loss track at one of the BLM. Most of the losses occur within 500 μsec, i.e. about 1000 turns. Details from expanding in the time scale is goven in figure 4(b). The loss event has a somewhat periodic structure. It is easily identified that the frequency of the period is 260 kHz which corresponds to the vertical tune. The possible reasons of causing the lossed includes horizontal residual and leakage field of injection magnets, injected beam launching condition, coupling of the storage ring, and small vertical aperture chambers used for insertion devices. The results demostrated that BLM is very helpful for injection study to optimize the injection conditions. In this experiment, signal reading from some of the BLMs nearby injection kickers are interfered while injection kickers are firing. This problem is eliminated by gating technique. It is expected that after the grounding improvement is finished for the BLM system, the interference will be further suppressed.

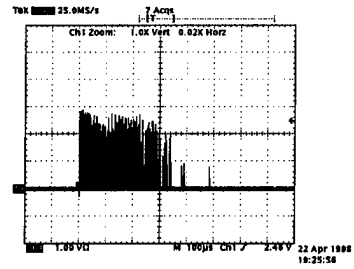

(a)

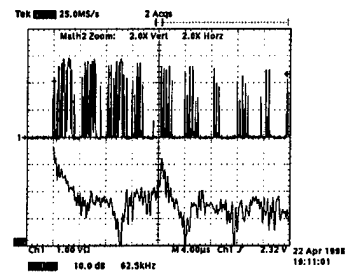

(b)

Figure 4. BLM applied in injection losses study, (a) Injection loss pattern; (b) tune observance by beam loss monitor.

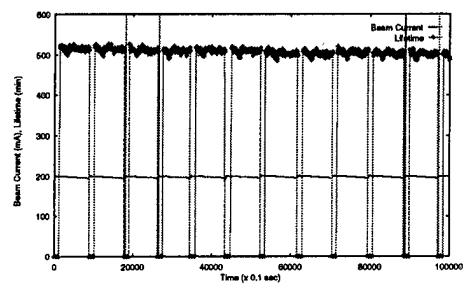

(a) Beam current and lifetime for top-off mode test at 1.3 GeV

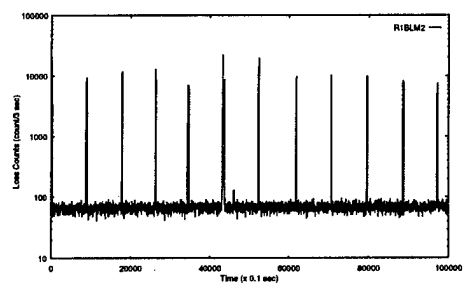

(b) Loss counts at R1BLM2

Figure 5. Beam losses observation for top-off mode test.

Top-off mode injection has been test in early 1996. Figure 5(a) shows beam current and lifetime during the test. Figure 5(b) shows the loss counts observed by R1BLM2. Loss peaks occur at the instant of injection. Discontinuity on lifetime display is due to the reasons

that lifetime calculation is stop during injection and the data length for lifetime estimation needs aabout 3 minute to produce the fist lifetime data.

3.2 Beam losses during users shift

It has also been examined that BLM and vacuum gauges reading provide complementary information to identify and interpret many beam loss phenomena. Corrlation between archived BLMs data and other machine parameters is also important in understanding the dynamic mechanism of machine characteristics.

3.3 Resonance line crossing observation

Resonance line crossing is usually occurred while tuning lattice parameters, changinf of insertion devices, beam energy ramping, etc. Figure 6 shows the scenario of resonance line crossing during 1.8 Tesla wiggler gap change. The wiggler gap change form 22.5 mm to 23 mm, and then close back to 22.5 mm. The loss counts at downstream of wiggler and injection septum illustrated that strong loss peak, at wiggler gap near 50 mm, were due to resonance line crossing during wiggler gap change.

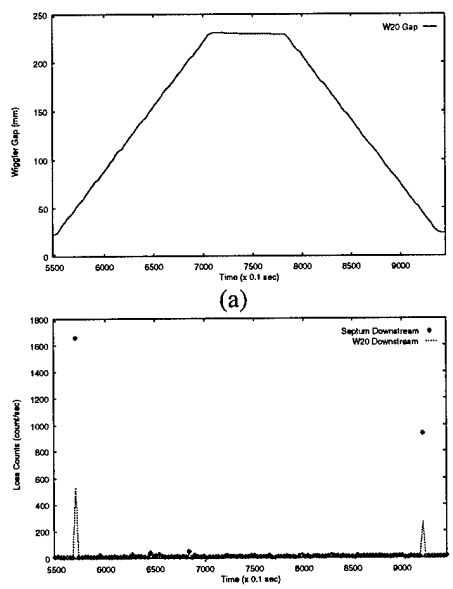

Figure 6. Resonance line crossing during W20 change gap. (a) Wiggler gap; (b) Loss count of BLM at downstream of septum and wiggler.

3.4 Tune mapping

Optimizing machine lattice requires systematic studing of its corresponding tune space [2,3]. Also, tune scan is also useful for studying insertion devices caused nonlinear resonance. Preliminary test result is shown in figure 7. The procedure is to reduce vertical aperture by scaper in association with the changing quadrupole strength of Q1 and Q2 for desired tune. Scan the various tunes and collect loss counts. The preliminary results are shown in figure 7. It is clearly shown that a tune trajectory crossing tune space, as shown in figure 7, corresponds to a third order resonance line.

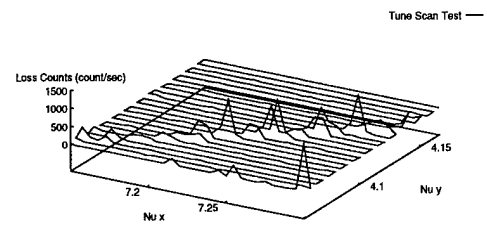

Figure 7. First tune scan test at Taiwan Light Source

3.5 Other applications and future plan

BLM is useful for studying the trapping phenomenon of micro-particles or ions. This study is in progress at TLS. Adding time frame generator will equip the scaler with capability to record dynamic loss for injection and tune scan study.

4. CLOSING REMARKS

BLM system provides an additional diagnostic tool which may help to locate problems in trouble shooting and finding possible reasons for poor beam lifetime in routine operation. BLMs system is also helpful in commissioning insertion devices.

5. ACKNOWLEDGMENTS

The author thanks the staffs of the instrumentation and control group to help setup the system. The authors would like to show their appreciation to all the personnel of the light source division of SRRC who devote the BLM system related in direct or indirect.

REFERENCES

[1] K. Wittenburg, F. Ridoutt, "Experience with the Electron and Proton Beam Loss Monitor (BLM) Systems at HERA", Proceeding of the 5th European Accelarator Conference, 1612 (1996) and reference therein.

[2] H. Schmickler, "Tune Scans in LEP", CERN SL/95-67 (BI), 1995 and reference therein.

[3] D. Robin, et al., "Observation of Nonlinear Resonance in the Advanced Light Source", LBL-36427, 1994 and reference therein. D. Robin, et al., "Reduction of Nonlinear Resonance Excitation from Insertion Devices in the ALS", LBL-36435, 1995 and reference therein.

METHODS OF ORBIT CORRECTION SYSTEM OPTIMIZATION*

Yu-Chiu Chao, Thomas Jefferson National Accelerator Facility

Abstract

Extracting optimal performance out of an orbit correction system is an important component of accelerator design and evaluation. The question of effectiveness vs. economy, however, is not always easily tractable. This is especially true in cases where betatron function magnitude and phase advance do not have smooth or periodic dependencies on the physical distance. In this report a program is presented using linear algebraic techniques to address this problem. A systematic recipe is given, supported with quantitative criteria, for arriving at an orbit correction system design with the optimal balance between performance and economy. The orbit referred to in this context can be generalized to include angle, path length, orbit effects on the optical transfer matrix, and simultaneous effects on multiple pass orbits.

1 INTRODUCTION

In designing orbit correction systems simple rules such as phase advance counting are often followed in placing monitors and correctors. While such rules work well with smooth, periodic betatron functions and phase advances, one may encounter difficulty using them in areas where large betatron variations contribute significantly to response matrix elements compared to pure phase contributions, or in areas where smooth periodicity is absent. When these problems are present, it is difficult to arrive at a *global and quantitative* design criterion for the orbit correction system based on phase advance counting. Here we present a self consistent program based on response matrices. It ensures the *globally consistent* application of the same quantitative criteria for observability, controllability and non-degeneracy defined by the designer, independent of the smoothness of the local lattice.

The program starts by evaluating the observability of the monitor system to ensure knowledge of the orbit to the same level everywhere. An algorithm for adding monitors is introduced in case of deficiency in observability. The redundancy of the monitor system is then evaluated and an algorithm for monitor minimization introduced to ensure that a minimally necessary set is obtained that would not place unjustified demands on the corrector system. We follow by evaluating the controllability of the corrector system to ensure control of the orbit to the same level everywhere. An algorithm for adding correctors is introduced in case of deficiency in controllability. The overall redundancy of the corrector system is then evaluated and an algorithm for corrector minimization introduced to ensure that a minimally necessary set is obtained that would not lead to large local orbits due to correction using near-singular response matrices. The application of this program to the CEBAF accelerator, where localized deficiencies in monitors and overall redundancies in correctors have been identified and corrected, will be described.

* Work supported by the U.S. Department of Energy, contract DE-AC05-84ER40150.

2 NOMENCLATURE

For simplicity we limit our discussion to the x-plane only with the usual index assignments of 1, 2, 6 for position, angle and momentum. Generalization is straightforward.

2.1 Error-to-monitor response matrix M^{EM}

The error-to-monitor response matrix M^{EM} summarizes the orbit disturbance at any monitor caused by any physical error which can affect any of the beam orbit coordinates:

$$O_i = \sum_j M_{ij}^{EM} \bullet E_j$$

where O_i is the orbit disturbance at the i-th monitor and E_j the magnitude of the j-th physical error, including injection errors, magnetic field errors, misalignments etc.. The elements of M^{EM} consist of optical transfer elements M_{11}, M_{12}, and M_{16} from the sources of error to the monitors. In constructing M^{EM} for subsequent analysis, one must identify all the major potential sources of errors that the entire orbit correction system is designed to correct. This usually includes quadrupole offsets, large dipole field errors, suspected misalignments etc.. Any estimate on the relative magnitude of such errors can be incorporated into M^{EM} by properly scaling individual columns.

2.2 Error-to-all-location response matrix M^{EA}

The error-to-all-location response matrix M^{EA} summarizes the orbit disturbance at all representative locations caused by the physical errors described above. These locations, not tied to any physical elements, should effect a dense coverage of the entire beam line and will be collectively denoted by a set C_A.

$$O_i = \sum_j M_{ij}^{EA} \bullet E_j$$

where O_i is the orbit disturbance at the i-th location.

2.3 Corrector-montior response matrix M^{CM}

The corrector-monitor response matrix M^{CM} summarizes the orbit disturbance at any monitor by any corrector.

$$O_i = \sum_j M_{ij}^{CM} \bullet K_j$$

where K_j is the magnitude of the j-th corrector kick.

2.4 All-location-to-montior response matrix M^{AM}

The all-location-to-monitor response matrix M^{AM} summarizes the orbit disturbance at any monitor caused by coordinate error at any representative location in the set C_A.

$$O_i = \sum_j M_{ij}^{AM} \bullet K_j$$

where K_j is the magnitude of the error at the j-th location.

2.5 Corrector-to-all-location response matrix M^{CA}

The corrector-to-all-location response matrix M^{CA} summarizes the orbit disturbance at all representative locations caused by any corrector.

$$O_i = \sum_j M_{ij}^{CA} \bullet K_j$$

2.6 Singular value decomposition (SVD)

SVD is the process of decomposing a matrix M into the product of three matrices U, W and V:

$$M = U^T \bullet W \bullet V$$

U and V afford useful physical interpretation when applied to response matrices. The rows of V represents orthonormal combinations of the "actuators", either errors or correctors, whose effects are magnified by the diagonal elements of W before being realized as orthonormal orbit patterns represented by the rows of U. SVD allows us to decompose the response matrix into decoupled cause-effect relations between linear combinations of the actuators and monitors, with the magnification factors contained in W. The diagonal elements of W are called singular values and the condition number N_M^{svd} of M is the ratio between the largest and the smallest singular values.

2.7 Null space vectors

The null space vectors E_M for a given matrix M are the vectors which are projected into 0 by M:

$$M \bullet E_M = 0, \qquad |E_M| = 1$$

Notice we choose to have all E_M's normalized.

2.8 Pseudoinverse and projected components

The pseudoinverse $M^\dagger$ of a given matrix M is defined as

$$M^\dagger = (M^T \bullet M)^{-1} \bullet M^T$$

The pseudoinverse is related to the projection operator Π_M, which decomposes any vector X into components X^M and $\overline{X}^M$ respectively inside and outside the subspace spanned by the column vectors of M, through

$$\Pi_M = M \bullet M^\dagger ,$$

$$V^M = \Pi_M \bullet X , \qquad P_M^X = |X^M|/|X|$$

$$\overline{X}^M = X - \Pi_M \bullet X , \qquad Q_M^X = |\overline{X}^M|/|X|$$

where we have also defined the fractional components $P^X{}_M$ and $Q^X{}_M$ of X inside and outside the subspace spanned by M.

2.9 Gram determinant and orthogonality

The Gram determinant G_M of a matrix M is given by

$$G_M = \mathrm{Det}\,(M^T \bullet M) \qquad \text{row dim.} > \text{column dim.}$$

$$= \mathrm{Det}\,(M \bullet M^T) \qquad \text{column dim.} > \text{row dim.}$$

$$G_M = \left(\prod_j S^M{}_j\right)^2$$

where $S^M{}_j$ is the j-th singular value of M. The normalized Gram determinant $\overline{G}_M$ is defined as

$$\overline{G}_M = G_M/L_M , \qquad 0 \le \overline{G}_M \le 1$$

$$L_M = \prod_j \left(\sum_i M_{ij}^2\right) \qquad \text{row dim.} > \text{column dim.}$$

$$= \prod_i \left(\sum_j M_{ij}^2\right) \qquad \text{column dim.} > \text{row dim.}$$

3 THE OPTIMIZATION PROGRAM

In the following we outline the entire optimization program using the quantitative measures defined in the previous section. It should be noted that the general philosophy of accelerator design demands the following numerology to hold: $N_E > N_M > N_C$, where N_E, N_M and N_C are the total number of potential errors, monitors and correctors respectively. Thus the matrix M^{EM} always has more columns than rows and the opposite is true for M^{CM}. One can start the program with an arbitrary initial monitor-corrector configuration and iterate until all criteria are satisfied. A set of candidate locations for monitors and correctors should be identified, for example at all quadrupole locations, in case additional monitors or correctors are demanded in an iteration. These sets will be denoted C_M and C_C in the following. We will also denote by C_A the set of all representative locations used for establishing M^{EA}. Various cutoff numbers will be used for terminating iterations. Their physical meaning will be briefly described, but not quantitatively elaborated.

3.1 Eliminating monitor deficiency

1. Determine cutoff number R in units of orbit displacement, a measure of the error-induced orbit anywhere that is undetectable by existing monitors.
2. Obtain null space vectors $E_{M^{EM}}$ of M^{EM}, calculate $V^A = M^{EA} \bullet E_{M^{EM}}$ for all $E_{M^{EM}}$.
3. If any element of any V^A is greater than R, identify index j of the largest such element in V^A.
4. Add to monitor list the candidate monitor in C_M closest to the location represented by the j-th location in C_A.
5. Iterate steps 2-4 until all elements of V^A are less than R.

6. Perform SVD on M^{EM}, obtain the row vector v of V with the smallest singular value, calculate $V^A = M^{EA} \bullet v$.
7. Iterate steps 3, 4 and 6 until all elements of V^A are less than R.

3.2 Minimizing monitor redundancy

1. Determine cutoff numbers R and S with $0 < R < 1$, $0 < S < 1$. R is a measure of the extent to which all error-induced orbits contribute to a single monitor, and S is a measure of the orthogonality of the monitors.
2. Calculate all N_M fractional components $Q^{X_i}_{M^{EM}}$, with X_i the vector representing unit orbit peak at the i-th monitor.
3. Eliminate all monitors whose corresponding $Q^{X_i}_{M^{EM}}$ exceed (1-R).
4. Calculate the normalized Gram determinants $\bar{G}_{M^{EM}}$, continue if it is less than S to the N_M-th power.
5. Perform SVD on M^{EM}, obtain the row vector u of U with the smallest singular value, identify the largest component of u and its index i.
6. Eliminate the i-th monitor.
7. Iterate steps 4-6 until $\bar{G}_{M^{EM}}$ is greater than S to the N_M-th power.

3.3 Eliminating corrector deficiency

1. Determine cutoff number R and S, $0 < R < 1$. R measures the fraction of an error-induced orbit pattern uncorrectable by the correctors. S measures corrector limits.
2. Perform SVD on M^{EM}, obtain all row vectors u of U.
3. Calculate all N_M fractional components $Q^{u_i}_{M^{CM}}$, and all N_M pseudo-inverted vectors $K_i = M^{CM\dagger} \bullet u_i$ with u_i the i-th row vector of U. Identify the maximum K_i^{max} of each K_i.
4. Continue if any $Q^{u_i}_{M^{CM}}$ is greater than R, or any K_i^{max} is greater than S. In the former case identify the u_i with the largest $Q^{u_i}_{M^{CM}}$, calculate $T_i = u_i - \Pi_{M^{CM}} \bullet u_i$. In the latter identify the u_i with the largest K_i^{max} and set $T_i = u_i$.
5. Calculate the normalized inner product between Ti and all the column vectors of M^{AM}. Identify index j with the largest inner product.
6. Add the candidate corrector in C_C closest to the location represented by the j-th location in C_A.
7. Iterate steps 2-6 until all $Q^{u_i}_{M^{CM}}$ are less than R and all K_i^{max} are less than S.

3.4 Minimizing corrector redundancy

1. Determine cutoff numbers R and S, R measures the evenness in the corrector effect distribution among monitors. S with $0 < S < 1$ measures the orthogonality of the corrector effects on the monitors.
2. Identify correctors forbidden from removal.
3. Perform SVD on M^{CM}, if the condition number $N^{svd}_{M^{CM}}$ is greater than R, or the normalized Gram determinants $\bar{G}_{M^{CM}}$ is less than S to the N_C-th power, continue.
4. Identify the row vector v of V with the smallest singular value and the index j of the largest element in v.
5. If the j-th corrector is not forbidden, remove it. If it is, remove the largest non-forbidden corrector in v.
6. Monitor $Q^{u_i}_{M^{CM}}$ and K_i^{max} defined in the previous program relative to their respective cutoff numbers to ensure freedom from deficiency.
7. Iterate steps 2-6 until $N^{svd}_{M^{CM}}$ is less than R and $\bar{G}_{M^{CM}}$ is greater than S to the N_C-th power.

3.5 Alternative to corrector redundancy

A more advantageous alternative to the last corrector reduction program aimed at eliminating excessive orbit correction caused by near-degeneracy is to introduce "virtual monitors" which automatically keep the correction result confined and free of singular behavior. The algorithm for adding virtual monitors is discussed in [1].

4 APPLICATION TO CEBAF ACCELERATOR

4.1 Monitor deficiency

The program 3.1 for eliminating monitor deficiency was applied to the existing set of BPM's in CEBAF. It was discovered that all elements V_A are within a limit of 3 mm, with the exception in the East Extraction Region with the elements of V_A exceeding 15 mm for all beam passes, causing orbit excursions undetectable from available data. This is supported by simulation and operation data. It was determined that additional BPM's be installed according to this program as the potential orbit error can cause emittance distortion on the order of 10% due to suspected higher order field in nearby dipoles.

4.2 Corrector redundancy

A corrector reduction program at CEBAF was performed based on the program 3.4 above. There have been operation and simulation evidences that an overly dense coverage of the beam line by correctors led to excessive correction in the lower arcs and poor reproducibility in the spreaders and recombiners. 66 correctors were removed from a total of about 860 while the corrector deficiency criteria were monitored at each step to prevent over-reduction. The machine has been operating with this reduced corrector set and no compromise in orbit correctability has been observed.

5 REFERENCES

[1] 'Orbit Correction Using Virtual Monitors at Jefferson Lab', Y. Chao et al, these proceedings.

AUTOMATED PATH LENGTH AND M_{56} MEASUREMENTS AT JEFFERSON LAB

D. Hardy, J. Tang, R. Legg, M. Tiefenback, M. Crofford, and G. A. Krafft
Thomas Jefferson National Accelerator Facility
12000 Jefferson Ave., Newport News, VA 23606

Abstract

Accurate measurement of path length and path length changes versus momentum (M_{56}) are critical for maintaining minimum beam energy spread in the CEBAF (Continuous Electron Beam Accelerator Facility) accelerator at the Thomas Jefferson National Accelerator Facility (Jefferson Lab). The relative path length for each circuit of the beam (1256m) must be equal within 1.5 degrees [1] of 1497 MHz RF phase. A relative path length measurement is made by measuring the relative phases of RF signals from a cavity that is separately excited for each pass of a 4.2 μs pulsed beam. This method distinguishes the path length to less than 0.5 degrees of RF (<280 μm) and gives the direction of the path length error. The development of a VME based automated measurement system for path length and M_{56} has contributed to faster machine setup time and has the potential for use as a feedback parameter for automated control.

1 INTRODUCTION

CEBAF is a 4 GeV electron accelerator producing CW beams for nuclear physics research. The accelerator consists of a 45 MeV injector and two parallel 400 MeV linacs. The linacs each contain 20 cryomodules each of which have 8 superconducting cavities. The beam is circulated a total of five times to achieve 4 GeV of total acceleration. The cavity phases are set to provide maximum acceleration using first pass beam. To keep higher passes on crest, the path length of each pass must be adjusted to less than 1.5 degrees. When performed locally in the service buildings measurements of path length and M_{56} can be imprecise and are time consuming. This paper describes the implementation of the hardware and software used to perform and automate the path length and M_{56} measurements using the EPICS (Experimental Physics and Industrial Control System) at Jefferson Lab.

2 MEASUREMENT METHODS

2.1 Description of Path Length and M_{56} Measurements

At CEBAF the beam is relativistic after the first superconducting cavity so the path length is a time of flight measurement of the whole electron bunch. The distance for each pass of the machine is measured in an integral number of 20 cm RF periods. The path length measurement method finds the length that each pass deviates within 1 RF period. M_{56} is a measurement of the degree that the path length changes for a given momentum change (ΔP)

$$M_{56} = \Delta \text{path length} \frac{\Delta p}{p}$$

The path length and M_{56} of the arcs are found using a precision phase detector [3] to measure the time of arrival of the electron bunches at a 1497 MHz cavity monitor [1] (M_{56} cavity). Because the beam induced voltage in the cavity is in phase with the bunch current, a measurement of the phase of the RF from the cavity is a direct measurement of the time of arrival of the electron bunches. An M_{56} cavity is located at the end of each linac, thus all five passes of the beam propagate through the cavity. A macro pulse with a duration less than the circulation time (4.2 μsec) is established at a 60 Hz rep rate. This pulse separately excites the cavity each time it completes one circulation. A difference in path length between passes is measured as a phase difference between the RF from each pass.

3.2 Path Length Theory of Operation

The phase of RF coming from the pickup cavity is adjustable relative to a 1497 MHz reference with a programmable phase shifter. The signal is then mixed with the RF reference where the voltage output (V_{out}) of the mixer is:

$$V_{out} = \text{cavity RF} \times \text{Reference Signal}$$

$$V_{out} = A_1 \sin(\omega t + \phi_1) A_2 \sin(\omega t + \phi_2)$$

The high frequency components are removed by a low pass filter. V_{out} is now dependent only upon the beam current and the phase difference between the RF from the cavity and the RF reference.

$$V_{out} = A_1 A_2 / 2 \ \sin(\phi_1 - \phi_2)$$

To perform a path length measurement the phase shifter is adjusted so that $(\phi_1 - \phi_2)$ is near 0, and using the small angle approximation

$$V_{out} \cong A_1 A_2 / 2 \ (\phi_1 - \phi_2)$$

The reference phase ϕ_2 is a constant, therefore any indicated phase change is due to a change in ϕ_1 from the cavity. The macro pulse separately excites the cavity for each pass and a separate measurement for V_{out} for each

0-7803-4376-X/98/$10.00 © 1998 IEEE

pass results. A change in phase of the cavity RF (ϕ_1) for any pass will result in a change in V_{out} for that pass (Figure1).

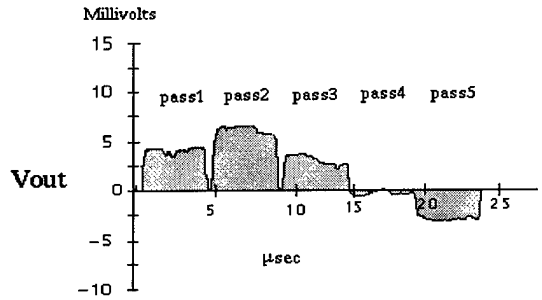

Figure 1 Relative Phase Measurement Between Passes

The cavity is calibrated by using the phase shifter to adjust ϕ_2 through a range of phases in the near-linear region of the output of the phase detector where $\sin(\phi_1-\phi_2)$ is close to 0. The slope of V_{out} as a function of $\Delta(\phi_1-\phi_2)$ in mV/degree is found. During a measurement this constant is used to find the path length difference for any change in V_{out} between passes.

3 PATH LENGTH MEASUREMENT SYSTEM

3.1 Path Length / M_{56} Measurement Hardware

The cavity is a simple pill box cavity, resonating the TM_{010} mode at 1497 MHz. Constructed of stainless steel in order to minimize drifts due to temperature, Q_0 is approximately 3000 and the geometric shunt impedance is 180 Ω [2]. The signal from the cavity is sent to the isochronous measurement chassis as shown in Figure 2.

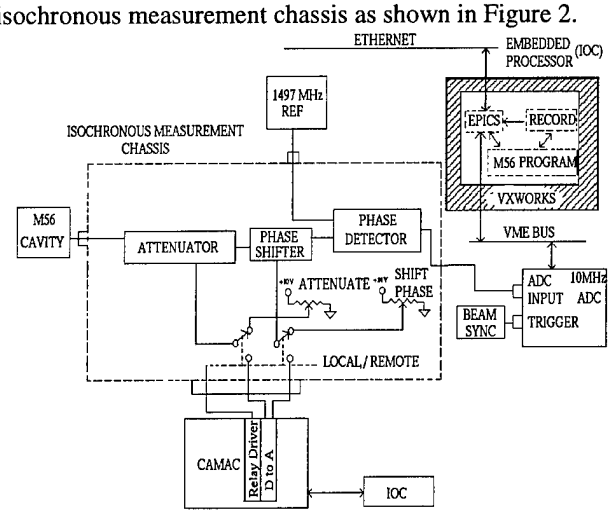

Figure 2 Schematic of Path Length Measurement System

The EPICS controls system is used to control an RF switch, a phase shifter, attenuator, and a 10 MHz ADC. The output signal from the phase detector is sent to the ADC which digitizes the M_{56} wave form when triggered by the 60 Hz beam sync signal.

2.2 Path Length / M_{56} Measurement Software

The path length program performs a selected number of averages on the digitized waveform and stores the averaged waveform in a EPICS wave form database record. The record is then parsed into segments for each pass, and the average of each parsed segment is found and a single value representing the cavity voltage for each pass is obtained. Three calibration factors are needed and stored for path length measurements. The first is the phase shifter setting found when pass1 is adjusted to 0 phase. The second is the attenuator setting for minimum attenuation. The third is a calibration of the phase detector with beam in the cavity with $A_1A_2/2\ \sin(\phi_1-\phi_2)$ in the near-linear region. With the output of the detector adjusted to 0 phase for pass 1, a relative path length measurement is made from one pass to the next. The cavity voltage for each pass is multiplied by the calibration factor in degrees/mV. The display screen shown in Figure 3 is used to initiate a path length measurement and display the result.

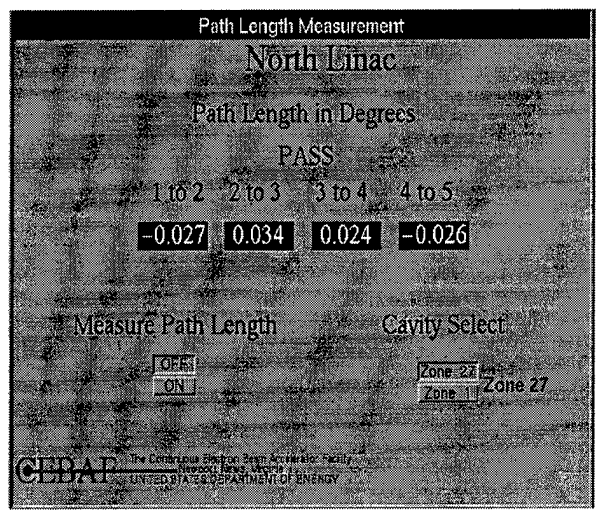

Figure 3 Path Length Measurement Screen

The relative path length between passes is measured in degrees. The update rate depends upon the number of averages selected on the M_{56} expert page, with 50 averages selected an update rate of approximately 2 seconds has been observed.

M_{56} measurements are made using the display screen shown in Figure 4. M_{56} is measured by performing one path length measurement at the nominal operating energy and another with a small energy offset ($\Delta P/P$). The program calculates the M_{56} for each pass and displays the results.

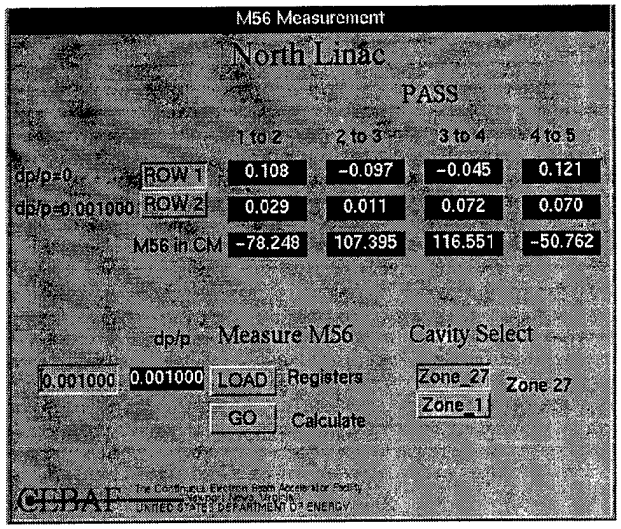

Figure 4 M_{56} measurement screen

4 PATH LENGTH MEASUREMENT RESULTS

In each arc at CEBAF there is a dogleg magnet system that is used to adjust the path length to set the energy cresting for the next linac. The dogleg control bus consists of a dipole and two shunts that allow the path length to be adjusted by up to 8 degrees in either direction from the designed orbit (Figure5).

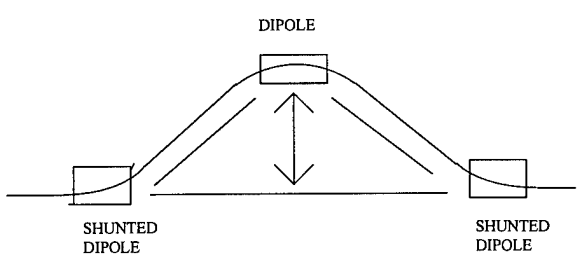

Path Length adjusted in either direction from Designed orbit by changing bend angle

Figure 5 Dogleg System

To test the accuracy of path length measurements, a range of path lengths from from +4 to -3 degrees in 0.5 degree increments was introduced into the dogleg of the second arc. The corresponding path length measured was as shown in figure 6. The accuracy of the measurement (as indicated by one standard deviation of no greater than .12 degrees) allows the system to diagnose path length error well below the design requirements of 1.5 degrees.

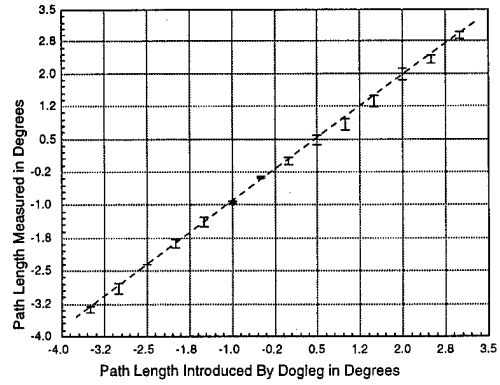

Figure 6 Path Length Introduced vs Measured

5 CONCLUSIONS

The novel use of relative phase measurements to perform path length and M_{56} and measurements results in a system that performs path length measurement in less than 3 seconds and gives a 2σ measurement error of <.25 degrees (< 140 μm). Presently an M_{56} measurement requires an operator to make the energy change. In the future the path length program will work at 30 Hz allowing M_{56} measurements to have the same speed performance as the path length program. Another feature of the system is that it gives the direction of the measured path length. This allows for quick calculation of needed corrections to the optics. Future developments may include automatic correction of path length and M_{56}

REFERENCES

[1] G. A Krafft, "Notes on the energy Spread at CEBAF", TN#90-269

[2] R. Ursic, K. Mahoney, C. Hovater, A. Hutton, C. Sinclair, "CEBAF Beam Loss Accounting", TN#95-034

[3] G. A. Krafft, M. Crofford, D. R. Douglas, S. L. Harwood, R. Kazimi, R. Legg, W. Oren, K. Trembay, and D. Wang, Proc. 1995 Particle Accelerator Conf., pp 2429-2431

ANALYZING MEASUREMENTS OF NONLINEAR TRANSFER FUNCTIONS WITH TSCHEBYSHEV POLYNOMIALS

G. A. Krafft, TJNAF, 12000 Jefferson Ave., Newport News, VA 23606

Abstract

Recently, due to advances in computers and data aquisition systems, the following type of measurement has become more common: (1) Impress a given modulation on a device to be tested. (2) Acquire a data stream, usually at equally spaced sample intervals, of the response of the system to the modulation. (3) Fit the data thereby acquired to some nonlinear function set that might (or might not!) describe the response of the device. In this paper it is pointed out that by choosing to modulate the test parameter sinusoidally, and by fast-Fourier transforming the acquired data stream, one unambiguously determines the Tschebyshev expansion of the response function around the working point, potentially yielding quantitative information about high nonlinear orders in the system response. The need for data fitting is thereby eliminated. A detailed example, the analysis of the nonlinear phase-phase transfer function in the Jefferson Lab injector, is presented.

1 ANALYSIS

The accelerator at Jefferson Lab acts like a LINAC in that the particle orbit never entirely closes on itself. Therefore, to analyse the performance of the accelerator, measurements of the beam transfer maps take on fundamental significance; there is no notion of tune as in a ring. In the course of analyzing such beam transfer maps, in particular the phase-phase transfer map between the chopping system and main linac in the injector, a convenient means was found for characterizing the system response, including nonlinearities that might exist in the transfer map. This type of analysis may be applied generally to measurements where one perturbs some parameter, e.g. the orbit around the working point of an accelerator, and measures the system response to that perturbation at the same time.

In general, consider a measurement where a parameter, x, is modulated between two limits, and simultaneously the response of the system under test is recorded. An interesting case is when the modulation is sinusoidal

$$\delta x = \Delta x \cos(\omega t),$$

where Δx is the amplitude of the modulation and ω is the angular frequency of the modulation. For a given amplitude Δx, the response defines a function with dimensionless argument on the domain [-1,+1] by $Y(\delta x/\Delta x) = y(\delta x)$. If this function is expanded in an orthogonal series of Tschebyshev polynomials

$$y(\delta x) = Y(\delta x/\Delta x) = \sum_{n=1}^{\infty} a_n T_n(\delta x/\Delta x),$$

then using the standard identity defining Tschebyshev polynomials, $T_n(\cos\theta) = \cos(n\theta)$, the amplitudes of the expansion coefficients appear directly as the size of the peaks in the Fourier analysis of the output data

$$a_n = \frac{1}{\pi}\int_0^{2\pi} Y(\cos\omega t)\cos(n\omega t)d(\omega t).$$

Examples of the types of distortions that correspond to two of the Tschebyshev modes are shown in Fig. 1. In these plots, the Tschebyshev modes are displayed, including a random noise component added to the ordinate, to model noise in the measurements, the peak to peak amplitude of the noise being one tenth of the mode amplitude. If the modulation is performed at a certain frequency $f = \omega/2\pi$, and the noise level is the same as appears in the mode pattern figures, then by Fourier analysis of the output of the phase detector, one obtains the power spectra in Figs. 2 and 3. Modulation in the $n = 1$ mode gives output only at the first harmonic, modulation in the $n = 2$ mode gives output only at the second harmonic, modulation in the $n = 3$ mode gives output only at the third harmonic, and so forth. Conversely, if one sinusoidally modulates the input parameter and Fourier analyzes the output response around a particular working point, the response function is resolved into its Tschebyshev amplitudes, the expansion coefficient being the Fourier amplitude of the corresponding harmonic of the modulation frequency.

In Figs. 1, the total number of points is 1020, and it is assumed for concreteness that the sample rate is 60 Hz. A 1 Hz modulation was done, and it is clear that the signal to noise in the measurement is good in a total measurement time of 17 sec. It is also clear that this technique unambiguously establishes the response function, at least in a neighborhood of the working point, *without the need of doing some form of nonlinear least fitting.*

2 MEASUREMENT SCHEME

It has been known for many years that a good way to measure relative time-of-arrival of charged accelerator bunches is to use longitudinal pickup cavities and precision RF phase detectors. Such devices are used to set up, check, and optimize the bunch length of the bunches emerging from the Jefferson Lab injector [1]. In the "best" case, one could in principle compress the bunch length up to the limit given by the injected longitudinal emittance, the maximum permitted extracted energy spread, and Liouville's theorem on conservation of phase space area. In practice, nonlinearities in the bunching process, for example, from nonlinearities in the RF fields, cause this best case limit to seldom be

0-7803-4376-X/98/$10.00 © 1998 IEEE

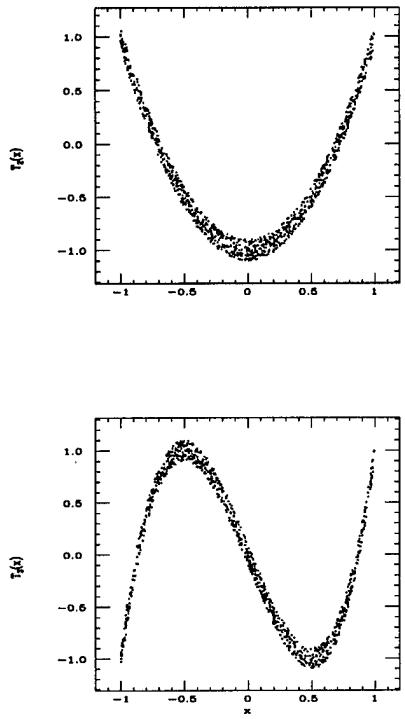

Figure 1: Mode patterns for $n = 2$ and $n = 3$; $T_1(x) = x$.

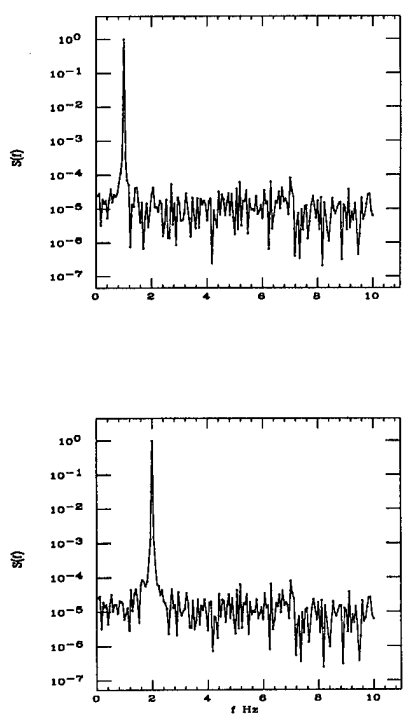

Figure 2: Modulation spectra for $n = 1$ fundamental and $n = 2$ second harmonic.

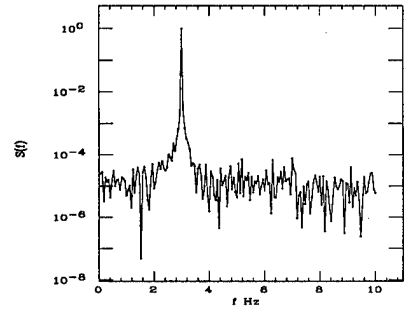

Figure 3: Modulation spectrum for $n = 3$.

achieved. Having a means to quantify and correct the bunch length is clearly useful for speeding and automating the optimization process. Tschebyshev analysis of the phase-phase transfer map (M_{55}) provides a systematic means of quantifying the nonlinearities as the amplitude of certain modes in phase-phase space. Given the measured amplitudes, it is clear that the bunch length is made smaller to the extent that the individual amplitudes can be made smaller.

In terms of the Tschebyshev modes, the $n = 1$ mode gives the slope of the phase transfer function. Making the $n = 1$ term in the expansion zero ($a_1 = 0$), is equivalent to the demand that the bunch should be going through a longitudinal waste ($\sigma_{55} = 0$). Demanding that $a_2 = 0$, means that bunch particles starting at the front of the bunch, the back of the bunch, and the middle of the bunch all arrive at the same time, given that a_1 has previously been corrected and the higher order terms are smaller than these. In this case the nonlinear transfer matrix element T_{555} is zero for the bunching system. Setting a_3 to zero, provides the first term that can correct asymmetries between the front and back of the bunch.

The level of correction that has been achieved in the references can be categorized. For example, Dowell, *et. al.*, [2] and Carlsten [3] have corrected the $n = 1$ and $n = 2$ modes. Likewise, Krafft [1] has corrected through $n = 3$, at least for the low space charge case reported.

3 EXPERIMENTAL RESULTS

At Jefferson Lab, for many years it has been possible to measure the phase-phase correlation function (M_{55}) between the beam chopping system in the injector and strategically placed longitudinal pickup cavities in the injector. An illustrative case is presented in Figures 4 and 5. In Fig. 4 an experimental aquisition of a 600 point phase-phase correlation function is given by the unconnected dots. Each dot was obtained on a separate beam pulse and the modulation of the input phase was chosen to be in a triangle wave so that uniform filling of the display is obtained [4].

Next the modulation was changed to be fully sinusoidal, all other conditions remaining the same. By the above anal-

ysis, the correlation function should be resolved into its Tschebyschev modes by examining the Fourier amplitudes of the output phase modulation. In Fig. 5, a Fourier analysis of the output phase is given which clearly shows the correct harmonic structure. The modulation frequency was 65 Hz, which is aliased to 5 Hz with a 60 Hz sample rate, and the total number of points was 1020 (17 sec). The resulting Tschebyshev expansion coefficients are shown in Table 1. Fig. 4 shows the function that results when the modes up to $n = 5$ are synthesized. The expansion clearly reproduces the measured phase-phase correlation function.

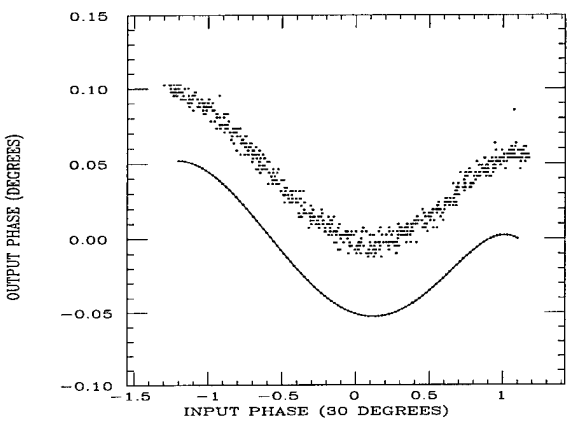

Figure 4: Experimental phase-phase transfer function obtained at the Jefferson Lab injector, and its synthesis using the Tschebyshev expansion (displaced for comparison).

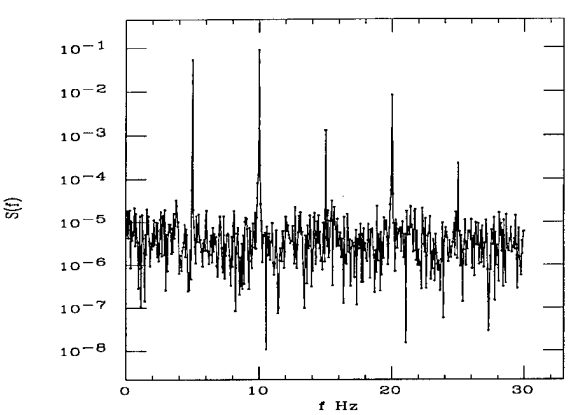

Figure 5: Output phase spectrum, f=65 Hz.

Because as part of the measurement process the power spectrum is obtained, one can estimate the relative error of

n	a_n (°)
1	-0.458
2	0.599
3	0.072
4	-0.182
5	-0.031

Table 1: Expansion coefficients for phase-phase transfer function in Fig. 4.

the measurements. Clearly, the peak at $n = 5$ can be distinguished with a S/N about 10 in Fig. 5. As the expansion coefficient is $a_5 = -0.031°$, the distortion in arrival time cleanly measured is $a_5 * 668$ psec$/360°$, or 58 fsec. It is possible to discern modulations perhaps one-fifth intense, leading to an overall resolution of order 25 fsec. This experimental result has precision comparable to the optical techniques that have been used to determine bunch length, but the present measurement provides much more information which can be used to tune the bunch length, in that the types of distortion in the phase space are given directly.

4 CONCLUSIONS

The conclusions of this work are:

- Nonlinear transfer maps may be conveniently analysed experimentally by performing modulation measurements, and by quantifying the results obtained using Tschebyshev polynomials.
- The nonlinearity is minimized when the magnitude of the expansion coefficients is minimized.
- Measuring the phase-phase correlation function provides a useful means of obtaining data to minimize the bunch length.

It should be noted that the Tschebyshev expansion techniques mentioned above are useful in quantifying measurements of transverse beam optical nonlinearities using transverse modulation of the beam. Multiple dimensions may be analyzed in the same way using multiple modulation frequencies. This work supported by U. S. DOE Contract No. DE-AC05-84ER40150.

5 REFERENCES

[1] Krafft, G. A., *Proc. of the Microbunches Workshop*, AIP Conf. Proceedings No. 367, pgs. 46-55 (1995).

[2] Dowell, D. H., Hayward, T. D., and Vetter, A. M., *Proc. 1995 Particle Accelerator Conference*, pgs. 992-994 (1995).

[3] Carlsten, B. E., *Proc. of the Microbunches Workshop*, AIP Conf. Proceedings No. 367, pgs. 21-35 (1995).

[4] Bowling, B. A., *et. al.*, "The CEBAF Injector Phase Transfer Function Measurement System", in preparation.

BEAM-BASED PHASE MONITORING AND GRADIENT CALIBRATION OF JEFFERSON LABORATORY RF SYSTEMS

M. G. Tiefenback and K. Brown,
Thomas Jefferson National Accelerator Facility*,
12000 Jefferson Avenue, Newport News, VA, USA, 23606

Abstract

Beam-based monitoring was instituted at Jefferson Lab in December of 1994 to correct the RF system phase setpoints against drifts of the master oscillator system, while running transparently to normal beam setup and delivery operations. As then implemented, the master oscillator distribution was subject to large thermal drifts, but no means existed of tracking the distribution of drifts, nor of identifying phase errors for individual cavities following maintenance activities. The background process implemented is capable of cresting each of the 312 cavities in the linacs to within approximately ± 2 degrees. In addition, during dedicated system measurement operations, the RF cavity gradients have been calibrated with beam to within a tolerance of approximately $\pm 5\%$. These beam-based results are in many cases more than 20% different from commissioning results using RF measurement techniques.

1 INTRODUCTION

The Continuous Electron Beam Accelerator Facility (CEBAF) consists of two recirculating electron linacs and the associated beam transport lines. Each linac provides a nominal energy gain of 400 MeV, up to five passes, for a final energy of 4 GeV. The injector provides three interleaved 499 MHz electron pulse trains with independent current control, one for each of the three experimental halls.

2 CRESTING THE LINAC PHASES

During accelerator commissioning, phase drifts in the master oscillator distribution hampered multipass operations, requiring re-adjustment of linac phase setpoints as often as several times per hour. Residual dispersion in the machine rendered detailed setup or measurement operations very difficult. As a result, correction processes called "energy locks," supported by analogous "orbit locks," were instituted [1, 2], providing 0.1 Hz bandwidth feedback stabilization of the beam position and energy at selected points within the system.

The energy locks stabilized the energy gain for the first pass beam, but not the accelerating phase (or the energy spread) of the beam. In November of 1994, we measured the resolution and stability of the energy lock process as a beam energy monitor and found that the scatter of measurements of the relative beam energy was approximately 5×10^{-5}. This performance was adequate to support an automatic cresting process for the phase setpoints of the RF system. The algorithm is described below. All individual cavity, cryomodule global, and linac global setpoints (available as single parameters in the control system) are available to the process. The resulting "AutoKrest" program [3] became the "phase lock" for CEBAF operations, and has been of great use in documenting residual phase drifts and faulty hardware in the system. The process has been stable for use while delivering CW beam to experiments, but as target requirements for energy stability become more stringent, we are less able to run the process during regular beam delivery.

2.1 Measurement Algorithm

The time scale of changes in the RF system (tens of minutes) and response time of the energy locks (5 seconds for each of the several updates required for convergence after an energy shift) implied that data for the cresting process would be very sparse. Accordingly, we chose an algorithm requiring the practical minimum (two) of data points. This provided the ability to crest a single RF phase in approximately one minute with the algorithm given below.

The RF system of a linac is divided into the energy lock cavities, the cavity or multiple cavities under test (which might include the energy lock cavities), and the rest of the linac (if any). For the first-order determinations required, the cavities of the energy lock process were presumed on-crest. The phase of an individual RF system is given relative to zero as the on-crest value, with ψ as the (slowly varying) error of the setpoint from that zero point. The total linac energy E, fixed by the energy lock process to within approximately 5×10^{-5}, is

$$E = E_{\text{other}} + E_{\text{lock}} + E_{\text{test}} \cdot \cos(\psi) + \text{error}.$$

If one adjusts the phase setpoint of the test system by $\pm\Psi$, successively, after some simplification one obtains

$$\frac{E_{\text{lock}}(+) - E_{\text{lock}}(-) + \text{error}}{2E_{\text{test}}} = \sin\psi \cdot \sin\Psi.$$

2.2 Precision

The differential resolution of beam energy is better than 10^{-4} of the total linac energy gain. With 160 cavities in each linac, the precision with which the relative energy gain of any cavity can be measured is better than 1%. For the case of a single RF cavity, using degree rather than radian measure for the phases and the small-angle expansion for the sine function, and including the overall error in energy

* This work is supported by the United States Department of Energy under contract DE-AC05-84-ER40150

determinations, we may write the relation above as:

$$\psi \cdot \Psi = \left(\frac{180}{\pi}\right)^2 \cdot \frac{E_{\text{lock}}(+) - E_{\text{lock}}(-)}{2E_{\text{test}}} \pm \sim 20$$

The uncertainty for a single cavity cresting measurement is equivalent to approximately 20 square degrees. Using a 10 degree shift in the cavity phase results in an overall energy shift (presuming a starting value near crest) of only 10^{-4}, and an anticipated error in determination of the crested phase setpoint of approximately 2 degrees. These estimates are confirmed by monitoring of successive determinations of the crest phase of given RF systems and by monitoring of the total system energy.

The most frequent problem with this algorithm is the influence of other components in the RF system, which also affect the energy lock gradient setpoints (other cavities going out of gradient lock, manipulation by operators, etc.).

2.3 *AutoKrest Implementation*

Implementing AutoKrest as a Unix process accomodated the need for for frequent modification during development. However, the other Unix control processes (energy and orbit locks) had user interfaces limited to the single screen from which they were invoked. To allow multiple users to control or monitor the progress of AutoKrest without spawning interfering processes, multiple instances of AutoKrest were prevented by using lock files as flags in the file system. The lock file contents provide CPU, process ID, and certain other useful information for later queries of the system to verify the status of the process. This has proven to be very useful and robust. A control interface usable from multiple operator screens was implemented using the Tcl/Tk language as extended to communicate with the EPICS database fields of the control system. To speed implementation, we began writing a Unix-based data acquisition, sequencing, and analysis task and an operator interface to connect the Unix program through a set of EPICS records accessible to a computer interface screen.

Because there was no other easily monitorable parameter to determine the status of the energy lock, we chose to monitor the gradient setpoints used by the lock to stabilize the overall system energy. These were updated at a nominal 0.2 Hz rate. We determined that it would be sufficient for AutoKrest to acquire data until the standard deviation of the last three data points was less than a threshold value. If a cavity or the rest of the RF system were particularly noisy, or if some other stimulus were being applied to the beam energy, the series of energy lock setpoints would not stabilize. This was the primary protection against AutoKrest introducing phase setpoint errors into the RF system.

The master oscillator system has been stabilized since AutoKrest was introduced, and this protection is marginal, as we have found examples of RF system behavior which can mislead AutoKrest. Several enhancements are planned to improve the performance of AutoKrest, notably the incorporation of an AC coupled operation mode (as used in [4]) and algorithmic improvements to allow use of all available data for consistency checks.

3 RF GRADIENT CALIBRATIONS

The fine energy resolution in the arcs has also been used to check the gradient calibration of the RF systems in both linacs last summer and again this spring. The gradient calibration for each RF system was obtained from the careful measurement of many independent pieces of hardware during cavity and RF commissioning, and was subject to many different sources of error. Calibration with beam yields an overall system response which is not subject to cumulative error buildup. In the first calibration of the linacs, one entire 8-cavity cryomodule was found in which the gradients had been overestimated by from 25% to 30%. Errors of this magnitude were few, and some have been found to be due to aging of RF modules left in service for two years before recalibration.

3.1 *Protocol and Errors*

The path we have taken to date is based on a null technique: with a reference cavity turned off, adjust the linac energy to the desired value; then successively turn each cavity in the linac off while supplementing its energy gain using the reference cavity. After a relative calibration of each cavity against the reference cavity, the absolute calibration is obtained from the known total beam energy.

The dominant error source is the variability of the total beam energy from random variations within the linacs. With the energy lock off, the energy is sometimes stable at the 5×10^{-5} level, but at other times may oscillate at a level as high as 10^{-3} with a period of a few minutes. We have not yet traced the source of this behavior. Comparison of each cavity against the reference takes approximately 20 seconds, and we periodically monitor the total linac energy to allow correction for drifts. We now track the background beam energy to about the $1\text{–}2 \cdot 10^{-4}$ level, so this source introduces errors of about 2% of a typical gradient for the first linac and 3% for a typical cavity in the other linac.

Each cavity in the 400 MeV linacs gives 2 to 4 MeV to the beam. The 2.5 MeV average is roughly 0.6% of the total energy of the beam in arc 1 and 0.3% of the total energy in arc 2. Turning each cavity off to make a differential energy measurement is possible, but can introduce errors from exceeding the linear field region of the bpms and of the quadrupoles. The errors from this type of measurement appear to be greater than those involved in the null measurement described above. Adjusting the arc dipole current to maintain the beam position would be reasonable but for the need to check for drifts in the total energy from the rest of the linac and because the solid iron dipoles need excessive (on the time scale of these measurements) amounts of time to settle in field after changes in current.

One weakness of the technique used is that it relies upon linearity between the gradient setpoint and the actual cavity gradient. As this is one of the primary bench tests for the

RF module calibration, we have considerable confidence in it. We have not yet made specific online linearity tests, although we plan to do so.

3.2 *Stability of Results*

The first attempts at this gradient calibration were in April, 1996, with both linac calibrations being completed in May, 1996. The measurements were useful in identifying some spurious gradient calibrations. After downloading corrections to the RF modules, we repeated the measurements in mid-summer. The correction factors found in the May 1996 calibration run are shown in Fig. 1. In addition to apparent errors from some of the commissioning analysis, we found some isolated cases of hardware which had drifted significantly in calibration. One set of 8 RF modules which had been in service for the two years since the earliest commissioning of hardware was replaced with freshly calibrated modules and recalibrated as a test. One slot had a gradient change of 15%. This shift was due to drift of the response of the gradient measurement diode. Verification of calibration for new modules is desirable to avoid such a reintroduction of errors. In the results shown below, some corrections made after the May measurements showed up inversely in the 1997 measurements, after routine replacement of the RF modules.

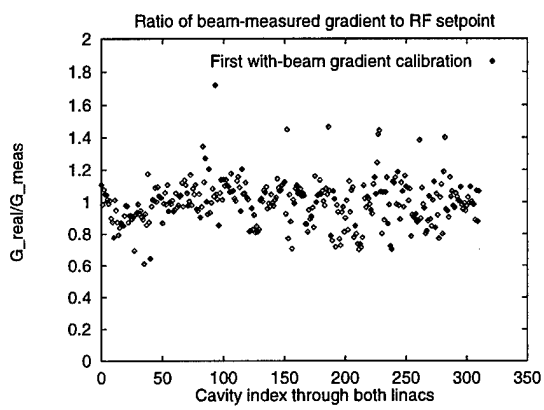

Figure 1: First measurement of linac gradient errors

The 1996 and 1997 gradient data are in good agreement for most of the linac cavities (Fig. 2). We had not recognized the necessity of tracking drifts in the two linacs as of the May, 1996, calibrations, and some of the fine structure visible in the later data may be an artifact of these drifts. Many large outliers are in slots in which RF modules were changed between the calibration runs. Systematic module installation records were not kept until recently, so we cannot determine whether all of the discrepancies occurred at module changes.

4 OUTLOOK

AutoKrest remains an essential tool for identifying and compensating for phase drifts, which also aids in targeting corrective actions. Improvements in the algorithm and sensing techniques will enable the necessary monitoring to be completed during periodic experimental hall accesses.

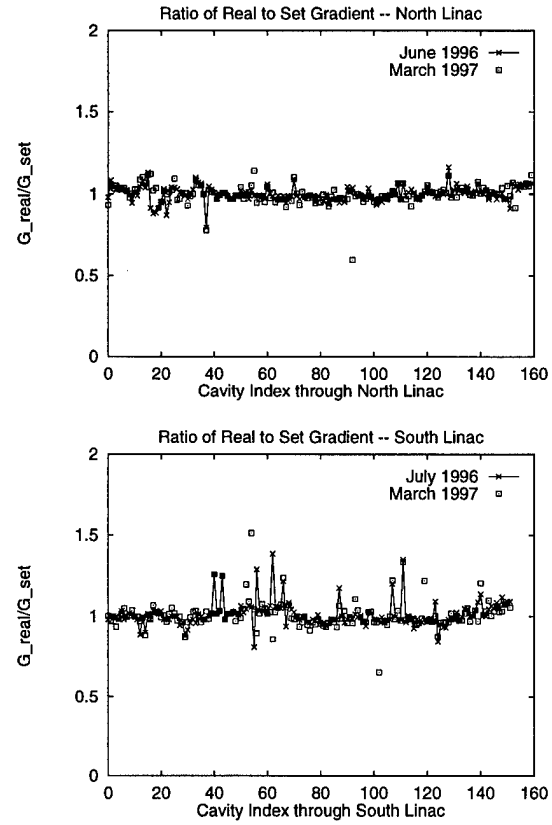

Figure 2: Measured Gradient ratio comparison from June/July, 1996, to March, 1997, for the North and South Linacs at CEBAF. Note the persistence of fine structure over the nine month interval between measurements.

The crest phase setpoint and detuning angle mixer offset (part of the tuner tracking process) are routinely measured when RF modules are replaced. The crest measurement already requires beam and it is desirable to check the gradient calibration against a few reference cavities at the same time to prevent the "inverse error" problem noted above. It is also desirable to dedicate the few hours required for a gradient calibration check at the start of each run period, as many RF modules will have been replaced with freshly calibrated ones. This provides an opportunity for a final validation before they are qualified for service.

5 REFERENCES

[1] "High Level Application Prototyping", J. van Zeijts, Tech. Note CEBAF-TN-94-038

[2] "Rapid Application Development Using the Tcl/Tk Language", J. van Zeijts, Proceedings of the 1995 Particle Accelerator Conference and International Conference on High-Energy Accelerators

[3] "Automated RF Cresting at CEBAF", M. G. Tiefenback and Kurt Brown, Tech. Note CEBAF-TN-96-020

[4] "Linear Optics Correction in the CEBAF Accelerator," V. A. Lebedev, *et al.*, these proceedings.

A HIGH POWER FARADAY CUP TO MEASURE EXTRACTED BEAM CURRENT FROM THE BATES SOUTH HALL RING

J. Shaw
University of Massachusetts, Amherst, MA 01003

R. Averill, S. Kowalski, S. Sarkar, C. Sibley, S. Sobczynski, W. Turchinetz
Bates Linear Accelerator Center, Middleton, MA 01949

Abstract

A water-cooled Faraday cup has been installed at the Bates Linear Accelerator Center in order to measure the extracted beam current from the pulse-stretcher ring in the South Experimental Hall. The Faraday cup is designed to dissipate 100kW of heat and is thus well-matched to the beam characteristics of Bates (50 μA at 1 GeV). The device has been placed on a cart-and-rail system so that it can be remotely driven into and out of the beam line. We expect the Faraday Cup to serve as an absolute calibration source for beam current measurements to better than 0.1% accuracy. This will allow for very high precision cross section measurements and the isolation of small interference response functions with reduced systematic uncertainty.

1. PROJECT PURPOSE

One of the primary experimental programs at the Bates Linear Accelerator over the next few years will be the measurement of interference response functions in (e,e'p) reactions. A system of four small magnetic spectrometers with full out-of-plane capability ("OOPS") has been constructed so that these response functions may be extracted simultaneously in one spectrometer setup. Due to the very small cross sections involved, even small systematic uncertainties may result in large errors in the extracted response function. For this reason, a program has been undertaken at Bates to minimize these systematic uncertainties. As part of this program, a water-cooled Faraday cup has been installed in the experimental hall in order to measure the incident beam charge to at least 0.1% accuracy.

Accurate measurement of the extracted beam current from the Bates South Hall Pulse-Stretcher Ring ("South Hall Ring") represents a significant challenge due to the very small beam currents involved. In the past, pulsed-beam experiments at Bates have employed ferrite toroid monitors which are ideal for measuring typical pulsed-beam currents of 1-3 mA peak. However, these devices are not sensitive enough to measure the peak currents of 5-50 μA from the South Hall Ring. In this case, an intercepting device represents the most accurate montior available.

2. HISTORY AND CHARACTERISTICS OF THE FARADAY CUP

The Faraday Cup was originally constructed thirty years ago for use at the electron linear accelerator at the National Bureau of Standards.[1] The badly damaged device was acquired as surplus material by Bates laboratory. Since then, it has been completely refurbished. Design changes have been implemented in order to modernize, and hopefully improve the reliability of, some of the key systems of the Faraday Cup.

A schematic of the Faraday Cup is shown in Figure 1. The device consists of a cylindrical lead tub with eight-inch-thick walls (nine inches at the rear of the cup). Inside the lead tub is a stainless-steel core where a large fraction of the incident beam energy is absorbed. This core consists of sixteen stainless-steel plates ranging in thickness from one-sixteenth inch in the front to one inch at the back. Water cicrulates around the plates to provide cooling. Cooling water also circulates through tubing in the lead tub. The water is provided by a closed-loop system at a rate of up to 12 g.p.m., depending on the heat load. The system can easily accomodate the 50 kW maximum heat load from the South Hall Ring (1 GeV at 50 μA). The core and tub present approximately a 41 R.L. absorption path for the incoming electrons so that a negligible fraction of the beam esacpes through the cup. Surrounding the lead tub is an aluminum shell which can be biased to several kV in order to bend low-energy charged particles back to the cup for collection. The entire assembly is housed inside an aluminum vacuum can. The vacuum is maintained at approximately 10^{-6} torr by an ion pump. The high vacuum is needed in order to prevent the incident electrons from being neutralized by positive ions, resulting in a loss of charge. The Faraday Cup must be electrically insulated from the vacuum tank to prevent excessive leakage currents. In the Bates implementation, this is achieved by four self-adjusting ceramic feet which support the weight of the tub. Ceramic standoffs are also placed on the top and sides of the vacuum tank. The water connection to the cup employs a ceramic break and a six-foot length of (rubber) hose in order to eliminate current losses through the cooling water. The zero-current of the installed Faraday cup has been measured to be 5 nA.

0-7803-4376-X/98/$10.00 © 1998 IEEE

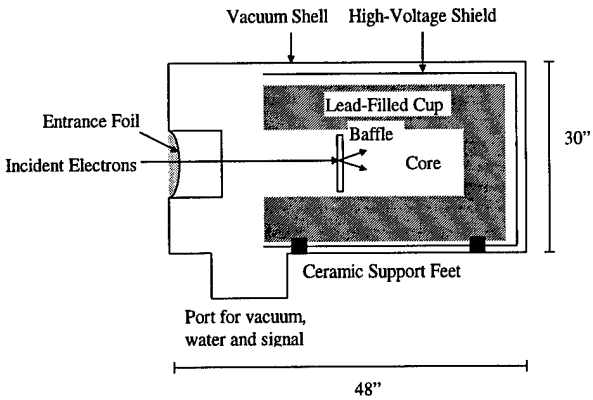

Figure: 1 Schematic of the Faraday Cup.

The electron beam enters the Faraday Cup through a 12 mil thick aluminum entrance foil. The foil is separated from the scattering baffle by a distance of approximately 24 inches in order to minimize the solid angle in which backscattered electrons may leave the cup. A series of permanent magnets ("catcher magnets") also help to reduce the number of escaping backscattered electrons.

The entire Faraday Cup has been placed on a moveable cart so that it can be remotely driven into and out of the beamline.

3. SOURCES OF ERROR AND FARADAY CUP CALIBRATION

The main source of error in the beam charge measurement is expected to be due to secondary electrons produced by scattering in the entrance foil. It has been known for a long time that the fractional error for this process follows a 1/E law, where E is the incident electron energy.[1] At the NBS, the beam energy was limited to 120 MeV and, at this energy, the error from this source was just 0.1%.[1] The higher energy beam employed at Bates will lead to correspondingly lower errors.

We plan to calibrate the Faraday Cup using pulsed beam and one of our ferrite toroids as a null monitor. This method has been employed elsewhere.[1,2] Briefly, the method is as follows. The output from the ferrite toroid is directly proportional to the beam current. We define the integrated, pedestal-subtracted, output from the toroid per unit charge collected from the Faraday Cup as:

$$C = k\frac{Q_T}{Q_{CUP}} \tag{1}$$

Now, suppose that we feed the current from the cup back through the toroid. We may then write,

$$\delta C = k\frac{(Q_T - Q_{CUP})}{Q_{CUP}} \tag{2}$$

The fractional Faraday Cup error is then given simply by,

$$\frac{\delta C}{C} = \frac{(Q_T - Q_{CUP})}{Q_T} \tag{3}$$

The third equation follows only if the constant, k, is the same in equations (1) and (2). This is not strictly correct as k has a small current dependence. Therefore, the result of equation (3) is exact only when the measurements implied by equations (1) and (2) are extrapolated to zero current.

Although we have not fully commissioned the Faraday Cup, an early test measurement appears promising. Figure 2 shows the response for a beam pulse for both the toroid and the Faraday Cup. The total charges measured by each device agree to within five percent.

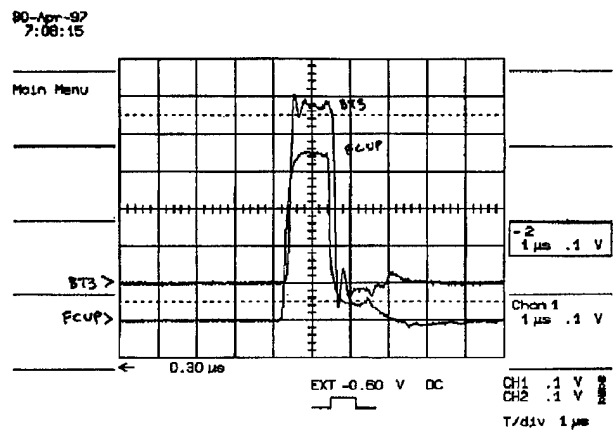

Figure: 2 Oscilloscope trace of the Faraday Cup signal (FCUP) and a ferrite toroid (BT3) for a beam pulse. The veritcal scale is 2mA/division while the horizontal scale is 1 microsecond/division.

4. FUTURE PLANS

In the near future, we will fully commission the Faraday Cup using the method outlined above. The availability of pulsed beam at Bates will allow us to quickly and accurately calibrate the Faraday cup for use in continuous-beam experiments which use extracted beam from the South Hall Ring. Due to the much higher beam energies at Bates as compared with NBS, secondary foil scattering should be greatly reduced, leading to improved accuracy in the beam charge measurement. We expect to achieve accuracies of better than 0.1%, thus practically eliminating the beam charge measurement as a source of systematic error in the OOPS physics program.

REFERENCES

[1] J.S. Pruitt, NIM **92**, 285, (1970).
[2] J.F. Hague, R.E. Jennings and R.E. Rand, NIM **24**, 456, (1963).

PHOTOEMISSION INSTABILITIES: THEORY AND EXPERIMENT

Joseph T. Rogers, Laboratory of Nuclear Studies, Cornell University, Ithaca, NY 14853, USA

Abstract

Synchrotron radiation in electron-positron colliders and synchrotron light sources ejects photoelectrons from the beam chamber walls. The resulting cloud of slow photoelectrons interacts with the beam, and may generate a transverse coupled bunch instability. In some high current storage rings a photoemission effect causes the dominant transverse instability, with a sub-millisecond risetime. Two types of photoemission instabilities have been observed. In CESR, photoelectrons are trapped by the combination of a quadrupole electrostatic field from the distributed ion pumps and the field of the bending magnets. This ``trapped photoelectron instability" has a very long range, is nonlinear in beam current, and is predominantly horizontal. In the Photon Factory and BEPC, photoelectrons moving freely across the chamber interact with the positron beam to produce a transverse instability. This ``free photoelectron instability" occurs for bunch-to-bunch intervals smaller than the transit time (a few tens of nanoseconds) of photoelectrons across the chamber, occurs in the absence of external fields, is approximately linear in bunch current, and is predominantly vertical. Numerical simulations of both effects reproduce the observed behavior of the beam, as does an analytical calculation of the trapped photoelectron instability. Experiments to observe these instabilities in other storage rings are underway. There is both theoretical and observational evidence that other types of instabilities due to photoemission may be important. We will discuss the consequences of the photoemission instabilities for the design and operation of high current storage rings.

1 ELECTRON EMISSION PROCESSES

The two main sources of electrons in the beam chamber of a high energy electron or positron storage ring are photoemission and secondary emission. Ionization of the residual gas is negligible source of electrons in comparison to these.

1.1 Photoemission

Electrons are ejected from the beam chamber walls by synchrotron radiation photons. The quantum efficiency of the photoemission process depends on the reflection coefficient of the chamber surface, the angle of incidence of the photons, the photon energy, and the material and surface conditions of the chamber. The reflection coefficient can become large at the shallow angle of incidence typical of synchrotron radiation intercepting beam chamber surfaces. The quantum efficiency tends to increase at low photon energy, and for small angles of incidence, because of the greater probability that an electron liberated close to the surface will penetrate to the surface. Measurements [1] and scaling laws [2] of the photoemission yield have been published, but the dependence on angle of incidence is not fully consistent between different measurements.

As an example, the values of parameters relevant for photoemission in CESR are listed in Table I.

Table I: Photoemission parameters for CESR

parameter	value
beam energy	5.3 GeV
bending radius	88 m
photon critical energy	3.7 keV
$I_{pe}/(I_{beam}/dl)$ (normal incidence)	0.04 m^{-1}
angle of incidence (approx.)	30 mrad
$I_{pe}/(I_{beam}/dl)$ (30 mrad)	0.04 - 0.2 m^{-1}
$I_{pe}/(I_{beam}/dl)$ (from obs. instability)	0.06 m^{-1}

The photoemission rate $I_{pe}/(I_{beam}/dl)$ is calculated by integration over the photon spectrum [1,3], assuming an Al_2O_3 surface on the aluminum vacuum chamber. The uncertainty in the photoemission rate at 30 mrad incidence is due to the uncertainty in the dependence of yield on incidence angle. The photoemission rate in the last row of Table I is inferred from a comparison of the observed photoelectron instability growth rate in CESR and the results of a computer simulation. This is a very large photoelectric current!

1.2 Secondary emission

Secondary electrons may be produced by primary electrons which are accelerated by the close passage of a positron bunch. The secondary electron yield (SEY) depends on the primary electron energy and the material. Aluminum chambers with an Al_2O_3 surface layer have an SEY which reaches a maximum of approximately 2.5 at a primary electron energy of approximately 390 eV [4,5]. All other accelerator vacuum chamber materials have a much lower maximum SEY (typically 1.0 to 1.2).

2 TRAPPED PHOTOELECTRON INSTABILITY

2.1 Observations in CESR

An anomalous transverse coupled bunch instability has been observed for many years in CESR [6,7,8]. The absolute value of the growth rate is largest at the intermediate currents encountered during injection, and becomes dramatically smaller at higher currents. The growth rate of the positron beam is very reproducible and is independent of the residual gas pressure. The instability is not as reproducible for electrons. The instability is predominantly horizontal. Coupled bunch modes at positive frequencies are damped; those at negative frequencies tend to grow. The absolute value of the growth rate decreases monotonically with mode frequency.

0-7803-4376-X/98/$10.00 © 1998 IEEE

If the beam consists of trains of bunches spaced by 28 ns or less, the bunches within a train move coherently.

The anomalous instability is present only when the distributed ion pumps (DIPs) are powered [8]. It disappears immediately when the DIPs are turned off. The growth rate is proportional to the number of DIPs powered and to the DIP anode voltage [9].

CESR contains DIPs in all bending magnets. A series of slots allows gas to flow from the beam chamber to the pump chamber. The slots also allow the DC electric field produced by the DIP anode to leak into the beam chamber, as demonstrated by numerical computation of the potential [10,3].

Some CESR DIPs have copper shields with offset slots, which shield the beam chamber from the DIP field. These shielded pumps have no effect on the beam.

The observations are consistent with the hypothesis [11] that slow electrons trapped in the beam chamber are responsible for the anomalous instability. These electrons are produced primarily through photoemission and are *trapped* in the combined dipole magnetic field and quadrupole electrostatic leakage field from the distributed ion pumps. Repeated passages of the beam eject these photoelectrons. In this way the transverse position of the beam modulates the trapped charge density, which in turn produces a time-dependent force on the beam.

Photoelectrons in the CESR chamber are confined to very small orbits in the horizontal plane by the 0.2 T field of the dipole magnets. The quadrupole component of the leakage field from the DIP slots confines the electrons vertically, much like a Penning trap. Because of the horizontal dipole component of the pump leakage field, the trapped electrons undergo an **E×B** drift down the length of the magnet, with a velocity of the order of 10^3 m/s, and are lost from the magnets in a few milliseconds. Electrons are removed by interactions with the beam on a time scale of tens of microseconds [3], so electron loss by drift is negligible. The cyclotron frequency of the trapped electrons is 5.6 GHz, so their cyclotron motion is unimportant at the frequencies of the coupled bunch modes. The vertical motion of the electrons, with frequencies of several MHz, dominates the dynamics.

2.2 Computer simulation

A computer simulation of photoelectron trapping was produced to calculate the coupled bunch growth rate and tune shift in CESR [3]. In this model, the trajectories of electron macroparticles moving under the influence of the electric field of the distributed ion pumps, a bunched beam, and the space charge of the other photoelectrons are calculated. Only vertical motion of the electrons is allowed because of the strong dipole magnetic field.
Macroparticle velocities and positions and the electric field are updated each time step of 0.5 ns. If the trajectory of the macroparticle has taken it outside the chamber boundaries, it is removed. Secondary emission is modeled by injecting one or more macroparticles, depending on the secondary emission efficiency, which is a function of the incident macroparticle energy. During the beam passage, smaller time steps are used in which several photoelectron macroparticles are injected with a uniform distribution of velocities. A value of the photoemission efficiency for the aluminum chamber which nearly reproduces the measured current dependence of the instability growth rate. This value is consistent with the extrapolation of the photoemission rate measured at DCI [1] to CESR parameters shown in Table I.

Figure1 shows the calculated electron charge density 10 ns after the passage of a leading bunch in the present CESR pattern of 9 trains of 2 bunches, with bunches in a train separated by 28 ns. The pumping slots are to the left, and the beam is at the origin. Newly emitted photoelectrons are evident as bands at the top and bottom of the chamber. Photolectrons which have been slowed by the space charge of the leading photoelectrons may be trapped on low-amplitude trajectories. The passage of subsequent bunches eventually ejects these trapped electrons.

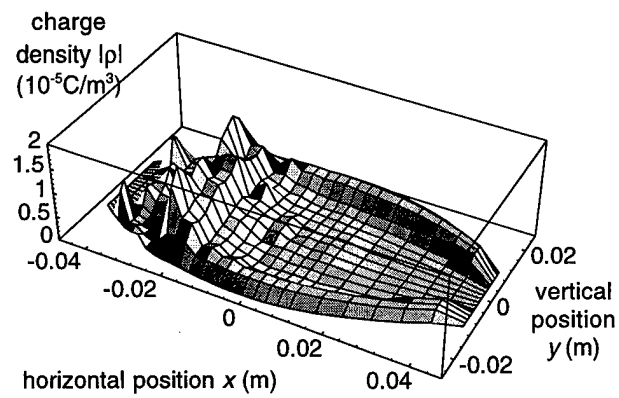

FIG. 1 Calculated charge density in the CESR beam chamber 10 ns after the passage of a bunch.

The growth rate of the lowest frequency coupled bunch mode was calculated from the force on the horizontally oscillating beam. The growth rate for the 9×2 bunch pattern is shown in Fig.2. The error bars on the simulation points show the effect of the limited number of macroparticles. The simulation shows chaotic behavior which leads to a large scatter in the calculated growth rates

. *2.3 Analytical model*

An approximate analytical model of photoelectron trapping which predicts the scaling of the growth rate with frequency and with current has been produced [12]. The time-varying force on the beam occurs because the strength of the repeated small kicks which remove the trapped electrons depends on the beam position. Because the electrons move in the nonlinear potential produced by the DIP and space charge, these kicks occur at nearly random phases of the trapped electron oscillation, and the motion of the electrons resembles diffusion. We model the diffusive motion of the electrons using a continuous Fokker-Planck equation.

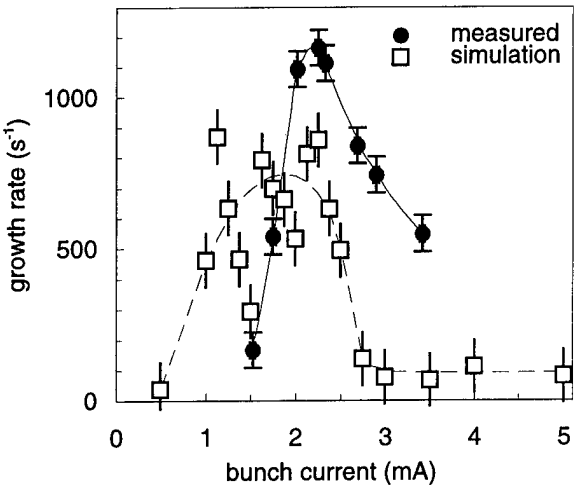

FIG. 2. Horizontal betatron growth rates in s^{-1} vs. bunch current in mA for the lowest frequency mode, measured in CESR and calculated by the simulation program. The curves are meant only to guide the eye.

We reduce the problem to a single spatial dimension by assuming that there is no variation of the forces or the diffusion constant in the region of trapped electrons, because the electrons are confined to a small band within the region between the beam and the DIP slots, as demonstrated by the numerical simulation, and further simplify the problem using the fact that the vertical oscillation period of the trapped electrons is much shorter than the characteristic time for electrons to diffuse out to the chamber wall. The phase space distribution will be approximately symmetric with respect to the phase of the oscillation.

The calculated growth rate is shown in Fig. 3 for the lowest frequency horizontal mode. These growth rate curves, plotted as a function of bunch charge, agree well with observations in CESR [7,9] The same model constants are used to fit three bunch data from 1985 and 9×2 bunch data from 1995.

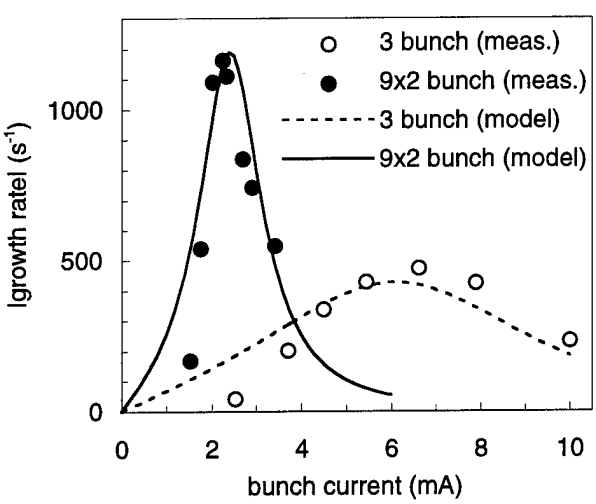

FIG. 3. Horizontal betatron growth rates in s^{-1} vs. bunch current in mA for the lowest frequency mode, measured in CESR (points) and calculated by the photoelectron model (curves).

3 ELECTRON CLOUD (FREE PHOTOELECTRON) INSTABILITY

In contrast with the trapped photoelectron instability observed in CESR, strong evidence for a *free* photoelectron instability (electron cloud instability or "ECI") has been observed in the Photon Factory and BEPC. This instability, in contrast with the CESR instability, occurs in the absence of magnetic and electrostatic fields; occurs only for positron beams, because electron beams repel the photoelectrons; is strong in the vertical direction; and increases with beam current. It is short-range in nature, because the photoelectrons move rapidly to the chamber walls. This free photoelectron instability is not observed in CESR, which operates with widely spaced bunches.

3.1 Observations in Photon Factory

A vertical coupled bunch instability has been observed with positron beams in the Photon Factory [13]. This instability has a very low threshold current (15 - 20 mA), shows a spectrum of betatron sidebands that is broad in frequency, and persists when a gap is introduced into the bunch pattern. The instability is observed with as few as 37 successive bunches followed by 275 empty buckets. The bands of excited betatron sidebands move to lower frequency as the beam current increases, indicating that the instability is not due to electromagnetic modes in beam chamber structures.

When an electron beam is used in the PF, a vertical instability with a higher current threshold and a completely different spectrum is observed. This latter instability is consistent with ion trapping, and is suppressed by a gap in the bunch pattern

The instability in the PF is consistent with an interaction of the positron beam with free photoelectrons. The electron beam is unaffected because the photelectron are repelled by the beam. A computer simulation of the electron cloud instability [14] (described below) reproduces the behavior of the observed instability.

3.2 Observations in BEPC

An instability similar to the one seen in the PF has been observed at BEPC by an IHEP/KEK collaboration in an extensive set of measurements [15]. As in the PF, the instability is vertical, appears only with positron beams, shows a broad distribution of betatron sidebands, and persists with a large gap in the bunch pattern. It has a low current threshold, similar to that in the PF.

The dependence of the instability threshold and beam spectrum on a large number of parameters was investigated. It was found that these did depend on the vertical chromaticity, the bunch spacing, the beam energy, the horizontal beam emittance, and the RF frequency (which moves the horizontal closed orbit).

The current threshold was observed to increase from 10 mA to 40 mA with only alternate RF buckets filled. This is consistent with the evidence from computer simulations, which show that the average electron density increases with decreasing bunch spacing [3,16]. The dependence of the instability threshold on energy is

weaker than that expected for an instability generated by electromagnetic wake fields. Further analysis of the large body of data is continuing, and more measurements are planned.

3.3 Computer simulations

Computer simulations of the electron cloud instability have been used to reproduce the observed effects [14] and to design beam chambers for new storage rings [16]. These simulations track electron macroparticles under the influence of the fields of the beam and electron space charge, and include photoemission and secondary emission models. The effective "wake" due to the electron cloud is determined by displacing a single bunch from the design orbit and calculating the force on subsequent bunches. This wake potential may then be Fourier transformed to determine the effective impedance.

4 LESSONS FROM THE SIMULATIONS

4.1 Role of bunch pattern

The transit time of the electrons across the beam chamber sets a time scale for the electron cloud instability. The electrons pass across the chamber in approximately 10 to 100 ns. The free photoelectron instability only occurs when the bunch spacing is smaller than this time interval. In contrast, the trapped photoelectron instability seen in CESR is seen even with a single bunch in the storage ring, because the electrons are trapped for many turns of the beam.

In the electron cloud instability, the cloud is established in approximately 100 ns, and disappears after a similar time in the absence of beam. The instability is thus expected to be insensitive to a gap in the bunch pattern, as is observed in the PF and BEPC.

For very closely spaced bunches, the presence of a trapping potential is unimportant, as the chamber will contain a high electron density with or without such a potential. Fig. 4a shows the calculated electron charge density in the CESR chamber in the presence of the DIP leakage field, as a function of bunch spacing and charge, and Fig. 4b shows the calculated charge density in the absence of the DIP leakage field

4.2 Bunch length

In the dipole magnets, cyclotron motion of the electrons may be excited by successive bunch passages [16]. Large horizontal momenta are possible after repeated beam passages. This effect is suppressed if the bunch passes in a time that is longer than one cyclotron period. This bunch length condition is satisfied for existing and planned storage rings.

4.3 Secondary emission

If the secondary emission yield is sufficiently high, an avalanche of secondary electrons can occur [16]. The electron density then increases until it is limited by its own space charge. This density is much higher that the density in the absence of runaway secondary emission, and may produce a much higher instability growth rate. With a lower SEY, the contribution of secondary electrons to the electron density may still be important.

In the regime where electron trapping is important (*i.e.*, long bunch spacing), secondary emission has a negligible effect [3,12].

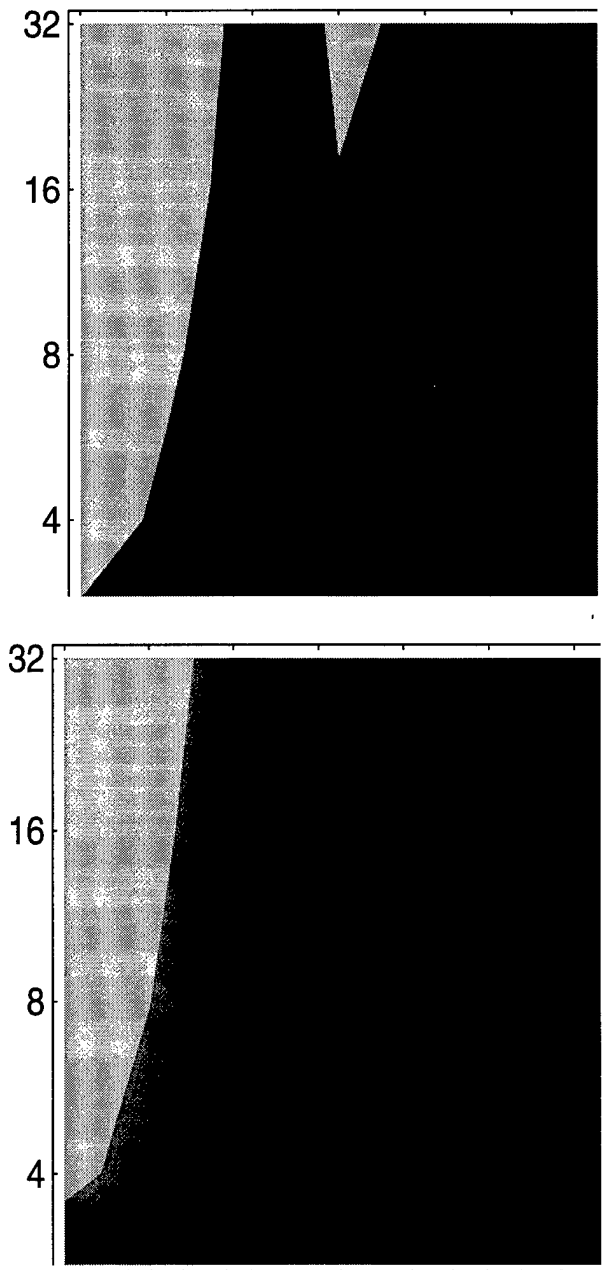

FIG 4. (a) Calculated electron charge density in the CESR chamber in the presence of the DIP leakage field, as a function of bunch spacing (ns) and bunch charge (10^{10} e). Contours are 1 nC/m, with black representing zero. (b) Calculated charge density in the absence of the DIP field.

4.4 Space charge

In the trapped electron instability, the electron "lifetime" is of the order of 10μs. The trapped electron density increases until limited by its own space charge. Space charge is always important in this instability [3,11,12].

In contrast, the electron lifetime in the electron cloud instability is of the order of 100 ns. In the absence of a secondary emission runaway condition, space charge is relatively unimportant [16].

5 CONTROL OF THE INSTABILITIES

The photoelectron instabilities may be controlled by

- Eliminating any trapping potential. In newly designed storage rings the DIPs have been isolated from the beam chamber by lengthening the pumping slots. In CESR, the DIP voltage has been reduced from 7.3 kV to 1.9 kV. The photoelectron trapping instability growth rate is found to be proportional to the DIP voltage [9].
- Using an antechamber to absorb sychrotron radiation far from the beam.
- Suppressing secondary emission with low SEY materials (such as Cu or stainless steel) or coatings (such as TiN, used in PEP-II).
- Increasing the bunch spacing. This may be impractical due to other design constraints, but is a very effective way to suppress the electron cloud instability.
- Damping the instability with beam feedback. This has been done in CESR and is planned for all of the new high current storage rings.

6 CONCLUSIONS

The photoelectron instabilities may be the dominant transverse instabilities in high current electron and positron storage rings. The calculated and measured growth rates, of the order of 1 ms^{-1}, are high and close to the maximum that may be controlled with present beam feedback systems. Good observations have been made in CESR, the Photon Factory, and BEPC, but observations in other machines, particularly ones with different chamber geometries, would be very useful. The basic mechanisms are understood, but more work is necessary to gain a detailed understanding. Computer simulations have successfully reproduced the features of the instability, but these are time consuming, and a means of simply estimating the threshold and growth rate of the electron cloud instability is lacking at present. The growth rate is fast, but the instabilities can be controlled with a combination of chamber geometry, materials, and beam feedback.

7 ACKNOWLEDGMENTS

The author wishes to thank and acknowledge the contributions of T. Holmquist, K. Ohmi, M. Furman, Z.Y. Guo, S. Heifets, J. Byrd, M. Billing, D. Sagan, D. Hartill, D. Rice, E. Chojnacki, and Y. Li as well as the other members of the CESR Operations Group.
The work at CESR has been supported by the National Science Foundation.

REFERENCES

[1] Gröbner, et al., J. Vac. Sci. Technol. **A7**, 223 (1989).
[2] Kobayashi, Proc. 5th Symp. Accelerator Sci. & Technol., 250 (1984).
[3] Holmquist, M.S. thesis, Cornell Univ. (1996).
[4] Landolt-Börnstein II/6, Springer-Verlag (1959).
[5] von Ardenne, Tabellen der electronenphysik, ionenphysik und übermikroskopie, Deutscher Verlag de Wissenschaften (1956).
[6] Sakazaki, R.M. Littauer, R.H. Siemann, and R.M. Talman, IEEE Trans. Nucl. Sci. 32, 2353 (1985).
[7] Sakazaki, Ph.D. thesis, Cornell Univ. (1985).
[8] Littauer, Cornell LNS report CLNS 88/847 (1988).
[9] Hartill, T. Holmquist, J.T. Rogers, and D.C. Sagan, Cornell LNS report CBN 95-3 (1995).
[10] Sagan and J.J. Welch, Cornell LNS report CBN 92-1 (1992).
[11] Rogers, Proc. 1995 Particle Accelerator Conf., Dallas, 3052 (1995).
[12] Holmquist and J.T. Rogers, "The trapped photoelectron instability in electron and positron storage rings", submitted to Phys. Rev. Lett. (1997).
[13] Izawa, Y. Sato, and T. Toyomasu, Phys. Rev. Lett. **74**, 5044 (1995).
[14] Ohmi, Phys. Rev. Lett. **75**, 1526 (1995).
[15] Guo, et al., "The Experimental Study on Beam-Photoelectron Instability in BEPC", this conference.
[16] Furman and G.R. Lambertson, Proc. 1996 European Particle Accelerator Conf., Barcelona, 1087 (1996), and "The Electron-Cloud Instability in PEP-II", this conference.

COMMISSIONING OF THE APS REAL-TIME ORBIT FEEDBACK SYSTEM

J. Carwardine, G. Decker, K. Evans Jr., A. Hillman, F. Lenkszus, R. Merl, A. Pietryla
Advanced Photon Source, Argonne National Laboratory
9700 South Cass Avenue, Argonne, Illinois 60439 USA

Abstract

A unified global and local closed-orbit feedback system has been implemented at the Advanced Photon Source in order to stabilize both particle and photon beams. Beam stability requirements in the band up to 50Hz are 17μm in the horizontal plane and 4.4μm vertically. Orbit feedback algorithms are implemented digitally using multiple digital signal processors, with computing power distributed in 20 VME crates around the storage ring. Each crate communicates with all others via a fast reflective memory network. The system has access to 320 rf beam position monitors together with x-ray beam position monitors in both insertion device and bending magnet beamlines. Up to 317 corrector magnets are available to the system.

The global system reduces horizontal rms beam motion at the x-ray source points by more than a factor of two in the frequency band from 10mHz to 50Hz.

1 SYSTEM DESCRIPTION

1.1 Hardware Architecture

The real-time orbit feedback system is implemented digitally using multiple digital signal processors (DSPs). A total of twenty VME crates are distributed around the circumference of the 40-sector APS storage ring to manage interfaces to beam position monitors (BPMs) and correctors, and to compute orbit corrections.

Figure 1 shows an overview of a typical crate. Each crate accesses locally available BPMs and correctors. A 68040 processor runs standard EPICS software, and one or more TMS320 DSPs perform orbit correction calculations at a 1kHz system sampling rate. Data from each crate is shared with all other crates via a synchronous reflective memory network running at 29MBytes/second.

A 21st VME crate serves as master and performs real-time analysis of data collected from the other crates.

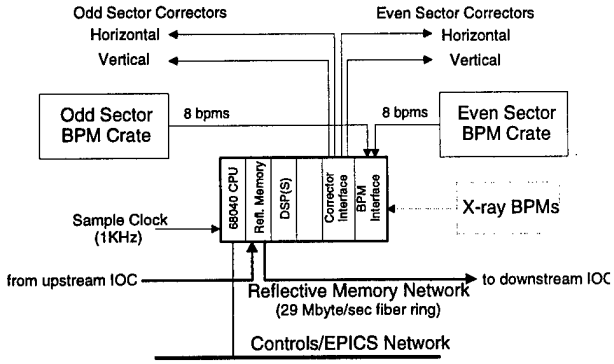

Figure 1: Architecture of a typical orbit feedback crate.

1.2 Software Architecture

The 68040 EPICS processor interfaces the DSP(s) to the control system and provides the means to monitor and control feedback algorithms running on the DSP. Data structures residing in dual-ported RAM on the DSP board are used to communicate commands and return status and data. The EPICS processor uses state programs to interface database variables with the shared data structures.

The reflective memories contain a shared data structure that is replicated at each node and is accessible to all processors in the feedback system. At each sample tic the DSP fetches BPM data from the BPM interfaces, computes the error in position, and writes the error values to assigned locations in the reflective-memory shared data structure. When all other DSPs have written their BPM errors, the DSP reads in the complete BPM error vector from the reflective memory and computes and writes new corrector values.

The master feedback crate provides global controls to the other 20 feedback crates by writing to specific locations in the reflective-memory shared data structure. In addition, it provides analysis tools such as 'dspscope' which functions like a digital scope, and 'ac voltmeter' which performs a sliding discrete Fourier transform in real time, both tools working on 40 channels of data.

1.3 RF Beam Position Monitors

The APS storage ring contains 360 rf BPMs, of which 320 are available to the real-time feedback system. In order to improve spatial resolution and minimize measurement error, it is preferable to use as many of the available BPMs as possible in the global correction algorithm. However computational resources are limited, and there is a trade-off between the number of BPMs in the algorithm and the overall sampling rate. The present configuration uses 160 BPMs and updates at 1kHz [1].

1.4 X-ray Beam Position Monitors

In addition to the rf BPMs, the APS is implementing x-ray BPMs on all the insertion device (ID) and bending magnet (BM) beamlines. These are intended to provide an absolute measure of the x-ray beam position for control of the x-ray source points.

1.5 Correctors

Each sector of the storage ring has a total of eight corrector magnets per plane. All of these could be made available to the orbit feedback system. One corrector magnet in each sector surrounds an Inconel vacuum chamber and has significantly higher effective bandwidth than the remain-

0-7803-4376-X/98/$10.00 © 1998 IEEE

ing correctors which surround a thick aluminum vacuum chamber. Only the high bandwidth correctors are presently used in the global correction algorithm (38 per plane).

Additional (low bandwidth) correctors will be used by the real-time feedback system for local steering of the insertion device and bending magnet x-ray source points.

1.6 Global Feedback Algorithm

As described elsewhere [2], singular value decomposition (SVD) is used to generate the required inverse response matrix. However, since we are using 160 BPMs and only 38 correctors, there may be no advantage to removing singular values from the matrix inverse calculation. Consequently, in this case, the SVD approach yields the same solution as the classical pseudo-inverse.

Use of a weighted pseudo-inverse is under consideration for local steering algorithms [1].

1.7 Regulator Design

The feedback loop regulator presently uses a digital implementation of simple analog elements; either an integrator or a bandpass filter are presently used. At the 1kHz sampling rate, the dynamics of the corrector magnets and of the inherent zero-order hold of the regulator each make comparable contributions to the open-loop dynamics. Consequently, a simple analog-equivalent regulator is sub-optimal and the closed-loop bandwidth is lower than could otherwise be achieved. In addition to redesigning the regulator, we are considering the implementation of a first-order hold in the corrector magnet power supply.

1.8 'DC' Mode of Operation

The real-time system can be configured to correct frequencies down to DC or to correct only dynamic orbit errors, leaving slow effects to an existing workstation-based system [3]. In 'DC' mode, integral feedback is used.

1.9 'Highpass' Mode of Operation

In this mode, the real-time system is used to supplement the existing workstation-based slow global feedback system which samples at 0.1Hz. Bandpass feedback is used in the real-time system to provide integral gain at higher frequencies but to roll off the gain at lower frequencies and decouple it from the workstation-based system. The highpass -3dB point is 20mHz.

The advantage to using the workstation-based system for slow effects is that it is better able to manage the effects of BPM systematic drift and random errors which appear at very low frequencies [3]. Techniques presently incorporated into this system (such as BPM 'despiking') will be incorporated into the real-time system at a later date.

The disadvantage of using both systems together is that the overall gain below 0.1Hz is less than could otherwise be achieved with the real-time system alone.

Beam-current dependence of the BPMs is also handled by a workstation-based system which varies the BPM offset calibrations as the current in the storage ring decays. This system is compatible with the real-time system in both 'DC' and 'highpass' modes.

In order to minimize the turn-on transient of the highpass filter, the system is energized with a highpass -3dB point considerably higher than the operating value (giving a much faster transient decay time). The break point of the highpass filter is then ramped down with the loops closed.

2 GLOBAL FEEDBACK PERFORMANCE

The performance of the global system is viewed in terms of the net improvement in beam motion power spectral density (PSD) as measured at the ID x-ray source points, with data averaged over many source points.

Figure 2 shows the effect of the real-time feedback on the horizontal PSD, when operating in 'DC' mode with integral feedback. The -3dB point is approximately 25Hz, with an improvement of 20dB below 3Hz. The maximum improvement gives a measure of the uncorrectable beam motion. Since the system can only correct the first 38 modes of beam motion, the system noise floor is determined by a combination of BPM noise, drift, and real orbit motion in higher modes [1].

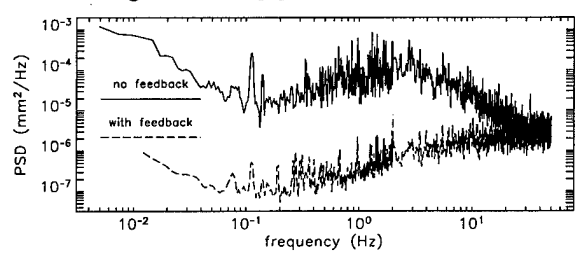

Figure 2: Horizontal power spectral density ('DC' mode).

The performance in 'highpass' mode in both horizontal and vertical planes is shown in Figure 3. Spikes at 0.1Hz are a consequence of the slow feedback system, but contribute little to the overall rms beam motion.

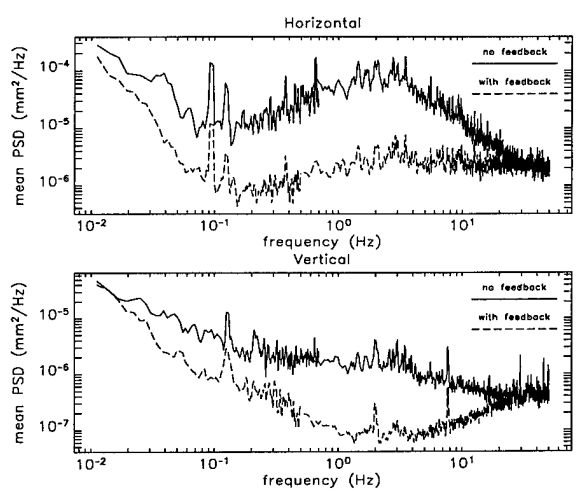

Figure 3: Power spectral density ('Highpass' mode).

The cumulative rms beam motion integrated from 10mHz is shown in Figure 4. In the band up to 50Hz, horizontal beam motion is reduced from typically 20μm to 10μm rms, and from 4μm to 3μm rms vertically.

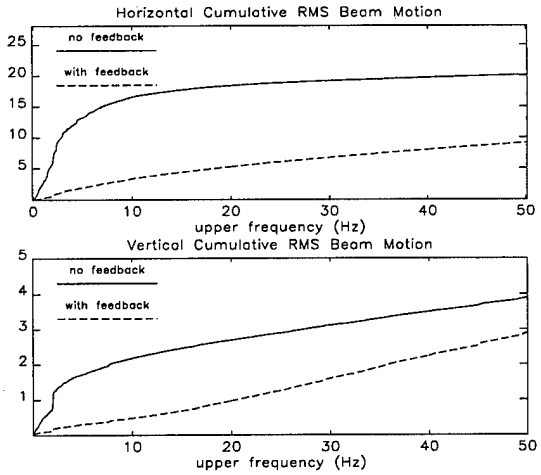

Figure 4: Cumulative rms beam motion above 10mHz ('Highpass' mode).

3 LOCAL FEEDBACK

Tests of local bump feedback using the low bandwidth correctors have revealed subtle differences in the frequency responses of the magnets used in the bumps. These differences are caused by eddy current effects in the various vacuum components surrounding each magnet. Closure of the local bump is very sensitive to these differences, and to achieve bump closure above a fraction of a hertz, the bump coefficients must be frequency dependent. So far, producing the right frequency dependence for the coefficients has proved extremely difficult.

Depending on the performance of the global (rms) algorithm, it is possible that local control may only be needed to make steering changes at the x-ray beamlines. Indeed, in order for continuous local feedback at the x-ray source points to be successful, long-term information from the x-ray BPMs must be more reliable than that provided by a large number of rf BPMs.

Since steering changes only require information from the local (rf or x-ray) BPMs for a short period of time, a low bandwidth local bump could be successfully implemented with good closure as originally planned. The bump would only be used during steering changes and disabled otherwise. An alternative is to implement a second global algorithm for the low bandwidth correctors, using rf BPMs from the entire ring and x-ray BPMs from the local beamlines. Since the system already takes care of reading BPMs from the entire ring, this is an attractive option.

4 DIAGNOSTIC CAPABILITIES

4.1 AC Lock-In Measurements

Various machine parameters (such as response matrices) can be measured by driving a global corrector at some frequency (e.g. 83.3Hz) and measuring only that frequency component in the BPM signals. This technique has the advantage that a low noise measurement can be made in a much shorter time than would be required with a comparable DC measurement. The real-time feedback system provides on-line capabilities to perform measurements using 38 correctors and 320 BPMs.

4.2 Lattice Null Measurements

The real-time feedback system offers some novel measurement opportunities. When running closed loop, the desired orbit is maintained automatically as machine conditions (such as quadrupole strength) are changed. Under these conditions, on-line measurement of quadrupole offsets or other machine parameters (such as beta function) could be considered even during user studies [4].

4.3 Identifying Sources of Beam Motion

The real-time feedback system plays a key role in identifying and localizing sources of orbit motion. The large number of BPMs available provides us with the ability to identify not only the existence of sources (from the orbit power spectrum), but also provides a means for identifying their location. By examining the relative power spectra of the drives to the 38 correctors, it is be possible to identify and localize sources of orbit motion in real time to within a sector of the machine [1]. Further localization to the girder-level (1/200th of the machine) is considered achievable.

The technique of examining the corrector reference waveforms has already been used to correctly identify a glitching power supply. Figure 5 shows the feedback system's response to the glitch. Several time steps are overlaid by sector number, with the glitch appearing at only one time step. Using only BPM data, it was possible to correctly identify the corrector power supply which glitched.

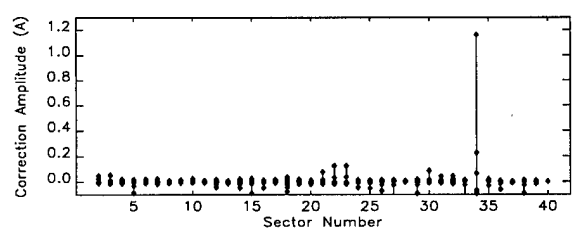

Figure 5: Glitching power supply identified on-line using BPM data alone.

5 ACKNOWLEDGEMENTS

We thank J. Galayda and L. Emery for their continuing support and insight into orbit correction.

This work was supported by the U.S. Department of Energy, Office of Basic Energy Sciences, under Contract No. W-31-109-ENG-38.

6 REFERENCES

[1] J. Carwardine, K. Evans, "Evaluation of the Global Orbit Correction Algorithm for the APS Real-Time Orbit Feedback System," these proceedings.

[2] Y Chung, "Beam Position Feedback System for the Advanced Photon Source," Proc. of the 1993 Beam Instrumentation Workshop, *AIP Conference Proceedings No. 319*, pp.1-20 (1994).

[3] L. Emery, M. Borland, "Advances in Orbit Drift Correction in the Advanced Photon Source Storage Ring," these proceedings.

[4] J. Galayda, private communication.

CONTROL OF MULTIBUNCH LONGITUDINAL INSTABILITIES AND BEAM DIAGNOSTICS USING A DSP-BASED FEEDBACK SYSTEM

D. Teytelman, R. Claus, J. Fox, H.Hindi, R. Larsen, I. Linscott, S. Prabhakar, W. Ross, A. Young, Stanford Linear Accelerator Center, P.O. Box 4349, Stanford, CA 94309
A. Drago, M. Serio, INFN - Laboratori Nazionali di Frascati, P.O. Box 13, I-00044 Frascati (Roma), Italy
G. Stover, Lawrence Berkeley National Laboratory, 1 Cyclotron Road, Berkeley, CA 94563

Abstract

A bunch-by-bunch longitudinal feedback system has been designed and built to control coupled-bunch instabilities in the PEP-II machine. A prototype system has been installed at the Advanced Light Source at LBNL. Programmable DSPs allow longitudinal feedback processing in conjunction with data acquisition or instrumentation algorithms. Here we describe techniques developed for different beam and system diagnostics, such as measurements of the modal growth and damping rates and measurements of the bunch-by-bunch currents. Results from the Advanced Light Source are presented to illustrate these techniques.

1 SYSTEM OVERVIEW

The multibunch longitudinal feedback system for use by PEP-II, ALS, and DAΦNE is designed using a modular family of analog and digital VME and VXI modules. The principles of operation and detailed description of the system design are given in earlier publications [1], [2], [3].

2 TRANSIENT RECORDING TECHNIQUES

One interesting feature of the programmable system is the capability to use the memory and features of the digital signal processors for machine and system measurements. The programmable algorithms in the DSP can be completely user specified, so that a program can excite the beam for a short interval, run different control algorithms at various times (such as injection) or simply record the bunch motion as the feedback system operates. Such digital data records provide a very powerful diagnostic capability to observe and quantify the motion of the particles in the storage ring. The record functions allow a snapshot of the controlled beam motion, from which the system noise floor and the power spectrum of external disturbances driving the beam can be obtained. Observing the motion as the feedback system is turned off displays the growth rates of the unstable modes, while recording the motion when the feedback signals are turned back on reveals the net damping in the system. Frequency domain information can be computed from these time-domain data sets via use of Fourier transform techniques.

An example measurement using this grow-damp technique is illustrated in Figure 1. In this experiment at the LBL Advanced Light Source the beam is initially stable under the action of the feedback system. Under software control the feedback gain is set to zero, and after a holdoff interval the DSP processors start recording the bunch motion. For $t_{holdoff} < t < t_{on}$ the growing bunch oscillations are recorded, and at t_{on} the feedback gain is restored to the operating value. The motion (now a damping transient) continues to be recorded until t_{max}, at which time the DSP's stop recording, but continue computing the feedback signal (controlling the beam). The data records are stored in a dual-port memory which is accessible to an external processor (the total record length is 960 samples of each of 324 bunches).

If the data is arranged in a 2 dimensional array of bunch vs. sample number, each row (containing the oscillation coordinate of each of 328 bunches sampled on a single turn) can be Fourier analyzed to express the bunch coordinates in a modal representation. This Fourier transform is computed for each sampling time (turn number) in the array. Figure 1 presents such a growth-damp modal plot (taken at the LBL Advanced Light Source) which shows the presence of two modes of oscillation in the transient. The growth rates and damping rates for each mode can be found from this data set via the numeric fitting of exponential curves to the data. The modal plot directly shows the action of the feedback system in turning the net growth rate from positive to negative at the time the feedback system is switched back on [4].

Another method of analyzing the transient time-domain data is to concatenate the sampled bunch phases over a

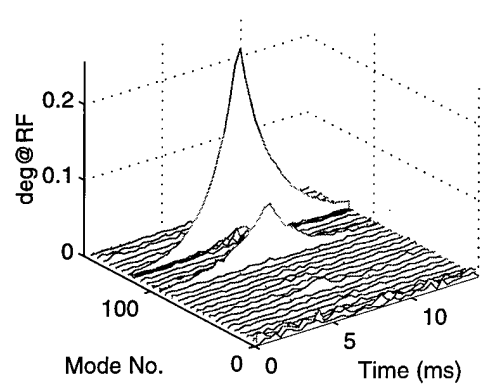

Figure 1: Plot of a turn by turn FFT of the bunch data, revealing two unstable modes (mode 95 and 124) of 328 bunches in the ALS over a 12 ms time interval. The feedback system is on for t<0 and t>6 ms, and off for 0<t<6 ms. Unstable bunch motion grows during the feedback off interval. The total machine current was 120 mA.

0-7803-4376-X/98/$10.00 © 1998 IEEE

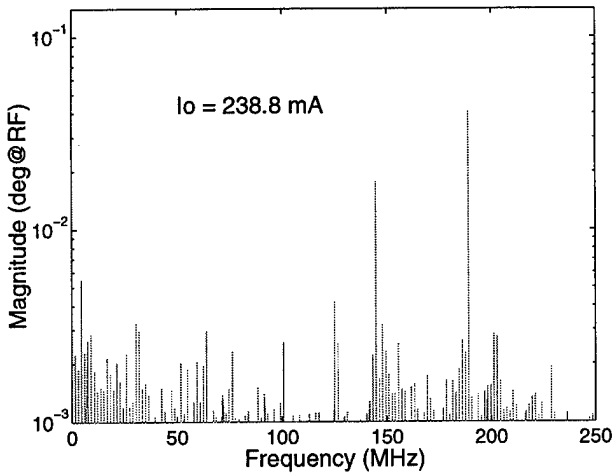

Figure 2: Magnitude of high-resolution FFT of growing transient in Fig. 1, showing all the spectral components over a 250-MHz bandwidth.

few milliseconds and take the FFT of the resulting vector. The beam pseudospectrum resulting from a single 4-8 ms transient covers the entire 250 MHz range of the modes with a resolution of 250-125 Hz. The distance of the sidebands from the revolution harmonics gives us the frequency shifts of the modes, and the width of the sidebands gives us an equivalent way of calculating their growth rates. Figure 2 shows the magnitude of the FFT of the bunch-phase signal over the last 4 ms of mode growth from a transient measurement at the ALS. The beam pseudospectrum spans 250 MHz with a frequency resolution of 250 Hz - the figure shows several large spectral components due to the unstable coupled-bunch motion [5]. The pseudospectrum contains information around every revolution harmonic in the 250 MHz span, though the revolution harmonics themselves are suppressed due to the sampling of the bunch motion in the feedback system.

Fig. 3 zooms in on a 70 kHz section of the 250 MHz spectrum in Fig. 2. It shows that the most unstable mode is an

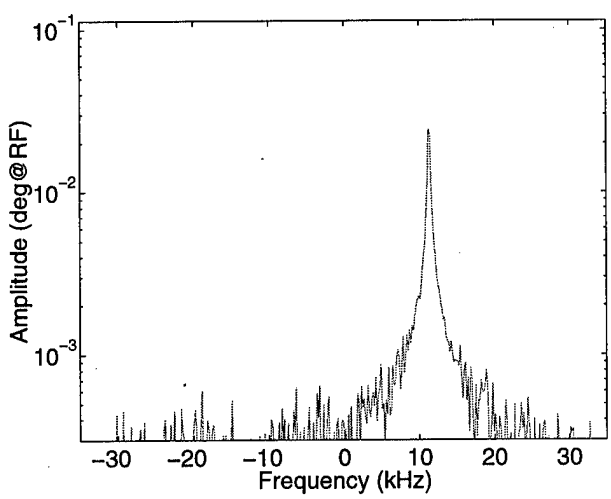

Figure 3: 70 kHz section of the high resolution spectrum in Fig. 2, showing an unstable upper sideband and a damped lower sideband at $204 f_{rev}$.

upper sideband at $204 f_{rev}$ (and therefore a lower sideband at $328 - 204 = 124 f_{rev}$), with a linewidth corresponding to the previously measured growth rate. The lower sideband is damped to the noise floor by the TM-011 cavity mode. The next most unstable mode in figure 2 is an upper sideband at $233 f_{rev}$ (and therefore a lower sideband at $95 f_{rev}$). In contrast to these transient techniques, a measurement using a heterodyned spectrum analyzer would take at least a few minutes to perform the 328 narrowband sweeps required to produce an equivalent spectrum, by which time the oscillations would have reached a damped or saturated steady state. For the PEP-II machine, with a harmonic number of 3592, the advantage of the transient - base technique over several thousand narrowband heterodyned measurements is even greater.

3 BUNCH-BY-BUNCH CURRENT MEASUREMENT TECHNIQUES

Analysis of the modal patterns is complicated by any non-uniformity of the fill pattern. An important piece of data for such analysis is the bunch current distribution. Two different techniques have been developed that allow the longitudinal feedback system to measure the bunch-by-bunch current distribution. The first method requires a system dedicated to the current measurement (the system is reprogrammed to act as a current monitor). A second approach has been developed which allows measurement of the per bunch current without affecting the longitudinal feedback processing.

3.1 Dedicated current measurement technique

In the feedback mode of operation the system is set up to detect the phase of the bunches with respect to a reference oscillator using a double balanced mixer. If the reference oscillator phase is set to a nominal bunch synchronous phase the digitized signal corresponding to bunch k is

$$s_k = G q_k \sin\phi_k$$

In the above equation q_k is the charge, ϕ_k is the phase of bunch k, and G represents the front-end gain. To measure beam currents the phase of the reference oscillator is shifted by 90°. Then at the A/D converter we get

$$s_k = G q_k \cos\phi_k$$

If every bunch is riding on an identical synchronous phase this method directly measures the charge per bunch, however if there is a beam loading transient each bunch has a unique synchronous phase and the s_k does not simply measure the per bunch charge. In order to extract the bunch current from this measurement each bunch signal is sampled at 70 kHz in the DSP farm. These signals exhibit significant variations due to synchrotron oscillations as well as low frequency synchronous phase motion. The DSP array is programmed to downsample the data using windowed peak detection with a 256 sample window. As a result we obtain a 3.6 second long record at a 270 Hz sampling rate. A windowed peak detection algorithm eliminates noise due to the synchrotron motion, but

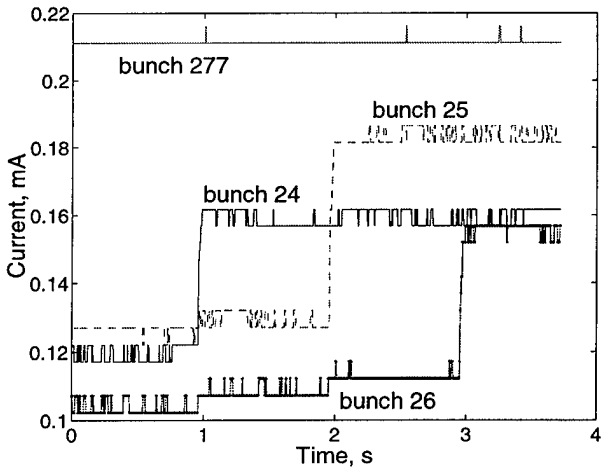

Figure 4: The bottom traces show injection into 3 consecutive buckets 2 ns apart, while at the top previously injected bunch is shown.

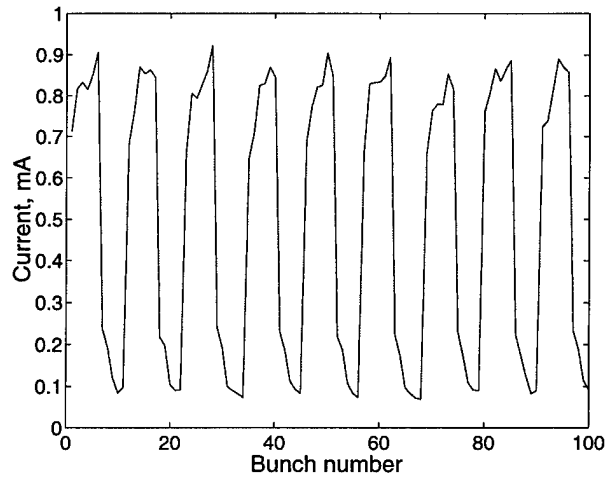

Figure 5: Current measurement for a square wave fill

synchronous phase motion at the line frequency is still present. The output of the peak detector is post-processed off-line using a 5-sample median filter. The sensitivity of this approach is 5 μA with 2.5 μA RMS noise. Full-scale range is 1.2 mA/bunch. Figure 4 shows current monitor data taken during injection at the ALS. The consecutive bunches are being injected at 1 Hz rate.

3.2 Frequency-division current measurement method

A technique has been developed that allows current measurement in conjunction with feedback processing. In the frequency-division method the front-end reference oscillator is operated at a nominal synchronous phase, which maximizes the phase detector sensitivity to synchrotron motion. A sinusoidal phase modulation ($f_{cm} = 2kHz$) is applied to the local oscillator at a frequency significantly below the synchrotron resonance and a second modulation frequency ($f_{sweep} = 70Hz$)is used to sweep the operating point of the phase detector. The input signal at the A/D for small motion ($\sin x \approx x$) is given by

$$s_k = Gq_k(\phi_k + \sin\omega_{cm}t + \sin\omega_{sweep}t)$$

A time record of all bunches is taken by the DSPs and processed off-line using envelope detection. The signal envelope of each bunch is bandpass filtered around the fast modulation frequency, and the magnitude of the peaks in the envelope waveform represents the current of that bunch. Figure 5 shows the current versus bunch number for the square wave fill that is used to study mode coupling. During this current measurement the feedback system continues to control the beam instabilities. The resolution of this technique is found to be 7 μA with a 1 mA/bunch full-scale.

5 SUMMARY

The time domain transient techniques illustrated require only a few milliseconds of beam motion and are essentially invisible to users of the storage ring. The information obtained from the analysis of the time domain data reveals growth rates and damping rates of beam modes, bunch current distributions and is very useful in adjusting the feedback system or as a quick check on its operation. The general-purpose signal processing capabilities of the DSP farm allow new instrument modes and new measurements to be rapidly developed and integrated into the system software.

6 ACKNOWLEDGEMENTS

The authors thank J. Hoeflich, J. Olsen, G. Oxoby of SLAC and W. Barry, J. Byrd, J. Corlett, G. Lambertson of LBL for numerous thoughtful discussions and direct contributions of technical expertise. We also thank Boni Cordova-Grimaldi of SLAC for her patient fabrication of electronic components. Work supported by DOE contract DE-AC03-76SF00515

7 REFERENCES

[1] G. Oxoby, et al., 'Bunch-by-Bunch Longitudinal Feedback System for PEP-II,' presented at the 4th European Particle Accelerator Conference (EPAC94), London, England, June 27 - July 1, 1994.

[2] A. Young, et al., 'VXI based Multi-Bunch Detector and QPSK modulator for the PEP-II/ALS/DAFNE Longitudinal Feedback System', Proc. 1997 PAC.

[3] M. Tobiyama, et al., 'Initial Test of a Bunch Feedback System with a Two-Tap FIR Filter Board,' Proc. Beam Instrumentation Workshop, 1996.

[4] J. Fox, et al., 'Observation, Control, and Modal Analysis of Longitudinal Coupled-Bunch Instabilities in the ALS via a Digital Feedback System', Proc. Beam Instrumentation Workshop, 1996.

[5] S. Prabhakar, et al., 'Observation and Modal Analysis of Coupled-Bunch Longitudinal Instabilities via a Digital Feedback Control System,' to be published in 'Particle Accelerators'.

GLOBAL ORBIT FEEDBACK UTILIZING ANALOG AND DIGITAL TECHNOLOGIES

O. Singh, Y. Tang, S. Ramamoorthy, S. Krinsky, L.H. Yu
NSLS, Brookhaven National Laboratory.

Abstract

At the NSLS, an analog global orbit feedback system is used in regular operations, and a digital global orbit feedback system is available in machine physics studies on the X-Ray Ring. Here, we discuss the relative merits of utilizing analog and digital technology in orbit feedback. Results of experiments are reported characterizing the performance of our analog and digital systems when operated individually or together. We give our thoughts on plans for future development of the orbit feedback systems at the NSLS.

1 INTRODUCTION

The analog global orbit feedback systems have been operational on the NSLS storage rings since 1991. These are based on correcting only a few harmonics near the tune [1] and they utilize only one-third of the available pues and trims. The analog systems provide an order of magnitude reduction in orbit motion using inexpensive hardware. The analog feedback controller is wideband and provides a stable feedback system with orbit correction bandwidth of 200 hz [2, 3]. From dc to 2 hz, the harmonic content of the orbit is corrected by a factor of 100, but at higher frequencies, the correction reduces linearly with frequency reaching to unity at 200 hz. We are also developing a digital orbit feedback system [4, 5] which has been used during machine physics studies in the X-ray storage ring. It employes up to 25 eigenvectors and all available pues and trims. The digital feedback system provides a significant improvement in slow orbit variation (less than 1 Hz), however, its correction bandwidth of 20 hz provides only moderate improvement for fast orbit motion.

We have three basic modes of operating the orbit feedback systems: (1) Run only the analog orbit feedback system as is the case during regular operation. (2) Run only digital feedback system, presently only in machine studies. In this case, the digital feedback system uses up to 25 eigenvectors and is highly effective in correcting orbit drift. The eigenvalues of the response matrix (trim excitation to pue response), with no feedback, are given in Table 1. (3) First the analog feedback is turned on, and then the digital feedback is turned on. In this mode, the digital feedback system uses a modified response matrix obtained with the analog system on. Using about 10 eigenvectors, the combined system provides additional orbit correction beyond that provided by the analog system alone. The eigenvalues of the response matrix, with analog feedback on, are given in Table 2. Fig. 1 and Fig. 2 provide improvement results for horizontal orbit motion in the slow drift and in fast orbit oscillation, respectively. The fast orbit oscillations are due to the NSLS booster, cycling at about 0.7 Hz.

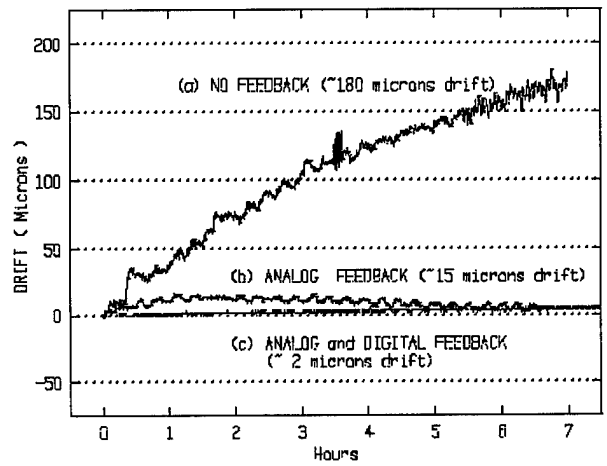

Figure 1: Horizontal orbit slow drift with (a) No feedback, (b) Analog feedback only and (c) Analog and Digital feedbacks.

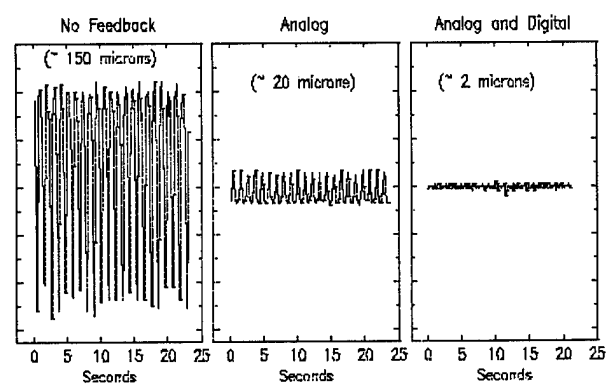

Figure 2: Horizontal orbit fast motion due to cycling NSLS Booster with (a) No feedback, (b) Analog feedback, and (c) Analog and Digital feedbacks.

We have observed that the vacuum chamber moves when it is heated by synchrotron radiation [3]. In the horizontal plane, the amount of this chamber motion is large at some pue locations, resulting in significant orbit measurement errors. This motion must be taken into account in order to use the digital system to improve the horizontal orbit. During studies, when the digital feedback is on, we observe that the photon beam monitored at the diagnostic beamline X28 shows a larger horizontal beam excursion with digital feedback on, although motion appears to be smaller on the PUEs (see Fig. 1). We are in process of studying the chamber motion and plan to incorporate a correction for PUE

0-7803-4376-X/98/$10.00 © 1998 IEEE

motion in order to implement the digital feedback system effectively.

2 ANALOG VS DIGITAL

The set up of our analog and digital orbit feedback systems is shown in Fig. 3. The plant P represents the trim to pue response, the controller C_a is the analog feedback element and the controller C_d is the digital feedback element. The digital feedback controller C_d has two configurations, one without analog feedback and other with analog feedback.

If the background orbit motion is represented by N as shown in Fig. 3, with both analog and digital feedbacks off, the orbit is given by the uncorrected background orbit motion N. With feedbacks on, it can be easily shown that the residual orbit is $[N/(1+P(C_a+C_d))]$ and the performance of a feedback depends on the value of $(1+P(C_a+C_d))$. At dc, this expression has a value of 100 and the noise reduction will be by two order of magnitude.

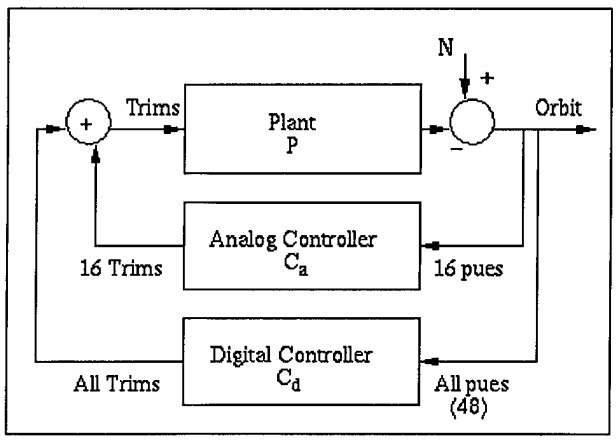

Figure 3: NSLS X-ray ring orbit feedback systems.

Let us comment upon some of the relative merits of analog and digital feedback, based upon our experience, which is constrained by existing hardware. The Bittner-Biscardi receivers provide a very precise, low noise analog output, with a bandwidth of larger than 2 khz. The analog feedback systems we have built utilizing the output of the receivers achieve high resolution and wide bandwidth in a straightforward and economical manner. For our relatively small storage rings, utilizing 16 (X-ray ring) or 8 (VUV ring) pues and trims is easy, and provides for a significant improvement in orbit stability. One downside of the analog system is the restriced flexibility in the choice of pues and trims, which limits studies of the dependence of system performance on the design choices of pues, trims and filters. For large rings, requiring more pues and trims, the analog approach may become less attractive.

In our implementation of a digital system, the achievement of submicron resolution, low noise, and high bandwidth has been more difficult than in the analog system. The noise level in the analog to digital converter (ADC) hardware results in a measurement error of a few microns. The bandwidth of the digital controller is presently limited in our case due to ADC sampling limit of 550 Hz, and the speed of the cpu processor used to compute and implement the orbit correction. However, these difficulties may be less restricting when designing a new system, and also will be eased by the rapid progress being made in digital components. On the other hand, the great flexibility made possible by the digital approach has already provided us with important benefits. We can easily add or remove pues or trims from the feedback, to assess their effect. Also, we can easily choose from different orbit correction algorithms, and vary the number of eigenvectors included in the correction. In this way, we have achieved new insight into the optimum conditions for feedback, which has even allowed us to improve the analog vertical feedback on the X-ray ring (see Fig. 4). In studies of digital feedback it was noticed that there are 8 vertical eigenvalues of magnitude greater than unity (see table 1), while existing analog feedback was only using 8 PUES and 6 eigenvectors. Based on this observation, we modified the analog vertical orbit feedback to include 16 PUES and 8 eigenvectors, improving the orbit correction by about a factor of 3. The improvement results are shown in Fig. 4.

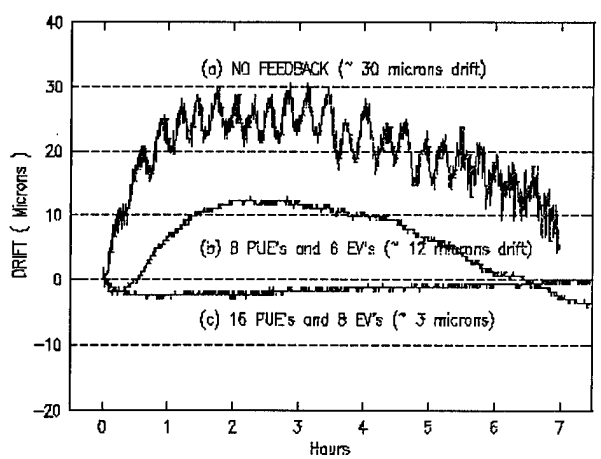

Figure 4: X-Ray vertical orbit drift with (a) No feedback, (b) Analog feedback with 8 PUEs and 6 eigenvectors, and (c) Analog feedback with 16 PUEs and 8 eigenvectors.

3 FUTURE PLANS

In short term, we plan to study the performance of digital feedback system by upgrading it with a) new ADC orbit measurement system which will have lower noise level by an order of magnitude, and will sample at a higher rate of about 1 Khz; and b) new cpu processor which is faster by a factor of 3. Simulation of feedback system has shown that these improvements should increase the digital feedback bandwidth from 20 hz to 40 hz. We will, also, study the improvement resulting from incorporating correction of pue motion due to vacuum chamber movement.

In long term, we will look into an orbit correction system which utilizes digital feedback only. We expect this sys-

Eigen number	Horizontal	Vertical
01	17.62	26.88
02	11.23	16.36
03	3.07	4.89
04	2.97	4.65
05	2.09	3.68
06	1.68	3.44
07	1.64	3.01
08	1.53	2.58
09	1.19	.30
10	.98	.29
11	.95	.29
12	.72	.28
13	.70	.28
14	.63	.28
15	.62	.28
16	.45	.23
17	.34	.13
18	.28	.13
19	.27	.12
20	.26	.12
21	–	–
22	–	–

Table 1: Eigenvalues of horizontal and vertical response matrix with no feedback. For vertical, note that there are 8 eigenvalues of magnitude greater than unity.

Eigen number	Horizontal	Vertical
01	1.34	.30
02	1.27	.29
03	1.06	.29
04	.89	.29
05	.74	.28
06	.71	.28
07	.62	.28
08	.59	.23
09	.48	.20
10	.40	.14
11	.32	.13
12	.30	.13
13	.28	.12
14	.28	.12
15	.27	.12
16	.24	.11
17	.23	.11
18	.20	.11
19	.05	.10
20	.05	.10
21	–	–
22	–	–

Table 2: Eigenvalues of horizontal and vertical response matrix when analog feedback is ON with 16 pues and 8 eigenvectors. Only 10 eigenvectors are utilized by the digital feedback in this case.

tem will sample and process orbit data at a rate of several khz. Also, this system should integrate with an orbit measurement system which incorporates correction for PUE's motion.

4 ACKNOWLEDGEMENTS

This work was performed under the auspices of the U.S. Department of energy undercontract DE-AC02-76CH00016.

5 REFERENCES

[1] L.H. Yu, R. Biscardi, J. Bittner, A.M. Fauchet, S. Krinsky, R.J. Nawrocky, J. Rothman, O. Singh and K.M. Yang, " Real Time Orbit Feedback System for NSLS X-ray Ring", Proc. IEEE Particle Accelerator Conf., San Franscisco, Vol 4, p. 2542, 1991.

[2] O. Singh, "Electron beam stabilty and beam peak to peak motion data for NSLS X-ray Storage Ring", Proc. IEEE Particle Accelerator Conf., Washington, D.C.,Vol. 3, p. 2254,1993.

[3] J. Safranek, O. Singh and L. Solomon, "Orbit Stability Improvement at the NSLS X-ray Ring", Proc. IEEE Particle Accelerator Conf., Dallas, Tx, Vol 4, p. 2711,1995.

[4] A. Friedman and E. Bozoki," A Digital Feedback System for Transverse Orbit Stabilization in the NSLS Rings", NIM A352, p. 393, 1995.

[5] E. Bozoki, A. Friedman, S. Rammamorthy, O. Singh and Y. Tang, " Operations with the Digital Orbit Feedback System in the NSLS X-ray Ring", Proc. of the fifth European Particle Accelerator Conf., Sitges (Barcelona), Vol 3, p. 1911, 1996.

EVALUATION OF THE GLOBAL ORBIT CORRECTION ALGORITHM FOR THE APS REAL-TIME ORBIT FEEDBACK SYSTEM

J. Carwardine and K. Evans Jr.
Advanced Photon Source, Argonne National Laboratory
9700 South Cass Avenue, Argonne, Illinois 60439 USA

Abstract

The APS real-time orbit feedback system uses 38 correctors per plane and has available up to 320 rf beam position monitors. Orbit correction is implemented using multiple digital signal processors. Singular value decomposition is used to generate a correction matrix from a linear response matrix model of the storage ring lattice. This paper evaluates the performance of the APS system in terms of its ability to correct localized and distributed sources of orbit motion. The impact of regulator gain and bandwidth, choice of beam position monitors, and corrector dynamics are discussed. The weighted least-squares algorithm is reviewed in the context of local feedback.

1 OVERVIEW

A real-time orbit feedback system has been implemented at APS in order to meet the rms beam stability requirements of 17μm horizontally and 4.4μm vertically in a frequency band up to 50Hz [1]. Both local and global feedback will be provided, with the global system planned to be available for user operations shortly.

The global system uses 38 correctors and has access to up to 320 beam position monitors (BPMs). An additional 279 correctors are available for local feedback. The feedback system is implemented digitally using 20 VME crates distributed around the 40 sectors of the storage ring. A reflective memory network provides synchronous data transfer between the crates, and in particular gives each crate access to data from every available BPM in the ring. Orbit corrections are computed at a 1kHz rate.

2 GENERAL CONSIDERATIONS

In principle, only 38 BPMs are needed to compute the 38 corrector settings, in which case the error at each BPM is corrected exactly. In practice however, using this exact solution can lead to orbit blow-up between the BPMs resulting in ineffective correction of global orbit errors.

The smoothness of the corrected orbit can be improved by singular value decomposition (SVD) to remove small singular values, but this occurs at the expense of the exact correction at the BPMs.

If more BPMs are used in the algorithm, the smoothness of the solution is improved, and the robustness to BPM measurement errors is increased. Since at APS there are many BPMs available to the orbit feedback system, we have chosen to increase the number of BPMs in the algorithm rather than reduce the number of singular values in the correction matrix. The workstation-based slow feedback system [2] uses all available BPMs in its algorithm; there is no penalty in doing this because the correction rate is only 0.1Hz. For the real-time system, on the other hand, there is a trade-off between the correction rate and the number of BPMs sampled. In this case using a larger number of BPMs requires more time be taken up accessing and subsequently processing the additional values.

The present configuration uses 160 BPMs in order to significantly reduce the susceptibility to measurement errors [2]. Ultimately, the same "despiking" algorithm used in the slow feedback system [2] will also be implemented in the real-time system.

3 CORRECTION OF DISTRIBUTED SOURCES

Dynamic orbit errors are generated by many sources distributed randomly around the storage ring. Ground vibration is assumed to couple principally through the quadrupole triplets. The resulting orbit motion can be analyzed in terms of SVD modes. Most of the energy appears in a relatively small number of modes. Up to 38 modes can be corrected with the APS real-time global system.

3.1 Measured SVD Modal Content

The SVD modal content of the APS random orbit motion has been measured using the real-time feedback system by examining the orbit power spectrum. Dynamic orbit errors were corrected with the real-time feedback system using inverse response matrices containing different numbers of singular values. The resulting power spectral density at x-ray source points was measured as a function of the number of singular values retained.

Results from the measurement are presented in Figure 1, where the residual power spectral density is shown as a function of the number of singular values retained in the correction matrix. It is clear there is a large effect from including relatively few singular values and a continued improvement as more singular values are included. Results are comparable with predicted SVD modal content [3].

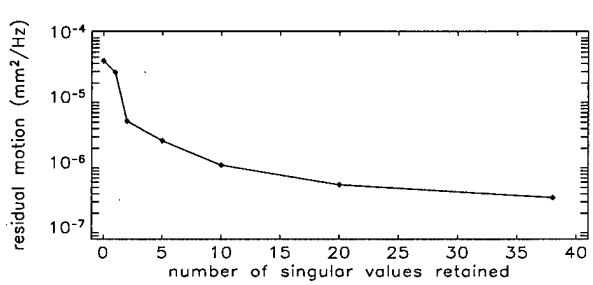

Figure 1: Residual uncorrected orbit at 1Hz vs. number of singular values retained.

3.2 *Regulator Gain*

The fact that some orbit motion remains uncorrectable means that the feedback system sees a noise floor well above the noise floor of the BPMs themselves. It can be shown that each mode is attenuated with the full gain of the regulator, but once the correctable modes have been reduced below the level of the noise floor, there is little to be gained from further increases in regulator gain.

This effect has been measured at APS using the real-time feedback system. Figure 2 shows the attenuation in beam motion as a function of regulator gain. This shows that just over 20dB attenuation in beam motion is achieved with 28dB of regulator gain, but there is very little improvement in beam motion when the regulator gain is increased beyond this point.

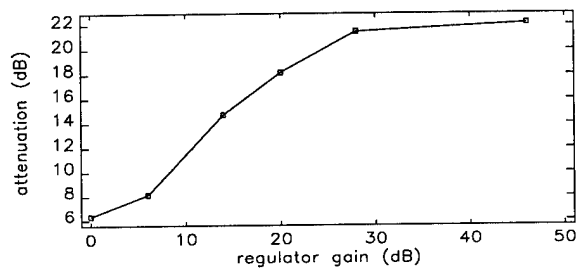

Figure 2: Attenuation of beam motion vs. regulator gain.

3.3 *Regulator Bandwidth*

The system presently operates with a closed loop bandwidth around 25Hz [1]. So far, little effort has been put into optimizing the regulator bandwidth; nevertheless, APS orbit stability specifications are met in both planes down to below 10mHz with the feedback system running.

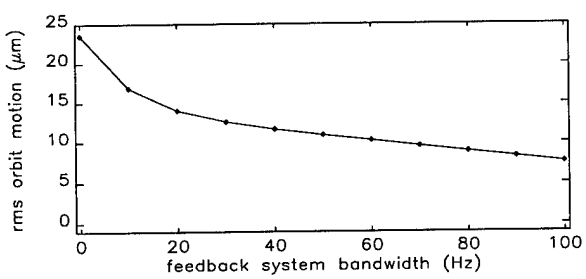

Figure 3: Projected APS horizontal beam motion vs. system bandwidth (10mHz to 100Hz).

Beam stability will improve further as the regulator bandwidth is increased; we expect that the bandwidth could be increased by a factor of two with an improved regulator design.

Yet further bandwidth improvements could be realized by increasing the sampling rate to 2kHz which will be possible when additional processing power is brought on line. Figure 3 shows how the horizontal rms beam motion is projected to improve as the regulator bandwidth is increased. The data is based on the measured power spectral density and includes beam motion from 10mHz to 100Hz [1].

4 CORRECTION OF LOCALIZED SOURCES

Recent observations have shown that the effort applied by the global feedback correctors varies significantly from corrector to corrector. This seems to indicate the existence of localized sources of beam motion, and it is hoped that the observed variations can be used to track down the sources of motion.

Simulations using the accelerator code Xorbit [4] have been run to determine how a localized source of motion influences the corrector power. The pattern of corrections applied by the algorithm is shown to depend on the proximity of the source to the correctors and on the number of singular values retained in the algorithm. In the 'ideal' case where the source of the motion is one of the global correctors themselves, the correction is shown to be highly localized [1].

A more realistic situation occurs when the source of the disturbance is between two correctors. Figure 4 shows the relative corrector power for a simulated source between the correctors in sectors 20 and 21. For the case where all singular values are retained, the source can be localized to within a sector of the machine. Figure 4 shows an Xorbit simulation of the response to an orbit disturbance between the global correctors in sectors 20 and 21.

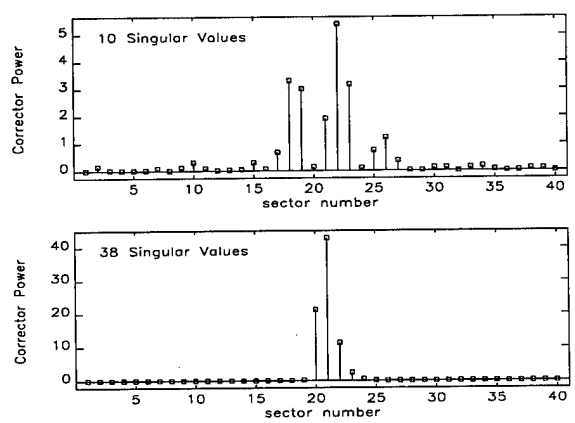

Figure 4: Correction of simulated source in sector 20.

Similar patterns of corrector power were measured in the storage ring with the real-time feedback system running. Figure 5 shows the actual horizontal corrector power by sector, measured in a band around 0.1Hz. It remains to be established whether there exists a localized source of motion at 0.1Hz in sector 37, as indicated by the data.

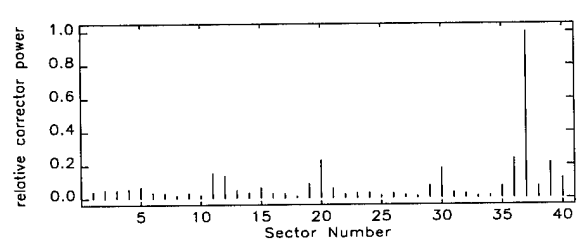

Figure 5: Measured horizontal corrector power at 0.1Hz.

5 LOCAL/GLOBAL FEEDBACK

X-ray beam position monitors are installed on each insertion device and bending magnet x-ray beamline. There are a number of options for including these in a local feedback algorithm in order to control position and angle of the x-ray source points.

An option recently considered is the determination of a global matrix which has the objective of exactly correcting the x-ray source points while simultaneously minimizing the global rms orbit. The algorithm assumes a system with N monitors, of which P must be controlled exactly, while using M correctors, where $P < M < N$. If only the P monitors are considered, then there exists a plane of solutions in M-P dimensions which produces an exact correction at these locations. The M-P degrees of freedom in the solution are available to correct the remaining N-P locations in a least-squares sense.

The algebra associated with this algorithm is straightforward, and the solution can be written in the form of a constant (response) matrix. However, it can be shown that the same numerical solution can be approached using the classical 'weighted least-squares' algorithm, where the P monitors are given a high weighting relative to the remaining N-P monitors. The weighted least-squares method differs from the pseudo inverse algorithm by the introduction of the weighting matrix, and has the form

$$\Delta \underline{c} = [(\mathbf{W.R})^T \mathbf{W.R}]^{-1} (\mathbf{W.R})^T \mathbf{W}\, \Delta \underline{x},$$

where **W** is a (diagonal) weighting matrix, **R** is the forward response matrix, and $\Delta \underline{c}$ and $\Delta \underline{x}$ are vectors of corrector and BPM changes.

The weighted least-squares algorithm offers the capability of achieving simultaneous local and global control using a single global system together with an appropriate response matrix. The capability to do weighting already exists in our orbit correction software [5], and limited tests on the storage ring using x-ray and rf BPMs have established this algorithm does indeed work as described.

6 CORRECTOR DYNAMICS

The APS system is designed to perform both local and global orbit feedback. In order to prevent instabilities from arising, it is necessary to decouple the two feedback loops, either dynamically or spatially.

If all correctors do not have the same dynamics, then it is very difficult to decouple the two loops spatially. This can be shown by considering the error from one iteration of the orbit correction algorithm, in which case the residual static orbit error is given by

$$\mathbf{E} = \Delta \underline{x} - \mathbf{R}\, (\mathbf{R}_{inv}\, \Delta \underline{x}),$$

where **R** and $\mathbf{R}_{inv}$ are the forward and inverse response matrices, and $\Delta \underline{x}$ is the vector of initial BPM errors (a linear orbit response is assumed). Corrector dynamics can be incorporated into a diagonal matrix **H(s)** containing transfer functions for each corrector. The dynamic error is then

$$\mathbf{E(s)} = \Delta \underline{x} - \mathbf{R\, H(s)}\, (\mathbf{R}_{inv}\, \Delta \underline{x}).$$

A simple algebraic transformation converts this to

$$\mathbf{E(s)} = \Delta \underline{x} - \mathbf{P(s)\, R}\, (\mathbf{R}_{inv}\, \Delta \underline{x}).$$

If all correctors have the same dynamics, then both the **P(s)** and **H(s)** matrices are identity matrices multiplied by a scalar transfer function, and corrector dynamics appear directly on the residual orbit error. However, if the correctors have different dynamics, then **P(s)** is nondiagonal and there is no simple relationship between corrector dynamics and the residual orbit error. Viewed in SVD terms, if the correctors have different dynamics, then the SVD modes are no longer decoupled dynamically, even though they remain decoupled in a static sense.

At the APS, the correctors assigned to local feedback have a much slower response than those assigned to global feedback because of strong eddy current effects in the APS vacuum chamber (the global correctors have an Inconel vacuum chamber). The design of compensation filters for the slow correctors has proved to be very challenging, and consequently a spatial decoupling algorithm may not be achievable at the bandwidths required for global feedback.

The alternative is to decouple the two systems in frequency space, with the local feedback system taking care of only slow effects, and the global system taking care of dynamics effects. It may in fact be appropriate to only use local feedback when user steering is requested [2], in which case the global system could be used for both dynamic and slow effects, but would only take care of dynamic effects when steering requests are being applied.

7 ACKNOWLEDGMENTS

We thank J. Galayda and L. Emery for their continuing support and insight into orbit correction.

This work was supported by the U.S. Department of Energy, Office of Basic Energy Sciences, under Contract No. W-31-109-ENG-38.

8 REFERENCES

[1] J. Carwardine et al., "Commissioning of the APS Real-Time Orbit Feedback System," *these proceedings.*

[2] L. Emery, M. Borland, "Advances in Orbit Drift Correction in the Advanced Photon Source Storage Ring," *these proceedings.*

[3] Y. Chung, "Beam Position Feedback System for the Advanced Photon Source," *Orbit Correction and Analysis in Corcular Accelerators, AIP Proc. 315, 1993.*

[4] K Evans, Jr., "Xorbit Reference Manual," *http://www.aps.anl.gov/asd/oag/manuals/xorbit/xorbit.html.*

[5] K. Evans, Jr. "Corbit Reference Manual," *http://www.aps.anl.gov/asd/oag/manuals/corbit/corbit.html.*

CHARACTERIZATION AND EQUALIZATION OF THE AC RESPONSES OF THE CORRECTOR MAGNETS FOR THE APS LOCAL ORBIT FEEDBACK SYSTEM

C. Doose and S. H. Kim
Advanced Photon Source, Argonne National Laboratory
9700 South Cass Avenue, Argonne, Illinois 60439

Abstract

Local feedback for the APS storage ring uses local bumps to control the position and angle of the positron beam through each x-ray source point. Induced eddy currents in the aluminum vacuum chamber dominate the AC characteristics of the corrector magnetic fields. Small differences in the geometries at each magnet location change the eddy current effects and result in bump closure errors which must be reduced in order to minimize the coupling between each of the many local loops and the global control loop. By a combination of flux-damping coils, flux-shielding copper sheets, and a set of steel laminations for end-flux clamping, the differences of the eddy current effects between two corrector magnets were reduced from 0.18 Gm/A to 0.035 Gm/A in the frequency span of 0.1-100 Hz.

1 INTRODUCTION

Around the 40 sectors of the Advanced Photon Source (APS) storage ring [1], 360 rf beam position monitors (BPMs) and 318 horizontal/vertical corrector magnets have been installed for both local and global orbit correction feedback systems [2]. The local feedback systems control the position and angle of the positron beam locally at the source points for the x-ray beams. The corrector magnets, which correct local orbit bumps up to 0.1 mrad from DC to 30 Hz, induce eddy current in the relatively thick aluminum vacuum chamber and other metallic components. The effects of the eddy current in the magnet laminations, which have a thickness of 0.64 mm, are negligibly small [3].

The local feedback system uses four correctors, two on each side of an insertion device. The sections of the vacuum chamber near the two corrector magnets, BH1 and BH2 on a girder upstream or downstream of the insertion device, are machined differently for the vacuum port and flange couplings, which changes the eddy current effects. Therefore, when the two magnets are energized with certain ratios of the magnet current, the differences in the eddy current effects result in bump closure errors as a function of frequency. The closure errors must be reduced in order to minimize coupling between each of the many local loops and the global control loop.

2 AC RESPONSE MEASUREMENTS

The two corrector magnets BH1 and BH2 were measured on a storage ring spare girder assembly that has all the eddy-current-related components, including the aluminum vacuum chamber. The two magnets were connected in series to a bipolar power supply/amplifier, Kepco BOP 20-20M [4], in order to have a common-current phase reference for the measurement. The power supply was driven in a current-controlled mode by a random frequency signal from a Hewlett Packard 35670A four-channel analyzer [4]. The signals from two "printed circuit" coils located in each magnet gap inside the vacuum chamber were processed using the analyzer to obtain the response of the integrated magnetic field strength to the magnet current in the frequency domain.

Figure 1 shows the magnitudes of the vertical field strength $B\ell(\omega)/I(\omega)$ of magnet BH2, and that of the difference between BH1 and BH2. The frequency span for the measurements was 0.1-100 Hz with a resolution

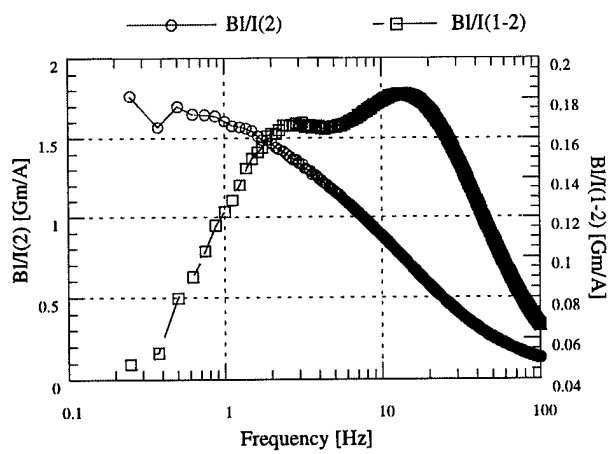

Figure 1: Magnitudes of the vertical field strength per current $B\ell(\omega)/I(\omega)$. $B\ell/I(2)$ for magnet BH2 and $B\ell/I(1\text{-}2)$ for the difference between magnets BH1 and BH2.

of 0.125 Hz, and rms magnet current for the frequency span was 10 A. The corresponding spectra of the phase shift for the field strength are plotted in Fig. 2. Magnet BH1, located closer to the stainless steel flange of the vacuum chamber at the end section of the girder, has 5-

0-7803-4376-X/98/$10.00 © 1998 IEEE

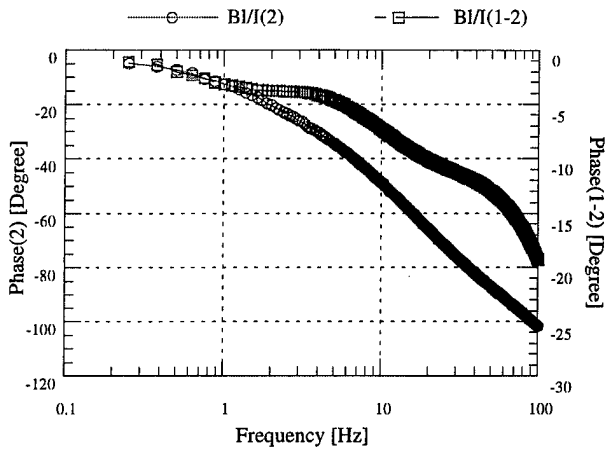

Figure 2: Phase delays of the vertical field strength per current $B\ell(\omega)/I(\omega)$. Phase(2) for magnet BH2 and Phase(1-2) for the difference between magnets BH1 and BH2.

20% less attenuation and phase shift of the magnetic field compared to those of magnet BH2.

3 EQUALIZATION OF THE AC RESPONSE

Three methods of compensation were used to equalize the response of BH1 on the AC magnet current to that of BH2. The first method installed a one-turn flux-damping coil (4/0 cable) around the "back leg" of the flux-return core near the midplane of the magnet in Fig. 3. (The upper half of the two-dimensional cross section for the steel lamination, magnet coils, and vacuum chamber is shown in Fig. 3. The flux lines in the figure are for a DC current.) The damping coil was most effective in changing the response in the frequency band of 4-15 Hz.

The second method shielded and damped the magnetic flux using 1-mm-thick copper sheets as shown in the left two poles in Fig. 3. The copper sheets were cut approximately 7 cm × 2.5 cm to fit on the pole tips of the magnet. The copper sheets were effective in changing the response above 15 Hz.

The third method used a set of U-shaped steel laminations (approximate cross section of 1.2 cm × 1 cm) hung on top of the magnet core across the 7-cm-long magnet near the center pole. This method was effective in the overall frequency band. The laminations diverted a small fraction of the flux from the air gap of the magnet similar to a flux shunt or end-flux clamping scheme.

Using a combination of these three methods for magnet BH1 significantly reduced the differences in the magnitude and phase delay between the two magnets. The results of the combination are plotted in Fig. 4. The difference in phase delay is now less than 1°, and the difference in magnitude is now less than 0.035 Gm/A, a fivefold reduction compared to 0.18 Gm/A before the compensation.

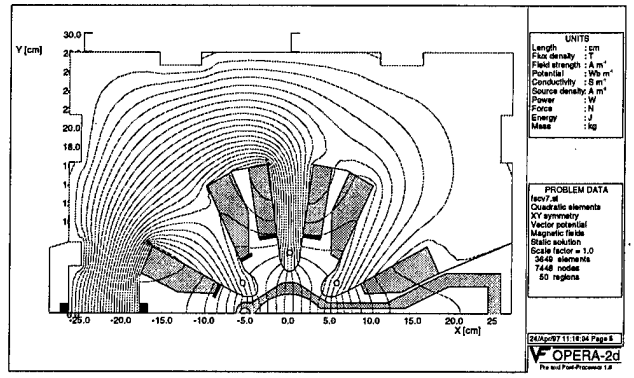

Figure 3: Upper half of the 2-D cross section of the magnet laminations, magnet coils, and vacuum chamber along with flux lines for DC current. The flux-damping coil and copper sheets for the flux shielding on two magnet poles are shown

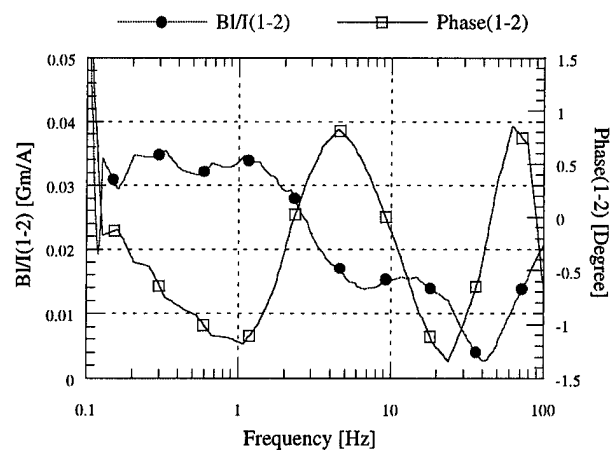

Figure 4: The differences of the magnitude, $B\ell/I(1\text{-}2)$, and phase delay, Phase(1-2), of the AC responses between magnets BH1 and BH2 with the three methods of flux compensation.

4 CONCLUSION

To minimize the local orbit closure errors, AC response differences in the vertical field strengths of two corrector magnets were reduced from 0.18 Gm/A to 0.035 Gm/A in the frequency span of 0.1-100Hz. This was achieved by three methods of flux compensation: damping, shielding, and shunting. Similar compensation methods for the correction of horizontal field have to be tested. The methods need to be simplified for easy installation in the storage ring.

5 ACKNOWLEDGMENTS

The authors gratefully acknowledge J. Galayda for his encouragement and suggestions for the work. This work was supported by the U.S. Department of Energy, Office Basic Energy Sciences, under Contract No. W-31-109-ENG-38.

6 REFERENCES

[1] J. N. Galayda, "The Advanced Photon Source," Proc. of the 1995 PAC, IEEE 95CH35843, 4 (1996).

[2] J. Carwardine et al., "Commissioning of the APS Real-Time Orbit Feedback System," these proceedings.

[3] Y. Chung and J. Galayda, "Effect of Eddy Current in the Laminations on the Magnet Field," LS Note 200, ANL, 1992.

[4] An explicit reference to a particular product does not imply that other vendors might not be able to supply equivalent products.

SIMULATION OF THE APS STORAGE-RING RF SYSTEM

C. Schwartz, A. Nassiri, Y. Kang, and R.L. Kustom
Advanced Photon Source, Argonne National Laboratory
9700 South Cass Avenue, Argonne, Illinois 60439 USA

Abstract

A simulation model for the APS storage ring rf system has been developed that includes the effects of cavity impedances, longitudinal beam dynamics, and generator klystrons. The model predicts multiple-bunch longitudinal beam behavior and is used for feedback system design and stability analysis.

1 INTRODUCTION

Presented here is a description of a computer-based model used to simulate the Advanced Photon Source (APS) 7-GeV storage ring rf system. Relevant system parameters are given in Table 1. The Matlab®-Simulink® software package was used for implementing the model. Some useful features of this package used for this model include the ability to have subsystem components or blocks that are nonlinear, time-varying, and/or mixed (discrete with continuous time). Also, different blocks can have different sampling rates. The overall model includes the cavity, the beam, the generator (klystron), and feedback and feedforward electronics (Figure 1).

The motivation behind the simulation effort is twofold. First, simulation is required in order to predict the beam's longitudinal dynamics, especially when there are significant gaps in beam current between bunches or between groups of bunches and when the charge significantly varies from bunch to bunch [1]. Second, the efficacy of the present and proposed low-level control schemes can be tested with such a model.

Table 1: RF System Parameters

Bunch revolution frequency, f_0	271.56 kHz	
Harmonic number, h	1296	
Cavity shunt impedance, R	5.6 MΩ	
Unloaded Q, Q_0	40000	
Cavity coupling, β	3.5	
Number of cavities	16	
Number of klystrons	4	
Momentum compaction, α	2.28 E-4	
	OPERATION	
Average beam current, I_0	100 mA	300 mA
Gap voltage (whole ring), V_{rf}	8.0 MV	12.0 MV
Stable phase (from rf crest)	47.1°	63.0°
Synchrotron frequency	1.70 kHz	2.30 kHz
Cavity detuning from fundamental, Δf	-7.22 kHz	-17.6 kHz

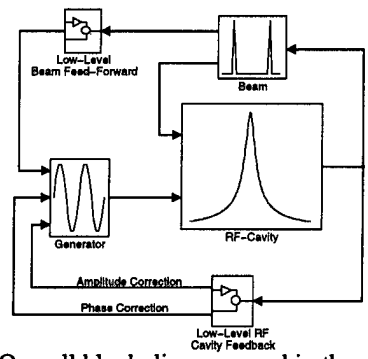

Figure 1: Overall block diagram used in the simulation.

In order to meet these requirements, the model simulates the continuous-time cavity voltage, as powered by both the (controllable) generator and the beam image-current, and the turn-by-turn, multiple-bunch difference equations of longitudinal motion that describe the effect of the cavity on the beam. Work is in progress to include cavity higher-order mode (HOM) resonances, so that a complete picture of beam stability can be obtained through simulation.

Several simplifications are made in order to speed up computer run-time. To avoid running the simulation at MHz frequencies, all signals are decomposed into their baseband, in-phase and quadrature (I and Q) projections in the vector plane that rotates at the angular radio-frequency ω_{rf} [2]. Rather than directly simulating error-inducing beam injection, the cavity fields are set in an errorless steady state, and the beam bunch phases are then allowed to oscillate, using some initial phase-error condition(s). In addition, the number of bunches used in the simulation is intentionally limited, so as to speed up the run-time.

2 MODEL COMPONENTS

2.1 Cavity

The cavity fundamental-resonance impedance is modelled as a linear, second-order harmonic oscillator, or RLC circuit, parameterized in the complex frequency domain (s) by:

$$Z = \frac{2\sigma R s}{s^2 + 2\sigma s + (\omega_{rf} + 2\pi\Delta f)^2}, \qquad (1)$$

where $\sigma = \frac{(\omega_{rf} + 2\pi\Delta f)}{2Q}$. Other parameter values for Eq. (1) used in the simulation can be found in Table 1. The linear, time-invariant property of this model permits a superposition of the rf and beam image-current as inputs to the cavity block of Figure 1.

In order to empirically verify the standard [1] cavity model of Eq. (1), a cold-model-cavity measurement near

0-7803-4376-X/98/$10.00 © 1998 IEEE

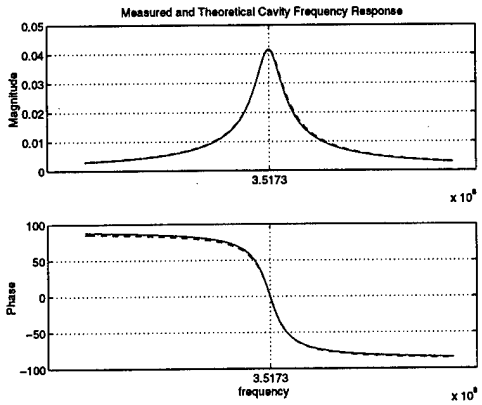

Figure 2: Measured frequency response (solid) and theoretical (dashed).

the rf fundamental was performed using an HP network analyzer. The resulting observed resonant frequency, Q, and gain were then used as parameters for Eq. (1). Plots of both data sets are given in Figure 2, showing that the model is well borne out by experiment.

For the simulation, the cavity shunt impedance is scaled so that the effects of all sixteen cavities (on the beam) are lumped into one resonance. This simplification is justified given the small synchrotron tune (Table 1); i.e., for a given bunch, effectively small longitudinal motion occurs within one revolution, therefore the even smaller motion that occurs between successive cavities can be ignored.

2.2 *Beam*

As each bunch passes through the cavity, the beam block shown in Figure 1 inputs a sample of the cavity voltage in order to update that bunch's phase, as governed by the following difference equations (modified from [3] to allow for time-varying cavity voltage):

$$\Delta\phi^{i}_{n+1} = \Delta\phi^{i}_{n} - \frac{\alpha\omega_{rf}T_o}{V_o}\Delta V^{i}_{n+1} \qquad (2)$$

$$\Delta V^{i}_{n+1} = \Delta V^{i}_{n} + (V_a)^{i}_{n} - V_c\cos\phi_s \qquad (3)$$

All quantities denoted with a superscript (bunch number) and a subscript (that bunch's pass through the cavity) refer to bunch-sampled continuous-time (rf) parameters. Otherwise, variables refer to constants, such as V_o, the stable beam energy (7.0 GeV) given here in volts, and ϕ_s, the stable phase w.r.t. the peak of the cavity voltage set-point V_c. For the ith bunch at its nth turn, ΔV^{i}_{n} denotes the deviation from V_o, and $\Delta\phi^{i}_{n}$ denotes the *beam* phase deviation from its nominal zero-reference [1]. The quantity $(V_a)^{i}_{n}$ thus represents the accelerating voltage for bunch i at its turn n, and it is given by the I/Q projection of $(V_c)^{i}_{n}$ onto $\Delta\phi^{i}_{n}$.

The beam block outputs beam-image current, partitioned into a number of segments corresponding to the number of bunches being simulated and the number and size of gaps in current. The amplitude of a given bunch over all turns is taken as constant, i.e., no quadrupole oscillations are assumed; however, the phase varies as described above. In addition, the amplitude of the image current over each revolution period is, of course, fill-pattern dependent.

For example, in typical operation 36 or 48 bunches may be uniformly concentrated in four groups about the ring, thereby creating a uniform, but gapped, fill pattern. Also used are non-uniform gapped fill patterns, for example, ones with a small leading group of successive bunches (i.e., no empty buckets between them) followed by a small gap, and then a large number of bunches and a large trailing gap. Such a fill pattern and the AM and PM modulations it induces on the cavity voltage are shown in Fig. 3(a-c), respectively. The stable, steady-state synchronous phases of individual bunches are thus also fill-pattern-dependent, and the simulation is a tool to determine these [1]. Certain fill patterns are empirically known to induce coupled-bunch instabilities, for which certain cavity HOMs have been implicated [4]. Although the HOM effects have not been (as yet) included in the simulation model, some fill patterns have been shown to cause instability even through the cavity fundamental.

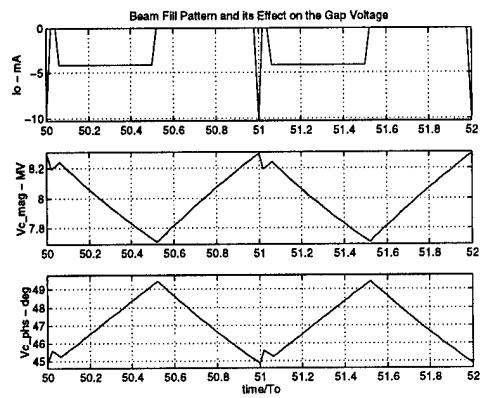

Figure 3: The asymmetric gapped fill pattern, shown over two revolutions (a), induces AM and PM modulations of the cavity gap-voltage shown in (b) and (c), respectively. The nominal cavity set points are 8.0 MV and 47.1°.

2.3 *Klystron*

In present operations, with DC beam current less than 160 mA, there is no need to drive the klystrons into power-saturation. However, this AM-limiting saturation effect, due to the klystron, its power supply, or both, is foreseen as operation approaches the full available power (3 MW). The saturation effects are under study and will be incorporated into the model. Presently, a linear klystron is assumed.

2.4 *Low-Level RF System [5]*

Two cavity feedback loops are now in operation in the storage ring: a low-bandwidth cavity tuning loop and a cavity-phase-sum feedback loop. The first loop is omitted from the model. Its has a relatively low bandwidth (less than 1 kHz) requiring too much additional simulation time to resolve its dynamic effect on the beam. Moreover, beam phase errors induced during injection (transient beam load-

ing) are well accounted for as perturbations to the cavity and beam steady state, as already mentioned.

The actual cavity-phase-sum loop compares the sum-signal of a group of four cavity phase measurements to a setpoint and feeds back the error through a PID controller to adjust the phase of their dedicated klystron. For the simulation the summing nature of the phase loop is of course omitted. The loop bandwidth has been measured to be near 7 kHz [6], corresponding roughly to the cavity bandwidth. The time-delay for the largest rf-station-to-cavity distance is 6 μs; it is included in the model as the nominal cable delay.

To date, a simple gain-scheduling algorithm has proven sufficient to insure the magnitude of the cavity gap voltage. However, since a cavity-amplitude feedback is foreseen, this loop is added to test its effect. To demonstrate the added utility of a beam phase-error feedforward, this loop has been added as well. Presently, the longitudinal motion of the beam is monitored using a dedicated storage ring BPM pickup button, so that a beam-phase signal could be incorporated into the overall low-level system with relative ease.

3 SOME SIMULATION RESULTS

Figures 4-5 are useful to visualize operation with 100 mA and 300 mA. For a given V_{rf} (Table 1) and an optimally detuned cavity (i.e. zero loading-angle), one can see the limit on stored beam due to the Robinson stability criterion (shaded area) and the limit due to available power (dashed line). Thus, while stability for dipole oscillations is guaranteed, still a beam feedforward aids in damping these oscillations more quickly as can be seen from Figure 6 (dash-dot case). Of course, for arbitrary beam offsets across all bunches and for cases when each bunch has its own synchronous phase, such a system may damp the oscillations of one bunch while driving those of another bunch. A bunch-by-bunch feedback system then becomes an attractive solution.

4 ACKNOWLEDGMENTS

The authors would like to Jeff Stepp (formerly of APS), A. Regan of LANL, and R. Tighe of SLAC, the latter having provided us with key help and with a portion of his Matlab code. In addition, K. Harkay of APS provided technical insight, and X. Jiang, also of APS, assisted with the cavity measurements. This work is supported by the U.S. Department of Energy, Office of Basic Sciences, under Contract No. W-31-109-ENG-38.

5 REFERENCES

[1] P. B. Wilson, "Fundamental-Mode RF Design in e^+e^- Storage Ring Factories," SLAC-PUB-6062, in *Frontiers of Particle Beams: Factories with e^+ e^- Rings*, M. Dienes, ed., 1993.

[2] B. R. Cheo et al. "Dynamic Interactions Between RF Sources and LINAC Cavities with Beam Loading," *IEEE Trans. Elec. Dev.* **ED-38**, No. 10, 2264 (1991).

[3] D. A. Edwards and M. J. Syphers, *An Introduction to the Physics of High Energy Accelerators*, Wiley-Interscience, 1993.

[4] K. C. Harkay et al., "Compensation of Longitudinal Coupled-Bunch Instabilities in the Advanced Photon Source Storage Ring," these proceedings.

[5] J. D. Stepp and J. F. Bridges, "General Overview of the APS Low-Level RF Control System," *Proceedings of the 1993 Particle Accelerator Conference*, pp. 1157-1159, 1993.

[6] D. Horan et al., "Phase-Loop Bandwidth Measurements on the Advanced Photon Source 352-MHz RF Systems," these proceedings.

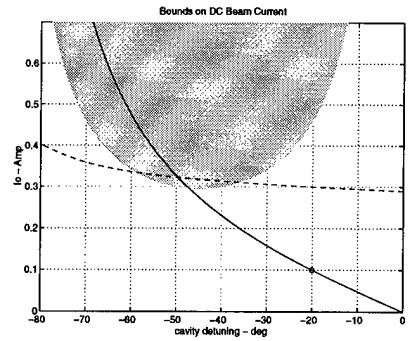

Figure 4: Bounds on beam current I_0, when cavities are detuned optimally (solid line), assuming V_{rf} = 8.0 MV. The shaded area is due to the Robinson instability, and the dashed curve is due to the available power (assumed < 3 MW). The o marks operation at 100 mA.

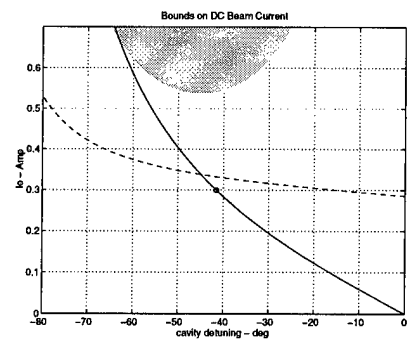

Figure 5: Bounds on beam current I_0, when cavities are detuned optimally (solid line), assuming V_{rf} = 12.0 MV. The shaded area is due to the Robinson instability, and the dashed curve is due to the available power (assumed < 3 MW). The o marks operation at 300 mA.

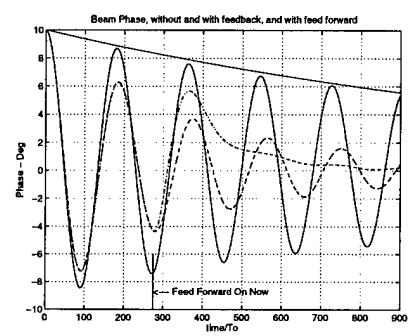

Figure 6: When all bunches are offset by 10°, the error oscillates (solid), damped with an envelope given by $10e^{-t/Td}$ (also shown). With LLRF feedback the damping improves (dashed), and even more so with the beam feedforward on (dash-dot).

MULTIPLE CONTROL FOR FEEDBACK TUNING OF THE ADVANCED PHOTON SOURCE STORAGE RING/BOOSTER RF CAVITIES

T. L. Smith
Advanced Photon Source, Argonne National Laboratory
9700 South Cass Avenue, Argonne, Illinois 60439 USA

Abstract

A method for tuning rf cavities that has fewer rf reflected power conditions and is easier for accelerator operators to use is presented. This method will also prepare the rf cavity tuning for future higher beam currents. The results and installation methods are discussed.

1 INTRODUCTION

The Advanced Photon Source (APS) is a 7-GeV synchrotron radiation facility. The storage ring uses sixteen single-cell rf cavities, and the booster uses four, five-cell rf cavities [1]. These cavities employ a plunger-type tuning system. At present, if the rf drive to these cavities is turned off or tripped off, the tuner movement is electronically inhibited to prevent the tuner from racing to either limit. In the absence of rf, the cavity water cooling system will quickly return the cavity resonance to its original "cold state" condition. When rf is returned to the cavity, the tuner will be at the wrong position and a certain amount of reflected power will always occur until the tuner phase loop can correct the tuner position. A system has been devised using VXI-based relay matrix cards and additional feedback loops that will drive the cavity resonance back to the "cold state" condition when the rf is removed. Several control modes, including a method for manual control of the tuners, have been built into the system. The storage ring single-cell cavities are divided into four sectors (sectors 36, 37, 38, and 40), each employing four cavities. This multiple control feedback tuning design has now been installed in sector 38. The other sectors will be updated in the near future. The following information is derived from the sector 38 data.

2 TUNING CONTROL

The cavity tuner uses a gear-driven potentiometer that varies with the tuner position and can give a voltage readout which corresponds to the tuner position inside the cavity. With the rf off, the tuner could be tuned to a position where the cavity resonance would match the storage ring rf drive frequency and the potentiometer reading noted. This is done for each cavity and the voltage readings are used as *setpoints* in the "cold state" tuning loop (see Figure 1). From this point on, these numbers will hold valid if the cavity volume is not disturbed, the cavity cooling water temperature is held constant, and the storage ring rf drive frequency does not change.

In normal operation (rf on), for each cavity, the output of low-level rf phase detection circuitry indirectly drives the tuning plunger. A VXI-based 8 × 8 relay matrix card is

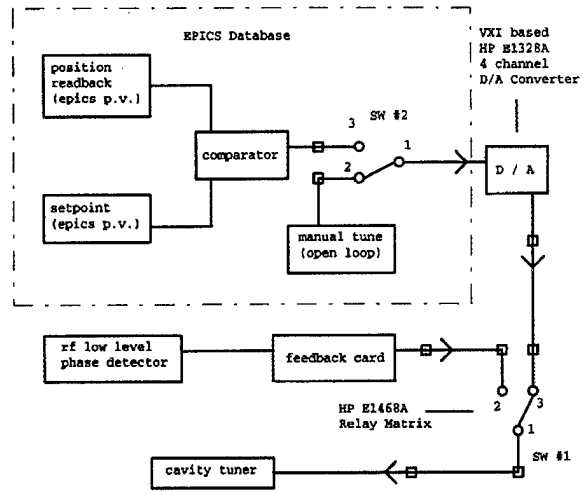

	SW #1	SW #2
RF On (Normal Operation)	1 - 2	X
RF Off	1 - 3	1 - 3
Manual Tune	1 - 3	1 - 2

Figure 1: Tuning control for each cavity.

electrically inserted between the rf phase detection circuitry and the tuner input (see Figure 2). Depending upon selection, the manual tune control *or* the output of the cold tuning loop drives one channel of a four-channel, VXI-based D/A converter. This D/A converter will drive the tuner, through the relay matrix, unless the rf low-level phase feedback loop is selected for control.

These selection processes take place in the software via the EPICS control system [2]. *The tuners are never allowed to freerun.* Power levels per cavity are monitored, and if the level drops below a certain adjustable value, normally set at approximately 900 watts, the software will assume the rf is off. This condition will switch the relay matrix to the "cold state," allowing the cavity tuners to quickly tune to a preset condition and wait for the return of rf. Each cavity is judged individually. If that cavity rf drive level is above 900 watts, the cavity tuner will be instantly controlled by the low-level rf phase loop and tune accordingly, negating the changing cavity resonance effects caused by the rising cavity temperatures.

The selection of manual tuning control will be used infrequently and for experimental purposes. The manual tuning of an rf cavity at high power could easily result in a high reflected power condition, the tripping of an rf system, and the loss of beam in the accelerator. It is the

0-7803-4376-X/98/$10.00 © 1998 IEEE

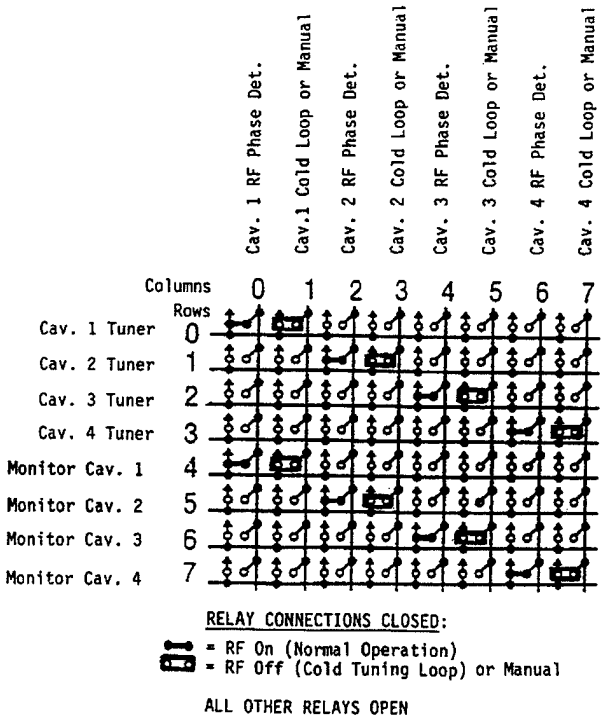

Figure 2: Relay matrix connections.

responsibility of the person selecting manual tuning to guard against this situation. To prevent operators from selecting manual tuning for cavities under power and accidentally leaving these cavities unattended, the following processes have been implemented in the software to aid against possible high reflected power conditions:

1. If rf is on (rf phase detection loops active), when rf is turned off or tripped off, all manual tuners will be automatically put back into auto, reset by the cold tuning loop, and wait for the return of rf.
2. If rf is off (cold tuning loop active), when rf is turned on, all manual tuners will be automatically put back in auto and tuned up properly with the rest of the sector.

3 CONTROL SCREENS AND OPTIMIZATION

Excluding the manual control, the changes in the tuning control in sector 38 have gone basically unnoticed to the operators since the rf phase loops and the cold tuning loops switch automatically. An existing operator screen has been modified for the addition of the manual tuning capability (see Figure 3).

An engineering screen for each cavity was added to make the parameter adjustments required for a timely stable lock up of the cold tuning loop (see Figure 4). A two-speed adjustable system is used for controlling the tuners. The setpoint is predetermined and stored in the database. The tuner position voltage is constantly monitored from the gear driven tuner potentiometer. The difference between the tuner position and the set-point is constantly calculated, and when it is above the fast range setting, the tuner will move in fast speed.

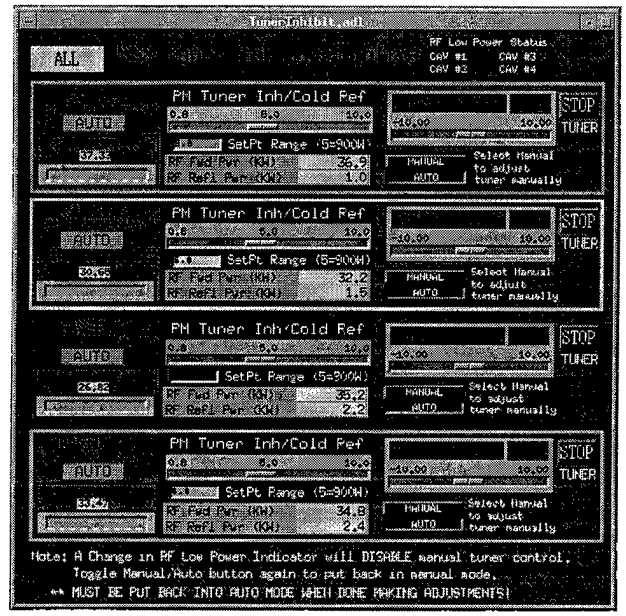

Figure 3: Operator screen for manual adjustments.

Tests were performed with a variety of adjustments, and a position showing the best overall speed and stability was obtained (see Figure 5). Figure 4 shows sector 38 cavity #1 in normal feedback control (rf phase loops on). If rf was turned off or tripped off, the cold loop would drive the tuner, and the tuner position would match the setpoint in approximately 2.5 seconds.

Figure 5 is one second per division and shows the lockup time of the cold tuning loop to be approximately 2.5 seconds. This time will change slightly with different power levels in the cavity. Channel 1 is a measurement of when the rf drive power leaves the cavity, prompting the cold tuning loop to begin. Channel 1 is the trigger for this measurement. Channel 2 is a measurement of the signal applied to the tuner input. The tuner is in fast speed for 1.3 seconds, slow speed for 0.8 seconds, and shows a tuner ini-

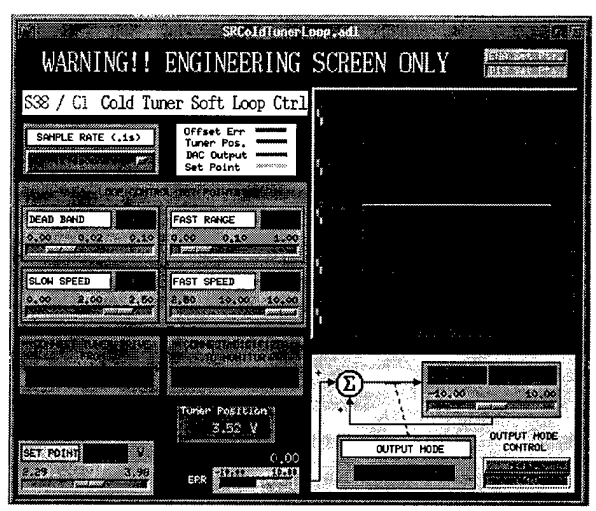

Figure 4: Cold tuning loop engineering screen.

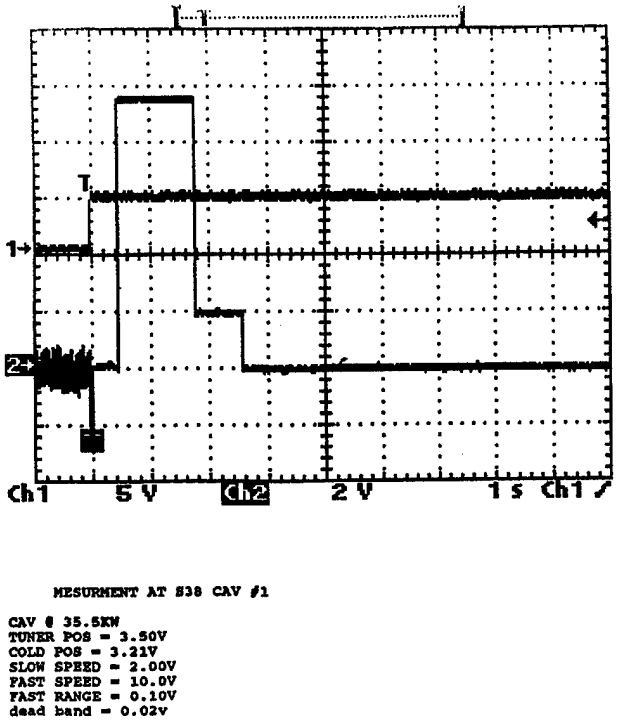

Figure 5: Lockup time of cold tuning loop.

tial response time of 0.4 seconds. This lockup time seems to be adequate, but a faster and more stable time could be acquired if more accelerator studies time was dedicated.

4 DISCUSSION

At the present time, the maximum beam current used in the APS is approximately 100 mA. The rf systems are running at high power levels to sustain this beam current. If the rf is turned off or tripped off in sectors 36, 37, or 40, the tuners will inhibit. When the rf is turned back on, some tuners will lock after a period of time and some will require manual help (by adjusting setpoints) to achieve phase lock. This problem will become increasingly more apparent as the accelerator beam current improves from 100 mA toward 300 mA.

At present in sector 38, all four cavities will automatically lockup and tune immediately upon the return of any level of rf.

5 ACKNOWLEDGMENT

I want to thank Nicholas DiMonte for his continuous support and interest in the software control programming and graphical display design. This work was supported by the U.S. Department of Energy, Office of Basic Energy Sciences, Under Contract No. W-31-109-ENG-38.

6 REFERENCES

[1] A. Nassiri et al., "An Overview of the APS 352-MHz RF Systems," these proceedings.

[2] L. R. Dalesio, M. R. Kraimer, A. J. Kozubai, "EPICS Architecture," Proc. of ICALEPCS '91, Tsukuba-Shi, Ibaraki, Japan, KEK Proceedings 92-15, pp. 278-282, December 1992.

AN EXAMPLE OF A DIGITAL SYNTHESIS APPROACH TO DSP DESIGN: THE AGS TRANSVERSE DAMPER*

K.A.Brown, G.Smith, V.Wong
Brookhaven National Laboratory
Upton, NY 11973

1 INTRODUCTION

Using Verilog HDL [1] and Synopsys, the digital signal processing of the AGS Transverse Damper was designed and fitted to an Altera Flex 10k FPGA. Using a control point specification style in the high level description greatly simplified the design by placing the burden of specifying the controller on the digital synthesizer.[2] The basic design and low level simulation are presented as well as the design methodology.

The purpose of the AGS Transverse Damper [3] [4] is to control instabilities and injection errors that may arise in high intensity proton beams being accelerated in the AGS. The system block diagram for the DSP is shown in Figure 1. The inputs to the system come from a normalization unit. This normalization unit takes two signals as input, a sum of beam position signal plates, and a difference from the plates. The output of the normalization unit is the difference divided by the sum. This Quotient is sent to the first ALU (as Qin[11..0]). Taking differences between position measurements the system acts as a notch filter.

The Second ALU computes a running sum of the output of the first ALU. This then acts to remove any offsets in the Quotient (and thus this part acts as a high pass filter - removing any baseline components to the signal). The depth of the first FIFO (between adder and subtract units) basically determines the low pass behaviour. The multiplier serves the purpose of overall loop gain for the system (the complete system is a real-time feedback system). The FIFO on the output is used to provide the correct amount of delay for the system.

The specifications for the design of the system are enumerated below . At power up time the FIFO's are initialized and filled with zeros.

1. 12 bit system (adder is 16 bit)
2. frequency range for clocks is 3 to 5 MHz.
3. Controls are for Gain, Initialization, Mux Selects, and external excitation.
4. number systems are all 2's complement.

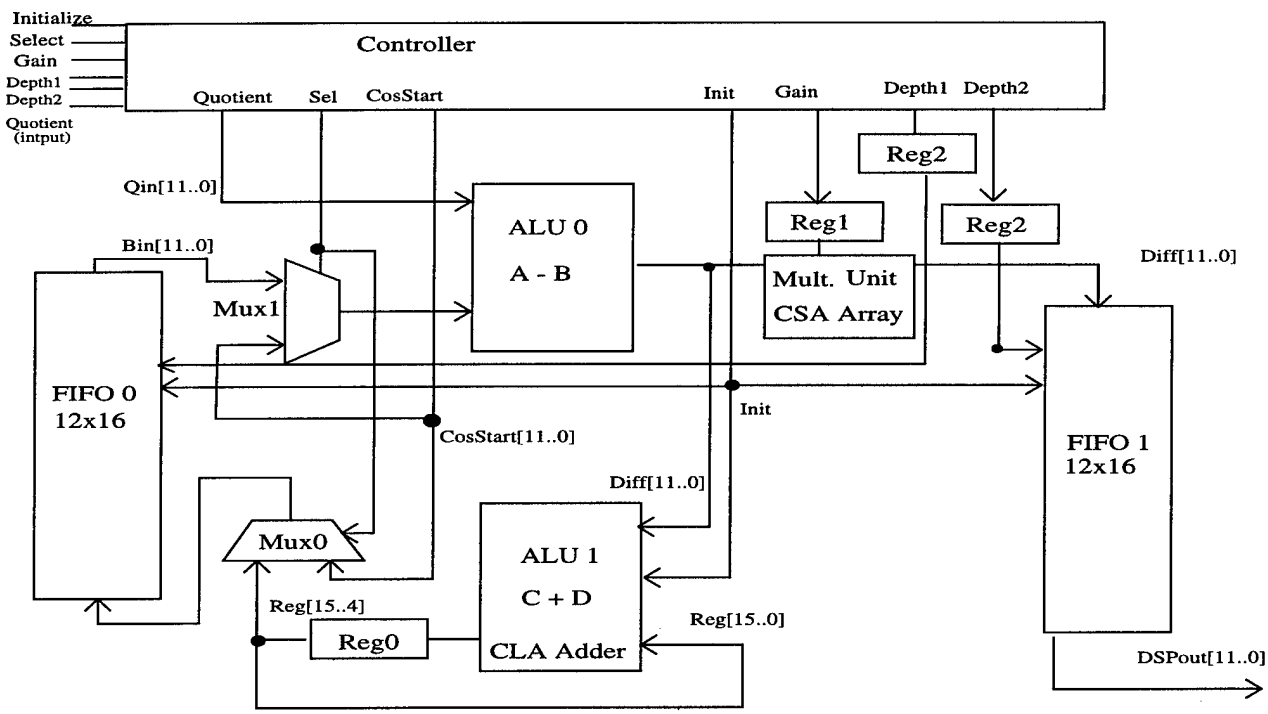

Figure 1: Block Diagram for AGS Damper DSP

* Work performed under the auspices of the U.S. Dept. of Energy

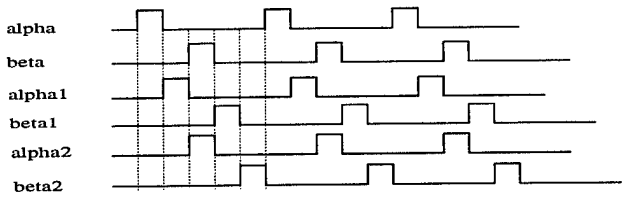

alpha => used for top level testing
beta => used for top level testing
alpha1 => used for second level triggering
beta1 => used for second level triggering
alpha2 => not used
beta2 => used for lowest level triggering

Figure 2: Multiphase timing for two level hierarchy

The design of the system is a two level hierarchy. So the triggering of the system is multiple phase. Figure 2 shows the timing sequences for the system.

2 DISCUSSION

The control point specification style requires a very structured approach to the design specification.[2] The basic idea behind this style is the designer never goes into the details of building or writing specifications for the system state diagram. They need only specifiy the state tables for the state diagram and these become the control points, the inputs and outputs of a black box. This black box the synthesizer constructs based on the state tables. The benefit of this approach is seen in figure 1. The controller unit is the black box. The inputs and outputs of the controller unit are specified, but the specification of the controller itself is left up to the synthesizer. We then only need to design the specifications for the individual submodules. To illustrate this a portion of the verilog specification is shown below:

```
module damper( //input parameters );
// input/output declarations put here
...
// control points
...
wire [ws+3:0] Sout; // ALU 1 Output
reg [ws+3:0] Rout; // Reg.0 Output
...
wire [ws-1:0] Dout; // ALU 0 Output
...
// asynchronous assignments
...
// instantiate submodules
mux #(1) TestSel(SEL, 1'b0, Select, testsel);
...
// Control points are passed to the submodules as so:
// this example is a carry lookahead adder, 16 bit.

add_clh16 #(ws+4) Add_1(alpha1,
Dout[0], Dout[1], Dout[2], Dout[3], Dout[4], Dout[5], Dout[6], Dout[7],
Dout[8],Dout[9], Dout[10],Dout[11], Dout[11],Dout[11],Dout[11],Dout[11],
Rout[0], Rout[1], Rout[2], Rout[3], Rout[4], Rout[5], Rout[6], Rout[7],
Rout[8], Rout[9], Rout[10], Rout[11], Rout[12], Rout[13], Rout[14], Rout[15],
Carryin, Cout,
Sout_0, Sout_1, Sout_2, Sout_3, Sout_4, Sout_5, Sout_6, Sout_7, Sout_8,
Sout_9, Sout_a, Sout_b, Sout_c, Sout_d, Sout_e, Sout_f);

// now do the work ...
always @(posedge alpha1 or posedge beta1 or posedge init) begin
...
```

2.1 Project Submodules

Each block inside figure 1 corresponds to a submodule, such as the carry lookahead adder whose instantiation is shown above. It is beyond the scope of this paper to describe each one. It should suffice to explain the basic organization of one. For this example we will continue with the carry lookahead module, which is the basic module for adders and multipliers (which can be built with trees of carry save adders and end with a final full adder). This basic idea can be extended to be used for subtration and division, although these algorithms are more complicated.

Figure 3 shows the block diagram for a 16 bit carry lookahead adder. For 16 bit addition a simple ripple carry adder would not work since it needed more than 100 nsec to finished a calculation. So going to something faster was needed. Below portions of the specification are shown. It is intended only to provide a flavor for how the specificaions can easily be made to follow the flow of the block diagram.

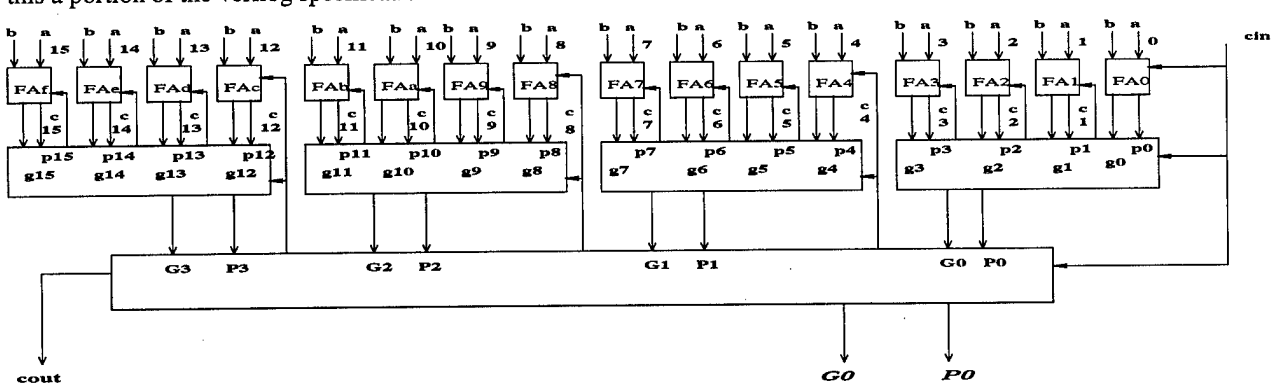

G0 = g3 | (p3 & g2) | (p3 & p2 & g1) | (p3 & p2 & p1 & g0)
P0 = p3 & p2 & p1 & p0
c1 = g0 | (p0 & cin)
c2 = g1 | (p1 & g0) | (p1 & p0 & cin)
c3 = g2 | (p2 & g1) | (p2 & p1 & g0) | (p2 & p1 & p0 & cin)
c4 = G0 | (P0 & cin)
...

Figure 3: Carry Lookahead Adder

```
module add_clh16(clka, // parameters );
//declarations, inputs/outputs, wires, etc.
  assign g0 = A[0]&B[0], g1 = A[1]&B[1],
         g2 = A[2]&B[2], g3 = A[3]&B[3];
  assign g4 = A[4]&B[4], g5 = A[5]&B[5],
         g6 = A[6]&B[6], g7 = A[7]&B[7];
...
  assign p0 = A[0]^B[0], p1 = A[1]^B[1],
         p2 = A[2]^B[2], p3 = A[3]^B[3];
...
  assign P0 = p3&p2&p1&p0;
  assign P1 = p7&p6&p5&p4&P0;
...
  assign G0 = g4|(p4&g3)|(p4&p3&g2)|
                (p4&p3&p2&g1)|(p4&p3&p2&p1&g0);
  assign G1 = g8|(p8&g7)|
                (p8&p7&g6)|
                (p8&p7&p6&g5)|
                (p8&p7&p6&p5&g4)|
                (p8&p7&p6&p5&p4&g3)|
                (p8&p7&p6&p5&p4&p3&g2)|
                (p8&p7&p6&p5&p4&p3&p2&g1)|
                (p8&p7&p6&p5&p4&p3&p2&p1&g0);
...
always @ (posedge clka )
  begin
     sum <= A ^ B;
carry[0] <= (g0)|((p0)&cin);
carry[1] <= (g1)|((p1)&(g0))|((p1)&(p0)&cin);
carry[2] <= (g2)|((p2)&(g1))|
                ((p2)&(p1)&(g0))|
                ((p2)&(p1)&(p0)&cin);
carry[3] <= (g3)|((p3)&(g2))|
                ((p3)&(p2)&(g1))|
                ((p3)&(p2)&(p1)&(g0))|
                ((p3)&(p2)&(p1)&(p0)&cin);
...
  end
endmodule
```

3 CONCLUSIONS

These techniques allowed the design and simulation of a complex system to be done relatively quickly. The synthesizer is often much better at optimizations than most human beings, and the use of implicit specifications gives the synthesizer the freedom to build a circuit which fits the design requirements. Of course the designer must learn how to define the specifications such that the desired result is obtained. The real benefit of this approach is it allows for the design process to become more dynamic. It is not difficult nor very time consuming to alter the design or even change specifications. It allows the designer to design and simulate as realistically as possible the circuits they are going to build. The amount of time actually spent testing the hardware on the bench is reduced considerably. It certainly has drawbacks. The engineer now needs to learn a complicated language and become proficient in that language. The software needed to do this is expensive and needs to be configured and maintained. It also requires alot of computing power and resources in order to run well. For a large production company building DSP's or microprocessors, they simply cannot exist without software tools such as these, and necessarily make the investment. For a small lab it is understandably difficult to consider such an investment.

Results of the simulation are shown in figure 4.

4 ACKNOWLEGEMENTS

This work was done as a class project in a graduate course on Digital System Synthesis, taught by Prof. David Smith of the Dept. Computer Science, SUNY at Stony Brook. A number of students did work in relation to this work. In particular Karpagavinayagam Ramesh built a Wallace Tree adder, which was experimented with in this design.

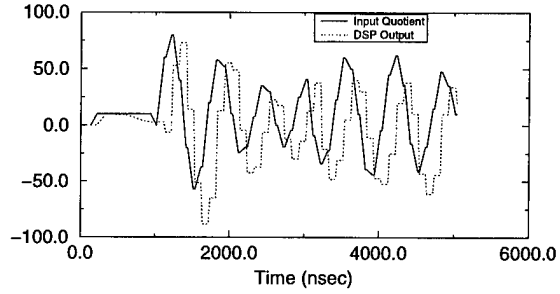

Figure 4: Simulation Results

5 REFERENCES

[1] Verilog HDL; A Guide to Digital Design and Synthesis by Samir Palnitkar, SunSoft Press, 1996.

[2] Dr. D. Smith, SUNY at Stony Brook Dept. Computer Science, Class notes from Graduate course on Digital Systems Synthesis, Fall 1996.

[3] G.A. Smith, T. Roser, R. Witkover, V. Wong, "Transverse Beam Dampers for the Brookhaven AGS" AIP Conference Proceedings 319, Beam Instrumention Workshop, Santa Fe, NM 1993, pp309-318

[4] G.A.Smith, V. Castillo, T. Roser, W. Van Asselt, R. Witkover, and V. Wong, "Digital Transverse Beam Dampers for the Brookhaven AGS", Proceedings of the 1995 Particle Accelerator Conference and International Conference on High-Energy Accelerators, pp2678-2680

LONGITUDINAL COUPLED BUNCH INSTABILITIES ON THE NSLS X-RAY RING

R.W. Klaffky, W. Broome, R. D'Alsace, S.L. Kramer, M.G. Thomas, J.M. Wang *
National Synchrotron Light Source, Brookhaven National Laboratory, Upton, NY 11973

Abstract

Studies have demonstrated that an 862 MHz RF cavity higher order mode (HOM) cause longitudinal coupled-bunch (LCB) dipole and quadrupole oscillations at specific RF tuner positions with associated increases in longitudinal, horizontal, and vertical electron beam sizes. In the XRF2 cavity a reconfiguration of damping antennae removed the 862 MHz HOM. High speed I(t) stripline measurements showed that a strong quadrupole oscillation resulted when the HOM was induced in the XRF3 cavity. The reason that a symmetric six bunch pattern was found to be effective in damping this mode is explained.

1 INTRODUCTION

The NSLS X-Ray Storage Ring is a national user facility producing high intensity, high brightness synchrotron radiation at 60 X-Ray beamlines. Four 52.88 MHz cavity resonators driven by 125 kW amplifiers restore the synchrotron radiation energy loss of the electron bunches[1]. Beginning in January 1998, the storage ring will operate predominantly in two user modes: 440 mA at 2.584 GeV and 260 mA at 2.8 GeV with the standard asymmetric pattern of 25 bunches filled followed by 5 bunches empty. There will continue to be limited single bunch operation at 130 mA for timimg experiments. Symmetric bunch patterns of 3,5,6,10,15 and 30(all bunches filled) are used during machine studies periods.

For a symmetric distribution of m coupled electron bunches with identical charge in each bunch, the beam spectra will have the frequency components:

$$f^{+}_{\mu,n} = nmf_{rev} + sf_{rev} + \mu f_s$$

$$f^{-}_{\mu,n} = nmf_{rev} + s'f_{rev} - \mu f_s$$

where s, s' are the mode numbers satisfying $s + s' = m$, f_s is the synchrotron frequency, and μ is the multipole number of the coupled bunch mode. For the NSLS X-Ray Storage Ring the revolution frequency f_{rev} is 1.76 MHz and the synchrotron frequency f_s is 5 kHz.

This paper investigates the coupling between symmetric bunches that occurs when an RF cavity HOM of high quality factor overlaps one of the above $f_{\mu,n}$ frequencies.

2 EXPERIMENTAL TECHNIQUES

Signals summed from the horizontal plates of an X-ray storage ring stripline were used to record the beam-induced power spectrum. In addition, high speed I(t) stripline measurements[2] were performed to study the longitudinal bunch profile during an LCB instability driven by a high Q 862 MHz HOM in the NSLS XRF3 system. S_{21} transmission measurements were made during shutdown periods using the cavity input loop and an RF monitor loop to characterize the major cavity HOMs as a function of tuner position. A pinhole camera and Spiracon on an X-ray bending magnet diagnostic port (X28) recorded transverse beam sizes[3].

3 LCB MEASUREMENTS OF THE NSLS XRF2 SYSTEM

The tuner positions of the 4 X-ray cavities are varied during X-ray injection, ramping and stored beam conditions to maintain a constant detune angle. It was noted in 1995 that some of the experimental beam lines detected steps in beam intensity that correlated with particular XRF2 tuner positions. Studies using symmetric bunch patterns revealed that at a tuner positions of 3.6V (98.6mm) and 4.1V (117.6mm) a strong 862 MHz cavity HOM observed in S_{21} measurements could account for a large μ = +1(dipole) mode on the +9 revolution line above the RF line at 846.2 MHz. This mode corresponds to a monopole mode calculated using URMEL. A weaker μ = +1 mode appeared on the +8 revolution line at 860.3 MHz for the 3.6V tuner position. In Figure 1 S_{21} transmission measurements are shown for the 3.6 V tuner position. The 862 and 860 MHz revolution lines intersect HOMs at these frequencies causing LCB instabilities.

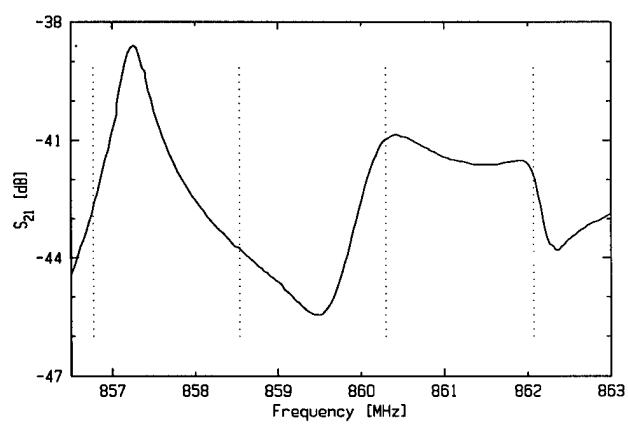

Figure 1: Transmission measurements for the XRF2 cavity with tuner at 3.6V. The revolution lines are shown by vertical dots.

At a tuner position of 4.1V, the 862 MHz revolution line intersects the 862 MHz HOM causing an LCB instability,

* Work performed under the auspices of the U.S. Department of Energy

as shown in Figure 2.

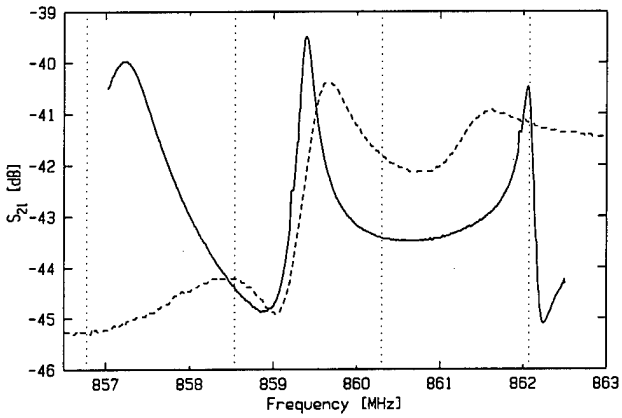

Figure 2: Transmission measurements for the XRF2 cavity with tuner at 4.1 V. The dashed line shows the modes after a reconfiguration of the damping antennae.

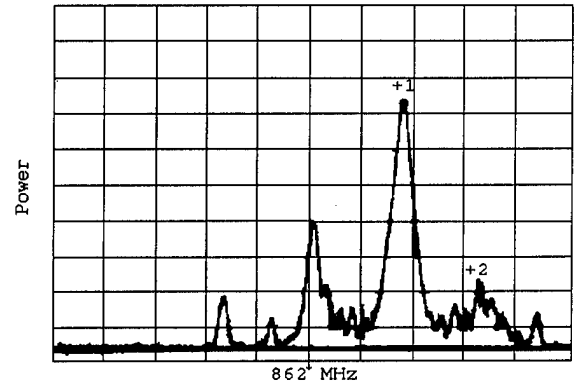

Figure 3: The μ = +1(dipole) sideband on the 862 MHz revolution line for XRF3 tuner position of 4.48V.

The 862 MHz mode was subsequently damped, as indicated by the dashed line in Figure 2, by changing the antennae configuration to resemble that of XRF1 where no 862 MHz LCB was observed. The damped S_{21} curve shows that the newly oriented XRF2 antennae reduced the Q value of the 862 MHz mode and shifted the peak frequency away from the revolution line thereby removing the LCB instability. The damping antennae also removed the 860 and 862 MHz LCB instabilities at the 3.6 V tuner position. Prior to the reorientation of antennae, the tuner range had been adjusted so that the tuner positions causing these LCB instabilities were avoided during operations.

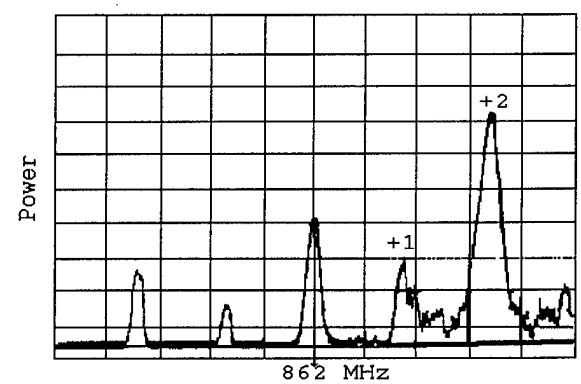

Figure 4: The μ = +2 (quadrupole) sideband on the 862 MHz revolution line for XRF3 tuner position of 4.51 V.

4 LCB MEASUREMENT OF THE NSLS XRF3 SYSTEM

The XRF3 system was found to have a very narrow (Q=9000) HOM at 862 MHz for a tuner position of 4.51V (127mm). At a tuner position of 4.48V (125.9mm) a strong μ = +1 sideband occured on the 862 MHz revolution line. As the tuner position was increased to 4.51V, the μ = +2 (quadrupole) sideband increased while the μ = +1 (dipole) sideband decreased. These sidebands are shown in Figures 3 and 4. In this tuner range, transmission data shows that the 862 MHz HOM peak has a 29 kHz/mm increase in frequency with tuner insertion length.

When these sidebands were present, an RF monitor loop on the cavity showed that a 862 MHz line increased by 54 dB putting it 20 dB above any of the other spectral lines from 117 MHz to 1617 MHz. When the quadrupole sideband was present the longitudinal bunch profile was measured with the stripline signal as shown in Figure 5. There was a clear quadrupole oscillation with a 1.1 nanosecond spacing of the lobes on the time axis, in agreement with a 1.1 nanosecond spacing expected for strong modulation with an 862 MHz HOM.

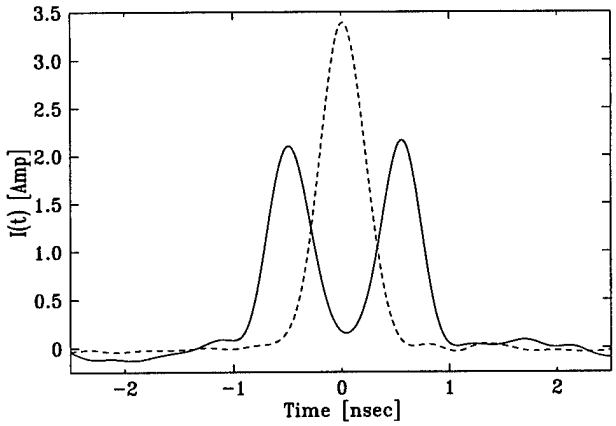

Figure 5: The bunch current distribution[2] measured at two phases of the quadrupole coupled bunch oscillation.

In addition to an increase in the longitudinal dimension of the beam, there were large increases in the transverse dimensions. For a 30 bunch pattern at 300 mA the horizontal beam size(1-σ) increased from 380 to 621 μm and the vertical size from 41 to 52 μm.

5 DAMPING OF THE 862 MHZ LCB INSTABILITY WITH SYMMETRIC SIX BUNCH FILL

For a symmetric six bunch fill (m=6), the 862 MHz LCB instability corresponds to $s = s' = 3$ modes. As a result, the f^+ and f^- frequencies occur above and below the 862 MHz revolution line. The growth rate of the LCB oscillation is proportional to

$$[ReZ(f^+) - ReZ(f^-)]$$

where Z is the cavity impedance. Since the f^+ and f^- dipole and quadrupole frequencies only differ by $2f_s$ and $4f_s$ respectively, $Z(f^+)$ and $Z(f^-)$ are approximately equal. As a result there is damping of the 862 MHz LCB oscillation for six bunch fills. This was evident from a comparison of the current thresholds for the 862 MHz LCB for 5 bunchs and 6 bunches. With the XRF3 tuner set to 4.51 V, the 862 MHz LCB instability threshold occured below 50 mA for 5 bunches. However, it was not observed on the stripline signal or on an XRF3 monitoring loop signal at the maximum six-bunch current of 240 mA.

6 CONCLUSION

It has been demonstrated that the 862 MHz HOM in the XRF2 and XRF3 cavities cause LCB oscillations with associated increases in longitudinal and transverse beam dimensions. Antennae have been successful in damping this mode in the XRF1, XRF2, and XRF4 cavities. A strong 862 MHz HOM remains in XRF3. Up to this point, the XRF3 tuner range has been adjusted so that the LCB induced by this HOM occurs at a tuner position traversed early in the fill to minimize its impact on user experiments. Longitudinal feedback measurements have been undertaken to study the feasibility of damping this mode, and the possibility of reconfiguring the XRF3 damping antennae will also be considered.

7 REFERENCES

[1] M.G.Thomas, et.al.,"NSLS X-Ray System RF System Upgrade", Proceed. of 1993 PAC, p1419 (1993).

[2] S.L.Kramer, et.al.,"Bunch Current Density Measurements in the VUV Light Source", Proceed. of 4-th EPAC, p1696 (1994).

[3] J.Safranek, and P.M.Stefan,"Emittance Measurement at the NSLS X-Ray Ring", Proceed. of 1996 EPAC, (1996).

AGS SLOW EXTRACTED BEAM IMPROVEMENT*

I. Marneris, G. Danowski, J. Sandberg, A. Soukas
Brookhaven National Laboratory, Upton, New York 11973 USA

Abstract

The Brookhaven AGS is a strong focusing accelerator which is used to accelerate protons and various heavy ion species to an equivalent proton energy of 29 Gev. Since the late 1960's it has been serving high energy physics (HEP - proton beam) users of both slow and fast extracted beams. The AGS fixed target program presently uses primary proton and heavy ion beams (HIP) in slowly extracted fashion over spill lengths of 1.5 to 4.0 seconds. Extraction is accomplished by flattoping the main and extraction magnets and exciting a third integer resonance in the AGS. Over the long spill times, control of the subharmonic amplitude components up to a frequency of 1 kilohertz is very crucial. One of the most critical contributions to spill modulation is due to the AGS MMPS. An active filter was developed to reduce these frequencies and it's operation is described in a previous paper [1]. However there are still frequency components in the 60-720 Hz sub-harmonic ripple range, modulating the spill structure due to extraction power supplies and any remaining structures on the AGS MMPS. A recent scheme is being developed to use the existing tune-trim control horizontal quadrupole magnets and power supply to further reduce these troublesome noise sources. Feedback from an external beam sensor and overcoming the limitations of the quadrupole system by lead/lag compensation techniques will be described.

1 THEORY OF OPERATION

Slow extraction from the AGS is accomplished on the 26/3 third order resonance. A set of four sextuples arranged in a +,-,+,- configuration excites the resonance just after the AGS Main Magnets are flattoped at the desired energy. The beam horizontal and vertical tunes, average radius, chromaticity and skew parameters are set to nominal values. The beam momentum spread is adjusted by RF phase-back and at RF turn-off the beam is effectively debunched. The debunched beam is brought to extraction radius by slightly sloping the flattop of the MMPS. The extracted beam orbit is set by local orbit deformations and by three (3) stages of septa comprised of electrostatic, thin copper magnetic, and thick copper magnetic ejection. Extraction is accomplished in the horizontal plane. Once the extracted beam is established, a (secondary emission chamber C10SEC) intensity signal is used for measurement and for analog feedback to a slow spill servo loop that dynamically adjusts the MMPS flattop. Since the AGS MM time constant is 3.0 seconds, it has a corresponding load breakpoint frequency of 0.05 Hz and thus can do a good job of average spill rate and length control and very little for higher frequency components.

2 CORRECTION SYSTEM DESIGN AND RESULTS

The AGS includes a set of 12 horizontal, tune-trim quadrupoles (QH), one per superperiod, that program the fractional tune of the machine during injection, acceleration and extraction. An equivalent set of 12 is used for the vertical plane. The magnets are laminated and have a small number of turns/pole to reduce their inductance. They are installed outside the vacuum with a 6 inch, 0.063 inch wall, stainless steel round vacuum pipe. The 12 magnets are connected in series to a single, bipolar power supply (PS). The string inductance is 18 millihenry, and the resistance is 0.2 ohms. The PS is a wide-band, switchmode type with a basic switching frequency of 44 kHertz. It includes a DCCT-sensed current feedback loop and a passive LC output filter. For our application, a wide band voltage loop within the current loop was implemented with the idea of feeding back the beam harmonics 180 degrees out of phase, to try to cancel them out. The beam harmonics were measured from the external beam sensor C10SEC. It was also essential to normalize the beam harmonic components to the averaged beam intensity because the amplitude of the harmonics changes with beam intensity variations. A lead/lag compensation was implemented to ensure stability and a bandwidth of 2 kilohertz of the system open loop transfer function. The normalized beam harmonics were then fed back to the lead/lag compensated voltage loop of the QH PS. It should be stated that the QH PS is 600 to 700 feet away from the beam harmonics signal of the C10SEC external beam sensor. As a result it was essential to split the electronics

* Worked performed under the auspices of the U.S.D.O.E.

of the lead/lag network in the two different locations. For the purpose of this paper we will refer to location A as the location of the beam harmonics signal, and location B as the location of the QH PS. **Fig 1.** is the signal flow graph of the overall system.

$G1(s)=\frac{G7(s)}{1+G7(s)\cdot H7(s)}$ is the measured voltage closed loop transfer function of the horizontal quadrupole power supply.

G2(s) is the transfer function of the lead/lag compensation network at location B.

G5(s) is the measured transfer function of the normalized beam harmonics at location A, versus the actual voltage output of the QH magnet PS monitored at location A.

G6(s) is the transfer function of the lead network at location A.

$G3(s)=G1(s)\cdot G2(s)\cdot G5(s)\cdot G6(s)$ is the system open loop transfer function.

$G4(s)=\frac{G3(s)}{1+G3(s)}$ is the system closed loop transfer function.

V1(s) is the zero reference to our overall system to minimize the harmonics, fed at location A.

V2(s) is the normalized beam harmonics at location A.

FIG 1.

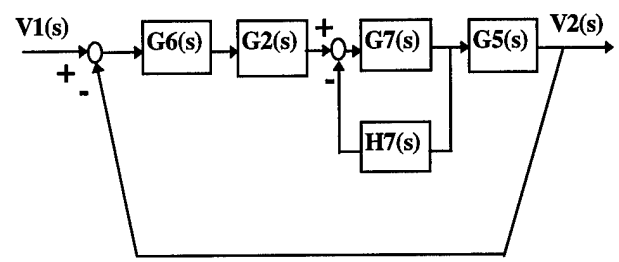

Y1(f), is the gain in (db) and **P1(f)** is the phase in (degrees), of the measured voltage closed loop transfer function **G1(s),** of the QH PS. See **FIG. 2 and FIG. 3.**

Y5(f), is the gain in (dB) and **P5(f)** is the phase in (degrees) of the measured transfer function of the normalized beam harmonics **G5(s)** at location A, versus the actual voltage output of the QH PS monitored at location A. See **FIG. 2 and FIG. 3.**

Y7(f), is the gain in (dB) and **P7(f)** is the phase in (degrees), of the open loop transfer function **G1(s)*G5(s)** without a phase lead/lag. See **FIG. 4 and FIG. 5.**

Y8(f), is the gain in (dB) and **P8(f)** is the phase in (degrees), of the overall lead/lag compensation transfer function **G2(s)*G6(s),** at both locations A, B. See **FIG. 4 and FIG. 5.**

Y3(f), is the gain in (dB) and **P3(f)** is the phase in (degrees), of the system open loop transfer function **G3(s)** including the lead/lag compensation network. See **FIG. 4 and FIG. 5.**

Y4(f), is the gain in (dB) and **P4(f)** is the phase in (degrees), of the system closed loop transfer function **G4(s).** See **FIG. 6 and FIG. 7.**

The results of this control system are shown in **FIG. 8.** **Mr,2** is the normalized beam harmonics (C10SEC) in percent at location A, without the implementation of this new control system. **Mr,1** is the normalized beam harmonics **(C10SEC) in percent** at location A, with the implementation of this new control system. Note that we were able to correct the harmonics by a factor of 2 to 4 from 60 Hz to 720 Hz. The data shown **in FIG. 8 were taken on 1-27-97** during our heavy ion run. The lead/lag compensation used at the time was not exactly the one shown in **FIG. 4.** The new one was improved to eliminate oscillations **at 1080 Hz** and to increase the improvement of the **C10SEC harmonics over the band of 120 Hz to 720 Hz.**

FIG 2. GAIN PLOTS

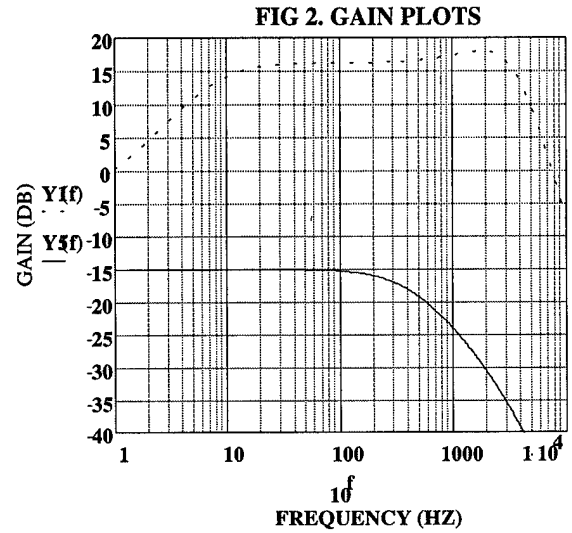

FIG. 3 PHASE PLOTS

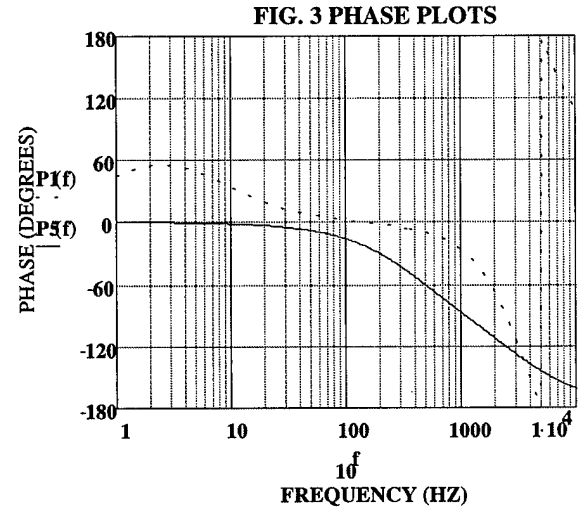

FIG.4 GAIN PLOTS

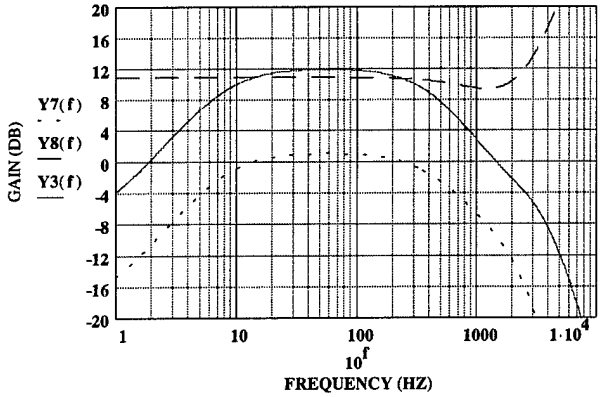

FIG. 5 PHASE PLOTS

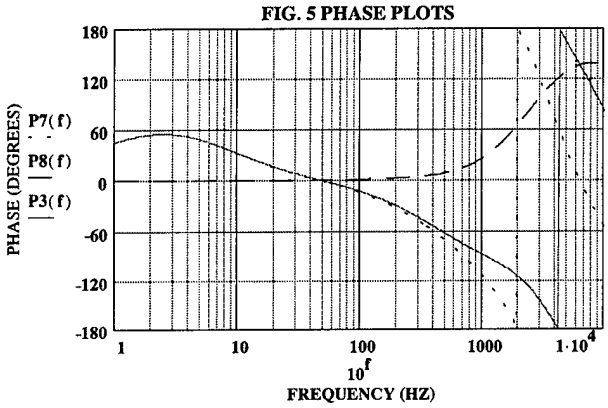

FIG. 6 GAIN PLOTS

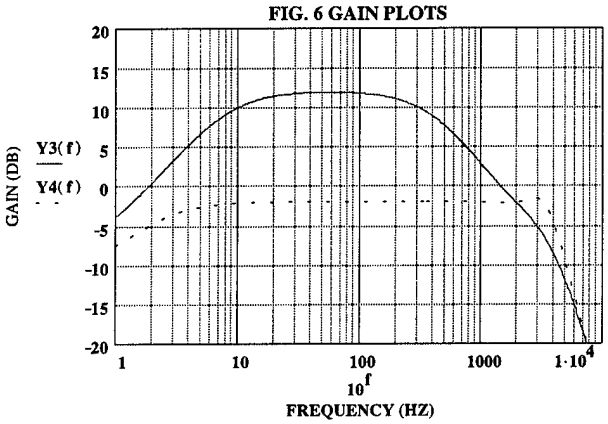

FIG. 7 PHASE PLOTS

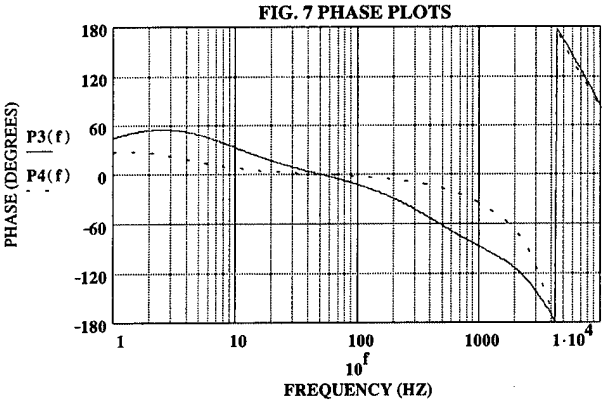

FIG. 8 RESULTS

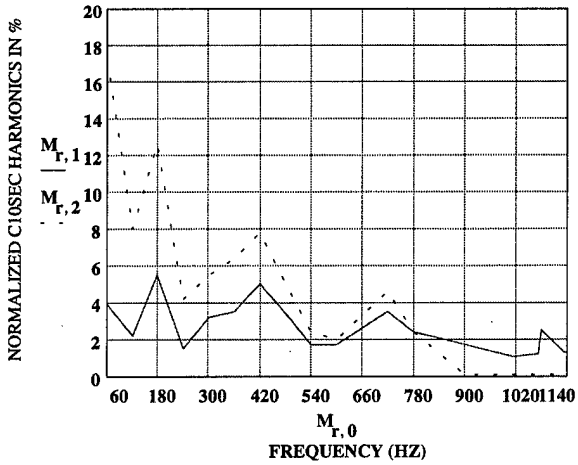

3 FUTURE PLANS

The results on **FIG. 8** show a small oscillation at **1080 Hz**. This is because the phase of the open loop transfer function **G3(s)** is more than 180 degrees, at this frequency. Design modifications were made to the lead/lag transfer function **G2(s)*G6(s),** to ensure stability and maintain the open loop gain. This is one of the reasons we decided to split the lead/lag compensation in the two different locations, A and B, mentioned above. As a result we will retest our correction system one more time with the proton slow extracted beam, to ensure we can get a **factor of 4** correction on the harmonics from **60 Hz to 720 Hz** without any oscillations at the zero dB point of the open loop gain **Y3(f).**

4 ACKNOWLEDGMENTS

The authors wish to thank W. Eng for his engineering support of the power supply. We also thank R. Bonati, M. Bannon, S. Savatteri and J. Funaro for their technical support in this project.

REFERENCES

[1] The active filter voltage ripple correction system of the brookhaven ags main magnet power supply. (WAR11) 1995 Particle Accelerator Conference.

RF CONTROL SYSTEM FOR THE SC CAVITY OF THE TESLA TEST FACILITY INJECTOR

A. Mosnier, S. Chel, B. Phung Ngoc, J.M. Tessier
CEA/DSM, CEA-Saclay, 91191 Gif-sur-Yvette Cedex, France

Abstract

The superconducting cavity of the TTF injector, which operates in pulsed mode, must accelerate the non relativistic electron beam to an energy of 10 to 15 MeV. Lorentz forces and microphonics detunings are the major sources of cavity field fluctuation. In order to achieve amplitude and phase stabilities much smaller than 10^{-3} and 1 degree, an analog feedback system, mainly based on a self excited loop and I/Q modulators, has been developed. After a description of the RF control module, various measurements without and with beam are reported.

1 INTRODUCTION

The SC cavities in the TESLA Test Facility have to operate in pulsed mode at high gradients, each klystron driving 16 cavities. Although the capture section consists in one single standard 9-cell TESLA cavity, driven by a 300 kW klystron, the main issues for the RF feedback system, namely Lorentz force within the beam pulse detuning, microphonics pulse-to-pulse detuning, except calibration of the vector sum, needed for a multiple cavities RF drive, have been successfully tested with beam, in agreement with the expected dynamic behaviour. It can be shown [1] that the beam energy spread can be kept much below the 10^{-4} level and without excessive extra power, assuming the following precautions have been taken [2]:

1. due to Lorentz forces, the RF generator must track the varying cavity frequency during the filling time, and the cavity must be pre-detuned, such that operating frequency and cavity frequency are approximately equal at half the beam pulse, giving minimal amplitude and phase errors when the loops are opened
2. due to microphonics, the phase feedback loop must be closed during the filling time, following a pre-determined phase law $\phi(t)$, to ensure minimum RF power requirements

Although a digital RF control system is certainly better suited for large scale SC linacs, an analog system was chosen for the capture cavity, because of simplicity for one module and of swiftness to bring into operation.

It is worthwhile noting that for the capture cavity, where the beam is running off-crest, the pre-detuning must be re-adjusted for compensation of the cavity detuning caused by the reactive component of the beam loading. By integration of the dynamics equations in the longitudinal plane, an average phase shift of about -30 degrees with respect to the RF wave is found for an accelerating field of 15 MV/m and an injection energy of 250 keV, resulting in a net beam detuning of almost 200 Hz. Fig. 1 shows for example the development of the field phase error during the RF pulse, when only the amplitude feedback loop is closed. Without beam, the pre-detuning Δf is set to its optimal value +80 Hz for a Lorentz force detuning parameter K = 1 Hz/(MV/m)^2 and a mechanical cavity time constant τ_m = 1 mS. With beam, if Δf is kept to the same value (+80 Hz), the phase error grows continuously and reachs large value at the end of the pulse, leading to non optimal performances once all the loops are closed. Conversely, if Δf is re-adjusted to take into account the off-crest beam effect (+80 -200 = -120 Hz), a small phase error is then recovered. For optimal performance of the capture cavity RF control, we conclude that it is essential to set the proper pre-detuning, sum of the Lorentz force and beam detunings, when the beam is on.

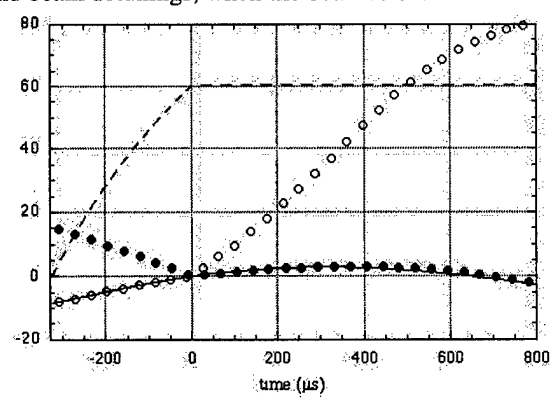

Figure 1 : Cavity phase (in degrees) a)without beam Δf = 80 Hz (solid line), b)with beam Δf = 80 Hz (empty circles), c)with beam Δf = -120 Hz (solid circles)

2 LOOPS DESCRIPTION

The RF control is based upon a self-excited loop, which ensures the cavity frequency tracking during the filling time (see Fig. 2). The attenuator sets the operating field amplitude, whereas the phase-shifter cancels out the phase shifts due to cables and components. The field vector is controlled by means of an I/Q modulator.

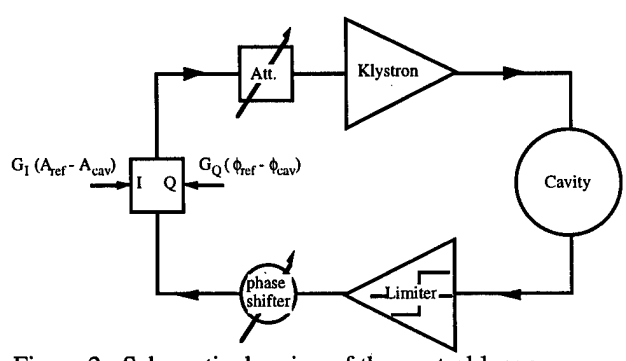

Figure 2 : Schematic drawing of the control loops.

Since the main perturbations come from cavity detuning (Lorentz forces, microphonics), the injection of an out-of-phase signal by the modulator will compensate automatically phase and amplitude of the field. The starting phase of the self oscillator is fixed by simply injecting a very low level reference signal. A klystron phase loop (not drawn on the figure), including a phase modulator, has been added to compensate any phase shift of the klystron. While the in-phase loop is closed just before the beam pulse, the out-of-phase loop is closed from the beginning of the RF pulse, otherwise the pulse to pulse detuning due to microphonics would give rise to large phase jitter, just when the beam is coming. The phase setting is of course a time varying signal, which is fixed to the average of previous measurements during the cavity filling and to zero during the beam pulse.

3 HARDWARE

The low level RF system has to fulfill different purposes:

- to set up the RF field in the resonator
- to stabilize amplitude and phase of the field by means of feedback loops
- to provide different informations, as reflected and transmitted power, field errors, etc

The gain cross-over frequency is about 25 kHz of the open loop transfer functions, mainly determined by the pole of the cavity. The bandpass RF filter and video notch filter (damping the nearest parasitic mode) contribute to a phase shift of 10°. Besides the resonator pole, the higher frequency poles (BW>1MHz RF components, cables, error amplifiers) give the minimal phase shift at the gain cross-over frequency. For the desired specifications of steady state error magnitude and degree of stability during the beam time, loops gain is held higher than 40 dB with a phase margin of 80° (Fig. 3).

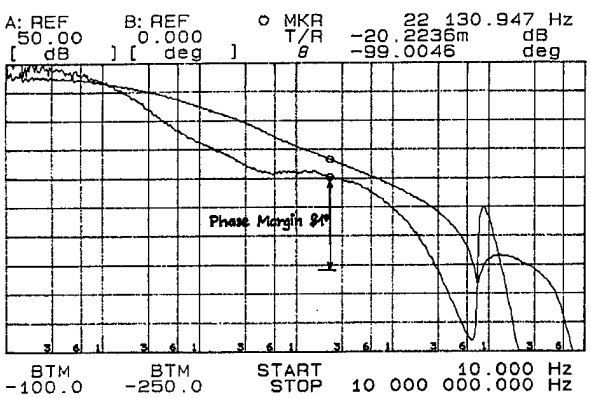

Figure 3 : Open-loop transfer function

The most important RF component is the CPM (Complex Phase Modulator), which has three different applications in this low level RF system :

- to provide continuous 360° unambiguous phase shifts for the self excited loop, for the phase setting of the RF field at the beginning of the pulse and for the global phase setting with respect to the beam.
- to control the cavity field through the I and Q ports. The I-ports behaves as a constant phase amplitude modulator (Fig. 4), while the Q-port behaves as a variable amplitude modulator (Fig. 5), ensuring a nearly total decoupling between the two feedback loops.

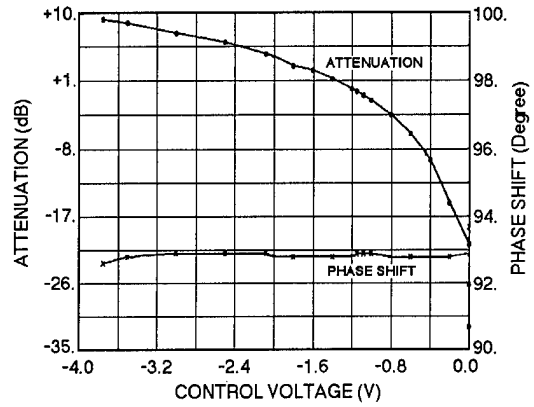

Figure 4 : CPM port I control

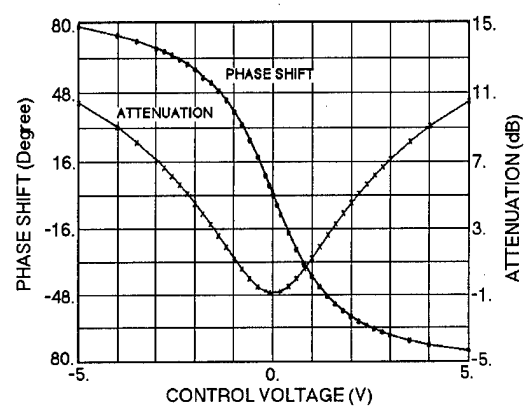

Figure 5 : CPM port I control

In order to suppress the strong modulation, which can be generated through the self excited loop by the $8\pi/9$ mode of the cavity, a RF bandpass filter (centered on 1302 MHz with a BW of ±2 Mhz) has been inserted at the cavity output and audio notch filters have been added in the feedback loops, giving a total attenuation of this parasitic mode of 43 dB. The reactive RF peak power has also been limited, in order to avoid high RF power peaks and over-oscillations for equivalent phase errors of 25°.

4 SOFTWARE

The operation of the RF feedback system is controlled by EPICS routines. The first goal is to tune correctly the different loops : to search for the right phase of the self excited loop while keeping klystron phase shift constant during the RF pulse, to search for the minimum error between the reference and the field amplitude, to reduce the field phase error at the beam injection time and to adjust the phase setting during the cavity filling. They have also to insure a survey while the system is running : monitoring of the control voltages of the loops, and re-adjustment, if necessary, of the frequency of the cavity, by minimizing the reactive RF power. All parameters and measurements, needed for remote-control, can be reached from a main control panel (Fig. 6).

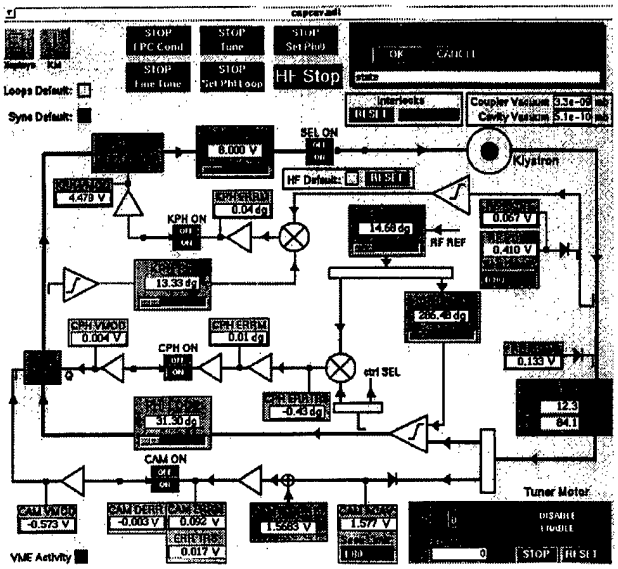

Figure 6 : Main control panel open to operators

5 RESULTS

Most of the tests at DESY in February 1997 on the TTF capture cavity have been performed at an accelerating gradient of 12.5 MV/m, first without beam and last with a beam current of 6 mA.

5.1 Without beam

The optimal cavity tuning, giving minimal phase error fluctuation during 800 µs after the filling time, was first searched. The time varying phase reference was then adjusted, in order to match the cavity phase variation during the filling time. Fig. 7 shows the different relevant signals, recorded from a digital oscilloscope. The incident RF power decreases suddenly after the filling time to about one quarter of its initial value, because there is no beam load. The field amplitude and the time varying phase reference, reversed signal of the cavity phase can also be seen. Only a small amount of extra RF power was needed to stabilize the cavity phase. The loop gains have been set to 200 for the I-loop and to 100 for the Q-loop, with a sufficient phase margin of 80°. Fig. 8 shows a zoom on the phase error, which looks well behaved when the pre-detuning has been properly set. With 0.6° per square, we deduce a phase fluctuation lower than ± 0.1° , while the amplitude fluctuation was measured lower than $\pm 4\ 10^{-4}$ during the flat top.

5.2 With beam

The same measurements were made with an accelerated beam current of about 6 mA. Unfortunately, the pre-detuning was not corrected to take into account the beam detuning effect. A zoom on the field phase (Fig. 9) reveals clearly the incorrect cavity tuning. Nevertheless, and thanks to the efficiency of the feedback loops, amplitude and phase errors are found about identical to the previous ones, without beam : $\pm 4\ 10^{-4}$ peak-to-peak, for the amplitude and ± 0.1° peak-to-peak for the phase. These fluctuations come mainly from high frequency noise, which would be uncorrelated from cavity to cavity and then would result in much lower beam energy spread.

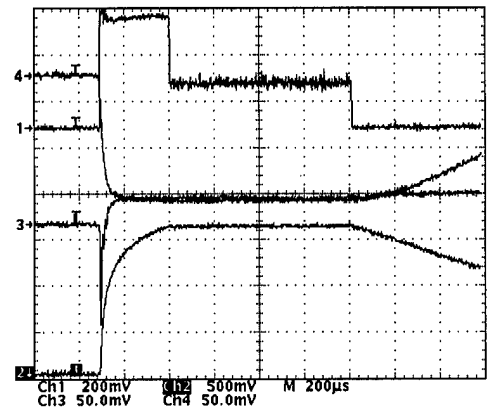

Figure 7 : Without beam, incident power (trace 1), field amplitude (2), field phase (3), phase reference (4)

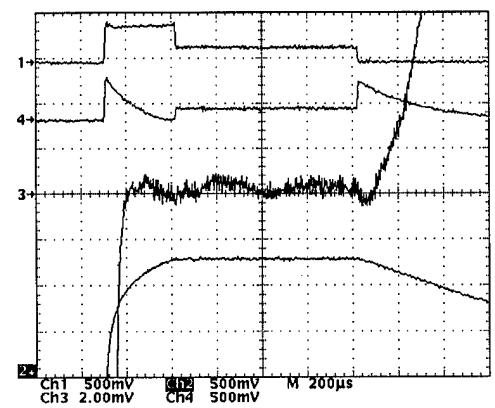

Figure 8 : Without beam, incident power (trace 1), field amplitude (2), field phase (3), reflected power (4)

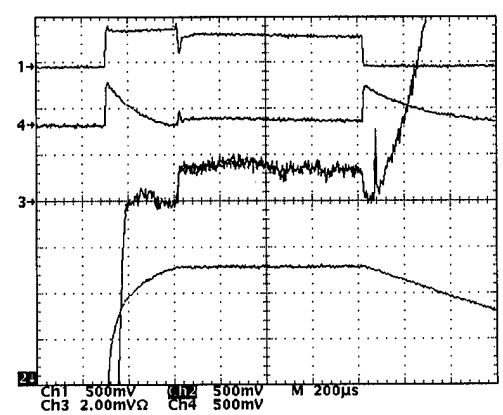

Figure 9 : With beam, incident power (trace 1), field amplitude (2), field phase (3), reflected power (4)

REFERENCES

[1] 'Stabilisation de champ dans des cavités supraconductrices en régime pulsé', J.-M. Tessier, Ph-D thesis, 1996.

[2] 'Energy Spread Sources in TESLA and TTF', A. Mosnier and J.-M. Tessier, TESLA report 95-5

[3] 'Design of the Digital RF Control System for the TESLA Test Facility', S. Simrock et al., Proc. of the 1996 European Part. Acc. Conf., Sitges.

EMITTANCE PRESERVATION IN THE PS COMPLEX

B. Autin, L. Giulicchi, A. Jansson, M.Lindroos, A. Lombardi, M. Martini, K. Schindl
CERN, CH-1211 Geneva 23, Switzerland

Abstract

As the LHC injectors have to provide bright beams, all the potential sources of emittance blow-up must be eliminated. One such source arises from the mismatch of the betatron focusing at the interface of a transfer line with a circular machine. Measurements and corrections of this effect have been performed in the line downstream of the linac where space charge plays an important role and between the booster and the PS ring where four beams are recombined and have to be matched simultaneously.

1 INTRODUCTION

Emittance preservation is a subject of concern for many high energy machines. In the case of the CERN PS complex, the most severe tolerances are imposed by the LHC beam. A program has therefore been set-up to investigate the sources of beam blow-up and to measure and correct the emittance with the required precision. The LHC injector chain consists of a total of four accelerators: linac, booster, PS and SPS. The tolerance on the beam size blow-up measured at 1 σ is smaller than 20% at the end of each of the accelerators. In a given linear machine and at low space-charge, the normalized emittance is a constant of the motion as far as external fields are concerned and can only be affected by instabilities. At the interface between two machines, the emittance may increase if the injection trajectory is not tangent to the closed orbit and if the focusing of the transfer line does not match the focusing of the accelerator. The first mechanism produces an oscillation of the centre of gravity of the beam; this is the problem of coherent oscillations [1]. The second effect produces a beam envelope oscillation and is the subject of this paper.

2 THEORETICAL BACKGROUND

A focusing error related to a quadrupole field can be treated within the general framework of first order perturbations. The position x and its derivative with respect to the curvilinear abscissa s are replaced by new normalised variables

$$q = \frac{x}{\sqrt{\beta}} \qquad \dot{q} = \frac{dq}{d\mu} \tag{1}$$

where β is the β-function at the point of abscissa s and μ the betatron phase advance at the same point. The betatron motion is thus described by a harmonic oscillator whose motion in phase space is a circle of radius the square root of the emittance, ε.

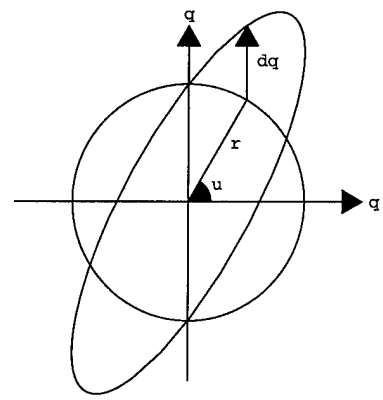

Figure 1: Effect of a quadrupolar error in the normalized phase plane.

A magnet of infinitesimal length ds and of focusing error k at a point of phase μ produces a kick

$$d\dot{q} = k\beta q \, ds \tag{2}$$

This kick changes the betatron emittance, considered not as the area of the ellipse but as a measure of the oscillation amplitude, and the phase of each particle by the quantities

$$d\varepsilon = 2\dot{q}\, d\dot{q} \qquad d\mu = \frac{q\, d\dot{q}}{\varepsilon} \tag{3}$$

whose detailed form can be written

$$\frac{d\varepsilon}{\varepsilon} = \sin 2\mu k\beta \text{ ds} \qquad \text{d}\mu = \frac{1+\cos 2\mu}{2} k\beta \text{ ds} \tag{4}$$

After the kick, the circle is transformed into an ellipse (see Fig. 1). The total focusing error is given by the integral over s of the above expressions. The term independent of μ in the phase perturbation is not relevant in this context because it corresponds to a global rotation of all the particles and does not change the shape of the ellipse which is characterized by the vector:

$$V = \int_0^L \begin{pmatrix} \sin 2\mu \\ \cos 2\mu \end{pmatrix} k\beta \, ds \tag{5}$$

where L is the length of the transfer line. The quadrupoles act in the horizontal and vertical planes simultaneously and the focusing error is corrected by minimizing the norm of

0-7803-4376-X/98/$10.00 © 1998 IEEE

the four-component mismatch vector

$$W = \int_0^L \begin{pmatrix} \beta_h \sin 2\mu_h \\ \beta_h \cos 2\mu_h \\ -\beta_v \sin 2\mu_v \\ -\beta_v \cos 2\mu_v \end{pmatrix} k\, ds \qquad (6)$$

The derivation of the vector W has been based on the classical action-angle perturbation theory. The mismatch can be measured [2] and expressed in terms of the Courant Snyder invariants characterized by β and α functions. The contribution of m discrete and local gradient errors, k_j, in quadrupoles (of length l_j at μ_j) to the α and β functions at a monitor (i) can be written as the sum over the m correctors

$$\begin{pmatrix} \frac{\Delta\beta}{\beta_i} \\ \Delta\alpha_i - \alpha_i \frac{\Delta\beta}{\beta_i} \end{pmatrix} = \sum_{j=1}^{m} \begin{pmatrix} k_j\, l_j \beta_j \sin 2(\mu_i - \mu_j) \\ k_j\, l_j \beta_j \cos 2(\mu_i - \mu_j) \end{pmatrix} \qquad (7)$$

where Eq. (7) can be derived from of Eq. (6).

The correction procedure, called Micado [3], is based on an iterative reduction of the norm of the residual vector. The correction matrix A has as many columns as correctors; each column is the mismatch vector W produced by a unit error; this error can be a focusing strength expressed in m^-2 or a current in Ampere. b is the measured mismatch vector at the interface between the transfer line and the machine. x is the unknown correction vector; at the first iteration, it contains one component attached to the best corrector; at the n-th iteration, the $n-1$ previous correctors are maintained, the best new corrector is chosen and all the corrections are recalculated. The procedure is stopped when the norm is limited by experimental errors.

3 LINAC LINE

The transfer line between linac and booster can be conceptually divided in three parts: the first part (from the output of the linac to the first bending) is space-charge dominated as the beam coming out of the linac is still strongly bunched (some 10 ° at 200 MHz); the second part (between the two bendings) is in a medium space-charge regime, and the third part (up to the last of two emittance measuring lines) is in a low space-charge regime as the beam is almost completely debunched. The matched input ellipse to the booster has been back-traced to the emittance measuring line defining slit where the matching is monitored. The matching is performed by the last four quadrupoles. The purpose of our work, which goes under the name of the Automated Beam Shaping (ABS) project, is the automatic correction of the transverse ellipse parameters at the defining slit.

The application of Micado requires the evaluation of the mismatch vector and correction matrix. The mismatch vector is derived by measuring the emittance of two consecutive cycles to acquire data on the horizontal and vertical planes and comparing it to the target value. The correction matrix represents the sensitivity of the mismatch vector components to small changes in quadrupole input currents.

Considering the limited accuracy introduced by space-charge effects, the evaluation of the quadrupole matrix is one of the most critical points in the application of the ABS procedure.

The evaluation of the matrix has been performed using two methods: the first method is to compute the sensitivity matrix using a beam dynamics model implemented in Trace 3D software tool [4] , the second by experimental measurements.

The matrix has been built by evaluating the mismatch vector components for $\pm 5\%$ change in the quadrupole currents, fitting them with a parabolic function and finally computing the derivative on the reference current value.

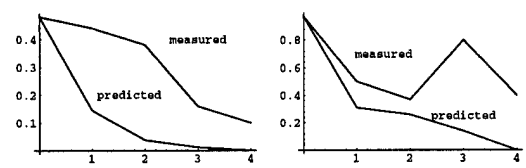

Figure 2: Theoretical and measured norms of the combined total mismatch vector in the linac line after compensation with 1, 2, 3 and 4 correctors.

In Fig. 2 the theoretical and the measured norm of the mismatch vector are shown. The norm has been reduced by a factor of five using four correctors. The correctors may be less efficient if the initial mismatch is big. Tests with a norm of the order of unity, clearly not within the scope of first order perturbations, could be nevertheless reduced by a factor of two using two correctors.

4 TRANSFER BETWEEN BOOSTER AND PS

4.1 Layout of the transfer line

To fill the CPS, the four PS booster beams are ejected sequentially. The present recombination scheme results in non-negligible differences in optical parameters for the four rings at the beginning of the common beam-line section [5]. A solution exists for curing these differences and it is likely to be implemented in the near future.

After the recombination, the beams ideally follow the same trajectory. From here the beam can be sent to different destinations, either ISOLDE, CPS or the PSB measurement line. The latter is equipped with three SEM-grids for transverse optics measurements.

4.2 Theoretical model

As space charge at 1 GeV is negligible for optics calculations an analytical package, *BeamOptics* [6], has been used for the modelling. An advantage with this analytical program is that it can directly generate the the correction matrices.

The inherent difference in the optics between the four booster rings gives a lower limit to the PS injection mismatch. If we try to minimize the mismatch for one of the beams, this will result in increased mismatch in the other beams. A better approach is to try to distribute this effect over the four beams as evenly as possible. This can

be achieved by putting the correction matrices for the individual beams together in a global matrix.

4.3 *Experimental results*

The correction method has been tested with positive results in the Booster measurement line. The measurements were made in the horizontal plane only, since the quadrupole settings for the line have to be different for horizontal and vertical measurements. The vertical correction was set to zero, i e the vertical mismatch vector was constrained not to change. The results for the correction, Fig. 3, show a significant reduction of the horizontal mismatch.

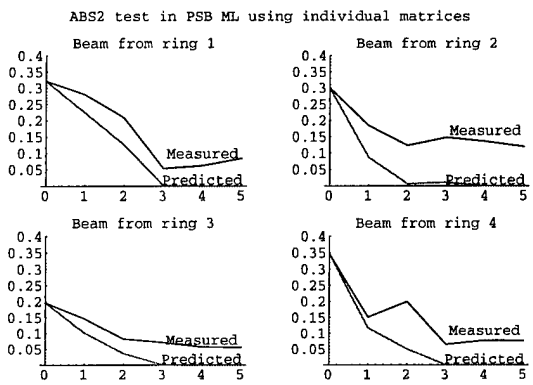

Figure 3: Results in the PSB Measurement line, using individual matrices. The absolute value of the horizontal mismatch vector is plotted as a function of number of correctors used.

Tests have also been performed in the PS ring, using three SEM-grids and a beam stopper. In this case both horizontal and vertical Twiss parameters can be measured with the same optics and it is possible to check if the correction is effective in both planes or not. The results are shown in Fig. 4.

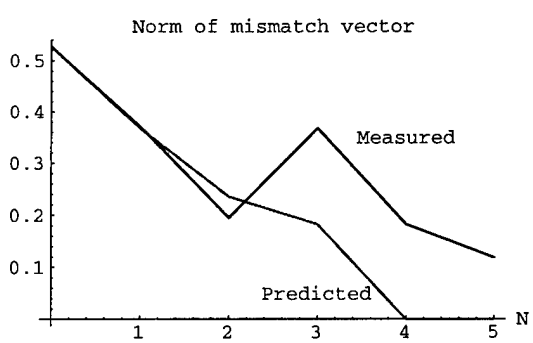

Figure 4: Results in the PS ring using up to 5 corrcetors in the booster-PS transfer line. The measurement was performed using beam from PSB ring three. The absolute value of the total mismatch vector is plotted as a function of number of correctors used.

5 CONCLUSIONS

The good general agreement between theory and measurements in the linac line, the booster measurement line and in the CPS ring confirms the validity of the approach to the problem of mismatch minimization. In the cases tackled, the initial mismatch was rather small, but there are indications that the procedure may diverge for larger values. It is possible to compensate for this by an iterative procedure where the initial mismatch is reduced with one or two correctors. The measurement is then repeated followed by new corrections. First tests of such a procedure show significant improvement of the convergence.

It should be stressed that the results presented here have been achieved using existing measurement software, offline calculated corrections, which were manually transferred to the quadrupoles. This procedure will be replaced in the near future by a dedicated, but generic software concerning machine part and type of correction. The method can then be made available for the daily work of maintaining the quality of the operational beams. Furthermore, the present very time consuming iterative procedure can be fully tested.

6 ACKNOWLEDGEMENTS

Many thanks to the TRIUMF laboratory for supplying the laminated quadrupoles for the linac line. Many thanks also to Michel Arruat and Olav Tungesvik of our division for prompt and highly reliable software support.

7 REFERENCES

[1] B. Autin, V. Ducas, A. Lombardi, M. Martini, E. Wildner: 'Automated beam optics correction for emittance preservation', Proc. LHC Workshop on LHC Injectors published by Particle Accelerators (1997).

[2] M. Martini, H. Schonauer: 'Emittance measurement', Proc. LHC Workshop on LHC Injectors published by Particle Accelerators (1997).

[3] B. Autin and Y. Marti, 'Closed orbit correction of AG machines using a small number of magnets', CERN ISR-MA/73-17.

[4] K. R. Crandall , 'TRACE 3-D documentation', Los Alamos Accelerator Code Group, LA-UR-90-4146

[5] A. Jansson and M. Lindroos: 'Mismatch between the PSB and CPS due to the present vertical recombination scheme', CERN/PS 97-14, Proc. LHC Workshop on LHC Injectors published by Particle Accelerators (1997).

[6] B. Autin, T. d'Amico, M. Martini, E. Wildner, 'Analytic lattice design with BeamOptics', These Proceedings.

OBSERVATION OF A LONGITUDINAL COUPLED BUNCH INSTABILITY WITH TRAINS OF BUNCHES IN CESR

Michael Billing*, Cornell University, Ithaca, NY USA

Abstract

A longitudinal coupled bunch instability has been observed in the operation of CESR with multiple trains of bunches. The instability threshold is dependent on the number of bunches per train and the spacing between those bunches. The threshold is also sensitive to parameters in the RF system leading to the conclusion that the RF cavities play a significant role in the dynamics. A summary of these observations is presented along with the design and status of a feedback system to stabilize the beams.

1 OBSERVATIONS

CESR has been operating as an electron-positron high energy physics collider using trains of bunches since February of 1995 [1]. Operating with nine trains of two bunches as the beam currents increased to above 230 to 250 mA in both beams, a reduction of the filling rate of the counter-rotating electron beam was first noticed as was an associated reduction of the vertical beam-beam tune shift parameter during collisions. These effects were traced to the growth of a self-limiting longitudinal coupled bunch dipole oscillation which increased the horizontal aperture required by the injected electrons and which caused the collision point of the bunches to oscillate about the minimum vertical beta point. The colliding beam vertical tune shift parameter continued to decline above 280 mA total current in both beams and the oscillation amplitude grew to be approximately a one sigma energy oscillation at 300 mA total current in both beams. This instability was also observed with either positron or electron beams separately; the following observations reported in this paper have been made with nine trains of equally populated bunches.

Above the instability threshold, observations of the frequency spectrum of a beam position monitor (BPM) showed the rapid growth of synchrotron sidebands of the rotation harmonics. Since the spacing between trains of bunches in CESR in nine train patterns is not uniform but has a three-fold symmetry, the amplitude of synchrotron lines above threshold tends to exhibit a three-fold periodicity at low frequencies and also at frequencies near one divided by twice the bunch-to-bunch time spacing within the train. The specific spectral lines which have amplitudes that grow most rapidly above the instability threshold depend on the number of bunches per train and the spacing of the bunches within the train. For a few bunch train patterns with positrons alone investigations were made using a BPM signal gated for individual bunches and comparing the relative phases of each of the bunches. As an example in the case of 9 trains of 2 bunches having a 28 ns spacing the bunches within a train have been observed to oscillate nearly 180 degrees out of phase with respect to each other, while in the case of a 42 ns spacing between bunches the phase difference between the bunches in the same train is nearer to 45 degrees. The rapid variation of the phase of the longitudinal oscillation between bunches in the same train is indicative of a high frequency mode or modes in one or more structures within the storage ring as being responsible.

The threshold current for the onset of the instability is a function of the number of bunches within a train and the spacing between the bunches within the train. In CESR the standard filling patterns allow the bunches within each train to be spaced in increments of 14 ns with up to 5 bunches permitted per train. Figures 1 through 3, respectively, show the instability threshold for the total stored current vs. bunch spacing for 9 trains of 2, 3 and 4 bunches per train for beams of positrons alone and for beams of both positrons and electrons in the standard horizontal electrostatically separated closed orbits (Pretzels) with a 2.4 mr half crossing angle at the interaction region. (N.B.. measurements with two beams and four bunches per train have not yet been made and in addition the configuration of 9 trains of 1 bunch is not longitudinally unstable.) The threshold current plotted in Figures 1 through 3 is the highest threshold current that has been measured for each set of bunch spacings; over long periods of time it has been observed that this threshold can vary downward by as much as 10-15%. From Figures 1 through 3 we see that there is more than a factor of two variation in the measured threshold currents for all the different bunch spacings within the nine trains and in some cases the threshold current more than doubles when the electron beam is stored indicating some cancellation of the RF fields with counter-rotating beams.

In addition to the instability current threshold depending on the number and spacing of bunches, it has been observed that there is a slight dependence on the amplitude of the Pretzel which extends around the entire circumference of CESR. After further investigation using horizontal bumps in CESR it has been observed that those bumps which displace the beam within the 500 MHz RF cavities are the major contributors to instability's dependence on Pretzel amplitude. For some bunch train patterns it was observed that changing the RF cavity temperatures by a few degrees C or changing the RF tuning angles on the order of 20 to 40 degrees can make very slight differences in the current threshold. Observations of beam induced RF signals on field probes in 16 of the 20 cells show the presence of a few modes in each cell in the frequency range of 1.8 to 3 GHz which have Q's in excess of 10,000. Modes with these high Q's have damping times for the RF fields which are 3 to 6

* Work supported by the National Science Foundation.

times the spacing between trains, easily permitting the wakefields to couple the motion of one train to the next. So the RF cavities must be considered to have at least a partial role in the dynamics which causes the present longitudinal dipole coupled bunch instability. Additional measurements indicate that the current threshold seems to be generally unaffected by changes in the synchrotron oscillation frequency or bunch length which is consistant with modes having frequencies less than 3 GHz.

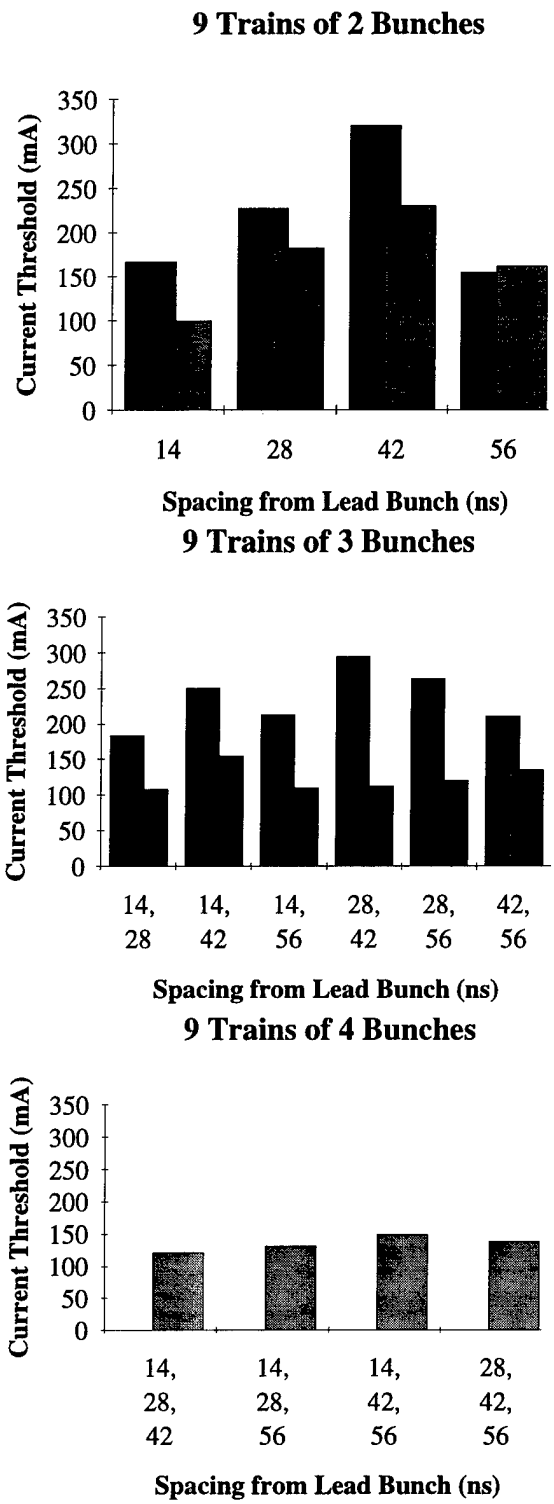

Figures: 1, 2 and 3. Current Threshold vs. Bunch Spacing for Various Numbers of Bunches per Train. Lighter bars are for single positron beam currents only and darker bars are for total current for both positron and electron beams.

Damping measurements for different coherent oscillation patterns of the trains of bunches have been made by exciting different synchrotron sidebands separately, modulating either the phase of an RF cavity or voltage on a stripline kicker and then allowing the motion to decay.[2] The signal from a beam position monitor (BPM) at a location of non-zero dispersion is viewed on a spectrum analyzer tuned to the coherent mode frequency in general yielding a decay which is not purely exponential. Although the decay of the BPM signal is not exponential, the decay envelope can be bounded above by an exponential curve; this curve is then used to give the characteristic damping rate for this synchrotron sideband. Measurements of several different synchrotron sidebands of single positron beams having different numbers of bunches and different spacings indicate that the natural damping rate at zero current is in the range of 200 to 900 sec^{-1} and the growth rate of the instability is between 1 and 9 sec^{-1} mA^{-1} depending on bunch pattern.

2 CURES

When this longitudinal coupled bunch instability was first encountered, CESR was operating with nine trains of two bunches having a 28 ns spacing. After learning that two bunches per train with a 42 ns spacing had a higher current threshold, the routine operation of CESR was changed to this bunch spacing. Since CESR has no longitudinal feedback cavities, the use of a transverse deflection from the horizontal stripline kicker (in routine use for horizontal feedback) which is located at a point with non-zero dispersion was determined to be a means of generating a path length change. This kicker is capable of independently deflecting bunches with as little as a 14 ns spacing allowing the creation of a bunch-by-bunch feedback system. A low noise phase sensitive detector has been developed to detect the energy-phase oscillation of each bunch. A prototype longitudinal feedback system has been assembled using this phase sensitive detector, the horizontal stripline kicker plus 150 MHz bandwidth RF amplifiers and digital processing electronics of the same type as is used with the transverse bunch-by-bunch feedback systems.[3] This feedback system was put into operation in February 1997 and it produces a damping rate of approximately 1.5 sec^{-1} mA^{-1} with the present feedback loop gain limited by noise and interference in the phase detection circuit. Although improvements of this phase detection circuit are underway to allow higher gain and damping rates, this prototype bunch-by-bunch longitudinal system has already permitted colliding beam operation with total two beam currents above 325 mA.

A final version of the longitudinal bunch-by-bunch feedback system is planned for operation beginning in the summer of 1997. In this design the linear RF amplifiers will be replaced by two FET pulsers each followed by a

transmission line impedance transformer; the combination of these is capable of delivering 14 ns long pulses of 1.5 KV into the 50 Ω stripline kicker. This more than ten times the peak voltage capability of the present RF amplifiers. To limit the power dissipation in the pulsers, the pulsers will operate at full amplitude and be modulated with a duty cycle proportional to a phase error signal when it exceeds a threshold level. Simulations of this feedback pulser configuration indicates this should function quite successfully and produce a linear damping of large amplitude oscillations (as compared to exponential damping for conventional proportional feedback systems.) A prototype pulser has been tested and the final design is in production. The digital processing electronics will also be replaced with a new design that incorporates such features as an internal steady state, bunch-by-bunch phase offset correction circuit to compensate for the bunches in the trains operating at slightly different phases due to beam loading of the RF system and a more sophisticated bunch-by-bunch digital filtering section to improve the signal to noise ratio. This feedback system should increase the damping rate by at least a factor of ten and should be capable of stabilizing total two beam currents in excess of the 600 mA CESR+ phase 2 and 1 A CESR+ phase 3 design levels.[1]

Plans are also underway to procure a low Q 1.1 GHz accelerating cavity as a longitudinal bunch-by-bunch feedback kicker. The cavity and RF amplifier is based on the design for a longitudinal feedback system for DAΦNE.[4] This configuration for CESR would simplify the horizontal and longitudinal feedback loops which presently share the same feedback kicker. This cavity is expected to be installed in CESR in the fall of 1997.

One other change to CESR which is likely to improve the longitudinal dipole coupled bunch instability threshold will be the installation of four single superconducting RF (SRF) cells over the next two years to replace the 20 normal conducting RF cells in the present RF system.[5] The loaded Q's of these cells are below 100 for all higher order modes. Since the present RF system contributes significantly to the total impedance of CESR and since it also is known to be an important source of the impedance which drives this instability, installing the entire SRF system will decrease the overall impedance of CESR and should likely increase the threshold current for this instability.

3 CONCLUSIONS

The longitudinal coupled bunch dipole instability that has been observed in the operation of CESR with multiple trains of bunches has limited the total colliding beam currents. With the installation of a prototype longitudinal bunch-by-bunch feedback system the instability threshold has been raised. An improved version of this feedback system should be capable stabilizing the total current in the two beams in excess of 1 A for CESR.

4 ACKNOWLEDGMENTS

I wish to gratefully acknowledge the work of my colleagues in the Operations Group at CESR who has contributed to our understanding of these phenomena and production of a longitudinal feedback system for CESR. I also wish to acknowledge the help of the CESR operators in these studies.

REFERENCES

[1] D. Rubin, "CESR Status", this conference.

[2] M. Billing, "Introduction to Beam Diagnostics", Fourth Annual Accelerator Instrumentation Workshop, Berkeley, CA, AIP Conf. Proc. No. 281, 72-3.

[3] J. T. Rogers et al, "Operation of a Fast Digital Transverse Feedback System in CESR", Proc of 1995 Part Acc Conf, (RAE14), 2426.

[4] R. Boni, "Experimental Tests of the DAFNE RF Feedback System", Proc of 1996 European Part Acc Conference.

[5] S. Belomestnykh, "Development of Supercon-ducting RF for CESR", this conference.

A DESIGN AND PERFORMANCE ANALYSIS TOOL FOR SUPERCONDUCTING RF SYSTEMS

T. Schilcher, S.N. Simrock, DESY, Notkestr. 85, 22603 Hamburg, Germany
L. Merminga, D.X. Wang, TJNAF, 12000 Jefferson Avenue, Newport News, VA 23606

Abstract

Superconducting rf systems are usually operated with continuous rf power or with rf pulse lengths exceeding 1 ms to maximize the overall wall plug power efficiency. Typical examples are CEBAF at the Thomas Jefferson National Accelerator Facility (Jefferson Lab) and the TESLA Test Facility at DESY. The long pulses allow for effective application of feedback to stabilize the accelerating field in presence of microphonics, Lorentz force detuning, and fluctuations of the beam current.

In this paper we describe a set of tools to be used with MATLAB and SIMULINK, which allow to analyse the quality of field regulation for a given design. The tools include models for the cavities, the rf power source, the beam, sources of field perturbations, and the rf feedback system. The rf control relevant electrical and mechanical characteristics of the cavity are described in form of time-varying state space models. The power source is modelled as a current generator and includes saturation characteristics and noise. An arbitrary time structure can be imposed on the beam current to reflect a macro-pulse structure and bunch charge fluctuations. For rf feedback several schemes can be selected: Traditional amplitude and phase control as well as I/Q control. The choices for the feedback controller include analog or digital approaches and various choices of frequency response. Feed forward can be added to further suppress repetitive errors. The results of a performance analysis of the CEBAF and the TESLA Linac rf system using these tools are presented.

2 INTRODUCTION

In the field of accelerator physics many sophisticated computer simulation codes have been developed in the past decades. They are mainly used to verify and optimize designs for the beam transport system but also codes for accelerator components such as magnets, rf cavities, and electron sources are readily available. There is however no sufficiently generic simulation code for the design of rf control systems available [1].

The authors of this paper have started the project of developing a generic rf system simulation code with emphasis on superconducting rf systems. This tool is to be used for the design and performance assessment of new or existing rf systems. The ultimate goal is a tool which supports on-line diagnostics during the commissioning phase and during routine operation of the rf system.

The tools make use of the high level programming language MATLAB and SIMULINK which are available at most accelerator facilties. MATLAB provides a natural environment for analysis, algorithm prototyping, and application development which is complemented with SIMULINKs graphical user interface for construction of block diagram models using "drag-and-drop" operations.

The rf system design and performance analysis tool is freely available via world wide web at "http://tesla.desy.de/rf_model/". The authors appreciate feedback from potential users of this software on their specific needs so that the tool can be made more universal. Presently the models have been used to study the rf systems at Jefferson Lab [2], the rf system for the TESLA Test Facility [3], the superconducting option for ESS and the recirculating linacs for the muon-collider.

3 CONCEPTUAL DESIGN

The concept of the rf system design tool is based on a combination of an interactive user interface with graphical blocks for rf sub-systems and initialization files for the

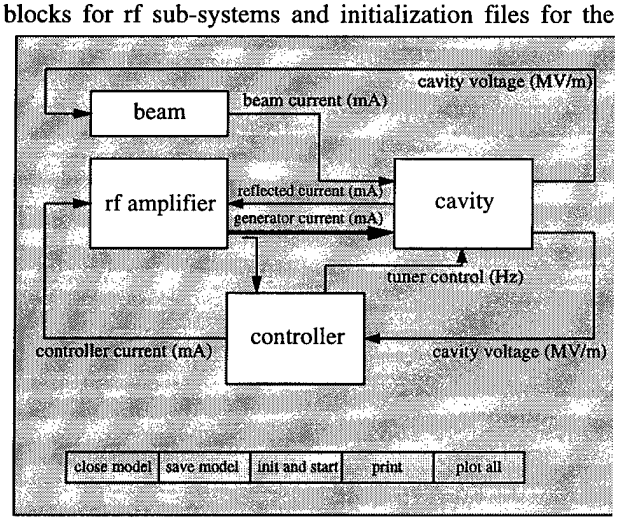

Figure 1: RF Sub-systems and interconnections at level 1

system parameters. The key features of the rf system design tool are:

- main blocks for major rf sub-systems
- fixed interconnection structure between sub-systems
- well defined interface between sub-systems
- multi-level tree structure within sub-systems
- separate initialization files for sub-system parameters

The main blocks and interconnection structure are shown in Figure 1. The rf amplifier which is modelled as a current source drives the rf cavity. The beam current is

0-7803-4376-X/98/$10.00 © 1998 IEEE

superimposed to the generator current with opposite phase. The cavity blocks calculates the response of the cavity to the two driving currents. The output of the cavity is the time-varying accelerating field in units of MV/m. In the controller block, the cavity gradient and phase are compared to the desired setpoints and the amplified error signal controls the generator current. Provision has been made to allow for cavity-beam-cavity interaction which is important for circular machines and recirculating, energy-recovering linacs.

3.1 Tree Structure

From the main panel the user can access the sub-systems. The controller block consists of the feed forward, the feedback, and the tuner sub-system control blocks which appear on level 3. The level below the sub-system level is user defined and it is planned to provide an extensive library of user defined blocks which describe actual rf system components.

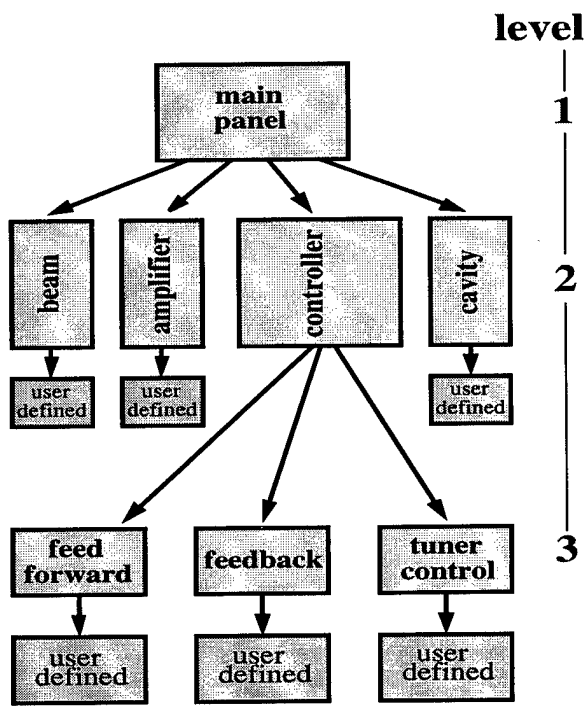

Figure 2: Tree Structure of the RF Simulation Tool

3.2 Files and Nomenclature

The rf system model consists of several m-files for the graphical blocks and the initialization files. The filenames include the project name and the block name. The following blocks must exist for a complete model:

- project.m
- project_cavity.m & project_cavity_init.m
- project_amplifier.m & project_amplifier_init.m
- project_feedforward.m & project_feedforward_init.m
- project_feedback.m & project_feedback_init.m
- project_tuner.m & project_tuner.m
- project_beam.m & project_beam_init.m
- project_plot.m

It is possible to mix blocks from several projects but is important that the block name and the corresponding initialization file match to ensure the correct setting of parameters.

4 RF SUB-SYSTEM BLOCKS

The rf sub-systems contain user-defined blocks with accompanying initialization files. These rf system specific blocks are added to a library which can be exchanged between various users since the interface between the sub-systems is well defined.

4.1 Beam

The beam can be modelled with arbitrary time-varying amplitude and phase as specified in a table. It is also possible to use pulse generators for a repetitive pulse structure and add a noise source to simulate bunch charge fluctuations. The beam library contains blocks for the cw beam at Jefferson Lab and the pulsed beam for injector I and injector II at the TESLA Test Facility.

4.2 Amplifier

It is possible use the measured non-linear characteristics of a klystron to create an input-output mapping table. The present klystron library contains a linear amplifier with a hard power limit.

4.3 Cavity

The use of superconducting cavities implies that Lorentz Force detuning and microphonics are included in the model. The state space representation of a cavity including Lorentz Force detuning is given by:

$$\begin{bmatrix} \dot{v}_r \\ \dot{v}_i \\ \Delta\dot{\omega} \end{bmatrix} = \begin{bmatrix} -\omega_{1/2} & -(\Delta\omega+\Delta\omega_T) & 0 \\ \Delta\omega+\Delta\omega_T & -\omega_{1/2} & 0 \\ -\frac{2\pi\cdot K}{\tau_m} v_r & -\frac{2\pi\cdot K}{\tau_m} v_i & -\frac{1}{\tau_m} \end{bmatrix} \cdot \begin{bmatrix} v_r \\ v_i \\ \Delta\omega \end{bmatrix} + \frac{R\omega_{rf}}{2Q} \cdot \begin{bmatrix} 1 & 0 \\ 0 & 1 \\ 0 & 0 \end{bmatrix} \cdot \begin{bmatrix} I_r \\ I_i \end{bmatrix}$$

where v_r, v_i : real and imaginary component of the cavity voltage ,
I_r, I_i : real and imaginary component of the total current (generator + beam)
$\Delta\omega+\Delta\omega_T = \omega_0-\omega_{rf}$, $\omega_0 = \omega_0(t)$: resonance frequency of the cavity ,
ω_{rf} : operating frequency , $\omega_{1/2} = \omega_{rf}/(2Q)$: half width of resonance ,
$\Delta\omega_T$: detuning by frequency tuner , τ_m : mechanical time constant ,
K : Lorentz force detuning constant .

The cavity library supplies a model for the cavities at Jefferson Lab and the TESLA Test Facility. For the TTF rf system a model of 8 cavities with different parameters including calibration errors for incident wave and vector-sum has been developed.

4.4 Controller

The Controller is composed of the subsystems feedback, feed forward, and tuner control. The feedback library includes model for amplitude and phase control and IQ control. It is possible to mix analog and digital design. In the digital design the possibility of the use of state

estimators is foreseen.

5 SELECTED SIMULATION RESULTS

5.1 TESLA Test Facility

RF System modelling is of great importance for the design of the TTF rf system since the vector-sum of 8 (later 16) cavities will be controlled in presence of Lorentz Force detuning, microphonics, and heavy beam loading. The model allows to predict the performance of the digital rf feedback system [3] in presence of parameter variations. The simulation results in Figure 3 show an attempt to operate the cavities at different gradient by variation of the loaded Qs. The simulation allows to monitor the maximum field in each cavity and optimize the system to operate close to the maximum operable gradients of each cavity.

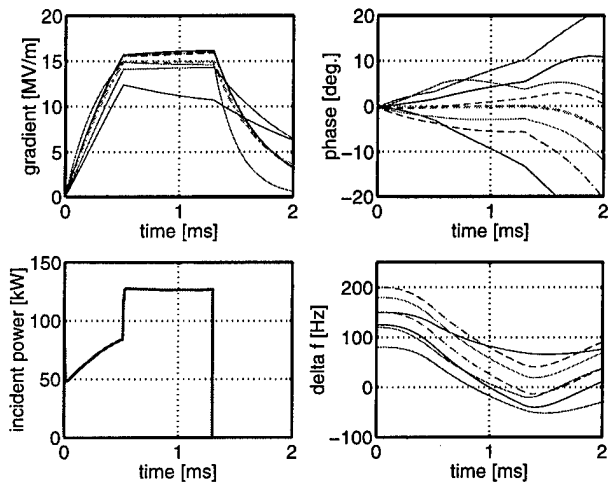

Figure 3: Operation of the TTF cavities at different gradients with different loaded Q and with 8mA of beam loading. The vector-sum is regulated to 15 MV/m.

5.2 Jefferson FEL RF System

A high average power Free-Electron Laser (FEL) is presently under construction at Jefferson Lab. The driver accelerator of the first phase of the FEL program, is a recirculating energy-recovering 42 MeV, 5mA cw superconducting rf electron accelerator.

The start up of the beam in the FEL is an interesting example of rf optimization as it must be done in a way that leaves the rf stable and robust, must be compatible with transport of space charge (and lack therefore) dominated beams and must be compatible with recirculation and energy recovery.

We have examined three different start up scenarios and we present here simulation results from one of them. In this scenario the average beam current is increased from 0 to 5 mA by first increasing the repetition frequency in factors of 2 at constant charge per bunch of 35 pC. When the beam repetition frequency reaches the operating frequency of 37 MHz, resulting in an average current of 1.3 mA, the current is further increased by linearly increasing the charge per bunch from 35 pC to 135 pC, for a total of 5 mA. Figure 4 displays beam current, amplitude and phase of the cavity fields as function of time, for the injector cavities with no energy recovery, and the linac cavities with energy recovery.

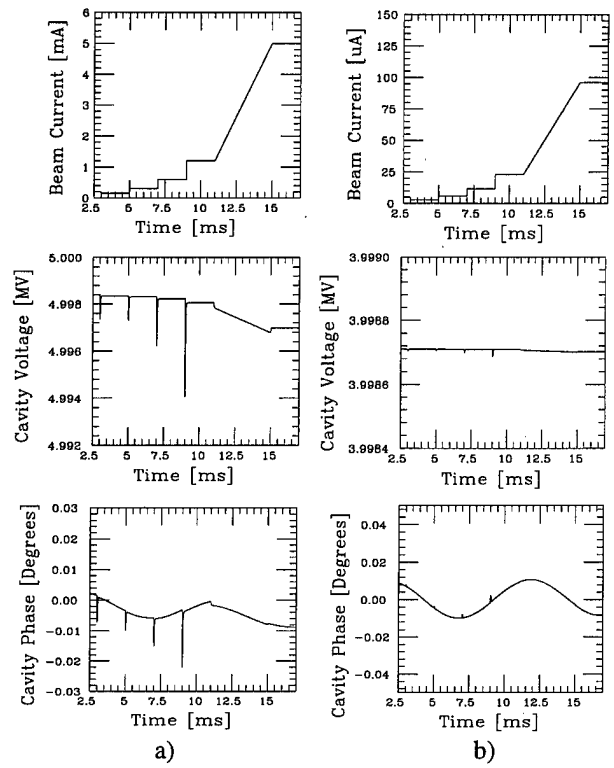

Figure 4: Jefferson Lab FEL RF system startup response in a) injector and b) linac.

6 CONCLUSION

An rf system design and performance analysis tool has been developed as a joint effort between DESY and Jefferson Lab. It has been successfully used to predict the performance of various rf system. The generic design of this tool allows its use for the simulation of a variety of different rf system with focus on superconducting cavities and relativistic beams. A well defined interface will allow the exchange of user defined sub-system blocks with the according initialization files among different users. This hopefully will help to reduce redundant efforts in rf system modelling in the future.

7 ACKNOWLEDGEMENTS

We gratefully acknowledge numerous helpful discussion with J.D. Delayen, L. Doolittle, and A. Gamp.

8 REFERENCES

[1] R. A. Jameson, EPAC 96, pp. 210-212
[2] L. Merminga et. al., EPAC 96, pp. 2079-2081
[3] S.N. Simrock et al., EPAC 96, pp. 349-351

OBSERVATION AND CURE OF LONGITUDINAL COUPLED-BUNCH INSTABILITIES IN THE FERMILAB MAIN RING

S. Assadi,I. Kourbanis, D. McGinnis, J. Steimel
Fermi National Accelerator Laboratory†
P.O. Box 500, Batavia, IL 60510, USA

Abstract

One goal of the Fermilab Main Ring accelerator during the Fixed target run is to keep the longitudinal beam oscillations as small as possible. It is found that when the proton beam intensity reaches a certain value, longitudinal beam oscillations rapidly grow. This motion can be explained by the longitudinal beam instability model. Installed active feedback system has successfully eliminated the instabilities and record intensities are achieved. We discuss the observations that indicate the damper systems are necessary. The results of the instability growth measurements are compared with a simple model.

1 INTRODUCTION

Longitudinal bunched beam modes and their electromagnetic interaction with the beam were first described by Sacherer [1]. For M equidistant bunches, there are M coupled bunch modes characterized by n-waves $0 \leq n \leq M-1$ around the storage ring. The theory of longitudinal bunched beam contain radial as well as within-bunch modes. Normally only the lowest radial and azimuthal modes are observed. This could be due to the fact that higher order modes are Landau damped. As mentioned, the interaction between charged particles and their environment, such as RF cavities, kickers and bellows can drive the beam unstable resulting in unwanted longitudinal coherent beam oscillations. These oscillations will cause the eventual growth in longitudinal emittance. Longitudinally, the beam is accelerated by two fields: One is externally powered in RF cavities, the other comes from the wake fields which are proportional to the beam intensities. For low intensities, the wake potential is small enough that its effect can be neglected. As the beam intensity increases, the wake potential produced by the frontal bunches in the RF cavities need to be considered in the particle equation of motion. In the Main Ring, the wake potential for the higher order cavity modes can reach several kV for a beam with 2E12 particles per bunch while the peak fundamental RF voltage is about 4MV per turn. By making comparisons, it is concluded that the observed beam behavior can be fully explained by a relatively simple simulation model. An active feedback system has reduced the 225 MHz signal associated with the longitudinal instabilities.

2 EXPERIMENTAL RESULTS

Data are collected by observing signals from a resistive wall monitor with a Tektronix 2 GHz digitizer. The digitizer is triggered every 32 turns to capture ~10 synchrotron period worth of longitudinal profiles of the bunches (Fig.1). The resulting time series is then broken up into 1000 realizations. Each realization contains the turn by turn data for each bunch which are then individually Fourier transformed. The phase shift $\Delta\varphi$ of the perturbing bunch motion with respect to a reference bunch is $2\pi n/M$. We can then infer the wake field structure by calculating the wavenumbers $k_n=\Delta\varphi_n/\Delta x$ (Fig.2).

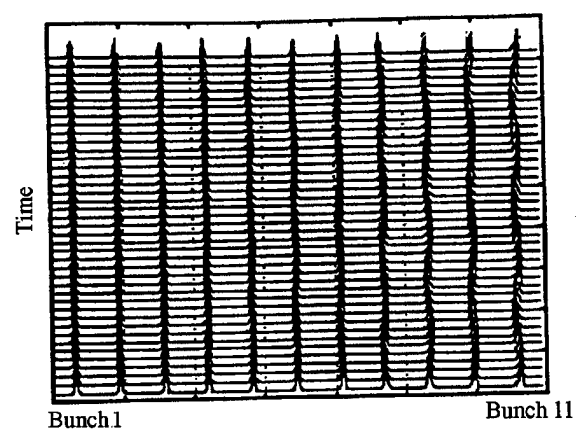

Fig.1) Waterfall plot of the first 11 bunches.

Another comparison can be made through the bunch length growth of both simulation and experiments with and

† Operated by the URA Inc.,under contract with the U.S. Department of Energy.

0-7803-4376-X/98/$10.00 © 1998 IEEE

without the dampers. With the assumption of a Gaussian distribution, the density function $f(\tau)=f_o\exp(-\tau^2/2\sigma_\tau^2)$ can be Fourier transformed. σ_τ is the width parameter of a standard Gaussian distribution. From the first and third harmonic line of the spectrum, one can obtain the bunch length. $\sigma_\tau = 1/(2\omega_{53})(f(\omega_{53})/f(\omega_{159}))$.Fig. 3 shows the growth of the bunch length as the instabilities develops.

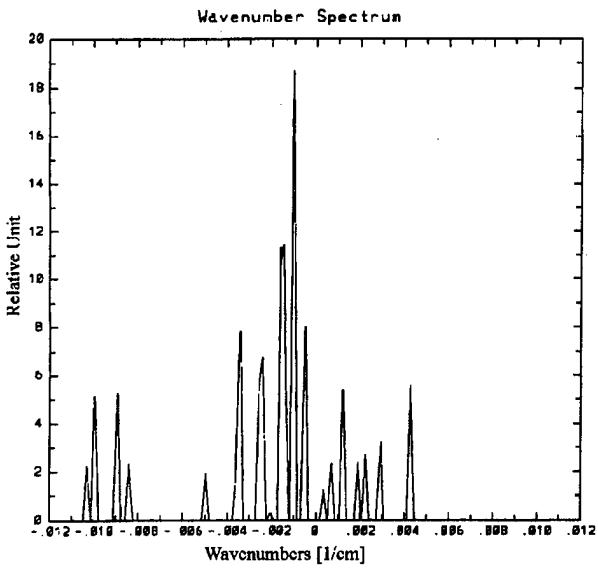

Fig.2) Measured two peaks associated with dipole and quadrupole oscillations between bunches 11 and 1 is shown.

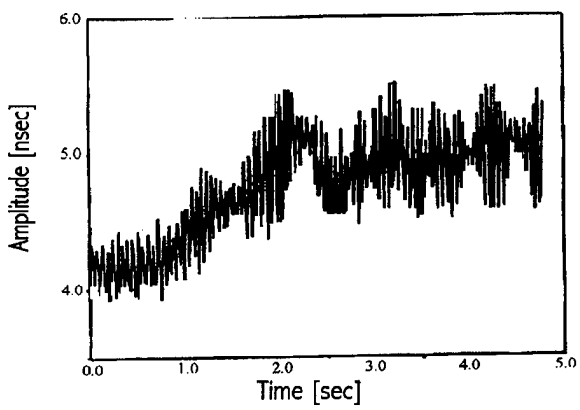

Fig.3) 150 Gev bunch length increases as the longitudinal coupled bunch instabilities occurs.

To understand the extend of short range wake fields, the beam is given an initial kick by a programmable digital phase shifter which shifts the phase of all 18 RF cavities by 20 degrees for 200 μsec (10 turns). The centroid position of each bunch can be found and compared with the unkicked case. The decay time τo for the oscillation is much longer than the bucket width (T_{RF}). The decay time for the higher order cavity modes can then be calculated. For example, the τ_{250} Mhz cavity mode is found to be ~.5μsec which is less than 21μsec revolution period but much larger than a bucket width .

3 SIMULATIONS

A simulation program similar to a simple resonator is written in MathWorks Simulink. Wake fields are accumulated continuously from bunch to bunch. Here 5 batches of 84 bunches are considered to be consistent with the experimental measurements. A Gaussian beam intensity distribution is assumed in the simulation. The bunch length for each bunch of 2e10 particles are calculated each turn. The bunch length of the 11th macro particle is shown in Fig. 4. As measured experimentally in (Fig.2) the wake potential is not proportional to bunch number. This is due to the fact that the higher order mode frequencies are not an integer number of RF. The vector addition of the induced electric field can be positive or negative, which leads to increase or a decrease in the oscillation of the centroid of the bunches (Fig.5,6).

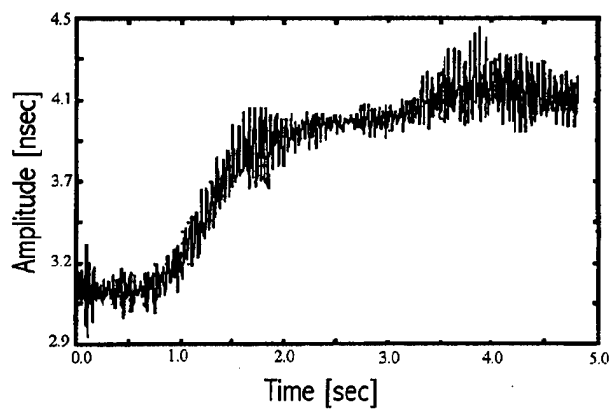

Fig. 4) Simulation of bunch length blowup vs Time.

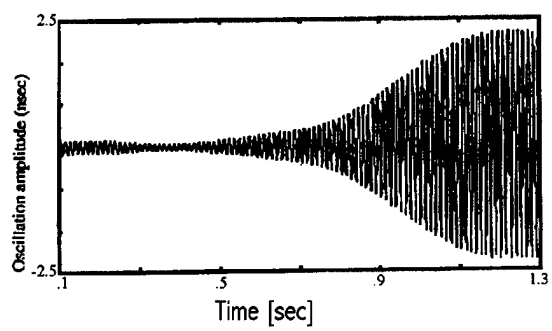

Fig.5) Simulation of 11th bunch centroid from bucket center. For the RF frequency of 53 MHz, 1 ns is equal to 19 degrees of phase.

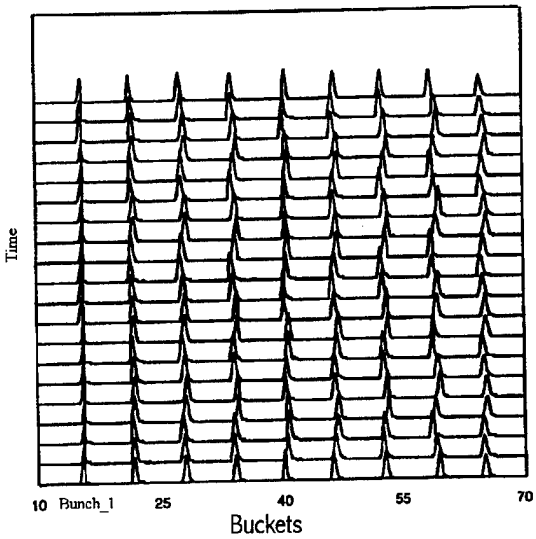

Fig.6) Waterfall plot of the simulated data after 1.3 sec shows the trailing bunches are affected by the cumulative frontal wake fields.

4 ACTIVE FEEDBACK

The *filter method* is used for longitudinal coupled bunch damping in the Main Ring. The longitudinal pickup and kicker together with specially shaped narrow band bandpass filter centered around revolution harmonic is used. The filter contain a notch centered exactly around the revolution harmonic. This notch serves the dual purpose of suppressing the unequal bunch line and providing a 180 degrees phase shift such that both upper and the lower sidebands are damped. Figures 7-9 shows

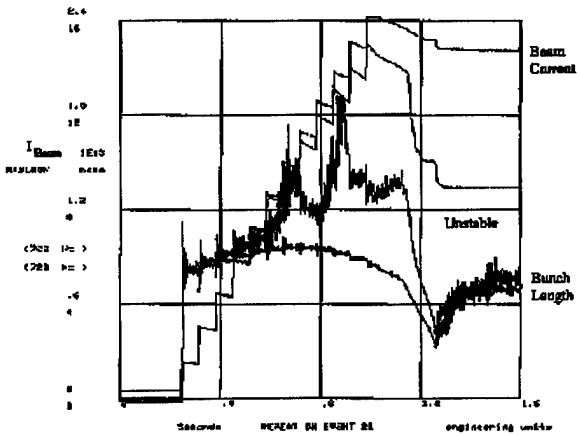

Fig.7) Current and bunch length of both stable and unstable beams are shown.

the effectiveness of the damping system.

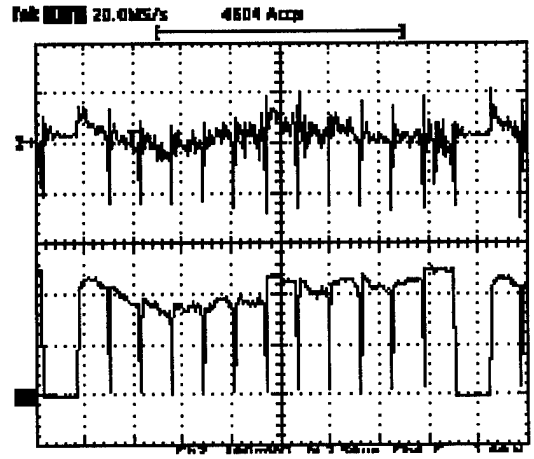

Fig.8) Dampers off: Phase (top) and amplitude (bottom) of beam intensity for 12 batches are nonuniform due to the instabilities.

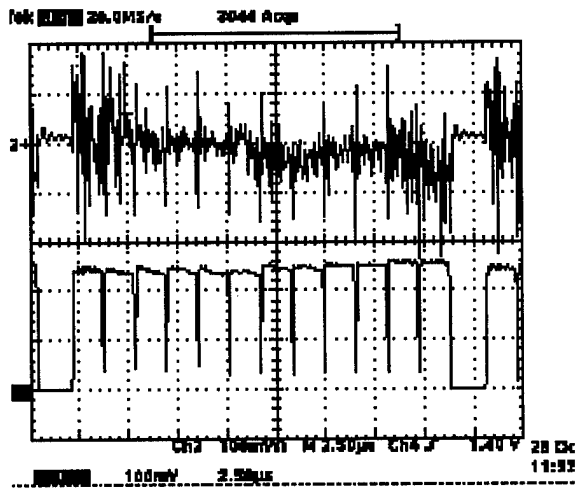

Fig.9) Dampers on: Phase (top) and amplitude (bottom) of beam intensities for the 12 batches are shown to be uniform.

5 CONCLUSION

A higher order mode impedance in the RF is verified to be the source and drive the beam unstable longitudinally. Simulation results agree with the measurements of the coupled-bunch instabilities. Oscillations are reduced by an active feedback system.

REFERENCE

[1] F.J. Sacherer, IEEE Trans. Nuclear Sci.,NS-28 (1973).

DIGITAL LOW LEVEL RF SYSTEMS FOR FERMILAB MAIN RING AND TEVATRON

B.E. Chase, B. Barnes, K. Meisner, Fermilab†, P.O. Box 500, Batavia, IL 60510

Abstract

New Low Level RF systems are successfully operating the Fermilab Main Ring and Tevatron. The upgrade replaces aging CAMAC and NIM components, and increases system accuracy, reliability, and flexibility. VXI LLRF systems feature a custom three channel direct digital synthesizer (DDS) module capable of independent or ganged operation in both frequency and phase modulation. Frequency and phase values are computed at 100Khz by the module's Analog Devices ADSP21062 (SHARC) digital signal processor. The DSP concurrently handles feedforward, feedback, and beam manipulations. Higher level state machines and the control system interface are handled at the crate level using the VxWorks operating system. This paper discusses the hardware, software, and operational aspects of these LLRF systems.

1 SYSTEM HISTORY

CAMAC and NIM (CNIM) platform LLRF systems have served Fermilab accelerators well for many years. The new Main Injector and Recycler accelerators, future Tevatron 36 on 36 collider HEP, and increasingly complex operating scenarios and study programs require significant and correspondingly complex new LLRF system functionality. Many future LLRF requirements are difficult to implement in the CNIM platform.

CNIM LLRF systems are very hardware intensive, with a large number of distributed specialty modules and cabling complexity for parallel digital data, timing, and DC through RF analog signals. Frequent upgrades introduce hardware changes and new EMI issues, and often require adding hardware in limited physical space.

Limited CNIM processing power means important LLRF feedforward control programs are manually tuned tables written to CAMAC curve generators. They do not incorporate fundamental accelerator physics and are not responsive to actual accelerator parameters. More complex control algorithms like the Main Ring LLRF synchronous phase angle program are accomplished by a combination of curve tables and electronic "tricks". This can produce errors that exceed the operating range of feedback loop components, and means scenarios like Main Ring (and future Main Injector) deceleration become unduly elaborate and esoteric implementations.

Future beam transfers between the Main Injector and Tevatron (transfer cogging) and collision point control in the Tevatron (collision point cogging) argue for replacing the CNIM cogging LLRF system, [*1] if only because simultaneous CNIM support of both cogging processes is difficult and very hardware intensive.

CNIM LLRF state machines execute in many modules. Minor system upgrades involve significant state machine hardware re-engineering, plus rematching RF amplitudes, group delays, and phase offsets. It is effectively impossible to duplicate and test CNIM system operation in a lab environment.

2 VXI SYSTEM COMPONENTS

The VXI platform facilitates LLRF system development and improves performance by shifting implementation into powerful hardware and software. The systems consist of modules in a single VXI mainframe and a custom interface chassis. About a dozen cables provide the control system network connection, accelerator time and data, TTL I/O, and LLRF outputs.

The front ends are National Instruments cpu-030 VXIbus embedded computers running VxWorks. The VXIcpu-030 is configured for slot 0 operation and runs a Startup Resource Manager with strict interpretation of the VXIbus specification to verify and configure all system devices. NIcpu-030 code libraries and an ethernet port provide all communication with control system host computers through the usual ACNET protocol. All cpu-030 software is downloaded over the network.

Fermilab VME and VXI Universal Clock Decoder (UCD) modules receive and process Tevatron clock (TCLK), Beam Synch clock, and MDAT [*2] accelerator timing and data. The UCDs synchronize LLRF system processes and provide ACNET interface timing resources.

An Interface Technologies IO100VXI digital I/O module generates TTL signals to other systems. It drives local comfort displays on a custom interface chassis that also filters and distributes the system RF outputs.

A Fermilab Direct Digital Synthesizer (DDS) with a SHARC DSP generates three LLRF outputs, and is a key component discussed in following sections. All VXI DDS modules receive a 50Mhz LO signal and 25Mhz DSP clock from a single ovenized crystal Oscillator module. The OSC module also sources the VXI backplane CLK10 signal. DSP software is downloaded over the network through the cpu-030.

A two channel 200Khz 16bit ADC module connects directly to the DDS via the local bus DSP serial port.

A lab VXI development system exactly duplicates operational systems and is used extensively to verify functionality before installation in the accelerators.

---

† Operated by Universities Research Association Inc. under contract with the U.S. Department of Energy

VXI LLRF Block Diagram

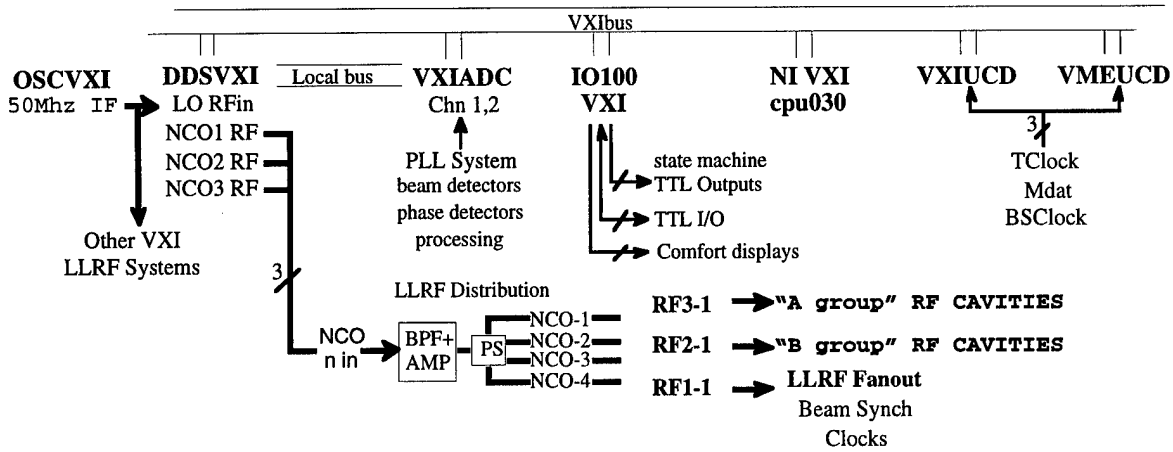

3 DDS HARDWARE

The VXI Direct Digital Synthesizer (DDS) is a custom module designed to provide LLRF frequency and phase control. It has three RF synthesizer channels controlled by an Analog Devices ADSP21062 (SHARC) DSP. Frequency and phase control for the RF channels can be independent or ganged. The DDS is a VXI slave with full interrupt and VXI trigger capability. High speed serial and link port DMA data paths are provided over the VXI local bus for real time feedback.

Each synthesizer channel consists of a Numeric Controlled Oscillator (NCO), two DACs, and an IQ modulator. The NCO is a Harris HSP45106 with 32 bit center frequency and 16 bit phase control registers which provide milli-Hertz and 100 micro-radian resolution. NCO outputs are 16 bit sine and cosine values. The TTL sine and cosine values drive separate 12 bit DACs. The nominal 3MHz DAC outputs are filtered to remove alias spectra, and drive the I and Q ports of the Mini-Circuits MIQC-88M modulator. The 50MHz OSC module drives the modulator LO port, and clocks the NCOs at 25MHz. The modulator RF output is the upper sideband 53MHz signal that is amplified to +17 dBm and output to the DDS front panel. A coupled port is provided for monitoring.

This configuration provides the following benefits. The lower sideband, LO leakage and IF harmonics are spaced at 3MHz intervals from the 53MHz RF drive. These signals are greater than -40dBc and are easily filtered outside the DDS module. Close in spurs are small due to the low distortion and quantization noise of the 12 bit DACs. Phase noise is near the extremely low level of the crystal oscillator. Phase control accuracy is very precise, as any nonlinearities in the IF path produce harmonics which are again attenuated by the bandpass filter. Synchronism between the NCOs on frequency register writes is essential for maintaining coherent phase. A virtual NCO (NCOALL) is decoded by hardware to generate common register write and control strobes.

PLL output signals are presently digitized with the two channel ADC module. ADC serial data is transferred over the VXI backplane local bus to DSP memory by the SHARCs DMA controller. Data can also be transferred from a 4 channel 12bit 25Mhz ADC module over the backplane using the SHARC local bus. These transfers are also under DMA control, and can run at 25Mbytes/sec.

4 DDS SOFTWARE

The DSP and its software create the RF bucket while controlling bucket area, beam energy, and azimuthal positions. It must do this as gently and with as little RF phase noise as possible to avoid heating the beam. This requires that DSP code execution is very deterministic, frequency and phase calculations are smooth and accurate, and that sidebands created in the process are small and outside the RF cavity bandwidth.

The feedforward frequency program (Frf) is calculated from real time bend bus current broadcast at 720Hz.

$$F_{rf} = F_E\Big|_{(\Delta r=0)} = F_\infty \beta = F_\infty \left(1 + \frac{K}{r^2}\right)^{\frac{-1}{2}}$$

where $F_\infty = \dfrac{hc}{2\pi R_0}$

The DSP interpolates Frf at 100KHz with a 7.5Hz lowpass 2760 tap FIR filter. Frequency feedback is also applied at 100Khz. The synchronous phase angle is calculated from I dot and the RF cavity gradient Vg.

$$\phi_s(t) = \sin^{-1}\left(\frac{2\pi R_s}{ecV_g\beta_s}\frac{dE_s}{dt}\right)$$

DDS phase control provides many LLRF system beam control processes. There are seven phase control input categories grouped by function and bandwidth requirements. 720hz adiabatic inputs are: static OFFSETs for transfer phasing, group delay COMPENSATION, Φs CALCULATIONs, SLOW arbitrary WAVEFORMs for counterphasing, and bucket COGging waveforms. Non-adiabatic 16.6Khz inputs are: STEPs for transition jumps

and FAST arbitrary WAVEFORMs. The DSP applies all categories simultaneously and several categories have multiple inputs. All DDS phase control data is interpolated and output at 100Khz. Lock stepping of the three process rates is done by a scheduler that is phase locked to the 720Hz MDAT link with a software PLL.

Asynchronous DSP processes such as cogging or transition crossing are driven by hardware and software interrupts. Priorities for these interrupts are set lower than the 720hz/16.6Khz/100Khz synchronous processes. The cpu-030 host communicates with the SHARC via its message and vector interrupt (VIRPT) registers. The model follows a C call in that DSP input parameters are written to message registers, and the interrupt is generated when a DSP function pointer is written to the VIRPT. DSP return and error values are placed back in the message registers. All DSP code is a continuation of the object models formed in the cpu-030 libraries.

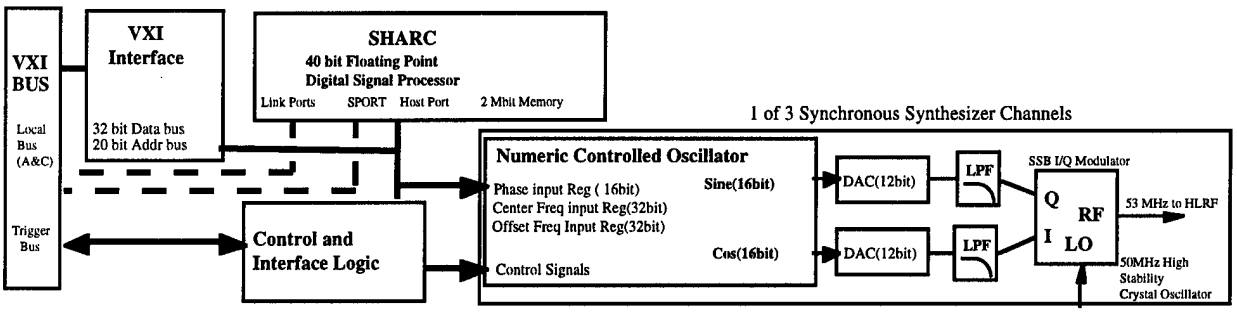

5 VXI SYSTEM OPERATION

Finite state machine implementation in front end and DSP software is a key VXI LLRF system feature that has demonstrated many advantages. The system VXIUCD sources backplane interrupts and triggers from directly decoded TCLK events and events + delays. These high priority LLRF system events are state machine excitations connected to corresponding callback functions. Users describe system operation in common accelerator language on a dedicated console application program. The user requests are sent to the front end with normal Acnet protocol to condition state machine outputs. State machines can also use VXIUCD MDAT 720hz accelerator data as conditional inputs.

One category of conditional inputs is used to completely reconfigure LLRF state machines for any specific accelerator cycle, and every cycle can support all functionality. Fermilab LLRF systems constantly evolve to support new operating scenarios and study programs that must be completely parasitic to normal operation. The state machine configuration inputs and the lab development system have proven invaluable for verifying new system functionality.

State machine outputs are largely IO100VXI digital I/O module TTL signals, and VIRPT calls to the DDS module. A state machine logging feature provides state execution timing, output values, and messages that offer intelligent problem diagnostic capability. Automatic test suites for component verification and run time fault detection are incorporated with no additional hardware.

6 SUMMARY

The VXI platform's accurate real time control has improved LLRF system performance. The DDS Frf calculation has decreased the MRLLRF frequency error from ±12Khz to ±350hz. This allowed a corresponding reduction of the beam PLL gain and CLBW, and reduced phase noise in the MRRF system. Accurate Frf has been exploited by state machine options that run the DDS open loop at specific frequencies. This feature is used anywhere the magnet current is constant, to eliminate transfer PLLs and replace CNIM flattop oscillators and RF switches.

The accurate DSP synchronous phase angle calculation eliminated MRLLRF problems from limited range feedback loop components, and allowed MR beam deceleration back through transition for the first time.

The VXI platform has streamlined LLRF systems by replacing dozens of CNIM modules and hundreds of cables. Adding basic accelerator physics to deterministic and responsive processors has improved performance, increased functionality, and minimized tuning. Concentrating LLRF state machines into easily managed code libraries has facilitated performance upgrades. Basic state machine control for parasitic MR slip stacking studies was added in hours. Transfer and collision point cogging were decoupled by adding cogging support to the VXI MRLLRF and TVLLRF systems in an upgrade that required no hardware modifications.

ACKNOWLEDGMENTS

The LLRF Group thanks Charlie Briegel for help with the ACNET interface, and Keith Engell for work on the LLRF console application.

REFERENCES

[1] K. Meisner, "RF Synchronous Transfer Into Specific Buckets Between Fermilab Main Ring and Tevatron Accelerators", IEEE PAC proceedings (1995)

[2] D. Beechy and R. Ducar, "Time And Data Distribution Systems At The Fermilab Accelerator", Nuclear Instruments and Methods in Physics Research A247 (1986)

DAMPING OF INJECTION OSCILLATIONS

V. M. Zhabitsky
Joint Institute for Nuclear Research, 141980 Dubna, Moscow Region, Russia

Abstract

The increasing dimensions and beam intensities of the new circular accelerators and colliders impose special demands on the performance of injection and transverse feedback systems. Injection errors blow up the emittance of a beam. The emittance increment with active feedback depends on the combination of injection error amplitude, tune spread and extra damping (above the needs for stability) by the feedback. A description of the transverse feedback system (TFS) for damping of injection oscillations is given. The TFS includes a subsystem for damping of transverse instabilities and a pulse subsystem for damping of injection errors with high damping rate. The optimization of the subsystem parameters is discussed, and the results obtained for damping rate of the beam are presented.

1 INTRODUCTION

Transverse feedback system (TFS) is used now to damp not only coherent transverse instabilities but also injection oscillations. As rule, two separate subsystems are used: one subsystem for damping of instabilities and a pulse subsystem for damping of injection errors. Each subsystem consists of one pick-up (PU), delay, filter and power amplifier in feedback path, and a kicker (DK) (see Fig. 1).

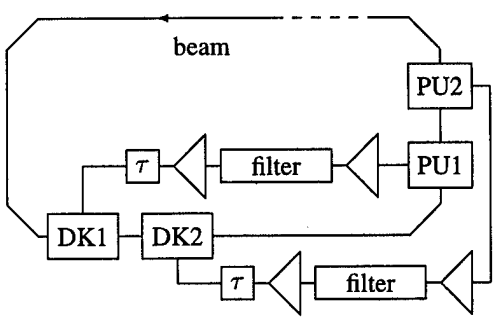

Figure 1: Damper scheme

The kicker corrects the beam angle, and this correction depends on the deviation of the beam from the closed orbit in the PU location. The gain of TFS amplifier is chosen to provide the needs for an amplitude decrease per revolution. All parameters of two subsystems are calculated independently. Clearly, these estimations can be used as a first approximation. Indeed, each kicker corrects the beam angle in accordance with its PU signal. But a change of beam angle per revolution is determined by two corrections produced by two kickers. This change depends also on PU signals due to "feedback via the beam". Hence, the damping rate depends on the feedback gains and betatron phase advances between pick-ups and kickers. Further the theoretical description of the feedback with two subsystems is given.

2 THEORY

2.1 Basic Equation

The arrangement for damping of transverse beam oscillations is sketched in Fig. 1. A pulse subsystem for damping of injection errors consists of a pick-up PU1 and a kicker DK1. Subsystem for transverse instabilities includes a feedback loop with a pick-up PU2 and a kicker DK2. Each pick-up measures bunch transverse deviation and the kicker corrects the beam angle. The kicker should change the angle of the same bunch that was measured by the PU. The delay τ in the feedback loop is adjusted to provide such a synchronization.

Taking into account the results obtained in [1, 2] the study of the transverse coherent motion bunch dynamic is started for independent bunches. In this case the bunch coupling, which occurs due to resistive wall instability, is neglected and the matrix method becomes suitable for the beam motion description.

Let the column matrix $\widehat{X}[n,s]$ determine the bunch state at the n-th turn at point s of the circumference C_0. The first element of this matrix equals the beam deviation $x[n,s]$ from the closed orbit and the second one is $x'[n,s]$. After a short DK the x' value of the beam is changed by $\Delta x'[n,s_K]$, while deviation remains the same as before the DK at point s_K^-. Hence, after DK at point s_K^+, the beam state is

$$\widehat{X}[n,s_K^+] = \widehat{X}[n,s_K^-] + \widehat{T}\Delta\widehat{X}[n,s_K], \qquad (1)$$

where $\widehat{T}$ is the 2×2 matrix in which $T_{21}=1$ and the other elements are zero. The kick is determined with column matrix $\Delta\widehat{X}[n,s_K]$, where the first element equals $\Delta x'[n,s_K]$ and the second one has an arbitrary value. It will be assumed further that $\Delta x'[n,s_K]$ is proportional to the beam deviation $x[n,s_P]$ in the pick-up:

$$\Delta\widehat{X}[n,s_K] = \frac{\mathbf{K}}{\sqrt{\beta_P\beta_K}}\widehat{X}[n,s_P], \qquad (2)$$

where β_P and β_K are the transverse betatron amplitude functions in the PU and DK locations, and $\mathbf{K}$ is the gain of the feedback loop.

Let us introduce the unperturbed revolution matrix $\widehat{M_0}$ from point s_{P1} of the PU1 location to point $s_{P1}+C_0$, the transfer matrix $\widehat{M_P}$ from point s_{P1} to point s_{P2} of the PU2 location, the matrix $\widehat{M_1}$ from point s_{P2} to point s_{K1} of

0-7803-4376-X/98/$10.00 © 1998 IEEE

the DK1 location, the matrix $\widehat{M}_K$ from point s_{K1} to point s_{K2} of the DK2 location, and the transfer matrix $\widehat{M}_2$ from point s_{K2} to point $s_P + C_0$. By using these matrices it is not difficult to calculate the transformation of the bunch state matrix $\widehat{X}[n, s_{P1}]$ after the circumference pass with two angle corrections. For each kick the relations (1) and (2) should be used. Putting together the terms, the beam state at the PU1 location at the $(n+1)$-th turn is then

$$\begin{aligned}\widehat{X}[n+1, s_{P1}] &= \widehat{M}_0 \widehat{X}[n, s_{P1}] + \\ &+ \frac{\mathbf{K}_1}{\sqrt{\beta_{P1}\beta_{K1}}} \widehat{M}_2 \widehat{M}_K \widehat{T} \widehat{X}[n, s_{P1}] + \\ &+ \frac{\mathbf{K}_2}{\sqrt{\beta_{P2}\beta_{K2}}} \widehat{M}_2 \widehat{T} \widehat{M}_P \widehat{X}[n, s_{P1}] \,. \end{aligned} \tag{3}$$

Eq.(3) fully describes the beam dynamics in an accelerator with two feedback subsystems considered.

2.2 General Solution

Equation (3) is solved using Z-transform [3, 4] for $\widehat{X}[n, s]$:

$$\begin{aligned}\widehat{\mathbf{X}}(z) &= \sum_{n=0}^{\infty} \widehat{X}[n, s] z^{-n} \,; \\ \widehat{X}[n, s] &= \sum_k \mathrm{Res}\left[\widehat{\mathbf{X}}(z_k) z_k^{n-1}\right] \,, \end{aligned} \tag{4}$$

where z_k are the singular points of $\widehat{\mathbf{X}}(z)$. The motion of the particles will be stable if $|z_k| < 1$.

The beam motion parameters are fully determined by the singular points z_k : the number of oscillations per turn $\{\mathrm{Re}Q_k\}$ equals $\arg(z_k)/2\pi$, the damping factor D_k equals $|z_k|$, and the damping time τ_D is

$$\frac{T_0}{\tau_D} = -\ln|z_k|. \tag{5}$$

Using Z–transform for Eq.(3) we get

$$\widehat{\mathbf{X}}(z) = \frac{z\widehat{I} - \widehat{\mathbf{M}}^{-1}(z) \det \widehat{\mathbf{M}}(z)}{\det\left(z\widehat{I} - \widehat{\mathbf{M}}(z)\right)} z\widehat{X}[0, s_{P1}], \tag{6}$$

where

$$\begin{aligned}\widehat{\mathbf{M}}(z) = \widehat{M}_0 &+ \frac{\mathbf{K}_1}{\sqrt{\beta_{P1}\beta_{K1}}} \widehat{M}_2 \widehat{M}_K \widehat{T} + \\ &+ \frac{\mathbf{K}_2}{\sqrt{\beta_{P2}\beta_{K2}}} \widehat{M}_2 \widehat{T} \widehat{M}_P \,. \end{aligned} \tag{7}$$

$\widehat{I}$ is the unit matrix; $\widehat{X}[0, s_{P1}]$ is the initial beam state matrix. The singular points z_k in (6) are found from the equation [3, 5]:

$$\begin{aligned}&\det\left(z_k\widehat{I} - \widehat{\mathbf{M}}(z_k)\right) = \\ &= z_k^2 - z_k \mathrm{Tr}\widehat{\mathbf{M}}(z_k) + \det \widehat{\mathbf{M}}(z_k) = 0. \end{aligned} \tag{8}$$

For damper system with one correction at every turn (for example, $\mathbf{K}_2 = 0$), Eq. (8) for z_k becomes [5]

$$\begin{aligned}z^2 - (2\cos(2\pi Q_0) + \mathbf{K}_1 \sin(2\pi Q_0 - \psi_{PK}))\, z + \\ +1 - \mathbf{K}_1 \sin\psi_{PK} = 0, \end{aligned} \tag{9}$$

where Q_0 is the number of unperturbed betatron oscillations per revolution in the transverse plane, and ψ_{PK} is the betatron phase advance from the PU1 to the DK1. The damper with one correction at every turn is known as a classical feedback system that has been used widely in synchrotrons (see, for example, [6]). It is easy to find the roots of Eq.(9). They correspond to the eigen frequencies with the number of oscillations per turn in the neighbourhood of $\mathrm{Re}Q_0$. If $|\mathbf{K}_1| \ll 1$, then in linear approximation the damping time is

$$\frac{T_0}{\tau_D} = \frac{1}{2}|\mathbf{K}_1 \sin\psi_{PK}| \,.$$

This decrement formula is well known. The best damping will be for PU and DK locations such that

$$|\sin\psi_{PK}| = 1 \,, \tag{10}$$

i.e. if the phase advance ψ_{PK} from PU to DK equals an odd number of $\pi/2$ radians.

3 RESULTS

In order to simplify the final expressions, all further results are shown for a damper system considered (see Fig. 1) when the relations (10) for the phase advances from PU1 to DK1 and from PU2 and DK2 are fulfilled. In this case Eq. (8) for z_k becomes

$$\begin{aligned}z^2 - (2 - (\mathbf{K}_1 + \mathbf{K}_2))\, z\cos(2\pi Q_0) + \\ +1 - (\mathbf{K}_1 + \mathbf{K}_2) + \mathbf{K}_1\mathbf{K}_2 \sin^2\psi_P = 0 \,, \end{aligned} \tag{11}$$

where ψ_P is the phase advance of the betatron oscillation of the particle on its way from PU1 to PU2. Eq. (11) coincides with the single correction equation (9) if $\mathbf{K}_1$ or $\mathbf{K}_2$ equals zero. The roots of Eq. (11) are

$$\begin{aligned}z_{1,2} &= (1 - \overline{\mathbf{K}})\cos(2\pi Q_0) \pm \\ &\pm\ i\sqrt{\left(1 - \overline{\mathbf{K}}\right)^2 \sin^2(2\pi Q_0) - \Delta^2} \,, \end{aligned} \tag{12}$$

where

$$\begin{aligned}\overline{\mathbf{K}} &= \frac{1}{2}(\mathbf{K}_1 + \mathbf{K}_2) \,, \\ \Delta^2 &= \overline{\mathbf{K}}^2 \cos^2\psi_P + \frac{1}{4}(\mathbf{K}_1 - \mathbf{K}_2)^2 \sin^2\psi_P \,. \end{aligned}$$

The solutions (12) can be used to compute the damping time and the other beam motion parameters. Thus, the damping time and the number of oscillations per revolution are

$$\frac{T_0}{\tau_D} = -\frac{1}{2}\ln|(1 - \overline{\mathbf{K}})^2 - \Delta^2| \,, \tag{13}$$

$$Q = Q_0 - \frac{\Delta^2 \cot(2\pi Q_0)}{4\pi|(1 - \overline{\mathbf{K}})^2 - \Delta^2|} \,. \tag{14}$$

The relation (14) is valid if the deviation of Q from Q_0 is small ($2\pi|Q - Q_0| \ll 1$).

Note, that all basic properties of solutions (12) depend on the phase advance ψ_P and the gains $\mathbf{K}_1$, $\mathbf{K}_2$. If the phase advance ψ_P from PU1 to PU2 equals an integer number of π radians ($\psi_P = n\pi$) then we obtain the same expressions as for a classical feedback system. But the damping rate will be higher because the sum angle correction per turn is provided by two kickers. It is necessary to emphasize that for all feedback gains in such systems ($\psi_P = n\pi$) there is an additional phase advance per turn for the particle betatron oscillations. This negative effect does not allow to use such damper for a fast correction of injection errors during few revolutions. Regime of injection angle suppression per one turn can be realized only if the bunch injected crosses one of the kickers with zero position error and the kick value is strongly proportional to the bunch amplitude error. This regime is used for all injection schemes in synchrotrons but the kicker pulse amplitude is generated in accordance with calculated value by hand and not with a pick-up signal passed on to the feedback processing and power electronics which drives the kicker.

If the phase advance ψ_P from PU1 to PU2 equals an odd number of $\pi/2$ radians ($\psi_P = (2n+1)\pi/2$) then the locations of pick-ups and kickers are the same as for a fast feedback system that has been proposed for UNK-I [7]. Note, that for $\mathbf{K}_1 = \mathbf{K}_2$ the solution (12) coincides with the similar expression for a fast feedback system that has been discussed in [5]. Only for these PUs and DKs locations ($\psi_P = \pi/2$) and gains ($\mathbf{K}_1 = \mathbf{K}_2$) the Δ value equals zero. Hence, in accordance with Eq. (12) and Eq. (14) the tune Q does not depend on the gain and the damping rate will be

$$\frac{T_0}{\tau_D} = -\ln|1 - \overline{\mathbf{K}}| \, .$$

If $|\overline{\mathbf{K}}| = 1$ then injection oscillations are completely cancelled after the kickers' pass and this result does not depend on the betatron phases of a particle crossing PU1, PU2, DK1 and DK2.

The damper with $\Delta = 0$ can be used for a multiturn suppression of injection oscillations. The scheme may be the following. The bunch injected crosses DK1 and DK2 which correct partially the initial oscillation amplitude. The pulse amplitudes for DKs should be calculated by hand in accordance with the initial beam state, the kickers' locations and the degree of the initial oscillation amplitude suppression (for example, on 60%; this value depends on a dynamic aperture in an accelerator). Because two kickers are used with not 100% correction then the pulse amplitude for DKs generators is lower in comparisons with a traditional one kicker injection scheme. After kickers' pass, the feedback is turned on: the pick-ups PU1 and PU2 measure the residual bunch deviation; these values are used in the feedback loops for angle corrections by DK1 and DK2, and so on. This scheme for damping of injection oscillation can be valid for a large hadron accelerators in order to decrease the power generated for injection kickers.

4 CONCLUSION

The consideration of damping regimes allows one to maintain that every turn correction with two subsystems is preferable. The best conditions for damping are achieved for those locations of pick-ups and kickers when the phase advances of the betatron oscillation of the particle on its way between pick-ups and kickers equal an odd number of $\pi/2$ radians. In this case a special regime can be realized for suppressing as initial injection amplitude of oscillations as residual errors and transverse instabilities.

5 REFERENCES

[1] V. M. Zhabitsky. Theory of multi-bunch resistive wall instability damping using feedback system with a digital filter. In *EPAC94. Proceedings of the Fourth European Particle Accelerator Conference, London, 27 June to 1 July 1994*, volume 2, pages 1090–1092. World Scientific, 1994.

[2] V. M. Zhabitsky, I. L. Korenev, and L. A. Yudin. Multi-bunch resistive wall instability damping with feedback. *JINR P9–92–309, Dubna*, 1992.

[3] V. M. Zhabitsky. The Z-transform application for solving the problem of free beam oscillation damping in the accelerator. *JINR P9–91–91, Dubna*, 1991.

[4] W. McC. Siebert. *Circuits, Signals, and Systems.* The MIT Press, 1986.

[5] V. M. Zhabitsky, I. L. Korenev, and L. A. Yudin. Transverse feedback system with digital filter. In *Proceedings of the 1993 Particle Accelerator Conference, Washington, USA*, pages 2543–2545. IEEE, May 1993.

[6] L. Vos. Damping of coherent oscillations. *CERN SL/96–66 (AP), Geneva*, 1996.

[7] I. N. Ivanov, V. M. Zhabitsky, I. L. Korenev, L. A. Yudin, and L. I. Kopylov. Requirements to the feedback system to damp resistive instability (I Stage UNK). In *XVth International Conference on High Energy Accelerators. July 20–24, 1992, Hamburg, Germany*, Proceedings Supplements. Int. J. Mod. Phys. A, pages 1034–1036. World Scientific, 1993.

STRATEGY FOR DEVELOPING FAST BUNCH FEEDBACK SYSTEMS FOR KEKB

E. Kikutani, and M. Tobiyama, KEK - High Energy Accelerator Research Organization,
Oho 1-1, Tsukuba-shi Ibaraki, 305 Japan

Abstract

KEKB, an asymmetric collider project for the B-physics, is now under construction at KEK Japan. In order to overcome the problem due to expected coupled bunch instabilities, we are developing bunch feedback systems. In these feedback systems we will use signal process systems based on the simple 2-tap filters. The fabrication of the prototype of the signal process board has completed and it worked well in the feedback experiments performed in AR at KEK.

1 INTRODUCTION

Recently, many storage rings which store very high current are in operation or under construction. In these rings, coupled bunch instabilities can be a serious problem in their operation. Several sources, such as cavity impedance, finite conductivity of the beampipe, some ion/electron cloud, $\cdots$ can cause these instabilities. One way to cure them is the use of bunch feedback systems that can treat multiple bunches. However, it is not a easy way to design such feedback systems, because the number of bunches is very large and, consequently, the bunch interval should become very short in these machines.

KEKB, which is an asymmetric e^+e^- collider for B-physics, is one example of such machines. In KEKB, about 5000 bunches/ring (harmonic # is 5120) are stored in the ring of 3019 meters in circumference and the bunch spacing is only 60cm. For several years, we have been developing bunch feedback systems which meet these severe conditions. At present, design of major hardware parts has completed and we have just started to integrate them to a system.

At this stage, discussions with the people who are developing similar feedback systems are very fruitful. For example, in PEP-II[1] and DAΦNE[2], they are developing the same kind of feedback systems. Since these feedback systems must satisfy a number of tight conditions, the hardware that satisfy them can not have wide variety. In fact, the front-end circuit for the bunch-position detection is more or less similar among these three examples. But we can find several differences in some hardware schemes as summarized in the table below.

	KEKB	PEP-II	DAΦNE
L. kicker	d.tube/cavity	d.tube	cavity
electronics	hard-base	soft-base	soft-base

The first example of the differences is the design of the longitudinal kicker. For PEP-II, they will use the drift-tube type of kickers[3] that is very wide-banded. These kickers have already been installed in APS at LBNL and they successfully damp the longitudinal oscillation. In DAΦNE, they are developing a very low-Q cavity[4] which has higher shunt impedance than the drift tube kicker. The second example of the difference in hardware scheme is the signal process system. Even though it is common to all of them to use the digital technology, there are some differences. In PEP-II and DAΦNE, the signal processing in the longitudinal plane is done with a system based on Digital Signal Processors (DSP). Since this system is programmable, it is very flexible. In KEKB, on the other hand, we will not use the DSPs but use hardware-based systems. In this paper, we describe our basic strategy of developing the feedback systems particularly paying attention to this signal processing system.

2 SIGNAL PROCESSING OF THE KEKB SYSTEM

2.1 *Basic idea - 2-tap digital filters*

The basic idea in designing our signal process system is to use the concept of the 2-tap digital filter. Since we closely discussed the features of the 2-tap digital filter in other papers[5][6], we briefly review its characteristics. In many feedback systems, the feedback-kick is given to a bunch after the phase of the betatron (or synchrotron) oscillation is rotated by the angle $\pi/2$ (mod 2π). Inspired by this usual method, we recognize that it is possible to damp the oscillation by kicking the bunch after the phase is rotated by $3\pi/2$. But, in this case, the sign (=direction) of the kick should be inverted; otherwise, it becomes an exciter not a damper. The idea proposed by F. Pedersen[7] is to combine two feedback loops in parallel; one is of $\pi/2$-delay the other is of $3\pi/2$ delay with the inverted sign. It is very advantageous for us to use this combining method because it can work as a DC-cut filter. Naturally, we need not prepare two feedback systems for these two cases actually. The combination can be realized by a simple subtract operation performed in digital components.

2.2 *Outline of the design*

Guided by our basic idea explained above, we made a conceptual design of the signal process system. Considering very simple algorithm of the 2-tap filter we judged it to be reasonable to make this logic by hardware. This choice enables us to construct a very fast processing system, i.e. a bunch-by-bunch signal processing with the bunch frequency of 500MHz is feasible with this system.

At the practical design stage, we found that

- it will be advantageous to fabricate a de-multiplexer which can reduce the signal rate of 500MHz to easy-

0-7803-4376-X/98/$10.00 © 1998 IEEE

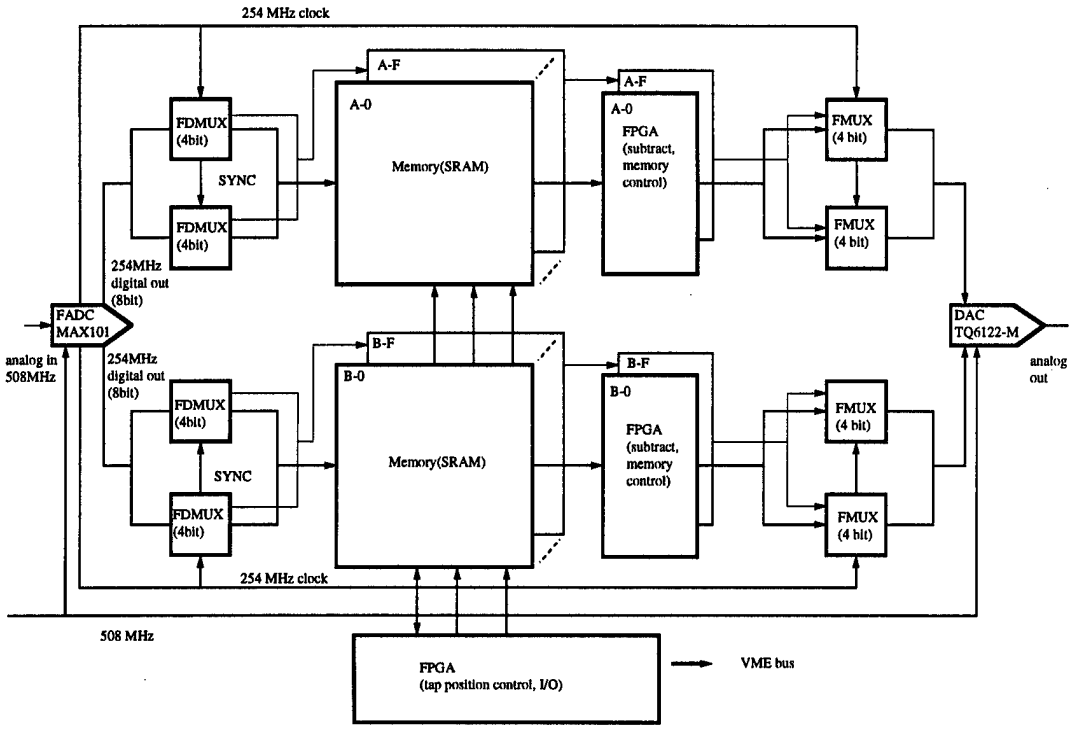

Figure 1: Block diagram of the signal process board. The output of the ADC is fed into the de-multiplexer fabricated as a custom LSI (FDMUX). It reduces the signal rate from 254 MHz to its 1/16. The output of the 2-tap filter, which is made up with the memory and the FPGAs, is fed into the multiplexer (FMUX) that is the counter-part of FDMUX.

manageable frequencies. It can be realized Ga-As LSI chips. Since we were not able to find such LSI commercially, we decided to fabricate it as a custom LSI as well as its counter-part, the high speed multiplexer.

- A set of circuitry for one plane can be packed in only one board, even though it treats 5120 bunches by using the de-multiplexer. The size of the board is almost the same as that of the 3-height VME board.

A block diagram of this signal process board is given in Figure 1. As we described this system in other paper[8] in detail, here we explain it very briefly. The board has an A-to-D converter for the input, two arrays of memory chips with subtract logics and a D-to-A converter for the output. The interface between the ADC and the memory is a pair of the FDMUXs. The 2-tap filter scheme is realized by these two arrays of memory and the subtract logic. The length of the memory is 1 Mbyts/array. A pair of FMUXs interfaces output of the filter and the DAC. The board itself has a non-standard size, but it is equipped with a VME interface. The tap positions of the 2-tap filter are easily set through this interface. Additionally, the content of the memory can be read out also through this VME interface when the system is at "not running" status.

2.3 *Evaluation of this scheme*

In our hardware-based scheme, we can stuff a large portion of the technical difficulties due to the high-speed into the custom LSIs. They can reduce the signal rate from roughly 500MHz (in our practical application we use 254 MHz of the input signal) to its 1/16, and vice versa. Then, outside of the LSIs, almost all the signal transportation is in only 16 MHz. The cost of the fabrication of these LSIs is a little expensive but thanks to this custom LSI, we can construct very fast devices without serious difficulties. This can be one of the strategies of making a system when the number of within-laboratory staffs is considerably limited. The high cost of these LSIs is paid by following two facts,

- The 2-tap signal process board can be commonly applicable to the longitudinal and transverse systems. If we used a slower system, it might not be usable for the transverse systems.
- By slightly changing the design, we can make a very powerful memory systems as explained in the next section. There must be many potential applications of this memory system.

3 THE MEMORY BOARD

3.1 *Design of the memory board*

If we remove the output part (FMUXs and the DAC) from our 2-tap filter board and add more memory chips in place of it, the board becomes a very fast, large-size transition memory system. We call it "the memory board". It has the common mother board with the 2-tap signal process board. The amount of the memory is increased from 1 Mbytes to 20Mbytes. This can store the history of oscillation of 5120 bunches over 4096 turns.

3.2 *Application of the board*

There are a wide range of the applications of this memory board. Several examples are a bunch-by-bunch current monitor and a bunch by bunch tune meter. The 4096 turns of data of oscillation is sufficient enough to determine the tune.

Another application of the memory board is to store the time-domain data of oscillations of many bunches. It should be a powerful tool for studying the behavior of bunches under mulitubunch operation. We are planning to use this system in the photo-electron instability experiments to be performed at BEPC in Beijing, China[9].

4 PRESENT STATUS

4.1 *The 2-tap filter board*

In the last autumn the first version of the 2-tap signal-process board completed. By using this board and other components, we have performed feedback experiments in AR at KEK. A detailed description of these experiments is given in another paper in these proceedings[10]. In these experiments we were successfully damped the longitudinal oscillation with the 2-tap filter board.

What we must describe here is a function of the 2-tap filter board as a medium-size transient memory. As explained above, it has 1Mbytes of the memory. That can record behaviors of bunches over 1600 turns when the number of bunch is 640, where 640 is the harmonic number of AR. Utilizing this function, we were able to perform several experiments of accelerator physics. The preliminary reports of these experiments are given in these proceedings[11][12].

4.2 *The memory board*

The fabrication of first prototype of the memory board has completed just after the experiments in AR. It will be exported to China this summer for the experiments at BEPC.

5 FUTURE PLANS

According to the general schedule of KEKB, the commissioning of LER will be started at the middle of next year. Until this time, we must carry out the following things:

- fabrication of the DAΦNE-type kickers
- development of the control software

5.1 *The longitudinal kicker*

We made the feedback experiments in AR with the drift-tube type of the longitudinal kicker. The experimentally-estimated shunt impedance is consistent with the calculation[13]. In this sense, the experiment was successful. But we still hope higher shunt impedance because the reduction of the number of the kickers as well as that of power amplifiers is seriously desired for practical and economical reasons. The cost for these amplifiers will take a large part of the total budget for the feedback systems.

Then we next try to construct the DAΦNE type kickers whose estimated shunt impedance is about twice of the drift-tube kicker of 2-inner electrodes. The operating frequency of the kicker in KEKB is very close to that in DAΦNE. Then the kicker will be usable with small correction in the design.

5.2 *The control software*

The accelerator control system of KEKB is based on EPICS[14], in which hard-ware accesses are done through VME computers. As described above, our signal process board and the memory board have the VME interface. Since these boards are "user-made" we must code the "device support" for practical operation. Particularly, it is essential to write a flexible support program for the memory board, because it will be used for various purposes.

6 SUMMARY

We fabricated the signal process systems for our bunch feedback systems. This system is based on hardware logic and can work at the bunch frequency of 509MHz. One of the main features of system is that we developed a custom LSI for fast de-multiplexing and multiplexing. The fabrication of these custom LSI is a little expensive. But thanks to these LSIs, we can made not only the feedback electronics but also a powerful transition memory board. It can be a powerful tool for the beam diagnostics.

7 ACKNOWLEDGEMENTS

The authors would like to give thanks to all the members of the bunch-feedback developing group of PEP-II. They thank also the DAΦNE feedback group. The discussions with them is very fruitful for us.

8 REFERENCES

[1] "PEP-II An Asymmetric B-Factory", LBL-PUB-5379, SLAC-418, CALT-68-1869, UCRL-ID-114055,UC-IIRPA-93-01.
[2] R. Boni et al., in Proceedings of EPAC96, p.1881.
[3] J.N. Corlett et al., in proceedings of EPAC94, p.1625.
[4] R. Boni et al., Particle Accelerators, 52 (1996) 95.
[5] E. Kikutani and Y. Minagawa, KEK-Report 94-5.
[6] Y. Minagawa et al.,in Proceedings of EPAC96, P.1890.
[7] F. Pedersen, talk given at Workshop on Multibunch Feedback - Filters and Signal Processing, November 1992, Erice.
[8] E. Kikutani et al., The proceedings of EPAC96 p.1893.
[9] Z.Y. Guo, in Proceedings of EPAC96, p.1042.
[10] M. Tobiyama et al.,: these proceedings (session 4P63).
[11] H. Fukuma et al., in these proceedings (session 2V9).
[12] S. Matsumoto et al., in these proceedings (session 6B6).
[13] M. Tobiyama et al., The proceedings of the 7-th Beam Instrumentation Workshop, Argonne, Il. AIP Prceedings 390.
[14] N. Yamamoto et al., in Proceedings of PAC95, p.2205.

STUDY OF BUNCH BY BUNCH FEEDBACK SYSTEM IN TRISTAN-AR

M. Tobiyama and E. Kikutani
Accelerator Laboratory, High Energy Accelerator Research Organization(KEK),
1-1 Oho, Tsukuba 305, Japan

Abstract

Beam tests of the KEKB bunch by bunch feedback system prototypes have been performed in the TRISTAN-AR on both longitudinal and transverse planes. A two-tap FIR filter system consisting of hardware logic's realized the function of the phase shift by 90 degrees, the suppression of the static component and the delay of up to a few tens of turns in longitudinal plane with 508 MHz of system clock. The transverse systems were purely analog system without any digital signal processing part. More than 100 bunches with maximum current of 376 mA have been accumulated successfully with the bunch spacing of 2 ns. The growth time and the growing modes of the transverse instabilities has also been measured with the memory function of the two-tap FIR filter. It suggests that the bunch-by-bunch feedback system is a powerful tool to explore the source of the instabilities.

1 INTRODUCTION

The KEKB rings are designed to accumulate huge beam current with many bunches. Even with the great care on the reduction of the possible impedance sources around a beam, unexpected impedance may remain high and may cause strong coupled bunch instabilities. The method to analyze and suppress the instabilities has the key to achieve the expected quality of the rings. A straightforward and the only realistic method is to apply bunch by bunch feedback based on very fast digital technology with the wide bandwidth up to 255 MHz and large power to supply enough negative impedance. The target of the KEKB bunch feedback systems has been set to achieve the damping time of about 1 ms both on the transverse and the longitudinal planes for the minimum bunch spacing of 2 ns.

The feedback system consists of three major parts: a front-end circuit to detect the bunch positions, a signal processing system, and kickers and wideband amplifiers with large power. The front-end circuit need to detect the individual bunch positions without disturbed by the signals from the preceding bunches with enough resolution. The signal processing system is a simple digital filter with the function of signal delay which correspond to phase rotation thorough 90°, and the noise elimination if necessary. The kickers should have enough shunt impedance over the necessary bandwidth without HOM's.

We have installed prototype systems in TRISTAN accumulation ring (TRISTAN-AR) and examined the feasibility of the system during the AR high beam current accumulation study. Related parameters of the TRISTAN-AR for the high current study are listed in Table 1.

Circumference	377.26	m
RF Frequency f_{RF}	508.58	MHz
Harmonic number	640	
Tune ν_x, ν_y	10.16, 10.23	
Beam Energy E	2.5	GeV
Typical RF voltage	1	MV
Typical Synchrotron tune ν_s	0.22	
Longitudinal damping time τ_ϵ	21.6	ms
Transverse damping time τ_x, y	43.1	ms
Natural bunch length σ_z	2	cm

Table 1: Main parameter of TRISTAN-AR

2 EXPERIMENTAL SETUP

2.1 Transverse system

A block diagram of the transverse feedback system prototype at TRISTAN-AR is shown in Fig. 1.

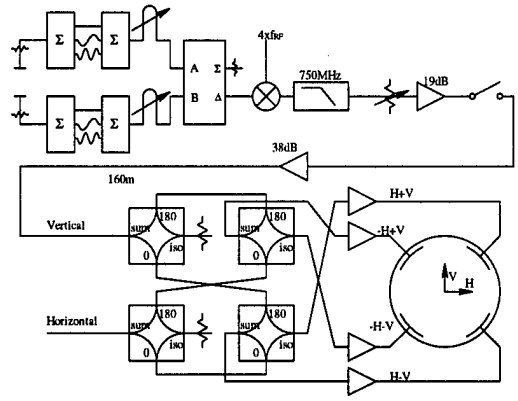

Figure 1: Block diagram of the transverse feedback system prototype installed in AR.

Signals from a button electrode is divided into three branches by a power combiner and summed up again by the other power combiner. As the lengths of the delay cables which connect the two combiners are chosen to be of α + nλ (n=0,1,2), where α is constant and λ is the wavelength of the detection frequency, this system works as an FIR bandpass filter with the first center frequency of nλ/c. The detection frequency is chosen to be the 4-th harmonic of the RF frequency. The differential of the two sine-like burst signal by the 180°-hybrid is multiplied by the reference signal which is quadruple of the RF signal with a double balanced mixer (DBM). Higher-frequency components are rejected by a low pass filter (LPF) of which cutoff frequency is 750 MHz.

0-7803-4376-X/98/$10.00 © 1998 IEEE

The stripline kicker has four electrodes with the length of 30 cm and the opening angle of 60° rotated 45° from horizontal plane. As it was impossible to prepare amplifiers which have bandwidth from 95 kHz to 255 MHz, we divided the bandwidth into two parts; from 95 kHz to 25 MHz (lower-band) and from 20 MHz to 255 MHz (higher-band) and used two stripline kickers for each amplifier sets. Totally, four lower-band amplifiers and four higher-band amplifiers were used. The maximum power output for each amplifiers was 200 W.

The damping times for the bunch current of 4 mA are estimated about 400 μs for the horizontal plane and about 800 μs for the vertical plane.

2.2 *Longitudinal system*

Figure 2 shows a block diagram of the longitudinal feedback system prototype.

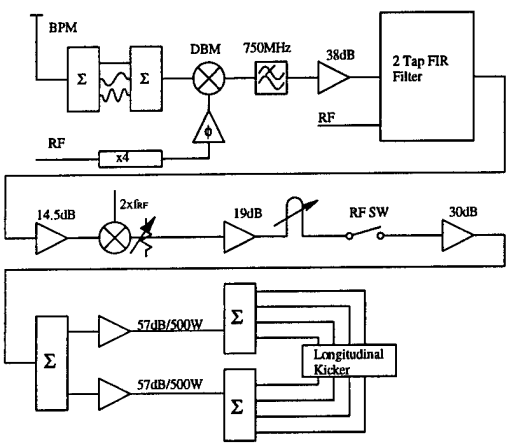

Figure 2: Block diagram of the longitudinal feedback system prototype installed in AR.

The longitudinal position of a bunch is measured with a wideband phase detection system. Using same BPF and the DBM as the transverse system, the sine-like burst signal from a bunch is multiplied by the quadruple of the RF signal. This time the nominal phase is adjusted to be 90° shifted from that of the bunch. By rejecting the higher-frequency component with the LPF, baseband signal of a synchrotron oscillation is detected as the form of $\sim I_b \Phi \sin(\omega_s t)$ if the amplitude Φ is small.

The signal process is performed with a two-tap FIR filter realized by a simple hardware system. Detailed description of the filter system is written in the reference[1]. We have used a four cells of series-drift-tube type longitudinal kicker just same structure as used in ALS at LBNL[2]. Total shunt impedance was about 1.6 kΩ and the maximum feedback voltage was 1.7 kV/turn.

3 BEAM TEST OF THE FEEDBACK SYSTEMS

General information of the high beam current study of AR is written elsewhere[3]. We therefore concentrate only the subject concerning to the feedback experiments here.

3.1 *Transverse feedback experiment*

We have encountered heavy coupled bunch instabilities both in horizontal and longitudinal planes and could not accumulate bunch train without the transverse feedback systems. Maximum number of stored bunches was less than 25 bunches.

With the transverse feedback system on, we successfully accumulated more than 300 bunches with the bunch spacing of 2 ns and the bunch current of 1 mA. Table 2 shows the maximum number of accumulated bunches on the bunch train mode with the bunch spacing of 2 ns together with the state of each feedback system.

Bunch current	H: off V: off	H: On V: off	H: off V: On	H: On V: On
1 mA	18	20	—	> 300
2 mA	20	70	20	> 170
4 mA	25	25	65	> 100

Table 2: Maximum number of stored bunches with the bunch train mode. H means horizontal system and V means vertical system.

The maximum stored beam current of 376 mA with the transverse feedback system on was achieved with the bunch train mode of 4 mA per bunches. We also applied the feedback system to the equally filled mode such as 8 ns or 10 ns spacing mode and succeeded to suppress the instabilities.

We have measured the growth and damp of the instabilities in time domain employing the memory function of the two-tap FIR filter complex. As the filter has 1 Mb of memory, we have recorded the oscillation of all the bunches about 1600 turns. The growth time of the instabilities just after turning off the feedback system was about 2 $\sim$ 3 ms for both horizontal and vertical planes, much faster then the radiation damping time. The damping time just after turning on the feedback was less than 1 ms for horizontal plane, about 2 ms for vertical plane, which are consistent with the rough estimates of the damping times. By arranging the data in a two dimensional array of bunch number vs. revolution time and making the Fourier transform of each rows, we get the change of the modes of the oscillation of the bunches in time domain. Figure 3 shows an example of the growing modes of vertical instabilities starting 3 ms after turning off the vertical feedback system. The filling pattern was equally spaced mode with 5 bunch spacing, 2 mA/bunch. Clearly only one mode corresponding to 10.2 MHz is growing rapidly.

In the horizontal plane, three modes corresponding to 9.4 MHz, 22.2 MHz and 25 MHz were growing rapidly.

3.2 *Longitudinal feedback experiment*

As it was impossible to accumulate the multi-bunched beam without transverse feedback system, we always turned on the transverse systems with the maximum gain during the longitudinal experiments. We have at first tuned

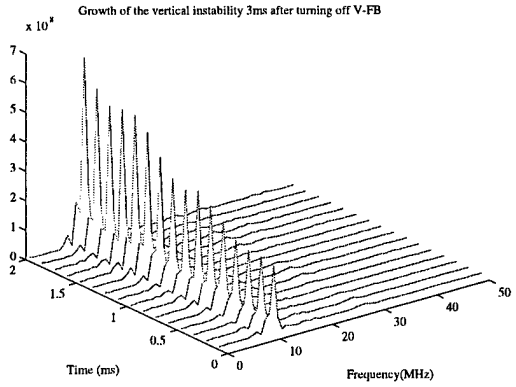

Figure 3: Growth of the vertical coupled bunch oscillation observed with the two-tap FIR filter.

the tap positions of the two tap filter to have the maximum gain with the positive feedback loop. Also the phase of the kicker was adjusted with the same situations.

In the bunch train mode with the bunch spacing of 4 ns and the bunch current of 2 mA, the synchrotron oscillation was successfully damped up to 6 bunches. However, when we injected the 7-th bunch, it occurred strong quadrupole oscillation in the 7-th bunch and was impossible to damp, though the first sideband was suppressed. It obviously shows there is huge longitudinal impedance in the ring.

In the equally spaced bunched mode with 10 bunches space and 2 mA/bunch, we successfully suppressed the longitudinal oscillation. However, if we once turned off the feedback system, we could not re-capture the oscillation when turning on the feedback until the total current has reduced from 120 mA to 90 mA. This shows that the maximum feedback voltage was insufficient. With the equally spaced mode with 5 bunch space and 1 mA/bunch, we also successfully suppressed the oscillation. This time we easily re-captured the oscillation after turning off the feedback system. Figure 4 shows the beam spectrum with the longitudinal feedback off and on.

During the high-current study at AR, we monitored the temperatures of the vacuum components and the high power components of the feedback systems. No fatal troubles has occurred during the experiment. We also checked the status of the components after the experiment and got no damage at all except the final power combiner to the longitudinal kickers.

4 SUMMARY

We have installed the transverse and longitudinal feedback systems which are prototypes for KEKB rings in the TRISTAN-AR and examined the feasibility with the high beam current study. As the instabilities were fairly stronger than expected before the experiment, it was unexpectedly heavy examination for our feedback systems.

The analog transverse feedback systems worked very well. With the two-tap FIR filter as the memory board, we observed the growth and damp of the modes of the oscillation. Also our system worked as the instrumentation tool for other experiments, such as the first ion trapping experiment[4]. They clearly observed the individual oscillation of bunches in the bunch train with 2 ns spacing.

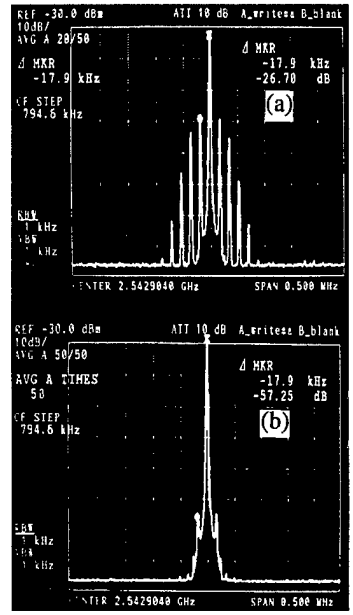

Figure 4: Beam spectrums (a) with longitudinal feedback off (b) with longitudinal feedback on. Without the feedback, there appeared many synchrotron sidebands corresponding to the strong longitudinal oscillations. The amplitude of the first sideband has reduced down to -30dB with the longitudinal feedback. The total beam current was about 120 mA.

The longitudinal system worked, though it also showed the insufficient feedback voltage for the oscillation with large amplitude. Invest much more power in the final amplifier and the use of kickers with larger shunt impedance will be necessary for the KEKB rings.

5 ACKNOWLEDGMENTS

The authors would like to express their sincere appreciation to Prof. T. Kasuga and Dr. T. Obina of KEK-PF for numerous thoughtful discussions. We thank Dr. Y. Funakoshi who spent much time to operate the accelerator during our experiments.

6 REFERENCES

[1] E. Kikutani, *et al*, in proceedings of the 5th European Particle Accelerator Conference, Sitges, Spain, 1996, p.1893.

[2] J. N. Corlett *et al.*, in proceedings of the 4th European Particle Accelerator Conference, London, UK, 1994 p. 1625.

[3] Y. Funakoshi, these proceedings.

[4] H. Fukuma, *et al.*, these proceedings.

APT LLRF CONTROL SYSTEM MODEL RESULTS*

A. Regan, Los Alamos National Laboratory, LANSCE Division, Los Alamos, NM, USA and
C. Ziomek, Z-TEC, Albuquerque, NM, USA

Abstract

The low-level RF (LLRF) control system is an essential component of the RF system for the Accelerator Production of Tritium (APT). Requisite for good performance at a reasonable cost is system modeling prior to actual hardware build. Models have been created to help establish the LLRF control system baseline design. These models incorporate common signal processing functions and control functions as well as mixed continuous and discrete-time analysis. Components include klystron saturation curves, waveguide delays, realistic resonant cavity equivalents, and LLRF proportional, integral, and differential (PID) control transfer functions. They predict the performance of the LLRF system in the presence of beam noise, excitation of non-fundamental modes which occur in the superconducting cavities, and pulsed beam situations. This paper will describe the basic model and will present results for a variety of operating scenarios.

1 MODEL DESCRIPTION

The functionality of the low-level RF (LLRF) control system for the APT was described in reference 1. In order to best design this system we have relied on computer modeling to predict system response to a variety of inputs during different operational scenarios. The software used is MATRIXX™, a graphical modeling and analysis control system program. In MATRIXX™, common signal-processing and control functions such as transfer functions, limiting, dead band, etc. are all available. It allows both linear and nonlinear functions, as well as mixed continuous and discrete-time analysis (e.g., digital control of a continuous-time plant) and it provides iconic programming (functional blocks, signal flow connectors). We have developed LLRF control system models for a variety of reasons: 1) specification of RF components; 2) verification of system design and performance objectives; 3) optimization of control parameters; and 4) testbed for exploratory control system development. This modeling has been utilized and proven on a number of LLRF control system designs: GTA; AFEL; Boeing's APLE; University of Twente's FEL. It is now being used as a tool for the design of the APT LLRF control system.

The graphical modeling approach allows the model to be built as a combination of "superblocks," each representing the transfer function of its individual components. The overall system model schematic is represented by the top-level block diagram shown in figure 1. Represented as baseband in-phase and quadrature signals, the model includes an ideal current-source beam with noise, a multi-mode accelerator cavity (single gap), a non-linear klystron (with saturation and ripple), waveguide and transmission line delays, and a LLRF controller with feedback and feedforward characteristics. The level of detail available to represent individual components within the RF system (including the accelerating cavity) can be significant. With such a model, we have been able to predict how a particular LLRF control system design will react to a variety of operational scenarios. These include the presence of beam noise, klystron high voltage power supply ripple, and beam pulsing or fault shutdown.

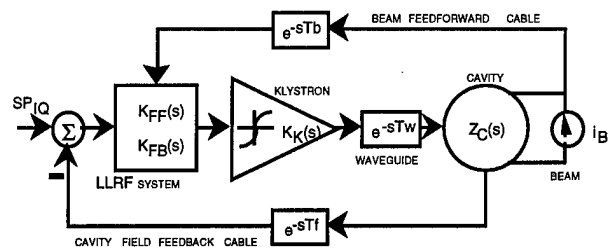

Figure 1. LLRF control system model block diagram.

2 MODEL RESULTS

Model analysis provides for certain parameters to be modified depending on the scenario being tested. These external parameters allow easy modification of the core model to investigate different operational cases. Figures 2 through 6 show the results of modeling the case of normal turn-on of the RF into the cavity followed by turn-on of the beam, as well as the case of rapid beam shutdown (due to pulsing or a beam abort).

As seen in figure 2, there is an initial RF turn-on transient in the cavity field and a spike in the field amplitude and phase errors. Figure 2 shows the type of field amplitude and phase errors we can expect for this turn-on/ CW operation. As seen, the beam turn-on causes a +1/-2% field amplitude error and a +1/-0.5° field phase error. The LLRF control system in this model utilizes just a cavity field feedback signal. An optional beam feedforward feature for tighter control is discussed at the end of this paper.

Figure 3 shows that the klystron saturates until the field gets close to its nominal value when the loop achieves control and the cavity field and klystron forward

* Work supported by US Department of Energy.

amplitude settle to their nominal levels (ready for beam). Field errors are now close to zero. Reflected amplitude is identical to the forward amplitude without beam, indicating the large mismatch due to strong overcoupling without beam. When the beam is turned on, at t = 500 μs, the klystron forward output increases to compensate for the beam loading and the klystron saturates once more. Again, the cavity field and klystron forward amplitude eventually settle to their nominal levels.

Since any beam noise will drive modes other than the fundamental in the superconducting cavities, we wanted to study the effects of these other modes. Figures 3 and 4 show the results when we include the two modes nearest to the fundamental. The klystron output does not match perfectly to these other modes in the cavity, and consequently, the reflected signal (figure 3) does not drop to zero as expected when the beam is present. Note the relative magnitudes of the plots in figure 4. Because the steady-state magnitude of the fundamental is approximately 3400 times that of the 698 MHz mode and even greater than that of the 681 MHz mode, their effects are fairly minimal. With a 2 MHz filter built into the feedback control system (to eliminate the possiblity of attempting to control a fedback mode signal which would have the wrong phase and thereby cause the control system response to blow up) the transient-induced modes damp out over time.

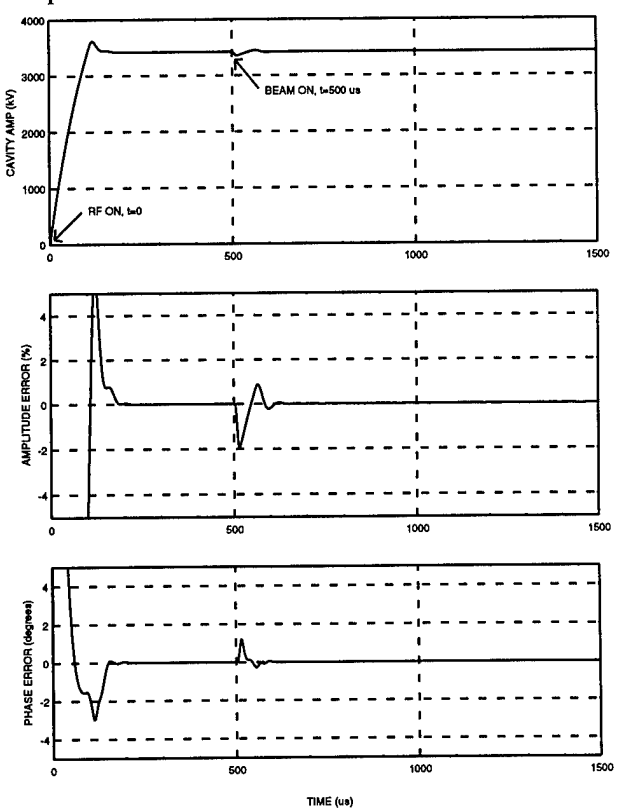

Figure 2. Normal RF and beam turn-on. Cavity field, amplitude and phase errors.

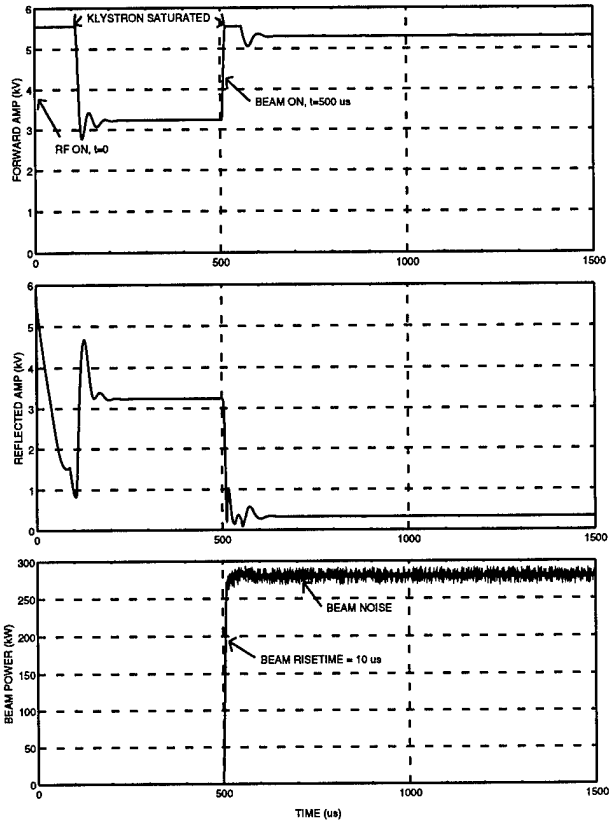

Figure 3. Normal RF and beam turn-on. Forward signal out of klystron, cavity reflected signal, beam power in the cavity.

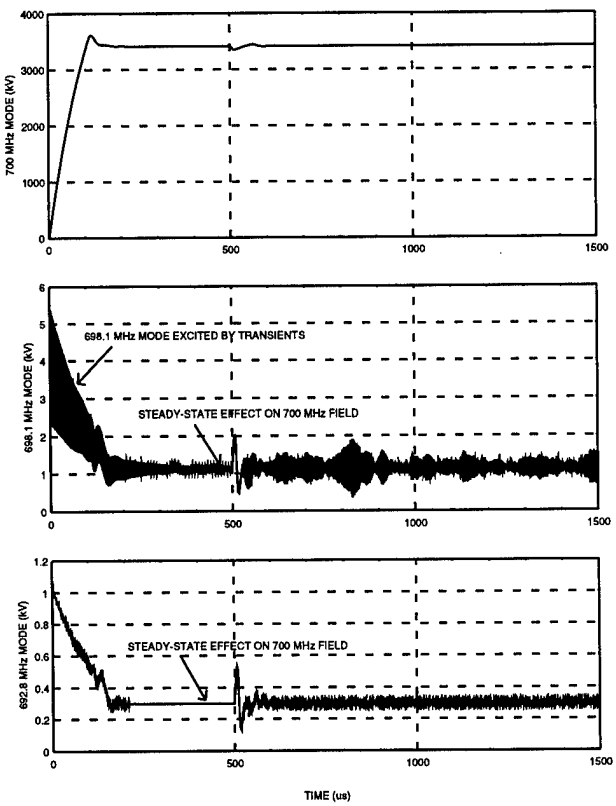

Figure 4. Normal RF and beam turn-on: cavity modes excited.

Another case investigated with the model was the effect of rapid beam shutdown. This might occur intentionally due to pulsing of the beam, perhaps for cavity conditioning, or unintentionally, due to a beam abort caused by some system error requiring fast beam shutdown. As seen in figures 5 and 6, without beam feedforward, there is a large transient when the beam is turned off, while the RF remains on. However, this transient is short-lived and should not cause any problems to the cavities.

When the beam is off and the transient passed, the cavity and the klystron return to the states they were in prior to the beam turn-on, and are ready for beam re-introduction. This model indicates that if the beam is turned off, the control system requires it to remain off for at least 50 μs before turning it on again in order to reach a controlled steady-state field in the cavity.

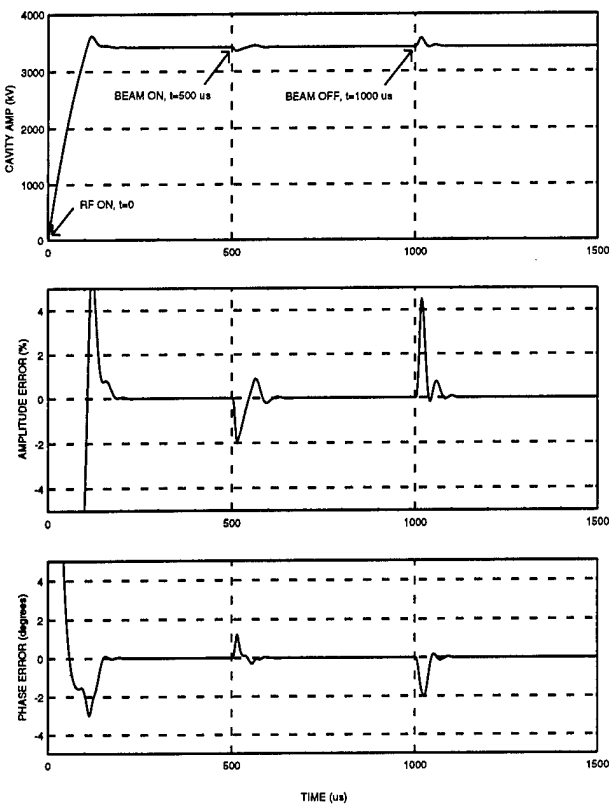

Figure 5. Beam turn-off effect on cavity field, error signals.

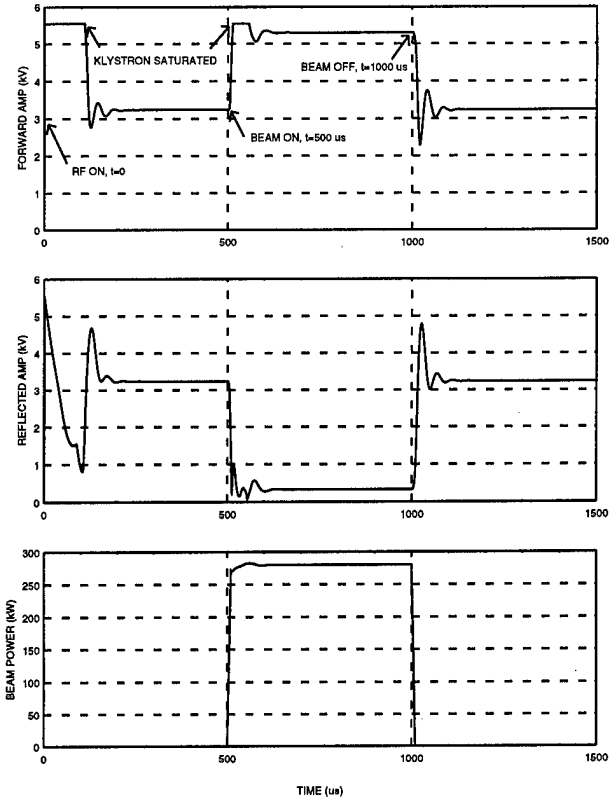

Figure 6. Beam turn-off effect on forward signal out of klystron, cavity reflected signal. Beam power shown.

We have also done some modeling to predict the effectiveness of a beam feedforward feature in the LLRF control system. These models predict that we can reduce the turn-on and turn-off transients that occur in the amplitude and phase errors to +1/-0.5% and +0.3/-0.5° respectively.

3 CONCLUSIONS

The modeling effort has been extensive for the APT project. The basic LLRF control system model has been proven on past projects and gives a solid foundation upon which to base our LLRF control system design. We are now in the process of developing VXIbus modules which perform the control functions defined by the models.

REFERENCES

[1] Regan, A.H., et al, "APT LLRF Control System Functionality and Architecture," Linac96 Proceedings, Geneva, Switzerland, August 1996, pp. 225-227.

[2] Ziomek, C.D., et al, "Low-Level RF Control System Issues for an ADTT Accelerator," ADTT Conference Proceedings, Las Vegas, NV, July, 1994.

[3] Cheo, B.R. and Jachim, S.P., "Dynamic Interactions Between RF Sources and Linac Cavities with Beam Loading," submitted to IEEE Trans. Elec. Dev., 1990.

ALGORITHMS AND IMPLEMENTATIONS OF APT RESONANT CONTROL SYSTEM*

Yi-Ming Wang† and Amy Regan, Los Alamos National Laboratory,
P.O. Box 1663, Los Alamos, NM 87545, USA

Abstract

A digital signal processor is implemented to control the resonant frequency of the RFQ prototype in APT/LEDA. Two schemes are implemented to calculate the resonant frequency of the RFQ. One uses the measurement of the forward and reflected fields. The other uses the measurement of the forward and transmitted fields. The former is sensitive and accurate when the operation frequency is relatively far from the resonant frequency. The latter gives accurate results when the operation frequency is close to the resonant frequency. Linearized algorithms are derived to calculate the resonant frequency of the RFQ efficiently using a fixed-point DSP. The control frequency range is about 100kHz for 350MHz operation frequency. A frequency agile scheme is employed using a dual direct digital synthesizer to drive the klystron at the cavity's resonant frequency (not necessarily the required beam resonant frequency) in power-up mode to quickly bring the cavity to the desired resonant beam frequency. This paper will address the algorithm implementation and error analysis, as well as related hardware design issues.

1 INTRODUCTION

Resonant control of the RFQ and superconducting RF cavities requires accurate measurement of the RF cavity resonant frequency. For a digital implementation of the resonant control system in APT/LEDA, an efficient and accurate algorithm is needed to provide a real time error signal to the cavity water cooling system within a desired bandwidth. The algorithm proposed in this paper utilizes the vector measurement of the forward, reflected, and transmitted fields to calculate the complex load impedance or admittance. Knowing the complex load impedance and the loaded quality factor Q of the cavity, the discrepancy of the operating frequency and the resonant frequency can be derived accordingly. A simple linear relationship between the imaginary part of the load admittance and error signal (difference between operating frequency and the cavity resonant frequency) is derived by linearizing a general quadratic relation between the imaginary load admittance and resonant frequency. Numerical simulations reveal that the difference between the full solution and approximated linear solution is negligible within the frequency range we are interested ($f_0 \pm 100$Hz).

2 SYSTEM IMPLEMENTATION

Figure 1 is a block diagram of the resonant control module for APT/LEDA.

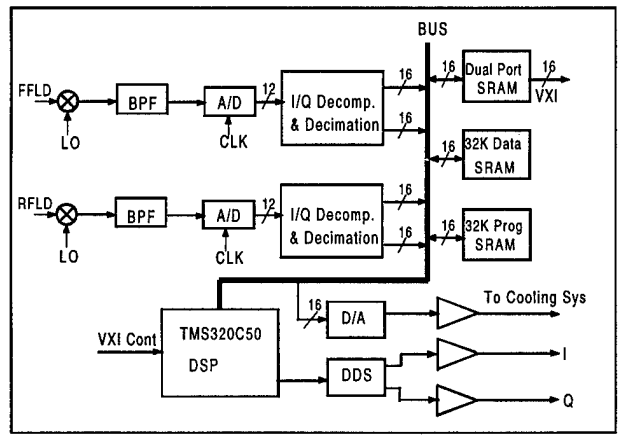

Figure 1. Block Diagram of Resonant Control Module

The RF frequency is 350MHz for APT/LEDA. The LO is 300MHz. The A/D converter clock is 40MHz. Since the IF frequency is 50MHz, the output of the A/D converter is a data stream consisting of the repeat pattern of measured I, Q, -I, and -Q components. The output of the A/D converter is fed into a multiplexer that switches every other sample into two parallel paths to separate the I and Q components. Then, each channel of the data stream is multiplied by +1 or -1 to remove the alternating sign accordingly. The outputs are the measured I and Q components of the input RF signal. The major advantage of the above described digital I/Q demodulation scheme is the single analog signal path for both I and Q components that ensures a perfect gain-matching between the I and Q signals. Secondly, since the sampled signal is at the IF frequency (50MHz), analog DC offsets and drifts do not affect the accuracy of the digital I/Q demodulation. A dual DDS is used to generate two off-phase error correction sine waves for I/Q modulation in the frequency agile mode.

* Work supported by US Department of Energy.

3 RESONANT CONTROL ALGORITHM

The resonant control algorithm of APT/LEDA is based on the vector measurement of the forward, reflected or transmitted fields. Figure 2 depicts a simplified transmission model for a cavity driven system. The complex load impedance of the cavity is Z_L. The transmission line impedance is Z_0. The forward and reflected field are measured at z_1 and z_2 respectively, which are between $z=0$ and $z=l$. Here l is the length of the transmission line from klystron to cavity.

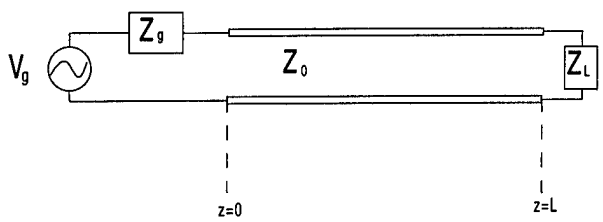

Figure 2. Waveguide with a length of L and load Z_L.

Using the transmission theory[1], we can show that the load impedance is related to the measured forward and reflected fields as

$$Z_L = \frac{V(l)}{I(l)} = Z_0 \frac{V^+(z_1)e^{\gamma(z_1-l)} + V^-(z_2)e^{-\gamma(z_2-l)}}{V^+(z_1)e^{\gamma(z_1-l)} - V^-(z_2)e^{-\gamma(z_2-l)}} \tag{1}$$

From (1), we have

$$Y_L = \frac{1}{Z_L} = Y_L^r + jY_L^i \tag{2}$$

For a parallel RLC resonant circuit, Y_L is

$$Y_L = \frac{1}{R}[1 + j(\frac{\omega RC\omega_0}{\omega_0} - \frac{RC}{\omega LC})]. \tag{3}$$

Using $\omega_0 = \frac{1}{\sqrt{LC}}$ and $Q_0 = RC\omega_0$, we have

$$Y_L = \frac{1}{R}[1 + jQ_0(\frac{\omega}{\omega_0} - \frac{\omega_0}{\omega})]. \tag{4}$$

For $Q_0 >> 0$, and $\frac{|\omega - \omega_0|}{\omega_0} << 1$, it can be shown that

$$\omega_0 - \omega = \Delta\omega \approx -\frac{\omega}{2Q_0}\frac{Y_L^i}{Y_L^r} \tag{5}$$

Eq. (5) is used to determine the difference between the resonant frequency and the operation frequency.

4 SIMULATION RESULTS

To verify the validity of the algorithm, a simulation was conducted using Eq. (5) and Eq. (1) to get the error signal vs. Frequency with a random noise added to the measured fields(20dB Signal-to-Noise Ratio). The results are shown in Figure 3. This result shows that Eq. (5) together with Eq. (1) gives a satisfactory result within the frequency range we are interested.

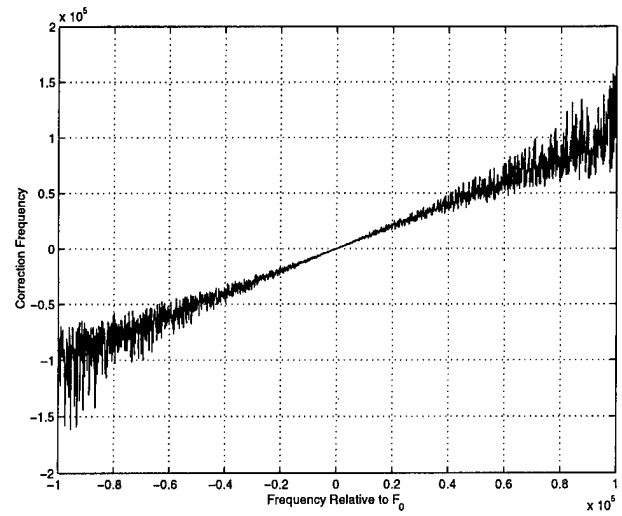

Figure 3. The result with noise in the measurement.

In figure 3, the correction frequency is obtained when the SNR (Signal-to-Noise Ratio) of the measured field is 20dB. Notice that the perfect gain-matching in our digital I/Q demodulation scheme ensures the equal effect of noise on both I and Q channels. Thus, we can represent the measured field as $(1+r)F$, where r is noise, F is the complex field without noise. Mathematically, this means that the noise correlation coefficient between two channels (I and Q) is one.

One important feature in Figure 3 is that the correction frequency never crosses zero on both sides of the resonant frequency f_0. This indicates that no ambiguity can exist regarding the sign and/or direction the correction frequency required. Next we investigated the correlated and uncorrelated I/Q noise on robustness of the algorithm. Here, we assumed that the SNR of the measurement is only 3dB. Figure 4 is for a completely correlated noise case. Figure 5 is for a completely uncorrelated noise case. It is very important to notice that the correction frequency never crosses zero on both sides of the resonant frequency for the case with the completely correlated noise for I/Q components. This means that when we implement this algorithm in this case, we always have a correct sign for the error signal. In contrast, the correction signal for the completely uncorrelated case back does across zero on both sides of the resonant frequency, potentially leading to ambiguity.

As mentioned before, the digital I/Q decomposition scheme implemented in our system ensures the perfect gain-matching for the I and Q channels which results in the completely correlated noise for the I and Q channels.

Therefore, the algorithm applied to our system is very robust.

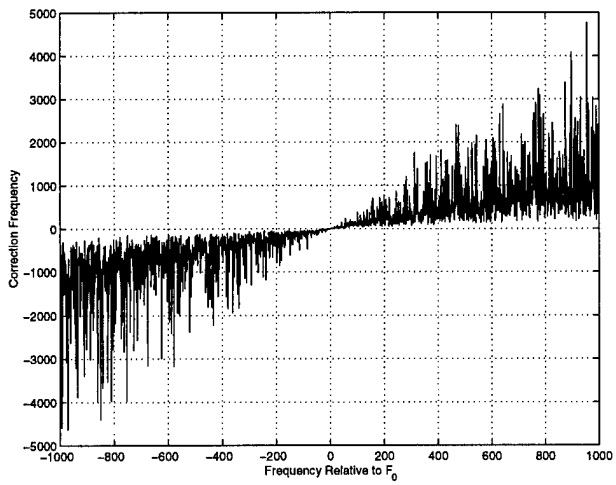

Figure 4. Result for the correlated noise case.

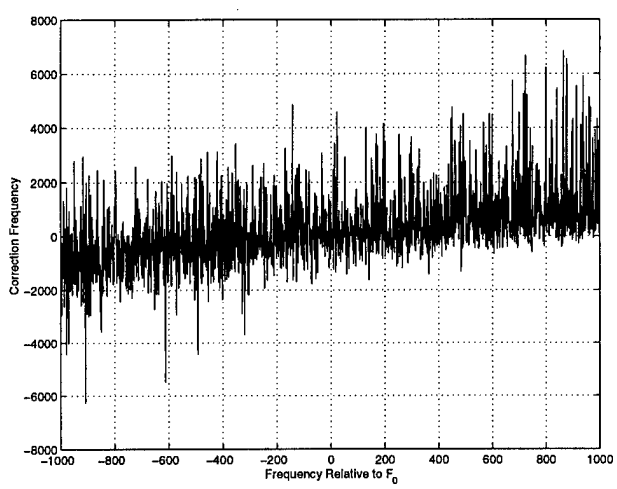

Figure 5. Result for the uncorrelated noise case.

5 OTHER CONSIDERATIONS

Here, all formulas are derived based on the forward and reflected fields. Similar formulas can also be derived from the forward and transmitted fields. Mathematically, they are equivalent. But some practical issues should be addressed when we decide which set of formulas to use in the system implementation. One limitation comes from the finite resolution of the A/D converter. For a 12bit A/D converter, as used in our system, the dynamic range of measurement is around 60dB. However, due to some instrumentation limitations, such as isolation of the directional coupler, the dynamic range of the measured signal could be 10 to 20 dB lower than the theoretical dynamic range of the A/D converter. Given the above consideration we don't want the magnitude of the measured field to change dramatically during normal operation.

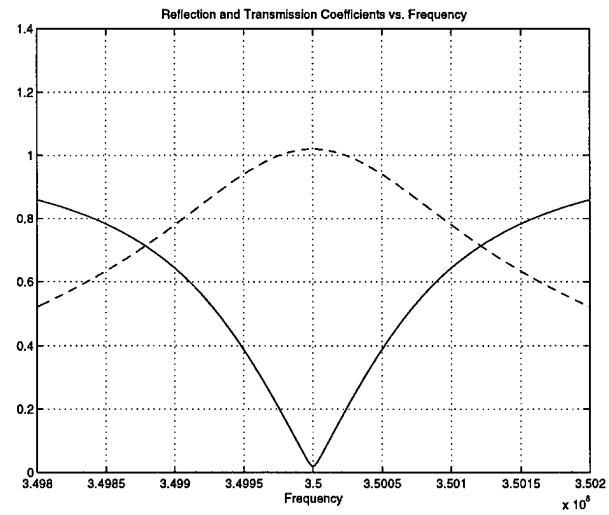

Figure 6. Magnitude of the reflection and transmission coefficients vs. frequency.

Figure 6 depicts the magnitude of the reflection and transmission coefficients for an equivalent RLC load with $Q = 3000$ and $f_0 = 350\,\text{MHz}$. From Figure 6, we can see that using the reflected field algorithm is good when the frequency is relatively far from resonance but the accuracy of the measurement will deteriorate when the frequency is close to resonance. However, on the other hand, the accuracy of the transmitted field algorithm is higher when the frequency is close to resonance and lower when the frequency is away from resonance. Based on the above observation, both algorithms are implemented in our system. The reflected field algorithm will be activated when the frequency is relatively far from resonance and the transmitted field algorithm will be activated when the frequency is close to resonance.

6 CONCLUSIONS

An efficient and simple algorithm that is suitable for the implementation in a digital signal processor is proposed. The simulation results reveal that the algorithm is very robust when implemented with the digital I/Q demodulation scheme used in our system. The algorithm gives a good result with a noise level at 20dB SNR.

REFERENCES

[1] Cheng, K.C., 'Field and Wave Electromagnetics', Second Edition, Addison-Wesley, 1989.

[2] Ziomek, C. and Corredoura, P., 'Digital I/Q Demodulator', PAC'95, 1995.

STATUS OF THE PEP-II TRANSVERSE FEEDBACK SYSTEMS*

W. Barry, J. Corlett, M. Fahmie, J. Greer, G. Lambertson, C. Pike, Lawrence Berkeley National Laboratory, Berkeley, CA 94720.

The feedback systems for controlling transverse coupled-bunch instabilities in both the high and low energy rings of the PEP-II collider are complete and installed on site. Presently, the high energy ring of the collider is beginning commissioning. The commissioning of the high energy ring transverse feedback system is expected to begin sometime in the next few weeks. Design specifications and the basic system concept are reviewed. Selected bench-test results for various system components are discussed including results from the sum-signal orbit offset cancellation electronics.

I. INTRODUCTION

The PEP-II B-Factory is a high-luminosity, asymmetric electron-positron collider for studying and determining the origin of CP violation in the B-meson system[1]. The collider consists of a 9 GeV high-energy storage ring (HER), and a 3.1 GeV low-energy storage ring (LER). Presently, the HER is being commissioned while construction of the LER continues with an expected completion date of April, 1998.

Because of the high average beam currents (1 A HER and 2.14 A LER), active feedback systems for controlling longitudinal[2] and transverse[3] coupled-bunch instabilities are required. The storage rings are designed to accommodate a large number of bunches, up to 3316 in buckets separated by 2.1 ns (476 MHz RF). As a result, a broad and dense spectrum of transverse coupled-bunch modes are driven by the higher-order transverse modes of the RF cavities and the transverse resistive-wall impedance. In order to effectively damp and control growth of these modes, the transverse feedback systems must be broad-band with the capability of providing bunch-by-bunch correction. Systems for both the HER and LER which have been modeled after the ALS transverse bunch-by-bunch system[4], have been designed, constructed and installed at the PEP-II sector 4 straights. In this paper, the system concept and specifications are reviewed with emphasis placed on some of the more challenging hardware designs and results.

II. SYSTEM SPECIFICATIONS

Nominally, PEP-II will operate with every other bucket filled (238 MHz bunch rate) and a small ion clearing gap. In this case, the minimum required bandwidth for the feedback system is 119 MHz. However, the feedback systems, as indicated in table 1, have been designed to have a bandwidth of 250 MHz in order to accommodate the possibility of operating with every bucket filled. One exception is the stripline kickers which are designed to cover the DC - 119 MHz band because they are more power efficient than shorter versions which would cover the DC - 238 MHz band. These may be replaced with a 238 MHz design, and if needed, more power amplifiers may be added if the 476 MHz bunch-rate becomes a likely operating scenario.

Parameter	Description	Value
E	Beam energy	3.1 GeV
f_{rf}	RF frequency	476 MHz
I_b	Average current	3.0 A
f_0	Orbit frequency	136.3 kHz
β_{av}	Average β	10 m
ν_f	Fractional tune	0.9
τ_b	Bunch spacing	4.2 ns
Z_{rw}	R-wall impedance	4.85 MΩ/m
α_0	Growth rate of m = 0 mode	3200 sec^{-1}
$\partial V/\partial x$	Req'd feedback gain	14.6 kV/mm
R_s	Kicker shunt impedance	24 kΩ
P_k	Available kicker power	240 W
V_{max}	Max. available kick	3.4 kV
y_{max}	Max. mode amplitude	0.23 mm
V_{mode}	Voltage to excite y_{max}	71.3 kV-turn
Δf_{min}	Req'd bandpass	13.6 kHz-119 MHz
–	Electronics bandpass	10 kHz-250 MHz
–	Kicker bandpass	DC - 119 MHz
σ_y	Vert. beam size	0.16 mm
-	Req'd dynamic range	23 dB
-	Actual dynamic range	42 dB
y_{os}	Allowable effective orbit offset	1.8 mm

Table 1. Accelerator and feedback system parameters for assumed worst-case transverse coupled-bunch mode.

The transverse feedback systems are conservatively designed to handle a worst-case scenario which assumes a 3.0 A beam in the LER at a fractional tune of 0.9 (nominal LER current and tune are 2.14 A and 0.64 respectively). In this case, the fastest growing coupled-bunch mode is the m = 0 mode driven by the vertical resistive-wall impedance. Under these conditions, the maximum controllable mode amplitude is 0.23 mm.

*Supported by the US Department of Energy under Contract number DE-AC03-76SF00098 (LBL) and DE-AC03-76SF00515 (SLAC)

For nominal current and tune, the controllable amplitude is considerably greater. In any case, if the feedback system is operating from the time filling of the storage ring commences, it is unlikely that the modal voltage of 71.3 kV required to reach the amplitude limit of 0.23 mm could accumulate apart from interruption of the feedback loop. It should also be noted that simulations indicate[5] that any expected injection transients are easily damped by the feedback system. This is because the amplitudes of the normal coupled-bunch modes corresponding to the Fourier decomposition of the transient are extremely small. Injection transients can however produce large transient voltages which can saturate the feedback system. For this reason, damping of injection transients usually starts out in saturated mode where a fixed kick is given to the injected bunch until it is damped to a point where proportional feedback takes over.

The required dynamic range is based on the requirement that the amplitude of betatron oscillations be damped to 0.1σ. For the case in Table 1, a 23 dB dynamic range is required to cover mode amplitudes ranging from the maximum of 0.23 mm down to $0.1\sigma_y = 0.016$ mm. The actual dynamic range of the system corresponds to that of an 8 bit D/A, 42 dB. From the required and actual dynamic ranges, the maximum allowable effective orbit offset of 1.8 mm can be inferred. The effective orbit offset signal depends on the true closed-orbit offset, various electronic gain imbalances, fill pattern, and the effect of the offset rejection circuitry to be described.

III. FEEDBACK SYSTEM OVERVIEW

The PEP-II transverse feedback system concept matches quite closely that of the current ALS system and is described in the references. Therefore, only a brief review for orientation purposes is given here with features that are unique to the PEP-II systems pointed out in more detail.

The overall feedback system concept is shown in figure 1. The system utilizes two sets of button pickups separated by some angle in betatron phase for detecting beam moment, $I\Delta x$. The appropriate vector sum of these is taken to produce a correction signal that is 90 degrees out of phase with respect to beam position at the kickers. This condition results in resistive (no tune shift) damping and is adjustable to allow for changes in tune.

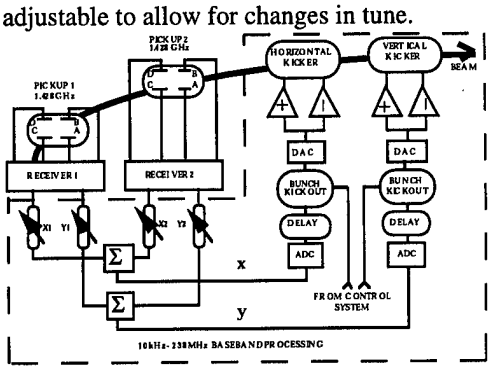

Figure 1. PEP-II transverse feedback system concept.

The beam moment signals are detected at the third harmonic of the RF (1.428 GHz) in order to take advantage of the good sensitivity of the button pickups at this frequency. The signals are demodulated to baseband with heterodyne receivers that also contain orbit offset rejection circuitry. Baseband processing consists of an analog system (shown as x and y attenuators) for proportional summing of the two pickup signals and a digital system that provides the necessary pickup-to-kicker timing delay. In addition, the digital electronics features circuitry for changing the sign and gain of the feedback for a given single bunch. This feature is used to trim the charges of single bunches to obtain a uniform fill or kickout an unwanted bunch entirely. Separate horizontal and vertical stripline kickers are used to apply the baseband correction kick to the beam. The kicker electrodes are individually driven with opposite polarities by 120 W, 10 kHz - 250 MHz, solid-state, Class-A, commercial amplifiers. Two components of the PEP-II systems not common to or differing from the present ALS system which presented particularly interesting design and implementation challenges are the receivers with orbit offset cancellation and the digital processors. These components are described in more detail below.

IV. RECEIVER DESIGN

The PEP-II transverse feedback system receiver design is shown in figure 2. Beam signals induced on each pickup are first bandpass filtered then processed in a microwave monopulse comparator hybrid to produce x and y beam moment signals at the 1.428 GHz carrier frequency. Subsequently, the signals are down-converted to baseband using standard heterodyne detection.

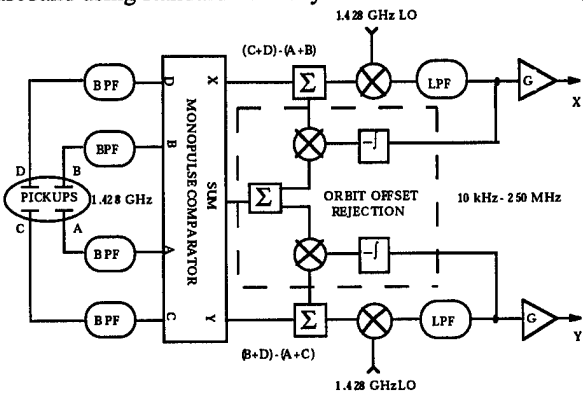

Figure 2. Receiver design.

Of special interest is the orbit offset rejection circuitry in the dashed box. In general, the x and y moment signals contain unwanted common -mode components that can saturate the feedback system. This common-mode signal is due to static beam orbit offset and, equivalently, imbalances in the gains of the button pickups and the electronics associated with them. The common-mode or offset signal has frequency components at integer multiples of the orbit frequency only and is spectrally indistinguishable, apart from an overall

amplitude factor, from the sum signal which is independent of betatron motion. Thus, to remove the common-mode component of the moment signal, some fraction of the sum signal from the comparator is added to or subtracted from it. As shown in figure 2, this process is automated in a feedback loop (which resides in a separate chassis). Figure 3 shows a typical bench measurement of the orbit-offset rejection performance. Here, the large pulse is the baseband receiver output for a simulated offset single bunch and the smaller trace is the bunch signal with the orbit offset rejection turned on. In this case, the rejection is about 20 dB. Because of differences in receiver components, the rejection from unit to unit was found to range from 15 dB to 26 dB over a large range of currents and offsets. If one assumes 15 dB of rejection and 1 dB of electronic imbalance, the system will handle a beam offset of 8mm and still meet the damping specifications in table 1.

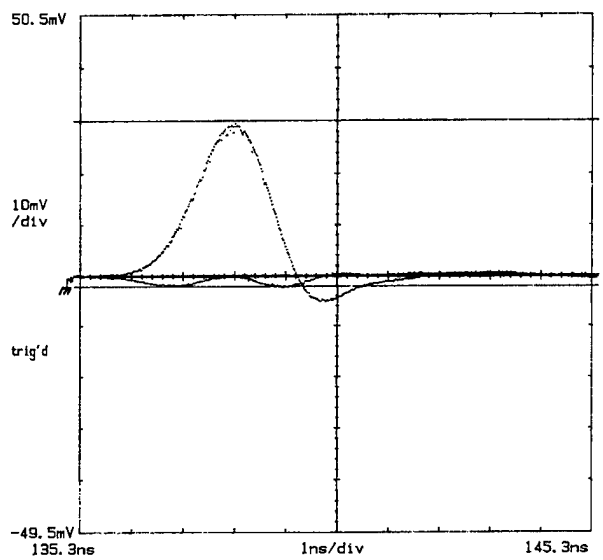

Figure 3. Orbit offset cancellation performance.

V. DIGITAL COMPONENTS

The digital components of the system basically consist of a fast analog-to-digital converter, circuitry for blanking or changing the sign of the feedback for a given bunch, a circular memory buffer to provide a pickup-to-kicker time delay of up to 8 microseconds, and a fast differential output digital-to-analog converter for driving the pre-amps/power amps. These features provide for the necessary system timing, single-bunch charge trim/kickout, and single-bunch tune measurement without the effects of feedback.

The baseband analog signal is sampled at 476 megasamples per second into 8-bit bi-polar digital form. The sampled data is then directed to a module, which on command, passes the data unaltered or inverts the sign for bunch kickout/trim, or simply blanks the feedback completely. These functions are selectable on a bunch-by-bunch basis. In this manner, any number of selected bunches may be kicked out, trimmed, or left uncontrolled simultaneously. The processed values are programmably delayed up to 8 microseconds, in steps of 2.1 nsec, by storing them in a circular buffer. The buffer is implemented with a fast ECL RAM array and EClips (tm) ECL logic devices. On alternate memory cycles, the values are written to the RAM array (into incrementing addresses) and then a previously stored value is read out from an offset address. The address offset is programmable and determines the amount of delay applied to the feedback signal. The delayed signal is then converted back into analog format by the fast digital to analog converter.

VI. CONCLUSION

The broadband transverse feedback systems for the PEP-II storage rings are complete, bench-tested and installed on site. The systems are modeled after the present ALS transverse feedback system which has been running successfully for user operations for almost two years. The design philosophy, as with the ALS system, has been one of simplicity, reliability, and user friendliness. Given our ALS experience, we look forward to the successful commissioning and operation of the PEP-II systems in the upcoming weeks.

VII. ACKNOWLEDGMENTS

The authors wish to thank the many members of the LBL/SLAC-ALS/PEP-II feedback systems collaboration for many enlightening discussions and useful suggestions.

VIII. REFERENCES

[1] "PEP-II Conceptual Design Report", LBL-PUB-5379, SLAC-418, CALT-68-1869, UCRL-ID-114055, UC-IIRPA-93-01, June, 1993.

[2] J. D. Fox, et al., "Observation, Control, and Modal Analysis of Longitudinal Coupled-Bunch Instabilities in the ALS via a Digital Feedback System", AIP Proceedings of the 1996 Beam Instrumentation Workshop, Argonne IL, May 1996.

[3] W. Barry, et al., "Design of the PEP-II Transverse Coupled-Bunch Feedback System", Proceedings of the 1995 IEEE Particle Accelerator Conference, Dallas, TX, May, 1995

[4] W. Barry, et al., "Commissioning and Operation of the ALS Transverse Coupled-Bunch Feedback System", Proceedings of the 1995 IEEE Particle Accelerator Conference, Dallas, TX, May, 1995.

[5] J. Byrd, "Simulations of the PEP-II Coupled-Bunch Feedback Systems", Proceedings of the 1995 IEEE Particle Accelerator Conference, Dallas, TX, May, 1995.

BEAM TEST OF THE ACCELERATION SYSTEM WITH THE DDS IN HIMAC SYNCHROTRON

M.Kanazawa, K.Noda, E.Takada, M.Kumada, A.Itano,
National Institute of Radiological Sciences, Chiba, 263 Japan
S.Watanabe, Center for Nuclear Study, School of Science, University of Tokyo, Tokyo, 188 Japan
Y.Morii, Toshiba Corporation, Chiyoda-ku, Tokyo, 100 Japan

Abstract

We have examined the acceleration efficiency as a function of B-clock step size from 0.1 to 2.0 Gauss/pulse at HIMAC synchrotron. The result showed good acceleration efficiency with 0.2 Gauss/pulse, even if we haven't used feedback. Larger width case shows significant loss, suggesting a limitation due to stepwise change of acceleration frequency.

1 INTRODUCTION

Accurate and stable operation of the acceleration system of the synchrotron is very important in the medical accelerator like the HIMAC[1]. Further the quick and easy operation for beam energy switch is also required. To obtain these required performances, we have moved to the digital acceleration system[2] with a direct digital synthesizer (DDS) at the design stage of the HIMAC synchrotron[3]. The rapid development of digital technology permit the utilization of the DDS as an RF signal generator of the acceleration system of the synchrotron. With the DDS, control of the acceleration frequency can be as precise as below 10^{-5} in $\Delta f/f$. This comes from the clock accuracy with a crystal in the DDS, whose frequency accuracy is sufficient enough for the acceleration system of the synchrotron. To maintain this precision in the acceleration frequency, the DDS is controlled with digital data directly. There is no analog signal between the programmed frequency data in the pattern memory and the controlling data of the DDS. When the feedback loop of the acceleration frequency is required with the phase and radial position of the accelerated beam, these beam signals must be digitized. In spite of these advantage of frequency accuracy, the output frequency of the DDS is swept with step wise function. In the analog system with the voltage controlled oscillator (VCO), it is easy to make smooth the step wise frequency function with a low pass filter for the controlling signal of a VCO. If the frequency step is large, it may deteriorate an adiabatic condition of the acceleration process, and make longitudinal emittance growth, consequently the acceleration efficiency may become worse. To see these effect, we have tested the effect of the step height in the acceleration frequency.

2 ACCELERATION SYSTEM AND ITS PARAMETERS

In the HIMAC synchrotron, injected beam of 6 MeV/u can be accelerated up to 800 MeV/u for ion with charge to mass ratio of 0.5. Corresponding acceleration frequency is from 1.05 MHz to 7.9 MHz with harmonic number of 4. Acceleration period is 1.0 second to the maximum energy with maximum ramp speed of 1.7 T/s in the main dipole field. The momentum spread of the injected beam is 0.1%. Acceleration voltage of 6 kV can be obtained, whose value is enough to accelerate the beam with above momentum spread. In this condition filling factor of rf bucket is 60% at beginning of the acceleration with maximum ramp speed. In the pattern operation of the acceleration system, the data are generated by use of clock pulse (50kHz) at flat base and top. During acceleration period, the frequency data is given as a function of the magnetic field of the main dipole magnet. This frequency pattern is generated by use of the field clock (B-clock). The single clock corresponds to 0.2 Gauss increment or decrement in the magnetic field of the main magnet in the current system. This single clock changes acceleration frequency 204 Hz and 56 Hz at the beam energy of 6 MeV/u and 800 MeV/u, respectively. In figure 1, ratio of above jump step versus rf bucket height is shown as a function of beam energy, where the step width of the field clock is 0.2 Gauss. This shows that the relative frequency jump is large at low energy.

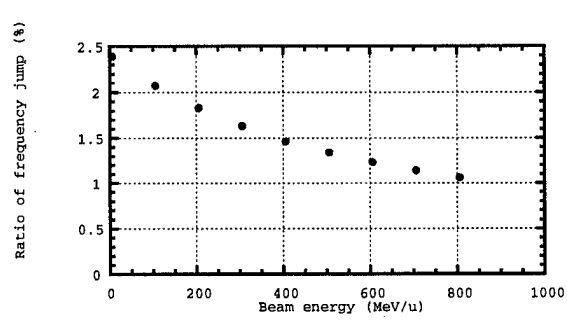

Figure 1 Ratios of the frequency jump height with 0.2 Gauss field clock to rf bucket half height as a function of beam energy. The acceleration voltage is 6 kV and the ramp speed of the dipole field is 1 T/sec.

0-7803-4376-X/98/$10.00 © 1998 IEEE

3 BEAM TEST

To see the effect of the B-clock step on the acceleration performance, we have tested acceleration efficiency with several step widths from 0.1 to 2 Gauss/pulse. For each step width we have made corresponding pattern data of the acceleration system i.e. acceleration frequency, ferrite bias current, acceleration voltage. Concerning the other patterns such as the current pattern of main dipole magnets, quadruple magnets, we haven't changed during this experiment. The test was performed with the flat top energy of 230 MeV/u, and maximum ramp speed of 0.9 T/s. We have used the constant acceleration voltage of 6 kV. With this low maximum ramp speed, we can test with B-clock step of 0.1 Gauss. In figure 2-1 accelerated beam intensity is shown with 0.2 Gauss B-clock step, where we haven't used beam phase feedback. Bunch shape at flat base is shown with same condition in figure 2-2.

Increasing the B-clock step width, beam loss occurred at low energy region as shown in figure 3. If we turn on the beam feedback the acceleration efficiency can be improved. In figure 4, acceleration efficiencies, as defined by beam intensity ratio of flat top and just after injection, are shown for various B-clock step widths in both the cases with and without the feedback. This shows deterioration of acceleration efficiency at larger B-clock step width than 0.2 Gauss/pulse without feedback. When we use the feedback we can improve the efficiency. With the condition of 0.4 Gauss/pulse, beam loss become large especially in the case that there is no feedback of beam phase. If there is the phase feedback the situation is improved very much. This will indicate that the frequency jump excite the synchrotron oscillation which can be damped with the phase feedback loop. If the jump becomes large, higher harmonics of the beam oscillation will be excited strongly. For this higher component the phase feedback can't work, and this is the reason of large beam loss with large B-clock step even if there is the feedback. The bunch shapes at flat top without feedback are shown in figure 5-1, and with feedback in figure 5-2. To see the emittance growth of the accelerated beam with different B-clock step, bunch widths(FWHM) are shown in figure 6 with and without the phase feedback. If we increase the B-clock step, we can observe the increment in the bunch width in the case of no feedback. At the flat base this value is 106 degree. If we assume adiabatic damping in the acceleration, this bunch width will decrease to 88 degree. This value is consistent with the observed value in the case of 0.1 Gauss/pulse. With the feedback, the bunch width is same to the value of 0.1 Gauss/pulse. This indicate that the feedback suppresses the emittance growth effectively in the acceleration process.

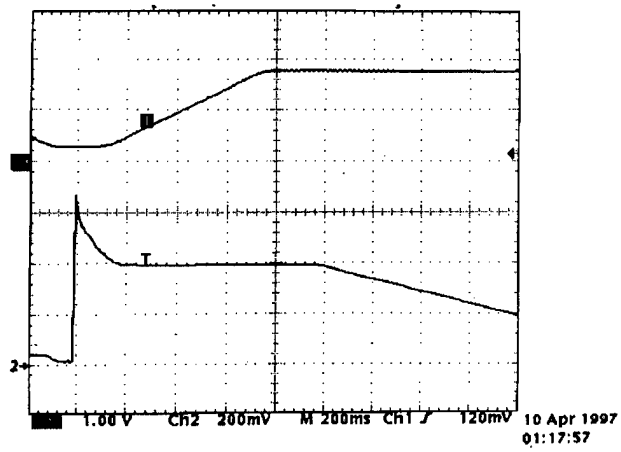

Figure 2-1 Beam intensity data (lower trace) from the injection to the flat top with B-clock step of 0.2 Gauss. Decrease of beam intensity at flat top is due to the slow beam extraction. Upper trace is current pattern of the dipole magnet. Horizontal scale is 200ms/div.

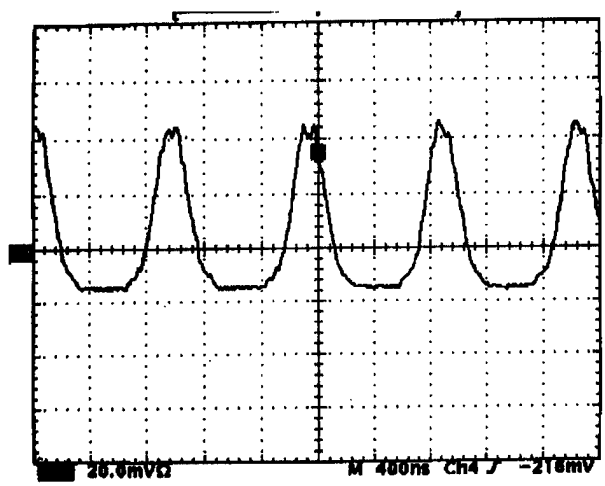

Figure 2-2 Beam bunch shape at flat base (15 msec after rf capture). Horizontal scale is 400 ns/div.

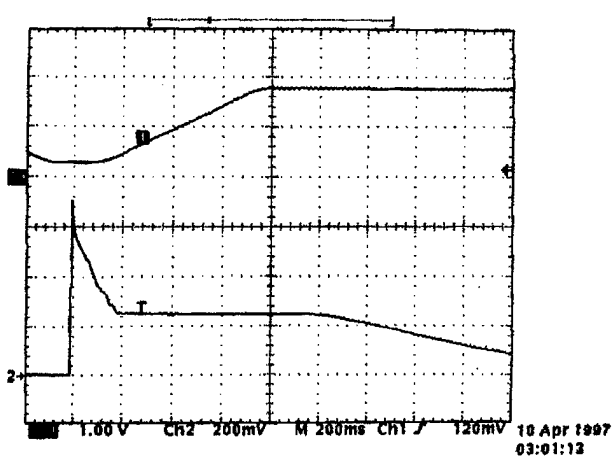

Figure 3 Beam acceleration with 0.4 Gauss/pulse instead of 0.2 Gauss/pulse in the B-clock. Traces are same as figure : 2-1.

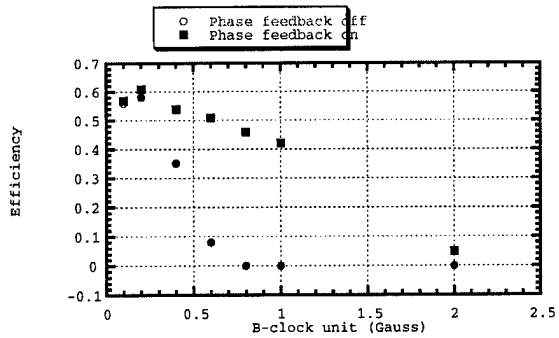

Figure 4 Dependence of acceleration efficiency on the step width of the B-clock.

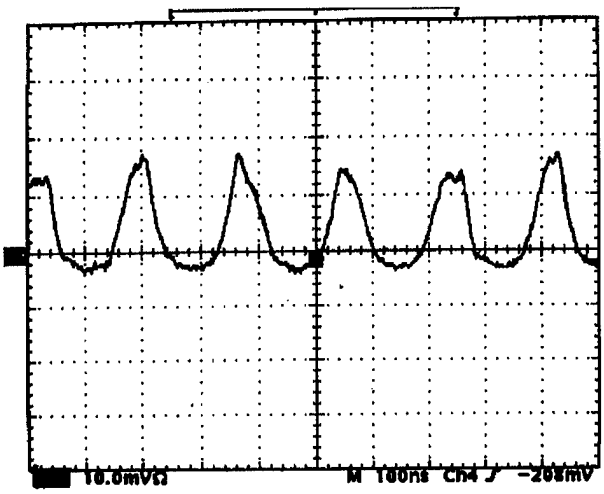

Figure 5-1 Beam bunch shape at flat top with B-clock step of 0.4 Gauss, where feedback was not used. Horizontal scale is 100 ns/div.

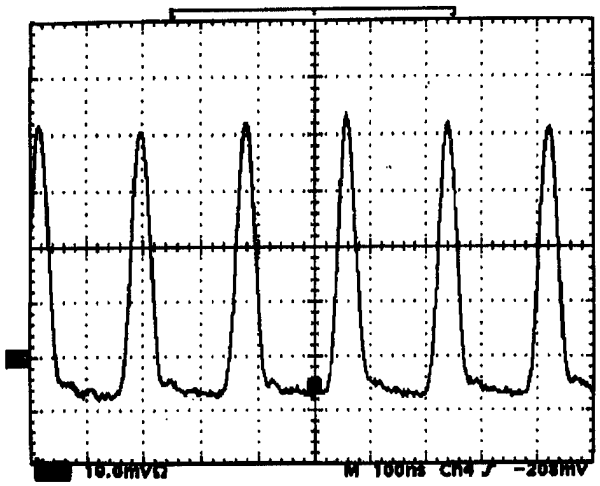

Figure 5-2 Same figure as figure:5-1 with feedback.

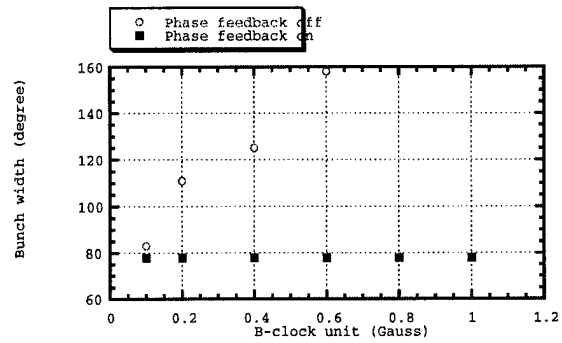

Figure 6 Beam bunch width (FWHM) at flat top.

4 SUMMARY

The B-clock step of 0.2 Gauss/pulse seems to be precise enough to achieve good acceleration efficiency, though we can observe small longtudinal emittance growth in the case of no phase feedback. With the step of 0.1 Gauss, we can't observe any difference in the acceleration efficiency and in the beam bunch shape between the cases with and without the feedback.

5 ACKNOWLEDGEMENTS

The authors are grateful to Mr.T.Kondo for his support in preparation of the pattern data. They would like also to express thanks to the operating crews of Accelerator Engineering Corporation for the operation of HIMAC facility. They also give thanks for other members of their division.

REFERENCES

[1] Y.Hirao, et al.,'Heavy Ion Synchrotron for Medical Use', Nucl.Phys.A538,541c(1992)

[2] M.Kanazawa, et al.,'Beam Monitors for RF Feedback Control in HIMAC Synchrotron', Proc. of the Workshop on Advanced Beam Instrumentation, 504(1991).

[3] K.Sato, et al., 'Status report on HIMAC', EPAC 1994,p.412. S.Yamada, et al., 'Commissioning and performance of the HIMAC medical accelerator', PAC 1995, p9.

TRANSVERSE BEAM FEEDBACK SYSTEM IN THE PLS

J. Y. Huang, M. K. Park, M. Kwon, M. Yoon and I. S. Ko
Pohang Accelerator Laboratory, POSTECH
Pohang 790-784, Korea

Abstract

A bunch by bunch transverse feedback system, as a complement of the longitudinal feedback system required for the suppression of the coupled bunch beam instabilities, has been developed and undergoing testing in the PLS. Major components are two beam oscillation detectors, betatron phase adjuster, notch filters and a stripline kicker. Each system component and its functions are described with simple trigonometric calculations. Preliminary result of the beam test has shown 30 dB damping of the beam oscillation.

1 INTRODUCTION

The PLS is a 2 GeV electron synchrotron light source dedicated to the beamline users since 1995. During the operation, various kind of beam instabilities have been observed. In particular, low frequency beam oscillation around 100Hz and the longitudinal coupled bunch instability induced by higher order modes of rf cavities (HOM) are typical [1]. For the suppression of these instabilities, a PEP-II type longitudinal feedback system [2] will be developed.

Although the transverse coupled bunch instability has not caused any problem in PLS, inserting of the narrow gap chambers for the planned insertion devices will generate large transverse resistive wall impedance, and, consequently, the spontaneous transverse coupled bunch instability will be possible. It is also well experienced in ALS that a transverse feedback system is required as a complement for the longitudinal feedback system to suppress the coupled bunch instabilities properly [3].

A PLS transverse feedback system is developed and is undergoing testing now. It operates as a bunch by bunch feedback system in time domain [3][4]. Frequency domain bandwidth of the system is 250 MHz, which is the highest coupled bunch oscillation frequency observable from 500 MHz bunch train. The PLS transverse feedback system consists of pickup electrodes, signal processing electronics, power amplifiers, and a stripline kicker. Fig. 1 shows an overview of the transverse feedback system. The first beam study has shown 30 dB damping of the beam oscillation in full bandwidth. In this paper, we describe the design and the preliminary test result of the transverse feedback system.

2 FEEDBACK SYSTEM

Two fast beam oscillation detectors are used for the control of $\pi/2$ phase relation between the pickup signal and the feedback kicker signal. Signal detection is done at the third harmonic of 500 MHz rf frequency (1.5 GHz). A notch filter made with two coaxial delay lines is used to suppress the DC beam signal [4]. Overall bandwidth of the system is 100 kHz to 250 MHz. Four 100 watt power amplifiers are used to drive the feedback kicker providing 65 dB total system gain. Each system component and its functions are described with simple trigonometric calculations and the test results are discussed in the following sections.

2.1 Pickup Electrodes

Two orbit BPMs, 6PM6 and 7PM6, are selected as the pickup electrodes, which have been reserved for beam diagnostics. They are located at the finite dispersion function region and 70 degrees apart in the betatron phase. High frequency capacitance of a pickup electrode is 2 pF, and the rise-fall time of the pickup signal is much shorter than 2 ns bunch seperation. RF response of a pickup electrode is also clean without any resonant spectral structure up to 12 GHz [5]. With two selected BPMs, $\pi/2$ betatron phase relation between the pickup electrode and the kicker can be controlled by adjusting attenuators a_1 and a_2.

When two pickup electrodes are φ_0 apart in betatron phase, beam signals x_1 and x_2 can be written as

$$x_1 = a_1\sqrt{\beta_1}\, sin(\varphi_1(s)), \tag{1}$$

$$x_2 = a_2\sqrt{\beta_2}\, sin(\varphi_1(s)+ \varphi_0), \tag{2}$$

and the sum signal x is

$$\begin{aligned} x &= x_1 + x_2 \\ &= [(a_1\sqrt{\beta_1} + a_2\sqrt{\beta_2}\, cos\varphi_0)^2 + a_2^2\beta_2 sin^2\varphi_0]^{1/2} \\ &\quad \times sin(\varphi_1(s)+\Delta\varphi) \end{aligned} \tag{3}$$

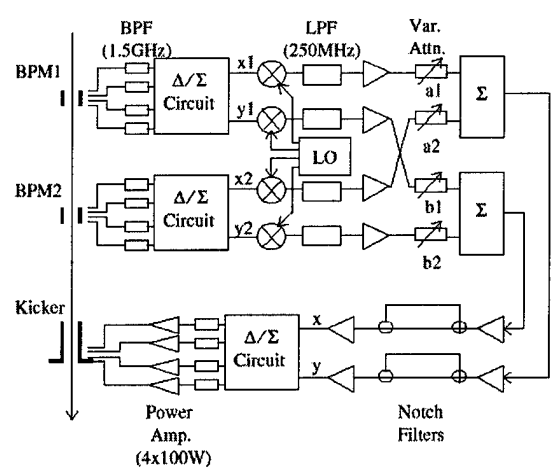

Figure 1: An overview of the transverse feedback system

where the phase change $\Delta\varphi$ is

$$\Delta\varphi = \tan^{-1}[a_2\sqrt{\beta_2}\sin\varphi_0/(a_1\sqrt{\beta_1} + a_2\sqrt{\beta_2}\cos\varphi_0)]. \quad (4)$$

By adjusting a_1 and a_2, we can control $\Delta\varphi$ as much as 2π. Since we select BPMs located at the same betatron functions, where β_h=2.1326 and β_v=3.3119, the betatron phase delay is controlled only by the ratio of the attenuations a_2/a_1.

2.2 Signal Processing Electronics

Pickup signals are delivered to the frontend electronics via phase matched coaxial cables. Since the beam signal is largest at the third harmonic (-10 dBm at 100 mA) of 500 MHz rf frequency, 1.5 GHz band is selected for the detection of beam oscillation. The rf detection electronics consists of 1.5 GHz ± 300 MHz band pass filters, rf hybrids, mixers, 1.5 GHz local oscillator, and the 250 MHz low pass filter at the mixer output. Detected signals of BPM1 and BPM2 are combined in the power divider with attenuation coefficients a_1 and a_2, which are calculated from Eq.(4). Four attenuators a_1, a_2, b_1, b_2 are computer controlled to accommodate the change of operation tunes. DC component of the beam signal, which appears as the revolution harmonics of the beam spectrum, is suppressed by two correlator notch filters. A notch filter is made with two coaxial delay lines which differ in delay time by the ring revolution period T. Output signal $x(t)$ can be written as the difference of two input signals with attenuations α and β as

$$x(t) = \alpha x_0(t) - \beta x_0(t-T). \quad (5)$$

Since the notch depth is sensitive to the mismatch of the delays and attenuations of two delay lines, they are precisely adjusted by a variable delay line and a variable attenuator to obtain the best notch depthes. To see how the notch frequency and the notch depth is sensitive to the delay error δT and the mismatch of attenuation α and β of delay lines, we consider the frequency domain spectrum:

$$x(\omega) \propto [\alpha^2+\beta^2-2\alpha\beta\cos(\omega T+\omega\delta T)]^{1/2}. \quad (6)$$

The notch frequency shift is $\delta f = \omega\delta T/2\pi T = f_{rev}\delta T/T$ and the notch depth R, defined as x_{max}/x_{min}, is

$$R = (\alpha+\beta)/(\alpha-\beta). \quad (7)$$

When β/α is adjusted within 1%, the notch depth is -46dB.

Phase change by the notch filter should also be considered in tuning the phase delay between pickup and kicker of the feedback system. From Eq. (5),

$$x(t) = [(\alpha-\beta\cos^2(2\pi\nu_x) + \beta^2\sin^2(2\pi\nu_x)]^{1/2} \times \sin(\omega t+\Delta\varphi), \quad (8)$$

where the phase change $\Delta\varphi$ is

$$\Delta\varphi = \tan^{-1}[\beta\sin(2\pi\nu_x)/(\alpha-\beta\cos(2\pi\nu_x))]. \quad (9)$$

In practice, we can set $\alpha = \beta = 1$, and the phase shift by the notch filter is

$$\Delta\varphi = \tan^{-1}[\cot(2\pi\nu_x)] = \pi/2 - \pi\nu_x. \quad (10)$$

For the PLS system, ν_x = 14.28 and ν_y = 8.18, and consequently $\Delta\varphi_x = 0.22\pi$, $\Delta\varphi_y = 0.32\pi$.

2.3 Power Amplifier

Beam induced transverse kick voltage $V_\perp$ by the transverse impedance $Z_\perp$ is given by

$$V_\perp = I_0\delta x Z_\perp \quad (11)$$

where δx is amplitude of the transverse oscillation and I_0 is the beam current. The required power of the kicker should provide more power than the beam induced power P_b to damp the oscillation:

$$P_b = V_\perp^2/2R_k \quad (12)$$

where R_k is the kicker shunt impedance.

For the PLS, the transverse HOM impedance $Z_\perp$ of the cavity is practically less than 10 MΩ and the shunt impedance R_k of the transverse feedback kicker is 6.5 kΩ at 250 MHz. When I_0 = 100 mA and δx = 1 mm, $V_\perp$ = 1 kV and P_b = 77 watt respectively. We need minimum 310 watt power amplifier when the beam current reaches 400 mA. Four 100 watt, 50 dB gain power amplifiers are purchased for the PLS transverse feedback system. The 3 dB bandwidth of the amplifier is 10 kHz to 230 MHz.

2.4 Kicker

A four-stripline type kicker is used for both horizontal and vertical kick instead of the seperate horizontal and vertical electrodes because of the lack of free space in the storage ring. Striplines are 17mm wide and 300mm ($\lambda/4$ of 250 MHz) long, and are carefully assembled to make 50 Ω stripline impedance. The transverse kicker shunt impedance R_k is given by [6]

$$R_k T^2 = 2Z_L(2gv/h\omega)^2\sin^2(\omega l/v) \quad (13)$$

where Z_L is the line impedance (50 Ω) of the stripline, g is the stripline coverage factor, v is the beam velocity, l is the length of striplines, and h is the distance between striplines. It is 6.5 kΩ at 250 MHz cutoff frequency for the PLS kicker.

3 TESTS AND RESULTS

3.1 Tune-up

Before turning on the feedback system, all the system components are tuned up with beam signal. Frontend and backend signal line lengths and the overall delay are adjusted within several ten picoseconds with individual line length adjusters. Phase of the local oscillator signal is also adjusted to get the maximum detection at the mixer. Using a line length adjuster and a variable attenuator, the depth and the frequency of notches are fine-tuned with the beam signal. Harmonic rejection is better than 25 dB in all harmonics from DC to 250 MHz.

3.2 Tests

Since the spontaneous transverse beam instability is hardly observed in the PLS, we have driven the beam at the betatron resonance frequency using a signal generator, power amplifiers and the stripline kickers of the tune measurement system. At the resonance frequency, a coherent beam oscillation is excited with the 4 mm peak to peak amplitude as shown in Fig. 2. When the feedback system is turned on after all tune-ups, the beam oscillation disappears in the beam image monitor. Snapshots of the oscillating beam and damped beam are also shown in Fig. 2. In the beam spectrum, betatron sidebands are also damped around 30 dB in the full bandwidth of the system as shown in Fig. 3. The remaining sideband amplitude is maintained by the resonance excitation of the beam.

For the better performance of the system, we have changed pickup electrodes to 7BPM2 and 8BPM2 where the dispersion function is zero and the betatron functions are much larger than 6BPM6 and 7BPM6 (β_h=11.0844 and β_v=6.711). Unfortunately, after the BPMs are changed, transverse feedback system is not working as good as before. High frequency sidebands above 150 MHz are not damped efficiently. It seem to be very sensitive to the change of the machine tune. Further beam study and tune-ups has to be performed for the normal operation of the PLS transverse feedback system.

4 CONCLUSION

A transverse feedback system is developed and is undergoing testing now in the PLS. With pickup electrodes at low betatron functions and finite dispersion, we demonstrate the 30dB suppression of the betatron sidebands in DC to 250 MHz band. When the pickup electrodes are changed to the large beta and dispersion free region, however, the feedback system does not work as good as before. Further beam studies and tuning works have to be performed for the normal operation.

Figure 2: Beam images before and after feedback-on. Because of the automatic gain control of CCD camera, beam image after damping looks larger than before.

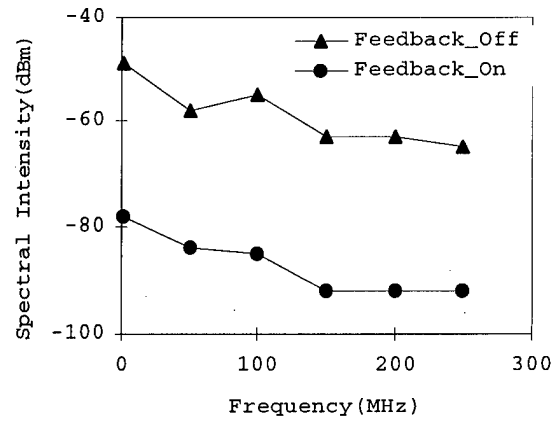

Figure 3: Betatron sidebands plotted for feedback on and feedback off.

5 REFERENCES

[1] M. Kwon et. al., "Instability Studies in the Pohang Light Source," Proc. of 1996 EPAC, Sitges (1997).

[2] J. Fox et. al., "Operation and Performance of a Longitudinal Damping System Using Parallel Digital Signal Processing," Proc. of 1994 EPAC, London, (1994).

[3] W. Barry et. al., "Commissioning of the ALS Transverse Coupled Bunch Feedback System," Proc. of 1995 PAC, London (1994).

[4] J. Galayda, "Performance of a Correlator Filter in Betatron Tune Measurement and Damping on the NSLS Booster," IEEE Trans. Nucl. Sci., NS-32, No.5 (1985).

[5] J. Y. Huang et. al., "Electron and Photon Beam Diagnostics in the PLS Storage Ring," AIP Conf. Proc. 333 (1995).

[6] D. A. Goldberg and G. R. Lambertson, "Dynamic Devices: A Primer on Pickups and Kickers," AIP Conf. Proc. 249 (1992).

THE DESIGN OF THE ELETTRA FAST LOCAL FEEDBACK SYSTEM

C. J. Bocchetta, D. Bulfone, A. Galimberti, D. Giuressi, M. Lonza,
R. Sergo, C. Scafuri, L. Tosi, R. Visintini
Sincrotrone Trieste, SS 14 - Km 164.5, 34012 Basovizza, Trieste, Italy

Abstract

The stability of the electron beam position is one of the main issues for third generation synchrotron radiation sources. A fast local feedback system based on digital signal processing techniques has been designed and installed on ELETTRA. After a characterization of the main system components, the design choices are presented. The software environment used for system development and measurements is described.

1 INTRODUCTION

The full exploitation of the high brilliance photon beams produced by third generation synchrotron radiation sources relies on the transverse stability of the electron orbit at the Insertion Device (ID) source points [1]. The main beam perturbations consist of slow drifts and vibrations up to some tens of Hz. In order to achieve the requested performance, active orbit feedback systems are typically used [2].

At ELETTRA, where the development of such systems has been considered since the design phase of the facility [3], a fast local orbit feedback has been developed and preliminarly installed on two out of the five IDs installed. The system presently works in the vertical plane but its operation can be extended to the horizontal one with no hardware modifications. High resolution Photon Beam Position Monitors (phBPM) are adopted. Taking advantage of the recent technology developments, digital signal processing techniques [4] are used for the system controller. They improve system reproducibility and flexibility by allowing to easily change the orbit correction algorithm and/or compensating scheme.

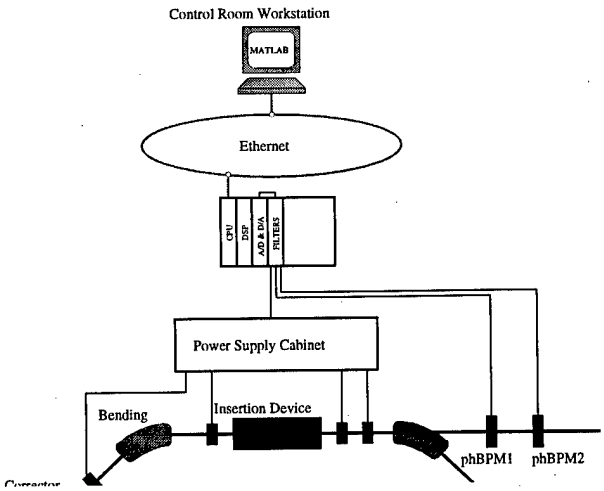

Figure 1: The local feedback layout.

2 SYSTEM LAYOUT

The ELETTRA local feedback system layout is shown in fig. 1: two phBPMs detect the photon beam position in the front-end and four corrector magnets move the electron beam inside the ID straight section. The phBPM signals are sampled by A/D converters and processed by a Digital Signal Processor (DSP) based system which implements the control algorithm. The D/A converters re-transform the resulting output samples in analog signals which drive the power supplies of the corrector magnets. An Ethernet connection allows to communicate with the control system [5] workstations and to remotely control the DSP operation.

2.1 The Photon Beam Position Monitors (phBPM)

The two phBPMs [6] are located in the ELETTRA front-end. They have a separation of 1 m and the first one is located 9 m from the corresponding ID centre. Excellent performance in terms of mechanical stability has been achieved by fixing the monitor supports directly in the rock below the concrete floor of the storage ring. The operation of the monitors is based on the photoemission effect of four blades spaced 90° from each other. Their particular configuration alows to intercept only the fringes of the beam and to sustain the radiation flux and the thermal load. The two monitors are rotated by 45° one respect to each other (fig. 2). In order to avoid non-linearity and cross-talk between planes the photon beam must be placed close to the centre of the photoemitting elements: a motorized x-z translation system has been developed for this purpose.

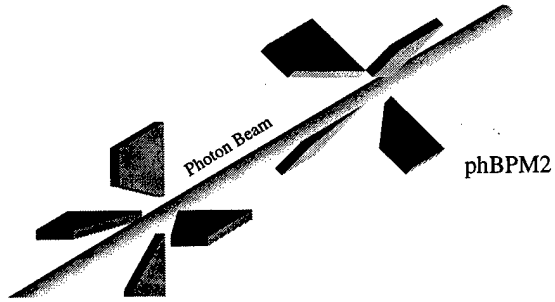

Figure 2: Photon BPM layout.

Each blade signal is proportional to the overall photon flux produced by both the ID and bending magnets. Since only the ID component has to be considered the bending one must be rejected. Its contribution is proportional to the electron beam current and can be evaluated when the ID is still open.

0-7803-4376-X/98/$10.00 © 1998 IEEE

The signals from the blades are pre-processed by high precision electronics located close to the front-end which provides a submicron sensitivity. They are then conditioned and amplified in order to assure good noise rejection in the transmission to the Controller.

2.2 Corrector Magnets and Power Supplies

The ELETTRA combined horizontal-vertical inverted U-shaped corrector magnets [7] are used also for the feedback system. The corresponding power supplies must therefore provide both DC and AC currents. The maximum allowed frequency of the AC current depends on the DC offset and is limited by the output voltage of the power supplies (65 V peak). AC amplitudes of 400 mA up to 50 Hz and 200 mA at 100 Hz can be obtained for the maximum 12 A of DC current. The feedback input signal is enabled by a solid state switch and is added to the DC setting coming from the control system in the regulation part of the power supply. The phase delay induced by the eddy currents generated in the stainless steel vacuum chamber by the AC magnetic field has been measured. It is about 1 degree at 60 Hz and 2 degrees at 100 Hz.

2.3 The Controller

The Controller is based on the VME bus standard. The eight analog signals coming from the two phBPMs are conditioned and filtered to avoid aliasing effects by a home-developed board with 4th order low-pass filters. The same board provides also filtering and conditioning for the output analog signals going to the power supply cabinet. A single board is in charge of the A/D-D/A conversion: it features a maximum rate of 200 ksamples/s on each independent channel with a resolution of 16 bits. The DSP board mounts a TMS320C40 processor at 40 MHz (50 MHz on the new boards) and its computing power could be enough to run the correction algorithms on both the vertical and horizontal planes at the sampling rate of 8 kHz. An additional CPU board acts as a bridge between the DSP and Ethernet. The A/D-D/A and the DSP boards are connected by a mezzanine bus (Modular Interface eXtension, MIX), while the VMEbus is used for the communication between the DSP and the bridge board.
The programs running in the DSP are written in "C" language. A complete development environment and a special Ethernet communication protocol called SwiftNet [8] allow to compile, download, run and debug the programs in the DSP from UNIX workstations.

3 THE MATLAB-DSP ENVIRONMENT IN ELETTRA (MADE)

The local feedback project has been supported through all its phases by an effective workbench based on Matlab [9] called MADE (MAtlab-Dsp environment in ELETTRA). Matlab is a computing interactive environment suited for data analysis, dynamic system design and simulations. The Matlab standard command set has been expanded in order to communicate with the DSP system directly from any control room workstation. The communication relies on SwiftNet. The newly developed commands take the form of Matlab Mex-files and are associated with specific software running on the DSP. They allow to:

- setup the VME boards (sampling frequency setting, A/D converters calibration, etc...)
- acquire input/output signals
- generate arbitrary output waveforms
- control the local feedback system operation and parameters (filters, controller parameters, open-close loop, etc...)
- acquire data preprocessed by the DSP (spectra, rms values, frequency responses, etc...)
- monitor the control variables.

The ELETTRA control system remote procedure call libraries have also been integrated with Matlab and allow to access the accelerator equipment through simple command line instructions [10]. The control of both the accelerator and local feedback system from the same workspace minimizes the time needed for measurements and tests.

4 SYSTEM MODELLING AND SIMULATION

The feedback setup allowed a quick and effective dynamic characterization of the overall chain made of power supply, magnet, vacuum chamber and phBPM. The frequency response of the system has been measured on the real machine by modulating one vertical corrector with sinusoidal signals at different frequencies generated by the DSP and acquiring the beam oscillations detected by the phBPMs with the DSP itself.
The phBPM does not introduce any appreciable cut-off at the working frequencies (0 - 200 Hz). The dynamic behaviour of the chain is dominated by the corrector magnet and power supply.
A polynomial model in z has been calculated which best fits the frequency response of the system: a third order model is sufficient to characterize it up to 200 Hz. Fig. 3 shows the response of the model compared with the real one.

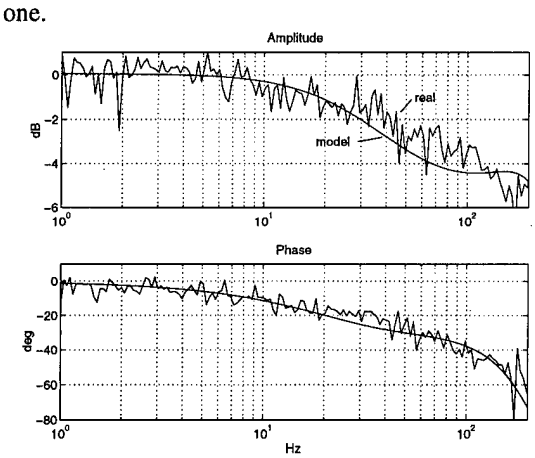

Figure 3: Frequency response of the real system compared with the third order model.

Starting from this model several simulations have been carried out using both Matlab and Simulink [11] to better understand the closed-loop behaviour of the system. The model block diagram is shown in fig. 4. The delay represents the time lag due to the processing and conversion time: it is estimated to be equivalent to two samples, which means 250 μs at the nominal 8 kHz

sampling rate. The controller implemented for the first tests is a PID [12] standard regulator with transfer function:

$$R(z) = K_P + \frac{K_I}{1-z^{-1}} + K_D(1-z^{-1})$$

A first-order low-pass filter with cut-off frequency f_C has been added before the PID in order to limit the dynamics of the signal at the higher frequencies and to avoid non-linearity of the power supply.

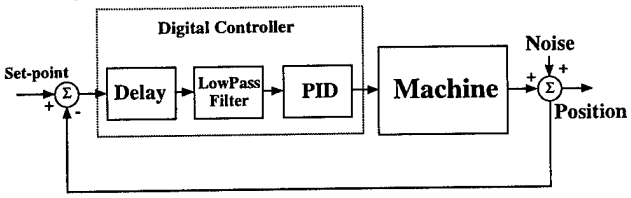

Figure 4: Block diagram of the model used to simulate the closed-loop system behaviour.

As the sampling frequency is much higher than the working frequencies, the model does not take into account neither the anti-aliasing nor the reconstruction analog filters.

Fig. 5 is an example of the simulated frequency response of the closed-loop system and the corresponding open-loop Nyquist diagram.

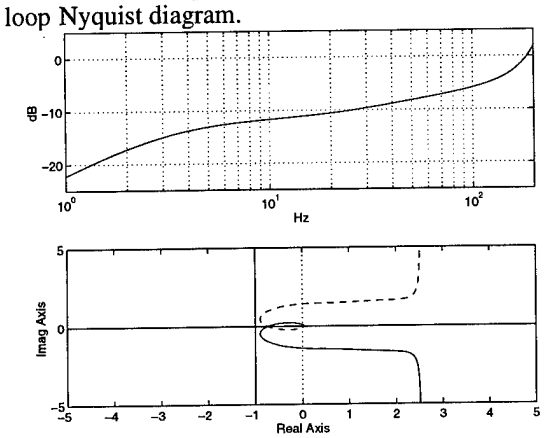

Figure 5: Closed-loop frequency response and open-loop Nyquist diagram of the simulated system (K_P=3, K_I=0.01, K_D=10, f_C=150 Hz).

5 CONCLUSIONS

The ELETTRA fast local feedback system uses phBPMs as position monitors and U-shaped combined corrector magnets as actuators. The magnet power supplies provide both DC and the AC current needed by the feedback system. The Controller is based on commercial DSP VME boards and is completely integrated in the ELETTRA control system.

A powerful software environment suited for digital signal processing applications, called MADE, has been developed and boosted the whole project.

A system model that fits the experimental data has been calculated and is used to predict its closed-loop behaviour. The described fast local orbit feedback system has been installed and the first operational results are presented in [13].

6 ACKNOWLEDGEMENTS

The authors would like to thank M. Vento and M. Zaccaria for their technical skill.

REFERENCES

[1] H. Winick: 'Synchrotron Radiation Sources, a Primer', World Scientific, 1994.

[2] E. S. Bozoki et al.: 'Orbit Correction and Analysis in Circular Accelerators', AIP Conference Proceedings 315, Upton, NY 1993.

[3] D. Bulfone et al.: 'Design Considerations for the ELETTRA Beam Position Feedback Systems', Proc. 2nd European Particle Accelerator Conference, Nice, France, 1990.

[4] J. G. Proakis and D. G. Manolakis: 'Digital Signal Processing', Prentice Hall, 1996.

[5] D. Bulfone: 'Status and Prospects of the ELETTRA Control System', Nucl. Instr. and Meth. A 352, p. 63, 1994.

[6] A. Galimberti et al.: 'Photon Beam Position Monitors suitable for a Local Feedback System at ELETTRA', Proc. 5th European Particle Accelerator Conference, Sitges, Spain, 1996.

[7] D. Tommasini et al.: 'Design, Construction and Testing of the Corrector Magnets for ELETTRA', Proc. 4th European Particle Accelerator Conference, Sitges, Spain, 1996.

[8] 'SwiftNet Host Software User's Guide', Pentek, Inc. 55 Walnut Street, Norwood, NJ 07648, 1995.

[9] 'Matlab User's Guide', The MathWorks, Inc. 24 Prime Park Way, Natick, Mass. 01760-1500, 1994.

[10] C. Scafuri: 'Integration of Matlab into the ELETTRA Control System', ST/M-TN-97/1, Sincrotrone Trieste, 1997.

[11] 'Simulink User's Guide', The MathWorks, Inc. 24 Prime Park Way, Natick, Mass. 01760-1500, 1995.

[12] G. F. Franklin: 'Feedback Control of Dynamic Systems', Addison-Wesley Pub. Co., 1994.

[13] C. J. Bocchetta et al.: 'First Operational Results with the ELETTRA Fast Local Feedback System', these Proceedings.

FIRST OPERATIONAL RESULTS WITH THE ELETTRA FAST LOCAL FEEDBACK SYSTEM

C. J. Bocchetta, D. Bulfone, A. Galimberti, D. Giuressi, M. Lonza,
R. Sergo, C. Scafuri, L. Tosi, R. Visintini
Sincrotrone Trieste, SS 14 - Km 164.5, 34012 Basovizza, Trieste, Italy

Abstract
A fast local feedback system has been installed on two of the ELETTRA beamlines. The first operational results are presented and compared with the performance foreseen with a simulated model of the system.

1 INTRODUCTION

The design of the ELETTRA fast local orbit feedback is described in [1]. The system performance and the first operational experience gained are presented in this paper. Static and "dynamic" closed bump leakage are measured and closed-loop behaviour is characterized and compared with simulation results obtained from a developed system model. On the base of the beam noise spectra measured at ELETTRA, a technique called "harmonic suppression" is presented which specifically damps persistent harmonic components.

2 THE LOCAL BUMP

The correction is made by four corrector magnets which move the beam to the desired position and angle inside the ID straight section and make a closed bump in order to localize the orbit change. The displacement x_j produced at the BPM location *j* by a kick θ_i applied to the corrector *i* is given by:

$$x_j = \frac{\sqrt{\beta_i \beta_j}}{2 \sin \pi Q} \theta_i \cos(\pi Q - |\Delta\varphi_{ij}|) \qquad (1)$$

Considering the generic "kick vector" Θ applied to the four correctors, the corresponding electron orbit change $\mathbf{X}_E$ measured on the 91 BPMs outside the bump is calculated by a superposition of the single corrector effects,

$$\mathbf{X}_E = \mathbf{R}_{E(91x4)} \cdot \Theta$$

where $\mathbf{R}_E$ is the response matrix whose elements are derived from (1). The same vector produces also a change in the position of the light beam measured by the photon Beam Position Monitor (phBPM) and represented by the vector $\mathbf{X}_P$,

$$\mathbf{X}_P = \mathbf{R}_{P(2x4)} \cdot \Theta$$

where $\mathbf{R}_P$ is the response matrix whose elements can be calculated geometrically from the position and angle inside the ID straight section. To have the closed bump condition, there must be a sub-space of the corrector vector space whose transform (represented by $\mathbf{R}_E$) is zero (a null space); in order to have two degrees of freedom for setting the wanted positions on the two phBPMs, this null space must be two-dimensional. As a consequence the matrix $\mathbf{R}_E$ must have rank two. Decomposing the matrix $\mathbf{R}_E$ with the SVD [2] algorithm we obtain:

$$\mathbf{R}_E = \mathbf{U}_{(91x91)} \cdot \mathbf{D}_{(91x4)} \cdot \mathbf{V}^T_{(4x4)}$$

where **U** and **V** are unitary matrixes and **D** is a rectangular matrix with the leading four diagonal elements λ (the singular values) in decreasing order:

$$\mathbf{D}_{(91x4)} = \begin{pmatrix} \lambda_1 & 0 & 0 & 0 \\ 0 & \lambda_2 & 0 & 0 \\ 0 & 0 & \lambda_3 & 0 \\ 0 & 0 & 0 & \lambda_4 \\ & & \mathbf{0} & \end{pmatrix} \qquad \mathbf{V}_{(4x4)} = \begin{pmatrix} \mathbf{K}_1 & \mathbf{K}_2 & \mathbf{N}_1 & \mathbf{N}_2 \end{pmatrix}$$

For the rank reduction condition λ_3 and λ_4 must be zero; as a result $\mathbf{N}_1$ and $\mathbf{N}_2$ can be considered a base of the null space. In other words two degrees of freedom are used to fix the source point and the other two to close the bump.
Let us call the "bump matrix" $\mathbf{B}_{(4x2)}$ a matrix that when multiplied by the vector **X** of the two wanted phBPM positions gives the corrector kicks which move the light beam by **X** and satisfies the closed bump condition.
It is easy to show that:

$$\mathbf{B}_{(4x2)} = \begin{pmatrix} \mathbf{R}_P \\ \mathbf{K}_1^T \\ \mathbf{K}_2^T \end{pmatrix}^{-1} \cdot \begin{pmatrix} \mathbf{I}_{(2x2)} \\ \mathbf{0} \end{pmatrix}$$

The two matrixes $\mathbf{R}_E$ and $\mathbf{R}_P$ can be calculated from the machine parameters and magnets settings.

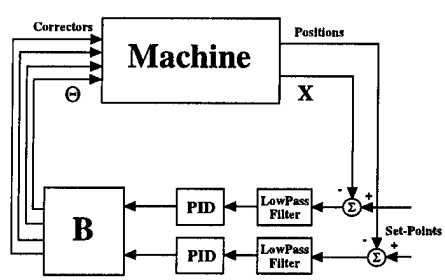

Figure 1: Block diagram of the correction scheme showing the bump matrix B decoupling action.

Nevertheless a completely empirical approach has been used for our system. They are determined by exciting separately the four correctors of the bump and measuring the corresponding BPM and phBPM positions. The advantage of this method is that no knowledge is required of machine optics parameters and/or calibration coefficients for the bump matrix allowing a rapid generation of $\mathbf{R}_E$ and $\mathbf{R}_P$ whenever required. This would be useful if new machine files are used. The procedure

0-7803-4376-X/98/$10.00 © 1998 IEEE

takes a few seconds for each beam-line and can be carried out after each injection.

In order to improve the accuracy, this method can be modified by performing the calculation in two steps. In the first we measure only $\mathbf{R}_E$. Secondly the two column vectors $\mathbf{N}_1$ and $\mathbf{N}_2$ are used to set the correctors. Let's call n_{ij} the position variation measured by the phBPM j due to $\mathbf{N}_i$; the bump matrix can be calculated as:

$$\mathbf{B}_{(4x2)} = \begin{pmatrix} \mathbf{N}_1 \, \mathbf{N}_2 \end{pmatrix} \cdot \begin{pmatrix} n_{11} & n_{21} \\ n_{12} & n_{22} \end{pmatrix}^{-1}$$

Two major advantages are associated with the second step of the method. As $\mathbf{N}_1$ and $\mathbf{N}_2$ impose closed bumps the other beamlines are not perturbed by the procedure which can be carried out during user operations at different ID gap values. Non linearities due to sextupoles outside the bump are avoided. The bump matrix transforms the four-input (correctors) by two-output (phBPM) system into a two-by-two system with decoupled channels, where the control algorithm is independently applied (fig. 1).

3 FIRST OPERATIONS AND RESULTS

The local orbit feedback has to stabilize the photon beam counteracting fast beam oscillations and slow beam drifts. When the feedback is running, slow corrections create an offset in the settings of the D/A converters which reduces the amount of AC dynamic range available for fast corrections. In order to compensate such effects the DC components of the D/A converters are periodically "discharged" and transferred to the "normal" DC settings of the corrector power supplies through the ELETTRA control system [3].

3.1 Static Leakage measurements

Preliminary tests with real matrices acquired from the machine confirmed the existence of the rank reduction condition; λ_3 and λ_4 are actually not zero because of machine non-linearities and measurement errors but are much smaller than λ_1 and λ_2 (e.g. λ_1=3935, λ_2=2304, λ_3=6, λ_4=5). To evaluate the leakage, i.e. the propagation of the closed bump error, the beam orbit has been measured before and after the application of a bump. The rms of the difference orbit outside the bump was about 1 μm, namely comparable with the resolution of the BPMs.

3.2 Closed Loop measurements

The behaviour of the closed-loop on the machine is in good agreement with simulations [1]. Fig. 2 shows the measured spectra before and after closing the loop. The Proportional Integral Derivative (PID) [4] parameters (K_P, K_I, K_D) as well as the low pass filter cut-off frequency f_C have been empirically determined with the aid of the model to optimize the response in the range 0 - 200 Hz. Attenuation of about 9 dB of the 50 Hz component, 6 dB of the 100 Hz and 3 dB of the 150 Hz have been obtained and confirm the predictions given by simulation on the model.

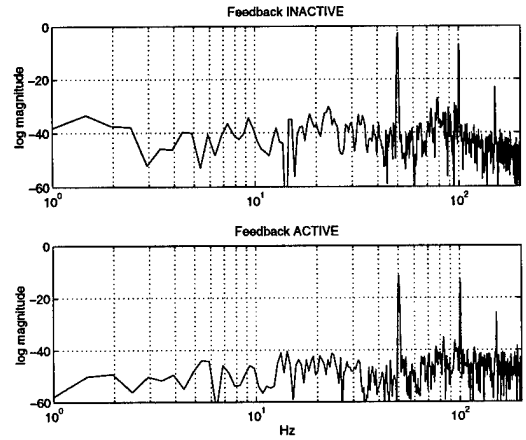

Figure 2: 0-200 Hz noise spectra with loop open and closed (K_P=3, K_I=0.01, K_D=10, f_C=150 Hz).

Closed-loop operation has also been optimized in the 0 - 40 Hz range (fig. 3).

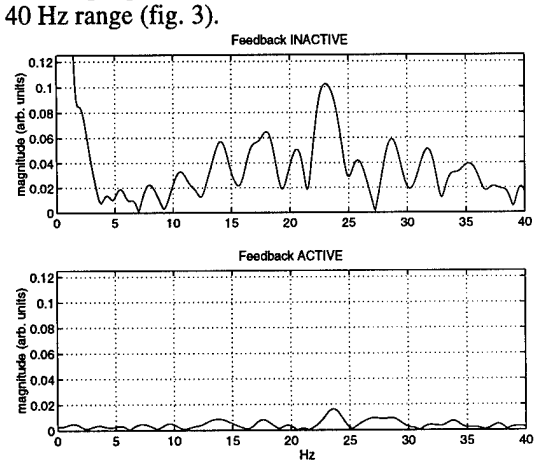

Figure 3: 0-40 Hz noise spectra with loop open and closed (K_P=10, K_I=0.01, K_D=0, f_C=30 Hz).

A time domain measurement has been performed by perturbing the beam orbit with a square wave at 5 Hz generated by another DSP based system modulating the current of a corrector magnet not involved in the feedback. The results are shown in fig. 4.

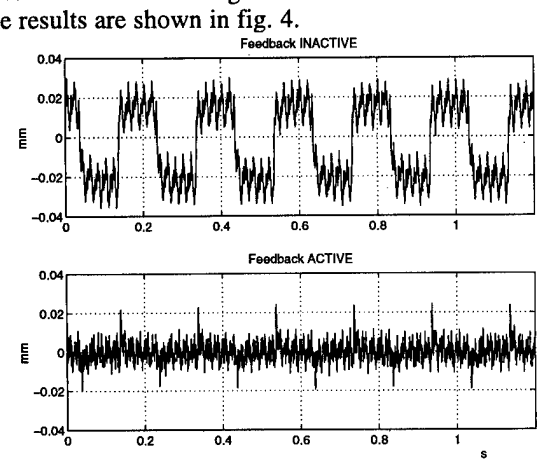

Figure 4: Open and closed-loop time domain measurements perturbing the beam with a 5 Hz square wave.

One of the main goals of a local orbit feedback system is to decouple the activity of the different beamlines. Perturbations induced on a given beamline by a gap change of another insertion device must be eliminated. Fig. 5 shows the position acquired on the phBPM of the beamline 6 during a gap change of ID_3 without and with feedback on ID_6 (before the implementation of the improved insertion device compensation scheme [5]) .

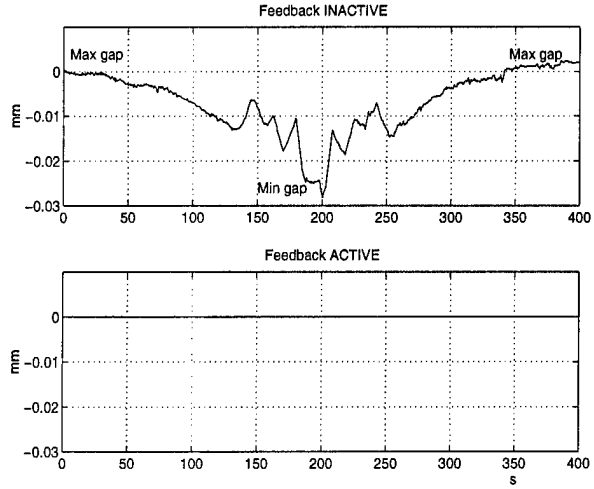

Figure 5: Effect of changing the gap of ID_3 on beamline 6 without and with the feedback active on ID_6.

3.3 Dynamic Leakage measurements

"Dynamic" leakage of the bump closure can drive instabilities when multiple active feedback loops are concurrently running on different beamlines. In order to evaluate the closed bump dynamic error of the feedback system, the photon beam position has been observed on the phBPM of another beamline. Signals before and after the closure of the loop have been recorded and analyzed, but no perceptible difference has been noticed.

4 THE HARMONIC SUPPRESSOR

A newly implemented technique, called "harmonic suppression", has been applied to damp the 50 Hz component and its harmonics which can be clearly identified in the beam position spectrum acquired by the phBPM. It consists of a selective digital filter with programmable delay and gain centered at the frequency to damp. The delay is calculated in order to get a overall system open-loop rotation of 360° at the chosen frequency. Simulation results are very promising and show the possibility of implementing multiple harmonic suppressors centered at different frequencies together with a standard PID regulator for the non-periodic components. The first tests on the machine with a single harmonic suppressor (fig. 6) running on the DSP system have confirmed the simulations. Other tests with one harmonic suppressor associated to a PID regulator have been carried out with success.

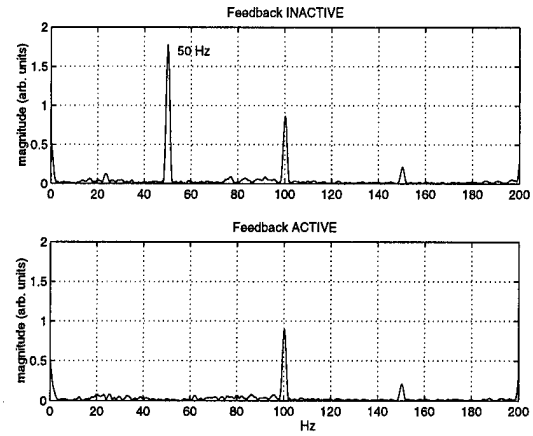

Figure 6: Experiment closed-loop operation running a single harmonic suppressor centered at 50 Hz.

5 CONCLUSIONS

A fast local orbit feedback system has been developed and implemented on two of the ELETTRA beamlines. All additional beamlines will have the system installed by the end of this year.

An empirical method has been developed for the generation of the bump matrix. Its application produces no perceptible leakage of the local correction.

First closed-loop tests have been performed using a standard PID regulator and an attenuation bandwidth of 0-150 Hz has been achieved. The results are in good agreement with the simulations.

Persistent harmonic components of the beam noise have been effectively damped by dedicated harmonic suppressors.

The concurrent utilization of the above techniques should provide the best way to counteract the beam noise spectra measured at ELETTRA.

6 ACKNOWLEDGEMENTS

The authors would like to thank M. Vento and M. Zaccaria for their technical skill.

REFERENCES

[1] C. J. Bocchetta et al.: 'The Design of the ELETTRA Fast Local Feedback System', these Proceedings.

[2] G. H. Golub and C. Reinsch: 'Singular Value Decomposition and Least Squares Solutions', Numer. Math. 14, pp. 403-420, 1970.

[3] D. Bulfone: 'Status and Prospects of the ELETTRA Control System', Nucl. Instr. and Meth. A 352, p. 63, 1994.

[4] G. F. Franklin: 'Feedback Control of Dynamic Systems', Addison-Wesley Pub. Co., 1994.

[5] R. P. Walker et al.: 'Operation of Insertion Devices in ELETTRA and Plans for Future Devices', these proceedings.

COMMISSIONING EXPERIENCE WITH THE PEP-II LOW-LEVEL RF SYSTEM*

P. Corredoura, S. Allison, R. Claus, W. Ross, L. Sapozhnikov, H. D. Schwarz, R. Tighe, C. Yee, C. Ziomek
Stanford Linear Accelerator Center, Stanford, Ca 94309, USA

Abstract

The low-level RF system for PEP-II is a modular design housed in a VXI environment and supported by EPICS. All signal processing and control is done at baseband using in-phase and quadrature (IQ) techniques. Remotely configurable RF feedback loops are used to control coupled-bunch instabilities driven by the accelerating mode of the RF cavities. A programmable DSP based feedback loop is implemented to control DC phase variations across the klystron and to adaptively cancel modulations caused by klystron power supply ripple at selected power line harmonics between 60 Hz and 10 kHz. The system contains a built-in baseband network analyzer which allows remote measurement of the RF feedback loop transfer functions and automated configuration of these loops. This paper presents observations and measured data from the system.

1. INTRODUCTION

The PEP-II low-level RF (LLRF) system [1] is based on 6 types of custom VXI modules, an off-the-shelf slot 0 controller/processor and an Allen Bradley (AB) VME scanner (figure 1). The processor is a National Instruments 68030 running the VxWorks real-time operating system which is supported by EPICS. The AB scanner supports a serial communication link with the Allen Bradley hardware used for slow interlocks (temperatures, water flows, power supply monitoring), control of cavity tuner stepper motors and control of the klystron high voltage power supply (HVPS). The clock/RF distribution module generates the 471.1 MHz LO and digital system clocks. The arc/interlock module detects window arcs, VXI faults and handshakes with the HVPS triggers and beam abort system [3].

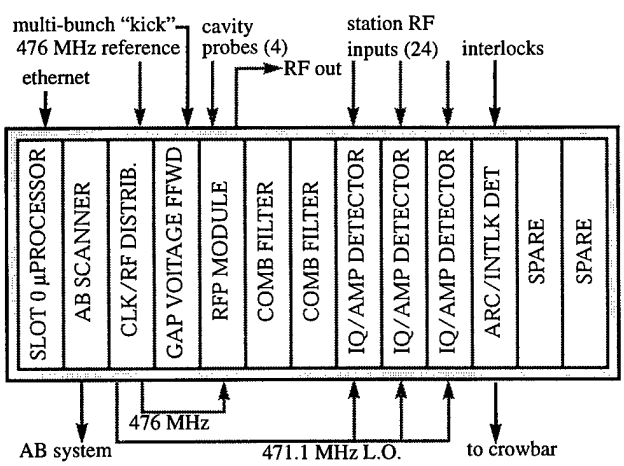

Fig. 1. PEP-II low-level RF system VXI crate topology

The IQ&A detector modules are 8 channel RF receivers using a digital in-phase and quadrature (IQ) down conversion technique for precise narrow-band measurements and a parallel diode detector used for wide-band amplitude detection [5] required for fast RF interlocks. Narrow-band (50 Hz) IQ measurements are transmitted to the EPICS database at a 2 Hz rate for station RF displays and the "slow" feedback loops (cavity tuners and cathode voltage control.). The klystron RF output is measured by a special IQ channel which transmits directly to the DSP in the RF Processing module via a VXI local bus serial link. This DSP runs a state space feedback loop across the klystron, drive amplifier, and RF modulator which keeps the phase shift across this path constant and cancels output phase and amplitude ripple caused by power line harmonics appearing on the HVPS output at a 1% level.

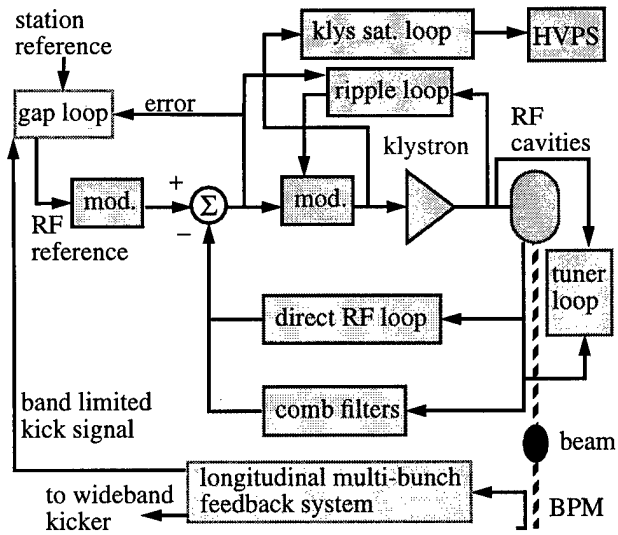

Fig. 2. Block diagram of RF feedback loops used in the PEP-II low-level RF system. Multi-cavities not shown.

The RF Processing module (RFP) contains the hardware necessary to support the wideband RF feedback loops needed to control longitudinal coupled-bunch instabilities caused by the accelerating mode of the RF cavities. Analog IQ demodulators are used to detect the RF voltage in each cavity. A programmable analog network allows combining the detected IQ signals from up to four cavities to form a station gap voltage vector sum signal. Programmable analog modulators allow remote adjustment of loop gains/phases for both direct and comb filter loops. A built in baseband arbitrary function generator/recorder forms a programmable network analyzer capable of performing initial cavity tuning, configuring the combining network, measuring RF feedback loop transfer functions and injecting test signals into the RF system. To our knowledge this feature is a first for storage ring RF systems and has proved to be extremely useful.

*Work supported by Department of Energy, contract DE-AC03-76SF00515

The comb filter modules operate in parallel with the direct RF feedback loop providing additional loop gain for a narrow band about the synchrotron sidebands covering the first ~30 revolution harmonics. A programmable 32 tap finite impulse response (FIR) filter is used to equalize the system group delay variation caused by the damped fundamental cavity resonance. The total comb loop delay is adjusted to equal exactly one ring revolution via a programmable FIFO. A built-in history buffer which automatically stops when a system fault is detected records the comb filter output for the previous 7000 turns. The comb modules communicate with the RPF module via differential analog signals carried over the VXI local bus.

The last module of the PEP-II LLRF family is the gap voltage feed-forward module [2]. This module has two functions. It receives the error signals (I&Q) of the direct RF feedback loop from the RFP module (as VXI local bus differential analogs) and generates the station baseband IQ reference through an adaptive learning algorithm. The resulting station references (I&Q) track the RF cavity transients caused mainly by the ion clearing gap in the bunch train and prevent the klystron from saturating. The second function of this module is to phase modulate the station RF reference by a band-limited "kick" signal sent from the PEP-II longitudinal multi-bunch feedback system. The "kick" is sent via a dedicated fiber optic link which transmits 10 bits of information at a 10 Ms/S rate. As with the comb filters, the kick signal is equalized by a 32 FIR filter and delayed with a FIFO to make the total group delay equal to two ring turns. Hardware in this module and in the longitudinal system kick source allow remote measurement of the "kick" transfer function for each RF station. The IQ station references are delivered to the RFP module as differential analog signals over the VXI local bus.

2. SYSTEM CONFIGURATION

The process of setting up a PEP-II RF station is quite involved. Through the use of the built-in measurement capability and the complete programmability of all adjustment parameters, this process has been highly automated. Matlab scripts running on a workstation have been written to access the EPICS database, control the necessary hardware and perform the substantial amount of signal processing required to configure the system. The procedure for bringing up a station is as follows:

TUNE RF CAVITIES - Klystron drive power is set to 25% of the saturated level to allow for the addition of band limited noise to the drive signal. The station is turned on at 100 kW klystron output power. The built-in network analyzer is used to measure the transfer function of each cavity. This measurement is fit to a model and the center frequency is extracted. The required cavity tuner movement is calculated and implemented. This process repeats for each cavity until all cavities are within 10 kHz of 476 MHz. We have found that variations in the cavity supply water temperature of 1°C prevent us from getting any closer without using the tuner loop. Next the tuner loop phase offsets are nulled and the tuner loop is activated. Cavity frequency measurements are repeated but adjustments are now made to the cavity probe phase offset. Drift in the water temperature no longer causes a frequency shift. This procedure is capable of bringing each cavity to within 300 Hz of the system RF frequency (476 MHz), corresponding to an acceptable 1° error in the cavity transmission phase. The cavity combining network in the RFP is then adjusted to null out phase variations caused by differences in cable lengths, sum the cavity voltages while conserving any gap voltage variations observed in the set of cavities due to variations of cavity Q and β. All cavities are now tuned, tuner loop phase offsets nulled and the combining network is optimized. This process takes about 30 minutes.

CONFIGURE DIRECT RF FEEDBACK LOOP - To insure a constant phase shift across the klystron the "ripple" loop must be enabled. Otherwise changes in the HVPS output voltage would translate to a change in the loop phase of the direct RF feedback loop. An automatic gain control (AGC) loop is planned which will keep the large signal gain of the klystron and the ripple loop modulator constant as the HVPS voltage is varied. To set the gain and phase shift of the direct loop the built-in network analyzer is again used to measure the open loop response. The measured response is fit to a model and the adjustment required to obtain phase margins of 67° (determined to be the optimum) is calculated. After updating the direct loop modulator the open loop response is again measured to verify that the proper settings have been achieved. If the response is OK the loop is closed and the closed loop response is measured. This procedure takes 10 minutes.

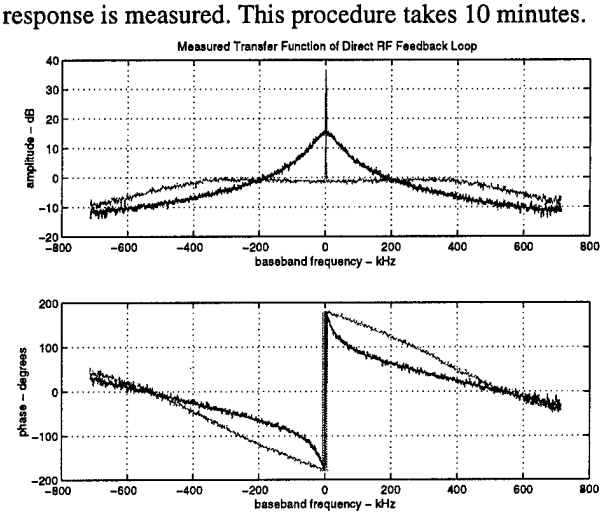

Fig. 3. Measured open/closed loop response of direct loop.

CONFIGURE THE COMB FILTER LOOP - Since the comb loop operates in parallel with the direct loop, the direct loop must be operating before the comb loop can be set up. The first step is to determine the group delay equalizer tap settings. The comb filters are placed in "thru" mode (no filtering) and equalizer taps are loaded with a single full scale tap weight, the remaining 31 taps are set to zero. The network analyzer then measures the open loop

response of the comb filter path. The response information is used to calculate the necessary tap weights to equalize the delay and roll the gain off above 2.5 MHz. The new taps are loaded and the equalized response is measured (figure 4). Next the comb filters are activated and the open loop response is measured. The response covering the first few comb peaks is fit to a model and the desired comb modulator coefficients are determined and loaded. The open loop response is then verified. If the open loop response is acceptable the loop is closed. The closed loop response (reflecting the damped cavity impedance) is then measured.

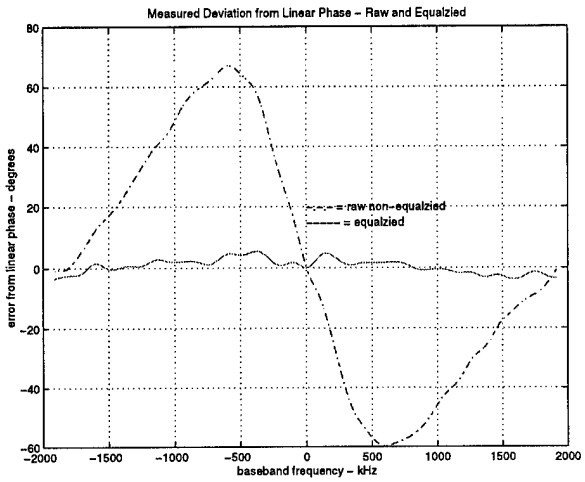

Fig. 4. Measured response without/with equalization.

3. KLYSTRON "RIPPLE" LOOP

To correct for DC phase variations across the klystron and cancel output modulation caused by HVPS output ripple a feedback loop using state-space control and adaptive noise cancellation techniques has been developed [6]. This new approach has several advantages over a typical klystron phase loop used in most storage rings. Mainly this method is completely compatible with IQ signal processing and does not require addition of analog phase detectors. The loop runs on a AT&T 1610 DSP in the RF processing module. The DSP receives band limited (10 kHz) klystron output RF data (I&Q) at a 23 kHz rate from a dedicated channel of an IQ&A detector module via a dedicated serial link. The DSP also measures the I&Q baseband drive signals using two 12 bit ADCs. The design of this loop has been described previously[1].

The current version of this loop keeps the phase shift across the RF modulator, drive amplifier and the klystron constant while cancelling both AM and PM from 14 sinusoidal noise sources. This number is limited by the amount of computations to be carried out before the next data sample arrives (every 43μs). Most of the processor time is used calculating the inverse tangents (drive phase and klystron output phase) and the square root (klystron output amplitude). We expect to increase the number of harmonics allowed by writing a new arctan function which is limited to 10 bits of precision, the current arctan supports 36 bits. During initial testing of this loop we were able to maintain the phase length of the drive chain and klystron to within 1° and reduce the amplitude of the targeted sidebands by ~30dB.

4. STATION OPERATION

Operator interface to the PEP-II RF system is achieved via EPCIS panels [4]. The main RF panel (figure 5) displays the most important system parameters (klystron and cavity RF power, gap voltages, vacuum levels, cavity tuner positions), has "buttons" for controlling the station mode and accessing other more detailed panels. Because of the system's complete programmability we have been able to add features which significantly reduce the required amount of operator involvement. Each station is capable of "autoprocessing". The user sets up the desired processing endpoints (maximum klystron power, maximum cavity voltage and vacuum level) and the EPICS processor will ramp the power up until the warning vacuum level is reached, power is then reduced. This procedure continues until the desired maximum set points are reached. To process new (dirty) cavities a method of sweeping the drive frequency +/- 160 kHz has been implemented by loading FM IQ files into the built-in network analyzer's programmable source. The system can also of reset itself after a fault.

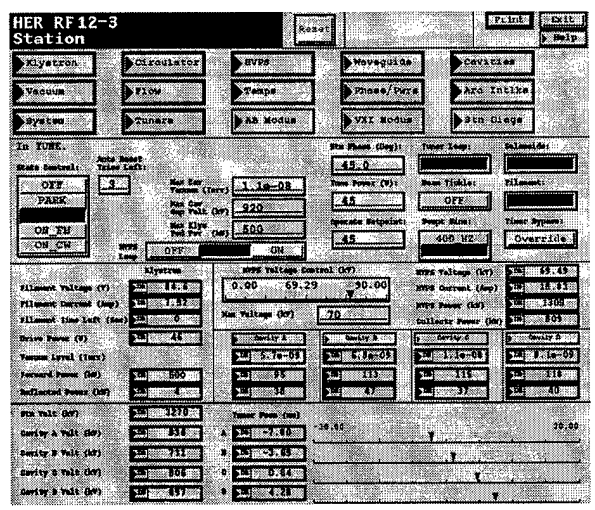

Fig. 5. Main EPICS panel for a PEP-II RF station.

5. REFERENCES

[1] P. Corredoura et al, "Low Level System Design for the PEP-II B Factory", Proceedings of the 1995 IEEE Particle Accelerator Conference.

[2] W. Ross, R. Claus, L. Sapozhnikov, "Gap Voltage Feed-Forward Module for the PEP-II Low-Level RF System", this conference (PAC 97)

[3] R. Tighe, "Arc Detection and Interlock Module for the PEP-II Low Level RF System", PAC 97

[4] S. Allison, R. Claus, "Operator Interface for the PEP-II Low Level RF Control System", PAC 97

[5] C. Ziomek, P. Corredoura "Digital I/Q Demodulator", Proceedings of the 1995 IEEE Particle Accelerator Conference.

[6] P. Corredoura "Development of Digital Control for the PEP-II Klystrons", SLAC PEP-II Tech Note #60, 1994.

[7] Thanks to Khoi Ha of Hytek Services for providing us with superior printed circuit board layout design support.

DESIGN AND VERIFICATION OF CONTROLLERS FOR LONGITUDINAL OSCILLATIONS USING OPTIMAL CONTROL THEORY AND NUMERICAL SIMULATION: PREDICTIONS FOR PEP-II

H. Hindi, S. Prabhakar, J. Fox, D. Teytelman,
Stanford Linear Accelerator Center, Stanford University, Stanford, CA 94309, U.S.A

Abstract

We present a technique for the design and verification of efficient bunch-by-bunch controllers for damping longitudinal multibunch instabilities. The controllers attempt to optimize the use of available feedback amplifier power - one of the most expensive components of a feedback system - and define the limits of closed loop system performance. Our design technique alternates between analytic computation of single bunch optimal controllers and verification on a multibunch numerical simulator. The simulator identifies unstable coupled bunch modes and predicts their growth and damping rates. The results from the simulator are shown to be in reasonable agreement with analytical calculations based on the single bunch model. The technique is then used to evaluate the performance of a variety of controllers proposed for PEP-II.

1 INTRODUCTION

The programmable digital signal processor based longitudinal feedback system described in [1] is currently being installed at PEP-II. In this paper, we present results from a study of the rms noise performance of the feedback system and closed loop damping rates, for PEP-II. The results were obtained using optimal control theory [2],[3] together with multibunch numerical simulation [4].

2 DESIGN APPROACH

For feedback design, the overall beam-feedback system can be abstracted into the block diagram in fig.1. The objective

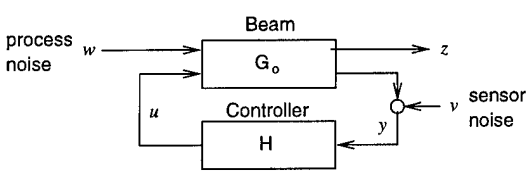

Figure 1: System block diagram.

of the feedback is to damp the unstable modes of the beam, minimize steady state phase oscillations z in the presence of process noise w, and reject dc to allow each bunch to ride on its own synchronous phase. This must be done using the minimum amplifier power u and without amplifying the sensor noise v. The closed loop system, which we call G, has 2-inputs (w & v) and 2-outputs (z & u). When designing a controller H for Go, all four components of G (Gzw, Gzv, Guw, and Guv) must be taken into account.

2.1 Single Bunch Beam Model

Due to the very large number of bunches in the beam, it is computationally infeasible to directly design a controller by treating the whole beam as a single system. Therefore a decentralized or "bunch-by-bunch" approach is used instead, where the feedback for each bunch is computed using measurements of that bunch only. So, the controllers are designed for the following open loop model Go: a single bunch beam, which is essentially a discrete-time simple harmonic oscillator with only radiation damping and a resonance at the synchrotron frequency. Fig.2 is the frequency response of Go for the PEP-II low energy ring (LER), on which we focus our study. Estimates for the noise statis-

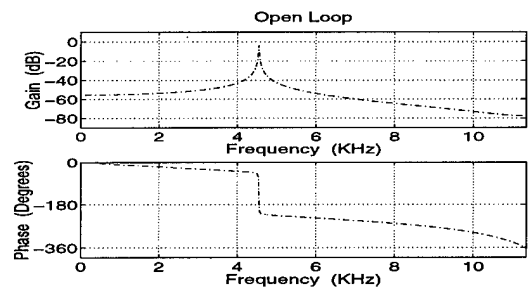

Figure 2: Single bunch beam model.

tics were obtained by scaling the values measured at the Advanced Light Source at LBNL.

2.2 Trade Off Analysis

LQG controllers [2],[3] minimize rms beam motion z for given rms feedback amplifier power u. They are optimal with respect to this rms criterion. As the available rms u is varied, one obtains a curve which defines the limits of performance of the system, see fig.3. A similar curve can be obtained for the FIR controllers [2] proposed for PEP-II by simply varying the loop gain. One can then inspect these curves, pick a desirable operating point, and design the corresponding controllers.

We expect the rms performance of the multibunch beam to be close to the rms performance of a single bunch with the average damping rate of all the modes. To a good approximation, this may be taken to be the radiation damping rate. The controllers were therefore designed for the radiation damped beam. To check that these controllers also stabilize the unstable modes, tradeoff curves were plotted for the most unstable beam mode as well, producing the

0-7803-4376-X/98/$10.00 © 1998 IEEE

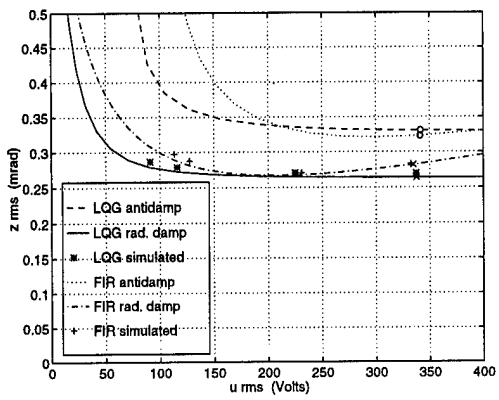

Figure 3: LQG & FIR Tradeoff curves.

remaining curves in fig.3.

3 RESULTS

The tradeoff curves show that the performance of the FIR controllers is quite close to optimal for a large range of operating conditions.

In this section we compare two controllers, one FIR and one LQG, which were designed to provide: a quiet beam in steady state, fast damping of unstable modes, some robustness to parameter variations and effective feedback without saturating the power amplifier on sensor noise. The rms performance of these two controllers is marked on the tradeoff curve with 'x's and 'o's.

3.1 Controllers

Fig.4 shows the frequency responses of two controllers tha we used in H for the single bunch LER model Go. FIR con-

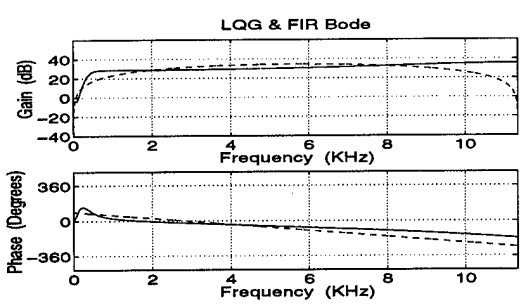

Figure 4: Controller frequency responses.

trollers (dashed) act as approximate differentiators; LQG controllers (solid) minimize rms beam motion using minimum rms amplifier power and are designed using optimal control theory. Both controllers provide dc rejection, which is a strict requirement.

3.2 Closed Loop Performance

Fig. 5 shows the four closed loop frequency responses, Gzw, Gzv, Guw, and Guv obtained with the FIR controllers

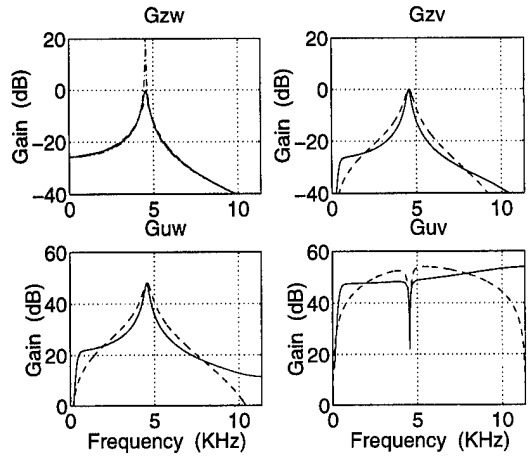

Figure 5: Closed loop frequency responses.

(dashed) and LQG controllers (solid). The (scaled) open loop response Go is plotted in dash-dot with Gzw. We note that the peak of Gzw is higher for the LQG than the FIR, showing that it provides lower damping than the FIR. The peaks of the other three responses are quite comparable. The LQG responses are narrower for Gzv and Guw, but broader for Guv. The following observations can be made for both controllers: There is a sharp notch in Guv, showing that the closed loop system rejects sensor noise at the synchrotron frequency. The fact that Guv is considerably larger than Guw over most of the frequency range, shows that the contribution of sensor noise v to amplifier voltage u is larger than that of process noise w. Thus at PEP-II the feeback system is sensor noise dominated.

4 LONGITUDINAL SIMULATION RESULTS

A phase-space tracking simulation program is used to identify HOM-driven unstable coupled bunch modes in PEP-II and predict their growth rates. The action of the longitudinal feedback system is also simulated, so as to predict its damping effect. However, the dynamics of the fundamental cavity resonance are not simulated, and the fundamental is assumed to be rigid.

The rms noise performance of four pairs of controllers (FIR & LQG) were verified on the numerical simulator. These controllers ranged from the "knee" to the right end of the tradeoff curves. The results of the simulation, shown with '*'s and '+'s in fig.3, are in good agreement with the curves for the radiation damped bunch, as expected.

The simulated experiment illustrated in figure 6 starts at t = 0 with the 1658 bunch, 2.25A, LER beam at equilibrium. Noise excitation produces growth of unstable beam motion until feedback is turned on at t = 18ms. From this point on the bunch phases are passed through feedback filters and fed back as voltage kicks that damp the oscillations down to steady state.The longitudinal oscillations are projected onto symmetric beam eigenmodes by taking FFTs of the bunch phases on each turn [5]. The figure traces the

evolution of the amplitudes of 1746 coupled bunch modes (folded at mode 873) over the whole grow/damp transient. We can see that there is a spectrum of unstable modes that grow from the noise floor in the absence of feedback. These modes are damped back down fairly rapidly once the 4-tap FIR feedback is turned on. Symmetric beam calculations indicate that modes 644-818 should be unstable at the design current, with growth rates ranging from 0 to 0.2 per ms. Exponential fits to the growing transients in the figure yield modes 677-689 and 758-789, growing at rates from 0.15 to 0.23 per ms. Exponential fits to the damping transients (after t = 18ms) yield damping rates clustered around 1 per ms. These rates were consistent with those obtained from the single bunch model analytical design. In

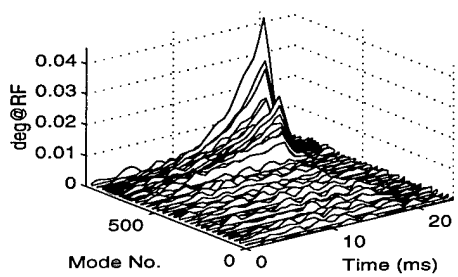

Figure 6: Growth and damping of unstable modes.

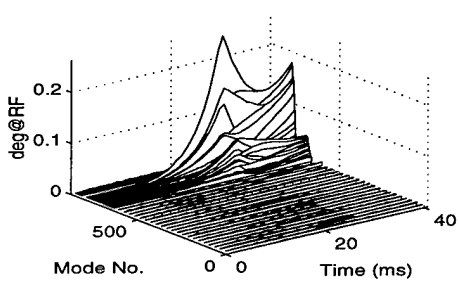

Figure 7: Instability due to saturated feedback.

fig.7, the simulation displayed in figure 6 is repeated with an LQG controller coming on 8ms later than before. As before, two bands of modes (677-689 and 758-789) show unstable growth in the absence of feedback. As a result of the delay in turning on the feedback, most modes grow to amplitudes 5-6 times larger than in the previous simulation before they are acted upon by the controller. The feedback power amplifier is thus heavily saturated, and hence fails to control the unstable modes. The threshold for saturation induced failure of the feedback system is approximately at 0.4 deg of rms beam motion for this controller.

5 SUMMARY AND CONCLUSION

We have presented a general technique for the design and verification of decentralized controllers for stabilizing longitudinal coupled bunch instabilities in a circular accelerator. The technique involves estimating growth rates of unstable modes using numerical simulation, analytical design of controllers for a radiation damped single bunch model, and verification of the controllers' performance on a multi-bunch beam simulation. This allowed the use of optimal control theory and trade off analysis to obtain the limits of the closed loop rms performance of the PEP-II feedback system in the presence of process and sensor noise.

It has been shown that the technique of designing controllers for a radiation damped single bunch model yields accurate calculations of the rms performance of the multi-bunch beam. The simulations show that it is possible to stabilize HER and LER beams under the estimated noise conditions with 1.5KW of amplifier power per ring. However, as demonstrated in fig.7, more power might be needed to control oscillations of the order of 8 mrad ($\approx$0.4 degree at rf) due to saturation of the back end. Reflections at the kickers, cable losses, and other nonidealities could also be larger than expected.

The damping rates calculated from the single bunch model were also consistent with those of coupled bunch modes in the numerical simulations. The tradeoff analysis showed that the feedback systems for the PEP-II beams are expected to be sensor noise dominated, for the gains required to produce good damping of unstable modes. The four-tap FIR controllers studied here were comparable to the LQG controllers in rms noise performance. They yielded better damping rates at the high end of the gain spectrum at the expense of only a 10-20% increase in rms beam motion. They also have better robustness to parameter variations, though this is not a significant issue for the conditions of PEP-II due to the fact that modal tune shifts are small in the two rings.

6 ACKNOWLEDGEMENTS

We would like to thank Robert Rimmer and John Byrd for very helpful discussions. This work was supported by DOE contract # DE-AC03-76SF00515.

7 REFERENCES

[1] G. Oxoby, et al.,'Bunch-by-bunch longitudinal feedback system for PEP-II', EPAC '94, London,England.

[2] H. Hindi, et al.,'A formal approach to the design of multi-bunch feedback systems: LQG controllers', EPAC '94, London,England.

[3] Astrom and Wittenmark, *Computer Controlled Sytems*, Prentice Hall, 1990

[4] K. Thompson,'Simulation of longitudinal coupled-bunch instabilities', Feb. 1991, Asymetric B-factory collider note, ABC-24.

[5] S. Prabhakar, et al.,'Observation and modal analysis of coupled-bunch longitudinal instabilities via a digital feedback control system,'to be published in 'Particle Accelerators'.

GAP VOLTAGE FEED-FORWARD MODULE FOR PEP-II LOW LEVEL RF SYSTEM*

W. Ross, R. Claus, L. Sapozhnikov
Stanford Linear Accelerator Center, Stanford, CA 94309, USA

Abstract

The Gap Voltage Feed-Forward (GVFF) Module produces adaptively generated inphase (I) and quadrature (Q) reference signals for a single RF station. This module measures the periodic (1-turn) beam induced cavity transients caused by the presence of an ion clearing gap in the beam. A reference waveform is generated to minimize the direct feedback error signal transient caused by the gap. In addition, the GVFF module receives a fiber-optically connected, band-limited 'kick' signal from the Longitudinal Feedback System. The kick signal modulates the I and Q components of the RF reference causing the station to act as a 'sub-woofer' for the Longitudinal Feedback System. This process dampens low order coupled-bunch instabilities induced by the fundamental mode of the accelerating cavities. The GVFF Module also includes hardware for remote measurement and adjustment of the 'kick' transfer function.

1. INTRODUCTION

The Gap Voltage Feed-Forward (GVFF) Module is a C-size VXI circuit board which is installed in a 13-slot VXI Chassis containing the various modules of the Low-Level RF system [1]. An RF Station consists of this VXI chassis, a safety interlock chassis, a klystron, an RF drive amplifier, and either two RF cavities for Low Energy Ring (LER) stations or four RF cavities for High Energy Ring (HER) stations. The PEP-II B-Factory contains five RF Stations for the HER and three RF Stations for the LER. The RF Stations are positioned around the 2200 meter circumference ring as shown in Figure 2. There is one GVFF module in each RF Station.

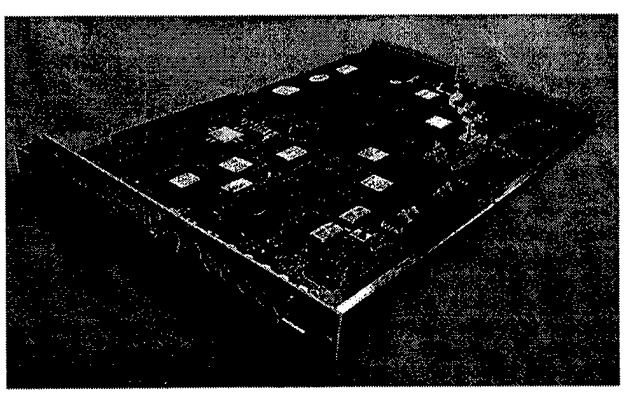

Figure 1: Photograph of GVFF module.

*Work supported by Department of Energy, contract DE-AC03-76SF00515

The primary function of the GVFF module is to generate a periodic reference signal which sets the amplitude and phase for the 476 MHz klystron RF drive signal. The desired amplitude and phase for each RF Station is defined in an EPICS data base which can be read by a DSP processor in the GVFF module. The reference signal is a two dimensional signal of I (in-phase) and Q (quadrature) components. Its period corresponds to one turn through the ring, or 7.34 μSec.

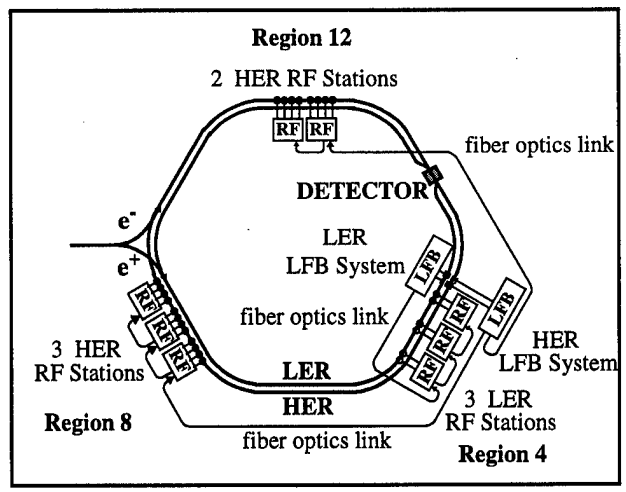

Figure 2: Interconnect between RF Stations and Longitudinal Feedback Systems.

Figure 3 shows the direct feedback loop of an RF Station. The stored circulating beam in either ring consists of a series of electron or positron bunches and an unfilled area called an ion clearing gap. When the gap passes through the cavities, a large voltage transient occurs which would normally saturate the feedback loop. The GVFF module monitors the direct feedback loop error signal to detect the periodic gap transient. The GVFF module applies an adaptive digital signal processing algorithm to generate a reference waveform which combines the EPICS specified amplitude and phase for the RF station (DC component) with a 'gap transient' compensating waveform (AC component) to minimize the gap transient as seen in the loop error signal.

The secondary purpose of the GVFF module is to interface the LLRF systems and the Longitudinal Feedback (LFB) system for each ring. Two LFB systems are installed in Region 4 of the PEP-II B-Factory, one serving the HER and one serving the LER. These LFB systems dampen the coupled bunch synchrotron oscillations which are driven by parasitic higher-order modes of the RF cavities.

0-7803-4376-X/98/$10.00 © 1998 IEEE

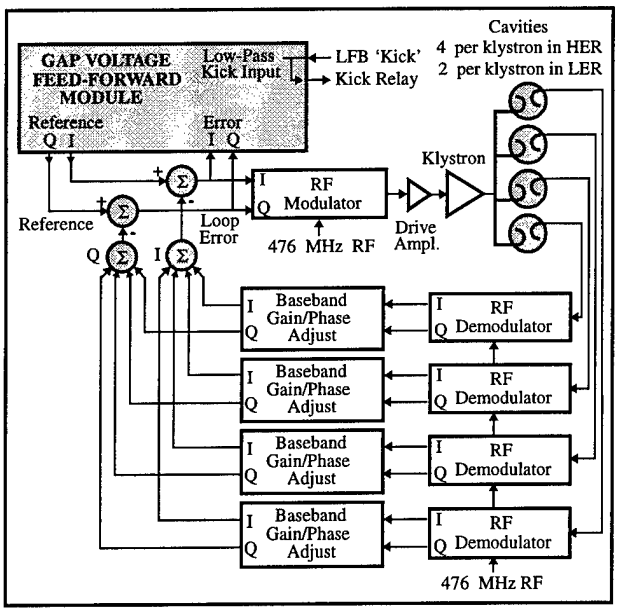

Figure 3: Block diagram of direct feedback loop for one RF Station.

The LFB Systems use their own 'kicker' arrays to dampen the higher-order mode oscillations. However, to dampen the larger low-order mode oscillations, each LFB system low-pass filters its analog kick signal, digitizes it and transmits it to the RF Stations via fiber optics cables, as shown in Figure 2. The RF Stations serve as high-power, low frequency drivers for the LFB systems. The GVFF modules act as interfaces between the LFB systems and the LLRF systems. The GVFF module transforms the kick signal by means of a cosine table and a sine table, so that Cos(kick) and Sin(kick) signals are applied to the real and imaginary inputs of a complex multiplier. The complex multiplier modulates the reference I and Q signals to vary primarily the phase of the klystron drive RF signal.

The GVFF module also measures the open and closed loop responses of the LLRF/LFB loop. A 512K word 'play' memory is loaded via the EPICS control interface with a stimulus signal. On demand of the EPICS control interface, the play memory plays out the stimulus waveform, while a 'record' memory collects the 'kick' waveform samples received from the LFB system. For open loop response, the stimulus signal replaces the LFB kick signal in driving the Cosine/Sine transform. For closed loop measurement, the stimulus signal is added to the LFB kick signal to drive the Cosine/Sine transform. The loop response can be tuned via a programmable 32-tap equalizing filter in the GVFF module.

2. ARCHITECTURE

Figure 4 shows a block diagram of the GVFF module. The digital signal processor (DSP) operates at slower than real-time in computing the reference waveform. Therefore, a pair of 512 word Input FIFOs are used to collect up to 3 turns of error waveform, initiated by a 'Turn Trigger' pulse which occurs once per turn. When the FIFOs have data available, the DSP is interrupted. The DSP reads the error signal data from the FIFOs and inputs this to its adaptive

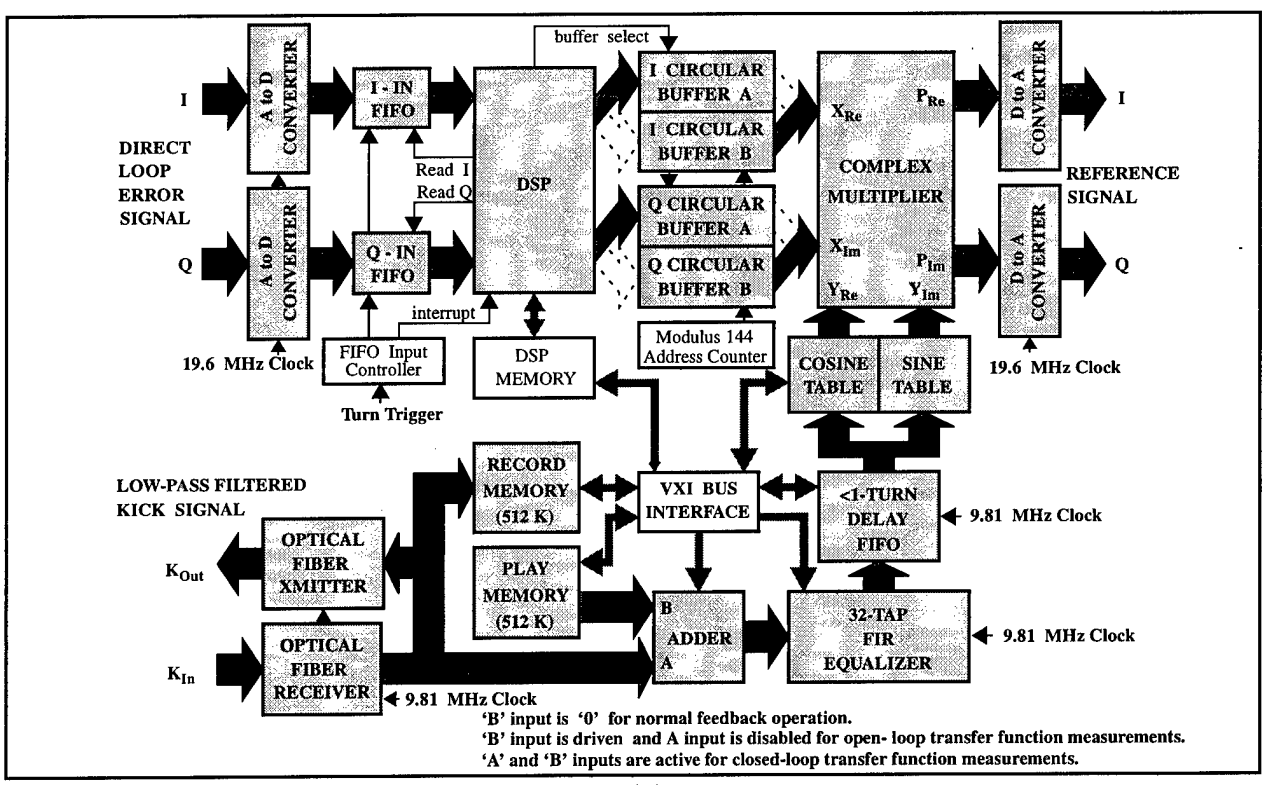

Figure 4: Block diagram of Gap Voltage Feed-Forward Module.

algorithm which calculates one turn of `reference' waveform. The result is placed into the inactive region of the circular buffers. The DSP then toggles the buffer selector to put the new reference waveform 'on-line'. The DSP begins the next iteration of its adaptive process by re-arming the Input FIFO controller.

The circular buffers repetitively play out the latest reference waveform, on a one-turn period. This reference waveform is then modulated by the LFB kick signal via the complex multiplier.

The low-pass filtered kick samples from the LFB system drive one input of the digital adder. The other input of the adder is driven from the 'play' memory. Either input may be disabled by the EPICS control interface to put the GVFF module into normal feedback mode, open loop transfer function measurement mode or closed loop transfer function measurement mode. The 'equalizer' is a programmable 32-tap FIR filter. It is required to correct kick signal phase distortion induced by the low-pass analog filter in the LFB system. The Delay FIFO time-delays the kick signal so that the delay due to the position of the RF station in the ring and the sum of data processing delays add up to exactly one turn. The Cosine/Sine tables convert the kick signal to I/Q components to cause primarily phase modulation of the station RF drive signal.

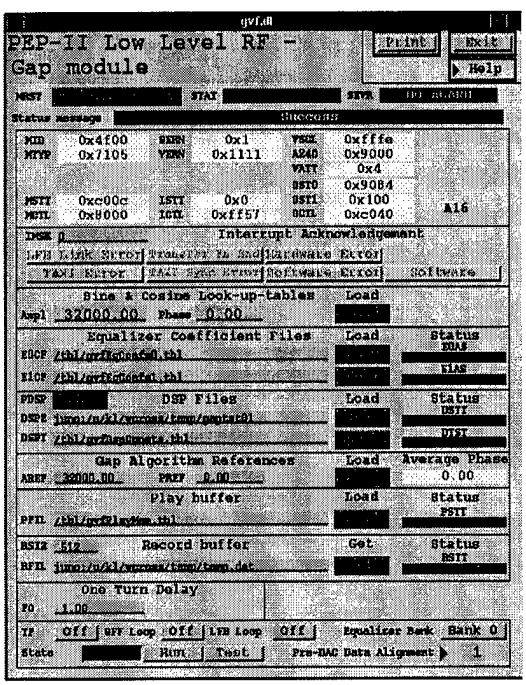

Figure 5: EPICS panel for Gap Voltage Feed-Forward Module control.

3. CONTROL

The various modules in the Low-Level RF System are controlled by EPICS control panels [2]. The EPICS shell runs on a remote workstation and establishes network connectivity to the XVI Control Processor in each of the LLRF VXI chassis. The control panel for the GVFF module is shown in Figure 5. Controls are provided for loading equalizer filter coefficients, down-loading or reading back the Record and Play memories, loading and starting DSP programs, loading the Cosine and Sine tables, setting the loop delay value, and setting the GVFF module into its various operating modes.

4. ADAPTIVE ALGORITHM

The DSP adaptive algorithm used to generate the reference waveform is outlined below:

- Arm Input FIFO and wait for 'data ready' interrupt.
- Average across the N turns of collected error signal data to compute one turn of 'averaged' I and Q error signals.
- Remove the DC components from the I error signal and the Q error signal:

  $NewErr_I[0..n] <= NewErr_I[0..n] - DC_I$

  $NewErr_Q[0..n] <= NewErr_Q[0..n] - DC_Q$
- Compute difference equations using constants α (forgetting factor) and β (adaptive rate):

  $Y_I[0..n] <= \alpha * (Y_I[0..n] + \beta * NewErr_I[0..n])$

  $Y_Q[0..n] <= \alpha * (Y_Q[0..n] + \beta * NewErr_Q[0..n])$
- Get 'AREF' and 'PREF' (station amplitude and phase) parameters from the EPICS data base, and convert to I_{ref} and Q_{ref}.
- Compute the new Reference waveform, placing the result into the inactive regions of I circular buffer and Q circular buffer:

  $NewReference_I[0..n] <= Y_I[0..n] + I_{ref}$

  $NewReference_Q[0..n] <= Y_Q[0..n] + Q_{ref}$
- Toggle the ping-pong circular buffers to put the new reference signal 'on-line', and loop back to top.

5. GVFF MODULE TEST CAPABILITY

A set of test programs has been developed for the GVFF module, and a tester board has been built which generates a synchronized 'kick' test pattern, feeding this to the GVFF module through a fiber optics link. To facilitate testing, the GVFF module includes an additional data path from the complex multiplier output to the 'record' memory (not shown in Figure 4). This allows most of the GVFF module to be tested in an automated manner.

6. REFERENCES

[1] P. Corredoura et. al. "Low Level RF System Design for the PEP-II B Factory", SLAC-PUB-95-6855, Oct 1995, Stanford Linear Accelerator Center, Stanford, CA 94309, USA.

[2] S. Allison et. al., "Operator Interface for the PEP-II Low Level RF System", this conference (PAC 97).

VXI BASED MULTIBUNCH DETECTOR AND QPSK MODULATOR FOR THE PEP-II/ALS/DAΦNE LONGITUDINAL FEEDBACK SYSTEM*

A. Young, J. Fox and D. Teytelman
Stanford Linear Accelerator Center, Stanford, CA 94309, USA

Abstract

The PEP-II/ALS/DAΦNE feedback systems are complex systems implemented using analog, digital and microwave circuits. The VXI hardware implementation for the Front-end and Back-end analog processing modules is presented. The Front-end module produces a baseband beam phase signal from pickups using a microwave tone burst generator. The Back-end VXI module generates an AM/QPSK modulated signal from a baseband correction signal computed in a digital signal processor. These components are implemented in VXI packages that allow a wide spectrum of system functions including a 120 MHz bandwidth rms detector, reference phase servo, woofer link to the RF control system, standard VXI status/control, and user defined registers. The details of the design and implementation of the VXI modules including performance characteristics are presented.

1 INTRODUCTION AND OVERVIEW

The multi-bunch feedback system was designed as part of a multi-lab collaboration for use at the PEP-II, ALS and DAΦNE machines. It is a programmable system implemented in a family of VXI and VME modules and operates at sampling rates up to 500 MHz. The beam motion is phase detected at a 6*RF frequency and processed in the Front-end VXI module. The output of the Front-end module is a baseband signal (DC-500 MHz) representing all the coupled-bunch modes of beam motion. The baseband signal is digitized and downsampled in the Downsampler VXI module. A distributed DSP function is implemented in an array processor constructed of VME based DSP modules. The recombination of the parallel computation results, and the output D/A converter are contained in a Hold Buffer VXI module. The baseband D/A output is then up-converted to 9/4 RF frequency and AM-QPSK modulated in a Back-end VXI module. The VXI packaging allows construction of mixed analog, digital and microwave functions, with a general purpose computer interface for configuration, control and monitoring functions. An extensive EPICS-based control software system is used to operate the feedback system. The system can also be used to measure bunch-by-bunch currents in the machine [1].

2 IMPLEMENTATION

Figure 1 shows a simplified block diagram of the feedback system. Most of the digital functions (DSP, Downsampler, Holdbuffer) has been discussed in previous papers [2,3]. The master oscillator shown generates the phase-locked 6*RF and 9/4*RF oscillators (PEP-II configuration) using a divided RF/4 signal from the master timing VXI module [4]. The RF/4 signal is multiplied via a step-recovery diode and the resulting spectral comb is filtered to provide both 6*RF and 9/4*RF signals in phase syncronisism to the beam. The system oscillator contains a small daughter board that controls switches, and other diagnostic functions. The control for these functions is through an interface data bus from the Front-end module. The system oscillator also has the capability of generating a simulated beam impulse so the system can be tested and calibrated off line.

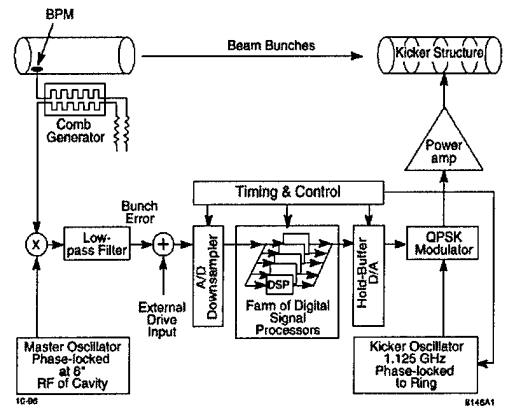

Fig. 1. Block Diagram of the Longitudinal Feedback System.

The heart of the Front-end beam signal processing is a stripline comb generator that is a passive band pass structure contained in the master oscillator chassis. The impulse response of this device is a finite length 4 cycle tone burst at the 6th harmonic of the ring RF (2856 MHZ for PEP-II). Figure 2 illustrates a four tap, -30dB, comb generator tuned for the PEP-II system. A four tap comb generator generates a unique beam phase signal for every bucket in the PEP-II system. This device is made from a copper-clad teflon material and then gold plated to lower the losses.

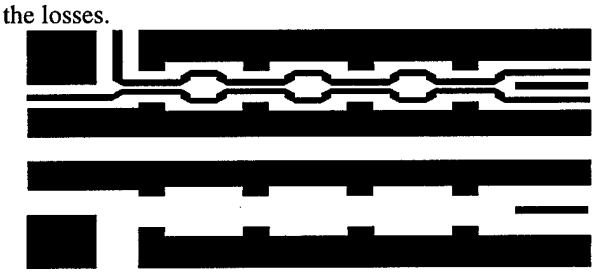

Fig. 2. Stripline Comb Generator.

The Front-end module shown in figure 3 contains a phase detector (operating at 6*RF) to detect synchrotron motion of each bunch. This circuit is implemented with 400 MHz band-width to provide bunch to bunch isolation.

* Work supported by Department of Energy, contract DE-AC03-76SF00515

The module has a low frequency DC coupled phase servo to adjust the reference phase of the system to the average synchronous phase of the bunches. The final major component is a beam motion detector circuit that provides a bandwidth limited (120 MHz) measurement of the excitation of the beam. The VXI interface in this module allows remote operation and calibration of all module functions. For example, the phase servo circuit can be operated and set up remotely using an auto calibration code that allows an operator to just push a button and the servo will be initialised to the best operating point.

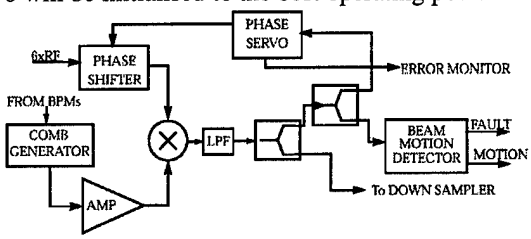

Fig. 3. Block Diagram of Front-end Module

The Back-end module transforms the baseband correction signal computed by the DSP farm into a signal within the frequency band of the power amplifiers and kicker (see figure 4). The center frequency of the kicker structures are designed to fall at 9/4, 11/4 or 13/4 of the machine RF frequency to minimize the coupling impedance the kicker presents to the beam [5,6]. The module transforms a CW carrier at the kicker center frequency into an AM-QPSK (quad phase shift keyed) modulated signal. The pure QPSK signal provides a DC kick on every bunch. The QPSK signal is amplitude modulated by the base-band correction signal that contains the feedback correction for every bunch. The output of this module is a signal spanning the entire coupled-bunch mode spectrum. For test purposes the QPSK modulator can be put into a single state (0, 90, 180, 270) by programming the gray counter using the VXI interface. The signal is then amplified using a solid state amplifier (produced by Milmega, LTD.). The VXI interface is used to control all module functions, such as adjusting the output signal's amplitude and manipulating the QPSK modulator diagnostic states for testing and calibration purposes. A broadband 120 MHz rms detector provides a check on the amount of kicker motion that is delivered to the amplifier. A separate low-frequency "WOOFER" channel sends a 10 MS/s bandwidth limited digital correction signal to the RF system via a fiber optic data link [7].

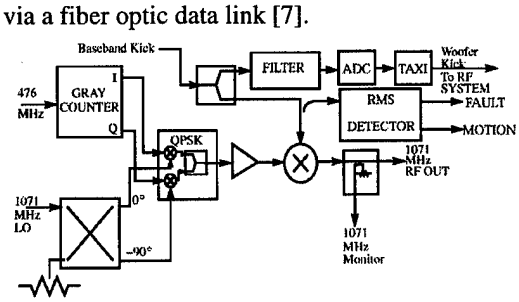

Fig. 4. Block Diagram of the Back-end Module

The woofer system has many operating modes, including diagnostic measurements of open-loop and closed-loop transfer functions between the longitudinal feedback system and the RF. To perform these tasks, the Woofer channel has six modes of operation. In typical operation the baseband kick signal is sent to the RF system using a serial fiber-optic link. In diagnostic modes the Back-end woofer channel can record the kick signal in a circular buffer or inject a test excitation in the signal path signal to the RF system. The woofer channel also has an input port where an external woofer signal can be summed with the kick signal and then transmitted to the RF system. The VXI interface allows operators to run and configure the woofer channel and synchronise the woofer path with the digital RF system.

3 RESULTS

Figure 5 shows a set of oscilloscope waveforms from the Front-end module in which simulated beam motion is growing at mode zero. The upper trace is the detected synchrotron motion of each bunch at baseband, showing a mode-zero signal growing as a linear ramp. The middle trace shows the output of the rms motion detector, which reveals the growing motion of the beam. The lower trace shows a comparator output of the beam motion detector. The Front-end module contains a comparator whose threshold can be set remotely to any degree of beam motion. This motion-over-threshold signal can be used to send an alarm or trigger the DSP farm to record a growing or runaway beam instability.

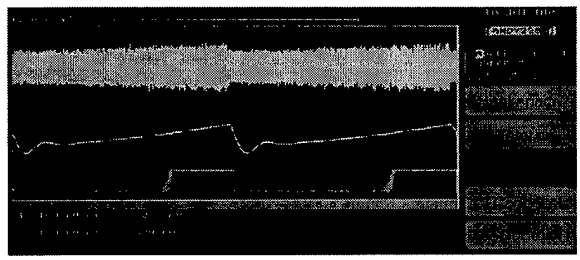

Fig. 5. Hardware simulated beam instabilities at mode 0

The kicker structures are designed to have impedance minima at multiples of the machine RF/2, and impedance maxima at odd multiples of RF/4. The four state QPSK modulation scheme sequences an input CW carrier at 9/4 RF (1071 MHz) through the phase states of 0, 90, 180, 270 at the machine RF rate (476 MHz). This produces a form of modulation with a large sideband at the RF*2 frequency, with an upper sideband at 2.5*RF. The spectrum in figure 6 shows the two sidebands, plus the suppressed carrier at 9/4 RF.

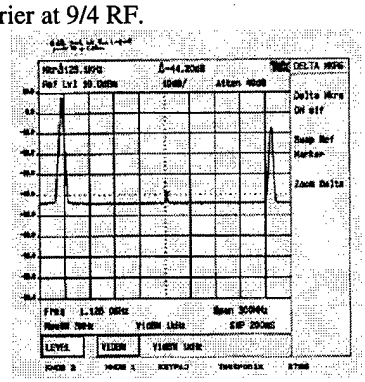

Fig. 6. Back-end kick QPSK spectrum (10dB/div).

Figure 7 shows oscilloscope waveforms of the baseband correction signal (top) and the resulting AM-QPSK output of the Back-end module (bottom). This photo is of six consecutive bunches with 2ns spacing as is used in the every-bucket ALS configuration. It is important to note that the 9/4*RF phase inverts for negative correction values.

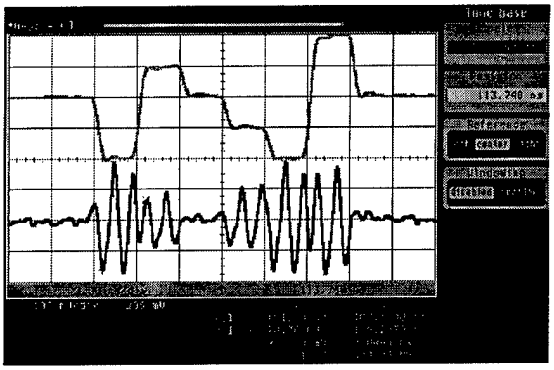

Fig. 7. Baseband correction signal and resulting amplitude and AM-QPSK modulated signal (Time Scale= 2ns/div).

4 SOFTWARE IMPLEMENTATION

The longitudinal feedback system is operated via a graphical computer interface on the users' host that communicates with real time software tasks in the remote processors over a network. The graphical interface was constructed using the EPICS software package that communicate via a register based protocol with the real time operating system VXWorks running in remote hosts located in the VXI/VME crates. The majority of the analysis codes used for machine diagnostics are written in MATLAB.[8]

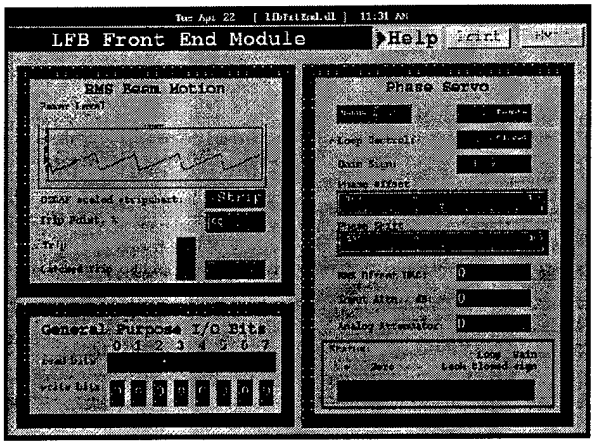

Fig. 8. The EPICs Panel

Figure 8 is an example of the EPICS control panel for the-Front-end module (the Back-End and System Oscillator have similar panels). The left sub-panel in Figure 8 is the beam motion detector showing a mode-zero signal growing in magnitude in a manner similar to figure 5. A threshold trip value can be programmed and the over-threshold trip is read and latched. The right sub-panel in Figure 8 controls the DC reference phase servo of the bunch motion detector. An automated task that can be run by pressing the auto button, locates an optimum phase and closes the servo-loop.

5 SUMMARY

The performance characteristics and features of the Front-end and Back-end include:

- SLAC designed generic VXI interface in both front and Back-end modules,
- automated DC phase servo,
- 118-MHz bandwidth , 20 dB dynamic range beam motion detector operating in both front and Back-end modules,
- 400 MHz Bandwidth phase detector,
- 42 dB of dynamic range in the Back-end.

The VXI packaging has allowed us to design a modular feedback control system and has simplified communication to and from these modules. The front and back end module designs have incorporated numerous features based on the operational experience from 20 months of running at the ALS. Two longitudinal feedback systems have been installed in PEP-II for the high and low energy rings. Five other systems have been produced for the ALS and DAΦNE machines.

6 ACKNOWLEDGMENTS

The authors wish to extend their appreciation to K. Krauter, R. Larsen, I. Linscott, J. Olsen, and W. Ross for their discussions of topics contained in this paper. Greg Stover of LBL made invaluable contributions in the system testing at the ALS. A. Drago and M. Serio of INFN-LNF have made an enormous contributions in the component testing and discussions of topics contained in this paper. Also D. Anderson, B. Cordova-Grimaldi and G. Dalit are recognized for their technical support of all phases of the construction.

7 REFERENCES

[1] S. Prabhakar, et al., "Use of Digital Feedback System as a Bunch by Bunch Current Monitor: Results from ALS" PEP-II AP note No. 96.29, SLAC.

[2] E. Kikutani, et. al., "Recent Progress in Development of Bunch Feedback System for KEKB", Proc. PAC 95, Dallas, pp. 2726-2728.

[3] G. Oxoby, et al, "Bunch by Bunch Longitudinal Feedback System for PEP-II," Proc. EPAC 94, pp. 1616-1618, London.

[4] W. Ross, "PEP-II Longitudinal Feedback System Timing Board Functional Specification", SLAC Internal Document, 5/97.

[5] J. Corlett, et al., "Longitudinal and Transverse Feedback Kickers for the ALS", Proc. EPAC 94, pp. 1625-1627, London.

[6] A. Gallo, et. al., "Simulations of the Bunch-by-Bunch Feedback Operation with a Boadband RF Cavity as Longitudinal Kicker", DA•NE Tech. Note G31, April 1995.

[7] W. Ross, R. Claus and L. Sapozhnikov, "Gap Voltage Feed-Forward Module for LLRF System", PAC 97, Vancouver (this conference) SLAC PUB # 7478.

[8] R. Claus, et al., "Software Architecture of the Longitudinal Feedback System for PEP-II, ALS and DAΦNE", Proc. PAC 95, Dallas, pp. 2660-2662.

LOCAL FEEDBACK EXPERIMENT IN THE TAIWAN LIGHT SOURCE

C. H. Kuo, K. T. Hsu, Jenny Chen, K. K. Lin , C. S. Chen, R. C. Sah
Synchrotron Radiation Research Center
No.1 R&D Road VI, Hsinchu Science-Based Industrial Park, Hsinchu, Taiwan, R.O.C.

Abstract

A highly-effective digital global feedback system has been developed to control closed-orbit error in the Synchrotron Radiation Research Center (SRRC). However, the beam orbit in SRRC is intrinsically so stable that a digital local feedback system may be preferred for some operating conditions. Consequently, a prototype digital local feedback loop has been developed and tested for suppressing orbit disturbances at the source point of a photon beamline. This prototype consists of a local orbit bump whose strength is dynamically controlled to preserve the beam trajectory. The measured bump response is used in this feedback system, and the controller uses a PID algorithm . Digital filtering is used to reduce the noise in beam position measurements. The hardware of the local feedback system is integrated with that of the global feedback system.

1 INTRODUCTION

A digital local feedback system (DLFB) [5, 6] has been developed to suppress orbit disturbances caused by low-frequency drift and insertion devices. First, a linear response matrix is measured by taking beam position monitor (BPM)reading when the corrector are individually perturbed. Then, this response matrix is used to design a local orbit bump. The feedback controller is based on PID algorithm [4]. Digital filtering [1] techniques were used to removed noise of electron beam position reading, to compensate eddy current effect of vacuum chamber, and to increase bandwidth of orbit feedback loop. The infrastructure of digital feedback system is composed of orbit acquisition system, gigabit fiber links, digital signal processing hardware and software, high precision digital-to-analog converters. The experimental results is presented in this report.

2 BPM DATA ACQUISITION AND CORRECTOR CONTROL

The configuration of feedback system is presently distributed in two VME crates. In the future, it will be configured to three nodes for operational version. Every crate will play its own role as beam position server, corrector server, and computation server. This arrangement is convenient for routine machine operation and DLFB system development. The sampling rate of system had been improved to 1 KHz. The single board computers of BPM and corrector control node had been upgraded to PowerPC with LynxOS from 68020 with pSOS$^+$. High precision data input and output have been upgraded to 16 bit. The sampling rate of BPM data acquisition is easy to upgrade with present hardware.

3 LOCAL BUMP DEVELOPMENT ALGORITHM

The local bump is generated based on the beam response with respect to the corrector strength change in the storage ring. The theory of measured bump is based on the relation given in Eqs. 1.

$$y_{a2} = \delta_2 \frac{\sqrt{\beta_a \beta_2}}{2\sin \pi\nu} \cos(\pi\nu - |\Phi_a - \Phi_2|) \qquad (1)$$

where β_a , β_2 are beta function and Φ_a, Φ_2 are phase advance. δ_2 is the magnitudes of the kicks.

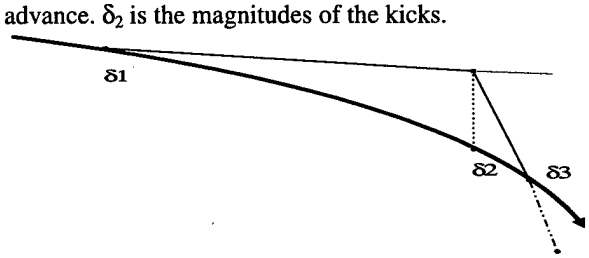

Figure 1: Three magnet bump.

A local orbit feedback system is based on a four-magnet local bump and is the major feedback mechanism to stabilized the beam trajectory in both angle and displacement. This four magnet bump is composed of two three-magnet bumps. Kicks of 3 magnet bump δ_1, δ_2 and d_3 are indicated in figure 1. The three magnet bump ratio is measured by two BPMs situated outside of the bump region.

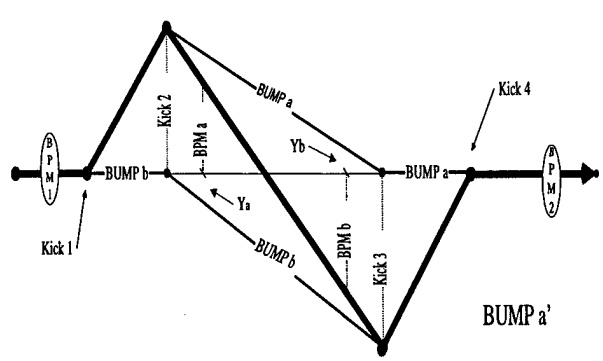

Figure 2: BUMP a' of 4 magnet bump.

The bump ratio transformation between the bump strengths and beam positions is straightforward in the two independent three-magnet local bumps, a and b. Bump a and bump b are combined to form a four magnet bump, as shown in figure 2. The beam response with respect to the applied bump indicated in figure 2 follows the relations below:

$$[\Delta Y] = [T][\Delta K]$$

$$[T] = [\Delta Y][\Delta K]^{-1}$$

$$\delta \propto [T]^{-1}$$

where ΔK is kick deviation of strength, T is transformation between BPMs and Kicks, ΔY is BPM deviation of orbit, and matrix δ is a local bump ratio. $[T]^{-1}$ is proportional to bump ratio. Two BPMs must be selected between bump a and bump b in order to decouple these two bumps. In this way, this particular pair of 3 magnet bump is extended and become a 4 magnet bump. Contribution ratio of bump a and bump b to this four magnet bump can be subsequently determined through the following calculation.

$$\begin{bmatrix} Y_a \\ Y_b \end{bmatrix} = \begin{bmatrix} a_{11} & a_{12} \\ a_{13} & a_{14} \end{bmatrix} \cdot \begin{bmatrix} \delta_a \\ \delta_b \end{bmatrix}$$

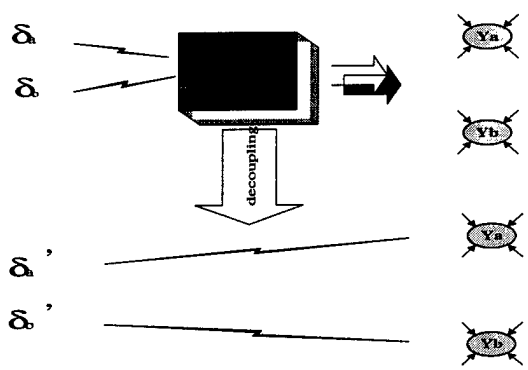

Figure 3: Decoupling of two 4-magnet bump.

$$\begin{bmatrix} b_{11} & 0 \\ 0 & b_{22} \end{bmatrix} = \begin{bmatrix} c_{11} & c_{12} \\ c_{21} & c_{22} \end{bmatrix} \cdot \begin{bmatrix} a_{11} & a_{12} \\ a_{21} & a_{22} \end{bmatrix}$$

Letting $c_{11} = c_{22} = 1$, we get

$$c_{12} = -\frac{a_{12}}{a_{22}} \qquad \delta_a' = \delta_a - \frac{a_{12}}{a_{22}}\delta_b$$

$$c_{21} = -\frac{a_{21}}{a_{11}} \qquad \delta_b' = -\frac{a_{21}}{a_{11}}\delta_a + \delta_b$$

4 CONTROL ALGORITHM

The control algorithm is applied to position error vector [5]. Control algorithm of the digital local feedback is executed in corrector and computation VME crates. The conventional PID controller function G(z) is given by

$$G(z) = K_p + \frac{K_i}{1 - z^{-1}} + K_d (1 - z^{-1})$$

where K_p, K_i, K_d are the proportional, integral, and derivative controller gains, respectively. The gain coefficients should be positive value for negative feedback. The desired response of feedback system can be adjusted by PID parameters to achieve control goals. Steady state error of local feedback system is close to zero when the open loop DC gain is large enough.

5 PERFORMANCE OF DIGITAL LOCAL FEEDBACK LOOP

The effectiveness of the local feedback system in suppressing orbit error was tested by introducing perturbation from two sources, the EPBM and U5. The results are shown in figure 4 and 5. The cutoff frequency of LPF is 60 Hz, and the combination of PID parameters are chosen to fulfill control goals in minimizing orbit change due to any type of perturbation. The PID parameters was not optimized yet. It will be modified together with promoting the bandwidth of feedback. Following description is based on the parameters $K_p = 0.3$, $K_i = 0.07$ and $K_d = 0.0$.

5.1 EPBM Perturbation

There are two recently installed devices at the storage ring. One is a elliptical polarization from bending magnet (EPBM). Orbit will be changed due to the bump leakage of EPBM [7]. The orbit changed without and with DLFB, while EPBM is working, is indicated in figure 4. The displacement of orbit is much smaller when the digital local feedback is turned on in comparison with the case when it was off.

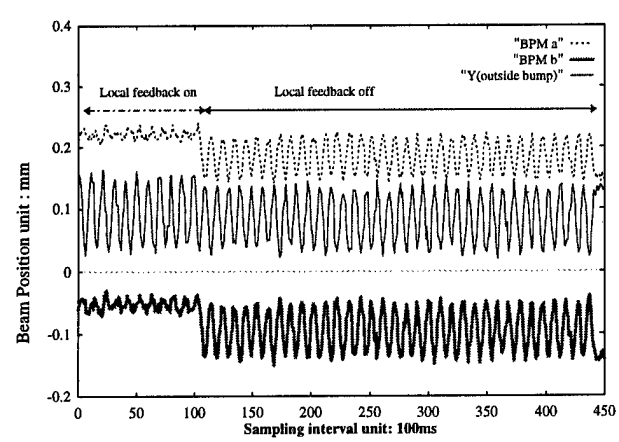

Figure 4: Difference orbit between feedback on and off with perturbation source: EPBM.

5.2 *U5 Perturbation*

Another instrument is a 4-meters long undulator with 5 cm period (U5). Orbit will be changed due to beta beating and field errors of the insertion devices. The orbit is changed without and with DLFB while adjusting the U5 gap as indicated in figure 5. The difference orbit is defined to be the orbit changed between cases when gap is 219 mm and that of 20 mm. The displacement of orbit was much smaller when the digital local feedback was turned on in comparison with the case when it was off.

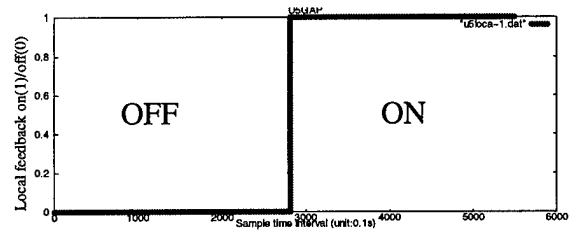

(a) Local feedback on/off

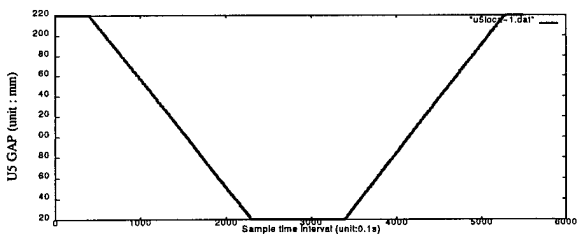

(b) U5 gap

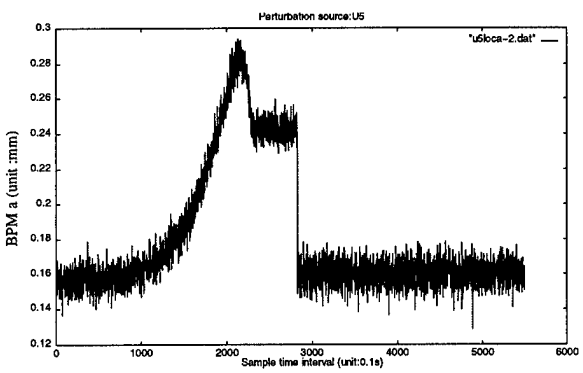

(c) BPM a (inside bump)

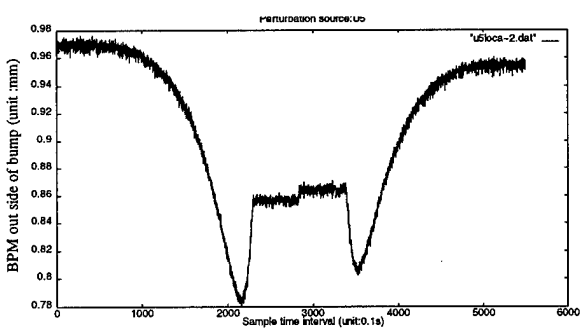

(d) BPM 1 (outside bump)

Figure 5: Difference orbit between undulator open and closed with feedback on/off.

Feedback on(1)/0ff(0) is indicated in figure 5(a), and U5 gap motion is indicated in figure 5(b). BPM readings associated with the applied local bump is shown in figure 5(c). The others arbitrarily picked up BPM readings indicates that the orbit drift at that particular location is a obvious one , and the result is shown in figure 5(d).

5 CONCLUSION

A digital local feedback system has been developed at SRRC. The performance of this system will be improved as the hardware is upgraded and as we gain further operational experience.

6 ACKNOWLEDGEMENTS

The author would like to thank C. T. Chen, C. C. Kuo and members of the Light Source Division for their support.

REFERENCES

[1] J. G. Proakis and D. G. Manolakis: Introduction To Digital Signal Processing, Macmillan 1988.

[2] M. J. Grimble: Dynamical Systems And Automatic Control, Prentice Hall 1993.

[3] Y. Chung, G. Decker and K. Evans, Jr.: Closed Orbit Correction Using Singular Value Decomposition of the Response Matrix." Proceedings of 1993 IEEE Particle Accelerator Conference, Washington, D.C., P. 2263, 1993.

[4] B. C. Kuo: Automatic Control Systems, Prentice Hall , p.691, 1995

[5] C. H. Kuo and K. T. Hsu: First Experiments of the Digital Global Feedback in SRRC, Proceedings of 1996 IEEE Particle Accelerator Conference, Barcelona, 1996.

[6] C. H. Kuo and K. T. Hsu: Digital Global Orbit Feedback System Developing in SRRC, Proceedings of 1997 IEEE Particle Accelerator Conference, Vancouver, 1997.

[7] K. K. Lin: A Dynamic Local Bump System For Producing Synchrotron Radiation With An Alternating Elliptical Polarization, Proceedings of 1997 IEEE Particle Accelerator Conference, Vancouver, 1997.

DIGITAL GLOBAL ORBIT FEEDBACK SYSTEM DEVELOPING IN SRRC

C. H. Kuo, K. K. Lin, C. J. Wang, Jenny Chen , J. S. Chen
C. S. Chen , and K. T. Hsu
Synchrotron Radiation Research Center
No.1 R&D Road VI, Hsinchu Science-Based Industrial Park, Hsinchu, Taiwan, R.O.C.

Abstract

The digital global orbit feedback system for the storage ring of SRRC has been upgraded in terms of its feedback bandwidth extension by increasing its data acquisition sampling rate and compensating eddy current effect of vacuum chamber with filter. This orbit feedback system has been applied incorporate with the insertion devices operation, such as U5 undulator and engineering model adjustable phase undulator. Eliminate orbit drift and low frequency oscillation is to continue effort.

1 INTRODUCTION

Work to improve beam stability continues during 1996 with improvement of the orbit feedback system. New BPM and data acquisition system is installed in the storage ring. In this paper , we will discuss the results of global beam position feedback experiments conducted on new insertion device in Synchrotron Radiation Research Center. Any vibrations and orbit drift that lead to distortions in the closed orbit will result in a larger effective emittance. Together with the brightness reduction, beam motion induced incident light position and angle varying can degrade the advantages of using synchrotron light. Insertion devices are essential to produce high brilliance synchrotron radiation, however it influences the electron orbit and the lattice of storage ring. Global feedback system is used to eliminate these undesirable effects. From control points of view, global feedback is an typical multiple input multiple output (MIMO) problems. Technical, it is difficult to implement an analog matrix operation consisting of large amount of BPMs and correctors. Consequently, digital processing was used here to implement global feedback system.

BPM resolution has to be better than 3 um, decoupling the interference between global and local feedback loops [7], integrating these two feedback loops for better tunability, bandwidth of 10 - 100 Hz is necessary to suppress vibration and power supply ripple related beam motion, etc. The global feedback system is integrated with the existed control system. BPMs data and correctors readback are updated into control system dynamic database in the period of 100 msec. Digital global feedback system is bounded on I/O as well as computation. It is important to arrange the real time task and to arbitrate computer bus properly in order to optimize system performance.

2 CONTROL ALGORITHM

The global orbit feedback system includes 19 BPMs and 18 correctors in the vertical plane for this study. The response matrix of the system was measured by vertical beam displacement while sequentially varying the corrector strengths, and then is inverted by SVD [1, 2] skill. This method is part of the extension of local feedback technique. The advantage of the method used in this system is that it isn sensitive to the beam instability while measuring the response matrix.

A schematic diagram of the feedback system is shown in figure 1. The position error vector [Δy] is filtered by a LPF [4] in order to compensate the system response dominated by eddy current effect of vacuum chamber. Filters are also used to extend close loop bandwidth and to eliminate processing noise.

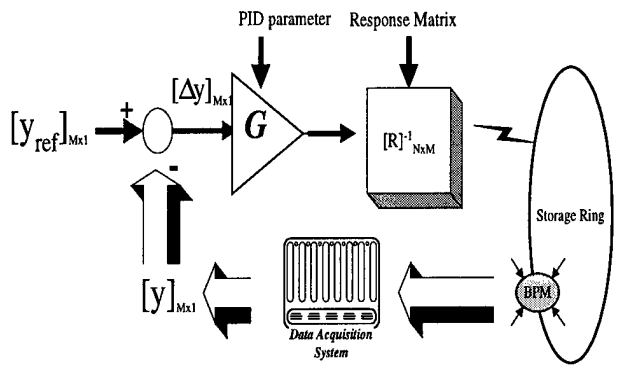

Figure 1: Block diagram of digital global feedback.

Then control algorithm is applied to position error vector. Control algorithm of the digital global feedback is executed in corrector and computation VME crate. The conventional PID controller function G(z) is given by

$$G(z) = K_p + \frac{K_i}{1 - z^{-1}} + K_d (1 - z^{-1})$$

where K_p, K_i, K_d are the proportional, integral, and derivative controller gains, respectively. The gain

0-7803-4376-X/98 /$10.00 © 1998 IEEE

coefficients should be positive value for negative feedback. The desired response of feedback system can be adjusted by PID parameters to achieve control goals. Steady state error of global feedback system is close to zero when the open loop DC gain is large enough. Therefore long-term drift can be completely corrected. Output vector from PID controller is multiplied with the inverse-model matrix (R^{-1}) and is sent to correctors for mend orbit.

3 SYSTEM STRUCTURE

The hardware configuration of the corrector control system in SRRC is described in figure 2. The low layer is a VME system based single board computer which includes a PowerPC 603 CPU board and I/O interface cards. The CPU board consists of a PowerPC microprocessor, 32 megabyte on-board memory, RS-232, PMC and Ethernet ports. The frontend devices are connected to this system via interfaces for analog I/O, digital I/O etc. An power PC based server system is used as the TFTP file server for download OS and mounted disk of network file server (NFS). All application programs are put on server disk. These programs are developed and debugged on client node to relief loading of server. The real-time multi-tasking kernel on the VME bus single board computer. It provided a satisfactory performance, reliability, and a rich set of system services. New device is easy to be created by that only modify device table file as if on line editing. The system can automatically boot and execute different applications in each VME node with the same operation system environments. The upload process will be removed when global feedback is on. This process handle device (analog input) and send acquisition data to database when receives the broadcast upload message from the Ethernet in each 0.1 second. The system timing had been improved to 1 ms by VME interrupt.

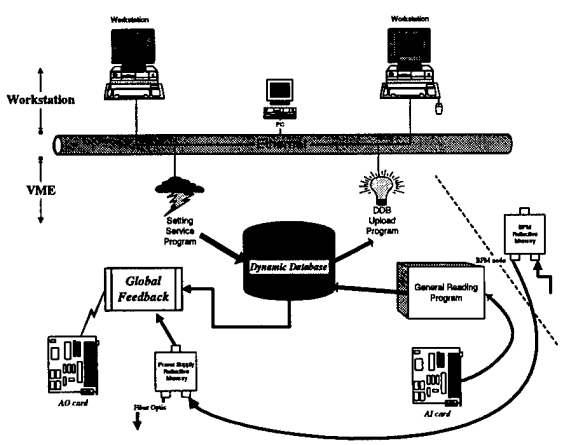

Figure 2: System diagram of corrector node.

Intrinsically, the performance of feedback system is limited by BPM resolution. The BPM processing electronics are based switched electrodes design, which is widely used around synchrotron radiation facilities. The BPM data is acquired by 16 bit A/D cards which are installed at one VME crate. The crate is used as orbit server. The orbit server provides fast beam position information to be used for feedback loop. It also provides slow orbit information for centralized database. The fast orbit information is sent via gigabit fiber linked reflective memory to corrector and computation needs in the VME crates.

Present system consists of two VME crates, i.e. orbit server VME crate, and corrector and computation VME crate. Within corrector and computation server, a VME bus to ISA bus adapter is used to provide PC and VME crate communication. The bus adapter is fit onto slot 1 of VME crate as system controller. All programs were developed and debugged on PC and downloaded to DSP board. The DSP board carrying TMS320C40 module handles all signal processing, including a digital low pass filter (LPF) and PID controller [5]. It takes 1 ms to complete feedback processes including operation of PID, digital low pass filtering, matrix operation, BPMs data reading from reflective memory, and corrector settings. The corrector setting had been upgrade to 16 bit DAC to achieve sub-μrad steering resolution. All parameters can be remotely adjusted from graphical users interface of control system.

4 ERFORMANCE OF DIGITAL GLOBAL FEEDBACK LOOP

Test results of the global feedback system has been done with changing the gap of insertion devices and externally applied perturbation. The results are shown in figure 3, 4 . The cutoff frequency of LPF is 60 Hz, and the combination of PID parameters are chosen to fulfill control goals to minimize orbit change due to any type of perturbation. The PID parameters was not optimized yet. It will be modified together with promoting the bandwidth of feedback. Following description was based on the parameters $K_p = 0.8$, $K_i = 0.03$ and $K_d = 0$.

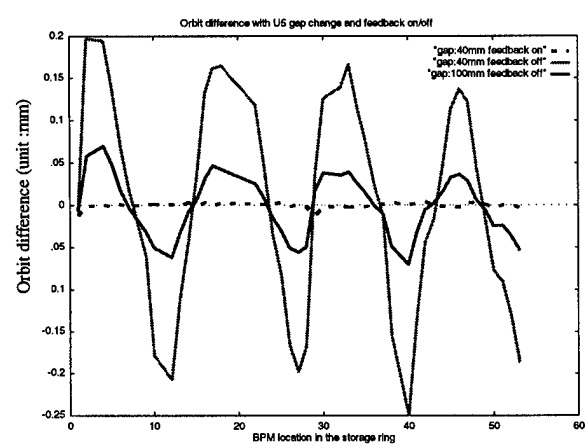

Figure 3: Orbit difference with U5 gap change and feedback on/off.

There is a new installed insertion device at the storage ring. One is a 4-meters long prototype undulator with 5 cm period (U5). Orbit will be changed due to beta beating and field error of the insertion device. The orbit changed without and with DGFB while adjusting the U5 gap as indicated in figure 3. The difference orbit is defined to be the orbit changed at 100 mm and 40mm from 219mm of U5 gap. The displacement of orbit was much smaller when the digital global feedback was turned on in comparison with the case when it was off.

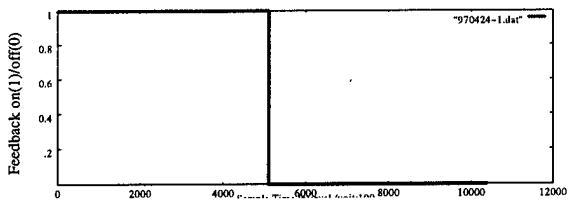

(a)

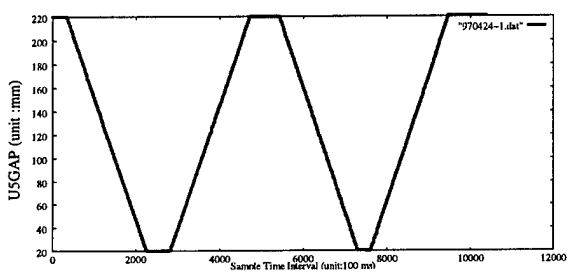

(b)

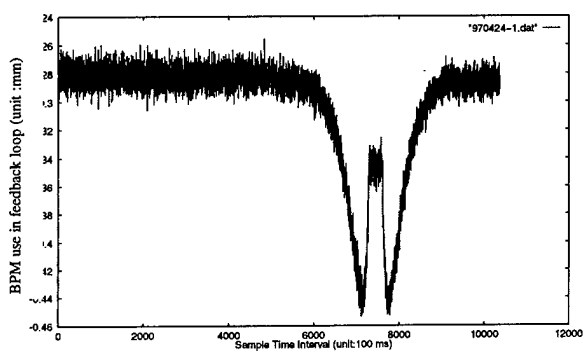

(c)

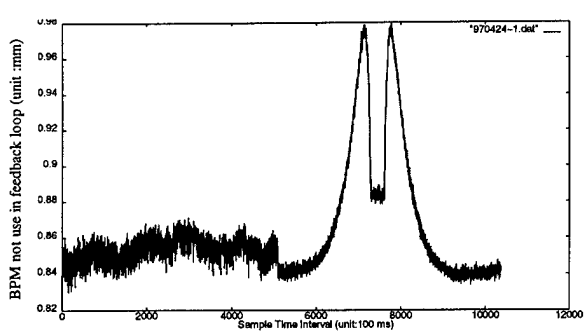

(d)

Figure 4: Difference beam position between undulator open and close with feedback on/off.

At present, only 19 out of 53 BPMs and 18 correctors were used in the vertical feedback system. It was noticed that at some of the BPM locations when gap change from 219 mm to 20 mm, as indicated in figure 4., the beam orbit difference were relatively larger than others. These BPMs were found to be those which were not included in the feedback loop. Orbit difference is showed in figure 4(c) when BPMs is in feedback loop. Conversely, is showed in figure 4(d). Further study is needed in order to improve the performance of the feedback system. However, its seems that feedback loop will deteriorate beam quality. This isn a general case, this is cause by feedback loop parameters mistune. Increase robustness of the feedback system by various techniques is under way.

5 CONCLUSION

Performance of the DGFB system will be improved as we gain operation experience and hardware upgraded. Furthermore, horizontal DGFB will be implemented in analog with the vertical DGFB. The configuration of feedback system will be distributed in three VME crates for operational version. Every crate will play its own role as beam position server, computation server, and corrector server. This arrangement is convenient for routine machine operation and DGFB system development.

6 ACKNOWLEDGEMENTS

The authors would like to thanks C. T. Chen, C. C. Kuo and R. C. Sah for their help. Supports form the staffs of the light source division are also highly appreciated.

REFERENCES

[1] W. Press et al., Numerical Recipes in C, Cambridge University Press, p.60, 1989.

[2] V. C. Klema and A. J. Laub, The Singular Value Decomposition: Its Computation and Some Applications" IEEE Transaction On Automatic Control, Vol. AC-25, No.2, April 1980.

[3] Y. Chung, G. Decker and K. Evans, Jr., losed Orbit Correction Using Singular Value Decomposition of the Response Matrix." Proceedings of 1993 IEEE Particle Accelerator Conference, Washington, D.C., P. 2263, 1993.

[4] J. G. Proakis and D. G. Manolakis, Introduction To Digital Signal Processing, Macmillan 1988.

[5] B. C. Kuo: Automatic Control Systems, Prentice Hall , p.691, 1995.

[6] C. H. Kuo and K. T. Hsu: First Experiments of the Digital Global Feedback in SRRC, Proceedings of 1996 IEEE Particle Accelerator Conference, Barcelona, 1996.

[7] C. H. Kuo and K. T. Hsu: Local Feedback Experiment in the Taiwan Light Source, Proceedings of 1997 IEEE Particle Accelerator Conference, Vancouver, 1997.

DEVELOPEMENT OF A DIGITAL LONGITUDINAL DAMPER FOR THE TLS STORAGE RING

W.K.Lau, S.J. Lin, M.S. Yeh, L.H. Chang, T.T. Yang, K.T. Hsu, M.H. Wang, C.C. Kuo,
Synchrotron Radiation Research Center No.1 R & D Rd. VI, Hsinchu, Taiwan

Abstract

A digital longitudinal damper is being developed in SRRC to stabilize the longitudinal coupled-bunch instabilities observed in the TLS storage ring. It is a bunch by bunch feedback system designed for 200 bunches at 2 ns bunch interval. Designs of the bunch phase detection circuit, the digital electronics and the 1125 MHz wideband rf system for correction of phase errors are presented in this article. The core of the digital electronics is a DSP array that ultilizes commercially available DSP modules performing parallel processing at a data throughput of 500 Mbytes/sec. This will greatly reduce the time required for both hardware and software developments. A prototype operating at one eighth of the data rate of the final system is under construction to evaluate the system design.

1 INTRODUCTION

Longitudinal coupled-bunch instabilities (LCBI) ocurred in the TLS storage ring electron beam are driven by cavity high order modes (HOMs) [1]. Since the bunch current is below the microwave instabilities threshold, LCBI is the main obstacle in preserving low emittance at higher beam current. Further, sudden amplitude changes of such instabilities are undesirable to the users because photon flux through slits fluctuate significantly [2]. In order to reduce the amplitude fluctuation of the instabilities, the original HOM damping antenna on each of the two cavities was replaced by an auxilliary tuner for detuning the troublesome HOMs [3]. Improvement of photon beam stability by an order of magnitude is achievable. However, the amplitudes of the LCBI are still significant. An active longitudinal damper is indispensable to suppress the instabilities effectively.

The damping system and some major subsystems designs will be described in section 2. The status of the project will be discussed in section 3.

2 SYSTEM DESIGN

The damping system being developed is a DSP based bunch by bunch feedback system. That is, the phase of each bunch is individually locked to the master clock signals [4]. For a system manipulating hundreds or thousands of bunches, a feedback system based on digital signal processing tecniques takes the advantage of simplicity in hardware structure in comparison with the mode by mode feedback. Also, the flexibility of such system allows conductions of various tasks with the same hardware design. For example, the longitudinal feedback system can be used to analyze the dynamics of the longitudinal dipole motions of the bunched electron beam.

The design of this longitudinal damper is conceptually similar to the ALS or PEPII system. In order to reduce the system development time and considering the ease of software development and maintenance, we employ very well developed commercial DSP modules that support real time parallel signal processing. Also, efforts have been made to simplify the interface between A/D (D/A) converter and the DSP modules. This interface circuit has the functions of down sampling, demultiplexing, multiplexing and data I/O control of the DSP modules. As shown in Figure 1, front end of the system is a phase detection circuit operating at 6 times of the rf frequency. The phase errors are digitized by an 8 bits flash A/D conveter at 500 Ms/sec and the data are then down sampled and distribute to the individual chips in the DSP array by the demutiplexer and a controlled FIFO memories. The array consists of eight DSP modules, each module has four DSP chips that perform digital filtering (e.g. FIR filters) such that the phase error information of the bunches can be extracted. The processed data are reorganized in a proper sequence again by the controlled FIFO memories and the multiplexer. The digital signal in this sequence is convertered back into a single analog signal by a fast D/A converter. This analog signal modulates the 1125 MHz rf system that is used to drive the feedback cavity. It is a low Q cavity providing a fast changing kick voltage to the beam. System design parameters are listed in Table 1.

Table 1. Parameters of the TLS Longitudinal Damper

rf frequency	500 MHz
bunch interval	2 ns
bunch numbers	200
synchrotron tune	0.0115
beam pickup frequency	3000 MHz
phase detection range	±15° max.
kicker frequency (bandwidth)	1125 MHz (250 MHz)
maximum kicker strength	200 volts
down sampling factor	16
number of filter taps	5
numbers of DSPs	32

0-7803-4376-X/98/$10.00 © 1998 IEEE

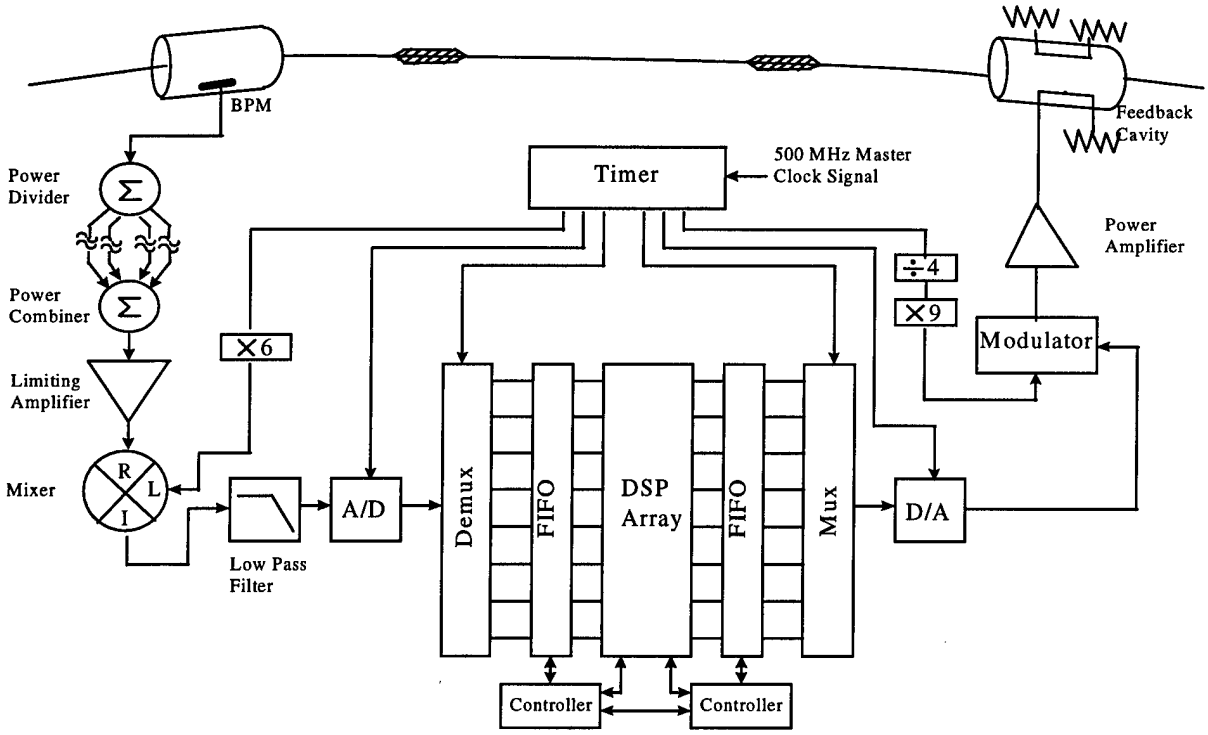

Figure 1. Functional Diagram of the TLS Longitudinal Damper

2.1 Bunch Phase Detection

Bunch signal picked up from a BPM electrode is used to generate short burst so that the phase error can be detected by common mixer techniques (see Figure 1). Since the bunch interval is 2 nsec. and the phase detector is designed to operate at 3 GHz, the dynamic range of detector is limited to ± 15° of the rf signal. Duration of the burst is limited to 1.4 nsec so that the detected phase error of one bunch can not be interferred by the signals of the neighboring bunches. This 3 GHz burst train is generated by a pair of four way broadband power dividers (combiners) connected by four short coaxial cables. The length of each cable is adjusted to have a group delay of 333 psec longer than the next cable. The phases of the short bursts relative to a 3 GHz reference signal are measured by a double balanced mixer. The 3 GHz reference signal is an Elisra MW15700 active multiplier which multiplies the 500 MHz master by six times and therefore phase locked to the clock signal. The IF output from the mixer are filtered by a 250 MHz low pass for anti-aliasing.

2.2 The wideband RF System

The rf system used to correct the phase errors of the bunches is designed to operate at 1125 MHz. The 1125 MHz signal to the power amplifier is locked to the rf frequency. It is generated by dividing the rf frequency four times and multiplied nine times (by another Elisra MW15700 active multiplier). In order to provide at less 250 MHz bandwidth for phase modulation, the 200 Watts Hughes instrumentation TWTA that have instantaneous bandwidth from 1 to 2 GHz is employed. The design of the modulator is not finalized yet. Since the modulation bandwidth of an I & Q modulator is inherently wide, the possibilty of using such network as phase modulator is under study.

The longitudinal kicker is essentially a pill-box cavity in TM_{010} mode except that it is heavily damped by coupling rf power out with large area magnetic coupled loops external rf absorbers. One of the coupling loop is used to couple the power output from the TWTA into the feedback cavity. Numbers of N-type rf coaxial feedthroughs are used to separate vacuum from the atmosphere. The advantages of using external loads are: (1) one can adjust the gain and bandwidth of the system by simply changing the loading condition of the cavity even it is in vacuum. (2) power combination can be made simply by connecting a TWTA to another coupling loop. From the cold tests we have done for a prototype kicker, a loaded Q of 4 can be obtained. The theoretical shunt impedance is approximately 100 Ω.

A vacuum compactable high power version that made of stainless steel with embedded cooling channel is currently under construction. Other issues that may affect the kicker performance such as beam loading, beam induced voltages etc. are under study in detail.

2.3 Digital Signal Processing

The core of the longitudinal damper is the DSP array. In our design, it consists of eight VME DSP modules. Each module can have four TMS320C40 40 MHz floating point parallel DSP as the processing elements. Since the chip have six 20 Mbytes/sec bidirectional communication ports, it allows communications between processors or direct data I/O controlled with external circuits. We use the 4 chips DBV44 DSP boards produced by Loughborough Sound Images as an example. It has eight uncommitted communication ports available via the front panel that can be used as the direct data I/O to the processors. On-board JTAG implementation enables cluster of C40 DSPs to be debugged in parallel. Software support such as the C source debugger, C compiler and the DSP function library are considered as the advantages of using such modules. Since floating point calculation is not necessary in our usage, it is considered to be a drawback of using C40 as the processing elements because it needs two extra cylcles to conveter the 8 bits fixed point data to floating point data and convert them back.

The A/D conveter we used is the MAX101 8 bits flash A/D converter that operates at 500 Ms/sec. It has dual 250 MHz outputs that are 180° out of phase. One of the main task is to make down sampling and distribute the data to the DSP array in a proper order. This is done by the demultiplexer and the controlled FIFO (first-in first-out) memories. The FIFO controller is programmed by PLD (Programmable Logic Devices). An overview of the digital signal processing electronics is shown in Figure 3.

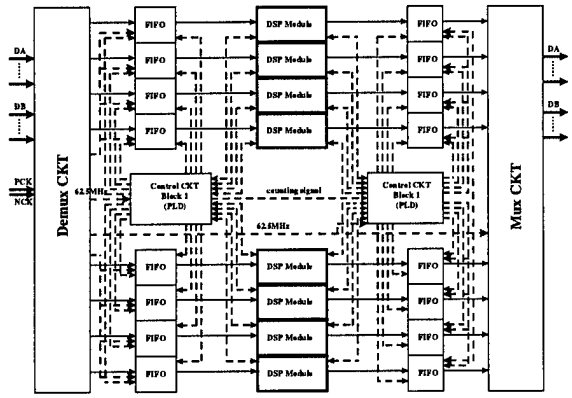

Figure 3. An Overview of the Digital Signal Processing Electronics.

Figure 4 shows demultiplexer circuit done by the serial to parallel converter MC100E445. A multiplexer for processed data reorganization is just the reverse of the demutiplexer logic. The fast D/A converter generates the analog modulation that is used to correct the beam. The TQS TQ6122 8 bits, 1 Gs/s digital-to-analog converter will be used for this purpose.

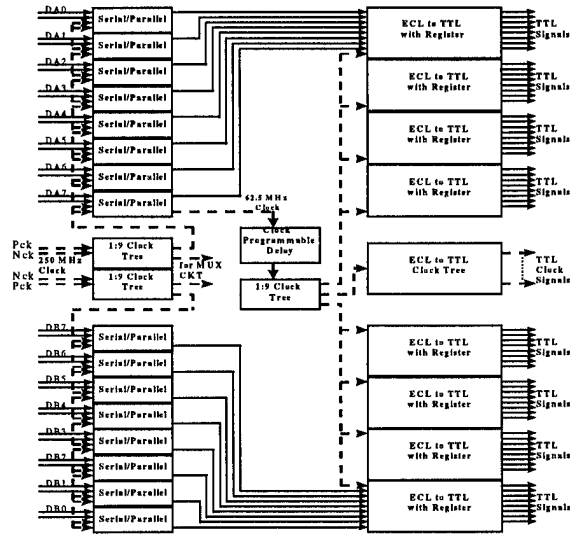

Figure 4. Functional Drawing of the Demultiplexer

3 STATUS OF THE PROJECT AND THE PROTOTYPE SYSTEM

A prototype system is being built to demonstrate the validity of the design as discussed in the previous section. Since we use one DSP board (with PCI bus and installed on a PC), this system can only operate at 62.5 MHz that is one eighth of the full speed of the final system. It can handle 25 equally spaced bunches. The MAX101 fast A/D converter circuit board has been built, tested and performs correctly. Since the designs of the D/A converter and the modulator are not finalized yet. We will use the Merrimac JEM-2B 1125B QPSK modulator that can be driven directly by the ECL signal in the multiplexer of this prototype system. This QPSK has a norminal data rate of 50 Mbits/s but still works fine at 62.5 Mbits/s.

The final system is scheduled to start commissioning by the end of this year.

REFERENCES

[1] W.K. Lau et al," Study of Longitudinal Coupled-Bunch Instabilities in the SRRC Storage Ring" Dallas, PAC 1995 proceedings.

[2] Y.C. Liu et al,"Performance of the TLS at SRRC", Barcelona, Proceedings of EPAC 1996.

[3] Ch.Wang et al,"Experience with HOM Frequency Tuners for the DORIS-I Cavities at SRRC", these proceedings.

[4] J.D. Fox et al,"Operation an Performance of a Longitudinal Damping System using Parallel Digital Signal Processing", Proceedings of EPAC 1994.

OPTIMISING INJECTION INTO CELSIUS WITH A STEERING FEEDBACK AND BETA-MATCHING SYSTEM

Ahmad Mohammadzadeh, The Svedberg Laboratory, S-75121 Uppsala, Sweden

Abstract

In order to provide reproducible conditions, a steering feedback system consisting of two beam position monitors and two steering magnets is installed in the beam line immediately upstream of the injection point into CELSIUS. Moreover, a 1 mm Aluminium wire placed vertically on the horizontally moving stripping foil mechanism measures the beam profile and the emittance. This allows adjusting upstream quadruples to optimise injection conditions. Preliminary operational result is presented.

1 INTRODUCTION

CELSIUS[1] is a cooler-storage ring accelerator for ions from the Gustaf Werner Cyclotron. It is primarily intended for nuclear and particle physics experiments with stored, cooled and accelerated ion beams interacting with extremely thin internal targets. The ring consists of four 90 degrees arcs and four straight sections. One straight section is used for injection into the ring.

There are two modes of injection into CELSIUS[2]. These are called multi-turn injection and stripping injection. The injection takes place when the bumper magnets displace the position of the closed orbit on the injection straight section during injection.

A very important task, on which beam development effort are taking place, is to make it possible to combine proton therapy and operation of CELSIUS at the same time. Thus to combine WASA (Wide Angle Shower Apparatus) and proton therapy, we need to use the electron cooler to accumulate 180 MeV protons, which are injected by multi-turn injection without stripping. We have stored 10^9 180 MeV protons by this kind of injection, to be compared with more than 10^{11} with the usual method of stripping injection. Thus we need to improve the efficiency of the multi-turn injection without stripping, which has to be used for polarised protons, 180 MeV protons, and heavy ions.

Slow drifts in the cyclotron and the beam line magnets make it necessary to adjust the CELSIUS injection parameters from time to time during experiments in CELSIUS. Here we demonstrate how the two beam position monitors, that are installed in the CELSIUS injection line and will be used to automatically adjust steering magnets, to keep the incoming beam path centered. This will also make it possible to adjust the focusing of the beam without at the same time getting unwanted changes in its position and angle at the injection point. A 1 mm aluminium wire has also been attached vertically to the stripping foil mechanism system. This system is equipped with a movable arm to measure the horizontal emittance and profile of the incoming beam. The beam parameters will be deduced by scanning upstream quadruples.

[1]visitor from Atomic Energy Organisation of Iran (AEOI), Nuclear Research Center for Agriculture and Medicine, Karadj, Iran

2 HARDWARE

2.1 *Stripper Foil and Telescope*

A new stripper foil mechanism equipped with a vertical 1 mm aluminum pin had been designed, constructed and installed at the CELSIUS entrance. This new mechanism has space for three different stripper foils of different thicknesses in order that suitable foil thicknesses can be used for different ions that can be stripping injected. The foils have an open vertical edge. The two thin foils are of carbon, the thick one is of aluminium. The position of the foils is adjusted remotely through the control system.

The stripper telescope consists of a pair of detectors 15 cm apart. They are installed near and outside the beam line close to the CELSIUS entrance. Each detector is consisted of a 0.5 cm thick, 4 by 5 cm plastic scintillator and a light-guide mounted onto a photomultiplier(PM). The two detectors are in coincidence to reduce the background count rates generated by them. The faces of the scintillators are perpendicular to the direction of the particles in the beam line. The scintillators emit light as the secondary particles pass through them. The emitted light is collected by the PMs and the PMs signals are transmitted through a discriminator to a counter. A counter registers the number of counts per second and resets itself just before the new pulse arrives from the cyclotron.

2.2 *Beam Position Monitors*

The two dual axis beam position monitors installed in the beam line immediately upstream of the injection point into CELSIUS have a pair of hollow electrodes each on which the signals are induced. Each hollow tube is diagonally cut (about 45°) and insulated to make two electrodes. The two BPMs are installed 3.5 meters apart in a drift space to have sufficient lever arm to measure the angles and positions. The induced signals which are linearly related to the beam positions are first pre-amplified, then fed to an amplitude detector and via a multiplexer to an analog to digital convertor(ADC). Finally, the signals from the ADC are sent to the work station through the Digital Signal Processor interface (Fig.-1). The detection electronics has 8 channels and produces charge independet horizontal and vertical positions in each BPM [3].

0-7803-4376-X/98/$10.00 © 1998 IEEE

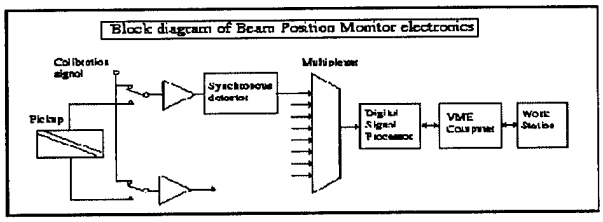

Figure 1: *Block Diagram of BPM Electronics*

3 PROFILE AND EMITTANCE MEASUREMENT

In order to convert the beam flux density as a function of position into a measurable signal, we scanned the incoming beam with a 1 mm aluminum pin at the CELSIUS entrance[4]. A scintillator and a photomultiplier installed near and outside the beam line, detect the secondary particles emitted as the step motor driven pin scans across the beam 0.8 mm every 3 seconds and produces a signal proportional to the number of particles intercepting the pin. It is assumed that the transverse particle density is a near-Gaussian distribution. The spatial r.m.s. beam width at the scanning point, $\sqrt{\sigma_{11}(1)}$, can be determined, (Fig.-2).

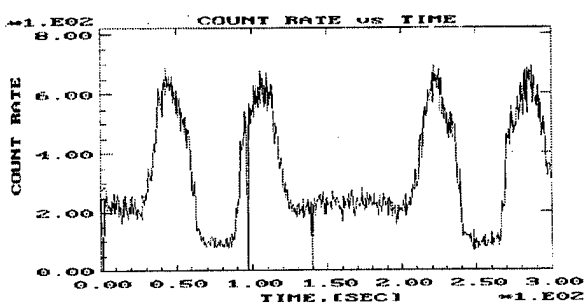

Figure 2: *Beam profiles and emittance measurements at the CELSIUS injection. The stripper pin was scanned across the beam by two in-and-out cycles.*

If a beam has matrix $\sigma(0)$ at some point, z_0, and matrix $\sigma(1)$ at some other point, z_1, downstream, the transformation of the beam between z_0 and z_1 is given by a transfer matrix R:

$$R = \begin{pmatrix} R_{11} & R_{12} \\ R_{21} & R_{22} \end{pmatrix} \quad (1)$$

such that

$$\sigma(1) = R\sigma(0)R^T \quad (2)$$

where R^T is the transpose of R. Since it is only $\sigma_{11}(1)$ that we can measure at the scanning point, we write out the expression for this element as a function of the incoming beam $\sigma(0)$ as

$$\sigma_{11}(1) = R_{11}^2\sigma_{11}(0) + 2R_{11}R_{12}\sigma_{12}(0) + R_{12}^2\sigma_{22}(0) \quad (3)$$

The elements of $\sigma(0)$ can be deduced from a set of three measurements of $\sigma_{11}(1)$ obtained from beam conditions described by three different transfer matrices[5]. To vary the transfer matrices, we change the parameters of the magnetic beam line elements by varying the gradients of the upstream quadruples Q_F30 and Q_F31. By doing so, the size of the beam spot at the pin position varies as described by eq. (3) along with the transfer matrix just defined. The elements of the matrix were extracted from a set of profile measurements taken at several quadrupole settings[4]. In fact we took eight independent width measurements rather than just three to obtain the matrix element of $\sigma(0)$, namely $\sigma_{11}(0), \sigma_{12}(0), \sigma_{22}(0)$, and the data were subjected to least-squares analysis.

In a test run the r.m.s. value of the horizontally measured beam profile at the CELSIUS entrance have been evaluated to be $\sqrt{\sigma_{11}} = 1.5$ mm.

The beam emittance, often defined as

$$\varepsilon = \sqrt{\det\sigma} = \sqrt{\sigma_{11}\sigma_{22} - \sigma_{12}^2} \quad (4)$$

can deduced from the beam's matrix parametrized by the Twiss parameters in the following way

$$\sigma = \varepsilon \begin{pmatrix} \beta & -\alpha \\ -\alpha & \gamma \end{pmatrix} \quad (5)$$

with $\alpha = -\sigma_{12}/\varepsilon, \beta = \sigma_{11}/\varepsilon$, and γ_{22}/ε, where $\beta\gamma - \alpha^2 = 1$. Using the beam matrix elements the emittance is calculated to be $\varepsilon = 5.3\,10^{-6}\,\pi$m-rad which is roughly consistent with emittance measurements close to the cyclotron.

4 AUTOMATIC ALIGNMENT

An automatic position measurement and correction system has been developed. First the response of the BPMs to steering magnets STM_F10 and STM_F11 upstream, are determined by changing their excitations and observing the changes of the BPMs signals. This yields the response matrix.

Inverting this matrix and multiplying it with the beam position deviation vector yields the correctors excitations needed to correct the position to its desired value. This system was tested by changing the current in an upstream bending magnet and letting the feedback system correct. Figure-3 shows the beam positions in the first two rows, and the actual corrector excitations in the third and fourth. We clearly see that an externally induced perturbations deviate the beam from its desired position, but then the correction system automatically brings the beam back to the desired position.

Tests of this system show that it is possible to correct the beam positions within a few pulses arriving from the cyclotron with an error of about 220 μm[4]. The beam reproducibility measured by the BPMs have an r.m.s. of about 150 μm as shown figure-4.

5 ACKNOWLEDGEMENTS

The Author wishes to express his gratitude to the International Atomic Energy Agency (IAEA) for their sponsor-

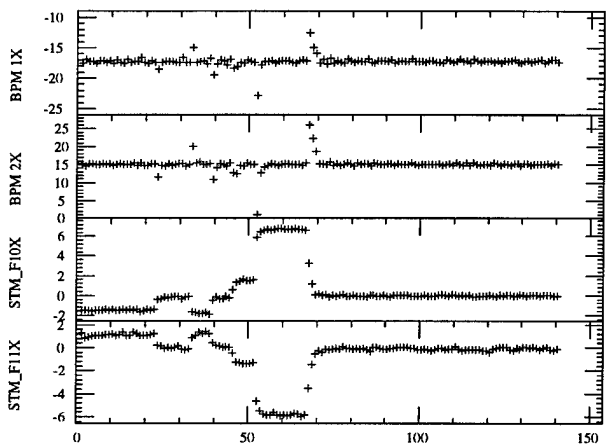

Figure 3: *The top two rows show the beam positions, and the bottom two rows represent the deviation and steering feedback correction in both BPMs.*

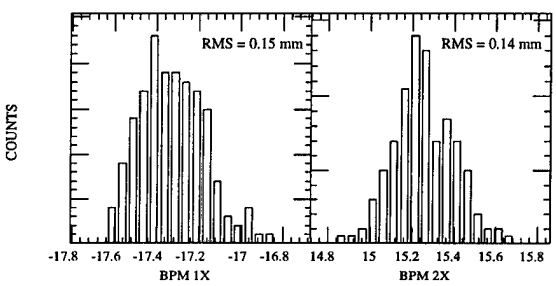

Figure 4: *The center of mass distribution of the pulses as measured by the BPMs*

ship. Special thanks to the director of the Svedberg Laboratory, L. Nilsson, and the technical director, D. Reistad for their hosting and supporting. I am grateful to my home institute AEOI especially my supervisors, M. Haji-Saied and H. Afarideh for creating such an opportunity for me. The step by step supervision and support of V. Ziemann through out this project is deeply appreciated. Thanks to T. Bergmark, and M. Bengtsson for making the BPMs work. The information about diagnostics reported here profitted greatly by discussions with J. Zlomanczuk.

6 REFERENCES

1. *PROGRESS REPORT,* 1987-1991, The Svedberg Laboratory, Uppsala, Sweden.

2. D. Reistad, *Injection, cooling, and accumulation of ions from the Gustaf Werner cyclotron into the CELSIUS cooler-storage ring.* Proc. 14th International Conference on Cyclotrons and their Applications, Cape Town, South Africa, 8-13 October 1995, John C. Cornell, editor, World Scientific, 1996, page 350. (TSL-note 95-23)

3. T. Bergmark and M. Bengtsson, *private communications,* TSL, Uppsala, Sweden.

4. V. Ziemann, *private communications,* TSL, Uppsala, Sweden.

5. K.T. McDonald and D.P. Russell, *Method of Emittance Measurement,* Joseph Henry Laboratories, Princeton University, Princeton, NJ 08544.

DEVELOPMENT OF DIGITAL FEEDBACK SYSTEMS FOR BEAM POSITION AND ENERGY AT THE THOMAS JEFFERSON NATIONAL ACCELERATOR FACILITY

J. Karn, M. Chowdhary, A. Hutton, V. Lebedev, R. Legg, P. Letta,
H. Shoaee, W. Watson, and J. van Zeijts
Thomas Jefferson National Accelerator Facility
12000 Jefferson Avenue, Newport News, VA 23606 USA

Abstract

The development of beam-based digital feedback systems for the CEBAF accelerator has gone through several stages. As the accelerator moved from commissioning to operation for the nuclear physics program, the top priority was to stabilize the beam against slow energy and position drifts (< 1 Hz). These slow drifts were corrected using the existing accelerator monitors and actuators driven by software running on top of the EPICS control system. With slow drifts corrected, attention turned to quantifying the higher frequency disturbances on the beam and to designing the required feedback systems needed to achieve the CEBAF design stability requirements. Results from measurements showed the major components in position and energy to be at harmonics of the power line frequencies of 60, 120, and 180 Hz. Hardware and software was installed in two locations of the accelerator as prototypes for the faster feedback systems needed. This paper gives an overview of the measured beam disturbances and the feedback systems developed.

1 INTRODUCTION

CEBAF is a 4 GeV electron accelerator producing CW beams for nuclear physics research. The accelerator consists of a 45 MeV injector and two parallel 400 MeV linacs. The beam is recirculated through both linacs four additional times to achieve 4 GeV of total acceleration. Multiple beams can be extracted after selected orbits and delivered to any, or each, of the three experimental halls. The ultimate stability requirements of the beam on target is 2.5×10^{-5} rms relative energy spread and maintaining an rms beam position within a 20 μm window.

2 SLOW LOCKS

During the commissioning of the accelerator a series of slow locks were developed to stabilize the beam against slow energy and position drifts (< 1 Hz). The locks made use of the existing beam position monitors, corrector dipoles, and SRF cavities. These monitors and actuators were controlled by a TCL/TK [1] software package running on top of the EPICS control system. A total of 15 independently controlled slow locks are used to set and maintain the orbit from the injector to the experimental halls. Three energy locks maintain the energy of the injector and each of the two linacs. Twelve orbit locks maintain the orbits in the injector, each of the nine recirculation arcs, and two of the three experimental hall transport lines. The long term relative momentum stability is typically kept to $\pm5\times10^{-5}$ in the first two CEBAF arcs. Position stability is typically maintained around ±100 μm, the resolution of the beam position monitors.

The original slow lock software has recently been upgraded to a more powerful CDEV based package [2]. The new software resolved several problems regarding CPU usage, operator friendliness, multiple lock interaction, and improved exception handling. In addition, external processes like automatic cresting of the linac RF cavities, are speeded up significantly using the new package. The result is a slow lock package that is an essential part of the long term stability of the accelerator.

3 BEAM STABILITY MEASUREMENTS

With slow drifts corrected, attention turned to quantifying the higher frequency disturbances. Two techniques were developed for measuring beam motion at various frequency ranges. The first method involved raising the trigger rate for the BPMs from 60 to 500 Hz. A data acquisition routine running on the IOC local to the desired BPMs recorded 60 seconds worth of data. The buffered data was then downloaded off the IOC for analysis using MATLAB [3]. FFTs of the data produced frequency spectrums up to 250 Hz.

Location	X mm.	Y mm.	X' mrad	Y' mrad	ΔE/E
Injector	2.0	0.9	0.27	0.20	1.2x10-3
East Arc	0.5	0.2	0.04	0.08	0.3x10-3
West Arc	0.4	0.3	0.02	0.06	0.2x10-3

Table 1: Magnitude of 60 Hz. motion at various locations in the accelerator.

Measurements were made at key locations in the accelerator over a period of three months. The data

0-7803-4376-X/98 /$10.00 © 1998 IEEE

showed the major components in position and energy to be at harmonics of the power line frequencies of 60, 120, and 180 Hz. The magnitude of the 60 Hz. component at various locations in the accelerator is listed in Table 1.

The second method for measuring beam disturbances was aimed at investigating higher frequencies. This technique made use of a new design of BPMs being integrated into the accelerator. These new Switched Electrode Electronics BPMs (SEEs) are VME-based and capable of being read at up to 114 kHz by a low level IOC routine. Data was collected at 7.1 kHz. over a 2.3 second time span [4]. A sample of this is shown in Figure 1. The amplitudes and phases of the known power line harmonics (60, 120, and 180 Hz.) were determined and these components were subtracted from the original signal. An FFT of the remaining signal was performed and plotted in Figure 2. This data shows the higher power line harmonics but at a much lower amplitude. An expanded plot of frequencies below 150 Hz. is shown in Figure 3. The amplitudes of the power line harmonics are summarized in Table 2.

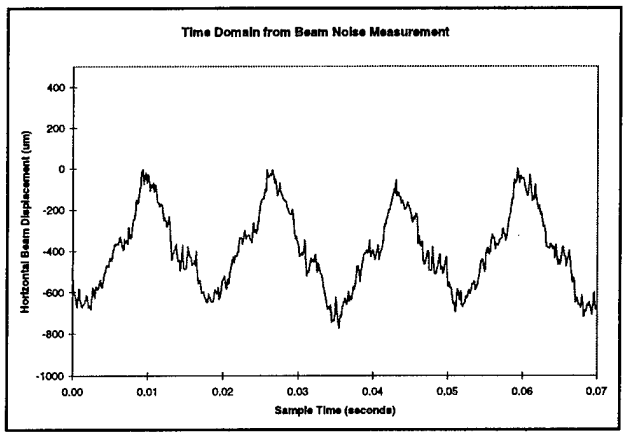

Figure 1: Horizontal beam position collected at 7.1 kHz.

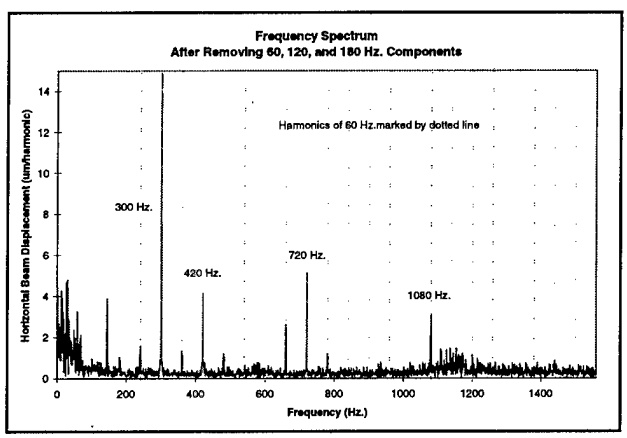

Figure 2: FFT following removal of 60, 120, and 180 Hz. contributions.

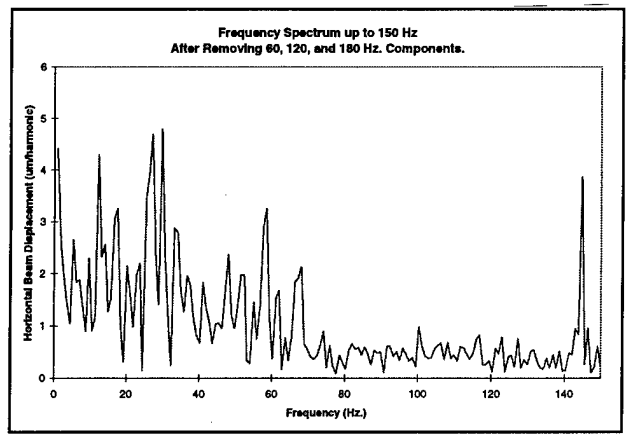

Figure 3: Expanded view of lower frequencies..

Component	Amplitude (μm)	sigma (μm)
60 Hz.	246.3	14.7
120 Hz.	23.5	1.6
180 Hz.	54.5	0.8
Sum of higher harmonics	25.5	0.6

Table 2: Magnitude of power line harmonics

4 PROTOTYPE FAST FEEDBACK SYSTEMS

To begin developing software and testing algorithms for faster feedback systems, hardware was installed in two locations of the accelerator. One system provided energy and position feedback for the beam leaving the Injector. The second system provided energy and position feedback for the beam after the first pass through the first linac. Each system consisted of a single VME crate housing an MVME167 CPU, a DAC for driving the actuators, and the specialized modules used for the SEEs.

Energy corrections to the beam were made using pairs of the installed SRF cavities. The VME DAC was used to drive a vernier input on the RF control module. The distances between the DAC and the RF control module exceeded 800 feet in some places and special filters had to be added to reduce higher frequency transmission noise.

Position corrections to the beam were made using air-core corrector dipoles powered by a modified version of the standard CEBAF trim supply. The magnets were a pair of simple saddle coils designed to wrap around the existing vacuum pipe in the areas of interest. The magnets had a design strength of 750 G-cm in order to provide the corrections needed for a maximum beam energy of 845 MeV. The trim supplies were modified to accept and external voltage input. This input was driven by the VME DAC. Tests on this setup showed the load had an impedance of $3.85\Omega + 2\pi f(7.4mH)$ [5]. The trim supply voltage limit of 60 volts was able to compensate for the impedance changes for frequencies up to 500 Hz. This setup provided an inexpensive method for orbit

correction, made use of available hardware, and provided an acceptable bandwidth.

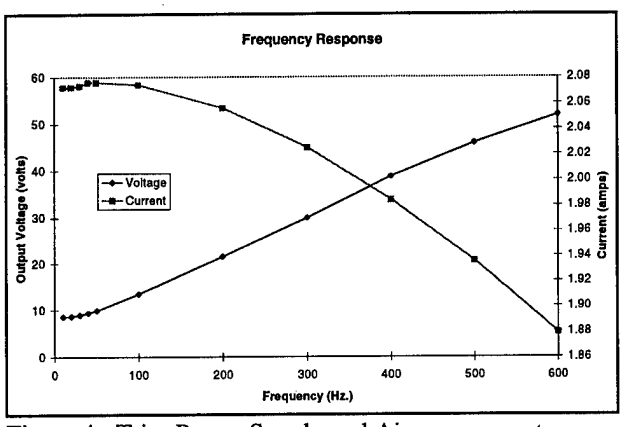

Figure 4: Trim Power Supply and Air-core corrector frequency response at 2 amps.

The SEE BPMs resided in locations from zero to high dispersion. The state matrix (x, x′, y, y′, and ΔE/E) could then be calculated using the known M_{12}s of the transport matrix. The corrections were calculated using a state space modeling and the required signal sent to the actuators. Early tests performed with beam have been successfully made at an SEE BPM acquisition rate of 60 Hz.

The optics for two of the experimental hall transport lines were changed to improve the sensitivity of feedback systems. The new optics increased the beta functions and dispersion by a factor of two. The betatron phase advance was also increased to $\pi/2 + n\pi$ between actuators and monitors. This optics change achieved 2 to 3 times better resolution in comparison with the original optics.

5 FUTURE WORK

Future development includes making the tools used for measuring beam noise into a user friendly package. Such a tool would provide operators a diagnostic for identifying and locating sources of beam instabilities. In past tests on the prototype feedback systems, the acquisition rate limit of 60 Hz. was set by the SEE low level software. Upgrades to this software will eventually allow them to be read at up to 1 kHz. Also being investigated is the use of feed-forward to suppress the power line harmonics [4].

6 CONCLUSIONS

With low frequency disturbances on the beam under control the development of *faster* feedback systems has begun. Measurements made using multiple techniques show the main source of position and energy variations are at the power line harmonics of 60, 120, and 180 Hz. Hardware has been installed in two locations to begin prototyping the feedback systems needed to suppress the observed disturbances. Both setups have been successfully operated at acquisition rates of 60 Hz. Future work involves running these systems at the higher rates needed to achieve the CEBAF ultimate design goals.

7 ACKNOWLEDGMENTS

This work was supported by the U.S. DOE under contract number DE-AC05-84ER40150.

REFERENCES

[1] J. K. Ousterhout, *Tcl and the Tk Toolkit*, Addison-Wesley Professional Computing Series (1994)

[2] J. van Zeijts *et al.*, *Design and Implementation of a General Slow Orbit Control Package at Jefferson Lab*, these proceedings.

[3] *Matlab Reference Manual*, Copyright The Math Works, Inc., 1984-1993.

[4] V. Lebedev, *Feedback System for Energy and Beam Position Stabilization*, Jefferson Lab Memo, 1996.

[5] R. Legg, *et al.*, *Fast Feedback Corrector System*, Jefferson Lab Tech Note #96-005, 1996.

DESIGN AND IMPLEMENTATION OF A SLOW ORBIT CONTROL PACKAGE AT THOMAS JEFFERSON NATIONAL ACCELERATOR FACILITY

J. van Zeijts, S. Witherspoon, and W. A. Watson

Thomas Jefferson National Accelerator Facility

Abstract

We describe the design and implementation of a C++ client/server based slow orbit and energy control package based on the CDEV[1] software control bus. Several client applications are described and operational experience is given.

1 INTRODUCTION

The slow orbit control system at Jefferson Lab. was initially implemented as several Tcl[2] scripting applications[3, 4]. This was a good interim solution when most resources needed to be spent on commissioning the low level control system. To develop more robust high level applications an effort was started to convert the most demanding applications to C++. The first project completed was the conversion of the DIMAD[5] based on-line optics database from Tcl to a C++ client/server framework[6]. That effort included the first application of the CDEV client/server framework in operations. Next we started the conversion of the slow orbit/energy control and auto-steering applications.

2 REQUIREMENTS

The general orbit control package requirements are summarized in a Software Requirements Document[7]. The requirements call for locking beam positions and energy at a maximum rate of 1Hz. The focus is on extensive exception handling, and particular attention is given to the determination of misbehaving responders.

3 DESIGN & IMPLEMENTATION

Here we describe the various parts needed to build an operational lock. The CDEV library has available a robust and flexible generic client/server framework[8]. We use this to design a multiple client and multiple server implementation. External control of the each server is handled by sending CDEV messages. We describe the design of each part and its implementation.

3.1 Lock Server

The Lock Server contains a set of related locks which are handled by a 'Lock Manager' described below. Each lock can potentially be using a different algorithm. Multiple named instances of Lock Servers may exist on the network.

• Lock Manager

The Lock Manager handles the scheduling and interaction of the related locks. The simplest instance is a periodic manager which periodically triggers each lock in series. For steering applications we provide an 'On Demand' manager. Lock to Lock interaction is handled in more involved managers. We plan to support SLAC type adaptive handlers[9].

• Type/Algorithms

Multiple lock types are supported. They are mostly distinguished by the use of different algorithms for locking and steering the beam. The basic algorithm is Singular Value Decomposition for calculating the state of the system. Standard feedback control state space algorithms are supported. For demanding applications in orbit steering we use a special purpose algorithm[10]. The locks can be configured to any of the applicable types.

3.2 Configuration Server

The configuration of each lock is kept in a Database server. There is once instance of this server. This database keeps a set of configurations, where each configuration has a list of named locks and a lock manager type. Each lock has a list of responders and actuators and selection information, and has an algorithm type.

3.3 Optics Information & Model Server

The response matrices needed for the operation of the locks are retrieved from a 'Model' server. These models can represent the design optics, or contain measured data. In the simulated control system environment these models can produce simulated beam position readings.

3.4 'Gold' Orbits Server

The Gold Orbit Server is the centralized repository for the 'gold' orbits. This is a set of orbits to which the machine should be steered. Access to this server is needed by safe/restore clients and by all the steering and feedback applications. In particular, each lock can be notified when the gold orbit changes. The server provides 'xGold' and 'yGold' attributes for all beam position monitors. The use of this server has significantly improved the management of the operational gold orbit values.

3.5 Error Logging

A centralized client/server facility will be used to report errors[11]. This facility accepts error messages

0-7803-4376-X/98 /$10.00 © 1998 IEEE

from clients distributed throughout the control system. Query messages and GUI query tools are used to monitor the state of any one of the systems.

3.6 Alarm Reporting

Alarm reporting will be done using the EPICS alarm handler program running over CDEV. Operators will hear an audible alarm when actuators go out of range or a feedback loop stops running because of a control system or hardware alarm.

3.7 Data Logging

The multiple lock servers present data to the outside world in a form such that standard CDEV data logging tools can be used. We use the generic StripTool application and will use the upcoming CDEV archiving standard.

3.8 User Interfaces

Even though the locks can in principle be operated by sending CDEV commands from the command line, this is clearly not sufficient for an operational interface. We use the Tcl/Tk tool box to provide lightweight graphics interfaces. The Tcl interpreter is dynamically extended with commands to access arbitrary CDEV devices and send/receive arbitrary cdevData packets. Asynchronous monitoring fits well in the Tcl event model.

4 OPERATIONAL IMPLEMENTATIONS

Here we describe the lock servers which are in use in operations at JLAB.

4.1 OpsLock Server

This server contains the default set of operational slow feedback loops. We have 3 slow energy locks and multiple slow orbit feedback loops, including orbit feedback locks in front of the experimental hall targets.

4.2 ArcDiagnostics Server

This server runs in calculate only mode and is used to diagnose energy shift problems throughout the machine. A momentum deviation is calculated for each of the 9 arcs and displayed on a strip chart tool.

4.3 OpsSteering Server

This server is configured with beam steering algorithms for the linacs and the arcs.

5 CLIENT IMPLEMENTATIONS

5.1 Operator Control GUI Client

The main operational interface is shown below. Operators can start/stop a feedback loop and get a status readback from both for the lock status and the beam status. All operational servers can be accessed from this main panel. An expert panel allows selection/deselection of elements and changing lock parameters. Multiple instances of these browsers can be up at the same time and changes are coordinated by the CDEV server monitoring capability.

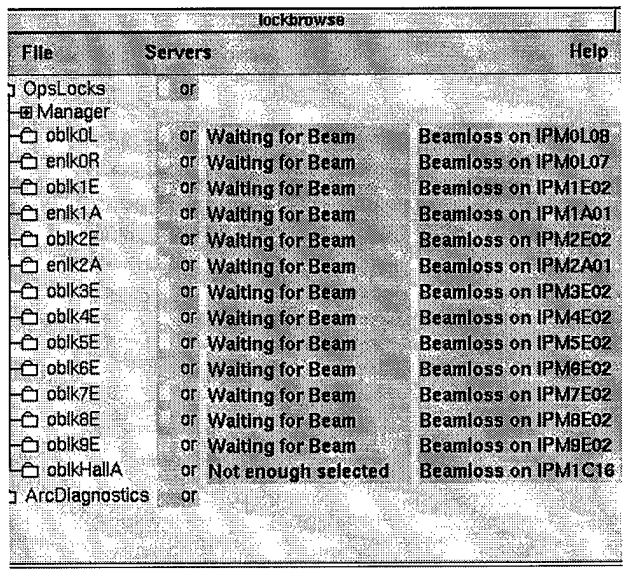

Figure 1: Main Operations Lock Overview Panel

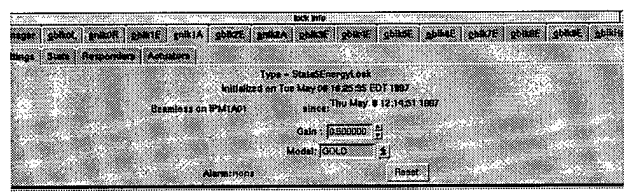

Figure 2: Expert State of Lock Display

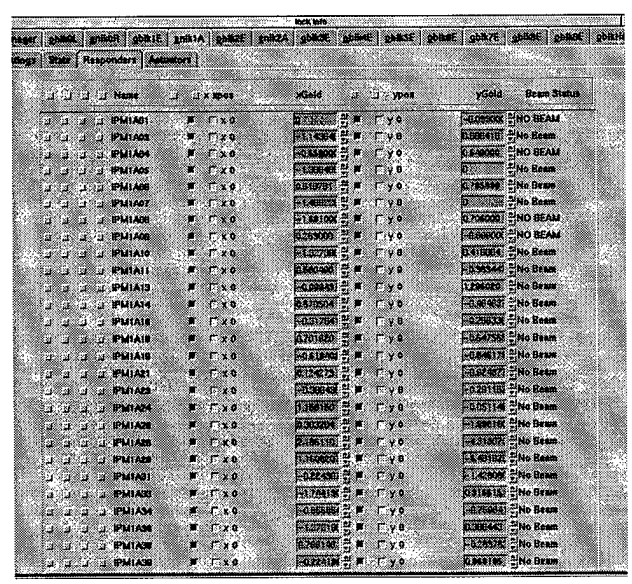

Figure 3: Responder Configuration Panel

5.2 Lock Database Configuration Tool

A browser GUI was developed to query and set the lock database. Persistent changes to the configurations can be made from this panel.

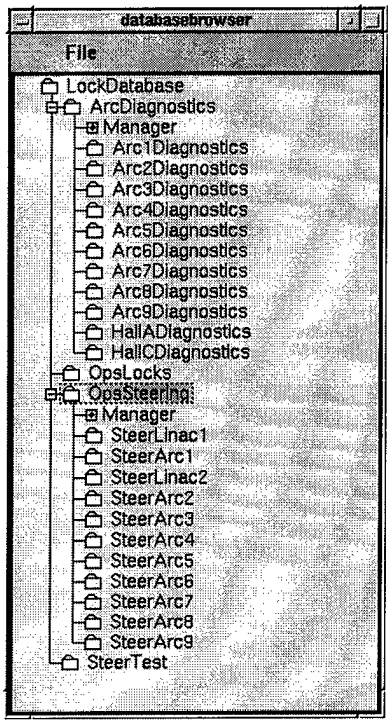

Figure 4: Lock Database Configuration GUI

5.3 Strip Chart Client

For operational diagnostics purposes we can use a standard CDEV tool like the StripTool to display a live strip chart of parameters calculated by any of the Lock servers. Here we show the dp/p momentum deviation for 2 arcs in the CEBAF accelerator.

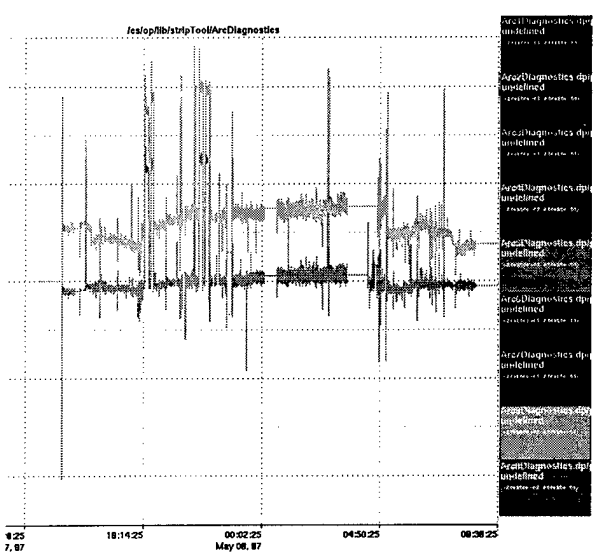

Figure 5: ArcDiagnostics Strip Chart

6 COMMISSIONING

Before releasing the code in operations it needs to be tested exhaustively. We take advantage of the CDEV device/attribute paradigm which gives us the ability to re-route control system devices to different servers. We build a 'fake' control system server and point the control system devices to this by a simple change in the routing information database. The application code is not changed. All the exception handling can be exercised by manipulating the fake control system to trigger arbitrary exceptions.

7 UPGRADES

The Database server will be backed up by an object-oriented persistent database. The code for any of the Database clients will need no change when we switch the database server to this. Likewise we can move from the current gold orbit server, to a persistent database server with no change in client code.

8 ACKNOWLEDGMENTS

We would like to acknowledge Walt Akers for providing the code and documentation for the CDEV Generic Server engine. This work is supported by the U.S. Department of Energy, contract DE-AC05-84ER40150.

9 REFERENCES

[1] W. A. Watson, 'A Portable Accelerator Control Toolkit', PAC 1997 Proceedings.

[2] J. K. Ousterhout, 'Tcl and the Tk Toolkit', Addison-Wesley Professional Computing Series (1994).

[3] J. van Zeijts, 'Rapid Application Development Using the Tcl/Tk Language', PAC 1995 Proceedings, Vol 4 p 2241.

[4] J. Karn et al., 'Development of Digital Feedback Systems for Beam Position and Energy at the Thomas Jefferson National Accelerator Facility'.

[5] R. Servranckx et. al., DIMAD Manual.

[6] B. Bowling et. al., 'Integrated On-Line Modeling at CEBAF', PAC 1995 Proceedings.

[7] J. van Zeijts, 'Software Requirements for Slow Locks', Jefferson Lab., internal document.

[8] W. Akers, The CDEV Generic Server, Jefferson Lab. CDEV Documentation. www.jlab.org/cdev/doc_1.5/cdevGenericServer.html

[9] T. Himel, 'Requirements and Design Overview for Adaptive Cascaded Feedback'. SLAC Preprint, October 1991.

[10] Y. Chao, 'Prosac Algorithm', CAP 96, 319.

[11] J. Chen, CMLOG documentation, Jefferson Lab., internal document.

ROBINSON-TYPE CRITERIA FOR BEAM AND RF CAVITY WITH DELAYED, VOLTAGE-PROPORTIONAL FEEDBACK

Shane Koscielniak, TRIUMF, 4004 Wesbrook Mall, Vancouver B.C., Canada

Abstract

We generalize the Robinson stability criteria, for a charged particle beam interacting with the radio-frequency cavity resonator that is responsible for accelerating it, to the case that the resonator is equipped with a delayed voltage-proportional feedback.

1 INTRODUCTION

Robinson[1] gave criteria for the stability of a charged particle beam interacting with the RF cavity resonator that is responsible for accelerating that beam. A widely adopted procedure[3] for high current beams, to avoid the power-limited instability, is to reduce the apparent cavity impedance by feedback. Inevitably, the feedback is delayed; and this introduces exponential terms into the system characteristic equation. We give a general, exact, analytic procedure for determining whether there are poles/zeros in the right-half complex plane (RHCP); and apply the method to find analogues of the Robinson stability criteria when the resonator is equipped with a delayed feedback. Of course, one should determine the stability of the delayed-feedback-resonator alone, before analysis with beam. The beam instability criteria are explained, in physical terms, in Ref. [6] using the theory of Sacherer[2]. This article is a precis of a more pedagogic exposition given in References [5, 6].

1.1 Nyquist stability criterion

Let $s = \sigma + j\omega$ be the Laplace frequency and $j = \sqrt{-1}$. If the system transfer function $F(s)$ has any poles fall in the RHCP, then the system is unstable. We adopt the usual convention of the complex plane that positive rotations are counter-clockwise. Nyquist realized that the difference in number of poles and zeros in the RHCP is equal to the number of counter-clockwise encirclements of the origin by the locus of the function $F(s)$ as s varies along a counter-clockwise semi-circular contour in the RHCP with the imaginary axis as diameter. Hence, Nyquist reduced the stability analysis to merely counting up loops about the origin. Given that we are searching for poles, it often simplest to decompose F into a numerator and denominator. Then, for the stability analysis, we investigate under what conditions the denominator has zeros in the RHCP. F shall now stand for the denominator of the transfer function.

1.2 Analytic stability criterion

We want a criterion that is easy to apply, and preferably algebraic rather than geometric – so that curve sketching is avoided. We divide $F(s)$ into a real part $\mathcal{A} = \Re[F]$ and an imaginary part $\mathcal{B} = \Im[F]$. It is clear that we want the locus of F to rotate counter-clockwise, and so we consider the angular rotation rate $d\,Arg(F)/d\omega = [\mathcal{A}\mathcal{B}' - \mathcal{A}'\mathcal{B}]/[\mathcal{A}^2 + \mathcal{B}^2]$ which is positive for positive rotations. Fortunately, we do not need to consider this quantity for all values of ω.

1.2.1 Criterion for poles and no zeros

In order to encircle the origin, the curve traced by $F(\omega)$ has to move through the four quadrants of the complex plane; and to do this there must be places where either $\mathcal{A}$ or $\mathcal{B}$ changes sign. Hence we are interested in the roots ω_A of $\mathcal{A} = 0$ and the roots ω_B of $\mathcal{B} = 0$. We state conditions so that F has only poles but no zeros, that is criteria that ensure the counter-clockwise encirclement of the origin.

$$\mathcal{A}(\omega_B) \times \mathcal{B}'(\omega_B) \;>\; 0 \quad \text{and/or} \tag{1}$$

$$\mathcal{B}(\omega_A) \times \mathcal{A}'(\omega_A) \;<\; 0\,. \tag{2}$$

These conditions are sketched in the R.H.S. of Figure 1.

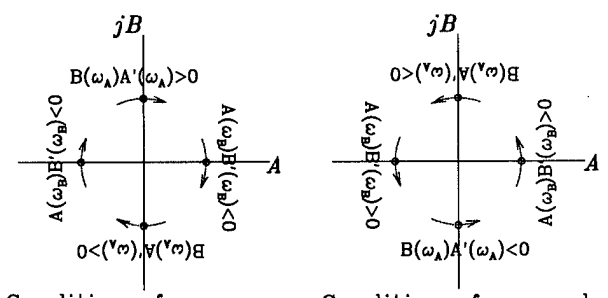

Figure 1: Geometric interpretation of stability criteria.

The stability criterion $\mathcal{A}\mathcal{B}' - \mathcal{B}\mathcal{A}' > 0$ does not have to be satisfied at all the roots ω_A and ω_B; but it must be satisfied at those which can cause encirclement of the origin. If there is no root ω_A between the nearest neighbour roots $\omega_B(n)$ and $\omega_B(n+1)$, then there is no encirclement. Hence, we should only apply the stability criteria where the roots *alternate*; that is where $\omega_B(n+1) > \omega_A > \omega_B(n)$ for condition (1), or where $\omega_A(n+1) > \omega_B > \omega_A(n)$ for condition (2).

1.3 The problem of delay

By delay, we mean that the value of some quantity at time t is related to the value of some other quantity at an earlier time $t - T$, where T is the delay interval. It is simple to show that the Laplace transform of $F(t - T)$ is $\exp(-sT)F(s)$ provided that $F(t) = 0$ for $t < T$. The Nyquist criterion is applicable to the exponential function because it is the limit of a polynomial: $\exp(-sT) = (1 - sT/N)^N$ as $N \to \infty$ where N is an integer. Suppose we set $T = 0$ and find a finite set of roots. Roots which satisfy $\omega T \ll 1$ will not be much shifted when we allow τ

0-7803-4376-X/98/$10.00 © 1998 IEEE

to become finite; we call them the 'LF roots.' When $T > 0$, there will also be an infinite set of HF roots; and these are usually periodic or approximately so; of these, usually only a very small subset can cause encirclement of the origin.

2 RESONATOR WITH DELAYED FEEDBACK

In the neighbourhood of resonance, a cavity behaves like a simple LCR parallel resonator. Let the original resonance angular frequency be Ω, the shunt resistance R_s and the time constant be $\tau_c = 1/\alpha = 2Q/\Omega$ where Q is the quality factor. Let us suppose the resonator is equipped with a delayed feedback of gain A/R_s. We suppose the delay interval is τ. Let dots placed above a variable denote derivatives with respect to time, t. The voltage, V, and driving current, I, obey the equation:

$$\ddot{V} + 2\alpha[\dot{V}(t) + A\dot{V}(t-\tau)] + \Omega^2 V = 2\alpha R_s \dot{I} \ . \quad (3)$$

For simplicity, suppose that $|A| \gg 1$ and that A does not cause any phase-shift. Also, for brevity, let us write $2\alpha A = B$ and $2\alpha R = C$. We introduce a dimensionless 'time' $u = \Omega t$, and dimensionless variables $b = B/\Omega$, $T = \Omega\tau$ and $c = C/\Omega$. Let primes denote derivatives with respect to u. We form the Laplace transform to find:

$$[s^2 + bse^{-sT} + 1]V(s) = csI(s) \ . \quad (4)$$

The eigen-values of the equation obtained by setting $I(s) = 0$ are the natural free-oscillation frequencies of the system.

2.1 *Criteria for stability*

We set $s = j\omega$ and form $F = \mathcal{A} + j\mathcal{B}$. It is easiest to locate the roots ω_B of $\mathcal{B} = 0$. We need to find one low frequency root and an infinite, periodic set of high frequency roots.

2.1.1 Low frequency root

If $\omega_B = 0$ is the only root for which $\mathcal{A}(\omega_B) > 0$ then we find the condition $\mathcal{A}\mathcal{B}' > 0$ implies $b > 0$. However, if $T > \pi/2$ then there will be two or more roots ω_B for which $\mathcal{A}(\omega_B) > 0$; and so $b > 0$ is not an essential condition. In fact, b must change sign periodically as T increases, and the maximum allowed gain b passes through zero at $\omega_n^2 = 1$ or $T = (2n+1)(\pi/2)$.

2.1.2 High frequency roots

The other roots of $\mathcal{B}$ occur at $\omega_n = (2n+1)\pi/(2T)$ with $n = 0, 1, 2, \ldots$ a positive integer. We find the condition:

$$\mathcal{A}\mathcal{B}' = [1 - \omega_n^2 + b\omega_n(-1)^n][-b\omega_n T(-1)^n] > 0 \ . \quad (5)$$

This need not be satisfied for all n. However, it must be satisfied for the two adjacent n which cause $\mathcal{A}$ to change sign. The exact conditions depend on the delay T.

The inequality $\Omega\tau = T \leq \pi/2$ is a special case: a sufficient condition for stability is $\mathcal{A}(\omega_0)\mathcal{B}'(\omega_0) > 0$ with $\omega_0 = \pi/(2T)$; which implies:

$$0 < B\tau < \left[(\pi/2) - (2/\pi)(\Omega\tau)^2\right] \ . \quad (6)$$

The case $T = \Omega\tau > \pi/2$ is more complicated. Suppose that $T \approx m\pi$ where m is the nearest integer. We establish the quantities T_{crt} and b_{max}:

$$T_{crt} = m\pi\sqrt{1 - 1/(4m^2)} \quad \to m\pi \quad (7)$$

$$(-1)^m b_{max} = \pi/T_{crt} \quad \to 1/m \quad \text{for large } m \ . \quad (8)$$

T_{crt} is a 'critical' value of the delay. Below T_{crt}, the limiting gain is the solution of $\mathcal{A}_{m-1} = 0$. Above T_{crt}, b is the solution of $\mathcal{A}_m = 0$. Exactly at T_{crt} the limiting stable gain is equal to b_{max}. Now we may state the extremal gain conditions.

$$(2m-1)\pi/2 \leq T \leq T_{crt} \Rightarrow b = (-1)^m[1-\omega_{m-1}^2]/\omega_{m-1} \ . \quad (9)$$

$$T_{crt} \leq T \leq (2m+1)\pi/2 \Rightarrow b = (-1)^m[\omega_m^2 - 1]/\omega_m \ . \quad (10)$$

The gain stability boundary is sketched in figure 2. If the gain b (with appropriate sign) is smaller than given in conditions (9, 10) then all natural oscillations are self damped.

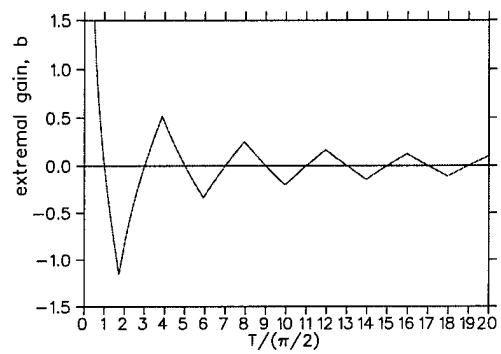

Figure 2: Maximum values of gain, b compatible with stability versus delay T.

2.2 *Radio-frequency system*

If the resonator appears as a real load when driven at Ω, then one must take the cases $T = \Omega\tau = m\pi > T_{crt}$. Hence the gain limit is given by:

$$(-1)^m \times A = Q/m = (\tau_c/\tau)(\pi/2) \ . \quad (11)$$

Other choices are possible: take the condition $\omega_{\rm rf}\tau = m\pi$ where $\omega_{\rm rf} \neq \Omega$ is the desired drive radio-frequency. Below transition, $\omega_{\rm rf} < \Omega$ and so $T > m\pi$. Let us introduce the detuning angle by the definition:

$$\tan\Psi = (\Omega^2 - \omega^2)/(2\alpha\omega) = Q(\Omega-\omega)(\Omega+\omega)/(\Omega\omega) \ . \quad (12)$$

Let $T = m\pi + (\Omega - \omega_{\rm rf})\tau \approx m\pi + (\tau/\tau_c)\tan\Psi$ and substitute in (10). $\Psi > 0$ because $\omega_{\rm rf} < \Omega$. In the limit of large m, the extremal gain is approximately

$$A(-1)^m \approx (Q/m)\left[1 - (2/\pi)(\tau/\tau_c)\tan\Psi\right] \ , \quad (13)$$

3 ANALOGUES OF THE ROBINSON CRITERIA

We consider small perturbations about the steady state, and develop the analysis in terms of the transfer functions for phase and amplitude modulations of the carrier frequency. Let us suppose the gain, A, has been chosen consistent with

the delay τ. The drive current is the sum of a generator component and the fundamental beam current component $\mathbf{I}_b^0 = jI_b^0 e^{j\Phi_b}$. It is customary[4] to define $I_V^0 = V^0/R$ and introduce the ratio $Y_b = I_b^0/I_V^0$. Let $w = \omega_{\rm rf}\tau + \theta$ where θ is a fixed arbitrary phase-shift in the feedback. We define the synchrotron frequency Ω_s *sans* the usual trigonometric factor and also define $\omega_s^2 = \Omega_s^2 \cos\Phi_b$. Using the beam response equations of References[4, 5], for small dipole oscillations of the bunch about the steady state phase, Φ_b, the system matrix is given by:

$$\begin{bmatrix} m_{11} & m_{12} & -Y_b\cos\Phi_b \\ m_{21} & m_{22} & +Y_b\sin\Phi_b \\ -\Omega_s^2\sin\Phi_b & -\Omega_s^2\cos\Phi_b & s^2+\Omega_s^2\cos\Phi_b \end{bmatrix} \begin{bmatrix} a_v \\ \phi_v \\ \phi_b \end{bmatrix} = \ldots$$

$$m_{11} = +m_{22} = 1 + s\tau_c + Ae^{-s\tau}\cos w \quad (14)$$

$$m_{12} = -m_{21} = Ae^{-s\tau}\sin w + \tan\Psi\,. \quad (15)$$

The natural frequencies are obtained by setting the determinant equal to zero, leading to $c_4s^4+c_3s^3+c_2s^2+c_1s+c_0 = 0$ where the polynomial coefficients contain exponential terms. We set $s = +j\omega$ to find $F = \mathcal{A} + j\mathcal{B}$.

3.1 Low frequency roots

$\mathcal{B}$ has three low frequency roots.

3.1.1 Root at $\omega = 0$

The quantity $\mathcal{A}(0)\mathcal{B}'(0)$ is is easiest to interpret when $w = m\pi$ and m is even, in which case the criterion:

$$[(1+A)^2 + \tan^2\Psi - Y_b\tan\Psi] \times [\tau_c - A\tau] > 0\,. \quad (16)$$

We know $A\tau < \tau_c$; and so it follows that $Y_b\tan\Psi < (1+A)^2 + \tan^2\Psi$ is a necessary condition for stability. This is formally identical with Robinson's 'power limited' stability criterion; and this was anticipated because delay cannot change the nature of a d.c. instability – for d.c. signals, an arbitrarily long delay does not change the signal.

3.1.2 Roots at $\pm\omega_s$

ω_s is an exact root of $\mathcal{B}$ when $w = m\pi$. Let us evaluate

$$\mathcal{A}(\omega_s)\mathcal{B}'(\omega_s) = 4\Omega_s^2 Y_b[1 + (-1)^m A\cos(\omega_s\tau)]\,\omega_s \times [\omega_s\tau_c - (-1)^m A\sin(\omega_s\tau)]\tan\Psi\,. \quad (17)$$

This quantity can become negative, indicating instability, in a variety of ways. Suppose m is even. Without feedback, the real part of the cavity impedance is positive (i.e. dissipative) at synchrotron upper and lower sidebands, and the difference is proportional to $\omega_s\tau_c \times \tan\Psi$. With feedback, the real part of the impedance at the sidebands becomes proportional to $[\omega_s\tau_c - (-1)^m A\sin(\omega_s\tau)] \times \tan\Psi$. However, from the stability of the cavity without beam we know

$$\tau_c > A\tau \geq A\sin(\omega_s\tau)/\omega_s\,. \quad (18)$$

Hence, from (17) we conclude the stability conditions:

$$\tan\Psi > 0\,, \quad (19)$$

$$1 + A\cos(\omega_s\tau) > 0\,. \quad (20)$$

The inequality (19) is the first Robinson criterion and it tells us to detune the cavity in the correct sense: $\Omega > \omega_{\rm rf}$ when below transition energy.

Suppose feedback phasing is adjusted so that the real part of the at the drive frequency is positive. For sufficiently long delay and high synchrotron frequency, one finds that at the upper and lower synchrotron sidebands of the drive frequency, the real part of the impedance looks like a *negative* resistance. Condition (20) determines if this situation occurs; from which we conclude $\omega_s\tau < \pi/2$ or $\omega_s < \omega_0$.

3.2 High frequency roots

To simplify matters we shall consider the case of very large gain, that is $|A| \gg 1$. The $\omega_n = (2n+1)\pi/(2\tau)$ where n is an integer are exact roots of $\mathcal{B} = 0$ if $w = m\pi$. When $\omega = \omega_n$ and $w = m\pi$, then

$$\mathcal{A} = -\Omega_s^2 Y_b\tan\Psi + (\omega_n^2 - \Omega_s^2\cos\Phi_b) \times \times [A^2 - 2(-1)^{m+n}A\tau_c\omega_n + (\tau_c\omega_n)^2 - \tan^2\Psi] \quad (21)$$

$$\mathcal{B}' = 2A\tau(-A + (-1)^{m+n}\tau_c\omega_n)(\omega_n^2 - \Omega_s^2\cos\Phi_b) \quad (22)$$

To simplify, let m be even. The transfer functions are only valid for small modulation frequencies and so we set $n = 0$. Now $\omega_0 > \omega_s$ and $A < \omega_0\tau_c$ from Eqn. (11), and so:

$$\left(\frac{Q\pi}{\Omega\tau} - A\right)^2 > \tan^2\Psi + \frac{(\Omega_s\tau)^2 Y_b\tan\Psi}{(\pi/2)^2 - (\Omega_s\tau)^2\cos\Phi_b}\,. \quad (23)$$

This condition implies that the maximum, stable feedback gain is reduced under conditions of heavy beam loading. The condition is only accurate under the condition of long delay: $\Omega\tau \gg \pi/2$. If relation (23) is violated, then a coherent oscillation occurs at the frequency $\omega_0 = \pi/(2\tau)$ because the dipole mode frequency is shifted away from the nominal synchrotron frequency by the very large reactance at the sidebands of the carrier that occurs if $|\tau_c\omega_0 - A| \approx \tan\Psi$. Essentially, the reactive impedance raises the coherent frequency to a point high enough that it can oscillate in synchronism with a spontaneous high frequency oscillation of the resonator-with-feedback. Despite the fact that the feedback is in-phase at the carrier, at this sideband frequency ω_0 the feedback is in quadrature so making the effective impedance look very reactive.

Reference[5] generalizes all results to the case of arbitrary w and θ and A.

4 REFERENCES

[1] K. Robinson: *Stability of beam in RF*, CEAL-1010, 1964.

[2] F. Sacherer: *Methods for computing bunched-beam instabilities*, CERN/SI-BR/72-5.

[3] D. Boussard: *Control of cavities with beam loading*, IEEE Trans. Nucl. Sci. Vol. NS-32. No.5, Oct. 1985, pp. 1852-1856.

[4] S. Koscielniak: *Analytic criteria for stability ...*, Particle Accelerators. Vol.48, No.3, pp. 135-168 (1994).

[5] S. Koscielniak: *Algebraic version of Nyquist stability criterion applied to systems with delayed feedback*, TRI-DN-97-2.

[6] S. Koscielniak: *Explanation of the delay-limited Robinson-type instability*, TRI-DN-97-3R.

STUDY OF ORBIT FEEDBACK SYSTEMS FOR THE TESLA LINEAR COLLIDER

R. Lorenz, I. Reyzl, S. Sabah, TU Berlin, Einsteinufer 17, D - 10587 Berlin, Germany

Abstract

In order to reduce the influence of magnet vibrations which can cause luminosity reduction in the TESLA Linear Collider, several feedback loops are planned to control the beam orbit and to keep the beams in collision. The complete control system for orbit correction can be divided into three different feedback systems: in the main linac a slow feedback system is intended to cancel perturbations in the low frequency range which are mainly due to ground motion. In the beam delivery section a fast feedback system is to be installed to compensate disturbances containing higher frequency components, mainly from pulse-to-pulse quadrupole vibrations and potentially also due to microphonics and Lorentz-force detuning in the superconducting cavities. At the interaction point a fast feedback system will keep the two beams in collision, using the beam-beam-deflection signal. The paper summarizes design studies for all three orbit correction schemes and the main components are discussed in detail.

1 INTRODUCTION

TESLA 500 is a e^+e^- linear collider study using superconducting Nb accelerating structures operating at 1.3 GHz [1]. Very low wakefields and a high accelerating efficiency with a gradient of 25 MV/m are major advantages of this design. At a center of mass energy of 500 GeV TESLA 500 is aiming for a nominal luminosity of $6 \cdot 10^{33}$ cm^{-2} s^{-1}, where at the interaction point (IP) the requested transverse beamsizes are $\sigma_x^\star = 845$ nm and $\sigma_y^\star = 19$ nm. The repetition rate is 5 Hz and the bunch train consists of 1130 bunches separated by 708 ns.

In order to keep the two beams in collision and to avoid emittance growth due to motions of different components several feedback loops will be installed in TESLA. Due to the flat shape of the beam the vertical movement of quadrupoles and above all the jitter of the final doublet is of particular significance.

The conceptual design of the orbit control in TESLA consists of three different feedback systems:
In the lower frequency range the beam is perturbed by vibrations mainly due to ground motion which is almost natural noise below 1 Hz [2]. A slow feedback system in the main linac working at the repetition frequency of 5 Hz will cancel their influence on the beam orbit up to a tenth of the repetition rate. The beam offset will be steered by means of corrector coils.

Assuming a noisy environment, after a certain time the pulse to pulse beam movement can result in unacceptable beam seperation at the IP. Therefore a fast feedback is necessary, working in the MHz-range, to regulate the beam offset after a few bunches of a train and to keep the two beams in collision. Due to the bunch spacing of 708 ns - another main advantange of TESLA - the fast feedback will provide a bunch to bunch correction of the beam orbit. The fast feedback will also compensate disturbances in the kHz range caused by quadrupole vibrations within a pulse, and potentially by Lorentz force detuning and microphonics in the superconducting cavities. It does not need to correct the relativly large orbit changes over many pulses which are already eliminated by the slow feedback system.
Two fast feedback systems are planned: before the beam enters the final focus system, a feedback in the beam delivery section (BDS) will eliminate the beam offset caused by the movement of upstream elements, especially in the linac. A fast IP - feedback will keep the two beams in collision using the beam-beam-deflection signal. Fast kicker magnets will provide the requested kicks for steering the beam.

All feedback systems will be digital allowing the realization of an advantageous data base driven feedback. The data received are recorded and can be used for further statistics. Figure 1 shows the schematic concept of a digital feedback. In case of the fast feedback, all operations in the different blocks of Fig. 1 and the signal transmission have to be done within the bunch spacing. In this

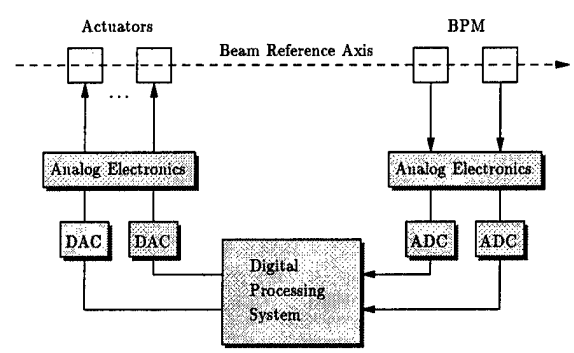

Figure 1: Schematic diagram of digital feedback systems

paper a brief description of all three feedback systems, of their main components and of the considered feedback algorithms is given.

2 MAIN COMPONENTS

2.1 Beam Position Measurement

The first device in the feedback loop shown in Fig. 1 is an electromagnetic pick-up to obtain a signal proportional to

0-7803-4376-X/98/$10.00 © 1998 IEEE

the beam position. Cylindrical cavities excited in the first dipole-mode by an off-axis beam are under consideration for this purpose in all feedback systems.

In the main linacs the slow feedback system will make use of the beam position monitors (BPM) installed at every cold quadrupole. To avoid interferences from the accelerating cavities, they were designed for a resonant frequency of 1.517 GHz. A loaded Q of about 900 is realized by using CrNi as a cavity material to measure individual bunches. Design details and test results at the TESLA Test Facility Linac (TTFL) are summarized in [3].

Monitors which are under development for the free-electron laser at the TTFL [4] might be installed in the BDS. Their signal processing scheme for detecting the 12 GHz signal will be slightly modified: another field-sensitive filter using waveguide components will be installed at the electronics front-end resulting in an improved common-mode rejection. In addition, all components especially the analog-to-digital conversion have to be optimized with respect to the processing time.

A cavity with a TM_{110}-frequency of about 2 GHz is designed for the IP, mainly because of the beam pipe diameter. The signal processing scheme is similar to the TTFL-monitors, but has to be optimized with respect to the processing time. In addition, special care has to be taken of the signal resulting from the incoming beam (see also section 2.4).

Table 1 summarizes some important design parameters of these three cavity monitors. The stability per day should be in the order of the resolution for all monitors.

	location of the BPM		
parameter	**Linac**	**BDS**	**IP**
Bunch separation		708 ns	
Resolution	10 μm	1 μm	5 μm
Bandwidth	1.5 MHz	12 MHz	5 MHz
TM_{110}-frequency	1.52 GHz	12.0 GHz	1.95 GHz
Cavity radius	115.2 mm	14.6 mm	90 mm
Cavity length	52 mm	8.6 mm	50 mm
Beam pipe radius	39 mm	5 mm	24 mm

Table 1: Design parameters for all cavity monitors

2.2 *Slow Feedback*

Disturbances in the low frequency range are mainly due to ground motion, causing quadrupole displacement and leading to beam emittance growth. In order to eliminate the effects of displaced elements a slow feedback system working on the repetition frequency of 5 Hz has been developed [6].

For the orbit correction the position and the angle of the beam trajectory in both transverse plans will be controlled. The conceptual design of this pulse-to-pulse orbit control is based on tools of Optimal Control Theory taking into account the stochastic nature of the beam movement and of the sensor noise. The feedback loop can be divided into four main operations: measurement taken by BPM's – estimation of the beam's position and angle – calculation of actuator strength – correction by use of corrector coils. The loop contains an optimal filter (Kalman Filter) to estimate the beam's position and angle and an optimal controller to determine the corrector settings [7].

Results of simulation runs show that the feedback algorithm provides a good orbit control in the requested range. The feedback loop damps frequency disturbances up to 0.4 Hz quite well, where a DC bias rejection of -50.8 dB was achieved. Including an integral part in the controller improves the DC bias rejection, but its disadvantage is a higher amplification in the frequency range between 0.5 Hz and 1.9 Hz. An assumed beam offset of 5 σ_y at the end of the linac requires a kick of 0.55 μrad; for a 250 GeV beam the corrector must provide a magnetic field of $4.57 \cdot 10^{-4}$ Tm. This can be done by the standard correction coils installed in the linac.

2.3 *Fast Feedback in the BDS*

A fast feedback system will be located in the tuning and diagnostic section of the BDS to correct the orbit before the beam enters the final focus system. This bunch to bunch feedback is also able to compensate disturbances like fast vibrations of quadrupoles, microphonics and Lorentz-force detuning caused by the superconducting cavities which cannot be detected and controlled by the slow feedback system. It will consist of two monitors to detect the beam position and angle and fast kickers to provide the requested kick for steering the beam. The feedback is determined with tools of classical control theory. The closed loop includes also a noise filter to suppress the sensor noise affecting the beam position measurements. This noise filter is based on the Maximum Likelyhood estimator which is equivalent to least square fitting if the noise is independent, gaussian distributed and with constant standard deviation [8]. In contrast to the Kalman Filter used in the slow feedback, the dynamic of the noise does not have to be known. Results of simulations are shown in Fig. 2: the influence of sensor noise, obviously, can be decreased by the noise filter.

2.4 *IP Feedback*

The vertical offset of the two beams at the IP is the most harmful effect of misplaced elements. A 2% luminosity reduction from beam centrouid motion is expected to occur in 1 ms, assuming a ground motion model on noisy environment. Therefore a fast feedback system is necessary to keep the beams in collision. The offset of the two colliding beams will be measured precisely with the beam-beam scattering method which has already been used in the SLC for single bunches [5]. For TESLA the kick angle α per σ_y^* estimated from beam-beam simulations is approximately given by

$$\alpha \quad [\text{mrad}]: \quad (\Delta y_{IP}/\sigma_y^*) \times 0.047\,\text{mrad} \qquad (1)$$

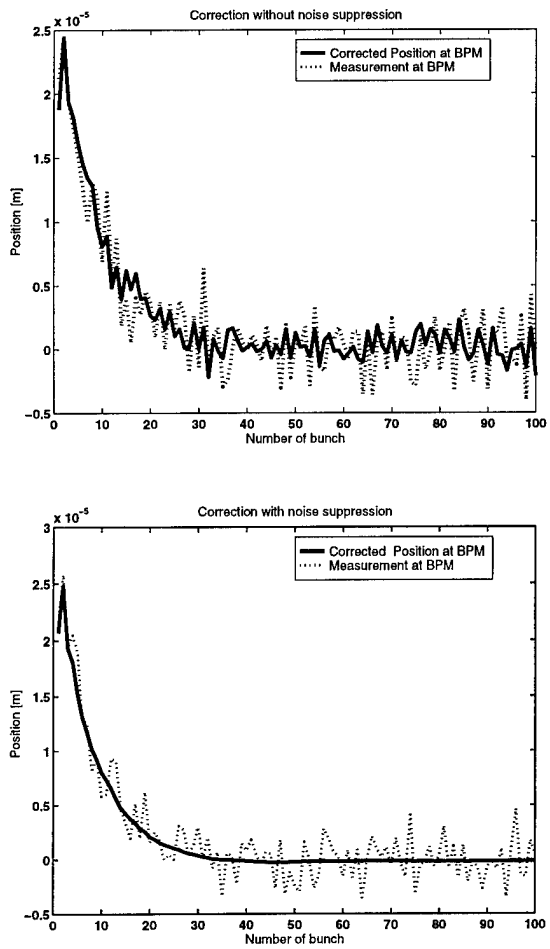

Figure 2: Simulation plots of fast feedback (BDS): Position and measurement 1) without and 2) with noise suppression. For scaling reasons, the offset of the pilot bunch (45 μm) is not shown.

with $\sigma_y^\star = 19$ nm beam spot size and Δy_{IP} beam-beam separation at the IP.

In order to reduce the processing time of the feedback loop, the locations of the BPM's and the kickers have to be as close as possible to the IP. If the BPM is located at the position of the final doublet separated by 3 m from the IP, a separation of one $\sigma_y^\star$ will result in an offset of about 140 μm. Therefore the required resolution of the BPM can be relaxed and will be about 5 μm. Within one pulse a bunch-to-bunch measurement of both outgoing beams can be used to get a precise measurement of the offset of the two colliding beams.

The sinusoidal part of the trajectory is given by the difference of the pick-up signals for one bunch taken before and after the IP; the sum determines the requested kick to steer the beam calculated by tools of classical control theory. The orbit feedback at the IP shall be able to remove a separation up to $10\,\sigma_y^\star$. Assuming a distance of 4 m between a kicker and the IP this will result in a requested kick of 0.023 μrad for each kicker. Therefore a magnetic field of $2 \cdot 10^{-5}$ T is required for an energy of 250 GeV.

2.5 *Correctors*

In the digital system, fast Digital-to-Analog Converters will convert the signals back into analog values for the correctors. These signals have to be amplified in a broadband power amplifier. In the slow feedback system corrector coils are used to steer the beam from pulse to pulse. For the fast feedback system the installation of feedback kickers successfully used in the HERA ring at DESY is planned [9]. The magnetic field of the 0.9 m long stripe line kicker is about 10^{-4} Tm providing a kick of 0.12 μrad at an energy of 250 GeV.

3 ACKNOWLEDGEMENTS

It is a pleasure to thank our colleagues from DESY Hamburg for their help and for their hospitality. Special thanks are extended to R. D. Kohaupt and R. Brinkmann for the uncountable discussions and intensive help, and H. Henke from TU Berlin for his support.

4 REFERENCES

[1] J. Rossbach, "Options and Trade-Offs in Linear Collider Design", IEEE Conference Proc. of the PAC 95, Dallas, Texas

[2] V. D. Shiltsev, "Alignment and Stability in Future Machines", IEEE Conference Proc. of the EPAC 96, Sitges, Spain

[3] R. Lorenz et.al., "First Operating Experiences of Beam Position Monitors in the TESLA Test Facility Linac", this Conference

[4] R. Lorenz et.al., "Beam Position Monitors inside the FEL-Undulator at the TESLA Test Facility Linac", this Conference

[5] P. Bambade, R. Erickson, "Beam-Beam Deflections as an Interaction Point Diagnostics for the SLC", SLAC-PUB-3979, May 1986

[6] I. Reyzl, "Simulation of Feedback for Orbit Correction", IEEE Conference Proc. of the EPAC 96, Sitges, Spain

[7] G. F. Franklin, J. David Powell, Michael L. Workman, *Digital Control of Dynamic Systems*, 2nd ed., Addison-Wesley, 1990

[8] J. Honerkamp, *Stochastische dynamische Systeme*, VCH Verlagsgesellschaft mbH, Weinheim, Germany, 1990

[9] J. Rümmler, " Feedback Kickers in the DESY Rings", IEEE Conference Proc. of the EPAC 94, London

OBJECT ORIENTED PROGRAMMING INTERFACES FOR ACCELERATOR CONTROL*

L.T. Hoff
Brookhaven National Lab
Upton, NY, 11973-5000, USA

Abstract

A current trend in control system design is to provide an object oriented programming interface for application developers. This talk will discuss important aspects and features of object oriented APIs for accelerator control systems, and explore why such interfaces are becoming the norm.

1 INTRODUCTION

Several years ago, the AGS controls group was given the task of developing software for the RHIC accelerator. Like the AGS, the RHIC control system needs to control and monitor equipment distributed around a relatively large geographic area. A local area network connects this equipment to a collection of UNIX workstations in a central control room. Similar software had been developed for the AGS about a decade earlier, but isn't well suited for RHIC use for a number of reasons.

The AGS software was designed to work within AGS parameters. The AGS software expects data updates at AGS operating rates. This rate is typically every 3 or 4 seconds. The AGS software does not allow large (greater than about 40 Kbytes) data transfers. The AGS software enforces a very rigid format for grouping related data. In addition, the AGS software was written for a proprietary hardware platform. An aggressive porting effort was well underway to make the software usable on typical UNIX workstations. However, it seemed that this effort would not be complete in time.

More importantly, all software for AGS operations had been written by the controls group. A different paradigm was expected for RHIC software development. The RHIC Accelerator Physics group is composed of experienced programmers. Not only are these physicists fully capable of writing physics applications, they expect to do so. The controls group is expected to provide training and assistance in using control system software. This necessitates a succinct, well-defined application programming interface (API).

The AGS software represents accelerator equipment as collections of control points. These collections of control points are called "logical devices". Other control systems focus more on individual control points, rather then on related groups of control points. The AGS approach contains the rudiments of an object oriented system. It is not truly object oriented, since the "logical devices" do not contain the methods for translating the control points into commands to accelerator equipment.

Rather than adapt the AGS software for RHIC use, the controls group opted to start with a clean slate. To develop software that would address the shortcomings of the AGS software, while preserving the useful features that evolved through years of use.

2 INFLUENCES

The ideas for the RHIC API were necessarily shaped by trends in industry. The network management protocol SNMP[1] was becoming more popular. Network management shares many characteristics with accelerator control. The simple, flexible interface of SNMP allows it to control and monitor a wide variety of network devices distributed around a large region. When Marshall T. Rose designed the SNMP interface, he commented "I wanted to make an interface so simple that no one could complain about it."[2]

Accelerator control systems began mimicking industry trends. A new control system was developed for the European Synchrotron Radiation Facility (ESRF) [3]. This control system provides an interface even simpler than SNMP. SNMP has separate SET and GET functions for controlling and monitoring devices. The ESRF control system provides a single function, dev_putget(), for both operations. Like SNMP, the ESRF control system is object oriented. Accelerator equipment is represented as collections of related control points. These collections are called Device Servers. Each Device Server contained methods for translating the control points into commands to accelerator equipment.

Widespread application of object oriented programming techniques were becoming the norm. In particular, the C++ language was emerging as the most popular object oriented programming language. C++ had already become the standard programming language for application development at the AGS[4]. The RHIC Accelerator Physics group members were all well versed in object oriented analysis and design as well as object oriented programming.

Concepts such as abstract data types began appearing in class libraries. The Free Software Foundation made available a general purpose class library called libg++. This library contains classes to represent

* Work performed under the auspices of the U.S. Department of Energy

rational and complex numbers. These classes are designed so that they can be manipulated without the user knowing how the data is represented. Such classes contain methods to coerce their values into C++ native data types. This might be necessary for interfacing with legacy code, or for doing I/O.

3 GOALS

Combining the requirements for RHIC operations, lessons learned from prior AGS experience, and adopting useful industry trends, the following goals were set for RHIC software.

3.1 Flexible

The inflexibility of the AGS software limited its usefulness for RHIC. Conventional wisdom held that control system software requirements were such that accelerator-independent software was not feasible. However, both Vsystem[5] and EPICS[6] proved that this was not the case. Both of these systems are in use, or are expected to be put into use at a number of different sites.

3.2 Portable

The ongoing porting effort of the AGS software could not be ignored. To try to avoid this hardship for RHIC software, a decision was made to use popular industry standards whenever possible. While this strategy is not foolproof it does increase the chance that the software will run on a variety of hardware platforms.

3.3 Easily configurable

The AGS software uses a central database to describe the location and functionality of distributed software. This database defines the data size and type, and even where in memory to find the data in each remote system. This rigid design severely limits the ability to incrementally upgrade or deploy remote systems.

3.4 Succinct API

Since AGS software development was contained within the controls group, there was little incentive to simplify, or fully document the various programming interfaces. This information is transmitted informally to new members when they joined the group. There are no external customers for the API. If external customers are expected, the API must be succinct enough so that it can be easily documented, and so that training can be easily provided.

3. 5 Object Oriented

AGS applications programmers found object oriented programming techniques essential. Object oriented programming techniques often allowed for more easily supporting last minute changes without restructuring the application. An object-oriented API can be more succinct than a procedural equivalent. Since certain state information can be contained within an object, there is less need to clutter the API by passing state information back and forth across the interface. Functionality such as error handling and recovery can often be separated from the main functionality of the interface. This frees the application writer to concentrate on interfacing with equipment, not on dealing with control system or network weaknesses.

3. 6 Abstract data types

To work with data in the AGS control system, the application programmer needs to know the size and type of the data. Since this information resides in a database, this becomes somewhat awkward. Using database information, the data must be coerced to fit the data type the programmer wishes to use. To simplify this process, all data may be automatically coerced to a float type. This method is not without pitfalls. It forces the use of slower floating point arithmetic, and precludes data types such as character strings. In addition, the AGS software made assumptions about byte ordering and padding. These assumptions added to the difficulty of porting to new platforms.

Abstract data types, such as the ones in libg++ avoid these shortcomings. Data can be stored in convenient internal representations. The data can be coerced as needed to the most appropriate native data type. Abstract data types can be flexible enough to represent vectors or scalars, character strings, and even data structures. This can vastly simplify application code by avoiding the need for complex "switch" statements.

4 ESRF

The ESRF control system was written in C using a technique called Objects in C. This technique was chosen in lieu of using an object oriented programming language such as C++. At that time, C++ was not supported for the hardware platforms used at ESRF.

A single function, dev_putget(), handles monitoring and controlling accelerator equipment. A vector version handles commands to groups of devices, and an asynchronous version provides for a delayed response.

The ESRF control system does not provide a true abstract data object. Instead, there is a generic data pointer type, DevArgument, and separate type information, DevType. This already succinct API could be made even more succinct with a true abstract data object.

The ESRF directory service is not embedded within the dev_putget() function. There is a separate dev_import() function call which activates the directory service. This function returns a handle which must be used in subsequent dev_putget() calls. This function is roughly analogous to a C++ constructor. The returned handle is similar to a pointer to a C++ object. The directory service indicates whether the service provider is local or remote. If the service provider is remote, the directory service provides network addressing

information. In this case, SUN RPC is used to handle parameter passing between the possibly different hardware platforms.

5 ADOIF

The RHIC control system API is called AdoIf[7]. This is an acronym for ADO interface. ADO is itself an acronym for Accelerator Device Object.

AdoIf was written entirely in C++. There is no other language binding for the API. Users are expected to be C++ programmers.

AdoIf provides three functions for controlling and monitoring accelerator equipment. Set() is used to change a current setting. Get() is used to retrieve a current setting or a current reading. GetAsync() is used to be notified of a future change to a setting or reading.

The name GetAsync() has been the source of some confusion. This may be replaced by the name subscribe() in the future. This name is consistent with the paradigm that new data is published to all subscribers.

Set() and Get() have vector equivalents for sending commands to groups of devices.

Data is represented by the C++ class Value. Value objects are abstract data objects. The Value class stores data internally in the most efficient manner. Users may coerce the data into native C++ data types as needed. The Value class also supports an ASCII dump method, which eases the task of writing generic utility programs. Such programs never need to know what type or size the data is. They can merely get the data, then display it in ASCII.

AdoIf has been used on a variety of UNIX workstations, using both RISC and CISC processors, and both Big-Endian and Little-Endian architectures.

The directory service is undergoing a transition from a file-based system to a server-based system. In either system, environment variables allow custom configurations. A custom configuration might combine real accelerator equipment with simulated accelerator equipment. In this way software can be tested even before the accelerator equipment is installed, or when the accelerator is not running.

6 CDEV

The Control Device API (CDEV)[8], is not a complete control system. Instead it is an abstract control system API which may use one or more underlying control systems. Issues such as data translation to different hardware platforms may be handled by the underlying control system.

CDEV was also written in C++. There is an effort underway to support portions of CDEV in Java, another object oriented language. Recently, a C language binding was added to CDEV. This was added at the request of some CDEV users, but does not change the object oriented nature of CDEV.

CDEV provides three messages which are analogous to AdoIf's Set(), Get(), and GetAsync() functions. They are "set", "get", and "monitorOn". All accelerator equipment is expected to respond to these messages.

Data is represented in the cdevData class. Like the Value class, this class provides methods for data coercion to native types, as well as an ASCII dump method.

The directory service is provided by the cdevDirectory class. This class directs requests to the appropriate underlying service provider. This may be a particular control system, a database, or other data acquisition software. By default, there is a single directory service. To provide custom configurations, users may register additional directory services with the CDEV system.

7 CONCLUSION

Several trends in API design are identified. The reasons for these trends are explored. All of these trends ease the job of application programming. Succinct APIs are easier to learn. Object oriented features make it easier to focus on the task on hand. Such features make it less necessary to focus on control system or network weaknesses, or data conversion. Portability allows control system software to run on a variety of hardware platforms. This allows users to choose hardware based on price and performance, rather than on compatibility grounds. Flexible directory services allow software to be written and tested using either real or simulated accelerator equipment. Identifying these common themes help applications programmers from different facilities to speak the same language, and perhaps even share software.

The underlying technology that shapes these trends continues to evolve. Emerging technologies, such as CORBA[9], may become more widely used. Such technologies will undoubtedly steer future trends in programming interface design.

REFERENCES

[1] RFC 1057 A Simple Network Management Protocol (SNMP), Case, Fedor, Schoffstall, and Davin, May 1990.

[2] The Simple Book: An Introduction to Management of TCP/IP-based Internets, Marshall T. Rose, Prentice-Hall, 1991. ISBN 0-13-812611-9

[3] A. Goetz, W.-D. Klotz, J. Meyer, Proc. Int. Conf. Accelerator and Large Experimental Physics Control Systems, Tsukuba, Japan, 1991, KEK Proc. 92-15 pp. 514-519.

[4] Joseph F. Skelly, Proc. Int. Conf. Accelerator and Large Experimental Physics Control Systems, Tsukuba, Japan, 1991, KEK Proc. 92-15 pp. 500-504.

[5] P. Clout, Nuclear Instruments and Methods in Physics Research A 352 (1994) pp. 442-446 North Holland.

[6] Dalesio, Kraimer, and Kozubal, Proc. Int. Conf. Accelerator and Large Experimental Physics Control Systems, Tsukuba, Japan, 1991, KEK Proc. 92-15 pp. 278-281.

[7] L.T.Hoff, J.F.Skelly, Nuclear Instruments and Methods in Physics Research A 352 (1994) pp. 185-188 North Holland.

[8] J. Chen et al, Proc. 1995 Int. Conf. Accelerator and Large Experimental Physics Control Systems, Chicago, Ill. USA, pp. 97-104.

[9] http://www.omg.org

A PORTABLE ACCELERATOR CONTROL TOOLKIT

William A. Watson III, Thomas Jefferson National Accelerator Facility

Abstract

In recent years, the expense of creating good control software has led to a number of collaborative efforts among laboratories to share this cost. The EPICS collaboration is a particularly successful example of this trend. More recently another collaborative effort has addressed the need for sophisticated high level software, including model driven accelerator controls. This work builds upon the CDEV (Common DEVice) software framework, which provides a generic abstraction of a control system, and maps that abstraction onto a number of site-specific control systems including EPICS, the SLAC control system, CERN/PS and others. In principle, it is now possible to create portable accelerator control applications which have no knowledge of the underlying and site-specific control system. Applications based on CDEV now provide a growing suite of tools for accelerator operations, including general purpose displays, an on-line accelerator model, beamline steering, machine status displays incorporating both hardware and model information (such as beam positions overlaid with beta functions) and more. A survey of CDEV compatible portable applications will be presented, as well as plans for future development.

1 INTRODUCTION

In almost any book or journal on software development one will find reference to the explosion in the quantity of software development, and the cost and difficulty in developing necessary software in a timely fashion. A typical rule of thumb for accelerators is that the control system costs 10% of the total project, with half of that going to software. In addition, as much as 5% to 10% of operating manpower may go towards ongoing software improvements.

In a decade of declining research budgets, this expense has driven an increasing interest in software sharing within many areas of the research community, including the accelerator controls community.

1.1 EPICS

One example of a successful collaboration to develop accelerator control software is EPICS (Experimental Physics and Industrial Control System). This software, whose history is described in another paper at this conference [1], is now in use at several accelerator sites including the Advanced Photon Source at Argonne, Thomas Jefferson National Accelerator Facility (Jefferson Lab), the B factory upgrades at SLAC and KEK, and several smaller machines.

EPICS provides a framework for developing low level device controls, including hardware interfacing and low level control algorithm development. Many device drivers are shared within the collaboration, as are modular software components for creating control processes. Programs within an EPICS system are tied together by a network infrastructure (the channel access library) based upon reading, writing, and monitoring changes in named variables. A named variable can refer to a hardware I/O point, or a variable within an algorithm

The toolkit contains a number of utility programs which plug into this software bus, including synoptic displays with interactive editors, a save/restore utility, archiving (data logging) and data browsing programs, and an alarm interface. Many commercial and freeware packages have also been interfaced to this bus via a callable library (e.g. a spreadsheet and the tcl/tk toolkit).

Including astronomy sites and large physics detectors, the EPICS collaboration includes over a hundred users and application developers, and represents a notable software sharing effort. For the most part, this sharing is limited to those who use EPICS as the core of their control system.

1.2 SOSH

SOSH (for Software Sharing) is a name given to a series of workshops on the general topic of software sharing for accelerators and large physics detectors. The original meetings were held in conjunction with the International Conference on Accelerator and Large Experimental Physics Control Systems (ICALEPCS).

The current thrust of these workshops is to (1) develop a framework within which shareable applications can be built, (2) develop shareable utility applications (e.g., display or manipulate named control system quantities), and (3) develop accelerator or detector specific control applications. The framework includes a common (abstract) interface to the local control system, with common standards for names of classes of devices and their attributes (or a way of aliasing these to a common set).

At the "Workshop on Software Sharing" following ICALEPCS '93 in Berlin, 19 invited participants agreed in a joint statement that "there is no fundamental reason (from operation and machine points of view) why ... the primary functions in the draft list could not be implemented by common generic (configurable) software and/or using appropriate common software tool kits". [2]

This list of functions included 13 topics related to the application environment including user interface development, on-line help, a sequencer, data logging, archiving, and system configuration. This is the area well covered in a portable way (within EPICS) by the EPICS toolkit.

What is more remarkable is that the participants stated that accelerator applications were equally shareable: magnet cycling (and super cycles), orbit measurement and correction, tune measurement and correction, chromaticity measurement and correction, RF gymnastics, machine

0-7803-4376-X/98 /$10.00 © 1998 IEEE

simulations, injection, matching, and extraction. To date, these sorts of applications have seen only limited portability, yet represent an even larger software development effort than all of EPICS at major accelerator labs like CERN, FNAL, and SLAC.

2 DISTRIBUTED SOFTWARE TECHNOLOGY

2.1 A Software Bus

If these applications are to be shareable among a large number of laboratories running different (mostly custom) control systems, there needs to be a well defined common interface through which they can connect. This interface is often referred to as a "software bus". Just as hardware modules pass data over a backplane bus, so too software modules (programs) pass information over the software bus.

In May of 1995, CERN hosted a workshop titled "A Softwarebus Common to Accelerators and Large Experimental Physics Control Systems". Twenty-five participants agreed that (1) applications "above the bus" (host side vs. hardware side) held the most promise and benefit for sharing, and (2) CDEV, a C++ framework developed at Jefferson Lab, [3] should be investigated as the framework through which these applications could access the control system. Two additional workshops in the previous 2 years have continued to focus upon CDEV as an enabling technology for portable accelerator control applications.

There are two ways in which a software bus can be defined, and both are used in practice. In one, the *network protocol* is defined, including how resources are located (discovered) on the network, what types of messages between programs are supported, and how these messages are formatted on the network. In the second way, an *application programming interface* (API) is defined, which specifies a set of routines to be called for communicating with other programs. The protocol on the network is not defined, and in fact multiple protocols may be used. The second technique is equivalent to defining a *virtual accelerator*, as presented by Kanaya at ICALEPCS '93. [4]

There are many software buses of each type in existence today, and it is difficult to choose one to be a standard; in fact the choice is somewhat a matter of preference. The choice of CDEV as a potential standard interface was driven by these requirements of the bus:

- ability to connect to legacy control systems
- high performance, with fully asynchronous behavior
- support for a high level view of the control system, dealing with named accelerator devices (magnet, bpm) each with multiple attributes (field, x-position, beam current) instead of a view consisting of hardware addresses or low level control points
- support for object oriented programming, and in particular the C++ language
- support for rich messaging (complex queries with complex replies)

2.2 CDEV

CDEV (Common DEVice) provides an interface (API) to a virtual control system with a simple flavor — the system consists of a set of named devices to which messages may be sent. The client program has no knowledge of the device's software or hardware implementation (location, control system type), and only knows (or discovers at run time) the list of messages to which the device responds.

CDEV is implemented as a C++ framework that provides a standard interface between an application and one or more underlying control packages or systems. It serves as an adaptor, or middleware, between a portable application and a local control system. In addition, it provides a number of features not provided by many control systems.

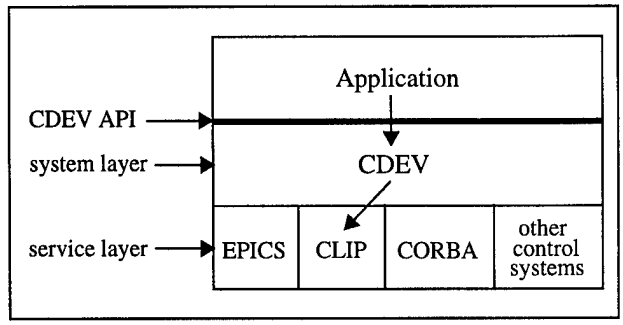

Figure 1: CDEV multi-service architecture.

CDEV does not specify which networking protocol is used between client and server, and can in fact support multiple protocols simultaneously (Figure 1). When used with the EPICS channel access protocol, CDEV can locate hundreds of device/attribute pairs per second, and receive thousands of value changes per second. The overhead of using CDEV instead of the native EPICS API is negligible and well offset by the additional functionality provided, even if portability is not a desired goal.

When used with another custom TCP/IP based protocol (CLIP) developed at Jefferson Lab, CDEV can deal with complex queries to (for example) a model server returning arrays of two-dimensional transfer matrices between specified devices. The client application remains unaware of which protocol is involved.

Additional interfaces to other control systems may be added to CDEV with a modest amount of programming, ranging from a couple of weeks of learning and coding for a simple system, to a few months for a complex system. SLAC has interfaced CDEV to its control system on VAX/VMS computers, and CERN/PS has done likewise for an IBM/AIX system. This is an extremely small amount of effort to support portable software.

2.3 Alternatives to CDEV

One possible alternative to CDEV which was considered (and continues to be evaluated) is CORBA, the Common Object Request Broker Architecture, which defines standards for object-oriented distributed-programming communication mechanisms. [5] Implementations of CORBA

are available from multiple vendors on all major platforms, and the latest version of the standard addresses interoperability among vendors.

While CORBA is well accepted in the marketplace, there are several problems with making it the software bus for control systems, and performance is one. CORBA is about 10 times slower at locating resources on a network than can be achieved with custom protocols — primarily because the location services deal with only a single resource at a time. In contrast, EPICS and CLIP buffer requests for name resolution, achieving much higher throughput for large, complex applications such as interactive displays containing a thousand or more variables.

Another CORBA difficulty is the complexity of the API for dynamic invocation (talking to remote objects whose interface is not compiled into the current program). This dynamic binding capability (discussed further in the next section) is a key feature of many utilities.

Nevertheless, CORBA continues to be of interest. One avenue often discussed is to use CDEV over CORBA, and to use CORBA only to locate servers and to transport messages. In this case one would use a custom (accelerator device) resource locator and CDEV as the API and higher level framework. CDEV could easily support this simultaneously with the existing direct support of other protocols.

3 UTILITY APPLICATIONS

3.1 Name Based I/O

There are a large number of useful controls applications which deal only with named values, and are not accelerator specific. These include operator displays (graphical — a meter showing magnet current, or text based — a list of all magnet setpoints and currents), data archiving (current in the magnet for the last year), or save and restore (of the magnet setpoint). These control system values are referenced by a single name (e.g. magnet7-setpoint) or through a pair of names (magnet7, setpoint) corresponding to device name and attribute name.

Because of the proven usefulness of the EPICS utility programs (which are name based), one development activity has been to port those tools to CDEV, allowing them to be used with non-EPICS servers and protocols.

3.2 Converting EPICS tools

Two EPICS applications [6] have already been converted from calling the EPICS channel access library to making CDEV calls.

stripTool Strip chart graphical application, with 8 colored pens. Interactively choose variables, including wildcards. Save / restore of display definitions.

alh Alarm handler; monitors the alarm (error) status of the referenced values and summarizes the errors in a tree hierarchy. Indicates alarm through color, blink, and beep.

In addition, the following EPICS tool is in the process of conversion; others will be converted as time allows.

dm Display manager; one of the two synoptic display programs in EPICS, with the ability to display values as text, color (of a graphic), or through widgets such as meters and push buttons. Menus and push buttons support executing scripts or bringing up additional displays.

3.3 New CDEV tools

Several new utilities have been developed or are currently being developed within the CDEV framework:

xact X-windows Automated Correlation Toolkit. Modeled after the SLAC correlation package, this utility can step 1 or 2 variables, and measure hundreds of other variables at each step. As part of each step or measurement, additional actions may be performed including time delay, wait for a value to settle, or invoke a script. Plans include automated min/max optimization of one parameter (done routinely at SLAC with their software).

zplot Another tool modeled after a SLAC utility, this program displays attributes of devices (such as *bdl*, the integral field in a magnet) as a function of position along the beam (z) in the machine. While this appears to be specific to accelerators, the attribute representing position could easily be replaced by any other collating parameter.

xarr Archive data browser. Originally developed to directly read EPICS archive data files, this program is being converted to a CDEV based client/server architecture. *StripTool* will also be modified to initialize immediately with archived data from the server, and to allow scrolling backwards in time. Additional features in the new archive system are planned. [7]

cmlog A distributed error logging system. Includes a logging daemon for each host (Unix and VxWorks), a database server, client logger and browser libraries, a Motif browser, a tcl browser, and (soon) a Java browser. Logging client library supports filtering (suppression of repeating errors). Browser supports interactive suppression of uninteresting errors.

4 CDEV COMPONENTS

CDEV is (1) a standard API for communicating with devices, (2) a C++ framework implementing this API, (3) a Java package implementing a (subset of) this API, and (4) a set of applications and libraries useful in building distributed systems. This section will briefly review the highlights of each, emphasizing recent developments.

4.1 C++ Library

The mainstay of CDEV is a C++ class library for developing both applications and adaptors to additional control systems. The library includes:

- *directory services:* look up devices by name or by type, including wildcard matching; discover at run time supported attributes and messages; get type for given device
- *asynchronous messaging*: high throughput, buffered I/O; callback mechanism, time-outs
- string and composite self describing binary data messages, with support for multiple architectures (byte swapping)
- I/O operation *grouping* and *synchronization*
- *collections,* for operations on vectors of devices, with support for passing the device array intact to the underlying control system for higher performance on some systems
- *virtual I/O:* use of multiple control systems from a single calling interface
- support for EPICS, CLIP (plus others at their sites)
- base class for integrating new control systems
- extensive documentation

4.2 Java Package

The Java package is written in 100% Java, allowing applets to be written to run inside of commercial web browsers. [8] It supports the same calls as in C++ for sending messages to devices, with network support for the CLIP protocol also in 100% Java. The package currently does not include support for groups or collections.

In addition to the Java-cdev package, there is also (in beta form) a graphics library for producing animated displays along the lines of those produced by dm (above).

4.3 tcl/tk

It has been the experience at Jefferson Lab and elsewhere that the *tcl* scripting language and its *tk* graphics toolkit provide an extremely productive environment for rapid prototyping of control applications. [9] Tcl has been interfaced to CDEV, allowing scripts to access the entire control system and accelerator model at Jefferson Lab.

4.4 Network Components

The latest extensions to CDEV include a set of network components useful in building up a large distributed system. These components include:

NameServer Supports the mapping from a named resource to server address and port. A CDEV device may be implemented as a single resource, or as a set of resources on different servers. Communication with the name server is asynchronous and buffered, locating resources 10 times faster than CORBA.

Gateway Allows multiple applications to connect to the control system through a single point, producing only a single connection to any real-time system. Performs protocol conversion from the external protocol (CLIP) to the site-specific protocol. Currently used to connect Java applets to the control system. (See Figure 2.)

Server Shell A skeleton server program which can be used to build a new CLIP server by writing a single routine to handle one message. All connection management and message queueing and routing is handled by the shell. Used to implement the NameServer, Gateway, and the model server Artemis (described in the next section).

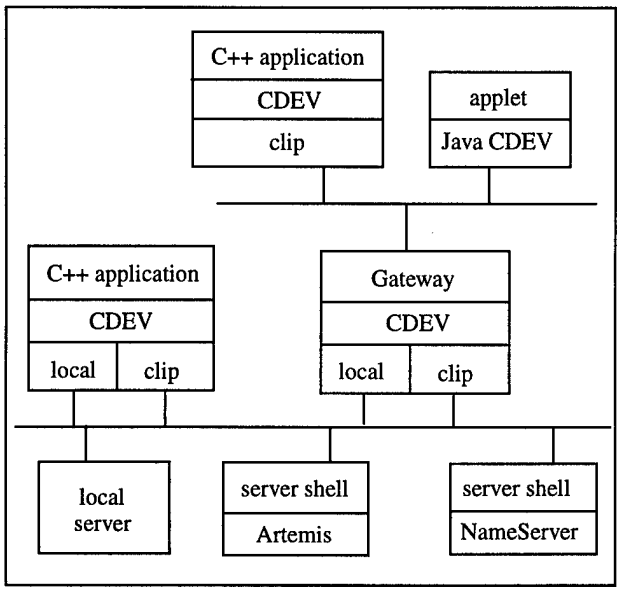

Figure 2: CDEV network components, showing logical network connections for two protocols, with gateway connected applets and applications.

5 ACCELERATOR APPLICATIONS

A certain amount of success has been achieved in the past in sharing beam optics modeling codes, such as MAD, DIMAD, PARMELA, and also analysis codes, such as RESOLVE. These applications are off-line applications with no connection to a control system, yet do represent a notable software sharing success.

Sharing of on-line applications is somewhat more difficult, and has met with only limited success. Much of the lack of success can be attributed to the lack of a common interface to the control system.

5.1 Standards or Conventions Needed

The model design codes mentioned above have been successful in moving from site to site because they provide significant capabilities, while enforcing few constraints upon the users. Each program has a simple naming convention for devices, and for classes of devices, and for attributes of devices. For example, DIMAD defines a quadrupole magnet as something of type "quadrupole" having characteristics "L" (length), "K1" (strength, in $1/m^2$), and "aperture" (radius in meters). Instance names are restricted to eight significant characters, and everything is case insensitive.

These are exactly the types of conventions which need to be standardized in order to allow portable on-line applications -- conventions on names of classes of devices, and conventions upon what capabilities (such as read and write attributes) these devices support.

5.2 CLASSIC

Among recent attempts to standardize the definitions of accelerator objects is the CLASSIC project. [10] CLASSIC is an acronym for Class Library for Accelerator System SImulation and Control. Its goal is to provide:

- a C++ class library for accelerator design, simulation and operation
- a mechanism for C++ code sharing and standardization in the accelerator community, and
- a platform to exchange new ideas in code development.

The collaboration includes SLAC, CERN, FNAL, DESY, Jefferson Lab, and the University of Maryland.

CLASSIC includes a standard input file format with mnemonic type codes for all accelerator elements, memory structures to represent these beamline components and composite beam lines, representations of lattice transfer maps, representations of misalignments, interfaces to algorithms, and an interface to the on-line control system (the plan is to use CDEV). This is still a work-in-progress, with the initial software being tested within the framework of a new version of MAD.

5.3 Unified Accelerator Libraries

UAL [11] is another effort to develop an environment for portable accelerator control applications. One major thrust of this effort is to standardize descriptions of accelerator structures. Unlike the CDEV and CLASSIC projects, UAL does not standardize upon C++ as the programming language, but instead uses the scripting language PERL as the glue to bind together a set of programs in potentially multiple languages into a cohesive system.

At this point, the UAL project anticipates using CORBA as the software bus through which applications will gain access to the control system.

5.4 CDEV Compliant Accelerator Software

In addition to the general purpose utility applications listed in the previous section, there are a small number of accelerator optics applications already finished:

Artemis Artemis is an accelerator beam optics server for simulation and control. [12] It provides first- and second-order transport matrices, beam envelop propagation, and particle ray tracing. It currently uses DIMAD as a back-end, but is adaptable to other modeling engines. It uses CDEV to obtain current lattice settings and to service clients.

Atlast Atlast (AuTomated Lock And Steering Toolkit) is a modular program for beam based energy and orbit corrections. [13] It uses CDEV to monitor beam position monitors, obtain model information, and drive actuators. Multiple algorithms are allowed, with support for SVD and Prosac. [14]

6 SUMMARY

Progress has been made in forming a new multi-lab collaborative effort in high level accelerator applications development. The CDEV framework has been used to support a diverse set of on-line tools, including modified EPICS applications, new utilities, and a small number of beam based applications. Portability of applications between EPICS and non-EPICS control systems has been demonstrated.

New developments at Jefferson Lab, SLAC, and other labs will continue to expand the set of CDEV compliant applications, and the work of affiliated groups like the CLASSIC collaboration will further increase the amount of software runnable at sites supporting a CDEV adaptor.

7 ACKNOWLEDGMENTS

Work supported by the U.S. Department of Energy, contract DE-AC05-84ER40150.

8 REFERENCES

[1] 'Experience with EPICS in a wide variety of applications', M. Kraimer, ANL; M. Clausen, DESY; W. Lupton, KECK; and C. Watson, Jefferson Lab, these proceedings, PAC '97.

[2] 'Panel Session on Software Sharing', 'About the Saturday Workshop', B. Kuiper, ICALEPC 1993 Proceedings, Nucl. Instr. and Meth. in Phys. Res. A 352 (1994) 513–515.

[3] 'An Object-Oriented Class Library for Developing Device Control Applications', J. Chen, W. Akers, G. Heyes, D. Wu, and C. Watson, ICALEPCS 1995 Proceedings. See also http://www.jlab.org/cdev/.

[4] 'Virtual accelerator and fundamental guidelines towards sharable software for accelerator control systems', N. Kanaya, ICALEPCS 1993 Proceedings, 497–500.

[5] Re CORBA, see http://www.omg.org/omg00/wicorba.htm.

[6] Private communication. *StripTool* converted by C. Larrieu, Jefferson Lab; *alh* by Janet Anderson, Argonne National Lab.

[7] 'Design of a new EPICS archive system' presented at the Vancouver spring 97 EPICS collaboration meeting by Matt Bickley.

[8] 'A Java Package for Building Client Applets to Access TJNAF Accelerator Data Across the Internet', C. Quach, master's thesis, Christopher Newport University, 1997.

[9] 'Rapid Application Development Using the Tcl/Tk Language', J. van Zeijts, PAC 1995 Proceedings, Vol. 4 p. 2241.

[10] 'The Classic Project', F. C. Iselin, Computational Accelerator Physics Proceedings, 1996, 325–330.

[11] 'Unified Accelerator Libraries', N. Malitsky, R. Talman, Computational Accelerator Physics Proceedings, 1996, 337–342.

[12] 'The Use of Artemis with High Level Applications', B. Bowling, H. Shoaee, S. Witherspoon, ICALEPCS 1995.

[13] "Design and Implementation of a General Slow Orbit Control Package atJefferson Lab", J. van Zeits et al., this conference.

[14] 'Prosac Algorithm', Y. Chao, CAP 96, 319.

EXPERIENCE WITH EPICS IN A WIDE VARIETY OF APPLICATIONS

Martin R. Kraimer
Argonne National Laboratory, 9700 South Cass Ave., Argonne, Illinois 60439
Matthias Clausen
Deutsches Elektronen Synchrotron (DESY), 85 Notkestrasse, Hamburg, 22603, Germany
William Lupton
W. M. Keck Observatory, 65-1120 Mamalahoa Highway, Kamuela, Hawaii 96743
Chip Watson
Thos. Jefferson National Accelerator Facility, 12000 Jefferson Ave., Newport News, Virginia 23606

Abstract

Currently more than 70 organizations have obtained permission to use EPICS, a set of software packages for building real-time control systems. In this paper representatives from four of these sites discuss the reasons their sites chose EPICS, provide a brief discussion of their control system development, and discuss additional control system tools obtained elsewhere or developed locally.

1 INTRODUCTION

The Experimental Physics and Industrial Control System (EPICS) [1] is currently in use at over 70 sites in Asia, Europe, and North America. It is used in accelerator facilities, astronomy, commercial industry, and industrial research. EPICS is the successor to the Ground Test Accelerator Control System (GTACS) that was developed at Los Alamos National Laboratory (LANL). EPICS resulted from a collaborative effort between the GTA controls group and the APS controls group. Over the last few years other sites have started using EPICS and contributing to its development.

Since EPICS is a collection of software components that can be used to develop a control system rather than a "turnkey" system, each site normally extends EPICS at the low level—i.e., custom record, device, and driver support—and adds support for high-level applications. This paper describes how four sites have used and extended EPICS.

2 ADVANCED PHOTON SOURCE

The Advanced Photon Source (APS) is a third-generation synchrotron light source located at Argonne National Laboratory. With regards to APS, this paper discusses the following: 1) APS/LANL cooperative development on input/output controller (IOC) software, 2) APS/LANL cooperative development on general-purpose high-level tools, 3) implementation of the APS accelerator control system, and 4) high-level applications developed by the APS accelerator physicists.

2.1 APS/LANL Cooperative IOC Software Development

During the last three months of 1989, APS evaluated GTACS by having a member of the controls group study the code and give tutorials explaining what he was learning. Most of the time was spent evaluating both the code which runs in the IOCs and Channel Access [2], the code which provides network-independent access to the IOCs. The result was a decision to use GTACS to build the APS control system. APS and LANL agreed to start cooperative development on improvements and on new general-purpose high-level tools [3].

While studying the GTACS code, APS identified many places where improvements could be made. The most important was the ability to add new record, device, and driver support without modifying core software. Although LANL also wanted the same or nearly the same improvements, GTA had already started commissioning and the GTA developers did not have time to implement these improvements. At that point the LANL and the APS staffs met and agreed on a design. APS then implemented the changes with input from LANL.

During the early years a lot of new hardware support was developed. If support for a device was developed at one site it was normally used at the other site. Improvements were folded into the common system. A VXI resource manager was implemented at LANL and used extensively at both sites. GPIB support was developed at APS and used at both sites. There was almost no duplication of effort in any area from Channel Access down to the device/driver software.

2.2 APS/LANL Cooperative Development on General-Purpose High-Level Tools

APS and LANL jointly decided on high-level tools which were needed but not yet available. The first tools to be developed were a general-purpose display manager/editor, an alarm handler, and an archive tool.

At that time a display manager/editor already existed but it ran only on VAX/VMS using a proprietary windowing system. LANL had already started design of an X-based replacement. When LANL/APS agreed to cooperate, the one point on which agreement could not be reached was whether this tool should be built directly on Xlib or on Motif. LANL, for performance reasons, wanted just Xlib. APS, for ease of development, wanted Motif. The end result is that two display managers/ editors were developed and are being used successfully. Each EPICS site normally chooses only one.

0-7803-4376-X/98/$10.00 © 1998 IEEE

The alarm handler tool was proposed and designed by APS, LANL reviewed it before development was started, and APS developed the tool. It is used at most EPICS sites.

The archiver was designed and implemented at LANL, reviewed at APS before development began, and implemented at LANL. It is used at many EPICS sites. Archiving is a difficult and many-faceted subject. Some EPICS sites use the LANL-developed archiver but many sites use other archive tools. New archive tools are currently being considered by several EPICS sites.

2.3 Implementation of the APS Accelerator Control System

The accelerator control system currently has 165 IOCs containing approximately 160,000 records. The main control room (MCR) has 10 Ultra Sparc workstations each equipped with two video monitors. The control system network has ten satellite hubs which are dual connected to a central hub using FDDI. Each IOC is connected to two hubs using a redundant fiber Ethernet transceiver. Each MCR workstation is connected via FDDI to a network hub.

The APS accelerator control system was developed by control engineers using the EPICS-supplied toolkit. The controls group assigned engineers to subsystems based on the APS technical groups, i.e. linac, rf, diagnostics, power supplies, and vacuum. For each subsystem one engineer was assigned overall responsibility for all controls-related activities, i.e., hardware and software. This engineer interacted closely with the group responsible for the subsystem itself. For example, the engineer discussed requirements with the people in the group, attended group meetings, etc. Controls group engineers are responsible for all controls-related activities from engineering-related display screens to the hardware that interfaces to the equipment.

In addition to EPICS-supplied support, the control engineers needed custom record, device, and driver support for their IOCs. Although they sometimes asked the APS EPICS developers for help, they developed most of the support themselves, implementing 13 special record types, 48 device support modules, and 2 drivers. In addition, a number of sequence programs and subroutines for the subroutine record were written.

The APS controls system makes extensive use of GPIB devices. BITBUS is used as a low-level subnet. Many of the special record and device support modules were created for GPIB and BITBUS devices. One of the EPICS tools developers created general-purpose GPIB support and helped with the BITBUS driver, but the rest of the support was developed by the control engineers.

An APS-developed event system, consisting of VME event generators and event receivers interconnected with 100-Mbaud fiber optic links, provides the means of distributing medium resolution/accuracy timing events throughout the facility. Special record support was developed to integrate the event system with EPICS, including the ability to synchronize time stamps across IOCs.

Other major APS control applications developed using the EPICS toolkit include fast timing, BPM control and monitoring, charge and current monitors, and the orbit feedback system.

2.4 High-Level Applications Developed by the APS Accelerator Physicists

The APS accelerator physicists have developed a set of high-level tools grouped under the collective name of Self Describing Data Sets (SDDS). The SDDS toolkit can read and write data in EPICS database records. Though most of the applications do rather simple operations, the combination of these and others from the SDDS postprocessing toolkit allow arbitrarily complicated analysis of data and control of the accelerators at the Advanced Photon Source. These tools are general and can be applied to devices other than accelerators under control of EPICS.

Initially adopted for complex physics simulation programs, it was clear that the SDDS file protocol would excel in data-collecting software as well. Typically, an EPICS tool would write EPICS data to an SDDS file with each readback written to a column of names corresponding to the EPICS database record name. Single value data that describe the experimental conditions might be written to the file as parameters. Once collected, the EPICS data can be further analyzed and plotted with any of the SDDS tools. One can regard the SDDS tools as the layer between the EPICS control system and more functional analyzing tools and scripts, with SDDS protocol files as an intermediary.

The various tools are joined together via a scripting language, originally C shell, now Tcl/Tk. Most of the accelerator physicists can write Tcl/Tk scripts to diagnose problems or to solve new controls problems. Before new control strategies become operational, a Tcl/Tk-based tool is prepared for use by operations.

3 DEUTSCHES ELEKTRONEN SYNCHROTRON (DESY)

Shortly after commissioning the HERA (Hadron-Electron Ring Accelerator) storage ring it was obvious that some of the components developed for the cryogenic control system needed immediate performance and reliability improvements (the MKS-2 group is responsible for the cryogenic systems). One major problem was related to random crashes of one of the subsystems responsible for transfer and conversion of data between the in-house fieldbus called SEDAC and the cryogenic process control system. It was obvious that the replacement component should not only match the requirements for this special application but also open the door to a new standard of control applications tools. In 1993 EPICS was chosen because of its process control and record-oriented structure.

3.1 Conversion of Cryogenic System to EPICS

Along with EPICS, a new UNIX operating system environment (replacing VMS) and VxWorks real-time kernels (instead of iRMX) had to be learned within six months in order to replace the existing subsystem. From installation of the various software packages to the start of the first running period of an EPICS system at DESY took about eight months. The HERA cryogenic controls system must be extremely reliable because the superconducting magnets run 24 hours a day, every day for at least six months at a time. The first EPICS system met these stringent requirements and was considered an unqualified success.

Once the EPICS IOCs were in operation, it was possible to make use of the new freedom these systems provided the system designers and the operators. Online access to all the individual data was now possible as well as the chance to establish new ways of archiving process data for long-term storage. This led to the first new development for the EPICS system. An archive record, the archiver (still under VMS), and a viewer (based on IDL) were programmed to improve the quality of the archived data, storing on significant change instead of at a fixed time (i.e., every 60 sec). The analysis of problems was now possible with a much higher resolution than before. In addition, other EPICS tools such as display managers (first edd/dm, later medm) became so popular that the operators became involved in the process.

3.2 DESY Utilities

The next major use of EPICS at DESY was for monitoring utilities. The installed system of Siemans program logic controllers (PLCs) had improved the stability of HERA operations; however, it lacked adequate operator interfaces and tools like an archiver and alarm handler. In addition, the distributed nature of the installation necessitated that displays be distributed throughout the DESY site and into the halls of the 6.3-km-long HERA tunnel. EPICS was chosen to provide these services. The initial goal was to provide tools to the utilities group that would enable them to create their own environment for supervisory control. Students were trained to create hundreds of graphic screens. Special tools (scripts) were prepared to create EPICS databases from the PLC configuration databases. But the most difficult job was preparing the interface to the H1 network of the PLCs. Nearly half a man-year was spent writing the software to interface H1 and the common driver interface (CDI), which is DESY-developed software that provides an easy-to-use EPICS interface to various fieldbuses.

This system has grown continuously since it began operation. Even more important than this growth is the acceptance of the new control environment by the operators who, until EPICS arrived, had not had any contact with computer-based controls. The HERA water system is now monitored by engineers who use the archive viewer to supervise their water pumps and to tune their control loops.

Recently new systems went into operation to monitor the quality of DESY's main power supply. Three 10-kV transformers are monitored to catch any power glitch and freeze the current reading into an EPICS waveform record, which is then read by an archive process and stored in a raid array for later analysis.

In addition to the supervisory controls for the HERA water systems (based on H1 communication) another fieldbus, Profibus, is supported. Profibus is a German standard widely used for small- and medium-sized PLC applications. At DESY the Profibus-based PLCs control the air condition systems and small general-purpose systems. An EPICS interface was quickly implemented due to experience gained on the previous work.

3.3 Collaboration with Other Institutes

In addition to the utilities group, the machine controls and process controls groups were demanding more support from the MKS-2 group. The modular nature of the EPICS toolkit made it possible to distribute the various jobs to collaborators outside DESY like the Institutes of High Energy Physics in Protvino, Russia and Beijing. China. DESY staff trained the new collaborators in order to coordinate the work and reintegrate the new software into EPICS. Thanks to their excellent collaborative efforts, many new features were developed and are now in operation. One of these areas was the controls for the magnet power supplies for the Tesla Test Facility (TTF) which is the test bench for the next generation of linear colliders at DESY based on superconducting cavities.

To implement the TTF cryogenics controls, several functions necessary for process controls, such as the PID algorithm, had to be added or modified in the EPICS toolkit. All these modifications have been in operation for several months and are providing stable operations for TTF cryogenics.

3.4 ORACLE

The need to handle EPICS databases for multiple IOCs and different versions of databases for different EPICS releases was the driving force behind creation of a relational database for configuring and storing record information. An ORACLE database was designed to support both the old report structure and the new ASCII type of EPICS databases. The interface to configure individual records as well as record prototypes and prototype record groups was written in ORACLE-Forms to facilitate configuration of complete databases without requiring in-depth knowledge of the record structures. New records are created by merely supplying default values.

In operation since February 1997, this tool is the basis for a new phase of database generation at DESY since it is now possible to train people quickly. The database functionality was recently expanded to integrate configuration data for the alarm tools and the global database structure

following the idea that a record belongs to a *device* within a *location* of a *facility*. This type of information can also help generate information for the CDEV API from Jefferson Lab (see section 4), a feature that is attracting growing interest at DESY.

Cryogenic operators without any knowledge of the EPICS control architecture are now preparing the EPICS database, creating graphics, and providing the information to create sequence programs. This would not have been possible without the ORACLE-based record configuration tools.

3.5 Current and Future EPICS Projects

Another project that is nearly finished is providing EPICS services to PC-based fast ADC boards. This will allow access to PC-based information from any X-terminal or PC. In addition, the data stored in the ADC boards will be written to the central raid-array so that everyone can retrieve the data.

While the above-mentioned projects are relatively small, the next big project is in the planning phase: The original process control system for the HERA refrigerator will be phased out within the next two to three years. The replacement time schedule will be very tight. Thousands of lines of sequence programs will be converted into the native EPICS language of the sequencer; the internal structures of the DDC controls will be converted into EPICS records; and the functionality of the partly redundant processors will be analyzed and, if necessary, implemented for the IOCs.

The network is based on distributed Ethernet switches on an FDDI backbone. The Ethernet workstation connections are evolving towards switched 100baseT connections, again on the FDDI backbone.

EPICS installations at DESY are still growing because of the reliability and rich functionality of its software. The software distributed to the collaborators is very stable and can be used for production after making local modifications, and the collaboration provides help and support for all installed software. Common development efforts, such as the joint Argonne-DESY- CERN improvements to the medm graphical user interface, are made known to a wide audience.

4 THOMAS JEFFERSON NATIONAL ACCELERATOR FACILITY

Thomas Jefferson National Accelerator Facility (Jefferson Lab, formerly CEBAF) made a decision to adopt EPICS, following an extensive review of its control system, in 1993. At that time it was recognized that the in-house-developed TACL control system would have difficulty scaling up to full machine operation without extensive work, and it was decided that there would be immediate and long-range advantages in joining the EPICS collaboration [4]. Conversion began in the midst of accelerator commissioning.

As much of the existing control system (over 90%) was CAMAC-based, Jefferson Lab quickly implemented support for CAMAC based I/O devices, using the IEEE standard 758-1979 to define the interface between EPICS and an arbitrary CAMAC interface. This allowed the use of existing IEEE-compliant software device drivers available for parallel crate controllers. Further development of IEEE routines for a CAMAC serial highway interface allowed integration of the remaining I/O.

In migrating from TACL to EPICS, much of the design of the original system was preserved, and support for CAMAC interrupts was not needed (i.e., not used in the original system and not implemented in the conversion). The following year, LANL modified the CAMAC driver for the serial highway to add support for interrupts and for multiple serial highways (controllers). Jefferson Lab further extended CAMAC capability by adding support for multiple processors sharing a single serial highway for compute-bound configurations.

Over the past three years, a wide variety of hardware has been integrated into the control system, including GPIB, VME, and RS-232 devices. In most cases this has required writing additional device drivers; in approximately 15-20% of the cases device drivers were obtained from the EPICS community. EPICS has proved very flexible in this regard.

Because CEBAF was further into its commissioning schedule than APS, it was the first site to scale EPICS up to a single integrated system with tens of thousands of database records, hitting the 100,000 mark in 1994. With only a few minor problems, this more than tenfold increase in the size of the largest system was accomplished smoothly, giving every indication that an additional order of magnitude is achievable.

The current configuration of the control system contains 70 IOCs and 160,000 records providing an interface to 50,000 hardware I/O points. Compared with APS, Jefferson Lab has fewer single-board computers (by more than a factor of 2), and has consequently had to deal more with loading issues (this is partly budget driven, as this is the second control system for a relatively young site). Many problems were encountered in the first two years related to poor behavior of the EPICS software under low memory conditions. This has been solved with additional memory and some software improvements. Some remaining problems still under investigation may be related to CPU loading and/or network loading.

4.1 Accelerator Controls

The EPICS toolkit is quite flexible and is not specific to accelerator operations. It provides extremely flexible name-based control of a wide variety of hardware I/O points. Much of the work done by the controls group at Jefferson Lab has been in adding accelerator-specific software on top of, and alongside of, EPICS.

Due to the time pressure of ongoing accelerator commissioning in 1994-1995, it was necessary to rapidly pro-

duce a handful of accelerator applications to provide high-level accelerator setup and control. In particular, beam steering, linac optics setup, cavity phase cresting, and machine settings management were urgently needed. In order to provide operator-friendly tools, the Tcl/Tk scripting language and its graphics library were adopted. An interface between Tcl and the EPICS channel access network library was implemented, and this provided the basis for a rapid prototyping environment with name-based I/O and full graphics support [5].

Experience with this environment is extremely positive. While some of the more demanding applications, such as beam feedback and an online accelerator model, have been rewritten in C++ to improve performance and capability, additional Tcl- based tools continue to be written. The most recent work includes an automated turn on of the entire injector, written by the accelerator operations group (not software engineers), and an accelerator optics tuning package which looks at the Courant-Snyder invariant as a function of beam pathlength.

In creating these accelerator control applications, it was unavoidable that work done at other laboratories was to some extent duplicated. Several attempts were made to port software from other systems to Jefferson Lab, but most online applications had too many dependencies upon the other laboratories' control systems (non-EPICS). This was one of several motivations in creating a new framework for control system applications called CDEV [6]. Additional motivations include isolating high-level applications from the details of the low-level control system implementation, and organizing named I/O points into devices.

CDEV is a C++ and Java framework for developing device control applications and provides a definition of a virtual control system which is independent of local implementation. It allows applications to be shared between EPICS sites like Jefferson Lab and APS, and non-EPICS systems such as SLAC and CERN. One unique feature of CDEV is that it supports multiple protocols (concurrently, if desired), and in particular it includes support for the EPICS channel access protocol, allowing CDEV applications to access EPICS-named variables through a device-oriented API. CDEV has also been shown to map well onto the SLAC and CERN/PS control systems.

A small number of new CDEV applications have been written at Jefferson Lab (e.g., beam steering, a correlation measurement package), and a few of the EPICS applications have already been modified to call CDEV instead of Channel Access (stripTool converted at Jefferson Lab, alarm handler at APS, display manager an ongoing joint project between LANL and Jefferson Lab). As these tools are finished, they may be used immediately at CERN and other non-EPICS sites which have implemented the CDEV adapter.

It is hoped that as this suite of control system-independent accelerator applications grows, additional non-EPICS sites will contribute to creating a reusable suite of high-level accelerator control software [7].

For some of the non-hardware portions of the control system (e.g., on-line accelerator model, error log, and archive data log query processing), the "software bus" used in EPICS does not provide a sufficiently rich protocol, and Jefferson Lab has implemented an additional message oriented protocol under CDEV for these applications. The protocol is also implemented in Java, allowing Web-based applets full live access (typically restricted to read-only) to all control system data through a gateway program on the Web server.

A final significant area of accelerator-specific developments is a fast feedback system for beam energy and orbit corrections [8]. This system may eventually provide feedback at more than 2 kHz to fully suppress observed 60-Hz and 180-Hz noise. Feedforward is also under investigation. A prototype state space formalism-based tool has been implemented which executes at 60 Hz, with plans to scale this to 540 Hz in the next six months. These speeds are outside of the range at which EPICS is an appropriate solution, and the current implementation uses separate tasks running on the same processor as EPICS (a separate processor may be used for highest rates). These tasks are controlled and monitored through EPICS, allowing a uniform view of this mixed system. Early performance results are quite encouraging.

4.2 Physics Controls

EPICS is also being used in the control of the three major physics detectors at Jefferson Lab. The data acquisition system CODA is also accessible through CDEV, and joint development projects between the accelerator and physics divisions on the use of EPICS and CDEV are further improving software reuse within the extended EPICS community. The most recent development in this area is a new error message logging facility co-developed by these two teams.

5 KECK OBSERVATORY

The W. M. Keck Observatory operates the twin Keck 10-meter optical telescopes on the summit of Mauna Kea in Hawaii. Both telescopes have identical control systems, entirely implemented using EPICS [10].

The Keck I telescope was commissioned in 1992 using an in-house control system. This system was functional but had various problems and was hard to extend. When the Keck II telescope was funded in early 1994, it was decided not to propagate the Keck I system to the new telescope but instead to produce a new control system that would scale to the planned future use of the two telescopes for optical interferometry. Since EPICS had already been selected by the Gemini 8-meter telescopes project, and there was already interest in EPICS throughout the astronomical community, it made sense to consider it for the Keck II control system.

Various low-level design studies were carried out in 1994 and the formal decision to use EPICS was made at a design review in March 1995. Development proceeded rapidly (with much help from LANL staff) and Keck II saw "first light" in January 1996, becoming fully operational in October 1996. Keck I was retrofitted with the new control system in March 1997 and both telescopes are now (independently) running identical software versions.

Unlike the accelerators described elsewhere in this paper, the Keck EPICS systems have relatively small numbers of IOCs, records, and I/O points. Each telescope currently has three IOCs, with about 2000 records total per telescope, of which about 850 are attached to hardware. In contrast to many accelerator systems, there is little duplicated hardware and a lot of algorithmic code runs on the IOCs, both in subroutine records (including two extended versions of the subroutine record supplied by the Gemini project) and in custom records (thirteen custom records have been implemented in-house).

In addition, EPICS is being used for the Keck adaptive optics program, which will add two or three IOCs per telescope. Looking further into the future, it will also be used for coordinating the two telescopes and several outrigger telescopes as an optical interferometer.

5.1 EPICS for Telescope Control

The main telescope control servo runs at 40 Hz, a low enough frequency to permit standard EPICS record processing to be used for reading hardware and performing the necessary encoder and servo processing. This processing has many inputs and outputs and it was decided early on that it would be necessary to write custom records with many fields. (Even if the new genSub record had been available at the time, it is probable that the same number of custom records would need to have been written.)

The time interval between the timing pulse that latches the telescope encoders (and triggers EPICS record processing) and the velocity demand being written to the drives is termed the critical region. This critical region is required to be less than 1 ms. In order to achieve this specification, the custom records use precalculated coefficients to perform critical processing as fast as possible and then forward link to the next record in the chain. Once critical processing is complete, the coefficients for the next iteration are calculated. As downstream records finish processing, the records that forward linked to them continue with their noncritical processing.

The main telescope control described above accounts for five of the thirteen custom records. Five more are used for the "pointing code," the rigorous astrometry that determines where the telescope should be at a given time. The three remaining records handle some standard conversions that, while logically appropriate for subroutine records, require more inputs and outputs than can be handled by such records.

In the early days, several LANL contractors wrote EPICS device and driver support for devices not already supported by EPICS. One generally-applicable product which has resulted is drvAscii/sioSup, which uses a C printf()-like format string in a record's PARM field to describe a prompt and an expected response. This allows control of many serial devices without having to write any C code (and is similar in concept to the ANL generic GPIB support).

5.2 Use of Standard EPICS Tools

Nearly all databases are generated using Capfast; there are still one or two snippets that use the LANL DCT tool or which are hand-edited in the ANL .db format. Experience with Capfast has in general been positive: the end result is wonderful but the drawing tool causes some gnashing of teeth.

At first, the LANL display manager was used extensively. However, use of Tcl/Tk and the commercial dataViews package—interfaced via the Keck-specific KTL library (described below) to Channel Access—for user interface screens is increasing. DM continues to be used primarily for engineering screens.

The EPICS alarm handler and archiver have been used extensively, and both have been invaluable. There have been some user acceptance problems with the alarm handler but this is probably due to insufficient attention being given to the configuration files. The m4 macro processor is used to combine subsystem alarm handler configuration files into a single telescope-wide file.

5.3 Locally-Developed Tools

Keck is only partially an EPICS shop. Owing to the freedom afforded the university groups who build its instruments, several different messaging systems and control APIs are in use. In order to alleviate this problem, the Keck Task Library (KTL) [11] API was defined in 1991. KTL shares some features with CDEV in that the API is independent of the underlying services and an internal API permits run-time activation of shareable libraries containing service-specific code. Like CDEV and Channel Access, all I/O is name-based, an object being identified by a service name (which identifies the shareable library) and a service-specific keyword name. Keck requires all telescope and instrument subsystems to provide a KTL library; as with CDEV, this permits KTL applications (mostly GUIs) to use a single API to control multiple heterogeneous underlying systems. Recent GUI development has used a Tcl/Tk/KTL extension called KTCL.

The EPICS archiver can log binary data at high rates and is used for collecting 40-Hz servo data. This data is imported using arrIDL (described below) and analyzed using IDL. The archiver can also log ASCII data at specified intervals but this produces files which are verbose and hard to handle. To address these difficulties, a simple archiver (EZAR) was written. EZAR can log both events and periodically sampled data in a comma-separated ASCII format. It is useful where ease of access to archived data is more important than efficient collection of the data.

The ANL BURT tool was evaluated as a means of loading and restoring calibration data. However, it seemed more sophisticated than warranted by Keck requirements and instead a simple PVLOAD tool was written. PVLOAD parses a file of EPICS channel assignments (including support for array-valued fields) and then uses Channel Access to set the values. A complementary PVSAVE tool is planned but has not yet been implemented.

Sequence programs are used for managing complex interactions such as subsystem initialization and fault handling. They are also used, at a higher level, for managing groups of subsystems. When implementing the latter, it was necessary to add a feature to the sequencer program to permit queueing of Channel Access monitors. This change will be made available to the EPICS Consortium.

Finally, IDL is used extensively for the analysis of engineering data. Accordingly, an EPICS extension to import EPICS archiver data into IDL has been written. This extension, arrIDL, is based on the C code from the LANL arrtk extension.

6 CONCLUSIONS

As shown in Table 1, EPICS has been successfully used to implement controls for medium to large facilities. APS, TJNAF, and Keck are using EPICS for most of their controls. DESY is using it mainly for cryogenic controls and facility monitoring.

Each site uses the same EPICS core, but has implemented special low-level software to communicate with hardware and/or fieldbuses connected to other control systems. The EPICS design makes it easy to add such support without having to modify the EPICS core.

Similarly, each site has developed high-level software that exists above the EPICS core software; the existence of the Channel Access client library has made this possible.

Table 1: Control System Sizes

	APS	DESY	TJNAF	Keck
# of Workstations	~10	~8	~10	~6
# of IOCs	165	31	70	6

7 ACKNOWLEDGMENTS

The work at Argonne was supported by the U.S. Department of Energy, Office of Basic Energy Sciences, under Contract No. W-31-109-ENG-38.

The W. M. Keck Observatory is operated as a scientific partnership between the California Institute of Technology and the University of California. The observatory is made possible by the generous financial support of the W. M. Keck Foundation.

The work at TJNAF was supported by the U.S. Department of Energy, under Contract No. DE-AC05-84ER40150.

8 REFERENCES

[1] L. R. Dalesio et al., "The experimental physics and industrial control system architecture: past, present, and future," Proc. of ICALEPCS '93, Berlin, Germany, *NIM A* **352**, pp. 179-184, (1994).

[2] J. O. Hill, "Channel Access: A Software Bus for the LAACS," Proc. of ICALEPCS '89, Vancouver, British Columbia, Canada, *NIM A* **293**, pp. 352-355 (1990).

[3] L. R. Dalesio et al., "Distributed Software Development in the EPICS Collaboration," Proc. of ICALEPCS '95, Chicago, Illinois, pp. 360-366 (1997).

[4] W. A. Watson et al., "The CEBAF accelerator control system: migrating from a TACL to an EPICS based system," Proc. of ICALEPCS '93, Berlin, Germany, *NIM A* **352**, pp. 118-121 (1994).

[5] J. van Zeijts, "Rapid Application Development Using the Tcl/Tk Language," Proc. of the 1995 PAC, pp. 2241-2243 (1996).

[6] J. Chen et al., "CDEV: An Object-Oriented Class Library for Developing Device Control Applications," Proc of ICALEPCS '95, Chicago, Illinois, pp. 97-104 (1997).

[7] W. Watson, "A Portable Accelerator Control Toolkit," these proceedings.

[8] M. Chowdhary et al., "A Fast Feedback System for CEBAF," Proc. of ICALEPCS '95, Chicago, Illinois, pp. 429-434 (1997).

[9] W. Lupton, "Software Infrastructure for the Keck II Telescope," in Telescope Control Systems, Proc. of SPIE, Vol. **2479**, pp. 140-151 (1995).

[10] W. Lupton, H. Lewis, K. Tsubota, A. Honey, S. Quady, "The Keck II Telescope Control System," Optical Telescopes of Today and Tomorrow, Proc of SPIE 1996 (to be published).

[11] W. Lupton, A. Conrad, "The Keck Task Library (KTL)," ADASS '92, PASP Conference Series **52**, pp. 315-319 (1993).

THE PROCEDURE EXECUTION MANAGER AND ITS APPLICATION TO ADVANCED PHOTON SOURCE OPERATION

M. Borland
Advanced Photon Source, Argonne National Laboratory
9700 South Cass Avenue, Argonne, Illinois 60439 USA

Abstract

The Procedure Execution Manager (PEM) combines a complete scripting environment for coding accelerator operation procedures with a manager application for executing and monitoring the procedures. PEM is based on Tcl/Tk, a supporting widget library, and the dp-tcl extension for distributed processing. The scripting environment provides support for distributed, parallel execution of procedures along with join and abort operations. Nesting of procedures is supported, permiting the same code to run as a top-level procedure under operator control or as a subroutine under control of another procedure. The manager application allows an operator to execute one or more procedures in automatic, semi-automatic, or manual modes. It also provides a standard way for operators to interact with procedures.

A number of successful applications of PEM to accelerator operations have been made to date. These include start-up, shutdown, and other control of the positron accumulator ring (PAR), low-energy transport (LET) lines, and the booster rf systems. The PAR/LET procedures make nested use of PEM's ability to run parallel procedures. There are also a number of procedures to guide and assist tune-up operations, to make accelerator physics measurements, and to diagnose equipment. Because of the success of the existing procedures, expanded use of PEM is planned.

1 INTRODUCTION

The motivation for creating PEM is the observation that many accelerator operations take the form of written or memorized procedures. It is not unheard of for accelerator operators to control a sophisticated accelerator with the guidance of a checklist written on paper. While this works, it is a long way from being automated. Sometimes automation of an activity is hampered by lack of computer control of a part of the facility or by the difficult nature of the equipment being controlled. Even in such cases, a combination of automatic and manual steps can often be used to produce partially automated operation. This partially automated procedure can include instructions to and advice for the operator and, as such, will result in a greater uniformity of operation. For example, some PEM scripts used at APS will set up a diagnostic device, then ask the operator to perform a specific tuning operation that would be difficult if not impossible for a computer to perform with current technology.

PEM's ability to execute procedures in parallel was similarly developed from the observation that often times several operations can be done simultaneously. For example, one can standardize DC magnets while warming up pulsed power supplies. With a small system, this can be done manually. However, with a large system this becomes difficult, and operators tend to do things somewhat sequentially, with attendant loss of time. For this reason, a design goal for PEM was to allow parallel procedure execution.

Finally, many procedural activities have individual steps that are themselves procedures. These steps may in some circumstances be performed separately as a standalone procedure. Based on this observation, another design goal for PEM was that any procedure should be easily embeddable within another.

Given that some procedures require human input and guidance, even while largely automated, PEM has three modes in which it may execute a procedure. *Automatic* mode accepts no human input at any point. *Semi-automatic* mode accepts human input at the beginning of a procedure, in order to allow selection of options and changing of parameters. *Manual* is like *Semi-automatic* except that at each defined step of the procedure the user must press a button indicating that he wants to proceed. A procedure that is called from within another procedure is run in *Automatic* mode, thus removing any user interaction. In this case, the calling procedure is responsible for providing input to the called procedure in place of human input. PEM procedures may switch modes internally to circumvent this, but it is uncommon and is discouraged.

Another principle underlying the creation of PEM is the desire and need to separate the interface from the algorithm, in order to make higher-level automation possible. For example, some storage ring facilities use orbit correction algorithms that are embedded in a graphical user interface, making it impossible to automate. Orbit correction and beamline steering at APS [1,2] are performed from several graphical user interfaces (GUIs) (including PEM), all of which use a common generic feedback program to execute the actual correction. This feedback program has no GUI and is used not only for orbit correction but for other tasks that are mathematically identical. The PEM orbit steering procedures also use Tcl/Tk library routines that are shared with various GUI applications.

When a developer creates a new PEM procedure, he does not create a GUI. PEM provides a GUI, as well as mechanisms for determining what mode the interface is in, so that procedures may run outside of a GUI environment. Typically, the developer of even a complicated PEM procedure will only create an initialization dialog box. This dialog box will appear only when the procedure is run in the proper context (i.e., by a person).

2 PEM OPERATOR INTERFACE

The PEM manager GUI consists of five areas. The first is a scrollable text window for status and error message reporting. The second is a scrollable list of available procedures. The third is a scrollable text box used to display detailed information about individual procedures.

0-7803-4376-X/98 /$10.00 © 1998 IEEE

The fourth is a scrollable list of currently executing procedures. Finally, there are various buttons that select execution mode, lock and unlock execution, start procedures, and abort procedures.

PEM is configured by a file that contains a list of procedure names, along with optional arguments that specify default values for the procedure. These arguments are specified using a convention given in the next section. From this configuration file, PEM creates a procedure selection list. Clicking on the name of any procedure in this list causes the manager application to display information about the procedure, if the programmer has supplied any.

Prior to executing a procedure, the user may select the execution mode, i.e., *Automatic*, *Semi-Automatic*, or *Manual*. The manager application also features an execution lockout that reduces the chance of accidentally executing a procedure. Once a procedure has been selected, the mode chosen, and the lockout released, the user clicks on the **Execute** button to execute the procedure. Following this, PEM launches a subprocess to execute the procedure. The name of the subprocess appears in a list of executing processes that is part of the manager window. The user may select any process from this list and abort it using the **Abort** button on the manager window.

PEM automatically creates an execution dialog to show the progress of the subprocess. Except in *Automatic* mode, the subprocess automatically displays an initialization dialog if one has been set up by the programmer; this is described below in Section 3.2. The execution dialog has its own scrollable text window for status output, as well as a scrollable area showing the names of the procedure steps as they are executed (again, except in *Automatic* mode). These names are coded green when being executed and red when halted for user interaction. The dialog has a **Continue** button and **Done** button that are used in *Manual* mode to proceed from step to step and to acknowledge termination of the procedure. There is also a button to acknowledge errors.

3 PEM PROGRAMMING FACILITIES

PEM provides a number of facilities for creation of procedures [3]. All PEM procedures are written in Tcl/Tk and may be used outside of PEM like any other Tcl/Tk code. Because we have many other Tcl/Tk procedures, we distinguish PEM procedures with the letters **Mp** (Machine procedure) in the name. The **Mp** designation indicates either that a procedure is part of the PEM environment or it uses aspects of that environment. The PEM environment defines several procedures that the programmer invokes when writing machine procedures. Among these are **APSMpStep**, **APSMpParallel**, **APSMpJoin**, **APSMpAbort**, and **APSMpInterface**. These procedures and other aspects of the PEM development environment are described below.

3.1 Argument Passing

In order to make Tcl/Tk procedures easier to use and upgrade, we have adopted a procedure calling convention. A procedure call is always of the form: *procName* [*fixedArgs*] [*variableArgs*], where items in square brackets may be absent for any particular procedure. *fixedArgs* are arguments that must be given in an established order; not doing so will result in a Tcl error. *variableArgs* are always optional, may come in any order, and take the form of tag-value pairs, specifically *-tag value*. The vast majority of procedures have only variable arguments in order to enhance code readability.

3.2 Initialization Dialogs

As described above, PEM's interaction with the user is context-dependent. At the beginning of each PEM procedure, the programmer inserts an **APSMpStep** with an **init** tag and the name of a procedure (the "initialization" procedure). In *Manual* and *Semi-Automatic* modes, PEM executes the initialization procedure, which typically brings up a GUI dialog to allow the user to specify initial parameters for execution of the main procedure. If a PEM procedure is called by another PEM procedure, the mode is set to *Automatic,* and hence the initialization dialog is never invoked. Instead, the calling procedure is responsible for providing proper initialization for the called procedure. The argument-passing mechanism discussed in the previous paragraph is important here, since it allows a procedure to be called with only the arguments needed in a given context. When a procedure is executed as a subroutine, it is generally supplied with a large number of arguments to substitute for the parameters normally supplied by a user.

3.3 Labelling of Steps

The second function of **APSMpStep** is to permit labeling of sections of a procedure, in order to define steps within the procedure. A step may comprise any number of actual operations. When a procedure is invoked in *Manual* and *Semi-Automatic* modes, the PEM execution dialog shows the progress of the script through these labeled steps. In *Manual* mode, the user must press the **Continue** button on the PEM dialog to permit execution of each step.

Labelling of steps also permits PEM to ensure servicing of user abort requests. When a user asks to have a PEM procedure aborted (via the PEM manager application), this request is serviced at the next occurrence of a Tcl/Tk **update** or **tkwait** call. Such a call is guaranteed to happen prior to each step of the procedure.

3.4 Parallel Processes

Creating parallel processes with PEM is simply matter of providing the **APSMpParallel** procedure with the Tcl/Tk command that is to be executed. One may also specify the host machine on which to execute the command and the PEM mode under which the command should be executed. The defaults are to execute the command on the present host and in the present PEM mode. (In most cases, the mode is set to *Automatic*.) For each process created in this fashion, **APSMpParallel** returns a unique identifier that may be used to control the process.

Having created one or more PEM parallel processes, it is typical to want to wait for these processes to complete.

This is done using **APSMpJoin.** If **APSMpJoin** is not used within a procedure that creates parallel processes, an implied join is performed prior to returning from the procedure. **APSMpJoin** takes a single argument, namely the identifier of a process for which to wait. A series of **APSMpJoin** statements is used to ensure that all parallel processes are complete. Each **APSMpJoin** returns a catchable error. In the case of an error, the programmer may elect to abort other parallel processes.

Aborting parallel processes is accomplished using **APSMpAbort.** This procedure accepts a list of identifiers for processes to abort or it can abort all processes. It can also be used to set up a conditional abort, wherein if any of the listed parallel processes returns an error, then all of the listed processes are aborted. This prevents blocking of **APSMpJoin** on one process when another process has encountered an error.

4 EXAMPLES

4.1 PAR/LET Start-Up Procedures

This was one of the first applications of PEM and is the most mature and sophisticated one to date. The PAR/LET consists of three main systems: the PAR itself, the linac-to-PAR transport line (LTP), and the PAR-to-booster transport line (PTB). While the LTP and PTB are simple and nearly identical, the PAR is somewhat complicated. The LTP and PTB both contain only DC magnets, vacuum hardware (including remotely controlled valves), and various diagnostics (including insertable screens). The PAR contains these components, plus two rf systems and four pulsed power supplies.

The PTB and LTP each have seven low-level machine procedures for functions like turning power supplies on and off, conditioning magnets, and clearing the aperture of obstructing valves and screens. These functions are implemented as stand-alone machine procedures and may be individually executed from PEM. In addition, there are start-up and shut-down procedures for the LTP and PTB that make use of these low-level procedures.

The PAR procedures show a similar structure, with the addition of procedures for the rf and pulsed magnet systems, for a total of 17 procedures. Again, these are potentially stand-alone procedures but are also integrated into a pair of start-up and shut-down procedures. The relatively time-consuming operations of pulsed power supply warm-up and DC magnet conditioning are run in parallel.

Finally, at the highest level there is a pair of start-up and shut-down procedures for the entire PAR/LET system. These execute the PAR, PTB, and LTP procedures in parallel. In addition, the start-up procedure guides the operator through several manual steps necessary to obtain beam.

4.2 APS Ring Procedures

One difficult aspect of APS ring operation has been tuning up injection for high efficiency. A tuning procedure was developed by physicists in the course of machine studies and subsequently implemented as a PEM procedure. Because much of the tuning involves an operator looking at a scope trace, insertable screen, or similar diagnostic, this might at first seem a difficult task for automation. However, if the goal is simply to improve convenience for the operator and standardize operational methods, PEM is quite useful in this application. Specifically, the PEM procedure walks the operator through the tune-up. For some steps, the procedure helps the operator by inserting a screen into the beam or bringing up a needed control system display. For such steps, it gives instructions on what to look at and what to try to achieve. This procedure makes use of the *Manual* execution mode of PEM and is not intended to be embedded within another procedure.

Beamline steering in the APS involves a complicated series of steps to ensure that the orbit is maintained within acceptable tolerances. This procedure is implemented using PEM and makes use of the ability to switch execution mode inside of a procedure. It does this in order to allow operators to complete activities using other interfaces. In this way, PEM allows the use of other code as part of a procedure without any "real" connection between PEM and the other code. Again, there is no intention of embedding this type of procedure in a larger one.

5 CONCLUDING REMARKS

The success of the PAR/LET procedure makes it clear that such procedures are desirable for the other systems. It is also clear that more effort is involved in writing a procedure robust enough that it can be embedded deep inside another procedure for automatic execution. The problem is partly one of anticipating all of the potential problems with the hardware. Still, we intend eventually to write start-up and shut-down procedures for all of the systems. In principle, this would allow starting up or shutting down the entire facility with a single operation, though the procedures are clearly desirable even if one never wants to run them all in parallel.

Since PEM was designed with multi-workstation and multi-operator tasks in mind, it would be desirable to be able to execute procedures on the least loaded workstation of a cluster. This would be particularly useful for computationally intensive procedures. Presently, the multi-workstation capabilities in PEM are disabled due to problems with IPC software from the vendor.

6 ACKNOWLEDGMENT

PEM was implemented by C. W. Saunders, formerly of APS, based on concepts developed by M. Borland and C. W. Saunders. Several of the scripts described above were created or contributed to by L. Emery (APS). Work is supported by the U.S. Department of Energy, Office of Basic Energy Sciences, under Contract No. W-31-109-ENG-38.

7 REFERENCES

[1] L. Emery, M. Borland, "Advancements in Orbit Drift Correction in the Advanced Photon Source Storage Ring," these proceedings.

[2] M. Borland, "Applications Toolkit for Accelerator Control and Analysis," these proceedings.

[3] C. W. Saunders, "PEM-Procedure Execution Manager," http://www.aps.anl.gov/asd/oag/manuals/APSPEM/APSPEM4.html.

DATA WAREHOUSE ON THE WEB FOR ACCELERATOR FABRICATION AND MAINTENANCE

A. Chan, G. Crane, I. MacGregor and S. Meyer

Stanford Linear Accelerator Center, Stanford, CA 94309 U.S.A.*

Abstract

A data warehouse grew out of the needs for a view of accelerator information from a lab-wide or project-wide standpoint (often needing off-site data access for the multi-lab PEP-II collaborators). A World Wide Web interface is used to link legacy database systems of the various labs and departments related to the PEP-II Accelerator. In this paper, we describe how links are made via the 'Formal Device Name' field(s) in the disparate databases. We also describe the functionality of a data warehouse in an accelerator environment. One can pick devices from the PEP-II Component List and find the actual components filling the functional slots, any calibration measurements, fabrication history, associated cables and modules, and operational maintenance records for the components. Information on inventory, drawings, publications, and purchasing history are also part of the PEP-II Database [1]. A strategy of relying on a small team, and of linking existing databases rather than rebuilding systems is outlined.

1. DATA WAREHOUSE—DO WE NEED IT?

In an accelerator laboratory we are inundated with data related to the fabrication and maintenance of the machine, such as hardware, personnel, finance [2]—yet it is more often than not quite difficult to obtain such related information in a useful format. To resolve a maintenance problem, one may need to log onto diverse computer systems and run different database software, frequently devoting much time to trying out obscure search strings.

Such compartmentalization of databases of the various accelerator departments evolved because different software was used to suit particular problems and situations. Although there is growing recognition to achieve database implementation under the same database software, we will still be faced to some degree with these differences. [3]

Another reason for this compartmentalization is that databases developed by the departments, of necessity, focus on their area of business functions. This short-term focus can be mitigated by recognizing the need to make linkages to the overall accelerator during the design of the database. However, the implementation of a data warehouse is required for a lab-wide view of decision support information for the accelerator.

2. DATA WAREHOUSE—FOR AN ACCELERATOR ENVIRONMENT

A data warehouse can be simply defined as [4] "a single, complete, and consistent store of data obtained from a variety of sources and made available to end users in a way they can understand and use in a business context."

There are 3 main architectures for a data warehouse (see Fig. 1), although in reality what is implemented is most likely a mixture of these different types. The data layers that Fig. 1 refers to are conceptual, rather than physical.

For the single-layer architecture, its strength is that data is only stored once, which avoids the need to synchronize multiple copies of data. Its weakness is that contention can occur between the online transaction processing systems and the decision support systems.

For the two-layer architecture, its strengths lie in solving the contention between the online transaction processing systems and the decision support systems. It addresses the fact that end-user needs for information are different from what is easily available from real-time data.

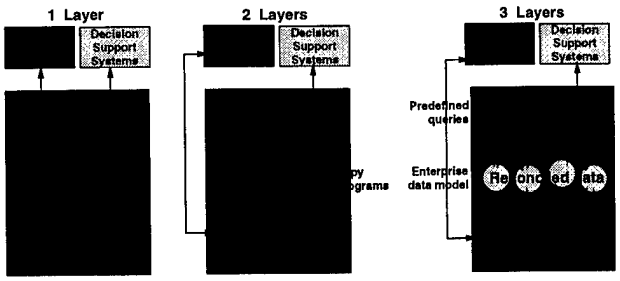

Figure 1 -- Types of implementation of data warehouse

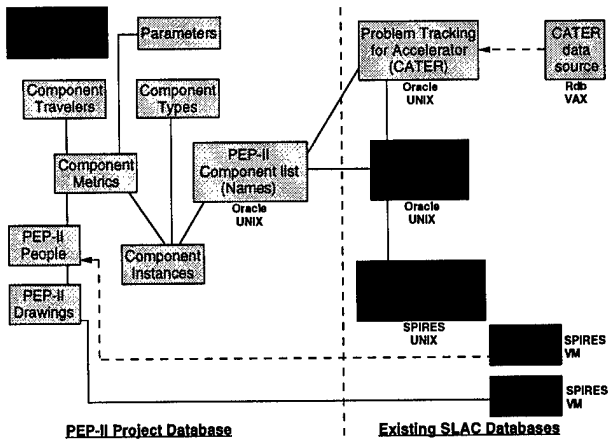

Figure 2 -- Linked SLAC accelerator databases

*Supported by the U.S. Department of Energy under contract DE-AC03-76SF00515.

However, there is a high level of data duplication in the two-layer approach (with a tendency to become 'spaghetti code').

For the three-layer architecture, its strengths lie in the reconciled layer which is based on enterprise data modeling (i.e., a normalized database). This reconciled layer can support new, unanticipated end-user needs. The derived layer can be used to fill most end user needs, being the equivalent of predefined queries. The enterprise data modeling is a much more committed effort, and needs to be done incrementally.

At SLAC, we have mostly implemented the single layer and two-layer approaches.

The World Wide Web (WWW) technology has made it possible to access and link disparate databases, allowing the data warehouse to be a reality for us, and at a fraction of the programming effort in today's resource-scarce environment.

3. LINKING THE LAB DATABASES

Figure 2 is an overview of the lab's major accelerator-related databases that we have linked for the accelerator data warehouse. These systems are:

- the PEP-II Component system, containing the formal device names, component fabrication history and calibrations. This is integrated into the PEP-II project-wide database which is in Oracle, most of it developed using Oracle*CASE tools
- the problem tracking database for the accelerator (CATER), which is in VAX Rdb and replicated into Oracle tables
- the cable plant database (CAPTAR) in Oracle
- the equipment tracking database for Controls (DEPOT) in SPIRES

Via WWW Common Gateway Interface (CGI) scripts, these databases are linked together using common data elements (i.e., variations of formal device names shown in Table 1). The WWW interface gives excellent 'drill-down' capabilities. Since linkages of the different databases are done by the CGI scripts, huge savings in programming time are realized as we do not have to create physical tables to join the databases.

Table 1. Linkage of data elements.

PEP-II Component List	*Primary* QUAD	*Micro* PR02	*Unit* 6072
Problem Tracking for Accelerator (CATER)	*Area* HER LER	*Micro* PR02	*Primary Unit* (not a required field)
Cable Plant (CAPTAR)	*System Function* QUAD:PR02,6072		
	Micro LI09	*Crate* CR02	*Model* 233-002-00
Equipment Tracking for Controls (DEPOT)	*Location* LI09/CR02		*Model* 233-002

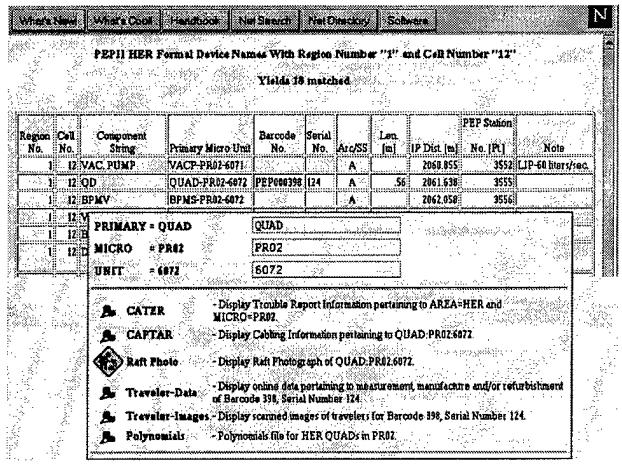

Figure 3 -- WWW screens of PEP-II Components List , and menu choices for each formal device identified by 'Primary, Micro, Unit'

Users can query the PEP-II Component List on WWW, and the search results will contain hypertext references that request information from the other database systems. In Fig. 3, among the search results returned for components in Region 1 Cell 12 is the Primary/Micro/Unit QUAD PR02 6072 (the three fields comprising the formal device name), which has a hypertext link that produces a menu with additional hypertext links to:

⇒ the CATER database summary and detail screens for Area HER or LER, Micro PR02 (Fig. 4).

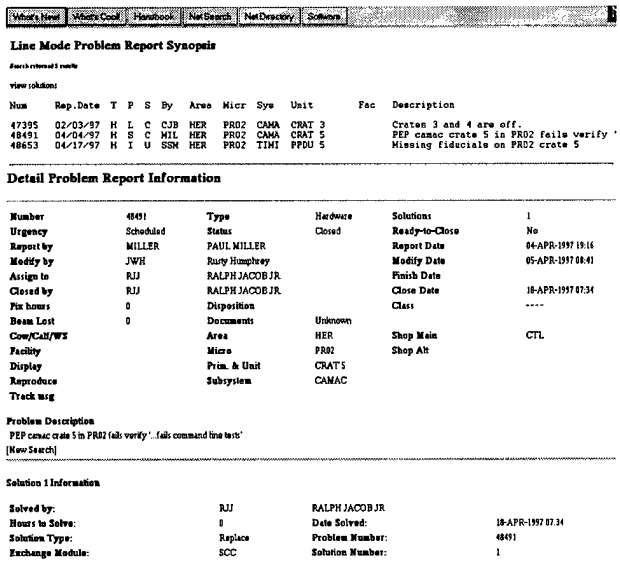

Figure 4 -- Summary and detail WWW screens of accelerator problem report database (CATER) linked from 'Area HER, Micro PR02' in figure 3

⇒ the CAPTAR database of cables linked to QUAD PR02 6072. From the Micro field, one can obtain crate profiles which are database reports in WWW tables (Fig. 5)

⇒ the DEPOT database with summary screen of the history of modules in this crate location, and detail screens of the maintenance records of each module is linked from the CAPTAR crate profile. In Fig. 5, this link is shown for Micro LI09 Crate CR02 Model 233-002.

⇒ the scanned paper fabrication and alignment travelers, online calibration measurements, drawings, photos, polynomials files, etc.

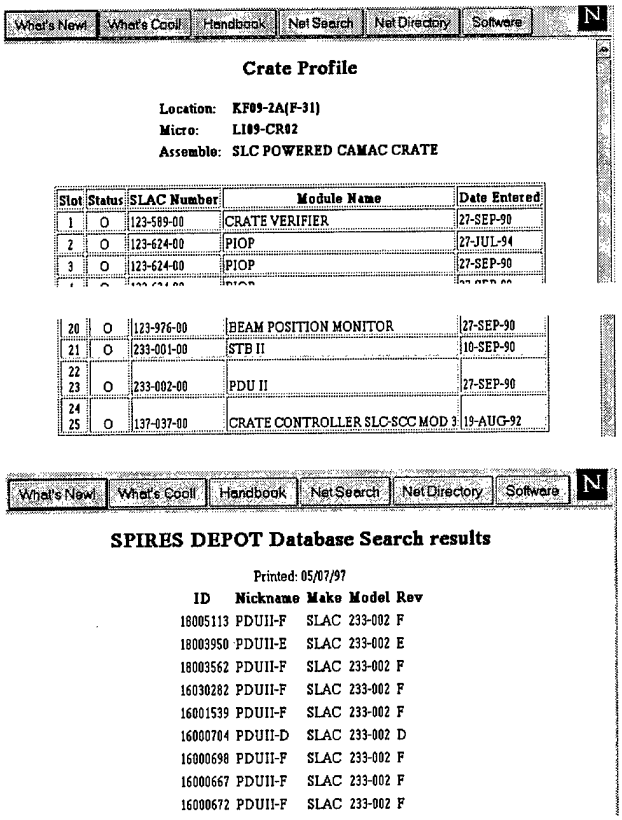

Figure 5 -- WWW screen of crate LI09/CR02 -- crate profile from cable plant database (CAPTAR), and linked history of modules in the Equipement Tracking for Controls database (DEPOT) which leads to maintenance history screens

4. LESSONS AND ISSUES

This accelerator-wide view of the information delivered through the WWW interface has been popular with users, enabling more efficient work.

There are a few key issues that have enabled us to get to this stage for an accelerator data warehouse

- We 'web-ified' both new or existing main disparate databases at the lab. This provided immediate benefits to the departments, and they were very willing to work with us.
- We approached each system with a lab-wide view of the information-not a departmental view.
- We focused on linking the existing departmental databases-not on rebuilding systems. Re-engineering is a major effort that our scarce programming resources cannot easily undertake, so we have left that effort to the departments-though, hopefully, there is coordination amongst related database work.
- We built incrementally, for each increment giving quick turnaround and visible benefits to the users and the departments.
- We relied on experience database programmer(s) for data modeling.

With the ability now to link databases via a few common data fields, the integrity of the data stored in these fields need to be enhanced by cleansing the data and/or applying better database constraints. But this effort becomes easier when the benefits are now apparent to the users (even if it may not benefit their own department immediately).

In the future, we would like to rely more on commercial WWW-database tools (such as Oracle Designer2000, etc.), and less on CGI scripts which are time consuming and less secure.

The URL for the PEP-II Project Database is:
http://www.slac.stanford.edu/accel/pepii/db.htm

5. ACKNOWLEDGMENTS

We are grateful for the continued support of the PEP-II management. We thank the people in PEP-II and the various Technical Division departments who manage the different databases, and who helped us analyze the linkages of these different systems. We also thank the student programmers who contributed to the WWW interface. We have drawn many lessons from discussions with members of the International Accelerator Database Group (IADBG).

REFERENCES

[1] A. Chan, G. Crane, I. MacGregor, S. Meyer, "The PEP-II/*BABAR* Project-Wide Database Using World Wide Web and Oracle*CASE", Proceedings of 1995 International Accelerator Database Group Workshop, Argonne National Lab, November 6-8, 1995.

[2] J. Poole, "Databases for Accelerator Control–An Operations Viewpoint", Proceedings of 1995 Particle Accelerator Conference, Dallas, May 1–5, 1995, p. 2157.

[3] J. Poole, "Summary and Conclusions of the IADBG Workshop on Databases for Accelerators", Proceedings of 1995 International Accelerator Database Group Workshop, Argonne National Lab, November 6-8, 1995.

[4] Barry Devlin, "Data Warehouse: from Architecture to Implementation", Addison-Wesley, 1997.

COSY INFINITY VERSION 7

Martin Berz, Department of Physics and Astronomy and National
Superconducting Cyclotron Laboratory, Michigan State University, East Lansing, MI 48824

Abstract

An overview over the features of version 7 of the code COSY INFINITY is given. The code allows the computation and manipulation of maps of arbitrary order for arbitrary arrangements of fields, and it is currently distributed to about 200 registered users. We present several features of the code, among which are the conventional analysis tools including various techniques for symplectic tracking, normal form methods, hardware and reconstructive aberration correction, and achromat design. We also discuss several new techniques which include efficient methods to treat fringe fields, a variety of methods to directly use measured field data for the computation of maps, as well as the computation and analysis of spin dynamics.

1 INTRODUCTION

This paper provides background of the code COSY INFINITY and its language, and examples of some of the features in COSY INFINITY[1]. These include methods for symplectic tracking[2][3], normal forms[2][4], and reconstructive correction of spectrographs[5]. New features include the SYSCA fast fringe field methods[6][7][8][9], the computation of maps from arbitrary measured fields, the computation and analysis of spin dynamics[10][11] which is getting more important due to the increasing number of studies connected to the acceleration of polarized particles, as well as the tools used for the design of fifth order achromats[12][13][14], and the new remainder-enhanced differential algebraic method[15][16][17][18][19]. Besides these features based on new techniques, there are also a variety of other new tools of a more technical nature. These are connected to standard problems of accelerator design, to interactive graphics, as well as to several improvements of existing tools. A good overview over the key features of the code can be found in the extensive demo that is part of the COSY shipment. Information about COSY can also be obtained at www.beamtheory.nscl.msu.edu/cosy.

2 THE CODE COSY

COSY INFINITY is a code for the simulation, analysis and design of particle optical systems. Since the first official version in 1989, a total of seven releases with an increasing number of features have been provided, and currently there are a total of about 160 registered users as shown in Figure 1. COSY is based on differential algebraic methods, which are described in detail elsewhere[2][20][21], and which lately have been widely used also in most of the other newly emerging codes.

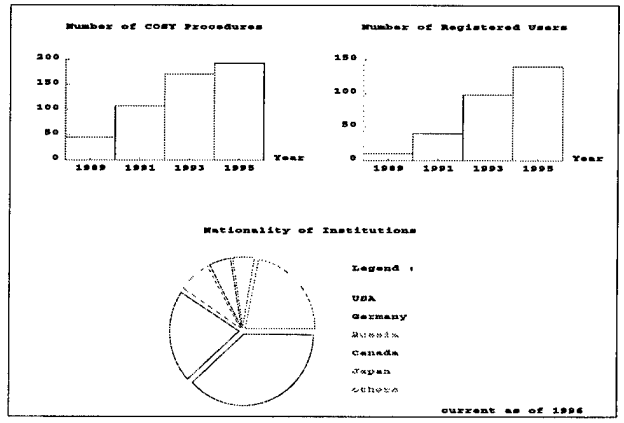

Figure 1: Some statistics about COSY INFINITY (picture generated with COSY's graphics environment and part of the COSY Demo).

For the sake of portability, the code is based on standard FORTRAN 77, which is still the most widespread language on the computers used for accelerator design and simulation. Since the code employs its own programming language which is object oriented and has the flavor of PASCAL, COSY's programmers and users are free from FORTRAN. The COSY language has very simple syntax which makes programming easy, and its elements are as follows:

```
BEGIN ;      END ;          {Begins and ends program}
INCLUDE ;    SAVE ;         {Includes and saves     }
                            {          compiled code}
VARIABLE ;                        {Declares a local }
                                  {         variable}
PROCEDURE ;  ENDPROCEDURE ;       {Declares a local }
                                  {        procedure}
FUNCTION ;   ENDFUNCTION ;        {Declares a local }
                                  {         function}
< assignments > ;            {Sets value of variable}
< procedure calls > ;        {Calls previously      }
                             {     defined procedure}
IF ;         ENDIF   ;       {Executed once if      }
                             {      argument is true}
WHILE ;      ENDWHILE ;      {Executed while        }
                             {      argument is true}
LOOP ;       ENDLOOP ;       {Stepping argument     }
FIT ;        ENDFIT ;        {varying arguments to  }
                             {        fit conditions}
```

Except for the last one, the flow control statements are rather standard. The unique FIT block is used for efficient utilization of COSY's various optimizers. The ENDFIT statement contains the number of the optimizer to be used and the objective quantities, as well as the tolerance and the maximum number of iterations allowed. The statements in the block are executed over and over again, where for each

0-7803-4376-X/98/$10.00 © 1998 IEEE

pass the optimization algorithm changes the values of the variables listed in the FIT statement and attempts to minimize the objective quantity.

A language environment makes the assembly of beamlines and the control of program flows very straightforward. For example, all standard particle optical elements are just represented by a procedures call, and user-made particle optical elements can have the same form. Groups of elements can be represented by new procedures, and the entire lattice can itself be represented by a procedure. There is also a conversion tool that allows to transform any lattice in standard MAD input to such a COSY procedure. In a similar way, commands for common tasks are also expressed as procedure calls.

The compiler for this language comprises about 6,000 of the approximately 25,000 lines of COSY's FORTRAN code. It has a completely rigorous syntax and error analysis and is comparable in speed to other compilers. The compiled code is stored in a binary file, which can either be saved for inclusion in later code or executed directly. The object oriented features of the code allow a direct use of the differential algebraic operations contained in the 16,000 line DA package.

3 THE FAST FRINGE FIELD CALCULATION

COSY has several options to take account of the fringe field. One is to compute the exact fringe field through DA integration of the equations of motion. In this case, the accuracy is limited only by the accuracy of the numerical integrator, which is adjusted via automatic step size control. While this method provides a very detailed fringe-field calculation, the computational expense becomes quite high. One of the other approaches to compute fringe-field in COSY is the SYSCA method. It is based on a combination of geometric scaling in TRANSPORT coordinates and symplectic rigidity scaling[6][7][8][9].

It uses parameter dependent symplectic representations of fringe-field maps stored on files to approximate the fringe field via symplectic scaling. This method computes fringe fields with a very high accuracy, yet its computational expense is two or three orders of magnitude less than direct integration and in the same terrain as that of main field only calculation. While the reference file can be produced by a user in COSY according to the detailed shape of the fringe fields at hand, one standard reference file comes as part of the COSY shipment. The SYSCA fringe-field mode is especially helpful in the final design stages of a realistic system after approximate parameters of the elements have been obtained by neglecting fringe fields or with other rough fringe-field calculation.

4 THE MEASURED FIELD DATA ELEMENT

One of new elements in COSY INFINITY, the measured field data element, allows the computation of the map of any magnetic field supplied by midplane measured data. The measured data has to be supplied at equi-distant grid points in cartesian coordinates.

The necessary interpolation method has to guarantee the differentiability to fit with the differential algebraic computation. Because of this, the evaluation of the field strength in the element in COSY is done by Gaussian interpolation, which is a powerful special case of a wavelet transform:

$$B_y(x,z) = \sum_{i_x,i_z} \mathrm{B}_{i_x,i_z} \frac{1}{\pi \mathrm{S}^2} \exp\left[-\frac{(x-x_{i_x})^2}{\triangle x^2 \mathrm{S}^2} - \frac{(z-z_{i_z})^2}{\triangle z^2 \mathrm{S}^2}\right],$$

where B_{i_x,i_z} are the supplied measured data. Since the gaussian function falls off quickly, the time consuming summation over all the gaussians can be replaced by the summation of only the neighboring gaussians, which is in the vein of other wavelet transforms and greatly improves efficiency.

The method is used extensively in the simulation of the S800 Spectrograph at NSCL/MSU[5], construction of which has just been completed, as well as the various spectrographs at CEBAF.

5 SPIN DYNAMICS

In version 7, features to analyze spin motion have been added in COSY[10][11]. The classical equation of motion for spin has the form

$$\frac{d\vec{s}}{dt} = \vec{w} \times \vec{s};$$

for details, see [11]. The solution is a linear orthogonal transformation depending on orbital variables, thus

$$\vec{s}_f = \hat{A}(\vec{z}) \cdot \vec{s}_i, \quad \text{where} \quad \hat{A}(\vec{z}) \in SO(3).$$

The motion of a particle with spin can be described as a nine dimensional motion, neglecting spin-orbit coupling, as

$$\begin{pmatrix} \vec{z} \\ \vec{s} \end{pmatrix}' = \vec{F}(\vec{z},\vec{s},s) = \begin{pmatrix} \vec{f}(\vec{z},s) \\ \hat{W}(\vec{z},s)\cdot\vec{s} \end{pmatrix}$$

$$\begin{pmatrix} \vec{z}_f \\ \vec{s}_f \end{pmatrix} = \vec{M}(\vec{z}_i,\vec{s}_i,s) = \begin{pmatrix} \mathcal{M}(\vec{z}_i,s) \\ \hat{A}(\vec{z}_i,s)\cdot\vec{s} \end{pmatrix}$$

To reduce dimensionality and utilize linearity, it is advantageous to set up the equation of motion for $\hat{A}$. Insertion yields the equation of motion for the 3×3 spin matrix depending on only the six orbital variables:

$$\hat{A}'(\vec{z},s) = \hat{W}(\vec{z},s) \cdot \hat{A}(\vec{z},s).$$

The COSY spin features have been used extensively at DESY and a variety of other places.

6 OTHER FEATURES

A recent application of COSY was the design of higher order achromats, and recently some extensive work connected to fifth order achromats has been done[12][13][14].

The new remainder-enhanced differential algebraic (RDA) method combines the rigor of interval computations and a reduction of blow-up due to its use of Taylor polynomials. For the purposes of beam physics, it allows the determination of rigorous bounds for the remainder term of Taylor maps, and combined with methods to determine approximate invariants of the motion, it can be used for guaranteed estimates of stability times in circular accelerators[15][16][17][18][19].

7 ACKNOWLEDGMENTS

The author is grateful for the efforts that a large number of people have made towards the development of COSY. In the past these have included mainly Roger Servranckx, Georg Hoffstätter, Weishi Wan as well as many COSY users, and recently our thanks go to Kyoko Makino.

8 REFERENCES

[1] M. Berz. COSY INFINITY Version 7 reference manual. Technical Report MSUCL-977revised, National Superconducting Cyclotron Laboratory, Michigan State University, East Lansing, MI 48824, 1996.

[2] M. Berz. *High-Order Computation and Normal Form Analysis of Repetitive Systems, in: M. Month (Ed), Physics of Particle Accelerators*, volume AIP 249, page 456. American Institute of Physics, 1991.

[3] M. Berz. *Symplectic Tracking in Circular Accelerators with High Order Maps*, page 288. World Scientific, 1991.

[4] M. Berz. Differential algebraic formulation of normal form theory. In *M. Berz, S. Martin and K. Ziegler (Eds.), Proc. Nonlinear Effects in Accelerators*, page 77. IOP Publishing, 1992.

[5] M. Berz, K. Joh, J. A. Nolen, B. M. Sherrill, and A. F. Zeller. Reconstructive correction of aberrations in nuclear particle spectrographs. *Physical Review C*, 47,2:537, 1993.

[6] G. Hoffstätter and M. Berz. Efficient computation of fringe fields using symplectic scaling. In *Third Computational Accelerator Physics Conference*, page 467. AIP Conference Proceedings 297, 1993.

[7] G. Hoffstätter and M. Berz. Accurate and fast computaton of high–order fringe field maps via symplectic scaling. *Nuclear Instruments and Methods*, 363:124, 1995.

[8] G. H. Hoffstätter. *Rigorous bounds on survival times in circular accelerators and efficient computation of fringe–field transfer maps*. PhD thesis, Michigan State University, East Lansing, Michigan, USA, 1994. also DESY 94-242.

[9] G. Hoffstätter and M. Berz. Symplectic scaling of transfer maps including fringe fields. *Physical Review E*, 54,4, 1996.

[10] M. Berz. Differential algebraic description and analysis of spin dynamics. In *Proceedings, SPIN94*, 1995.

[11] V. Balandin, M. Berz, and N. Golubeva. Computation and analysis of spin dynamics. In *Fourth Computational Accelerator Physics Conference*. AIP Conference Proceedings, 1996.

[12] W.Wan and M. Berz. Design of a fifth order achromat. *Nuclear Instruments and Methods*, 352, 1994.

[13] W. Wan. *Theory and Applications of Arbitrary-Order Achromats*. PhD thesis, Michigan State University, East Lansing, Michigan, USA, 1995. also MSUCL-976.

[14] W. Wan and M. Berz. An analytical theory of arbitrary order achromats. *Physical Review E*, 54,3:2870, 1996.

[15] M. Berz and G. Hoffstätter. Computation and application of Taylor polynomials with interval remainder bounds. *submitted to Interval Computations*, 1997.

[16] M. Berz and G. Hoffstätter. Exact bounds of the long term stability of weakly nonlinear systems applied to the design of large storage rings. *Interval Computations*, 2:68–89, 1994.

[17] K. Makino and M. Berz. Remainder differential algebras and their applications. *in: Computational Differentiation: Techniques, Applications, and Tools*, SIAM, 1996.

[18] M. Berz. Differential algebras with remainder and rigorous proofs of long-term stability. In *Fourth Computational Accelerator Physics Conference*. AIP Conference Proceedings, 1996.

[19] K. Makino. Rigorous integration of maps and long-term stability. In *1997 Particle Accelerator Conference*. these proceedings, 1997.

[20] M. Berz. Differential algebraic description of beam dynamics to very high orders. *Particle Accelerators*, 24:109, 1989.

[21] M. Berz. Arbitrary order description of arbitrary particle optical systems. *Nuclear Instruments and Methods*, A298:426, 1990.

A SOLVING MODULE OF AN EXPERT SYSTEM FOR NONLINEAR BEAM DYNAMICS

S. Andrianov, A. Dvoeglazov, SPbSU, Bibliotechnaja pl.2, 198904 St.Petersburg, Russia

Abstract

In this paper we describe basic concepts which are took as a base of an expert system for an investigation of nonlinear behavior of particle beams. Modelling process for beam line design is based on the matrix formalism for Lie algebraic tools and computer algebra methods. This allows to use an object-oriented approach for describing both physical and mathematical objects. [1]

1 INTRODUCTION

It is known that human problem solving is much characterized by its enormous range as by the huge amounts of detailed specific knowledge that can be effectively mobilized for a particular domain. For scientific modelling problems one comes up tedious and time consuming calculations that are a source of numerous errors. That is why it is necessary to rearrange the main amount of work to be done from a researcher to computer. This aim can be reached in different ways. We consider one of these based on symbolic representation of necessary information. This approach allows to create databases and corresponding environment and use them if necessary [1]. The most proper tools for this is the matrix formalism for Lie algebraic methods [2].

2 THE BASIC MATHEMATICAL DEFINITIONS

It is known that any dynamical system can be described with the help of a Lie transformation (map) $\mathcal{M}(U;t|t_0)$:

$$X = X(X_0, U; t|t_0) = \mathcal{M}(U;t|t_0) \circ X_0,$$

where X and X_0 are current and initial phase vectors, U is a control vector, t is an independent variable (for example, the length along a reference orbit). For the general case of nonautonomous systems we can write

$$\mathcal{M}(F|U;t|t_0) = \mathrm{T}\exp\left\{\int_{t_0}^{t} \mathcal{L}_{F(X,U,\tau)} d\tau\right\}, \qquad (1)$$

where T exp is a chronological exponent operator, $\mathcal{L}_F$ is a Lie operator, associated with some function (for example, a right part of a ODEs system) $F(X,U;t)$. From (1) we can proceed to the Magnus representation in the form of a routine exponential operator for a new Lie operator:

$$\mathcal{M}(G|U;t|t_0) = \exp\left\{\mathcal{L}_{G(X,U;t|t_0)}\right\},$$

where the function $G(X,U;t|t_0)$ can be calculated with the help of a continuous analog of the well known CBH formula. Thus one can build the following chain of mappings:

$$F(X,U;t) \Longrightarrow \mathcal{L}_{F(X,U;t)} \Longrightarrow$$

$$\Longrightarrow \mathcal{M}(F|U;t|t_0) = \mathrm{T}\exp\left\{\int_{t_0}^{t} \mathcal{L}_{F(X,U;\tau)} d\tau\right\} \Longrightarrow$$

$$\Longrightarrow \mathcal{M}(G|U;t|t_0) = \exp\left\{\mathcal{L}_{G(X,U;t|t_0)}\right\}. \qquad (2)$$

Let $F(X,U;t)$ be represented in the form

$$F(X,U;t) = \sum_{k=0}^{\infty} \mathbf{P}^{1k}(U;t)\, X^{[k]}, \qquad (3)$$

where $X^{[k]} = \underbrace{X \otimes \ldots \otimes X}_{k-times}$ is the Kronecker power of X of k–th order and $\mathbf{P}^{1k}(U;t)$ are coefficient matrices of the dimensions $\left(n \times \binom{n+k-1}{k}\right)$.

The mapping (2) and the expansion (3) generate the next mapping

$$\mathbf{P}^{1k}(U;t) \Longrightarrow \mathbf{G}_k(U;t|t_0),$$

where $\mathbf{G}_k(U;t|t_0)$ is a coefficient matrix for homogeneous polynomial of k-th order $G_k(X,U;t|t_0)$ and

$$\mathcal{L}_G = \sum_{k=0}^{\infty} \mathcal{L}_k, \quad \mathcal{L}_k = \mathcal{L}_{G_k}, \quad G_k = \mathbf{G}^k X^{[k]}.$$

The matrices $\mathbf{P}^{1k}$ (system matrices) are defined from initial physical model. The matrices $\mathbf{G}_k$ can be called system matrices too. Their form and the order N, $k \leq$ N depend on an approximating model, which is chosen by a researcher as the series in (3) must be truncated . In this case we proceed to so called N–jet approach. After this it is convenient to use the Dragt–Finn factorized representation [3]

$$\mathcal{M} = \ldots \circ \mathcal{M}_k \circ \ldots \circ \mathcal{M}_1 = \tilde{\mathcal{M}}_1 \circ \ldots \circ \tilde{\mathcal{M}}_k \circ \ldots, \qquad (4)$$

where $\mathcal{M}_k$ ($\tilde{\mathcal{M}}_k$) is a new map associated with a new Lie operator $\mathcal{L}_k$ ($\tilde{\mathcal{L}}_k$), $\mathcal{L}_k = \mathcal{L}_{H_k(X,t)}$, $H_k(X,t) = \mathbf{H}_k X^{[k]}$. According the matrix representation for Lie transformation we can write

$$\mathcal{M}(F|U;t|t_0) \circ X_0 = \sum_{k=0}^{\infty} \mathbf{M}^{1k}(F|U;t|t_0)\, X_0^{[k]}.$$

Matrices $\mathbf{M}^{1k}(F|U;t|t_0)$ are called solving matrices. So we can give the following definition.

[1] This work is supported by the Russian Foundation for Fundamental Researches 96-02-17335

Definition 1 . *Let $\mathcal{M}(F|U;t|t_0)$ be a Lie transformation generated by a dynamical system with the vector field $\mathcal{F}(X,U,t) = \mathcal{L}_{F(X,U,t)}$. The creation of the chain*

$$\begin{bmatrix} \textit{coordinates systems} \\ + \\ \textit{approximating} \\ \textit{external control fields} \end{bmatrix} \Longrightarrow \begin{bmatrix} (X,U) \\ + \\ \textit{an independent} \\ \textit{variable - "time" } t \end{bmatrix}$$

$$\Longrightarrow [\mathbf{P}^{1k},\ k \leq N] \Longrightarrow [\mathbf{G}_k,\ k \leq N]$$

$$\Longrightarrow [\mathbf{H}_j,\ j \leq N] \Longrightarrow [\mathbf{M}^{1j},\ j \leq N]$$

will be named solution process in the matrix formalism.

For $\mathbf{M}^{1k}$ we used symbolic formulae which have only algebraic character (see [2]). As a starting–point we can consider both motion equations in the form of ODEs and Hamiltonian description. For N–jet representations we have

$$\mathcal{M}\,(F|U;t|t_0) \Longrightarrow \mathcal{M}_{\mathrm{N}}\,(F|U;t|t_0):$$

$$\mathcal{M}_{\mathrm{N}}\,(F|U;t|t_0) \circ X_0 = \sum_{k=0}^{\mathrm{N}} \mathbf{M}^{1k}\,(F|U;t|t_0)\, X_0^{[k]}.$$

So our main goal is to calculate $\mathcal{M}_{\mathrm{N}}\,(F|U;t|t_0)$ (in the terms of $\mathbf{M}^{1k}\,(F|U;t|t_0)$) for given set of $\mathbf{P}^{1k}$, $k \leq \mathrm{N}$ which describes a designed beam line.

3 SOLVING MODULE DESCRIPTION

3.1 Structure of a Solving Module

Symbolic character of all objects: from $\mathbf{P}^{1k}$ up to $\mathbf{M}^{1k}$ allows us to create databases of these matrices and corresponding database management system. Besides these matrices we must create rules according which one has to manipulate by these objects for his goal. This set of rules is the basic contents of proposed solving module. As above mentioned the necessary operations have mainly algebraic character. These operations we can separate on several submodules:

- Submodule of algebraic manipulations over noncommutative variables, which are necessary for evaluation of similar to CBH expansions and so on [4].
- Submodule of matrix algebra extended by including the Kronecker sum and product. All operations are made for abstract forms of matrices [5].
- Submodule for integration procedures for calculation of $\mathbf{G}_j$ and $\mathbf{H}_j$, $j \leq \mathrm{N}$ (for example, for the Magnus representation) and other necessary integration procedures. For this purpose it is convenient to create a database of formulae for some set of support functions [2].
- Submodule for the factorization procedures (see (4)).
- Submodule for formation of the solving matrices $\mathbf{M}^{1k}$ for a selected initial variant of the beam line [8].
- Submodule for finding of explicit solutions for some classes of the Lie transformations [7].
- Submodule of manipulations by system matrices $\mathbf{P}^{1k}$ for an investigation of symmetry properties of the dynamical system under study (the level of building of a protoproject) and so on.
- Submodule for calculation of the invariants and symmetries for the designed beam line (the level of formation of beams with desired characteristics) [6].
- Submodule of calculation of envelope beam matrices (σ – matrices) and distribution functions in phase and/or configuration spaces [8].
- Submodule for maps construction including space charge [9].
- Submodule of calculation of object functions and condition functions for an optimization procedure. Here the optimal control theory and nonlinear programming methods are used .
- Submodule for numerical calculations for a selected set of system parameters – **dynamics level** and numerical optimization – **optimization level**.
- Submodule (if it is necessary and possible) for testing of modelling with the help of known packages (for example, such as $MARYLIE$, $COSY$, MAD) and/or using general mathematical packages (for solving, for example, ODEs) [10].
- Submodule for visualization of calculation results.

3.2 A Hierarchy of Submodules

For the effective working of all submodules we must create databases of ready objects. The symbolic forms of these objects allow to do it and a researcher can fill up these databases simultaneously with accumulation of his knowledge.

The submodules are combined into a solving module which is surrounded by a human interface. This interface can be provided by a special language for a restricted problem class or by more wide language which can be adapted under transfer from one problem to another. In this case we can talk about an object–oriented interface. For realization of the modelling process one must go through the following steps:

- to select transport system elements in desired N–order approximation (including all effects which are necessary) — to define the system 0matrices $\mathbf{P}^{1k}$, $k \leq \mathrm{N}$;
- to build Magnus representation (if it is necessary) — to calculate the matrices $\mathbf{G}_k$, $k \leq \mathrm{N}$;
- to calculate the matrices $\mathbf{H}_k$, $k \leq \mathrm{N}$ for factorized representation (4);
- to create (step by step) the solving matrices $\mathbf{M}^{1k}$, $k \leq \mathrm{N}$;

So we can separate all submodules into four levels. The zero level group – the kernel level – is intended for manipulations by noncommutative variables and for realization of matrix algebra procedures (extended by the Kronecker product and sum [5]). The first level group of submodules is intended for preparing of all matrices which are

necessary for next steps. The second level submodules are meant for symbolic manipulation for preparing corresponding databases and program packages. Here the basic objects are matrices from which we build desired solutions for a beam line considered as a dynamical system. These three groups of submodules can be realized with the help of computer algebra codes (i.e. such as $REDUCE$, $MAPLEV$, $MuPAD$). The third level submodules play the main role for our problem. Namely, the final result of this submodules group is a map generated by the transport system under study. There are some differences from usual approaches for this problem. According to this approach a particular map can be extracted from a corresponding database. If the desired solving matrices are absent in this database than one must turn to corresponding calculation submodules and make necessary calculations with the help of the two first group of submodules.

3.3 *Organization of Calculations*

Naturally, all above mentioned operations must be provided with a suitable interface. Here we should note that the interface problem is created not only for convenience of a user. The main role of this interface to optimize the modelling process, to provide adaptivity and efficiency of all manipulations [11]. Modern systems of visual programming (what is known as Rapid Application Development systems) such as $DELPHI$, C^{++} $Builder$ are given necessary tools for this. It is obviously that an expert system can be designed only by a researchers group which consists of adepts in different scientific domains. Only their co–operation can be lead to the desired goal: creation of an expert system (more exactly a prototype of the expert system). The complexity of the modelling process and of physical behaviour of particles in beam lines (first of all in nonlinear systems) make very difficult a formalization process and creation of a rules set.

4 REFERENCES

[1] S.N.Andrianov: 'Computer Algebra and Object–Oriented Programming', Abstr. of the Int. Conf. on Interval and Comp. Algebra in Sci. and Engineering', SPb, 1994, p.41.

[2] S.N.Andrianov: 'Algebraic Approach to Perturbation Theory and Computer Algebra', Proc. of the Int. Workshop "New Computer Technology in Control Syst.", Pereslavl–Zalesky, Russia, 1994, p.10.

[3] A.J.Dragt, J.Finn: 'Lie Series and Invariant Functions for Analytical Symplectic Maps', J.of Math. Phys., **17**, 1976, p. 2215.

[4] P.V.Koseleff: 'Formal Calculus for Lie Methods in Hamiltonian mechanics', Ph.D. Thesis, Ecole Polytechnique, 1993.

[5] S.N.Andrianov: 'Group–Theoretical and Algebraic Modelling of Control Systems for Particle Beam', Problems of Mechanics and Control Processes, issue 15, S.-Petersburg, SPbSU, 1992, p.7 (in Russian).

[6] S.N.Andrianov:'Construction of Approximate Symmetries and Invariants for Dynamical Systems', Proc. of the Second Int. Workshop on Beam Dynamics & Optimization – BDO'95, SPb, 1996, p.25.

[7] S.N.Andrianov: 'σ– Matrix Application for Solving of Problems of Charged Particle Beams Transport', Mathematical Theory for Technology Objects, Leningrad, LSU, 1982, p.114 (in Russian).

[8] S.N.Andrianov: 'The Explicit Forms for Lie Transformations', Proc. of the Fifth European Particle Conference EPAC'96, SITGES (Barcelona), Spain, 1996, p. 998.

[9] S.N.Andrianov: 'Analytical Simulation of Space Charge in Ion–Optical Systems', Proc. of the First Int. Workshop on Beam Dynamics & Optimization – BDO'94, SPb, 1995, p.19.

[10] S.N.Andrianov, A.I. Dvoeglazov: 'A Solving Module for Hamiltonian Dynamical Systems', Proc. of the Third Int. Workshop on Beam Dynamics & Optimization – BDO'96, SPb, will be published.

[11] S.N.Andrianov: 'Dynamic Modeling in Beam Dynamics', Proc. of the Second Int. Workshop on Beam Dynamics & Optimization – BDO'95, SPb, 1996, p.25.

DESIGNING A PORTABLE ARCHITECTURE FOR INTELLIGENT PARTICLE ACCELERATOR CONTROL

W. Klein, C. Stern, Vista Control Systems, Inc., 134B Eastgate Dr., Los Alamos, NM 87544 and
G. Luger, E. Olsson, University of New Mexico, Albuquerque, NM 87131

Abstract

We present a portable system for intelligent control of particle accelerators. This system is based on a hierarchical distributed architecture. At the lowest level, a physical access layer provides an object-oriented abstraction of the target system. A series of intermediate layers implement general algorithms for control, optimization, data interpretation, and diagnosis. Decision making and planning are organized by knowledge-based components that utilize knowledge acquired from human experts to appropriately direct and configure lower level services. The general nature of the representations and algorithms at lower levels gives this architecture a high degree of potential portability. The knowledge-based decision-making and planning at higher levels gives this system an adaptive capability as well as making it readily configurable to new environments. Significant successes of this work are reported in [1, 2].

1 DESIGNING AN ARCHITECTURE

To be most useful, control architectures should be flexible enough to incorporate the important tools necessary for robust control, and should include design features which support the application of those tools in a timely and transparent manner. Our control architecture attempts to meet the following six requirements:

1. The use of conventional control techniques where appropriate. Conventional control is the best solution for a large class of problems, and consists of established, well developed, robust techniques for dealing with linear and approximately linear small systems.

2. The use of high-level control knowledge from experts in the field. More complex control systems include high-level knowledge and information obtained through knowledge-engineering sessions with a human expert. This knowledge is preserved in the form of symbolic data sets (rules, relations, objects, etc.) and is manipulated through sophisticated, high-level reasoning mechanisms. This knowledge-based component encodes internal control information about how and when to use classes of control algorithms and heuristics and for storing configuration information for PID, neural network, fuzzy control, etc.

3. The use of supervisory control for dealing with macro state transitions. For instance, in beam line tuning, if a failure in an upstream monitor forces the use of stripline data in judging beam intensity and distribution, a downstream controller may need to use a control algorithm which is less precise, faster, and less sensitive to intermittent failure or noise. Supervisory control can also be used for control over different internal control subsystems.

4. Support for real time reactive control. In this case, "real time" means the ability to compute and perform "satisfactory" or "good enough" decisions that are not delayed due to control system response.

5. The control of complex systems through the use of a hierarchical distributed architecture. To perform intelligent control that optimizes behavior in complex systems, a control architecture should support the ability to coordinate the individual partitions of the system to achieve an overall goal. This is especially true when controllers operate on platforms distributed throughout a plant. A distributed architecture requires structures for relaying information between nodes, synchronizing information, coordinating timing, etc. A distributed control system may also require global access to certain data structures including process models, diagnostic systems, alarm systems, and hardware.

6. Portability across classes of similar control problems. For a system to be truly portable, domain specific algorithms should work at many facilities with limited modification. The control system should have a working model of the domain that allows it to accomplish similar goals at numerous facilities with different specific hardware designs, but similar classes of control elements.

2 PHYSICAL ACCESS LAYER

The *Physical Access Layer*, or PAL, is what allows the control system access to hardware, portability, dynamic construction of representation, filtering of data, coordination of hardware, and conflict detection. The PAL is permanent and static, but hierarchical structures in the PAL can be built dynamically at run time. Learning can occur in the PAL in various feature detectors and pattern recognition components, as well as in recording attributes of specific physical devices.

The Physical Access Layer provides a mechanism for controllers and optimizers to access the physical system. Access to hardware is supported through a single layer

0-7803-4376-X/98 /$10.00 © 1998 IEEE

for a number of reasons. First, the control system can be ported to multiple systems whose hardware varies in implementation detail but not functionality. A globally available, uniform interface to hardware keeps controllers and solvers from having to explicitly represent low-level handlers and hardware handshaking mechanisms. The PAL is one of the only shared global repositories of information in the control system. This makes it an ideal mechanism for conflict resolution.

The PAL also plays an important role in transforming raw data into a representation for higher level reasoning. This translation may be simple filtering of data, as in noise reduction, pattern classification, and error detection or it can be more sophisticated. In particular, the PAL is responsible for providing initial feature detection, fuzzification, data analysis, and discretization of information. This is particularly important in the context of a knowledge-based or symbolic system where raw numeric data is often inappropriate for manipulation. For instance, the PAL can be used to transform image data into a set of relevant image features, e.g., background noise, average pixel intensity, or existence of a defect.

The PAL is also useful for detecting, preventing, and resolving resource conflicts in a distributed control system. If an obvious resolution exists, the PAL provides coordination instructions to the conflicting units. Otherwise, the PAL can simply report the conflict and allow resolution to occur within the control system itself.

A further purpose of the PAL is to support an abstract translation mechanism between the low-level control system interface accessible through Vsystem channels [3] and the control architecture's multi-representational interface. The PAL accesses Vsystem directly through a library of Vsystem API calls encapsulated in a channel class library built using object-oriented programming techniques in C++. Simple channels are represented as objects with enhanced features including data validation, recording and retrieving defaults, time delayed action, equipment limit checking, and value stepping.

The PAL is designed for fast parallel operation. Each object that can receive messages from outside the PAL is run as a separate thread. Messages are received in a single message handler and immediately distributed to a message buffer associated with the recipient object.

PAL objects are not confined to representing physical devices. They may also be used to implement abstract devices defined as the collection and interacting behavior of a group of other objects. Abstract objects can be used to build control knobs that transform a single signal into a set of signals to many devices. Tuning knobs are sometimes used in accelerator control when the relationship of a set of quadrupoles and their effect on the beam at a downstream location can be determined by a series of non-linear functions. Tuning then occurs by manipulating a single knob to affect a single beam parameter while maintaining other beam properties, e.g., magnifying the beam without increasing divergence.

3 DISTRIBUTED COMPONENT CONTROL

Our system is based upon a distributed hierarchical architecture designed to incorporate a wide variety of representations, both analytical and knowledge-based, into a single control framework. At the heart of the architecture is a group of knowledge-based *controllers* that apply control from a local viewpoint. These controllers are hierarchically organized in a structural/functional hybrid design [4].

Controllers are responsible for making decisions about how control actions will be performed, what those actions will be, when they occur, and how their performance will be measured. Controllers are also responsible for reasoning about system state, diagnosing errors in control solutions, decomposing goals into tasks and actions, and initiating any necessary human interaction. Knowledge is encoded in each controller as a set of relations (n-ary predicates) and a set of operators that manipulate those relations. The predicates describe relationships between controller variables, facts about process state, task decomposition relationships, and message parameters for controller communication.

In addition to controllers that encode information about domain specific elements, algorithms, and experience, we also use *solvers* for component-based application of specific algorithms. Solvers encode pieces of algorithms which can be put together (again in a hierarchical manner) for run-time construction of control algorithms. Consider, for example, a search procedure for a search algorithm such as simple hill-climbing for optimizing beam transmission. The procedure is broken into three parts, a component for generating data points that must be measured during search, a component for measuring the data points using appropriate elements in the domain, and a parent controller which coordinates actions of the two children in a way that produces hill-climbing. A different algorithm, such as Newton's method, can be constructed by merely substituting the parent controller for one that applies a different top-level procedure. Different child controllers may also be substituted when operating different sets of control elements or in cases where specific constraints (e.g., noise handling, speed, etc.) are important [5].

4 TELEO-REACTIVE BEHAVIOR

Controllers built for tuning beam lines were designed to carry out reactive plans to maintain robustness and to support dynamic re-planning based on changing goals or world states. Reactivity was obtained by using a teleo-reactive (TR) rule structure. The TR architecture was

originally designed as a control system for autonomous robots. [6] The purpose of teleo-reactive programs, also called TR trees, is to encode a plan for achieving a goal and allow reactive execution of control actions based on observed world state. TR plans are coded as ordered lists of condition-action pairs. Each condition specifies a state of the environment that must be true in order to perform the action. The TR plan is executed by checking the preconditions of each TR rule in the tree in order. If a rule has a satisfied precondition, its associated action is taken. World state is then reevaluated and the tree is cycled again. Only the rule with highest ordering whose conditions are satisfied is activated at each iteration.

Each control action is intended to make a condition for a higher ordered rule true. Control algorithms are provably correct if the union of all rule preconditions identifies the universe of possible world states, and if all actions guarantee the eventual satisfaction of a higher precondition. TR trees allow reactive plan execution, since the action that corresponds with the observed world state is taken at each time step. If the world state changes to a state further from the goal state, a lower level rule automatically activates and control moves the state closer to the goal. If a benevolent world state occurs, causing the world state to jump closer to goal, the control system skips unnecessary control actions.

5 LEARNING

Learning is intended to occur in our control architecture at many levels. Rather than regarding learning as a centralized activity, the framework supports the use of local learning techniques in different structures. This view of adaptive behavior fits in with the overall distributed local-control scheme on which the entire architecture is based [5].

Low-level learning in the form of pattern recognition and feature detection can occur in the PAL through the use of adaptive filters attached to feedback objects. Neural networks, fuzzy classifiers, and other adaptive systems can identify system behavior and store learned information as network weights, fuzzy sets, etc. These filter parameters can be stored at the controller level and passed back to the PAL during future tuning.

Conventional adaptive control methods can be used at the solver level to enhance the locally adaptive nature of the system. Well understood techniques exist for applying such algorithms as adaptive PID, Kalman filters, etc. Controller-level learning involves deeper knowledge-level issues. Since these modules operate over longer time scales and often contain strategic or goal oriented information, high level learning algorithms such as case based learning and decision tree induction are appropriate [5].

One area of learning which we have begun to study in detail is model refinement. Model refinement is the process of identifying system behavior with some uncertainty, and then refining the model through observation as well as active experimentation to reduce uncertainty or adapt the model to changing conditions. Physicists often use complex model refinement techniques to work from an analytic model, as coded in TRANSPORT, COSY, etc., and iterate between beam tuning and model adaptation and search. Our goals are to adapt these methods within the framework of our automatic control system.

5 SUMMARY

We have described a distributed, hierarchical architecture for beamline control combining heuristic, knowledge-based, and conventional control methods. This hybrid architecture integrates a variety of reasoning, search, and pattern recognition methodologies. Preliminary tests, reported in [1, 2] indicate the potential for emulating and often exceeding the performance of skilled human operators. Continuing research includes extending the diagnostic, model refinement, planning, and learning components of the system.

ACKNOWLEDGMENTS

This work was supported by a DOE SBIR contract (#DE-FG05-95ER81897) to Vista Control Systems, Inc. We thank Mike Kroupa, Bob Knight, and Bob Westervelt of Vista. We thank Andy Jason of LANL and Xijie Wang of BNL-ATF for helping us understand accelerator physics.

REFERENCES

[1] Klein, W., Stern, C., Kroupa, M., Westervelt, R., Luger G., and Olsson, E. 1997. Tuning and Optimization at Brookhaven and Argonne: Results of Recent Experiments, *Proceedings of the Particle Accelerator Conference*, American Physical Society.

[2] Klein, W., Stern, C., Luger, G., and Olsson, E. 1997. An Intelligent Control Architecture for Accelerator Beamline Tuning, *Proceedings of Innovative Applications of Artificial Intelligence*, Cambridge: MIT Press.

[3] Clout, P. 1993. The status of Vsystem. *Proceedings of the Third International Conference on Accelerator and Large Experiment Physics Control Systems*, Germany.

[4] Acar, L. and Ozgunner, U. 1993. Design of Structure-Based Hierarchies for Distributed Intelligent Control. In Antsaklis et al., *An Introduction to Intelligent and Autonomous Control*, Boston: Kluwer.

[5] Klein W. 1997. *A Software Architecture for Intelligent Control*, Ph.D. Dissertation, Computer Science Department, University of New Mexico.

[6] Nilsson, N. 1994. Teleo-Reactive Programs for Agent Control. *Journal of Artificial Intelligence Research* 1:139-158.

A HYBRID NUMERICAL METHOD FOR ORBIT CORRECTION

Greg White, Tom Himel, Hamid Shoaee *
Stanford Linear Accelerator Center, Stanford University, Stanford CA 94305

Abstract

We describe a simple hybrid numerical method for beam orbit correction in particle accelerators. The method overcomes both degeneracy in the linear system being solved and respects boundaries on the solution. It uses the Singular Value Decomposition (SVD) to find and remove the null-space in the system, followed by a bounded Linear Least Squares analysis of the remaining recast problem. It was developed for correcting orbit and dispersion in the B-factory rings.

1 INTRODUCTION AND PROBLEM STATEMENT

The main objective in accelerator steering is to minimize deviations of the beam from the center of the beam pipe, that is, to minimize the rms of the orbit. There may be other objectives such as minimizing the corrector strengths, or dispersion, but these are generally secondary. What follows can be generalized very easily to include these secondary objectives, but for illustration only orbit correction will be discussed.

For practical purposes of online orbit correction in a linear accelerator, its reasonable to assume that there is only a linear relationship between a corrector magnet's strength (the extent to which it bends the beam) and the beam's position when measured horizontally or vertically by any "down-stream" Beam Position Monitor (BPM). The magnitude of this influence can be computed or measured, and recorded, for all magnets to all BPMs in the accelerator. This coefficient is sometimes called, informally, T_{12}, the subscripts refer to the position of this coefficient in the larger "Transport matrix" discussed in [5] and elsewhere, which describes to the first-order the action-response relationship between control elements of a beam-line.

The problem of accelerator steering can then be posed as a system of simultaneous linear equations relating M BPMs to N magnets used for orbit correction.

$$\begin{aligned} T_{12}^{11}\Delta\theta_1 + T_{12}^{12}\Delta\theta_2 + \cdots + T_{12}^{1N}\Delta\theta_N &= \Delta BPM_1 \\ T_{12}^{21}\Delta\theta_1 + T_{12}^{22}\Delta\theta_2 + \cdots + T_{12}^{2N}\Delta\theta_N &= \Delta BPM_2 \\ &\vdots \\ T_{12}^{M1}\Delta\theta_1 + T_{12}^{M2}\Delta\theta_2 + \cdots + T_{12}^{MN}\Delta\theta_N &= \Delta BPM_M \end{aligned}$$

where ΔBPM_i, $i = 1 \ldots M$, is the desired change in the ith BPM, and $\Delta\theta_j$, $j = 1 \ldots N$, is the sought change in the bend angle of the jth corrector magnet to achieve that change. A suitable vector of the N $\Delta\theta$ values which solves this system would then constitute a solution to the steering problem for the M BPMs.

* Work supported by the Department of Energy, contract DE-AC03-76SF00515

The equations are often written in matrix form, which lends itself to solution by numerical methods:

$$\begin{bmatrix} T_{12}^{11} & T_{12}^{12} & T_{12}^{13} & \cdots & T_{12}^{1N} \\ T_{12}^{21} & T_{12}^{22} & T_{12}^{23} & \cdots & T_{12}^{2N} \\ & & \vdots & & \\ T_{12}^{M1} & T_{12}^{M2} & T_{12}^{M3} & \cdots & T_{12}^{MN} \end{bmatrix} \cdot \begin{bmatrix} \Delta\theta_1 \\ \Delta\theta_2 \\ \vdots \\ \Delta\theta_N \end{bmatrix} = \begin{bmatrix} \Delta b_1 \\ \Delta b_2 \\ \vdots \\ \Delta b_M \end{bmatrix}$$

In practice though, there is a barrier constraint; that each $\Delta\theta$ does not result in exceeding the practical maximum strength for that magnet. That is, each element in the unknown vector of $\boldsymbol{\Delta\theta}$ has an upper limit.

So, we could characterize this as a linear least squares problem

$$\|\mathbf{Ax} - \mathbf{b}\|_2 \tag{1}$$

$$\text{subject to } \mathbf{x}_j \leq \mathbf{x}_j^{\max}$$

for which a solution $\mathbf{x}$ can be found by least-squares inversion of $\mathbf{A}$ giving $\mathbf{x} = \mathbf{A}^\dagger\mathbf{b}$. $\mathbf{b}$ would be the vector of all the desired changes to the BPMs values, $\mathbf{x}$ is the vector of necessary changes in corrector magnet strengths as bend angles, and $\mathbf{A}$ is the matrix of all the ratios between a corrector strength and its concomitant beam monitor value. Specifically, $\mathbf{A}$ is the matrix of the T_{12}s in the system, where each column of $\mathbf{A}$ represents a single corrector.

Posed as a linear system then, the problem lends itself to questions such as "is there a solution $\mathbf{x}$, if so is there a family of solutions, and if there is, which is the "best" solution according to some criteria, if there is no solution, is there at least some optimum compromise?"

These questions are all related to the property of *rank*, the maximal number of linearly independent columns in $\mathbf{A}$, and the ratio of this rank to the number of unknowns in $\mathbf{x}$. The term *singularity* is also often used particularly for square matrices. There are a number of separate theoretical methods to answer these questions, but one, the SVD has become popular because its very robust and is easily applicable to all of these questions.

The SVD though does not respect barrier conditions so its not possible to include the magnet limits in the problem posed to classical SVD algorithms, and it is this drawback we address later.

2 THE SINGULAR VALUE DECOMPOSITION

The SVD technique is based on a factorization of $\mathbf{A}$ which we shall summarize as follows: $\mathbf{A} = \mathbf{U\Sigma V^T}$ where $\mathbf{A}$ is M rows $\times$ N columns, $\mathbf{U}$ is an $M \times M$ column-orthogonal matrix, $\boldsymbol{\Sigma}$ is an $M \times N$ diagonal matrix of positive or 0 values, and $\mathbf{V}$ is an $N \times N$ column-orthogonal matrix, i.e. $\mathbf{U^TU} = \mathbf{V^TV} = \mathbf{I}$. Since V is square it is also row-

orthogonal.

$$(\mathbf{A}) = (\mathbf{U}) \cdot \begin{pmatrix} \sigma_1 & & & \\ & \sigma_2 & & \\ & & \ddots & \\ & & & \sigma_N \end{pmatrix} \cdot (\mathbf{V^T}) \quad (2)$$

The elements σ_j are the *singular values* of $\mathbf{A}$. The condition-number of $\mathbf{A}$ is given by the ratio of the largest of the singular values to the smallest. The rank of $\mathbf{A}$ is given by the number of non-0 singular values, and so the nullity (explained more fully below) of $\mathbf{A}$ is given by the number of 0 valued singular values. Given the above properties of orthogonality, the pseudo-inverse of A is given by $\mathbf{A}^\dagger = \mathbf{V}\mathbf{\Sigma}^\dagger\mathbf{U^T}$. $\mathbf{\Sigma}$ is a diagonal matrix, so its inverse is the diagonal matrix of reciprocals of its elements. This then is the simple method of solving a linear system given in eq 1: using the formalism used in Press et al[2]:

$$\mathbf{A}^{-1} = \mathbf{V} \cdot diag(1/\sigma_j) \cdot \mathbf{U}^T \quad (3)$$

The properties of these matrices for diagnosing algebraic problems are well explored, particularly by Golub and Riensch [1]. The interpretation of results under the conditions $M < N, M = N$ and $M > N$ are very practically explained in Press et al, and Strang[3] describes Linear Algebra in general, and its geometric interpretation in particular.

3 THE SOLUTION SPACE

To illustrate our method of finding solutions which respect barrier conditions lets look at the case of the under-determined system, one in which there are simply less equations than unknowns, $M < N$, or the rank of $\mathbf{A}$ is insufficient to find a single perfect solution. This may have been due simply to there being more correctors than BPMs, or more subtly because of correctors and BPMs being poorly separated in phase space, or one sub-set of correctors having roughly the same influence on the BPMs as some other sub-set. All of these conditions would cause degeneracy in the transformation matrix $\mathbf{A}$.

The SVD will return at least $N - M$ 0 or small σ_j's. There may also be additional 0 σ_j due to rank deficiency. Call the number of 0 singular values k.

One must also set σ_j that are very close to 0 to 0, since those are probably dominated by numerical error. If these values are allowed to remain they will tend to attract the computation in 3 toward a null-space vector. Specifically what constitutes "close to 0", is related to computational precision and accuracy of original data. Guidelines for deciding appropriate cut-off values are given in the literature.

The SVD can easily be used to select a 'particular solution' and it will be the solution which is smallest in the least squares sense: one simply sets all the 0 valued σ (after editing for computational precision) to 0 rather than $1/\sigma_j$.

$$\mathbf{x} = \mathbf{V} \cdot [diag(1/\sigma_j)] \cdot (\mathbf{U}^T \cdot \mathbf{b}) \quad (4)$$

If we now wanted to look at alternative solutions, perhaps because the particular solution involved exceeding the limit of some corrector, we can look more closely at the geometric interpretations of $\mathbf{U}$ and $\mathbf{V}$. To do this lets make explicit the ideas of range and null-space. If there are alternative solutions $\mathbf{x}$, $\mathbf{A}$ must be singular or $M < N$, and then there must be some sub-space $\mathbf{x}$ for which $\mathbf{A} \cdot \mathbf{x} = \mathbf{0}$. This is the null-space of $\mathbf{A}$, and its dimension is called the "nullity" of $\mathbf{A}$. The space that can be reached by $\mathbf{A}$ multiplied by any $\mathbf{x}$ at all is called the "range" of $\mathbf{A}$. The rank of $\mathbf{A}$ is equivalent to the dimension of this range.

The non-0 singular values define the dimensions of these sub-spaces. Specifically, the columns of $\mathbf{U}$ that correspond to same-numbered non-0 valued elements of $\mathbf{\Sigma}$ form a set of orthonormal basis functions for the range of $\mathbf{A}$, call this matrix $\mathbf{U_1}$. A basis is a set of vectors which spans the same sub-space as the original matrix. It is orthonormal in the sense that it is a set of mutually orthogonal unit vectors, and so makes up a necessary and sufficient description of the sub-space.

The columns of $\mathbf{V}$ that correspond to 0 valued elements of $\mathbf{\Sigma}$ form a set of orthonormal basis functions for the null-space of $\mathbf{A}$, call this matrix $\mathbf{V_0}$.

Using $\mathbf{V_0}$ one can compute alternative solutions by adding to the particular solution $\mathbf{x}$ linear multiples (or "combinations") of columns v_j drawn from $\mathbf{V_0}$, giving $\mathbf{x}'$ and the overall value $\mathbf{Ax}'$ won't be different from $\mathbf{Ax}$.

Taking this process further, how can we find those specific alternative solutions which do not exceed some specific barriers?

4 BOUNDED LEAST SQUARES SEARCH

Recall that the objective is to find a vector $\mathbf{x}$ which minimizes $\|\mathbf{Ax} - \mathbf{b}\|_2$ - a linear least squares problem. This is equivalent to minimizing the RMS of the beam orbit when $\mathbf{A}$ is the "transport matrix" of an accelerator. But the problem is made difficult to solve by the classical linear least squares algorithm implementations such as LSSOL[4] if there is degeneracy in the equations $\mathbf{A}$. Degeneracy significantly compounds the effects of rounding error in numerical computations.

One way to overcome the problem would be to remove the trouble-some null-space from $\mathbf{A}$, and search for solutions $\mathbf{x}$ in the remaining sub-space. The constraints on the solution would also have to be transformed in to the coordinates of that, re-cast, problem. When a solution is found it would be transformed back again into the original coordinates.

To delineate these transformations, define the basis functions that will be used to generate them:

$\mathbf{U_1} \stackrel{\text{def}}{=}$ columns $\mathbf{u_j}$, for which $\sigma_\mathbf{j} \neq \mathbf{0}$: An orthonormal basis for the range of $\mathbf{A}$. $\mathbf{U_1}$ is $M \times N - k$.

$\mathbf{U_0} \stackrel{\text{def}}{=}$ columns $\mathbf{u_j}$, for which $\sigma_\mathbf{j} = \mathbf{0}$: An orthonormal basis for the orthogonal complement of the range of $\mathbf{A}$. $\mathbf{U_0}$ is $M \times k$.

$\mathbf{V_0} \stackrel{\text{def}}{=}$ columns $\mathbf{v_j}$, for which $\sigma_j = 0$: An orthonormal basis for the null-space of $\mathbf{A}$. $\mathbf{V_0}$ is $N \times k$.

$\mathbf{V_1} \stackrel{\text{def}}{=}$ columns $\mathbf{v_j}$, for which $\sigma_j \neq 0$: An orthonormal basis for the orthogonal complement of the null-space of $\mathbf{A}$. $\mathbf{V_1}$ is $N \times N - k$.

$\mathbf{\Sigma_1} \stackrel{\text{def}}{=} \sigma_j$, for which $\sigma_j \neq 0$: The extent of each dimension of the range of $\mathbf{A}$. $\mathbf{\Sigma_1}$ is a square diagonal matrix of non-0 singular values and is $N - k \times N - k$.

Then define the orthogonal sub-space of $\mathbf{A}$:

$$\mathbf{A_1} \stackrel{\text{def}}{=} \mathbf{U_1 \Sigma_1} \tag{5}$$

The solution vector being sought must similarly be interpreted in the coordinates of orthogonal complement of the null-space of $\mathbf{A}$:

$$\mathbf{x_1} \stackrel{\text{def}}{=} \mathbf{V_1^T x} \tag{6}$$

$\mathbf{x_1}$ will be $N - k \times 1$.

Then the minimization can be re-written to exclude the null-space:

$$\begin{aligned} & \|\mathbf{Ax} - \mathbf{b}\|_2 \\ \iff & \|\mathbf{U_1 \Sigma_1 V_1^T x} - \mathbf{b}\|_2 \\ \iff & \|\mathbf{A_1 x_1} - \mathbf{b}\|_2 \end{aligned} \tag{7}$$

This is then a least squares problem of smaller dimension - those dimensions in the null-space of $\mathbf{A}$ have been removed.

To incorporate the barriers on the original problem, $\mathbf{x_j} \leq \mathbf{x^{max}}$, where $\mathbf{x^{max}}$ are the limits on changes to the corrector magnet settings, we need to pose those barriers also in the recast coordinates. From the interpretation of $\mathbf{V_1}$, and the definition of $\mathbf{x_1}$ given in 6, and since the inverse of an orthogonal matrix is its transpose, then

$$\mathbf{x} = \mathbf{V_1 x_1} \tag{8}$$

$\mathbf{V_1}$ then is the matrix whose rows each define a general linear constraint on $\mathbf{x_1}$. Each corresponding row vector multiplication $\mathbf{V_{1j} x_1}$ must not exceed $x_j^{\max}$.

Altogether, the linear least squares problem in the recast coordinate space is to minimize:

$$\|\mathbf{A_1 x_1} - \mathbf{b}\| \tag{9}$$

$$\text{subject to } \mathbf{V_1 x_1} \leq \mathbf{x^{max}}$$

This can be solved by any linear least squares solver that accepts a linear constraints matrix as part of the problem parameters, such as LSSOL. When some $\mathbf{x_1}$ is found, it can be transformed back into regular coordinates by 8.

5 PERFORMANCE

Both the SVD and the Linear Least Squares method for non-singular matrices are known to be very robust.

Although the decomposition operation itself is fairly expensive, it need at least only be computed once and then all orbit corrections using the same transport matrix can proceed from it.

We do not submit the recast problem to a constrained linear least squares solver in the case that the SVD solution, by 4, finds solutions that are in bounds, since the minimum solution has already been found. Also, the linear least squares technique in the case of negligible degeneracy is equivalent to the SVD when all of the singular values are used.

The hybrid method has been tested in simulation and been in operation in the SLC linac for some time with success. It was developed for the B-factory, which will be commissioned in the summer of '97, when heavier requirements will be made of its ability to deal with degenerate matrices. It is also part of a larger project in which dispersion is corrected simultaneously with orbit [6].

6 THANKS

Our very warm thanks are extended to Prof. SVD, Gene Golub for pointing us down the hybrid path, and to Jeff Corbet and Martin Lee. And Haitham Hindi, who is to formal argument what a buzz-saw is to a match-stick.

7 REFERENCES

[1] Golub G., Reinsch C. Singular Value Decomposition and Least Squares Solutions, in Wilkinson J.H. and Reinsch C. 9 (editors) Handbook for Automatic Computation, vol II. Springer. 1971.

[2] Press W.H., Flannery B.P, Teukolsky S.A., Vetterling W.T. Numerical Recipes, The Art of Scientific Computing. Cambridge University Press. 1989.

[3] Strang, G Linear Algebra and its Applications. Harcourt Brace Jovanovich. 1988.

[4] Gill P. E., Hammarling S.J., Murray W., Saunders M.A., Wright M.H., LSSOL, Systems Optimization Laboratory, Stanford University. 1986.

[5] Sheppard J. C., Lee M. J., Ross C., Seeman J. T., Stiening R. F., Woodley M. D. Beam Steering in the SLC Linac, Proceedings of PAC 1985.

[6] Chi Y., Donald M., Shoaee H., White G., Yasukawa L.A. An Orbit and Dispersion Correction Scheme for the PEP-II. Proceedings of PAC 97.

ELECTRON MULTIPACTOR CODE FOR HIGH-POWER RF DEVICES

S. Humphries, Jr., Department of Electrical and Computer Engineering,
University of New Mexico, Albuquerque, NM 87131 and
D. Rees, APT Program, Los Alamos National Laboratory, Los Alamos, NM 87545

Abstract

We have developed an integrated software system, TrakRF, to model electromagnetic fields and charged particle orbits in high-power RF devices. Our primary application is simulation of electron multipactoring near RF vacuum windows for the APT (Accelerator Production of Tritium) Program. In this paper we describe features of the codes and initial multipactor calculations for superconducting cavity arrays. The finite-element frequency-domain solver can determine resonant modes in cavities and waveguides. TrakRF directly determines power dissipation and phase shifts in lossy materials. In addition, the program handles scattered waves in open structures with free-space boundaries based on matched termination layers. TrakRF has advanced particle tracking capabilities to investigate a variety of innovative window designs. The program can simultaneously apply three independent solutions for electrostatic, magnetostatic and RF fields. The finite-element methods allow an accurate representation of electron collisions with surfaces.

1 INTRODUCTION

TrakRF is an integrated finite-element software system to model charged particle trajectories in combined electrostatic, magnetostatic and electromagnetic fields. The program is an extension of the Trak 3.0 [1] gun design code. New capabilities include frequency-domain calculations of electromagnetic fields in both resonant cavities and open spaces and particle tracking in time-dependent fields. A unique feature is the ability to combine up to three independent numerical solutions for static electric and magnetic fields and RF modes. The present version handles two-dimensional fields in planar or cylindrical geometries.

The software was developed to investigate contributions of multipactoring to breakdowns on RF windows in high-power accelerators. A cooperative program on Accelerator Production of Tritium to maintain the US nuclear weapons stockpile has recently been initiated at Los Alamos National Laboratory (LANL) and the Savannah River Site [2]. The goal is a continuously operating proton linac that produces a 1.3 GeV beam with an average current of 100 mA (130 MW beam power). The accelerator demands powerful RF systems with high reliability. A critical area of concern is the possibility of breakdowns on RF vacuum windows that must transmit MW power levels. To address the issue, an experimental and theoretical program of window testing and development has been initiated at LANL [3]. Starting in October 1996, the University of New Mexico has supported this effort through the development of particle and radiation diagnostics to warn of impending breakdowns and computer codes to help understand the role of stray electrons in window failure.

2 CONFORMAL MESHES AND STATIC FIELD COMPUTATIONS

All static and dynamic field calculations in TrakRF are carried out on conformal triangular meshes modeled on those used in SuperFish [4]. As an example, Fig. 1 shows a mesh of triangular elements for the calculation of resonant modes in the five cell $\beta = 0.64$ superconducting cavities designed for the APT accelerator. The advantage is apparent - the edges of elements conform closely to curved and angled material boundaries. As a result, each element is uniquely associated with a material. This is an important feature in a particle tracking code because it allows an accurate identification of surface collisions. Section 3 reviews some advantages of the finite element formulation in RF calculations. In static field solutions, there are three major advantages over finite-difference calculations: 1) the finite element method gives accurate field values near metal surfaces, 2) the technique correctly represents field discontinuities at the boundaries of dielectrics and ferromagnetic materials, and 3) it is easy to implement Neumann conditions on angled and curved boundaries.

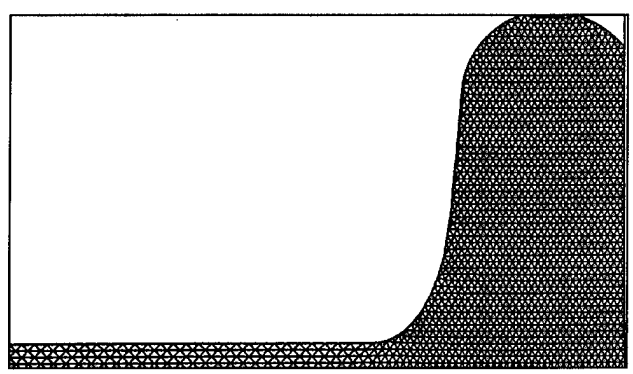

Figure 1. Conformal triangular mesh for the LANL 5 cell superconducting cavity

TrakRF uses the standard mesh generator and static field solvers of the TriComp system [5]. This suite of finite-element programs runs on IBM-standard personal computers. Boundary information is entered through an interactive drafting program or from drafting like AutoCAD. The basic electrostatic and magnetostatic solvers use the linear finite-element formulation described in Refs. [6] and [7] with solutions by successive over-relaxation.

0-7803-4376-X/98 /$10.00 © 1998 IEEE

They analyze files of boundary and material information to produce output files of vertex coordinates and corresponding values of electrostatic or vector potential.

3 RF FIELD COMPUTATIONS

The derivation of finite-element equations for two-dimensional frequency-domain RF fields is reviewed in Ref. [7]. As an example, consider the equations for a planar structure with no variation in z with electric field polarization E_z. The associated differential equation is

$$-\nabla\times\left(\frac{1}{\mu}\nabla\times E\right)=-\varepsilon\omega^2 E+j\omega J_o, \qquad (1)$$

where ω is the angular frequency of the radiation. The quantities μ and ε may have may have complex values to represent losses from resistivity or non-ideal materials. The current source J_o contains information on the amplitude and phase of drive regions. The finite-element equations for wave propagation at the test vertices are derived from area integrals of Eq. 1 over surrounding elements and vertices. The result is

$$E_{zo}\left(-\sum_i W_i+\omega^2\sum_i\frac{\varepsilon_i a_i}{3}\right)+\sum_i E_{zi}= j\omega\sum_i\frac{J_i a_i}{3}. \qquad (2)$$

In general, the quantities E_{zi} are complex numbers to represent amplitude and phase. The index *i* refers to the vertices and elements surrounding a test vertex marked *o*. The quantities ε_i, μ_i and J_i are the material properties and current density of the elements. Expressions for the geometric coefficients W_i are given in Ref. [7]. Equation 2 represents a large set of coupled linear equations, one for each mesh vertex. The set is solved in TrakRF using sparse matrix inversion methods. The complex values of E_{zi} give the physical electric field at a given RF phase. Numerical derivatives give the magnetic field components B_x and B_y.

A significant advantage of the finite-element method is the ability to define ideal absorbing layers of arbitrary shape to represent free-space boundary conditions. The procedure is to set up a thin layer of width δ on the outside of the solution volume. The imaginary part of the dielectric constant in the layer is assigned the value $\varepsilon'' = -\sigma/\omega$, where the conductivity is matched to the impedance of the adjacent medium,

$$\sqrt{\frac{\mu}{\varepsilon}}=\frac{1}{\sigma\delta}. \qquad (3)$$

The performance of absorbing layers equals or exceeds that of look-back techniques [8]. The advantages are that termination layers can have any shape or orientation and do not place restrictions on the time step in time-domain solutions.

Figure 2 shows an example of a resonant calculation, the π mode of the LANL five-cell superconducting cavity array for proton beams with $\beta = 0.64$. The outer radius is 19.4 cm and there is a 20 cm beam pipe on the left that is not shown. A small capacitive probe (bottom-right) drives the mode. The program searches for the zero crossing of the imaginary part of the response of a sensor near the outer radius. The predicted frequency of 701.6 MHZ is in good agreement with SuperFish and MAFIA results.

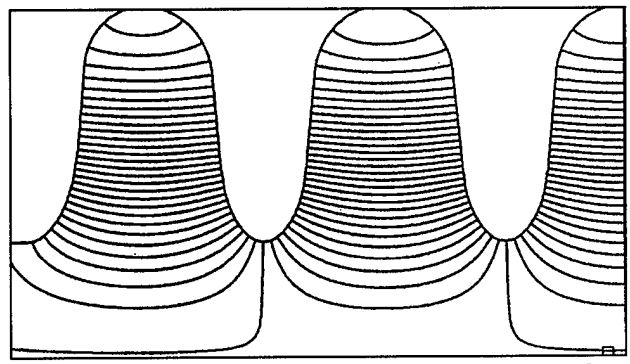

Figure 2. Electric field lines - π mode of the LANL β = 0.64 5-cell superconducting cavity array. f = 701.6 MHz.

4 CHARGED-PARTICLE ORBIT CALCULATIONS

Charged-particle orbit calculations in TrakRF are straightforward. They involve Runge-Kutta integrations using numerically-calculated field components. The main challenge is organization of the broad range of possibilities. The program can handle three numerical field solutions on independent conformal meshes: electrostatic, magnetostatic, and electromagnetic. The motivation for this versatility is to model stray electron control near RF windows using sweeping fields. Field geometries can be mixed in any combination. The static solutions may have either rectangular geometry (variations in x and y with infinite extent in z) or cylindrical (variations in r and z with azimuthal symmetry). There are four possibilities for electromagnetic fields: rectangular geometries with primary field components E_z or H_z or cylindrical systems with solutions for E_θ or H_θ. TrakRF uses a reference three-dimensional Cartesian coordinate system and organizes interpolations of the numerical field solutions to derive total values of **E** and **B** at the position and elapsed time of the particle. The three field solutions can be assigned translations and rotations within the three-dimensional reference system.

The basic method to initiate particle orbits is through a parameter listing file generated by spreadsheets or user-written programs. The file specifies charge, mass, initial kinetic energy, position and direction cosines. When electromagnetic fields are present there is the option to assign a reference phase. Each particle initially has a multiplication factor of unity. TrakRF can handle up to 1000 orbits in a run. The program can also generate a variety of particle distributions. Working from user-supplied numerical tables, TrakRF creates arbitrary distributions in energy, position, and direction. The program

has several options to stop orbits, including maximum distance and elapsed time. It is also possible to set up stopping planes along the Cartesian axes for high-accuracy interpolations of crossing particle parameters.

An important feature for the multipactor application is orbit modification when a particle enters a material element. Element characteristics are identified by the status of the corresponding mesh region. Regions can be individually set to one of three conditions: *Vacuum*, *Material* or *Secondary*. A particle stops if it enters a *Material* element on any of the three field meshes. For *Secondary* elements, the orbit is returned to its position before entering the surface and assigned a low momentum in the opposite direction. The particle multiplication factor is multiplied by the secondary emission coefficient of the material. This quantity is either a constant value or derived from a user-generated numerical function of the incident kinetic energy. Orbits that reach the end of their lifetime with multiplication factors much larger than unity are susceptible to multipactoring.

5 BENCHMARK CALCULATIONS

We carried out an extensive set of runs to investigate multipactoring in the $\beta = 0.64$ and $\beta = 0.82$ single-cell test cavities at LANL. We used the energy-dependent secondary emission coefficients for clean niobium tabulated in Ref. [9]. Electrons were emitted during the acceleration half-cycle from twelve equally-spaced positions on the upstream wall. Nineteen electrons were generated at each position in the phase range from -180° to 0° in 10° intervals. Each run tracked a total of 228 electrons for 150 ns (105 RF periods). The multiplication factor for individual electrons increased or decreased from unity depending on the history of interactions with the niobium walls. The global multiplication factor is the sum of individual values divided by the number of initial electrons. When the value was less than unity most individual factors were small and there was no orbit that stayed in resonance for a large number of cycles. Although particles started at discrete locations, resonant electrons migrated large distances; therefore, the runs gave a good indication of average cavity properties.

Figure 3 shows global multiplication factors as a function of the RF electric field amplitude at the center of the cavity over the range 1.0 to 6.0 MV/m. The $\beta = 0.82$ cavity was safe below about 4.2 MV/m, but exhibited strong electron multiplication at higher gradient. Dangerous orbits generally started near the outer wall of the cavity. Here, the combination of electric field amplitude and transit distance gave resonant electrons that struck the walls with kinetic energy in the range 200-1000 eV. The increasing electron density resulted mainly from first order multipactoring, where critical electrons struck the cavity about once each half RF cycle. Global multiplication factors as high as 10^{14} were observed for the 150 ns runs. The $\beta = 0.64$ cavity had a lower critical field of about 3.6 MV/m.

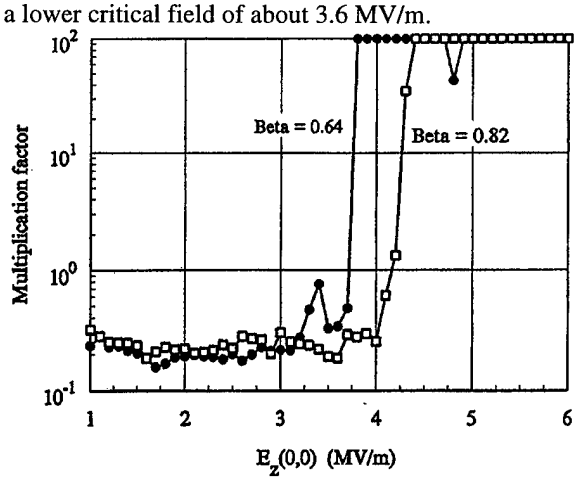

Figure 3. Global multiplication factor – electron multipactoring in the LANL single cell tests cavities as a function of peak on-axis field. The values at the top range from 10^{11} to 10^{14}.

REFERENCES

[1] S. Humphries, Jr., J. Comp. Phys. **125**, 488 (1996).

[2] G. Lawrence, *et.al.*, *Conventional and Superconducting RF Linac Design for the APT Project* in **Proc. 1996 Int'l. Linear Acc. Conf.** (Geneva, 1996), to be published.

[3] D. Rees, P.J. Tallerico and M. Lynch, IEEE Trans. Plasma Sci. **25**, 1033 (1996).

[4] K. Halbach and R.F. Holsinger, Particle Acc. **7**, 213 (1976).

[5] TriComp software source code courtesy of Field Precision, Albuquerque, NM.

[6] P.E. Allaire, **Basics of the Finite Element Method** (W.C. Brown Publishers, Dubuque, 1985).

[7] S. Humphries, Jr., **Field Solutions on Computers** (CRC Press, Boca Raton, 1998), Chap. 14.

[8] See, for instance, K.S. Kunz and R.J. Luebbers, **The Finite Difference Time-Domain Method for Electromagnetics** (CRC Press, Boca Raton, 1993), Chap. 18.

[9] D.R. Lide (ed..), **Handbook of Chemistry and Physics, 74th Edition** (CRC Press, Boca Raton, 1993), 12-107.

EIGENMODES OF MICROWAVE CAVITIES CONTAINING HIGH-LOSS DIELECTRIC MATERIALS

S. J. Cooke, University of Maryland, College Park, MD 20742 and
B. Levush, Vacuum Electronics Branch, Code 6840, NRL, Washington DC 20375

Abstract

The numerical determination of the electromagnetic field eigenmodes of a microwave cavity containing regions of high-loss dielectric material is of technological importance to many areas, including high power microwave generation, particle accelerator design and microwave sintering of ceramic materials. This problem has proved problematic to numerical techniques [1], causing poor convergence and long computation times when highly lossy materials are present. The Jacobi-Davidson algorithm [2] applied to this problem is shown to be capable of extracting a set of eigenmodes, even for the cases of degenerate eigenvalues and low ohmic-Q cavity modes. Details of the theory and numerical solution using 2-dimensional (planar circuit) and 3-dimensional electromagnetic operators will be presented.

1 INTRODUCTION

Many scientific and engineering problems require the determination of a selected number of the eigenvalues, and possibly eigenvectors, of a large system of linear equations. Typical examples arise in electromagnetics when a field is represented by discrete values and the determining equation is discretised in some manner, for example by finite difference, finite element or finite integration methods. The ease with which such problems may be solved depends on the size of the problem, but also is strongly dependent upon the distribution of the eigenvalues and whether they are real or complex.

Methods for eigenvalue and eigenvector computation for large, linear systems of equations by iterative methods frequently require that the matrices be self-adjoint (Hermitian). Such methods can often be applied with some success for systems having eigenvalues with relatively small imaginary parts, however the theoretical basis for convergence is not well defined and poor convergence often results. Many basic properties of the solutions of self-adjoint eigensystems do not hold in the general case, and more rigourous techniques must be used if convergence is to be ensured.

2 EIGENVALUE FORMULATION

Two electromagnetic eigenproblems will be considered here. Firstly, a 2-dimensional planar circuit model will be used to provide realistic test examples of moderate size, for which solutions may be readily visualised. Secondly, a full 3-dimensional model is described and examples given to show the effectiveness of the Jacobi-Davidson method on larger problems.

2.1 2D planar circuit model

Simple electromagnetic planar circuits considered here are those for which an exact two-dimensional representation can be found in terms of a single field component. The class includes many structures of practical use, for example rectangular waveguides with H-plane bends and junctions, which may contain columnar structures of metal or dielectric. Such circuits have no structure in the third dimension other than parallel bounding planes of metal, and possess only modes having an electric field perpendicular to the plane.

For such a circuit having no structure in the y direction, the following eigenvalue problem may be derived

$$\left\{\nabla_\perp^2 + \omega^2\epsilon(\mathbf{r}_\perp)\mu_0\right\} E_y(\mathbf{r}_\perp) = 0$$

The cavity frequencies, ω, and mode structures, $E_y(\mathbf{r}_\perp)$, may be obtained as solutions of this eigensystem. Metallic wall boundary conditions in the x–z plane may be included in the numerical implementation of the differential operator. The transverse Laplacian operator is self-adjoint, and therefore if the permittivity and permeability functions are real then the eigensystem is symmetric, and the spectrum will contain only real eigenvalues.

2.2 3D complex cavity model

A 3-dimensional electromagnetic operator was derived using the finite integration method [3]. The eigenvalue form derived from Maxwell's equations is (in normalised units) the vector equation [1]

$$\text{curl}\, \mu^{-1}\text{curl}\, \mathbf{E} - \text{grad div}\, \epsilon\mathbf{E} = \omega^2\epsilon\mathbf{E}$$

where the discretised components of $\mathbf{E}$ form the eigenvector, and ω^2 is the eigenvalue of the numerical implementation of the operator. The divergence term is included to remove the multiply degenerate *static* solutions with eigenvalue zero which result from the freedom of E to include a component corresponding to the gradient of an arbitrary scalar field.

The finite integration method defines field components using the Yee cell arrangement, shown in figure 1, for which the differential operators take a particularly simple form, and takes account of the permittivity and permeability of each
cell.

2.3 LOSSY MATERIALS

Regions of complex permittivity, representing Ohmic loss in these materials, make the discretised eigensystems non-Hermitian, and therefore critically change the characteris-

0-7803-4376-X/98 /$10.00 © 1998 IEEE

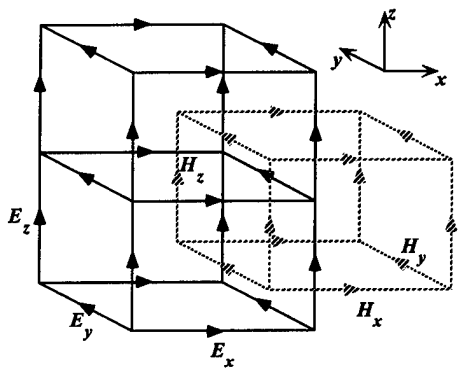

Figure 1: Yee cell structure of 3D discretisation

tics of the solution. The solution for non-Hermitian systems may often be obtained using methods derived for Hermitian systems, provided that the system deviates only slightly from a Hermitian problem. Here, this corresponds to small values of the loss tangent of the dielectric materials, and solutions for such cases frequently converge using Hermitian methods. If highly lossy materials are to be modelled successfully, a more rigourous approach is necessary.

3 NON-HERMITIAN EIGENSYSTEMS

A generalised linear matrix eigensystem can be written in the form

$$\mathbf{Ax} = \lambda \mathbf{Bx} \tag{1}$$

The column vector $\mathbf{x}$ satisfying (1) is an eigenvector of the system $\{\mathbf{A},\mathbf{B}\}$, with corresponding eigenvalue, λ. For matrices which are not Hermitian, it is possible to formulate a second, related eigenproblem as follows.

$$\overline{\mathbf{y}}\mathbf{A} = \lambda\overline{\mathbf{y}}\mathbf{B} \text{ or } \overline{\mathbf{A}}\mathbf{y} = \overline{\mathbf{B}}\mathbf{y}\overline{\lambda} \tag{2}$$

where $\overline{\mathbf{y}}$ is a row vector. The vector $\overline{\mathbf{y}}$ satisfying (2) is a *left*-eigenvector of the system $\{\mathbf{A},\mathbf{B}\}$, with corresponding eigenvalue, λ. For a given generalised eigensystem described by $\{\mathbf{A},\mathbf{B}\}$, pairs of left- and right-eigenvectors have equal eigenvalues, though the eigenvectors are not necessarily equal.

The left and right eigenvectors possess a mutual orthogonality relationship, such that each left (right) eigenvector with corresponding eigenvalue λ is orthogonal to each right (left) eigenvector with a different corresponding eigenvalue.

4 THE JACOBI-DAVIDSON METHOD

The Jacobi-Davidson technique is applicable to eigenproblems of the generalised form (1). Here, it has been extended to operate with independent left and right subspaces, so that the left and right eigenvectors may be represented effectively for non-Hermitian problems. In the standard method, a single subspace is used to span the space containing the desired left *and* right eigenvectors, for which the theory is well described by Sleijpen *et al.* [4]. At each step, the subspace is updated by obtaining an estimate of the correction to each approximate eigenvector using Jacobi's orthogonal component correction (JOCC) method derived from the residual error. For systems which are not self-adjoint, the left and right eigenvectors corresponding to an eigenvalue will in the general case not be parallel, and the subspaces spanned by the eigenvectors corresponding to a given set of eigenvalues will be different. Therefore separate subspaces should be maintained and updated for the solution of non-Hermitian systems. This has been suggested in connection with the original Davidson method for use with non-normal matrices [5].

The modified Jacobi-Davidson method for non-Hermitian systems operates as follows. The large eigensystem is projected at each iteration into the current stored left and right subspaces, and the small projected problem solved exactly to obtain estimates of the solution through a Ritz procedure. Separate subspace corrections are obtained using JOCC steps on the left and right eigenvector residuals, and incorporated in the subspaces. Both corrections may be obtained from a single procedure, and little computational overhead is involved in obtaining the second correction as a by-product of calculating the first.

5 EXAMPLE GEOMETRIES

To test the effectiveness of the method in solving for eigenfrequencies and field eigenmodes of cavities, results from a number of test examples will be given. The ability of an algorithm to converge can depend on the characteristics of the structure of the cavity. For example,

- symmetry of the structure can lead to degeneracy of eigenvalues
- materials with high loss-tangent can give rise to non-real eigenvalues in the spectrum
- the number of unknowns in the solution may influence the convergence

The test examples are intended to include sufficient complexity with regard to these criteria in order to ascertain the effectiveness of the eigenvalue solver for electromagnetic problems.

5.1 2D geometries

Two-dimensional (planar circuit) problems are simple to visualise, and permit accurate solutions to be obtained for relatively complex structures with a moderate number of unknowns, typically 10^4 to 10^5. Two examples are given here.

5.1.1 Lossy structure with degenerate modes

The first example consists of a 2mm×2mm square column of lossy dielectric material located centrally in a 20mm×20mm square cavity, discretised on a 100 × 100

cell grid. The dielectric constant of the block was assumed to be $\epsilon_r = 10 - 2i$.

The following table shows the real and imaginary components of the complex eigenfrequency and the cavity-Q for each of the first eight cavity eigenmodes. Degenerate eigenvalues converged to the limit of numerical round-off error.

Mode	Complex Freq./GHz		Q
1	6.2145185	0.48687	6.38
2/3	13.8931731	0.807264	8.60
4	16.6253632	0.370592	22.43
5/6	19.8161824	0.636433	15.56
7	20.5588852	0.485044	21.19
8	23.1571167	0.394130	29.37

5.1.2 Loaded cavity test structure

Figure 2 shows an eigenmode of a cavity in a cylindrical geometry, loaded with a lossy ceramic ring. The permittivity of the ceramic was ϵ_r=12.24, with loss tangent 0.3. Though convergence time increased for this structure, the eigenmodes were successfully identified. Localised modes in the ceramic having Q<4 were also observed.

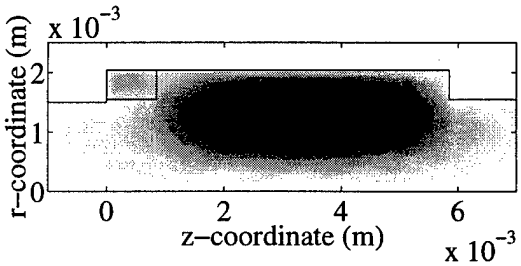

Figure 2: Gyroklystron cavity mode at 93.37GHz

The following table shows good agreement for two similar cavities between eigenmodes determined by (a) this calculation and (b) a scattering matrix calculation:

Mode:		TE_{011}	TE_{012}	TE_{012}	TE_{012}
(a)	f	93.377	103.095	92.867	102.517
	Q	174.198	51.941	187.077	53.654
(b)	f	93.491	103.396	92.929	102.736
	Q	168.767	46.864	169.635	47.045

These values are also in excellent agreement with experimental cold-test data.

5.2 3D geometries

Three-dimensional geometries increase the problem complexity in a number of ways

- vector field increases the number of unknowns in the solution by a factor of three
- many more cells are necessary to fill a 3-dimensional region while maintaining solution accuracy
- more coupling terms arise in the matrix operator

5.2.1 Cubic cavity with high degeneracy

A perfectly cubic cavity with a symmetric discretisation provides an excellent test for separation of degenerate eigenvalues. This method successfully identified the six-fold (real) eigenvalue degeneracies of this structure, correct to round-off error (approx 10^{-14}).

5.2.2 Lossy structure with degenerate modes

The final test example follows Schmitt *et al.* [1] and consists of a cavity 20mm×20mm×10mm with a lossy dielectric block 7mm×7mm×8mm located centrally on the square cavity floor. The dielectric constant of the block was taken as $\epsilon_r = 10 - 2i$. Calculations were performed using a 40×40×10 cell mesh with approximately 4.8×10^4 unknowns, slightly coarser than the reference example. The following agreement was obtained.

Mode	Freq./GHz		Q	Freq./GHz [1]	
1	6.1384	0.2810	10.92	6.161	0.278
2/3	9.0865	0.7790	5.83	9.091	0.780
4/5	11.316	0.7583	7.46	11.39	0.759
6	11.416	1.0386	5.49	11.42	1.104
7	13.250	1.1593	5.71	13.25	1.161
8	13.618	0.8746	7.78	13.66	0.870
9/10	13.667	0.8750	7.81	13.78	0.860

The method used here is, however, better applicable to such non-Hermitian systems, and converges uniformly even for loss tangents greater than one.

6 CONCLUSION

The Jacobi-Davidson method for eigenvalue determination has been modified to operate with separate left and right subspaces, and shown to successfully identify eigenmodes of complex cavities containing highly absorbing materials. The method does not transform the matrix operator directly, and so may be used if the operator and its adjoint are available in functional form. Additionally, there is no requirement for estimation of extreme eigenvalues, and the solution may be seeded for iterative refinement. The method has been shown to be an attractive algorithm to aid the design of microwave cavities containing highly absorbing materials.

7 ACKNOWLEDGEMENTS

This work was supported by the Office of Naval Research. The computational work was supported in part by a grant of HPC time from the DoD HPC Center NAVO.

8 REFERENCES

[1] D. Schmitt, R. Schuhmann, and T. Weiland. The complex subspace iteration for the computation of eigenmodes in lossy cavities. *Int. J. Num. Model.: Electronic Networks, Devices and Fields*, 8:385–398, 1995.

[2] A. Booten and H. A. van der Vorst. Cracking large-scale eigenvalue problems, part I: Algorithms. *Computers in Physics*, 10(3):239–242, May/June 1996.

[3] M. Bartsch *et al.* Solution of Maxwell's equations. *Computer Physics Communications*, 72:22–39, 1992.

[4] G. L. G. Sleijpen and H. A. van der Vorst. A Jacobi-Davidson iteration method for linear eigenvalue problems. *SIAM J. Matrix Anal. Appl.*, 17(2):401–425, 1996.

[5] E. R. Davidson. Super-matrix methods. *Comp. Phys. Commun*, 53:49–60, 1989.

STATUS OF UNIFIED ACCELERATOR LIBRARIES

Nikolay Malitsky and Richard Talman,
Laboratory of Nuclear Studies, Cornell University, Ithaca, NY 14853

Abstract

The Unified Accelerator Libraries (UAL) form an object-oriented programming toolkit for developing distributed accelerator software. At this time the UAL joins accelerator programs DA, PAC, and TEAPOT thereby implementing a set of fundamental accelerator data structures and algorithms: an accelerator lattice model, element-by-element particle tracking, differential algebra, and others. The Application Programming Interface (API), written in Perl, provides a universal homogeneous environment for invoking, customizing, and extending diverse accelerator algorithms, and integrating them with other computer software. It can be considered a model of the Accelerator Simulation Facility based on the CORBA Business Object Facility and the UAL framework.

1 BASIC CONCEPTS AND ARCHITECTURE

The Unified Accelerator Libraries toolkit is designed as a customizable and extendible environment for developing mission-critical applications. This goal is achieved by the fundamental Model/View/Controller (MVC) paradigm[1]. Following the MVC pattern, the UAL is partitioned into three categories: Accelerator Objects (accelerator model, bunch, *etc.*), Physics (analysis, optimization and correction algorithms, *etc.*), and Application Programming Interface ('input language'). Each accelerator program is considered as a separate self-contained class, that may have its own internal organization and methods. Connection with the UAL is by common data objects of the first category. At this time the UAL joins three object-oriented accelerator programs (as shown in Fig. 1): Platform for Accelerator Codes (PAC)[2], Thin Element Program for Optics and Tracking (TEAPOT)[3], and Differential Algebra (DA)[4].

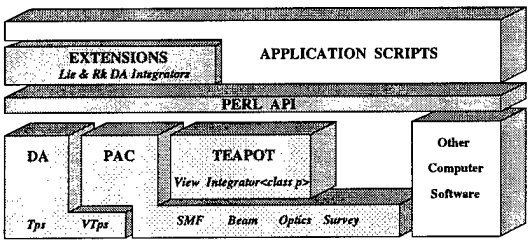

Figure 1: Unified Accelerator Libraries Environment.

The PAC is a collection of Accelerator Objects that can be shared, exchanged,or converted by other codes and processes. TEAPOT and DA are the implementations of the two different theoretical algorithms for simulating particle motion in accelerator elements. The UAL distributed architecture makes it possible to merge these diverse approaches seamlessly to provide optimal conditions for studying accelerator performance. Moreover, the present TEAPOT tracking engine is developed as a C++ template that can be instantiated either to provide the original functionality or as a DA integrator. The 'input language' is a key part of accelerator programs. According to the Standard Input Format (SIF)[5] (and the MVC paradigm) it may be divided into two major parts: the Accelerator Description and Actions. Accelerator is a complex system that includes many elements of different physical types, each having many attributes, all organized in a more or less hierarchical fashion. The second part, Actions, have traditionally consisted of an even more heterogeneous collection of commands and directives. This has resulted in the creation of diverse 'input languages' and formats, each requiring a 'proprietary', 'embedded' parser to perform the conversion from human readable ASCII files to the internal data structures. To resolve the problem we have introduced an Application Programming Interface (API) based on the standard object-oriented interpreter (e.g. PERL) and the UAL Accelerator Objects:

API = PERL + UAL Accelerator Objects

This approach makes it possible to include other 'input languages', such as MAD[5] and COSY[6], and provides a description of *all* accelerator elements and access to *all* accelerator methods. One can consider such a homogeneous shell as a foundation for establishing the Catalog of Accelerator Designs and Scenarios. Especially, it seems interesting for storing 'start-up' scripts of future Simulation Facilities.

2 APPLICATIONS

The last several years have witnessed a new phase in accelerator physics' evolution that is characterized by two tendencies: focus on new physical effects and devices (e.g. spin and helical dipole) and research on combined heterogeneous effects (beam-beam + machine nonlinearities + tune modulation + ...) on accelerator integral characteristics (luminosity, period of long-time instability, and others). The very flexible and extendible organization of the UAL environment is addressed to solving these kinds of tasks. In 1996/97 it has been applied by several groups to test its capabilities:

- **CESR**, Wilson Laboratory:
  - instantiation of uniform accelerator description that can be initialized from scripts or embedded C/C++ wrappers of control data;

0-7803-4376-X/98 /$10.00 © 1998 IEEE

- preliminary simulation of beam-beam performance for Möbius accelerator;

- **RHIC**, Brookhaven National Laboratory:
  - evaluation of performance with a helical magnet;
  - investigation of tune modulation;
- **Recycler**, Fermi National Laboratory:
  - evaluation and comparison of several theoretical models for combined function magnets;

3 CORBA INTEGRATION

An interesting and challenging accelerator task is steering theoretical and experimental activities in a common direction toward the development of an intelligent model-based control system. In the SSC laboratory, the Accelerator Simulation Facility (ASF) project was initiated by G.Bourianoff[7]. Since that time accelerator scientists and software developers in FNAL and TJNAF[8] have achieved significant progress, but the portability and interoperability of present simulation facilities are still active problems. To address them we have combined two components, Common Object Request Broker Architecture (CORBA)[9] and Unified Accelerator Libraries (UAL):

ASF = CORBA + UAL

CORBA is an industrial standard for object-oriented distributed systems, introduced and developed by a consortium, the Object Management Group (OMG), that includes over 700 companies. Accelerator software based on the CORBA implementations automatically becomes a part of the modern technological process and inherits many powerful CORBA benefits:

- standard distributed object infrastructure;
- uniform object-based interface and high-level language bindings;
- natural integration with Java mobile environment for developing the 3-tier Object Web systems;
- component portability and interoperability;
- local/remote transparency;
- natural integration with existing systems;
- 15 famous unified Services[10];
- Common Business Objects and a Business Object Facility[11];

The OMG Business Object Facility (BOF) is a logical product of the consistent CORBA evolution from interoperability to collaboration. The BOF is designed as a foundation of industry-specific frameworks and applications. Based on this specification, OMG members are currently developing domain frameworks for Finance, Manufacturing, Telecom, Electronic Commerce, and others. The accelerator community should be ready to initiate similar efforts. Figures 2 and 3 demonstrate parallelism between an OMG Business Object Component and an Accelerator Simulation Facility. The central concept of the BOF is a cooperative Business Object Component. According to the MVC pattern, Business Object Components consist of three kinds of objects (as shown in Fig. 2)[12]: Business Objects, Business Process Objects, and Presentation Objects.

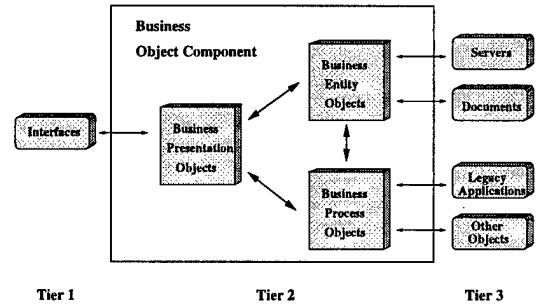

Figure 2: OMG Business Objects.

Components exist at several levels of abstraction: Enterprise Model, Domain Model, Business Object, and Atomic Concepts. They may be implemented by subtyping from existing components of the same level or by combining lower level components. To specify a Business Object Model (BOA) and to facilitate the application development process, the BOF provides also the Component Definition Language (CDL). CDL extends the CORBA Interface Definition Language (IDL) to represent the higher level concepts found in the BOA. In the BOF terminology, the ASF is an Accelerator Business Component at the Domain level (Fig. 3) that includes three cooperative objects: Accelerator, Control, and Interface.

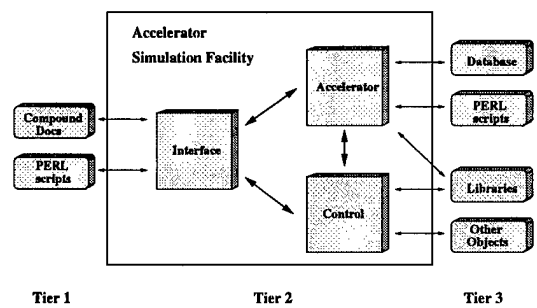

Figure 3: Accelerator Business Objects (Domain Model).

An Accelerator Business Object can be implemented from PAC Accelerator Objects, and TEAPOT tracking engine or other accelerator simulation codes. The next step in the UAL development will be the integration of TEAPOT matching and correction algorithms to become a part of the Control Business Object. The ASF will provide two different Interfaces: Perl scripts and Graphical User Interface based on the CORBA Compound Documents (containers of ORBlets). Communication between different components is by PAC Accelerator Objects. All components (and their subcomponents) may reside in one or more computers. The CORBA local/remote transparent mechanism makes these details invisible to users and significantly sim-

plifies the transformation of conventional codes into distributed facilities(Fig. 4).

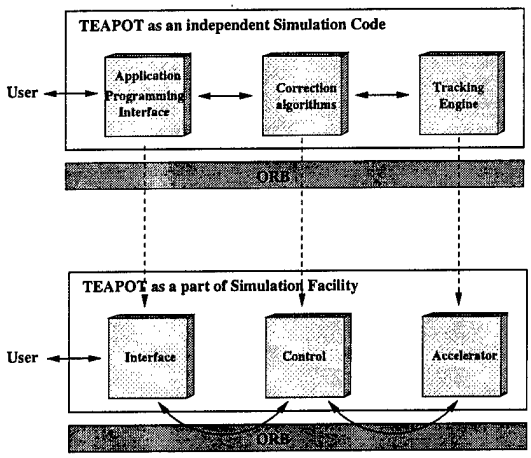

Figure 4: Simulation Code vs. Simulation Facility.

To exercise the connections between different systems, we have implemented a tiny tracking demo available over the Internet that provides the simplest remote control to the DA library (Fig. 5 and 6). Despite its simplicity, this example demonstrates two interoperability features of the CORBA architecture: high-level language bindings (Java and C++), ORB vendor independence (VisiBroker and HP ORB plus).

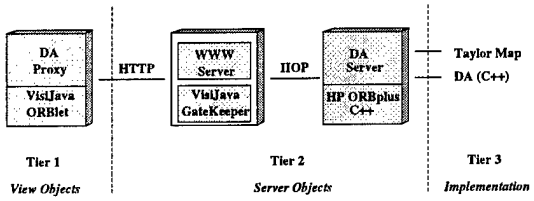

Figure 5: The 3-tier Object Web tracking demo.

4 ACKNOWLEDGEMENTS

One of the authors (N.Malitsky) would like to thank the members of the Nile project, Mike Athanas, Dan Riley, Mark Rondinaro, and Greg Sharp, for useful discussions and valuable suggestions.

5 REFERENCES

[1] G.E.Krasner and S.T.Pope. A cookbook for using the model-view-controller user interface paradigm in Smalltalk-80, Journal of Object-Oriented Programming, 1(3):26-49, August/September 1988.

[2] N.Malitsky, A.Reshetov, G.Bourianoff. PAC++:Object-Oriented Platform for Accelerator Codes, SSCL-675, June 1994.

[3] L.Schachinger and R.Talman. Teapot: A Thin-Element Accelerator Program for Optics and Tracking, Particle Accelerators, **22**, 35(1987).

[4] N.Malitsky and A.Reshetov, to be published.

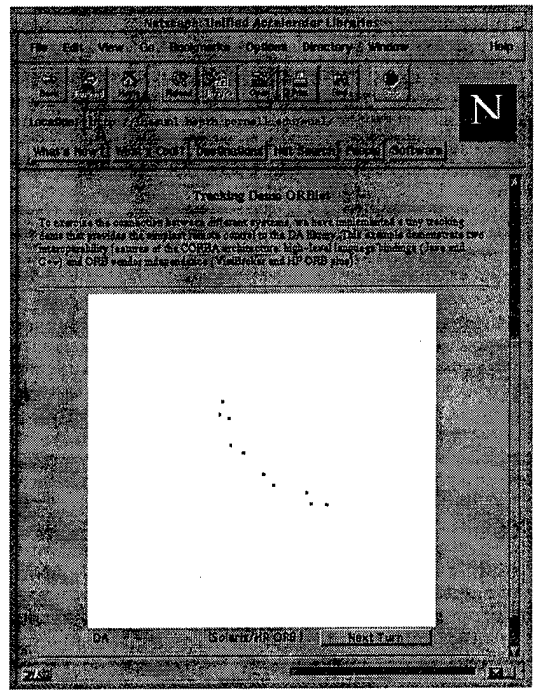

Figure 6: Tracking demo ORBlet.

[5] D.C.Carey and F.C.Iselin. Standard Input Language for Particle Beam and Accelerator Computer Programs, Snowmass, Colorado, 1984.

[6] M.Berz. COSY INFINITY, Refernce Manual, Technical Report 28881, LBL, 1990.

[7] G.Bourianoff, A.Reshetov, N.Malitsky. Object-Oriented Approach for the Design of the Simulation Facility of the SSC, SSCL-677, July 1994.

[8] C.Watson, J.Chen, D.Wu, W.Akers. Introduction to CDEV, Version 1.5, TJNAF, December 1996.

[9] CORBA 2.0/IIOP, OMG Technical Document formal/97-02-25.

[10] CORBAservices: Common Object Services Specification, 1996.

[11] BODTF-RFP 1 Submission, Business Object Facility, 1997.

[12] R.Orfali, D.Harkey, J.Edwards. Instant CORBA, Wiley Computer Publishing, 1997.

INNOVATIVE ASPECTS OF THE SDL CONTROL SYSTEM

W.S. Graves, S.K. Feng, P.S. Pearson, J.D. Smith
National Synchrotron Light Source, Brookhaven National Lab, Upton, NY 11973

Abstract

The Source Development Lab at BNL consists of a 230 MeV electron linac and 10m long wiggler for short wavelength FEL development. The control system is based on that in use at the NSLS. Two new extensions of the control system using VXI equipment are described. The first extension is the replacement of patch panels and lab oscilloscopes to monitor RF equipment. Instead, the RF waveforms are fed through a multiplexor into VXI digitizers. The waveforms can then be monitored remotely on any control console. The second extension is the replacement of the analog RF hardware needed to process beam position monitor signals. A digital system based on very fast (sub-nanosecond) VXI waveform digitizers is under development. The difficult operations requiring precise time alignment are then done in software.

1 INTRODUCTION

The control system extensions discussed below are designed to increase the level of detail and the amount of information available to experimenter and accelerator operator alike. Most control rooms have several lab oscilloscopes which are manually switched among different signals on a patch panel as needed. This method is very limited in its ability to capture and store information, and lacks the flexibility needed to change signals rapidly from any location. The new system under development greatly expands the number of channels that may be used, automates their operation so that remote locations can switch signals, and integrates the data and its analysis into the main control system. It also takes advantage of the latest high-speed digitizers to simplify the often cumbersome analog signal processing needed before digitization. These digitizers have many features that expand their utility beyond data acquisition, such as waveform integration and differentiation, FFT, standard pulse width and height measurements, a variety of digital filters, and auto-advance mode whereby many waveforms may be acquired in rapid succession.

The sections below briefly sketch the NSLS control system, and then give a detailed description of the new extensions including hardware, software, and current status of development.

2 NSLS CONTROL SYSTEM

The control system at the Source Development Lab (SDL) is based on the system in use at the NSLS. The main NSLS facility consists of two storage rings, and an injection system comprised of a linear accelerator and Booster ring. It has been in operation since 1979 and the control system has gone through several major upgrades [1, 2, 3].

The hardware architecture of the NSLS control system is a two-level distributed system consisting of HP Unix workstations connected by ethernet to VME-based microprocessor subsystems. The VME systems control and monitor the hardware status while the workstations are used as operator IO consoles.

Host level applications use X11 and a Motif graphical interface. Standard interface libraries are used to give application programs a simplified high level interface to the hardware.

At the lower level real-time software performs hardware control, data acquisition, error reporting and closed loop algorithms. It provides a standard interface to the high level programs on the host computers independent of differences at the hardware equipment level.

The micro system uses a Motorola single board computer with an ethernet interface, battery backed memory and a utility board which provides extra timers, serial ports, bus-interrupter module, video display generator, software selectable switches and diagnostic LEDs. Each VME micro has its own set of specific I/O interface and control requirements.

The complexity and diversity of the hardware used in the facility makes each micro unique at the hardware control level. To present a uniform hardware interface to the host level applications a standard set of commands for control and data acquisition has been defined. Each hardware item to be monitored or controlled is treated as one or more standard devices. For instance, the fast digitizers described below are each treated as several devices; one to send digitization rate, another for trigger levels, and a third to set voltage ranges.

3 VXI EXTENSIONS TO VME MICROS

The VME equipment has interfaces to both CAMAC and VXI crates. Most of the analog and digital I/O at the SDL is carried using legacy CAMAC equipment. The VXI equipment is dedicated to waveform acquisition and analysis.

The first extension to the NSLS control system being tested at the SDL is the ability to measure and record many voltage waveforms using the control system. This is accomplished using an RF multiplexor (MUX) and fast VXI waveform digitizers. The digitizers are essentially oscilloscopes mounted in a VXI crate. Their advantages over standard lab oscilloscopes are that:

- they are designed to be remotely controlled,

0-7803-4376-X/98/$10.00 © 1998 IEEE

- they have the memory and bus bandwidth needed for high speed data transmission,
- they can maintain precise timing information synchronous with accelerator timing signals,
- they may be integrated with other sophisticated VXI equipment such as timing and signal generators.

Figure 1 shows the layout of the VME and VXI crates used to control the digitizers. In the VXI crate there are two Tektronix 4-channel 1 GS/s TVS641 digitizers used for general purpose data acquisition, and one two channel 5 GS/s TVS625 digitizer used for beam position monitor (BPM) processing [4]. In addition there is a card for communication with the controlling VME crate, and a 1.5 GHz RF MUX with 32 input channels and 8 output channels. The 8 outputs are sent to the two 4-channel digitizers. Thus this system can simultaneously monitor 8 of 32 waveforms in addition to the BPM processing.

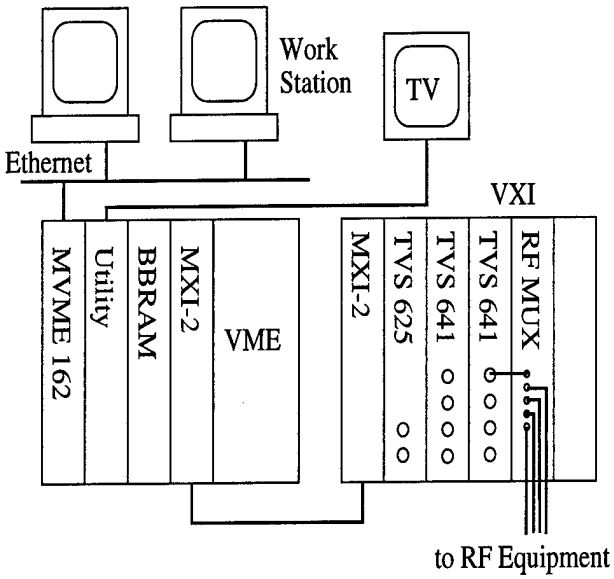

Figure 1: VME and VXI hardware at SDL.

4 LOW-LEVEL CONTROLS

The communication between the VME CPU and the VXI devices is done via VME-MXI-VXI hardware and software. The VME-MXI-VXI hardware requires simple initializations to configure/enable the address maps. Afterwards, the MXI system becomes a transparent VME chassis extender.

A resource manager configures the VXI devices, performs a system self-test and diagnostic sequence, configures the system's address map, commander/servant hierarchies, allocates IRQ lines, and initiates normal operation.

Both the waveform digitizer and RF MUX provide a VXI word-serial protocol for commands and data transfers. The software provides routines to read and write VXI message-based devices, to detect protocol errors, and a watchdog timer to limit the transfer time between CPU and VXI devices.

Early in the evaluation stage tests of data transfer rates were done on different combinations of hardware platforms using a MVME162 CPU running VxWorks. Using GPIB controllers in the VME and VXI crates, the DMA data transfer rate was 12 kbytes/s from the TVS625. Using high performance MXI connections we measured a 21 kbytes/s transfer rate using the word-serial protocol. We then developed a Fast Data Channel (FDC) driver to replace the word-serial protocol. This FDC driver (without DMA) performed roughly a factor of ten faster than the word-serial protocol. Utilizing the digitizers' auto-advance mode to transfer multiple waveforms without software intervention, the FDC driver without DMA performed at 883 kbytes/s for 100 records of data.

5 HIGH LEVEL CONTROLS

Figure 2 shows the main user interface to the SDL Scope Control and Monitor program. The program is being developed using the XRT/Graph package under X11 and Motif. Devices are selected by clicking the appropriate pushbutton on the screen.

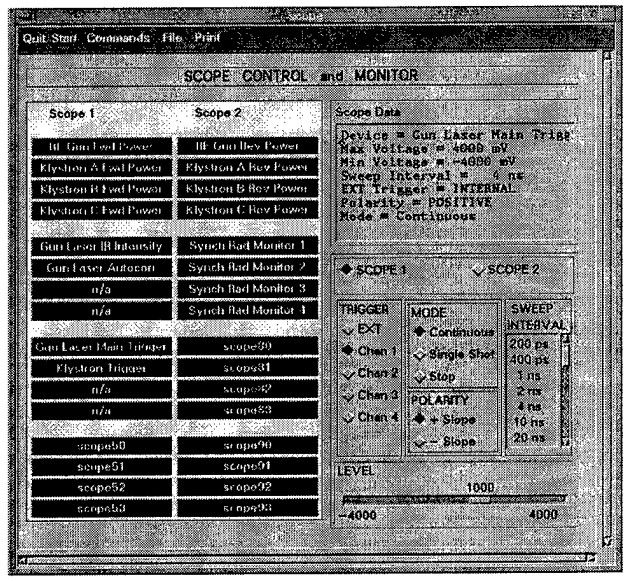

Figure 2: User interface to waveform digitizers.

To view the trace from any device the Start pushbutton is selected. Figure 3 shows an example of the screen that then appears. The program graphs an array of data read from the scope micro device. It also provides the ability to alter the voltage range, trigger source and mode, and digitizer sample rate for each device that is being displayed.

The graph data is automatically updated in real time, is resizable, and zoom and print functions allow the user to study the data more closely. Any graph may be saved to file, for later recall and display.

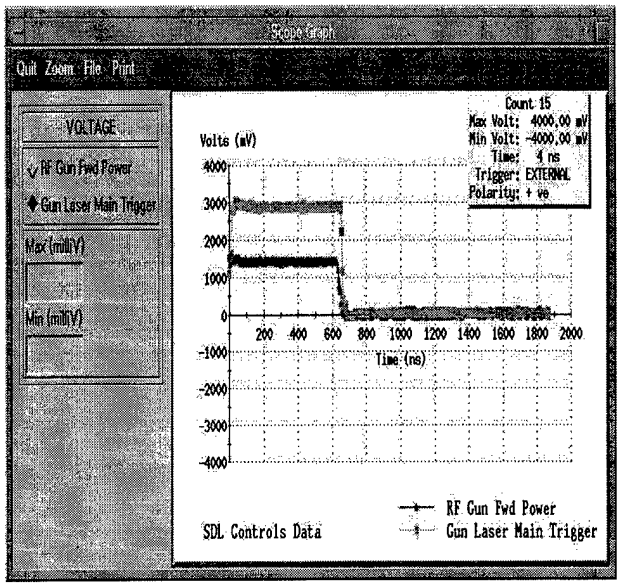

Figure 3: Data plot showing acquired waveform.

6 BEAM POSITION MONITOR PROCESSING

Another new aspect of the SDL control system is digitization and software processing of BPM signals. This is described in more detail in a companion paper [4]. The premise is to use the high speed and sophisticated trigger and analysis capabilities of the TVS series digitizers to replace an expensive assortment of RF processing equipment normally required for BPM signals.

The raw signal from each pickup electrode is digitized with sufficient time and amplitude resolution to eliminate the need for signal preprocessing. There are several methods[5] of obtaining the beam position from the raw signal. Each method is usually implemented in dedicated analog RF hardware due to the very short time pulses (few ns) characteristic of BPM signals. However, the new VXI system has 0.2 ns spacing between points, allowing the processing to be done in software following digitization. This allows experimentation with each method, and the most appropriate may be chosen after testing. Digital filters may be applied to improve signal-to-noise ratio and sensitivity.

This is a cost effective and flexible approach that may be modified at later times without additional hardware expense. Initial tests are now in progress on the VUV ring at the NSLS.

7 CONCLUSIONS

The new capabilities of the control system at the SDL have been described. This consists primarily of the installation of high speed digitizers mounted in VXI racks. In combination with a RF MUX and appropriate high and low level software, this equipment significantly extends our ability to monitor hardware performance and perform real-time analysis.

The data displays permit the operator to quickly observe waveforms from many different pieces of equipment and will be useful both for troubleshooting routine operations and for collecting experimental data. Having the information integrated with the main control system will facilitate data logging, operational record keeping, and allow well-defined synchronization of data from many sources.

The very fast digitization rates allow direct acquisition and processing of beam position monitor signals. This eliminates the need for expensive traditional fast analog signal conditioning.

8 ACKNOWLEDGEMENTS

This work performed under DOE Contract DE-AC02-76CH00016.

9 REFERENCES

[1] Y.N. Tang et al. The high level programmer and user interface. In *1993 IEEE Particle Accelerator Conference.*

[2] S. Ramamoorthy, J.D. Smith. NSLS control monitor and its upgrade. In *1993 IEEE Particle Accelerator Conference.*

[3] J. Smith, S. Ramamoorthy, Y.N. Tang. NSLS control system upgrade. *Nucl. Inst. and Meth. A*, 250:95–99, 1994.

[4] W.S. Graves, S.K. Feng, P.S. Pearson, J.D. Smith. Digital processing of RF signals from beam position monitors. In *this conference.*

[5] R.E. Shafer. Beam position monitoring. In *1989 Accelerator Instrumentation Workshop.* (AIP, 1990)

CONTROL AND OPERATIONAL MODELS FOR VACUUM EQUIPMENT

P.M. Strubin and N. Trofimov, CERN, CH-1211 Geneva 23, Switzerland

Abstract

Operational models which describe the behaviour and the physical values associated with the vacuum equipment as seen by an operator have been studied for some time at CERN. Recently, they have been completed by control models, which define in a formal way the data structures required to access the physical values described in the operational model. The control models also define the operations that an application program has to send to the vacuum equipment to modify its state. Object Modelling Techniques (OMT) have been used to formalise the description of the models.

In order to test the validity of the concepts, we have made a working prototype in the LEP accelerator. This prototype is being built on top of the CERN SL-Equip equipment access package and uses the "cdev" C++ library, developed at TJNAF, for the interface to application programs. SL-Equip is used for data transmission between front-end computers and vacuum equipment. We use the "cdev" networking facilities to communicate between the workstation and the front-end computers, and the "cdev" generic server as the framework for implementing the vacuum controls software. These packages were used in order to minimise the required software investment, but also to prove that these models are hardware and software independent.

1 INTRODUCTION

Recent experience, when developing a common man machine interface for vacuum controls for all accelerators at CERN [1], made evident that a significant amount of work was induced by the variety of vacuum equipment and access methods. Whereas the interface presented to the operator is identical for all accelerators, the underlying programs are quite different. The work presented here is aiming at hiding the differences between equipment to the application programmer as well as to provide him with a clear description of how to control the vacuum equipment. Starting from the operational model [2], a control model is defined, which makes use of building blocks which we call components. These components provide a uniform way of representing physical data from which the application program interface can be derived.

The application interface is built from a device server using the CDEV interface library. This server is the key to present the control model in a coherent way to the application programs.

2 MODELS

There are two concepts of a model which have to be clearly defined, the operational model and the control model.

2.1 The operational model

The operational model refers to the following:

- a narrative description of what the primary function and behaviour of the device is;
- the enumeration of the various physical values of interest which can be observed by means of the hardware and firmware installed in the control unit of the vacuum device. There is no assumption about any data type, we simply refer to variables and units applicable to the physical values;
- the state that a given vacuum device can take in normal operation, documented with the reasons which can lead to a change of state (actuation, time-out, interlock, fault, etc.);
- the commands (actuation) the vacuum device can accept to modify its state and possible restrictions to these commands;
- the settings of the various physical values of interest and the calculation parameters that the device needs to operate according to its specifications.

The operational model does not imply computer control and is therefore applicable to manual or computer controlled operation. It does not depend on a particular make of the device, although some real implementation may not fulfil all aspects of the operational model. Finally, there should be no controls related definitions or concepts in its description.

2.2 The control model

The control model refers to the following:

- define in a formal way the data structures required for the application programs to access the various physical values described in the operational models, including related information like time-stamp or validity;
- define in a formal way the data structure required for the application programs to recognise and handle abnormal operating conditions or faults;
- describe in an semi-formal, although exhaustive, way the transitions between the possible states defined in the operational models of the vacuum devices as a result of external or internal events, typically using some form of state transition diagrams;
- define in a formal way the procedures (operations) required by the application programs to send the events (actuation) required for operating the vacuum devices;

0-7803-4376-X/98/$10.00 © 1998 IEEE

- define in a formal way the aggregation of the above mentioned data structures to emulate the modelled vacuum devices. This aggregation is referred to as configuration.

All formal definitions must be independent from any programming language, but should be easily translated into a real language.

3 REQUIREMENTS OF APPLICATION PROGRAMS

All application programs must be able to control vacuum devices in an identical way, using the same configuration. Main functionality related to vacuum equipment which should be accessible via the model is to evaluate the current state of a device, to be able to modify it and to acquire all relevant physical values.

Auxiliary information for the evaluation of the current state, like the time when the state was last observed or changed and the reason for a change must be provided to the application programs. If a request to change state fails, the application programs must be able to work out the reason of the failure.

Similarly, the application programs must be able to obtain, together with the relevant values from the physical process, the time a value was last evaluated, the limits of validity, the resolution and the units in which a physical value is represented.

4 CONTROL MODELS OF VACUUM DEVICES

A vacuum device will in general be a piece of vacuum equipment, like a gauge or a pump, associated to its corresponding power supply or controller and connected to the control system of an accelerator through an appropriated network.

4.1 Functional components

Functional components define a common way to represent the functions and data available in a vacuum device. They can be looked at as building blocks through which access to the information of specific devices can be granted. We do not describe real data access channels here.

For the purpose of vacuum equipment modelling, we define seven basic types of the functional components. Each component type represents certain device capability and holds a number of data items, or properties, that applications can observe and, in some case, modify.

For example, Continuous Input (CInput) models the analogue measurement capability. It provides read only access to the measured value of the associated physical value, as well as some related properties, such as the valid range, the units of measurement, achievable resolution, etc. A pressure returned from a gauge can typically be represented by a Continuous Input.

It is possible to describe these functional components using class hierarchy and association:

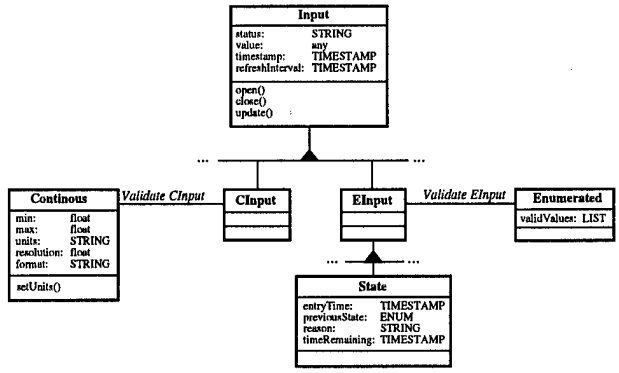

Figure: 1 Example of components used to feed data into a model

Components are defined as a result of the analysis of the requirements of application programs. They may be extended to include more information, but care must be taken not to try to adapt the functionality of the vacuum devices to the any arbitrary definition of components.

4.2 Control models

A control model is based on a set of functional components and a state model. Hence, the control models for vacuum devices are built by aggregating functional components around a generic vacuum device class. The behaviour of a controlled vacuum device is described by its state model. The generic vacuum device class is the way to provide the interface to this state model for an application.

A configuration database describes which physical values can be read, which need settings and what type of components are used to access the physical values. This is not to be confused with the database describing the topology (or grouping) of equipment.

5 INTERFACE TO APPLICATION PROGRAMS

The application programs only know a device via its control model. The exact level at which the model becomes first visible in a control system depends on the system architecture and specific design choices made in the equipment interface. It should be at the lowest possible level in order to minimise unnecessary data transfer and reformatting.

A software process (or a number of processes) maintains an image of the state and of the data generated by a vacuum device for the application programs and forwards data from the application programs to the vacuum device, using the data structures described in the control model.

The representation of the various data structures for an application within a specific implementation is derived from the control model.

6 CLASS HIERARCHY FOR VACUUM DEVICES

Analysis of the control models reveals the common functionality and capabilities between vacuum devices. This leads to the definition of a class hierarchy in which the common features are placed at the top. Specialisation of these generic classes provides the interface to more specific vacuum equipment, like gauges. Common functionality, like pressure measurement, can be added as another abstract class, from which "gauges" would inherit. Finally, further specialisation will lead to the classes representing the real equipment.

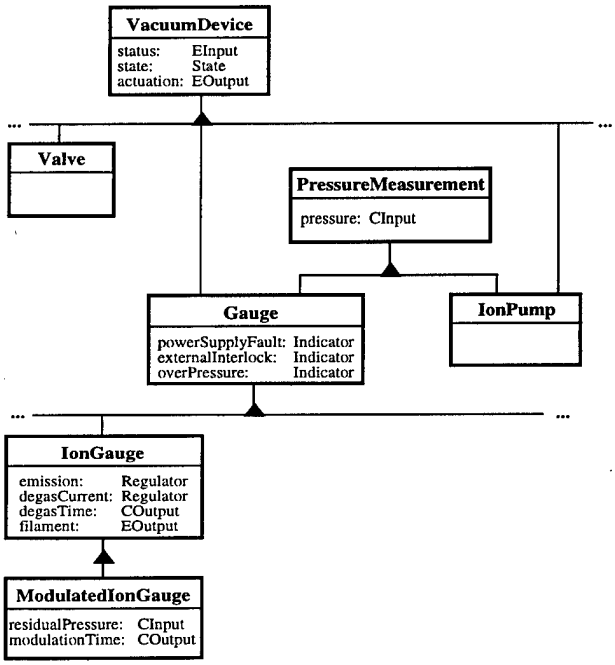

Figure: 2 Part of the Device Class Hierarchy

7 IMPLEMENTATION OF A PROTOTYPE IN LEP

The prototype implementation in the LEP control system employs the client-server architecture (Fig. 3). The VacModel servers are running on the front end computers (LynxOS on VME/PowerPC) and provide a model based view of the vacuum equipment for the applications running in the workstations (HP-UX). The VacModel server uses the standard LEP equipment access software (SL-Equip) [4] to communicate with the equipment, and the existing Oracle database as primary source of all the configuration data.

The server implementation is based on the "CDEV Generic Server Engine", a collection of C++ classes developed at TJNAF [3]. The CDEV (Control DEVice) class library aims at providing an object-oriented interface between an application and underlying accelerator control software. Basic concepts of the CDEV application programming interface are very close to our control model definition, so the mapping is rather simple and straightforward.

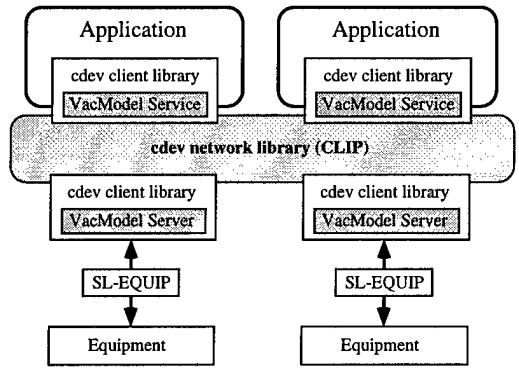

Figure: 3 Overview of implementation

The device class hierarchy (Fig 2) can easily be expressed in the CDEV Device Definition Language and the components of the control model map directly to the CDEV device attributes. Using standard CDEV messages, an application can read, write or monitor values of the components' properties. All required communication functionality is provided by the CDEV library classes. The specific VacModel software essentially binds the CDEV framework to the LEP database and equipment access environment.

8 CONCLUSIONS

Operational models have already been successfully applied in several projects, but the large variety of access methods meant that a significant amount of work was required whenever a new device was added or an application was ported to a different environment. Control models aim at minimising this effort and the first prototype implementation in LEP shows that this is quite possible.

This prototype was built using existing "general purpose" libraries, like CDEV and SL-Equip, which demonstrates that a generic description of equipment leads itself to an easy implementation on real hardware and software platforms.

9 REFERENCES

[1] 'A data driven graphical user interface for vacuum applications', L. Kopylov, M. Mikheev, N. Trofimov (IHEP Protvino), P. Strubin, M. Steffensen (CERN), ICALEPCS 1995, Chicago, USA.

[2] 'Using models to allow for object oriented programming of the vacuum control systems', R. Gavaggio, M. Steffensen and P. M. Strubin, EPAC 1994, London, UK.

[3] 'CDEV: An Object-Oriebnted Class Library for Developing Device Control Applications', J. Chen, G. Heyes, W. Akers, D. Wu and W.A. Watson (CEBAF), ICALEPS 1995, Chicago

[4] 'The Equipment Access Software for a Distributed UNIX-Based Accelerator Control System', N. Trofimov, S. Zelepoukine, E.Zharkov (IHEP Protvino), P. Charrue, C. Gareyte, H. Poirier (CERN), ICALEPS 1993, Berlin

PC-BASED APPLICATIONS PROGRAMMING ON THE SRS CONTROL SYSTEM

B.G.Martlew, H.L.Owen, M.J.Pugh, W.R.Rawlinson, S.L.Smith
CLRC Daresbury Laboratory, Warrington, WA4 4AD, UK.

Abstract

The CERN PC-based ISOLDE control system has been installed at the SRS electron storage ring at Daresbury Laboratory. The use of Windows NT for the control consoles together with PC and VME front-end computers running under several operating systems has resulted in a flexible and reliable system for accelerator control. The implementation and philosophy of control application programs, based around a suite of Microsoft Visual Basic and Excel programs, is described. In particular, the use of Excel to provide adaptable programs online allows rapid generation of new control functions; orbit correction and servoing at the application level are described as examples of this.

1 ISOLDE CONTROLS ON THE SRS

1.1 Overview

Over the last few years there has been a policy of gradual upgrade of the SRS control system from a 32-bit mini-computer based system using 1970's technology to a modern PC based system. The ISOLDE ion-separator beamline at CERN was chosen as the model for this upgrade because of its use of a simple client/server paradigm and its philosophy of making maximum use of standard, commercial PC hardware and software [1,2]. Presently, the control system is a hybrid of the old mini-computers and the new ISOLDE PC system.

1.2 SRS Enhancements

Since its introduction on the SRS the ISOLDE system has been enhanced in several ways.

1.2.1 Conversion of operator console to Windows NT

The original system used Windows 3.11 as the client system. This suffered from severe resource limitations and considerable difficulty in multi-tasking. For these reasons it was decided to switch to Windows NT. This has proved to be a very much more stable system which can successfully multi-task many control system applications as well as simplifiying system installation and maintanence.

1.2.2 OS-9 VME systems as Front End Computers (FEC)

The original DOS FEC has been supplemented by porting the server code to OS-9. This was originally necessary in order to interface to an existing VME/OS-9 based sub-system used for control of the storage ring beam steering and orbit diagnostics systems [3]. It has since proved to be a very versatile and inexpensive (especially in 3U format) alternative to DOS-based PCs.

1.2.3 Support for LabVIEW based FECs

Recently the RF group developed a monitoring system based around a PC running Windows 95 and LabVIEW. It is now possible to access this as though it was an ISOLDE style FEC by the development of suitable interface software. This technique is described fully in [4].

1.3 Access to Plant Data

The control system provides two basic methods for accessing plant information: an Application Programming Interface (API) implemented as a Win32 Dynamic Link Library (DLL), and a Dynamic Data Exchange (DDE) server that can provide periodic updating of requested plant information. Alternatively, any standard networking or inter-process communication mechanism available may be utilised in specialised applications. These three alternatives will be discussed in more detail.

The present layout of the PC-based part of the SRS Control System is shown in figure 1.

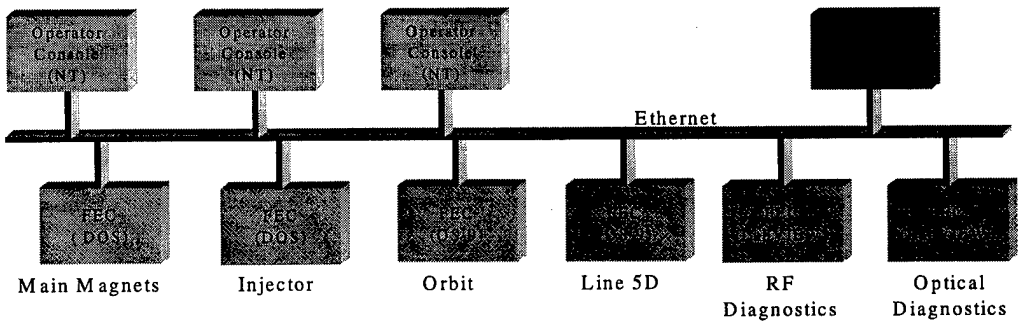

Figure 1: Layout of the upgraded SRS Control System

0-7803-4376-X/98/$10.00 © 1998 IEEE

1.3.1 Win32 API

API calls are the most versatile way of providing access to plant data from the operator consoles. However, their use does demand some programming knowledge as well as a detailed understanding of the under-lying operation of the system. API calls can be used from any programming tool or system that supports access to DLLs.

1.3.2 DDE Server

DDE is a mechanism to simplify the transfer of small quantities of data between different applications. In addition it supports the concept of hot-links, which automatically update client programs whenever new data becomes available. For example, the contents of a cell in an Excel worksheet can be set to update at a user-specified rate. However, it is relatively slow, it is not easy (though possible) to set new values via DDE and it can only be used by those applications that have been specifically written to support DDE.

1.3.3 Network/Inter-Process Communications

The two techniques described above cope with the great majority of requirements but some specialised applications need to be able to transfer large data files (eg. images or waveform data) or to use complex data structures not easily supported by the standard ISOLDE mechanisms. In these cases use may be made of standard TCP/IP sockets or file sharing to access data.

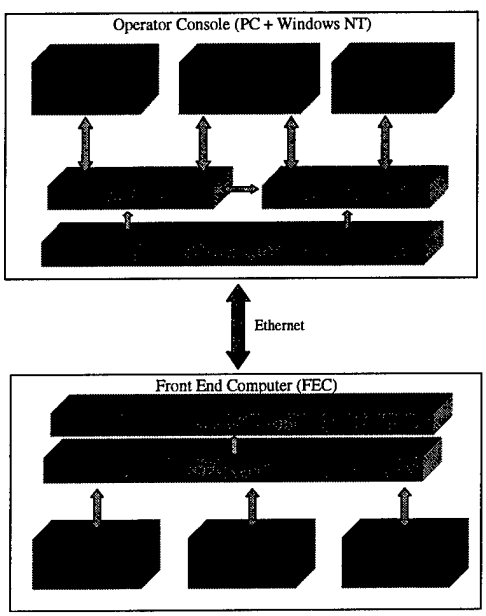

Figure 2: Data Flow from Console to FEC

These three mechanisms, either separately or together, can be used to construct control system application using any of a wide range of application development tools (MS VC++, Visual Basic, MS Excel, Tcl/Tk and LabVIEW have been used on the SRS). Figure 2 illustrates the data flow between application and FEC when using the standard ISOLDE interface

2 CASE STUDIES

2.1 DDE and OOP in Excel

One of the principal advantages of the ISOLDE system is the ease and flexibility of program development. The features of Microsoft Excel, which is already widely used for the analysis and presentation of scientific data, have been taken advantage of by using the two principal ISOLDE data interfaces - DDE hotlinks and API function calls.

2.1.1 DDE Hotlinking

DDE hotlinks are a straightforward method of providing data for instant analysis within an Excel worksheet. For example, a simple status monitor has been written which automatically updates beam current, beam lifetime and other information. Similarly, other monitoring is possible, for instance dynamic orbit displays; by adding formulae to the worksheet cells, dynamically updating calculations can be provided to aid data analysis for control system users. The use of Excel allows users to write custom applications online during experiments, which dramatically reduces the development time required for new applications.

2.1.2 Object Modules

Although the ISOLDE API function calls can be used directly within Visual Basic and Excel, code is not simple to read and consequently debugging is harder. To overcome this, wrapper functions have been written in Excel using Visual Basic for Applications to give an object interface to equipment. Parameters which have single numeric read and write values, for instance individual steering magnets, use the PROPERTY LET and PROPERTY GET functions to give transparent reading and writing. Simultaneous reading or writing of multiple values, such as reading the orbit, is accomplished using Methods provided by SUB procedures. Sets of related parameters are grouped, using the SRS naming convention, into Excel modules. The whole set of modules is grouped into a single workbook (the APM - Application Programming Modules) which may be referenced by a user application. Example command syntaxes are:

ZM.VSTR(4) = 2.83	sets 2.83A on storage ring magnet (ZM) vertical steer (VSTR) number 4.
A = ZB.HBPM(8)	reads value from storage ring monitor (ZB) horizontal BPM (HBPM) number 8 into variable A.
ZM.HSTR_Apply B	applies current values in amps in array B to all horizontal storage ring steering magnets.

2.1.3 Scaleability

New parameters can be prototyped at the application level. For instance, in the SRS some horizontal and vertical steering magnets are provided on common multipole elements in the lattice: Individual coil settings are calculated at the VME level, giving 'virtual' parameters at the ISOLDE level. Skew quadrupoles have been implemented at the application level, with the APM keeping track of values which have been applied; once these are tested at the application level, they can be implemented at the VME level to improve speed. The advantage of this system is that to the user the command syntax remains the same.

Additional functionality can be provided with extra properties and methods which are not appropriate to direct parameters. For instance, closed-orbit bumps are provided at the VME level as virtual parameters. However, when setting large amplitude bumps the sequential application of the individual steering currents making the bump can cause unacceptable orbit deviations and risks instabilities in the beam. To overcome this, bumps can be ramped in 1mm steps using a simple APM Method. Overall, the modules offer a simple, scaleable system to interface between Excel and the ISOLDE front-end system.

2.2 Prototyping SVD and other servo correction systems

Similarly to individual parameters, more complex machine control algorithms are easily protoyped at the application level. For example, the use of singular-value decomposition (SVD) techniques is presently being developed to replace the present system of locally servoing the source beamlines. The new system will perform simultaneous correction of the electron beam orbit and the beamline vertical tungsten vane monitors (TVM), and prototyping within Excel has proved invaluable in studying and optimising the usage and weighting of correctors and monitors.

2.3 Quadrupole Realigment

2.3.1 The Need for Realignment

The daily operational cycle of beam injection and subsequent decay of stored beam causes thermal cycling of the storage ring magnet elements. This in turn gives rise to a repeated expansion and contraction of the elements which causes the storage ring quadrupoles to 'walk' over extended periods of time. The consequent steering effect of the misaligned quadrupoles eventually becomes beyond the practical limit of correction for the steering magnets. Magnet realignments are performed at periodic intervals; in the SRS correction is performed approximately every 6-12 months using a combination of survey and beam-based correction.

2.3.2 Automation Using Excel

Since only a few magnets can be moved at a time, due to operational restrictions, choosing the optimum set to move is of great importance to best compensate errors affecting both the working points used in the machine. Previously, only manual prediction and simulation of solutions was possible, limiting the number that could be explored. However, the use of the Excel Solver allows the rapid calculation of all possible solutions; the quadrupole moves can then be simulated on the storage ring with scaled corrector magnets in each of the machine modes. The combination of rapid data collection and analysis afforded by ISOLDE and Excel has greatly improved the efficiency and reliability of magnet realignment.

3 FUTURE DEVELOPMENTS

The APM discussed in 2.1.2 above is presently only useable from within Excel. However, since it is written using standard Visual Basic for Applications code it will be a simple exercise to port it to Visual Basic 4.0 and compile it as an OLE server. This will allow the encapsulated objects to be used from any OLE-enabled application and will also remove the need to reference the APM in every Excel application that requires it.

Also, several applications written using the APM are now in regular use and could be converted into full Visual Basic 4.0 applications to improve performance and maintainability.

4 ACKNOWLEDGEMENTS

We wish to thank CERN PS division for permission to use the ISOLDE Control System software. In particular we thank Ivan Deloose for his help and advise on software installation and Alberto Pace for useful discussions.

6 REFERENCES

[1] I.Deloose, A.Pace, "The ISOLDE Control System", Proc. of the 1993 International Conference on Accelerator and Large Experimental Physics Control Systems, Berlin.

[2] B.G.Martlew, M.J.Pugh, W.R.Rawlinson, "Present Status of the SRS Control System Upgrade Project", Proc. of the 1996 European Particle Accelerator Conference, Sitges, Spain.

[3] W.Rawlinson, B.G.Martlew, M.J.Pugh, M.McCarthy, "Development of a VME-Based Control System for the SRS Orbit Feedback Project", Proc. of the 1994 European Particle Accelerator Conference, London, pp. 1785-1787.

[4] M.J.Pugh, A.R.MacDonald, "Implementation of a New RF Monitoring System for the SRS Using LabVIEW", these proceedings.

THE USAGE OF TRANSIENT RECORDERS IN THE DAILY HERA MACHINE OPERATION

R. Bacher, M. Clausen, P. Duval and L. Steffen, DESY, Hamburg, Germany

Abstract

Many parameters of HERA machine components such as RF systems or quench protection as well as important beam parameters are continuously measured using transient recorders. In general, these recorders are not synchronized among one another and sample the data with very different rates ranging from 200 Hz to 50 MHz. At present, work is going on to integrate the different existing transient recorders into a global system. The article reviews the transient recorder hardware in operation at HERA. In addition, the proposed trigger distribution based on the HERA Integrated Timing system as well as the software concept to archive, retrieve and display the data will be described.

1 INTRODUCTION

The HERA accelerator complex is a proton-electron collider. A proton beam of more than 70 mA is injected at an energy of 40 GeV into a ring of superconducting magnets and accelerated to 820 GeV. Electrons are transferred to HERA at 12 GeV and ramped to 27 GeV using conventional magnets. Typical electron currents are about 40 mA. A successful fill remains stored in HERA about half a day. Less than 50 % of the time scheduled for physics experiments can be used for data taking. The remaining fraction is mainly dominated by the filling, ramping and tuning processes. In particular, the filling of protons takes a long time. Therefore, the most unfavourable situation in the daily operation of HERA is the loss of one or even both circulating beams. If the origin of the beam loss can be uniquely identified, improvements of the machine operation or the technical components can be performed. However, a loss not understood contains the risk of a new loss during the following run. Besides a reduction of the running efficiency, losses can generate dangerous situations for the superconducting magnets and radiation-sensitive components close to the beam pipe of the physics detectors.

To identify the reasons for beam losses, many parameters of HERA machine components like RF systems or quench protection as well as important beam parameters are continuously measured using transient recorders. In general, these recorders are not synchronized among one another and sample the data with very different rates ranging from 200 Hz to 50 MHz. This lack of synchronization often does not allow us to disentangle the temporal or causal development of a beam loss. At present, work is going on to integrate the different existing transient recorders into a global system. In addition, a new universally usable recorder is currently being developed. This article reviews the transient recorder hardware in operation at HERA. The proposed trigger distribution based on the HERA Integrated Timing system as well as the software concept to archive, retrieve and display the data will be described.

2 EXISTING TRANSIENT RECORDER SYSTEMS

At present, more than 100 parameters such as phase and amplitude of the different electron RF transmitters as well as of the feeding HV power supplies are recorded at different locations along with the electron current. Commercially available PC boards (Bakker BE 490) with 8 inputs each are used. The sampling rate and the storage capacity per channel are 100 kHz and 20k byte, respectively. The analog signals are converted by a 12-bit ADC. The data recording can be stopped by an external or an internal trigger. The software runs on top of Windows 3.1 and has no networking functionality. The different PC's can be remotely controlled via PCAnyWhere. Only a couple of parameters of the proton RF system are continuously measured. The system is controlled and operated by a front-end DOS-PC sampling the data every some milliseconds. An external trigger is not implemented.

The HERA quench protection system for the superconducting magnets is the most prominent user of transient recorders. For diagnostic purposes more than 1400 voltages measured across the magnets and with respect to ground are stored in case of a quench. The transient recorder boards used have been developed at DESY as dedicated measuring devices. The boards are distributed in the HERA tunnel along the magnets. The sampling rate and the number of data samples per channel are 250 Hz and 1k, respectively. A 12-bit ADC measures the voltages between +5 V and -200 V or +25 V and -1000 V. A cluster of about 20 boards is read out by a VME-CPU via a commercial field bus (CAN). The data taking is stopped one second after the corresponding CAN broadcast message. The control, archiving and display software has been written at DESY using C and Visual Basic.

The proton beam diagnostics makes extensive usage of dedicated post-mortem memories. The proton beam loss rates are measured at about 250 locations every 5 ms. A history of 128 data samples is stored as well as 128 average loss rates integrating over 128 measurements. At almost the same locations, the proton

0-7803-4376-X/98/$10.00 © 1998 IEEE

beam orbit is recorded. Horizontally and vertically, the last 1024 turns are stored as well 256 closed orbit data samples gained by averageing over 128 turns. In each case, data taking is stopped by a common hardware trigger released from the beam loss detection or the quench protection system. The data are read out via DESY standard field bus lines (SEDAC) by a DOS-PC belonging to the HERA control network. Front-end control and display application software are written in C and VisualBasic, respectively.

The current pulses of the 12 kickers and septum magnets necessary to eject the beams from the booster accelerator PETRA and to inject the beams into HERA are recorded at every transfer process. Standard HP digital scopes and PC ADC boards from National Instruments are used. The sampling rates differ from 250 kHz for septum pulses to 5 MHz and 50 MHz for kicker pulses. Per pulse 512 data samples are taken. The Scopes are controlled by PC's via GPIB. A LabView application displays the traces.

3 DEVELOPMENTS FOR FUTURE USAGE OF TRANSIENT RECORDER SYSTEMS

At present, work is going on in order to enhance the profit which can be gained from the usage of transient recorder systems.

- Improved functionality of the power supply controllers to store permanently with 12-bit resolution the set value of the current as well as the actual values of current and voltage. The sampling rate will be less than 1kHz. More than 1000 data samples per channel can be stored. The data stored in about 680 controllers will be read out via SEDAC lines by a server responsible for all magnets and currently under development.
- Enlarging the number of measured parameters. A couple of signals from the electron and proton multi-bunch feedback and the electron tune controller will be recorded in the future. In addition, the currents of the electron and proton reference bunches as well as more parameters of the HV power supplies for the electron RF transmitters will measured continuously.
- Implementation of networking capability into the software of the Bakker BE 490 boards. The software has been completely re-written at DESY to support the VxWorks operating system on PC hardware. This allows us to integrate the boards into the HERA control system keeping the same flexibility as in the original Windows 3.1 environment
- Development of a low-cost multi-purpose transient recorder at DESY with moderate sampling rate. A cluster of 8 or 16 channels will share the same clock and memory. The probes with the ADC's can be configured according to the dedicated measuring requirements (isolation to ground, amplitude and band width of input signals). Analog and digital electronics can be separated by about 20 m. In addition, 12 digital input ports are offered per cluster, which can be logically combined to generate stop trigger conditions. Also a simple threshold as well as a software trigger functionality will be foreseen. The sampling rate will be about 100 kHz which is twice the revolution frequency of HERA. The sampling process can be synchrozid to the HERA clock system if requested. It is proposed to connect the clusters to a field bus e.g. CAN or to an Ethernet line.
- HERA-wide trigger distribution for a simultaneous stopping of data tating of all or a subset of all transient recorder systems. The HERA Integrated Timing (HIT) system offers the possibility of distributing events along HERA. Independent of location at HERA, the HIT system guarantees the synchronization of the events. Two trigger conditions are foreseen: (1) proton beam loss and (2) electron beam loss. The generation of triggers can be inhibited by additional conditions like beam energy or beam current thresholds as well as by a operator or control system request. In addition, triggers can be released by software events.
- Integration of all different transient recorder and post-mortem systems into the HERA control system which will be described in the following section.

4 SOFTWARE ARCHITECTURE FOR AN INTEGRATED ARCHIVE SYSTEM

A common application to remotely operate the various transient recorders and post-mortem systems e.g. to set a trigger threshold is not practicable. The systems are mostly part of complex technical systems and will be operated by dedicated applications.

However, starting the archiving of the data after a freeze trigger and the retrieving of the data for display and analysis puposes must be handled in a common way. Due to the very different hardware and software concepts a heterogeneous software architecture as shown in Fig. 1 with the following specifications has been chosen:

- client-server prinicple,
- modularity, distribution of functionality over 3 software layers (front-end, middle and application layer) reflecting the different needs of the different systems, easily adding of components in all layers,
- distributed archiving, shared usage of all archives, no standard data base format,
- standardized interface to the network using in-house Remote Procedure Calls (RPC) based on IP sockets,
- open for a wide range of platforms (UNIX-like systems, Windows NT),
- open to add commercial data bases such as Oracle or future software standards like JAVA applets.

Attached to each Archive Server is a set of Device Servers reflecting different transient recorders. If

the data taking of any transient recorder channel (Device) is stopped by an external or internal trigger the corresponding Archive Server will ask an Event Server for a unique event number (Unix time stamp). All requests even from different Archive Servers within a short time interval are tagged by the same event number. The Archive Servers start their archive processes locally and store all data delivered from the Device Servers in a unique way. A standardized gobal data header is added to each archive and a local header is added to the data set of each device which has stopped sampling. The global header contains all information to characterize and select the archive event, e.g. the event number, the number of stored data sets or a comment. The local header consists of individual information such as sampling rate, number of data samples or number of pre-trigger values which are necessary to display the data. During the archiving the Archive Server does not accept any other event number. After the completion of an archiving process the corresponding Archive Server reports to the Event Server the names of the Device Servers which have delivered data for this particular event.

The Event Server stores a list of all event numbers and the additional information obtained from the various Archive Servers. It creates automatically an event code which contains encoded information to be used by filtering routines. A similar event code is generated at the Archive Server level.

All triggers distributed by the HIT system are marked with the current HIT time stamp (Trigger Server), i.e. the actual value of the revolution counter. This time information allow us to correlate data sets generated even by different trigger sources.

To display data by an application client, first a query is sent to the Event Server to obtain the event numbers and the contents of the archives stored within a certain time interval. In a second step the Archive Servers are asked to provide more specific informations about the data sets stored as available from the global and local data headers. Finally, the application requests the measured data to be displayed.

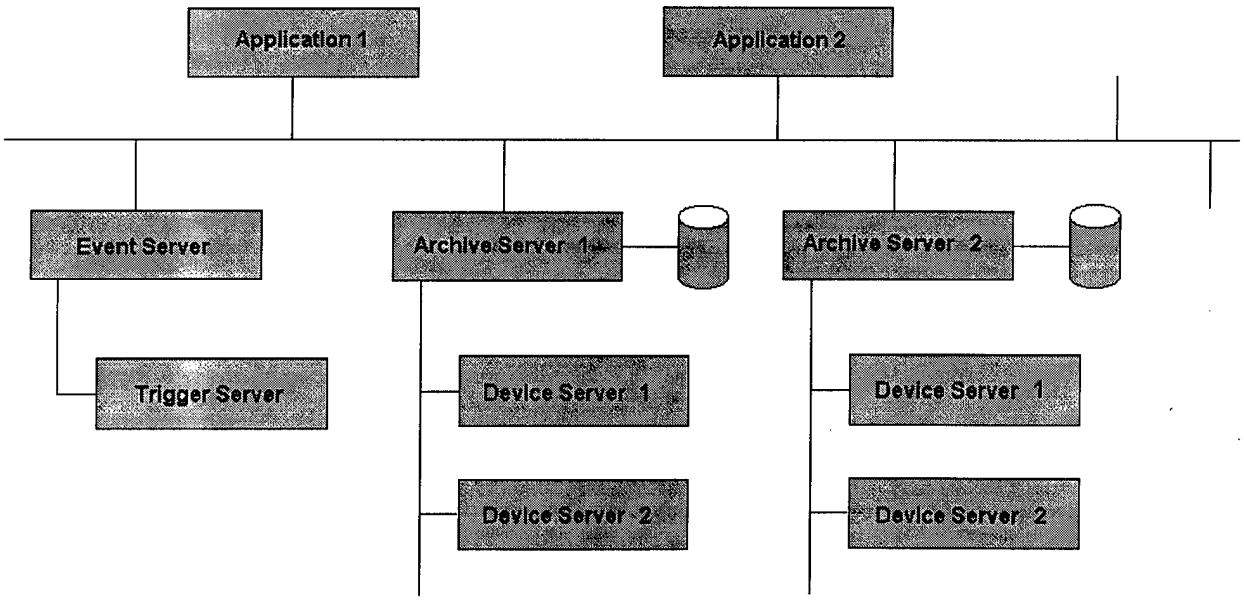

Figure 1: Software Architecture for an Integrated Transient Recorder Archive System

5 STATUS AND OUTLOOK

The software modules described in sections 3 and 4 are currently developed. The production of the hardware to distribute triggers via the HIT system is almost finished. The design work for the low-cost multi-purpose transient recorders has been started. It is expected that all transient recorder and post-mortem systems already existing will be integrated into a common system at the beginning of the 1998 running period of HERA. Additional systems will be added in the future according to the availability of the new hardware components.

6 ACKNOWLEDGEMENTS

The encouraging help and engagement of K.-H. Meß (low-cost multi-purpose transient recorder) and S. Pätzold and H.-T. Duhme (trigger distribution) is gratefully acknowledged.

A HIGH RELIABILITY CONTROL SYSTEM

J. Callahan, J. Collins, A. Qualls, IUCF, 2401 Milo B. Sampson Lane, Bloomington, IN 47408
W. Hunt, Indiana University Computer Science Dept., Bloomington, IN 47405

Abstract

This paper describes part of an innovative control system developed for the Cooler Injector Synchrotron (CIS). This system achieved specifications oriented to accelerator applications which could not be met with commercial hardware and hence may be of interest to other laboratories. The system displays high levels of performance, reliability, maintainability, and repeatability. It is VME based and employs fiber optic data transmission for high noise rejection; actively redundant modules with automatic switch over for high reliability; and built in test and self diagnosis with centralized failure and system health monitoring for rapid maintenance. Several modules, designed and manufactured at IUCF, are described. This paper focuses on the Non-ramping Controls Subsystem.

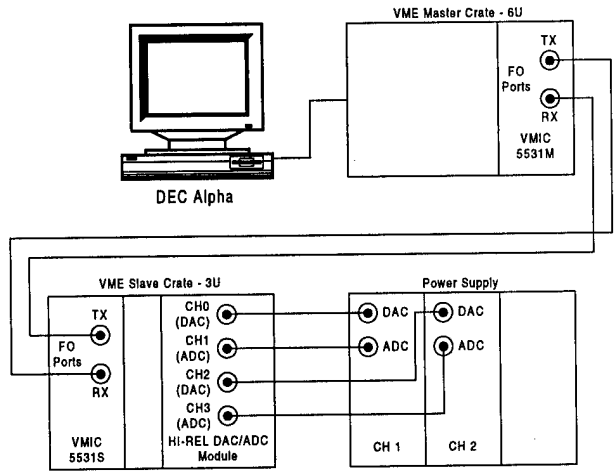

Figure 1 Beamline DAC/ADC - Overall System Design

1 OVERALL SYSTEM

There were four major goals which drove the CIS control system design: precision, repeatability, reliability, and maintainability. The overall system architecture was driven by the requirement for a precise control system. Electromagnetic Interference (EMI), which is intense in our environment, limits the precision of DACs and ADCs connected to power supplies over long copper cables. To combat this we designed the system as a fiber optic star network with the DACs and ADCs located near or in the power supplies themselves. (Figure 1). Locally, each DAC/ADC module has opto-isolation to avoid interaction among power supplies. The central computer, a DEC Alpha, drives two VME 6U communications crates located adjacent to the computer. The communications crates are populated with VMIC 5231M fiber optic (FO) communications modules which are linked to remote 3U and 6U crates by fiber optic cables. Each remote crate has a VMIC 5231S FO module which plugs into the local VME backplane. The remote crates can hold up to ten HI-REL DAC/ADC modules. Another consideration in providing precise control is to avoid interactions between power supplies. When DACs/ADCs controlling multiple power supplies have large common mode signals on the control lines, unwanted interactions between the supplies can result. To prevent this interaction, the DAC/ADC modules were designed with optically isolated data and a low capacitance power supply module which were also designed and manufactured at IUCF. This approach provides near total noise immunity (160dB @ 60 Hz) and permits highly accurate control of power supplies and other devices.

2 REPEATABILITY

Repeatability refers to being able to reproduce runs, perhaps years later. We frequently run different energy levels and different particles and, historically, it has taken many hours to re-tune the cyclotrons and cooler after each energy/particle change. There are several reasons for this including magnet hysteresis, but a significant cause is drift in the DAC/ADCs and the power supplies, as well as calibration differences when DACs and power supplies are replaced after failures. There are two kinds of drift which are important here. One is temperature drift induced by changing temperatures, the other is long term drift induced by changes in component characteristics over time. Our DAC/ADC modules display 3 ppm/°C of temperature drift. To attain this level, at reasonable cost, we were forced to design our own DAC/ADCs. These modules operate by generating a ramp whose end points are tied to voltage references of great temperature stability (3 ppm/°C). The input and output voltages are then compared (Figure 2) to the ramp in order to set the output voltage (DAC) or measure the input voltage (ADC). A byproduct of this design is that the same channel can serve as either a DAC or an ADC depending on an external switch selection. The modules which we have produced have four channels which can be set to any combination of DAC or ADC (Figure 2).

0-7803-4376-X/98/$10.00 © 1998 IEEE

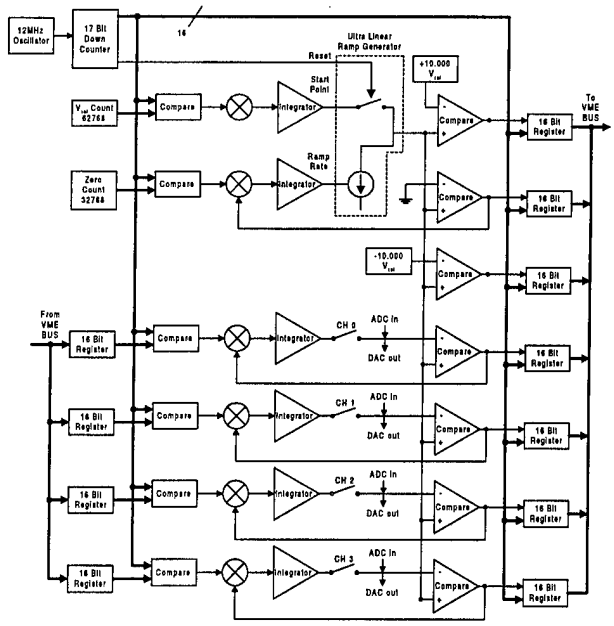

Figure 2 16 Bit, 4 Channel DAC/ADC Block Diagram

3 REDUNDANCY

To combat long term drift, we take advantage of a feature which was originally designed for reliability reasons, as will be described presently. Each DAC can be read back by the central computer and its output compared to its input, providing a direct measure of drift. If the DAC is in calibration, the computer examines the output of the power supply as measured by the ADC. If drift is detected here, we know that either the ADC or the power supply is in error, but not which. However, each power supply is controlled by two DAC/ADC modules in an actively redundant configuration. The central computer therefore has the ability to compare the output of two separate ADCs. If both agree, to within calibration accuracy, we know that the power supply has probably drifted or malfunctioned. If the ADC's differ, we know the problem is with the ADCs. If the problem is with the ADC, the central computer has the ability to switch the module to it's backup and the primary module can then be removed and repaired or recalibrated. This feature also permits us to automatically scan the system and determine that all DACs/ADCs and power supplies are functioning and are within specifications. A key requirement of this approach is to calibrate power supplies and DACs/ADCs which are nearing their calibration limits.

4 COMMUNICATIONS LINK

The communication modules which link the DAC/ADC modules to the main computer do not have automatic switch over. To protect against communications failure, the primary and backup DAC/ADC modules are located in different crates. A failure in the communications module, backplane, or backplane power supply is detected by the module as a loss of communication. If the FPGA detects a loss of communications it switches to the backup module. The master communications modules at the main computer are also located in two separate 6U VME crates so that a failure of the primary crate results in a switch over of all primary modules to their backups. The only common point in the system is the Alpha computer itself which is not duplexed.

5 RELAIABILITY

Another major design goal is reliability. Beam time is expensive. We wanted CIS to be highly reliable and we were also laying ground work for the proposed Light Ion Synchrotron and for possible medical applications of proton therapy which require high reliability. The first step in "reliability by design" is to insure that individual modules have as high a reliability as possible. Good design, careful component selection, and heavy parts derating yield a high reliability design. The next step is carefully controlled manufacture to insure that the design reliability is actually achieved. At IUCF, we developed an ISO9000 compliant production facility (as yet unaudited) with full Electrostatic Discharge (ESD) protection to produce these modules. We have had approximately 50 units in service for 9 months with no failures to date.

5.1 MEAN TIME BETWEEN FAILURE (MTBF)

However, when large numbers of modules are used in a system, the overall system MTBF is additive and hence, can be quite low, even when the individual MTBFs are high. One of the best ways to improve system MTBF is to provide active redundancy. Active redundancy provides a back up module which takes over automatically when the primary module fails. What makes active redundancy so attractive is that the probability of failure of two devices, in a given interval, is the product of the individual failure rates. When those rates are low, the product is extremely low. If failures are detected immediately and the failed unit replaced quickly, the system MTBF can approach years. In CIS, critical devices are controlled by two DAC/ADC modules. The primary module is normally in control. The DAC/ADC module has a field programmable gate array (FPGA) designated the "health" FPGA which continuously monitors fourteen (14) parameters within the module. If these parameters go out of established ranges, a failure is detected. The primary DAC/ADC module then relinquishes control to the backup. The switch over occurs in less than a millisecond and will not usually be noticed by the controlled device at all. The failure information is sent to the main computer. The primary unit is also monitored by it's backup module via a "heartbeat" line. If the primary unit fails catastrophically or loses power, the back up unit takes over automatically. As mentioned previously, the main

computer can also direct a changeover to the backup module if the primary module drifts out of calibration.

5.2 MEAN TIME TO REPAIR (MTTR)

Maintainability determines mean time to repair and consists of two components: diagnosis and repair time. Typically time spent diagnosing failures contributes 90% of MTTR. In order to minimize MTTR, we designed in a number of built in test features to facilitate diagnoses of problems. For active redundancy to be effective, it is necessary to detect failures and replace the offending module. The DAC/ADC modules report their health and primary/backup status to the main computer and display it on front panel LEDs. The failed unit can then be replaced. The modules have a "hot swap" capability which allows us to replace a failed module without turning off power to the crate. We expect an order of magnitude reduction of MTTR from approximately 3.1 hours to typically 15 minutes.

6 CONCLUSION

The non-ramping control system displays high reliability and very low drift. Other portions of the CIS control system are described in other papers.

NUCLOTRON CONTROL SYSTEM

V.Andreev, V.Gorchenko, A.Kirichenko, A.Kovalenko, I.Kulikov, V.Monchinsky, S.Romanov, B.Sveshnikov, A.Tsarenkov, B.Vasilishin, M.Voevodin, V.Volkov
141980, Laboratory of High Energies
Joint Institute for Nuclear Research, Dubna, Russia

Abstract

The superconducting synchrotron, named the Nuclotron is based on miniature iron-shaped field SC-magnets. It was put into operation in March 1993 at the Laboratory of High Energies of the Joint Institute for Nuclear Research in Dubna. Eleven runs of the new accelerator have been performed by the present time.The Nuclotron Control System (NCS) project, which is still under development, started in 1992 and has provided an efficient support for the machine commissioning through all its phases. This paper presents the current status of the whole system and some details of cryogenics, beam injection, and main power supplies subsystems.

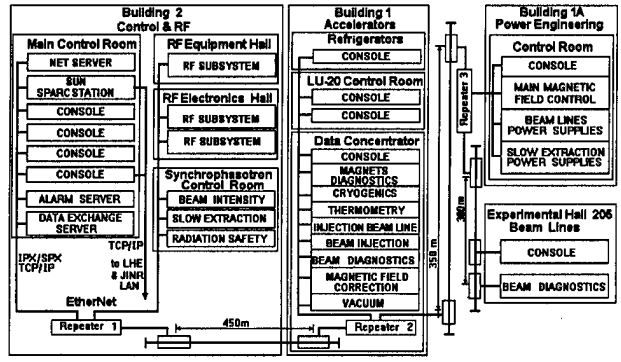

Figure 1: Basic structure of NCS

1 INTRODUCTION

The Nuclotron [1] is intended to accelerate nuclei and multicharged ions including the heaviest ones (uranium) up to an energy of 6 Gev/u for the charge to mass ratio Z/A = 1/2. There are 96 dipole, 64 quadrupole, 32 correcting multipole SC-magnets in the Nuclotron magnetic ring with a circumference of 251.5 m. The maximum value of the magnetic field is about 2 T.

2 NCS STRUCTURE

2.1 General

The Nuclotron Control System in its present form, together with the Main Control Room and the local consoles, comprises the following subsystems: cryogenics, thermometry, magnet diagnostics, an injection beam line, beam injection, beam diagnostics on the first turns, magnetic field correction, vacuum, circulating beam diagnostics, radio frequency, main power supplies, and radiation safety. The slow extraction and external beam diagnostics subsystems are still under development. Each subsystem is autonomous, i.e. the corresponding accelerator component can be put into operation and tested in this way.

The basic structure of NCS is shown in Fig.1. The control system architecture is hierarchical in nature and consists of two physical levels, an Operator Control Level and a Front End Level.

2.2 Operator Control Level

The Operator Control Level supplies all the appropriate man-machine tools for operators to run the accelerator. High performance workstations, together with general-purpose server computers, are used at this top level. The workstations act as operator consoles, while the servers provide the communication process, data storage, printing utilities, a common database, alarm service, a program library, and data exchange between the Nuclotron and its experiments.

The NCS is a distributed system, in which subsytems are geographically separated by as much as 500 m. The common backbone of the system is an Ethernet Local Area Network (LAN). It runs IPX/SPX and TCP/IP communication protocols and connects console computers to the Front End Level and physicists workstations. As the system has four geographically separated parts, LAN is divided into four independent segments. A LAN bridge on the basis of SUN Sparc station is used to filter communication between the General JINR Ethernet and Nuclotron network.

The database includes static and dynamic ones. The static database contains the information necessary to drive all the devices connected to the control system. The complete information set about the status of the whole machine is available in the dynamic runtime database. It is updated each accelerator cycle. The archive database keeps a long-term history of machine parameters. The status of all the equipment is recorded into log files once 30 minutes for further analysis. Access to the database information is gained by the consoles independently in order to display relevant parameters about the elements required by the operators. The library of database access routines named the Data Viewer has been developed. These applications allow users to select data sets for visual observation or color graphic printing on remote workstations. Multiple Data Viewers can be activated simultaneously.

The alarm server monitors continuously any changes of the state of predefined equipments and detects fault conditions; anomalies are displayed on an alarm screen and duplicated by multimedia audio devices for the operator to take an appropriate action. Alarm messages are archived

0-7803-4376-X/98/$10.00 © 1998 IEEE

for retrieval and off-line inspection.

An information management subsystem was designed and is now under implementation to interchange information between the NCS and the Nuclotron experimentalists. The element tables in the dynamic database are duplicated at the data exchange server in order to be available to the physicists. This information can be both observed on display screens, and processed and written on disks together with experimental data for future off-line physics analysis. Some data are broadcasted via cable TV channels. The same subsystem also sends experimental information, such as background levels and detector counting rates to the NCS. The Nuclotron operators use this information to adjust the machine.

2.3 *Front End Level*

The Front End Level deals with real-time controls. At present, the total number of points for measurement and control are about 3000. This number will be increased by about 20The expected average rate of real-time acquisition is 90 kByte/s.

This level comprises both industrial rack-mountable PCs from ADVANTECH, equipped with I/O boards and data acquisition modules, and intelligent CAMAC crate-controllers with embedded micro-PCs. These ones, as a rule, are diskless systems, and they can be installed in harsh environments. The controller developed by our own staff is based on an OCTAGON micro-PC. An onboard Ethernet interface allows software downloading and remote device control. The main part of the existing hardware interface is in the CAMAC standard. All CAMAC modules of the total number up to 600 were developed and manufactured at the LHE, JINR. However, we are planning to implement more extensively acquisition and control boards in the industrial PC standard.

3 SUBSYSTEMS

3.1 *Cryogenics and Thermometry*

The parameters under control are the quality of a two-phase flow (the mass vapour content of helium in the supply headers), the density and flow rate of two-phase cryoproduct flows. The principle of measurement is based on the dependence of the resonance frequency of an oscillating RF-resonator with a high Q-factor on the dielectric permeability of the controlled flow [2] . At the same time, the subsystem provides a helium pressure measurement in direct and back flows, the helium and nitrogen levels and pressure in the separators and storage tanks, as well.

The temperature measurement is one of the central points in the cryogenic subsystem. This makes it possible to monitor and control cool-down and warm-up of the accelerator magnets, to support operational conditions during machine runs, to indicate the deviations of cooling parameters from nominal ones, and to carry out temperature diagnostics of the cryogenic components during accidents (quenches, vacuum breakdowns, etc.). The subsystem provides the temperature measurements of the Nuclotron elements at more than 600 control points. The measurement range is from 4 to 300 K with the resolution of 25 mK at temperatures of 4 K. Fig.2 illustrates the operation of the subsystem.

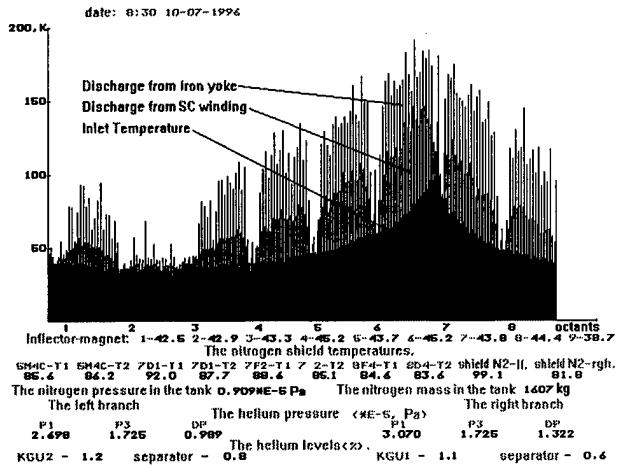

Figure 2: The temperature distribution along the Nuclotron ring after 48 hours of cooling-down

3.2 *Beam Injection*

The subsystem has been set up to control and monitor the equipment on a beam transport line, power supplies, a superconducting inflector magnet, inflector plates, beam instrumentation elements in the ring, timing and synchronization.

In order to observe the beam behaviuor during injection and at the initial stage of beam circulation, various monitoring devices were made for the subsystem. The diagnostics of the beam injection transport line include 2 wire collector profilometers, 1 wire collector beam current monitor, 2 destructive screen monitors, and 2 Faraday cups. The beam profile monitor consists of X- and Y-wire planes. Each plane has 32 golden tungsten wires 0.1 mm in diameter separated by 2 mm. The beam current monitor has one plane with wires connected in parallel. Image processing technique based on fluorescent screens, CCD cameras, and frame-grabbers ensures the following possibilities: fluorescent screen selection and setting inside the beam, video tuning, background subtraction, pseudo-color for displays, the ability to save and restore specific images, snapshot and live mode selection (Fig. 3).

The accelerator ring diagnostics are composed of 5 wire collector profilometers, 21 electrostatic position pick-ups, 1 electrostatic intensity pick-up, 1 magnetic pick-up, 4 destructive screen monitors, 4 Faraday cups. Two of five profilometers are placed at the entrance and the exit of the inflector magnet. We are planning to measure emittance using the profilometers at the end of the transport line, at the inflector magnet entrance, and in the first straight section of the ring. It will allow us to adjust more exactly injected

beam matching to the ring lattice. Using the position and intensity pick-ups with fast (10-50 MHz) buffered ADCs of 8-bit resolutions, beam information for each revolution can be acquired. It is possible to obtain transverse and longitudinal information for 800 first turns in parallel with orbit acquisition. Fig.4 shows some parameters of the subsystem.

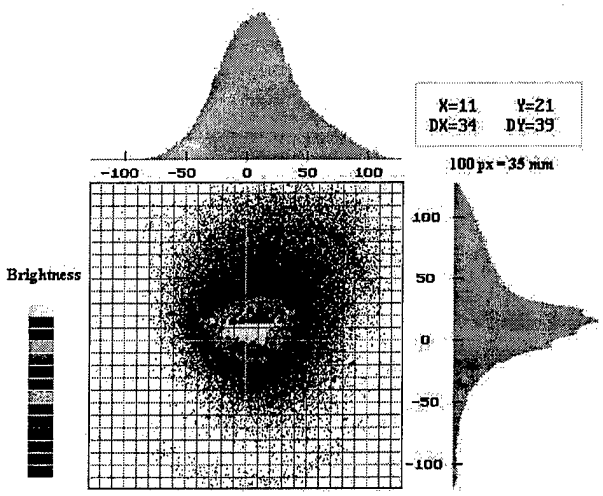

Figure 3: Beam image acquired by the injection subsystem

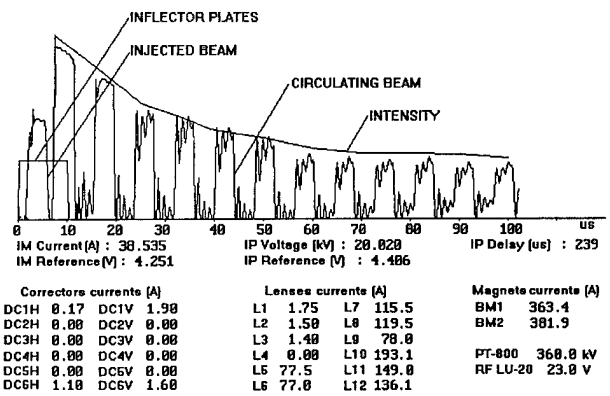

Figure 4: Some parameters of the injection subsystem

3.3 *Main Magnetic Field Control*

The dedicated control subsystem for pulsed power supplies of the magnets was designed, allowing the reproduction of the desired B and Q fields to better than 5×10^{-4} at injection.

The bending (BM), focusing (QF) and defocusing (QD) magnets are powered by three supplies. The BMs are driven by supply of a 6.3 kA nominal current. The QFs and QDs are connected in series and powered by supply of 6 kA. Besides, an additional supply of 200 A for the QFs is used to keep the required ratio I_{QD}/I_{QF} during the accelerator cycle.

The BM magnetic field shape is set by a pulse function generator which produces a reference burst (Bo-train) with a 0.1 Gs resolution. This train increments a pattern analog function generator based on a 16-bit DAC. A real B-train off the reference bending magnet and the corresponding analog function are used for feedback loop. The current magnetic field of the BMs is used as reference function for the focusing and defocusing magnets, i.e. the BM power supply is a master and the QF and QD supplies are slave ones. The QF and QD trains are utilized for control as described above. Fig.5 shows the magnetic field cycle parameters.

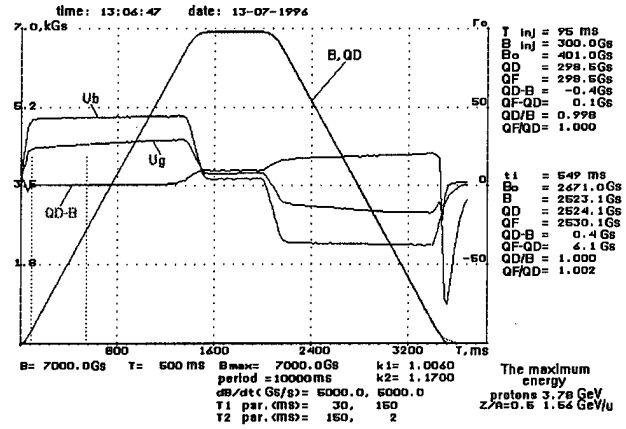

Figure 5: Example of magnetic field cycle parameters

4 CONCLUSION

At present, though not at its final dimension, the control system is fully operational and has the proposed functionality. An essential step to provide the accelerator with a high performance and flexible computer control environment has been accomplished. Up to now, 28 computers and 35 CAMAC chassis are installed in the control system.

5 ACKNOWLEDGEMENTS

We would like to thank our colleagues who have contributed to the NCS project. The authors are grateful to L.Sveshnikova for her help in preparing this paper.

6 REFERENCES

[1] A.D.Kovalenko, "Status of the Nuclotron", Proceedings of the Fourth European Particle Accelerator Conference (EPAC 94).

[2] A.I.Alexeev et al,"Application of Radio Frequency Method to Measurements in Cryogenics", Cryogenics, 1991, Vol.31, pp.1020-1029.

USE OF A VIRTUAL ACCELERATOR FOR A DEVELOPMENT OF AN ACCELERATOR CONTROL SYSTEM

Noboru Yamamoto
KEK,High Energy Accelerator Research Organization
1-1 Oho,Tsukuba, Ibaraki,JAPAN 305

Abstract

Concept of Virtual accelerator is introduced to develop beam control application programs in the KEKB accelerator control system. A virtual accelerator is a computer process which simulates behavior of a beam in an accelerator and responds to the accelerator control program under development in a same way as an actual accelerator do. Users of the virtual accelerator can test their control algorithm and user interface without affecting the operation of the accelerator.

EPICS(Experimental Physics and Industrial Control System) jointly developed by LANL and APS/ANL will be used as a base of KEKB accelerator control system. In the EPICS based control system, a device is represented as a collection of records in a EPICS runtime database. A control program on a host computer can access devices in the system only through names of record fields, called 'channel'. This abstraction allows us to construct a virtual accelerator control system. Channel access interfaces was implemented into the modeling program SAD[1] to realize this idea. Sample application of the method will be also presented.

1 USE OF VIRTUAL ACCELERATOR CONCEPT.

1.1 Accelerator Model in an accelerator control system.

A concept of a virtual accelerator(VA) had been discussed within the SAD program development team [1] since the early stage of the development of SAD modeling code. It is one of goal in the SAD project to develop a environment in which one can access both an accelerator model and a machine using same user interface and the users cannot easily distinguish them. A user of the program writes a script to analyze data for the model. VA concept in SAD allows to use this program for the operation of REAL accelerator without any modification or with tiny modification.

In the TRISTAN operation, we learned importance of modeling program in the accelerator control system[4]. Comparison of the measured data and results of simulation by modeling code gives us a deeper understanding of the an accelerator and were essential to improve performance of the accelerator. Since the TRISTAN control system was designed long before SAD was developed, data files are the only way to exchange data between two environment. It work, but takes time and human intervention. This experience suggests that tighter integration of modeling program and control system is necessary in the future accelerators such as KEKB[5]. If we can use same operator interface to control both "REAL" and "VIRTUAL" accelerators, we can directly compare the results of measurement and the simulation in same environment.

1.2 VA as a RAD(Rapid Application Development) tool

Tightly integrated modeling code in a control system, or a virtual accelerator, is also useful as a RAD tool in the construction of an accelerator control system. Application programmer and/or an accelerator physicist can develop a code without waiting for the completion of hardware installation. Realistic response using the VA will help the development of high level applications in the control system.

Figure 1 shows a sample application developed with the VA. User can display the horizontal and vertical orbits of KEKB-LER(Low Energy Ring) and can also issue several commands, such as "correct orbit", to the control system. This application, in principle, can be used with the real KEKB-LER when it is ready to operate. MEDM is used to build a user interface in this case. Shell sciripts and SAD scripts are used to describe behaiviour of the application.

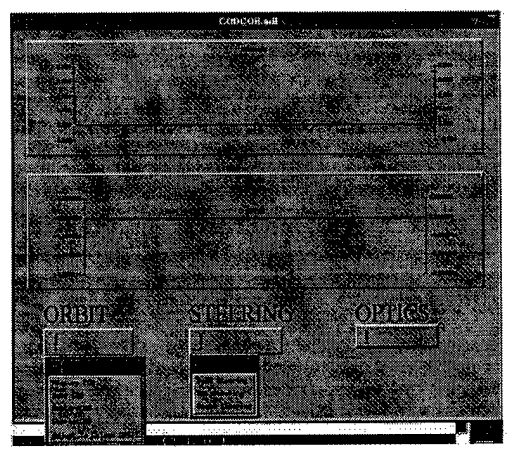

Figure 1: Sample application using VA.

1.3 VA as a "Flight simulator"

It is also useful to use VA as a "Flight simulator". Trainee of the accelerator operation can learn the response of the system even in a situation which should not occur in the real machine.

In the commissioning of the new accelerator, it is necessary to examine new algorithm to optimize performance of the beam. "Flight simulator" allows accelerator physicist to examine his/her algorithm without disturbing the operation.

0-7803-4376-X/98/$10.00 © 1998 IEEE

2 A CONTROL SYSTEM WITH VA.

To realize VA concept in the accelerator control system, a modeling program and control system architecture should have the following features.

1. Control system should have a layer to hide hardware detail from the an application program. Application should access control devices through a logical names but not through hard coded hardware address. Without this layer it is difficult to develop an application which can access both "real" and "virtual" accelerators using same program interfaces.

2. Modeling program can access the information on the control system. And the control system can access data in a process running the model.

3. A control system should allow multiple instance of virtual accelerators at same time. So that multiple users can develop their control application without interference between them.

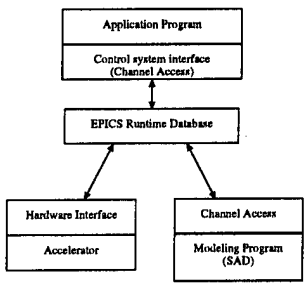

Figure 2: EPICS Database allows application program to access hardware devices and data on a simulation process in a unified way.

2.1 *EPICS runtime database and channel access.*

We have decided to use EPICS(Experimental Physics and Industrial Control System) as a infrastructure of the KEKB accelerator control system[6]. Runtime database and channel access, which are key parts of the EPICS system, provides a layer which we discussed in the previous section. Figure 2 shows how EPICS runtime database hides a diffrence between "REAL" and "VIRTUAL" accelerators from the application program.

2.2 *SAD: an accelerator modeling program*

SAD is a computer program complex for accelerator design. It has been developed in KEK since 1986. The major functions are:

1. Structural Definitions of Beam Line and Component[10].

2. Ritch Matching Functions

   (a) Optics matching

   (b) Optical/Geometrical matching

   (c) Off-momentum matching

   (d) Finite-amplitude matching

   (e) Spin matching

3. SAD Script Programming Interface in Mathematica[11] Style. Major functions for lists and structural operations. Built-in, system- and user-defined functions for accelerators

4. 6D full-symplectic particle tracking for Dynamic aperture survey with/without Synchrotron radiation effect.

5. Taylor map by automatic differentiation and Lie algebraic map for Nonlinear Analysis

6. Emittance Calculation using 6D Beam-matrix method[2]

7. Anomalous Emittance Calculation [3]

8. Spin depolarization(SODOM)

SAD has proven to be powerful and useful in designs, simulations, commissioning and improvement of TRISTAN, KEKB, FFTB, ATF, JLC, NLC, and others. Various packages for accelerator studies are written for SAD scripting language. These packages will be used in the operation of KEKB.

2.3 *EPICS interface in SAD*

EPICS CA interface was implemented in the SAD. Using this interface SAD can directly access data in the control system. This interface is also used to put a response from VA, which is one of process running SAD, into EPICS database. CA interface in SAD has just three functions, $CaOpen$, $CaRead$ and $CaWrite$. These functions can take a list as a its argument to take advantage of asynchronous operation in EPICS CA. For example, if you have a list of EPICS channel names,

$$channels = \{"BPM1", "BPM2", \ldots\},$$

a single call of $CaOpen$,

$$CaOpen[chnnels]$$

will return a list of opened channel ids. $CaWrite$ function can take this list of channel ids and returns a list of current values of these channels. This list handling allows SAD to read data from EPICS database efficiently.

However these interface allows to construct VA, you need to prepare EPICS database definition files for each instance of VAs and needs to load these databases onto IOC(Input Output Controller, VME CPU running EPICS core software). We are now developing another mechanism to support VA using the portable CA server program developed at LANL. The "portable CA server" is a collection of

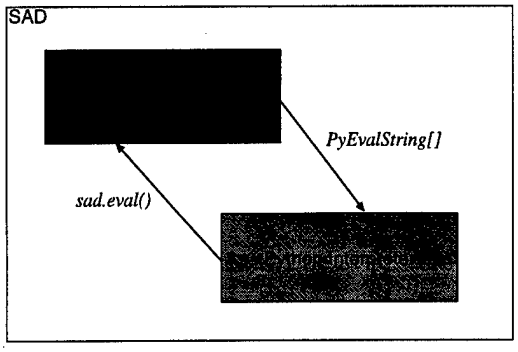

Figure 3: SAD code includes both SAD/FFS interpreter and Python interpreter in it. Two interpreters can exchange a expression as a string for evaluation.

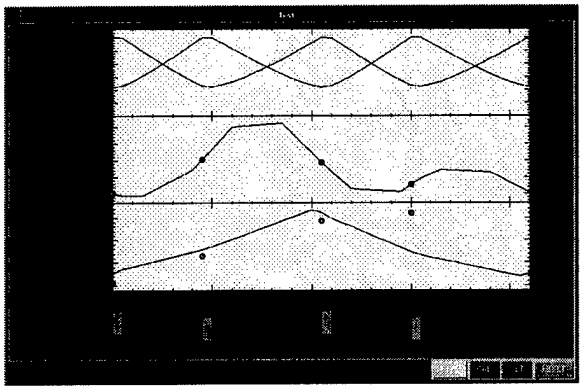

Figure 4: SAD can use Python/Tk to provide GUI.

C++ classes to support development of CA server on Unix platform. Using this framework, you can create SAD-CA bridge software, which takes CA request, get a data from SAD processes and returns these value to the CA clients. The SAD-CA bridge can also create channels connected to the SAD process dynamically. It allows unlimited numbers of VA instances in the control system.

2.4 Python/Tk in SAD

Python is "an interpreted, interactive, object-oriented programming language"[8]. Like Tcl/Tk[9] it can be used as an extension language for applications that need a programmable interface. Python has Tk bindings, Tkinter.py, so that you can create GUI using the Python. Figure 3 shows how Python is embedded in SAD program. SAD passed a string including any Python expression to Python core and Python core evaluate it. Python core can also pass a string which represents SAD/FFS scripts to SAD for evaluation. It provides basic mechanism to exchange data between two interpreters. Wrapper functions are written on this basic mechanism.

K. Oide [12] wrote a sample user interface for the orbit correction as shown in Figure. 4.

3 CONCLUSION

We have implemented a basic mechanism to realize VA concept in the KEKB accelerator control system. Using the this mechanism, a few sample application program were written. Futher development is needed to allow multiple instance of VAs and its dynamic creation.

4 REFERENCES

[1] "SAD home page", http://www-acc.kek.jp/SAD/sad.html. ; K.Hirata, An introduction to SAD, Second Advanced ICFA Beam Dynamics Workshop, CERN 88-04 (1988).

[2] K.Ohmi, K.Hirata and K.Oide, From the beam-envelope matrix to synchrotron-radiation integrals,Phys.Rev.E49, 751 (1994).

[3] . K.Oide and H.Koiso,Anomalous equilibrium emittance due to chromaticity in electron storage rings, Phys.Rev.E49, 4474 (1994).

[4] "Integration of the Modeling Program with Accelerator Control Systems in TRISTAN", Proceedings of the 1995 International Conference on Accelerator and Large Experimental Physics Control Systems, Chicago, Illinois, pp. 423-428

[5] S-I Kurokawa, " Status of TRISTAN-II Project", Proceedings of the 1993 Particle Accelerator Conf, pp. 2004-2006; S-I Kurokawa, "KEKB status and Plans", 1995 Particle Accelerator Conference and International Conference on High-Energy Accelerators, Dallas, Texas,USA, May 1-5, 1995.

[6] T.Katoh et al., "Status of the KEKB accelerator control system development", Proceedings of the 1995 International Conference on Accelerator and Large Experimental Physics Control Systems,Chicago, Illinois,1995, pp. 899

[7] L.R. Dalesio, et al., "EPICS Architecture", ICALEPCS 91, KEK Proceedings 92-15, (1992) pp.278-282.; L. Dalesio et al. "The Experimental Physics and Industrial Control System Architecture," ICALEPCS 93, Berlin,Germany, Oct. 18-22, 1993.

[8] "Python Language Home Page", http://www.python.org

[9] "Why Tcl?", http://sunscript.sun.com/tcltext.html

[10] D.C. Carey and F.C. Iselin, "A standard input language for particle beam and accelerator computer program"

[11] S. Wolfram, "Mathematica: A system for Doing Mathematics by Computer",Second Edition, Addison-Wesley Publishing Company, 1991

[12] Katsunobu Oide, KEK, in private communications.

OPERATION LOGGING SYSTEM USING THE DATABASE FOR THE SYNCHROTRON RADIATION BEAM LINES AT THE PHOTON FACTORY

Noriichi KANAYA, Seiji ASAOKA and Hideki MAEZAWA

Photon Factory
High Energy Accelerator Research Organization (KEK)
1-1, Oho, Tsukuba, 305, Japan

Abstract

The operation Logging System has been designed and built using the Oracle database for the twenty-two synchrotron radiation beam lines at the 2.5 GeV positron storage ring at the Photon Factory, where X-ray/VUV synchrotron radiation experiments are simultaneously carried out. The operation Logging System has a real-time capability to automatically store the database with all possible operational events of all vacuum valves/shutters and interlock signals, and all static operational data, including the pressures of the beam lines and the storage ring, and related operational data which represent the physical behaviors of the beam lines. By retrieving any combination of operational data, the system allows to reproduce the physical behaviors that have occurred in the beam lines.

1 INTRODUCTION

There are twenty-two synchrotron radiation beam lines at the 2.5-GeV positron storage ring, Photon Factory at the National Laboratory for High Energy Physics. These beam lines feed synchrotron radiation to the experimental hall where experiments such as surface physics, x-ray lithography, microscopy and crystal structure analysis are simultaneously carried out. These beam lines are simultaneously in operation, providing intense synchrotron radiation beams.

These beam lines are automatically controlled by the twenty-two computers connected to a VAX Station 4000/90, running under VAX/VMS, through an optical-fiber network with a star configuration [1]. The host collects all operational data and control data of the beam lines. The operational and control data have been automatically stored in the logging file system to retrieve later specific combinations of behaviors of beam line components.

There have been further necessities to allow clients, such as the staff of the Beam Line Group or operators of the storage ring at the Photon Factory, to retrieve any combinations of control data for the beam lines. A new logging system has thus been designed and implemented using the Oracle database. The Logging System for the synchrotron radiation beam lines has a real time capability to fetch any event real our experience with the Logging System based on the database for the synchrotron radiation beam lines at the Photon Factory.

2 SYSTEM DESCRIPTION

It is crucial for the Beam Line Group to be capable of improving the performance of the beam lines by using the Logging System. In addition, they must be capable of identifying later when, how, what, where and which device was controlled in order to predict any sign that suggests any presence of malfunctioning behavior of a beam line component beforehand. When a beam line component is unexpectedly malfunctioning, the Logging System must provide play-back control-information that leads to a swift recovery of the problem with the component. This is also true for predictive maintenance; for example, the Beam Line Group monitors the closing/ opening times of more than ninety vacuum valves at an accuracy of 0.1 seconds or less are ranging within ordinal closing/opening times every day in order to ensure the safety of synchrotron radiation experiments. For these reasons, all control data, including the operational status of the beam lines to be controlled and the set-up values for the beam lines, have to be automatically logged into the on-line Logging System being incorporated with the Beam Line Control System [1]. For a large accelerator, a logging system using a database has been also in operation[2].

Each beam line has a number of components and sensors to be controlled, including vacuum valves, interlock devices (Cooling water flow sensor, fast/slow vacuum sensors, pneumatic-pressure sensor, atmosphere sensor, Open-Request signal from the storage ring, and from the experimental hall), vacuum pressure gauges of the storage ring and the beam lines, valve driving units). These components are controlled and monitored by a computer of the beam line control system.

There are two categories of data available from the beam line control system: event data and static data. Each dada has a time stamp with an accuracy of 20 ms. The first category includes "asynchronous event data". The event data are obtained from digital ON/OFF signals generated by the vacuum valves, shutters together with time-stamps. Event data also include driving signals for controlling these vacuum valves and shutters, and the status signals of safety

0-7803-4376-X/98/$10.00 © 1998 IEEE

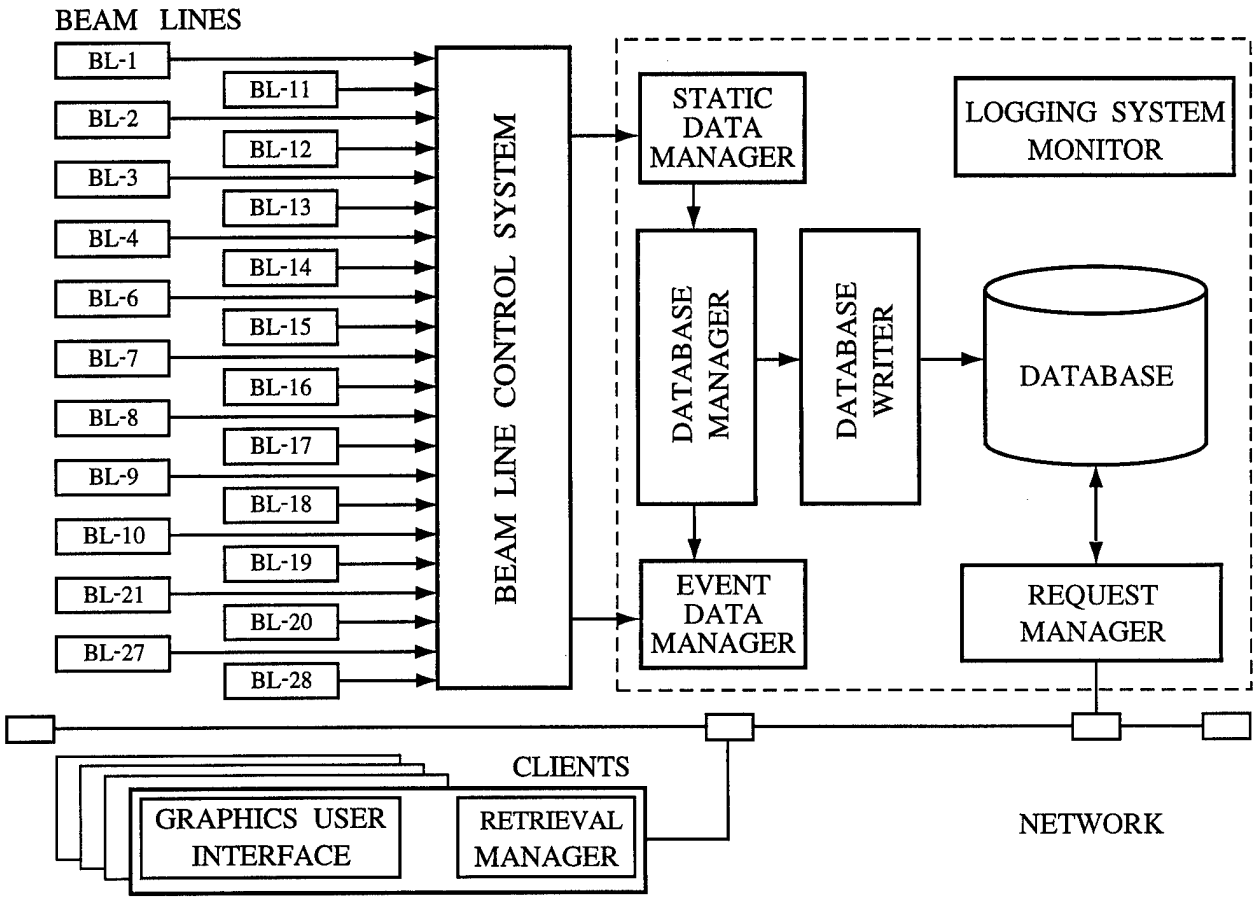

Figure: 1 Block diagram of the Operation Logging System for Synchrotron Radiation Beam Lines at the Photon Fctory, KEK.

interlock signals. Event type of data are obtained at any instance of time when a component changes its status; for example, when a valve opens it simultaneously generates 'status-open-on' signal and 'status-close-off' signals. There are approximately 2000 pick-ups in total. The maximum event rate typically occurs at 9 AM every morning when all beam lines have to simultaneously close/open due to radiation safety reason before and after a beam injection, generating a number of event signals. The maximum rate of event signals reaches ~300 events/sec. This also happens when one of the interlocks is triggered in the case that an unexpected failure occurs [3]. It is very important for the Logging System not to miss any event signal.

The second category includes static analogue data: static data comprises analogue data that are periodically measured at a specified interval ranging from 3 seconds to one minute. The static data includes a beam current of the storage ring, pressures signals which are measured at the middle point of the beam line and the storage ring at an interval of three seconds. These should be stored in the Logging System. The total amount data to be logged into the database reaches approximately 35 million items, consuming 1.5 GB of disk space per year.

Figure 1 shows a block diagram of the operation Logging System. When an operational condition changes or when the status of a device changes, the beam line control

system automatically notifies event data representing the device status of the Event manager running on the VAXStation 4000/90 (~30MIPS, 80 MB of memory). The VAX has two 2GB disks for the system, database management, user applications, and a 4.5GB-disk for storing only operational data of the beam lines, allowing at least three years of data to be on-line.

Upon receiving event data, the Event Manager attaches a time stamp to the event data, and makes compliance checks in terms of validity of the event data that contains a device code and condition status code. If the event data have valid codes, the Event manager forwards the event data to the Database Manager.

The Static Data Manager fetches static data at specified time intervals associated with the devices to be measured. The Static Data Manager attaches a time stamp and device code to the measured value, and then sends it to the Database Manager. The Database Manager specifies a data-table name to which event data/static data is stored, depending on the event data code and condition status code. Then, the Database Manager sends a set of data to the Database Writer that stores the data to the specified table in the database. Data tables and index tables in the on-line database are separately assigned for each set of valves and interlocks, pressures and a beam current. All operational data stored in the database are archived for at least three years.

A Graphics Interface for operators is a client on the network which is implemented using Motif widgets on a VAX/Station 4000/90. An operator can choose any items associated with devices to be searched. The Retrieval Manager encapsulates these items into a packet, and queries the Logging System across the network. Then the Retrieval Manager receives reply from the database through the Requet Manager, transfering the reply to the Graphics User Interface to display the results.

3 CONCLUSION

The Logging System using database for the synchrotron radiation beam lines at KEK was designed and implemented in the late 1994, and come into actual operation in the beginning of 1995 to replace the existing logging file system. The Logging System based on the database has been reliably operating for several years, providing better performance than the ancestor logging file system, even to the degree of acquiring real-time event operational data from the beam lines. The Logging System provides a means to improve the performance of the beam lines[4], and is useful for determining the cause of a problem in a beam line.

4 ACKNOWLEDGEMENTS

The authors wish to express their gratitude to the staff of the Photon Factory Light Source Division for operating the beam liens and the storage ring.

REFERENCES

[1] N.Kanaya, "Design of the Distributed Control System for Beam Lines at the Photon Factory", IEEE Trans.Nucl. Sci.,Vol.NS-31, No.3, pp.957-962, June, 1984.

[2] R.Billen, "LEP Accelerator Logging System using on-line database," NIM, Sec. A, pp.296-299, 1994.

[3] N.Kanaya, S.Asaoka, S.Sakanaka and H.Maezawa, "Experience with the Ultra-High-Vacuum Protection system for the Synchrotron Radiation Beam Lines with High Power Wigglers/Undulators at the Photon Factory," in these proceedings.

[4] N.Kanaya, in preparation (noriichi.kanaya@kek.jp).

INTEGRATING COMMERCIAL AND LEGACY SYSTEMS WITH EPICS

J.O. Hill, LANL P.O. Box 1663, Los Alamos, NM 87545 USA
K.U. Kasemir, Universität Osnabrück, Fachbereich Physik, D-49069 Osnabrück, Germany
J.B. Kowalkowski, ANL 9700 South Cass Avenue, Argonne, IL 60439 USA

Abstract

The Experimental Physics and Industrial Control System (EPICS) is a software toolkit, developed by a worldwide collaboration, which significantly reduces the level of effort required to implement a new control system. Recent developments now also significantly reduce the level of effort required to integrate commercial, legacy and/or site-authored control systems with EPICS. This paper will illustrate with an example both the level and type of effort required to use EPICS with other control system components as well as the benefits that may arise.

1 INTRODUCTION

1.1 What is EPICS

EPICS is a process control and data acquisition software toolkit in use at over 70 sites world wide. The software is designed for general utility and has been successfully installed into a wide range of applications including particle accelerators, experimental physics detectors, astronomical observatories, municipal infrastructures, petroleum refineries, and manufacturing. A scalable, fault-tolerant system that follows the "standard model"[1] can be created with the toolkit. Compilers and filters are used to instantiate control algorithms in front-end computers from function block and state-machine formalism-based input. EPICS communication occurs within a software layer called channel access (CA) that follows the client server model and employs the internet protocols (Figure 1).

Figure 1

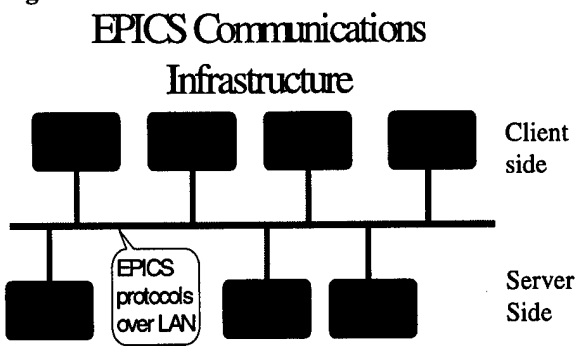

A mature set of client-side tools provide operator interface, alarm handling, archival tasks, backup, restore, state sequencing, and other capabilities. There is also an expanding library of hardware device drivers that have been written for use with EPICS. Recently we have seen a number of sites working on generic physics and control theory applications that will interface directly with EPICS. All of these components taken together form a toolkit that allows control system installation with a minimum of low level coding. Details can be obtained on the world-wide web[2] and from previous papers[3][4][5][6]. EPICS is very unusual among control system software packages in that it has been developed by a collaborative effort of several laboratories and industrial partners[7].

2 INTEGRATING WITH EPICS

2.1 Manipulating EPICS Process Variables

Many 3rd party products have been integrated with EPICS. These include LABVIEW, PVWAVE/IDL, SLGMS, WING Z, MATLAB, TCL/TK, DATAVIEWS, MATHMATICA, and the SDDS toolkit. All of these facilities have the ability to read and write external named data. To integrate with EPICS, a simple code that translated these requests into requests to read, write, and monitor an EPICS process variable must be written. With this translation code installed, the 3rd party product becomes an EPICS client side tool that can directly manipulate EPICS process variables.

Recently, many components of EPICS have been ported to the PC environment[8]. This has opened new opportunities to integrate EPICS with the many inexpensive "shrink-wrapped" software components that are available for the PC today. PC versions of the EPICS libraries have been packaged as Microsoft Dynamic Link Libraries (DLLs). This allows these EPICS components to be called directly from almost any PC program with macro language capabilities such as Excel, Visual Basic, and many others. This does however require writing small amounts of code.

A Microsoft Direct Data Exchange (DDE) server for EPICS has also recently been written. Many PC based programs can read, write, and monitor named data through this interface. Many 3rd party PC products can now integrated without writing *any* additional code. For instance, to access an EPICS process variable with Microsoft's Excel we simply add a line as follows to our spreadsheet.

==CaDDE|Get!'HighlyImportantMagnetCurrent'

0-7803-4376-X/98/$10.00 © 1998 IEEE

2.2 Your Data Can be an EPICS Process Variable

Recently a server level "Applications Programmers Interface" (API) has been added to EPICS. After writing a small amount of translation code conforming to this API, any named data appears in the EPICS process variable name space and can be directly manipulated as an EPICS process variable. This allows a legacy system to leverage the many EPICS client side tools that are capable of directly manipulating EPICS process variables. For example, the LANSCE control system at LANL and the D3 control system at DESY both can export their data into EPICS using this mechanism.

To export data into EPICS as an EPICS process variable one must provide at least the functions in Table 1.

Table 1

	Function
1	named process variable exists in subsystem test
2	create (or locate) instance of process variable
3	read from process variable
4	write to process variable

It is also necessary to inform EPICS when a process variable is modified so that any clients monitoring that variable will receive an update. To be compatible with the widest range of EPICS clients a subsystem must also be ready to respond to client requests for a standard set of process variable attributes such as limits, units, time stamp, and alarm status.

2.3 Adding New Function Blocks

A typical EPICS system has a real-time database resident in a processor with direct access to the process IO. This real-time database is made up of interconnected function blocks which implement the logic specific to a particular application of the system. A wide range of function blocks are supplied with the system. They provide execution semantics associated with various types of process IO, calculation, multiplexing, fan-out, delay, data reduction and many others. This list can be extended by writing a record support module that plugs into well defined software interface within the EPICS system.

2.4 Adding New Device Drivers

There are also well defined interfaces within EPICS for adding new device drivers. To install a new device driver the programmer must write a set of functions conforming with the device support API of a particular function block.

3 AN EXAMPLE

A demonstration of the famous nonlinear cart and pendulum problem from control theory was implemented on a portable laptop PC using only EPICS, the EPICS DDE server, and demonstration copies of two commercial products for the PC (Figure 2).

Figure 2

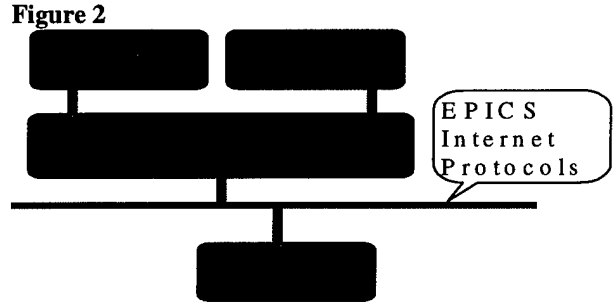

An evaluation copy of National Instrument's "Lookout" was used to implement the operator console for the demonstration. An evaluation copy of "MATLAB" from Math Works was used to implement a model of the cart and pendulum dynamic system (Figure 3), and also an LQR feedback compensator for this system (Figure 4). The dynamics of the system can be seen in Equations 1 and 2. All communication between MATLAB and Lookout occurred with the assistance of an EPICS server and an EPICS DDE server. The model and the compensator were updated in "pseudo real-time" in response to force input u from the operator console. The demonstration system can be controlled in a manual mode (without the aid of the LQR compensator) and also a closed loop mode (with the aid of the LQR compensator). The model is updated within MATLAB 100 times a second in response to a periodic DDE update for the force input u from the EPICS server.

Figure 3

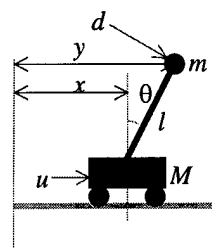

$$(M+m)\ddot{x}+ml(\ddot{\theta}\cos\theta-\dot{\theta}^2\sin\theta)=u \qquad 1$$

$$m(\ddot{x}\cos\theta+l\ddot{\theta}-g\sin\theta)=d \qquad 2$$

Figure 4

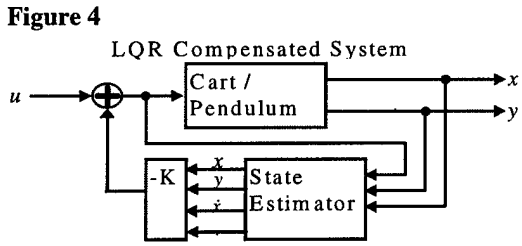

The demonstration was implemented in 2 man weeks by an individual integrating these products together with EPICS for the first time. Most of the labor was devoted to drawing the operator screen within Lookout, modeling the linearized cart and pendulum system in MATLAB, and designing an LQR compensator using the MATLAB control systems toolbox. No new EPICS code was written for this demonstration. Figure 5 shows the response of the

compensated system to a step on the *u* force vector on the cart.

4 CONCLUSIONS

EPICS is an open modular system that was designed for extension. Nearly all components within the system are replaceable. It is possible to manipulate EPICS process variables from a system that knows very little about EPICS. Likewise a system mostly unaware of EPICS can export its data into EPICS as EPICS process variables. Within two weeks one of the authors was able to integrate two commercial PC based components and create a non-trivial control theory demonstration that was updated in pseudo real time and hosted solely on a laptop PC platform. The public interface to EPICS only supports sending read, write, and monitor messages to a process variable and its associated attributes. This interface is both primitive and concise. It has been suggested that this interface is therefore old technology and not suitable for new projects, and we will counter that it is compatible with a large number of commercial and legacy systems that exist today. When optimizing and debugging a control process it is important for operators to be able to directly examine and record the internal state of the system. We have positive expectations for emerging high level object oriented standards, but we also see the continuing value of a high performance process variable based interface.

[1] B. Kuiper: 'Issues in Accelerator Controls', Proc. ICALEPCS, Tsukuba, Japan, 1991, pp 602-611.

[2] W. McDowell et al.: 'EPICS Home Page', "http://www.aps.anl.gov/asd/controls/epics/EpicsDocumentation/WWWPages/EpicsFrames.html"

[3] L. Dalesio et al.: 'The Experimental Physics and Industrial Control System Architecture: Past, Present, and Future', Proc. ICALEPCS, Berlin, Germany, 1993, pp 179-184.

[4] L. Dalesio et al: 'The Los Alamos Accelerator Control System Database: A Generic Instrumentation Interface', Proc. ICALEPCS, Vancouver, Canada, 1989, pp 405-407.

[5] J. Hill: 'Channel Access: A Software Bus for the LAACS', Proc. ICALEPCS, Vancouver, Canada, 1989, pp 352-355.

[6] J. Hill: 'EPICS Communication Loss Management', Proc. ICALEPCS, Berlin, Germany, 1993, pp 218-220.

[7] M. Knott et al: 'EPICS: A Control System Software Co-development Success Story', Proc. ICALEPCS, Berlin, Germany, 1993, pp 486-491.

[8] Chris Timossi performed the initial port of several of the EPICS components to the PC environment.

Figure 5

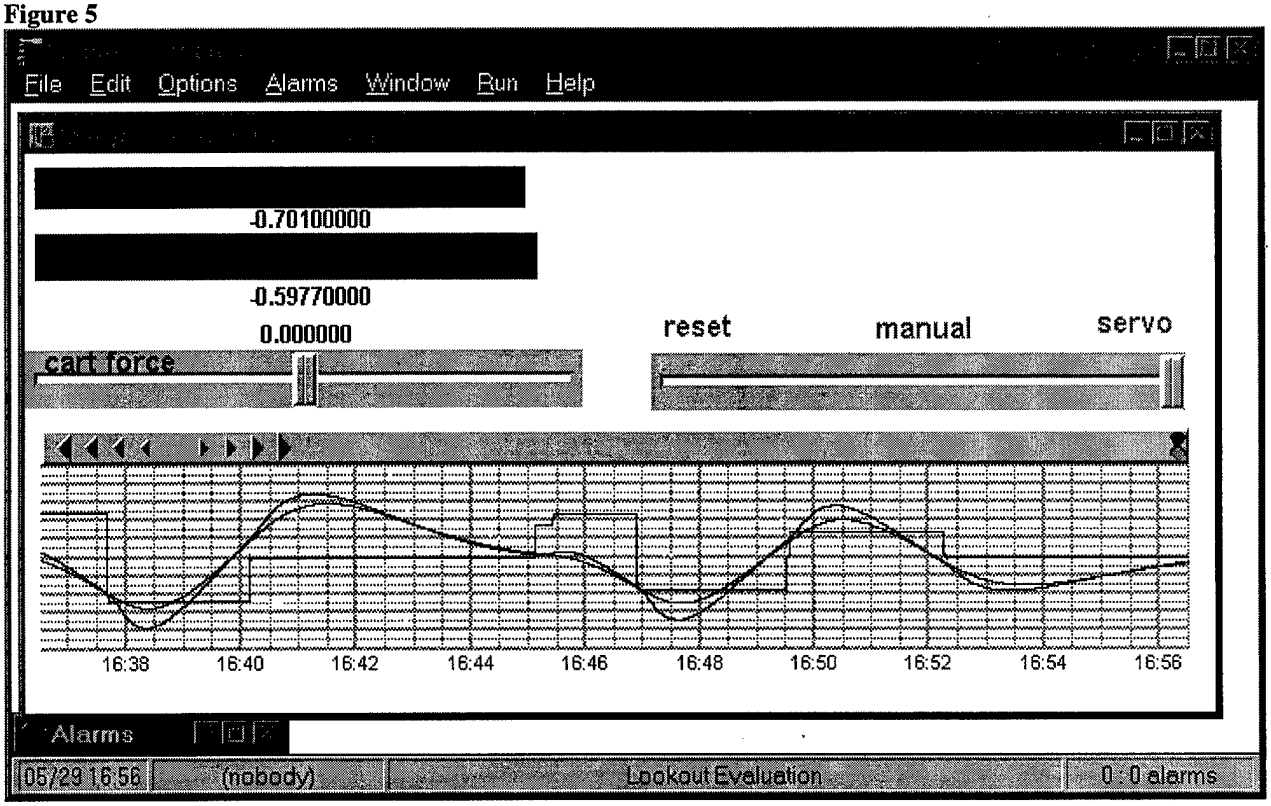

COMPLETION OF THE LANSCE PROTON STORAGE RING CONTROL SYSTEM UPGRADE -- A SUCCESSFUL INTEGRATION OF EPICS INTO A RUNNING CONTROL SYSTEM

S.C. Schaller, E.A. Bjorklund, N.T. Callaway, G.P. Carr, J.A. Faucett, M.A. Oothoudt, and D.J. Ostrem, Los Alamos Neutron Science Center, Los Alamos National Laboratory
Los Alamos, NM 87545

Abstract

The Los Alamos Neutron Scattering Center (LANSCE) Proton Storage Ring (PSR) control system upgrade is complete. In previous work, much of a PDP-11-based control system was replaced with the Experimental Physics and Industrial Control System (EPICS) controls. Several parts of the old control system which used a VAX for operator displays and direct access to a CAMAC serial highway still remained. The old system was preserved as a "fallback" if the new EPICS-based system had problems. The control system upgrade completion included conversion of several application programs to EPICS-based operator interfaces, moving some data acquisition hardware to EPICS Input-Output Controllers (IOC's), and the implementation of new gateway software to complete the overall control system interoperability. Many operator interface (OPI) screens, written by LANSCE operators, have been incorporated in the new system. The old PSR control system hardware was removed. The robustness and reliability of the new controls obviated the need for a fallback capability.

1 INTRODUCTION

At the 1995 International Conference on Accelerator and Large Experimental Control Systems in Chicago, Illinois, we reported on the success of the first steps in upgrading the LANSCE PSR control system to an EPICS-based system [1]. In this paper, we report the completion of this upgrade.

The original PSR control system [2] was based on PDP-11 front-end computers that polled data from CAMAC crates on local serial highways. Another serial highway was used to continuously update a live database in a central VAX computer. The central VAX ran application programs which used the live database to update operator interface screens. Although this system was highly reliable, it confronted us with a number of problems. These problems included the reliability of the serial highways, limitations in expanding the PDP-11 memory, complications and delays in adding new data and control channels, difficulties in implementing new applications programs, slow response to knob commands, and aging computer hardware.

As part of a general upgrade to the Proton Storage Ring in 1994, we began an upgrade of the PSR controls. Following an extensive review [3], we decided to replace the old PSR control system completely with an EPICS-based [4] system. Time and manpower constraints, however, prohibited a complete conversion in time for the 1995 production period.

In the 1995 PSR upgrade (Fig. 1), we replaced the PDP-11's with EPICS Input-Output Controllers (IOC's). The VAX to PDP-11 serial highway was thus effectively replaced by Ethernet. Budgetary considerations required us to retain the local CAMAC serial highways and crates. Several hardware devices on the VAX to PDP-11 serial highway could not be implemented on IOC's immediately. The requirement to handle these devices, plus the need to fall back to the original control system, meant that we needed to keep the PDP-11's, the central VAX database, and the original operator interfaces available.

To keep old and new databases consistent for a possible fallback, we implemented migrator software which recorded changes to the EPICS databases in the central PSR database. In a further complication, the separate LANSCE linac control system (LCS) [5] had to be able to acquire both PSR and EPICS data and to provide LCS data to the EPICS operator interface (OPI) screens. Thus we had a series of gateways and migrators that allowed the three control systems to interact effectively [6].

2 THE REMAINING UPGRADE

During the 1995 production period, we verified the usability and reliability of the new EPICS-based controls. There was no need to maintain a fallback capability. Thus at the end of this period, we were ready to completely replace the original PSR control system in time for the 1996 production period. In late 1995 we began the final upgrade tasks. The final PSR control system configuration looks like Fig. 1 without the PSR VAX serial CAMAC highway.

2.1 Hardware

Hardware and/or CAMAC crates that had resided on the VAX to PDP-11 serial highway were moved to IO-based serial highways. This hardware included beam position monitors (BPM's) and ring buncher RF generation equipment. We also removed the specially-designed PSR knob units that lived on the VAX highway. Knob

0-7803-4376-X/98 /$10.00 © 1998 IEEE

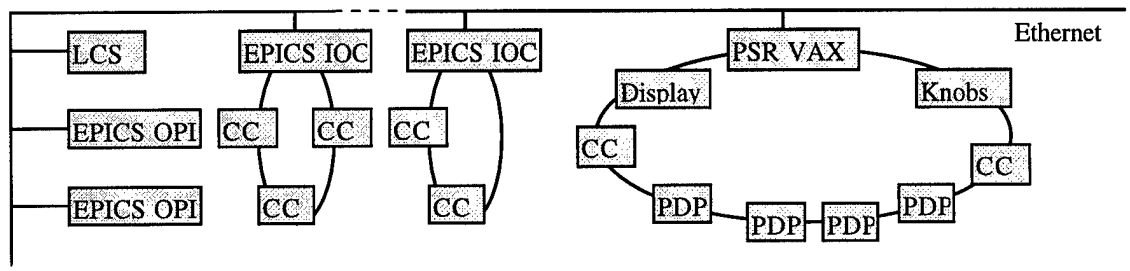

Fig. 1: PSR Controls in 1995. "LCS" is the Linac Control System. "CC" is a CAMAC crate. The ovals are CAMAC serial highways. The PDP-11's were for fallback. For 1996, the PSR VAX highway was removed.

functionality would now be provided by LCS knobs through the LCS-to-EPICS gateway software.

Through diagnostics available on the EPICS IOC's we developed a better understanding of the control algorithms in the front-end computers. This was information that was not easily available in the PDP-11 front ends. With this information we improved some closed loop controls, replaced some slow ADC's which had contributed to unstable conditions, and improved our ability to override commands and limit overshoot. Many of these problems had not been evident in the old system because of the general slowness of the old system to knob commands.

In addition to, but not directly connected to the PSR upgrade, was the initiation of a magnet/power supply continuous quality improvement program. This program was a joint effort between software, electronics, and power supply staff. It was successful in identifying problem areas that affected magnet performance and reliability and led to some of the previously indicated control system changes.

2.2 *Software*

In conjunction with the move of hardware from VAX serial highway to IOC's, we developed several new OPI-based applications. Some of these were implemented via the EPICS display manager (dm) interface builder and some were done using the Tcl/Tk language. The most difficult was the reimplementation of a closed orbit program which used BPM's to set the ring benders. Parts of this program were implemented in Fortran -- one of the few uses of this language in the upgrade. The loss monitor program, which had been implemented in Tcl/Tk for the 1995 run, was reimplemented as a dm screen. This program displays a great deal of frequently changing data, and measurements showed that the Tcl/Tk widgets were updating rather slowly. The operations team had to compromise on losing some minor functionality, but they gained much improved performance for this heavily used screen.

During the initial upgrade phase, we had begun to teach members of the operations staff to design and implement their own dm screens. The dm program is a graphical GUI builder and is quite intuitive. This process continued during the last year. Operators have developed a series of run permit screens for both the PSR and the LCS systems (the latter through the EPICS-to-LCS gateway) which is now the primary means of diagnosing linac and PSR problems.

We used the opportunity of the upgrade completion to extend the suite of diagnostics available for the new PSR control system. In particular, we incorporated IOC nodes in the standard LCS network diagnostics, using the LCS-to-EPICS gateway to acquire data and test hardware. Other network information was also made available through EPICS screens. Heartbeat channels were added to all the EPICS IOC's and a dm screen was developed to show the overall IOC status.

As an equipment diagnostic as well as a control system diagnostic, we developed a Tcl/Tk program called line-by-line that allows wildcard access to any set of PSR or linac channels. This program is an expert-level diagnostic and also provides hooks to low-level IOC diagnostic information.

As a result of eliminating the fallback capability, we were able to remove all of the old PSR software from the central PSR VAX. We no longer had to keep the old PSR database current. However, we also lost our connection from the LCS system through the old LCS-to-PSR gateway that allowed control of EPICS channels through the PSR/EPICS migrators. To fill this gap, we implemented a new LCS-to-EPICS gateway which is a VAX-based EPICS channel-access client. LCS knob performance on EPICS channels has improved remarkably. In addition, the performance of the EPICS-to-LCS gateway was improved by using multiple asynchronous data takes in the LCS system.

3 EXPERIENCE

Several operational aspects of the new PSR control system are worthy of note. Much of what follows was gleaned from the programmer-on-call notes for the 1996 production period.

Hardware problems continued to trouble us, but less than in the 1995 production period. Because of the unpredictability of some magnet power supplies, we added open/closed-loop switches for the power supply interface screens. In addition, we found instances where IOC closed-loop controls were fighting with internal power supply closed-loop controls. Studying the detailed

implementation of magnet power supplies in the EPICS databases, we found some cases of incorrect wiring that had existed for years.

Operator interface hardware on the EPICS OPI's caused some difficulties. The optical mice that came with the Sun workstations proved a poor choice in a control room environment. The optical mouse pads never seemed to be where they were needed. Mechanical mice are now being used. Printing hardcopy images of OPI screens also took some time to sort out. It took careful selection of a set of both dm and Tcl/Tk standard colors before the monochrome hardcopy looked acceptable.

Although Tcl/Tk provided a quick means of prototyping operator interfaces while still allowing significant algorithmic content, both its syntax and its performance leave something to be desired. At least one Tcl/Tk screen was converted to a dm screen to get better performance (see above). The obscure Tcl/Tk syntax can make program maintenance somewhat daunting – especially at three o'clock in the morning.

Providing a reliable, smooth (i.e., "bumpless") reboot capacity for IOC's continues to be something of a problem. The IOC's record setpoints, deadbands, and alarm deltas on a central file server for use in later boots. But we have seen occasions where, for unknown reasons, the save file does not get written. In addition, one must specify what parameters should be saved in the off-line database. This can lead to problems, especially with newly-added devices. Work continues on the bumpless reboot problem.

Because gateways try to make two disparate control systems see eye-to-eye, they can be the source of many difficulties. The LCS-to-EPICS gateway returns EPICS data to LCS applications and gives them control over EPICS channels. LCS applications expect a well-defined raw data format as well as an engineering unit format. Since EPICS has only an engineering unit format, some approximations are made that can cause loss of precision and also possible overflow. The LCS archiver expects to acquire EPICS data on a demand-driven basis. If the EPICS deadbands are too small, LCS archiver requests can generate significant amounts of network traffic even for channels that are only recorded infrequently. The EPICS channel status and severity fields do not translate well to the VMS condition code statuses used by LCS. This ambiguity can cause errors to appear even if there are none. For example, a problem occurred when an uninitialized EPICS setpoint channel had to be read before issuing knob-based command pulses.

The EPICS-to-LCS gateway is a bit more complicated since it must provide an EPICS channel-access server in a VMS (not an IOC) environment. This task was accomplished by modifying an earlier version of the channel-access server code. Problems have arisen because the IOC environment is multi-threaded while the VMS environment is not. To avoid waiting on all first requests for data (since LCS is a demand-driven system), we have decided to return invalid data on first requests. This works well for dm or Tcl/Tk programs that are monitoring data, but can cause problems for programs that expect good data on their first acquisition. We are currently in the process of reimplementing the EPICS-to-LCS gateway using the new EPICS server-level application programmers interface [7].

One final difficulty occurred in moving some Fortran code from a VAX (little-endian) to a Sun (big-endian). An actual argument was integer*4 while the formal argument was integer*2. This worked on a VAX, but not on a Sun.

4 CONCLUSIONS

Late last fall we finished the 1996 LANSCE production period using the completely converted PSR control system. The control system availability was estimated to be approximately 99.73%. Out of 2740 hours of production, the PSR control system was reported to be unavailable only 7.3 hours. Since 7 hours of this time was due to fused field wiring, the EPICS system availability was actually much higher and easily comparable to the 1994 and 1995 availabilities of 99.7% and 99.9% respectively.

5 ACKNOWLEDGMENTS

The authors wish to thank the following members of the LANSCE-8 EPICS software team without whose help the final phase of the upgrade project would have been seriously delayed: L.R. Dalesio, J.O. Hill, D.M. Kerstiens and R.M. Wright. This work has been supported by the U.S. Department of Energy.

REFERENCES

[1] M.A. Oothoudt, et al., *Proceedings of the 1995 International Conference on Accelerator and Large Experimental Physics Control Systems*, FERMILAB Conf-96/069 (1996) 217.

[2] P. Clout, et al., Nucl. Instr. and Meth. A247 (1986) 116.

[3] M. A. Oothoudt, et al., Evaluation of PSR Control System Upgrades, AOT-6 Technical Report AOT-6-94-25, Los Alamos National Laboratory, 1994.

[4] L. R. Dalesio, et al., Nucl. Instr. and Meth. A352 (1994) 179.

[5] G. P. Carr, et al., *Proceedings of the 1987 Europhysics Conference on Control Systems for Experimental Physics*, CERN Yellow Report 90-08 (1990) 107.

[6] S.C. Schaller and M.A. Oothoudt, *Proceedings of the 1995 International Conference on Accelerator and Large Experimental Physics Control Systems*, FERMILAB Conf-96/069 (1996) 943

[7] J.O. Hill, *Proceedings of the 1995 International Conference on Accelerator and Large Experimental Physics Control Systems*, FERMILAB Conf-96/069 (1996) 136

AUTOMATING ELETTRA OPERATION WITH "ONE BUTTON MACHINE"

D. Bulfone, F. Potepan*, C. Scafuri
Sincrotrone Trieste, SS 14 - Km 164.5, 34012 Basovizza, Trieste, Italy

Abstract

ELETTRA has reached good operational stability. Repetitive tasks, like the injection procedure, can be automated in order to maximise the beam time delivered to users. One button machine is a task spawner that executes different tasks concurrently, following a pre-defined control flow logic. It uses conventional UNIX routines for process execution and communication, and a Motif interface. A description of its various features is presented, covering operator intervention during flow execution, error recovery and step-by-step help when manual operation is selected. Operational results are given.

1 INTRODUCTION

ELETTRA has provided synchrotron radiation to the users since the commissioning year 1994. The set of control room tasks that drive the machine to a well-known state suitable for user operations is fully defined and tested. The One Button Machine (1bm) Project has been specifically developed in order to automate such procedures, simplify the operator's job and increase the beam time delivered to the users.
Each procedure is decomposed into a series of "actions" dealing with a specific machine subsystem operation. Actions are implemented by dedicated software "modules". A manager, called 1bm, regulates the execution of the various modules and interacts with the operator through a graphical user interface.

2 THE 1BM PROGRAM

1bm [1] [2] is a programmable UNIX task manager that spawns, communicates and controls the logical flow of a predefined set of processes. Its user interface is based on the standard Motif look and feel, which is already adopted for the ELETTRA control room programs.

2.1 The Programmable Module Manager

The term "module" will be used throughout this article synonymous with process, task or application program, referring to any executable spawned by 1bm.
The execution of a module is usually allowed after the successful termination of a specific set of modules. The logical constraints are expressed by means of simple boolean expressions based on the module termination result. By using the negated values in the expressions specific modules can be triggered in case of failure conditions. This can be exploited by error recovery schemes.
An important feature of the manager is its capability to spawn many modules concurrently in order to reduce the overall time needed by a procedure.
The manager spawns the modules according to the rules written in a configuration file. This file, which implements a given procedure, is modified by means of a normal text editor but only the operations officer has the privileges necessary to modify it.
1bm acts as an independent "finite state machine" for each spawned module. Fig. 1 is a representation of its state transition diagram. Shaded arrows denote manual operator intervention. The following states are defined:

- INITIAL: it is the initial state of every module, i.e. a module that was never executed before.
- FROZEN: module execution has been formerly blocked by the operator.
- RUNNING: the module is being executed for the first time.
- ERROR: the module execution failed and terminated with an unrecoverable fatal error.
- WARNING: the module execution failed and terminated with a recoverable error.
- DONE: the module was successfully executed.
- RECOVER: the module is being re-executed after a recoverable error.

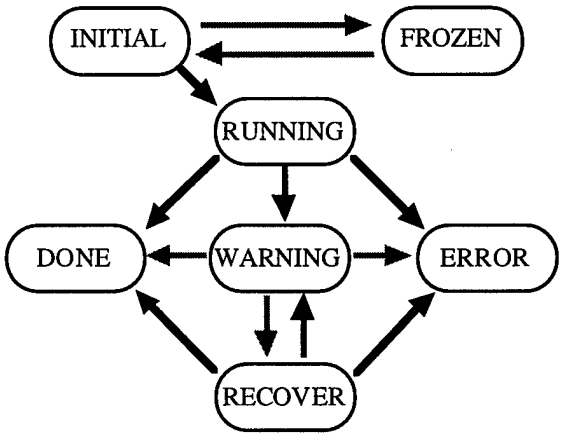

Figure 1: 1bm module state transition diagram.

2.2 The User Interface

The user interface, which is based on the standard Motif libraries, is well decoupled from the modules and not influenced by their execution or failure. Only data necessary to perform routine operations are shown by default, while details can be requested if necessary. The list of modules foreseen for a given procedure is initially displayed (fig. 2). Each module has a colour coded label that shows its current status, during

* now at Integrated Computer Solutions Incorporated, 201 Broadway, Cambridge, MA 02139.

0-7803-4376-X/98/$10.00 © 1998 IEEE

execution. The panel also contains the main controls of 1bm: two buttons to formerly "freeze/thaw" the execution of selected modules, a button to start the whole procedure and a panic button to force the immediate termination of a module or all of them.
The following additional information panels are available for each module in the list:
- a window with a brief description of the parameters passed for the execution of the module and their actual values.
- two scrolled message windows showing, respectively, the redirected standard output stream from the module and a special subset of error messages. These are used to closely follow the execution of the module.
- a help window containing the information needed when manual operator intervention is eventually required. Such information is defined in the configuration file of the given procedure. There are also three buttons on the lower part of the window that force the manual transitions foreseen in case a module is in the warning state.

3 MANUAL OPERATOR INTERVENTION

Manual intervention of the operator is requested when module execution fails, but no fatal error has been detected. In this case the module switches to the warning status. The operator detects this condition and, with the help of the corresponding information window, attempts to manually terminate the module's action by means of the standard programs available on the control room consoles or by direct intervention on the equipment. On the base of the achieved result the operator eventually forces a module state transition to the correct current status (DONE or ERROR) or re-execute the module. The 1bm programmable manager then automatically continues or terminates the on going procedure depending on the logic specified in the configuration file.

4 1BM MODULES

Any UNIX executable, binary object or shell script, can be a 1bm module so that already developed and well tested control room programs are easily integrated and re-used. Only four simple rules are adopted:
- modules must be based on standard UNIX conventions, libraries and system resources;
- module's execution parameters are taken from the command line;
- any information or error message must be printed on the standard output;
- modules must terminate clearly, returning to the calling environment a defined exit code indicating the success or failure of their execution.

4.1 Special Strings

1bm recognizes some special strings sent by a module to the standard output and displays them on a dedicated section of the associated message window. This feature is useful in case of problems to quickly identify what is going wrong. A set of definition files and a module skeleton making use of such special strings is available for writing new modules. The use of special strings is however absolutely not mandatory for a module to be integrated in 1bm.

5 INJECTION PROCEDURE

The injection procedure is performed once a day during "user shift" periods. The operator has first to dump the beam, open the insertion devices (ID) gaps, close the front-end shutters and valves, set the injection elements, cycle the magnets and load the machine files.

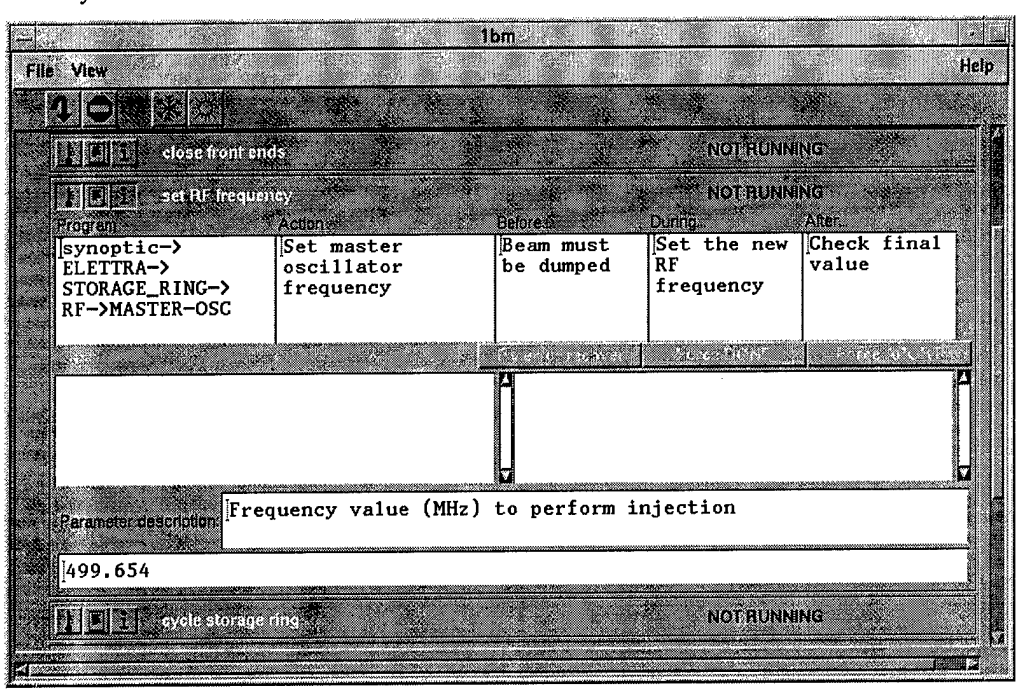

Figure 2: 1bm Motif user interface.

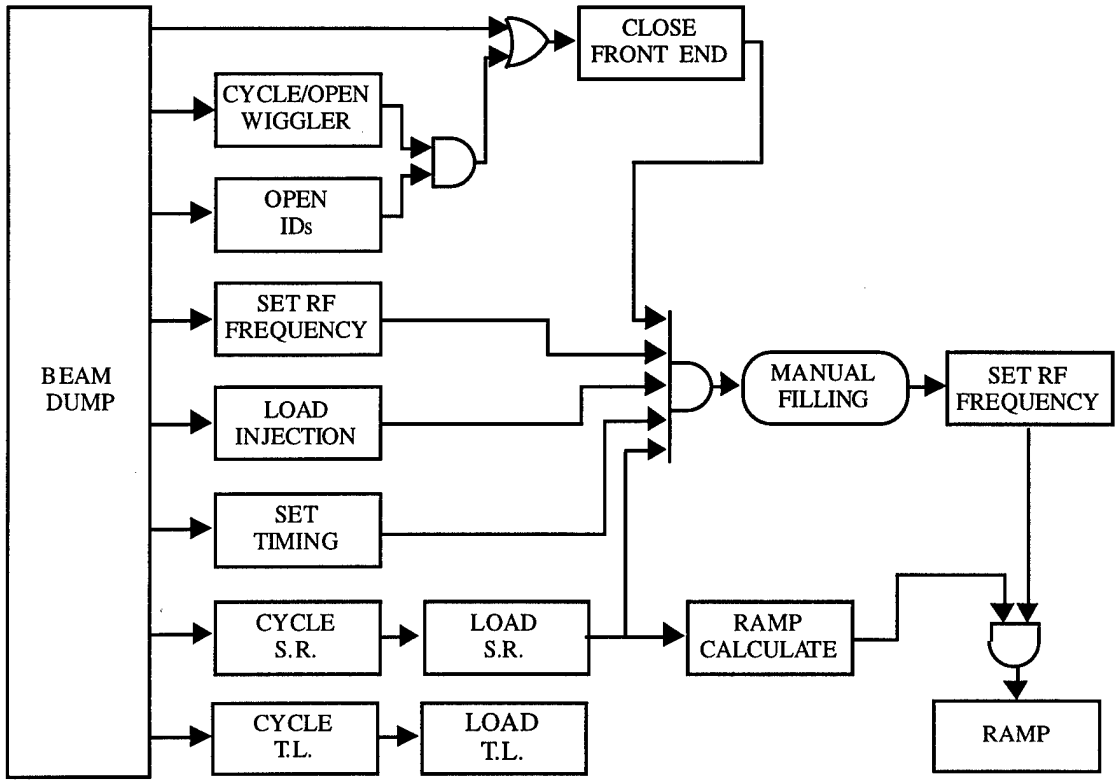

Figure 3: ELETTRA injection procedure logic flow diagram.

After filling the ring with the requested current value, he has to execute a ramp to the final energy, close the ID gaps, correct the orbit to zero position and slope at the centre of the IDs and open the front-end shutters and valves to provide light to the users.

The injection procedure has been almost completely automized by 1bm [3]. The implemented logical flow involving many concurrent tasks is shown in fig. 3.

The average time spent from "beam dump" to "manual filling" has been reduced from about 40 minutes to less the 20 minutes. This time cannot be reduced further since it is fixed by equipment hardware constraints. The main duty of the operator is to fill the ring with the requested current value.

Some newly developed 1bm modules are now under commissioning in order to automize also the energy ramping of the ring after the manual filling. First results are quite good as the total injection procedure time, including manual filling, has been cut down to 26 minutes.

6 CONCLUSIONS

1bm has been preliminarly installed in the ELETTRA control room since mid 1996 and has been routinely used to perform the injection procedure since the beginning of 1997. More and more modules are being integrated and the preparation of the machine for user operations has been considerably speeded up. Injection is carried out by a single operator and the rate of human errors has been minimized. The adoption of a well defined configuration file guarantees that the machine is always operated with the desired parameters and increases reproducibility.

The spectrum of applications for 1bm is not restricted to machine operation. It can be successfully used every time a logically ordered execution of related modules is required, just specifying a different configuration file.

Future extensions deal mostly with the automatic error recovery: a simple convention should be defined when error messages are sent from a module to 1bm and a smart error recovery performed by the Programmable Module Manager. Only unsuccessful commands will then be performed in order to save the time needed for a complete re-execution of the module.

7 ACKNOWLEDGEMENTS

We would like to thank the ELETTRA Operators and the Operations Group for their useful comments and suggestions.

REFERENCES

[1] F. Potepan: 'Automize Machine Operation at Control Room Level: One Button Machine Program', ST/M-TN-96/3, Sincrotrone Trieste, 1996.

[2] D. Bulfone et al.: 'Controls in the Past Year of ELETTRA Operation', Proc. Int. Conf. on Accelerator and Large Experimental Physics Control Systems, Chicago, Illinois, 1995.

[3] C. Scafuri: 'Automatic Machine Operations', Proc. 4th Annual Workshop on European Synchrotron Light Sources, Trieste, 1996.

OPERATOR INTERFACE FOR THE PEP-II LOW LEVEL RF CONTROL SYSTEM*

S. Allison, R. Claus Stanford Linear Accelerator Center, Stanford University, Stanford, CA 95309 U.S.A.

Abstract

This paper focuses on the operational aspects of the low level RF control system being built for the PEP-II storage rings at SLAC. Subsystems requiring major operational considerations include displays for monitor and control from UNIX workstations, slow feedback loops and control sequences residing on microprocessors, and various client applications in the existing SLAC Linear Collider (SLC) control system. Since commissioning of PEP-II RF is currently in-progress, only those parts of the control system used during this phase are discussed is detail. Based on past experience with the SLC control system, it is expected that effort expended during commissioning on a solid user interface will result in smoother transition to full reliable 24-hour-a-day operation.

I. INTRODUCTION

The PEP-II RF system 1 consists of 5 klystrons, each with 4 cavities, for the high energy ring (HER) and 3 klystrons, each with 2 cavities, for the low energy ring (LER). Currently, two of the HER RF stations are undergoing commissioning[2].

For controls, each RF station has a VXI crate containing a VXI-based microprocessor running VxWorks, Allen-Bradley (AB) VME scanner card, and a collection of custom VXI modules used for low level RF controls, monitoring, and machine protection on arc and power faults. Outside the VXI crate, AB hardware is used for both the high voltage power supply (HVPS) and machine protection on slower changing inputs. UNIX workstations and a DEC computer are used for the operator interface and higher level applications. During commissioning, UNIX workstations are the primary X-terminals in use. During operation, other types of X-terminals, some with touchpanels, will supplement the workstations.

The interface between the user and the hardware is constructed using the Experimental Physics and Industrial Control System (EPICS) took kit[3] To meet requirements, additional software is being developed in-house or at other labs to supplement the standard EPICS software distribution. The tasks running on each RF VXI processor, also known as an Input Output Controller (IOC), provide data-scanning for updating the database, data archival for bumpless reboot, message logging, control loops, state transitions, calibration sequences, and channel access, allowing other hosts to access the database.

In addition to software on the IOC, other EPICS-based packages are used on the UNIX stations for client operator interface (OPI) applications including the EPICS display editor and manager (EDD/DM)[4], a stripchart tool, and various channel access tools. Existing SLC control system applications are being modified to perform channel access and to incorporate EPICS messages into the SLC message log.

II. IOC SOFTWARE

The RF IOC software was developed for an efficient and easily maintainable hardware interface. For the custom VXI modules, one EPICS record per module was developed, encapsulating all data and functions of that module. For the AB interface, software developed at APS and LANL was implemented as-is or modified slightly for the machine protection and high voltage systems[5]. For the AB stepper motor card, device support software for the existing stepper motor record was developed. Additional software on top of this lower-level interface is being added to allow a user without detail knowledge of the control hardware to operate the RF station.

The EPICS database is the bedrock of the RF control sys-tem. Some subsystems such as machine protection monitoring are implemented with just database records. To allow quick changes with minimal software impact, all RF stations use the same database and startup files, with distinctions defined by environment variables. The following packages are being added to supplement the basic database and provide a more usable system:

Subroutine, Calculation, and Sequence Records

Subroutine and calculation records provide data processing and analysis. An example of their usage is in the calculation of phase, power, and other related parameters from input in-phase and quadrature count values at 24 locations in the RF station at 2 hz. Also, for each component of the RF station, records providing summaries of severities and trips are processed on change and allow quick determination of trouble spots.

Sequence records perform a series of simple control steps in a particular order with optional delays. Functions performed by sequence records include station reset, which executes the 12 steps needed to reset after a trip, reinitialization of the cavity tuner stepper motors, calibration of various system coefficients, and DAC update.

SEQUENCE TASKS

For more complex control sequences and loops, sequence tasks are being developed instead of a series of subroutine and sequence database records. Sequence tasks include one per *Work supported by Department of Energy, contract DE-AC03-76SF00515 cavity for cavity tuning, high voltage control for either station processing or to maintain the klystron drive power, DAC calibration, and station state control for transitioning to a desired run mode such as

0-7803-4376-X/98 /$10.00 © 1998 IEEE

OFF, ON, PARK for allowing beam through the cavities while the station is offline, and TUNE or FM for station processing while no beam.

For all sequence tasks, common features are incorporated especially for the user interface. Metered descriptive error messages are logged on abnormalities such as hardware errors and trips. Informational messages are logged on state changes, atlimit conditions, and other warnings. These conditions are also updated in the database as strings for real-time display.

For control loops, ring buffers containing the most recent values of the loop parameters are kept as compress records in the database for diagnostic display purposes. Standard data-base records are provided so that the user can to turn the loop on and off, reset the loop to known good values, and change the loop period, gain, maximum actuator delta allowed in one cycle, and any other loop-specific constant.

Bumpless Reboot

Bumpless reboot is an IOC software package developed at LANL that saves all input constants, states, and other data as they are changed and then restores them as part of IOC initialization performed during reboot. This package is not part of the standard EPICS distribution but is considered critical for RF station operation and thus was implemented early in the project. To enhance the user interface, an optional informational message is now logged whenever an input is changed, providing a trail for debugging and determining system usage.

Since so many fields in the database are modifiable, it is unreasonable to save every possible value since this would affect IOC performance due to the overhead of database monitoring and file IO. As a result, users must identify up-front what items they plan to change on the fly. As yet, this limitation has not proved to be too restricting

Message Logging

In addition to messages logged by subroutine records, sequence tasks, and bumpless reboot, errors are also logged by various EPICS system and database tasks. The message logging mechanism provided by the standard EPICS distribution does not integrate well with the existing SLC message logging, a system familiar to the users and heavily used. As a result, a remote procedure call (RPC) client task was developed which forwards all messages to a server in the SLC control system.

III. OPI APPLICATIONS

The PEP-II control system is built from both EPICS and the SLC control system. Both systems are high performance, distributed database-driven systems using microprocessors running real-time operating systems and performing control and monitoring of nearby hardware. Both provide similar basic client applications such as data archival, alarming, correlation plots, backup and restore, and knobbing. Since users are already familiar with SLC applications, the only EPICS UNIX OPI tools enlisted for PEP-II are those with either no equivalent or with highly-desirable features not available in the SLC control system. Currently, these tools include EDD/DM from LANL and a strip chart tool from TJNAF. EPICS channel access tools are also used by MATLAB data analysis programs written and used only by the RF engineers.

EDD/DM

EDD/DM provides real-time graphical displays. Though already rich in options, additional features are being added to EDD/DM by LANL to meet PEP-II requirements. Because of the variety of X-terminals in use, displays are now automatically scaled depending on screen size. To match similar capabilities on the SLC control system, the user now has the ability to select a printer or save-to-file. New kinds of buttons for selecting files, toggling a binary state, and printing have been added. The name behind any dynamic button is now made visible on request and put into the workstation paste buffer for use by other applications.

The same displays are used, whenever possible, for all stations, with distinctions defined by macros. Except for diagnostic displays, all displays have a similar look and are consistent in the use of color-coding, button and data-display sizes, and placement of common items on all displays like the title, exit, print, and help buttons. The displays are hierarchical so the user starts at the high-level displays, which show overall summaries and statuses, and works down to the lower-level displays, providing more detail for a smaller part of the machine. In general, when going from one display to another, the parent display is killed to prevent clutter and manage resources. Buttons on the lower-level displays allow the user to go back up.

Since displays must work on touchpanel X-terminals by people standing in a crowded and cluttered control room, the mouse usage is minimized by employing more realestate for display and control selections rather than using mousedriven popup or pulldown menus. The size of many control buttons and spacing between buttons are made for fingers rather than cursors. Currently, the displays have too much information and very few graphics per page, convenient for commissioning but not ideal for normal operation since the displays take too long to activate and are too dense.

Colors are limited to a handful and, if possible, are combined with other attributes such as text and flashing for color-challenged users. For both summaries and individual items, green means OK, yellow means warning but with time for action, flashing yellow means a trip is imminent, red indicates the item is currently tripped and keeping the station off, flashing red indicates the item is the first to trip the station, and magenta means a hardware or software problem. Currently, all display backgrounds are light-colored with informational text in darker colors

though this may change once operation is transferred to the dimly lit control room.

In general, monitored data is displayed in black text with the current status shown using a colored rectangular box around the value. A small "DB" box resides next to the value which the user can select to get detailed database and other related information. These database displays have proved to be valuable for quick debugging and verification during commissioning.

An example display follows:

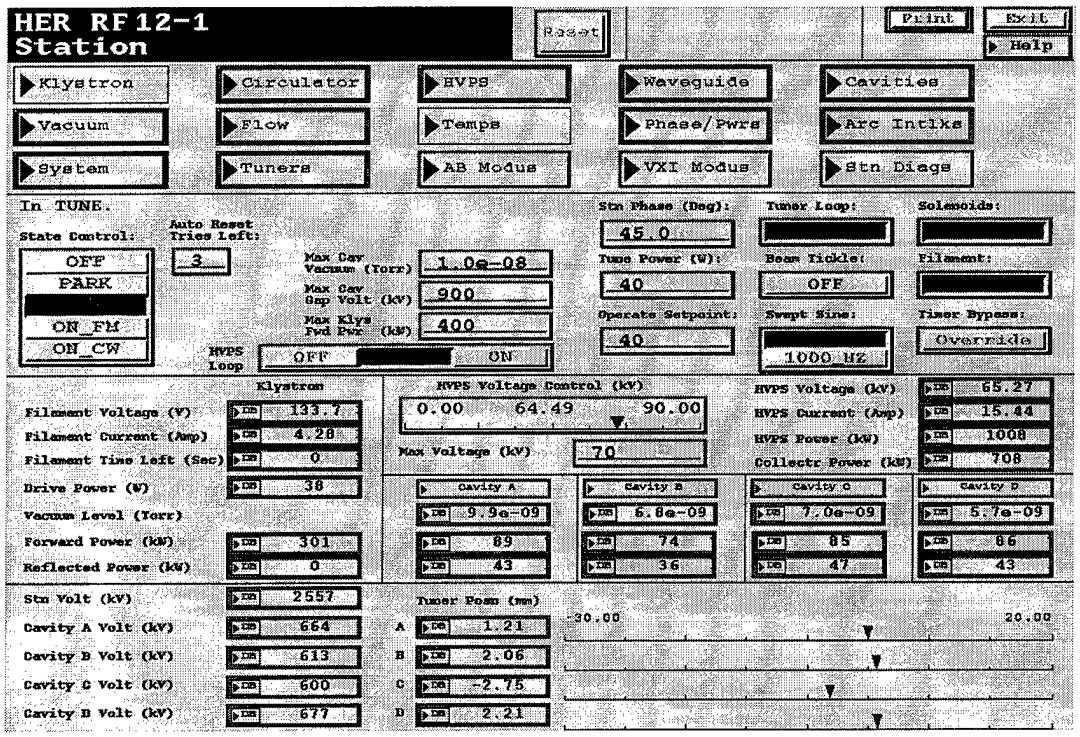

STRIP CHART TOOL

The strip chart tool is used during commissioning to monitor RF processing parameters such as cavity vacuums and gap voltages. Buttons on EPICS display allow users to start a variety of canned strip charts. Once active, the users may change any plot setup parameter for tailoring to their specific needs. This tool is quite popular and there are plans to allow it access to SLC control system data.

IV. SLC CONTROL SYSTEM

Channel access has been incorporated into a subset of SLC control system client applications to access the RF databases. EPICS database record naming conventions were developed so that the existing user interface could be adopted with few changes. During commissioning, the two mostly widely used applications are data archival and message logging. Other applications such as configuration save/restore, correlation plots, alarm handling, and multiknobs will be used later during full operation. For data archival, a channel access history buffer process was developed that periodically samples a subset of RF analog data points and saves them to files in the same format as SLC data. The user can then request plots of specific channels for any time period using the existing interface for SLC history. Canned plots of the more popular histories are available with one button push. An RPC server task was developed to receive messages from the IOCs and forward them to the SLC message handling facility. The existing message display system, with its rich set of features, can then be used to search for and list specific messages.

V. ACKNOWLEDGEMENTS

We would like to acknowledge P. Corredoura, T. Himel, D. Kerstiens, K. Krauter, R. Sass, and M. Zelazny for their efforts in either specifying or implementing the EPICS user interface. We would like to thank the SLC controls group for their help and patience during integration, and the EPICS collaboration for their invaluable assistance.

REFERENCES

[1] P. Corredoura et.al., "Low Level System Design for the PEP-II B Factory", Proceedings of the 1995 IEEE Particle Accelerator Conference.

[2] P. Corredoura et.al., "Commissioning Experience with the PEP-II Low-Level RF System", these Proceedings.

[3] Dalesio et.al., "The Experimental Physics and Industrial Control System Architecture: Past, Present, and Future", ICALEPCS, October 1993.

[4] P. Stanley, "EDD/DM User's Manual 2.4", March 1997.

[5] Stein et.al., "Data Exchange from Allen-Bradley PLC-Based Systems to EPICS, ICALEPCS, October 1995.

NETWORK UPGRADE FOR THE SLC: PEP-II NETWORK

M. Crane, M. Call, S. Clark, F. Coffman, T. Himel, T. Lahey, E. Miller, R. Sass
Stanford Linear Accelerator Center, Stanford University, Stanford CA 94309

Abstract

The PEP-II control system required a new network to support the system functions. This network, called CTLnet, is an FDDI/Ethernet based network using only TCP/IP protocols. An upgrade of the SLC Control System micro communications to use TCP/IP and SLCNET would allow all PEP-II control system nodes to use TCP/IP. CTLnet is private and separate from the SLAC public network. Access to nodes and control system functions is provided by multi-homed application servers with connections to both the private CTLnet and the SLAC public network. Monitoring and diagnostics are provided using a dedicated system. Future plans and current status information is included.

I. INTRODUCTION

The PEP-II control system is a combination of the SLC Control System and EPICS[1]. Together these two control systems provide a way to match an application with a control system methodology which best matches the applications needs. The SLC Control System is based on a DEC Alpha OpenVMS central host (MCC) with distributed microprocessor (SLCmicro) front ends and networked displays. The displays use TCP/IP, but the SLCmicros use a SLAC-developed communications system. EPICS for PEP-II is based on Sun UltraSparc Solaris servers with distributed microprocessor front ends (IOC), all based on TCP/IP and Ethernet. A common network is needed to serve these and other PEP-II control system nodes. We expect that this single new network will show a cost savings over time due to the commercial availability of products, new advances to those products, and standard diagnostic tools and experience.

II. COMMON PROTOCOLS

All EPICS IOCs and operator interfaces (OPI)s, as used in the PEP-II control system, use Ethernet as the physical layer. Since the IOCs and local OPIs are distributed around the PEP-II ring, some sort of Ethernet-based technology must be available in these parts of the ring. Parts of EPICS also run on the MCC central host, so MCC must be able to acquire data from IOCs around the ring. The display portions of the SLC control system are TCP/IP-based using the X-windowing system. There are various Ethernet-based X-terminals distributed around the PEP-II ring, so Ethernet must be provided for these terminals. Various other systems such as GPIB controllers and other commercial instrumentation use Ethernet and TCP/IP to communicate.

An upgrade of the SLCmicros and the SLC Control System to use TCP/IP and Ethernet would provide a common communications path for the PEP-II control system. There are about 70 Intel Multibus I based Intel 386/486 single board computers, or SLCmicros, in the SLC Control System. Communications between the MCC central host and the SLCmicros currently use a SLAC-developed network called SLCNET. The anticipated amount of additional bandwidth required for PEP-II SLCmicros is greater than the current available bandwidth on SLCNET. This, combined with the desire for common physical layer interfaces such as FDDI/Ethernet, and the potential cost savings in maintenance and commercial upgrades, brought us to the conclusion that SLCmicros should be updated to use TCP/IP and Ethernet.

A new Multibus I single board computer from Radisys has been chosen as the replacement card for the current SLC micro hardware. This new card, named the Skater card or EPC (Embedded PC), is actually a PC-based computer with an embedded Ethernet interface mounted on a Multibus I card. The EPC is cost effective in that the card is less expensive that the current SLCmicro hardware and allows memory to be upgraded using standard SIMM memory. This hardware/software upgrade has allowed us to modify our SLCmicro code to operate on a PC-like computer, use Ethernet and TCP/IP, but retain our investment in Multibus/CAMAC systems. The software to do this upgrade is the subject of another PAC97 paper.[2]

III. MACHINE TO MACHINE NETWORK

The network to support these TCP/IP-based nodes must provide enough throughput to run the control system and have available bandwidth for future applications. The fact that this network is compatible with the SLAC public networks and the Internet makes it very important to isolate this network. Bandwidth on this network is reserved for control system usage only. Traffic includes control system computers communicating with control system computers and operators/users communicating with their systems. This excludes someone's everyday work traffic such as e-mail, editing, and WWW access. There is also the need to protect the control system nodes from non-users and would-be hackers, since these nodes provide the basis for a 'factory' with an expected uptime of 99%.

The CTLnet is a separate network from all other networks at SLAC. To allow users to access their systems on this network, there are three gateway machines which the user can log onto as shown in figure 1. CTLnet uses an RFC 1918 Private Internet Address as an added measure

*Work supported by Department of Energy, contract DE-AC03-76SF00515

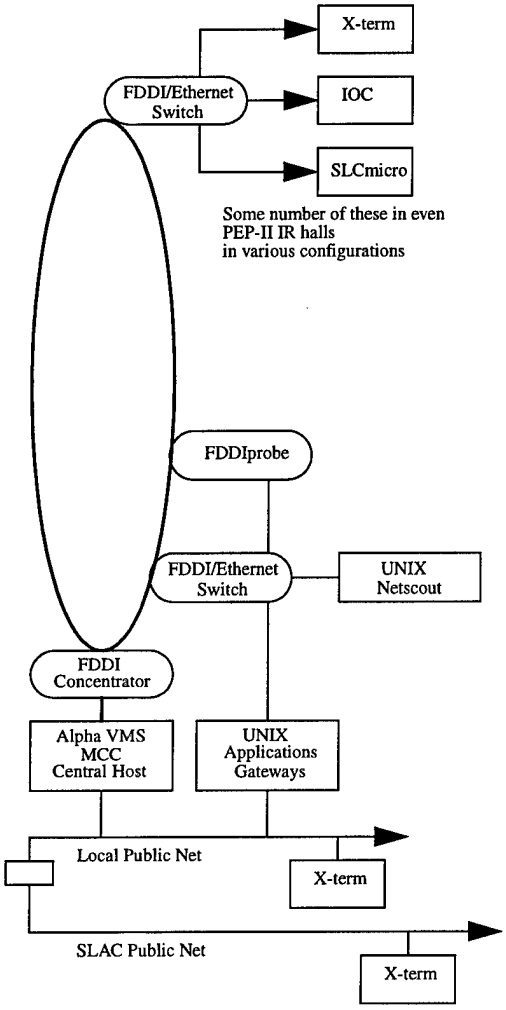

Fig. 1. PEP-II CTLnet.

to promote the idea that this is not a normal public network. The Private IP subnet addresses for CTLnet were chosen so that they would overlay a real SLAC subnet, and that SLAC subnet was reserved for future use. This precaution was taken to allow us to move from the Private IP address space to normal SLAC address space if problems should arise. This capability has already been utilized during commissioning. A router has been installed to allow packets from select internal nodes to be presented to the SLAC public network. This allows users to initially connect their EPICS OPI and IOCs in the control network while maintaining their normal development environment. As the UNIX application gateways are improved, we will implement the unrouted private addresses.

Making this network separate also allows a better understanding of the local network traffic since all traffic is generated and consumed within the local address space. This also keeps CTLnet traffic from "cluttering up" the public networks.

IV. APPLICATION GATEWAYS

There are three application gateway machines which provide user access to CTLnet and the control systems resident there. These gateways are multi-homed systems with a network connection to the local SLAC public network and a separate connection to CTLnet. These gateways are not configured as routers, so traffic does not pass directly through them from one network to another. The user must first log onto a gateway and then log onto an internal CTLnet node. Note that the normal SLAC network environment is not available on CTLnet, including public printers and file servers, since this traffic is blocked by the gateways.

MCC is the OpenVMS central-host gateway for the SLC Control System. This gateway provides the X-window touch panel interface for access to the SLC Control Program (SCP). The SCP X-window traffic can be directed to a user's X-terminal on either network, allowing access from a user's office at SLAC or from somewhere on the CTLnet. When a user is logged onto MCC, internal CTLnet nodes are accessible with such tools as telnet and ftp. Some EPICS functions are also available on MCC, such as the launching of EPICS displays.

There are two UNIX gateways which provide access to the EPICS control system. Like MCC, these EPICS OPIs allow a user to log on and start a display to an X-terminal on either network. The EPICS application then gathers data from IOCs on CTLnet and displays the information to the user. The full complement of tools to run EPICS reside locally on these gateways, so they can operate with no outside references such as the SLAC UNIX environment. This allows the PEP-II control system to be completely removed from the SLAC public network if such a need arises. The tools include support for IOC booting, math tools, display tools, and basic UNIX administration applications.

The gateways are also the common interface for other types of network-based instrumentation such as spectrum analyzers, GPIB instruments, etc. This list will most certainly grow as time passes.

V. FDDI AND ETHERNET

The requirements for the new network made the physical layer choices relatively straightforward. There are clusters of Ethernet-based nodes spread around the PEP-II ring and in the Main Control Center. There was an existing fiber optic cable plant connecting nearly all the cluster locations. The VMS host already had an FDDI interface and software. A high speed backbone was needed which could provide control system growth over the next few years and provide a flexible local interface to Ethernet-based nodes. Fault tolerance is required for single area power failures. The availability of commercial diagnostic and monitoring systems was required to keep failures and

downtime to a minimum. There is also a need to continue the backbone down the linac as a future expansion adding another four miles to the total backbone length.

FDDI matches these needs very well. FDDI is a high speed backbone to connect stations nearly 1000 meters apart using fiber optics, connected as a dual FDDI ring to provide single area fault tolerance. There is an abundance of commercially available support tools and experience for both the FDDI hardware and software. The VMS host supports DEC hardware and TCP/IP using Multinet for the FDDI interface.

The network backbone initially includes the Main Control Center (MCC) and the periphery of PEP-II with the total ring distance of approximately one and one half miles. Nearly all of the Ethernet-based nodes are located in the even-numbered interaction regions. A Cisco Catalyst 1200 switch, which has one dual-access FDDI port and eight 10baseT (twisted-pair) Ethernet ports, is installed in each even-numbered interaction region to support the Ethernet requirements. Each Catalyst switch is located so that most or all of its Ethernet customers can be reached within the standard 100-meter limit of a 10baseT twisted-pair cable run. We assume that 10baseT Ethernet connections will generally be used, unless there is some overriding need for a specific node to use some other type of connection. We will use a dedicated port from the Catalyst for each SLCmicro and EPICS IOC. For other devices, we may choose to use either a dedicated port from the Catalyst or shared port from a multiport repeater (hub) connected to the Catalyst. This will depend mainly on the number of Ethernet devices and their geographical distribution relative to the Catalyst. The hubs provide 12 10baseT Ethernet connections from a single Catalyst 10 baseT port and can be monitored remotely.

The MCC central host has an FDDI interface connected to the PEP-II network via an FDDI concentrator. The UNIX gateway machines will be connected via Ethernet ports on a Catalyst switch in the Main Control Center.

VI. MONITOR AND DIAGNOSTICS

The monitoring and diagnostic system for this network is modeled after the SLAC network monitoring facilities. A separate, dedicated system must be implemented for this private network rather than using the public SLAC services.

The system uses the SNMP protocol to access information from Ethernet hosts and network devices such as the Cisco Catalyst switch, hubs, and others. The FDDI information comes from a NetScout FDDIprobe using the RMON protocol. NetScout management software running on a SUN station completes the system.

Other tools are also available to look at specific traffic on the CTLnet. These tools include portable lanalyzers and the normal UNIX-style network utilities.

VII. FUTURE PLANS

The first expected expansion will be the extension of the FDDI backbone down the SLC linac. Fiber is already installed and reserved for this usage. The expected plan would be to install FDDI/Ethernet switches and add these new sections to the existing FDDI ring. Then as time, schedule (and budget) permit, new EPC SLCmicros would be installed and enabled to use Ethernet. There are nearly 70 existing micros, so an incremental installation plan with accompanying SLCNET decommissioning must be devised for each micro.

VIII. SYSTEM STATUS

The network has been installed for six months now and is being used for PEP-II commissioning. As mentioned earlier, the network is currently routed as a public network to allow developers easy access to their normal development environment while commissioning. The router was installed since the EPICS application gateways are not yet on-line to support the developers. This has fallen behind partially because the new Sun hardware uses Solaris 2.5, whereas all of the EPICS work so far at SLAC has been with SunOS.

The monitoring systems are installed but not completely configured, so accurate information is not yet available.

Delays in developing software and hardware for the EPC SLCmicro has caused PEP-II to use the standard SLCNET SLCmicro for commissioning. The Ethernet-based software will be released when more testing has been completed. It is expected to install the new EPC SLCmicros as time permits.

IX. REFERENCES

[1] L. Dalesio et.al., The Experimental Physics and Industrial Control System Architecture: Past, Present, and Future, Proc. ICALEPCS, Berlin, Germany, 1993.

[2] M. Crane et.al., Network Upgrade for the SLC: Control System Modifications, PAC, Vancouver, BC, Canada, 1997.

X. TRADEMARKS

*OpenVMS is a trademark of Digital Equipment Coporation.
*Alpha ia a trademark of Digital Equipment Coporation.
*UltraSPARC is a trademark of SPARC International, INC.
*Solaris and SunOS are trademarks of Sun Microsystems, INC.
*Catalyst and MultiNet are trademarks of Cisco Systems, INC.
*NetScout is a trademark of NetScout Systems, INC.

NETWORK UPGRADE FOR THE SLC: CONTROL SYSTEM MODIFICATIONS

M. Crane, R. MacKenzie, R. Sass, T. Himel
Stanford Linear Accelerator Center, Stanford University, Stanford CA 94309

Abstract

Current communications between the SLAC Linear Collider control system central host and the SLCmicros is built upon the SLAC developed SLCNET communication hardware and protocols. We will describe how the Internet Suite of protocols (TCP/IP) are used to replace the SLCNET protocol interface. The major communication pathways and their individual requirements are described. A proxy server is used to reduce the number of total system TCP/IP connections. The SLCmicros were upgraded to use Ethernet and TCP/IP as well as SLCNET. Design choices and implementation experiences are addressed.

I. CURRENT SLC CONTROL SYSTEM

The current SLC Control System micro communication services are based on the SLCNET communications protocol. The SLCNET system was developed at SLAC in the 1980's and consists of a master node and up to 255 slave nodes connected by custom hardware and software. The master, or VMS central host is a DEC Alpha computer running the OpenVMS operating system. The slaves, or SLCmicros, are Intel ix86 single board computers in Multibus I crates running the iRMX real time operating system. The SLCNET clock rate is one megahertz and the protocol used is SDLC.

Message passing is supported between individual processes on the VMS host to individual tasks on the SLCmicros. The most prevalent VMS host process is the SLC Control Program or (SCP), of which there can be many running concurrently. The SCP provides the main user interface to the SLC Control System. There are also stand-alone processes which communicate directly to the SLCmicros to collect error reports, distribute database and timing information. All together this involves 50-100 processes on the VMS host communicating with 1-10 tasks on the SLCmicros. The basic tools to boot, debug, and query diagnostic information from the SLCmicros are also available over SLCNET.

The VMS host is equipped with Ethernet and FDDI interfaces which provides support for TCP/IP. The VMS host TCP/IP stack is Multinet which provides communications to various network nodes used in the control system such as EPICS nodes, X-terminals and others. The SLCmicros do not presently support Ethernet or TCP/IP.

II. ENTER ETHERNET AND TCP/IP

The decision to upgrade the SLC Control System VMS host and SLCmicros to use TCP/IP protocols was based on projected bandwidth requirements, hardware availability, and maintenance issues. Please refer to the network upgrade paper for more information[1]. The upgrade of the SLC Control System and the SLCmicros would make TCP/IP the common communications protocol for all PEP-II control system nodes.

This upgrade project required that code be modified or written for both the VMS host and the SLCmicros. This code supports both SLCNET and TCP/IP communications paths since we plan to upgrade as schedule and budget constraints permit. There are some applications that require significant modifications and others that require complete new software to use TCP/IP.

The TCP stream-based protocol was chosen for nearly all the applications since a reliable data stream with flow control is required. TCP connections are setup once and remain for the lifetime of the SLCmicro task or VMS host process. This reduces connection overhead. Since the VMS host and the SLCmicros enjoy the same byte alignment, the data will be passed in little-endian order.

The Multinet package on the VMS host supports both TCP/IP BSD3.4 socket interface and the standard VMS QIO interface. The SLCmicro uses the Fusion TCP/IP stack ported to the iRMX operating system

III. A PROXY SERVER

On the VMS host there can be 50 SCPs plus 10-20 stand-alones running concurrently while there are about 70 SLCmicros in the system. Using direct TCP connections would require 2000-3000 connected sockets on the VMS host. This number of connections would consume to many system resources. The problem was solved by implementing a proxy server that provides data flow between the VMS host and the SLCmicros. The proxy server has two connections to each SLCmicro and a single connection to each VMS host processes communicating to the SLCmicros. This limits the number of VMS host TCP connections to just the number of communicating processes.

The proxy server works by appending a destination header to the users data stream. This header has routing information which allows the proxy server to forward the data transfer to the correct destination. Proxy server 'KEEPALIVE' is also supported to allow an application to check that the proxy server connection is complete and the

*Work supported by Department of Energy, contract DE-AC03-76SF00515

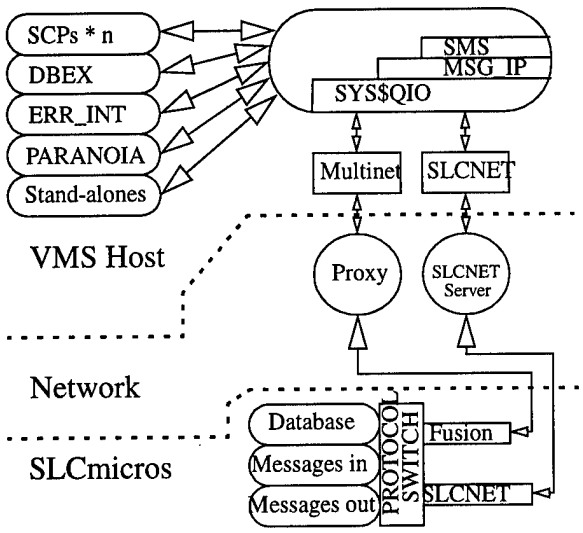

Figure 1. SLC Control System Micro Data Communications

proxy server is operational.

IV. MESSAGE SERVICE

The SLC Message Service (SMS) is a message service which securely delivers messages between the VMS host and SLCmicros. It is a design goal to have TCP/IP communications fit into the existing message service in a transparent manner. Meeting this design goal means making TCP behave like SLCNET (from the user's perspective). This is tricky because SLCNET is a reliable, connectionless, datagram protocol unlike TCP which is stream based.

SMS works in a command/response mode. A VMS host computer process issues a command and one or more SLCmicros may optionally respond. A command is sent to SLCmicro(s) by a host computer process (e.g. a SCP) and the process then optionally waits for a reply.

Each SCP process on the VMS host is a "Single-Process Client" which makes an active connection request to a server. SMS supports any mixture of direct connections to SLCmicros and connections via proxy servers.

The TCP/IP communications code is implemented as a flexible MSG_IP layer below the existing SMS code. This layering makes it possible for both new and existing applications to call the MSG_IP layer directly for TCP/IP services without going through SMS.

V. DATABASE DISTRIBUTION

DBEX is the database executive which communicates database changes between the SLCmicros and the VMS host. This VMS based stand-alone process is the source of most of the network communications traffic in the SLC Control System. DBEX also downloads the database to the SLCmicros at boot time.

DBEX receives data from VMS mailboxes (data destined for the SLCmicros), SLCNET interrupts (data from the SLCmicros) and now TCP/IP interrupts (data from the SLCmicros).

DBEX does not support any direct TCP/IP connection to SLCmicros. Instead, all messages flow through the proxy server. DBEX is a TCP/IP 'client' in that it initiates connections to the proxy server by calling MSG_IP_SEND which transparently makes the connection and sends a KEEPALIVE message. DBEX sends these messages periodically to make sure that the proxy server is alive. If the connection to the proxy server has been broken, the MSG_IP layer automatically tries to re-establish the connection. If a response to the KEEPALIVE message is not received within a given amount of time, an error message is logged in the error log stating that the proxy server is dead.

DBEX calls the MSG_IP layer to receive data using VMS asynchronous I/O methods. Mailbox data is sent to the SLCmicros using MSG_IP_SEND which performs connection management and error logging transparent to DBEX.

VI. ERROR LOGGING

ERR_INT (error interceptor) is the VMS based stand-alone process which receives error messages from SLCmicros, logs them into the error log file and places them into the error message global section.

As was the case with DBEX updates, all error messages from TCP/IP SLCmicros flow through the proxy server. ERR_INT is also a TCP/IP 'client' and uses the MSG_IP layer to send KEEPALIVE messages to the proxy server.

Error messages are received from the SLCmicros in a similar manner to DBEX by using MSG_IP layer. When a message is received, an event flag is set and ERR_INT receives the data portion of the message. The message is then logged and placed into the global section.

VII. PARANOIA

The VMS PARANOIA process is responsible for performing 'check' functions and for receiving unsolicited messages from the SLCmicros. Check functions are issued by PARANOIA to check whether an SLCmicro is up and communicating by sending a check request to the SLCmicro and waiting for a reply. If no reply is received, the SLCmicro is marked as off-line in the SLC database. Check functions also tell the SLCmicro to update various device information and send a reply back to the VMS host.

Unsolicited messages are service requests sent by SLCmicros to the VMS host. Typically, PARANOIA receives these requests and forwards them on to another VMS process which provides the requested service.

As is the case with DBEX database updates, all PARANOIA messages flow through the proxy server. PARANOIA is also a TCP/IP 'client'. KEEPALIVE messages are not needed because the check functions periodically send messages to the proxy server which insures that

the proxy server connection is kept open. Check function messages are sent to a list of SLCmicros using SMS calls instead of the MSG_IP layer. Check function replies and unsolicited messages are received using the MSG_IP layer methods described above.

VIII. DIAGNOSTICS AND TOOLS

There are SLCNET diagnostic tools provided to monitor the activities of both the SLCNET network and the SLCNET based SLCmicros. The tools which support the SLCmicro itself are modified to use both protocols, or are replaced with new TCP/IP functionality.

SLCmicro booting will be accomplished using the standard TCP/IP BOOTP and TFTP protocols which are supported by both TCP/IP stacks. The boot sequence is built into the SLCmicro EPROM and run only at bootstrap time to load and execute the image.

Standard ethernet and IP diagnostic tools are used to trouble shoot network and low level communications problems. These tools include ethernet protocol analyzers, UNIX-style tools such as ping, tcpdump, and netstat. Scripts have been developed for the protocol analyzers to trap SMS and proxy server traffic for development and debugging purposes.

SLCNET provides a means to acquire communications information from the SLCmicros which provide users and technicians needed diagnostic data. This same information is provided from a TCP/IP-based SLCmicro using an embedded HTTP server. This server simply gathers data from the ethernet driver, SNMP variables from Fusion, image filename, boot date/time, and sends it to a requestor. This information is displayed in a format similar to the SLCNET tool for consistency. Some of this information is also written to the database to make it available for display by the SCP.

Commercial TCP/IP based debuggers have been tested during the development phase of the project but the familiarity of the SLC debugger still makes it a good choice. It is possible to modify the SLC debugger to use TCP/IP. No final decision has been made yet.

IX. SLCmicro

A new Multibus I single board computer from Radisys was chosen as the replacement card for the current SLC micro hardware. This new card, named the Skater card, or EPC (Embedded PC), is actually a PC based computer with an Ethernet interface on a Multibus I card. Fusion, a third party TPC/IP stack was integrated with iRMX and our code development system to provide a fast and maintainable communications interface for the SLCmicro.

A difficult part of the EPC upgrade was getting the current SLCmicro image to boot and run on a PC-like platform. The modifications to the memory map for the actual SLCmicro image were substantial but everything did have a place. The lack of a Non Maskable Interrupt (NMI) on the EPC caused a re-design of the most critical section of the SLCmicros code. This section of code wakes up at 360hz to set up for the next beam crossing and must do so very reliably.

The TCP/IP modifications to the SLCmicro code were straight forward since nearly all the communication needs are handled by a handful of routines. All of the I/O routines were changed to reference a single set of routine contained in one file, making a single place to modify how a SLCmicro communicates, SLCNET or TCP/IP. A flag is set at boot time specifying if this SLCmicro is a TCP/IP SLCmicro or a SLCNET SLCmicro. If the flag is set to SLCNET then message flow is as it has been for SLCNET. If the flag is set to TCP/IP new code is used to setup the TCP connections to the proxy server and then keep the connections up. There are two connections to the proxy server, one for database flow and one for messages and error reports. These connections are kept for the life time of the tasks or are re-connected when errors occur.

X. STATUS / EXPERIENCES

All major applications have been ported to TCP/IP in both the VMS host and the SLCmicro and are being tested now. Connections from the VMS host and the SLCmicro via the proxy sever are operational and being tested using a mixed system of SLCNET and TCP/IP SLCmicros. SLCNET is still being used for timing data transfer, SLCmicro booting, and debugging.

A some issues came up during the upgrade process. The SMS message service was designed with limited functionality so that when a process had needs that were not met, shortcuts were taken. An example would be, asynchronous I/O completion where the solution was to make VMS system calls directly instead of going through the SMS layer to talk to SLCNET. This lack of good 'layering' made it necessary to modify individual applications instead of just modifying a unified SMS layer. The lesson learned is that good interface design and evolution saves a lot of time in the long run.

Quite a bit of time was spent porting the TCP/IP stack to our SLCmicro compilers and the iRMX operating system. It was difficult to integrate this large body of source code into our production system and then make it work well. The porting of the SLCmicro image to the EPC card was also a challenge due to the newness of the EPC card and the constraints of PC-type hardware.

XI. REFERENCES

[1] M. Crane et.al.,Network Upgrade for the SLC: PEP-II Network, PAC, Vancouver, BC, Canada, 1997.

XII. TRADEMARKS

*OpenVMS is a trademark of Digital Equipment Corporation.
*Alpha ia a trademark of Digital Equipment Corporation.
*Fusion is a trademark of Pacific Softworks, Inc.
*iRMX is a trademark of Radisys Corporation.

USING WWW IN SRRC CONTROL SYSTEM

J.S. Chen

Synchrotron Radiation Research Center

No.1 R&D Road VI, Hsinchu Science-Based Industrial Park, Hsinchu, Taiwan

Abstract

The SRRC (Synchrotron Radiation Research Center - in Taiwan) control system is built in DEC VMS and DEC OSF/1 UNIX system. Considering that there are many other computer systems in our lab (like SUN and IBM PC....) , and all of these can not directly connected to the control system, so a hardware platform and OS independent system is necessary. The WWW is one of the choice to solve the problem.

The SRRC light source WWW site (http://www-icg.srrc.gov.tw) is built with Microsoft IIS2.0 on Windows NT 4.0 . All of the program is written with JAVA to support runtime interactive ability. Using WWW browser, the user can monitor and control every individual storage ring devices. This paper describes the detail of the hardware and software structure.

1 HARDWARE STRUCTURE

The hardware structure is shown in figure 1. WWW server in a PC base computer (Intel Pentium 133) runs on Microsoft Windows NT4.0 . The database server is a DEC Alpha computer, running on OSF/1 Unix. At the bottom, several ILCs (VME base controller) directly connected to hardware device (eg. RF, BPM...).

2 SOFTWARE STRUCTURE

The software structure is sketched in figure 2. WWW browser side program is written with JAVA Applet. It can, and only can, communicate with www server , and the www server side program is also written with JAVA language. The advantage of server side program written with JAVA is its portability. It can be easily transferred to other platform (e.g. from IBM PC to Sun workstation) and do not need to change even a single line of the program. The disadvantage is the slower speed. Because the JAVA application is slower than C or C++. However, this is the limitation of every www applications, so the slow speed factor is acceptable.

There are three service modules in WWW server. The broadcast service module reads some of the most important machine parameters (beam current, beam lifetime, BPM reading, ...) into www server and store it in computer's RAM. When any browser request these data, www server can directly transmit it to browser. In this way, the network traffic is decrease. Because when many browsers request data at the same time , the www server just need to read once from database server. This broadcast service program is set to read these machine parameters every 10 seconds.

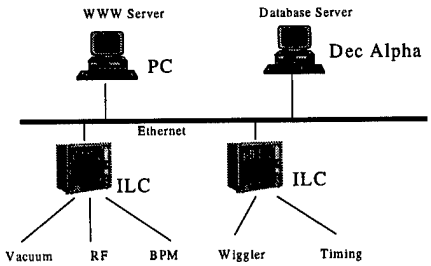

Figure 1

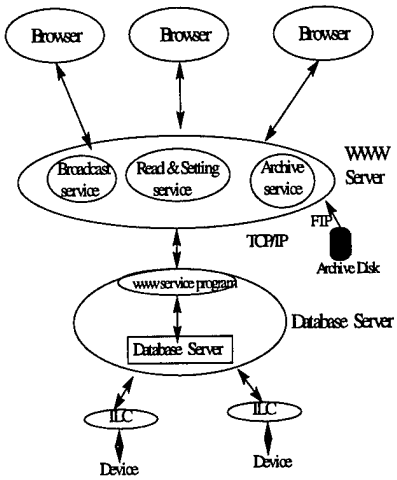

Figure 2

The second module is reading and setting service module. This module can accept the browser read and setting commands. By using this service the browser can not only to read the machine parameter but also to control every devices of the machine. Of course, there are several security protect for this function. Only when the machine operator open the privilege to a specify user , and the user is allowed to control particular devices .

0-7803-4376-X/98/$10.00 © 1998 IEEE

The third module is archive service module. Since our history archive data is stored in DEC VAX system, so this module use FTP to connect the archive disk , getting data and transmitting it to browser side program.

The Database server side WWW service program is written with C, and running in background, it can be connected to database. Since this database is a port of SRRC control system , so through this path the program in www browser can fully control the device (reading and setting).

3 JAVA PROGRAM IN WWW BROWSER

There are three groups programs in www browser. All these programs are write with JAVA . The first group is realtime broadcast monitor programs. These include beam current and beam lifetime curve display program , (as shown in figure 3) , BPM bar chart display program , vacuum bar chart display program . All these programs will automatically update the screen every 10 seconds. The user in WWW browser can received the newest machine status on line .

The second group is monitor and monitor & setting program. The monitoring program is using the graphic like interface, as illustrated in figure 4 to present the machine status. All the SRRC machine status (e.g. every power supply, every insertion device ...) can be see in the WWW browser. The monitoring and setting program is equipped with setting function onto the monitoring program. Using this program, the WWW browser user can control several particularly device, if the machine operator open the privilege for this user. Considering the network traffic, the monitor process running on WWW browser updates the screen every 5 seconds.

The third program is history archive display program. This program allows WWW browser user to select the device and read the data archive . Typical example is given in figure 5 in which two power supplies archive data is displayed for 97/4/25 to 97/4/27 duration.

4 CONCLUSION

Using the technique of WWW and JAVA, we have supported an easy way to monitor and control our accelerator system. Although the speed is slower than the original control program developed in workstation. However, in some of the important application cases , it is shown to be very useful.

REFERENCE

[1] F.Momal, C.Pinto-Pereira "Using World-Wide-Web for Control System "AT Division CERN, 1211 Geneva 23

[2] JAVA SDK page, http://www.sunsoft.com

[3] IIS 2.0 www server page, http://www.microsoft.com

[4] Netscape's Home page, http://home.netscape.com

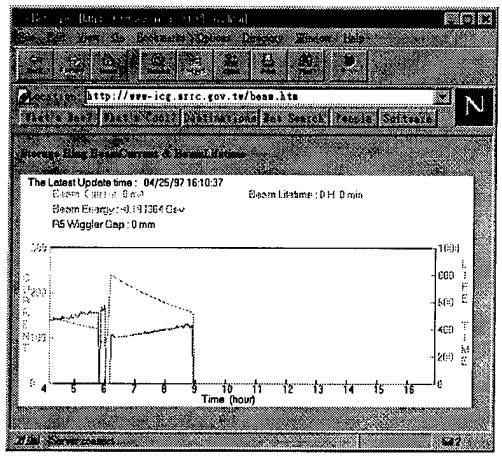

Figure 3

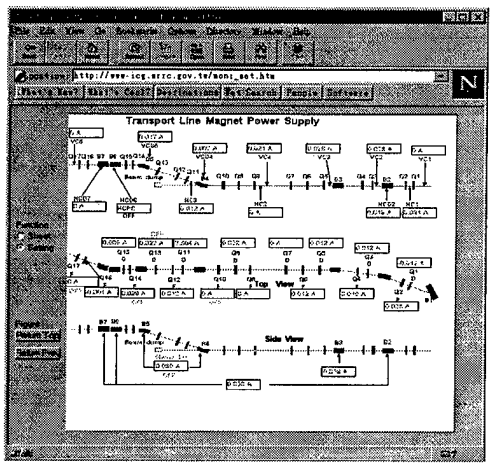

Figure 4

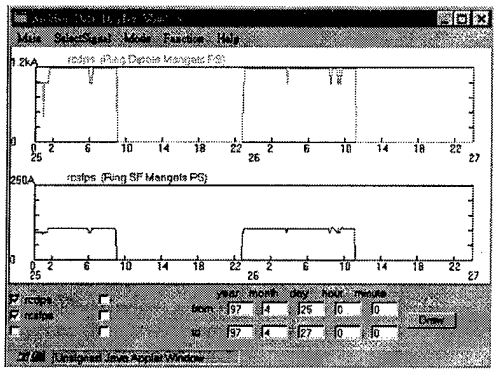

Figure 5

THE DESIGN OF THE CONTROL SYSTEM FOR ANKA

S. Avsec, B. Jeram, G. Mavric, M. Plesko, M. Smolej, J. Stefan Institute, Ljubljana, Slovenia
e-mail: mark.plesko@ijs.si

Abstract

ANKA is a low budget light source. It has to be built with minimal cost. This includes a short construction period to keep the personnel cost low. The use of ANKA as an industrial light source on the other hand places tight constraints on the reliability of its components and its operation. In the creation of the control system one has to minimise in-house development and maximise the use of commercial-quality products. Here, the term commercial-quality applies equally to off-the-shelf-products and to products in the public domain or from other accelerator centres that are field proven and are documented at a level equal to commercial products.

It has been our goal to search for the simplest model and thus the most reliable one. Our extensive investigations have shown that none of the actions and responses of the control system for ANKA need a real-time operating system. Therefore, we have disposed of the whole middle layer of the control system including VME crates in favour of a fieldbus network which connects the individual devices directly to the console computers. The consoles will be PCs running Windows NT. The fieldbus candidate is LonWorks from Echelon which provides plug-and-play and requires almost no additional development. On the software side we have opted for TACO, an object oriented control system environment developed at the ESRF.

1. DESIGN CONSIDERATIONS

The 2.5 GeV electron storage ring ANKA[1] is being constructed at the Forschungszentrum Karlsruhe in Germany and will be used primarily for industrial applications. Such a light source operates for 10 years and more. This asks for a control system that is upgradeable, scaleable and simple to maintain. Therefore, the following considerations have been given top priority in the design of the control system.

§1. Employ standards that will last over the lifetime of the project and solutions that will be supported for a long time.

The control system architecture should allow heterogeneity if necessary, but should not be based on it in its basic form. Simplicity requires that there is only one operating system and a uniform and consistent developing environment:

§2. Use a uniform operating and development environment.

The same is true for the control system electronics. It should not be adapted for each possible device, but rather such devices should be chosen that easily support standard electronics:

§3. Minimise the number of electronic boards.

The cheapest solutions are commercial "off the shelf" solutions. They are well tested and therefore reliable, well documented and thus simplify development. Their price is heavily outweighed by savings in personnel time and cost.

§4. Minimise in-house development and maximise the use of commercial components.

Here, the term commercial applies also to products in the public domain or from other accelerator centres that are field proven and are documented at a level equal to commercial products.

2. THE COMPONENTS OF THE CONTROL SYSTEM

2.1 PCs, Windows NT and Java

Although PC hardware and in particular PC software is significantly cheaper than their workstation equivalents, there are other more important reasons in favour of PCs:

- PCs are used for accelerator control in several laboratories (CERN[2], DESY[3,4], KEK[5])
- PCs have become equivalent to workstations in features if not in power
- PC hardware has become sufficiently reliable
- excellent development tools exist at low price
- commonly known graphical user interface (GUI) tools, e.g. Visual Basic, allow for easy prototyping and testing
- rugged industrial packages exist, if needed in an accelerator environment.

For the operating system, the obvious candidate is Windows NT, because:

- it has all attributes of a modern multitasking operating system
- it supports all standard network protocols
- it is stable and reliable
- it has built-in graphical elements (mouse, events, objects, etc.)
- users are already familiar with it from before
- through the object linking and embedding (OLE) mechanism it is possible to interface the control system into spreadsheets (e.g. Excel) and graphical programming tools (e.g. Visual Basic).

The programming language Java may look a bold choice at the moment, but we have to look into the future. Java, which may be described as the next generation object oriented language after C++, has been accepted by the

0-7803-4376-X/98/$10.00 © 1998 IEEE

whole industry. This year has witnessed an explosion of Java applications and development tools. It is just a matter of time that state-of-the-art development environments for Java, similar to Delphi or Optima, will be available on PCs and other platforms. We are currently evaluating several promising development tools.

Java allows furthermore for true portability and complete platform independence, even between UNIX and Windows. All investment in Java source code will therefore never become obsolete. Having been born for network computing, Java simplifies control over the network by being built into World Wide Web browsers. The fact that Java is an interpreted language is not a problem, as computing power is not such an important issue in accelerator control.

2.2. The TACO Control System Architecture

There are many implementations of control systems that were developed in-house by accelerator laboratories, which are too site-specific to be taken into consideration for ANKA. Of interest are general control system architectures. Among those that deal with the console and control layers and the communication between them are TACO and EPICS and maybe the commercial Vsystem.

We have evaluated the performance of TACO [6] (see Appendix A) and have found that it fulfils all needs of ANKA. TACO has been already ported to the hardware platform of our choice - PCs. This has been done both for the Linux and Windows NT operating systems, while the other two systems, EPICS and Vsystems don't support a full PC solution so far. Although richer in features, they rely on expensive hardware, VME and Digital, respectively.

TACO, developed at the ESRF, is a control system architecture that deals with the console and control layers and provides communication between them. TACO is object oriented and is being currently upgraded by the ESRF to support the newest developments in distributed objects technology like CORBA, etc. Other laboratories (SLS, Soleil) are seriously considering to join a collaboration based on TACO, therefore we can expect further tools and applications developed that we can use "out-of-the-box" for ANKA.

Due to the small size and lower control data flow of ANKA, TACO will run directly on the PCs. TACO relies on a client/server architecture. In the case of ANKA, both the clients and the servers will run on PCs, albeit not necessarily on the same machine. The device servers will collect the data gathered through the field bus or will send commands into the field bus. Each device server will be responsible for a certain group of equal devices, represented logically as objects. The clients will run on any operator console and will, through the applications programming interface (API), communicate with any device server running anywhere. This will allow that control system information will be available all around the ANKA intranet, be it in offices or on beamlines and even anywhere in the Internet. Security provisions will ensure that no dangerous action can be performed outside of the control room.

In a joint effort with the ESRF and the SLS to upgrade TACO, we will extend the communication model of TACO from RPC to CORBA. In addition, the API will provide true objects and will be available to Java with a Java-CORBA implementation. All controls will be done through Java applications or applets that will run in the enviroment of a WWW brower like Netscape or MS-Explorer. The client-side of the control system will be thus completely platform independent and due to its object-oriented structure portable to other acelerator facilities.

2.3. The Fieldbus

Our extensive investigations have shown that most of the actions and responses of the control system can happen on a time scale of 1s, with the exception of:

1. ramping: the power supply current has to be increased in 1 ms steps
2. feedback loops: signals have to be processed and acted upon in the 100 Hz range
3. knobs: fine tuning with knobs needs about 25 actions and displays per second

The first task can be solved by intelligent power supplies or by cheap micro controllers, one attached to each power supply. The second tasks requires a dedicated system which has to be developed on separate hardware anyway. There are no short term plans for feedback systems in ANKA, but if they will have to be built, they will run on their own in specialised hardware and just be connected to the control system for exchanging messages. Knob control may be very useful. But there are just two knobs that an operator can handle at the same time, therefore the necessary responses can be achieved within a non-real-time operating system task at high priority.

As there is no need for a real-time operating system, we can dispose of the whole middle layer of the control system including VME crates. For this we need a field bus network to connect the individual devices directly to the console computers.

There are two low-cost solutions on the market:

- CAN-bus[7], a fast, low-function bus for real-time network systems
- LonWorks[8], an intelligent decentralised network for automation and control

After first evaluations we have a preference for LonWorks, because it offers a complete network system in hardware and software with all the necessary development and network management tools. LonWorks already implements layers 1-6 of the ISO/OSI model and thus transparently connects controlled devices and control room consoles without any need for network programming. Many types of electronic boards are available from third parties (RS-232, ADCs, etc.), others can be easily assembled. LonWorks thus reduces field bus development practically to mere network designing.

2.4. The Interface to the Devices of ANKA

Following §3, we define a set of I/O boards that will exist and be supported in advance. To our mind, these should suffice to control all standard ANKA devices with the possible exception of dedicated diagnostic and instrumentation tools. But even there, one should try to fall back to the standard boards.

- ADC/DAC (16-bit) + 16 digital I/O for power supplies
- 16-channel ADC (12-bit) for temperature, vacuum, RF, diagnostics, etc.
- 64 digital I/O or similar
- RS-232 interface
- GPIB interface

For the local control of beamlines, a few extra boards will be made available: timer/counter, stepper driver, shaft encoder, etc.

3. FIRST TESTS WITH LONWORKS

The purpose of the tests were to determine the operating parameters of the LonWorks network in a real environment and test the ability of a single Neuron module to control the power supplies of dipole magnets. Especially time critical is the ramping process, at which several modules should synchronously (within 1 ms time-jitter) increment their output value once per millisecond.

The tests were made at the synchrotron of the University of Bonn. In the short available period of time, we have done the following:

1. Measurements and comparisons of the network transmission rate and Neuron chip board behaviour in a non-noisy and a very noisy environment were made;
2. Writing a prototype application to ramp a power supply and set and read its current;
3. Creating a set-up where machine parameters can be tuned through mechanical knobs and checking response times at very high network loads;
4. Attaching a micro controller board to a Neuron chip and programming the micro controller to either drive or simulate PS ramping and control;

Several types of communication between Neuron-chip and peripheral (custom made) devices have been tested (Neurowire, Muxbus, bit shifting and serial RS232 communication) and the response and data throughput times measured.

Our tests have not shown any severe limitations of the LonWorks and so far in no case exclude the idea of using them for the control system. In opposite: the tests have proven, that the LonWorks are relatively simple to handle, operate and maintain, and easy to connect among each others or with peripheral devices.

LonWorks simplify the tedious work of programming the network communication, putting all of its essentials in form of firmware into the Neuron chip. The powerful Neuron C language enables the user to quickly build and program a large and complicated communication network, which can easily be extended or modified. The integrated debugger is a useful tool to test and follow the events in the system.

4. CONCLUSIONS

Building an accelerator control system is no art anymore. It has become possible to take a few industry solutions and just work on the implementation and the interfacing. All existing accelerator control system models do their job, which has been proven by the fact that all accelerators work. It has been our goal to search for the simplest model and thus the most reliable one.

Due to the relatively small size of ANKA, we have found that instead of having relatively dumb devices and a strong middle layer, we bring intelligence to the devices and avoid the middle layer completely. This is possible also because most equipment has already some intelligent control. It is just necessary to combine them with a proper field bus.

Maximal portability and longevity has been achieved by choosing tools and products that will remain alive even after a new generation of PCs or a change of operating systems. Such an approach reduces cost and saves development time, too.

5. ACKNOWLEDGEMENTS

During our work, we enjoyed in the friendly cooperation with the ANKA team at the Forschungszentrum Karlsruhe. Furthermore, we thank prof. Husmann and his collegues for kindly allowing us to run tests at the Bonn synchrotron and for giving us all the necessary support there. We thank the company Echelon Munich for loaning the LonBuilder development kit for the time of our tests.

6. REFERENCES

[1] H.O. Moser et al., ANKA Conceptual design, Forschungszentrum Karlsruhe, June 12th, 1995.
[2] Ivan Deloose, PS/CO Note 96-53, Sep. 20th, 1996.
[3] P. Duval, R. Schmitz, Controlling DESY Accelerators with PCs, PCaPAC Workshop, DESY Hamburg, 1996.
[4] C.M. Fu, M. Clausen, G. Csuka, PC Hardware in Realtime Controls, PCaPAC Workshop, DESY Hamburg, 1996.
[5] A. Abe, private communication.
[6] A. Götz et al., TACO: An object oriented system for PC's running Linux, Windows/NT, OS-9, LynxOS or VxWorks, presented at the PCs and Particle Accelerator Control (PCaPAC) Workshop, DESY Hamburg, 1996.
[7] Road Vehicles - Interchange of Digital Information - Controller Area Network (CAN) for High Speed Communication, Document Iso/DIS 11898, International Standardization Organization (1991).
[8] The '95-'96 Echelon LonWorks Product Databook, Echelon Corporation, 1995.

AUTOMATED STARTUP OF THE CEBAF 45 MEV INJECTOR

D. Kehne, P. Letta, B. Dunham, R. Kazimi, Thomas Jefferson National Accelerator 12000 Jefferson Avenue, Newport News, VA 20606

Abstract

In order to improve the speed and reproducibility of restoring the beam in the Continuous Electron Beam Accelerator Facility (CEBAF) 45 MeV injector [1] after a full or partial shutdown of the accelerator, a program has been written using the Tcl/Tk [2] scripting language to automate most of the required steps. The procedure is separated into four main parts. The first part performs preliminary checks that verify that the hardware is set correctly and then turns on the main interlocked systems including high power magnets and RF. The second step turns on the gun high voltage. The final steps turn on the beam and verify that the beam quality is satisfactory by measuring the transmission, orbit, transverse beam size, and bunch length. Minor corrections for phasing are also performed in the program. In order to identify inefficiencies in the startup, each is timed and parameter changes are logged so that system drifts can be tracked. This paper describes the software implementation, the logic to achieve a successful startup, and efficiency results.

1 INTRODUCTION

A major goal of accelerator operations is the minimization of downtime. During a typical startup, there are several contributors to delays. First are component or system failures. Second are day to day drifts in the beam setup. Finally come distractions to the operations crews.

To alleviate these delays, a program has been developed that automates the startup of the CEBAF nuclear physics injector. The program is written in the object oriented language Tcl/Tk, which has been used successfully in several other high level applications at CEBAF [3]. As will be described later, full automation, though near, has not yet been achieved.

2 MOTIVATION AND PHILOSOPHY

Though the ultimate goal of the injector automatic startup program, AutoStart, has always been to achieve full automation, it was understood from the beginning that the program itself would be a tool used to identify obstacles impeding startup. Some of these obstacles include lack of repeatibility, recurring hardware or software failures and, procedural errors. In view of this, a further set of goals was developed. These are:

- Rapid identification of component or system failures
- Standardization of startup sequence
- Verification of beam quality
- Automatic record keeping to identify points of recurring failure and areas that are delaying startup.

Personnel from the injector group and the operations group were chosen to develop the AutoStart program. This was done for several reasons. First, when the development of the AutoStart program began, the sofware group was overloaded with work on higher priority low and high level applications. Second, the startup documents were written by the members of the injector group. Having the document authors convert those procedures to programs allowed each step to be examined critically and changed if necessary. Finally, an automatic startup program follows the steps that a human operator follows and the insight of experienced operators was desired to aid in identifying some of the subtleties of actual startups.

3 EVOLUTION OF THE PROGRAM

3.1 Degree of Automation

The program began as a series of startup procedures in which each step provided instructions for the operator to carry out. The steps have been gradually automated and streamlined. After concern was expressed that operator skills would diminish if familiarity with the turn on procedure was reduced, easy access to an explanation of each step and instructions to perform each step manually, were provided. Priority for implementation has been based on ease of automation and degree of gain. In general, the program evolved so that those steps that were most time consuming or tedious for an operator to perform were automated first.

3.2 Structure

The program was initially designed to parallel the three states of the Personnel Safety System (PSS) of the accelerator. The Controlled Access PSS state, in which high power system operation is prohibited, allows personnel to enter the accelerator enclosure. The next higher state is Power Permit. In this state personnel are excluded from the accelerator enclosure and high power systems, with the exception of the electron gun, can be turned on. The highest state of the PSS is Beam Permit which allows gun high voltage turn on and beam operation. Since during machine access times operations crews are busy with other tasks, an early version of the program that was initiated while in Controlled Access was found to be ineffective. The program structure was

0-7803-4376-X/98/$10.00 © 1998 IEEE

modified so that all functions occur after the PSS reaches Power Permit.

4 LAYOUT AND DESCRIPTION

The four main parts of the program are: system turn on, gun HV turn on, beam turn on, and beam check out.

4.1 Startup Screen

The main AutoStart screen is shown in Fig. 1. The buttons to activate each of the four subprograms are positioned horizontally to minimize screen space. While the program is running, a log file is kept, detailing the progress of the startup, including any faults that may occur. When the System Turn On subprogram is activated, a timer is started that records the overall length of time that the startup takes. Each subprogram is timed as well. Options to enter comments concerning the program, view the log file, and initiate detailed checkout programs are provided under the menu.

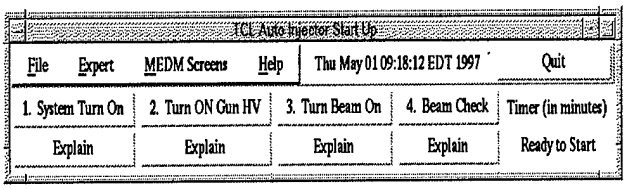

Fig. 1. The main injector AutoStart screen shows the buttons that activate the four main parts of the program.

4.2 System Turn On

The System Turn On portion of the program performs the following functions:

- Turn on of all injector RF cavities
- Turn on and hysteresis cycling of the arc dipole magnets
- Opening of all accelerator valves
- Hysteresis cycling of injector solenoids and quadrupoles.

The System Turn On screen is shown in Fig. 2. Flag indicators along the top of the screen are yellow during execution and turn green or red indicating either success or failure. Status of the program is provided in text boxes below the status indicators. Each function can be activated individually by the operator or automatically. Since the turn on of the rf cavities and dipoles can to up to 10-20 minutes each, an independent process is launched to allow parallel turn on. Stray fields generated by the accelerator arc dipoles are the reason that these must be on for successful injector startup. Due to inconsistent response times, the arc dipole routines have caused the most difficulties, even causing crashes of the control system. This problem is being currently addressed.

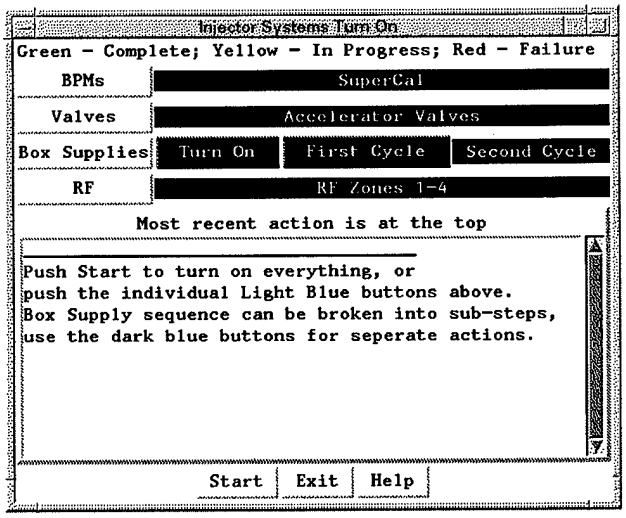

Fig. 2. The System Turn On control screen is shown.

4.2 Gun HV Turn On

When the system turn on section is complete, the program waits for acknowledgement from the operator that the PSS state has changed to beam permit. At this point, the control electrode is set to suppress electron emission and the gun high voltage is automatically turned on. In addition, all interlocks preventing beam turn on are verified to be clear. The gun high voltage turn on screen is is similar to the System Turn On screen with indications given for success or failure.

4.3 Beam Turn On

Beam turn on requires only one action: change of the gun control electrode to allow electron emission. The program requests via a textbox that the operator do this manually. This is the only true administrative break point in the program that prevents "one button" startup.

4.4 Beam Check Out

To verify that the injected beam properties are satisfactory, a minimum set of checks is done automatically. Determining a minimum set has been more challenging than was first thought. More checks were added as errors were found over the span of months. Out of this emerged a nearly complete and detailed set of automated checks that were slowing down the startup. This complete set was then reduced to four diagnostic checks. The beam current is checked automatically by inserting a Faraday cup and comparing the signal with the standard. Orbit is checked for perturbations outside a range of +/-2 mm for all beam position stripline monitors. Several critical locations have allowable errors of +/- 0.25 mm. The transverse profile is checked by automatically triggering a wire scan at a high dispersion point. This verifies proper phasing of the acceleration cavities and transverse matching of the injector to the accelerator. The final step activates a program to measure the phase transfer function in the low energy end of the injector.

This verifies that the bunching is correct. This program has been automated to a large degree. However, since the output of the diagnostic is a complex plot of the phase transfer function, optimization of the phases still relies on operator feedback. The complete diagnostic list is now offered as an menu option. Options for running the complete injector diagnostic checkout, opening useful control screens and the standard options described earlier are accessible via a menu.

4.4 Efficiency Tracking

Since one goal of the AutoStart program is to reduce the startup time of the injector and accelerator, a plotting routine [4] is accessible from the menus that gives a plot of run times for each section of the program as well as the overall run time. Such a plot is shown in Fig. 3 with actual data of the time taken to measure the phase transfer function described in the preceding section. Sufficient data has not yet been collected on all portions of the startup but general observation has produced the following results. In the absence of faults, system turn on takes 10 minutes, gun HV and beam turn on takes 2 minutes, and beam checkout takes 5 minutes for a total of about 20 minutes. However, for typical startups, system turn on takes 20 minutes, Gun HV and beam turn on still take 2 minutes (few failures in these steps), and beam checkout requires 20 minutes, including adjustments of the injector rf phasing. This produces a time for typical injector turn on of 45 minutes from a state of controlled access to beam delivery to the linac. The major time consuming portions of the startup are turn on and cycling of the dipoles, and measurement and adjustment of the phase compression. Improvement of the efficiency of the latter could reduce the startup time by up to 15 minutes.

5 PLANNED IMPROVEMENTS

The first and obvious goal, to be implemented within the next three months, is the interfacing of the PSS with the accelerator control system EPICS. This will allow nearly full automation of the startup. In fact, the necessary modifications have been made and await the hardware implementation. Full automation of the bunching setup is also in progress. This would include automatic adjustment of the rf phases to optimize phase compression. Next, a quick method of analyzing past data for fault occurrance is necessary to make the program useful as an error tracking tool. Finally, extension of the automatic startup to the entire accelerator is planned. In view of the fact that the dipole turn on routine is complete, the most difficult portion to be written is the beam verification sequence for the entire accelerator.

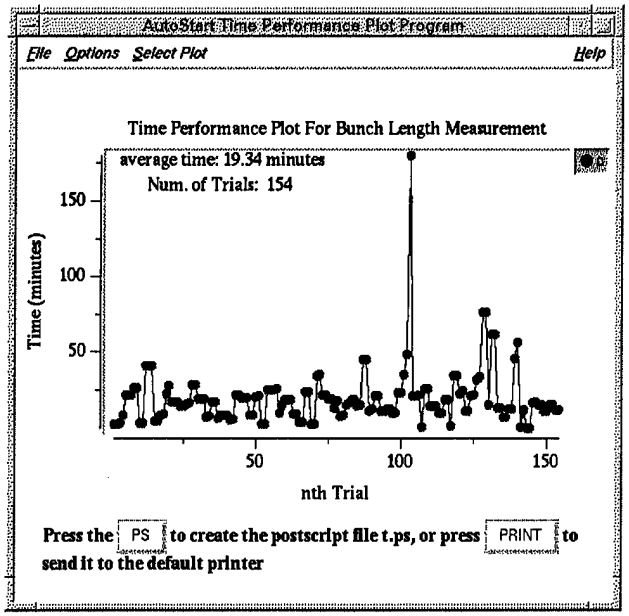

Fig. 3. Performance plots such as shown here can be accessed from the menu in the AutoStart main screen.

6 CONCLUSION

A partially automated injector startup program has been written for the CEBAF nuclear physics injector by members of the Injector and Operations Groups. Currently, hardware obstacles prevent full automation but these are being removed.

7 ACKNOWLEDGEMENTS

The authors gratefully acknowledge the critiquing of the AutoStart program provided by the operations staff, the periodic prodding of A. Hutton and C. Sinclair, and the assistance of the software group. Work supported by the U.S. DOE under contract number DE-AC05-84ER40150.

REFERENCES

[1] R. Abbott, et al, *"Design, Commissioning, and Operation of the Upgraded CEBAF Injector,"* Proceeedings of the 1994 International LINAC Conference, Aug. 21-26,1994, Tsukuba, Japan p. 777.

[2] J. K. Ousterhout, *Tcl and the Tk Toolkit*, Addison-Wesley Professional Computing Series (1994).

[3] J. van Zeijts, *"Rapid Application Development Using the Tcl/Tk Language,"* Proceedings of the 1995 Particle Accelerator Conference, May 1-5, 1995, p. 2241.

[4] B. Gold and B. Dunham, CEBAF TN-96-057.

APPLICATIONS TOOLKIT FOR ACCELERATOR CONTROL AND ANALYSIS

M. Borland
Advanced Photon Source, Argonne National Laboratory
9700 South Cass Avenue, Argonne, Illinois 60439 USA

Abstract

The Advanced Photon Source (APS) has taken a unique approach to creating high-level software applications for accelerator operation and analysis. The approach is based on self-describing data, modular program toolkits, and scripts. Self-describing data provide a communication standard that aids the creation of modular program toolkits by allowing compliant programs to be used in essentially arbitrary combinations. These modular programs can be used as part of an arbitrary number of high-level applications. At APS, a group of about 70 data analysis, manipulation, and display tools is used in concert with about 20 control-system-specific tools to implement applications for commissioning and operations. High-level applications are created using scripts, which are relatively simple interpreted programs. The Tcl/Tk script language is used, allowing creating of graphical user interfaces (GUIs) and a library of algorithms that are separate from the interface. This last factor allows greater automation of control by making it easy to take the human out of the loop. Applications of this methodology to operational tasks such as orbit correction, configuration management, and data review will be discussed.

1 INTRODUCTION

Every accelerator facility faces the challenge of creating high-level applications for controlling and diagnosing the operation of the accelerators. Traditionally, this has taken the form of compiled programs specifically coded for each application and accelerator. A more efficient approach is to solve one's problems using generic and configurable programs. This reduces programming effort and speeds the production of usable applications. It takes advantage of the fact that many accelerator control problems involve similar operations, e.g., orbit correction is really no different from other slow feedback problems. Similarly, many graphical display tasks (e.g., plotting an orbit or plotting vacuum pressure around a ring) involve identical operations.

While one need not use stand-alone generic programs and a scripting environment in order to have generic, multi-use code, it is very convenient to do so. Having algorithms available in the form of ready-made programs rather than as a library of subroutines is far more convenient and allows more rapid development. Individual compiled programs can conveniently be used in stand-alone fashion or coordinated by a script. This coordination creates a high-level application, typically with a GUI, out of reusable low-level components. In the rush to create GUI applications, we must not forget that sophisticated users frequently require more power and flexibility than is easily provided using GUIs. The use of scriptable, command-line-oriented tools satisfies this need in addition to aiding development of GUI scripts. Indeed, at APS many GUIs have their genesis in work done by experts using command-line-oriented tools.

2 SDDS TOOLKIT

The advantage of configurable programs is amplified when many such programs use a common data file protocol. These programs can then properly be called a program "toolkit." At APS, the Self-Describing Data Sets (SDDS) file protocol [1,2,3,4] is used not only for many program configuration tasks, but also for storage of experimental, archival, and simulation data. Briefly, self-describing data gives access to data by name and class only, without reference to position or concern about the presence of data items that are not of interest.

The SDDS Toolkit, comprising about 70 generic programs, provides the muscle for many script applications. The disadvantage of scripts is that they are slower than compiled programs. We mitigate this problem by using the SDDS Toolkit for computationally intensive operations. Operations available include graphics, fitting, winnowing, Fourier analysis, filtering, smoothing, interpolation, cross-referencing, sorting, histogramming, statistics, equation evaluation, and others.

3 INTERFACES VS. ALGORITHMS

A goal of our high-level applications effort is a high level of automation. This is often at odds with the desire to create GUI applications, since these tend to be written assuming the presence of a button-pressing user. We have found that separating the algorithm from the interface is most difficult when it comes to error and status reporting. Interactive applications need to report errors and status differently than noninteractive applications.

A workable way to handle status messages is the use of callback routines passed to an algorithm by a calling routine. In an interactive context, a procedure can be passed the name of a status updating procedure that it can use to provide operator status reports. In a noninteractive context, the same procedure can be passed, for example, the name of an empty callback routine that does nothing other than return.

The Tcl/Tk error catching mechanism is convenient for handling errors in a multi-level procedure context. When an error is encountered in a Tcl/Tk procedure, a return can be made with an error code that is 'caught' by the calling procedure. This procedure can either display an error message or return a catchable error itself. Most of our procedures do the latter only. Only the highest-level, GUI-related procedures display error messages when they catch an error.

In a separate paper in this conference [5], we discuss the Procedure Execution Manager (PEM), a Tcl/Tk envi-

0-7803-4376-X/98/$10.00 © 1998 IEEE

ronment for procedure execution. PEM was developed to allow procedures to easily operate with varying levels of operator involvement. For example, operator interaction with a PEM procedure is (normally) automatically confined to the highest-level procedure. In different contexts, the same code will automatically accept operator input or input from a calling procedure. Error and status messages are posted to a single area regardless of the level from which they originate.

4 OTHER TOOLS

APS uses the EPICS [6] controls system. In addition to the SDDS Toolkit, there are EPICS-specific programs that are used in creating high-level applications. Among these are 20-odd EPICS-specific SDDS-compliant programs [2], which include data-collection tools, experiment execution tools, save/restore tools, a general-purpose feedback program (discussed below), and others. These tools are all used by multiple GUI applications.

For displaying live data that is a function of position around a storage ring or in a transport line, the program ADT (Array Display Tool [7]) is used. ADT is configured by an SDDS file that tells it what process variables to display and an optional additional file that supplies information on how to draw the accelerator lattice. ADT allows saving and recalling of data to memory or files, tracking of minimum and maximum values, computation of statistics, differencing of current and saved data, and other features. It is most commonly used to view the orbit in the APS ring. In several cases, scripts use SDDS tools to create ADT configuration files on the fly to display context-dependent data.

5 EXAMPLES

In this section, we present applications of the above methods, all drawn from routine APS operations. All of these applications rely solely on the SDDS-compliant programs and Tcl/Tk scripts, unless otherwise noted. These examples illustrate how much may be accomplished with a set of tools like those in use at APS.

5.1 General-Purpose Workstation-Based Feedback

As mentioned, one of the EPICS-specific SDDS tools is a general-purpose feedback program that is configured by SDDS files. This compiled C program is used for controlling rf gap voltages under beamloading conditions, for providing specialized power supply regulation, for correcting the global orbit, for local beamline steering, and for correcting transport line beam trajectories. The program itself has no GUI, but is run in its various instances by different GUIs. Some of these are simply configurable instances of the same GUI, while others are custom-made for specific applications. One GUI allows on-the-fly creation of a simple one-readback, one-actuator feedback loop.

The orbit correction system for the APS storage ring [8] is broken into several parts. One script is used to edit configuration files specifying which correctors and beam position monitors to use. This script also performs singular value decomposition (using a compiled program) to create the inverse matrix file, starting with a forward matrix from either simulation or experiment. The job of using the inverse matrix to perform orbit correction is performed by another, independent script. The advantage of this arrangement is that either of these functions may be performed by any means desired, i.e., one could have several scripts that perform the actual correction or several that prepare input data. This is convenient during development of new algorithms, as it allows one to work on only that part of the system that is of interest. In addition, it allows use of interfaces for multiple applications; for example, the same script that prepares input for the workstation-based global correction scripts also prepares input for the real-time feedback system [9].

5.2 Configuration Management

Accelerator configuration or settings management is a problem that all accelerator facilities face. At APS, the "save/compare/restore" or SCR system is built using SDDS files, SDDS tools, and Tcl/Tk. For each of 15 major subsystems, a "request file" is available that lists and describes the process variables (PVs) that are important for that system. In addition to being used to acquire PV values from the controls system, the request file gives tolerance data, protection status, categorization, and other information that determines how each PV is treated in compare, restore, and review operations. Adding new PVs or a new major subsystem is largely a matter of adding entries to a request file or creating a new request file.

Partial review, restore, and comparison operations are supported via several mechanisms. Operators may choose categories and subcategories from those defined in the request file. Since these may change with time, the actual categorizations are extracted from the saveset and used to configure the GUI. Operators may also choose to select PVs based on "filter files," which are lists of PVs with a specific functional relationship (e.g., all PVs relevant to steering a certain beamline). For some subsystems, graphical display of comparison operations is available; addition of more such displays is planned.

In addition to the main SCR script, several other applications make savesets using the same procedure that the main SCR script uses. This procedure permits any application to make "backup" data giving the state of the accelerator prior to making a change. If the operator needs to recover from the change, he then uses the main SCR script rather than another, redundant interface. If the GUI SCR script were not designed with separation of interface and algorithm in mind, this feature would not be as simple to implement in as many contexts.

5.3 Data Review

Another function required at accelerator facilities is review of archival data. All archival data collection for accelerator operation is performed using SDDS-compliant EPICS programs. This includes simple time-series data collection, alarm logging, and glitch- or beam-dump-triggered data collection. The data collection processes are managed using UNIX cron jobs. This includes daily starting of jobs, automatic restarting of jobs following a crash,

and daily postprocessing of data. Postprocessing includes recovery of any corrupted files that might result from a system crash, compression of the data, and in some cases analysis of the data.

Normally, users access this data through Tcl/Tk GUIs. In most cases, a common GUI is used for accessing all the time-series data, another for all the alarm log data, and so on. In several cases, customized Tcl/Tk GUIs have been provided for certain systems that have unusual or specific display requirements (often involving preprocessing of data prior to display). Users requiring even more access can make use of the same Tcl procedures used by the GUIs to find the data of interest (typically by specifying the group the data belongs to and the time interval of interest). There is also a mechanism for exporting data to user files in various formats, such as SDDS or spreadsheet format.

Another application of this data is the automatic creation of GIF images for display on the World Wide Web. About 150 different plots are created at intervals of one to 15 minutes, displaying data from the APS storage ring vacuum, absorber, and rf systems. These plots are created using the same SDDS graphics program that is used to create plots from Tcl/Tk scripts. The Experimental Facilities Division at APS has created a Web interface that permits on-demand plotting of SDDS data from their systems using SDDS tools and Perl scripts [10].

Several types of glitch-based data collection jobs are used, again based on SDDS-compliant EPICS tools. These collect data at a relatively high rate in a circular buffer, until one or more glitch or trigger events are seen. Following the event, data collection continues for a specified period, after which the data is added to the log file. A single interface is used for all of the glitch data, with customized plotting and analysis available for some data sets. For example, orbit glitches are logged for the APS storage ring (a glitch is defined as a change in a beam position reading over a defined threshold at one or more locations). The user may select events based on cause (e.g., x orbit motion, beam loss), then plot the raw data, plot difference orbits, or perform analysis to find the most likely corrector to have caused the motion.

A third type of data collected in large quantities at APS is alarm information. The most typical use of this data is to determine when a certain piece of equipment tripped. The GUI provided as an interface to this data provides simple printouts of events and the times they occur; it also creates histograms of alarm density and total alarm counts per channel within a defined period. A related tool provides probability analysis of alarm data, indicating, for example, whether an observed alarm rate during one period is improbable compared to the alarm rate in another period.

5.4 Digital Scope Control and Data Acquisition

APS has a number of remotely-controlled digital oscilloscopes used for monitoring pulsed magnet waveforms, rf signals, current monitor signals, and the like. At present, two of these instruments are controlled using Tcl/Tk scripts and SDDS tools. The scripts perform configuration save and restore operations for the scope and essentially arbitrary associated equipment (e.g., multiplexers). Recently, we have implemented waveform documentation software that sets up equipment (e.g., a pulsed power supply) in a standard way, then acquires and archives waveform data. This permits tracking of changes in the response of such equipment.

5.5 Accelerator Measurements

A number of accelerator measurements have been implemented as GUI scripts that were originally developed by physicists using SDDS tools. To a large extent, we simply wrapped a GUI around the algorithm created by the physicist. Among the applications developed for the APS storage ring are measurement of small orbit and tune changes due to undulator gap changes, measurement of BPM offsets using orbit bumps and variation of quadrupole strength, measurement of the beam motion spectrum, and automated timing of BPMs.

6 CONCLUSIONS

The combination of the SDDS toolkit, SDDS-compliant EPICS tools, and Tcl/Tk has proven very effective in the development of high-level applications for APS operations. True reusability of programs is made possible through the use of self-describing data and proper generalization of program functions, saving programmer effort and speeding the development of new applications. Separation of the user interface and the algorithm has made it possible to reuse code and automate operations. The command-line orientation of the SDDS tools enhances use by experts, provides easy integration into scripts, and permits rapid use of expert-developed algorithms in GUIs.

7 ACKNOWLEDGMENTS

Contributions to the above work have been made by a number of individuals at APS, including J. Carwardine, L. Emery, K. Evans, C. Saunders, and N. Sereno. Work is supported by the U.S. Department of Energy, Office of Basic Energy Sciences, under Contract No. W-31-109-ENG-38.

8 REFERENCES

[1] M. Borland, "A Self-Describing File Protocol for Simulation Integration and Shared Postprocessors," Proc. of the 1995 Particle Accelerator Conference, Dallas, Texas, pp 2184-2186 (1996).

[2] L. Emery, "Commissioning Software Tools and the Advanced Photon Source," ibid, pp 2238-2240.

[3] M. Borland et al., "Doing Accelerator Physics Using SDDS, UNIX, and EPICS," *Proc. of ICALEPCS* '95, pp 382-391 (1997).

[4] M. Borland et al., "The Self-Describing Data Sets File Protocol and Toolkit," ibid, pp 653-662.

[5] M. Borland, "The Procedure Execution Manager and Its Application to Advanced Photon Source Accelerator Operation," these proceedings.

[6] L. R. Dalesio, et. al., "EPICS Architecture," *Proc. of ICALEPCS* '91, KEK Proceedings 92-15, pp 278-282 (1992).

[7] K. Evans, private communication.

[8] L. Emery et. al., "Advances in Orbit Drift Correction in the Advanced Photon Source Storage Ring," these proceedings.

[9] J. Carwardine et. al., "Commissioning and Performance of the APS Real-Time Orbit Feedback System," these proceedings.

[10] M. Ramanathan, private communication.

A BUNCH CLOCK FOR THE ADVANCED PHOTON SOURCE

Frank R. Lenkszus and Robert J. Laird
Advanced Photon Source, Argonne National Laboratory
9700 South Cass Avenue, Argonne, Illinois 60439 USA

Abstract

A bunch clock timing module has been developed for use by Advanced Photon Source beamlines. The module provides bunch pattern and timing information that can be used to trigger beamline data collection equipment. The module is fully integrated into the control system software (EPICS) which automatically loads it with the storage ring fill pattern at injection time. Fast timing outputs (1 ns FWHM) for each stored bunch are generated using the storage ring low-level rf and revolution clock as input references. Fiber-optic-based transmitters and receivers are used to transmit a 352-MHz low-level rf reference to distributed bunch clock modules The bunch clock module is a single-width VME module and may be installed in a VME crate located near beamline instrumentation. A prototype has been in use on the SRI CAT beamline for over a year. The design and integration into the control system timing software along with measured performance results are presented.

1 INTRODUCTION

The need arose to provide bunch timing for a time-resolved experiment at the APS. The primary requirements were to provide a timing trigger for each bunch stored in the machine and to provide a means for adjusting the timing of the bunch triggers to compensate for propagation delays.

We considered both a centralized bunch clock generator with individual time delays for multiple beamlines and distributed bunch clock generators. The module described in this paper may be used either way. We presently plan to provide a separate module for each beamline, i.e., distributed bunch clocks. The reasons are twofold: it is much easier to distribute a clean, stable rf reference than a train of impulses, and separate bunch clock generators allow the tailoring of trigger sequences to individual experimental requirements.

2 DESCRIPTION

The bunch clock accepts both the storage ring revolution clock and 352-MHz low-level rf as inputs. It provides two NIM-level outputs that have a sequence of pulses corresponding to bunches stored in the ring. The output pulses are synchronized to the low-level rf input and hence are synchronized to the beam. Each output bunch pulse is approximately 1 ns wide.

Coarse and fine programmable delays are provided to adjust the output timing to the arrival of beam at the experimental apparatus. The coarse delay is specified in low-level rf tics and is variable from 0 to 1295 (the ring has 1296 rf buckets). The fine delay has a range of 0 to 4.6 ns with a resolution of approximately 18 ps per step. The combination of the two delays permit the output to be shifted up to a full revolution period with 18 ps resolution.

The module also provides a raw bunch clock output. When used with multiple programmable external delays, the output provides the basis for a centralized bunch clock generator.

3 CIRCUIT

The bunch clock circuit is shown in Fig. 1. It is based on an arbitrary bit pattern generator. The contents of an on-board RAM is shifted out a bit at a time at the storage ring rf frequency. Each bit in the RAM corresponds to a storage ring rf bucket The shifting process is synchronized with the revolution clock such that the bit sequence starts over at each revolution clock. The RAM is loaded with the bunch pattern at injection time.

Two inputs are required: the revolution clock and the low-level rf reference. The revolution clock is resynchronized with the rf reference. The resynchronized revolution clock is delayed by a counter which produces an output delayed by a programmable number of rf clock periods. This counter provides the coarse delay. The delayed revolution clock resets a divide-by-16 counter that advances the RAM address counter. The 16 data outputs of the 256-word RAM are loaded into a shift register which runs at the rf reference rate. The output of the shift register is fed to a programmable digital delay chip which controls the fine delay with a resolution of approximately 18 ps per step.

The delayed shift register output is buffered through NIM output buffers that drive the front panel bunch clock output connectors. In addition, the shift register output is buffered and brought out as the "raw bunch clock" signal. This signal may be used with external circuits to provide additional outputs.

It takes 81 16-bit RAM memory locations to hold the 1296-bit storage ring bucket pattern. The RAM address counter is compared to the value "81" and reset when that value is reached.

It is absolutely necessary that the revolution clock arrive at the front panel within an acceptable time window relative to the rf reference input to assure stable operation. A timing circuit compares the received revolution clock arrival time with the rf reference. A status indicator available as a front panel LED indicates whether or not the timing is acceptable. The revolution clock may be shifted one-half an rf period by a two-position front panel "skew" switch.

0-7803-4376-X/98/$10.00 © 1998 IEEE

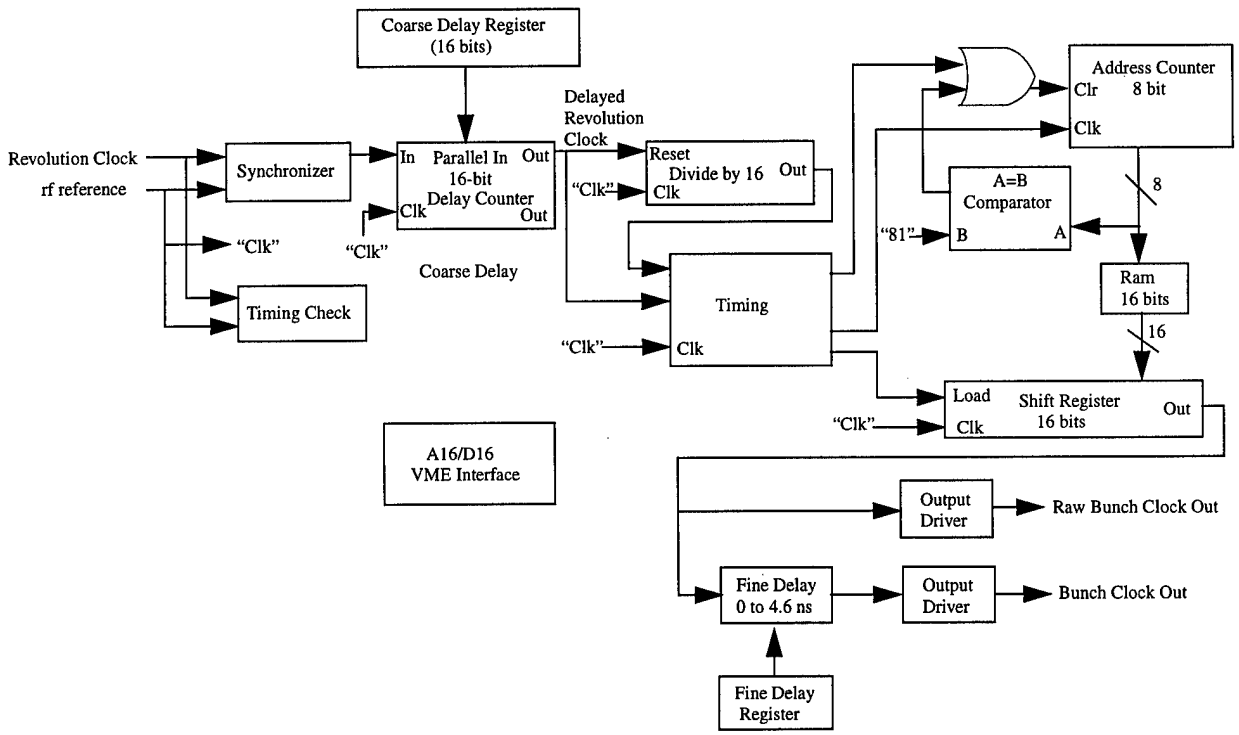

Figure 1: Storage ring bunch clock block diagram.

Since the revolution clock is used only to reset the divide-by-16 counter that advances the RAM address counter, the circuit has the interesting property that it will continue to produce a synchronized bunch pattern output even if the revolution clock is momentarily lost. This is neither the normal nor desired mode of operation. This property, however, illustrates the choice of a design that provides a modicum of fault tolerance.

A VME interface provides read/write access to the bunch pattern RAM and to registers that set the coarse and fine delays. Status readbacks are provided that indicate whether or not the rf reference and revolution clock inputs are receiving signals.

4 IMPLEMENTATION

Most of the circuit is implemented with emitter-coupled logic (ECL). The VME interface and RAM addressing logic are implemented in PLDs. The edge speed of ECL, 125 to 300 ns, dictates the use of controlled impedance lines on the printed circuit board. As a result, the circuit was implemented on an 8-layer board. In addition, the fast edge speed requires that printed circuit line stub lengths be held to a minimum.

The logic is fully synchronous. A great deal of care has been taken in distributing the clock and minimizing clock skew. Differential clock drivers with guaranteed within-device clock skew of less than 50 ps are used to provide clocks to various parts of the circuit. In addition, printed circuit board trace lengths have been adjusted to minimize skew at critical parts of the circuit. As part of a test of internal timing margins, we are able to run the bunch clock generator reliably at 480 MHz. In fact, the bunch clock generator may actually be capable of running in excess of 500 MHz. The 480-MHz limit is imposed by a module that generates the revolution clock. If the revolution clock input is removed, the bunch clock will run at a rate in excess of 550 MHz.

The circuit is implemented in a single-width VME card. An on-board DC-to-DC convertor provides the -5.2 Volts required by the ECL logic.

5 SOFTWARE

Software has been written to seamlessly integrate the bunch clock generator into the APS control system. An EPICS device driver, database, and graphical control screens have been developed which provide access to all the bunch clock generator features.

The bunch clock generator programming model is straightforward and consists of five registers. The registers are control/status, RAM address, RAM data, fine delay, and coarse delay. The EPICS driver provides a convenient interface to these registers through EPICS process variables.

EPICS process variables are provided to enable/disable the bunch clock output, clear the bunch pattern RAM, set and reset a bit in RAM corresponding to a desired bucket number, return a waveform listing the filled bucket numbers, and return a waveform showing the bunch pattern as an array of ones and zeros.

The set and reset process variables accept a bucket number as the input value. The driver computes the RAM location and bit number corresponding to the desired bucket number and sets or resets the resultant bit in the computed RAM location.

The storage ring injection timing system writes the value of each bucket number to the bunch clock set bucket number process variable as part of the storage ring injection process. Thus, the bunch clock generator RAM contents track the injected bunch sequence as bunches are injected into the storage ring.

The bunch clock generator RAM contents need to be cleared upon loss of beam. An EPICS state program implements the logic to perform this function. The state program monitors storage ring beam current. When the beam current drops below a setable threshold for more than 5 seconds, the bunch clock clear bunch pattern process variable is written, causing the device driver to clear the RAM contents.

In addition, upon causing the bunch pattern waveform record or the filled bucket numbers waveform records to be "processed" (an EPICS euphemism for causing a database record to perform its intended function), the device driver reads the RAM contents and computes and returns either bucket numbers or the bunch pattern depending on which process variable is processed.

6 RF REFERENCE DISTRIBUTION

Since the bunch clock generator is intended to be located near the beamline, an important consideration in the design is delivering the rf reference to the bunch clock generator front panel. While a coax cable such as phase-stabilized HELIAX® may be used (and in fact this is exactly what we used initially), we designed a pair of single-mode fiber optic modules to deliver the rf reference to distributed bunch clocks from a central location.

7 PERFORMANCE

Tables 1 and 2 summarize measured performance. Temperature measurements were done in an environmental chamber at 23 +/- 10 degrees C.

The measured value of 34 ps/degree C/km should be compared to an estimated 19 ps/degree C/km for HELIAX® LDF2-50.

Table 1: Temperature Measurements

	ps/degree C
Fiber transmitter	7
Fiber receiver	0
Single mode fiber	34/km
Bunch clock	10 (estimated)

All jitter measurements were made with a 20-GHz sampling oscilloscope. The quoted rms jitter is as calculated by the oscilloscope. Peak-to-peak jitter was measured by placing the oscilloscope in infinite persistence and measuring the peak-to-peak spread over a two-minute period.

Table 2: Jitter Measurements

	rms	peak to peak
Bunch clock	3.4 ps	21 ps
Fiber transmitter - 525m fiber cable - fiber receiver	3.2 ps	25 ps
In situ at Sector 3	5.3 ps	36 ps

The end-to-end measurement for the fiber transmitter and receiver for a short (2 m) cable resulted in essentially the same values as reported for the 525-m fiber length.

The in situ measurement was done at the SRI CAT. The cable run to this location is approximately 115 m. A HELIAX® cable with 352 MHz driven from the same location as the fiber was used as a reference. We believe this overestimates the jitter somewhat.

8 CONCLUSIONS

The bunch clock generator was placed in production in January 1996. It has been successfully used for several time-resolved experiments at SRI CAT. A second bunch clock is scheduled to be installed at the BESSRC CAT in May of this year. It is anticipated additional units will be installed as more beamlines move into production.

9 ACKNOWLEDGMENTS

Work is supported by the U.S. Department of Energy, Office of Basic Energy Sciences, under Contract No. W-31-109-ENG-38

EMBEDDED CONTROLLERS, FIELD BUS AND A MODULAR IO CONCEPT: CENTRAL ELEMENTS OF BESSY II CONTROLS *

J. Bergl, B. Kuner, R. Lange, I. Müller, R. Müller, G. Pfeiffer, J. Rahn, H. Rüdiger
BESSY, Berlin, Germany

Abstract

Wherever applicable IO nodes connected by a field bus (FB) have apparent advantages: Simple and flexible installation and cabling, easy signal conditioning as well as data filtering and process security provided by intelligent actuators and sensors. The cost of a complex 3rd control system layer may be a high development effort. At BESSY several design principles of this layer control the risk: A few multi purpose IO cards form a modular set. Multiple IO bus connectivity provides high installation flexibility. 'Controller Area Network' (CAN) is the FB connected to the VME system of the standard model control system. Communication is provided by a small set of software modules designed to be easily adapted to hardware changes. The communication protocol with BESSY IO modules is a small and efficient subset of the 'CAN Application Layer' (CAL) standard.

1 ADVANTAGES OF A FIELD BUS LAYER

A reliable automated and flexible control system is essential for the effective operation of complex installations like a 3rd generation light source. A wide variety of solutions with emphasis on different properties can make up such a control system. Today the distributed architecture of console workstations on the same fast network as local process computers is widely accepted as *standard model.*

The amount of device control directly handled by local process computer IO cards compared to the data transmission via additional field bus networks connecting intelligent sensors and actuators is less settled. The advantages of a predominantly field bus based architecture obviously overcompensates the drawbacks with respect to the requirements at BESSY:

Installation is Simplified.

+ *Short signal cables*: The DAC can be placed as close as possible to the power supply. Combined with properly specified components analog signals with 16 bit resolution become meaningful.
+ *Secure and cheap connection*: The field bus protocol guarantees reliable data transmission via shielded twisted pair cable even in noisy environments.
+ *Electrical independency*: Cross talk via common ground or bus backplane does not exist.

Intelligent Actuators and Sensors can be Utilized.

+ *Data preprocessing*: Raw measured values are converted to relevant physical quantities.
+ *Asynchronous data collection*: Autonomously aquired data can satisfy requests immediately.
+ *Data sharing*: Field bus multicast facility allows task synchronisation and interlocks.
+ *Autonomous control applications*: The embedded controller may generate ramp functions, perform regulation loops and monitor device status.

Process Security is Improved.

+ *Separate CPU per device*: Equipment specific software and configuration is very localized and simple.
+ *Stateful recovery*: Service is not interrupted by higher level system crashes, actual IO status and setpoints are provided to the rebooting systems.
+ *Independent trouble shooting*: Replacement of faulty or suspicious hardware does not affect other devices.

Nevertheless increased complexity and development effort should not be underestimated: A field bus communication has to be developed that matches the standard network protocol (at BESSY EPICS/Channel Access). Real time databases and program configurations of local process computer and embedded controller require additional data and link definitions. The intelligent subsystem makes task distribution as well as identification of failures more difficult.

2 SMART IO HARDWARE SET

The modular set of hardware (Fig. 1) satifying most of the requirements is remarkable small. Thus the software development, configuration and maintainance effort becomes calculable.

2.1 Highly Integrated IO Components

+ *Multipurpose Analog IO Card*: This versatile module with high quality components is optimized to control power supplies with high stability. Features are 16 Bit DAC, 4 mux 15+sign Bit ADC, 8 Bit digital in, 8 Bit digital out, low thermal drift components combined with fully isolated analog and digital stages as well as two bus and one device connectors.
+ *Flexible Digital IO*: Card has 16 Bit digital in, 16 Bit, digital out and the same set of connectors. Bus interface unit, programmable array logic, input/output stage are fully separated segments on board.
+ *Embedded Controller*: The Piggyback Module equipped with i386EX CPU and CAN Controller can be attached to the IO Cards via ISA Bus Connector.

*Funded by the Bundesministerium für Bildung, Wissenschaft, Forschung und Technologie and by the Land Berlin

0-7803-4376-X/98/$10.00 © 1998 IEEE

+ Bus *Adapters/Connectors* and *Carrier Boards* allow to use the basic components in a variety of VME, ISA 96 and CAN bus configurations.

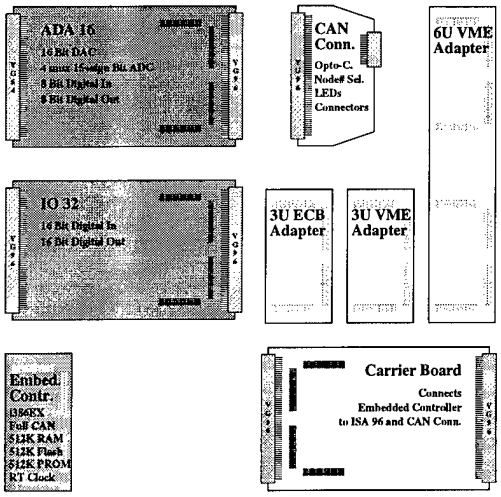

Figure 1: Components of the Modular IO Set

2.2 *Configuration Flexibility*

Whereever possible devices have been specified with slot, connector and power supply for the interface. Therefore the most common configuration is a standard IO card equipped with embedded controller, plugged into the device and attached to the CAN via bus connector (Fig. 2, top).

Unexpensive ISA 96 crates provide access to special devices exclusively equipped with analog signals or requiring more than one IO card. The embedded controller is connected to the ISA bus by a carrier board. Software is identical to the previous case. The interfaces are plugged into the ISA bus with their bus connectors (Fig. 2, middle). For a more efficient use of the ISA 96 crate the backplane can be divided into 4 independent segments of 5 slots.

6U and 3U VME bus adapters allow to use the interfaces also at the local process computer level directly (Fig. 2, bottom).

2.3 *Network Setup*

The CAN field bus has a mature protocol on an inexpensive chip available from multiple sources. Industrial support as well as increasing connectivity to industrial devices [1] make CAN a reasonable choice. The multicast facility is required for synchronisation of corrective actions [2] and used for device protection interlocks.

On the embedded controller board the Intel 82527 Full CAN Chip is used to free CPU and development effort from CAN object management. The selected VME CAN card (VCAN2 from *esd*) is equipped with a MC 68 000 16 MHz CPU and two Philips PCA 82C200 Basic CAN chips capable of handling 2048 CAN objects each and providing gateway functionality between two CAN segments [2].

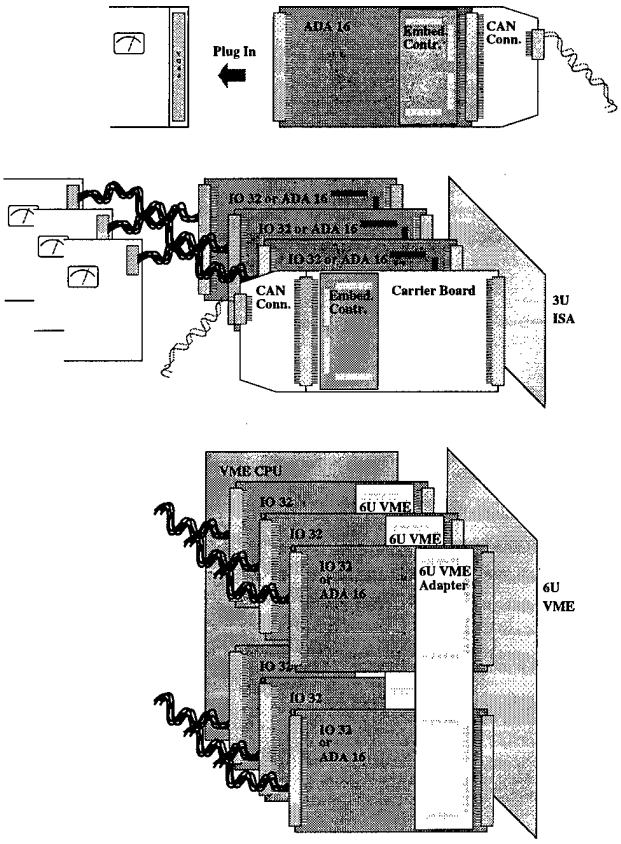

Figure 2: Basic Configuration Options

3 ADAPTIVE SOFTWARE DESIGN

Using CAN as major building block of the control system a CAN communication software is required that allows for hardware changes as well as for different protocols.

3.1 *Uniform Data Link Layer*

A simple programmers interface (SCI - *Simple CAN Interface*) has been defined hiding specifics of the installed hardware and providing a protocol independent data link layer. SCI reduces the effort of data transmission from a CPU to a certain CAN segment to function calls like 'Create CAN Object' assigned to a port #, 'Read' and 'Write' with different synchronisation behaviour.

On the VME side SCI is a library portable between different operating systems and capable of multithreading. Presently the VCAN2 card of *esd* is supported. The portable SCI board support driver utilizes the vendor supplied memory mapping of CAN objects. Integration of e.g. CAN *Industry Pack* modules could be done by embedding the appropriate driver (e.g. from [3]) into SCI.

SCI used by the embedded controller is a C–library of Intel specific code. It features the transparent handling of several Full CAN chips that may be used on the same CAN segment to increase the number of available CAN objects.

3.2 *Multiple CAN Protocols Supported*

The asynchronous communication between VME master and IO node requires read, write, buffering and busy/retry mechanisms for identifiable chunks of data.

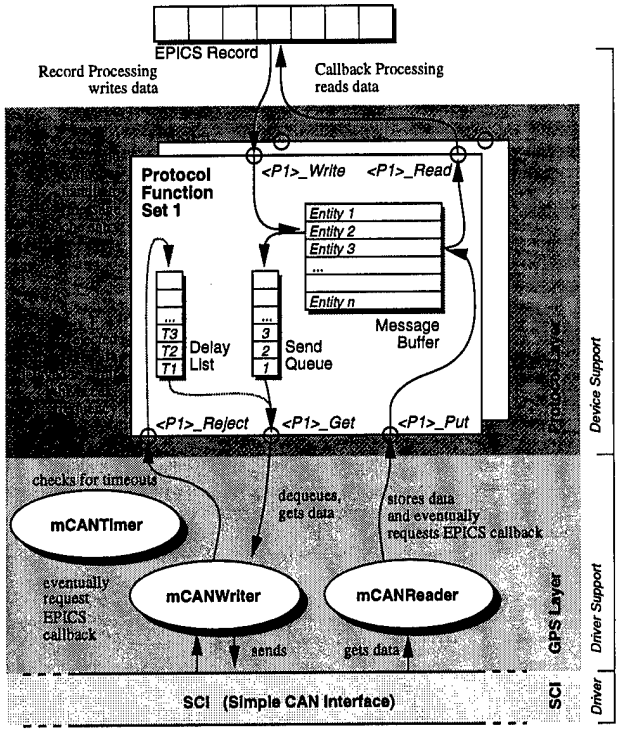

Figure 3: Sketch of the Multi Protocol Handler

In addition to the transmission engine the software has to support different communication protocols (Fig. 3). In the CAL [1] standard a *CAN Message Specification* (CMS) is given. Any protocol can be identified as conformal to the CANopen CAL/CMS implementation conventions or not.

Base protocol for data exchange between VME and embedded controller is a minimal and efficient subset of CAL/CMS called *lowCAL*. Protocol support and communication handler run symmetric both on VME motherboard and embedded controller CPU (Fig. 4).

The communication protocol for the CAN interface of the RF power amplifier Siemens S5 PLC has been specified to deliver *lowCAL* conformal messages. Other commercial CAN modules following the CAL/CMS specification (e.g. PT 100) have been integrated with minimal effort.

A PC CAN card in combination with the equivalent development environment for PCs and the embedded controller allow to interface PC based (otherwise standalone) control applications with the same software bundle.

The CAN interface to a commercial motor controller (MOCON) used for the insertion device gap drives does not fully comply with CAL/CMS. Consequently a variant of *lowCAL* has been implemented. The software would also be able to support proprietary protocols like SDS (*Smart Distributed Systems*) or *DeviceNet*.

Development and maintainance of autonomous control

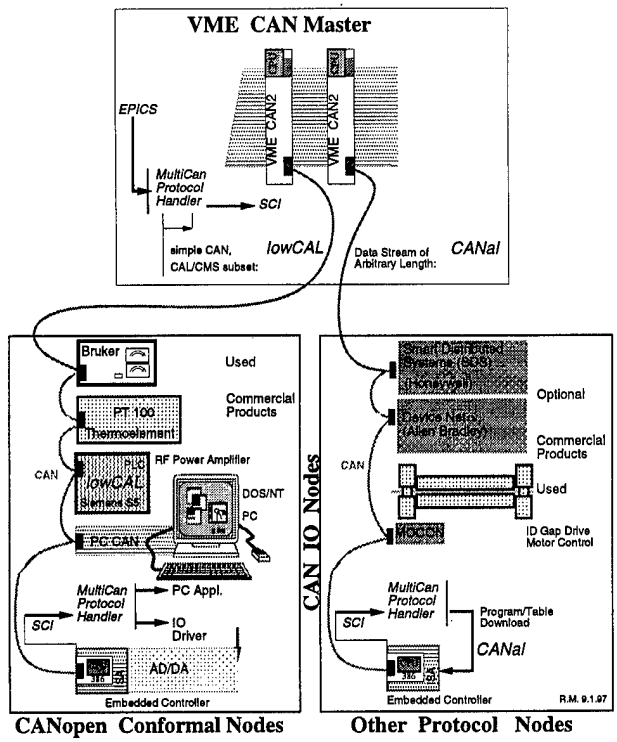

Figure 4: Supported CAN Communication Protocols

tasks performed by the embedded controller is drastically simplified if code and configuration data can be downloaded from a host via the CAN connection. It is foreseen to implement the appropriate protocol supporting data streams of arbitrary length (*CANal*) (Fig. 4).

4 EXPERIENCES AND SUMMARY

Today 30% of the planned control system installation is operational and fulfills the specified requirements (speed, robustness etc.). The installation process is rapid – partly due to the amount of about 80% CAN based IO nodes mostly in 'Plug In' configuration. The CAN communication software design revealed its power while connecting commercial CANopen conformal sensor devices. Portable implementation has been proven by an independent installation at another laboratory (SLS).

5 REFERENCES

[1] CAN in Automation International Users and Manufacturers Group e.V.: *CAN Application Layer for Industrial Applications (CAL)*, CiA e.V., Nürnberg, 1995.

[2] J. Bergl, B. Kuner, R. Lange, I. Müller, R. Müller, G. Pfeiffer, J. Rahn, H. Rüdiger, *Controller Area Network (CAN) — a Field Bus Gives Access to the Bulk of BESSY II Devices*, Proceedings of the 1995 ICALEPCS, Chicago, 1995, p. 1017

[3] See `http://www.ast.cam.ac.uk/~anj/epics/`, section 'UKIRT/Gemini CANbus driver'

RHIC BEAM PERMIT AND QUENCH DETECTION COMMUNICATIONS SYSTEM[1]

CHARLES. R. CONKLING JR., *Brookhaven National Laboratory*

Abstract

A beam permit module has been developed to concentrate RHIC[2] subsystem sensor outputs, permit beam, and initiate emergency shutdowns. The modules accept inputs from the vacuum, cryogenic, power supply, beam loss, and superconducting magnet quench detection systems. Modules are located at equipment locations around the RHIC ring. The modules are connected by three fiberoptic communications links; a beam permit link, and two magnet power supply interlock links. During operation, carrier presence allows beam. If a RHIC subsystem detects a fault, the beam permit carrier terminates - initiating a beam dump. If the fault was a superconducting magnet quench, a power supply interlock carrier terminates - initiating an emergency magnet power dump. In addition, the master module triggers an event to cause remote sensors to log and hold data at the time-of-failure.

1. Work preformed under the auspices of the U.S. Department of Energy.
2. Relativistic Heavy Ion Collider

INTRODUCTION

Brookhaven National Laboratories Alternating Gradient Synchrotron, and Booster have room temperature magnets that are not effected by beam losses. RHIC has superconducting magnets, and there is sufficient beam energy to damage the magnets. The possible beam damage, and use of superconducting magnets, created the requirement for a beam permit and quench detection communications system. RHIC has two rings, therefore, the RHIC permit and quench communications system has three functions:

- Beam permit: single permit link to permit beam entry and presence in both rings.
- Yellow magnet interlock: yellow quench link protects yellow ring magnets.
- Blue magnet interlock: blue quench link protects blue ring magnets.

There were similar requirements in the design of the Fermilab Tevatron a decade earlier. The author wishes to acknowledge the work of Robert J. Ducar of the Fermilab, Accelerator Controls Section. Mr. Ducar developed two CAMAC modules to meet the requirement, the CAMAC 200 PERMIT CONCENTRATOR and CAMAC 201 PERMIT LINK GENERATOR. The RHIC permit system design is based upon these two Fermilab modules. The major differences between between the two systems are the inclusion of the quench protection system, modules based on VME specifications, and the use of complex programmable logic devices which were not available a decade ago.

The RHIC beam permit/quench detection communications system concentrates RHIC subsystem sensor outputs to allow beam entry, and its continued presence. RHIC subsystem inputs include vacuum, cryogenic, beam loss monitors, power supply status, safety, and superconducting magnet quench detection systems. These subsystems report their status to the permit/quench system. If any permit/quench input or interconnecting cable fails, all modules terminate their local permit level output, and if a quench input failed, the associated power supply interlock. In addition, the master module generates a beam dump command, and triggers an abort event transmission. While the beam permit system is considered an emergency system, the beam permit system will be normally be used to purge the accelerator at the end-of-cycle.

PERMIT/QUENCH COMMUNICATIONS SYSTEM MODULES

One beam permit/quench module becomes the master by its location, and printed wire board jumper patch. To initialize the beam permit/quench communications system, both yellow and blue magnet quench detector inputs must be active. On an event link command, the master module initiates two 10 MHz carriers; yellow and blue QUENCH_LINK. Slave modules receive the QUENCH_LINK carriers (input or upstream), test local magnet quench detector inputs, and retransmit the QUENCH_LINK carriers (output or downstream). The QUENCH_LINK carriers return to the master module in less than 0.5 sec (if all magnet quench detector outputs are asserted). If the master module detects the QUENCH_LINK carriers at its upstream inputs 0.5 seconds after start, the QUENCH_LINK carriers are maintained, and all modules enable their power supply interlock outputs.

Once the quench links have been established, the superconducting magnets can be energized, the permit link may be established. The PERMIT_LINK is similar to the QUENCH_LINK, an event link command initiates the carrier at the master module. The master and slave modules concentrate local beam permit inputs and pass the permit carrier if conditions permit. If the master module detects the PERMIT_LINK carrier at its upstream input, the PERMIT_LINK carrier is maintained, and all modules enable their local permit outputs.

The three permit/quench links are constructed from standard AGS/RHIC event link communications components. The module carrier input and output buffers are EIA RS-422, differential TTL components. All module

0-7803-4376-X/98/$10.00 © 1998 IEEE

RS-422 inputs are transformer coupled for galvanic isolation. The RS-422 links are converted to fiberoptic if the link exceeds 25 meters. Multi-mode fiberoptic links are used for long distance transmissions. During the first loop around the RHIC ring, the fiberoptic link receivers require approximately 8 msec to detect carrier, and unblank. As there may be 40-50 fiber optic links around the RHIC ring, there is an initial permit/quench link loop delay of 300-400 msec. After the fiber optic receiver's have unblanked, the fiber optic, copper wire, and integrated circuit propagation delays will not exceed 2 beam revolutions.

After the PERMIT_LINK is established, any module detecting a permit input, or upstream PERMIT_LINK carrier failure terminates its local permit level and PERMIT_LINK carrier output. The PERMIT_LINK carrier failure propagates around the RHIC ring, terminating local permit level and PERMIT_LINK carrier outputs. When the master module detects an upstream PERMIT_LINK carrier failure, its local permit level, and PERMIT_LINK carrier outputs are terminated. Blue and yellow beam dump commands are initiated, and an event link abort event code is triggered. The PERMIT_LINK carrier failure continues to propagate from the master module to the module that initiated the failure, terminating local permit levels and PERMIT_LINK carrier outputs. Within 2 beam revolutions, all modules have detected the failure, the beam dump initiated, and local permit levels terminated.

If the module input failure was a quench input, the associated local power supply interlock level and QUENCH_LINK carrier are terminated in addition to the PERMIT_LINK. However, the yellow and blue quench links are not coupled, a quench detection in one magnet ring doesn't propagate to the other ring. The ring that contains a quenching magnet is "crowbared," a stressful process, the other ring will be slowly "ramped" down.

A permit/quench module contains:

- VMEbus interface; D8(OE), D16, A16 data transfers
- Six, fail-safe, optically isolated, permit inputs; subsystems must drive a 50 ohm line termination. Permit inputs may be disabled by VMEbus command, and masked during operation. Masks are controlled by event link event codes.
- Two, fail-safe, optically isolated, quench inputs; subsystems must drive a 50 ohm line termination. Quench inputs can be permanently deactivated by module jumper patch, however there is no VMEbus control of quench inputs.
- Four, RS-422, 10 MHz carrier inputs; permit, yellow quench, blue quench, and event links. Inputs are is transformer coupled for galvanic isolation, and terminated in 100 ohms. The permit/quench modulation is on-off, while the event link modulation is bi-phase-mark.
- A 32-bit time stamp is register is provided for each permit, quench, and permit upstream carrier input. The module time stamp counter is driven by a 1 MHz clock derived from the event link, and the counters are synchronized by an event link event code.
- Three, RS-422, 10 MHz carrier outputs; permit, blue quench, and yellow quench links.
- Pulse output; trigger event link abort event code. Output will drive a 50 ohms termination to a TTL level.
- Five, fail-safe, level outputs; blue and yellow beam dump, local permit level, and blue and yellow power supply interlock. Outputs will drive a 50 ohms termination to a TTL level. These outputs are negated on initialization, or link failure, and are asserted approximately 0.5 seconds after link initialization. The transition from assertion to negation initiates, power supply emergency shut-down, beam dump, and local shutdowns.
- Interface to RHIC event link [1]; event link event codes control permit and quench initialization, time stamp counter synchronization, and permit input masks. Eight masks are available to disable permit inputs. During various machine operating phases, permit inputs may be masked. For example, a loss monitor near the injection kicker may be masked during injection, when losses may exceed the normal operating threshold.

V120 MODULE

The permit/quench module was named V120 by the BNL AGS/RHIC Accelerator Controls Section. The module is a standard 4U x 6HP VME module. The module is a VMEbus slave, responding to D8(OE), and D16 short address transfers. The front panel contains 16 LED status indicators. All input/output connections are made through the user pins in the VME P2 connector. The logic was implemented in three Altera EPM9320, complex programmable logic devices (CPLD). The three CPLD's contain a total of 960 logic cells. The EPM9320 is in-system programmable. Each CPLD has an individual programming connector, and is programmmed after the module is assembled. The EPM9320 was selected after the logic failed to partition in smaller CPLD's. The remainder of the module integrated circuits are primarily VMEbus, and module input/output buffers.

T120 TRANSITION MODULE

All RHIC/AGS VME chassis have a rear transition module mounting panel. The transition module mounting panel accepts 21 4U x 6HP modules, with 80 mm deep printed wiring boards. The V120 input/output connections are through the VME chassis backplane P2 connector. A ribbon cable connects the T120 transition module to the rear side of P2. The T120 module is an 8U x 6HP module. All permit/quench module system input/output connectors are contained on the T120 transition module. These include the permit/quench link, event link, beam dump, and event trigger connectors. The transition module contains the RS-422 differential input isolation transformers and terminators, and single ended input/output termination's, but

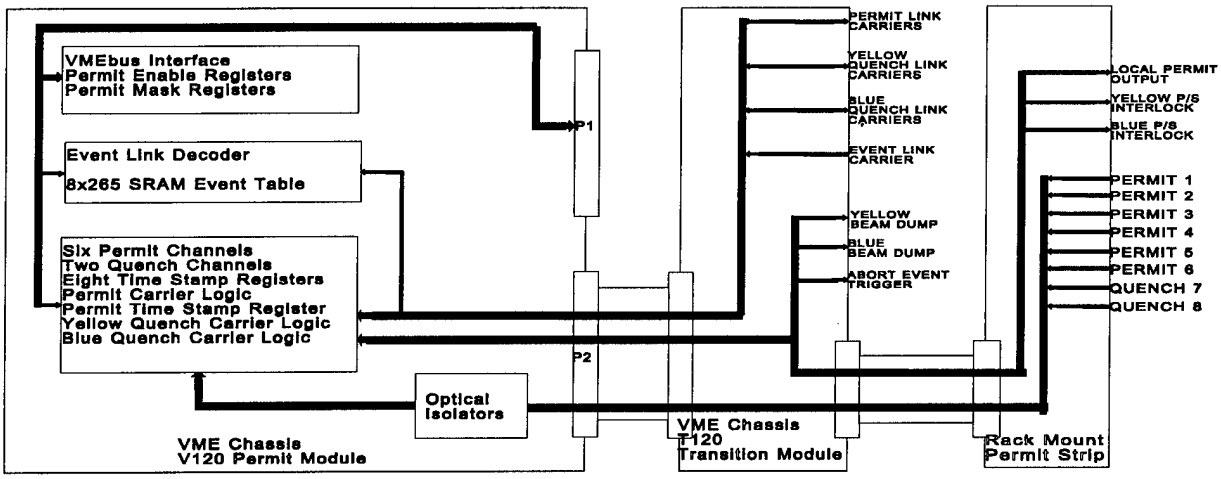

Single Module of Permit Communications System

no active circuitry. The link connectors are twin-BNC, and single ended connectors are Lemo NIM/CAMAC connectors.

The T120 contains connectors that are thought of as system connectors - controlled by the controls group. The RHIC subsystem input/outputs are contained on a rack mounted chassis. The transition module contains a 25-pin subminiature connector to connect the chassis.

RACK MOUNTED PERMIT INPUT CHASSIS

All subsystem permit and quench input/outputs are made on a 1RU rack mounted chassis. The chassis is normally mounted on the rack cabinet rear rack rails, with assess to the chassis is through the rack cabinet rear door. The chassis contains 11 Lemo NIM/CAMAC connectors; 8 permit and quench inputs, and 3 outputs. The outputs are permit level, and yellow and blue power supply interlocks. A 25-pin subminiature connector connects to the transition module cable. The chassis contains no active circuits, just single ended cable terminations.

1996-1997 RHIC SEXTANT TEST

Nine V120 modules were operating during the RHIC Sextant Test. A limited number of inputs were provided by quench detection systems, main power supply, and vacuum. Both yellow and blue quench links were operating. The yellow line contain test beam, while the blue line was used to complete the magnet power circuit for this test. Vacuum was the only permit input during the test. The power supply interlocks were active, and the permit output was used to control the switching magnet at the end of the AGS to RHIC transfer line. Beam couldn't be switched into the RHIC sextant unless the local permit output near the switching magnet was asserted.

REFERENCES

[1] B. R. Oerter , C. R. Conkling, *Accelerator Timing at Brookhaven National Laboratory*, Proceedings of the 1995 Particle Accelerator Conference

THE RHIC REAL TIME DATA LINK SYSTEM*

H. Hartmann, Brookhaven National Laboratory, Upton, NY 11973 USA

Abstract

The RHIC Real Time Data Link (RTDL) System distributes to all locations around the RHIC ring machine parameters of general interest to accelerator systems and users. The system, along with supporting host interface, is centrally located. The RTDL System is comprised of two module types: the Encoder Module (V105) and the Input Module (V106). There is only one V105 module, but many (up to 128) Input Modules. Multiple buffered outputs are provided for use locally or for retransmission to other RHIC equipment locations. Machine parameters are generated from the V115 Waveform Generator Module (WFG) or from machine hardware and coupled directly through a fiber optic serial link to one of the V106 input channels.

1 BACKGROUND

Many magnet excitation currents will be related to the beam energy or similarly to the main magnet dipole current. To avoid manual adjustment of hundreds of excitation currents to track the main magnet dipole current, the RTDL System provides for the distribution of real time data on the main magnet dipole current and other machine parameters in a form that can be used directly by equipment control hardware.

2 INTRODUCTION

The RTDL machine parameter frames are transmitted on a serial self clocking link using a modified Manchester code (bi-phase mark). Each frame has the following format:

* 1 start bit
* 8 bit parameter ID field
* 24 bit parameter Data field
* 1 parity bit
* 1 stop bits

The transmission rate is 10Mb/s and 3.5μs are required to transmit each parameter data frame. All frames are transmitted synchronous with the 720 Hz RHIC Event (every 1.39 ms). The 8 bit parameter ID field allows up to 255 different frames to be defined, and sufficient time exists for transmission of all 255. The system transmits a continuous bi-phase mark "one" (the 10Mhz carrier) during idle periods. This scheme of transmission is the same as the Event Link currently being used in the AGS/Booster Timing System, and therefore can take advantage of existing fanout and repeater circuits.

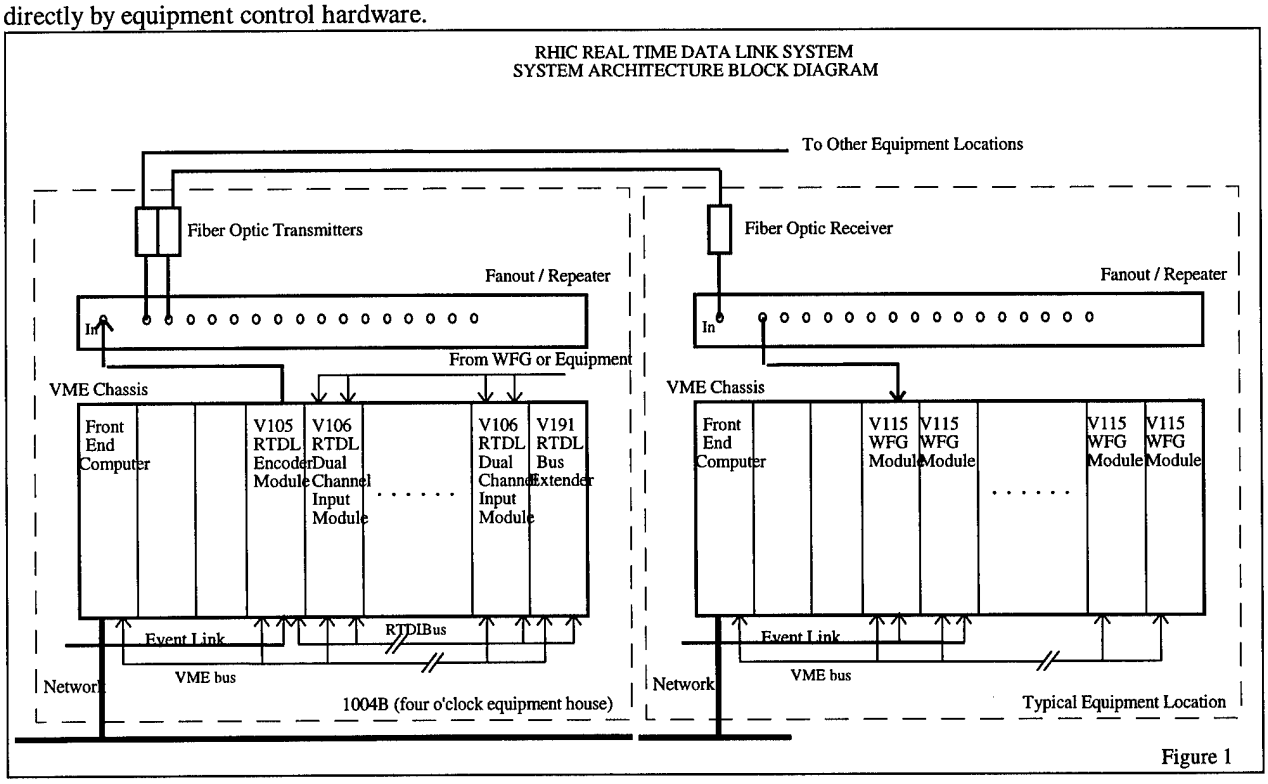

Figure 1

* Work performed under the auspices of the U.S. Dept. of Energy.

3 SYSTEM ARCHITECTURE

The RHIC RTDL System is located in the 4 o'clock equipment house (1004B). A standard 6U 84HP VME Chassis has sufficient space to support the V105 module, the necessary V106 modules to support 30 RTDL frames, the standard Front End Computer (FEC) running VxWorks operating system used in all RHIC VME chassis, and a V108 utility module. Additional frames can be added with extension chassis. The V105 initially drives a fanout/repeater module which provides multiple buffered TTL differential outputs. These outputs are used locally within the 4 o'clock equipment house, and others drive fiber optic transmitters for optical transmission to other RHIC equipment locations. Local receiving modules are isolated from the V105 module by transformer coupling at the receiving modules input.

At each equipment location, the optical transmission is converted to single-ended TTL, and buffered as differential TTL. A fanout/repeater is utilized to generate multiple outputs. General purpose V108 Utility modules which receive the RTDL frames may be located in these area, as well as specially designed modules such as the V115 WFG, which have direct RTDL inputs. A block diagram of the overall system architecture is shown in figure 1, and the front panel layout for each module is shown in figure 2.

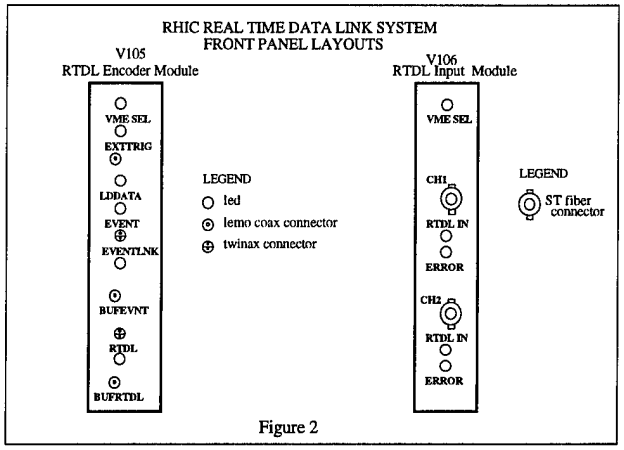

Figure 2

A hardware block diagram for the V105 and V106 modules is provided in figure 3. The V105 Module contains a VME bus interface, RHIC event link interface, the custom interface (local) bus control circuitry, the parameter ID SRAM and the link encoder circuitry. The V106 module contains a VME bus interface, the direct machine parameter input interface and a custom interface (local) to the V105 module through user defined pins on the VME bus P2 connector.

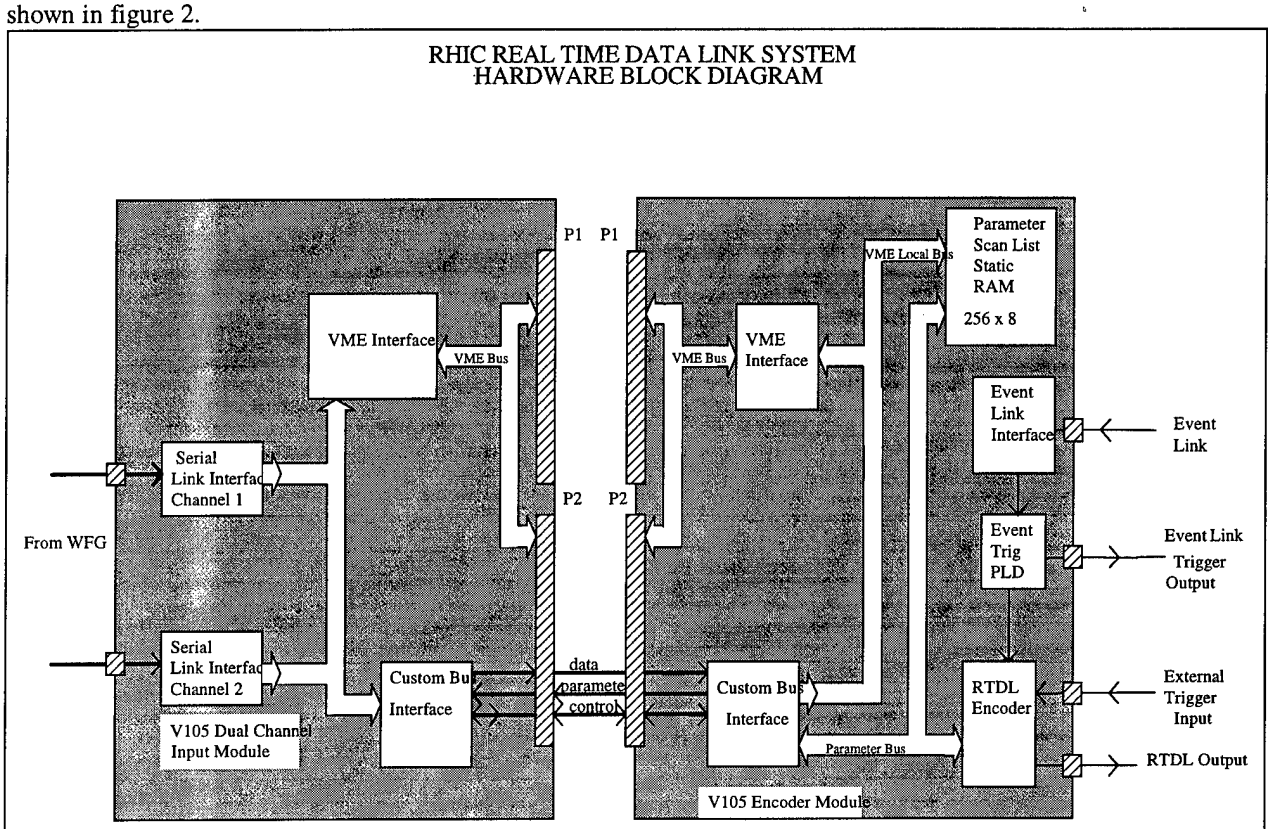

Figure 3

4 THEORY OF OPERATION

4.1 V105 Encoder Module

The V105 Module is a standard VMEbus 6U x 160mm module. It occupies 4HP of a standard 84HP VME chassis. This module directly outputs the encoded machine parameters onto the link. It accepts parameter data from the V106 modules via the custom interface bus. The V105 module controls the handshaking protocol on this bus.

The V105 Module converts each machine parameter acquired from the V106 from a serial NRZ into a serial bi-phase mark code for transmission. Parameter frames are permanenetly assigned a parameter ID code. Parameter transmission priority is defined in the parameter ID SRAM. The V105 module contains a RHIC Event Link interface which decodes the 720 Hz event, and initiates a transmission cycle synchronous with this event. For RTDL System diagnostic purposes, an external user supplied trigger or a RHIC Event Link trigger (other than the 720 Hz event) can initiate a transmission cycle. There is no system limitation that frames be transmitted in sequential order.

When the transmission cycle has been triggered, the following will occur:

a. A parameter ID code, which was previously defined in the SRAM, will be made available on the custom interface bus for all V106 modules to read.
b. The channel whose parameter ID matches the one placed on the bus, places its' machine parameter data on the custom interface bus.
c. Data is latched into the encoder modules' output register.
d. The RTDL encoder is triggered and the data is encoded and transmitted as one frame.
e. This process continues until all defined frames have been transmitted. The "end of list" is defined as 00h.

If any channel has not responded within 1μs, an interrupt will
be generated, and the parameter ID of the nonresponsive channel will be stored in the status register.

The V105 Module is a VMEbus slave. Status/ID registers (64 bytes), scan list RAM (256 bytes), and configuration registers are mapped to VME A16 space on a jumper selectable 512 byte boundary (A16..A9). VME data transfers supported include D16 and D08(EO), except for the scan list RAM, which allows D08(EO) only. BLT (block mode transfer) is not supported.

4.2 V106 Input Module

The V106 Module is a standard VMEbus 6U x 160mm module. It occupies 4HP of a standard 84 HP VME chassis. Each module has two input channels. Parameter data to be transmitted on the link can be input from one of two sources:

a. various system sources on unique serial fiber optic links .
b. written to the individual channel via the VMEbus interface.

Separate registers are provided on each input channel for storing both the machine parameter data and VME supplied data. A command to each channel input selects the source of the data to be transmitted on the link. A strobe, synchronous with the 720 Hz event, transfers the content of the selected source register for each input channel to its respective output register. The content of both the machine parameter data register and the VME register can be read through the VMEbus interface. The parameter ID for each input channel is jumper selectable on the input module, and can be read via the status register.

When the V105 module initiates a transmission cycle and places a parameter ID on the custom interface bus, the following will occur:

a. All input channels will decode the parameter ID.
b. The channel that matches the code placed on the bus places the contents of its output data register on the custom interface bus and completes the data transfer by asserting a data acknowledge strobe.
c. Custom interface bus cycles continue until all channels have been polled.

The V106 Module is a VMEbus slave. Status/ID registers (64 bytes) and configuration registers are mapped to VME A16 space on a jumper selectable 256 byte boundary (A16..A8). VME data transfers supported include D16 and D08(EO). BLT (block mode transfer) is not supported.

5 REFERENCES

[1] Ducar, R. J. , *CAMAC 166 Module - MDAT Transimitter,* Fermi National Lab Controls Hardware Release No. 45.3, 8/25/88.

[2] Hartmann, H. , *Specification for the RHIC Real Time Data Link System* , 10/23/93, unpublished.

EVALUATION OF IEEE 1394 SERIAL BUS FOR DISTRIBUTED DATA ACQUISITION*

T. J. Shea, J. A. Mead, P. Cerniglia, C. M. Degen
Brookhaven National Laboratory, Upton, NY 11973

Abstract

One trend in accelerator instrumentation is the digitization of signals further upstream in the signal processing chain. In some systems, this leads to distributed data sources that must be interconnected in a standard way. IEEE 1394 Serial Bus provides a possible interconnection standard for these systems. With Serial Bus, data acquisition is implemented via memory to memory transfers within a distributed 64 bit address space. Because this functionality is provided in silicon, software overhead is significantly reduced. This technology is under evaluation for use in the RHIC position monitor system. Using this example system, the suitability of IEEE 1394 for the accelerator environment will be described. Also, the results from recent tests will be presented.

I. INTRODUCTION

Before the introduction of card modular packaging like CAMAC and VXI, electronic instrumentation was typically housed in separate chassis and interconnected with cables. Modular systems introduced standard packaging that allowed inter-module communication via a well defined parallel backplane. Additional benefits include compactness and the convenience of a shared power supply. Although this packaging works for most accelerator instrumentation systems, some applications could benefit from the old separated chassis solution. Examples include: systems with large components that make inefficient use of circuit board real estate, distributed systems that must consolidate data from digitizers located close to the signal sources, and high performance devices that must operate in a controlled environment. After the decision is made to remove devices from the backplane environment, the requirement for data communication remains.

In this brief paper we cannot compare the many communication standards that could connect separate chassis. Of the many standards available, the IEEE1394 Serial Bus[1] offers a reasonable trade-off between cost, performance, and distance. Also, the standard is based on a memory mapped model that allows simple bridging to existing VME/VXI systems. Silicon support and industry acceptance is growing. The RHIC beam instrumentation group is evaluating IEEE1394 for use in the position monitor system.

* Work supported by the U.S. Department of Energy

II. OVERVIEW OF IEEE1394 SERIAL BUS

Some of the most important Serial Bus features are listed below:

- Memory mapped model based on the IEEE 1212 Command and Status Register (CSR) standard with a 64 bit addresses.
- 100, 200, or 400 Mbits/s bandwidth. Work is in committee to extend the standard to 3.2 Gbit/s.
- Hot pluggable and self-configuring.
- Asynchronous (guaranteed delivery) and isochronous (guaranteed bandwidth and latency) data transfers are supported.
- Up to 4.5 meters between nodes, 72 meter total length. Work is in progress to extend to much longer distances.
- Cable or backplane environments. The cable environment is specifically designed for low emission and susceptibility.
- Point-to-point signal transmission. Each node re-clocks data before re-transmission.
- Cost effective: Silicon cost $30USD/node in 1997.

The memory mapped model makes the protocol fairly efficient. In fact, memory to memory transfers between nodes can be supported in silicon with no software overhead. However, latency is only guaranteed at the 125 μs level. To maintain efficient media use, split transactions are supported. When bridging Serial Bus to a backplane bus that does not support split transactions (like VME), some decoupling must be provided to avoid backplane bus time-outs.

Although this standard was developed for short haul communications in consumer-oriented multimedia systems, it has potential for longer distance operation and for industrial applications. A 1394 system with 100 meter hops over plastic optical fiber has been demonstrated as part of the home network initiative[2]. The noise immunity and isolation provided by this solution would be welcome in the accelerator environment. One of the earliest deployments of 1394 in an industrial application is an electrical power network simulator developed by Sederta for

0-7803-4376-X/98/$10.00 © 1998 IEEE

HydroQuebec[3]. Installed at Mitsubishi in Kobe, Japan in July 1996, the first system consists of 8 SUN workstations with two 1394 interfaces each, 75 VME based PowerPC CPU nodes with two 1394 interfaces each, and 120 I/O nodes each containing 4 Industry Pack sites and one 1394 interface.

III. RHIC POSITION MONITOR APPLICATION

The RHIC position monitor system includes over 600 channels (planes) of electronics, each housed in their own chassis. Because there are only six major equipment buildings external to the tunnel, most channels will be located in the tunnel, adjacent to their corresponding position monitor. This arrangement improves performance and tremendously reduces cable cost. Where the position monitors are located near the equipment buildings or in high radiation areas, signals will be cabled out of the tunnel on pairs of high quality, phased matched coax. The electronics chassis will be identical for all channels. The distributed chassis will be mounted above the magnet cryostats while the others will be rack mounted.

Each channel contains two 16 bit samplers operating at a nominal rate of 78 kSamples/s (the revolution frequency of RHIC). An onboard DSP provides buffer maintenance, digital filtering, local control, and built in self test features. Data communication between the position monitor modules and the VME based control system will be provided by approximately four independent IEEE1394 buses per VME system. Each bus will contain about 12 nodes with each node separated by up to 20 meters. Achieving reliable communication over these distances in an accelerator's EMI environment is the early goal of our evaluation program.

Each distributed channel will continuously update a circular buffer with averaged beam position records. These records are typically calculated at a rate of about 100Hz. The buffer will be located in VME-resident memory that is bridged to a portion of the Serial Bus' 64 bit address space. In addition, a subset of channels may be selected to stream turn-by-turn position samples into VME memory. To allow efficient use of bus bandwidth, the Serial Bus asynchronous block transfer capability will be used. Although isochronous transfers would provide the most efficient bus utilization, guaranteed delivery is more important at this low level of the data acquisition chain. Therefore, the system will allow a retransmission of corrupted packets (as identified by the built in 32 bit CRC circuitry). This capability is only available to asynchronous transfers because they include an acknowledgment packet for every transfer.

Two 1394 mezzanine cards have been designed and constructed for this application. The first, an Industry Pack supporting the 100Mbit/s rate has been used to exercise basic 1394 functionality and to demonstrate packet transmission over a 20 meter long cable. The second, a PCI Mezzanine Card (PMC) is a candidate for use in the final system and will be used in a 12 node demonstration system by late 1997.

IV. THE 1394 INDUSTRY PACK

The Industry Pack 1394 module (IP1394) is a double wide Industry Pack[4] that uses the first generation Texas Instruments 1394 chip set, namely the TSB12C01A link layer controller and the TSB11C01 physical layer controller. A block diagram of the IP1394 is shown in Figure 1.

This module was constructed in 1995 and primarily used as a stepping stone to the final module, the PMC1394, which will be described later in this paper. The Industry Pack Interface Bus permitted us to use an existing VME-based carrier board, which contains a DSP96002[5]. The DSP96002 assembles/disassembles packets to/from the 1394 bus and provides bridging between 1394 and VME address spaces.

The TSB12C0l link layer controller provides all necessary control and status registers, as well as three FIFOs for sending and receiving packets. To transmit a packet, quadlets are written to the Asynchronous Transmit FIFO, or the Isochronous Transmit FIFO, depending on the type of transaction required. These FIFOs are written one quadlet at a time until the complete packet is in the FIFO. The TSB12C01A then requests the bus through the TSB11C01. The TSB11C01 arbitrates for the bus and upon successful arbitration forwards the packet from the TSB12C01 onto the 1394 bus. Incoming packets are received by the TSB11C01, retransmitted out its other two ports, and forwarded to the TSB12C01 if the bus and node number are a match. To read the incoming packets, the General Receive FIFO on the TSB12C01 is read, one quadlet at a time until the entire packet is received.

The major limitation of the IP1394 is its lack of galvanic isolation between the Link Layer Controller and Physical Layer Controller. This creates ground loop problems when attempting to use multiple IP1394

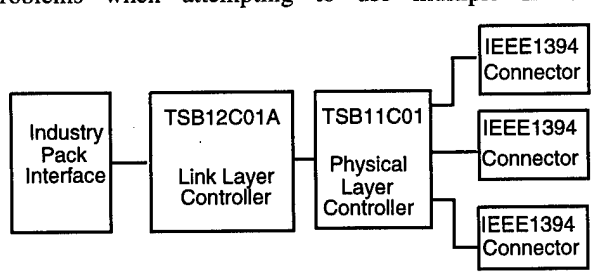

Figure 1. Block Diagram of IP1394

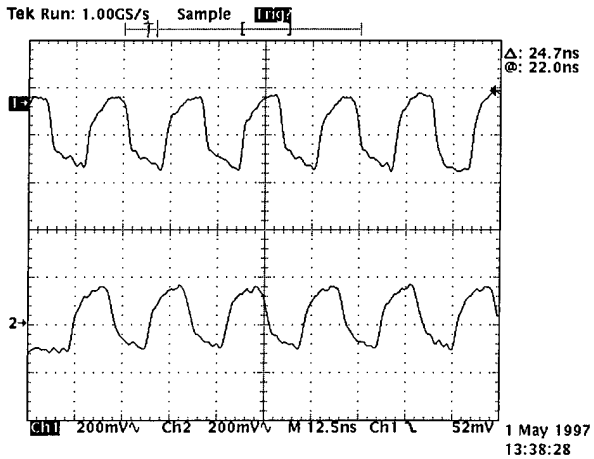

Figure 2. 100 Mbit/s data over 20m cable (top: input, bottom: output)

modules powered from different supplies. This problem has been addressed in the PMC1394 module.

Figure 2 shows a sample waveform of the 1394 strobe line transmitted by the IP1394 for a single data quadlet packet over a 20 meter cable. The cable was specifically designed by C&M Corporation for 1394 transmissions up to the 200Mbit/s rate. Signal fidelity at 100 Mbit/s is good enough to expect adequate reliability.

V. THE 1394 PMC BOARD

The 1394 PMC[6] board (PMC1394) uses the Texas Instruments TSB12LV21 (PCILynx) and TSB21LV03 (PCIPhysical) chip set with the isolation feature implemented. The PCILynx IC provides a high performance IEEE1394 interface with the capability to transfer data between the 1394 physical link interface, the PMC bus interface and external devices connected to the local bus interface. It contains the link layer controller (LLC) which is the control for transmitting and receiving 1394 packet data between the FIFO and physical layer IC at 100, 200 or 400 Mbps and allows access to the physical IC control and status registers. The PMC interface supports 32 bit burst transfers up to 33 Mhz. The PCILynx IC also includes a DMA controller with 5 DMA channels, as well as a local bus interface consisting of RAM, ROM, AUX, ZV (video), and GPIO (general purpose I/O). Only RAM and GPIO are implemented on the PMC1394 board. There are 4 GPIO ports with status monitoring LEDS and 32K x 16 bits of RAM. The board includes a 2K serial eeprom allowing the loading of configuration registers and unique identification codes.

The IEEE1394 cable carries data at various rates and also sources/sinks power to/from remote nodes. This allows nodes that either do not have their own source of power or have their power turned off to continue to function as repeaters in the IEEE1394 network. The PMC1394 board conforms to the requirements set forth

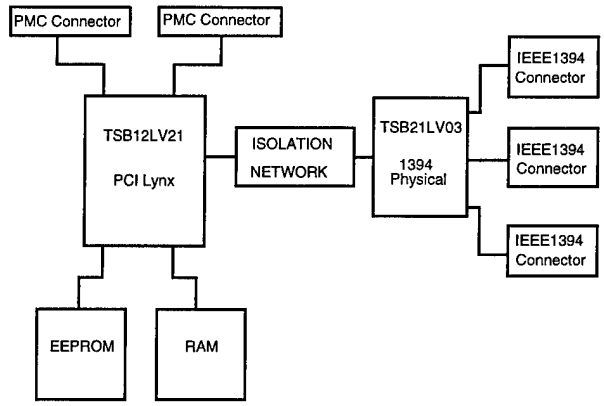

Figure 3. Block diagram of the PMC1394

in the IEEE1394-1995 specifications for isolation concerning shield termination, cable power isolation and signal isolation. The board achieves signal isolation by using the method known as a bus holder galvanic isolation barrier. It consists of a series isolation capacitor between each of the PCILynx and PCI Physical IC's signal lines with CMOS bus holders on each side of the capacitor. Control lines are isolated by using opto-isolators. Power isolation is handled by a DC-DC converter for 1394 cable power. The cable shield is isolated per the specification by connecting the outer cable shield to ground through a parallel combination of a 1 M ohm resistor and a 0.1 microfarad capacitor to provide a relatively high impedance coupling at low frequencies and a relatively low impedance coupling at high frequencies.

VI. FUTURE WORK

A demonstration system consisting of 12 nodes with a hop length of up to 20 meters will provide confirmation of a reliable operation. This demonstration in a high EMI environment will be required before procurement of the RHIC position monitor electronics. Performance optimization will then commence.

VII. REFERENCES

[1] IEEE 1394-1995, High Performance Serial Bus, D8.

[2] Private communication, Patrick Yu, NEC Corporation.

[3] Private communication, Christophe Brayet, Sederta Corporation. See also http://www.sederta.com.

[4] VITA 4-1995, Draft 1.0.d.0 IP Module Draft Standard.

[5] J.A. Mead, T.J. Shea, A DSP Based Data Acquisition Module for Colliding Beam Accelerators, Proc. 6th Int'l Conf. On Signal Processing, Boston, MA, 10/24-26/95 pp. 455-459.

[6] IEEE 1386.1, Physical/Environmental Layers for PCI Mezzanine Cards, PMC.

PRECISION TIMING CONTROL SYSTEM

Robert E. Meller
Cornell University, Ithaca, NY 14853 *

1 INTRODUCTION

Operation of the CESR storage ring with complex bunch patterns has made necessary more flexible timing controls. Multiple trains of bunches based on a fundamental spacing of 14 ns are used in both the injector and the storage ring. Hence, a generally programmable trigger pattern is needed for electron gun pulsing, beam detection, beam feedback gating, and RF phase control. To achieve this, an upgrade of the previous CESR timing system[1] using small-feature CMOS logic has been built. The new system has a time delay resolution of 10 ps and RMS jitter of 14 ps. The delay transfer function is linear to within 30 ps, and is monotonic over 32 bits of range. The use of programmable large-scale integrated circuits and the VME packaging system results in a system that is contained in 4 crates and occupies a fifth of the volume of its predecessor.

1.1 Design objectives

The previous CESR timing system had a resolution of 160 ps, which was soon found to be inadequate. It consisted of several hundred circuit cards, most of which were 8-bit timers. These were connected point-to-point with coaxial cables to obtain concatenated delays of sufficient length and precision. The precision functions were implemented with ECL logic, and hence there were a large number of power supplies which were also the main source of failure. The system had grown to occupy a volume of about 2 cubic meters, a quarter of which was power supplies.

The main objective of the timing upgrade was to improve the resolution and flexibility of the system. Resolution of 10 ps was chosen as a practical limit of the CMOS technology that is easily available. The system must also be able to generate arbitrary bit patterns at a 14 ns clock rate. Another objective was flexible configuration of the system from data files rather than by point-to-point connections, and testing of the system by software. Additional objectives were standard and compact packaging with a minimum number of power supplies.

2 SYSTEM DESIGN

2.1 Clock frequency

The fundamental period for CESR bunch loading is 14 ns, corresponding to a frequency of 71.4 MHz and 183 buckets per CESR revolution. This frequency is within reach of LSI logic devices, but it is very inconvenient for synchronous interconnection of a large system. A period of 42 ns was chosen for the timing system clock, corresponding to a frequency of 23.8 MHz. This frequency is the lowest common multiple of the revolution frequencies of CESR and the injection synchrotron. Multiplication of the clock to 71.4 MHz is only done where bit patterns are needed.

2.2 Logical organization

The standard timing channel is based on a 20 bit counter which operates synchronously at the 42 ns clock period. The counter is loaded from either of two 20 bit registers, which can control either pulse delay, width, or period. The counter has a start and stop input, and can be programmed to issue pulses singly or periodically when started, with or without a software enable. Both phases of the clock are used to give the output pulse 21 ns delay resolution. The range of the counter is about 44 ms, which exceeds the 16.7 ms injection cycle time. This unit provides most of the needed timing functions, and is implemented in a single CMOS logic array, with 8 channels on a single 6U VME card.

Eight trigger signals are bussed cratewide through the P2 backplane, and each standard timing channel has a pair of programmable gates which derive the start and stop inputs as coincidence functions of any of the 8 triggers. Each standard channel has the capability of driving a trigger signal on its own card, and each trigger signal is passed between the card and crate backplane by a bidirectional buffer. Hence, each trigger signal can be driven externally, or by a timing channel either cardwide or cratewide. This permits any portion of the system with complex cross-connections to be confined to a single card, without using cratewide connection resources.

The precision timing channel consists of a standard channel, followed by two optional modules for the precision functions: The precision delay performs a 12 bit phase shift of the 42 ns clock, which gives 10 ps delay resolution. The pattern generator multiplies the phase-shifted clock to 71.4 MHz and uses it to clock a bit pattern from a random-access memory. Two precision channels are provided on a single 6U VME card, along with a power converter which provides low-ripple +5 V for the precision components. The precision output drivers issue both the 71.4 MHz clock and the bit string so that the timing of complex bit patterns can be reconstructed by the receiver without the distortions caused by cable dispersion: When a pulse signal is sent down a cable, each pulse develops a tail which interferes with the timing of any closely following pulse. However, since the clock is periodic, the effect of dispersion is only a uniform phase shift. If the bit string is resynchronized to

* Work Supported by the National Science Foundation

the clock at the destination, then the dispersion of the bit string signal is irrelevant as long as it satisfies a setup time relationship with the clock signal.

Each timing crate is self-contained, and supports between 32 and 128 timing channels. Hence, each crate is an independent timing system, and typically requires only a clock input and two trigger inputs to synchronize it with other timing crates. This allows the overall timing system to be substantially de-centralized.

2.3 *Software control*

The VME bus controller is a MVME162 microcomputer. This unit has a 68040 microprocessor with extensive resources of RAM and ROM. The microprocessor code is stored in battery-protected static RAM, and will run automatically when the crate is powered up. The entire configuration of the timing system is down-loaded from the CESR control system via a custom serial interface when the system is initialized. The configuration consists of mode controls and interconnections for the standard timing counters, formulae for the numbers to be loaded into the timing registers, bit patterns to be loaded into the pattern generator RAMs, and also test masks to be used to verify installation of the correct timing hardware. After the initial configuration, the serial interface transmits commands from the control system. These commands are usually adjustments to timing numbers or channel enables/disables, but can include reconfiguration of any parameters except the hardware tests.

The MPU code which performs real-time control of the timing channels is executed at 60 Hz, synchronous with the accelerator injection cycle. During the idle period between injections, the MVME162 program performs all necessary setup for the next injection cycle. These operations include enabling or disabling timing outputs, loading values into the timing registers, loading bit patterns, and possibly reconfiguring the modes and connections of the timing channels. During the injection cycle, the MVME162 services command requests.

2.4 *Automatic testing*

When the system is initialized, each timing channel is polled for a hardware identification number. This indicates the card type, and also identifies the optional components associated with it, such as the output driver and any precision timing modules. Each module socket has pins that are reserved for identification codes that are unique to each module type. Before a channel is initialized, its polled identification is compared against a number downloaded with the other initialization data. Hence, the possibility of unknowingly installing incorrect hardware is eliminated.

The output pulse drivers support two test functions: The pulse output is continuously checked against the logic input to detect short circuits or driver failures. The output is also applied to a coarse aperture (42 ns) sampling gate. The sampling trigger is generated centrally and routed to all channels via the P2 backplane. These are used to implement a logic analyzer which can be used to examine timing outputs from any control system terminal.

2.5 *Mechanical design*

The system is built on the VME 6U format, with both P1 and P2 backplanes extending over 21 card slots. Each crate has 16 slots reserved for timing cards and 4 slots for support functions. The output pulse drivers are on separate 3U VME cards which plug into the back of the P2 backplane connectors. This allows a variety of logic standards to be used with one type of timing card, and also simplifies repair and noise isolation.

Each crate has a self-contained power supply, and the entire system is operated on +5 VDC. The +/- 12 VDC supplies are used only by output pulse drivers which are required to issue non-TTL logic levels. The precision timing cards require forced air to operate, which is provided by a single-height fan pack mounted below the crate.

3 METHODOLOGICAL DETAILS

3.1 *Phase shifter design*

The essential component of the precision phase shifter is a linear phase detector. The phase of two clock signals is compared, and the phase of the slave clock is adjusted through a phase-locked loop to make the measured phase equal to the command phase. Conceptually, the phase detector consists of two latches: One latch is set by each of the clock signals, and when both are set, they are reset simultaneously. If the latches are implemented in CMOS logic, then the output levels are VDD and 0, and when the two outputs are subtracted in a differential amplifier, the result is VDD $\Delta\phi/(2\pi)$. The phase shift can be made independent of VDD by obtaining the phase command from CMOS data latches also: The 12 bit command is latched in a CMOS register and converted to analog by a R-2R ladder network. Hence the digital phase command N gives an analog result of VDD (N - 2048)/4096 in offset binary code. If this and the phase detector output are nulled in a bridge circuit, the resulting transfer function is $\Delta\phi = 2\pi$ (N - 2048)/4096, and is independent of voltage. This was implemented with a custom metal-film resistor network which combines the DAC ladder network with the necessary matched balancing resistors for the phase detector pulses.

The use of a precision bridge network means that the accuracy of the phase shifter only depends on the accuracy of the phase detector. Standard flipflops are generally not suitable for this use, however, since the internal timing paths are not constant. For example, a D-type flipflop may have different signal paths from reset to Q, depending on the level of the clock input. The design currently in use uses a high-speed logic array to anticipate the latch states and steer the correct signal edges through a CMOS multiplexer, thus emulating an ideal CMOS latch with constant

internal delays.

Assuming an ideal latch circuit, the limits on phase detection linearity are due to crosstalk and damping of transitions. Damping is significant because the logic transition waveforms subtract out of the phase detector function only if they damp out completely before the next transition. The damping time of the transitions depends mainly on the parasitic inductance of the integrated circuit package. With a 42 ns clock period, the damping time available in the worst case is 10 ns, and this is not sufficient even with surface-mount circuit packaging. The damping problem has been solved by only operating the phase detector on alternate cycles and doubling the gain.

Crosstalk between the two phase pulses is more problematical. The most significant coupling is through the power supply, and 6 decoupled VDD circuits are used in this design. However, there is a risk of capacitive coupling wherever there is a logic element shared between the two phase detector channels. This problem is compounded by general ignorance of the internal design of commercial integrated circuits. The author's opinion is that most of the nonlinearity displayed in figure 1 is due to this type of crosstalk. A custom integrated circuit implementation of an ideal linear phase detector is under design and nearing completion.

3.2 *Pattern generator design*

The pattern generator is straighforward except for the frequency multiplier. The multiplier uses a phase-locked loop design with a phase detector similar in principal to the one used in the phase shifter. This type of phase detector has the advantage that if a good differential amplifier is used to subtract the phase pulses, then the phase output is DC at zero phase, and hence free of subharmonics which would modulate the oscillator.

4 PERFORMANCE

The test results were obtained from two precision timing channels: One channel is used to phase-lock the low-noise crystal oscillator which serves as the CESR RF frequency source. The oscillator is 500 MHz, or 21 times the clock frequency. The second timing channel is used as a trigger for an HP54120A sampling oscilloscope. The data points are the mean and σ of 500 sample histograms taken of the RF waveform for various settings of the phase command to the oscillator. Hence, the phase mean is the transfer function of the first timing channel, but the noise is substantially from the second channel.

Figure 1 shows the RF phase as the phase shifter is advanced by whole wavelengths through a full clock cycle. An ideal linear transfer function would give identical phase for each measurement. Figure 2 shows the phase shifter wrapping from full count to zero, and hence that the gain is accurate to 12 bits and that the transfer function is monotonic over this transition.

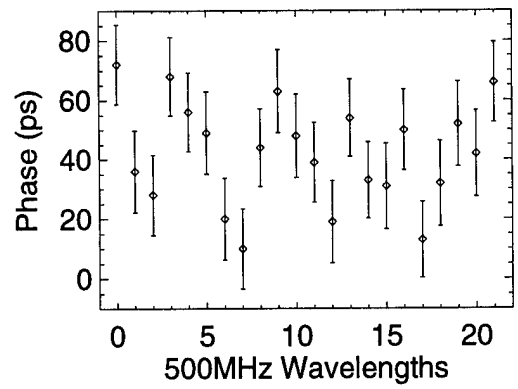

Figure 1: Phase of 500 MHz RF shifted by an integer number of wavelengths.

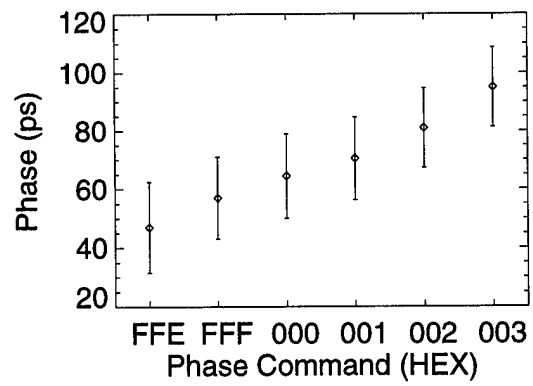

Figure 2: Phase shifter output across major carry transition.

5 ACKNOWLEDGEMENTS

Thanks to Meredith Williams for printed circuit design, and to Peter Quigley for integrated circuit design.

6 REFERENCES

[1] R. E. Meller, IEEE Trans. Nucl. Sci., Vol. NS-26, No. 3, p. 4152 (June 1979)

IMPLEMENTATION OF A NEW RF MONITORING SYSTEM FOR THE SRS USING LABVIEW

M.J.PUGH, A.R.MACDONALD, CLRC, Daresbury Laboratory, Warrington, WA4 4AD, UK.

Abstract

The SRS Computer Control System is undergoing a programme of upgrade from a system of Concurrent Computer Corporation mini computers to a network of PCs [1]. The old RF monitoring system, based on CAMAC hardware, has been replaced with two Industrial PC front end computers running Windows 95 and controlling Hewlett Packard instrumentation and Eurotherm Temperature Controllers. Measurements on the new system are now performed using the data acquisition software LabVIEW® combined with standard PC cards for GPIB and serial communication. This paper describes the hardware and software used in this project, and also how it has been interfaced onto the existing SRS ISOLDE PC control system.

1 INTRODUCTION

The Daresbury SRS is a second-generation light source based on a 2 GeV electron storage ring. The current control system upgrade programme, based on the CERN PS ISOLDE Control system [2,3], is being introduced progressively. The main magnet power converters and steering system have now been in routine operation on the new control system for some time [4].

One of the new projects taking place is the development of an RF monitoring system using LabVIEW® on a PC running Windows. This will be used for monitoring the RF systems' parameters as well as control of the klystron voltage ramp procedure and will be integrated into the ISOLDE system.

2 THE UPDATED SRS RF MONITORING SYSTEM

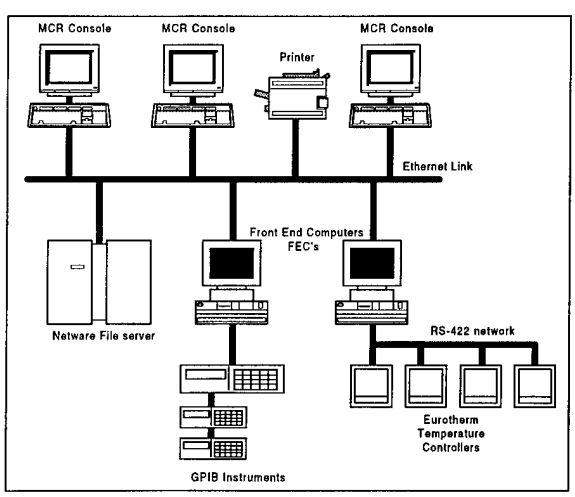

Figure 1: Diagram showing the layout of the system.

An overview of the new system can be seen in Figure 1. Both of the new RF Front End Computers (FECs) are installed, along with all the instrumentation within a single nineteen inch rack.

2.1 RF Power level monitoring

Upon the SRS RF system, twenty three independent RF power signals are currently monitored. This is achieved by using an Industrial enclosed Pentium 100MHz PC, as the Front End Computer, to perform all the processing of the signals and control of the ISA hardware inserted within it, and external Hewlett Packard 3488A Switch/Control unit and 437B Power meter. Windows '95 is used as the operating system.

Each signal is connected to the HP Switch/Control unit and fed through, in turn, to the HP power meter. The resulting power levels are analysed by the National Instruments LabVIEW® data aquisition and control software on a GPIB bus through a National Instruments AT-GPIB/TNT(PnP) 16bit card. All the power levels received are displayed on a graphical representation of the SRS RF system, showing the exact position of the signal in the RF system and the status within a predetermined range.

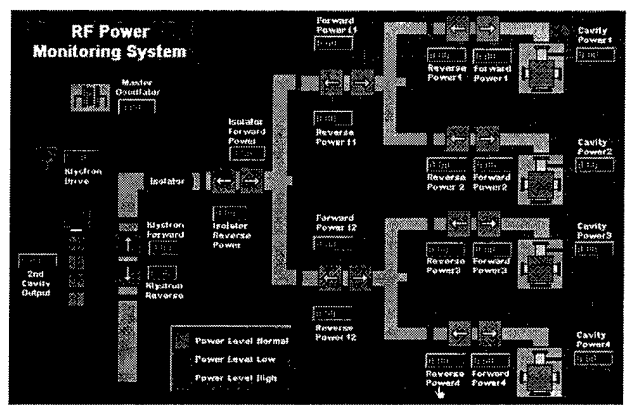

Figure 2: RF Power Monitoring application on the remote console in the SRS control room.

All of the power signals are displayed in watts and a colour coded status warning is included.

2.2 RF system Klystron Efficiency and Flow Monitoring

The second of the two FEC's analyses data from the RF systems water cooling network of flow meters. Seven flow meters are present in the network. This PC is also

Pentium powered installed within an Industrial enclosure running at 133 MHz but using Windows NT Workstation Version 4.0 as its operating system. Again, all the programming is done using LabVIEW® to read back the rates of flow from each of the seven meters in turn and display the outputs on a graphical front end display. Using the rate of flow of the cooling water through the klystron, along with the differential temperature change of the klystron's output, (the differential temperature change being available through a TCP/IP connection from the temperature monitoring LabVIEW® program running on FEC1), it is possible to calculate the klystron's efficiency.

$$\textbf{Efficiency} = \frac{\textbf{Output Power (in KW)}}{\textbf{Input Power}} \times 100\%$$

$$= \frac{\textbf{K} \times \textbf{Differential Temperature change} \times \textbf{flow}}{\textbf{Klystron Voltage} \times \textbf{Current}}$$

Where :

Differential Temperature Change = differential change in temperature calculated in the Temperature Monitoring LabVIEW® vi (Degrees Celsius).

K = 0.3172 if Flow is measured in gallons/minute
= 0.06979 if Flow is measured in litres/minute

This can also be displayed remotely on the control room console.

2.3 RF system temperature monitoring

The temperature monitoring system uses the same Industrial P100 PC as its Front End Computer. There are nineteen temperature levels that are monitored within the RF system through an RS-232 and RS-422 link using three different types of hardware monitors.

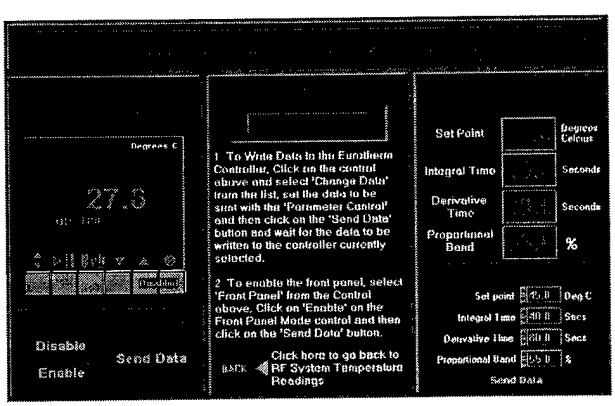

Figure 3: The LabVIEW® cavity body temperature control application for a Eurotherm 902s Controller.

On each of the four cavity bodies are Eurotherm 902s controllers, on the cavity windows are infra-red temperature detectors and to monitor the rest of the RF system, an Anafaze Independent Alarm Scanner (IAS) is used. The latter simply scans through all of its connected thermocouple inputs and downloads the data to the FEC via the RS-232 COM port on the rear of the FEC. The Eurotherm 902s controllers not only monitor the temperatures of each of the four cavity bodies but can alter the temperatures by changing the rate of flow of cooling water through the cavity bodies. The controllers are communicated with via a National Instruments 2-port RS-485 interface 16bit card. Remote operation of the cavity body temperature control is available from the SRS control room only by specified users with password protection.

3 KLYSTRON VOLTAGE RAMP PROCEDURE

3.1 Updated procedure for ISOLDE control system

The second Front End PC also controls and monitors the klystron voltage ramp procedure; parameter name PROG. This is achieved through LabVIEW® using National Instruments NI-DAQ software and an AT-MIO-16XE-50 data aquisition ISA card, as shown in Figure 4.

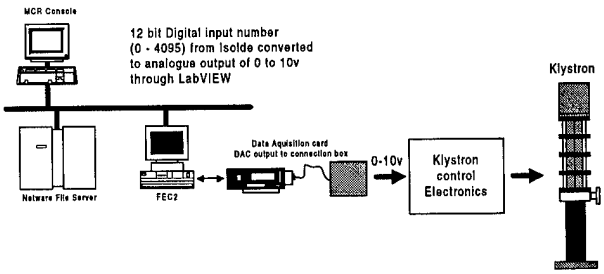

Figure 4: Diagram of hardware used for controlling klystron voltage.

The ISOLDE control system sends the FEC a ramp table over the etherlink connection. This table is in the form of a series of consecutively increasing numbers along with a time in which the step up in voltage should occur. A LabVIEW® program interprets the input table and converts the control values to a voltage out between zero and ten volts through the 16-bit DAC on the data aquisition card. (Using the on board ADC on the same card, the output voltage is analysed.) This voltage is then connected to the klystron voltage control electronics.

4 INTEGRATING TO THE ISOLDE CONTROL SYSTEM

4.1 Porting The ISOLDE Software to Windows NT.

As it was intended to implement the RF control system using LabVIEW® running under Windows 95/NT, it was necessary to port the 16-bit DOS based front end software and equipment modules written in 'C' to Windows NT. This has been done using the 32-bit Visual C++ Version

2.0. Network connections are now handled through the Winsock API rather than the PC/TCP socket library used under DOS and has been made multi-threaded to handle network requests and user input more effectively. All configuration information is now stored in the system registry, but the software still makes use of Excel CSV formatted database files.

4.2 OLE Database Server

It has been necessary to store the most recently monitored values in memory to be read back when a parameter is requested. This is because the SRS ISOLDE system has a timeout of 2 seconds for an acquisition, which is shorter than the time it takes to read a power level. Ideally, this would have been done by using LabVIEW® as an OLE server and the FEC process retrieving the value through an OLE method. However, as LabVIEW® can only act as an OLE client, this has been achieved by using a separate out-of-process OLE server which LabVIEW® writes to and the FEC reads from. The OLE server has been implemented using Visual Basic and is flexible in that extra parameters can be added simply by inserting an extra line into the parameter database file.

4.3 Klystron Ramp and Temperature Control

There is an element of control required through the ISOLDE system for ramping the klystron and controlling the cavity temperatures. A separate LabVIEW® VI has been written to cope with this and communicates with the FEC process using TCP, residing on the same computer. This LabVIEW® VI can then control the hardware using the same sub-VIs which are used for local control.

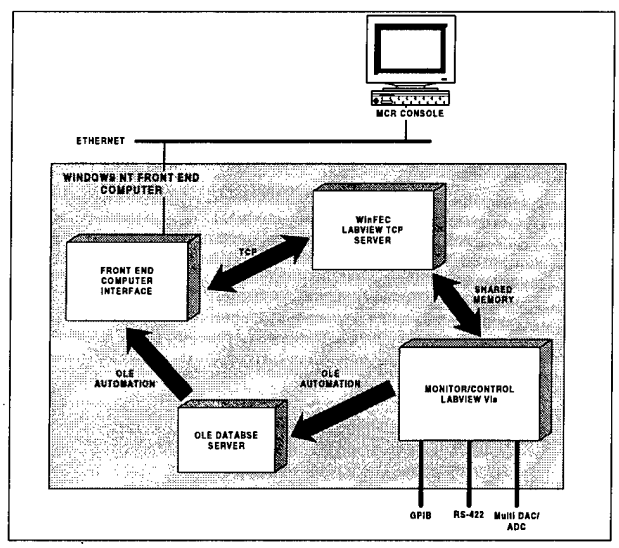

Figure 5: Diagram showing data flow in a Windows NT FEC.

An equipment module has been written to allow klystron ramp tables to be loaded remotely from the control room which can be executed or aborted on request. This software has only been tested with the DAC output connected to a chart recorder but gives expected results. It is planned to integrate this into the ramping of the main dipole magnets which are already controlled through the ISOLDE system. The temperature control software has been implemented but is untested.

Due to some doubts over the stability of software running on a Windows PC using LabVIEW®, the Windows NT machine has been set up so that the PC automatically reboots itself if the program crashes. On restarting, the software will load again and can continue to operate as before. This could be done without losing a user beam as the DAC outputs are not reset.

An overview of the software used to provide the interface to the Daresbury ISOLDE system can be seen in Figure 5.

5 CONCLUSIONS

Although there is still some work to be done in completing this project, it has been successful up to now. The RF power and temperature parameters can be monitored locally and in the control room over the network with a clear graphical representation of the RF system. The cavity temperatures can be controlled locally and the klystron voltage can be ramped.

There are already plans to re-use the Windows NT ISOLDE software to integrate small stand-alone systems onto the main control system, including beam profile measurements made in the SRS Synchrotron Light Area. LabVIEW® still has its own problems though as it is very memory and processor hungry and there are still some doubts over its stability. However, it would have been unlikely that such a project could have been undertaken by a non-programming specialist, if it had been implemented as a traditional front end computer using 'C'.

REFERENCES

[1] Planned Upgrades to the SRS Control System, B.G.Martlew, M.J.Pugh, W.R. Rawlinson, Proceedings of the 4th European Particle Accel. Conf. London 1994, pp 1788-90.

[2] I.Deloose, A.Pace, "The ISOLDE Control System", Proc. of the 1993 International Conference on Accelerator and Large Experimental Physics Control Systems, Berlin.

[3] I.Deloose, "Dynamic Link Libraries to access the Windows RPC Server, Error Server and Excel Databases", European Organization for Nuclear Reasearch, PS/CO/Note 93-01.

[4] B.G.Martlew, M.J.Pugh, W.R.Rawlinson, "Present Status of the SRS Control System Upgrade Project", Proc. of the 1996 European Particle Accelerator Conference, Sitges, Spain, pp1769-71.

COMMISSIONING OF SPRING-8 LINAC CONTROL SYSTEM

H. Sakaki, H. Yoshikawa, T. Asaka, T. Hori, Y. Itoh, A. Kuba,
A. Mizuno, S. Suzuki, T. Taniuchi, K. Yanagida, H. Yokomizo
SPring-8 Project Team, Kamigori, Ako-gun, Hyogo 678-12 JAPAN

Abstract

After a year from the installation of linac components, we have started the beam commissioning and accelerated the purpose energy. We think that the installation time is much short. As one of the answer of this, we follow the success of automatic RF conditioning. It works very good job, and the RF conditioning had finished for 400~550 hours. The conditioning system is based on VME computers and Work Station (WS).

And, at the beam commissioning, we have designed new type beam fluctuation monitor using image process. This monitor is very useful for the measurement of energy fluctuation.

In this paper we report the history of the construction and the beam commissioning on the linac control system.

Table 1: SPring-8 Linac I/O boards.The VME CPU board is operated by OS-9. These VME boards are installed into the VME cage which is taken aganist EMI.

Name	Function	Number of boards
MVME147s	CPU(68030)	21
AVME9350	AI(16ch)	34
AVME9210	AO(6ch)	25
DVME-DIN3	DI(64ch)	53
DVME-DOUT3	DO(64ch)	31
VPAK601	MotorControl(2ch)	55
EVME-GPIB21	GPIB	18
ADVME2210	JPEG image	1

1 THE HISTORY OF THE CONSTRUCTION

The SPring-8 injector linac was completed at end of July 1996, and the beam commissioning has begun since 1st August. At 8th August 1996, we succeed in the 1 GeV electron acceleration which is the purpose energy. Figure 1 shows the history of our project. Left parts shows hardware installation history, and right part shows software installation. The installation of hardware had started since June 1995. And the pre-alignment had started since October. Since February in 1996, the consistency test between hardware and software had started.

The linac is 140 meter long, and have many number of parameters. Table 1 shows the number of linac control parameters. These parameters is controlled by VME computers which are commercial product.

The total number of man-days that required for the consistency testing was about 10 people. Though the testing done a small number of people, we had no big trouble, and

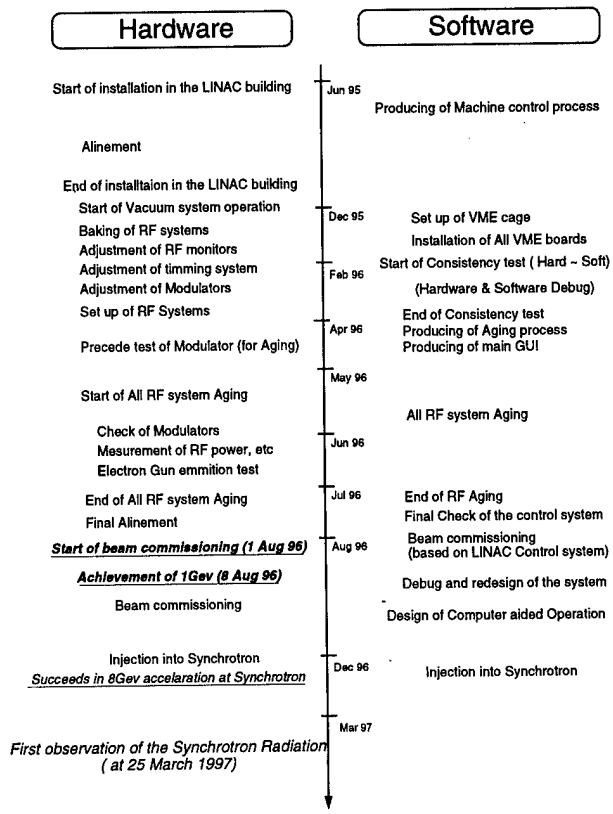

Figure 1: History of the soft and hard construction.

we could do the testing and checking smoothly. This test had done for about two month. In the testing, we took care of the electronic noise of linac component.

A rehearsal for the non beam linac operation has begun since a last week of July. And, we had started on the beam commitioning since August 1th.

2 THE PF CONDITIONING SYSTEM

2.1 *Guide line of automatic RF conditioning*

We choose 80MW klystron (Toshiba E3712, 2856MHz) RF system. The number of E3712 are 13, and usually drive one about ~60MW, ~60pps, ~3μsec[1]. We must achieve near this power until the beam commissioning. However, if the conditioning start, we have to work night and days for this plan. Because, the conditioning staff have very few. For these problems, we designed the automatic RF conditioning system[2]. Figure 2 shows sequence for the automatic RF conditioning system. This sequence was get from the precede test of RF component. These sequence was operated in the VME computers.

0-7803-4376-X/98/$10.00 © 1998 IEEE

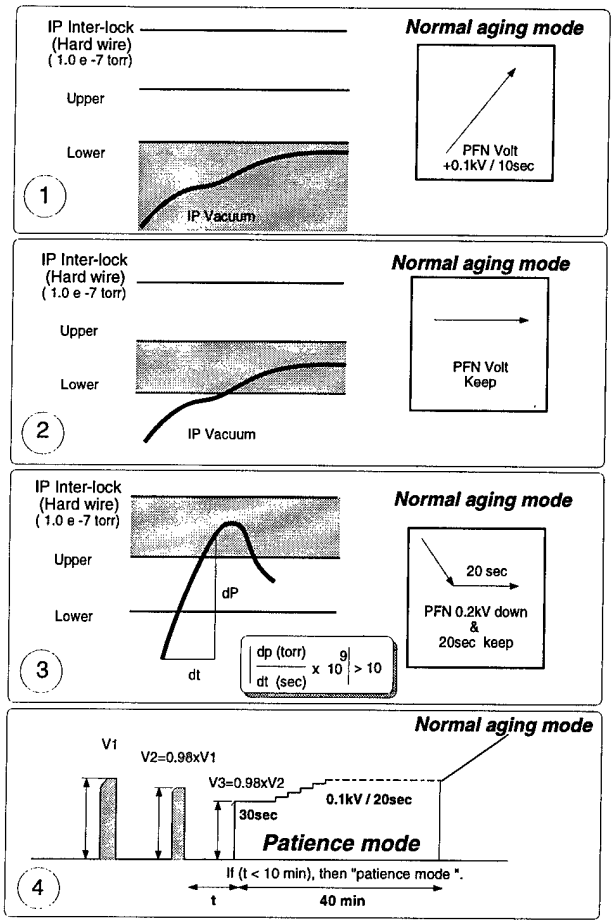

Figure 2: The sequence of automatic conditioning. This sequence is based on an expert in linac operation. He has operated many linac for about 30 years.

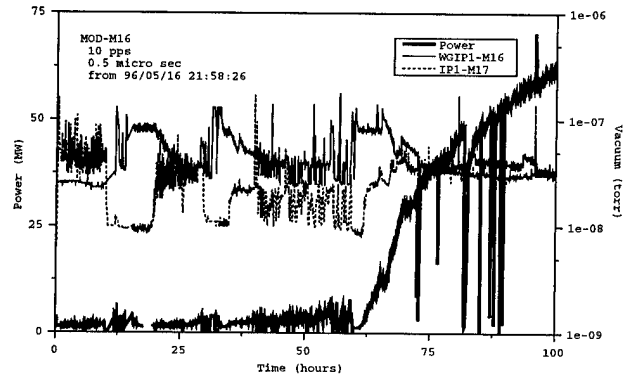

Figure 3: Process of automatic conditioning.

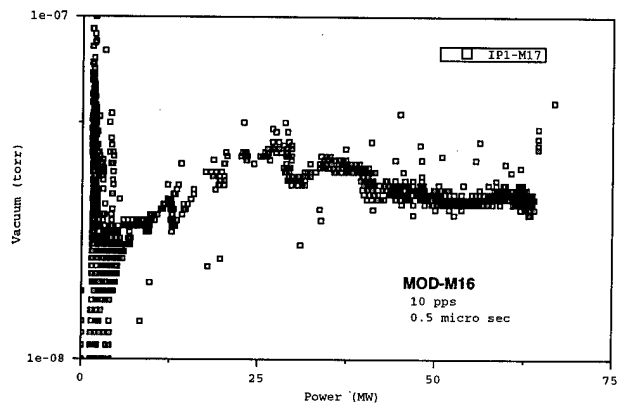

Figure 4: the spectrum of automatic conditioning. The value of vacuum is at near the accelerator tube.

2.2 *The result of conditioning system*

The automatic RF conditioning system is very stable and good job, so that all the RF conditioning has finished for ~550 hours. It is very short time. Figure 3 shows a progress of automatic RF conditioning. The pulse width is 0.5 micro sec. Firstly, the RF system generate discharges at a low-level power. At the these power, the RF-window have many kind of out-gas mechanism, so it operated more carefully and wasted long time. Figure 4 is the spectrum of RF conditioning. The horizontal axis means input power of the RF conditioning, and the vertical axis means the vacuum value of input power. As stated above, low-level input power causes the electronic discharge on the RF window, and the spectrum shows bad vacuum on this power domain. At first, we had designed an automatic RF conditioning system using fuzzy logic[3]. However, we could not ready for it.

3 MEASUREMENT OF THE BEAM FLUCTUATION

3.1 *Guideline of fluctuation monitor*

At the beam commissioning and the injection into synchrotron, we have to supply the very stable beam which have the no fluctuation. However we are able to measure two type beam fluctuations on that. One is a beam current fluctuation, other is a beam energy fluctuation. The measurement of current fluctuation is comparative simplicity. But the energy fluctuation does not. So we designed the beam energy fluctuation monitor using image process.

Figure 5 shows the guideline of measurement system. The current monitor(OSC) and screen monitor are watched by CCD camera which made as NTSC (National Television System Committee) regulation. The video switch collects all NTSC video signal and send to the VME camera interface board. At the VME board, the video signal convert digital-value and compress JPEG (Joint Photographic Expert Group) data file. The data file is send to WS using the SCD (SPring-8 Linac Control Datagram) [4].

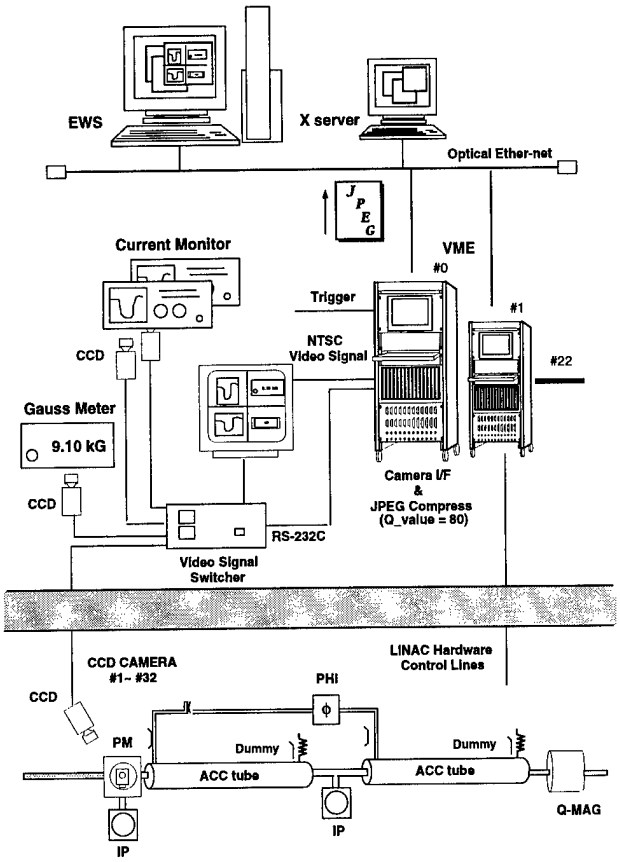

Figure 5: Guidline of the analyzer system. The image data is compressd into the VME board.

3.2 *Human interface and the measurement data*

Figure 6 shows the human interface of the monitor. The image data is send from a VME computer to the WS. The monitor is recognize the highest intensity part on image data as the beam center part, and recording. If this part have big fluctuations, then we can understand the beam energy also fluctuate. Figure 7 shows result of energy monitoring at the 1GeV bending magnet. So that we can say that the beam energy fluctuation is under 0.3% at 1GeV. Probably, this fluctuation is cause from the RF phase fluctuation at every klystrons. Because, we do not control the RF phase fluctuation.

4 CONCLUSION

The SPring-8 linac had completed, and the beam commissioning has started. Since the commissioning, the linac control system has no big troubles, and be stable. Special mention should be made of the automatic RF conditioning system. It worked very good job, and we got plenty time.

Now, we design the injection control system which based on the image monitor. It may be that the system is going to use some mathematical theories. To use it, so that we will be able to get more simple operation[5]. And, we will try to control the RF phase fluctuation.

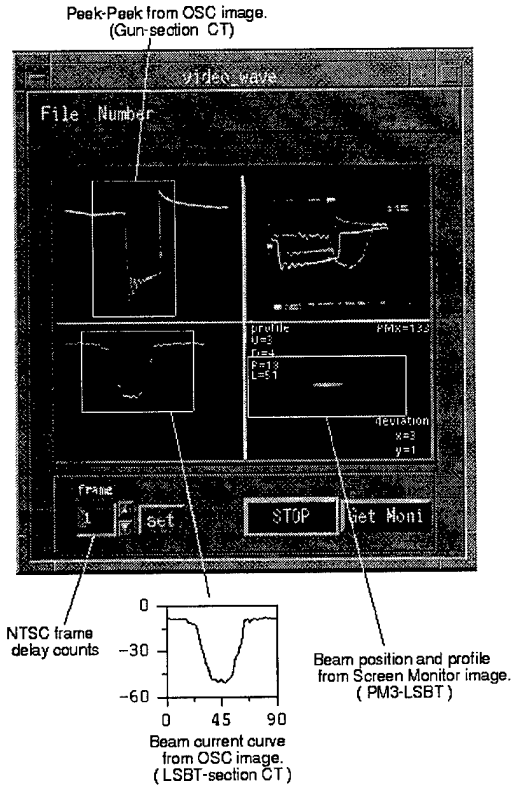

Figure 6: Human interface of the monitor.

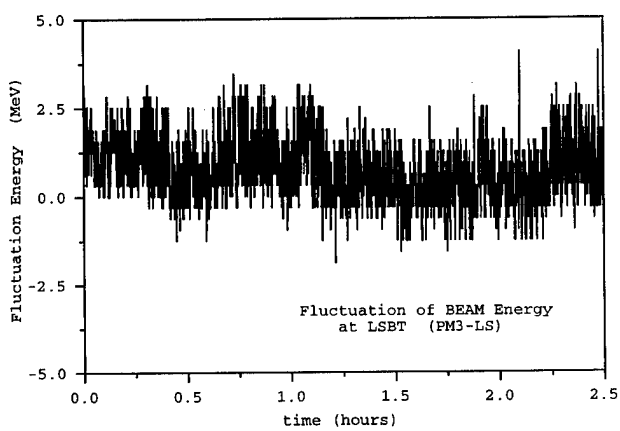

Figure 7: Fluctuation of beam energy at the 1GeV energy place.

5 REFERENCES

[1] K.Satoh et al., Proc. of THE 20TH LINEAR ACCELERATOR MEETING IN JAPAN, p263-265,(1995).

[2] H.Sakaki et al., Proc. of THE 21TH LINEAR ACCELERATOR MEETING IN JAPAN, p50-52, (1996).

[3] H.Sakaki et al., Proc. of ICALEPCS'95, p726-732, (1997).

[4] H.Sakaki et al., Proc. of PAC'95, p2208-2210, (1996).

[5] H.Sakaki et al., Proc. of IWCSMSA96, in Tsukuba, (1996).

IMPROVEMENTS TO THE LANSCE ACCELERATOR TIMING SYSTEM

L.J. Rybarcyk and F.E. Shelley, Jr., LANSCE Division,
Los Alamos National Laboratory, Los Alamos, NM 87545

Abstract

The Los Alamos Neutron Science Center (LANSCE) 800 MeV proton linear accelerator (linac) operates at a maximum repetition rate of twice the AC power line frequency, i.e. 120 Hz. The start of each machine cycle occurs a fixed delay after each zero-crossing of the AC line voltage. Fluctuations in the AC line frequency and phase are therefore present on all linac timing signals. Proper beam acceleration along the linac requires that the timing signals remain well synchronized to the AC line. For neutron chopper spectrometers, e.g., PHAROS at the Manuel Lujan Jr. Neutron Scattering Center, accurate neutron energy selection requires that precise synchronization be maintained between the beam-on-target arrival time and the neutron chopper rotor position. This is most easily accomplished when the chopper is synchronized to a stable, fixed frequency signal. A new zero-crossing circuit which employs a Phase-Locked Loop (PLL) has been developed to increase the phase and frequency stability of the linac timing signals and thereby improve neutron chopper performance while simultaneously maintaining proper linac operation. Results of timing signal data analysis and modeling and a description of the PLL circuit are presented.

1 INTRODUCTION

The Los Alamos Neutron Science Center (LANSCE) 800 MeV proton linear accelerator (linac) provides pulsed beams of protons for direct use and for production of spallation neutrons. Employing Time-of-Flight (TOF) techniques and an assortment of instruments, experimenters at the Manuel Lujan Jr. Neutron Scattering Center (Lujan) use the pulsed neutron beams in a variety of research areas. One of those instruments, the PHAROS high-resolution chopper spectrometer [1], employs two rotating mechanical choppers. A "T0" chopper is used for background suppression of prompt gamma rays and high energy neutrons while a fast monochromating Fermi chopper is used for neutron energy selection. For the Fermi chopper to be effective, its rotor position must remain precisely synchronized to the proton beam arrival time on the spallation target. Lack of synchronization results in lower "good data" rates and wasted beam time. The finite bandwidth of the combined chopper rotor and drive system implies that precise synchronization is most easily achieved when the linac reference clock frequency is fixed and stable. However, this is not the optimal timing scenario for linac operation.

The linac is a pulsed machine which operates at a maximum repetition rate of 120 Hz, i.e., twice the AC power line frequency. Presently, the accelerator RF systems operate at a duty factor of about 10%. Each machine cycle occurs a fixed delay after each zero-crossing (ZX) of the AC line voltage. This was done to maximize performance of the linac. The gains of certain klystrons used in the Side Coupled Linac (SCL) are sensitive to their operating point relative to the AC line phase. These sensitivities are due to defects in the AC powered filaments and result in gain variations of ±15% over one full 60 Hz cycle. This constrains linac operations to remain well synchronized to the AC line.

Using the ZX reference signal the Master Timing System (MTS) generates all the logic timing signals used in triggering the ion sources, beam deflectors, linac RF amplifiers and other accelerator pulsed-power systems. Therefore, these timing signals contain phase and frequency fluctuations present in the line. This results in optimal linac operation but inefficient chopper operation.[1]

Recent measurements on the linac revealed that a several hundred microsecond window is available in which machine cycles could occur relative to the actual AC line ZX and not impact accelerator performance. This led to the possibility of operating the accelerator on a version of the ZX signal which had been filtered to reduce unwanted phase and frequency jitter, thereby resulting in a more stable reference signal for the choppers to follow. The bandwidth of the filter was selected to prevent the cumulative phase error between the raw and filtered signals from exceeding this available window. A simple Phase-Locked Loop (PLL) circuit consisting of a Phase Detector (PD), Loop Filter (LF), Voltage Controlled Oscillator (VCO) and frequency divider was chosen to provide the narrow-band filtering of the raw ZX signal.

2 DATA ACQUISITION, MODELING AND ANALYSIS

The AC power grid which supplies electrical energy to the accelerator is fed by variable output generators which

[1] A provision does exist for starting each cycle on a trigger which occurs within a 75 μs window after the ZX. The PHAROS neutron spectrometer uses this feature along with an option to define the Proton Storage Ring extraction time to achieve proper synchronization of the beam-on-target arrival time and the Fermi chopper rotor position. However, the chopper uses the ZX signal as a reference and will therefore attempt to follow all the variations present in this signal.

0-7803-4376-X/98/$10.00 © 1998 IEEE

respond to continuously fluctuating loads. This results in a frequency modulated 60 Hz AC waveform [2]. Both the magnitude and rate of change of the frequency variations are important. To determine the correct amount of filtering to be applied to the raw ZX signal, a simple data acquisition system was employed to collect pulse-to-pulse time variations and a simple PLL model was developed for analysis of these data.

The ZX signal is a nominal 120 Hz pulse train. However, the existing ZX circuit did not contain any prefiltering to remove unwanted higher harmonics present in the AC line and also at times introduced unwanted 60 Hz modulation of the output pulse train. A new circuit incorporating a band-pass filter and precision comparator was therefore assembled to provide an accurate ZX signal for this analysis. A CAMAC module (single input, dual scalar with an internal 2 MHz clock) was available which allowed the time difference between adjacent pulses (~8333 μs) to be measured without dead time. These data were recorded and stored in event files for off-line analysis. A typical spectrum of the time difference between adjacent ZX pulses is shown in Figure 1.

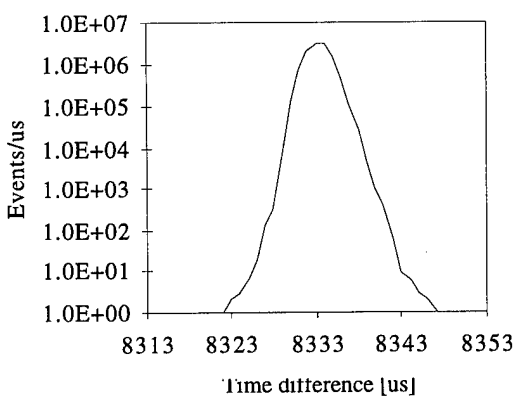

Figure: 1 Typical distribution of time differences between adjacent zero crossings for a 24 hour period.

A simple PLL model was developed for the analysis. The basic information available was a sampled data set of the time difference between adjacent zero-crossings. Although these time differences, i.e., sampling intervals, are not constant, the variations are small enough that to a good approximation the sampling frequency is 120 Hz. Each measurement was reduced to the time (phase) error between the actual and ideal waveforms by subtracting off the time interval of the 120 Hz sampling frequency. These data were then used as input to the PD in the PLL model. Because the data were sampled, a discrete-time PLL model [3] was used. This is shown schematically in Figure 2. This is a linear model of a 2nd-order PLL which is initially locked, i.e. no loop error, at the desired frequency of 120 Hz. In the actual PLL phase detector, the input and clock signals are combined to produce a pulse-width modulated error signal. In this model the phase detector is

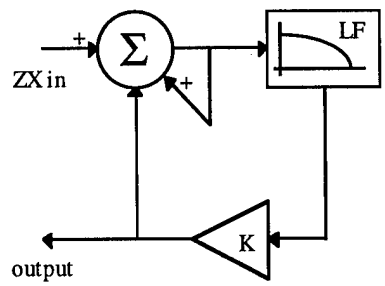

Figure: 2 Block diagram of discrete-time PLL model used in analysis of ZX data.

represented by a summing junction which produces weighted impulses at the sampling frequency. To properly account for the accumulated phase difference between the actual loop input and VCO output signals, the error signal is summed back into the junction. The LF is a discrete time representation of a passive lag filter. Using the weighted impulse approximation, the phase error in the VCO output signal is then simply proportional to the output of the LF. This loop output served as the other PD input signal. Finally, the overall loop gain, K, is represented by a single gain block.

The PLL model was used in combination with the ZX data to evaluate the impact of different loop parameters on the cumulative phase (loop) error distributions. A FORTRAN program was written to simulate the PLL using the aforementioned model. Approximately twenty-four hours of contiguous zero-crossings were analyzed in order to get a representative picture of the phase error distribution that might be accumulated in a typical day. Results of the analysis suggested a 3 dB cutoff frequency (f_{3dB}) of 0.3 Hz and a damping factor (ζ) of 0.7 would produce a cumulative phase error distribution within the several hundred microsecond window.

3 NEW ZERO-CROSSING HARDWARE

A block diagram of the new Zero-Crossing Detector is shown in Figure 3. The detector consists of three major components: the pre-filter, the PLL, and the fault detection circuit. The pre-filter section performs the functions of reducing the AC line voltage to a manageable level and curtailing the line voltage sine-wave impurities. To accomplish these functions the pre-filter employs a transformer circuit, two 2-pole low-pass filters [4], and a 8-pole Butterworth switched capacitor band-pass filter [5]. All components and filter cutoff frequencies were selected to obtain a minimum phase shift at 60 Hz. Once the pre-filter has conditioned the input, the zero-crossing is detected in the PLL section using a precision comparator. This section also contains two PLL's [6] as well as the detection and pulse-shaping circuit. One PLL is used to

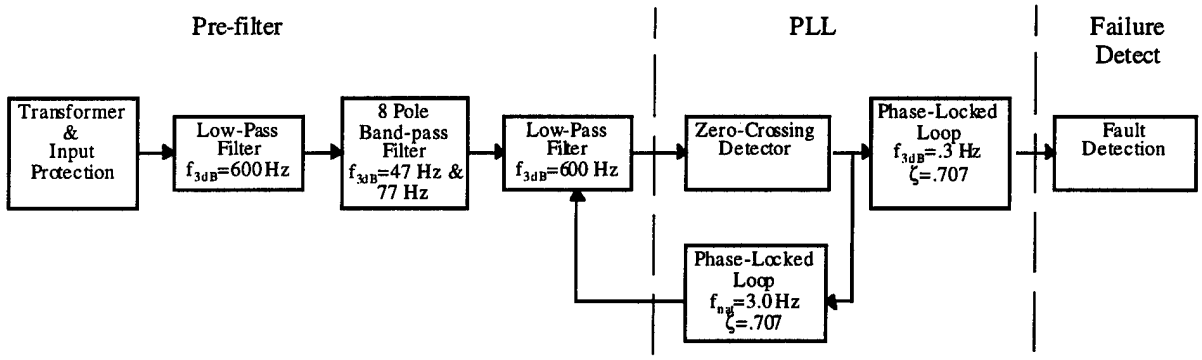

Figure: 3 Block diagram of New Zero-Crossing Hardware.

generate the clock needed for the band-pass filter other PLL performs the narrow-band filtering of the zero-crossing pulse train. The type of phase detectors used in both PLL circuits are Phase Frequency Detectors (PFD). The PFD has several advantages over other phase detectors [6]. However, the PFD will cause the VCO output to go to its maximum value if one of the phase detector inputs is missing. Provisions to handle this failure mode were made in the fault detection circuitry. Loop filters for the two PLL's differ in filter order and implementation. The PLL which provides the clock for the band-pass filter was implemented using a fifth-order low-pass filter as described in Reference [7]. Using the method found in Reference [6], a natural frequency (f_{nat}) of 3.0 Hz and a ζ of 0.707 were measured for this PLL. A ζ of 0.707 and a much lower f_{3dB} of 0.3 Hz were achieved for the other PLL using a traditional passive lag filter with an additional pole to reduce jitter. The jitter was seen as power in the side bands when looking at the output using a spectrum analyzer [6]. Following the filtering action of the PLL, the pulse train enters the fault detection circuit where the time delay from pulse to pulse is checked for instantaneous frequency shifts. When a fault is detected, an oscillator, which was synchronized to the last known good zero-crossing pulse, is switched into operation. Provisions were made for the circuitry to automatically switch back to the detected zero-crossing once the fault is cleared.

4 SUMMARY

The accelerator timing system at the LANSCE facility has been upgraded. The reference timing signal used by the MTS is now produced by a new ZX circuit employing a PLL. This new circuit produces a more stable reference signal for the neutron choppers to follow without impacting linac performance. It also affords the option of improving the stability of the ZX signal even further by reducing the bandwidth of the filter through simple implementation to track the ZX center frequency. The component replacement. This option will be pursued as the sources of the linac's AC line phase sensitivities are better understood and mitigated.

5 ACKNOWLEDGMENTS

The authors would like to thank Andrew Browman for his contributions to the modeling, analysis and design of this system and Jerry Potter for his contributions to the data acquisition and zero-crossing hardware.

REFERENCES

[1] R.A. Robinson, M. Nutter, R.L. Ricketts, E. Larson, J.P. Sandoval, P. Lysaght, and B.J. Olivier, "A New Chopper Spectrometer for Neutron Brillouin Scattering and Low-Angle Neutron Inelastic Scattering: PHAROS (Phase I)," in "Proceedings of ICANS-XII," Rutherford Appleton Laboratory report 94-025, Vol. I (May 24- 28, 1993), p.44-51.

[2] V.W. Bolie, R.M. Brugger and R.N. Silver, "Neutron Chopper Phasing for a Quasi-Periodic Pulsed Neutron Source," Nucl. Instr. and Meth. A236 (1985) pp. 85-94.

[3] J.P. Hein and J.W. Scott, "z-Domain Model for Discrete-Time PLL's," IEEE Trans. Circuits and Systems, vol. 35, pp. 1393-1400, Nov. 1988.

[4] Y.J. Wong. *Function Circuits Design and Application,* New York. McGraw-Hill Inc. 1976.

[5] N. Sevastopoulos and R. Markell. "A Simple Method of Designing Multiple Order All Pole Bandpass Filters by Cascading 2nd Order Sections", Linear Technology 1990 Linear Applications Handbook, pp. AN27A1-AN27A16.

[6] R.E. Best, *Phase-locked Loops Theory, design, and Application*, Second edition, New York. McGraw-Hill Inc. 1993.

[7] N. Sevastopoulos and P. Karantzalis. "Unique Applications for the LTC1062 Lowpass Filter", Linear Technology 1990 Linear Applications Handbook, pp. AN24A1-AN24A8.

A COMPONENTS DATABASE DESIGN AND IMPLEMENTATION FOR ACCELERATORS AND DETECTORS*

S. Meyer and A. Chan, Stanford Linear Accelerator Center, Stanford, CA, 94309

Abstract

Many accelerator and detector systems being fabricated for the PEP-II Accelerator and *BABAR* Detector needed configuration control and calibration measurements tracked for their components. Instead of building a database for each distinct system, a Components Database was designed and implemented that can encompass any type of component and any type of measurement. In this paper we describe this database design that is especially suited for the engineering and fabrication processes of the accelerator and detector environments where there are thousands of unique component types. We give examples of information stored in the Components Database, which includes accelerator configuration, calibration measurements, fabrication history, design specifications, inventory, etc. The World Wide Web interface is used to access the data, and templates are available for international collaborations to collect data off-line.

1 RATIONALE

In the early design stage of the PEP-II/*BABAR* Project Database, it was recognized that many very different kinds of measurements needed to be recorded for many different kinds of components of the accelerator and detector systems. At that time, it was decided that flexibility to store this diverse set of data was paramount in order to avoid redesigning the database for each set of measurements and each component type.

2 THE DESIGN

2.1 Items to be stored

The items to be stored describe the components, information about function and installation of components, the processes by which they are manufactured, refurbished, and measured, performance measurements which are recorded on paper and on-line travelers and information to track who did what and when it was done.

This was distilled into the following datasets:

- Components
- Component-Types
- Travelers
- Traveler-Tasks
- Metrics
- Functions
- Installation-Data
- Parameters
- People - The people dataset was previously developed as part of other PEP-II/*BABAR* Project database systems[1] including meetings, drawings, and publications as well as basic personnel information.

This vertical design using separate tables linked together to describe components and metrics allows for the required flexibility to store the diverse data of the many accelerator and detector systems. Rather than creating a new table with different columns for each traveler, new travelers with different metrics for different components can be stored as new rows in these few tables without creating multitudes of tables with new columns for the all of the travelers.

The horizontal design would have, for example, a table with a column for magnet current, a column for coil temperature, a column for iron temperature, a column for ambient temperature and so forth. In the vertical design, that we use here, rather than columns for each metric, there are rows in the table PARAMETERS like:

- Magnet Current
- Coil Temperature
- Iron Temperature
- Ambient Temperature

Each of the metrics is linked to one of the rows of the PARAMETERS table. Creating a new kind of metric is as simple as adding a new line to the bulleted list above.

An Entity-Relationship Diagram of the PEP-II/*BABAR* Components/Functions/Metrics database is shown in Fig. 1.

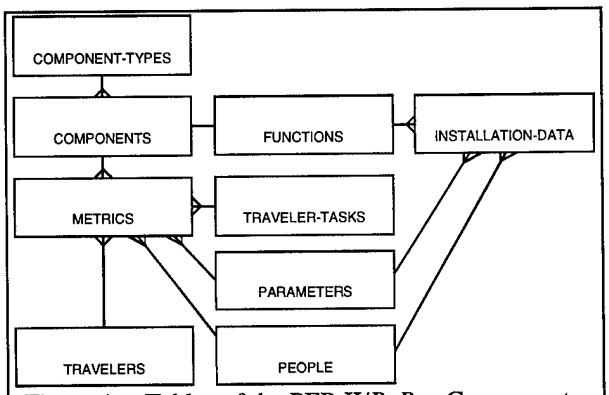

Figure 1 -- Tables of the PEP-II/*BABAR* Components, Functions and Metrics Database

* Work supported by Department of Energy contract DE-AC03-76SF00515.

2.2 The datasets

- The Components dataset stores basic information generic to all components -- serial number, barcode number, component type and so forth. This is the COMPONENTS table.
- The Component-Types dataset contains a description of each kind of component. This is the COMPONENT_MASTER_LISTS table. Each record in the components table refers to one of these component-types. Examples are
  - ◊ HER Quadrupole - 550
  - ◊ HER Main Bend
  - ◊ LER Main Bend
  - ◊ *BABAR* Calorimeter Crystal
  - ◊ Drift Chamber Wire
- The Travelers dataset contains the names and identifying number of the each "process" to be performed on all components. These processes include manufacturing, refurbishing, and measuring the components. This is the TRAVELERS table. Each measurement refers to one of these travelers to describe the measurement Examples are:
  - ◊ *BABAR* Calorimeter Crystals / Performance Measurements with Phototube
  - ◊ HER Dipole Magnets / Resistance and Temperature Measurements
- The Traveler-Tasks dataset contains the steps of each Traveler. This is the TRAVELER_TASKS table. Each measurement refers to one of these traveler-tasks to describe the measurement. Examples are:
  - ◊ Resistance and Temperature Measurements at 10 Minutes
  - ◊ Integrated Gradient vs. Current
- The Metrics dataset contains all measurements of all components on all travelers. This is the COMPINFO_METRICS table. Columns include Date-Measured, Measured-By, Metric-Value and columns to refer to the other tables to describe the measurement.
- The Functions dataset contains a record for each "Formal Device Name" in the ring, as well as a few devices not in the beam-line. This is the FUNCTION_DEVICE_NAMES table. There is an FDN for each magnet, vacuum pump, vacuum chamber and other items that make up the accelerator. Each FDN may have an actual device assigned to it by a reference to the components table.
- The Installation-Data dataset contains information about the installation of the FDNs. This is the INSTALLATION_DATA table. This data includes dates when various items were installed, and notes by the installers. In addition, a history is maintained of components that have filled each slot.
- The Parameters dataset contains basic descriptions of measurements. This is the PARAMETERS table. The Metrics and Installation-data datasets refer to this table. Examples are:
  - ◊ Current
  - ◊ Voltage
  - ◊ Passed LY Test
- The People dataset contains basic personnel information about people. This is the PEPII_PERSONS table. Many other tables refer to this one to indicate who did something.
- The components/travelers/metrics database has been used for all sorts of components for the PEP-II ring as well as parts of the *BABAR* detector:
  - ◊ Calorimeter Crystals
  - ◊ Instrumented Flux Return Modules
  - ◊ Drift Chamber Wires

Calorimeter Crystal	Traveler Number:	013-00 R1	Spreadsheet Version:	2	Drawing Number:	SA 341-992-02

cm00

Assembly Identification						
Assembly Serial Number	Assembly Barcode	Supplier	Date Manufactured	Date Received	Component Comments	Type
050A	BCAL01123	Hilger Analytical	25-Mar-97	11-Apr-97		BS-8
073A	BCAL01124	Hilger Analytical	25-Mar-97	11-Apr-97		BS-8
067A	BCAL01125	Hilger Analytical	25-Mar-97	11-Apr-97		BS-8
073B	BCAL01126	Hilger Analytical	25-Mar-97	11-Apr-97		BS-8
078B	BCAL01127	Hilger Analytical	25-Mar-97	11-Apr-97		BS-8
069A	BCAL01128	Hilger Analytical	25-Mar-97	11-Apr-97		BS-8
059A	BCAL01129	Hilger Analytical	25-Mar-97	11-Apr-97		BS-8
071B	BCAL01130	Hilger Analytical	25-Mar-97	11-Apr-97		BS-8

Figure 2 -- Example Excel Input Template - Calorimeter Crystals Identification Traveler

Calorimeter Crystal	Traveler Number:	013-02 R2	Spreadsheet Version:	2	Drawing Number:	SA 341-992-02

cm02

Assembly Identification									Measurements with Phototube						
Assembly Serial Number	Assembly Barcode	Date Measured	Measured By	Wrap Type	Wrapping Comment	Tuning	Reference crystal #	Source	Light Output 511	Sigma 511	File Name (scan curve)	Comments	Passed LO Test	Passed Uniformity Test
050A	BCAL01123	21-Apr-97	PV	R		N	3367	Na-22	39.02	1.379225	BCAL01123.scn		Y	Y
073A	BCAL01124	21-Apr-97	PV	R		N	7360	Na-22	37.57	0.800103	BCAL01124.scn		Y	Y
067A	BCAL01125	21-Apr-97	PV	R		N	3367	Na-22	36.20	1.437436	BCAL01125.scn		Y	Y
073B	BCAL01126	21-Apr-97	PV	R		N	7360	Na-22	37.04	1.060394	BCAL01126.scn		Y	Y
078B	BCAL01127	21-Apr-97	PV	R		N	3367	Na-22	36.46	1.142953	BCAL01127.scn		Y	Y
069A	BCAL01128	21-Apr-97	PV	R		N	7360	Na-22	37.87	1.265278	BCAL01128.scn		Y	Y
059A	BCAL01129	21-Apr-97	PV	R		N	3367	Na-22	39.04	1.367011	BCAL01129.scn		Y	Y
071B	BCAL01130	21-Apr-97	PV	R		N	7360	Na-22	37.25	1.365912	BCAL01130.scn		Y	N

Figure 3 -- Example Excel Input Template Calorimeter Crystals Phototube Traveler

3 HOW IT IS USED

3.1 Loading

Due to the distributed, international locations where the data is collected, a method was needed to allow off-line collection of data. In order to accomplish this, an MS Excel template was developed that could be loaded by a loader program (Fig. 2, Fig. 3). With little modification to the template, any manufacturing, refurbishing or measuring traveler can be loaded. Some on-line data acquisition systems that were developed after the template was developed, were written to create data files in the format of the Excel template, thus avoiding the need to type the data into Excel. For those data files created before the template was developed, custom programs were created to load them.

Calorimeter Crystals

Crystals Info

013-00	BABAR Calorimeter Crystals / Parent Traveler			
		Identification		
Serial Number	Barcode	Date Measured	Measured By	Type
18K4.9B5.14	BCAL00001	05-MAY-97	Va'vra, Paul Michael	B5-9
18K4.9B5.16	BCAL00002	05-MAY-97	Va'vra, Paul Michael	B5-9
19K4.9B5.40	BCAL00003	05-MAY-97	Va'vra, Paul Michael	B5-9
18K4.9B5.27	BCAL00004	05-MAY-97	Va'vra, Paul Michael	B5-9

Figure 4 -- Example Generic Traveler Output on WWW Calorimeter Crystals Identification Traveler

3.2 Reporting

The World-Wide-Web is used extensively to make reports available to the international collaboration (Fig 4). UNIX utilities such as GNUPLOT are used to provide charts and histograms of data for display directly on the WWW browser (Fig 5). In addition, on any of the reports, the data can be downloaded to a tab-delimited file on the user's local disk drive. This tab-delimited file is suitable for loading into a spreadsheet program such as MS Excel for local calculations, and charting (Fig 6).

4 LIMITATIONS

4.1 Query Time on World Wide Web

The use of the World Wide Web for reports leads to a limitation on run time for queries. Most WWW browsers will time out after 5 minutes have elapsed from the time the HTTP request is submitted to the server. Reports must be completed prior to expiration of the time-out period. Efforts to improve the efficiency of the SQL to alleviate the problem will not scale to hundreds or thousands of records. Using the CGI scripting language to

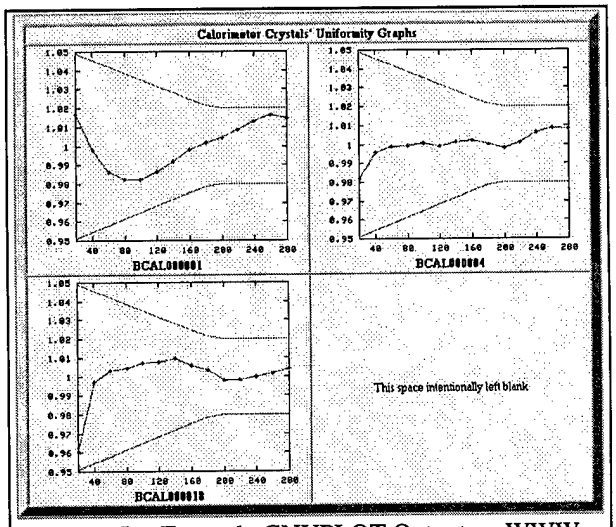

Figure 5 -- Example GNUPLOT Output on WWW Calorimeter Crystals Uniformity Plots

SLAC Magnetic Measurements - INTEGRATED FIELD STRENGTH MEASUREMENTS							
Date:							
Magnet Name: 007							
Test Operator: Dix, Brendan							
Magnet Standardization Currents (Amps)							
100	950	100	950	100	950	100	
Measurement Currents (Amps)							
500	550	600	650	700	750	800	850
900	950	900	800	700	600	500	
BL Measurements for the Test Magnet							
I(A)	VTXC (VS)	sigVTXC (VS)	ratio VTXC/VTR	sig VTXC/VTR	BL (TM)	sigBL (TM)	BL/I (TM/KA)
500.46	0.73542	0.00003	0.99894	0.00005	0.76342	0.00003	1.52543
550.46	0.80890	0.00004	0.99901	0.00009	0.83970	0.00004	1.52549

Figure 6 -- Example Output from WWW as Tab-Delimited Data in a Spreadsheet File

retrieve a portion of the data and provide hyperlinks to see the "next page" and "previous page" is one solution.

4.2 Improving Query Time by Rotation of Tables

While simplifying the design of the database, the use of the normalized "vertical" table design complicates the SQL even for "simple" queries as most of the tables must be linked in order to select the appropriate data. Two solutions that may be applied once the data is loaded and stabilized are:

- Separate data into "subset" tables of identical design. Each logical set of data is copied to its own table to reduce the time to search for the required data -- if a given subset table has only data for a given traveler, then the traveler tables need not be linked.
- Rotate the data into custom-designed tables. This simplifies the queries by reducing the number of tables involved and the number of rows that must be fetched.

5 ACKNOWLEDGMENTS

The authors gratefully acknowledged the continued support of the PEP-II/*BABAR* management and the assistance of various people in PEP-II and Technical Division departments.

6 OUR ADDRESS

The URL for the PEP-II Project Database is:
http://www.slac.stanford.edu/accel/pepii/db.htm

REFERENCES

[1] A. Chan, G. Crane, I. MacGregor, S. Meyer, 'The PEP-II/BaBar Project-Wide Database Using World Wide Web and Oracle*CASE', Proceedings of 1995 International Accelerator Database Group Workshop, Argonne National Lab, November 6-8, 1995.

ARC DETECTION AND INTERLOCK MODULE FOR THE PEP-II LOW LEVEL RF SYSTEM*

R. Tighe, Stanford Linear Accelerator Center, Stanford University, Stanford, CA 94309 USA

Abstract

A new arc detection and interlock generating module for the SLAC PEP-II low-level RF VXI-based system has been developed. The system is required to turn off the RF drive and high voltage power supply in the event of arcing in the cavity windows, klystron window, or circulator. Infrared photodiodes receive arc signals through radiation resistant optical fibers. Gain and bandwidth are selectable for each channel to allow tailoring response. The module also responds to interlock requests from other modules in the VXI system and communicates with the programmable logic controller (PLC) responsible for much of the low-level RF system's interlock functionality.

1 SPECIFICATION AND DESCRIPTION

The PEP-II low-level RF system VXI-based Fast Interlock module (figure 1) performs several functions related to monitoring and protecting the RF system. The module serves as the sole VXI module responsible for transmitting any VXI module generated faults to trip the klystron high voltage system. Each Fast Interlock module resides in a VXI crate adjacent to each RF station. An additional hardware subsystem known as the 'Local Panel' has been configured to serve as an intermediary between the interlock handling subsystems of the VXI Fast Interlock module, the Allen-Bradley (Milwaukee, WI) PLC, and the high voltage power supply (HVPS) controller[1].

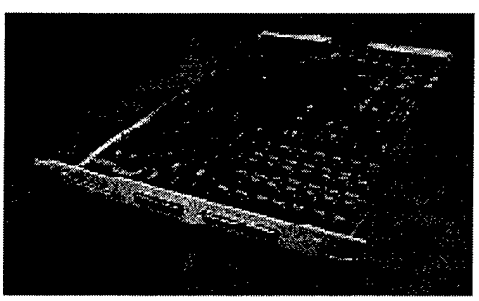

Figure 1. VXI Fast Interlock Module

The Fast Interlock module communicates directly with the Local Panel and indirectly through it to the Allen-Bradley system and the high voltage power supply controller.

*Work supported by U.S. Department of Energy Contract DE-AC03-76SF00515

Fiber optic cables monitor for high power arcing near the cavity windows and at the klystron and circulator.

2 I/O FACILITIES

The Fast Interlock module provides a means of communicating with several external systems. The control system can operate the HVPS, klystron filament and solenoid supplies, and beam abort requests as well as Allen-Bradley system monitoring and fault resetting. The ethernet fiber signals from the control system are brought into the shielded rack and passed on to the Fast Interlock module by a National Instruments (Austin, TX) VXIcpu-030. The Fast Interlock module then issues the commands over fiber optic cable to the nearby instrumentation rack containing the Local Panel.

In the event of a fault it can be necessary to abort the beam to prevent instabilities from the undriven RF cavities. A global beam abort system receives the request to abort the beam from the Fast Interlock module and the request is maintained until either the cavities of that station are parked or the station is returned to normal operation.

An uncommitted external input for tripping of the system is available.

3 ALLEN-BRADLEY COMMUNICATIONS

The RF system is monitored by an Allen-Bradley PLC/5 industrial controller. This Allen-Bradley controller monitors numerous temperatures, digital inputs, and analog voltages. If any of the monitored levels goes outside its prescribed range a fault signal is sent to the Fast Interlock module which then turns off the high voltage. The controller also sends a 'heartbeat' signal over a fiber optic cable to the Fast Interlock module. Should this pulse train fail to appear at the Fast Interlock module after a suitable time, the Fast Interlock module will assume the controller is faulty and issue a command to turn off the high voltage.

The processing nature of the Allen-Bradley system precludes its use as a fast interlock generator. The system loops through its monitored signals approximately once every 15 ms. This is adequate to respond to 'slow' problems, like faulty temperatures, arising in the RF system, but is not adequate as a means of tripping the

0-7803-4376-X/98/$10.00 © 1998 IEEE

system in the fast manner required such as when an arc is detected.

A separate chassis serves to collect the many fiber optic connectors, both inputs and outputs. Each arc detection fiber input connects here. The fiber connections for the control of the filament supply, HVPS, solenoid, Allen-Bradley reset, Allen-Bradley heartbeat, Allen-Bradley summary, and beam abort signal are on this chassis. The optical signals are converted to electrical signals and transmitted over ribbon cable to the Fast Interlock module nearby.

4 COLLECTOR POWER DETECTION

The klystron forward power is detected in the external chassis and an analog output sent to the Allen-Bradley system for use in tripping the system if the collector power is too high. This is determined by subtracting the klystron forward power from the high voltage supply's voltage-current product and assuming that the difference is absorbed in the collector.

5 INTERLOCK HANDLING

All critical fast interlock logic resides in hardware on the Fast Interlock module. The fault logic is independent of the crate controller microprocessor and network. Should there be a network problem or crate controller hang-up the Fast Interlock module will still function to trip the HVPS in case of a fault. All faults are configured in a fail safe manner so as to trip the system in event of module failure. The fiber optic outputs must provide continuous light output in order for the 'on' signal to be valid. Power loss to the module leads to the turning off of the high voltage. The primary interlock function is through the permissive for the HVPS that is issued from the Fast Interlock module. Other modules in the crate may be configured to issue interlock requests to the Fast Interlock module by asserting a TTL backplane trigger. These faults may be generated for reasons of excessive RF amplitude detected on any number of monitored signals such as klystron reflected power.

The high voltage permissive is removed by the Fast Interlock module when any of the fault sources is in the faulted state. The VXI backplane trigger, the loss of the Allen-Bradley heartbeat or summary, a detected arc, or even a software generated forced fault may all drive the fault line. A 'first fault' register is provided in the event of a rapid succession of faults in order to distinguish the precipitating fault. The current status as well as latched fault status is available to read out in the event that a fault is persistent. A front panel trigger is provided when a fault is detected for additional diagnostic purposes.

The VXI backplane fault requires special handling by the Fast Interlock module since it is a fault that is both generated by and monitored by the module. Upon detecting any type of fault the Fast Interlock module asserts the backplane TTL trigger for the benefit of the other modules. In the event another module in the crate is forcing the fault the Fast Interlock module must remove its assertion and check for persistent assertion by the other module and maintain the fault if that assertion is there.

6 ARC DETECTION

Seven 100 foot lengths of fiber optic cable bring the arc detection light to the Fast Interlock module. In a high energy ring installation four are from cavities, one is from the klystron window, and another is from the circulator, the seventh is a spare channel. A low energy ring installation has two fewer cavities to monitor. The detector is a Honeywell HFD-3854 PIN photodiode with a peak response wavelength of 850 nm. Each channel has both adjustable gain and bandwidth setting jumpers. The fastest response time is about 1μs. The slowest can be up to 10μs. Slower settings enable controlled timing of the trip. The circulator manufacturer specifies a 5μs trip time to allow for burning up the arc instigating debris. Three gain settings along with adjustable trip settings at the comparator input allow flexible selection of trip levels for good protection without nuisance trips. The photodiode output is amplified in two stages to achieve a gain of about 155dB. The two feedback stages are implemented in a 'T' topology (figure 2) to allow moderate component values and reduced stray capacitance.

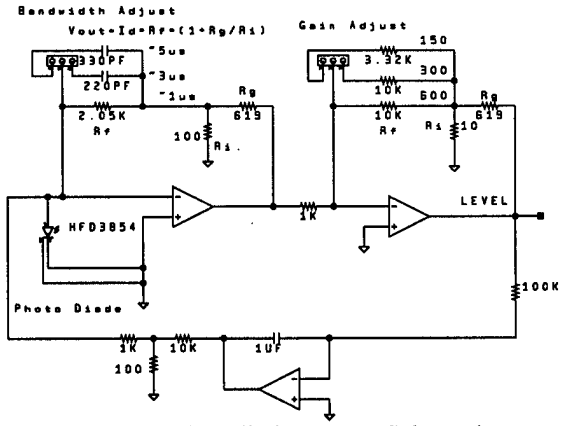

Figure 2. Photodiode Preamp Schematic

Each channel has slow DC removal (>1ms) to allow the use of high gain without regard to the offsets that would normally restrict such a gain. Only fast transient light

events are triggered. The unbiased response time of the photodiode is fast enough that no reverse biasing is required. The resulting speed increase from reverse biasing would be small compared to overall response time anyway, and dark current noise would increase. The noise equivalent power is approximately .05μW (-43dBm). The preamp output is buffered and available at the front panel of the external chassis for testing and monitoring purposes.

The two-stage output is then transmitted differentially to the VXI module portion of the fast interlock system. Each of the channels may be bypassed through a jumper located on the VXI module itself. Remote readback of the bypassed status is provided.

The fiber optic cable for the arc detection is Spectran (Avon, CT) HCR with 200 micron core. The cable is UL rated OFNP -- Nonconductive Optical Fiber plenum cable, no conduit is required and it meets safety standards for flammability and smoke generation. The cable is radiation resistant and should be able to reside in the PEP-II tunnel without degradation. The cable has been tested elsewhere with up to 50 krads without degradation[2]. Radiation dose in the PEP-II beam tunnel where the fiber resides is estimated to be approximately 30krad/year [3]. The only component of the Fast Interlock system to reside in the beam tunnel is the radiation hardened fiber optic cable. Less than one third of the length of each cable resides in the tunnel radiation area. Test data shows approximately 1dB induced loss per 30m of exposed cable after a brief exposure to 3krads [4]. Fiber optic cable of this type is known to recover over a period of time subsequent to the dose. This provides assurance that the arc detection system will not be significantly 'blinded' by beam loss events.

7 CRATE TEMPERATURE AND VOLTAGE MONITORING

A programmable data acquisition system (DAS) monitors the crate temperature and power supply voltages and generates an interrupt in the event of an out of tolerance value. Once programmed, the DAS reads through its channels comparing the inputs to programmed limits without control system attention.

The peak detected levels from the arc detection channels are available through the control system to assist in remote trip level setting and noise monitoring.

8 CONCLUSION

A VXI-bus based Fast Interlock module is in use in the PEP-II low-level RF system. It is required to handle numerous sources of faults and transmit trip requests rapidly and reliably. The crucial interlock logic resides entirely in hardware and operates autonomously despite computer or network difficulties.

9 REFERENCES

[1] P. Corredoura, et al., "Commissioning Experience with the PEP-II Low-Level RF System", these proceedings.

[2] E.R. Beadle, "Fiber Optics in the BNL Booster Radiation Environment", Proceedings of the 1991 Particle Accelerator Conference, pp. 1493-1495.

[3] Liu, J. ,Mao, S. , "Radiation Dose to an Electronic Device under RF Penetration", SLAC Memorandum, May 1996.

[4] West, R.H., "A Local View of Radiation Effects in Fiber Optics", Journal of Lightwave Technology, Vol. 6, No. 2, February 1988.

AUTOMATIC LATTICE PARAMETERS MEASUREMENT TOOLS AT SRRC

Jenny Chen, C. S. Chen, C. H. Kuo, K. K. Lin, K. T. Hsu
Synchrotron Radiation Research Center
No. 1 R&D Road VI, Hsinchu Science-Based Industrial Park, Hsinchu, Taiwan, R.O.C.

Abstract

In order to acquire necessary machine parameters information within reasonable time, supporting tools for automatic lattice parameters measurement is implemented in SRRC. Signal waveform detection, spectrum analysis, and associated control circuits were installed and tested, and the application programs were developed. These application program tool boxes can be activated with simple pop-up operation on workstation. Detailed functions and their status are presented in this report.

1. INTRODUCTION

Acquiring necessary machine parameters information within reasonable time for machine study is important due to limited available machine shift. Consequently, supporting tools for automatic machine related parameters measurement is implemented in SRRC. Hardware component include devices for signal waveform recording, spectrum analysis, and control circuits. Developed software package consists of tools for instrument control, data acquisition, analysis, and visualization of measured parameters. Typical applications of this package are tune identification, resonance diagram for working point evolution, measured lattice function display, and filling pattern of the stored electron bunched in the ring. Real-time display of absolute orbit and difference orbit with persistence display option have shown to be a powerful tool for orbit study. These tools are planned to be adopted to the injector together with the integration of accelerator control system.

2. CONTROL SYSTEM ENVIRONMENTS

SRRC control system is a two level hierarchical computer system [1,2]. It is connected to the equipments through VME crate system. For complex instruments, such as spectrum analyzer, connection with the control system is made by using GPIB-ENET adapters. NI-488.2M software installed on workstation is used to drive the system. Applications on workstation can access every accelerator device whichever is connected with the VME crates or GPIB-ENET. At presentation layer, UIM/X graphical user interface builder [3] was used to develop the operation interface.

3. TUNE MEASUREMENT UTILITIES

The tune measurement system is currently using HP4396A spectrum/Network analyzer to acquire spectrum information of the beam signal and is running in list scan mode [2,4]. The full screen is divided into three sections for synchrotron frequency, vertical and horizontal betatron frequency measurement respectively without lossing its resolution. The excitation is achieved by using a random noise generator with 5 MHz bandwidth to shake the beam and the power level of the noise was properly adjusted to satisfied the beam condition.

The spectrum analyzer is connected to control system via GPIB-ENET adapter. The tune measurement program is able to give command and to drive the spectrum analyzer with the aid of NI488.2M library. The related parameters setting is done through operator interface as shown in figure 1. The parameters include frequency scanning range, beam excitation enable/disable and power level controlling, ... etc.

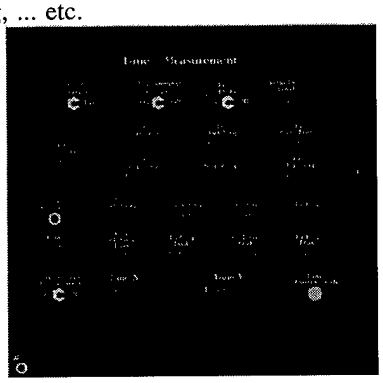

Figure 1. Tune measurement system parameters control page

Figure 2 shows the tune evolution while 1.8 Tesla wiggler closing its gap from 230 mm to 22.5 mm. The vertical tune drifted from 4.1 to 4.15, and the horizontal tune does not change.

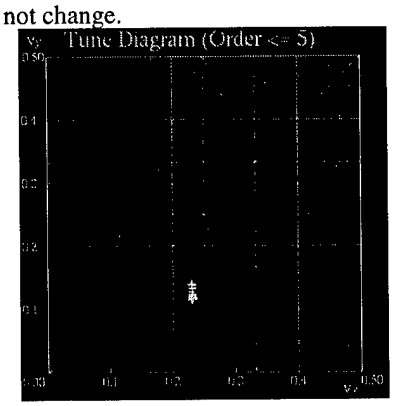

Figure 2. Tune diagram and tune evolution during W20 gap change

3. ORBIT DISPLAY UTILITIES

Orbit display is usually required in routine operation and machine study. A bar chart display of beam position monitor (BPM) reading has been in service since storage ring commissioning. However, requirement for acquiring orbit difference in association with particular machine parameter changes has been raised as the machine study activity increase. Since there are a lots of requirement for orbit display, therefore a real-time display urilities was developed to satisfied various requirements. The utility provides display of absolute and difference orbits supported with persistent mode option. Color grading display will be supported in new versions. The line style can be dot line and line-dot. Data averaging is also supported by the package. The updating period without any average is less than 0.5 sec. Typical example of the display is shown in Figure 2.

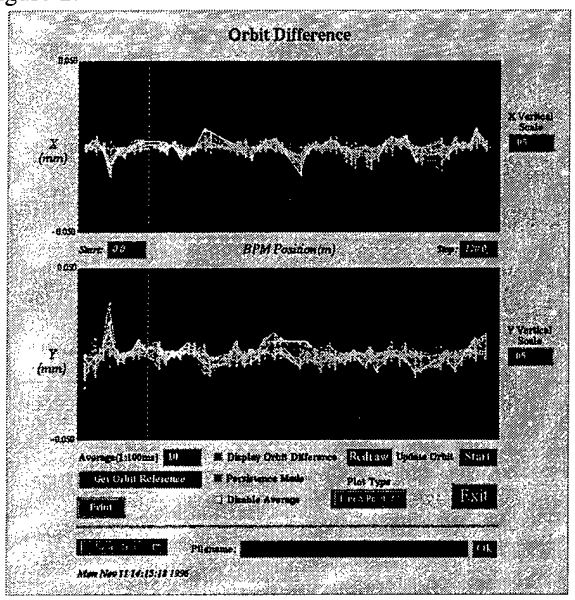

Figure 3. Real-time difference orbit display

4. LATTICE FUNCTION MEASUREMENT TOOLS

Lattice functions information is very important for machine optimization especially for low emittance ring. Measuring lattice function is a tedious work without automation. In order to solve this problem, tools to support lattice function measurement has been developed recently. The package provides betatron function, dispersion function, eta function, and chromaticity measurement. Figure 4 gives typical display for betatron function measurement. The measured raw data as well as processed data can be save for later use.

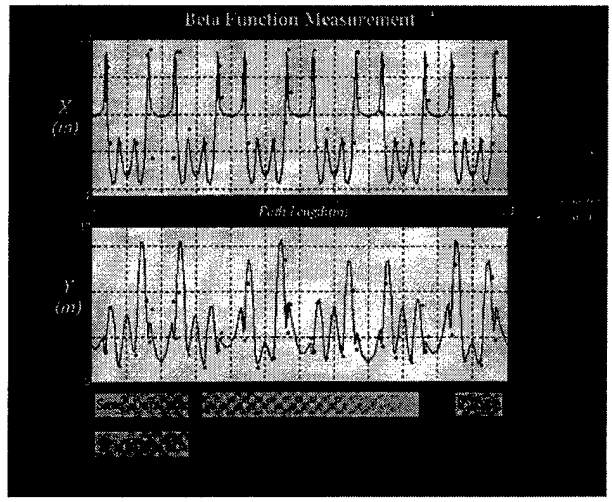

Figure 4. Measured betatron function (point) and theoretical betatron function (line).

5. FILLING PATTERN MEASUREMENT

Filling pattern plays a crucial role which affects the performance of the accelerator system due to coupled-bunch instabilities. A real-time filling pattern diagnostic tool is in developing stage. The system is composed of a VMEbus form factor 500 MHz digitizer using external clock comes from master oscillator. The signal picked up by the stripline electrode is digitized by the fast ADC. Each data point reading value of the acquired data is proportional to the amount of charge accumulated inthe corresponding bunch. The data is then sent to workstation to display the filling pattern and for various uses. Figure 5 shows a preliminary result of the acquired filling pattern. There are 200 buckets in the TLS.

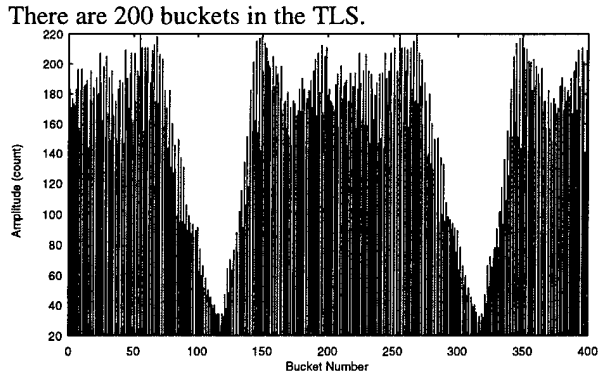

Figure 5. Preliminary real-time filling pattern acquisition results

6. DISCUSSIONS AND CONCLUSIONS

Automatic machine parameters measurement system is developed in SRRC. The system provides a convenient way to measured some of the major lattice related parameters for beam physics study. The system includes various data instruments interface and presentation tools. Extending its functions and improving its performance will be one of the major work in the coming months. It will also be implemented in the renewed control system

which will integrate both the injector and the storage ring operation. A digital receiver based tune meter is under developing in order to further improve the time required of tune measurement related study. Commercial available visualization tools is planned to integrate with the control system to provide various display option and manipulation of the raw data. The tools kits is expected to be very useful to save precious machine time and increase the productivity of machine specilists

7. ACKNOWLEDGMENTS

The authors express their thanks the staff of the instrumentation and control group and operation group for their collaboration. The helps from H. P. Peace, C. H. Kuo and Richard Sah are also highly appreciated.

REFERENCES

[1] C. J. Wang, et al., "The design schemes of graphic user interface database and intelligent local controller in the SRRC control system", Nucl. Instrum. and Meth. in Phys. Res. A352 (1994) 300- 305).

[2] Jenny Chen, et al., "Virtual Instrumentation Interface for SRRC Control System", Proceedings of the 1995 IEEE Particle Accelerator Conference, 2256, May 1995.

[3] UIM/X are trademarks of Visual Edge Software Ltd.

[4] J. A. Hinkson, M. Chin, C. H. Kim, H. Nishimura, "Automatic Tune Measurement in the Advanced Light Source Storage Ring Using LabVIEW APPLICATION", Proceedings of the 1994 European Accelerator Conference.

ORBIT CORRECTION USING VIRTUAL MONITORS AT JEFFERSON LAB*

Yu-Chiu Chao, Bruce Bowling, Johannes van Zeijts, William A. Watson III, Sue Witherspoon,
Thomas Jefferson National Accelerator Facility

Abstract

An orbit correction algorithm is developed to achieve the following goals for the CEBAF accelerator at Jefferson Lab.: 1). Preprocessing of orbit input to account for estimated misalignment and monitor errors. 2). Automatic elimination of blind spots caused by response matrix degeneracy. 3). Transparency of exception handling to interchangeable generic steering engines. 4). CEBAF-specific demands on control of injection angle, path length, orbit effects on optics, simultaneous multiple pass steering, and orbit control at un-monitored locations. All of the above can be accomplished by the introduction of virtual monitors into the processed input orbit, whose theoretical basis is to be discussed in this report. Implementation of all or part of these features and operational experience during the CEBAF variable energy runs will also be discussed.

1 INTRODUCTION

At Jefferson Lab the particular optics configuration and operation constraints impose unique demands on the orbit correction program as elaborated in the abstract. These demands can be met with a universal orbit processing algorithm before specific steering engine is called and ideally the need for human intervention on exception handling is minimized. The algorithm interprets the underlying orbit from monitor and correction element data while performing estimates on misalignment and monitor errors by a well defined procedure. The resulting underlying orbit, including position, angle, path length and other orbit-dependent information, becomes source of steering constraints not only at locations of existing monitors, but at *any location* deemed necessary to have the orbit constrained or corrected, either due to need of blind spot elimination or due to explicit constraints on angle, path length etc. This enhanced set of orbit constraints, or *virtual monitors*, is fed into any generic steering engine with no a priori knowledge of either the specifics of the orbit control goals or the need of exception handling. In the following report this program is outlined and its theoretical basis discussed. Application at CEBAF is also described.

2 ORBIT CORRECTION ISSUES

2.1 The generic linear orbit correction problem

All linear orbit correction problems, regardless of the constraints, can be represented conceptually as

$$X_i = \sum_j M_{ij} \bullet C_j \qquad (1)$$

where X_i is orbit error at the i-th BPM, C_j the strength of the i-th corrector, and M_{ij} the linear response linking X_i and C_j. The core of any steering algorithm amounts to inverting or pseudo-inverting M such that the corrector changes ΔC_j can be found to cancel the orbit error X_i,

$$\Delta C_j = \sum_i M^{\dagger}{}_{ij} \bullet X_i \qquad (2)$$

with different algorithms having different emphases on the weighting scheme, response matrix near-singularity, corrector strength constraints, etc.

2.2 The more generalized orbit correction problem

For the most general orbit correction problem we generalize X_i to any of the coordinate errors including position, angle, path length, etc., as well as quantities derivable from orbit errors such as spurious dispersion caused by angle error at non-zero chromaticity. We can also generalize C_j to any orbit correction devices, as well as energy and devices having different effects on different beam passes. The response matrix elements M_{ij} therefore can be any of the linear transfer matrix elements or linearized second order transfer elements, possibly relating a single corrector to multiple pass beam coordinates. The generalized orbit errors need to be realized by quantities *not directly observable* by the BPM's. They serve as virtual BPM's when included in Eqn (1) with proper weighting.

2.3 Response matrix singularity

When the response matrix is near singular so that some linear combination of the correctors has almost undetectable response at all the monitors but large response elsewhere, naive correction schemes fail by producing excessive corrector strengths and undetected orbit bumps. Corrector reduction or strength constraint can solve this problem [1], as is done by many algorithms. It is not the optimal solution since usually a combination of correctors, not a single one, causes the problem. Indiscriminately limiting or eliminating correctors kills not only the offending combination, but also the useful ones, especially those needed for injection fixes. If however we impose a constraint on the orbit at a strategically chosen location which couples only to the offending combination, we would constrain the offending combination while allowing the useful ones to function. Such orbit constraints at arbitrary locations constitute another instance of the virtual monitors. A well defined algorithm to determine where these virtual monitors should be placed will be described later [1].

2.4 Transparency of singularity handling and other generalized constraints to generic steering algorithms

In light of the above discussion, the goal of the proposed algorithm is thus to construct the input generalized orbit error X_i, generalized corrector strength C_j, and generalized response matrix M_{ij} which, through the introduction of virtual monitors, take into account all the steering constraints described in section 2.2 and automatically remove singularities described in section 2.3. The input data for

* Work supported by the U.S. Department of Energy, contract DE-AC05-84ER40150.

subsequent steering algorithm contain both virtual and real orbit and response matrix, indistinguishable under the format of Eqn (1). They can be given to different steering algorithms with any level of singularity handling and a consistent singularity-free outcome conforming to all additional constraints should be expected.

2.5 Errors in input data

A major problem affecting orbit correction is the inherent errors in the input data. Without an effective filtering mechanism, such errors can distort the underlying physical picture and compromise the correction. In the current context such filtering mechanism is also critical for constraints on the virtual monitors since the latter can inherit errors from the physical data. The success of using virtual monitors thus depends on the ability to screen out errors in interpreted orbit data, to be discussed in the next section.

3 INTERPRETING THE UNDERLYING ORBIT AND ERRORS

We have to answer the following question: Given a set of *physically* monitored orbit errors, how does one derive the generalized orbit errors for the *virtual* monitors? A complete set of orbit information of all beam coordinates at *any* location can be known given the following: corrector strengths, monitor readings, monitor errors, field and alignment errors, and injection errors. The last 3 errors, being unobservable, have to be estimated from the first 2 and the model. The distinction between the injection and all the other misalignment type errors is artificial, depending on choice of starting point. We therefore focus on two types of errors: monitor error and alignment type error. The effect of all alignment type error on the orbit X_1 at the p-th monitors is

$$K^p = \delta X_1^p = \sum_a \sum_i M_{1i}^{ap} \bullet \delta X_i^a \tag{3}$$

where δX_i^a is the misalignment induced error in the i-th coordinate at location indexed a. M_{1i}^{ap} is the transfer matrix element linking such error to the p-th monitor.

The effect a monitor error has on the *apparent* orbit at the p-th monitor is simply its offset at that monitor

$$\Delta^p = \delta X_1^p . \tag{4}$$

Although not part of the real orbit, this error will be included as input to any orbit correction algorithm.

It can be shown that with all the above errors included, the best orbit correction that can be achieved by any algorithm represented by Eqn (1) is limited by the residual error E:

$$\begin{aligned} E &= \Pi^{\perp}_{M_{CM}} \bullet K - \Pi^{\backslash\backslash}_{M_{CM}} \bullet \Delta \\ \Pi^{\perp}_{M_{CM}} &= M_{CM} \bullet \left(M_{CM}^T \bullet M_{CM}\right)^{-1} \bullet M_{CM}^T \\ \Pi^{\backslash\backslash}_{M_{CM}} &= I - \Pi^{\perp}_{M_{CM}} \end{aligned} \tag{5}$$

where M_{CM} is the response matrix linking all correctors to all monitors, $\Pi^{\perp}$ and $\Pi^{\backslash\backslash}$ are projection operators mapping any vector into components outside and inside the subspace spanned by the column vectors of M_{CM}, and K and Δ are the error vectors of Eqns (3) and (4). Eqn (5) is intuitively obvious since no corrector system can eliminate an orbit error pattern which is outside the corrector's reach, while only the part of a "fake" orbit error pattern due to monitor offsets that is *correctable* will lead to real but unobserved residual orbit errors after correction. An important task for any intelligent orbit correction algorithm is to distinguish the signature of these two very different sources of errors before applying correction. This can not be achieved exactly since the problem is usually underconstrained. An algorithm developed to obtain consistent estimates however proved successful in a wide range of cases. This is described in the following sections.

3.1 Alignment biased solution

We start with the extreme assumption that any discrepancy between observed orbit, corrector strength, and model

$$Y_i = X_i - \sum_j M_{ij} \bullet C_j \tag{6}$$

is predominantly attributable to monitor errors. We then perform singular value decomposition (SVD) on the response matrix M_{AM} from a wide range of alignment error locations and coordinates to all monitors

$$M_{AM} = U^T \bullet W \bullet V .$$

The matrix V consists of orthonormal combinations of alignment errors which have decoupled effects in the monitor space represented by U. These effects U_i are then compared to Y_i of Eqn (6) in turn to identify the error combination responsible for Y_i. This is iterated to build a matrix N of combined error effects to account for Y_i

$$\begin{aligned} N_{ij} &= U_i^j \quad N^{\dagger} = N \bullet \left(N^T \bullet N\right)^{-1} \\ S_j &= \sum_i N^{\dagger}{}_{ji} \bullet Y_i \\ Y_i &\rightarrow Y_i - \sum_j N_{ij} \bullet S_i \end{aligned} \tag{7}$$

It was indicated that the orbit discrepancy Y_i is reduced at each iteration as more alignment errors are included, and thus will represent progressively more contribution due to monitor errors. Y_i is also used to update the weighting of monitors at every iteration to speed up the distinction of major monitor errors above noise level. The iteration is terminated when the algorithm detects an unnatural jump in the alignment error magnitude S_j in Eqn (7), signaling a monitor error being misinterpreted as alignment-induced.

3.2 BPM biased solution

We start with the extreme assumption that the orbit discrepancy of Eqn (6) is predominantly attributable to alignment type errors. We perform the same iteration process as described in the last section. The only difference is that the monitor weightings are not updated, and since the monitor errors are assumed to be more reliable, the iteration terminates when the orbit discrepancy is below a specified limit.

3.3 Interpolation between the biases

An entire spectrum of orbit interpretations can be interpolated between these two extremes. Such interpolation

also represents a compromise between globally and locally-oriented interpretations of the data, since the more alignment error one introduces to account for the discrepancy, the more emphasis is given to satisfying the short range observation at the expense of global consistency. This algorithm allows user defined criteria for choosing a desired interpolation, for example, the one with minimal combined RMS of alignment and monitor errors.

The introduction of alignment errors amounts to enhancing the fitting parameters in a rigid injection fit, with only responses from injection to monitors. We can represent this enhanced response with a matrix U_0 which contains at least the injection responses, and maybe any number of responses to alignment errors. The final residual correction error becomes, with input of the interpreted orbit:

$$E = \Pi^{\perp}_{M_{CM}} \bullet K + \Pi^{\backslash\backslash}_{M_{CM}} \bullet \Pi^{\perp}_{U_0} \bullet K - \Pi^{\backslash\backslash}_{M_{CM}} \bullet \Pi^{\backslash\backslash}_{U_0} \bullet \Delta \quad (8)$$

where the projection operators $\Pi^{\perp}$ and $\Pi^{\backslash\backslash}$ are as defined in Eqn (5). Depending on the predominance of alignment or monitor error, changing the content of U_0, amounting to interpolation between the two biases, can help offset the effects of K or Δ and reduce the overall residual error.

4 IMPLEMENTING VIRTUAL MONITORS

Once the interpretation of the underlying orbit is decided, we have the complete information of beam coordinate at any location. The virtual monitors described below use this information as input to the steering algorithms.

4.1 Generalized steering constraints realized as virtual monitors

Very often not only the orbit at the monitors are targeted for correction, but also injection angle at the end of the line, orbit at unmonitored locations, or even overall path-length need to be constrained simultaneously. Knowing the interpreted beam coordinate everywhere, one can easily include these as orbit errors at virtual monitors, and feed this together with the relevant response matrix elements and weighting to a generic steering algorithm. The latter has no need to know a priori that the input contains more than pure position data at the real monitors.

Another type of steering constraint happens with orbit dependent optics. When the orbit is changed, the higher order optical elements pick up extra contributions. We are especially interested in the effects of chromaticity-like elements T_{ij6}, the orbit effect of which on the linearized elements M_{i6} between points a and b can be expressed as

$$\delta M^{ab}_{i6} = \sum_{j\neq 6}\sum_{k}\sum_{c} 2T^{cb}_{ijk} M^{ac}_{j6} \delta X^{c}_{k} + \sum_{j}\sum_{c} 2T^{cb}_{ij6} \delta X^{c}_{j} \quad (9)$$

where we sum over all the locations c with appreciable coordinate change and/or T_{ij6}. The second term in the sum of Eqn (9) becomes dominant with large chromaticity-like optical elements and a steering constraint on the overall M_{i6} can be realized again through virtual monitors which simply have as response matrix elements the product of these T_{ij6}'s and the ordinary M_{i6}'s.

4.2 Virtual monitors created for singularity control

To combat the problem of excessive correction due to response matrix singularities, an algorithm is developed which automatically places extra constraints in the form of virtual monitors coupling strongly to the singular corrector combinations. It is outlined in the following.

1. Determine cutoff numbers R and S, R measures the evenness in corrector effect distribution among monitors reflected in SVD condition number. S with $0 < S < 1$ measures orthogonality of the corrector effects.
2. Form a set C_M of locations densely covering the beam line of interest, not necessarily tied to any physical elements. Form the response matrix M_{CA} from all correctors to these locations.
3. Perform SVD on the corrector-to-monitor response matrix M_{CM}, if the condition number $N^{svd}_{M^{CM}}$, i.e., the ratio between the largest and the smallest singular values, is greater than R, or the normalized Gram determinant $\overline{G}_{M^{CM}}$ [1] is less than S to the power of the number of correctors, continue.
4. Identify the row v of V with the smallest singular value.
5. Apply the matrix M_{CA} to the vector v. Identify its largest component with index j.
6. Place a virtual monitor at the j-th location in the set C_A.
7. Iterate steps 3-6 until $N^{svd}_{M^{CM}}$ and $\overline{G}_{M^{CM}}$ satisfy the conditions specified in step 3.

Once all the virtual monitors are identified, the interpreted orbit at these locations are added to the input orbit for the steering algorithm. The steering result should be automatically free of singularity.

5 STATUS OF APPLICATION

The algorithm described in this report has been prototyped in Mathematica and tested on a wide range of CEBAF machine data. From these tests the error analysis algorithm of Section 3 performed satisfactorily. It was used to identify BPM offsets and misalignments in various areas. Singularity-induced excessive correction has been observed in the lower arcs at CEBAF and verified by simulation. The algorithm of Section 4 for eliminating such problems using virtual monitors has been tested against simulation and found to perform extremely well. Inclusion of generalized steering constraints such as angle and path length has been tested in simulation. Inclusion of higher order optical effects has not been tested. Application to simultaneous multiple pass steering has been tested separately.

Implementation under the on-line control system [2] is being carried out. With the degree of versatility and robustness to be built into the production version, it is expected to meet the unique demands for global orbit control at CEBAF.

6 REFERENCES

[1] 'Methods of Orbit Correction System Optimization', Y. Chao, these proceedings.

[2] 'A Portable Accelerator Control Toolkit', William A. Watson III, these proceedings.

PULSE SELECTION CONTROL FOR THE IR FEL PHOTOCATHODE DRIVE LASER

K. Jordan, R. Evans, O. Garza, R. Hill, M. Shinn, J. Song, D. Venhaus
Thomas Jefferson National Accelerator Facility, 12000 Jefferson Ave., Newport News, VA, 23606

Abstract

The method for current control of a photocathode source is described. This system allows for full remote control of a photocathode drive laser for resulting electron beam currents ranging from less than one microamp to a full current of five milliamps. All current modes are obtained by gating the drive laser with a series of electro-optical cells. The system remotely generates this control signal by assuming a mode of operation with the following properties selectable: Current mode as continuous or gated, micropulse density, macropulse gate width from single shot to 1ms duration, macropulse synchronization to A/C line voltage (60 Hz) or an external trigger, 60 Hz phase and slewing through 60 Hz when applicable. All selections are derived from programable logic devices operating from a master-oscillator resulting in a discrete, phase stable, pulse control for the drive laser. Complete system documentation is available at http://www.jlab.org/fel

1 INTRODUCTION

A Free Electron Laser is under construction in Newport News Virginia. This facility will begin commisioning in the fall of 1997.

1.1 Driver Accelerator

A schematic representation of the infrared demonstration FEL[1] (IR Demo FEL) is shown in Fig. 1. Electrons are produced at 350 keV by a DC photocathode gun[2] driven by a Nd:YLF laser[3] and accelerated to 10 MeV in a superconducting RF (SRF) "cryounit", an accelerator of about 1 m active length. These electrons are then accelerated to 42 MeV by another SRF accelerator, a "cryomodule" (essentially 4 cryounits). The FEL is placed at the exit of the linac, the electron beam is deflected around the two optical cavity mirrors and then has two possible paths. One is straight ahead into a beam dump used for initial commissioning and tune up. The other is into a recirculation loop based on the isochronous achromats used in the Bates accelerator[4]. This latter path allows the electron beam to be recirculated for energy recovery and deceleration in a 10 MeV dump[5,6].

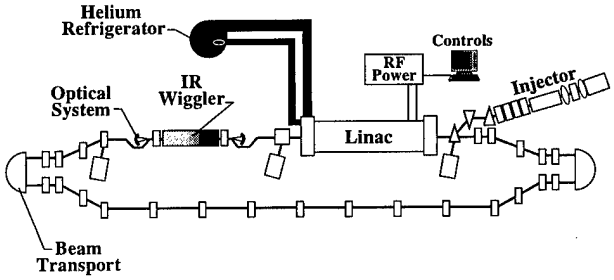

Figure 1. Schematic Layout for IRFEL

Since many of the electron beam properties such as charge/bunch and time structure are a reflection of the laser's beam, some attention has been devoted to its characterization. Equally important has been the development of robust pulse selection techniques capable of delivering the temporal formats (for both micropulse and macropulses) required for commissioning and operation of the FEL. Unlike the usual laser laboratory environment, the drive laser must run unattended for long periods of time, and have remote control and monitoring of its output. As is common in the industry, the pulse selection equipment we purchased was not capable of remote control, so a system was developed and implemented to add that capability. This paper describes our approach and the results.

2 PHOTOCATHODE DRIVE LASER

A schematic representation of the drive laser transport system is shown in Fig. 2. Our drive laser is a frequency-doubled Antares™ mode locked Nd:YLF laser from Coherent, Inc. It differs from the standard product in its operating frequency of 74.85 MHz (1/20th the SRF cavity frequency) and modifications to the laser's optical components to allow insertion of an electro-optic modulator (EOM) before the frequency doubler. The purpose of this EOM is to drop the micropulse repetition frequency to 37.425 MHz, which yields the highest laser gain for our existing machine design. This EOM is a fixed-frequency device and will not be discussed here. Instead, we will concentrate on two EOMs located downstream of the laser, which control the macropulse structure and micropulse frequencies $\leq$ 37.425 MHz. These EOMs are identical and along with their associated electronics were purchased from Conoptics, Inc. (Danbury, CT). They are of the transverse electric type, using KD*P crystals with a total path length of 160 mm and an aperture of 2.9mm. They are "dry" EOMs, the ends of the crystals are AR-coated, rather than immersed in index-matching fluid. Earlier attempts to use "wet" EOMs were abandoned when we determined the fluid caused thermal blooming for average input intensities exceeding about 25 W/cm^2 (for ~ 45 ps FWHM pulses). The EOMs require a DC bias and fast-slewing voltage source (~ 160V). This, and the pulse control unit (also known as a synchronous countdown) were purchased from the same vendor (model 25D and 305, respectively).

0-7803-4376-X/98 /$10.00 © 1998 IEEE

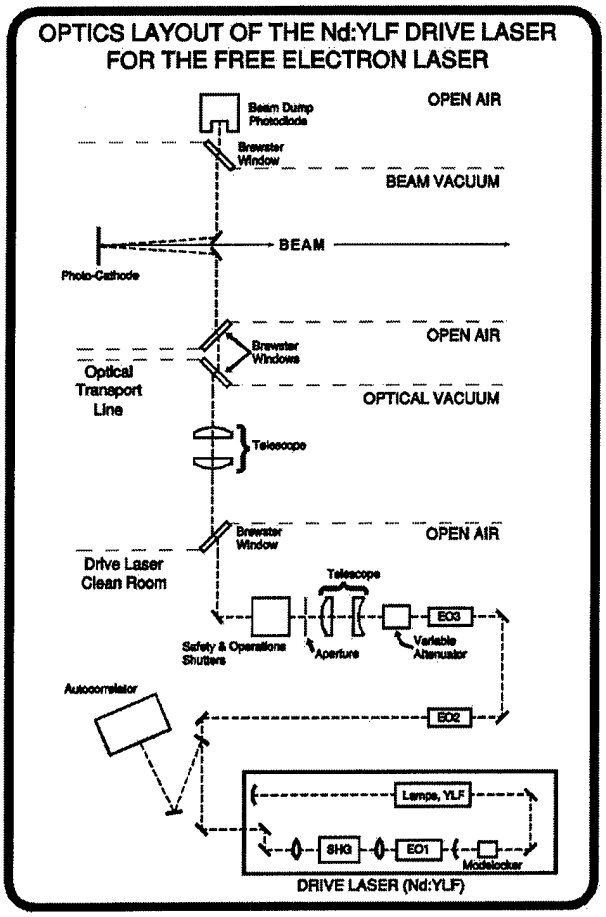

Figure 2. Drive Laser Transport System

2 PULSE CONTROL ELECTRONICS

The pulse control electronics enable full duty cycle control from 100% to less than 0.02% while holding the charge per bunch constant. A system level block diagram is shown in Figure 3. The space charge dominated optics require that the charge per micropulse be between 60pC and 135 pC for clean transmission.

2.1 Pulse mode Gate width

Commissioning of the electron beam will be done beginnning with average electron beam currents of less than 1 μAmp. This minimizes the burn through hazards associated with initial threading of the electron beam. There are 16 choices of gate widths. These gate widths are easily reprogrammed in the Programable Logic Devices (PLDs). The different electron beam diagnostic devices require varying average beam currents. The BPM'srequire a minimum current while the multislit emittance monitor[7] is limited to a fraction of the full beam current.

The rising and falling edge of the gate pulse is preset to occur at the trough of the optical pulses. This enables the system to be setup, once all cables are in place, such that the first and last optical pulse do not get truncated.

2.2 CW Frequency

The electron machine and FEL wiggler are designed to operate with an average beam current of 5 milliamps. The machine optics are designed for bunch charges ranging from 135pC - 60 pC, which in the injector is heavily space charge dominated. The average electron beam current for CW operation is controlled by using a variable attenuator in conjunction with the Conoptics unit to divide the drive laser output frequency by factors of two. This function is implemented in the Conoptics model 305. We have modified this chassis by adding a daughter board with opto-couplers in order to interface to the EPICS control system. This system is able to operate at 40th subharmonic of the superconducting RF cavity frequency 1497MHz and below; 37.425MHz, 18MHz, 9MHz, 4MHz, 2MHz, & 1MHz.

2.3 60 Hz Line Synchronization

The line frequency synchronization system is designed to allow the operation crew to readily check for 60 Hz interference from motors or transformers too close to the beamline. The EPICS interface allows the operator to either single step or sweep the macropulse through 22.5 degree steps of the 60 Hz wavelength. In the sweep mode the operator can optimize the sweep freqency such that the beam, when observed on a beam viewer the spot should appear stable in the absense of any stray 60 Hz fields. In the event that there is excessive 60 Hz magnetic fields in the area of the electron beam transport, the beam spot will appear rhythmically unstable, with an amplitude proportionate to the magnitude and position of the 60 Hz interference.

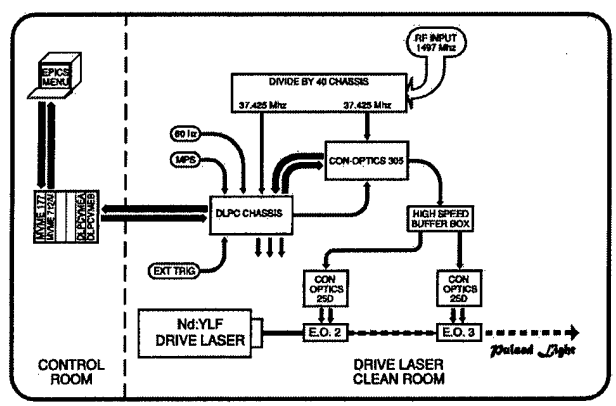

Figure 3. Block Diagram of Pulse Control Electronics

2.4 Machine Protection Interface

The electron accelerator has four distinct beam modes for comissioning and operation: 1. Injector startup; this is average current limited by a ceramic beam viewer (cromox) to less than 100nAmp. 2. Multi-slit Emitance measurement; this device is average power limited to dissipate 100 watts or less. 3. Tune-up beam; For

general beam startup the macropulse is set to 250 microseconds at a CW fequency of 18.7125 Mhz. This is the minimum beam for reliable operation of the beam position monitors. 4. Unlimited; All protection systems are active and the beam is allowed to run at any current up to the design value of 5 milliamp at an energy of 43 MeV.

A single fast shut down interface now exists; when any of a number of faults occurs, the system sets the laser to pulsed mode and removes the gate pulse shutting down the drive laser and hence the electron beam in a few microseconds. In addition to the EOM shutter a mechanical shutter also closes.

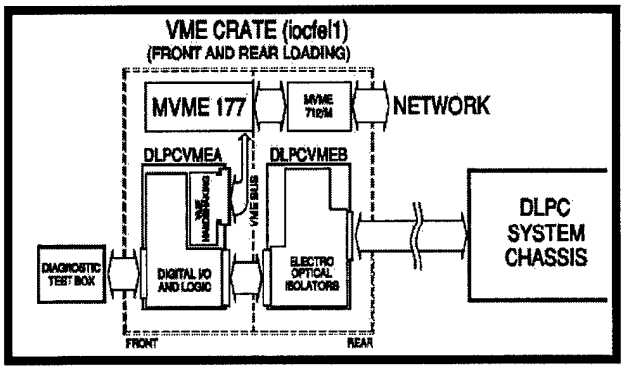

Figure 4: Simplified Diagram of Remote Inteface System

2.5 Remote Interface

The Drive Laser Pulse Control System (DLPC) is operated remotely from a VME based microcontroller located in the FEL Control Room (Area 7). This VME crate is fitted with two custom built VME modules which bridge the gap between the DLPC system and the VME system (see figure A). The DLPC control cable connects to a board fitted in the rear plane of the crate (DLPCVMEB). The function of this module is to optically isolate all electrical connections from the DLPC chassis and rout them through the user-defined pins of the P2 connector of the VME Bus. These control signals are driven by a simple VME slave module (DLPCVMEA), which is fitted into the front plane of the VME crate. The DLPCVMEA module is classified as an A16:D16:D8 device. The DLPCVMEA also has the ability to display all of it's current setting to a Diagnostic Test Box which is easily inserted and removed at any time. The two boards (DLPCVMEA and DLPCVMEB) working together empower all functions of the Pulse Control System to be governed by the IOC of the VME crate (iocfel1). The IOC is made accessible to the network using a standard Ethernet adapter, and can be communicated with from any number of locations. From this point, all command functions and status readback items can be observed and/or modified by other systems if and when appropriate, such as the Machine Protection System and Instrumentation and Controls by the Operators.

3 FUTURE DEVELOPMENTS

This system as described is operational in the Injector Test Stand (ITS) for the FEL. Beginning in June of 1997 the ITS will be moved to the new FEL building. Commisioning will begin in the new facility in early fall 1997. Also, the system described is the first attempt at fulfilling the design requirements for a pulse control system for the FEL. It was designed and built around other key devices involved with the operation of the drive laser. In some regaurds, the functionality of the Pulse Control System is limited by these devices. The primary example of this effect is the lack of communication between the DLPC Chassis and the Con-Optics 305 Chassis. More specifically, the DLPC synthesizes the signal used by the C/O-305 to gate the micropulse stream. The problem arises when low frequencies are chosen for the micropulse stream. In this condition, if the operator chose a gate width less than the period of the drive laser output no light would be emitted. This can easily be resolved in either PLD code or software.

4 ACKNOWLEDGEMENTS

Work supported by the U.S. Department of Energy under contract number DE-AC05-84-ER40150 and the Office of Naval Research.

5 REFERENCES

[1] C. L. Bohn, *et al.*, "Recirculating Accelerator Driver for a High-Power Free-Electron Laser: A Design Overview", these proceedings.

[2] H. Liu, *et al.*, "Design of a high charge CW photocathode injector test stand at CEBAF", Proc. 1995 Particle Accelerator Conf. Dallas TX 1995.

[3] S. Benson and M.D. Shinn, "Development of an Accelerator-Ready Photocathode Drive Laser at CEBAF" Proc. 1995 Particle Accelerator Conf. Dallas TX 1995.

[4] J. Flanz, G. Franklin, S. Kowalski and C.P. Sargent, MIT-Bates Laboratory, Recirculator Status Reports, 1980 (unpublished); described in R. Rand, "Recirculating Electron Accelerators" (Harwood, New York, 1984) pp 107-109 and pg 155.

[5] D. Neuffer et al., Nucl. Inst. and Meth. A **375** 123 1996.

[6] Laser Processing Consortium "Free-Electron Lasers for Industry", available from the FEL Dept. Office, Jefferson Lab, Newport News, VA. 1995.

[7] P. Piot, J. Song, R. Li, G.A. Krafft, D. Kehne, K. Jordan, E. Feldl, and J.-C. Denard "A Multislit Transverse-Emittance Diagnostic for Space-Charge-Dominated Electron Beams" these proceedings.

EXPERIENCE WITH VSYSTEM IN A WIDE VARIETY OF APPLICATIONS

Peter N. Clout, Robert T. Westervelt, Vista Control Systems, Inc., 134B Eastgate Dr., Los Alamos, NM 87544

Abstract

Vsystem [1-3] has been developing rapidly with the demands of industrial and research users as well as with promising research into smart controls [4-8]. A significant development has been the fielding of V3.0 on VxWorks, Digital UNIX, Concurrent power/UX, and Solaris as well as our traditional platforms. One application running is with Vaccess on all three of VxWorks, VAX/OpenVMS, and Alpha/OpenVMS in one system. Other applications use Digital UNIX and Concurrent Power/UX. Our new version of the logger has been running in a power plant for over a year, acting as a black-box flight recorder, recording data at 33Hz and 100Hz. We are also installing a power-plant training system emulating the operator's home system with Vdraw and Vaccess running under Digital UNIX. For a new contract for an equipment vendor, we have finished the port of the full Vsystem package to Windows 95 and Windows NT. We made the first tests of charged-particle beam line automation and optimization with a generic automation package. This package has been developed against realistic models and exemplifies on-going research and development at our company.

1 VSYSTEM ARCHITECTURE

The Vsystem architecture is quite unlike any other product. It consists of a software bus/database, Vaccess, that connects all the computers in the system regardless of their architecture or operating system. Any computer can have 0-65,000 separate databases mapped in individual global sections; any process on any computer can access any field of any channel in the system. Vaccess is event-driven, which means that any process can request notification of changes of any field of any channel in any database. Equally, any field can be changed dynamically (except name, type, and array dimension). In V3.2, due late this year, dynamic channel creation will be supported. Figure 1 gives a picture of this software architecture and it can be seen that it is very much like plugging independent modules into a backplane of an I/O crate. This gives modularity and isolation through the operating system.

A key aspect in the use of this architecture is to use channels for calculated information so that it can easily be displayed and logged. An additional advantage of this architecture is that in place of the I/O connection, one can put a model of the accelerator and generate a training system or a log file playback utility and look at earlier operations. With the sophisticated database resolution mechanism, the playback and training systems can coexist on the same network as the production system.

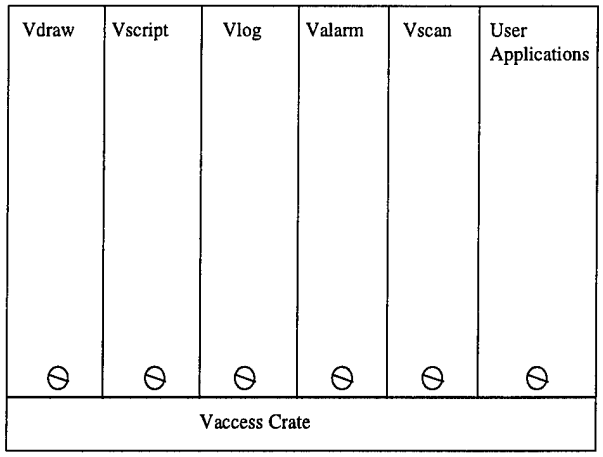

Figure 1: The Vsystem Architecture

2 INDUSTRIAL APPLICATIONS

2.1 Metal Casting and Rolling Mills

We have a number of applications in the metals industry where plants are being modernized with modern, fast controls in order to significantly improve efficiency and quality. These systems all use fast I/O, VME, VXI, and RTP Corp. as well as PLCs for the slower I/O. The fastest loops, controlling the roller pressure of the roller stands and the looper positions between the roller stands, run at one millisecond intervals in VME crates under either Digital VxWorks or Wind River VxWorks. In order to reduce unnecessary risk, the next level of computers are VAX's and Alphas running OpenVMS. All these systems have been in operation for some time and are performing well. Vsystem allows the implementers to map databases in all parts of the system. As a result, channels that relate mainly with activities in the OpenVMS computers, the less deterministic systems, can be placed in databases in these OpenVMS systems. This results in higher performance and less load on the highly deterministic VxWorks systems.

2.2 Power Plant Training Systems

Another client is a Power Plant Training School where they bring in operators for training from plants of several European countries. This training system has a super-computer running the plant model and communication with our system through reflective memory in a VME

0-7803-4376-X/98/$10.00 © 1998 IEEE

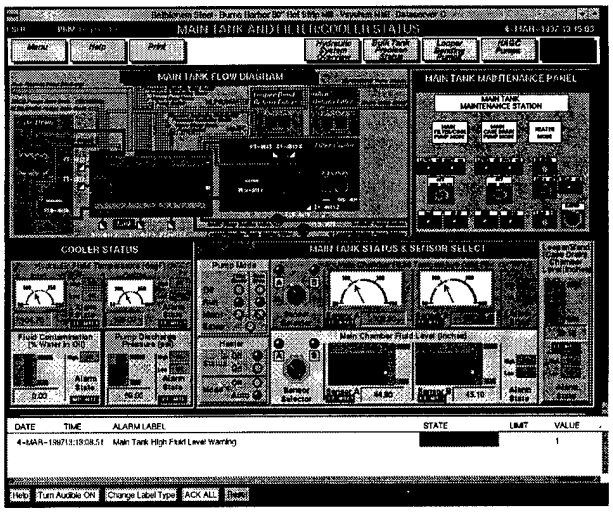

Figure 2: An Example Operator Window from a Hot Strip Mill.

crate. An Alpha single-board VME computer running Digital UNIX provides the second step of the link through to a Vaccess database in a workstation running Digital UNIX. Here also the operator interface emulation is implemented with Vdraw.

We used Vdraw to emulate older proprietary digital control systems from the student's home plant and added to Vdraw a few features to fully accomplish this. One new feature allows the operator to use a key to tab around the active areas on the screen. Another is the "picture-in-a-picture" (PIP) feature that makes it possible to include a portion of a Vdraw picture in a Vdraw window and to dynamically change this as the value of a channel changes. In this way, 12 segment files defining faceplates are used to create 15,000 screens through relationship tables, special Vaccess channels and handlers in the Vaccess database.

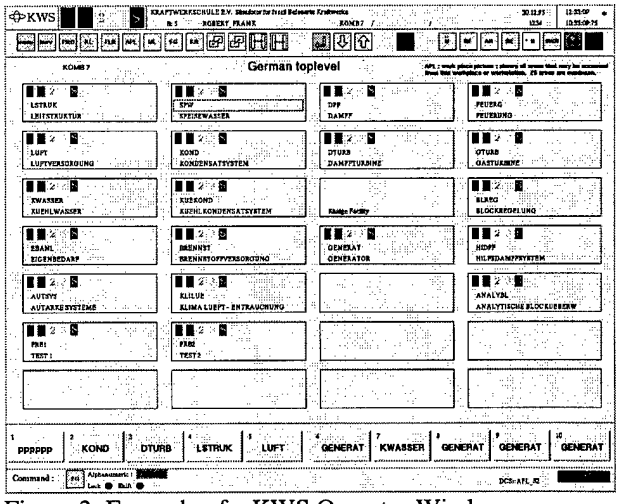

Figure 2: Example of a KWS Operator Window Constructed Automatically.

This saved the creation and maintenance of 15,000 individual pictures by hand. One of these pictures is shown in figure 2. Thus, the whole operator interface system is *automatically* defined for this emulation, including window relationships, content, and so forth. In addition, a custom, industrial keyboard has been integrated into the system in addition to the regular keyboard, to better represent the systems being emulated.

2.3 Wafer Processing Machines

Semiconductor foundries use machines from several different vendors to process the silicon wafers. Until very recently, all the vendors had their own operator interface, which led to confusion for the operators moving from one machine to the next. Sematec, the US semiconductor industry consortium, generated a man-machine interface standard for these machines and we have implemented this for one of our customers to the Sematec Standard. This was done with the standard Vdraw with some minor additions to the package to support touch screens. Figure 3 shows one of the MMI screens.

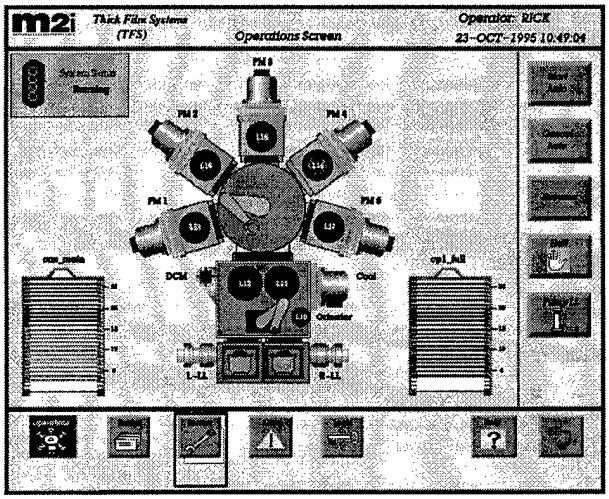

Figure 3: One of the Semiconductor Processing Machine Screens

2.4 Black Box Flight Recorder

Another application is the recording of plant operation data in a circular buffer on disk so that the engineers have high time resolution data to study. Such a system has been running at a European Nuclear Power Plant for over a year and two more systems are currently going into petrochemical plants.

These applications emphasize the performance of Vlogger. Logging over 13,000 values a second continuously into a 3-day long buffer makes the buffer large and thus the users needed search tools to find the point of interest and other tools to access and save this data. We have a full graphical user interface with an API for programming and an SQL interface for searching. Vtrend gives a graphical look at the data, as shown in Figure 4, and this can be started automatically at the point of the search.

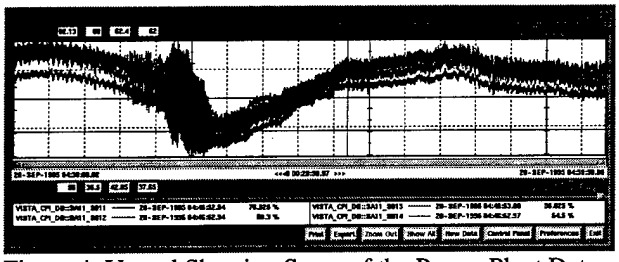

Figure 4: Vtrend Showing Some of the Power Plant Data

3 AUTOMATION

The architecture of Vsystem lends itself naturally to automate operations [4-8]. We are in the process of developing tools to tackle the control problems in an accelerator and apply solutions with the aim of complete automation and automatic optimization of an accelerator. These tools are not specific to one or a few control technologies but form a general framework within which to include appropriate control technologies. The goal is to improve on the performance of the operator and physicist. The first tests have now been carried out at the ATF accelerator in Brookhaven and the Atlas facility at Argonne. We expect that this work will lead to new members of the Vsystem family of products

4 IMPACTS ON VSYSTEM

All the examples given are industrial applications. This is not to ignore the research applications where Vsystem is used but rather to show the many common requirements between research and production environments. There are some important differences however.

In industrial production, productivity is easily measured and monitored by all layers of management. Imagine that the stock of all laboratories was quoted on some stock exchange and market analysts were monitoring performance in papers published and prizes won for outstanding research. This is essentially the case for industry. Profit, a combination of productivity, costs and sales, is the dominant measure of success. The only argument is whether one should take a long-term investment view or a short-term one. As a result, reliability is essential for any component of the plant. Here, perhaps, is one of the biggest impacts on Vsystem from the marketplace.

Another impact is the diversity of operating systems that customers demand support for. While many new applications are using OpenVMS because it is proven for continuous operations, some customers have migrated to UNIX. In addition, support is required for hard real-time operating systems like VxWorks and other customers are using Windows 95 and Windows NT. Vsystem supports all these operating systems.

For larger applications, the PIP feature of Vdraw gives the basis for automated generation of operator screens through a data description of the machine. This saves considerable configuration and maintenance effort and thus cost.

5 CONCLUSION

It is clear from this short paper that Vsystem has found a market in industrial systems where the requirements are often more stringent than in typical accelerator control systems. Even so, Vsystem has not lost any functionality or performance and thus is an even better solution for accelerator control systems for accelerators of all sizes. A recent performance benchmark by a user measured 8.2×10^6 floating point numbers/second put to the Vsystem database on a Pentium Pro 200MHz running Windows NT.

Excellent documentation and support makes Vsystem especially suitable for small and medium sized projects with limited staff. All the evidence suggests that with similar resources, better and more comprehensive control systems result than with any other solution. Certainly, existing users benefit from the continual additions to the Vsystem package. For example, Vsystem now fully supports many operating systems on many computer architectures.

6 REFERENCES

[1] P. N. Clout: 'The Influence of industrial Applications on a Control System Toolbox', Proc. ICALEPCS'91, KEK Proc. 92-15 (1992) 287-290

[2] P. N. Clout: 'Status of Vsystem', NIM A 352 (1994) 442-446

[3] P. N. Clout: 'Status of Vsystem', Proc. IWCSMSA'96, KEK, Tsukuba, in press

[4] C. R. Stern, W. B. Klein, G. F. Luger, M. Kroupa: 'Adcuctive Model Refinement for Accelerator Control', Proc. Conf. Computing for Accelerator Physics, 1966.

[5] W. B. Klein, C. R. Stern, G. F. Luger, E. T. Olsson: 'An Intelligent Control Architecture for Accelerator Beamline Tuning', Proc IAAI '97, In Press.

[6] W. B. Klein, R. T. Westervelt, G. F. Luger: 'Developing a General Purpose Intelligent Control Systems for Particle Accelerators', J. Intelligent and Fuzzy Systems, 1997, In Press

[7] W. B. Klein, C. R. Stern, G. F. Luger, E. T. Olsson: 'Designing a Portable Architecture for Intelligent Particle Accelerator Control', Proc. this Conf.

[8] C. R. Stern, W. B. Klein, M. Kroupa, R. T. Westervelt, G. F. Luger: 'Tuning and Optimization at Brookhaven and Argonne: Results of Recent Experiments Using a Portable Intelligent Control System', Proc. this Conf.

TUNING AND OPTIMIZATION AT BROOKHAVEN AND ARGONNE: RESULTS OF RECENT EXPERIMENTS

W. Klein, C. Stern, M. Kroupa, R. Westervelt, Vista Control Systems, Inc., and
G. Luger, E. Olsson, University of New Mexico

Abstract

Vista Control Systems Inc. is developing a portable system for intelligent accelerator control. Our system is general purpose and has been designed to be reused at multiple accelerator facilities. This portability arises from the hierarchical object-oriented nature of the architecture. The control system employs a multi-level organization in which knowledge based inferencing is used to dynamically configure a variety of optimization and control algorithms. We discuss results from recent beamline tuning tests at the Brookhaven National Laboratory ATF and the ATLAS facility at Argonne. Results are analyzed along a number of dimensions, including portability, performance as benchmarked against human tuning, adaptive behavior, noise handling, integration of control subsystems, and support for rapid knowledge capture and utilization.

1 THE ARCHITECTURE

This system is based on a hierarchical distributed architecture. At the lowest level, a physical access layer (PAL) provides an object-oriented abstraction of the target system. A series of intermediate layers implement general algorithms for control, optimization, data interpretation, and diagnosis. Decision making and planning are organized by knowledge-based components that utilize knowledge acquired from human experts to appropriately direct and configure lower level services. The general nature of the representations and algorithms at lower levels gives this architecture a high degree of portability. The knowledge-based decision-making and planning at higher levels also supports a real-time capability for adaptation to unexpected events and changing environments [1, 2, 3].

2 DESCRIPTION OF EXPERIMENTS

We carried out experiments at two accelerator facilities: Brookhaven National Laboratory's Accelerator Test Facility (ATF), and Argonne National Laboratory's Advanced Tandem Linear Accelerator Site (ATLAS). The experiments were designed to address common beam line tuning tasks which are currently performed strictly through human interaction. These experiments vary in their difficulty, but each tests some features of the control architecture These experiments vary in their difficulty but each tests some set of features of the control architecture such as knowledge based control, use of solvers (optimizers) for low level control, integration of knowledge based and analytic methods, component based programming, and task decomposition and delegation.

The Brookhaven ATF consists of a beam source, a linear accelerator, a transport line, and three experimental beam lines. Electrons are generated from a pulsed laser striking a cathode and are initially accelerated by an RF device known as a klystron. This beam source generates short bunches of electrons at a rate of 1.5, 3, or 6 Hz. Electrons travel from the source through a solenoid magnet and then a short distance into the accelerator tube. After exiting the accelerator, the beam travels through a beam line section to an achromat, then through another short beam line, and finally into one of the beam lines in the experimental hall.

Our tuning experiments were directed to experimental beam line 3, whose purpose is to support research with a free electron laser (FEL). The FEL is a device which produces a laser beam from a interaction caused by accelerated electrons passing an undulator or wiggler. In order to cause the FEL to laze efficiently, the beam must be carefully transported from the beam source, through the accelerator, and into the entrance of the FEL. At the entrance, the beam must have a specific size and shape. Tuning must also produce a waist condition inside the undulator. A waist is related to a beam's sigma matrix [1]. To date, no human operator has successfully achieved vigorous lasing in the FEL.

Our first experiments tuned and conditioned the beam to the end of the H beamline. This involved transporting the beam to a set of beam position monitors (BPMs) at the end of the H line, and then producing a minimum spot in the X and Y axis at the first BPM. For a variety of reasons, we have not yet attempted to use the control system to tune the source or the klystron themselves.

Argonne's ATLAS is a heavy-ion facility whose main purpose is to conduct experiments using isotopes of a wide variety of single elements. Ions can be generated from a high voltage platform and accelerated by the PII accelerator, or from a second platform and accelerated by a large tandem VandeGraf accelerator. A single beam line transports ions from either source down to a target area in one of many experimental lines.

At ATLAS, our tuning experiments were directed to the PII line between the high voltage platform and the PII accelerator. Ions leave the platform in a stream, are

0-7803-4376-X/98 /$10.00 © 1998 IEEE

transported through a short section of beam line, through an achromatic bend which turns the beam 180°, and then through a section designed to chop and bunch the beam into packets and prepare it for the PII accelerator.

A standard tuning procedure for the PII linac breaks control into four sequential parts: tuning the PII0 line, tuning the PII1 achromat, tuning the PII2 beam line, and then refining the entire tune to produce proper beam conditions at the exit to the PII linac. Tuning procedures for ATLAS are similar to those at ATF. The existence of faraday cups and wire-scanning profile monitors, as well as a shortage of tuning elements, caused the full beam tuning to differ significantly. Our task was to port the control system from the ATF to ATLAS and tune the entire PII beam line.

3 FIRST STEPS AT BROOKHAVEN

To steer through the accelerator, it is required to put the beam on center in order to maximize beam intensity and minimize distortions of beam structure. This task is particularly challenging because of the lack of diagnostics inside the accelerator, making the task of correct steering wholly dependent on metrics of the beam's quality as it exited the accelerator.

We used a variety of algorithms during steering optimization. These employed an evaluation function combining metrics of beam intensity, spot size, and beam structure based on data from a profile monitor after the accelerator. Algorithms included two knob hill climbing, gradient descent, and a genetic algorithm.

The two knob hill climbing algorithm achieved tuning results that were comparable to, and in some cases exceeded, the best human tuning efforts. A key to the successful application of these algorithms was the proper sequencing of tuning actions. Heuristics derived from human experts proved effective in selecting the next tuning element and action for the tuning sequence.

The second task at Brookhaven was to steer as well as possible through a set of quadrupole magnets. A beam that passes through a quadrupole magnet off center is steered to a degree proportional to the magnetic field strength and magnitude of the offset. This is undesirable since quadrupoles are used primarily for focusing. The control system was generally more successful at this task than human operators. Minimization of quadrupole steering requires a tedious repetition of steps, including manipulation of quadrupole field strengths after each adjustment of steering magnets to measure the strength of quadrupole steering. Humans exhibit little patience for the number of steps required to effectively perform this task, and as a result, often do an inadequate job.

By the time of our last visit to Brookhaven in March 1997 we were able to build individual subsystems to perform each of the required control tasks at a level of performance comparable to that of the human operator. At the time what we lacked was a methodology for coordinating the sequencing of control operations, i.e., for executing a control *plan*, that would take the beam from the source to the FEL.

4 PORTING TO ARGONNE

The primary effort in porting the PAL from the ATF to ATLAS was in modifying Vsystem channels [3] encoded in various objects to point to appropriate values in the ATLAS control database. Similarities between magnet types were reflected by similar channel structures between the facilities. We added new classes to the PAL [2] for Faraday cups and slits, and modified existing classes for profile monitors and steering, quadrupole, and dipole magnets. We estimate that porting the control system was accomplished in approximately one person week of programming time.

5 NOISE HANDLING

Noise is significant in inhibiting effective beam tuning at ATLAS, where the difference between peak intensities of two beam profiles taken in series can exceed 50%. Background noise in a single profile or pulse is high, causing simple feature detection algorithms to fail. Human operators ignore noise without use of conscious thought. Experienced tuners understand the difference between incidental beam loss due to aberration and recurring loss from source instabilities. Experts are good at identifying relevant features from noisy distributions.

The control architecture does not deal with noise in a single standard way, but divides the problem into various levels based on correspondence between noise frequency and knowledge necessary for its interpretation and filtering. The initial processing of information in the control architecture occurs in the PAL, where data filtration is necessary to respond to higher level beam feature measurement requests. The PAL allows the control system to select from a variety of tools to deal with observed noise. The PAL performs initial averaging of the beam data retrieved from both Faraday cups and profile monitors. Averaging is through software internal to the PAL and PAL manipulation of various device drivers and hardware features. The controller selects an averaging level based on signal to noise ratio versus the time delay necessary for taking extra samples.

To compensate for pulse-to-pulse noise, we implemented a solver-level algorithm for taking measurements based on prediction. The solver worked by tracking control actions performed in succession, and comparing new values to the projected trajectory. The trajectory was defined by a vector of first and second derivatives calculated from changes in control values from changes

in beam measurements. This predictive algorithm is simple and works well for well-behaved functions whose measured derivatives offer good local approximations.

6 GOAL REDUCTION AND REACTIVITY

The beam tuning experiments at ATLAS illustrate a control architecture designed to respond to and implement user goals. Goals are given to a high-level controller which decomposes them and delegates action to other controllers. As these units meet conditions outside their locus of responsibility, they request assistance from their parent. Parents coordinate the activity of child controllers based on an understanding of the tasks each can accomplish [1]. The controllers coordinating beam sections implement plans adopted from human experts. Plans are carried out in a reactive manner using the teleo-reactive (TR) paradigm [3].

Two events in our experiments at Argonne were particularly noteworthy. We interviewed the resident tuning [1] expert to learn the proper sequence of actions necessary to tune the PII beamline. This physicist found the TR condition-action rule representation particularly intuitive and was able to directly encode appropriate tuning algorithms. The second was the observation of the control system exhibiting spontaneous adaptive behavior that had not been intentionally preprogrammed. In performing a sequence of focusing actions the control system would regularly backtrack to steering whenever quadrupole steering would cause excessive movement of the beam centroid and a consequent loss of beam transmission.

7 COMPARISONS OF PERFORMANCE

The two knob hill climbing algorithm achieved results that were comparable to, and in some cases exceeded, the best human tuning efforts. A key to the successful application of these algorithms was the proper sequencing of tuning actions. Heuristics derived from human experts proved effective in controlling the selection of the next tuning element and tuning action in the sequence.

During our visit to Argonne in late March we demonstrated the feasibility of a larger scale integration of control components to perform an extended tuning task. The control system used a total of 18 controllers and solvers to tune a sequence of three transport sections. It used four teleo-reactive controllers [3], corresponding to the three sections of the beamline and a supervisory controller, to orchestrate the sequence of control actions and to alternate back and forth between control and diagnostic elements in different sections. On two separate days of testing, and under somewhat different beam conditions, this system achieved beam transmission levels equaling or exceeding the best tunes of human operators in roughly comparable amounts of time (Table 1). In every case, human operators could not improve the tune achieved by the control system, indicating that the control system had found each time at least a local optimum.

Control Element	Our Tune	Operator Tune
STP001_X	-0.65	-0.69
STP001_Y	-0.20	-0.14
QDP001_X	4.09	3.91
QDP001_Y	4.29	4.02
STP002_X	0.05	0.07
STP002_Y	-0.10	-0.12
Transmission	3.55 mA	3.65 mA
PMP001 Sigma_X	3.0513	
PMP001 Sigma_Y	5.3918	

Table 1. Comparing Control System and Operator Tunes at Argonne's ATLAS Facility[1].

8 SUMMARY

Over the past two years we have used more than four weeks of beam time running experiments at Brookhaven and Argonne. The result of this effort was construction of individual control components capable of a single tuning task such as producing a waist in the beam or minimizing steering through a sequence of quad magnets. In almost every case, performance achieved in these individual tuning tasks was comparable to the best tunes achieved by human operators. A good portion of our more recent effort has been spent coordinating the activity of these control subsystems to adaptively execute sustained sequences of control actions of the type required to tune the entire accelerator from source to target. At present, experiments using a teleo-reactive mode of execution have been very successful and suggest that this architecture may be well suited to the kind of control coordination demanded by the dynamic nature of the accelerator tuning task.

ACKNOWLEDGMENTS

This work was supported by a DOE SBIR contract (#DE-FG05-95ER81897) to Vista Control Systems, Inc. We thank Andy Jason of LANL, Richard Pardo of Argonne-ATLAS and Xijie Wang of BNL-ATF for helping us understand accelerator physics.

REFERENCES

[1] Klein W. 1997. *A Software Architecture for Intelligent Control*, Ph.D. Dissertation, Computer Science Department, University of New Mexico.

[2] Klein, W., Stern, C., Luger G., and Olsson, E. 1997. Designing a Portable Architecture for Intelligent Particle Accelerator Control, *Proceedings of the Particle Accelerator Conference*, American Physical Society.

[3] Klein, W., Stern, C., Luger, G., and Olsson, E. 1997. An Intelligent Control Architecture for Accelerator Beamline Tuning, *Proceedings of Innovative Applications of Artificial Intelligence*, Cambridge: MIT Press.

SPIN TRACKING STUDY OF THE AGS*

Haixin Huang, Thomas Roser, Alfredo Luccio
Brookhaven National Laboratory, Upton, NY 11973, USA

Abstract

In the recent polarized proton runs in the AGS, a 5% partial snake was used successfully to overcome the imperfection depolarizing resonances. Although some depolarization at intrinsic resonances are expected, the level of the depolarization does not agree with a simple model calculation. A spin tracking program is then used to simulate the real polarized proton beam in the AGS. The results show that, due to the linear coupling introduced by a solenoidal 5% partial snake, the polarized beam will be partially depolarized also at the so-called coupling resonance, which is related to the horizontal betatron tune. The synchrotron oscillation also affect the beam polarization to a smaller extent.

1 INTRODUCTION

The acceleration of polarized beam will encounter depolarizing resonances whenever the spin precession frequency exactly matches the frequency with which the protons encounter depolarizing horizontal magnetic fields. In the recent polarized proton run in the AGS, a 5% partial snake [1] was used to overcome the imperfection depolarizing resonances [2]. Fig. 1 shows the measured absolute value of the vertical polarization at $G\gamma = n + \frac{1}{2}$ up to $G\gamma = 22.5$ (solid points). For these measurements, the betatron tunes were set at $\nu_x = 8.80$, $\nu_y = 8.70$, and the acceleration rate α was about 1.1×10^{-5}. The pulsed tune-jump quadrupoles were not used in this experiment. As shown in Fig. 1, the depolarization resulted only from the three intrinsic resonances, located at $G\gamma = 0+\nu_y, 24-\nu_y$, and $12+\nu_y$, which the 5 % partial snake could not overcome. The observed level of depolarization at the intrinsic resonances were -65%, 63% and -49%, respectively.

Although some depolarization at intrinsic resonances are expected, the level of the depolarization does not agree with a simple model calculation. When calculating the intrinsic resonance depolarization, one has to take into account the beam distribution. Suppose the beam distribution is Gaussian, the effective polarization after passing through the resonance becomes,

$$\frac{P_f}{P_i} = \frac{[1 - \frac{\pi|\epsilon(\varepsilon_0)|^2}{\alpha}]}{[1 + \frac{\pi|\epsilon(\varepsilon_0)|^2}{\alpha}]}, \qquad (1)$$

where P_f and P_i are the polarization before and after the resonance crossing, respectively, $\epsilon(\varepsilon_0)$ is the resonance strength with rms emittance ε_0, and α is the resonance crossing rate. The measured normalized 95% emittance

* Work performed under the auspices of the U.S. Dept. of Energy

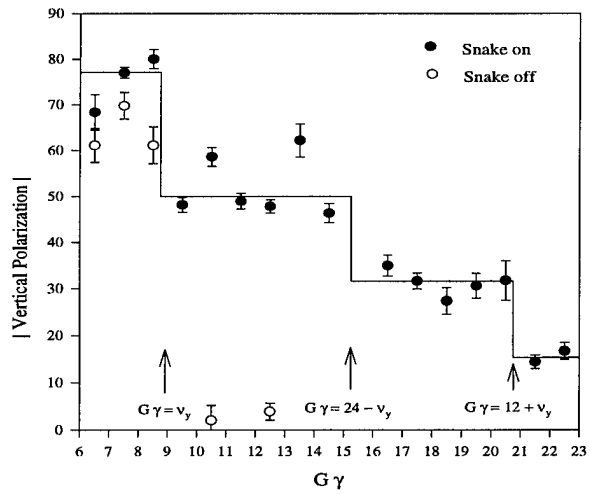

Figure 1: The measured absolute value of the vertical polarization at $G\gamma = n + \frac{1}{2}$ up to $G\gamma = 22.5$ (solid points). The acceleration rate α is about 1.1×10^{-5}.

$\varepsilon_{N,95\%}$ in the AGS is about 25~30 π mm-mrad; the acceleration rate α is 1.1×10^{-5}; and the resonance strengths of $0 + \nu_y$, $24 - \nu_y$ and $12 + \nu_y$ given by DEPOL [3] for a $\varepsilon_N = 10\pi$ mm-mrad beam are 0.0154, 0.00062 and 0.0054, respectively. With these numbers, the polarization after crossing each of the three resonances are $\frac{P_f}{P_i} = -0.94$ at $0+\nu_y$, $\frac{P_f}{P_i} = 0.90$ at $24-\nu_y$, and $\frac{P_f}{P_i} = -0.61$ at $12+\nu_y$, respectively. They are different from the measured values. Thus a spin tracking simulation is needed to understand the spin dynamics when a partial snake is inserted in the ring.

DEPOL [3], a program written by E.D. Courant, calculates the depolarizing resonance strength by Fourier analysis. The inputs of DEPOL are the outputs of a machine code such as MAD or SYNCH. DEPOL is simple but it requires a smooth lattice condition which is not satisfied by a ring with a snake inserted. Moreover, there is no way to include the effect of synchrotron motion, and linear coupling effect of a solenoidal snake. So a spin tracking program is needed to analyze the data obtained from the AGS partial snake experiment.

2 SPIN TRACKING PROGRAM

A tracking program SPINK [4] is used to track the polarized proton beam in the AGS. The idea is to track a group of protons, randomly generated with certain distribution in the phase space, through the machine lattice. Each proton is characterized by four transverse coordinates, two longitudinal coordinates and three spin components. Orbit matrices are built from a TWISS file, output of MAD.

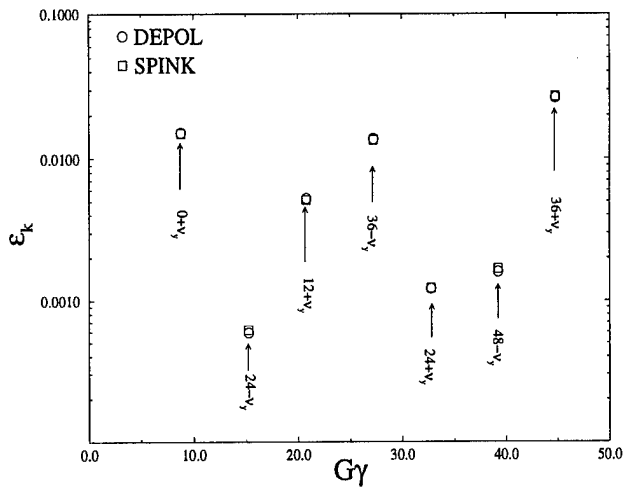

Figure 2: The comparison of results of DEPOL and SPINK for intrinsic resonances. The acceleration rate α used for SPINK is 4.5×10^{-5}.

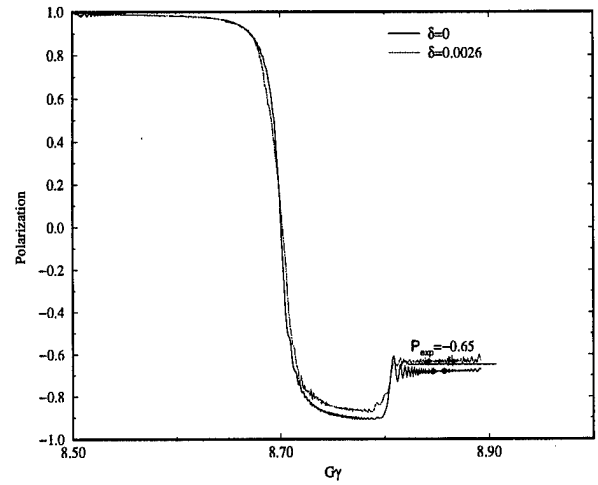

Figure 3: The simulation of crossing $G\gamma = 0 + \nu_y$, where $\nu_x = 8.80$ and $\nu_y = 8.70$. The momentum spread $\delta = 0.0026$ corresponds to emittance 0.8 eVs. The transverse emittances $\epsilon_x = \epsilon_y = 30\pi$ mm-mrad. The final polarization $P = -0.63$, which agrees with the experimental value $P_{expt} = -0.65$ within the error bar ± 0.05. The acceleration rate α is 1.1×10^{-5}.

Spin matrices are built for each piecewise constant magnet, which includes bending magnets (both separate function and combine function), quadrupoles (both regular and skew), snakes, rf cavities, spin flippers.

SPINK can be used to check the strength calculated by DEPOL if the resonances are well-separated and are not too strong. The first condition insures that the polarization is stable at the beginning of the tracking. The second condition should be met to avoid complete spin flip.

Suppose the initial polarization P_i is 1, then the resonance strength can be extracted from the final polarization $\langle P_f \rangle$ simulated by the tracking:

$$|\epsilon_k| = \sqrt{-\frac{2\alpha}{\pi} \ln \frac{(1 + \langle P_f \rangle)}{2}}, \qquad (2)$$

where $\langle P_f \rangle$ is the average of the polarization over a number of turns after crossing the resonance.

An example is given for the AGS lattice without partial snake. The betatron tunes are set to be $\nu_x = 8.717$ and $\nu_y = 8.766$, respectively. The same TWISS file is used as inputs for DEPOL and SPINK. For the imperfection resonances, the random error is chosen as Δy= 0.3 mm. For the intrinsic resonances, the particle is chosen on the boundary of the 10 π mm-mrad normalized emittance. The intrinsic resonance strengths are plotted in Fig. 2. The results of SPINK for the imperfection and intrinsic resonances agree well with those of DEPOL.

3 TRACKING FOR THE AGS BEAM

The SPINK program is then used to simulate the real polarized proton beam in the AGS. In the simulation, the betatron tunes, acceleration rate and the normalized longitudinal emittance are chosen as the experiment values; and for the simplicity, the two transverse emittances are set at the same value $\varepsilon = 30\pi$ mm-mrad. A group of 200 particles randomly chosen with a Gaussian distribution in transverse phase space and a parabolic distribution in longitudinal phase space are used in the tracking. The tracking results for $0 + \nu_y$, $12 + \nu_y$ and $24 - \nu_y$ are plotted in Figs. 3, 4 and 5, respectively.

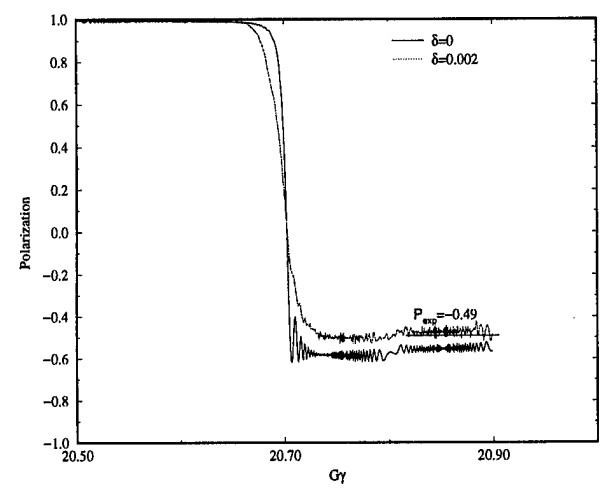

Figure 4: The simulation of crossing $G\gamma = 12 + \nu_y$, where the beam condition is the same as $G\gamma = 0 + \nu_y$. The momentum spread $\delta = 0.002$ corresponds to emittance 0.8 eVs. The final polarization $P = -0.47$, which agrees with the experimental value $P_{expt} = -0.49$ within the error bar ± 0.05.

Figs. 3 and 4 clearly show that there is an extra resonance adjacent to the intrinsic resonance, which causes depolarization. This additional resonance can be easily understood as a linear coupling effect. The solenoidal partial snake introduces considerable linear coupling between the two transverse betatron motions. Due to the coupling,

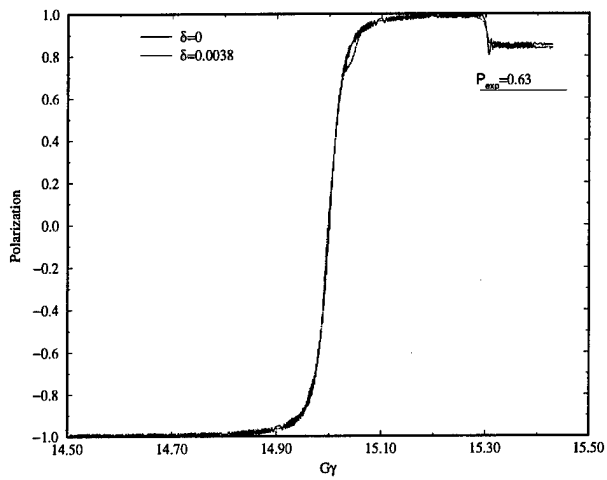

Figure 5: The simulation of crossing $G\gamma = 24 - \nu_y$, where the beam condition is the same as $G\gamma = 0 + \nu_y$. The momentum spread $\delta = 0.0038$ corresponds to emittance 0.8 eVs. The final polarization $P = 0.83$, which is higher than the experimental value $P_{expt} = 0.63$.

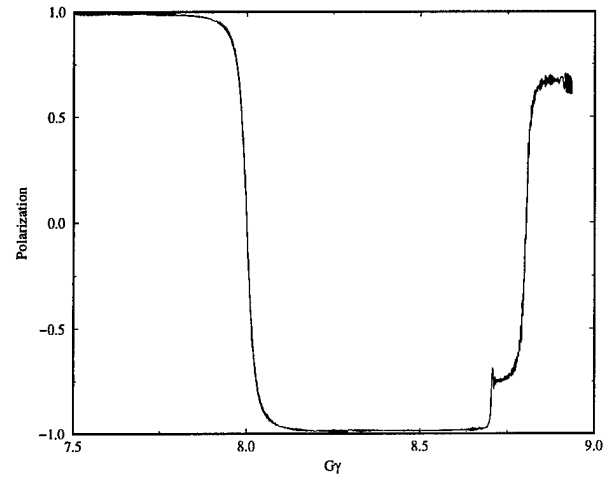

Figure 6: The simulation results for $\nu_y = 8.80$ and $\nu_x = 7.70$. $\varepsilon_x = \varepsilon_y = 30\pi$, $\delta = 0$, $\alpha = 1.1 \times 10^{-5}$.

the vertical betatron motion also has a component with the horizontal betatron frequency. As a consequence, the beam will see an additional resonance, the so-called coupling resonance. Besides the linear coupling effect, the synchrotron motion also affect the beam polarization but to a smaller extent. The results show good agreement with the experimental data.

The simulation results for $24 - \nu_y$ are shown in Fig. 5. The coupling resonance is very weak as expected and there is no visible effect. The unexpected high depolarization at $G\gamma = 24 - \nu_y$ is believed to be caused by the coincidence with the AGS transition energy (For AGS, $\gamma_t = 8.5$, which corresponds to $G\gamma_t = 15.24$. When $\nu_y = 8.70$, the intrinsic resonance is located at $G\gamma = 24 - \nu_y = 15.3$). Further simulation study is needed to understand this depolarization.

The coupling resonance strength can be decreased by separating the betatron tunes. Thus it seems that the linear coupling can be diminished by well-separated betatron tunes. The betatron tunes of the AGS can be separated by more than one unit, so a simulation with $\nu_x = 7.70, \nu_y = 8.80$ is performed (see Fig. 6). Although there is no depolarization at $G\gamma = 0+\nu_x = 7.70$, beam depolarization happens at $G\gamma = 1 + \nu_x = 8.70$ and the depolarization level is about the same as the one with $\nu_x = 8.80, \nu_y = 8.70$ (see Fig. 3). Because there is only one coupling element, the solenoidal partial snake, in the AGS, the coupling kick has all Fourier components $G\gamma = N \pm \nu_x$ and with the same amplitude. Whichever Fourier component is closest to the vertical betatron tune, it will pick up the strength of the intrinsic resonance and become the strongest coupling resonance.

The ratio of the coupling resonance strength to the intrinsic resonance strength with a 5% partial snake and 0.1 unit tune separation is about 0.06. With a larger tune separation of 0.3, the ratio goes down to 0.03. This ratio makes it impossible to cross those strong intrinsic resonances ($0 + \nu$, $12 + \nu$, and $36 \pm \nu$) at a single speed without losing polarization. A novel energy-jump method has been tested in the AGS to cross the coupling resonance and the results are summarized in [5].

4 CONCLUSION

As shown in the simulations, it is clear that depolarization level after crossing the strong intrinsic resonances is due to the combined effect of the coupling resonance and synchrotron oscillation. The coupling resonance strength can be decreased by separating the betatron tunes. However, separating the two tunes for more than 0.5 unit does not help. Spin tracking is a very useful tool to understand the experimental data and to prepare for the future experiments. Further simulation is going on for the AC dipole methods[6].

5 REFERENCES

[1] T. Roser, in *High-energy spin physics: 8th international symposium,* ed. K.J. Heller, Minneapolis, 1988, AIP Conference Proceedings No. **187**(AIP, New York, 1989), p.1442.

[2] H. Huang, et al., Phys. Rev. Lett. **73**, 2982 (1994).

[3] E.D. Courant and R. Ruth, BNL report, BNL-51270(1980).

[4] A. Luccio, BNL Report, BNL-52481(1995).

[5] H. Huang, et al., These Proceedings.

[6] M. Bai, et al., These Proceedings.

AN INTERACTIVE BEAM LINE SIMULATOR MODULE FOR RHIC*

W. W. MacKay, Brookhaven National Laboratory, Upton NY, 11973-5000

Abstract

This paper describes the interactive simulation engine, **bl**, designed for the RHIC[1] project. The program tracks as output to shared memory the central orbit, Twiss and dispersion functions, as well as the 6×6 beam hyperellipsoid. Transfer matrices between elements are available via interactive requests. Using a 6-d model, optical elements are modeled with a linear transfer matrix and a vector. The vector allows simulation of misalignments, shifts in field strengths, and beam rigidity. Currently only a linear model is used for elements. In addition to the usual magnets, a foil element is included which can shift the beam's rigidity (resulting from a change of charge and energy loss), as well as increase the momentum spread and emittance. Running as a Glish[2] client, **bl** can be interfaced to other programs, such as an orbit plotter and a power supply application to give a quick prediction of the beam orbit from actual operating currents in the accelerator. Various strengths and offsets may be changed by sending Glish events to **bl**.

1 INTRODUCTION

My intention in writing this program was to provide a program that would quickly track a beam through a section of beam line. Of particular interest are modeling of injection and first turn in RHIC. The requirements were that:

1. It should track the central trajectory, beam envelope, and optics functions for various magnet settings and initial beam conditions.
2. It should read the standard RHIC lattice definition files, with additional information on how to combine these files using a database.
3. It should be interactive, so that it could be used as a simulator. Initial conditions and various elements should be able to be tweaked with a quick turn-around from retracking the beam. It should be able to return requested transfer matrices between elements.
4. It should be able to be interfaced into the control system.
5. It should produce binary output, both to disk files and to shared memory.

The program does not print out results or plot them; separate programs have been written for these purposes. An X-windows plotting program, **plot_bl**, plots the data from shared memory and can be tied to **bl** through Glish.

* Work performed under the auspices of the US DOE.

Glish is a system with three components: a scripting language specifying what programs to run and how to interconnect them, libraries that can be linked with programs to allow them to communicate by sending and receiving events, and an interpreter process for executing Glish scripts and providing interprocess communication via Glish events.

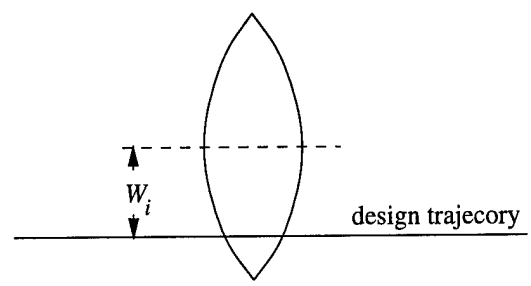

Figure 1: Schematic of an offset element.

2 TRACKING METHOD

The program **bl** is fully 6-dimensional with the transpose of a trajectory vector given by

$$\vec{X}^T = (\, x \quad x' \quad y \quad y' \quad z \quad \delta \,), \tag{1}$$

where $\delta = \Delta p/p$ is the fractional momentum deviation from the design particle. The program tracks the central trajectory through the ith element by the equation:

$$\vec{X}(s_i) = \mathbf{M}_i \vec{X}(s_{i-1}) + \vec{V}_i, \tag{2}$$

where $\mathbf{M}_i$ is the usual linear matrix for the element, s_i is the path length at the downstream end of the element, and $\vec{V}_i$ is a constant vector for that element. The vector $\vec{V}_i$ may be used to specify misalignment of the element. For an offset misalignment given by $\vec{W}_i$ (see Fig. 1), the corresponding vector is

$$\vec{V}_i = (\mathbf{I} - \mathbf{M}_i)\vec{W}_i. \tag{3}$$

The 6×6 beam hyperellipsoid Σ is tracked by the equation

$$\Sigma_i = \mathbf{M}_i \Sigma_{i-1} \mathbf{M}_i^T. \tag{4}$$

The Twiss functions: β_x, α_x, γ_x, β_y, α_y, γ_y, dispersion functions: η_x, η'_x, η_y, η'_y, η_z, and phase advances: ψ_x, ψ_y may also be tracked through the beam line.

In order to keep calculations to a minimum, three separate Glish events are used to invoke independent tracking of trajectory, hyperellipsoid, and optics functions, since the user may not want all the possible information. If only a steering magnet is changed, the user may care to retrack just the trajectory.

0-7803-4376-X/98/$10.00 © 1998 IEEE

3 TYPES OF ELEMENTS

At present, the kinds of optical elements which **bl** understands are drift, rotation about beam axis (SROT), quadrupole, dipole corrector, sector dipole with gradient and edge focusing, foil, and tcelement (a general purpose fixed element described below). The transfer matrices for drift, quadrupole, SROT, and sector dipole elements are essentially the same as used in the MAD program[3]. Even though the gradient dipoles in our transfer line are rectangular dipoles, we have approximated them by sector dipoles with gradients and half-angle wedges. Since the bend angles are relatively small ($< 3°$ per magnet) the errors for a single-pass beam are negligible. The constant vector of a magnet element is a tunable quantity through Glish events.

Additional tunable parameters for quadrupoles are the strength and tilt about the beam axis.

The horizontal corrector dipole has the same matrix element as a normal rectangular dipole, but with the vector component

$$\vec{V}^T = (\, l\theta/2 \quad \theta \quad 0 \quad 0 \quad 0 \quad 0\,), \tag{5}$$

where l and θ are the respective length and bend angle of the corrector. Vertical correctors are handled in a similar way. The bend angle of a corrector is a tunable parameter.

Since the bend angle through a dipole is given by

$$\theta = \frac{q}{p}\int B\, dl, \tag{6}$$

an increase in magnetic field $\Delta B/B$ is equivalent to an opposite shift in momentum $\Delta\delta \simeq -\Delta B/B$. We can simulate the correct steering effect by using Eq. (3) for the dipole a shift with

$$W_\delta = \frac{\theta - \theta_0}{\theta_0}, \tag{7}$$

where θ_0 is the designed bend angle. The additional tunable parameters for a dipole are θ and the gradient strength.

The foil element simulates the effect of a thin foil or flag on the beam by allowing one to set the $\Delta p/p$ component of the V_i vector to indicate a shift in momentum from dE/dx energy loss. It is also possible to use this feature to simulate a change in rigidity ($= p/q$) due to stripping of electrons from partially stripped ions. The change in rigidity in this case gives an effective shift

$$\frac{\Delta p}{p} = \frac{q_i}{q_f} - 1, \tag{8}$$

where q_i and q_f are the respective charge states upstream and downstream of the foil. Since foils can also increase the emittance of the beam, increases in angular divergence, $\Delta\Sigma_{x'x'} = \Delta\Sigma_{y'y'}$, and momentum spread, $\Delta\Sigma_{\delta\delta}$, are allowed.

Sometimes it is necessary to model an element which does not fit into the standard set of elements (drift, dipole, quadrupole, ...). This kind of "trajectorially challenged" element (tcelement) may have a transfer matrix obtained by differentiating trajectories that have been integrated through a mapped fringe field. Another simple tcelement is needed to shift coordinates from an injection beam line onto the circulating beam of a storage ring such as RHIC (see Fig. 2). This coordinate shift is a zero-length element whose matrix is the identity element, and the shift of coordinates is specified by the vector $\vec{V}$. This capability of specifying coordinate shifts makes it easy to model injection including the steering effects through ring quadrupoles (Q1 and Q2) upstream of the kicker magnet.

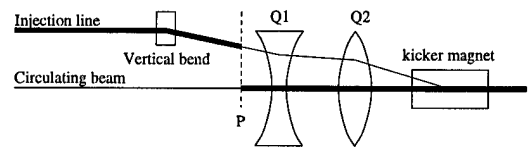

Figure 2: A zero-length tcelement is placed at location P to provide a shift of coordinate system from the injection line to the circulating beam in each RHIC ring. The heavy lines indicate the design trajectories used by **bl**.

As an example, Fig. 3 shows a section of beam line from the last part of the AtR[4] (AGS-to-RHIC transfer line) followed by a few cells of RHIC.

4 SPECIFICATION OF A MODEL

Probably the hardest part of any tracking code is reading the lattice specification which is frequently in some rather arcane format. The standard RHIC lattices are defined in several SYBASE databases[5]. A program was written which could output data into different formats required by several tracking codes. I have opted to use the format which writes the data into files with an SDS[6] binary format containing C-structures.

There are four such files: "Blue" for the clockwise (CW) ring, "Yellow" for the counterclockwise (CCW) ring, "BTransfer" for the transfer lines to the CW ring, and "YTransfer" for the transfer lines to the CCW ring. Both of the "Blue" and "Yellow" descriptions are given in a clockwise order starting at the southernmost interaction region. The reason the "Yellow" file is backwards is that most tracking codes use right-handed coordinate systems. In order to model injection into the CCW ring through the first turn, we want to concatenate information from two files and put a tcelement in between to shift coordinate systems. One important thing to note is that the injection point, specified as the marker YEND is in the middle of the "Yellow" file. Incidentally this "tcelement" with a constant vector does not fit into the standard RHIC SDS format.

Another database **bl_models** is used to specify to **bl** how to concatenate all this information. Four rows in a database table *bl_lattices* keyed by the *model* name "yinj" specify the file concatenation:

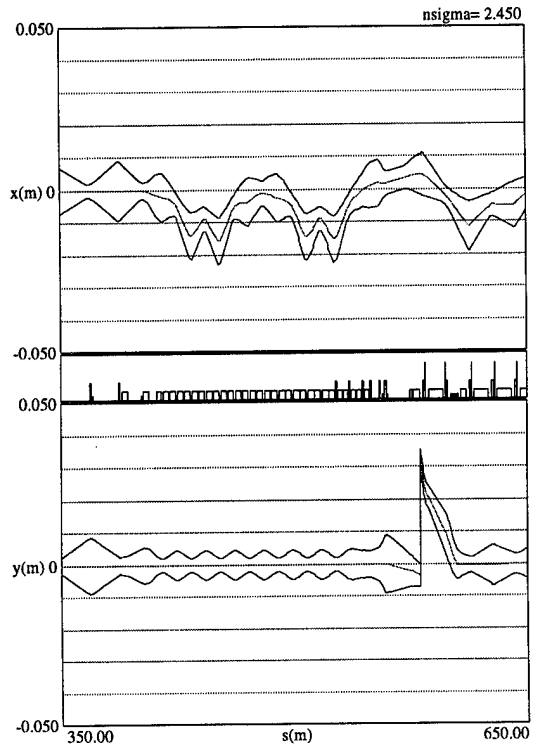

Figure 3: Beam envelope for 95% beam calculated by **bl**. The top (horizontal) plot shows the effect of mistuning the 90° magnet buss by +0.4% The bottom (vertical) plot shows a discontinuity due to a shift of reference coordinates just downstream of the Lambertson septum magnet. Notice the steering in the two following quadrupoles. The middle key indicates locations of magnets with increasing heights ordered as corrector, dipole, quadrupole, and sextupole.

1. Read in all of "YTransfer".
2. Read in the tcelement INJSPLICE from another table in **bl_models**.
3. Read "Yellow" backwards from YEND to the beginning of the file.
4. Read "Yellow" backwards from the end up to YEND.

Other ways of concatenating files and tcelements may be specified in the table *bl_lattices*.

Since speed is important, **bl** concatenates elements together, unless they are specified as interesting in either of two more tables:

1. *bl_tweaks* to specify that an element has tunable parameters, and
2. *bl_monitors* to specify that the user is interested in receiving output at this location.

Elements which are listed in the *bl_tweaks* table have both ends automatically elevated to monitor status. Clearly various schemes of concatenation may be wanted for a given model. The *bl_tweaks* and *bl_monitors* tables are keyed by both a model name and a scheme name.

5 FUTURE PLANS

Although **bl** has been used by a few control-room application codes, the direct input of magnet values from the magnet manager remains to be completed. In order to speed up communication, we plan to add our standard control system interface, so that **bl** may communicate directly with the control system. This new interface should simplify the connection to the magnet manager.

A simple rf element will be added to allow orbit calculation as the frequency is shifted. The vector $\vec{V}_i$ can allow for relative phase-shifts between cavities. Events will be added to calculate closed orbits and periodic solutions. Tunes, momentum compaction, etc. will be calculated.

We plan to develop a model of actual misalignments of the transfer lines and rings, so that they may be used to initialize **bl** and improve our online simulation capability.

6 REFERENCES

[1] Steve Peggs, "RHIC Status", these proceedings.

[2] V. Paxson, *The Glish 2.5 User Manual* (1994).

[3] H. Grote and F. C. Iselin, "The MAD Program (Methodical Accelerator Design) Version 8.1 User's Manual", CERN/SL/90-13(AP).

[4] N. Tsoupas et al., "Focusing and Matching Properties of the AtR Transfer Line", these proceedings.

[5] C. Trahern, "LAMBDA Manual", RHIC/AP/12 (1983).

[6] E. Lutz and C. Saltmarsh, "ISTK Overview and the SDS Document", RHIC/AP/29 (Obtainable from www.rhichome.bnl.gov/AP/ap_notes).

MODELING RHIC USING THE STANDARD MACHINE FORMAT ACCELERATOR DESCRIPTION*

F. Pilat, C. G. Trahern, J. Wei, T. Satogata, S. Tepikian
Brookhaven National Laboratory, Upton, NY 11973, USA

Abstract

The Standard Machine Format (SMF)[1][2] is a structured description of accelerator lattices which supports both the hierarchy of beam lines and generic lattice objects as well as those deviations (field errors, alignment errors, etc.) associated with each component of the as-installed machine. In this paper we discuss the use of SMF to describe the Relativistic Heavy Ion Collider (RHIC) as well as the ancillary data structures (such as field quality measurements) that are necessarily incorporated into the RHIC SMF model. Future applications of SMF are out-lined, including its use in the RHIC operational environment.

1 INTRODUCTION

The description of circular accelerator lattices has two major phases. In the design stage before and during construction, generic elements and beam lines are commonly used. In the latter phase of construction and on into operations the generic description is usually discarded in favor of a "flat" view of the machine where each component in the ring has its own characteristics such as magnetic field deviations or misalignment. In the flat view of the machine one can not easily recover the symmetry properties of the original design in case one wishes to investigate the lattice's basic properties anew. If in order to carry out these investigations one does then go back to the original design lattice, one often finds that essential details (unrelated to non-generic quantities such as field errors) have not been incorporated. The maintenance of an accurate generic description along with the detailed flat description becomes a quandary. The Standard Machine Format (SMF) [1][2] was created to unify these two phases of development in a single set of data structures. In this paper we discuss the use of SMF to manage the design and operation of the Relativistic Heavy Ion Collider (RHIC). We first discuss the definition of SMF, and then describe the particular ways in which the various RHIC data stores are incorporated.

2 SMF DATA STRUCTURES

The Standard Machine Format consists of four levels of description (classes):

1. Parameter
2. Generic Element
3. Line
4. Lattice

Parameters are names which are assigned specific values. *Generic Elements* are defined as structures having attributes appropriate to the accelerator object. For example, a bending magnet has length, strength, edge fields, etc. Each type of generic element incorporates specific attributes which are assigned values. Attributes may be assigned values using parameter names which subsequently take the parameters' values. New attributes can easily be added to the list. A *Line* is a structure composed of generic elements and other lines. A Line is a generic structure like the previous levels of description. Finally, *Lattice* is a sequential list of Lattice Elements which retains the memory of the hierarchical tree of lines contained in the lattice even while being a flat description. A Lattice Element is derived from one of the Generic Elements but contains in addition the deviations from its generic value of magnetic field strength, alignment, etc.

3 RHIC DATA STORES

Figure 1 provides a schematic view of the data stores and processes required to construct the RHIC SMF. The top level of the figure shows the basic data structures required, namely optics, name correlation, magnetic field and survey measurements. The RHIC accelerator physics group has responsibility for the optics design. This is maintained in an *Optics Model* [3] within a relational database. However, a complete model of RHIC also requires information about magnetic field and survey alignment data which are controlled and maintained by other groups within the RHIC organization. Consequently, the construction of the SMF requires the communication of the data from these other groups which must then be correlated with the basic optics model. Because magnets and other equipment to be installed in the accelerator have been named differently by the various groups, we have to resort to a *NameLookup* structure to resolve the correlation problem. Finally, the raw measurement data from the other groups must be processed before it can be incorporated into our lattice SMF model. We now discuss each of these component data stores in turn.

3.1 Optics Model and NameLookup

The lattice database at RHIC had its beginnings in the SSC Central Design Group. This database structure has been discussed previously [3], and we will not go into the details here. It should be sufficient to note that the optics description provided by the database is modeled after the Standard Input Format (SIF) [4] (incorporated into MAD and many other programs). The lattice database is used to maintain the design of the machine. From this hierarchical description a flat C structure is generated by a program using the *Self-describing Data Standard* (*SDS*)

* Work performed under the auspices of the U.S. Department of Energy

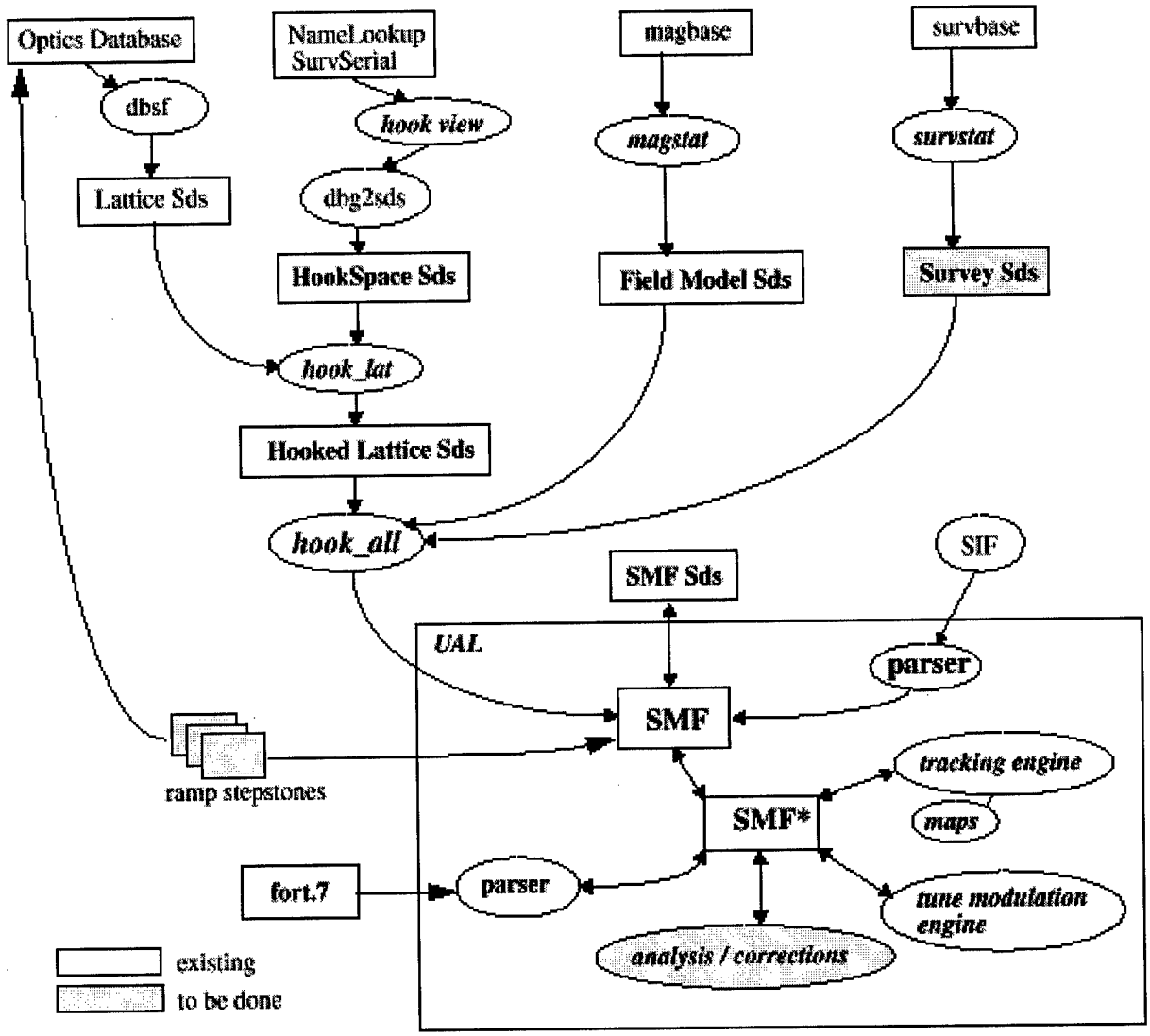

Figure 1: Overview of RHIC SMF

[5] for its data representation. This lattice SDS file acts as an information tree for RHIC installation and configuration as it is used as input to the construction of the *NameLookup* structure.

The first pass in the generation of *NameLookup* is made with a C++ program. It is then loaded into the database as a relational table, and the completion of filling is accomplished by joining the NameLookup table with other tables in the RHIC configuration databases. For example, the correlation of the site name of a magnet with its serial number defined at the factory is stored in the NameLookup table after a join to tables in the magnetic field quality database. The NameLookup table is the primary source of name correlation for installation and operations. (Since NameLookup is needed independently of the SMF for installation and operations, we have not tried to re-design what is clearly a very convoluted data flow in order to make the SMF creation process simpler.)

3.2 HookSpace and HookedLattice

The next stage is the construction of the so-called HookSpace and HookedLattice structures. HookSpace is created by selecting a subset of the NameLookup data as well as some extra construction details of the quadrupole/corrector assemblies which are only stored in the magnetic field quality database. HookSpace is then melded with the flat lattice SDS structure via a C++ program (*HookLat*) to create a HookedLattice SDS structure. The HookedLattice is a flat SDS data structure with all the data as well as the informational links necessary to construct the four levels of the SMF.

3.3 Magnetic Field Quality

The RHIC Magnet Production Group maintains an extensive field quality database [6] based on warm and cold tests of the super-conducting magnets used in RHIC. This database was created mainly for the purposes of magnet construction and testing. Weekly reviews of the quality of new magnets are conducted based on this data.

Accelerator physicists use a copy of this database (re-generated weekly from the source maintained by the Magnet Group) on their relational database server to analyze field quality for its implications for the stability of beam dynamics. A significant level of computation is required to convert the raw field quality data into a form more useful for this purpose. The result of these computations is saved as a flat SDS C structure called *FieldModel*. Each magnet in FieldModel is keyed to the HookedLattice structure by its magnet serial number. FieldModel contains for each magnet both the values of all deviations for each magnetic multipole tested at various currents as well as the mean and standard deviations of the ensemble of magnet measurements.

3.4 Survey and Alignment

The RHIC Survey and Alignment group has prepared a database structure to record the results of all alignment activities before and after installation of equipment in the RHIC tunnel. The raw data is stored in a set of relational database tables, and programs are used to determine deviations from the ideal locations defined by the lattice design. At present the alignment results are not incorporated in the SMF. In a manner similar to the FieldModel, we will eventually construct an *AlignmentModel* SDS structure appropriately keyed to the lattice so that this data may also be included in the fourth level of the RHIC SMF.

4 SMF GENERATION PROCESS

By joining the HookedLattice structure with the magnetic field quality (and eventually, the alignment) data, we are ready to produce the RHIC SMF. The C++ program *HookAll* reads the information contained in HookedLattice, associates magnetic errors to individual elements from FieldModel, and fills the four level SMF structures.

If a magnet is installed and has been measured cold, we use individual measurements, otherwise we assign the average of measured data relative to that particular type of magnet (DRG, main arc dipole, QRG, main arc quadrupole, QRI, interaction region triplet, and so on for all magnet types). The model can be dynamically updated as soon as new data for magnets are stored in the database. An interesting new feature of the SMF description is that any element (at the GenericElement level) contains Body and End parts. One can then associate body and end harmonics to each thick element without having to add non physical thin multipole elements to the lattice for the sole purpose of carrying errors. This results in a cleaner description where only physical elements are represented.

Once the RHIC SMF is instantiated (see again Figure 1) one can access the UAL (Unified Accelerator Libraries) package [2] and use its tools and physical libraries. A tool has been developed that writes (and reads) an SMF in memory to (from) an SDS file, allowing an external representation of the SMF classes. More recently [2] an ascii external representation of the SMF has been written using the Perl language. The SMF representation can be automatically converted to an SMF* representation which closely maps the Teapot internal structures, allowing us to use the physical libraries of Teapot++: the teapot tracking engine along with its newer map and tune modulation capabilities. For reasons of backwards compatibility a parser from SIF (Standard Input Format) to SMF has been written as well as a parser from and to the "fort.7" teapot machine file. The latter has been widely used in RHIC for a variety of applications and it is important to retain the capability of accessing it from SMF.

We used the SMF representation of RHIC to perform short term tracking and compared the outcome with results from previous simulations run on Fortran Teapot. The SMF/Teapot++ results are in perfect agreement with the SIF/Fortran Teapot.

5 CONCLUSION

The model of the accelerator provided by the SMF is the most complete and detailed available. It does not assume that magnetic elements are approximated by "thin" kicks, and without loss of generality allows for unusual structural details that may only be needed for special applications such as the insertion of maps. We have used this model in tracking studies to understand the effect of measured multipole fields on the RHIC dynamic aperture and additionally for the study of tune modulation, spin rotators and other non-linear effects. In the future the SMF will become part of the online model of RHIC. Currently, the SMF representation for RHIC is large, easily encompassing over 10 MB of memory, and we expect to see some performance degradation as the size of the SMF increases. Fortunately, it is possible to use the model at either generic or fully instantiated levels, and this makes it possible to adjust some of the simpler operational parameters in a way distinct from those requiring more detailed studies. The advantages of having a single accurate representation of the machine rather than several versions requiring heterogeneous methods to manage them is expected to pay for the added discipline and complication that the model introduces.

6 REFERENCES

[1] N. Malitsky, R. Talman, et.al., "A Proposed Flat Yet Hierarchical Accelerator Lattice Object Model", Particle Accel. **55**, 313(1996).

[2] N. Malitsky, R. Talman, "Status of Unified Accelerator Libraries", PAC 97, These Proceedings.

[3] S. Peggs et.al., SSC-N-606, March, 1989; C.Trahern, J.Zhou, ICALEPCS Proceedings, Tsukuba, Japan, Nov. 1991, pp.538-541.

[4] D.C. Carey and F.C. Iselin, "Standard Input Language for Particle Beam and Accelerator Computer Programs", Snowmass 1984.

[5] C. Saltmarsh, "ISTK Overview and the SDS Document", RHIC AP Note 29, June 1994.

[6] D.McChesney, internal RHIC memo; J.Wei et.al. "Field Quality Evaluation of the Superconducting Magnets of the Relativistic Heavy Ion Collider", PAC, Dallas, 1995

3-D NUMERICAL FIELD CALCULATIONS OF CESR'S UPGRADED SUPERCONDUCTING MAGNETS

Z. Greenwald, S. Greenwald *
Laboratory of Nuclear Studies, Cornell University, Ithaca, NY 14853

Abstract

A 3-D numerical code BST.c was used to calculate the spatial magnetic fields generated by a current carrying wire. In particular, the code calculates the fields of wire loops wrapped on a pipe similar to superconductive magnet structures. The arrangement and dimensions of the loops can be easily modified to create dipoles, quadrupoles, skew magnets etc., and combinations of the above. In this paper we show the calculated 3-D fields of ironless superconducting quadrupole dipole combination designed for CESR phase III upgrade (which will be manufactured by TESLA). Since the magnet poles are made of loops, the fields at the edges are not only distorted but have a component, B_z, in the z direction as well. This B_z field can cause X-Y coupling of the beam. In order to calculate the coupling, the particle trajectories through the whole magnet were computed. The code is also used to calculate local fields errors due to possible manufacturing imperfections. An example of a rotational error of one pole is shown.

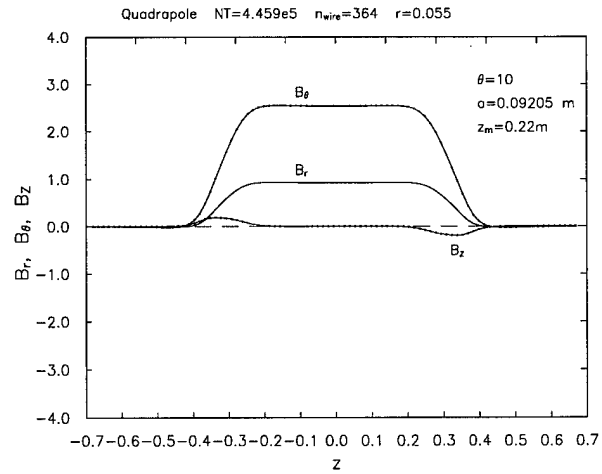

Figure 1: Magnetic Field of the TESLA Quadrupole for $r < a$

1 INTRODUCTION

3-D Numerical magnetic field calculation code BST.c was developed in order to study the possible problems associated with the rounded ends of the wire loops of the superconductive magnets, planned for CESR upgrade III. The algorithm and details of the code BST.c are described in CBN 97-10 [1]. The code calculates the spatial magnetic field surrounding current carrying wire loops.

2 *QUADRUPOLES*

Each one of the superconducting quadrupoles, to be installed next to the interaction point, for CESR upgrade III [2] is made out of four loops of wire ribbons which are wrapped on a pipe. The loops touch each other and create four poles. (The current flows in opposite direction in each loop). All the consecutive ribbon layers have the same perimeter. The straight part of the loops (ideal magnet) lies along the z axis for $-z_m < z < z_m$ .The ends of the loops are elliptical causing magnetic field distortion at the ends including a component of magnetic field, B_z, in the z direction. In order to suppress the field distortion (higher order multipoles), created at the rounded ends of the loops, each loop is divided into three sub concentric loops. The fields of this magnet, calculated by the 3-D code BST.c, are shown in Figures 1-5. Figure 1 shows the field components B_r, B_θ, B_z along the z axis for $r = 0.055$, $\theta = 10°$, with pipe radius $a = 0.092\ m$. Figures 2,3 show the field components at the end ($z = 0.33\ m$) along the r and θ axis correspondingly. Figures 4,5 show 3D presentation of B_r and B_z along z and r axis, $0 < r < 1.5a$, $\theta = 0$. Since the superconducting magnet does not have iron, the field calculated for $r > a$ is the field outside the magnet. This field is not small, as can be seen in Figures 4,5. Its effect on the nearby interaction point detector may be significant. Note, despite the subdivision of each loop, there is still a component, B_z at the ends for $-z_m < z < (z_m = 0.23)$ which increases with r, as can be seen in Figures 2,3,5. Also, there is some distortion left in B_r and B_θ at the ends which will introduce higher order multipoles.

3 HIGHER ORDER MULTIPOLES

In order to find the extent of the parasitic multipoles we expand the field component $B_r(\theta) = \sum_{m=1}(A_m \cdot \sin(m\theta) + B_m \cdot \cos(m\theta))$. $A_2 \sin(2\theta)$ is the ideal quadrupole component where $A_{(m,m\neq 2)}$ is the m multipole amplitude and B_m is the m sqew pole amplitude. The normalized amplitude A_m/A_2 of the multipoles, obtained by Fourier transformation, at the end of the magnet ($z = 0.33\ m$) and very large displacement ($r = 0.8a$), is shown in Figure 6. The expanded scale (right side axis) shows that the strongest remaining multipole $m = 6$ is less than 3% of the quadrupole strength at this location. The other multipoles $m = 10$ is less than 2% and $m = 14$ is less than 1%. The total effect of each multipole is obtained by integration of each multipole intensity along the whole length of the magnet.

* Work supported by the National Science Foundation

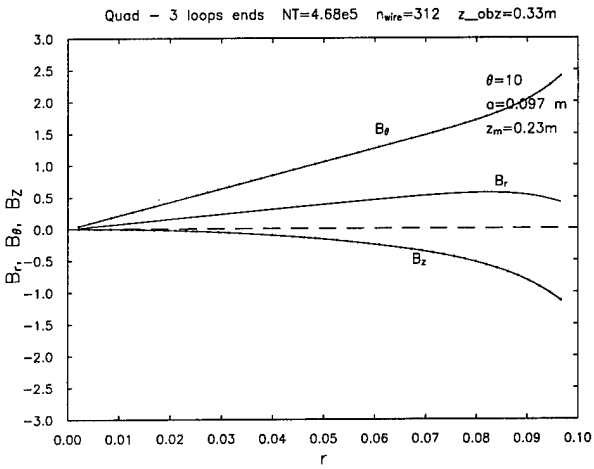

Figure 2: Magnetic Field of the Quadrupole along r

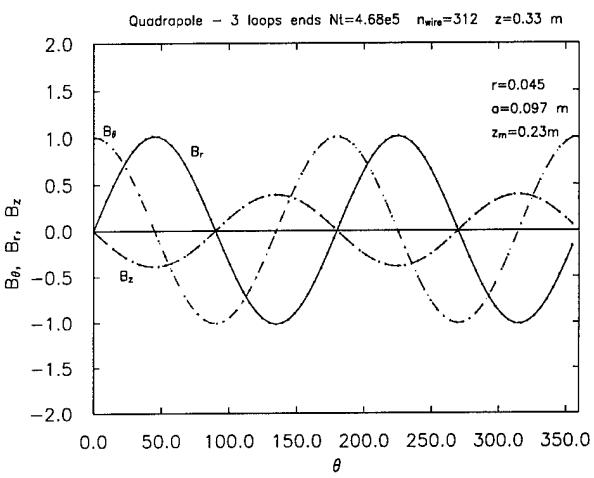

Figure 3: Magnetic Field of the Quadrupole along θ

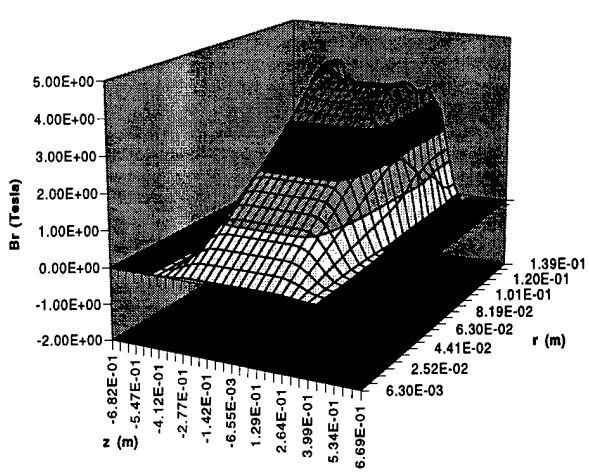

Figure 4: Magnetic Field B_r of the TESLA Quadrupole along z for $0 < r < 1.5a$

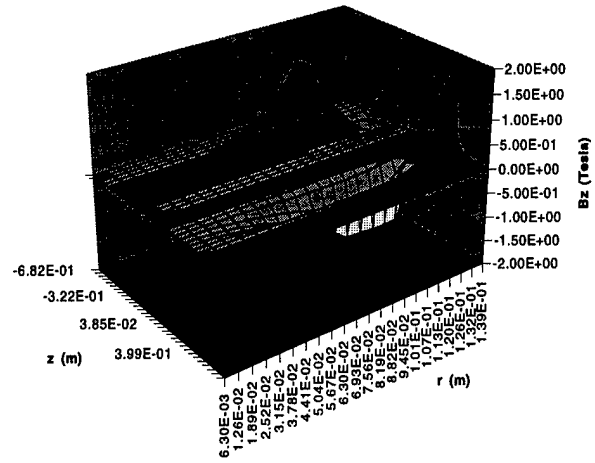

Figure 5: Magnetic Field B_z of the TESLA Quadrupole along z for $0 < r < 1.5a$

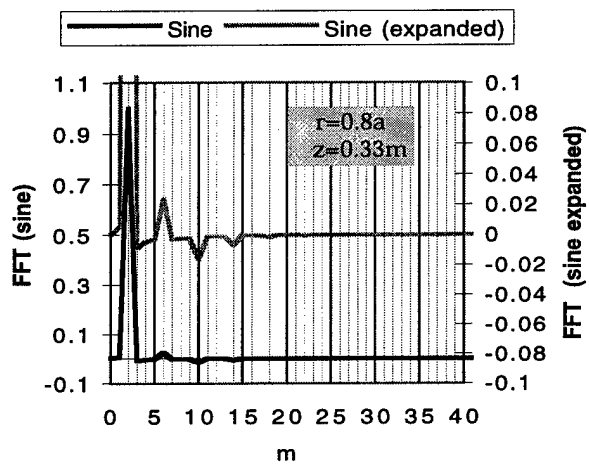

Figure 6: Relative strength of the higher order multipoles at $r = 0.8a$ and $z = 0.33$.

4 WINDING ERRORS

Magnetic field deviation due to misalignment of wires can be easily calculated. An example of the field errors of a magnet with the center of one loop shifted by 1° is shown in Figure 7. ΔB_i $i = (r, \theta, z)$ is the difference between the ideally symmetric magnet to the one with the shifted loop in Tesla. The error $\frac{\Delta B_r}{B_r}$ in this example is 1.8%.

Shifting the coils of one loop as in the above example will cause a localized error in the azimuthal direction over the length of the whole magnet. Because the error is localized in θ, its total effect on the integrated multipoles will be relatively small [4].

5 QUADRUPOLES AND DIPOLE COMBINED

An option which will save space and cryogenic cooling is to wind the dipole magnet, needed for misalignment com-

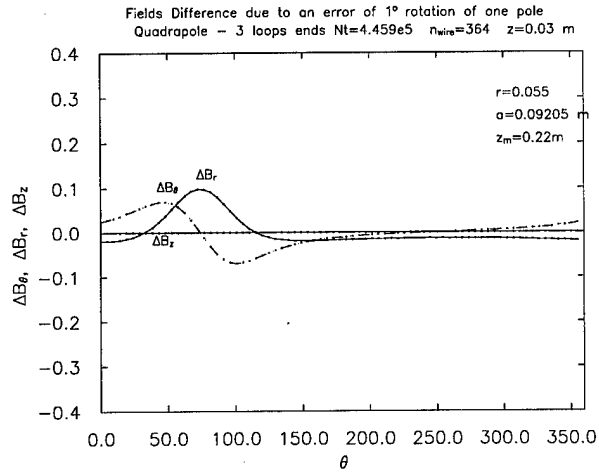

Figure 7: Field errors due to 1° shift in the center of one loop

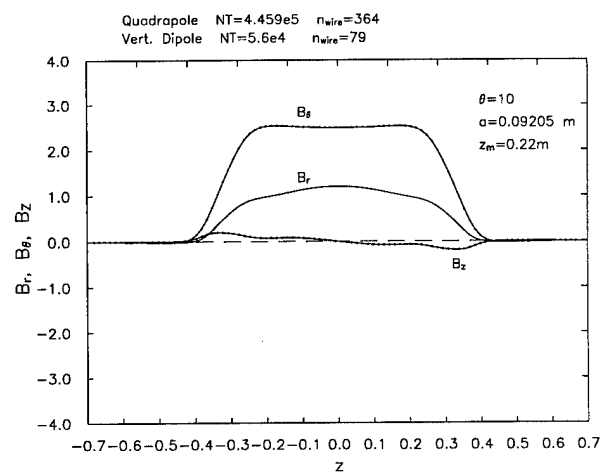

Figure 8: Combined Field of the above Quadrupole and Dipole at $r = 0.055\ m$.

pensation, on top of the quadrupole. The basic dimensions of the dipole are determined by the outside diameter of the quadrupole and its length. These constraints make the dipole loops ellipse-like, almost without straight sections. The combined field of the quadrupole and (without subdivisions of the dipole loops) dipole can be seen in Figure 8. The total field obtained is distorted by the dipole. A more complex dipole winding is being designed. For additional field calculation see CBN 96-09 [3].

6 THE SUPERCONDUCTIVE QUADRUPOLE TRANSFER MATRIX

The particle trajectory through the whole magnetic field including the fringe fields at the edges, total length of 83 cm, was calculated by solving the equation of motion numerically. The magnetic fields were recalculated at each step by the 3-D numerical code BST.c. Using these results the transfer matrix ,T, of the horizontal quadrupole magnet was calculated.

$$T = \begin{pmatrix} 0.3082 & .6854 & 0.0 & 0.0 \\ -1.4932 & -0.0799 & 0.0 & 0.0 \\ 0.0 & 0.0 & 1.885 & 1.650 \\ 0.0 & 0.0 & 2.237 & 2.460 \end{pmatrix}$$

From the transfer matrix it can be seen that there is no coupling between the horizontal and vertical motion. The main reason that there is no coupling is that the magnetic field B_z has opposite polarities at the ends of the magnet, as seen in Figures 2,4. Also the particle's azimuthal angle changes very little through the whole magnet. Therefore the effect of the B_z field on the particle motion is canceled out. The exact transfer matrix can be used in simulation of the whole storage ring instead of the thin lens approximation.

7 SUMMARY

The strength of the higher order multipoles characterizes the quality of a superconducting magnet. The sources for these multipoles can be the rounded ends of the wire loops and manufacture winding errors. In order to calculate the multipoles, especially those generated by manufacture errors, a 3-D code like the BST.c is needed. This code has no restrictions on the wire layout. Also, in designing combined magnets where the layout of the wires is complex, the flexibility of the code is essential. A study of the expected coupling between horizontal and vertical motion due to B_z component at the magnet ends was done by calculating the transfer matrix.

8 ACKNOWLEDGMENT

We would like to thank Gerry Dugan and David Sagan for very helpful discussions. Thanks also to David Rice Gerald Codner and David Rubin for helping prepare this paper.

9 REFERENCES

[1] Z. Greenwald, "3-D Numerical Code for Field Calculation of Super Conducting Magnets." CBN 97-10. (Available on the web at http://www.lns.cornell.edu)

[2] J. J. Welch, G. F. Dugan, E. Nordberg, D. H. Rice, "The Superconducting Interaction Region Magnet System for the CESR Phase III Upgrade." This conference.s

[3] Z. Greenwald, S. Greenwald, "3-D Numerical Field Calculations of Magnets." CBN 96-09.

[4] G. Dugan, "Construction Error Tolerances for CESR Phase III IR Quadrupoles." CBN 97-3.

WAKE FIELDS OF A BUNCH ON A GENERAL TRAJECTORY DUE TO COHERENT SYNCHROTRON RADIATION

M. Dohlus, A. Kabel, T. Limberg
DESY, Notkestr. 85, 22603 Hamburg, Germany

Abstract

If short bunches travel along trajectories with small bending radii a simple geometrical condition permits strong longitudinal and radial wake fields to act: electromagnetic fields emitted by a particle can 'overtake' on a shorter straight trajectory and interact with particles ahead. The bunch then starts to radiate coherently. The electromagnetic fields along the bunch have strong gradients and in general increase emittance. Investigations for the Tesla Test Facility Free Electron Laser have shown that the wrong choice of compressor parameters can increase the emittance by more than a factor of ten when compressing down to 50μm bunch length.

We present a formalism and numerical code to calculate the resulting electromagnetic fields on a general trajectory. Shielding effects of the vacuum chamber have been included. We present first results for the TTF-FEL undulator magnet and calculations of the influence of transition regions (bunch entering and leaving a homogeneous magnetic field).

1 INTRODUCTION

In [1] it has been shown:
1) The 'overtaking length' $L_o = (24\sigma_s R^2)^{1/3}$ is a measure for the interaction length inside of a bending magnet (with the bending radius R and the bunch length σ_s). Usually the overtaking length is large compared to σ_s but not very small compared to the dimensions of the configuration (e.g. R).
2) The longitudinal wake (per length) in the center of the bunch scales as $W_{||} = 1 \Big/ \left(\varepsilon(2\pi)^{3/2}3^{1/3}\sigma_s^{4/3}R^{2/3}\right)$. This leads e. g. to a wake in the order of 1 MV/m for an 1nC bunch with σ =0.1mm on a curvature R=1m.
Additionally in [2] it has been demonstrated:
3) Shielding by horizontal conducting plates in the distance h starts to be effective if the 'shielding length' $L_s = (\sigma_s^2 + h^2)/(2\sigma_s)$ is of the same order as the 'overtaking length'. L_s is the path length for the electromagnetic field emitted by a particle and reflected from the wall to reach the particle one sigma behind it.
4) The length of transient regions (e.g. bunch entering and leaving a= homogeneous magnetic field) is of the order of L_o. As the transient lengths may be comparable to magnet lengths their effects have to be taken into account for beam dynamic simulations. An analytical formulation for the longitudinal wake of 1D bunches in an arc has been derived in [3].
5) The wake due to coherent synchrotron radiation (including transient effects) has been taken into account in the calculation of emittance increase for the case of a bunch compressor in the TESLA Test Facility FEL [4].

This approach [2] is not self-consistent: the wake fields are calculated for a source distribution in pre-defined motion $\vec{r}_{s,i}(s)$ (s is length parameter of path, i is index of sub-bunch). The source bunch has no transversal dimensions (1D bunch) and does not change its longitudinal profile (rigid bunch). Two- or three-dimensional bunches are composed from one-dimensional line charges. The simulation of the shielding effects due to infinitely conducting plates in the horizontal plane is taken into account by mirror charges.

Our *new formulation*, described in chapter two, takes into accont:
1) 2D bunch distributions with longitudinal profile $\lambda(s,t) = \lambda(s - v_s t)$ and profile $\eta(\tilde{z})$ in $\vec{e}_z$ direction. $\vec{e}_z$ is a constant unity vector that is essentially perpendicular to the plane of motion (the motion is not restricted to be exactly in a plane!), $\tilde{z} = z - \vec{r}(s)\cdot\vec{e}_z$ describes the offset to the central path $\vec{r}(s)$ in $\vec{e}_z$ direction;
2) The 2D approach avoids the field singularities of the 1D approach [2] and is therefore better capable of the simulation of fully three dimensional source distributions (using an array of 2D bunches). So called 'space charge forces' are taken into account.
3) The new formulation is better suited for numerical integration (even for 1D bunches).

Chapter three describes the calculation of energy spread increase for the case of a single bending magnet and following drift space for different bunch lengths and bending radii. In chapter four, first results for a micro-bunch entering the TTF-FEL are presented.

2 CALCULATION OF THE LORENTZ FORCE

The action of the electromagnetic field caused by a source (index s) to a charged test particle (index t) is described by the *Lorentz force equation*:

$$\frac{1}{q_t}\vec{F}_t = \vec{E}_s + \vec{v}_t \times \vec{B}_s \ . \tag{1}$$

Using the scalar and vector potentials $\vec{E}_s = -\nabla V_s - \dot{\vec{A}}_s$, $\vec{B}_s = \nabla \times \vec{A}_s$ this force can be split into two terms:

$$\frac{1}{q_t}\vec{F}_t = \underbrace{\nabla\left(\vec{v}_t\cdot\vec{A}_s - V_s\right)}_{\frac{1}{q_t}\vec{F}_{At}} + \underbrace{\left(-\dot{\vec{A}}_s - \vec{A}_s\left(\vec{v}_t\cdot\nabla\right)\right)}_{\frac{1}{q_t}\vec{F}_{Bt}} \ . \tag{2}$$

The first term is a gradient field, the second term vanishes for bunches in linear motion. As the space charge and

0-7803-4376-X/98/$10.00 © 1998 IEEE

current density distributions are determined, the scalar and vector potentials can be directly obtained from the *retarded potential equation*. For a two dimensional bunch with the density $\lambda(s - v_s t)\eta(\tilde{z})$ the scalar and vector potential integrations lead to:

$$\frac{4\pi\varepsilon}{q_t}\vec{F}_{At} = \int \left\{G_1(s')\vec{R}_{xy} + G_2(s')\vec{e}_z\right\}\left(1 - \vec{\beta}_t \cdot \vec{\beta}_s\right) ds', \tag{3}$$

$$\begin{aligned}\frac{4\pi\varepsilon}{q_t}\vec{F}_{Bt} &= \beta_t\beta_s \int \left(\left\{G_1\vec{R}_{xy} + G_2\vec{e}_z\right\}\cdot(\vec{e}_t - \vec{e}_s)\right)\vec{e}_s ds' \\ &- \beta_t\beta_s \int G_3(s')\frac{\partial\vec{e}_s}{\partial s'}ds' \\ &+ (\beta_s - \beta_t)\int G_4(s')\vec{e}_s ds'\end{aligned} \tag{4}$$

with

$$\begin{aligned}G_1(s) &= \int \left\{\lambda/R^3 + \dot{\lambda}/(c_0R^2)\right\}\eta(\tilde{z})d\tilde{z} \\ G_2(s) &= \int \left\{\lambda/R^3 + \dot{\lambda}/(c_0R^2)\right\}\tilde{z}\,\eta(\tilde{z})d\tilde{z} \\ G_3(s) &= \int \lambda/R\,\eta(\tilde{z})d\tilde{z} \\ G_4(s) &= \int -\dot{\lambda}/(c_0R)\,\eta(\tilde{z})\tilde{z}\end{aligned}$$

and $\vec{R} = \vec{r}_t - \vec{r}_s(s') - \tilde{z}\vec{e}_z$, $\vec{R}_{xy} = \vec{R} - (\vec{e}_z \cdot \vec{R})\vec{R}$, $\vec{\beta}_s = \beta_s\vec{e}_s = \vec{v}_s/c_0$, $\vec{\beta}_t = \beta_t\vec{e}_t = \vec{v}_t/c_0$, and $\lambda = \lambda(s' + \beta_s R - v_s t)$.

For this derivation we used the chain rule with the boundary conditions $\|\vec{r}_s(s = \pm\infty)\|^{-1} = 0$. The main contribution to the longitudinal force is given by the integral (3). The last term in (4) vanishes if source and observer particle have the same velocity. The first term vanishes for particles in circular motion if source and observer are on the same orbit. The remaining part (proportional to the curvature $\|\partial\vec{e}_s/\partial s\|$) gives the so called 'centrifugal space charge force'. In the following calculations, all integrals have been solved numerically without further restrictions.

3 TRANSITIONS FOR LONGITUDINAL WAKES AND ENERGY SPREAD GROWTH IN BENDING MAGNETS

The field calculation simulates the bunch as a set of gaussian sub bunches—each with a different energy, different initial conditiones and an individual path. The trajectories of these sub-bunches are not effected by the calculated fields.

An independent set of bunch slices, initially lined up, is traced through the bending magnet and experiences the energy variations due to the longitudinal fields. Due to the strong longitudinal variation of the fields, the slice centroids follow different paths and a 'centroid emittance' developes.

For the tracking, the bending magnets and drift spaces are cut into slices and the wake fields are calculated and the consequent energy changes are applied at the end of each slice.

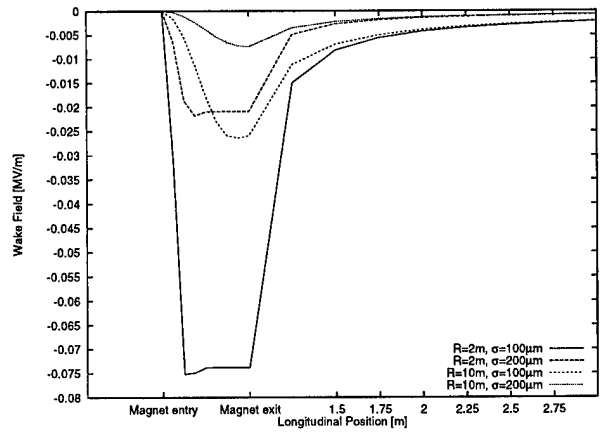

Figure 1: Longitudinal wake field at bunch center vs. longitudinal position.

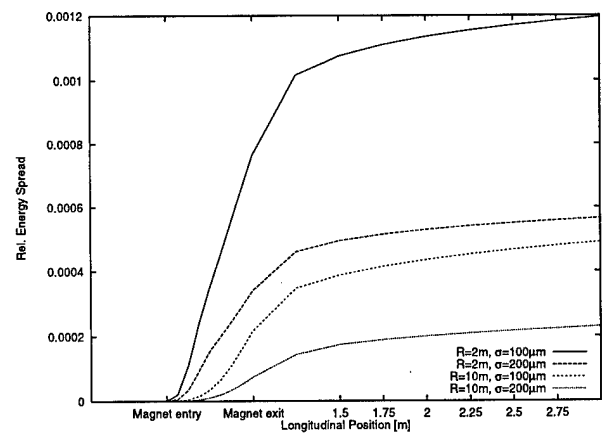

Figure 2: Energy spread vs. longitudinal position.

Fig. 1 and 2 show the longitudinal wake field at the bunch center and the resulting energy spread growth for different bunch lengths and bending radii vs. longitudinal position for a very simple set-up, comprising a bending magnet of length .5m and a drift space of length 2.0m. It can be seen that there is no steady-state region for the larger bending radius. The asymptotic behavior of the field past the magnet's exit is independent of the bunch's history and can be shown to be $\lambda/(2\pi\epsilon r)$, where λ is the 1D charge density and r is the distance from the magnet's exit.

4 FIRST CALCULATIONS OF AN UNDULATOR

The longitudinal charge distribution of a bunch traversing an FEL undulator changes drastically due to the micro-bunching of the SASE process. In the TTF-FEL case, the incoming bunch has a homogeneous peak-shaped distribution with an RMS-length of about 50μm. Micro-bunching along the undulator then produces a chain of micro-bunches with a periodicity of the wavelength (6.4nm). As first results of undulator field calculations, we present here

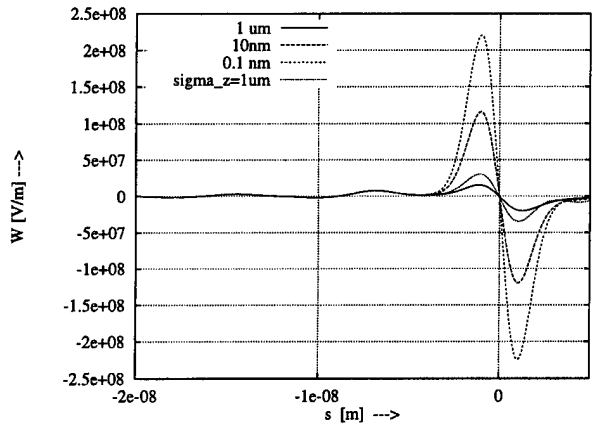

Figure 3: Longitudinal wake for a micro-bunch (3 nm FWHM) in the TTF-FEL undulator for different transverse offsets of the observation point vs. longitudinal position.

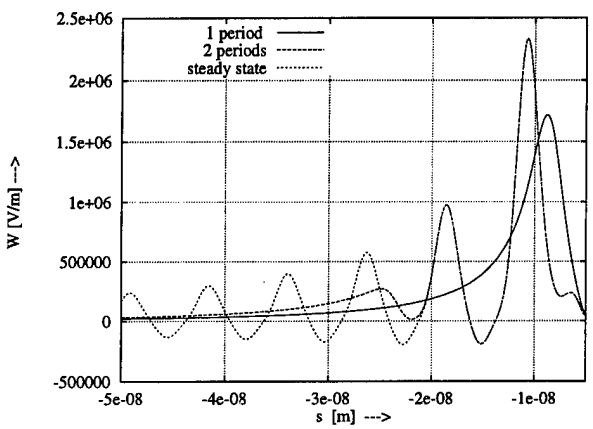

Figure 4: Longitudinal wake for a micro-bunch (3 nm FWHM) in the TTF-FEL undulator for different numbers of periods into the undulator vs. longitudinal position.

calculations of the longitudinal wake of a microbunch, modeled as a gaussian distribution with a FWHM of 3.2 nm, half the distance between micro-bunches. The undulator has a period length of 2.7cm and a field strength of 0.5 Tesla. Fig. 3 shows the longitudinal wake field for different transverse offsets in a range between 0.1nm and 1μm. The curve labeled '$\sigma_z = 1\mu$m results from a centered bunch with a non-zero transversal extension. The fields are calculated at a position 20 undulator periods into the undulator, where a steady state regime is reached. The strong logarithmic dependence indicates a space charge like force to be the cause of the peak around the bunch center (s=0). For an evaluation of bunch energy loss, the transverse bunch distribution has to be folded with these curves.

Fig. 4 shows with higher resolution the region ahead of the bunch, (negative s in these plots means ahead) starting with the second peak, for the bunch being at different numbers of periods into the undulator. There is no significant dependance on vertical offsets in this region.

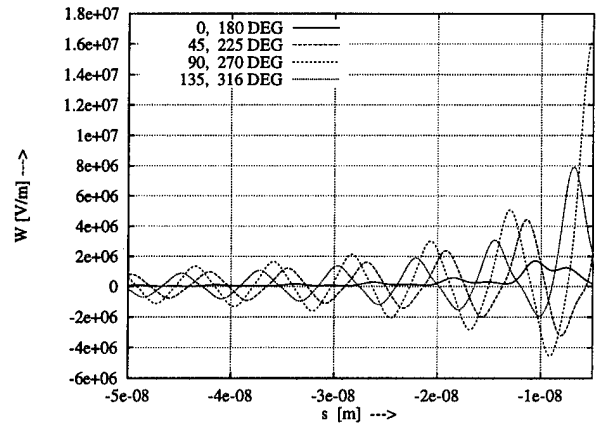

Figure 5: Longitudinal wake for a micro-bunch (3 nm FWHM) in the TTF-FEL undulator for different bunch positions within an undulator period in the steady state regime vs. longitudinal position.

Fig. 5 then varies the bunch position within an undulator period in the steady state region, the bunch position expressed in degrees of that period. At the zero crossings (90 and 270 degrees), the strength of the focussing field has its maximum.

5 SUMMARY

A new formalism for the calculation of wake fields acting on bunches travelling on arbitrarily curved trajectories makes the proper treatment of magnets possible where, unlike in bending magnets, the particle trajectory is not a circle: undulators, quadrupoles etc.. First results for the case of a micro-bunch in the TTF-FEL undulator are shown.

The longitudinal wake fields and the energy spread growth in the transition regimes of a bending magnet are calculated for different bunch lengths and magnet strengths. It can be seen that for bends whose length is considerably shorter than the bending radius no steady-state regime region exists.

6 REFERENCES

[1] *Y. Derbenev, J. Rossbach, E. Saldin, V. Shiltsev: 'Microbunch Radiative Tail-Head Interaction', TESLA-FEL 95-05, September 95.*

[2] *M. Dohlus, T. Limberg: 'Emittance Growth due to Wake Fields on Curved Bunch Trajectories', presented at XVIII International Free Electron Laser Conference (Rome, 1996); DESY print TESLA-FEL 96-13.*

[3] *E. L. Saldin, E. A. Schneidmiller, M. V. Yurkov: 'On The Coherent Radiation of an Electron Bunch Moving in an Arc of a Circle', DESY Print October 1996, TESLA-FEL 96-14.*

[4] *A VUV Free Electron Laser at the TESLA Test Facility at DESY. Conceptual Design Report. DESY Print June 1995, TESLA-FEL 95-03*

APPLICATION OF THE GSM METHOD AND TD COMPUTATION OF THE LONG RANGE WAKE IN LINEAR ACCELERATOR STRUCTURES

A. Jöstingmeier, M. Dohlus, DESY, D-22607 Hamburg, Germany and
C. Rieckmann, A. S. Omar, TU Hamburg-Harburg, D-21071 Hamburg, Germany

Abstract

For a proper design of linear colliders it is important to know the transverse long range wake which can either be computed directly in TD or alternatively from the corresponding higher order resonant modes. In this contribution, the resonant modes of the first, third and sixth dipole passband of the 180-cell accelerating structure used for the S-band linear collider at DESY have been analyzed using an accurate and numerically efficient generalized scattering matrix (GSM) method. Furthermore, the MAFIA program package has been applied to calculate the wake function in time domain (TD). The agreement of both methods turns out to be excellent. From the results one can predict that the sixth dipole passband significantly contributes to the transverse wakefield.

1 INTRODUCTION

At several high energy physics laboratories around the world strong efforts are currently made to design an e^+e^- linear collider with an initial center of mass energy of about 500 GeV [1]. In most of the designs trains of bunches are accelerated by long tapered multi-cell structures which are similar to disc-loaded circular waveguides. In order to avoid deflections of the beam which decrease the efficiency of the collider or even may lead to cumulative beam instabilities, one has to control the wakefield excited by previous bunches in the train. Higher order modes corresponding to the first and sixth dipole passband are mainly responsible for this phenomenon.

For a closed cavity the wake function can be computed from its resonant modes [2]. The contribution of each mode to the wakefield is characterized by the so-called loss parameter. In reality accelerator cavities are not closed because the beam pipe is open. Nevertheless, the computation of the wake function presented in [2] can also be used to approximate the spectral components of the wake below the cutoff frequency of the beam pipe. Therefore the beam pipe has to be modeled sufficiently long so that the cavity modes do not depend on the position of the short.

The GSM method has been proved accurate and numerically efficient for the investigation of a large variety of waveguide and cavity problems [3], [4]. In the field of linear accelerators, this method has also successfully been applied. E.g., the beam loading in a tapered X-band accelerating structure driven by monopole modes has been analyzed using the GSM method [5].

Dipole modes corresponding to the first passband of a 180-cell structure which has been designed for the S-band linear collider at DESY [6] have been studied in [7] and [8] using the GSM method and a discrete network model, respectively. However, in [7] only the first dipole passband has been considered. Furthermore, instead of the original structure a simplified model has been assumed which consists of 30 packages containing 6 identical cells each. The numerical results have demonstrated that this assumption leads to a wide scattering of the loss parameters which is however an artifact of the calculation model.

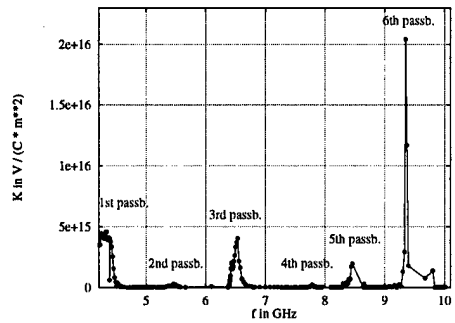

Figure 1: Normalized longitudinal loss parameters corresponding to dipole modes of the 30-cell structure.

In this contribution, the GSM method is applied to determine the loss parameters corresponding to the resonant modes of the first, third and sixth dipole passband of the S-band linear collider structure. As a reference method the MAFIA program package which is based on a grid discretization of Maxwell's equations is used to compute the wake function as it develops in time. The contributions of the individual resonant modes to the wakefield are then obtained by means of Fourier transform.

2 LOSS PARAMETER COMPUTATION OF DIPOLE MODES

For a qualitative estimate of the loss parameters covering several higher order dipole passbands we have analyzed a 30-cell structure which consists of every sixth cell of the original structure. The results presented in Fig. 1 underline the importance of the sixth dipole passband which contains the modes with the highest loss parameters. Furthermore Fig. 1 shows that besides the first, third and sixth passband the resonant modes corresponding to other passbands can be neglected.

In Fig. 2 the loss parameters of the 180-cell structure corresponding to the first passband are presented. This passband contains more than 100 modes with considerably high loss parameters.

It is worth noting that in the frequency range from about

0-7803-4376-X/98/$10.00 © 1998 IEEE

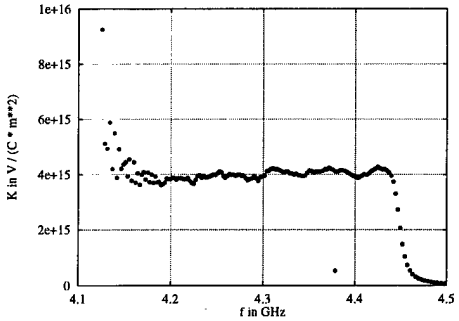

Figure 2: Normalized longitudinal loss parameters corresponding to the first dipole passband of the 180-cell structure.

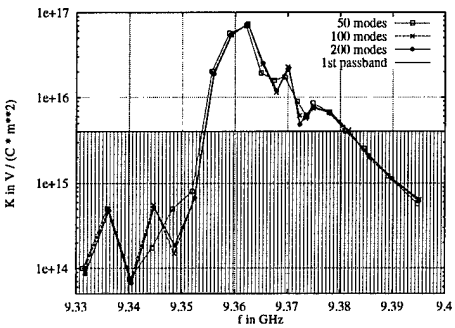

Figure 3: Normalized longitudinal loss parameters corresponding to the sixth dipole passband of the 180-cell structure.

4.15 GHz to 4.44 GHz all modes (despite of one single mode) have nearly the same loss parameter. The odd mode at $f = 4.3785$ GHz is not an intrinsic mode of the tapered periodic structure. It is rather characterized by the interaction of the first few cells with the beam pipe. Note that this mode is also observed in the loss parameter distribution of the 30-cell structure, see Fig. 1.

Fig. 3 shows the results of a detailed investigation of the sixth dipole passband of the original structure in the immediate vicinity of the mode with the highest loss parameter. An extensive study of convergence has been carried out in order to demonstrate the accuracy of the method. It has turned out that the loss parameters are stable if more than 100 waveguide modes are used in the GSM method.

The level of the loss parameters corresponding to the first dipole passband ($\approx 4 \cdot 10^{15}$ V/(C m^2)), which is also given in Fig. 3, is about 20 times less than the peak loss parameter observed in the sixth dipole passband ($\approx 8 \cdot 10^{16}$ V/(C m^2)).

The loss parameters belonging to the third dipole passband, which have also been calculated, are in the same order of magnitude as those corresponding to the first dipole passband. However, the contribution of the third dipole passband to the wake function is very small which will be shown below.

Figs. 4 and 5 present the loss parameter of the dipole

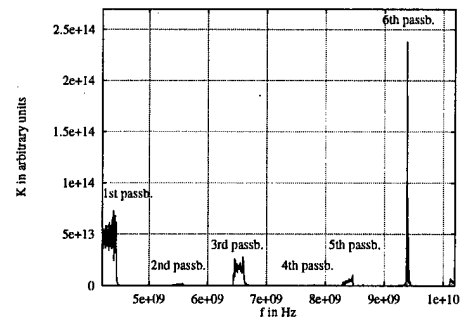

Figure 4: Fourier transform of the transverse wake function calculated in TD.

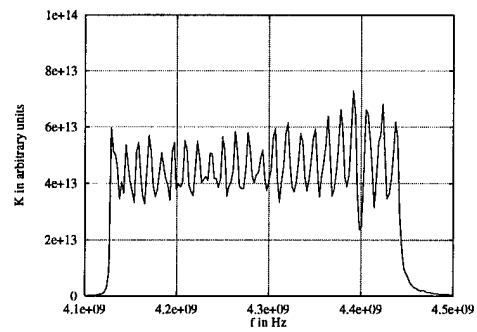

Figure 5: Detailed representation of the Fourier transform shown in Fig. 4 in the frequency range corresponding to the first dipole passband.

modes in the frequency range from 4.2 GHz to 10.2 GHz and those which correspond to the first dipole passband, respectively, as a result from the MAFIA calculations. In both Figs., the frequency resolution of the Fourier transform is 6 MHz so that individual modes cannot be recognized. Nevertheless the MAFIA results agree very well with those of Figs. 1 and 2 which have been computed using the GSM method. Nevertheless one has to keep in mind that the results which are shown in Fig. 1 correspond to a 30-cell structure.

The sum of all loss parameters $\sum k_\nu$ corresponding to a particular passband can be obtained directly from the mode computation or by the peak value of the envelope of the filtered normalized longitudinal wake function. The sums corresponding to the first, third and sixth passband obtained by the GSM method, MAFIA calculations and a discrete network model [8] are compared in Table 1. From this table it can be concluded that the three methods are in good agreement.

3 COMPUTATION OF THE TRANSVERSE LONG RANGE WAKE FUNCTION

Figs. 6, 7 and 8 present the long range wake functions corresponding to the first, third and the sixth dipole passband, respectively. These curves can either be obtained by superimposing the corresponding resonant modes (GSM method) or by applying

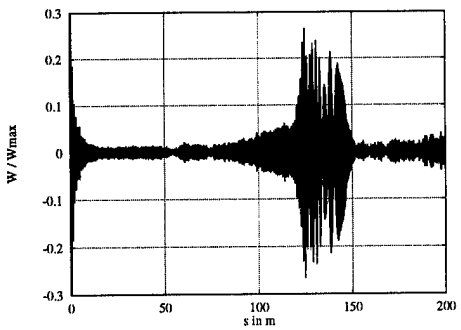

Figure 6: Transverse long range wake corresponding to the first dipole passband of the 180-cell structure.

Table 1: Sums of the loss parameters corresponding to the individual passbands.

	$\sum k_\nu$ in 10^{17} V/(Cm^2)		
	band 1	band 3	band 6
GSM	5.85	2.41	2.09
MAFIA	5.84	2.30	1.98
[8]	5.69	—	—

bandpass filters with appropriate passbands to the wake functions (MAFIA).

From the results it can be concluded that wakefield corresponding to the third dipole passband is negligible. The recoherence lengths of the first and sixth dipole passband are 120 m and 100 m, respectively. These values are consistent with the densities of the corresponding mode spectra which are 2.5 MHz and 3.0 MHz, respectively.

The recoherence phenomenon can effectively be suppressed by artificially reducing the quality factor of the dipole modes down to 3000 [8]. On the other hand, keeping in mind that the bunch to bunch distance in the S-band linear collider is 8 m, the wake function corresponding to the first *and* sixth dipole passband is not sufficiently decohered when the following bunch enters the structure. Consequently these modes have to be taken into account in beam dynamics simulations.

4 CONCLUSIONS

The GSM method has been applied to the computation of various dipole passbands corresponding to multi-cell linear accelerator structures. A detailed study of the first, third and sixth dipole passband of the 180-cell structure used for the S-band linear collider at DESY has shown that the maximum loss parameter is observed in the sixth dipole passband. The validity of the results which have been obtained using the GSM method has been confirmed by the MAFIA program package. The computation of the wake functions corresponding to the individual passbands has shown that the sixth dipole passband has to be considered in beam dynamics simulation whereas the contribution of the third dipole passband can be neglected.

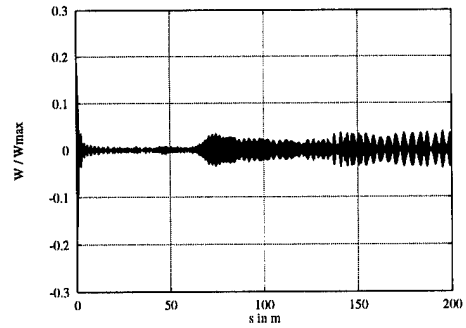

Figure 7: Transverse long range wake corresponding to the third dipole passband of the 180-cell structure.

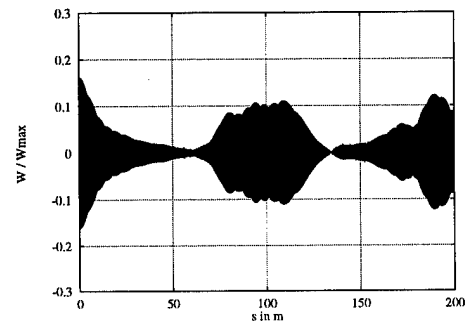

Figure 8: Transverse long range wake corresponding to the sixth dipole passband of the 180-cell structure.

5 REFERENCES

[1] G.A. Loew (ed.) "International linear collider technical review committee report," SLAC-R-95-471, 1995

[2] K.L.F. Bane, P.B. Wilson and T. Weiland, "Wake fields and wake field acceleration in physics of high energy particle accelerators," AIP Conf. proc., n0. 127, pp. 876–927, 1985.

[3] T. Itoh, Generalized scattering matrix technique," Numerical Techniques for Microwave and Millimeter-Wave Passive Structures, Wiley, New York, pp. 622–636, 1989.

[4] J. Esteban and J.M. Rebollar, "Characterization of corrugated waveguides by modal analysis," IEEE Trans. Microwave Theory Tech., vol. 39, pp 937–943, 1991.

[5] S.A. Heifets and S.A. Keifets, "Longitudinal electromagnetic fields in an aperiodic structure," SLAC-PUB-5907, 1992.

[6] N. Holtkamp, "Status of S-band technology at DESY," Proc. LC95, pp. 121–143, 1995.

[7] U. van Rienen, "Higher order mode analysis of tapered disc-loaded waveguides using the mode matching technique," Particle Accelerators, vol. 41, pp. 173–201, 1993.

[8] M. Dohlus *et al.*, "Higher order mode damping by artificially increased surface losses," Deutsches Elektronen-Synchrotron DESY, DESY-96-169, 1996.

ENHANCEMENTS TO THE LONGITUDINAL DYNAMICS CODE ESME

J. MacLachlan, J.-F. Ostiguy
Fermi National Accelerator Laboratory *, P.O. Box 500, Batavia, IL 60510

Abstract

ESME is a program developed at Fermilab for simulating both single particle and multi-particle dynamics in proton synchrotrons. The code has evolved incrementally for more than fifteen years, accumulating many useful features and some internal inconsistency in the process. In the latest revision (8.2), a significant effort has been made to eliminate inconsistency and ambiguity in the determination of phases for multiple RF systems. The use of frequency and phase curves is now more transparent. Other additions or improvements include additional features for time domain calculation, low noise distributions to extend multi-particle capability, run-time memory allocation and portable graphics. A Web page has been established to facilitate the distribution of the source code and documentation. Further information, bug reports and fixes will be made available through this resource.

1 INTRODUCTION

ESME is a computer program which follows the evolution of a distribution of particles in energy and azimuth as it is acted upon by the radio frequency system(s) of a proton synchrotron. The code was initially developed during the years 1981-82 for the design of the Tevatron Antiproton Source and documented for general use in 1984. In 1986, provisions were made for longitudinal coupling and space charge to investigate the usefulness of a γ_T-jump in the Fermilab Booster. Since then, various incremental improvements have been made. Recently, due to users interest and anticipation of the use of the code to help model longitudinal phase space manipulations required for operation of the new Recycler Ring and future Tevatron luminosity upgrades, a number of improvements were made including better support for user-defined frequency curves, new distributions with low numerical noise, dynamic memory allocation and portable graphics taking better advantage of color displays.

2 CODE DESCRIPTION

2.1 Single Particle Dynamics

At the heart of ESME is a pair of single particle difference equations

$$\theta_{i,n} = \left[\frac{\tau_{s,n-1}}{\tau_{s,n}}\theta_{i,n-1} + 2\pi\left(\frac{\tau_{i,n}}{\tau_{s,n}} - 1\right)\right] \quad (1)$$

$$E_{i,n} = E_{i,n-1} + eV(\phi_{s,n} + h\theta_{i,n}) - eV(\phi_{s,n}) \quad (2)$$

where h is the harmonic number and the subscripts s and i denote respectively quantities related to the synchronous particle and to particle i. Thus, $\tau_{s,n}$ is the synchronous period at turn n, $\tau_{i,n}$ is the period for particle i at turn n and $E_{i,n}$ and $\theta_{i,n}$ are respectively the energy and azimuth of particle i at turn n. Coupling between the longitudinal and transverse dynamics enters into this system of equations through the relation $\tau_{i,n} = L_{i,n}/(c\beta_{i,n})$. The dependence of the orbit path length L on the momentum is set by externally specified coefficients of the series expansion of L in powers of $\Delta p_i/p_0$.

2.2 Collective Effects

In the context of this paper, we define collective effects as any effect in which the distribution influences single particle motion. ESME can model the following types of collective effects: (1) reaction of the beam environment, (2) space charge and (3) feedback systems (e.g. from bunch centroid to RF phase or bunch width to RF amplitude). In all cases, only the effect on longitudinal dynamics is modeled.

In its normal mode of operation, ESME treats space-charge and the coupling to the beam environment in the frequency domain. The frequency representation is a natural one for high energy proton synchrotrons where collective effects are often dominated by a few narrow cavity resonances. Longitudinal impedances can be of two types: a simple resonance for which it is sufficient to specify three parameters i.e. frequency, strength and width, or a user-specified table of the complex longitudinal impedance $Z_{\|}(\omega)$ at different frequencies.

The charge distribution $\lambda(s)$ is obtained by projecting the phase space distribution. The relatively small number of particles ($10^4 - 10^7$) used for a typical simulation results in small scale spatial density fluctuations. For relativistic particles in a smooth cylindrical beam pipe, one can show that the longitudinal electric space charge field is given by [1]

$$E_s(s) = -[1 + 2\log(b/a)]\frac{\lambda'(s)}{4\pi\epsilon_0\gamma^2} \quad (3)$$

where $\lambda'(s)$ is the derivative of the longitudinal line charge distribution and b/a is the ratio of vacuum chamber to beam radii. Note that the presence of a derivative in equation (3) indicates that small scale fluctuations will produce high electric fields and "spurious" emittance growth.

ESME implicitly assumes that the RF frequency *does not change significantly over a turn.* This allows the beam current to be treated as a periodic function and its spectral contents to be efficiently calculated using the FFT. The finite number of harmonics used for the FFT acts as a low-pass filter that mitigates spurious emittance growth due to

* Operated by the Universities Research Association, Inc., under contract with the U.S. Department of Energy.

loca fluctuations. Optionally, the distribution can also be smoothed using a variety of methods, e.g. high order polynomial fitting.

In certain situations, the frequency domain representation may be inappropriate. The canonical example is the situation where the revolution period changes significantly during a period smaller than the fill time of the cavities. To deal with this situation, ESME can model simple resonances in the time-domain. However, more complicated environment responses must still be handled through $Z_{\|}(\omega)$.

3 NEW FEATURES AND ENHANCEMENTS

3.1 *Frequency and Phase for Multiple RF Systems*

ESME provides for several independent RF voltages representing either Fourier components of a complex waveform or the output of physically independent RF systems. Voltage, frequency, and phase may have arbitrary programs. The phase of each RF system consists of a programmed phase with a default of zero, an optional synchronizing phase, and an optional phase feedback term. In the simplest case of a single RF voltage with a programmed phase of zero, the synchronizing phase $\vartheta_s = \varphi_s/h$, where h is the harmonic number and φ_s is the conventionally defined synchronous phase. The synchronous trajectory can be moved freely with respect to the central orbit by using phase curves, frequency curves, or specified momentum offset for such processes as momentum stacking and phase displacement acceleration. The resulting complexity of definining the phase variables correctly prompts more questions than any other general feature; fortunately it is hidden in many typical applications.

3.2 *Low Noise Distributions*

Assuming a rotation period T and M identical evenly spaced bunches, the Fourier spectrum of the beam current consists a train of impulses of period MT^{-1} modulated by the transform $B(\omega)$ of the bunch profile. At high frequencies, $B(\omega)$ has a tail which is approximately constant and proportional to the inverse square root of the number of particles in the beam, $N_p^{-1/2}$. The bunch-lengthening and bucket distortion effects resulting from the lower frequency part of the spectrum can be simulated with a modest number of macroparticles n_p sufficing to produce the general form of $B(\omega)$. However, if effects such as microwave or negative mass instabilities are to be included with the intention of generating meaningful quantitative information, the noise in the spectrum of the starting distribution should be the Schottky noise of the real beam not the numerical noise corresponding to n_p. Since $N_p/n_p \simeq 10^{13}/10^7$ the numerical noise must be reduced by a few orders of magnitude. ESME can now produce quieter distributions without increasing the number of particles by populating the phase space using quasi-random distributions derived from Sobol [2] sequences of appropriate dimensionality.

The high frequency tail for quasi-random distributions is proportional to n_p^{-1} rather than $n_p^{-1/2}$. Unfortunately, the mapping (1-2), even in the absence of collective effects, reintroduces high frequency noise. Nevertheless, the distribution will generally remain quieter than one generated by pseudo-random numbers. Thus, the technique is useful but getting reliable results requires caution.

3.3 *Memory Management*

ESME is written in Fortran 77. The code utilizes a number of large arrays to store phase space coordinates, longitudinal distributions, etc. Communication between various modules relies heavily on large COMMON blocks. With the availability of inexpensive memory, users have become eager to run simulations with increasingly large number of particles. The old structure of the code required recompilation resulting in a proliferation of executables. To avoid this situation, the memory management has been extensively modified to support dynamic memory allocation. This was accomplished without making dramatic structural changes by passing pointers through COMMON blocks rather than actual arrays. CRAY style rather than "standard" Fortran 90 syntax was used. While the former is a de-facto standard under most UNIX f77 compilers, Fortran 90 is still not widely used. Porting the code to Fortran 90 should be a straightforward task if this ever becomes an issue.

3.4 *Graphics*

Over the years, ESME has been modified many times to support various graphic packages. Prior to the current version, ESME relied on HIGZ, a library developed at CERN Although support for HIGZ remains available, we have opted to migrate to the PGPLOT library and to use it for future development. PGPLOT is compact, supports a wide variety of devices, is free for non-commercial use, distributed in source form and currently runs under every flavor of UNIX. A Windows NT port exists and should make it possible to support that platform. The new graphics code makes better use of color, in particular to distinguish among different classes of particles. New types of plots are supported including more informative phase space density contour plots and mountain range plots of the beam spectrum evolution.

3.5 *Internet Resources*

A Web page has been established to enable users to report bugs and new releases in a timely manner. The URL is `http://www-ap.fnal.gov/ESME`. At the time this article was written, the current version was 8.2. Source code, documentation and binaries for various platforms should be available from the above address within a few days of this conference.

4 CONCLUSIONS AND FUTURE PROJECTS

ESME does not claim to be taking advantage of the most recent advances in software technology. However, as it stands it is a mature well-proven tool that occupies a specialized niche. Our objectives for the near future are (1) fix problems that are reported (2) to the extent that fundamental changes in the structure of the code are not required, add new features that will allow users to solve practical problems. In an upcoming release, we intend to provide a mode where all calculations will be performed consistently in the time-domain; the beam environment reaction will be specified through a calculated or measured wake potential. This should be useful in situations where the Fourier representation is not economical e.g. a ring populated with a large number of short intense bunches.

5 ACKNOWLEDGEMENTS

The modifications described in this paper were in part implemented during a visit to CERN in November 1996. The authors would like to thank Roland Garoby and Stephen Hancock of the CERN PS RF group for their useful comments and hospitality. Thanks are also due to Ioanis Kourbanis for his insights and patience in testing the new code.

6 REFERENCES

[1] A. M. Sessler and V. K. Neil, "Longitudinal Resistive Instabilities of Intense Coasting Beams", NIM 36, No. 4, pp 429 - 436 (April 1965)

[2] Sobol' I.M. USSR Computational mathematics and mathematical Physics, 7,4, 86-122.

[3] Information about the PGPLOT library can be found at `http://astro.caltech.edu/~tjp/pgplot`.

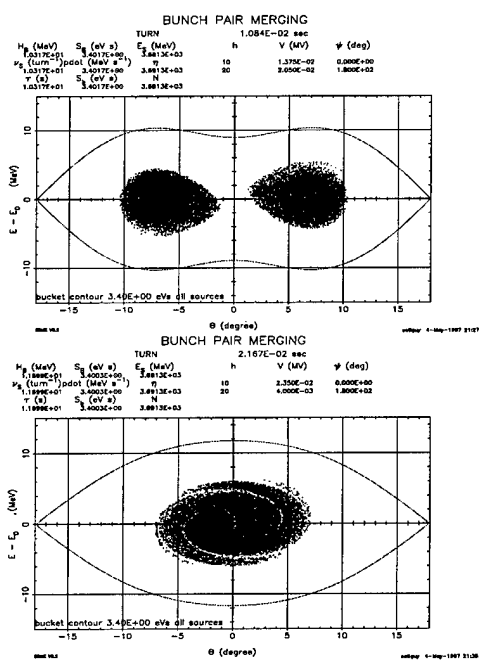

Figure 1: Adiabatic merging of h=20 bunches into h=10 bunch in CERN PS

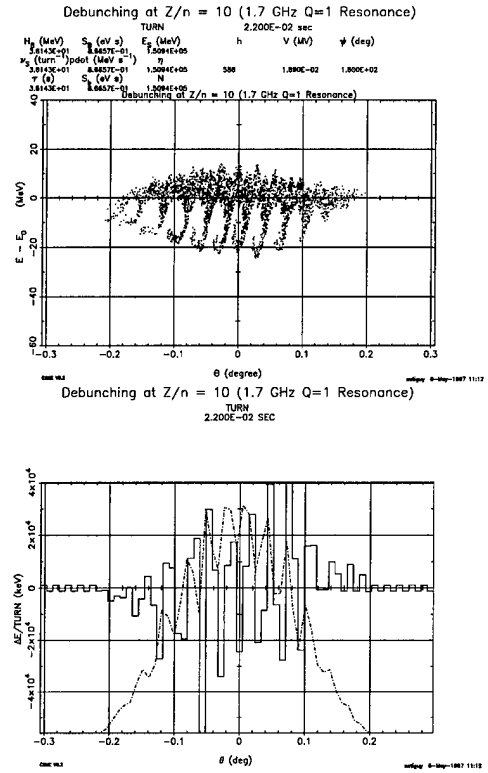

Figure 2: Well developed microwave instability. Lower plot shows azimuthal charge distribution (...) and longitudinal electric field (—).

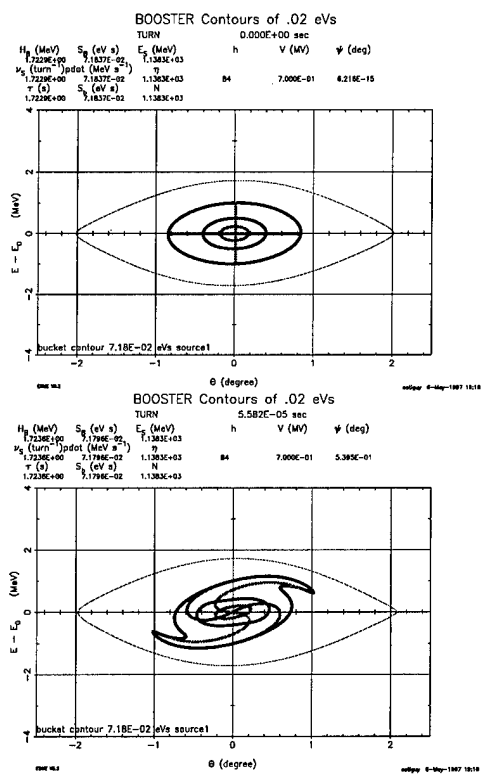

Figure 3: Distortion of .02, .005, and .002 eVs contours caused by locating all cavities at one place in rapid cycling booster ring

OPTICS ELEMENTS FOR MODELING ELECTROSTATIC LENSES AND ACCELERATOR COMPONENTS I. EINZEL LENSES

George H. Gillespie[a] and Thomas A. Brown[b]
[a]G. H. Gillespie Associates, Inc., P.O. Box 2961, Del Mar, CA 92014, U.S.A.
[b]Center for Accelerator Mass Spectrometry, LLNL, P.O. Box 808, Livermore, CA 94551, U.S.A.

Abstract

A set of optical models for a variety of electrostatic lenses and accelerator columns has been developed for the computer code TRACE 3-D. TRACE 3-D is an envelope (matrix) code including space charge often used to model bunched beams in magnetic transport systems and radiofrequency (RF) accelerators when the effects of beam current may be important. Several new matrix models have been developed that allow the code to be used for modeling beam lines and accelerators with electrostatic components. The new models include (1) three einzel lenses, (2) two accelerator columns, (3) three electrostatic deflectors (prisms), and (4) an electrostatic quadrupole. A prescription for setting up the initial beam appropriate to modeling 2-D (continuous) beams has also been developed. The new models for (1) are described in this paper, selected comparisons with other calculations are presented, and a beamline application is summarized.

1. INTRODUCTION

TRACE 3-D uses the first-order transfer matrix (R-matrix) formalism to compute changes to the beam matrix (σ-matrix) [1]. However, rather than using the R-matrix for an entire optical element, TRACE 3-D divides each element into a series of small (longitudinal) segments and the calculation then steps through the beamline one segment at time. The effective transfer matrix may be modified in each segment.

The capability of TRACE 3-D to model longitudinal changes in parameters within an element allows one to include effects that are not possible with a strictly first-order code; e. g., space charge forces (applying impulses at each step) and permanent magnet quadrupole fringe field effects are included in the standard version of TRACE 3-D [1]. This "longitudinal" capability has been used in this work to incorporate changes in the beam energy as a function of position in the electrostatic elements, as well as to calculate fringe fields and retain the space charge model for all elements.

Three different electrode geometries for einzel (or unipotential [2]) lenses have been modeled and are illustrated in Figure 1. All of the lenses have cylindrical symmetry about the z axis, indicated by the dashed line in Figure 1. In addition, the einzel lenses are symmetric about their mid-points, corresponding to the point $z = 0$.

2. OPTICS MODELING

The optics of particles near the axis of cylindrically symmetric electrostatic elements is determined by the axial potential distribution $V(z)$. The first-order electric fields are given by

$$E_x(x,y,z) = +\,[(1/2)\,(\partial^2 V(z)/\partial^2 z)]x \quad , \tag{1}$$

$$E_y(x,y,z) = +\,[(1/2)\,(\partial^2 V(z)/\partial^2 z)]y \quad , \tag{2}$$

and

$$E_z(x,y,z) = -\,(\partial V(z)/\partial z) \quad . \tag{3}$$

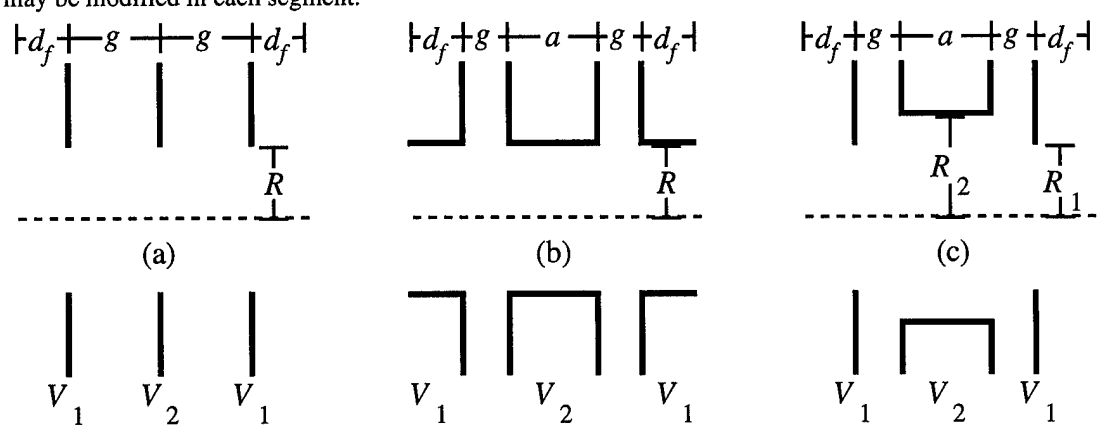

Figure 1. Electrode geometries for the three einzel lens models. Different potential functions are used to describe (a) a three-aperture lens, (b) a three-tube lens and (c) a two-aperture, center-tube lens.

0-7803-4376-X/98/$10.00 © 1998 IEEE

The fields given above satisfy Maxwell's equation $\nabla \bullet \boldsymbol{E} = 0$ for any $V(z)$. The R-matrices describing the first-order optics may be computed directly from these fields. Our method follows that given in reference [3].

2.1 R-Matrix Elements

The region over which the fields (1)-(3) act is divided into small steps of length Δz and two R-matrices are computed for each step. The first R-matrix, together with an increase in the beam energy, computes the effects of a uniform electric field acting over a distance of Δz. The non-trivial elements of this R-matrix are

$$R_{13} = R_{24} = 2\Delta z /[1+(\eta_-)^{1/2}] \quad , \tag{4}$$

$$R_{22} = R_{44} = R_{66} = 1/(\eta_-)^{1/2} \quad , \tag{5}$$

and

$$R_{56} = \Delta z /\gamma^2 \quad , \tag{6}$$

where

$$\eta_- = V(z)/V(z - \Delta z) \quad , \tag{7}$$

and γ is the relativistic energy factor of the beam at z.

The second R-matrix computes the effective thin lens for the focusing effect of the field applied as an impulse. The non-trivial elements of this R-matrix are

$$R_{21} = R_{43} = - [\eta_-\eta_+ - 2\eta_- +1]/(4\eta_-\Delta z) \quad , \tag{8}$$

where

$$\eta_+ = V(z +\Delta z)/V(z) \quad . \tag{9}$$

The formulas given by Equations (4)-(9) can be used to model any electrostatic element whose potential is given at discrete positions on the axis. In this work, analytic forms for the on-axis potential functions are used for computing the R-matrix elements.

2.2 Potential Functions

The potential as a function of z for the einzel lenses illustrated in Figure 1 may be written in terms of the electrode potentials V_1 and V_2 as

$$V(z) = V_1 + [(V_2 - V_1)/2]\, \phi(z) \quad , \tag{10}$$

where $\phi(z)$ is an even function of z, and goes to zero as z approaches $\pm\infty$. The function $\phi(z)$ depends only on the geometry (electrode spacings and dimensions) of the lens.

For the three-aperture lens illustrated in Figure 1(a), we use a potential that is a special case of the potential for the two-aperture center-tube lens, Figure 1(c). (That potential is described further below.) When the two radii are equal, and the center tube has the zero length, the formula for $\phi(z)$ is given by

$$\phi(z)= (2/\pi)(g)^{-1}\{A\} \quad , \tag{11}$$

where

$$A=(z+g)\tan^{-1}[(z+g)/R]+(z-g)\tan^{-1}[(z-g)/R]-(2z)\tan^{-1}[(z)/R].$$

For the three-tube lens illustrated in Figure 1(b), we use the following formula for $\phi(z)$

$$\phi(z)= R\,(\omega' g)^{-1}\ln\{A/B\} \quad , \tag{12}$$

where

$$A = [\cosh(2\omega z/R)+\cosh[(\omega a/R)+(\omega' g/R)]] \quad , \tag{13}$$

and

$$B = [\cosh(2\omega z/R)+\cosh[(\omega a/R)-(\omega' g/R)] \quad . \tag{14}$$

The constants ω=1.31835 and ω'=1.67. This form of the potential is based upon a parameterization of a single two-cylinder (acceleration) lens [4]. The potential was obtained from the superimposition of potentials for 2 back-to-back, two-cylinder lenses, with the end electrodes set to V_1, and the adjacent electrodes set to V_2 [5]. When $\omega'=\omega$=1.318, the potential given by (12)-(14) is the same as that used by Lu, Ben-Zvi and Cramer [3] and other authors. The use of ω'=1.67 provides better agreement with numerical solutions to Laplace's equation for certain cases [4].

For the two-aperture center-tube lens illustrated in Figure 1(c), we use a potential given by El-Kareh and El-Kareh; see Equation (6.5) of reference [2]. Specifically,

$$\phi(z)= (2/\pi)(g)^{-1}\{A-B\} \quad , \tag{15}$$

where

$$A = (z+g+a/2)\tan^{-1}[(z+g+a/2)/R_1] + (z-g-a/2)\tan^{-1}[(z-g-a/2)/R_2] + 2R_1 \quad , \tag{16}$$

and

$$B = (z+a/2)\tan^{-1}[(z+a/2)/R_1] + (z-a/2)\tan^{-1}[(z-a/2)/R_2] + 2R_2 \quad . \tag{17}$$

When $R_1 = R_2 = R$ and $a = 0$, these results reduce to that given by Equation (11) above.

The fields are modeled to a distance d_f before and after each lens, so that the full length of a lens is $2(g+d_f)+a$. In the calculations described here, the value of $d_f = fR$ (or fR_1), where f is the TRACE 3-D fringe field extension factor, PQEXT [1].

3. COMPARISONS WITH OTHER WORK

Several calculations have been carried out using the einzel models described above for comparison to other results available in the literature. Table 1 gives the focal length f obtained from TRACE 3-D for the 3-tube lens, together with results from numerical calculations by Adams and Read [5], all expressed as the ratio $f/(2R)$.

Table 1. Focal length to aperture ratio for 3-tube einzel lenses. Results for two fringe field factors f are given.

V_2/V_1	$f/(2R)$=-1/[2R R_{21}] [this work] f=2.5	f=10.0	$f/(2R)$ [5]
-0.5	0.632	0.629	0.628
0.0	2.832	2.842	2.843
0.8	131.524	141.267	141.752
2.0	11.462	11.169	11.261
9.0	1.288	1.301	1.312

4. BEAMLINE DIAGNOSTIC APPLICATION

The three–tube einzel lens model described above has been used in developing a diagnostic model of the low–energy injection system for the Center for Accelerator Mass Spectrometry (CAMS) at the Lawrence Livermore National Laboratory (LLNL). Figure 2 illustrates a TRACE 3-D simulation of the injection beamline. In the first step of the model development, iterative adjustment of the TRACE 3-D source emittance and voltage on the second einzel lens of the zoom–lens section (element 6 in Figure 2) resulted in a simulation of the beamline that was consistent with measured beam profiles at the equivalent of positions 4/5 and 7/8 in Figure 2 (the first einzel lens was turned off for this test).

The second einzel lens voltage required in the model to produce a beam waist at position 7/8 was 27.4 kV. This value is within 1.5% of the measured 27.8 kV required in the laboratory. Given the uncertainties in the DAC/ADC conversion factors, the difference between the two values is not significant. Since the superposition derivation of Equation (12) is valid for $g/a \leq 1/3$ and $a/2R \geq 1/2$, and the physical dimensions of the second einzel lens are such that $a/2R = 1.1$ and $g/a = 0.1$, this level of agreement was expected.

In the second step of this development, a full model of the injection system has been constructed. This model has been used in understanding and optimizing the transport of various ions through the low–energy injection system and into the CAMS accelerator.

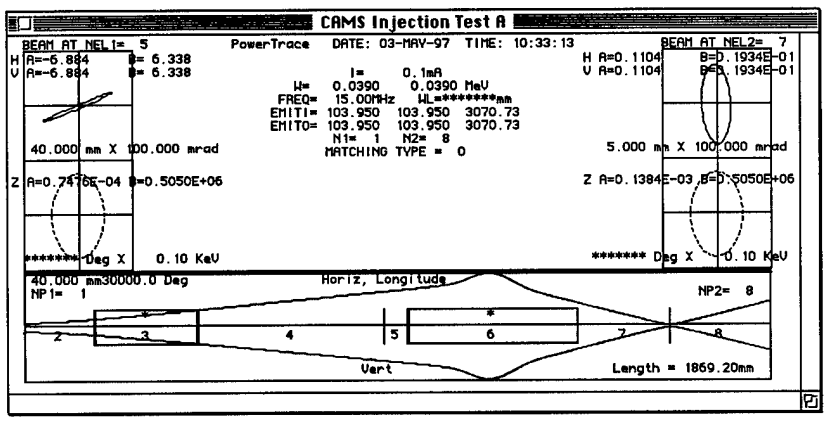

Figure 2. TRACE 3-D output for the zoom–lens section of the modeled low–energy injection line. This figure shows the results obtained after adjustment of the source emittance and second einzel lens voltage to match the measured beam profiles at the equivalent of positions 4/5 and 7/8.

5. SUMMARY

Several optical elements for electrostatic accelerator devices have been developed. The elements have been integrated into a version of the TRACE 3-D code that works within the Shell for Particle Accelerator Related Codes (S.P.A.R.C.) software environment [6]. A detailed summary of the einzel models used for the code has been presented. Focal length calculations show good agreement with other results from the literature. The utility and accuracy of the einzel lens models has been demonstrated in the development of a diagnostic model of the low–energy injection line at the LLNL Center for Accelerator Mass Spectrometry. Details for other elements will be published in future papers.

ACKNOWLEDGMENTS

The assistance of Barrey W. Hill in developing new components for the S.P.A.R.C. interface is gratefully acknowledged. This work performed in part under the auspices of the U.S. Department of Energy at the Lawrence Livermore National Laboratory under contract W-7405-Eng-48.

REFERENCES

[1] K. Crandall and D. Rusthoi, "TRACE 3-D Documentation," Los Alamos National Laboratory Report LA-UR-90-4146, 92 pages (1990).

[2] A. B. El-Kareh and J. C. J. El-Kareh, Chapter VI "The Electrostatic Unipotential Lens," *Electron Beams, Lenses and Optics*, Vol. 1, Academic Press, New York, 186--228 (1970).

[3] J.-Q. Lu, I. Ben-Zvi and J. G. Cramer, "LYRAN A Program for the Analysis of Linac Beam Dynamics" Nucl. Instru. Meth. Phys. Res. A 262, 200-6 (1987).

[4] F. H. Read, A. Adams and J. R. Soto-Montiel, "Electrostatic Cylinder Lenses I Two Element Lenses," J. Phys. E 4, 625-632 (1971).

[5] A. Adams and F. H. Read, "Electrostatic Cylinder Lenses II Three Element Einzel Lenses," J. Phys. E 5, 150-155 (1972).

[6] G. H. Gillespie and B. W. Hill, "A Graphical User Interface for TRACE 3-D Incorporating Some Expert System Type Features," 1992 Linear Accelerator Conference Proc., AECL-10728, 787-789 (1992).

THE PARTICLE BEAM OPTICS INTERACTIVE COMPUTER LABORATORY FOR PERSONAL COMPUTERS AND WORKSTATIONS

George H. Gillespie, Barrey W. Hill, Hendy Martono, John M. Moore,
Nathan A. Brown, Michael C. Lampel and R. Chris Babcock
G. H. Gillespie Associates, Inc., P.O. Box 2961, Del Mar, CA 92014, U.S.A

Abstract

The Particle Beam Optics Interactive Computer Laboratory (PBO Lab) is a new software concept to aid both students and professionals in modeling charged particle beams and particle beam optical systems. The PBO Lab has been designed to run on several computer platforms and includes four key elements: (1) a graphic user interface shell, (2) a graphic beamline construction kit for users to interactively and visually construct optical beam lines, (3) a knowledge database on electric and magnetic optics elements, including interactive tutorials on the physics of charged particle optics and on the technology used in particle optics hardware, and (4) a set of charged particle optics computational engines that computes transport matrices, beam envelopes and trajectories, fits parameters to optical constraints, and carries out similar calculations for the graphically-defined beam lines. The primary computational engines in the first generation PBO Lab are the third-order TRANSPORT code, the multiple ray tracing program TURTLE, and a new first-order matrix code that includes an envelope space charge model with support for calculating single trajectories in the presence of the beam space charge. Progress on the PBO Lab development is described and illustrations from the Windows 95 implementation are presented.

1. INTRODUCTION

The increasing variety of accelerator applications in research and industry places a growing demand upon scientists and engineers involved in developing new accelerator and beamline designs. Particle optics simulation codes play a key role in the design process and enhanced software tools offer the promise of improved productivity for beamline designers. Another benefit of improved software tools is a significant reduction in the time required to train new researchers in the use of optics simulation programs. This paper summarizes progress on one such new tool: The Particle Beam Optics Interactive Computer Laboratory (PBO Lab). An object oriented programming (OOP) approach has been adopted for the PBO Lab and the architecture of the software has been developed specifically to run on several different operating systems. An overview of each of the primary components of the PBO Lab has been presented elsewhere [1]. Here we describe the first two key elements of the PBO Lab listed in the abstract: the graphic user interface shell and the beamline construction kit.

One emphasis in the PBO Lab is on assisting users in the set up and running of the optics programs without requiring any knowledge of the format, syntax, or similar requirements of the input. Beamlines and accelerator systems are graphically constructed on the computer screen using drag and drop icons. Default parameters are incorporated for all required inputs so that both the topology of the beamline and a complete set of input data are defined automatically during the graphical construction. Setting up a particular design is reduced to editing the values of parameters, which are displayed in windows together with the parameter descriptions. Different parameter set options are available for defining optical elements, and a variety of units options may be used. Expert system type rules provide guidance for editing input parameters, and additional displays, such as effective focal lengths and phase space plots, provide users with further useful feedback on their input. The graphic user interface shell and the beamline construction kit focus on these objectives.

2. GRAPHIC USER INTERFACE (GUI) SHELL

The conceptual foundation for the PBO Lab GUI shell is derived from a unique graphic user interface designed specifically for codes used in the accelerator community, known as the Shell for Particle Accelerator Related Codes (S.P.A.R.C.) [2]. A new multi-platform (MP) version of the S.P.A.R.C. environment has been developed to support a number of different operating systems [1]. S.P.A.R.C. MP is written in C++ and has been constructed using a modular approach that provides a good framework for implementing a cross platform version of the GUI. Figure 1 illustrates the PBO Lab GUI running on the Windows 95 operating system.

0-7803-4376-X/98/$10.00 © 1998 IEEE

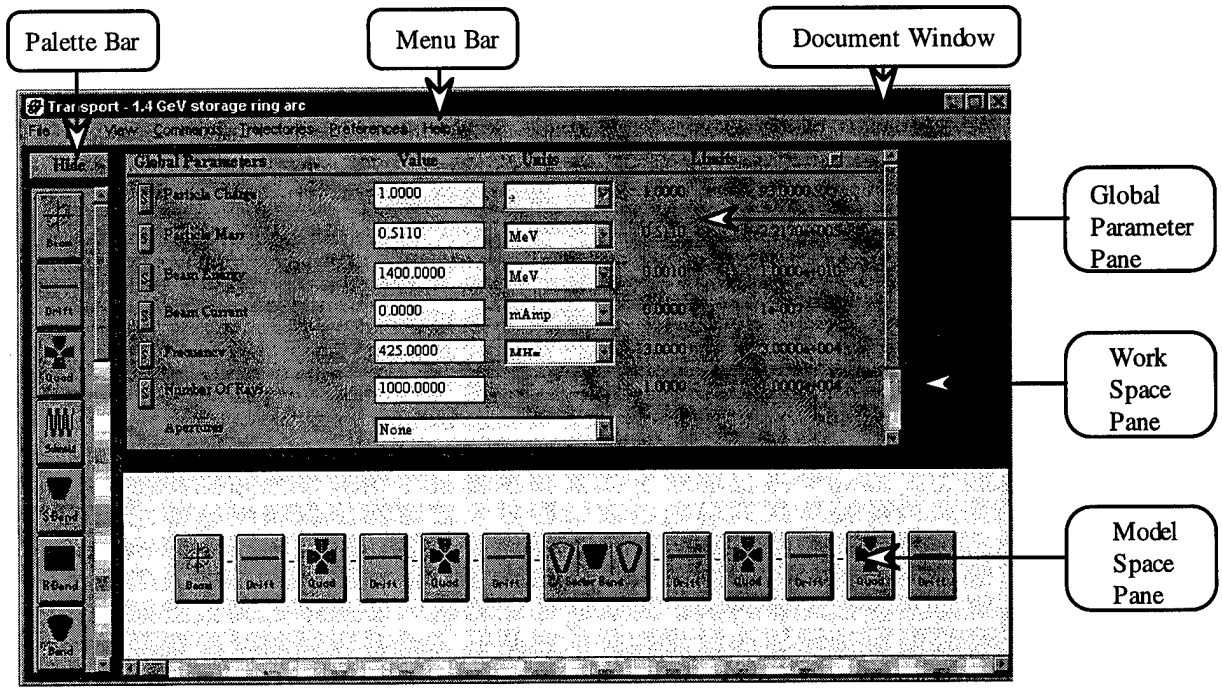

Figure 1. Example of the PBO Lab graphic user interface for TRANSPORT using S.P.A.R.C. MP.

Parameter values are edited using Data Tables in the Global Parameter Pane or in Piece Windows for individual beamline components. A Piece Window is accessed by "double clicking" on the icon of the desired beamline component. Figure 2 illustrates a Piece Window for the Quad element of TRANSPORT [3] or TURTLE [4]. The PBO Lab Piece Windows have several features that assist users in editing input data.

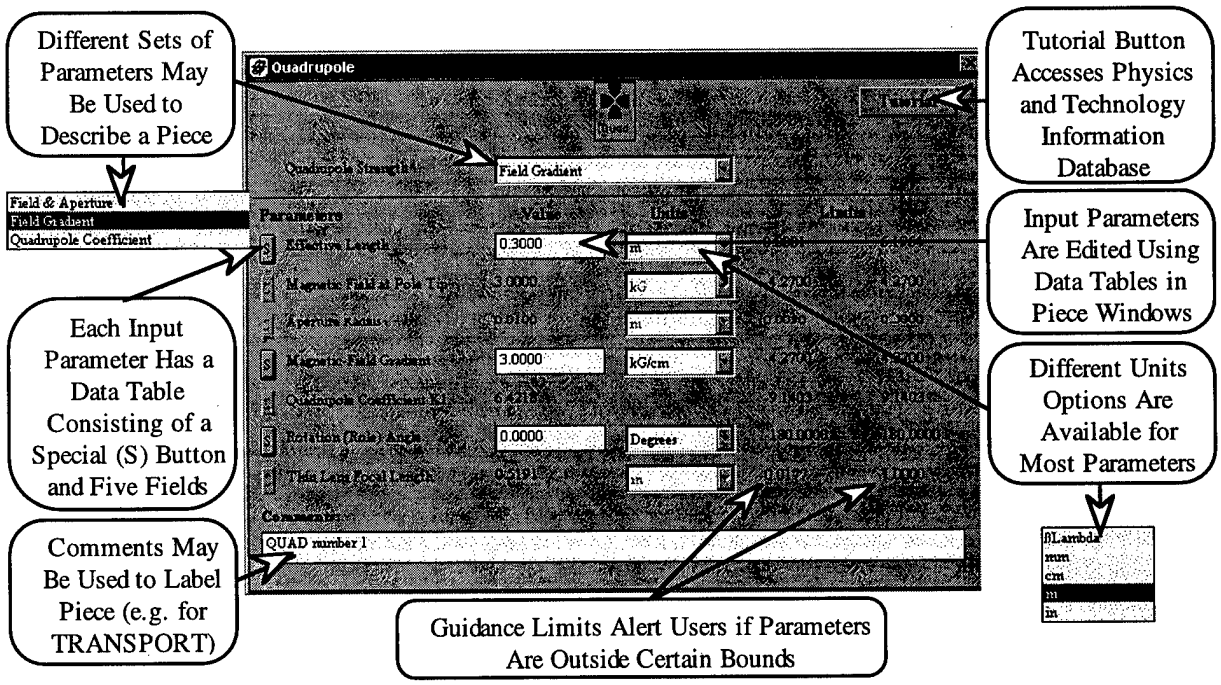

Figure 2. Example of PBO Lab Piece Window for editing parameters of a magnetic quadrupole element.

3. BEAMLINE CONSTRUCTION KIT

The construction of a beamline using S.P.A.R.C. MP follows the basic approach used in the original S.P.A.R.C. environment [1]. A beamline is built by selecting and dragging (with the mouse) the icons from the Palette Bar for individual transport elements and dropping them onto the Model Space Pane. Graphical representations of components (Piece icons) are then displayed on this pane. Figure 1 illustrates a Model Space beamline composed in this way that contains drifts, quadrupoles and a bending magnet. Transport elements (Pieces) can be snapped to either end of the beamline and may also be inserted into the middle of the beamline, by selecting a drop location that is near one of the connection lines between elements on the beamline.

Individual Pieces or groups of Pieces on the beamline may be selected for use in other beamline construction tasks. Once a selection is made, it may then be Copied, Cut, Deleted, or dragged up to the Work Space Pane for future use. Pieces from the Work Space may be inserted in, or dropped onto the ends of, the beamline on the Model Space. Selected Pieces may also be defined as "Sublines" to be used in constructing beamlines composed of repetitive elements (e.g. a lattice). A number of operations on Sublines are being developed, such as Expand, Invert and Rotate operations. A powerful object model has been developed [5], which very efficiently describes either hierarchical (Subline), flat (single Piece), or mixed beamline representations, that forms the basis for this graphic functionality. Figure 3 illustrates an example of Subline use, where the arc shown in Figure 1 has been defined as a Subline and then replicated 5 times. Sublines may contain additional Sublines, as well as individual Pieces.

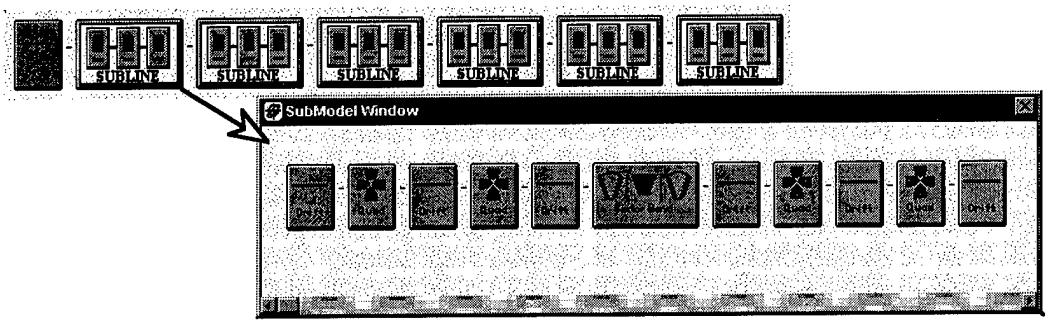

Figure 3. Using Sublines to construct a beamline composed of a repetitive group of elements.

4. SUMMARY

The Particle Beam Optics Interactive Computer Laboratory promises improved productivity for scientists and engineers involved in the analysis or design of accelerators and a significant reduction in the time required to train new researchers in the use of optics programs. Substantial progress has been made in developing the PBO Lab into a useful tool, including the integration of TRANSPORT into the S.P.A.R.C. MP environment running in the Windows and Solaris operating systems.

ACKNOWLEDGMENTS

The authors are indebted to Dave Carey for assistance in defining the requirements for the PBO Lab needed to support the TRANSPORT and TURTLE codes. We also thank Karl Brown for useful comments on early versions of the PBO Lab and TRANSPORT GUI. The assistance of James Gillespie in the design of the software architecture for the PBO Lab is gratefully acknowledged. Portions of this work have been supported by the U. S. Department of Energy under SBIR grant number DE-FG03-94ER81767. Windows is a trademark of Microsoft and Solaris is a trademark of Sun Microsystems.

REFERENCES

[1] G. H. Gillespie, B. W. Hill, N. A. Brown, H. Martono and D. C. Carey, "The Particle Beam Optics Interactive Computer Laboratory," AIP Conference Proceedings 391, 264-269 (1996).

[2] G. H. Gillespie, "The Shell for Particle Accelerated Related Codes (SPARC) - A Unique Graphical User Interface," AIP Conference Proceedings 297, 576-583 (1993).

[3] D. C. Carey, K. L. Brown and F. Rothacker, "Third-Order TRANSPORT - A Computer Program for Designing Charged Particle Beam Transport Systems," Stanford Linear Accelerator Center Report No. SLAC-R-95-462, 295 pages (1995).

[4] D. C. Carey, "TURTLE (Trace Unlimited Rays Through Lumped Elements) A Computer Program for Simulating Charged Particle Beam Transport Systems," Fermi National Accelerator Laboratory Report No. NAL-64, 45 pages (1978).

[5] B. W. Hill, H. Martono and J. S. Gillespie, "A Object Model for Beamline Descriptions," AIP Conference Proceedings 391, 361-365 (1996).

LORENTZ GROUP LIE ALGEBRA MAP OF ULTRA-RELATIVISTIC RADIATING ELECTRON

H. Kawaguchi, K. Tsubota and T. Honma
Graduate School of Eng., Hokkaido Univ., Kita 13, Nishi 8, Kita-ku, Sapporo 060, Japan

Abstract

This paper discusses a precise numerical integrator for ultra-relativistic radiating electron motion. It is firstly shown that the covariant form Lorentz force equation of motion possesses the Lorentz group Lie algebra structure and the Lorentz-Dirac equation of motion as well. After that, a precise numerical integrator for radiating electron is constructed based on the Lie algebra properties. Numerical examples show that this integrator can be effectively used not only for the ultra-relativistic electron motion but also for a non-relativistic electron motions in pure magnetic field as well.

1 INTRODUCTION

One of the precise integrators for charged particle, the symplectic integrator, shows us its powerful properties for integration of the Hamilton systems. The leading principle for obtaining precise solutions is the conservation of the symplectic structure of the system. Here, we know that radiating electrons do not belong to the Hamilton systems when its velocity is very close to the light speed (ultra-relativistic velocity), because of radiation dumping effects. For that situation, any different kind leading principle are required, if one want to obtain precise solutions.

From this point of view, this paper considers of a numerical integrator for the ultra-relativistic radiating electron.

2 LORENTZ GROUP LIE ALGEBRA PROPERTIES OF EQUATION OF MOTION

The ordinary Lorentz force equation of motion (without the radiation reaction force) is expressed in the following covariant form (MKSA),

$$mc\frac{du^\mu}{ds} = eF^\mu_\nu u^\nu \,, \tag{1}$$

then one can find that the electromagnetic field tensor F^μ_ν possesses special structure,

$$F^\mu_\nu = \begin{pmatrix} 0 & E_x/c & E_y/c & E_z/c \\ E_x/c & 0 & B_z & -B_y \\ E_y/c & -B_z & 0 & B_x \\ E_z/c & B_y & -B_x & 0 \end{pmatrix} , \tag{2}$$

or

$$F^\mu_\nu = \frac{\mathbf{E}}{c} \bullet \mathbf{K} - \mathbf{B} \bullet \mathbf{S} \,, \tag{3}$$

where $\mathbf{K}$ and $\mathbf{S}$ are the boost and rotation operators, which construct one of irreducible representations of the Lorentz group Lie algebra[1],

$$\mathbf{K} = (K_x, K_y, K_z) \,,$$
$$K_x = \begin{pmatrix} 0&1&0&0 \\ 1&0&0&0 \\ 0&0&0&0 \\ 0&0&0&0 \end{pmatrix}, K_y = \begin{pmatrix} 0&0&1&0 \\ 0&0&0&0 \\ 1&0&0&0 \\ 0&0&0&0 \end{pmatrix}, K_z = \begin{pmatrix} 0&0&0&1 \\ 0&0&0&0 \\ 0&0&0&0 \\ 1&0&0&0 \end{pmatrix}, \tag{4}$$

$$\mathbf{S} = (S_x, S_y, S_z) \,,$$
$$S_x = \begin{pmatrix} 0&0&0&0 \\ 0&0&0&0 \\ 0&0&0&-1 \\ 0&0&1&0 \end{pmatrix}, S_y = \begin{pmatrix} 0&0&0&0 \\ 0&0&0&1 \\ 0&0&0&0 \\ 0&-1&0&0 \end{pmatrix}, S_z = \begin{pmatrix} 0&0&0&0 \\ 0&0&-1&0 \\ 0&1&0&0 \\ 0&0&0&0 \end{pmatrix}. \tag{5}$$

The representation (3) can be naturally understood if we remember that the four velocity vector u^μ is exactly confined by the following identity,

$$u^\nu u_\nu = 1 \,, \tag{6}$$

that is to say, Eq. (1) merely tells us that the four velocity is governed by the Lorentz transformation along the particle trajectory and then the field tensor F^μ_ν plays the role of the Lorentz group Lie algebra. (This situation can be expressed in Fig. 1. The terminal point of the four vector is always on unit sphere in 4D Minkowski space and its trajectory moves along "vector" F^μ_ν.)

$$F^\mu_\nu = \frac{\mathbf{E}}{c} \bullet \mathbf{K} - \mathbf{B} \bullet \mathbf{S}$$

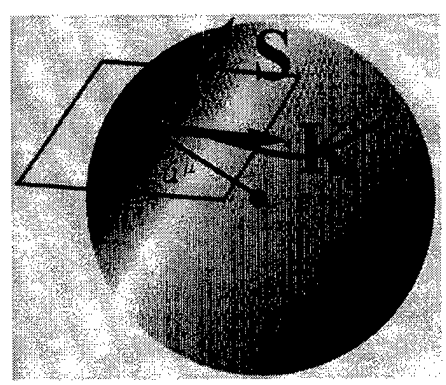

Figure 1: Trajectory of terminal point of four vector.

There also exists similar situation in the radiation dumping phenomena. The ultra-relativistic radiating electron is governed by the Lorentz-Dirac equation of motion [1, 2, 3],

$$mc\frac{du^\mu}{ds} = eF^\mu_\nu u^\nu + \frac{e^2}{6\pi\epsilon_0 c}\left(\frac{d^2u^\mu}{ds^2}u_\nu - \frac{d^2u_\nu}{ds^2}u^\mu\right)u^\nu \,, \tag{7}$$

Then, the radiation reaction term (the second term) also has similar structure as the field tensor and can be expressed by using the irreducible representations, **K** and **S**,

$$mc\frac{du^\mu}{ds} = eH^\mu_\nu u^\nu \tag{8}$$

where

$$\begin{aligned} H^\mu_\nu &\equiv F^\mu_\nu + G^\mu_\nu \\ &\equiv F^\mu_\nu + \frac{e}{6\pi\epsilon_0 c}\left(\frac{d^2u^\mu}{ds^2}u_\nu - \frac{d^2u_\nu}{ds^2}u^\mu\right) \end{aligned} \tag{9}$$

3 CONSTRUCTION OF PRECISE INTEGRATOR FOR RADIATING ELECTRON

The foregoing discussion tells us that the four velocity vector u^μ satisfies,

$$u^\mu(s) = \exp\left(\frac{e}{mc}F^\mu_\nu s\right)u^\nu(0) \tag{10}$$

That is to say, the exponential fuction is operating on u^μ as the Lorentz transformation. Then, one more integral of Eq. (10) yields the following transformation rule of the four dimensional particle coordinates x^μ,

$$x^\mu(s) = x^\nu(0) + \int_0^s d\sigma \exp\left(\frac{e}{mc}F^\mu_\nu \sigma\right)u^\nu(0) \tag{11}$$

Unifying Eqs. (10) and (11), we obtain the following transformation formula,

$$\begin{bmatrix} x^\mu(s) \\ u^\mu(s) \end{bmatrix} = \begin{bmatrix} 1 & \int_0^s d\sigma \exp\left(\frac{e}{mc}F^\mu_\nu \sigma\right) \\ 0 & \exp\left(\frac{e}{mc}F^\mu_\nu s\right) \end{bmatrix} \begin{bmatrix} x^\nu(0) \\ u^\nu(0) \end{bmatrix} \tag{12}$$

To be iteratively used for the infinitesimal interval ds, the transformation (12) gives us a numerical integral formulation which exactly utilizes the Lorenz transformation of u^μ along the particle trajectory.

And then, almost same formula is also obtained for the radiating electron,

$$\begin{bmatrix} x^\mu(s) \\ u^\mu(s) \end{bmatrix} = \begin{bmatrix} 1 & \int_0^s d\sigma \exp\left(\frac{e}{mc}H^\mu_\nu \sigma\right) \\ 0 & \exp\left(\frac{e}{mc}H^\mu_\nu s\right) \end{bmatrix} \begin{bmatrix} x^\nu(0) \\ u^\nu(0) \end{bmatrix} \tag{13}$$

4 FORMULAS OF IRREDUCIBLE REPRESENTATION

Before proceed to concrete numerical calculations, some useful formulas of the irreducible representations of the Lorentz group Lie algebra are summarized for later reference here. If we denote arbitrary unit vectors as **e** and **b**, the following formula are satisfied,

$$\begin{aligned} (\mathbf{e}\bullet\mathbf{K})^3 &= (\mathbf{e}\bullet\mathbf{K}) \\ (\mathbf{b}\bullet\mathbf{S})^3 &= -(\mathbf{b}\bullet\mathbf{S}) \end{aligned} \tag{14}$$

$$\begin{aligned} [S_i,\ S_j] &= \epsilon_{ijk}S_k \\ [S_i,\ K_j] &= \epsilon_{ijk}K_k \\ [K_i,\ K_j] &= -\epsilon_{ijk}S_k \end{aligned} \tag{15}$$

where ϵ_{ijk} denotes the Levi-Civita pseudotensor. Moreover, one can readily confirm the following identities too,

$$\begin{aligned} (\mathbf{b}\bullet\mathbf{S})(\mathbf{e}\bullet\mathbf{K})(\mathbf{b}\bullet\mathbf{S}) &= 0 \\ (\mathbf{e}\bullet\mathbf{K})(\mathbf{b}\bullet\mathbf{S})(\mathbf{e}\bullet\mathbf{K}) &= 0 \end{aligned} \tag{16}$$

These formula can be effectively used in calculations of exponential function in the formulas (12) and (13).

5 EXAMPLES OF NUMERICAL CALCULATION

The first example is an electron motion in pure magnetic field, especially no radiation dumping case. In this case, the identity (6) shows us special aspect, i.e., the formula gives us numerical solutions which exactly satisfy the momentum conservation law. Adding to this, we find that the exponential function in Eqs. (10) and (11) can result in the following reduced expression,

$$\begin{aligned} u^\mu(s) = &\left[1 - (\mathbf{b}\bullet\mathbf{S})\sin\left(\frac{eB}{mc}s\right)\right. \\ &\left. + (\mathbf{b}\bullet\mathbf{S})^2\left(1 - \cos\left(\frac{eB}{mc}s\right)\right)\right]u^\mu(0) \end{aligned} \tag{17}$$

which makes the calculation time much shorter (where **b** is normalized unit vector of **B** and B is its absolute value). The position x^μ is also expressed in the same manner. The figure 2 shows a typical example, the 3D electron motion in so-called magnetic mirror profile. In Fig. 3, velocity changes during the motion, which are caused by numerical errors, are indicated for the ordinary Runge-Kutta method and presented one, respectively. The initial electron energy is taken to be 200 MeV. The simulation result shows us that the presented method indeed can exactly conserve the particle momentum.

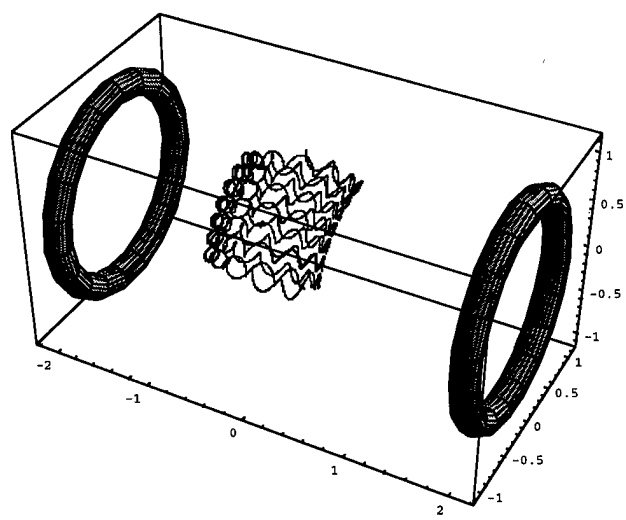

Figure 2: Electron motion in magnetic mirror profile (200 MeV).

The next example is the main purpose of this paper, the ultra-relativistic radiating electron. An electron orbit,

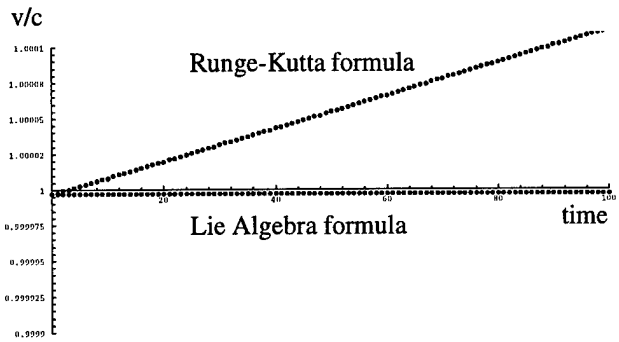

Figure 3: Velocity change caused by numerical error.

which has strong radiation dumping, is shown in Fig. 4. The initial electron energy is taken to be 500 GeV. In this case, the ordinary Runge-Kutta method cannot work because the calculation is very sensitive for numerical errors. On the other hand, the presented method still works well. The figure 5 shows the change of the Minkowski norm during the motion, which shows that the identity (6) exactly satisfied even in this energy region (non-Hamilton systems).

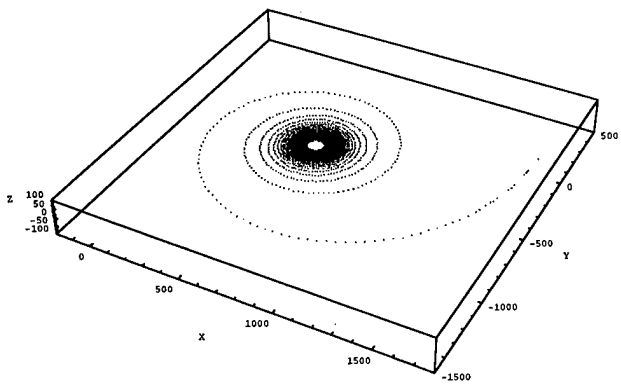

Figure 4: Ultra-relativistic radiating electron motion (500 GeV).

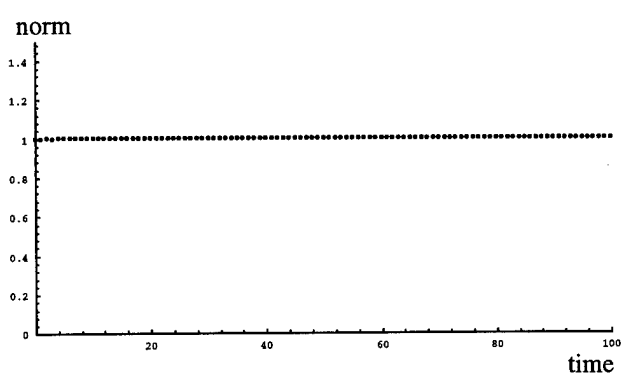

Figure 5: Change of Minkowski norm.

6 SUMMARY

This paper has presented a precise numerical integrator for the ultra-relativistic radiating electron based on the Lorentz group Lie algebra. Some simple numerical calculations show its validity. However, serious problem still exists in the ultra-relativistic electron orbit calculation. It is well-known that the Lorentz-Dirac equation is itself approximation for the case of weak radiation dumping[3]. To fully treat strong radiation dumping some more modifications are required.

7 REFERENCES

[1] J.D. Jackson, Classical Electrodynamics, 2nd Ed., (Wiley, New York 1975).

[2] W.K.H. Panofsky and M. Phillips, Classical Electricity and Magnetism (Addison-Wesley, Cambridge 1961).

[3] L.D. Landau and E.M. Lifshitz, Classical Theory of Fields, (Pergamon, Oxford, 1971).

PLATO: A PROGRAM LIBRARY FOR THE ANALYSIS OF 4D NONLINEAR TRANSVERSE MOTION*

M. Giovannozzi†, INFN Sezione di Bologna, Italy
E. Todesco, A. Bazzani, Dipartimento di Fisica Università di Bologna, Italy
R. Bartolini, CERN, 1211 Geneva 23, Switzerland

Abstract

The PLATO (Perturbative Lattice Analysis and Tracking tOols) program, a program library for analyzing four-dimensional betatronic motion in circular particle accelerators is presented.

The routines included in this library provide both the resonant and the nonresonant perturbative series that approximate nonlinear motion (normal forms); standard numerical tools such as the Lyapunov exponent, frequency analysis and evaluation of the dynamic aperture are also available. To ensure the highest flexibility, the code is fully compatible with standard tracking programs commonly used in the accelerator physics community.

1 INTRODUCTION

The discrete formalism of nonlinear mappings, based on the Lie algebraic tools, has been introduced in accelerator physics in recent years [1], and relevant applications have been made (see Ref. [2] for a review). A perturbative approach for nonlinear one-turn maps has been proposed [3–7], generalizing the Birkhoff series to the case of mappings. The theory of nonresonant normal forms allows one to derive analytical expansions for the amplitude-dependent tuneshift and for the phase-space distortion. Recently, resonant normal forms have been developed, providing a classification of the geometry of resonances [8, 9], and have been applied to derive analytical quality factors to optimize the lattice [10]. On the computational side, efficient arbitrary-order codes have been written to automatically evaluate the coefficients of the one-turn map [11] and the perturbative series for generic maps, both in the nonresonant [5, 12] and resonant [12] cases.

Moreover, sophisticated numerical tools borrowed from celestial mechanics have proved to be useful indicators of the nonlinear motion: computation of the Lyapunov exponent [13, 18], frequency analysis[14–16], evaluation of the global dynamics through tune footprints [10, 15], and so on.

In this paper we outline the main features of PLATO (Perturbative Lattice Analysis and Tracking tOols), a code developed for the analysis of four-dimensional nonlinear betatron motion.

* Work partially supported by EC Human Capital and Mobility Contract No. ERBCHRXCT940480.

† Present address: CERN PS Division

2 GENERAL FEATURES

2.1 Main aims

The routines in the program library can be grouped into three categories.

Interface with tracking codes used in the accelerator physics community (MAD [19] and SIXTRACK [20]).

Analysis of tracking data obtained via numerical simulations (element-by-element tracking). These data are processed to evaluate the dynamic aperture, the nonlinear tunes, and the maximal Lyapunov exponent.

Normal forms analysis and related perturbative tools (nonresonant and resonant normal forms, quality factors and resonance analysis).

2.2 Structure of the code

The code is written in standard FORTRAN 77 and structured as a program library of 136 modules. Two main programs are available. The first allows tracking simulations to be performed using sophisticated numerical tools for post-processing. The second carries out perturbative computations on the truncated one-turn map. Help files allow the user to eventually modify his version of the code to fit his needs and to design his own personal version of the main program. A long write-up is also available in the form of an ASCII file.

3 LATTICE INPUT

An accelerator is made up of a sequence of magnets. One record is sufficient to describe the physical properties (length, magnetic field, etc.) of each component. A plain sequence of such records is enough to describe a machine but, in practice, the assembling of such a file for a complex machine such as the Large Electron Positron collider (LEP) or the planned Large Hadron Collider (LHC) is tedious and inefficient.

As the MAD program [19] contains a simple and powerful language to deal with accelerator structures and, in addition, MAD is used to officially maintain the lattices of LEP and LHC, we have decided to use the MAD input data in defining the lattice parameters.

Interface with MAD The MAD program allows a lattice structure – in the form of a simple sequence of records describing the elements of the machine – to be dumped to a disk file. Starting from a MAD input file, a second file with the sequential structure of the accelerator can be produced. This output file is the input that provides the lattice to our library.

Interface with SIXTRACK Since a translation program

is available to convert a MAD to a SIXTRACK input file, we decided not to develop any routine which uses the SIXTRACK input files. On the other hand, it is possible to read in the polynomial maps produced by SIXTRACK through the Differential Algebra package [11] as well as the tracking-data files. This allows the analysis through the tools implemented in PLATO.

4 TRACKING ANALYSIS

One of the main aims of the library is to carry out element-by-element tracking of an accelerator structure and to perform a sophisticated analysis of the obtained data. The linear part of the code is based on the standard transfer matrices formalism. Nonlinear magnets are always considered as thin elements in the kick approximation. This approach allows one to derive an approximate map that is exactly symplectic: this is crucial for simulating hadron machines where the motion is conservative.

The main program contains several routines that perform the following operations.

Dynamic aperture evaluation. The dynamic aperture is the volume of the domain around the closed orbit where the particles remain confined. The numerical computation of the dynamic aperture is very CPU-time consuming. Let ρ_1 and ρ_2 be the nonlinear invariants in the planes (x, p_x) and (y, p_y) respectively, the dynamic aperture reads

$$V(N) = 4\pi^2 \int\int \chi(\rho_1, \rho_2)\, d\rho_1 d\rho_2 \qquad (1)$$

where $\chi(\rho_1, \rho_2)$ is one if the initial condition with nonlinear invariants (ρ_1, ρ_2), is stable for N turns, and is zero elsewhere. In Ref. [17] we have discussed different approaches to compute the integral (1) and these algorithms are included in the library.

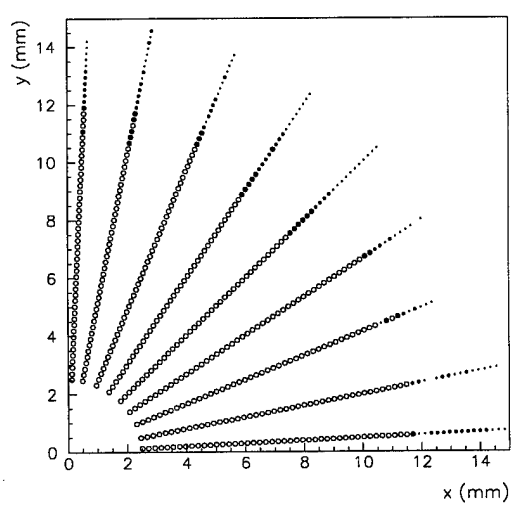

Figure 1: Long-term diagram for a 4D LHC model; particles stable for at least 10^5 turns (empty circles) and lost between 10^2 and 10^5 turns (black circles of decreasing size).

A typical graphic output is shown in Fig. 1, where the plane (x, y) of initial conditions (p_x, p_y are set to zero) is scanned along a polar grid. Different markers correspond to stable or unstable particles.

Tune evaluation. The tune is the ratio of the betatron to the revolution frequencies. It is a crucial parameter since it can drive resonances that endanger the beam stability. During the last decade, efficient methods to compute the tune, have been proposed [14–16] and they are implemented in PLATO. The indicator of 'chaoticity', based on the variation of the instantaneous tune over the orbit [15, 18], is also implemented.

Tune footprint. The tune footprint [10, 15] of a magnetic lattice can be generated by starting with a large set of initial conditions distributed in the phase-space, determining their nonlinear tunes with a high precision, and plotting the result in the tune plane. This technique gives a vivid picture of the resonance net which governs the stability of the system. Fig. 2 shows a typical tune footprint, generated by PLATO, relating to a simple LHC model [10].

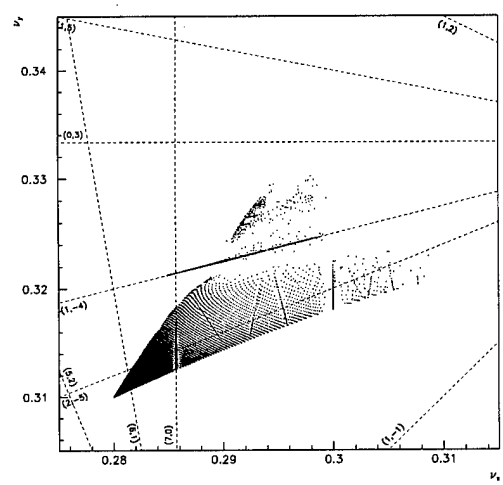

Figure 2: Tune footprint and resonance lines up to order 7 for the LHC cell lattice with random errors.

Lyapunov evaluation. The Lyapunov exponent is a measure of the rate of divergence of nearby orbits, thus giving an indication of the local 'chaoticity' of a dynamic system [13, 18]. The evaluation of the maximal Lyapunov exponent through the nearby-particles method and the renormalization technique is implemented in the program library.

5 NORMAL FORMS ANALYSIS

A wide set of routines in PLATO is dedicated to the computation of nonresonant and resonant normal forms [12] and other related quantities [6, 8, 10]. Below we will describe the most important quantities that can be computed for a generic complicated lattice.

Truncated one-turn map. The complex coefficients of the one-turn map can be calculated inside the library given the lattice input file; the truncation order $j_1 + j_2 + j_3 + j_4 \leq N$ depends on the number of nonlinear elements, on the maximum available memory, and on the speed of the platform

used.

Nonresonant normal forms. Once the map coefficients are stored, the conjugating function Φ that transforms the one-turn map into its normal form $\mathbf{U}$ [3–7] can be calculated. A detailed survey of the algorithms used to evaluate the normal form series are given in Refs. [6, 12]. The Hamiltonian is a function of the amplitudes (ρ_1, ρ_2) in the normalized space only. An analytic expression for the nonlinear tunes is given by the derivative of the Hamiltonian with respect to the amplitudes:

$$\nu_{x,y}(\rho_1, \rho_2) = \frac{\partial}{\partial \rho_{1,2}} h(\rho_1, \rho_2).$$

Single-resonance normal forms. In this case one selects a single resonance $(q\nu_x + p\nu_y)$ with $q \in \mathbf{N}$ and p integer. The normal form is the Lie series of an interpolating Hamiltonian that is a function of the amplitudes and of one linear combination of angles:

$$h = \sum_{k_1,k_2,l} h_{k_1,k_2,l}\, \rho_1^{k_1+lq/2} \rho_2^{k_2+l|p|/2} \cos\left[l(q\theta_1 + p\theta_2) + \varphi_{k_1,k_2,l}\right].$$

The coefficients of these Hamiltonians give important information about the resonance strength , the position of the resonance line in the space of invariants, the width of the resonance and the eigenvalues of the fixed lines.

Double-resonance normal forms. In this case one selects two different resonances $(q_1\nu_x + p_1\nu_y)$ and $(p_2\nu_x + q_2\nu_y)$. The Hamiltonian is not integrable, but can be used to work out the position and the stability of the fixed points that arise when the two single resonances are crossing [8, 9].

Quality factors. In many optimization problems it is necessary to analyse different versions of a lattice to select the one with the best dynamic aperture. An efficient solution is to find a quality factor (QF) having a good correlation with the dynamic aperture and which can be calculated in a short time. The QF can then be used to rate the performance of a lattice [10]. Three QFs based on nonlinear maps and normal forms are directly implemented in the library:

$\underline{Q_1}$ – the norm of the nonlinear part of the map evaluated at the amplitude A;

$\underline{Q_2}$ – the average tuneshift at amplitude A evaluated through nonresonant normal forms;

$\underline{Q_3(p,q)}$ – the norm of the resonant part of the interpolating Hamiltonian of the single-resonance normal form evaluated at the amplitude A.

A detailed description of the definition of the quality factors can be found in Ref. [10], where these techniques have been used to propose a sorting method for the LHC. Fig. 3 shows the correlation between the dynamic aperture and the three quality factors for a simplified version of the LHC lattice, including only random sextupolar errors.

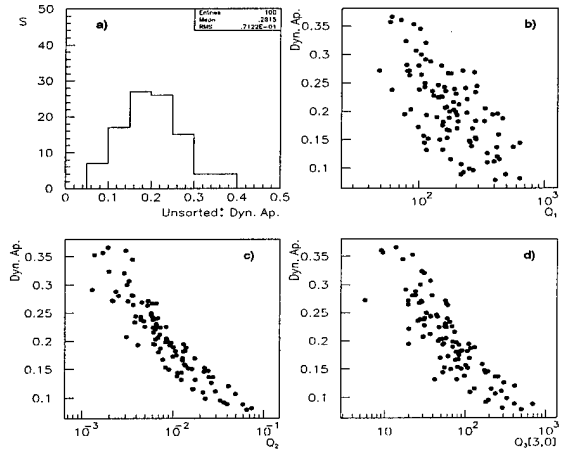

Figure 3: (a) Distribution of the dynamic apertures for an LHC cell lattice with random errors (100 seeds). Correlation between the dynamic aperture and the quality factors Q_1 (b), Q_2 (c) and $Q_3(3,0)$ (d).

6 REFERENCES

[1] A. Dragt and J. M. Finn, J. Math. Phys. **17** (1976) 2649–60.

[2] A. Dragt, Nucl. Instrum. and Methods Phys. Res., A **258** (1987) 339–354.

[3] A. Bazzani, P. Mazzanti, G. Servizi and G. Turchetti, Nuovo Cimento, **B102** (1988) 51.

[4] A. Bazzani, Celestial Mech. **42** (1988) 107.

[5] E. Forest, M. Berz and J. Irwin, Part. Accel. **24** (1989) 91.

[6] A. Bazzani, E. Todesco, G. Turchetti and G. Servizi, CERN 94–02 (1994).

[7] E. Forest and J. Irwin, in: 'Non linear problems in future particle accelerators', edited by W. Scandale and G. Turchetti, World Scientific, Singapore (1990) 46–52.

[8] E. Todesco, Phys. Rev. **E50** (1994) R4298.

[9] E. Todesco, Physica **D95** (1996) 1–12.

[10] M. Giovannozzi, R. Grassi, W. Scandale and E. Todesco, Phys. Rev. **E52** (1995) 3093.

[11] M. Berz, Part. Accel. **24** (1989) 109.

[12] A. Bazzani, M. Giovannozzi and E. Todesco, Comput. Phys. Commun. **86** (1995) 199.

[13] F. Schmidt, F. Willeke and F. Zimmermann, Part. Accel. **35** (1991) 249.

[14] E. Asseo, J. Bengtsson and M. Chanel, *in* Proc. Fourth European Signal Processing Conference, eds. J.L. Lacoume, A. Chehikian, N. Martin, J. Malbos (North Holland, Amsterdam, 1988) p. 1317.

[15] J. Laskar, C. Froeschlé and A. Celletti, Physica **D56** (1992) 253.

[16] R. Bartolini, A. Bazzani, M. Giovannozzi, W. Scandale, E. Todesco, Part. Accel. **52** (1996) 147–77.

[17] E. Todesco and M. Giovannozzi, Phys. Rev. **E53** (1996) 4067–76.

[18] E. Todesco, M. Giovannozzi, W. Scandale, Part. Accel. in press (1997).

[19] H. Grote and F.C. Iselin, CERN SL (AP) 90–13 (Rev. 4) (1995).

[20] F. Schmidt, CERN–SL (AP) 94–56 (1994).

PARALLEL ALGORITHMS FOR THE ANALYSIS OF NONLINEAR BETATRONIC MOTION*

M. Giovannozzi†, INFN, Sezione di Bologna, Italy
E. McIntosh, CERN, 1211 Geneva 23, Switzerland

Abstract

The dynamic aperture represents the volume in phase-space in which stable motion occurs. This is a key parameter to define the performance of a circular machine. The computation of this volume requires CPU-intense numerical simulations.

In this paper, some original parallel algorithms to speed-up the evaluation of the dynamic aperture are presented. A detailed analysis of different algorithms is carried out. Furthermore, the dependence of the CPU-time on the phase-space parameters as well as the load balancing of the proposed techniques are studied.

1 INTRODUCTION

The particles circulating in superconducting accelerators experience nonlinear forces which produce strong instabilities and losses. These effects could prevent safe operation of the machine with a consequent reduction of the overall performance.

The main parameter to quantify these harmful effects is the so-called dynamic aperture (hereafter DA); this is the volume in phase-space in which stable motion occurs. A large dynamic aperture implies a wide stable region where one can operate without experiencing particle losses.

In a previous paper [1], the problem of computing the DA in the presence of strong nonlinear perturbations was analysed. Some algorithms were described and numerical simulations were carried out to test the precision of the proposed techniques. All these tools were implemented in PLATO [2], a program library developed to analyse nonlinear phenomena in accelerator physics.

To further improve the efficiency in the computation of the dynamic aperture, in the sense of improving the accuracy and/or the CPU-time needed by the calculations, a promising approach is to convert the sequential tools developed so far into parallel algorithms [3].

Nowadays, computer systems with a relatively large number of processors (10 to 100) are widely available, either as workstation clusters, shared memory multiprocessor machines, or scalable parallel-processing systems with physically distributed memory. At CERN, for instance, there are several such systems of each type and, in particular, there is a MEIKO CS-2, a scalable parallel computer with 128 processors, developed with the support of the European Union, in the framework of the ESPRIT III Programme, and installed at CERN in 1994.

* Work partially supported by EC Human Capital and Mobility contract Nr. ERBCHRXCT940480.

† Present address: CERN PS Division

2 DYNAMIC APERTURE: DEFINITION AND NUMERICAL COMPUTATION

To define the dynamic aperture, the first step is to consider the phase-space volume of the initial conditions which are bounded after N turns:

$$\int\int\int\int \chi(x, p_x, y, p_y)\, dx\, dp_x\, dy\, dp_y, \qquad (1)$$

where $\chi(x, p_x, y, py)$ is the characteristic function of the set, i.e. it is unity if (x, p_x, y, p_y) is stable and zero otherwise. Since in 4D the invariant curves (i.e. 2D KAM tori) do not separate different domains of phase-space, the concept of a last invariant curve surrounding stable initial conditions is no longer valid [4, 5]. Although, from a purely theoretical point of view, the dynamic aperture could be a rather peculiar set, numerical simulations of lattices modelling circular machines showed that these situations are not typical [6, 7, 8, 9]. This means that, in general, there exists a connected region of initial conditions which are stable for a given number of iterations.

Two methods can be used to compute the integral in Eq. (1) (see Ref. [1] for more details).

Method 1: direct integration To exclude the disconnected part of the stability domain in the integral (1), we have to use polar variables. A scan of the four phase-space variables is performed and the DA evaluated by averaging the value of the maximum stable amplitude over the angular variables.

Method 2: integration over the dynamics A scan along two phase-space variables is performed. The information on the two neglected directions can be recovered via an average procedure.

3 PARALLEL ALGORITHMS TO EVALUATE THE DA

In both algorithms to evaluate the DA, the computation is split into two stages: firstly the last stable radius, as a function of the phase-space parameters, is determined, and secondly the DA is evaluated. It is clear that the algorithm has a natural parallel structure. Two procedures can be designed [3]:

Parallel algorithm 1: direct approach The direct method implies a scan over the four variables. The most efficient way to parallelise such a structure is to assign to each processor the task of performing the radial scan along a given direction in the 4D phase-space to determine the maximum stable amplitude. A procedure determines which processor, among the group of N_{proc} units, will perform the scan

along which direction. Once the first unstable initial condition is reached, the processor stops and it becomes available to compute along a different direction. The results obtained by the different processors are then gathered together (each processor is unaware of the results obtained by the others) and only one CPU is used to perform the evaluation of the DA.

Parallel algorithm 2: integration over the dynamics The integration over the dynamics allows us to compute the DA by scanning over two phase-space variables. The only difference with respect to the direct method is the evaluation of an average to recover the information from the neglected variables. As for the direct method, the most efficient way to parallelise this algorithm is to assign to each processor the task of determining the last stable radius for a given direction.

4 LOAD BALANCE

An important issue in the definition of a parallel algorithm is the load balance between the different processors; clearly, the optimal solution is to have an equal amount of work for each of the CPUs. Two principal methods of assigning work, static and dynamic, each with two variants, have been implemented and evaluated [3].

Static Cyclic allocation: the cases over which the parallelization is performed are divided into blocks of length N_{proc}. the jth processor will only work on the cases with $j + kN_{proc}$ where $0 \leq k \leq [N_{cases}/N_{proc}]$. This approach is rather appealing due to its simplicity.

Dynamic allocation with a Master: this technique allows very high computational efficiency even in those situations where the difference in CPU-time needed for different cases is relevant. As soon as a processor is available, it will start the calculations on the current case. The procedure designed to balance the work-load is based on a master-slave structure [3]. The drawbacks are the fixed overhead of $1/N_{proc}$, the overhead due to the communications between the master and the slaves, and a possible bottleneck if many slaves request a new iteration at the same time. In the cases considered, with N_{proc} typically between 20 and 80, these effects were negligible with respect to the improvement introduced by the more optimal load-balance.

Atomic Dynamic allocation: this technique provides the same advantage as dynamic load balancing as described above, but without the fixed overhead of a master processor. Every processor uses a global shared variable to label the different cases. This method is also extremely simple, but can be implemented only on systems with a global shared memory capability such as the MEIKO CS-2.

The last method has been implemented using the MEIKO Atomic library, while the others are based on the MPI library [10].

5 MEIKO DESCRIPTION

The MEIKO CS-2 computer is a distributed-memory, scalable, parallel system using SPARC micro-processors and a MEIKO-developed interconnection which enables programs to read and write memory in remote nodes without context switching. The CERN CS-2 has 64 nodes, each with two 100 MHz HyperSPARC processors (rated at over 100 Specint92 per processor) and 128 MB of memory. Each node has a local disk for temporary data storage and paging or swapping as well as SCSI connections for additional peripheral equipment.

The CS-2 service is at present used for the support of data recording and event reconstruction for high energy physics experiments, and for event-parallel simulation using a specially developed version of the GEANT program [11]. It also provides a Parallel Interactive Analysis Facility (PIAF [12]). Currently under development is a system (GRACE [13, 14]) for the automatic generation of Feynman diagrams in parallel.

6 RESULTS

The different algorithms presented in Section 3 have been tested using a realistic lattice of the CERN Super Proton Synchrotron (SPS). The model simulates the special machine conditions used during the experimental sessions dedicated to dynamic aperture studies [15].

As a first step, the performance of the first parallel algorithm applied to the model of the SPS was analysed. For such computations, ten steps in the angular variables were used, while the number of iterations has been fixed to 1000. As far as the number of radial initial conditions is concerned, the step between two successive points was specified: the program then increases the value of the radial variable until an unstable condition is met. The simulations have been used to test how the CPU-time needed to compute the DA scales as a function of N_{proc}, independently of the different type of implementation. The results are shown in Fig. 1.

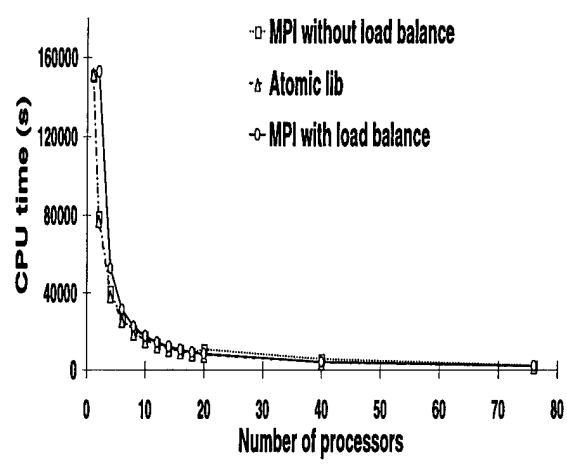

Figure 1: Performance of the first parallel algorithm. The total CPU-time is depicted as a function of N_{proc}.

Independent of the implementation, the CPU-time decreases with the number of processors. In this respect the performance seems to be optimal. As expected, using the

MPI library has some drawbacks: one processor is used as a master, therefore the total number of active CPUs is reduced by one with respect to the other methods. This effect is clearly visible on the plot. As soon as the N_{proc} exceeds 10 units, this negative effect disappears and the beneficial effect of a good load balance makes this particular implementation more efficient than using MPI alone without load balance and practically at the same level as the algorithm based on Atomic library.

To quantify the impact of the load balance approach on the efficiency of the algorithm, we plot the normalised mean CPU-time, namely:

$$\mu(N_{proc}) = \frac{1}{N_{proc}} \sum_{i=1}^{N_{proc}} \frac{\tau_i}{\tau_{max}}, \qquad (2)$$

where $\tau_{max} = \max_{j=1,\cdots N_{proc}} \tau_i$, and τ_i represents the total CPU-time used by the ith processor. In the ideal case of perfect load balance $\mu(N_{proc}) = 1$. The results are reported in Fig. 2.

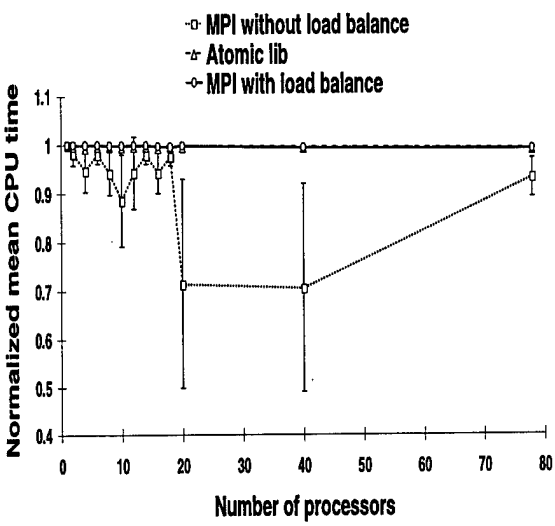

Figure 2: Load balance for the first parallel algorithm. The average CPU-time μ is shown as a function of N_{proc}. The error bars are computed using the standard deviation of the CPU-time for the different processors.

The difference in performance between the three implementations is clearly seen. For the algorithm without any built-in load balance control, the results are rather poor: the normalised mean time fluctuates wildly, especially when the number of processors is greater than 20. Correspondingly the CPU-time performance (see Fig. 1) becomes worse than the other algorithms.

On the other hand, the other two approaches behave very well: in both cases μ is almost constant as a function of N_{proc} and very close to one. In this respect the implementation based on MPI and the one using the Atomic library are almost equivalent, because the time spent in communications is negligible with respect to the CPU-time required for computations.

Similar tests have been carried out on the second parallel algorithm giving similar results as far as the speed-up and the load-balance are concerned.

7 CONCLUDING REMARKS

In this paper parallel algorithms to evaluate the dynamic aperture together with their performances using a realistic model of the CERN SPS have been discussed. The results show that the algorithms are optimal and that the problem of load balance can be efficiently solved. The solutions based on the MPI and Atomic library have very similar performance: although the latter gives a CPU-time shorter by some percent than the version implemented with MPI, the overall results are comparable.

8 REFERENCES

[1] E. Todesco and M. Giovannozzi, Phys. Rev. **53**, 4067 (1996).

[2] M. Giovannozzi, E. Todesco, A. Bazzani and R. Bartolini, CERN PS (PA) **96–12** (1997).

[3] M. Giovannozzi and E. McIntosh, Int. J. Mod. Phys. C , in press (1997).

[4] A. Bazzani, E. Todesco, G. Turchetti and G. Servizi, CERN **94–02** (1994).

[5] J. D. Meiss, Rev. Mod. Phys. **64**, 795 (1992).

[6] W. Scandale, in *Third European Particle Accelerator Conference* , edited by H. Henke (Edition Frontiéres, Gif sur Yvette, 1993) pp. 264.

[7] F. Zimmermann, in *Fourth European Particle Accelerator Conference* , edited by V. Suller and C. Petit-Jean-Genaz (World Scientific, Singapore, 1995) pp. 327.

[8] F. Galluccio and F. Schmidt, in *Third European Particle Accelerator Conference*, edited by H. Henke (Edition Frontiéres, Gif sur Yvette, 1993) pp. 640.

[9] M. Giovannozzi, R. Grassi, W. Scandale and E. Todesco, Phys. Rev. E **52**, 3093 (1995).

[10] M. Snir, S. Otto, S. Huss-Lederman, D. Walker, and J. Dongarra, MPI: The Complete Reference (The MIT Press, Cambridge, 1995).

[11] Application Software Group, CERN Program Library Long Writeups **Q123**.

[12] T. Hakulinen and F. Rademakers, to be published in the Proceedings of *HPCN 95, High Performance Computing and Networking Conference*, Milan - Italy, 2-5 May, 1995.

[13] T. Kaneko, Comput. Phys. Comm. **92**, 127 (1995).

[14] F. Yuasa, D. Perret-Gallix, S. Kawabata and T. Ishikawa, to be published in the Proceedings of *Fifth International Workshop on Software Engineering, Artificial Intelligence and Expert Systems for High Energy and Nuclear Physics*, Lausanne - Switzerland, 2-5 Sep., 1996.

[15] W. Fischer, M. Giovannozzi and F. Schmidt, Phys. Rev. E **55**, 3057 (1997).

FURTHER IMPROVEMENTS IN TRACE 3-D

D.P. Rusthoi, W.P. Lysenko, Los Alamos National Laboratory, Los Alamos, NM,
and K.R. Crandall, Amparo Corporation, Santa Fe, NM*

Abstract

TRACE 3-D, an interactive beam-dynamics program that calculates the envelopes of a bunched beam (including linear space-charge forces) through a user-defined transport system, has undergone several upgrades in physics, coding, and capabilities. Recent modifications include centroid tracking (and misalignment capabilities) and an improved beam description that allows study of some nonlinear effects such as wakefields. The Fortran code has been made portable and runs on numerous platforms. It can be used with a variety of graphics packages. The additional beamline elements, new commands, expanded fitting capabilities, improved beam description, and coding modifications have extended TRACE 3-D's usefulness and applicability to the accelerator community. These changes are documented in the third edition of *TRACE 3-D Documentation.*

1 INTRODUCTION

TRACE 3-D, a first-order accelerator design code that was first written as a two-dimensional version in the early 1970's, has been expanded extensively over the years and adapted to run on numerous systems using different versions; however, there is now one official version that is documented and available on most workstations, PC, and Macintosh platforms. Some of the code's newer features are described below.

2 NEW CAPABILITIES

Included among new capabilities added to TRACE 3-D are centroid tracking, aperture calculations, quadrupole misalignments, additional matching types, a rotation/translation element, a wiggler element, vertical bend option, graphic scale flexibility, and a number of new commands. The addition of wakefield calculations is described in the following section.

2.1 Centroid Tracking

TRACE 3-D now tracks the transverse beam-centroids and plots them in the beam profile box ('+' for the x-centroid and '*' for the y-centroid). The phase-space ellipse centers are also plotted on the corresponding phase-space plots. The code ignores centroid calculations unless an offset is entered or a beamline element causes the centroid to shift off-axis. The example in Fig. 1 shows the typical TRACE 3-D graphic page output with a beam offset generated from random quadrupole misalignments.

2.2 Aperture Calculation

The maximum extent of the beam inside each element is now calculated in the two transverse planes by adding to the beam centroids the transverse profiles multiplied by a user-supplied "aperture factor." Given these maximum extents within each element, TRACE 3-D calculates the minimum radius required for a circular beampipe that will transport the beam without scraping. At each point where the minimum radius is largest, the code writes the transverse profiles and the corresponding centroids to an aperture file (when the command is issued). For example, an aperture factor of 3.13 supplied by a user for a TRACE 3-D beam (normally $\sqrt{5}$ times the rms beamsize) will yield maximum-extent values for a 7-σ beam.

2.3 Quadrupole Misalignments

The quadrupole element, which used to be specified by only two parameters (gradient and length), has been expanded to include three additional parameters specifying misalignment (rotation or translation) in the transverse plane. If translation is specified, transverse offsets in one or both planes may be entered; if rotation is specified, an angle specifying the amount of rotation about the beam axis may be specified. It is also possible to specify random misalignments (either rotation or translation).

2.4 Matching Types

Three new matching/fitting options were added, bringing the total of matching types to fourteen. One new matching type finds the values of two variables that produce a round output beam—identical magnitude Twiss parameters in x and y—useful when trying to get a circular spot on a beam target. Another new matching type varies the input beam-ellipse parameters (BEAMI) to obtain a specified output beam (BEAMF). A third type enables the user to adjust one or more variables in a periodic transport system to achieve a specified phase advance in one or more phase planes, e.g., setting the quadrupole gradients in a drift-tube linac to get a certain value for the zero-current phase advance in x and y. There may be three quadrupoles involved, but all identical, so the user might have "repeat" elements or use the variable-coupling option. If one wants to achieve a specified phase advance with current, an iterative techinque is required because this option does not automatically keep the beam matched as it adjusts the variable.

* Research supported by the U.S. Department of Energy, Office of Energy Research, through the Division of High Energy Physics and Division of Mathematical, Information, and Computational Sciences

2.5 Rotate / Translate Element

The rotate element was expanded to provide both a rotation and a translation capability (and is backward compatible with earlier files containing rotation elements). The expanded element allows the user to select a plane (viz., *x-y, y-z, z-x*) specifying rotation about the axis normal to that plane (roll, pitch, yaw) and/or translation in that plane.

2.6 Wiggler Element

A new element was added to simulate a wiggler by using a series of alternating bends and drifts (bend-drift-bend-drift), where odd-numbered bends are defined as positive and even-numbered bends as negative. The user supplies the overall length of the wiggler, a field strength and dipole gap to be applied to each bend, plus the length of and distance between each bend.

2.7 Graphic Scales Flexibility

When input and output beams vary significantly in size, one can enter different scales for the input and output phase-space plots. This can be seen in the example of Fig. 1 where both transverse and longitudinal phase-space plots have different input and output scales. Additionally, phase-space plots can be generated at any point along the beamline by entering values for NEL1 and NEL2 (displayed at top of phase-space plots). Another option, useful for viewing portions of long transport files, is the profile close-up plot, generated by specifying values for the profile box, NP1 and NP2 (also displayed in Fig. 1). These plotting options do not affect beam-dynamics calculations.

2.8 New Commands

Several new commands were added, some of which are mentioned here. The *aperture* command, previously discussed, was modified not only to calculate the minimum radius of a circular beampipe required to transport the beam without scraping, but also to calculate the maximum beam extent for both transverse planes within (inside) each beamline element. An "*unmatch*" command was added to allow a user to conveniently return to pre-match values of matching variables should the results of a matching calculation provide an unacceptable solution. To check the parameter values of a particular element in the transport, a *query* command was added to obtain a display of parameter values of a specific element. Now that TRACE 3-D tracks beam centroids, the *centroid* command was added to enable a user to display the centroid at any point. A *mini-help* command is now available to assist when adding new beamline elements, and a *newfile* command brings in new datafiles to allow for comparisons.

3 NEW PHYSICS

3.1 Wakefield Calculation

There is a parallel version of TRACE 3-D that can simulate some nonlinear effects, such as wakefields, related to the variation of the beam bunch along the longitudinal direction [1,2]. This code is compatible with the standard version and will produce the same results for problems not involving wakefields. The two codes may be merged in the future.

In the wakefield code, the beam bunch is divided into a number of slices longitudinally. We describe each slice by its 6-D centroid and 6x6 sigma matrix, and follow the collection of centroids and sigma matrices down the beamline. Whenever the code needs to generate output or compute space charge, it combines the slices into a single 6-D centroid and 6x6 sigma matrix and uses the existing code structure. The bunch-slice centroids and sigma matrices are transported as usual by the various elements in the beamline. However, space charge and the new wakefield elements get a modified treatment. In the case of space charge, we take into account the effect of space charge on the slice centroids. Of course, the overall centroid is not affected by space charge. Wakefield

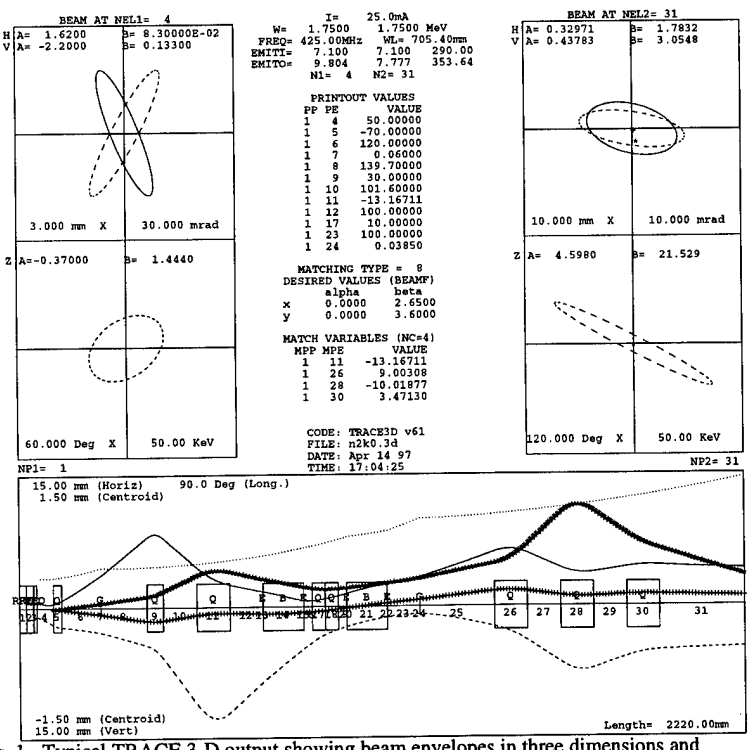

Fig. 1. Typical TRACE 3-D output showing beam envelopes in three dimensions and beam centroid profiles in *x* and *y* due to random quadrupole misalignments.

effects are taken into account with new zero-length elements, similar to how bend edges are handled. The wakefield element parameters specify wakefield functions, which determine forces acting on a given bunch slice caused by slices ahead of the given bunch slice. There are three wakefield elements: one each for monopole, dipole, and quadrupole wakefields. These wakefield elements are user-specified elements and may easily be changed to model other effects that depend on longitudinal position within a beam bunch. Unlike some existing particle codes, this approach allows for the distance between bunch slices to vary throughout the simulation. This is useful for studying wakefield effects in a regime where space charge is important.

3.2 Space Charge

It was found that when one tried to design an achromatic bend with current, the beam did not remain achromatic downstream. The problem was discovered in the space-charge calculation used when the beam ellipsoid was tilted with respect to the coordinate axes. The beam is first "stretched" in the longitudinal direction by multiplying the z-coordinate by γ. The beam is then rotated to be upright, the space-charge impulses applied, the inverse rotation applied, and the z-coordinate divided by γ. The beam "stretching" and "unstretching" transformations are now symplectic.

4 NEW CODING

4.1 Standard FORTRAN 77

Previously, different versions of the code were maintained in different formats for various computer platforms, resulting in machine dependencies and versions differing in capabilities and documented features. TRACE 3-D has now been rewritten using Standard FORTRAN 77 (with exception of the NAMELIST extension—now standard in Fortran 90)[†], and is capable of being compiled on almost any system. This standard version of the code is maintained by the Los Alamos Accelerator Code Group and corresponds to the published documentation.

4.2 Plotting Routines

All external plotting calls have been placed in short subroutines at the end of the source code. The code can still be used with PLOT10 on systems using the Tektronix terminal or systems emulating a Tektronix 4000-series terminal. On Unix systems, we supply a set of replacement routines for the PLOT10 library that produce PostScript and run a PostScript viewer. More recently, we compiled TRACE 3-D with a set of "freeware" graphics available off the Internet from CalTech (http://astro.caltech.edu/~tjp/pgplot/) called PGPLOT. The PGPLOT graphics routines have drivers written for X-Windows, the Macintosh, Windows95, Windows NT, and a host of other platforms. The code comes with two sets of plotting subroutines: one for PLOT10 users and/or PostScript replacement calls, and one for PGPLOT users.

[†] Old TRACE 3-D datafiles may need slight modification to be read by NAMELIST extensions on some Windows and Macintosh systems.

5 CODE / DOCUMENTATION AVAILABILITY

TRACE 3-D Documentation [3], now in its third edition (May 1997), includes a description of the code, the transport elements and their transfer matrices, the dynamics calculations, and complete instructions for the user, including a number of examples. Fifteen appendices give detailed information on the physics and coding. The documentation is available on-line as a Microsoft Word document or as a PostScript file. Both code and documentation may be accessed by anonymous FTP via connection to the Los Alamos Accelerator Code Group FTP Server, *PC-AOT-1.ATDIV.LANL.GOV* (IP Address 128.165.32.190), with username *TRACEUSER* and password *ftptrace* (password is in lower case). The TRACE directory contains readme files and subdirectories for documentation, the source code, and downloadable executables for various platforms. A hardcopy of the documentation is provided upon request.

A special interface for the Macintosh [4], developed by the MACcelerator Project in Del Mar, California, has been written and is commercially available using the standard version of TRACE 3-D under a license agreement with the Los Alamos National Laboratory. Among other advantages, there is a minimal amount of alpha-numeric (keyboard) input used for setting parameter values, and no text or command-line input is required.

6 ACKNOWLEDGMENTS

The authors express their appreciation to members of the Los Alamos Accelerator Code Group who help maintain and distribute TRACE 3-D and its documentation, and provide technical assistance to users as needed.

REFERENCES

[1] W.P. Lysenko, D.P. Rusthoi, K.C.D. Chan, G.H. Gillespie, and B.W. Hill, "Wakefields in the TRACE 3-D Code," Proceedings of the 18th International Linac Conference held August 26-30, 1996 in Geneva, Switzerland.

[2] W.P. Lysenko, D.P. Rusthoi, K.C.D. Chan, G.H. Gillespie, and B.W. Hill, "TRACE 3-D Code Improvements," Proceedings of the 1996 Computational Accelerator Physics Conference held September 24-27, 1996 in Williamsburg, Virginia.

[3] TRACE 3-D Documentation, K.R. Crandall and D.P. Rusthoi, LA-UR-97-886, Los Alamos National Laboratory Report, May 1997.

[4] G.H. Gillespie and B.W. Hill, "A Graphical User Interface for TRACE 3-D Incorporating Some Expert System Type Features," 1992 Linear Accelerator Conference Proceedings (Ottawa) AECL-10728, 787-789.

APPLICATIONS OF THE GENERAL PARTICLE TRACER CODE

S.B. van der Geer, M.J. de Loos, Pulsar Physics,
Flamingostraat 24, 3582 SX Utrecht, The Netherlands

Abstract

The General Particle Tracer (GPT) code provides a new 3D simulation package to study charged particle dynamics in electromagnetic fields. Because of its modern implementation, GPT can be conveniently customized without compromising its ease of use, accuracy or simulation speed.

The most common use of GPT is accelerator and beam line design, especially the calculation of non-linear 3D space-charge effects. A typical example is the study of the effect of different bunch charges in a bend system.

One of the advanced GPT features is the possibility to solve additional differential equations while tracing particles. Using this mechanism, the generated EM wave power spectra in an undulator and the effect of beam-loading in a traveling wave linac are calculated self-consistently with the particle trajectories.

GPT is currently being applied to the design of the energy recovery system of the 2 MeV, 12 A Free Electron Maser under construction at FOM-Rijnhuizen. The required 99.8 % beam recovery and the initial energy spread of 300 keV ensure this to be a challenging GPT project.

1 INTRODUCTION

Particle tracking is a very powerful tool in the design of accelerators or beam lines. Computers however used to be too slow to trace the amount of particles needed to obtain good statistics in a reasonable amount of computing time. Therefore the particle tracking method was often abandoned and especially matrix/optical methods became popular. These alternative methods however have their limitations. Especially when space-charge effects are important, they are inaccurate or can not be used at all.

Because of enormous advances in computer technology, it is currently possible to track thousands of particles through complex electromagnetic fields taking all 3D effects and space-charge forces into account. This offers much more accurate and reliable results than matrix codes. The General Particle Tracer (GPT [1]) offers all of these capabilities in a very user friendly and easy to customize package. Due to the general character of the code and its flexibility, GPT is suited for a large number of purposes.

The main features of GPT, new additions to the package and selected cases that highlight the capabilities of GPT are presented.

2 THE GPT CODE

2.1 A brief description

The purpose of the General Particle Tracer software package [2] is to aid in the design of accelerators and beam lines by using modern, particle tracking techniques. GPT is a 3D particle tracer developed to simulate charged particle dynamics in electromagnetic fields.

The GPT inputfile language supports the use of variables, functions and algebraic expressions, thus giving the user great flexibility. Automatic parameter scanning is also incorporated. GPT has a large set of standard elements, i.e. sector magnets, quadrupoles, solenoids and accelerating structures. Additional elements can easily be developed and exchanged with other users. Elements can be positioned anywhere and with any orientation in 3D space. The effect of fringe fields can also be simulated.

GPT tracks macro particles through the electromagnetic fields and offers complete freedom in the initial particle distribution. The space-charge forces are calculated from full 3D relativistic particle-particle interaction [3]. To ensure both accuracy and speed, an embedded fifth order Runge-Kutta method with adaptive stepsize control [4] is used to solve the equations of motion of the particles in the time domain. Additional differential equations can be solved while tracking the particles, ensuring self-consistent results.

The data-analysis and plotting capabilities of GPT complete the possibilities of the package. GPT is written in ANSI-C for portability and runs on UNIX platforms and PC's. Furthermore a user interface with on-line help and graphical output is available for Windows 95/NT.

2.2 Different types of particles

GPT has always been capable of simulating any type of particle. Electrons, positrons and ions can all be simulated. In addition, the new GPT kernel is capable of simulating different types of particles simultaneously and can calculate all 3D space-charge effects among the particles.

Particle sets can be used to sort different types of particles. For example electron and positron beams can be simulated simultaneously. The merging and colliding of various beams can be simulated.

0-7803-4376-X/98/$10.00 © 1998 IEEE

2.3 *Field maps*

Field maps are a convenient tool to import electromagnetic fields, for example obtained with a Poisson solver, into GPT. Electrostatic and magnetostatic field maps for 2D, 2.5D and 3D problems can be imported. The specified fields must lie on a equidistant rectangular grid, allowing the code to immediately find the enclosing square or cube. All interpolations are performed bilinearly to further improve the simulation speed. Furthermore, standing and traveling wave resonant cavities can also be simulated.

3 APPLICATIONS

To demonstrate a few of the capabilities of the GPT package the following cases are examined: Basic beam line and accelerator design, simulation of a free-electron laser and the highly specialized design of a depressed collector.

3.1 *Beam line design*

One of the main applications of GPT is beam line design. It is especially useful for high accuracy simulations including space-charge. This example presents a beam injection system, which in its normal mode is isochronous [5]. The system uses a minimum number of magnetic components, 3-4 dipoles, 2 quadrupole triplets and 6 sextupoles.

Figure 1 shows the evolution of the rms-bunchlength in the system. The simulations are performed for different settings of the bunch charge, hereby affecting the space-charge forces. Without space-charge, the simulations agree with the predictions of the TRANSPORT code [6]. Space-charge has a large effect on the bunchlength in the second part of the system. However, due to the careful positioning of the various beam line components, the final increase remains restricted to a few percent.

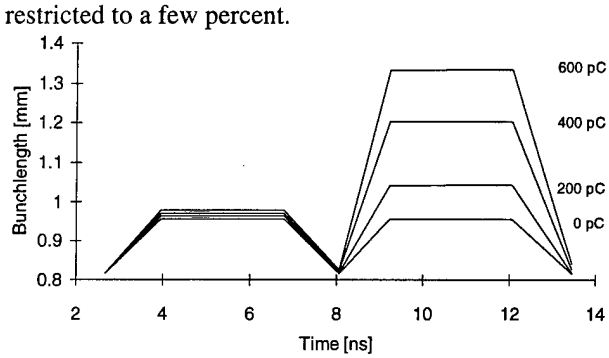

Figure 1: The effect of space-charge on the evolution of the bunchlength in an isochronous bend system.

An important consideration in the design of this type of system is the effect of energy spread in the initial beam. Figure 2 shows the influence of energy spread on the rms-bunchlenth, at the exit of the system. The various lines represent different bunch charges.

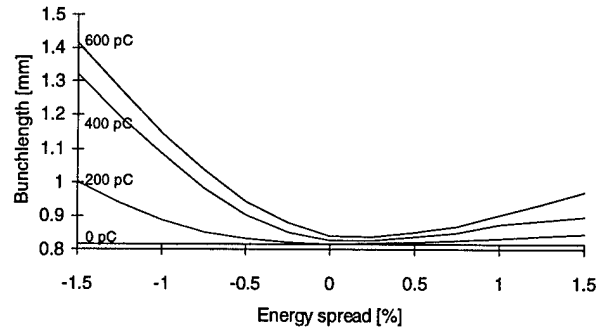

Figure 2: Bunchlength as function of initial energy spread at the exit of an isochronous bend system. The corresponding bunch charges are indicated.

3.2 *Accelerator design*

The FELIX accelerator consists of a standing wave prebuncher and a traveling wave buncher followed by two RF-linac sections [7]. Because of the low energy of the electrons emitted by the gun (100 keV), space-charge effects are very important in the first section of the beam line.

A free-electron laser (FEL) employing a RF-linac accelerator as injector, is very sensitive to the amplitude and phase of the RF power applied to different parts of the injector. The microbunches need to be reproduced exactly alike and at the same intervals to build up the radiation in the optical cavity. Furthermore the shift in average energy during a macropulse due to imperfect stability of the RF sources should be small compared to the energy spread within a single microbunch.

In FELIX the buncher and linac are fed from a common source. Figure 3 shows the final energy as function of the RF phase. The different lines represent the difference in operating phase of the linac in degrees from the top of the wave. Between -5° and -10° the output energy is almost independent of the input RF phase. This operating phase will produce the greatest micropulse to micropulse reproducibility.

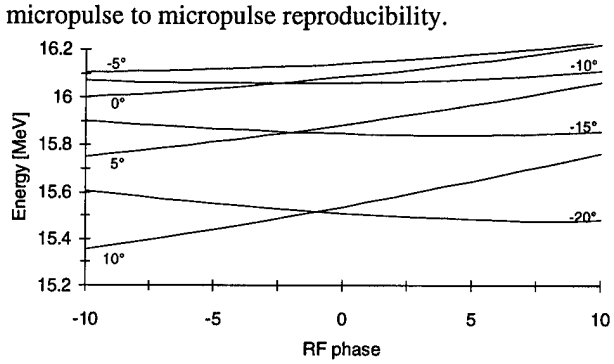

Figure 3: Output energy after the buncher and linac of FELIX as function of RF phase for various operating points of the linac.

GPT has the possibility to solve additional user-specified differential equations while tracking the particles. Using this option, the beam-loading field in the constant gradient FELIX linac is calculated from the

particle trajectories in the above results. This method ensures that the beam-loading wave has the correct phase.

3.3 Free Electron Lasers

The complete FOM Fusion FEM [8] beam line has been simulated using the GPT code. During the commissioning of the first part of the beam line, the settings predicted by the simulations were proven to be accurate within a few percent.

Additional differential equations for the amplitude and phase of the various longitudinal and transverse modes in the waveguide of the FEM are solved while tracking the particles. This enables multi-mode, multi-frequency examination of the modes in the cavity and their influence on the particle trajectories. The method was used to optimize both beam transport and output power.

Figure 4 shows the energy of the individual particles going through the step-tapered undulator of the FEM. The particles, on average, lose energy to build up output power, at the cost of an introduction of an energy spread of 300 keV.

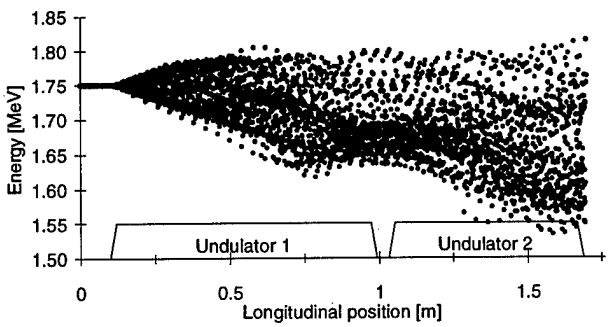

Figure 4: Snap shot of the energy of individual particles of the beam on flowing through the FEM undulators. The loss in average energy is contributed to the radiation.

3.4 FEM depressed collector design

Currently the GPT code is being used to design the 2 MV electrostatic decelerator and depressed collector of the FOM Fusion FEM [8]. The design is complicated due to the required 99.8 % collection efficiency, the space-charge forces of the 12 A continuous beam and the energy spread of 300 keV generated by the undulator.

The electrostatic decelerator has been modeled in GPT using analytical expressions. The cylindrical symmetric electrostatic fields of the depressed collector [9] are imported into GPT using a 2D field map. In the simulation shown in Figure 5, an additional external magnetic field generated by the fields of two solenoids positioned above and below the collector are used to minimize the backstream of electrons. The asymmetric bending scheme requires a 3D treatment, even for a cylindrical symmetric collector.

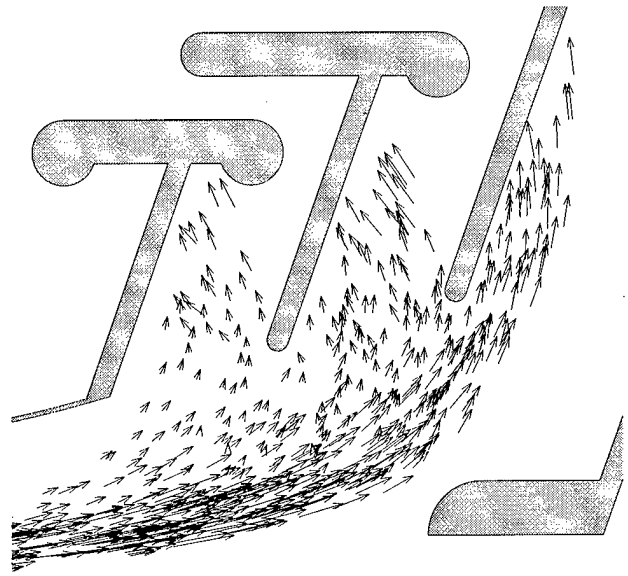

Figure 5: Primary electrons in the FEM depressed collector. The tail of the vector is proportional to the energy of the particle. The energy of the incoming beam ranges from 75 keV to 425 keV.

In the actual collector the beam will be rotated slowly by two sets of coils to homogeneously distribute the dissipation over the collector plates. The analysis of the effect of scattered primaries and secondaries is scheduled to take place in the upcoming months.

4 CONCLUSION

The high accuracy, the possibility to add custom code, the large number of standard elements and the user friendly interface, all make GPT an attractive analysis tool. Also the possibility to add self-consistent differential equations makes GPT a powerful tool for the design of accelerators and beam lines, and even FEL's. The current status of the GPT project can be found on the web at *http://www.pulsar.nl/gpt.*

5 ACKNOWLEDGEMENTS

The authors gratefully thank Prof. W.A. Gillespie and C.A.J. van der Geer for their contributions to this paper.

6 REFERENCES

[1] M.J. de Loos, et al, Proc. 5th Eur. Part. Acc. Conf., Sitges, (1996) pp. 1241.
[2] GPT User Manual, Pulsar Physics, Flamingostraat 24, 3582 SX Utrecht, The Netherlands.
[3] Ch. Bourat, CGR-MeV, Thesis, (1988).
[4] W.H. Press, et al., Numerical Recipes in C, Cambridge Univ. Press, 2nd edition, (1992) pp. 714.
[5] W. A. Gillespie, Nucl. Inst. Meth. Phys. Res., A 374, (1996) pp. 395-400.
[6] K.L. Brown, et al, CERN Report 80-04, (1980).
[7] P.W. van Amersfoort, et al, Nucl. Inst. Meth. Phys. Res., A 318, (1992) pp. 42.
[8] A. van der Linden, et al., Proc. 4th Eur. Part. Acc. Conf, London, (1994) pp. 849.
[9] A. Smirnov, Private communication.

THE COMPUTER PROGRAM LIAR FOR THE SIMULATION AND MODELING OF HIGH PERFORMANCE LINACS*

R. Assmann, C. Adolphsen, K. Bane, P. Emma, T.O. Raubenheimer,
R. Siemann, K. Thompson, F. Zimmermann
Stanford Linear Accelerator Center, Stanford University, Stanford, CA 94309

Abstract

High performance linear accelerators are the central components of the proposed next generation of linear colliders. They must provide acceleration of up to 750 GeV per beam while maintaining small normalized emittances. Standard simulation programs, mainly developed for storage rings, do not meet the specific requirements for high performance linacs with high bunch charges and strong wakefields. We present the program LIAR ("LInear Accelerator Research code") that includes single and multi-bunch wakefield effects, a 6D coupled beam description, specific optimization algorithms and other advanced features. LIAR has been applied to and checked against the existing Stanford Linear Collider (SLC), the linacs of the proposed Next Linear Collider (NLC) and the proposed Linac Coherent Light Source (LCLS) at SLAC. Its modular structure allows easy extension for different purposes. The program is available for UNIX workstations and Windows PC's.

A major objective of the LIAR project is to provide an open programming platform for the accelerator physics community. We invite interested scientists to join this project. The LIAR home page and the ONLINE version of the user's manual can be accessed under:

http://www.slac.stanford.edu/grp/arb/rwa/liar.htm

1 THE LIAR PROJECT

The LIAR ("LInear Accelerator Research code") project was started at SLAC in August 1995 in order to provide a computing and simulation tool that addresses the needs of high performance linear accelerators. Its first objective was to implement advanced simulations for the main linacs of SLC (50 GeV) and NLC (500 GeV) at SLAC. Since then it has been applied to the LCLS project at SLAC (15 GeV), the CLIC project at CERN and to studies of a possible future 2.5 TeV linac. The program can be applied to a broad range of problems that vary widely in energy and beam parameters. Interested scientists are explicitly invited to join the LIAR project and to contribute new features (commands).

2 DISTRIBUTION

The LIAR code is put into the public domain and can be used and distributed freely. However, we expect that publications that contain LIAR results make proper reference to the user's guide [1]. In addition we ask that any extensions and modifications to this program are made available to the scientific community for free usage. The most recent information on LIAR is available through its home page on the World Wide Web:

http://www.slac.stanford.edu/grp/arb/rwa/liar.htm

Please check for changes in the User's Manual or use the ONLINE manual with the most recent information. The LIAR source code and executables are available through its AFS site:

/afs/slac.stanford.edu/public/software/liar/release

This directory is world-readable and can be used to download the LIAR files. The present release version of LIAR is 1.9. New versions and updates will be put into this directory. Bug fixes will generally not result in a new version number. The existing version of LIAR will just be updated. Every 1-2 months, however, a new version will be released that contains all the old features plus the new commands that have been added since the last release. If existing commands are enhanced or significantly changed they will be available under a new name. The original commands with their old functionality will be available with their original names. We thus will try to maintain backward compatibility.

3 PORTABILITY

The LIAR code is mainly written in standard Fortran 77. It, however, takes advantage of the STRUCTURE and RECORD extensions that are available in most Fortran compilers. The code is stand-alone, apart from a few system calls (random number generator, time) that need to be adjusted to the actual computer system. No specific libraries are required for the compilation. LIAR version 1.9 is presently running under those operating systems:

- UNIX: (IBM AIX 3.2, etc.).
  Computer: UNIX RISC workstations.
- Windows 95 / Windows NT: (Personal Computers).
  Computer: > Pentium 133 MHz, > 32 MB RAM.
  Compiler: Microsoft Powerstation Fortran 4.0.

The code is easily ported, as long as Fortran compilers are available that support the STRUCTURE and RECORD extensions.

4 ACCELERATOR PHYSICS IN LIAR

The LIAR program models both single and multi-particle beam dynamics in the presence of strong wakefields and beam acceleration. It is essentially a tracking program that

* Work supported by the Department of Energy, contract DE-AC03-76SF00515.

is enhanced by a large number of utility, analysis and optimization routines. Those routines allow adjusting the simulation to a realistic model and estimating the linac performance after the application of optimization routines. The underlying theory and concepts of LIAR are described in the user's manual [1]. Here we give a list of important features:

- Full implementation of quadrupoles, RF structures, dipole correctors, beam position monitors (BPM's), magnet movers and their errors.
- Fully coupled beam transport.
- Single-particle Twiss parameters.
- Consideration of all chromatic and dispersive effects.
- Transverse and longitudinal dipole wakefields.
- Transverse quadrupole wakefields.
- Calculation of wakefield effects within a single bunch (short-range wakefields) and within a bunch train (long-range wakefields).
- Charge sensitive beam transport (e.g. bunch train with electron and positron bunches).
- Calculation of beam offsets, emittances, β-mismatch, effective luminosity reduction, etc. at all BPM's.
- Calculation of full phase space at freely definable Marker points.
- Steering trajectory correction.
- Automatic generation of freely definable position feedbacks.
- General multi-device knobs.
- Automatic emittance bump optimization.
- Advanced beam-based alignment algorithms (dispersion-free steering, alignment using magnet movers, ...).
- Multi-particle beam optics diagnostics to determine beam phase advance, wakefield growth of betatron oscillations, etc.
- Output and plotting routines for all lattice and optics parameters and all observables.

Machine specific parameters are defined interactively by the user (beam current, bunch length, ...) or are defined in external input files (lattice, wakefield functions, ...). Though the required input format is fixed, the names of input files are chosen by the user. Lattices can be specified in the TRANSPORT or MAD format.

5 EXAMPLE

If LIAR is called without command line parameters it enters into interactive mode:

```
 ___      ___
 |||      |||
 |||      ___   ______    ____
 |||      |||  _||||||   _||||
 |||      |||  |||  ||   |||
 |||____  |||  |||__||_  |||
 |||||||  |||  ||||||||  |||   Version 1.9
 ------------------------------------------
 L I near   A ccelerator   R esearch  code
 S L A C   1996    ---    Ralph Assmann
                          Karl Bane
                          Tor Raubenheimer
                          Kathy Thompson
LIAR>
```

and commands can be entered. Alternatively LIAR can be run in batch mode, reading its input from a file. Let's consider the example of a simple SLC simulation. We go through in steps. Many of the commands shown here have more parameters than are specified. If parameters are not explicitly given, they are set to their default values. Command lines are automatically continued if an input line is ended with a comma.

In the first two commands we initialize all internal data structures to zero, we switch off the debug level and we set the output unit to the standard output:

```
RESET, all
SET_CONTROL, debug   = 0,
             outlun  = 6
```

Then we read the lattice from a transport input deck and define the injection energy:

```
READ_TRNS, infile  = 'input/slc.trns',
           energy  = 1.19
```

In the next step the RF-phases for BNS damping are defined and the acceleration and lattice is rescaled accordingly. Note that two different RF-phases are specified along the linac with the switch at 800 m:

```
SET_RF, energy   = 46.6,
        scale    = .t.,
        phase1   = 22.,
        lswitch1 = 800.,
        phase2   = -16.5
```

Next we calculate the Twiss parameters, specifying the initial values:

```
CALC_TWISS, betax   = 3.40,
            betay   = 3.08,
            alphax  = 0.156,
            alphay  = 0.066
```

After that we need to define the initial conditions for the beam setup. We define an initial beam offset y, the injection energy and energy spread, the normalized emittances and the Twiss values:

```
SET_INITIAL, y        = 200.d-6,
             energy   = 1.19,
             espread  = 0.014,
             nemitx   = 3.0d-5,
             nemity   = 0.3d-5,
             betax    = 3.40,
             betay    = 3.08,
             alphax   = 0.156d0,
             alphay   = 0.066d0
```

Everything is prepared now to set-up the beam. We specify the bunch population, the bunch length, the number of bunches, the number of slices per bunch and the number of mono-energetic beam ellipses per slice:

```
SET_BEAM, current  = 4.d10,
          blength  = 1100.d-6,
          nb       = 1,
          ns       = 20,
          nm       = 3
```

Next we must define the wakefields. They are read in from external input files. We only define short-range wakefields:

```
SET_SR_WF, file = 'input/srwf_slc.dat'
```

Before we track the beam through the lattice, we misalign all quadrupoles vertically by 200 μm RMS:

```
ERROR_GAUSS_QUAD, name     = '*',
                  y_sigma  = 200.e-6
```

Now we can finally track the beam through the lattice:

```
TRACK
```

and measure the normalized beam offsets at the BPM's:

```
MEAS_BPM, file = 'output.data',
          norm = .t.
```

The output is saved into a file. As already mentioned, many more parameters and commands are available in LIAR. For example the command TRACKC would have tracked the beam through the lattice while applying a 1-to-1 trajectory correction. The complete reference information is available in the LIAR manual [1].

During the execution of the commands LIAR provides extensive information. For example the progress of the tracking is indicated by a "trackometer":

```
T R A C K O M E T E R :
~~~~~~~~~~~~~~~~~~~~~~
0   10   20   30   40   50   60   70   80   90   100 %
|____|____|____|____|____|____|____|____|____|____|
^^^^^^^^^^^^^^^^^^^^^^^^^^^^^^^^^^^^^^^^^^^^^^^^^^^^
```

At the end of the tracking, summary information is printed to the standard output. We just show the first few lines:

```
End of tracking   A N A L Y S I S :
~~~~~~~~~~~~~~~~~~~~~~~~~~~~~~~~~~~~

Beam energy
   - acceleration:    E_0   =    1.190 GeV   -->   E_f   =   45.998 GeV
   - spread:          E_sig =     .016 GeV   -->   E_sig =     .126 GeV
   - rel. spread     SIGE/E =    1.322 %     -->  SIGE/E =     .274 %
Beam blow-up
   - Emittance (b1):  g_x   =    0.000 %           g_y   =  205.158 %
```

The observables are defined in [1]. We just mention a few of the summary results: emittance growth in the linac, lattice mismatch, RMS trajectory offsets, beam energy, ... In addition most of the results are saved at every BPM location. They can be printed out into files, for example in order to study the emittance growth along the linac.

6 SUMMARY

The computer program LIAR ("LInear Accelerator Research code") is a numerical modeling and simulation tool for high performance linacs. Amongst others, it addresses the needs of state-of-the-art linear colliders where low emittance, high-intensity beams must be accelerated to energies in the 0.05-1 TeV range. LIAR is designed to be used for a variety of different projects. It has been applied to and checked against the existing Stanford Linear Collider (SLC), the linacs of the proposed Next Linear Collider (NLC) and the proposed Linac Coherent Light Source (LCLS) at SLAC.

LIAR allows the study of single- and multi-particle beam dynamics in linear accelerators. It calculates emittance dilutions due to wakefield deflections, linear and non-linear dispersion and chromatic effects in the presence of multiple accelerator imperfections. Both single-bunch and multi-bunch beams can be simulated. It is possible to simultaneously study the acceleration of positive and negative charges in a linac. Diagnostic and correction devices include beam position monitors, RF pickups, dipole correctors, magnet movers, beam-based feedbacks, multi-device knobs and emittance bumps. Several basic and advanced optimization schemes are implemented. Present limitations arise from the incomplete treatment of bending magnets and sextupoles.

A major objective of the LIAR project is to provide an open programming platform for the accelerator physics community. We invite interested scientists to join this project. Due to its design, LIAR allows straight-forward access to its internal FORTRAN data structures. The program can easily be extended and its interactive command language ensures maximum ease of use. Presently, versions of LIAR are compiled for UNIX and MS Windows operating systems. An interface for the graphical visualization of results is provided. Scientific graphs can be saved in the PS and EPS file formats. In addition a Mathematica interface has been developed. LIAR now contains more than 40,000 lines of source code in more than 130 subroutines.

In the future we will add the ability to include bunch compression into the simulation.

7 REFERENCES

[1] R. Assmann et al., "LIAR - A Computer Program for the Modeling and Simulation of High Performance Linacs", SLAC/AP-103 (1997).

LEGO: A MODULAR ACCELERATOR DESIGN CODE *

Y. Cai, M. Donald, J. Irwin and Y.T. Yan
Stanford Linear Accelerator Center, Stanford University, Stanford, CA 94309 USA

Abstract

An object-oriented accelerator design code has been designed and implemented in a simple and modular fashion. It contains all major features of its predecessors: TRACY and DESPOT. All physics of single-particle dynamics is implemented based on the Hamiltonian in the local frame of the component. Components can be moved arbitrarily in the three dimensional space. Several symplectic integrators are used to approximate the integration of the Hamiltonian. A differential algebra class is introduced to extract a Taylor map up to arbitrary order. Analysis of optics is done in the same way both for the linear and non-linear case. Currently, the code is used to design and simulate the lattices of the PEP-II. It will also be used for the commissioning.

1 INTRODUCTION

There were many accelerator design and simulation codes used for designing lattices for the PEP-II[1] largely due to the complexity of the design. It has been always a dream during the design stage to have one code that can handle everything correctly: purposely off-aligned quadrupole inside a solenoid detector, two beams inside a common quadrupole and non-linear chromatic effects with coupling. It is clear that a code with object-oriented design and implementation is the most natural and powerful approach to handle even more complicated modeling efforts during the commissioning and operation of the machines.

We started to design and implement LEGO two years ago to generate an environment to simulate single charge particle dynamics as a primary goal. The first requirement for the design was that all physics calculation directly related to particles shall be handled in a local coordinate system mounted on the accelerator components. The second requirement was to use differential algebra methods to generate maps and analyze beam dynamics whenever appropriated[2].

We also wanted any applications developed in this environment to be applied to real accelerators in the same way as a simulated machine. Finally, we tried very hard to make our design as simple and modular as possible.

2 BASIC CORE LIBRARY

The core library consists of several inter related modules. They are the parser, beamline, processor, integrator and patch. These modules are designed to be used most effectively as parts of a library. However, they can be used independently as well. For example, a beamline can be constructed directly without using the parser module.

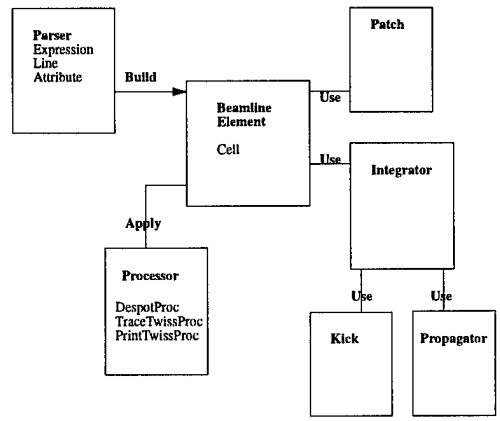

Figure 1: Main Lego Modules

The parser module is for decoding lattice input files. The main function of this module is to read a given input lattice file into tables of parameters, element attributes and symbolic beamlines which then build a beamline with a tree structure for LEGO. The module can be used to parse many common input formats used in the accelerator community, for instance the MAD input. We will discuss some implemented formats later in the section on interfaces.

The beamline module is the core of the library. It defines many components commonly used in accelerators and holds places for the integrators and patches required for physics calculation. It also provides the interface and hook for processors to access elements and travel through the tree-structured beamline sequentially. Together with the processor, they form a visitor pattern[3]. This creates a separation between the beamline and its operations. This is a very desirable feature of a library because additional operations on the beamline can be added using a processor without recompiling the core library.

The processor module is the key of the library. A processor uses the hooks provided by the beamline to manipulate the data of elements and beamline. Most data processing performed on elements, integrators or patches is handled by processors. Applications often use processors to interface with the beamline. One of the most important processors in the module sets up the DESPOT integrators for tracking. Actually, we can replace the engine of the computation simply by sending another processor to set up another type of integrators, for example TRANSPORT matrices. Linear and non-linear analysis procedures are unaffected by the swapping of integrators.

The integrator module defines the physics of the beam-

* Work supported by the Department of Energy under Contract No. DE-AC03-76SF00515 and DE-AC03-76SF00098

transport. An integrator is introduced for the integration of the local Hamiltonian through the body of element including fringe field if needed. Since there are many ways to approximate the integration, the choice of what kind of integrators to use for a given type of element is left for users. In the module, we provide a few processors to set up a consistent set of integrators for instance, DESPOT or TRANSPORT matrices. The integrator makes it possible to separate the description of physical components and how they are used in the calculation of physics. This feature is considered to be one of the major achievements of the library.

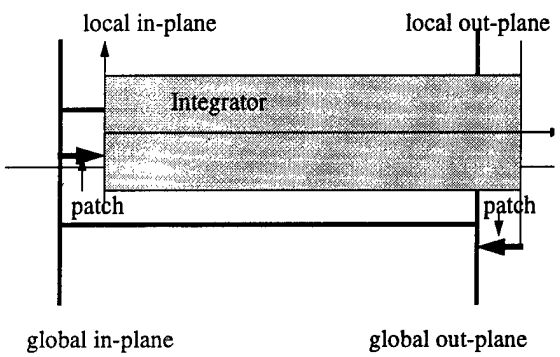

Figure 2: Lego Concept

The patch module handles element or beamline misalignment. Typically, there are two patches for each misaligned component. One is for the entry right before entering the element and another for the exit. Similar to the integrator, the choice of patches can be made by users. A proper selection of the patch allowed us to handle purposely off-aligned quadrupoles inside the solenoid detector.

Many important features have been implemented and tested in the library, for example:

- geometry and survey,
- symplectic integrator,
- synchrotron radiation,
- linear optics,
- element by element tracking,
- non-linear map extraction to arbitrary order,
- fast map tracking,
- non-linear map analysis.

In additional to these closely related modules, we have many independent modules, such as differential algebra, matrix, vector, geometry, fitting and map modules.

3 DESIGN FEATURES

There were many tradeoffs made during the design stage. The most important one is the introduction of the integrator class. In principle, we could carry integrators in a processor while going through a beamline. However, this approach will slow down multi-turn tracking significantly because an integrator needs to be constructed in the element before each calculation. In our design, integrators are saved on the beamline so that setting up integrators only has to be done once.

Similar to the integrator, we also decided to save patches on the beamline for the reason of speed. Actually we gain more than just the speed. Stored patches also allow us to place an element on an existing geometry. This feature is crucial when we are dealing with two beams in the same detector or magnet.

Integrators and patches may be used to carry parameters of the differential algebra. For example, when we study beam-based alignment of quadrupoles the patches for the quadrupole magnets are replaced with parameterized ones so that we can calculate the response of the beam trajectories to their alignemnts. This mechanism of extracting responses is very powerful and conceptually simple.

In the element class, we have built up an inheritance structure that reflects a building-block concept and the perturbative nature of the accelerator theory. The first layer is called "chart" to note the zeroth-order perturbation, namely those elements needed to define geometry and coordinates system. Then the second layer is for components which carry additional attributes for the optics and higher order perturbations.

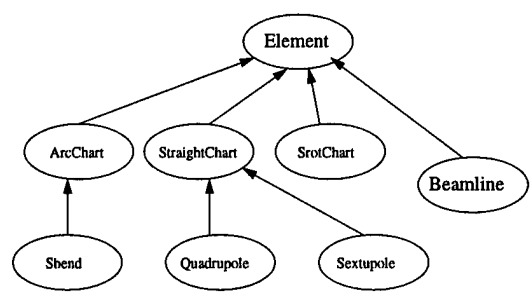

Figure 3: Lego Element Classes

4 APPLICATIONS

Building upon the core library, we have written many useful application programs. They are commonly used to evaluate the performance of the machines when many aberrations are present. Among them, the simplest procedures adjust tunes with two families of quadrupoles and chromaticities with sextupoles. To make a global coupling correction, we implemented a scheme of four families of skew quadrupoles to zero out the four coupled elements in an one-turn matrix.

For control of the closed orbit, we have implemented the widely used three-bump method. Recently, we added a more powerful scheme correcting orbit and dispersion simultaneously using orbit steering correctors based on eigen-vector decomposition and the MICADO method[4].

Finally, to prepare for the commissioning of the high energy ring(HER) this year, we wrote a beam-based alignment package to determine misalignments of quadrupoles and offsets of beam position monitors. The method of analysis is to fit the beam trajectories for several quadrupole configurations differing by a large percentage in strength while treating the circular accelerator as a single-passage beamline.

Similar to the beam-based alignment scheme, by kicking the beam with correctors and then measuring the beam positions, we can work out the errors of strength in quadrupoles and correctors and gains of beam position monitors. This scheme can be applied to both storage ring and transport beamline.

All the application packages have been simulated for the PEP-II lattice under various conditions and have worked well. They will be applied to the HER soon.

5 INTERFACES

In order to use the applications effectively, we wrote many interfaces to the control system of PEP-II and other existing programs. First, in the parser module, we have implemented two builders for decoding MAD input decks and skeleton decks used in the control system. We are defining our own standard input format to accommodate the new types of element allowed in LEGO.

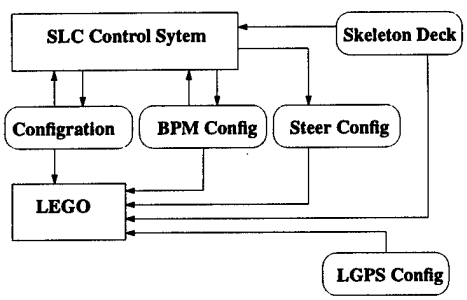

Figure 4: Interface to the control system

Furthermore, we have added the feature of loading configurations and beam position monitor files from the control system to the LEGO beamline so that we can build an off-line model easily in the control room and then apply the application programs to the accelerators. This feature also complys with the requirement that an application be used in the same way for both simulated and real machines.

Since the RESOLVE program has proved very useful for commissioning of accelerators, we have developed interfaces[5] so that we can use RESOLVE as a graphical tool to identify machine errors. We plan also to add a graphical user interface for the applications mentioned earlier.

We have linked Zlib[6] to LEGO for extracting non-linear parameterized maps and for non-linear map analysis.

6 SUMMARY

We have created an object-oriented environment for simulating accelerators. It becomes a very efficient tool box to develop new applications both for simulation and operation of accelerators. In this approach, we have achieved five important design specifications. Four of them are related to the modularity of design. They are:

- separation between input language and physical description of element,
- separation between description of element and computational usage of element,
- separation between beamline and its operations,
- separation between analysis of physics and underlining method of transport.

These separations make LEGO very flexible to use and adaptable to challenging design and simulation conditions, like the interaction region of the PEP-II.

The last achievement is the common interface both for simulated machines and real accelerator for all applications.

7 ACKNOWLEDGMENT

We would like to thank Scott Berg, Jim Holt, Chris Iselin, Leo Michelotti, Nick Walker and Johannes van Zeijts for many stimulating and passionate discussions about class design during the CLASSIC meetings. We benefited very much from those discussions. We would also like to thank E. Forest for explaining the physics and procedures implemented in TRACY and DESPOT.

8 REFERENCES

[1] "PEP-II: An Asymmetric B Factory," Conceptual Design Report, SLAC-418, June 1993.

[2] Y. Cai, J. Irwin, Y. Nosochkov and Y.T. Yan, "Computational Tools and Lattice Design for the PEP-II B-Factory," AIP Conference Proceedings 391, CAP 1996,

[3] E. Gamma, R. Helm, R. Johnson and J. Vlissides, "Design Patterns, Elements of Reusable Object-Oriented Software," Addison-Wesley Professional Computing Series, 1994

[4] M. Donald, Y. Cai, H. Shoaee and G. White, "An Orbit and Dispersion Correction Scheme for PEP-II," these proceedings.

[5] M. Lee *et at.*, "Lattice Commissioning Strategy for the B-Factory", these proceedings.

[6] Y.T. Yan, Y. Cai and J. Irwin, "A Flexible-Variable Truncated Power Series Algebra in Zlib," these proceedings.

LATTICE COMMISSIONING STRATEGY FOR THE B-FACTORY *

M. Lee, Y. Cai, J. Corbett, H. Shoaee, D. Whittum, G. White, Y. Yan
Stanford Linear Accelerator Center, Stanford, California 94309

Y. Zambre
SRI International, Menlo Park, CA 94025

Abstract

To prepare for the PEP-II turn on, we have studied one commissioning strategy with simulated lattice errors. Features such as difference and absolute orbit analysis and correction are discussed

1 INTRODUCTION

To prepare for the commissioning of the PEP-II injection line and high energy ring (HER), we have developed a system for on-line orbit analysis by merging two existing codes: LEGO [1] and RESOLVE [2]. With the LEGO-RESOLVE system, we can study the problem of finding quadrupole alignment and beam position (BPM) offset errors with simulated data. We have increased the speed and versatility of the orbit analysis process by using a command file written in a script language designed specifically for RESOLVE. In addition, we have interfaced the LEGO-RESOLVE system to the control system of the B-Factory. In this paper, we describe on-line analysis features of the LEGO-RESOLVE system and present examples of practical applications

2 THE RESOLVE PROCESS

Orbit analysis has been used for almost two decades to find errors in accelerator lattices [3,4,5]. One code that provides a interactive graphical user interface for orbit analysis is RESOLVE. RESOLVE was developed specifically to find errors in the beamline elements such as magnet strength and position. The orbit analysis procedure to find "modeling" errors is typically a two step process: The first step is to adjust the value of the modeling errors to produce a simulated orbit which matches to the measured orbit. The second step is to interpret this result. Up to now, both of these steps have been performed manually via the graphical interface provided by RESOLVE. In many cases, this manual application of RESOLVE can be a time consuming process. Our desire to speed up the error-finding procedure motivated the development of a command file language.

* Work supported by Department of Energy contract DE-AC03-76SF00515

3 THE LEGO-RESOLVE CONNECTION

LEGO is an object-oriented environment for integration of accelerator design, beam simulation and machine modeling codes. At present, we have connected RESOLVE with LEGO by means of a file-driven interface as shown in Fig. 1. A similar file-driven interface has also been implemented between LEGO and the B-Factory control system. With these file-driven connections, we also can use the RESOLVE Graphical User Interface for other on-line LEGO applications such as orbit correction and lattice calculation.

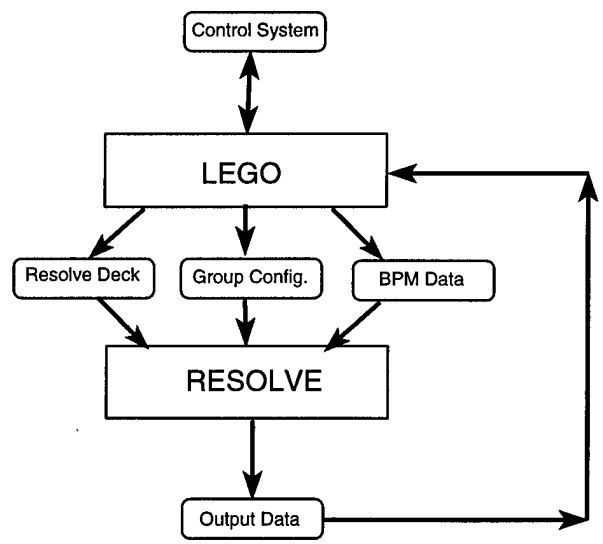

Figure 1. Schematic diagram of connections between LEGO, RESOLVE, and the Control System.

To use RESOLVE, we first create a directory for the input and output files. Then, we use LEGO to place the following input files in the RESOLVE directory: (1) a "beamline" file which describes the lattice, (2) a "groups" file which defines how the magnets are connected by common power supplies, and (3) "BPM" with the simulated or measured orbit data to be analyzed. After loading these files into the RESOLVE directory, the measured or simulated data can be analyzed either manually or automatically. To analyze data automatically, we need to create a "cmd" or command in the RESOLVE directory. At present, the command files are created

manually. Eventually, we will use LEGO to create command files automatically. Examples of input files for RESOLVE can be found at: "http://www. slac.stanford.edu /grp/ara/ ".

For a typical application, a "cmd" file contains the following commands: (1) select the region of beamline to be studied, (2) choose the elements with errors (such as quadrupole misalignments or BPM offsets), (3) delete the "bad" BPMs, (4) define the launch conditions (such as the initial beam position and angle), and (5) find the value of the errors. To find the errors, RESOLVE minimizes the sum of the squares of the discrepancy between the measured orbit and the simulated orbit at all BPMs. With these commands automatically read by RESOLVE, the error analysis process can proceed quickly. In some cases, on-line data processing of PEP-II orbit data will be possible during machine physics studies.

4 MULTI-CONFIGURATION ANALYSIS

In the past, RESOLVE was used primarily for analysis of the "difference orbit" to find optical errors [6,7,8,9]. The difference orbit is defined as the change in the orbit introduced by a kick from a dipole corrector. RESOLVE can be used to find the errors in the strength of quadrupole magnets by minimizing the sum of the least squares of the measured orbit changes and simulated orbit changes. In practice, we often measured the orbit change at all BPMs for every corrector in the beamline or ring. We also can solve for the values of BPM sensitivity errors with RESOLVE. We call this process "multi-track" analysis.

In the case of beam-based misalignment studies [9,10,11,12], we analyze orbit data taken for several configurations with different quadrupole magnet settings. There is one track for each configuration. Each track is not a "difference" orbit but an "absolute" orbit [10,11,12,13]. We call this process "multi-configuration analysis".

5 BEAM-BASED ALIGNMENT STUDY

Recently, we used the command file feature in RESOLVE to study beam-based alignment in the HER. The beam-based misalignment study in HER is the first time RESOLVE is used for multi-configuration analysis. In this study, LEGO was used to simulate the measured orbit for 10 different configurations. Each configuration is defined by a set of quadrupole strength values. A set of 10 orbits was produced by tracking with LEGO.

Each orbit or "track" was simulated for the same launch conditions (the beam is injected into HER with same position, angle, and energy), and every quadrupole magnet randomly misaligned. Two kinds of errors were introduced into the BPMs: offsets and noise. The BPM offsets were the same for all tracks, but the BPM noise was different for each track.

To simplify the analysis, we assume no quadrupole strength errors. Under this condition, we did not need a "groups" file for our analysis. Instead, we use the "set" option in each BPM file to set the strength of the quadrupoles for the corresponding track. Since the launch conditions, the quadrupole misalignment, the BPM offsets, and the beam energy are the same for all tracks, we use the "vary" option in the command file to declare them as variables. We use the interactive RESOLVE interface to read the beamline file, read the BPM files, and then to read the "cmd" file.

With these three actions, RESOLVE will solve for the misalignment and offsets automatically. The result will be displayed graphically in the output windows or written into an output file. LEGO can read this output file and can pass the information to the control system (see Fig. 1).

An analysis of simulated data provides us an example using the LEGO-RESOLVE system for on-line beam-based alignment studies. Examples of two tracks over one arc of HER are shown in Fig. 2, where the dots represent sampled BPM data, and the solid lines are the simulated trajectories in RESOLVE. This study provided us a way to study alignment errors and to see how the command file works for on-line data analysis.

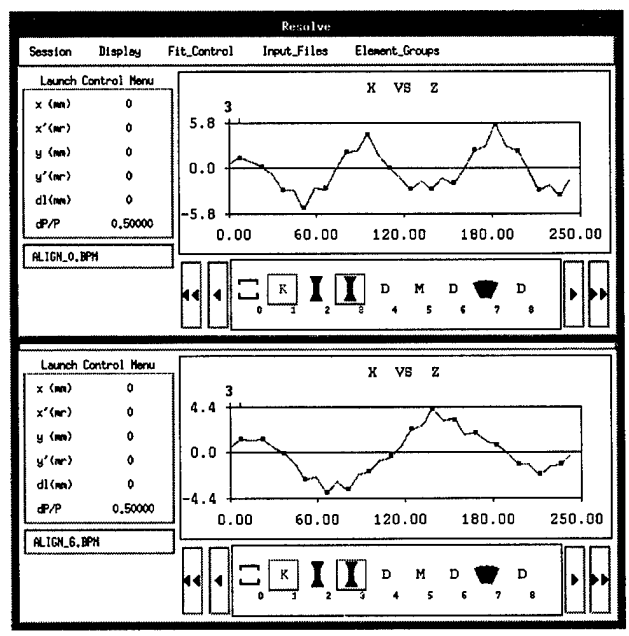

Figure 2. Typical trajectories used in our example.

6 A NEW ERROR-FINDING ALGORITHM

We have developed a new procedure for finding magnet alignment and monitor offset errors by means of an automated procedure. This method requires searching for the solution with the least-square error values as we vary the energy of the beam. To do an energy scan, we simply set the beam energy to a given value, and use RESOLVE to find the misalignment and offset errors for this energy. By comparing the solution over a range of beam energy values, we can make a choice on the best solution. With simulated rms. BPM noise value of 0.03 mm, we have been able to determine the beam energy error within 0.002% as shown in Fig. 3

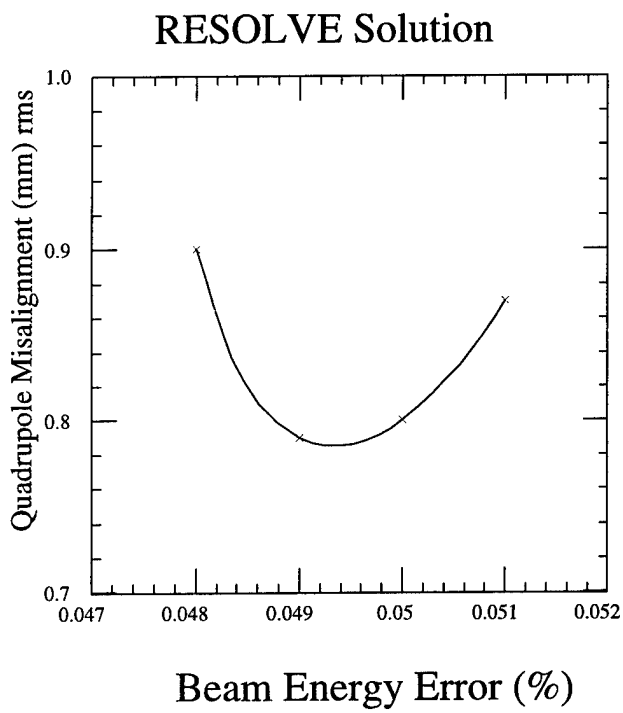

Figure 3. A plot of the solution for different beam energy error values for a case with simulated error of 0.05%.

7 SUMMARY

The combination of LEGO and RESOLVE has provided us with a state-of-the-art on-line accelerator modeling and analysis system. This system enables us to study error finding and correction strategies with simulated errors. These simulation studies give us a way to practice commissioning of the high-energy ring for PEP-II. The experience we gain from this practice increases our ability to find errors in the real machine. To find real errors in the PEP-II, we simply replace the simulated data with the measured data.

6 REFERENCES

[1]. Y. Cai, M. Donald, J. Irwin, and Y. Yan, "LEGO: A Modular Accelerator Design Code", see these proceedings.

[2]. M. Lee, Y. Zambre, and J. Corbett, "Accelerator Simulation Using Computers", International Conference on Current Trends in Data Acquisition and Control of Accelerators, Calcutta, India, 1991; SLAC-PUB-5701(A).

[3]. M. Lee, J. Sheppard, and M. Sullenberger, "Models and Simulations", Proceedings of the Europhysics Conference on Computing in Accelerator Design and Operation, Berlin, 1983; SLAC-PUB-3217(A).

[4]. M. Lee, et al., "Analysis of the Orbit Errors in the CERN Accelerators", Proceedings of the Europhysics Conference on Control Systems for Experimental Physics, Villiars, Switzerland, 1987; SLAC-PUB-4411(A).

[5]. M. Lee, "GLAD: A Generic Lattice Debugger", Proceedings of the International Conference on Accelerators and Large Experimental Physics Control Systems, Tsukuba, Japan, 1991; SLAC-PUB-5700(A).

[6]. J. Corbett, M. Lee, and Y. Zambre, "Automatic Beamline Calibration Procedures", Proceedings of the 3rd EPACS, Berlin, 1992; SLAC-PUB-5776(A).

[7]. J. Safranek and M. Lee, "Calibration of the X-ray Ring Quadrupoles, BPMs, and Orbit Correctors Using the Measured Orbit Response Matrix", AIP Conference Proceedings 315 on Orbit Corrections and Analysis in Circular Accelerators, Brookhaven, 1994.

[8]. J. Safranek, "Experimental Determination of Storage Ring Optics Using Orbit Response Measurements", NIM(A), vol. 388, no. 1 & 2, 1997.

[9]. G. LeBlac and W. J. Corbett, "Accelerator Modeling at SPEAR", see these proceedings.

[10]. C. E. Adolphsen, et al., "Beam-Based Alignment Technique for the SLC LINAC", Proceedings of the 1989 PAC, Chicago; SLAC-PUB-4902(A).

[11]. C. Adolphsen and T. Raubenheimer, "Method to Evaluate Steering and Alignment Algorithms for Controlling Emittance Growth", Proceedings of the 1993 PAC; SLAC-PUB-6233.

[12]. W. J. Corbett and V. Ziemann, "Procedure for Determining Quadrupole and BPM Offset Values in Storage Rings', Proceedings of the 1993 PAC; SLAC-PUB-6112(A).

[13]. K. Ott, "Quadrupole Misalignment Determination at BESSY", Proceedings of the 1996 EPAC, Barcelona, Spain.

TRANSVERSE WAKEFIELD ANALYSIS FOR THE NLC & JLC DETUNED STRUCTURES ON A PARALLEL COMPUTER *

Xiaowei Zhan and Kwok Ko†
SCCM Program, Stanford University, Stanford, CA 94305
† Stanford Linear Accelerator Center, Stanford University, Stanford, CA 94309

Abstract

The detuned structure (DS) has been proposed as one possible design to control the emittance growth of long bunch trains in linear colliders due to transverse wakefields. A DS typically consists of over a hundred cells with tapering from cell to cell of the order of few microns to decohere the dipole modes. The design parameters are targeted for two orders of magnitude reduction in the wakefield experienced by the trailing bunch. Field analysis of such a large heterogeneous structure is impractical with finite-difference schemes using structured grids. This paper presents the results from calculations performed on a parallel computer using a finite-element code based on an unstructured grid. We discuss the parallel implementation issues and show comparisons between simulation results and the wakefield data taken on both the NLC and JLC detuned structures.

1 INTRODUCTION

As all linear collider designs adopt acceleration of long bunch trains to increase luminosity the dilution of the beam emittance due to wakefield effects in the linac is an important problem to overcome in accelerator structure design. The detuned structure (DS) is considered as one viable option to suppress the long range wakefields that lead to cumulative beam break-up instability. In the DS the cell dimensions are tapered to provide a Gaussian distribution of the most harmful dipole modes so that their detuning results in a substantial decrease in the wakefield experienced by the trailing bunches. Both SLAC and KEK have a DS design for their proposed X-Band linear colliders (NLC and JLC). Fig. 1 (a) shows the cell geometry in a typical DS. The unit cell is formed between disks whose aperture a and thickness t vary along the structure according to the distributions shown in Fig. 1 (b). The tapering profile for a is to Gaussian detune the 1st dipole band while that for t applies to the higher bands (3rd and 6th). The cell radius b is then adjusted to tune the accelerating mode to 11.424 GHz at 120 degree phase advance across the cell length L.

2 FINITE ELEMENT WAKEFIELD ANALYSIS

Many wakefield calculations have been carried out to assess the effectiveness of the DS in wakefield reduction. But they have all been based on approximate methods because the size of the problem precludes a direct numerical approach until now. Also, previous analysis have mostly simplified the cell geometry so that ends of the disks are treated as flat than round. The methods used include equivalent-circuits [1], mode-matching [6], and the open-mode [5] expansion. Generally the wakefield results obtained from these studies agree qualitatively with measurements. Nevertheless it is of interest to obtain the wakefield from a direct simulation of the DS on a numerical grid that models closely the exact geometry and dimensions.

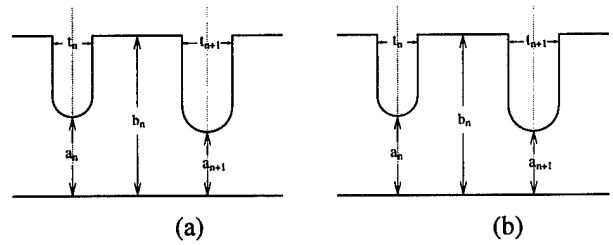

Figure 1: (a) The dimensions of a typical cell; (b) Variations of cell dimensions.

There are difficulties in applying numerical field solvers to the DS geometry especially if they are of the finite-difference (FD) type that employs a structured grid. First, to fit the gradual taper in a and b would require mesh sizes so small that the mesh becomes prohibitively large to be practical to simulate on any computer. One can exploit grading of the mesh sizes (non-uniform mesh) to reduce the number of mesh points. But over grading can lead to mesh cells with such disparate dimensions that convergence may become an issue for the solver. Also, structured grids are not capable of modeling curved boundaries accurately. Diagonal mesh can help to provide a better fit but the unusually large aspect ratio can cause the solution matrix to be ill-conditioned.

The finite-element (FE) method has been shown to be highly accurate and efficient in modeling accelerator structures [4]. The FE unstructured grid is able to fit small differences in geometry and to refine locally around curved boundaries without significant increase in the global number of elements or degrees of freedom (DOF). The DOF's can be further minimized without loss in accuracy through the use of higher-order elements. These improvements altogether are still not sufficient to reduce the problem size enough for the simulation to be practical on any high-end workstation. It becomes apparent that more efficient gridding (adaptive mesh refinement) and more powerful computing resources (parallel processing) are needed.

3 ADAPTIVE MESH REFINEMENT

In finite element analysis, the accuracy of the solution improves as the mesh is refined. The simplest refinement is

* Work supported by the Department of Energy, contract DE-AC03-76SF00515.

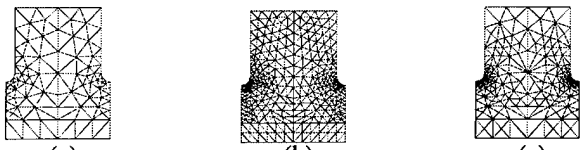

(a) (b) (c)

Figure 2: (a) Initial mesh; (b) Uniform refinement; (c) Adaptive refinement.

to subdivide each element over the entire mesh so the increase in DOFs scales with the number of subdivisions. A more cost effective way is to refine adaptively to keep the number of extraneous DOFs to a minimum. We use the local integral of the energy density gradient as a criteria to determine if local refinement is necessary, and stop the refinement when a specified tolerance is reached. This indicator turns out to be very effective from our numerical experiments in approximating the optimal mesh for a desired accuracy. Fig. 2 show an initial mesh, a uniformly refined mesh, and an adaptively refined mesh. The two refined meshes yield the same accuracy but the adaptively refined mesh has half the number of DOFs, thereby producing a significant savings in memory requirement and run time.

4 PARALLEL IMPLEMENTATION

The DS geometry is highly amenable to domain decomposition for parallel processing because the partitioning is straightforward. Each cell in the long structure is assigned a processing node. In the single program multiple data (SPMD) model, global data such as meshes and matrices are distributed to the nodes where global operations can be processed locally. As shown previously in Fig. 1 the cell is bounded by half-disks (subdomain) so that sharing of data between nodes is limited to the field quantities at the cell apertures. This way the communication between nodes is kept to a minimum, and is achieved using the message passing interface (MPI).

The discretization of the Maxwell's equations in the frequency domain by FE results in a generalized eigenvalue problem, $Kx = \lambda Mx$. Both M and K are large, sparse and symmetric while M is positive definite. We use the Lanczos algorithm in the solver for its superior convergence properties which is ideal for computing extremal eigenvalues of large problems [3]. With the shift-invert technique, in each Lanczos iteration one solves the linear system $\tilde{K}x = b$, where $\tilde{K} = K - \sigma M$, and σ is the shift introduced to accelerate convergence by better separating the eigenvalues. Since solving the linear system constitutes the most time-consuming operation in the entire program, its parallel implementation is important for high parallel efficiency.

One way to look at the linear system under the domain decomposition introduced earlier is to separate the DOFs into "interior" ones that reside inside a subdomain (cell) and "interface" ones that are shared by the neighboring subdomains. Since there is no coupling between the "interior" DOFs from different subdomains, and the "interface" DOFs are far less in number, $\tilde{K}$ can be reordered in the form

$$\tilde{K} = \begin{pmatrix} A & C^T \\ C & F \end{pmatrix},$$

where A is a block diagonal matrix with the ith diagonal block A_i resulted from the "interior" DOFs in the ith subdomain, while F consists of only the "interface" DOFs, and C provides the coupling between them.

The next step is to decompose the matrix $\tilde{K}$ as

$$\tilde{K} = \begin{pmatrix} I & 0 \\ CA^{-1} & I \end{pmatrix} \begin{pmatrix} A & C^H \\ 0 & G \end{pmatrix} \tag{1}$$

where $G := F - CA^{-1}C^H$ is the Schur complement [2].

Now, since A is block diagonal, $A^{-1}v$ can be computed in parallel without interprocessor communication.

Because the size of G is relatively small, and it is block tridiagonal, the communication overhead to form it to explicitly is not significant. Hence, through the decomposition (1), the linear system $\tilde{K}x = b$ can be solved efficiently in parallel.

The block decomposition (1) is particularly useful and flexible for providing a framework for parallel implementation of the linear solvers. It allows us to achieve the parallelism for solving the global linear system regardless of how the local linear systems are solved.

5 TRANSVERSE WAKEFIELDS IN THE NLC & JLC

One concern over the stability of long bunch trains in next generation linear colliders such as the NLC and the JLC is the deflection of the beam due to long-range transverse wakefields. The wakefield at distances of the order of the bunch spacing is mainly due to the resonant modes of the structure, and in the transverse case, is given by

$$W(s) = \frac{2}{N_c} \sum_{i=1}^{N} K_i \sin(\frac{\omega_i s}{c}) \tag{2}$$

where ω_i, K_i are the frequency and the kick factor of mode i respectively, N is number of modes excited by the bunch and N_c is the number of cells in the structure. The kick factor is determined from the synchronous voltage

$$V_i = \int_{z_{min}}^{z_{max}} E_z(r_o, z) \ \exp(j\frac{\omega_i}{c}z)dz$$

and the stored energy

$$U_i = \frac{1}{2}\epsilon \int |E|^2 \, dV + \frac{\mu^{-1}}{2} \int |B|^2 \, dV$$

via the expression

$$K_i = \frac{|V_i|^2}{4(\omega_i/c)U_i \, r_o^2 \, L}$$

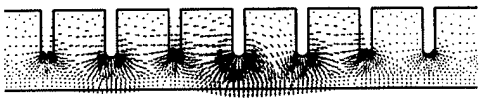

Figure 3: E-field (cell 163–170) of mode 166 for NLC DS.

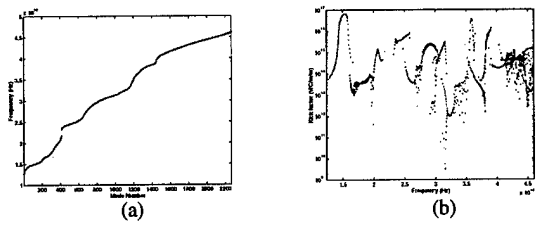

(a) (b)

Figure 4: Dipole modes for NLC: (a) frequency vs mode number; (b) kickfactor vs frequency.

Except for the open-mode method, other wakefield calculations have included only modes from the first two dipole bands although it is recognized that contributions from higher bands can be important as well. The open-mode analysis extends to the higher bands but thus far has considered only flat-ended disks in the cell geometry. The present work takes into account the exact cell geometry and includes as many higher band contributions as computation time would allow.

6 SIMULATION RESULTS

We have developed a new FE field solver using quadratic elements and including both parallelization and adaptive refinement features. Written in C++, the program is modular in structure and is compatible with any mesh generator. We used MODULEF to generate the mesh data for the NLC and JLC DS geometries. The program has been running on the Intel's Paragon XP/S 150 at Oak Ridge National Laboratory. This massively parallel computer has 1,024 nodes with two 75-MFLOPS i860 XP processors and 64 MBytes memory per node. Based on the one cell per node strategy described earlier, it is clear that memory rather than CPU is the limiting factor in our simulations.

The NLC X-Band DS is 1.8m long consisting of 206 cells and Fig. 3 shows the 166th mode in the first dipole band that is localized between cell 163 and 170 in that structure. We have computed the contributions from eleven bands for a total of 2266 modes with wall loss included. Figs. 4 show the frequencies of these modes and their kick-factors. Applying these data to the wakefield in (2) results in Fig. 5. Also shown are the measured data and the calculated result from equivalent circuit method. For the 150 cell JLC DS, we computed 1466 modes and the comparison between finite-element, measurement, and open-mode results is displayed in Fig. 6. Both the NLC and JLC wakefield analysis indicate a closer agreement between the finite-element result and measured data.

7 SUMMARY

This paper reports the first-ever direct field analysis of the transverse modes in a long tapered structure with realistic

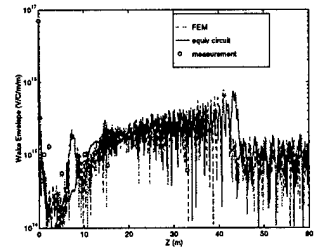

Figure 5: For NLC: Wake envelope comparison between FEM and equivalent circuit method; the circles are measured data.

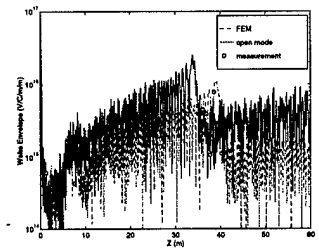

Figure 6: For JLC: Wake envelope comparison between FEM and open-mode method; the circles are measured data.

geometries and dimensions. The enabling capability is a new finite-element program that utilizes higher-order elements, adaptive refinement and parallel processing. The cpu time required for the NLC and JLC detuned structure calculations is in the ten's of hours even when contributions from thousands of modes are considered. In terms of parallel computing efficiency the speedup increase is close to linear. They lend support to our assertion that parallel computing is practical for accurately analyzing large heterogeneous systems.

8 ACKNOWLEDGMENTS

We are grateful to Drs. Cho Ng, Zenghai Li and Vinay Srivinas for their generous help and fruitful discussions. We'd like to thank Profs. Roger Miller and Gene Golub for their interests in the problem. We also acknowledge the use of Intel Paragons located in ORNL's CCS.

9 REFERENCES

[1] K. L. F. Bane and R. L. Gluckstern, *The transverse wakefields of a detuned X-band accelerator structure*, SLAC-PUB-5783, 1992.

[2] G.H. Golub and C.F. Van Loan, *Matrix Computations*, The John Hopkins University Press, Baltimore, 3rd edition, 1996.

[3] Y. Saad, *On the Rates of Convergence of the Lanczos and the Block Lanczos Methods*, SIAM J. Num. Anal. 17, 687-706, 1980.

[4] Eric Nelson, SLAC Report 92-16, 1992.

[5] M. Yamamoto, *Study of Long-Range Wake Field in Accelerating Structure of Linac*, KEK Report 94-9, 1995.

[6] S. A. Heifets and S. A. Kheifets, *Coupling impedance for modern accelerators*, AIP 249, 1992, pp. 151-235.

MAPA: IMPLEMENTATION OF STANDARD INTERCHANGE FORMAT AND USE OF ANALYZING LATTICES

Svetlana G. Shasharina† and John R. Cary,† Tech-X Corporation, 4588 Pussy Willow Court, Boulder, CO 80301

Abstract

MAPA (Modular Accelerator Physics Analysis) is an object oriented application for accelerator design and analysis with a Motif based graphical user interface. MAPA has been ported to AIX, Linux, HPUX, Solaris and IRIX. MAPA provides an intuitive environment for accelerator study and design. The user can bring up windows for fully nonlinear analysis of accelerator lattices in any number of dimensions. The current analysis methods of Lifetime plots and Surfaces of Sections have been used to analyze the improved lattice design of Wan, Cary and Shasharina (this conference). MAPA can now read and write Standard Interchange Format (MAD) accelerator description files and it has a general graphical user interface for adding, changing and deleting elements. consistency checks prevents deletion of used elements and creation of recursive beamlines. Plans include development of a richer set of modeling tools and the ability to invoke existing modeling codes through the MAPA interface.

1 MAPA AS A FRAMEWORK FOR STUDYING DYNAMIC SYSTEMS AND ACCELERATORS

MAPA was created in such a way, that many dynamical systems can be studied within it with the use of the same graphical user interface. In order to hook up a system to the code, users have to inherit it from `System-Map` tree class hierarchy and represent its attributes as parameters, options and strings.

Each system should be provided with the method int Advance(double* p) which describes the way the d-dimensional array of coordinates changes in one step of time. MAPA has many systems included already (non-linear maps, toroidal magnetic systems for plasma confinement and accelerators).

On the Fig. 1, we showed a typical view of the GUI. The upper left window has two systems, one of which is an accelerator (empty beamline by default). By clicking on the button, the user chooses the system, and brings the system control window (upper right on Fig. 1). This window has several menus for invoking methods for the system control and graphical analysis. Thus, the window for changing parameters can be brought up for dynamical changes of the system.

A special button in Menu allows reading description files, after which an corresponding accelerator is instantiated. We provided MAPA with parsers for reading both from the MAPA-native and SIF (MAD) format. This implies that the set of accelerator elements of MAPA is full enough: has all elements currently in use in MAD.

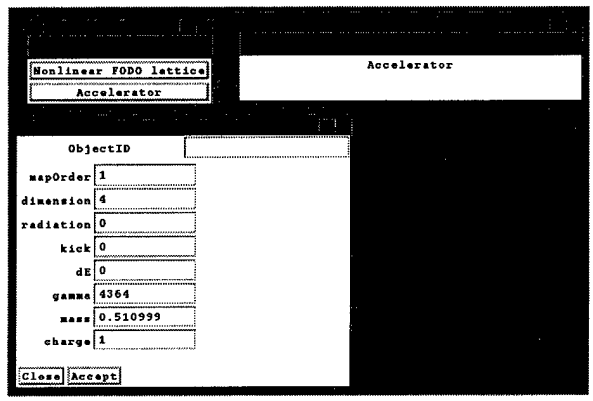

Fig. 1 A typical view of MAPA GUI: a window for choosing the system, control window and window for changing parameters.

2 GRAPHICAL ANALYSIS OF ACCELERATOR

MAPA has a rich set of graphical methods for analysis of accelerators. By invoking the menus described above, a user can bring up surfaces of sections (Fig. 2), which have means for starting orbits from clicks, or by choosing initial conditions in the slots, erasing orbits, zoom-in and out, and change the order the axis to see orbits in configuration space.

A special window can be brought up for dynamical changes of the beamline: adding, removing and changing the elements (Fig. 3).

Another powerful means for the accelerator study is a Lifetime plot (see Fig. 4, where different color indicate different confining properties of phase space locations).

Finally, MAPA can perform simulations relevant to the system, like Monte Carlo simulations (Fig. 5). As always, parameters of the calculations can be changed interactively and dynamically.

---

† also University of Colorado, Physics Dept., P.O. Box 390, Boulder, CO 80309

0-7803-4376-X/98/$10.00 © 1998 IEEE

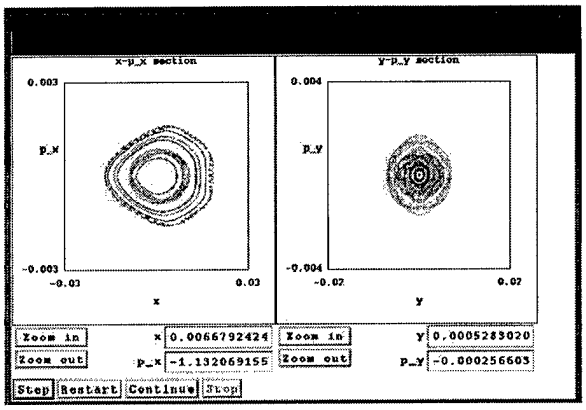

Fig. 2 Surfaces of section for ALS (Lawrence Berkeley Lab).

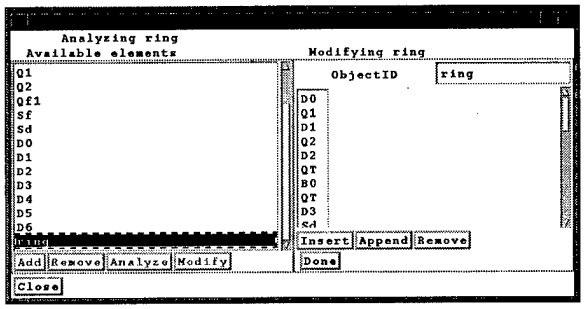

Fig. 3 A window for changing the beamline.

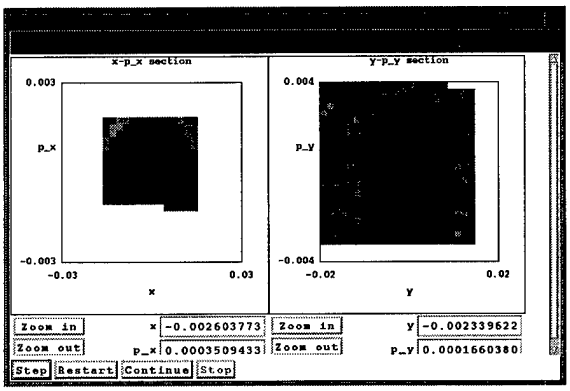

Fig. 4 Lifetime plots.

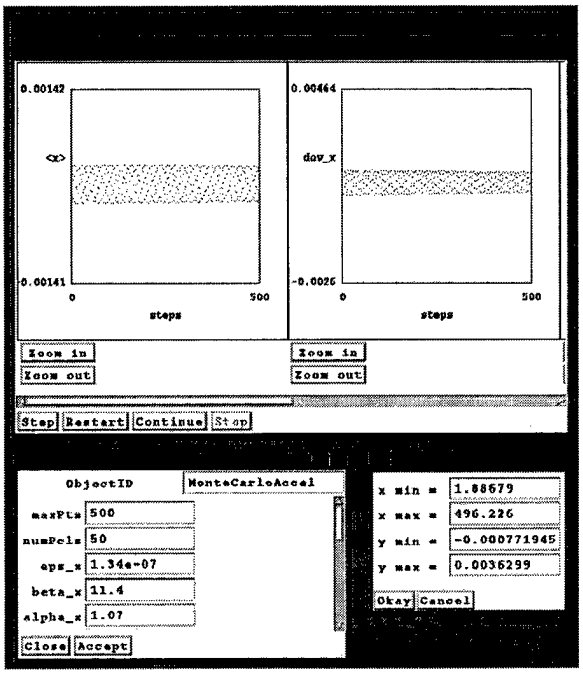

Fig. 5 Monte Carlo simulation for ALS.

3 SPECIAL FEATURE OF MAPA AND FUTURE PLANS

MAPA is a framework for studying dynaical systems. It is specially well suited for studying accelerators. All parameters of accelerator can be changed dynamically through a user friendly graphical interface. Several dynamical systems can be instantiated simultaneously for the ease of comparison. MAPA has a rich set of graphical analysis means. MAPA is easily extended and portable across many platforms. MAPA reads and writes MAD files.

Plans are at work to invoke Differential Algebra methods for rapid tracking and non-linear map analysis. Fitting facility will also be included soon.

ION OPTICAL STRAY FIELD ANALYSIS OF AN ESR DIPOLE

B. Schillinger, T. Weiland, Darmstadt University of Technology, Germany
B. Langenbeck, GSI, Germany

Abstract

The ion optical characteristics of the injection into the ESR are calculated up to second order. The three dimensional model of an ESR dipole magnet forms the basis of our computations. Special efforts have been spent on an accurate approximation of the lateral stray field over a distance of 2m, in which the ion beam enters the ESR dipole tangentially. The reference trajectory and the first and second order transformation coefficients are calculated solving the corresponding differential equations numerically. For this purpose we have developed a new ion optics section as part of the MAFIA postprocessing module P. The differential equations are set up and solved automatically using the simulated magnetic field distribution. The new implemented section is general and allows the easy calculation of beam trajectories and optical characteristics corresponding to arbitrary numerically calculated magnetic fields. As special feature also phase space monitors along a curved reference trajectory can be defined. We will give a short introduction into the method and discuss the results in case of the ESR injection.

1 INTRODUCTION

The location of the Experimental Storage Ring (ESR) [1] in the whole GSI accelerator complex requires an unusual beam guide for the injection. Between the inflector and the in-ring septum magnet the ion beam has to pass the lateral fringe field of a dipole magnet over a distance of two meters (figure 1). To get a better knowledge about the influence of this perturbation on the beam ellipse we have made a 3D simulation of one quarter of the whole dipole magnet. Further, we have used this simulation results as basis for numerical calculations of the curved injection line and the ion optical transfer map up to second order.

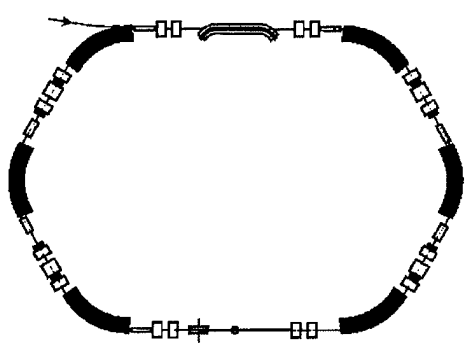

Figure 1: Layout of the ESR with injection line.

2 DIPOLE DIMENSIONS AND SIMULATION PARAMETERS

The bending system of the ESR consists of six 60° sector magnets with a maximum field strength of 1.6 T. In the following we choose a working point of 1 T. In this case the effective bending radius is 6.324 m in respect of an effective field boundary of 4 cm at the magnet ends [2].

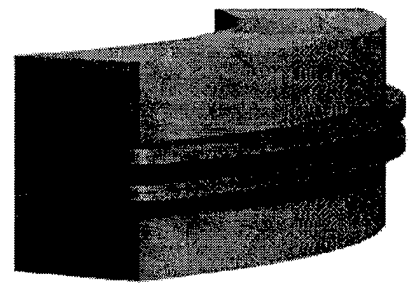

Figure 2: 3D view of an ESR Dipole magnet.

The magnet has a non-othogonal exit face (exit angle 7.5°), which leads to difficulties in view of the mesh generation. Therefore we use a coupled coordinate system [3] as indicated in figure 3. Further, we take advantage of the two symmetry planes and decided to shorten the simulated sector up to 17° in order to reduce the number of mesh points.

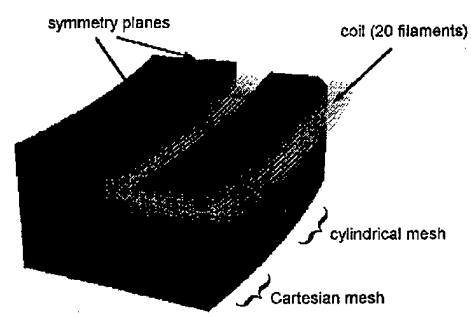

Figure 3: Approximated part of the dipole which is used for the field calculation.

3 OPTICS OF THE INJECTION

Being interested in the optics of the injection, we introduce a local coordinate system x, y, z along the injection line as shown in figure 4. The fixed global coordinate system ξ, ψ, ζ is placed at the intersection point of central tra-

0-7803-4376-X/98/$10.00 © 1998 IEEE

jectory and exit face, ζ points in normal direction of the dipole's mid plane.

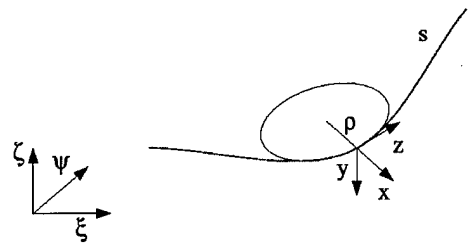

Figure 4: Global and local coordinate system.

In matrix notation the whole injection line can be subdivided in three parts: a drift space M_0 from the inflector magnet to the dipole, the stray field region of the dipole M_s and a drift space up to the septum magnet in the ring M_1. The combined map $\mathbf{x}^1 = M_1 M_s M_0 \mathbf{x}^0$ describes the optical transformation of an initial phase space vector $\mathbf{x}^0 = (x, x', y, y', l, \delta)^0$ located at the inflector magnet to a final vector $\mathbf{x}^1 = (x, x', y, y', l, \delta)^1$ located at the in-ring septum magnet.

Up to second order the combined map takes the expansion

$$x_i^1 = \sum_{j=1}^{6} (x_i^1 | x_j^0) x_j^0 + \sum_{j,k=1}^{6} (x_i^1 | x_j^0 x_k^0) x_j^0 x_k^0, i = 1, .., 6.$$

The first order coefficients $C_x = (x_1^1|x_1^0)$, $S_x = (x_1^1|x_2^0)$, $C_y = (x_3^1|x_3^0)$ and $S_y = (x_3^1|x_4^0)$, the so called principal trajectories, are solutions of the homogeneous differential equations

$$C_x''(s) + k_x(s) C_x(s) = 0, \quad C_y''(s) + k_y(s) C_y(s) = 0,$$
$$S_x''(s) + k_x(s) S_x(s) = 0, \quad S_y''(s) + k_y(s) S_y(s) = 0,$$

with boundary conditions $C(0) = 1, C'(0) = 0, S(0) = 0, S'(0) = 1$. The prime denotes derivation with respect to the path length s. The stiffness parameter functions $k_x(s)$ and $k_y(s)$ depend on the field expansion coefficients

$$h(s) = \frac{q}{p_0} B_y(s) \Big|_{x=y=0}$$
$$k(s) = \frac{q}{p_0} \frac{\partial B_y(s)}{\partial x} \Big|_{x=y=0}$$

and are given by $k_y(s) = -k(s)$ and $k_x(s) = h^2(s) + k(s)$.

The first order dispersion $D_x = (x_1^1|x_6^0)$ and the second order coefficients $q_{ijk} = (x_i^1|x_j^0 x_k^0)$ are solutions of the inhomogeneous differential equations

$$q_{ijk}''(s) + k_x(s) q_{ijk}(s) = f_{ijk}(s),$$

resp.

$$q_{ijk}''(s) + k_y(s) q_{ijk}(s) = f_{ijk}(s)$$

with boundary conditions $q_{ijk}(0) = 0$, $q_{ijk}'(0) = 0$ and varying driving functions $f_{ijk}(s)$. The driving functions depend on second order field derivatives in normal (x) and tangential (z) direction and are listed in [4, 5].

In our case the stiffness parameters and driving functions are non-constant and not analytically given. Therefore we will simultaneously integrate the reference trajectory, evaluate the stiffness parameters and driving functions and solve the introduced differential equations on the basis of the simulated field data. To assure the accuracy of the solution, we tested the procedure on an idealized dipole magnet with parallel ends[6].

4 SIMULATION RESULTS

4.1 Field Calculations

We have performed a nonlinear calculation of an ESR dipole magnet with the parameters introduced in section 2 using the static solver S of the MAFIA package[7], which has been modified to solve the field equations in a coupled coordinate system. Figure 5 shows the simulation results for the Field in the mid plane at an azimuthal cut compared with measurements. The two curves fit very well, the deviations are lower than 0.1%, which means that the simulated lateral fringe field can be used for further ion optical treatments. An additional reduction of the real shim height (4mm) will lead to a better correspondence of the simulation data and the measurments near the shims.

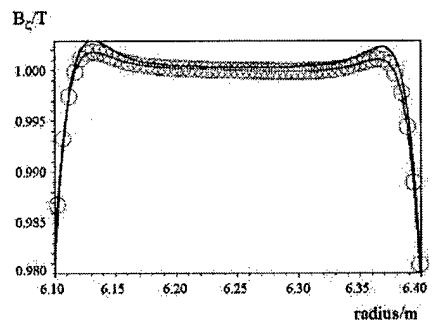

Figure 5: Simulated and measured magnetic flux density at the magnetic mid plane.

4.2 Optics of the Injection Line

We have integrated the reference trajectory for a particle rigidity of 6.234 Tm using the calculated field data (figure 6). The non-constant field expansion coefficients $h(s)$ and $k(s)$ are shown in figures 7 and 8. Further, the integrated principal trajectories are shown in figure 9 and the first order dispersion in 10. Finally table 5 summarizes the first order results for the combined transformation map $M_1 M_s M_0$ including the drift spaces M_0 and M_1 as introduced in section 3. The entire path length calculated is 4.13 m.

5 CONCLUSION

The presented calculations give new insight into the real characteristics of the ESR injection line and serve for the

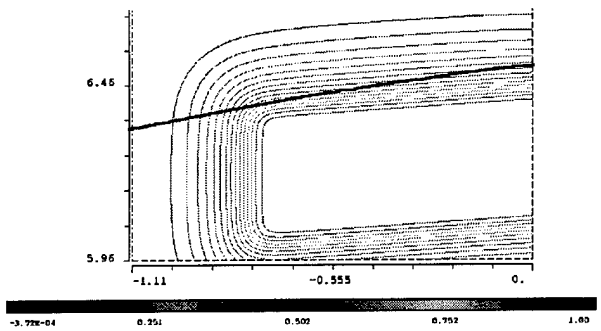

Figure 6: Magnetic flux density at the mid plane with calculated reference trajectory.

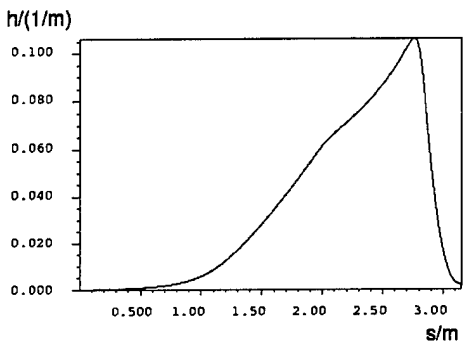

Figure 7: Parameter $h(s)$ calculated for the ESR injection line.

definition of corrective measures. The calculated coefficients will be used in TRANSPORT and MAD simulations of the ESR.

6 REFERENCES

[1] B. Franzke, et al., Commissioning of the Heavy Ion Storage Ring ESR, Proc. 2nd Europ. Part. Accel. Conf., Nice 1990, Vol.1, pp.46–48.

[2] M. Chen, et al., Field Measurements of the ESR Magnets, Proc. 2nd Europ. Part. Accel. Conf., Nice 1990, Vol.2, pp.1142–1144.

[3] B. Schillinger, T. Weiland, Beamtracking in Cylindrical and Cartesian Coordinates, CAP'96, to be published.

[4] K. L. Brown, A First and Second Order Matrix Theory for the Design of Beam Transport Systems, SLAC 75, 1967.

[5] K. G. Steffen, High Energy Beam Optics, Int. Publ., 1965.

[6] B. Schillinger, T. Weiland, B. Langenbeck, Ion Injection through fringe fields of dipole magnets, Proc. 5th Europ. Part. Accel. Conf.,Sitges(Barcelona) 1996, Vol.2, pp.1377–1379.

[7] MAFIA Manual Version 4.00, CST GmbH, Lauteschlägerstr. 38, D–64289 Darmstadt, January 1997.

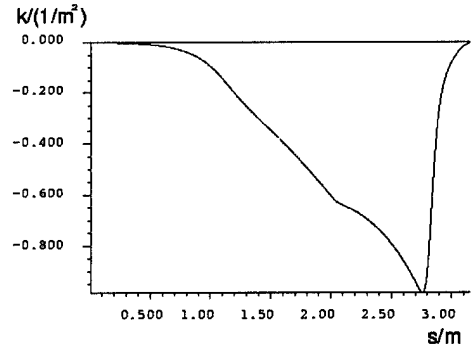

Figure 8: Parameter $k(s)$ calculated for the ESR injection line.

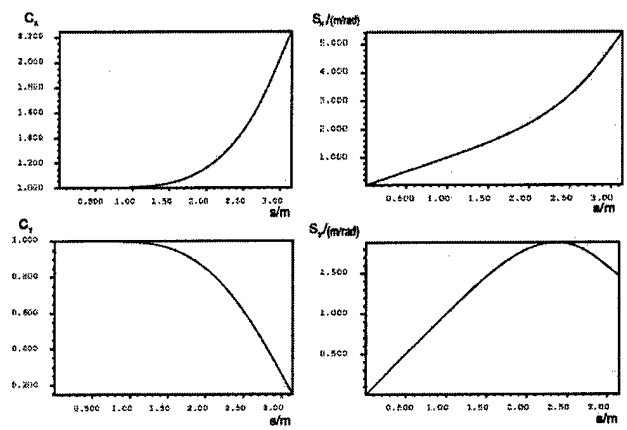

Figure 9: Principal trajectories of the ESR injection line.

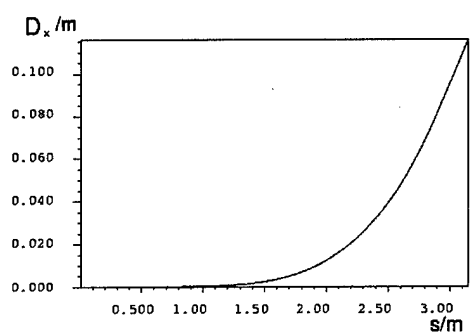

Figure 10: First order dispersion of the ESR injection line.

$(\mathbf{x}^1\|\mathbf{x}^0)$	x	x'	y	y'	l	δ
x	3.62	9.17	0	0	0	0.25
x'	1.40	3.82	0	0	0	0.14
y	0	0	-0.60	0.68	0	0
y'	0	0	-0.76	-0.80	0	0
l	0.15	0.32	0	0	1	3.6e-3
δ	0	0	0	0	0	1

Table 1: Calculated first order coefficients of the combined transformation map.

DEVELOPMENT OF THE ACCSIM TRACKING AND SIMULATION CODE

F.W. Jones, TRIUMF, 4004 Wesbrook Mall, Vancouver, B.C., Canada V6T 2A3

Abstract

Accsim is a synchrotron/storage-ring tracking and simulation program that was originally written to simulate charge-exchange injection and accumulation of an intense proton beam in a KAON factory accumulator ring. It has subsequently been developed and used for other injection studies and for applications such as the optimization of collimation systems. The code performs basic six-dimensional tracking of an ensemble of particles in a magnet lattice and incorporates models for various processes such as multiturn injection, phase-space painting, RF capture, space-charge effects, interactions with stripping foils and collimators, and tabulation of particle losses and beam form factors. After a brief review of Accsim's architecture and basic design, this paper gives an update on the current status of the code and describes the more recent additions that have been made.

1 OVERVIEW

Fast tracking For Accsim's role in finding optimal injection and accumulation schemes, perhaps with many design iterations for the ring lattice and injection system, an efficient and fully symplectic particle tracking method is of paramount concern. The initial requirement was for runs with up to 10^4 particles and $2 \cdot 10^4$ turns, and subsequently the particle capacity was raised to 10^5 in order to get sufficiently good statistics in the early stages of accumulation.

The basic transport mechanism uses first-order transfer matrices, possibly spanning many magnetic elements, punctuated by kicks representing thin lenses (up to octupole order), rf cavities, space charge effects, injection foil scattering, etc. The working coordinates $(x, x', y, y', \phi, \Delta E)$ are used, where ϕ is rf phase and ΔE is the energy difference from the synchronous energy. To achieve correct longitudinal tracking, the rf phase transport incorporates the path-length terms from the matrix formalism plus an additional term to account for particle velocity.

Utilization of DIMAD At the inception it was recognized that development time could be saved by using the lattice-design program DIMAD as a pre-processor for the ring to be studied. Usually a DIMAD-format input file for the lattice would already be available (or could be converted from a MAD file), and it was a matter of running DIMAD and then cutting the relevant matrix coefficients and optical parameters from the DIMAD output and pasting them into the Accsim input file. Later, this procedure was automated via a routine in Accsim that scans the DIMAD output and extracts all the necessary quantities. Although Accsim has grown in generality and in features, this dependence on DIMAD has been retained because it brings many benefits. It allows Accsim to concentrate on tracking and simulation and omit the considerable machinery needed for processing lattice definition files, calculating matrix terms and optical functions, fitting of element strengths, etc.

Injection foil Multiturn charge-exchange injection may lead to emittance growth due to multiple scattering during repeated traversals of the injection foil. The program provides a number of features for studying injection scenarios that reduce foil traversals by using "corner" or "postage-stamp" foils, collapsing orbit bumps, linear coupling etc. During tracking, each particle traversing the foil undergos an energy loss sampled from a pre-calculated Landau distribution. Coulomb scattering in the foil can be simulated using an iterated single-scatter model or a faster one-shot method using a plural scattering distribution. To simulate thick foils or internal targets a Molière scattering routine is also available.

Space charge Longitudinal space charge effects are accounted for in the usual way by binning particles to obtain the line density, optionally applying smoothing, deriving the space-charge potential per turn, and applying the appropriate energy kick, pro-rated by the fraction of a turn travelled, to each particle. This procedure is performed whenever the program encounters the `LSC` pseudo-element. These elements are usually placed at the rf locations and can be added at intermediate locations as well if accuracy requires. A transverse space charge package was developed for Accsim by H. Schönauer. It bins particles in "amplitude space" (ε_x vs ε_y) and for each bin derives a rectangular charge density distribution based on the x–y Lissajous motion of particles averaged over all relative betatron phases. The contributions to the space-charge potential are summed and least-squares fitting of a multipole expansion yields the coefficients needed to calculate the tune shifts for individual particles. These tune shifts are (optionally) applied to each particle by rotating it in phase space. By default this is done once per turn, but recently a `TSC` pseudo-element has been added to enable the calculation to be done once per lattice period.

Painting A major aspect of Accsim injection studies has been phase-space painting, whereby the desired final beam distributions are arrived at via mechanisms like collapsing orbit bumps, injection steering, injection energy ramping, or even guide-field ramping. Program options are available for simulating any or all of these, using time-vs-value arrays for the parameters to be varied. Realistic orbit bumps can be set up using programmed thin dipole elements.

Built-ins Accsim provides built-in graphics, with X11 and PostScript support, for producing rapid scatterplots of phase space and real space. There are also commands for calculating RMS, 95% and 99% emittances, producing loss-mode summaries, estimating foil heating, tabulating

0-7803-4376-X/98/$10.00 © 1998 IEEE

losses on apertures, and determining the extent and population of beam halos. For external graphics and analysis, Accsim has a plethora of diagnostic and logging options that allow virtually all of its data to be output at various intervals and ring locations as dictated by the user. On the large-scale output streams there is a binary-format option to reduce the data volume and processing time.

Development The above describes the basic machinery of Accsim. In the process of being used for many applications with differing requirements, the code has undergone a long series of ad-hoc modifications to implement an ever-growing list of features, a number of which will be reviewed in the following sections.

2 COLLIMATORS

The issue of controlling particle losses during accumulation of an intense beam prompted the development of Accsim's `COLLIMATOR` elements, which simulate the interaction of protons with blocks of material of specified length, position and orientation, and can be placed in appropriate drift spaces in the ring. The collimator routine performs the necessary ray-tracing in the drift region to determine hits on the absorber blocks and does detailed tracing of proton trajectories in the blocks, with treatments of multiple scattering, energy loss, and nuclear interactions.

Tracking in the block material uses a fixed, user-settable step size, over which the energy loss (from a Landau or Gaussian distribution) and multiple scattering angle (from a Molière distribution) are calculated. For each material, a net mean free path for nuclear interactions is derived from the elastic and inelastic cross sections, and sampled interaction lengths are generated from this. Elastic scattering events result in an angular deflection sampled from a forward diffraction peak. Inelastic interactions are considered simply to be "absorption" events: the proton is removed from tracking and no attempt is made to account for secondary particles produced.

The fixed tracking step size entails a small "quantization error" in the geometry, but it has significant advantages: (1) ray-tracing is much faster because exact boundary-crossing points do not have to be calculated, (2) numerical problems at boundaries are avoided (3) it guarantees that energy loss and multiple scattering calculations always have valid step sizes. Efficiency is also gained by using small-angle approximations wherever appropriate.

In general, the intention is not to provide an exhaustive simulation (better left to codes like GEANT) but rather to provide timely estimates of collimator performance and of downstream losses due to outscattering (particles hitting shallow on an absorber block and scattering back into the vacuum chamber).

Later additions to the collimator element included: circular-contoured entrance faces (helpful in reducing outscattering), arbitrary rotation angles of the blocks around the longitudinal axis, and tracking through a uniform magnetic field in the material (a possible technique for reducing outscattering by bending particles toward the interior of the absorber block).

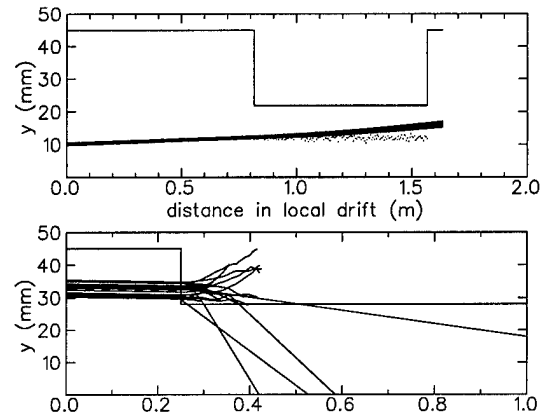

Figure 1: Proton trajectories from Accsim tracking in septum/absorber collimation system

3 MINI-WIRE SEPTUM

For efficient loss management in intense-beam scenarios, H. Schönauer[2] has proposed the use of a septum with very fine wires (~0.05mm) to deflect candidate particles to higher emittances (possibly with repeated traversals of the septum) so that they can be efficiently collected by a downstream absorber. We implemented a `SEPTUM` element in Accsim which tracks particles through the septum field, taking into account the curvature of the fine wires due to the field, the resultant wire position errors, and multiple scattering due to collisions with the wires. Accsim runs showed that such a septum/collector system could provide cleaner loss collection than a two-stage massive collimator system.

4 ACCELERATION

The treatment of acceleration in the program is at present intended primarily to model a synchrotron's injection and early acceleration phase, rather than to accurately follow a particle ensemble through a whole acceleration cycle. Since the transport matrix formalism represents a steady-state solution and does not admit of time-variation of fields, acceleration is simulated by updating the synchronous energy and synchronous phase on a turn-by-turn basis. To maintain synchronism and avoid artificial growth, the rf phase coordinate of each particle must also be changed by an amount equal to the increment in synchronous phase.

There are various options for specifying the guide field and rf programs including, most recently, a "machine program file" which consists of a free-format table with arbitrarily-spaced time values and parameter values chosen from the list: $(B, dB/dt)$, V_{rf}, ϕ_s, K_d, K_q. (The last two parameters are field strengths for optional thin dipoles and quads that can be used to produce programmed orbit bumps and programmed tunes.) By means of a variable "start time" input parameter, both the falling and rising portions of the magnet cycle can be reproduced, allowing injection to start during the falling portion if desired.

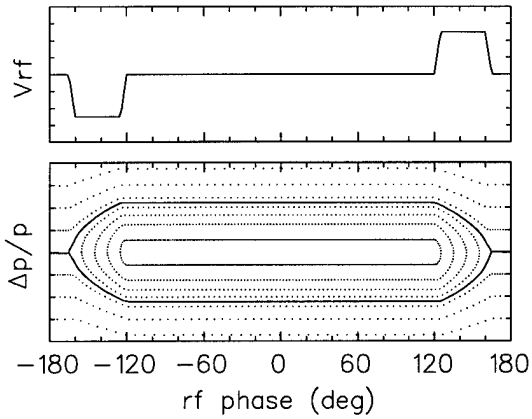

Figure 2: Barrier bucket rf waveform and longitudinal phase space trajectories

Accsim can also simulate guide-field ramping with the rf off, in which case energy and positional kicks are applied to the particles to reflect the changes in the reference energy and off-momentum orbits. This can be used to simulate H^- injection scenarios where this ramping is exploited for phase-space painting and also for carrying the injected particles on spiral trajectories away from the stripping foil.

5 BARRIER BUCKET

The use of a pulsed rf waveform, with short pulses at or near $\pm\pi$, defines a so-called barrier bucket, where particles in the bucket follow coasting trajectories except near the ends where they are bent around and reverse their direction of travel in longitudinal phase space. The resulting bunches have a line density profile that is mostly flat, and hence the longitudinal space charge forces, and the modulation of transverse space charge forces by the local charge density, are very small except near the ends of the bunch.

Features were added to Accsim in order to generate barrier-bucket rf waveforms using either trapezoidal or sinusoidal pulses, with parameters for pulse positioning, height and width, and rise and fall time.

6 MOMENTUM ANALYSIS

In the performance of phase-space rotations (for chromatic and space-charge tune shifts) and emittance calculations (for printing or transverse space-charge binning), Accsim must determine the phase-space ellipse for each particle. Formerly, this was done using the optical functions α, β, η read from DIMAD, which are valid for the linear lattice but may be inadequate if thin lenses have been added in Accsim and there is significant momentum spread. In particular, an accurate closed orbit is needed to avoid accumulation of errors during phase-space rotations.

Routines were written to perform a momentum analysis based on a nominal momentum deviation δ input by the user. A test particle is tracked through the Accsim lattice (DIMAD matrices + thin lenses) for five turns, and from the results a system of linear equations are derived that can

$\Delta p/p$	x_{co}	x'_{co}	α_x	β_x	Q_x
-0.0100	0.680	-0.144	2.191	10.452	6.749
-0.0050	0.320	-0.068	2.143	10.229	6.785
0.0000	0.000	0.000	2.103	10.043	6.821
0.0050	-0.275	0.058	2.069	9.884	6.857
0.0100	-0.502	0.106	2.041	9.758	6.893
	Error in quadratic				
-0.0050	0.002	0.000	-0.001	-0.003	0.000
0.0050	-0.002	0.000	0.000	-0.001	0.000

Table 1: Example of Accsim momentum analysis for a synchrotron lattice with added thin-lens sextupoles (co = closed orbit; y results omitted for brevity)

be solved for the closed orbit, ellipse parameters, and tunes. This is done for momenta $-\delta$, 0, $+\delta$ and for each parameter a quadratic is run through the three data points, thus giving a parameterization of the optics as a function of particle momentum. To check the goodness of fit, additional particles are run at $-\delta/2$, $+\delta/2$ and the errors with respect to the quadratics are printed.

7 MISCELLANY

There have been quite a number of other additions to the code that can only be summarized here: input linac distribution with microbunches; parameterized tails on injected distributions; rf harmonics; zoom window and coordinate readout for scatterplots; generalization from protons to arbitrary ion species (except in interactions with matter); `PICKUP` and `DAMPER` elements to model transverse damping; `VCHAMBER` element to simulate interactions with the vacuum chamber wall. Accsim has been ported to all the major UNIX platforms, including (soon) Intel/LINUX. Those interested in obtaining the code should connect to http://www.triumf.ca/compserv/accsim.html.

8 FUTURE

As part of a TRIUMF-CERN agreement, Accsim will continue to be developed in support of injection and collimation studies for LHC-era beams in the CERN PS Booster. The program is also being applied to injection simulations in various other design studies such as HIDIF, JHP, and the NSNS[3]. To support these applications, improvements in generality, features, and particularly in space-charge treatments, are being pursued.

9 REFERENCES

[1] F.W. Jones, G.H. Mackenzie, and H. Schönauer, "ACCSIM – A Program to Simulate the Accumulation of Intense Proton Beams," *14th Int. Conf. on H. E. Accelerators*, Tsukuba, Japan, 1989, in *Particle Accelerators* **31**:199 (1990).

[2] H.O. Schönauer, "Loss concentration and evacuation by mini-wire septa from circular machines for spallation neutron sources," *Particle Accelerator Conference*, Dallas (1995).

[3] A. Luccio, D. Maletic, F.W. Jones, "Proton Injection and RF Capture in the National Spallation Neutron Source," *these proceedings*.

A GRAPHICAL USER INTERFACE FOR RELAX3D

F.W. Jones, TRIUMF, 4004 Wesbrook Mall, Vancouver, B.C., Canada V6T 2A3

Abstract

The Laplace/Poisson solver Relax3d has been used extensively in cyclotron central region design and other accelerator and beam physics applications. It is typically run in an interactive mode where the user types in commands and parameters to initiate and control the solution process and to view or output the results. This paper describes a graphical user interface (GUI) that eliminates most of this typing and makes for more efficient user interaction. The use of a unique package called Expect (an extension to Tcl/Tk) allows the interface to be implemented as an independent front-end process that communicates with the running Relax3d program, thus requiring minimal modifications to Relax3d itself. Since Expect can control multiple processes, and since Relax3d results are often sent to some subsequent program for visualization, particle tracking, etc., there are interesting opportunities to integrate these post-processing tasks into the same GUI.

1 INTRODUCTION

In the field of Accelerator Physics there is a large legacy of Fortran codes, many still widely used, that were developed in the text-based environment of previous computing platforms. Many of these codes could benefit from the addition of graphical user interfaces. For batch programs that have many input parameters, or for interactive programs that have many different commands and command options, these interfaces can be tremendous labour-saving devices. Moreover, a well-designed GUI represents a program's parameters and functions and in a direct visual way that allows the user to largely dispense with reading voluminous documentation and memorizing mnemonics and keywords.

Relax3d[1], as one such Fortran code, is an ideal candidate for a point-and-click interface. It has a repertoire of around 30 interactive commands, many with parameters (up to 6). Its high level of interactivity has made Relax3d a popular and relatively easy-to-use program, but the process of working through the entire design, set-up, and solution process for a given problem, with initial trials, production runs, and checking and visualization of results, can involve a lot of typing and a certain sense of tedium.

2 INTERFACE OPTIONS

The X-based OSF/Motif toolkit, available on many computing platforms, was considered as a means for implementing a GUI. This raised some general concerns: (1) Motif and other toolkits impose an asynchronous event-driven protocol: applications must have an event loop as their core structure and must respond to any input event (e.g. a mouse click) that can occur. This represents a "clash of architectures" with many Fortran programs, which expect particular items of input at particular times and may be unreceptive to input at other times. Extensive modifications may be required to implement the GUI. (2) The interface code must, or should, be written in C or C++ (for various good reasons, GUI programming is rarely done in Fortran). This escalates the application to a mixed-language environment, where argument-passing and name-space protocols have to be followed carefully and are not always portable between platforms.

These issues can be dealt with, but the fatal problem for Relax3d is the need for the user to rebuild the Relax3d executable on-the-fly, to incorporate the user-written BND subroutine that defines the boundary conditions for a given problem. It would be unreasonable to expect that the Motif library, or some other toolkit library, would be available on the platform where Relax3d is being used. Moreover, linking in such a large and complex library could slow down the problem-solving process which often involves a number of trials with different BND routines.

A possible solution to this is to implement the Motif GUI as a separate program written in C, which would run as a distinct process (front-end) and would communicate with Relax3d (back-end) via UNIX pipes. This approach also avoids the mixed-language concerns and isolates the event-handling architecture in the front-end.

3 PROTOTYPES

A prototype of this loosely-coupled type of interface was written, with the help of the Motif GUI construction tool XDesigner, and tested on various UNIX platforms. A crucial requirement for this system was the need to interrupt long-running Relax3d computations, in order for the front-end to gain control and possibly make changes or corrections. Relax3d itself already has the mechanism for this, a handler for the INTERRUPT signal, usually sent by pressing CTRL-C on the keyboard.

It was no problem to have the front-end send the same interrupt signal, but but during testing it was found that under certain conditions the signal would consistently fail to get delivered to the Relax3d process, rendering it uninterruptable and leaving the user to either wait or kill the process and start again.

To try to isolate this fault, and also to investigate alternative toolkits, another interface with almost identical features was written using the popular Tcl/Tk scripting/GUI language. This interface was easily and rapidly prototyped, even without the help of an XDesigner-style GUI builder, because of Tcl's simple syntax and its interpretive shell which allows the Tk widgets to be deployed and configured

0-7803-4376-X/98/$10.00 © 1998 IEEE

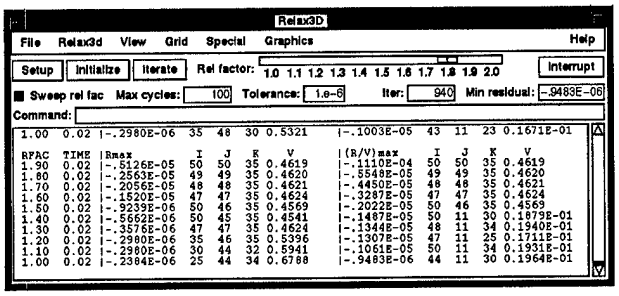

Figure 1: Main window

on-the-fly. This prototype worked well but did not solve the signal delivery problem, which appeared not to be an interface problem but rather a consequence of Relax3d reading input from a pipe rather than a terminal.

4 EXPECT

During the prototype development there arose another avenue of pursuit: a Tcl/Tk extension package called Expect[2]. This package was originally developed as a tool for communicating with pre-existing interactive programs, such as UNIX system utilities, in order to automate frequently-performed tasks.

As an extension, Expect provides all of the Tcl/Tk functionality together with a set of added commands that provide a flexible and programmable facility for launching and communicating with external programs. With the Tk widgets ready to hand, it proved to be an excellent environment for constructing a GUI for Relax3d. Best of all, the initial tests showed that Expect solved the interrupt signal problem. Expect does not use pipes, rather it creates UNIX *pty* (pseudo-terminal) devices to communicate with spawned processes, which thus behave just as if they are reading from and writing to a real terminal.

The other capabilities provided by Expect were the icing on the cake. Notable among them are: (1) the ability to spawn and communicate with multiple independent processes, (2) a programmable event-loop type of input processing to pattern-match against the output from spawned processes and take appropriate actions depending on what is received, (3) a timeout mechanism to keep the front-end from hanging while waiting for a spawned process to produce output, and (4) the ability to connect the user's terminal window directly to a spawned process. The importance of this last feature will be enlarged upon later.

Although most of the example Expect applications in the literature are fairly small and task-specific, further work on the Relax3d prototype showed that the system could be scaled up very nicely into a complete, multi-window interface.

5 INTERFACE OVERVIEW

The basic program functions, each corresponding to a Relax3d command, are invoked from the Main Window (see Figure 1). For efficiency, simple pushbuttons are provided for the most heavily-used commands: `Setup` to specify the problem type and grid parameters, `Initialize` to set the grid to initial values, `Iterate` to start the iteration process, and `Interrupt` to prematurely stop it in the manner discussed above. The relaxation factor, often an item to be experimented with, is set by a slider, and editable text input fields `Max cycles` and `Tolerance` are used to set stopping criteria based on number of iterations or maximum normalized residual. Using an Expect directive, the line-by-line output from Relax3d's iteration loop is captured and displayed in a scrolling text area, providing a complete record of the run. In addition, this output is scanned to extract the residual and display a running minimum in the `Min residual` text field.

The remaining program functions and settings are accessed via popdown menus on the menu bar. Some of these functions could be implemented directly in a few lines of Tcl/Expect code, whereas others were written as separate Tcl procedures that bring up independent dialog windows. These procedures all follow a common pattern: (1) If the window has not been created then create it, otherwise pop it up if it is iconized or off-screen. (2) When the user clicks one of the "action" buttons in the window, build the appropriate command string and send it to Relax3d's input stream. (3) Pattern-match the output from Relax3d and take appropriate actions such as sending more input or displaying error messages.

The following example, edited for brevity, shows part of this sequence for the Contour Plot procedure (Relax3d's `PLOT` command). The complete plot window is shown in Figure 2.

```
proc plot {} {
    ...
   # If plot window is already made, map it and return
   if [winfo exists .p] {
      wm deiconify .p; raise .p
      return
   }
   # Construct the plot window
   toplevel .p
   wm title .p "Contour Plot"
      ...
   checkbutton .p.yes -text "Label contours" \
      -variable clabel
   # Text fields for label spacing and plot magn:
   entry .p.spacing -textvariable spacing -width 5
   entry .p.mag -textvariable mag -width 4
      ...
   # Button to send Plot command and options to Relax3d:
   button .p.action.plot -text PLOT -command {
      set dolabel ""
      if {$clabel == 0} { set dolabel "-" }
      exp_send "PLOT $dolabel$spacing $mag \
               $xorig $yorig $ptype\r"
      # Pattern-match Relax3d o/p & diagnose errors:
      expect {
         "Option number" { }
         "*Relax3D > " { errmsg $expect_out(buffer)
                         return }
         ...
```

Tcl's string-oriented syntax makes it easy to assemble the appropriate command, with parameters taken directly from variables tied to the Tk widgets, and ship it to Relax3d with the `exp_send` directive. Then the `expect` loop checks for possible outcomes: a prompt for more input indicates that the command was accepted, whereas some text followed by the `Relax3d>` prompt indicates an in-

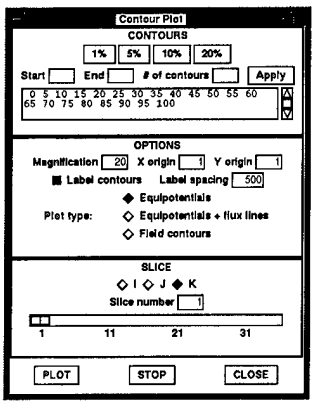

Figure 2: Contour plot window

valid command parameter and the captured error text is displayed in a message box.

Some other interesting features of this interface are: (1) A `Rebuild` button that shuts down the current Relax3d executable, builds a new one from the selected BND routine, starts it up, and connects the GUI to it. (2) An option for redrawing a contour plot on-the-fly as iterations proceed. (3) An `Interact` button that *connects the user's terminal window to the spawned Relax3d process*, allowing the user to assume "manual control" of Relax3d in case of any doubt as to what is going on. This utilizes Expect's `interact` command, a very powerful feature indeed for both users and developers, the more so because while the terminal is connected to Relax3d, the GUI remains connected and fully operational as well (the best of both worlds)!

6 BACK-END MODIFICATIONS

Relax3d itself has required some modifications to support a GUI front-end, but they are relatively few and straight forward. Some new "private" commands were added to allow the interface to inquire on the state of the program and the values of various set-up parameters after a problem set-up has been performed. Some procedures were modified to produce more diagnostic output that allows the interface to monitor their progress, and some "hand-shaking" was implemented where large amounts of data had to be transferred between the GUI and the program. None of the modifications interfere with the use of Relax3d in the normal terminal mode without the front-end.

7 VISUALIZATION

In the Expect environment, it was a natural progression from interfacing to the built-in graphics to interfacing to more powerful external facilities for producing graphics. Programs like GnuPlot, Mathematica, and MATLAB were investigated for this purpose and MATLAB was chosen for its excellent publication-quality 2d and 3d graphics facilities and its ease of use. It proved to be almost trivial to write the additional Tcl/Expect code to launch MATLAB from the Relax3d interface, modify Relax3d to write out slice data in a form digestible by MATLAB, and then build a prototype "MATLAB Plot" dialog window offering various 2d (contour, pseudocolour) and 3d (waterfall, mesh, surface, slice) plot types, with menus and sliders for colourmaps, viewing angles, etc. Once again, Expect's `interact` command is invaluable since it allows the user access to all of MATLAB's commands without disabling the GUI operation.

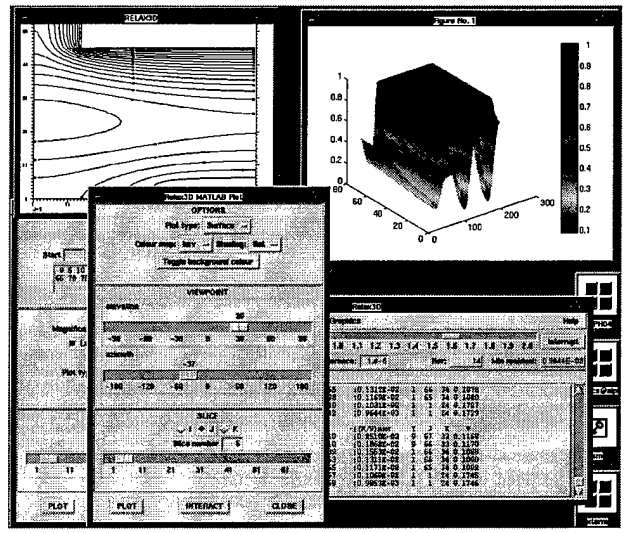

Figure 3: Relax3d session with MATLAB interface

8 CONCLUSION

The software technology used in the Relax3d GUI is sufficiently general and flexible to have a wide range of applicability to Accelerator Physics computing: lattice and beamline design codes, tracking and raytracing codes, and simulation codes are some obvious examples where efficient interactive run preparation and visualization facilities are desirable. In general, the Expect package can be thought of as a way to interlink computer programs to create problem-solving environments. Together with Tcl/Tk, it can provide a lot of functionality for a relatively modest investment of programming time.

Further development of the Relax3d GUI will likely concentrate on electric field plotting methods, volumetric visualization, and the development of a spreadsheet-style viewing facility for navigating through the grid to check boundary and solution values. Those wishing to obtain Relax3d and/or the first released version of the GUI can connect their Web browsers to `http://www.triumf.ca/-compserv/relax3d.html` for up-to-date information.

9 REFERENCES

[1] H. Houtman, F.W. Jones, and C.J. Kost, "Solution of Laplace and Poisson Equations by RELAX3D," *Computers in Physics*, July/August 1994.

[2] D. Libes, *Exploring Expect*, O'Reilly & Associates, 1995.

HESHBEAM — A PROGRAM WITH A GRAPHICAL USER INTERFACE FOR CALCULATION OF THE LUMINOSITY SPECTRUM AND THE DIFFERENTIAL LUMINOSITY

H. Heydari, H. Schulte*, Institut f. Theoretische E-technik, TU-Berlin, Germany

Abstract

The paper presents a program with a Graphical User Interface for solving the luminosity spectrum and the differential luminosity. Instead of using the particles-in-cells method, the code is based on analytical solutions and experimental results. The user creates with the GUI an input data file, which contains only a few numbers of parameters, such as the beam size at the IP, the number of particles and the center-of-mass energy. The beam, with a round or elliptical cross-section, is described by a uniform or a gaussian density function in transverse and longitudinal direction. In all cases the program makes use of the analytical solutions for the beam-beam energy loss, the deflection angle, the luminosity spectrum and the differential luminosity. The results for several Linear Collider designs and different disruption numbers are obtained and compared with other numerical solutions. The numerical examples demonstrate clearly the accuracy of this method.

1 INTRODUCTION

The luminosity $\mathcal{L}$ in Linear Colliders during the interaction of e^+e^- beams is not constant. At the interaction point (IP) $\mathcal{L}$ is dependent on the time and will be different from $\mathcal{L}_0$. There are two different kinds to analyse the change of luminosity:

1.) The first part we consider a spectral representation of the luminosity which is investigated in dependence of the center-of-mass-energy for the colliding electron and positron beams. On the basis of the beamstrahlung effect the energy loss influences the bending of the trajectories. The whole center-of-mass-energy decreases during the collision and define an energy range of an undisturbed E_{cm0} to a center-of-mass-energy with maximum radiation loss $E_{cm} = E_{cm0} - \delta_{max}$. In this range we assign every energy value to a luminosity number, this relation is called the luminosity spectrum $\mathcal{L}$. The spectral representation of the luminosity $\mathcal{L}$ is a function of the center-of-mass energy E_{cms}. We found, that the center-of-mass energy E_{cms} decreases during the penetration process ($E_{cms} \leq E_{0cms}$). This entails a spread of the luminosity spectra to smaller center-of-mass energies.

2.) Instead of the spectrum the luminosity is analysed in the time domain, usually with the derivation $\frac{d\mathcal{L}}{dt} = f(t)$. In the calculation we distinguish between two regimes, the weak-focusing regime corresponding to the disruption range $D =]0,1]$ and the transition region $D =]1,10]$. The disruption factor D can be defined as

$$D = \frac{N\alpha_s L\hbar c}{2\sqrt{3}m\gamma_v{}^2\sigma_{r_0}{}^2} = \frac{N\sigma_z r_e}{\gamma_v\ \sigma_{r_0}{}^2}\ , \tag{1}$$

with the lorentzfactor

$$\gamma_v = \frac{1}{\sqrt{1-\frac{v^2}{c^2}}}\ . \tag{2}$$

For the transition region we derived the equation

$$\frac{d\mathcal{L}}{dt} = \mathcal{L}_0 \frac{c}{\sqrt{\pi}\sigma_z} \frac{e^{-\frac{c^2 t^2}{\sigma_z^2}}}{(t-t_f)^2 \frac{9}{16}\frac{c^2}{\sigma_z^2}\frac{D}{2} + \frac{16}{9}A^2\frac{2}{D}}\ . \tag{3}$$

σ_{r_0}	:	beam cross-section without beam-beam loss
σ_z	:	beam length
N	:	particles per bunch
m	:	electron mass
r_e	:	electron radius
A	=	σ_z/β^*
β^*	:	betatron function at the IP
t_f	:	focal time

Figure 1 shows $\frac{1}{\mathcal{L}_0}\frac{d\mathcal{L}}{dt}$ as a function of time for the disruption $D = 0.7$, the time t is in units of σ_z/c.

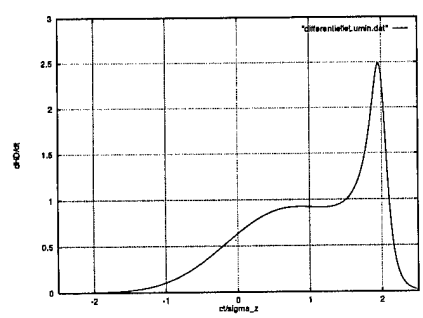

Figure 1: Differential luminosity $\frac{1}{\mathcal{L}_0}\frac{d\mathcal{L}}{dt} = f(ct/\sigma_z)$ for $D = 0.7$.

2 THE GRAPHICAL USER INTERFACE

The methods for solving the luminosity spectrum and the differential luminosity are being integrated into a single, flexible, easy-to-use software system, called HeShBeam. The interface is based on the tool Tcl/Tk due to J.Ousterhout [5] for developing graphical interfaces. It is independet of the numerical code. This software is intended to support all steps involved in the examination of

* schulte@tetibm1.ee.tu-berlin.de

0-7803-4376-X/98/$10.00 © 1998 IEEE

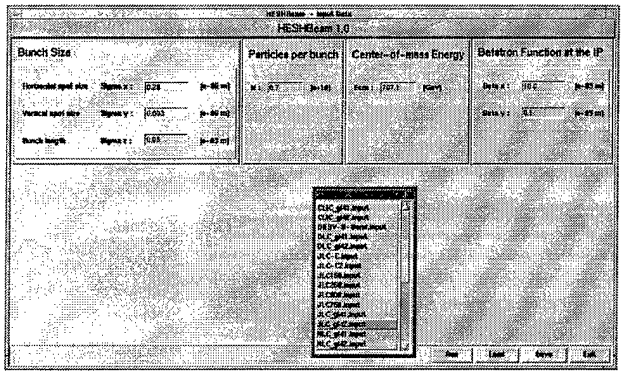

Figure 2: Input-window with file menue to open an existing file.

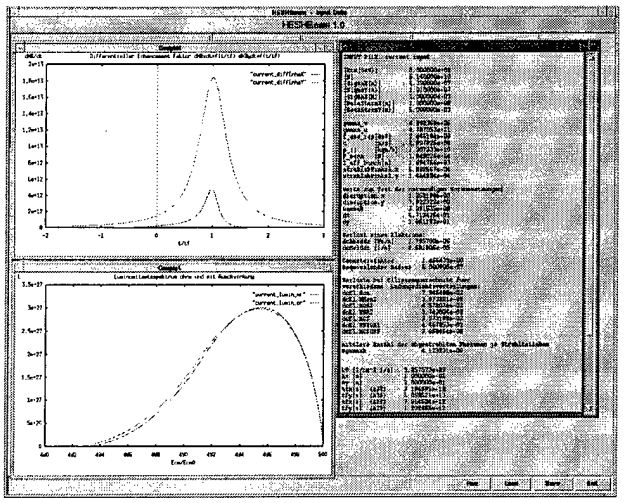

Figure 3: Result-windows: Table with average values, luminosity spectrum and the differential luminosity.

the luminosity change at the IP by state-of-the art numerics and visualization.
The first official version of HeShBeam has been released in January 1997, still isn't complete, the full version for Unix and Win95 will be available in June 1997.
HeShBeam is run in an interactive mode where the user types in commands and parameters to initiate and control the solution process and to view or output the results. First, the user creates with the input-window only a few numbers of parameters, such as the beam size at the IP $(\sigma_x, \sigma_y, \sigma_x)$, the number of particles per bunch N, the center-of-mass energy E and the betatron function at the IP (β_x^*, β_y^*). Each parameter-file can be saved and changed in the input-window (figure 2).

The menu in the input-window (figure 2) contains the commands `run`, `load`, `save` and `exit`. The command `run` starts the numerical calculation and the results appear in another window, as shown in the figure 3.

3 ALGORITHMIC KERNEL

Let us briefly discuss some of the essential steps of the algorithmic kernel of HeShBeam. The computer program is divided into subroutines carrying out the following task:

1. If the set of parameters satisfies

$$\frac{N\,\sigma_{x,y}}{\gamma_u\,\sigma_z} \gg 1 \quad , \tag{4}$$

then the beam is described by gaussian density functions

$$n_r(r,t) = \frac{1}{\sigma_r^2(t)} \exp\left(-\frac{r^2}{2\sigma_r^2(t)}\right) , \tag{5}$$

$$n_z(z_j) = \frac{1}{(2\pi)^{3/2}\sigma_{z_j}} \exp\left(-\frac{{z_j}^2}{2{\sigma_{z_j}}^2}\right) . \tag{6}$$

2. Which regime, the weak-focusing regime or the transition region ?

3. Determine the average relative beam-beam loss :

$$\delta_c = \frac{4}{3}\sqrt{\frac{3}{\pi}}\, 8 \ln\left(\frac{9}{8}\right) \frac{r_e^3 N^2 p_{\|} c}{B L m_0 c^2} \left(\frac{1+\beta}{2}\right)^2 \beta^{-3} , \tag{7}$$

with the total particle energy

$$E = mc^2 = \gamma_u m_0 c^2 \approx \frac{p_{\|}}{|\vec{u}|} c^2 , \tag{8}$$

and the effective length

$$L = 2\sqrt{3}\sigma_L = 2\sqrt{3}\,\gamma_v\,\sigma_z . \tag{9}$$

B : effective beam cross-section
β = v/c

4. The spectral representation of the luminosity $\mathcal{L}$ is a function of the center-of-mass energy E_{cms}. This entails a spread of the luminosity spectra to smaller center-of-mass energies. An expression of $x = \frac{E_{cms}}{E_{0cms}}$ which consists of two areas was determined.

$$\mathcal{L}(x) = \begin{cases} \mathcal{L}_1 & \text{for } 1-\delta_{max}/2 \le x < 1 \\ \mathcal{L}_2 & \text{for } 1-\delta_{max} \le x \le 1-\delta_{max}/2 \end{cases} \tag{10}$$

$$\mathcal{L}_1(x) = \mathcal{L}_0\big[(1-x) + (1-x)\cdot \cdot(\ln(\delta_{max}) - \ln(1-x) - 2\ln 2)\big] \tag{11}$$

$$\mathcal{L}_2(x) = \mathcal{L}_0\big[\delta_{max} - (1-x) - (1-x)\cdot \cdot(\ln(\delta_{max}) - \ln(1-x))\big], \tag{12}$$

where δ_{max} is the maximum energy loss of the beam-beam radiation.

5. Differential luminosity:
For the transition region we derived the equation

$$\frac{dH_D}{dt} = \frac{c}{\sqrt{\pi}\sigma_z} \frac{e^{-\frac{c^2 t^2}{\sigma_z^2}}}{(t-t_f)^2 \frac{9}{16}\frac{c^2}{\sigma_z^2}\frac{D}{2} + \frac{16}{9}A^2\frac{2}{D}} . \tag{13}$$

4 CONCLUSION

In this paper we have presented our program HeShBeam. The results obtained from ABEL, SCHROEDER, HeShBeam for TESLA1, SLC, NLC are in agreement, but there are some discrepancies with the results of RBEAM, TRACKIT, HeShBeam for TESLA1-3. More detailed analysis of our results is available [9][10], but due to space limitation it is not included here.

5 REFERENCES

[1] P. Chen. *Disruption effects from the interaction of round e^+e^- beams.* Phy.Rev.D,Volume 38,Number 3,S.987-1000. 1988

[2] H. Heydari. *Elektrodynamische Kontinuumstheorie der Strahl-Strahl Wechselwirkung.* Habilitation. TU-Berlin 1995

[3] H. Heydari, H. Schulte. *Calculation of the Luminosity Spectrum and the Differential Luminosity.* Fifth European Particle Accelerator Conference(EPAC).Barcelona 1996

[4] J.D. Jackson. *Klassische Elektrodynamik.* Walter de Gruyter. Berlin New York 1983

[5] J. K. Ousterhout. *Tcl und Tk: Entwicklung grafischer Benutzerschnittstellen fuer das X Window System.* Addision-Wesley (Deutschland) GmbH 1. Auflage, 1995

[6] S. Ritter. *The macroparticel code MACPAR to simulate the beam-beam interaction of high energy electron-positron-colliders* KEK Report 85-4. 1984

[7] D.V. Schroeder. *Beamstrahlung and QED Backgrounds in Future Linear Colliders.* PhD thesis. Stanford University 1990

[8] D. Schulte. *Untergrund durch inkohaerente Paarerzeugung in Linearbeschleunigern.* DESY Hamburg Maerz 1993

[9] H. Schulte. Studienarbeit, Inst.f.Theoretische E-Technik, TU-Berlin 1995

[10] H. Schulte. *Strahlung und Dynamik zweier sich durchdringender relativistischer Elektronenstrahlen.* Diplomarbeit, Inst.f.Theoretische E-Technik, TU-Berlin 1996

[11] J. Schwinger. Phy.Rev.75 S.1912-25. 1949

[12] K. Yokoya. KEK Report 85-9. 1985

TRACKING ROUTINES FOR ARBITRARY INSERTION DEVICES

Michael Scheer*, Godehard Wüstefeld, BESSY II Project
Rudower Chaussee 5, Geb. 15.1, 12489 Berlin, Germany

Abstract

A package of FORTRAN tracking routines for arbitrary insertion devices has been developed at BESSY and incorporated in the tracking code BETA [1]. A comparsion of computing time and tracking results for phase space and dynamical aperture calculations is presented.

1 INTRODUCTION

The 1.7 GeV synchroton light source BESSY II [1] (under construction) will be a low emittance machine with 16 straight sections. The variety of planned IDs requires flexible and adapted tracking tools to study their effects on the performance of the beam optics. Based on both analytical and numerical methods we have implemented several routines into the tracking code BETA [1].

2 METHODS AND IMPLEMANTION

The program BETA as well as our routines are written in FORTRAN. We have provided three user interface routines. Two routines pass control to the user at the beginning and the end of the main programm. The third one is the insertion device tracking routine IDTRCK_MODI which replaces the original routine IDTRCK of BETA. We also have provided a user common block to transfer variables within the user routines. When the program starts it calls our initialisation routine, which reads from a file the information needed for the insertion device tracking, i. e. the name, type and tracking mode, and the parameters of the ID.

For the time being we have two main sets of insertion device routines:

- symplectic mapping routines, based on Generating Functions
  - analytical Taylor expansion of Generating Function for devices with large bending radii
  - tracking with the linear transfer matrix of the ID
  - numerically fitted polynomial of the Generating Function for arbitray magnetic field configurations
- symplectic integration routine
  - analytically given arbitrary magnetic field configuration
  - arbitrary equially spaced 3D magnetic field map

For the user it is easy to implement his own routines into the interface routines. This allows a very flexible adaptation to special problems. The integration routines e.g. calls a routine which provides the magnetic field. This routine can be replaced by the user to provide his own insertion device description.

In the following subsections the routines of our package are described in more detail.

2.1 *Analytical Generating Function*

Several of our routines are based on Generating Functions. The advantage of this method is clearly that it is symplectic and it is well suited for mapping over final step length. That is different to integration methods which are valid only for infinitesimal step length.

The GF is approximately solved by a Taylor series expansion [2]. The Hamilton-Jacobi differential equation

$$\partial F/\partial z + H = 0,$$

with a Hamiltonian given by

$$H = (p_x - A_x/B\rho)/2 + (p_y - A_y/B\rho)^2/2 - A_z/B\rho$$

is solved for arbitrary magnetic fields described by the vector potential (A_x, A_y, A_z). The coefficients of the Taylor series are analytical expressions of the magnetic potential. This method shows good convergence for most of the ID fields. Step length over several periods of an ID can easily be done with good accuracy. Compared to the generating function $F = F(x, y, p_{xi}, p_{yi})$ given in [2] a better type is $F = F(x_i, y_i, p_x, p_y)$, where x_i, y_i are the initial positions and p_x, p_y are the final momenta of the particle. This has an advantage in solving the implicite coordinate relation for the GF and makes the tracking routines much faster.

For the formulation of the GF an analytical representaion of the ID field is required. This analytical formulas are manipulated with the algebraic computer code REDUCE [4]. Three FORTRAN modules are generated and inserted in a FORTRAN tracking code. Parameters like field strength, particle energy, period length and so on are kept as variables and will be defined in the FORTRAN code.

These modules have to be created for different ID field expressions. Presently we have a set of modules for planar IDs and two different helical IDs. One routine is for a Sasaki type of helical IDs [3]. The other module can be used for IDs described by a potential function of the type $V = a_1 \cos k_z z + a_n \cos nk_z z + b_1 \sin k_z z + b_n \sin nk_z z$. This is a very general field description [5]. The a, b coefficients are polynomials in x, y up to 7th order. In the longitudinal direction the sin- and cos-like terms can be

* scheer@bessy.de

[1] funded by the Bundesministerium für Bildung, Wissenschaft, Forschung und Technologie and by the Land Berlin

given by two Fourier components. The field potential is only approximately Maxwellian, but in combination with the Generating Function the mapping routine becomes symplectic.

This method based on analytical approximated GF tracking routines is also available as one of the option for IDs tracking simulation (planar and helical ID) in RACETRACK [6].

2.2 *Numerically fitted Generating Function*

The Generating Function $F(x_i, p_x, y_i, p_y)$ describes the mapping of a particle through an insertion device approximated by a four- dimensional polynomial of the 4th or 6th order [8], [9]. The coefficients of the polynomial are fitted from the start and end points for a set of particle trajectories passing through the device. The corresponding tracking and fitting is done by the program WAVE [7]. The coefficients of the fit are passed to the tracking routine via a data file. The method is described in a technical note and reference [9]. This method allows to track through an insertion device in a single step. The advantage of this numerical method is that it is not restricted to large bending radii and can e.g. be used for superconducting wavelength shifter. A disadvantage is that coefficients have to be derived for off momentum particles seperately. Another disadvantage is that besides BETA other programms are needed.

2.3 *Integration tracking routine*

The integration routine tracks the particle step by step through a given magnetic field. Within each step it calls the selected or user provided magnetic field routine passing the coordinates of the particle and getting back the magnetic field at this position. Then it transports the particle over one step assuming a constant field within this step. We usually track with 1 mm steps. The advantage of this method is its flexibility and reliability. It also offers the option to write out the particle trajectory inside the device. The main disadvantage is its time consumption.

If the field is given by a 3D field map, a large computer memory is required, but it offers the option to use measured or computer generated field maps.

3 PERFORMANCE STUDIES

To study the overall performance of the various insertion device tracking routines we have considered the planned undulator U42 for BESSY II with a period length of $\lambda_0 = 42mm$. The on-axis peak field is $B_0 = 0.69T$ at a full gap of $15mm$. The number of periods is 78. This type of device can be tracked with the original beta routine as well as with our routines. The analytical representation of the field is given by

$$\begin{aligned} B_x &= -k_x/k_y \quad B_0 \sin(k_x x)\sinh(k_y y)\cos(k_z z) \\ B_y &= \quad B_0 \cos(k_x x)\cosh(k_y y)\cos(k_z z) \\ B_z &= -k_z/k_y \quad B_0 \cos(k_x x)\sinh(k_y y)\sin(k_z z) \end{aligned}$$

with $k_y^2 = k_x^2 + k_z^2$.
The ration k_x/k_z has been set to $k_x/k_z = 0.2$.

3.1 *Computing time*

We started with an investigation of the computing time considering the standard BESSY II optics with the U42 as the only insertion device. The sextupoles were turned off for these runs. We used a DEC AlphaServer 2100 4/200 with 256 MByte memory running OpenVMS V6.2-1H3. During the test the machine was almost exclusively processing the tracking job. In case of the analytical GF routine one period was tracked in a single step. For the numerical GF routine the whole device was taken in a one step and the step length for numerical integration routine was set to one millimeter. Each tracking method was done in a first run with 1000 turns and in a second run with 11000 turns. Then the differences in CPU time and elapsed time of both jobs then correspond to 10000 turns. Finally we substracted the times used for tracking without any insertion device. This way we obtained the tracking time for the insertion device routines. The differences in the CPU and elapsed time were negligible, thus only the CPU time is shown in fig. 1.

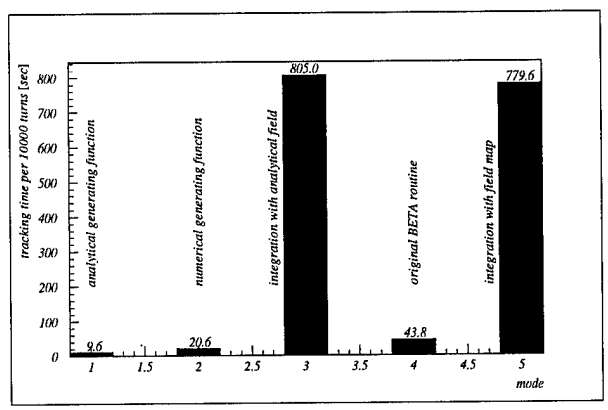

Figure 1: Tracking time for the various routines for 10000 turns.

3.2 *Tracking precision*

The tracking results of the routines were investigated by comparing phase space plots (linear optics with the U42 as the only ID). Fig. 2 shows in the upper windows two horizontal phase space plots. The first plot is done for different horizontal and vertical tunes. There is no significant difference between tracking results. For the second plot we set both tunes to the same value such that the resulting coupling resonance increased the differences between the various tracking schemes. Although the phase is slightly divergent our routines show a good agreement, i.e. the particle stays within the same phase space region. The behavior of the BETA tracking routine is different, the covered phase space is larger.

For an identical set of about 100 phase space coordinates at the entrance of the device we plotted in the lower

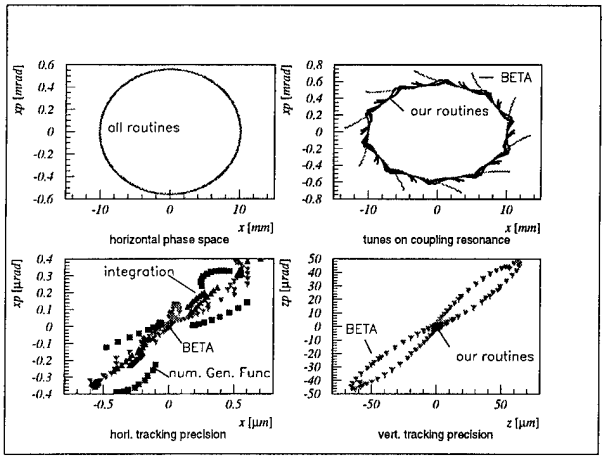

Figure 2: Comparison of tracking results for the original BETA routine and our Generating function and integration routines.

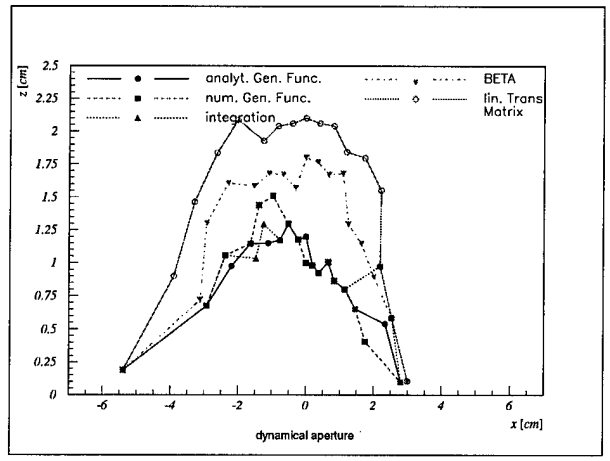

Figure 3: Comparison of dynamical apertures

windows of fig.2 the deviations with respect to the results for the analytical Generating Function at the exit of the ID (same phase space region as before). The differences in the horizontal coordinates x,xp are similar for all routines. But for the vertical coordinate z,zp the BETA routine shows a much larger discrepancy than the integration and numerical Generating Function routines. Their deviation is of the same size as for the horizontal coordinates.

3.3 Dynamical aperture

As a last comparison we calculated dynamical apertures for the BESSY II optics (including sextupoles) with the U42 as the only ID. We asked for 1000 stable turns. Fig.3 shows the results. Although our routines are based on different methodes and algorithms they show a good agreement. The original BETA routine shows a larger aperture. The largest aperture is obtained when the ID is tracked using the corresponding linear transfer matrix of the ID.

However, it should be noted that for vertical apertures larger than 1 cm, the simple formulas for the magnetic field of the device as given above yield unrealistic values. We obtain e.g. $B_y(0, 1cm, 0) = 1.6T$ and $B_y(0, 2cm, 0) = 6.7T$. For these extreme values the analytical field expansion is no longer valid. All tracking routines using this simple description of IDs deal with this problem. Hence the resulting vertical apertures are not reliable. On the other hand, this in general will cause no problems, since the hardware aperture is much smaller in most cases.

4 CONCLUSION

The package of our routines shows consistent results for the different methods and algorithms. Some significant differences were found with respect to the BETA insertion device tracking routine. The provided routines allow to study the influence of arbitrary insertion devices on the beam dynamics.

5 REFERENCES

[1] L. Farvacque, J. L. Laclare, A. Ropert, BETA User's Guide, ESRF-SR/LAT-88-08 (1987)

[2] G. Wüstefeld, "Particle Tracking with Generating Functions of Magnetic Fringing Fields", Proceedings of the IEEE 1995 Particle Accelerator Conference, Dallas (USA), 1995, p. 2868

[3] G. Wüstefeld, M. Scheer, "Canonical Particle Tracking and End Pole Matching of Helical Insertion Devices", these proceedings

[4] A. C. Hearn, REDUCE 3.6, A General Purpose Algebra System, ©A.C.Hearn, RAND,Santa Monica, CA 90407-2138,USA (reduce@rand.org)

[5] Simulation of Non-linear Beam Dynamic Effects due to an Electromagnetic Elliptical Wiggler R.P. Walker, B. Diviacco, L. Tosi (Sincrotrone Trieste), G. Wüstefeld, M. Scheer (BESSY), S. Werin (MAX-lab), these proceedings

[6] A. Wrulich, "RACETRACK", DESY Report 84-026 (1984); F. Iazzourene et al., "RACETRACK User's Guide, Version 4.00", ST/M-91/11, July 1991

[7] M. Scheer, WAVE, A code to track electrons through magnetic fields and calculate emitted synchrotron radiation, unpublished

[8] M. Scheer, G. Wüstefeld, Effects of a Superconducting Wavelength Shifter on the Planned Storage Ring BESSY II Technischer Bericht TB Nr.169, BESSY, Berlin (Germany) 1992

[9] M. Scheer, G. Wüstefeld, "Influence of a Wavelength Shifter on the Performance of the Synchrotron Light Source BESSY II', Proceedings of the EPAC 1992, Berlin (Germany)

SIMULATION OF MULTIPACTING IN RF CAVITIES AND PERIODICAL STRUCTURES

A.V. Grudiev, D.G. Myakishev, Budker INP, Novosibirsk 630090, Russia
V.P. Yakovlev, Omega-P Inc., 202008 Yale Station, New Haven, CT 06520*

Abstract

The code for multipacting simulations in axisymmetrical RF cavities, periodical structures and coaxial lines is presented. Physical model includes secondary emission simulations and particle trajectory integration in realistic RF fields. The code calculates multipacktor voltage levels and discharge distribution. The paper contains simulation results for 180 MHz cavity of INP microtron-recuperator as well as measured data for this cavity demonstrating good agreement with the calculations.

1 PHYSICAL MODEL AND ALGORITHM

Physical model and algorithm consist of two parts. The first part is the calculation of electrons trajectories in electromagnetic fields. The second part is the surface phenomenons simulation such as secondary emission and back-scattering of electrons.

1.1 Electrons trajectories

Since the density of electrons is supposed to be small, trajectories of electrons are calculated by means of integration of motion equations in axisymmetrical external electromagnetic field without taking into account space charge distribution. The code SLANS [1] is used for geometry input, finite element mesh generation and calculation of RF field in the nodes of the mesh. If there is an external electro- and magnetostatic field, the codes SAM [2] is used for its calculation in the same nodes. Using node values, field is interpolated by using finite element method and electron trajectory is calculated by Runge-Kutte's method of integration. The calculation of electron trajectory continues until the collision with the surface.

1.2 Surface phenomena

When the electron collides with the surface, two phenomena take place secondary emission and back-scattering [3]. Both of them are taken into account. The distributions of back-scattering coefficient and secondary emission coefficient versus the energy of arrival electron and the angle of its velocity vector with respect to the surface were taken from [3] and modeled by analytical functions for each type of material.

After each collision the decision about back-scattering of electron is made and the number of secondary electrons is calculated. The decision is made after comparison of the value of back-scattering coefficient for this collision with random number from the range [0;1]. If the random number is less then the value of back-scattering coefficient, the electron is scattered back. Back-scattered electrons have the same energy as arrival one and the opposite direction.

The number of secondary electrons is calculated using following procedure. If acts of emission of secondary electrons are supposed to be independent on each other, the process of emission can be described in term of Bernulli model of random processes [4] and then the probability of emission of n electrons is

$$P_n = \frac{(F\delta)^n}{n!}\exp^{-F\delta} \tag{1}$$

where δ - value of secondary emission coefficient for each collision, i.e. for the energy and the angle of the arrival electron, F - enhancement factor, which depends on the material and the condition of the surface. To determine the number of secondary electrons, a random number x from the range [0;1] is compared with value

$$x_k = \sum_{n=0}^{k} P_n \tag{2}$$

for k =0,1,2,... If x more then x_{k-1} and less then x_k, k is supposed to be the number of secondary electrons for this collision.

The energy and angular distributions of secondary electrons were taken from [3] for each type of material. Using those distributions, two equations are solved, to get the energy and the angle of each secondary electron:

$$\int_0^{E_2} F_E(E)dE = x_E \tag{3}$$

$$\int_0^{\Theta_2} F_\Theta(\Theta)d\Theta = x_\Theta \tag{4}$$

where E_2 - the energy of the secondary electron, Θ_2 - the angle between the secondary electron velocity vector and the normal vector to the surface in the point of collision, $F_E(E)$ and $F_\Theta(\Theta)$ - the energy and angular distribution of secondary electrons, x_E and x_Θ - random numbers from the range [0;1].

In our model the process of back-scattering and secondary emission is assumed to have no time delay between impact and scattering or emission because of in reality its values are negligible.

2 THE COMPUTER CODE MPS

Based on described above methods and algorithms, codes MPS (MultiPacting Simulation) was developed and tested.

* on leave from Budker INP, Novosibirsk, 630090, Russia

0-7803-4376-X/98/$10.00 © 1998 IEEE

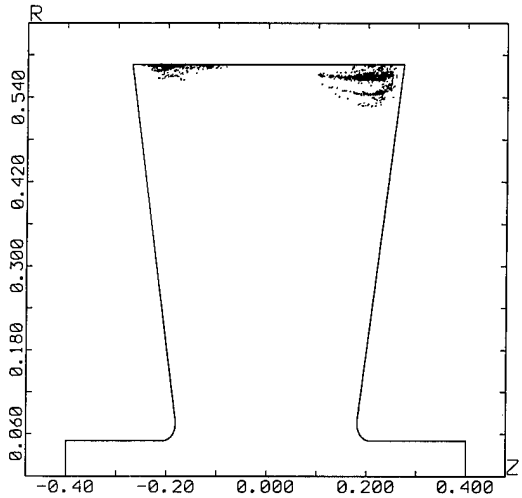

Figure 1: The geometry of 180 MHz cavity for microtron-recuperator and electrons inside.

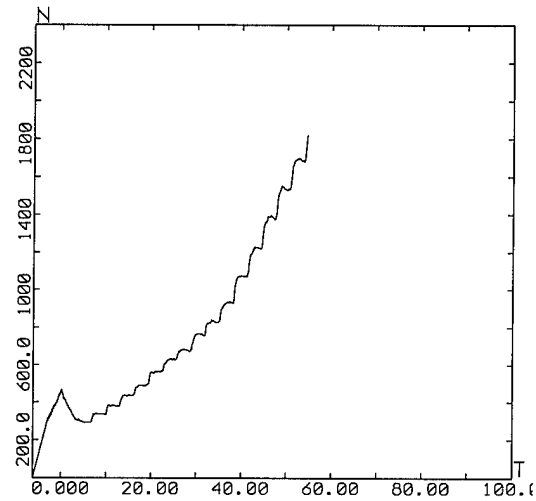

Figure 2: The time dependence of the number of electrons in the cavity.

To simulate multipacting in axisymmetric device, this code is run after saving data from SLANS and SAM to files. The following initial parameters have to be defined, before the start of the calculation:

- radio-frequency
- normalization of field in term of peak voltage for cavity or power for travelling wave structure
- materials of surface
- enhancement factor for each material
- elements of surface, where initial electrons will start
- number of initial electrons
- initial phase shifts of electrons
- number of RF-cycles to calculate
- step of integration

During the process of calculation, it is possible to monitor electrons dynamics inside the device and behavior of regions of multipacting in first output window (see Figures 1 and 4) and the time dependence of the number of electrons in the second output window(see Figure 2). If the number of electrons are increasing dramatically, the multipacting is supposed to take place in such a device under defined conditions.

3 TEST RESULTS

A few final tests were performed to check the code:

- Two parallel plates with homogeneous electric field
- 430 MHz E_{010}-mode toroidal cavity
- 180 MHz E_{010}-mode cavity for microtron-recuperator

3.1 *Two parallel plates*

Series of calculation were performed for two parallel plates with homogeneous electric field between plates:

$$E_z(t) = \frac{U}{d}\cos(2\pi f t) \qquad (5)$$

to determine multipacting zones on the parametric plane $(U; fd)$, where U - peak voltage between the plates, f - frequency of voltage, d - gap between the plates. Two zones was determined for two values of enhancement factor 1.5 and 2.0. This two zones and the experimental data [5] are shown on the Figure 3. The experimental data are presented by three curves: 1 - initial, 2 - intermediate, 3 - final. Each curve is for different time of discharge process, dur-

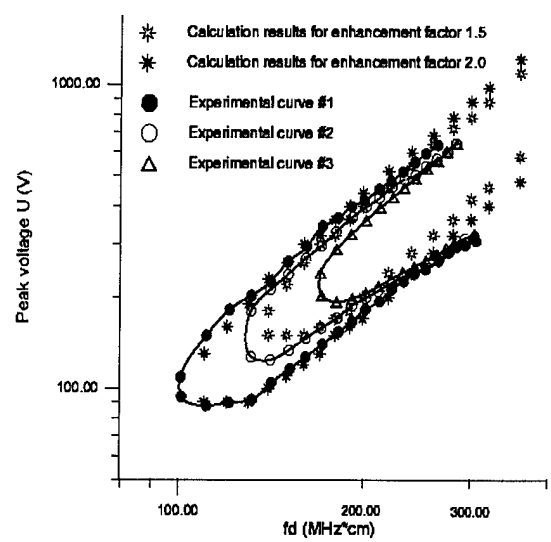

Figure 3: The results of the experiment and the simulation for parallel plates.

ing which the enhancement factor is getting smaller until the constant value is set up (curve 3). The Figure 3 demonstrates a good agreement between the experiment and the simulation for parallel plates.

3.2 *Toroidal cavity*

Simulation of multipacting in the 430 MHz E_{010}-mode toroidal cavity (see Figure 4) was made under various val-

ues of voltage along the axis, which is

$$U = \int_{-\infty}^{\infty} E_z(z)dz \qquad (6)$$

The multipacting zone was determined for two side high

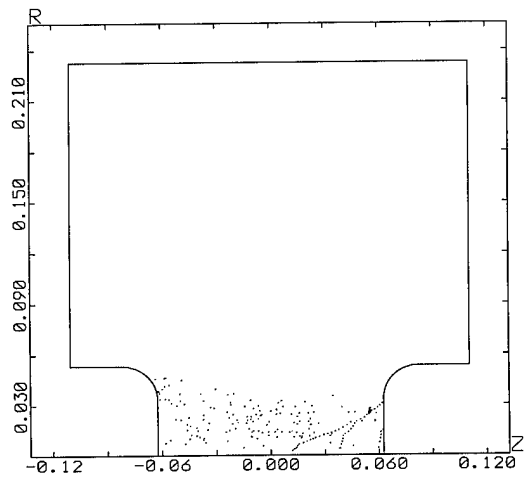

Figure 4: The geometry of 430 MHz toroidal cavity and electrons inside.

order multipacktor in the central gap. Obtained results were compared with measurements of electron current in the central gap under various axial voltage [6], which were carried out by using Faraday pick-up. The result of comparison is presented on the Figure 5.

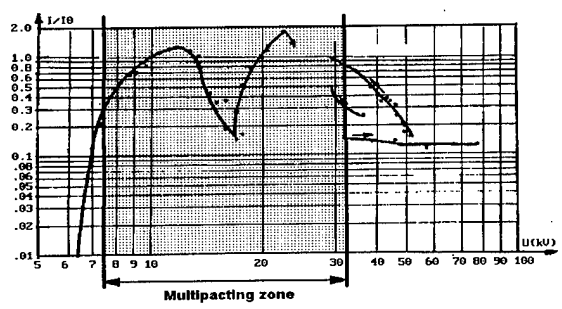

Figure 5: The results of measurement and calculation in the toroidal cavity.

The dotted area represents the calculated multipacting zone and the curve represents measured Faraday pick-up's current versus axial peak voltage. A good correlation between the calculation and the measurement can be seen.

3.3 *Cavity for microtron-recuperator*

The simulation of the multipacting in the 180 MHz E_{010}-mode cavity for microtron-recuperator [7] (the geometry of the cavity is shown on the Figure 1) was made under various values of axial voltage. On the Figure 1 the region of multipacting and the discharge distribution can also be seen as electrons cloud near the outer wall.

Multipacting was found for a few levels of axial voltage. Each levels corresponds to a different order of multipacting (see the Table).

n	F_m	U(kV)
1	0.99	930
2	1.33	550
3	2.26	370
4	3.7	280

Where n - order of multipacting, F_m - minimal enhancement factor for which multipacktor still take place under the axial voltage - U. The order of multipacting can be determined visually during the observation of electron dynamics or after analysis of time dependence of the number of electrons.

For this cavity the measurement of axial voltage levels was carried out [8] and following results were obtained. At first the multipacting levels were 380...580 kV and 800...1000 kV. The first zone disappeared after few minutes of RF processing. It appeared again after opening of the cavity but was processed easily as well. The second zone remained all the time, only it got very weak and narrower: 900...950 kV. As one can see, the comparison of the measurement with the calculation demonstrates a good agreement between them for the first and the second order multipacktors. The measurements of the higher order multipacktors were not carried out because of in reality the enhancement factor is not enough high to get the multipacting.

4 ACKNOWLEDGEMENTS

The authors thank V.G. Vesherevich and I.K. Sedlyarov of BINP for discussions and providing measurement data.

5 REFERENCES

[1] Myakishev D.G. and Yakovlev V.P., "An Interactive Code SuperLANS for Evaluation of RF-cavities and Acceleration Structures," Proceedings of IEEE Particle Accelerator Conference, May 6-9, 1991, V.5, pp.3002-3004.

[2] M.A.Tiunov, B.M.Fomel and V.P.Yakovlev, "Computer-Aided Electron Gun Design," Proceeding of the XIII International Conference on High Energy Accelerators, August 7-11, 1986, V.1, pp. 353-355.

[3] I.M.Bronshtein and B.S.Fraiman, "Secondary electron emission," Nauka Edition, Moscow, 1969.

[4] S.M.Rytov "Introduction to Statistical Radiophysics", Nauka Edition, Moscow, 1978.

[5] H.Tamagawa, "On the Mechanism of the High Frequency Vacuum Discharge," ETJ of Japan, June 1957, pp. 42-46.

[6] I.K.Sedlyarov and V.D.Shemelin, "Resonant Radio-Frequency Discharge in Toroidal Cavity," Preprint INP9-73, Novosibirsk, 1973.

[7] V.S.Arbuzov et al., "RF System of the CW Race-Track Microtron-Recuperator for FELs," Proc. of the 1993 Particle Accelerator Conference, V.2, pp 1226-1228.

[8] V.G.Vesherevich and I.K.Sedlyarov, BINP, Private Communication, 1996.

CONSIDERATION OF DC SPACE CHARGE EFFECTS IN THE MODAL ANALYSIS OF APERTURE-COUPLED CAVITIES

A. Jöstingmeier, M. Dohlus, DESY, D-22607 Hamburg, Germany and
C. Rieckmann, A. S. Omar, TU Hamburg-Harburg, D-21071 Hamburg, Germany

Abstract

The modal analysis of aperture-coupled cavities is frequently applied to the field theoretical analysis of high-power tube cavities and accelerating structures in high energy physics. Besides the rf electromagnetic field, dc space charge effects may also be important in such applications. Because there is no magnetic field related with dc space charges a straightforward application of the modal expansion method, which makes use of matching the aperture tangential magnetic field, to the investigation of dc space charge fields is not possible. In this contribution it is therefore demonstrated that the computation of the dc spectral component of the electric field due to space charges can also be included in the modal analysis of aperture-coupled cavities if instead of the aperture tangential magnetic field the corresponding normal electric field is matched. It is shown that even in this case the solenoidal electric eigenfunctions of the cavity have to be taken into account because of the waveguide coupling. Furthermore, the validity of the method is checked by applying it to a field problem for which a solution is already well-known from another analysis.

1 INTRODUCTION

In many high-power tubes, e.g. klystrons, travelling wave tubes and gyrotrons, the beam-field interaction takes place in one or more aperture-coupled cavities. In the analysis of such tubes space charge effects are often not taken into account [1]–[3] although it is well-known that this effect cannot always be neglected. This is especially the case if high charge densities are encountered, as e.g. in the output cavity of a klystron. In [4] a modal analysis of aperture-coupled cavities has been presented which takes space charge effects into account: By the application of the equivalence principle [5], the coupling-apertures are short-circuited and the nonvanishing tangential electric field there is replaced by two surface magnetic currents at both sides of the short circuit, which are equal in magnitude and opposite in direction. The electromagnetic field inside the cavity is then expanded with respect to the solenoidal *and* irrotational eigenfunctions of the corresponding completely shielded cavity including the effect of space charges in the analysis.

The method presented in [4] makes use of matching the aperture tangential magnetic field. Consequently this analysis cannot be used for the computation of the electric field at $\omega = 0$ which is just the electrostatic field generated by the space charges. In this contribution it is shown how the modal analysis is to be modified so that it can also be applied to the analysis of the electrostatic field. Nevertheless it turns out that even in this case solenoidal electric fields are excited due to the magnetic surface currents at the short-circuited coupling apertures.

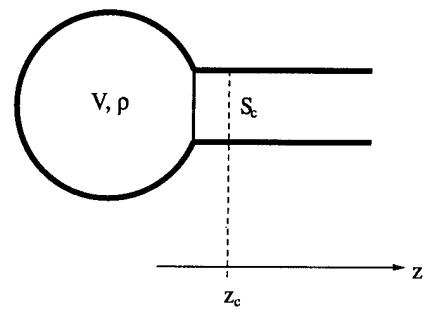

Figure 1: Cavity which is coupled to a single waveguide.

2 BASIC FORMULATION

For the sake of simplicity let us consider a cavity with only one coupling aperture as shown in Fig. 1. The extension of the method to more than one aperture is straightforward. In [4] the electromagnetic field inside the cavity is expanded in terms of the solenoidal ($\boldsymbol{e}_n$, $\boldsymbol{h}_n$) *and* irrotational ($\boldsymbol{f}_n$, $\boldsymbol{g}_n$) eigenfunctions of the corresponding completely shielded resonator:

$$\boldsymbol{E} = \sum_n^\infty a_n \boldsymbol{e}_n + \sum_n^\infty b_n \boldsymbol{f}_n \quad , \tag{1}$$

$$\boldsymbol{H} = \sum_n^\infty c_n \boldsymbol{h}_n + \sum_n^\infty d_n \boldsymbol{g}_n \tag{2}$$

The expansion coefficients b_n corresponding to the irrotational electric eigenfunctions are given by

$$\frac{b_n}{\bar{k}_{0n}} = -\frac{Z_0}{jk_0} \int_V \boldsymbol{J} \cdot \boldsymbol{f}_n^* \, dV \quad , \tag{3}$$

where Z_0, k_0, $\bar{k}_{0n}$ and $\boldsymbol{J}$ denote the intrinsic impedance of free space, the vacuum wavenumber which is proportional to the operating frequency, the eigenvalue corresponding to $\boldsymbol{f}_n$ and the current density, respectively. Keeping in mind that the irrotational electric eigenfunctions are related to potentials φ_n by

$$\boldsymbol{f}_n = \nabla \varphi_n \quad \text{with} \quad \varphi_n = 0 \quad \text{on} \quad S \quad , \tag{4}$$

where S is the surface of the corresponding completely shielded cavity, and by making use of the continuity equation

0-7803-4376-X/98/$10.00 © 1998 IEEE

$$\nabla \cdot \boldsymbol{J} = -jk_0c_0\varrho \quad , \tag{5}$$

where c_0 and ϱ are the free space velocity of light and the charge density, respectively, (3) can be reformulated:

$$\frac{b_n}{\bar{k}_{0n}} = -Z_0c_0 \int_V \varrho\varphi_n^* \, dV \tag{6}$$

Thus the coefficient b_n is simply given by the expansion of the charge density ϱ with respect to the potential φ_n. On the other hand, it can be shown that the irrotational magnetic eigenfunctions are not excited.

Although we consider an electrostatic problem the expansion coefficients a_n corresponding to the solenoidal electric cavity eigenfunctions $\boldsymbol{e}_n$ do not vanish due to the coupling apertures. From the modal analysis we obtain

$$a_n = j \int_{S_c} \left(\boldsymbol{E} \times \hat{\boldsymbol{k}}\right) \cdot \boldsymbol{h}_n^* \, dS \tag{7}$$

for $\omega = 0$ where S_c and $\hat{\boldsymbol{k}}$ are the coupling aperture and the unit vector in axial direction, respectively. Note that (7) still holds in the presence of a dc magnetic field due to a stationary current inside the cavity because electric and magnetic fields are decoupled for $\omega = 0$. For the field inside the waveguide only TM-modes have to be taken into account since the dc electric field of TE-modes vanishes. On the other hand, TM-modes have no magnetic field for $\omega = 0$ so that the waveguide field reads

$$\boldsymbol{E}_t = \sum_{\mu}^{\infty} A_\mu \nabla_t e_{z\mu} \exp[-k_\mu (z - z_c)] \quad , \tag{8}$$

$$E_z = -\sum_{\mu}^{\infty} A_\mu k_\mu e_{z\mu} \exp[-k_\mu (z - z_c)] \quad . \tag{9}$$

In (8) and (9), ∇_t, $e_{z\mu}$, k_μ and z_c are the transverse component of the nabla-operator, the axial electric field characterizing the μth TM-mode, the corresponding cutoff wavenumber and the axial coordinate of the coupling aperture, respectively. Inserting (8) into (7), which guarantees the continuity of the aperture tangential electric field, one arrives at

$$a_n = -j \sum_{\mu}^{\infty} A_\mu \int_{S_c} (\nabla_t e_{z\mu} \times \boldsymbol{h}_n^*) \cdot \hat{\boldsymbol{k}} \, dS \quad . \tag{10}$$

By making use of Maxwell's equation

$$\nabla \times \boldsymbol{h}_n = jk_{0n}\boldsymbol{e}_n \tag{11}$$

for the normalized cavity eigenfunctions $\boldsymbol{e}_n$ and $\boldsymbol{h}_n$, where k_{0n} is the corresponding resonant wavenumber, we find after some algebraic manipulations that the cavity expansion coefficients a_n are related with the waveguide mode amplitudes A_μ by a linear transformation:

$$a_n = \sum_{\mu}^{\infty} K_{n,\mu} A_\mu \quad \text{with} \tag{12}$$

$$K_{n,\mu} = k_{0n} \int_{S_c} e_{z\mu} \boldsymbol{e}_n^* \cdot \hat{\boldsymbol{k}} \, dS \tag{13}$$

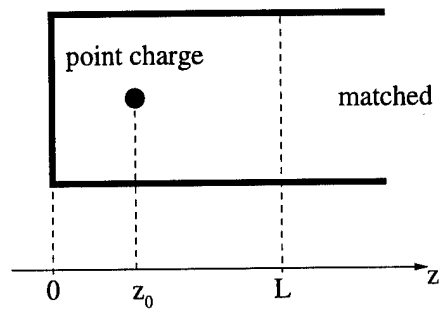

Figure 2: Short-circuited waveguide which contains a point charge.

Note that this transformation is purely real because the electric field is in phase throughout the whole structure for an electrostatic problem. Instead of matching the aperture tangential magnetic field, we exploit the continuity of the axial electric field which yields

$$\sum_{n}^{\infty} a_n \boldsymbol{e}_n \cdot \hat{\boldsymbol{k}} + \sum_{n}^{\infty} b_n \boldsymbol{f}_n \cdot \hat{\boldsymbol{k}} = -\sum_{\mu}^{\infty} A_\mu k_\mu e_{z\mu} \quad . \tag{14}$$

Applying Galerkin's procedure, we obtain an algebraic system of equations for the unknown expansion coefficients of the waveguide modes:

$$\sum_{\mu}^{\infty} \left(\frac{\delta_{\mu\nu}}{k_\nu} + \sum_{n}^{\infty} \frac{K_{n,\nu}^* K_{n,\mu}}{k_{0n}} \right) A_\mu = -\sum_{n}^{\infty} b_n \int_{S_c} e_{z\nu} \boldsymbol{f}_n \cdot \hat{\boldsymbol{k}} \, dS \quad , \quad \nu = 1, \ldots, \infty \quad , \tag{15}$$

where $\delta_{\mu\nu}$ denotes Kronecker-delta. Note that the b_n in the above equation are already determined by (6). In order to demonstrate the validity of the proposed method let us consider the structure shown in Fig. 2. This illustration presents a waveguide which extends uniformly in axial direction from $z = 0$ to infinity. This waveguide is assumed to be short-circuited and matched at $z = 0$ and $z \to \infty$, respectively. The field is excited by a point charge Q_0 which is located at $\boldsymbol{r}_{t0} + \hat{\boldsymbol{k}} z_0$. Let us now consider the structure as an artificial cavity with its coupling aperture located at $z = L$. The normalized eigenfunctions $\boldsymbol{e}_{mp}$ and φ_{rs} are

$$\boldsymbol{e}_{mp} = \sqrt{\frac{2}{k_{0mp} L (1 + \delta_{p0})}} \left[\frac{p\pi}{k_{0mp} L} \nabla_t e_{zm} \sin\left(\frac{p\pi}{L} z\right) - \hat{\boldsymbol{k}} \frac{k_m^2}{k_{0mp}} e_{zm} \cos\left(\frac{p\pi}{L} z\right) \right] \quad , \tag{16}$$

$$\varphi_{rs} = \sqrt{\frac{2}{\bar{k}_{0rs} L}} \frac{k_r}{\bar{k}_{0rs}} e_{zr} \sin\left(\frac{s\pi}{L} z\right) \quad , \tag{17}$$

where m and r denote the transverse order of $\boldsymbol{e}_{mp}$ and φ_{rs}, respectively. p and s are the corresponding longitudinal orders. Inserting (16) and (17) into (15), we arrive at the

following expression for the waveguide amplitude A_ν:

$$A_\nu = Z_0 c_0 Q_0 \frac{\sum_{s=1}^{\infty} \frac{2s\pi(-1)^s}{(\bar{k}_{0\nu s}L)^2} e_{z\nu}(\boldsymbol{r}_{t0}) \sin\left(\frac{s\pi}{L} z_0\right)}{\frac{1}{k_\nu} + \sum_{p=0}^{\infty} \frac{2}{k_{0\nu p}^2 L(1+\delta_{p0})}} , \quad (18)$$

for $\nu = 1, \ldots, \infty$. Substituting the separation conditions

$$k_{0mp}^2 = k_m^2 + \left(\frac{p\pi}{L}\right)^2 , \quad (19)$$

$$\bar{k}_{0rs}^2 = k_r^2 + \left(\frac{s\pi}{L}\right)^2 \quad (20)$$

into (18) and making use of the closed-form expressions [6]

$$\sum_{n=1}^{\infty} \frac{\cos(nx)}{n^2 - a^2} = \frac{1}{2a^2} - \frac{\pi}{2a} \frac{\cos[(x-\pi)a]}{\sin(\pi a)} \quad (21)$$

$$\sum_{n=1}^{\infty} \frac{n\sin(nx)}{n^2 - a^2} = \frac{\pi}{2} \frac{\sin[(x-\pi)a]}{\sin(\pi a)} \quad (22)$$

yields

$$A_\nu = -Z_0 c_0 Q_0 k_\nu e_{z\nu}(\boldsymbol{r}_{t0}) \exp(-k_\nu L) \sinh(k_\nu z_0) \quad . \quad (23)$$

E.g., inserting the amplitudes A_ν into (9), we get for the axial component of the electric field for $z > L$

$$E_z = \sum_{\mu}^{\infty} k_\mu^2 Z_0 c_0 Q_0 e_{z\mu}(\boldsymbol{r}_{t0}) \sinh(k_\mu z_0) \exp(-k_\mu z)\, e_{z\mu} \, . \quad (24)$$

Note that in the cavity expansion approach the length L of the artificial cavity does not enter the expression for the waveguide field. Therefore (24) holds as long as the cavity contains the point charge which means $z > z_0$. The result of the modal analysis is now compared with an integration of Poisson's equation by matching the electric potential and the displacement flux at the cross section of the waveguide which contains the point charge. For $z \neq z_0$ the electric potential V fulfills Laplace's equation $\nabla^2 V = 0$. Suitable series expansions for $z < z_0$ ($V^{(-)}$) and $z > z_0$ ($V^{(+)}$) are thus

$$V = \begin{cases} V^{(-)} = \sum_{n}^{\infty} V_n^{(-)} e_{zn} \sinh(k_n z) & , z < z_0 \\ V^{(+)} = \sum_{n}^{\infty} V_n^{(+)} e_{zn} \exp(-k_n z) & , z > z_0 \end{cases} \quad (25)$$

These expansions already satisfy the boundary condition at the shielding of the waveguide as well as at $z = 0$ and $z \to \infty$. From the matching conditions on S

$$V^{(-)}\Big|_{z=z_0} = V^{(+)}\Big|_{z=z_0} , \quad (26)$$

$$\hat{\boldsymbol{k}} \cdot \left(\boldsymbol{D}^{(+)} - \boldsymbol{D}^{(-)}\right)\Big|_{z=z_0} = Q_0 \delta(\boldsymbol{r}_t - \boldsymbol{r}_{t0}) , \quad (27)$$

where $\boldsymbol{D}$ denotes the displacement flux, it follows

$$V_n^{(+)} = k_n \frac{Q_0}{\varepsilon_0} e_{zn}(\boldsymbol{r}_{t0}) \sinh(k_n z_0) \quad . \quad (28)$$

Inserting (28) into (25) and calculating E_z for $z > z_0$ from $E_z = -\frac{\partial}{\partial z} V^{(+)}$, we arrive at the same result as has been previously derived with the modal expansion method as it should be. In this contribution it has been demonstrated that the computation of the dc spectral component of the electric field due to space charges can also be included in the modal analysis of aperture-coupled cavities if instead of the aperture tangential magnetic field the corresponding axial electric field is matched. It has been shown that even for $\omega = 0$ the solenoidal electric eigenfunctions of the cavity have to be taken into account because of the waveguide coupling. Furthermore, the validity of the method has been checked by applying it to a field problem for which a solution is already well-known from another analysis.

3 CONCLUSIONS

In this contribution it has been demonstrated that the computation of the dc spectral component of the electric field due to space charges can also be included in the modal analysis of aperture-coupled cavities if instead of the aperture tangential magnetic field the corresponding axial electric field is matched. It has been shown that even for $\omega = 0$ the solenoidal electric eigenfunctions of the cavity have to be taken into account because of the waveguide coupling. Furthermore, the validity of the method has been checked by applying it to a field problem for which a solution is already well-known from another analysis.

4 REFERENCES

[1] *K. E. Kreischer and R. J. Temkin, "Linear theory of an electron cyclotron maser operating at the fundamental," Int. J. Infrared Millimeter Waves, vol. 1, pp. 195–223, 1980.*

[2] *A. W. Fliflet, M. E. Read, K. R. Chu and R. Seeley, "A self-consistent field theory for gyrotron oscillators: application to a low Q gyromonotron," Int. J. Electronics, vol. 53, pp. 505–521, 1982.*

[3] *A. W. Fliflet, R. C. Lee and M. E. Read, "Self-consistent field model for the complex cavity gyrotron," Int. J. Electronics, vol. 65, pp. 273–283, 1988.*

[4] *A. Jöstingmeier, C. Rieckmann and A. S. Omar, "Frequency domain analysis of gyrotrons based on complete eigenfunction expansions," Conf. Digest 19th Int. Conf. on Infrared and Millimeter Waves (Sendai), pp. 345–346, 1994.*

[5] *R. F. Harrington, Time-Harmonic Electromagnetic Fields. New York: McGraw-Hill, 1961.*

[6] *R. E. Collin, Field Theory of Guided Waves. New York: IEEE Press, 1991.*

A SELF-CONSISTENT BEAM LOADED TRAVELING WAVE ACCELERATOR MODEL FOR USE IN TRACE 3-D

M. C. Lampel, G. H. Gillespie Associates, Inc., P. O. Box 2961 Del Mar, CA 92014

Abstract

An optics model of a constant gradient traveling wave (CGTW) accelerator structure has been implemented for TRACE 3-D. TRACE 3-D is an envelope code including space charge that is used to model bunched beams in magnetic transport systems and radio frequency (RF) accelerators when the effects of beam current might be significant. The new matrix model has been developed to allow incorporation of particle beam loading (current) effects on the accelerator gradient and the accelerator structure's beam focusing properties in a self-consistent manner. The beam loaded electric field for a CGTW accelerator structure is constant for only a particular design current (e.g. 0 current), otherwise it can be written as a function of accelerator attenuation and axial position along the structure. The variation of the electric field through the structure has been taken into account in the new model. CGTW structures differ substantially in focusing properties and beam loading properties from standing wave structures. Examples will be presented using the new TW model, propagating electron beams with different currents through the Stanford Linear Accelerator Center's 3 m structure. The results will be compared to the zero current TW structure model in TRANSPORT and the Tank model (a standing wave structure model) in TRACE 3-D. A computer demonstration of the new element will also be presented.

1 INTRODUCTION

TRACE 3-D [1] is an extremely popular first order optics code incorporating space charge effects in calculating the equivalent uniform beam envelope for particle beams. Implementation of a constant gradient traveling wave (CGTW) accelerator optics model into TRACE 3-D is useful to groups interested in generating models of entire CGTW beamlines using TRACE 3-D.

TRACE 3-D has several rf elements implemented into the standard version: rf gap, rfq cell, cavity, and the coupled cavity tank elements. These are all standing wave (SW) structures and possess focal properties differing from CGTW structures, due to the different fields seen by the particles as shown in Table 1.1. Note that for SW there is a transit time factor, T, and there appear backwards traveling wave components in the fields. In addition beam loading in CGTW structures is also different. Therefore, a model for this structure seemed desirable, particularly as many electron beam facilities rely on the SLAC 3 m structure [2] or a variation thereof.

The implementation of the model consisted of putting together two different pieces of the physics: 1) The R matrix elements for a CGTW; 2) The changing gradient as a function of accelerator structure parameters and beam parameters.

Field	CGTW Cavity	1'st Half SW Cavity	2'nd Half SW Cavity
E_z	$E_0\cos\phi$	$2E_0T[\cos\phi/2 + \sin\phi/\pi]$	$2E_0T[\cos\phi/2 - \sin\phi/\pi]$
E_r	$\frac{-\pi E_0 r\sin\phi}{2L}$	$-\pi E_0 Tr [\cos\phi/\pi + \sin\phi/2]/2L$	$\pi E_0 Tr [\cos\phi/\pi - \sin\phi/2]/2L$
B_θ	$\frac{-\pi E_0 \beta r\sin\phi}{2cL}$	$\pi E_0 T\beta r [\cos\phi/\pi - \sin\phi/2]/cL$	$\pi E_0 T\beta r [\cos\phi/\pi + \sin\phi/2]/cL$

Table 1.1: Comparison of averaged electric and magnetic fields in a single SW or TW cavity. Note SW terms have backwards traveling wave components. E_0 is the applied field strength, ϕ the phase, β and γ the relativistic factors, L the cavity length, and T the transit time factor.

Sections 2 and 3 describe the R-matrix and gradient models. Section 4 compares TRACE 3-D results to TRANSPORT, numerical integration, and theory to demonstrate the accuracy of the model. Section 5 discusses an application of the new model. Section 6 presents a brief summary and some conclusions.

2 R-MATRIX ELEMENTS FOR THE CGTW

Previously, the TRANSPORT [1] code has been modified to achieve better first order simulation of a CGTW structure [4,5]. TRANSPORT now has R-matrix elements based on the WKB approximation. The R-matrix elements derived in this manner for TRANSPORT are used in the TRACE 3-D model. The non-zero R-matrix elements can be found in [1]. These matrix elements have been implemented in the current TRACE 3-D model.

3 THE ELECTRIC FIELD GRADIENT

The electric field gradient for a CGTW structure depends on the applied field and the field generated by the beam. Several derivations of the field developed [6,7] are in the literature. We use the field as expressed by [7]:

$$G = G_0\cos\phi - (I_0 r/2)\ln[1 - (z/L)(1 - e^{-2\tau})], \quad \text{eq. 3.1}$$

where G is the net gradient, ϕ is the phase, G_0 is the applied gradient, I_0 is the average beam current, r the shunt impedance per unit length, L the structure length, τ the attenuation, and z the distance along the structure. The applied gradient is related to the input power, P, by:

$$G_0 = [rP/L)(1 - e^{-2\tau})]^{1/2} \quad \text{eq. 3.2}$$

0-7803-4376-X/98/$10.00 © 1998 IEEE

4 IMPLEMENTATION OF THE MODEL

The TRACE 3-D model was implemented by writing FORTRAN routines which first calculate the total gradient, G, across a step and then the R-matrix. The R-matrix elements are calculated assuming the gradient over the step is constant.

Several test calculations have been performed to demonstrate the accuracy of the model. First for the 0 current case a comparison to previous TRANSPORT and Runge-Kutta integration results obtained by Hurd and McGill [4] and Carey [5] was performed, as shown in Table 4.1. The initial energy is 100 MeV, the maximum energy gain is 3.19 MeV over a length of 290 cm (1.1 MV/m) and the phase lag is 30 degrees.

Element	Runge-Kutta	TRANSPORT	TRACE 3-D
$R_{11} = R_{33}$	1.197	1.197	1.198
$R_{12} = R_{34}$	0.307	0.307	0.307
$R_{21} = R_{43}$	1.386	1.386	1.395
$R_{22} = R_{44}$	1.179	1.179	1.180
R_{55}	0.653	0.653	0.651
R_{56}	2.059	2.060	2.058
R_{65}	-0.281	-0.281	-0.282
R_{66}	0.624	0.624	0.622

Table 4.1: Comparison of R-matrix Elements

The zero current comparison of the TRACE 3-D R-matrix to the TRANSPORT and numerically integrated values of the R-matrix elements is quite good. The largest discrepancy, for the $R_{21} = R_{43}$ elements, is 0.6%. This is within the accuracy of the input data for this model.

Next, as shown in Table 4.2, two models with SLAC accelerator structure parameters were built check beamloading [6,7]. The first case is a single 3 meter SLAC section. The second case is for two 3 meter SLAC sections. For both, the beam gains 70 MeV (from 5 MeV to 75 MeV) under the loaded conditions. The SLAC structure parameters used for these tests are: L = 3.01 meters; $\tau = 0.572$ nepers; $\lambda = 10.5$ cm; r = 57 Mohms/m. The phase lag is 0, the currents and energy gains are given in Table 4.2:

No. of CGTW Structures	Current (mA)	Beam Energy Theory (MeV)	Beam Energy TRACE 3-D (MeV)
1	0	80.2	80.2
1	255	70.0	70.1
2	0	113.4	113.4
2	544	70.0	70.2

Table 4.2: Beam Loading Calculations, Theory and TRACE 3-D

The two cases studied for beam loading effects also show good agreement between theory and TRACE 3-D. The largest difference of 0.3% for a beam loading of 544 mA occurs with a step size of 5 mm or less through the structure. This is within the accuracy expected.

5 BEAMLINE DESIGN APPLICATIONS

As an example of a beamline design application where use of a CGTW model makes a difference, take the model of a single 3 m SLAC section accelerating a 255 mA beam from 5 to 75 MeV. Input beam parameters, which are the same for both the CGTW and SW (TRACE 3-D Tank element) models are given in Table 5.1.

The two structures differ slightly in length because for the CGTW structure 3.01 m is exactly 86 cells long, each with phase advance of $2\pi/3$, while the SW structure is 3.0396 m long with 58 cavities whose phase advance is π. Because of this the accelerating gradient in the SW case also differs slightly from the CGTW case, but more importantly the input gradients differ because the CGTW model starts with an applied gradient for 0 current and then calculates the loaded gradient (see section 3). Table 5.2 gives a complete list of the structure parameters.

Input Parameter	Initial Value
Initial Energy	5 MeV
I_0	255 mA
$\varepsilon_x = \varepsilon_y$	4 π mm-mrad
$\alpha_x = \alpha_y$	0.1640
$\beta_x = \beta_y$	1.5907 mm/mrad
ε_z	21.22 π mm-mrad
α_z	-4.397
β_z	0.1584 mm/mrad

Table 5.1: Initial beam characteristics for CGTW and SW structure comparison. Emittances are 5 times r.m.s.

Other differences in how the structures are defined are the use of shunt impedance and attenuation (of the rf power through the structure) for the CGTW structure. Through the use of the shunt impedance, r, the attenuation, α, and the other input parameters, many possible traveling wave structures can be modeled with this new element.

Structure Parameter	CGTW	SW
Length	3.0100 m	3.0396 m
Phase	0	0
Applied Gradient	26.64 MV/m	23.03
No. of Cavities	86	58
Phase Adv./cav.	$2\pi/3$	π
Attenuation	0.572 nepers	n/a
Shunt Impedance	57 MΩ/m	n/a

Table 5.2: Structure parameters for CGTW and SW comparison.

Figures 5.1 and 5.2 show the different beam envelopes calculated for CGTW and SW cases. The SW structure is strongly focusing and brings the beam to a waist near the beginning of the structure, while the CGTW structure slightly defocuses the beam. Final values for the Courant-Snyder (Twiss) parameters are quite different as shown in the figures and as is apparent from the very different phase space ellipses in the upper right corners.

The R-matrices (including the first order effects of space charge) which TRACE 3-D calculates are shown in tables 5.3 and 5.4.

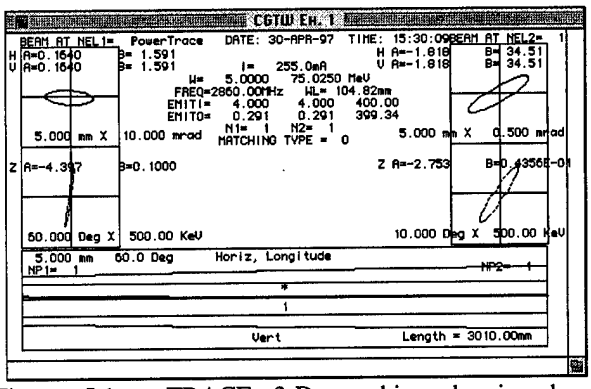

Figure 5.1: TRACE 3-D graphics showing beam envelope for CGTW case. The beam is slightly defocusing throughout the structure.

The differences between the two cases demonstrate the desirability to have both a traveling wave element available in TRACE 3-D as well as the existing standing wave elements. Many accelerator facilities around the world presently use traveling wave structures, of which the SLAC 3 m structure discussed in this paper is the most prevalent. The ability to make use of TRACE 3-D for modeling these facilities, with a reasonably accurate CGTW element, will improve the capacity of scientists, accelerator operators, and designers to explore different configurations and operating points quickly and efficiently.

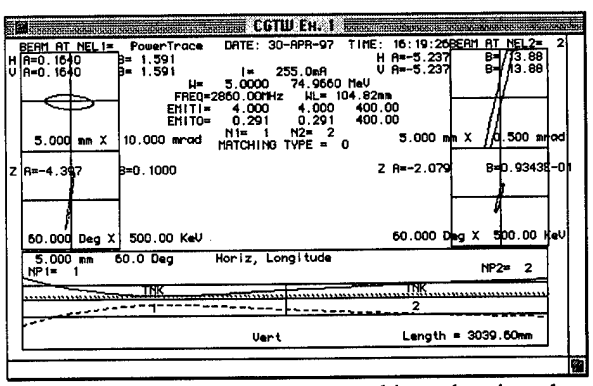

Figure 5.2: TRACE 3-D graphics showing beam envelope for SW case. Note that the scales for 5.1 and 5.2 are the same, and the phase ellipses on the right of both figures are quite different. The beam is focused to a waist near the beginning of the structure.

-0.6901	0.4728	0	0	0	0
-0.2905	0.0937	0	0	0	0
0	0	-0.6901	0.4728	0	0
0	0	-0.2905	0.0937	0	0
0	0	0	0	0.9992	0.0010
0	0	0	0	1.0640	0.0738

Table 5.3: R-matrix for SW element, with first order space charge effects folded in.

1.2564	0.6279	0	0	0	0
0.0604	0.0880	0	0	0	0
0	0	1.2564	0.6279	0	0
0	0	0.0604	0.0880	0	0
0	0	0	0	1.0059	0.0125
0	0	0	0	0.0444	0.0726

Table 5.4: R-matrix for the CGTW element, with first order space charge effects folded in.

6 CONCLUSIONS

This paper has presented a new traveling wave element for TRACE 3-D. It uses the same R-matrix as TRANSPORT but with the electric field recalculated at each step to account for beam loading effects. Electric field variation due to beam loading effects are calculated from theory. Several tests have been performed to compare the accuracy of this element to TRANSPORT and Runge-Kutta integration in the calculation of 0 current R-matrix elements, and to theory in the calculation of beam loading effects on energy gain. Good agreement has been found.

An example demonstrating the quite different behavior of CGTW and SW rf elements shows the utility of this new element in TRACE 3-D. Many different CGTW structure configurations can be modeled through different values of the accelerator structure parameters: Length, applied gradient, shunt impedance, and attenuation. Although not discussed in this paper, an extension of this work to model a constant impedance traveling wave structure would be quite simple.

The beam calculations presented were performed with a version of TRACE 3-D code that works in the Shell for Particle Accelerator Related Codes (S.P.A.R.C.) software environment[8].

REFERENCES

[1] K. Crandall and D. Rusthoi, "TRACE 3-D Documentation," Los Alamos National Laboratory report LA-UR-90-4146, 92 pages (1990)

[2] The Stanford Two Mile Accelerator, R. B. Neal, General Editor, W. A. Benjamin Inc., 1968.

[3] D. C. Carey, K. L. Brown, and F. Rothacker, "Third Order TRANSPORT a Computer Program for Designing Charged Particle Beam Transport Systems," SLAC-R-95-462, Fermilab-Pub-95/069.

[4] J. W. Hurd, J. McGill, "Modification of Acceleration Element in "TRANSPORT"," IEEE 1987 Particle Accelerator Conference, pp. 1198-1200, 87CH2387-9

[5] D. C. Carey, "The WKB Approximation and the Travelling-Wave Acceleration Cavity," IEEE 1991 Particle Accelerator Conference, pp. 1618-1620, 91CH3038-7.

[6] Perry B. Wilson, "High Energy Electron Linacs: Applications to Storage Ring RF Systems and Linear Colliders," SLAC-PUB-2884, 1982.

[7] G. A. Loew and R. Talman, "Lectures on the Elementary Principles of Linear Accelerators," Physics of High Energy Particle Accelerators, M. Month Ed., AIP Conference Proc. No. 105, 1982.

[8] G. H. Gillespie and B. W. Hill, "A Graphical User Interface for TRACE 3-D Incorporating some Expert System Type Features," 1992 Linear Accelerator Conference Proc., AECL-10728, 787-789 (1992).

MONTE CARLO SIMULATION OF A NONLAMINAR DC BEAM INCLUDING THE INFLUENCE OF SELF-FIELDS

G. Zapalac, Imatron Inc., 389 Oyster Point Blvd.,
So. San Francisco, CA

Abstract

We present a method to simulate the transport of a nonlaminar DC beam under the influence of self-fields. The simulation randomly populates an initial phase space distribution with n particles. These particles are propagated in steps through the transport region, and the particle positions at each step are used in an unbinned maximum likelihood fit for the beam profile distribution. The self-fields at the position of each particle are calculated using the fitted beam profile distribution. The total computation required by the simulation scales linearly with n. The simulation for an electron beam with a phase space given by the Kapchinskij-Vladimirskij distribution is in good agreement with the beam profile predicted by the Kapchinskij-Vladimirskij envelope equations.

1 INTRODUCTION

The optics for a charged particle beam that does not satisfy the condition $\beta = v/c \approx 1$ is influenced by the beam self-forces. These forces include the electrostatic repulsion between the like charges in the beam and the focusing due to the self-magnetic field. The beam self-forces may become an important consideration in the transport region near the output of the particle source for the beam. In some applications, an electron beam is delivered directly from the gun to the target with no further acceleration, and the electrostatic repulsion cannot be tolerated. The beam may then be neutralized by allowing it to ionize a dilute gas[1]. We will denote the ratio of electron to ion charge densities as the beam neutralization factor f. Typically, $f = 1$ immediately after the beam encounters the ionizing gas.

The evolution of the beam envelope for a uniform elliptical beam in the absence of longitudinal magnetic fields may be calculated by integrating the Kapchinskij-Vladimirskij (K-V) equations if the phase space of the beam is given by the K-V distribution[2]:

$$f(x,y,x',y') = \delta\left(\frac{x^2}{a^2} + \frac{y^2}{b^2} + \frac{a^2x'^2}{\epsilon_x^2} + \frac{b^2y'^2}{\epsilon_y^2} - 1\right). \quad (1)$$

The quantities a and b are the semi-axis of the uniform beam profile ellipse in the $x-y$ plane normal to the reference trajectory along the z direction. The slopes x' and y' yield the transverse momenta p_x and p_y in the $x-y$ plane, where $p_x, p_y << p_z$. ϵ_x and ϵ_y are the emittances (area/π) in the $x-p_x$ and $y-p_y$ planes. The K-V equations for $a(z)$ and $b(z)$ in the absence of external fields are given by[2]:

$$\frac{d^2a}{dz^2} - \frac{2K}{a+b} - \frac{\epsilon_x^2}{a^3} = 0$$

$$\frac{d^2b}{dz^2} - \frac{2K}{a+b} - \frac{\epsilon_y^2}{b^3} = 0$$

$$K = \frac{2Nr_e}{\beta^2\gamma}(1/\gamma^2 - f), \quad (2)$$

where r_e is the classical electron radius and N is the number of electrons per unit length of the beam. These equations are easily integrated in the presence of transverse magnetic fields.

A realistic beam is unlikely to satisfy the conditions required by the K-V equations. The initial transverse momentum distribution is more likely to be Maxwellian, and longitudinal magnetic fields may be present. This note describes a Monte Carlo simulation that in principle may be adapted to simulate an arbitrary beam under the influence of self-fields. The simulation has been investigated for a DC beam satisfying the K-V distribution; this allows the results from the simulation to be compared to the beam envelope predicted by the K-V equations.

2 MONTE CARLO SIMULATION

The simulation assumes that the profile of the current density in a plane normal to the reference trajectory may be modeled by a profile function $J(x,y;\vec{\alpha})$, where the parameters $\vec{\alpha}$ are allowed to evolve as the beam propagates. The profile function should be flexible enough to represent the beam profile within the transport region of interest. Choosing an appropriate profile function with a minimum number of parameters is not a trivial task and requires some physical guidance. The profile function chosen to represent the K-V beam is discussed in the next section.

The simulation randomly generates an ensemble of n particles that populate an initial beam profile $J(x,y;\vec{\alpha_0})$ and an initial transverse momentum distribution. These initial distributions must reproduce the beam emittance.

The initial beam profile is used by the simulation to calculate the beam self-fields at the position of each particle. For a round (azimuthally symmetric) beam these fields are easily obtained from the integral

$$2\pi\int_0^R J(\rho^2 = x^2+y^2;\vec{\alpha_0})\rho d\rho,$$

where R is the radial position of the particle. If the beam is not azimuthally symmetric, the fields must be obtained by numerical integration.

0-7803-4376-X/98/$10.00 © 1998 IEEE

Once the self-fields are calculated, the external fields are added and each particle is propagated by a short step dz. Because the self-fields scale with the dimensions of the beam, the step length is chosen to be a scale factor F_s times a parameter representing the size of the beam. If we were propagating a round beam, for example, we might choose this parameter to be the radius enclosing half of the particles. For the uniform elliptical beam used with the K-V distribution, we have chosen the minor semi-axis of the ellipse.

After the particles are propagated by dz, the new $x - y$ positions of the particles are used in an unbinned maximum likelihood fit to determine the parameters $\vec{\alpha}$ of the new beam profile $J(x, y; \vec{\alpha})$. We have used the downhill simplex method[3] to perform the fit, using the parameters from the previous step as initial values. The self-fields are recalculated at the new particle positions using the new beam profile, and the particles are each propagated through the next step. This process continues until the particles have been propagated through the desired transport region, yielding the solution $J(x, y; \vec{\alpha}(z))$ for the beam profile at each step.

The number of computations performed by the simulation scales linearly with the number of particles. For applications requiring a numerical integration of the beam profile, the computation requirements may become quite large. Fortunately, the simulation is ideally suited for distributed processing. Distributed processing has been implemented on the workstation network at Imatron. Several client processes on different CPUs each generate a fraction of the total number of particles. The clients calculate the fields and propagate the particles for each step. The positions of the particles for all of the clients are read over the network by a single server process, which performs the fit to determine the parameters $\vec{\alpha}$. Each client reads $\vec{\alpha}$ back from the server so that it can calculate the self-fields for propagating the particles through the next step.

3 SIMULATION USING THE K-V DISTRIBUTION

A beam with a K-V distribution in phase space has a uniform elliptical profile. We approximate a uniform profile by using a profile function similar to the Fermi-Dirac distribution. For a round beam we perform a one parameter fit to the radius a:

$$J(\rho^2 = x^2 + y^2; a) = \frac{I_0}{\aleph\left[1 + \exp\left(\lambda^2(\eta^2 - 1)\right)\right]}. \quad (3)$$

I_0 is the total current in the beam, λ controls the cutoff of the profile near the radius a, $\aleph = \pi a^2 \log(1 + \exp(\lambda^2))/\lambda^2$ is a normalization constant, and $\eta^2 \equiv \rho^2/a^2$. Eq. (3) may be immediately generalized to a uniform elliptical beam with semi-axes a and b by setting $\eta^2 = x^2/a^2 + y^2/b^2$ and $\aleph = \pi ab \log(1 + \exp(\lambda^2))/\lambda^2$. The beam profile $J(x, y; a, b)$ then becomes a two parameter fit to a and b.

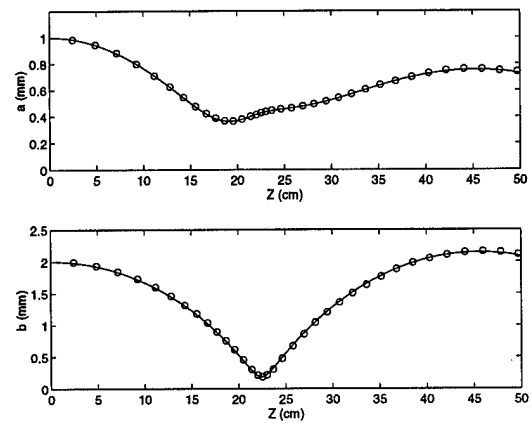

Figure 1: The beam envelope semi-axes predicted by the K-V equations (solid line) and the simulation (open circles) for a 0.635 Amp neutralized electron beam with a kinetic energy of 130 KeV and an emittance of $4.3 \times 10^{-4}\ \pi$ cm-radians.

The initial phase space is populated with n electrons using Eq. (1) with $\epsilon = \epsilon_x = \epsilon_y$. For each electron we generate three random numbers between 0 and 1 which we denote as s_1, s_2, and s_3. Let a_0 and b_0 be the initial semi-axes of the beam profile ellipse. We first map s_1 into the unit area underneath the normalized beam profile distribution and solve for η_s:

$$s_1 = \frac{\pi a_0 b_0}{I_0} \int_0^{\eta_s} J(x, y; a, b)\eta d\eta. \quad (4)$$

We then have:

$$\begin{aligned} \theta &= 2\pi s_2 \\ \phi &= 2\pi s_3 \\ x &= a_0 \eta_s \cos\theta \\ y &= b_0 \eta_s \sin\theta \\ x' &= \epsilon\sqrt{(1 - \eta_s^2)} \cos\phi / a_0 \\ y' &= \epsilon\sqrt{(1 - \eta_s^2)} \sin\phi / b_0. \end{aligned} \quad (5)$$

The electric and magnetic fields $\mathbf{E}$ and $\mathbf{B}$ are generated at the position of each electron by numerical integration of the beam profile. Each surface element $dS' = dx'dy'$ of the beam profile is treated as a filament of current at the position $\mathbf{r}' = (x', y')$ with the current $dI = J(\mathbf{r}'; a, b)dS'$. The current filament generates the fields $d\mathbf{E}(\mathbf{r})$ and $d\mathbf{B}(\mathbf{r})$ at the position $\mathbf{r} = (x, y)$ of an electron:

$$\begin{aligned} d\mathbf{E}(\mathbf{r}) &= \left(\frac{ec\mu_0}{2\pi\beta}\right) \frac{(\mathbf{r} - \mathbf{r}')}{|\mathbf{r} - \mathbf{r}'|^2} dI \\ d\mathbf{B}(\mathbf{r}) &= \left(\frac{e\mu_0}{2\pi}\right) \frac{\hat{z} \times (\mathbf{r} - \mathbf{r}')}{|\mathbf{r} - \mathbf{r}'|^2} dI. \end{aligned} \quad (6)$$

For a profile with elliptical symmetry, we make the substitutions $u = x/a$ and $v = y/b$ to map the ellipse onto a

unit disk in the $u - v$ plane. The disk is divided into two domains: a central core of radius $1 - \pi/4$ containing about 5% of the total area, and a surrounding annulus. The core is integrated by 21 point Gaussian quadrature. The annulus is further subdivided into square tiles using m radial divisions and $8m$ azimuthal divisions. Each tile is integrated by 9 point Gaussian quadrature. We have found that setting $m = 7$ provides a sufficiently accurate determination of the self-fields.

To obtain close agreement with the K-V envelope equation, we have set $F_s = 1/4$ and used several hundred electrons. Figure 1 shows the results from a simulation (plotted at 100 step intervals) of 840 electrons and the K-V envelope equation for a 0.635 Amp neutralized ($f = 1$) beam with a kinetic energy of 130 KeV and an emittance of 4.3×10^{-4} π cm-radians.

4 COMMENTS ON SIMULATING A MAXWELLIAN BEAM

Preliminary investigations are now in progress for a realistic electron beam with a Maxwellian momentum distribution that begins at a round cathode of radius a_0. The slopes x' and y' now have Gaussian distributions with $\sigma = \epsilon/(2a_0)$, where ϵ is the r.m.s. emittance[2]. The profile distribution is expected to include the profile from Eq. (3) because the beam is initially uniform.

5 ACKNOWLEDGEMENTS

The author has benefitted from discussions with R.E. Rand, K. Garewal, and T. Sanders.

6 REFERENCES

[1] 'Transport of Self-Field Dominated DC Low-Energy Electron Beams Through Low-Pressure Gases', R.E. Rand, M.C. Lampel, and D.Y. Wang, *J. Appl. Phys.* **62**(5), 1639 (1987).

[2] 'The Physics of Charged Particle Beams', by J.D. Lawson, published by Clarendon Press, 1977.

[3] 'Numerical Recipes in C', by Press, Teukolsky, Vetterling, and Flannery, published by Cambridge University Press, 1992.

USE OF THE LANA CODE FOR THE DESIGN OF A HEAVY ION LINAC

D.V. Gorelov, P.N. Ostroumov, INR, 117312, Moscow, Russia and
R.E. Laxdal, TRIUMF, 4004 Wesbrook Mall, Vancouver, B.C., Canada V6T 2A3

Abstract

The LANA computer code (Linear Accelerators Numerical Analysis) has been developed in INR, Moscow during the last several years and still is in further development. This code is designated for the design and simulation of various kinds of linear accelerators. Recently the code has been extensively used for the design and study of the *separated function* heavy ion DTL for the ISAC project at TRIUMF. The paper describes the mathematical models used in the LANA code including *space charge* effects and three-dimensional *realistic* accelerating field representation. In particular the procedure for drift tube geometry generation based on three-dimensional electromagnetic field distributions extracted from MAFIA is described in detail. The LANA code is also used to determine the influence of the *asymmetry* in the fields of the H-type structure on the beam dynamics.

1 INTRODUCTION

The LANA code has been developed at INR, Moscow during the last several years [1] as a powerful tool for the design and study of the beam dynamics in various linear accelerators [2, 3, 4].

The LANA code is especially useful for the simulation of complicated beam dynamics problems in linacs [5]. The completeness and flexibility of the graphics output and convenience of the operator's intervention during simulation allows research into new linac concepts. Recently the code has been applied successfully in the design of the Separated Function DTL for the ISAC project at TRIUMF [6].

2 MATHEMATICAL MODELS

The main simulation mode used in LANA assumes the so called *square wave* approximation of the accelerating field in the gaps of the DTL. This mode allows quick calculations with an accuracy sufficient for establishing gross specifications (ie. number and length of tanks, effective voltage, phase, stability requirements etc.) Therefore this regime is preferable for simulations of such procedures as phase scanning [3], Δt - procedure [3, 4], *variable energy* scans [6, 7], etc.

However this code permits detailed calculations with a *realistic field* distribution in the accelerating structure (a particular iterative procedure is described in section 2.4). Actually the mathematical background in both cases is identical, but in the case of *realistic fields* the accelerating cell is split longitudinally into a number of steps and the formulas for the *square wave* are applied for each step sequentially.

The *realistic fields* have to be calculated using some available electromagnetic codes like SUPERFISH for 2-D, MAFIA for 3-D [8] or other similar codes. The calculated field distributions inside the aperture of the accelerating channel can be imported to LANA. The data are interpolated linearly on all three coordinates where needed during the simulation. A more detailed description of the interpolation algorithm is given in [1, 9].

2.1 Linac Structure Representation

In the code the linac is considered as a number of independently fed cavities. This means that the accelerating field amplitude and phase can be different in sequential cavities. The linac to be simulated can be a combination of different available structure types such as DTL, IH, CCL, etc.

Each cavity can consist of several separate sections (modules). Focusing and/or bending magnet systems (in the horizontal plane) may be included in front of the first and after every section. The focusing system can include quadrupoles, solenoids and drifts. In addition to dipoles the bending magnet system can include a stripping foil. The stripping foil is simulated as a thin element with a predefined equilibrium charge state as well as parameters to account for transverse scattering and energy straggling.

2.2 Beam Representation

The LANA code uses a 3-dimensional multi-particle Monte Carlo model of the beam. All particles are traced separately, sequentially and independently, through the elements of the focusing and bending magnet systems, the drift spaces and the accelerating cells.

The interaction between the charged particles is estimated only at certain points along the accelerating cell, magnetic element or drift and is used as a constant up to the next point of the estimation. The space charge effects can be ignored in order to speed up the computations in the case of low current beams. The 3-D space charge calculation is valid for bunched beams only. The method [10] is based on analytic relations between charge density and electric field for the distribution with 3-D ellipsoidal symmetry in real space.

2.3 Formalism

Dipoles, quadrupoles, solenoids and drifts are simulated using standard matrix formalism [11]. The simulation of the accelerating gap is done using formulas of the *iteration*

0-7803-4376-X/98/$10.00 © 1998 IEEE

procedure [12]. This procedure has been redeveloped for the 3-D particle dynamics and space charge consideration.

The initial equation of the particle's motion in the accelerating gap is:

$$\frac{d}{dt}\left(\gamma \cdot \dot{\vec{x}}(t)\right) = \frac{e}{m_0} \cdot \vec{E}(\vec{x}(t)) \cdot cos(\varphi_0 + \omega t) + \frac{e}{m_0} \cdot \vec{E}_c(\vec{x}(t))$$

where: $\gamma = \frac{1}{\sqrt{1-\beta^2}}$ – the Lorentz factor, β – longitudinal relative particle velocity, c – speed of light, e – particle's charge, m_0 – particle's rest mass, $\varphi_0 + \omega t$ – phase of the accelerating field at the corresponding moment of time, $\vec{E}(\vec{x}(t))$ – amplitude of the accelerating field at the corresponding space coordinates, $\vec{E}_c(\vec{x}(t))$ – static electric field equivalent of the space charge force (with the magnetic field impact included).

This equation is solved numerically in LANA for both the transverse and longitudinal motion. The equivalent space charge electric field could be presented in the approximation of the elliptically symmetric charge distribution in configuration space:

$$\begin{cases} E_{cz} &= Q_z \cdot \zeta \\ E_{cx} &= Q_x \cdot x \\ E_{cy} &= Q_y \cdot y \end{cases}$$

where: $\zeta = \zeta_0 + z - z_c$, x and y are the particle displacements in the corresponding space coordinates relative to the center of the rms ellipsoid, $z_c(t)$ – current longitudinal coordinate of the center of the rms ellipsoid, ζ_0 is the initial longitudinal displacement of the particle from the center of the rms ellipsoid, and $Q_{z,x,y}$ – the functions of the parameters of the rms ellipsoid (constant for the current step of the integration of the particle motion).

All details about the the final formulas used in LANA can be found in [9].

2.4 *Procedure for DTL Design with Realistic 3-D Fields*

In order to perform the DTL geometry correction and beam dynamics simulation in the linac with a *realistic field* distribution several sequential stages of the calculations should be made:

1. Conceptual design of the accelerator in the *square wave* approximation.

2. General optimization of the physical tank geometry in order to satisfy the requirements of the rf power consumption distribution, the electric gradient distribution in the structure, the peak surface field distribution along the structure, etc. An example of such a study is described in detail in reference[8] for MAFIA simulation procedures.

3. The additional LANA geometry generation run should be performed using the correct values for the average accelerating gradients and the desired g/ℓ ratios in the sequential cells.

4. The electromagnetic field recalculation (with MAFIA or SUPERFISH codes for instance) should be done in order to provide self-consistent data for the next LANA geometry correction procedure.

5. The main geometry correction stage is performed at this point. This stage involves special algorithms of the longitudinal DTL geometry correction with the tracing of the reference particle through the *realistic fields*.

6. For the final check of this procedure and in order to have self consistent data an additional electromagnetic field recalculation should be done.

7. The last stage is to run LANA on this consistent set of field data.

This procedure actually converges at stage 5, so the final two stages provide an extra verification of the overall procedure.

3 EXAMPLE OF BEAM DYNAMICS SIMULATION

The most recent studies of the beam dynamics using LANA were done in application to the Separated Function DTL for the ISAC project at TRIUMF [6, 9]. A typical LANA graphic screen from these studies is shown in Fig. 1. This screen provides the beam phase space portraits and also transverse and longitudinal envelopes in the intermediate cell of the second IH tank of the DTL.

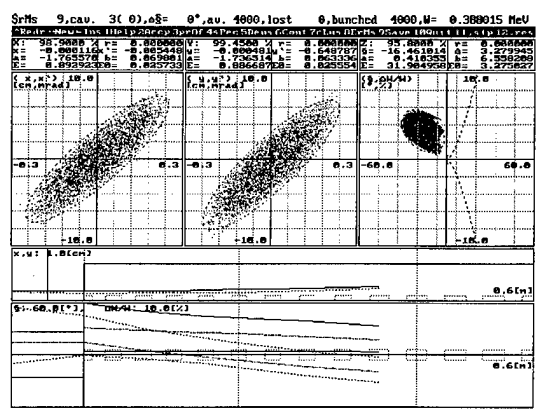

Figure 1: A typical PC screen of the LANA simulation session.

The simulation shown in Fig. 1 has been performed with *realistic fields* calculated from MAFIA. An example of the longitudinal electric field component, E_z, in the vertical plane of symmetry of the IH structure for the second cell of tank 2 is given in Fig. 2. This picture is typical for all other cells of the IH structure. A detailed study of the first IH tank field components and properties is done in reference[8].

One of the most interesting features of the beam dynamics study of the IH structure is the vertical asymmetry of the

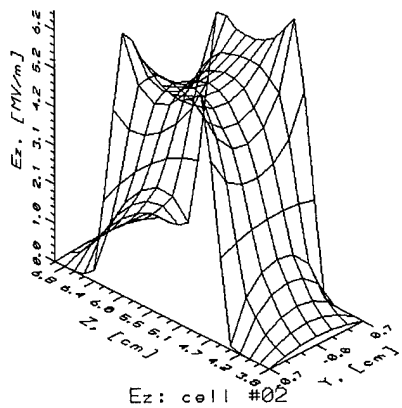

Figure 2: A typical MAFIA calculated 3-D field distribution in the accelerating gap.

stems geometry. This asymmetry produces a *dipole component* in the on axis vertical electric field. The overall effect, however, is negligible because of the alternating nature of the deflections. Fig. 3 provides the scaled integral of the effective E_y electric field component along the second IH tank. The corresponding markers represent the vertical divergence of the beam bunch center in the middle of each drift tube as calculated with LANA. Fig. 3 illustrates the self-compensation of the *dipole component* effect at the exit of the cavity. This result was proved by the actual beam dynamics simulation in the 3-D fields bv LANA.

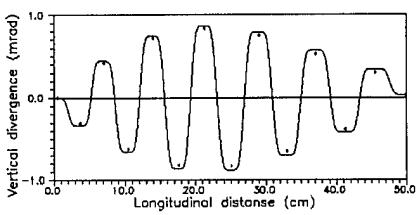

Figure 3: The overall accumulated dipole component effect in the IH structure.

The thin lens model of the rf defocusing is used in LANA in the *square wave* approximation, which coincides completely with the results of the simulation with 3-D *realistic fields* [9]. The relative difference between the transverse envelopes in these two approximations is always less then 3%.

The longitudinal dynamics is insignificantly changed as a result of the small change of the final optimized drift tube geometry for the *realistic field* case compared to the "generic" *square wave* case. These changes are concerned only with the position of the bunch in longitudinal phase space and its shape. While the energy spread increased by ~3%, the phase spread decreased by about the same relative amount.

4 CONCLUSION

The LANA code is a user friendly tool for the design and study of multi-cavity linacs. LANA offers the convenience of the PC platform, a graphical representation of the beam during the simulation process, the possibility of intervention during simulation and flexibility of several simulation models.

At the present time LANA is successfully used for the design of a high intensity H^- linac.

The LANA code is in continuous development and improvement in order to cover the widest possible range of different studies applied to various kinds of linear accelerators.

5 ACKNOWLEDGEMENTS

Special thanks to P. Bricault for very important and helpful discussions on various aspects of the DTL design and MAFIA simulations of the IH tanks. The authors would also like to thank G. Dutto for the attention to this work and kind help in different situations.

6 REFERENCES

[1] D.V. Gorelov and P.N. Ostroumov, 'The LANA Computer Code for the Beam Dynamics Simulation in Multi-Cavity Linacs', INR Internal Report, 1993-1994.

[2] S.K. Esin *et al.*, 'Linear Accelerator for Production of Radioactive Beams', proc. of Linear Accelerators Conf. 1992, Ottawa, 1992.

[3] S.K. Esin *et al.*, 'Commissioning/Operating of the Moscow Meson Factory Linac', proc. of International Linac Conf. 1994, Tsucuba, Japan, Vol. 1, p. 31, 1994.

[4] M. Popovic *et al.*, 'Measurements of the Longitudinal Beam Parameters in the Fermilab Linac', proc. of International Linac Conf. 1994, Tsucuba, Japan, Vol. 2, p. 896, 1994.

[5] D.V. Gorelov and P.N. Ostroumov, 'Application of LANA Code for Design of Ion Linac', proc. of European Particle Accelerators Conf. 1996, Barcelona, Spain, Vol. 2, p. 1271, 1996.

[6] R.E. Laxdal, 'A Separated Function Drift Tube Linac for the ISAC Project at TRIUMF' , these proceedings.

[7] R.E. Laxdal and D.V. Gorelov, 'Optimization and Design Specifications for Tank1 of the ISAC Drift Tube Linac', TRIUMF Design Note TRI-DN-ISAC-97-4, 1997.

[8] D.V. Gorelov, 'MAFIA Studies of the ISAC DTL Tank1', TRIUMF Design Note TRI-DN-ISAC-97-5, 1997.

[9] D.V. Gorelov, 'Beam Dynamic Simulation with 3-D Realistic Fields Using LANA Code', TRIUMF Design Note TRI-DN-ISAC-97-6, 1997.

[10] A.D. Vlasov, 'Theory of the Linear Accelerators', Atomizdat, Moscow, 1978. (in russian).

[11] K.L. Brown *et al.*, 'TRANSPORT. A Computer Program for Designing Charged Particle Beam Transport Systems', CERN, Geneva, 1980.

[12] B.P. Murin *et al.*, 'Ion Linear Accelerators. V.1. Problem and Theory'. Edited by B.P.Murin, Atomizdat, Moscow, 1978. (in Russian).

RELATIVISTIC KLYSTRON TWO-BEAM ACCELERATOR SIMULATION CODE DEVELOPMENT

S. M. Lidia, Lawrence Berkeley National Laboratory, and
R. D. Ryne, Los Alamos National Laboratory

Abstract

We present recent work on the development and testing of a 3-D simulation code for relativistic klystron two-beam accelerators (RK-TBAs). This code builds on our previous experience with 1-D and 2 1/2-D relativistic klystron simulators. We adopt a new approach utilizing symplectic integration techniques to push particles, coupled to a circuit equation framework that advances fields in the cavities. Space charge and current effects are calculated using an electrostatic PIC algorithm.

1 INTRODUCTION

Current development of relativistic klystrons for two-beam accelerator applications [1] demand a high degree of simulation detail. These devices are long (extraction sections of tens to hundreds of meters), employ both solenoid and quadrupole focusing elements, and may use detuned RF output structures for longitudinal stability. In the LLNL/LBNL RK-TBA design, the beam receives periodic re-acceleration from induction cells, followed by energy extraction in the output RF structures. The beam phase space cycles rapidly through a sequence of different states, and there exist numerous instabilities that ultimately limit the device's RF power extraction efficiency. The breaking of azimuthal symmetry in the transport lines and RF cavities, and the high degree of longitudinal bunching, necessitate a fully 3-D simulation capability. For a short device, a 3-D electromagnetic particle-in-cell (PIC) code would be an appropriate simulation tool. However, these new devices are quite long, so that full PIC studies become exceedingly expensive and impractical for beamline design.

We are building a simulation code that incorporates well established symplectic tracking techniques for single particle motion [2] and an electrostatic beam frame PIC algorithm, with a circuit equation solver for the cavity modes.

In section 2 of this paper, we describe the general framework and formalism used by the code. In section 3, we present results from the simulation of transport through a beamline comprised of magnetic quadrupoles, induction accelerating cells, and an RF output cavity.

2 CODE FORMALISM

The code uses a Hamiltonian framework to advance the positions and canonical momenta of the particles. The equations of motion for particles following a given design orbit (or fiducial) are solved exactly. All other particles are advanced by tracking their deviations in phase space about the fiducial. Deviations in transverse position and canonical momenta, arrival time, and energy all are tracked to 3rd order. Likewise, external fields are included as scalar and vector potentials, represented as 4th order Taylor series expansions about their values along the fiducial. Fringe fields and overlapping beamline elements are included automatically. Effects arising from self-fields are calculated by an electrostatic PIC solver in the beam's rest frame.

2.1 Particle Tracking

The total Hamiltonian is represented in the form

$$H_{tot} = H_{kin} + H_{ex} + H_{self}$$

where H_{kin} is the kinetic portion describing single particle motion in the absence of all fields, H_{ex} is the contribution to single particle motion from external electromagnetic fields, and H_{self} is the contribution from self-fields. The transfer maps due to the kinetic and external field sectors are calculated together, resulting in a total map for single particle motion. The map due to self-fields is then calculated separately.

These two separate mappings are applied to the particle phase space coordinates by using split operator techniques[1]. The prescription to advance the particles, which is accurate through 2nd order over the step size (t), is to apply the two mappings in an interleaved manner, viz.

$$M_{total}(t) = M_{single}(t/2)\, M_{self}(t)\, M_{single}(t/2).$$

Here M_{single} is the resultant single particle map, while M_{self} is the map from the self-field impulse. In terms of computational expense, calculating the map due to self-fields is by far the most costly step in this procedure. To increase the efficiency in the computation, we use as large a step size as possible, while maintaining sufficient accuracy (as determined, for example, by verifying that the

[1]Split operator techniques are based on splitting the Hamiltonian into pieces that can be solved exactly (or through some desired order of accuracy), and then combining the separate maps to produce an approximate map for the full Hamiltonian. Split operator symplectic integration algorithms (including the well known leap-frog algorithm of plasma physics simulations) are widely used in the treatment of Hamiltonian systems [3 4 5].

0-7803-4376-X/98/$10.00 © 1998 IEEE

results do not change significantly when the step size is further decreased.)

The self-fields are determined by numerically solving Poisson's equation on a 3-D Cartesian grid in the beam's rest frame. Standard fast Fourier transform techniques are used [6, 7]. For an accurate representation of the 3-D fields from a bunched beam, we must use grid sizes of up to 64 x 64 x 512 nodes, as well as 10^5 - 10^6 macroparticles. Even with this many particles, noise effects in the fields remain an issue.

2.2 Circuit Equation for RF Cavities

The RF structures are modeled by a decomposition of fields into the vacuum modes. Associated with each mode is a characteristic circuit equation describing the evolution of amplitude and phase. The beam-cavity interaction is modeled by specifying a small set of parameters: the mode frequency (w_o), the loaded Q (Q_L) of the mode, the [r/Q] of the mode, the driving frequency of the beam (w), and the overlap of the beam current density with the mode (i_b). The cavity voltage (V_c) then evolves according to

$$\ddot{V}_c + \frac{\omega_o}{Q_L}\dot{V}_c + \omega_o^2 V_c = \omega_o \left[\frac{r}{Q}\right] \dot{i}_b ,$$

where the overdots indicate time derivatives. We assume that both the current and the cavity voltage oscillate at the same frequency (w), and that amplitude variations in both occur on a much longer time scale than 1/w. Then, solving for steady state voltage levels, we find that

$$V_c = i_b Q_L \left[\frac{r}{Q}\right] \cos\psi \cos(\psi+\omega t) ,$$

where y is the tuning angle, defined by $\psi = Q_L\left(\frac{\omega_o}{\omega} - \frac{\omega}{\omega_o}\right)$.

This formalism is used to study the beam dynamics in both the RF output and the induction cell cavities. Besides the fundamental mode in the in the RF output structures, attention is paid to longitudinal modes in the induction cells, as well as transverse beam-breakup (BBU) modes in both cavities. The BBU modes have been identified as the cause of transverse instabilities which eventually limit the net efficiency of the RK-TBA. The longitudinal mode in the induction cell cavity has been studied [8] as a source of beam energy loss as it can couple to the fundamental harmonic of the RF beam current.

3 SIMULATION RESULTS

We present results of simulation through a section of a hypothetical RKTBA extraction section. The beamline is comprised of permanent magnet quadrupoles, induction cell acceleration cavities, and standing wave output structures. The parameters are shown in Table 1.

The RF output structure extracts 180 MW from the beam as it passes through, corresponding to a 300 kV drop in the beam voltage. There are five induction reacceleration cells per meter, each providing 60 kV to the beam. In this way, the beam energy is kept steady, period by period. Here, we attempt to model the steady-state behavior of the beam through the section.

Table 1 Parameters of RKTBA extraction section

Beam Parameters	
Average energy	3.88 MeV
DC current	600 A
RF current, frequency	1200 A, 11.424 GHz
FODO Lattice	
Lattice period	0.20 m
Phase advance / period (s_0)	72°
Occupancy factor	0.5
Induction Cell Parameters	
Cell Voltage	60 kV
RF Structure Parameters	
Frequency	11.424 GHz
Q_L	80
Steady-state output power	180 MW

The choice of a 1 m betatron period corresponds to the spacing between RF output structures. This *betatron node* scheme significantly reduces the transverse instability growth rate associated with the cavities. In Figure 1 we show the evolution of the transverse phase space through a 1 m section of the beamline. The transverse phase space distribution is seen to remain stationary, with only a small number of particles leaving the core to form a halo.

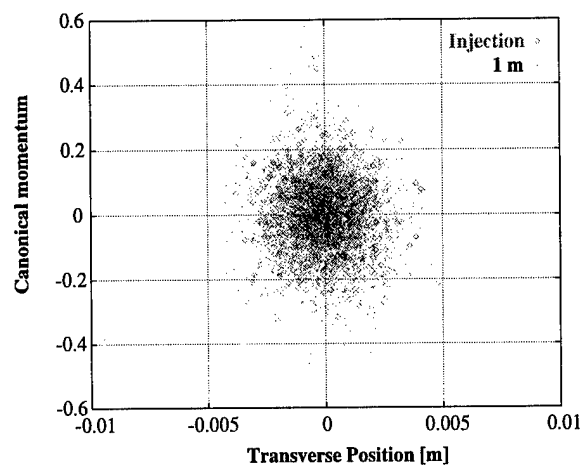

Fig. 1 Transverse phase space evolution

The beam upon injection was strongly bunched at the 11.424 GHz frequency, but was not otherwise matched in its longitudinal phase space. Longitudinal space charge forces act to debunch the beam, while the RF output structure can be phased to provide some focusing. Figure 2 shows the evolution of the longitudinal phase space as the beam passes through 1 m of beamline. The increase in energy spread due to space charge is readily apparent,

with nonlinearities due to the nonuniform (gaussian) distribution.

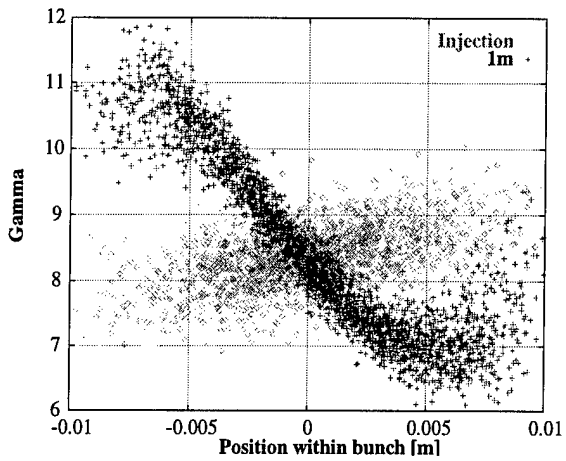

Fig. 2 Longitudinal phase space evolution

4 CONCLUSIONS

We have begun work on a new simulation code for relativistic klystron two-beam accelerators. This code tracks the full six dimensional phase space of the beam, and incorporates fields self-consistently. More work on transient power evolution in the RF cavities is being performed. Benchmarking of the code will concentrate simulations of transport, RF power extraction, and debunching effects in upcoming 35 GHz experiments.

5 ACKNOWLEDGMENTS

The authors wish to thank Glen Westenskow and Simon Yu for their continued support of this work, William Fawley for his useful advice on PIC simulations, and Enrique Henestroza and Tim Houck for their assistance in numerical modeling of cavities. One of the authors (SML) would like to thank the members of the LANSCE-1 group at LANL for hosting him while much of this work was performed. This work was performed under the auspices of the U.S. Department of Energy by LBNL under contract AC03-76SF00098.

REFERENCES

[1] D. Anderson, *et. al.*, *Design of a Linear Induction 1-MV Injector for the Relativistic Klystron Two-Beam Accelerator*, these proceedings.

[2] A. J. Dragt, *et. al.*, Ann. Rev. Nucl. Sci. **38** (1988), 455.

[3] E. Forest and R.D. Ruth, Physica D **43** (1990), 105.

[4] H. Yoshida, Phys. Lett. A **150** (1990), 262.

[5] E. Forest, J. Bengtsson, and M.F. Feusch, Phys. Lett. A **158** (1991), 99.

[6] C. K. Birdsall and A. B. Langdon, *Plasma Physics Via Computer Simulation*, Adam Hilger, Bristol, 1991.

[7] R. W. Hockney and J. W. Eastwood, *Computer Simulation Using Particles*, Institute of Physics Publishing, Bristol, 1988.

[8] S. Eylon, *et. al.*, *Longitudinal Impedance Measurements of an RK-TBA Induction Accelerating Gap*, these proceedings.

MEASURED AND THEORETICAL CHARACTERIZATION OF THE RF PROPERTIES OF STACKED, HIGH-GRADIENT INSULATOR MATERIAL

T.L. Houck, G.J. Caporaso, C.C. Shang, S.E. Sampayan, N.E. Molau
Lawrence Livermore National Laboratory, Livermore, CA 94551
M.L. Krogh, Allied Signal Corporation, FM&T, Kansas City, MO 64141

Abstract

Recent high-voltage breakdown experiments of periodic metallic-dielectric insulating structures have suggested several interesting high-gradient applications. One such area is the employment of high-gradient insulators in high-current, electron-beam, accelerating induction modules. For this application, the understanding of the rf characteristics of the insulator plays an important role in estimating beam-cavity interactions. In this paper, we examine the rf properties of the insulator comparing simulation results with experiment. Different insulator designs are examined to determine their rf transmission properties in gap geometries.

1 INTRODUCTION

Insulators comprised of finely spaced, alternating layers of dielectric and metal have demonstrated greater (from 1.5 to 4 times) vacuum surface flashover capability than insulators made from a uniform dielectric [1,2]. These high-gradient insulators (HGIs) have maintained similar capability in the presence of an electron beam [3]. The high field stress level in the presence of a beam permits greatly simplified gap designs for induction accelerators. In typical induction accelerator designs [4], the gap is shaped to accommodate an extended insulator hidden from the beam line-of-sight view. The gap shape must then be carefully designed to minimize field stress. A simplified gap design using the superior performance of the HGI technology has been suggested for the induction modules for a proposed TBNLC rf power source [5].

Collective beam instability associated with the gap's transverse beam impedance is of equal importance to surface flashover. Transverse impedance scales linearly with the gap width and inversely with the square of the beam line aperture [6]. Increasing the aperture to lower impedance is effective, but is not energy or cost efficient. HGI technology, by minimizing gap width and permitting less complicated gap designs, can reduce the induction core volume to achieve higher efficiency.

However, a concern with the use of the HGI in gap designs is the possible introduction of high-impedance resonances from the more complicated geometry of the insulator. Transverse impedance measurements were performed with HGI insulators positioned at the mouth of simplified cavity gaps. These measurements were then compared against solid insulators.

2 EXPERIMENTAL LAYOUT

The impedance measurements were performed by a standard technique [7] where the beam pipe is transformed into a coaxial TEM transmission line by inserting two center conductors and measuring transmission through the two-wire transmission line. The center conductors are driven through a 180° hybrid to excite transverse currents in the test cavity. Transmission through the beam line with the a test cavity inserted is compared to that of a smooth pipe of equal longitudinal length as the test cavity. Measurements of the S-parameters were made with an HP8510C Network Analyzer. The through-short-delay (TSD) calibration technique was used to remove the effect of the matching sections between the analyzer and beam pipe transmission line. The real part of the transverse impedance can be calculated from the measured S-parameters using [8]

$$Z_\perp = \frac{2\,c\,Z_o}{\omega\,\Delta^2}\left(\frac{\cos\theta}{S} - 1\right), \text{ where} \qquad (1)$$

$$S = \left|\frac{S_{21}}{S_{21}^{ref}}\right|, \text{ and } \theta = \arg\left[\frac{S_{21}}{S_{21}^{ref}}\right], \text{ and} \qquad (2)$$

$\Delta = 10.8$ cm is the wire separation. The superscript "ref" indicates the value measured for a smooth pipe, or reference, configuration. The characteristic impedance of the two-wire transmission line, Z_o, had a value of 359 Ω for the configuration used.

The test cavity represented a simplified induction module. The cavity geometry was a pillbox (14.6 cm ID and 25.4 cm OD) separated into two regions by a 3 mm thick ring of inside diameter of 23.5 cm, concentric with the cavity axis, and extending 2.25 cm across the cavity. A 6mm thick, 2.54 cm wide ring of ferrite (TDK PE11B) was positioned between the OD of the ring and the outer wall of the cavity. The ferrite was effective in reducing the Q of the trapped dipole modes to less than 3, a typical value for induction accelerator gap designs. A schematic of the test cavity is shown in Fig. 1.

The insulators were comprised of thin disks (0.5 mm) of polycarbonate or stainless steel, with inner diameter of 14.6 cm and outer diameter of 19.7 cm or 22.2 cm depending on the configuration. The distribution of disks was varied to produce different ratios of insulator to conductor and different number of alternating layers, or periods, for a specific ratio. A photograph of the pillbox test cavity with a 4:1 ratio stacked insulator is shown in Fig 2. One wall of the cavity was removed for the picture.

0-7803-4376-X/98/$10.00 © 1998 IEEE

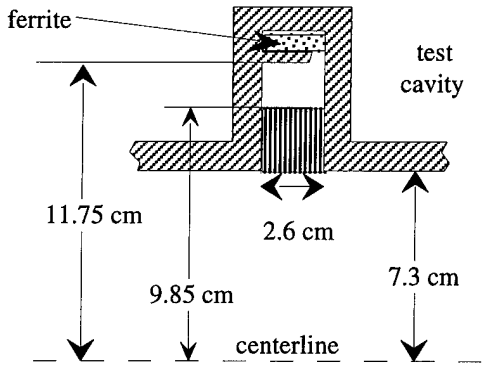

Figure 1. Schematic of the pillbox test cavity.

3 EXPERIMENTAL RESULTS

Impedance measurements of the test cavity with the 19.7 cm OD insulator and different ratios of dielectric to conducting material is shown in Fig. 2. The smaller peaks flanking the primary resonance at 1.35 GHz are related to the geometry of the transmission line and are not specific to the test cavity. Addition of microwave absorbers at the ends of transmission line pipe reduced these impedances while not affecting the primary or 350 MHz resonances. The TE/TM cutoff frequencies for traveling wave modes in the transmission pipe are 1.2/1.57 GHz respectively. The 350 MHz resonance is not affected by the structure of the insulator. Removal of the intermediate ring in the pill box also did not significantly change the impedance of this resonance, although the 1.35 GHz resonance was effectively removed. The number of layers, or periods, of polycarbonate were 9 for the 2:1, 7 for the 1:1, and .9 for the 1:2 ratios respectively. Data in Fig. 3 can be directly compared with computer simulations shown in Fig. 6.

Results for the 22.2 cm OD insulator are shown in Fig. 4. The impedance measurements are similar to the smaller OD insulator so an expanded view of the impedance spectrum around the primary resonance is given. The number of periods of insulator were 11 for the 4:1 ratio, 7 for the 3:1 ratio, 9 for the 2:1 ratio, and 7 for the 1:1 ratio. The affect of increasing the number of periods while maintaining the same ratio of dielectric to stainless steel is shown in Fig. 5. The impedance converged rapidly with increasing number of periods.

4 THEORETICAL CALCULATIONS

Impedance calculations were performed using a 2.5-D, full-wave, time-dependent, wakefield code with a dispersive model for the PE11b ferrite [9]. Two series of calculations were performed for the geometry of Fig. 1.

Fig. 6 displays the dipole impedance spectrum calculated by AMOS for a nominal solid insulator, and simulated stacked insulators with 2:1, 1:1, and 1:2 dielectric to metal thickness ratios. These results not only mimic the physics observed in the experiment, but also are in excellent quantity agreement with the experiment.

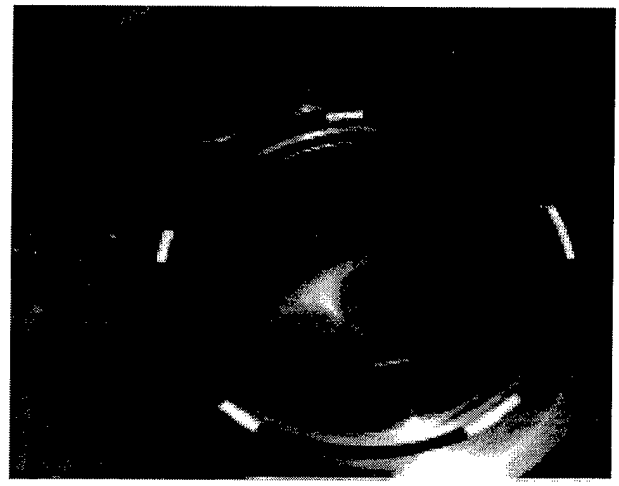
Figure 2. Photograph of test cavity with insulator. One wall of the cavity has been removed so that the insulator, intermediate ring, and damping ferrite are visible.

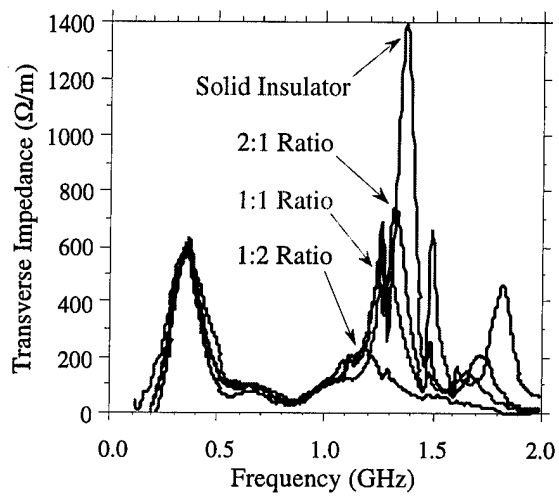

Figure 3. Impedance spectrum of the cavity with 19.7 cm OD insulator for different dielectric and conductor ratios.

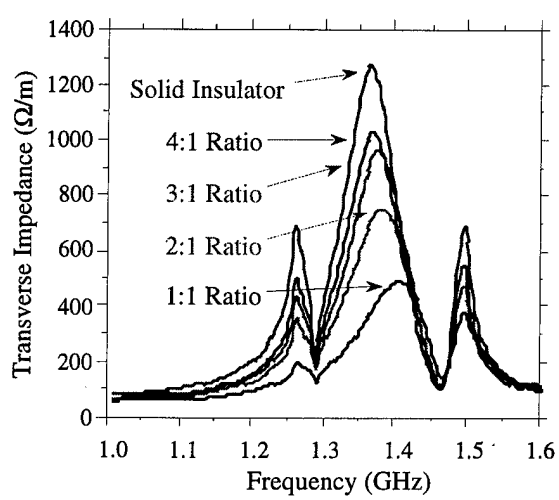

Figure 4. Effect on the primary resonance due to varying the ratio of dielectric to conducting material.

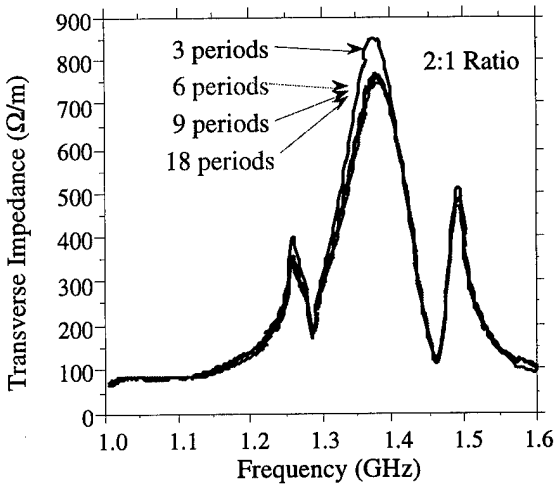

Figure 5. Effect on the primary resonance due to increasing the number of periods while maintaining the ratio of dielectric to conducting material.

Figure 7 illustrates the rapid convergence to a minimal impedance value for a fixed dielectric to conductor ratio as the number of layers,or periods, of dielectric is increased. Both experimental and theoretical predictions are consistent with the observation that the effect we see is a mode dependent and not a frequency dependent phenomenon.

5 CONCLUSIONS

Observations that can be made from the experimental measurements and simulations include:

(1) Geometry of the stacked insulator does not result in new resonances of significant impedance.

(2) The ratio of dielectric to conducting material is more important than the number of layers in the insulator in regards to the effect on impedance.

(3) For a specific ratio, the impedance converges rapidly to a final spectrum with increasing number of periods.

(4) AMOS accurately calculates the impedance spectrum associated with stacked insulators.

(5) To first order, the reduction of impedance can be related to the reduction in effective gap (dielectric) width.

(6) A possible second effect of the stacked insulator is a shifting of resonance field patterns leading to more effective damping by absorbers.

6 ACKNOWLEDGMENTS

We thank D. Prono (LANL), M. Burns (LANL), and R.E. Clough (LLNL) for their encouragement and support. We also thank C. Holmes for fabricating the test cavity and J. Dunlap for assistance with the impedance measurements. The work was performed under the auspices of the U.S. Department of Energy by Lawrence Livermore National Laboratory under contract W-7405-ENG-48 and by Allied Signal Corp. under contract DE-AC04-76-DP00613.

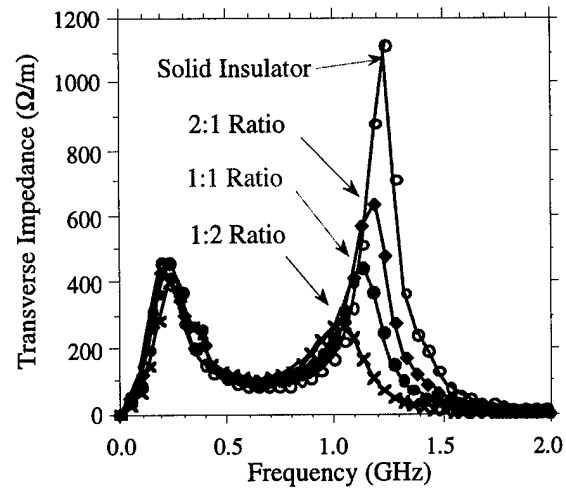

Figure 6. Impedance spectrum from AMOS calculations for actual experimental measurements. Refer to Fig. 3.

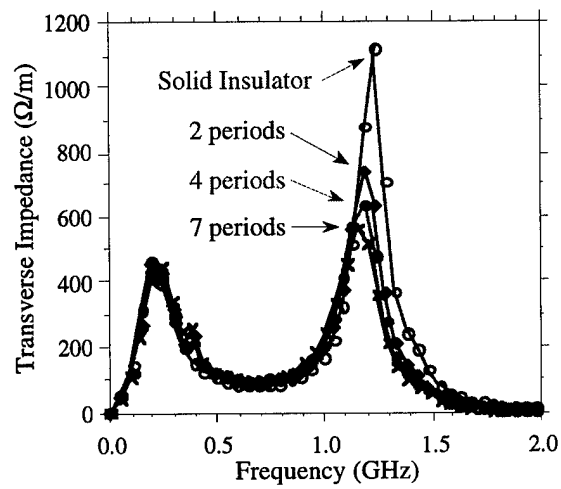

Figure 7. Simulation results illustrating the rapid convergence of the impedance spectrum with increased number of layers, or periods, of insulating material.

7 REFERENCES

[1] Juan M. Elizondo and A.E. Rodriguez, "Novel High Voltage Vacuum Surface Flashover Insulator Technology," Proceedings of the XVth International Symposium on Discharges and Electrical Insulation in Vacuum, Vde-Verlag, Berlin, Germany, pp. 198–202 (1992).

[2] S. Sampayan, et al., "High-Performance Insulator Structures for Accelerator Applications", these proceedings.

[3] S. Sampayan, et al., Proceedings 1995 Particle Accelerator Conference, (IEEE), New York, N.Y., pp. 1269–1271.

[4] M. Burns, et al., Proceedings 1991 Particle Accelerator Conference, (IEEE), New York, N.Y., pp. 2958–2960.

[5] J-S Kim, et al., "Stack Insulator Induction Gaps", these proceedings

[6] R.J. Briggs, et al., *Part. Acc.*, **18**, pp.41-62, 1985.

[7] L.S. Walling, et al., *Nucl. Inst. Meth.*, A281 (1989) 433.

[8] L.S. Walling et al., Proceedings of the 1990 LINAC, p. 704.

[9] J.F. Deford and G. Kamin, Proceedings of the 1990 LINAC, p. 384.

WAKE PROPERTIES OF A STRIPLINE BEAM KICKER

Brian R. Poole, George J. Caporaso, and Wang C. Ng
Lawrence Livermore National Laboratory

Abstract

The transport of a high current relativistic electron beam in a stripline beam kicker is strongly dependent on the wake properties of the structure. The effect of the beam-induced fields on the steering of the beam must be determined for a prescribed trajectory within the structure. A 3-D time domain electromagnetic code is used to determine the wake fields and the resultant Lorentz force on the beam both for an ultra-relativistic electron beam moving parallel to the beamline axis as well as a beam that follows a curved trajectory through the structure. Usually in determining the wake properties of the structure, a wake impedance is found for a beam that is moving parallel to the beamline axis. However, we extend this concept to curved trajectories by calculating beam induced forces along the curved trajectory. Comparisons are made with simple transmission line models of the structure. The wake properties are used in models to transport the beam self-consistently through the structure.

1 INTRODUCTION

The stripline beam kicker is designed to spatially separate a high current electron beam for transport into two separate beamlines. Figure 1 shows a schematic representation of the geometry under consideration.

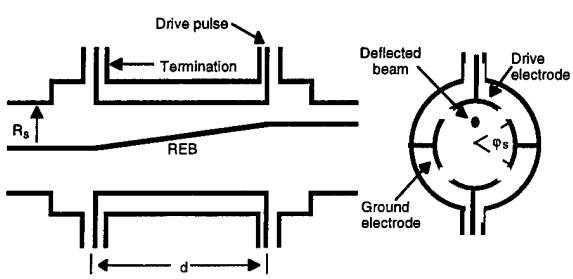

Figure 1. Kicker geometry and beam trajectory

An external pulse is applied to the downstream end of the kicker and the beam is deflected into one of two beamlines. The beam kicker is conceptually similar in design to a stripline beam position monitor.[1] However, the beam position monitor is typically used in high-energy accelerator applications with small beam current, to determine the transverse beam location by measurement of induced voltages on the striplines. In our application, the beam current is sufficiently large as to generate beam-induced voltages and currents on the strip transmission lines comparable with the externally applied voltages and currents. The dipole component of the beam-induced fields can contribute to the steering of the beam in addition to the externally applied steering fields. The wake impedance characterizes the strength of the interaction.

2 ANALYSIS

The wake impedance is a measure of the spectral characteristic of the integrated Lorentz force on a test charge, q traveling a fixed distance s, behind a source charge, Q. The concept of the wake potential and transverse wake impedance of a structure are discussed by DeFord,[2] and are defined as

$$\mathbf{W}(s) = \frac{1}{Q}\int_{-\infty}^{\infty} dz(\mathbf{E} + \mathbf{v}\times\mathbf{B})\Big|_{t=(s+z)/v} \qquad (1)$$

$$\mathbf{Z}_t(\omega) = \frac{j}{v}\int_{-\infty}^{\infty} \mathbf{W}_t(s)e^{jks}ds \qquad (2)$$

where $\omega = kv$.

This type of stripline structure has been discussed in some detail by Ng.[1] A simple model for the dipole wake impedance can be found using a simple transmission line model as shown in Figure 2.

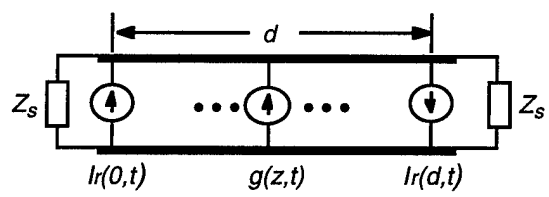

Figure 2. Transmission line model

To account for the curved trajectory of the beam within the structure, an equivalent shunt dipole current, $g(z,t)$ will be continuously setup along the transmission line to account for the change in the beam's dipole return current. The current sources at the ends of the structure represent the dipole gap return currents. Therefore, the transmission line equations representing this model are given by

$$\frac{\partial V}{\partial z} = -L\frac{\partial I}{\partial t} \qquad (3)$$

and

$$\frac{\partial I}{\partial z} = -C\frac{\partial V}{\partial t} + g(z,t) \qquad (4)$$

where

$$g(z,t) = \frac{2}{\pi R_s}\sin\left(\frac{\phi_s}{2}\right)\frac{\partial}{\partial z}\left[r(z)I_B(t - d/c - z/c)\right] \qquad (5)$$

and $r(z)$ represents the trajectory of the beam through the structure.

If the beam is moving at a constant offset in the structure, the only dipole current sources in the transmission line model are the upstream and downstream dipole gap return currents. The wakes are then found by application of Equations (1) and (2) to the fields along the transmission line and analytic expressions for the transverse dipole ($m = 1$) impedance is found for a matched transmission line as

$$Z_t(\omega) = \frac{8cZ_s}{\pi^2 R_s^2} \sin^2\left(\frac{\phi_s}{2}\right)\left(\frac{1}{\omega}\right)\left[\sin^2\left(\frac{\omega d}{c}\right) + j\sin\left(\frac{\omega d}{c}\right)\cos\left(\frac{\omega d}{c}\right)\right] \tag{6}$$

The effect of $g(z,t)$ is to set up waves continuously along the transmission line which interact with the test charge as opposed to the case when the beam is moving parallel to the axis and the perturbed current is only generated at the gaps at the beginning and end of the structure. The continuous source distribution will significantly alter the wake properties of the structure.

For example, if the beam enters on axis and is steered off axis by an externally applied field as in the beam kicker we expect a reduction in the transverse dipole impedance since no beam return dipole current is present at the upstream gap. Also, the presence of the continuous distribution of sources will lead to a superposition of waves with differing phases to interact with the test charge which can lead to a reduction in the impedance as well as a redistribution of the spectral content of the impedance associated with the structure. A beam transport model based on the effect of the distributed shunt current sources is being developed.[3]

3 MODELING

We use a 3-D finite-difference time-domain (FDTD) code, TSAR (Temporal Scattering and Response) to model the wake properties of the structure and compare the results with the simple transmission line model for the structure as described by Ng.[1] The code uses a 3-D grid composed of cubical cells for the FDTD analysis, with each cell being assigned a given material property. The cell size is typically chosen to resolve the shortest wavelength expected in the problem and is chosen small enough to accurately represent the smallest dimension in the model. In addition, to satisfy stability requirements for the FDTD field solver, the Courant condition for the time step must be satisfied. This condition is ($dt<dx/2c$) where dx is the length of a cell edge. It is also important to resolve the lowest frequency that the electron beam may excite, which determines the total number of time steps to be run for a specific problem.

In our numerical calculations, the length of the structure was 10 cm, the strip radius was 1.65 cm, the subtended angle of each of the 4 strips was 55 degrees and the enclosure radius was 1.9 cm. The structure was terminated with 25Ω resistors which were chosen based on a frequency domain calculation of the TEM impedance of the structure for our geometry. Even to represent the gross geometric characteristics of the structure using cubical cells requires a cell size of 0.5 mm making the computational size of this problem $8\text{x}10^6$ cells and requires a time step of .83 ps as dictated by the Courant condition. The axial ends of the problem space had MUR radiation boundary conditions imposed to prevent undesired reflections. The MUR boundary conditions were located 25 cm away from each end of the structure to allow a sufficient decay of evanescent waves. The problem was run for 16000 time steps.

For modeling purposes the trajectory of the beam was either a constant offset beam at a radius of 1 cm or a trajectory of the form

$$r(z) = \frac{r_0}{2}\left[1 - \cos\left(\frac{\pi z}{d}\right)\right] \tag{7}$$

where d is the length of the structure. In this case, the beam enters the structure on axis and leaves at an offset of r_0=1 cm. While this trajectory is somewhat artificial, it was required to have the beam enter and leave the problem space normal to the plane of the MUR radiation boundary conditions at the axial ends of the problem space for stability of the code. Figures 3a and 3b show comparisons of the analytic model of the offset beam with results obtained numerically through the modeling code for the transverse dipole impedance for a beam with a constant offset. As is seen, there is excellent low frequency agreement with the numerical results for the constant offset beam with the analytic dipole impedance. Figures 4a and 4b show the results due to the distributed source $g(z,t)$ arising from the trajectory defined in equation 7. Note that these plots do not include the contributions from the dipole gap currents. Again, there is excellent low frequency agreement between the distributed source model and the code results. These results must be subtracted from the constant offset impedance results to obtain the total curved trajectory dipole impedances. The effect of the curved trajectory, as expected was to reduce the impedance and redistribute the impedance spectra. The deviations at the higher frequencies may be due to the high frequency impedance of the wire resistors used in the FDTD code which are not included in the analytic model since we are assuming the striplines to be matched.

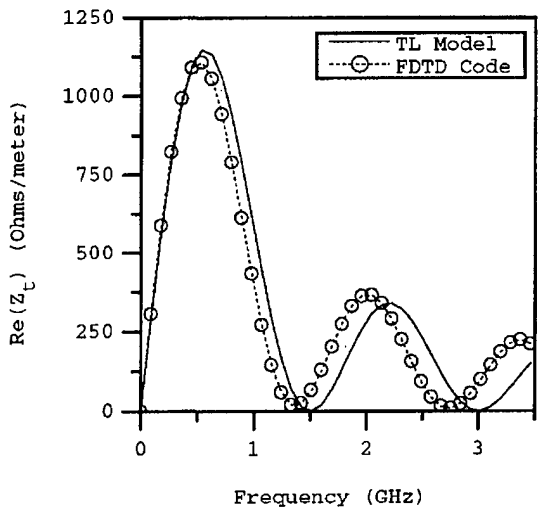

Figure 3a. Real part of impedance for offset beam

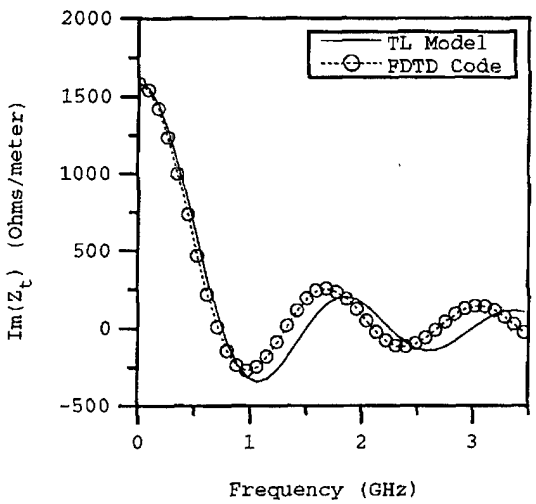

Figure 3b. Imaginary part of impedance for offset beam

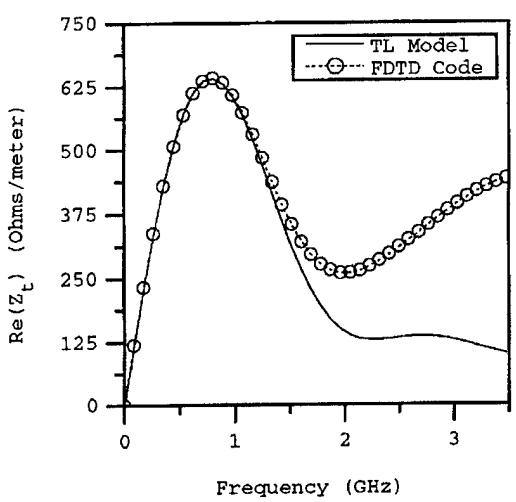

Figure 4a. Contribution to real part of dipole impedance for curved trajectory from distributed source term, $g(z,t)$

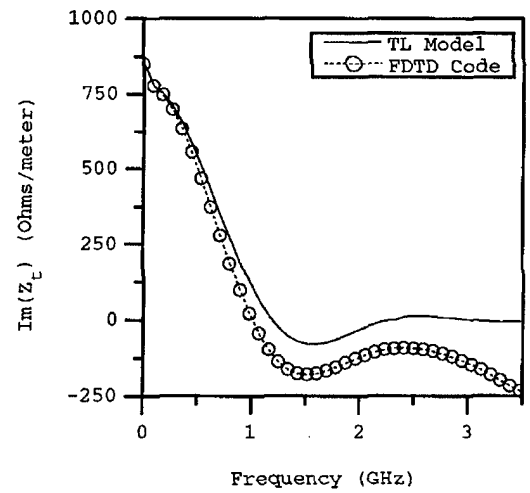

Figure 4b. Contribution to imaginary part of dipole impedance for curved trajectory from distributed source term, $g(z,t)$

4 CONCLUSION

The effect of including more complex beam trajectories in wake impedance calculations can have significant impact on the nature of the beam interaction. These effects are particularly relevant in the design of high-current beam transport systems where the beam induced fields may be large. It is found that the wake impedance spectra is altered due to the introduction of a continuous distribution of shunt transmission line currents to account for the change in dipole return current as the beam is deflected in the structure. The resultant superposition of waves generated by the distributed current sources is to redistribute the spectral content of the wake impedance. We see from our modeling the wake impedance at very low frequency is reduced by a factor of 2 indicating the effect of beam induced steering is not as significant as in the beam offset case.

5 ACKNOWLEDGMENT

Stimulating discussions with S. Nelson, C. Shang, and Yu Ju Chen of Lawrence Livermore National Laboratory are gratefully acknowledged. This work was performed under the auspices of the U.S. Department of Energy by the Lawrence Livermore National Laboratory under contract number W-7405-ENG-48.

6 REFERENCES

[1] K.-Y. Ng, *Particle Accelerators*, **23**, 93–102 (1988).

[2] J. F. DeFord, G. D. Craig *Particle Accelerators*, **37–38**, 111–121 (1992).

[3] G. J. Caporaso, Yu Ju Chen, B. R. Poole, "Transmission Line Analysis of Beam Deflection in a BPM Stripline Kicker," these proceedings.

BBU DESIGN OF LINEAR INDUCTION ACCELERATOR CELLS FOR RADIOGRAPHY APPLICATION[1]

C.C. Shang, Y.-J. Chen, G.J. Caporaso, T.L. Houck, N.E. Molau, S.D. Nelson, and W.C. Ng
Lawrence Livermore National Laboratory

J. Fockler, PSI

S. Gregory, Bechtel-Nevada

Abstract

There is an ongoing effort to develop accelerating modules for high-current electron accelerators for advanced radiography application. Accelerating modules with low beam-cavity coupling impedances along with gap designs with acceptable field stresses comprise a set of fundamental design criteria. We examine improved cell designs which have been developed for accelerator application in several radiographic operating regimes. We evaluate interaction impedances, analyze the effects of beam structure coupling on beam dynamics (beam break-up instability and corkscrew motion). We also provide estimates of coupling through interesting new high-gradient insulators and evaluate their potential future application in induction cells.

1 INTRODUCTION

The nature of the electromagnetic interaction of a charged particle beam in an accelerator beampipe with imperfections or perturbations in the beampipe wall is of fundamental importance to the design of an induction accelerator. These interactions van be characterized by an interaction impedance, which relates moments of the beam current to the work done on the beam by the beam-induced electromagnetic fields. The impedance quantities of interest may all be derived from the characteristic wake potential W, defined by the expression

$$W(s)=\frac{1}{Q}\int_{-\infty}^{\infty} dz'(E+v\times B)\Big|_{vt=s+z} \tag{1}$$

$$Z_t(\omega)=\frac{j}{v}\int_{-\infty}^{\infty} W_t(s)e^{jks}ds \tag{2}$$

Over the past fifteen years, several high current linear induction cells have been built and tested. One of the fundamental design objectives is to minimize the transverse dipole coupling impedance since the growth rate of beam breakup instability (BBU) is proportional to the transverse coupling impedance. A form factor,

$$\eta=\frac{\left(Z_t b^2\right)}{4wc} \tag{3}$$

where b is the beampipe radius and w is the gap width is a figure of merit from the viewpoint of BBU. η is tabulated in Figure 1 for existing cells in addition to new cell designs for advanced radiography including DARHT, and FXR-upgrade.

Cell	Beampipe radius	Gap	BBU frequency	Transverse impedance	Form factor	Characteristic
DARHT-1 Mod 2A	7.41 cm	1.91 cm	816 MHz	670 ohms/meter	1.6	Intrinsic n=2 mode
ETA-II	6.6 cm	1.5 cm	300 MHz	700 ohms/meter	1.7	BBU rings
FXR	7.3 cm	3.56 cm	800 MHz	1500 ohms/meter	1.9	Two cell types
ATA	6.725 cm	2.7 cm	800 MHz	1000 ohms/meter	1.4	Leakage current
DARHT-2 short pls	7.41 cm	2.0 cm	463 MHz	490 ohms/meter	1.1	Ferrite inset PE16 model
FXR/U	7.3 cm	3.56 cm	350 MHz	1000 ohms/meter	1.3	Two cell types

Figure 1. Table of induction cell form factors for existing and new induction cell designs.

2 WAKEFIELD ANALYSIS

There are several features characterizing existing linear induction accelerator (LIA) cell design. Characteristic in several designs is the presence of a shielded gap. The purpose of the shielded gap design is to provide an RF filter effect for BBU modes, in addition to preventing direct line of sight between beam and insulator. Another conventional approach involves application of corner reflectors comprising either of lossy ferrite of highly conducting electric materials. These design features have also been successfully employed to both damp and direct wakefields towards lossy induction core material.

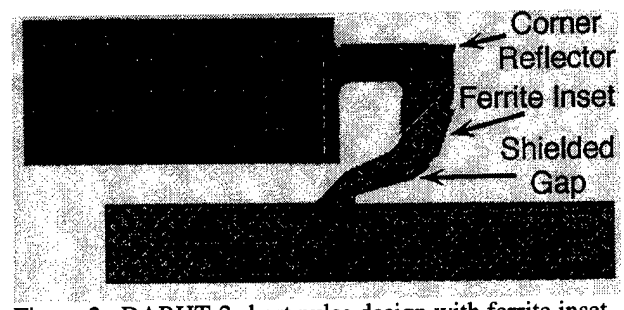

Figure 2. DARHT-2 short pulse design with ferrite inset.

Several new improvements in induction cell design hold the promise for additional suppression of beam break-up modes. Recently, we have examined the use of ferrite insets on the vacuum side of the insulator in designs for DARHT and AHF. The ferrite inset geometry must be designed to minimize field enhancement over the field stresses in the unperturbed cavity structure. Typical inset designs can be optimized for minimal field enhancement and recent work on DARHT-2 short pulse

[1] This work was performed under the auspices of the U.S. Department of Energy by the Lawrence Livermore National Laboratory under Contract No. W-7405-Eng-48.

design has maximum field enhancements over the unperturbed case of 27%. Another key consideration is to ensure that the damping ferrites are positioned on the anode electrode to avoid possible difficulties with field induced emission.

3 DAMPING FERRITE

A key requirement for accurate impedance calculations is highly realistic material data. Data for two well-known ferrites in the LIA community are the TDK PE11b [2] and TDK PE16. We measured the magnetic dispersion characteristics of PE16. We found that in the VHF to L-band microwave spectrum, it is more lossy than TDK PE11b. In impedance calculations, the difference is manifested as a 5-10% reduction in transverse impedance. Small differences in phase due to the thickness of the ferrite sample cause the fine structure (non-physical) in the data.

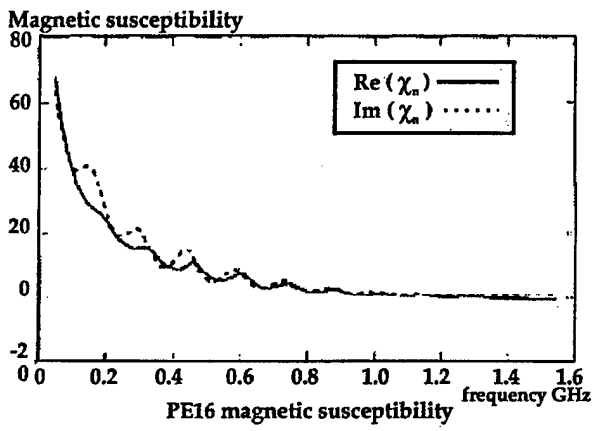

Figure 3. Magnetic dispersion for PE-16 ferrite material

4 CELL DESIGN

For two cell designs (DARHT short pulse and FXR-upgrade) the ferrite insets are employed. For the DARHT-2 design, a DARHT-1-like cell employing corner reflector yields an impedance spectrum with two BBU resonances (~270 MHz and ~750 MHz).

The utilization of the ferrite inset on the vacuum side obtains a low-Q spectrum in Figure 4. We found that placement of ferrite nearer to the gap yields this desirable frequency impedance dependence. We have also examined its application at FXR. For FXR, we see a similar effect in that we have a nominal impedance with conventional design featuring a BBU resonance at 800 MHz. Calculations using the damping ferrite inset on the vacuum side also obtains a low-Q impedance spectrum which we found for the DARHT-2 short pulse design. Wakefield calculations predict an upgraded FXR cell with $\eta = 1.3$. Impedance measurements at FXR are currently in progress.

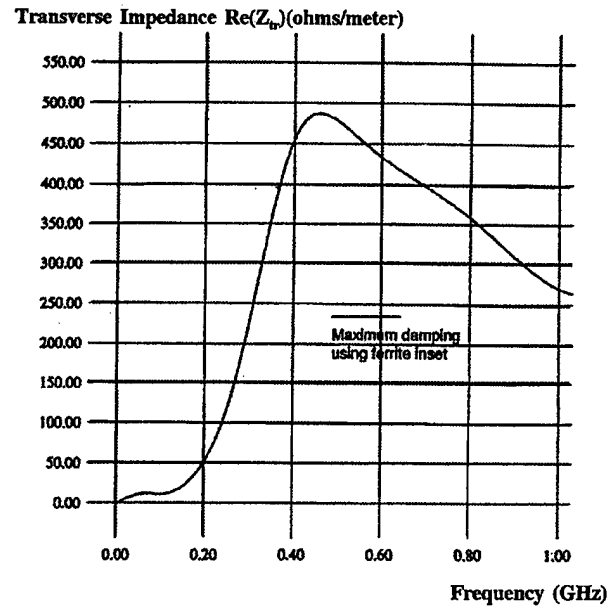

Figure 4. DARHT-2 short pulse dipole impedance spectrum with $\eta = 1.1$

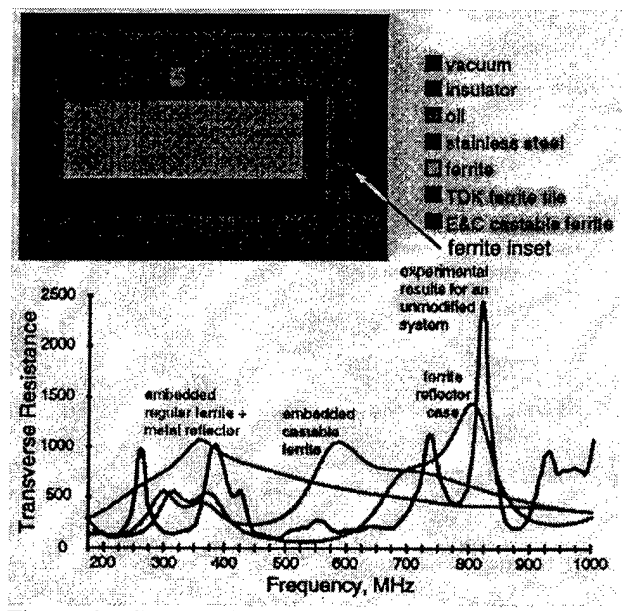

Figure 5. Computed impedance spectrum for FXR cell upgrade

5 BEAM DYNAMICS SIMULATIONS

Simulations of the beam breakup instability are required to evaluate the low-Q impedance spectrum characteristic of ferrite insets. The DARHT-2 short pulse configuration is similar to DARHT-1 except the cell and solenoid parameters are changed. The injected beam into the accelerator is at 4 MeV and 4 kA. The magnetic tune averaged at 700 G is chosen so that a beam with a 190 mm-mrad normalized edge emittance [3] is focused gently from 4.6 cm radius to about 0.6 cm radius within the first 7.5 meters, and is maintained at 0.6 cm radius through the rest of the machine.

In the simulations, the beam breakup instability is driven by misalignment of magnets. The DARHT-1

alignment specification [4] is used in the simulations. The 3-σ of random magnet tilts and random magnet offsets is 1.95 mrad and 0.45 mm, respectively. We assume that the injector and the induction cell voltages have 15 ns rise time and 70 ns flat-top with a small linear ramp. These voltage ramps introduce an ±1% energy variation to the beams, and hence corkscrew motion. Without any steering, the peak-to-peak (p-p) BBU amplitude and the corkscrew amplitude is 4 mm and 3 mm, respectively. Assume that beam position monitors are located between cell-blocks, and their resolution is 0.1 mm. We minimize the corkscrew amplitude by using the corkscrew tuning curve algorithm [5] and the averaged centroid displacement at alternating beam position monitors. We found that both the beam breakup instability and corkscrew motion are controllable with steering as shown in Figure 6. The BBU only appears in the first 10 ns of the flat-top portion of the pulse, and its p-p amplitude at the end of accelerator is 1.2 mm. The corkscrew amplitude is 0.6 mm. Note that the magnetic tune used in the simulation is relatively weak. Nevertheless, both the simulated BBU amplitude and corkscrew amplitude are small enough to satisfy the final focus requirement.

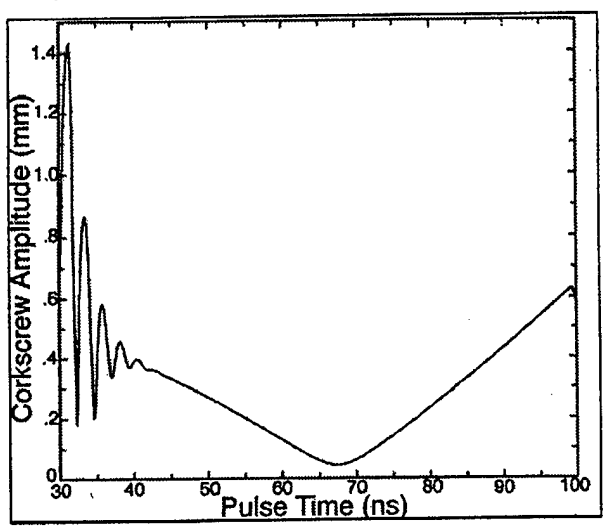

Figure 6. BBU and corkscrew motion at the end of the DARHT-2 accelerator for the short pulse option

6 HIGH GRADIENT INSULATOR STRUCTURE

It has been reported that a high gradient insulator structure, consisting of a periodic structure of alternating conductor and dielectric has voltage hold-off properties of up to 5 times conventional insulator technology [6]. In recent impedance experiments [7] it was shown that the impedance value has a strong dependence on dielectric-to-metal thickness ratio. Suitability for induction cell application also required evaluation of the radial length and position of the insulator in the gap and its effect on impedance. In Figure 7, by varying radial length and position we observe that a further reduction on the interaction impedance is achievable. The effect appears to be mode dependent.

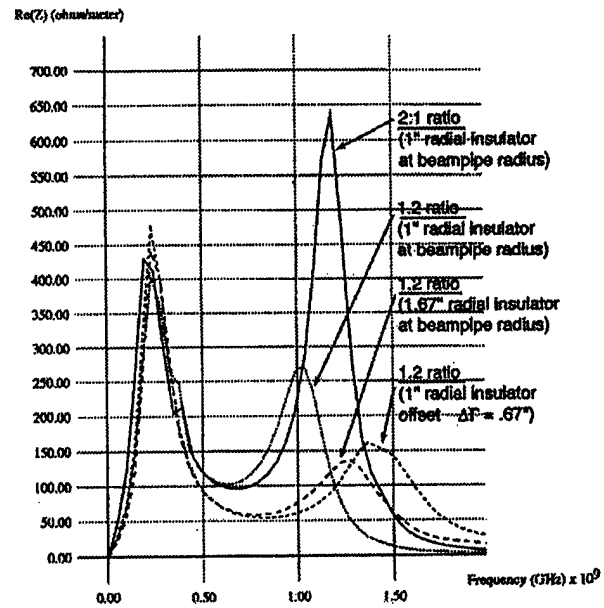

Figure 7. High gradient insulator structure in damped pillbox with ID=5.75", OD=10", and gap = 1"

7 CONCLUSION

Future induction accelerator designs may profit from new improvements involving ferrite damping materials and insulators to help achieve very low impedance structures with possibly more robust insulator performance. Experiments at FXR and AHF design and test activities are underway.

8 ACKNOWLEDGEMENTS

Stimulating discussions with J. Melton, J. Carlson, and J. Downing at LANL and G. Westenskow LLNL are gratefully acknowledged. We express appreciation to D. Prono and M. Burns at LANL, and R.E. Clough, LLNL, for their encouragement and support.

REFERENCES

[1] R.J. Briggs, et al., "Theoretical and Experimental Investigation of the Interaction Impedances and Q Values of the Accelerating Cells in the Advanced Test Accelerator", *Particle Accelerators*, 1985, Vol. 18.

[2] J. DeFord and G. Kamin, "Application of Linear Magnetic Loss Model of Ferrite to Induction Cavity Simulation", 1990 Linear Accelerator Conf., Sept. 1990, pp 384-386.

[3] T.P. Hughes, private communication.

[4] M.J. Burns, private communication.

[5] Yu-Jiuam Chen, "Control of Transverse Motion Caused by Chromatic Aberration and Mis-alignments in Linear Accelerators", to be published in *Nucl. Inst. Methods in Phys. Res. A.*

[6] S. Sampayan, et al., "High Performance Insulator Structures for Accelerator Applications", these proceedings.

[7] T. Houck, et al., "Measured and Theoretical Characterization of the RF Properties of Stacked, High Gradient Insulator Material", these proceedings.

A FLEXIBLE-VARIABLE TRUNCATED POWER SERIES ALGEBRA IN Zlib *

Y.T. Yan, Y. Cai, and J. Irwin
Stanford Linear Accelerator Center, Stanford University, Stanford, CA 94309 USA

Abstract

Zlib is a numerical library for Truncated Power Series Algebra (TPSA) and Lie Algebra for application to nonlinear analysis of single particle dynamics. The first version was developed in 1990 with the use of the One-Step Index Pointers (OSIP's). The OSIP's form the Zlib nerve that offers optimal computation and allow order grading as well as flexible initialization of the global number of variables for the TPSA. While the OSIP's are still kept for minimum index passing to achieve efficient computation, Zlib has been being upgraded to allow flexible and gradable local number of variables in each C++ object of the Truncated Power Series (Tps) class. Possible applications using Zlib are discussed.

1 INTRODUCTION

The first Zlib version was developed in 1990 [1] in Fortran language. Its development was aimed at fast computation of the one-turn Taylor map extraction of the Superconducting Super Collider (SSC) lattices and high-order nonlinear mapping analyses. The core is the Zlib nerve system which consists of the One-Step Index Pointers for minimum index pass to achieve efficient computation of the TPSA that involves some fundamental operations such as addition, subtraction, multiplication, division, inverse, sine, cosine, square root, power, exp, log, derivative, integral, etc. of the Tps's, and some derived operations such as concatenation, Poisson bracket, various formats of Lie generators in Cartesian or Action-Angle coordinates, map tracking, etc. The Tps orders were gradable. The Memories for the One-Step Index Pointers and necessary internal auxiliary arrays were dynamically allocated at the minimum required level per user's input for the maximum order and number of variables.

In 1993, the basic part (about 20%) of the Zlib Fortran subroutines were faithfully translated into C++ codes that form two fundamental classes of the TPSA [2]. These two classes were named ZSeries and ZMap which handles the algebra of truncated power series and vector truncated power series respectively. Recently at SLAC, aiming at further development in C++ for mapping analysis, while keeping the original Zlib One-Step Index Pointers for efficient index passing, we have been re-designing the Zlib based on a newly invented formulation [3] that allows for both order and variable grading. Major classes implemented and to be implemented are Tps (Truncated Power Series), Vps (Vector Tps), Aps (Tps in Action-Angle Variables), Lie and a variety of derived Lie classes. The truncated power series coefficients are commonly understood as a double type. Indeed, they can be a Tps type, too, making classes Tps<Tps>, Vps<Tps>, Lie<Tps>, etc. such that the canonical coordinate variables form a class of Tps of which each coefficient is another class of Tps of certain parameter variables whose optimal values are to be determined after parameterized mapping analysis.

2 ONE-STEP INDEX POINTERS

There are, fundamentally, three kinds of data structures used in programming the TPSA in beam physics community, the hybrid procedure of Cosy Infinity developed in late 1990's, the One-Step-Index-Pointer procedure of Zlib developed in 1990, and the Link-List procedure of MXYZP-PLK developed in 1990, The recent elegant TPSA "look-back table" description of Dragt is fundamentally similar to Zlib "One-Step Index Pointer".

Through appropriate labeling and indexing, a Tps can be represented by a one-dimensional array of real (double) numbers one-to-one corresponding to the coefficients of the Tps. For allowing order grading, low order coefficients would be indexed first, followed by the next high-order and then the next high-order coefficients until the preset (or derived) maximum order is reached. In a mathematical formula, an n-variable, P-order Tps can be written as

$$T(n,P) = C_0 + H(n,1) + H(n,2) + ... + H(n,P),$$

where $H(n,i), i = 1,2,...,P$, is the homogeneous polynomial of order i. and C_0 is the constant term. This formula allows for order grading (adding or truncating high-order terms does not affect the low order structure) but not for variable grading. Of course, in the above formula, one can let n be the fixed order and P be the maximum number of variables, then it allows for variable grading, but the order has to be fixed. Such a flexible-variable but fixed-order formulation is most suitable for use in Taylor map extraction. Indeed, the Zlib Fortran version developed in 1990 has two sub libraries, one for gradable number of variables (the TPALIB) and the other for gradable orders (the ZPLIB) [1].

The key to fast speed TPSA is to have One-Step Index Pointers prepared only once for repeated use such that for any coefficient involved in a given calculation, it can be identified with a minimum index path. Taking Tps multiplication as an example, let Tps C = A * B, where A and B are two given Tps's that may be with different orders, then the task is to obtain all of the coefficients of C to a

* Work supported by the Department of Energy under Contract No. DE-AC03-76SF00515

specified order derived from the orders of A and B and the preset cap order. To obtain $C[j]$ (jth-term of C), the "backward" scheme would go over a loop i to sum over exactly the number of contributing multiplication terms given by $A[aOSIP[i]] * B[bOSIP[i]]$, where $aOSIP$ and $bOSIP$ are One-Step Index Pointers (OSIP's) stored for repeated use to achieve fast multiplication.

3 FLEXIBLE NUMBER OF LOCAL VARIABLES

As has been described in the last section, the one-dimensional-array data structure for the Tps can either have variable grading or order grading but not both. If one chooses to have gradable orders, then the number of variables is fixed in the structure. Nonetheless, one can establish a set of order-gradable One-Step Index Pointers for each number of variables up to the maximum number of variables, and build up variable-crossing OSIP's that involves operations between two different number-of-variable structures. In addition to a fixed-variable version, Zlib has a C++ version with such a flexible-variable data structure. Therefore, for example, one can perform Tps multiplication directly between two Tps's A and B with nA and nB variables respectively, where nA may or may not be equal to nB. In comparison with the fixed-variable TPSA, such data structure allowing for operation among different number of variables would ease the flexible use of the TPSA dramatically. However, the price is paid with a larger memories for storing a larger set of the OSIP's. Also note that such a data structure does not allow variable grading though it allows for flexible number of variables.

To offset the large memories required for the OSIP's, We have been upgrading Zlib again based on a new formula give by [3]

$$\begin{aligned} T(n,P) &= C_0 + x_1 T(1,P-1) + x_2 T(2,P-1) + .. \\ &\quad + x_n T(n,P-1), \end{aligned}$$

where C_0 is the constant term and $x_1, x_2, ...x_n$ label the n variables respectively. The nice thing about this new formulation is that (a) it builds on the top of the above one-dimensional flexible-variable scheme such that the One-Step Index Pointers can still be used for achieving fast speed, (b) both the number of variables and the order are gradable simultaneously, and most importantly, (c) the OSIP's only need to be prepared and stored up to an order smaller than the maximum order desired by 1 or 2, saving memories dramatically. The most saving of memories comes from the Tps multiplication OSIP's. They only need to be prepared and stored up to an order that is smaller than the maximum order by 2. For detailed description of this new scheme, allowing both order and variable grading while still using One-Step Index Pointers, one can refer to the original article [3].

4 MAJOR CLASSES AND THEIR APPLICATIONS

Major classes in Zlib are Tps, Vps, Aps, Lie and its derivatives, and related parameterized classes Tps<Tps>, Vps<Tps>, Lie<Tps>. They are briefly described as follows.

The Tps Class

Tps is an abbreviated name for the truncated Power Series. It is the most fundamental class in Zlib. A Tps truncated at an order of P can be mathematically written as [1] [6]

$$U(\vec{z}) = \sum_{o=0}^{P} u(\vec{k}) \vec{z}^{\vec{k}},$$

where, assuming n variables, $\vec{z}$ represents the variables labeled as $z_1, z_2, ...z_n$, $\vec{k}$ represents the power indices $(k_1, k_2, ...k_n)$ and so $\vec{z}^{\vec{k}}$ represents $z_1^{k_1} z_2^{k_2} ... z_n^{k_n}$, and $\sum_{o=0}^{P}$ means summation over all possible monomials labeled by $\vec{k}$ with order given by $o = k_1 + k_2 + ... + k_n$ that is less than or equal to P.

The Tps class in Zlib is designed to manipulate Tps represented by the above-described coefficients. Both the order and the number of variables are local (object) member data, that is, each object of Tps can have its own order and number of variables that may be different from another Tps object.

Besides providing the basic functions for the other classes in Zlib, this class is frequently used for extracting Taylor maps for beamlines. With a suitable Tps initialization, one simply replace the the double type declaration of related variables with the Tps declaration in the tracking routine to obtain Taylor maps.

The Vps Class

Vps is an abbreviated name for the Vector truncated Power Series. A Vps truncated at an order of P can be mathematically written as [1] [6]

$$\vec{U}(\vec{z}) = \sum_{o=0}^{P} \vec{u}(\vec{k}) \vec{z}^{\vec{k}}, \tag{1}$$

that is, each component of the Vps is a Tps represented by coefficients described in the last section. For example, the ith component would be represented by

$$U_i(\vec{z}) = \sum_{o=0}^{P} u_i(\vec{k}) \vec{z}^{\vec{k}},$$

The Vps class in Zlib C++ version is designed to manipulate Vps described above. It can represent a Taylor map and therefore have member functions for concatenation and Taylor-map tracking.

The Aps Class

Aps is an abbreviated name for the truncated power series in action-angle variable space. A class named Aps in Zlib C++ version is actively under implementation. Some of the important member functions in this class are the nPB tracking and the extraction of the normalized resonance basis

coefficients which was coded before in Fortran and have been used intensively for PEP-II lattice studies [7].

The Lie Classes

Application of TPSA to nonlinear single-particle dynamics usually goes with the Lie algebraic analysis. Therefore, majority of the Zlib classes are to be for Lie algebras such as single Lie generators, Dragt-Finn factorizations [8], nonlinear normal forms [9], kick factorizations [10], integrable polynomial factorization [11], etc. Most of these functions are achieved with derived Lie classes.

The parameterized Classes

In mapping analysis of a beam line lattice, in addition to the canonical phase-space variables, we often would like to have parameter variables which are constant but not specified with a value. Their values are either to be determined after the analysis or are dynamical (time dependent) to allow additional studies such as for synchrotron oscillation, power supply ripple, and ground motion at lower computational price. Treatment of such parameterized map in Fortran is tedious and usually uses semi-parameterization methods. Although some fully parameterized (coefficients of the power series in canonical space are treated as power series in parameter space) algorithms were written for treating both linear (but nonlinear in parameter space) and nonlinear cases [12], there were no implementation of such fully parameterized methods in the Zlib Fortran version. However, with the object-oriented capability, it is easier to code such fully parameterized algorithms since one can consider each of the coefficients in the canonical space as an object of Tps instead of a double. These fully parameterized mapping methods are currently under active development in Zlib C++ version. The major part of this effort involves classes Tps<Tps>, Vps<Tps>, Lie<Tps> and more. We plan to make the Tps, Vps, and Lie classes as template classes so that no extra classes are needed for achieving these parameterized functions.

5 SUMMARY

Through several rounds of upgrading, we may have lead Zlib to the ultimate design of the TPSA in terms of speed and flexibility. The Zlib nerve system consisting of the One-Step Index Pointers provides very efficient computational speed. The implementation based on the newly discovered formula /citegrade given in Section III, allows flexible and gradable number of variables and orders.

Possible applications of Zlib are broad. Besides performing various nonlinear mapping analyses, it can be easily linked to a C++ tracking code to extract one-turn or one-section Taylor maps.

Zlib has been linked to LEGO (a modular accelerator design code) [13] for extracting nonlinear parameterized maps and for non-linear mapping analysis.

6 ACKNOWLEDGEMENT

We would like to thank Scott Berg, Alex Dragt, Jim Holt, Chris Islin, Leo Michelotti, Nick Walker, and Johannes van Zeijts for many useful discussions. Special thanks are given to N. Malitsky for his interest in translating the Zlib Fortran version into the first C++ version.

7 REFERENCES

[1] Y. Yan and C. Yan, "*Zlib — A Numerical Library for Differential Algebra,*" SSC Laboratory Report SSCL-300 (1990); Y.T. Yan, "*Zlib and Related Programs for Beam Dynamics Studies,*" in *Computational Accelerator Physics,* AIP Conf. Proc. No. 297, p.279 (1993), R. Ryne, eds.

[2] N. Malitsky, A. Reshetov, and Y. Yan, "*ZLIB++: an Object-Oriented Numerical Library for Differential Algebra,*" SSCL-659 (1994).

[3] Y.T. Yan, "*A New Formula for Ultimate Design of the Truncated Power Series Algebra with Both Order and Number-of-Variable Gradability,*" SLAC-PUB-7435, 1997; Y.T. Yan, "*Letter to the Editors,*" ICFA Beam Dynamics Newsletter, No. 13, P. 8, April, 1997, K. Hirata, J. Jowett, and S.Y. Lee eds.

[4] M. Berz, "*Differential Algebraic Description of Beam Dynamics to Very High Orders,*" *Particle Accel.* **24**, 109 (1989).

[5] L. Michelotti, "*MXYZPPLK: a C++ version of differential algebra,*" Fermi National Accelerator Laboratory Report FN-535 (1990).

[6] Y.T. Yan, "*Applications of Differential Algebras to Single-Particle Dynamics in Storage Rings,*" SSCL-500, in *The Physics of Particle Accelerator,* AIP Conf. Proc. No. 249, p. 378 (1992), M. Month and M. Dienes, eds.

[7] Y.T. Yan, J. Irwin, and T. Chen, "*Resonance Basis Maps and nPB Tracking for Dynamics Aperture Studies,*" Particle Accelerators, Vol. 55, p. 263 (1996).

[8] A. Dragt and J. Finn, "*Lie Series and Invariant Functions for Analytic Symplectic Maps,*" *J. Math. Phys.*, **17**, 2215 (1976).

[9] E. Forest, M. Berz, and J. Irwin, "*Normal Form Methods for Complicated Periodic Systems,*" *Particle Accelerators*, **24**, 91 (1989).

[10] J. Irwin, "*A Multi-Kick Factorization Algorithm for Nonlinear Maps,*" in *Accelerator Physics at the SSC,* AIP Conf. Proc. No. 326, edited by Y.T. Yan et al. (AIP, New York, 1995), p. 662; D. Abell and A.J. Dragt, to be published.

[11] J. Shi and Y.T. Yan, "*Explicitly Integrable Polynomial Hamiltonians and Evaluation of Lie Transformations,*" *Phys. Rev. E,* **48**, 3943 (1993).

[12] In Chapters 5 and 6 of Ref. 5.

[13] Y. Cai, M. Donald, J. Irwin, and Y.T. Yan, "*LEGO: A Modular Accelerator Design Code,*" in these proceedings.

A FIELD-CANCELLATION ALGORITHM FOR CONSTRUCTING ECONOMICAL PLANAR PERMANENT MAGNET (PM) MULTIPOLES WITH LARGE HIGH-QUALITY FIELD APERTURES*

R. Tatchyn
Stanford Synchrotron Radiation Laboratory, SLAC, Stanford, CA 94309, USA

Abstract

In recent years studies have been initiated on a new class of multipole field generators consisting of cuboid planar permanent magnet (PM) pieces arranged in bi-planar arrays of 2-fold rotational symmetry. These structures, first introduced for Free Electron Laser (FEL) applications, are based on reducing the rotational symmetry of conventional N-pole field generators from N-fold to 2-fold. One consequence of this reduction is a large higher-multipole content in a planar PM multipole's field at distances relatively close to the structure's axis, making it generally unsuitable for applications requiring a large high-quality field aperture. In this paper we outline an economical field-cancellation algorithm that can substantially decrease the harmonic content of a planar PM's field without breaking its biplanar geometry or 2-fold rotational symmetry.

1 INTRODUCTION

In recent years, the development of a novel class of PM multipole (N-pole) field generators has been initiated at SSRL [1,2,3,4]. The basic construction principle, depicted in Fig. 1, is to arrange N rectangular PM pieces, magnetized with their easy axis perpendicular to two opposed faces, into a biplanar array with N/2 pieces per plane. In general, while the pieces in each quadrant of the x-y plane can have arbitrary dimensions, x-placements, and magnetizations, the overall structural and field geometries possess symmetry with respect to the y-z and x-z planes, and the normal convention is to have each of the two sets of magnet surfaces closest to the x-z plane be coplanar. If we postulate an ideal N-pole generator to be a structure with N-fold rotational symmetry [5], the essential concept of planar PM multipoles is seen to be based on the reduction from N-fold to 2-fold rotational symmetry.

The entire class of planar PM multipoles can be grouped into two families: 1) N=4n; and 2) N=4n-2; where n e {1,2,..}. Thus, the first family includes the quadrupole (quad), octupole, dodecapole, etc., and the second family includes the dipole, sextupole, decapole, etc. From Fig. 1 it is seen that the basic criterion for this classification is field symmetry, viz., the N=4n family has

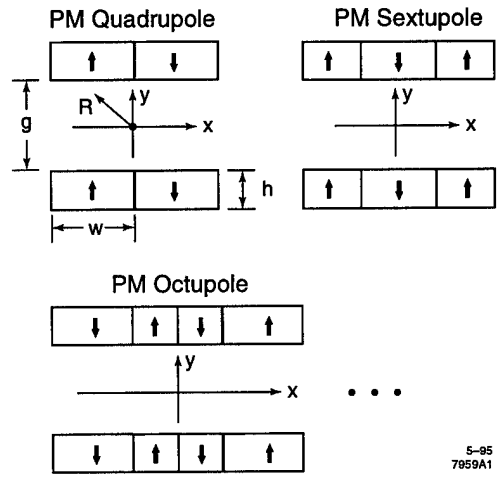

Fig. 1. Planar PM multipoles composed of pieces of equal height (h), with no lateral spacing between pieces. Symmetry axis (z axis), along which all the PM pieces have equal length L, is perpendicular to the page.

fields with odd symmetry vs. x, while the N=4n-2 family has even field symmetry. For each family, the corresponding magnetic scalar potential (for L>>g) in the vicinity of the symmetry axis can be approximated by a real Taylor series expansion as follows:

$$\phi_{4n} \cong C_{11}\, xy + E_{13}(xy^3 - x3y) + G_{15}(3xy^5 - 10x^3y^3 + 3x^5y) + \ldots; \qquad (1)$$

and

$$\phi_{4n-2} \cong B_{01}y + D_{21}(3x^2y - y^3) + F_{41}(5x^4y - 10x^2y^3 + y^5) + \ldots; \qquad (2)$$

where the subscripted capital coefficients are functions of the PM parameters. To configure a given N-pole, the dimensions, spacings, and magnetizations of the N pieces must be designed to eliminate all the multipole coefficients lower than the desired leading N-pole coefficient. As formulas (1) and (2) explicitly show, the field of each such N-pole will not only exhibit its leading N-pole coefficient, but will also contain an infinitude of higher-pole terms with strengths proportional to increasing integral powers of distance (R) from the z axis.

In the following sections, an economical algorithm for removing the dominant members of these higher terms as a means of restoring the high-quality field aperture of a planar PM multipole to values comparable to those of a conventional structure, is outlined.

* Work supported in part by the Department of Energy Offices of Basic Energy Sciences and High Energy and Nuclear Physics, and Department of Energy Contract DE-AC03-76SF00515.

2 APPROACHES TO PLANAR MULTIPOLE FIELD QUALITY IMPROVEMENT

In contrast to a rotationally N-fold symmetric N-pole, whose pole surfaces can be shaped to approximate to the optimum equipotential contours [6], the freedom of adjusting the parameters of planar PM multipoles to attain a comparable degree of field quality is rather limited. Specifically, the shapes of the PM pieces (all rectangular cross sections) cannot be modified, forcing all equipotential surfaces to be planar. Secondly, confinement to a plane prevents the rotation of the pieces as a means of approximating to a curved 2-dimensional equipotential contour. Under these constraints, the principal means of improving the field quality has to be associated with the adjustable degrees of freedom of the planar PM multipole, namely, the number, dimensions, x-placements, and magnetizations of the PM pieces. Approaching the problem from this perspective, eq's. (1) and (2) suggest a straightforward way of enhancing the field quality of a planar PM N-pole; namely, by the successive removal of its higher-pole field components [3].

The basic principle behind this approach is illustrated in Fig. 2. For an optimized planar PM quad with the field spectrum shown on the top left side, the octupole component

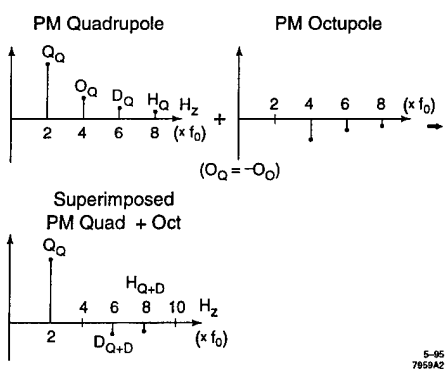

Fig. 2. Linear superposition of planar PM octupole and quadrupole rotating-coil spectra as a means of nulling the octupole component in the combined structure. f_0 is the coil rotation frequency.

can be nulled by centering a planar PM octupole whose leading field component, O_O, is equal and opposite to the quad's octupole component, O_Q, over the symmetry axis of the quad. We note that since the potential is given by the same canonical form for each structure (viz., by eq. (1)), making O_O=-O_Q will null the octupole component (E_{13} in our notation) for all values of R. Due to linear superposition, all the higher-pole components of the PM octupole will also tend to subtract from the corresponding higher-pole components of the quad. This procedure can be, of course, repeated to eliminate the next higher (dodecapole) component of the combined quad+octupole structure (see Fig. 3). Further repetition can be used to successively remove as many of the next-higher (or indeed, arbitrarily-located) field components as desired. Consequently, the same method can be used to purify the field of any planar PM N-pole. It is easy to show that if an individual PM multipole is used for each cancellation, the total number of PM pieces required for a quad with m successively nulled next-higher components would be $4+6m+2m^2$, and the corresponding number of pieces for a sextupole would be $6+8m+2m^2$. Clearly, the straightforward application of the cancellation procedure, as described up to this point, requires: 1) the vertical height of the initial N-pole structure to increase substantially; and 2) the number of pieces to go up rapidly with the required degree of purity. Both of these factors tend to li mit the practical implementability of this approach.

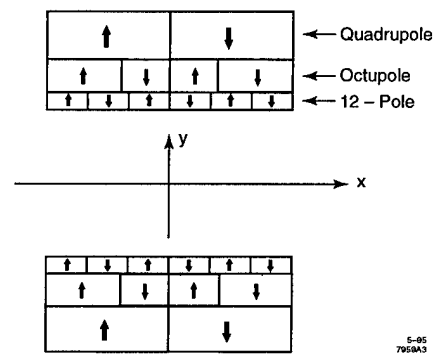

Fig 3. Planar PM quadrupole structure with nulled octupole and dodecapole field components.

3 AN ECONOMICAL FIELD-CANCELLATION ALGORITHM

The principle of the improved method (algorithm) to be introduced in the present paper can now be stated: by applying linear superposition to the PM magnet pieces themselves it is possible to generate fields equivalent to those of the improved structure of Fig. 3, but with a substantially reduced number of PM pieces, and without compromising the primary advantages of the basic N-pole structures of Fig. 1.

Referring to Fig. 3, the first requirement is that all the individual N-poles comprising the structure be of equal width. The second requirement is that all the PM pieces comprising the structure be of equal height. The third requirement, which underlies the superposition of the pieces is that each of the individual N-poles comprising the structure have the same gap. It is essential to note that under these constraints the field cancellations generated by the octupole and dodecapole can be maintained by suitable adjustments of the magnetization of their PM pieces. To illustrate the method, we can first consider the quadrupole and octupole structures in Fig. 3. Under the cited constraints, the octupole will be completely

superimposed over the quadrupole, yielding a structure with only eight pieces. The magnetizations of these pieces, however, will now be the linear sum of the magnetizations of the superimposed quadrupole and octupole structures, yielding a structure with the original quadrupole field component and a completely nulled octupole component. This has now been accomplished with eight pieces instead of twelve.

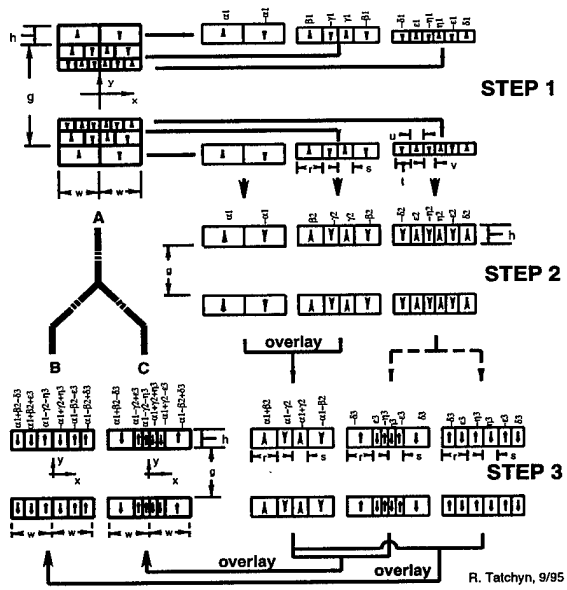

Fig. 4. Planar PM quadrupole field-cancellation algorithm for removing octupole and dodecapole components with a minimal number of pieces. Structures B and C are, apart from a scalar factor, equivalent to A.

We next take this new structure and superimpose the dodecapole structure over it in the same fashion. The new constraint is that the total width of the two pieces to the right of the dodecapole's y axis must be equal to the width of the piece to the right of the y axis of the new eight-piece structure. With this condition, a new twelve-piece structure is generated which has the original quadrupole component and completely suppressed octupole and dodecapole components. This has now been accomplished with only twelve pieces instead of the 24 shown in Fig. 3. Continuing in this fashion, it is straightforward to show that a planar PM quadrupole with m successively nulled next-higher components requires 4+4m pieces, and the corresponding number of pieces for the sextupole is 6+4m. In similar fashion, similar reductions in the complexity of higher N-poles can be achieved. A schematic flow chart of the field-cancellation algorithm described in the above paragraphs is shown in Fig. 4. In this picture the magnets are represented by equivalent magnetic charge sheets on their top and bottom surfaces, with the charge density magnitudes labeled by lower-case Greek letters. It is seen that a major penalty incurred by the proposed algorithm is the substantial reduction in the quadrupole strength of the reduced structures. As is evident for the quadrupole case, the algorithm generates two alternative paths; higher-N-pole optimization will involve even greater numbers of possible implementation options. The different possible configurations evidently provide the opportunity for further optimization, such as, e.g., minimizing the maximum/minimum spread in the values of magnetization while maximizing the dominant (N-pole) component in the final reduced structure.

4 SUMMARY

An economical field-cancellation algorithm has been described which will allow the fabrication of bi-planar quadrupoles and sextupoles with high-quality fields using a manageably small number of PM pieces. For higher order N-poles the number of pieces required to cancel a given number of successively-higher multipole components will also increase linearly; nevertheless, the practicability of fabricating octupoles and higher N-poles of this type should be considered a subject of continuing r&d. Since the removal of a large number of successive multipole components essentially increases the transverse region over which the N-pole's field is dominated by its leading N-pole field component, the fabrication of quadrupoles and sextupoles of the type described in this paper should lead to their introduction in storage ring applications. One potentially important application in this area is as distributed focusing elements installed into very-short-period, small-gap undulators (e.g., as a FODO lattice) [7]. The installation is rendered feasible by the very small vertical height of the biplanar N-poles (on the order of a millimeter), which, notwithstanding, doesn't prevent them from attaining focusing gradients on the order of several hundred T/m. If proven, this would allow short-period undulators of substantial length (viz., >>b) to be operated on storage rings, potentially transforming the optimality and economy of synchrotron radiation sources toward more favorable regimes.

5 REFERENCES

[1] R. Tatchyn, "Selected applications of planar permanent magnet multipoles in FEL insertion device design," Nucl.. Instrum. Meth. A341, 449(1994).

[2] R. Tatchyn, "Planar Permanent Magnet Multipoles for Particle Accelerator and Storage Ring Applications," IEEE Trans. Mag. 30(6), 5050(1994).

[3] T. Cremer, R. Tatchyn, "Planar Permanent Magnet Multipoles: Measurements and Configurations," in Proceedings of the 1995 Particle Accelerator Conference, IEEE Catalog No. 95CH35843, ms. FAP-20(on CD).

[4] J. Cobb and R. Tatchyn, "Tests of planar permanent magnet multipole focusing elements," Nucl.. Instrum. Meth. A347, 562(1994).

[5] D. C. Carey, "The Optics of Charged Particle Beams," Harwood, New York, 1987.

[6] K. Halbach, "Design of Permanent Multipole Magnets with Oriented Rare Earth Cobalt Materials," Nucl. Instrum. Meth. 169, 1(1980).

[7] R. Tatchyn, P. Csonka, A. Toor, "Perspectives on micropole undulators in synchrotron radiation technology," Rev. Sci. Instrum. 60(7), 1796(1989).

APERTURE CALCULATION OF AURORA-2D COMPACT ELECTRON STORAGE RING WITH A SUPERCONDUCTING WIGGLER

H. Tsutsui, T. Takayama, and T. Hori

Laboratory for Quantum Equipment Technology, Sumitomo Heavy Industries, Ltd.
2-1-1 Yato-cho, Tanashi-city, Tokyo, 188 Japan

Abstract

Dynamic apertures of AURORA-2D 700MeV compact electron storage ring with a 7 Tesla wiggler are calculated with a tracking program NABO which uses a sixth order Runge-Kutta method. Also dynamic apertures are calculated by a symplectic tracking program SAD to see the validity of using Runge-Kutta method. Sufficiently large dynamic apertures are obtained.

1 INTRODUCTION

AURORA-2[1,2] has two versions S and D. AURORA-2S is designed as a synchrotron radiation source for X-ray lithography. It has two 180 degrees 2.7 Tesla normal conducting bending magnets and two quadrupole magnets.

AURORA-2D is designed for scientific applications. It has two 180 degrees 2.7 Tesla normal conducting bending magnets, eight quadrupole magnets, and two 3 m straight sections. Up to two insertion devices can be installed in the straight sections. Two AURORA-2D accelerators were assembled in Hiroshima University and Tanashi works of Sumitomo Heavy Industries, Ltd. They successfully accumulated 30 mA at 700 MeV in the first operation without insertion devices. We think that the accumulated current will increase as the vacuum will become well. One 7 Tesla wiggler will be installed in the ring at Tanashi works and tested in July.

In this paper, we calculate dynamic apertures for AURORA-2D with a 7 Tesla super conducting wiggler. We used a particle tracking code NABO developed by Takayama. NABO is based on a sixth order Runge-Kutta method. It reads measured magnetic field data in median plane, calculates twiss parameters, makes chromaticity correction, and calculates dynamic apertures. Runge-Kutta method is powerful for treating measured magnetic field directly. But it is thought that a multi turn particle tracking by this method is risky because the symplectic condition is violated by numerical error. We also calculated dynamic apertures by a particle tracking program SAD[3] which satisfies the symplectic condition.

2 LATTICE PARAMETERS

Figure 1 shows the top view of AURORA-2D. It has two 180 deg. bending magnets (BM), four focusing quadrupoles (QF), and four defocusing quadrupoles(QD). Bending magnets have an edge angle to function as defocusing quadrupoles. Dipole and sextupole magnetic field components can be generated in QF's and QD's by auxiliary coils in them. Sextupole component in QF's and QD's may be used for chromaticity correction. One of the two straight sections is occupied with a 7 Tesla wiggler. The magnetic flux density in the wiggler were calculated by TOSCA. The wiggler is now under fabrication. Spectra of light from bending magnets and 7 Tesla wiggler are shown in figure 2.

For the calculation of natural chromaticities, the well known formula:

$$\xi = \oint \beta \eta K ds / 4\pi ,$$

is not applicable to small rings because the formula does not include the effect of the second order aberrations in bending magnets[4]. Though the natural chromaticities can be calculated by complicated linear theory, they were calculated by NABO and SAD tracking codes because of easiness. Table 1 shows the parameters of AURORA-2D. Necktie diagrams are shown in figure 3. Lattices are shown in figures 4 and 5.

3 DYNAMIC APERTURE

Chromaticities are corrected before the aperture calculation. Figures 6 and 7 show the results. The cross symbols are by NABO. The lines are by SAD. Ideal magnets are assumed in the calculation by SAD. Effect of the third order aberrations in BM's can be seen. Differences between the results of NABO and those of SAD are due to the imperfection of actual quadrupole field in QF's and QD's, and the errors of the measured data.

Dynamic apertures are shown in figures 8 and 9. They are at the center of the straight section. Solid lines are by NABO. Dots are by SAD. Broken lines show 10σ of the beam size. Vertical emittance is assumed to be the half of the natural emittance. Apertures by NABO are considerably smaller than those by SAD because NABO uses the measured data which has the physical limit. Vertical limits are due to the physical aperture in BM's, and the horizontal limits are due to the physical aperture in QF's.

Apertures become considerably small if the 7T wiggler is installed. Some part of 10σ volume is out of the aperture calculated by NABO. This is not so much

0-7803-4376-X/98/$10.00 © 1998 IEEE

problem because the vertical emittance is overestimated. If typical x-y emittance coupling of 0.01 is used, the 10σ volume become small in the vertical direction by a factor of 7 and is well within the aperture.

4 CONCLUSION

Dynamic apertures of AURORA-2D with a 7 Tesla wiggler are calculated by NABO and SAD. Apertures are sufficient for the practical operation.

5 ACKNOWLEDGEMENTS

The authors wish to thank Prof. Kamada and Dr. Ohmi of KEK for helping us to use SAD.

REFERENCES

[1] Toshitada Hori and Takeshi Takayama, '"AURORA2" Compact Advanced SR Ring as an X-ray Source', 4th International Conference on Synchrotron Radiation Sources and 2nd Asian Forum on Synchrotron Radiation 1995, pp. 148-158

[2] T. Takayama, H. Tsutsui and T. Hori, 'Compact Synchrotron Radiation Source 'AURORA-2' with 2.7T Normal Conducting Bending Magnets', EPAC'96 pp. 709-711

[3] 'Sad Home Page', http://www-acc-theory.kek.jp/SAD/sad.html

[4] W. Hardt, J. Jaeger and D. Moehl, 'A General Analytical Expression for the Chromaticity of Accelerator Rings', CERN PS/DL/LEAR/Note82-5 1982

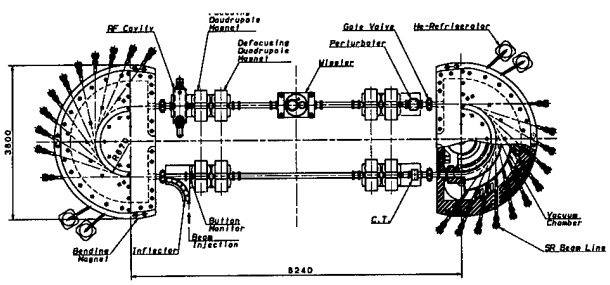

Figure 1 Top view of AURORA-2D with one wiggler

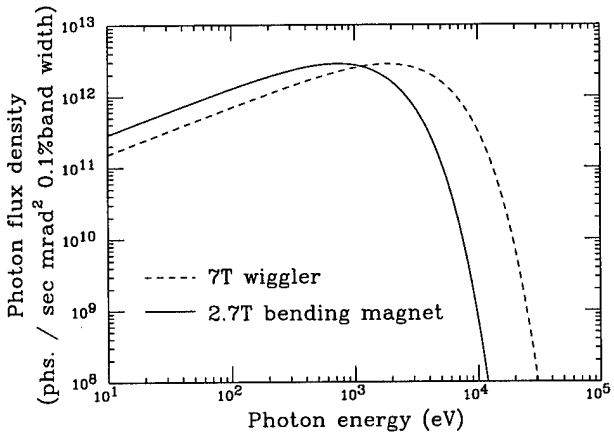

Figure 2 Spectra from bending magnets and 7T wiggler. Beam energy is 700MeV. Beam current is 300mA.

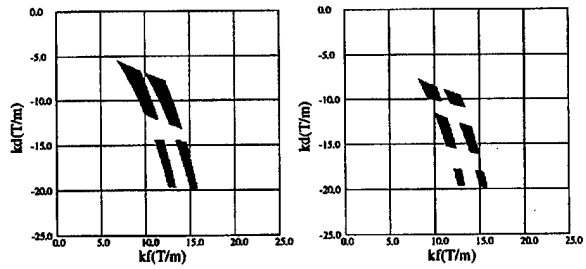

Figure 3 Necktie diagrams. The diagram of the left hand side is of no insertion device type. The diagram of the right hand side is of single 7T wiggler type.

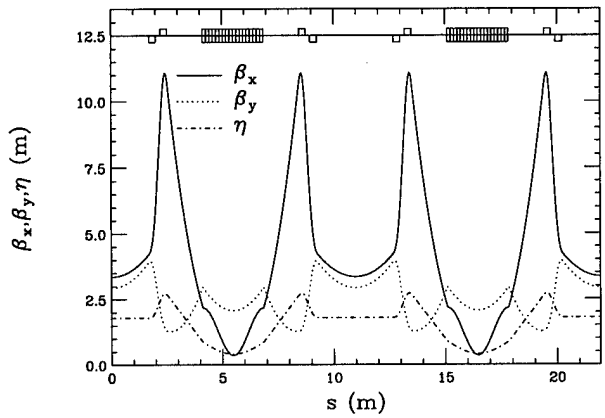

Figure 4 Lattice of no insertion device type

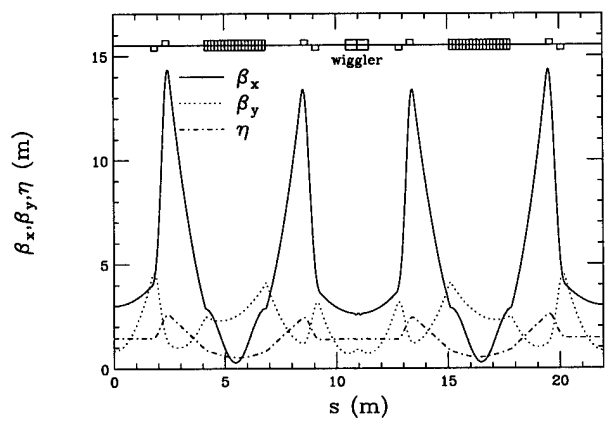

Figure 5 Lattice of single 7T wiggler type

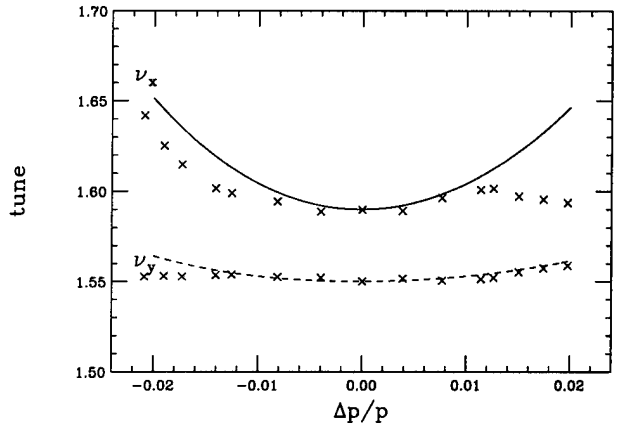

Figure 6 Tune plot of no insertion device type. Cross symbols are by NABO. Lines are by SAD.

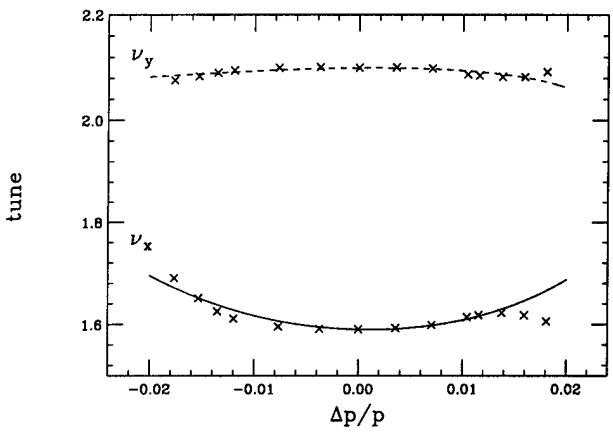

Figure 7 Tune plot of single 7T wiggler type

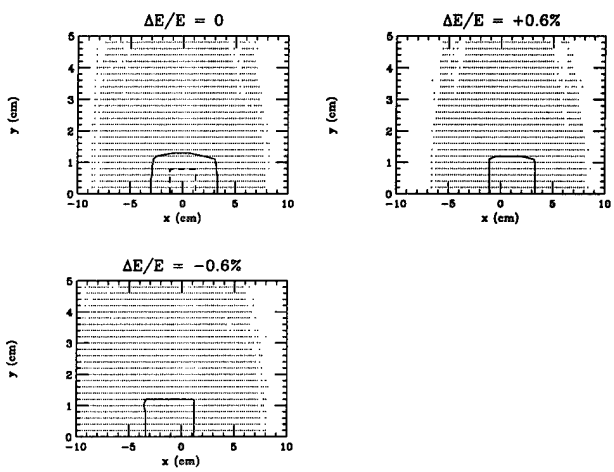

Figure 8 Dynamic aperture of no insertion device type. Solid lines are by NABO. Dots are by SAD. Broken line shows 10σ of the beam size.

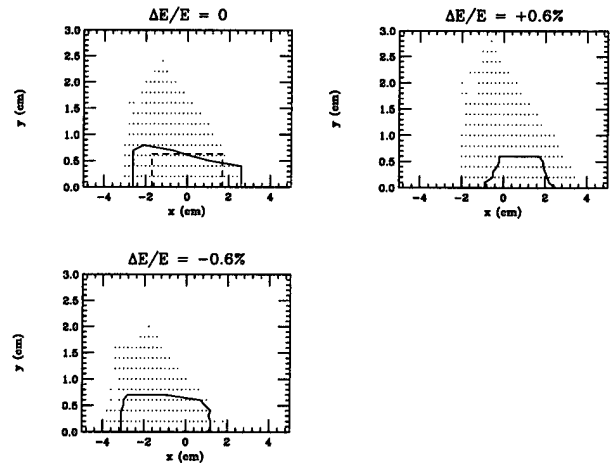

Figure 9 Dynamic aperture of single 7T wiggler type.

	A2D	*1W7T*	
Energy	0.7	0.7	GeV
Circumference	21.946	21.946	m
RF voltage	220	220	kV
Harmonic number	14	14	
RF frequency	191.243	191.243	MHz
Energy aperture	5.937	5.502	MeV
Energy loss	24.424	29.071	keV/turn
Synchrotron frequency	0.14651	0.15493	MHz
Momentum compaction	0.16528	0.18530	
Tune horizontal	1.590	1.590	
vertical	1.550	2.100	
Natural chromaticity			
horizontal	-1.4	-2.3	
vertical	-2.8	-3.8	
Natural emittance	474.022	934.564	πnm rad
Energy spread	0.421	0.444	MeV
Radiation damping time			
horizontal	5.873	5.599	msec
vertical	4.196	3.525	msec
longitudinal	1.836	1.487	msec
Bunch length	32.403	36.164	mm
Touschek lifetime at 1A	5.712	9.903	hour
Quantum lifetime	>1E+32	7.0E+24	hour
Field strength BM	2.7	2.7	Tesla
QF	9.4	10.9	Tesla/m
QD	-8.6	-12.3	Tesla/m

Table 1 Lattice parameters of AURORA-2D

NUMERICAL SIMULATION AND RF MODEL MEASUREMENTS OF THE NEW GSI IH-DTL*

B. Krietenstein, T. Weiland, TH Darmstadt, Darmstadt, Germany
U. Ratzinger, R. Tiede, GSI, Darmstadt, Germany
S.A. Minaev, MEPhI, Moscow, Russia

Abstract

Two IH drift tube linacs (IH1 and IH2) will be part of the new high current injector of the GSI accelerator facility in Darmstadt (Germany). In order to shorten the cavity design period, numerical simulations using MAFIA, as well as rf model measurements were used to determine the dimensions of these linacs.

In this paper we present results of the simulations and the measurements for IH1, which was the more complex structure.

1 INTRODUCTION

The main parts of the GSI accelerator facility are a heavy ion linear accelerator (UNILAC), a heavy ion synchrotron (SIS) and an experimental storage ring (ESR). To be able to fill the SIS up to its space charge limit, the first (prestripper) part of the UNILAC has to be replaced (see also [2], [3]). Besides an IH RFQ and an IH superlens, two IH drift tube linacs (IH1 and IH2) will be part of the new prestripper linac. They are designed to provide an effective voltage gain of 40.8 MV(IH1) and 42.4 MV, respectively, at a resonance frequency of 36.136 MHz.

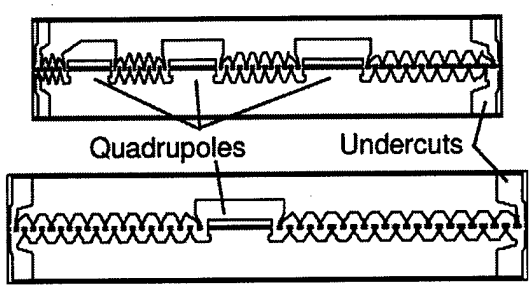

Figure 1: Layout of IH1 and IH2 after the optimization with MAFIA.

The design of these cavities based on numerical simulations using MAFIA[1] and measurements of a 1:5.88 scaled rf model. The main purpose of the simulations was the determination of main geometric parameters as the tank radius and the dimensions of the undercuts in the girders at the ends of the tanks. Furthermore, the initial guess for the capacity distribution along the drift tube structure could be improved in order to get a good start for the measurements. With help of the measurements, the gap voltage distribution could be optimized and the performance of tuning elements was studied.

* work supported by GSI - Gesellschaft für Schwerionenforschung, Darmstadt, Germany

[1] Solution of Maxwell's equations using a Finite Integration Algorithm (see [1]).

The beam energy along tank IH1 ranges from 120 keV/u to 748 keV/u. This range has not yet been covered by a single IH cavity of this type. Thus, the design was more difficult, especially as the gap voltage distribution given by LORASR beam dynamics calculations was not trivial.

2 SIMULATION

The procedure for the simulation was presented in [4]. As the longitudinal cut plane through the girders is a symmetry plane, only one half of the cavities had to be simulated. The main task herein is the calibration of the drift tubes for the calculation. Restrictions in memory size and computation time determine a rather coarse mesh in the drift tube region. The drift tubes consist of a tube and asymmetric bulges at the apertures for compensation of dipole components in the electric field (see also [6]). For the simulation, these tubes were replaced by tubes with octagonal cross-sections. These substitutes can be modeled with a 6×6 grid in the cross-section.

Table 1: Some data concerning the simulations.

Number of mesh points:	2-3 million
CPU-time:	36 hours
Machine:	IBM RS-6000 590

Furthermore, there are three drift tube sizes in tank IH1. Gaplengths and periodlengths at the low energy end of the tank are about 2-2.5 times smaller than at the high energy end. The correlated higher capacitive load at the entrance is partially compensated by the use of a quadrupole lens array, which allows to reduce the drift tube apertures at the low energy end. To avoid small meshsteps all drift tubes were modeled with the same radii. The change in the drift tube capacities then was compensated by variation of the gaplengths in the range of $\pm20\%$.

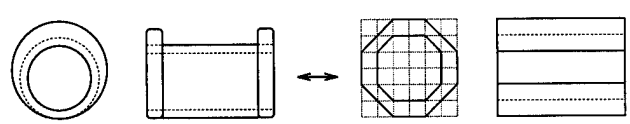

Figure 2: The real drift tube and its substitute. The octogonal cross-section can be discretized with only 3 cells along the radius.

3 SINGLE GAP INVESTIGATIONS

When designing an IH drift tube linac, it is important to know the characteristics of the gaps. Single gaps can be investigated as slices of the tank, measured from one drift tube center to the next, with magnetic boundary conditions ($\vec{B}_{\parallel} = 0$) in the cutting plane.

0-7803-4376-X/98/$10.00 © 1998 IEEE

In the following, we present results of single gap investigations for tank IH2.

3.1 Empty Tank

The fundamental mode of a cylindrical cavity is the H_{111}-Mode. With r being the cavity radius and L the cavity's length, the resonance frequency f writes

$$f = \frac{c_0}{2\pi}\sqrt{\left(\frac{\pi}{L}\right)^2 + \left(\frac{1.841}{r}\right)^2} \quad (1)$$

In the case of single slices with magnetic boundary conditions, $L \rightarrow \infty$ and f becomes

$$f = \frac{1.841 \cdot c_0}{2\pi r} \quad (2)$$

3.2 Tank with Girders

When girders are inserted, the capacity rises and the frequency decreases. Figure 3 shows, how the frequency varies with the girder distance

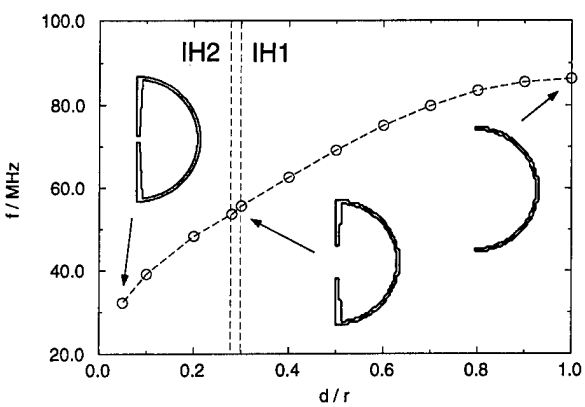

Figure 3: Variation of the resonance frequency with the distance of the girders. $d/r = 0.275$ is the distance of the girders in cavity IH2.

3.3 Tank with Drift Tubes Mounted on the Girders

The resonance frequency of a cavity slice with girders only is independent of the period length of the cell. When drift tubes are mounted with feet on the girders, the combination of period and gap length determines the frequency, which is further decreased. Figure 4 displays the frequencies of all gaps of cavity IH2.

These frequencies can be used to obtain a guess for the resonance frequency of the complete cavity IH2. If the frequencies are weighted linearly with the period lengths of the corresponding gaps:

$$f = \frac{1}{L}\sum_{i=1}^{N_{\text{Gaps}}} f_i \cdot l_i = 36.191\,\text{MHz} \quad (3)$$

L denotes the cavity length, f_i and l_i the frequency and period length of the indexed gap, respectively. The value for the frequency only differs from the actually measured

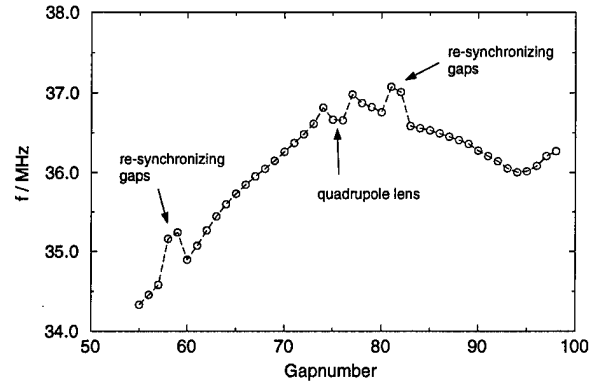

Figure 4: Local frequencies of all gaps of cavity IH2. The values result from single gap calculations.

and simulated frequency by less then half a percent, but this method does not include the effect of undercuts in the girders, which also decrease the frequency of the cavity.

For a direct comparison, table 2 shows, how the frequency changes in cavity IH2, when girders, drift tubes and their feet are mounted.

Table 2: Decrease in frequency, when girders, drift tubes and their feet are mounted.

Step	Frequency / MHz	Deviation
Empty cavity	86.373	0%
Girders added	53.698	-37.8%
Drift tubes and feet added	36.191 (34.332-36.979)	-58.1% (-60.3%-57.2%)

4 MEASUREMENTS

For the measurements at GSI, the perturbation method was used. The perturbing bead was a silver sphere of 2.5 mm radius for the measurements of tank IH2. As the drift tube apertures were too small in tank IH1, a metal cylinder of the same length, but only 0.8 mm diameter was used in order to get reliable results. Goals for the measurement were

- Determination of the resonance frequency
- Measuring and optimizing the gap voltage distribution
- Obtaining frequency range and gap voltage distortion of the tuning elements

The gap voltage distribution could be optimized within 5 steps by variation of the drift tube lengths, keeping the period lengths constant. The asymmetric gap geometry at the end of each drift tube containing a quadrupole triplet lens caused asymmetric electric gap fields with peaks close to the slim drift tube. A conical drift tube shape was introduced for these gaps, which makes the electric field distribution along the beam axis more symmetric (see figure 5).

The tuning method for tank IH1 will be the same as for tank IH2 (see [4]). Three plungers have successfully been tested. They are positioned between the quadrupole lenses and in the high energy section of IH1. A plunger at the low energy end showed a rupture in the tuning characteristics.

This was caused by a plunger resonance, which split the operating mode in a higher and a lower mode. For this reason, no plunger will be used at that position. The gap field distortion at the nominal frequency is neglectable.

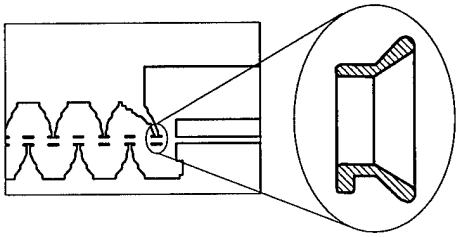

Figure 5: Conical drift tubes are used near the quadrupole lenses in order to reduce the peak field.

5 RESULTS

Figure 7 compares the simulated, the measured and the reference gap voltage distribution. In the fifth and final optimization step, the deviation of the measured voltages was $< 1\%$. The simulation's deviation is up to 15%. This is plausible, as the distribution reacts very sensitive on changes in the drift tube geometry and can be modified, even after the cavity is assembled. Figure 6 compares the deviation of the measured and the reference voltage for two optimization steps and the change in gaplengths between these two steps. Figure 6 demonstrates, how the gap voltage distribution can be tilted by variation of the drift tube geometries.

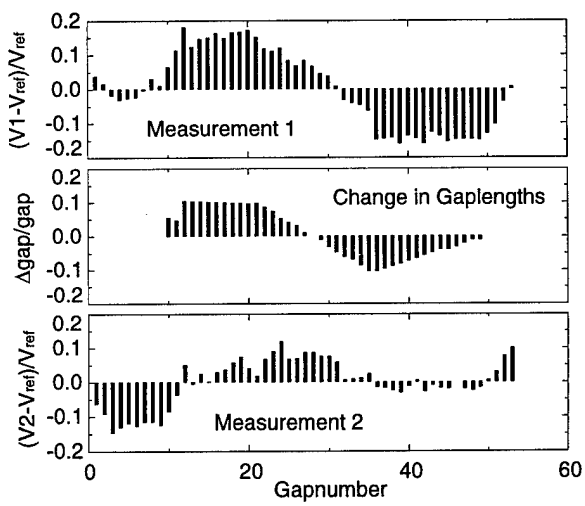

Figure 6: Relative deviation of the measured and the reference voltage distribution for two measurements and the relative change in the gaplengths between these measurements.

The more important point was the accuracy of the resonance frequency, as tuning was planned in the range from 0% to -0.5% only. Table 3 lists measured and calculated frequencies of the operating modes of tanks IH1 and IH2, respectively. Due to the detailed calibration of the drift tube substitutes, the agreement is excellent.

6 SUMMARY

With the help of measurements and simulations, the design of two new IH drift tube linacs could be completed within

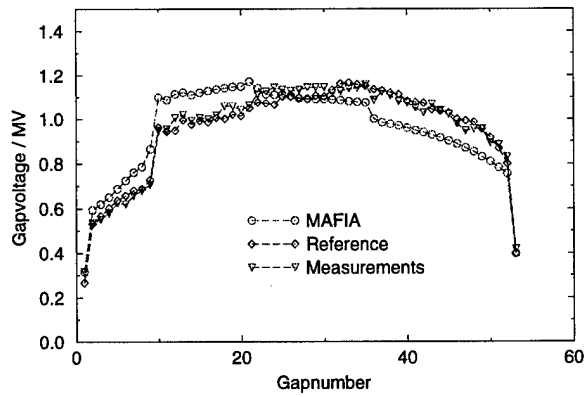

Figure 7: Calculated, measured and reference gap voltage distribution in cavity IH1

Table 3: Calculated and measured frequencies of the operating modes of IH1 and IH2

	IH1	IH2
MAFIA	36.255	36.275
Measurement	36.195	36.287
Rel. Dev. [%]	0.16%	0.03%

the project's schedule. The tanks and the girder structure could be ordered, even before the measurements started. While measured and simulated voltage distributions differ slightly, the frequencies agree very well.

It could be shown, that even such complex structures as tank IH1 with its three quadrupole lenses can be simulated numerically with good results.

7 REFERENCES

[1] The MAFIA collaboration, *User's Guide MAFIA Version 3.2*, CST GmbH, Lauteschlägerstraße 38, D-64289 Darmstadt, Germany.

[2] *Beam Intensity Upgrade of the GSI Accelerator Facility*, GSI-95-05, Report, June 1995, ISSN 0171-4546

[3] U. Ratzinger, *The New Prestripper Linac for High Current Heavy Ion Beams*, Proceedings of the XVIII International Linear Accelerator Conference, August 1996, Geneva, Switzerland, vol. 1, p. 288-292.

[4] B. Krietenstein, S.A. Minaev, U. Ratzinger, R. Tiede, T. Weiland, *Numerical Simulation of IH-accelerators with MAFIA and RF Model Measurements*, Proceedings of the XVIII International Linear Accelerator Conference, August 1996, Geneva, Switzerland, vol. 1, p. 243-245.

[5] E. Nolte et alt., *The Munich Heavy Ion Postaccelerator*, Nuclear Instruments and Methods 158 (1979),pp. 311-324

[6] U. Ratzinger, *Interdigital RF Structures*, Proceedings of the Linear Accelerator Conference 1990, Albuqerque, New Mexico, LA-12004-C, pp. 525-529.

BROAD-BAND IMPEDANCE OF LHC SHIELDED BELLOWS

Misha D'yachkov, TRIUMF, 4004 Wesbrook Mall, Vancouver, B.C., Canada V6T 2A3
and
Francesco Ruggiero, CERN, Geneva, Switzerland

Abstract

To compensate for thermal expansion the LHC ring has to accommodate about 2500 bellows which, together with beam position monitors, are the main contributors to the LHC broad-band impedance budget. In order to reduce this impedance to an acceptabe value the bellows have to be shielded. In this paper we compare different designs proposed for the bellows and calculate their transverse and longitudinal wake fields and impedances. Owing to the 3D geometry of the bellows, the code MAFIA was used for the wake field calculations. The results presented in this paper indicate that the latest bellows design, in which shielding is provided by sprung fingers which can slide along the beam screen, has impedances smaller than those previously estimated according to a rather conservative scaling of SSC calculations and LEP measurements. Several failure modes, such as missing fingers and imperfect RF contact, have also been studied.

1 INTRODUCTION

The bellows are the main contributors to the LHC broad-band impedance budget [1]. The LHC bellows design is based on the LEP and the SSC bellows [2]. Studies done for SSC bellows [3, 4] have shown that in order to reduce their impedances to acceptable values they have to be shielded. The number of particles per bunch in the LHC is even larger than in the SSC (1.05×10^{11} compared to 1.5×10^{10} in the SSC) and therefore the same applies to LHC bellows.

LHC beam screen has a race-track shape and, in order to provide even pressure on each finger touching the beam screen (for good RF contact), it has been proposed to make a transition from race-track to circular shape. The LHC bellows design has not been finalized yet and therefore the effect of the transition length on the impedance will be studied in this paper.

2 ANALYTICAL ESTIMATES

The fact that all transitions and discontinuities in the bellows are very small compared to the beam screen diameter makes it possible to estimate the impedances analytically. It should also be noted that since the r.m.s. bunch length in the LHC ($\sigma_l \geq 7$ cm) is larger than the beam screen radius ($b \approx 2$ cm), the beam spectrum lays well below the cut-off frequency of the beam screen $f_{\rm cutoff} = 2.405\, c/2\pi b =$ 5.74 GHz and therefore we are mostly interested in the low frequency limits of the impedances.

i) *Impedance of a step*: The small steps (an order of 1 mm) are unavoidable in the area where the sliding fingers touch the beam screen; an imaginary part of the longitudinal impedance Z_l of a single step can be estimated is given by the following analytic formula, which can be found in Ref. [5]:

$$Z_l/n = -iZ_0 \frac{\omega_0}{c} \frac{h^2}{4\pi^2 b} \left[2\ln(2\pi b/h) + 1\right]. \qquad (1)$$

The transverse impedance of an axially symmetric discontinuity can be obtained from the longitudinal one using the formula

$$Z_t = \frac{2c}{b^2\omega_0} \frac{Z_l}{n}. \qquad (2)$$

The resistive part of the impedances (both longitudinal and transverse) of a small step is very small at the typical beam spectrum and can be disregarded. The impedances of a long pill-box, calculated using formulae 1-2 are shown in Table 1 (we assumed that an average beta-function in the LHC is $\beta_{\rm av} = 89$ m)

Table 1: Impedance contributions from two small steps in the bellows at the contact areas between fingers and beam screen.

Step size	1 mm	2 mm	3 mm
L, nH	0.0340	0.118	0.243
Z_l/n, mΩ	0.00240	0.00835	0.0172
Z_t, kΩ/m	0.051	0.177	0.364
$2500 \times Z_l/n$, mΩ	6.00	20.9	42.9
$2500 \times Z_t \times \beta_{\rm av}$, M$\Omega$	0.127	0.443	0.910

ii) *The impedance of a gaps between fingers*: gaps between separate fingers as well as possible "missing fingers" also have a very small size compared to the beam pipe radius and therefore their effect can be estimated by calculating low frequency impedances of a narrow slot [5]. We found that low-frequency contribution of the gaps is very small compared to a contribution of the "step" which is unavoidable.

2.1 Power losses in bellows gaps

As it will be shown in this report, the impedance for different bellows design is well within the LHC impedance budget and the only effect which should be considered is the effect of power losses in the bellows and consequent heating. It is recommended that the total power loss in all bellows should not exceed 1 kW/ring [2], this number is much higher than the one used in the SSC design ($P < 190$ W).

The parasitic loss per bellows equals

$$P = k_l\, e^2 N^2 M f_{\rm rev}, \qquad (3)$$

0-7803-4376-X/98/$10.00 © 1998 IEEE

where k_l is the longitudinal loss factor, N the number of particles per bunch, M the number of bunches and f_{rev} is the revolution frequency. The loss factor is negligible in case of good RF contacts between bellows fingers and beam screen, but even a very small gap can contribute significantly to the power losses. The gap can be treated as a coaxial transmission line and thus we can derive the following formula for parasitic losses due to a gap Δ

$$P = \frac{\Delta}{b} \frac{Z_0 c}{4\pi^{3/2}\sigma_z} N^2 e^2 M f_{rev}. \quad (4)$$

Plugging typical LHC parameters we obtain the following expression for the power loss per gap:

$$P(\mathrm{W}) \simeq 30 \cdot \Delta(\mathrm{mm}). \quad (5)$$

Therefore, in order to have losses below 1 kW in 2500 bellows and taking into account that there are two sets of fingers, the maximum allowed gap is about $\Delta = 0.006$ mm.

2.2 *Power losses in other discontinuities*

Due to the fact that the frequency spectrum of the LHC bunch is concentrated in a region well below cutoff frequency of the pipe and the resistive part of the impedance is very small at these frequencies, we estimate that the power losses from all the steps in the bellows will be less than a few watts per ring and can be disregarded. Power losses in the gaps (< 1 mm) between fingers are also found to be small.

The situation when the RF contact is lost for all fingers in a single bellows is equivalent to the "gap" which was considered in the previous subsection. From Eq. (5) we see that, if we assume Δ = 1 mm, the power losses in a single bellows may be 30 W! However, it is unlikely that the RF contact will be lost at all fingers simultaneously. It is more likely that only one or two fingers break at the same time, therefore we need to estimate the power losses due to a few missing fingers. If the power losses due to the "missing" fingers will be higher than the maximum power of the cooling power in the region near the the broken contact, this may cause overheating of neighboring fingers and their subsequent breakup.

We can estimate the power losses in the case of "missing fingers" by representing them as a long slot. Our estimates show that these losses are negligible (which is consistent with the results of numerical simulations shown below).

3 NUMERICAL RESULTS

Due to the distinctive 3D geometry of the proposed LHC bellows designs and in order to be able to compare the results for different bellows models, it has been decided to use the MAFIA T3 module (3D time domain) for all calculations. Unfortunately, due to computing limitations, the minimum mesh size we were able to use in our calculations was only 0.5 mm in the transverse planes and 1 mm in the longitudinal direction, i.e., memory limitations were

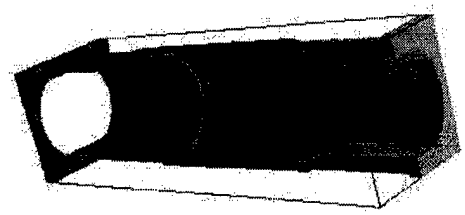

Figure 1: A typical geometry used in the calculations: smooth transition and two steps (pill-box).

our major constraint since the CPU time on the 200 MHz DEC Alpha station was only about 1-2 hours for a typical geometry.

In our simulations we used MAFIA T3 to calculate the wake fields generated by a test Gaussian bunch with charge Q=1 and r.m.s. length σ_z = 1 cm, displaced by 5 mm from the center of the beam pipe in both vertical and horizontal planes and traveling with the speed of light. The wake fields have been calculated with the step 1 mm and were truncated at 52 cm. The bunch length used in the simulations (σ_l = 1 cm) allowed us to obtain the impedance up to 10-12 GHz (about twice the LHC beam screen cutoff frequency f_{cutoff} = 5.74 GHz). On the graphs (Figs. 2-3) the impedance is shown up to 16 GHz, together with the spectrum of the σ_z = 1 cm bunch.

The displacement of the beam in the transverse direction was only 10 mesh points, and therefore one should expect additional errors (at least 15-20%) in the transverse impedances at low frequencies. These errors will be even bigger at higher frequencies. A typical geometry used in the calculations is shown on figure 1.

3.1 *Beam Pipe Transition*

In this section we study the effect of the transition length from the race-track shape to a circle, which is made in order to have the same pressure on each of the sliding fingers.

The low frequency impedances obtained from the results of the simulations for different transition lengths are shown in Table 2. It is interesting to note that the transverse impedances in horizontal and vertical planes are not only different, but have also different signs.

Both transverse and longitudinal impedances decrease sharply if the transition length changes from 0 to 10 mm, and only slightly if it increases from 10 to 35 mm.

Table 2: Low frequency impedances for different transition lengths.

Transition	0 mm	10 mm	20 mm	35 mm
Z_l/n, mΩ	0.0072	0.0035	0.0034	0.0028
$Z_t(v)$, kΩ/m	0.413	0.205	0.199	0.121
$Z_t(h)$, kΩ/m	-0.276	-0.138	-0.129	-0.079

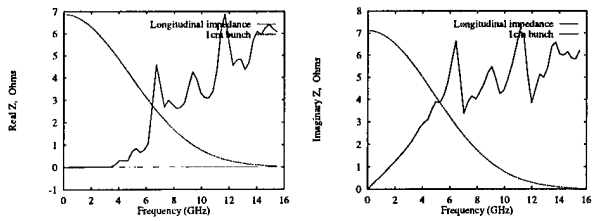

Figure 2: Longitudinal real and imaginary part of impedance for the case of 1 mm step, 10 mm transition and 2 missing fingers

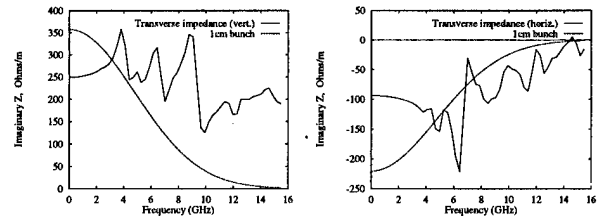

Figure 3: Imaginary part of transverse impedances (vertical and horizontal planes) for the same geometry (1 mm step + 10 mm trans. + 2 m.f.).

3.2 *Transition + step*

The results in the previous section did not include the effect of small steps unavoidable at the point of contact between beam pipe and sliding fingers. In this section we will calculate the impedances of a model bellows which includes smooth transitions and two steps (pill-box).

Using arguments from the previous subsection, the transition length was set to 10 mm and we calculated the wake fields and the impedances for two different values of the steps, namely 1 mm and 2 mm (keeping in mind that though the beam screen is only 1 mm thick some extra step may be required to allow a good RF contact with the fingers).

The low frequency impedances for the structures considered are presented in Table 3. A "missing finger" was also simulated as a long narrow slot. The width of the slot used in the simulations was 6 mm (which is in fact equivalent to the case of 2 missing fingers in the same place) though, as one can see from Table 3, the effect of this slot on the overall impedance is very small.

Table 3: Low frequency impedances of the model bellows with smooth transitions of 10 mm and two steps, for different step sizes and including the case of a missing finger (m.f.).

Step size	0 mm	1 mm	1 mm + m.f.	2 mm
Z_l/n, mΩ	0.0035	0.0061	0.0062	0.0134
$Z_t(v)$, kΩ/m	0.205	0.251	0.249	0.344
$Z_t(h)$, kΩ/m	-0.138	-0.088	-0.094	-0.007

As one can see from Table 3, the longitudinal impedance of the bellows with step $\Delta = 2$ mm is only 0.0134 mΩ, which results in $Z_l/n = 33.5$ mΩ for 2500 bellows (i.e., less than half the value of 80 mΩ previously allocated for bellows in the LHC impedance budget [1]) and $Z \times \beta_{av} = 0.910$ MΩ also smaller than the value originally used in Ref. [1].

4 CONCLUSION

The calculated impedances of the LHC bellows were found to be smaller than the values used in Ref. [1] (based on a rather conservative scaling of SSC calculations and LEP measurements).

It has been found that one of the most significant factors contributing to the impedance of the bellows is the size of the step at the point of contact between sliding fingers and beam screen. Therefore additional care should be taken to make this step as small as possible, but retaining at the same time a good RF contact between the fingers and the beam screen, in order to avoid parasitic power losses in the bellows. The gap between the sliding contacts and the beam screen should be less than 0.006 mm in order to keep the power losses in the bellows $P < 1$ kW.

The transverse wake fields and impedances of the bellows in the vertical and horizontal planes are not only different, but have also different signs (i.e., focusing in one plane and defocusing in the other). The effect of the gaps between fingers is found to be negligible.

5 ACKNOWLEDGMENTS

We would like to thank Alastair Mathewson and Ray Veness, of the LHC Vacuum Group, for useful discussions about the LHC bellows design and for providing us with their latest version.

6 REFERENCES

[1] F. Ruggiero, *Single-Beam Collective Effects in the LHC*, in Proc. "Workshop on Collective Effects in Large Hadron Colliders", Montreux, 1994, eds. E. Keil and F. Ruggiero, Particle Accelerators, Vol. 50, pp. 83–104 (1995).

[2] A. Chao, *Summary of the Impedance Working Group*, ibid, pp. 1–18 (1995).

[3] K. Ng and J. Bisognano, *An Estimate of the Contributions of Bellows to the Impedances and Beam Instabilities of the SSC*, ibid, p. 45 (1985).

[4] K.L.F. Bane and R. Ruth, *Bellows Wake fields and Transverse Instabilities in the SSC*, in "Report of SSC impedance Workshop", SSC-SR-1017, p. 11 (1985).

[5] S. Kurennoy, *Coupling Impedance of Pumping Holes*, Particle Accelerators, Vol. 39, pp. 1–13 (1992).

[6] S. Kurennoy and G. Stupakov, *A New Method for Calculating Low Frequency Coupling Impedance*, Particle Accelerators Vol. 45, pp. 95–110 (1994).

[7] S. Kurennoy, Report SSCL-636, Dallas (1993).

GdfidL: A FINITE DIFFERENCE PROGRAM WITH REDUCED MEMORY AND CPU USAGE

W. Bruns*, Technische Universität Berlin, Einsteinufer 17, 10587 Berlin

Abstract

Two new field solvers based on the FDTD Algorithm are described. One solver computes resonant fields in lossfree structures, the other computes time dependent fields, scattering parameters and wake potentials in lossy or lossfree structures. The program uses linked lists instead of three dimensional arrays to model the computational volume. The main advantage of this approach is: Grid cells are only needed in regions, which are not filled with electric or magnetic conducting materials. This may result in an appreciable reduction of memory and CPU usage. The modeling via the linked lists is described in detail and some examples of calculated realistic geometries are given.

1 GENERAL METHOD

GdfidL [1] is another Finite-Difference Code that approximately solves MAXWELLs equations by discretizing the curl operators. For homogeneous materials this discretization was invented by Yee [1]. In case of inhomogeneous dielectric or permeable materials, the discretization of the curl operators is the same as by Weiland [2].

1.1 Curl Equations with linked lists

The discretized curl operators are a recipe how to compute the time derivative of a field component in the grid from the values of the four surrounding dual components. By attaching a triple index i, j, k to each field component in the computational volume, the resulting difference equations are very simple. Eg. the $\frac{d}{dt}B_z$ component in a lossfree region is approximated as

$$\frac{d}{dt}B_z^{i,j,k} \approx \frac{\Delta_x(E_x^{i+1,j,k} - E_x^{i,j,k}) + \Delta_y(E_y^{i,j+1,k} - E_y^{i,j,k})}{\Delta_x \Delta_y} \tag{1}$$

One of the advantages of this simple difference equation is: it is easy to understand and easy to implement in a computer program by declaring triple indexed variables. However for many geometries this approach has a disadvantage: Grids cells are also assigned to regions where the material is ideal conducting.

GdfidL uses an equation that looks slightly more complicated: Cells do not carry a triple index, but only a single index: The $\frac{d}{dt}B_z$ component now looks as

$$\frac{d}{dt}B_z^l \approx \frac{\Delta_x(E_x^{n_y^+(l)} - E_x^l) + \Delta_y(E_y^{n_x^+(l)} - E_y^l)}{\Delta_x \Delta_y} \tag{2}$$

The indices $n_x^+(l), n_y^+(l)$ are the indices of the neighbour cell in positive $x-$, and $y-$direction of the cell with index l. These indices and four other indices $n_z^+(l), n_x^-(l), n_y^-(l), n_z^-(l)$ constitute the linked lists.

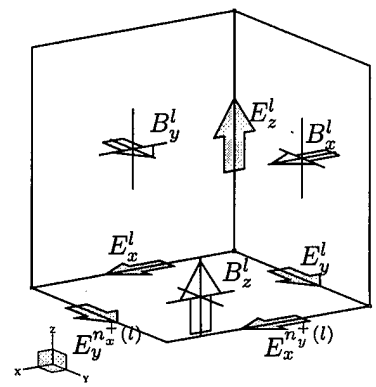

Figure 1: The l.th gridcell with its six field components. Additionally the two field components of neighbour cells are shown which are needed to compute the curl of E at the position of B_z^l.

Equations similiar to (2) for all components of B in the computational volume can be written as a single matrix equation:

$$\frac{d}{dt}\vec{b} = -\mathbf{C}^{\mathbf{e}}\vec{e} \tag{3}$$

Here $\vec{b}$ and $\vec{e}$ are arithmetic vectors containing all the field components of E and B.

The computation of $\frac{d}{dt}E$ is slightly more complicated but can also be written as a matrix equation with a matrix $\mathbf{C}^{\mathbf{h}*}$:

$$\frac{d}{dt}\vec{e} = [\varepsilon]^{-1}\mathbf{C}^{\mathbf{h}}[\mu]^{-1}\vec{b} = \mathbf{C}^{\mathbf{h}*}\vec{b} \tag{4}$$

1.2 Time domain

Given the discretized curl operators, the fields at the next timestep are computed from the previous fields by the leapfrog scheme [1].

1.3 Resonant fields

Resonant fields in principle can be found by exciting a structure with some broadband pulse and examinating the ringing of the fields. If one is interested in resonances that are not well separated in frequency, such an approach needs a long simulation time T, since the frequency resolution Δf of such an approach is $\Delta f = 1/T$.

GdfidL instead solves an eigenvalue problem that is directly derived from the discretized curl equations. The time

* bruns@tetibm2.ee.TU-Berlin.DE

[1] Pronounciation is: Gee-Dee-fidl

0-7803-4376-X/98/$10.00 © 1998 IEEE

derivatives in eqns. (3) (4) can be replaced by jω's following from the FOURIER transform. By substituting $\vec{b}$ in the second equation by the first equation, one gets:

$$-\mathbf{C}^{\mathbf{h}*}\mathbf{C}^{\mathbf{e}}\vec{e} = -\omega^2\vec{e} \tag{5}$$

This is an algebraic eigenvalue problem with a real positive semidefinite matrix $A = \mathbf{C}^{\mathbf{h}*}\mathbf{C}^{\mathbf{e}}$. The lowest nonzero eigenvalues and their corresponding eigenvectors are found by an algorithm of Tückmantel [4].

Since the eigenvalue problem is directly derived from the discretized MAXWELLian equations, no non-MAXWELLIAN solutions are found and GdfidL does not have to check for them.

2 SCATTERING PARAMETERS

GdfidL computes S-parameters by performing a time domain simulation and subsequently FOURIER transforming the histories of the tangential fields at the ports of the structure. Absorbing boundary conditions (ABCs) have to be applied where waveguides cross the boundary of the computational volume. GdfidL implements its ABCs as an expansion of the tangential fields in a limited number of orthogonal functions, which are the tangential fields of the TE, TM or TEM-modes in the waveguides. The result of this expansion is: The parts of the field that can be described as a superposition of the expansion functions have a reflection of less than 1% independent of frequency, the remaining part is totally reflected.

3 WAKE POTENTIAL COMPUTATION

3.1 Beam traversing ABCs

For wakepotential computations, a rigid beam is traversing the computational volume. For long range wakes, ABCs have to be applied at the two beampipes where the beam enters and exits the cavities. Since the primary field of the charge cannot be expanded in the waveguide modes, a special treatment is needed: With known velocity of the charge, the primary field of the charge at the ABCs is also known and can be subtracted from the total field. The remaining field consists of the scattered waves and is expanded in orthogonal functions.

As in case of scattering parameter calculation, a reflection of less than 1% is achieved for the parts of the field that can be described by the number of expansion functions selected, the remaining part is totally reflected. Since this algorithm guarantees that no reflection larger than one occurs for any field pattern of any frequency, no late time instability occurs even for wakepotential computation.

3.2 Inhomogeneous mesh in beam direction

GdfidL exactly integrates the charge dependent factor $\vec{G}$ in the update equation (6) for the electric field independent of the selected mesh spacing and of the used time step.

$$\vec{e}^{n+1} = \vec{e}^{n} + \Delta t \mathbf{C}^{\mathbf{h}*}\vec{b}^{n+1/2} - [\varepsilon]^{-1} \int_{t=n\Delta t}^{(n+1)\Delta t} \vec{G}(\tau)\, d\tau \tag{6}$$

The main advantage is: The time step Δt can be choosen as high as the stability limit allows; Therefore, a given time to simulate can be computed in less time steps.

4 EXAMPLES

4.1 Scattering parameters

Fig. 2 shows a short section of a disk loaded waveguide with attached input/ output couplers. For this case GdfidL needed 30% of CPU that would be needed if the field components were organized as triple indexed variables.

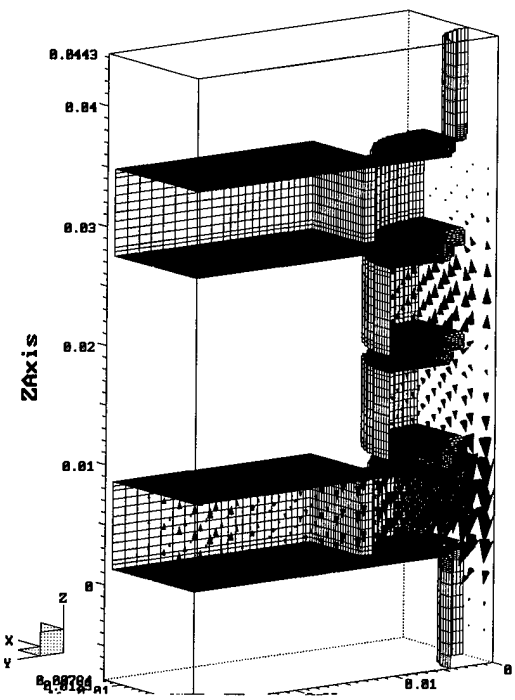

Figure 2: A quarter of a short section of a x-band linac. The shown field was excited by a GAUSSIAN pulse of the fundamental mode in the feeding waveguide left below. At the shown time, the excitation has already died, the visible field is mostly travelling upwards the cavity chain and partly back into the feed.

4.2 Long range Wakepotential

The computation of the long range wake in a simple test-geometry is shown here. It is a rectangular waveguide (w=1cm, h=0.5cm) where a rectangular cavity of depth b=0.5cm and length a=1cm is in. A relativistic GAUSSIAN line charge with $\sigma = 5$ mm is travelling in the center of the waveguide. In order to be able to compare with a code that does not allow inhomogeneous mesh in the direction of the

beam, a homogeneous grid with a spacing of Δ=0.5mm is used. In fig. 4 GdfidLs results are shown both for the short

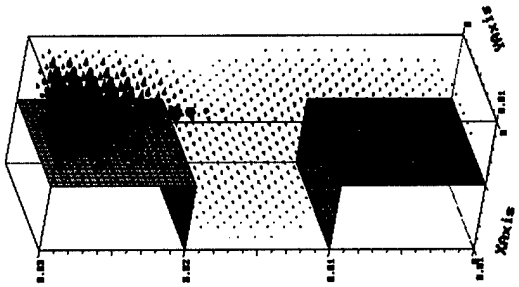

Figure 3: Primary and scattered field of a long GAUSSIAN line charge traversing the test geometry. The charge has entered the volume through an ABC at the right of the volume and is just exiting trough the left ABC. All other boundaries are electric.

and the long range wake. Fig. 5 shows the wake potential as it is computed when Mur's first ABC's [3] are applied. The short range wakes in both cases agree well, the long range wake obviously does not agree. GdfidL uses a timestep of $\Delta t = 0.928$ps and so needed 9094 timesteps for its computation of the wake in the range $0 < s < 2,5$ m.

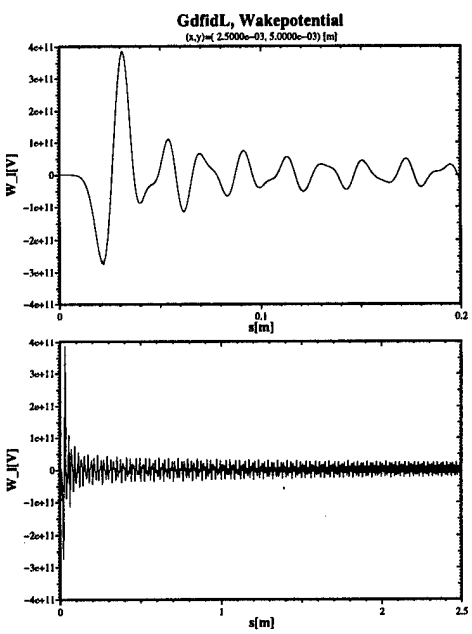

Figure 4: Above: short range wake; Below: Long range wake as computed by GdfidL.

5 AVAILABILITY

The executable programs of GdfidL for most UNIX systems are available free of charge from the author.

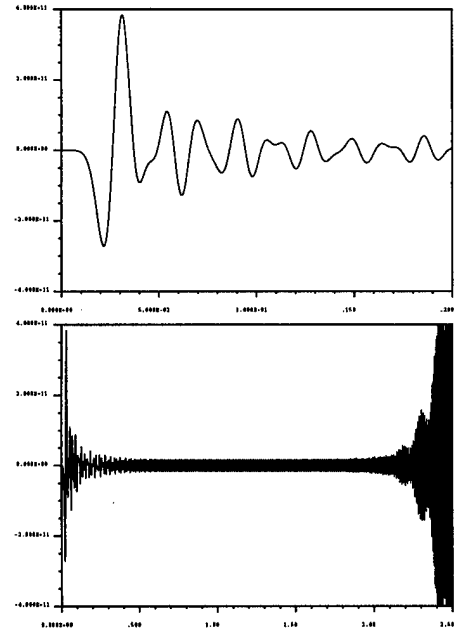

Figure 5: Above: short range wake; Below: Long range wake. Both are computed with Mur's first ABCs.

6 CONCLUSION

GdfidL implements a variant of the method of finite differences. The CPU and memory consumption is proportional to the field carrying volume. Resonant fields are computed without finding nonMAXWELLian solutions. Scattering parameters and long range wakepotentials are computed by applying broadband ABCs. For wakepotential computations, no restriction to homogeneous grids in the direction of the beam exists. No late time instability occurs.

7 ACKNOWLEDGEMENT

Part of the development of GdfidL has been supported by the RF group of the APS at Argonne National Laboratory.

8 REFERENCES

[1] Kane S. Yee, "Numerical solution of initial boundary value problems involving Maxwell's equations in isotropic media", *IEEE Transactions on Antennas and Propagation*, vol. 14, May 1966

[2] Thomas Weiland, "Eine Methode zur Lösung der Maxwellschen Gleichungen für sechskomponentige Felder auf diskreter Basis", *Archiv für Elektrotechnik und Übertragungstechnik, (Electronics and Communication)*, Band 31 (1977), Seiten 116-120

[3] Gerrit Mur, "Absorbing Boundary Conditions for the Finite-Difference Approximation of the Time-Domain Electromagnetic-Field Equations", *IEEE Transactions on Electromagnetic Compatibility*, vol. EMC-23, No. 4, November 1981

[4] J. Tückmantel, "An improved version of the eigenvector processor SAP applied in URMEL", CERN/EF/RF 85-4, 4 July 1985

EXPRESSION TEMPLATES FOR TRUNCATED POWER SERIES

John R. Cary and
Svetlana G. Shasharina, Tech-X Corporation, 4588 Pussy Willow Court, Boulder, CO 80301

Abstract

Truncated Power Series technique (Differential Algebra or DA) is a powerful tool for non-linear map analysis of accelerators. The most natural language for numerical DA's is C++, since it is object oriented and has operator overloading. Traditional C++, though, can be inefficient for scientific programming due to creation of many temporaries and extra loops in overloaded operators. Recent Expression Templates technique allows a user to combine the elegance of object oriented approach with the speed of procedural languages. The way it was created, it is not directly applicable for DA. We created a set of classes whose structure will be suitable for implementing DA vectors and maps. Classes realizing the Expression Templates technique are separated from the client classes, which allows their reuse for different mathematical concepts. Speed tests on KCC compiler showed that new C++ classes for DA have the same speed as hand-coded C.

1 PROBLEMS OF NUMERICAL IMPLEMENTATION OF DIFFERENTIAL ALGEBRA

Numerical differential algebra methods (see Ref. [1]) have found increasing use as they can be applied to arbitrary dynamical systems, for example accelerators or other beam and optics devices. The effect of passing of particles or rays through the system can be described mathematically by a map relating the final coordinates (coordinates in the most general sense: momentum, position, charge, mass etc.) to the initial. The map contains the information needed to evaluate such quantities of interest as nonlinear oscillation frequencies and chromatic aberrations. However, except for several trivial cases, it is impossible to find a closed mathematical solution for the map. But one can find solutions up to some order in distance from the central trajectory through perturbation theory based on power series expansion of the map. Numerical differential algebra methods permit one to carry out this perturbation theory for very high order maps, e.g., twelfth order in six variables, where there are millions of separate terms in the map.

For the purpose of this paper, one need to know only a couple of facts about DA vectors. In principle, it is an array of coefficients, obtained from Taylor expansion of functions in multidimensional space. These vectors can be added, subtracted, multiplied etc., and the result of most operations depends on the whole set of coefficients of operands. Thus, DA vectors can be represented by a vector-type class with overloaded operators. That is the reason why the implementation of DA methods is easiest within object oriented programming (see [2]), which provides a powerful triad: encapsulation, inheritance, and dynamic binding. C++ is especially well suited since it provides operator overloading.

Unfortunately, a big performance price must be paid to realize many of these benefits. Performance losses of a factor up to ten times (exact number depends on vector length) have been reported for codes rewritten in C++. The performance loss arises because usual C++ programming practices lead to the creation of many temporaries and the separation of complicated loops into loops with fewer operations. The latter is especially bad in current times, where RISC chips may have several arithmetic units that can be working simultaneously.

As a concrete example, we consider the evaluation of the addition among these vector objects in the following code fragment.

```
Vector y, a, b, c;
y = a + b + c;
```

With conventional Vector objects, usually defined as one-dimensional arrays, perhaps including array limits, with properly overloaded arithmetic operators, the typical C++ compiler generates code equivalent to:

```
int n = a.size();
Vector temp1 = new double[n];
for(int i=0; i<n; i++) temp1[i] =
a[i] + b[i];
Vector temp2 = new double[n];
for(int i=0; i<n; i++)
   Vector temp2[i] = temp1[i] + c[i];
for(int i=0; i<n; i++)
   y[i] = temp2[i];
delete [] temp1;
delete [] temp2;
```

The temporary storage variables temp1 and temp2 must each be created and destroyed. Indeed, the creation of temp2 is unecessary, but usually done by C++ compilers that are not optimized with regard to the return of user defined objects from operators and functions. In addition, there are three separate loops above, when only a single loop,

```
int n = b.size();
for(int i=0; i<n; i++) y[i] =
a[i]+b[i]+c[i];
```

is needed. The loss of efficiency due to creation of temporaries and having separate loops can be very significant. Whenever users use C-style similar to the coding above, it is called hand-coded C.

0-7803-4376-X/98/$10.00 © 1998 IEEE

In the next section, we describe how new C++ technique, called Expression Templates (Ref. [3]) allowed us to make C++ classes for DA elements as fast as hand coded C.

2 EXPRESSION TEMPLATES FOR DA VECTORS

We start from giving the a partial implementation for the DA vector class. From the operational point of view, it has only addition operator (all the rest can be implemented in a similar way). For the sake of brevity, we declared everything public. We also had to acquire an awkward way of formatting the code in order to preserve the format of the paper:

```
class DA {
public:
  double* data;
  int length;
  DA(int n) : length(n){data = new
double[n];}
  DA(){}
  DA(const DA& x) {
      length = x.length;
      data = new double[length];
      for(int i=0;i<length;++i)
        data[i] = x.data[i];}
  ~DA() {delete [] data;}
//  Access
  double& operator[](int i)
      {return data[i];}
  const double& operator[] (int i)
     const {return data[i];}
//  Assignment to expression
  template <class A> DA& operator=
      (const DAExpr<A>& result){
      for (int i=0;i<length;++i)
        data[i] = result[i];
      return *this;}
//  Assignment to DA
  DA& operator = (const DA& a){
      if (this == &a) return *this;
      delete [] data;
      length = a.length;
      data = new double[length];
      for(int i=0;i<length;++i)
        data[i] = a.data[i];
      return *this;}
//  Summation
  template <class A, class B>
  static double Add
     (const A& a, const B& b, int i)
     {return a[i]+b[i];}
};
```

This class has typical (for vector-like classes) members: `double* data` and `int length`, describing the set of coefficients and their number. It has a constructor from `int`, a copy constructor and a typical destructor. In order to insure a normal behavior of assignment, we need to provide assignment to `DA` with deep copying (memory management with garbage collection can change its implementation). To implement inlining of all expressions containing vectors, we need assignment to DA expressions. Class for DA expressions is template and relies on behavior of `operator[](int)`, which is governed by the type of the template parameter A:

```
template<class A>
class DAExpr {
private:
  A iter;
public:
  DAExpr(const A& a) : iter(a){}
  double operator[](int i) const
      {return iter[i];}
};
```

Assignment to `DAExpr` is a template member function of a no-template class. Not so many compilers provide this capability: KCC compiler (Ref. [4]) is the only one we know. If the compiler does not have template members, see Ref. [3] for the trick

Consider how all this should work in a simple example:

```
DA y, a, b;
y = a + b;
```

Since this operation will call for assignment of y to an expression (a+b), summation of two DA vectors should return a DA expression, whose type is determined by the performed operation. In this case it is a binary operation of + type (`DApAdd`) between two double arrays:

```
DAExpr<DABinOp<double*,double*,DApAdd
<DA,double*,double*> > >
operator+(const DA& a, const DA& b)
{typedef DABinOp <
double*,double*,DApAdd<DA,double*,
double*> >  ExprT;
return DAExpr<ExprT>
(ExprT(a.data,b.data));}
```

When the resulting expression is assigned to a vector, `operator[](int)`, sitting in the assignment operator, applies this operator to `DAOpBin` (since it is the filling of `DAExpr` in this case). Inside `DAOpBin::operator[](int)`, function `Op::Apply` is called (with `Op` in our case being `DApAdd`)

```
template<class A, class B, class Op>
class DABinOp {
private:
  A iter1;
  B iter2;
public:
  DABinOp(const A& a, const B& b)
        : iter1(a), iter2(b) {}
```

```
  double operator [] (int i) const
  {return Op::Apply(iter1,iter2, i);}
};
```

Function `Op::Apply` in the case of addition is member of a separate class `DApAdd` (we have to have separate classes for all arithmetic operations):

```
template <class C,class A,class B>
class DApAdd {
public:
  DApAdd() { }
  static inline double Apply
      (const A& a, const B& b, int i)
      {return C::Add(a,b,i);}
};
```

It does not provide any specific behavior. It relies on the class type `DA` to know how to perform its operations by calling `C::Add(a,b,i)`, where `C` is `DA` in our example. We have to provide full arguments `iter1`, `iter2` and index i for `Op::Apply`, because in some cases (like multiplication and many other operations and functions for DA vectors) calculation of i-th component of the resulting vector involves several components of operands and depends on i.

In case of operation y = a + b + c, the compiler actually does (a+b)[i]+c[i] = a[i]+b[i]+c[i], so that the two loops are fused in one, which makes operations as fast as hand-coded C.

One actually must define four + operators: one for each of the possible combinations of `DAVec` and `DAVExpr`. None of these operators contain loops. The template mechanism combines all of the expressions together into one assignment, where the loop occurs. Thus, all of the loops always collapse to a single loop.

The novelties here compared with simple vector classes of Ref. [3], are:

(a) We pass whole objects and index to `Apply` function in order to generalize to more complicated structures. Correspondingly, we had to make class `DApAdd` template.

(b) We separated implementation of operations from the ET structure, putting it into the class itself. This idea is similar to *Glommables* of Ref.[4].

(c) We had to introduce + between 2 expressions in order to deal with situations like y=(a+b)+(c+d).

We performed speed test for our classes on KCC compiler. The results for time to perform one addition are shown on the figure. The upper curve corresponds to C++, another two are: C++ with Expression Templates and hand-coded C, which are practically indistinguishable. The speed enhancement over traditional C++ is enormous!

REFERENCES

[1] M. Berz, "Differential Algebraic Description of Beam Dynamics to very High Order," Particle Accelerators, **24**, 109 (1989).

[2] S. Lippman, *C++ Primer, second edition* (Addison-Wesley, Reading, Massachusetts, 1991).

[3] T. Veldhuizen, "Using C++ Template Metaprograms," C++ Report, vol.7, No. 4, 36 (1995).

[4] http://www.kai.com.

[5] G. Furnish, " Disambiguated Glommable Expression Template," preprint UCRL-JC-126523 (February, 1997, LLNL), submitted to Computers in Physics.

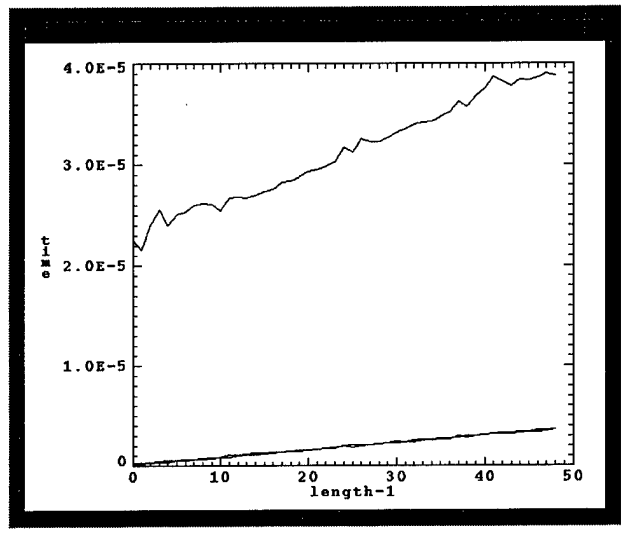

AUTHOR INDEX

A

Abramenko, N.I. 2773
Abramovich, A. 906
Abs, M. 3816, 3857
Adachi, T. 3470
Adolphsen, C. 439, 554, 608, 1673, 1676, 2119, 2186, 2256, 2580, 2852, 3027, 3042, 3192
Agafonov, A.V. 1299, 1302, 3141
Ahn, H. (JAERI) 648, 760
Ahn, H. (LANL) 1012
Ahrens, L. 69, 89, 98, 101, 959, 965, 1460, 1478
Aiello, G. Roberto 2113, 2122
Aizatsky, M.I. 3810
Akai, K. 2902, 2974, 2977, 2986, 3069, 3087, 3090
Akasaka, N. 455, 530, 533, 536, 1831, 2902, 2974, 2977, 2986, 3069
Akemoto, M. 587, 1319, 1322
Akre, J. 2067
Akre, R. 506, 1569, 3021, 3024, 3027
Alessi, J. 89, 162, 970, 1460, 2023, 2711
Alexahin, Y. 312
Alexeev, N.N. 261
Alford, O. 3562
Alforque, Rudy 3693
Allen, C.K. 1526
Allen, C.W. 596
Allen, M. 3004
Allen, T. 3796
Alley, R. 1981, 2849
Allison, Paul 1138, 1141, 1144
Allison, S. 439, 2359, 2470, 3027
ALS Stability Task Force 784
Alzofon, D. 2253
Amano, D. 1266
Amano, S. 757
Amatuni, A.Ts. 690, 693, 695
Ambrosia, M. 3872
Amelia, J.-C. 3816
Ames, F. 947
Amman, M. 3807
An, Y. 402, 880
Anamkath, H. 3796
Anders, A. 2678
Anderson, D.E. 590, 3734
Anderson, E.B. 369
Anderson, K. 3837
Anderson, S. (SLAC) 596
Anderson, S. (UCLA) 736, 1965
Anderson, S. (IUCF) 2968
Andersson, Å. 345
Ando, A. 757, 1385
Andreev, V.A. 1087, 1090
Andreev, V. (Dubna) 2452
Andrews, D.E. 3413
Andrianov, S. 2419
Anerella, M. 3338, 3356
Anferov, V.A. 78
Ang, Z. 3377
Ankenbrandt, C. 144, 396, 399
Anthouard, P. 1254, 1257
Ao, H. 1203
Appleton, Bill R. 20
Arai, S. 938
Arakaki, Y. 938, 1557
Arakawa, D. 1548, 1599, 1908
Araki, N. 201
Araki, S. 587
Archuleta, T.A. 2829
Arduini, G. 168, 171, 1858
Arensburg, A. 906
Areti, H. 3681
Ärje, J. 2672
Arnett, D. 2253
Arnold, J. 1813
Arroyo, F.C. 3476
Artoos, K. 3586
Arutunian, S.G. 695
Asaka, T. 2511, 2814
Asano, K. 2908, 3087, 3090
Asaoka, Seiji 2458, 3616
Aspenleiter, J. 2947, 3497
Assadi, S. 127, 1771, 2323
Assmann, R. 449, 497, 500, 503, 506, 608, 687, 1331, 1523, 2119, 2580
Atkinson, R. 439, 3042
Aune, B. 425
Ausset, P. 2720
Autin, B. 1362, 2314
Averill, R. 348, 2274, 3407, 3743
Avrakhov, P.V. 3126
Avramopoulos, H. 1042
Avsec, S. 2481
Ayzatsky, N.I. 651
Azorsky, N.I. 3126

B

Baartman, R. 956, 1415, 2675, 2778
Baba, H. 530, 593
Babcock, R. Chris 2562
Babzien, M. 621, 675, 2687
Bacher, R. 2446
Bagnato, O.R. 1209
Bai, M. 1346, 1460, 1478
Bailey, J.D. 1177
Bailey, R. 66
Bailey, V.L. 1251
Baine, M. 611
Baiod, R. 3272, 3278, 3288
Baird, S. 979, 982
Bajikar, S. 461
Baker, G.D. 190
Bakhtiari, Shervin 3842, 3845
Balakin, V.E. 3126
Balakirev, V.A. 651
Ball, M. 1481, 2081
Ball, M.J. (Penny) 3404
Balling, P. 1984
Baltadoros, D. 1042
Bane, K. 506, 509, 515, 554, 608, 903, 1673, 1738, 1789, 1873, 1876, 2189, 2580
Barale, P. 3312
Barbarosou, M. 1042
Barber, R.L. 1150
Bardy, J. 1254, 1257
Barillas, G. 3024
Barlow, D. 83, 193, 3309
Barnard, John J. 1929, 1932
Barnes, B. 2326
Barnes, John N. 86
Barnes, M.J. 1325, 1328
Barnes, P. 3075
Barni, D. 1126
Barov, N. 627, 1996
Barraza, Juan 2210
Barry, W. 772, 2344
Bartelson, L. 3461
Barth, W. 1897
Bartolini, R. 1469, 2568
Barton, D. 101
Bassato, G. 1129
Batskikh, G.I. 950
Battistella, A. 1129
Batygin, Y. 941, 1786, 1941
Bauer, G.S. 3785
Baumgartner, W. 439, 3042
Baynham, E. 3386
Bazzani, A. 2568
Beauvais, P-Y. 2720
Bechstedt, U. 1048
Bedermann, K. 3123
Beebe, E. 2711
Beebe-Wang, J. 970, 1882
Beeckman, W. 1045, 3816
Behne, D. 3622
Belkacem, A. 150
Bellato, M. 1129
Bellomo, G. 1126
Bellomo, P. 315

Belochitskii, P. 312, 1382
Belomestnykh, S. 1718, 3075
Belorgey, J. 3365
Belser, C. 3619
Ben-Zvi, I. 645, 675, 1197, 1971, 2687, 2790, 2793, 2843, 2846
Benapfl, M. 3568
Bendall, R.G. 1021
Benedikt, M. 1376, 1379
Benesch, J. 3108, 3758
Benjegerdes, R. 3212
Benson, S. 912
Benveniste, V.M. 2767
Berezin, A.K. 651
Bereznitsky, S.L. 261
Berg, G.P.A. 264, 2737, 3303
Berg, J.S. 107, 1712
Berg, W.J. 871
Bergbusch, P. 967
Berger, J.C. 2696
Bergl, J. 2493
Berkvens, P. 3571
Berlin, D. 979
Bernal, S. 1650, 1855, 1959, 2143
Bernard, M. 2823
Berners, D.P. 1296
Bertazzo, L. 1129
Bertenelli, F. 3586
Bertolini, L. 3562, 3619, 3622
Bertsche, K.J. 3263, 3283
Berz, Martin 2416
Besler, C. 315
Bestea, V. 3854
Bezzon, G. 1129
Bharadwaj, V. 315, 903, 2855
Bhat, C.M. 243, 1590, 3242, 3245, 3672
Biallas, G. 3333, 3752
Bickley, M. 2128
Biedron, S.G. 324
Bieniosek, F.M. 234, 1403, 3837
Bigelow, N.P. 2867
Biino, C. 80, 165
Billan, J. 3365, 3377
Billen, J.H. 1171, 3138
Biller, Ye.Z. 3810
Billing, Michael 2317
Billquist, P.J. 2702
Bilodeau, D. 2081
Bini, C. 572
Biryukov, V. 177, 179, 249
Bish, P. 3212
Bishofberger, K. 736
Bisoffi, G. 1087, 1129
Bisognano, J. 1641, 1644, 2128
Bissiato, E. 1087, 1129
Bizek, Hana M. 1493, 1496
Bjork, M. 2253
Bjorklund, E.A. 2464
Blackmore, E.W. 3831
Blank, M. 3150, 3180
Blas, F. 973
Blaskiewicz, M. 89, 959, 970, 1554, 1578, 1581
Blell, Udo 1727
Bleser, E. 89
Blind, B. 83, 193, 270, 1012, 1015, 3728
Bliss, N. 3598
Blokhin, A.I. 258
Blokland, W. 2032
Blondel, A. 366
Blosser, H. 1054, 1057, 1060
Blum, E.B. 3494
Blumberg, L. 159, 970
Bobyleva, L.V. 488
Bocchetta, C.J. 826, 829, 2353, 2356
Boer-Rookhuizen, H. 1063
Bogacz, S.A. 1697
Bogard, D. 2720
Bogdanovich, B. 276, 2773, 3869
Böge, M. 366, 1356, 1436, 1439
Boggia, A. 2729
Bohl, T. 1813, 1849
Bohn, C. 909, 1641, 1644, 2693
Boillot, J. 979, 982
Bollen, G. 947
Bolotin, I. 1313
Bolshakov, A.E. 261
Bong, E.L. 2253
Bong, P. 439
Bongardt, K. 988, 1846
Bonnafond, C. 1254, 1257
Borasi, F. 2696
Borchard, P. 3180
Borden, M.J. 187, 1012
Bordry, F. 66
Boriskin, V.N. 3810
Borland, M. 742, 2052, 2410, 2487, 3224
Bosch, R.A. 862
Boscolo, A. 2011
Bosland, P. 817
Bosotti, A. 1126, 3657
Bosser, J. 944, 979
Bossert, R. 3389
Botman, J.I.M. 1036, 1200
Bottura, L. 66, 3377
Bourat, C. 1191
Bourdon, J.C. 2823
Boussard, D. 2879
Bovet, C. 1987
Bowden, G. 464, 672, 3330
Bowling, Bruce 2526
Bowman, J. 3622
Boyce, R. 838
Bradley, S. 348, 2099
Bradley III, J. 1147
Brandt, D. 312
Braun, H.H. 479
Braun, J. 3123
Brautti, G. 2729
Bravin, E. 366
Breizman, B.N. 1635
Brennan, J.M. 69, 89, 396, 399, 967, 970, 1030
Brennan, S. 838
Bretin, J.-L. 225
Bricault, P. 925, 956, 1105, 1194, 2675
Brinkmann, R. 336, 1572, 1679
BRNBF Project Group 1224
Broadbent, A.J. 3413, 3494
Brodowski, J. 3233
Broere, J. 944, 3123
Bromberek, D. 2929
Broome, T.A. 1021
Broome, W. 2305
Brouet, M. 979
Brown, B.C. 994, 3242, 3245, 3254, 3257, 3260, 3263, 3269, 3286, 3288
Brown, I. 2678, 3752
Brown, K. (BNL) 69, 89, 98
Brown, K.(TJNAF) 2271
Brown, K.A. 1460, 2149, 2213, 2302
Brown, Nathan A. 1894, 2562
Brown, R.J. 2737
Brown, R.L. (SLAC) 2186
Brown, R.L. (BNL) 3230
Brown, Thomas A. 2559
Brown, V. 439
Brown, W. 2690
Browne, J.C. 1159
Browne, M. 439
Brugnoletti, B. 2253
Brumwell, F.R. 156
Brun, T. 190, 1159
Brunelle, P. 817, 1406
Brunet, J.-C. 3368, 3586
Brüning, O. 107, 1715, 1816, 1858
Bruno, D. 3449, 3452
Bruns, W. 2651
Bucalossi, J. 2717
Buhler, S. 2823
Buldakovsky, V.N. 184
Bulfone, D. 826, 2353, 2356, 2467, 3527
Buller, T.L. 2950
Bultman, N.K. 190
Bunce, G. 1460
Burke, D. 608

Burkhardt, H. 1532, 1813, 1819
Burla, P. 66
Burnham, B. 883
Burns, A. 1987, 2026
Burris, H.R. 611
Bushuev, A. 2838
Buttkus, J. 979
Buxton, W. 2155
Bylinsky, Y. 1135
Byrd, J. 769, 772, 775, 778, 1514, 1563

C

Cai, Y. 1454, 2583, 2586, 2636
Calame, J. 3144, 3159
Calder, R. 3586
Call, M. 2473
Callahan, J. 2449
Callaway, N.T. 1165, 2464
Callin, R.S. 3045
Calvani, H. 959
Camariuc, R. 3854
Cameron, P. 1460, 2152, 2215
Cammarata, Jim 3693
Campedel, C. 3586
Canella, S. 1129
Cao, Z. 3318
Capek, K. 2198
Capista, D. 144, 1721, 2061
Caporaso, G.J. 1248, 1260, 1305, 1308, 1861, 2627, 2630, 2633
Cappi, R. 973
Cardman, L. 2693
Carli, C. 944, 976, 1379, 1382
Carlier, E. 225, 1325
Carlson, Randolph L. 1867, 2826
Carlsten, B. 1914, 2832, 3129, 3132, 3135
Carr, G.P. 2464
Carson, J.A. 3291
Carter, A. 2099
Carwardine, J. 2281, 2290
Cary, John R. 2592, 2654
Caryotakis, G. 439, 2894
Casas-Cubillos, J. 3206
Caspers, F. 75, 107, 979, 982, 1587
Caspi, S. 3212, 3398
Cassel, R. 439, 3482
Castellano, M. 2137
Castillo, V. 2155
Castle, M. 3168
Catani, L. 2137
Cavallari, G. 1858
Cavenago, M. 1129
Ceci, N. 2169, 2729
Celata, C.M. 1926, 2761, 3807
Cerniglia, P. 2502
Cervellera, F. 1129
CESR Operations Group 372
Chae, Y.-C. 953, 1700
Chai, J.S. 3825
Chairman, D. 906
Chan, A. 2413, 2517
Chan, K.C.D. 1150, 1168, 3096
Chanel, M. 944, 982, 1587
Chang, C.H. 3536, 3539
Chang, H.P. 841
Chang, L.H. 1487, 1638, 1691, 2377, 3048, 3051, 3054
Chang, Peace 853, 1409, 1487, 3533
Chang, S.S. 1638, 2858, 3048, 3054
Chang, Y.I. 1638
Chao, A.W. 1523, 1563, 1738, 1834, 1873
Chao, Yu-Chiu 2125, 2262, 2526
Chaput, R. 817
Charlton, Lowell A. 86
Chase, B.E. 2326
Chattopadhyay, S. 687, 1984
Chautard, F. 479
Chavanne, J. 3506, 3509
Chehab, R. 2823
Chel, S. 817, 1709, 2311, 2823
Chen, Bingyi 1218, 1221
Chen, C.S. 2371, 2374, 2523, 3488, 3539, 3749
Chen, C.T. 3749
Chen, Chiping 1938
Chen, Huaibi 1215
Chen, J. (DULY) 2802, 3120
Chen, J. (SRRC) 3749
Chen, J.R. 847, 3642
Chen, J.S. 2374, 2479, 3488, 3539, 3749
Chen, Jenny 853, 2371, 2374, 2523, 3488, 3539
Chen, P. 687, 1789
Chen, S.-Y. 2657
Chen, Tong 2164
Chen, W. 3297
Chen, X. 402
Chen, Y.J. 1260, 1305, 1861, 1864, 2633
Cheng, D. 3619
Cheng, G.-T. 2183
Cheng, J. 3168
Cheng, W.-H. 422, 1514, 1614
Chepegin, V.N. 249
Cherepakhin, A. 234
Chernikov, V.I. 184
Chesnokov, Yu. 249
Chester, N. 3248, 3291
Chiang, I.H. 2149, 2213
Chiang, John 850
Chiba, T. 941, 2672
Chiba, Y. 3828
Chida, K. 1557
Chin, A.H. 1984
Chin, M. 2235, 2253
Chin, P. 1855
Chin, Y. 1545, 1566, 1596, 1656
Chiurlotto, F. 1087, 1129
Cho, M.H. 593, 823
Cho, Y. 953
Chohan, V. 973, 979, 982
Choi, E.H. 1870
Choi, J. 823
Choi, J.J. 3159
Chojnacki, E. 363, 3075, 3177
Chou, P.J. 464, 542, 672
Chou, W. 110, 113, 130, 991, 994, 1724, 3251
Chow, K. 3212
Chowdhary, M. 2383
Chu, C.M. 1346, 1481
Chubar, O. 3509
Chung, S.M. 3633
Chupp, W.W. 1926, 2755
Church, M. 1006, 2055
Cinnamon, J. 3678
Cisneros, G. 439
Clark, D.J. 1051
Clark, George S. 3336
Clark, J.C. 1260
Clark, S. 439, 2473, 3027
Clark, W. 1093
Clarke, J.A. 3386, 3503
Claus, R. 2284, 2359, 2365, 2470
Clausen, M. 2403, 2446
Clauser, T. 2169
Clayton, C. 678, 681, 687, 2870
Claytor, N. 150
Clément, M. 80, 165
Clendenin, J. 903, 2849
Clerc, G. 2899
Clifford, T. 101
Cline, D.B. 621, 675
Clout, Peter N. 2532
Coates, M.C. 3494
Coffman, F. 2473
Cohen, M. 906
Cohen, S. 1042
Cojocaru, G. 1123, 3854
Colby, E. 2873
Cole, M. 3177
Colestock, P. 16, 127, 2873, 3716
Collier, P. 66, 3206
Collins, B. 2253
Collins, D. 1051
Collins, I. 3586

Collins, J. 2449
Colomb, D. 3619
Colomp, P. 3571
Comunian, M. 1087, 1129, 1132
Conde, M. (ANL) 627, 633, 639, 1996
Conde, M. (UCLA) 2873
Conkling Jr., C.R. 2496
Connolly, R. 69, 98, 101, 2152, 2215, 2947
Constant, T. 439
Cooke, S.J. 2431
Coombs, R. 3386
Coosemans, W. 560, 3645
Copeland, M.R. 464, 672
Corbett, J. 342, 832, 838, 1457, 1490, 2586
Corcoran, P. 1245
Cordova, S.R. 1245
Corlett, J. 2116, 2344, 3639
Corlier, M. 817
Cornacchia, M. 838, 1457, 1490
Cornali, R. 1813
Cornelis, K. 171, 1813
Cornelius, Wayne D. 3636
Cornuet, D. 973
Corradini, E. 1087
Corredoura, P. 2359
Corsini, R. 563
Cortopassi, C. 3221
Corvin, C. 439, 3746
Courant, E. 405, 1030, 1371, 3359
Cours, A. 2941
Cozzolino, J. 3338
Craddock, M.K. 153
Craievich, A. 811
Cramariuc, R. 1123
Crandall, K. 915, 1099, 1150, 1162, 2574
Crane, G. 2413
Crane, M. 2473, 2476
Crawford, C. 243
Crisp, J. 2072, 2166
Crofford, M. 2265
Crosbie, E. 953
Cruikshank, P. 3206, 3368, 3586
Ctcherbakov, A. 1263, 1313
Cullen, J.R. 3583
Cummings, K. 1147, 3183, 3725
Cuttone, G. 2038
CYCIAE 30 Engineering Group 3834

D

D'Alsace, R. 2305
d'Amico, T. 566, 1362
D'Auria, G. 826, 1180, 1182, 1212, 2002
D'yachkov, M. 107, 1587, 2648
da Cruz, M.T.F. 2998
Daclon, D. 1212
Daclon, F. 826
Daems, G. 973
Dahl, L. 1897
Dahlerup-Petersen, K. 3206
Dainelli, A. 2169
Dalin, J.-M. 3586
Dallin, L.O. 716
Daly, E. 2014, 2253, 3619
Danby, G. 3233
Danilov, V.V. 1499, 1759, 1777
Danly, B. 2690, 3144, 3150, 3159, 3180
Danowski, G. 2308
Davies-White, W. 838
Davis, T. 1093
Dawson, C.L. 2956, 3598
de Jager, C.W. 1063
de Lamare, J. 1316
de Leeuw, R.W. 1200
de Lima, J.A. 2998
de Loos, M.J. 2577
De Martinis, C. 2002, 2038
de Mascureau, J. 1254, 1257
De Vito, Bill 3693
de Vries, J. 808, 1987, 3221
Dean, T. 439, 3027
Decker, F.-J. 449, 497, 500, 503, 506, 509, 608, 687, 1569, 1876, 3021
Decker, G. 698, 745, 2281
Decking, W. 778, 799
Degen, C. 2502
Degtyarev, I.I. 252, 255, 258
Dehler, M. 518
Dehning, B. 366, 3648
Deitinghoff, Horst 1900
Dejus, R. 3224
DeKamp, J. 278
Dekkers, D. 973, 979
Del Giusto, P. 1212
Delahaye, J.P. 482, 563
Delferrière, O. 2720
Dell'Orco, D. 3212
Dell, F. 69, 98, 219
Delsart, P. 1254, 1257
DELTA Group 724
Delvigne, T. 3857
Denard, J. 912, 2198, 2204
Deng, J.J. 1855, 1956, 1959
Den Hartog, P.K. 3224, 3556
Deregel, J. 3365
Derenchuk, V.P. 2737
Desavouret, E. 3395, 3713
Desforges, B. 3206
Desgranges, C. 2717
Desmon, M. 2823
Devin, A. 1254, 1257
Devlin, D.J. 2829
DeVolder, Barbara G. 2174
Devred, A. 3365
Dewa, H. (JAERI) 648, 760
Dewa, H. (Kyoto) 1087, 1129
Dey, J. 2032, 3018
Diaczenko, N. 3443
Dieperink, J.H. 225
Dietderich, D. 3212
Dietrich, J. 1048
Dikansky, N.S. 1795
Dikiy, N.P. 3840
DiMarco, J. 3269, 3272, 3389, 3395
Dimonte, N. 3690
Ding, X. 1968, 2802
Ding, Xiaodong 1215
Dinkel, John 234
Dinneen, T. 150
DiStefano, James 86
Diviacco, B. 1520, 3524, 3527
Doble, N. 80, 165
Dodd, E. 2657
Dodson, G. 348
Doets, M. 3630
Dohlus, M. 2008, 2550, 2553, 2612
Dolbilov, G.V. 1290, 3126
Dölling, R. 174, 246
Dombsky, M. 956, 2675
Donahue, J.B. 190, 1159
Donahue, R. 3807
Donald, M. 1454, 2583
Donaldson, A. 390, 1316
Dong, Lan 3300
Donohue, J.T. 900
Dooling, J.C. 156
Doolittle, L. 3758
Doose, C. 745, 2293, 3227, 3577
Doub, J.M. 3473
Douglas, D.R. 1351
Dovbnya, A.N. 651, 2820, 3810, 3840
Dovgenko, B.A. 3455
Dow, K. 348, 3407
Dowell, D.H. (CEA) 2684
Dowell, David H. (Boeing) 1888, 1891, 2950
Drago, A. 2284
Dragusin, M. 3854
Draznin, M. 906
Drewsen, M. 1560
Drivotin, O. 1944
Drozdovsky, A.A. 3848
Drozhdin, A.I. 116, 133

Drury, M. 3105, 3108
Du, Taibin 1221
Duan, Xiuming 1221
Ducas, V. 1362
Ducimetière, L. 225, 1325
Dudnikov, V.G. 2714
Duffy, P. 3562
Dugan, G. 318, 3215, 3380, 3383
Duke, Jonathan 204
Duke FEL Lab 24
Dunham, B. 1947, 2201, 2484, 2693, 3755
Durieu, L. 228
Dutto, G. 956, 1105, 2675, 2781
Duval, P. 2446
Duzenli, C. 3831
Dvoeglazov, A. 2419
Dwinell, R. 1051
Dykes, D.M. 2956, 3078
Dzengeleski, J. 3407

E

Earley, L.M. 3135
East, G. 1481
Ebeling, W. 985
Ebrahim, N.A. 897
Ecklund, S. 3330
Eckoldt, Hans-Joerg 3458
Economou, D. 1042
Edwards, H. 2873
Ego, H. 2971
Ehrlich, R. 3075
Ehst, D. 393
Eichenbaum, A. 906
Eichner, J. 439, 3042
Eickhoff, H. 3801
Einfeld, D. 336, 763, 1039, 3613
El-Shazly, M.N. 3607, 3610
Elizondo, J. 1308
Elleaume, P. 2210, 3506, 3509
Elliott, T. 3443
Elsener, K. 80, 165, 168, 171
Elzhov, A.V. 488
Emamian, M. 883
Emery, L. 742
Emma, P. 452, 608, 903, 1679, 2580, 2855
Endo, K. 3470
Endo, M. 820
Engelmann, G. 1813
Engels, O. 1078
Engwall, D. 2201, 2693
Erdt, W. 3368
Erickson, R. 596
Eriksson, M. 345, 3527
Eriksson, T. 979, 982, 1382
Ershov, O.V. 1090
Esarey, E. 611, 630
ESS Study Group 988
Etkin, A. 3230
Euteneuer, H. 1902
Evans, B. 3831
Evans, J. 3123
Evans, L.R. 61
Evans, R. 2529
Evans Jr., K. 2281, 2290
Evtushenko, Yu.A. 3455
Eyharts, P. 1254, 1257
Eyl, P. 1254, 1257
Eylon, S. 590, 2755, 2832, 3719, 3722
Eysselein, F.G. 3410
Ezura, E. 2902, 2974, 2977, 2986, 2992, 2995, 3069, 3087

F

Fabris, A. 826, 829, 1735
Fabris, R. 826
Facco, A. 1129, 3084
Fahmie, M. 808, 2344
Fainberg, Ya.B. 651
Faircloth, J. 883
Faltens, A. 195, 1926
Fan, Mingwu 3834
Fan, T.C. 3536, 3539
Fang, J.M. 621
Fang, S. 2049, 3057
Fang, Si J. 994, 3242, 3251
Fant, K. 3004, 3039
Farias, R.H.A. 811, 2096, 2238, 3324, 3740
Farkas, David 599
Farkhondeh, M. 348
Farrell, Ken 86
Fartoukh, S. 470
Fateev, A.A. 1290
Faucett, J.A. 2464
Faure, J. 2720
Faus-Golfe, A. 1356, 1442
Favale, A.J. 950
Favaron, P. 1129
Fawley, W.M. 1923, 1926
Fazio, M.V. 3135
Fedorov, V.M. 1299
Fedorova, A. 1502, 1505, 1508
Fedotov, Alexei V. 1744, 1747, 1750
Fedotov, M.G. 883
Fedotov, Yu.S. 255
Feher, S. 3389, 3395
Feinberg, B. 150
Feinerman, A.D. 461
Felch, K. 3180
Feldl, E. 912, 2198, 2204
Feng, P.K. 3452
Feng, S.K. 2437
Feral, B. 3586
Ferdinand, R. 2720, 2723
Ferguson, P.D. 190
Ferguson, Patrick 3129
Ferianis, M. 826, 2002, 2011
Ferioli, G. 171
Fernow, R. 408
Ferrando, O. 228
Ferraz, R.O. 3628
Ferreira, M.J. 811, 3324, 3628
Feschenko, A.V. 2078
Fidecaro, G. 168, 171
Filhol, J-M. 751
Filippas, T.A. 1042
Finocchiaro, Paolo 2038
Fiorito, R.B. 675
Firjahn-Andersch, A. 1081
Fischer, R. 611
Fischer, W. 69, 98, 101, 210, 222, 3341, 3359
Fischer, W.E. 3785
Fisher, A. 315, 2014, 2253, 2840, 2849
Fisher, J. 3108
Fitch, M.J. 2867
Fitzgerald, D.H. 1012, 1015, 1159, 1611, 2743
Fitzgerald, J. 2072
Flechtner, D. 1272, 1275
Fliflet, Arne W. 3153
Flood, Roger 2131
Flynn, G. 817, 1517, 1709
Fockler, J. 2633
Foley, K.J. 3230
Fong, Craig 1096
Fong, K. 1105, 2049, 3057
Fong, Martin 1096
Fontana, J.R. 675
Forrestal, J. 3669
Fortgang, C.M. 897, 3135
Fortuna, G. 1129
Foster, G.W. 363, 3257, 3260, 3263, 3280, 3286, 3392
Fowkes, R. 439, 2911, 3045, 3189, 3195
Fowler, W.B. 3254, 3257, 3260, 3263
Fox, J. 2284, 2362, 2368
Fox, W. 2737, 3303
France, A. 2720
Franco, G.S. 811
Franks, R.M. 3007
Franzini, P. 3413
Freedman, S.J. 2770
Freund, A. 80

Friedl, J. 724
Friedman, A. 1240, 1923
Friedrichs, C. 3473
Friesel, D. 264, 935, 2737, 2811, 3303
Frigola, P. 736
Frischholz, H. 2911
Fry, A.R. 2867
Fuja, R. 1269
Fujieda, M. 2992, 2995
Fujishima, S. 1066, 1069, 1075, 3419, 3422, 3428, 3440
Fujita, H. 339
Fujita, Y. 3819
Fukuma, H. 306, 1566, 1596
Fuller, R. 439, 2186, 3027, 3042
Fumelli, M. 2717
Funahashi, Y. 587
Funakoshi, Y. 301, 306
Funk, W. 1150
Furman, M.A. 1617
Furuya, T. 2908, 3087, 3090
Fusellier, J. 2823
Futami, Y. 3822

G

Gabriel, Tony A. 86
Gaedke, R. 3443
Gagliano, J. 3552, 3580
Gahl, J.M. 3725
Gai, W. 627, 633, 636, 639, 1996
Galambos, J.D. 1018, 3851
Galayda, J.N. 877
Galbraith, P. 3648
Galdi, V. 1753
Galimberti, A. 826, 2353, 2356
Gallardo, J. 405, 408, 616, 621, 675
Gallet, B. 3365
Gambalonga, S. 1129
Gamp, A. 3162
Ganetis, G. 3353, 3356, 3651
Ganguly, A.K. 3156, 3171
Gao, J. 1602, 1605, 1608
Gardner, C. 89, 962, 970
Gardner, I.S.K. 988, 1021
Gareyte, J. 1356
Garnett, R.W. 1150, 1165, 2743
Garoby, R. 973, 979, 2953
Garren, A. 411, 838, 868
Gärtner, W. 3410
Garvey, J.D. 3291, 3395
Garvey, T. 2823
Garza, O. 2529, 3681
Gassner, D. 2149
Gatignon, L. 80, 165
Gavidia, A. 2067
Gavrilov, N.G. 883
Gaydosh, M.. 3666
Gayet, P. 1858
Gazis, E.N. 1042
Gelbart, William Z. 3842, 3845
Gelbke, C.K. 34
Gelfand, N. 997
Geller, J. 2149
Genet, M. 3368
Genevey, P. 3365
Gentner, M. 330
Gentzlinger, R.B. 3096
Gentzlinger, Robert C. 2914
Gerken, E. 3725
Geschonke, G. 1858
Ghiroso, W. 1926
Ghosh, A. 3353, 3356, 3398
Giachino, R. 1813
Giannini, R. 979, 1382
Gikal, B.N. 3610
Gill, P.F. 3583
Gillespie, George H. 1894, 2559, 2562
Gilpatrick, J.D. 83, 1150, 2041, 2090, 2093, 2232
Gioumousis, A. 2253
Giovannozzi, M. 1445, 1451, 1469, 2568, 2571
Giove, D. 2002, 2038, 3657
Giulicchi, L. 2314
Giuressi, D. 2353, 2356
Glass, H.D. 3242, 3257, 3260, 3263, 3269, 3286
Glatz, J. 1897
Glazov, A. 1263
Glenn, J.W. 89, 965, 967, 1478, 2149, 2155
Glock, H.-W. 521, 527
Glover, M.G. 1021
Glover, T.E. 1984
Gluckstern, Robert L. 1744, 1747, 1750, 1950
Gluskin, E. 877, 3224
Gobin, R. 2720
Goddard, B. 309
Godlove, T. 1855, 1956, 1959
Goeppner, G.A. 2207
Goetz, S. 883
Gold, S. 439, 1319, 1322, 3027, 3042
Gold, Steven H. 3153
Goldberg, D.A. 3001
Goldstein, J.C. 897, 2174
Golkowski, Cz. 1272, 1275
Gonçalves da Silva, C.E.T. 811
Goodzeit, Carl L. 3404
Gorchenko, V. 2452
Gordon, D. 681
Gorelov, D.V. 1194, 2621
Goto, A. 930, 941, 1066, 1069, 1075, 2672, 3419, 3422, 3428, 3440
Gottschalk, S.C. 675
Gou, Z.Y. 1729
Gouffon, P. 3239
Gough, R. 2675, 2758, 2770, 3737
Gougnaud, F. 2823
Gould, H. 150
Gourlay, S.A. 3209, 3398
Gournay, J.F. 2823
Gover, A. 906
Govil, R. 654
Gower, F. 3796
Gracia, J. 315
Graf, M.A. 2767
Grafström, P. 80, 165
Granatstein, V.L. 3168
Grandinetti, R. 3651
Graves, W.S. 1197, 1993, 2437, 3497
Gray, E.R. 83, 915, 1153, 1162
Gray, R. 315
Green, M.A. 868, 3401
Greene, J. 2696
Greenslade, M. 3413
Greenwald, S. 2547, 3699, 3702, 3705
Greenwald, Z. 2547, 3705
Greenwood, J.B. 2705
Greer, J. 2344
Gregory, S. 2633
Grelick, A. 1269, 2941, 3174
Grier, D. 973
Grier, E. 2953
Grieser, M. 947
Griffin, J. 396, 399, 1724
Grimm, T.L. 663
Grimmer, J. 3556
Grippe, J. 439
Grishanov, B.I. 237
Grishin, V.K. 889, 3866
Gröbner, O. 979, 3542, 3586, 3589
Groeppner, G.A. 3552
Gros, P. 2720
Gross, R. 3743
Groß, P. 174
Grote, D.P. 1240, 1923
Grote, H. 1356, 1442
Gruber, J. 973, 979
Grudiev, A.V. 2609
Guerra, A. 3333
Guharay, S.K. 2681
Guigli, J. 2067
Guignard, G. 458, 473, 482, 566
Guilhem, D. 1254, 1257
Gulbekian, G.G. 3607, 3610
Guo, Z.Y. 1566, 1828

Gupta, R. 3344, 3347, 3356, 3362, 3398
Gustafson, R. 3260
Gustwiller, J. 1245
Guy, A. 1051
Guy, F.W. 1099
Gyr, M. 168, 171

H

Ha, K.M. 3479
Haber, I. 1240, 1923
Haberer, Th. 3801
Habs, D. 947
Haddock, P.C. 3135
Haebel, E. 1858
Hafizi, B. 666, 3153
Hagedoorn, H.L. 1036, 1200
Hagel, J. 458
Hagestedt, A. 763
Haggard, J.E. 3257, 3263, 3266
Hahn, A.A. 2166, 2226
Hahn, H. 210, 213, 216, 1706
Hahn, K. 1926
Hahn, U. 2134
Haid, D. 3669
Haimson, J. 2808
Haines, John 86
Halbach, Klaus 3728
Halbleib, J.A. 1245
Halvarsson, B. 2026
Hamilton, B. 1481, 2081
Hamm, R.W. 2811
Hammen, A.F.J. 1200
Han, Y. 3297
Han, Y.J. 3633
Hangst, J.S. 1560
Hanna, S. 439, 539, 3042
Hannaford, C. 3212
Hansborough, L.D. 2740
Hansen, B.C. 3872
Hansen, Robert J. 3153
Hansen, U. 3123
Hanson, A. 3096
Hanson, D.L. 1935
Hanus, X. 817, 1709
Hao, Y. 3297
Haouat, G. 1841
Haque, T. 3452
Hara, K. 3087, 3090
Hara, M. 2971
Harding, D.J. 3242, 3245, 3257, 3263, 3269, 3272, 3275, 3278, 3286, 3288, 3291
Hardy, D. 2265
Hardy, L. 751
Harkay, K. 953, 1575, 1700, 2052, 2944, 3577
Harkewicz, R. 2702
Harnden, W. 3212
Harold, M.R. 1021
Harris, G. 3580
Harrison, M. 69, 101, 219
Harrison, S.M. 3413
Harss, B. 2696
Hartemann, F.V. 2858
Harteneck, H. 3568
Hartill, D. 1718, 2164, 3236
Hartmann, H. 2499
Hartmann, W. 3123
Hartung, W. 3075
Haruyama, Y. 1557
Harwood, L. 3333
Hasegawa, K. 915
Hashimoto, S. 757
Hashimoto, Y. 584, 938
Hatanaka, K. 3359, 3416, 3434
Hatch, K. 3743
Hathaway, D. 3622
Hayano, H. 494, 584, 587, 2980
Hayes, T. 965
Haynes, W.B. 2914, 3096, 3135
Hays, T. 3075, 3177
He, P. 675
Heiberger, M. 3816
Heifets, S. 1503, 1620, 1682
Helm, R. 608
Hemery, J.-Y. 228, 979
Hemker, R.G. 2870
Hemmi, M. 941, 2672
Henderson, S. 291, 1472, 1542, 1765, 2029, 2164
Hendrickson, L. 452, 497, 608, 2122
Henestroza, E. 590, 1926, 2832, 3719, 3722
Henke, H. 251, 464, 542, 672, 2134
Henrichsen, K. 66, 3648
Herbeaux, C. 817
Herer, A. 3857
Herminghaus, H. 1042
Hernandez, M. 733, 2017, 2840
Herr, W. 168, 171, 309, 312
Herrup, D. 2058
Hershcovitch, A. 1792, 2678, 2711
Hertzbach, S. 608
Hess, C. 3395
Hettel, R. 838
Heydari, H. 2603, 2784
Hezel, T. 3512
Higashi, A. 3822
Higgins, S. 3755
Higley, H. 3212
Higo, T. 494
Hilbert, B. 3206
Hill, A. 3004
Hill, Barrey W. 1894, 2562
Hill, C. 944
Hill, J.O. 2461
Hill, R. 2529
Hillman, A. 2281
Himel, T. 2425, 2473, 2476
Hindi, H. 2284, 2362
Hinkson, J. 775, 2110, 2235, 2253
Hinode, F. 354, 578, 587, 2980, 2983
Hiramatsu, S. 1566
Hiramoto, K. 1653, 3294, 3813
Hirata, K. 384, 1780, 1783
Hirota, J.I. 3294
Hirshfield, J.L. 666, 3153, 3156, 3171, 3863
Ho, C.H. 2858, 3048
Ho, Wendy 3842, 3845
Hoag, H. 439, 539
Hock, J. 2149
Hodapp, T.R. 2232
Hodgkins, D.J. 2740
Hoff, Lawrence T. 2395
Hoff, Matthew D. 1096
Hofler, A. 2201
Hofmann, A. 838, 1813, 1858
Hofmann, Ingo 1852
Hogan, B. 3168
Hogan, M. 736
Hogge, J.P. 2690
Hogrefe, R. 3669
Holben, S. 3165
Holik, P. 439
Holmes, J.A. 1018
Holmes, Michael 796
Holmes, R. 3562
Holmes, S. 439, 3027, 3042, 3192
Holmes, S.D. 47, 997
Holt, J. 72, 997
Holtkamp, N. 581, 2008, 2078, 2104, 2726
Holtzapple, R.L. 509
Homeyer, H. 1078
Honda, T. 2084, 2146
Honma, T. (Chiba) 1557
Honma, T. (Hokkaido U.) 2565
Horan, D. 953, 2926, 2935, 2941, 3111, 3687, 3690
Hori, T. (Sumitomo) 1266, 2642
Hori, T. (SPring-8) 2511, 2814
Hornekær, L.H. 1560
Horsky, T.N. 2767
Horton-Smith, S. 1981
Hosino, M. 1557
Hosono, K. 1557
Hosoyama, K. 3087, 3090

Hou, R. 3297, 3318
Houck, T. 590, 2627, 2633, 3719, 3722
Hovater, Curt 2861
Howells, M. 778
Hower, N. 883
Hoyer, E. 3221
Hoyt, M. 3004
HRIBF Operations Staff 1227
Hsieh, H. 3619
Hsiung, G.Y. 3642
Hsu, Ian C. 850, 2047, 2183
Hsu, K.T. 841, 847, 853, 1487, 2259, 2371, 2374, 2377, 2523, 3488, 3539, 3749
Hsu, Y.J. 850, 3642
Hsue, C.S. 1409, 1487, 3533
Hsue, K.T. 1409
Hu, K.H. 3539
Hu, Shaoguang 1218, 1221
Hu, Wensheng 1218, 1221
Hua, D. 3807
Huang, Bingsong 3300
Huang, Fuhe 3300
Huang, H. (BNL) 89, 1460, 1478, 2155, 2538
Huang, H. (IHEP) 1566
Huang, J.Y. 823, 2107, 2350, 3015, 3479
Huang, N. 1388, 1448, 1780
Huang, Yuanzhong 1215, 3764
Hubbard, E. 3816
Hubbard, R.F. 611, 630
Hughes, Thomas P. 1144, 1867, 2826
Hülsmann, P. 521, 524, 527
Humphrey, R. 439
Humphries, D. 3315
Humphries Jr., S. 2428
Hunt, D. 3619
Hunt, W. 2449, 2737
Hurh, P.G. 2166, 3283
Hurn, T. 3816
Hus, J.L. 684
Husmann, D. 330, 1033, 1373
Huttel, E. 763, 3613
Hutter, G. 3123
Hutton, A. 281, 2383
Hwang, C.S. 3536, 3539
Hwang, J.Y. 2858
Hwu, K.H. 3749

I

Iazzourene, F. 826, 829, 1185
Ichac, J.-P. 2899
Igarashi, I. 1599
Ikegami, K. 1066, 1069, 1075, 3419, 3422, 3428, 3440
Ikegami, Masanori 1911
Ilhoff, E. 2241
Imai, Y. 3425
Imanishi, A. 938
Inabe, N. 1400, 2672
Indreias, I. 1123, 3854
Ingalls, W.B. 2743, 2764
Ingold, G. 3527
Ingrassia, P. 1460
Inoue, M. 339, 1203, 1206, 3294, 3819
Intensity Upgrade Study Crew 1009
Irwin, J. 360, 482, 512, 608, 1341, 2583, 2636
Isaeva, L.G. 883
Ishi, Y. (INS) 1962
Ishi, Y. (Mitsubishi) 2908, 3087
Ishikawa, Y. 3822
Ishimaru, H. 110
Ishkhanov, B.S. 889, 3866
Issinsky, I. 181, 184
Itano, A. 201, 2347
Ito, Y. 2511, 2814
Itoh, M. 859
Ivanenko, A.I. 3604, 3607
Ivanov, I.N. 491, 1391, 3126
Ivers, J.D. 1272, 1275
Iverson, R. 315, 687
Iwashita, Y. 339, 1203, 1206, 1798, 3294, 3819
Izawa, M. 1566, 2171, 2989, 3066

J

Jablonka, M. 2823
Jackson, A. 703, 778
Jackson, G.P. 3257, 3260, 3263, 3280, 3286
Jackson, J. 3233
Jacob, J. 1551
Jacobs, G. 2726
Jacobs, K. 348, 2099
Jaeschke, E. 713
Jagger, J. 363, 2699
Jahnel, L.C. 811, 2096, 2238, 3740
Jain, A. 3309, 3338, 3347, 3353, 3356, 3362, 3651
Jaisle, A. 3443
Jakob, A. 174, 246
Jakob, H. 2026
Janenko, V. 276
Jankowiak, A. 2140
Janssen, D. 2796, 2838
Jansson, A. 2314
Jansson, U. 1325
Jark, W. 3527
Jarvis, H. 608
Jason, Andrew 270, 3138, 3728, 3731
Jayamanna, K. 2675
Jeanneret, J.B. 153
Jenkins, D.M. 3413
Jenner, D. 2968
Jensen, C. 1281, 1284, 1287
Jensen, D. 3330
Jensen, E. 973, 2953, 3060
Jensen, K. 1105
Jeon, D. 1346, 1481
Jeong, S.C. 938
Jeram, B. 2481
Jiang, C.L. 2696
Jiang, X. 2932, 2938
Jimenez, M. 1858
Jin, L.H. 1388
Jin, Qingxiu 1218, 1221, 3764
Jobe, K. 1981
Jobe, R.K. 3021, 3027
Johnson, B.M. 2678
Johnson, C. 563
Johnson, D. (NSCL) 1054, 1057
Johnson, D. (LANL) 1611
Johnson, D.E. 997, 3272
Johnson, E.D. 1197, 1993
Johnson, J. 808
Johnson, Jeffrey O. 86
Johnson, K.F. 1150, 2232
Johnson, L. 439
Johnson, P.E. 2950
Johnson, R. 2110, 2122, 2253
Johnstone, C. 119, 396, 399, 411, 414, 1030
Johnstone, John A. 240
Joly, J.M. 2823
Joly, S. 1117, 1120, 2684
Jones, C.R. 2799
Jones, F.W. 1882, 2597, 2600
Jones, G. 3619
Jones, J. 2699, 2929
Jones, K.W. 1165
Jones, R. 439, 518, 545, 548, 551, 554
Jones, W.P. 2737
Jongen, Y. 1045, 3770, 3816, 3857
Jongewaard, E. 439, 3189
Jonker, M. 1813
Jordan, K. 912, 2204, 2529
Joshi, C. 11, 678, 681, 687
Jöstingmeier, A. 2553, 2612
Jowett, J.M. 312
Judd, D. 195
Judkins, J. 3004, 3039
Juillard, M. 817, 2823
Jung, D.H. 2107
Junquera, T. 2823

K

Kaan, A.P. 3630
Kabe, A. 3087, 3090
Kabel, A. 2550
Kagaya, S. 587
Kageyama, T. (RIKEN) 2672
Kageyama, T. (KEK) 2902, 2974, 2977, 2986, 3069
Kahn, S. 3309, 3350, 3356
Kaiser, K.-H. 1902
Kakiuchi, S. 3294
Kaljuzhny, V.E. 2008, 2104
Kaltchev, D. 153
Kamada, S. 1831
Kamigaito, O. 941, 2672
Kaminsky, V.I. 3869
Kamitsubo, H. 6
Kamiya, Y. 856, 2146, 2989, 3066
Kamps, T. 2134
Kanai, T. 3822
Kanaya, Noriichi 2458, 3616
Kanazawa, M. 201, 2347, 3819, 3822
Kando, M. 648, 760
Kane, Steve 3693
Kang, X. 264, 1346, 1481, 2968
Kang, Y. 461, 1575, 2296, 2699, 2929, 2932, 2935, 2938, 2941, 2944, 3687
Kao, C.C. 727
Kaplan, R. 1718, 3075
Karabarbounis, A. 1042
Karantzoulis, E. 826, 829
Karas', V.I. 651
Karasyov, S.P. 2229
Karl, F. 3651, 3693
Karliner, M. 2796, 2838
Karn, J. 2383, 3333
Kase, M. 941, 2672, 3327
Kashiwagi, S. 494, 587
Kasimer, K.U. 2461
Kassab, L.R.P. 3239
Kasuga, T. 1566, 1664
Katayama, I. 938, 1557
Katayama, T. 92, 930, 938, 1024, 1072, 1400, 1786, 1807, 3359, 3416, 3431, 3434, 3437, 3521
Kato, S. 1596
Kato, T. 3822
Katoh, M. 2084
Katsouleas, T. 681, 684, 687, 2870
Kawachi, K. 820, 3822
Kawaguchi, H. 2565
Kawaguchi, T. 1066, 1069, 1075, 3359, 3419, 3422, 3425, 3428, 3431, 3440
Kawakami, H. 938
Kawakita, T. 1203
Kawashima, Y. 2971
Kazacha, V.I. 488
Kazakov, S.Yu. 3126
Kazimi, R. 1947, 2484, 3755
Keane, J. 2069
Keesee, M. 2201
Kehne, D. 912, 2204, 2484, 2693, 3755
Keil, E. 104, 309, 363
Keil, J. 1373
Keller, R. 775, 778, 781, 784, 787
Kelly, Darren R.C. 3547
Kelly, E. 3362
Kennedy, K. 3568, 3619
Keppler, P. 165
Kerby, J. 3398
Kerns, J. 3619
Kersevan, R. 3559, 3592
Kerslick, G.S. 1272, 1275, 3117
Kester, O. 947
Kewisch, J. 69, 98, 222
Khabarov, M.V. 3607
Khan, S. 1703, 1810
Khlebnikov, A.S. 3518
Kiang, L. 1481
Kidman, R. 3096
Kihara, T. 1798
Kijima, Y. 2908, 3087
Kikutani, E. 306, 1566, 1596, 2332, 2335
Kim, C. 778, 790, 808
Kim, C.K. 3633
Kim, Eun-San 384
Kim, J.-S. 3719, 3722
Kim, J.-W. 1066, 1069, 1075, 3419, 3422, 3425, 3428, 3440, 3825
Kim, J.K. 2657
Kim, K-J. 1984
Kim, K.H. 2107
Kim, S. 3577
Kim, S.H. 745, 2293, 3227
Kim, T.Y. 1593
Kimura, W.D. 675
King, F. 3568
King, N.S.P. 3096
Kinkead, Allen K. 3153
Kinosita, H. 757
Kinross-Wright, J.M. 897
Kirbie, H.C. 1260
Kirby, G.A. 3209
Kirby, R. 3568
Kircher, F. 3365
Kirchgessner, J. 3075, 3177
Kirichenko, A. 2452
Kirk, H. 408
Kirsebom, K. 80
Kiselev, A.V. 2805
Kiselev, V. 1463, 1466
Kiselev, V.A. 651
Kishek, R.A. 3198
Kishiro, J. 1548, 1599, 1908
Kishiyama, K. 2110, 3622, 3625
Kitagawa, A. 3822
Kitamura, Hideo 3515
Klabunde, J. 1897
Klaffky, R.W. 2305
Klaus, F. 3123
Kleeven, W. 3816
Kleffner, C. 2078, 2726
Klein, H. 174, 246, 521, 524, 527, 988
Klein, W. 2422, 2535
Kleinman, H. 906
Klem, J. 168, 171
Klimine, P. 3407
KLOE Collaboration 3413
Knauf, A.B. 3710
Knott, M. 3669
Ko, I.S. 823, 2107, 2350, 3015, 3479, 3633, 3663
Ko, J.J. 1870
Ko, K. 387, 439, 2589, 3033
Koba, K. (KEK) 1548, 1599
Koba, K. (Miyazaki U.) 1908
Kobayashi, T. (JAERI-RIKEN) 2814
Kobayashi, T. (Tsukuba) 2902, 2974, 2977, 2986, 3069
Kobayashi, Y. 856, 1566, 2084, 2171
Koepke, K. 2873
Kohara, S. 941
Kohno, T. 201
Koiso, H. 1394
Kojima, Y. 3087, 3090
Koldenhoven, R. 3669
Kolomiets, A. 1090, 1129, 1905, 2735, 2965, 3848
Kondoh, S. 648, 760
Kondratiev, B.K. 2735
Konecny, R. 633, 636, 639, 1996
Konstantinov, S. 2838
Koontz, R. 439, 1319, 1322, 3021, 3027, 3042
Koop, I. 1063, 1433
Korhonen, T. 587
Korovin, O.P. 1511
Korsbjerg, T. 2920, 2923
Kos, N. 3586
Koscielniak, S. 956, 1102, 1647, 2389
Koseki, T. 856, 1756, 2146, 2989, 3066
Kostin, D.V. 1108, 2008, 2104
Kotaki, H. 648, 760
Kotov, V.I. 249

Kotseroglou, T. 687, 1981, 2849
Kouda, S. 3822
Kourbanis, I. 144, 1721, 2061, 2323
Koutchouk, J.-P. 66, 1356, 1442
Kovalenko, A. 184, 2452
Kowalkowski, J.B. 2461
Kowalski, S. 348, 2274
Koyama, K. 1203
Koyama, T. 375
Koziol, H. 973, 979
Kozlov, O. 181
Kozodaev, A.M. 2965, 3848
Kozyrev, E.V. 3114
Kponou, A. 1460, 2023, 2711
Krafczyk, G. 3291, 3461
Krafft, G.A. 739, 912, 2020, 2128, 2204, 2265, 2268
Kraft, G. 3801
Kraimer, Martin R. 2403
Krainz, G. 3206
Kramer, S.L. 748, 2305
Krasnopolsky, V.. 1263
Krasnykh, A. 1319, 1322
Krastelev, E.G. 3141
Krause, U. 3801
Krawczyk, Frank L. 2914, 3093, 3731
Krebs, Gary F. 793, 796
Kreischer, K.E. 2690
Krejcik, P. 608, 1623, 1626, 3030
Krevet, B. 3512
Kriens, Wilhelm 231
Krietenstein, B. 2645
Krinsky, S. 727, 1197, 2161, 2287
Kroc, T.K. 3269
Kroes, F.B. 1063
Krogh, M.L. 1308, 2627
Kroll, N. 429, 439, 518, 548, 551, 554
Kroupa, M. 2535
Kruchkov, J. 2838
Krueger, K. 1460
Krusche, A. 973
Krushelnick, K. 611
Krüssel, A. 763
Kuba, A. 2511, 2814
Kubo, K. 354, 494, 587, 1484, 2980, 2983
Kubo, T. 1066, 1069, 1075, 3419, 3422, 3425, 3428, 3440
Kubo, Tadashi 3467
Kubono, S. 938
Kudinov, V. 276
Kudo, Hirofumi 2146
Kuijer, L.H. 1063
Kukarnikov, S.I. 491
Kukhtiev, V. 1135
Kulik, I. 1129
Kulikov, A. 315, 1316, 2253, 3639
Kulikov, I. 2452
Kulipanov, G.N. 883
Kumada, M. 820, 2347, 3327, 3822
Kuner, B. 2493
Kuo, C.C. 841, 847, 850, 853, 1409, 1487, 1638, 2377, 3048, 3051, 3054, 3533
Kuo, C.H. 2259, 2371, 2374, 3749
Kuo, T. 2675
Kupper, R.R. 2737
Kurakin, V.V. 3848
Kurennoy, Sergey S. 1732, 1950, 3731
Kurita, N. 2014, 2110, 2253, 3639
Kurkin, G.Ya. 883
Kurnaev, O. 234
Kurokawa, S. 381, 1566, 1596
Kurz, M. 521, 527
Kusche, K.P. 621, 675
Kushnir, V.A. 651, 3810
Kustom, R. 461, 953, 1575, 2296, 2929, 2941, 2944, 3174
Kutner, V.B. 3604
Kuybeda, R.P. 3848
Kuzay, Tuncer 2210
Kuzmiak, M. 1391
Kwan, J.W. 1230, 2755
Kwan, Thomas J.T. 2174
Kwiatkowski, S. 2947
Kwon, M. 823, 2350, 3015
Kyser, R.H. 3159

L

Labrador, A. 1560
Labrouche, J. 1254, 1257
Lackner, H. 1251
Laclare, J.-L. 817, 1406, 1517
Ladeuze, M. 3816
Lagniel, J-M. 1120, 2720
Lahey, T. 2473
Lai, B. 461
Lai, C.Y. 1638
Lai, P.-C. 2047
Laird, R. 2490, 2926
Lalayan, M.W. 2104
Lamanna, G. 2169
Lambaise, R.F. 3452
Lambertson, G. 1617, 2344
Lambiase, B. 3449
Lamm, M.J. 3389, 3395, 3398
Lamont, M. 309
Lampel, M.C. 2562, 2615
Lancaster, J.A. 2799
Lange, R. 2493
Langenbeck, B. 2594
Langenbrunner, J. 1611
Langton, J. 2014, 2253
Lannoye, G. 3816
Larsen, R. 2284
Larson, D. 1403, 3248, 3837
Lash, J.S. 1245
Latham, P.E. 3150
Latypov, D. 3443, 3446
Latypov, T. 1263, 1311
Lau, W.K. 847, 1487, 1638, 1691, 2377, 2858, 3048, 3051, 3054
Lau, Y.Y. 3198
Lauckner, R. 66
Launspach, J. 1254, 1257
Laverty, M. 3057
Lavine, T. 439, 1676, 3027, 3042, 3192, 3675
Lawrence, G.P. 83, 1150, 1156
Lawson, W. 3168
Lawton, D. 1054, 1057
Laxdal, R. 956, 1102, 1105, 1135, 1194, 2621
Laycock, S. 3816
Lazarev, N.V. 2965, 3848
Lebedev, V. 1560, 2128, 2383
LeBlanc, G. 342, 345, 832
Leboutet, H. 1117
Lee, C.-H. 2183
Lee, D.H. 850
Lee, E. 195
Lee, J.C. 844
Lee, M. 2586
Lee, P.B. 657
Lee, R. (UC Irvine) 965
Lee, R. (TRIUMF) 1102
Lee, S. 687
Lee, S.C. 3663
Lee, S.Y. 264, 396, 399, 935, 1346, 1460, 1478, 1481, 2968
Lee, T. (Pohang) 823
Lee, T. (DULY Research) 2802, 3036, 3120
Lee, Y. 2667, 2675, 2770, 3737
Lee, Y.Y. 159, 162, 962, 970
Leemans, W. 630, 654, 657, 687, 1984
Legg, R. 2201, 2265, 2383, 2693, 3755
Leibfritz, J. 994, 3601
Leinbach, R. 3221
Leitner, M.A. 2758, 2764, 2770
Lemaire, J-L. 1120
Lenci, S. 3183
Lengeler, H. 988
Lenkszus, F. 2281, 2490, 2926
Lenz, J.W. 1099
Leonhardt, W.J. 3230, 3583
Leroy, P-A. 2720

Le Sage, G.P. 2858
Lessner, E. 327, 953
Letchford, A.P. 1846
Letta, P. 2383, 2484
Leung, K-N. 2675, 2758, 2761, 2764, 2767, 2770, 3737, 3807
Level, M.-P. 817, 1406, 1517
Levichev, E. 1463, 1466
Levin, L.A. 906
Levush, B. 2431, 3144, 3150, 3159, 3180
Levy, C.D.P. 2781
Ley, R. 944, 982
Leyman, D. 3816
LHC Magnet Team 3371
Li, L. 3297
Li, N. 3312, 3318
Li, Quanfeng 1218
Li, R. 1641, 1644, 2204
Li, S.P. 1566
Li, X. 633, 1996
Li, Y. (Maryland) 1855, 1959
Li, Y. (IHEP) 3297
Li, Yuezeng 1218, 1221
Li, Yulin 3559, 3592, 3595
Li, Zenghai 599
Liakin, D.A. 2965
Lidia, S. 590, 900, 2624
Liehr, M. 2708
Lietzke, A. 3212
Liiou, A.V. 2078
Likhachev, S.P. 3866
Liljeby, L. 947
Limberg, T. 491, 2550
Limborg, C. 838
Limon, P.J. 3389, 3395, 3398
Lin, Glory 850
Lin, K.K. 2259, 2371, 2374, 2523, 3749
Lin, Liu 811, 2096, 2238, 3740
Lin, M.C. 1638, 3048, 3051, 3054
Lin, S.J. 1638, 2377, 3048
Lin, X. 387, 3033
Lin, Y.K. 853
Lin, Yuzheng 1215, 1218, 1221
Lindgren, L-J. 345
Lindroos, M. 2314
Linebarger, W. 596
Ling, Guan Xia 1224
Linnecar, T. 1813, 1816, 1849
Linnik, A.F. 651
Linscott, I. 2284
Lipari, J. 1316
Lira, A.C. 811, 1209, 3476
Lisowski, P.W. 708, 3780
Littauer, R. 1472, 1542
Littenberg, L. 967
Litvinenko, V. 874, 883
Liu, C.Y. 3488
Liu, D.K. 1566
Liu, F. 2678, 3752
Liu, H. 1947, 2693
Liu, K.B. 3488
Liu, W.B. 1388
Liu, Y. 621, 675
Liu, Y.C. 847, 853, 2259, 2858
Lockey, R. 2711
Loew, G.A. 439
Loewen, R. 439, 539, 3042, 3189, 3192, 3195
Lokhovitskii, A.E. 252, 255, 258
Lollo, M. 1129
Lombardi, A. (CERN) 944, 2314
Lombardi, A. (INFN) 1087, 1129
Lonza, M. 826, 2353, 2356
Lorenz, R. 2134, 2137, 2392
Losito, R. 3063
Lou, W. 3236
Louie, W. 3338
Loulergue, A. 817, 2684
Lozowski, W.R. 2737
Lu, Fuhai 3162
Lucas, William 3595
Luccio, A. 92, 207, 962, 970, 1460, 1882, 2538, 3359
Luchini, K. 808
Ludewig, H. 970
Ludewigt, B.A. 3791
Luger, G. 2422, 2535
Luhmann Jr., N.C. 2858
Luijckx, G. 1063
Lujan, R.E. 3096
Luke, P.N. 3807
Lumpkin, A. 775, 871, 874, 883, 1700, 1999, 2052, 2207
Lund, S.M. 1240, 1260, 1929, 1932
Lundgren, S. 1051
Luo, G.H. 847, 850, 853, 1638, 3048
Lupton, William 2403
Lussignol, Y. 2823
Lyles, J. 3473
Lynch, D.R. 3494
Lynch, M. 1147, 3138
Lyneis, C.M. 1051, 2770
Lysenko, A.P. 1433
Lysenko, W. 1917, 2574
Lyudmirskiy, E.A. 249

M

Ma, L. 1566, 2075
Ma, R. 3831
Maas, R. 1063
Maccaferri, R. 944, 979
MacDonald, A.R. 2508
Macedo, D. 2096
Macek, R. 190, 1012, 1015, 1159, 1611
MacGregor, I. 2413
Machida, S. 1656, 1670, 1908, 1962, 2995
Machie, D. 3108
MacKay, W. 69, 98, 101, 210, 222, 2541
Mackenzie, G. 956, 2675
Mackenzie, R. 2476
MacLachlan, J. 1590, 2556
MacLaren, S. 1926
Madey, J.M.J. 24, 883, 2799
Madlung, J. 1081
Madsen, N. 1560
Maenchen, J.E. 1245
Maeng, A.H. 3663
Maezawa, Hideki 2458, 3616
Mahler, G. 2155
Mahoney, K. 3565, 3678, 3681, 3684
Maidment, J.R. 985
Maier, R. 1048
Mailian, M.R. 695
Mainaud, H. 560
Maines, J. 3224
Mais, H. 1825
Maisheev, V.A. 249
Majka, Dick 967
Major, J. 165
Makarov, A. 3248, 3291
Makarov, I.G. 3114
Makdisi, Y.I. 1460
Makino, K. 1336
Makoveev, V.K. 1391
Maksimchuk, A. 2657
Malafronte, A.A. 2998
Malagari, M. 1042
Malamud, E. 363
Maletic, D. 970, 1882
Malitsky, N. 375, 2434
Maloney, M. 3096
Mamaev, G. 1263, 1311, 1313
Mamaev, S. 1263, 1311, 1313
Mammarella, F. 956
Mammosser, J. 3102, 3108
Mancini, D. 461
Mane, V. 69, 98, 2158
Mangra, D. 745, 2938
Manka, C. 611
Mansur, Louis K. 86
Manvell, Benjamin 3595
Margaritescu, A. 1123, 3854
Marghitu, S. 1123, 3854
Marhauser, F. 521, 527
Mariam, F. 1460, 3359

Marin, A. 3645
Marks, N. 3386
Marks, S. 802, 3221
Marlats, J.-L. 817
Marneris, I. 2308
Marone, A. 3353
Maroulis, D. 1042
Marriner, J. 72, 144
Marsh, K. 678, 687
Marshall, T. 642, 666
Martens, M.A. 72, 136
Marti, F. 278, 1054, 1057
Martin, D. (Bucharest) 1123, 3854
Martin, D. (SLAC) 1457, 1490
Martin, P.S. 139, 243, 3242, 3245, 3269, 3272, 3275, 3278, 3288
Martin, S. 1048
Martinez, D.G. 2232
Martinez, F. 1093
Martinez, R. 2232, 3309
Martini, M. 1362, 2314
Martins, M.N. 2998
Martlew, B.G. 2443
Martono, Hendy 2562
Marutsuka, K. 267, 1908
Marx, M. 491
Maryokhin, S.V. 2229
Mashaw, A. 3737
Mashiko, K. 339
Maslov, M.A. 258
Massmann, P. 2717
Massoletti, D. 778, 808
Masunov, E.S. 2835
Mathewson, A. 3586
Matsuda, Kooji 3813
Matsumoto, H. 455, 530, 533, 581, 587, 593
Matsumoto, S. 306, 1596
Matsuoka, M. 1203
Matufuji, N. 3822
Matuk, C.A. 2767
Maury, S. 944, 976, 979, 982, 1382
Mavric, G. 2481
May, M.P. 3257, 3263, 3280, 3286
Mazarakis, M.G. 1245
Mazur, P. 3389, 3392
McAllister, B. 348, 2099
McCammon, D. 2968
McCormick, D. 1981, 2189, 2253
McCullough, R.W. 2705
McCurdy, A.H. 3159
McDaniel, B. 1472, 1542
McDonald, M. 2675
McDowell, W. 953, 3669
McGee, M.W. 3283
McGhee, D. 953
McGill, R. 2253
McGinnis, D. 144, 1721, 2323
McIntosh, E. 2571
McIntosh, P.A. 2223, 2956, 3078
McInturff, A.D. 3212, 3389
McIntyre, Gary 3693
McIntyre, P. 3443, 3446
McJunkins, P. 3443
McMahan, M.A. 1051
McManamy, Thomas J. 86
McMichael, G.E. 156
Mead, J. 2502
Mecklenburg, B. 2808
Meddahi, M. 309, 312, 1813
Medvedko, A.S. 3455
Medvedko, E.A. 2113, 3455
Medvedyeva, Ye.P. 3840
Meincke, O. 1858
Meisner, K. 2326
Meitzler, C.R. 3872
Melissinos, A.C. 2867
Meller, Robert E. 2505
Mencik, M. 2823
Mendonsa, R. 3796
Menegat, A. 464, 672, 3036, 3045
Meneghetti, J. 3619
Meng, W. 3233
Menge, P.R. 1245
Menshov, A.A. 2078
Méot, F. 121, 1987
Merinov, I. 2244
Merl, R. 745, 2281
Merle, E. 1254, 1257
Merminga, L. 1694, 2320
Merrill, F. 1611, 2743
Metzger, C. 979, 982
Metzmacher, K. 973, 979, 1328
Meyer, D. 1269
Meyer, E.A. 2740
Meyer, J. 883
Meyer, S. 2413, 2517
Meyerhofer, D. 2840
Michelini, P. 3527
Michelotti, L. 997
Michnoff, R. 2218
Mikhailichenko, A. 318
Mikhailov, S.F. 883
Mikhailov, V. 181, 184
Mikkelsen, U. 80, 165, 168
Mikkelson, K. 1245
Miles, J. 1356
Militsyn, B. 1063
Miller, E. 2473
Miller, R. 439, 518, 539, 548, 551, 554, 599, 2687, 2790, 2840, 2843, 2846, 2849, 2852, 2855, 3042
Miller, T. 3619
Millich, A. 563
Milloch, M. 1212
Millos, G. 3568
Mills, J.A. 3230
Mills, Mark R. 2122
Milocco, A. 1212
Milovanov, O.S. 2104
Milton, B.F. 3775
Milton, S. 324, 877, 1700, 2699, 3577
Milward, S.R. 3209, 3494
Minaev, S.A. 2645
Minamihara, Y. 3221
Minato, T. 3425
Minister, J. 439
Minty, M.G. 354, 357, 449, 506, 509, 608, 1563, 1569, 1741, 1873
Minuzzi, F.A. 3628
Mirzojan, A.N. 2078
Mishra, C.S. 139, 997, 1771, 3269
Mistry, N.B. 3559, 3592, 3595
Mitchell, D. 3389
Mitchell, M. 3021, 3024
Mitra, A. 1105, 2953, 3060, 3063
Mitrochenko, V.V. 651, 2817, 2820, 3810
Mitsuhashi, T. 766, 859, 2084
Mitsumoto, T. 1066, 1069, 1075, 3419, 3422, 3428, 3440
Mitsunobu, S. 2908, 3087, 3090
Miura, A. 530
Miura, T. 2983, 3066
Miyachi, T. 938
Miyahara, Y. 891
Miyamoto, S. 757
Miyatake, H. 938
Miyazawa, Y. 941, 2672
Mizuno, A. 2511, 2814
Mizuno, H. 2902, 2974, 2977, 2986, 3069, 3767
Mochihashi, Akira 1664
Mochizuki, T. 757
Moe, H. 953
Mohammadzadeh, Ahmad 2380
Möhl, D. 944, 976, 979, 982, 1382
Moir, D.C. 1138, 1141, 1144, 2829
Moisio, M.F. 1129
Mokhov, N. 116, 124, 133, 393, 414, 3672
Molau, N.E. 2627, 2633
Molinari, G. 944
Møller, S.P. 80, 165, 1027, 2920, 2923
Molodozhentsev, A.Y. 491, 1391
Momal, F. 3206
Monchinsky, V. 184, 2452
Montag, C. 485
Montoya, Debbie I. 2914
Moog, E. 2207, 3224

Moor, E.J.F. 3494
Moore, C.D. 141
Moore, C.I. 611
Moore, John M. 2562
Moraru, R. 3854
Morcombe, P. 883
Moretti, A. 3018
Morgan, G. 3356, 3362
Morgillo, A. 3353
Mori, W. 681, 684, 687, 2870
Mori, Y. 920, 1656, 1670, 1908, 1962, 2992, 2995, 3306
Morii, Y. 2347, 3828
Morikawa, T. 1066, 1069, 1075, 3419, 3422, 3428, 3440
Morita, Y. 3087, 3090
Morpurgo, G. 1858
Morris, J. 3209
Morrison, L. (ANL) 2929
Morrison, L. (LBNL) 3212
Morrison, M. 3212
Morrissey, D.J. 198
Mortazavi, P. 3494
Morton, P. 1611
Morvillo, M. 75, 107
Moser, H.O. 763, 3512
Mosnier, A. (Saclay) 467, 817, 1661, 1709, 2311, 2823
Mottershead, C. Thomas 1397
Mouat, M. 3831
Mueller, A.C. 1120
Mugge, M. 3622
Mulder, H. 944, 979, 982
Mulhollan, G.A. 2849
Muller, Tom 3693
Müller, I. 2493
Müller, R. 2493
Müller, W.F.O. 524
Mullins, L. 3562
Muñoz, M. 814
Murai, T. 3087
Murakami, T. 3822
Muratore, J. 3347, 3353, 3356, 3362
Muratore, P. 3338
Murokh, A. 736
Muto, M. 584, 3306
Myakishev, D.G. 2609
Myers, S. 1
Myers, T.J. 950

N

Naba, T. 2983
Nadji, A. 817, 1406, 1517
Nagatsuka, Toshiya 856
Nagl, M. 2078, 2726
Naidenov, V.O. 1511
Naito, F. 2902, 2974, 2977, 2986, 3069
Naito, T. 584, 587
Nakagawa, T. (RIKEN) 941, 2672
Nakagawa, T. (Mitsubishi) 2102
Nakai, H. 3087
Nakajima, K. 648, 760
Nakamura, N. 856, 1756, 2146
Nakanishi, H. 648, 760, 2902, 2974, 2977, 2986, 3069, 3087
Nakayama, H. 1394, 2992, 2995
Nakayama, K. 3828
Nam, S.H. 823, 2107, 3479
Nam Soon-Kwon 1593
Namkung, W. 593, 823
Nantista, C. 439, 1676, 2186, 2256, 2852, 3027, 3042, 3192
Naqvi, S. 3117
Naranjo, A. 1093
Nassiri, A. 461, 1575, 2052, 2296, 2941, 2944, 3111, 3120, 3174, 3491
Nath, S. 915, 1150, 1153, 1162, 1171
Nation, J.A. 1272, 1275, 3117
Naumann, O. 1551
Nawrocky, R.J. 2069
Naylor, Graham 2210
Neel, J. 817
Nelson, E.M. 1837
Nelson, R. 3165
Nelson, S.D. 2633
Neri, F. 193, 273, 1012, 1015, 3788
Nesterenko, I.N. 1433, 1762
Nesterov, V. 439
Nesterovich, A. 276, 2773, 3869
Neubauer, M. 3004, 3039
Neuenschwander, R.T. 811
Neuffer, D. 417, 624, 1537, 2905
Ney, S. 3096
Nezhevenko, O.A. 3013, 3114, 3153, 3156, 3186
Nezrick, F. 2867, 2873
Ng, C. 387, 1738, 2116, 2189, 3033, 3562
Ng, K.-Y. 396, 399, 405, 994, 1000, 1003, 1030, 1481
Ng, Wang C. 2630
Nghiem, P. 330, 817, 1406, 1517
Nguyen, D.C. 897, 1990
Nguyen, K. 3144, 3180
Nguyen, M.N. 3482
Nguyen, V. 3102
Nguyen-Tuong, V. 3105
Ni, G. 3297
Ni, Yi 3764
Nicol, T.H. 3257, 3263, 3710
Nielsen, J.S. 1560
Nielsen, R. 953
Niibe, M. 757
Niki, K. 938, 3306
Nikiforov, A.A. 3114
Nikitina, I. 3586
Nikitina, L. 3586
Nishi, M. 3813, 3819
Nishimura, H. 778, 784, 799, 805
Nissley, L. 3816
Nitsch, F. 3123
Njegomir, M.M. 190
Nobes, S. 3209
Noble, R.J. 393
Nobrega, F. 3389, 3398
Noda, A. 339, 1203, 1206, 3294, 3819
Noda, K. 201, 820, 1557, 2347, 3819, 3822
Nogiec, J.M. 3395, 3464, 3713
Nolen, J. 2696
Nomura, M. 402, 880, 2787
Nomura, T. 201, 938
Noomen, J.G. 1063
Noonan, J. 3552, 3580
Nordberg, E. 3075, 3383
Nordby, M. 3330, 3639
Norek, G. 953
Norem, J. 363, 396, 399, 1030
Noriega, R. 2253
Normann, L. 1813
Nosochkov, Y. 838
Novicova, T.A. 889
Novikov, A.V. 2732
Novikov, S.A. 184
Novitski, I. 3398
Novokhatski, A. 467, 1661, 1709
Nuhn, H.-D. 838

O

O'Day, S. 1006
O'Shea, P.G. 1278, 1891, 1993, 2799
O'Sullivan, M. 3681
Oakeley, O. 883
Obina, Takashi 1664
Odagiri, T. 1557
Ogata, A. 648, 760
Ogawa, H. 3327, 3822
Ogitsu, T. 3365
Oh, J.S. 581, 593
Ohashi, Y. 2971
Ohkawa, T. 1024
Ohkubo, Y. 533
Ohmi, K. 1566, 1596, 1667, 1831
Ohmori, C. 1656, 1670, 1908, 1962, 2992, 2995
Ohshima, T. 2971
Ohtomo, K. 1072

Ohtomo, Kiyotaka 3816
Oide, K. 494, 587, 1394, 1484, 1798, 3660
Okada, M. 938
Okamoto, H. 339, 1203, 1798, 1911
Okamura, M. 1460, 3341, 3359, 3431, 3437
Okugi, T. 584, 587, 1484
Okuma, S. 730
Okuno, H. 1066, 1069, 1075, 3327, 3419, 3422, 3440
Oliveira, L.H. 3476
Olsen, B. 101
Olsen, D.K. 1018, 1177, 2775, 3851
Olsen, Jeff J. 2122
Olsen, R. 3485
Olson, C.L. 1935
Olsson, E. 2422, 2535
Omar, A.S. 2553, 2612
Omeich, M. 2823
Onishchenko, I.N. 651
Ono, S. 1557
Oothoudt, M.A. 1165, 2064, 2464
Oproiu, C. 1123, 3854
Oren, T. 3755
Ormond, Kern W. 1822
Orris, D. 3389, 3395, 3713
Osborn, J. 3312, 3318, 3321
Oshita, E. 730
Osmanov, N. 736
Ostiguy, J.-F. 1403, 2556, 3257, 3260, 3263, 3272, 3278, 3286
Ostojic, R. 3209, 3696
Ostreiko, G.N. 3114
Ostrem, D.J. 2464
Ostroumov, P. 1135, 2078, 2621, 2732
Otter, Alan J. 3336
Ottinger, M.B. 1653
Ovsyannikov, D. 1944
Owen, H. 333, 2443
Oyaizu, M. 938
Ozelis, J.P. 3389

P

Pabst, M. 1846
Pachnik, J. 3395, 3713
Padamsee, H. 2884, 3075, 3177
Padmore, H. 3221
Pagani, C. 1126, 3657
Pakter, Renato 1938
Palanque, S. 817
Palmer, D.T. 1968, 2687, 2790, 2840, 2843, 2846, 2849, 2855
Palmer, R. 286, 405, 408, 3401
Palmieri, V. 1129
Pamela, J. 2717
Pan, K.T. 3539
Pantell, R.H. 675
Paoluzzi, M. 979
Papadakis, N.H. 1042
Papanicolas, C.N. 1042
Papis, J.P. 2049
Pappas, G.C. 390
Paramonov, V. 1135, 2726, 2959, 2962
Pardine, C. 811, 1209, 3010
Pardo, R.C. 2696, 2702
Parisi, G. 1090, 1900
Park, D. 3633
Park, H.J. 3015
Park, M.K. 2350
Park, S. 874, 883
Park, Sanghyun 835, 2840
Parker, J.M. 3625
Parker, R. 66
Parker, R.K. 3159
Parkhomchuk, V.V. 1795
Parma, V. 3368, 3374
Parodi, R. 1126
Parsa, Z. 642, 1502, 1505, 1508, 1917
Parzen, G. 1421, 1424, 1427, 1430
Pascholati, P.R. 2998
Pasotti, C. 826, 1185, 1735, 3099
Pasquinelli, R.J. 1403, 3804, 3837
Passchier, I. 1063
Patavalis, N. 1042
Paton, K. 3831
Patteri, P. 572, 2137
Patterson, J. 883
Patterson, J.M. 439
Paul, A.C. 1260
Paul, M. 2696
Pawel, Steve J. 86
Payet, J. 330, 817, 1406, 1517
Pearson, C. 439, 2911, 3192
Pearson, P.S. 2437
Peaupardin, P. 817
Pedersen, F. 973, 979, 982, 1382
Pedersen, J. 973
Peggs, S. 56, 69, 95, 98, 101, 219, 222, 405, 1030, 2158, 3359
Pei, A. 1481, 2968
Pekeler, M. 2917
Pekker, M.S. 1635
Pelaia, T. 1472, 1542
Pellegrini, C. 678, 736, 1457, 1490, 1968, 2687, 2802
Pellico, W. 3716
Pelzer, W. 1078
Pendzick, A. 2213
Peng, Q. 378, 3297
Pengo, R. 1129
Pénicaud, J.-P. 817
Peoples Jr., J. 29
Peperkorn, I. 2078, 2726
Perelstein, E.A. 488
Perevedentsev, E.A. 1759
Perez, F. 763, 1039
Perin, R. 3371
Perini, D. 3410
Perkins, L.T. 2761, 3807
Perraudin, C. 1117, 1191
Pershin, V.I. 1090, 3848
Pershing, D. 3144
Persov, B.Z. 3114
Peschardt, E. 309
Peters, C. 1926
Peters, J. 2726
Peterson, K. 953
Peterson, T. 3392, 3395
Petillo, J. 3144
Petracca, S. 1753, 1783
Petri, H.R. 2737
Petrov, S.P. 3455
Petrov, V. 1795, 2796, 2838
Petrov, V.A. 491
Pett, J. 66
Pewitt, E.G. 3269, 3275
Peyrot, M. 3374
Pfeffer, H. 994, 3461
Pfeiffer, G. 2493
Phillips, L. 3102, 3108, 3752
Phillips, R. 439
Phinney, N. 497, 506, 608
Phinou, P. 1042
Phung Ngoc, B. 2311, 2823
Picard, D.S. 2761
Pickles, T. 3831
Picoli, R.A. 1209
Picon, J.C. 1254, 1257
Piech, R. 2929
Pierini, P. 1126
Pietryka, M. 315, 439, 3666
Pietryla, A. 2281
Pike, C. 2344
Pikin, A. 2711
Pilat, F. 69, 95, 98, 101, 222, 2544, 3359
Pile, G. 1269
Pillai, C. 2064, 2743
Piller, Chip 2131
Pinayev, I.V. 883
Pinchasi, Y. 906
Pinto, I. 1753
Piot, P. 912, 2198, 2204
Pipersky, P. 3221
Pirozhenko, V.M. 950
Pisent, A. 1087, 1129, 1132
Pittana, P. 3099

Pivarč, J. 3604
Pivarč jun., J. 3604
Placidi, M. 366, 1987, 3648
Planner, C.W. 1021
Plate, D. 3221
Plesko, M. 336, 763, 2481
Plotnikov, V.K. 2965, 3848
Plum, M. 187, 190, 1012, 1015, 1611
Podgorny, F.V. 237
Podlech, H. 947
Podobedov, B.V. 1629
Poelker, B.M. 2861, 2864
Poggi, M. 1129, 2169
Pogorelsky, I. 621, 645, 675
Poirier, R. 956, 1105, 2953, 3060, 3063
Polk, I. 3230
Pomasan, Yu. 276
Pomatsalyuk, R.I. 2229
Poncet, A. 3368, 3586
Poole, Brian 1861, 2630
Pope, R. 439, 3042, 3192
Popenko, V.A. 3810
Popik, V.M. 883
Popov, E.O. 1511
Popovic, M. 396, 399, 1030, 1403, 3837
Poppensieker, K. 3801
Porcellato, A.M. 1087, 1129
Poreye, V. 3816
Portante, L. 2998
Porter, T. 439
Postma, O. 3630
Potepan, F. 2467
Potier, J.P. 476
Potter, J.M. 1099
Potukuchi, P. 3072
Pouchkov, S. 1263
Poukey, J.W. 1245
Power, J. 633, 639, 1996
Power, J.F. 193, 2041, 2232, 3731
Pozimski, J. 174, 246
Pozzer, A. 1212
Prabhakar, S. 2284, 2362
Prasuhn, D. 1048
Preble, J. 3108
Prelec, K. 2711
Price, J.S. 2864
Prichard, B. 1611
Prieels, D. 3816
Prior, C.R. 1021
Pritzkau, D. 672, 1626, 3036
Proch, D. 3081
Prokesh, K. 1391
Prokopenko, S.Yu. 2229
Pros, M. 2011
Proudlock, P. 66
Pruss, S.M. 3286
Ptitsin, V. 3359, 3500
Puchkov, S. 1311, 1313
Pugachov, G.D. 3840
Pugh, M.J. 2443, 2508
Putnam, S.D. 1251
Pynn, R. 1159

Q

Qin, Q. 1448, 1566
Qing, Q. 1356
Qiu, Joe X. 1971
Qualls, A. 2449
Quigley, P. 3075
Quimby, D.C. 675
Qunell, D. 1281, 1287

R

Rabedeau, T. 838
Radoiu, M. 3854
Radu, A. 1123
Rafael, F. 811, 1209, 2096, 3324
Rahmani, H. 1042
Rahn, J. 2493
Raia, Guido 2038
Raich, U. 973
Raimondi, P. 449, 452, 503, 509, 608, 687, 1981, 2189
Raino, A. 2729
Rajagopalan, S. 2802
Rakowsky, G. 727, 3497
Ramamoorthy, S. 2287
Ramsell, C.T. 663
Rao, M.G. 3105
Raparia, D. 162, 970, 2023
Raridon, R.J. 2775
Raskopin, A.M. 2965
Ratner, L. 1460, 1478
Ratti, A. 216, 1706
Ratzinger, U. 947, 1897, 2645
Raubenheimer, T. 473, 482, 503, 599, 605, 687, 1197, 1563, 1626, 2580
Rawlinson, B.R. 2443
Rawnsley, W.R. 2049
Ray, B.D. 1165
Redd, D.B. 273
Redden, D.P. 3872
Reece, C. 3105
Reece, K. 89, 1460
Rees, D. 1147, 2428, 2889, 3183, 3725
Rees, G.H. 988, 1021
Reeve, Paul 3336
Regan, A. 1150, 2338, 2341
Reginato, L. 590, 1296
Rehm, K.E. 2696
Reichanadter, M. 243
Reiche, S. 736, 1365
Reichel, I. 1819
Reidelbach, K. 246
Reigle, D. 3669, 3690
Reilly, J. 3075
Reis, D. 2840
Reiser, M. 1526, 1650, 1855, 1953, 1956, 1959, 2143, 2681, 3168
Ren, F. 3297
Rennich, Mark J. 86
Rensfelt, K.G. 947
Repkov, V.N. 883
Repnow, R. 947
Reppond, A. 3872
Reshetnyak, N.G. 2820
Reuter, E. 315
Reymermier, C. 3586
Reyzl, I. 2392
Riabko, A. 1346, 1481
Rice, D. 3236, 3383, 3705
Richards, L. 3443
Riche, A. 563
Richter, M. 3801
Rickard, M.L. 2758
Ridlon, Rae N. 2826
Rieckmann, C. 2553, 2612
Ries, T. 1194
Rifflet, J.M. 3365, 3374
Rifkin, J. 439, 2186, 3042, 3192
Rijllart, A. 3206
Rimmer, R.A. 3001, 3004, 3007, 3039
Rinckel, T. 3303
Ringwall, A. 3330
Risbud, S. 3183
Risselada, T. 1356, 1442
Ritson, D. 113
Riunaud, J.-P. 228, 973, 979
Rizawa, T. 3828
Rizzi, V. 1212
Robert, C. 2899
Roberts, J.E. 190
Robertson, H.P. 3684
Robin, D. 778, 799
Robinson, K.E. 675, 3201
Rodger, E.S. 3230
Rodier, J. 2823
Rodionov, D.A. 3866
Rodrigues, A.R.D. 811, 2096, 3324, 3740
Rodriguez-Mateos, F. 3206
Rogers, J. 318, 369, 1822, 2276, 3215
Rohmig, P. 3368, 3374
Rohrer, U. 3785
Röjsel, P. 345

Rokni, S. 687
Romanov, S. 2452
Romas'ko, V.P. 2820
Romeu da Silva, A. 811
Ronnigen, R. 1054
Root, L. 956, 1102
Ropert, A. 754
Roques, A. 1254, 1257
Rosa, A. 811
Rose, C.R. 193, 1012, 1293, 2044, 2093, 2232
Rose, J. 967
Rosenberg, A. 906
Rosenberg, R.A. 3552
Rosenzweig, J. 627, 678, 736, 1365, 1965, 1968, 2802, 2873, 2876
Roser, T. 89, 207, 396, 399, 1030, 1460, 1478, 2538, 3359
Roshal, A.S. 2835
Ross, J.S.H. 3413
Ross, M. 608, 1626, 1981
Ross, W. 2284, 2359, 2365
Rossa, E. 1987
Rossbach, J. 719
Rossi, C. 826, 1180, 1182, 1212, 2002
Rossmanith, R. 763, 1039, 3512
Roster, W. 439
Rotela, E. 2207, 2929
Rovang, D.C. 1245
Rovelli, Alberto 2038
Roy, A. 3072
Roy, G. 312, 1819, 1858
Roybal, P. 1093
Roybal, W. 1147, 3183, 3725
Royer, J.P. 973
Rubin, D. 318, 372, 3075, 3236, 3654
Rüdiger, H. 2493
Ruggiero, A. 970, 1114, 1578, 1581
Ruggiero, F. 75, 107, 1712, 1753, 1816, 2648
Rukoyatkin, P. 181
Rule, D.W. 675
Rümmler, J. 237
Rusnak, B. 2914, 3096
Russell, A.D. 3275, 3278, 3288
Russell, G.J. 190
Russell, Steven J. 2005, 2177
Rust, K.R. 273
Rusthoi, D.P. 2574
Ruth, R. 439, 482, 539, 548, 554, 605, 1676, 3042, 3192
Ryan, W. 2152, 2215
Rybaltchenko, K. 3645
Rybarcyk, L. 1150, 2514, 2743
Ryne, R.D. 2624

S

Saadatmand, K. 2767
Sabah, S. 2392
Saban, R. 3206
Sabbi, G. 1682, 3398
Sachtschale, R. 883, 1278, 2799
Sachwitz, M. 2137
Safa, H. 3096
Safranek, J. 748, 799, 838, 841
Sagan, David 1765, 1768
Sah, R.C. 847, 850, 853, 2371
Saito, K. 2995
Saito, M. 1557
Sajaev, V. 1463, 1466
Sakai, F. 648, 760
Sakai, H. 2902, 2974, 2986, 3069
Sakaki, H. 2511, 2814
Sakamoto, N. 1066, 1069, 1075, 3419, 3422, 3428, 3440
Sakamoto, T. 587
Sakanaka, S. 354, 2980, 2983, 2989, 3616
Saldin, E.L. 575, 1658
Salzborn, E. 2705, 2708
Sampayan, S.E. 1308, 2627
Sampson, W. 3353, 3356
Sandberg, J. 2308
Sander, O. 1015, 1611, 2743
Sanders, D.M. 1308
Sandweiss, J. 675
Sano, Masami 3816
Sapozhnikov, L. 2359, 2365
Saraph, G.P. 3168
Sarkar, S. 2241, 2274
Sasaki, Shigemi 802
Sass, R. 2473, 2476
Sassowsky, M. 973
Sato, H. 267, 1009, 1460, 1908
Sato, K. 3327
Sato, S. 201
Sato, Y. 1566, 3822
Satogata, T. 69, 98, 101, 210, 2544
Satoh, K. 2983, 3066, 3828
Satoh, Kotaro 306, 2087
Satoh, Takemi 3816
Savino, Ray 3693
Sawada, S. 2992, 2995
Scafuri, C. 826, 2353, 2356, 2467
Scandale, W. 1445, 1469, 1816
Scanlan, R. 3212, 3398
Scarpa, F. 1129
Schächter, L. 1272
Schaefers, F. 3527
Schaffer, H. 3796
Schaffner, S. 2128
Schaller, S.C. 2464
Schaper, J. 336, 763
Scheblein, J.A. 3230
Scheer, M. 1418, 1520, 2606, 3527
Scheitrum, G.P. 3045
Schempp, A. 947, 1078, 1081, 1084, 1897, 2726
Schiffer, J.P. 1560, 2696
Schilcher, T. 2320
Schillinger, B. 2594
Schindl, K. 973, 2314
Schlabach, P. 3248, 3257, 3263, 3392
Schlapp, M. 2702, 2705, 2708
Schlarb, H. 1572
Schlueter, R. 802, 3221, 3230, 3315
Schmalzle, J. 3356
Schmerge, J. 2840
Schmickler, H. 66, 1858, 2026
Schmidt, C.W. 1403, 3837
Schmidt, F. 1356, 1436, 1439
Schmidt, R. 66, 3206, 3209, 3648
Schmitz, S. 569
Schmor, P. 956, 2675, 2781
Schnase, A. 1048
Schneider, G. 3586
Schneider, H. 1048
Schneider, J.D. 1168, 2740
Schneidmiller, E.A. 575, 1658
Schoenlein, R.W. 1984
Schoessow, P. 633, 639, 1996
Schönauer, H. 973, 1587
Schrage, D. 1093, 3625
Schreiber, H.J. 2137
Schriber, S.O. 1159
Schröder, G.H. 225, 1325
Schroeder, C.B. 684
Schryber, U. 3785
Schubert, J. 1060
Schulte, H. 2603
Schultheiss, C. 3452
Schultheiss, T. 3177
Schütt, P. 3162
Schwalm, D. 947
Schwartz, C. 2296, 3111
Schwarz, H. 2359, 3004, 3007, 3039
Scorzato, C. 811
Seamen, J.F. 1235
Sears, J. 3075
Sebek, James J. 835
Sedlak, J. 1391
Sedlyarov, I. 2796, 2838
Seeman, J.T. 315, 1563, 1876
Segel, R.E. 2696
Seidel, M. 434, 439, 500, 554, 2119, 2189
Seidl, P. 1923, 1926
Seitz, Gerald J. 2826
Sekutowicz, J. 3081

Sellier, J.C. 3365
Senichev, Yu. 1111, 2923
Sennyu, K. 2908, 3087
Senyukov, V.A. 3869
Seo, K. 3425
Seo, K.W. 3663
Serafini, L. 1365, 1965, 1968, 2876
Serdobintsev, G.V. 3114
Sereno, N.S. 1700
Sergo, R. 2353, 2356
Serio, L. 3206
Serio, M. 2284
Sermeus, L. 1328
Serre, C. 979
Servranckx, R.V. 153
Sery, Andrey 557
Sessler, Andrew M. 422, 1614
Settakorn, Chitrlada 733, 2017
Sexton, I. 3586
Sgobba, S. 3586
Shafer, R. 83, 1150, 1293, 2232, 3309
Shahal, O. 906
Shamovsky, V.G. 1795
Shang, C. 2627, 2633, 3183
Shank, C.V. 1984
Shapiro, A.H. 2914, 3096
Shapiro, M. 2690
Shapiro, V.E. 1368
Shaposhnikova, E. 1813, 1816, 1849
Sharma, S. 363, 2207, 2929, 3574
Sharonov, S. 3395, 3464, 3713
Shasharina, Svetlana G. 2592, 2654
Shatilov, D.N. 1762
Shatunov, Y. 1433, 3359, 3407, 3500
Shaw, J. 2241, 2274
Shchelkunoff, S.V. 3114
Shcherbakov, A. 1311
Shea, T.J. 2152, 2215, 2502
Sheehan, J. 2687
Sheffield, R.L. 897
Shelley Jr., F.E. 2514
Shen, S. 3625
Shen, W. 3443, 3446
Sheng, I. 2207, 2929, 3574
Shepard, K.W. 3072
Sheppard, J.C. 903
Sherman, J.D. 2723, 2740, 2746
Sherrill, B.M. 198
Sheu, J.T. 3488
Shevtsov, V.Ph. 491
Shi, P. 1560
Shi, Ping 2075
Shibuya, S. 1962
Shiloh, J. 906
Shiltsev, V.D. 237, 420, 1475, 1774, 1777, 2805
Shin, H.M. 1870
Shinn, M. 2529, 2693
Shinoe, Kenji 2146, 3066
Shintake, T. 455, 530, 533, 536, 593, 1981
Shirai, T. 339, 1087, 1203, 1206, 3294, 3819
Shirakabe, Y. 938
Shirakata, M. 267, 1908
Shlakhov, I.N. 2229
Shoaee, H. 1454, 2383, 2425, 2586
Shoji, Y. (KEK) 267, 1908
Shoji, Y. (Himeji) 757, 1385
Shu, Deming 2210
Shu, Q.-S. 624, 2905
Shukla, S. 144
Shulze, M. 1611
Shurter, R.B. 2232
Shurter, R.P. 2829
Shvedov, O.V. 3848
Shvedunov, V.I. 1108, 1902, 3866
Shvets, G. 657, 669
Shvetsov, V.S. 3126
Sibley, C. 2099, 2241, 2274, 3407, 3743
Sidorenko, V.N. 1090
Sidorov, G.I. 1391
Sieber, T. 947
Siemann, R.H. 464, 497, 500, 602, 672, 687, 1629, 2164, 2580, 3036
Siemko, A. 3377
Sievers, P. 3377
Siggins, T. 3752
Sikora, John 1765
Sikora, R. 2152
Silbar, Richard R. 1529
Silke, C. 3816
Silva, A.R. 1209, 3476
Silva, M.B. 3628
Sim, J. 3242, 3395, 3713
Siman-Tov, Moshe 86
Simon, D.J. 979
Simon, R. 763
Simonin, A. 2717
Simonov, E.A. 1762
Simpson, J. 633, 636, 639
Simrock, S. 2320, 2905
Sinclair, C.K. 2693, 2864, 3761
Singh, O. 727, 2161, 2287, 3455, 3494
Skachkov, V.S. 2965, 3848
Skaritka, J. 621, 675, 1197, 2687, 2843
Skoczen, B. 3368
Skopik, D.M. 716
Skrinsky, A.N. 883
Sloan, T. 264, 1481
Smaluk, V. 1463, 1466
Smedley, J. 2790
Smirnov, A. 1795, 3407
Smirnov, A.V. 894, 3518
Smirnov, V. 2244
Smith, D.L. 1245
Smith, G.A.(BNL) 2149, 2215, 2302
Smith, G.A.(FNAL) 3257, 3263
Smith, H. 439
Smith, H.V. 1150, 2746
Smith, I. 1245
Smith, J.D. 2437
Smith, J.R. 1251
Smith, K.D. 3209, 3413, 3494
Smith, R. Scott 2164
Smith, S. 439, 2110, 2113, 2116, 2122, 2253
Smith, S.L. 2443
Smith, T.L. 2299, 2938, 2941
Smith, V. 2253
Smithwick, J. 3212
Snell, Charles M. 2174
Snydstup, L. 2711
Sobczynski, S. 2274
Sobenin, N.P. 1108, 2008, 2104
Søby, L. 1587
Soika, A. 3443
Sokolowski, J.S. 906
Solita, L. 3669, 3690
Solomon, L. 727, 3497
Sommer, M. 817, 1406
Sommer, W.F. 190
Sondericker, Jack 3693
Song, J. 912, 2204, 2529
Song, J.J. 461, 1575, 2941, 2944
Soong, S.B. 2241
Soukas, A. 2308, 3449
Soutome, K. 1385
Sparveris, N. 1042
Spence, W.L. 506, 1673
Spencer, J. 439, 608
Spencer, N. 439
Spentzouris, L. 16
Spielman, R.B. 1235
Spinka, H.M. 1460
Sprangle, P. 611, 630
Sprehn, D. 439
Springer, R.W. 2829
SRC Staff 865
Srinivasan-Rao, T. 2790
Stagno, V. 2169
Stanek, M. 596
Stanford, G. 956, 1105
Staples, John W. 1096, 1174
Stefan, J. 2481
Stefan, P.M. 727, 3497, 3515
Steffen, L. 2446
Stege, R. 2253

Steier, C. 1033
Steimel, J. 144, 1721, 2323
Stein, P. 2711
Steiner, R. 3801
Steininger, R. 763
Stellfeld, D. 1816
Stepin, V.D. 651
Stern, C. 2422, 2535
Stettler, M. 2041, 2044, 2093, 2232
Stevens, A.J. 219
Stevens, R.R. 2723, 2740, 2743, 2746, 2764
Stevens, T. 3619
Stevenson, Nigel R. 3842, 3845
Stiliaris, E. 1042
Still, D. 1721, 2061
Stinson, G. 956
Stirling, W.L. 2714
Stitts, E. 3681
Stockhorst, H. 1048
Stoddard, R.D. 1308
Stoltz, P. 669
Stover, G. 2284, 3734
Stowell, G. 2808
Strait, J.B. 124, 3209, 3389, 3395, 3398
Strasser, P. 938
Street, A.J. 3209, 3413
Strong, Edward 2131
Strozinsky, R. 3021
Strubin, P. 2440
Struve, K.W. 1235
Stuart, B. 886
Stupakov, G. 449, 1563, 1632, 1635, 1685, 1688, 1834, 2180
Stygar, W.A. 1235, 1245
Suda, M. 3822
Suetake, M. 306
Suetsugu, Y. 1566, 1596
Sugai, I. 187
Sugimura, T. 339, 1206, 3819
Suh, J.H. 3479
Suk, H. 1650, 1855, 2143
Sukenobu, S. 3828
Sullivan, Gary 1144
Sullivan, M. 296, 3330, 3562
Summers, D. 624
Sun, Baogen 1664
Sun, Baoyu 1218
Sun, D. 1403, 3018
Sun, J. 3297
Sun, Jingqing 1218, 1221
Sun, Xiang 1221
Sun, Y. 3300, 3312, 3318
Suwada, T. 2253
Suzuki, C. 536
Suzuki, S. 2511, 2814
Svandrlik, M. 826, 829, 1735, 3099
Sveshnikov, B. 2452
Svirtun, V. 3580
Swan, T. 3622
Swenson, D.A. 1099, 3872
Swift, G. 883, 1278
Sylvester, C. 3392, 3395
Syphers, M. 95, 207, 1478, 2155, 3359
Syversrud, D. 1051
Szczech, J. 2702

T

Tabor, M. 3816
Tachikawa, T. 1045, 3816
Tadano, M. 2084
Tadokoro, M. 3294, 3819
Tajima, T. (Texas) 1653
Tajima, T. (KEK) 2908, 3087, 3090
Takada, E. 201, 2347, 3822
Takagi, A. 2992, 2995
Takagi, H. 1908
Takahashi, H. 402, 880, 2787
Takahashi, J. 2998
Takahashi, T. 2908, 2989, 3087, 3090
Takaki, Hiroyuki 856, 2146
Takanaka, M. 1807
Takano, M. 587
Takao, M. 1385
Takashima, T. 2971
Takata, K. 494
Takayama, K. 1548, 1599, 1908
Takayama, T. 2642, 3816
Takeda, H. 1171
Takeda, S. 494, 587
Takeda, Shigeru 581, 3660
Takeda, Y. 938
Takeuchi, N. 859
Takeuchi, Y. 581, 2902, 2974, 2977, 2986, 3069
Takii, T. 730
Taleyarkhan, Rusi 86
Tallerico, P. 1147, 3138
Tallerico, T. 2213
Talman, R. 375, 1472, 1542, 2434
Tamura, F. 3767
Tamura, Kazuhiro 1664
Tan, Cheng-Yang 2221
Tanabe, J. 3312, 3318, 3321
Tanabe, T. 1557, 2992, 2995
Tanabe, Toshiya 3515
Tanabe, Y. (KEK) 2992, 2995
Tanabe, Y. (Toshiba) 3828
Tanaka, H. 1385
Tanaka, J. 938
Tanaka, M. 69
Tanaka, M.H. 938
Tanaka, Y. 1066, 1069, 1075, 3419, 3428, 3440
Tang, C. 1729, 3081
Tang, H. 599, 608, 2849
Tang, J. 2265
Tang, Y. 2287
Tani, K. 1266
Taniuchi, T. 2511, 2814
Tanke, E. 944
Tantawi, S. 439, 3042, 3189, 3192, 3195
Tarakanov, V.P. 1299
Taratin, A. 165
Tarnetsky, V.V. 3114
Tartaglia, M. 147, 3395
Tatchyn, R. 2192, 2195, 2639, 3530
Tatum, B.A. 1227
Taurigna-Quere, M. 2823
Tavares, P.F. 811, 2096, 2238, 3740
Tawada, M. 1394
Taylor, B.D. 2867
Taylor, C. 3212
Taylor, T. 315
Taylor, T.M. 3209, 3696
Tazzioli, F. 2137
Tecker, F. 366, 3645, 3648
Tejima, Masaki 2087
Temkin, R.J. 2690
Temnykh, A. 1718, 1768, 3218, 3654, 3708
Tenenbaum, P. 439, 479, 608
Teng, L. 1359, 2699
Tenishev, S. 2229
Tenyakov, I. 1263, 1311, 1313
Tepikian, S. 69, 98, 101, 222, 405, 2544, 3359, 3651
Terasawa, M. 757
Terebilo, A. 1457, 1490
Terechkine, I. 994, 3248, 3291
Terekhov, A.S. 1063
Terunuma, N. 494, 584, 587
Teryaev, V.E. 3126
Teryoshkin, Y. 1263
TESLA collaboration 425
Tessier, J.M. 2311
Teytelman, D. 2284, 2362, 2368
Theuws, W.H.C. 1036, 1200
Thevenot, M. 1254
Thiessen, H.A. 273, 1012, 1015, 1611, 3788
Thivent, M. 973
Thomas, M.G. 2305
Thomas, R. 3362
Thomlinson, W. 3494
Thompson, K. (SLAC) 608, 2580
Thompson, K. (ANL) 953, 2699

Thompson, P. 69, 98, 101, 3353
Thomson, J. 1563
Thorson, I. 956
Thur, W. 2067
Tian, Bo 3764
Tiede, R. 2645
Tiefenback, M. 2128, 2265, 2271, 3758
Tieger, D. 348
Tighe, R. 2359, 2520
Tikhomirov, A.V. 3610
Tille, T. 2784
Tillghman, A. 439
Timlin, C. 3413
Timm, M. 515
Timossi, C. 805
Ting, A. 611, 630
Tinsley, D. 1287
Tkatchenko, A. 330, 817, 1406
Tkatchenko, M. 817
Tobiyama, M. 306, 1566, 1596, 1664, 2332, 2335
Toda, M. 2992, 2995
Todesco, E. 1445, 1469, 2568
Toelle, R. 1048
Tojyo, E. 938
Tokumoto, S. 2983, 2989, 3066
Toldo, F. 3449
Tolstoluzhsky, A.P. 651
Tomicich, A. 1212
Tomimasu, T. 730
Tominaka, T. 1066, 1069, 1075, 3359, 3416, 3419, 3422, 3428, 3431, 3434, 3437, 3440
Tomitani, T. 3822
Tomizawa, M. 938, 1962
Tomlin, R. 144
Tommasini, D. 763
Tompkins, J.C. 3389, 3395, 3713
Tomura, H. 3822
Tong, Dechun 1215, 1218, 1221, 3764
Tongu, E. 730
Tonguu, H. 339, 1206
Tonisch, F. 2137
Toole, L. 1147
Tordeux, M.-A. 817
Torikoshi, M. 820, 3819, 3822
Tortschanoff, T. 3374
Tosi, L. 826, 829, 1520, 2353, 2356, 3527
Tosin, G. 3324
Tovo, E. 1087
Tovo, T. 1087
Townsend, M. 3209
Toyama, T. 1548, 1599, 1908
Trahern, C. 69, 101, 2544
Trakhtenberg, E. 3224, 3556
Tran, H.J. 1647
Tranquille, G. 944, 979, 982
Trassl, R. 2705, 2708
Travish, G. 736, 1126
Trbojevic, D. 69, 98, 101, 219, 396, 399, 405, 1030, 1371, 3651
Treadgold, J. 3209
Tremaine, A. 736
Tribendis, A. 2796, 2838
Trimble, D.O. 1308
Trofimov, N. 2440
Trombly-Freytag, K. 3713
Tron, A. 2244, 2247
Trotz, S. 2690
Trower, W.P. 1108
Troyanov, E.F. 249
True, R. 3153, 3180, 3186
Trzeciak, Walter 865
Tsarenkov, A. 2452
Tschalaer, C. 348
Tsentalovich, E. 348, 2241
Tsoupas, N. 69, 98, 207, 210, 213, 222, 1460, 2152, 3359
Tsubota, K. 2565
Tsubuku, H. 3822
Tsutsui, H. 1266, 2642
Tsygankov, E. 276
Tumanov, K.D. 3604
Tuozzolo, J. 213, 2149, 3233
Tur, Yu.D. 2820, 3810, 3840
Turchin, V.I. 2735
Turchinetz, W. 348, 2274
Turlington, Larry 2131
Turner, J. 315, 1569
Turner, L.R. 3491
Turner, William C. 422
Tuyn, J. 979
Tzeng, K-C. 2870
Tzeng, R.H. 3051

U

Ueda, A. 2084
Ueda, T. 648, 760
Ueng, T.S. 847
Uesaka, M. 648, 760
Uesugi, T. 1656, 2992, 2995
Uggerhøj, E. 80, 165
Uhm, Han S. 1870, 3147
Ullmann, J. 3096
Ullrich, H. 973
Umezawa, M. 3294, 3813
Umstadter, Donald 2657
Underwood, D. 207, 1460
Underwood, K.K. 497
Urakabe, E. 3819
Urakawa, J. 354, 444, 494, 578, 584, 587, 1484, 2980
Ursic, R. 912, 2131
Uskov, V.V. 651
Uvarov, V.L. 2229, 3810, 3840
Uythoven, J. 1858
Uzat, W. 3057
Uzunoglou, N. 1042

V

Valbuena, R. 3586
Valentino, V. 2169, 2729
Valishev, A.A. 1433
Valter, H. 3123
van Amersfoort, P.W. 1063
van Asselt, W. 89, 1460, 1478, 2155
van den Brand, J.F.J. 1063, 3630
van den Putte, M.J.J. 1063
van der Geer, S.B. 2577
van der Laan, J.B. 1063
Van der Schueren, A. 979
Van Duppen, P. 947
Van Ginneken, A. 393, 417
van Leeuwen, E. 3630
van Oers, W.T.H. 2781
van Oort, J. 3212
van Rienen, U. 524
van Steenbergen, A. 616, 621, 675
Van Vaerenbergh, P. 3506
Van Weelderen, R. 3368
van Zeijts, J. 2128, 2383, 2386, 2526
Vandeplassche, D. 1045, 3816
Vanecek, D. 590, 3722
Varfolomeev, A. 736
Variale, V. 2169, 2729
Variola, A. 2002, 2823
Varisco, G. 3657
Vasiliev, V.V. 3848
Vasilishin, B. 181, 2452
Vasserman, I. 3224
Vazquez, L. 1825
Védrine, P. 3365, 3374
Veness, R. 3586
Vengrov, R.M. 1090, 3848
Venhaus, D. 2529
Venturini, M. 1855, 1953
Verdier, A. 312, 1442
Veremeenko, V.F. 3455
Vetter, A.M. 2950
Vetterlein, R. 3761
Vierlbeck, D. 3123
Vilaithong, R. 2761
Villate, D. 1254, 1257
Vincent, D. 3374
Vincent, J. 1054, 1057
Vinokurov, N.A. 883

Vinzenz, W. 3123
Vishnevskiy, N.K. 249
Visintini, R. 826, 2353, 2356, 3527
Vlasenko, S.I. 1263
Vlieks, A. 439, 3042, 3189, 3192, 3195
Vlogaert, J. 3368, 3410
Vobly, P.D. 883, 1795
Vodinas, N. 1042
Voevodin, M. 184, 2452
Vogel, G. 2032
Vogel, V.F. 3126
Voigt, S. 763
Voisin, L. 1254, 1257
Volfbeyn, P. 657, 1984
Volk, J.T. 3254, 3257, 3260, 3263, 3280, 3286
Völker, F. 973
Volkov, V.I. 184, 2452
Volkov, V.N. 1795, 2796, 2838
vom Stein, P. 2796, 2838
von Hahn, R. 947
Vondrasek, R.C. 2702
Vormann, H. 1084
Vorobiev, P. 3407
Voronin, V.S. 1302
Vossenberg, E. 225, 1325
Vretenar, M. 944
Vylet, V. 439, 3675

W

Wada, M. 938
Wagner, A. 1813, 1858
Wagner, R. 2657
Wagner, U. 3368
Wait, G.D. 1325, 1328
Wakasugi, M. 3521
Wakisaka, K. 730
Wakita, K. 730
Walbridge, D. 3242, 3248, 3269, 3272
Walckiers, L. 66, 3377
Walker, R.P. 826, 829, 1520, 3524, 3527
Walstrom, P. 193, 3309, 3788
Walters, D. 2699, 3552, 3580
Walther, R. 1039
Walz, D. 608, 687
Wan, W. 1801
Wanderer, P. 3309, 3338, 3347, 3350, 3353, 3356
Wang, C.-T. 2047
Wang, C.J. 2374, 3488, 3539
Wang, Ch. 1638, 1691, 3048, 3051, 3054, 3536
Wang, Changbiao 3171, 3863
Wang, Chaoen 3533, 3539
Wang, Chun-xi 360
Wang, D. 1388
Wang, D.X. 1976, 2020, 2320
Wang, F. 348, 2099
Wang, G. 687
Wang, G.W. 1729
Wang, J. (ANL) 953, 2699
Wang, J. (SLAC) 1676, 2852
Wang, J.G. 1650, 1855, 1956, 1959, 2143
Wang, J.M. 2305
Wang, J.Q. 1566
Wang, J.W. 439, 539, 548, 554, 3042
Wang, L.F. 1566, 1828
Wang, M. 3297
Wang, M.H. 1409, 1487, 2377, 3533
Wang, P. 874, 883
Wang, Q. 3117
Wang, S.H. 1566, 1729, 1828
Wang, T.F. 1670, 2696
Wang, T.S. 1611
Wang, W.C. 2633
Wang, X.J. 621, 1971, 2687, 2790, 2793, 2843, 2846
Wang, Xiaoping 3300
Wang, Yi-Ming 2341
Wangler, T.P. 915, 1150, 1153, 1156, 1162, 3138
Warsop, C.M. 988
Washio, M. 1266
Watanabe, I. 1557
Watanabe, K. 593
Watanabe, S. 2347
Watanabe, T. (Tokyo) 648, 760, 1557
Watanabe, T. (Himeji) 757
Watson, W.A. (Chip) 2128, 2383, 2386, 2398, 2403, 2526
Weaver, J. 2840
Weber, R. 3837
Wei, F. 826
Wei, J. 69, 98, 222, 396, 399, 2158, 2544, 3651
Wei, Z.T. 1388, 1448
Weiland, T. 515, 524, 2594, 2645, 3162
Weinacht, D. 1159
Weir, J.T. 1260
Weisse, E. 168, 171
Weisz, S. 1356, 1442, 3696
Welch, D.R. 1245, 1867, 1935
Welch, J. 3236, 3380, 3383, 3654, 3708
Wells, S. 2241
Welz, J. 956, 2778
Wendt, D. 3443
Wendt, M. 2134
Weng, W.T. 42, 162, 970, 1885
Wengrow, A.B. 2758, 2764
Wenninger, J. 366, 3645
Werin, S. 345, 1520, 3527
Westenskow, G.A. 590, 1260, 3719, 3722
Westervelt, R. 2532, 2535
Whealton, J.H. 2714, 2775
Wheeler, S.J. 654
White, G. 1454, 2425, 2586
White, M. 327, 953, 1269, 3174
White, V. 461
Whitham, K. 3796
Whitney, R. 3761
Whittum, D. 351, 500, 542, 602, 687, 900, 2119, 2189, 2586, 3045
Wiatrzyk, J.M. 3209, 3413
Wiedemann, H. 733, 838, 2017, 2840
Wiemerslage, G. 3556
Wienands, U. 315
Wieskamp, T.F. 1308
Wight, G.W. 2781
Wilcox, D. 3183
Wilde, S.B. 2767
Wildner, E. 1362
Wilkinson, C. 1012, 1015, 1611
Wille, K. 2140
Willeke, F. 51
Willen, E. 624, 3347, 3356, 3359, 3362
Williams, B. 228
Williams, D. (SLAC) 390
Williams, D. (LBNL) 2675, 2758, 2761, 2764, 2767, 2770
Williams, L.R. 3368
Williams, N.W. 1460
Wilson, I. 482, 518
Wilson, N.G. 3625
Wilson, P.B. 439, 482, 545, 605, 3042
Wilson, Z. 439, 1319, 3027, 3042
Winick, H. 37, 2687, 2840
Winn, D. 363
Wiseman, M. 3108, 3761
Wisnivesky, D. 811, 1209, 3010, 3476
Witherspoon, S. 2386, 2526
Witkover, R. 101, 2149, 2155, 2215, 2218
Wokas, T. 3248
Wolf, R. 66, 3377
Wolf, Z. 3330
Wolff, D. 3461
Wong, V. 2302
Wood, F. 3159
Woodle, M. 1197, 2687, 2790, 3494
Woodley, M. 497, 903, 1673, 2855
Woody, C. 967
Worm, T. 80

Wright, E. 439
Wright, E.L. 2808
Wrulich, A. 826, 829, 1185, 1188
Wu, G. 3245
Wu, H. 92, 3359
Wu, X. 195, 198
Wu, Y. 874, 883
Wu, Y.Z. 321, 378
Wuensch, W. 518
Wurtele, J.S. 422, 657, 684, 1614
Wüstefeld, G. 1418, 1520, 2606, 3527
Wutte, D. 2758, 2764, 2770, 3737
Wyss, C. 3347

X

Xiao, A.M. 1448
Xiao, Liling 3764
Xie, Ming 660
Xie, Z. 1051, 2662, 2702, 2770
Xu, S. 3556
Xu, X. (SLAC) 3045
Xu, X. (IHEP) 3312

Y

Yakimenko, V. 675, 2687
Yakover, I.M. 906
Yakovlev, V.P. 2609, 3114, 3153, 3156, 3186
Yamada, S. 201, 820, 3819, 3822
Yamaguchi, A. 3828
Yamamoto, M. 2995
Yamamoto, Noboru 2455, 3660
Yamazaki, Y. 2902, 2974, 2977, 2986, 3069
Yan, Y. 2583, 2586, 2636
Yanagida, K. 2511, 2814
Yang, B. 871, 874, 883, 1700, 1999, 2052, 2207, 3574
Yang, J. 1266
Yang, Ming-Jen 2035
Yang, T.T. 1638, 2377, 2858, 3048, 3051, 3054
Yang, Yue 1218
Yano, Y. 930, 941, 1066, 1069, 1075, 2672, 3419, 3422, 3428, 3440
Yaramishev, S. 1090, 1129, 1905
Yarba, V. 3248, 3291
Yarigin, S.N. 2008, 2104
Yatagai, T. 859
Yazynin, I.A. 252, 255, 258
Yee, C. 2359
Yee, D. 3318, 3321
Yeh, M.S. 2377, 3048
Yeremian, A.D. 439, 599, 608, 1676, 2840, 2849, 2852, 2855, 3042
Yin, B. 3297
Yocky, G. 2189
Yokomizo, H. 2511, 2814
Yokosawa, A. 1460, 1478
Yokouchi, S. 1066, 1069, 1075, 3419, 3422, 3428, 3440
Yokoya, K. 1566, 1596
Yonezawa, H. 533
Yoon, M. 823, 2107, 2350
Yoribayashi, Y. 578
York, R.C. 195, 198, 663, 1855
Yoshida, Masato 3467
Yoshii, M. 1548, 1908, 2992, 2995
Yoshikawa, H. 2511, 2814
Yoshimoto, S. 3087
Yoshioka, M. 581
Yoshizawa, J. 3822
Yosiyuki, T. 1557
Young, A. (SLAC) 2284, 2368, 3027
Young, A. (LBNL) 3221
Young, E. 1472, 1542
Young, L. 1093, 1150, 1162, 1920, 2746, 2749, 2752, 3138
Young, P. 1403, 3018, 3837
Younger, F. 3321
Yourd, R. 3312, 3318
Yu, C.H. 1388
Yu, D. 886, 1968, 2802, 3036, 3120
Yu, I.H. 3015
Yu, L.-H. 1197, 2287
Yu, S. 590, 2832, 3719, 3722
Yuan, D. 2675
Yunn, B. 1694, 2128
Yurkov, M.V. 575, 1658

Z

Zagel, J.R. 2166
Zakutin, V.V. 2820
Zaltsman, A. 967
Zangrando, D. 826, 3524
Zante, A. 3796
Zapalac, G. 2618
Zaplatine, E. 2920, 2923
Zapryagaev, I.A. 3114
Zarecky, M. 3761
Zaremba, S. 1045, 3816, 3857
Zarucheiskiy, V.G. 249
Zaugg, T.J. 2723, 2740
Zavadtsev, A.A. 2008, 2250, 3860
Zawislanski, Peter T. 3807
Zeitlin, M. 1502, 1505, 1508
Zelenski, A. 2781
Zelinski, J. 439
Zeller, A.F. 198
Zeno, K. 89
Zhabitsky, V.M. 2329
Zhan, Xiaowei 2589
Zhang, C. 1566, 1780, 1828
Zhang, Dunan 3300
Zhang, F.Q. 3470
Zhang, J. 3297
Zhang, S.Y. 89, 970, 1584, 1885, 2155
Zhang, T.B. 666
Zhang, Tainjue 3834
Zhang, W. 210
Zhang, X.L. 1566, 1596
Zhao, G. 3297
Zhao, S. 2908, 3087
Zhao, X. 1346
Zhao, Y. 408
Zheng, L. 3297
Zholents, A. 315, 808, 1801, 1804
Zhou, F. 1566, 1729
Ziemann, V. 1412, 1879
Zimmermann, F. 452, 608, 1514, 1563, 1626, 1741, 1789, 1876, 1981, 2189, 2580
Zimmermann, H. 1081
Zinin, E.I. 883
Ziomek, C. 439, 2338, 2359, 3027
Ziomi, L. 1129
Zisman, M. 315, 3312, 3318
Zitvogel, E. 2149, 2215, 2218
Zlobin, A.V. 3389, 3395, 3398
Zlunitsyn, E.S. 3810
Zolfaghari, A. 348
Zolotorev, M. 1801, 1804, 1984, 2180
Zorzano, M.P. 1825
Zotter, B. 1813, 1858
Zou, Y. 1650, 1855, 1959
Zou, Yang 1218, 1221
Zumbro, John D. 1397
Zumbro, M.V. 1012, 2064
Zviagintsev, V. 3084
Zwart, T. 348, 2241
Zykov, A.I. 3810
Zyngier, H. 778

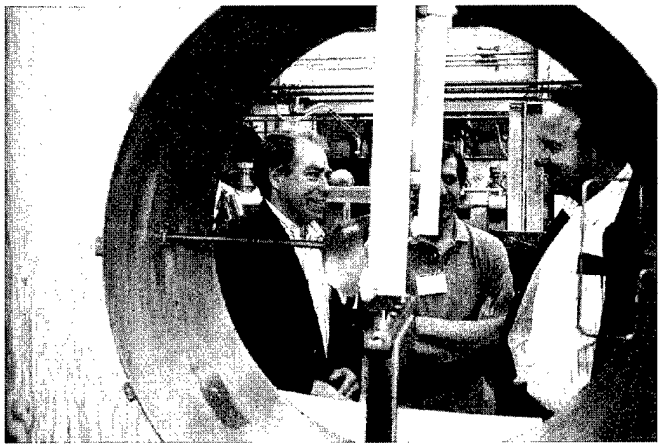

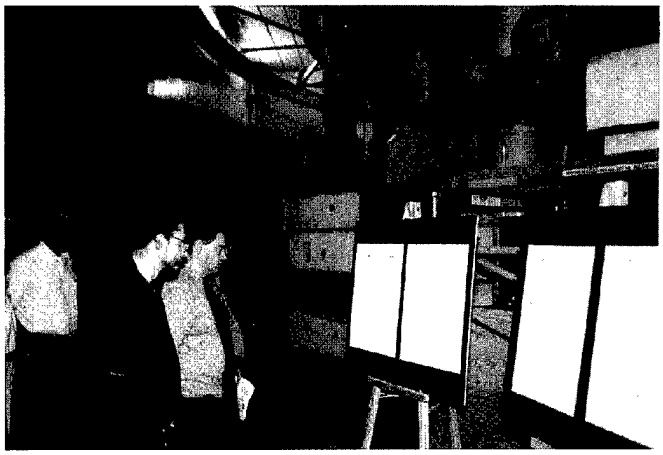

EXIT